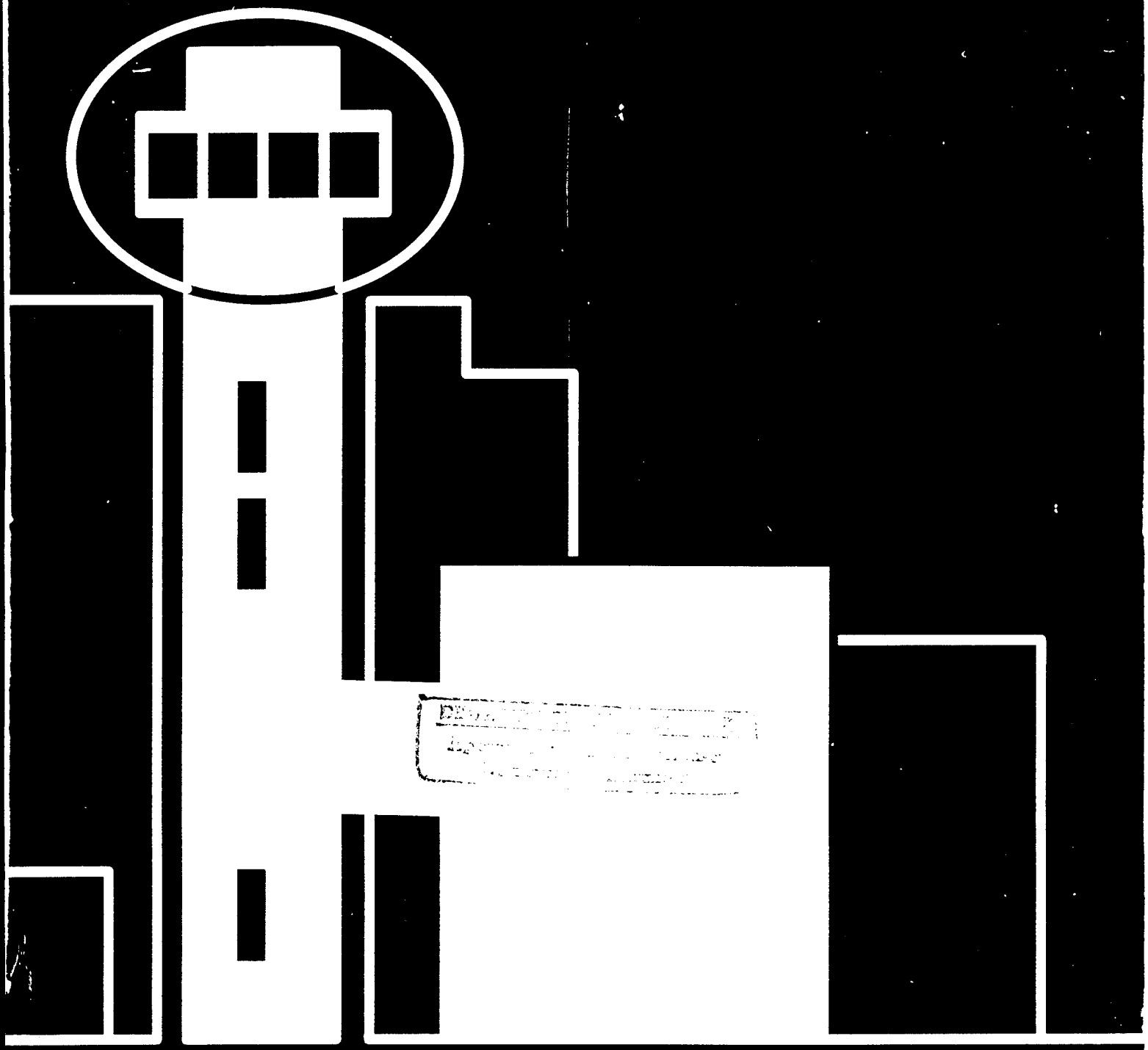
Proceedings of the 1995 Particle Accelerator Conference and International Conference on High-Energy Accelerators




J-R
REGISTR



IEEE

The American Physical Society

Proceedings of the 1995 Particle Accelerator Conference

N00014-95-1-0791

Volume 1 of 5

Papers from the sixteenth biennial Particle Accelerator Conference, an international forum on accelerator science and technology held May 1–5, 1995, in Dallas, Texas, organized by Los Alamos National Laboratory (LANL) and Stanford Linear Accelerator Center (SLAC), jointly sponsored by the Institute of Electircal and Electronics Engineers (IEEE) Nuclear and Plasma Sciences Society (NPSS), the American Physical Society (APS) Division of Particles and Beams (DPB), and the International Union of Pure and Applied Physics (IUPAP), and conducted with support from the US Department of Energy, the National Science Foundation, and the Office of Naval Research.

19960705 127

PROCEEDINGS OF THE 1995 PARTICLE ACCELERATOR CONFERENCE

Abstracting is permitted with credit to the source. Libraries are permitted to photocopy beyond the limits of U. S. copyright law for private use of patrons those articles in this volume that carry a code at the bottom of the first page, provided the per-copy fee indicated in the code is paid through the Copyright Clearance Center, 222 Rosewood Drive, Danvers, MA 01923. Instructors are permitted to photocopy isolated articles for noncommercial classroom use without fee. For other copying, reprint, or republication permission, write to the IEEE Copyright Manager, IEEE Operations Center, 445 Hoes Lane, Piscataway, NJ 08855-1331. All rights reserved. Copyright © 1996 by the Institute of Electrical and Electronic Engineers, Inc.

IEEE Catalog Number: 95CH35843 (softbound)
95CB35843 (casebound)

Library of Congress Number: 88-647453

ISBN Softbound: 0-7803-2934-1
ISBN Casebound: 0-7803-2935-X
ISBN Microfiche: 0-7803-2936-8
ISBN CD-ROM: 0-7803-2937-6

Additional copies of this publication are available from

IEEE Operations Center
445 Hoes Lane
P. O. Box 1331
Piscataway, NJ 08855-1331 USA

Phone: 1-800-678-IEEE (1-800-678-4333)
1-908-981-1393
FAX: 1-908-981-9667
Telex: 833-233
e-mail: customer.service@ieee.org

The CD-ROM version is available from

Dan Rusthoi, PAC95 Treasurer
Los Alamos National Laboratory
P. O. Box 1663 - M/S H811
Los Alamos, NM 87545 USA

Phone: 505-667-2796
FAX: 505-667-0919
e-mail: drusthoi@lanl.gov

Volume 1

Plenary and Special Sessions

CEBAF Commissioning and Future Plans *(Invited) — Hermann A. Grunder* 1 MAD01
The Advanced Photon Source *(Invited) — John N. Galayda* 4 MAD02
Commissioning and Performance of the HIMAC Medical Accelerator *(Invited) — S. Yamada* 9 MAD03
Accelerator Field Development at Novosibirsk (History, Status, Prospects) *(Invited) — A. Skrinsky* 14 MAD04
A Personal Perspective of High Energy Accelerators *(Invited) — Gustav-Adolf Voss* 27 FPD01
Photon-Photon Colliders *(Invited) — Andrew M. Sessler* 30 FPD02
Transmutation and Energy Production with High Power Accelerators *(Invited) — G.P. Lawrence* 35 FPD03
The Large Hadron Collider *(Invited) — L.R. Evans* 40 FPD04
Frontiers of Particle Physics *(Invited) — L. Okun* 45 FPD05
R. R. Wilson Prize Lecture: Pretzels *(Invited) — R. Littauer* ..... manuscript not submitted MXG01
Experimental Studies of Longitudinal Dynamics of Space-Charge Dominated Electron Beams *(Invited) — D.X. Wang* 48 MXG02
High-Energy High-Luminosity $\mu^+ \mu^-$ Collider Design *(Invited) — Robert B. Palmer, Richard Fernow, Juan C. Gallardo, Y.Y. Lee, Yagmur Torun, David Neuffer, David Winn* 53 MXG03
Cosmic Acceleration Mechanisms *(Invited) — J. Arons* ..... manuscript not submitted MXG04

Accelerator Applications

Hadron Particle Therapy *(Invited) — Jose R. Alonso* 58 WPE01
Micromechanics via Synchrotron Radiation *(Invited) — H. Guckel* 63 WPE02
Radionuclide Production for the Biosciences *(Invited) — Thomas J. Ruth* 67 WPE03
X-Ray Lithography - Status and Projected Use *(Invited) — W.A. Johnson* ..... manuscript not submitted WPE04
Microelectronic Applications for RF Sources and Accelerators *(Invited) — Cha-Mei Tang* 70 WPE05
A High-Gradient Electron Injector to an X-Ray Lithography Ring *(Invited) — D. Yu* ..... manuscript not submitted FAG01
X-Ray Holography *(Invited) — I. McNulty* ..... manuscript not submitted FAG02
Medical and Surgical Applications of FELs *(Invited) — Benedikt Jean* 75 FAG03
Medical Uses of Monochromatic X-Rays *(Invited) — Frank E. Carroll* 80 FAG04
Texas Regional Medical Technology Center — *R. Sah, T.D. Cain, E.K. Cleveland, K. Saadatmand, M.E. Schulze, R.A. Winje* 83 FAG05
A Proposed 100-400 MeV Beam Facility at Fermilab — *C. Johnstone, C. Ankenbrandt, S. Bjerklie, D. Boehnlein, M. Foley, T. Kroc, J. Lackey, A. Lennox, A. Leveling, E. McCrory, M. Popovic, C. Schmidt, K. Vaziri* 86 FAG06
Cyclotrons for Isotope Production — *B.F. Milton, N.R. Stevenson* 89 FAG07
European Heavy Ion ICF Driver Development — *G. Plass* 92 FAG08
A 3-Stage Cyclotron Complex for Driving the Energy Amplifier — *P. Mandrillon, N. Fietier, C. Rubbia* 95 FAG09
Accelerator-Based Gamma Neutron Transmutation of Radionuclides as a New Technology for the Nuclear Fuel Cycle — *I.P. Eremeev* 98 FAG10
A High-Average-Power FEL for Industrial Applications — *H.F. Dylla, S. Benson, J. Bisognano, C.L. Bohn, L. Cardman, D. Engwall, J. Fugitt, K. Jordan, D. Kehne, Z. Li, H. Liu, L. Merminga, G.R. Neil, D. Neuffer, M. Shinn, C. Sinclair, M. Wiseman, L.J. Brillson, D.P. Henkel, H. Helvajian, M.J. Kelley* 102 FAG11
X-Ray Radiation by Relativistic Electrons in Condensed Media on Base of MSU Race-Track Microtron — *V.K. Grishin, A.S. Chepurnov, K.A. Gudkov, B.S. Ishkhanov, S.A. Kosterin, E.V. Lasutin, S.V. Blazhevich, N.N. Nasonov* 105 FAG12
Applications of MeV Proton and Deuteron Linear Accelerators — *George H. Gillespie, Gerald E. McMichael* 107 FAG13
Accelerator Requirements for Fast-Neutron Interrogation of Luggage and Cargo — *B.J. Micklich, C.L. Fink, T.J. Yule* 110 FAG14

Energy Varying Resonant Beam Extraction from the Synchrotron — *K. Hiramoto, M. Tadokoro, J.I. Hirota, M. Nishi, K. Noda* 113 TAB03
Radiotherapy Process Integration Using a Compact Photon Source Together with Fluence Control and Patient Imaging — *D. Tronc, F. Dugardin, J.P. Georges, R. Letoumelin, J.L. Pourre* 116 TAB04
A 1.5 GeV Compact Light Source with Superconducting Bending Magnets — *A.A. Garren, D.B. Cline, M.A. Green, D.E. Johnson, J.J. Kolonko, E.M. Leung, D.D. Madura, L.C. Schachinger* 119 TAB06
Applications of Industrial Electron Accelerators at Samsung Heavy Industries — *Bumsoo Han, Keeman Kim, Kihun Joh, Sungmyun Kim, Byungmun Kim, Heunggyu Park, Jongpil Park, Jinsoo Kim, Wongu Kang, Kyungwoo Kang, Yuri Kim, Sangil Lee, Younghee Kim* 122 TAB09
Application of Accelerated Electron Beams for Rubber and Polymer Modification — *A. Shalnov, B.Yu. Bogdanovich, A. Ignatyev, V. Senyukov* 125 TAB13
Status on Low Energy (10 MeV Range) X-band Linacs Developed Worldwide — *A.V. Michine* 128 TAB15
Linear Accelerator for Radiation Chemistry Research at Notre Dame — *K. Whitham, S. Lyons, R. Miller, D. Nett, P. Treas, A. Zante, R.W. Fessenden, M.D. Thomas, Y. Wang* 131 TAB17
IREN Status: New Electron Linac Driven Intense Resonance Neutron Source — *A. Krasnykh* 134 TAC01
A Cost Estimation Model for High Power FELs — *George R. Neil* 137 TAC03
Details of the Initial Part of the Tungsten Ion Linac for Particle Track Membranes Production — *V. Kushin, T. Kulevoy, N. Nesterov, A. Oreshnikov, S. Plotnikov, D. Seleznev, V. Zubovskiy* 140 TAC05
A Series of Ion Accelerators for Industry — *B.N. Sukhina, N.I. Alinovsky, I.L. Chertok, S.N. Chumakov, N.S. Dikansky, A.D. Goncharov* 143 TAC06
A Pulsed Source of Neutron Focus for Fundamental and Applied Research in High-Energy Electron Accelerator Centres — *I.P. Eremeev* 146 TAC11
Moderator/Collimator for a Proton/Deuteron Linac to Produce a High-Intensity, High-Quality Thermal Neutron Beam for Neutron Radiography — *R.C. Singleterry Jr., G.R. Imel, G.E. McMichael* 149 TAC12
Experimental Set-up for Multiplication Coefficient Fluctuation Study vs Accelerator Parameter Deviations on the JINR Pulsed Acclerator Driven Neutron Source — *V. Belkovets, A. Ivanov, A. Kaminsky, A. Krasnykh, N. Malakhov, L. Menshikov, Yu. Popov, V. Piataev, N. Pilyar, V. Rudenko, L. Somov, A. Sumbaev, V. Tarabrin* 152 TAC16

Synchrotron Light Sources and Free Electron Lasers

European Synchrotron Radiation Storage Rings *(Invited)* — *H. Zyngier* 155 TPG01
Development of the JAERI FEL Driven by a Superconducting Accelerator *(Invited)* — *E.J. Minehara, M. Sugimoto, M. Sawamura, R. Nagai, N. Kikuzawa* 159 TPG02
Status of New Light Sources in Russia *(Invited)* — *G. Kulipanov* ..... manuscript not submitted TPG03
Free Electron Laser Research in China *(Invited)* — *Jialin Xie* 162 TPG04
Accelerator Physics Trends at the ESRF — *A. Ropert, L. Farvacque, J. Jacob, J.L. Laclare, E. Plouviez, J.L. Revol, K. Scheidt* 167 TPG05
Commissioning of the PLS 2 GeV Storage Ring — *M. Yoon, J.Y. Huang, J.S. Jang, M. Kwon, T. Lee, S.H. Nam* 171 TPG06
Femtosecond X-Rays from 90° Thomson Scattering — *W. Leemans, R. Schoenlein, A. Chin, E. Glover, R. Govil, P. Volfbeyn, S. Chattopadhyay, K.-J. Kim, C.V. Schank* 174 TPG07
Design of a Diffraction Limited Light Source (DIFL) — *D. Einfeld, J. Schaper, M. Plesko* 177 TPG08
Updated Pans for DIAMOND, a New X-ray Light Source for the UK — *V.P. Suller, J.A. Clarke, J.B. Fitzgerald, H.L. Owen, M.W. Poole, X. Queralt, S.L. Smith* 180 TPG09
Design Optimization for an X-Ray Free Electron Laser Driven by SLAC Linac — *Ming Xie* 183 TPG10

The FERMI FEL Project at Trieste — *D. Bulfone, F. Cargnello, G. D'Auria, F. Daclon, M. Ferianis, M. Giannini, G. Margaritondo, A. Massarotti, A. Rindi, R. Rosei, C. Rubbia, R. Visintini, R.P. Walker, A. Wrulich, D. Zangrando, F. Ciocci, G. Dattoli, A. De Angelis, A. Dipace, A. Doria, G.P. Gallerano, F. Garosi, L. Giannessi, E. Giovenale, L. Mezi, P.L. Ottaviani, A. Renieri, E. Sabia, A. Segreto, A. Torre, M. Castellano, P. Patteri, S. Tazzari, F. Tazzioli, F. Cevenini, A. Cutolo* 186 TPG11

Studies on a Free Electron Laser for the TESLA Test Facility — *J. Rossbach* 189 TPG12

MIT Microwiggler for Free Electron Laser Applications — *P. Catravas, R. Stoner, J. Blastos, D. Sisson, I. Mastovsky, G. Bekefi, X.-J. Wang, A. Fisher* 192 TPG14

DORIS III as a Dedicated Source for Synchrotron Radiation — *H. Nesemann, W. Brefeld, F. Brinker, W. Decking, O. Kaul, B. Sarau* 195 FAA02

Beam Lifetime and Beam Brightness in ALS — *C. Kim, A. Jackson, A. Warwick* 198 FAA03

Asynchronized Energy Ramping at SRRC Storage Ring — *Gwo-Huei Luo, L.H. Chang, Y. Cheng, K.T. Hsu, C.C. Kuo, W.C. Lau, Ch. Wang, P.K. Tseng, Y.C. Liu* 201 FAA04

Emittance Measurements in the ALS Booster Synchrotron — *D. Massoletti, C.H. Kim, A. Jackson* 204 FAA05

Compton Scattering in the ALS Booster — *D. Robin, C. Kim, A. Sessler* 207 FAA06

Beam Stability at SRRC Storage Ring — *W.T. Weng, H.P. Chang, J.R. Chen, Y. Cheng, K.T. Hsu, C.C. Kuo, J.C. Lee, K.K. Lin, Y.C. Liu, G.H. Luo, K.L. Tsang* 210 FAA07

Commissioning of the Duke Storage Ring — *V.N. Litvinenko, Y. Wu, B. Burnham, J.M.J. Madey, F. Carter, C. Dickey, M. Emamian, J. Gustavsson, N. Hower, P. Morcombe, S.H. Park, P. O'Shea, R. Sachtshale, D. Straub, G. Swift, P. Wang, J. Widgren* 213 FAA08

Pulsed VUV Synchrotron Radiation Source — *S.H. Kim, Y.S. Cho, T.Y. Kim, K.H. Chung* 216 FAA10

Merits of a Sub-Harmonic Approach to a Single-Pass, 1.5-Å FEL — *W.M. Fawley, H.-D. Nuhn, R. Bonifacio, E.T. Scharlemann* 219 FAA12

Operation of the ELETTRA Injection Linac in the FEL Mode — *G. D'Auria, C.J. Bocchetta, M. Plesko, C. Rossi, L. Tosi, R.P. Walker, A. Wrulich* 222 FAA13

Free Electron Laser - FEL - Study in Institute of Nuclear Physics of MSU — *V.K. Grishin, B.S. Ishkhanov, T.A. Novikova, V.I. Shvedunov* 225 FAA14

A Chirped-Pulse Regenerative-Amplifier FEL for the Gamma-Gamma Collider — *K.C.D. Chan, J.C. Goldstein, D.C. Nguyen, H. Takeda* 228 FAA16

Alignment and Magnet Error Tolerances for the LCLS X-Ray FEL — *H.-D. Nuhn, E.T. Scharlemann, R. Schlüter* 231 FAA17

Electron Transport and Emittance Diagnostics in CIRFEL — *J. Krishnaswamy, I.S. Lehrman, R. Hartley, R.H. Austin* 234 FAA19

Study on Accelerator Noise Effects on a Far-Infrared FEL Oscillator — *Shinian Fu, Yinbao Chen, Zhibin Huang* 237 FAA21

Status of the UCLA High-Gain Infrared Free Electron Laser — *M. Hogan, C. Pellegrini, J. Rosenzweig, G. Travish, A. Varfolomeev* 240 FAA23

Accelerator Design for the High-Power Industrial FEL — *D.V. Neuffer, S. Benson, J. Bisognano, D. Douglas, H.F. Dylla, D. Kehne, J. Fugitt, K. Jordan, Z. Li, H.-X. Liu, L. Merminga, G. Neil, M. Shinn, C. Sinclair, M. Wiseman, M. Cornacchia* 243 FAA25

Free Electron Laser Amplifier Experiment Based on 3.5 MeV Linear Induction Accelerator — *Ding Bainan, Deng Jianjun, Hu Shenzong, Shi Jinsui, Zhu Wenjun, Li Qing, He Yi* 246 FAA26

A High Duty Factor Electron Linac for FEL — *T.D. Hayward, D.H. Dowell, A.M. Vetter, C. Lancaster, L. Milliman, D. Smith, J. Adamski, C. Parazzoli* 248 FAA27

A Kilowatt Class Visible Free Electron Laser Facility — *J.L. Adamski, D.H. Dowell, T.D. Hayward, C.G. Parazzoli, A.M. Vetter* 251 FAA28

Self-Consistent Analysis of Radiation and Relativistic Electron Beam Dynamics in a Helical Wiggler Using Lienard-Wiechert Fields — *M. Tecimer, L.R. Elias* 254 FAA29

First Lasings at Visible and IR Range of Linac-Based FELs at the FELI — *T. Tomimasu, E. Oshita, S. Okuma, K. Wakita, K. Saeki, A. Zako, T. Suzuki, Y. Miyauchi, A. Koga, S. Nishihara, A. Nagai, E. Tongu, K. Wakisaka, A. Kobayashi, M. Yasumoto* *257* *FAA30*

The Northrop Grumman Compact Infrared FEL (CIRFEL) — *I.S. Lehrman, J. Krishnaswamy, R.A. Hartley, R.H. Austin* 260 FAA31

A Proposed NSLS X-Ray Ring Upgrade Using B Factory Technology — *E.B. Blum* 263 FAR01

A Low Emittance Lattice for the NSLS X-Ray Ring — *J. Safranek* 266 FAR02

Design of a 1.2 GeV Synchrotron Light Source for X-Ray Lithography at Samsung Heavy Industries — *Keeman Kim, Bumsoo Han, Kihun Joh, Sungmyun Kim, Byungmun Kim, Heunggyu Park, Jongpil Park, Jinsoo Kim, Wongu Kang, Kyungwoo Kang, Yuri Kim, Sangil Lee, Younghee Kim* 269 FAR03
ANKA, A Synchrotron Light Source for Microstructure Fabrication and Analysis — *H.O. Moser, M. Ballauff, V. Bechtold, H. Bertagnolli, J. Bialy, P. v. Blanckenhagen, C. Bocchetta, W. Bothe, C. Coluzza, A.N. Danilewsky, K.D. Eichhorn, B. Eigenmann, D. Einfeld, L. Friedrich, M. Haller, N. Holtkamp, V. Honecker, K. Hümmer, E. Huttel, J. Jacob, V. Kashikin, J. Kircher, H. Klewe-Nebenius, A. Knöchel, A. Krüssel, G. Kumpe, K.D. Möller, J. Mohr, M. Nagaenko, F.J. Pantenburg, M. Plesko, J. Schaper, K. Schlösser, G. Schulz, S. Schuppler, H. Schweickert, I. Seidel, Y. Severgin, I. Shukeilo, L. Steinbock, R. Steininger, M. Svandrlik, G. Williams, K. Wilson, J. Zegenhagen* 272 FAR06
An Undulator at PETRA II - A New Synchrotron Radiation Source at DESY — *K. Balewski, W. Brefeld, U. Hahn, J. Pflüger, R. Rossmanith* 275 FAR07
Electron Storage Ring, KSR for Light Source with Synchrotron Radiation — *A. Noda, H. Dewa, H. Fujita, M. Ikegami, Y. Iwashita, S. Kakigi, M. Kando, K. Mashiko, H. Okamoto, T. Shirai, M. Inoue* 278 FAR08
A Lattice for the Future Project of VUV and Soft X-Ray High Brilliant Light Source — *H. Takaki, Y. Kobayashi, K. Matsuda, Y. Kamiya* 281 FAR09
Millimeter Wave Coherent Synchrotron Radiation in a Compact Electron Storage Ring — *J.B. Murphy, E. Blum, R. Heese, J. Keane, S. Krinsky* 284 FAR10
Commissioning of the Argonne Positron Accumulator Ring — *M. Borland* 287 FAR11
APS Storage Ring Commissioning and Early Operational Experience — *G. Decker* 290 FAR13
New Specifications for the SOLEIL Project — *M.-P. Level, P. Brunelle, A. Nadji, M. Sommer, H. Zyngier, J. Faure, P. Nghiem, J. Payet, A. Tkatchenko* 293 FAR14
A Combined Magnet Lattice of the Synchrotron Light Source ISI-800 — *I. Karnaukhov, S. Kononenko, A. Shcherbakov, V. Nemoshkalenko, V. Molodkin, A. Shpak* 296 FAR16
Progress of the ISI-800 Project — *E. Bulyak, S. Efimov, A. Gevchuk, P. Gladkikh, I. Karnaukhov, S. Kononenko, V. Kozin, V. Markov, N. Mocheshnikov, A. Mytsykov, A. Shcherbakov, Yu. Telegin, A. Zelinsky, V. Molodkin, V. Nemoshkalenko, A. Shpak* 299 FAR17
Reduction of Open-Loop Low Frequency Beam Motion at the APS — *G. Decker, Y.G. Kang, S. Kim, D. Mangra, R. Merl, D. McGhee, S. Sharma* 303 FAR19
Horizontal-Vertical Coupling Correction at Aladdin — *R.A. Bosch, W.S. Trzeciak* 306 FAR20
One and a Half Years of Experience with the Operation of the Synchrotron Light Source ELETTRA — *C.J. Bocchetta, D. Bulfone, F. Daclon, G. D'Auria, A. Fabris, R. Fabris, M. Ferianis, M. Giannini, F. Iazzourene, E. Karantzoulis, A. Massarotti, R. Nagaoka, N. Pangos, R. Richter, C. Rossi, M. Svandrlik, L. Tosi, R. Visintini, R.P. Walker, F. Wei, A. Wrulich* 309 FAR21

Low and Intermediate Energy Accelerators

First Generation ISOL Radioactive Ion Beam Facilities *(Invited)* — *D.K. Olsen* 312 RPG01
Latest Developments in Superconducting Cyclotrons *(Invited)* — *H.W. Schreuder* 317 RPG02
Synchrotron-Driven Spallation Sources *(Invited)* — *P.J. Bryant* 322 RPG03
Heavy Ion Cooling Rings *(Invited)* — *J.S. Hangst* ..... manuscript not submitted RPG04
Commissioning the MIT-Bates South Hall Ring — *K. Jacobs, R. Averill, S. Bradley, A. Carter, G. Dodson, K. Dow, M. Farkhondeh, E. Ihloff, S. Kowalski, B. McAllister, W. Sapp, C. Sibley, S. Sobczynski, D. Tieger, C. Tschalaer, E. Tsentalovich, W. Turchinetz, A. Zolfaghari, T. Zwart* 327 RPG05
The AmPS Ring: Actual Performance and Future Plans — *G. Luijckx, R. Bakker, H. Boer Rookhuizen, C. de Jager, F. Kroes, J. van der Laan, R. Maas, J. Noomen, Y. Wu* 330 RPG06
Feasibility Study for Using the FNAL Antiproton Source as a Low Energy Proton-Antiproton Collider — *Mike Church, Stephan Maury* 333 RPG07
CIS, A Low Energy Injector for the IUCF Cooler — *D.L. Friesel, S.Y. Lee* 336 RPG08
The R&D Works on the High Intensity Proton Linear Accelerator for Nuclear Waste Transmutation — *N. Ito, M. Mizumoto, K. Hasegawa, H. Oguri, J. Kusano, Y. Okumura, M. Kawai, H. Ino, H. Murata, Y. Touchi* 339 RPG09
Development of the RFD Linac Structure — *D.A. Swenson, K.R. Crandall, F.W. Guy, J.W. Lenz, A.D. Ringwall, L.S. Walling* 342 RPG10

Proposed Upgrade of the NSCL — *R.C. York, H. Blosser, T. Grimm, D. Johnson, D. Lawton, F. Marti, J. Vincent, X. Wu, A.F. Zeller* 345 RPG11
ISAC-1: Radioactive Ion Beams Facility at TRIUMF — *P.G. Bricault, R. Baartman, J.L. Beveridge, G.S. Clark, J. Doornbos, G. Dutto, T. Hodges, S. Koscielniak, L. Root, P.W. Schmor, H.R. Schneider* 348 RPG12
First Beam Tests of the INS Split Coaxial RFQ for Radioactive Nuclei — *S. Arai, A. Imanishi, K. Niki, M. Okada, Y. Takeda, E. Tojyo, N. Tokuda* 351 RPG13
Accelerator Complex for a Radioactive Ion Beam Facility at ATLAS — *J.A. Nolen* 354 RPG14
The Lattice Design of Indiana University Cyclotron Facility Cooler Injector Synchrotron — *D. Li, X. Kang, D.L. Friesel, S.Y. Lee, J.Y. Liu, A. Pei, A. Riabko, L. Wang* 357 TAP03
Design Study of AntiProton Accumulation and Deceleration Ring in the KEK PS Complex — *S. Machida, M. Yoshii, Y. Mori, N. Tokuda, Y. Ishi* 360 TAP04
Feasibility Study of a 1-MW Pulsed Spallation Source — *Y. Cho, Y.-C. Chae, E. Crosbie, M. Fathizadeh, H. Friedsam, K. Harkay, D. Horan, S. Kim, R. Kustom, E. Lessner, W. McDowell, D. McGhee, F. Mills, H. Moe, R. Nielsen, G. Norek, K.J. Peterson, A. Rauchas, K. Symon, K. Thompson, D. Warner, M. White* 363 TAP05
ORIC Central Region Calculations — *J.D. Bailey, D.T. Dowling, S.N. Lane, S.W. Mosko, D.K. Olsen, B.A. Tatum* 366 TAP07
An Internal Timing Probe for Use in the MSU K1200 Cyclotron — *J.D. Bailey, J. Kuchar, F. Marti, J. Ottarson* 369 TAP08
Axial Injection and Phase Selection Studies of the MSU K1200 Cyclotron — *J.D. Bailey* 372 TAP09
Study and Redesign of the NSCL K500 Central Region — *S.L. Snyder, F. Marti* 375 TAP10
Heavy Ion Acceleration Strategies in the AGS Accelerator Complex -- 1994 Status Report — *L.A. Ahrens, J. Benjamin, M. Blaskiewicz, J.M. Brennan, C.J. Gardner, H.C. Hseuh, Y.Y. Lee, R.K. Reece, T. Roser, A. Soukas, P. Thieberger* 378 TAP11
Observation of Intensity Dependent Losses in Au(15+) Beams — *M. Blaskiewicz, L.A. Ahrens, H.C. Hseuh, T. Roser, Y. Shoji, K. Zeno* 381 TAP12
High Intensity Proton Operations at the Brookhaven — *M. Blaskiewicz, L.A. Ahrens, E.J. Bleser, J.M. Brennan, C.J. Gardner, J.W. Glenn, R.K. Reece, T. Roser, M.J. Syphers, W. VanAsselt, S.Y. Zhang* 383 TAP13
Fast Extracted Proton Beams at Low Energies in the CPS East Experimental Area — *R. Cappi, L. Durieu, J.-Y. Hémery, M. Martini, J.-P. Riunaud, Ch. Steinbach* 386 TAP14
Ion-Optics Systems Of Multiply Charged High-Energy Ions For High Emittance Beams — *V.O. Naidenov, L.A. Baranova, G.M. Gusinskii, A.V. Matyukov, S.Ya. Yavor* 389 TAP16

High Energy Hadron Accelerators and Colliders

The Status of the Fermilab Main Injector Project *(Invited)* — *D. Bogert, W. Fowler, S. Holmes, P. Martin, T. Pawlak* 391 MPG01
Status and Future of the Tevatron *(Invited)* — *V. Bharadwaj* 396 MPG02
The RHIC Project - Status and Plans *(Invited)* — *M. Harrison* 401 MPG03
HERA Status and Plans *(Invited)* — *R. Brinkmann* 406 MPG04
The CERN Heavy Ion Accelerating Facility *(Invited)* — *H.D. Haseroth* 411 MPG05
UNK Status and Plans *(Invited)* — *G. Gurov* 416 MPG06
Reduction of Particle Losses in HERA by Generating an Additional Harmonic Tune Modulation — *O.S. Brüning, F. Willeke* 420 MPG07
Acceleration of Lead Ions in the CERN PS Booster and the CERN PS — *F. Blas, P. Bossard, R. Cappi, G. Cyvoct, R. Garoby, G. Gelato, H. Haseroth, E. Jensen, D. Manglunki, K. Metzmacher, F. Pedersen, N. Rasmussen, K. Schindl, G.C. Schneider, H. Schönauer, L. Sermeus, M. Thivent, M. van Rooij, F. Völker, E. Wildner* 423 MPG09
Highly Efficient Deflection of the Divergent Beam by Bent Single Crystal — *V.I. Baranov, V.M. Biryukov, A.P. Bugorsky, Yu.A. Chesnokov, V.I. Kotov, M.V. Tarakanov, V.I. Terekhov, S.V. Tsarik, O.L. Fedin, M.A. Gordeeva, M.P. Gur'yev, Yu.P. Platonov, A.I. Smirnov* 426 MPG10
Potential Accelerator Improvements Required for the Tevatron Upgrade at Fermilab — *G. Jackson, G.W. Foster* 428 MPG11
Beyond the LHC: A Conceptual Approach to a Future High Energy Hadron Collider — *M.J. Syphers, M.A. Harrison, S. Peggs* 431 MPG12

132 nsec Bunch Spacing in the Tevatron Proton-Antiproton Collider — *S.D. Holmes, J.A. Holt, J. Johnstone, J. Marriner, M. Martens, D. McGinnis* 434 WAP01
Aluminum Beam Tube for the Super Collider: An Option for No-Coating & No-Liner — *W. Chou* 437 WAP02
Variable Bunch Spacing in Super Collider — *W. Chou* 440 WAP03
Fermilab Collider Run 1B Statistics — *V. Bharadwaj, J. Crawford, R. Mau* 443 WAP04
Optimizing the Luminosity in the Tevatron by Independently Moving the Horizontal and Vertical Beta Stars Longitudinally — *M.A. Martens, G.P. Goderre* 446 WAP05
A Model of the Fermilab Collider for Optimization of Performance — *Elliot S. McCrory, Peter W. Lucas* 449 WAP06
Coupling in the Tevatron — *Norman M. Gelfand* 452 WAP07
Calculating Luminosity for a Coupled Tevatron Lattice — *J.A. Holt, M.A. Martens, L. Michelotti, G. Goderre* 455 WAP08
Remarks Concerning the γ-Production Probability of High Relativistic Dirac-Electrons in the Positron Bunch — *Huschang Heydari* 458 WAP09
Field Quality Evaluation of the Superconducting Magnets of the Relativistic Heavy Ion Collider — *J. Wei, R.C. Gupta, A. Jain, S.G. Peggs, C.G. Trahern, D. Trbojevic, P. Wanderer* 461 WAP10
High Intensity Proton Beams in a Multi-cycled SPS — *A. Faugier, X. Altuna, R. Bailey, R. Blanchard, T. Bohl, H. Burkhardt, P. Collier, K. Cornelis, N. Garrel, A. Hilaire, M. Jonker, R. Keizer, M. Lamont, T. Linnecar, G. de Rijk, G. Roy, H. Schmickler, J. Wenninger* 464 WAP12
The SPS as Accelerator of Pb^{82+} Ions — *A. Faugier, X. Altuna, R. Bailey, R. Blanchard, T. Bohl, E. Brouzet, H. Burkhardt, P. Collier, K. Cornelis, G. de Rijk, F. Ferioli, A. Hilaire, M. Lamont, T. Linnecar, M. Jonker, C. Niquille, G. Roy, H. Schmickler* 467 WAP13
Experimental Evidence for Multi-pass Extraction with a Bent Crystal — *B. Dehning, K. Elsener, G. Fidecaro, M. Gyr, W. Herr, J. Klem, W. Scandale, G. Vuagnin, E. Weisse, S. Weisz, S.P. Møller, E. Uggerhoj, A. Freund, R. Hustache, G. Carboni, M.P. Bussa, F. Tosello* 470 WAP14
Storage Ring for Enhanced Antiproton Production at Fermilab — *G. Jackson, G.W. Foster* 473 WAP16

Circular Electron Accelerators and Colliders

LEP Status and Plans *(Invited)* — *S. Myers* 476 WPG01
CESR Status and Plans *(Invited)* — *David L. Rubin* 481 WPG02
PEP II Status and Plans *(Invited)* — *John T. Seeman* 486 WPG03
KEKB Status and Plans *(Invited)* — *Shin-ichi Kurokawa* 491 WPG04
DAΦNE Status and Plans *(Invited)* — *G. Vignola* 495 WPG05
Electron-Positron Colliders at Novosibirsk *(Invited)* — *N. Dikansky* 500 WPG06
BEPC Status and Plans *(Invited)* — *Shu-Hong Wang* 506 WPG07
The First Attainment and Routine Use of Longitudinal Spin Polarization at a High Energy Electron Storage Ring — *D.P. Barber* 511 WPG08
Experiments with Bunch Trains in LEP — *O. Brunner, W. Herr, G. von Holtey, E. Keil, M. Lamont, M. Meddahi, J. Poole, R. Schmidt, A. Verdier, C. Zhang* 514 WPG09
Trapped Macroparticles in Electron Storage Rings — *F. Zimmermann, J.T. Seeman, M. Zolotorev, W. Stoeffl* 517 WPG10
A Compact-High Performance NLC Damping Ring Using High Magnetic Field Bending Magnets — *D.B. Cline, A. Garren, M. Green, J. Kolonko, D. Madura* 520 WPG11
Application of Precision Magnetic Measurements for Control of the Duke Storage Ring — *B. Burnham, V.N. Litvinenko, Y. Wu* 524 RAA01
Wiggler Insertion of the PEP-II B-Factory LER — *J. Heim, L. Bertolini, J. Dressler, O. Fackler, B. Hobson, M. Kendall, T. O'Connor, W. Stoeffl, T. Swan, A. Zholents, M.S. Zisman* 527 RAA03
Status of the High Energy Ring of the PEP II B-Factory — *U. Wienands, E. Reuter, J.T. Seeman, W. Davies-White, A. Fisher, J. Fox, L. Genova, J. Gracia, C. Perkins, M. Pietryka, H. Schwarz, T. Taylor, T. Jackson, C. Belser, D. Shimer* 530 RAA04
Design of the PEP-II Low-Energy Ring — *M.S. Zisman, R.B. Yourd, H. Hsieh* 533 RAA05
Injection Envelope Matching in Storage Rings — *M.G. Minty, W.L. Spence* 536 RAA06
A Mathematical Model for Investigating Chromatic Electron Beam Extraction from a Pulse Stretcher Ring — *Yu.N. Grigor'ev, A.Yu. Zelinsky* 539 RAA07

The Dynamical Aperture of ISI - 800 — *S. Efimov, I. Karnaukhov, S. Kononenko, A. Shcherbakov, A. Tarasenko, A. Zelinsky* 542 RAA08
The Influence of Residual Vertical Dispersion on LEP Performance — *P. Collier, H. Schmickler* 545 RAA10
Operational Procedures to Obtain High Beam-Beam Tune Shifts in LEP Pretzel Operation — *R. Bailey, P. Collier, T. Bohl, H. Burkhardt, K. Cornelis, G. De Rijk, A. Faugier, M. Jonker, M. Lamont, G. Roy, H. Schmickler, J. Wenninger* 548 RAA11
Synchrotron Phase Space Injection into LEP — *P. Collier* 551 RAA12
Systematic Studies of the LEP Working Point — *P. Collier, H. Schmickler* 554 RAA13
Modification of the LEP Electrostatic Separator Systems for Operation with Bunch Trains — *B. Balhan, A. Burton, E. Carlier, J.-P. Deluen, J. Dieperink, N. Garrel, B. Goddard, R. Guinand, W. Kalbreier, M. Laffin, M. Lamont, V. Mertens, J. Poole, H. Verhagen* 557 RAA15
Low Emittance Lattice for LEP — *Y. Alexahin, D. Brandt, K. Cornelis, A. Hofmann, J.P. Koutchouk, M. Meddahi, G. Roy, A. Verdier* 560 RAA17
Radiation Damping Partitions and RF-Fields — *M. Cornacchia, A. Hofmann* 564 RAA18
Experiments on Beam-Beam Depolarization at LEP — *R. Assmann, A. Blondel, B. Dehning, A. Drees, P. Grosse-Wiesmann, H. Grote, M. Placidi, R. Schmidt, F. Tecker, J. Wenninger* 567 RAA19
Measurements of Impedance Distributions and Instability Thresholds in LEP — *D. Brandt, P. Castro, K. Cornelis, A. Hofmann, G. Morpurgo, G.L. Sabbi, J. Wenninger, B. Zotter* 570 RAA20
A Preliminary Lattice Design of a Tau-Charm Factory Storage Ring in Beijing — *N. Huang, L. Jin, Y. Wu, G. Xu* 573 RAA21
Low Energy Ring Lattice of the PEP II Asymmetric B-Factory — *Y. Cai, M. Donald, R. Helm, J. Irwin, Y. Nosochkov, D.M. Ritson, Y. Yan, E. Forest, A. Zholents* 576 RAA22
Damping Rates of the SRRC Storage Ring — *K.T. Hsu, C.C. Kuo, W.K. Lau, W.T. Weng* 579 RAA23
Performance of the SRRC Storage Ring and Wiggler Commissioning — *C. Kuo, K.T. Hsu, G.H. Luo, W.K. Lau, Ch. Wang, H.P. Chang, L.H. Chang, M.H. Wang, J.C. Lee, C.S. Hsue, W.T. Weng, Y.C. Liu* 582 RAA24
Detector Solenoid Compensation in the PEP-II B-Factory — *Y. Nosochkov, Y. Cai, J. Irwin, M. Sullivan, E. Forest* 585 RAA25
Swamp Plots for Dynamic Aperture studies of PEP-II Lattices — *Y.T. Yan, J. Irwin, Y. Cai, T. Chen, D. Ritson* 588 RAA26
Lattice Design for the High Energy Ring of the SLAC B-Factory (PEP-II) — *M.H.R. Donald, Y. Cai, J. Irwin, Y. Nosochkov, D.M. Ritson, J. Seeman, H.-U. Wienands, Y.T. Yan* 591 RAA27
The APS Booster Synchrotron: Commissioning and Operational Experience — *S.V. Milton* 594 RAA28
A Preliminary Design for a Tau-Charm Factory — *J. Norem, E. Crosbie, J. Repond, L. Teng* 597 RAA29
A Spin Control System for the South Hall Ring at the Bates Linear Accelerator Center — *T. Zwart, P. Ivanov, Yu. Shatunov, R. Averill, K. Jacobs, S. Kowalski, W. Turchinetz* 600 RAA31
Beam-Based Alignment of Sextupoles with the Modulation Method — *M. Kikuchi, K. Egawa, H. Fukuma, M. Tejima* 603 RAA33

Linear Colliders and Advanced Accelerator Concepts

The Stanford Linear Collider *(Invited)* — *Paul Emma* 606 WAG01
Options and Trade-Offs in Linear Collider Design *(Invited)* — *J. Rossbach* 611 WAG02
Test Facilities for Future Linear Colliders — *Ronald D. Ruth* 616 WAG03
Channel Guided Lasers for Plasma Accelerators *(Invited)* — *H.M. Milchberg, C.G. Durfee III, T.M. Antonsen, P. Mora* 621 WAG04
Inverse Cerenkov Accelerator Results *(Invited)* — *W.D. Kimura* 626 WAG05
Measurements of Plasma Wake-Fields in the Blow-Out Regime — *N. Barov, M. Conde, J.B. Rosenzweig, P. Schoessow, G. Cox, W. Gai, R. Konecny, J. Power, J. Simpson* 631 WAG06
Experimental Study of Electron Acceleration by Plasma Beat-Waves with Nd Lasers — *F. Amiranoff, F. Moulin, J. Fusellier, J.M. Joly, M. Juillard, M. Bercher, D. Bernard, A. Debraine, J.M. Dieulot, F. Jacquet, P. Matricon, Ph. Miné, B. Montès, R. Morano, P. Poilleux, A. Specka, J. Morillo, J. Ardonceau, B. Cros, G. Matthieussent, C. Stenz, P. Mora* 634 WAG07
A Broadband Electron Spectrometer and Electron Detectors for Laser Accelerator Experiments — *C.E. Clayton, K.A. Marsh, C. Joshi, C.B. Darrow, A.E. Dangor, A. Modena, Z. Najmudin, V. Malka* 637 WAG08

Photon Acceleration from Rest to the Speed of Light — *C.H. Lai, T. Katsouleas, R. Liou, W.B. Mori, C. Joshi, P. Muggli, R. Brogle, J. Dawson* 640 WAG09
A Constant Gradient Planar Accelerating Structure for Linac Use — *Y.W. Kang, P.J. Matthews, R.L. Kustom* 643 WAG10
Pulse to Pulse Stability Issues in the SLC — *C. Adolphsen, R. Assmann, F.J. Decker, P. Emma, J. Frisch, L.J. Hendrickson, P. Krejcik, M. Minty, N. Phinney, P. Raimondi, M.C. Ross, T. Slaton, W. Spence, R. Stege, H. Tang, F. Tian, J. Turner, M. Woodley, F. Zimmermann* 646 WAG11
HOM-Free Linear Accelerating Structure for e+e- Linear Collider at C-Band — *T. Shintake, K. Kubo, H. Matsumoto, O. Takeda* 649 WAG12
SLAC/CERN High Gradient Tests of an X-Band Accelerating Section — *J.W. Wang, G.A. Loew, R.J. Loewen, R.D. Ruth, A.E. Vlieks, I. Wilson, W. Wuensch* 653 WAG13

Linear Colliders

Performance of the 1994/95 SLC Final Focus System — *F. Zimmermann, T. Barklow, S. Ecklund, P. Emma, D. McCormick, N. Phinney, P. Raimondi, M. Ross, T. Slaton, F. Tian, J. Turner, M. Woodley, M. Placidi, N. Toge, N. Walker* 656 RPB01
Direct Measurement of Transverse Wakefields in the SLC Linac — *P. Krejcik, R. Assmann, F.-J. Decker, S. Hartman, R. Miller, T. Raubenheimer* 659 RPB02
Feedback Performance at the Stanford Linear Collider — *M.G. Minty, C. Adolphsen, L.J. Hendrickson, R. Sass, T. Slaton, M. Woodley* 662 RPB03
Vibration Studies of the Stanford Linear Accelerator — *J.L. Turner, C. Adolphsen, G.B. Bowden, F.J. Decker, S.C. Hartman, S. Matsumoto, G. Mazaheri, D. McCormick, M. Ross, R. Stege, S. Virostek, M. Woodley* 665 RPB04
SLAC Modulator Availability and Impact on SLC Operation — *A.R. Donaldson, J.R. Ashton* 668 RPB05
The SLC as a Second Generation Linear Collider — *J.E. Spencer* 671 RPB06
Status of the Design for the TESLA Linear Collider — *R. Brinkmann* 674 RPB07
The TESLA Test Facility (TTF) Linac - A Status Report — *H. Weise* 677 RPB08
The Infrastructure for the TESLA Test Facility (TTF) - A Status Report — *S. Wolff* 680 RPB09
The Status of the S-Band Linear Collider Study — *N. Holtkamp* 683 RPB12
The S-Band Linear Collider Test Facility — *N. Holtkamp* 686 RPB13
Beam Dynamics Studies for the SBLC — *M. Drevlak, R. Wanzenberg* 689 RPB14
S-Band HOM-Damper Calculations and Experiments — *M. Dohlus, M. Marx, N. Holtkamp, P. Hülsmann, W.F.O. Müller, M. Kurz, H.-W. Glock, H. Klein* 692 RPB15
The S-Band 36-Cell Experiment — *B. Krietenstein, O. Podebrad, U. v.Rienen, T. Weiland, H.-W. Glock, P. Hülsmann, H. Klein, M. Kurz, C. Peschke, M. Dohlus, N. Holtkamp* 695 RPB16

Volume 2

Linear Colliders (cont'd)

Parameters for the SLAC Next Linear Collider — *T. Raubenheimer, C. Adolphsen, D. Burke, P. Chen, S. Ecklund, J. Irwin, G. Loew, T. Markiewicz, R. Miller, E. Paterson, N. Phinney, M. Ross, R. Ruth, J. Sheppard, H. Tang, K. Thompson, P. Wilson* 698 RPC01
A Damping Ring Design for the SLAC Next Linear Collider — *T.O. Raubenheimer, J. Byrd, J. Corlett, R. Early, M. Furman, A. Jackson, P. Krejcik, K. Kubo, T. Mattison, M. Minty, W. Moshammer, D. Robin, B. Scott, J. Spencer, K. Thompson, P. Wilson* 701 RPC02
A Bunch Compressor for the Next Linear Collider — *P. Emma, T. Raubenheimer, F. Zimmermann* 704 RPC03
A Final Focus System for the Next Linear Collider — *F. Zimmermann, K. Brown, P. Emma, R. Helm, J. Irwin, P. Tenenbaum, P. Wilson* 707 RPC06
Optimization of the NLC Final Focus System — *F. Zimmermann, R. Helm, J. Irwin* 710 RPC07
The SLAC NLC Extraction & Diagnostic Line — *J. Spencer, J. Irwin, D. Walz, M. Woods* 713 RPC08

CLIC - A Compact and Efficient High Energy Linear Collider — *H. Braun, R. Corsini, J.-P. Delahaye, G. Guignard, C. Johnson, J. Madsen, W. Schnell, L. Thorndahl, I. Wilson, W. Wuensch, B. Zotter* 716 RPC09
CLIC Test Facility Developments and Results — *R. Bossart, H. Braun, F. Chautard, M. Comunian, J.P. Delahaye, J.C. Godot, I. Kamber, J.H.B. Madsen, L. Rinolfi, S. Schreiber, G. Suberlucq, I. Wilson, W. Wuensch* 719 RPC10
Generation of a 30 GHz Train of Bunches Using a Magnetic Switch-Yard — *B. Autin, R. Corsini* 722 RPC11
A New Family of Isochronous Arcs — *G. Guignard, E.T. d'Amico* 725 RPC12
Updating of Beam Dynamics in the CLIC Main Linac — *G. Guignard* 728 RPC13
Improved CLIC Performances Using the Beam Response for Correcting Alignment Errors — *C. Fischer* 731 RPC14
Experimental Studies of a CERN-CLIC 32.98 GHz High Gradient Accelerating Structure Driven by the MIT Free Electron Laser Amplifier — *P. Volfbeyn, I. Mastovsky, G. Bekefi, I. Wilson, W. Wuensch* 734 RPC15
Design of a Relativistic Klystron Two-Beam Accelerator Prototype — *G. Westenskow, G. Caporaso, Y. Chen, T. Houck, S. Yu, S. Chattopadhyay, E. Henestroza, H. Li, C. Peters, L. Reginato, A. Sessler* 737 RPC16
Beam Dynamics Issues in an Extended Relativistic Klystron — *G. Giordano, H. Li, N. Goffeney, E. Henestroza, A. Sessler, S. Yu, T. Houck, G. Westenskow* 740 RPC17
Engineering Conceptual Design of the Relativistic Klystron Two-Beam Accelerator Based Power Source for 1-TeV Next Linear Collider — *L. Reginato, C. Peters, D. Vanecek, S. Yu, F. Deadrick* 743 RPC18
Design of Inductively Detuned RF Extraction Cavities for the Relativistic Klystron Two Beam Accelerator — *E. Henestroza, S.S. Yu, H. Li* 746 RPC19
Beam-Based Optical Tuning of the Final Focus Test Beam — *P. Tenenbaum, D. Burke, S. Hartman, R. Helm, J. Irwin, R. Iverson, P. Raimondi, W. Spence, V. Bharadwaj, M. Halling, J. Holt, J. Buon, J. Jeanjean, F. Le Diberder, V. Lepeltier, P. Puzo, K. Oide, T. Shintake, N. Yamamoto* 749 RPC20
Fermilab Contributions to the FFTB — *V. Bharadwaj, A. Braun, M. Halling, J.A. Holt, D. Still* 752 RPC21
HV Injection Phase Orbit Characteristics for Sub-Picosecond Bunch Operation with a High Gradient 17 GHz Linac — *J. Haimson, B. Mecklenburg* 755 RPC22

New Acceleration Techniques

Electron Acceleration in Relativistic Plasma Waves Generated by a Single Frequency Short-Pulse Laser — *C.A. Coverdale, C.B. Darrow, C.D. Decker, W.B. Mori, K.-C. Tzeng, C.E. Clayton, K.A. Marsh, C. Joshi* 758 RAB01
Theory and Simulation of Plasma Accelerators — *W.B. Mori, K.-C. Tzeng, C.D. Decker, C.E. Clayton, C. Joshi, T. Katsouleas, P. Lai, T.C. Chiou, R. Kinter* 761 RAB02
An Injector-prebuncher for a Plasma Electron Accelerator — *M. Lampel, C. Pellegrini, R. Zhang, C. Joshi, W.M. Fawley* 764 RAB03
Measurements of the Beatwave Dynamics in Time and Space — *A. Lal, K. Wharton, D. Gordon, M.J. Everett, C.E. Clayton, C. Joshi* 767 RAB04
A Novel Technique for Probing theTransverse Interactions Between an Electron Beam and a Plasma — *D. Gordon, A. Lal, C.E. Clayton, M. Everett, C. Joshi* 770 RAB05
Studies of Intense Laser Propagation in Channels for Extended Length Plasma Accelerators — *T. Katsouleas, T.C. Chiou, W.B. Mori, J.S. Wurtele, G. Shvets* 773 RAB08
UV Laser Ionization and Electron Beam Diagnostics for Plasma Lenses — *R. Govil, P. Volfbeyn, W. Leemans* 776 RAB10
Plasma Wakefield Acceleration Experiments in Overdense Regime Driven by Narrow Bunches — *T. Kozawa, T. Ueda, T. Kobayashi, M. Uesaka, K. Miya, A. Ogata, H. Nakanishi, T. Kawakubo, M. Arinaga, K. Nakajima, H. Shibata, N. Yugami, Y. Nishida, D. Whittum, Y. Yoshida* 779 RAB13
The Wake-Field Excitation in a Plasma-Dielectric Structure by a Sequence of Short Bunches of Relativistic Electrons — *I.N. Onishchenko, V.A. Kiseljov, A.K. Berezin, G.V. Sotnikov, V.V. Uskov, A.F. Linnik, Ya.B. Fainberg* 782 RAB15

A Beam Focusing System for a Linac Driven by a Traveling Laser Focus — *A.A. Mikhailichenko* 784 RAB18
2 x 2 TeV μ+μ- Collider: Lattice and Accelerator-Detector Interface Study — *N.M. Gelfand, N.V. Mokhov* 787 RAB19
Muon Cooling and Acceleration Experiment at TRIUMF — *S.A. Bogacz, D.B. Cline, P.H. Sandler, D.A. Sanders* 790 RAB20
Helical Siberian Snakes — *E. Ludmirsky* 793 RAB21
Performance of Achromatic Lattice with Combined Function Sextupoles at Duke Storage Ring — *V.N. Litvinenko, Y. Wu, B. Burnham, J.M.J. Madey, S.H. Park* 796 RAB22

Accelerators and Storage Rings, Misc.

Matreshka High-Intensity Accelerator of Continuous Particle Beams — *F.A. Vodopianov* 799 TAR02
The Amplitude and Phase Control of the ALS Storage Ring RF System — *C.C. Lo, B. Taylor, K. Baptiste* 801 TAR03
Integral Dipole Field Calibration of the SRRC Storage Ring Combined Function Bending Magnets — *J.C. Lee, Peace Chang, C.S. Hsue* 804 TAR04
Improved Mobile 70 MeV Race-Track Microtron Design — *V.I. Shvedunov, A.I. Karev, V.N. Melekhin, N.P. Sobenin, W.P. Trower* 807 TAR05
The Improvement of Energy Measurement in BTS Transport Line by Using Beam Tracing Method — *M.H. Wang, J.C. Lee* 810 TAR06
Design Study of PAL-Stretcher Ring — *I.S. Ko, G.N. Kim, J. Choi, M.H. Cho, W. Namkung* 813 TAR07
Thermomechanical Analysis of a Compact-Design High Heat Load Crotch Absorber — *I.C. Sheng, S. Sharma, R. Rotela, J. Howell* 816 TAR08
Novosibirsk Tau-Charm Factory Design Study — *N. Dikansky, V. Parkhomchuk, A. Skrinsky, V. Yakimenko* 819 TAR11
Development of a RAMI Program for LANSCE Upgrade — *K.C.D. Chan, A. Browman, R.L. Hutson, R.J. Macek, P.J. Tallerico, C.A. Wilkinson* 822 TAR12
Accelerator Waveform Synthesis and Longitudinal Beam Dynamics in a Small Induction Recirculator — *T.J. Fessenden, D.P. Grote, W.M. Sharp* 825 TAR13
Progress Toward a Prototype Recirculating Induction Accelerator for Heavy-Ion Fusion — *A. Friedman, J.J. Barnard, M.D. Cable, D.A. Callahan, F.J. Deadrick, S. Eylon, T.J. Fessenden, D.P. Grote, D.L. Judd, H.C. Kirbie, D.B. Longinotti, S.M. Lund, L.A. Nattrass, M.B. Nelson, M.A. Newton, T.C. Sangster, W.M. Sharp, S.S. Yu* 828 TAR14
Three Dimensional Simulations of a Small Induction Recirculator Accelerator — *D.P. Grote, A. Friedman, I. Haber* 831 TAR15
A Dynamic Momentum Compaction Factor Lattice in the FERMILAB DEBUNCHER Ring — *D.N. Olivieri, M. Church, J. Morgan* 834 TAR16
Mechanical Design of Recirculating Accelerator Experiments for Heavy-Ion Fusion — *V. Karpenko, J. Barnard, F. Deadrick, A. Friedman, D. Grote, S. Lund, J. Meredith, L. Nattrass, M. Nelson, G. Repose, C. Sangster, W. Sharp, T. Fessenden, D. Longinotti, C. Ward* 837 TAR17
The PEP-II Project-Wide Database — *A. Chan, S. Calish, G. Crane, I. MacGregor, S. Meyer, J. Wong, A. Weinstein* 840 TAR18
Chromaticity Compensation - Booster Sextupoles — *S.A. Bogacz, K.-Y. Ng, J.-F. Ostiguy* 843 TAR20
Overview of $\mu^+\mu^-$ Collider Options — *D.B. Cline* 846 TAR21
HIRFL Status and HIRFL-CSR Proposal — *Ye Fang, Wang Yifang* 850 TAR22

Particle Sources and Injectors

A Review of Polarized Ion Sources *(Invited)* — *P.W. Schmor* 853 MPE01
Sources for Production of Radioactive Ion-Beams *(Invited)* — *Helge L. Ravn* 858 MPE02
The TRIUMF High-Curent DC Optically -Pumped Polarized H^- Ion Source — *A.N. Zelenski, C.D.P. Levy, K. Jayamanna, M. McDonald, P.W. Schmor, W.T.H. van Oers, J. Welz, G.W. Wight, G. Dutto, Y. Mori, T. Sakae* 864 MPE03

Lifetime Test on a High-Performance DC Microwave Proton Source — *J. Sherman, D. Hodgkins, P. Lara, J.D. Schneider, R. Stevens Jr.* 867 MPE04
Performance Enhancement of a Compact Radio Frequency Ion Source by the Injection of Supplemental Electrons — *R.F. Welton, G.D. Alton, D. Becher, G.D. Mills, J. Dellwo, S.N. Murray* 871 MPE05
A High-Current Position Source — *V.V. Gorev* 874 MPE06
Polarized Electron Sources *(Invited)* — *J.E. Clendenin* 877 MPE08
High Brightness Electron Sources *(Invited)* — *Richard L. Sheffield* 882 MPE09
Polarization Studies of Strained GaAs Photocathodes at the SLAC Gun Test Laboratory — *P. Sáez, R. Alley, J. Clendenin, J. Frisch, R. Kirby, R. Mair, T. Maruyama, R. Miller, G. Mulhollan, C. Prescott, H. Tang, K. Witte* 887 MPE10
Experimental Results of the ATF In-line Injection System — *X.J. Wang, T. Srinivasan-Rao, K. Batchelor, M. Babzien, I. Ben-Zvi, R. Malone, I. Pogorelsky, X. Qiu, J. Sheehan, J. Skaritka* 890 MPE11
High Power Testing of a 17 GHz Photocathode RF Gun — *S.C. Chen, B.G. Danly, J. Gonichon, C.L. Lin, R.J. Temkin, S.R. Trotz, J.S. Wurtele* 893 MPE12
Analytical Model for Emittance Compensation in RF Photo-Injectors — *L. Serafini, J.B. Rosenzweig* 896 MPE13
Emission, Plasma Formation, and Brightness of a PZT Ferroelectric Cathode — *S. Sampayan, G. Caporaso, D. Trimble, G. Westenskow* 899 MPE14

Radio Frequency Guns and Linac Injectors

Design and Testing of the 2 MV Heavy Ion Injector for the Fusion Energy Research Program — *W. Abraham, R. Benjegerdes, L. Reginato, J. Stoker, R. Hipple, C. Peters, J. Pruyn, D. Vanecek, S. Yu* 902 WPA01
K^+ Diode for the LLNL Heavy Ion Recirculator Accelerator Experiment — *S. Eylon, E. Henestroza, F. Deadrick* 905 WPA02
A Single Bunch RFQ System for Heavy Ions — *J. Madlung, A. Firjahn-Andersch, A. Schempp* 908 WPA03
The Design of Low Frequency Heavy Ion RFQ Resonators — *A. Schempp, H. Vormann, U. Beisel, H. Deitinghoff, O. Engels, D. Li* 911 WPA04
A VE-RFQ-Injector for a Cyclotron — *A. Schempp, O. Engels, F. Marhauser* 914 WPA05
Fermilab Linac Injector, Revisited — *M. Popovic, L. Allen, C.W. Schmidt* 917 WPA06
New RF Structures for the Fermilab Linac Injector — *M. Popovic, A. Moretti, R.J. Nobel* 920 WPA07
High-Power RF Operations Studies with the CRITS RFQ — *G.O. Bolme, D.R. Keffeler, V.W. Brown, D.C. Clark, D. Hodgkins, P.D. Lara, M.L. Milder, D. Rees, P.J. Schafstall, J.D. Schneider, J.D. Sherman, R.R. Stevens, T. Zaugg* 923 WPA08
Beam Dynamics Studies of the Heavy Ion Fusion Accelerator Injector — *E. Henestroza, S.S. Yu, S. Eylon, D.P. Grote* 926 WPA09
First Tests at Injector for the S-Band Test Facility at DESY — *M. Schmitz, W. Herold, N. Holtkamp, W. Kriens, R. Walther* 929 WPA12
RF Phasing of the Duke Linac — *Ping Wang, Nelson Hower, Patrick G. O'Shea* 932 WPA13
Simulations and Measurements of the TTF Phase-1 Injector Gun — *T. Garvey, M. Omeich, M. Jablonka, J.M. Joly, H. Long* 935 WPA14
Experimental Studies on Cold Cathode Magnetron Gun — *A.N. Dovbnya, V.V. Zakutin, V.F. Zhiglo, A.N. Opanasenko, V.P. Romasko, S.A. Cherenshchikov* 938 WPA15
Secondary Emission in Cold-Cathode Magnetron Injection Gun — *S.A. Cherenshchikov, A.N. Dovbnya, A.N. Opanasenko* 939 WPA16
Design of a High Charge CW Photocathode Injector Test Stand at CEBAF — *H. Liu, D. Kehne, S. Benson, J. Bisognano, L. Cardman, F. Dylla, D. Engwall, J. Fugitt, K. Jordan, G. Neil, D. Neuffer, C. Sinclair, M. Wiseman, B. Yunn* 942 WPA17
CANDELA Photo-Injector Experimental Results With a Dispenser Photocathode — *C. Travier, B. Leblond, M. Bernard, J.N. Cayla, P. Thomas, P. Georges* 945 WPB01
A Multi-Cell RF Photoinjector Design — *Sanghyun Park* 948 WPB02
On the Frequency Scalings of RF Guns — *Leon C.-L. Lin, J.S. Wurtele, S.C. Chen* 951 WPB03
Waveguide Broad-Wall Coupling for RF Guns — *Leon C.-L. Lin, S.C. Chen, J.S. Wurtele* 954 WPB04

Charge and Wavelength Scaling of RF Photoinjectors: A Design Tool — *J. Rosenzweig, E. Colby*.....957 WPB05
A Photocathode RF Gun Design for a mm-Wave Linac-Based FEL — *A. Nassiri, T. Berenc, J. Foster, G. Waldschmidt, J. Zhou*.....961 WPB06
The RF Gun Development at SRRC — *C.H. Ho, W.K. Lau, J.I. Hwang, S.Y. Hsu, Y.C. Liu*.....964 WPB07
Design and Construction of High Brightness RF Photoinjectors for TESLA — *E. Colby, V. Bharadwaj, J.F. Ostiguy, T. Nicol, M. Conde, J. Rosenzweig*.....967 WPB08
Jitter Sensitivity in Photoinjectors — *Patrick G. O'Shea*.....970 WPB09
Asymmetric Emittance Beam Generation Using Round Beam RF Guns and Non-linear Optics — *G. Fiorentini, C. Pagani, L. Serafini*.....973 WPB10
The Argonne Wakefield Accelerator High Current Photocathode Gun and Drive Linac — *P. Schoessow, E. Chojnacki, G. Cox, W. Gai, C. Ho, R. Konecny, J. Power, M. Rosing, J. Simpson, N. Barov, M. Conde*.....976 WPB11
Witness Gun for the Argonne Wakefield Accelerator — *J. Power, J. Simpson, E. Chojnacki, R. Konecny*.....979 WPB12
Microwave Measurements of the BNL/SLAC/UCLA 1.6 Cell Photocathode RF Gun — *D.T. Palmer, R.H. Miller, H. Winick, X.J. Wang, K. Batchelor, M. Woodle, I. Ben-Zvi*.....982 WPB13
Subpicosecond, Ultra-Bright Electron Injector — *Bruce E. Carlsten, Martin L. Milder, John M. Kinross-Wright, Donald W. Feldman, Steven Russell, John G. Plato, Alan Shapiro, Boyd Sherwood, Jan Studebaker, Richard Lovato, David Warren, Carl Timmer, Ronald Cooper, Ronald Sturges, Mel Williams*.....985 WPB15
Energy Spread Compensation in an Electron Linear Accelerator — *Yu.D. Tur, A.N. Dovbnya, V.A. Kushnir, V.V. Mitrochenko, D.L. Stepin*.....988 WPB16
On Enhancement of Limited Accelerating Charge — *Yu. Tur*.....990 WPB17
Magnetic Pulse Compression Using a Third Harmonic RF Linearizer — *D.H. Dowell, T.D. Hayward, A.M. Vetter*.....992 WPB20
A Comparison of L-Band and C-Band RF Guns as Sources for Inline-Injection Systems — *Juan C. Gallardo, Harold G. Kirk, Thomas Meyerer*.....995 WPB21
Progress in the Study and Construction of the TESLA Test Facility Injector — *R. Chehab, M. Bernard, J.C. Bourdon, T. Garvey, B. Jacquemard, M. Mencick, B. Mouton, M. Omeich, J. Rodier, P. Roudier, J.L. Saury, M. Taurigna-Quere, Y. Thiery, B. Aune, M. Desmons, J. Fusellier, F. Gougnaud, J.F. Gournay, M. Jablonka, J.M. Joly, M. Juillard, Y. Lussignol, A. Mosnier, B. Phung, S. Buhler, T. Junquera*.....998 WPB22

Particle Sources

Hollow Beam Profile in the Extraction System of ECR Ion Source — *Y. Batygin, A. Goto, Y. Yano*.....1001 WPC01
Ion Sources for Use in Research and Applied High Voltage Accelerators — *S. Nikiforov, V. Golubev, D. Solnyshkov, M. Svinin, G. Voronin*.....1004 WPC03
Direct Fast Beam Chopping of H- Ion Beam in the Surface-Plasma H^- Ion Source — *K. Shinto, A. Takagi, Z. Igarashi, K. Ikegami, M. Kinsho, S. Machida, M. Yoshii, Y. Mori*.....1007 WPC07
Emittance Measurements of the High Intensity Polarized Ion Source at IUCF — *V. Derenchuk, R. Brown, H. Petri, E. Stephenson, M. Wedekind*.....1010 WPC08
Report on EBIS Studies for a RHIC Preinjector — *E. Beebe, A. Hershcovitch, A. Kponou, K. Prelec, J. Alessi, R. Schmieder*.....1013 WPC09
Development of a Volume H^- Ion Source for LAMPF — *D.R. Swenson, R.L. York, R.R. Stevens Jr., C. Geisik, W. Ingalls, J.E. Stelzer, D. Fitzgerald*.....1016 WPC10
Generation of High Purity CW Proton Beams from Microwave-Driven Sources — *David Spence, Keith R. Lykke*.....1019 WPC11
Computational Studies for an Advanced Design ECR Ion Source — *G.D. Alton, J. Dellwo, R.F. Welton, D.N. Smithe*.....1022 WPC12
Pulsed Ion Sources of Duoplasmatron Type with Cold and Hot Cathodes — *A. Glazov, V. Krasnopolsky, R. Meshcherov, V. Masalov*.....1025 WPC13
Double Pulse Experiment with a Velvet Cathode on the ATA Injector — *G. Westenskow, G. Caporaso, Y. Chen, T. Houck, S. Sampayan*.....1027 WPC16

Emittance Measurements for the Illinois/CEBAF Polarized Electron Source — *B.M. Dunham, L.S. Cardman, C.K. Sinclair* 1030 WPC17
The NLC Positron Source — *H. Tang, A.V. Kulikov, J.E. Clendenin, S.D. Ecklund, R.A. Miller, A.D. Yeremian* 1033 WPC18
Ferroelectric Cathodes as Electron Beam Sources — *D. Flechtner, G.S. Kerslick, J.D. Ivers, J.A. Nation, L. Schächter* 1036 WPC19
Studies of Linear and Nonlinear Photoelectric Emission for Advanced Accelerator Applications — *R. Brogle, P. Muggli, P. Davis, G. Hairapetian, C. Joshi* 1039 WPC20
A Derivative Standard for Polarimeter Calibration — *G. Mulhollan, J. Clendenin, P. Sáez, D. Schultz, H. Tang, A.W. Pang, H. Hopster, K. Trantham, M. Johnston, T. Gay, B. Johnson, M. Magugumela, F.B. Dunning, G.K. Walters, G.F. Hanne* 1043 WPC21
Analysis of Positron Focusing Section for SPring-8 Linac — *A. Mizuno, S. Suzuki, H. Yoshikawa, T. Hori, K. Yanagida, H. Sakaki, T. Taniuchi, H. Kotaki, H. Yokomizo* 1046 WPC22
R & D Activity on High QE Alkali Photocathodes for RF Guns — *P. Michelato, A. Di Bona, C. Pagani, D. Sertore, S. Valeri* 1049 WPC23
Development of an Accelerator-Ready Photocathode Drive Laser at CEBAF — *S. Benson, M. Shinn* 1052 WPC24

Linear Accelerators

Analytical Formulae for the Loss Factors and Wakefields of a Disk-loaded Accelerating Structure — *J. Gao* 1055 RPA03
Design Parameters for the Damped Detuned Accelerating Structure — *K. Ko, K. Bane, R. Gluckstern, H. Hoag, N. Kroll, X.T. Lin, R. Miller, R. Ruth, K. Thompson, J. Wang* 1058 RPA04
Operation of PLS 2-GeV Linac — *W. Namkung, I.S. Ko, M.H. Cho, J.S. Bak, J. Choi, H.S. Lee* 1061 RPA06
Radiation Measurements at the Advanced Photon Source (APS) Linear Accelerator — *H.J. Moe, J.H. Vacca, V.R. Veluri, M. White* 1064 RPA07
Positron Focusing in the Advanced Photon Source (APS) Linear Accelerator — *Y.L. Qian, M. White* 1067 RPA08
Bunch Length Measurements at the Advanced Photon Source (APS) Linear Accelerator — *N.S. Sereno, R. Fuja, C. Gold, A.E. Grelick, A. Nassiri, J.J. Song, M. White* 1070 RPA10
Performance of the Advanced Photon Source (APS) Linear Accelerator — *M. White, N. Arnold, W. Berg, A. Cours, R. Fuja, J. Goral, A. Grelick, K. Ko, Y.L. Qian, T. Russell, N.S. Sereno, W. Wesolowski* 1073 RPA11
TW Accelerating Structures with Minimal Surface Electric Field — *O. Nezhevenko, D. Myakishev, V. Tarnetsky, V. Yakovlev* 1076 RPA12
A 100 MeV Injector for the Electron Storage Ring at Kyoto University — *T. Shirai, M. Kando, M. Ikegami, Y. Iwashita, H. Okamoto, S. Kakigi, H. Dewa, H. Fujita, A. Noda, M. Inoue, K. Mashiko* 1079 RPA13
Phase Control and Intra-Pulse Phase Compensation of the Advanced Photon Source (APS) Linear Accelerator — *A.E. Grelick, N. Arnold, K. Ko, N. Sereno, M. White* 1082 RPA14
Error Sensitivity Study for Side Coupled Muffin Tin Structures using a Finite Difference Program — *Warner Bruns* 1085 RPA15
Design of Input Couplers and Endcells for Side Coupled Muffin-Tin Structures — *Warner Bruns* 1088 RPA16
Accelerator Archeology - The Resurrection of the Stanford MARKIII Electron Linac at Duke — *P.G. O'Shea, F. Carter, C. Dickey, N. Hower, V.N. Litvinenko, R. Sachtschale, G. Swift, P. Wang, Y. Wu, J.M.J. Madey* 1090 RPA17
Cold Model Test of Biperiodic L-Support Disk-and-Washer Linac Structure — *Y. Iwashita, A. Noda, H. Okamoto, T. Shirai, M. Inoue* 1093 RPA18
Compact Low Energy CW Linac with High Beam Current — *A. Alimov, A. Chepurnov, O. Chubarov, D. Ermakov, K. Gudkov, B. Ishkhanov, I. Piskarev, V. Shvedunov, A. Shumakov* 1096 RPA19
C-Band Linac RF-System for e+e- Linear Collider — *T. Shintake, N. Akasaka, K.L.F. Bane, H. Hayano, K. Kubo, H. Matsumoto, S. Matsumoto, K. Oide, K. Yokoya* 1099 RPA20
Initial Operation of the UCLA Plane Wave Transformer (PWT) Linac — *R. Zhang, P. Davis, G. Hairapetian, M. Hogan, C. Joshi, M. Lampel, S. Park, C. Pellegrini, J. Rosenzweig, G. Travish* 1102 RPA21

The UCLA Compact High Brightness Electron Accelerator — *P. Davis, G. Hairapetian, M. Hogan, C. Joshi, M. Lampel, S. Park, C. Pellegrini, J. Rosenzweig, G. Travish, R. Zhang* 1105 RPA22
A Semi-Automated System for the Characterization of NLC Accelerating Structures — *S.M. Hanna, G.B. Bowden, H.A. Hoag, R. Loewen, A.E. Vlieks, J.W. Wang* 1108 RPA23
SLAC Accelerator Operations Report: 1992-1995 — *R. Erickson, C.W. Allen, T.K. Inman, W. Linebarger, M. Stanek* 1111 RPA24
Beam Current Limitation in Microwave Accelerators — *A.V. Mishin, I.S. Shchedrin* 1114 RPA25
Installation and Commissioning of the e+/e- Injector for DAΦNE at Frascati — *K. Whitham, H. Amankath, J. Edighoffer, K. Fleckner, E. Gower, S. Lyons, D. Nett, D. Palmer, R. Sheppard, S. Sutter, P. Treas, A. Zante, R. Miller, R. Boni, H. Hsieh, F. Sannibale, M. Vescovi, G. Vignola* 1116 RPA26
Recent Studies of Linac for Production of Radioactive Beams in the INR — *I.N. Birukov, I.V. Gonin, D.V. Gorelov, A.N. Iljinov, V.A. Moiseev, P.N. Ostroumov, A.V. Tiunov* 1119 RPR01
RFQ Cold Model Studies — *P.G. Bricault, D. Joffe, H.R. Schneider* 1122 RPR02
Simulation of the TRIUMF Split-Ring 4-Rod RFQ with MAFIA — *P.G. Bricault, H.R. Schneider* 1125 RPR03
A Low-charge-state Injector Linac for ATLAS — *K.W. Shepard, J.W. Kim* 1128 RPR05
Progress of the Heidelberg High Current Injector — *C.-M. Kleffner, S. Auch, M. Grieser, D. Habs, V. Kößler, M. Madert, R. Repnow, D. Schwalm, H. Deitinghoff, A. Schempp, E. Jaeschke, R. von Hahn, S. Papureanu* 1131 RPR06
The New Concepts in Designing the CW High-current Linacs — *B.P. Murin, G.I. Batskikh, V.M. Belugin, B.I. Bondarev, A.A. Vasiljev, A.P. Durkin, Yu.D. Ivanov, V.A. Konovalov, A.P. Fedotov, I.V. Shumakov* 1134 RPR07
A Versatile, High-Power Proton Linac for Accelerator Driven Transmutation Technologies — *J.H. Billen, S. Nath, J.E. Stovall, H. Takeda, R.L. Wood, L.M. Young* 1137 RPR08
A Compact High-Power Proton Linac for Radioisotope Production — *H. Takeda, J.H. Billen, S. Nath, J.E. Stovall, R.L. Wood, L.M. Young* 1140 RPR09
Potentialities of Electron and Ion Beam Accelerators for Long-Lived Nuclear Waste Transmutation — *A. Shalnov, N. Abramenko, B. Bogdanovich, M. Karetnikov, A. Nesterovich, A. Puchkov* 1143 RPR10
RFQ Design for High-Intensity Proton Beams — *R. Ferdinand, J.-M. Lagniel, P. Mattei* 1146 RPR11
Methods for Increasing of Beam Intensity in Undulator Linear Accelerator — *E.S. Masunov* 1149 RPR12
Linac Integrated Scheme Using RF Energy Storage and Compression — *A.V. Smirnov* 1152 RPR13
Magnetic Field Influence on RF-Structures Electrodynamic Characteristics and Sparking Limit — *A. Shalnov, N. Abramenko, B. Bogdanovich, M. Karetnikov, A. Nesterovich, M. Tubaev* 1155 RPR15
Calculations on the Possibility of the Simultaneous Acceleration of Ions with Different Charge States in a RFQ — *H. Deitinghoff* 1158 RPR18
Phase-Scan Analysis Results for the First Drift Tube Linac Module in the Ground Test Accelerator: Data Reproducibility and Comparison to Simulations — *K.F. Johnson, O.R. Sander, G.O. Bolme, S. Bowling, R. Connolly, J.D. Gilpatrick, W.P. Lysenko, J. Power, E.A. Wadlinger, V. Yuan* 1161 RPR19
Accelerator Systems Optimizing Code — *C.C. Paulson, A.M.M. Todd, M.A. Peacock, M.F. Reusch, D. Bruhwiler, S.L. Mendelsohn, D. Berwald, C. Piaszczyk, T. Meyers, G.H. Gillespie, B.W. Hill, R.A. Jamison* 1164 RPR20
Unexpected Matching Insensitivity in DTL of GTA Accelerator — *V.W. Yuan, O.R. Sander, R.C. Connolly, J.D. Gilpatrick, K.F. Johnson, W.P. Lysenko, D.P. Rusthoi, M. Smith, R. Weiss* 1167 RPR22
Current Losses and Equilibrium in RF Linear Accelerators — *Nathan Brown, Martin Reiser* 1170 RPR23
MMF Linac Upgrade Possibilities for the Pulsed Neutron Source — *S.K. Esin, L.V. Kravchuk, A.I. Kvasha, P.N. Ostroumov, V.L. Serov* 1173 RPR24
Moscow Meson Factory DTL RF System Upgrade — *S.K. Esin, L.V. Kravchuk, A.I. Kvasha, V.L. Serov* 1175 RPR25

Pulsed and High Intensity Beams and Technology

Heavy Ion Fusion 2 MV Injector *(Invited)* — *S. Yu, S. Eylon, E. Henestroza, C. Peters, L. Reginato, D. Vanecek, F. delaRama, R. Hipple, J.D. Stoker, D. Grote, F. Deadrick* 1178 TAE01
Linac-Driven Spallation-Neutron Source *(Invited)* — *Andrew J. Jason* 1183 TAE02

High Average Power, High Current Pulsed Accelerator Technology *(Invited)* — *Eugene L. Neau* 1188 TAE03
Studies of Localized Space-Charge Waves in Space-Charge Dominated Beams *(Invited)* — *J.G. Wang, M. Reiser* 1193 TAE04
Design of the Jupiter Accelerator for Large X-ray Yields — *J.J. Ramirez* 1198 TAE05
Design and Power Flow Studies of a 500-TW Inductive Voltage Adder (IVA) Accelerator — *M.G. Mazarakis, J.W. Poukey, J.P. Corley, D.L. Smith, L. Bennett, J.J. Ramirez, P. Pankuch, I. Smith, P. Corcoran, P. Spence* 1201 TAE06
COBRA Accelerator for Sandia ICF Diode Research at Cornell University — *David L. Smith, Pete Ingwersen, Lawrence F. Bennett, John D. Boyes, David E. Anderson, John B. Greenly, Ravi N. Sudan* *1204* *TAE07*
Beam Injector and Transport Calculations for ITS — *Thomas P. Hughes, David C. Moir, Paul W. Allison* 1207 TAE08
Status of the AIRIX Induction Accelerator — *Ph. Eyharts, Ph. Anthouard, J. Bardy, C. Bonnafond, Ph. Delsart, A. Devin, P. Eyl, J. Labrouche, J. Launspach, J. De Mascureau, E. Merle, A. Roques, P. Le Taillandier, M. Thevenot, D. Villate, L. Voisin* 1210 TAE09
Pulse Modulators for Ion Recirculator Cells — *T.F. Godlove, L.K. Len, F.M. Mako, W.M. Black, K. Sloth* 1213 TAE10
A High Charge State Heavy Ion Beam Source for HIF — *S. Eylon, E. Henestroza* 1216 TAE11
Design and Operation of a 700kV, 700A Modulator — *J.D. Ivers, G.S. Kerslick, J.A. Nation, L. Schächter* 1219 TAE12
The 3 MEV, 200 KW High Voltage Electron Accelerator for Industrial Application — *N.G. Tolstun, V.S. Kuznetsov, A.S. Ivanov, V.P. Ovchinnikov, M.P. Svinjin* 1222 TAE13
Klystron Modulator for Industrial Linac — *Yu.D. Tur, V.I. Beloglazov, E.A. Khomyakov, V.P. Krivchikov, V.B. Mufel, V.V. Zakutin* 1225 TAE14
Optimization of High-Current Ion Beam Acceleration and Charge Compensation in Two Cusps of Induction Linac — *Vyacheslav I. Karas', Nadya G. Belova* 1227 WAA01
2,5-Dimensional Numerical Simulation of Propagation of the Finite Sequence of Relativistic Electron Bunches (REB) in Tenuous and Dense Plasmas — *V.I. Karas', Ya.B. Fainberg, V.D. Levchenko, Yu.S. Sigov* 1230 WAA02
Kinetic Simulation of Fields Excitation and Particle Acceleration by Laser Beat Wave in Non-Homogeneous Plasmas — *V.I. Karas', Ya.B. Fainberg, V.D. Levchenko, Yu.S. Sigov* 1233 WAA03
An Upgraded Proton Injection Kicker Magnet for the Fermilab MIR — *J. Dinkel, R. Reilly* 1236 WAA05
Fermilab Main Injector Abort Kicker System — *C.C. Jensen, J.A. Dinkel* 1239 WAA07
Analysis of the Electrical Noise from the APS Kicker Magnet Power Supplies — *J.A. Carwardine, J. Wang* 1242 WAA08
Design and Test Results of Kicker Units for the Positron Accumulator Ring at the APS — *J. Wang* 1245 WAA09
Development of a Modular and Upgradeable Fast Kicker Magnet System for the Duke Storage Ring — *R.J. Sachtschale, C. Dickey, P. Morcombe* 1248 WAA10
High Current High Accuracy IGBT Pulse Generator — *V.V. Nesterov, A.R. Donaldson* 1251 WAA11
Analysis and Design Modifications for Upgrade of Storage Ring Bump Pulse System Driving the Injection Bump Magnets at the ALS — *G.D. Stover* 1254 WAA14
Eddy Currents Induced in a Muon Storage Ring Vacuum Chamber Due to a Fast Kicker — *W.Q. Feng, E.B. Forsyth* 1257 WAA15
High Pulse Power Modulator for a S-Band Transmitter — *J. DeCobert, B. Binns, R. Campbell, A. Hawkins, D. Wang, A. Zolfaghari* 1260 WAA16
Modulator for Klystron 5045 — *N.S. Dikansky, V. Akimov, B. Estrin, K. Gubin, I. Kazarezov, V. Kokoulin, N. Kot, A. Novokhatsky, Yu. Tokarev, S. Vasserman* 1263 WAA17
High Voltage Nanosecond Generators for SIBERIA - 2 — *A. Kadnikov, V. Deviatilov, V. Korchuganov, Yu. Matveev, D. Shvedov* 1266 WAA18
High Gradient Insulator Technology for the Dielectric Wall Accelerator — *S. Sampayan, G. Caporaso, B. Carder, Y. Chen, C. Holmes, E. Lauer, D. Trimble, J. Elizondo, M. Krogh, B. Rosenblum, C. Eichenberger, J. Fockler* 1269 WAA19
Status of the First Stage of Linear Induction Accelerator SILUND-21 — *A.A. Fateev, G.V. Dolbilov, I.I. Golubev, I.N. Ivanov, V.V. Kosukhin, N.I. Lebedev, V.A. Petrov, V.N. Razuvakin, V.S. Shvetsov, M.V. Yurkov* 1272 WAA20

EMIR-M Installation in the Mode of Operation with Plasma Opening Switch — *V.P. Kovalev, V.M. Korepanov, B.M. Lavrent'ev, R.N. Munasypov, B.A. Filatov* 1274 WAA21

Magnet Technology

New Developments in Niobium Titanium Superconductors *(Invited)* — *D.C. Larbalestier, P.J. Lee* 1276 TPE01
Superconducting Magnets *(Invited)* — *R. Perin* 1282 TPE02
Assembly and Commissioning of the LHC Test String *(Invited)* — *P. Faugeras* 1288 TPE03
Construction and Testing of Arc Dipoles and Quadrupoles for the Relativistic Heavy Ion Collider (RHIC) at BNL *(Invited)* — *P. Wanderer, J. Muratore, M. Anerella, G. Ganetis, A. Ghosh, A. Greene, R. Gupta, A. Jain, S. Kahn, E. Kelly, G. Morgan, A. Prodell, M. Rehak, W. Sampson, R. Thomas, P. Thompson, E. Willen* 1293 TPE04
Permanent Magnet Design for the Fermilab Main Injector Recycler Ring — *G.W. Foster, K. Bertsche, J.-F. Ostiguy, B. Brown, H. Glass, G. Jackson, M. May, D. Orris, Dick Gustafson* 1298 TPE05
Recent Advances in Insertion Devices *(Invited)* — *E. Gluskin, E.R. Moog* 1301 TPE06
Permanent Magnet Beam Transport *(Invited)* — *R.F. Holsinger* 1305 TPE07
Statistical Analyses of the Magnet Data for the Advanced Photon Source Storage Ring Magnets *(Invited)* — *S.H. Kim, D.W. Carnegie, C. Doose, R. Hogrefe, K. Kim, R. Merl* 1310 TPE08
The Magnet System for the BESSY II Injector Synchrotron — *T. Knuth, D. Krämer, E. Weihreter, I. Chertok, S. Michailov, B. Sukhina* 1316 TPE09
Segmented High Quality Undulators — *J. Chavanne, P. Elleaume, P. Van Vaerenbergh* 1319 TPE10
Design of the PEP-II Low-Energy Ring Arc Magnets — *T. Henderson, N. Li, J. Osborn, J. Tanabe, D. Yee, R. Yourd, W. Du, Y. Jiang, Y. Sun* 1322 FAP01
Prototype Developement of the BESSY II Storage Ring Magnetic Elements — *T. Becker, D. Krämer, S. Küchler, U. Strönisch, V. Korchuganov, N. Kuznetsov, E. Levichev* 1325 FAP02
Design, Construction, and Procurement Methodology of Magnets for the 7-GeV Advanced Photon Source — *A. Gorski, J. Argyrakis, J. Biggs, E. Black, J. Humbert, J. Jagger, K. Thompson* 1328 FAP03
The Main Injector Trim Dipole Magnets — *R. Baiod, D.J. Harding, D.E. Johnson, P.S. Martin, S. Mishra* 1331 FAP04
The Main Injector Chromaticity Correction Sextupole Magnets: Measurements and Operating Schemes — *C.M. Bhat, A. Bogacz, B.C. Brown, D.J. Harding, Si J. Fang, P.S. Martin, H.D. Glass, J. Sim* 1334 FAP05
Magnetic Field Measurements of the Initial Fermilab Main Injector Production Quadrupoles — *D.J. Harding, R. Baiod, B.C. Brown, J.A. Carson, N.S. Chester, E. Desavouret, J. DiMarco, J.D. Garvey, H.D. Glass, P.J. Hall, P.S. Martin, P.O. Mazur, C.S. Mishra, A. Mokhtarani, J.M. Nogiec, D.F. Orris, J.E. Pachnik, A.D. Russell, S.A. Sharonov, J.W. Sim, J.C. Tompkins, K. Trombly-Freytag, D.G.C. Walbridge, V.A. Yarba* 1337 FAP06
Magnetic Field Measurements of the Initial Fermilab Main Injector Production Dipoles — *D.J. Harding, R. Baiod, B.C. Brown, J.A. Carson, N.S. Chester, E. Desavouret, J. DiMarco, J.D. Garvey, H.D. Glass, P.J. Hall, P.S. Martin, P.O. Mazur, S. Mishra, A. Mokhtarani, J.M. Nogiec, D.F. Orris, J.E. Pachnik, A.D. Russell, S.A. Sharonov, J.W. Sim, J.C. Tompkins, K. Trombly-Freytag, D.G.C. Walbridge, V.A. Yarba* 1340 FAP07
The Fermilab Main Injector Dipole and Quadrupole Cooling Design and Bus Connections — *J.A. Satti* 1343 FAP08
Design of the Fermilab Main Injector Lambertson — *D.E. Johnson, R. Baiod, D.J. Harding, P.S. Martin, M. May* 1346 FAP09
Three-Dimensional End Effects in Iron Septum Magnets — *J.-F. Ostiguy, D.E. Johnson* 1349 FAP10
Design and B-field Measurements of a Lambertson Injection Magnet for the RHIC Machine — *N. Tsoupas, E. Rodger, J. Claus, H.W. Foelsche, P. Wanderer* 1352 FAP11
The APS Direct-Drive Pulsed Septum Magnets — *S. Sheynin, F. Lopez, S.V. Milton* 1355 FAP12
Development of the Pulse Magnets for the Booster Synchrotron of SPring-8 — *H. Yonehara, H. Suzuki, T. Nagafuchi, M. Kodaira, T. Aoki, N. Tani, S. Hayashi, Y. Ueyama, T. Kaneda, Y. Sasaki, H. Abe, H. Yokomizo* 1358 FAP13
Magnetic Design of the LNLS Transport Line — *R.H.A. Farias, Liu Lin, G. Tosin* 1361 FAP14
Construction and Characterization of Combined Function Quadrupoles — *G. Tosin* 1364 FAP15

Dipole Magnets for the SLAC 50 GeV A-Line Upgrade — *R. Erickson, S. DeBarger, C.M. Spencer, Z. Wolf* 1366 FAP16
Design and Testing of the Magnetic Quadrupole for the Heavy Ion Fusion Program — *R. Benjegerdes, A. Faltens, W. Fawley, C. Peters, L. Reginato, M. Stuart* 1369 FAP17
Design and Construction of a Large Aperture, Quadrupole Electromagnet Prototype for ILSE — *M. Stuart, A. Faltens, W.M. Fawley, C. Peters, M.C. Vella* 1372 FAP18
A Permanent Race-Track Microtron End Magnet — *A.I. Karev, V.N. Melekhin, V.I. Shvedunov, N.P. Sobenin, W.P. Trower* 1375 FAP19
Planar Permanent Magnet Multipoles: Measurements and Configurations — *T. Cremer, R. Tatchyn* 1378 FAP20
Temperature Considerations in the Design of a Permanent Magnet Storage Ring — *K. Bertsche, J.-F. Ostiguy, W.B. Foster* 1381 FAP21
3D Numerical Analysis of Magnets and the Effect of Eddy Current on Fast Steering — *T. Nagatsuka, T. Koseki, Y. Kamiya, Y. Terada* 1384 FAP22
MEB Resitive Magnets Prototypes Manufacturing — *G. Batskikh, G. Mamaev, T. Latypov, I. Tenyakov, Y. Tereshkin* 1387 FAP24

Volume 3

Magnet Technology (cont'd)

Quench Antennas for RHIC Quadrupole Magnets — *T. Ogitsu, A. Terashima, K. Tsuchiya, G. Ganetis, J. Muratore, P. Wanderer* 1390 FAQ02
Superconducting 8 cm Corrector Magnets for the Relativistic Heavy Ion Collider (RHIC) — *A. Morgillo, J. Escallier, G. Ganetis, A. Greene, A. Ghosh, A. Jain, E. Kelly, A. Marone, G. Morgan, J. Muratore, W. Sampson, P. Thompson, P.J. Wanderer, E. Willen* 1393 FAQ03
Superconducting Sextupoles and Trim Quadrupoles for RHIC — *P. Thompson, M. Anerella, G. Ganetis, A. Ghosh, A. Greene, R. Gupta, A. Jain, E. Kelly, M. Lindner, G. Morgan, J. Muratore, W. Sampson, P. Wanderer, E. Willen* 1396 FAQ04
Study of UNK Quench Protection System on the String of 4 UNK Superconducting Magnets — *A. Andriishchin, O. Afanasiev, V. Gridasov, A. Erochin, E. Kachtanov, K. Myznikov, V. Sytchev, L. Vassiliev, O. Veselov, N. Yarygin* 1399 FAQ06
Two Alternate High Gradient Quadrupoles; An Upgraded Tevatron IR and a "Pipe" Design — *A.D. McInturff, J.M. van Oort, R.M. Scanlan* 1402 FAQ07
Superconducting Focusing Solenoid for X-band Klystron — *T. Ogitsu, T. Higo, H. Mizuno, Y. Imai, T. Inaguchi, T. Minato, T.H. Kim, T. Uemura, S. Yokoyama, Z. Wolf, D. Jensen, P. Radusewicz* 1405 FAQ08
A High Gradient Superconducting Quadrupole for a Low Charge State Ion Linac — *J.W. Kim, K.W. Shepard, J.A. Nolen* 1408 FAQ09
Status of the High Brilliance Synchrotron Radiation Source BESSY-II — *E. Jaeschke, S. Khan, D. Krämer, D. Schirmer* 1411 FAQ12
Harmonic Generation FEL Magnets: Measured B-fields Compared to 3D Simulations — *W.S. Graves, L. Solomon* 1414 FAQ13
Measurement of Ramp Rate Sensitivity in Model Dipoles with Ebanol-Coated Cable — *C. Haddock, V. Kovachev, D. Capone* 1417 FAQ14
Combined Element Magnet Production for the Relativistic Heavy Ion Collider (RHIC) at BNL — *S. Mulhall, H. Foelsche, G. Ganetis, A. Greene, E. Kelly, S. Plate, E. Willen* 1420 FAQ15
Field Quality Control Through the Production Phase of the RHIC Arc Dipoles — *R. Gupta, A. Jain, S. Kahn, G. Morgan, P. Thompson, P. Wanderer, E. Willen* 1423 FAQ16
The Ellipitical Multipole Wiggler Project — *E. Gluskin, D. Frachon, P.M. Ivanov, J. Maines, E.A. Medvedko, E. Trakhtenberg, L.R. Turner, I. Vasserman, G.I. Erg, Yu.A. Evtushenko, N.G. Gavrilov, G.N. Kulipanov, A.S. Medvedko, S.P. Petrov, V.M. Popik, N.A. Vinokurov, A. Friedman, S. Krinsky, G. Rakowsky, O. Singh* 1426 FAQ17
Results of Magnetic Measurements and Field Integral Compensation for the Elliptical Multipole Wiggler — *D. Frachon, P.M. Ivanov, E.A. Medvedko, I. Vasserman, O. Despe, Y.G. Kang* 1429 FAQ18

Status of ELETTRA Insertion Devices — *R.P. Walker, R. Bracco, A. Codutti, B. Diviacco, D. Millo, D. Zangrando* 1432 FAQ19
Expected Radiation Spectra of a 30-m Long Undulator in SPring-8 — *M. Takao, Y. Miyahara* 1435 FAQ20
Analytical Formulation of a Quasi-periodic Undulator — *M. Takao, S. Hashimoto, S. Sasaki, Y. Miyahara* 1438 FAQ21
High-Field Strong-Focusing Undulator Designs for X-Ray Linac Coherent Light Source (LCLS) Applications — *S. Caspi, R. Schlueter, R. Tatchyn* 1441 FAQ23
Wigglers at the Advanced Light Source — *E. Hoyer, J. Akre, D. Humphries, T. Jackson, S. Marks, Y. Minamihara, P. Pipersky, D. Plate, G. Portmann, R. Schlueter* 1444 FAQ24
Design of End Magnetic Structures for the Advanced Light Source Wigglers — *D. Humphries, J. Akre, E. Hoyer, S. Marks, Y. Minamihara, P. Pipersky, D. Plate, R. Schlueter* 1447 FAQ25
Passive End Pole Compensation Scheme for a 1.8 Tesla Wiggler — *L.H. Chang, Ch. Wang, C.H. Chang, T.C. Fan* 1450 FAQ26
Insertion of Helical Siberian Snakes in RHIC — *A. Luccio, F. Pilat* 1453 FAQ28
Modeling of WLS Field with Piecewisely Constant Magnets — *Zuping Liu, Aihua Zhao* 1456 FAQ29
A BESSY-1 6 Tesla WLS Effect Compensation Scheme — *Zuping Liu, Aihua Zhao* 1459 FAQ30
16 Tesla Block-Coil Dipole for Future Hadron Colliders — *Peter M. McIntyre, Weijun Shen* 1462 FAQ31
Automated Methods of Field Harmonic Signal Extraction and Processing for the Magnets in Superconducting Supercollider — *T.S. Jaffery, J. Butteris, M. Wake* 1465 FAQ32

Radio Frequency Technology

Review of the Development of RF Cavities for High Currents *(Invited)* — *J. Kirchgessner* 1469 FAE01
Performance of Normal Conducting Structures for Linear Colliders *(Invited)* — *Toshiyasu Higo* 1474 FAE02
High Gradient Superconducting RF Systems *(Invited)* — *J. Graber* 1478 FAE03
Development and Advances in Conventional High Power RF Systems *(Invited)* — *P.B. Wilson* 1483 FAE04
The Upgraded RF System for the AGS and High Intensity Proton Beams *(Invited)* — *J.M. Brennan* 1489 FAE05
Phase-Stable, Microwave FEL Amplifier — *Bruce E. Carlsten, Michael V. Fazio, W. Brian Haynes, Lisa M. May, James M. Potter* 1494 FAE06
1.2 MW Klystron for Asymmetric Storage Ring B Factory — *W.R. Fowkes, G. Caryotakis, E. Doyle, E. Jongewaard, C. Pearson, R. Phillips, J. Sackett, E. Wright, H. Bohlen, G. Huffman, S. Lenci, E. Lien, E. McCune, G. Miram* 1497 FAE07
Analysis of Multipacting in Coaxial Lines — *E. Somersalo, P. Ylä-Oijala, D. Proch* 1500 FAE08
An Accelerator Resonantly Coupled with an Energy Storage (ARES) for the KEKB — *Y. Yamazaki, K. Akai, N. Akasaka, E. Ezura, T. Kageyama, F. Naito, T. Shintake, Y. Takeuchi* 1503 FAE09
Non Integer Harmonic Number Acceleration of Lead Ions in the CERN SPS — *D. Boussard, T. Bohl, T. Linnecar, U. Wehrle* 1506 FAE10
Analysis and Results of the Industrial Production of the Superconducting Nb/Cu Cavities for the LEP2 Project — *E. Chiaveri, C. Benvenuti, R. Cosso, D. Lacarrere, K.M. Schirm, M. Taufer, W. Weingarten* 1509 FAE11
Performance Experience with the CEBAF SRF Cavities — *C. Reece, J. Benesch, M. Drury, C. Hovater, J. Mammosser, T. Powers, J. Preble* 1512 FAE12
Beam Test of a Superconducting Cavity for the CESR Luminosity Upgrade — *H. Padamsee, P. Barnes, S. Belomestnykh, K. Berkelman, M. Billing, R. Ehrlich, G. Flynn, Z. Greenwald, W. Hartung, T. Hays, S. Henderson, R. Kaplan, J. Kirchgessner, J. Knobloch, D. Moffat, H. Muller, E. Nordberg, S. Peck, M. Pisharody, J. Reilly, J. Rogers, D. Rice, D. Rubin, D. Sagan, J. Sears, M. Tigner, J. Welch* 1515 FAE13

Radio Frequency Power Sources

Development of Input & Output Structures for High Power X-Band TWT Amplifiers — *S. Naqvi, Cz. Golkowski, G.S. Kerslick, J.A. Nation, L. Schächter* 1518 TAQ01
Characterization of a Klystrode as a RF Source for High-Average-Power Accelerators — *D. Rees, D. Keffeler, W. Roybal, P.J. Tallerico* 1521 TAQ02
Choppertron II — *T.L. Houck, G.A. Westenskow, J. Haimson, B. Mecklenburg* 1524 TAQ03

The Resistive-Wall Klystron as a High-Power Microwave Source — *Han S. Uhm* 1527 TAQ04
Operating Conditions of High-Power Relativistic Klystron — *Han S. Uhm* 1530 TAQ05
Spurious Oscillations in High Power Klystrons — *B. Krietenstein, K. Ko, T. Lee, U. Becker, T. Weiland, M. Dohlus* 1533 TAQ06
In-House Repair of a 30 Megawatt S Band Klystron — *R. Sachtschale, P.G. O'Shea, M. Ponds, G. Swift* 1536 TAQ07
Development of a High Power 1.2 MW CW L-Band Klystron — *K. Hirano, Y.L. Wang, T. Emoto, A. Enomoto, I. Sato* 1539 TAQ08
Ultrarelativistic Klystron - a Future Super Power UHF Generator — *F.A. Vodopianov* 1542 TAQ10
A 200 KW Power Amplifier and Solid State Driver for the Fermilab Main Injector — *J. Reid, H. Miller* 1544 TAQ11
A 476 MHz RF System for the Storage Mode of the AmPS Ring — *F. Kroes, P. de Groen, E. Heine, B. Heutenik, A. Kruijer, B. Munneke, R. Pirovano, T. Sluijk, J. Verkooyen* 1547 TAQ12
Lifetime Experience with Low Temperature Cathodes Equipped in Super Power Klystrons — *Rudolf Backmor* 1550 TAQ13
Microwave System of PLS 2-GeV Linac — *H.S. Lee, O.H. Hwang, S.H. Park, C.M. Ryu, W. Namkung* 1553 TAQ14
Klystron-Modulator System Performances for PLS 2-GeV Linac — *M.H. Cho, J.S. Oh, S.S. Park, W. Namkung* 1556 TAQ15
Klystron Modulator Operation and Upgrades for the APS Linac — *Thomas J. Russell, Alexander Cours* 1559 TAQ16
Prospects for Developing Microwave Amplifiers to Drive Multi-TeV Linear Colliders — *V.L. Granatstein, G.S. Nusinovich, J. Calame, W. Lawson, A. Singh, H. Guo, M. Reiser* 1561 TAQ17
Design of 100 MW, Two-Cavity Gyroklystrons for Accelerator Applications — *J.P. Calame, W. Lawson, J. Cheng, B. Hogan, M. Castle, V.L. Granatstein, M. Reiser* 1563 TAQ18
Design of Three-Cavity Coaxial Gyroklystron Circuits for Linear Collider Applications — *W. Lawson, G. Saraph, J.P. Calame, J. Cheng, M. Castle, B. Hogan, M. Reiser, V.L. Granatstein, H. Metz* 1566 TAQ19
Numerical Simulation of Magnicon Amplifier — *V. Yakovlev, O. Danilov, O. Nezhevenko, V. Tarnetsky* 1569 TAQ21
RF-Power Upgrade Systems with Energy Compression for Electron Linacs — *A. Shalnov, B.Yu. Bogdanovich, A. Ignatyev, V. Senyukov* 1572 TAQ23
RF-Power Upgrade System with Resonant Loading — *A. Shalnov, B. Bogdanovich, A. Ignatyev, V. Senyukov* 1575 TAQ24
High-Power Test of Traveling-Wave-Type RF-Pulse Compressor — *S. Yamaguchi, A. Enomoto, I. Sato, Y. Igarashi* 1578 TAQ25
Active Radiofrequency Pulse Compression Using Switched Resonant Delay Lines — *Sami G. Tantawi, Ronald D. Ruth, A.E. Vlieks* 1581 TAQ26
Design of a Multi-Megawatt X-Band Solid State Microwave Switch — *Sami G. Tantawi, Terry G. Lee, Ronald D. Ruth, A.E. Vlieks, Max Zolotorev* 1584 TAQ27
Reduced Field TE01 X-Band Traveling Wave Window — *W.R. Fowkes, R.S. Callin, S.G. Tantawi, E.L. Wright* 1587 TAQ28
Design and High-Power Test of a TE11-Mode X-Band RF Window with Taper Transitions — *Y. Otake, S. Tokumoto, H. Mizuno* 1590 TAQ29
Feasibility Study of Optically Coupling RF-Power at mm Waves — *B. Littmann, H. Henke* 1593 TAQ30
A Low-Frequency High-Voltage RF-Barrier Bunching System for High-Intensity Neutron Source Compressor Rings — *T.W. Hardek, D. Rees, C. Ziomek* 1596 TAQ31
Temporal Evolution of Multipactor Discharge — *R. Kishek, Y.Y. Lau, R.M. Gilgenbach* 1599 TAQ32
Stabilizing a Power Amplifier Feeding a High Q Resonant Load — *A.K. Mitra, R.L. Poirier, J.J. Lu, R. Hohbach* 1602 TAQ33
Study of 14 GHz VLEPP Klystron With RF Absorbing Drift Tubes — *G.V. Dolbilov, N.I. Azorsky, A.A. Fateev, N.I. Lebedev, V.A. Petrov, V.P. Sarantsev, V.S. Shvetsov, M.V. Yurkov* 1605 TAQ34
24-MW, 24-μs Pulse RF Power Supply For Linac-Based FELs — *E. Ohshita, Y. Morii, S. Abe, S. Okuma, K. Wakita, T. Tomimasu, I. Ito, Y. Miyai, K. Nakata, M. Hakota* 1608 TAQ35
Initial Operation of an X-Band Magnicon Amplifier Experiment — *S.H. Gold, A.K. Kinkead, A.W. Fliflet, B. Hafizi* 1611 TAQ37

Superconducting RF

The Effects of Tuning and Terminating on the Operating Mode of Multi-Cell Coupled Cavity — *Zubao Qian* 1614 TPP01

Response of Superconducting Cavities to High Peak Power — *T. Hays, H. Padamsee* 1617 TPP02

Development of HOM Damper for B-Factory (KEKB) Superconducting Catities — *T. Tajima, K. Asano, T. Furuya, M. Izawa, S. Mitsunobu, T. Takahashi, N. Gamo, S. Iida, Y. Ishi, Y. Kijima, S. Kokura, M. Kudo, K. Sennyu, S. Tachibana, H. Takashina, N. Taniyama* 1620 TPP03

Microscopic Examination of Defects Located by Thermometry in 1.5 GHz Superconducting Niobium Cavities — *J. Knobloch, R. Durand, H. Muller, H. Padamsee* 1623 TPP04

RF System for the NSLS Coherent Infrared Radiation Source — *W. Broome, R. Biscardi, J. Keane, P. Mortazavi, M. Thomas, J.M. Wang* 1626 TPP06

Development of TESLA-type Cavity at KEK — *M. Ono, E. Kako, S. Noguchi, K. Saito, T. Shishido, M. Wake, H. Inoue, T. Fujino, Y. Funahashi, M. Matsuoka, T. Suzuki, T. Higuchi, H. Umezawa* 1629 TPP07

Study of Luminous Spots Observed on Metallic Surfaces Subjected to High RF Fields — *T. Junquera, S. Maïssa, M. Fouaidy, A. Le Goff, B. Bonin, M. Luong, H. Safa, J. Tan* 1632 TPP09

Test Results for a Heat-Treated 4-Cell 805-MHz Superconducting Cavity — *Brian Rusnak, Alan Shapiro* 1636 TPP10

An Advanced Rotating T-R Mapping & its Diagnoses of TESLA 9-Cell Superconducting Cavity — *Q.S. Shu, G. Deppe, W-D. Möller, M. Pekeler, D. Proch, D. Renken, P. Stein, C. Stolzenburg, T. Junquera, A. Caruette, M. Fouaidy* 1639 TPP11

Improvements to Power Couplers for the LEP2 Superconducting Cavities — *J. Tückmantel, C. Benvenuti, D. Bloess, D. Boussard, G. Geschonke, E. Haebel, N. Hilleret, S. Juras, H.P. Kindermann, J. Uythoven, C. Wyss, M. Stirbet* 1642 TPP12

Arcing Phenomena on CEBAF RF-Windows at Cryogenic Temperatures — *Tom Powers, Peter Kneisel, Ray Allen* 1645 TPP13

Surface Scanning Thermometers for Diagnosing the TESLA SRF Cavities — *T. Junquera, A. Caruette, M. Fouaidy, Q.S. Shu* 1648 TPP14

Microwave Surface Resistance of YBaCuO Superconducting Films Laser-Ablated on Copper Substrates — *J. Liu, K. Asano, E. Ezura, M. Fukutomi, S. Inagaki, S. Isagawa, K. Komori, S. Kumagai, H. Nakanishi, M. Tosa, K. Yoshihara* 1652 TPP16

Room Temperature RF

Transverse Coupling Impedance Measurement Using Image Current — *D. Sun, P. Colestock, M. Foley* 1655 WPP01

Decreasing Transient Beam Loading in RF Cavities of U-70 Accelerator — *O.P. Lebedev* 1658 WPP02

RF System for Bunch Lengthening — *R. Biscardi, G. Ramirez* 1660 WPP03

Electromagnetic Field Vector Components Precise Measurements in Accelerating Structures — *M.A. Chernogubovsky, M.F. Vorogushin* 1663 WPP04

A New Tuning Method for Traveling Wave Structures — *T. Khabiboulline, V. Puntus, M. Dohlus, N. Holtkamp, G. Kreps, S. Ivanov, K. Jin* 1666 WPP05

RF Systems for RHIC — *J. Rose, J. Brodowski, R. Connolly, D.P. Deng, S. Kwiatkowski, W. Pirkl, A. Ratti* 1669 WPP07

A New RF System for Bunch Coalescing in the Fermilab Main Ring — *J. Dey, I. Kourbanis, D. Wildman* 1672 WPP08

Higher Order Modes of the Main Ring Cavity at Fermilab — *J. Dey, D. Wildman* 1675 WPP09

RF Measurements and Control of Higher Order Modes in Accelerating Cavities — *V. Veshcherevich, S. Krutikhin, I. Kuptsov, S. Nosyrev, A. Novikov, I. Sedlyarov* 1678 WPP10

RF System of VEPP-4M Electron-Positron Collider — *E. Gorniker, P. Abramsky, V. Arbuzov, S. Belomestnykh, A. Bushuyev, M. Fomin, I. Kuptsov, G. Kurkin, S. Nosyrev, V. Petrov, I. Sedlyarov, V. Veshcherevich* 1681 WPP11

Storage Ring Cavity Higher-Order Mode Dampers for the Advanced Photon Source — *Paul Matthews, Yoon Kang, Robert Kustom* 1684 WPP12

Reduction of Multipactor in RF Ceramic Windows Using a Simple Titanium-Vapor Deposition System — *K. Primdahl, R. Kustom, J. Maj* 1687 WPP13
Cooling the APS Storage Ring Radio-Frequency Accelerating Cavities Thermal/Stress/Fatigue Analysis and Cavity Cooling Configuration — *K. Primdahl, R. Kustom* 1690 WPP14
RF Cavities for the Positron Accumulator Ring (PAR) of the Advanced Photon Source (APS) — *Y.W. Kang, A. Nassiri, J.F. Bridges, T.L. Smith, J.J. Song* 1693 WPP16
The Proposal of Complex Impedance Termination for Versatile HOM Damper Cavity — *V.V. Paramonov* 1696 WPP17
The Magnetron-Type Varactor for Fast Control in Accelerator RF Systems — *M.I. Kuznetsov, V.V. Paramonov, Yu.V. Senichev, I.B. Enchevich, R.L. Poirier* 1699 WPP18
The Distortion of the Accelerating Field Distribution in Compensated Structures due to Steady-State Beam Loading — *V.G. Andreev, V.V. Paramonov,* 1702 WPP19
The Indiana University Cooler Injector Synchrotron RF System — *A. Pei, M. Ellison, D. Friesel, D. Jenner, X. Kang, S.Y. Lee, D. Li, J. Liu, A. Riabko, L. Wang, K. Hedblom* 1705 WPP20
The Indiana University Cooler Injection Synchrotron RF Cavity — *A. Pei, M. Ellison, D. Friesel, D. Jenner, X. Kang, S.Y. Lee, D. Li, J. Liu, A. Riabko, L. Wang, K. Hedblom* 1708 WPP21
Determination of Resonant Frequency and External Q Values for the Bessy II HOM-Damped Cavity — *Frank Schönfeld, Bengt Littmann* 1711 WPP22
106 MHz Cavity for Improving Coalescing Efficiency in the Fermilab Main Ring — *J. Dey, I. Kourbanis, D. Wildman* 1714 WPP23
On the Higher Order Mode Coupler Design for Damped Accelerating Structures — *Jie Gao* 1717 WPQ01
High Power Window Tests on a 500 MHz Planar Window for the CESR Upgrade — *M. Pisharody, P. Barnes, E. Chojnacki, R. Durand, T. Hays, R. Kaplan, J. Kirchgessner, J. Reilly, H. Padamsee, J. Sears* 1720 WPQ02
Operational Peformances and Future Upgrades for the ELETTRA RF System — *A. Fabris, A. Massarotti, C. Pasotti, M. Svandrlik* 1723 WPQ04
X-Band High Power Dry Load for NLCTA — *K. Ko, H. Hoag, T. Lee, S. Tantawi* 1726 WPQ05
Development of a High-Power RF Cavity for the PEP-II B Factory — *R.A. Rimmer, M.A. Allen, J. Saba, H. Schwarz, F.C. Belser, D.D. Berger, R.M. Franks* 1729 WPQ06
A Design of Input Coupler for RF-Cavity — *T. Nagatsuka, T. Koseki, Y. Kamiya, M. Izawa, Y. Terada* 1732 WPQ07
Design of the KEKB RF System — *K. Akai, E. Ezura, Y. Yamazaki* 1735 WPQ08
RF Characteristics of ARES Cold Models — *N. Akasaka, K. Akai, T. Kageyama, T. Shintake, Y. Yamazaki* 1738 WPQ09
Design of Traveling Wave Windows for the PEP-II RF Coupling Network — *N.M. Kroll, C.-K. Ng, J. Judkins, M. Neubauer* 1741 WPQ10
Impedance Spectrum for the PEP-II RF Cavity — *X.E. Lin, K. Ko, C.-K. Ng* 1744 WPQ12
Measurement and Analysis of Higher-Order-Mode (HOM) Damping in B-Factory R-F Cavities — *D.A. Goldberg, M. Irwin, R.A. Rimmer* 1747 WPQ13
Planar Structures for Electron Acceleration — *H. Henke* 1750 WPQ14
Precise Fabrication of X-Band Detuned Accelerating Structure for Linear Collider — *T. Higo, H. Sakai, Y. Higashi, T. Takatomi, S. Koike* 1753 WPQ15
Development of a Beam-Pipe HOM Absorber for the ATF Damping Ring — *F. Hinode, S. Sakanaka* 1756 WPQ16
Development of a HOM-Damped Cavity for the KEK B-Factory (KEKB) — *T. Kageyama, K. Akai, N. Akasaka, E. Ezura, F. Naito, T. Shintake, Y. Takeuchi, Y. Yamazaki, T. Kobayashi* 1759 WPQ17
Possible Cavity Construction Techniques for the DIAMOND Storage Ring — *D.M. Dykes, D.S.G. Higgins* 1762 WPQ18
The Design of the 26.7 MHz RF Cavity for RHIC — *J. Rose, J. Brodowski, D.P. Deng, S. Kwiatkowski, W. Pirkl, A. Ratti* 1765 WPQ19
A Design Upgrade of the RF Cavity and Its Power Window for High Current Operation of the NSLS X-Ray Storage Ring — *P. Mortazavi, M. Thomas* 1768 WPQ20
A Ferrite Loaded Untuned Cavity for a Compact Proton Synchrotron — *J.I. Hirota, K. Hiramoto, M. Nishi, Y. Iwashita, A. Noda, M. Inoue* 1770 WPQ21
On the Theory of Two Coupled Cavities — *N.I. Aizatsky* 1773 WPQ22

Measurement of Multipacting Currents of Metal Surfaces in RF Fields — *D. Proch, D. Einfeld, R. Onken, N. Steinhauser* 1776 WPQ24
Optimization of CLIC Transfer Structure (CTS) Design to Meet New Drive Beam Parameters — *A. Millich* 1779 WPQ25
A High-Power Multiple-Harmonic Acceleration System for Proton- and Heavy-Ion Synchrotrons — *P. Ausset, G. Charruau, F.J. Etzkorn, C. Fougeron, H. Meuth, S. Papureanu, A. Schnase* 1781 WPQ26
A Bunch Lengthening RF Cavity for Aladdin — *K.J. Kleman* 1785 WPR01
Design of a High-Power Test Cavity for the ATF Damping Ring — *S. Sakanaka, F. Hinode, M. Akemoto, S. Tokumoto, T. Higo, J. Urakawa, T. Miura, Y. Hirata, K. Satoh* 1788 WPR02
Design of an RF System for the ATF Damping Ring — *S. Sakanaka, F. Hinode, M. Akemoto, H. Hayano, H. Matsumoto, K. Kubo, S. Tokumoto, T. Higo, J. Urakawa* 1791 WPR03
Development of a Damped Cavity with SiC Beam-Duct — *T. Koseki, M. Izawa, Y. Kamiya* 1794 WPR04
HOM Absorber for the KEKB Normal Conducting Cavity — *Y. Takeuchi, K. Akai, N. Akasaka, E. Ezura, T. Kageyama, F. Naito, T. Shintake, Y. Yamazaki* 1797 WPR05
PEP-II B-Factory Prototype Higher Order Mode Load Design — *R. Pendleton, K. Ko, C. Ng, M. Neubauer, H. Schwarz, R. Rimmer* 1800 WPR07
High-Power RF Window and Coupler Develoment for the PEP-II B Factory — *M. Neubauer, K. Fant, J. Hodgson, J. Judkins, H. Schwarz, R.A. Rimmer* 1803 WPR08
Input Coupler for the KEKB Normal Conducting Cavity — *F. Naito, K. Akai, N. Akasaka, E. Ezura, T. Kageyama, T. Shintake, Y. Takeuchi, Y. Yamazaki* 1806 WPR09
Minimum Wakefield Achievable by Waveguide Damped Cavity — *Xintian E. Lin, Norman M. Kroll* 1809 WPR10
PLS RF System Operation During the Commissioning — *M. Kwon, I.H. Yu, H.J. Park, D.H. Han, M. Yoon, Y.S. Kim* 1812 WPR11
Acoustic Experimental Studies of High Power Modes in Accelerating Structure of Kurchatov SR Source — *M. Gangeluk, A. Kadnikov, Yu. Krylov, S. Kuznetsov, V. Moisseev, V. Petrenko, V. Ushkov, Yu. Yupinov* 1815 WPR13
Computer Simulations of a Wide-Bandwidth Ferrite-Loaded High-Power Waveguide Termination — *J. Johnson, R. Rimmer, J. Corlett* 1818 WPR14
Effects of Temperature Variation on the SLC Linac RF System — *F.-J. Decker, R. Akre, M. Byrne, Z.D. Farkas, H. Jarvis, K. Jobe, R Koontz, M. Mitchell, R. Pennacchi, M. Ross, H. Smith* 1821 WPR15
Broadband Coax-Waveguide Transitions — *T. Rizawa, R. Pendleton* 1824 WPR16
Rectangular Microtron Accelerating Structure — *N.P. Sobenin, V.N. Kandrunin, V.N. Melekhin, A.I. Karev, V.I. Shvedunov, W.P. Trower* 1827 WPR17
Investigation of the Biperiodic Accelerating Structure For The Free Electron Laser Buncher — *N.P. Sobenin, S.N. Yarygin, D.V. Kostin, A.A. Zavadtsev* 1830 WPR18
Ferromagentic Cores Made from Amorphous Material for Broad-Band Accelerating System — *I. Bolotin, V. Budilin, A. Glazov, V. Krasnopolsky, V. Skuratov* 1833 WPR19
A New Structure with Continuous RF Acceleration and Focusing — *J.J. Manca, M.C. Fallis, J.P.J. Manca* 1835 WPR20
Spark Location in RF Cavities — *Q. Kerns, M. Popovic, C. Kerns* 1838 WPR21
RF System for the Duke 1 GeV Storage Ring — *Ping Wang, Peter Morcombe, Ying Wu, Grigori Kurkin* 1841 WPR22

Injection, Extraction and Targetry

Matching Section to the RFQ Using Permanent Magnet Symmetric Lens — *M. Kando, M. Ikegami, H. Dewa, H. Fujita, T. Shirai, H. Okamoto, Y. Iwashita, S. Kakigi, A. Noda, M. Inoue* 1843 WAQ01
Conceptual Designs of Beam Choppers for RFQ Linacs — *Subrata Nath, Ralph R. Stevens Jr, Thomas P. Wangler* 1846 WAQ02
The Role of Space Charge in the Performance of the Bunching System for the ATLAS Positive Ion Injector — *R.C. Pardo, R. Smith* 1849 WAQ03

Experimental Investigations of Plasma Lens Focusing and Plasma Channel Transport of Heavy Ion Beams — *A. Tauschwitz, S.S. Yu, S. Eylon, L. Reginato, W. Leemans, J.O. Rasmussen, R.O. Bangerter* ... 1852 WAQ04
A Low Energy Ion Beam Transport System with Variable Field Permanent Magnetic Quadrupoles — *Y. Mori, A. Takagi, M. Kinsho, T. Baba, K. Shinto* ... 1855 WAQ06
A Comparison of Two Injection Line Matching Sections for Compact Cyclotrons — *T. Kuo, R. Baartman, L. Root, B. Milton, R. Laxadal, D. Yuan, K. Jayamanna, P. Schmor, G. Dutto, M. Dehnel, K. Erdman* ... 1858 WAQ07
Stripping Injection Into the New Booster Ring at IUCF — *K. Hedblom, D.L. Friesel* ... 1861 WAQ08
Accurate Tuning of 90^0 Cells in a FODO Lattice — *K. Bertsche, N. Mao* ... 1864 WAQ09
Design Principles for High Current Beam Injection Lines — *H. Liu, D. Neuffer* ... 1867 WAQ11
Survey and Analysis of Line-Frequency Interference in the CEBAF Accelerator — *M.G. Tiefenback, Rui Li* ... 1870 WAQ12
Location and Correction of 60 Hz in the CEBAF Injector — *R. Legg, D. Douglas, G.A. Krafft, Q. Saulter* ... 1873 WAQ14
PEP-II Injection Transport Construction Status and Commissioning Plans — *T. Fieguth, E. Bloom, F. Bulos, T. Donaldson, B. Feerick, G. Godfrey, G. Leyh, D. Nelson, M. Ross, D. Schultz, J. Sheppard, P. Smith, C. Spencer, J. Weinberg* ... 1876 WAQ15
Beam Transport Lines at BESSY-II — *D. Schirmer, M. v.Hartrott, S. Khan, D. Krämer, E. Weihreter* ... 1879 WAQ17
Matching the Emittance of a Linac to the Acceptance of a Racetrack Microtron — *R.W. de Leeuw, M.C.J. de Wijs, J.I.M. Botman, G.A. Webers, W.H.C. Theuws, C.J. Timmermans, H.L. Hagedoorn* ... 1882 WAQ19
The Extraction Orbit and Extraction Beam Transport Line for a 75 MeV Racetrack Microtron — *R.W. de Leeuw, H.R.M. van Greevenbroek, J.I.M. Botman, G.A. Webers, C.J. Timmermans, H.L. Hagedoorn* ... 1885 WAQ20
Electromagnetic, Thermal and Structural Analysis of the Fermilab Antiproton Source Lithium Collection Lens — *S. O'Day, K. Anderson* ... 1888 WAQ22
A New Concept in the Design of the LHC Beam Dump — *J.M. Zazula, M. Gyr, G.R. Stevenson, E. Weisse* ... 1891 WAQ24
Loss Concentration and Evacuation by Mini-Wire-Septa from Circular Machines for Spallation Neutron Sources — *H. Schönauer* ... 1894 WAQ25
Status of the Radioactive Ion Beam Injector at the Holifield Radioactive Ion Beam Facility — *D.T. Dowling, G.D. Alton, R.L. Auble, M.R. Dinehart, D.L. Haynes, J.W. Johnson, R.C. Juras, Y.S. Kwon, M.J. Meigs, G.D. Mills, S.W. Mosko, D.K. Olsen, B.A. Tatum, C.E. Williams, H. Wollnik* ... 1897 WAQ26
A New Fast Rise Time Kicker System For Antiproton Injection Into The Tevatron — *B. Hanna, J. Dinkel, C. Jensen, D. Qunell, R. Reilly, D. Tinsley, J. Walton* ... 1900 WAR01
Design of the MI40 Beam-Abort Dump — *C.M. Bhat, P.S. Martin, A.D. Russell* ... 1903 WAR02
Study on the Metallic Coating of the Ceramic Chamber for the ATF Damping Ring Kicker Magnets — *N. Terunuma, H. Nakayama, J. Urakawa* ... 1906 WAR03
Prospect of the Fast Extraction from KEK-PS for the Long Base Line Neutrino Experiment — *H. Sato, Y. Shoji, T. Kawakubo* ... 1909 WAR04
Helium Beam Acceleration in the KEK Proton Synchrotron with a Newly Developed Injection System for Positive/Negative Ions — *I. Sakai, A. Takagi, Y. Mori, S. Machida, M. Yoshii, T. Toyama, M. Shirakata, Y. Shoji, H. Sato* ... 1912 WAR05
Fast and Reliable Kicker Magnets for the SLC Damping Rings — *T.S. Mattison, R.L. Cassel, A.R. Donaldson, G. Gross* ... 1915 WAR06
Status of the Nuclotron Slow Extraction System — *V.I. Chernikov, I.B. Issinsky, O.S. Kozlov, V.A. Mikhailov, S.A. Novikov* ... 1918 WAR09
The RHIC Injection Fast Kicker — *E.B. Forsyth, G.C. Pappas, J.E. Tuozzolo, W. Zhang* ... 1921 WAR10
The Active Filter Voltage Ripple Correction System of the Brookhaven AGS Main Magnet Power Supply — *I. Marneris, R. Bonati, J. Geller, J.N. Sandberg, A. Soukas* ... 1924 WAR11
The Injection Kicker System for the Muon G-2 Experiment — *G.C. Pappas, E.B. Forsyth, W. Feng* ... 1927 WAR12
The AGS Accelerator Complex with the New Fast Extraction System — *M. Tanaka, E.J. Bleser, J.W. Glenn, Y.Y. Lee, A. Soukas* ... 1930 WAR13
DESY III - Dump System with One Fast Kicker — *J. Ruemmler* ... 1933 WAR14

Utilizing a Pulsed Deflector for Extraction of Pulsed Beams from the TRIUMF Cyclotron — *R.E. Laxdal* 1936 WAR15
Requirements for a Beam Sweeping System for the Fermilab Antiproton Source Target — *F.M. Bieniosek, K. Anderson, K. Fullett* 1939 WAR17
Measurement and Reduction of Quadrupole Injection Oscillations in the Fermilab Antiproton Accumulator — *F.M. Bieniosek, K. Fullett* 1942 WAR18
Results from Experiments of Crystal Extraction of 900 GeV Proton Beams from the Tevatron Collider — *G. Jackson, D. Carrigan, D. Chen, C.T. Murphy, A. Bogacz, S. Ramachandran, J. Rhoades, A. McManus, S. Baker* 1945 WAR19
High Energy Beam Line Based on Bending Crystal — *V.M. Biryukov, Yu.A. Chesnokov, V.N. Greth, A.A. Ivanov, V.I. Kotov, V.S. Selesnev, M.V. Tarakanov, V.I. Terekhov, S.V. Tsarik* 1948 WAR20
Observation of the Influence of the Crystal Surface Defects on the Characteristics of the High Energy Particle Beam Deflected With a Bent Monocrystal — *V.I. Baranov, V.M. Biryukov, Yu.A. Chesnokov, V.I. Kotov, M.V. Tarakanov, S.V. Tsarik* 1949 WAR21
Beam Extraction with Using of Volume Reflection Effect in Crystals — *I. Yazynin* 1952 WAR22
Use of a Bent Crystal for Beam Extraction in a Slow Extraction Mode — *A.A. Asseev, M.Yu. Gorin* 1955 WAR23
Computer Simulation of the Tevatron Crystal Extraction Experiment — *Valery Biryukov* 1958 WAR24

Power Supplies

PEP-II Magnet Power Conversion Systems — *L.T. Jackson, A.H. Saab, D.W. Shimer* 1961 RPP01
The AGS Main Magnet Power Supply Upgrade — *J.N. Sandberg, R. Casella, J. Geller, I. Marneris, A. Soukas, N. Schumburg* 1964 RPP02
Performance of the Ramping Power Supplies for the APS Booster Synchrotron — *J.A. Carwardine, S.V. Milton, D.G. McGhee* 1967 RPP03
A Distributed Dipole Power Supply System for the EUTERPE Electron Ring — *A.H. Kemper, Boling Xi, R.W. de Leeuw, W.H.C. Theuws, J.I.M. Botman, C.J. Timmermans, H.L. Hagedoorn, R.G.J. Oude Velthuis* 1970 RPP04
A 20 Ampere Shunt Regulator for Controlling Individual Magnets in a Seriesed String — *E.J. Martin, N. Dobeck, G.S. Jones, M.K. O'Sullivan* 1973 RPP06
A Multi-Channel Corrector Magnet Controller — *G.E. Leyh, A.R. Donaldson, L.T. Jackson* 1976 RPP07
Advances in Power Supply and Control System for Electrostatic Accelerators — *S.N. Chumakov, A.D. Goncharov, A.N. Malygin, V.P. Ostanin, B.N. Sukhina, V.S. Tupikov* 1979 RPP08
Mode Analysis of Synchrotron Magnet Strings — *M. Kumada* 1982 RPP09
Autotransformer Configurations to Enhance Utility Power Quality of High Power AC/DC Rectifer Systems — *Sewan Choi, Prasad N. Enjeti, Ira J. Pitel* 1985 RPP11
Performance of a 2-Megawatt High Voltage Test Load — *D. Horan, R. Kustom, M. Ferguson* 1988 RPP12
Early Operating and Reliability Experience with the CEBAF DC Magnet Power Supplies — *W. Merz, R. Flood, E.J. Martin, M. O'Sullivan* 1991 RPP13

Cryogenics, Vacuum, Alignment and Other Technical Systems

CEBAF Cryogenic System *(Invited)* — *Claus H. Rode* 1994 RPE01
The Large Hadron Collider Vacuum System *(Invited)* — *B. Angerth, F. Bertinelli, J.-C. Brunet, R. Calder, F. Caspers, P. Cruikshank, J.-M. Dalin, O. Gröbner, N. Kos, A. Mathewson, A. Poncet, C. Reymermier, F. Ruggiero, T. Scholz, S. Sgobba, E. Wallén* 1999 RPE02
Large Medical Gantries *(Invited)* — *J.B. Flanz* 2004 RPE03
Alignment Considerations for the Next Linear Collider *(Invited)* — *Robert E. Ruland* 2009 RPE04
Reliability of the LEP Vacuum System: Experience and Analysis — *P.M. Strubin, J.-P. Bojon* 2014 RPE06
On the Electron Beam Lifetime Problem in HERA — *D.R.C. Kelly, W. Bialowons, R. Brinkmann, H. Ehrlichmann, J. Kouptsidis* 2017 RPE08
Design and Testing of a High Power, Ultra-High Vacuum, Dual-Directional Coupler for the Advanced Photon Source (APS) Linear Accelerator — *S.O. Brauer, A.E. Grelick, J. Grimmer, R.D. Otocki, Y.W. Kang, J. Noonan, T. Russell* 2020 RPE09
A Pulse Septum Magnet with Low Outgassing Rate — *Yuan Ji Pei, W.M. Li, D.M. Jiang, X.Q. Wang* 2023 RPE10

Surveying the Monument System at Lawrence Berkeley Laboratory's Advanced Light Source Accelerator — *W. Thur, T. Lauritzen* 2026 RPE12
Induced Radioactivity of Thick Copper and Lead Targets Irradiated by Protons, ^{4}He and ^{12}C Nuclei with Energy 3.65 GeV/Nucleon — *A.A. Astapov, V.P. Bamblevski* 2029 RPE13
The PEP-II High Power Beam Dumping System — *A. Kulikov, J. Seeman, M. Zolotorev* 2032 RPE14
Cryogenic Thermometry in Superconducting Accelerators — *V.I. Datskov, J.A. Demko, J.G. Weisend, M. Hentges* 2034 MPP01
Cryogenic Operation and On-line Measurement of RF Losses in the SC Cavities of LEP2 — *G. Winkler, Ph. Gayet, D. Güsewell , Ch. Titcomb* 2037 MPP02
Pressure Measurement for the UNK-1 Vacuum System — *A. Kiver, V. Komarov, K. Mirzoev, V. Terekhov, A. Vasilevsky* 2040 MPP03
Total Pressure Measurements in the ELETTRA Storage Ring According to the Performance of the Sputter-Ion Pumps — *F. Giacuzzo, J. Miertusova* 2042 MPP04
Insertion Device Vacuum Chamber for the ELETTRA Storage Ring — *J. Miertusova, N. Pangos* 2045 MPP05
Bellows Design for the PEP-II High Energy Ring Arc Chambers — *M.E. Nordby, N. Kurita, C.-K. Ng* 2048 MPP07
A Zero-Length Bellows for the PEP-II High-Energy Ring — *M. Nordby, E.F. Daly, N. Kurita, J. Langton* 2051 MPP08
Processing of O.F.E. Copper Beam Chambers for PEP-II High Energy Ring — *E. Hoyt, M. Hoyt, R. Kirby, C. Perkins, D. Wright, A. Farvid* 2054 MPP09
Stretchforming Vacuum Chambers for the PEP-II B-Factory High Energy Storage Ring — *E.F. Daly, D. Bostic, A. Lisin, M. Palrang, C. Perkins, K. Skarpaas* 2057 MPP10
Beam Vacuum Chambers for Brookhaven's Muon Storage Ring — *H.C. Hseuh, L. Snydstrup, W.S. Jiang, C. Pai, M. Mapes* 2060 MPP11
Test Results of Pre-Production Prototype Distributed Ion Pump Design for the PEP-II Asymmetric B-Factory Collider — *F.R. Holdener, D. Behne, D. Hathaway, K. Kishiyama, M. Mugge, W. Stoeffl, K. van Bibber, C. Perkins, E.F. Daly, E. Hoyt, M. Hoyt, M. Nordby, J. Seeman, D. Wright* 2064 MPP12
Design of the PEP-II Low Energy Ring Vacuum System — *D. Hunt, K. Kennedy, T. Stevens* 2067 MPP13
The Vacuum Upgrade of the CERN PS and PS Booster — *M. van Rooij, J.-P. Bertuzzi, M. Brouet, A. Burlet, C. Burnside, R. Gavaggio, L. Petty, A. Poncet* 2069 MPP15
The Vacuum System for Insertion Devices at the Advanced Photon Source — *E. Trakhtenberg, E. Gluskin, P. Den Hartog, T. Klippert, G. Wiemerslage, S. Xu* 2072 MPP16
Test Results of a Combined Distributed Ion Pump/Non-Evaporable Getter Pump Design Developed as a Proposed Alternative Pumping System for the PEP-II Asymmetric B-Factory Collider — *F.R. Holdener, D. Behne, D. Hathaway, K. Kishiyama, M. Mugge, W. Stoeffl, K. van Bibber, C. Perkins, E.F. Daly, E. Hoyt, M. Hoyt, M. Nordby, J. Seeman, D. Wright* 2075 MPP20

Volume 4

Cryogenics, Vacuum, Alignment and Other Technical Systems (cont'd)

Ground Motion Measurements in HERA — *V. Shiltsev, B. Baklakov, P. Lebedev, C. Montag, J. Rossbach* 2078 TAA01
Alignment of Duke Free Electron Laser Storage Ring — *M. Emamian, N. Hower, Y. Levashov* 2081 TAA02
Beamline Smoothing of the Advanced Photon Source — *H. Friedsam, M. Penicka, S. Zhao* 2084 TAA03
Improvement of the Alignment System for the KEK 2.5-GeV Electron Linac — *Y. Ogawa, A. Enomoto, I. Sato* 2087 TAA04
A Mechanical Feedback System for Linear Colliders to Compensate Fast Magnet Motion — *C. Montag, J. Rossbach* 2090 TAA06
A Microstrip Based Position System for the Alignment of the TTF Cryostat — *D. Giove, A. Bosotti, C. Pagani, G. Varisco* 2093 TAA07
Beam-Based Magnetic Alignment of the Final Focus Test Beam — *P. Tenenbaum, D. Burke, R. Helm, J. Irwin, P. Raimondi, K. Oide, K. Flöttmann* 2096 TAA08

Alignment and Survey of the Elements in RHIC — *D. Trbojevic, P. Cameron, G.L. Ganetis, M.A. Goldman, R. Gupta, M. Harrison, M.F. Hemmer, F.X. Karl, A. Jain, W. Louie, S. Mulhall, S. Peggs, S. Tepikian, R. Thomas, P. Wanderer* 2099 TAA09
RF Radiation Measurement for the Advanced Photon Source (APS) Personnel Safety System — *J.J. Song, J. Kim, R. Otocki, J. Zhou* 2102 TAA11
Radiation Shielding of the Main Injector — *C.M. Bhat, P.S. Martin* 2105 TAA12
The Safety Interlock System of Synchrotron Radiation Research Center — *T.F. Lin, J.P. Wang* 2108 TAA14
Radiological Protection Policy Aspects Concerning the Preliminary Design and Operation Modus of the Athens RT Microtron Facility — *B. Spyropoulos* 2111 TAA15
SLAC Synchronous Condenser — *C. Corvin* 2114 TAA16
Printed-Circuit Quadrupole Design — *Terry F. Godlove, Santiago Bernal, Martin Reiser* 2117 TAA17
Microprocessor Controlled Four-Axis Goniometer — *A. Bortnyansky, M. Klopenkov, M. Pavlovets, M. Svinin, P. Kovach, J. Dobrovodsky* 2120 TAA18
Optically Induced Surface Flashover Switching for the Dielectric Wall Accelerator — *S. Sampayan, G. Caporaso, B. Carder, M. Norton, D. Trimble, J. Elizondo* 2123 TAA20
Measurements of Magnet Vibrations at the Advanced Photon Source — *V. Shiltsev* 2126 TAA21
The Vacuum System for the PEP II High Energy Ring Straight Sections — *U. Wienands, E. Daly, S.A. Heifets, A. Kulikov, N. Kurita, M. Nordby, C. Perkins, E. Reuter, J.T. Seeman, F.C. Belser, J. Berg, F.R. Holdener, J.A. Kerns, M.R. McDaniel, W. Stoeffl* 2129 TAA22
Compact X-band High Power Load Using Magnetic Stainless Steel — *Sami G. Tantawi, A.E. Vlieks* 2132 TAA27
Progress on Plasma Lens Experiments at the Final Focus Test Beam — *P. Kwok, P. Chen, D. Cline, W. Barletta, S. Berridge, W. Bugg, C. Bula, S. Chattopadhyay, W. Craddock, I. Hsu, R. Iverson, T. Katsouleas, P. Lai, W. Leemans, R. Liou, K.T. McDonald, D.D. Meyerhofer, K. Nakajima, H. Nakanishi, C.K. Ng, Y. Nishida, J. Norem, A. Ogata, J. Rosenzweig, M. Ross, A. Sessler, T. Shintake, J. Spencer, J.J. Su, A.W. Weidemann, G. Westenskow, D. Whittum, R. Williams, J. Wurtele* 2135 TAA28
Measurement of the Electric Field Uniformity in an Electrostatic Separator — *Weiran Lou, James J. Welch* 2138 TAA29
Analysis and Redesign of RF Filter Bar to Relieve Thermal Stresses — *E.G. Schmenk, K.W. Kelly, V. Saile, H.P. Bluem* 2141 TAA32
Loaded Delay Lines for Future R.F. Pulse Compression Systems — *R.M. Jones, P.B. Wilson, N.M. Kroll* 2144 TAA33

Controls and Computing

Integrating Industrial and Accelerator Control Systems *(Invited)* — *R. Saban* 2147 WAE01
Control System for Fermilab's Low Temperature Upgrade *(Invited)* — *B.L. Norris* 2152 WAE02
Databases for Accelerator Control - An Operations Viewpoint *(Invited)* — *J. Poole* 2157 WAE03
Taking an Object-Oriented View of Accelerators *(Invited)* — *Hiroshi Nishimura* 2162 WAE04
The CEBAF Control System *(Invited)* — *William A. Watson III* 2167 WAE05
MECAR (Main Ring Excitation Controller and Regulator): A Real Time Learning Regulator For The Fermilab Main Ring Or The Main Injector Synchrotron — *R. Flora, K. Martin, A. Moibenko, H. Pfeffer, D. Wolff, P. Prieto, S. Hays* 2172 WAE07
Framework for a General Purpose, Intelligent Control System for Particle Accelerators — *R.T. Westervelt, W.B. Klein, G. Luger* 2175 WAE08
Automatic Beam Steering in the CERN PS Complex — *B. Autin, G.H Hemelsoet, M. Martini, E. Wildner* 2178 WAE09
Integrated On-Line Accelerator Modeling at CEBAF — *B.A. Bowling, H. Shoaee, J. van Zeijts, S. Witherspoon, W. Watson* 2181 WAE10
A Self-Describing File Protocol for Simulation Integration and Shared Post-Processors — *M. Borland* 2184 WAE11
Analytic Computation of Beam Impedances in Complex Heterogenous Accelerator Geometries — *S. Petracca, I.M. Pinto, F. Ruggiero* 2187 WAE12
Comparison of CONDOR, FCI and MAFIA Calculations for a 150MW S-Band Klystron with Measurements — *U. Becker, T. Weiland, M. Dohlus, S. Lütgert, D. Sprehn* 2190 WAE13

Controls

The BEPC Control System Upgraded — *J. Zhao, X. Geng, Y. Yu, B. Wang, C. Wang, J. Xu, W. Liu, H. Luo, Y. Wang, M. Zhan* 2193 MPA01
Control System of PLS 2-GeV Linac — *I.S. Ko, W. Namkung* 2196 MPA02
Control System of the Synchrotron Radiation Source SIBERIA-2 — *A. Valentinov, A. Kadnikov, Y. Krylov, S. Kuznetsov, Y. Yupinov* 2199 MPA04
Control System for the Holifield Radioactive Ion Beam Facility — *B.A. Tatum, R.C. Juras, M.J. Meigs* 2202 MPA05
Control System Design for KEKB Accelerators — *S.-I. Kurokawa, T. Katoh, T.T. Nakamura, T. Mimashi, N. Yamamoto* 2205 MPA06
Design of SPring-8 Linac Control System Using Object Oriented Concept — *H. Sakaki, H. Yoshikawa, Y. Itoh, A. Kuba, T. Hori, A. Mizuno, H. Yokomizo* 2208 MPA07
The Slow Control System of the Muon g-2 Experiment — *Arnold Stillman* 2211 MPA09
The Duke Storage Ring Control System — *Y. Wu, B. Burnham, V.N. Litvinenko* 2214 MPA10
EPICS at Duke University — *C. Dickey, B. Burnham, F. Carter, R. Fricks, V. Litvinenko, A. Nagchaudhuri, P. Morcombe, R. Pantazis, P. O'Shea, R. Sachtschale, Y. Wu* 2217 MPA11
The Integration of Two Control Systems — *M. Bickley, K. White* 2220 MPA12
Upgrade of NSLS Timing System — *O. Singh, S. Ramamoorthy, J. Sheehan, J. Smith* 2223 MPA15
Accelerator Timing at Brookhaven National Laboratory — *B. Oerter, C.R. Conkling* 2226 MPA16
The RHIC General Purpose Multiplexed Analog to Digital Converter System — *R. Michnoff* 2229 MPA17
The Datacon Master - Renovation of a Datacon Field Bus Communications System for Accelerator Control — *T.M. Kerner, R. Warkentien* 2232 MPA18
Upgrade of the Controls for the Brookhaven Linac — *W.E. Buxton* 2235 MPA19
Commissioning Software Tools at the Advanced Photon Source — *L. Emery* 2238 MPR01
Rapid Application Development Using the Tcl/Tk Language — *Johannes van Zeijts* 2241 MPR02
Accelerator Operation Management Using Objects — *H. Nishimura, C. Timossi, M. Valdez* 2244 MPR03
Orbit Control at the ALS Based on Sensitivity Matrices — *H. Nishimura, L. Schachinger, H. Ohgaki* 2247 MPR04
Error Handling in the NSLS Control System — *Susila Ramamoorthy, Pauline Pearson, John Smith* 2250 MPR07
History Data Collection, Retriving and Display in the NSLS Control System — *Y.N. Tang, J.D. Smith* 2253 MPR08
Virtual Instrumentation Interface for SRRC Control System — *Jenny Chen, C.H. Kuo, Gloria Huang, J.S. Chen, C.J. Wang, K.T. Hsu, G.J. Jan* 2256 MPR10
User-Friendly Interface for Operator in the Controls of UNK Beam-Transfer Line. — *Yu. Karshev, Yu. Fedotov, V. Komarov, I. Lobov* 2259 MPR11
Macmon: A Monitoring Program for ELETTRA — *Emanuel Karantzoulis, Mark Plesko* 2262 MPR12
Device Control at CEBAF — *S. Schaffner, D. Barker, V. Bookwalter, B. Bowling, K. Brown, L. Doolittle, T. Fox, S. Higgins, A. Hofler, G. Lahti, P. Letta, B. Montjar, N. Patavalis, J. Tang, W. Watson, C. West, D. Wetherholt, K. White, S. Witherspoon, M. Wise* 2265 MPR13
Automated Frequency Tuning of SRF Cavities at CEBAF — *M. Chowdhary, L. Doolittle, G. Lahti, S.N. Simrock, R. Terrell* 2268 MPR14
Operational Monitoring of the CEBAF RF System — *J. Karn, B. Dunham, M. Tiefenback* 2271 MPR15
Operating Experience with the New TRIUMF RF Control System — *K. Fong, M. Laverty, S. Fang* 2273 MPR16
Managing Control Algorithms with an Object-Oriented Database — *M. Bickley, W. Watson* 2276 MPR19
Design of the Commissioning Software for the AGS to RHIC Transfer Line — *C.G. Trahern, C. Saltmarsh, T. Satogata, J. Kewisch, S. Sathe, T. D'Ottavio, S. Tepikian, D. Shea* 2279 MPR20

Computer Codes

A Relational Database for Magnets and Measurement Systems at the Fermilab Magnet Test Facility — *J.W. Sim, B.C. Brown, H.D. Glass, D.J. Harding, C.S. Mishra, A.D. Russell, K. Trombly-Freytag, D.G.C. Walbridge* 2282 MPB05

Software for a Database-Controlled Measurement System at the Fermilab Magnet Test Facility — *J.W. Sim, R. Baiod, B.C. Brown, E. Desavouret, H.D. Glass, P.J. Hall, D.J. Harding, C.S. Mishra, J.M. Nogiec, J.E. Pachnik, A. Russell, K. Trombly-Freytag, D.G.C. Walbridge* 2285 MPB06
BBAT: Bunch and Bucket Analysis Tool — *D.-P. Deng* 2288 MPB08
MASTAC - New Code for Solving Three-Dimensional Non-linear Magnetostatic Problems — *M. Rojak, E. Shurina, Yu. Soloveichik, A. Grudiev, M. Tiunov, P. Vobly* 2291 MPB09
The Computer Code BPERM for Wakepotential & Impedance Calculations — *T. Barts, W. Chou* 2294 MPB10
RESOLVE at CEBAF — *Byung C. Yunn, Rui Li, Stefan Simrock* 2297 MPB11
New Graphic User Interface for the Charged Particle Beam Program PARMILA — *George H. Gillespie, Barrey W. Hill* 2300 MPB14
XWAKE 1.1: A New Impedance and Wake Field Software Package — *G.W. Saewert, T.G. Jurgens* 2303 MPB15
The Los Alamos Accelerator Code Group — *Frank L. Krawczyk, James H. Billen, Robert D. Ryne, Harunori Takeda, Lloyd M. Young* 2306 MPB16
Beam Simulation and Radiation Dose Calculation at the Advanced Photon Source with SHOWER, an Interface Program to the EGS4 Code System — *L. Emery* 2309 MPB17
An Interactive Version of the PBGUNS Program for the Simulation of Axisymmetric and 2-D, Electron and Ion Beams and Guns — *Jack E. Boers* 2312 MPB18
Vector Computer Used for Calculation of 3D Magnetostatic Fields — *E.P. Zhidkov, M.B. Yuldasheva, I.P. Yudin, O.I. Yuldashev* 2314 MPB19
Impedance Study for the PEP-II B-factory — *S. Heifets, A. Chao, E. Daly, K. Ko, N. Kurita, X. Lin, C. Ng, M. Nordby, C. Perkins, J. Seeman, G. Stupakov, U. Wienands, D. Wright, M. Zolotorev, E. Henestroza, G. Lambertson, J. Corlett, J. Byrd, M. Zisman, T. Weiland, W. Stoeffl, C. Bolser* 2317 MPC01
Pressure Stability under a Pump Failure — *S.A. Heifets, J. Seeman, W. Stoeffl* 2319 MPC02
Investigation of the Beam Impedance of a Slowly Varying Waveguide — *R.M. Jones, S.A. Heifets* 2321 MPC03
Optimal Transport of Low Energy Particle Beams — *Christopher K. Allen, Samar K. Guharay, Martin Reiser* 2324 MPC04
Simulation of the Space Charge Effect in RHIC — *G.F. Dell, S. Peggs* 2327 MPC05
Magnetic Shielding for the D0 Detector Solenoid Upgrade — *J.-F. Ostiguy, R. Yamada* 2330 MPC07
Trapped Modes in the PEP-II B-Factory Interaction Region — *E. Henestroza, S. Heifets, M. Zolotorev* 2333 MPC08
A Proof of Principle of a Storage Ring with Fifth-Order Achromatic Bending Arcs — *Weishi Wan, Martin Berz* 2336 MPC09
Analytic Electrostatic Solution of an Axisymmetric Accelerator Gap — *John K. Boyd* 2339 MPC13
3D-Finite Difference Analysis of Planar Loop Couplers as Beam Electrodes in Stochastic Cooling Systems — *R. Schultheis, H.L. Hartnagel, B. Franzke* 2342 MPC15
Some Remarks on the Location of Higher Order Modes in Tapered Accelerating Structures with the Use of a Coupled Oscillator Model — *G. Romanov, S. Ivanov, M. Dohlus, N. Holtkamp* 2345 MPC16
The New Possibilities of SuperLANS Code for Evaluation of Axisymmetric Cavities — *D.G. Myakishev, V.P. Yakovlev* 2348 MPC17
Transverse EM Fields in a Detuned X-band Accelerating Structure — *S.A. Heifets, S.A. Kheifets, B. Woo* 2351 MPC18
RF Cavity Computer Design Codes — *P.A. McIntosh* 2353 MPC19
Arbitrary Order Transfer Maps for RF Cavities — *Johannes van Zeijts* 2356 MPC20
The Computation of the Dynamic Inductance of Magnet Systems and Force Distribution in Ferromagnetic Region on the Basis of 3–D Numerical Simulation of Magnetic Field — *N. Doinikov, V. Kukhtin, E. Lamzin, B. Mingalev, Yu. Severgin, S. Sytchevsky* 2359 MPC21
Advanced Electromagnetic Design of Cavities for High Current Accelerators — *Frank L. Krawczyk* 2361 MPC22
Modified PARMILA Code for New Accelerating Structures — *H. Takeda, J.E. Stovall* 2364 MPC23
Tracking Particles with Wake Fields and Space Charge Effects — *A.J. Riche* 2367 MPC24
On the Importance of Fourth Order Effects on Wakefield Calculations for Short Bunches — *Zenghai Li, Joseph J. Bisognano* 2370 MPC25

Coupling Impedances of Muffin-Tin Structures with Closed and Open Sides — *M. Filtz* 2373 MPC28
Explicit Soft Fringe Maps of a Quadrupole — *John Irwin, Chun-xi Wang* 2376 MPC31

Instrumentation and Feedback

Bunched Beam Cooling for the Fermilab Tevatron *(Invited)* — *Ralph J. Pasquinelli* 2379 RAE01
Fast Digital Dampers for the Fermilab Booster *(Invited)* — *James M. Steimel Jr.* 2384 RAE02
Fast Feedback for Linear Colliders *(Invited)* — *L. Hendrickson, C. Adolphsen, S. Allison, T. Gromme, P. Grossberg, T. Himel, K. Krauter, R. MacKenzie, M. Minty, R. Sass, H. Shoaee, M. Woodley* 2389 RAE03
Instrumentation in Medical Systems *(Invited)* — *W.T. Chu* 2394 RAE04
Laser Diagnostics of a One-Dimensional Ordered Ion Beam — *R. Calabrese, V. Guidi, P. Lenisa, U. Tambini, E. Mariotti, L. Moi* 2399 RAE05
Determining Electron Beam Parameters from Edge Radiation Measurement Results on Siberia-1 Storage Ring — *O.V. Chubar* 2402 RAE06
Absolute Energy Measurement in e- e+ Linear Colliders — *Blaine E. Norum, Robert Rossmanith* 2405 RAE07
INR Activity in Development and Production of Bunch Shape Monitors — *S.K. Esin, A.V. Feschenko, P.N. Ostroumov* 2408 RAE08
Conceptual design of a Charged Particle Beam Energy Spectrometer Utilizing Transition Radiation Grating — *X.Z. Qiu, X.J. Wang, K. Batchelor, I. Ben-Zvi* 2411 RAE09
An Analysis of the Operational Performance of the Automatic Global Horizontal Beam Position Control System on the SRS at Daresbury — *J.B. Fitzgerald, B.G. Martlew, P.D. Quinn, S.L. Smith* 2414 RAE10
A Prototype Fast Feedback System for Energy Lock at CEBAF — *M. Chowdhary, G.A. Krafft, H. Shoaee, S.N. Simrock, W.A. Watson* 2417 RAE11
Operation and Performance of the PEP-II Prototype Longitudinal Damping System at the ALS — *D. Teytelman, R. Claus, J. Fox, H. Hindi, J. Hoeflich, I. Linscott, J. Olsen, G. Oxoby, S. Prabhakar, W. Ross, L. Sapozhnikov, A. Drago, M. Serio, J. Byrd, J. Corlett, G. Stover* 2420 RAE12
Commissioning of the ALS Transverse Coupled-Bunch Feedback System — *W. Barry, J. Byrd, J. Corlett, J. Johnson, G. Lambertson, J. Fox* 2423 RAE13
Operation of a Fast Digital Transverse Feedback System in CESR — *J.T. Rogers, M.G. Billing, J.A. Dobbins, C.R. Dunnam, D.L. Hartill, T. Holmquist, B.D. McDaniel, T.A. Pelaia, M. Pisharody, J.P. Sikora, C.R. Strohman* 2426 RAE14
Measuring and Adjusting the Path Length at CEBAF — *G.A. Krafft, M. Crofford, D.R. Douglas, S.L. Harwood, R. Kazimi, R. Legg, W. Oren, K. Tremblay, D. Wang* 2429 WXE01
Simulations of the BNL/SLAC/UCLA 1.6 Cell Emittance Compensated Photocathode RF Gun Low Energy Beam Line — *D.T. Palmer, R.H. Miller, H. Winick, X.J. Wang, K. Batchelor, M. Woodle, I. Ben-Zvi* 2432 WXE03
Small Gap Undulator Experiment on the NSLS X-Ray Ring — *P.M. Stefan, S. Krinsky, G. Rakowsky, L. Solomon* 2435 WXE04
Measurements of Longitudinal Dynamics in the SLC Damping Rings — *R.L. Holtzapple, R.H. Siemann, C. Simopoulos* 2438 WXE05
Single Bunch Collective Effects in the ALS — *J.M. Byrd, J.N. Corlett, T. Renner* 2441 WXE06
Experiments of Nanometer Spot Size Monitor at FFTB Using Laser Interferometery — *T. Shintake, K. Oide, N. Yamamoto, A. Hayakawa, Y. Ozaki, D. Burke, R.C. Field, S. Hartman, R. Iverson, P. Tenenbaum, D. Walz* 2444 WXE07
Transverse Electron Beam Size Measurements Using the Lloyd's Mirror Scheme of Synchrotron Light Interference — *O.V. Chubar* 2447 WXE08

Instrumentation

Charge Balancing Fill Rate Monitor — *J.L. Rothman, E.B. Blum* 2450 MPQ01
Sensitivity and Offset Calibration for the Beam Position Monitors at the Advanced Photon Source — *Y. Chung, D. Barr, G. Decker, K. Evans Jr., E. Kahana* 2452 MPQ03
An Sampling Detector for the RHIC BPM Electronics — *W.A. Ryan, T.J. Shea* 2455 MPQ04
RHIC Beam Position Monitor Characterization .....

— *P.R. Cameron, M.C. Grau, M. Morvillo, T.J. Shea, R.E. Sikora* 2458 MPQ05
Duke Storage Ring Tune Measurements System using Razor Blade and Photomultiplier — *V.N. Litvinenko, B. Burnham, N. Hower, P. Morcombe, Y. Wu* 2461 MPQ06
The Development of Beam Current Monitors in the APS — *X. Wang, F. Lenkszus, E. Rotela* 2464 MPQ07
Overall Design Concepts for the APS Storage Ring Machine Protection System — *A. Lumpkin, R. Fuja, A. Votaw, X. Wang, D. Shu, J. Stepp, N. Arnold, G. Nawrocki, G. Decker, Y. Chung* 2467 MPQ08
Status of the Synchrotron Radiation Monitors for the APS Facility Rings — *A. Lumpkin, B. Yang* 2470 MPQ09
Initial Diagnostics Commissioning Results for the Advanced Photon Source (APS) — *A. Lumpkin, D. Patterson, X. Wang, E. Kahana, W. Sellyey, A. Votaw, B. Yang, R. Fuja, W. Berg, M. Borland, L. Emery, G. Decker, S. Milton* 2473 MPQ10
Initial Tests of the Dual-Sweep Streak Camera System Planned for APS Particle-Beam Diagnostics — *A. Lumpkin, B. Yang, W. Gai , W. Cieslik* 2476 MPQ11
A Transverse Tune Monitor for the Fermilab Main Ring — *P.J. Chou, B. Fellenz, G. Jackson* 2479 MPQ13
Recalibration of Position Monitors With Beams — *Kotaro Satoh, Masaki Tejima* 2482 MPQ14
Simulation of PEP-II Beam Position Monitors — *C.-K. Ng, T. Weiland, D. Martin, S. Smith, N. Kurita* 2485 MPQ15
Prototype Bunch Killer System At SRRC — *G.J. Jan, Jenny Chen, C.H. Kuo, T.F. Lin, K.T. Pan, Glory Lin, K.T. Hsu* 2488 MPQ16
Beam Diagnostics for the Amsterdam Pulse Stretcher AmPS — *J.G. Noomen, H. Boer-Rookhuizen, N. Dobbe, J. v.Es, E. Heine, F. Kroes, J. Kuijt, J. v.d.Laan, A. Poelman, H. Nieuwenkamp, T. Sluijk* 2491 MPQ17
Non-Destructive Beam Profile Measuring System Observing Fluorescence Generated by Circulating Beam — *T. Kawakubo, E. Kadokura, T. Kubo, T. Ishida, H. Yamaguchi* 2494 MPQ18
The Closed Orbit Measurement of SRRC Booster During Ramping — *T.S. Ueng, K.T. Hsu, K.H. Hwu, K.K. Lin* 2497 MPQ19
Lattice Function Measurement with TBT BPM Data — *Ming-Jen Yang* 2500 MPQ20
Optimal Placement of Profile Monitors in a Mismatched FODO Lattice — *K. Bertsche* 2503 MPQ21
SSRL Beam Position Monitor Detection Electronics — *J. Sebek, R. Hettel, R. Matheson, R. Ortiz, J. Wachter* 2506 MPQ22
Single-Turn Beam Position Monitor for the NSLS VUV Electron Storage Ring — *R.J. Nawrocky, S.L. Kramer* 2509 MPQ23
Design of the Button Beam Position Monitor for PEP-II — *N. Kurita, D. Martin, S. Smith, C. Ng, M. Nordby, C. Perkins* 2512 MPQ25
Study of Fast Electron Beam Profile Monitor System — *Ian Hsu, C.I. Yu, C.C. Chu* 2515 MPQ26
The Average Orbit System Upgrade for the Brookhaven AGS — *D.J. Ciardullo, J.M. Brennan* 2518 MPQ30
Feasibility Study of an Orbit Feedback System for the KEKB Facility — *Y. Funakoshi, M. Tejima, H. Ishii* 2521 MPQ31
Turn-by-Turn Beam Position Measurement for 1.3 GeV Booster Synchrotron — *T.S. Ueng, K.T. Hsu, C.S. Fang, Y.M. Chang, K.K. Lin* 2524 MPQ32
Beam Position Monitor for the LNLS UVX Synchrotron Light Source — *F.S. Rafael, E.K.C.S. Hayashi* 2527 MPQ33
Transition Radiation Electron Beam Diagnostic Study at ATF — *X.Z. Qiu, X.J. Wang, K. Batchelor, I. Ben-Zvi* 2530 TPB01
Machine Parameter Measurement of the Amsterdam Pulse Stretcher AmPS — *Y.Y. Wu, R. Maas* 2533 TPB03
Wire Setup Calibration of Beam Position Monitors — *D. Wang, B. Binns, M. Kogan, A. Zolfaghari* 2536 TPB04
Beam profile data analysis for the RHIC Injection Line — *Ping Zhou* 2539 TPB05
Energy Spread of Ion Beams Generated in Multicusp Ion Sources — *M. Sarstedt, P. Herz, W.B. Kunkel, Y. Lee, K.N. Leung, L. Perkins, D. Pickard, M. Weber, M.D. Williams, E. Hammel* 2542 TPB07
A 2 MHz 3-Port Analog Isolation and Fanout Module — *Edward R. Beadle* 2545 TPB08
A General Purpose Fiber Optic Link with Radiation Resistance — *Edward R. Beadle* 2548 TPB09
DSP Based Data Acquisition for RHIC — *T.J. Shea, J. Mead, C.M. Degen* 2551 TPB12

Ion-Chamber Beam-Loss-Monitor System for the Los Alamos Meson Physics Facility — *M. Plum, D. Brown, A. Browman, R. Macek* 2554 TPB13
Development of Beam Position Monitors for Heavy Ion Recirculators — *F.J. Deadrick, J.J. Barnard, T.J. Fessenden, J.W. Meredith, J. Rintamaki* 2557 TPB14
Laser Compton Polarimetry of Proton Beams — *A. Stillman* 2560 TPB15
Phase and Synchronous Detector Theory as Applied to Beam Position and Intensity Measurements — *J.D. Gilpatrick* 2563 TPB16
Testing Coaxial Switches of BPM using a High-Resolution RF Detector — *Takao Ieiri* 2566 TPB17
A Beam Size Monitor Based on Appearance Intensities for Multiple Gas Ionization — *T. Katsouleas, J. Yoshii, W.B. Mori, C. Joshi, C. Clayton* 2569 TPB18
Beam Profile Measurement in the Presence of Noise — *K. Bertsche, J. Palkovic* 2572 TPB19
Beam Shaping Using a New Digital Noise Generator — *H. Stockhorst, G. Heinrichs, A. Schnase, S. Papureanu, U. Bechstedt, R. Maier, R. Tölle* 2574 TPB20
The RHIC Transfer Line Cable Database — *E.H. Scholl, T. Satogata* 2577 TPB21
Characterization of Beam Position Monitors for Measurement of Second Moment — *S.J. Russell, J.D. Gilpatrick, J.F. Power, R.B. Shurter* 2580 TPB22
Beam Diagnostic Systems and Their Use in the New IUCF Beam Line — *W.P. Jones, M. Ball, J. Collins, T. Ellison, B. Hamilton* 2583 TPB24
Tomographic Method of Experimental Research of Particle Distribution in Phase Space — *V.V. Kalashnikov, V.I. Moisseev, V.V. Petrenko* 2586 TPB25
Design of the Beam Profile Monitor System for the RHIC Injection Line — *R.L. Witkover* 2589 TPB26
Beam Intensity Observation System at SRRC — *C.J. Wang, C.H. Kuo, J.S. Chen, Jenny Chen, K.T. Hsu, G.J. Jan* 2592 TPB29
Performance of the Advanced Photon Source (APS) Linac Beam Position Monitors (BPMs) with Logarithmic Amplifier Electronics — *R.E. Fuja, M. White* 2595 TPC01
Preliminary Calculations on the Determination of APS Particle-Beam Parameters Based on Undulator Radiation — *A. Lumpkin, B. Yang, Y. Chung, R. Dejus, G. Voykov, G. Dattoli* 2598 TPC03
Coherent Synchrotron Radiation Detector for a Non-Invasive Subpicosecond Bunch Length Monitor — *G.A. Krafft, D. Wang, E. Price, E. Feldl, D. Porterfield, P. Wood, T. Crowe* 2601 TPC04
A Beam Test of Button-Type Beam Position Monitor for the ATF Damping Ring — *F. Hinode, H. Hayano, M. Tejima, N. Terunuma, J. Urakawa* 2604 TPC05
Application of a Transverse Phase-Space Measurement Technique for High-Brightness, H- Beams to the GTA H- Beam — *K.F. Johnson, R.C. Connolly, R.C. Garcia, D.P. Rusthoi, O.R. Sander, D.P. Sandoval, M.A. Shinas, M. Smith, V.W. Yuan* 2607 TPC06
Precision Intercomparision of Beam Current Monitors at CEBAF — *R. Kazimi, B. Dunham, G.A. Krafft, R. Legg, C. Liang, C. Sinclair, J. Mammosser* 2610 TPC07
Damped Button Electrode for B-Factory BPM System — *T. Obina, T. Shintake, Y.H. Chin, N. Akasaka* 2613 TPC08
Beam Monitors for the S-Band Test Facility — *W. Radloff, M. Wendt* 2616 TPC09
Low Energy Regime for Optical Transition Radiation Emission — *D. Giove, C. De Martinis, M. Pullia, P. Mangili* 2619 TPC10
Recovery of CTF Beam Signals from a Strong Wakefield Background — *Yan Yin, Elmar Schulte, Tord Ekelöf* 2622 TPC11
A Low-Cost Non-Intercepting Beam Current and Phase Monitor for Heavy Ions — *J.M. Bogaty, B.E. Clifft* 2625 TPC12
Transverse Emittance Systematics Measured for Heavy-Ion Beams at ATLAS — *J.A. Nolen, T.A. Barlow, K.A. Beyer, K.A. Woody* 2628 TPC13
Beam Position Monitors in the TESLA Test Facility Linac — *R. Lorenz* 2631 TPC14
Energy Measurement of Relativistic Electrons by Compton Scattering — *Ian Hsu, C.-C. Chu, C.-I. Yu, C.-I. Chen, A.-T. Lai, Y.-C. Liu, P.-K. Tseng, G.-Y. Hsiung, R.-C. Hsu, C.-P. Wang, R.-C. Chen* 2634 TPC15
Tests of a High Resolution Beam Profile Monitor — *J. Norem, J. Dawson, W. Haberichter, R. Lam, L. Reed, X.-F. Yang, J. Spencer* 2637 TPC16
Airix Alignment and High Current Beam Diagnostics — *D. Villate, Ch. Bonnafond, A. Devin, E. Merle* 2640 TPC17
A New Beam Intensity Monitoring System with Wide Dynamic Range for the Holifield Radioactive Ion Beam Facility — *M.J. Meigs, D.L. Haynes, C.M. Jones, C.T. LeCroy* 2643 TPC18

Diagnostic Beam Pulses for Monitoring the SLC Linac — *F.-J. Decker, M. Stanek, H. Smith, F. Tian* 2646 TPC20
Observation of Thermal Effects on the LEP Wire Scanners — *J. Camas, C. Fischer, J.J. Gras, R. Jung, J. Koopman* 2649 TPC21
CEBAF Beam Loss Accounting — *R. Ursic, K. Mahoney, C. Hovater, A. Hutton, C. Sinclair* 2652 TPC26
Nanometer Resolution BPM Using Damped Slot Resonator — *S.C. Hartman, T. Shintake, N. Akasaka* 2655 TPC29
An Automatic Tune-Measurement System for the CELSIUS Ring — *T. Lofnes* 2658 TPC31

Feedback

Software Architecture of the Longitudinal Feedback System for PEP-II, ALS and DAΦNE — *R. Claus, J. Fox, I. Linscott, G. Oxoby, W. Ross, L. Sapozhnikov, D. Teytelman, A. Drago, M. Serio* 2660 RPQ01
Digital I/Q Demodulator — *C. Ziomek, P. Corredoura* 2663 RPQ02
RF Feedback Simulation Results for PEP-II — *R. Tighe, P. Corredoura* 2666 RPQ03
TM0,1.5,0 Mode Cavity for Longitudinal Bunch Feedback Kicker — *T. Shintake* 2669 RPQ04
Low Level RF System Design for the PEP-II B Factory — *P. Corredoura, R. Claus, L. Sapozhnikov, H. Schwarz, R. Tighe, C. Ziomek* 2672 RPQ05
Experiment of the RF Feedback using a Parallel Comb Filter — *S. Yoshimoto, E. Ezura, K. Akai, T. Takashima* 2675 RPQ06
Digital Transverse Beam Dampers for the Brookhaven AGS — *G.A. Smith, V. Castillo, T. Roser, W. Van Asselt, R. Witkover, V. Wong* 2678 RPQ07
Design of the PEP-II Transverse Coupled-Bunch Feedback System — *W. Barry, J. Byrd, J. Corlett, M. Fahmie, J. Johnson, G. Lambertson, M. Nyman, J. Fox, D. Teytelman* 2681 RPQ08
Simulations of the PEP-II Transverse Coupled-Bunch Feedback System — *J.M. Byrd* 2684 RPQ09
Fermilab Booster Low Level RF System Upgrades — *Robert C. Webber* 2687 RPQ10
Energy Stability in a High Average Power FEL — *L. Merminga, J.J. Bisognano* 2690 RPQ11
Automated Beam Based Alignment of the ALS Quadrupoles — *G. Portmann, D. Robin, L. Schachinger* 2693 RPQ13
First Results with a Nonlinear Digital Orbit Feedback System at the NSLS — *Eva Bozoki, Aharon Friedman, Susila Ramamoorthy* 2696 RPQ14
Local Beam Position Feedback Experiments on the ESRF Storage Ring — *Y. Chung, E. Kahana, J. Kirchman, A. Lumpkin, J. Meyer, E. Plouviez, K. Scheidt, E. Taurel, A. Ando, S. Sasaki, A. Taketani* 2699 RPQ15
Implementation of the Global and Local Beam Position Feedback Systems for the Advanced Photon Source Storage Ring — *Y. Chung, D. Barr, G. Decker, J. Galayda, J. Kirchman, F. Lenkszus, A. Lumpkin, A.J. Votaw* 2702 RPQ16
The RHIC Accelerating Cavity Prototype Tuner — *A. Ratti, J.M. Brennan, J. Brodowski, E. Onillon, J. Rose* 2705 RPQ17
Ramp Tuning of the APS Booster Synchrotron Magnet Power Supplies — *S.V. Milton, J.A. Carwardine* 2708 RPQ18
Orbit Stability Improvements at the NSLS X-Ray Ring — *J. Safranek, O. Singh, L. Solomon* 2711 RPQ19
Digital Orbit Feedback Compensation for SPEAR — *J. Corbett, R. Hettel, D. Keeley, D. Mostowfi* 2714 RPQ21
Digital Orbit Feedback Control for SPEAR — *R. Hettel, J. Corbett, D. Keeley, I. Linscott, D. Mostowfi, J. Sebek, C. Wermelskirchen* 2717 RPQ22
Beam Position Feedback Systems for the PF Storage Ring — *N. Nakamura, K. Haga, T. Honda, T. Kasuga, M. Katoh, Y. Kobayashi, M. Tadano, M. Yokoyama* 2720 RPQ23
The New Booster Synchronization Loop — *E. Onillon, J.M. Brennan* 2723 RPQ25
Recent Progress in the Development of the Bunch Feedback Systems for KEKB — *E. Kikutani, T. Kasuga, Y. Minagawa, T. Obina, M. Tobiyama* 2726 RPQ26
60 Hz Beam Motion Reduction at NSLS UV Storage Ring — *Om V. Singh* 2729 RPQ27
The CEBAF Fiber Optic Phase Reference System — *K. Crawford, S. Simrock, C. Hovater, A. Krycuk* 2732 RPQ29
RF System Modeling for the High Average Power FEL at CEBAF — *L. Merminga, J. Fugitt, G. Neil, S. Simrock* 2735 RPQ30

Beam Positioning and Monitoring in the Racetrack Microtron Eindhoven — *W. Theuws, R.W. de Leeuw, G.A. Webers, J.I.M. Botman, C.J. Timmermans, H.L. Hagedoorn* 2738 RPQ31
Multi-Bunch Systems at DESY — *Rolf-Dieter Kohaupt* 2741 RPQ32

High Energy Accelerator Beam Dynamics

Results of Final Focus Test Beam *(Invited)* — *V.A. Alexandrof, V. Balakin, A. Mikhailichenko, K. Flöttmann, F. Peters, G.-A. Voss, V. Bharadwaj, M. Halling, J.A. Holt, J. Buon, J. Jeanjean, F. LeDiberder, V. Lepeltier, P. Puzo, G. Heimlinger, R. Settles, U. Stierlin, N. Akasaka, H. Hayano, N. Ishihara, H. Nakayama, K. Oide, T. Shintake, Y. Takeuchi, N. Yamamoto, F. Bulos, D. Burke, R. Field, S. Hartman, R. Helm, J. Irwin, R. Iverson, P. Raimondi, S. Rokni, G. Roy, W. Spence, P. Tenenbaum, S.R. Wagner, D. Walz, S. Williams* 2742 TAG01
Comparison of Measured and Calculated Dynamic Aperture *(Invited)* — *F. Willeke* 2747 TAG02
Ion Effects in Future Circular and Linear Accelerators *(Invited)* — *T.O. Raubenheimer* 2752 TAG03
Nonlinear Wave Phenomena in Coasting Beams *(Invited)* — *P.L. Colestock, L.K. Spentzouris, F. Ostiguy* 2757 TAG04
The Cure of Multibunch Instabilities in ELETTRA — *M. Svandrlik, C.J. Bocchetta, A. Fabris, F. Iazzourene, E. Karantzoulis, R. Nagaoka, C. Pasotti, L. Tosi, R.P. Walker, A. Wrulich* 2762 TAG05
Nonlinear Analyses of Storage Ring Lattices Using One-Turn Maps — *Y.T. Yan, J. Irwin, T. Chen* 2765 TAG06
Precise Determination and Comparision of the SPS Dynamic Aperture in Experiment and Simulation — *W. Fischer, F. Schmidt* 2768 TAG07
Coherency of the Long Range Beam-Beam Interaction in CESR — *Alexander B. Temnykh, James J. Welch* 2771 TAG08
Effect of Quadrupole Noise on the Emittance Growth of Protons in HERA — *T. Sen, O. Brüning, F. Willeke* 2774 TAG09
Nonlinear Mode Coupling Analysis in the Tevatron — *S. Assadi, C.S. Mishra* 2777 TAG10
Lattice Design for KEKB Colliding Rings — *H. Koiso, K. Oide* 2780 TAG11
Entropy and Emittance Growth — *Patrick G. O'Shea* 2783 TAG12
Analysis of Optical Stochastic Cooling Including Transverse Effects — *K.-J. Kim* 2786 TAG13

Volume 5

Linear and Nonlinear Orbit Theory

Reduction of Non Linear Resonance Excitation from Insertion Devices in the ALS — *D. Robin, G. Krebs, G. Portmann, A. Zholents, W. Decking* 2789 FAB01
Sum Betatron Resonances under Linear Coupling of Oscillations — *P.N. Chirkov, I.I. Petrenko* 2792 FAB02
Linear Orbit Parameters for the Exact Equations of Motion — *G. Parzen* 2795 FAB03
Tune Modulation Due to Synchrotron Oscillations and Chromaticity, and the Dynamic Aperture — *G. Parzen* 2798 FAB04
Normal Mode Tunes for Linear Coupled Motion in Six Dimensional Phase Space — *G. Parzen* 2801 FAB05
Fast Symplectic Mapping and Quasi-invariants for the Large Hadron Collider — *R.L. Warnock, J.S. Berg, E. Forest* 2804 FAB06
Nonlinear Dependence of Synchrotron Radiation on Beam Parameters — *G.H. Hoffstätter* 2807 FAB07
Effects of Imperfections on the Dynamic Aperature and Closed Orbit of the IPNS Upgrade Synchrotron — *E. Lessner, Y.-C. Chae, S. Kim* 2811 FAB09
Paraxial Expansion of a Static Magnetic Field in a Ring Accelerator — *Lee C. Teng* 2814 FAB10
Experimental Determination of Linear Optics Including Quadrupole Rotations — *J. Safranek* 2817 FAB11
Perturbation of Beam Energy Due to Steering and Pretzel Orbit — *W. Lou, M. Billing, D. Rice* 2820 FAB12
Lattice Studies for a High-Brightness Light Source — *D. Kaltchev, R.V. Servranckx, M.K. Craddock, W. Joho* 2823 FAB14

Transfer Maps Through Ideal Bends (Again?) — *Leo Michelotti* ... 2826 FAB15
Skew Chromaticity in Large Accelerators — *S. Peggs, G.F. Dell* ... 2829 FAB20
The Effect and Correction of Coupling Generated by the RHIC Triplet Quadrupoles — *F. Pilat, S. Peggs, S. Tepikian, D. Trbojevic, J. Wei* ... 2832 FAB22
The Beam Envelope Equation - Systematic Solution for a FODO Lattice with Space Charge — *Edward P. Lee* ... 2835 FAC01
Analytic Second- and Third-Order Achromat Designs — *Chunxi Wang, Alex Chao* ... 2838 FAC02
Measurement of Chromatic Effects in LEP — *D. Brandt, P. Castro, K. Cornelis, A. Hofmann, G. Morpurgo, G.L. Sabbi, A. Verdier* ... 2841 FAC03
The Lattice of the CERN Large Hadron Collider — *W. Scandale, B. Jeanneret, J.-P. Koutchouk, X. Luo, F. Méot, R. Ostojic, T. Risselada, C. Rufer, T. Taylor, T. Trenkler, S. Weisz* ... 2844 FAC04
Sorting Strategies for the LHC Based on Normal Forms — *W. Scandale, M. Giovannozzi, R. Grassi, E. Todesco* ... 2847 FAC06
Algorithms to get a Circulating Beam — *André Verdier, Frank Richard* ... 2850 FAC07
Non-Linear Chromaticity Correction with Sextupole Families — *André Verdier* ... 2853 FAC08
Simulation of Charged Particle Transport in Nonlinear Axisymmetrical Electrostatic Potential — *I.P. Yudin, V.V. Andreev* ... 2856 FAC09
Stochastic Effects in Real and Simulated Ion Beams — *Jürgen Struckmeier* ... 2860 FAC10
Magnetic Field Correction in Nuclotron — *I.B. Issinsky, V.A. Mikhailov, V.A. Shchepunov* ... 2863 FAC12
Effects of the CHESS Wigglers on a Beam with an Angular Offset — *James J. Welch* ... 2866 FAC14
Particle Tracking with Generating Functions of Magnetic Fringing Fields — *Godehard Wüstefeld* ... 2868 FAC16
Computation of Lattice Maps Using Modular BCH and Similarity Composition Rules — *J. Irwin* ... 2871 FAC18
Treatment of Wiggler and Undulator Field Errors in Tracking Codes — *W. Decking, O. Kaul, H. Nesemann, J. Roßbach* ... 2874 FAC19
Experimental Study of the Duke Storage Ring Dynamic Aperture — *Y. Wu, V.N. Litvinenko, B. Burnham, J.M.J. Madey* ... 2877 FAC20

Beam-Beam Interaction and Beam Cooling

A New Model of the e+e- Beam-Beam Interaction — *K.D. Cromer, B.E. Norum* ... 2880 RAP01
A Study of Beam-Beam Interactions at Finite Crossing Angles for a B-Factory — *K. Hirata, K. Ohmi, N. Toge* ... 2883 RAP02
Simulation of Beam-Beam Effects in Tevatron — *C.S. Mishra, S. Assadi, R. Talman* ... 2886 RAP03
The Dynamic Beta Effect in CESR — *David Sagan* ... 2889 RAP04
Lifetime and Tail Simulations for Beam-Beam Effects in PEP-II B Factory — *D.N. Shatilov, A.A. Zholents* ... 2892 RAP05
Gamma Ray Sources Based on Resonant Backscattering of Laser Beams With Relativistic Heavy Ion Beams — *E.G. Bessonov, Kwang-Je Kim* ... 2895 RAP06
Observations of the Effects of the Beam-Beam Interaction on the Orbits of Stored Beams in CESR — *E. Young* ... 2898 RAP07
Calculations on Depolarization in HERA due to Beam-Beam Effects — *M. Böge, T. Limberg* ... 2901 RAP08
A Map for the Thick Beam-Beam Interaction — *J. Irwin, T. Chen* ... 2904 RAP09
Transient Beam Loading in the SLC Damping Rings — *M.G. Minty, R.H. Siemann* ... 2907 RAP10
Studies of Halo Distributions Under Beam-Beam Interaction — *T. Chen, J. Irwin, R.H. Siemann* ... 2910 RAP11
The Effect of Phase Advance Errors Between Interaction Points on Beam Halos — *T. Chen, J. Irwin, R.H. Siemann* ... 2913 RAP12
Compensation of the "Pacman" Tune Spread by Tailoring the Beam Current — *Miguel A. Furman* ... 2916 RAP14
Disruption Effects on the Beam Size Measurement — *P. Raimondi, F.-J. Decker, P. Chen* ... 2919 RAP15
Flat Beam Spot Sizes Measurement in the SLC-Final Focus — *P. Raimondi, F.-J. Decker* ... 2922 RAP16
Polarization Correlations in the SLC Final Focus — *F.-J. Decker* ... 2925 RAP17
Supercooling of Bunched Beams by Coherent Synchrotron Radiation — *M. Bergher* ... 2928 RAP19

Analysis of the Tevatron Collider Beam Spectrum for Bunched Beam Stochastic Cooling — *G. Jackson* 2931 RAP20
Asymmetric Hopf Bifurcation for Proton Beams with Electron Cooling — *X. Kang, M. Ball, B. Brabson, J. Budnick, D.D. Caussyn, P. Colestock, G. East, M. Ellison, B. Hamilton, K. Hedblom, S.Y. Lee, D. Li, J.Y. Liu, K.Y. Ng, A. Pei, A. Riabko, M. Syphers, L. Wang, Y. Wang* 2934 RAP21
Space Charge Effects and Intensity Limits of Electron-Cooled Bunched Beams — *S. Nagaitsev, T. Ellison, M. Ball, V. Derenchuk, G. East, M. Ellison, B. Hamilton, P. Schwandt* 2937 RAP22
Stability Conditions for a Neutralised Electron Cooling Beam — *J. Bosser, S. Maury, D. Möhl, F. Varenne, I. Meshkov, E. Syresin, E. Mustafin, P. Zenkevich* 2940 RAP23
Neutralisation of the LEAR Electron-Cooling Beam: Experimental Results — *J. Bosser, F. Caspers, M. Chanel, R. Ley, R. Maccaferri, S. Maury, G. Molinari, G. Tranquille, F. Varenne, I. Meshkov, V. Polyakov, A. Smirnov, O. Stepashkin, E. Syresin* 2943 RAP24
Crystalline Beam Properties as Predicted for the Storage Ring ASTRID and TSR — *Jie Wei, Xiao-Ping Li, Andrew Sessler* 2946 RAP25

Instabilities and Cures

Impedance Matrix - an Unified Approach to Longitudinal Coupled-Bunch Feedbacks in a Synchrotron — *S. Ivanov* 2949 TPQ01
The Coupling Impedance of Toroidal Beam Pipe with Circular Cross Section — *H. Hahn* 2952 TPQ02
Bunch Lengthening Study in BEPC — *Z. Guo, Q. Qin, G. Xu, C. Zhang* 2955 TPQ03
Practical Criterion of Transverse Coupled-Bunch Head-Tail Stability — *S. Ivanov, M. Pozdeev* 2958 TPQ04
A Code to Compute the Action-Angle Transformation for a Particle in an Arbitrary Potential Well — *J. Scott Berg, Robert L. Warnock* 2962 TPQ07
Study of Longitudinal Coupled-Bunch Instabilities in the SRRC Storage Ring — *W.K. Lau, M.H. Wang, K.T. Hsu, L.H. Chang, Ch. Wang, C.C. Kuo* 2965 TPQ08
Suppression of the Transverse Oscillation in the SRRC Storage Ring by RF Knockout Method — *J.C. Lee, M.H. Wang, K.T. Hsu, R.J. Sheu, G. Lin, C.S. Hsue* 2968 TPQ09
The Observation of Longitudinal Coupled Bunch Motion on Streak Camera at SRRC — *M.H. Wang, K.T. Hsu, W.K. Lau, C.S. Hsue, H.J. Tsai, H.P. Chang, J.C. Lee, C.C. Kuo* 2971 TPQ10
Resistive-Wall Instability Experiment in Space-Charge Dominated Electron Beams — *H. Suk, J.G. Wang, M. Reiser* 2974 TPQ11
Mode-Coupling Instability and Bunch Lengthening in Proton Machines — *K.Y. Ng* 2977 TPQ12
Longitudinal Wakefield for Synchrotron Radiation — *J.B. Murphy, S. Krinsky, R.L. Gluckstern* 2980 TPQ14
Review of Beam Instability Studies for the SSC — *W. Chou* 2983 TPQ15
Collective Effects in the NLC Damping Ring Designs — *T. Raubenheimer, K.L.F. Bane, J.S. Berg, J. Byrd, J. Corlett, M. Furman, S. Heifets, K. Kubo, M. Minty, B. Scott, K.A. Thompson, P.B. Wilson, F. Zimmermann* 2986 TPQ16
Emittance and Energy Control in the NLC Main Linacs — *C. Adolphsen, K.L.F. Bane, K. Kubo, T. Raubenheimer, R.D. Ruth, K.A. Thompson, F. Zimmermann* 2989 TPQ17
Digital Signal Processing for the APS Transverse and Longitudinal Damping System — *D. Barr, W. Sellyey* 2992 TPQ19
Longitudinal Coupling Impedance of a Hole in an Infinite Plane Screen — *Yong-Chul Chae* 2995 TPQ20
Investigation of Resistive Wall Instability in the 7-GeV APS Storage Ring — *Yong-Chul Chae* 2998 TPQ21
Longitudinal Instability Analysis for the IPNS Upgrade — *K. Harkay, Y. Cho, E. Lessner* 3001 TPQ22
Transverse Instability Analysis for the IPNS Upgrade — *K. Harkay, Y. Cho* 3004 TPQ23
Longitudinal Emittance Measurements in the Fermilab Booster — *D.A. Herrup* 3007 TPQ25
Analog Dampers in the Fermilab Booster — *D.A. Herrup, D. McGinnis, J. Steimel, R. Tomlin* 3010 TPQ26
A Study of the Longitudinal Coupled Bunch Instability in the Fermilab Main Ring — *K. Junck, J. Marriner, D. McGinnis* 3013 TPQ28
Inference of Wake Field Structure by Driving Longitudinal Coupled Bunch Modes in Main Ring — *S. Assadi, K. Junck, P. Colestock, J. Marriner* 3016 WAB01
Simulation of Transverse Coupled Bunch Instabilities — *S. Khan* 3019 WAB03
The Transition Jump System for the AGS — *W.K. van Asselt, L.A. Ahrens, J.M. Brennan, A. Dunbar, E. Keith-Monnia, J.T. Morris, M.J. Syphers* 3022 WAB04

Measurements of Longitudinal Phase Space in the SLC Linac — *R.L. Holtzapple, F.-J. Decker, R.K. Jobe, C. Simopoulos* 3025 WAB05
Observation of Induced Beam Oscillation from Actively Displaced RF Accelerating Structures — *John T. Seeman, Henk Fischer, William Roster* 3028 WAB06
Measurement of the Effect of Collimator Generated Wakefields on the Beams in the SLC — *K.L.F. Bane, C. Adolphsen, F.-J. Decker, P. Emma, P. Krejcik, F. Zimmermann* 3031 WAB07
Beam Trajectory Jitter in the SLC Linac — *Chris Adolphsen, Tim Slaton* 3034 WAB08
Emittance Growth due to Decoherence and Wakefields — *M.G. Minty, A.W. Chao, W.L. Spence* 3037 WAB09
A Weak Microwave Instability with Potential Well Distortion and Radial Mode Coupling — *Alex Chao, Bo Chen, Katsunobu Oide* 3040 WAB10
Wake Field and the Diffraction Model Due to a Flat Beam Moving Past a Conducting Wedge — *A.W. Chao, H. Henke* 3043 WAB11
Operating Experience with High Beam Currents and Transient Beam Loading in the SLC Damping Rings — *M.G. Minty, R. Akre, P. Krejcik, R.H. Siemann* 3046 WAB12
Deflecting Forces for the Case of Multi Mode Beam - RF Cavity Interaction in Linear Accelerators — *V.G. Kurakin* 3049 WAB14
Photoelectron Trapping Mechanism for Transverse Coupled Bunch Mode Growth in CESR — *J.T. Rogers* 3052 WAB15
Electron Cooler Impedances — *A. Burov* 3055 WAB16
Wall Impedances for Low and Moderate Energies — *A. Burov* 3058 WAB17
Impedance Analysis of the PEP-II Vacuum Chamber — *C.-K. Ng, T. Weiland* 3061 WAB18
Microwave Instabilities in Electron Rings with Negative Momentum Compaction Factor — *S.X. Fang, K. Oide, K. Yokoya, B. Chen, J.Q. Wang* 3064 WAB20
Microwave Stability at Transition — *J.A. Holt, P.L. Colestock* 3067 WAC01
Experimental Observations of Nonlinear Coupling of Longitudinal Modes in Unbunched Beams — *Linda Klamp Spentzouris, Patrick L. Colestock, Francois Ostiguy* 3070 WAC02
Damping Rate Measurements in the SLC Damping Rings — *C. Simopoulos, R.L. Holtzapple* 3073 WAC04
Transverse Multibunch Instabilities for Non-Rigid Bunches — *J. Scott Berg, Ronald D. Ruth* 3076 WAC05
Simulations of Transition Crossing in the Main Injector — *C.M. Bhat, J.A. MacLachlan* 3079 WAC06
Impedance Budget for the KEK B-Factory — *Y.H. Chin, K. Satoh* 3082 WAC07
Single-Beam Collective Effects in the KEK B-Factory — *Y.H. Chin, K. Akai, Y. Funakoshi, K. Oide, K. Satoh* 3085 WAC08
Beam Transfer Function and Transverse Impedance Measurements in the Fermilab Main Ring — *P.J. Chou, G. Jackson* 3088 WAC09
Experimental Studies of Transverse Beam Instabilities at Injection in the Fermilab Main Ring — *P.J. Chou, G. Jackson* 3091 WAC10
Longitudinal Multibunch Feedback Experiment with Switched Filter Bank — *A. Pei, M. Ball, M. Ellison, X. Kang, S.Y. Lee, D. Li, J. Liu, A. Riabko, L. Wang* 3094 WAC12
Field Propagation Effects and Related Multibunch Instability in Multicell Capture Cavities — *M. Ferrario, A. Mosnier, L. Serafini, F. Tazzioli, J.-M. Tessier* 3097 WAC13
Cure of Transverse Instabilities by Chromaticity Modulation — *T. Nakamura* 3100 WAC14
A Fast Beam-Ion Instability — *F. Zimmermann, T.O. Raubenheimer, G. Stupakov* 3102 WAC15
Simulations of the Longitudinal Instability in the New SLC Damping Rings — *K.L.F. Bane, K. Oide* 3105 WAC16
High-Intensity Single Bunch Instability Behavior In The New SLC Damping Ring Vacuum Chamber — *K. Bane, J. Bowers, A. Chao, T. Chen, F.J. Decker, R.L. Holtzapple, P. Krejcik, T. Limberg, A. Lisin, B. McKee, M.G. Minty, C.-K. Ng, M. Pietryka, B. Podobedov, A. Rackelmann, C. Rago, T. Raubenheimer, M.C. Ross, R.H. Siemann, C. Simopoulos, W. Spence, J. Spencer, R. Stege, F. Tian, J. Turner, J. Weinberg, D. Whittum, D. Wright, F. Zimmermann* 3109 WAC17
Alignment Tolerance of Accelerating Structures and Corrections for Future Linear Colliders — *K. Kubo, C. Adolphsen, K.L.F. Bane, T.O. Raubenheimer, K.A. Thompson* 3112 WAC18
Refinements to Longitudinal, Single Bunch, Coherent Instability Theory — *S.R. Koscielniak* 3115 WAC19
Simulations of Sawtooth Instability — *R. Baartman, M. D'Yachkov* 3119 WAC20
Characterisation of a Localised Broad-Band Impedance Phenomenon on the SRS — *S.F. Hill* 3122 WAC21
Cavity-Beam Instabilities on the SRS at Daresbury — *P.A. McIntosh, D.M. Dykes* 3125 WAC22

Bunch Lengthening Thresholds on the Daresbury SRS — *J.A. Clarke* ... 3128 WAC23
Estimation of Collective Instabilities in RHIC — *W.W. MacKay, M. Blaskiewicz, D. Deng, V. Mane, S. Peggs, A. Ratti, J. Rose, T.J. Shea, J. Wei* ... 3131 WAC24
RHIC Injection Kicker Impedance — *V. Mane, S. Peggs, D. Trbojevic, W. Zhang* ... 3134 WAC25
KRAKEN, a Numerical Model of RHIC Impedances — *S. Peggs, V. Mane* ... 3137 WAC26
Lattice Design of Beijing Light Source — *N. Huang, L. Jin, D. Wang, L. Wang, A. Xiao, G. Xu* ... 3140 WAC27
A Theoretical Study of the Electron-Proton Instability in a Long Proton Pulse — *Tai-Sen F. Wang* ... 3143 WAC28
Recent Progress on Beam Stability Study in the PSR — *T. Wang, P. Channell, R. Cooper, D. Fitzgerald, T. Hardek, R. Hutson, A. Jason, R. Macek, M. Plum, C. Wilkinson, E. Colton* ... 3146 WAC29

Low Energy Accelerator Beam Dynamics

Halos of Intense Proton Beams *(Invited)* — *Robert D. Ryne, Salman Habib, Thomas P. Wangler* ... 3149 RAG01
Polarized Proton Beams *(Invited)* — *T. Roser* ... 3154 RAG02
Beam Dynamics in Heavy Ion Fusion *(Invited)* — *Peter Seidl* ... 3159 RAG03
Crystalline Beams *(Invited)* — *John P. Schiffer* ... 3164 RAG04
Injecting a Kapchinskij-Vladimirskij Distribution into a Proton Synchrotron — *E. Crosbie, K. Symon* ... 3167 RAG05
Halo of a High-Brightness Electron Beam — *G. Haouat, N. Pichoff, C. Couillaud, J.P. De Brion, J. Di Crescenzo, S. Joly, A. Loulergue, C. Ruiz, S. Seguin, S. Striby* ... 3170 RAG06
Studies on Halo Formation in a Long Magnetic Quadrupole FODO Channel First Experimental Results — *P.-Y. Beauvais, D. Bogard, P.-A. Chamouard, R. Ferdinand, G. Haouat, J.-M. Lagniel, J.-L. Lemaire, N. Pichoff, C. Ruiz* ... 3173 RAG07
Radial Mode Evolution in Longitudinal Bunched Beam Instability — *S.Y. Zhang, W.T. Weng* ... 3176 RAG08
Stability of a Breathing K-V Beam — *Robert L. Gluckstern, Wen-Hao Cheng* ... 3179 RAG09
Hamiltonian Formalism for Space Charge Dominated Beams in a Uniform Focusing Channel — *A. Riabko, M. Ellison, X. Kang, S.Y. Lee, J.Y. Liu, D. Li, A. Pei, L. Wang* ... 3182 RAG10
Simulation Studies of the LAMPF Proton Linac — *R.W. Garnett, E.R. Gray, L.J. Rybarcyk, T.P. Wangler* ... 3185 RAG11
Functional Dependence of Wakefunctions for v < c — *Zenghai Li, Joseph J. Bisognano* ... 3188 RAG12
Betatron Transients Caused by Rapid Changes in the Closed Orbit — *James J. Welch* ... 3191 RAG13
Phenomenology of Crystalline Beams in Smooth Accelerators — *A.F. Haffmans, D. Maletic, A.G. Ruggiero* ... 3194 RAG14
Beam Dynamics in the 1.3 GeV High Intensity ESS Coupled Cavity Linac — *M. Pabst, K. Bongardt* ... 3197 TPA01
Final Bunch Rotation and Momentum Spread Limitation for the ESS Facility — *K. Bongardt, M. Pabst* ... 3200 TPA02
Design Criteria for High Intensity H^--Injector Linacs — *K. Bongardt, M. Pabst* ... 3203 TPA03
Measurements of Vacuum Chamber Impedance Effects on the Stored Beam at CESR — *M. Billing, Z. Greenwald, W. Hartung, W.R. Lou, M. Pisharody, J. Rogers, D. Sagan, J. Sikora* ... 3206 TPA04
The Study of Nonlinear Effects Influenced by Space Charge in High Intensity Linac — *A.A. Kolomiets, S.G. Yaramishev, P.R. Zenkevich, A.P. Korolev* ... 3209 TPA05
Beam Size Versus Intensity for Resonant Extracted Beam at the Brookhaven AGS — *K.A. Brown, R. Thern, H. Huang* ... 3212 TPA06
Review of Longitudinal Perturbation Formalism — *S.Y. Zhang* ... 3214 TPA08
Klystron Power Specifications Based on Transient Beam Loading Analysis in Damping Rings — *M.G. Minty, R.H. Siemann* ... 3217 TPA09
Transverse Combining of Four Beams in MBE-4 — *C.M. Celata, W. Chupp, A. Faltens, W.M. Fawley, W. Ghiorso, K.D. Hahn, E. Henestroza, C. Peters, P. Seidl* ... 3220 TPA10
Ion Core Parameters in the Bending Magnets of Electron Storage Rings — *E. Bulyak* ... 3223 TPA12
Ion Driven Effects in the Intence Electron Beam Circulating in Storage Rings — *E. Bulyak* ... 3226 TPA13
Disk-Loaded Waveguides for Accelerating High Intensity Short Pulse Electron Beams — *N.I. Aizatsky* ... 3229 TPA14
The Description of High Current Beam Dynamics Using Lie Algebraic Methods — *A.I. Borodich, A.A. Khrutchinsky, V.I. Stolyarsky* ... 3232 TPA15

Chaos, a Source of Charge Redistribution and Halo Formation in Space-Charge Dominated Beams — *Jean-Michel Lagniel, David Libault* 3235 TPA17
Transport of a Partially-Neutralized Ion Beam in a Heavy-Ion Fusion Reactor Chamber — *Debra A. Callahan, A. Bruce Langdon* 3238 TPR01
Emittance Growth from Rotated Quadrupoles in Heavy Ion Accelerators — *John J. Barnard* 3241 TPR02
Wakefield Effects on the Beam Accelerated in a Photoinjector: Perturbation Due to the Exit Aperture — *J.-M. Dolique, W. Salah* 3245 TPR04
Influence of the Photoinjector Exit Aperture on the Wakefield Driven by an Intense Electron Beam Pulse: a Theoretical Approach — *J.-M. Dolique* 3248 TPR05
Invariability of Intense Beam Emittance in Nonlinear Focusing Channel — *Y.K. Batygin* 3251 TPR06
Beam Transport for Uniform Irradiation: Nonlinear Space Charge and the Effect of Boundary Conditions — *D. Bruhwiler, Yuri K. Batygin* 3254 TPR07
Transport of Bunched Beams with Space Charge Through a Periodic Lattice — *M.F. Reusch, D.L. Bruhwiler* 3257 TPR08
Modeling Space Charge in Beams for Heavy-Ion Fusion — *W.M. Sharp* 3260 TPR09
Impedance of Periodic Irises in a Beam Pipe — *Shicheng Jiang, Robert L. Gluckstern, Hiromi Okamoto* 3263 TPR11
Frequency Dependence of the Polarizability and Susceptibility of a Circular Hole in a Thick Conducting Wall — *Wen-Hao Cheng, Alexei V. Fedotov, Robert L. Gluckstern* 3266 TPR12
Spatial-Temporal Hysteresis Effects in an Intense Electron Beam — *A.V. Agafonov, A.N. Lebedev, V.S. Voronin* 3269 TPR13
General Wave Equation in the Electrostatic Approximation — *A.V. Agafonov* 3272 TPR14
Space Charge Effects at KEK-Booster Synchrotron — *Chihiro Ohmori, Toshikazu Adachi, Tadamichi Kawakubo, Motohiro Kihara, Isao Yamane* 3275 TPR16
On the Relaxation of Semi-Gaussian and K-V Beams to Thermal Equilibrium — *S.M. Lund, J.J. Barnard, J.M. Miller* 3278 TPR18
Transverse-Longitudinal Energy Equilibration in a Long Uniform Beam — *I. Haber, D.A. Callahan, A. Friedman, D.P. Grote, A.B. Langdon* 3282 TPR19

Beam Dynamics, Misc.

Variants of Optics Schemes and Accelerator Configurations for Athens Microtron: Preliminary Considerations — *A.V. Tiunov, V.I. Shvedunov, I.V. Surma, K. Hizanidis, C. Kalfas, C. Trikalinos, J. Tigelis* 3285 RAQ01
Study of Beam Decoherence in the Presence of Head-Tail Instability Using a Two-particle Model — *G.V. Stupakov, A.W. Chao* 3288 RAQ02
Beam Distribution Function after Filamentation — *T.O. Raubenheimer, F.-J. Decker, J.T. Seeman* 3291 RAQ03
Measurement of the Interaction Between a Beam and a Beam Line Higher-Order Mode Absorber in a Storage Ring — *W. Hartung, P. Barnes, S. Belomestnykh, M. Billing, R. Chiang, E. Chojnacki, J. Kirchgessner, D. Moffat, H. Padamsee, M. Pisharody, D. Rubin, M. Tigner* 3294 RAQ04
A New Analytical Model for Axi-symmetric Cavities — *D. Burrini, C. Pagani, L. Serafini* 3297 RAQ05
Impurity Growth in Single Bunch Operation of PF — *M. Tobiyama, A. Higuchi, T. Mitsuhashi, T. Kasuga, S. Sakanaka* 3300 RAQ06
Coupling Impedance of a Periodic Array of Diaphragms — *G.V. Stupakov* 3303 RAQ09
Coupling Impedance of a Long Slot and an Array of Slots in a Circular Vacuum Chamber — *G.V. Stupakov* 3306 RAQ10
Dark Currents for CEBAF Linacs — *Byung C. Yunn* 3309 RAQ11
Improvements in Bunch Coalescing in the Fermilab Main Ring — *J. Dey, I. Kourbanis, D. Wildman* 3312 RAQ13
Slow Extraction of Particles Using a Thin Target for Driving for Resonance — *Yu. Severgin, W. Belov, A. Makarov, M. Tarovik* 3315 RAQ14
Properties of a Transverse Damping System, Calculated by a Simple Matrix Formalism — *S. Koscielniak, H.J. Tran* 3317 RAQ15
A Concept for Emittance Reduction of DC Radioactive Heavy-Ion Beams — *J.A. Nolen, J.C. Dooling* 3320 RAQ16

Measurements of the Octupole-Induced Amplitude-Dependent Frequency Shift in SPEAR — *P. Tran, C. Pellegrini, J. Yang, M. Cornacchia, J. Corbett* ... 3323 RAQ17
Radiation Damping in Focusing-Dominated Systems — *Zhirong Huang, Pisin Chen, Ronald D. Ruth* ... 3326 RAQ18
Colliding Crystalline Beams — *A.F. Haffmans, D. Maletic, A.G. Ruggiero* ... 3329 RAQ20
Helical Spin Rotators and Snakes for RHIC — *V.I. Ptitsin, Yu.M. Shatunov, S. Peggs* ... 3331 RAQ21
Effects of Enhanced Chromatic Nonlinearity during the AGS gt-Jump — *J. Wei, J.M. Brennan, L.A. Ahrens, M.M. Blaskiewicz, D.-P. Deng, W.W. MacKay, S. Peggs, T. Satogata, D. Trbojevic, A. Warner, W.K. van Asselt* ... 3334 RAQ22
Effect of Parametric Resonances on the Bunched Beam Dilution Mechanism — *L. Wang, M. Ball, B. Brabson, J. Budnick, D.D. Caussyn, G. East, M. Ellison, X. Kang, S.Y. Lee, D. Li, J.Y. Liu, K.Y. Ng, A. Pei, A. Riabko, D. Rich, T. Sloan, M. Syphers* ... 3337 RAQ23
Parametric Resonances and Stochastic Layer Induced by A Phase Modulation — *J.Y. Liu, M. Ball, B. Brabson, J. Budnick, D.D. Caussyn, P. Colestock, V. Derenchuk, G. East, M. Ellison, D. Friesel, B. Hamilton, W.P. Jones, X. Kang, S.Y. Lee, D. Li, K.Y. Ng, A. Pei, A. Riabko, T. Sloan, M. Syphers, L. Wang* ... 3340 RAQ24
Nonlinear Space Charge Effect of Gaussian Type Bunched Beam in Linac — *Yinbao Chen, Shinian Fu, Zhibin Huang, Zhenhai Zhang* ... 3343 RAQ25
Emittance Growth Caused by Bunched Beam with Nonuniform Distributions in Both Longitudinal and Transverse Directions in Linac — *Zhibin Huang, Yinbao Chen, Shinian Fu* ... 3346 RAQ26
The Envelopes of Beam Motion in the Charged Particle Cyclic Accelerator — *Yu.P. Virchenko, Yu.N. Grigor'ev* ... 3349 RAQ28
A Semi-analytical Approach to the Design of Low Energy Cylindrically Symmetric Transport Lines — *Pedro F. Tavares* ... 3352 RAQ29
Stability of Trapped Ions in Electron Storage Rings in View of Parametric Resonance — *Y. Miyahara* ... 3355 RAQ30
Entropy and Emittance of Particle and Photon Beams — *K.-J. Kim, R.G. Littlejohn* ... 3358 RAR02
Effect of the Coupling Slots on Beam Dynamics in Accelerator Structure of Moscow CW RTM — *V.I. Shvedunov, A.S. Alimov, A.S. Chepurnov, O.V. Chubarov, D.I. Ermakov, A.V. Tiunov, P.L. Tkachev* ... 3361 RAR04
The Electron Beam Orbit Sensitivity on the Photon Flux of the Photon Beam Line — *Ian Hsu, G.H. Luo, K.L. Tsang, C.C. Chu, C.I. Yu, W.T. Weng, S.C. Chung* ... 3364 RAR05
Ground Motion in LEP and LHC — *L. Vos* ... 3367 RAR07
Cosmic Particle Acceleration at Very High Energies — *K.O. Thielheim* ... 3370 RAR09
Trapped Modes in the Vacuum Chamber of an Arbitrary Cross Section — *Sergey S. Kurennoy, Gennady V. Stupakov* ... 3373 RAR11
A General Approach for Calculating Coupling Impedances of Small Discontinunities — *Sergey S. Kurennoy, Robert L. Gluckstern, Gennady V. Stupakov* ... 3376 RAR12
Polarizabilities of an Annular Cut and Coupling Impedances of Button-Type Beam Position Monitors — *Sergey S. Kurennoy* ... 3379 RAR13
The Effect of Coupling on Luminosity — *D. Sagan* ... 3382 RAR15
RFQ-DTL Matching Solutions for Different Requirements — *D. Raparia* ... 3385 RAR16
Low-Dispersion γ_t Jump for the Main Injector — *K.Y. Ng, A. Bogacz* ... 3388 RAR17
Wakefields and HOMs Studies of a Superconducting Cavity Module with the CESR Beam — *S. Belomestnykh, W. Hartung, G. Flynn, J. Kirchgessner, H. Padamsee, M. Pisharody* ... 3391 RAR18
Comparison of the Predicted and Measured Loss Factor of the Superconducting Cavity Assembly for the CESR Upgrade — *S. Belomestnykh, W. Hartung, J. Kirchgessner, D. Moffat, H. Muller, H. Padamsee, V. Veshcherevich* ... 3394 RAR19
Control of Trapped Ion Instabilities in the Fermilab Antiproton Accumulator — *Steven J. Werkema* ... 3397 RAR20
Longitudinal Emittance Oscillation in a Superconducting Drift Tube Linac — *J.W. Kim, K.W. Shepard* ... 3400 RAR21
Electric Fields, Electron Production, and Electron Motion at the Stripper Foil in the Los Alamos Proton Storage Ring — *M. Plum* ... 3403 RAR22
Electron Clearing in the Los Alamos Proton Storage Ring — *M. Plum, J. Allen, M. Borden, D. Fitzgerald, R. Macek, T.S. Wang* ... 3406 RAR23

Advanced Photon Source Insertion Device Field Quality and Multipole Error Specification — *Yong-Chul Chae, Glenn Decker* 3409 RAR24
Study of Field Ionization in the Charge Exchange Injection for the IPNS Upgrade — *Yong-Chul Chae, Yanglai Cho* 3412 RAR25
Lattice Considerations for a Tau-Charm Factory — *L.C. Teng, E.A. Crosbie* 3415 RAR26
Effects of Vertical Aperture on Beam Lifetime at the Advanced Photon Source (APS) Storage Ring — *Hana M. Bizek* 3418 RAR27
Rebucketing After Transition in RHIC — *D.-P. Deng, S. Peggs* 3421 RAR29
Closed-Orbit Drifts in HERA in Correlation with Ground Motion — *V. Shiltsev, B. Baklakov, P. Lebedev, C. Montag, J. Rossbach* 3424 RAR30
Simulation of the Acceleration of Polarized Protons in Circular Accelerators — *Yu. Shatunov, V. Yakimenko* 3427 RAR31

CEBAF Commissioning and Future Plans

Hermann A. Grunder
Director
Continuous Electron Beam Accelerator Facility
12000 Jefferson Avenue, Newport News, VA 23606-1909 USA

I. INTRODUCTION

With first beam on target in July 1994 , the Continuous Electron Beam Accelerator Facility (CEBAF) in Newport News, Virginia began capitalizing on years of planning and work to create a laboratory devoted to the exploration of matter that interacts through the strong force, which holds the quarks inside the proton and binds protons and neutrons into the nucleus. This event is made more remarkable in that the accelerator is available to physicists on schedule and within cost. The success of the project is due largely to a reasoned approach to its planning and the extraordinary work of scores of talented and motivated individuals.

A. Why CEBAF Now?

Just as Quantum Mechanics and Coulomb's Law explained atoms as bound states of electrons and nuclei, and molecules as bound states of atoms, it is CEBAF's scientific goal to use the theory of Quantum Chromodynamics (QCD) to describe nucleons as bound states of quarks and gluons and nuclei as bound states of nucleons. This machine and its capabilities will enable us to fill in what are some of the most glaring gaps in our understanding of nature. In the "molecular physics" of nuclei it is our goal to understand the physical mechanisms and novel features in terms of known basic theory, to answer questions such as "Why do we have nucleons instead of a quark-gluon soup?", "What is the origin of the NN force", and "What are the short distance nuclear degrees of freedom?" In the atomic physics of quarks and gluons we seek to understand quark confinement, discover gluonic degrees of freedom; and understand why we only see quarks in qqq and $q\bar{q}$ configurations?

What makes the time right for a facility such as CEBAF? Key ingredients have come together including the theory of Quantum Chromodynamics, superconducting accelerator technology, advances in detector technology, and new capabilities for rapid data acquisition to make it possible for us to answer these questions.

When D. Allan Bromley and his committee met in 1983, they specified what the parameters of the beam for such a machine should be based on the Barnes Panel. They called for a machine with an energy of 4 GeV that could be upgraded to 6 GeV, a current of 200 μA, and energy spread of $\Delta E/E \leq 10^{-4}$, emittance of 2×10^{-8} (geometric at 45 MeV), and a duty factor of 100%, creating a continuous wave accelerator. When paired with the appropriate experimental instrumentation, such a machine provides a tool for the world physics community of unmatched capability.

In a recent popular movie "Field of Dreams", the main character hears a voice that tells him "If you build it, they will come." Though in that movie the voice referred to a baseball field, it could have applied to CEBAF as well. The physics community has responded with enthusiasm. Currently, CEBAF's user group has about 1100 members. Five hundred thirteen users from 114 institutions in 24 countries are collaborators on approved experiments. CEBAF's Program Advisory Committees have already approved 3 years of experimentation in each of the three halls with the following profile.

Table 1

Totals of Approved Experiments by Physics Topic

Topic	Number
Nucleon and Meson Form Factors and Sum Rules	11
Properties of Nuclei	28
N* and Meson Properties	24
Strange Quarks	12
TOTAL	75

CEBAF offers its user community three experimental halls which can run experiments simultaneously, with complementary capabilities and equipment. Hall C, the first to come on-line, is equipped with a High Momentum Spectrometer (HMS) which has a large solid angle, a moderate resolution (10^{-3}) and a maximum acceptance of 7 GeV/c. It also has a Short Orbit Spectrometer (SOS) with a large momentum acceptance and a very short (7.4m) optical path for use in detecting particles having a short lifetime, such as low momentum π's and K's. The HMS has already achieved its design specifications and the SOS spectrometer will begin operation shortly. The initial experimental program will include an investigation of the validity of the quark counting rules in the photodisintegration of the deuteron, measurements of the neutron electric form factor, and studies of kaon electroproduction. Hall C is also the area envisioned for the installation of specialized detectors designed to investigate specific problems such as hypernuclear physics and the strange quark content of the proton (via parity-violating $\vec{e}\vec{p}$ scattering).

Hall A, scheduled to begin operation in early 1996, is equipped with two optically identical high resolution (10^{-4}) magnetic spectrometers (HRS) having a relatively large solid

* Supported by U.S. DOE contract #DE-AC05-84ER40150

0-7803-3053-6/96/$5.00 ©1996 IEEE

angle and a maximum momentum of 4 GeV/c. The detector packages have been optimized differently: one for detecting electrons and one for detecting hadrons. The Hall A experimental program will conduct detailed investigations of the structure of nuclei, and look at the elastic, inelastic, and weak structure of the nucleon. Such measurements will provide stringent tests for microscopic models of the nucleon, including the strange quark contributions to their charge and magnetization distributions.

Hall B, scheduled to begin operation in late 1996, is equipped with a large acceptance detector (CEBAF Large Acceptance Spectrometer, or CLAS), designed to carry out experiments which require the detection of several only loosely correlated particles in the hadronic final state, and measurements at limited luminosity. A major focus of the research program in Hall B is the investigation of the quark-gluon structure of the nucleon. The CLAS detector will also be used in a variety of other investigations requiring data on multiparticle final states.

B. Machine configuration and design

In planning what CEBAF's accelerator would look like , there was thought given not only to what the physics community wanted now, but what they were likely to want in the future. What was needed was a continuous wave electron accelerator. However, that offered a number of challenges. The first was controlling the power cost for such a machine, a challenge that was best met by utilizing superconducting radiofrequency (SRF) cavities. Though other more mature technologies existed that would allow the necessary specifications, SRF would allow "growth" in the capabilities of the machine since it was a technology at a promising beginning, not a successful end. The next hurdle was limiting the capital expense of such a machine, which was done by using beam recirculation. The final challenge was leaving some room for upgradabilty of the machine. This was done through the design of arcs that could accommodate 20 GeV beam, with their limitation being synchrotron radiation and the resulting degraded beam quality. Thus the CEBAF accelerator was born.

The system itself is an impressive array of hardware and software. The accelerator system consists of 338 SRF cavities, each with its own klystron, in 42 1/4 cryomodules. The injector will consist of three independent electron sources to allow independent current, independent pulse sequence and independent polarization to meet the needs of the user community. Our helium liquifier is the largest 2 K° system in the world with 5000W at 2.1° K at 97% availability. It is a closed system with two temperatures, 50° K and 2° K. The instrumentation and control system consists of 100,000 i/o points. The system is currently operational running under the EPICS control system. The beam transport system in the arcs and the beam switchyard consists of 2,241 magnets (dipoles, quadrupoles, and correction magnets), 4.5 km of vacuum line and the necessary beam dumps and LCW system.

C. Commissioning and status

To bring such a collection of state of the art equipment together into a functioning system was not an easy task. There were a number of challenges along the way to make things interesting. With the SRF cavities themselves, we needed to achieve and maintain high gradient and high Q factor in a production environment. We have successfully met that challenge, producing, installing and commissioning the cavities with characteristics that are twice the CEBAF specifications for both these parameters. This experience and performance makes CEBAF the recognized world leader in SRF technology.

The machine control system offered its own challenges including a successful mid-construction migration to the EPICS control system. Currently the hardware upgrade is complete, and the RF, magnets and diagnostics have successfully been migrated to EPICS. The injector is now in the process of conversion, with plans to convert the gun control later in Spring and the Central Helium Liquifier in August.

The injector has also exceeded specifications, producing currents of 340 μA, as compared to the specified 200 μA. The injector will offer the capability to produce three independent interleaved beams, though this capability is not fully operational yet. It can start up from a cold state in about ten minutes.

Along with our challenges, the commissioning has offered its share of successes. On March 20, 1995, we achieved an energy of 3.2 GeV, the equivalent of 4-pass beam. We have also delivered continuous wave beam to allow the commissioning of coincidence capabilities in Hall C.

D. Looking toward the future

Even though CEBAF has just begun operations, we are already looking toward the future. Our highest priority over the next five years is to run the presently approved experimental program. However, we and our user community are looking toward increasing the science that is possible using the CEBAF accelerator. The existing capabilities of our SRF cavities have us aiming for gradually pushing the current machine's energy from 4 to 6 GeV. Our user community has also recommended, and NSAC has supported, an evolutionary upgrade of CEBAF to the 10 GeV range. This upgrade would be particularly cost effective, since it can be achieved by adding additional cavities in existing free spaces in the linacs and upgrading the performance of those cavities that have lesser gradients.

* Supported by U.S. DOE contract #DE-AC05-84ER40150

CEBAF has also been active in partnership with industry to apply its SRF technology for an accelerator-driven free electron laser. There are industrial applications for cost-effective, high average power sources of coherent infrared and ultraviolet light. These include primarily materials processing that will enable new and value-added products. Industrial partners have identified SRF technology as the route to such a device for industrial processing, and thus an industry-driven alliance, the Laser Processing Consortium, was organized to develop, test and apply high average power FELs. The program plan has two phases; Phase 1, a UV and IR demonstration at a few (2-3) kw, and Phase 2, an industrial prototype of 10-100 kw. The conceptual design for Phase 1 is being reviewed by the Department of Energy, and funding opportunities are being explored.

As the nation's newest laboratory, CEBAF has worked hard to become a center of scientific and academic excellence that benefits not only the nation's scientific community but the nation's economic competitiveness as well. With continued sound planning, with the dedication of its excellent staff, and with the continued development of cutting edge technology, the phenomenal contributions that can come from such a facility will be realized.

Note added: On May 9, 1995, in the week immediately following the Conference, CEBAF attained its full design energy of 4 GeV.

* Supported by U.S. DOE contract #DE-AC05-84ER40150

The Advanced Photon Source*

John N. Galayda
Argonne National Laboratory, 9700 South Cass Avenue, Argonne, IL 60439

Abstract

The Advanced Photon Source (APS) is a 7-GeV third-generation synchrotron radiation storage ring and full-energy positron injector. Construction project funding began in 1989, and ground breaking took place on 5 May 1990. Construction of all accelerator facilities was completed in January 1995 and storage ring commissioning is underway. First observation of x-rays from a bending magnet source took place on 26 March 1995. Nearly all performance specifications of the injector have been reached, and first observations indicate that the reliability, dynamic aperture, emittance, and orbit stability in the storage ring are satisfactory. Observation of radiation from the first of 20 insertion device beamlines is scheduled for October 1995. Start of regular operations is expected to take place well before the APS Project target date of December 1996.

I. INTRODUCTION

The APS accelerator systems consist of:

- 250-MeV electron linac
- 450-MeV positron linac
- 450-MeV positron accumulator ring
- 0.4 to 7-GeV booster synchrotron
- 7-GeV, 100-mA low-emittance (8 nm-rad) positron storage ring (see Figure 1)

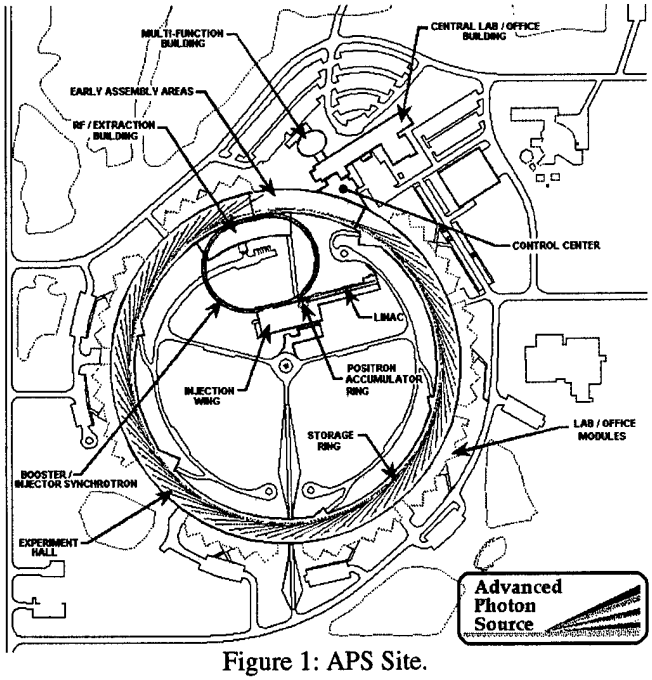


Figure 1: APS Site.

The purpose of the Advanced Photon Source (APS) at Argonne National Laboratory is to provide extremely brilliant beams of x-rays for basic and applied research in areas such as materials science, biology, and medicine. It is one of a large and growing number of "third generation" light sources [1], designed to make best use of the tuneability and monochromaticity of synchrotron radiation from undulators. At present, x-ray beamlines are being designed and constructed for 20 of the 35 available straight sections of APS by 17 collaborative access teams, or CATs. The CATs include participants from 104 universities, 37 industrial research organizations, and 16 research laboratories. Independent researchers will have access to the CAT beamlines for up to 25% of the available operating time. Protein crystallography, characterization of the structure of viruses, and x-ray microscopy are a few of the experimental capabilities of APS beamlines.

These experimental opportunities are made possible by the very high flux of photons of selectable wavelength which can be brought to bear on a sample under investigation. The quantitative measure of this intensity is "brilliance," peak 4-dimensional transverse phase space flux density of photons in a 0.1% bandwidth. The APS storage ring was designed with a Chasman-Green lattice to produce an 8-nm-rad damped emittance so as to provide high brilliance from its undulators. The 7-GeV energy and 8-mm vertical physical aperture [2] in the insertion device straight sections were chosen to enhance the tuning range of undulators. For example, APS undulator "A" [3], which will be installed in 18 APS beamlines, will produce $1x10^{17}$ to $2x10^{18}$ photons/(sec mm^2 mrad^2 0.1%bw) in the energy range 44 keV to 3 keV. Special-purpose insertion devices such as the elliptical motion wiggler [4] will provide unique additional capabilities.

II. SCHEDULE AND COST

The APS Project began in FY 1989 with funds sufficient to begin architectural design. Groundbreaking took place in May of 1990. Site preparation was completed one year later, at which point construction of the injector buildings began. Linac installation began in April of 1992 and was completed in October of 1993. Positron accumulator ring installation was completed in January of 1994, and booster synchrotron installation was complete two months later. Storage ring installation activities began in April 1993, when construction of the first segments of the storage ring tunnel was completed. Storage ring installation was completed in January of 1995.

The total construction cost of the APS is $467.2 million. Cost of construction of the accelerator systems was $150 million, with $44 million allotted to the injector, $91 million allotted to the storage ring, and the remainder allocated to common facilities and activities such as central controls, survey activities, and magnet measurement. Figure 2 depicts the funding history of the Project, as well as major milestones since 1989.

* Work supported by the U.S. Department of Energy, Office of Basic Energy Sciences, under Contract No. W-31-109-ENG-38.

0-7803-3053-6/96/$5.00 ©1996 IEEE

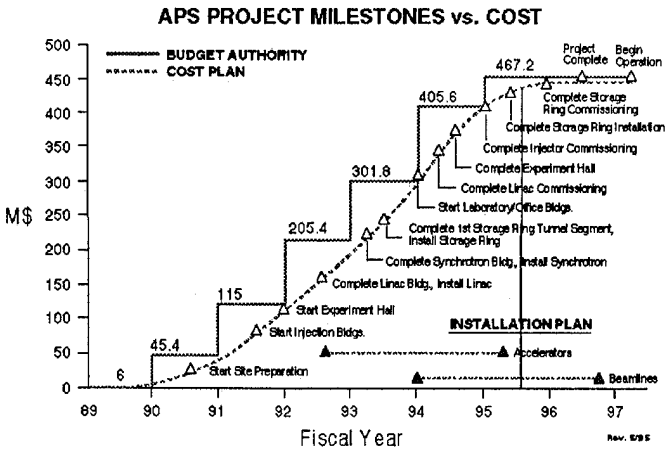


Figure 2: APS Project Budget Schedule.

III. COMMISSIONING CHRONOLOGY

Linac commissioning [5] began with the production of 50-MeV beam on 7 October 1993. The linac has supplied electrons for commissioning the downstream accelerators since January 1994, while positron production studies were pursued in parallel. Performance specification for positron current was achieved by 31 July 1994 and the specified positron energy was achieved in February 1995.

Positron accumulator ring (PAR) commissioning [6] began 27 February 1994, and stored beam was achieved 17 April 1994. The PAR has run reliably, supplying electrons for booster and storage ring commissioning since April 1994. Positron injection studies have been postponed until installation of a septum magnet capable of 60-Hz operation in June 1995.

Booster commissioning [7] began 21 April 1994. Difficulties arose with the regulation bandwidth of the ramping power supplies, causing a rather slow approach to specified performance. Acceleration to 1 GeV was achieved 24 August 1994, and 4-GeV beam was produced 18 October 1994. First 7-GeV beam was produced 22 January 1995. After extensive improvements to the power supply regulation [8,9], the booster has run very reliably at 7 GeV for storage ring commissioning since February 1995.

A 4-GeV beam was transported through two sectors of the storage ring on 30 October 1994, before installation of the ring was complete. First 7-GeV beam was delivered to the completed storage ring 20 February 1995. Commissioning proceeded smoothly [10] from first turn on 18 March to first observation of bending magnet radiation from a stored 4.5-GeV beam on 26 March 1995. Storage at 7 GeV was achieved on 15 April 1995.

IV. LINAC DESCRIPTION AND STATUS

The APS staff functioned as general contractor and final assembler of the linac. The gun was purchased from Hermosa Electronics. Klystrons are Thomson 35-MW units operated at 2856 MHz. After the vendor for the modulators went bankrupt, the linac group completely reworked the modulator design and finished construction [11]. Accelerating waveguide and SLED cavities follow SLAC design and were purchased from Schonberg Engineering. Quadrupoles and bending magnets were purchased from Danfysik.

The first accelerating waveguide of the electron linac is powered by a dedicated modulator and is followed by four more 3-meter waveguides powered by a single klystron with SLED. The electron beam is brought to a focus on a 7-mm-thick tungsten target from which 8-MeV positrons are collected for acceleration. The positron linac is essentially a duplicate of the electron linac, followed by an additional set of four accelerating sections excited by a klystron and SLED to produce 450-MeV beam. The positron production target may be retracted to allow acceleration of electrons to 650 MeV.

Almost all major performance criteria for the linac have been met, with the exception of the energy spread of the positron beam (1% desired, 1.6% measured); it is expected that optimization of focusing near the production target will yield the desired 30 nsec x 8 mA positron macropulses at 450 MeV.

V. POSITRON ACCUMULATOR RING DESCRIPTION AND STATUS

The DC magnets for the PAR were purchased from Danfysik, and DC supplies were built by Inverpower and Dynapower; pulse magnets and supplies, vacuum beam pipe, rf cavities, and amplifiers were all built to APS designs, mostly by local machine shops.

The PAR is a 30.7-meter circumference storage ring, the design of which is inspired by the positron intensity accumulator (PIA) ring; its lattice has twofold symmetry with two dispersion-free straights for rf and injection/extraction. Almost all the vertical focusing is supplied by the 25-degree edge angle of the eight zero-gradient dipole magnets. Special attention was given to clamping the end fields of these magnets to control soft-edge focusing effects.

The PAR is intended to collect 24 pulses from the linac at 60 Hz, capturing with a 1st harmonic (9.77 MHz) rf system, and finally compressing longitudinally with a 12th harmonic rf system before extraction to the booster. Because the beam from the linac has rather long macropulses, the PAR uses fluorescent flags for first-turn diagnostics rather than rf beam position monitors.

Commissioning studies have led to a very comprehensive and accurate model of PAR optics, as well as a set of convenient and powerful software tools for commissioning [12,13]. Measurements of ring properties such as corrector response matrix, dispersion function, tunes, chromaticities, rf voltage, etc. were first performed as automatic scripts which invoke the software tools; these scripts may now be used by Operations Group personnel for troubleshooting.

At present the PAR performance has been excellent with electrons. Injection tests at 30 Hz have yielded better than 95% capture efficiency. Current accumulation requirements for the PAR have been exceeded; over 190 mA of beam has been stored. Positron accumulation tests will begin in June.

VI. BOOSTER SYNCHROTRON DESCRIPTION AND STATUS

APS staff developed the design and manufacturing procedures for the booster dipoles and quadrupoles. APS also functioned as general contractor for magnet fabrication, buying copper conductor and sheet iron, and placing contracts with industry for stamping of laminations and coil winding. Dipole laminations were stacked and welded at Argonne, while other magnet laminations were stacked and welded by local industry. Final assembly was carried out by APS staff.

The booster vacuum system is an APS design, using stainless conflat vacuum seals. It has achieved 10 nT pressure.

The booster has four 5-cell, 352-MHz accelerating cavities manufactured by Interatom. They are identical to cavities used in the ESRF storage ring. The cavities are powered by a Thomson klystron and Universal Voltronics high voltage power supply.

The lattice of the booster synchrotron is a 40-cell FODO, using zero-gradient dipoles. Twelve dipoles are deleted from the lattice to create four zero-dispersion straight sections symmetrically placed around the ring. A single bunch is injected directly onto the closed orbit. The booster is designed to operate at 2 Hz, ramping 450 MeV to 7,000 MeV and back during beam accumulation in the PAR.

Booster commissioning was prolonged because the ramping power supplies had insufficient regulation bandwidth. The power supply regulators were completely reworked [8,9]. During booster operation, a computer program running on an operator console workstation modifies the ramp commands to adapt to lines changes and other environmental factors. Though the modification of the ramping regulators is not complete, at present the booster is running very reliably with negligible beam loss at injection due to power supply tracking errors.

VII. STORAGE RING DESCRIPTION AND STATUS

A standard sector (Figure 3) of the APS storage ring has ten quadrupoles, seven sextupoles, eight correctors, and nine rf beam position monitors. The magnets in a sector are supported on five girders.

Construction of the magnets of the APS storage ring followed the pattern of the booster magnets; APS personnel executed the design, procured the raw materials, and developed the manufacturing technique. Commercial vendors were given the task of manufacturing subassemblies such as coils and welded cores. Final assembly was carried out by APS personnel. The storage ring dipoles were an exception; Tesla assembled completed magnets from stamped laminations and copper conductor supplied by APS.

The magnet designs were strongly influenced by the shape of the vacuum chamber, which has an antechamber connected to the beam chamber by a 10-mm-high, 127-mm-long channel. In order to accommodate the chamber, quadrupoles were designed with no iron connecting the top and bottom yokes. For the same reason the sextupole magnet yokes are three separate pairs of poles, arranged so that there is no iron in the plane of the stored beam on the outboard side of the ring. The corrector magnet yokes are shaped like sextupoles with windings on the poles to create vertical and horizontal steering fields. Magnet quality exceeded specification [14].

Table 1: Storage Ring Parameters

Nominal Energy	7.0 GeV
Nominal circulating current, multibunch	100 mA
Maximum circulating current, multibunch	300 mA
Maximum circulating current, single bunch	5 mA
Harmonic number	1296
Natural emittance	8.2×10^{-9} m-rad
Natural energy spread, rms	9.6×10^{-4}
Bunch length, rms, natural	5.3 mm
Max energy	7.7 GeV
Circumference	1104 m
Radio frequency	351.93 MHz
Number of periods	40
Length of insertion region	6.72 m
Length available for insertion device	5.2 m
Bending radius	38.9611 m
Betatron tunes	
Horizontal	35.22
Vertical	14.30
Synchrotron tune	0.0072
Natural chromaticities	
Horizontal	-64.7
Vertical	-26.4
Maximum beta functions	
Horizontal	24.1 m
Vertical	21.4 m
Beta functions at insertion symmetry points	
Horizontal	14.2 m
Vertical	10.0 m
Maximum dispersion	0.40 m
Ring acceptance	
Horizontal	22.8×10^{-6} m-rad
Vertical	20.3×10^{-6} m-rad
Vertical acceptance with undulators	1.6×10^{-6} m-rad
Beam size at insertion symmetry points, rms	
Horizontal	0.34 mm
Vertical, 10% emittance ratio	0.09 mm
Momentum compaction factor	2.28×10^{-4}
Transition Gamma	66.24
Bucket $\Delta E/E$ (BM only)	2.8%
Damping time	
Horizontal	9.46 ms
Vertical	9.46 ms
Longitudinal	4.73 ms
Radiation loss per turn, dipoles	5.45 MeV
Bending magnet critical energy	19.5 keV
Radiation loss per turn, insertion devices, max.	1.25 MeV

The quality of the magnet alignment and ring survey [15] is very good in the storage ring and indeed in the other accelerators as well. Data analysis indicates that alignment of neighboring magnet fiducials, relative to a "smoothed" reference line, is about 90 microns in the horizontal plane and 70 microns in the vertical. Stability of the storage ring is satisfactory, with less than 2.5 mm settlement between June 1993 and

September 1994, even though construction of the APS office buildings is still in progress. Settling has decelerated in those areas removed from ongoing construction.

Five girders support the magnets in a superperiod of the storage ring: two for the dipoles and neighboring sextupoles, two for the triplets of quadrupoles adjacent to the undulator straights, and one for the high-dispersion straight. These girders are supported on wedge jacks. Their lowest frequency vibrational resonance is near 12 Hz and may be described as a horizontal rigid-body motion of the girder, with the wedge jacks beneath the girders acting as springs. This resonance will be damped by a factor of 10 by insertion of Anatrol 227 viscoelastic material beneath the girders [16]. This is expected to reduce the rms horizontal motion of the girders from values as high as 300 nanometers to 50-80 nanometers (4-50 Hz) under normal conditions. Stability of the girders with respect to vertical vibrations is very good.

The storage ring vacuum system is made up of 240 aluminum chambers extruded by Taber Metals. The extrusions were machined and bent by Ideal Tool, Inc. Vacuum seals are SMC aluminum conflats at the ends of the chambers and Helicoflex seals for the rf beam position monitor electrodes. *In situ* bakeout is possible by circulating 150° C water through the chambers. Glidcop synchrotron radiation absorbers intercept the bending magnet radiation. Each chamber has approximately 7 meters (1400 l/sec) distributed non-evaporable getter (NEG) strips installed. High-power bending magnet radiation absorbers have an additional 220 l/sec ion pump and a 1000 l/sec lumped NEG pump.

The rf transmitters in the storage ring are nearly identical to that of the booster. The storage ring cavities consist of four groups of four single cells, powered by two transmitters for 100-mA operation. At least three transmitters are necessary to attain the ultimate design goal of 300 mA at 7 GeV. Four transmitters are installed, affording one spare for 300-mA operation. The cavity design is, to a very good approximation, a 500-MHz KEK rf cavity, scaled up in dimensions to 352 MHz. Cavities were fabricated from massive OFHC copper forgings by Interatom.

Storage ring and injector diagnostics [17] include flags, loss radiation monitors, visible-light synchrotron radiation monitors, and rf beam position monitors (BPMs) for the transport lines and rings. Booster and storage ring rf BPMs can archive up to 16,000 single-turn measurements and average them for a closed orbit reading. They use AM-PM conversion to provide output signals proportional to beam position and independent of beam current. They have been extremely useful in commissioning and will be integrated in a digital global feedback orbit control system for the storage ring which will collect and distribute beam position data at 4-kHz update rate for a 200-Hz closed-loop bandwidth [18,19].

The diagnostics functions and indeed other accelerator systems have been well served by the EPICS control system. The health and growth of the EPICS user community has been an important asset of the control system's utility [20].

VIII. STORAGE RING COMMISSIONING

Commissioning activities to date have included extensive use of the rf BPM system and the independent current control of every quadrupole. The first shifts were dedicated to confirming the adequacy of radiation shielding by forcing loss of known quantities of beam at prescribed locations [21]. Measurements of the response of the first-turn beam trajectory to corrector magnets were used to identify beam optics problems such as magnet polarity errors and power supply problems, to set the integer part of the betatron tunes, and to correct the first turn trajectory.

A notable demonstration of the utility of the diagnostics, controls and application tools is shown in Figure 4. It shows the average of 40 single-turn beam position measurements using rf BPMs in the high dispersion regions of the ring, displayed as a function of turn number. The result is a real-time (1-Hz update) display of the rf capture process, used to set the correct radiofrequency and phase of the rf system. This application was written by Glenn Decker in about one hour during a commissioning shift.

Once stored beam was obtained, scripts for automated orbit correction, tune measurement and chromaticity measurement were written and run. Operation of the 1-BM bending magnet radiation beamline continued, to validate the shielding and to cross-calibrate rf BPMs and correctors against x-ray BPMs. Finally a horizontal emittance measurement was made at 1-BM, which agrees within error bars with the expected value. Vertical emittance measurements are still being analyzed; they are consistent with linear coupling below the 10% design specification.

Thus far no effort has been devoted to stacking, so all measurements have been performed with less than 0.4-mA stored beam current. Commissioning has begun before completion of *in situ* bakeout of the vacuum system, which will be continued after repair of water-to-air leaks in the chamber

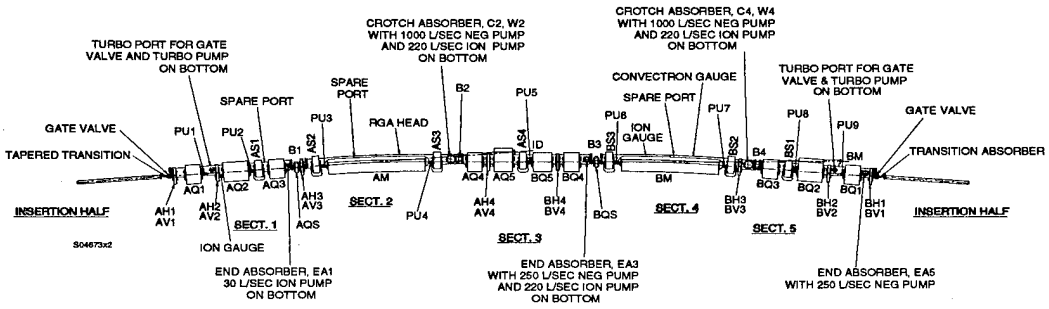


Figure 3: One Sector of the Storage Ring

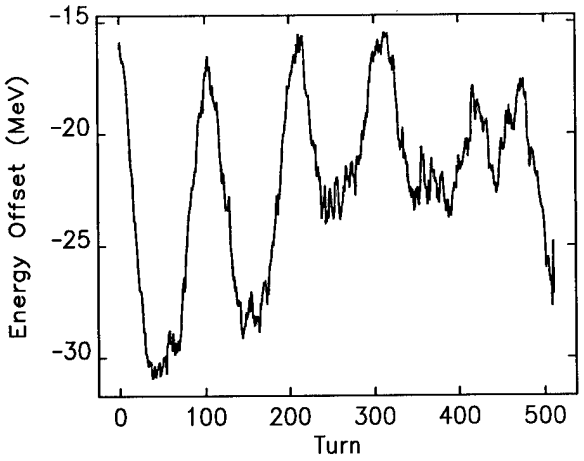


Figure 4: An operator's display of the rf capture process in the storage ring.

cooling/bake connections. For the present, the average ring pressure is about 30 nTorr, though the baked sectors have attained 0.1 nTorr. Beam lifetime at low current is dominated by the base pressure and is measured to be about six hours. The random and systematic noise of the rf BPMs was measured to be 0.25 micron/$\sqrt{\text{Hz}}$ with 300 μA stored beam. Correcting for this noise, the stability of the vertical beam position in the storage ring was measured to be 4.5 microns rms in the bandwidth 1-20 Hz. This satisfies the stability goal without use of feedback. The horizontal beam motion, at 32 microns rms 1-20 Hz, exceeds the stability target at present. Completion of installation of the viscoelastic damping material beneath the girders will bring horizontal beam stability into specification as well.

IX. FUTURE PLANS

Attempts to accumulate higher current will begin in May. Two-week commissioning periods will be separated by two-week maintenance periods through the summer, during which installation of x-ray beamline front-end components will continue and orbit stability and control will be investigated. First observation of undulator radiation is scheduled for October.

In the longer term, commissioning and machine studies will address operation with emittances down to 4 nm-rad [22], top-up operation of APS, and the limits on minimum gap of undulators in the storage ring [23].

X. ACKNOWLEDGMENT

The author wishes to express his gratitude for the outstanding performance of the Argonne APS Accelerator Systems Division during construction and commissioning. I am grateful to SSRL, ESRF, and NSLS for making beam studies time available for testing diagnostics and orbit feedback. While many other members of the APS Project and DOE also deserve thanks, these proceedings seem the right place to publicly thank the APS Accelerator Advisory Committee for their dedication and advice: George Brown, Don Edwards, Alan Jackson, Quentin Kerns, Sam Krinsky, J. L. Laclare, Boyce McDaniels, J. M. Paterson, Bob Siemann, Ron Sundelin, and Bruno Zotter.

XI. REFERENCES

[1] Synchrotron Radiation Sources - A Primer, H. Winick ed. Singapore, World Scientific Publishing Co., 1994.

[2] E. Traktenberg, et al., "The Vacuum System for Insertion Devices at the Advanced Photon Source," these proceedings.

[3] R. J. Dejus, et al., "Undulator A Characteristics and Specifications: Enhanced Capabilities," Argonne National Laboratory Report ANL/APS/TB-17, May 1994.

[4] E. Gluskin, et al., "The Elliptical Motion Wiggler Project," these proceedings.

[5] M. White, et al., "Performance of the Advanced Photon Source (APS) Linear Accelerator," these proceedings.

[6] M. Borland, "Commissioning of the Positron Accumulator Ring for the Advanced Photon Source," these proceedings.

[7] S. V. Milton, "The APS Booster Synchrotron: Commissioning and Operational Experience," these proceedings.

[8] J. A. Carwardine, et al., "Performance of the Ramping Power Supplies for the APS Booster Synchrotron," these proceedings.

[9] S. V. Milton and J. A. Carwardine, "Ramp Tuning of the APS Booster Synchrotron Magnet Power Supplies," these proceedings.

[10] G. Decker, "APS Storage Ring Commissioning and Early Operational Experience," these proceedings.

[11] T. Russell and A. Cours, "Klystron Modulator Operation and Upgrades for the APS Linac," these proceedings.

[12] L. Emery, "Commissioning Software Tools at the Advanced Photon Source," these proceedings.

[13] M. Borland," A Self-Describing File Protocol for Simulation Integration and Shared Post-Processors," these proceedings.

[14] S. Kim, et al., "Statistical Analyses of the Magnet Data for the Advanced Photon Source Storage Ring Magnets," these proceedings.

[15] H. Friedsam, et al., "Beamline Smoothing of the Advanced Photon Source," these proceedings.

[16] G. Decker, et al., "Reduction of Open-Loop Low Frequency Beam Motion at the APS," these proceedings.

[17] A. Lumpkin, et al, "Initial Diagnostics Commissioning Results for the Advanced Photon Source (APS)," these proceedings.

[18] Y. Chung, et al., "Local Beam Position Feedback Experiments on the ESRF Storage Ring," these proceedings.

[19] Y. Chung, et al., "Implementation of the Global and Local Beam Position Feedback Systems for the Advanced Photon Source Storage Ring," these proceedings.

[20] W. Watson, "The CEBAF Control System," these proceedings.

[21] L. Emery, "Beam Simulation and Radiation Dose Calculation at the Advanced Photon Source with shower, an EGS4 Interface," these proceedings.

[22] A. Ropert, "Accelerator Physics Trends at the ESRF," these proceedings.

[23] P. Stefan, et al., "Small Gap Undulator Experiment on the NSLS X-ray Ring," these proceedings.

COMMISSIONING AND PERFORMANCE OF THE HIMAC MEDICAL ACCELERATOR

S. Yamada, Research Center of Heavy Ion Therapy, National Institute of Radiological Sciences, 4-9-1 Anagawa, Inage-ku, Chiba 263, JAPAN

Heavy ions show the excellent dose concentration especially at a position located deep in a human body. This character of heavy ions are well suited for the medical treatment of the cancer. A heavy ion synchrotron complex, HIMAC, has been constructed at NIRS for this purpose. The HIMAC accelerator consists of an injector linac, a couple of synchrotron rings, long and complicated beam transport lines, three treatment rooms and four experimental rooms. The maximum energy of the synchrotron is determined so that the residual range of silicon ions exceeds 30 cm in water. The clinical trials of the cancer treatment started on June 21 using a 290 MeV/u carbon beam, and 21 patients were treated by the end of February 1995.

1. INTRODUCTION

During the last 19 years, clinical trials have been carried out at NIRS with fast neutrons and protons as well as conventional X-rays and gamma rays. Based on the long experience of radiotherapy, NIRS decided to construct a heavy ion accelerator, HIMAC, for medical use[1],[2]. The main reason to adopt heavy ion therapy is the excellent dose localization both in transverse and longitudinal directions. In the longitudinal dose distribution, a very sharp Bragg peak is observed around the end point of heavy ions as shown in Fig. 1. Such a distribution is much more effective in the treatment of deeply seated tumors than exponentially decreasing dose distribution of X and γ rays. High relative biological effectiveness (RBE) of heavy ions at the Bragg peak is expected to be efficacious even on the radio-resistive tumors. Another high LET characteristics, a low oxygen enhancement ratio (OER), seems also very attractive. These characteristics of heavy ions were shown to be very effective in medical treatment by clinical trials at LBL[3].

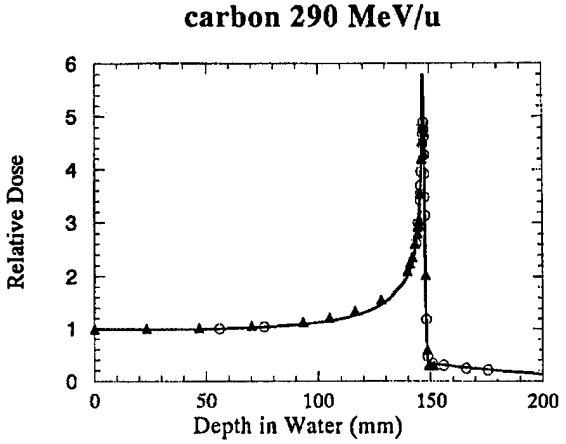


Fig. 1: A typical example of dose distribution of heavy ions in water.

The HIMAC project was approved in 1987 as one of the major project of "Comprehensive 10 year Strategy for Cancer Control" promoted by Japanese government since 1984. The construction of the injector started in the same fiscal year of 1987. The maximum energy of HIMAC is designed to be 800 MeV/u for light ions with q/A = 1/2 so that silicon ions reach 30 cm deep in a human body. Ion species of He, C, Ne, Si *etc.* are required for the clinical treatment. In the facility, there are three treatment rooms one of which has both vertical and horizontal beam lines. The other two treatment rooms are equipped with a vertical and a horizontal beam lines, respectively.

The beam tests of the accelerator started in November 1993 and the basic experiments for cancer treatments was begun in February 1994. The first clinical irradiation was carried out on June 21 and the treatment was successfully completed for three patients in August 1994. The patients have cancer cells in the head or the neck. It takes about 90 seconds for a single fractional treatment with 290 MeV/u carbon beam, while the precise patient-fixing procedure requires about 20 minuets. Three treatments per week and total of 18 treatments for each patient were planned to destroy perfectly tumor cells. The interim report of the heavy ion treatment for the first three patients shows excellent results just as expected. Radiation damage on the inside surface of the mouth seems very small in spite of the perfect damage of tumors.

Table 1: Requirements for the HIMAC beam

Ion species	^{4}He to ^{40}Ar
Maximum energy	800 MeV/u (q/A=1/2)
Minimum energy	100 MeV/u
Beam intensity*	1.2×10^{10} pps for ^{4}He
	2.0×10^{9} ^{12}C
	8.5×10^{8} ^{20}Ne
	4.5×10^{8} ^{28}Si
	2.7×10^{8} ^{40}Ar
Beam duration	400 ms (typical)
Repetition rate	1/2 Hz for each ring
Beam emittance	10 π mm mrad
Momentum spread	$< \pm 0.2\%$
Field size	22 cm (Max. diameter)
Dose uniformity	$\pm 2\%$
Maximum range	30 cm
Dose rate	5 Gy/min. (Max.)

*Extracted beam intensity per ring.

0-7803-3053-6/96/$5.00 ©1996 IEEE

In the second series of the clinical trials, heavy ion therapy was applied to cancers at the head or neck, the lungs and the central nerve system. Eighteen patients were treated in the second series extended to the end of February 1995. In the third series of the trials, much more patients will be treated with other types of cancers, for examples, the uterus, the liver, the prostate *etc.*

2. HIMAC FACILITY

The medical requirements for the output beam properties of HIMAC are summarized in table 1. The minimum output energy is required because of the treatment of superficial cancers. A cutaway view of the facility is shown in Fig. 2. As shown in the figure, the upper ring provides a vertical beam (600 MeV/u max.) to the treatment rooms A and B, and a horizontal beam with the same energy to the experimental room for biology. The extracted beam from the lower ring (800 MeV/u max.), on the other hand, goes horizontally to the treatment rooms B and C, and experimental room for physics and general purposes. Since a branch of the lower high energy beam transport (HEBT) line merges into the upper HEBT line, the output beam of the lower synchrotron can be provided vertically to the treatment rooms A and B. In order to get a high efficiency of the treatment room usage, it is required to switch the accelerated beam from one treatment room to the other room within 5 minuets. The reproducibility of the beam position should be better than ±2.5 mm at the isocenter. Such precise beam positioning is realized with a special sequence in the switching magnet excitation. An energy change of the synchrotron is also required once in a day to select the optimum residual range for different patients. After changing the beam energy, the dose uniformity in the irradiation field will be checked, whereas no such check is scheduled after the beam course switching.

There are two other experimental rooms for the medium energy (6 MeV/u) experiments and for the secondary beam experiments. A beam line for generating the radioactive beam will be installed in near future. Positron emitters, such as ^{11}C, will be effective in checking the irradiated area.

In the following subsections, brief descriptions are given for major components of HIMAC.

A. Ion Sources

We have two types of ion sources: a PIG and an ECR sources. A PIG source is a hot cathode type and operated in a very short pulse with a relatively long time interval. Such an operation mode increases appreciably an arc impedance resulting in a high arc voltage. The performance of the PIG source is excellent including the lifetime of the source[4].

An ECR source is a single stage type and energized with a 10 GHz microwave source of 2 kW max. The source is equipped with a sextupole permanent magnet of 9 kG at a pole tip.[5] The output beam intensities and emittance are satisfactory for the treatments. Since the ECR source is very stable and easy to operate, the ECR source is preferable in the daily operation for the clinical treatment.

Both sources are installed independently on high voltage decks of 60 kV max. and provide ions with 8 keV/u to the next acceleration stage.

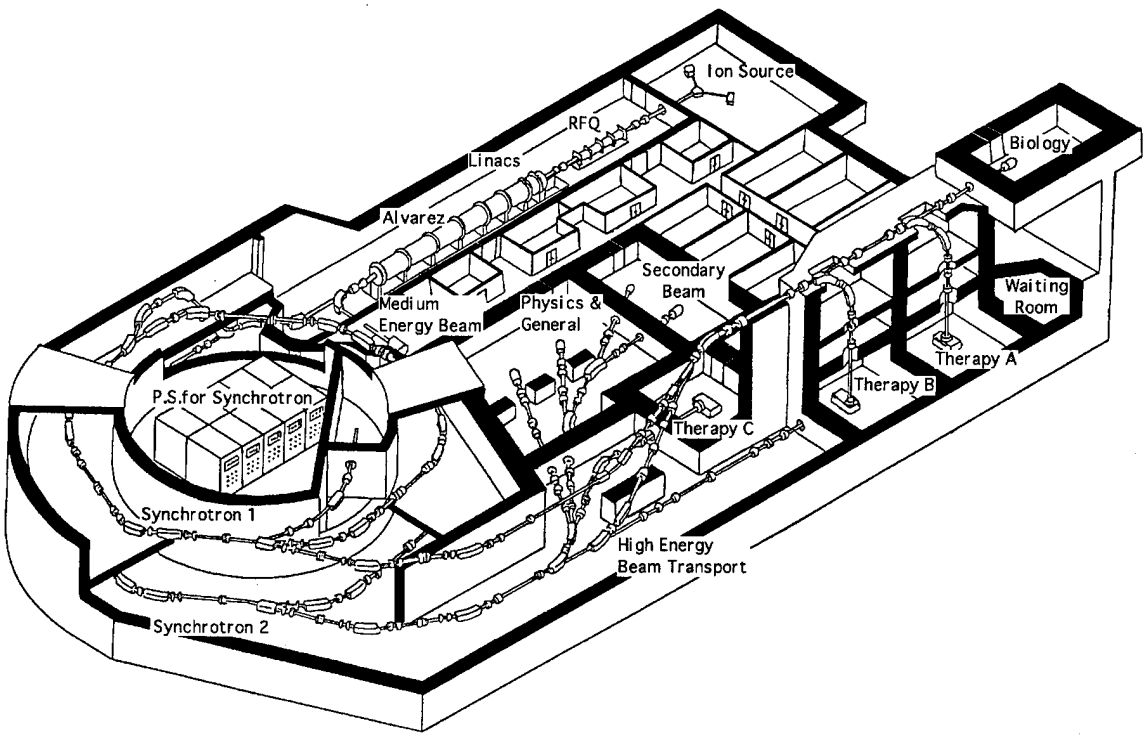


Fig. 2: A Bird's eye view of the HIMAC facility.

B. Linacs

The injector consists of a 100 MHz RFQ, an Alvarez linac, a debuncher to reduce the momentum spread of the output beam, and beam transport lines connecting them[6].

An RFQ linac accelerates heavy ions with $q/A \geq 1/7$ from 8 keV/u to 800 keV/u. The RFQ is a conventional four vane type and has a vane length of 7.2 m. Since the vane length is very long comparing with the tank diameter, a filed distribution must be carefully tuned along longitudinal direction. About 40 side tuners are introduced for this purpose and realize very small field error of 4.9% and 2.6% for longitudinal and transverse directions, respectively. An acceptance and anaccelerating rate are 0.6 π mm¥mrad (normalized) and 0.76 MV/m, respectively.

The RFQ is followed by an Alvarez type linac (DTL) operated with the same frequency of 100 MHz. Both linacs are operated with a very low duty factor of 0.3% at maximum. The transverse phase space matching between the RFQ and the DTL is accomplished with a quadrupole magnet quadruplet installed in a 1.9 m long beam transport line. The DTL tank is 24 m long and separated into three independent rf cavities. The diameter of the cavities is about 2 m and change from one cavity to the next in order to obtain reasonable values for transit time factors. Since a transverse emittance of the output beam from the RFQ is thoroughly small, a FODO type focusing sequence is adopted for Q-magnets in the drift tubes. The magnets have laminated cores and are excited with the same flat-top-duty of 0.3% max.

At the output end of the DTL, a 100 $\mu g/cm^2$ thick carbon stripping foil is inserted to improve a charge to mass ratio of the ions. Only one stripping stage is adopted at a relatively high ion energy of 6 MeV/u because of the reliability of the system and of advantages for future expansion to the acceleration of heavier ions.

C. Synchrotrons

The main accelerator of HIMAC consists of two independent synchrotron rings with the same circumference of 130 m. The two ring structure of the synchrotron makes it possible to provide a treatment room simultaneously with a horizontal and a vertical beams having different energies. As a future extension, two stage acceleration of the heavier ions is planned.

A pulse magnet located in a MEBT line between the linac and the synchrotron switches the output beam from the injector to the upper and lower synchrotron rings. The two synchrotron rings are operated independently from each other except that the magnets must be excited 180° out of phase. The synchrotron is a separated function type with a FODO type focusing structure. The ring consists of 12 unit cells, whereas the superperiodicity of the ring is 6. A bending angle and a radius of the sector type dipole magnet are 30° and 6.5 m, respectively. The dipole field changes from 0.11 T at injection energy to 1.5 T at maximum with a ramping rate of 2 T/s (max). The effective length of the dipole magnets are adjusted by shimming cores at both ends of the pole tips. Design value of the betatron tunes are 3.75 and 3.25 for horizontal and vertical directions, respectively. The actual values, however, are chosen typically at 3.68 and 3.13 in a daily operation.

A current pattern of the synchrotron magnets is controlled with digital processors and a repetition rate can be varied from 0.3 to 1.5 Hz. A typical operation pattern is 200 ms for a flat base, 700 ms for rise and falling time and 400 ms for a flat top. A multiturn injection scheme is adopted to increase the circulating beam current by a factor of 20 and a third order resonant extraction scheme is employed to realize a rather long beam duration of 400 ms.

The rf system is required to cover a wide frequency range from 1 to 8 MHz. The maximum acceleration voltage is estimated to be 10 kV for ions with a charge to mass ratio of 1/2. A fully digital control system (sampling rate of 500 kHz) is adopted for the feed back loop of the phase and the beam position. The rf frequency essentially varies with a B-clock pulse generated at every 0.2 G change in bending field. Feed back loops of a phase and a beam position are adopted to adjust the frequency. The whole control system works very well and even a very low intensity beam of a few hundred particles per second can be stably accelerated without $\Delta\phi$ and Δr feedback loops.

D. Irradiation apparatus

In order to realize a large and uniform irradiation field, a wobbler scanning method is adopted. As shown in Fig. 3, a pair of wobbling magnets is installed in the beam line to make a circular trajectory at the isocenter. A scatterer with a proper thickness is used to smooth out the transverse dose distribution. Other important elements of the irradiation apparatus are a ridge filter and a range shifter. The ridge filter has a profile like a saw-tooth and broaden the momentum

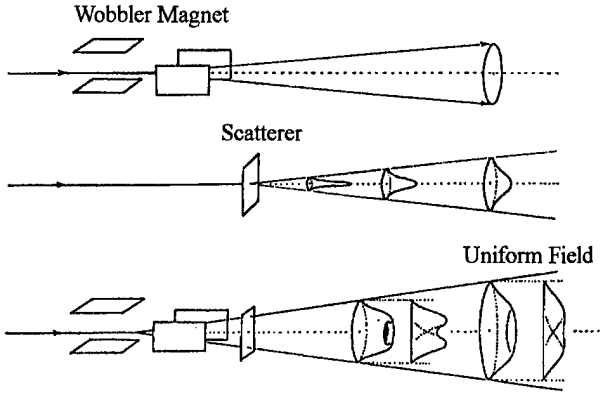


Fig. 3: A schematic explanation for field broadening with a pair of wobbling magnets.

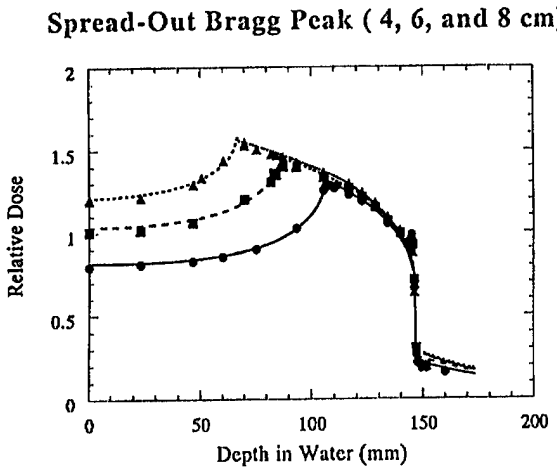


Fig. 4: Examples of physical dose distribution of the spreaded out Bragg peak.

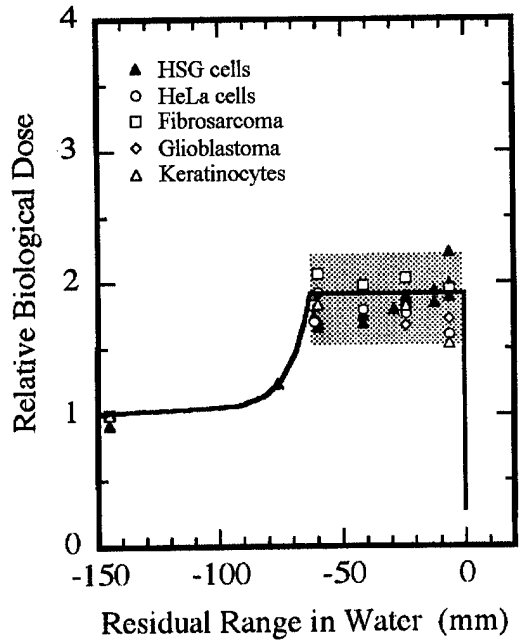


Fig. 5: An example of the biological dose distribution for a spreaded out Bragg peak.

spread of the ions through it. The ion beam with large momentum spread results in a spreaded out Bragg peak, which is necessary in a treatment of large size of tumors. Examples of the spreaded out dose distribution with the ridge filters are shown in Fig. 4. An example of the biological dose distribution for a spreaded out Bragg peak is also shown in Fig. 6 together with typical results of biological experiments. The range shifter, on the other hand, is made of plastic plate and changes the effective energy on a patient.

3. BEAM PERFORMANCE

The first beam from the injector has been obtained in late March 1993 with singly charged He ions. Beam tests have been begun for dual synchrotron rings in November 1993 with doubly charged He ions. The ions were accelerated to 230 MeV/u with a repetition rate of 1/2 Hz for each ring. Tests of the slow extraction from both rings were successfully completed in December and the extracted beams were transported to three treatment rooms within a few days. The length of the extracted beam spill was typically 300 ms. After careful tuning of the whole system including the measurements of biomedical effects of the carbon ions, clinical trials of the heavy ion cancer therapy started in late June 1994 with 290 MeV/u carbon beam.

In Fig. 6, an example of oscilloscope signals is given for a bending magnet excitation pattern (top), a pulse magnet for beam extraction (2nd), beam signal in the synchrotron ring (3rd) and the extracted beam signal (bottom). In the signal of the extracted beam, the very big intensity fluctuation can be observed. This fluctuation is due mainly to a current ripple of the synchrotron magnets, since no feedback system works to stabilize the extracted beam intensity. High frequency components of the beam ripple are suppressed appreciably after careful tuning of the synchrotron magnet power supplies. At the flat top, voltage ripples of the power supplies of Q_F and bending magnets are kept extremely low values of less than 1×10^{-6} and 1×10^{-5} , respectively (50 Hz). A beam ripple, however, remains at high level. The fluctuation of the bending filed may affects on the beam ripple through the sextupole magnets for chromaticity correction. By reducing the sextupole filed, satisfactory beam spill is obtained as shown in Fig. 7.

Stability and reproducibility of the whole accelerator system are excellent. Even in the early stage of the accelerator operation, it takes only 3 hours to get the accelerated beam in a treatment room. Most part of the tuning time are spent in tuning of the ion source and LEBT elements.

4. FUTURE DEVELOPMENTS

This facility is open for many researchers who are interested in the heavy ion science as well as heavy ion therapy. The accelerator is required to accelerate heavier ions with a variety of energies and with high quality. In order to meet these demands, third ion source of 18 GHz ECR source is now under developments. Ions from these three ion sources will be accelerated simultaneously with so called time sharing acceleration scheme and delivered to a medium energy experimental room, the upper synchrotron ring and the lower synchrotron ring.

A secondary beam will be available within a few years to investigate the possibility of precise check of the ion stopping position in a human body. The positron emitters, such as ^{11}C, are considered to be effective for this purpose. The beam course will be open for other scientific fields.

Further sophisticated irradiation schemes, such as a spot scanning method or a three dimensional irradiation method, are also important in improving the effectiveness of the heavy

ion therapy. An irradiation treatment synchronized with human breathing is our first target to reduce the unwanted irradiation to the normal cells around the tumor. The treatment will be realized with a quick response of the rf-knockout beam extraction from the synchrotron ring[7].

5. ACKNOWLEDGMENTS

The author express his sincere gratitude to Drs. Y. Hirao and K. Kawachi for their continuous encouragement and fruitful discussions. He is also grateful to Drs. H. Ogawa, K. Sato, F. Soga and other members of HIMAC accelerator group for valuable discussions and assistance.

6. REFERENCES

[1] Y. Hirao *et. al.*, NIRS-M-89, 1992.
[2] K. Sato *et. al.*, European Particle Accelerator Conference, 1994, to be published.
[3] J. R. Castro *et. al.*, Int. J. Rad. Oncol. Bio. & Phys., **29**, 647 (1994).
[4] Y. Sato *et. al.*, Rev. Sci. Instrum., **63 (4)**, 2904 (1992).
[5] A. Kitagawa *et. al.*, Rev. Sci. Instrum., **65 (4)**, 1087 (1994).
[6] S. Yamada *et. al.*, 1994 Linac Conference, Tsukuba, Japan, p768.
[7] K. Noda *et. al.*, European Particle Accelerator Conference, 1994, to be published.

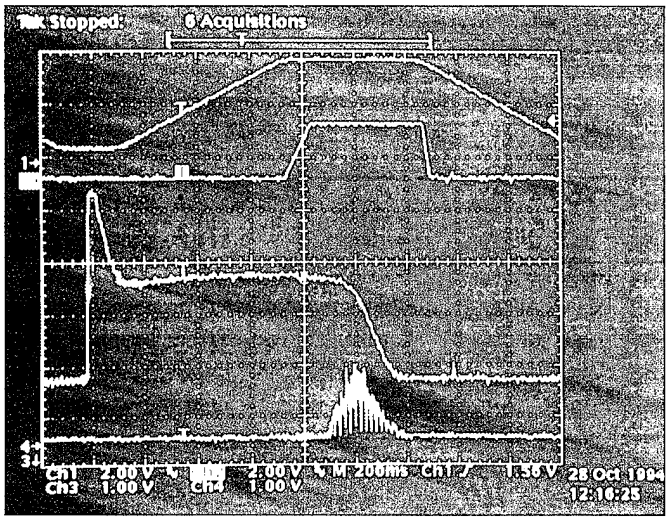


Fig. 6: A typical oscilloscope view of the synchrotron acceleration cycle: An excitation pattern of the synchrotron magnet (top), a bump field (2nd), a beam signal in the ring (3rd) and an extracted beam signal (bottom).

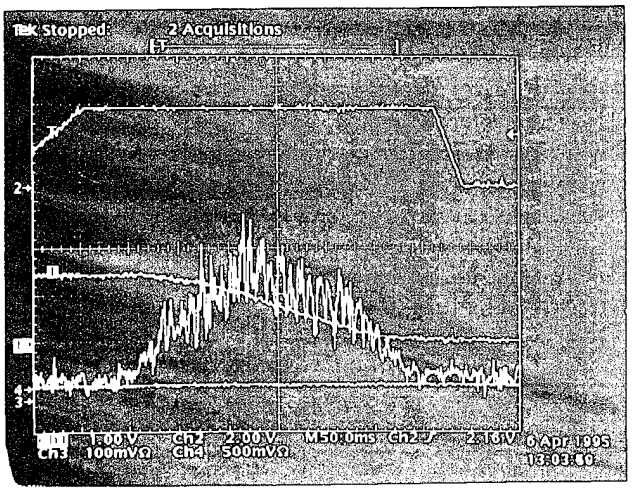


Fig. 7: An example of the beam spill from the synchrotron (bottom) together with a circulating current (middle) and a waveform of the bump magnet (top).

ACCELERATOR FIELD DEVELOPMENT AT NOVOSIBIRSK (HISTORY, STATUS, PROSPECTS)

A. Skrinsky
Budker Institute of Nuclear Physics, Novosibirsk, Russia

Abstract

In this talk an attempt is made to present INP contribution to the accelerator field in inventions, discoveries, theoretical and experimental studies of related phenomena, in design, construction and application of accelerator complexes. There are presented only events and aspects where the Institute was a pioneer or achieved the ultimate results to the moment of their publication.

Our team was arranged initially as the Laboratory of New Acceleration Methods, of the Institute of Atomic Energy (Moscow), under leadership of Prof. G. Budker. Then, at 1958 the Laboratory was transformed in to the Institute of Nuclear Physics and we moved to Novosibirsk. Through many years, till his passing away in 1977, Prof. G. Budker remained the director of our Institute, which is now named after him.

I. COLLIDING BEAMS

The INP high energy physics prospects and experiments are based, from the very beginning, on colliding beams, mainly. This activity started just upon D. Kerst's proton collider suggestion and G. O'Neil's proposal to use radiation damping for electron beams storing and compression. And the first years our efforts (since 1957) were focused on physics development, design and construction of electron-electron collider VEP-1.

Many laboratories throughout the world became active in the direction, and, upon the first beams storing at AdA (Frascati), two of them, Stanford-Princeton group and Novosibirsk group, were the first in reaching the real HEP experiments stage. These two groups carried out electron-electron scattering experiments in 1965-1967.

1.1. At VEP-1 collider, the maximum energy was 2×0.16 GeV, and maximum luminosity 3×10^{27} cm^{-2} sec^{-1}, and elastic scattering and double bremsstrahlung experiments were performed [1].

The main achievement of these Princeton-Stanford and Novosibirsk experiments was the proof of real possibility to perform colliding beams experiments for elementary particle physics.

1.2. The world first electron-positron experiments were performed at Novosibirsk collider VEPP-2 at 1967: the ρ-meson parameters were measured via electron-positron annihilation in to two pions [2]. Afterwards, many electron-positron colliders were and are in operation, starting, still in 1960s, of ACO (Orsay) and CEA (Cambridge), bringing a lot of very important results and discoveries.

The VEPP-2 collider was in operation for electron-positron experiments 1967 - 1970, providing energy up to 2×0.7 GeV and luminosity up to 2×10^{28} $cm^{-2}sec^{-1}$. The main results are related to ρ-, ω-, φ-mesons parameters and decay modes studies, discovery of multi-hadron production above main

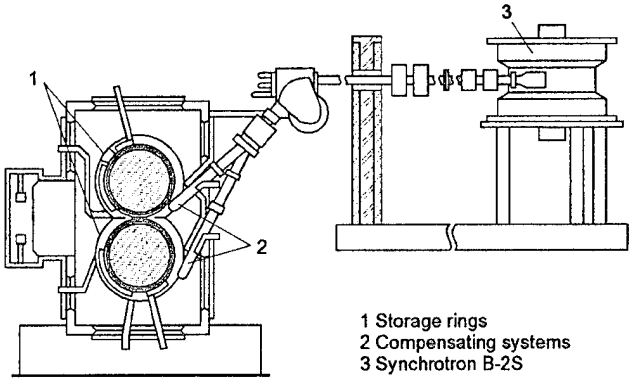


Figure 1. Layout of the VEP-1 Installation

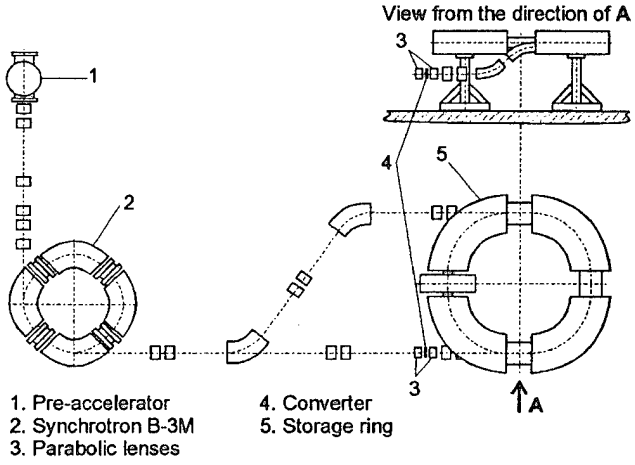


Figure 2. Layout of the VEPP-2 Installation

vector mesons region and first observation of two-photon e^+e^- pair production, which was the world start of two photon physics [3].

1.3. The next Novosibirsk e^+e^- collider VEPP-2M, which can be considered as the world first electron-positron "pre-Factory", started to operate for experiments at 1975 [4]. The energy range was just the same as of VEPP-2, but the luminosity reached was more than 100 times higher: up to 5×10^{30} $cm^{-2}sec^{-1}$. The initial VEPP-2 storage ring served for a long time as VEPP-2M booster. Up to now, through all these long years, VEPP-2M remains the main (practically the only) supplier of electron-positron physics results in its energy range [5], with several consequent steps in accelerator and detector upgrades, including construction of special more effective booster BEP.

It is worthwhile to pay special attention to the 8 Tesla superconducting wiggler magnet installed at (such a low energy storage ring!) VEPP-2M, [6] which is in use for about 15 years to increase the radial emittance and the radiation

0-7803-3053-6/96/$5.00 ©1996 IEEE

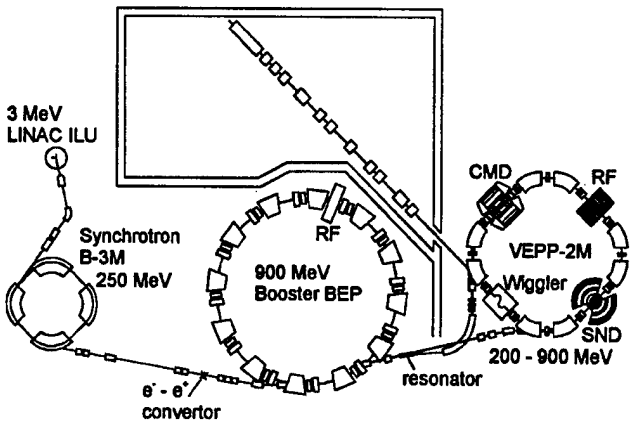


Figure 3: Layout of VEPP-2M Complex

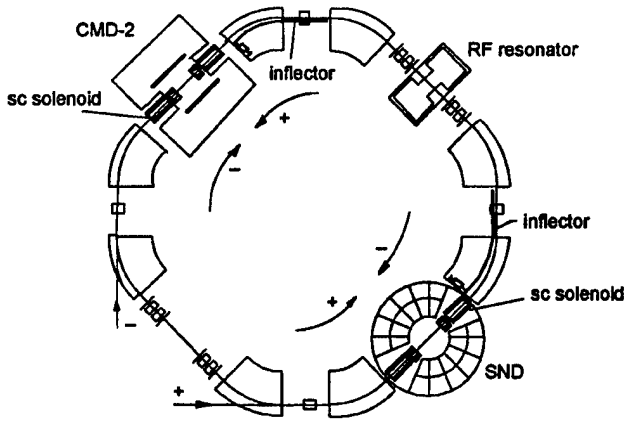


Figure 4: Layout of the VEPP-2M storage ring.

decrements for luminosity enhancement and for suppression of intra-beam scattering.

The best intensity results reached up to now are 0.8×10^{11} per bunch and 3×10^{11} per bunch for VEPP-2M and BEP, respectively.

The physics results obtained are rich. But it is worth to underline specifically the experiments, related to the achieving, study and use of polarized beams [7] (Ch. 5).

Currently, two new modern detectors, CMD-2 with superconducting magnet spectrometer and SND with advanced crystal, high granularity, three layers electromagnetic calorimeter, carry out new set of front-line experiments. The main aims for the experiments are the very high precision measurement of hadron production in e^+e^- experiments (to be able to derive interesting physics from new muon "g-2" experiment at BNL and to obtain α_s from Z-experiments at CERN) and study of rare, in many cases, still non-observed in processes light vector mesons sector.

1.4. Now in preparation is a new VEPP-2M upgrade (so-called "round beams" option) as the way to rise additionally its luminosity [8,9] and to prepare solid background for our Phi Factory.

The option implies several important issues:

a) Equal - small! - beta values at Interaction Region $\beta_x = \beta_z = \beta_0$;
b) Equal horizontal and vertical emittances, excited via quantum fluctuations independently up to the level, required for desired luminosity $\varepsilon_x = \varepsilon_z$;
c) Equal betatron tunes with "zero" coupling ("no" tunes splitting) $Q_x = Q_z$;
d) Small positive (for e^+e^-) non-integer tune fraction {Q};
e) Low (tunable) synchrotron frequency Q_s.

Items a), b), and c) lead to the conservation of angular momentum in transversal motion, thus converting this motion to "one-dimensional" one, with less beam-beam resonances, which can cause beam blow-up and/or degrade its lifetime. Items d) and e) proved in computer simulations to be useful in rising the maximal beam-beam tune shift ξ_{max}, which does not damage luminosity. We hope to raise this value, at least, up to 0.1, in comparing with 0.05 - the best achieved up to now for flat beams.

The additional useful effect arises due to the simple fact, that beam-beam tune shift for given counting bunch density is two times lower for round beams than for smaller dimension of flat beam.

Now we plan to implement the round beams option at the collider VEPP-2M. The main change will be the replacing of quadrupole focusing at two interaction regions, equipped with modern running detectors, to solenoidal focusing (9 Tesla), that will give at the same time equal transverse emittances.

This move will let us learn - just now - such non-traditional storage ring optics and study its tolerances, and reach real gain in ξ_{max} and in luminosity, rising it from current $5\times10^{30}cm^{-2}s^{-1}$ to $1\times10^{32}cm^{-2}s^{-1}$. This improvement will give also a possibility to operate detectors at already very high fluxes of useful events.

1.5. Since 1980 the higher energy e^+e^- collider VEPP-4 is in operation at Novosibirsk [10]. Its maximal energy is 5.5 GeV per beam, and highest luminosity till now was 5×10^{30} $cm^{-2}s^{-1}$. The main physics results [11,7] are related to the Y family complementary studies, best full hadron cross-section measurements in the energy range, two-photon physics, and especially high precision mass measurements (Ch. 5).

Now, upon complete restoration after heavy miss-happening and upon major upgrade, the collider came in operation. The main improvement is arranging of interaction region section as a double-arm high resolution, high efficiency spectrometer for electrons and positrons, which remain after reaction $e^+e^- \rightarrow e^+e^- + X$ (the so called two-photon processes).

It was proved experimentally, the X mass resolution reached in double-tagging is below 10 MeV for X masses 0.5-2.5 GeV/c^2 with efficiency around 30%. Such experiments would open, in particular, very important window in to the hadron spectroscopy in this mass region - complementary to the hadron beam and e^+e^- annihilation experiments. This approach would be of special importance for the separation of glueballs, four-quark states and "normal" two-quark states.

1.6. For number of years, the new generation of e^+e^- colliders (the super-high luminosity factories) are under development, in particular, at INP [12]. Now The VEPP-5 complex is under design and construction at Novosibirsk,

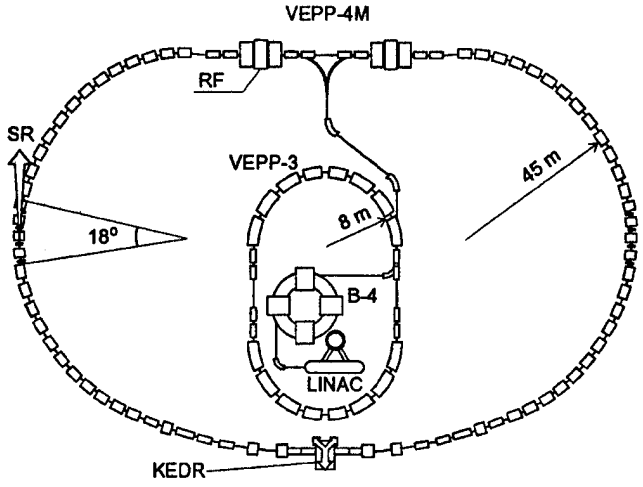


Figure 5: VEPP-4M

which include the new injector facility to produce up to 10^{10} positrons and electrons per second with excellent emittances, the Φ Factory and the Charm/Tau Factory (the injector facility will feed the VEPP-4 collider, also).

1.6.1. The Novosibirsk Phi Factory project [13,9] takes the full use of round beams approach and, additionally, combines both interaction regions at opposite azimuth in one, providing the very complicated and costly detector for CP violation studies with doubled luminosity. Each bending part of this storage device consists of two stores of dipole and quadrupole magnets; equal sign particles at the outer ends of solenoids are separated by magnetic field, while the opposite sign ones are separated electrostatically.

Such "Four-wing Butterfly" provides two options of operation. If number of equi-distant bunches of electrons and positrons is odd, the collisions occur alternatively (electron-positron, then positron-electron, etc.). Equal signs collision regions happens at a quarter of D_{bb} from IR, but the orbit separation is made magnetically, hence, much faster.

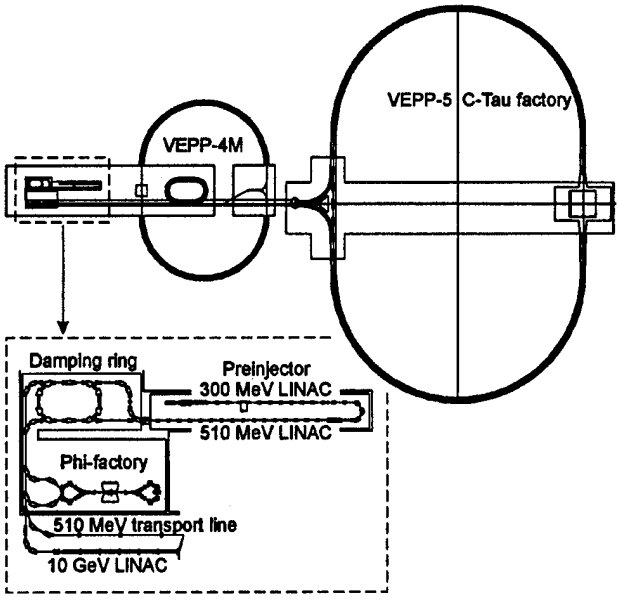


Figure 6: General Layout of the VEPP-5 complex

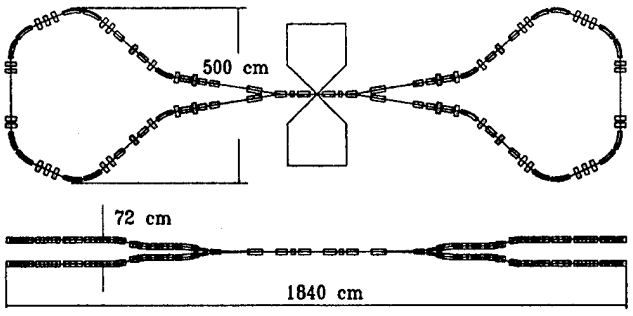


Figure 7: Layout of the Novosibirsk Phi Factory.

The usual luminosity estimation (at β_0=1 cm, bunch-bunch distance D_{bb}=400 cm) gives for this case 5×10^{33} $cm^{-2}s^{-1}$. If number of bunches is made even, the collisions occur with uni-directional electron and positron bunches overlapping before each collision, thus providing compensation of coherent electric and magnetic fields. The beta-values at the collision point remain as small as in a previous mode, thus it opens possibility, with acceptable tolerances, to diminish emittances and/or to rise bunches intensity, thus reaching several times higher luminosity. (The e^+e^- luminosity is accompanied in this case by equal parasitic e^-e^- plus e^+e^+ luminosity.)

1.6.2. The Charm/Tau Factory [14], which is a regular double ("two-stores") race-track storage ring with one Interaction Region, will be equipped with two, 2 meter long, 10 Tesla solenoids. At acceptably high beams emittances (a^2/β) about 1.5×10^{-5} cm (rms), excited in special wiggler sections installed at technical (opposite to IR) straight sections, the option gives at 2 GeV per beam luminosity 1×10^{34} $cm^{-2}s^{-1}$.

For this project, two additional options are in preparation, with enhanced monochromaticity and with longitudinal polarization.

Usual electron-positron colliders provide already very good effective "mass-of-event" resolution: $\sqrt{2}\sigma_E \approx 5\times10^{-4}$. But there are resonances in annihilation channel, like Ψ and Υ quarkonia, with much smaller energy widths, and it is of very interest to enhance substantially collider monochromaticity. This idea appeared at Novosibirsk immediately upon J/Ψ particle discovery, and different options were studied.

The general idea is quite simple and straightforward. At the interaction region with very small (vertical) betatron size, energy dispersion is introduced, of opposite sign for electrons and positrons. Effective mass-of-event spread will be smaller than beam energy spread in proportion to the ratio of betatron size to "energy" size.

For our Charm/Tau factory, based on usual two-stores double ring with single IR, a flexible monochromatization option is foreseen. To excite energy dispersion at IR while keeping it zero at ring parts, in the long straight section on both sides of IR, independently for e^- and e^+, weak radial magnetic field is introduced, which changes its sign "in resonance" with vertical betatron oscillations. For additional vertical emittances suppression and for raising the beam energy spread, special wigglers are introduced in opposite to IR straight sections.

There is a hope to get $L = 1\times10^{33}$ $cm^{-2}s^{-1}$ for $\sigma_{Mass} = 40$ keV and $L = 5\times10^{31}$ $cm^{-2}s^{-1}$ for $\sigma_{Mass} = 5$ keV. Of course, all the problems with field stability etc. are assumed been solved. The final tracing of current energy is worth to arrange by the continuous bunch-by-bunch resonant depolarization.

This monochromatic option of Charm/Tau Factory provides quite inspiring physics potential:

to produce narrow Ψ resonances with much lower non-resonant admixture – for the study of rare and difficult-to-separate decays;

to complete charm-quarkonia spectroscopy;

to measure directly with high precision the full width of charm quarkonia states;

to produce, for example, 400 clean η_c per second - via $e^+ e^- \rightarrow \Psi \rightarrow \gamma \eta_c$;

to study τ-lepton pair production near threshold, 0.5 pairs/sec at threshold, 3000 $\tau\tau$ atom/day – possibly sensitive to the New Physics;

to measure τ mass with ultimate accuracy;

to set τ-neutrino mass limit lower than 1 MeV;

to study charmed baryons threshold behavior;

to ease substantially the study of possible DDbar mixing and CP violation (with adding a detector of a micron coordinate resolution);

to measure masses with ultimate accuracy, using resonant depolarization; etc

II. LINEAR COLLIDER DEVELOPMENT

Since 1960's we did understand that the only way to hundreds of GeV electron-positron collider is to switch to linear single-pass colliders. And at International Seminar on High Energy Physics Prospects (Morges, 1971) these considerations were presented [15]. We considered there two options: the use of superconducting linacs with energy recuperation, and the normal conducting pulsed linacs approach. As more promising we scored the superconducting option.

But we were able to present the self-consistent physics project of VLEPP linear collider at 1978 only, based on normal conducting pulsed linacs, when many important - basic - issues of the approach were specified and principal solutions found [16,17]. Among the major issues were:

single bunch high efficiency energy extraction;

transversal single bunch instability and its curing by along-the-bunch energy gradient (BNS damping);

achievability of 100 MeV/m acceleration gradients;

the beamstrahlung as basic. and flat beams to cure;

beam-beam single pass instability limit;

the possibility to produce short intense bunches of very low emittances - good enough for subsub-micron vertical size at final focus.

We did start the wide range R&D for this project, approved by the state authorities in principle. This project is stopped now because of dramatic changes in the country. But many important additional steps were made and are in progress now in linear collider physics, techniques and technologies, to be ready for the moment of Decision on World Linear Collider (when/if this happens).

Especially important steps made are:

development of 15 GHz grided klystrons with 1 MV DC power supply and permanent magnets focusing structure - power of 50 MW at 90 dB amplification achieved at the prototypes;

design and proof of effective peak power multiplication;

design and prototyping of nanometer range beam position monitors and movers;

the idea and algorithm development for adaptive linac positioning;

effective cure of beam emittance stochastic blow-up by proper along-the-bunch energy distribution.

The concept of photon-photon and photon-electron option of linear collider was proposed and is now under development with INP active participation [18].

Very slowly, but construction of 20 meter long test section is progressing at the Branch of our Institute at Protvino. If successful, VLEPP components will be used for post acceleration of electron and positron beams for VEPP-4 and Charm/Tau Factory injection.

We also participate actively, from the very beginning, in Final Focus international experiments at SLAC.

III. ELECTRON COOLING

The synchrotron radiation cooling was crucial for the success of electron-electron and electron-positron colliders. It does not exist practically for heavier particles at modest energies. The first cooling method, applicable to protons, was proposed at INP by G. Budker at 1965 [19]. It was the electron cooling, when at some straight section of proton storage ring intense a "cold" electron beam of the same mean velocity accompanies the proton beam. In the common rest frame it looks as plasma relaxation with hot protons and cold electrons, with relaxation time short enough for applications. The initial aim of the proposal was storing of high proton currents for proton-proton collider. But immediately upon the invention, again at INP, it was proposed to use electron cooling for storing of antiprotons to arrange proton-antiproton collisions of high luminosity. The dedicated proton-antiproton complex for 46 GeV (total) was designed and, partly, constructed [20]. But upon construction of the FNAL Main Ring, which could carry out antiproton experiments of comparable energy as stationary target ones, we gave up this intention and converted project in to electron-positron collider VEPP-4.

The idea of electron cooling was met by the world community with interest, but for the next 9 years nobody tried to develop and to apply the idea. During these years the physics of electron cooling was studied at INP theoretically [21], a dedicated proton storage ring NAP-M (Russian abbreviation for "Storage ring for AntiProtons - a Model") was designed and built, and a special device to produce electron beam of perfect parameters was developed, constructed and installed at NAP-M.

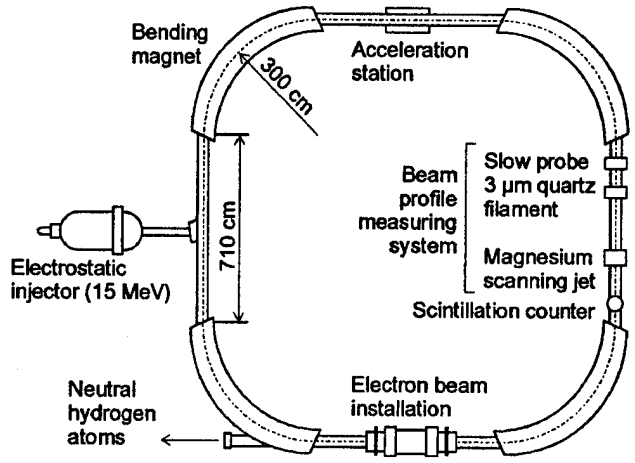


Figure 8. Layout of the proton cooler ring NAP–M

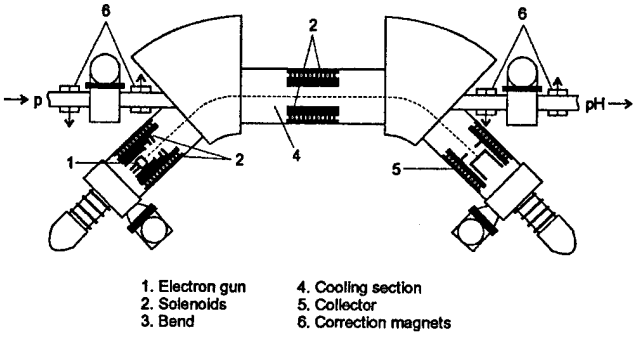


Figure 9. Layout of the electron-beam device for electron cooling.

The world situation changed dramatically at 1974, after first successful experimental demonstration of the electron cooling [22].

In the next years the intense experimental and theoretical studies of the electron cooling were undertaken at INP [23,24]. The main results of these efforts are:

the discovery, explanation and theory of super-fast and ultra-deep cooling - because of very low longitudinal electron temperature and "magnetization" of electron transversal velocities; as a result, 100 times faster cooling, then our initial hopes;

record results, reached at NAP-M (1979): cooling time – 3 milliseconds, longitudinal proton temperature - 1 Kelvin, transversal proton temperature - 50 Kelvin;

longitudinal ordering ("crystallization") of deeply cooled proton beam, and consequent suppression of intra-beam scattering.

Additionally, the special installation to study single-pass ("linear") electron cooling was built. The main results of these studies were [25]:

effective decrement reached was close to the theoretical limit $\Omega_{eplasma} * m_e/M_p$ - few meters of cooling length for 1 MeV protons;

very substantial difference was discovered and explained for low temperature decrements of H^+ and H^- (for H^- and antiprotons everything is much better) - because of non-perturbative effects.

In parallel, intense search for areas of useful application of electron cooling was in progress at INP, and the great potential of coolers for elementary particle and nuclear physics was discovered and presented [26,24].

Now the electron cooling is in use at many laboratories throughout the world for antiproton and ion experiments, in some cases, with our active participation.

IV. IONIZATION COOLING AND MUON COLLIDERS

The ionization cooling was for a long time under consideration in different laboratories. We at INP got interested in this method since the end of 1960s, having in mind muon-muon colliders [27]. For us it was clear, that the muons are the only particles, for which ionization cooling might be of crucial importance: for them, there are no nuclear interactions and no bremsstrahlung at the parameters of interest.

We presented the ionization cooling as the way to reach high luminosity at hundreds of GeV muon-muon collider at 1971, at the same Morges Seminar [15]. The scheme presented did include the steps:

to obtain a very large number of protons with tens of GeV energy in rather short bunches;

to produce with maximum efficiency muons with 1 GeV energy, using nuclear cascade for pion production, strong focusing at conversion target and at pion decay channel;

to cool muons in special hundred kilogauss pulsed storage ring, using ionization energy losses. If the targets are at azimuths with very small beta-functions, the final emittance of muon beam shell be small enough to be injected into the main muon accelerator with small aperture and to be well compressed in interaction points;

to accelerate muons rapidly in some accelerator; if the muon energy is increasing several times of $m_\mu c^2$ during their rest frame time τ_0, most of the muons will be accelerated up to final energy. It is possible to use a linear accelerator, or to use a fast pulsed synchrotron;

to arrange collisions at storage ring (or cyclic accelerator) with 100 kGs guide field (In the case of pulsed ring, the collider can serve at the same time as main accelerator.) In such ring it is possible to have several thousand of useful turns before muon decay.

Then we considered the most important aspects and details of ionization cooling in 1980 and 1981 [24]. But only quite recently muon colliders and ionization cooling attracted the interest of several groups. The next step should be the development of practical test facility and experimental proof of possibility to reach really high efficiency of transforming of protons in muon beam of low emittance (corresponding to the ionization cooling limits); the facility should include an advanced proton-to-pions conversion system.

The immediate goal for this efforts could be to supply high intensity, low emittance muon beam for ultra-high precision muon g-2 experiment at BNL.

V. POLARIZED BEAMS IN COLLIDERS AND ACCELERATORS

Polarized beams became one of the focuses in INP activity since mid-1960s, initially in theoretical considerations and inventions, and in a few years, in experiments and applications.

5.1. Just upon theoretical discovery of synchrotron radiation polarization mechanism for electrons (positrons) in homogenous magnetic field [28], intense studies of the process in "practical" accelerator fields started at INP. It was proved, the process does exist in this case [29], but does appear a specific mechanism of depolarization due to "machine" spin resonances, under influence of energy jumps caused by quantum fluctuation of radiation in presence of vertical orbit perturbation [30]. Then the practical method of calculation of polarization time and equilibrium polarization degree in arbitrary complex fields was developed [31], based on the discovery of existence of closed spin orbit $\vec{n}(\theta)$ for any closed "coordinate" orbit [32], followed by design of corresponding perturbation theory [33]. It was shown, that depolarization rate is higher if the dependence of $\vec{n}$ on energy for the storage ring under consideration is higher. Afterwards, a very effective method of depolarization suppression was proposed and designed (section 5.7).

A special attention was paid to the very high energy storage rings, because of suspicions in HEP community appeared on complete deterioration of polarization if the beam energy spread becomes (much) larger then energy separation (440 MeV for electrons) of main machine depolarizing resonances, what happens around 30 GeV. It was shown [34], that by proper correction of spin-resonansing harmonics of the storage ring radial magnetic field it is possible to reach good polarization degree even (then future) LEP ring. Especially effective approach could be the following: to install at few azimuths of (long) storage ring with "very" low magnetic field the high field asymmetric wigglers and local spin-chromaticity correctors.

Electron beam radiatively polarized for the first time was reached at our storage ring VEPP-2 and at ACO at 1970 [35]. In this experiment external RF resonant depolarization was used for the first time, afterwards proved to be such an efficient tool in applications (section 5.3). The process of radiative polarization, the depolarizing factors and their curing were studied in details at other INP storage rings [36].

5.2. An important part in all the polarization dealings is development of polarization degree and (local) polarization direction measurement methods at storage rings without beam loss, especially for electrons and positrons. Most of them were proposed at INP, but are in use everywhere:

spin-dependence of energy exchange due to intra-beam scattering [37];

effective for low energies - up to 2-3 GeV - used at VEPP-2, ACO, VEPP-3, SPEAR, BESSY;

up-down asymmetry in backward scattering of circularly polarized laser photons [37] effective for higher energy range 2 to 100 GeV - used at SPEAR, DORIS, CESR, VEPP-4, PETRA, PEP, TRISTAN, LEP;

same asymmetry in helical undulator photons scattering - used at VEPP-2M [38];

same asymmetry in synchrotron radiation photons scattering (upper vs. lower parts) [39]; specifically effective for simultaneous measurements for both colliding beams - used at VEPP-4;

spin-dependent fraction of synchrotron radiation [40]; effective for high energies and high (local) magnetic field - successfully tested at VEPP-4 [40];

may be of specific interest for continuous (or instant) measurements at very high energy storage rings with the use of specific e^+e^- pair detector [41].

5.3. Implementation of RF induced resonant beam depolarization, started at VEPP-2 experiments, 1970, was an important step in the field. It gave possibility to depolarize electrons and positrons without any changes in their orbital motion (for example, without machine resonance crossing by energy change), what is helping a lot, at all labs, in beam polarization studies.

But the most productive application is the very high precision measurement (up to 1×10^{-6}) of mean beam energy at colliders [4] by scanning measurement of spin precession frequency of electrons and positrons. This method gave us possibility to measure at VEPP-2M and at VEPP-4 the masses of $K^{+/-}$, K^0, ω, Ψ, Ψ', Y, Y', Y'' [7]. The accuracy of Y meson reached at 1985 was 1×10^{-5}, and still remains the world best in the area.

The method was successfully applied at CESR, DORIS and LEP colliders.

Upon solving difficult and tricky technical problems (field stability, higher statistics, etc.), it would be possible to enhance additionally (up to 2 orders) the accuracy of mass measurements.

The same approach was used for precise comparison of e^+ and e^- magnetic moments. But even better results were obtained with the use of RF simultaneously induced spin resonance without depolarization. If to switch off the amplitude of spin-precession exciter just at the moment of resonance crossing, the spins of both beams particles will precess in horizontal plane coherently for many cycles. If to restore the RF amplitude at the resonant frequency and scan frequency back, the final direction and degree of polarization depend on relative phase of electrons and positrons precession. This approach gave possibility to prove equality of electron and positron magnetic moments at VEPP-2M collider with the accuracy 1×10^{-11} [42].

5.4. RF depolarizers and flippers. Physical measurements of spin dependent phenomena demand very often a fast polarization reverse or full depolarization of the beams while orbital beam parameters are not changed. To achieve these goals, special RF devices were suggested and developed (1970,1980). To reverse the polarization of the stored beam, the frequency of an RF electromagnetic field is swept adiabatically across a resonance with the spin precession frequency. An amplitude of the RF field and its configuration

requirements depend on a direction of polarization, the beam energy and conditions of experiments.

For electrons, in the simplest case of the transverse polarization a RF solenoid provides the adiabatic rotation of the polarization in the energy region up to few GeV. On higher energy the use of electromagnetic field which is transverse to the beam trajectory is more effective, because in this case the spin rotation angle is proportional to spin tune

$$\nu_s = \gamma \cdot \frac{\mu_{an}}{\mu_0} >> 1.$$

Under such consideration the RF-power about 1-3 kW is enough for the robust polarization reverse at any existing storage ring.

The same RF-devices on a low power can give the fast beam depolarization due to a natural or external noise when the frequency of the excited field coincides with the spin precession frequency [33].

With a proper choice of the depolarizer's parameters a synchronous detecting of the beam depolarization indicates the spin tune with an accuracy of the spin tune spread

$$\delta\nu_s \approx 10^{-5} \div 10^{-6} \quad .$$

5.5. Since longitudinal beam polarization is more interesting for physical experiments, special spin rotators are used to bring polarization along particle momentum in the Interaction Point. A number of the spin rotators with different field combinations were proposed in the middle of the 70's. A real design of the rotator must be safe for the beam and minimized for beam polarization losses. These requirements have demanded a creation of new calculating methods for the spin and particle motion in the nontraditional complicate field configuration.

A special attention was paid to the rotator which rotates the spin by 180 degree on passage around any axis [43]. Such rotator creates the stable longitudinal polarization at the opposite point of the orbit and excludes in principle the depolarizing spin resonances because in this case the spin tune is always equal to 1/2.

A combination of two Siberian snakes (located at contra sides of the machine and with the rotation axises which are perpendicular to each other) provides also spin tune equal to 1/2 and the polarization along the guiding field in the arcs. This configuration is very stable against the radiative depolarizing effects for electrons, and opens the way for the polarized proton acceleration up to the high energy. A few pairs of the snakes make the TeV polarized protons available. Now programs with the high energy polarized protons are under development at BNL (RHIC) and DESY (HERA). A compact design of the snakes and spin rotators based on a helical superconducting magnets was suggested at INP [1994; 44].

5.6. A step in polarization related development at storage rings, which we consider as very important and even crucial, was made in 1969, when the way to reach longitudinally polarized colliding beams was discovered and proved theoretically [32]. Opposite to the common sense of that time that only transversal to the orbit plane spin direction can repeat at every turn continuously, it was shown that for any closed orbit $\vec{r}(\theta)$ the corresponding closed spin "orbit" $\vec{n}(\theta)$ does exist, which is as stable out of spin resonances as in the usual purely transversal case. Hence, by adding of some combination of longitudinal and transversal magnetic fields along the storage ring orbit (so called spin rotators of different kind) it is possible to arrange any stable spin direction at a given azimuth. In particular, longitudinal polarization in interaction region of a collider can obtained, and for both beams in a time.

The simplest spin rotators use some distribution of radial magnetic fields, which bend the beam orbit in vertical direction. In this case, if at the electron-positron interaction region the vertical inclination of the orbit is

$$\frac{\pi}{2} \cdot \frac{1}{\gamma} \cdot \frac{\mu_0}{\mu_{an}} = \frac{\pi}{2} \cdot \frac{440}{E_{MeV}},$$

colliding beams are longitudinally polarized.

Of course, the practical spin rotation layout is strongly dependent on the beam energy and specificity of the storage ring [45,14].

Quite recently, very good degree of longitudinal polarization was achieved at HERA electron ring.

5.7. Just upon the first presentation of INP linear collider approach it was understood, that the use of helical undulator radiation of spared electrons and positrons, is possible to reach polarized e^+e^- collisions [46,17]. The longitudinally polarized photons of several MeV hit the targets, the upper half of $e^+(e^-)$ is collected and at the end of 1 GeV pre-accelerator we get longitudinally polarized $e^+(e^-)$ with high degree of polarization and reasonable monochromaticity. After passing spin rotators vertically polarized $e^+(e^-)$ are injected in to cooler rings. Upon reaching final normalized emittance and passing proper spin rotators, the particles enter their main linacs and collide at the detector with arbitrary chosen helicities.

5.8. The possibility to arrange (at a given azimuth of a storage ring) stable longitudinal polarization, opens the way to polarize, say, stored antiprotons, using difference in cross-section for different helicities - the so called spin filtering [26,47]. To achieve the aim, it is worth to use gas (gas-jet) proton target, polarized in the direction of antiproton velocity.

The best layout is to use super-thin target regime (Ch. 7) with electron cooling.

Quite recently, this approach was successfully tested for protons at GSI (Darmstadt).

VI. EXTREME ACCELERATION GRADIENTS

In the process of our search of the ways for linear colliders, it was understood and proved experimentally, that acceleration gradients at the level of 100 MeV/m can be achieved at properly designed normal conducting accelerating structures in short pulse mode (Ch. 2).

One of the ways to power such linacs is to use stored energy of extremely high energy proton beams - the so called "proton klystron" approach [48,17].

To achieve much higher accelerating gradientsÑup to 1 GeV/m - it is almost inevitable to use plasma based devices. For decades, this direction was studied theoretically and experimentally in many labs, and several approaches were studied. Among them: smokotron, laser beam excitation, two laser beams beat-wave acceleration, plasma wake field acceleration (PWFA).

The last one - PWFA - up to now was based, in considerations and experiments, on driver electron beams of modest energy - the most natural transition from electron beams of klystrons, which excite usual linacs. But, in our understanding, it is not the way to extreme gradients: we need to use as high energy - "rigid" - beams as economically possible, with high linear density and low emittance. This is the way to overcome plasma and beam-plasma (local) instabilities and toreplace efficiently the accuracy of solid surfaces, which shape fields in usual linacs [49,50]. And a very important component of the whole approach is to arrange a proper focusing channel to keep the beams "very carefully" aligned.

One of the key elements of the approach is to find the way to introduce proper micro-bunching in to the driver beam - at about 1 mm wave length.

The way proposed to solve this problem is to use very low emittance beams and transversal cutting. The general layout looks as following. At some part of the beam channel with high beta value, say, in vertical direction, we arrange local RF structure acting on the traveling bunch with the vertical force linearly depending on the position along the bunch (zero action at the bunch center). The resulting transversal vertical momentum should much higher than due-to-emittance internal moments in the bunch. Upon passing long enough free space, the different head-to-tail constituents of each bunch will be positioned differently in vertical direction. At this stage a target-cutter is placed, the holes of which are absolutely transparent but the other parts of the target destroy beam components completely. At the same place a vertically focusing lens is placed (focal length is 2 times smaller than RF section to target distance). At the same distance after the target the same RF structure is located, which compensates the vertical moments of bunch components. Hence, at the exit of this section, each driver bunch will be transformed in a seris of microbunches - properly shaped and properly positioned.

Additionally, the way to arrange sequential acceleration, using spiral delay-lines, to reach proportionally higher energy than of driver beam was proposed.

Modest scale experiments to test the approach and to understand related problems more clearly, we hope to start 1997, using the very appropriate BEP booster beam of VEPP-2M complex.

In case of success in the approach development, it would be worth to consider LHC beam (and the beam of the Next Super Collider) to drive such 1 GeV/m plasma linac to get direct proton, antiproton, muon, pion and kaon beams of multiplied energy.

It is worth to study also application of the approach for e^+e^- ($e\gamma$, $\gamma\gamma$) linear collider of ultimate energy, if the ultra-low emittance intense beams plasma acceleration happens to be reachable in principle.

VII. SUPER-THIN INTERNAL TARGETS

Interesting prospects for high luminosity, high sensitivity experiments were found [51], if to use the "super-thin" internal target regime at storage rings, when the stored beam parameters degradation due to multiple interactions with components of the target are suppressed by strong cooling (radiative, electron,...), but the only source of beam losses are single interaction with the target. The regime was tested at VEP-1, and then applied for electron-nuclear interactions at VEPP-2 and VEPP-3, especially for studies of interactions with polarized deuterons. Now the special polarized electron storage ring NEP is prepared as part of VEPP-2 complex at INP, and we do participate actively in the project to arrange polarized electrons experiments in this regime at AmPS (NIKHEF, Amsterdam).

Wide variety of super-thin target experiments with antiprotons and ions under electron cooling were proposed [26,24], most of them are now carried out or in preparation at different labs.

VIII. BEAM DYNAMICS

(SELECTED TOPICS)

Of course, beam physics studies (experiments and theory) through all this years was a core subject in our efforts in high energy accelerators area. Some aspects were mentioned in sections above. Let us just mention several other crucial topics.

8.1. The non-linear dynamics is of very importance for storage rings in general (because of very long life-time needed) and especially for colliders with very strong non-linear high harmonics in beam-beam interaction.

Specifically, of bright impression were the experiments in which transition from "dynamic" to "stochastic" behavior of particle motion in storage ring under multiple resonances influence were studied, and conditions and ways to avoid such transition were tested and proved [52].

8.2. Incoherent beam-beam effects are under continuos study from 1963 - the first collisions at VEP-1 [1,53]. The studies of $\{Q_x, Q_z, Q_s\}$ "maps" gave us not only to operate successfully our first colliders, but together with the development of low-beta insertions and general structures led to the pre-Factory VEPP-2M. Now this understanding is the background for real Factory projects.

It was discovered that in low-beta interaction conditions or at finite angle crossing, longitudinal beam-beam effects can become not only visible, but crucial [54].

Coherent beam-beam effects were under theoretical study and the ways to prevent the consequent luminosity limitation were found [55].

8.3. The single beam coherent instabilities and their curing were at INP always under attention as one of the key issues in reaching high intensities and luminosities.

One of the first effect analyzed was resistive wall phenomenon for single "rigid" bunch, for the first time obtaining stability condition [56].

The unexpected effect was discovered in interaction of bunches with perfectly terminated lines, coupled to the transverse motion of bunches electromagnetically [57]: coherent oscillations become not unstable, but damp very fast _ the higher intensity the faster! This effect is in use in most of our storage rings.

The important effect analyzed and cured was (single) the phase instability of a bunch under interaction with RF cavity (or some parasitic resonant cavity) [58]. Its increment is proportional to

$$R(\Omega_0-\omega_s)-R(\Omega_0+\omega_s)\ ,$$

where $R(\omega)$ is real part of the longitudinal impedance at frequency ω; Ω_0 is the revolution frequency or its harmonics; ω_s is synchrotron oscillations frequency. Correspondingly, to reach phase stability, the resonant frequencies of all the cavities should be shifted down from the revolution one.

Transverse betatron instability driven by beam interaction with compensating particles (electrons, positive and negative ions) was discovered and investigated for high intensity proton beam (two beam instability) [59]. This instability was damped by negative feed back. Now these instabilities are limiting intensity in many proton storage rings.

The very latest event was the development of advanced theory of transverse head-tail instability with strong mode coupling [60], and design of special kind feedback system, which should rise the instability threshold in this difficult regime. The test experiments are currently under way at LEP collider.

IX. FREE ELECTRON LASERS

Synchrotron radiation sources for more than 20 years were in development and use at INP, including many novel and advanced storage ring conceptions and insertion devices, like superconducting wigglers (1978), permanent magnet undulators, fast switching electromagnetic undulators, etc.. Some of them are in operation at many dedicated SRS throughout the world. But this subject deserves much more attention than is possible to pay to it here [61].

Some very brief words will be said about free electron laser developments, only. We are active in the field since the first demonstration of free electron lasing at Stanford, 1977.

9.1. The first INP contribution was the invention of special FEL version: the Optical Klystron [1978; 62], especially well suited for storage ring FEL operation. Successful operation of OK at VEPP-3 storage ring [63]. At this OK the lasing at 0.24 micron was achieved - the shortest among all the FELs up to now. Important achievement was also the very narrow band-width - up to 2×10^{-6}.

Now we collaborate actively in the development and construction of dedicated storage ring at Duke University.

9.2. But the main goal in the field for INP now - the construction at Novosibirsk of high power laser for infrared to visible - up to 100 kW CW operation, based on dedicated microtron-recuperator [64]. Many novel concepts are incorporated in the project.

Energy recuperation not only improves 10-20 times wall-plug power efficiency, but converts 50 MW, 50 MeV very radiation difficult and costly installation to reasonably modest one.

One of the most problematic component of any high power laser, the mirror system, is replaced by so-called electron radiation output. The single-pass radiation process is divided in two stages:

- the optical klystron structure and resonant cavity: to introduce proper laser wave length micro-bunching in each electron bunch;
- out of the optical resonator the properly matched long undulator is installed, to radiate coherently about 1% of electron beam energy, with all the optical operations placed far away, where the light beam size is enlarged enough already.

The immediate application of this laser will be high scale photochemistry studies and technology developments. Among the more distant applications the most inspiring is to develop ground-based high efficiencyand high scale power supply for future satellites, including geo-stationary ones.

XII. HIGH POWER TECHNOLOGICAL ELECTRON ACCELERATORS

The development, design, construction and supply of high power, MeV energy range electron accelerators for technological applications [65] for decades is for INP a subject for care and an important source of additional investment in our basic research in high energy physics, fusion studies, etc.

To date, compact accelerators of two types - DC rectifier based and pulsed RF single-cavity based ones - are in serial production and more than 90 of them do operate successfully in technological lines of many countries, including more than 10 countries of "far abroad" (Japan, Germany, Poland, China,

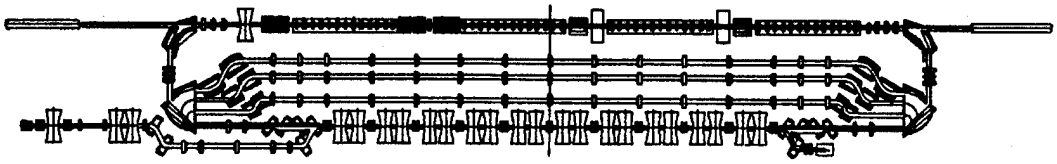


Figure 10. Layout of the Novosibirsk high-power FEL project.

Korea, etc.). Its mean power ranges from 20 kW to 100 kW, and energy, from 0.7 MeV to 3 MeV. The wall-plug efficiency for 100 kW DC accelerator exceeds 85%.

Now we are ready to supply DC accelerators up to 0.5 MW mean power, and RF ones, up to 4 MeV, 30 kW.

XIII. CONCLUSION.

Unfortunately, this brief history of the accelerator field development at Novosibirsk INP is very incomplete, albeit too lengthy already. Even such important, well known and widely used INP concepts and devices, as charge exchange proton (ion) injection, high brightness negative ion sources, high field electron/ion optical elements like X-lenses and lithium lenses, girocon and magnicon high power pulsed and CW RF generators, single bunch injection/ejection systems applicable and important from VEP-1 to LHC, electrostatic parasitic collision regions orbit separation, were not even touched here.

Of course, this development happened thanks to efforts and achievements of very many of our INP colleagues, most of whom could not be mentioned even in references. But we need to praise again A.M. Budker, who laid the background for the whole building.

REFERENCES

[1.1] E.A. Abramyan *et al.*, "Work on Colliding Electron-Electron, Positron-Electron Proton-Proton Beams at the Institute of Nuclear Physics." Proc. of the IV Int. Conf on High Energy Accelerators, Dubna, 1963, p.274.

[1.2] G.I. Budker *et al.*, "Accelerator Developments in Novosibirsk". Proc. of the V Int. Conf. on High Energy Accelerators, Frascati, 1965, p. 389.

[1.3] G.I. Budker *et al.*, "The quantum electrodynamics test in electron-electron scattering". Sov. Nucl. Phys. vol.6 (1967) 1221.

[2.] V.L. Auslender *et al.*, "The electron-positron storage ring VEPP-2 status". Proc. of the V Int. Conf. on High Energy Accelerators, Frascati, 1965.

[2.2] V.L.Auslender *et al.*, "Investigation of the ρ-meson Resonance with Electron-Positron Colliding Beams". Phys. Lett., 25B (1967) 433.

[3.1] V.E. Balakin *et al.*, "Investigation of the ϕ-mesom Resonance by e+e- Colliding Beams". Phys. Lett., 34B (1971) 328.

[3.2] L.M..Kurdadze *et al.*, "Observation of multihadronic events in e+e- collisions at the energy of 1.18-1.34 GeV". Phys. Lett., 42B (1972) 515.

[3.3] V.E.Balakin *et al.*, "Evidence for electron-positron Pair Electroproduction". Phys. Lett., 34B (1971) 663.

[4] V.M. Aulchenko *et al.*, "The first experiments on the electon-positron storage ring VEPP-2M". V International High Energy Physics Symposium, Warsaw, 1975, p. 163.

[5.1] L.M.Barkov *et al.*, "Electromagnetic Pion Form Factor in the Timelike Region". Nucl. Phys., B256 (1985) 365.

[5.2] A.D. Bukin *et al.*, "Φ-meson: Precise mass measurements and ω-ϕ interference observation". Sov. Nucl. Phys., vol.27, N.4, p.976, 1975.

[5.3] L.M. Kurdadze *et al.*, "Decays of ρ-meson studies". Sov. Nucl. Phys., vol. 35 (1982) 352.

[5.4] V.P. Druzhinin *et al.*, "Search for Rare Radiative Decays of ϕ-meson at VEPP-2M". Z. Phys., C37 (1987) 1.

[6] V.V. Anashin *et al.*, "Superconducting wiggler with 7,5 T field for e+e- collider VEPP-2M". Proc. of IX All-union conf. on charged particle accelerators, Dubna, 1984, v. 2, p. 262.

[7] A.N. Skrinsky, Yu. M. Shatunov, "Elementary particles precise masses measurements by means storage rings with polarized particles". Sov. UPhN-1989.-vol.158, N 2. p.315-326; Particle World, 1990.

[8] A. Filippov *et al.*, "Proposal of the Round Beams Lattice for VEPP-2M collider". HEACC'92, Humburg, v. II, p. 1145.

[9] A. Skrinsky, "VEPP-2M status and prospects and Phi-Factory project at Novosibirsk". II DAΦNE Workshop, Frascati, 1995 (Proceedings in publication).

[10.1] VEPP-4 Group, "Status report on the colliding beam facility VEPP-4". Proc. XI Inter. Conf. on high energy accelerators, Geneva, 1979, p. 38.

[10.2] VEPP-4 Group, "Electron-positron Storage Ring VEPP-4. Status and Prospects". Proc. XII Inter. Conf. on high energy accelerators, Batavia, 1983, p. 179.

[10.3] V.V. Anashin *et al.* "VEPP-4M status". VII All-Union Accelerator Conference, Proc. Dubna, 1992, vol. 1, p. 295-300.

[11.1] S.E.Baru *et al.*, "New measurement of Upsilon-meson mass". Z.Phys. C 30 (1986) p.551.

[11.2] A.E. Blinov *et al.*, "Search for decay Upsilon-meson into rho-0 and pi-0". Phys. Lett. B, 1990, 245, 311-314.

[11.3] S.E. Baru *et al.*, "Measurement of Two-Photon Widths of the η, η' and a2 mesons". Z. Phys. C48 (1990) 581-585.

[11.4] S.E. Baru *et al.*, "The Search for Narrow Resonances in the Reaction e+e- to hadrons at Center of Mass Energy Range between 7.23 and 10.34 GeV". Z.Phys. C49 (1991) 239-243.

[11.5] A.E. Blinov *et.al.*, "Pion pair production in photon-photon collisions". Z.Phys. C53 (1992) 33-39.

[11.6] S.E. Baru *et al.*, "Total Cross Section of Two Photon Production of Hadrons". Z.Phys. C53 (1992) 219-224.

[11.7] S.E. Baru *et al.*, "Measurement of the leptonic width and the muon-pair branching ratio of the Y_{1s} with the MD-1 detector '. Nucl. Phys. B (Proc.Supplements) 1992, 27, 89-93.

[11.8] S.E. Baru *et al.*, "Determination of the Upsilon (1S) leptonic width". Z. Phys. C56 (1992) 547.

[11.9] A.E. Blinov *et.al.*, "Measurement of inclusive Lambda production in e+e- interactions". Z. Phys. C62 (1994) 367.

[11.10] S.E. Baru *et al.*, "Experiments with the MD-1 detector at the e+e- collider VEPP-4 in the energy region of Upsilon-meson". Preprint BudkerINP 95-36, 1995, Novosibirsk; Submitted to *Physics Reports*.

[11.11] V.M. Aulchenko *et al.*, "Detector KEDR tagging system for two-photon physics". NIM A355 (1995) 261.

[12] A. Skrinsky, "Electron-positron factories". The 1990 ICFA Seminar "Future perspectives in high energy physics", Protvino, USSR, 1990; XXV International High Energy Physics Conference, Singapore.

[13] L. Barkov *et al.*, "Phi-factory project in Novosibirsk Particle accelerators". -1990.-v.311, N 1-4.-p.177-182.

[14] A. Skrinsky, "Advanced physics potential of electron-positron factories (accelerator aspects)". La Thuile 1995 Conference, (Proceedings in publication).

[15] A. Skrinsky, "Colliding Beams Program in Novosibirsk". International Seminar on Prospects in High Energy Physics; Morges, 1971.

[16] V.E. Balakin, G.I. Budker, A.N. Skrinsky, "A possibility for a super high energy electron-positron colliding beams facility". International Seminar on High Energy Physics and Thermonuclear Fusion, Novosibirsk, 1978 in the book: *High Energy Physics and Thermo-Nuclear fusion problems* (in a memory of G.I.Budker), M.: Nauka, 1981, p.11-21. VI All-Union Accelerator Conference, Dubna, 1978-Dubna 1979, vol.1, p.27-34.

[17] A. Skrinsky, "Accelerator and instrumentation prospects of elementary particle physics". XX Intern. Conf. on High Energy Physics, Madison, 1980. New York, 1981, v.2, p.1056-1093 Uspekhi Fiz. Nauk, 1982.

[18] I.F. Ginzburg *et al.*, "Colliding photon-electron and photon-photon beams on the single-pass e+e- colliders". NIM 205 (1983)47. V.E. Telnov, "Introduction to photon-photon and photon-electron linear colliders". Proc. of Workshop on Physics and Experiments with Linear e+e- colliders. Hawaii, 1993.

[19] G.I. Budker, "Efficient method for damping of particle oscillations in proton and antiproton storage ring". Atomnaya Energia 22 (1967), 346-348.

[20] VAPP-NAP Group, "Proton Antiproton Colliding Beams". VIII Inter. Conf. High Energy Accelerators, Geneva, CERN 1971 p.22-25.

[21] Ya.S. Derbenev, A.N. Skrinsky, "The Physics of Electron Cooling". ser. Soviet Physical Reviews, v. 3, pp 165 - 237.

[22] G.I. Budker, Ya.S. Derbenev, N.S. Dikansky, V.I. Kudelainen, I.N. Meshkov, V.V. Parkhomchuk, D.V. Pestrikov, B.N. Sukhina, A.N. Skrinsky, "Experiment on electron cooling". IEEE Trans. Nucl. Sci., 1975, NS-22, 2093-7.

[23.1] N.S. Dikansky, N.Kh. Kot, V.A. Lebedev, V.V. Parkhomchuk, D.V. Pestrikov, A.N. Skrinsky, B.N. Sukhina, "The study of fast electron cooling". VI All-Union Conference on Acceleration of Charged Particles Dubna, 1978, Moscow, Nauka).

[23.2] N.S. Dikansky, V.I. Kudelainen, V.A. Lebedev, I.N. Meshkov, V.V. Parkhomchuk, A.A. Sery, A.N. Skrinsky, B.N. Sukhina. "Ultimate possibilities of electron cooling". Preprint INP 88-61 1988.

[24.1] V.V. Parkhomchuk and A.N. Skrinsky, "Methods of cooling of beams of charge particles". Phys. Elementary Part. Atomic Nucl., 1981, 12,557-613.

[24.2] V.V. Parkhomchuk and A.N. Skrinsky, "Electron cooling: physics and prospective applications". Reports on Progress in Physics, 1991, v.54.n.7 919-47.

[25] N.S. Dikansky, N.Kh. Kot, V.I. Kudelainen, V.A. Lebedev, V.V. Parkhomchuk, A.A. Sery, A.N. Skrinsky, B.N. Sukhina, "Influence of sign of ion charge on the friction force at electron cooling". Preprint INP 87-102.

[26] G.I. Budker, A.N. Skrinsky, "Electron cooling and new perspectives in the physics of elementary particles", Uspekhi Fiz. Nauk, 1978, 124, 561-595.

[27] G.I. Budker, "Colliding beams prospects". XV International Conference on High Energy Physics, 1970, Kiev.

[28] A.L. Sokolov, I.M. Ternov "Radiative polarization of electrons in magnetic field". Sov. Phys. Doklady, 8 (1964) 1203

[29] V.N. Baier, V.M. Katkov, "Polarization in non-homogeneous field". Nucl. Phus., 3 (1966) 81.

[30] V.N. Baier, Yu.F. Orlov, "Electrons in a magnetic field quantum depolarization". Int. Acc. Conference Proc., Fraskati, 1965. USSR Academy of Scienses Reports, 1965, N 4, p.165.

[31] Ya.S. Derbenev, A.M. Kondratenko, "General formulas for radiative polarization". Sov.JETP, 37 (1973) 968.

[32] Ya.S. Derbenev, A.M. Kondratenko, A.N. Skrinsky, "Spin stability in arbitrary magnetic fields". Preprint INP 2-70, Novosibirsk, 1970. Sov. Phys. Doklady, 15 (1970) 583.

[33] Ya.S. Derbenev, A.M. Kondratenko, A.N. Skrinsky, "Spin resonances crossings". Sov. JETP, 33 (1971) 658.

[34] Ya.S. Derbenev, A.M. Kondratenko, A.N. Skrinsky, "Polarization in ultra-high energy storage rings". Part. Accel., 9 (1979) 247.

[35] V.N.Baier Radiative polarization. Sov. Phys. Uspekhi, 14 (1972) 695.

[36] S.I. Serednyakov *et al.*, "First polarization results at VEPP-2M". Sov. JETP, 71 (1976) 2025.

[37] V.N. Baier, V.M. Khoze, "Methods for polarization measurements". Atomic Energy, 25 (1968) 440.

[38] E.L. Saldin, Yu.M. Shatunov, "Helical undulator for polarization measurements". Proc. of VI Sov. conf. on particle accelerators, Dubna, 1978, v. 1, p. 124.

[39] A.E. Blinov *et al.*, "Measurements of particle polarization in storage ring by method of synchrotron radiation scattering at colliding beams". NIM, v. A241 (1985) 80.

[40] S.A. Belomesthnykh *et al.*, "An observation of spin dependence of synchrotron radiation intensity". Nucl. Instrum. Methods 227 (1984) p. 173-181.

[41] A.E. Bondar, A.N. Skrinsky, "On the method of the polarization measurement by the spectral density of synchrotron radiation". Preprint INP 82-14, Novosibirsk, 1982.

[42.1] S.I. Serednyakov *et al.*, "Comparison of electron and positron magnetic moments". Phys. Lett., B66 (1977) 102.

[42.2] E.S. Gluskin *et al.*, "Precise comparison of electron and positron anomalous magnetic moments". Phys. Lett., B198 (1987) 302.

[43] Ya.S. Derbenev *et al.*, "Project of Obtaiining Longitudinally Polarized Colliding Beams in the Storage Ring VEPP-4 at Energies up to 2×2 GeV". XII Intern. Conf. on High Energy Acceleratots, Fermilab, 1986, p. 410.

[44] V.I. Ptitsin, Yu.M. Shatunov, "Helical spin rotators and snakes". XI Intern. Symposium on High Energy Spin Physics, Blumington, 1994.

[45] A.N. Skrinsky, "Longitudinally Polarized Colliding Beams". Intern. Conf. on Instrumentation for Colliding Beam Physics, Stanford, SLAC-Report 250, 1982, p. 230.

[46] V.E. Balakin, A.A. Mikhailichenko, "The Conversion system for obtaining highly polarized electrons and positrons". Preprint INP 79-85, Novosibirsk, 1979. XII Intern. Conf. on High Energy Accelerators, 1982, Batavia, p. 127-130.

[47] I.N. Meshkov, S.G. Popov, A.N. Skrinsky, "Precise Experiments Possibilities by Super-Thin Internal Target Experiments on Rings with Electron Cooling". X Intern. Conf. on High Eneergy Accelerators, Protvino, 1977, v. 2, p. 141.

[49] V.L.Militsyn *et al.*, "Experimental plasma wake-field accelerator project". Physics of Fluids, B 5 (7), 1993, p. 2714.

[50] A. Skrinsky, "Plasma Wake Field Acceleration". CERN-USA-Japan Accelerator School, Hawaii, 1994 (in publication).

[51] S.T. Belyaev, G.I. Budker, S.G. Popov, "The possibility of using storage rings with internal thin target". Proc. of the 3rd Intern. Conf. on High Energy Physics and Nuclear Structure, New-York, 1969. Plenum Press, 1970, p. 603.

[52] G.N. Kulipanov *et al.*, "Influence of nonlinearities on betatron oscillations". II All-Union accelerator conference, Moscow, 1970, v. 2, p. 353-361.

[54] Ya.S. Derbenev, A.N. Skrinsky, "Longitudinal beam-beam effects". III All-Union accelerator conference, Moscow, 1972, v. 1, p. 386.

[55] N. Dikansky, D. Pestrikov, "Nonlinear Coherent Beam-Beam Oscillations in the Rigid Bunch Model". Preprint INP 90-14, Novosibirsk, 1990; Proc. of the 2nd European Part.Accel.Conf., v. 2, p. 1644.

[56] N. Dikansky, A. Skrinsky, "Single bunch resisitive wall instability". Atomnaya Energiya, 1966, 21, p. 176.

[57] V.L. Auslender *et al.*, "Fast coherent transverse damping at VEPP-2". Atomnaya Energiya, 1967, v. 22.

[58] N.S. Dikansky *et al.*, "Interaction of coherent oscillations of the beam with internal systems". Atomnaya Energiya, 1967, v. 22.

[59] G. Dimov *et al.*, "Transversal instability of proton beam due to interaction with plasma in cyclic accelerators". All-Union Accelerator Conference 1968, v. 2 pp. 285 - 288.

[60] V.V. Danilov, E.A. Perevedentsev, "Feedback system for elimination of the transverse mode coupling instability". CERN Report, SL/93-38, 1993 (AP).

[61.1] G.N. Kulipanov, A.N. Skrinsky. "A Synchrotron Radiation Utilization: Status and Prospects". Sov. Uspehi Fiz. Nauk, vol. 122 p. 369, 1977.

[61.2] V.V. Anashin *et al.*, "Compact storage rings Siberia-AS and Siberia-SM synchrotron radiation sources for lithography", Rev. Sci. Instr. v. 60 N 7 p. 1767 (1989).

[61.3] V.N. Korchuganov *et al.*, "Optimization of parameters of a dedicated synchrotron radiation source for technology", Nucl. Instr. and Meth. 208 p. 11 (1983).

[61.4] G.N. Kulipanov *et al.*, "Superconducting 'snake' for the dedicated SR source Siberia-1". Proc. of the Intern. conf. on X-ray and VUV synchrotron radiation, Stanford, 985. Amsterdam: North-Holland, 1986, -p. 99-104.

[61.5] G.N. Kulipanov, A.N. Skrinsky, "Synchrotron radiation sources". INDO-USSR seminar on synchrotron radiation source (SRS): Physics, technology, utilization, Indore, 1989.-Indore, 1989, - p. 1-28.

[62.1] N.A. Vinokurov, A.N. Skrinsky, "An Optical Range Generator Klystron by Ultra-Relativistic Electrons". Preprint INP 77-59. Novosibirsk, 1977.

[62.2] N.A. Vinokurov, A.N. Skrinsky. "An Optical Klystron". In book. *Relativistic High frequency electronics,* p.204. Gorky, Inst. of Appl. Physics AS USSR,1981.

[62.3] N.A. Vinokurov, A.N. Skrinsky, "About a Power Limit for an Optical Klystron on an Electron Ring". Preprint INP77-76. Novosibirsk,1977.

[62.4] N.A. Vinokurov, A.N. Skrinsky, "About a Power Limit for an Optical Klystron". The VI All-Union Accelerator Conference Proceedings. Vol.2, p. 233. Dubna, (1980).

[63.1] V.N. Litvinenko, "Storage ring FELs and the prospects". Nucl. Instr. and Meth. A304 p.40 (1991).

[63.2] N.G. Gavrilov *et al.*, "Electromagnetic undulators for the VEPP-3 optical klystron". Nucl. Instr. and Meth., A282 (1989), pp. 422-423.

[63.3] I.B. Drobyazko, G.N. Kulipanov, V.N. Litvinenko, I.V. Pinayev, V.M. Popik, I.G. Silvestrov, A.N. Skrinsky, A.S. Sokolov, N.A. Vinokurov, "The Lasing in the Visible and Ultraviolet Regions in an Optical Klystron Installed on the VEPP-3 Storage Ring". Nucl. Instr. and Meth., A282 (1989), pp. 424-430.

[63.4] G.N. Kulipanov, V.N. Litvinenko, I.V. Pinaev, V.M. Popik, A.N. Skrinsky, A.S. Sokolov, N.A. Vinokurov, "The VEPP-3 Storage Ring Optical Klystron: Lasing in the Visible and Ultraviolet Regions". Nucl. Instr. and Meth., A296 (1990), pp. 1-3.

[63.5] V.N. Litvinenko and N.A. Vinokurov, "Lasing spectrum and temporal structure in storage ring FELs: theory and experiment". Nucl. Instr. and Meth., A304 (1991), pp. 66-71.

[63.6] M.-E. Couprie, N.G. Gavrilov, V.N. Litvinenko, G.N. Kulipanov, I.V. Pinaev, V.M. Popik, A.N. Skrinsky, N.A. Vinokurov, "The Results of Lasing Linewidth Narrowing on VEPP-3 Storage Ring Optical Klystron". Nucl. Instr. and Meth., A304 (1991), pp. 47-52; A308 (1991), pp. 39-44.. IEEE Journal of Quantum Electronics, v.27 (1991), #12, pp. 2560-2565.

[63.7] N.A. Vinokurov, "Free electron lasers with electron storage rings". Proc. of the 2nd Eur. Part. Accel. Conf. v.1 (1990), pp. 112-114. Nucl. Instr. and Meth. A308 (1991), pp. 24-27.

[63.8] N.A. Vinokurov, "The storage ring free electron lasers". Proc. of the 3rd Eur. Part. Accel. Conf. v.1 (1992), pp. 103-105.

[64.1] G.I. Erg *et al.*, "The project of high power free electron laser using race-track microtron-recuperator". Preprint BudkerINP 93-75, Novosibirsk, 1993.

[64.2] N.G. Gavrilov, E.I. Gorniker, G.N. Kulipanov, I.V. Kuptsov, G.Ya. Kurkin, A.D. Oreshkov, V.M. Petrov, I.V. Pinaev, I.K. Sedlyarov, A.N. Skrinsky, A.S. Sokolov, V.G. Vesherevich, N.A. Vinokurov, P.D. Vobly, "Project of CW Race-Track Microtron-Recuperator for Free Electron Lasers". Nucl. Instr. and Meth. A304 (1991) pp. 228-229. *IEEE Journal of Quantum Electronics*, v.27 (1991), #12, pp. 2626-2628.

[65] V.L. Auslender, R.A. Salimov, A.N. Skrinsky *et al.*, "Powerful Electron Accelerators for a Radiation Technologies". Report on All-Union Conf. for Radiation Technologies, Obninsk, 1984.

A Personal Perspective of High Energy Accelerators

by Gustav-Adolf Voss

At the beginning of this year I retired from the position of Head of the Accelerator Department at "Deutsches Elektronen Synchrotron- DESY", which I had held for the last 22 years. I want to thank the organizers of this conference for the invitation to give a talk on "A Personal Perspective of High Energy Accelerators". This gives me a chance to thank my teachers, my colleagues and friends, whom I have found during the 37 years in which I have been working in the field of accelerators and who have helped to make my life so exciting and wonderful.

My first teachers were Stanley M.Livingston, Ken Robinson and Tom L.Collins. It is widely known, that Livingston had built the first working cyclotron as his Ph.D. thesis under Lawrence . It is also known that Lawrence was inspired with the idea of the cyclotron by reading Rolf Wideroe`s paper on the first linear accelerator, back in 1927. And Rolf Wideroe, although he is 93 years old by now, is still healthy and full of ideas, which he sometimes tries out on me. As you see, accelerator science does not yet have a long history.

Ken Robinson was the legendary genius, who developed most of the theory of electron synchrotrons and storage rings single-handedly and in whose unpublished papers, found after his death, the basics of the free electron laser had already been developed, 10 years ahead of time. Tom Collins was Assistant Director at the Cambridge Electron Accelerator, my first real place of work. He developed the "Collins-Straight-Section" and furthered my technical education.
After 14 years at the CEA I went to the Deutsches Elektronen-Synchrotron DESY from where I have now formally retired.

Among my first friends and colleagues from the CEA times one finds - besides the already mentioned Stan Livingston, Ken Robinson and Tom Collins - such well known names as Karl Strauch, John Rees, Ewan Paterson, Herman Winick and Albert Hoffman.

When I started my professional life in the accelerator field, life was different. The first atomic bomb had been exploded not much more than a decade earlier and the prestige of the nuclear physicist was much higher than it is today. The goals of particle physics were less questioned and there was less competition for public research funds. For accelerator builders, bureaucracy had not yet been invented, at least not in America. Those were the golden days.

Accelerator science and technology were in their infancy. Strong focusing had just been invented by Courant, Livingston and Snyder and independently by Christophilos, but there was hardly anyone who understood tolerance problems, nonlinear resonances, dynamic apertures and other aspects of theoretical machine physics and, at the same time, equally well the engineering aspects of those machines, their costs and their potential technical pitfalls. If there is not one single person, who has at least some rudimentary understanding of all these aspects, it is very difficult to find the right compromises in building accelerators. So, with hindsight, some of these early machines look rather awkward: Huge tunnel cross sections, fantastic magnet support systems which were sometimes so complicated, that it became a real problem to turn on these machines, big and expensive air conditioning systems for the ring tunnel, which would not tolerate much power dissipation in the ring tunnel and thereby made other installations expensive and complicated. Radiation safety was another area, where lack of understanding and technical perspective produced technical abominations.
It was Bob Wilson, I believe, who was the first all-round accelerator builder, to set a new style. Bob was a penny pincher when it came to building accelerators, surpassed perhaps only by Wolfgang Paul of Bonn University in Germany. Both of these two outstanding physicists were and still are my heroes. Paul was most unhappy when he saw money squandered "as if it was play money in a Monopoly game", and to Wilson it was a challenge to see what he could get away with technically in his wish to save money. Project leaders like Wilson and Paul (Paul built the first strong focusing synchrotron in Europe) had to have a good understanding of the risks they were taking when they cut all the trimmings of accelerators down to the bone. They put the other people on their projects at ease by assuming the full responsibility for all major decisions themselves .

What happens, if you do not have competent project leaders with full authority and power to make the decisions on how the money is spent? The first result is usually a cost overrun: People working on the project don´t want to be blamed if the machine does not work when completed. So they insist on extra safety margins in those parts they are responsible for. And that means more money spent. Then, the schedule also begins to slip, because the number of changes increases, changes which are a result of insecurity, trying to play it safe. And so it goes on. And this sorry state of affairs is not helped by imposing organization experts or military brass. Also, large numbers of reviews and vast herds of reviewers can no longer save the situation. This little piece of wisdom should be obvious to everyone, particularly to those in power to make major decisions.

How refreshing and exhilerating on the other hand is the situation, where you have very little money but the urgent will to do new and exciting physics with a new machine. Where competent people "steal, rob and cheat" to scratch the resources together to get their project built in the fastest way imaginable, at a bargain price and in record time. Some of our most productive electron positron storage rings have been built that way.
By claiming that some of our most productive machines have been built in situations where very little money was available, I do not want to give the impression that I have a contempt for wealth. Wealth makes great opportunities. Tunnels which have been built in the olden days with 5 times the necessary cross

0-7803-3053-6/96/$5.00 ©1996 IEEE

section make it now possible to install a second or even a third machine. Laboratories used to inflated budgets can now build new machines with very little new money. Stepping into such a situation, making use of all that wealth, can make you an instant hero. It is the change of style which makes those golden opportunities.
Wealth can manifest itself in buildings, in money but also in staff. After all, many laboratories today spend much more money on salaries than on electricity bills and new equipment. In some places it seems to be difficult to focus a significant portion of the staff on the actual problems at hand. Personnel management is something very few of us have studied. Some people in responsible positions do it right instinctively, some succeed by the sheer power of their enthusiasm and power of conviction, but many do it wrong or not at all. If it were possible to focus only half of the staff on the real important things at hand, in most places there would be no staff shortage, rather the opposite. Some smaller exceptional labs seem to be doing fine, but others need change. Several stories come to my mind to illustrate how much the output of a lab depends on spirit and motivation: The rapid cycling Princeton Penn proton synchrotron had a staff of more than 300 when they were told one day to close down the place. In the year after this announcement they gradually reduced the staff to 25, while at the same time running a full proton program and at the same time also developing the techniques for heavy ion acceleration. That was the most productive year they ever had in their whole history.

In some places what seems to be needed is a change in the style of management .
Style of course is also subject to the external forces, with which we have to live. We are no longer allowed to do business the way it could be done 40 years ago. Innumerable reports, review committees and other checks apparently have to accompany many major projects. There are laudable exceptions and I myself have enjoyed such blissful conditions during the last two decades of my professional life. But in other not so happy situations things are quite bad: This reminds me of large interlock chains which people sometimes arrange in order to improve equipment safety. After all, this is given by the product of the probability of the failure of all the components of the system, and if there are only enough interlocks in series you must be safe. This of course is only true if each single interlock is tested with the same rigor and sincerity which you want to have applied to the system. Coming back to reviews and reports, each of them, to be meaningful, should have a depth, a competence and a sincerity fully matched to that of the project leader whose head is always on the block. I believe, this is rarely the case.

Things certainly were different 25 years ago. Professionally, the most formative years for me were those between 1967 and 1972, when the very small group of people: Bob Averill, Albert Hofmann, Roy Little, Harry Mieras, Ewan Paterson, Ken Robinson, Karl Strauch, Herman Winick and myself embarked on the CEA-By-pass project. Since money for a multi-GeV electron-positron storage ring was not available, we had the idea of using the old 6 GeV electron synchrotron, modifying it and using it for storage of counter rotating electron and positron beams. This way we hoped to be the first to do colliding beam experiments in the multi-GeV region. And all that had to be done with almost no extra funds.

Nothing came easy and to everybody involved these were the most grueling but also the most rewarding years. The CEA had an alternating gradient magnet focusing system and synchrotron radiation led to a horizontal anti-damping of betatron oscillations. Special damping magnets, invented by Robinson, the world's first wiggler magnets, were necessary for stable beam storage. Damping magnets, actually, are considerably more sophisticated than ordinary wiggler magnets, because they need a very strong gradient field at the location of the beam.
The 100 MeV positron linac had much too small an energy to inject and accumulate positrons in the synchrotron. A special multicycle operation became necessary, where the synchrotron cycled between the injection energy of 100 MeV and a peak energy of 3 GeV. Synchrotron radiation at the high energy part of each cycle damped injection oscillations sufficiently to allow beam accumulation.
A special by-pass to the synchrotron had to be invented, to create enough space for a meaningful detector with the world`s first low beta interaction region for high luminosity. Nothing of all this worked from the beginning and it was an uphill battle all along. In the course of this work we did a number of things which were great fun: We decided that with certain precautions it would be perfectly safe to be in the tunnel with a stored 2 GeV 1 mA beam. This can make a huge difference to the set-up and adjustment of a machine. The very small aperture beam pipes of the by-pass could be adjusted simply by watching beam life times, a total of 48 distributed sextupole magnets could be adjusted simply by watching Q-changes, when they were shorted by hand. Vertical beam height at the interaction point could be minimized by taking polaroid pictures of the photon -beam from a carbon fiber at the interaction point and by adjusting the rotational tilt of some of the critical magnets. Synchrotron radiation monitors are much easier to install and align if you can see the light, adjust the mirrors and the lenses for optimum focusing. Before we did all this, of course, we had carefully assessed the situation and determined that what we were doing was absolutely safe, albeit not very conventional. My teacher Tom Collins always maintained that the safest thing in the world is a person who really understands all aspects of what he is doing and acts accordingly in a responsible, conservative way. The emphasis is on understanding all aspects and acting accordingly. No tiger could be trained to do that. As an aside: Studying the personel roster of a lab with a challenging project a few weeks ago, I found 2 accelerator physicists, and 10 full time radiation safety officers!

The By-pass project was an almost impossible mission and I secretely made the vow, that if I ever should get out of it without loosing face, I would never again get myself involved in another major project. Well, we measured the first multi-hadron production cross sections, results which nobody believed at that time because the cross sections were so unexpectedly large. But, it turned out, they were right! And I went to DESY and - against my better instincts - got involved with PETRA and - together with Bjoern Wiik - with HERA. Particularly the 20 GeV e+ - e- storage ring PETRA became an exhilerating experience for the DESY staff and for me.

Scheduled for a 4 year construction period, the staff became so concerned with keeping the self imposed schedule, that each of the people responsible for a particular component worked ahead to leave time for unforseen problems. Thus, the schedule could be revised twice and moved forward. The machine was actually turned on 2 years and 8 months after authorization. Also, staying within the authorized budget of 100 MDM had become such an overriding issue, that only 80% of this amount had been committed at the time of first successful beam storage, leaving a comfortable cushion for later improvement work. No inflationary increases needed to be claimed. For some obscure reason R.R. Wilson´s rule seemed to be true also in this case: Construction time and project costs seem to go hand in hand.

Accelerators have become more efficient and much more economical over the last 30 years. I once had to give a talk on the evolution of new technologies and costs in the accelerator field and discovered, that we have gained at least a factor of ten in GeV/ M$, when we compare inflation adjusted prices of the first multi-GeV machines with machines we build today. And it is not so much the new technologies like superconducting magnets or superconducting rf which cause these savings but it is mostly the better understanding of what is and what is not really necessary in accelerator building.

The big question is now, how will we go on? How will we build tomorrow´s accelerators with an order of magnitude higher energy at a cost which society is willing to pay? There is one school which believes, that what we need now are new ideas. Many people of this school aim at ultra high accelerating gradients: A table top multi GeV accelerator is their dream. Thinking about such machines can be great fun and very entertaining. Of course, it should not be the size of an accelerator but its costs which must be minimized. What most of the people studying ultra high gradient ideas overlook is, that not only energy but also luminosity has to be increased. We are talking about colliders at very large center of mass energies, which require very high luminosities to produce a meaningful counting rate. There are many good reasons why this then translates into very large beam power. The aspect which then becomes increasingly important is the over-all power efficiency of these machines. None of all the new accelerating ideas (and I myself have contributed to this effort) shows much promise in this respect.
So we are probably left with the old principles: Superconducting proton storage rings for proton-proton collisions and more or less conventional linear colliders for electron positron collisions. How then can we possibly build a machine with ten times the center of mass energy at a cost society is willing to pay? I believe that the only answer is an extreme economizing of standard technology, plus a large all-encompassing international collaboration, plus lots of luck. The LHC has just passed that hurdle. I only hope, that ways may be found to avoid the missing magnet concept under which it was approved.
The problem of getting the next linear collider for electron positron collisions approved looks more formidable. Despite a large number of international workshops I have not seen, over the last 6 years, much convergence of ideas and concepts. With everybody just following his own pet idea, it is hard to see how a big international collaboration can be formed and find approval from the respective governments. Part of the problem may be, that linear collider studies have not yet reached the degree of maturity where a proposal can be written. We may have to wait until detailed technical lay-outs and in particular prices are better known and we must hope that a merging of ideas and designs will then occur. If there is not one single government willing to start such a project but if instead international concensus is required from the beginning, such convergence must be reached. The basis, I believe, must be proven technology and economy. As long as these two aspects cannot be substantiated by hard facts and numbers, one cannot write a proposal, not to mention any hope of approval.
I hope very much, that an international consensus can be found soon. I love our science and I am fascinated by it, even if the gap between our machine science and technology and the latest theoretical ideas like superstrings seems to widen all the time and the energies to check a particular "final" theory seem to be dishearteningly out of reach. There are enough open questions within the energy range we can cover in the next decade.And as long as the field finds so many bright and motivated young people as evidenced by this conference, we need not worry!

*PHOTON-PHOTON COLLIDERS**

Andrew M. Sessler
Center for Beam Physics
Lawrence Berkeley Laboratory, Berkeley, CA 94720 USA

Since the seminal work by Ginsburg, *et al.*, the subject of giving the Next Linear Collider photon-photon capability, as well as electron-positron capability, has drawn much attention [1]. A 1990 article by V.I. Telnov describes the situation at that time [2]. In March 1994, the first workshop on this subject was held [3]. This report briefly reviews the physics that can be achieved through the photon-photon channel and then focuses on the means of achieving such a collider. Also reviewed is the spectrum of backscattered Compton photons—the best way of obtaining photons. We emphasize the spectrum actually obtained in a collider with both polarized electrons and photons (peaked at high energy and very different from a Compton spectrum). Luminosity is estimated for the presently considered colliders, and interaction and conversion-point geometries are described. Also specified are laser requirements (such as wavelength, peak power, and average power) and the lasers that might be employed. These include conventional and free-electron lasers. Finally, we describe the R&D necessary to make either of these approaches viable and explore the use of the SLC as a test bed for a photon-photon collider of very high energy. *

I. INTRODUCTION

From earliest times, man has known that light does not affect light. In modern terms, if you shine one flashlight on a wall, and direct the beam of a second flashlight through the beam of the first flashlight, shaking the second beam up and down, no matter how violently, will not affect the first beam. Maxwell formalized this in his famous electrodynamic equations, from whose linearity we would quickly deduce the above-described phenomenon. Of course, none of this is true in quantum mechanics, and the scattering of light upon light (Delbruck scattering), a quantum electrodynamic effect (QED), was first proposed in 1933 [4]. This phenomenon was first observed in 1954, and an experiment is now under way to carefully study this and other nonlinear QED effects [5].

As the energy of the light increases, not only do QED phenomena occur, but particle physics begins to play a role, so that in the light-light scattering, diverse pairs of particles are produced. In photon-photon colliders, the intensity of the light is so strong and the energy so high, that the collider becomes interesting for elementary particle physics.

*Work performed under the auspices of the U.S. Department of Energy, Office of High Energy and Nuclear Physics, under Contract No. DE-AC03-76SF00098.

In this report, we discuss the elementary particle physics and experimental detectors (Section II), the kinematics, cross sections, and geometrical constraints of gamma-ray production and collision (Section III), conventional lasers (Section IV), free-electron lasers (Section V), and an R&D program (including the possible conversion of the SLC to a photon-photon collider) (Section VI).

II. ELEMENTARY PARTICLE PHYSICS AND EXPERIMENTAL DETECTORS†

The structure functions of the photon, probed by deep inelastic scattering from a photon target, are a fundamental and largely unresolved area of investigation in quantum chromodynamics (QCD). Clearly, the electron-photon collision option would provide the paramount facility for these studies. In another important area of QCD, photon-photon collisions would allow studies of the top quark threshold region that would complement studies performed in electron-positron collisions. Here some unique measurements are possible by using polarized photon beams. Large circular polarization allows direct observation of p-wave toponium, not possible in electron-positron collisions, while linear polarization may make possible very sensitive measurements of the strong coupling constant.

Studies of W boson pair production in photon-photon collisions provide the most sensitive tests for quartic anomalous interactions of the electroweak gauge bosons. The photon-photon option also provides unique advantages for Higgs boson studies. The two-photon width of a Higgs boson is most directly measured; the width is a fundamental probe both of (1) the electroweak theory and (2) electrically charged, ultraheavy quanta (which would affect the two-photon rate if their mass is generated by the Higgs boson). The search for supersymmetric Higgs bosons is also enhanced by the photon-photon option. In electron-positron collisions, the heavy scalar and pseudoscalar of the minimal supersymmetric model must be produced together in the same event, requiring energy greater than the sum of their masses, but in photon-photon collisions, they can be produced and observed individually. The circular polarization of the photon beams is an important asset in these studies, both enhancing the signal and suppressing the background. Linear photon polarization may also be useful, since it would allow direct measurement of the parities of the Higgs bosons, which might not be directly measured in any other way.

0-7803-3053-6/96/$5.00 ©1996 IEEE

III. GAMMA RAY PRODUCTION AND COLLISION

Photons of high energy, equivalently gamma rays, may most readily be obtained by Compton backscattering. The general scheme of a photon-photon collider, with the Compton collision occurring at the "conversion point" (different from the collision point) is shown in Fig. 1.

1. The Conversion and Collision

The scattered photon differential cross section is:

$$\frac{1}{\sigma_c}\frac{d\sigma_c}{dy} \equiv f(x,y) =$$

$$\frac{2\sigma_0}{x\sigma_c}\left[\frac{1}{1-y}+1-y-4r(1-r)+2\lambda P_c rx(1-2r)(2-y)\right]$$

$$\sigma_0 = \pi\left(\frac{e^2}{mc^2}\right)^2 = 2.5\times10^{-25}\,cm^2$$

where λ = electron helicity, P_c = photon circular polarization,

$$r = \frac{y}{x(1-y)} \quad , \quad y = \frac{\omega}{E_0} \quad ,$$

$$\omega = \frac{\omega_m}{1+\left(\frac{\theta}{\theta_0}\right)^2} \quad , \text{ and } \quad x = \frac{4E_0\omega_0}{m^2c^4} \quad .$$

The total Compton cross section is:

$$\sigma_c = \sigma_c^{np} + 2\lambda P_c \sigma_1 \quad ,$$

$$\sigma_c^{np} = \frac{2\sigma_0}{x}\left[\left(1-\frac{4}{x}-\frac{8}{x^2}\right)\ell n(x+1)+\frac{1}{2}+\frac{8}{x}-\frac{1}{2(x+1)^2}\right]$$

$$\sigma_1 = \frac{2\sigma_0}{x}\left[\left(1-\frac{2}{x}\right)\ell n(x+1)-\frac{5}{2}+\frac{1}{x-1}-\frac{1}{2(x+1)^2}\right] \quad .$$

σ_c is hardly affected by $2\lambda P_c = 1$ or $2\lambda P_c = 0$, but the spectrum very much depends upon $2\lambda P_c$.

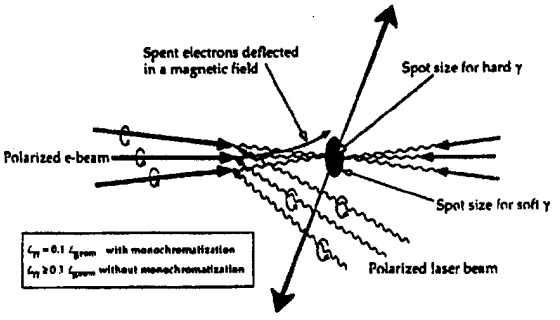


Figure 1: A schematic drawing indicating the conversion point from infra-red photons to gamma rays and the collision point or the gamma rays.

The geometry of conversion and collision produces a significant hardening of the spectrum. If we let ℓ be the distance between the conversion and collision point, and introduce the parameter ρ by $\rho = \ell / \gamma a_e$, where a_e is the radius of electron beam, then the luminosity spectrum strongly depends on beam parameters, but only through the parameter ρ.

If we introduce the geometrical luminosity $L_{ee} \equiv N^2 f / 2\pi a_e^2$, the resulting spectral luminosities are shown in Fig. 2.

It can be seen that laser photon polarization and electron helicity have a large effect upon the specific luminosity. This feature is important for experiments. Employing this analysis, we arrive at Table 1.

2. Laser Characteristics

In determining laser parameters, there are several considerations. The first is wavelength. Incident photons, ω_0, cannot be too energetic. If they are, then pairs are produced. The condition is

$$x \equiv \frac{4E_0\omega_0}{m^2c^4} > 2(1+\sqrt{2}) \approx 4.8$$

The best is to choose x close to 4.8 or $\lambda = 4.2E_0$ (TeV) μm.

The pulse length of the laser should equal that of the electron bunch (and its pulse structure should match that of the electrons). The amount of energy in one pulse or, equivalently, the laser peak power is given by the desire

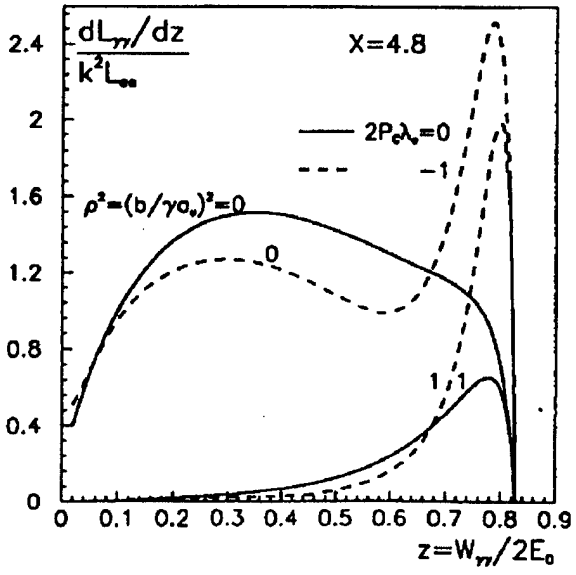


Figure 2: The spectral luminosity of γ–γ collisions. The curves represent unpolarized electrons or photons and fully polarized photons on helicity unity electrons. Two different distances between the conversion point and the collision point are considered. [From V. Telnov, Nucl. Instrum. Methods **A355**, 3 (1995)].

Table 1. Luminosity for various collider projects at 250 GeV × 250 GeV. Direct conversion to a photon-photon collider is given in the first column; the second assumes only the final focus is modified; while the third column gives the luminosity if, further, the electron beam emittance is reduced by the factors given in the last two columns. (The table was developed by V. Telnor, K.-J. Kim, P. Pielini, and the author.)

Machine	Direct Operation	Modified FF	Reduced Emittance	Emittance Reduction Factor	
TESLA	2.59E+32	9.20E+32	1.84E+33	1.00	4.00
SBLC	2.23E+32	4.12E+32	1.43E+33	3.00	4.00
JLC	5.47E+32	9.48E+32	1.90E+33	2.00	2.00
NLC	5.32E+32	1.11E+33	1.93E+33	2.00	1.50
CLIC	1.89E+32	4.33E+32	1.06E+33	2.00	3.00
VLEPP	4.93E+32	1.97E+33	1.97E+33	1.00	1.00

to have one γ-ray per electron. Then $N_{ph} = \pi w^2 / \sigma_c$. The energy in the laser pulse is $W = N_{ph} \cdot \hbar\omega_0$. The photon Rayleigh length should be the length of the electron bunch, that is $\ell_e = \pi w^2 / \lambda$. Combining $N_{ph} = \lambda \ell_e / \sigma_c$, independent of electron bunch radial size (provided $a_e < w$). More careful treatment puts a π upstairs. The pulse energy W is $hc\ell_e / \sigma_c$ or $W \sim 251_e$ (cm) J. For various projects W ~ 1 to 4 J, $\tau \equiv (1_e/c) \sim 1$ to 5 ps.

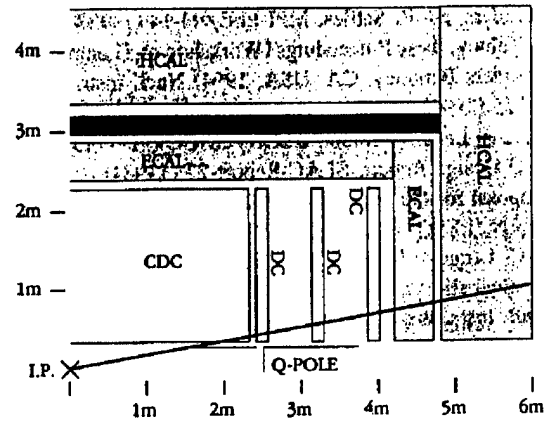
Finally, we recall that the laser should be able to vary the polarization of the output beam.

3. Detector Configurations

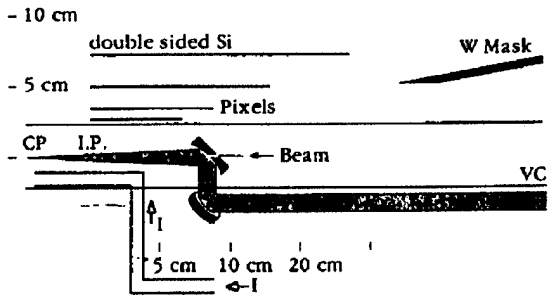
So far, only minimal thought has been given, and much more work is needed, on the detector aspects of a photon-photon collider. A first consideration is presented in Fig. 3.

It is not necessary, but highly desirable, to separate the used electrons from the γ-rays. Since the distance between these two points is, at best, a few centimeters, very high magnetic fields (within the detector!) are needed. Figure 4 shows some possible ways to generate such fields while minimizing the external fields.

Alternatively, a plasma lens (over-focusing the electrons and, therefore, greatly reducing spurious collisions) might be ideal, as it has no external magnetic field. Getting in the gas (for the plasma), and then removing it may, however, introduce too much mass into the detector.



(a)



(b)

Figure 3: (a) A schematic layout of the IP in a photon collider, with drift chambers and electromagnetic calorimeter. (b) Details of the region around the IP. [From F. Richard, Nucl. Instrum. Methods **A355**, 92 (1995)].

IV. SOLID-STATE LASERS

Several laser possibilities can meet the requirements for a photon-photon collider. Recall that backwards Compton scattering requires an input laser with the following properties: wavelength for electron energy of E_o (TeV) ($\lambda = 4.2\ E_o\ \mu m$), laser power (P > 1 TW), pulse length (τ = 1 ps), helical polarization, and pulse structure of about 100 pulses with a rep rate of about 200 Hz or 20 kW of average power.

Solid-state lasers can easily satisfy the first four requirements. But they cannot yet satisfy the average (as contrasted with the peak) power requirements. On the other hand, solid-state lasers without chirped pulse compression have produced an average power of 500 W.

Thus it is necessary to marry these two technologies, perhaps by having diode pumping of a Nd glass laser that is then used to drive a (wide band) Ti sapphire laser with a compressible pulse.

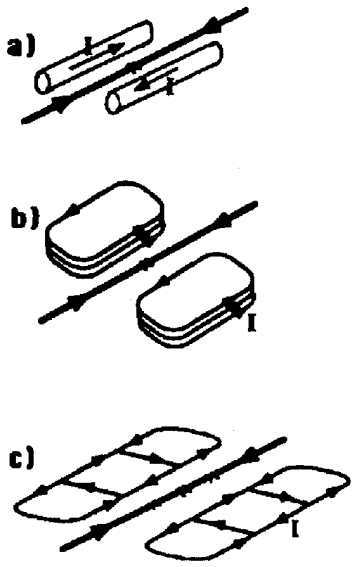


Figure 4: Possible setups for generating the strong transverse magnetic fields required to separate the electrons from the photons. [From D. Miller, Nucl. Instrum. Methods **A355**, 101 (1995)].

Generation of the pulse structure required for a collider can readily be accomplished. A possible scheme is shown in Fig. 5.

Getting the laser light to the electron beam, so as to have Compton backscattering, deep inside a detector is one of the major challenges of a photon-photon collider.

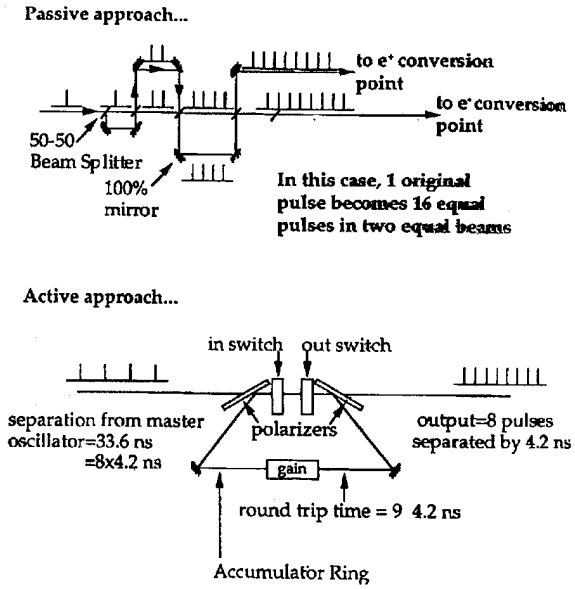


Figure 5: Two possible schemes for generating the train of laser pulses needed for a collider [From C.E. Clayton *et al.*, Nucl. Instrum. Methods **A355**, 121 (1995)].

Possible schemes are shown in Fig. 6, but this subject requires much work.

V. FREE-ELECTRON LASERS

Free-electron lasers (FELs) are a possibility for a photon-photon collider; however, it is true that FELs have neither achieved the requisite peak power nor average power. Various possibilities have been considered [6] such as:

1. 10 FELs each driven by 3–4-kA, 150-MeV, induction-accelerated e-beam.
2. MOPA with amplifier driven by 1-GeV, 2.5-kA, induction-accelerated e-beam.
3. Photon compression of a ~100-ns induction-accelerated e-beam of 100 MeV and 1 kA.
4. Oscillator, with rf-accelerated e-beam and with high-power output switching.

The first possibility is the most extensive (and the most expensive) but the most likely to be successful. On the other hand, the last approach, an oscillator, is least expensive but requires the most R&D (to learn how to

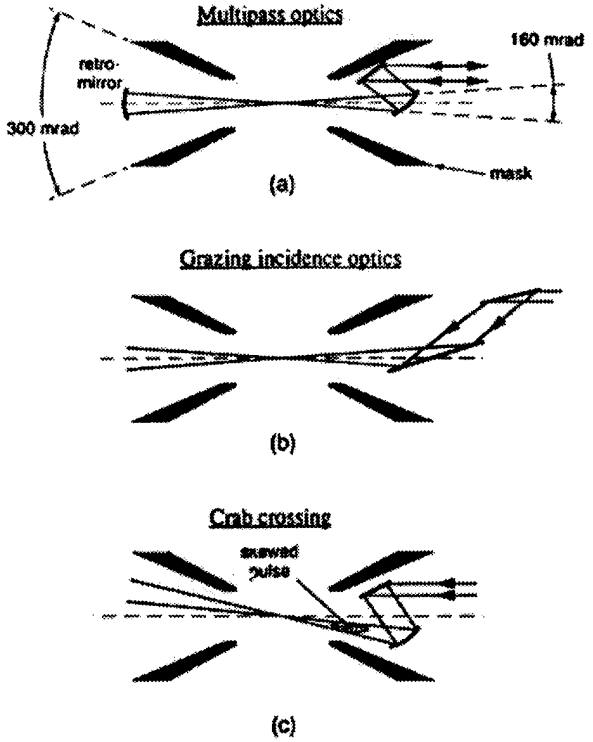


Figure 6: Three possible arrangements of the laser-focusing optics within the vertex detector: (a) an optical arrangement that uses the same laser pulse at both conversion points, (b) grazing-incidence optics that reduce the effect of collision debris upon the mirrors, (c) a crab-crossing geometry that even further reduces the effect of debris. [From C.E. Clayton *et al.*, Nucl. Instrum. Methods **A355**, 121 (1995)].

Table 2. Parameters for an FEL Pulse Compression Scheme.

Beam

$1 = 1$ kA
$E = 100$ MeV
$\Delta E/E = 10^{-3}$
$\varepsilon_N = 50 \times 10^{-6}$ πm – r
$\lambda_\beta = 11.3$ m

Conventional Tapered Planar Wiggler

$\lambda_w = 4.0$ cm
$K = 1.4$
$L_{sat} = 16$ m
$L_W = 25$ m

Output

$P_{out} = 1.6$ GW
$E_{out}(1.4\ ns) = 2.24$ J

circulate MW of power in contrast with the present achievement of only 1 W).

A pulse-compression scheme, very similar to that done with solid-state lasers, would seem to be a good way to take advantage of the fine average power capability of an FEL (without pressing it excessively on peak power) [7]. The scheme has the parameters shown in Table 2.

It is easy to show that the pulse-compression scheme, for light of wavelength λ (~1 μm), compressed from pulse length T (~1 ns) to pulse length τ (~1 ps), requires fluctuations in frequency limited by a number of relations, the most restrictive being $\Delta\omega/\omega < \lambda/4\pi cT$. This requires $\Delta\omega/\omega < 2\times10^{-7}$

For an FEL, it is easy to show that variation in input beam energy (measured by γ) or current (I) will lead to an error in frequency (at the output) of

$$\frac{\Delta\omega}{\omega} = -\left(\frac{\lambda}{Tc}\right)\left(\frac{Lw}{\lambda_w}\right)\phi\rho\left[\frac{1}{3}\frac{\Delta I}{I} - \frac{\Delta\gamma}{\gamma}\right] ,$$

where L_W is the length of the wiggler, λ_W is the wiggler wavelength, φ is the phase change due to the FEL, and ρ is the FEL parameter. For our example,

$$\frac{\Delta\omega}{\omega} \sim 10^{-5}\left[\frac{1}{3}\frac{\Delta I}{I} - \frac{\Delta\gamma}{\gamma}\right] ,$$

and thus with a 1% tolerance on beam characteristics, pulse compression can be accomplished.

VI. AN R&D PROGRAM

The relevant R&D has both immediate and long-term aspects. It should consist of work on:

1. Detectors and masking
2. High-power lasers including FELs
3. Special final-focus components
4. Bright sources of polarized electrons
5. High-power, low-loss optical components.

The SLC can provide a realistic test bed for a higher energy γ-γ collider and, furthermore, would provide interesting new particle physics. Many of the problems faced by developing detectors, the final focus geometry, and high-power lasers for SLC-II are almost the same as those for a higher-energy collider. The cost-effective upgrade of the SLC to allow for e^+–e^-, e-γ, and γ-γ collisions will provide an opportunity to the international HEP community that we cannot afford to miss.

In sum, then, the R&D program consists of work on solid-state lasers and free-electron lasers, experiments in the FFTB, development of a low rep-rate collider at SLC, and finally implementation of the high rep-rate, high-luminosity γ-γ collider at SLC.

VII. CONCLUSIONS

To the HEP community, the basic question is, "How seriously do you take the γ-γ, γ-e, and e-e capability"? There are many possible answers and consequences:

1. "Not at all." Then you don't need to build and instrument a second interaction region.
2. "As an add-on." Then the luminosity $L_{\gamma\text{-}\gamma}$ = (1/10) $L_{e^+\text{-}e^-}$ (and is probably not very interesting). If you change the final focus, then $L_{\gamma\text{-}\gamma}$ = (1/4 to 1/5) $L_{e^+\text{-}e^-}$.
3. "Very seriously." Then one designs rather different damping rings and, as a consequence, can achieve $L_{\gamma\text{-}\gamma} = (1/2)\, L_{e^+\text{-}e^-}$.

If the answer, A, is such that $2 \le A \le 3$, then an R&D program should be initiated now.

REFERENCES

†Section II is taken from W. Barletta *et al.*, Nucl. Instrum. Methods in Phys. Res. ***A355***, 1 (1955).

1. I.F. Ginsburg *et al.*, Nucl. Instrum. Methods in Phys. Res. ***205***, 47 (1983); I.F. Ginsburg *et al.*, *ibid* **219**, 5 (1984).
2. V.I. Telnov, Nucl. Instrum. Methods in Phys. Res. ***A294***, 72 (1990).
3. S. Chattopadhyay and A.M. Sessler, ed., Proceedings of the Gamma-Gamma Workshop, Berkeley, March 1994, Nucl. Instrum. Methods in Phys. Res. ***A355*** (1995).
4. M. Delbruck, Z. Phys. ***84***, 144 (1933).
5. C. Bula *et al.*, "Study for QED at Critical Field Strength at SLAC," Proposal for Experiment E144 (1992).
6. P. Morton & S. Chattopadhyay, Nucl. Instrum. Methods ***A355***, 138 (1995).
7. K.-J. Kim, A.M. Sessler & M. Xie, to be published.

TRANSMUTATION AND ENERGY PRODUCTION WITH HIGH POWER ACCELERATORS*

G. P. Lawrence, Los Alamos National Laboratory, Los Alamos, NM 87545 USA

Accelerator-driven transmutation offers attractive new solutions to complex nuclear problems. This paper outlines the basics of the technology, summarizes the key application areas, and discusses designs of and performance issues for the high-power proton accelerators that are required.

I. INTRODUCTION

Stimulated by advances in spallation neutron sources, several groups worldwide are now evaluating the potential of accelerator-driven transmutation technology (ADTT) to provide new solutions to pressing nuclear problems [1,2]. Applications include destruction of nuclear waste (ATW), burnup of plutonium from weapons and spent reactor fuel (ABC), production of tritium (APT), and accelerator-driven fission-energy production (ADEP) using the Th232/U233 cycle. Several ADTT variants are being pursued, with technical details differing significantly. While the principal focus in this paper is on the set of concepts developed at Los Alamos, and on their associated accelerator requirements and design issues, some information on other ADTT approaches is provided to suggest the breadth of investigation.

ADTT concepts (except for APT) are based on a high-power proton beam driving a subcritical fissioning assembly through a spallation neutron source. APT is a special case in which thermalized spallation neutrons convert He3 or Li6 into tritium in a blanket that contains no fissile material; there is no neutron multiplication or power generation. Principal elements of an ADTT system are illustrated in the Los Alamos scheme shown in Fig.1. An 800-MeV linac delivers a high-

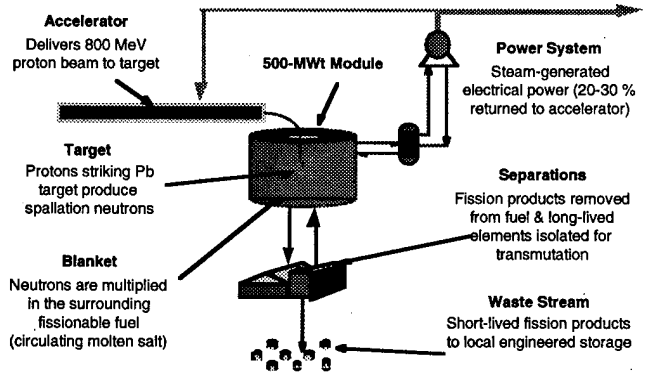


Fig. 1 General features of Los Alamos ADTT concepts.

current proton beam to a liquid Pb target, producing large numbers of spallation neutrons. These are thermalized and multiplied in a surrounding graphite-moderated blanket containing fissionable fuel and nuclear wastes in the form of circulating fluoride salts dissolved in a molten-salt carrier. Neutron multiplication in the blanket is typically in the range 10-20, which corresponds to a k_{eff} of 0.90 - 0.95, and power multiplication factors of 20 - 40. The energy produced in the high-temperature salt generates electricity with high efficiency (> 0.4); a fraction (20 - 30%) of the power is returned to the accelerator to produce the beam, with the balance available for export to the grid. Pu and other actinides in the blanket are burned to completion, while fission products are continuously removed from the circulating salt by physical, electrical, and chemical processing, and separated into long-lived and short lived isotopes. Long-lived products are returned to the blanket for transmutation, while short-lived fission products are sent to local engineered storage.

The advantage of accelerator-driven subcritical systems, in comparison with reactors is that they greatly broaden the design and operating space for the fissioning assemblies, in terms of safety and stability (fast shut-down and insensitivity to reactivity transients), superior neutron economy (extra neutrons for fission product burning), external neutrons (allowing deep burn with safe control margins), complete fuel utilization, and essentially total elimination of Pu.

II. ACCELERATOR REQUIREMENTS

Accelerator requirements for ADTT systems cover a broad range, from 400 - 1600 MeV proton energy, and 10 - 300 MW beam power. At the high end of the power range, only CW RF linacs currently provide realistic solutions. Present concepts are based on conventional (copper) accelerating structures, but the continuing development of superconducting RF (SRF) technology may in future provide cost advantages and technical attractions for some applications. At lower beam power levels, the competition is between pulsed conventional RF linacs, CW SRF linacs, high-current cyclotrons, and possibly induction linacs.

Critical relationships governing choice of beam energy and current for a given beam power requirement are the energy dependence of the spallation neutron production efficiency, and the accelerator electrical efficiency. Fig. 2 shows the calculated neutron efficiency for a stopping-length, tungsten target, plotted along with the number of spallation neutrons per proton. The former increases rapidly to a plateau beginning at about 1200 MeV, and then declines gradually at high energies as competing nuclear channels open up. For a fixed beam power in a conventional RF linac, the "wall-plug" to beam power efficiency declines with increasing energy. Because of the competing neutron-production and accelerator efficiencies, there is an optimum beam-energy band that yields the best overall plant efficiency. This band is broad and shifts to higher values as neutron requirements increase. Parameterized models based on these relations and incorporating key cost factors (per Watt of installed RF power, per meter of accelerating structure, etc.) are used to optimize ADTT system designs. In combination with beam physics constraints these

* Work supported by the US Department of Energy

0-7803-3053-6/96/$5.00 ©1996 IEEE

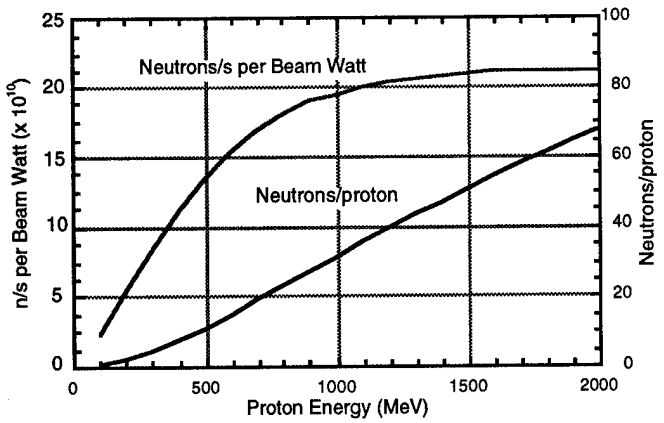


Fig. 2 Neutrons/s per beam Watt, neutrons per proton, for a beam incident on axis of cylindrical W target 50-cm diam. x 100-cm long.

models guide the choice of beam current and energy and help with the selection of other parameters, such as RF field gradient, and cavity frequency. In SRF linacs, the elimination of cavity wall losses modifies the argument, since accelerator electrical efficiency becomes nearly independent of energy. In cyclotrons, because of the repeated acceleration of beam by the same cavities, the accelerator efficiency dependence on energy is similar in shape to that of linacs, but at 20 times lower currents.

III. ADTT CONCEPTS

A. Target/Blanket Concept

All Los Alamos concepts for ADTT systems assume the beam from a single high-power linac is distributed to six 500-MWt subcritical assemblies, providing a total blanket power of 3000 MWt. Fig. 3 shows a typical module. The beam is delivered vertically through a vacuum window to an axial liquid Pb/Bi target, which provides spallation neutrons to the surrounding graphite-moderated blanket. The blanket contains materials to be burned in the form of fluorides dissolved in a molten LiF/BeF_2 salt carrier. Outside the blanket is a graphite reflector to minimize neutron leakage. The average power density in the core is 6 W/cm^3, and the average neutron flux is $1.2x10^{14}$ n/cm^2. The molten salt blanket is based on technology developed at ORNL in the 1960s.

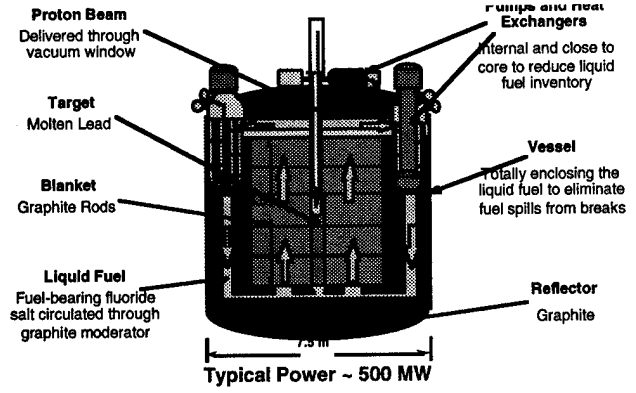


Fig. 3 ADTT molten salt target/blanket concept

In contrast with Los Alamos ADTT schemes, the thermal "energy amplifier" scheme proposed by the CERN group assumes a 10 MW beam driving a single 400-MWt target/-blanket subcritical assembly. The CERN concept uses liquid lead not only for the target but also as the blanket coolant, and uses solid (MOX) fuel elements [2]. The liquid lead technology has been extensively developed in Russia.

B. Transmutation of Nuclear Waste (ATW)

ATW systems are designed to destroy the nuclear waste from commercial power plants. Spent LWR fuel, is preprocessed to remove U and Zr, which is recycled. Th232 or weapons-Pu is added to the residue to provide the desired neutron multiplication, and the mixture is inserted into the blanket to be burned. Pu and higher actinides are fissioned, and long-lived fission products are transmuted to shorter lived or stable isotopes. With an 800-MeV, 200-mA CW linac driver, 1200 MWe is produced in the target/blanket modules; 450 MWe is used to power the accelerator, leaving 750 MWe available to the power grid. Each ATW system can handle the spent fuel of 4 LWRs of equal thermal power. Fission pro-ducts are continuously extracted from the blanket and separ-ated into two groups. Long-lived isotopes (Tc99, I129, Cs135, & others), which are the species of long-time-scale concern for the biosphere, are returned to the blanket for transmutation, while short-lived species (Cs137, etc.) are sent to engineered storage for natural decay (30-yr halflife).

C. Plutonium Burning (ABC)

The scheme for destruction of weapons-Pu provides a deep burn, destroying >99% of the material, with no fuel fabrication and reprocessing. The feed is pure Pu, which is inserted continuously in the blanket to maximize the burn depth; no new Pu from fertile isotopes is generated during the process. The ABC residue is useless for weapons purposes and can be sent to a geologic repository, or the fission products can be separated for transmutation. Using an 800-MeV, 100-mA CW linac, an ABC plant produces 1200 MWe, with 300 MWe needed to power the accelerator and 900 MWe available for the grid. An alternative Pu-burning system, proposed by General Atomics, is a hybrid reactor/accelerator scheme. Three modular helium-cooled gas reactors (MHRs) burn the weapons-Pu until the buildup of fission-products exceeds a specified value, generating electricity with high efficiency. The residual material is then burned to very low Pu levels in an accelerator-driven MHR.

D. Energy Production (ADEP)

The Los Alamos energy production concept (ADEP), converts plentiful Th232 into U233 and burns it in a molten-salt blanket, while concurrently transmuting the long-lived fission products that are generated. The fuel is natural Th, which is completely utilized without excess fissile fuel breeding. The system can be started with low-enrichment U, weapons-Pu, spent LWR fuel, or power from the grid. A representative ADEP system has beam requirements and electric power distribution similar to ABC. Preliminary economic analysis shows that ADEP plants could be competitive with

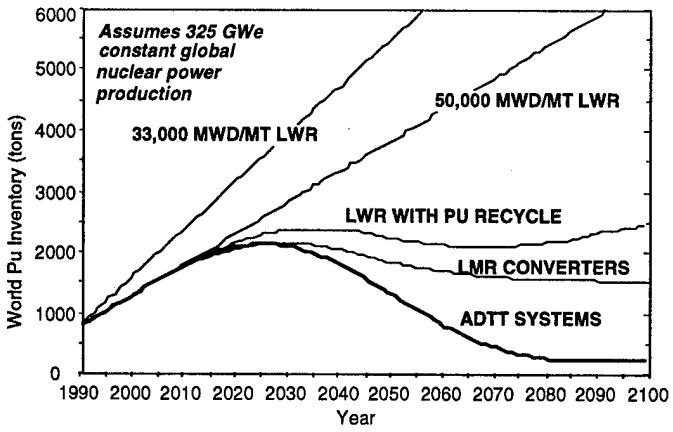


Fig.4 Estimated world Pu inventory for fission energy systems based on LWR, LMR, and ADTT fuel cycles.

conventional LWRs when all fuel cycle costs are included, and the need for long-term geologic storage of radioactive wastes would be drastically reduced.

A major benefit of ABC and ADEP systems is that they would destroy completely the Pu from decommissioned weapons, burn down the rapidly growing inventory of Pu in the spent fuel of the world's power reactors, and would not produce any new Pu. Fig.4 indicates how ADTT systems compare with several kinds of reactors and reactor fuel cycles in terms of the projected growth of world Pu inventory.

IV. CONVENTIONAL RF LINACS

A. Designs and Architectures

Representative Los Alamos high-power linac designs [3] for producing the same neutron source strength are shown in Fig.5 Both begin with low-energy linacs consisting of a microwave-driven H^+ injector, a 7-MeV 350-MHz RFQ, and a 20-MeV 350-MHz DTL. The high-energy system consists of a 100-MeV, 700-MHz CCDTL (coupled-cavity drift-tube linac) [22] followed by a 700-MHz side-coupled linac that accelerates the beam to full energy. Both use a focusing lattice with a 10-$\beta\lambda$ period, and have an average accelerating gradient (E_0T) of 1.0 MV/m. An important design feature for attaining very low beam losses is a large ratio of structure aperture to rms beam size. The aperture ratio increases from 13 at 100 MeV to 26 at 1000 MeV, and is obtained through a combination of low beam emittance and high focusing strength per unit length. Other features of the design are 1) there are no significant acceptance transitions above 20 MeV, and 2) the focusing lattice tune is nearly independent of current, which simplifies beam turn-on.

The accelerator in Fig.5-top provides a 100-mA, 1000-MeV beam (100 MW) using a single low-energy linac. The version in Fig.5-bottom provides a 750-MeV beam at 150 mA (112.5 MW), using a funneling scheme. Electric power requirements for the funneled and non-funneled system are similar, because the increased electrical efficiency of the high current solution is offset by its lower neutron production efficiency. Construction costs of the funneled system are lower because of the reduced accelerator and tunnel length. In addition to cost, funneling [5] provides other advantages, including filling all RF buckets in the high-energy linac, thus minimizing the charge per bunch. Preliminary experiments [11] have confirmed funneling principles, but a more comprehensive operational demonstration is needed.

Two different ADTT linac concepts for 1.5-GeV linacs have been described by ITEP and MRTI in Moscow. The ITEP design for a 300-mA system [14] avoids funneling by using a low-frequency RFQ (75 MHz) that can accelerate the current in a single channel. A 150-MHz DTL accelerates the beam to 150 MeV, and a 900-MHz disk-and-washer (DAW) CCL takes the beam to 1.5 GeV. Because of the low RFQ frequency, only one out of every 12 RF buckets in the CCL contains a bunch, so the charge per bunch is an order of magnitude greater than in the LANL design. The CCL gradient is comparable to the LANL choice, but because the current is higher, the overall RF efficiency is greater, 0.89. Aperture factors are estimated to range from 5.5 to 8.7.

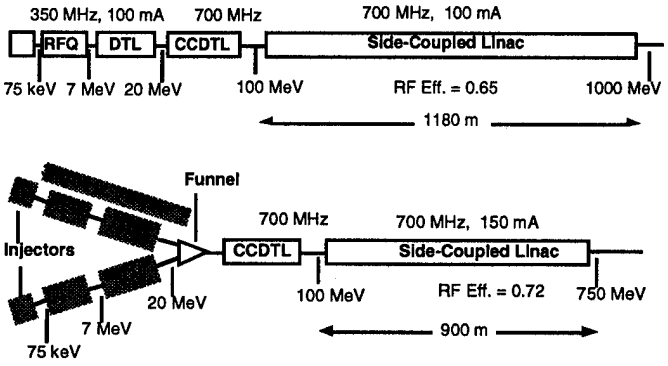


Fig 5 Representative Los Alamos ADTT linac designs.

MRTI has proposed a novel linac architecture [13] based on the use of 5 - 7 Tesla superconducting solenoids external to the accelerating structures to provide beam envelope control, thus completely separating the accelerating and focusing functions. The low energy linac begins with a 350-MHz HILBILAC accelerating a 250-mA beam to 3 MeV. This structure is followed by a conventional 350-MHz DTL accelerating the beam to 100 MeV, and finally a high energy DAW CCL operating at 1050 MHz. The external focusing scheme offers advantages in terms of beam dynamics and overall efficiency, but the superconducting solenoids could introduce operational complication.

B. Beam Physics, Beam Losses, and Halo

In high intensity ADTT linacs, a major concern is activation from beam loss in the accelerator [21]. Advances in theory and control of high-current beams achieved in the past decade (high structure frequencies, strong focusing, ramped gradients, careful matching, avoidance of large acceptance transitions, equipartitioning, etc.) provide a starting design framework for managing rms beam properties [12], but attention must also be paid to the small fraction of particles far from the core (the halo) [8,17]. Allowed beam losses are in the range 0.1 nA/m to 1 nA/m, depending on proton energy, to assure contact maintainability. This translates to 10^{-8}/m to 10^{-9}/m beam loss allowances for high-intensity ADTT linacs.

To reach such a low loss levels, the apertures in the accelerating structures and focusing elements must be large enough to contain not only the beam core but also the halo.

Experience with the LAMPF proton linac provides the best information on the potential for achieving ultra-low losses in ADTT linacs. Activation measurements following several-month operating periods at 1-mA average current show that these losses are very low through most of the CCL ($< 2x10^{-7}$/m), leading to radiation levels < 5-10 mR/hr, compatible with hands-on maintenance. ADTT linacs need to achieve fractional loss levels 10-100 times lower, a challenging objective, but one that is achievable with the much larger aperture factors attainable in modern linac designs, the greatly improved understanding of matching and emittance control, and the greater precision of beam diagnostics and control.

Much work has been done recently on understanding the factors producing beam halos, and on how to design linacs to minimize halo growth [7,16,18,23]. Several groups are carrying out analysis and simulation using a model picturing a resonant interaction between beam-edge particles and a core undergoing density and size oscillations due to transverse or longitudinal mismatches . Simulations with very large numbers of particles (10^6 - 10^7), using massively-parallel computers, have progressed from simple 1-D cases to 3-D representations of FODO channels including accelerating gaps. These simulations generally confirm the principal analytical results, which are that halo production depends strongly on the degree of mismatch, and to a weaker extent on tune depression. They also show there is a limiting radial amplitude for halo particles, at a few times the core rms radius.

C. Electrical Efficiency

To minimize operating costs, the electrical efficiency of ADTT linacs must be high. Two main factors are involved, the RF generator dc-rf conversion efficiency [6], and the cavity efficiency (beam loading). With regard to the first factor, contemporary high-power klystrons have efficiencies around 0.55-0.60 when control margin is accounted for. In advanced RF generator concepts currently being investigated (klystrode, magnicon, advanced klystron), there is the expectation that the dc-rf efficiency could be raised as high as 0.75.

To maximize the second factor, there are three parameters to consider, accelerating gradient, cavity shunt impedance, and beam current. Cost models show that a low structure gradient (1.3-1.5 MV/m) is generally optimum for CW operation, a result of the high cost of RF power relative to other elements of the linac as well as the dominance of electric power cost in the the total operating cost. The gradient also affects capital cost through length-related factors. Cavity shunt impedance can nominally be increased by going to higher-frequency structures, but in practice this improvement is restricted by the need to maintain large cavity apertures for low beam loss. The optimum operating frequency for the high-energy part of an ADTT linac (CCL) is from 600 to 1000 MHz. For conventional copper linacs, beam currents need to be $\geq$ 100 mA for highest cavity efficiencies.

E. Availability; RAM Modeling

With the incorporation of accelerators into materials production/destruction and power generating roles, a systems assessment of reliability, availability, and maintainability (RAM) becomes an important aspect of design. The requested availability of the production plant is typically > 75%, so the linac must have an availability > 85%. The use of RAM models (based on fault-trees and component reliability statistics or estimates) in system design is being incorporated in accelerator design for ADTT applications.

RF station availability is one of the major concerns for a linac having 200-400 klystrons. With projected tube lifetimes of 25,000 hours, failure rates can be on the order of 2-3 per week. A station fault can cause a large enough local energy deficiency to interrupt acceleration. New Los Alamos linac designs are studying the concept of dividing the accelerator into "super-modules" which each include an extra RF tube; the coupled accelerating structure acts as an RF combiner. When an RF tube fails, the remaining units increase their output power to compensate, allowing the failed unit to be serviced or replaced without a significant beam interruption.

V. CYCLOTRONS

The CERN ADTT group is studying Th232/U233 ADEP schemes [2] which have beam drive requirements in the 10-20 MW range. For such relatively modest beam requirements, the possibility of using cyclotron technology comes into play. The CERN group, is developing a concept based on a 3-stage cascade of cyclotrons [20], with each chain delivering a 10 mA beam at 1,000 MeV (10 MW). Cyclotron designers at PSI are also assessing the feasibility of such a machine [4]. In one scheme, depticted in Fig. 6, the cascade begins with two 10-MeV isochronous cyclotrons injecting 5-mA beams into a 120-MeV intermediate-energy 4-sector cyclotron. This machine delivers a 10-mA beam to a 10-sector ring cyclotron that accelerates the protons to approximately 1000 MeV. The final stage is an extension of the 590-MeV ring cyclotron design at

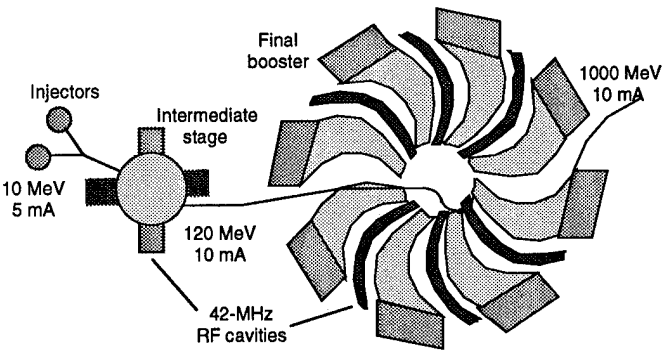


Fig. 6 CERN/PSI multi-stage cyclotron scheme for producing a 10 MW beam at 1 GeV.

PSI, which has recently been upgraded to operate at 1.5 mA. The operating frequency of the cascade is 42 MHz.

The perceived advantages of a cyclotron scheme for the 10-MW power range are compactness and high power effi-

ciency at relatively low beam currents. The latter property derives from the large number of beam orbits passing through each RF cavity; a cavity efficiency of 0.70 is achieved with a 10 mA beam, leading to an overall machine efficiency of 0.40, similar to that of a 200-mA linac. The CERN ADEP scheme would drive a single target/-blanket module with a 10-MW beam, producing 400 MWt, which would generate 155 MWe. About 25 MW would be needed to run the accelerator system, leaving 130 MWe for export to the grid.

Design issues for an advanced high-power cyclotron lie in the details of transverse and longitudinal beam dynamics, in achieving large orbit separations for low-loss extraction, and in how to supply the large RF power needed in each cavity to provide the requisite energy gain per turn. To obtain low extraction losses, the number of turns in the high-energy cyclotron must be low (140), implying an energy gain of 6 MeV per turn. For reference, extraction losses in the upgraded PSI cyclotron are $< 2 \times 10^{-4}$ at 1.0 mA, which is a tolerable. In addition to the localized extraction loss there is concern over distributed beam loss inside the cyclotron from beam halo.

Cyclotron designers believe that 10 mA is achievable in an advanced cyclotron using conventional (pole-edge) focusing and conventional RF cavities. To go further would probably require a strong-focusing system using very high energy gain per turn, as in a separated orbit cyclotron (SOC). Such a system, which might require superconducting RF cavities and superconducting magnets, could be based on the design developed for a small superconducting SOC prototype being built at U. Munich for heavy ion beams [19].

VI. SUPERCONDUCTING RF LINACS

The growing maturity of superconducting RF (SRF) technology provides a potentially attractive alternate approach for high-intensity proton linacs [15]. The advantages of an SRF accelerator would be significantly reduced operating costs because of the elimination of RF wall losses, higher gradients which could reduce linac length, and larger structure apertures, which would reduce the beam loss threat. The operating power advantage increases as the beam power requirement decreases; for a 100 MW beam requirement, the electric power reduction is about 20%.

A possible SRF-based design to compete with the 100-MW linac concepts in Fig.5 might involve a conventional low-energy linac (to 100 MeV), followed by a high-energy SRF linac based on multi-cell elliptical cavities. Preliminary design parameters could be 1.2 GeV, 80 mA CW, 700-MHz SRF cavities combined in groups of 2-4 (depending on β), with each group fed by a 250-to-400-kW power coupler.

Design issues specific to high-intensity proton linacs [9] include the complexity of structure assembly, long-term availability, the necessity for low-temperature (2-4K) refrigeration , the lack of proven medium-β accelerating structures, and power coupler limitations. In addition, it is necessary to gain experience in operation of prototype SRF cavity systems with high-current beams. The practical gradients that can be realized will generally be bounded by the power coupler performance. This technology has made significant advances in the past year or so, and many believe that 300-500 kW per coupler will soon be practical.

VII. ACKNOWLEDGEMENTS

The author thanks F. Venneri and E. Heighway of the Los Alamos ADTT Group for helpful updates on transmutation technology and applications, and colleagues in the Accelerator Division for useful comments on the draft of this paper.

VIII. REFERENCES

[1] C.D. Bowman, "Overview of the Los Alamos Accelerator-Driven Transmutation Technology Program", Proc. of 1994 International Conf. on Accelerator-Driven Transmutation Technologies and Applications, Las Vegas, July 25-29, 1994.

[2] C. Rubbia, "The Energy Amplifier Concept: A Solid-Phase Accelerator -Driven Subcritical Th/233U Breeder for Nuclear Energy Production with Minimal Actinide Waste", ibid.

[3] G. Lawrence, "Los Alamos High-Power Proton Linac Designs", ibid.

[4] Th. Stammbach, S. Adam, H.R. Fitze, W. Joho, and U. Schryber, "Potential of Cyclotron-Based Accelerators for Energy Production and Transmutation", ibid.

[5] S. Nath, "Funneling in LANL high intensity Linac Designs," ibid.

[6] M. Lynch, et al., "Important Requirements for RF Generators for Accelerator-Driven Transmutation Technologies", ibid.

[7] R. Ryne, "Recent Results in Analysis and Simulation of Beam Halo", ibid.

[8] M. Reiser, "Beam Physics Design Strategy for a High-Current RF Linac", ibid.

[9] J.R. Delayen and C.L.Bohn, "Overview of Superconducting RF Technology and its Application to High-Current Linacs", ibid.

[11] K.F. Johnson, et al., "The Single-Beam Funneling Demonstration: Experiment and Simulation", Proc. 1990 Linear Accelerator Conf., Albuquerque, NM, September, 1990, pp. 701-703.

[12] T.P. Wangler, et al., "Linear Accelerator for Production of Tritium: Physics Design Challenges", ibid. pp. 548-552.

[13] B.P. Murin, et al., "High-Current Low-Energy RF Ion Acceler-ator", ibid, p. 707-709.

[14] I.M. Kapchinsky, et al., "Linear Accelerator for Plutonium Conversion and Transmutation of NPP Wastes", Proc. 1993 Particle Accelerator Conf., Washington DC, May 1993, pp. 1675-1680.

[15] J.R. Delayen et al. "Design Considerations for High-Current Superconducting Ion Linacs", ibid., pp. 1715-1717.

[16] J.S. O'Connell, et al, "Beam Halo Formation from Space-Charge Dominated Beams in Uniform Focusing Channels", ibid, p. 3657-3659.

[17] R.A. Jameson, "Design for Low Beam Loss in Accelerators for Intense Neutron Source Applications", ibid., p. 3926-3930.

[18] J.M. Lagniel, "Chaotic Behaviour Induced by Space Charge", Proc. 1994 European Particle Accel. Conf., London, June 1994.

[19] U. Trinks, "Exotic Cyclotrons – Future Cyclotrons", Proc. CERN Accelerator School, LaHulpe, 1994, to be published.

[20] C. Rubbia, P. Mandrillon, and N. Fetier, "A High-Intensity Accelerator for Driving the Energy Amplifier for Nuclear Energy Production", Proc. 1994 European Particle Accelerator Conference, EPAC94, London, June, 1994, 270-272.

[21] G.P. Lawrence, "Critical Design Issues of High-Intensity Proton Linacs", ibid. 236-240.

[22] J.H. Billen et al., "A Versatile High-Power Proton Linac for Accelerator-Driven Transmutation Technologies", Proc. 1995 Particle Accelerator Conf., Dallas, TX, May 1-5, 1995.

[23] R.D. Ryne, "Halos of Intense Proton Beams," ibid.

THE LARGE HADRON COLLIDER

L.R. Evans, European Organization for Nuclear Research, CH - 1211 Geneva 23, Switzerland

The Large Hadron Collider (LHC) project was approved by the CERN Council in December 1994. The machine will provide proton-proton collisions with a centre of mass energy of 14 TeV and an unprecedented luminosity of 10^{34} cm^{-2} s^{-1}. In order to achieve the design energy within the constraint of the 27 km circumference LEP tunnel, the magnet system must operate in superfluid helium below 2 K, with a dipole field of 8.4 Tesla. In addition, space limitations in the tunnel as well as cost considerations dictate a two-in-one magnet design, where the two rings are incorporated into the same cryostat. The machine will also provide heavy (Pb) ion collisions with a luminosity of 10^{27} cm^{-2} s^{-1} using the existing CERN ion facility. Space will be kept above the LHC for the eventual reinstallation of components of the LEP machine to provide future e-p collisions if the physics case justifies it.

I. INTRODUCTION

The CERN Large Hadron Collider will provide proton-proton collisions with a centre of mass energy up to 14 TeV with a nominal luminosity of 10^{34} cm^{-2} s^{-1} and heavy ion (Pb-Pb) collisions with a luminosity of up to 10^{27} cm^{-2} s^{-1}. The reference design of the LHC has been presented at several conferences and two design reports exist [1, 2]. The main parameters of the machine for proton-proton operation are given in Table 1.

In view of the fact that the machine will be installed in the existing 27 km circumference LEP tunnel, considerable technological innovation is needed to fit the two rings into the tunnel cross section whilst leaving enough space for an eventual lepton ring. The LHC will be installed on the tunnel floor after removal of the LEP ring. However, space will be kept free above the LHC for the future installation of a lepton machine using LEP components for e-p collisions (Figure 1).

The basic layout of the LHC mirrors that of LEP, with eight long straight sections each approximately 500 meters in length available for experimental insertions or utilities (Figure 2). Two high luminosity proton-proton experiments are located at diametrically opposite straight sections, Point 1 (ATLAS) and Point 5 (CMS). Two more low-beta insertions are located at Point 2 (ALICE, Pb ions) and Point 8 (B-physics), which also contain the two injection systems. The beams cross from one ring to the other at these four locations.

The remaining four long straight sections do not have beam crossings. Points 3 and 7 are used for beam "cleaning" and collimation. The beam abort system is located at Point 6 and Point 4 remains spare.

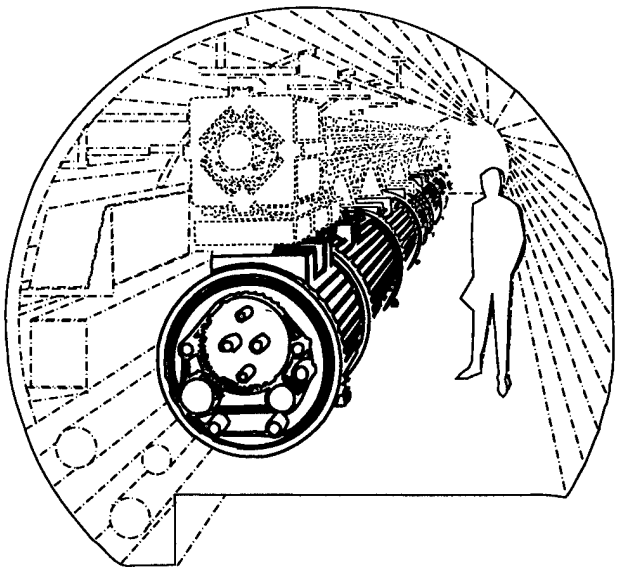


Figure 1: LHC with space for a future lepton machine

Table 1

Energy	*(TeV)*	7.0
Dipole field	*(T)*	8.4
Coil aperture	*(mm)*	56
Distance between apertures	*(mm)*	180
Luminosity	*(cm^{-2} s^{-1})*	10^{34}
Beam-beam parameter		0.0032
Injection energy	*(GeV)*	450
Circulating current/beam	*(A)*	0.53
Bunch spacing	*(ns)*	25
Particles per bunch		$1x10^{11}$
Stored beam energy	*(MJ)*	332
Normalized transverse emittance	*(μm)*	3.75
R.m.s. bunch length	*(m)*	0.075
Beta values at I.P.	*(m)*	0.5
Full crossing angle	*(μrad)*	200
Beam lifetime	*(h)*	22
Luminosity lifetime	*(h)*	10
Energy loss per turn	*(keV)*	6.9
Critical photon energy	*(eV)*	45.6
Total radiated power per beam	*(kW)*	3.7

0-7803-3053-6/96/$5.00 ©1996 IEEE

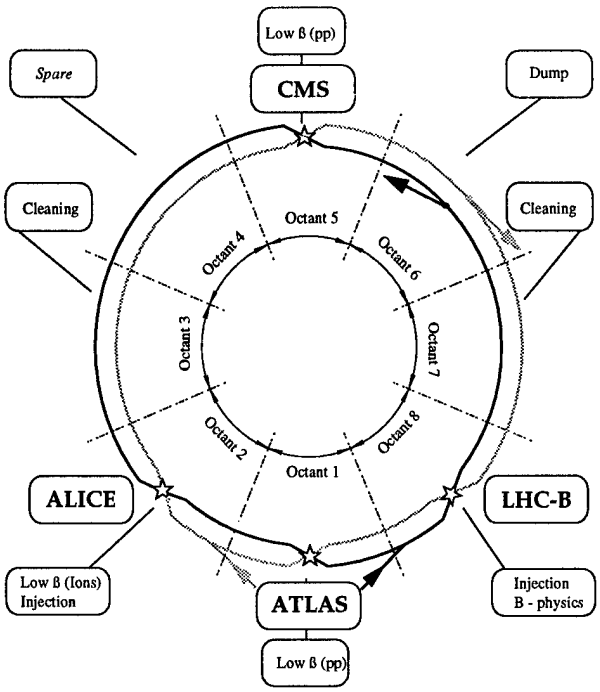


Figure 2: Schematic layout of LHC

II. INJECTORS AND INJECTION PROCESS

The existing accelerator chain (Linac/Booster/PS/ SPS) will be used for LHC proton injection. The achievement of the small transverse emittance, high bunch intensity and bunch spacing shown in Table 1 requires substantial modifications in the PS and Booster. In the Booster a new harmonic h=1 system will be needed for acceleration with a superimposed h=2 system for bunch shaping in order to minimize the space charge effects. In addition, in order to reduce the Laslett detuning in the PS at injection, the booster energy must be upgraded from 1 GeV to 1.4 GeV (kinetic).

In the PS, the main hardware addition will be a harmonic 84 (40 MHz) RF system for rebunching the beams with the correct time structure for the LHC. In the SPS, the main additions are an 80 MHz (700 kV) RF system for capturing the injected beam and a 400 MHz superconducting RF system (6 MV peak) in order to match the bunches to the LHC buckets.

Two new extraction systems at Points 4 and 6 of the SPS are needed together with two new transfer lines at 450 GeV/c to Point 8 of the LHC (counter clockwise beam) and Point 2 (clockwise beam). Injection into the LHC is made horizontally with copper septum/kicker systems. Both injections are made into the outside ring.

The filling sequence starts with the injection of three bunch trains with the right spacing between bunches (25 nsec) into the SPS on three successive PS cycles each separated by 3.6 seconds, filling one third of the SPS circumference. The SPS then ramps to 450 GeV/c and transfers each batch (each containing 4×10^{13} protons) to one or the other of the LHC rings. This is repeated 12 times per ring with a cycle time of 16.8 seconds.

During the injection process the low-beta insertions are detuned in order to reduce the beta values to a tolerable level in the insertion quadrupoles. Once both rings are filled, the beams are accelerated to the nominal collision energy in about 20 minutes.

III. MACHINE LAYOUT

A. The regular arcs

The arcs contain 23 regular lattice periods per octant. Each lattice period, 106.9 meters in length, is made up of six two-in-one dipoles, each with a magnetic length of 14.2 meters [3]. Each dipole contains short sextupole and decapole correctors in order to compensate for unwanted field harmonics. The lattice quadrupoles are 3 meters long with a maximum gradient of 250 T/m and are powered separately from the dipoles. The coil aperture is the same as that of the dipoles (56 mm). The quadrupoles are integrated into "short straight sections" which also contain a closed orbit correction dipole, chromaticity correction sextupoles and some free space for either an octupole or a skew quadrupole. The short straight section also contains a beam pick-up monitor and a cryogenic service unit for the production of the primary superfluid helium needed to cool each half-cell.

The nominal phase advance per cell is 90 degrees although it will be possible to split the horizontal and vertical tunes by a few units in order to make the machine less sensitive to systematic coupling.

B. The dispersion suppressors

The transitions from each of the arcs to the long straight sections are made through "dispersion suppressors". Each dispersion suppressor consists of two perturbed lattice periods with four dipoles per period instead of six and four independently powered quadrupole units. In order to reduce the number of high current feedthroughs, each quadrupole unit consists of a main quadrupole powered in series with the lattice together with a low current trim quadrupole 1.5 meters long, independently powered to allow for optics variations during squeezing of the insertions to their final configurations.

C. The low-beta insertions

The layout of a low beta insertion is shown in Figure 3 together with the optical functions during collision ($ß^* = 0.5$ m). The insertion is antisymmetric and consists of a matching section (the outer triplet) for detuning the optics, and an inner triplet focusing the beams to the interaction point. Between the two, a pair of recombination dipoles bring the beams into a common channel with a small crossing angle ($\pm$ 100 µrad) at the interaction point. The outer triplet quadrupoles are two-in-one magnets with the

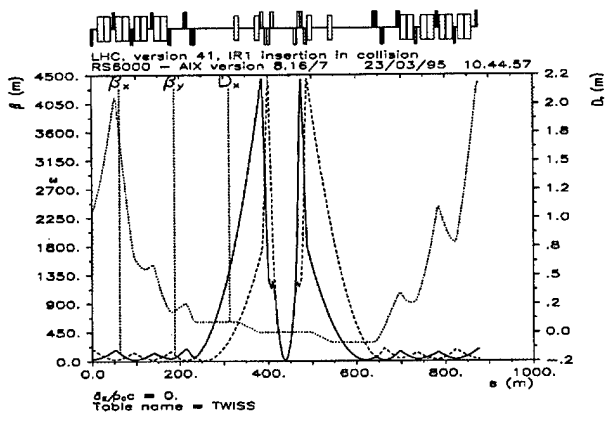


Figure 3: Low-beta insertion

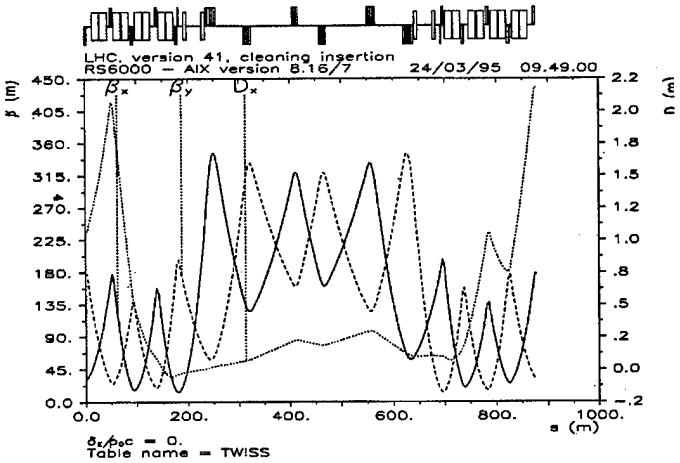


Figure 4: Cleaning insertion

same cross section as the regular lattice quadrupoles whereas the inner triplet quadrupoles are single bore with the aperture increased from 56 mm to 70 mm (gradient 250 T/m). In the two high luminosity insertions, a free space of ± 23 meters between the two inner triplets is available for the experiments, whereas for the other two insertions this space is reduced to ± 21 meters to allow more room for injection.

During injection and acceleration, the insertion is "detuned", bringing the maximum beta value down from its collision value of about 4500 m to below 400 m.

D. The cleaning insertions

The rôle of the cleaning insertion is to allow for collimation and cleaning of the beam halo in order to minimize the background in the experimental detectors as well as the beam losses in the cryogenic parts of the machine. Two such insertions are foreseen at Points 3 and 7.

The insertion consists of a "pseudo FODO" structure containing only classical magnets (Figure 4). At each end of the insertion there is a double dogleg consisting of a pair of dipoles of opposite polarity which increases the beam separation from 180 mm to 210 mm. This ensures that the spray of neutral secondaries from collimators between the dipoles is directed away from the downstream arc and also makes the design of the two-in one warm quadrupoles easier.

E. The beam abort insertion

The purpose of the abort insertion is to dump the beams in a clean and safe way at the end of physics runs or to protect the machine in case of hardware failure or beam instability. The optics of the insertion is shown in Figure 5.

The optics is designed to provide a very long (340 m) drift region at the centre of which is placed a vertically deflecting double Lambertson septum. The beam dump kickers located at the beginning of the straight section deflect the beams horizontally across the septum in which they are vertically extracted from the machine.

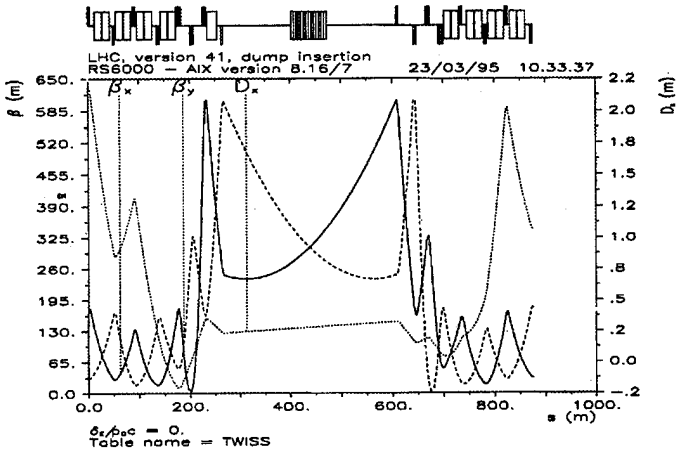


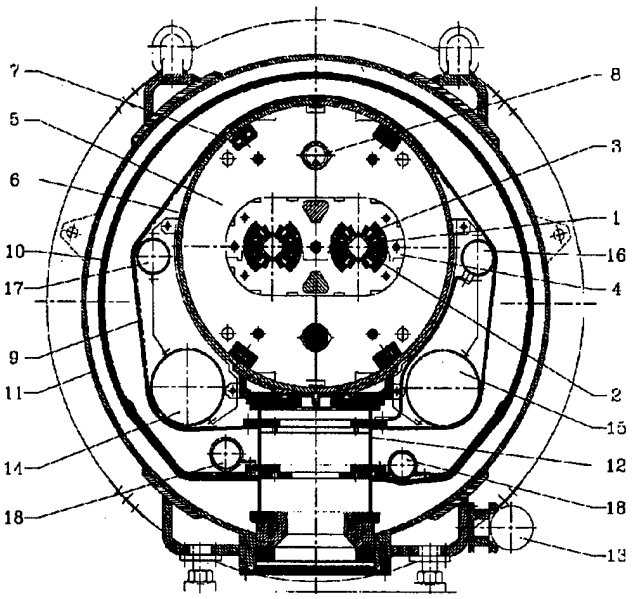
Figure 5: Dump insertion

IV. MAGNETS

A. Overall design

The magnet system [4] contains many innovative features in order to reduce cost and to fit the two rings into the constrained geometry of the LEP tunnel. The basic structure of both dipoles and quadrupoles are the two-in one design, where the two beam channels are incorporated into a single iron yoke and cryostat (Figure 6) and operating in superfluid helium to achieve the very high guide field required. In order to retain the large bursting force of more than 500 tons per meter the coils must be very firmly clamped in a rigid mechanical structure. Combined aluminium collars have been chosen instead of the alternative separate stainless steel collars in order to minimise the pre-stress required at room temperature and to ensure the best possible parallelism between the dipole fields in the two channels.

The main characteristics of the dipole magnet are given in Table 2. The regular lattice and dispersion suppressors will require 1232 dipoles and 368 normal quadrupoles as well as special quadrupoles in the matching and insertion regions.



1. Beam screen, 2. Beam pipe, 3. Superconducting coils, 4. Non-magnetic collars, 5. Iron yoke, 6. Shrinking cylinder/ HeII vessel, 7. Sc. bus-bars, 8. Heat exchanger pipe, 9. Radiative insulation, 10. Thermal shield (55 to 75 K), 11. Vacuum vessel, 12. Support post, 13. Alignment target, 14. 1.8 K GHe pipe, 15. 20 K GHe pipe, 16. 4.5 K GHe pipe, 17. 2.2 K GHe pipe, 18. 50÷75 K GHe pipe.

Figure 6: Cross section of the dipole magnet.

Table 2

Dipole Parameters

Operational field	*(T)*	8.4
Coil aperture	*(mm)*	56
Magnetic length	*(m)*	14.2
Operating current	*(A)*	12000
Operating temperature	*(K)*	1.9
Coil turns per beam channel:		
inner shell		30
outer shell		52
Distance between aperture axes	*(mm)*	180
Outer diameter of cold mass	*(mm)*	560
Overall length of cold mass	*(mm)*	15140
Outer diameter of cryostat	*(mm)*	980
Overall mass of cryomagnet	*(t)*	31
Stored energy for both channels	*(MJ)*	7.2
Self-inductance for both channels	*(mH)*	110

In order to achieve the unprecedented value for an accelerator magnet of 8.4 Tesla in the dipoles, the magnets must be cooled to 1.9 K, below the lambda point of helium. The magnet cryostat must therefore be of an advanced design in order to limit the heat influx to the 1.9 K cold mass. This requires two layers of thermal insulation to intercept the radiated heat at temperature levels of 50 K and 4.5 K as well as a careful design of the cold mass support structure. The cryostat also serves to carry the considerable amount of cryogenic piping, thus obviating the need for a separate line.

B. Hardware status

A considerable amount of development work on the dipoles and quadrupoles has already been done. More than a dozen short models have been constructed and tested. All of these models have exceeded 9 T with the best reaching 10.5 T.

Four 10 meter long industrially built prototypes have been tested. All magnets have exceeded 9 T with some training. Detailed results are given elsewhere in these proceedings [5]. In addition, two full size quadrupoles have been designed and constructed under a CERN-CEA/Saclay collaboration agreement. Both magnets have reached their design gradient with very few training quenches.

Two long dipoles and a short straight section containing one of the quadrupoles have been assembled into a "string", simulating the basic half-cell, cryogenically cooled, powered and protected in an identical way to the real machine. This unit became operational at the end of 1994 and has run at the LHC nominal design field for an extended period. More details can be found elsewhere in these proceedings [6].

V. CRYOGENICS

Cooling the 30'000 tons of material in the LHC magnets poses a particular challenge. The elementary LHC cooling loop matches the periodicity of the machine lattice and corresponds to the half-cell of 53 m length (Figure 7). Static superfluid helium pressurised at 1 bar permeating the magnet laminations is cooled by heat exchange with saturated superfluid helium flowing through a tube running through the magnet chain over the whole length of the half-cell. Sub-cooled helium (2.2 K) is tapped from line A, expanded to saturation through a Joule-Thomson valve and sent to the end of the loop from where it returns, gradually vapourising as it gathers heat in the heat exchanger tube. The whole loop including heat exchanger tube and phase separator is maintained at saturation pressure by line B, through which cold helium vapour is pumped back to the cryoplant.

An important advantage of using the latent heat of vapourisation is that the temperature of each magnet is independent of its distance from the cryoplant. A key technology for the attainment of large capacity refrigeration in this temperature range is the development of cold sub-atmospheric helium compressors. The design of these units builds on previous experience at the Tore Supra tokamak and at CEBAF. In view of the importance of this technology, CERN has launched in collaboration with CEA in Grenoble a comprehensive development programme on the design, construction and testing of a prototype LHC multistage cold compressor box.

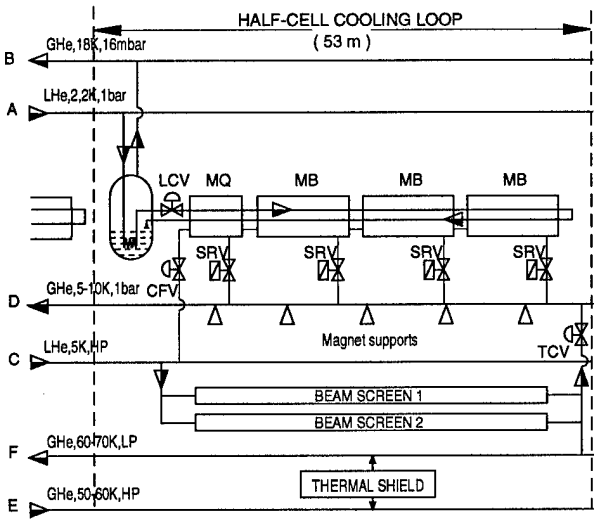


Figure 7: The elementary cooling loop

The four existing LEP cryoplants, each of 12 kW capacity at 4.5 K will be boosted to 18 kW and supplemented by a further four units of the same capacity. The eight cryogenic units will be concentrated at the four even LEP pits where adequate infrastructure including compressor buildings and cooling towers already exist. Consequently, the whole octant, 3.4 kms in length must be supplied with liquid helium from the even points.

VI. THE RF SYSTEM

The radiofrequency system will be installed at Point 8. In order to ensure sufficiently short bunches in collision and avoid RF noise diffusion, a voltage of 16 MV per beam at the second harmonic (400.8 MHz) of the SPS frequency is needed. This will be provided by a set of eight superconducting cavities. A prototype cavity has been built and installed in the SPS for tests, where three such cavities will also be needed to match the longitudinal phase space between the two machines. During acceleration, it is necessary to increase the bunch area from the SPS value of 1 eV.s. to 2.5 eV.s. in order to obtain a good intrabeam scattering lifetime at collision energy.

VII. VACUUM

The LHC beam vacuum poses particular problems [7]. Due to the synchrotron radiation emitted by the protons (~ 4 kW per ring at 7 TeV) and the heating due to the image currents in the wall of the vacuum chamber, the magnet cold bore at 1.8 K must be shielded from the beam, otherwise the required cryogenic power would become excessive. (1 Watt at 2 K needs approximately 1 kW at room temperature.) An inner liner cooled to around 20 K through tubes carrying high pressure gas will therefore be installed inside the cold bore.

Synchrotron radiation impinging on this liner will cause gas to be desorbed from the bulk material which will in turn be cryopumped to the surface of the liner. This is particularly undesirable especially for hydrogen. Once a surface layer of this gas builds up the pressure will rise to that of the vapour pressure of hydrogen at the temperature of the liner, more than two orders of magnitude higher than required for an adequate beam lifetime. In order to avoid this, slots must be cut in the liner so that hydrogen can be cryopumped by the cold bore surface at much lower temperature.

VIII. CONCLUSIONS

The considerable amount of R&D accomplished over the past few years have validated the main technical choices for the construction of the LHC. In particular, the two-in-one magnet structure operating in high field in helium II has proved to be a cost effective and viable solution for obtaining the required performance.

The main lattice parameters and the allocation of long straight sections have now been fixed. The detailed design of the specialised insertions is making good progress.

IX. ACKNOWLEDGEMENTS

It is a pleasure to acknowledge the outstanding contribution of Giorgio Brianti to this project.

X. REFERENCES

[1] The LHC Study Group, Design Study of the Large Hadron Collider, CERN 91-03 (1991)

[2] The LHC Study Group, The Large Hadron Collider Accelerator project, CERN AC/93-03 (LHC) (1993).

[3] J.P. Koutchouk et al., The Lattice Lay-out and Optics of LHC version 4.1, SL/Note 95-38 (AP), unpublished (1995).

[4] R. Perin and J. Vlogaert, Magnets for the Large Hadron Collider, Proc. European Conference on Applied Superconductivity, Göttingen, Germany (1993).

[5] R. Perin, Superconducting magnets, these proceedings.

[6] P. Faugeras, Assembly and Commissioning of the LHC Test String, these proceedings.

[7] A. Mathewson, Vacuum Technology for Superconducting Colliders, Proc. 1993 Particle Accelerator Conference, 3823 (1993).

FRONTIERS OF PARTICLE PHYSICS

L. Okun, ITEP, Moscow, 117259, Russia

I. THREE SCALES IN PARTICLE PHYSICS

Among the known energy scales in particle physics, it is natural to single out the three most important ones: the hadronic scale $\sim$ 1 GeV, the electroweak scale, often called the Fermi scale, $\sim 10^2$ GeV, and the Planck scale $\sim 10^{19}$ GeV.

The hadronic scale is set by the mass of light hadrons: ρ-mesons and nucleons. The Fermi scale is set by the Fermi coupling constant G_F or by the value of the hypothetical higgs vacuum expectation value $\eta = (\sqrt{2}G_F)^{1/2} \approx 246$ GeV (in units $\hbar, c = 1$).

The Planck scale is set by the Planck mass m_P expressed in terms of G_N, $\hbar$, c ($m_P = \sqrt{\hbar c/G_h} \approx 10^{19}$ GeV), where G_N is the Newton gravitational constant.

II. THE TOP QUARK MASS: ITS DIRECT AND INDIRECT VALUES

The most important experimental achievement of recent years is definitely the discovery of the top quark at the Tevatron. We anxiously waited for it for two decades. Now we have this long-awaited fundamental fermion with its largest and most natural value of mass (in the Fermi scale). But our understanding of particle physics does not seem to have changed substantially by its discovery.

What were the main hopes connected with the top, besides the obvious completion of the third generation? They were based on the expectation that by measuring directly the top mass m_t with accuracy, say, better than 10 GeV, and by comparing it with the value of m_t derived indirectly from the precision measurements of the electroweak radiative corrections, we would be able to figure out the most probable value of the mass of the higgs m_h. (Both m_t and m_h enter into the expressions for electroweak radiative corrections to such electroweak observables as m_W/m_Z and the decay amplitudes of the Z boson, which were and are measured with highest achievable precision by UA2, CDF, D0, four famous detectors at LEP, and SLD at SLAC.)

A discrepancy between the direct and indirect values of m_t could even have served as a signal of new physics. We have now

$$m_t(\text{direct}) = 180 \pm 12 \text{ GeV},$$

$$m_t(\text{indirect}) = (160, 180, 200) \pm 9 \pm 5 \text{ GeV}.$$

The direct value is derived by a straightforward averaging of CDF and D0 results; the indirect by a global fit of all electroweak observables in the framework of the Minimal Standard Model. The three central values correspond to $m_h = 60$, 300, and 1000 GeV, respectively; ± 9 is statistical uncertainty, ± 5 is due to the uncertainty in $\bar{\alpha} \equiv \alpha(m_Z) = 1/128.89(9)$.

We see that we are, in a sense, unlucky: the direct value is right in the center of the indirect interval.

III. THE HIGGS AND SUPERSYMMETRY

If the higgs is heavy, then farewell to supersymmetry, which requires a light higgs. Theorists of course would prefer a light higgs, with $m_h < 130$ GeV, accompanied by many supersymmetric partners of our particles: neutral and charged.

There may be a hint of the existence of light squarks and gluinos, with masses of order 100 GeV. I refer here to the 2σ discrepancy between experimental data and theoretical expectations on the decay of Z bosons into $b\bar{b}$ pairs. Another discrepancy which may be cured by light sparticles is the difference in the values of the strong coupling constant $\alpha_S(m_Z)$ extracted 1) from the global fit of the Z boson decays (0.125(5)) and 2) from the sum rules involving masses and electronic decay widths of the known upsilon states, and also from deep inelastic scattering (0.110).

If the higgs is very light, below 95 GeV, it could be produced and detected at LEP 200 (or more precisely LEP 195; note that LEP 210 could reach $m_h = 110$ GeV). (The lightest charginos could be also detected by LEP 200.) For the discovery of a heavier higgs, the Next Linear Collider, with energy 2×250 GeV would be the best. The point is that a light higgs decaying mainly into $b\bar{b}$, $\tau\bar{\tau}$, and $\gamma\gamma$ is a very difficult target for the LHC. If the higgs is not light enough for LEP 200, then the discovery of this pivotal particle will be postponed until the next century. Many of us will pass away with a question mark in our minds on the central point of particle physics—on the origin of mass and symmetry breaking in Nature.

IV. NEUTRINO OSCILLATIONS

Great progress has been made in recent years in neutrino physics, first of all in solar neutrinos. As you know, there are several major kinds of solar neutrinos: so called boron neutrinos (from the β decay of ^8B), beryllium neutrinos (from the electron capture in ^7Be), and proton neutrinos (from the reactions $pp \to de^+\nu_e$ and $pe^-p \to d\nu_e$.) In spite of having different names, all of them are ordinary electron neutrinos ν_e and differ only by their energy spectra.

For many years the Homestake chlorine experiment, which is sensitive to the boron and beryllium neutrinos, has signalled a flux about one-third of what was expected. This was traditionally considered to be a deficit of boron neutrinos. The water detector Kamiokande, sensitive to boron neutrinos only, has shown a deficit close to half. But the most intriguing are the data from two gallium detectors sensitive mainly to proton and beryllium neutrinos (Gallex and Sage) which see a signal of about two-thirds of that expected. The main suspects are now beryllium neutrinos, which seem almost to disappear on their way to the detectors. The most probable explanation for this disappearance is the transformation of ν_e into ν_μ or ν_τ or in a new unknown sterile form ν_s during the travel inside the sun.

In order to undergo such transformations, the neutrinos must have a nonvanishing mass difference, $\Delta m^2 \approx 10^{-5}$ eV^2. An-

0-7803-3053-6/96/$5.00 ©1996 IEEE

other interesting phenomenon is the deficit of muonic neutrinos created in the atmosphere of the earth. This deficit, seen at Kamiokande, may be caused by the transformation $\nu_\mu \to \nu_\tau$ and/or $\nu_\mu \to \nu_s$. There are two CERN experiments searching for the $\nu_\mu \to \nu_\tau$ transformation; they are short-based. Additional long-base experiments using beams of neutrinos from accelerators and far away detectors may be very interesting. It is not clear at present what is the scale at which the neutrino masses are determined in Nature. Possibly it is the Grand Unification Scale around 10^{16} GeV.

V. OTHER FRONTIERS

I have touched on a number of the experiments which mark the frontiers of present day particle physics. I don't have time to speak about many other extremely important experiments, which either have been carried out or will start running in the near future. I can only list some of them:

- Studies of CP violation, especially in the decays of B mesons.
- Studies of hadron structure with lepton beams. (Recently, a vast new kinematical region was opened by HERA.)
- Studies of soft and hard hadron collisions.
- Attempts to create the quark-gluon plasma in heavy ion collisions (many physicists hope to see it at RICH).
- Quantitative measurements of the heavy flavour hadron's properties.
- Spectroscopy of light flavour hadrons, including glueballs.
- Searches for very rare decays of kaons and muons, which may uncover flavour-changing neutral currents and/or higher order electroweak effects.
- Searches for the dark matter particles in space and on the earth.

VI. THREE FUNDAMENTAL CONSTANTS

The frontiers of particle physics are multidimensional and have a very complex topology. Assume all of the experiments listed above have already been performed and are immortalized in the Particle Properties Data volume. Particle physics will still be far from complete. This follows from the simple fact that none of the above experiments deals with gravity—one of the most fundamental physical forces. Since Newton, we have known that this force, both on the earth and in the skies, is characterized by the same Newtonian coupling (interaction) constant G_N.

Our century has brought us a plethora of physical constants—particle masses, interaction constants, scales, etc. But it seems obvious that the most fundamental of them, in addition to G_N, are c, the maximal velocity of particles in vacuum, and $\hbar$, the quantum of action and of angular momentum (in fact, the latter is $\hbar/2$). The numerical values of G_N, $\hbar$, and c, when expressed in grams, seconds and meters, have no deep meaning, because grams, seconds and meters are man-made units: they were fixed historically, but physically are quite arbitrary. What is of paramount importance is the very existence of G_N, $\hbar$, and c.

VII. THE CUBE OF THEORIES

Consider three orthogonal axes x, y, and z. Put $1/c$ on x, $\hbar$ on y, and G_N on z at equal distances from the origin. Now we are ready to contemplate the cube of physical theories associated with the name of Matvey Bronshtein, the Soviet theorist executed in 1938 at the age of 32.

At the origin we have non-relativistic mechanics (NM). When velocity is on the order of c, we have special relativity (SR). When action or angular momentum is on the order of $\hbar$, we have Quantum Mechanics (QM). Thus we have marked three corners of a square in the xy plane. The fourth corner represents quantum field theory (QFT) which came from the merging of SR and QM.

VIII. THE STANDARD MODEL OF QFT

QFT is the quintessence of present day particle physics. All experimental frontiers discussed or mentioned above are described in the framework of QFT, in its language. Non-relativistic atomic, molecular, and solid state physics, classical electrodynamics, optics, etc., are limiting cases of QFT. It also describes nuclear phenomena, and strong and weak interactions of hadrons and leptons. All of these treasures of knowledge have a rather bureaucratic dry name: the Standard Model. The SM is based on a famous gauge symmetry group $SU(3) \times SU(2) \times U(1)$. The gauge bosons—photon, $W^\pm$, and Z^0 bosons and gluons—each have couplings which in units $\hbar$, c are dimensionless. Their squares are denoted by α, α_W, and α_S for electromagnetic, weak, and strong interactions, respectively. These couplings are functions of momentum transfer q^2: they are running. For example, $\alpha(q^2 = 0) = 1/137.039895(61)$, while $\alpha(m_Z^2) = 1/128.89(9)$.

In spite of all its successes, the Standard Model is far from being the Ultimate Theory of Physics. It has a few dozen free dimensionless parameters (or even more if superparticles exist), while we expect that the Ultimate Theory will have no free parameters at all. The Higgs mechanism of the origin of masses still awaits its experimental test. But what is much more important, the SM does not incorporate gravity.

IX. QUANTUM GRAVITY AND THE TOE

As you remember, the Newton constant G_N is not in the xy plane, it is on the z axis, where it represents non-relativistic gravity (NG). By merging NG and SR, Einstein created general relativity (GR)— the relativistic theory of gravity. He spent the subsequent forty years of his life trying to create a unified theory of electromagnetism and gravity in the xz plane. As electromagnetism is a part of QFT, it is common knowledge today that the unified theory of electromagnetism and gravity should be a part of the Theory of Everything (TOE), which should be created by merging GR with QFT, in particular by creating Relativistic Quantum Gravity, which also would be a part of the TOE.

Note that the inclusion of the Newton constant G_N brings to the cube of theories the dimensions of mass, energy, momentum, length and time, which cannot be constructed from $\hbar$ and c alone. The mass, corresponding to G_N, was first calculated by Planck at the turn of our century and is called the Planck mass:

$m_P = \sqrt{\hbar c/G_N} \approx 10^{19}$ GeV, and the corresponding Planck length $l_P \approx 10^{-33}$ cm.

The enormous value of m_P compared with the heaviest known masses ($\sim 10^2$ GeV) and with the energies of our accelerators may make you despair. No imaginable technology will ever bring such center-of-mass energy to a physical laboratory. Even daydreaming about experiments at Planck energy is out of the question. And at the same time it looks as if the answers to the most fundamental questions in physics are hidden at the Planck scale.

What are the brightest and the most active young theorists doing nowadays? They are trying to create the future TOE by brainstorming. Since the early eighties their main hope has been superstrings—tiny objects with a characteristic Planck length l_P. They have developed a special branch of mathematics to describe these objects and their interactions.

In connection with superstrings a question is under discussion in the literature. Do we really need three basic dimensional constants c, $\hbar$, and G_N, or would only two of them be sufficient: c and l_P—the length of the string, while $\hbar$ is redundant? According to that point of view, string theory deals only with space and time, but not with energy, momentum, or mass. Momentum for instance has the dimension of inverse length, while action has that of area. The fact that action has, in certain units, the dimension of area does not mean that action can be discarded as a physical quantity and that its role can be assigned to area. It seems to me that statements to the contrary stem from a kind of blurring of such notions as parameters, dimensions, units, and fundamental dimensional constants. For superstrings there should be no free dimensionless parameters. As for the natural units, they are $\hbar$, c, and l_P Thus, the equations should contain neither dimensionless parameters, nor fundamental dimensional constants. However, to connect superstrings with the traditional parts of physics, one needs all three fundamental dimensional constants: $\hbar$, c, and G_N.

Creating the TOE is a very hard and a very risky job. Many physicists looking from outside complain that a whole generation of young theorists has lost contact with real-world physics, have become pure mathematicians. I am not qualified enough to be a judge. Maybe there is some truth in these complaints. But the process of increasing specialization is a universal phenomenon in all scientific fields, and Planck physics is no exception.

X. FROM QFT TO TOE

While we cannot reach the Planck scale with beams of particles, we may reach it with beams of thought, beams of ideas. If somebody is able to think constructively about the Planck scale, the farthest frontier of physics, let him do it.

On the other hand, the richness of particle physics indicates that it would be impossible to formulate the TOE without experimental inputs. How can one make such an input to the region of 10^{19} GeV while being limited to 10^3 GeV or even 10^6 GeV? A possible answer is logarithmic dependence on energy, such as demonstrated by the running alphas. In the Standard Model, masses are also running logarithmically with energy. Thus, by starting with a broad interval of initial conditions at, say, 10^{17} GeV, one ends up with m_t lighter than 200 GeV and m_h lighter than 130 GeV in a minimal supersymmetric standard model. Hopefully the main vehicle is the logarithm.

There is also slight chance of small power terms of order E/m_P. Note that the CPT theorem has been proved only in the framework of QFT, which deals with pointlike particles. It may be not true for strings. Then small differences between masses of particles and corresponding antiparticles would appear. Of course, if we are unlucky and they are proportional to $(E/m_P)^2$, we will be unable to observe them.

XI. THE FUNDAMENTAL IMPORTANCE OF THE FERMI SCALE PHYSICS

Thus we need experimental inputs in order to extrapolate them logarithmically to the Planck scale. But is it not enough to have as inputs the data which have already been obtained? The answer is a definite NO! We have too many loose ends. We still have not seen higgs (or higgses) and superparticles. We still do not know the mechanisms of symmetry breaking at the Fermi scale. We know that this scale starts at masses of W and Z bosons, stretches to the top mass, to the value of the hypothetical higgs vacuum expectation value $\eta = 1/(\sqrt{2}G_F)^{1/2} \approx 246$ GeV (in units $\hbar, c$) and further through the spectrum of supersymmetric particles to multiTeV energies.

Without full understanding of physics at the Fermi scale, we will be unable to construct the logarithmic superhighway to the Planck scale, to the ultimate theory of physical world, including the origin of the universe. That is why we so deeply feel the loss of the SSC. (The first version of this talk had a dedication: *In memory of the SSC.*) That is why most of all we need the energy and luminosity of the future sub-TeV and multi-TeV accelerators!

EXPERIMENTAL STUDIES OF LONGITUDINAL DYNAMICS OF SPACE-CHARGE DOMINATED ELECTRON BEAMS*

D. X. Wang†, Institute for Plasma Research, University of Maryland, College Park, Maryland 20742

A comprehensive experimental program was carried out at the University of Maryland Beam Transport facility to study the longitudinal beam physics of space-charge dominated bunches. This investigation included the behavior of (a) bunches with parabolic line charge profile, (b) bunches with rectangular line charge profile, and (c) local perturbations (slow and fast waves) in rectangular bunches. The major experimental results are presented in this paper.

I. INTRODUCTION

High-intensity charged particle beams have many applications such as high energy linear accelerators, radioactive waste burners, induction linacs as Heavy Ion Inertial Fusion (HIF) drivers, free electron lasers (FEL), and high power microwave generators. In many cases high beam current and power are desired, and the beam dynamics is in a space-charge dominated regime. The appearance of the strong space-charge force complicates the beam dynamics, may degrade the beam quality and limit applications. The objective of this project was to understand the longitudinal beam physics of space-charge dominated beams.

The space-charge force is a collective effect due to the repulsive coulomb interaction between particles. It is a function of the space-charge distribution and the boundary conditions and is always defocusing. The space-charge force is often nonlinear and time-dependent. In general, beam dynamics becomes space-charge dominated if the beam size is primarily determined by the space-charge, instead of the emittance. This condition usually occurs at relatively high beam current and non relativistic energies. For coasting beams this means that the space-charge wave velocity is much larger than the velocity spread, i.e. $c_s >> \Delta v$, (more than 30 times larger in our experiments) where the wave velocity is $c_s = \sqrt{egI/4\pi\varepsilon_0 mv\gamma^5}$, I is the beam current, v is the beam velocity, and g is a geometry factor that will be discussed later. The longitudinal space-charge field which can be expressed analytically as [1]

$$E_z(z,s) = -\frac{g}{4\pi\varepsilon_0\gamma^2}\frac{\partial\Lambda(z,s)}{\partial z}, \qquad (1)$$

where Λ is the line charge density, z is the longitudinal coordinate in the beam frame, and s is the travel distance. Equation (1) was derived for a coasting beam under long wavelength approximation and is widely used for bunched beams where the bunch length 2Z is much longer than the beam diameter 2a. The geometry factor g is an important parameter in longitudinal dynamics that is introduced by the boundary conditions and represents the transverse and longitudinal coupling. The g factor is treated as a constant in Eq. (1) though in practice it is a variable of time since the beam radius varies in time and along the bunch. Generally, the space-charge field can be obtained by solving Maxwell's equations numerically for a given boundary and charge distribution.

Our experiments were chosen to explore the beam behaviors in different dynamic regimes. The first series of experiments were conducted to study linear behavior with a parabolic line charge profile having a linear space-charge force given by Eq. (1) [2, 3]. The second series of experiments were performed with a rectangular bunch (uniform line charge density) to investigate the nonlinear behavior since there is little space-charge force at the flat region but very strong force on the ends that causes rapid edge expansions [4]. Finally, space-charge wave experiments were carried out to study the linear wave behavior on a "coasting" beam, i.e. fast and slow waves as propagation of localized velocity and density perturbations [5, 6, 7].

The experimental configuration will be briefly described first. Then three series of experiments will be discussed separately with brief introductions of theoretical models, and important experimental results are presented. At the end, a short summary is given.

II. EXPERIMENTAL CONFIGURATION

The experiments were performed at the University of Maryland Electron Beam Transport facility consisting of a short-pulse electron beam injector, a 5-meter periodic solenoid-focusing transport channel, and an upgraded diagnostic system [8]. A schematic drawing of the experimental setup is shown in Fig. 1. The key components included a gridded electron gun that can produce parabolic beams and localized perturbations on beams and can vary the beam energy and current by adjusting operating parameters; five fast wall-current monitors with 1.2 GHz bandwidth and three time-resolved energy analyzers, installed along the channel; a compact induction module producing a quadratic time-dependent accelerating voltage.

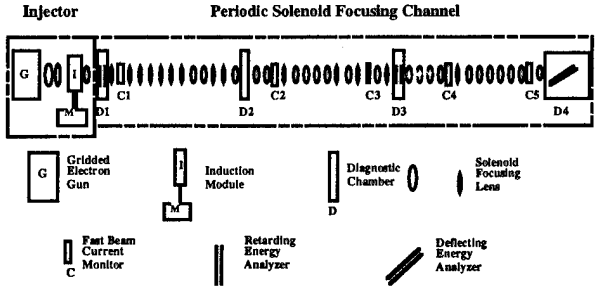


Fig. 1. Schematic of experimental setup.

Typical beam parameters were a few keV in beam energy, a few tens of mA in current, a few tens of ns in pulse duration, about 5 mm in beam radius, and beam pipe radius of 19 mm.

* Supported by Department Of Energy

† Present address: CEBAF, Newport News, VA 23606

0-7803-3053-6/96/$5.00 ©1996 IEEE

III. PARABOLIC BUNCH EXPERIMENT

The longitudinal dynamics of a parabolic bunch can be described by a longitudinal envelope equation [9. 10], written as

$$\frac{d^2Z}{ds^2}-\frac{2gZ_iI_p(0)}{\beta_0^3I_0}\frac{1}{Z^2}-\frac{\varepsilon_L^2}{Z^3}=0, \qquad (2)$$

where 2Z is the full longitudinal bunch length, $2Z_i$ is the initial bunch length, $I_0=4\pi\varepsilon_0 m_e c^3/e=17kA$ for electrons, I_p is the peak current, and ε_L is the longitudinal emittance of the beam. If the beam is space-charge dominated, the third term in Eq. (2) is negligible comparing to the second term. On the other hand, this condition defines a space-charge dominated beam for parabolic bunches. Then an analytical solution can be readily found by integrating Eq. (2) twice [3]. According to this 1-D envelope model the parabolic shape is preserved and the velocity distribution remains linear. The bunch length, or the peak current and the slope of the velocity distribution are determined by Eq. (2).

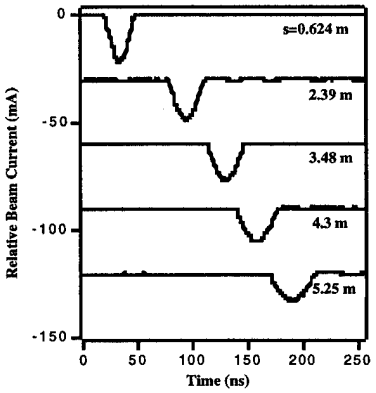


Fig. 2. Beam current signals of a parabolic bunch at different locations along the channel without a velocity tilt.

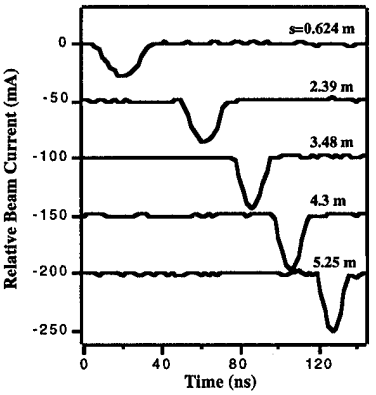


Fig. 3. Beam current signals of parabolic bunch with an initial tilt Z'=-0.092.

In the experiment, a parabolic beam with a constant velocity was produced and launched into the channel. Current profiles of a drift parabolic bunch, measured at different channel locations, is shown in Fig. 2. Also the parabolic beams were compressed by the induction accelerating voltages with various slopes. A typical case is shown in Fig. 3. For each case, the bunch lengths were obtained by fitting the current profiles with the parabolic curves, and are plotted in Fig. 4 in comparison with the results from the envelope equation where a constant g was used. The experiment and theory were in very good agreement. To verify the transverse dependence of the g factor, the focusing strength was varied, giving different beam radius, and the result is plotted in Fig. 5. The velocity distribution was also measured and plotted in Fig. 6 for a drift expanding beam, showing the linearity predicted by the theory. In the experiment, it was observed that the longitudinal envelope was insensitive to the transverse mismatching oscillations, which was later confirmed by a 2-D simulation of particle code [11].

IV. RECTANGULAR BUNCH EXPERIMENT

For rectangular beams, i.e. a uniform line charge density, the longitudinal space-charge force is highly nonlinear, with little force at the flat region but very strong forces at the ends [12, 13]. In general, the 1-D cold fluid model can be employed to describe the longitudinal beam dynamics. The fluid equations can be written as

$$\frac{\partial\Lambda}{\partial t}+v\frac{\partial\Lambda}{\partial z}+\Lambda\frac{\partial v}{\partial z}=0$$
$$\frac{\partial v}{\partial t}+v\frac{\partial v}{\partial z}\approx\frac{e}{m\gamma^3}E_z=-\frac{eg}{4\pi\varepsilon_0 m\gamma^5}\frac{\partial\Lambda}{\partial z} \qquad (3)$$

where Λ is the line charge density and v is the particle velocity in the beam frame. Analytic solutions can be obtained by the method of characteristics in the practically interested regime. One of the important properties of the fluid equations is the time-reversibility, i.e. Eqs (3) are invariant by changing the sign of t (therefore, changing the sign of v as well).

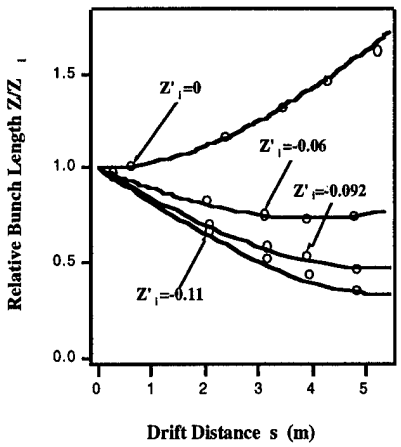


Fig. 4. Normalized bunch length vs. drift distance for parabolic beams with different initial tilts, where the circles represent experiment while the solid curves are from envelope calculation.

For an initial rectangular beam with a constant velocity, the beam edge erodes towards the beam center at a speed of c_s and expands towards vacuum at $2c_s$, due to the strong space-charge force at the ends. The density profile is quadratic and the velocity distribution is linear at the ends, while the center region remains non-perturbed. There is a "cusp" point where the edge erosions reach the

beam center and the velocity distribution becomes linear along the entire bunch . Utilizing the time reversibility the initial rectangular bunch shape can be reconstructed by imparting an appropriate linear velocity tilt at the "cusp" location, which changes the sign of the velocity in the beam frame. The detailed description and a schematic of this process can be found in Ref. [3].

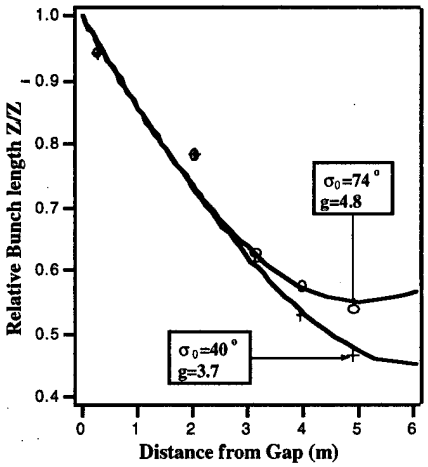


Fig. 5. Normalized bunch length vs. drift distance for different focusing strengths where the circles and the crosses represent experiment while the solid curves are from calculations.

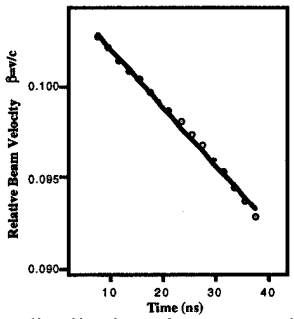


Fig. 6. Velocity distribution along a parabolic bunch after certain distance of the drift expansion, where the circles represent experiment while the solid line for linear fit.

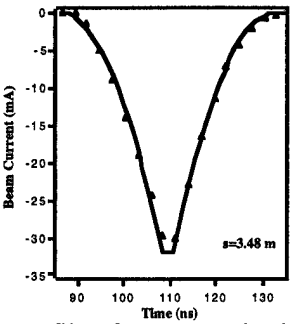


Fig. 7. Current profile of a rectangular bunch just before the cusp point, after certain drift distance.

In the reconstruction experiment, we first demonstrated the linear velocity distribution at the "cusp" point by adjusting the bunch length so that the "cusp" point appeared at the second energy analyzer. Figure 7 shows the current profiles of an expanding rectangular bunch just before the cusp point. The velocity distribution was also measured and is shown in Fig. 8, which was very linear as predicted by the theory. The measurement result (circles), simulation (triangles), and calculations (solid line) were in very good agreement. Here beam energy, current and pulse duration were 2.5 keV, 35 mA, and 17.5 ns, respectively. In the experiment the pulse duration was carefully adjusted to let the cusp point happen at the second energy analyzer.

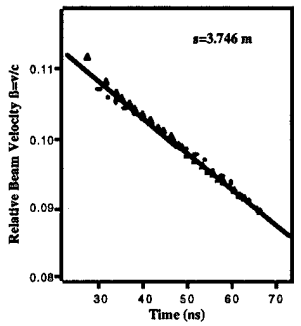


Fig. 8. Velocity distribution along a rectangular bunch after certain distance of drift expansion, where circles represent experiment while solid curve theory.

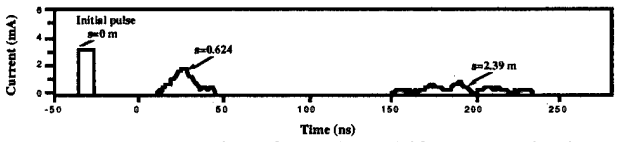


Fig. 9a. Current profiles for a short drift rectangular bunch without induction acceleration voltage.

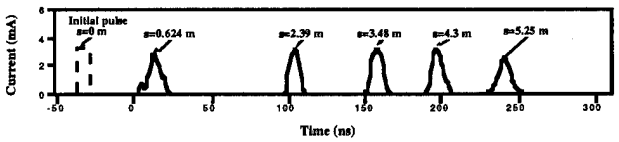


Fig. 9b. Current profiles along channel for a short drift rectangular bunch with an appropriate velocity tilt imparted by induction module.

Due to the short distance (0.34 m) between the gun and induction module where a linear velocity tilt was imposed, a 300 eV, 3.3 mA. and 7 ns beam was used to increase the wave velocity and slow down the traveling speed. Without application of the induction acceleration and velocity tilt the beam expanded rapidly and disappeared at the third current monitor, shown in Fig. 9a. The bunch length at the second current monitor was consistent with the calculation, though the noise became substantial due to the very low beam current. With a proper induction acceleration to impart the linear velocity tilt, the bunch shape was reconstructed, shown in Fig. 9b. The distinguishing features of the reconstruction process were that the peak current in the flat region remained the same, the leading and falling edges became steep, and the flat top maintained a constant velocity. In the experiment we also varied the beam pulse duration, the slopes of the velocity tilt, and the beam center energy after the induction module. In each case the beam behaved consistently with the theory. Due to the low beam current, the measurement of constant velocity distribution predicted at the reconstruction point was not available.

It is noted that the time reversibility is a general property of the fluid equations. Therefore, in principle, the

reconstruction process can be performed any where as long as the appropriate velocity distribution was generated. In practice, however, it is easiest to generate a linear ramp of acceleration.

V. SPACE-CHARGE WAVE EXPERIMENTS

The initial localized perturbations were introduced to the beam by creating small positive voltage bumps on the cathode-grid pulse, which generated both initial localized velocity and density perturbations. These initial perturbations propagated as space-charge waves, i.e. fast and slow waves moving forward and backward in the beam frame, respectively. In the experiment, we generated not only a pair of fast and slow waves, shown in Fig. 10, but also single fast and single slow waves. An analytical solution was found to interpret the experimental observations [5]. Figure 11 shows the current signals of the space-charge waves from the energy analyzer. The signals represented the perturbed electrons with an energy above the average beam energy, where the left bump corresponded to the fast wave and the right to the slow wave. The fast and slow waves had separated after a drift distance. In obtaining this set of traces, the only difference was change of the gun operating condition that determined the different initial perturbations of the velocity and the density. In general two space-charge waves in the form of localized perturbations were generated with different amplitudes in the velocity and the density, depending on the initial conditions.

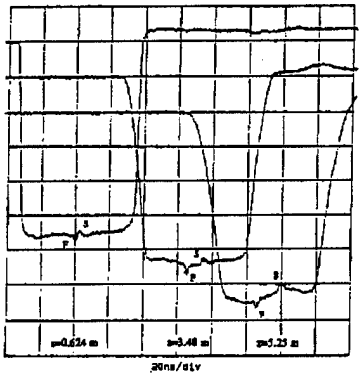


Fig. 10. Current profiles along channel with initial perturbation propagating as fast and slow waves.

The localized fast and slow waves propagated away from each other at speed of c_s in the beam frame. By measuring the time interval between the two waves and the traveling distance of the beam, the wave velocity can be determined by a linear fitting, shown in Fig. 12 and calculated from a formula $\Delta t=2c_s s/(v_0^2-c_s^2)$, where Δt was the time interval between the fast and slow waves, s was the drift distance, and v_0 was the beam velocity. From the measured wave velocity, the geometry factor can be found according to the relation between c_s and g given above. An average beam radius was measured using a movable florescent screen and a CCD camera, shown in Fig. 13. The measured radius was in a very good agreement with calculation under smooth approximations [14]. The result showed that g=2lnb/a, where b was the pipe radius and a was the average beam radius, which was consistent with the theory under the assumption of a constant volume charge density [1]. This also implies that the space-charge field is a constant across the transverse cross section.

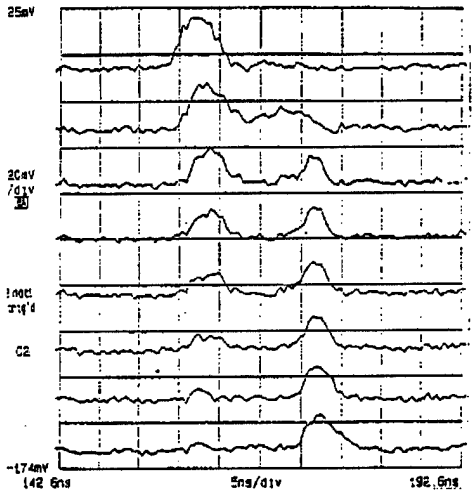


Fig. 11. Current signals are perturbed electrons at one of the retarding energy analyzers. Initial perturbation becomes two waves, fast and slow, after certain drift distance.

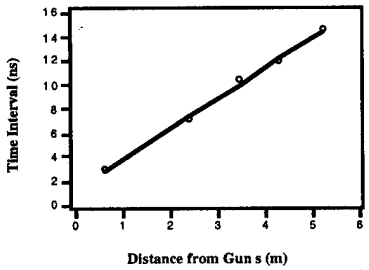


Fig. 12. Time intervals between fast and slow waves vs. drift distance, where the circles represent experiment and the solid line is linear fit.

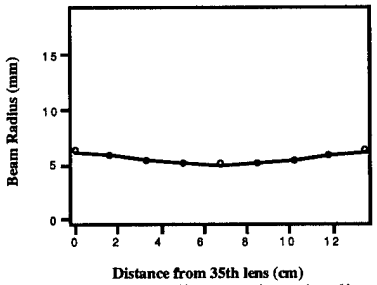


Fig. 13. Measured beam radius vs. longitudinal distance.

The experiments were also conducted to investigate the wave behaviors at ends of the rectangular bunch, where the ends were referred to as the boundary between the flat region and the finite edge. The initial perturbation was moved to very close to the beam end. The slow wave hit the eroding end shortly and split into reflected and transmitted waves, shown in Fig. 11. The reflected slow wave became a fast wave moving forward. Due to the edge expansion and erosion, the reflected wave and the edge moved forward at the same wave speed. The transmitted wave could not reach the zero density point because the zero density point kept moving out at twice of the wave speed. Figure 12 plots the time interval between the fast

wave and the reflected wave and the fast and the transmitted waves. The wave velocity of the reflected wave changed as approaching the beam end and became c_s afterwards while the transmitted wave remained at a constant wave velocity c_s. In the experiment, a single fast wave with rather large amplitude was launched close to the bunch front end, and the clear reflection and transmission were seen [15]. It was also qualitatively observed that the steeper the edge, the stronger the reflection.

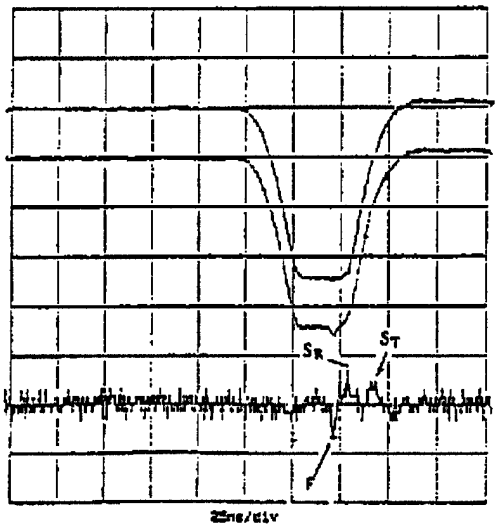


Fig. 14. Current profiles after certain drift distance with and without perturbation (top two traces, respectively), showing the original fast wave (F), the reflected slow wave (S_R), and the transmitted slow wave (S_T), while the bottom trace is the difference of the two top traces.

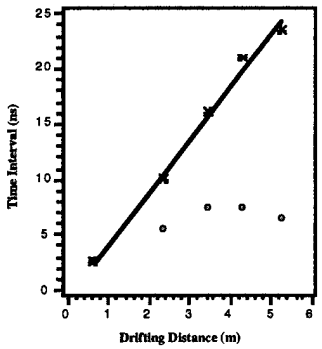


Fig. 15. Time separations between the original fast wave and the transmitted slow wave (stars), and between the original fast wave and the reflected slow wave (circles), vs. drift distance.

VI. CONCLUSION

The self-consistent parabolic profile and linear velocity distribution were experimentally verified. The experimental results were in very good agreement with the envelope model. The linear velocity distribution at the cusp point, predicted by the fluid model was experimentally obtained for a drift rectangular bunch. The pulse reconstruction of rectangular bunch, based on the time-reversibility was experimentally demonstrated. Both single fast and single slow space-charge waves were generated in the experiment. In general, a pair of fast and slow waves was generated with different amplitudes, depending on the initial perturbation conditions. The geometry factor was experimentally determined for space-charge dominated coasting beams, which was consistent with the theory under assumption of a constant volume density, rather than a constant radius for the emittance dominated beams. The reflection and transmission of the waves at the beam ends were observed in the experiment.

Overall, 1-D models worked surprisingly well. A constant g factor was a good approximation for both parabolic and rectangular beams. The longitudinal dynamics was insensitive to transverse mismatch oscillations.

VII. ACKNOWLEDGMENT

The author would like to express deepest gratitude to his dissertation adviser, Prof. M. Reiser and co-adviser Dr. J. G. Wang for their guidance. He thanks the former colleagues at Maryland, in particular Dr. D. Kehne and H. Suk for their contributions to this project and Dr. I. Haber of NRL for permitting the use of his SHIFTZ code and many fruitful discussions. The author would also like to acknowledge the Division of High Energy Physics and the Division of Advanced Physics and Technology of DOE for their support.

VIII. REFERENCES

[1] M. Reiser: Theory and Design of Charged Particle Beams, Wiley & Sons, New York.

[2] J. G. Wang, D. X. Wang, and M. Reiser, Appl. Phys. Lett., **62**(6), pp. 645-647, 8 Feb. 1993.

[3] D. X. Wang, J. G. Wang, D. Kehne, and M. Reiser, Appl. Phys. Lett., **62**(25), pp. 3232-3234, 21 June 1993.

[4] D. X. Wang, J. G. Wang, and M. Reiser, Phys. Rev. Lett. **73**(1), pp. 66-69, July 4, 1994.

[5] J. G. Wang, D. X. Wang, and M. Reiser, Phys. Rev. Lett., **71**(12), pp. 1836-1839, September 20, 1993.

[6] J. G. Wang, H. Suk, D. X. Wang, and M. Reiser, Phys. Rev. Lett., **72**(13), pp. 2029-2032, March 28, 1994.

[7] J. G. Wang, D. X. Wang, H. Suk, and M. Reiser, Phys. Rev. Lett., **74**(16), pp. 3153, April 17, 1995.

[8] J. G. Wang, D. X. Wang, and M. Reiser, Nucl. Instr. & Meth. in Phys. Res. A 316, pp. 112-122, 1992.

[9] L. Smith, "ERDA summer study for heavy ion inertial fusion" (ed. R. O. Bangerter, W. B. Herrmannsfeldt, D. L. Judd, and L. Smith), LBL-5543 (1976), pp. 77-79.

[10] D. Neuffer, IEEE Trans. on Nuclear Science, **26**(3), pp. 3031-3033, June 1979.

[11] A. Faltens, E.P. Lee, and S.S. Rosenblum, J. Appl. Phys., **61**(12), 5219 (1987).

[12] I. Haber, private communications.

[13] D.D. Ho, S.T. Brandon, and E. P. Lee, Particle Accelerator, Vol. **35**, 15 (1991).

[14] H. Suk, M. Reiser, J. G. Wang, and D. X. Wang, Appl. Phys. Lett., **76**(7), pp. 3970-3974, 1 October 1994.

[15] J. G. Wang and M. Reiser, in these proceedings.

HIGH-ENERGY HIGH-LUMINOSITY $\mu^+\mu^-$ COLLIDER DESIGN

Robert B. Palmer, Richard Fernow, Juan C. Gallardo, Y. Y. Lee, Yağmur Torun,
Brookhaven National Laboratory, P. O. Box 5000, Upton, New York 11973-5000
David Neuffer, CEBAF, Newport News, VA, 23606
David Winn, Fairfield University, Fairfield, CT, 06430-5195

Abstract

We discuss the design of a high luminosity ($10^{35}\ cm^{-2}\ s^{-1}$), high energy (2 + 2 TeV) $\mu^+\mu^-$ collider, starting from the proton accelerator needed to generate the muon beams and proceeding through the muon storage ring.

INTRODUCTION

Lepton (e^+e^-) colliders have the valuable property of producing simple, single-particle interactions with little background, and this property is essential in the exploration of new particle states. However, extension of e^+e^- colliders to multi-TeV energies is severely performance-constrained by beamstrahlung, and cost-constrained because two full energy linacs are required[1]. On the other hand μ's (heavy electrons) have negligible beamstrahlung, and can be accelerated and stored in rings.

The liabilities of μ's are that they decay, with a lifetime of 2.2×10^{-6} s, and that they are created through decay into a diffuse phase space; in addition the decay products are likely to create large backgrounds at the final focus points making the detector design a challenge. The first problem is overcome by rapidly increasing the relativistic γ factor; at 2 TeV for example, the lifetime is 0.044 s, sufficient for storage-ring collisions. The second can be dealt with by cooling. The possibility of μ colliders has been introduced by Skrinsky et al.[2], Neuffer[3], and others. More recently, several workshops and collaboration meetings have greatly increased the level of discussion[4],[5]. In this paper we discuss the beam dynamics problems encountered in one particular scenario for a 2 + 2 TeV collider. Tb.I shows parameters for the candidate design and Fig.1 shows a schematic overview of the machine. This scenario includes a high-intensity μ-source, μ-cooling, and acceleration and storage in a collider. The complete cycle is repeated at 30 Hz.

Table I
Summary of Parameters of 2 + 2 TeV $\mu^+\mu^-$ Collider

Beam energy	TeV	2
Beam γ		19,000
Repetition rate	Hz	30
Muons per bunch	10^{12}	2
Bunches of each sign		1
Normalized rms emittance ϵ_n	mm mrad	50
Average ring mag. field B	T	6
Effective turns before decay		900
β^* at intersection	mm	3
Luminosity ˇ	$cm^{-2}s^{-1}$	10^{35}

SYSTEM COMPONENTS

Proton Driver

The μ-source driver is a high-intensity rapid-cycling (30 Hz) proton synchrotron. The protons are targeted to produce pions, which are then allowed to decay into the required muons. A recent study[6] suggests that an optimum proton energy may be 10 GeV. In this case, with some conservatism (we allow an extra factor of two for potential loss), we require a total of about 10^{14} protons at 30 Hz. This specification is almost identical to that studied[7] at ANL for a spallation neutron source. The only difference is the number of bunches: 2 of 5×10^{13} instead of 1 of 10^{14}, one of which is for making μ^-, the other for μ^+. Both are brought on to the same target.

In order to minimize the longitudinal emittance of the produced pions it is desirable to target relatively short bunches of protons with rms bunch length less than 3 ns (1 m). An RF sequence must thus be designed to phase rotate the bunch prior to targeting. The total final momentum spread, based on the ANL parameters (95% phase space of 4.5 V s per bunch), is modest (6 %, or 2.5 % rms), but if the compression were to take place in a relatively low-field, fast-cycling synchrotron, then the space charge tune shift just before extraction would be very large ($\approx$ 1.5). A separate superconducting compression ring is thus needed (reducing the tune shift to $\approx$ 0.15), or some other more exotic solution must be found. Some possible parameters of the main components of the proton driver are given in Tb. II.

Table II
Proton Driver parameters

Linac	Energy	MeV	330
	Gradient	MeV/m	4-5
	Frequency	MHz	1200
Booster 1	Energy	GeV	2.2
	Circ.	m	190
	Frequency	MHz	2.2-3
Booster 2	Energy	GeV	10
	Circ.	m	690
	Frequency	MHz	9
Buncher	Energy	GeV	10
	Circ.	m	70
Final	rms emittance	mm mrad	62
	rms long. phase space	V sec	0.7
	rms bunch length	nsec	3
	rms dp/p	%	2.5

0-7803-3053-6/96/$5.00 ©1996 IEEE

Target and Pion Capture

The target could be Cu (24 cm by 12 mm diameter) or Be (70 cm by 2 cm diameter), although Cu would be preferred because of its higher pion multiplicity. Pions are captured from the target by a high-field hybrid solenoid that surrounds it. A field of 28 T, and radius of 7.5 cm are consistent with what is currently available[8]. The pions can then be matched, using a suitable tapered field[9] into a long (350 m) solenoidal decay channel. A field of 7 T and radius of 15 cm for the decay channel seems reasonable and matches the capture acceptance.

Monte Carlo studies indicate that such a system captures almost 40% of the produced pions. Using the Wang[10] formula for pion production, the program calculates a yield of 0.22 μ's, of each sign, per initial proton. However, for a Cu target, a higher multiplicity is expected and would consequently give, yet, a higher yield.

Phase Rotation Linac

The pions, captured by a solenoid focus system (and the muons into which pions decay) have a huge energy spread, from 0 - 3 GeV (rms/mean $\approx$ 100%), and would be difficult to transport and to handle in any subsequent system. It is thus proposed to introduce a linac along the decay channel, whose frequencies and phases are chosen to deaccelerate the fast particles and accelerate the slow ones; i.e. to phase rotate the muon bunch. Tb.III gives the parameters of these linacs. After phase rotation the rms bunch

Table III
Parameters of Phase Rotation Linacs

Linac	Length m	Frequency MHz	Gradient MeV/m	Phase degrees
1	50	24	2	36
2	50	24	2	0
3	250	6	2	43
4	60	24	2	81

length is 6 m, and the rms momentum spread is reduced to about 15 %. Unfortunately at such frequencies the linacs cannot phase rotate both signs in the same bunch: hence, the need for two bunches. The phases must be set to rotate the μ^+'s of one bunch and the μ^-'s of the other.

Ionization Cooling

Cooling Theory

For collider intensities, the phase-space volume must be reduced within the μ lifetime. Cooling by synchrotron radiation, conventional stochastic cooling and conventional electron cooling are all too slow. Optical stochastic cooling[11], electron cooling in an plasma discharge[12] and cooling in a crystal lattice[13] are being studied, but are not by any means certain. Ionization cooling of muons[14] seems relatively straightforward.

In ionization cooling, the beam loses both transverse and longitudinal momentum as it passes through a material medium. Subsequently, the longitudinal momentum can be restored by coherent reacceleration, leaving a net loss of transverse momentum. Ionization cooling is not practical for protons and electrons because of nuclear scattering (p's) and bremsstrahlung (e's) effects in the material, but is practical for μ's because of their low nuclear cross section and relatively low bremsstrahlung.

The equation for transverse cooling (with energies in GeV) is:

$$\frac{d\epsilon_n}{ds} = -\frac{dE_\mu}{ds}\frac{\epsilon_n}{E_\mu} + \frac{\beta_\perp (0.014)^2}{2\,E_\mu m_\mu\, L_R} \qquad (1)$$

where ϵ_n is the normalized emittance, $\beta_\perp$ is the betatron function at the absorber, dE_μ/ds is the energy loss, and L_R is the material radiation length. The first term in this equation is the coherent cooling term and the second term is the heating due to multiple scattering. This heating term is minimized if $\beta_\perp$ is small (strong-focusing) and L_R is large (a low-Z absorber).

From Eq.1 we find a limit to transverse cooling, when heating due to multiple scattering balances cooling due to energy loss, at $\epsilon_n \approx 0.6\ 10^{-2}\ \beta_\perp$ for Li, and $\epsilon_n \approx 0.8\ 10^{-2}\ \beta_\perp$ for Be.

The equation for energy cooling is:

$$\frac{d(\Delta E)^2}{ds} = -2\,\frac{d\left(\frac{dE_\mu}{ds}\right)}{dE_\mu} < (\Delta E_\mu)^2 > + \frac{d(\Delta E_\mu)^2_{\text{strag}}}{ds} \qquad (2)$$

Where the first term is the cooling (or heating) due to energy loss and the second term is the heating due to straggling.

Cooling requires that $\frac{d(dE_\mu/ds)}{dE_\mu} > 0$. But at energies below about 200 MeV, the energy loss function for muons, dE_μ/ds, is rapidly decreasing with energy and there is thus rapid heating of the beam. Above 400 MeV the energy loss function increases gently, thus giving some cooling, though not sufficient for our application.

In the long-path-length Gaussian-distribution limit, the heating term (energy straggling) is given by[15]

$$\frac{d(\Delta E_\mu)^2_{\text{strag}}}{ds} = 4\pi (r_e m_e c^2)^2 N_o \frac{Z}{A}\rho\gamma^2\left(1-\frac{\beta^2}{2}\right) \qquad (3)$$

where N_o is Avogadro's number and ρ is the density. Since the energy straggling increases as γ^2, and the cooling system size scales as γ, cooling at low energies is desired.

Energy spread can also be reduced by artificially increasing $\frac{d(dE_\mu/ds)}{dE_\mu}$ by placing a transverse variation in absorber density at a location where position is energy dependent, i.e. where there is dispersion. The use of such wedges can reduce energy spread, but it simultaneously increases transverse emittance in the direction of the dispersion. Six dimensional phase space is not reduced. But it does allow the exchange of emittance between the energy and transverse directions, and it can do this either way.

Cooling System

We require a reduction of the normalized transverse emittance by almost three orders of magnitude (from 2×10^{-2} to 3×10^{-5} m-rad), and a reduction of the longitudinal emittance by more than an order of magnitude. This cooling is obtained in a series of cooling cells. Each cell consists of a section of Be ($\approx 0.7\,m$) or Li ($\approx 2\,m$) placed in a region of the lattice with a low $\beta_\perp$, a linac ($200\ MeV$), and a matching bend with dispersion where wedges can be introduced to interchange longitudinal and transverse emittance. The energy would be restricted to a value

between 200 and 400 MeV, so as to avoid the energy dE/dx heating below 200 MeV, but minimize the straggling heating at higher momenta. About 20 such cells would be needed.

For the early cells, when the emittance is still large, a sufficiently low $\beta_\perp$ can be obtained with solenoids. In later cells, when the emittance is lower and a lower $\beta_\perp$ is required, current carrying cooling rods ($\approx$ 2 m long, if Li) which serve both to maintain the low $\beta_\perp$ and reduce the beam energy could be employed. In a Li rod, with surface fields of 10 T (as achieved in Li lenses at Novosibirsk, FNAL and CERN [16]), a $\beta_\perp$ of 1.7 cm can be achieved, and the emittance is reduced to about 10^{-4} m. But this is still a factor of $\approx$ 3 above the emittance goal of Tb.I. A final stage might consist of short sections of Be at even lower $\beta_\perp$ insertions. Alternatively, the additional transverse emittance reduction can be obtained by cooling more than necessary longitudinally, and then exchanging transverse and longitudinal phase-space with a thick wedge absorber.

In all these cells, lattices are required with adequate momentum acceptance, matching in and out of the low beta insertions, appropriate momentum compaction and control of emittance growth from space charge, wake field and resistive wall effects. In addition it would be desirable to economize on linac sections by forming groups of cells into recirculating loops.

Acceleration

Following cooling and initial bunch compression (of the order of 0.2 m) the beams must be accelerated to full energy (2 TeV). A single linac of this energy would work, but would be expensive, and would not utilize our ability to recirculate μ's in rings. A conventional synchrotron cannot be used because the muons would decay before they were accelerated. A fast cycling synchrotron could be used but, because it would be limited to low magnetic fields, would be very large. The best solution seems to be a recirculating linac (similar to CEBAF). If acceleration is done in 20 recirculations, then only 100 GeV of linear accelerator is required.

In practice, a cascade of at least 3 recirculating linacs (e.g., with maximum energies of 20 GeV, 200 GeV and 0.2 TeV) would be needed. The μ-bunches would be compressed on each of the return arcs, and be bunched finally to the required length of 3 mm at full energy. The two higher energy recirculators must be superconducting for two reasons: the store time is far too long for conventional cavities, and the wall power consumption with conventional cavities would be too high. The total muon beam power is 38 MW. It is hoped to achieve at least 30% efficiency with superconducting cavities, giving a wall power consumption of 127 MW. The gradients assumed are below those assumed for TESLA. They may be over conservative in view of the shorter pulse duration in this application than assumed in TESLA. The muon linac beam dynamics is complicated by transverse HOM because of the large number of muons per bunch, about a factor of 100 higher than electrons in TESLA. The HOM power is estimated to be $\approx$ 100 W/m. As in the TESLA design, this would required a coupler section to remove this HOM power.

At the higher energies, space charge effects will not be a problem, but as the bunches are compressed wake field and resistive wall effects become serious. Preliminary studies suggest that, with a slight decrease in Q/Z (by widening the irises), and with BNS damping, such effects can be controlled.

μ Storage Ring

After acceleration, the μ^+ and μ^- bunches are injected into the 2-TeV storage ring, with collisions in two low-β^* interaction areas. The beam size at collision is $r = \sqrt{\epsilon_n \beta^*} \approx 2\,\mu m$, similar to hadron collider values. The bunch populations decay exponentially, yielding an integrated luminosity equal to its initial value multiplied by an "effective" number of turns $n_{effective} = 150\,B$, where B is the mean bending field in T. With 9 T superconducting magnets, an average B of 6 T might be obtained, yielding an $n_{effective} \approx 900$. The magnet design is complicated by the fact that the μ's decay within the rings ($\mu \rightarrow e\bar{\nu}\nu$), producing electrons whose mean energy is approximately 1/3 of that of the muons. These electrons travel to the inside of the ring dipoles, but radiate a substantial fraction of their energy, as synchrotron radiation, towards the outside of the ring. A warm tungsten, or other heavy metal, liner of about 2 cm thickness will be required to intercept this radiation.

A relatively conventional lattice has been designed [17], but the rf requirements to maintain the required 3 mm rms bunch length in such a lattice would be large. A low momentum compaction lattice of the type discussed by S.Y. Lee et al[18] might thus be preferred. A preliminary study[19] of resistive wall impedance instabilities indicate that 3 mm bunches of 2×10^{12} muons would have an unacceptable transverse microwave instability. A fully isochronous lattice, with conventional BNS[20] damping, would solve the problem, but is not possible because of the effects of the large angles of trajectories in the insertion regions. The proposed solution is to employ RF quadrupoles to apply the BNS damping[21].

Another problem is the design of chromatic correction for the very low beta ($\beta^* = 3\,mm$) insertions. A triplet design would have maximum beta's of 200-400 km in both directions, and chromaticity ($1/4\pi \int \beta dk$) of 2000-4000. If no correction is employed, as in the lattice in reference [17] then the momentum acceptance ($\approx 10^{-5}$) is much less than that easily obtained by the ionization cooling. It seems clear that a local correction of chromaticity[22] would be required. A preliminary automated[23] study of such a correction system, using a doublet at the final focus, gave momentum acceptances of ± 0.1 % and ± 0.6 % in the two directions, where the β_{max}'s were 1.2 and 0.2 million m respectively. A similar design with the triplet (β_{max}'s both 0.4 million m) would be expected to give about 0.3 % in both directions. More sophisticated designs [24] should do better. But this estimate is only for a single pass device like a linear collider; the performance for a storage ring remains to be seen.

Detector Background

For the physics user there is a problem of background from μ-decays that occur near the intersection point, and from scattering of any muon halo circulating in the ring.

A first Monte Carlo[25],[26] study assumed a final triplet with interspersed strong dipole bending magnets. These magnets, it was hoped, would help deflect background tracks coming from further down the beam. No chromatic correction scheme or machine lattice was included in this study. Background track den-

sities initiated by muon decays are indicated in Tb. IV. In this study it was assumed that the detector pixels in the inner tracker were 20 μm by 20 μm, and in the central tracker: 50 μm by 300 μm. The track densities are high, but they result from very low energy electrons that would be eliminated in any track reconstruction. Given the fine subdivision of the assumed detector,

Table IV
Detector Backgrounds from μ decay. σ is the density of tracks and ρ is the occupancy.

Location	outside		inside	
	σ cm^{-2}	ρ %	σ cm^{-2} %	ρ
inner tracker	170	0.07	480	0.19
central tracker	3.2	0.05	2.3	0.03
outer tracker	1.7	-	0.3	-

the occupancies do not look impossible.

In a second study of this problem [27], it was found that much of the background in the first study had come from synchrotron radiation of electrons in the bending magnets near the intersection point. Removal of these magnets reduced the peak track densities by factors of between 2 and 5, and reduced the total by an even larger factor. Clearly, more studies are needed, but it seems probable that ways will be found to further improve the situation.

These studies have also shown that severe background can be generated by scattering of tails in the muon beam. A collimation system will be required in a straight section far from the detectors (presumably a quarter way around the ring). No such system has yet been designed.

CONCLUSION

- The scenario for a 2 + 2 TeV, high luminosity collider is by no means complete. Much work remains to be done. More theoretical studies are needed on optimization of pion production, muon phase rotation, cooling scenarios, the collider lattice, radiation effects, and detector background. Technical studies are needed on the design of liquid lithium rods, targeting, high field solenoids, low-frequency high-gradient linacs, multibeam magnets for the recirculation, and high field magnets for the collider. But no obvious show stopper has yet been found.
- An experimental demonstration of ionization cooling should be made. A letter of intent[28] for such an experiment has been submitted to the BNL AGS.
- If the problems can be overcome, then a $\mu^+\mu^-$ collider may be the best route to study physics at energies higher than those accessible at the LHC or NLC. A 2 + 2 TeV $\mu^+\mu^-$ machine with a luminosity of $10^{35}\ cm^{-2}sec^{-1}$ would have a physics reach greater than either of these machines, yet it would be small enough to fit on the BNL or FNAL sites. Its relative cost, however, remains to be seen.
- Efforts are now needed on the design of a "Demonstration Muon Collider" that would employ an upgraded existing proton source, could have a center of mass energy of 0.5 TeV, and might have a luminosity of the order of $10^{32}\ cm^{-2}sec^{-1}$. Such a machine, besides being a stepping stone to a higher energy machine, would have the unique capability of searching for the direct channel production of the supersymetric Higgs particles A and H.

ACKNOWLEDGMENTS

We acknowledge important contributions from our colleagues W. Barletta, J. D. Bjorken, S. Caspi, A. Chao, D. Cline, Y. Cho, D. Douglas, R. Helms, J. Irwin, F. Mills, N. Mokhov, O. Napoly, R. Noble, J. Norem, H. Padamsee, Z. Parsa, C. Pellegrini, A. Ruggiero, R. Scanlan, A. Sessler, M. Syphers, A. Tollestrup, W. Willis, and Y. Zhao.

This research was supported by the U.S. Department of Energy under Contract No. DE-ACO2-76-CH00016 and DE-AC03-76SF00515.

References

[1] D. V. Neuffer, R. B. Palmer, Proc. European Particle Acc. Conf., London (1994); M. Tigner, in Advanced Accelerator Concepts, Port Jefferson, NY 1992, AIP Conf. Proc. **279**, 1 (1993).

[2] E. A. Perevedentsev and A. N. Skrinsky, Proc. 12th Int. Conf. on High Energy Accelerators, F. T. Cole and R. Donaldson, eds., (1983)485; A. N. Skrinsky and V.V. Parkhomchuk, Sov. J. of Nucl. Physics **12**, (1981) 3.

[3] D. Neuffer, IEEE Trans. **NS-28**, (1981) 2034.

[4] Proc. of the Mini-Workshop on $\mu^+\mu^-$ Colliders: *Particle Physics and Design*, Napa CA, D. Cline ed., Nucl Inst. and Meth. A **350** (1994) 24; Proceedings of the Muon Collider Workshop, February 22, 1993, Los Alamos National Laboratory Report LA- UR-93-866, H. A. Theissen ed., (1993) and 2^{nd} *Workshop on Physics Potential & Development of* $\mu^+\mu^-$ *Colliders*, Sausalito, CA (1994), to be published.

[5] Transparencies at the *2 + 2 TeV* $\mu^+ - \mu^-$ *Collider Collaboration Meeting*, Feb 6-8, 1995, BNL, compiled by Juan C. Gallardo.

[6] R. B. Palmer et.al., *Monte Carlo Simulations of Muon Production*, submitted to the Sausalito Proceedings.

[7] Y. Cho, et. al., ANL-PUB-081622, *Proc. Int. Collab. on Advanced Neutron Sources*, Abbingdon, UK., May 24-28 (1993).

[8] Physics Today, Dec (1994), p21-22

[9] R. Chehab, J. Math. Phys. **5**, (1978) 19

[10] C. L. Wang, Phys. Rev. **D10**, (1974) 3876; C. L. Wang, Phys Rev **D9**, (1973) 2609 and Phys. Rev. **D10**, (1974) 3876.

[11] A. A. Mikhailichenko and M. S. Zolotorev, Phys. Rev. Lett. **71**, (1993) 4146; M. S. Zolotorev and A. A. Zholents, SLAC-PUB-6476 (1994)

[12] Ady Hershcovitch, Brookhaven National Report AGS/AD/Tech. Note No. 413 (1995)

[13] Z. Huang, P. Chen, R. Ruth, SLAC-PUB-6745, *Proc. Workshop on Advanced Accelerator Concepts*, Lake Geneva, WI , June (1994); P. Sandler presentation at Sausalito Workshop, to be published; A. Bogacz, private communication.

[14] Initial speculations on ionization cooling have been variously attributed to G. O'Neill and/or G. Budker see D. Neuffer, Particle Accelerators, **14**, (1983) 75; D. Neuffer,

Proc. 12th Int. Conf. on High Energy Accelerators, F. T. Cole and R. Donaldson, eds., 481 (1983); D. Neuffer, in Advanced Accelerator Concepts, AIP Conf. Proc. 156, 201 (1987).

[15] U. Fano, Ann. Rev. Nucl. Sci. 13, 1 (1963).

[16] G. Silvestrov, Proc. Muon Collider Workshop, February 22, 1993, LANL Report LA-UR-93-866 (1993); B. Bayanov, J. Petrov, G. Silvestrov, J. MacLachlan, and G. Nicholls, Nucl. Inst. and Meth. **190**, (1981) 9; Colin D. Johnson, Hyperfine Interactions, **44** (1988) 21; M. D. Church and J. P. Marriner, Annu. Rev. Nucl. Sci. **43** (1993) 253.

[17] N.M.Gelfand, *A Prototype Lattice Design for a $\mu^+\mu^-$ Collider*, Fermilab TM-1933, April 1995.

[18] S.Y. Lee, K. Y. Ng, D. Trbojevic, FNAL Report FN595 (1992); Phys. Rev. **E48**, (1993) 3040.

[19] M. Syphers, private communication.

[20] V. Balakin, A. Novokhatsky, V. Smirnov, Proc. of the 12^{th} Int. Conf. on High Energy Accelerators, Fermilab, (1983), p. 119; V. Balakin and A. Novokhatsky, *Beam Dynamics in the VLEPP Linear Accelerator*, Int. Conf. of High Energy Accelerators, Novosibirsk (1986).

[21] A. Chao, *Theory of Collective Beam Instabilities in Accelerators*, Wiley and Sons, New York (1993).

[22] K. L. Brown , J Spencer, SLAC-PUB-2678 (1981) presented at the Particle Accelerator Conf., Washington, (1981) and K.L. Brown, SLAC-PUB-4811 (1988), Proc. Capri Workshop, June 1988 and J.J. Murray, K. L. Brown, T.H. Fieguth, Particle Accelerator Conf., Washington, 1987.

[23] Bruce Dunham, Olivier Napoly, *FFADA, Final Focus. Automatic Design and Analysis*, CERN Report CLIC Note 222, (1994); Olivier Napoly, *CLIC Final Focus System: Upgraded Version with Increased Bandwidth and Error Analysis*, CERN Report CLIC Note 227, (1994).

[24] Oide, SLAC-PUB-4953 (1989); J. Irwin, SLAC-PUB-6197 and LBL-33276, Particle Accelerator Conf.,Washington, DC, May (1993); R. Brinkmann, *Optimization of a Final Focus System for Large Momentum Bandwidth*, DESY-M-90/14 (1990).

[25] N. V. Mokhov, *MARS10*, FNAL Report FN-508 (1989); *MARS12*, Proc. SARE Workshop, Santa Fe, Jan 1993; *MARS95*, FNAL FN-628.

[26] N. Mokhov, submitted to the Proceedings of the Sausalito Workshop.

[27] N.M. Gelfand and N.V.Mokhov, *2×2 TEV $\mu^+\mu^-$ Collider Lattice and Accelerator-Detector Interface Study*, Proceedings of this conference.

[28] R. Fernow et.al., *A possible ionization cooling experiment at the AGS*, BNL-61577 (1994).

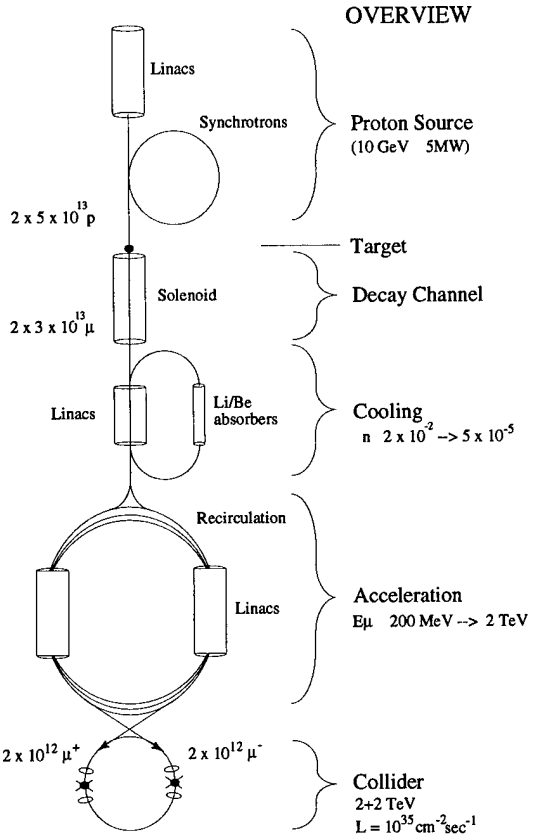


Figure. 1. Schematic overview of a $2 + 2$ TeV $\mu^+\mu^-$ collider

HADRON PARTICLE THERAPY [*]

Jose R. Alonso, Lawrence Berkeley Laboratory, Berkeley, CA 94720

I. INTRODUCTION

Radiation therapy with "hadrons" (protons, neutrons, pions, ions) has accrued a 55-year track record, with by now over 30,000 patients having received treatments with one of these particles. Very good, and in some cases spectacular results are leading to growth in the field in specific well-defined directions. The most noted contributor to success has been the ability to better define and control the radiation field produced with these particles, to increase the dose delivered to the treatment volume while achieving a high degree of sparing of normal tissue. An additional benefit is the highly-ionizing character of certain beams, leading to greater cell-killing potential for tumor lines that have historically been very resistant to radiation treatments.

Until recently these treatments have been delivered in laboratories and research centers whose primary, or original mission was physics research. With maturity in the field has come both the desire to provide beam facilities more accessible to the clinical setting of a hospital, as well as achieving highly-efficient, reliable and economical accelerator and beam-delivery systems that can make maximum advantage of the physical characteristics of these particle beams. Considerable work in technology development is now leading to the implementation of many of these ideas, and a new generation of clinically-oriented facilities is beginning to appear.

We will discuss both the physical, clinical and technological considerations that are driving these designs, as well as highlighting specific examples of new facilities that are either now treating patients or that will be doing so in the near future.

II. HISTORICAL DEVELOPMENTS[1]

A. Fast Neutron Therapy

Being neutral, and hence not interacting electromagnetically with matter, fast neutrons impart their energy to matter through nuclear reactions. It is the recoils from elastic collisions, and nuclear disintegration products that contribute to the dose to biological tissue. Depth dose distribution for 30 MeV neutrons resemble the spectrum of an 8 MeV photon beam, with an exponential falloff (50% attenuation in about 15 cm of water). The character of the radiation, however, because of the low energy of the recoiling particles, is said to be "high LET" (Linear Energy Transfer, a measure of the energy deposited in tissue by the particle). The high ionization density creates more severe local destruction to biologically-active molecules.

E.O. Lawrence always had a great interest in finding medical applications for his cyclotrons, and early work on the production and biological characterization of fast neutrons led, in 1938 to the initiation of a treatment program. A total of 226 patients were treated with neutrons produced from the 30" and 60" cyclotrons between 1938 and 1941. The treatments were interrupted by WW II, but an analysis of the outcome of this treatment program, performed after the war, revealed that although early response was not bad; the high-LET late effects, in the form of complications to normal tissue and organs, were extremely severe. These observations led the medical researchers to conclude that the program should not be continued until further studies of early and late effects could be performed [2].

In fact, it was not until 1970 that the resistance in the medical community was overcome sufficiently that a program was started at the Hammersmith Hospital in London, using a 60 Mev cyclotron. Careful work by Mary Catterall and her co-workers [3] yielded some of the answers that had eluded the earlier researchers, and formed the basis for a substantial program of treatment with fast neutrons. Today, eight centers in Europe, five in the US, five in Japan and Korea, and one in South Africa are treating patients using cyclotrons, D-T generators and linacs [4]. Neutrons are produced by 30 to 70 MeV protons striking a beryllium target, or 14 to 50 MeV deuterons on beryllium, or in the case of the D-T generators, 14 MeV neutrons come from 200 keV deuterons striking the tritiated target.

Current results from these programs clearly indicate that certain classes of patients can benefit by the use of fast neutrons [4]. Salivary gland and paranasal sinus tumors are controlled much better than with photons, and promising results were obtained in some other sites, for example soft tissue sarcomas and prostatic adenocarcinomas. Late effects now seem to be better understood, and carefully-crafted treatment plans can minimize the deleterious effects.

B. BNCT (Boron Neutron Capture Therapy)[5]

The principle is quite simple: attach a nucleus with a high thermal-neutron capture cross section to a pharmaceutical that is preferentially absorbed by tumor tissue, then flood the area with thermal neutrons. The increased number of nuclear disintegrations in the tumor provides the dose concentration that will produce an improved clinical effect. This idea was first proposed in 1935 [6,7], and a clinical program treating brain tumors was undertaken at reactors at MIT and Brookhaven between 1951 and 1961. This program was not successful, mainly because the hoped-for increase in dose to the tumor could not be obtained due to poor uptake ratio of the pharmaceutical and the non-optimal spectral distribution of the neutrons [8]. This concept, too, lapsed into disfavor and was not resurrected until 1970 when a Japanese group [9] reported very promising results using a new class of drugs, and an intra-operative procedure to directly expose the tumor to the thermal neutrons. Considerable activity is now taking

0-7803-3053-6/96/$5.00 ©1996 IEEE

place in this field, with new families of pharmaceuticals promising even higher tumor-uptake ratios, and tailoring of neutron spectra, starting with epithermal neutrons, and using brain tissue itself to moderate the neutrons to the desired thermal spectrum at the site of the (deep-seated) tumor[10]. BNCT is being eyed with much hope as an effective treatment for gliomas, tumors that have been notoriously resistant to any other form of therapy.

C. *Protons*

Protons were recognized by Bob Wilson in 1947[11] as having excellent potential for radiation therapy due to the 1/E nature of the energy-loss process. As the proton slows down it loses proportionately more energy, the greatest energy-deposition in the medium occurring just as the particle stops (the so-called "Bragg Peak"). By adjusting the proton energy so it will penetrate to and stop in a tumor, most of the radiation damage is done in the tumor itself, while the normal tissue traversed on the way to the tumor is largely spared. The comparative rigidity of the proton allows it to travel in an almost straight path to its stopping point, providing for good localization of the dose. Multiple scattering and range straggling will broaden the stopping point somewhat, but at depths of 15 to 20 cm, dose-falloffs of 8 to 10 mm are possible. Shallower depths are proportionately better. Note that proton therapy is considered as a "low-LET" modality, the ionization density for the stopping proton beam is comparable with that of a photon beam.

The first use of protons in therapy was performed at the Berkeley 184" Synchrocyclotron[12] in 1952, for pituitary treatments. Rotational therapy (twisting the head about the pituitary as a center of rotation) was used with a high-energy beam, not trying to stop the beam because of uncertainty in the tissue-thickness on the way to the target. The first Bragg-Peak therapy was performed at Uppsala in 1956[13] using their 230 MeV Synchrocyclotron. Noteworthy programs in Russia[14] and Japan[15] also pioneered many of the techniques for using protons in therapy. In 1965 the 170 MeV Synchrocyclotron at Harvard was converted from its nuclear physics use into a dedicated medical facility, and became the site for the longest-running and very successful program in radiosurgery and therapy with protons [16,17]. Extremely high success rates were obtained with ocular melanomas, and chordomas and chondrosarcomas, tumors very close to critical structures (optic nerve and spinal chord, respectively). For successful treatment beam had to be placed with millimeter accuracy to prevent unacceptable complications. These treatments were possible because of the sharp stopping of protons in these relatively shallow target volumes. To date over 16,000 patients have been treated at these and other, newer facilities, with good indications of success in a wide range of tumors. Of all the hadron modalities, protons are the most widely accepted today, and significant growth is occurring with many proton therapy facilities in planning and construction[18].

D. *Pions*

Fermi recognized the possible use of pi-minus mesons in medicine; formal proposal of their use for radiation therapy was made by Peter Fowler in 1961[19]. The pion exhibits the same Bragg curve stopping behavior as the proton (although being lighter does suffer more from multiple scattering), but the π- is captured as it stops causing the capturing nucleus to disintegrate, adding a "star dose" of high-LET radiation to the Bragg Peak. Early characterization and dosimetry work was done at Berkeley (184") and CERN (SC), but it was not until the meson factories at Los Alamos, PSI and TRIUMF were built that sufficient flux was available to contemplate a medical therapy program. Programs were conducted at all three[20,21,22] and over the last 20 years 1000 patients have received pion treatments. Noteworthy is the "Piotron"[22] built at PSI from an idea proposed by Kaplan at Stanford years earlier[23]. To increase the dose rate, this "pion concentrator" consisted of a 60-channel "orange-peel" type spectrometer, collecting pions from a conical section 60° from the beam axis and bringing 60 beamlets to an image-point of the target. A positioner brought the patient to this point, and moved the patient around so all points in the treatment volume were exposed to this concentrated spot.

On the whole, the clinical results from these programs were good, but not outstanding. The general consensus of the researchers is that while pions are effective, they do not seem to show clinical results that are much better than other hadron beams. Considering the size and expense of machines needed to produce high fluxes of pions, it is unlikely that a practical, cost-effective hospital-based pion therapy facility will ever be built. The TRIUMF program, the last of the three still in operation, will stop accruing patients in 1995.

E. *Heavy Ions (C, Ne, ...Si)*

With the commissioning in 1974 of the Bevalac in Berkeley, the use of ions heavier than protons for therapy became a possibility. In fact, funding for the transfer line between the SuperHILAC and the Bevatron, critical link in the creation of this composite machine, was provided by life-sciences with the object of investigating the potential of heavy ions for medical applications. To achieve the necessary 30 cm range in tissue requires energies of 400 MeV/amu for carbon or 600 MeV/amu for neon ions, energies not available before the Bevalac came into being.

These ions are heavier than protons, will scatter less and so provide sharper edge-definition for the radiation field. On the other hand, the nuclear mean-free-path is comparable to the treatment depth so that a significant amount of the beam can be lost to nuclear reactions, mostly peripheral transfer reactions, producing light fragments that travel beyond the stopping point of the primary beam. This "tail dose" becomes appreciable for heavier ions at depths greater than about 20 cm.

Since ionization density varies as the square of the ion

charge, heavy ions have higher LET than protons. Based on a fairly arbitrary threshold, it is argued that the slowing-down region (called the "plateau") for carbon ions is "low-LET" while the "peak" is higher LET, offering the best advantage of normal-tissue sparing and good tumor-killing. On the other hand, researchers at LBL observed that neon ions would provide a better test of high-LET effects, and in fact this is the ion primarily used in the Bevalac program. Note that heavier ions than neon will exhibit very high ionization in the slowing region, and an "overkill" in the stopping region, so were not considered for any but the most superficial of tumors, in which little or no normal tissue would have to be traversed. A few such tumors were treated with silicon and argon beams.

Between 1974 and 1993, the year the Bevalac closed, over 400 patients were treated with these ions. Many different tumor types were treated, to get an overall view of the benefits that might be obtained. Castro, the lead physician in this program, reports promising results[24] in many sites, but particularly for advanced prostate carcinomas, as well as soft-tissue osteo-sarcomas, tumors that are normally very resistant to radiation treatments. However, statistics are low, and it is clear that more experience is necessary before the overall clinical utility of heavy ions can be established. Results have been encouraging enough, though, that two major efforts have been launched to continue the trials begun at the Bevalac. The HIMAC facility in Chiba, Japan is now treating patients, and a program at GSI in Darmstadt, Germany, is preparing a medical area and will begin treating patients in about two years. Both of these programs will be described further later in this paper.

III. LESSONS LEARNED

A. Dose Localization

Tumor control is significantly improved when the dose can be more precisely placed. Spectacular improvements in cure rates have resulted from the advent of CT and MRI diagnostic devices that have for the first time allowed accurate definition of target volume. Radiation therapy is still lagging in its ability to place the desired radiation dose into the optimally-defined target volume. Dose concentration with photons is obtained by multi-port treatments, irradiating the patient from different angles with the beams overlapping in the tumor region. The current generation of compact linacs used for x-ray therapy are installed on a gantry so can be easily rotated in a vertical plane about the patient lying on a table at the center of the beam arc. The overlap region, however, cannot without great difficulty be made to conform to the irregular shape of the tumor volume, so a significant amount of normal tissue is exposed to a higher-than-desired dose.

The Bragg Peak and the ability, in principle, to place stopping particles in any coordinate of the body gives ions a natural advantage over photons to improve further the selectivity and precision of radiation therapy. The juxtaspinal (i.e. chordoma) treatments are a case in point. In many cases the tumor surrounds the spinal chord, so the desired treatment volume would be a toroid. By controlling the stopping point to come short of entering the chord, ions can deliver a treatment that keeps dose to the chord to an acceptable level. Such a treatment is essentially impossible with photons.

In practice, even with ions, treating an arbitrarily-shaped volume without involving normal tissue in the high-dose field is technologically very complex, in fact no patients have been treated yet with such a fully "three-dimensional" system. Typically the maximum outline of the treatment volume is defined by a shaped collimator, the maximum penetration is contoured by a "bolus compensator" placed in front of the patient, then the range is modulated by a ridge-filter that spreads stopping particles over the maximum thickness of the tumor. This "delta-Z" is the same for all parts of the field, defining a cylindrical section of uniform high dose. The normal tissue in this cylinder outside the tumor volume receives the same dose as the tumor.

In fact, technology does exist to overcome this limitation, but it is very complex and requires much development and testing prior to being mature enough to use with actual patients. In addition, the implementation of such scanning systems place many constraints on the accelerator performance, requirements often not found in conventional accelerator designs. These will be discussed below.

B. High LET

Heavy-ion and neutron treatment results do show that high LET can kill tumors that have resisted other forms of treatment. Normal tissue is also damaged more by these particles, and in particular side effects can show up many months after the treatment has been completed. Maximum effectiveness then requires an extremely delicate balance, and also the need to keep to an absolute minimum the involvement of normal tissue in the high-LET radiation field. Again, this requires the most sophisticated delivery systems. Defining this balance in the treatment plan requires the greatest possible knowledge of the response of both normal and tumor tissues to the radiation in question; much of this information is not available now.

Much more research is required to optimize the use of high-LET radiation, but the potential benefits for patients with difficult tumors could be very high. Adding to the complexity is the extra degree of freedom in the mass (or charge) of the ion that is used. On the other hand, this flexibility can add further to the benefits available from a finely-tuned treatment plan customized for each patient. A technique, called "predictive assays"[25] can assist in selecting the appropriate treatment: samples of tumor and normal tissue are taken from the patient and are exposed to different radiations to determine the response of these particular cell types. The treatment plan, and even the best ion to use, can be selected by this means.

IV. DESIGNING FOR OPTIMUM EFFECTIVENESS

The best conformation of the radiation dose to the clinically-defined target volume can be achieved if careful attention is paid to the design of the accelerator and beam-delivery systems. Paramount for proton and ion therapy is the preservation of beam quality to prevent loss of sharpness due to range straggling and multiple scattering. Range variations should take place by adjusting the energy of the beam outside the treatment room, not by degraders; and lateral spreading should use magnetic deflection rather than scattering systems. Precise three-dimensional dose deposition requires very fine control over the instantaneous beam current, and the ability to quickly adjust the coordinates (x,y,z) of the stopping beam with high accuracy. Considering that a typical target volume may be subdivided into 10^6 volume elements that must be independently irradiated to a ±2% dose accuracy in less than 2 minutes, the complexity of the delivery system becomes apparent. A close coupling of the accelerator performance and the delivery system is the only way of assuring success. Performance specifications for the accelerator have been carefully studied, and although quite stringent, do fall within today's state of the art[26].

The ease of treatment afforded by placement of photon sources on a gantry has indicated that all modern treatment facilities should have this capability. Treating in the supine position not only adds to patient comfort, but is critical for use of the essential diagnostic information from CT and MRI scanners. Proton gantries are large, in many cases larger than the accelerator, but nonetheless feasible. A heavy-ion gantry is unmanageable with today's technology, but fixed beams at different orientations can come close to providing the necessary flexibility.

V. NEW FACILITIES

A. Fast Neutrons

The state-of-the-art neutron therapy facility is embodied in the gantry-mounted superconducting deuteron cyclotron[27] built by Henry Blosser for the Harper Hospital in Detroit. The 48.5 MeV, 15 μA deuteron beam strikes an internal beryllium target producing a neutron dose rate of 40 cGy/min. As the whole cyclotron rotates around the patient there is no need to extract the beam from the cyclotron, nor for any beam-transport system. In full use since early 1992, about 150 patients per year are now treated.

B. BNCT

If the clinical advantages of BNCT are demonstrated, a hospital-based program will most likely be implemented with accelerator technology rather than with reactors. Neutrons are produced by protons striking lithium or beryllium targets, the epithermal spectrum is obtained with a suitably-designed moderator. To treat a patient in a reasonable time (less than one hour) the p-Li reaction will require a proton beam current between 10 and 100 mA (average) at 2.5 MeV, the p-Be requires somewhat less current (5-10 mA) at around 20 MeV. High duty-factor RFQs and electrostatic generators are being developed for the lower energy application, while high-current cyclotrons might meet the need for the higher energy. R&D is progressing, and these systems should be ready for patient treatments in a few years.

C. Protons

The first hospital-based proton facility at Loma Linda has been operational since 1990, and has treated over 1000 patients[28]. A 250 MeV (weak-focusing) synchrotron delivers beams to three gantry rooms and two fixed-beam rooms. Although not now using advanced delivery systems, the flexibility of the accelerator allows for their implementation when it is felt the technology is suitably tested for reliable use with patients. The accelerator and ancillary technical systems have demonstrated extremely high reliability, and stand as a demonstration of the readiness for introducing complex accelerator systems into hospital settings.

The Paul Scherrer Institute in Switzerland is now commissioning a compact gantry system with a line-scanning system that will be capable of treating 3-dimensional volumes[29]. Attached to the high-current, 600 MeV cyclotron, this proton-therapy facility uses only a tiny fraction of the available beam, degrades it to 200 MeV, followed by cleanup by collimation and momentum-selection prior to entering the gantry system. Patient treatments are expected to start this summer.

Construction is well underway for a new facility at the Massachusetts General Hospital in Boston. A 235 MeV cyclotron will deliver beam to one gantry and one fixed-beam room. Energy variation is obtained by degrading the beam followed by collimation and momentum selection. The compact cyclotron is being built by IBA (Belgium), field mapping starts in June 1995. Patients treatments should start in 1998.

About ten other facilities are in operation today, many of them low-energy (≈70 MeV) cyclotrons dedicated to eye treatments. Several projects are in various planning stages, in Texas, Italy, Russia and Japan[18].

D. Heavy Ions

The HIMAC facility in Chiba, Japan stands as the premier facility dedicated to hadron therapy today. This large complex consists of two 800 Mev/amu synchrotrons one above the other, injected by a 6 MeV/amu Alvarez linac[30]. Ions from helium to silicon can be delivered to one of three treatment rooms, equipped with horizontal and vertical beam ports. For accurate patient positioning, a CT scanner has been installed in each treatment room. As described earlier in these proceedings[31], this facility has now completed its commissioning, and since October 1994 has treated 21 patients with carbon beams. The beam-delivery system is closely patterned after that used for many years at the Bevalac, a two-dimensional system based on wobbler magnets[32], but

it is anticipated that a more advanced system will be implemented in future years.

GSI, in Darmstadt, is beginning serious work on a patient treatment facility. Clearly defined as a technology demonstration effort, rather than an outright clinical program, new and innovative techniques are being developed and will be tested with patients[33]. Pulse-to-pulse energy variation has been demonstrated from the SIS synchrotron, and a scanning system is now operational that has demonstrated spectacular abilities in painting beam into complex shapes. Excellent conformation to defined target volumes should be achieved. In addition a technique, first developed in Berkeley[34] for using positron emission from radioactive ions to localize the stopping point of the treatment beam is being implemented. Patient treatments are expected to start in 1997.

Planning for other heavy-ion facilities is progressing as well: the AUSTRON project in Austria will consist of a carbon synchrotron built in conjunction with a spallation neutron source, the TERA project in Milan plans initially for a proton synchrotron that can be upgraded to carbon capability with addition of a new injector, and the Hyogo Prefecture will build a carbon-ion treatment facility close to the SPRING-8 site. Start of this last project has been slightly delayed by the recent Kyoto earthquake, but the determination to proceed with the project has not been affected.

VI. SUMMARY

Hadron therapy is a maturing field, with strengths and weaknesses that have been clearly identified. For certain tumor types, particles have become the treatment of choice, and hospital-based implementation of these techniques are coming on line. Focused R&D programs in critical areas of beam-delivery, treatment planning and radiobiology are underway at many centers around the world, increasing the scientific and technological base needed to best utilize these modalities.

Cancer is a highly complex disease; effective control requires a wide arsenal of treatment techniques. The flexibility and precision of hadron therapy are powerful tools in this arena, and promise to provide great improvements in our health-care when fully understood and implemented.

VII. REFERENCES

[*] This work was supported in part by a grant from the National Cancer Institute, NIH, and in part by the US Department of Energy, under DOE Contract No DE-AC03-76SF00098.

Many references cited below come from the proceedings of the November 1993 conference in Como, Italy entitled "Hadrontherapy in Oncology" U. Amaldi and B. Larsson, editors, Elsevier (1994). This volume is referred to as "HiO."

[1] Much of the historical material is drawn from the excellent summary by M.R. Raju, "Hadrontherapy in a historical and international perspective," in "HiO" pp 67-79.

[2] Stone RS Am J Roentgen 59 (1971) 771.

[3] Caterall M et al. Br Med J 2 (1975) 653.

[4] Richard F, Wambersie A, "Fast neutrons and the LET-factor" in "HiO" pp 173-198.

[5] D. Gabel, W. Sauerwein, "Clinical implementation of BNCT in Europe," in "HiO" pp 509-517.

[6] Taylor HJ, Goldhaber M, Nature 135 (1935) 341.

[7] Locher GL. Am J Roentgen Radium Ther 36 (1936) 1

[8] Slatkin DN. Brain 114 (1991).

[9] Hatanaka H, "Boron neutron capture therapy for tumors," in "Glioma," Karim ABMF, Laws ER editors, Springer Verlag 1991.

[10] Zamenhof R et al. in "Progress in Neutron Capture Therapy for Cancer," Allen BJ, Moore DE, Harrington BV editors, Plenum Press 1992, pp 21-26.

[11] Wilson RR. Radiology 47 (1947) 487.

[12] Tobias CA et al.. Am J. Roentgenol Radium Ther Nucl Med 67 (1952) 1.

[13] Larsson B et al. Acta Chir Scand 125 (1963) 1.

[14] Minakova, EI. "The Russian protontherapy program," in "HiO" pp 102-108.

[15] Tsujii H et al.. Int J Radiat Oncol Biol Phys 25 (1992) 49.

[16] Constable IJ et al. Radiat Res 65 (1976) 304.

[17] Gragoudas ES et al. Am J Ophthalmol 83 (1987) 665.

[18] Janet Sisterson, editor "Particles" Newsletter issued semiannually. Sisterson@huhepl.harvard.edu.

[19] Fowler PH, Perkins DH. Nature 189 (1961) 524.

[20] Von Essen CF et al. Int J Radiat Oncol Biol Phys 13 (1987) 1389.

[21] Blattmann H. "Pions at Los Alamos, PSI and Vancouver," in "HiO" pp 199-207.

[22] Lam GKY et al. see [21].

[23] Kaplan HS et al. Radiology 108 (1973) 159.

[24] Castro JR. "Heavy Ion Therapy: the Bevalac Epoch," in "HiO" pp 208-216.

[25] Burkard W, Larsson B. "Towards individualization and optimization of radiation therapy: biological behaviour of tumor cells derived from human tumor biopsies," in "HiO" pp 735-741.

[26] Chu WT et al. "Performance specifications for proton medical facility," LBL-33479, 1993.

[27] Maughan RL et al. "Facility for fast neutron therapy at the Harper hospital," in "HiO" pp 377-385.

[28] Coutrakon G et al. "A performance study of the Loma Linda proton medical accelerator," in "HiO" pp 282-306.

[29] Scheib S et al. "Spot scanning with protons at PSI: experimental results and treatment planning," in "HiO" pp 471-480.

[30] Kawachi K et al. "Heavy ion medical accelerator facility in Japan," in"HiO" pp 229-240.

[31] Yamada S. "Commissioning and performance of the HIMAC medical accelerator," proceedings of this conference.

[32] Renner TR, Chu WT. Med Phys 14 (1987) 825.

[33] Kraft G et al. "The Darmstadt Program HITAG: heavy ion therapy at GSI," in "HiO" pp 208-216.

[34] Llacer J et al. Med Phys 17 (1990) 151.

MICROMECHANICS VIA SYNCHROTRON RADIATION

H. Guckel, University of Wisconsin-Madison,
Department of Electrical & Computer Engineering, 1415 Johnson Drive, Madison, WI 53706

A significant portion of micromechanics deals with actuators: devices which modify their environment. Manufacturing techniques for this class of devices involve 3-dimensionality, tolerances, IC-compatibility, a broad material base and cost effectiveness. Photoresist based processing with x-ray exposures via synchrotron radiation has many of the required attributes for actuator manufacturing. This is particularly true for exposures with 20 KeV x-rays where structural heights to 10 cm have been obtained and where x-ray mask issues simplify. Tests with this type of tool have brought significant advances in linear actuators and have been used to fabricate a micro electro mechanical system, a dynamometer on a chip, for magnetic micromotor testing.

I. INTRODUCTION

Micromechanical devices fall into two categories: sensors and actuators. Sensors are devices which measure some property of their environment. They should do this non-invasively. This implies small physical size and low power dissipation. Both attributes are shared with microelectronic devices. The successful adaptation of microelectronic processing procedures for sensor fabrication is therefore not surprising. Actuators are devices which modify their environment. A good actuator with defined performance specification does this at minimum physical size and minimum power dissipation. This implies that an actuator may in fact not be a physically small device but is constructed by using micromechanical tools. An appropriate tool for actuator fabrication must address at least five issues. Thus, actuators are always three-dimensional devices. The processing tool must recognize that. If a microactuator is a scaled version of a larger device the tolerances must also scale. Since typical mechanical tolerances are in the 100 ppm range the microactuator tool must accommodate this. The material base for microelectronics is relatively small and inadequate for actuators. A good actuator tool must be able to accommodate materials which extend from metals to ceramics to polymers. Actuators are components. Systems which use these components are of economic benefit. Control issues for systems made from actuators demand electronics. In some applications, for instance, capacitive sensing, co-fabrication of microelectronic components must be possible for the actuator tool. In other cases co-packaging of commercially available microelectronics is adequate. The fifth point is perhaps the most important one: the actuator processing sequence must be cost effective. Since many actuators and microactuators may be fabricated using precision engineering tools which are typically serial, photoresist based processing tools may meet the cost effectiveness requirement because they are fundamentally parallel.

All photoresist based processes use a mask to transfer geometric information to a photoresist layer which is located on a planar substrate. The exposed or unexposed photoresist regions are removed during development. The geometry which is produced is therefore prismatic and actuators based on photoresist technology are prismatic actuators. The performance for this type of device may be estimated. Thus

$$F_{out} \leq \rho_E V_A \tag{1}$$

where F_{out} is the output force, ρ_E the stored energy density and V_A the active volume in which the energy is stored. The active volume may be related to the physical volume, V, by a filling fraction, α.

$$\alpha = \frac{V_A}{V} \tag{2}$$

However, since the geometry is prismatic the physical volume becomes the product of the actuator area, A, and the structural height, H. Hence, Equation (1) becomes

$$\frac{F_{out}}{A} \leq \rho_E \alpha H \tag{3}$$

The output force per unit chip area is a figure of merit for a particular design. It depends on the actuation mechanism which is used: electrostatics, magnetics or pneumatics and hydraulics. The energy density increases from electrostatics to hydraulics. The required three-dimensionality does the same thing which explains the large activity in electrostatics. The filling fraction is in part related to the resolution of the lithography process. A large structural height improves performance. A high performance actuator tool is therefore identified as a thick photoresist technology with high geometric resolution.

II. LIGA-LIKE PROCESSES

Thick photoresist processes must face the initial difficulty of photoresist application. The traditional spin coating in a single coat is not very feasible because of solvent evaporation problems. Multiple coats reduce yield and increase processing cost. The first successful attempts to produce photoresist thicknesses of 500 μm or so were

0-7803-3053-6/96/$5.00 ©1996 IEEE

reported by W. Ehrfeldt and his co-workers [1]. He used the in situ polymerization of poly methyl methacrylate or PMMA to form an x-ray sensitive photoresist layer, which he used in a process called LIGA. His application procedure, a form of casting, has the problem that polymerization involves a volume shrinkage, roughly 20%, and that this shrinkage together with the adhesion requirement results in a heavily strained photoresist. This problem, strain induced due to polymer shrinkage, is the nemesis of many thick photoresist processes and limits the maximum attainable height.

The strain issue for thick photoresists has recently been solved by using a solvent bonding approach [2]. In this technique commercially available, cell cast photoresist sheets of convenient thickness are used. These sheets are essentially strain free and can be analyzed for strain and molecular weight prior to usage. They are next cut to size via water jet machining and are then solvent bonded to the selected substrate. After curing the height is adjusted by precision milling. Figure 1 illustrates the result.

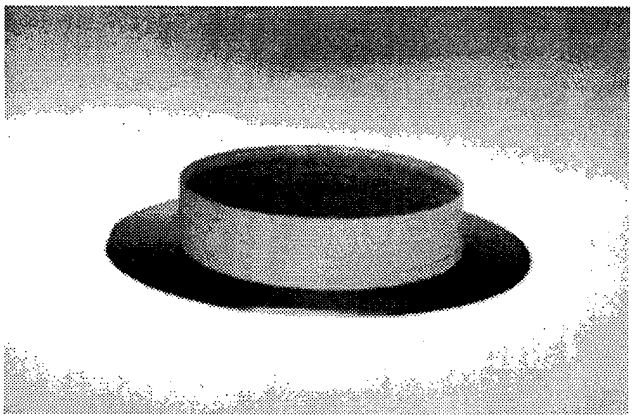


Figure 1: 2" diameter PMMA disks on a 3" silicon wafer. The absence of wafer bending is noteworthy. The photoresist height is 1.6 cm.

The photoresist of Figure 1 must be exposed through a suitable mask. This requires photon energies which are associated with absorption lengths which are comparable to the photoresist thickness. For PMMA, a photoresist with reasonable mechanical properties, poor optical sensitivity and excellent optical resolution, this can only be done by using x-ray photons. The type of photon follows from Figure 2.

Since the absorption length is roughly 100 μm at 3,000 eV exposure depth at this energy are restricted to 500 μm or so. This condition changes to 5 cm at 20,000 eV where the absorption length is 1 cm. The dose which is required for

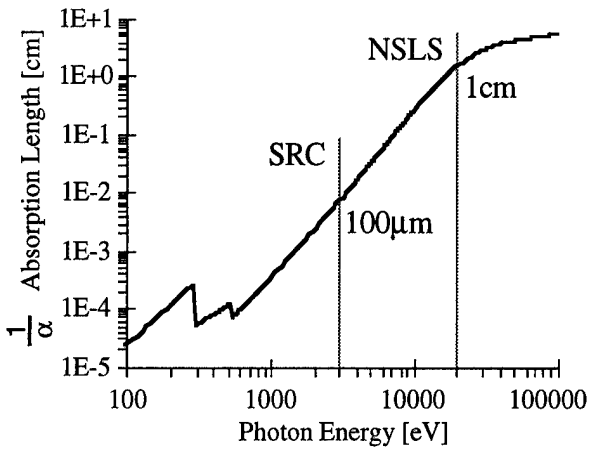


Figure 2: Absorption length for PMMA versus photon energy.

PMMA and a particular developer is 1.6 x 10^3 Joules/cm^3. Since this dose is large a high brightness source, synchrotron radiation is required. In fact, Figure 2 refers to Aladdin, the Wisconsin storage ring at 1 GeV and Brookhaven's 2.6. GeV machine for hard x-rays. The use of x-rays for exposure eliminates the standing wave problem which limits optical exposures. The use of synchrotron radiation contributes excellent collimation which results in vertical photoresist flanks.

A comparison between low and high energy exposures results in conclusions which favor high energy fluxes. The mask for low energy exposures involves a mask blank which is typically 1 μm in thickness and made of low atomic number material, say, Si_3N_4. The absorber is gold at 2 to 4 μm thickness. The mask by necessity involves a small area and yields a cost effective tool only if x-ray exposures are minimized. This normally requires injection molding from an x-ray generated master die. The A in LIGA stands for Abforming or injection molding.

High energy exposures use a mask blank which is simply a standard silicon wafer. The absorber is again gold in the 10 to 50 μm range. A large area mask is therefore possible. This mask can be used to expose photoresists on both sides of a wafer which produces perfect front to back alignment. Moreover, several of these wafers can be stacked and exposed at the same time. The need to use injection molding lessens and, under the right circumstances, disappears as a cost issue.

The exposed photoresist is developed. Since a free standing photoresist sheet can be used PMMA parts with submicron tolerances can be produced. This is illustrated in Figure 3.

If the photoresist is attached to a substrate with a plating base the photoresist recesses can be filled with electroplated metals. This converts the PMMA mold to a metal mold of fully attached parts. This process, electroplating, is represented by the letters GA in the acronym LIGA and completes the original LIGA processing sequence.

The LIGA process as outlined here does not meet the requirements for an actuator processing tool. The process is basically 2-dimensional and obtains its tolerances from the x-ray mask and the ability to print and develop the PMMA. This is troublesome for mechanically weak shapes, for instance optical gratings, which must survive developing and plating. The process does have a large material base. It becomes cost effective via injection molding and via high energy exposures.

The process can be improved by combining surface micromachining and LIGA. In this process, SLIGA, sacrificial layers are used to form metal parts which are either fully attached, partially attached or can be removed from the substrate. Since the metal parts are quite thick they do not distort when freed. Thus, free parts may be assembled onto fixed parts. Assembly improves the tolerance issue because assembly in effect subtracts two mask dimensions from each other. Since incremental mask tolerances are typically submicron, devices with submicron assembled tolerances can be produced. This is particularly important for bushing clearances where 0.25 μm tolerances have been achieved with shaft diameters of 100 μm and rotor holes of 100.5 μm at structural heights of several hundred micrometers. The extreme edge acuity of the x-ray exposure permits this excellent performance. Assembly does of course also improve the 3-dimensionality to the processing tool. This aspect of the tool will increase dramatically when SLIGA with multiple, sequential x-ray masks; MEMS-LIGA; becomes available. This should occur within the next few months.

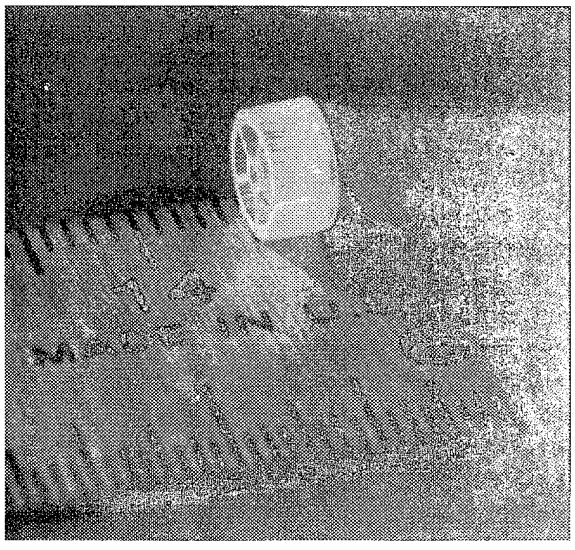


Figure 3: PMMA parts

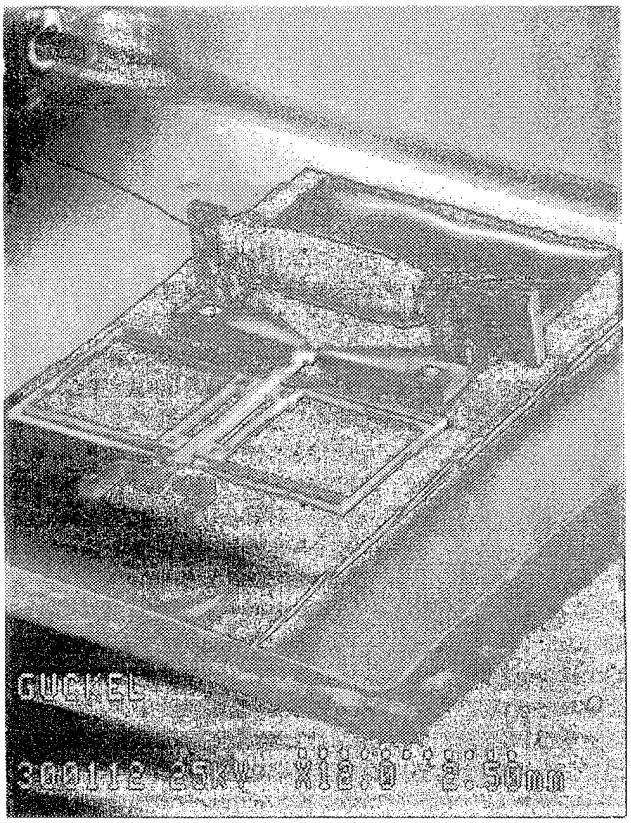


Figure 4: Linear magnetic actuator.

III. MAGNETIC ACTUATOR PROGRESS

The SLIGA processing sequence is being tested by constructing electromagnetic actuators. The material of choice for this project is a permalloy with 78% Ni and 22 % Fe. This alloy was chosen in order to minimize magnetostricitve effects which compromise magnetic properties. The measured as plated magnetic behavior for the alloy involves a saturation flux density of 10,000 Gauss with a coercivity of 0.3 Oersted and a pemeability of roughly 2000. The material is therefore a soft magnet. The permalloy also has good mechanical properties: it is hard and has high yield strength. Because of this it makes a very good material for mechanical springs which play an important role in actuator construction.

Linear actuators have application areas which extend from microrelays to positioning systems. The "right" actuator for these areas is required to have a throw in excess of 100 μm with a position independent output force of at least 1×10^{-3} Newton. It should move 100 μm in 1 millisecond and cannot consume more than 10×10^{-3} watt. A device which meets and exceeds these specifications is shown in Figure 4 [3].

The device uses magnetic pole pieces and spring mounts which are fixed to the substrate. The spring with a spring constant of 3 N/m is fabricated separately and assembled on the spring mounts with a tolerance of 0.25 μm. The coil is fabricated by winding up to 1000 turns of 25 μm diameter magnet wire on a SLIGA permalloy staple.

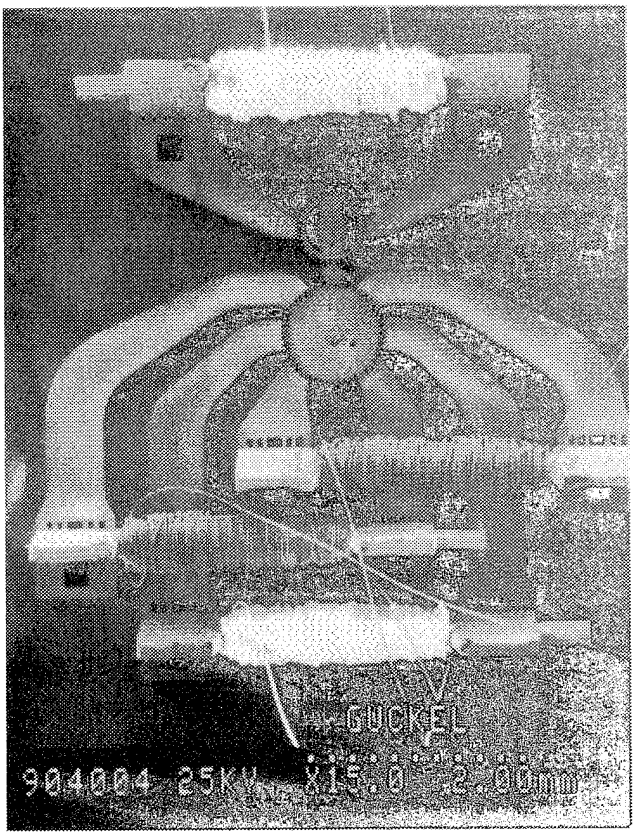


Figure 5: Permalloy dynamometer formed from three phase motor, idler gear and electromagnetic brake.

It is then inserted into the pole pieces and forms an inductance of several millihenry at closure with 10 Ohms per 100 turns of resistance. The change in inductance with position is near 1 x 10^{-6} henry per micrometer of travel. This allows not only inductive position sensing but also experimental output force measurements which are useful for closed loop operation. The device has a fundamental resonance at 400 cps, a quality factor of 400 in air and consumes 200 x 10^{-6} watt at resonance with a movement of 350 μm. The measured performance is acceptable for several practical applications.

In rotational machines the transition from components to systems has been achieved. Figure 5 shows a recent result which is in the form of a dynanometer.

The driver in this case is a three phase reluctance motor with a rotor which has 50 involute gear teeth. These teeth interact with a stator with teeth in order to form a stepping motor which can move one rotor tooth at a time. This start-stop motion is difficult to achieve in small devices because of stiction problems. If the motor is excited with 3-phase sinusoids steady rotational speeds are achieved and coupled into the idler gear. The idler drives the brake gear which is located in an electromagnet which controls the motor load via DC-current through its coil. The desired speed range extends to 10,000 rpm with maximum input currents of 20 mA and tip force outputs in the millinewton range. The machine is needed to collect data on the behavior of micromotors under load.

IV. CONCLUSIONS

LIGA or LIGA-like processing forms a tool which has major implications on not only actuator and microactuator fabrication but also on precision engineering where it competes favorably with precision discharge machining techniques. The experimental and theoretical feasibility studies for high energy x-ray exposures have produced results which have improved the utility and cost effectiveness of this type of manufacturing. Practical high performance actuators are but one of many possible products which this type of activity can and will provide.

V. REFERENCES

[1] E.W. Becker, W. Ehrfeld, P. Hagmann, A. Maner, and D. Münchmeyer, "Fabrication of Microstructures with High Aspect Ratios and Great Structural Heights by Synchrotron Radiation Lithography, Galvanoforming, and Plastic Moulding (LIGA Process)," Microelectronic Engineering, vol. 4, 1986, pp. 35-56.

[2] H. Guckel, K.J. Skrobis, J. Klein, T.R. Christenson, and T. Wiegele, "Deep X-ray Lithography for Micromechanics," in Proceedings of *Québec '93 - SPIE*, Québec City, Canada, 15-21 August 1993.

[3] H. Guckel, T.R. Christenson, T. Earles, J. Klein, J.D. Zook, T. Ohnstein, M. Karnowski, Solid State Sensor and Actuator Workshop, Hilton Head Island, South Carolina, June 13-16, 1994, pp. 49-52.

Radionuclide Production for the Biosciences

Thomas J. Ruth
UBC/TRIUMF PET Program

I. INTRODUCTION

The use of radionuclides in the bioscience can be broken down into three general categories, imaging, radiotherapy and radiotracers. Imaging can be further divided into positron emission tomography (PET) and single photon emission tomography (SPECT). These topics are beyond the scope of this paper and will not be described here.

All of these uses rely on the fact that the radionuclides are used at tracer concentration. In order to be used as tracers the radionuclides and the compounds to which they are attached must obey the tracer principles which state that:

- the tracer behaves or interacts with the system to be probed in a known, reproducible fashion,
- tracer does not alter or perturb the system in any fashion and
- the tracer concentration can be measured.

In radiotherapy, the second principle is, in a strict sense, broken since the point of delivering the radiotoxic substance is to have the emitted radiation cause damage to the undesirable surrounding tissues. However, in order for the radiotoxic substance to localize it must be follow the known chemical behaviour without perturbing that pathway.

The following are some typical radionuclides used in each of the broad categories:

^{11}C is a positron emitting radionuclide with a half-life of 20 minutes. It is generally produced as $^{11}CO_2$ which can be converted into a wide variety of labelling agents such as $^{11}CH_3I$ or $H^{11}CN$. Since all biological compounds contain carbon ^{11}C finds wide spread use as a tracer in PET.

^{13}N is also a positron emitting radionuclide. However it is used in applications other than PET imaging, for example it is widely used in botany studies to determine the kinetics of nitrogen uptake in a variety of plant systems.

^{123}I emits -rays with an energy of 159 keV which is ideally suited with imaging in SPECT cameras. In addition the ease with which an iodine atom can be inserted into a compound makes ^{123}I extremely versatile as a radiotracer in SPECT.

^{186}Re is a ß- emitter with a low abundant γ-ray with an energy of 140 keV. The 1 MeV γ-rays and its 90 hour half-life make it a promising radiotoxic nuclide for therapy. As a chemical analogue of technetium, rhenium possesses similar chemical properties as ^{99m}Tc and can thus be used with some of the same compounds that have been developed for imaging tumours.

Most of the radiotracers have relatively short half-lives (less than a few hours to at most a few days). There are definite advantages in using short-lived radionuclides, for example there is a low radiation dose associated with each study, serial studies are possible (sometimes on the same day for tracers such as ^{11}C) and the radioactive waste disposal problems are minimized if not eliminated. The disadvantages include the need for an accelerator nearby or within easy shipping distance for the longer lived species and rapid chemical procedures are required, especially for the more complex compound formation.

II. RADIONUCLIDE PRODUCTION

The rate of production is dependent on the number of bombarding particles, the number of target nuclei and the cross section of the reaction. The length of bombardment is also important since the production of short lived nuclei can reach saturation rather quickly. In order to optimize the production of a particular radionuclide the following production considerations must be taken into account:

- the threshold energy for the desired reaction,
- the energy where the maximum yield occurs,
- the chemical form of the target nucleus,
- the physical form of the target nucleus,
- the chemical form of the desired product,
- the physical form of the desired product, and
- the ease of separation of product from the target.

To illustrate this approach we can look at the case where ^{18}F is needed as fluoride. The two most widely used nuclear reactions for producing ^{18}F are the $^{20}Ne(p,\alpha)^{18}F$ and the $^{18}O(p,n)^{18}F$. Both reactions have a relatively low threshold energy (0-2 MeV) and the maximum yield occurs under 10 MeV. However, the (p,n) reaction has a much higher cross section so that the quantity of ^{18}F that can be produced expressed as mCi/μAh is more than double for a thick target reaction using protons of about 12 MeV in comparison to deuterons of comparable energy [1]. Thus having selected the mode of production and the energy, the next issue is to examine the chemical and physical forms of the target and product. The most convenient target material for producing ^{18}F as fluoride is a water target enriched in ^{18}O. The resulting ^{18}F is produced directly as the fluoride ion which can be extracted from the target water by simple ion exchange columns.

III. ACCELERATORS

Through the 1970's most radionuclides that were produced for the biomedical community utilized cyclotrons designed for physics applications. These machines usually accelerated four particles and were cumbersome to operate when it came to

0-7803-3053-6/96/$5.00 ©1996 IEEE

changing particles which was necessary since the preferred reactions for the PET radionuclides required both protons and deuterons (e.g. $^{14}N(p,)^{11}C$ and $^{14}N(d,n)^{15}O$). In the late 1970's the cross sections for proton induced reactions for the PET radionuclides ^{18}F and ^{15}O were explored and found to give higher yields than the corresponding deuteron reactions. These results and the fact that all of the commercially available radionuclides produced for nuclear medicine are also produced by proton induced reactions led the participants of the Heidelberg Workshop on Targetry and Target Chemistry to conclude that proton only cyclotrons could meet the needs of the PET/nuclear medicine communities [2]. The primary drawback to this possession was the fact that some of the reactions required the use of enriched target materials which were not always readily available or easily recovered. More recently the availability issues have been resolved for the most part.

Another factor that has influenced the expansion of PET was the development of negative ion cyclotrons which were made possible by the demonstration of the principle of accelerating negative hydrogen ions and extracting the protons by electron stripping [3]. The first negative ion cyclotron was built at UCLA and the University of Manitoba in the mid 1960's [4,5]. TRIUMF, Canada's National Laboratory for Nuclear and Particle Physics was established around the design of a 500 MeV negative ion cyclotron [6]. By the late 1970's The Cyclotron Corporation (TCC) had designed and built several negative ion cyclotrons for the producing the commercial radioisotopes and for neutron radiotherapy (CP42 and CP45) [7]. After CTI took over TCC's holdings they built a small negative ion cyclotron producing protons of 11 MeV [8].

The advantages of a negative ion machine include the simplicity with which the protons can be extracted, the near quantitative extraction efficiency, the ability to vary the extraction energy easily and the ability to extract multiple beams simultaneously.

At the same time these events were occurring the development of external ion sources added another advantage to the negative ion machines. These new ion sources produced very high beam currents with low emittance, the centre region is not disturbed with replacement of the ion source, the vacuum tank does not have to opened during repairs of the ion source and high vacuum is more easily maintained with an external ion source which is differentially pumped.

A. How Big?

In selecting an accelerator for producing radionuclides for biomedical research the hardest question to answer is how big an accelerator is needed? The real question is what energy since the smaller the machine the less valuable space is required. The obvious answer to this question is in the definition of the program involved. For example, a program to produce the commercial radioisotopes such as ^{123}I and ^{201}Tl requires a machine capable of providing protons of about 30 MeV while a clinical PET program can have its needs met with an accelerator with 10-13 MeV protons. PET research programs may a higher energy accelerator.

B. Alternatives.

Along with the research into using high beam power targets came a renewed interest in low energy alternatives. Several different approaches were examined. One proposed using a low energy tandem cascade accelerator to generate protons and deuterons of 3-4 MeV [9]. While the cross sections for the various reactions are low at these energies the idea was to make up the low production rate with higher beam current. The use of deuterons of 3-4 MeV has proven useful not only for the tandem cascade accelerator but also in a small dedicated 3 MeV cyclotron used just to make ^{15}O-labelled compounds. Another approach proposed using ^{3}He as the accelerated particle. The advantage to this machine would be the low neutron flux associated with the reactions [10].

In addition to these new machines an interest in linear accelerators has also been generated [11]. The major advantage with these machines would be the low cost, low weight and low radiation generated by the machine, thus they would require less shielding around the machine itself. Regardless of the source of the accelerated particles the targets would be similar except for the very low energies where new concepts have had to be explored due to the large energy loss as the projectiles pass through matter (e.g. isolation foils) at the low energies.

C. Yields.

The actual yields from most target systems is generally less than the theoretical predictions. This is especially true for gas target systems. Possible reasons for low yield at high beam currents in gas targets could be the interaction of the produced radionuclide with the target chamber walls, gas density reduction due to beam heating of the gaseous target material and thus the lack of optimization of the energy of the projectile. It has been clearly demonstrated that gas density reduction is a major contributor to loss of yield as a function of beam current.

IV. FUTURE

The future growth area for nuclear medicine is predicted to be in radiotherapy. While most radiotoxic nuclides emit particles and are thus neutron rich and are generally produced in a reactor, there is keen interest in producing these radiotoxic nuclides via particle accelerators because of the inherent ability to produce a radionuclide of differing chemical element with accelerators, thus increasing the potential specific activity.

A. NBTF.

No discussion of the production of radionuclides for the biosciences can be complete without some mention of the

proposed National Biomedical Tracer Facility, the NBTF. The nuclear medicine community in the US has seen a need for a dedicated accelerator facility that would be capable of produced a wide range of radionuclides for research proposes. Presently these radionuclides are prepared at the national labs but this approach has proven to unsatisfactory due to limited operated schedules and a lack of control of what is produced. The commercial suppliers are not interested in supplying radionuclides that have low or no profit margin. Thus new promising what to radiotherapy are being stymied because of the lack of availability of some radionuclides. The proposed NBTF would conceivably go a long way toward relieving this problem. The proposal is to build an accelerator cable of generating at least two beams of protons of up to 500 μA each with variable energies up to 80 MeV. The machine would be available throughout the year operating 24 hours per day, 7 days per week for a minimum of 48 weeks. In addition to the production of radionuclides, the mission of the NBTF would include education and training in nuclear and radiochemistry, research in target and target chemistry and research in the use of new radiopharmaceuticals. Having been reviewed for the Department of Energy (DOE) by the National Academy of Sciences' Institute of Medicine, the DOE is reviewing a number of Project Definition Studies from a number of sites throughout the US [12]. It is still not clear whether the resources to build a new facility will be made available.

V. ACKNOWLEDGEMENTS

The author wishes to acknowledge the helpful comments and efforts of colleagues at TRIUMF, especially Drs. Michael Adam and Stefan Zeisler and Salma Jivan, Tamara Hurtado and Ken Buckley. Support from TRIUMF and the Medical Research Council of Canada is also gratefully acknowledged.

VI. REFERENCES.

[1] Ruth, TJ, Wolf AP, Radiochim. Acta (1979); 26: 21-24.

[2] Proc. 1st Workshop on Targetry and Target Chemistry, Heidelberg (1985).

[3] Rickey ME, Smythe R, Nucl. Instr. Meth, (19620; 66: 18-19.

[4] Wright BT, IEEE Trans. (1966); NS-13: 72.

[5] Burgerjon JJ, Nucl. Instr. Meth. (1966); 43: 381.

[6] Burgerjon JJ, Nucl. Instr. Meth. (1985); B10/11: 951-956.

[7] Hendry GO, Kuo TYT, Ramsey F, Jenkins K, et al. 9th Int. Conf. Cyclotrons and their Appl. Les eds. de Physique, Paris (1982):125.

[8] Wieland BW, Hendry GO, Schmidt DG, J. Label. Cmpds. Radiopharm. (1985); 23: 1187.

[9] Shefer RE, Klinkowstein RE, Welch MJ, Brodack JW, Proc. 3rd Workshop on Targetry and Target Chemistry, Vancouver, (1990).

[10] Dabri AE, Hagan WK, Swenson DA, Krohn KA, Proc. 3rd Workshop on Targetry and Target Chemistry, Vancouver, (1990).

[11] Hamm RW, Proc. 3rd Workshop on Targetry and Target Chemistry, Vancouver, (1990).

[12] Isotopes for Medicine and the Life Sciences, SJ Adelstein and FJ Manning, eds. Nat. Acad. Sci. Press (1995).

MICROELECTRONIC APPLICATIONS FOR RF SOURCES AND ACCELERATORS

Cha-Mei Tang

Current address: National Institute of Standards and Technology, Gaithersburg, MD 20899
Permanent address: Plasma Physics Division, Naval Research Laboratory, Washington, DC 20375-5346

Abstract

Lithographic microfabrication techniques have been applied to the development of cathodes. In this paper, we limit the discussion of microfabricated cathodes to gated field-emitter arrays, ferroelectric and microminiature therm-ionic vacuum cathodes. These cathodes have made significant advancements in the last few years. They share in common the potential of being temporally and spatially modulated at high frequencies by low voltages with low input power requirements. These properties not only provide opportunities to improve rf power sources and accelerators, but also provide opportunities to make new commercial products.

I. INTRODUCTION

Various lithographically fabricated cathodes are emerging with potentially exciting characteristics for rf power sources and accelerator applications. In this paper, we will discuss three cathodes produced by microfabrication methods: gated field-emitter arrays (FEAs), ferroelectrics and microminiature thermionic vacuum (MTV) cathodes. The emission mechanism for each of these devices is different. Significant advancements have been made in these cathodes in the last few years, and each cathode has its own advantages, disadvantages and applications for which they are best suited. These cathodes also have the potential for major commercial applications. Vast opportunities still exist for additional research in this area.

These microelectronic cathodes share some common potential properties. In some cases, future development is required to reach these potentials. (i) The emission from these cathodes may be temporally and spatially modulated. (ii) The modulation frequency may be high. (iii) The voltages that are required to drive the modulation may be less than 100 V. (iv) The power that is required to drive the modulation may be low.

II. GATED FIELD-EMITTER ARRAYS

Gated FEAs have been under development for almost thirty years. They are based on the principle of field-emission, in which electrons tunnel through a surface potential barrier reduced by the application of high ($3\text{-}6\times10^9$ V/m) electric fields at the solid-vacuum interface. A sche-matic of the field-emission model is shown in Fig. 1. Field-emission was first derived by Fowler and Nordheim,[1] who found the relation

$$I \propto E^2 \exp(-b/E), \qquad (1)$$

where I is the emission current, E is the electric field on the surface and b is related to the work function of the material. Current from field-emission has sharp turn-on and a sharp rise.

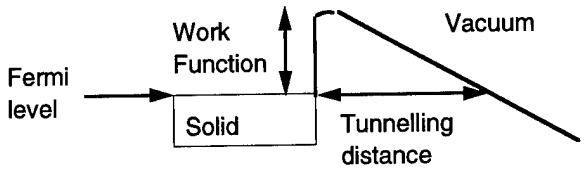


Figure 1. Schematic of field-emission.

For field emission devices to be practical, the emission has to be controlled by modest gate voltages. This can be accomplished by utilizing field enhancement at sharp corners and points and by placing the extracting electrode close to the emission site. This was first achieved by C. A. Spindt at SRI in the late 1960s by applying microfabrication technology, including thin-film deposition, photolithography, electron lithography, and wet and dry etching processes.[2] Using these techniques, Spindt fabricated an array of nearly-identical molybdenum (Mo) cones on silicon (Si) substrates. The grid or gate electrode is insulated from the substrate by silicon dioxide (SiO_2), as shown in Fig. 2. Recently, Spindt[3] fabricated FEAs with gate opening diameters as small as 0.3 μm, with tip-to-tip separation of 0.5 μm. These tips emitted on average 3 μA per tip at a gate voltage of 45 V.

A wide variety of field-emitter arrays have been developed. The most common emitter shapes are cones, wedges, edges and cones on columns. The most often used emitter materials are metals (Mo or W), semiconductors (Si and GaAs), diamond, single-crystal tungsten fibers formed by eutectic composites and graphite. Three examples will be given below.

At MIT/Lincoln Laboratory, the holographic method[4] was used to pattern gate openings as small as 0.16 μm in diameter with a tip-to-tip separation of 0.32 μm. The emitter is formed by vapor deposition similar to the Spindt approach. They measured on average 1 μA per tip at a gate voltage around 30-35 V.

MCNC has been developing silicon field emitters in the shape of cones on columns,[5] see Fig. 3. Emitter heights from 0.5 μm to 10 μm with approximately 1 μm gate diameter have been demonstrated. The thick insulator decreases the capacitance between the gate and the substrate. Average currents as high as 30 μA per tip were measured at a gate voltage of 85 V.

At Varian, single crystal GaAs edge emitters with an air-bridge have been fabricated (Fig. 4). Among its many good qualities such as an emitter material,[5] single crystal GaAs can provide more uniform edge emission and does not require ultra high vacuum. Varian has fabricate structures with emitter to gate distances of 0.3-0.4 μm. The air-bridge can be used to guide the electrons away from the gate (if anode voltage is low) and can

0-7803-3053-6/96/$5.00 ©1996 IEEE

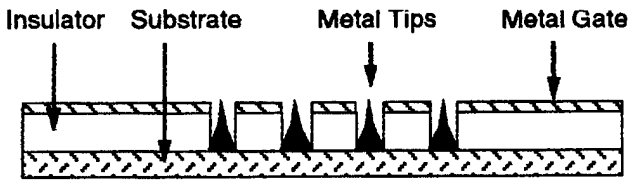


Figure 2. Schematic of Spindt cathode.

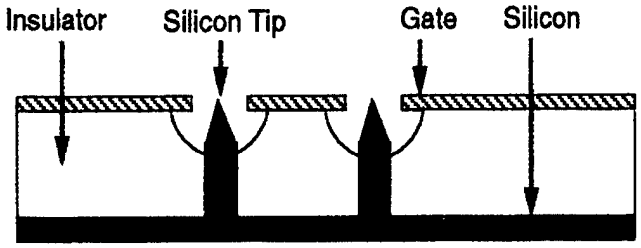


Figure 3. Schematic of MCNC silicon cones on column field-emitters.

protect the emitter edge from back-ion bombardment.

Some of the properties of FEAs that encouraged their development through out the years are: (i) The electron emission can be turned on with low gate voltages, and (ii) the emitters can be x-y addressed. These properties are appropriate for the development of flat-panel displays. Coupled with the potential visual quality of a CRT, low power consumption and low cost, the field-emitter display is emerging as a serious contender in the large market of flat-panel displays.[7] Many field-emitter display demonstration models have now been developed throughout the world.

The first successful microwave experiment utilizing FEAs was in a gyrotron oscillator built by M. Garven for her Ph.D. thesis, completed in 1994.[8] She designed the gun such that the FEAs are shielded from back-ion bombardment. The electron beam was accelerated up to 40 keV with beam power up to 1 kW. The FEA life times approached 100 hours. She measured 50 db power gain in the DC mode and operated in a gate modulated pulsed mode up to 1 kHz.

The development of a density modulated wideband inductive output amplifier in the 1-10 GHz regime with moderate power levels utilizing FEAs has been advocated primarily by R. K. Parker.[9] Inductive output amplifiers, where the rf output circuit is separated from the beam collection electrode resulting in an increase of power and bandwidth, was first proposed by Haeff and Nergaard in the 1940s.[10] The klystrode^{TM}, also an inductive output tube, was developed by Sharder and Preist.[11] It uses a cavity-driven cathode-grid region to form a modulated electron stream that is then accelerated in a high-voltage electron gun. Density modulated beams were shown to be capable of producing microwave power more efficiently, in a more compact size and at a higher power than velocity modulated devices.

The frequency, f_T, at which the short-circuit current gain attains unit magnitude, is often used as an estimate for the frequency of operation. It is defined as

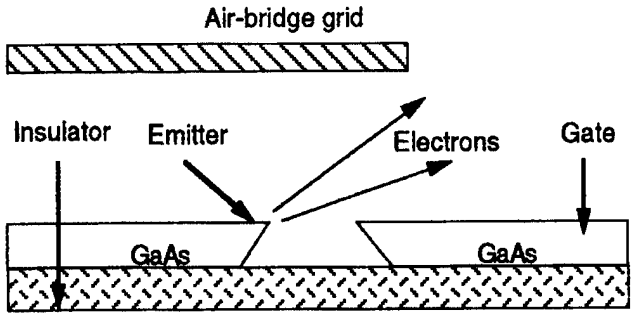


Figure 4. Schematic of Varian single crystal edge emitter with air-bridge.

$$f_T = (\Delta I/\Delta V)/C_{in}, \tag{2}$$

where ΔV is the change of the gate voltage, ΔI is the resultant change in emitted current and C_{in} is the input capacitance.

The use of FEAs in an inductive output amplifier has many advantages:

i. The frequency of operation is not limited by the distance between the emitter and the extracting grid, which is typically less than 1 μm.

ii. Fowler-Nordheim field-emission has high transconductance, $\Delta I/\Delta V$. Reduction of ΔV reduces input power and an increase of ΔI increases output power. Thus, high transconductance leads to high gain.

iii. Various FEA designs and fabrication methods have steadily decreased the input capacitance. Decrease of C_{in} increases the frequency as shown by Eq. (2). Decrease of C_{in} also decreases the input power requirement and thus increases the gain.

iv. FEAs have demonstrated high current densities,[12] up to 1 kA/cm^2. High current density improves the beam propagation.

Currently two emission gated microwave amplifiers are under development which have the same objective but use slightly different approaches, i.e., twystrode and klystrode. The common objectives of the two microwave amplifier programs are: frequency of operation at 10 GHz, with 50 W output power, 10 db gain, efficiency of 50% before energy recovery with electron beam energy of 2.5 keV, to be completed by early 1997. The preliminary designs under consideration are hollow beams with peak current about 160-170 mA to be confined by a high axial magnetic field of 1-5 kG. The interaction length of the tubes will be approximately 1 cm with radius much less than 1 mm. The designs have to be somewhat flexible to accommodate various FEAs from different suppliers.

The twystrode tube will be developed in the Electronics Science and Technology Division of the Naval Research Laboratory under the guidance of R. A. Parker. A series of twystrode experiments has been performed by M. A. Kodis with other types of cathodes to establish the understanding of the physics of the twystrode.[13] For the emission gated twystrode amplifier experiment, a variety of field-emitters will be procured.

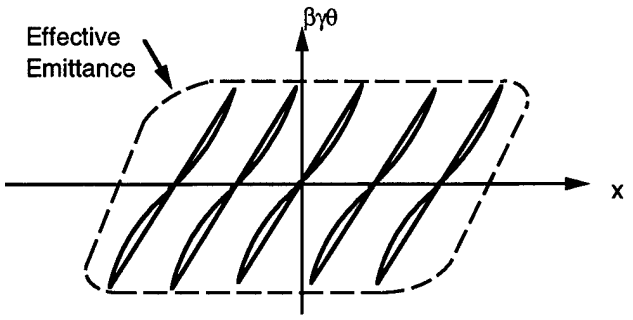


Figure 5. Schematic of normalized emittance of an array of field-emitters.

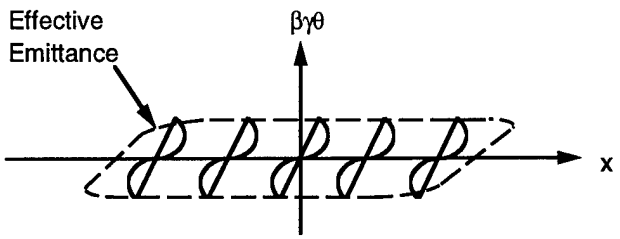


Figure 6. Schematic of normalized emittance of an array of field-emitters with lenses.

The Klystrode tube is to be developed by Varian. The FEAs are to be supplied by SRI, MIT/Lincoln Laboratory, MCNC and Varian.

The FEA requirements for the 10 GHz emission gated microwave tubes are very demanding.

(i) Currently, FEAs have only demonstrated beam modulation at 1 GHz. Optimism that beam modulation can be achieved at 10 GHz is based on (a) verification of the concepts to be used in the design of 10 GHz FEAs and (b) the development of new and improved processing techniques. Modulated beam at high frequencies may also be obtained by methods other than gate modulation.[14]

(ii) Back-ion bombardment may be prevented by proper tube design. This was demonstrated by the gyrotron experiment. The tubes must be designed such that the ions will be directed away from the FEAs. For the Varian GaAs edge emitter, the air-bridge also protects the emitter.

(iii) For uniform emission and tip protection, a resistive substrate is commonly used. However, this method cannot be used for high frequency gate modulated emission because it would reduce the transconductance. For the 10 GHz experiments, improvements in fabrication and reductions in the size of the array ($<<$ 1 mm^2) will increase the possibility of finding good chips.

(iv) Emittance is an issue to be addressed in the next generation of experiments. A large magnetic field is required to confine the beam in the two present experiments. However, this is not a long term solution because of the size and weight introduced by the magnet. The normalized emittance of a single cone field emitter is very good,[15] on the order of 10^{-4} π mm-mrad calculated by EGUN2.[16] The emittance is a function of the gate voltage and the field-emitter geometry. The phase space diagram of the normalized emittance associated with a single cone field emitter tip is in the shape of a propeller, shown in Fig. 5. The effective normalized emittance of an array of field-emitters is the area enclosed by the dashed curve in the phase space diagram.[17] Reduction of the normalized effective emittance can be accomplished by fabricating lenses at each emitter, decreasing gate diameter to decrease the gate voltage and/or lowering the work function of the emitter to decrease the gate voltage. The resultant reduced effective normalized emittance is shown in Fig. 6. Various lens configurations have been simulated[17,18] and experimentally attempted.[18,19] Extensive fabrication development effort is still required to develop field-emitters with integrated lenses.

The demand of the FEAs for microwave and accelerator applications is challenging because of the high current density, high frequency and high voltage requirements. If the two proof-of-principle twystrode and klystrode experiments are successful, it would be a significant advancement in the field and would lead the way for high power devices.

The gigatron[20] is a high power amplifier concept that can reduce the space charge effect of high current density by the utilization of a ribbon beam generated from spatially and temporally modulated emission. It is compact and has high efficiencies. Originally, FEAs were the only potentially available cathode. Advancements in emission gated cathodes towards high current density and high modulation frequency may someday enable the realization of the gigatron concept.

III. FERROELECTRIC CATHODES

The development of ferroelectric material for use as a "strong" emission cathode started in 1987 when Gundel and co-workers reporting high current densities of more than 100 A/cm^2 in the absence of an external extraction field, after its discovery at CERN earlier in the year.[21] The most commonly studied ferroelectric cathodes are composed of lead lanthanum zirconate-titanate (PLZT) and lead zirconate-titanate (PZT or LZT). These ceramic materials can be polished to a thicknesses of 50 μm to 1 mm, with lithographically patterned electrodes on one side and a blank electrode on the other.

Large polarization vectors can be formed inside the ferroelectric. The initial value of P_s is obtained by prepoling a ferroelectric sample at high temperature under the influence of a modest dc electric field. Each P_s domain is related to the electric field by a hysteresis, shown in Fig. 7. Ferroelectric emission is different from classical thermionic, field, secondary or photo emissions. A simplified schematic of the emission process is shown in Fig. 8. The conceptual model shown assumes the sample is represented by a single-domain structure with two possible directions of the polarization vector P_s.

In Fig. 8a., the polarization is set up such that the polarized charges on the surface are neutralized by screening electrons and screening holes. When the electric field of sufficient strength is suddenly switched, the polarization vectors will switch. For submicrosecond polarization switching, the screening electrons will be emitted,[22] before the screening charges can flow away over the surface or through the bulk of the ferroelectric material, shown in Fig. 8b. The spontaneous polarization[23] can be as large as 20 μC/cm^2 resulting in the accumulation of a screening

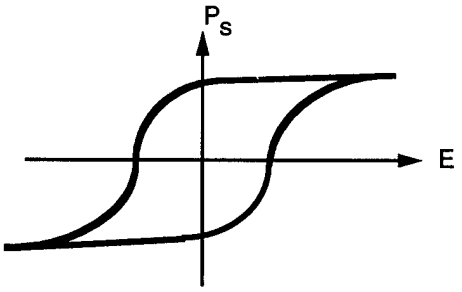


Figure 7. Hysteresis of ferroelectric materials.

charge density of 10^{18} electrons/cm^2.

The voltage required for switching of the electric field E is shown to be dependent on the thickness of the ferroelectric. For ferroelectric samples 1 mm thick,[23–25] the amplitude of the voltage pulse usually has to be greater than 1 kV with pulse lengths ranging from 100-1000 ns. The voltage pulses required to switch thinner ferroelectrics are less: (i) 100 μm thick[26] PLZT requires 300-400 V, (ii) 30-45 μm thick[27] PZT requires 75 V and (iii) 1 μm thick[26] PZT requires 10-40 V.

The polarization switching can also be produced by mechanical pressure pulses, thermal heating and laser illumination. Enhanced laser-induced emission from ferroelectrics is different from photoemission, because strong self-emission of energetic (> 10 keV) electrons was observed without an extraction field, and a threshold laser energy is needed.[28,29] Laser induced emission requires regular polarization switching in order to maintain a constant emission level. Otherwise, emission decays after some tens of pulses toward zero. The details of laser induced emission has not yet been satisfactorily explained.

The ferroelectrics are robust ceramic materials.[21] The ease of use is comparable to the best metallic cathode. They can be touched and transported through air. They do not need a good vacuum so they can work in a low-pressure gas or plasma. This emission mechanism is unique and has properties appropriate for rf sources and accelerator applications.

The current density from ferroelectrics could be high, for example, 100 A/cm^2 at CERN[21] and 70 A/cm^2 at Cornell.[25] Current density was reported to be as much as two orders of magnitude larger than the Child-Langmuir limit. One explanation is that the electrons are emitted with high energies (250 eV at MCNC[26] to 10 keV at CERN[28]).

High normalized beam brightness was reported[23] from an LTZ-2 disk. A gate voltage pulse of 1-2 kV was applied across a 1 mm thick disk 2.5 cm in diameter. For an anode voltage of 10 kV, the detected current was 15 A. The normalized emittance is 5 mm mrad and the normalized beam brightness is 1.2×10^{11} A/m^{2}rad^2, which exceeds the brightness of thermionic cathodes.

Ferroelectrics may potentially be very useful for accelerators and rf sources. Again, ferroelectrics may also have wide commercial applications.[21] For the ferroelectric to be practical as a large area cathode, the turn-on voltages have to be reduced for obtaining the desirable current density. Ferroelectric formed by thin film deposition is under development at MCNC to obtain large area, thin ferroelectrics.[26] Ferroelectrics provide many research opportunities.

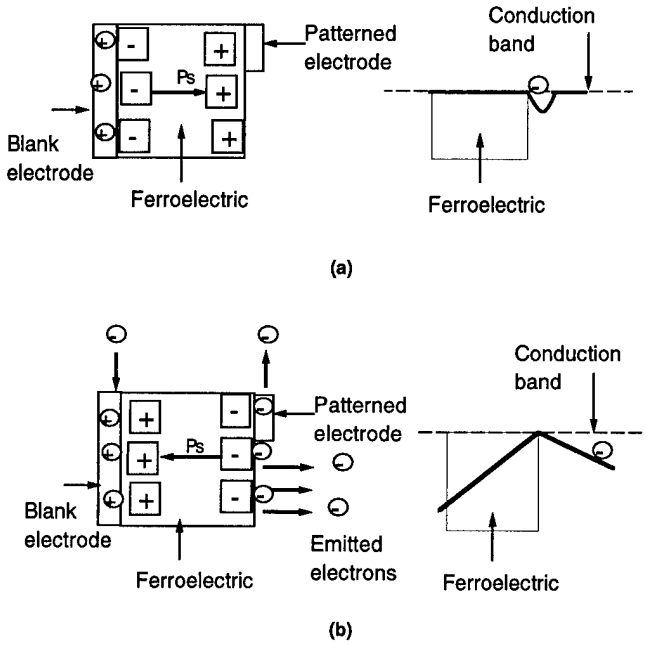


Figure 8. Schematic of ferroelectric emission mechanism: (a) no emission and (b) emission.

IV. MICROMINIATURE THERMIONIC VACUUM (MTV) CATHODE

Thermionic cathodes can also be miniaturized and large arrays of them can be fabricated so that they can be controlled spatially and temporally with low voltages.[30] A thin tungsten filament coated with low work function material suspended as an air-bridge can be heated to high temperatures by applying a low voltage across the filament. For a filament $15 \times 30 \times 1.5$ μm^3 in size and input power of 70 mW, 16 μA of current was collected by a planar anode at 100 V at a distance of a few microns from the cathode.[30] The advantages of the MTV cathode are the small size of individual components, ruggedness, radiation hardness, environmental and temperature insensitivity, the short distance between the cathode and grid, and the small capacitance between the cathode and the grid. MTV may be able to go to high frequencies, but the current density will not be as high as with FEAs.

V. SUMMARY

In summary, microfabrication methods have introduced exciting cathodes, each with its best suited applications. (i) FEAs have been under development for almost thirty years. FEAs will be entering the commercial market in the application of field-emitter displays. The FEA performance requirements for rf amplifier application are challenging, but not out of reach. The first concentrated effort to develop rf amplifiers with FEAs has been launched. Successful results will initiate significant growth in this field. (ii) Since ferroelectric cathodes with "strong" emission were only discovered in 1987, some aspects of the emission processes are not yet well understood. Ferroelectric cathodes, however, are already finding their way into accelerator related

applications. It is an active area of research. (iii) MTV cathodes provide more flexibility than conventional thermionic cathode. They are still in the early stages of development.

VI. Acknowledgements

This work is supported by National Institute of Standards and Technology and Naval Research Laboratory/Office of Naval Research.

References

[1] R. H. Fowler and L. Nordheim, Proc. Roy. Soc. (London), **A 119**, 173 (1928).
[2] C. A. Spindt, J. Appl. Phys. **39**, 3505 (1968).
[3] C. A. Spindt, private communications.
[4] C. O. Bozler, C. T. Harris, S. Rabe, D. D. Rathman, M. A. Hollis and H. I. Smith, J. Vac. Sci. Technol. **B12**, 629 (1994).
[5] L.N. Yadon, D. Temple, W. D. Palmer, C. A. Ball, G. E. McGuire, C. M. Tang and T. A. Swyden, JVST, April-May (1995).
[6] S. Bandy, C. K. Nishimoto, C. Webb, G. Virshup, M. Riaziat, L. Partain, C. Yuen and C. Shih, Vacuum Electronics Annual Review Proc., Crystal City, VA, June 29-July 1, 1993, p. VI-37.
[7] H. F. Gray, Information Display **9**, No. 3, 9 (1993).
[8] M. Garven, Ph. D. Thesis, Dept. of Physics and Applied Physics, University of Strathclyde, UK, 1994.
[9] R. K. Parker and R. H. Abrams, *1992 Government Microcircuit Applications Conference (GOMAC), Digest of Papers*, vol. XVIII, pp. 29-32, 1992.
[10] A. V. Haeff and L. S. Nergaard, Proc. of I.R.E. **28**, 126 (1940).
[11] D. H. Preist and M. B. Shrader, Proc. IEEE **20**, 126 (1982).
[12] C. A. Spindt, C. E. Holland, A. Rosengreen and I. Brodie, IEEE Trans. on Electron Devices **ED-38**, 2355 (1991).
[13] M. A. Kodis, N. R. Vanderplaats, E. G. Zaidman, B. Goplan, D. N. Smithe and H. P. Freund, Tech. Digest of the 1994 IEEE Intl. Elec. Devices Meeting, San Francisco, CA, 795 (1994).
[14] C. M. Tang, Y. Y. Lau and T. A. Swyden, Appl. Phys. Lett. **65**, 2881 (1994).
[15] C. M. Tang, M. Goldstein, T. A. Swyden and J. E. Walsh, in press Nucl. Instrum. and Methods A, 1995.
[16] W. B. Herrmannsfeldt, EGUN - An Electron Optics and Gun Design Program, SLAC Report 331 (1988).
[17] C. M. Tang, A. C. Ting and T. A. Swyden, Nucl. Instrum. and Methods A **A318**, 353 (1992).
[18] C. M. Tang, T. A. Swyden and A. C. Ting, J. Vac. Sci. Technol. B **13**, 571 (1995).
[19] J. Itoh, K. Morikawa, Y. Tohma and S. Kanemaru, Revue "Le Vide, les Couches Minces" – Supplément au No 271 – Mars-Avril 1994, p. 25.
[20] P. M. McIntyre, H. M. Bizek, S. M. Elliott, A. Nassiri, M. B. Popovic, D. Pararia, C. A. Swenson and H. F. Gray, IEEE Trans. on Elec. Dev. **36**, 2720 (1989).
[21] H. Riege, Nucl. Instrum. and Meth. A **340**, 80 (1994).
[22] L. Schachter, J. D. Ivers, J. A. Nation and G. S. Kerslick, J. Appl. Phys. **73**, 8097 (1993).
[23] B. Jiang, G. Kirkman, and N. Reinhardt, Appl. Phys. Lett. **66**, 1196 (1995).
[24] H. Gundel, J. Handerek, H. Riege, E. J. N. Wilson and K. Zioutas, Ferroelectrics **94**, 337 (1989).
[25] J. D. Ivers, L. Schachter, J. A. Nation, G. S. Kerslick, and R. Advani, J. Appl. Phys. **73**, 2667 (1993).
[26] O. Auciello, M. A. Ray, D. Palmer, J. Duarte, and G. E. McGuire, Appl. Phys. Lett. (in press, April 1995).
[27] J. Asano, T. Imai, M. Okuyama and Y. Hamakawa, Jpn. J. Appl. Phys. **31**, 3098 (1992).
[28] K. Geissler, J. Handerek, A. Meineke, H. Riege and K. Schmidt, Phys. Lett. A **176**, 387 (1993).
[29] H. Gundel, H. Henke, A. Meineke, H. Riege, K. Schmidt, and J. Handerek, Nucl. Instrum. and Meth. A **340**, 102 (1994).
[30] L. P. Sadwick, et al., Tech. Digest of the 1994 IEEE Intl. Elec. Devices Meeting, San Francisco, CA, 779 (1994).

MEDICAL AND SURGICAL APPLICATIONS OF FELS

Benedikt Jean, MD, PhD *(Invited Paper)*
Experimental Ophthalmic Surgery, University of Tübingen, FRG

Abstract: Every medical laser application is based upon the compromise between efficiency and collateral adverse effects.The optimizing strategies of preclinical investigations of IR lasers can be dramatically improved by using FEL technology, allowing the free combination of wavelength, pulselength and energy. The new approach is illustrated by the results from photoablation of three different types of tissue (cornea, dental hard substances and atheromatous plaques). FEL technology enables the optimizing of physical and biological parameters and reducing risks while minimizing time and costs involved.

I. INTRODUCTION

Among the many laser/tissue interactions which have been introduced into microsurgery over the past 15 years, photoablation, the contact free removal of tissue is probably the most spectacular: Never before have we been able to remove tissue with a precision better than one micron, far beyond the resolution of the surgeon's naked eye. In ophthalmic microsurgery, techniques to reshape the cornea, to correct myopia, to remove pathologic tissue on a micron, - or submicron scale have been developed with the 193 nm excimer laser [1].

Photoablation is possible at wavelengths ranging from the far-UV to the Far-IR. The typical fluences required, range from 180 mJ/cm^2 for the far UV to 1 J/cm^2 in the mid IR. Photoablation has been achieved with pulselengths ranging from femtoseconds to microseconds and, apart from the three decisive parameters (pulselength, wavelength and fluence) the pulse repetition rate influences the roughness of the ablated surface. The basic principles of photoablation however, have not yet been investigated systematically over a wider wavelength range [2].

In the past, the preclinical investigation of new laser sources depended upon their technical availability: pulselength, wavelength and energy are technically related to each other and they allowed no or only minimal variation of the parameters. Laser surgical procedures for fistulation surgery in ophthalmology, angioplasty, dental surgery, a.s.o. were iteratively optimized, as a function of the mere availability of laser sources. The Deutsche Forschungsgemeinschaft (German Research Council) alone, has invested a total of 21 million marks (15 million $) in experimental laser devices for medicine over a 7-year period (1985-92) for investigational laser equipment (data provided by DFG).

Any medical laser application is based upon the compromise of efficiency and the correlated adverse effects of each set of laser parameters. **The surgical requirements**, however, are often contradictory: A high ablation rate is required in dental surgery, while it must be minimal to reshape the human cornea; cutting through vascularized tissue (e.g. brain surgery) requires some amount of surface coagulation (thermal "damage") in order to achieve hemostasis while for avasular tissues, wound healing is best when there is no thermal damage. Higher pulse repetition rates reduce surface roughness while, at the same time they increase the overall thermal load on the target site. The absorption coefficient of the target material not only determines the penetration depth of the radiation but also the ablation related shockwave.

Since the FEL has been made available for biomedical research [3], its unique possibility of independently combining wavelength tuneability with any energy and any pulselength allows a new approach. In this manner it is the ultimate research tool for preclinical investigations of new laser sources or new combinations of parameters.

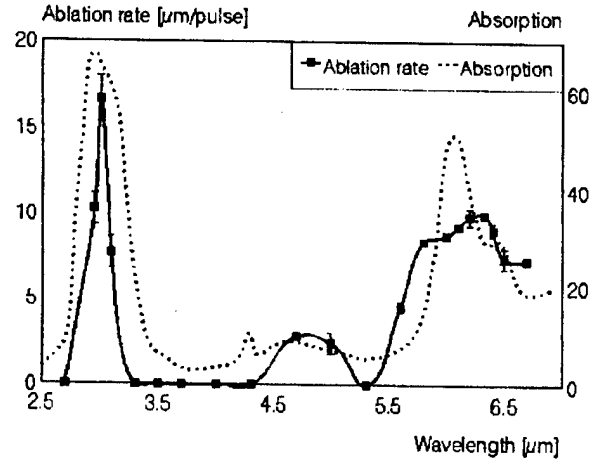


Fig.1: Ablation rate as a function of wavelength

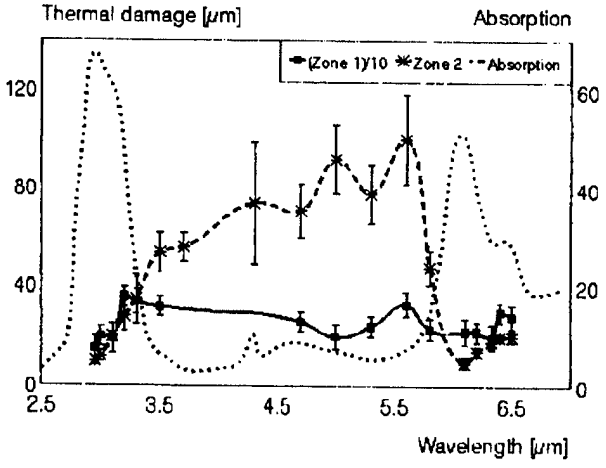


Fig. 2: Thermal damage as a fucntion of wavelength

II. RESULTS

As a typical example for <soft> tissue, with high water content, corneal tissue was chosen to perform the first systematic investigations of IR photoablation with the FEL at Vanderbilt University, between 2.7 μm and 6.5 μm thus including the two water absorption bands around 3 μm and 6 μm.

The **ablation efficiency** (Fig 1), as measured by the depth of the ablation crater, is found to be related to the absorption spectrum of the material [4]: at high absorption, ablation efficiency is high, at minimal absorption it is lowest for aconstant fluence. However, even at minimal absorption, ablation is possible, but with the disadvantage of extrem thermal damage.

The collateral thermal damage is relatively uniform in the IR but markedly more pronounced than in the UV. Collateral thermal damage, measured by the extent of the eosinophilic zone (Fig. 2, zone 2) at the bottom of the ablation area, is inversely related to target material's absorption [5].

The water absorption spectrum beyond 6 μm shows an increase up to 15 μm and decreases slightly between 15 and 50 μm. This spectral range is covered by the FELIX Free-Electron Laser at FOM, Nieuwegein/the Netherlands. According to our expectations, the first sucessful photoablation in the far IR was performed in corneal tissue at 15 μm and 70 μm [6].

The relevance of those findings lie in the fact that, for the first time, photoablation was investigated over a wide range of wavelength variation, providing a solid basis for the development of new and the verification of existing **models, adding a predictive element** to shorten the preclinical optimizing strategy for new laser sources. As a next step, variation of pulselength will be studied as soon as FEL technology permits.

It has recently been proved that the FEL can also be used as an ideal stress wave generator, allowing the study of shock wave related damage in vitro [8]; this approach may provide the first systematic access to the assessment of **pressure related cellular damage** and its relevance in surgery.

Apart from the predominant water absorption in the human cornea (with its 85 % of water), at 6.45 μm the amid II collagen absorption peak allows **selective interaction** with the incident laser light. This suggestion was the first to be made with regard to selective corneal photoablation in the IR [9].

Dentin and enamel are typical target materials for the study of photoablation with the FEL in bone-like biological materials with low water content: Presently the 2.94 μm Er:YAG laser uses the 30 % water content of enamel and dentin as a main absorber in order to achieve photoablation. The highest absorptions, however, are around 9.5μm for hydroxyapatite, the main constituent (approx. 50 %) of enamel and dentin. A major problem of the 2.94μm radiation is the appearance of thermally induced cracks in the enamel around the ablation site, leading to caries, since they provide favourable environment for bacteria. The 9.5 μm wavelength was investigated with FELIX: As expected, the ablation efficiency was maximal and the collateral thermal damage minimal at maximal absorption (Fig.3). At maximal absorption, the penetration depth is minimal and thus the volume of tissue heated per puls is minimal too [14]. As a consequence, the appearance of thermal cracks was also minimal, their size being beyond the diameter of bacteria. Furthermore, at 9.5 μm, the ablation threshold requires a minimal fluence; this, in return, is an element of selectivity limiting photoablation to enamel/dentin while neighbouring gingiva cannot be ablated. This adds an element of inherent safety to the surgical use of this wavelength.

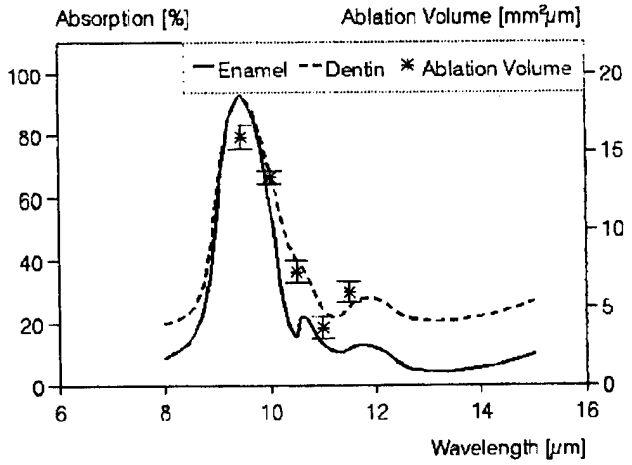


Fig. 3: Absorption spectrum of dentin and enamel and ablated volume

Removal of atheromatous plaques for recanalization of obliterated cardiac vessels (laser angioplasty) is another minimally invasive surgical task with highest socio-economic relevance. So far only a few selected wavelengths, available with solid state lasers, have been tried in the IR. While the ablation efficiency should be high, the stress wave induced damage to the vessel wall should be minimal and perforation of the vessel, a deadly complication, must be avoided under all circumstances. As plaques show a rather inhomogenous composition (apatite and cholesterol), the ''selectivity'' of the absorption for the materials to be removed must be high enough to contrast with the absorption properties of the underlying vessel wall (high watercontent) to avoid perforation. Fig. 4 show that the efficiency as well as the selectivity criterion (Fig.5), can be met by using 9.5 μm [15].

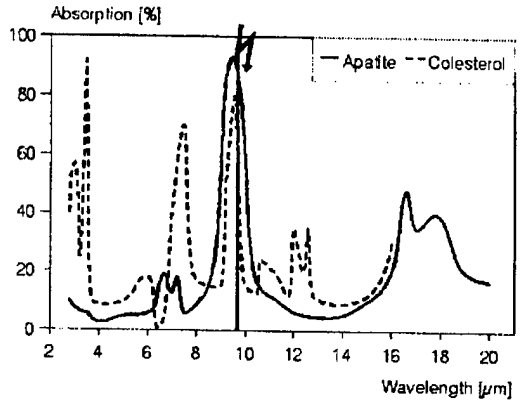


Fig. 4: Absorption spectrum of colesterol and apatite

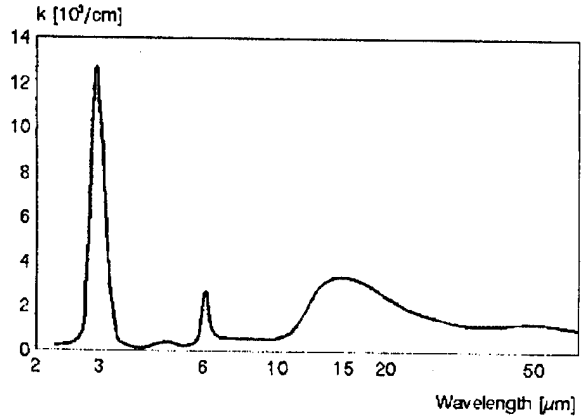
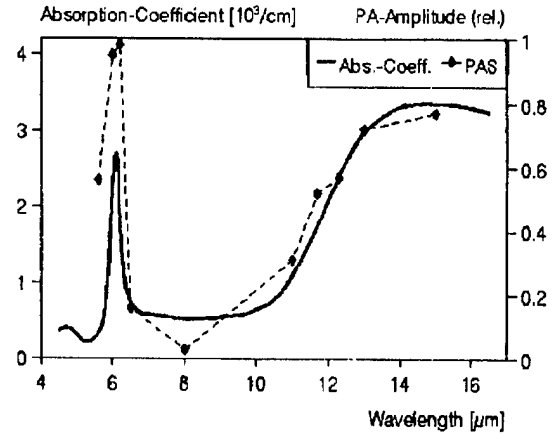


Fig. 5: Absorption coefficient of (ocean) water

As the pressure gradient over the time of the shock wave is related to the target material's absorption, the incident radiation can be tuned off the absorption peak to reduce the harmful collateral pressure gradient which causes micro lesions on the vessel endothelia eventually triggering thrombosis and restenosis. Such studies are in progress.

Discrimination of different tissues which cannnot be targeted selectively by specific absorbers (e.g. if they all have a high water content) is another central goal of microsurgery: a non contact photoacustric spectroscopy (NCPAS) set up, recently suggested for <smart> laser controle [10] captures the sound wave emitted, rather than the pressure signal from the ablation site. It has proved its feasibility to assess the ablation rate, the ablation zone diameter, the fluence and, in particular, its ability to disciminate between different target materials by on-line measurement of the center gravity of the FT signal. In this manner NCPAS measures the absorption coefficient of every ablated volume of tissue; it can be used to stop a laser automatically when it hits a tissue, not to be removed (e.g. a nerve in connective tissue). The FEL was used to study the photoacustic signal as a function of absorption coefficient in the IR [11].



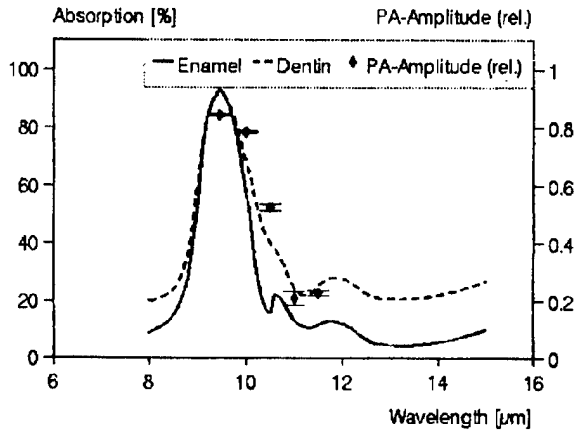


Fig.6: Amplitude of photoacustic signal as a function of wavelength (target material: cornea (top); dentin (bottom)).

Never before have we been able to study efficiency and adverse effects or any of the compromises of a new set of laser parameters so carefully in vitro. As another consequence, we can now minimize surgical risks for the first in-vivo applications on patients dramatically; at the same time, the FEL enables us to minimize costs and time invested in experimental and preclinical applications in medicine and surgery.

The biological adverse effects, rather than the physical parameters describing efficiency and related damage, are the decisive criteria in the assessment of the usefulness of new combinations of parameters for specific medical and surgical applications. The study of such biological adverse effects and the cell's sensitivity to them, however, requires a large data basis, in order to integrate the wide variation of biological parameters. While radiation biology has been systematically investigating the effects of ionizing radiation for years, very little is known about the interference of coherent laser light with living cells.

Advanced automated flow-cytometry [12] allows the assessment of such effects on a large number of cells in very short time by analysing intracellular fluorescent markers, tracing and measuring simultaneously 6 key metabolites. A self classifying software, developed by

VALET [13] identifies typical damage patterns and correlates them to biochemical pathways as a function of the external stimuli, e.g. the incident laser radiation. A recent pilot study, (supported by the US-ONR), performed in the Far UV and mid IR proved the feasibility of the approach, to assess distinct biochemical damage patterns (Jean, Valet in preparation).

III. CONCLUSION

The FEL as a research tool in biomedical laser research allows a new approach to the optimization of laser/tissue interactions by applying a 5 step procedure to bypass conventional time consuming and expensive strategies:

- absorption spectroscopy of the target material
- determination of a ''promising'' selective interaction with distinct absorbers
- assessment of physical parameters of ablation efficiency and collateral damage
- investigation of related biological and functional biochemical adverse effects.
- preclinical and clinical use

Taken together, FEL technology has opened a new era of systematic and prospective investigation of laser-tissue-interactions and their optimization prior to clinical use. Its enormous potential for reducing time and costs involved and also for minimizing typical risks, associated with its clinical investigations on patients, will play a major role in the development of future minimally invasive surgical techniques in many branches of surgery and interventional medicine.

An important impact on medical laser industries can be expected by reducing typical risks and costs of the conventional iterative optimization strategies which have been the rule so far, thus favouring competitiveness on national and international markets.

Where tuneability of the laser and free combination of parameters for optimal parameter selection are clinically required, the FEL may also gain importance **as a therapeutic tool at a few medical and surgical centers.** Since 1994, the first medical unit on top of an FEL has been under construction at Vanderbilt University. The FEl's future as a clinical tool, however, will depend upon advances in engineering to reduce costs and complexity of current FEL technology and thus to promote its advantages when competing with alternative technology such a optic parametrical oscillators.

Aknowledgment: We are indebted to Prof. Charles A. Brau, Director of the FEL Center at Vanderbilt University for his continuing support and encouragement and Prof v.d.Wiel and W.v.Amersfoort at FOM-FELIX, Nieuwegein/the Netherlands for granting access to the laser. This work received support from US-ONR grant # 00014-91-0109 and the European Union HCM grant ERB 4050PL940877.

IV. REFERENCES

[1] S. L. Trokel, R. Srinivasan, B. Braren. Excimer laser surgery of the cornea. *Am J Ophthalmol,* vol. 96, pp. 710 (1983).

[2] T. Bende, B. Jean, M. Matallana, T. Seiler, Ch. A. Brau. Photoablation with the Free-Electron Laser between 2.8 and 6.7 microns wavelength. *Invest Ophthalmol (suppl),* 34, 4, pp. 1246 (1993).

[3] C. A. Brau. The Vanderbilt University Free Electron Laser Center. *Nuclear Instruments and Methods in Physics Research,* A 3183R-1 N.Y.Elsevier Science Publisher (1992).

[4] B. Jean ,T. Bende. Photoablation with the Free-Electron Laser between 2.7 and 6.7 µm. *Corn Refr surg,* vol.10, 4, pp. 433-438 (1994).

[5] T. Bende, R. Walker, B. Jean. Photoablation in Porcine Corneas with the Free-Electron Laser between 2.7 and 6.7 µm wavelength - Thermal Collateral Damage. *Corn Refr Surg*, vol. 11, 2, pp. 129-136 (1995).

[6] B. Jean, R. Walker, T. Oltrup, T. Bende, W.v. Amersfoort. Free Electron Laser (FEL): Photoablation, Thermal Gradients and Damage in the FAR IR (10 µm to 65 µm). *Invest Ophthalmol (suppl),* 35, 4, pp. 2155 (1994).

[7] M. Ostertag, R. Walker, T. Bende, B. Jean. Optimizing Photoablation Parameters in the Mid IR - a Predictive Model for the Description of Experimental Data. *SPIE's International Symposium of Biomedical Optics '95 (supp) accepted* (1995).

[8] D. C. Lamb, L. Reinisch , J. Tribble, R. H. Orsoff ,T. J. Flotte, A.G. Doukas. The FEL As The Ideal Stress-Wave Generator. *SPIE's International Symposium of Biomedical Optics '95 (supp)* (1995).

[9] G. Edwards, L. Regan, M. Copeland, L. Reinisch, J. Davidson, B. Johnson *et al.* Tissue ablation by a Free-Electron Laser tuned to the amide II band, *Nature,* vol. 371, pp. 416-419 (1994).

[10] B. Jean ,T. Bende, M. Matallana. Non Contact Photoacustic Spectroscopy. *German J Ophthalmol,* vol 2, pp. 404-408 (1993).

[11] B. Jean, M. Matallana, M. Ostertag, R. Walker,T. Bende, W.v. Amersfoort IR Laser photoablation of Cornea Measured by Noncontact Photoacustic Spectroscopy. *Invest Ophthalmol (suppl),* 36, 4, pp. 987, 4562-543 (1995).

[12] G. Valet, H. H. Warnecke, H. Kahle. Automated Diagnosis of Malignant and Other Abnormal Cells by Flow Cyrtometry using DIAGNOSI program systems. In: Clinical Cytometry and Histometry; G. Burger, JS. Ploem, K. Goerttler (eds). Academic Press London, pp. 58-65 (1987).

[13] G. Valet, M.Valet, D. Tschöpe, H. Gabriel, G. Rothe, W. Kellermann, H. Kahle. White Cell and Thrombocyte Disorders. *Clin Flow Cytom.* vol. 677, Ann. NY Acad of Sci (1993).

[14] M. Ostertag, R. Walker, H. Weber, W.v. Amersfoort, B. Jean. Photoablation of Dental Hard Substances at the Absorption Maximum of 9.4 μm of Hydroxyapatite. International Free-Electron Laser Conference and 1st Annual FEL User Workshop, August, Stanford (1994).

[15] M. Ostertag, R. Walker, K. Karsch, M. Wehrmann, B. Jean. Photoablation on Atherosclerotic Plaque with 9.5 μm Wavelength. International Free-Electron Laser Conference and 2nd Annual FEL User Workshop, August, New York (1995); accepted.

Medical Uses of Monochromatic X-rays

Frank E. Carroll, M.D.
Vanderbilt University Medical Center
Department of Radiology and Radiological Sciences
and
Department of Physics and Astronomy
Nashville, TN

BACKGROUND:

At a time in which medical costs are straining the economic welfare of our country, do we need another new technology to diagnose and treat diseases? To answer that question we must explore any shortcomings of our present system and assess the benefits that we might hope to derive from the costs of another layer of expensive technology. If our longevity and quality of life can be significantly altered by development of monochromatic x-rays, then by all means we must pursue this holy grail.

ARE MONOCHROMATIC X-RAYS USEFUL?

Present day diagnostic x-ray systems suffer from many ills. Among these are: (1) the delivery of relatively high radiation doses; (2) limited resolution; and (3) less than optimal sensitivity and specificity secondary to the acceptance of scattered radiation, a suboptimal radiation spectrum and the failure to effectively use energy discriminant information.

Boone and Siebert have developed a method for calculating a Figure of Merit (FOM) designed to establish whether or not monochromatic x-rays (MXR's) are an improvement over standard x-ray beams [1]."It embodies parameters related to image quality in the numerator and radiation integral dose to the patient in the denominator. In this manner, maximizing image quality and minimizing radiation dose amount to maximizing the FOM." Their work in the area of angiography concludes that "monochromatic x-ray beams are capable of delivering the same image quality at about half the radiation dose to the patient compared to conventional x-ray tubes". In other areas and using other techniques, we can improve significantly even on the FOM seen in angiography, as the figures used in that procedure are those obtainable using standard image intensifiers and digital subtraction techniques.

If we were able to produce tunable MXR's we could reduce radiation dose to a patient for many reasons: (1) Softer x-rays would be absent from the beam thereby lowering entry dose ; (2) Higher energy photons would also be eliminated reducing the amount of scatter seen by the detector; (3) Enhancements to imaging would be gained by using phase contrast imaging; (4) Scatter reduction would be appreciable using time of flight imaging; (5) Selection of the MXR energy most suited to the tissues being studied takes advantage of energy discriminant information; and (6) Inherent differences in the linear attenuation of some tissues can be used more effectively. By combining tunable MXR's with rapid gating of detectors to accomplish direct "3-D" digital acquisition and computer generated "2-D" reconstructions and image screening, we could be light years ahead of our present inadequate system. But first we must produce a usable beam.

VANDERBILT'S APPROACH TO THE PRODUCTION OF MONOCHROMATIC X-RAYS:

Why Use the Free Electron Laser?

The FEL is unique in that it is **simultaneously** a dual source of electrons and photons . Both its high brightness electron beam and its high intensity infrared (IR) output are delivered in picosecond pulses. Since the electrons are mostly at the same energy and the IR photons are mostly at the same frequency, X-rays produced by Thompson scattering (when one redirects the IR and e-beams into a head-on collision) will mostly be at the same energy [2]. Since the FEL is tunable, the X-rays will be tunable. Additionally, since the IR and e-beam interaction zone is small (50 microns), the "source" of the x-rays is for all intents and purposes, a point source radiating into a forward-directed cone of radiation. This creates an ideal geometry for imaging (i.e.- a circular beam covering 10 cm or more at 10 meters distance). Fluxes generated (10^8 x-ray photons/mm^2 /second) are equivalent to those available from standard diagnostic x-ray tubes [3,4]. Therefore, the FEL can deliver tunable, near-monochromatic x-rays in picosecond pulses with high flux and in an ideal geometry for imaging. Why use anything else?

0-7803-3053-6/96/$5.00 ©1996 IEEE

WHAT ARE SOME OF THE ANTICIPATED DIAGNOSTIC USES?

Sorting out tissues by attenuation:

Among the anticipated uses for MXR's is the diagnostic evaluation of the breast for malignancies. If use of the MXR's created a benefit of only a twofold improvement in the FOM, one could halve the radiation dose delivered in one of the most common x-ray examinations performed today. However, there is an additional advantage to be gained, in that the interaction of X-rays with matter in the mid-teen keV range tends to favor photoelectric scattering rather than Compton scattering. Because of this, there is a "trough" for reduction in radiation dosage in the 14-18 keV region, allowing further reduction in dose from 6 to 50 times.

Furthermore, if we are to derive maximal benefit from use of MXR's, we must learn more about how these x-rays interact with the "target". To that end, specimens of breast tissues were studied at the Brookhaven National Laboratories, National Synchrotron Light Source (NSLS) using MXR's from 14 to 18 keV. Prior work by Johns and Yaffe between 20 and 100 keV had shown that cancerous tissues absorbed MXR's more "avidly" than do normal tissues at energies below 30 keV [5]. Our work confirmed and extended their findings by showing that cancers tend to exhibit a higher effective Z at energies lower than 20 keV, and that they absorb approximately 11% more MXR's than do normal tissues through the 14-18 keV range [6]. Unfortunately, this fact alone would not assure visualization of tumors using standard "2-D" imaging by plain film mammography. However, direct digital acquisition of data with motion of patient and detector (given our beam must remain stationary) allows for "3-D" imaging and the ability to study the breast (or any organ) slice by slice without superimposition of confusing shadows. Computers can offer assistance by searching voxel by voxel (voxel = a picture element (pi**xel**) with a finite depth (**vo**lume)) for tissues exhibiting a high attenuation and flagging these for further perusal by the radiologist. Computers can also search for minute calcifications, stellate tissue aberrations, and asymmetry of the breasts assisting enormously in every day screening.

This same methodology can be applied to any organ system in the body (e.g.- lung, liver, brain, etc.) to diagnose aberrant high attenuation tissues within relatively homogenous organs or to permit precise three-dimensional localization of tumors for procedures such as stereotactic brain surgery.

Time of flight imaging:

As x-rays traverse tissues they are, of course, scattered to some extent. These scattered x-rays offer little useful information for imaging purposes and comprise 65-95% of the detected intensity in standard radiography. If we were able to utilize only the unscattered portion of the beam (i.e. the photons which pass through the tissues unscathed, called "ballistic photons"), we could improve conspicuity of lesions another 6 to 9 times due to improvement in the signal/noise ratio. In an imaging setting, ballistic photons may be expected to exit the tissues within 10 to 100 picoseconds. Scattered photons, on the other hand, exit in a nanosecond time regime. Rapid gating of an imaging chain with a multichannel plate and CCD to accumulate only ballistic photons has already been accomplished using x-rays from a laser-produced plasma [7].

Phase contrast imaging:

The x-ray absorption coefficients of light elements are very small, yet if one uses an x-ray interferometer and some "3-D" imaging techniques, phase shifts in the x-ray beam traversing the tissues can be elicited by light elements which are large enough to be detected. This technique is approximately 100 times more sensitive to the presence of these light element than absorption contrast imaging [8]. Since x-ray interferometers to date have been made from large and highly perfect single-crystal blocks, they have been quite small [9,10,11]. This lends itself to performance of X-ray microscopy and computed tomography only of small specimens. Whether or not this can be scaled up to a large enough size to allow imaging of large body appendages or the whole body remains to be seen. However, the ability to image tumors directly without the injection of contrast agents holds great promise and warrants the pursuit of larger interferometers.

Subtraction Imaging in Angiography:

Dual energy digital subtraction imaging has had some limited success in the study of vascular anatomy using contrast injections and filtered standard beams. As Boone and Seibert have noted a change to MXR's will allow a reduction in radiation dose and by imaging just above and just below the k-edge of iodine a reduction in the amounts of contrast needed for a study.

Other applications:

Veterinary use, X-ray microscopy and holography are other potential uses for these MXR's, but will not be discussed here.

THERAPEUTIC USES ANTICIPATED:

The union of chemotherapy and radiotherapy in order to deliver "more bang for the buck" to tumors is within the reach of MXR's and new experimental drugs. One can deliver multiple small doses of a drug over a time period of days or weeks. And if the material accumulates incrementally within a malignancy, one has a clear-cut method for delivering metals

into a tumor. By substituting metallic ions into the drug's molecular labyrinth and selecting a metal with a k-edge near that of the MXR's deliverable, one can stimulate the production of focal concentrated radiation damage in a tumor by knocking k-shell electrons loose from the drug by resonance with the MXR's.

Several drugs are under investigation including metalloporphyrins (By J. Nelson, M.D. at the University of Washington, Seattle) , IUDR and BUDR (iodinated and brominated deoxyuridines) and monoclonal antibodies in other laboratories. Localization of which site needs to be irradiated with MXR's can be accomplished by magnetic resonance imaging, if a small percentage (5-10%) of the metal substitute is replaced by a metal with a magnetic moment making the site of drug accumulation discoverable in the MR scans. This combination of drug with radiation can be a particularly useful mode of therapy in brain tumors. Localized lesions are amenable to excision and stereotactic attack, but infiltrating tumors that have worked their way in among adjacent cells cannot be approached any other way surgically. Chemoradiotherapy offers a reasonable alternative for treatment here , as the metal containing drug will accumulate only in the cancerous cells and not the normal tissues.

FUTURE NEEDS:

Compact FEL's will be needed if these devices are to be used in a hospital setting. The current devices are large, temperamental, and expensive. A single use machine could easily be fabricated for the production of MXR's alone. If one were to add hard x-ray optics to a compact FEL, we would expand the utility of MXR's tremendously [12].

Quantum efficient, fast detectors with high resolution are currently under development [13]. These will assist in the reduction of radiation dose to the patient. However, we may come to a point whereby the radiation dose is limited by quantum mottle. We may be unable to define the edges of anatomic structures if we too severely limit the number of photons available to the detector.

SUMMARY:

If we take advantage of time of flight imaging, phase imaging, energy discrimanant information, inherent absorption differences of tissues, fast gated digital detectors, computer enhancements and reconstruction of data , and new chemoradiotherapeutic agents, monochromatic x-rays will have a shining future in medicine.

*This work is supported by ONR Grant #420-632-3913 and a grant from the Eastman Kodak Corp., Rochester, NY.

REFERENCES:

1.-Boone JM, Seibert JA. A Figure of Merit Comparison between Bremsstrahlung and Monoenergetic X-ray Sources for Angiography. Journal of X-ray Science and Technology. 4:334-345, 1994.

2.-Carroll FE, Waters JW, Price RR, Brau CA, Roos CF, Tolk NH, Pickens DR, Stephens WH. Near-monochromatic x-ray beams produced by the free electron laser and Compton backscatter. Invest Radiol25:465-471, 1990.

3.-Dong WW, Brau CA, Waters JW, Tompkins PA, Carroll FE, Price RR, Pickens DR, Roos C. Current Status of the VU MFEL Compton X-ray Program. Journal of X-ray Science and Technology 4:346-352, 1994.

4.-Tompkins PA, Brau CA, Dong WW, Waters JW, Carroll FE, Pickens DR, Price RR. The Vanderbilt University Free Electron Laser X-ray Facility. SPIE Proceedings 1736:72, 1992.

5.-Johns PC, Yaffe MJ. X-ray characterization of normal and neoplastic breast tissues. Phys Med Biol 32:675-695, 1987.

6.-Carroll FE, Waters JW, Andrews WW, Price RR, Pickens DR,Willcott R, Tompkins P, Roos C, Page D, Reed G, Ueda A, Bain R, Wang P, Bassinger M. Attenuation of Monochromatic X-rays by Normal and Abnormal Breast Tissues. Invest Radiol29:266-272, 1994.

7.-Gordon CL. Time gated imaging with and ultrashort pulse laser-produced plasma x-ray Source. Optics Letters, May '95 (in press).

8.-Momose A, Takeda T, Itai Y. Phase-contrast x-ray computed tomography for observing biological specimens and organic materials. Rev. Sci. Instrum. 66:(2) 14734-1436, 1995.

9.-Hart M. The Application of Synchrotron Radiation to X-ray Interferometry. Nucl Instrum and Meth. 172:209-214, 1980.

10.-Bonse U , Hart M. An X-ray interferometer. Appl Phys Lett 6:(8) 155-156, 1965.

11.-Bonse U , Hart M. An X-ray Interferometer with Long Separated Interfering Beam Paths. Appl Phys Lett 7:(4) 99-100, 1965.

12.-Carroll FE. Use of Monochromatic X-rays in Medical Diagnosis and Therapy. What is it Going to Take? Journal of X-ray Science and Technology 4:323 333, 1994.

13.-Wang PW, Haglund RF, Kinser DL, Margul HC, Tolk NH, Weeks RA. Luminescence induced by ion deposition in synthetic Sio_2 glasses, Diffusion and Defect Data 53-54:463-468, 1987.

Texas Regional Medical Technology Center

R. Sah, T.D. Cain, E.K. Cleveland, K. Saadatmand, M.E. Schulze, and R.A. Winje
Texas National Research Laboratory Commission
2275 North Highway 77, Waxahachie, Texas 75165

Abstract: **A linear accelerator was partially completed as part of the SSC construction project. The related assets will be incorporated into a world-class medical center dedicated to providing proton-beam radiation therapy for cancer patients. The Texas National Research Laboratory Commission is collaborating with the University of Texas Southwestern Medical Center at Dallas on this project. The linac will be used to inject beam into a new proton synchrotron, which will provide protons at energies up to 350 MeV. A unique feature of this facility will be the capability to enhance the precision of the radiation therapy through the use of proton radiography. A Conceptual Design Report has been completed for this project. The Department of Energy has provided funds for this project subject to an environmental assessment.**

I. INTRODUCTION

When the Superconducting Super Collider (SSC) construction project was terminated in 1993, the U.S. Department of Energy (DOE) funded Project Definition Studies for the purpose of finding good uses for the existing SSC assets. One Project Definition Study described the Regional Medical Technology Center (RMTC). This proposed project will use the SSC linear accelerator assets, including the partially-completed linac and its building, for medical purposes. As part of the SSC Termination Settlement, the DOE placed $65 million in escrow with the Texas National Research Laboratory Commission (TNRLC), for the purpose of building the RMTC.

II. PROJECT DESCRIPTION

The first portion of the SSC linac, including the first tank of the drift-tube linac (DTL), will be completed for the purpose of providing a 13-MeV H^- beam. This injection linac will be placed in the SSC Linac Building, located on the West Campus, near Waxahachie, Texas. The H^- beam will be injected into a proton synchrotron located in a new RMTC building. The synchrotron will accelerate the protons to energies up to 350 MeV, in order to treat cancer patients and to provide a capability for proton radiography. The beam delivery system includes a high-energy beam transport line, two gantry treatment rooms, and two fixed-beam rooms. Double-scattering systems will provide beam spreading in the nozzles.

The system specifications for the RMTC are given in Table 1. They are based on the clinical requirements for the facility.

Table 1 **System Specifications**

Specification	Value
Injection	
Injection energy	13.4 MeV
Injection pulse current	17 mA
Injection pulse length	2.35 μs
Number of turns injected	4
Proton therapy	
Proton beam energy	70 - 270 MeV
Design extracted current	30 nA
Guaranteed extracted current	20 nA
Duty cycle	50%
Proton radiography capability	
Proton beam energy	70 - 350 MeV
Extracted beam current	1 nA
Repetition rate	1.5 Hz
Extraction system	Resonant (half integer)
Circumference	29.4m

The H^- beam is injected into the synchrotron using a stripper foil, and 4 turns of beam is injected in 2.35 μs. For proton therapy, the synchrotron accelerates the beam to energies up to 270 MeV. The machine design parameters are selected to provide 30 nA of average extracted beam current. This ensures that the guaranteed average extracted current of 20 nA will be achieved. A duty cycle of 50% is appropriate for many beam delivery systems, including raster scanning.

The capability for proton radiography is an important design goal for the RMTC. Proton radiography is the formation of images by the detection of low intensity proton beams which have passed entirely through the patient's body. This technique can be used to check the final alignment of the collimated proton beam relative to the treatment volume within the patient. It can also provide a check of the estimated proton-beam stopping power of body tissues. Higher energy beams (up to 350 MeV) are provided for radiography, but only very low beam currents are required.

0-7803-3053-6/96/$5.00 ©1996 IEEE

A maximum repetition rate (i.e., synchrotron cycling frequency) of 1.5 Hz has been selected in order to provide a design beam current of 30 nA. A half-integer resonant extraction system will provide a slow beam spill from the synchrotron. Great care will be taken to assure a smooth beam spill, one that will be suitable for a raster-scan beam-delivery system. For example, the dipole-magnet power-supply specification includes a very stringent current-ripple requirement, in order to control the time structure of the beam spill.

Figure 1 shows the injector linac, and Figure 2 shows the new RMTC Building.

Table 2 gives some specifications for the RMTC subsystems.

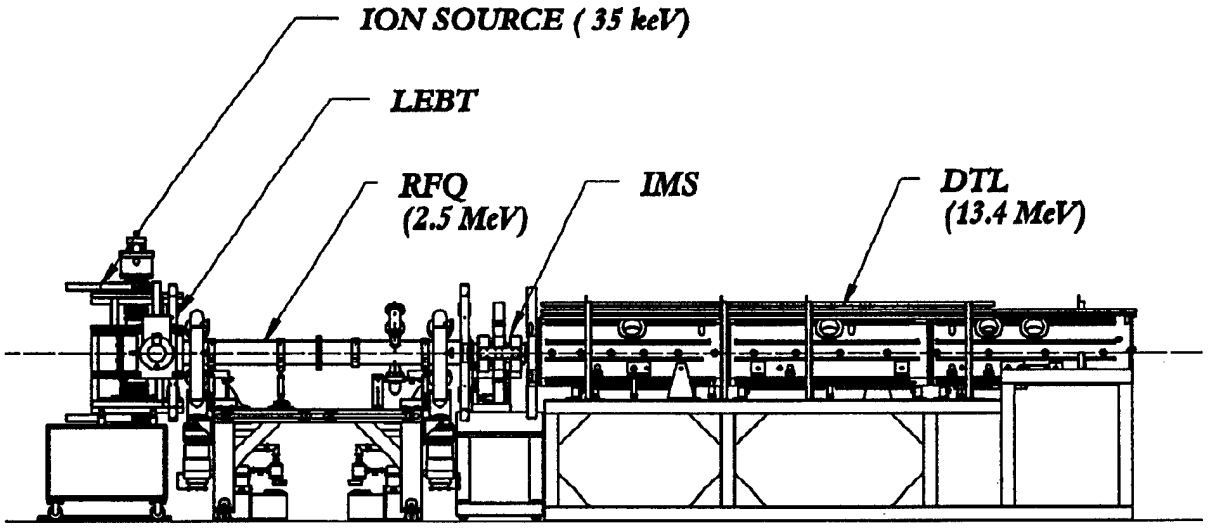


Figure 1 Injector linac

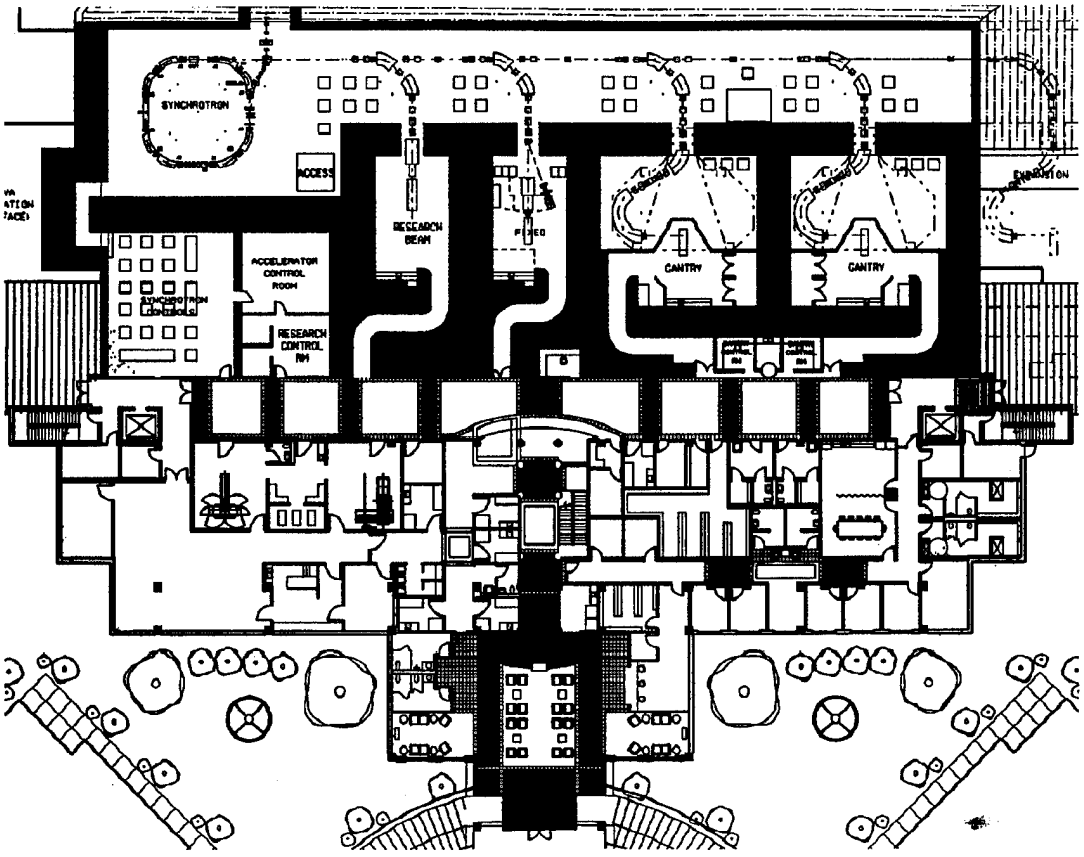


Figure 2 RMTC building

Table 2 **Subsystem Specifications**

Specification	Value
Injector	
Type	H^- linac
Energy	13.4 MeV
Design pulse current	25 mA
Guaranteed pulse current	17 mA
Design pulse length	10 μs
Guaranteed pulse length	2.35 μs
Synchrotron	
Horizontal betatron tune	1.56
Vertical betatron tune	1.58
Harmonic number	1
Radiofrequency	1.708 - 6.995 MHz
Dipole gap	60 mm
Good field region (FW)	80 mm x 50 mm (H x V)
Beam delivery systems	
Gantries	Conventional
Source to axis distance	3 m
Beam spreading system	Double scattering

The linac must provide a pulse current of 17 mA, in order to permit the synchrotron beam current to reach its design value of 30 nA. The design value for the linac pulse current is conservatively set at 25 mA. The design value for the linac-beam pulse length is set at 10 μs.

The harmonic number for the synchrotron has been selected to be 1. The radiofrequency must be swept over a rather wide frequency range, in order to capture beam at 13.4 MeV (injection) and to deliver beam at up to 350 MeV kinetic energy. The full gap of the synchrotron dipole magnets is 60 mm.

Two beam-treatment rooms will be outfitted with isocentric gantries of a "conventional" design, as opposed to a "corkscrew" design. These gantries feature a source-to-axis distance of 3 m. For the start of RMTC operations, a double-scattering system will provide beam spreading in the nozzles.

III. PROJECT STATUS

The technical staff at the TNRLC has completed a Conceptual Design Report that includes a technical design, a detailed cost estimate, a summary schedule, and a management plan. The U.S. Department of Energy has nearly completed an environmental assessment for the RMTC.

A Proposed 100-400 MeV Beam Facility at Fermilab

C. Johnstone, C. Ankenbrandt, S. Bjerklie, D. Boehnlein, M. Foley, T. Kroc, J. Lackey, A. Lennox, A. Leveling, E, McCrory, M. Popovic, C. Schmidt, K. Vaziri
Fermi National Accelerator Laboratory*
P.O. Box 500, Batavia, IL 60510 USA

*Abstract**

An extraction beamline and an experimental area have been designed for the Fermilab Linac. The design exploits attributes of the Linac in order to adapt it to a wide range of applications and purposes. Charge stripping of H^- ions enables beam manipulations which contribute enormously to the capabilities and flexibility of the facility. The proposed Linac Experimental Area would provide facilities for research and development in accelerator physics, medical physics, health physics, and atomic physics.

I. INTRODUCTION

Some of the same characteristics which make the Fermilab Linac well-suited for its primary role as an injector for a synchrotron--short duty cycle, fixed beam parameters and even high intensity--would seem to limit its utility for other applications, which often require much lower intensity and flexible control of parameters. The facility design presented here circumvents many of these limitations in a variety of ways. The most important method is charge stripping of the H^- beam, which allows intensity, transverse phase space distributions, and momentum spread to be simultaneously controlled over wide ranges. For example, this technique allows intensity to be adjusted from a few protons/pulse to more than 10^{13} protons/pulse, emittances to be controlled from .1-6π mm-mrad, and momentum spread. to be reduced well below its normal value. In addition, the controls system developed for the Linac allows for pulse-to-pulse changes in output energy from 100-400 MeV in discrete steps [1].

Construction of such a facility at Fermilab became especially practical and economical following the recent upgrade of the Fermilab Linac. The Linac Upgrade Project raised the Fermilab Linac beam energy from 200 to 400 MeV, making it more useful for the proposed research. It also left behind considerable civil construction and resources (magnets, utilities, etc.). Furthermore, the proposed program could use the many beam cycles which are presently available on the Fermilab Linac without interfering with the high energy physics program.

A workshop[2] was held at Fermilab in October, 1993 to examine the research potential of such a facility and to gauge outside interest. A number of research groups in the aforementioned subfields of physics participated actively, and several groups subsequently submitted written proposals and expressions of interest. The proposed activities would foster symbiotic interactions and cooperation among these subfields of physics. Much of the proposed medical research requires an operationally flexible, well-calibrated proton beam, which is currently not available in this energy regime. Likewise, a well-characterized beam offers special opportunities for health physics research, particularly in the areas of dosimetry, radiation damage, and optimization of shielding. Thus an important goal was to design a beam having variable parameters but well-established properties. The overall design of the area promotes cooperative initiatives between diverse research efforts and thereby achieves a number of advantages, as detailed in the following sections.

II. PERFORMANCE GOALS AND BEAM OPTICS

A major design challenge was to deliver a wide range of beam parameters required by the proposed experimental program without perceptible impact on the laboratory's high energy physics program or on accelerator operational resources. In order to meet the required beam specifications and to satisfy operational constraints, the extraction beamline was designed to regulate intensity, phase-space attributes, and momentum spread in a precise, reliable, and operationally simple, manner.

Performance goals that can be realistically achieved with the present beamline design when the full capability of the Fermilab Linac is taken into consideration are given in the table below.

Table 1. Operational Parameters of the Linac Experimental Area.

Beam Energy Range	100-400 MeV
Intensity Control	few protons/pulse [3] to 10^{13} protons/pulse
Emittance Selection	.1π to 6π mm-mrad
Pulse Length	picosecs [3] to 40μsec
Transverse Beam Size	.5 mm to 75 mm
Momentum Spread, $\Delta p/p$	0.3%-0.05%
Energy Calibration [4]	$\pm 10^{-4}$
Determination of $\Delta p/p$ [5]	$\pm 10^{-5}$

*Operated by the University Research Association, Inc. under contract with the US Department of Energy.

0-7803-3053-6/96/$5.00 ©1996 IEEE

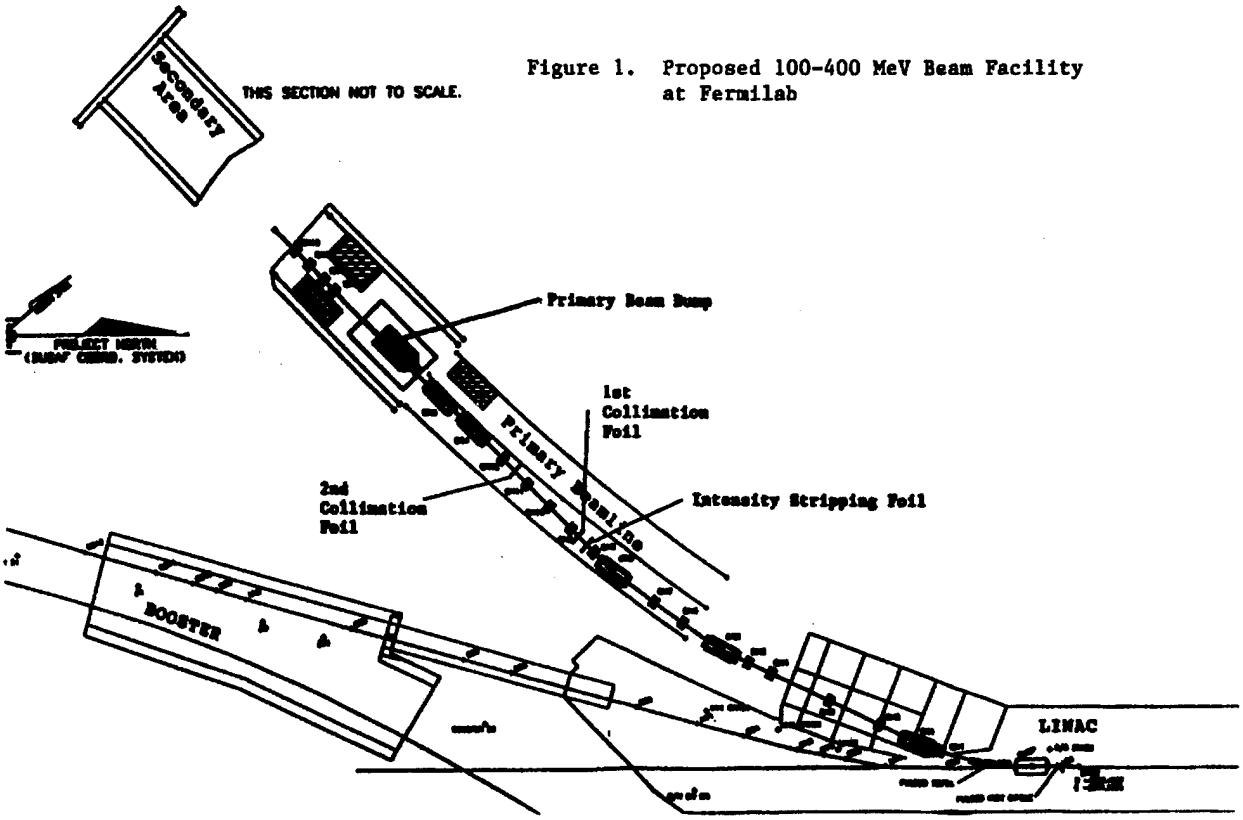


Figure 1. Proposed 100-400 MeV Beam Facility at Fermilab

III. BEAM OPTICS

A. Beam Extraction

The Linac can generate beam pulses from 1-60 μsec long at a repetition rate of 15 Hz. For extraction, a pulsed magnet system will deflect individual complete beam bursts through a bend angle of 15^0 toward the proposed experimental area. This approach not only maintains operational simplicity but also minimizes the impact on accelerator operations and the laboratory's high energy physics program. However, it also necessitates a shielded enclosure and a primary beam dump capable of coping with the full Linac intensity. A plan view of the primary beamline is given in Figure 1.

B Beam Intensity

To control the beam intensity, the instantaneous beam current can easily be varied by about a factor of two and the duration of the beam pulse by about a factor of sixty. The H^- intensity can be further reduced when necessary by stripping foils of varying thicknesses. The intensity of the H^- beam can be limited by the transmission foil to a fraction of a percent of the initial Linac (by thicknesses in the range 50-300 $\mu g/cm^2$ for 400-MeV beam).

Downstream of the foil, the beam contains protons as well as H^- atoms. Two dipoles of equal strength and opposite polarity just upstream of the primary dump separate the two charge species. The unwanted charge species (usually protons) is deposited in the beam dump while the intensity-moderated beam (H^-) is transported through the dump and into a secondary experimental beamline and area (see Figure 1). The beam optics downstream of the stripping foil successfully transports beams of both polaritites to their intended destinations.

C. Transverse Beam Properties and Momentum Spread

After the beam intensity is attenuated by the transmission foil, the transverse beam parameters and momentum spread are adjusted by means of strategically located stripping-foil collimators. Two stripping collimators with pinholes are used to control phase space attributes such as emittance and divergence. For example, the acceptance of stripping collimators with .5 mm pinholes separated by 3m is 0.1 mm-mrad for transmission of an H^- beam. Since the collimators are located at highly dispersed horizontal foci, momentum spread is also adjustable. The initial momentum spread of the full Linac beam (~.2%) can be reduced by about a factor of 4 or 5 through the use of pinhole collimators (Figure 1).

D. Beam Energy

The beam energy can be varied by allowing the beam to drift through unpowered or misphased individual sections of the Linac. Almost continuous control over the output energy can be attained through inter-tank phasing. The Linac quadrupoles are pulsed at 15 Hz, and the timing of the pulse can be adjusted to maintain the usual Linac transverse focussing as the beam energy varies.

IV. OVERVIEW OF APPLICATIONS

The potential for medical research, in particular for activities related to proton therapy, is especially compelling. For example, the development of pulsed-beam scanning techniques has been proposed for delivering uniform doses that conform accurately to irregular three-dimensional tumor volumes. Also, there is considerable interest in proton radiography and tomography, particularly in conjunction with proton therapy, to produce images of patients immediately preceding treatment. Other proposed applications would take advantage of the versatile beam parameters to test beam delivery techniques and of the well-known properties of the beam to cross-calibrate dose-measuring devices.

The broad spectrum of proposed applications in accelerator researach ranges from basic beam characterization and device calibration to development of new beam detectors and other advances in accelerator technology. To illustrate the symbiotic nature of the proposed program, precise experimental techniques and tools pioneered in the field of atomic physics will not only further experiments in atomic physics, but also serve as the basis for new accelerator diagnostic tools, such as, for example, the advanced laser techniques developed for the study of relativistic H^- beams [4,5]. The same laser apparatus and setup proposed for atomic physics research will make possible accurate and absolute determination of a class of beam and device parameters which address accelerator performance issues. In a similar vein, the well-calibrated beam desired for medical applications offers special opportunities for health physics research in the areas of dosimetry, radiation damage, and shielding optimization.

IV. SUMMARY

The design of a multipurpose Linac experimental facility that satisfies a variety of experimental requirements on beam intensity, phase space distributions, and momentum spread is described. The present design boasts flexible and independent control over all of these parameters, primarily by selective stripping of an H^- beam. This versatile facility design meets requirements of numerous applications and experiments in medical, accelerator, health, and atomic physics, for both basic research and applied technology.

IX. REFERENCES

[1] Elliott McCrory and Chuck Schmidt, private communication.

[2] Chuck Ankenbrandt and Carol Johnstone, editors, *Proceedings of the 400-MeV Beam International Workshop,* Fermilab, October 1993.

[3] A few protons/pulse is achieved by neutralizing the H- beam using a laser and then extracting and stripping the neutrals in a foil. Laser intensity is lowered until only a few neutrals; i.e. a few protons/pulse are generated. Picosecond pulse lengths can also be attained using laser photodetachment.

[4] E. P. MacKerrow, et al, "Laser Diagnostics for H^- Beam Momentum and Momentum Spread," *Proceedings of the 400-MeV Beam International Workshop,* Fermilab, October 1993., 147.

[5] P. G. Harris, et. al., "Measurement and Reduction of Momentum Spread in the LAMPF Linac Beam," Nucl. Inst, and Meth., A292, 254-258 (1990).

Cyclotrons for Isotope Production

B.F. Milton and N.R. Stevenson,
TRIUMF, 4004 Wesbrook Mall, Vancouver,
B.C., V6T 2A3, Canada

Abstract

Cyclotrons continue to be efficient accelerators for radio-isotope production. In recent years, developments in the accelerator technology have greatly increased the practical beam current in these machines while also improving the overall system reliability. These developments combined with the development of new isotopes for medicine and industry, and a retiring of older machines indicates a strong future for commercial cyclotrons. In this paper we will survey recent developments in the areas of cyclotron technology, and isotope production, as they relate to the new generation of commercial cyclotrons. We will also discuss the possibility of systems capable of extracted energies up to 100 MeV and extracted beam currents of up to 2.0 mA.

I. Introduction

For many decades accelerators have been used to produce proton rich isotopes, as a complement to the neutron rich isotopes produced in reactors. Initially this production was done in a parasitic mode, on accelerators originally constructed for nuclear physics research. However over the past couple of decades there has been a large number of commercial facilities designed solely for the production of isotopes. In particular the production of isotopes with long enough half-lives that regional distribution is practical, and yet sufficiently short that "just-in-time" production is required, has developed into a specific market. In this market cyclotrons in the energy range of 20 to 40 MeV have become the accelerator of choice, primarily because of their power efficiency and compactness. While the production of PET isotopes represents a significant new market, the requirements of these very short lived isotopes (eg. ^{18}F), leads to different approaches, not considered in this paper.

The first generation of commercial cyclotrons were primarily proton machines that were very similar to the original research machines. In order to simplify operation and reduce costs these machines were often run with the isotope production target inside the cyclotron magnet (ie. no extracted beam). In the 1970's it was recognized that the old trick of accelerating H^-, and extracting by stripping, offered the advantages of separating the target and accelerator without the difficulties of positive ion extraction. The CP42 built by TCC [1] was the first commercially available cyclotron to exploit these advantages. While these machines demonstrated themselves to be able work horses, over the following decade, many short comings in the design were identified. Recognizing the possibilities presented, Ion Beam Applications (IBA) in Belgium, followed by Ebco Technologies in Vancouver, developed the Cyclone 30 [2] and the TR30 [3] cyclotrons respectively. These machines are sometimes referred to as the third generation commercial cyclotrons. Since the initial introduction of these machines, they have dominated the market, and are now available in several different configurations to meet specific market niches.

II. Market Requirements

In North American and Asia the cyclotron produced isotope business has grown about 20% per year for the past decade, predominantly reflecting the increased use of ^{201}Tl in the US and ^{123}I products in Japan. While the Japanese market is expected to continue to grow (10%/yr) for the next few years, many people have predicted that the ^{201}Tl usage in North America will decline although no evidence of this has yet emerged. While other products continue to be developed, none have truly blossomed. Therefore the market stability is hard to predict, and this generates uncertainty when making decisions about future facilities.

The production of short lived isotopes, as is the case for most commercial cyclotron production, imposes certain important characteristics to the business. In particular;

- Irradiation, processing and shipping are on a"just-in-time" basis.
- Round the clock operation
- Weekly scheduling with much flexibility to handle customer requirements and recover from system failures.
- Costs are dominantly fixed, ie. little scaling with the level of production (for a given facility).
- Radiation dose accumulated by maintenance and repair personnel represents a serious cost component.

To respond to these requirements, the cyclotron system needs to be reliable, flexible, and designed to minimize personnel dose. As the market for isotopes matured, producers learned that the increased cost of production enhancing features in these areas could be quickly recovered. The principle production enhancing developments in third generation cyclotrons are:

- A magnet design that guarantees strong vertical focussing for reduced losses during acceleration.
- H^- acceleration to allow extraction by stripping, which is basically lossless and allows easy energy variability.
- Targets located in separate caves, since these represent the most radioactive components of the system.
- Good vacuum (low 10^{-7}) inside the acceleration tank to reduce beam losses from gas stripping of the H^-.
- External ion source, which improves the vacuum, the ease of operation and the reliability.
- Modular systems, with a lot of hardware (eg power supplies) located outside the vault.
- Use of low activation materials, and a reduced dependence on materials that are subject to radiation damage.
- Use of more power efficient designs.
- Improved beam quality and stability to reduce hot spots on the target.

0-7803-3053-6/96/$5.00 ©1996 IEEE

	1989	1992	1995
Europe	8 H^+ 2 H^-	8 H^+ 4 H^-	8 H^+ 5 H^-
North America	13 H^+ 1 H^-	13 H^+ 4 H^-	13 H^+ 5 H^-
Asia-Pacific (exc. China)	5H^+	5 H^+ 4 H^-	4 H^+ 5 H^-
Total H^+ Total H^-	26 3	26 8	25 15
Total No. Cyc.	29	34	40

Table I
Installed and operating commercial cyclotrons used for isotope production

- More sophisticated control system using PLCs and commercial graphics based user interface.

Table I shows the number of commercial cyclotrons installed for commercial isotope production. As can be seen, since the introduction of these machines in 1988 all new commercial isotope production machines have been in this class of third generation of cyclotrons. (Note: A couple of proton cyclotrons with internal targets have been sold during this period, for a highly specialized isotope production use.)

The fact that at TRIUMF we have a CP42 (2^{nd} gen.) and a TR30 (3^{rd} gen.) operating along side one another provides a unique opportunity to directly compare the two. Both machines are run by the same staff, and have similar schedules, however as shown in figure 1 there is a significant difference in the total charge delivered by the two machines.With continued improvements on the third generation machines their outputs have substantially increased during the last five years. Table II shows some representative make rates available over the years (note: the values given are for typical production and not best available). At the present time Nordion International in Vancouver is upgrading its TR30, so that it will be capable of delivering in excess of 1 mA of beam on target. This represents a considerable increase in the production capability, at very little additional costs. It is also quite remarkable considering that this TR30 was originally designed to operate at 350 μA.

A comparison of accumulated personnel dose between the two cyclotrons also shows a dramatic difference. As seen in figure 2 there is nearly an order of magnitude improvement over the previous generation, particularly when compared on a dose per charge delivered basis. This improvement represents both a significant cost saving and an improved work environment for the staff. It is also believed that proposed new dose rules will increase the pressure to retire the existing first generation machines, and replace the capacity using third generation machines.

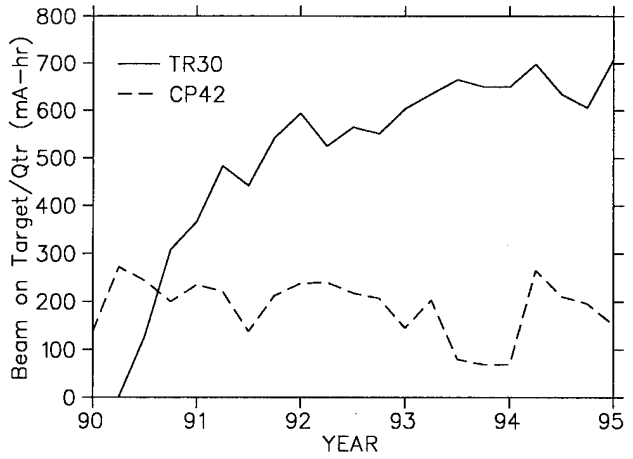


Figure. 1. Total charge delivered on target each quarter by the TR30 and CP42 cyclotrons located at TRIUMF, and owned by Nordion Int.

Year	Cyc.	Current (μA)	Energy (MeV)	Make-Rate (mCi/beam-hr) [EOB+56hrs]
1989	CS30 CP42	350 180	26.5 29	190 160
1992	CYC30 TR30	360 360	29 29	320 320
1994	TR30	440	29	400
1995	TR30	900	29	800

Table II
Make Rates of ^{201}Tl for representative Commercial Cyclotrons

III. Future Developments

The increased beam current available allows more flexibility in scheduling, improved profitability, and reduced strain on systems when not operated at peak capacity. Work at TRIUMF on a model of the TR30 injection system has all ready demonstrated 2 mA of H^- injected and accelerated to 1.1 MeV [4]. This work indicates that the 1 mA machines now being developed, are still a long way from any fundamental limits. Active work on ion source development and low energy injection systems may make this type of capability commercially available in the next few years.

An isotope with increasing potential for clinical PET studies is ^{82}Sr/^{82}Rb generator systems. As a generator system, it again lends itself to distribution from a central facility, making it very different from most other PET isotopes, that basically require an on site production facility. Presently this isotope is produced in North America on higher energy accelerators employing spalla-

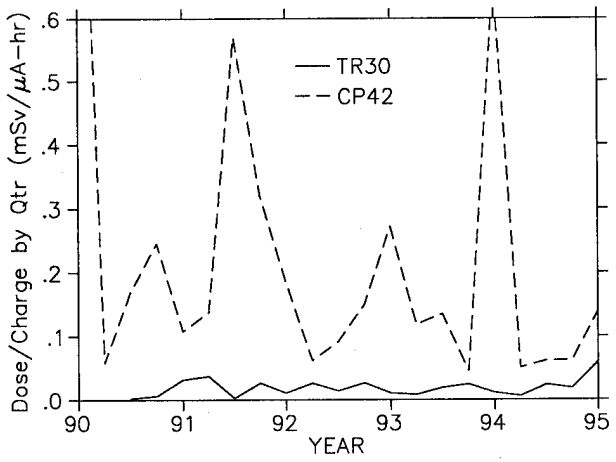


Figure. 2. Accumulated personnel radiation dose, by quarter for the TR30 and CP42 cyclotron.

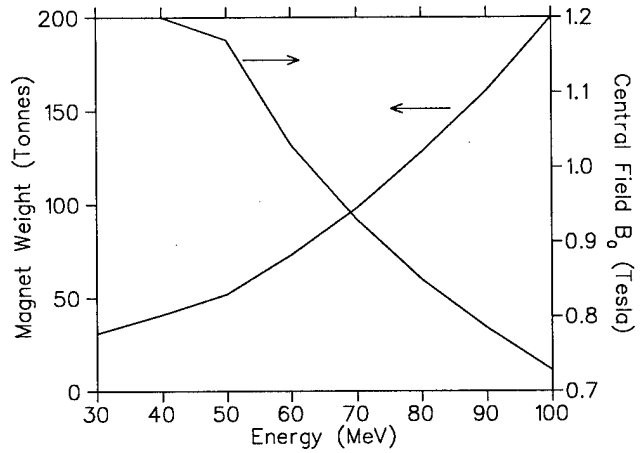


Figure. 3. Required Magnet Sizes as a function of Energy for a H^- Cyclotron. The electomagnetic stripping losses have been constrained to be less than 2%.

tion from molybdenum, or by bombardment of rubidium metal with 60-80 MeV protons [5]. The ability to produce this generator has been a strong driving force in the design of cyclotron systems under consideration for the U.S. National Biomedical Tracer Facility [6]. Preliminary studies indicate that the design principles used in the current generation of cyclotrons could be extended to the required 80 MeV (figure 3). The dominant factor limiting the practical energy of a H^- cyclotron, is electromagnetic stripping of the H^- during acceleration. In order to reduce activation of the accelerator systems, caused by the resulting beam spill, these losses should be kept to the few percent level. This requires substaintialy lower central magnetic field values (B_0) with increasing energy, which in turn leads to a very rapid rise in magnet size. While these considerations do not provide a hard limit on the maximum possible energy, 80 MeV seems to be a practical compromise between the still increasing production cross-section and the accelerator size.

It seems inevitable that commercial cyclotron systems of the future will continue the trend towards higher beam currents, increased flexibility, and a diversity of available beam energies, to produce a broadening range of isotopes. At present it appears that extensions of existing technologies are capable of dealing with the forseeable needs, however uncertainty in the market place may delay implementation.

The authors would like to thank W. Dickie, Nordion Int. Inc., for his input.

References

[1] G.O. Hendry *et. al.*, "Design and Performance of a H^- Cyclotron,*Proc. of the 9th Int. Conference on Cyclotrons and their Applications*, 1981, p. 125.

[2] Th. Vanderlinden, E. Conrad, Y. Jongen, "Three Years of Operation of CYCLONE 30 in Louvain-La-Neuve", *Proc. 2nd European Particle Accelerator Conference*, Nice, 1990, p. 437.

[3] B.F. Milton *et. al.*, "Commissioning and First Operation of a 500 μA, 30 MeV H^- Cyclotron: The TR30", *Proc. of the IEEE Particle Accelerator Conference*, San Francisco, 1991, p. 65.

[4] T. Kou, proceedings of this conference

[5] M.R. Cackette *et al.*, Appl. Radiat. Isot. **44**, No. 6, p 917 (1993).

[6] "National Biomedical Tracer Facility Planning and Feasibility Study", R. A. Holmes, Society of Nuclear Medicine publication, 1991.

EUROPEAN HEAVY ION ICF DRIVER DEVELOPMENT

G. PLASS, CERN, Geneva, Switzerland

Abstract

Approaches in Europe to heavy ion induced Inertial Confinement Fusion are oriented toward the linac-plus-storage ring technique. Despite the very limited support of this work, technical progress was achieved in some important areas. For the immediate future, a substantial intensity upgrade of the GSI accelerator facilities at Darmstadt is being implemented, leading to specific energy depositions of the order of 100 kJ/g and plasma temperatures of 10 to 20 eV. For the longer term, a conceptual design study of a heavy ion based Ignition Facility is being initiated.

I. INTRODUCTION

The quest for 'new' or 'alternative' energy sources for mankind is getting a new impulse since the late eighties through the increasing concern about the climatic consequences of the ever growing use of fossile fuels and the consequential increase of CO2 concentration in our atmosphere.*Global greenhouse warming*, on the timescale of 50 or 100 years is perceived as an immediate danger whereas the limits of the reserves (for coal) would only be felt after several centuries.

Fusion energy is the ultimate, CO2-free, resource for mankind, be it in the form of solar energy where and when sun shines, or from fusion processes confined in man-made machines. Fusion energy from the latter is relatively clean, producing, for the fusion reactions most easily controllable, only a limited amount of radioactive waste of moderate life-time.

Of the two confinement schemes known to date, Magnetic Confinement and Inertial Confinement, the first has been developed during the past fourty years to conditions that make thermonuclear burn and break-even a clear goal for the next generation of experimental Tokomac-type devices. Experiments towards Inertial Confinement Fusion (ICF) driven by laser beams were largely motivated by the need to understand the implosion mechanism in large-scale devices and to check the relevant computational tools, but provided the ground also for the present confidence in the feasibility of ICF. The solid-state-laser driven National Ignition Facility should advance this development to pellet ignition at small gain.

Heavy-ion drivers for ICF, the alternative to laser drivers, are recognized (ref.1) as the only scheme where reasonable extrapolations of present-day technology promise efficiency and reliability sufficient for an energy producing plant. These conjectures ought to be backed up by more data and oriented development work. It is in this optique that the development of a heavy-ion driven Ignition Facility has been undertaken.

II. RECENT ACTIVITIES IN EUROPE

2.1 Driver development

An exploratory investigation of the linac-plus-storage ring version of a heavy-ion driver was conducted in the early eighties and has led up to the HIBALL sytems studies concluded by 1985 (ref.2). Thereafter, studies of a variety of subjects oriented towards an eventual HIF facility were coordinated in a program "High Energy Density in Matter produced by Heavy Ion Beams" centered at the GSI laboratory at Darmstadt. A few of the subjects studied are listed below:

- The initial 'funneling' stages of a heavy ion linac, ion sources (ref.3) and
- RFQ accelerators for heavy ions (ref.4) and
- the merger of several stages with minimum loss of phase-space density into one main linac.
- A two-beam RFQ (Fig.1, ref.5).
- The IH structure, a new type of heavy-ion linac structure (ref.6).
- Focusing in the final beam transport by pulsed lenses (ref.7) or plasma lenses (ref.8,).
- Charge-exchange cross-sections are being measured (ref.9) and beam losses in rings due to charge-exchange scattering computed(ref.10).
- Beam experiments at the CERN-PS, with a Laslett tuneshift of ~1 due to space-charge showed only small emittance blow-up(ref.11).
- In beam experiments at the GSI-ESR (ref.12), the beam remained stable at local densities exceeding the Keil-Schnell criterium by a factor of 5.

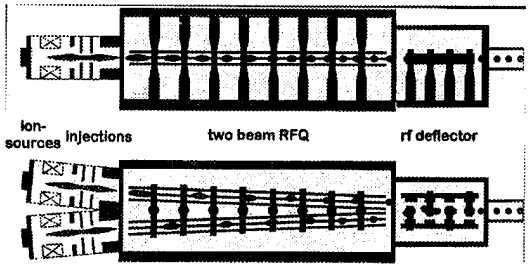


Figure 1: Two beam funneling experiment.

2.2 Target physics

A very substantial programme of computational target physics (beam-plasma interaction, opacities, radiation symmetrization in indirect drive targets, environmental problems, etc.) which cannot be presented within the limits of this paper, is under way in several institutions, e.g. DENIM (Madrid), ENEA (Frascati), MPI (Garching) as well as the Universities of Darmstadt and Frankfurt.

0-7803-3053-6/96/$5.00 ©1996 IEEE

III. A TWO-STAGE PROGRAMME

The current activities can be described in terms of a two-stage programme:

- the GSI laboratory has launched an intensity upgrade project (ref.13) which will allow, by end 1998, filling of the GSI-SIS synchrotron with heavy ions up to its space-charge limit, and
- a feasibility study is now under way of a heavy-ion driven Ignition Facility.

The GSI intensity upgrade project consists of three items to be implemented between 1995 and 1998, viz. the replacement of the first-stage Wideroe structure by a new front-end consisting of new ion sources, an RFQ and a modern IH structure, various improvements of the efficiency of the UNILAC linear accelerator, and the installation in the SIS synchrotron of an electron cooler. The number of ions per pulse produced to-day and the expected space-charge limit are shown in Fig. 2, whereas Fig. 3 shows the specific energy deposited and the plasma temperatures to be reached at the three stages.

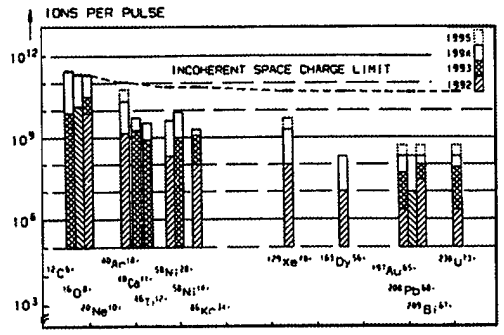


Fig. 2: Present & expected ion beam intensities in SIS.

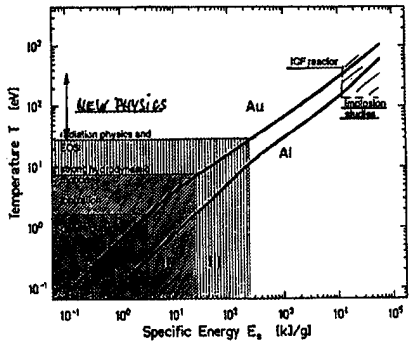


Figure 3: Plasma temperatures as a function of the specific energy deposition.

The Ignition Facility should, in a staged approach, bridge the gap (see Fig. 3) of two orders of magnitude in specific energy deposition, and one order of magnitude in plasma temperature, between the performance of the upgraded GSI machines and the parameters required for ignition of an ICF pellet. It shall serve the purposes of:

- the exploration of issues of accelerator design which cannot be tackled with existing machines,
- the exploration of a large programme of target physics,
- and finally, the demonstration of a heavy ion ICF driver and the demonstration of pellet ignition by heavy ions, in indirect drive mode, at moderate gain.

For the medium-term future, the Ignition Facility will provide the basis for the design of a Demonstration ICF Energy Plant.

IV. STUDY OF A HEAVY-ION DRIVEN IGNITION FACILITY

This feasibility study (ref. 14) was launched by the management of four laboratories, i.e. DENIM (Madrid), ENEA (Frascati), GSI (Darmstadt), and KFK (Karlsruhe), and will very likely be supported by the European Union. Other laboratories with relevant experience are expected to join the collaboration.

Within the coming two to three years the feasibility and approximate cost shall be examined of a laboratory facility which ultimately can achieve ignition of DT pellets. The initial target parameters of the facility are given in the Table

Ion energy	6 GeV (Bi ions)
Ion range	0.05 g/cm^2
Driver energy	2 MJ
Beam pulse shape	prepulse 15 - 25 ns, 20 TW main pulse 6 - 7 ns, 300 TW
Spot size	2 mm, 2 opposite converters
Pointing tolerance	.1-.2 mm
Timing tolerance	<.5 ns
Target (indirect drive)	pellet diameter $\leq$ 2mm pellet mass $\leq$ 1.5 mg DT
Predicted gain	10 - 30

and displayed in Fig. 4, but the final specifications and a reasonable staging, which is part of the charge to the study group, remain to be defined in interaction between driver and target experts. The facility must be considerably more modest than the power generating facilities considered in earlier systems studies: although the ion energy will be of the same order of magnitude, the total deposited beam energy is chosen such as to provide only for low target gain, and reaction chambers, beam spot dimensions, and (low) repetition rate will be adapted to laboratory studies.

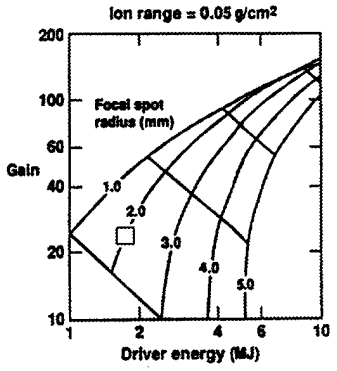


Figure 4: Gain curves for indirectly driven targets (Livermore group).

Recent advances and results do contribute to reducing the scale of the facility. It is now established that 'indirect drive' targets (Fig. 5) with only two converters at opposite ends can, with the help of internal screens, provide the necessary uniformity of pellet illumination (ref. 15, 16). The number of beams in final transport can then be chosen with respect to the Maschke transport limit, and the geometrical layout is simplified. Following accelerator experiments (ref. 12), it is expected that the Keil-Schnell criterium for longitudinal beam stability can be passed by about one order of magnitude in local beam density, for short dwelling times in any case. In other experiments, the beam was shown to survive for the time necessary for final bunching with small emittance blow-up (ref.11) even when integer transverse resonance lines were crossed due to space-charge. Routine operation (albeit at low intensity) of heavy ion linacs using the IH structure (ref. 17) indicates that the linac length may be considerably reduced.

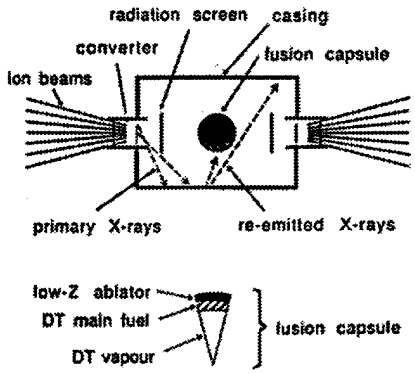


Figure 5: Indirect-drive target (ref. 15).

Conceptually, the facility will consist of one pulsed high-current linac (~100 mA) fed by a funnel system (Ref. 18) of preaccelerators, in turn fed from 8 (possibly 16) ion sources, which injects into a small number of storage and buncher rings. The beam bunches of up to 10 ns duration are, through transport channels of different lengths, directed at the two converters of an indirect drive target, where they must impinge simultaneously.

Examination of the merits of various types of structures for the different stages of accelerators (RFQ, IH, SCDTL, etc.) has been launched along with the work on storage ring, bunching and final transport, so that a consistent set of accelerator parameters will become available in the near future.

V. ACKNOWLEDGEMENTS

This brief report summarizes many discussions with the co-authors of the ICF proposal (ref.14) and the persons responsible for the GSI project (ref.13), and in particular N. Angert, S. Atzeni, K. Blasche, R. Bock, D. Böhne, B. Franzke, I. Hofmann, H. Klein, and D. Möhl.

VI. REFERENCES

1) Fusion Policy Advisory Cttee; Final report, Sept.1990; US DoE, Wash.DC,

2) HIBALL II, report KfK 3840 (1985) Kernforschungszentrum Karlsruhe, FRG

3) K. Volk et al., GSI 94-10 (1994) p. 34; GSI Darmstadt, FRG

4) H. Deitinghoff et al., GSI 94-10 (1994) p.33

5) A. Firjahn-Andersch et al. GSI 94-10, p.28

6) U. Ratzinger, Nuovo Cimento 106 A (1993) p. 1583

7) P. Spiller et al., Nuovo Cimento 106A (1993) p.1719

8) M. de Magistris, M. Stetter et al., Nuovo Cimento 106A (1993) p.1643,17256)

9) R. Schulze et al.,GSI 94-10 (1994) p.14; GSI Darmstadt, FRG

10) D.Budicin; I. Hofmann et al., Nuovo Cimento 106A (1993) p. 1621,1671

11) R. Cappi et al., Proc. EPAC 94 (1994) p. 279

12) I. Hofmann et al., Proc. EPAC 92 (1992) p. 783

13) D. Böhne et al. The GSI Intensity Upgrade Programme GSI 95-06 (1995)

14) S. Atzeni et al. Proposal for a Heavy Ion Ignition Facility GSI 95-03 (1995)

15) S. Atzeni, Nuovo Cimento 106A (1993) p.1489

16) J.D. Lindl, Nuovo Cimento 106A (1993) p.1467

17) H. Haseroth, this Conf.

18) A. Schempp, private comm.

A 3-stage Cyclotron complex for driving the Energy Amplifier

P.Mandrillon, N.Fietier, Laboratoire du Cyclotron, Nice, France, C.Rubbia, CERN, Switzerland

I. INTRODUCTION

The goal of this accelerator complex is to provide a 10 MWatt proton beam for driving the Energy Amplifier recently proposed by C.Rubbia [1]. It is lower (by one order of magnitude) than the requirements of most of the accelerator-driven projects based on c-w linacs [2]. Therefore, the requirements for the Energy Amplifier open an alternative solution based on ring cyclotrons [3] [4] producing a continuous beam. Thus taking into account the present development of high-intensity cyclotrons (cf. PSI [5]), a three-stage cyclotron accelerator is a possible solution. It comprises:

- **the injector(s)** which should be able to deliver a 10 mA beam in a given phase width. a solution based on two 5mA compact isochronous cyclotrons (**CIC**) working in parallel is proposed.
- **the intermediate stage (ISSC)** which is a four-separated-sector cyclotron accelerating the injected beam up to 120 MeV.
- **the final booster (BSSC)** which has ten separated sectors and six cavities raising the kinetic energy up to about 1000 MeV.

II. DESIGN CONSIDERATIONS

Acceleration of intense beams requires an very efficient extraction process free of beam loss. The main parameters of the intermediate stage and the final booster should satisfy the following design criteria :

- **Single turn extraction :** A large radial gain per turn is requested, i.e. an high energy gain per turn, in order to get an effective turn separation on the extraction radius.
- **Flat-topping RF cavities** : In this multi-stage cyclotron complex, the extraction efficiency and the energy spread of a given accelerator stage depends on the pulse length and energy spread of the beam extracted from the previous stage. Therefore the only way of decreasing the energy spread for a given longitudinal particle density and phase width, is to use flat-topping accelerating cavities, namely, two additional RF resonators working on a harmonic of the main RF cavity frequency in order to obtain an "as flat as possible" accelerating voltage wave form. Usually these cavities work on a third harmonic mode.
- **Matching the three stages :** In order to avoid any beam loss, matching conditions must be satisfied between the different stages for further acceleration : in particular the RF frequency of the booster should be a multiple of that of the injector. In order to simplify the overall design of the RF system, a good choice is to operate all the machines with the same RF frequency, i.e. 42 MHz in the proposed design.

The main parameters of the intermediate stage and the final booster of the 42 MHz option are presented in Table 1. The equilibrium orbits and their properties have been calculated numerically using realistic computed magnetic field maps.

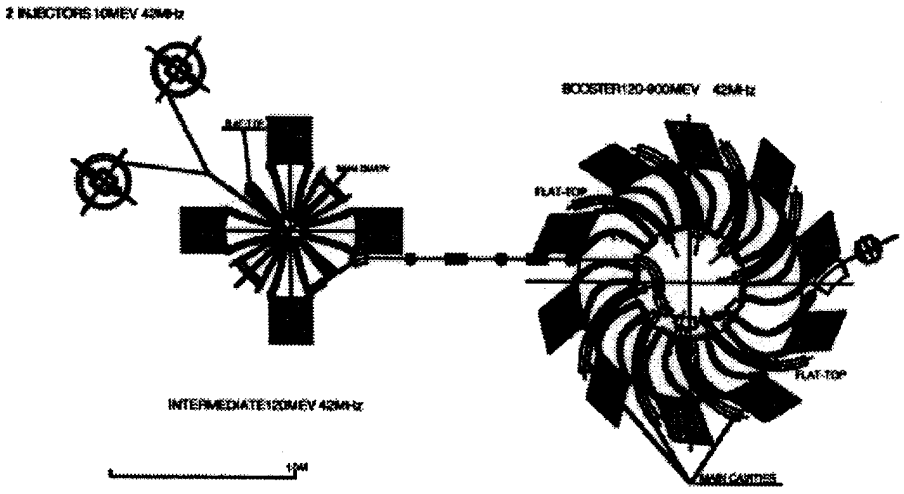


Figure 1 : General lay-out of the accelerator complex

0-7803-3053-6/96/$5.00 ©1996 IEEE

Table 1 : Main parameters for the 42 MHz design

Accelerator type	ICC	ISSC	BSSC
Injection (MeV)	0.1	10	120
Extraction (MeV)	10	120	990
Frequency (MHz)	42	42	42
Harmonic	4	6	6
Magnet gap (cm)	6	5	5
nb. sectors	4	4	10
sector (inj/ext)(deg)	15/32	26/31	10/20
sector spiral ext. (deg)	0	0	12
nbr. cavities	2	2	6
Peak Volt. injection (kV)	110	170	550
Peak Volt. extraction (kV)	110	340	1100
nbr. flat-top cavities	2	2	2
Flat-top frequency	126	126	210
FT Volt. injection (kV)	13	20	22
FT Volt. extraction (kV)	13	40	44
Radial gain ext.(mm)	16	12	10

III. THE INJECTORS

We propose a solution based on 2 compact cyclotrons. Therefore an axial injection is needed for each cyclotron with the following advantages :

- the use of an high extraction voltage,i.e. about 100 KV.
- the choice of a multicusp ion source for the production of negatively charged ions. This source is cumbersome and could not be installed in the central region of the cyclotron.
- getting a high brightness beam accelerated by the cyclotron requires a careful 6D matching (the two transversal and the longitudinal phase space), in particular it is necessary to use a buncher in a way to avoid too strong effects of the space charge.
- better vacuum which allows to use high RF voltages.

This compact cyclotron solution implies combining the output beam of 2 injectors delivering 5 mA working at the same frequency as the intermediate stage and the final booster. It is then necessary to superpose the bunches of the two 5 mA beams produced by each injector to obtain a single 10 mA beam in the ISSC. In order to reduce the space charge effects, it could be attractive to combine an H^+ beam (extracted by stripping H^- ions) and an H^- beam (extracted by a conventional channel). These two beams are synchronised so that the bunches are superposed in a straight portion of the ISSC injection line. A stripper is installed at the end of the injection line, before the beam enters the ISSC magnetic field in order to get a H^+ beam.

The RF system consists of two accelerating and two flat-topping cavities. In order not to worsen space-charge effects by phase compression, a constant voltage distribution along the cavity gaps is desired.

Refined 3-D computations of the magnetic field have been carried out in particular in the injection and extraction regions. As opposed to the intermediate and booster cyclotrons, a closed magnet configuration with a return yoke is used in order to make the cyclotron more compact. A general view of the injector cyclotron is visible in Figure 2.

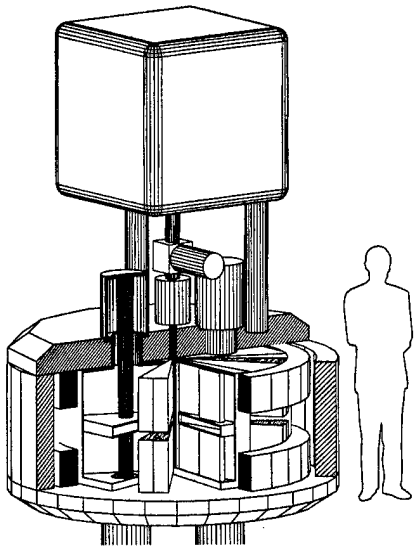


Fig. 2 : General view of the injector cyclotron

IV. THE INTERMEDIATE STAGE

A four-separated-sector cyclotron (cf. Fig. 3) has been chosen because of the following features :

- the acceleration to a sufficiently-high injection energy for the booster can be achieved in about 200 turns due to the possibility to install between the sectors cavities providing a high accelerating voltage.
- the flat-topping of the RF voltage is easy to achieve.
- the strong magnetic focusing provided by the four identical C-shaped sector with a constant small gap (5 cm).
- the possibility to install an efficient extraction channel in the field-free valleys.

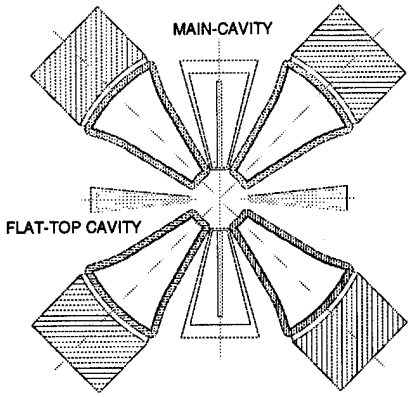


Figure 3 : Top view of the ISSC

The injection energy into the ISSC is certainly one of the most important parameters which influences the overall performances of the cyclotron complex. The space charge effects are strong at low energy. They are present in both transversal and longitudinal directions of the beam. Figure 4 shows the simulation of the evolution of a 20 mA beam in the horizontal plane during the first 16 turns in the ISSC.

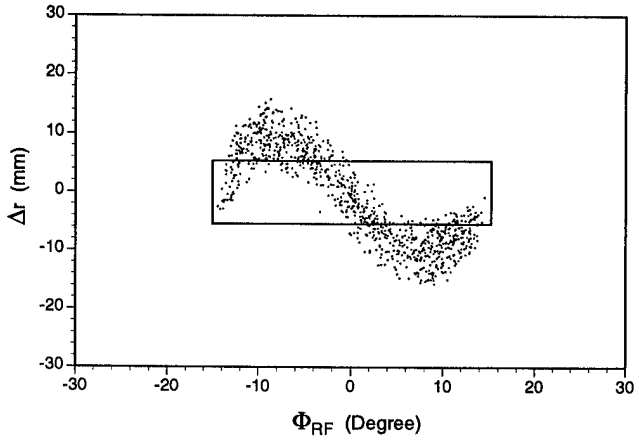


Figure 4 : Space charge effects after 16 turns (initial conditions at injection in the rectangular box).

V. THE FINAL BOOSTER

The lay-out of the booster can be seen in Figure 5. The magnet of the final booster consists of 10 identical C-shaped sector magnets with a strong spiral needed in order to obtain sufficient vertical focusing at high energy. As in the ISSC cyclotron design, no trimming coils are used for generating the radial magnetic field increase required by isochronism. This effect is obtained by increasing the sector width with radius.

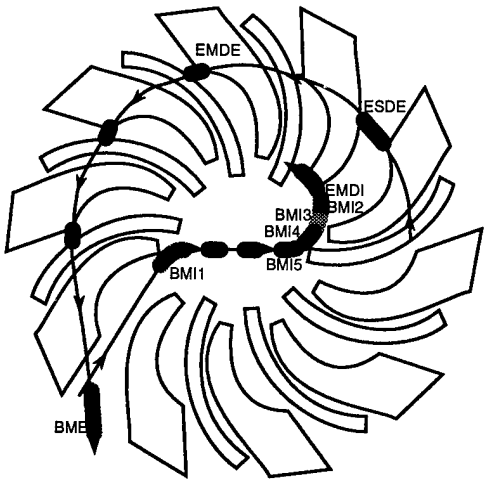


Figure 5 : Lay-out of the BSSC

Acceleration of the beam is provided by 6 main resonators located in the valleys giving an energy gain per turn of 3.0 MeV at injection and 6.0 MeV at extraction giving a voltage (or phase compression) ratio of 2.0. Single-gap cavities are used for both accelerating and flat-topping cavities. Since the beam phase width can be reduced to 15 degrees at the intermediate cyclotron exit, fifth harmonic operation has been selected for the flat-top cavities. This enables to decrease the flat-top cavity power compared to operation on the third harmonic. Measurements on the accelerating cavity model have been carried out in order to check and determine precisely the cavity characteristics. A very good agreement has been found between theoretical and experimental results. The injection channel and extraction channels of the BSSC are shown on the Fig. 5.

VI. CONCLUSIONS

An essential aspect of this accelerator complex is the overall efficiency which depends mainly on the RF performances. For a 10 mA beam the power to be delivered to each main cavity of the BSSC is estimated to be about 2.05 MW (1.45 MW beam power and 0.60 MW cavity loss), which correspond to about 2.9 MW electrical power (assuming a 70% DC to RF conversion efficiency). Further optimisations of the cavity shape which are in progress show that a global efficiency slightly greater than 40 % is within the reach.

The authors would like to express their thanks to the members of the AT-ET Group for the many useful discussions during these studies.

VII. REFERENCES

[1] F.Carminati et al, An Energy Amplifier for Cleaner and Inexhaustible Nuclear Energy Production Driven by a Particle Beam Accelerator, CERN/AT/93-47 (ET), 1st November 1993.

[2] R.A.Jameson et al., Accelerator-driven transmutation technology for energy-production and nuclear-waste treatment, 3rd EPAC, Berlin 1992, pp. 230-234.

[3] P.Bonnaure, P.Mandrillon, H.Rief, H.Takahashi, Actinide transmutation by spallation in the Light of recent cyclotron development, ICENES 86, Madrid, July 1986.

[4] C. Rubbia, P.Mandrillon, N.Fiétier, A High Intensity Accelerator for Driving the Energy Amplifier for Nuclear Energy Production, 4th EPAC, London 1994, pp. 270-272.

[5] Th. Stammbach et al., Potential of cyclotron based accelerators for energy production and transmutation, Int. Conf. on Accelerator-driven transmutation technologies and applications, Las Vegas, July 1994.

ACCELERATOR-BASED GAMMA NEUTRON TRANSMUTATION OF RADIONUCLIDES AS A NEW TECHNOLOGY FOR THE NUCLEAR FUEL CYCLE

I.P.Eremeev, International Business Nucleonic, Moscow, Russia

ABSTRACT

A new transmuting technology for incinerating long-lived nuclear waste and breeding fissile fuel is proposed as an application of the physical approach [1, 2]. The physical parameters of the technology, such as a transmuting rate, an intensity of photoneutrons generated in the gamma transmutation process, an energetic "cost" of a transmutation event have been determined by multigroup calculations. It is shown that the approach proposed allows any long-lived radionuclide (both transuranium actinide and fission product) to be transmuted at a much greater rate than that of its build-up in any operating NPP reactor at a much less energy consumption than an energy accompanying their production in a reactor core. To realize the technology proposed requirements to a cyclic electron accelerator have been formulated.

I. THE GNT METHOD

The problem of radioactive waste (RW) would be solved cardinally, if it were a success in finding such feasible and economically expedient method, which would allow, on the one hand, long-lived fission radionuclides (FR) to be transmuted to stable isotopes and actinide radionuclides (AR) to be incinerated or transmuted to isotopes fissionable by thermal neutrons and, on the other hand, additional fissile fuel to be produced to compensate at least in part the energy consumption for RW transmutation.

The approach proposed provides an unique opportunity to do it.

The method of gamma neutron transmutation (GNT) is based on photoneutron reactions (γ, xn) induced by magnetic bremsstrahlung (synchrotron) radiation of an ultrarelativistic electron beam turned periodically in a uniform or spatially periodic magnetic field [1, 2]. The possibility of industrial use of the GNT method, its distinctions and advantages as compared with the known ones stem from the properties of magnetic bremsstrahlung (MB) such as a great integral intensity raising as the third power of electron energy, a high spectral and spatial densities, a specific shape of the spectrum falling exponentially in the high-energy range with the relatively low average energy of γ-quanta.

These properties provide the great spatial and spectral densities of RW transmutation and photoneutron production.

The opportunity to use of MB for transmuting FR follows from the fact that long-lived FR, such as Sr-90 and Cs-137, are neutron-rich to be on the verge of nuclear stability and to have the cross-section of neutron capture near to zero. In the MB gamma field they loss the excess neutrons through the (γ, xn) reactions and transform into a stable state either directly during the above reactions or via the β-decay of short-lived daughter nuclei.

Photoneutrons produced in this process could be used to transmute by the reaction (n, γ) : (a) FR with a noticeable cross-section of neutron capture, such as Tc-99, J-129 and Cs-135; (b) even-even and odd- odd AR, such as Np-237, Pu-238 and Pu-240, to isotopes fissionable by thermal neutrons.

It is desirable that Pu-242 should be also transmuted in the MB gamma field so that the chain of production and accumulation of minor actinides (Am, Cm) were broken.

To reach the maximum intensity and hence the maximum rate of transmutation it is essential that a "critical" energy of the MB spectrum be comparable with the (γ, n) threshold energies $E_{\gamma n}$ of nuclei transmuted. For medium-mass nuclei with A = 90-150 and for transuranium actinides they are equal to $E_{\gamma n}$ = 6 - 12 MeV. Therefore, the electron energies required are E = 50-100 GeV at magnetic fields on the orbit H = 2-6 T. Under such conditions, the spectral density of generated gamma radiation in the energy range of a giant dipole resonance in the cross-section of the (γ, xn) reactions becomes sufficient to ensure a value of the transmuting rate suitable for industrial use.

II. CHARACTERISTICS OF THE METHOD

The spectral density of gamma transmutation in the MB field with allowance in a first approximation for the contributions from the Compton scattering of γ-quanta and the bremsstruhlung of Compton electrons and electron-positron pairs is described by the expressions:

$$N_{tr}(E_\gamma) = N_\Sigma \frac{\Sigma_x \sigma_{\gamma,xn}(E_\gamma)}{\sigma_\gamma(E_\gamma)}\left(1 - e^{-\Sigma_\gamma(E_\gamma) l}\right)\Phi_\gamma(E_\gamma)$$

where

$$\Phi_\gamma(E_\gamma) = \Phi_{\gamma 0}(E_\gamma) + \sum_{i=1}^{3}\Phi_{\gamma i}(E_\gamma)$$

$$\Phi_{\gamma 0}(E_\gamma) = k_0 \eta_\gamma(E_\gamma / E_c)\frac{1}{E_\gamma}$$

N_Σ is the MB integral intensity; $\sigma_\gamma(E_\gamma)$ and $\sigma_{\gamma,xn}(E_\gamma)$ are the total cross-section and the cross-section of the (γ, xn) reactions for γ-quanta of an energy E_γ, respectively; $\Phi_{\gamma 0}(E_\gamma)$ is the spectrum of MB γ-quanta normalized to unity; $\Phi_{\gamma i}(E_\gamma)$ are the spectra of γ-quanta for the above processes; $\eta_\gamma(E_\gamma / E_c)$ is the MB spectral function; $E_c \propto E^2 H$ is the so-called "critical" energy determining the position of the maximum in the MB spectrum; k_0 is the normalization factor; l is the target dimension along the MB beam, $l >> 1/\Sigma_\gamma(E_{\gamma n})$. The spectral density of photoneutrons emitted in the gamma transmuting processes can be determined from the expressions in [2].

The spectral density of gamma transmutation and photoneutrons produced and, hence, their integral intensity are

0-7803-3053-6/96/$5.00 ©1996 IEEE

determined by the (γ, n) reaction threshold, the shape of the giant resonance of the reaction (γ, xn) and the value of the function $\eta_\gamma(E_\gamma / E_c)$ (see [2]).

The rate of gamma transmutation, the spectra of photoneutrons emitted hereby, the integral intensity of neutron production and other parameters of the GNT method were calculated by numerical integration for 40 energy groups in the range $E_{\gamma n} \le E_\gamma < 32$ MeV for a typical FR Sr-90 and for AR such as Pu-240 or Pu-242. In view of the absence of any data on $\sigma_{\gamma,xn}$ for FR and AR the cross-sections for their nearest even-even analogs Sr-88 [3] and U-238 [4, 5] were used in the calculations. Allowance was made for both the contribution from the above secondary processes and the production of photoneutrons in a Be moderator surrounding from above and below a plane target of radionuclides transmuted. In the case of Be the data [6, 7] were used.

The parameters were estimated for MB formed by an electron beam with E = 100 GeV and a current of 0.1 A in a uniform magnetic field H = 2 T (E_C = 13.3 MeV). It is proposed that electron bunchs should turn in a certain cyclic accelerator (storage ring) assembled as a magnetic and accelerating sectioned structure. In each of the sections the MB would be formed by a bending magnet within an angle of 3.6°. The radiation losses of electrons would be about $5 \cdot 10^{-3}$ E to be compensated by afteracceleration within the following accelerating section. Under these conditions the MB integral intensity would be $N_\Sigma = 8.2 \cdot 10^{21}$ q/s within 2π-radian, the MB flux being $F_\Sigma = 3 \cdot 10^{17}$ q/cm^{2}s with a 50 m length of the radiation exit channel.

The spectra of the photoneutrons are shown in Fig. 1 and 2 for the cases of the plane model FR (Sr-90) and AR targets (U-238) and for the same targets surrounded by the Be moderator of neutrons. It is seen that in the last case the spectral yield of photoneutrons grows considerably owing to production in the Be moderator by gamma radiation scattered from the plane targets.

The calculated parameters are presented in Tables 1 and 2. The symbols in the tables denote as follows: N_{tr}^γ and N_n^γ are the intensities of gamma transmutation and photoneutron production, respectively, in the target in the field of incident MB gamma radiation; $N_{tr}^{\gamma'}$ and $N_n^{\gamma'}$ are the same in the field of scattered radiation; N_{tr} and N_n are the total intensities of the above processes with allowance for the contributions from $\Phi_{\gamma i}(E_\gamma)$ and the neutron multiplication in the Be moderator through both (γ, xn) and $(n, 2n)$ reactions; Q_γ is the specific energy consumption per transmutation event. The productivity of the GNT method is defined by the sum of $N_{tr} + N_n$. It was made allowance for the contribution from the $(n, 2n)$ reaction approximately and only for Be.

The results were compared with those determined from the data on amounts of various FR and AR in spent fuel from NPP reactors (see, for example, [8]) and summarized in Table 3. The symbols in Table 3 denote as follows: $T_{1/2}$ is the half-life of the i-th radionuclide; q^i is its yield in g per GW × day of thermal energy output; N_r^i is the rate of build-up of this radionuclide per GW of thermal power; Q_f^i is the specific

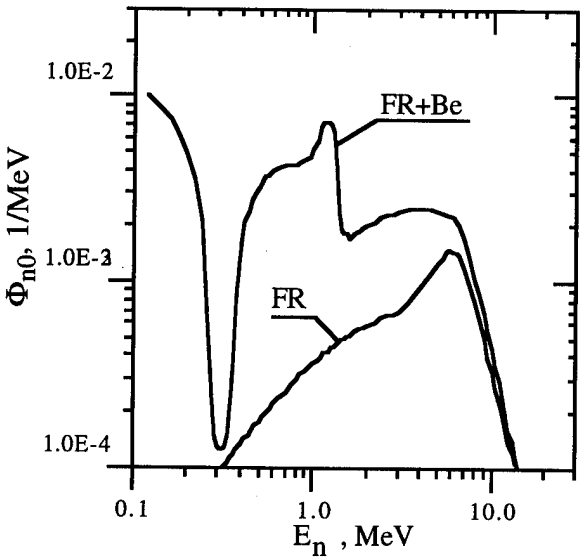


Fig. 1. The photoneutron spectra Φ_{n0} (E_n) from the model FR target (Sr) without a moderator and in Be moderator enveloping it.

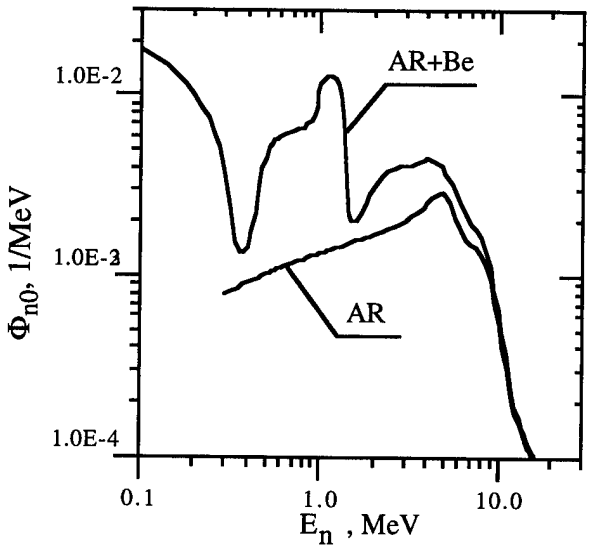


Fig. 2. The photoneutron spectra Φ_{n0} (E_n) from the model AR target (U-238) without a moderator and in Be moderator enveloping it

energy output per nucleus of the i-th radionuclide; $< Q_f^i >_i$ is the same averaged over FR or AR. The total rate of RW build-up amounts to about $1{,}8 \cdot 10^{19}$ nucl./GW ·s.

The comparison of the data presented shows that the GNT method allows the transmuting rate to be made essentially higher than the accumulation rate of any radionuclide in any operating NPP reactor: for RW with a maximum yield, such as Sr - 90 and Cs-137 by a factor of 4-5 and such as Pu - 240 and Pu - 242 by a factor of 10-15, for other RW - more than 30 times.

Table 1. The GNT parameters expected for FR-Be systems.

Parameter	FR	Be	FR + Be
N_{tr}^{γ} , 1/s	1.7· 10^{19}	–	1.7· 10^{19}
N_{n}^{γ} , n/s	2.0· 10^{19}	–	2.0· 10^{19}
$N_{tr}^{\gamma'}$, 1/s	1.8· 10^{18}	–	1.8· 10^{18}
$N_{n}^{\gamma'}$, n/s	2.0· 10^{18}	3.6· 10^{19}	3.8· 10^{19}
N_{tr} , 1/s	1.9· 10^{19}	–	1.9· 10^{19}
N_{n}^{2n} , n/s	to be determ.	4.3· 10^{19}	4.3· 10^{19}
N_{n} , n/s	2.2· 10^{19}	3.6· 10^{19}	5.8· 10^{19}
$N_{tr}+N_{n}$ =12.0· 10^{19} 1/s; Q_{γ} =270 MeV/nucl.			

Table 2. The GNT parameters expected for AR-Be systems.

Parameter	AR	Be	AR + Be
N_{tr}^{γ} , 1/s	1.8· 10^{19}	–	1.8· 10^{19}
N_{n}^{γ} , n/s	3.3· 10^{19}	–	3.3· 10^{19}
$N_{tr}^{\gamma'}$, 1/s	4.2· 10^{18}	–	4.2· 10^{18}
$N_{n}^{\gamma'}$, n/s	7.0· 10^{18}	4.1· 10^{19}	4.8· 10^{19}
N_{tr} , 1/s	2.2· 10^{19}	–	2.2· 10^{19}
N_{n}^{2n} , n/s	to be determ.	5.2· 10^{19}	5.2· 10^{19}
N_{n}^{f} , n/s	to be determ.	–	–
N_{n} , n/s	4.0· 10^{19}	4.1· 10^{19}	8.1· 10^{19}
$N_{tr}+N_{n}$ =15.5· 10^{19} 1/s; Q_{γ} =210 MeV/nucl.			

The energetic value of a transmuting event can be estimated from the expression:

$$Q_{\gamma} = \frac{N_{\Sigma} < E_{\gamma} >}{N_{tr} + N_{n} / \left(1 - k_{eff}\right)}$$

where $< E_{\gamma} >$= 0.3 E_c is the average energy of the MB spectrum and k_{eff} is the multiplication factor of neutrons in a blanket (for that of FR + Be k_{eff} = 0).

Under the above conditions and for a nonmultiplicating matter of the blanket Q_{γ}amounts to about 210 MeV per AR nucleus and 270 MeV per FR nucleus. It can be somewhat minimized at the expense of a more optimal choice of the parameter E^2H for each of radionuclides to be transmuted as well as the more exact allowance for the processes of multiple scattering of γ-quanta and the $(n, 2n)$ reaction in the Be moderator. The contributions from processes $(n, 2n)$ in FR targets and $(n, 2n)$, (n, f) in AR targets should be included also.

As follows from the data of Table 3, the specific energy output averaged over RW with allowance for their cumulative yield amounts to about 5700 MeV per AR nucleus and about 4600 MeV per FR nucleus.

If we assume that the efficiency of energy transformation in designed NPP reactors and storage rings were raised in the future up to k_{NPP} = 0.38 and k_{ACC} = 0.65, respectively, we would obtain a ratio of the specific energy consumption for transmutation to the specific energy output $Q_{\gamma} / k_{NPP} k_{ACC} < Q_f >$ = 0.15 and 0.24 in the case of AR and FR, respectively. This means that 15 - 25 % of electricity generated by an NPP unit should spent to transmute any RW produced by this unit.

For a multiplicating blanket whose composition is similar to the AR - FR percentage in spent fuel it is not difficult to ensure the multiplication factor k_{eff} = 0.8 - 0.95 for thermal neutrons (with the system remaning conservatively subcritical). In consequence the values of Q_{γ} would be reduced considerably (by a factor of 5-20). This means that the above estimate for the NPP unit power spent to transmute RW produced by the unit itself should be considered as an upper limit of its possible values. In this case the productivity of the method $N_{tr}+N_{n}$ would grow much more than the total rate of build-up of FR and AR (see Table 3). Therefore the opportunity would arise to realize the breeding of fissile fuel and thereby to compensate at least in part for the energy consumption for transmutation.

III. CONCLUSION

The data presented demonstrate that the method proposed for gamma neutron transmutation of RW allows: (a) any long-lived radionuclide both AR and FR to be transmuted, with FR transmuted to a stable form; (b) the rate of transmutation to be made much greater than that of RW build-up in any operating NPP reactor; (c) the energetic value of a transmuting event to be made economically attractive; (d) the partial compensation of the energy consumption for transmutation to be obtained at the expense of the breeding of fissionable isotopes in the flux of neutrons produced.

One can expect that this method would be cleanest as compared with the known ones, because the fission is not here a basic nuclear reaction.

In realizing the method, the challenges are: (a) development and creation of a 50-100 GeV cyclic electron accelerator (a storage ring) with an efficient system of multiple afteracceleration to compensate for the beam radiation losses; (b) development and creation of RF systems capable of generating and transfering dozens MW of RF power to the beam with an efficiency of at least 60-65%; (c) development of methods and creation of facilities for the ejection of powerful MB beams from the accelerator vacuum chamber onto RW targets of great activity.

The problems concerning chemical extraction and separation of RW, radiation protection and safety of these processes which are also very important are complicated to solve. Nevertheless, all they must be overcome, if we wish to create a high technology for the closed nuclear fuel cycle ("wasteless nuclear technology") and thereby to provide the safe and ecologically clean future.

Table 3. The characteristics of the RW build-up process determined for the NPP reactors of WWER-440, WWER-1000 and RBMK

Fission radionuclides (FR)

Parameter	Sr-90	Zr-93	Tc-99	Pd-107	I-129	Cs-135	Cs-137
$T_{1/2}$, years	29.0	$9.5 \cdot 10^5$	$2.1 \cdot 10^5$	$6.5 \cdot 10^6$	$1.6 \cdot 10^7$	$2.3 \cdot 10^7$	30.1
Transmut. type	γ	γ	n	γ	n	n	γ
q^i, g/GW·day	17.3	20.8*	26.6*	8.35*	5.29	40.1	37.4
N_r^i, 10^{18} nucl./GW·s	1.33	1.56	1.86	0.544	0.286	2.07	1.90
Q_f^i, Mev/nucl.	4700	4000	3350	11500	21900	3000	3300

Total rate of FR build-up per GW thermal power: $\sum_{i=1}^{7} N_r^i = 9.55 \cdot 10^{18}$ nucl./GW·s

Energy output per FR nucleus averaged over FR: $< Q_f^i >_i^{FR} = 4580$ MeV/nucl.

Actinide radionuclides (AR)

Parameter	Np-237	Pu-238	Pu-239	Pu-240	Pu-241	Pu-242	Am-241
$T_{1/2}$, years	$2.6 \cdot 10^6$	87.8	24380	6537	14.54	$3.9 \cdot 10^5$	433
Transmut. type	n	n	n	$n(\gamma)$	n	$\gamma(n)$	$\gamma(n)$
q^i, g/GW·day	9.31	2.54	160.6	73.3	35.8	14.8	3.20
N_r^i, 10^{18} nucl./GW·s	0.274	0.074	4.69	2.13	1.04	0.426	0.092
Q_f^i, Mev/nucl.	22800	84400	1350	2950	6050	14700	67800

Total rate of AR build-up per GW thermal power: $\sum_{i=1}^{8} N_r^i = 8.75 \cdot 10^{18}$ nucl./GW·s

Energy output per AR nucleus averaged over AR: $< Q_f^i >_i^{AR} = 5720$ MeV/nucl.

* The interpolation on Sr-90 and Cs-137.

REFERENCES

[1] I.P. Eremeev. JETP Lett., Vol. 27, No 1, p. 10, 1978.

[2] I.P. Eremeev. Paper to be presented to this Conference.

[3] A. Lepretre , H. Beil, R. Bergere et.al. Nucl. Phys., Vol. A 175, p. 609, 1971.

[4] J.T. Caldwell, E.J. Dowdy, B.L. Berman, R. A.Alvarez, P. Meyer. Phys. Rev., Vol. C 21, p. 1215, 1980.

[5] A. Veyssiere, H. Beil, R. Bergere, P. Carlos, A.Lepretre, K.Kernbach. Nucl. Phys., Vol. A 199, p. 45, 1973.

[6] B.L. Berman, R.L. Van Hemert, C.D. Bowman. Phys. Rev., Vol. 163, p. 958, 1967.

[7] R.J. Hughes et al. Proc. Int. Conf. Photonuclear Reactions and Applications, p. 151. Asilomar, 1973.

[8] S.N. Begichev, A.A. Borovoi, E.V. Burlakov et. al. Preprint IAE- 5268/3. Moscow, 1990.

A High-Average-Power FEL for Industrial Applications†

H. F. Dylla, S. Benson, J. Bisognano, C. L. Bohn, L. Cardman, D. Engwall, J. Fugitt, K. Jordan, D. Kehne, Z. Li, H. Liu, L. Merminga, G. R. Neil, D. Neuffer, M. Shinn, C. Sinclair, M. Wiseman, CEBAF, L. J. Brillson, Xerox, D. P. Henkel, AS&M, Inc., H. Helvajian, Aerospace Corp., M. J. Kelley, DuPont

Abstract

CEBAF has developed a comprehensive conceptual design of an industrial user facility based on a kilowatt UV (150–1000 nm) and IR (2–25 micron) FEL driven by a recirculating, energy-recovering 200 MeV superconducting radio-frequency (SRF) accelerator. FEL users—CEBAF's partners in the Laser Processing Consortium, including AT&T, DuPont, IBM, Northrop-Grumman, 3M, and Xerox—plan to develop applications such as polymer surface processing, metals and ceramics micromachining, and metal surface processing, with the overall effort leading to later scale-up to industrial systems at 50–100 kW. Representative applications are described. The proposed high-average-power FEL overcomes limitations of conventional laser sources in available power, cost-effectiveness, tunability and pulse structure.

Introduction

The Laser Processing Consortium—a collaboration involving nine U.S. corporations and companies, seven research universities, and a national accelerator laboratory—intends to develop a profitable, production-scale capability to use laser light in manufacturing. We propose to develop a cost-effective, high-average-power free-electron laser (FEL) that would deliver light at wavelengths fully adjustable across the infrared (IR), ultraviolet (UV), and deep ultraviolet (DUV) portions of the spectrum [1]. Such an FEL would address markets totaling hundreds of billions of dollars by fundamentally improving industry's abilities to: modify polymer film, fiber, and composite surfaces; process metal surfaces and electronic materials; micromachine metals, ceramics, semiconductors, and polymers; and non-destructively evaluate industrial processes.

In principle, energy in the form of laser light offers distinct advantages for manufacturing. Laser light's coherence and high brightness allow delivery of high power densities onto material substrates. Its monochromaticity allows precise matching to narrow-band absorption. In short pulses, it can modify surfaces without the counterproductive side effect of bulk heating. Moreover, environmentally benign laser processing can replace wet-chemistry processing methods that produce enormous amounts of dilute aqueous waste.

Conventional lasers suffer limitations in cost, power, and choice of wavelength. Therefore industry needs a fundamental improvement in laser technology: a laser that can affordably deliver precisely controlled light at average power levels that are orders of magnitude higher than now available, and at wavelengths fully selectable across the IR, the UV, and especially the DUV. An FEL driven with a superconducting radio-frequency (SRF) electron accelerator can meet these cost and performance requirements.

A production-scale manufacturing FEL's driver accelerator is its key subsystem and technological challenge especially since industrial applications require continuous-wave (cw) light.

With the maturity of SRF technology at laboratories such as CEBAF, CERN, DESY, and KEK, it is clearly demonstrated that high average power, cw electron accelerators can be built and operated. A comparatively small, CEBAF-type SRF accelerator would be ideally suited to drive a cost-effective FEL for industrial applications.

Therefore we propose a two-phase program of developing SRF-based FELs for industry. In Phase 1, we plan to build and commission at CEBAF a demonstration-and-development user facility centered on a kilowatt-scale FEL which will operate across the IR, UV, and DUV for industrial application. The Phase 1 FEL is hereafter called the UV Demo, since its UV/DUV capability is the major focus of commercial interest. In Phase 2, we will scale up from this UV Demo and build a 50 to 100 kW version, a prototype for cost-effective use at industrial sites.

Industrial application of high-power laser light

Most prospective light-based manufacturing will involve modifying materials' surfaces and will take place in the UV. The appeal of surface modification as a final, high-value-adding step has been recognized for several decades. Numerous desired product enhancements stem from improvements in the performance of surfaces, including interfaces subsequently made from them. Chemical treatments, coatings, and platings are widely applied, mature technologies. Familiar examples are to be found in anti-stain carpets, improved corrosion resistance in auto bodies, modern food packaging, and composite materials. In fact, a major share of U.S. industrial output depends on surface or interface characteristics in the final product or on surface processing as a means of manufacture. These industries now depend on wet-chemical (e.g., solvent coating, plating, etching) or mechanical (e.g., grinding, burnishing) processes, but light-based processing is now also a prospect. Surface modification by light can add value to existing products, serve as the value basis for new products, or be incorporated into special interfaces of packaging materials or structural composites. Such modified surfaces can be formed by physical or chemical rearrangements caused by intense, carefully tailored energy absorption in the transformed region, especially energy in the form of UV light.

Existing UV sources—including lamps that provide incoherent light, harmonically converted Nd-doped solid state lasers, and excimer lasers—suffer severe limitations for such work. None offers high enough average power, a cw duty factor, or low enough cost per delivered kilojoule for general production purposes, and the light output from the coherent sources is not available at, or tunable to, wavelengths overlapping specific absorption bands of interest.

Nonetheless, a few conventional lasers—UV excimer lasers in particular—have seemed to offer tantalizing promise. Since excimers became available about ten years ago, many researchers have used them for surface processing. Absorption coefficients in the 10^4–10^5 cm^{-1} range result in

0-7803-3053-6/96/$5.00 ©1996 IEEE

essentially all the energy being deposited in the outermost few hundred nanometers. Consequently, novel materials or material states can be created on the surface while leaving the desirable properties of the bulk intact. Further, with a proper choice of conditions, laser-induced ablation can remove material, allowing micromachining to the dimensional scale of the light wavelength itself.

Commercially viable applications for conventional-laser materials processing, have been limited primarily to cutting and welding tasks. With increased reliability in pulsed lasers, especially pulsed excimers, other applications have been developed including lithography, pulsed-laser deposition/etching, and micrometer-scale machining/surface texturing.

Certain specialized applications with excimer lasers have been notably cost-effective: those requiring limited irradiation doses at one of four fixed excimer laser wavelengths, and those requiring relatively few intense pulses for high-fluence ablation. The low-duty cycle of these lasers limits their applicability to large-area processing. The pulse intensity unnecessarily affects a large volume of material by removing or altering bulk material, thereby damaging the surrounding area via thermal and plasma effects and wasting incident laser energy. To mitigate these effects, the laser fluence is commonly reduced, which is tantamount to significantly increasing the processing time. Given the low (sub-kilohertz) repetition rate of high-power conventional lasers, the additional processing time makes the application too costly. High-fluence laser processing does have applications in advanced-materials development, but more applications become possible if each processing step can be made to affect less material.

So despite some limited successes, despite industrial potential markedly superior to that of other light sources, despite the intrinsic utility of laser light, and despite substantial R&D investment by industry, conventional laser technology is not destined to improve U.S. manufacturing capability in any fundamental way. Commercially available excimer lasers present perhaps the best illustration: they remain limited to tenths of kilowatts, tens of cents per kilojoule, and a few isolated specific wavelengths, while large-scale exploitation of UV surface processing will require sources providing at least a few tens of kilowatts, light that costs a few tenths of a cent per kilojoule, and full wavelength tunability.

UV Demo FEL

The UV Demo FEL briefly described in this section will provide light that will allow users to demonstrate and develop laser applications like those listed in Table 1.

Table 1
Representative Industrial Applications of FELs

Polymer Surface Processing	Electronic Materials Processing	Metal Surface Processing
Surface texturing	Flat-panel displays	Laser glazing and annealing
Surface amorphization	Large-area photovoltaics	Metglass coatings

Requirements for the UV Demo appear in Table 2. Figure 1 contrasts UV Demo performance in power and wavelength with that of conventional lasers. Delivered photons are expected to cost in the $1/kJ range. For the much higher-power Phase 2 device, the cost is expected to drop to below $0.01/kJ.

Table 2
Output Requirements for the UV Demo

	User Requirement	Design Goal
Wavelength range	190–300 nm 3000–20000 nm	160–1000 nm 2500–25000 nm
Power	1 kW	1.7 kW
Optical beam quality	<2× diffraction-limit	1.2× diffraction-limit
Bandwidth	4 × Fourier limit	Fourier-limited

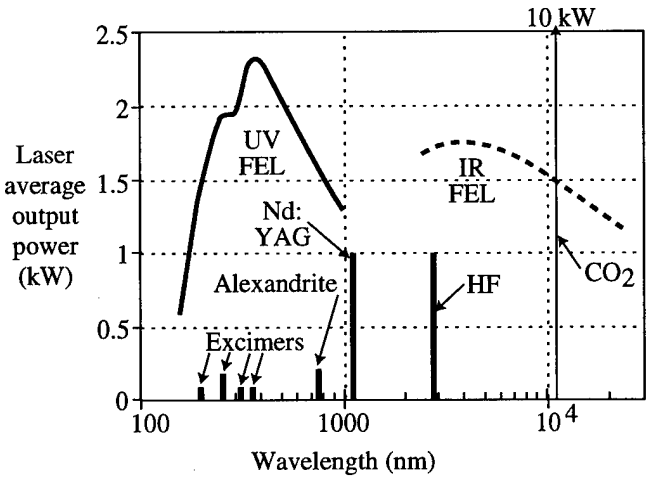


Figure 1. Power vs. wavelength for the UV Demo FEL

In addition to the characteristics shown in Table 2, the FEL will provide a picosecond pulse (at 37 MHz) ideally suited for rapid thermal annealing or ablation of near-surface regions. This pulse length matches the characteristic times of surface vibrations and surface molecular rearrangements. It is much shorter than the nanosecond time scales of vaporization or thermalization. These undesirable effects therefore do not appear, and surface processing with the UV Demo is highly efficient.

A schematic of the UV Demo appears in Figure 2. The injector consists of a Nd:YLF-laser-driven 500 kV DC photoemission electron source, a copper cavity to bunch the beam, and a two-SRF-cavity cryomodule [2]. It feeds a 10 MeV beam into the driver linac consisting of three CEBAF-type cryomodules, each containing four pairs of integrally linked 1.5 GHz SRF accelerating cavities [3]. The injected beam will:

- Accelerate through the driver linac, which will provide a nominal energy gain of 96 MV.
- Recirculate back to the injection point by transiting clockwise through the low-energy recirculator line for a second acceleration pass.
- Enter an FEL wiggler at up to 200 MeV to yield about 0.5% of the beam power in the form of laser light. Approximately 13% of the light will be outcoupled from the

optical cavity for applications in a dedicated user laboratory.

- Decelerate through two energy-recovery passes in the linac and deposit its remaining energy in a cooled, shielded copper beam dump at about 10 MeV. Energy freed during deceleration appears as rf-field energy at the operating frequency of the cavities and is used to accelerate other electrons. Thus, energy recovery greatly enhances (by more than an order of magnitude) the operating efficiency of the device.

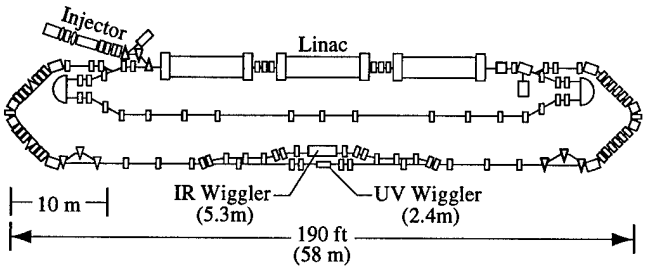


Figure 2. Layout of the UV demo FEL

We are trying to achieve cost-effective operation during Phase 1 in preparation for the Phase 2 scale-up to a production-scale device. The existing CEBAF accelerator combines SRF technology with electron-beam recirculation, and thus there is a base of experience from which to draw. Energy recovery adds efficiency and eliminates the need for large-scale radiation-management measures. A 200 MeV beam at 5 mA without energy recovery would require a megawatt-scale beam dump, but a beam decelerated to approximately its original injection energy requires far less: for the UV Demo, a 50 kW beam dump. Recirculation lowers capital cost by minimizing the number of superconducting components, lowers operating cost by reducing the cryogenic load, and substantially reduces system footprint size.

Table 3 lists some of the key machine specifications for both the driver accelerator and the UV laser.

Table 3
UV Demo FEL Specifications

Driver Accelerator		Wiggler and Optical Cavity	
Electron kinetic energy	100–200 MeV	Wiggler length	2.38 m
Pulse repetition frequency	2.3–37.4 MHz	Wiggler wavelength	3.3 cm
Charge/bunch	135 pC	Maximum field	0.75 T
Bunch length	0.2 psec	Wiggler gap	11.5 mm
Peak current	270 A	Optical cavity length	64.09 m
Average current	5 mA		

Phase 2: Technology Scale-Up

Successful demonstration and development efforts at the kilowatt scale in the Phase 1 industrial user facility will focus and intensify needs for systems operating at much higher power levels, and will also provide hard data and practical experience for meeting these needs. In Phase 2 we will build a prototype of a 50 to 100 kW industrial UV FEL system suitable for cost-effective production at individual industrial sites, and at regional processing centers serving multiple manufacturers.

The prototype must be cost-effective, robust, reliable, and easy to operate. For an operational commercial system, the capital cost and the operating cost are key considerations which lead to an overall figure of merit, the cost per delivered kilojoule. A key goal is to produce UV light in the 0.2 cents per kilojoule range, two orders of magnitude cheaper than that obtained with conventional lasers.

Although detailed analysis of Phase 2 can only be prepared based on actual Phase 1 data and experience, preliminary analysis has been carried out. It is clear that developing the capability for higher powers will require attention to:

- Injector performance. The injector is a challenge because of the desire for high average current with a long cathode life, and because of the high brightness specifications on the required electron beam. Average current more than an order of magnitude higher than that for Phase 1 will place increased demands on the electron source, so a critical goal during Phase 1 will be to develop a high-intensity, high-quality source.
- Optical cavity performance. The optical cavity is a challenge because of the high intracavity intensity exacerbated by relatively high mirror-coating absorptions at short wavelengths which can lead to deleterious mirror deformation.
- Operating frequency, the choice of which requires tradeoff between SRF cavity design, transport characteristics of the lattice design, RF source efficiency, and cryogenic system performance.
- Lattice design, including optimizing the number of recirculation passes.

Details of our cost analysis for high-power FELs are given in a companion paper [4].

Summary

The Laser Processing Consortium has identified industrial applications of UV laser light that involve surface modification of polymers, metals, and electronic materials. Substantial commercial development of these applications that would incorporate the benefits of light-based manufacturing is impeded by the present lack of cost-effective, high-average power UV sources.

The consortium has proposed a two-phase plan for developing high-average-power UV sources that meet the industry cost goals based on SRF-linac-driven free-electron lasers.

References

[1] Laser Processing Consortium, Proposal: "High-Power Ultraviolet and Infrared Free Electron Laser for Industrial Processing" (1994).

[2] H. Liu, S. Benson, J. Bisognano, P. Liger, G. Neil, D. V. Neuffer, C. Sinclair, and B. Yunn, Nucl. Instr. Meth., A339 (1994) 415.

[3] D. V. Neuffer, S. Benson, J. Bisognano, D. Douglas, et al., these Proceedings (1995).

[4] G. R. Neil, these Proceedings (1995).

†Supported by U.S. DOE Contract #DE-AC05-84ER40150 and the Commonwealth of Virginia.

X-RAY RADIATION BY RELATIVISTIC ELECTRONS IN CONDENSED MEDIA ON BASE OF MSU RACE-TRACK MICROTRON

V.K.Grishin, A.S.Chepurnov, K.A.Gudkov, B.S.Ishkhanov, S.A.Kosterin, E.V.Lasutin
Institute of Nuclear Physics, Moscow State University, 119899 Moscow, Russia
S.V.Blazhevich, N.N.Nasonov
Kharkov Institute of Physics and Technology, 310108 Kharkov, Ukraine

I. PROGRAM OF STUDY

The development of effective sources of monochromatic sharp-directed X-ray radiation is stimulated by important applications in medicine, Roentgen lithography, crystallography and mikroelement analysis. Possible methods of generating the X-ray radiation are actively studied now. These methods are alternative to the traditional method based on synchrotron radiation. Spectrum and angle features of radiation of fast electrons channelling in crystals, resonance radiation of relativistic electrons in dielectric layerous structures and so on are under insistent theoretical and experimental attention [1]. The essential advantage of mechanisms mentioned above is the possibility to use a low energy beams of electrons (order of 1 - 10 MeV) and to produce also a radiation with the higher spectrum density.

A great number of processes of interaction of fast charged particles and photons with matter leads to new physical effects in the radiation. The effects are for example diffractive radiation of oscillator [2]. Another examples of these effects are the interference of parametric and the Cherenkov radiations [3] and the interference of parametric radiation and coherent bremsstrahlung [4]. Due to this the study of the processes of fast electrons radiation is of interest for fundamental physics and for various applied research.

There is information about the program and the first experimental results of processes of X-ray radiation at the electron accelerator of NPI MSU in this paper.

The electron accelerator of NPI MSU is the first stage of the Race-Track Microtrone with the electron energy up to 180 MeV [5]. The first stage produces the continuous electron beam of 6.6 MeV with maximum current up to 100 mkA. The beam has a little energy spread (about 10^{-3}) and a little transverse emittance (to 5 mm*mrad).

The high quality beam allows to perform different studies of the X-ray radiation of charged particles in amorphous and crystal structures. It is very interesting to investigate the process of radiation which occurs due to scattering of the Coulomb field of fast electrons off atomic shells in substance. This radiation is called polarisation bremsstrahlung (PB). It is mainly studied in rarefied substances where the radiation has a noticeable effect (in the laser discharge in gases ,for example). A number of effects for instance the effect of the suppression of radiation can be observed in dense substances in the low frequency part of the spectrum (in amorphous media) [6]. Another forwarding circumstance is the interference of PB with ordinary bremsstrahlung. The influence of this circumstance becomes conspicuous at not too little observation angles. Besides the dependence of the radiation intensity on the sign of the particle charge is revealed.

Other group of questions is associated with the study of the X-ray radiation in crystall media. Particularly scattering of the Coulomb field of fast particles by the crystall planes leads to the appearance of the parametric radiation (PR). Like the channelled radiation PR is now considered as one of the most perspective effects for creating a tuneable source of the X-ray radiation [7]. The interference of PR with coherent bremsstrahlung and the interference of PR and transition radiation which appears on the crystal surface are the forwarding effects leading to interesting physical law-governed natures. Notice that PR has a high polarisation degree. But the direction of the photon polarisation is an oscillating function of the observation angle. So such and mentioned above effects can be studied only with the high quality beams which are proper for the new generation accelerators with continuous beam.

II. EXPERIMENT AND DISCUSSION

As the first step to accomplish the program presented the study of the features of X-ray radiation of fast electrons in amorphous media was chosen. Notice that the amorphous substances are of certain interest from the point of view of creating materials with new parameters of its structure.

Experimental setup was traditional for such experiments [8]. It included a chamber with windows where the scattering target was placed, input and output beam tubes, the beam focusing system and the beam quality control system, Si(Li) cooling detector, the Faraday cup, monitor, combined protection system and a number of additional equipment. The chamber and the beam control system allowed to measure the photons radiated at the angles 0, 45, 90, 135 degrees respectively to the beam. In the experiments with the target prepared from an amorphous material the observed radiation is the combination of the polarisation bremsstrahlung and the ordinary bremsstrahlung. PB is practically isotropic in difference from bremsstrahlung. As an analytical estimation predicted PB can be 2 or 3 times more than a simple bremsstrahlung at the 45 degrees angle. The last circumstance results in a favourable condition to observe PB.

The first stage of the experiments just finished was devoted to the measurements with a dense foil from amorphous carbon (the foil density 2.4; the foil amorphous structure is confirmed by special measurements). The foil of 10 by 10 square mm, thickness 100 mkm was placed at the 45

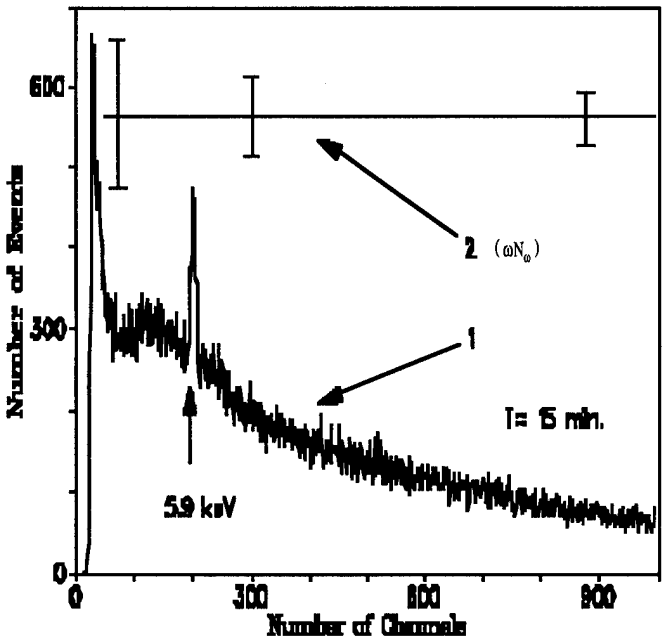
0-7803-3053-6/96/$5.00 ©1996 IEEE

degrees angle respectively to the electron beam and perpendicularly to the observation line. Allocating and turning the target were achieved by means of a special holder. To reduce the common radiative background, the target heating and to eliminate the nonlinear errors in the detecting system the measurements were carried out with the beam current of several nA. Even at such a little current due to the continuous character of the beam the information rate was about 1 kHz. This allowed to reduce a real exposition time to 2 h, including a background measurement time (notice that on the pulse accelerators with analogous average current the information rate does not exceed 10 Hz).

High quality of the beam (low emittance) allowed also to decrease a common background level for turning and focusing the particles to the target were brought about without any additional collimation of the beam.

The background created by the beam directly into the chamber was measured in the second position of the target. In this case it scattered the beam but the X-ray radiation did not income to the detector. By the way the background level appeared to be small enough.

Let us state the direct results of the first study. They are unexpected and lessonful. The main results are presented on the Fig.



Curve 1 is the intensity of summary radiation at different energies of the X-ray quanta. The peak with energy 5.9 keV corresponds to the K-line of iron. Its traces are on the surface of the carbon foil. On curve 2 there is a value ωN_ω (in arbitrary units) which is equal to the product of frequency of photons and the radiation spectrum density. This curve is obtained by subtracting the background and correcting the results taking into account the detector spectrum sensitivity ε dependence on the photon energy (in relative units the ε value changes according to special measurements from 0.57 at E_ω=13.92 keV to 0.38 at E_ω=3.3 keV) and the absorption of the X-ray radiation in the target. The confidence intervals take into attention also the discrepancies produced while correction of the results.

The ωN_ω value of the radiation measured is constant with good precision. This shows that the radiation has exclusively bremsstrahlung character, and PB is suppressed completely. The theoretical predictions point out the effect of the suppression in the energy range below 5 keV (the density effect [6]) and fast decrease of the ωN_ω value in the energy range beyond 10 keV. However these predictions are in essence made for very dense gas consisting of separated atoms. Really in carbon in condensed state four electrons of atom are mutual. This results in comparable values of the effective screening radius and the interatomic distance. The latter leads to an amazing effect: the PB suppression in the whole frequency range.

III. CONCLUSION

Thus the first experiment revealed some interesting details and questions. What is an amorphous media (from point of view of the PB experiment)? What is a screening radius ? Obviously we can receive the different answers for the media consisting of the light and heavy atoms. In this case the observations of PB may discover some new features. But this conclusions will be made after the additional processing of both experimental and theoretical studies.

IV. REFERENCES

[1] V.A.Bazylev, N.K.Zhevago. Izluchenie byctryx chastits v veshchestve i vo vneshnikh poliakh, -M., Nauka, (1987)

[2] V.G.Baryshevsky, I.Ya.Dubovskaya. J. Phys. C. Solidi State Phys. **16** (1983) 3665.

[3] N.N.Nasonov, A.G.Safronov. Physica Status Solidi B, **168** (1991) 617.

[4] V.L.Kleiner, N.N.Nasonov, A.G.Safronov. Physica Ststus Solidi B, **181** (1994) 223.

[5] S.A.Alimov, A.S.Chepurnov, O.V.Chubarov et al. Moscow CW Race-Track Microtron, Preprint INP MSU-93, M., (1993).

[6] N.N.Nasonov, A.G.Safonov. ZhTF, **62** (1992) 1.

[7] A.Shchagin, V.Pristupa, N.Khizhnyak. Phys. Lett. A, **148** (1990) 485.

[8] W.Lotz, H.Genz, P.Hoffmann et al. Nucl. Instr. and Meth. in Phys. Res. **B48** (1990) 256.

APPLICATIONS OF MEV PROTON AND DEUTERON LINEAR ACCELERATORS

George H. Gillespie
G. H. Gillespie Associates, Inc., P. O. Box 2961, Del Mar, California 92014, U.S.A.
and
Gerald E. McMichael
Argonne National Laboratory, 9700 South Cass Avenue, Argonne, Illinois, 60439 U.S.A.

ABSTRACT

There are a number of applications, either proposed, currently under development or already reduced to practice, that utilize proton or deuteron beams in the 1-10 MeV energy regime. These applications have been reviewed and the accelerator requirements summarized. In terms of the beam time-structure, nearly all of the applications fall into three broad categories. (1) Beams that utilize nanosecond pulses at low duty factors (<0.5%) are required for a variety of material composition interrogation concepts using neutron time-of-flight techniques. (2) Pulsed beams, in the microsecond regime, are also used for material characterization utilizing (non-time-of-flight) characteristic nuclear signatures, where a low duty factor is used to suppress backgrounds. (3) High duty factor and continuous beams are needed for several applications, including neutron radiography (NR) and boron neutron capture therapy (BNCT), in which a high total current is required, or for which the time structure of the beam is unimportant. Linear accelerators of various types can meet most of the requirements for each category, but the high average power machines of the last category of applications require further development. The primary results of this review are presented, and an assessment of the current development status of radiofrequency accelerators to meet the high-duty-factor requirements is given.

I. CLASSIFICATION OF APPLICATIONS

To put different applications into the perspective of potential accelerator technologies, it is useful to classify the applications in terms of their accelerator requirements. There are a number of important accelerator parameters that need to be considered in developing a classification scheme. Previous authors have reviewed the requirements for particular application areas [1-3], or for a specific accelerator technology [4,5]. Beam energy and beam current play a major role in defining appropriate accelerators for a given application. The required time structure of the beam can be equally important. In terms of the beam time structure, nearly all of the applications fall into the three broad categories defined in the abstract. Figure 1 summarizes the accelerator requirements, classified using these key parameters, for the applications reviewed for this work. Each of the applications is described briefly below.

In addition to the beam current, energy and time structure, other accelerator requirements must be considered for most practical applications. The site requirements of an application, for example, location in a hospital or at a remote test site, or a requirement for a mobile system, can impact accelerator specifications. It is also useful to distinguish applications according to whether or not they require the production of neutrons. Applications for which the accelerator beam is used to provide a neutron source have certain common elements: targets that use (p,n) or (d,n) reactions, moderators to customize the neutron spectrum, frequently with collimators to localize the neutron flux, and detectors or imaging systems for measuring neutron or associated particle, yields or spectra.

II. NANOSECOND PULSE APPLICATIONS

Beams that have nanosecond pulses at low duty factors are required for a variety of material interrogation concepts using neutron time-of-flight (TOF) and/or coincidence techniques. Prominent among the applications of this category are those involved with the detection of contraband, primarily explosives or narcotics [6]. Two primary approaches are being investigated: pulsed fast neutron analysis (PFNA) and fast neutron spectroscopy (FNS).

To detect and measure the relative concentrations of oxygen, carbon and nitrogen, FNS utilizes a broad white spectrum of neutrons in the 0.75-4 MeV region [7]. TOF measurements are used to determine the neutron attenuation, as a function of neutron energy, by comparing the target-in to target-out spectra. PFNA utilizes the delayed coincident measurement of the gammas produced by the inelastic scattering of fast neutrons [8]. A monoenergetic pulsed beam of neutrons is used and the spatial distribution of oxygen, carbon, nitrogen, and chlorine can be measured. PFNA can be useful in characterizing the condition of nuclear weapons [9] and these techniques may also have applicability to non-proliferation and other inspection needs.

Compact tandem Van de Graaffs, Pelletrons, and other electrostatic linacs provide sufficient beam energy, and can be pulsed to produce the required beam time structure. However, the high current required for most FNS applications is pushing the state of the art for electrostatic machines.

III. MICROSECOND PULSE APPLICATIONS

Pulsed beams in the microsecond regime are also used for material interrogation utilizing (non-time-of-flight) characteristic signatures. A low duty factor is used to suppress backgrounds.

0-7803-3053-6/96/$5.00 ©1996 IEEE

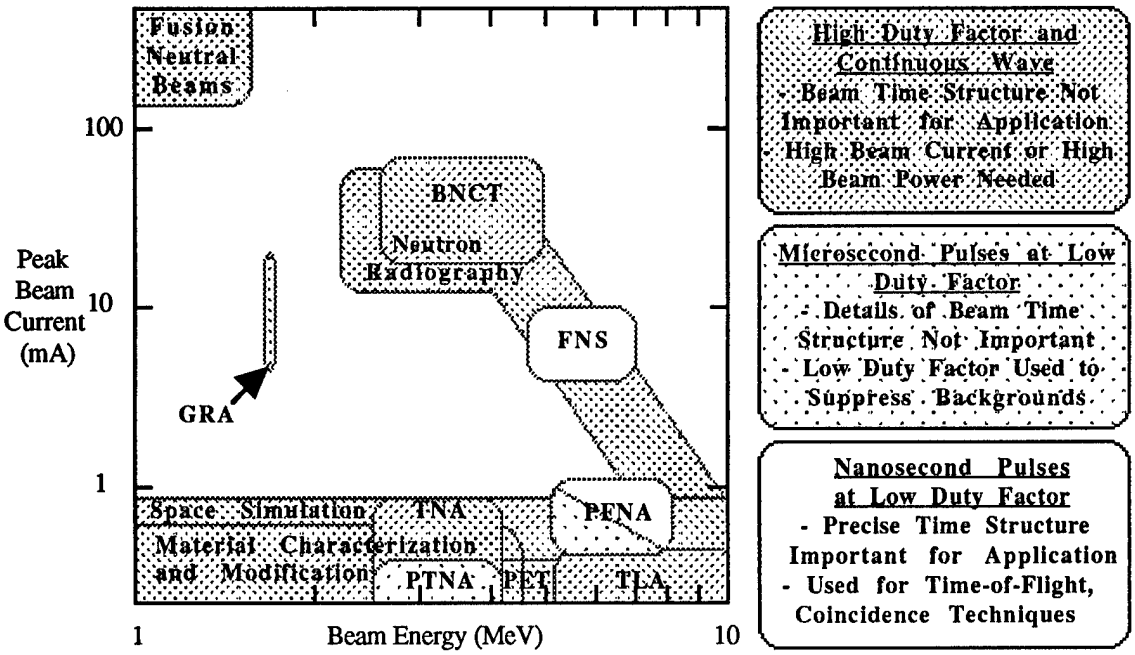


Figure 1. Scheme for classification of applications, using 1-10 MeV proton and deuteron beams, according to the accelerator requirements. Applications plotted in the central region of the vertical axis, the high current regime (1 mA ≤ I ≤ 100 mA), use a logarithmic scale for peak beam current. The moderate (0 < I < 1 mA) and very high (100 mA < I < ∞) current regimes are approximate, and the plots are only intended to suggest a rough measure of the relative scale.

Pulsed thermal neutron activation (PTNA), as well as a variation of PFNA, use a pulse of fast neutrons injected into the sample to be interrogated. In PTNA, the neutrons are allowed to thermalize, and the delayed gamma rays from the thermal (n,γ) reactions are examined to determine the composition of the sample. The pulse length, typically 10-50 μsec, is not critical, but the time between pulses needs to be of the order of the neutron capture time, typically a few 100 μsec. The pulsing technique suppresses the background from prompt gammas produced by inelastic collisions of the fast neutrons during the pulse on-time. The prompt gammas can be used in a non-TOF variant of the PFNA technique (see Section III). By selecting different time gates for the gamma detectors, PTNA and PFNA may be combined [6]. In addition to detecting contraband in luggage [8,10], PTNA can be used for measuring the pollutant constituents of bulk coal and determining the composition of other solids [11].

Electrostatic linacs can meet the needs of these applications, as can radiofrequency quadrupole (RFQ) linacs. Pulsed, high current RFQs have also found a number of specialized, one-of-a-kind applications [3,4] not shown in Fig. 1.

IV. HIGH DUTY FACTOR APPLICATIONS

High duty factor, including continuous, beams are important for several applications. Neutral beams for heating fusion plasmas require very high currents. The International Thermonuclear Experimental Reactor (ITER), if the designers decide to use neutral beam heating, would need several tens of amperes (CW) of 1-1.5 MeV deuterons. This is a formidable amount of power and will likely require an approach using multiple beams in an electrostatic quadrupole linac.

There are a number of applications that utilize beams of less than a milliampere. Materials characterization and modification encompass several applications in this energy regime, as well as at lower energies. Ion implantation [12], surface hardening [13], lifetime killing of minority charge carriers [2], and the alteration of surface chemical properties [2], are representative examples of materials modification applications. In this energy region, and higher, the production of radioisotopes [14], for positron emission tomography (PET), and thin layer activation (TLA), for corrosion and wear analysis [15], are finding increased application. Simulation of the space radiation environment [16] spans the energy regime considered. Electrostatic or RFQ linacs can provide most required beams.

Among the high-duty-factor applications illustrated in Figure 1, three require relatively high beam current: gamma resonance absorption (GRA) for explosives detection [10], neutron radiography (NR) for a variety of uses [17], and boron neutron capture therapy (BNCT) for cancer treatment [18]. A high current is required for these applications in order to meet practical, operational needs associated with the total doses desired (high through-put or short exposure times). The time structure of the beam is not important, and the duty factor may be selected to optimize the performance of the system.

BNCT offers a promising hope in the treatment of certain cancers, and initial clinical trials at reactor facilities, especially in Japan, are encouraging. While the BNCT prospects are

good, a large investment in accelerator technologies to optimize the delivery of the neutrons may be premature. In contrast, the utility of NR is established for several applications. Reactor-based facilities are used for examining aircraft parts. Ordinance inspection is of current interest, but requires remote siting and has hazards for reactor-based approaches. Transportable, low-fluence NR systems, based on radioactive sources, D-T tubes and cyclotrons, have been developed. Other applications are waiting for better mobile systems.

Electrostatic linacs may be able to meet the requirements of BNCT and NR, but the high currents required are a challenge. RFQs probably offer the best approach for both BNCT and NR. One RFQ-based system of modest duty factor (1 mA average current) has been built to further explore practical NR uses [5]. However, development work will be required to make economic, portable RFQs, with the 10-60 mA continuous beams needed for many applications. The target, moderator and collimator assemblies for these high-duty-factor systems will also require development [19]. The Argonne Continuous Wave Linac (ACWL) can provide a 2 MeV continuous beam, of over 20 mA of deuterons [20]. With modifications, 3.5 MeV protons at the same current and duty factor could be produced. The ACWL offers a unique facility to develop and test technology for both NR and BNCT.

V. SUMMARY

Applications that utilize proton or deuteron beams in the 1-10 MeV energy regime have been reviewed and the accelerator requirements summarized. The beam energy, peak beam current requirements, and the beam time structure, all impact the appropriate selection of accelerator technologies. Linear accelerators can meet most of the requirements. However, the high current (1 mA $\leq$ I $\leq$ 100 mA) and high-duty-factor applications challenge the state-of-the-art. Both neutron radiography and boron neutron capture therapy and fall into this category. RFQs offer the potential to meet the requirements, although developments are needed in several areas. The ACWL offers a unique test bed for developing a number of key technologies needed for NR and BNCT.

ACKNOWLEDGEMENTS

This data was assembled as part of work completed under Argonne National Laboratory contract number 942662401 and DOE contract number W-31-109-Eng-38, and was refined for an introductory course on accelerator applications given at the U. S. Particle Accelerator School held in January, 1995.

REFERENCES

[1] T. Gozani, "Advances in accelerator based explosive detection systems," Nucl. Instr. Meth. Phys. Res. B 79, 601-604 (1993).

[2] J. Asher, "MeV ion processing applications for industry," Nucl. Instr. Meth. Phys. Res. B 89, 315-321 (1994).

[3] R. W. Hamm, "Commercial Applications of Linacs," Proceedings of the 1990 Linear Accelerator Conference, Albuquerque, LA-12004-C, 558-562 (1990).

[4] A. Schempp, "The Application of RFQs," 1992 Linear Accelerator Conference Proceedings, Ottawa, AECL-10728, 2, 545-549 (1992).

[5] R. W. Hamm, "Neutron Production with Compact Ion Linacs," SPIE Proc. 2339, 170-174 (1995).

[6] B. J Micklick, C. L. Fink and T. J. Yule, "Accelerator Requirements of Fast-Neutron Interrogation of Luggage and Cargo," these proceedings (1995).

[7] T. G. Miller and W. H. Makky, "Application of Fast Neutron Spectroscopy / Radiography (FNS/R) to Airport Security," SPIE Proc. 1737, 184-196 (1992).

[8] Z. P. Sawa, "PFN GASCA technique for detection of explosives and drugs," Nucl. Instr. Meth. Phys. Res. B 79 , 593-596 (1993).

[9] G. Vourvopoulos, F. J. Schultz, and P. C. Womble, "Nondestructive Characterization of Nuclear Weapons Using Pulsed Neutrons," presented at 6th European Conference on Non Destructive Testing, Nice, (1994).

[10] L. Grodzins, "Nuclear techniques for finding chemical explosives in airport luggage," Nucl. Instr. Meth. Phys. Res. B 56/57, 829-833 (1993).

[11] G. Vourvopoulos, "Multi-Parameter On-Line Coal Bulk Analysis," Journal of Coal Quality 12, 96-101, (1993).

[12] J. Ungrin, "Industrial Applications of Low-Energy Linacs," Proceedings of the 1994 International Linac Conference, 659-663 (1994)

[13] C. Ascherson,"Surface hardening by proton irradiation," Nucl. Instr. Meth. Phys. Res. B 79, 680-686 (1993).

[14] V. Valkovic and G. Moschini, "Some advances in medical applications using low energy accelerators," Nucl. Instr. Meth. Phys. Res. B 56/57, 1274-1278 (1993).

[15] I. O. Konstantinov and B.V. Zatolokin, "Monitoring Wear and Corrosion in Industrial Machines and Systems: A Radiation Tool," IAEA Bulletin, 1, 16-18 (1994).

[16] K. Murray, W. J. Stapor and C. Castenada, "A proton beam facility for single event research," Nucl. Instr. Meth. Phys. Res. B 56/57, 1256-1259 (1991).

[17] *Neutron Radiography (4) Including Radioscopy and Complementary Inspection Methods Using Neutrons*, ed. J. P. Barton, Gordon and Breach (1993).

[18] R. F. Barth, A. H. Soloway, R. G. Fairchild, and R. M. Brugger, "Boron Neutron Capture Therapy for Cancer - Realities&Prospects," CANCER 70, 2995-3007 (1992).

[19] X.-L. Zhou, and G. E. McMichael, "Design of Neutron Beams at the Argonne Continuous Wave Linac (ACWL) for Boron Neutron Capture Therapy and Neutron Radiography," presented at Accelerator-Based Neutron Sources for BNCT Workshop, 14 pages (1994).

[20] G. E. McMichael and T. J. Yule, "Argonne CW Linac (ACWL) - Legacy from SDI and Opportunities for the Future," presented at the ADTT Conference (1994).

ACCELERATOR REQUIREMENTS FOR FAST-NEUTRON INTERROGATION OF LUGGAGE AND CARGO

B. J. Micklich, C. L. Fink, and T. J. Yule, Argonne National Laboratory, Argonne, IL 60439 USA

Several different fast-neutron based techniques are being studied for the detection of contraband substances in luggage and cargo containers. The present work discusses the accelerator requirements for fast-neutron transmission spectroscopy (FNTS), pulsed fast-neutron analysis (PFNA), and 14-MeV neutron interrogation. These requirements are based on the results of Monte-Carlo simulations of neutron or gamma detection rates. Accelerator requirements are driven by count-rate considerations, spatial resolution and acceptable uncertainties in elemental compositions. We have limited our analyses to luggage inspection with FNTS and to cargo inspection with PFNA or 14-MeV neutron interrogation.

I. INTRODUCTION

Fast-neutron interrogation techniques are being examined for detection of illicit substances, such as explosives and narcotics, in luggage and cargo containers. Fast-neutron techniques are attractive because they can be used to determine the concentrations of the light elements [hydrogen, carbon, nitrogen, and oxygen] which are the primary constituents of these materials. Explosives and drugs are characterized by elemental densities and density ratios that are different from most other substances likely to be found in legitimate cargo.

This paper discusses two different fast-neutron techniques. The first uses an accelerator to produce nanosecond pulsed beams of deuterons that strike a target to produce a pulsed beam of neutrons with a continuum of energies. Elemental distributions are obtained by measuring the neutron spectrum after the source neutrons pass through the items being interrogated. This technique, first investigated by Overley[1] for bulk material analysis, is best suited for examination of luggage or small containers with transmissions greater than about 0.01. The second technique uses an accelerator or sealed-tube source to produce monoenergetic fast neutrons. The characteristic gamma rays emitted due to fast- or thermal-neutron interactions with the material being interrogated allow the determination of elemental densities. Two variations[2,3] of this technique are considered here. This technique is suitable for examination of large containers because of the good penetration of the fast neutrons and the low attenuation of the high-energy gamma rays.

II. FAST-NEUTRON TRANSMISSION SPECTROSCOPY

Fast-Neutron Transmission Spectroscopy (FNTS) uses standard time-of-flight techniques to measure the energy spectrum of neutrons emitted from a collimated ^{9}Be(d,n) continuum source before and after transmission through the sample. An unfolding algorithm determines the areal densities (density integrated along the line of sight, with units of number density per cm^2), and the uncertainties, of the various elements present in the sample. Projection data from several angles are then reconstructed to provide two-dimensional images, one for each element, of a slice through the sample. The elemental reconstructions are then combined and processed through a detection algorithm. Only a few projections and coarse resolution are used to minimize interrogation time while still obtaining a reconstruction that provides enough separation between objects to maximize the success rate of an explosive detection algorithm. The use of this method as applied to explosive detection is discussed in Reference [4].

The accelerator requirements for an FNTS system involve tradeoffs between many parameters, including: the accelerator energy (size), the time available for sample examination, maximum allowable detector count rates, spatial resolution required for adequate explosive detection, and neutron yield and spectrum versus deuteron energy. There are also limits on how well elemental densities can be determined at lower deuteron energies. In general, one would like to have as high a detector count rate as possible to minimize sample irradiation time, consistent with acceptable errors due to dead time and spectral distortion. This limits the detector count rate to about one-tenth of the accelerator pulse repetition rate. Given a detector count rate, one can then determine the required neutron source rate from the left-hand side of

$$R / (\langle T \rangle \langle \varepsilon \rangle) = \text{source n/s} = S_n \, \Delta\Omega \, I_p \, \tau_p \, f \qquad (1)$$

where R = maximum detector count rate
$\langle T \rangle$ = average transmission
$\langle \varepsilon \rangle$ = average detector efficiency
S_n = zero-degree neutron emission (n/sr-s-μA)
$\Delta\Omega$ = detector solid angle (sr)
I_p = peak current (μA)
τ_p = pulse time width (s)
f = accelerator pulse repetition rate (1/s)

The right-hand-side of Eqn. [1] can then be used to determine the required accelerator current once the deuteron energy, pulse width, and pulse repetition rate have been chosen. A typical time-of-flight system would have a flight path of 5 m, limiting f to 10^6/s (to avoid wrap-around), thus making R = 10^5/s. If the required spatial resolution inside the interrogated object is 2 cm, the detector size would be 4 cm if

0-7803-3053-6/96/$5.00 ©1996 IEEE

the object is placed midway between source and detector. The required accelerator current as a function of deuteron energy is shown in Table 1 for transmission through 3 cm of RDX high explosive. While lower deuteron energies would lead to a smaller accelerator and thus smaller system footprint, the declining neutron yield means that more current is required.

Table 1. Deuteron current required for a neutron count rate of 10^5/s in a 4-cm detector as a function of deuteron energy (for 5 m flight path, f = 10^6/s, and $\langle\varepsilon\rangle = 0.15$).

E_d (MeV)	Y_n (n/sr -μC)[a]	$\langle I_d\rangle$ (μA)[b]	I_p (mA)[c]
2.6	$2.62\cdot10^8$	120	60
3.0	$4.35\cdot10^8$	69	35
3.4	$6.41\cdot10^8$	45	22
3.8	$8.83\cdot10^8$	31	16
4.2	$1.17\cdot10^9$	24	12
4.6	$1.50\cdot10^9$	18	9.1
5.0	$1.87\cdot10^9$	15	7.3
5.4	$2.31\cdot10^9$	12	5.9
5.8	$2.80\cdot10^9$	9.6	4.8
6.2	$3.35\cdot10^9$	7.9	4.0
6.6	$3.97\cdot10^9$	6.6	3.3
7.0	$4.66\cdot10^9$	5.6	2.8

[a] Neutron yield data from Ref. [5].
[b] Average deuteron current
[c] Peak deuteron current (2 ns pulse at 10^6 repetition rate)

III. PULSED FAST-NEUTRON ANALYSIS

This technique uses nsec pulses of monoenergetic neutrons produced by accelerating deuterons onto a deuterium gas target. The neutron beam is scanned vertically across the cargo container by a movable collimator. Scanning along the length of the container is accomplished by moving the container horizontally. Depth information is obtained using time-of-flight between the accelerator pulse and the arrival of a gamma ray in NaI detectors located outside the container. Since the neutrons produced have velocities of about 4 cm/ns, the accelerator pulse must be at most a few ns if the voxel depth (thickness) is to be about 10 cm. The 4.44-MeV gamma from the first excited state in ^{12}C and the 6.13-MeV gamma ray from the second excited state in ^{16}O are used to generate a qualifier that indicates the presence of contraband.

The signal obtained from this technique depends sensitively on the incident neutron energy used, as can be seen in Fig. 1. Neutron energies greater than 6.5 MeV are required to detect ^{16}O, with the optimum energy being between 8.2 and 8.25 MeV (requiring a deuteron energy of about 5.0 MeV). However, since the inelastic scattering cross sections vary rapidly in this energy range, the energy stability of the accelerator and the pulse-forming network which generates the nsec-width pulses must create an energy variation of less than 10 keV.

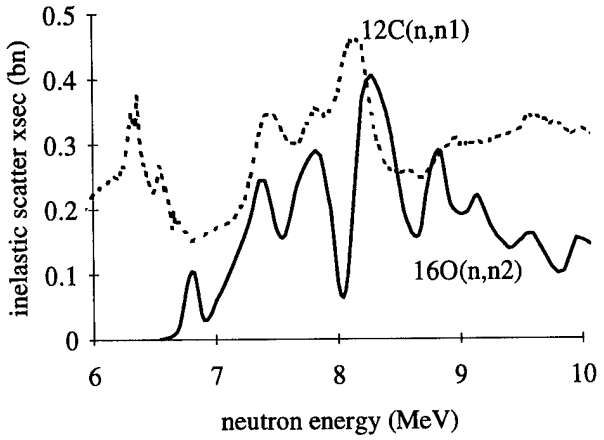


Figure 1. Inelastic scattering cross sections for the first excited state in carbon and second excited state in oxygen.

Equation 1 can be rewritten for PFNA in the form

$$R = \{\langle T_n\rangle \langle T_\gamma\rangle\} [S_n I_p \tau_p f \Delta\Omega_n] \{S_\gamma \Omega_\gamma\} \langle\varepsilon_\gamma\rangle \qquad (2)$$

where S_γ = gamma source (gammas/sr-n)
Ω_γ = detector solid angle from gamma source
$\langle T_\gamma\rangle$ = average gamma transmission to detector

This is the same as Eqn. 1, with the factor $\{S_\gamma\ \Omega_\gamma\}\langle T_\gamma\rangle$ added to account for the production and transport of gamma rays. We used the radiation transport code MCNP[6] to calculate the ^{12}C and ^{16}O gamma signals from a cargo container loaded with sugar at a density of 0.5 g/cm^3 with and without a ball of cocaine with radius 25 cm centered 75 cm from the front face. The count rates as a function of time are shown in Figure 2, and the count rates at the front of the sphere are given in Table 2. The actual count rates are obtained by multiplying the data in Table 2 by the estimated neutron source rates. For an average beam current of 100 μA, and a beam energy of 5.5 MeV, the number of neutrons incident on the region defined by the cocaine ball is $2.5\cdot10^{10}\cdot\Delta\Omega_n\cdot\langle\varepsilon_\gamma\rangle$. Assuming that the ball occupies a solid angle of 0.023 sr and that the gamma-ray detection efficiency is 0.2, one calculates count rates of 57 and 33 cps for the C and O lines in sugar, and 72 and 15 cps for the C and O lines in cocaine.

The required number of counts to detect the difference in the C/O ratios in sugar and cocaine will depend on the background and on the accuracy to which we need to know the ratio. If we assume a signal-to-background ratio of 1, and a 20% accuracy in determining the C/O ratio, then we will need approximately 300 counts in the ^{16}O(n,n2) peak for the cocaine case. This implies a counting time of 300/15 = 20 s.

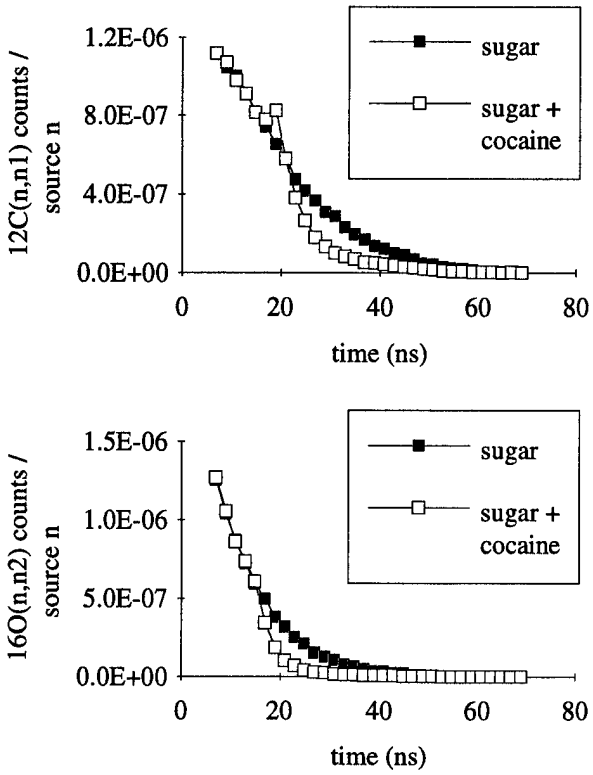


Figure 2. MCNP simulation results for 4.44-MeV gammas from ^{12}C (top) and 6.13-MeV gammas from ^{16}O (bottom) detected at the middle of the top of a container containing sugar or sugar plus cocaine sphere.

Table 2. PFNA count rates for sugar and sugar + cocaine calculated with MCNP (normalized to 1 source n/s).

	Sugar	Cocaine
$^{12}C(n,n1)$	$6.5 \cdot 10^{-7}$	$8.2 \cdot 10^{-7}$
$^{16}O(n,n2)$	$3.8 \cdot 10^{-7}$	$1.8 \cdot 10^{-7}$
Ratio	1.7	4.6

IV. 14-MeV NEUTRON INTERROGATION

In this technique 14-MeV neutrons are produced by a sealed-tube (d,t) source. Collimators generate a fan-shaped neutron beam that illuminates a vertical slice of the cargo container. The horizontal position is varied by moving the cargo container. The vertical position and depth of the voxel are also defined by collimators, behind which are located the gamma-ray detectors. The neutron source is operated in a pulsed mode with each pulse lasting several tens of microseconds. The inelastic 4.44-MeV and 6.13-MeV gamma rays from carbon and oxygen are detected during the active portion of each pulse. Prompt activation gamma rays characteristic of chlorine and nitrogen (PGNAA - Prompt Gamma Neutron Activation Analysis) and capture gamma rays from hydrogen (DGNAA - Delayed Gamma Neutron Activation Analysis) are detected between pulses.

The same analysis that was applied to PFNA in Section III can be used for 14-MeV interrogation. While the source neutrons have slightly greater penetrability, the gamma ray signals are lower because the inelastic scattering cross sections are lower, about 0.2 bn for $^{12}C(n,n1)$ and 0.1 bn for $^{16}O(n,n2)$. These cross sections are flat in this energy region. The neutron source rates for these types of (d,t) tubes are presently limited to approximately $8 \cdot 10^9$ n/s/sr in the forward direction, which is lower than the $1.9 \cdot 10^{10}$ n/s/sr assumed for PFNA. These tubes have the advantage of size and cost compared to a 5-MeV accelerator. A major disadvantage is their limited lifetime.

V. SUMMARY

The accelerator requirements for FNTS are determined primarily by detector count rates and not by fundamental accelerator limits. The main requirement for accelerator designers is to reduce size and cost. For PFNA and 14-MeV neutron interrogation methods, the gamma-ray count rates are directly proportional to the accelerator current. These techniques could make use of increased accelerator current.

VI. ACKNOWLEDGMENTS

This work was sponsored by the U. S. Federal Aviation Administration Technical Center under contract DTFA03-03-X-00021 and by the Office of National Drug Control Policy, Counterdrug Technology Assessment Center under contract 6-CO-160-00-195.

VII. REFERENCES

[1] J. C. Overley, *J. Appl. Radiat. Isot.* **36** (1985); *Nucl. Instr. Meth. Phys. Res.* **B24/25** (1987).

[2] Z. P. Sawa and T. Gozani, *Proc. 1st Int'l Symp. on Explosive Detection Technology*, Atlantic City, NJ (May 1992); D. L. Brown, R. Loveman, J. Bendahan, and M. Schulze, *Proc. Int'l Symp. on Contraband and Cargo Inspection Technology*, Washington, DC (Oct. 1982).

[3] M. J. Hurwitz, R. C. Smith, W. P. Noronha, and K.-C. Tran, *Proc. Int'l Symp. on Contraband and Cargo Inspection Technology*, Washington, DC (Oct. 1992).

[4] B. J. Micklich, A. H. Novick, M. K. Harper, and D. L. Smith, *Nucl. Instr. Meth. Phys. Res.* **A353** (1994); C. L. Fink, B. J. Micklich, T. J. Yule, P. Humm, and L Sagalovsky, *13th Int'l Conf. on the Application of Accelerators in Research and Industry*, Denton, Texas (Nov. 1994).

[5] J. W. Meadows, "The Thick-Target $^{9}Be(d,n)$ Neutron Spectra for Deuteron Energies Between 2.6 and 7.0 MeV," *Nucl Instr. Meth. Phys. Res.* **A324** (1993).

[6] "MCNP - A Generalized Monte Carlo Code for Neutron and Photon Transport, Version 3A," LA-7396-M, Rev. 2, Los Alamos National Laboratory (Sept. 1986).

Energy Varying Resonant Beam Extraction from the Synchrotron

K. Hiramoto, M.Tadokoro, J.I. Hirota, M. Nishi
Hitachi Research Lab., Hitachi, Ltd.
1-1, Omika-chou, 7-chome, Hitachi-shi, Ibaraki-ken, 319-12, Japan

K. Noda
National Institute of Radiological Sciences
4-9-1, Anagawa, Inage-ku, Chiba 263, Japan

Abstract

Two different operating schemes for the energy varying beam extraction from the synchrotron are presented based on the resonant extraction scheme in which the transverse RF perturbation is applied for increasing the amplitude of the betatron oscillations with keeping the separatrix of the resonance constant. The first operating scheme is that the primary acceleration is followed by the second acceleration, during which the beam is extracted by the above extraction scheme. In order to keep the separatrix constant during the extraction, the currents of the magnets are ramped with keeping the mutual ratio. In the other operating scheme, the currents of the magnets are ramped from the injection energy level to the maximum level and the beam is extracted with a constant energy at an intermediate stage. The ramping pattern can be commonly used for the beam extraction at the different energy level.

1. INTRODUCTION

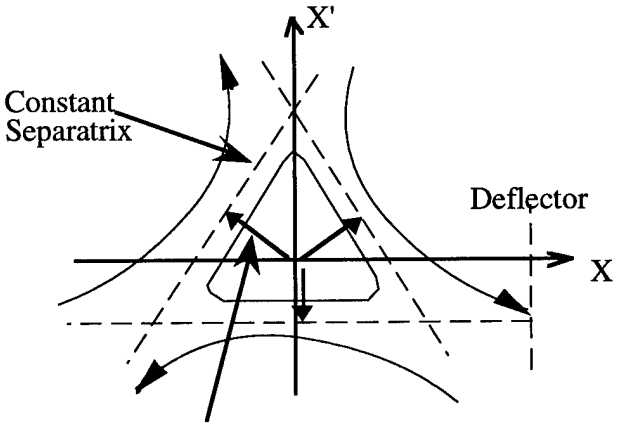
A high energy ion beam has been considered to be very effective for the cancer therapy because it shows a relatively sharp Bragg peak in the patient body. Presently, sixteen dedicated ion accelerators is being operated worldwide[1].

The depth of the Bragg peak depends on the energy of the ion beam. Accordingly, it is necessary to change the beam energy and its width when irradiating the different depth of the patient or treating the different patient. In most of the current ion accelerator systems for the cancer treatments, the beam is extracted at a fixed energy from the particle accelerator and, the beam energy and its width are controlled by the degrader and ridge filter installed at the end of the beam transport system. However, it has been pointed out that the degrader and ridge filter cause the beam loss of more than about 50%[2]. One of the reason why the degrader and ridge filter are applied is considered that practically it has not been so easy to change flexibly the extraction beam energy at the accelerator.

The synchrotron has a capability for accelerating and extracting the beam at several energy leves below the possible maximum beam energy. Then, for example, in GSI it is planned to use the energy variation of the synchrotron from pulse to pulse for the medical application[3]. For the energy variation, generally, it is necessary to prepare the several different and complex operating patterns of the magnets during the acceleration and extraction. Especially, in the conventional slow beam extraction scheme, the different current patterns of the several magnets are needed for each extraction energy. In order to simplify the operation of the extraction, we have presented a new beam extraction scheme[4]- [7] in which the separatrix of the resonance is kept constant for an extraction energy by maintaining the constant magnet currents and the transverse RF perturbation is applied to the beam. Since the magnet currents are kept constant, the operation is quite simple. This extraction scheme has also other features that the low emittance beam can be extracted and the extracted current is not affected significantly by the ripple of the magnet current in the synchrotron. Then, by using the above extraction scheme, we present new operating schemes for varying the beam energy during an extraction operation or for each repetitive extraction .

2. BASIC RESONANT EXTRACTION SCHEME

For energy varying extraction, we apply the resonant extraction scheme in which the separatrix of the resonance of the betatron oscillations is kept constant and the transverse RF perturbation is applied to the beam to make the amplitude of the betatron oscillations increase and finally reach the separatrix.



Amplitude Growth of the Betatron Oscillations by the Transverse RF Perturbation

Fig.1 Phase Space of the Present Extraction Scheme

The phase space of the beam by the present extraction scheme is shown schematically in Fig. 1. When the particles reach the separatrix because of the transverse RF perturbation, the nonlinear resonance occurs and those particles are extracted from the deflector. Since the separatrix of the resonance of the betatron oscillations is kept constant, the orbit gradients of the

0-7803-3053-6/96/$5.00 ©1996 IEEE

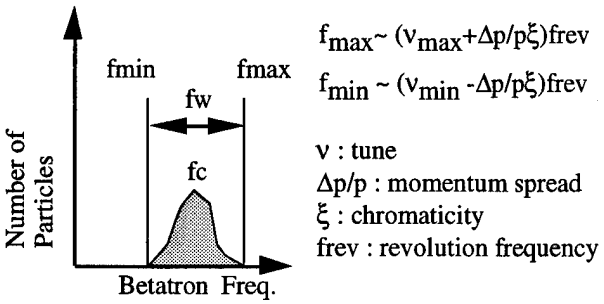


Fig.2(a) Frequency Spread of the Betatron Oscillations

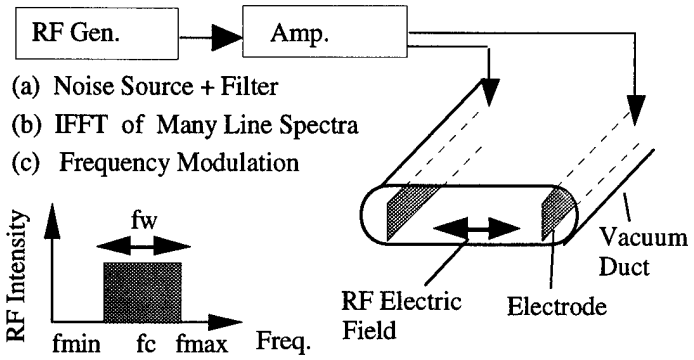


Fig.2(b) Transverse RF Perturbation applied to the Beam

extracted particles at the deflector position are kept almost constant. Therefore, the time integrated emittance can be reduced significantly.

Generally, the betatron tune varies with the betatron amplitude under the nonlinear magnetic field and the momentum of the particles because of the chromaticity. Then, the tune spectrum of the beam at the resonant extraction spreads, as shown in Fig.2(a). Therefore, in order to increase the amplitude of the betatron oscillations, it is effective to apply the transverse RF perturbation having a band width covering the spread betatron frequencies, as shown in Fig.2(b). The following methods can be applied to make the RF perturbation have an adequate central frequency fc and frequency width fw.

(a) Filtering a random noise
(b) Inverse Fourier transformation of many line frequency spectra with different random phases
(c) Frequency modulation

The extraction using the above RF perturbation (c) has been already studied experimentally in HIMAC and the feature of the low emittance extraction has been confirmed[6].

Since the separatrix of the nonlinear resonance is determined by the magnet currents, these currents are kept constant during the extraction for a fixed energy. Furthermore, even in the case of changing the extraction energy, it is not necessary to alternate the ratio of the several magnet currents.

The intermittent structure of the extracted current can be also improved significantly even under the condition that the magnet current includes a low frequency ripple[6][7]. In the conventional extraction varying the separatrix size, the number of the extracted particles per unit time is expressed as NV where N(1/mm·mrad) is the number of particles on the unit area near the separatrix and V(mm·mrad/s) the speed of varying separatrix size. Since V is small in this scheme, its value is modulated by the ripple of the magnet currents. This results in the intermittent extraction. In the present extraction, the number of the extracted particles per unit time is expressed as NVrf where Vrf(mm·mrad/s) is the outgoing speed of the particles on the separatrix. Since the value of N is small, a relatively large value of Vrf is needed to obtain a sufficient flux. As a result, the separatrix change due to the magnet current ripple does not make the extraction flux vary significantly. Furthermore, it has been also pointed out that this extraction scheme can be applied to the breath synchronized irradiation in the cancer treatments because the fast switching of the extraction is possible due to the RF perturbation[6].

3. OPERATING SCHEMES FOR VARYING BEAM EXTRACTION ENERGY

In order to make it simple to change the beam extraction energy, we present following two different schemes which employ the above resonant extraction scheme using the transverse RF perturbation under the constant separatrix.

(1) Energy Varying Extraction during One Pulse Operation

The operating patterns of the beam momentum and the magnet currents are schematically shown in Fig. 3. These operating patterns consist of the primary and secondary accelerations. Psi and Pei (i=1,2 - - n) shown in the figure

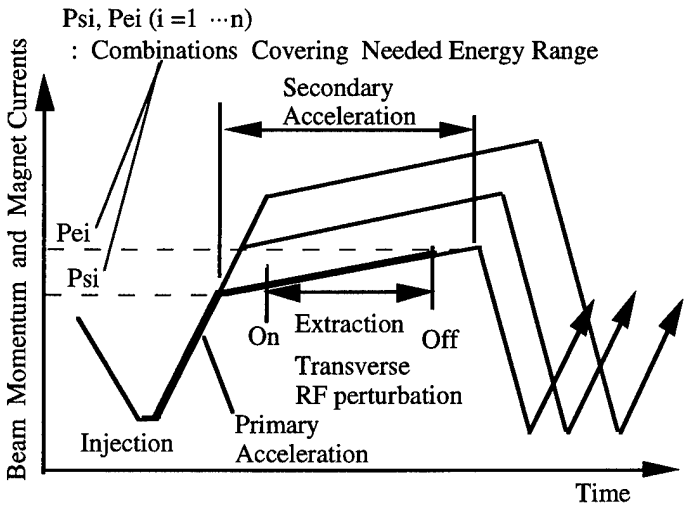


Fig. 3 Operating Pattern for Varying the Beam Energy during the Extraction

denote the beam momenta at the initiation and termination of the second acceleration. The beam extraction is done during the second acceleration. The separatrix of the resonance is generated by using the nonlinear magnet such as a sextupole magnet at the initiation of the second acceleration. If needed, the tune is varied after the primary acceleration by controlling the quadrupole magnets. The currents of the nonlinear magnets as the resonance exciter are increased with maintaining the ratio between the currents of the several magnets so as to keep the separatrix of the resonance constant during the second acceleration. It is necessary that the frequency spectrum of the transverse RF perturbation covers the spread frequency width due to the nonlinearity of the betatron oscillations and the momentum spread. On the other hand, it is

desirable that the transverse RF perturbation has a needed minimum frequency width because the needed RF power increases with the frequency width fw. Since the frequency spectrum of the betatron oscillations varies with changing the beam energy, the central frequency fc of the transverse RF perturbation should be shifted during the second acceleration with keeping a constant frequency width fw. This can be realized easily by applying the recent RF or digital technique. If the energy changing width is narrow during the second acceleration, that is, the frequency spectra of the betatron oscillations does not vary significantly, it is possible that the transverse RF perturbation with a constant central frequency and wide frequency width is applied during the second acceleration.

The initiation and termination of the extraction can be controlled by turning on and off the RF perturbation. Accordingly, the momentum range of the extracted beam can be also selected between Psi and Pei. The combinations of the Psi and Pei (i=1,2 - - n) are chosen between the minimum and maximum energy levels of the extraction. In the case of the medical use, generally, it may be useful to determine the combination of the Psi and Pei for each patient. On the other hand, if several combinations of the Psi and Pei (i=1,2 - - n) covering the needed energy ranges are chosen and the machine tuning is performed in advance, it is possible to change the extraction beam energy more flexibly. Furthermore, the time of the machine tuning can be reduced by using the operating pattern of the primary acceleration commonly for the different combinations of the Psi and Pei (i=1,2 -- n) .

(2) Varying Energy Extraction per Pulse to Pulse Operation

In the following, the operating scheme for varying beam energy per pulse to pulse operation is presented. The operating patterns of the beam momentum and the magnet currents are

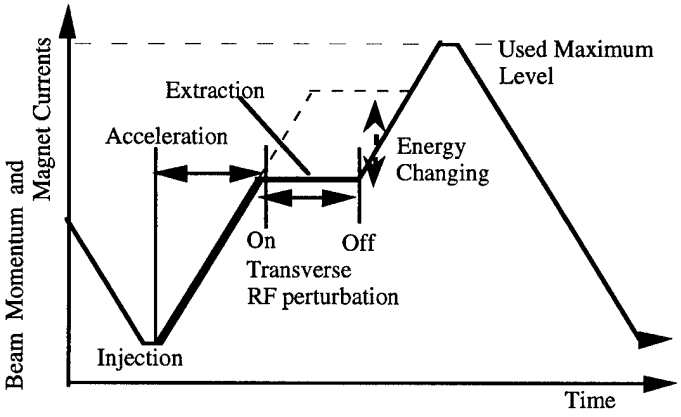


Fig. 4 Operating Pattern for Varying the Beam Energy per Pulse to Pulse Operation

schematically shown in Fig. 4. The beam is extracted at a constant energy after the acceleration. For the magnets used during the acceleration, the currents are also ramped up to the maximum beam energy level after the extraction. The operating patterns during the acceleration and after the extraction are used commonly when changing the extraction beam energy.

The extraction is initiated by turning on the transverse RF perturbation. In this operating scheme, in order to decrease the power of the transverse RF perturbation, it is also desirable that the transverse RF perturbation has a needed minimum frequency width fw and its central frequency fc is alternated when changing the extraction energy. During the extraction, the separatrix for the resonance of the betatron oscillations is kept constant. As a result, the orbit gradient of the extracted beam is almost constant and the time averaged emittance can be very small. If the same separatrix size can be applied to the extraction at the different energy levels, the ratio between the currents of the magnets can be kept constant. Then, the machine tuning for changing the extraction energy becomes more flexible. Furthermore, this constant separatrix for the different extraction energy makes the energy dependence of the characteristics of the extracted beam vanish. As a result, the tuning of the electrostatic deflector and the magnets of the beam transport system can be significantly simplified.

4. CONCLUSIONS

In order to make it more flexible to change the beam extraction energy at the synchrotron for medical use, we presented the following different operating schemes using the resonant beam extraction scheme in which the transverse RF perturbation is applied for increasing the amplitude of the betatron oscillations while maintaining the constant separatrix.

In the first operating scheme, the primary acceleration is followed by the second acceleration. The separatrix of the resonance is kept constant by maintaining the ratio between the currents of the magnets during the second acceleration. Then, the beam is extracted by applying the transverse RF perturbation for reaching the betatron oscillations to the separatrix. The operating pattern of the primary acceleration is used commonly. By preparing about ten operating patterns for the second acceleration in advance, it is possible to select flexibly the extraction energy between the needed minimum and maximum energy.

In the other operating scheme, the beam is extracted with a constant energy after the acceleration. The magnet currents during the extraction are kept constant for the constant separatrix. After the extraction, the currents of the magnets for the acceleration are ramped to the maximum level. This ramping pattern before and after the extraction is used commonly for the extraction at the different energy levels.

5. REFERENCES

[1] J.M. Sisterson, Abstracts of the XX PTCOG Meeting, p19(1994)

[2] W. T. Chu, et al., Rev. Sci. Instrum. 64 (8),p2055,August, 1993

[3] K. Blasche, et al., Proc. of the 4th European Particle Accelerator Conference, p133, London, U.K, 1994

[4] K. Hiramoto, et al., Nucl. Instrum. Methods. A322, p154 (1992)

[5] M. Tomizawa, et al., Nucl. Instrum. Methods. A326, p399 (1993)

[6] K. Noda, et al., Proc. of the 4th European Particle Accelerator Conference, p982, London, U.K, 1994

[7] K. Hiramoto, et al., Proc. of the Particle Accelerator Conference, p309, Washington D.C., USA, 1993

RADIOTHERAPY PROCESS INTEGRATION USING A COMPACT PHOTON SOURCE TOGETHER WITH FLUENCE CONTROL AND PATIENT IMAGING

D. Tronc, F. Dugardin, J.P. Georges, R. Letoumelin, J.L. Pourre
General Electric Medical Systems, BP 334, 78 533 Buc Cedex, France

Abstract

Process integration, combining diagnostic, simulation and therapy in a single instrument will overcome many limitations in cancer care. But it asks for a miniturization of the high energy photon source. Such effort could open unforeseen developments as mobile "global therapy" units. Parameter values for the photon source will be achieved with an X-band linac integrated with target and collimator as a shielded compact sub-unit.

I. NEEDS AND OBJECTIVES

A. The needs (user's point of view):

The therapeutic treatment consists of 3 phases: diagnostic imaging, simulation of the dose delivery conditions, dose delivery. It is done today with 3 different instruments with inherent problems such as induced incompatibility of materials (today without standards) and difficulties in coordinating the phases into a coherent process. The use of multiple, independent systems creates an incoherence resulting in faults of treatment efficacy and safety, and a waste of time and discomfort for the patient. And, no effective treatment exists today for concave shape of tumor volume (prostate).

One needs to *integrate the 3 phases of treatment into one system and instrument.* The advantages are in level with industrial effort required from the manufacturer and adaptation required from users: (1) the necessary control for a dynamic conformal therapy adapted to concave shape of tumor volume becomes possible, (2) *the precise and simple control position for each treatment* becomes feasible, (3) sources of errors due to use of different instruments and non medical data transfer are eliminated, (4) the global cost for the process is decreased as one instrument on one site replaces 3 instruments on 3 sites.

Such instrument insures 'unité de lieu' (same place whatever the phase) but does not require time limitation and the imaging resources can be used at different levels of sophistication for a typical sequence as: diagnostic (3 arbitrary time units) – simulation (later, 2 time units) – treatments (later, over several weeks, for ex. 15 x 1 time units). Then the instrument is used at 75% for therapy and at 25% for imaging preparations.

B. The objectives (technological point of view):

A new concept for the delivery of dynamic conformal radiotherapy has been recently proposed under the "tomotherapy" name [1]. It arouses much interest as it proposes a combination in a single instrument of diagnostic and therapy. The proposal is to deliver therapeutic radation following the spiral scan method used on recent CT imaging units, as a modulated slice, while the patient moves through the gantry. This introduces a synergy between the large medical diagnostic engineering resources and the more modest medical therapy ones. However, weight and cost are large when the ratio of useful to available radiation is low as is the case in a "slice" delivery. Also the patient moves under a potentially harmful treatment.

One alternative keeps the conical radiation delivery and uses a multileaf collimator (MLC) and a pulse to pulse control [2]. See figure 1. This in turn leads to rather intricate 3D dosimetry. The emerging photon beam fluence is detected either behind the patient as is the case in portal imaging, or more simply before the patient at the MLC exit, as the patient view is available by perpendicular CT scan (meaning only a one-fourth rotation time delay). It acts as the key control for the treatment process. Dose delivery to a fixed patient combines slow longitudinal mechanical motions in the MLC [3] with quick azimuthal time modulation by pulse to pulse fast on/off electronic control. For treatment, patient view could be restricted to a slice (2D scan). For full diagnostic view the patient would move (3D helical scan).

Even if it is too soon to decide what is the solution best fitted to radiotherapy, it is clear that the association of a photon source with field fluence control and patient diagnostic imaging in a single global radiotherapy instrument is the key for more precise and simpler treatment process. This supposes a *miniturisation* of the source to make it much lighter and to allow its rotation on imaging rings of the fourth generation in continuous rotation. The necessary electrical power must be reduced to transfer through circular contacts. A first design presented below uses a 9.3 GHz linac to accelerate electrons at 6 MeV, a cooled target and a multi-leaf collimator (MLC).

C. Let us dream (a little) to future extensions

Such a miniaturized instrument able to integrate the whole radiotherapy process could be used as a "global radiotherapy mobile unit" similar to the radiology mobile unit used today. The fixed protection necessary for the outside world would be replaced by a dedicated and eventually protected parking space with access limitation or `site.' Such an approach could benefit under-equipped regions. For example, 2 mobile units (for reliability) would move from site to site within a large district area around a central hospital.

II. PHOTON SOURCE PARAMETERS VALUES

The following table summarizes the choices for the main parameter values. The photon megavoltage is modest, a necessary condition for compacity then low cost and general applicability (including optional mobile unit). In fact, it is this modest value compatible with many available beam input ports or with a basic generalization of therapy which allows the high frequency choice with dramatic effect on weight, cost, mobility. Before, conventional radiotherapy products were simpler (without imag-

0-7803-3053-6/96/$5.00 ©1996 IEEE

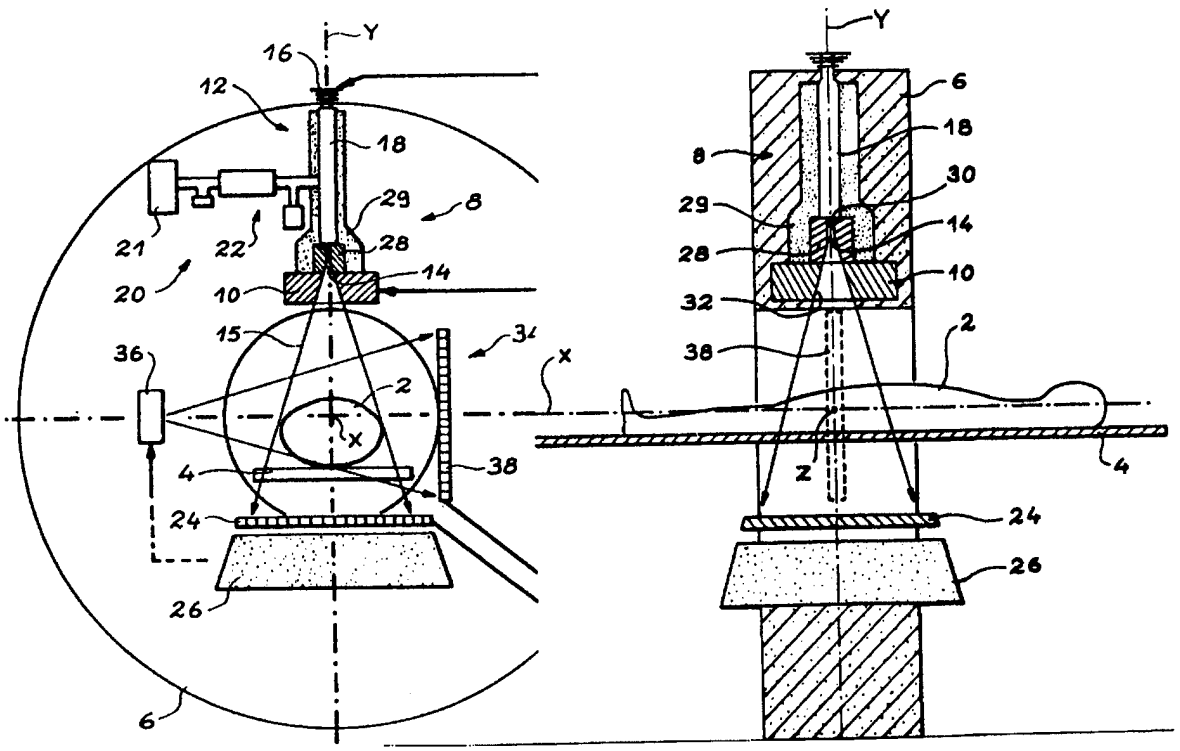


Figure 1. The 3D delivery case: the rotating ring which supports the photon source and the CT scan is seen in plane and in profile.

ing capabilities) but had to cover a whole range of energy up to 18 MeV, and this precluded RF higher frequency use.

Fundamental parameters	Values
Treatment volume envelope radius	200 mm
Patient clearance radius	500 mm
Source to axis distance	750 mm
Maximum external radius	1300 mm
Electron energy (photon megavoltage)	6 MeV
Electron beam peak/mean power	0.5 MW/0.38kW
High Energy Photon Source weight	<200 kg
HEPS electrical power required	<3kW
Dose rate on-axis at isocentre	>4 Gy/mn

III. X-BAND COMPACT LINAC AND SHIELDED TARGET AND COLLIMATION

The predesign uses the following formulae:

The dose on-axis D in Gray/min for a mean electron current i in μA at the energy V in MeV, delivered at the distance d in m, is empirically given by [4]:

$$D = 9 \times 10^{-}4 \times i \times \frac{V^{2.58}}{d^2}$$

The mean current i in μA is related to the pulse length τ in μs and to the repetition frequency F in Hz and to the peak current I in A:

$$i = \tau \times F \times I$$

The peak current I in A for the total peak power P in MW and for the Joule power P_J (necessary to create the electrical field leading to the energy gain) in MW and for the energy V in MeV is:

$$I = \frac{P - P_J}{V}$$

The Joule power loss P_J in MW leading to the energy gain V in MeV for the shunt impedance per unit length Z in MΩ/m and for an acceleration length L in m is:

$$P_J = \frac{V^2}{ZL}$$

with P = 1.2 MW at the section input (the magnetron delivering >1.3 MW), for V = 6 MeV and Z = 130 M Ω/m at 9.3 Ghz (SUPERFISH code gives more for the profile chosen but surface roughness and coupling and dynamics lower it), and for L = 0.4m: P_J = 0.69 MW, I = 0.083 A.

At τ = 3 μs and F = 250 Hz: i = 62 μA.

With d = 0.75m and V = 6 MeV: D = 10.1Gy/mn, more than 4Gy/mn required—and available even with field equalization (not used in the present project).

From the parameters defined above, one has to design the integrated electron linac plus the target plus the collimator, surrounded by a minimum shielding. The difficulties lie more in the integration than in any specific subcomponent. However, the magnetron, the triode gun, the beam capture and the beam radial control with minimum energy loss, the technology of target cooling presents challenges. The concept is to put the cooled target inside a rather thick shielding, then to shield more lightly the linac structure after assessment of the low stray X-rays production along it, by dynamic simulation to minimize beam loss

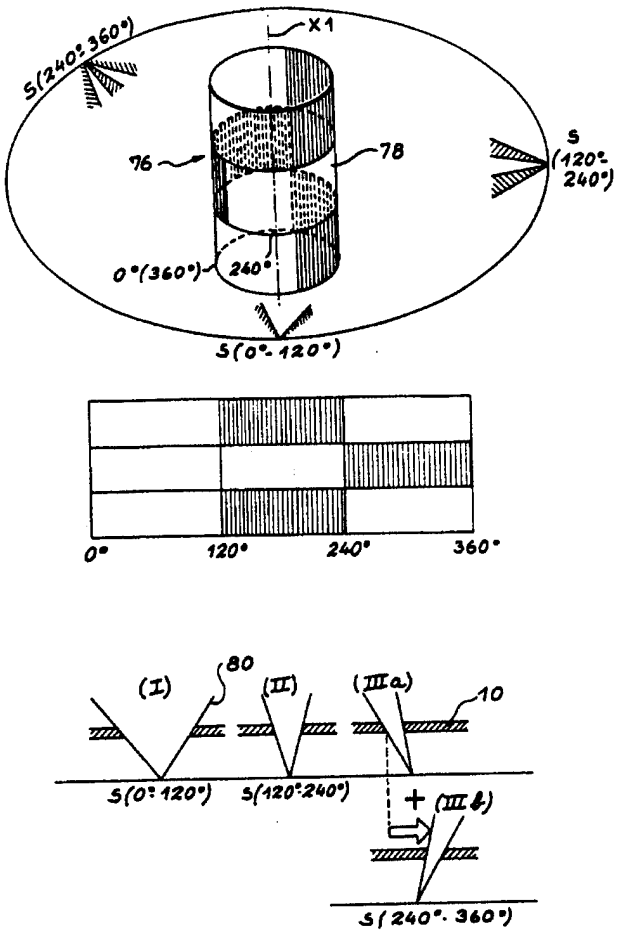


Figure 2. represents an oversimplified treatement of a cylinder mapped as rectangular 3 x 3 zones. The shaded ones are protected by proper collimation including at right summation (which requires then 2 turns around the cylinder).

before direct measurements. The MLC is set as near target as possible, to be part of the shielding and to be compact, but one is limited by the penumbra. The protected empty box between primary collimator and MLC upper boundary is used for optical simulation and optional beam flattening filter.

IV. CONCLUSION

This approach offers a solution to catch up with the needs on two lines: (i) the very sophisticated instrument aimed to better conform to tumoral sites following multiports delivery techniques developed in centers of excellence, (ii) the very compact and relatively cheap instrument able to cope with the 3 treatment stages necessary to deliver safe radiotherapy. Eventually such an instrument could move in a truck to cover a large area when few medical centers are available.

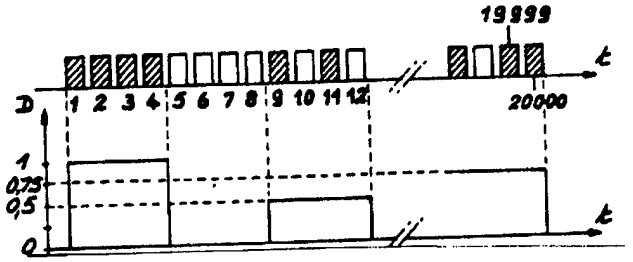


Figure 3. represents the fast pulse on/off control which leads to azimuthal dose modulation—here oversimplified to 4 possible levels only.

References

[1] T. Rock Mackie et al., "Tomotherapy: A new concept for the delivery of dynamic conformal radiotherapy," Med. Phys. 20(6) Nov/Dec 1993, 1709.

[2] D. Tronc, french patents 94 15 696 & 94 15 697

[3] T.R. Bortfield et al., X-ray field compensation with multileaf collimators, Int.J.Radiation Oncology Biol.Phys., vol.28, no.3, 1994, 723.

[4] J. Milcamps, CGR MeV int. report, 1982.

A 1.5 GeV Compact Light Source with Superconducting Bending Magnets*

A A. Garren[a,b,c], D. B. Cline[a,b], M. A. Green[c], D. E. Johnson[a], J J. Kolonko[a,b], E. M. Leung[d], D. D. Madura[d] and L. C. Schachinger[a]

a. Particle Beam Lasers, Inc., Northridge CA 91324
b. UCLA Center for Advanced Accelerators, Los Angeles CA 90095
c. Lawrence Berkeley Laboratory, Berkeley CA 94720
d. Martin Marietta Technologies Inc., Rancho Bernardo CA 92125

Abstract —This paper describes the design of a compact electron synchrotron light source for producing X-rays for medical imaging, protein crystallography, nano-machining and other uses up to 35 keV. The source will provide synchrotron light from six 6.9 tesla superconducting 60° bending magnet stations. In addition the ring, contains conventional quadrupoles and sextupoles. The light source has a circumference of 26 meters, which permits it to be located in a variety of industrial and medical facilities.

I. BACKGROUND

The machine presented here is designed primarily as a light source for industrial and medical applications. Modified versions of the design may have other applications as a damping ring or collider.

The ring is designed to produce X rays with energies up to 35 keV. To make the ring compact, its energy is limited to 1.5 GeV. This beam energy allows use of conventional quadrupoles and sextupoles without greatly increasing the ring circumference. In order to get useful quantities of X rays at 35 keV or above, the bending dipole should have a central induction above 6 T. For the machine described, with a bending induction of 6.9 T and beam energy of 1.5 GeV, the critical synchrotron-radiation energy is 10.3 keV. The lattice has been designed to optimize dynamic aperture, emittance, cost, and ring size, while providing adequate space for the rf and injection systems.

II. THE COMPACT STORAGE RING LATTICE

The racetrack-shaped ring has a hybrid magnet structure, consisting of superconducting dipoles and conventional quadrupoles and sextupoles. The two arcs are identical and each is symmetric about its center. The straight sections have the same length but different structure. Each is symmetric about its center, so the ring is reflection-symmetric about the line joining the center points. Figure 1 shows the ring layout.

Each arc consists of six 30° dipoles, four quadrupoles and six sextupoles. The dipoles are grouped into three pairs, each of which shares a single cryostat. Conceptually, the arc is built up from three cells, where the outer two cells are truncated beyond the two dipoles. Referring to Figure 1, the center cell consists of the magnet sequence (SFH QF SD B B SD QF SFH), the first cell is (B B SD QF SFH) and the last cell is (SFH QF SD B B). Here SFH is a half focusing chromaticity sextupole, QF a focusing quadrupole, SD a defocusing chromaticity sextupole, and B is a dipole.

The rectangular dipole has a field of 6.9 T and zero gradient. Vertical focusing comes from its edges. The cell has horizontal and vertical phase advances of 120° and 90° respectively; these values are obtained by adjusting the strength of QF and the distance between QF and B. The horizontal phase advance of three cells is 360°, so the arc is an achromat and the dispersion is zero in the straight sections (see Figure 2). The vertical phase advance is chosen to make the arc as short and the emittance as low as possible.

The straight section at the top of Figure 1 has a 1.6 meter drift in the center for injection. The straight section at the bottom of Figure 1 has seven quadrupoles, between which the rf modules would be located. Both straight sections are adjusted so that the periodic beta functions in the arc are brought to waists at the straight section centers. Consequently the emittance depends on the arc design only, not on the straight sections or the tunes. Table I presents the basic parameters for the Lattice.

The bottom straight section produces 3π horizontal and vertical phase differences between the centers of the two arcs. Thus, each magnet in one arc is paired with one in the other so as to partially cancell their nonlinear effects. The top straight section quadrupoles are adjusted to make the tunes favorable with respect to resonances, minimization of beam size and chromaticity and the provision of useful drift spaces.

Figure 2 shows the lattice and orbit functions of the ring, running clockwise from the center of the top straight section.

The following variations have been investigated:

1) The arc was composed of either three 60° dipoles or six 30° dipoles.
2) Values of the cell vertical phase advance of 120°, 90°, and 60° were compared.
3) The number and location of the defocusing chromaticity SD sextupoles have been varied.
4) Different ring tune values were compared.

* This work was performed with the support of the Office of High Energy and Nuclear Physics, United States Department of Energy under contract number DE-FG03-94ER81826 and LBL contract number DE-AC03-76SF00098.

0-7803-3053-6/96/$5.00 ©1996 IEEE

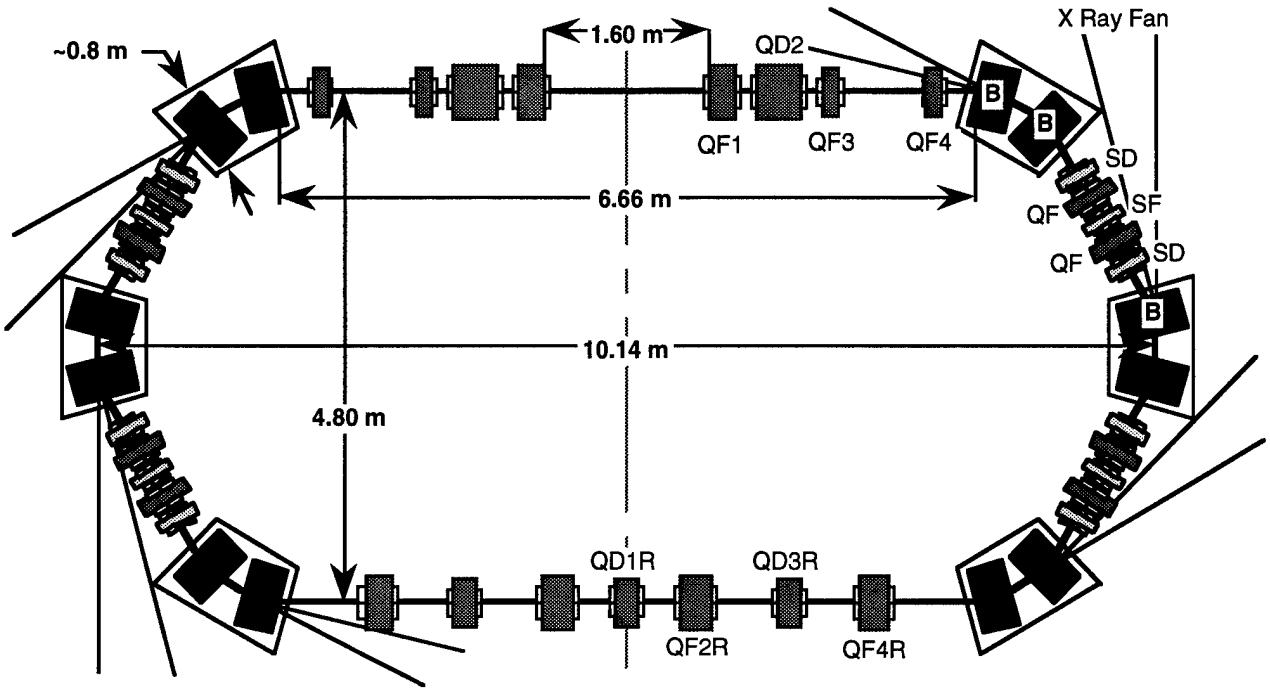


Fig. 1. A Compact Storage Ring with Superconducting Dipoles and Conventional Focusing Elements

Table I Lattice Parameters for the Compact Light Source

Maximum Stored Beam Energy (Gev)	1.50
Projected Injection Beam Energy (Gev)	0.10
Projected Beam Current (mA)	~20.
Circumference (m)	26.0
Bend Radius (m)	0.7257
Dipole Bend Angle (deg)	30.
Integrated Dipole Induction* (T m)	2.6197
Dipole Central Induction (T)	6.894
Dipole Magnetic Length along the Bend (m)	0.380
Critical Energy (keV)	10.3
Horizontal Natural Emittance* (μm)	2.34
Vertical Coupled Emittance* (μm)	1.17
Vertical Operating Emittance*(μm)	0.0234
Horizontal Tune	3.17
Vertical Tune	2.57
Horizontal Chromaticity	-2.22
Vertical Chromaticity	-5.24
Maximum Horizontal Beta Function (m)	3.09
Maximum Vertical Beta Function (m)	6.66
Maximum Dispersion (m)	1.29
Energy Loss per Turn* (MeV/turn)	0.617
RF Voltage (MV)	2.5
RF Frequency (MHz)	499.
Energy Spread (parts in 1000)	1.52
Bunch Length rms* (mm)	30.
Horizontal Damping Time* (ms)	0.412
Vertical Damping Time* (ms)	0.422
Energy Damping Time* (ms)	0.213
Quantum Lifetime (s)	2.2 10^8

* at the maximum design beam energy

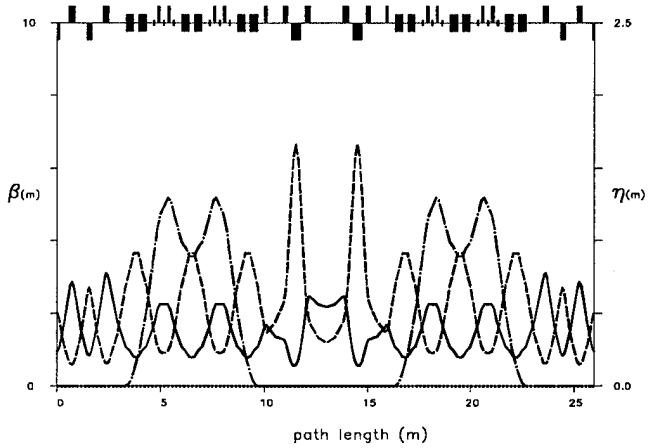


Fig. 2 Orbit Functions of the Compact Storage Ring. The solid, dashed, and dot-dashed curves show βx, βy, and η

The comparison of lattice alternatives for the ring, which included engineering and tracking studies, have led to the following conclusions:

1) The split-magnet configuration (six dipoles per arc) is far preferable to the unsplit one.in cost and field quality.
2) The best sextupole configuration is the one that has four SDs per arc.
3) The best vertical cell phase advance is 90^o: this value leads to the shortest feasible arc and the lowest emittance.
4) The best working point is at $\nu_x = 3.17$, $\nu_y = 2.57$.

Particles were tracked for 1,024 turns around the ring. Multipole errors were included in the dipoles consistent with the assumption of dipole field uniformity of 1 part in 10000 over a radial dimension of 28mm. The dynamic aperture was at least 25 sigma in both planes, considerably larger than the 15 sigma physical aperture of the magnets. This aperture should be more than large enough for beam lifetime.

III THE SUPERCONDUCTING DIPOLE

Fig. 3 shows a cross-section of the dipole. The design for the dipole is based on a concept proposed by Pavel Vobly at INP Novosibirsk.[2,3]. The dipole shown in Fig. 3 will generate a uniform field over a wide range of central inductions, provided that the current density in the shield coil system is correctly chosen with respect to the current density in the gap and crossover coil system. The shield coil current can be set so that the sextupole and decapole field components are zero, and the 14 pole component is very small. The excitation function can be modified by changing the height and slope of the shield coil.

The dipole has saturated iron in the poles. The shield coils keep the magnetic flux in the pole until it can be returned by an unsaturated iron return yoke. As a result, the field fall off at the end of the dipole is similar to that of conventional low field copper iron dipoles. Since the compact ring dipoles are only 376 mm long, the fall-off of the magnetic field at the end is important.

If one bases the coil design shown in Figure 3 on superconducting cable made from SSC inner conductor, the dipole will operate at about 87% of its critical current along the load line (based on a conductor packing fraction of 0.7 and an operating temperature of 4.4K). The SSC conductor can be cabled into conductor of almost any desired current for this application.

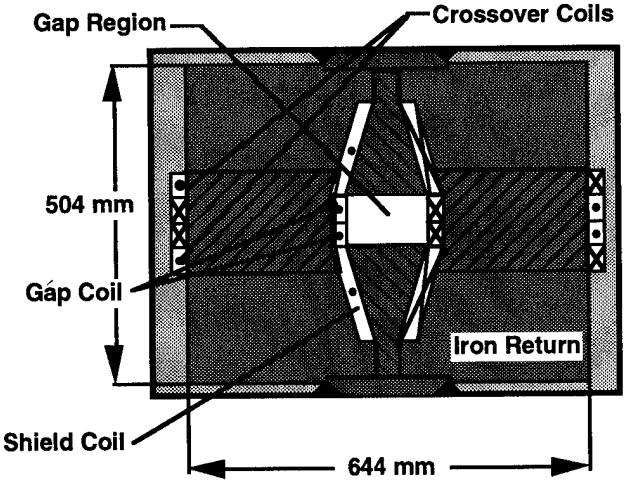


Fig. 3 Cross-section of a 6.9 T Vobly Type Dipole

IV. CONCLUSION

A 1.5 GeV compact synchrotron with superconducting bending magnets and conventional focusing elements can be made with a circumference of 26 meters. At 1.2 GeV, the proposed storage ring should perform even better. The ring appears to be suitable for industrial production of X rays at energies up to 35 keV. In this energy range there are a number of interesting potential uses for such a ring, which, it is expected, can be built for less than 12 million dollars.

The key to building a compact electron storage ring in the 1.2 to 1.5 GeV energy range is the development of a short superconducting dipole with field characteristics similar to that of conventional room temperature iron dominated dipoles. It appears that a Vobly type dipole is an attractive design for a compact X ray source.

REFERENCES

[1] D. B. Cline A. A. Garren, M. A. Green, et al, "A Compact Hard X Ray Source for Medical Imaging and Biomolecular Studies," to be published in NIM (1995), UCLA-CAA0112

[2] G. N. Kulipanov, N. A. Mezentsev, L. G. Morgonov, et al, "Development of a Superconducting Compact Storage Rings for Technical Purposes in the USSR," Rev. Sci. Instrum. 63 (1), p731 (1992)

[3] P. D. Vobly, private communication concerning compact synchrotron dipole magnet designs (1992)

Applications of Industrial Electron Accelerators at Samsung Heavy Industries

Bumsoo Han, Keeman Kim, Kihun Joh, Sungmyun Kim, Byungmun Kim, Heunggyu Park, Jongpil Park, Jinsoo Kim, Wongu Kang, Kyungwoo Kang, Yuri Kim, Sangil Lee, and Younghee Kim
Samsung Heavy Industries Daeduk R&D Center
Yousung-Gu, Moonjee-Dong 326, Daejeon, Korea 305-380

ABSTRACT

An industrial electron beam accelerator has been developed at Samsung Heavy Industries with the collaboration of Seoul National University and Russian Budker Institute of Nuclear Physics. The accelerator is a high voltage accelerator using rectifiers and able to deliver 40 mA of 1 MeV electrons in CW mode. Functionally, the accelerator is an electron irradiation processing device and an electron beam scanning system is employed for the uniform irradiation of the electron beam through the extraction window of the size 980 mm x 75 mm. The industrial applications of the electron irradiation processes include combustion flue gas purification process, treatment of industrial waste water containing refractory pollutant, treatment of semiconductor devices, and radio-chemical processes. The major features of the device and its industrial applications will be described.

I. INTRODUCTION

Samsung Heavy Industries Daeduk R&D Center is a part of SAIT (Samsung Advanced Institute of Technology) Daeduk site which is located at the central part of Korea. The accelerator laboratory at Daeduk R&D Center is devoted for the development of accelerator technologies and applications. Current research activities include the development of electron accelerators for irradiation processing purpose, applications of electron irradiation processing and the development of a synchrotron light source.[1]

As an initial step, an industrial electron accelerator[2] has been developed with the collaboration of Seoul National University and Russian Budker Institute of Nuclear Physics. The electron accelerator is designed for electron irradiation processing and it is a part of an electron irradiation processing facility. Practically, most of electron accelerators for irradiation processing are used for radio-chemical processes, which include treatment of heat-resistant electric cable, automobile tire, textile, polymer tube for heating purpose, foam sheet and thermo-shrinkable tube. Another interesting application is semiconductor treatment. After the electron radiation treatment, the switching speed of IGBT (Insulated Gate Bipolar Transistor) is improved by order of 2 magnitude. Though there are many other possible applications such as sterilization of food and medical waste, our major research object is focused on the application of the electron accelerator to environmental engineering. The combustion flue gas purification process is one of the actively studied subject for environmental applications. This technology could be a major impact on the flue gas purification technology for incineration plants and coal power plants. The treatment of industrial waste water containing refractory pollutant is also actively studied.

II. ELECTRON IRRADIATION PROCESSING FACILITY

The industrial electron beam accelerator developed at Samsung Heavy Industries is a high voltage accelerator using rectifiers. The original design of the accelerator was developed at Russian Budker Institute of Nuclear Physics. The nominal energy and current of the electron beam is 1 MeV and 40 mA, respectively. As a matter of fact, the electron accelerator is a part of the electron beam irradiation processing facility and an additional scanning system is required for the uniform irradiation of the electron beam to a certain area.

After a frequency converter changes the frequency of input current from 60 Hz to 480 Hz, a transformer coil system is employed to convert the voltage. The transformer system consists of one primary coil of 30-turn and 44 secondary coils of 3000-turn. In order to prevent discharge, the transformer coil system is filled with SF_6 gas. Each secondary coil generates the DC voltage of 20~25 kV with its own rectifier system from the input voltage of 360~390 V. In order to produce the high voltage for the acceleration of electrons, the outputs from 44 secondary coil systems are connected in series and 0.7~1 MV is delivered to an accelerating tube which is positioned at the center of the transformer coil system. The accelerating tube is made of 88 ceramic tubes and 87 stainless steel disks by alternately stacking them up and being bonded together. The pressure of the accelerating tube is maintained below 10^{-7} torr. The voltage distribution of the accelerating tube is manipulated by connecting appropriate resisters between stainless steel disks. The scanning system is used for the uniform spread of the accelerated electron beam through a Titanium extraction window. The physical size of the electron extraction window is 980 mm X 75 mm and the scanning frequencies of horizontal and vertical directions are 55 Hz and 925 Hz, respectively. Figure 1 shows the simplified diagram of the electron accelerator.

0-7803-3053-6/96/$5.00 ©1996 IEEE

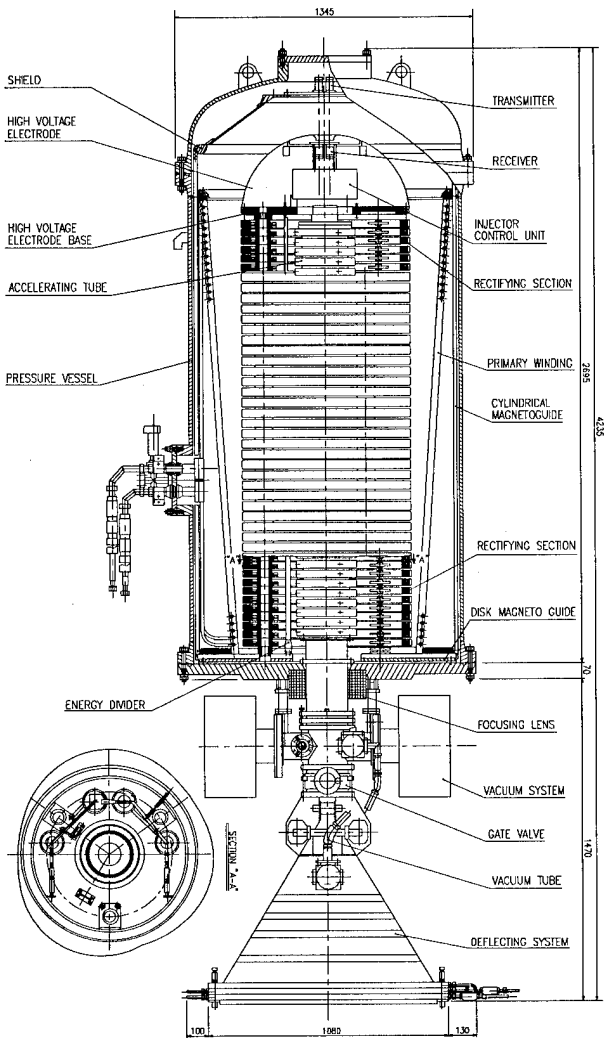


Figure 1. Simplified diagram of the electron accelerator.

III. COMBUSTION FLUE GAS PURIFICATION

One of the most prominent environmental applications is the combustion flue gas purification process[3] for the treatment of the flue gas from incineration plants and coal power plants.

Figure 2 shows the simplified schematic of the flue gas treatment. The irradiation of the electron beam produces radicals from the steam vapor inside the reactor, which react chemically with SO_X and NO_X gases and produce acids such as H_2SO_4 and HNO_3. The neutralization of the acids is the final process of the electron irradiation method. There are advantages of the electron irradiation method over conventional methods. Since the electron irradiation process is a dry process, no secondary waste water is produced as the by-product of the process. When ammonia gas is fed as the neutralizer, the by-product can be used as a fertilizer. The reduction of SO_X, NO_X, and HCl also can be done simultaneously and the fact that the area of the facility is much smaller than that of the conventional facility could be the most attractive advantage.

Bench scale tests using the flue gas with the flow rate of 4 Nm^3/hr promises the simultaneous reduction of SO_X and NO_X up to 90 % and 80 %, respectively. A pilot plant able to treat the flow rate of 200 Nm^3/hr is under construction for the treatment of the flue gas from a municipal incinerator.

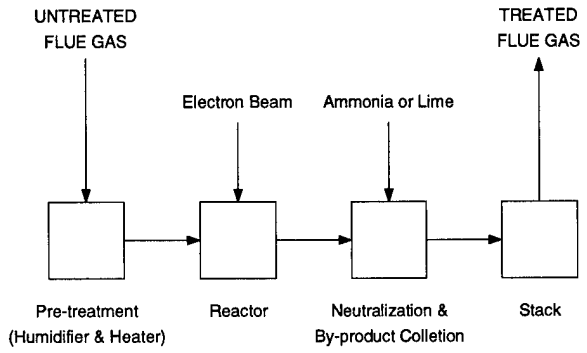


Figure 2. Simplified schematic of the combustion flue gas purification process.

IV. WASTE WATER TREATMENT

The treatment of municipal and industrial waste water becomes a more important subject in the field of environmental engineering.[4,5] The treatment of the industrial waste water containing refractory pollutant is actively studied in Samsung Heavy Industries.

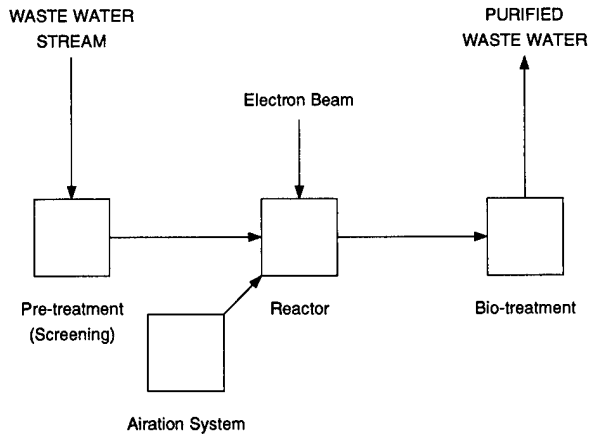


Figure 3. Simplified schematic of the industrial waste water treatment process.

Figure 3 shows the simplified schematic of the industrial waste water treatment. The irradiation of the electron beam to waste water produces radicals such as e^-_{aq}, H•, OH•, H_2•,

H_2O_2•, H^+, OH^-_{aq}, H_2O•, and O_2^-•. In order to improve the penetration depth of the electron beam to water, an air bubbling system is employed to help the effective distribution of the radicals. The radicals react chemically with chlorinated organic compounds and generate by-products such as H_2O, CO_2, chloride, aldehyde, and formic acids. The fact that the interaction by the radicals are effective to a wide range of pollutant is the one of advantages of the electron irradiation method. The effectiveness in biological sterilization and decolorization of dyes is another advantage. The method also shows the improvement in sedimentation and coagulation.

Figure 4 shows the preliminary result of application to dye waste water. The solid line shows the reduction of TOC (Total Organic Carbon) and the dotted line shows the efficiency of decolorization as functions of absorbed dose. The sampling of the waste water is performed from dyeing industry complex. As the dose increases, both of the decomposition of compounds and the bio-degradability increase.

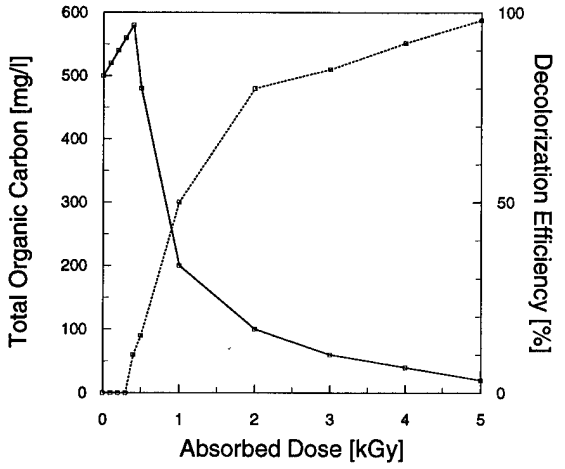


Figure 4. Effectiveness of the electron irradiation method for dye waste water. The solid line shows the reduction of TOC (Total Organic Carbon) and the dotted line shows the efficiency of decolorization as functions of absorbed dose.

V. CONCLUSION

The electron accelerator developed by Samsung Heavy Industries Daeduk R&D Center is used as a part of the electron irradiation processing facility. Our major applications of the electron irradiation processing facility are the subjects related with industrial and municipal waste management. The preliminary result of the flue gas treatment shows the possibility that the technology could become a major impact on the flue gas purification process for incineration plants. The bench scale test of the waste water purification process is also successful. However, both of the applications need more research works for practical applications. The research subjects of other radio-chemical processing techniques are performed by the collaboration with other institutes and industries.

VI. REFERENCES

[1] B. Han, K. Kim, K. Joh, S. Kim, B. Kim, H. Park, J. Park, J. Kim, W. Kang, K. Kang, Y. Kim, S. Lee, and Y. H. Kim, "Design of 1.2 GeV Synchrotron Light Source for X-ray Lithography at Samsung Heavy Industries," these proceedings.

[2] E. A. Abramyan, Industrial Electron Accelerators and Applications, Hemisphere Publishing Corporation, 1988.

[3] H. Namba, O. Tokunaga, T. Tanaka, Y. Ogura, S. Aoki, and R. Suzuki, "The Study on Electron Beam Flue Gas Treatment for Coal-Fired Thermal Plant in Japan," Radiat. Phys. Chem, vol. 41, 1993.

[4] N. Getoff, "Decomposition of Biological Resistant Pollutants in Water by Irradiation," Radiat. Phys. Chem, vol. 35, 1990.

[5] W. J. Cooper et al., "High Electron Beam Irradiation : An Innovative Process for the Treatment of Aqueous Based Organic Hazardous Wastes," Environ. Sci. Health, 1992.

APPLICATION OF ACCELERATED ELECTRON BEAMS FOR RUBBER AND POLYMER MODIFICATION.

A.Shalnov, B.Yu.Bogdanovich, A.Ignatyev, V.Senyukov.

Moscow State Engineering-Physics Institute, MEPhI, Moscow, 115409, Russia.

The radiation modification of polymer and rubber materials permits the proper changing of their characteristics to improve the operational and consumer properties of products. In particular, the radiation processing of polymer and rubber materials permits to increase their strength, wear-resistivity and to expand a range of working temperatures. Practical use of radiating updating polymer is possible in the various areas of manufacture, for example, graphic arts industry, automobile and tractor engineering, light industry and other.

The common feature of ionising radiation beams effect, in particular, electron, x-ray and bremsstrahlung on polymer chemical bands is a possibility of their braking and formation of chemically active radicals, spread throughout a processed material volume pursuant to distribution of an absorbed doze. The products of ionisation and excitation of molecules give an institute to new chemical bands, therefore changing the physics-chemical properties of an initial material. The process of macromolecules formation at the expense of free radicals connection permits to create the chains of complex structured polymer molecules. It results in improvement of elastic properties of a polymer material, expansion of a temperature range, in which it saves properties. However, except processes of molecules association during interaction of a polymer material with ionising radiation the processes of the molecules oxidenting and formations of products with shorter chains occur also. In view of this positive result (i.e. the improvement of operational properties of products manufactured from modified materials) can be received only at a determined ratio of products, formed as a result of these two processes, that is reached at quite determined value of an absorbed doze for each type of a material.

To research the polymer materials physical properties changing under electron beam radiation with energy 4...8 MeV and average current up to 100 μA were used for material processing. A conversion target was also used for creation of bremsstralung and mixed beams. However the efficiency of bremsstralung has appeared to be essentially smaller, than of an electron one.

A The nitrille rubbers modification.

The radiation-chemical modification of rubbers permits to improve considerably theirs limiting operational parameters. Thus the most essential increases appear for wear-resistivity (up to 5 times), limit of elasticity (up to 5 times) and working temperature range (up to 2 times). Such changes of the nitrille rubbers properties are stipulated by occurrence of additional cross-bands between polymer molecules under the ionising radiation beams influence.

For research of the rubber properties change under radiation modification the sample of rubbers marks 7-N068-1, IRP-3029, 7-IRP-1352, 7-V14 were used. These marks rubbers are widely used in automobile and tractor engineering, produced by industry of Russia. In particular, these rubbers are used for manufacturing various seals, shock-absorbers.

The main results of conducted researches on some marks rubbers properties changing are listed in the Table. These results are obtained for optimum values of absorbed dozes. It is necessary to note, that the range of an absorbed doze value variation, in which given parameters are reached, is about (30 ...50) % from the optimum value.

The obtained results show, that at all tested rubbers samples at an insignificant increase of a module of elasticity (i.e. increase of its rigidity) an essential increase of wear-resistivity and limit of elasticity is observed. In turn, the increase of a material limit of elasticity also increases the durability of products, manufactured from it, that works as seals and shock-absorbers.

The tests of bearings seals, made from rubber mark 7-N068-1 and been processed by electron beam, that were carry out at a specialised equipment have shown, that the such seals durability grows in 2 ...3 times in comparison with control samples.

B. The silicone rubbers modification.

The silicone rubbers are used in cases, when application of usual rubbers is not effective or is impossible because of significant deterioration of their properties. As a rule, it is connected with work at increased or lowered temperatures. The usual rubbers in these conditions either become very rigid and fragile (low temperatures), or become plastic with elasticity loss (high temperatures). The silicone rubber save serviceability in a wider temperature range: at lower and higher temperatures both.

In particular, pursuant to help data [1], the most widespread samples of the silicone rubbers serviceable (i.e. the changes of their properties are insignificant) at temperatures up to -35 ...-40 ℃ (see Fig.1). The radiating processing of the silicone rubbers results in improvement of their properties at low temperatures. A number of experiments on processing of the silicone rubber samples mark 9M4218 was conducted. The rubber of this mark is applied by the firm Caterpillar (USA) at seals manufacturing of the tractors.

The results of these experiments are shown in Fig.2. Here the graphs of a rubber module of elasticity relative value $E(t) / E_0$ va. sample temperature t for various values of an

0-7803-3053-6/96/$5.00 ©1996 IEEE

absorbed doze (here the size of an absorbed increased from sample A to sample C) are plotted. The dependence of a module of elasticity on temperature in a range from -40 up to -80 ℃ for processed samples appears to be smoother in comparising with untreated ones. The 50 % decrease of module of elasticity for processed samples is observed at temperatures on 15 ...20 ℃ below, than for an initial material.

C. Kaprolon modification.

The kaprolon, as well as the rubber, is widely enough used in engineering for manufacturing of various details. In particular, it is used for manufacturing of cartridges of sliding bearings and gears. In this case a special significance is given to such characteristics of a material, as a sliding friction factor, limit of elasticity, wear-resistivity.

The researches conducted have shown, that at optimum absorbed doze values the kaprolon parameters increases as following: module of elasticity - at 20 % , limit of elasticity - in 4 times and wear-resistivity - at 60 % .

D. Polymer materials for a graphic arts industry.

In a graph art industry a metal and a photo polymer high forms are used in printing process. Photo polymer forms materials like cellophot and flexophot are used. Thus the photo polymer high forms cost appears far below the cost of metal ones. Besides this advantage of the photo polymer forms there are a number of essential defects: a significant wear (it means low durability), that is due to insufficient strength of the photo polymer material and low operating temperature. These defects do not permit to use given materials in some technological processes required increased working temperature. The radiating processing of photo polymer high seal forms give a possibility to increase a limit of elasticity of a material in 4 ... 5 times, and working temperature up to 200 ° C. Such change of the material properties enables to increase the forms durability in 50 and more times for application in usual conditions. Moreover after modification they can be used in processes, where untreated forms are disabled. In a number of cases, it permits a complete replacement of the metal forms by the photo polymer ones.

E. Shoe industry.

A thermoplastic polyurethane is used in a footwear industry for manufacturing shoes. The special researches were conducted to define the opportunities of the polyurethane physical properties improvement, in particular, the wear-resistivity increase, with the help of radiation processing. The experiments been accomplished show following results. The radiation processing provides a possibility to increase a material wear-resistivity in 1,7 ...2 times.

The other physics-mechanical properties of the material do not change. The processed products cost grows not more than on 15 ...20 %.

Thus, the conducted researches of electron beams effects on polymer and rubber materials have shown a possibility of essential improvement of their operational properties, such as strength, wear-resistivity, work temperature. The real values of the appropriate materials parameters change may be up to several times.

REFERENCES

[1] V.K.Knyazev, N.A. Sidorov et al. Radiazionnaya stojikost materialov radiotechnicheskich construkziji, M: Sov. Radio, 1976.

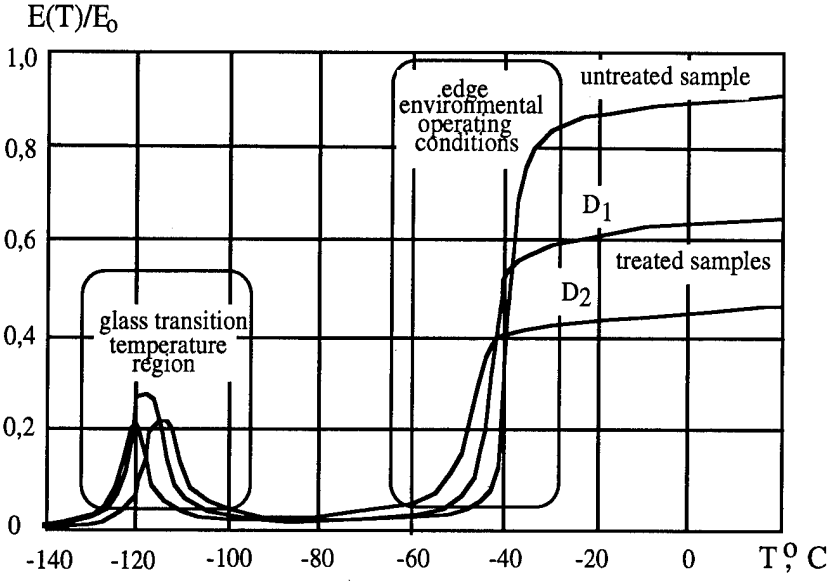


Fig. 1. The silicone rubber module of elasticity relative change E(T)/To vs. temperature T for various values of an absorbed doze (D1 < D2).

Material	Parameter increase, %		
	Wear-resistivity	Module of elasticity	Limit of elasticity
Rubber 7-N068-1	400 ...500	10 ...20	400 ...500
Rubber IRP-3029 7-IRP-1352	300	20 ...30	500 ...600
Rubber 7-V14	200	15 ...20	200 ...300

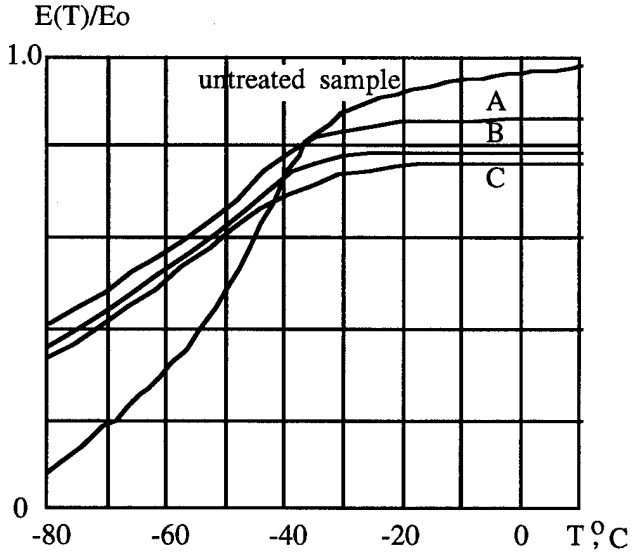


Fig.2. The silicone rubber (mark 9Ì4218, Caterpillar Inc.) module of elasticity Å(Ò)/Åî relative change vs. temperature Ò for various values of an absorbed doze of electron beam irradiation (absorbed doze increases from sample A to sample C)

STATUS ON LOW ENERGY (10 MEV RANGE) X-BAND LINACS DEVELOPED WORLDWIDE

A.V.Mishin
Schonberg Research Corporation
3300 Keller Street, Bldg. #101, Santa Clara, CA, 95054

Abstract

Portable X-band linear accelerators characteristics are analyzed. An attempt is made to summarize the commercial application areas in accordance with achievable beam basic characteristics using available microwave power sources, especially magnetrons. Guidelines for the further research and linac characteristics improvement in order to meet the customers' requirements are presented.

1. Introduction

The history of portable linear accelerators powered by X-band magnetrons started in the early 60s. The reason for entering into a shorter wavelength region to accelerate charged particles was quite obvious - to reduce the size and weight of accelerator head. Technological problems in building such a device were considerable enough to create some difficulties for a new generation of portable linac systems. Part of the problem was that a small, comparatively cheap, and reliable microwave power source was not reliable enough at power levels over 1 MW. However, magnetrons with power of 0.25 to 0.5 MW were successfully applied for accelerator technique. The necessity to operate at low power levels boosted up the technology of X-band accelerators and encouraged designers in the United States and Russia, where most of the work has been done, to generate new ideas for accelerator development. Therefore, during more than a thirty year period, interest in these unique machines has grown and been supported by few groups in the accelerator designers society. Currently, portable X-band accelerators are commercially available with a 1.5 MW magnetron. Recently, the 10 MeV level was approached and a beam over 12 MeV was delivered in a 1 m long section with the same magnetron. This opens new horizons for application in various fields- non-destructive testing, radiology, free electron laser technique, various radiation source simulations, well logging, etc.

2. X-band Linear Accelerator Models and Parameters

Small Accelerator Laboratory of Moscow Engineering Physics Institute under supervision of Dr. I.S. Shchedrin developed a number of X-band linacs U-30, 31, 32, 33, 34, 35, 36 [1, 2, 3]. All structures are travelling wave, except U-34 (Fig.1) [3] and powered by 0.25 or 0.5 MW magnetron.

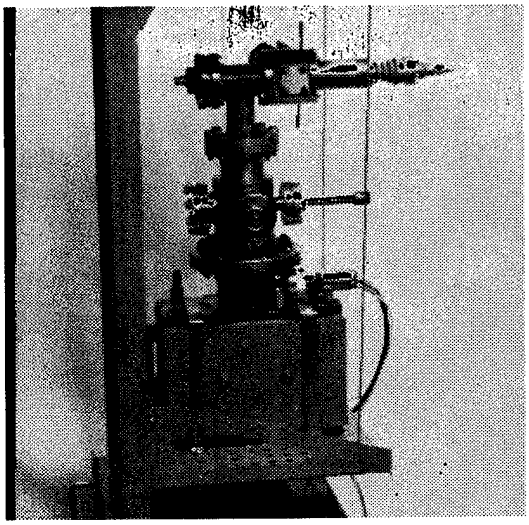


Figure 1: U-34 1 MeV, 30 mA, 11.6 cm SWF section designed for 0.5 MW magnetron.

Basically, these machines are not portable and once installed are not transported any more. New systems are being developed to improve portability of the units.

The linacs that were used as portable electron and/or X-ray sources in field are summarized in the following table.

0-7803-3053-6/96/$5.00 ©1996 IEEE

Accelerator &	Energy MeV	Current mA	Dose Rate R/min@1m	Magnetron MW	Acc. length m(TW/SW)	Mass kg	Application
[4] ISTOK,Russia	1	50	-	0.3	0.27 (SW)	-	test piece
UT-8A[5] VNIIAGG, Russia	6	0.5	-	0.5	2.0 (TW)	100	well logging
MINAC 1.5 SRC, USA [6]	1.5	30	2.5	0.2	0.4 (SW)	16	NDT, curing
MINAC 4 SRC,USA[6]	3.9	100	100	1.5	0.3 (SW)	25	NDT, curing
MINAC 6 SRC, USA [6]	6.0	50	300	1.5	0.5 (SW)	41	NDT, therapy

We have developed MINAC-9 [7] which was supposed to be a prototype of the system for electron beam therapy system in operating room [8]. Recently, a high gradient standing wave structure has replaced a second regular section of this two-section linac and allowed us to increase the achievable energy limit to 12.5 MeV using the same 1.5 MW magnetron.

One of the unique features of 9 and 13 MeV units is a possibility of smooth broad band energy regulation. We feel that this upgraded version of 9 MeV section is still not at the energy limit. A predicted limit with the same magnetron is around 15 MeV. Microwave design is shown on Fig.2.

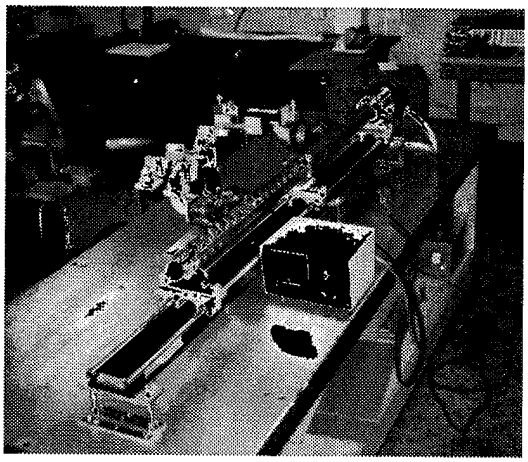


Figure 2: Design of 9 and 13 MeV MINAC system.

This is a working prototype with removed magnetic shield.

9 and 13 MeV accelerator testing is currently in progress. The characteristics are stable and reliable. 9 MeV accelerator section is recommended for NDT application and will be a good addition to a family of MINAC units.

This recent advances has developed some interest in this accelerators as potential injectors for portable free electron lasers.

3. Main applications of X-band portable linacs today include the following:

1. Non destructive examination of thick wall and dense components with equivalent thickness up to 30 cm of steel (example: MINAC 4/6). Real time data processing is possible in some cases.
2. Radiation therapy (MINAC 6/9/13)
3. Well logging (UT-8A, not used any more)
4. Electron beam curing (MINAC 1.5/4)
5. Injectors for portable FEL (MINAC 9/13) - new potential application.
6. Electron beam treatment of various objects (U30...U36, MINACS).

REFERENCES

1. I.S. Shchedrin, X-Band Linear Accelerators, Proceedings of All-Union Charged Particle Accelerators Seminar, Kharcov, 1985, p.6

2. I.I.Gozin, V.A.Poliakov, I.S.Schedrin Development of Linear Accelerator for High Energy Microscope Unit, Proceedings of 4th All-Union Meeting on Charged Particle Accelerators Industrial Applications, Leningrad, 1979, pp.207-213.

3. A.V. Mishin, Standing Wave X-Band Accelerator U-34-1 (in Russian), Abstracts of 12th Charged Particle Linacs Seminar, Kharkov, 1991.

4. M.M. Anuchina, et al., Small Size Pinched-off 1 MeV X-band Linac (translated from Russian), Voprosi Radioelectronici, ser. 1, Electronica, #9, 1961, pp.47-53.

5. A.I.Khaustov, E.V.Suvorov, Electron Linear Accelerator for Well Logging - Proceedings of All-Union Conference, "20 years of Isotopes and Radiation Sources Industrial Application", M., Atomizdat, 1968.

6. Russell G. Schonberg et al., Portable X-Band Linear Accelerator Systems, 1985, IEEE Transaction on Nuclear Science, V. NS-32, #5 .

7. A.V.Mishin, R.G.Schonberg, H.Deruyter, T.Roumbanis, Intraoperative X-band Linear Accelerator Structure Design, Proceedings of 4th European Particle Accelerator Conference, London, 1995.

8. M.L.Meurk, R.G.Schonberg, G.Haynes, and J.M.Vaeth, The Development of a Small, Economic Mobile Unit for Intraoperative Electron Beam Surgery, Am. J. Clin. Oncol. (CCT), p.p.459-464, 1993.

LINEAR ACCELERATOR FOR RADIATION CHEMISTRY RESEARCH AT NOTRE DAME

K. Whitham, S. Lyons, R. Miller, D. Nett, P. Treas, A. Zante
Titan Beta, Dublin, CA 94568
R. W. Fessenden, M. D. Thomas, Y. Wang
Radiation Laboratory, University of Notre Dame, Notre Dame, IN 46556

ABSTRACT:

An 8 MeV, S-Band linear accelerator has been delivered to Notre Dame by Titan Beta Corporation. This accelerator utilizes a variety of techniques to provide uniform dose repeatability, very low dark current, and high beam current over a range of pulse widths from 2 ns to 1.5 s. This paper describes the design and results of tests.

APPLICATION

The specifications for this LINAC were developed to meet the needs of basic research in Radiation Chemistry. Various types of samples will be irradiated, but the main application will involve production of short-lived chemical species in liquid samples (contained in a 1 cm silica cell) and their detection by optical absorption methods at visible and ultraviolet wavelengths (pulse radiolysis). Typically, the sample is irradiated by pulses every several seconds and the changes in photodetector output digitally recorded and averaged for improved signal-to-noise ratio. The special requirements include: a short pulse for study of very fast processes; enough charge accelerated to produce a sufficient chemical change; low pulse jitter relative to a trigger pulse; no current outside of the main pulse to avoid a complicated analysis of data; and a very low dark current so that, if the observation is carried out for a number of seconds, no additional irradiation will be occurring. The energy is selected to be high enough to penetrate several centimeters of material of moderate density without causing serious nuclear activation of the samples. Because the optical absorption at a number of wavelengths will be combined to form a spectrum, it is vital that the accelerated charge (dose) be accurately repeatable.

GENERAL DESCRIPTION OF THE LINAC SYSTEM:

The system is designed to have very repeatable shot to shot dose along with low pre and post pulse radiation.

The centerline shown in Figure 1 begins with a 130-140 kV gridded electron gun similar to the Stanford Linear Accelerator Center (SLAC) Injector gun. It includes a ceramic envelope capable of withstanding 150 kV DC in air, stainless steel electrodes and vacuum parts, and a replaceable 2 square cm dispenser grid cathode assembly.

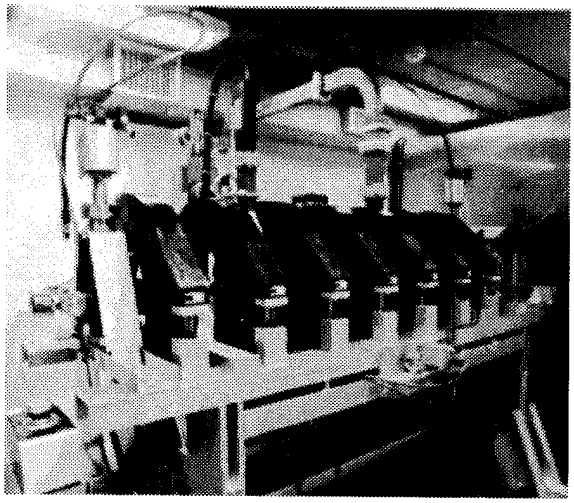


Figure 1

The gun is followed by a high vacuum tee with ion pump, an isolation vacuum valve and a fast beam current monitor.

A water cooled, temperature stabilized prebuncher cavity is next, followed by a drift space designed to compress 60% of the charge emitted from the electron gun into a longitudinal phase space of 60 degrees at injection into the accelerator guide.

The accelerator is a 2 pi/3 mode, temperature stabilized guide with a tapered velocity buncher designed to satisfy the performance as stated below.

A thin lens is placed after the gun as part of the beam transport system. A bucking coil is placed over the cathode region of the gun to cancel out any fringe fields from the coil system.

A series of accurately aligned Helmholtz coils are provided along the beamline to transport the beam and to provide a beam diameter of approximately 5 mm at the output of the accelerator.

0-7803-3053-6/96/$5.00 ©1996 IEEE

An ion pump is placed after the gun in the injection system and at the beginning of the accelerator to keep the operating vacuum in the proper range.

Evacuated RF waveguide is used in this system. This has many advantages for reliable and maintenance free operation.

The RF transmitter for the linac is comprised of a line- type modulator with all the necessary power supplies, controls, and monitors for operation of a SLAC model XK5 20 MW, 2856 Mhz klystron. Because of the requirement for a highly reproducible pulse to pulse dose rate, a very accurate switching power supply is used to charge the PFN.

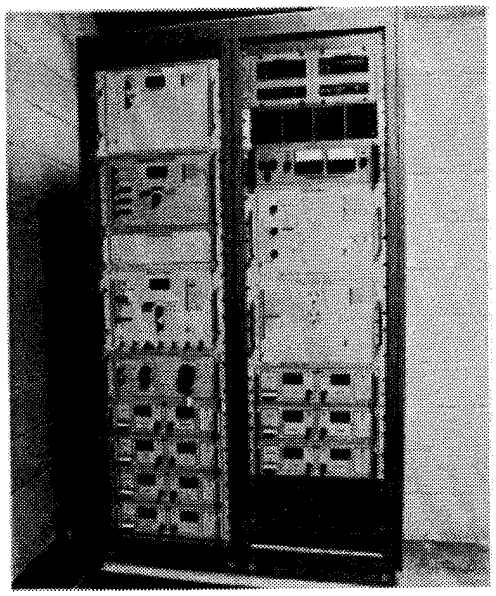


Figure 2

In addition, in order to be able to maintain dose repeatability within ± 1% between single pulses taken up to 30 minutes apart, the electron gun HV and control voltages and the PFN firing level are stabilized prior to triggering the pulse.

The need to minimize dark current required the use of a low dark current electron gun and the use of a pin diode switch to control the RF drive pulse with respect to the beam pulse.

A water cooling system is provided for maintaining the beam centerline components at 40 degrees C ± .4 degrees C and for removal of heat from the klystron, modulator, and magnetics.

Controls and monitors for system operation are mounted in a multiple bay vertical rack assembly in the control area. Some local control capability is provided for local service operations of the modulator. Figure 2 shows the control rack.

SPECIFICATION:

Frequency	2856 mHz
Input Power	18 mw (max)

STEADY STATE OPERATION:

Beam pulse width	1.5 s
Peak beam current	2 A
Energy	6 MeV

STORED ENERGY OPERATION:

Beam pulse width	2 ns to 10 ns
Beam current	4 A
Energy	8 MeV
Dark current	<10 pC
Pulse Jitter	± 100 pS
Dose Stability (pulse to pulse)	± 1%

PERFORMANCE:

The pulse current and time profile was determined using a terminated 50 ohm faraday target, a Heliax cable, and a Tektronix 644 digital oscilloscope. The integration feature was used to determine the charge in the pulse. The beam size was determined by coloration of glass plates and was checked by bleaching of blue cellophane. The beam characteristics at several pulse widths are

pulse width	peak current	beam size
2.8 ns	4.4 A	5 mm
10 ns	5 A	5 mm
100 ns	3.3 A	7 mm
1.7 s	2.2 A	10 mm

The time jitter of the beam pulse was determined by using the "infinite persistence" mode of the oscilloscope and measuring the width of the trace after recording a large number of pulses. The jitter was ± 125 ps.

The beam energy was measured with the 2.8 ns pulse by exposing a stack of glass plates and measuring the darkening with a spectrophotometer. A plot of absorbance against plate number gave the dose profile which could be extrapolated to the electron range.

Two measurements gave similar ranges of 5.15 g/cm2 for an energy of 8.9 MeV with the 4A 2.8 ns pulse. the microwave power setting was 18.6 MW.

The extraneous dose after the main pulse was determined from a recording on the digital oscilloscope which was checked by a photograph of the trace on a Tektronix 7104 with 7A29 plugin. It consisted of a slight tailing after the main pulse over about 20 ns with a total charge of 1% that of the main pulse. No echo pulses from reflections in the electron gun pulser were seen. The dark current was determined by use of an unterminated target and a Keithly electrometer. The current measured with high voltage on the electron gun but no rf for acceleration was 0.5 pA.

Dose repeatability was determined by integration of the current waveform on the 644 digital oscilloscope. Two different series were run using the 2.8 ns pulse. In the first, the pulse rate was set at 4 Hz and individual traces taken by manually arming the oscilloscope. the results are given below with an rms deviation of 0.45%. Then the accelerator was used single shot (with a single rf pulse) and pulses were recorded at about a 20 minute separation with the machine put at standby in between. The three pulses taken single shot are quite the same. This excellent behavior validates the care taken to stabilize the injector and modulator charging voltages.

1. Ten pulses taken with the repetition rate set at 4 Hz. The scope was triggered single shot and manually for each pulse and the area read. The average dose of 49.627 equals 10.9 nanocoulombs of charge.

49.435 .....49.410
49.859 .....49.820
49.930 .....49.510
49.255 .....49.530
49.905 .....49.620

average = 49.627
rms = 0.225 or 0.45%

2. Three single pulses taken with the machine turned off between pulses.

Time	Dose
9:24	49.345
9:47	49.574
10:02	49.570

CONCLUSIONS:

The system was installed, meets the specifications, and is in use at Notre Dame.

IREN STATUS: NEW ELECTRON LINAC DRIVEN INTENSE RESONANCE NEUTRON SOURCE *

Submitted by A. Krasnykh on behalf the JINR IREN Linac Team

Joint Institute for Nuclear Research, Dubna, Moscow District, 14980 Russia

Abstract

Recently, JINR (Dubna) decided to erect a new accelerator driven intense resonance neutron spectrometer [1] Specifications in terms of output parameters are as follow. The integral neutron yield is approximately 10^{15} neutrons per second. The neutron pulse duration is approximately $400ns$. The repetition rate is $150Hz$. IREN source consists of a S-band linac, a multiplying target as a converter and a plutonium subcritical core. The present status of the S-band linac systems will be addressed.

I. Introduction

Frank Laboratory of Neutron Physics is erecting a new pulse neutron spectrometer. The neutron source consists of three parts: a $200MeV$, $10kW$, $250ns$ S-band linac, a photoneutron target and a plutonium subcritical core.

The intense resonance neutron source, (so called IREN) [1], is designed for investigations in the resonance neutron energy range. It would also provide good opportunities for experiments with fast ($E_n \leq 5MeV$) and thermal neutrons, specifically for thermal neutron measurements in condensed matter physics. The new source would complement the experimental possibilities of the stationary neutron sources of Grenoble, Gatchina, etc., at which experiments with thermal neutrons are carried out, (as they were in the study of parity violation effects in neutron interactions), and also of the pulsed neutron sources — GELINA, FAKEL, ORELA, LU-50 — operating with linear electron accelerators, which provide optimum conditions for investigating various averaged effects over fast neutron range.

An idea to use the combination of an electron accelerator as an injector and a reactor core as a neutron multiplication target is not only a tribute to tradition [1] but also reflects our desire to have the advantage over other time-of-flight, high resolution, neutron spectrometers, specifically over proton accelerator-based ones. This combination would allow:

- reduction of the requirements for electron accelerator parameters and thus have a safer operating machine;
- reduction (by an order of magnitude or even more) of the construction cost;
- have a much cheaper operating machine, both with respect to power consumption and the number of the maintenance staff;
- use of the entire infrastructure of the now existing spectrometer, including buildings, flight paths, experimental pavilions, part of the research instruments and the accelerator power supply system.

The IREN project is optimized for investigations with resonance neutrons and designed to have the parameters given in Table 1 (for comparison, the parameters of the existing IBR-30 booster are also indicated).

Table 1

Parameters	IREN	IBR-30/ LUE-40
Electron beam energy, MeV	200	40
Average beam power, kW	10	2.5
Electron pulse duration, ns	250	1600
Repetition rate, Hz	150	100
Beam current, A	1.5	0.3
Neutron multiplication gain	28	200
Integral neutron yield, n/sec	10×10^{15}	0.5×10^{15}
Fast neutron pulse duration, ns	400	4500

II. Layout of the System

A schematic layout of the IREN facility is given in fig. 1. The same IBR-30 and LUE-40 building will be used for the placement all IREN systems. The electron gun (1) delivers a pulsed electron beam. The beam here is accelerated up to 200 keV. After that the beam is driven downstairs to buncher and then to the first acceleration section (2). The beam is accelerated with a high gradient of $35MeV/m$. The second section (5) is placed in floor hole directly after first one. The final beam energy will be $\approx 200MeV$. The focusing system consists of two parts. The solenoidal field (8) is applied between the end of e-gun and the entrance of the second section. Four pairs of quads (9) guide the beam to the target (10). The convertor is a source of photoneutrons produced in the (γ, n)- reaction as a result of electron bremsshtralung of the accelerator beam. The converter is surrounded by a core with fuel elements. Converter and core are located in the reactor hall of the IBR-30 building. The core is made up of 124 plutonium fuel elements, similar in construction to the fuel elements of the IBR-30. Fuel elements are combined in groups forming fuel assemblies.

III. Technical Aspects of the Electron Linac-Driven IREN Source

The linac project was designed in INP (Novosibirsk) by the A. Novokhatsky team [2]. A background of the design was the use of S-band SLAC 5045 klystrons. Both the injector of ϕ-factory

*Work supported by the JINR Plan Development of Facilities under JINR code# 0993-95/97

[1] JINR has a old facility IBR-30, which was build more 30 years ago and still operated up to now

0-7803-3053-6/96/$5.00 ©1996 IEEE

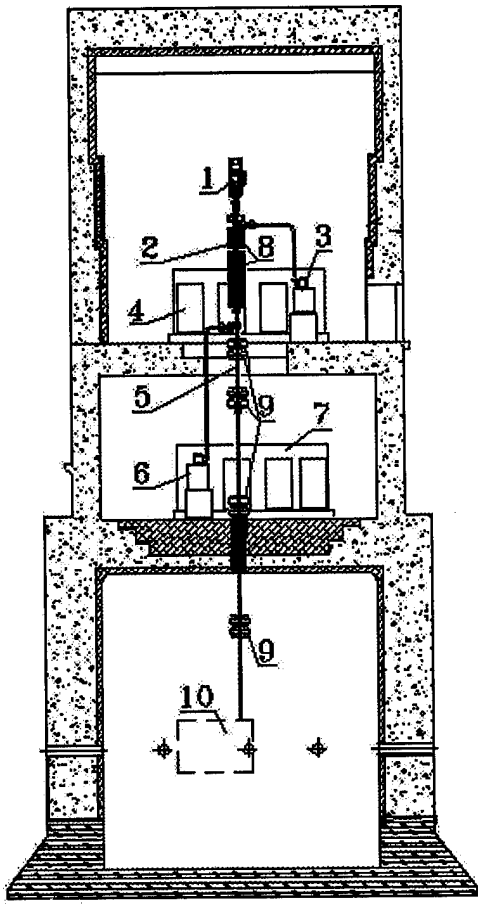


Figure. 1. Layout of the IREN facility

and the linac for IREN had been designed on the basis of the 5045 klystron used as high power pulse RF-sources.

A. The Electron Gun

A triode-type Koontz-like thermonic gun has been designed for a vertical placing. INP (Novosibirsk) will supply a cathode-grid node for the e-gun and a high voltage ceramic feedthrough while the rest of the e-gun nodes will be developed and manufactured at JINR. The electron gun consists of a high voltage DC power supply, a low voltage DC power supply for the grid driver, the grid driver itself, a high voltage insulator and a cathode assembly. The ceramic insulator in the gun is designed to withstand the maximum system voltage under normal atmospheric pressure. The cathode magnetic field on the cathode surface is zero. A vacuum pressure of about $10^{-9} Torr$ is provided by a pumping rate of about 60 liters per second.

The agreement regulating the working relationship between Frank Laboratory Neutron Physics and other JINR Laboratories for creation of the e-gun is at the final stage. The Contract with INP (Novosibirk) for manufacturing and shipping the high voltage feedthrough ($200kV$) and the cathode-grid unit has been prepared.

Table 2

Energy of electrons	$200keV$
Peak current	$10A$
Pulse width	$250ns$
Repetition rate	$150Hz$
Emittance less than	$0.01\pi \cdot cm \cdot rad$
Time jitter less than	$1ns$
Energy spread less than	$2keV$

B. Buncher, Accelerator Sections, SLED-cavities

These main linac elements will be designed, produced and shipped to JINR by INP (Novosibirsk) at the beginning of 1997.

The electron capture efficiency up to 55% in the energy range $\triangle E/E = 3\%$ can be reached with an initial current of $10A$. Parameters of the acceleration sections is shown in Table 3.

Table 3

Operation mode	$2\pi/3$
Operation frequency	$2856MHz$
Section length	$3030mm$
Number of accelerating cells in section	85
Period	$34.98mm$
Disk aperture radius	$25.6mm$
Cavity radius	$83.7mm$
Disk thickness	$6mm$
Overvoltage coefficient	1.7
Group velocity	0.02
Quality factor	$1.3 \cdot 10^4$
Shunt impedance on unit length	$53\mathrm{M}\Omega/m$
Accelerating gradient	$40MeV/m$

In the first quarter of 1995, obligations for the Contract on design, manufacturing, assembling and tuning of the IREN linac accelerating system were drawn up. INP (Novosibirsk) as the head organization, will design and create the buncher, two accelerating sections and the SLED-cavities for two klystrons, and will also carry out adjustment of the nodes which are being created at JINR. The work is being carried out according to the Contract time schedules.

The work on design of the RF-feeder is being performed at the Moscow Engineering Physics Institute and at the power stacks of "ISTOK" (Phryazino, Moscow region). This work is in the final stages: manufacturing of the feeder elements is almost complete and they could be shipped to JINR after "cool" tests at the nominal power of the 5045 klystron.

C. Modulators for the 5045 klystrons

The average modulator power consumption is $\approx 130 - 140kW$. Several units of the Russian M-250 modulator had been designed and manufactured for the updating of the ErPhI injector before the Russia industry collapsed. According to the Agreement between JINR and Armenia, there is a possibility to use different nodes of M-250's for the IREN source.

The main parameters of the M-250 and the modulator which is necessary to achieve (it was named as M-350) are shown in Table 5

Table 5

Parameter	M-250	M-350
Pulse power, MW	65	150
Tube voltage, kV	50-250	50-350
Output voltage of PFL, kV	20	23.5
Output pulse current, kA	3.6	6.3
Flat top pulse duration, μsec	8.0	3.5
Top flat unevenness, %	± 0.15	± 0.5
Repetition rate, Hz	100	150

The relatively high average power consumption ($\approx 150kW$) by the modulator of the 5045 klystron and the absence (in Russia) of a modulator scheme realization regarding such power have demanded the technical design project of a full scale, stand modulator. This project has been completed for the time being. The high power stand has been set up at the Frank Laboratory and a high power supply has been already created for the 5045 klystron modulator. Strategy for the creation of the 5045 klystron modulator based on Russian standards has been determined by the collaborators of JINR (Dubna), ErPhI (Armenia) and the Russian Institute of Powerful Radioconstruction (St. Petersburg). The scheme of the M-250 Russian modulator will be the basis for the design of the new M-350 modulator for the 5045 klystron (SLAC). It should be noted that several M-250 modulators were manufactured for the OLIVIN acceleration station and stocked at ErPhI. The basic technical decisions for the redesign scheme and equipment composition of the new M-350 modulator have been determined.

Two types of Russian thyratrons were shipped to SLAC (Stanford University) for the purpose of complex high power tests in order to study the possibility of using such thyratrons in the 5045 klystron modulator. For the time being, the first one has already been assembled on the high voltage stand and its tests have been begun. An item for pulse amplitude stabilization of the 5045 klystron modulator has been considered - that it be supplied from the industry network directly. A technical solution was suggested which does not demand the creation of a special highly stable supply. In this case, the suggestion provides for stability of the voltage amplitude in the tube when the modulator is supplied from the industry network used at JINR. It was shown that this task could be fulfilled with the least amount of engineering and industrial effort if the new technical decisions and the OLIVIN station elements could be used.

The relationships between the collaborators on decisions of the questions connected with the new modulator creation have been drawn up. The Armenian government has agreed to ship the part of the OLIVIN station equipment needed to arrange a full scale klystron stand at JINR as Armenia's share of the payment for the JINR budget. Right now this equipment is being prepared for transportation from ErPhI to JINR.

D. Focusing System

The technical specifications for the acceleration focusing system design has been coordinated with INP (Novosibirsk) and accepted by the Laboratory of Nuclear Problems team of JINR. The estimation of tolerances for the focusing system elements is being done according to the time schedule. The work on the construction of these elements has begun. A variant of the separate short focusing solenoids is being designed to reduce the amount of power value consumed from the network. Simultaneously, modelling of the hardware for the power supply system is being carried out.

E. General Layout of the Linac in Existing FLNP Building #43

Fixation of the main acceleration elements relative to the existing linac pavilion has been done. The engineering study of two new M-350 modulator placements at 9.5 m altitude has led to a high equipment concentration and increased demands for the production of an air cautioning system. As an alternative variant, placement of the modulator equipment on two building floors is being considered: the first klystron and its facility being housed at 15.6 m altitude and the second one housed accordingly at an altitude of 9.5 m.

F. Control System Design

Test stand studies of the instrumentation system prototype have begun on the IBR-30 and LUE-40 facilities. The system for measuring the general facility parameters (e-beam current, thermal neutron signal, RF power signals, etc.) can be measured for a definite time interval and stored for subsequent analysis in on-line experiments. A study of the influence of different machine operation modes on the neutron flow parameters is being performed.

IV. Acknowledgement

The JINR IREN linac team thank Mrs. A. Schaeffer for her help in preparing this report.

References

[1] IREN Project, Frank Lab of Neutron Physics, JINR, Dubna, 1994.

[2] Linear Accelerator for Intense Resonance Neutron Sourse (IREN), A. Novokhatski, et al., in Proceedings of the 2nd Workshop on JINR Tau-Charm Factory, p.197, D1,9,13-93-459, Dubna 1994.

A COST ESTIMATION MODEL FOR HIGH POWER FELS*

George R. Neil, Continuous Electron Beam Accelerator Facility, Newport News, VA 23606 USA

ABSTRACT

A cost estimation model for scaling high-power free-electron lasers has been developed for estimating the impact of system-level design choices in scaling high-average-power superconducting-accelerator-based FELs. The model consists of a number of modules which develop subsystem costs and derive as an economic criterion the cost per kilojoule of light produced. The model does not include design engineering or development costs, but represents the 2nd through *n*th device. Presented in the paper is the relative sensitivity of designs to power and linac frequency while allowing the operating temperature of the superconducting cavities to optimize.

INTRODUCTION

A spreadsheet-based cost estimation model for scaling high-power FELs has been developed motivated by a desire to uncover the elements with the highest cost leverage to guide a program to develop high-power FELs for industrial processing applications [1]. The point of comparison in this note is the cost per kilojoule of light delivered—the primary economic criterion industry will use to judge the advantage of an FEL for photon processing. There are, of course, other factors which will enter into any decision as to the applicability, practicality, or profitability of a high-power FEL system: reliability, unit power capability, pulse structure compatibility with the desired process, and ability to meet the desired output wavelength.

In this model we have assumed the FEL is an oscillator based on a continuous wave (CW) radio-frequency (RF) recirculating accelerator with energy recovery. The model includes both superconducting RF (SRF) cavities and normal conducting cavities for comparison. The FEL extraction efficiency is an input assumption. Beam average powers, subsystem losses, etc., are calculated self-consistently in the model. An adjunct calculation is performed to estimate the overall device electrical efficiency. The model can optimize cost per kilojoule of delivered light on the SRF operating temperature.

Table 1 shows a set of input machine parameters for a 200 nm output at 100 kW. The FEL single-pass efficiency has been taken as 1.2%, which results in a net FEL efficiency of 0.8% after allowing for mirror losses within the optical cavity. The fundamental limitation in achieving such efficiencies may be the beam transport considerations of the large FEL-induced energy spread.

*Work supported by DOE contract DE-AC05-84ER40150 and the Commonwealth of Virginia.

Table 1: Input parameters to the cost model for the cases shown in the results. Case 2 is used in Figs. 1 and 2.

Case	1	2	3	4	5
Power out (kW)	100	100	100	100	100
Wavelength (μm)	0.2	0.2	0.2	0.2	0.2
Energy (MeV)	250	250	250	250	250
Current (A)	0.05	0.05	0.05	0.05	0.05
Frequency (MHz)	**300**	**500**	**805**	**1100**	**1300**
Gradient (MV/m)	5	5	5	5	5
Temperature (K)	**4.5**	**4.2**	**2.9**	**2.5**	**2.3**
# of recirculations	2	2	2	2	2
Cells/cavity	5	5	5	5	5
# inj. cavities	2	2	2	2	2
Inj. energy (MV)	10	10	10	10	10
Availability (%)	.85	.85	.85	.85	.85

The subsections below discuss the cost estimating modules for each element.

RF Model We were guided by analyses in Reference 2 and CEBAF experience to estimate RF costs by summing two terms, one proportional to the RF power required (high voltage, regulation, mounting, klystrons, and circulators) and one proportional to the number of low-level controls. The low-level controls are frequency independent. Each system costs $65k connected in sets of eight, including procurement, calibration, and installation.

Cryogenics Model The cryogenics module is based on analyses due to C. Rode and D. Proch [3]. In that model, the heat loads consist of three elements: 1) the temperature-dependent surface resistance (BCS) losses, 2) temperature-independent residual losses due to surface resistance of impurities and defects, and 3) static loads which represent heat leakage through fundamental and higher-order-mode power couplers, tuners, and piping connections. The BCS losses in W/m are given by

$$P_{\mathrm{BCS}} = \frac{AE^2}{T}(f/500)^{1.1}\, e^{(-17.67/T)}$$

where $A = 2.6\times10^{-10}$ for the frequency f in MHz, gradient E in MV/m, and temperature T in K showing the exponential operating temperature dependence. The residual power dissipated is

$$P_{\mathrm{res}} = E^2/ZQ_{\mathrm{res}}$$

with a curve fit to existing cavities giving a shunt impedance $Z(\Omega/\mathrm{m}) = 380(f/500)^{0.9}$. Q_{res}, the residual quality factor, is taken as fixed at 3×10^9, although in many cases this has by now been exceeded using careful cleaning techniques at CEBAF. Static losses are given by

0-7803-3053-6/96/$5.00 ©1996 IEEE

$$P_{\text{static}}\,(\text{W/m}) = 8/\sqrt{\text{f}/500}$$

to account for the smaller surface area per meter at higher frequencies. From the total loss at the assumed temperature and gradient the refrigerator power can be calculated. Refrigerators become more efficient and cost-effective as unit size increases. Capital costs scale as $P^{0.7}$ and inversely with T since such operation is less efficient and requires subatmospheric helium transport. Electricity and cryogens are included in the efficiency and operating cost calculations.

SRF Cavities Model SRF represents a major fraction (40%–60%) of the system capital costs. Unfortunately there is a large uncertainty in this value as addressed in presentations at the 1990 TESLA Workshop [4], presumably due to different system designs as well as accounting structures between the laboratories. An expected dependency on frequency due to lower material costs at the higher frequencies does not emerge. For this note, we use \$600k/m independent of frequency.

Normal Conducting Cavities Model If an NC accelerator is assumed, a different cavity module is used and the cryogenic system cost and power consumption are eliminated. No added cost for the cooling system required to maintain the cavities in tune has been applied.

Other Models The cost of the injector exclusive of RF power is assumed to vary as the (beam power)$^{0.7}$. A cost per pass of acceleration is taken as \$1.2M for magnets, power supplies, alignment, and vacuum hardware.

Most wigglers to date have been "one off" so commercial costs include non-recoverable engineering. An exception is the 2.5 m wedge-pole hybrid design at APS, with a cost of ~\$600k. Allowing for procurement, alignment, integration, and controls, we use \$400k/m as the nominal cost. Caution is advisable since it is not obvious that wiggler costs should scale linearly with the length.

The model uses a rule of thumb that diagnostics and control should cost 10% of the systems they are controlling. An optical system cost of \$2500k and a fixed dump cost of \$200k were assumed.

Amortization In many companies capital costs are amortized by calculating present value and return on investment. In this model the capital is amortized at 13.3% per year, roughly corresponding to a 7% rate with an assumed ten-year life.

Operating Costs Operating costs include electricity, cryogens, supplies, and operating labor. Electric costs are assumed at a flat rate of 0.08 cents/kWh in the cited examples. It is assumed that FEL operation requires two people on shift. Maintenance is assumed handled by a separate contract at 1.5% of the system capital cost annually, consistent with CEBAF experience.

Figure 1 shows the relative capital cost contributions in Case 2. On the operating side amortization consumes 59% of the annual budget, followed by labor and electricity at 14% each, and maintenance and supplies at about 7% each.

Stability In addition to cost, the model estimates beam stability margins as a way to ensure some level of credit for changed accelerator performance. The calculations are based on some formulas by J. Bisognano [5]. Three relative margins are calculated: beam breakup (BBU) sensitivity, longitudinal wakefield effects, and transverse wakefield effects. Together they give guidance as to the possibility of operating at high average currents and thus high average powers.

Generally the most limiting effect is BBU, with the threshold current for instability taken to scale as

$$I_{\text{th}} \sim 1/\left[\omega^2 \times L_{\text{acc}} \times (R/Q)_{\perp}\right]$$

where ω is the linac frequency, L_{acc} is the accelerator length, and $(R/Q)_{\perp}$, the transverse impedance, has no explicit frequency dependence. No judgment is made relative to the lattice, since such a choice could be made (in principle, at least) independent of the cavity parameters.

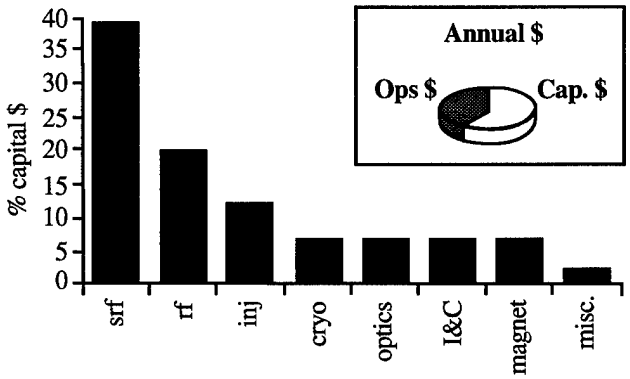


Figure 1. Cost factors. Relative capital cost contribution of each subsystem is shown with annual capital retirement vs. operating cost inset.

RESULTS

As expected, the cost per watt decreases monotonically with increasing power, as is shown in **Figure 2** for both the superconducting design at 500 MHz and the 180 MHz normal conducting design. The range shown for the superconducting design covers a nominal system cost down to what might be achieved using an aggressive approach to cost reduction to get photon costs down to \$0.002/kJ. The room temperature system suffers in comparison from the much higher RF power required due to wall losses, the cavity costs to achieve the same energy (due to low gradients), and the higher electrical costs to power the RF. At 180 MHz and a 2.8 MV/m gradient, the NC system has a BBU threshold which is twice a 500 MHz, 5 MV/m SC system but only 60% of a similar 350 MHz SC linac. Each of these systems could transport in excess of 100 mA (provided a suitable lattice is adopted) which should be sufficient to produce on the order of 100 kW of FEL output.

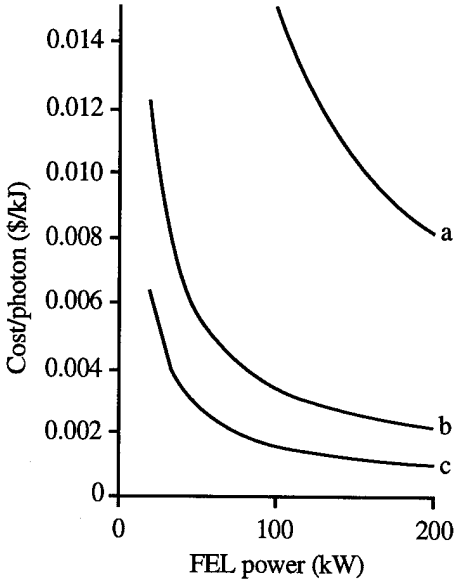


Figure 2. Photon cost versus power. The costs are calculated for a) 180 MHz normal conducting cavities, b) 500 MHz superconducting cavities using nominal values for the element costs, and c) 500 MHz superconducting cavities assuming an aggressive program to minimize costs: SRF cavities reduced to 67% nominal, RF reduced 47%, similar reduction factors for other elements.

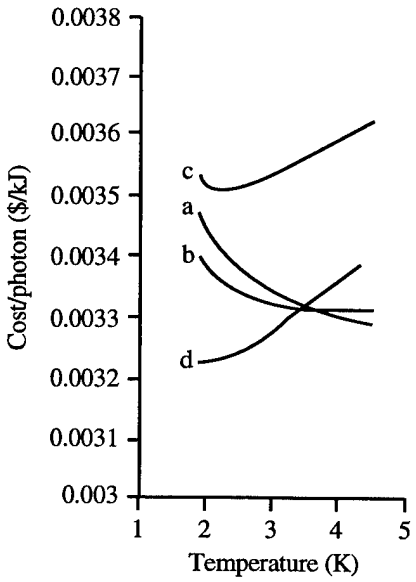


Figure 3. Photon cost as a function of temperature. The output power is assumed to be 100 kW. Costs are shown for: a) 300 MHz at 5 MV/m, b) 500 MHz at 5 MV/m, c) 1300 MHz at 5 MV/m, d) 1300 MHz at 7 MV/m. The lower-frequency cavities optimize around 4 K, and high-frequency cavities around 2 K. These curves all lie within the error bars of the cost model. The high gradient is shown for the 1300 MHz cavity because it is easier to achieve high-gradient operation in higher-frequency cavities due to the reduced surface area, which reduces the possibility for gradient-limiting imperfections.

For a given gradient and frequency the operating temperature can be optimized. Higher-frequency cavities want a lower operating temperature. Due to the competing factors of lower losses but lower refrigerator efficiency at lower temperature, the net frequency dependence of capital and operating cost is quite weak, lying within a 10% band. Uncertainties in the cost algorithm surely exceed this variance. For example, in **Figure 3** the cost per photon is plotted versus temperature The lower-frequency systems are seen to be the least expensive at 5 MV/m and around 4.5 K. If credit is taken for the higher gradients achievable at higher frequencies, the situation reverses and higher frequency cavities yield a less expensive system, as shown in curve d. It thus appears that the operating frequency should be chosen on the basis of issues such as transport robustness, maturity of the technology, and reliability of the equipment. For RF and cryogenics, this clearly favors operation below approximately 800 MHz in the technically mature commercial UHF band and at around 4.5 K for ~1 atm liquid helium transfer pressure leading to simplified and more reliable cryogenics. The conclusion of more extensive parameter variations not presented here is that significant effort should focus on the SRF cavities' capital cost followed by the RF systems. If electron transport to as many as four passes with energy recovery can be technically achieved then benefits accrue. High availability and low operating costs are also important.

The author would like to express his appreciation to J. Bisognano, H. F. Dylla, J. Fugitt, L. Harwood, C. Rode, and W. Schneider of CEBAF and M. J. Kelley of DuPont for valuable comments on this effort.

REFERENCES

1. Laser Processing Consortium, Proposal: High-Power Ultraviolet and Infrared Free-Electron Laser for Industrial Processing (Newport News, VA: CEBAF, May 1994).

2. D. W. Reid, Res. Chem. Intermed. **20** No. 1 (1994) 97–114.

3. C. Rode and D. Proch, Proceedings from 1989 IEEE Particle Accelerator Conference.

4. "SRF and RF Session Summaries", Proceedings from 1st TESLA Workshop.

5. J. Bisognano, "Impedance Formulas for Quick and Dirty Estimates," unpublished.

DETAILS OF THE INITIAL PART OF THE TUNGSTEN ION LINAC FOR PARTICLE TRACK MEMBRANES PRODUCTION

V. Kushin, T. Kulevoy, N. Nesterov, A. Oreshnikov, S. Plotnikov, D. Seleznev and V. Zubovskiy
ITEP, B.Cheremushkinskaya 25, Moscow 117259, Russia

Abstract

The data of designing, tuning and tests on the initial part of the heavy ion linac main systems, that are the 35 kV ion beam injector with the MEVVA-type ion source, the 5 MeV 3m long acceleration section with RFQ and the 0.4 MeV/amu 6m long pre-stripper section with the alternating phase focusing (APF), are presented. The injector produces intensive tungsten ion beam with the working charge of +4, the beam pulse length of 300 mcs and the repetition rate of 25 pps. The main construction feature of the sectionalized RFQ structure are the ceramic insulators as mechanic supports for the 4-rod modulated line. The high power tests data for the single cell of the RFQ structure are given. The APF prestripper section design is described.

I. INTRODUCTION

The RF linac-based technological complex for particle track membranes (PTM) industrial production is under developing now in Russia [1]. The dedicated heavy ion linac is developing in the anticipation of high demand for extra quality membrane products, especially for sterilizing ones. The productivity of the accelerator complex is expected to be not less than some hundred thousands m^2 of irradiated polymer film per year.

First, it must reach high production rate and capacity combined with high quality of irradiation (porosity $\geq$ 20%, irradiation nonuniformity $\leq \pm 5\%$, wide range of film thickness, i.e 10-30 μm). Secondly, the installation must be energetically effective. At last, the industrial linac must be extremely compact, reliable and convinient for maintainances by non-specialized enterprise personnel.

The schematic layout of the 1.7 MeV/amu heavy ion linac for industrial PTM production is shown in Fig.1.

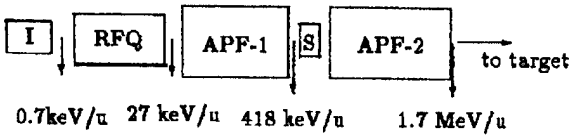


Figure. 1. The schematic layout of the linac

The heavy ion linac consists of five basic units:

- injection unit, which consists of the 35 kV injector based on metal evaporation vacuum arc ion source and beam formation and preminary acceleration section including electrostatic matching channel and RFQ accelerator section
- prestripper APF section,
- intermediate stripper section,
- poststripper APF section,
- exit beam formation line.

Pulse beams of tungsten ions with the designed charge of +4, being produced in the MEVVA type ion source, pass than through high voltage injector terminal of 35 kV and static matching channel. The RF matching of the beam, its bunching and preliminary acceleration is carried out in the 3m long RFQ. The main acceleration is executed in two alternating phase focusing (APF) sections, both 6 m long, up to the final energy of 1.7 MeV/amu. The intermediate beam recharge up to the equilibrium charge of +16 is provided in between two APF sections by a gas stripper at the energy of 0.42 MeV/amu. As the RFQ section so the APF prestripper section are supplied with pulse RF power at the industrially permitted frequency of 40.7 MHz (under maximum pulse length of 800 μs and repetition rate of 25 pps), though the stripped beam is accelerated at doubled frequency of 81.4 MHz. Exit beam sweep and formation at the irradiation target is provided by system of multipole lenses for acceptable pulse irradiation of a wide constantly moving roll of a polymer film. Maximum permissible number of parasitic pores comply with the case when the film porosity per one pulse does not exceed 0.8%. So the getting of optimum porosity of 20% corresponds to a pulse irradiation under variable angles of the incident ions with the repetition rate of 25 pps in accordance with restrictions on percentage of parasitic (doubled and more) pores.

II. INJECTOR

The injector for an industrial complex must maintain stable and reliable pulse supply for the linac structure with heavy ions. Comparatively low injection potential of $\leq$ 35 kV have been chosen for the exploitation convenience. The layout of the source design is shown in Figure 2.

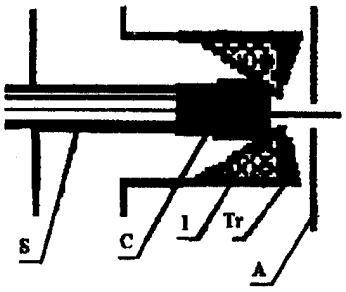


Figure. 2. The schematic design of the ion source

The elegant construction of the MEVVA-type ion source [2] has been developed for the operation with the pulse length of 400 μs and the repetition rate of 25 pps. It can provide at least some tens mA of total beam current taking into account the percentage of the designed W^{4+} component does not exceed one-third of total beam intensity. The cathode block construction gives a

0-7803-3053-6/96/$5.00 ©1996 IEEE

possibility of quick renewal of the used cathode by enterprise operating personnel.

Plasma being created by vacuum ark discharge penetrates then through the hole in the anode and the metal ion beam is extracted from its surface and formed by adding accel-decel system. The main problems for industrial applications of this type of ion source are stability, reproducibility and lifetime.

Mechanically the cathode (C) is a small tungsten cylinder of 30 mm long and 4 mm in diameter which is fixed at the copper mounting slug welded on a bellow. The slug sizes must also be extremely small to facilitate effective cathode cooling.

The bellow is used as a spring for the cylindric cathode clamping tightly to the inner surface of the aluminum-oxide insulator (I) with a cone hole. It gives a posibility to convey the cooling water as close as possible to the cathode surface. A spring support facilitates both reliable contact between cathode and insulator surfaces and stabilization of the cathode front surface placement during its burning-out. The described assembly is clamped to the stainless steel triggering electrode (Tr) whose construction permits to change the distance between the triggering electrode and cathode along the insulator surface for the searching of the optimum position. This position reduces to a trade-off of reliability of discharge initiation at small distances against the requirement to avoid insulator surface metallization at large distances. The cathode, the triggering electrod and the insulator are joined in the common cathode unit which provides fairly stable triggering and discharge regimes. Insulator metal spraying process is the one of main restricts for the source lifetime. The metal film is evaporated only during triggering discharges. In [3] was shown in assuming of the equality of trigger and main discharges duration that triggering and main discharge currents must satisfy the following relationship:

$$I_{tr}/I_d \geq k \cdot (\sqrt{\Delta t}/a), \qquad (1)$$

where I_{tr},I_d are triggerring and discharge currents correspondently, k - the factor depending on physical properties of the cathode material, Δt - the pulse duration of ark discharge, and a - the distance between C and TE along the insulator surface. In our case of a=3mm and I_d = 80 A, the $\frac{I_{tr}}{I_d} \geq 0.25$ (the arc current amplitude is defined from the requirement of the arc continuity during the required time). The source anode (A) mechanically is a copper ring with an axial hole of 10 mm in diameter. The anode-cathode distance of 6 mm was chosen.

The operating amplitude and duration of triggering pulse are 8 kV and 15 μsec correspondently. The igniting discharge is driven by the modulator with inductor current stabilizer (MAC). This modulator provides more stable arc and beam characteristics in comparison with LC pulse line modulator. MAC provides discharge current amplitudes up to 200 A. The discharge duration may be varied from 15 μsec (the triggering pulse duration) up to 900 μsec. The operating regime is maintained at the discharge arc current value of 80 A at pulse duration of 400 μsec.

Recent tests on improving of the operational stability under designed values of pulse length and repetition rate maintain stable regimes of the arc generator during several hours of nonstop work.

III. RFQ SECTION

The designed beam parameters of the RFQ section are listed in the table 1:

Table I
RFQ Section Design Parameters

Charge-to-mass ratio	1/46
Initial energy, keV/amu	0.7
Final energy, keV/amu	27
Resonant frequency, MHz	40.7
Aperture diameter,mm	4.6
Maximum field strength,kV/cm	173.7
Normalized acceptance, $\pi mm \cdot mrad$	2.5
Exit velosity spread, %	1.2
Exit phase spread, deg	20
Beam current limit, mA	6.1

The RFQ resonator construction includes four-rod modular line with stainless steel pole pieces and copper support bars fixed on the resonator jacket by means of ceramic insulators due to comparatevely small operating RF voltages on rods.

The use of RF insulators decreases transversal sizes of the structure markedly with no dramatic changes in the RF structure parameters. These insolators are placed on adjustment stages fixed at the resonator frame. Copper resonant spirals are tapped down between support bars and a frame to get designed frequency of 40.7 MHz. Electric coupling half-rings provide low impedance connection between the diametrally opposed rods for decreasing of sensitivity to misalignments and RF working mode stabilization. The cooling of the structure is furnished by distilled water which is running inside resonant spirals and cooling tubes fixed in support bars. Longitudinally the RFQ section construction includes four cells, 700 mm long each, joined with each other.

The structure is arranged inside a common electric shell of 700 mm in diameter and 3 m long.

During the RF cold tests with a single cell full-scale model the transversal and longitudinal electric fields between adjacent were tuned not worse than $\pm$ 2.5% and 1.1% correspondently.

Independent vacuum tests with a single cell of the RFQ structure (fig.3) have demonstrated acceptable electric strength of the ceramic insulators. During one week tests under repetition rate of 25 pps and pulse length up to 400μs fairly stable RF regimes were reached.

IV. PRESTRIPPER APF SECTION

The prestripper section is intended for the pulse acceleration of 2 mA tungsten ion beam with charge +4 to the exit energy of 418 keV/amu. It is also designed for the working at the industrially permitted frequency of 40.67 MHz.

The designed values of phase capture are 50^o and 1.0%. A rather small momentum spread allows to consider the APF channel as a narrow bandwidth filter that prevents beam parasitic components moving to the exit. It will probably improve the uniformity of polymer film irradiation at a target. On the other hand, comparatively small beam intensities per one pulse are desirable

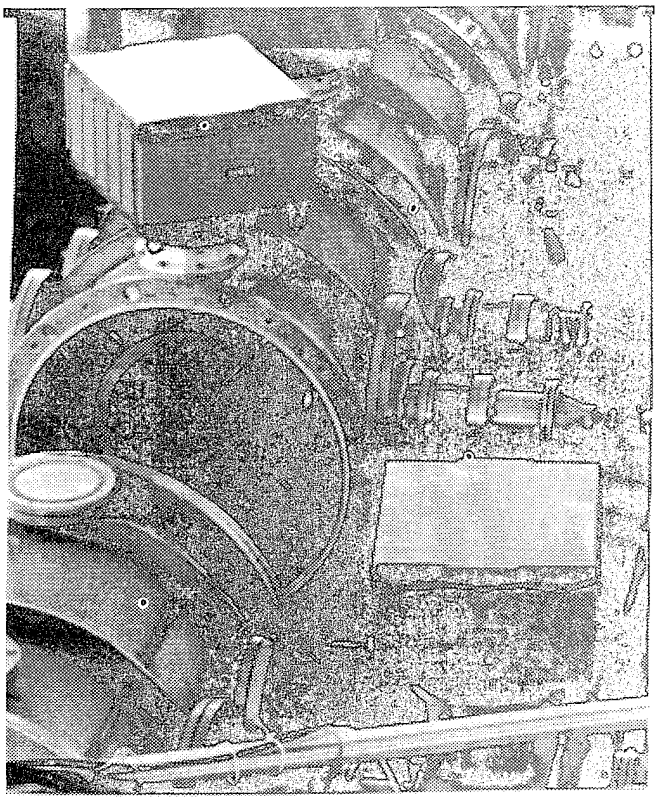


Figure. 3. The RFQ section test installation

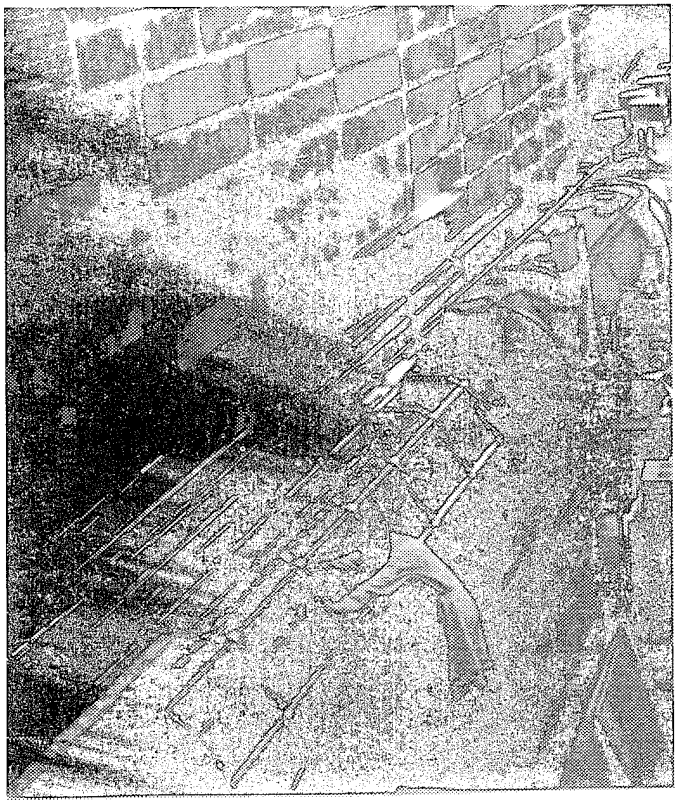


Figure. 4. Full-scale model of the APF prestripper section

Table II
APF Prestripper Section Design Parameters

Charge-to-mass ratio	1/46
Initial energy, keV/amu	27
Final energy, keV/amu	418
Resonant frequency, MHz	40.7
Aperture diameter,mm	7
Maximum field strength,kV/cm	100
Section length, m	6
Beam current limit, mA	2

to prevent the "multihole" statistic problem, although acceptable productivity is reached by repeated many times (25 pps) film irradiations at different angles.

The layout of the full-scale model of the 6m long prestripper APF section is shown in fig.4. The twin line Wideroe-type APF accelerating structure is placed inside the 6m long and 1.2m in diameter stainless steel vacuum tank. Both longitudinal resonant electrodes made of square hollow bars are arranged in horizontal plane symmetrically with respect to the accelerator axis and supported by vertical hollow (again for cooling) copper resonant rods. The drift tubes free of any focusing lenses are arranged and bolted by turns on both longitudinal bars. An output copper jacket of the resonator is fixed mechanically inside the 6-side stainless steel framework which furnished with wheels to move the structure into the vacuum tank.

The maximum value of the field gradient in accelerating gaps does not exceed 100 kV/cm for exploitation reliability. The section contains 84 drift tubes with outer diameters from 35 mm to 70 mm and the aperture diameter of 10 mm. The cold RF tests made on the full-scale model showed principal possibility of tuning the structure on required frequency and electric field distribution.

References

[1] I.B.Barsukov, I.V.Chuvilo, V.V.Kushin, S.V.Plotnikov, "Project of the Industrial Heavy Ion Linac for Particle Track Membrane (PTM) Production" Proc. of 1994 Intern. Linac Conf., Tsukuba, Japan, p.740.

[2] V.A.Batalin et al. "Vacuum arc ion source for the ITEP RFQ accelerator", Rev. Sci. Instr., 65(10), oct.1994, p.3104-3108.

[3] V.A.Batalin, et al. "MEVVA-25 ion source for tungsten ion accelerator." Proc. of the 14 Conference on Particle Accelerators, Abstracts, Protvino, Russia, 1994, p.14 (russian).

A SERIES OF ION ACCELERATORS FOR INDUSTRY

BN Sukhina,NI Alinovsky,IL Chertok,SN Chumakov,NS Dikansky,AD Goncharov
Budker Institute of Nuclear Physics, 630090, Novosibirsk, Russia

Ion accelerators intended for application to electronics industry, surface modification and other technologies are described. A series of the accelerators are characterized by horizontal ion beam position. The energy ranges from 20 KeV to 1.5 MeV. In the frame of this project, the ION-300, ION-1500 installations were designed, built and succesfully tested. The main rectifier and high voltage terminals of the accelerators have the power supply of the increased frequency. The high voltage terminals are supplied with a power up to 2.2 KW using special small-size resonant transformers. The accelerators are provided with ion beam separation on full energy, oil-free vacuum, high voltage isolation (SF_6), and an intellectual automatic control system with the IBM PC host computer. A special set of technical, hardware and software decisions allows us to meet the reliability requirements.

I. THE ION ACCELERATOR ION-1500 FOR INDUSTRY

Table 1. THE MAIN PARAMETERS.

Energy range , KeV	500-1500
Energy instability,	0.001
Ripple of accelerating voltage,	0,0005
Total ion current , mA	1.5
Output beam diameter , mm	10
Separating-magnet radius , mm	1300
Induction in sep.-magnet, Tl	1.0
Range of the masses , A.M.U.	1-80
Gas pressure, MPa	0.6
Dimensions L * B * H, m	5.5 * 3. * 1.7

A. THE DESIGN.

A general view of the installation is shown on Fig.1

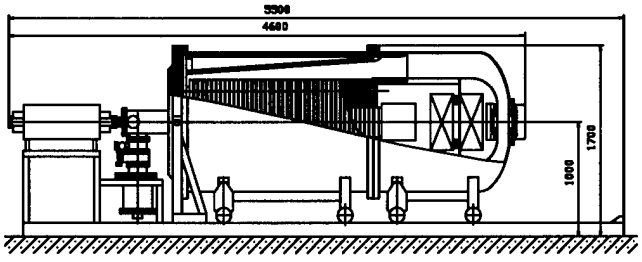


Figure. 1. The ION-1500 Schematic layout

The main units of the accelerator are: the main high voltage rectifier; the acceleration tube and the ion channel; the ion source located under the potential of the main rectifier; the high voltage terminal with a transformer for power transmission; a separating magnet with the power supply system; an oil free pumping system; a power supply system and a computer control system. The high voltage units of the accelerator are located in volume filled with gas SF_6 under a pressure to 0.6 MPa. The horizontal position of the accelerating tube gives some advantages to provide high operational characteristics of the accelerator.

B. THE MAIN HIGH VOLTAGE RECTIFIER

uses a single-phase cascade multiplier with an inductive connection, which has high loading ability / to 25 mA / and a small factor of ripple. The rectifier is supplyied from a controlling machine-generator at a frequency of 1 KHz. The use of the increased frequency allows us to decrease the weight of the rectifier and simplifies its design. The design of the horizontally located rectifier comprises consecutive connections of the identical sections in the form of disks, 40mm thick. Each section contains the secondary winding of the transformer, ballast and measuring resistors. The primary winding of the transformer is included in a resonant circuit, which is common for all the sections and separated from the sections by a gas insulating gap with a variable step to optimization the inductive connection. The rectifier voltage has the linear characteristics of numbers of sections. A high loading ability corresponds to large reservated energy in the condensers; therefore, its fast switching-off is provided in the case of breakdowns.

C. THE ACCELERATION TUBE

is installed horizontally on the axis of the secondary windings of the main rectifier. The section of the tube is made of ceramic and metal chevron-shaped rings. The ION-300 acceleration tube consists of one section, the ION-1500 acceleration tube consists of 5 sections of this type. The constant magnets are installed between the sections for reducing of the full energy of the secondary electrons, thus decreasing the radiation background. The tube doesn't contain organic materials. As a result, its the electrical strength and life time are substantially increased. For proportional distribution of high potential along the acceleration tube, a high voltage divider is used.

D. THE ION CHANNEL

is equipped with the devices for measureming of the beam parameters, such as, the magnetic-modulation meters of average beam current, a sliding meter of full beam current (the Faraday's cap), a beam profile monitor.

E. THE RF TYPE ION SOURCE

has the following parameters:

TABLE 2.

Energy of ions, KeV	10
Ion current, mA	1.5
Power consumption, W	300
Gas flow, cm3/h	15
RF frequency, MHz	50

0-7803-3053-6/96/$5.00 ©1996 IEEE

The quartz tube of the RF ion source has a silicon rubber sealing. The RF circuit is placed perpendicular to the axis of the quartz tube. A ferromagnetic extractor with two ceramic ring magnets has a constant magnetic field parallel to the direction of ion extraction. The generator, pyezoelectrical valve for gas supply consumption and a cylinder with a working gas are under the potential of a high voltage emitter and are isolated from the accelerating potential of the source by the ceramic tube. The source performance was tested for the following gases: H_2, He, N_2, O_2, CO_2, Ar, BF_3, and SF_6. The time up to failures, when working with oxygen, was more than 300 hours.

F. THE HIGH VOLTAGE TERMINAL

serves for ion source power supply. The electrical power (to 0.3 KW) for power supply of the terminal at a frequency of 20 KHz is transmitted by a resonant transformer of the armoured type, the primary and secondary circuits of which are inductively coupled and divided by a high voltage insulating gap. The high voltage gap is 105 mm, and the ferrite core-cups are 210 mm in diameter. The secondary coil of the transformer doesn't need the forced cooling, because it is placed in the insulation gas (SF_6). The terminal structure consists of a set of controlled functional modules [1], connected with the computer by a duplex fiber optic communication line. The feature of these modules is the use of the increased power supply frequency in combination with the magnetic nonlinear regulating elements: magnetic amplifiers characterized by high efficitncy, high specific power, ability of limiing the current of a short circuit. A set of the unified supply units is suitable for the supply of the RF ion source, duoplasmatron, or other similar devices.

G. THE MAGNET-SEPARATOR

of the dipole type (with the magnetic field recession parametr n=0) is used to separate the ion beam accelerated to a full energy. The magnet-separator consuming the constant current from a controlled machine generator working at a frequency of 1 KHz and a 8 KW power with subsequent transformation into constant current.

H. THE OIL-FREE PUMPING SYSTEM

consists of turbo-molecular pumps. The working vacuum is about 1 * E-4 Pa inside the acceleration tube.

I. THE COMPUTER CONTROL SYSTEM

provides: the direct control of the accelerator parametrs, the control of the ion source parameters, the measurement of the ion beam parameters, the emergency switching-off at overloading or high voltage breakdown. The control system consists of the central computer IBM PC / AT, a set of the functional modules in the CAMAC standards, and a series of special electronic units. The high voltage terminal is controlled via a duplex optic-fiber line by a pulse width-modulated signal. The of continuous ion currents to and after magnet-separator are measured by magnet-modulation meters of average current. The ion beam profile is measured with the help of a relocating gauge (thin wire). It is possible to measure the ion mass spectrum at the magnet-separator output and to display the data. The fast switch-off of the main high voltage rectifier is made by thyristors switch for time which is substantiolly less than the the period of the feeding network in order to prevent from the irreversible processes in its elements. The ions C^+, B^+ , and N^+ with an energy up to 1200 KeV and full ion current up to 1.5 mA are obtained. The acquired experience and the successful testing of the accelerator ION-1500 allow us to develop the "ION" type accelerators.

II. THE ACCELERATOR ION-300 FOR INDUSTRY

Table 3. THE MAIN PARAMETERS

Energy range, KeV	100-300
Maximum full current ,mA	5
Separating magnet radius, mm	600
Range of the masses, A.M.U	. 1-80
Maximum gas pressure, MPa	0,07
Dimensions LxBxH, m	3.1 * 1.5 * 2.0

A. THE DESIGN.

A general view of accelerator ION-300 is shown in Fig.2

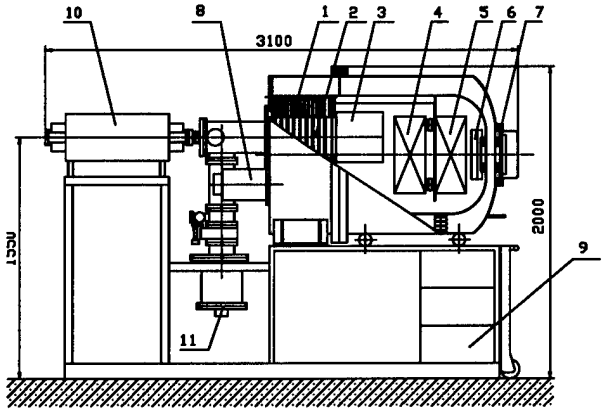


Figure. 2. The ION-300 schematic layout

1-the main high voltage rectifier; 2-the acceleration tube; 3-the ion source; 4,5-the high voltage terminal; 6,7-the power transmission transformer; 8-the tranformers; 9-the 3-phase powerful generator; 10-the magnet-separator; 11-the oil-free pumping system.

B. THE MAIN HIGH VOLTAGE RECTIFIER

used in the accelerator ION-300 works at a frequency of 20 KHz. The rectifier represents a capacitive voltage multiplier with a sequential feeding of the cascades. The feeding is made from a 3-phase powerful electronic generator. The frequency of voltage pulsation at the rectifier output is 120 KHz. This allowed us to considerably decrease the energy accumulated in the condensers of the rectifier column and to reduce the degree degradation of the insulators and metal electrodes of the tube, which is depends on the dicharge energy in the case of breakdown.

C. THE ION SOURCE

of the RF type and its unified two crate power supply system, which contains two network stabilizers, two control stations, and a set of the current and voltage sources are located in a high

voltage terminal under the potential of the main rectifier. The terminal electrical power supply is made irrespective of the main rectifier at 20 KHz via a resonant transformer, whose primary and secondary coils are divided by a high voltage gas insulating gap. With a 60 mm gap between the coils, such transformers can transmit the electrical power to 2.2 KW at a efficiency about 0,9.

D. THE DISTRIBUTED COMPUTER CONTROL SYSTEM

is specially designed for applying to electro-physical installations with subsystems, located under high potentials and working under the conditions of powerful electrical interference and breakdowns. The distributed control system [1] consists of the central computer IBM PC XT / AT and three throught six intelligent multifunctional control stations. Each local station controls directly one of the subsystems of the installation according to its functional purpose and design under high potential as well. All the stations are connected with the central computer by the duplex optic-fiber link. The program in the central computer consists of several subprograms working independently in the regimes of time division. The central processor-manager operates with peripheral processes, each of them controls one of physical subsystems of the installation. The peripheral processor one-paid module has a complete set of functional input/output devices to realize the control algorithms and stabilize the analog parameters, such as the accelerator energy, ion source current, magnet-separator current, etc. The control station is designed to withstand a powerful pulse interference. The processor-module has an automatic restart in the accidental situation [1].

III. REFERENCES

[1] SN Chumakov, AD Goncharov, AN Malygin, VP Ostanin, BN Sukhina, VS Tupikov, "Advances in power supply and control system for electrostatic accelerators", The 1995 Particle Accelerator Conference.

A PULSED SOURCE OF NEUTRON FOCUS FOR FUNDAMENTAL AND APPLIED RESEARCH IN HIGH-ENERGY ELECTRON ACCELERATOR CENTRES

I. P. Eremeev, International Business Nucleonic, Moscow, Russia

ABSTRACT: Hard magnetic bremsstrahlung radiation of relativistic electrons is suggested to be used according to the idea [1] to generate pulsed neutron fluxes by photonuclear reactions. The spectral and integral characterictics of the corresponding source have been determined by multigroup calculations for several targets as applied to present-day electron accelerators with an energy of more than 7 GeV. It is shown that the beam parameters of the accelerators allows one to generate the pulsed neutron fluxes of unprecedented space, time and spectral densities.

I. INTRODUCTION

Over many years leading research centres have exhibited an unremitting attention to improving the parameters of neutron sources based on charged particle accelerators. This is explained by both some unsettled fundamental problems and demands of applied investigations of practical importance.

The known methods allow the generation of pulsed fluxes of thermal and resonance neutrons which do not exceed $5 \cdot 10^{16}$ n/cm$^2 \cdot$ s at a pulse duration of much more than 10^{-6} s. To a great extent, these limits are dictated by a considerable exothermicity of the processes used and a high average energy of the spectrum of neutrons produced. The stage of slowing down features a significant neutron leakage and a strong dispersion of the originally short neutron pulse. For these reasons the source quality parameter defined as a ratio of the average the intensity $< N_n >$ to the square of the pulse duration falls by 3 to 6 orders of magnitude during slowing down. For the methods using acceleration of charged particles restrictions on the current and the energy release in a target are also of basic importance.

The approach proposed in this paper is free from the above short-comings to a considerable degree. It was described for the first time in [1].

II. THE METHOD OF NEUTRON FOCUS

The method is based on the (γ, n) reaction producing neutrons from the nuclei of a target placed in a beam of directed hard magnetic bremsstruhlung ("synchrotron") gamma radiation formed by a current of ultrarelativistic electrons in a spatially periodic magnetic field. The fundamental features and advantages of the method are due to a set of the following properties of magnetic bremsstruhlung (MB) radiation:

(a) a high spectral and spatial density of MB resulting from a high energy, a great averaged current and a very small electron beam cross-section in up-to-date accelerators;

(b) the pulsed nature of MB allowing the ultrashort neutron pulses with a typical duration of 10^{-9} s to be produced;

(c) a specific shape of the MB spectrum falling exponentially in the high-energy range and a relatively low energy of γ-quanta in the basic part of the spectrum.

Properties (a) and (b) provide a high space-time and spectral density of neutron generation and flux. Property (c) allows the optimization of the process with respect to radiation losses in the target.

A radically new property consists in a possibility to produce low-energy neutrons *without slowing down*. For this purpose light nuclei *with an anomalously low neutron binding energy*, such as Be and D, should be used as a target. These nuclei are characterized by not only the minimum value of the (γ, n) reaction threshold egual to 1.665 and 2.225 MeV, respectively, but also an abrupt growth of the reaction cross-section near the threshold. The latter dictates the specific shape of the photoneutron spectrum with a great density in the low-energy range. When the moderating stage is absent , there are no reasons for the loss of intensity and the pulse broadening mentioned above. This increases drastically the quality of the source of slow and resonance neutrons.

In the case of a space-periodic magnetic field H_w, when the values of the horizontal and vertical divergences of MB differed insignificantly, the geometry of the neutron production region would be considered approximately as axially symmetrical. Because the MB divergence and the area of the MB source are small, the radial dimension of the region should be much less than the longitudinal one determined by the path length of γ-quanta in the target. Such an axially simmetrical source with a high generation density was proposed in [1] to be named the "neutron focus" (NF).

The spectral density of photoneutrons producing in the NF is determined by the expressions:

$$N_n(E_n) = N_\gamma \frac{A}{A-1} \cdot \Theta_{\gamma,xn}(E_\gamma)\, \Phi_\gamma(E_\gamma), \qquad (1)$$

$$\Phi_\gamma(E_\gamma) = k \cdot \eta(E_\gamma/E_c)\, \frac{1}{E_\gamma}, \qquad (2)$$

$$\Theta_{\gamma,xn}(E_\gamma) = \frac{\sum_x \nu_x \sigma_{\gamma,xn}(E_\gamma)}{\sigma_\gamma(E_\gamma)} \left(1 - e^{-\Sigma_\gamma l}\right), \qquad (3)$$

$$E_n = \frac{A-1}{A}(E_\gamma - E_{\gamma n}), \qquad (4)$$

where N_γ is the integral intensity of the MB radiation; A is the mass of the target nucleus; E_γ , E_n and $E_{\gamma n}$ are the energies of γ-quantum, photoneutron and the (γ, n) reaction thershold, respectively; $\Theta_{\gamma,xn}(E_\gamma)$ is the spectral neutron-yield function; $\sigma_\gamma(E_\gamma)$ and $\sigma_{\gamma,xn}(E_\gamma)$ are the total cross-section and the cross-section of the (γ, xn) reactions for γ-quanta of energy E_γ , respectively; Σ_γ is the macroscopic cross-section of attenuation for γ-quanta in a target of length $l \simeq 3/\Sigma_\gamma(E_{\gamma n})$ along the MB beam; ν_x is the yield of neutrons in the γ, xn processes

0-7803-3053-6/96/$5.00 ©1996 IEEE

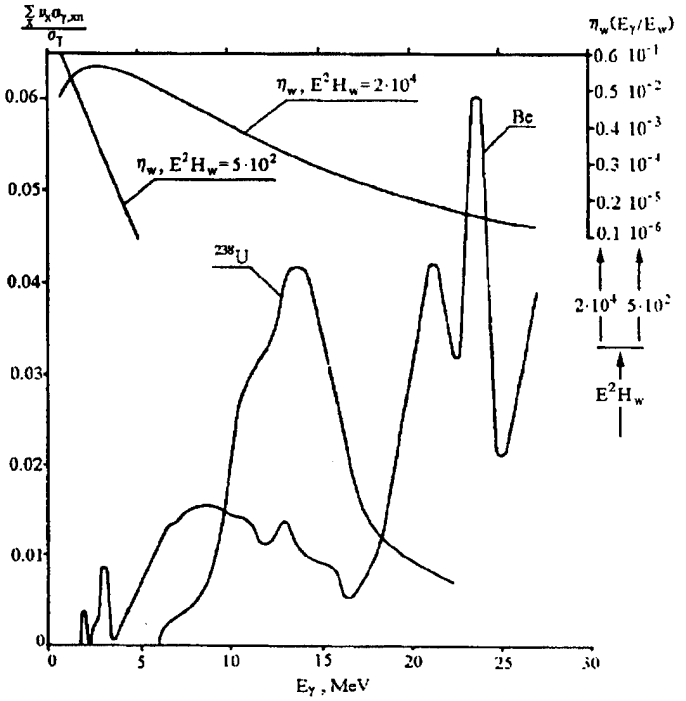


Figure. 1. The dependences of the ratio $\sum_x \nu_x \sigma_{\gamma,xn}/\sigma_\gamma$ on an energy of γ-quanta for Be, U-238 and the MB spetral function for $E^2H_w = 5 \cdot 10^2$ ($E_c = 340$ keV) and $2 \cdot 10^4$ ($E_c = 13.3$ MeV).

($\nu_x = 1, 2$) and photofission ($\nu_f = 3$); $\eta\,(E_\gamma/E_c)$ and E_c are the MB spectral function and the parameter determining the position of its maximum; k is the factor normalizing the MB spectrum to unity.

The spectral and integral intensities of photoneutrons produced are determined by the yield function $\Theta_{\gamma,xn}\,(E_\gamma)$ and the values of the parameters E_c and $E_{\gamma n}$. The energy dependence of the ratio $\sum_x \nu_x \sigma_{\gamma,xn}/\sigma_\gamma$ are shown in Fig.1 for Be and U-238. The MB spectral functions $\eta\,(E_\gamma/E_c)$ are given in the same figure for $E_c = 340$ keV and 13.3 MeV, corresponding to $H_w = 8$ T and the electron energy $E = 8$ GeV and 50 GeV, respectively. It is seen that for $E = 8$ GeV the value of η near $E_{\gamma n}$ for Be is as small as $10^{-2} - 10^{-3}$. It grows exponentially as the parameter E^2H_w increases to approach at $E = 50$ GeV the maximum values in the wide range of the γ, n resonances.

The photoneutron spectrum for the Be target calculated for $E = 8$ GeV and normalized to one γ-quantum is shown in Fig.2. The data of the precision measurements of the cross-sections for Be from [2] were used for the calculation. The spectrum exhibits a high density of neutrons in the resonance range and low values of the mean and boundary energies.. The extrapolation of the results of [2] to zero shows that a considerable density of neutrons should persist in the region below $E_\gamma - E_{\gamma n} = 0.5$ keV by virtue of the recoil of nuclei emitting photoneutrons. The kinematic corrections to the neutron energy E_n at angles of more than 90° for Be amount to 200 – 400 eV to be sufficient to shift the zero of the E_n scale to the region of the noticeable values of $\sigma_{\gamma,n}$ in the $E_\gamma - E_{\gamma n}$ scale. It should noted that for D this effect must

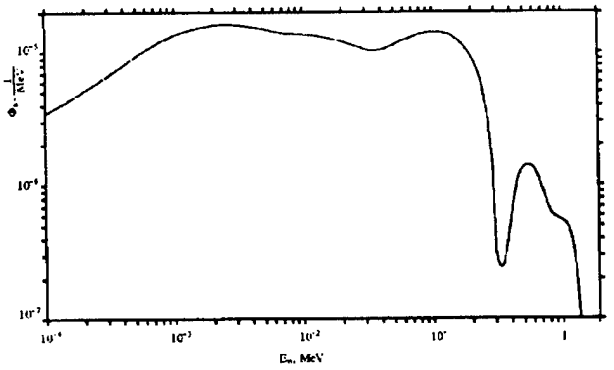


Figure. 2. The spectrum of photoneutrons emitted from the Be target at $E_c = 340$ keV.

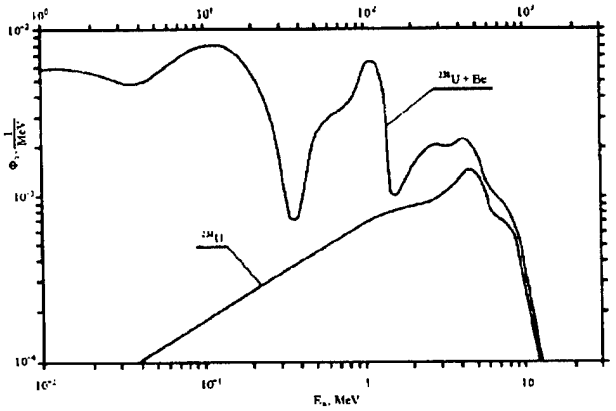


Figure. 3. The photoneutron spectra for the U-238 target and for the combined target of U-238 and Be enveloping it.

be considerably stronger.

The photoneutron spectrum for the Be target have been calculated too for $E = 50$ GeV.

The above results have been obtained under condition that the cross-sectional dimensions of a target are much smaller than the path length for γ-quanta scattered from the incident MB beam. Results for the opposite case are shown in Fig.3. The calculations were fulfiled for the U-238 target and for the same target enveloped by Be. The partial (γ, xn) cross-sections of U-238 were taken from [3], [4]. The allowance for the contribution of photoneutrons produced in the scattered gamma field have been made in the manner similar to [5]. Account was taken of the Compton scattering of γ-quanta and the bremsstruhlung of Compton electrons and electron-positron pairs. It is seen that the spectral density of resonance neutrons in the spectrum increases in the U-Be target almost by an order as compared to the "thin" Be target. In the case one should expect no broadening of a neutron pulse because the time of the scattering act do not exceed the MB pulse duration.

The integrated characteristics of the NF have been determined for the above cases and for a MB formed in a wiggler of a length $L_w = 7.5$ m and a field period $2d_w = 15$ cm by an electron beam with the average current $< I >= 0.01$ A at a pulse duration $\tau = 10^{-9}$ s and a circulation frequence 10^5 1/s. These parameters

are typical for modern storage rings such as APS, ESRF, Spring and TRISTAN in a single bunch regime. The results obtained are listed in Table. The table symbols are as follows: q_n^γ is the yield of photoneutrons per γ-quantum; q_n^e is the same per single electron passage through the wiggler; P_γ^w and $P_{\gamma n}^w$ are the integral flux of γ-quanta incident on a target for the exit channels length of 10 m and 20 m for $E = 8$ GeV and 50 GeV, respectively, and the same in the energy range $E_\gamma > E_{\gamma n}$ of Be; N_n and P_n are the integral intensity and the flux of photoneutrons, respectively; <...> are the same avereging over time; $< N_n > /\tau^2$ is the source quality parameter; Q_γ is the specific MB power released in the target and estimated approximately.

It is necessary to note that for the U – Be target allowance was made approximately for neutrons produced in the $(n, 2n)$ processes in Be and U. Therefore, the pulse duration is assumed to be equal to $\sqrt{\tau^2 + t_m}$, where t_m is the moderation time of neutrons with an average energy of the spectrum slowing down to the $(n, 2n)$ reaction threshold.

Parameter	E_c=340 keV	$E_c = 13.3$ MeV	
	Be	Be	U + Be
τ, s	10^{-9}	10^{-9}	$2.0 \cdot 10^{-9}$
q_n^γ, n/q	$1.4 \cdot 10^{-6}$	$4.7 \cdot 10^{-3}$	$7.8 \cdot 10^{-3}$
q_n^e, n/e	$1.0 \cdot 10^{-4}$	0.49	0.81
$< P_\gamma^w >$, $\frac{q}{cm^2 \cdot s}$	$1.4 \cdot 10^{18}$	$5.0 \cdot 10^{18}$	$5.0 \cdot 10^{18}$
$< P_{\gamma n}^w >$, $\frac{q}{cm^2 \cdot s}$	$7.3 \cdot 10^{14}$	$2.2 \cdot 10^{18}$	$2.2 \cdot 10^{18}$
N_n, n/s	$1.4 \cdot 10^{17}$	$4.7 \cdot 10^{20}$	$1.3 \cdot 10^{21}$
$P_n^{*)}$, $\frac{n}{cm^2 \cdot s}$	$8.2 \cdot 10^{13}$	$1.6 \cdot 10^{18}$	$5.0 \cdot 10^{17}$
$< N_n >$, n/s	$1.4 \cdot 10^{13}$	$4.7 \cdot 10^{16}$	$2.5 \cdot 10^{17}$
$< P_n^{*)} >$, $\frac{n}{cm^2 \cdot s}$	$8.2 \cdot 10^{9}$	$1.6 \cdot 10^{14}$	$1.0 \cdot 10^{14}$
$< N_n > /\tau^2$, $\frac{n}{s^2}$	$1.4 \cdot 10^{31}$	$4.7 \cdot 10^{34}$	$6.2 \cdot 10^{34}$
Q_γ, n/MeV	$1.2 \cdot 10^{4}$	480	180

*) P_n is the neutron flux on the target surface.

III. CONCLUSION

It is evident from the data presented that the neutron source proposed has considerable promise for the use in fundamental and applied investigations. This results from the NF properties such as a great pulsed flux in combination with an ultrashort duration, a specific shape of the spectrum with a maximum in the resonance neutron energy range, a possibility to change simply the spectral end point in the wide energy region by varying the electron energy and a minimum radiation loading the target as compared with the known methods.

The method can be best realized on SLAC and present-day storage rings with electron energies of at least 7 – 8 GeV, such as APS, PEP, PETRA, Spring and TRISTAN, using superconducting wigglers with a field amplitude of at least 5 T.

The variant with an uniform magnetic field, ranking below the NF in the flux and the space density, is superior to it in higher intensity which is achieved at the expence of the increased horisontal angle of MB ejection and in essentially less energy loading on the target. One can expect that this variant will turn out to be more promising for technological applications (see, for example, [5]).

References

[1] I.P. Eremeev. JETP Lett., Vol. 27, No 1, p. 10, 1978.

[2] B.L. Berman, R.L. van Hemert, C.D. Bowman. Phys. Rev., Vol.163, p.958, 1967.

[3] J.T. Caldwell, E.J. Dowdy, B.L. Berman et al. Phys. Rev., Vol. C 21, p. 1215, 1980.

[4] A. Veyssiere, H. Beil, R. Bergere et al. Nucl. Phys., Vol. A 199, p. 45, 1973.

[5] I.P. Eremeev. Paper to be presented to this Conference.

MODERATOR/COLLIMATOR FOR A PROTON/DEUTERON LINAC TO PRODUCE A HIGH-INTENSITY, HIGH-QUALITY THERMAL NEUTRON BEAM FOR NEUTRON RADIOGRAPHY

R.C. Singleterry Jr., G.R. Imel*, and G.E. McMichael**
*Argonne National Laboratory, P.O. Box 2528, Idaho Falls, ID 83403-2528 USA
**Argonne National Laboratory, 9700 South Cass Ave., TD/207, Argonne, IL 60439 USA

Abstract

Reactor based high resolution neutron radiography facilities are able to deliver a well-collimated (L/D $\geq$ 100) thermal flux of 10^6 n/cm^2·sec to an image plane. This is well in excess of that achievable with the present accelerator based systems such as sealed tube D-T sources, Van der Graaff's, small cyclotrons, or low duty factor linacs. However, continuous wave linacs can accelerate tens of milliamperes of protons to 2.5 to 4 MeV. The MCNP code has been used to analyze target/moderator configurations that could be used with Argonne's Continuous Wave Linac (ACWL). These analyses have shown that ACWL could be modified to generate a neutron beam that has a high intensity and is of high quality.

I. INTRODUCTION

Neutron Radiography (NR) has been the domain of thermal reactors until the present day. The reactor was the easiest and most economical method for the generation of a high quality, high intensity thermal neutron source. Today, reactors are becoming expensive to license and operate and are not portable. At the same time, charged particle accelerator technology is advancing, intensities are increasing, and hardware is decreasing in size. This paper investigates the use of a charged particle accelerator, the Argonne Continuous Wave Linac (ACWL) at Argonne National Laboratory in Illinois, to generate a high quality, high intensity thermal flux suitable for NR.

II. ACCELERATOR FACILITY

The original purpose of ACWL was as an accelerator development test stand for the Strategic Defense Initiative (SDI) as describe in Reference [1]. This mission has ended, so ACWL is being modified to investigate the use of accelerators in NR and Boron Neutron Capture Therapy with the current work concentrating on NR. ACWL was designed and built to accelerate negative deuteron ions in a radio frequency quadrupole accelerator in a Drift Tube Linac (DTF). The facility is being modified for water cooling versus the more expensive cryogenic cooling needed for the space environment of the SDI mission. If it is deemed that proton acceleration is needed, the particle generation equipment exists and can be fitted to ACWL readily. This analysis investigates what particle(s), particle energies, and particle currents are needed to perform NR with the intended goals.

III. NEUTRONIC ANALYSES

Various models of the new ACWL target facility were analyzed for neutronic properties with the MCNP code and ENDF/B-V continuous energy cross sections. The MCNP code system simulates many particle trajectories using a stochastic method. With these tools, analyses were performed to determine if ACWL with a suitable target could generate the beam needed to obtain the goals. The first step was to generate a source definition that modeled the neutron generation reactions. The target area and thickness were chosen to enable the target to dissipate the heat generated by the reaction. A moderator substance and configuration were designed to generate as many thermal neutrons as possible without contaminating the beam with gammas and higher energy neutrons. The beam tube was designed to transport those neutrons to the image plane and maintain its high resolution capability.

A. Source Model for the Li^7-proton Reaction

Since MCNP cannot analyze charged particles other than electrons, the model for the source was performed separately. The reaction of interest was the $Li^7(p,n)Be^7$ reaction. Experimentally based cross section data was given in Reference [2]. The resultant energy and direction of the outgoing neutron was calculated from the two-body equations as formulated in Reference [3]. Figure 1 shows the neutron source strength as a function of proton energy and laboratory angle. Continuous slowing down theory was used to model the protons while traveling through the target. Reference [4] was used for the stopping power of hydrogen ions in the target materials.

The neutron source strength was collapsed into a source definition recognized by MCNP. To do this, the angular variable was broken into evenly distributed angle bins from 0 to 180 degrees with the probability equal to the normalized source strength. To link the angular distribution to the neutron energy distribution for that angle, the dependant source mechanism in MCNP was used. Each angle bin was made dependant to an energy range and probability as shown in Figure 2. The energy range is the maximum and minimum energies shown in Figure 2 for each angle, while the probability distribution was set equal to the normalized source strength for that angle.

B. Target Design

Exact details of the target design are not necessary for this analysis. The materials that could scatter or absorb neutrons and their position are the important details modeled. The proton target is modeled as a right circular cylinder which projects enough

0-7803-3053-6/96/$5.00 ©1996 IEEE

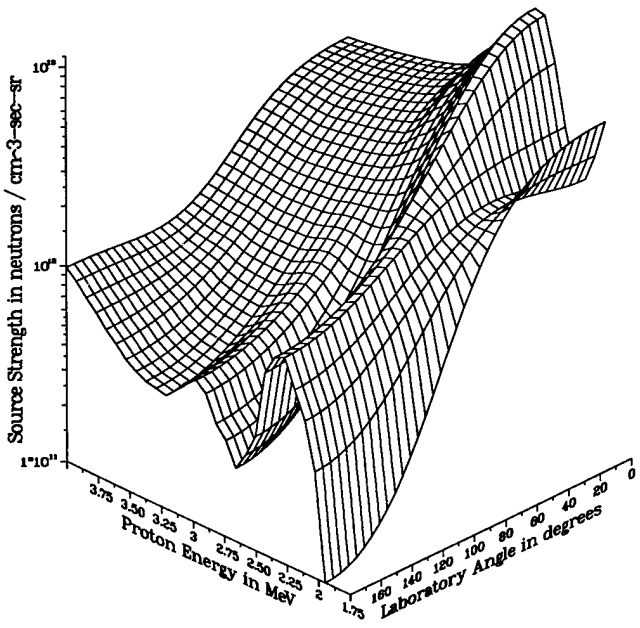


Figure. 1. The Neutron Source Strength as a Function of Laboratory System Angle and Proton Energy in Lithium

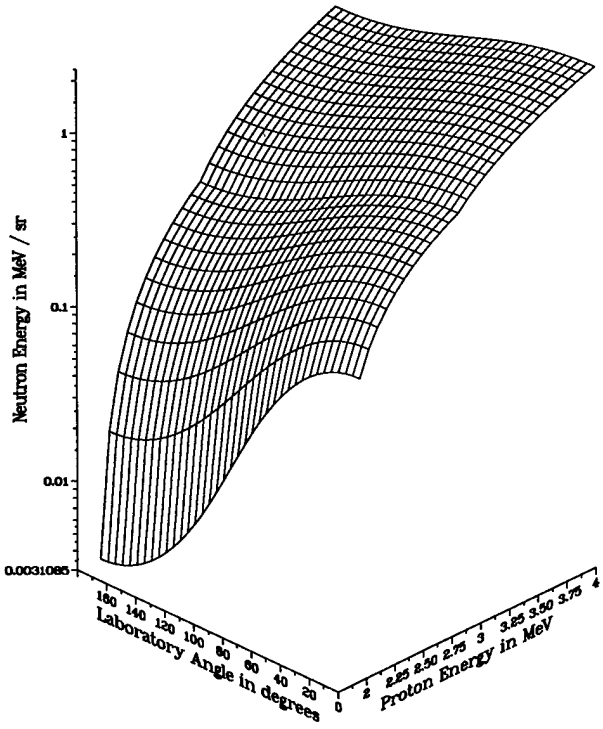


Figure. 2. The Neutron Energy Distribution as a Function of Laboratory System Angle and Proton Energy in Lithium

circular surface area to the proton beam so it absorbs approximately 1 $\frac{kW}{cm^2}$ of energy. The proton target is attached to a copper plate and sealed in a stainless steel 316 evacuated can that extends to the left hand edge of the model. The can is slightly larger than the proton beam to allow clear passage of the beam to the target.

C. Moderator and Reflector Design

The neutron energies from the source are between 2.5 MeV and 0.002 MeV. The goal is to have a large number of neutrons enter the beam tube with a mean energy of 0.0253 eV (thermal neutrons). The moderator must slow the neutrons down to these energies without absorbing the neutrons, spreading them through geometry effects, or having them escape. A low atomic weight, high density moderator is used to achieve the largest energy loss per collision possible to keep the geometry losses to a minimum. A reflector material is placed outside of the moderator to economize on neutrons.

The neutron source is very forward peaked. Tally surfaces were placed in the model to cover possible positions for apertures. To accelerate the MCNP calculation, gamma rays were not simulated in the models to determine placement of the aperture; however, in the final model, gamma rays were included.

D. Beam Tube Design

The objective is to obtain a collimated beam of neutrons having a thermal flux of 10^6 neutrons per cm^2·sec striking the image plane with an image quality category of I as described in Reference [5]. A first order approximation for the flux entering the beam tube is

$$\phi_0 = 16\phi_I \left(\frac{L}{D}\right)^2, \qquad (1)$$

where, ϕ_I is the flux at the image plane (10^6), L is the length of the beam tube, and D is the diameter of the aperture.

In order to achieve the goal of a high quality beam, an L/D of 100 is needed. From equation (1), this gives an attenuation of 1.6×10^5, or to achieve a flux of 10^6, the flux at the aperture must be 1.6×10^{11} neutrons per cm^2·sec. To absorb any stray or reflecting neutrons from or through the beam tube, a stainless steel can is lined with a thin layer of cadmium or other large cross section material (see Reference [6]). This lining keeps neutrons from entering or exiting the beam tube except at the aperture and the image and preserves the collimation of the beam.

IV. RESULTS

The results reported here are for a 2.5 MeV and a 4.0 MeV proton beam impinging on a lithium target with light and heavy water as the moderator and graphite as the reflector. The lithium target is 5 cm in radius and 0.1 cm thick and is placed at the center of a water box 50 cm on a side. A 5 cm thick graphite reflector was employed outside of the box . To keep the perturbation from the aperture small, the diameter was set to 4 cm. Figure 3 gives a representation of the geometry. The results from these models create a working set of parameters for determination of the feasibility of this effort. From this, a complete study of materials and configurations can be completed to design the actual target to be employed at ACWL.

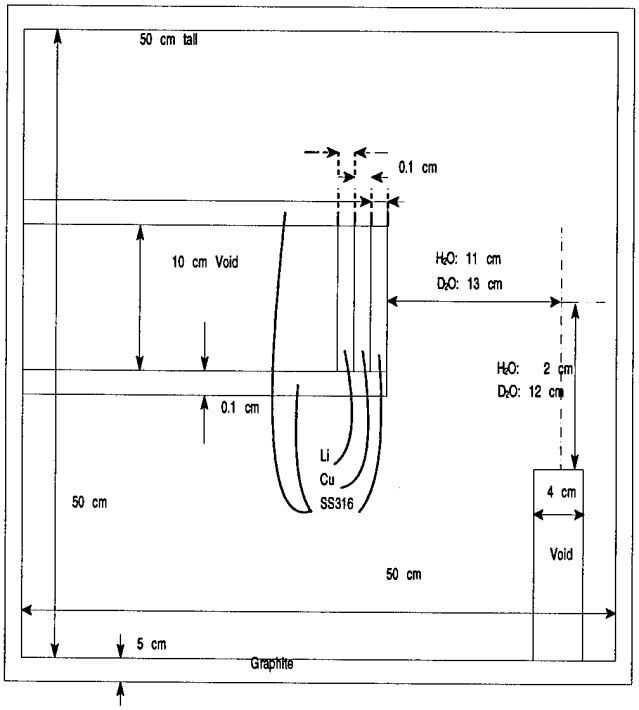


Figure. 3. Geometric Representation of the Physical Model

Table I
Thermal to Total Neutron Flux and Optimal Position

Proton Energy MeV	Slowing Down Material	$\frac{\phi_{th}}{\phi}$	Source Distance cm	Direction from Beam degrees
2.5	H_2O	0.319718	11	90
4.0	H_2O	0.308378	11	90
2.5	D_2O	0.012559	13	90
4.0	D_2O	0.012235	13	90

Table I shows the ratio of the thermal to the total neutron flux at the optimum position without the beam tube modeled. Table II shows the thermal neutrons per source neutron at the beam tube entrance (location given in Table I) and the proton current needed to achieve the objective of 10^6 n/cm2·sec of the assumed image plane.

V. CONCLUSION

With the MCNP code, it is possible to model the entire system. The problem that is encountered is the creation of a biasing scheme to cut the number of simulated particles needed to converge the model. The simplifications made in this model allowed short (6 to 20 CPU hours on a Sun Sparc 20) turn-around times but in no way encompassed all parameters needed to design a target and beam tube for high intensity and high quality NR. However, this study did determine that NR is feasible with light water at ACWL and showed approximate results that could be obtained. The next step is to investigate more moderating materials such as polyethylene and optimize the placement of the beam aperture. Once this work is finished, the design and construction of a target and beam tube for ACWL to assist in the research needed for portable NR devices can continue.

Table II
Thermal Neutrons per Source Neutron and Proton Current for High Intensity NR

Proton Energy MeV	Slowing Down Material	Thermal Neutrons n / Source n	Proton Current mA
2.5	H_2O	5.45353E-6	59.1
4.0	H_2O	4.66151E-6	69.1
2.5	D_2O	—	—
4.0	D_2O	—	—

References

[1] McMichael, G., *et. al.*; *CWDD Accelerator at Argonne – Status and Future Opportunities*; **Proceedings of the 1994 LINAC Conference**; Tsukuba Japan, August 21-26, 1994, page 131.

[2] Liskien, Horst and Paulsen, Arno; *Neutron Production Cross Sections and Energies for the Reactions $^7Li(p,n)^7Be$ and $^7Li(p,n)^7Be^*$*; **Atomic Data and Nuclear Data Tables, 15**, 57-84 (1975).

[3] Lamarsh, John R.; **Introduction to Nuclear Reactor Theory**, Addison-Wesley Publishing Company, (1966).

[4] Andersen, H.H. and Ziegler, J.F.; **Hydrogen, Stopping Powers and Ranges in All Elements**; Volume 3 of The Stopping and Ranges of Ions in Matter; Pergamon Press (1977).

[5] **Standard Method for Determining Image Quality in Direct Thermal Neutron Radiographic Examination**, Vol. 03.03 Nondestructive Testing, ASTM E 545-91, (1994).

[6] Von Der Hardt, P. and Röttger, H., Editors; **Neutron Radiography Handbook**; Commission of the European Communities; D. Reidel Publishing Company (1981).

EXPERIMENTAL SET-UP FOR MULTIPLICATION COEFFICIENT FLUCTUATION STUDY vs. ACCELERATOR PARAMETER DEVIATIONS on the JINR PULSED ACCELERATOR DRIVEN NEUTRON SOURCE *

V. Belkovets, A. Ivanov, A. Kaminsky, A. Krasnykh, N. Malakhov, L. Menshikov,
Yu. Popov, V. Piataev, N. Pilyar, V. Rudenko, L. Somov, A. Sumbaev and V. Tarabrin
Joint Institute for Nuclear Research, Dubna, Moscow District, 14980 Russia

Abstract

The conception of an electron beam-driven subcritical molten salt safety reactor (MSR) was presented at the International Conference on Accelerator-Driven Transmutation Technologies and Application (ADTT) [1]. The essence of the concept is the use of the MSR cascade system to reduce the driving power. The cascade reactor could allow diminishing of the beam power down to a value where the electron accelerator could be used. The question is how much the neutron multiplication coefficient may be used in the ultimate safety reactor design. The Joint Institute for Nuclear Research (Dubna) has a facility, which could be named as a prototype of the future accelerator driven subcritical reactor. It is the IBR-30 pulse reactor driven by the S-band electron linac (LUE-40). Here the neutron multiplication coefficient of ≈ 200 (the same as the value of subcriticality $k_{eff} = 0.995$) from the coupled facilities allows an integral yield of 0.5×10^{15} neutrons per second at a pulse width of 4 microseconds. These facilities form the JINR experimental set-up for the study on multiplication coefficient fluctuations vs. deviation of accelerator driven parameters, as well as for the steady state and transient regimes. The experimental set-up for these studies and the first results will be presented.

I. INTRODUCTION

The Accelerator-Driven Energy Production is a modern conception of the next generation of nuclear safety power plant development. The main idea of this conception is the development of a type of reactor that does not produce nuclear wastes. For complete freedom from a nuclear accident, the reactor should work in the deep subcritical regime. It is for this reason that an external neutron source is needed. The subcriticality value k_{eff} is a function of reactor design and thus determines the power required from the neutron source.

It is clear that the beam power will increase when the requirements of safety dictate. The problem of beam power reduction is a major problem in the Accelerator-Driven Energy Production for nuclear safety power plant development. As a possible solution this problem the cascade reactor conception was presented at the conference on ADTT [1] . The essence of the conception is an use of the MSR cascade system which can allow diminishing of k_{eff} at every cascade step. For the first time it was shown that the present proton accelerators, like the PSI [2] cyclotron or Los Alamos linac [3] , could be used for the pilot experiments. But

* This work was performed without any financial support

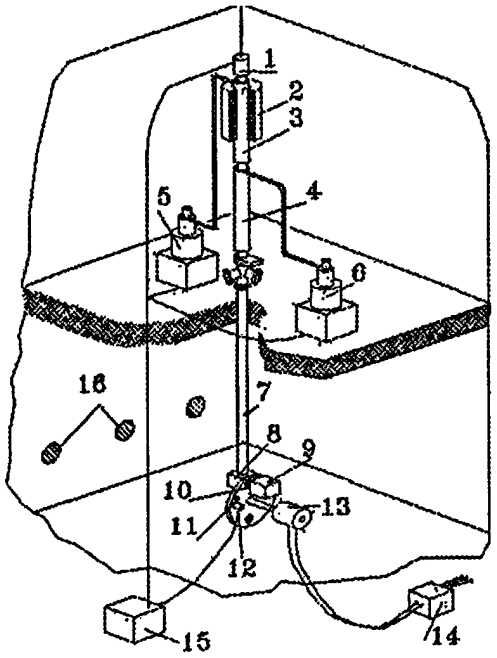


Figure 1. Layout of the linac-driven subcritical neutron pulse source: 1 - electron gun; 2 - solenoid; 3, 4 - traveling wave sections; 5, 6 - klystrons; 7 - beam line; 8 - $e - \gamma - n$ converter and 1st half of plutonium core; 9 - 2nd half of fuel elements; 10 - wheel with two fuel shells; 11 - permanent magnet; 12 - coil; 13 - motor; 14 - motor power supply; 15 - trigger system and 16 - neutron beam channels.

lifetime linac problems, beam loss problems, total efficiency and reliability, and other practical things urged to do the next step. The cascade MSR, as example, could allow diminishing of the beam power down to such value where the electron accelerator system could be used.

On the other hand the total multiplication coefficient should be a large enough to reduce the beam power also. In this case the accelerator-driven reactor should have have a minimal power fluctuation in the subcritical assembly during all times of operation. Next would like to discuss which factors could be influenced by the subcriticality coefficient fluctuation.

II. LAYOUT OF THE FACILITY

A schematic layout of the JINR facility is shown in fig. 1.

0-7803-3053-6/96/$5.00 ©1996 IEEE

Electron linac is situated in a vertical plane and consists of two S-band sections (3, 4) which are fed by two Russian KIU-12 klystrons (5, 6). After acceleration in the traveling wave section, the electron beam passes downstairs through the transport line (7) downstairs in the hard concrete box. Here the multiplying target system is located. Neutron beam lines (16) are placed outside the concrete box in a horizontal plane encircling 180^o degrees to the side of the electron beam line.

The target system consist of two parts. The first one is an $e-\gamma-n$ converter. The second one is a splitting into two separate volumes containing subcritical plutonium fuel elements (8, 9). There is rotating a wheel (10) with two fuel element shells. This wheel has a special electrical drive (13). There is a permanent magnet shell (11) on the wheel and a stator coil (12). These elements (11, 12) form a trigger (15) for accelerator pulse systems.

Typical values for the repetition rate are 100 Hz and 50 Hz.

III. PRELIMINARY STUDY RESULTS

IBR-30 is a pulsed subcritical facility. Here the multiplication coefficient can be periodically changed from low level $\approx$ 16 up to a nominal value $\approx$ 200. Therefore, there could be a possibility to study the real fluctuations of k_{eff} for different levels of multiplication coefficients. On the other hand, it should be taken into account that IBR-30 contains a wheel with a shell of fuel mass. This system can give a contribution to the neutron fluctuation as well. What could be the sources of neutron fluctuation? Because of the pulse source, there could be two kinds of fluctuation. The first one is short range fluctuations (SRF). Time interval of SRF is several times the pulse duration. The second is long rage fluctuations (LRF). The time scale of LRF is several times the repetition rate.

Neutron detector (fission chamber) records a signal which has a small periodical deviation during the all time the facility is being run. A typical value of the fluctuation in a nominal regime is about 4-6% and it is shown in fig. 2. This value is much more (up to 12%) for the transient regime.

The new diagnostic elements were installed in the control room in order to determine what the reason was for such periodical deviations. The general linac signals were collected for on-line pulse to pulse analysis. A linac mathematical model was made up to study the processes more correctly.

A. Linac Related RF Properties and Transient Beam Loading Problem of LUE-40

The average energy sag per one mA is $\approx$ $43keV/mA$. The first section has a buncher part 54 cm long and constant impedance structure as the regular part 400 cm long. The length of the second section is 314 cm. The filling time for both sections is $\approx 650ns$. In fig. 3 the output energy of the two sections and a summary RF-efficiency vs. beam current are shown. This is the steady state regime. Any transient regime shall take that into account.

The typical range of the beam current is 0.3-0.5 A. The time duration of the beam current is $\approx 1.8\mu s$ (i.e., $t_f \approx 1/3$ of t_{beam} and t_f is the filling rf - power).

In fig. 4 the experimental transient beam loading of the first rf-section is shown in arbitrary units. In practice the beam injection

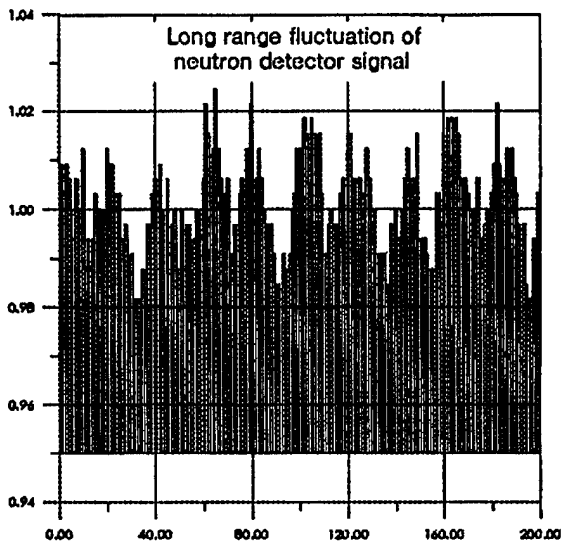


Figure 2. Long range neutron fluctuation vs repetition rate cycles.

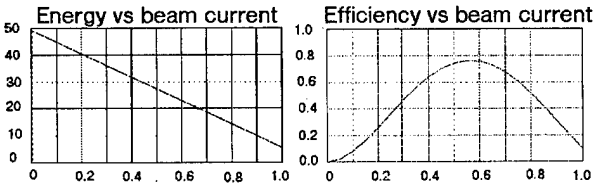


Figure 3. Output LUE-40 energy and rf-efficiency vs beam current.

starts before the end of the filling time in order to reduce the energy sag. The deviation of the output rf-signal during the pulse is $\approx$ 20 – 30%. The computer simulation of the rf-power sag for a beam injection at $t = t_f$ is shown in fig. 4 (3). To set the main parameters of the linac, the experimental results of relative power sag and filling time were used.

There are a several fluctuation sources. IBR-30 contains a mechanical system which consists of a DC power electromotor with a wheel. The motor generator feeds from an AC network. The rotational speed of the wheel can changed by the operator and tuned to be close to 100 Hz. On the other hand all power supplies of the linac systems feed from the 50 Hz AC network. The first fluctuation source is the beat frequency between the rotational speed of the wheel and network frequency. This is a long range fluctuation.

In our studies there was a possibility of simultaneously picking up several signals according to the phase of the network frequency (rf-system, beam current, amplitude of neutron detector signal etc.). Fluctuations of the neutron detector signal correlates with the phase of the AC network power is shown in fig. 5. Approximately 9, 000 events are shown in this plot and there is only a $\pm 4\%$ fluctuation of the neutron signal. This picture shows that 2% do not correlate with the phase of the network.

Above data were received when IBR-30 was running with 50

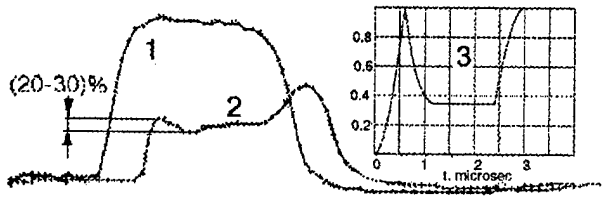


Figure 4. Transient beam loading in first section: 1 - P_{in} input rf-power; 2 - P_{out} output rf-power; 3 - computer simulation of the power sag for a beam injection at $t = t_f$.

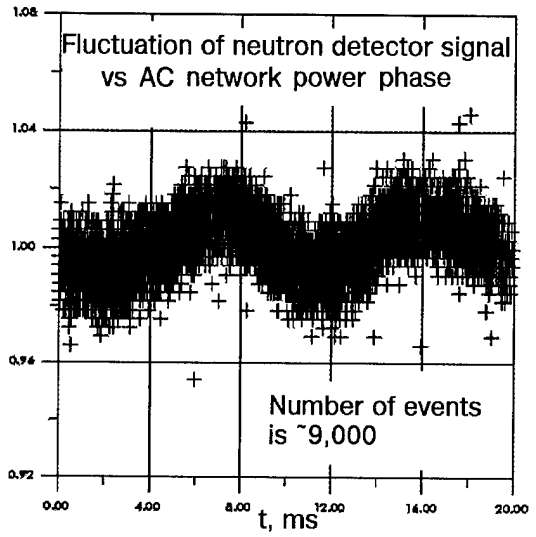


Figure 5. Fluctuation of neutron amplitude signal vs phase of network power.

Hz repetition rates. There was only short time to record a runaway (to get a nominal regime) regime of IBR-30 with 100 Hz repetition rate. It can be seen in fig. 6 when the velocity of wheel was equal the AC frequency of the network power and there was a period when phases almost did not change (region). In this regime the LRF of beam power and neutron signal were less than 1%.

IV. CONCLUSION

The first preliminary results for multiplication coefficient fluctuation study vs. accelerator parameter deviation on the JINR accelerator driven neutron source were carried out.

The experimental fluctuation of thermoneutron detector signal was correlated with the fluctuation of the beam power. The major source of the neutron signal fluctuation is the absence of the equiphase conditions the wheel rotation velocity and the network frequency.

The study should be continued with the signal of the fast neutron detector. The on-line experiments should be done in stable phase regime.

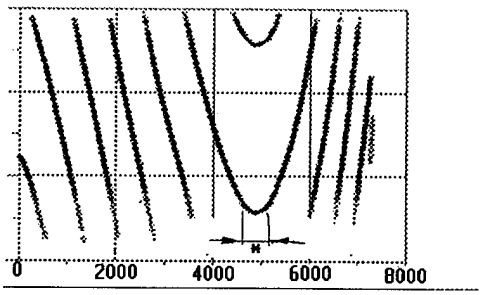


Figure 6. AC phase of network power supply vs number of cycles of IBR-30.

V. ACKNOWLEDGEMENT

Authors thank the IBR-30 operations group for their patience during the measurement preparations. They would like to thank the PAC and ICHEA organizing committee for their invitation to take part in this conference. Authors also would like thank the George Soros Foundation for making one of us (Dr. A. Krasnykh) to attend this conference. Finally, they also thank Mrs. A. Schaeffer for her help in preparing this report.

References

[1] Inter. Conf. on Accelerator-Driven Transmutation Technologies and Applications, Las Vegas, MGM Grand Hotel, 1994.

[2] S. Adam, et al., Potential of Cyclotron Based Accelerators for Energy Production and Transmutation, Inter. Conf. on Accelerator-Driven Transmutation Technologies and Applications, Las Vegas, MGM Grand Hotel, 1994.

[3] O. van Dyck, LAMPF Reliability History and Program, Inter. Conf. on Accelerator-Driven Transmutation Technologies and Applications, Las Vegas, MGM Grand Hotel, 1994.

EUROPEAN SYNCHROTRON RADIATION STORAGE RINGS[1]

H. Zyngier, LURE, Centre Universitaire de Paris Sud, Bât. 209 D, 91405 Orsay Cedex France

The list of European synchrotron radiation sources is updated. It shows several new facilities coming into operation, or very close to completion. Their characteristics show the present trends of the community.

New projects are announced. The capabilities are extended in the countries already equipped, and new countries are willing to build synchrotron radiation sources. All this confirms the vitality of the discipline.

I. OVERVIEW OF THE EUROPEAN SITUATION

The community of synchrotron radiation users is developping at a fast and regular pace. New techniques appear and new sources are constantly needed. Europe participates in this trend, as I shall show here by a survey of the West European sources.

In the exhaustive list [1] of sources throughout the world which has been compiled by V. Suller for the 1992 EPAC there were 70 rings planned, operating or in construction. Among them, 20 were European : 9 in operation, 6 under construction, and 5 projects. Since then, the operation column lost ADONE now closed, and gained DELTA, ELETTRA, ESRF and MAX II, making a total of 12 rings in operation. BESSY II went from the planned to the construction phase, and 5 new projects are presently announced. The situation is now 12 rings operating, 3 under construction, and 9 planned.

There is no general body in Europe comparable to the DOE or NSF, and no uniform policy governing the development of Science or scientific tools. Decisions concerning programs are made separately, and independently by the governments of European countries, and therefore the history of synchrotron radiation sources in Europe depends much on the local traditions of machine builders and machine users. A remarkable exception to this situation is the ESRF, an international facility on the model of CERN and the ILL, initiated by the European Science Foundation, and whose scientific goals were assigned after a wide study of european needs and capabilities made by over 140 scientists and engineers.

Moreover, some degree of synchronization is provided by informal links between actors in the field, in particular through conventions and meetings. A biannual European Particle Accelerator Conference (EPAC) held under the auspices of the European Physical Society provides a forum on the general field of accelerators. As far as synchrotron radiation storage rings are concerned, two annual informal workshops have already been held at the ESRF, and this tradition is likely to be continued in the future in other places.

Despite the independance of the actors, there appears to exist a certain logic in the distribution of storage rings between the different generations as defined by H. Winick [2] and between the different photon energy ranges. To simplify, I shall use a half logical, half chronological classification of the sources which seems more convenient for a small sample, and distinguish between two fundamental energy domains : the low energies, up to a few keV, referred to as "VUV", and the higher energies, above 1 keV, referred to as "X". Detailed references on the different rings can be found in [1] and I shall just add the more recent ones.

To begin with, there is no dedicated lithography ring. The experimental ring COSY has been abandoned, and HELIOS, built in Great Britain for IBM is now in the US.

II. PARTLY DEDICATED SOURCES

The first group counts four partly dedicated sources listed in Table 1. ELSA [3] in Bonn is an electron pulse stretcher. Six dipole ports are available, and approximately a quarter of the time is devoted to synchrotron light users. ASTRID [4] in Aarhus is an interesting machine, storing ions and electrons six months per year each. Three beamlines are operating, and a VUV undulator is under construction. There are plans for a dedicated ring. Then come two dutch sources, not yet operating. In Amsterdam, AmPS [5] has been functionning as a pulse stretcher since 1992, and EUTERPE, in Eindhoven aims at synchrotron radiation and beam physics studies. Both rings have projects for a low emittance mode.

This class of synchrotron radiation sources illustrates the importance of local situations. These active centers overcome funding difficulties by associating different communities around a single machine. The drawback is the time it takes to reach the objectives, and that is why two of theses rings are still in the "planned" state as far as synchrotron light itself is concerned.

Table 1 : Multipurpose sources.

Name	Country	First Beam	Emittance	Energy
ELSA	D	1988	900 nm	3.5 GeV
ASTRID	DK	1991	160 nm	580 MeV
AmPS	NL	1992	100 nm (5 nm)	900 MeV
EUTERPE	NL	> 1995	160 nm (8 nm)	400 MeV

[1]Work supported by CNRS-CEA-MESR.

0-7803-3053-6/96/$5.00 ©1996 IEEE

Table 2 : Established sources.

Name	Country	Generation	First Beam	Emittance	Energy	Dipole ports	Insertions	Particles
DORIS III	D	1	1973	430 nm	4.5 GeV	12	10	e^+
DCI	F	1	1976	1 300 nm	1.85 GeV	3	1	e^+
SRS	UK	2	1980	110 nm	2.0 GeV	9	2	e^-
BESSY I	D	2	1982	55 nm	800 MeV	24	3	e^-
MAX I	S	2	1985	50 nm	550 MeV	8	2	e^-
Super-ACO	F	3	1987	37 nm	800 MeV	8	4	e^+

III. SOURCES OF THE 80'S

The facilities listed in Table 2 delivered their first dedicated photon beams in the 80's. They span the three generations, and belong to two categories : three X-ray sources, and three VUV. The by-pass added to the 4.5 GeV collider DORIS [6] in Hamburg makes it an attractive source serving 10 insertion devices and 12 dipole ports. The stored particles are positrons. This particular feature is shared by the other former collider, DCI in Orsay, where it contributes to a long lifetime of over 100 h. The light coming from the three dipole ports from serve 16 experiments, and 6 others are fed from a 5 pole superconducting wiggler delivering a 50 mrad wide fan. The third X-ray ring, SRS [7] in Daresbury, is the first second generation source of this set, and its emittance is the smallest. It has 9 dipole ports, and 3 insertions in operation.

The VUV machines are more recent. The trend towards smaller emittances initiated at SRS is continued. Due to the lower energy, the Touschek effect reduces the lifetimes. BESSY, in Berlin with its 24 dipole ports and 3 insertions is very densely used, while MAX I, in Lund still has some possibilities for extension. Super-ACO, in Orsay shares the linac injector with DCI and also stores positrons. It works half time in the temporal mode, usually with two 100 mA bunches, and part time with the Free Electron Laser acting as a user UV source.

Super-ACO was the first third generation machine, that is designed from the start with a low emittance, and to accomodate several insertion devices. It remained the only one until the ESRF went on line.

This class of rings is actually the most complete. They exhibit the widest variety in energies, emittances, and sign of stored particles, as can be seen in the Table 2. But this table does not show the particular histories of these rings. Almost all of them have been modified and improved. Not only new beamlines have been added, have been reduced. They served as test benches for new techniques for the sources, and for the beamlines as well.

IV. SOURCES OF THE 90'S

The recent rings are listed in Table 3. They exhibit a small emittance, lower than 10 nm.rad, and rely much on insertions. ESRF [8] in Grenoble is the only facility dedicated to hard X-rays in the world. It will soon be joined in this energy range by the APS and SPring8. The italian VUV source ELETTRA [9] in Trieste is comparable to the ALS. Both ESRF and ELETTRA are currently delivering photons to their users. Two more are in the commissioning phase, DELTA in Dortmund, and MAX II [10] in Lund. BESSY II [11] in Berlin will start in 1997.

Apart from the ESRF, the rings of this set are oriented towards VUV and soft X-rays, but with a higher beam energy than the older ones to overcome the Touschek lifetime limitation, and to take advantage of the lower field in the insertions. The experience of the preceding machines has been used to make a big step forward towards ever smaller emittances.

I want to mention here an IR source of a completely different design. CLIO [12] in Orsay, is a linac based FEL, working for external users since 1992. Last year after having delivered 1 500 h of useful beam between 1.8 and 17.5 μm, the machine was upgraded, to reach 50 μm. It is now operating since february.

Table 3 : Present generation.

Name	Country	First Beam	Emittance	Energy
ESRF	F	1992	8 nm	6 GeV
ELETTRA	I	1993	4 nm	1.5 GeV
DELTA	D	1995	10 nm	1.5 GeV
MAX II	S	1995	9 nm	1.5 GeV
BESSY II	D	1997	6 nm	1.7 GeV

V. A NEW LIFE FOR ACO

Before beginning the survey of future machines, I would like to pay a tribute to the oldest collider. ACO, in Orsay which stored its first beam in october 1965, served as a collider solely first, then part time photon source since 1968, and from July 1976 dedicated source, until its last shut down in April 1988. Since then, the hall has been cleaned up, and it is managed by a foundation "Sciences ACO", devoted to cultural action, and to be a link between research, public, industries and the educational world.

VI. PLANS FOR THE FUTURE

A number of new projects are being studied in different countries. They are listed in Table 4. ANKA [13] is the only one definitely oriented towards industrial uses such as analysis and micromechanics. DIAMOND [14] in the UK and SOLEIL [15] in France should replace existing rings. The Danes consider a fully dedicated ring to join ASTRID, and the British are considering a VUV ring, SINBAD [14]. Spain with LLSB and Switzerland with SLS [16] are two new countries joining the club. Two more opportunities are being considered : using the radiation of PETRA and DAΦNE as used to be done with the first generation.

At this time, these projects are not funded. There is therefore no defined time schedule, and the characteristics are still subject to change. I shall therefore be cautious in driving conclusions as to possible trends. It seems that the VUV rings (with the exception of SINBAD) aim at a higher beam energy, in order to improve the lifetime, and perhaps also to cover a wider energy range. Also, the double bend based lattice appears often. Compared to the present series of rings, the emittance values are much more dispersed. To understand this, it must be borne in mind that the conditions vary much in the different countries. Germany has a large variety of sources, and the new project ANKA can be designed for a very specific use, namely industrial applications. Denmark, the United Kingdom and France have already working sources, with well trained communities of users who follow their own traditions, and need extensive access to synchrotron radiation. The situation of Switzerland and Spain who are creating a new domain of research is obviously different.

Table 4 : Projects.

Name	Country	Emittance	Energy	Lattice
ANKA	D	45 nm	2.5 GeV	DDBA
ASTRID II	DK	63 nm	1.4 GeV	DBA
DIAMOND	UK	15 nm	3.0 GeV	DBA
LLSB	E	10 nm	2.5 GeV	TBA
SINBAD	UK	< 10 nm	700 MeV	DBA
SLS	CH	3.2 nm	2.1 GeV	7BA
SOLEIL	F	4 nm	2.15 GeV	DB

VII. CONCLUSION

The early successes of the young rings ESRF, ELETTRA, and the ALS show that many of the challenges described by A. Jackson [18] at the Tsukuba Conference have been properly mastered. A strong confidence in the calculation codes to predict the emittances, the dynamic acceptance and the instability thresholds has been gained because no unknown effects have shown up. The techniques of heat absorption are well mastered.

On the other hand, realization of small vacuum chamber impedances remains an important issue. Also, some progress is still needed to stabilize the beams against instabilities and ground motion as well. But progress is going on, and new techniques for feedback and contact fingers are being tested.

All this is very encouraging for the success of the new projects. The main problem which remains is beyond our technical knowledge : funding.

VIII. REFERENCES

[1] V. Suller, "Review of the status of synchrotron radiation storage rings", Proceedings of EPAC 92 (Berlin), pp. 77-81.

[2] H. Winick, G. Williams, "Overview of synchrotron radiation sources worldwide", Synchrotron Radiation News, Vol. 4, n° 5, (1991) pp. 23-26.

[3] K. H. Althoff et al., "ELSA, one year of experience with the Bonn electron stretcher accelerator", Particle Accelerators, 27 (1990) pp. 101-106.

[4] E. Uggerhoj, "ASTRID. The Aarhus dual purpose storage ring for positive/negative ions and electrons", Journal de Physique IV, 4 (1994) pp. 349-356.

[5] R. Maas, G. Luijckx, "AmPS, the Amsterdam pulse stretcher as photon source", Proceedings of EPAC 92 (Berlin) pp. 480-482.

[6] H. Nesemann et al., "First experience with DORIS III", Proceedings of the 15th ICHEA (Hamburg 1992) p 549.
H. Nesemann et al., "DORIS III as dedicated source", this Conference (FAA 02).

[7] J.A. Clarke et al., "Update on commissioning and operations with the second superconducting wiggler at Daresbury", Proceedings of EPAC 94 (London), pp. 648-650.
M.V. Poole et al., "Updated plans for DIAMOND, a new X-ray light source for the UK", this conference (TPG 09).

[8] A. Ropert et al., "Towards an increased brilliance at the ESRF", Proceedings of EPAC 94 (London), pp. 582-584.

L. Farvacque et al., "Possible retuning of the ESRF storage ring lattice for reducing the beam emittance", Proceedings of EPAC 94 (London), pp. 612-614.
A. Ropert, "Accelerator physics trends at the ESRF", this conference (TPG 05).

[9] A. Wrulich, "ELETTRA status report", Proceedings of EPAC 94 (London), pp. 579-581.
C.J. Bocchetta et al., "ELETTRA commissioning and operation", Proceedings of EPAC 94 (London), pp. 57-61.

[10] A. Andersson et al., "The MAX II synchrotron radiation storage ring", NIM, A343, (1994) pp 644-649.

[11] D. Krämer et al., "Status of the high brilliance synchrotron radiation light source BESSY II", Proceedings of EPAC 94 (London).
E. Jaeschke, "Status of the high brilliance synchrotron radiation light source BESSY II, this conference (FAR 12).

[12] J.-M. Ortega et al., "CLIO : collaboration for an infrared laser at Orsay", NIM A285 (1997) pp. 97-103.
R. Prazeres et al., "CLIO, an infrared free electron laser facility", NIM B89 (1994) pp. 54-59.

[13] H.O. Moser, "ANKA, a synchrotron radiation light source for microstructure fabrication and analysis", this conference (FAR 06).

[14] M.V. Poole, V.P. Suller, "Proposals for new UK light sources", Proceedings of EPAC 94 (London), pp. 621-623.
M.V. Poole et al., "Updated plans for DIAMOND, a new X-ray light source for the UK", this conference (TPG 09).

[15] M.-P. Level et al., "New specifications for the SOLEIL project", this conference (FAR 14).

[16] W. Joho et al., "Design of a Swiss light source (SLS), Proceedings of EPAC 1994 (London) pp. 647-629.

DEVELOPMENT OF THE JAERI FEL DRIVEN BY A SUPERCONDUCTING ACCELERATOR

E.J.Minehara, M.Sugimoto, M.Sawamura, R.Nagai and N.Kikuzawa,
Free Electron Laser Laboratory, Department of Physics,
Japan Atomic Energy Research Institute
2-4 Shirakata-shirane, Tokai-mura, Naka-gun, Ibaraki-ken, 319-11 Japan

A prototype for a quasi-cw, and high-average power free electron laser (FEL) driven by a 15 MeV superconducting rf linac has been developed, and constructed at Tokai, JAERI. Expected cryogenic(stand-by loss<3.5W at 4.5K) and accelerating fields' performances (Eacc ~ 7MV/m and Q ~ $2\times10^{+9}$) of four JAERI superconducting accelerator modules have been demonstrated, and installed them in the FEL accelerator vault. A beam test and commissioning of the JAERI superconducting rf linac as an FEL Driver have been successfully performed to get an electron beam ranging from 10 to 20 MeV with nearly full transmisson. FEL opticals and beam transport elements around the undulator, which have been already assembled, are now under commissioning. Spontaneous emission in the wavelength of 20 μm to 80 μm or longer has been observed by using the Ge (Cu) and Ge (Ga) detectors and fast current amplifier system.

I. INTRODUCTION

As well known, a laser system consists of three major parts, i.e., a laser driver like a flash lamp, a gain medium like a glass or a crystal, and an optical resonator of paired mirrors. Since the invention of the laser in 1950's or 1960's, efficiency and average power level of the conventional lasers have been seriously limited to very low by their huge heat losses in the laser drivers and gain media, and damages in the mirrors. Because a free electron laser (FEL) has an high energy electron beam in alternating magnetic field as the gain media, we could neglect the heat losses in the FEL gain media. Unfortunately, as long as conventional normal conducting accelerators were used to produce the high energy electron beam as the FEL driver, we still have the large heat losses in the accelerator cavity wall of the FEL driver. Therefore, in order to make a highly-efficient, and high average power FEL, we resultantly have to minimize the heat losses in the driver to very low level in comparison with total rf power consumption. This is our motivation why we try to apply the superconducting rf linac accelerator to the JAERI FEL driver.

A developmental program [1,2] of the FEL system for a far-infrared region from the wavelength of 20 μm to 80 μm or longer has been undertaken at Japan Atomic Energy Research Institute (JAERI), Tokai. The purpose of the present JAERI FEL program lies in constructing a very long pulse or quasi-continuous wave (cw) superconducting rf linac electron accelerator, and demonstrating a high-average power FEL in the far-infrared wavelength region.

Because the wall losses and required rf power become minimal in the superconducting accelerator cavity, we may realize a quasi-cw and high-current rf linac driver, and hence a high-average power laser. Each major part of the program including future plans has been reported in other papers [3-8] in detail. Here, we present an outlook of the program including the present status and schedule.

II. INJECTOR

The injector of the JAERI FEL consists of a thermionic cathode electron gun with a pulsing grid, a sub-harmonic buncher (SHB), and a buncher. The accelerating voltage in the single gap electron gun is typically around 210KV, and the gun is usable from 200 to 240 KV. The cathode is mounted horizontally in a stainless-steel pressurized vessel with SF_6 gas to 2kg/cm^2 in order to prevent break down across a 45 cm-long insulating ceramic tube of the gun. The accelerating gap electrodes are fabricated in a re-entrant geometry to increase the accelerating gradient. Optimization of the geometry was made by computer-modeling of electron beams using E-GUN [9].

The injector was installed, and commissioned late August 1991, and is now operated routinely. An extensive study of pulse characteristics as a function of injector parameters has resulted in sets of optimized operating conditions which minimize pulse width at a time focus point while maintaining the beam quality as good as possible. The characteristics typically obtained are as follows: an electron beam ranging from 85 to 140mA with 4ns bunch length was extracted from the gun at the accelerating voltage of 210-240KV. The beam was successfully compressed to less than 70 ps at around the time focus point by the bunching system [1] in the injection beam line. Measured normalized emittance after the SHB was scattered around 10 to 20 π mmmrad. Transmission of the injector was measured to be around 100% by using the JAERI-made current core monitor.

III. SUPERCONDUCTING RF LINAC

The JAERI superconducting rf linac consists of two pre-accelerator modules of the single-cell cavity type and two main modules of the 5-cell cavity type. The resonant frequency of the cavities is 499.8MHz which is exactly the same with the buncher, and the sixth harmonic of SHB in the injector.

We decided to choose a so-called DESY concept of the cavity geometry and the fabrication technology refined

0-7803-3053-6/96/$5.00 ©1996 IEEE

by Siemens Energieerzeugung KWU for the JAERI FEL superconducting rf linac accelerator late September,1990. Design values of the accelerating field strength and Q-value for the cavities are 5MV/m, and 2×10^9, respectively. In the beginning of 1993, we have successfully demonstrated very good cryogenic (stand-by loss < 3.5W at 4.5K) and accelerating fields' performances (Eacc~7MV/m and Q~$2\times10^{+9}$) of four JAERI superconducting accelerator modules, and installed them in the FEL accelerator vault.

As a main coupler was designed to have a variable coupling coefficient over 3 and half decades, we could inject not only low current but also high current electron beams into the accelerator module without changing a rf matching condition in the coupler. In order to do some diagonostics, we could easily perform low and high rf power test anytime shortly utilizing the coupler. Typical peak RF power for the coupler was measured up to the 50kW without trouble in JAERI. The coefficient was designed to be adjusted by pushing and pulling a center conductor into the cavity.

Three sets of the higher mode couplers were designed, and fabricated to suppress unwanted and harmful TE and TM modes having a higher resonance frequency. Two monitor couplers were designed, and fabricated to use in monitoring and phase detecting in the feedback loop of a fast tuner. Slow and fast tuners were designed, and fabricated to tune a resonance frequency of the cavity in the module. The slow tuner consists of a stepping motor driver and an interface from the control system. The fast tuner consists of a piezo-electric actuator, a high voltage power supply, a feedback loop, an interface from the phase detector, and the control system. During the accelerator operation, the system keeps the phase constant wthin 1 degree, and keeps the amplitude constant within less than 1% .

IV. CRYOSTAT AND REFRIGERATORS

We have newly developed a multi-refrigerators system[5] integrated into the superconducting accelerator module cryostat to realize a independent, and highly-efficient system without any liquid coolant. Each accelerator module has own heat shield cooler and recondensor being equipped with refrigerators and compressors, independently. This modular structure of the module makes it possible to remove any single module for repairing, and to add more modules without warming other module.

A 4K closed-cycle He gas refrigerator mounted just above a liquid-He supply tower of the module was adopted to cool down and to recondense cold vapor of liquid He around a heat exchanger in the liquid He container. Required electricity of a conventional liquefier is around 1KW for 1W cooling at 4.5K, and the required of the JAERI recondensor 1.8KW. In order to run the recondensor ecomonically, we introduced a new heat buffering material of ErHoNi magnetic compound instead of Pb, and successfully reduced the required down to 0.9KW. A 40K/80K two-stage closed-cycle He gas refrigerator, which was mounted in a vacuum vessel of the module was adopted to cool down the 40K and 80K heat shields and other major components of the cryostat. These two kinds of the refrigerators are available commercially in Japan and other countries. The 4K refrigerator supported in a heavy steel frame can be winched up and down to remove the heat exchanger out of the liquid He container, and to insert the exchanger into the container. Cooling capacity of the 4K refrigerator is about 12W at 4.5K and 60Hz.

The 40K and 80K heat shields are used to prevent heat invasion from outside into the liquid He container. In order to minimize heat loads to the container, the heat shields work as a thermal anchor, and make the heat flow return route having a temperature higher than 4K for all heat bridges from the outside. The 40K/80K refrigerator used here provides two cooling stages with a typical pair of temperature of 40K and 80K and heat load capacities of 40W and 120W , respectively.

V. RF POWER SUPPLES

One of the largest merit of a super- conducting accelerating cavity is very low power loss, which makes it possible to use all-solid-state RF power amplifiers for all of the cavities[4]. Because the required voltage of the all-solid-state amplifiers is lower than that of a klystron and a tetrode, a more stable RF power is expected to be realized. We choose to use two sets of all-solid-state 50kW RF power amplifiers for the main accelerator modules, two sets of 6KW for the preaccelerators, and 4KW for the SHB, and 2KW for the buncher.

All sets of the power supply have been already installed, and have been ready to use at the experimental area since the middle of August 1992. Performance of the rf power supplies has been preliminarily measured to be better than 1% of amplitude and within 1 degree of phase stability at an rf power level of 50kW or more. We have had no malfunctioning of the rf power supply since the installation, and we expect no repairing and no maintenance in the rf amplifiers near future.

VI. ELECTRON BEAM TRANSPORT SYSTEM

The energy of electron beams accelerated by the linac usually ranges from about 10 to 20 MeV. A conceptual design of the transport system was done by using the beam optics code TRACE-3D [10]. High current beams have to be fed to the undulator under isochronous and achromatic conditions for efficient lasing of FEL. Because of the large amount of charge density, space charge effects would become serious in a long transport line and a beam waist. Since the code could take into account partially space charge effects, the transport system has been investigated by using the code.

A beam dump in preparation will be capable of handling about 40 mA of true average current or more, and 1 kW of beam power. Cooling of the dump is provided by air flowing in channels or pipes machined into an aluminum rod. About 30 cm-thick lead surrounds the dump to reduce the radiation levels during routine operation to natural background levels outside the shielding walls made of 150 cm-thick concrete.

VII. HYBRID UNDULATOR

A wedged-pole hybrid undulator will be used for the first lasing experiment of the JAERI FEL. The undulator was originally designed and built as a prototype undulator for the SPring-8 project [11]. This device is expected to generate brilliant photon beams of energy ranges around 10 keV by installation into the low emittance high energy storage rings such as the Spring-8 [12]. In order to fit the undulator into the JAERI FEL system, the undulator was characterized by three-dimensional field calculation and two-dimensional field mapping.

In order to characterize the undulator, a distribution of the multipoles was derived from the field distributions in the median plane of the undulator. A strip of the three-dimensional field distribution was obtained by using a conventional finite element method (FEM) calculation code ANSYS [13]. An experimental distribution was obtained by field mapping with commercially-available three-dimensionally measuring equipment.

Calculational and experimental distributions of the multipole components along the undulator axis were derived up to dodecapole components from the field distributions by a least-square fitting method. The calculated distributions of the multipoles quantitatively shows very good reproduction of the experimental distributions.

IX. ACCELERATOR VAULT

A new extension was completed to an old 5.5 MV electrostatic accelerator building as an FEL accelerator vault in March 1992. Two sets of the main accelerator module, the beam transport system, hybrid undulator, and FEL opticals were installed inside the vault in the beginning of 1993.

X. PRESENT STATUS AND FUTURE PLANS

In the beginning of 1993, we have successfully demonstrated expected cryogenic (stand-by loss < 3.5W at 4.5K) and very good accelerating fields' performances(Eacc > 7MV/m and Q > $2\times10^{+9}$) of four JAERI superconducting accelerator modules, and installed them in the FEL accelerator vault. In 1993, Optical resonators and beam transport systemwere already assembled, and installed in the accelerator vault.

Before ending of the 1994 Japanese fiscal year (before March 31st, 1995), a beam test of the JAERI superconducting rf linac FEL was successfully performed to get an electron beam of ten and several amperes of peak current after the main accelerator at around 15 MeV. Measured energy resolution of a pre-accelerated beam is about 3% of FWHM , and that of a fully-accelerated beam about 0.8% or less. Maximum transmission of the beam from the gun to the undulator is now obtained to be at around 100%. Since September 1994, we have tried several number of spontaneous and stimulated far-infrared (FIR) emission measurements. By utilizng Ge (Cu) and other detectors equipped with the JAERI made fast current amplifier [14], very stable and large, and intermittantly very large FIR signals were observed around 25 μm during the measurements.

After the current developmental program will be successfully ended, we plan to build a large-scaled high average power FEL facilitydriven by a superconducting rf linac with a 200MeV recirculating configuration, or to build a UV and shorter wavelength FEL facility without a recirculating configuration. After or before the second step, an industrial superconducting rf linac based FEL machine (Industrial SCFEL) will be built to demonstrate higher average power capabilities of the superconducting rf linac FEL driver. These three plans under consideration in JAERI are not approved yet by Japanese government.

XI. SUMMARY

In conclusion, we have presented the status and purpose of the JAERI quasi-cw, high-average power FEL program concerning the superconducting rf linac driver, and other FEL opticals. We reported our successful demonstration on the performances of the injector, rf power supplies, four JAERI superconducting accelerator modules, hybrid undulator, and Liquid He refrigerators, which have been installed for these four years. We are now active in transporting electron beams in the JAERI FEL, and in performing some lasing experiments in the optical resonator.

ACKNOWLEDGEMENT

The authors would like to thank Drs. N. Shikazono, M. Ishii, Y.Kawarazaki, Y.Suzuki, and S. Sasaki of JAERI for their continuous encouragement and interests in this work.

REFERENCES

[1] M.Sawamura et. al. ,Nucl. Instrum. Method A318 (1992)127.
[2] M.Ohkubo et. al. ,Nucl. Instrum. Methods A296 (1990)270.
[3] R. Kato, et al., in the Proceedings of Sixteenth International Free Electron Laser Conference, 1994, San Francisco.
[4] M. Sawamura, et al., ibid.
[5] N. Kikuzawa, et al., ibid.
[6] R. Nagai, et al., ibid.
[7] M.Sugimoto, et al., ibid.
[8] K. Sasaki, et al., ibid.
[9] W.B.Herrmannsfeldt, SLAC Report-226, November 1979.
[10] K. R. Crandall, et al., TRACE 3-D Documentation, LA-1054-MS, UC-32 and UC-28, 1987.
[11] H. Kamitsubo, Nucl. Instr. and Meth. A303 (1991) 421.
[12] S. Sasaki, et al., in the proceedings of Particle Accelerator Conference, 1991, San Francisco.
[13] Swanson Analysis Systems, Inc. Reference manual of ANSYS-386 Rev. 4.4.
[14] K.Berrymann, Stanford University, private communication.

FREE ELECTRON LASER RESEARCH IN CHINA

Jialin Xie, Institute of High Energy Physics, Chinese Academy of Sciences, P.O. Box 918, Beijing, 100039, China

China has endeavored in the field of FEL research since the mid-eighties. Compton regime, Raman regime, Electromagnetic Pumping, Cherenkov FEL, and Harmonic Generator FEL, etc. based on the RF linac accelerator, induction linac accelerator, pulsed-line accelerator, and storage ring have all been developed. These experimental projects are in various stages of development and are discussed in sequence. Theoretical analysis, numerical simulation and components research related to FEL also will be mentioned briefly.

INTRODUCTION

Free Electron Laser is well known for its stringent requirements on the quality of the electron beam taking part in the beam-wave interaction. Thus, research on FEL serves both the purposes of exploration of its potential applications and promotion of the development of accelerator physics and technology.

FEL research and development have been taking place in China since the mid-eighties.[1] The primary purpose is to study the physics and learn the technology. Now, after some facilities have been completed and lased to saturation, the applications of these facilities has become the object of exploration. Furthermore, in order to satisfy the requirements of various applications, the quality - such as the intensity and spectral stability, etc. - of the laser produced and the ease of operation of the system will come to attention and deserve research efforts.

In the following, the RF linac based Compton regime FEL, including Beijing IR-FEL of the Institute of High Energy Physics; FIR-FEL of the Institute of Atomic Energy; wide-band user facility of the Institute of Nuclear Physics, and FIR-FEL of the Academy of Engineering Physics will be presented first. Then, the Induction linac based Raman regime FEL amplifier of the Academy of Engineering Physics and the pulsed-line accelerator based Raman FEL, E.M. pumped oscillator and Cherenkov FEL of several institutes will be discussed. Finally, the storage ring based UV harmonic generator of China University of Science and Technology will be described. Also, theoretical achievements, computer-code developments and system components studies will be mentioned briefly.

I. IR-FIR FEL

1.1 IR-FEL of The Institute of High Energy Physics (BFEL) [2]

Figure. 1 shows the schematic layout of BFEL. This facility has a microwave electron gun with a LaB_6 cathode of <100> cut for high stability and high emission. The maximum energy of the electrons from the gun cavity is 1.2 MeV and the beam current is about 200 mA at the entrance of the linac with a bunch width of about 4 ps. The thermionic cathode microwave electron gun proves to be a very compact and convenient way for the production of short electron bunches with good beam quality for IR-FEL. However, it has the draw-back of back-bombardment that causes intensity variation of the beam current during the macropulse accompanied by energy variation due to the beam loading effect in the gun cavity. By using two deflecting magnetic fields along the gun cavity, the back-bombardment effect can be significantly reduced.[3] BFEL operates stablely at a macropulse length of 4.5 μs and repetition rate of 3.125 Hz.

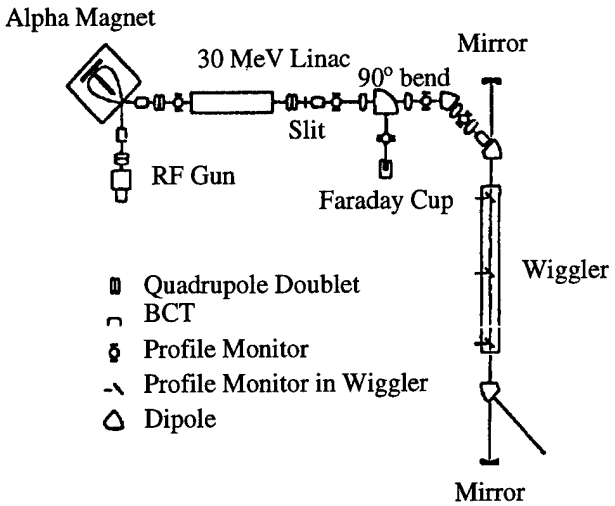


Figure 1: Schematic diagram of Beijing FEL

The electrons generated from the gun and compressed by the Alpha magnet are injected into an S-band, constant gradient unit relative phase velocity linac section and are accelerated to about 30 MeV. The linac section used is a modified SLAC-type constant gradient waveguide with four extra circular holes on some disks. These holes create a separation of the dispersion curves of EH_{11} mode but little perturbation of the dominant TM_{01} mode.[4] Thus, the

0-7803-3053-6/96/$5.00 ©1996 IEEE

BBU threshold value should increase with practically no effect on the acceleration process.

After passing through an achromatic and a nearly isochronous 90° beam transport system, electron bunches are injected into an undulator. The undulator is planar type with NdFeB permanent magnets, consisting of 50 periods of 1.5m long. The magnets have the size of 7.5 mm × 7.5 mm × 40 mm. The optical cavity is a near concentric resonator consisting of two ZnSe mirrors with ZnSe/TuF4 multilayer dielectric coating. After being extracted from the downstream mirror, the laser beam passes through a telescopic pipe and is sent to the diagnostic room.

The typical result of lasing is as illustrated in Figure 2. The laser builds up in about 2 μs corresponding to about 100 round trips in the optical cavity. The saturated output power level is about 2 KW at the HgGdTe detector. Since both the outcoupling factor and the macropulse duty factor are about 1%, the intra-cavity average optical power is estimated to be 200 KW and the peak power 20 MW. The spatial distribution of the laser at the diagnostic room as measured with a LMP-32 × 36 elements pyroelectric detector located in the focal plan of a lens, is about twice the diffraction limit as illustrated by Figure 3.

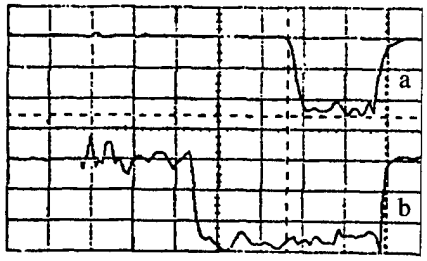


Figure. 2: BFEL macropulse at saturation (1 μs/div) (a) laser, (b) electron beam

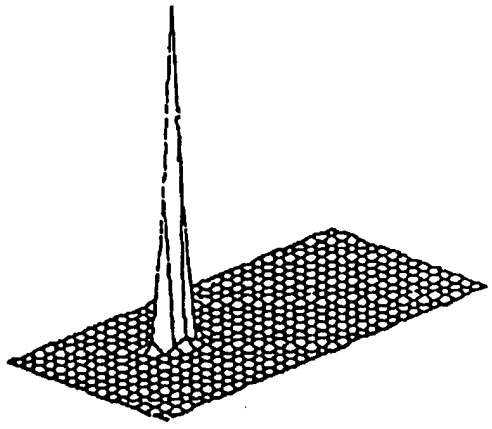


Figure. 3: Spatial distribution of the laser beam

The wave-length range of the system was, so far, limited by the spectral range of the reflectance of the mirror. An upgrading program is under way to expand the laser wavelength coverage and to improve the operational stability. To summarize, the general characteristics of the laser are given in Table 1.

Table 1: Summary of the laser characteristics

Total spectral range	9 - 11 μm
Output energy in optical macropulse	2 - 10 mJ
Average power in macropulse	200 KW
Peak power	200 MW
Spectral width	0.3 - 2%
Small signal gain	32%
Optical extraction efficiency	0.48%
Beam divergence	2 mrad

(1.2) FIR FEL of the Institute of Atomic Energy [5]

In the Institute of Atomic Energy (IAE), an L-band high brightness injector has been built and tested. It is planned to add some 3π/4 mode high gradient accelerator section to make it a driver of FIR-FEL.

The injector consists of a 100 KV, 3 ns triode electron gun, one-quarter wavelength reentrant coaxial resonator sub-harmonic buncher of 108 MHz and one TW 3π/4 mode buncher of 1300 MHz composed of 7 cavities. This particular mode was adopted for both the buncher and the accelerator section because of its high BBU threshold which is important for the high current operation of the system.

The performance up to now is given in the following

Injector energy	1.8 MeV
Micropulse current	> 50 A
Micropulse width	~ 40 ps
Normalized emittance	0.02 cm-rad

(1.3) Wide-band FEL User Facility of the Institute of Nuclear Physics and the Institute of Optics and Fine Mechanics [6]

A wide-band FEL user facility (SFEL) is being built at the Shanghai Institute of Nuclear Physics, China Academy of Sciences. The driver of SFEL consists of a triode electron gun, sub-harmonic buncher and a high gradient buncher as injector and SLAC type accelerator sections as accelerator. The injector produces micropulses of 59.5 MHz repetition rate of 6 - 10 ps long and 20 - 100 A current. The designed macropulse width is 6 - 8 μs.

SFEL uses three different undulators driven by three different energy electron beams to cover a wide wavelength range. The first beam is from the injector itself with energy of 2 - 3 MeV and produces FIR radiation with wave-length from 800 - 2000 μm. The second beam is produced after the electrons from the injector are accelerated by one accelerator section to an energy of about 30 MeV. This beam, after passing through the second undulator, produces Mid-IR radiation from 10 - 25 μm. The third beam, being accelerated by two more accelerator sections to an energy of 40 - 50 MeV produces radiation of 2.5 - 8 μm. The wave-length range is designed to cover the applications of FEL in life science, material science and bio-medical science. The use of RF grid controlled triode electron gun and buncher combination allows easy adjustment of bunch separation, which is of concern for time resolved experiments.

The above mentioned scheme is for the first phase of the project. To further extend the wave-length range to UV, three more accelerator sections and a storage ring will be added as the second phase.

The present status of SFEL is that the accelerator sections are available. Buncher is under measurement, gun and modulator being delivered and other components under construction.

(1.4) FIR FEL of China Academy of Engineering Physics [7].

Construction of an FIR-FEL facility using a thermionic microwave electron gun as injector operated at 1.3 GHz has been started at China Academy of Engineering Physics.

The electron beam from the injector has the following characteristics:

Energy	1.8 MeV
Peak micropulse current	10 A
Micropulse Width	~35 ps
Macropulse current	450 mA
Macropulse width	4 μs
Beam normalized emittance	15 π mm-mrad
Beam energy spread	<1.5%

II. MM-WAVE FEL

(2.1) Raman FEL Amplifier of China Academy of Engineering Physics (CAEP) [8]

The induction linac-based FEL amplifier (SG-1 FEL) of CAEP was started in 1987. Spontaneous emission experiment, constant parameter undulator, and variable parameter undulator amplifier experiments were carried out in sequence up to 1994.

SG-1 FEL amplifier is composed of an induction linac, beam transport system, undulator, microwave source, and diagnostic system as shown in Figure 4.

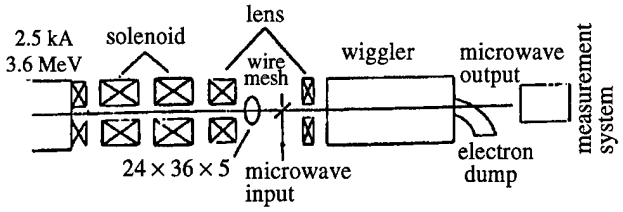


Figure. 4: Schematic layout of SG-1 FEL of CAEP

The induction linac is composed of a 4-cell injector and an 8-cell accelerator. Each injector cell provides 250 kV, 100 ns pulse voltages to give a total 1 MV for the diode gun with felt cathode. The electron beam is generated from the gun passing through an axial magnetic guiding field and is generated from the gun passing through an axial magnetic guiding field and is injected into the accelerator where each cell gives 300 kV acceleration.

The measured output electron beam parameters are:

Electron Energy	3.5 MeV
Electron Current	2.5 A
Energy Spread	2%
Emittance	0.43 cm-rad.
Beam Brightness	10^8 A/(m-rad)^2

The accelerated beam passes through a beam transport system of solenoid and lens of 2 m long and then goes through an emittance selector into the undulator. The current there is about 800 A.

The undulator is of electromagnetic type which has parabolic pole face for double focusing. The period of the undulator is 11 cm and length is 3.96 m with nominal field level of 3.1 KG. Every two period shares one separate power supply so that different tapered fields can be produced. Peak magnetic field is continuously variable from 1.4 - 3.4 KG on the axis while the two-period at the entrance and at the exit are lower strength for orbit control. The transmission efficiency of the undulator is greater than 80%.

Microwave source for SG-1 amplifier is a 20 kW, 34.4 GHz, 0.35 μs pulse-width magnetron. The microwave power entering the undulator region is about 7 kW. Rectangular wave-guide with TE_{01} mode is used for beam-field coupling. The amplified signal frequency and power are measured with dispersion line and crystal detector.

The experimental measurements of the SG-1 system were first performed with the amplification of the spontaneous emission. Power output of 400 mW at 100 A was obtained which compares reasonably with the result of 600 mW according to numerical simulation. Results of the amplification of a seeding signal are illustrated by Figures 5 through 7.

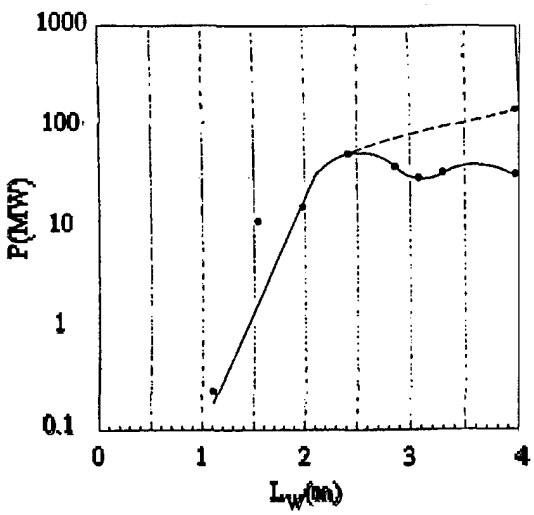


Figure. 5: SG-1 power output vs undulator length. Dashed line: Tapered undulator, Solid line: Constant parameter undulator (3.1 KG)

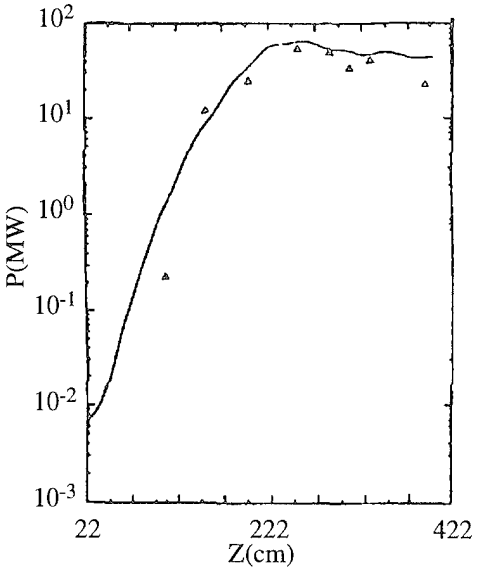
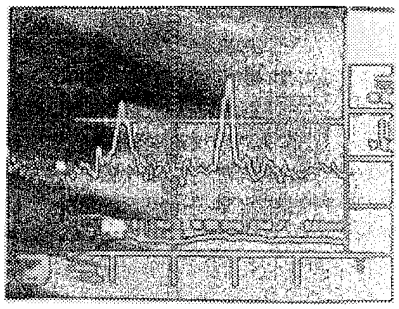
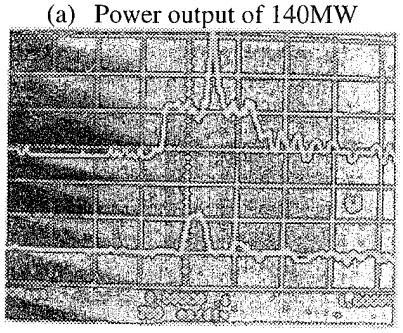


Figure. 6: Comparison between experiments (dots) and simulation (solid line)



(a) Power output of 140MW



(b) Upper trace-microwave drive, Lower trace-electron beam

Figure. 7: Output waveforms of SG-1 FEL

(2.2) Pulse-line Accelerator FEL and Electromagnetic Pumped FEL [8][9]

FEL with wavelength of several mm has been realized in China since mid-eighties. The Shanghai Institute of Optics and Fine Mechanics first produced a superradiant emission of 8 mm wavelength and 1 MW power with a 0.5 MV pulse-line accelerator. The Southwest Institute of Applied Electronics, in cooperation with the University of Electronic Science and Technology of China (UESTC), performed similar experiments with an annular beam of 0.7 MV, and radiation of 32 GHz was observed. Later, amplifier experiment without axial guiding magnetic field and with a 1.5 m, 3.45 cm period undulator and 280 A was carried out which produced output power of 7.6 MW at 37 GHz.[10]

Electromagnetic pumping FEL was first implemented in UESTC where a system that produced simulated radiation with an interaction region separated from the BWO pump wave generator was used.[11] The radiation generated by the BWO serves as an electromagnetic undulator which as the advantage of producing up-shifted frequency radiation with relatively low source voltage.

Electron beam of 0.6 MeV and 3 - 5 KA generated by a pulse-line accelerator passes through the slow-wave structure of BWO at the down-stream and generates microwave of 3 cm wavelength as an electromagnetic pump source for the FEL interaction region located at the up-stream. Stimulated radiation of 3 - 8 mm wavelength is produced at the output window and detected with a crystal detector.

(2.3) Cherenkov FEL

CFEL has been pursued in China in several institutes. [12] Here, only the case of multilayer dielectric loaded waveguide CFEL [13] will be given as an illustration. The calculated longitudinal field distribution with multi-layer dielectric in a plane waveguide shows that the first fundamental mode $TM^1{}_{01}$ has very favorable field distribution for beam-wave interaction. The dielectric loss is also found to be lower than the conventional waveguide and the interaction area is increased. The CFEL oscillator consists of five ceramic plates of 445 mm long, 0.6 mm at top and bottom, and 1.2 mm for the others in a 26 mm × 16 mm waveguide driven by a pulsed-line generator. The solid electron beam generated was cut into sheet beams by a metallic screen. About 80% of the generated beam entered the cavity. The useful beam current is 280 A at 500 KV. The radiation power of 33.4 GHz is in close agreement with that predicted from the dispersion relation. The output radiation power of 1.7 MW was measured with a calibrated crystal detector at the end of the dispersive delay line. The corresponding efficiency was about 1.2%.

III. UV FEL

FEL Harmonic Generator at Hefei National Synchrotron Radiation Laboratory [14]

At Hefei National Synchrotron Radiation Laboratory, a project has started to build an optical klystron installed in one of the straight sections. A third-harmonic of Nd glass laser of wavelength 3533 Å is used as input to produce third harmonic of 1178 Å VUV harmonic coherent radiation for application research.

The electron beam and the optical klystron parameters are given in the following:

Energy	301.6 MeV
Energy spread	1.74×10^{-4}
Beam current	50 mA
Bunch length	12.3 mm
Emittance	2.36×10^{-2} mm-mrad
Number of bunches	45
Rotating frequency	4.8 MHz
Energy damping time	0.195 s
For the optical klystron:	
Period	7.2 cm
No. of period	2×12
Field strength	0.3247 T
Gap	3 cm
Length of dispersion section	21.6 cm
Dispersion field strength	0.7837 T

It was estimated that with this arrangement, each bunch can produce 1.7×10^5 photons at 1178 Å coherently.

IV. THEORETICAL ANALYSIS AND NUMERICAL SIMULATION

Besides the construction of experimental facilities as given above, considerable theoretical work on FEL has been accomplished in China. A new analytical method of describing different kinds of longitudinal mode evolution was proposed. It is a one-dimensional, unified theory that includes the effects of pre-bunching, self-bunching and co-bunching caused by strong external field. Co-bunching is responsible for the emission of harmonics and synchrotron sidebands.[15] Linear space-charge wave theory was developed to analyze the bunching process and beam-wave interaction of FEL.[16] Several computer codes have been completed to guide the design and tune-up of the above mentioned facilities. For example, for SG-1, the simulation is made with a 3-D code, WAGFEL, which--besides other things--includes the space charge effect, transition region of undulator entrance effect, etc.[17] This code, after comparing with the experimental data of SG-1 FEL and also with ETA-ELF,[18] proves to be a reliable means to guide the experimental design.

V. COMPONENT DEVELOPMENTS

Various FEL component developments, such as super-conducting RF gun research, multiple cavity microwave electron gun, etc. are also being carried out. Peking University has started a super-conducting microwave electron gun project with Nb cavity operated at 1.5 GHz. The preliminary test of the prototype showed it can stand an accelerating field of 12.6 MV/m and a Q of 2×10^9 at 2.1K.[19] Figure 8 shows the 3-1/2 cavity thermionic cathode electron gun being developed jointly by Qinghua University and the Institute of High Energy Physics.[20] According to the simulation, the back-bombardment power is only one-eighth of the single cavity case through optimization of various parameters.

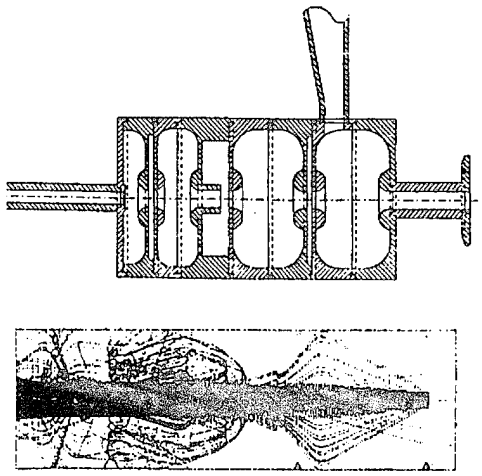


Figure 8: A 3-1/2 cavity RF gun under development. Schematic diagram of the cavity and electron orbits

REFERENCES

[1] Xs.W. Du, the First Asian Symposium on FEL (1993)
[2] J.L. Xie et al, Nuc. Instr. & Meth. A341 (1944) 34
[3] V. Kushnir and Gang Wang, private communication.
[4] C.G. Yao, IEEE NS32 (1985) 2968
[5] W.Z. Zhou et al, Nucl Instr. & Meth. A341 (1994) ABS 37
[6] X. F. Zhao et al, the First Asian Symposium on FEL (1993)
[7] K.S. Hu, private communication
[8] Z.X. Hui et al, the First Asian Symposium on FEL (1993)
[9] S.G. Liu, Proc. 17th Inter. Conf. on IR & MM (1992)
[10] K.S. Hu, High Power Laser and Particle Beam, 2 (1990) 158
[11] Z. Liang, Proc. of 7th National FEL Symposium (1991) 130
[12] C.L. Li, High Power Laser and Particle Beam, 3 (1991) 136; 147
[13] Q.Y. Wang et al, Appl. Phys. Lett. 59 (1991) 2378
[14] D.H. He et al, Proc. of 7th National FEL Symposium, (1991)
[15] M. Yu, High Power Laser and Particle Beam, 3 (1991) 127
[16] S.G. Liu, Inter. J. Electronics, 72 (1992) 161
[17] Z.H. Yang et al, High Power Laser and Particle Beams, 1 (1989) 60
[18] T.J. Orzechowski, Proceedings of the Beijing FEL Seminar, (1989) 347
[19] C.E. Chen et al, the First Asian Symposium on FEL (1993)
[20] C.X. Tang, private communication.

Accelerator physics trends at the ESRF

A. Ropert, L. Farvacque, J. Jacob, J. L. Laclare, E. Plouviez, J. L. Revol, K. Scheidt

European Synchrotron Radiation Facility, BP 220, F - 38043 Grenoble Cedex

Abstract

The operation of third generation synchrotron light sources at design target goals raises a number of challenging problems in accelerator physics. This paper will review the most recent advances made at the ESRF in some of these areas during the first two years of operation. The lattice performance is dominated by the non-linear effects induced by the requirement for a low emittance; the correction of these effects enables significant increase of the tunability and flexibility of the DBA lattice. Solutions to overcome the instability-related problems linked to the increase of intensity thresholds in multibunch and single bunch modes will be discussed. The achievement of a stability of the beam centre of mass in the micron range is a key issue for all third generation light sources. Present ESRF performances and limitations will be presented.

1. INTRODUCTION

Since the beginning of 1993, the ESRF has been operated in user service mode (USM). At present 25 beamlines are supplied with X-rays produced from insertion devices or bending magnets. In 1995, 5000 hours of operating time for users have been scheduled. In addition a provision of about 1400 hours is being made for machine dedicated time. Table 1 summarises the remarkable increase in performance achieved with respect to the design goals [1].

	design goals	served during USM	present peak performance
Intensity MB	100	150	185
(*in mA*) SB	5	5	25
		15 *(feedback)*	20 *(feedback)*
Lifetime MB	8	60 (100 mA)	70 (100 mA)
(*in hours*) SB	8	30 (5 mA)	30 (5 mA)
e^- emittances H	7	4	4
(*in nm*) V	0.7	0.04	0.04
Beam stability	*10 % of size*	1 % in H	1 % in H
	and divergence	10 % in V	10 % in V

Table 1

This illustrates the main accelerator physics trends currently being tackled: assessing the performance of a low emittance lattice and the lifetime related issues, pushing the current to higher limits, controlling the beam position stability. This paper will review the results achieved so far.

2. LATTICE RELATED ISSUES

The successful running-in of the Double Bend Achromat lattice used for the ESRF storage ring shows that the new lattices for third generation light sources are not over-sensitive, as feared in the past. The DBA lattice has proven to be very forgiving since it was possible to run it for two years with a wrong polarity on a harmonic sextupole (this was discovered by chance at the beginning of 1994). Since target performances of the lattice have by far been achieved, flexibility and tunability issues are now of prime concern in order to satisfy future needs that may arise.

2.1 Lattice flexibility

The lattice is currently run in a mode with alternating zero-dispersion high β and low β straight sections. One attractive way to decrease the horizontal emittance [2] by a factor of 2 and consequently increase the brilliance consists of allowing a finite dispersion all around the machine (Fig. 1).

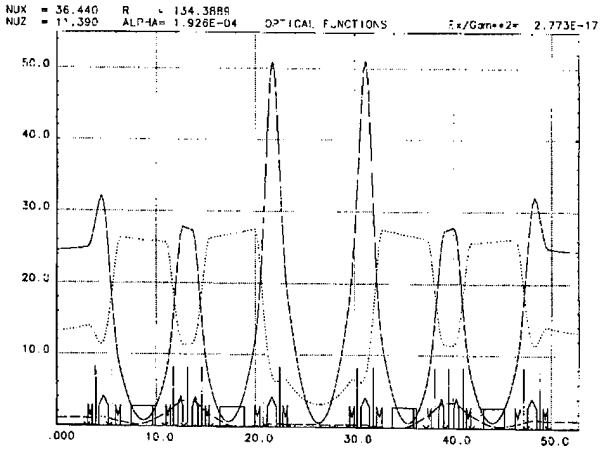


Figure 1

Low emittance settings can easily be derived by detuning the focusing quadrupole of the achromat. This new optics has been successfully tested and an emittance of 4 nm measured, compared to the 7 nm of the regular lattice, whilst keeping the 1 % coupling. The acceptance in momentum and the lifetime are comparable to those of the regular lattice. Ramping to maximum intensity of 185 mA was achieved without any sign of transverse instabilities. This low emittance version of the lattice replaced the standard version in March 1995 in multibunch.

Some of the numerous potentialities of the Double Bend Achromat lattice in terms of flexibility are currently being investigated [3], as illustrated by the examples below:

- The tuning of all straight sections to high βs or of a single straight section from high β to low β has been successfully tested on the machine. The decrease of the vertical β in all high β straight sections sections (from 12 m to 2.5 m) would ease the installation of undulators with smaller gaps than the standard 20 mm currently used. Preliminary tests are very promising.

0-7803-3053-6/96/$5.00 ©1996 IEEE

- Up until now, all efforts to provoke ion trapping, even in the most favourable conditions of low current and uniform filling of the ring, have been in vain. In order to favour the occurrence of ion-related effects, a weak focusing version of the lattice using uniform focusing and smooth β functions (horizontal/vertical tunes of 14.4/12.8) and providing a second generation type emittance (63 nm) has also been run. 50 mA could be stored with a bad lifetime of one hour. No ion-related effects have been observed so far.

- Finally, exciting perspectives could be opened with the ESRF lattice running in a quasi-isochronous mode with even negative momentum compaction. The likely advantages of such an optics in terms of instabilities look very attractive since, among others, it is naturally stable for head tail effects, and strong sextupoles are no longer necessary.

2.2 Enlargement of the acceptance in Δp/p and correction of resonances

Lifetime is a key issue for third generation sources, due to the much smaller emittances and insertion device gaps than machines of the previous generation. During lattice design, the achievement of a large dynamic acceptance and a low emittance took priority over longitudinal acceptance despite this being the key solution to a long lifetime, especially in the few bunch mode where Touschek related effects play a major role. Since the start of operation, the efforts to upgrade the design figure of 8 hours have been very successful thanks to the optimisation of machine tuning (careful choice of working point, optimisation of the sextupole distribution to enlarge the Δp/p acceptance, correction of all resonance lines in the vicinity of the working point [4]). The benefits from this strategy are demonstrated in Figure 2. Despite the large vertical chromaticity, large excursion possibilities are found in the tune diagram. When compared to the initial acceptance in momentum (-8σ/9σ), the enlargement (-18σ/22σ) is spectacular.

Although the correction of resonances is not usually practised in electron storage rings, the beneficial effects are evident. For each resonance line, the correction is performed by 2 pairs of correctors arranged so as to correct the driving term in amplitude and phase and to cancel the harmonic 0. The recent implementation of a global correction algorithm based on the use of the response matrix of each type of resonance minimises the cross-talk between corrections.

The correction of the 2 coupling resonances $\upsilon_x - \upsilon_z = 25$ and $\upsilon_x + \upsilon_z = 48$ enables the coupling to be decreased by a factor of 10 down to the 1 % range. The half integer stop-bands $2\upsilon_x = 73$ and $2\upsilon_z = 23$ are perfectly mastered since these resonances can be crossed without any beam loss. Their correction almost cancels the modulation of β functions induced by focusing errors and also the blow-up of the horizontal emittance which could reach values of 8.5 to 11 nm without corrections. At present, the correction of the integer quadrupolar stop-bands is less efficient since it is impossible to go below $\upsilon_x = 36.03$ or $\upsilon_z = 11.065$.

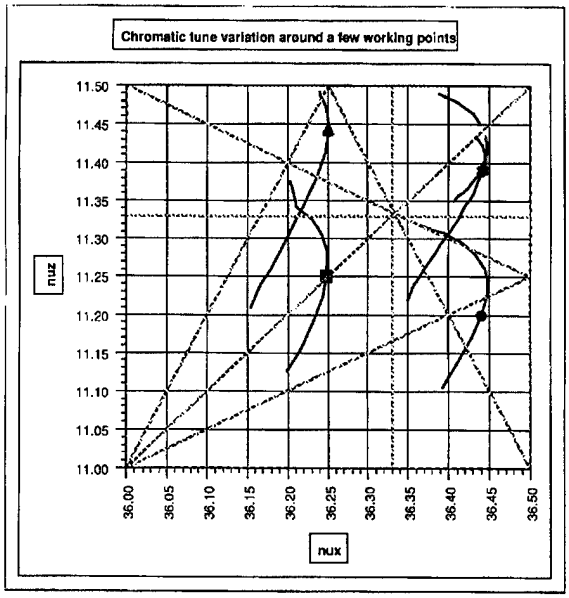


Figure 2

3. ULTIMATE CURRENT LIMITS

3.1 Multibunch case

Low instability thresholds resulting from the excitation of coupled bunch instabilities driven by the Higher Order Modes in the RF cavities effectively limit the maximum current to about 60 mA when the machine is filled in the uniform filling mode. A simple solution has been applied to nevertheless overcome the predicted threshold and go significantly beyond the 100 mA design current. It consists of adopting a non-uniform filling leaving an empty gap corresponding to two-thirds of the circumference. In addition to being less sensitive to transverse resistive wall instabilities, this filling pattern provides a stabilising effect thanks to the beam loading of the cavity at every passage of the bunch train. The induced amplitude modulation of the voltage increases with current and provides enough Landau damping via the spread of the synchrotron frequencies in the bunch train to damp coherent oscillations. Peak intensity could be pushed to 185 mA without any sign of instability thanks to this trick and the large over-compensation of the vertical chromaticity ($\xi_z = \Delta\upsilon/\upsilon)/(\Delta p/p) = 0.6$) applied to overcome resistive wall-related instabilities.

It must be emphasised that such a large positive chromaticity has obviously some impact on the optimisation of the dynamic aperture and the necessary sextupole strengths. The possibility of running the machine with natural chromaticity has been questioned. Initial tests have been carried out in that direction (20 mA stored with a negative chromaticity close to the $\xi_z = -2$ natural figure).

Another solution [5] to avoid the excitation of HOM-related instabilities consists of detuning the responsible HOMs away from the beam eigen frequencies by regulating the cavity temperatures to ±0.1 °C. This method enabled the intensity threshold to be doubled in the uniform filling mode and is currently applied when the machine is operated with 16 equally spaced bunches and cannot benefit from the beam loading damping effect.

3.2 Single bunch case

With regard to single bunch current limitations, the maximum current is limited, as predicted, by the fast head-tail instability, the threshold of which is chromaticity-dependent. As seen in Figure 3, the threshold can be pushed above 20 mA by varying the vertical chromaticity up to $\xi_z = +1$.

At zero chromaticity, the threshold for the transverse instability occurs at very low current (in the mA range) and the instability mechanism is due to the expected coupling between modes 0 and -1. At higher chromaticity, with short bunches like the ESRF ones, the interpretation of the interaction of the bunch with a broad-band impedance looks more questionable. The follow-up of the position of the maximum of the envelope of the synchrotron satellite amplitudes shows that all satellites are defocused by current and move in parallel. In particular, the maximum is not attached to a given satellite. It coincides with the line associated with m = -1 at zero current and $\xi_z = 0$ and with the line associated with m = -3 at $\xi_z = 0.6$ when approaching the threshold of 6 mA. This is far from the conventional mode coupling mechanism. At higher chromaticity, a large number of lines is involved and their follow-up is more difficult. The "damping" mechanism leading to higher thresholds still needs to be understood in detail.

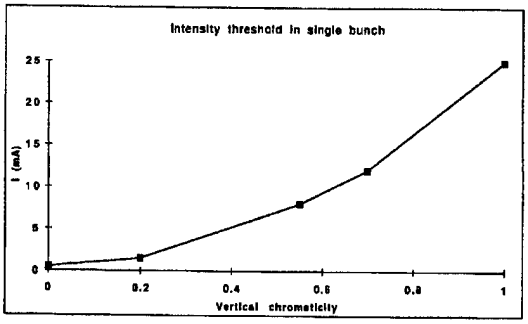


Figure 3

However such large chromaticities lead to large tune excursions associated with Δp/p deviations and accordingly to strong Touschek lifetime limitations. The use of a Digital Signal Processing based transverse feedback [6] enables large currents to be stored with still a reasonable chromaticity ($\xi_z = 0.6$). Up to 20 mA have been stored in that mode and 15 mA delivered to users with a lifetime of 15 hours in April 1995.

Following the recent commissioning of our streak camera, a campaign of measurements of single bunch parameters (bunch length, synchrotron frequency and phase evolution as a function of current and RF voltage) is under way. The main goal is to assess the predicted absence of bunch lengthening which was associated with the broadband impedance model used to fit the longitudinal wake field of a bunch passing through the vacuum vessels discontinuities. These measurements are being performed for the regular and the low emittance lattices which (among other contrasts) differ by their momentum compaction ($2.8\ 10^{-4}$ / $1.9\ 10^{-4}$).

Similar results are found for the 2 optics with a bunch lengthening of a factor of 2.75 between 1 mA and 17 mA. This independence of the bunch length on the optics indicates that the beam remains at the turbulent regime when the current is increased and that some lengthening and widening are required to keep it stable. The energy spread is evaluated from the analysis of gap scans of the 7^{th} harmonic of the ID6 machine undulator spectrum. Preliminary estimates confirm that some widening occurs. The objective is now to use in a self consistent analysis the updated data in order to derive a model of impedance and losses.

4. BEAM POSITION STABILITY

In order to avoid spoiling the small achieved emittances, stringent tolerances on the X-ray beam stability and reproducibility in position and angle have to be achieved (the target is set at 10 % in position and angle for both planes). Therefore, in order to stabilise the beam, the requirements on the measurement and correction of the beam position stand in the micron range for the vertical plane and are 10 times less severe in the horizontal plane.

As far as DC closed orbit control is concerned, the adopted strategy consists in correcting the orbit every 5 minutes in 3 steps: a global harmonic correction, a readjustment in position and angle in the straight sections where insertion devices are located and a retuning of the RF frequency. This brings the beam centre of mass stability to a few % of beam sizes over periods of one week. However, the stability of the sensors, i.e. the electron BPMs, is now the limiting factor in the control of beam stability, given the 0.04 nm vertical emittance routinely operated [7]. Among the many effects inducing motions of the sensors in the few micron range, contributions from the machine itself (crane, thermal effects,..) are dominating external influences (tides, water table motion,..) acting with long wavelengths. It appears that thermal effects on the vacuum vessels linked with beam intensity is the major limitation.

In AC mode, fast feedback systems can successfully be operated to minimise the beam displacements induced by vibrations amplified by the magnet girders (naturally of the order of 5 % of the beam sizes at frequencies higher than 1 Hz). However, they suffer the same limitations as the standard orbit correction, namely stability in position of the

sensors, mechanical stress on the vacuum vessel, electronics drifts.

Short-term improvements are expected from the installation of new BPMs between bellows at both ends of ID straight sections. The fast feedback system using BPMs will take advantage of their better mechanical stability. Provided similar improvements on the XBPM side could be achieved, angular stability, which is the dominant limiting factor, could be significantly improved by combining BPMs and XBPMs to increase the lever arm. However, the stabilisation of the beam centre of mass to better than 10 % of beam sizes and divergences with third generation light sources vertical emittances still remain a challenging R&D issue.

5. REFERENCES

[1] J. L. Laclare, "Target specifications and performances of the ESRF source", J. Synchrotron Radiation (1994)

[2] L.Farvacque, J. L. Laclare, P. Nghiem, J. Payet, A. Ropert, H. Tanaka, A. Tkatchenko, Proc. EPAC94, p. 612 (1994)

[3] L.Farvacque, T. Günzel, J. L. Laclare, C. Limborg, A. Ropert,"Flexibility of the ESRF lattice", to be published

[4] A. Ropert, 2nd Workshop on Synchrotron Light Sources, Grenoble (1994)

[5] J. Jacob, 2nd Workshop on Synchrotron Light Sources, Grenoble (1994)

[6] J. L. Revol, E. Plouviez, Proc. EPAC94, p. 1506 (1994)

[7] L. Farvacque, "Brainstorming on X-ray beam center of mass stability", N°5/94,ESRF

COMMISSIONING OF THE PLS 2 GEV STORAGE RING

M. Yoon, J.Y. Huang, J.S. Jang, M. Kwon, T. Lee, and S.H. Nam, Pohang Accelerator Laboratory, Pohang University of Science and Technology, San 31, Hyoja-Dong, Pohang, Korea 790-784

In Pohang, Korea, construction of a third-generation 2 GeV light source has been in progress since 1988. Installation of the storage ring components started in March 1993 and was completed in August 1994. Initially, only two super-periods out of 12 were baked out in-situ. From September to the end of 1994, the machine commissioning had been carried out. The initial injection energy for the commissioning was chosen to be 1.4 GeV because at this energy the injection kicker magnet can make a design bump, -21 mm. On September 8, the injected beam from the injector linear accelerator was circulated in storage ring more than 500 turns without RF. After accumulating the beam up to 76 mA on October 20, the injection energy was changed to the design value which is 2.0 GeV. At 2.0 GeV, amount of the bumped orbit which the kicker magnet can generate is -15 mm. Additional -6 mm bump is produced by four horizontal corrector magnets located on each side of the injection straight section. On December 24, 1994, the beam was stacked up to 300 mA, exceeding the commissioning goal of 100 mA. From January to March 1995, the ring had been shut down for in-situ bakeout. Since April, the second commissioning has been in progress. The PLS facility will be open to users in July 1995. In this paper, we present the current status of the PLS storage ring commissioning and the future plan for normal operation.

I. INTRODUCTION

The PLS is a third-generation synchrotron radiation facility. The construction project began in April, 1988 and the installation was completed in September, 1994. It was jointly funded by Pohang Iron and Steel Company (POSCO) and Ministry of Science and Technology (MOST) of Korean government. Total construction budget was approximately US $180M.

The PLS is located an area adjacent to the Pohang University of Science and Technology (POSTECH) campus in Pohang, which is about 400 km southeast of Seoul. Total area of the PLS facility is 650,000 m^2, which is large enough to accomodate possible future expansion. The facility itself is situated on stable mud-stone area. On April, 1991, a ground-breaking started and the building construction was completed in September, 1993.

The PLS consists of two major accelerators; a 2.0 GeV full energy injector linear accelerator and a 2.0 GeV storage ring. The linear accelerator is a conventional RF accelerator which provides a 2 A, 2 nsec long electron pulses with a nominal repetition rate of 10 Hz. The operating frequency is 2856 MHz and there are total 42 constant gradient accelerating columns and 10 energy doublers. The bunching of electrons is done by employing a 2856 MHz standing-wave prebuncher followed by a 2856 MHz traveling-wave buncher. The electron bunches leaving the first accelerating column are bunched within 5 degrees in phase. The construction of the linear accelerator was completed in December, 1993 and from January to June 1994, the commissioning had been conducted and the machine is now in normal operation mode so that it can provide an electron beam whenever storage ring demands.

The injection into the storage ring is done by four kicker magnets and one septum magnet, all located in one of the straight sections in the storage ring. Since the injector is located below ground, the output beam from the linear accelerator is transported vertically at an angle and this beam is then deflected vertically by the septum magnet to place it on the same level as the stored beam in the storage ring. The storage ring is 280.56 m in circumference and consists of 12 super-periods. The magnet lattice employs a triple bend achromat structure, with 36 dipole magnets, 144 quadrupoles and 48 sextupoles. The magnetic field of the dipole magnet is 1.058 T at 2.0 GeV, and the critical photon energy from the bending magnet is 2.8 keV.

The installation of the storage ring was started in March 1993 and was completed in August 1994. Actually, most of the storage ring components had been installed by March 1994 and in April, magnet alignment was started. By August, several iterations of survey and alignment had been carried out and as a result quadrupole magnets were aligned within 0.15 mm in rms. The commissioning of the storage ring and the beam transfer line was started in September 1994. In this report, we present the current status of the PLS storage ring commissioning. Status and plan of the beamline construction will also be described.

II. STORAGE RING COMMISSIONING

A. General Status

Prior to the commissioning, only the chambers in two super-periods out of 12 were baked out in-situ due to lack of time. The average vacuum pressure was mid 10^{-9} torr which was sufficient for commissioning purpose. An overall debugging of the control system had been performed during August. This includes a magnet power supply control, vacuum gate valve IN/OUT control,

0-7803-3053-6/96/$5.00 ©1996 IEEE

injection and RF control, and machine safety interlock debugging etc. On September 1, 1994, the commissioning of the beam transfer line was started. On the same day, the injected beam appeared at the first screen monitor located between kicker magnets in storage ring. For the initial commissioning, the electron beam energy was set to be 1.4 GeV because below this energy the storage ring kicker magnet can produce a design bump, -21 mm. This corresponds to -15 mm at 2.0 GeV. Therefore at 2.0 GeV, the additional kick is necessary and this can be produced by utilizing four horizontal corrector magnets located on each side of the injection straight.

The injection into the storage ring and the storage ring commissioning began on September 5. On the 8th, the signal from the stripline pickup monitor indicated that the injected beam was circulated in storage ring more than 500 turns without RF turned on, which is in agreement with the estimation. After turning on the RF and with some adjustment of magnet currents and RF frequency, the beam started being stored and as time went by the stored current increased gradually. Immediately after the beam stacking, the vaccum went up by more than two orders of magnitude. For the commissioning, the number of beam bunches was chosen to be 100 to 200 out of maximum 468 bunches. On September 28, the stored beam current reached to 27 mA where the vacuum interlock at the RF straight section prevents from further stacking; the interlock level of the vacuum was set to be at 10^{-6} torr. As the vacuum chamber is being scraped out by the photon beam, the storage ring vacuum has been improved slowly which in turn increased the stored beam current and lifetime.

In order to see the possibility of 2.0 GeV injection with DC bump, at 1.4 GeV the bumped orbit was reduced to -15 mm from -21 mm and on top of this a -4 mm DC bump was applied. The stacking was successful and with minor adjustment of injection conditions, the beam current reached up to 76 mA where again the vacuum interlock at RF was activated . Subsequently on October 24, the beam energy was changed to 2.0 GeV and on October 26, the current went up to 102 mA, exceeding the commissioning goal of 100 mA. Since then, the stored current increased continuously and on December 23, just one day before shut-down, it went up to more than 300 mA. Total beam dose obtained to that date was 8.5 ampere-hours and the beam lifetime was 45 minutes at 100 mA. Normally, the injection rate was 2 mA/sec, with the best perfomance of 3.5 mA/sec. The injection efficiency was approximately 25%.

The storage ring had been shut down from January to March, 1995 in order to bake out all the vacuum chambers in situ and to remove some of the beam profile monitors. After the bake-out, all magnets were resurveyed and aligned and by the end of March, the quadrupoles were aligned within 0.14 mm (rms) in horizontal and 0.09 mm (rms) in vertical directions, respectively.

On April 1, 1995, the second commissioning of the storage ring was started. The base pressure of the vacuum was of the order of 10^{-10} torr. Improvement of the beam lifetime was apparent after the bake-out; immediately after the beam storage, the lifetime at 100 mA was about 2 hours. At 13 ampere-hours of total dose, it became approximately 4 hours at 100 mA and at this current the vacuum pressure was low 10^{-8} torr.

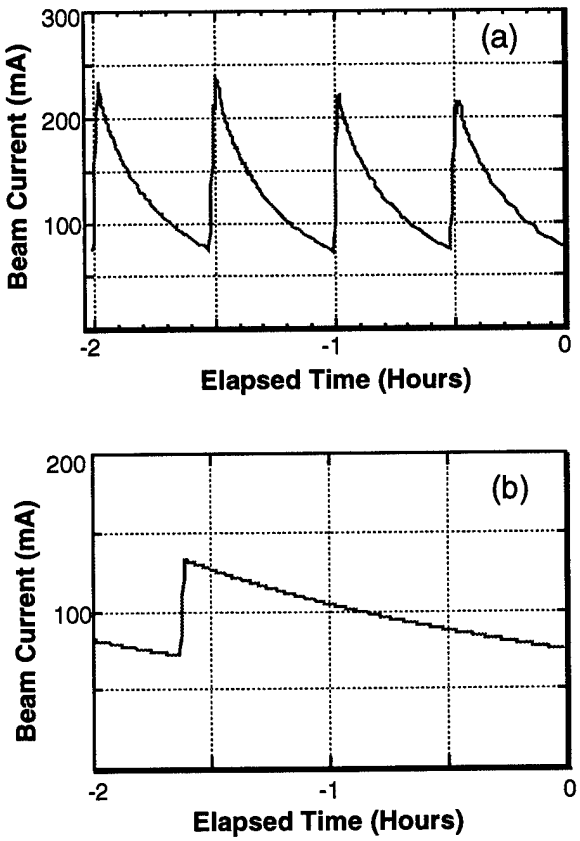


Figure 1: Stored beam current as a function of elapsed time. (a) The data was taken during the first commissioning before bake-out. (b)The data was taken during the second commissioning after bake-out.

In figure 1, the beam current is displayed as a function of time. Fig. 1(a) shows the beam current decay as a function of time when the total dose was approximately 6 ampere-hours and the data was taken before the bake-out. Fig. 1(b) shows a similar plot after the bake-out when the total dose was 10 ampere-hours. Comparing these two figures clearly indicates the increase in beam lifetime after the bake-out. In these two figures, the difference in total dose has some effect on the lifetime difference, but it is clear that the bake-out has more impact on it.

By the end of June 1995 when the second commissioning is scheduled to be completed, we expect the total dose to be 50 ampere-hours and our immediate goal is such that by that time the lifetime is more than five hours at 100 mA.

At present, there are three RF cavities installed in the storage ring, each provides 600 kV . And therefore, with three cavities, total voltage is 1.8 MV, satisfying the design value at 2.0 GeV. In view of our future upgrade to 2.5 GeV, we plan to install one additional cavity sometime at the end of 1995. See [1] for the RF system operation during the PLS commissioning.

B. Commissioning Diagnostics

Diagnostic instruments for the commissioning include the beam profile monitor, beam current monitor, tune monitor, beam position monitor, and stripline pickup etc. Initially we placed five beam profile monitors distributed around the ring. Except the one in the injection straight, the remaining four profile monitors were not impedance matched; the vacuum chamber cross sections were changed abruptly along the beam direction. Since these profile monitors were just to aid in obtaining the first turn on the very first day of commissioning, their large contribution to the impedance was not important. Originally, it was planned to remove the four profile monitors immediately after the first commissioning. However as the commissioning was in progress, it became clear that the profile monitors were very useful to check roughly the beam position from time to time, especially when the injection condition was changed. Because of this, it was decided to retain total three profile monitors permanently and therefore during shut-down period four monitors were removed to be replaced by two impedance-matched new ones. Another useful diagnostics during the commissioning was a number of radiation safety monitors attached on walls in various places of the storage ring. The radiation level of these monitors are closely monitored in the main control room. And therefore, the high radiation level at a certain location indicates the spot where the beam loss occurs.

In PLS, one beamline near the injection area is reserved for the photon beam diagnostics. It will be installed in the next shut-down period which is scheduled to be held sometime in this summer.

III. BEAMLINE STATUS

At present, two bending magnet beamlines have been installed; one for VUV experiments and one for hard X-ray experiments with photons at energies below 10 keV.

For the VUV beamline, two branches are attached to the exit beam port from a bending magnet, which has a horizontal divergence of 42 mrad. Of the two branches, one is a spherical grating monochromator (SGM) beamline for photoemission spectroscopy experiments and the other is a normal incidence monochromator (NIM) beamline for gas-phase experiments. The SGM will accept 10 mrad of white photon beam and provide photons between 13 and 1230 eV. Another 13.5 mrad of white beam can be used for the optics of NIM for 5 - 30 eV photons. At present, only SGM beamline has been constructed and NIM beamline will be installed sometime in 1996.

For the bending magnet X-ray beamline, there will be two experimental stations, each for X-ray scattering and XAFS, respectively. Each experimental station will be located inside a hutch for radiation shielding. X-ray scattering beamline will accept a 3 mrad wide X-ray beam from bending magnet. The X-ray photons will be focussed by a dynamically bent cylindrical Pt-coated sillicon mirror in front of a double crystal monochromator which monochromatizes X-rays between 4-12 keV. The monochromator is being assembled and is planned to be tested with a conventional sealed-tube X-ray source. At present, X-ray deflection beamline has been installed and XAFS beamline will be installed in 1996.

In PLS, there are ten available places for insertion devices to be installed. At present, one undulator (U7) has been designed and will have been constructed by early 1996. Its beamline will be installed in 1996. A decision has just been made to construct a helical undulator. Its design will start in the early 1996 and will be installed in 1997.

IV. SUMMARY

PLS construction was completed and it is now under commissioning. So far, the maximum beam current achieved was more than 300 mA. Total dose is 13 ampere hours and expected to be 50 ampere hours by the end of June. After in-situ bake out of vacuum chambers, the beam lifetime at this dose is more than four hours at 100 mA and this is continuously increasing. At present, two bending magnet beamlines have been constucted and one undulator beamline is scheduled to be installed in 1996. The PLS will be open to users starting from July 1995.

V. REFERENCES

[1] M. Kwon at al, in these proceedings

FEMTOSECOND X-RAYS FROM 90° THOMSON SCATTERING*

W. Leemans, R. Schoenlein, A. Chin, E. Glover, R. Govil, P. Volfbeyn, S. Chattopadhyay, K.- J. Kim, and C. V. Shank, Lawrence Berkeley Laboratory, Berkeley, CA 94720 USA

We report on progress on the femtosecond X-ray pulse generation experiment. The experiment involves a relativistic electron beam (50 MeV) with an rms bunch length of 10 ps containing 1 -2 nC of charge, and a ultrashort pulse (50 - 200 fs), high power (< 4 TW) 0.8 μm laser beam from a Ti:Al_2O_3 laser system. Both beams are focused down to about a 50 μm waist size and intersect at 90°. The laser field acts as an electromagnetic undulator for the relativistic electron beam generating radiation upshifted by 2 γ^2 and a pulse length given by the transit time of the laser beam across the electron beam. For a 50 MeV electron beam we expect 10^5 photons at 0.4 Å (25% bandwidth) in a cone angle of 6 - 10 mrad in about a 200 fs pulse.

I. INTRODUCTION

Scattering of femtosecond laser pulses off a low energy relativistic electron beam at 90° offers the possibility to generate ultrashort X-ray pulses. Experiments are under way in the Beam Test Facility of the Center for Beam Physics at LBL to demonstrate the generation, detection and practical utility of such pulses. The laser field acts as an electromagnetic undulator generating up-shifted radiation and, in this geometry, the x-ray pulse length is determined by the overlapped interaction length in time of the laser beam and the electron beam [1].

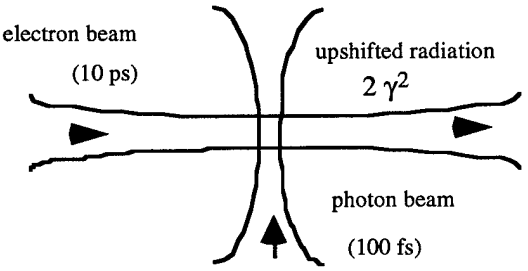


Figure 1: A generic lay-out of the 90° x-ray generation experiment. The laser beam is upshifted by $2\gamma^2$ and propagates in the direction of the electron beam.

We have previously reported on the design of this experiment which involves a relativistic electron beam and a high intensity short pulse laser [2]. The generic set-up is shown in Fig. 1. We next describe the details of the linac, laser system and experimental set-up, followed by up-to-date results of the experiment.

II. EXPERIMENT DESCRIPTION

* Supported by the Director, Office of Energy Research, Office of High Energy and Nuclear Physics, High Energy Physics Division, of the U. S. Department of Energy under Contract No. DE-AC03-76SF00098.

A. Electron Transport Line and Laser Beam Parameters

The experiment is conducted at the Beam Test Facility (BTF) which has been constructed by the Center for Beam Physics and is operated by the Center in support of its experimental R&D program. The BTF houses an electron beam transport line which transports the 50 MeV electron beam from the Advanced Light Source (ALS) into a dedicated experimental cave, and a terawatt laser system 3]. The measured electron beam parameters are given in Table 1.

Maximum Energy	50 MeV
Charge	1-2 nC/bunch
Bunch Length (σ_z)	10-15 ps
Emittance rms (unnorm)	0.35 mm-mrad
bunches/macropulse @ 125 MHz	1 - 10 (max 100)
Macropulse rep. rate	1 - 10 Hz

Table 1: Electron beam parameters

The transport line is equipped with two integrating current transformers for charge transport efficiency measurements, high bandwidth beam position monitors, fluorescent screens for transverse beam analysis and an optical transition radiation (OTR) diagnostic system [4]. The OTR system allows single bunch measurement of beam emittance, energy, and bunch length.

The main laser system parameters have been measured and are listed in Table 2.

Wavelength	0.8 μm
Energy/pulse	125 mJ
Pulse length	50 - 200 fs
Repetition rate	10 Hz
Timing jitter with respect to e-bear	2 ps

Table 2: Ti:Al_2O_3 laser system parameters.

The passively Kerr lens modelocked Ti:Al_2O_3 laser oscillator operates at 125 MHz (4^{th} subharmonic of the ALS 500 MHz linac masterclock frequency). After stretching the oscillator pulses by a factor 10^4 , a single pulse is selected and amplified through an 8-pass pre-amplifier and a 4 pass main amplifier. The pulse is compressed in a vacuum compressor to a nominal pulse width of 100 fs (FWHM) containing an energy of about 100 mJ. The beam is propagated into the BTF cave and focused with a spherical mirror.

B. X-ray source parameters

Theoretical properties of the X-ray source have been previously described [1, 2]. The frequency of the upshifted

radiation can easily be calculated from energy and momentum conservation:

$$\omega_r \cong \frac{2\gamma^2\omega_o}{1+K^2/2+\gamma^2\theta^2} \quad (1)$$

where the Compton shift has been neglected. Here γ is the Lorentz factor, K the wiggler strength, θ the angle of observation and ω_0 the incident laser frequency. The wiggler strength is given by

$$K = \frac{25.6}{c[cm/s]}\sqrt{I[W/cm^2]}\lambda[\mu m] \quad (2)$$

where I is the incident laser intensity and λ the laser wavelength. From Eqn. (2) it is clear that wavelength tuning can be achieved by reducing the laser spot size at the interaction point to obtain wiggler strengths on the order of 1. Since the x-ray yield depends linearly on the laser energy no photon flux reduction is expected. In addition, harmonic generation is expected to become important at such large wiggler strengths [5].

For our experimental parameters, the x-ray pulse width, bandwidth and total flux are calculated from the expressions given by Kim et al. [1] and are listed in Table 3.

Wavelength (Å)	0.4
Pulse length (fs)	200
# photons (25 % bandwidth)	1×10^5
Full angle cone (mrad)	6
Bandwidth (%)	25

Table 3: x-ray source parameters.

The main contributions to the bandwidth are from the finite electron beam emittance and limited number of wiggler periods seen by the electrons. The finite emittance effect causes a washing out of the typical angularly correlated wavelength distribution for a single radiating electron. Neglecting the finite wiggler period effect, the actual source bandwidth is obtained by taking the convolution of the single electron radiation pattern with a Gaussian distribution for the angles that the electrons make with respect to the laser beam. For a beam emittance of 0.35 mm-mrad and a spot size of 50 μm, the electron beam divergence is 6 mrad which leads to an intrinsic bandwidth on the order of 20 - 25 %.

III. EXPERIMENTAL RESULTS

We next describe in detail the main milestones that have been passed on the way towards generating femtosecond x-ray pulses.

A. Electron Beam Focused to less than 100 μm.

The electron beam has been focused down to a spot size less than 100 μm using a telescope consisting of two quadrupole triplets. The large bore (6") of the final magnet allows for small f-number focusing and reduces Bremsstrahlung production by beam halo scraping against the beam pipe. The electron beam profile at the interaction point has been measured using OTR and is shown in Fig. 2. The pointing stability was found to be better than 50 μm.

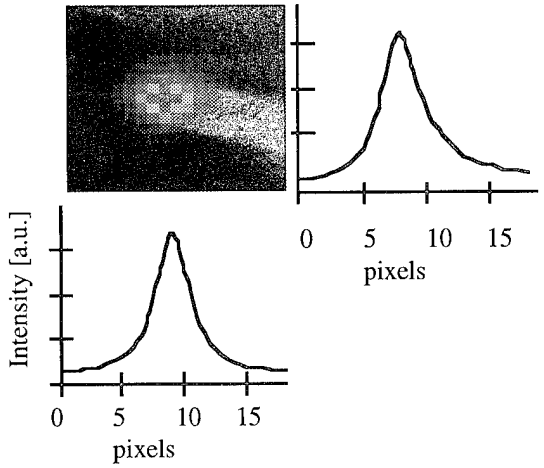


Figure 2: OTR image of the electron beam spot inside the X-ray interaction chamber with vertical (right) and horizontal (bottom) line-out. The actual spot size is probably less than the measured spot size σ_x = 115 as the present optical lens system is resolution limited to about 100 μm.

B. Electron and Laser Beam Synchronized

To ensure proper synchronization between the laser and the electron beam, a feedback system has been implemented to continually adjust the laser oscillator cavity frequency. The laser oscillator operates at 125 MHz (1/4 of the 500 MHz linac frequency). A 500 MHz signal synchronous with the laser oscillator is extracted from a photodiode signal using a 500 MHz bandpass filter. An error signal, which drives a piezo-controlled mirror mount, is then obtained by mixing this 500 MHz signal with the 500 MHz linac reference signal.

Using a streak camera with picosecond time resolution we have verified that locking of the laser oscillator to the electron beam was achieved with timing jitter performance of about 2 ps (Fig. 3).

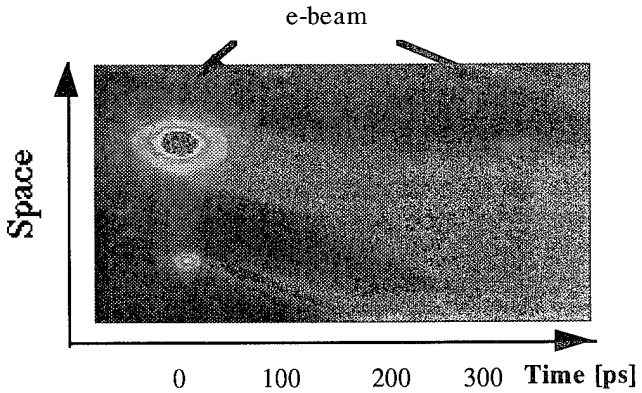


Figure 3: Time resolved streak camera image showing OTR radiation from the electron beam (main bunch and trailing bunch separated by 333 ps) and laser beam fiducial.

Optical transition radiation from the electron beam and laser oscillator pulses were simultaneously imaged onto the slit of the streak camera. A histogram of 50 consecutive shots is shown in Fig. 4.

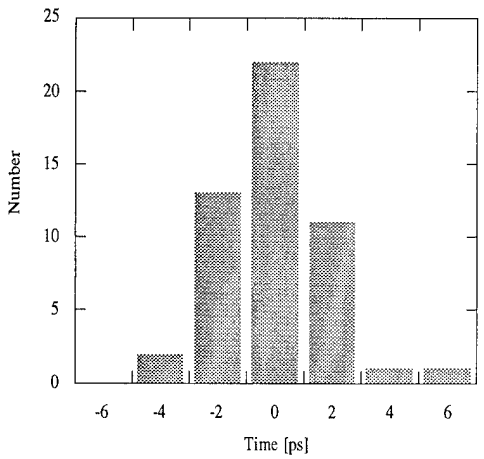


Figure 4: Histogram of separation in time between electron beam and laser beam as measured from streak camera images such as the one shown in Fig. 3.

An on-line timing signature of the electron beam and of the laser beam is obtained from a high bandwidth beam position monitor and an ultra-high speed photo-diode respectively. The 6 ps rise time diode detects laser light leaking through the final focusing mirror. Both those signals are then combined and monitored on a Tektronix SCD 5000 oscilloscope.

C. X-ray Measurements

A variety of x-ray diagnostics are being implemented and developed to measure wavelength, beam size and divergence, pulse length and polarization of the produced x-ray beam.

A 60° H-magnet separates the particle and photon beams after the interaction point. A 75 μm Be-foil isolates the beam line (high vacuum) from the x-ray diagnostic systems.

Spatial properties of the X-ray beam (spot size and divergence) are being measured using a slow scan CCD camera looking at a phosphor screen. Preliminary results using this phosphor indicate that the total x-ray background contribution (mainly due to Bremsstrahlung) is about two orders of magnitude below the expected signal level..

To determine the angular wavelength distribution of the x-ray photon beam we are using a 1 cm thick, 3 cm diameter cooled Ge-detector. The detector has been calibrated using the 26 keV and 60 keV emission lines from an Am^{241} source and has about a 2.5 % energy resolution at 30 keV. Since this detector is capable of detecting single photons, background levels need to be kept below a single photon per pulse for operating this detector. A 1 mm diameter, 2 cm long lead pinhole is used to spatially filter the background x-ray radiation incident on the detector and to reduce the signal level to a single x-ray photon per shot to avoid pile-up.

For initial pulse length measurements the transit time will be lengthened by changing the horizontal focusing strength of the quadrupoles, allowing the use of a diamond photodiode as well as an X-ray streak camera. A coincidence technique between the X-ray pulse and an optical pulse in a gas jet is being developed to measure shorter pulse durations [6]. In the absence of the laser, photo electrons will be produced in a Kr gas jet by tuning the source to produce 14.8 keV x-rays, about 500 eV higher than the K-shell energy of Kr-gas (14.3 keV). If the laser pulse arrives simultaneously with the x-ray pulse, the x-ray photo electrons will acquire an additional drift velocity component whose magnitude and direction depends on the phase and amplitude of the laser field at which the photo electron is born and the relative polarization of the laser with respect to the x-rays. The temporal overlap between the two pulses will therefore determine the emitted x-ray photo electron spectrum.

IV. SUMMARY

A status report has been given of the orthogonal Thomson scattering experiment at the BTF. Based on simple scaling laws we expect that about 10^5 x-ray photons with an energy of 30 keV will be produced for our current experimental parameters. Both the electron beam line and the laser system have been completed. The electron beam has been focused to a spot size less than 100 μm. The 25 ps (FWHM) electron and 100 fs (FWHM) laser pulses have been synchronized to a jitter level of about 2 ps. We have started looking at x-ray generation using a phosphor screen imaged onto a slow scan CCD camera as well as a Ge-detector and are poised to start intense x-ray measurements in the coming months.

V. ACKNOWLEDGMENTS

The authors wish to thank the ALS personnel for their help in the construction and operation of the Beam Test Facility, in particular Dennis Calais and Terry Byrne. We would also like to thank Leon Archambault for his engineering and technical support and Harvey Gould, Ali Belkacem and Norm Madden for their help with the Ge-detector.

VI. REFERENCES

[1] K.- J. Kim et al., NIMA 341, 351 (1994).
[2] W. Leemans et al., AIP Proc. 1994 Workshop on Advanced Accelerator Concepts, Lake Geneva, LBL-36369.
[3] W. Leemans et al., IEEE Proc. 1993 Part. Accel Conf, 83 (1993) and Proc. 1994 European Part. Accel. Conf.
[4] M. de Loos et al., Proc. 1994 European Part. Accel. Conf.
[5] E. Esarey et al., Phys. Rev E **48**, 3003 (1993).
[6] J.M. Schins et al., Phys. Rev. Lett 73, 2180 (1993).

Design of a Diffraction Limited Light Source (DIFL)

D. Einfeld, J. Schaper, Fachhochschule Ostfriesland, Constantiaplatz 4, D-26723 Emden
M. Plesko, Institute Jozef Stefan, Jamova 39, P.O.B. 100, SLO-61111 Ljubljana
e-mail: einfeld@alpha.fho-emden.de

Abstract:

Three synchrotron light source of the third generation have been commissioned (ESRF, ALS and ELETTRA). All machines have reached their target specifications without any problems. Hence it should be possible to run light sources with a smaller emittance, higher brilliance and emitting coherent radiation. A first disign of a Diffraction Limited Light Source has been performed. It is a 3 GeV storage ring with a modified multiple bend achromat (MBA) optics as a lattice leading to a normalized emittance of $\varepsilon_x = 0.5$ nmrad. The novel feature of this lattice is the use of horizontally defocussing bending magnets with different bending angles to keep the radiation integrals low. The circumference is 400 m including 12 straight sections with a lenght of 6 m. The dynamical behaviour should allow to store a beam of 100 mA with a lifetime larger 5 hours.

I. Introduction

The most important factor for synchrotron radiation users is the brilliance which is mainly determined by the cross-section of the beam and given by the square root of the emittance multiplied with the betatron function. However, even at zero emittances the phase space of the radiation from an undulator itself is finite due to diffraction effects. The corresponding emittance of the light beam is given by $\varepsilon_{phot} = \lambda/4\pi$, with λ being the wavelength at the peak flux. A light source is called diffraction limited if the emittance of the electron beam is smaller than that of the photon beam.

For a 3 GeV light source, the typical undulator radiations peaks at a wavelength of around 1 nm, or energy 1.2 keV, respectively. This means that for a diffraction limited light source, the emittance would have to be below 0.08 nm·rad.

The third generation light sources ALS, ESRF and ELETTRA have been commissioned in record times and are running very well and reliable. This proves that it should be possible to obtain a horizontal emittance which is an order of magnitude below the present one of these machines, i.e. around 0.5 nm·rad. With a coupling of 1%, the corresponding vertical emittance is 5 pm·rad. The diffraction limited emittance would thus be between the two vaules.

It is interesting to note that damping rings for the next generation electron-positron colliders have a similar emittance and a similar particle energy [1]. They can be kept much more compact, however, because the light sources need a larger circumference to accomodate straight sections for insertion devices.

2. Obtaining A Low Emittance

The optics influences the emittance via the partition number J_x, which is unity for a pure dipole field and via the H-function:

$$H = \gamma\eta^2 + 2\alpha\eta\eta' + \beta\eta'^2$$

which is determined by the shape of the horizontal betatron (β) and dispersion (η) functions within the bending magnets only. Low emittances can be reached if the $\beta(s)$ and $\eta(s)$ have a minimum there. In order to get the desired shape of the Twiss funktions in a unit cell a bending, a focussing and a defocussing magnet are needed. This can be achieved with four quadrupoles and a dipole with the deflecting angle φ [2] or by two qudrupoles and a bending magnet with a superimposed quadrupole strenge to focus the beam vertically [3],[4]. A light source includes undulators and wigglers and at the position of these insertion devices, in the long straight sections, the dispersion has to be zero. This requires a matching of the Twiss functions to the desired values within the straight sections. To get the smallest emittance the bending magnet with in the matching section must have a deflection angel around $\varphi/2$ [4],[5].

3. The Concepts of the MBA Lattice

The lattice of a multiple bend achromat (MBA) structure can be described as a set of several unit cells accompanied on each side by a matching section followed by a straight section. The matching sections assure that the dispersion is zero in the straight sections and that the beta-functions can be set to the requirements of either undulators (high beta) or wigglers (low beta). The dipoles within the unit cells have a deflection angle of φ, whereas the ones in the matching section deflect by $\varphi/2$.

The unit cell with a defocussing bending magnet has a threefold advantage:

1) the number of magnets per achromat is reduced;
2) the partition number J_x is larger than 1 and thus reduces the emittance;
3) the length of the cell is small, therefore reducing the total circumference.

The circumference of such a machine containing five unit cells within an achromat which performs an overall deflection of 30 degrees would be around 400 m.

0-7803-3053-6/96/$5.00 ©1996 IEEE

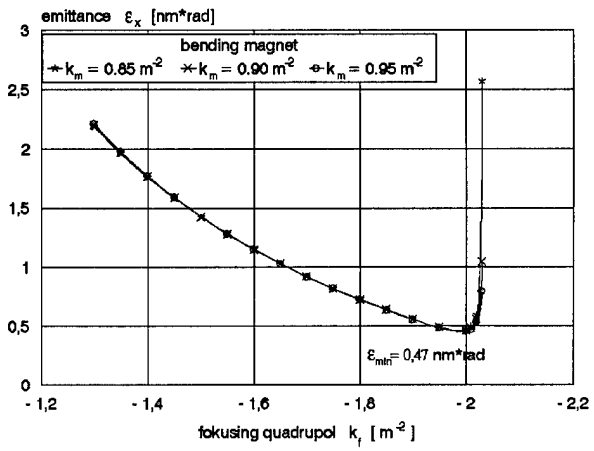


Fig. 1: The emittance of the DIFL unit cell as function of the focussing quadrupole strength at different defocussing strengths of the bend.

Accepting reasonable magnetic field strengths for the bending magnets determines more or less the length of the magnets. The only two free parameters which can be varied to minimize the emittance are the strength of the focusing quadrupole and the quadrupole strength of the bending magnet. Therefore it is easy to find the optimal setting (figure 1), resulting in an emittance of 0.47 nm·rad. The shape of the Twiss functions within a unit cell is shown in figure 2.

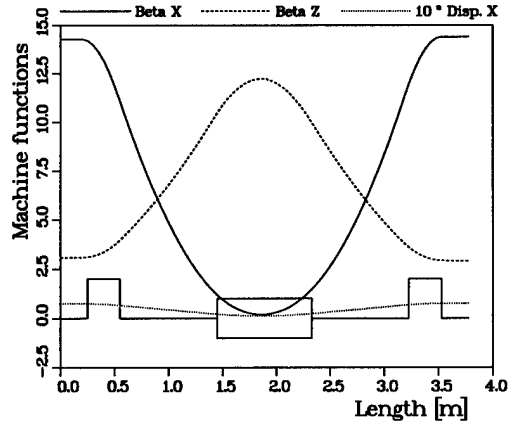


Fig. 2: The course of the machine functions within a unit cell.

The performance of the achromat is mainly determined by the unit cell. Its characteristics are given by the factors: emittance, partition number, working point, chromaticities and momentum compaction factor. The optimisation of the lattice is therefore first done on a hypothetical ring consisting of 72 unit cells. From figure 1 one can see, that the minimal emittance depends very weakly on the defocussing strength of the bend. Therefore it can be chosen such as to find an optics with a large dynamic aperture by keeping the total tune away from dangerous resonances. The results of tracking one particle over 100 turns through the hypothetical ring are shown in figure 3. Only chromatic sextupoles have been used. The tracking has been performed using the computer codes RACETRACK [6] and BETA [7]. The dependence on the particle momentum is negligeable.

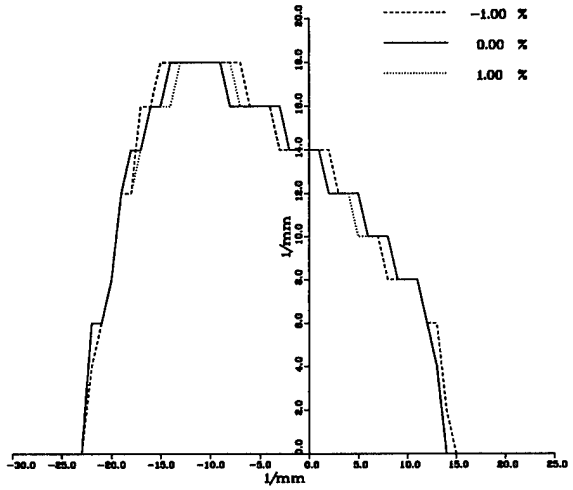


Fig. 3 The dynamic aperture of the MBA lattice composed of unit cells only.

The dynamic aperture is particularly large if one considers that it extends from -296 to 160 times the beam width in the horizontal plane and to +/-3680 times the beam height (at 1% coupling) in the vertical plane. Thus the overall dynamic properties of the MBA lattice are very promising.

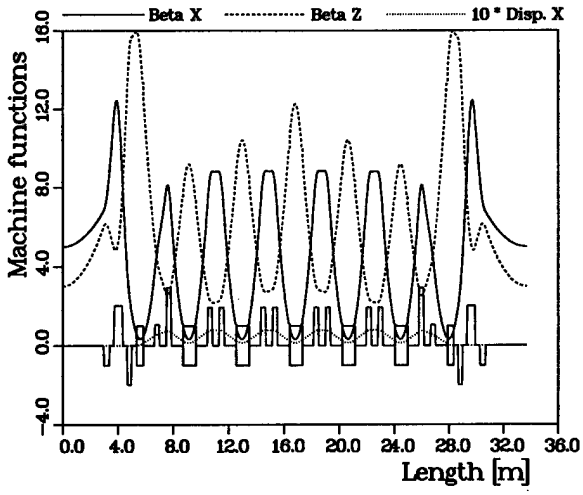


Fig. 4 The optical functions for one achromat of the DIFL lattice. Indicated are the position and sizes of bending magnets and quadrupoles. All units are in meters.

4. THE DIFL LATTICE

In the realistic lattice, twelve straight sections of 6m length each are introduced, leaving sufficient space for insertion devices. Four quadrupoles and a 2.5 degree bending magnet compose the matching section to set the dispersion to

zero and the horizontal and vertical beta functions in the straight sections to the desired values (figure 4).

With the matching, the emittance is increased by the presence of the outer two magnets from 0.47 nm rad to 0.56 nm rad. Assuming 1% coupling between planes, the beam sizes $\sigma_{x,y}$ are 54 μm and 4 μm in the horizontal and vertical plane, respectively. All damping times are around or below 9 ms, the relative energy spread is 8 10^{-4}, and even the natural chromaticities are not too large (-77 horizontal and -37 vertical).

Unfortunately, the dynamic aperture is reduced once the optics composed of unit cells only is modified to allow for dispersion-free straight sections.

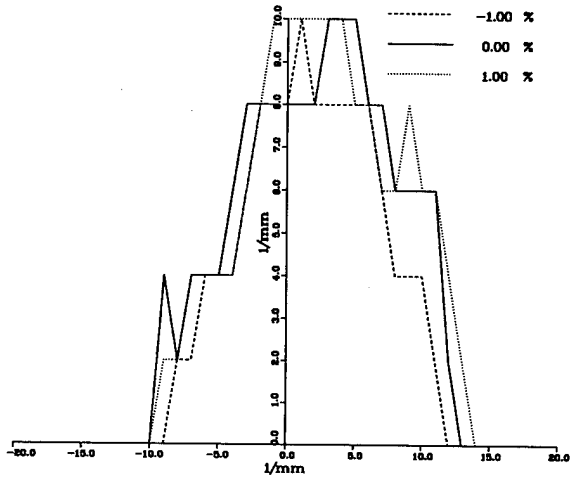


Fig. 5 The dynamic aperture of the DIFL lattice.

Even after reoptimizing the optics, the largest dynamic aperture obtained is 10 mm horizontally and 8 mm vertically (figure 5), certainly creating a challenge for the injection into the ring but not rendering the optics unfeasible, because once the injected beam is damped to the natural emittance, the dynamic aperture still corresponds to more than 100 times the beam size in both planes. This should be sufficient to accomodate Touschek scattering given that the dispersion is also quite small.

The plot of the tune shift with amplitude (figure 6) reveals that indeed the dynamic aperture vanishes due to the rapid change of the tune. With proper sextupole arrangements we hope to increase the dynamic aperture to larger values.

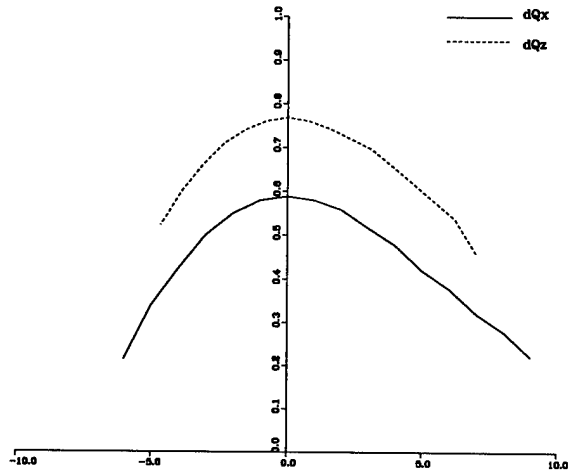


Fig. 6 The tune shift with amplitude of the DIFL lattice.

5. Conclusions

The presented multiple bend achromat (MBA) lattice provides a mean to obtain significantly lower emittances than with conventional DBA or TBA lattices. The advantages of the modified lattice are the small contribution of the outer magnets bending to the emittance, a large horizontal partition number which further reduces the emittance, a small number of quadrupole magnets, a short unit cell and good dynamic properties with only chromatic sextupoles. The scheme of the MBA optics can be applied to small compact rings as well as for the design of a diffraction limited light source.

6. References

[1] R.Brinkmann, A Study of Low-Emittance Damping Ring Lattices, DESY, M-90-09,July 1990

[2] DELTA, a Low Emittance Storage Ring as a Free-Electron-Laser Radiation Source, Proc. 1989 IEEE PAC (1989), p.780; Part. Accel. Vol. 33 (1990), p.27

[3] D.Einfeld, D.Husmann, M.Plesko, "An investigation of the QBA-Otpics for the storage ring LISA", Bonn University Bonn ME-92-02, Augisut 1992.

[4] D. Einfeld, M. Plesko, A modified QBA optics for low emittance storage rings, Nucl. Inst. Meth. in Phys. Res. A336 (1993) 402-416.

[5] D.Einfeld et al., "The Synchrotron Light Source ROSY", Proceedings of the PArticle Accelerator Conference PAC 93, Washington, 1993.

[6] User's Guide, Sincrotrone Trieste, ST/M-91/11, F.Iazzourene, C.J.Bocchetta, R.Nagaoka, L.Tosi, A.Wrulich, RACETRACK July 1991

[7] L.Farvacque, A.Ropert, BETA User's Guide, ESRF-SR/LAT 88-08

Updated Plans for DIAMOND, a New X-Ray Light Source for the UK

V P Suller, J A Clarke, J B Fitzgerald, H L Owen, M W Poole, X Queralt and S L Smith

CCL, Daresbury Laboratory, Warrington, Cheshire WA4 4AD, United Kingdom

Plans are being made to replace the 15 year old Daresbury SRS light source with a new 3rd generation ring at an energy of 3 GeV. An earlier concept was based on a TBA lattice which permitted simple inclusion of superconducting dipoles at the centre of selected achromats. A recent design review has recommended changing to a DBA version with the addition of two super long straights. An outline design of this racetrack light source is presented here.

I. INTRODUCTION

Although the 2 GeV SRS [1] continues to provide excellent quality synchrotron radiation supporting a major national facility containing almost 40 experimental stations, it is clear that the source has insufficient space for modern insertion devices and has an electron beam emittance (120 nm.rads) which will soon be too high to conduct state-of-the-art research. A major review of the needs of the domestic research community has established that the basic specification of a new source should be to provide high brilliance photons in the Soft X-ray region (0.2 - 5 keV) and high fluxes in the Medium X-ray region (1 - 30 keV), this radiation being generated by a suite of undulators and multipole wigglers. There is an additional requirement for a small number of superconducting dipole sources to provide high photon fluxes beyond 30 keV. High brilliance radiation at photon energies up to 30 keV will be adequately catered for by the UK's share of the European Synchrotron Radiation Facility in Grenoble, see [2]. This specification taken in conjunction with realistic designs for insertion devices leads to a proposed energy for the new source of 3 GeV.

II. THE PREVIOUS DESIGN

The original concept for DIAMOND [2] [3] was a 16 cell triple bend achromat (TBA) with a circumference of approximately 300 m. The scale of the facility to accommodate sufficient insertion devices for a large national user community led to the choice of 16 cells, whilst the 3 GeV energy arose by considering the spectral output to be produced by multipole wigglers with fields peaking at around 1.6 T. TBA lattice cells were chosen for their ability to produce a high brilliance light source in addition to permitting the simple replacement, when required, of the central dipole in chosen cells by a short superconducting dipole giving the same deflection as previously. Such dipoles will provide new research opportunities by utilising the high fluxes of hard X-rays which could be accepted by experiments placed within a few metres of the source point.

This TBA version of DIAMOND was used as an example for estimating the resources and timescales which would be required to replace the SRS with a modern facility. Subsequent refinement of the scientific case for DIAMOND led to a re-evaluation of the basic lattice structure and it became clear that more appropriate solutions could be derived for the electron beam source properties and for the lengths of the insertion device straights. As a result the lattice for DIAMOND has been recently changed to a double bend achromat (DBA) cell with a resultant improved specification.

III. A DOUBLE BEND ACHROMAT

In a DBA cell the quadrupoles in the zero dispersion straight may be regarded as free parameters able to adjust the overall betatron functions of the cell whilst the quadrupoles in the dispersive straights produce the condition of zero dispersion. When the betatron stability of the cell is plotted as a function of the values of the F and D quadrupoles making up the doublets at each end of the zero dispersion straight, the familiar neck-tie diagram divides into four distinct regions. Fig 1 shows this behaviour for the DBA cell which was used as a starting point for the updated DIAMOND structure.

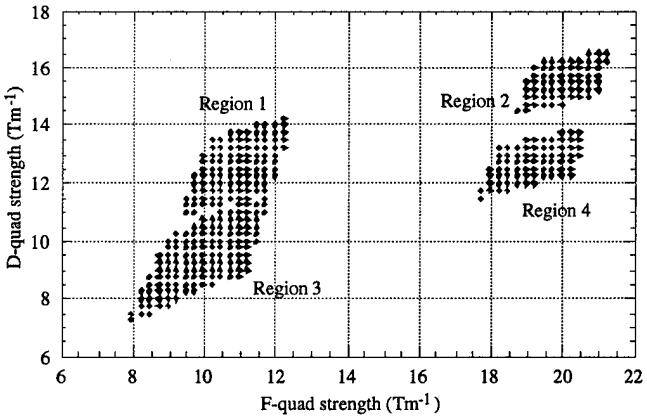


Figure 1: Stability islands of DBA cell with doublets in zero dispersion straight.

The natural beam emittance is expected to be strongly dependent on the horizontal betatron tune, but fig 2 shows how it is remarkably similar in each of the four regions. The lowest emittance results from operating at a horizontal phase

0-7803-3053-6/96/$5.00 ©1996 IEEE

advance per cell of either nearly 2π or 3π. It can be seen from fig 2 that an emittance of between 11-15 nm.rad is available over a useful region of tune space. The theoretical minimum emittance from a 16 cell DBA at 3 GeV is 6.5 nm.rad.

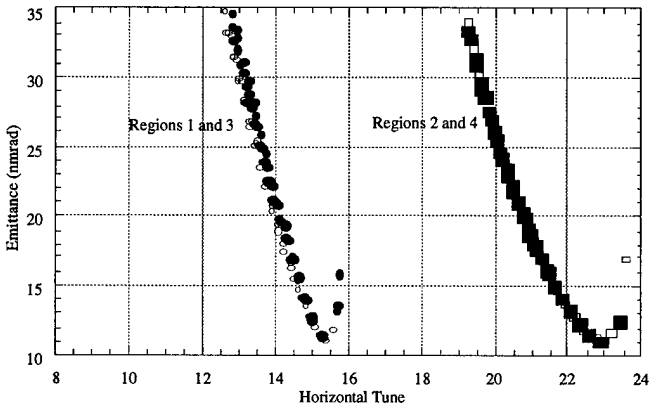


Figure 2: Variation of emittance with tune in different stability regions.

The betatron functions in the zero dispersion straights tend to take distinct values in the different regions of stability. Regions 2 and 4 have very low horizontal beta, whilst regions 1 and 3 have high beta. A range of vertical beta values, from low to high, is available in the regions. It is possible that selection of an operating region could be decided by the requirement for specific insertion devices to be matched to specific beta values. The DBA cell for DIAMOND was selected to be in region 2 to provide a low horizontal beta of less than 1.0 with a vertical beta of about 2.0

IV. FULL FEATURE LATTICE

The basic cell was then subjected to a series of modifications to produce a facility which meets the full specification of the end users. The most important of these requirements are:

a) Flexible control of beamsize in the insertion device straights. This is necessary to ensure that any conceivable insertion device, (multipole wiggler, undulator, wavelength shifter) can have the optimum beam size or divergence to produce the best source characteristics. It has been achieved by changing the doublets in the insertion device straights to triplets. Initially a very symmetric solution has been selected which sets high and low betas in alternate long straights.

b) Super-long straights. These will enable novel insertion devices to be accommodated in the long term future. Additionally they will allow the testing of new devices when configured in a by-pass mode, thereby minimising the impact of testing on the facility operation. Two super-long straights with free lengths of about 20m have been matched into the 16 cell ring by stretching two of the high beta insertion device straights and adding additional quadrupoles.

c) Superconducting lattice dipoles. As an upgrade route, future substitution of normal dipoles by equivalent deflection superconducting dipoles receives strong user support. Only selected cells would be treated, with a maximum limit of 4 cells. An interim high symmetry solution has been evaluated and is presented here, with replacement of both dipoles in each of 4 cells. Other options will be studied involving the substitution of only one dipole per cell.

The overall lattice for half of the new DIAMOND structure, incorporating all the above mentioned features, is shown in fig 3. It can be seen that a high degree of symmetry has been maintained and that the lattice functions remain well behaved. The major parameters of the source are listed in table 1.

TABLE 1

DIAMOND Major Parameters

Energy	3 GeV
Circumference	340 m
Natural Emittance	16.4 - 27.6 nm.rad
Cell Type	DBA
Dipole Field	1.4 T; (4.35 T)
No of Cells	16
Straight Length	14 x 5 m; 2 x 20 m
Betatron Tunes (h,v)	18.24, 6.63
Natural Chromaticities (h,v)	-46.9, -27.6
Beam Current	300 mA

V. SOURCE PERFORMANCE

The performance of DIAMOND, as measured by its photon output, will be the combination of the performance of the storage ring and of the insertion devices. These need to be well matched to their scientific application and are ideally designed to a precise specification. At this stage, therefore, it is only possible to describe the generic parameters of the insertion devices which could be installed in DIAMOND. These are listed in table 2. The performance of the ring itself is assumed to be as stated in table 1, and is realistically based on the results obtained by recent 3rd generation sources.

TABLE 2

Projected Insertion Devices

ID	Period (mm)	N	K (max)	Length (m)
U80	80	56	6.5	4.5
U48	48	93	2.3	4.5
U21	21	95	0.8	2.0
MPW-1.6	136	33	20.3	4.5

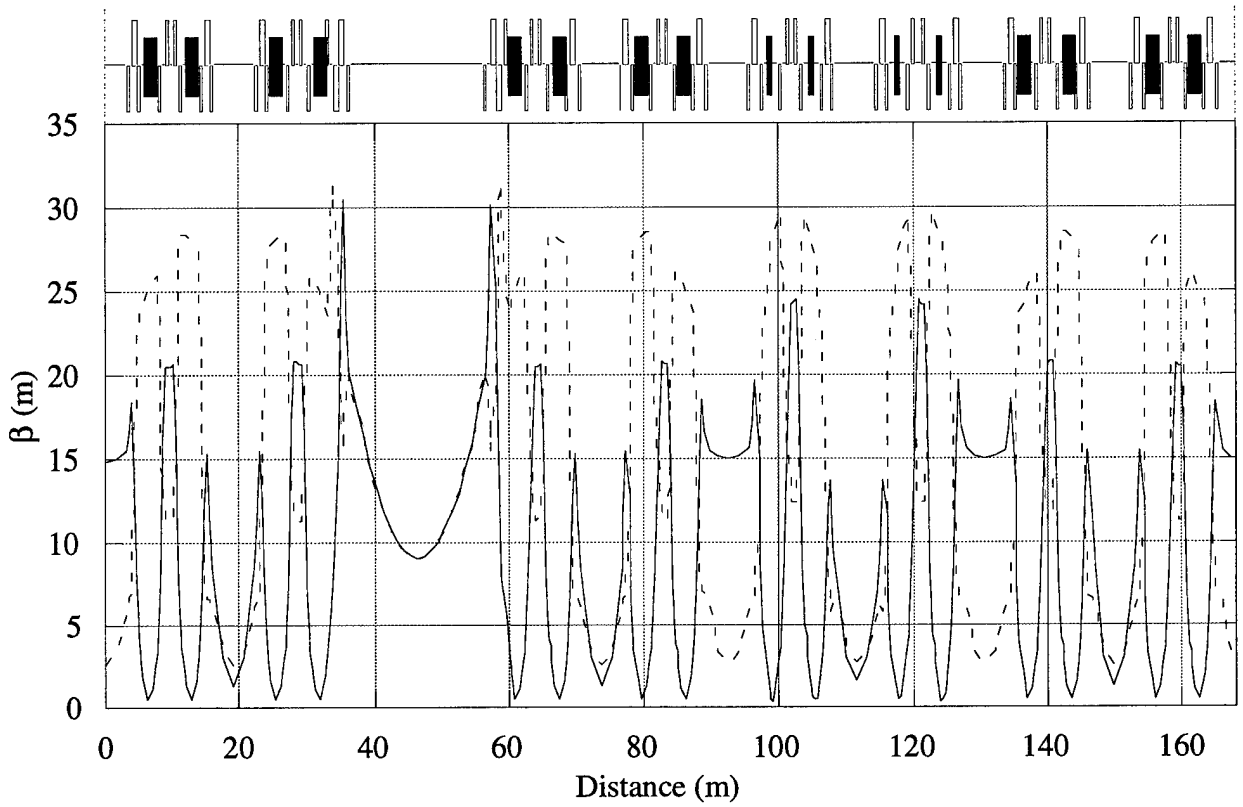


Figure 3: Lattice functions of normal, superconducting and long straight cells. The solid line shows the horizontal, the short dashes the vertical beta function.

The computed brilliances of the various sources which will be employed in DIAMOND are shown in fig 4.

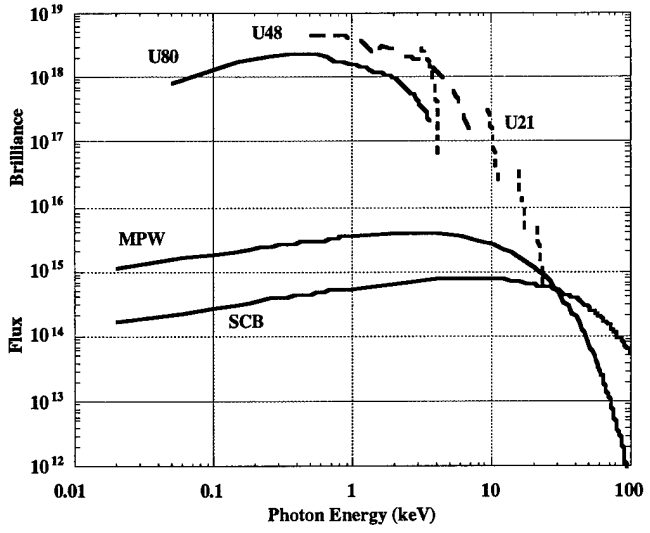


Figure 4: Flux (ph/sec/0.1% bandwidth) for the multipole wiggler (MPW) and superconducting dipoles (SCB); Brilliance (flux/mm^2/mrad^2) from the undulators.

VI. STATUS AND FUTURE PLANS

A re-estimated proposal for this updated version of DIAMOND will be submitted to the UK funding bodies in Autumn 95. If financial approval is obtained, the earliest likely starting date for construction would be in April 97. The intervening period will be used to continue lattice refinement, paying particular attention to its non-linear behaviour and to the effects of insertion devices. Engineering design of all major systems will also be carried out in this period. A 5 year construction period is foreseen, leading to first scheduled operation in 2002.

VII. REFERENCES

[1] P D Quinn, Proceedings of the 4th European Particle Accelerator Conference, London, 1994; pp 648-650: World Scientific Publishing, Singapore.

[2] V P Suller, Journal of Synchrotron Radiation; Vol 1, pp 5 - 11, 1994

[3] M W Poole and V P Suller, Proceedings of the 4th European Particle Accelerator Conference, London, 1994; pp 621-623: World Scientific Publishing, Singapore.

DESIGN OPTIMIZATION FOR AN X-RAY FREE ELECTRON LASER DRIVEN BY SLAC LINAC *

Ming Xie, Lawrence Berkeley Laboratory, Berkeley, CA 94720, USA

Abstract

I present a design study for an X-ray Free Electron Laser (FEL) driven by the SLAC linac. The study assumes the FEL is based on Self-Amplified Spontaneous Emission (SASE) and lasing is achieved in a single pass of a high current, high brightness electron beam through a long wiggler. Following a brief review of the fundamentals of SASE, I will provide without derivation a collection of formulas relating SASE performance to the system parameters. These formulas allow quick evaluation of FEL designs and provide powerful tools for optimization in multi-dimensional parameter space. Optimization is carried out for the SLAC FEL over all independent system parameters modeled, subjected to a number of practical constraints.

I. INTRODUCTION

An X-ray Free Electron Laser (FEL) driven by the SLAC linac, the Linac Coherent Light Source (LCLS) [1], was proposed to reach wavelengths down to a few Å with performance far exceeding other sources. At this wavelength range Self-Amplified Spontaneous Emission (SASE) [2][3][4] is the only working principle, since mirrors are not available to make an oscillator.

A SASE FEL, in its basic configuration, requires a high current, high brightness electron beam and a long wiggler. As the electron beam passes through the wiggler, the initial spontaneous radiation induces a longitudinal density modulation in the electron beam at the radiation wavelength scale, and as a result the spontaneous radiation becomes amplified in intensity and enhanced in coherence characteristics, leading to an exponential instability. As the optical power build up, electrons become trapped and rotate in the phase space bucket. Eventually the beam-wave interaction becomes nonlinear, putting the exponential power growth into saturation. For the LCLS, a power maximum can be reached with a wiggler a few tens of meters long.

Effectively a SASE FEL is a power amplifier. Its initiation, growth and saturation can be described simply by

$$P = \alpha P_n e^{z/L_g} < P_{sat} \qquad (1)$$

where P_n is the effective input noise power, α is the coupling coefficient representing the fraction of the noise power P_n coupled into the dominant mode exponentially growing in z (the distance along the wiggler) with a power gain length L_g, and P_{sat} is the saturation power. The input noise power is the frequency integrated synchrotron radiation power in an FEL gain bandwidth generated in the first gain length or so [2][5]. Corresponding to the saturation power, one may define a saturation length given by

$$L_{sat} = L_g \ln\left(\frac{P_{sat}}{\alpha P_n}\right) \qquad (2)$$

*This work was supported by the U.S. Department of Energy under contract No. DE-AC03-76SF00098.

which is the length of the wiggler required to reach the maximum output power. The quantities L_g, L_{sat} and P_{sat} are the major performance parameters for SASE.

II. MODELS AND FORMULAS

An FEL amplifier consists of three major components: an electron beam from an accelerator; a wiggler for beam-wave interaction; and a focusing system for electron beam confinement in the wiggler. In this paper, the electron beam distribution is assumed to be of Gaussian shape in four dimensional transverse phase space and in the energy variable, but uniform in longitudinal coordinate. The assumption of uniform longitudinal distribution is justified for the LCLS even though the electron bunch is only a few hundred femtoseconds long, since the ratio of the bunch length to the radiation wavelength is so large that the so called short pulse effects are negligible from the FEL interaction. Further assuming round beam with equal emittance in both transverse planes we may characterize the electron beam by four parameters: beam energy $E = \gamma mc^2$; current I; normalized rms emittance ε_n and rms energy spread σ_e. The wigglers are separated into two classes: planar and helical, each class is specified by two parameters: wiggler period λ_w and a dimensionless wiggler parameter: $K = 0.934\lambda_w[\mathrm{cm}]B_0[\mathrm{T}]$, where B_0 is the peak wiggler magnetic field.

The focusing system is assumed to have a transverse gradient invariant along the beam axis and characterized by a constant betafunction β. Such a system would give a constant beam envelope for the matched beam over the entire wiggler length. The focusing of this type is naturally provided in a wiggler, but may not be strong enough to have optimal FEL performance especially at short wavelength. To remedy this problem external focusing has been considered and alternating-gradient quadrupole was shown [6][7] to perform better than the constant gradient focusing. If this is true in general, the formulas provided in this paper would give conservative results.

Given electron beam and wiggler parameters, the radiation wavelength is determined by a resonance condition $\lambda = \lambda_w(1 + a_w^2)/2\gamma_0^2$ where $a_w = K$ for helical and $a_w = K/\sqrt{2}$ for planar wiggler, γ_0 is related to the average beam energy E_0.

To determine SASE performance given system parameters it is instructive to look first at the simplest model, the so called one-dimensional (1D) model [2][8]. The 1D model is an ideal case, which assumes the electron beam has a uniform transverse spatial distribution with zero emittance and energy spread. In this model the quantities appeared in Eq.(1) are given by

$$\begin{aligned} &\alpha = 1/9, \quad P_n \approx \rho^2 c E_0/\lambda \\ &L_g = \lambda_w/4\pi\sqrt{3}\rho, \quad P_{sat} \approx \rho P_{beam} \end{aligned} \qquad (3)$$

where ρ is a dimensionless parameter known as the Pierce parameter [8] defined by

$$\rho = \left[\left(\frac{I}{I_A}\right)\left(\frac{\lambda_w A_w}{2\pi\sigma_x}\right)^2\left(\frac{1}{2\gamma_0}\right)^3\right]^{1/3} \quad (4)$$

where $I_A = 17.045$ kA is the Alfven current, $A_w = a_w$ for helical wiggler and $A_w = a_w[J_0(\xi) - J_1(\xi)]$ for planar wiggler, $\xi = a_w^2/2(1+a_w^2)$, $J's$ are Bessel functions, electron rms beam size is determined by $\sigma_x = \sqrt{\beta\varepsilon}$, $\varepsilon = \varepsilon_n/\gamma_0$, and electron beam power is given by P_{beam}[TW] = E_0[GeV]I[kA].

Notice the Pierce parameter is proportional to the cubic root of the current density. Here we have replaced the current density by the peak value, $I/2\pi\sigma_x^2$, for a Gaussian beam. Thus the 1D model gives the highest possible FEL gain (shortest gain length) and can be used as a reference for the cases with non-ideal electron beam. In fact it can be shown from rigorous analysis [9][10][11] that the FEL gain length can be expressed by a universal scaling function

$$\frac{L_{1d}}{L_g} = F(\eta_d, \eta_\varepsilon, \eta_\gamma) \quad (5)$$

where

$$\eta_d = \frac{L_{1d}}{L_r},\ \eta_\varepsilon = \left(\frac{L_{1d}}{\beta}\right)\left(\frac{4\pi\varepsilon}{\lambda}\right),\ \eta_\gamma = 4\pi\left(\frac{L_{1d}}{\lambda_w}\right)\left(\frac{\sigma_e}{E_0}\right)$$

L_{1d} is the gain length given by the 1D model, Eq.(3), and Rayleigh range is defined by $L_r = 4\pi{\sigma_x}^2/\lambda$.

The universal scaling function, determined by fitting numerical solutions of the coupled Maxwell-Vlasov equations describing FEL interaction, is given by [11]

$$\frac{L_{1d}}{L_g} = \frac{1}{1+\eta} \quad (6)$$

where

$$\begin{aligned}\eta &= a_1{\eta_d}^{a_2} + a_3{\eta_\varepsilon}^{a_4} + a_5{\eta_\gamma}^{a_6} \\ &+ a_7{\eta_\varepsilon}^{a_8}{\eta_\gamma}^{a_9} + a_{10}{\eta_d}^{a_{11}}{\eta_\gamma}^{a_{12}} + a_{13}{\eta_d}^{a_{14}}{\eta_\varepsilon}^{a_{15}} \\ &+ a_{16}{\eta_d}^{a_{17}}{\eta_\varepsilon}^{a_{18}}{\eta_\gamma}^{a_{19}}\end{aligned}$$

and the 19 fitting parameters are given below.

$a_1 = 0.45$	$a_2 = 0.57$	$a_3 = 0.55$	$a_4 = 1.6$
$a_5 = 3$	$a_6 = 2$	$a_7 = 0.35$	$a_8 = 2.9$
$a_9 = 2.4$	$a_{10} = 51$	$a_{11} = 0.95$	$a_{12} = 3$
$a_{13} = 5.4$	$a_{14} = 0.7$	$a_{15} = 1.9$	$a_{16} = 1140$
$a_{17} = 2.2$	$a_{18} = 2.9$	$a_{19} = 3.2$	

Notice the maximum of the scaling function corresponds to $L_{1d}/L_g = F(0,0,0) = 1$, which gives the shortest gain length in the 1D limit. Thus the scaling parameters η_d, η_ε, and η_γ measure the deviation of the beam from the ideal case. Specifically, η_d is for gain reduction due to diffraction, a spatial 3D effect, η_ε and η_γ are for gain reduction due to electron's longitudinal velocity spread caused by emittance and by energy spread, respectively. Another scaling parameter related to the wavelength detuning has been optimized thus eliminated to give Eq.(5) and (6).

The saturation power obtained empirically by fitting simulation results is given by [12]

$$P_{sat} \approx 1.6\rho\left(\frac{L_{1d}}{L_g}\right)^2 P_{beam}. \quad (7)$$

A formula for noise power is not available for non-ideal beam. So the 1D formula in Eq.(3) will be used instead, which is shown by simulation [13] to give conservative estimate of noise power for non-ideal beam.

III. EVALUATION AND OPTIMIZATION OF LCLS DESIGN

Using the formulas given in the previous section, a computer code is developed to evaluate SASE performance given wiggler class (planar or helical) and seven independent system parameters: I(kA), ε_n(mm-mrad), σ_e(MeV), λ_w(cm), K, β(m), and λ(Å). With the code any one of the seven parameters can either be fixed at a given value, varied or optimized over a given range, in any combination. The criteria for optimization is to have the shortest possible saturation length in order to minimize the size and hence the cost of the project. Optimization for the LCLS is carried out in three steps.

A. *Wiggler Optimization*

A contour plot of L_{sat} vs. λ_w and K is shown for planar wiggler in Fig.1, where the three beam parameters: I, ε_n, and σ_e are fixed at nominal values given in table 1 for λ = 1.5 Å, and β is optimized (varied to give the shortest L_{sat}) throughout this section. The calculations shown in Fig.1 are for a generic planar wiggler. In reality, the accessible area in the λ_w-K space is limited by practical constraints, such as wiggler design, beam energy, etc. For the hybrid wiggler of Nd-Fe-B type λ_w and K are related by the Halbach formula [14]: $K = 3.2\lambda_w[\text{cm}]exp[-5.08g/\lambda_w + 1.54(g/\lambda_w)^2]$, where g is the full wiggler gap. There are two major practical constraints: one is on g, which limits the size of beam pipe thus should not be too small to cause wakefield problem; another constraint is on beam

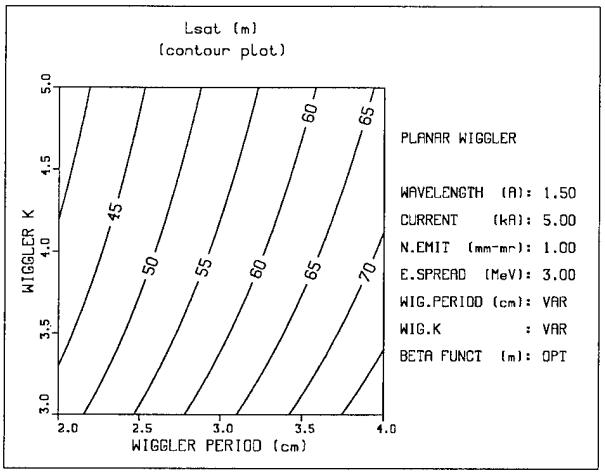


Figure 1. L_{sat} vs. λ_w and K for a generic planar wiggler.

energy, which should not exceed 15 GeV considering the availability of SLAC linac. Taking into account the two constraints, the optimized wiggler and focusing parameters: λ_w, K, and β, together with SASE performance parameters: L_g and L_{sat} are given in table 1 for three choices of g values. Also given in table 1 are the similar optimization results for a superconducting helical wiggler [15]. Beam energy is close to 15 GeV for all these cases.

Table 1. Parameters and Optimization Results

$\lambda = 1.5$Å, $I = 5$kA, $\varepsilon_n = 1$mm-mr, $\sigma_e = 3$MeV					
Hybrid Planar Wiggler					
g(cm)	λ_w(cm)	K	β(m)	L_g(m)	L_{sat}(m)
0.6	3.0	3.7	10	3.1	58
0.8	3.4	3.6	11	3.5	65
1.0	3.7	3.4	12	3.8	71
Superconducting Helical Wiggler					
g(cm)	λ_w(cm)	K	β(m)	L_g(m)	L_{sat}(m)
0.6	2.0	3.4	5.1	1.4	26
0.8	2.15	3.3	5.6	1.5	28
1.0	2.3	3.1	6.1	1.7	31

B. Effects of Beam Quality

The dependence of L_{sat} on I and ε_n is shown in Fig.2 for the hybrid wiggler, with both I and ε_n varied above and below the nominal values in table 1. Notice the tradeoff possibilities between the beam quality parameters: I and ε_n suggested by the contour lines.

C. Upgrade Pass

As seen from Fig.2, operation at $\lambda = 1.5$ Å strongly prefers high quality beam. However the requirement on beam quality is relaxed at longer wavelength. Thus one may envision an upgrade pass using the same wiggler optimized for 1.5 Å but starting at a longer wavelength with somewhat lower quality beam, and approaching 1.5 Å as beam quality improves. To illustrate this point in a single plot, let's consider a three-dimensional beam parameter space $\{I, \varepsilon_n, \sigma_e\}$. Suppose the operation starts from a point of lower beam quality {2.5kA, 2mm-mrad, 6MeV} and finish at a point of higher beam quality {5kA, 1mm-mrad, 3MeV} on a straight line pass in the 3D space. By defining a Beam Quality Factor (BQF), which goes from 0 to 1 linearly as the operation goes from the starting to the finishing points, we may visualize in Fig.3 the effect of such an upgrade pass over a broad wavelength range. Notice the factor of 2 change in each beam quality parameter between the two points.

IV. ACKNOWLEDGMENT

I thank Herman Winick for discussions on LCLS optimization scheme, Schlomo Caspi for providing parameters for the superconducting helical wiggler and Kwang-Je Kim for discussions on SASE physics.

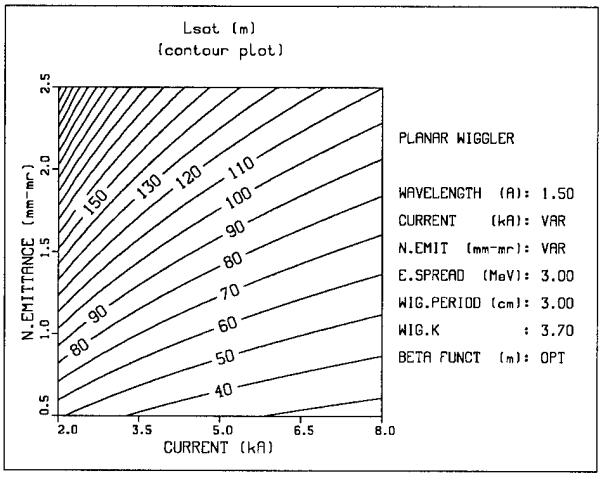


Figure 2. L_{sat} vs. I and ε_n for the hybrid wiggler with $g = 0.6$ cm.

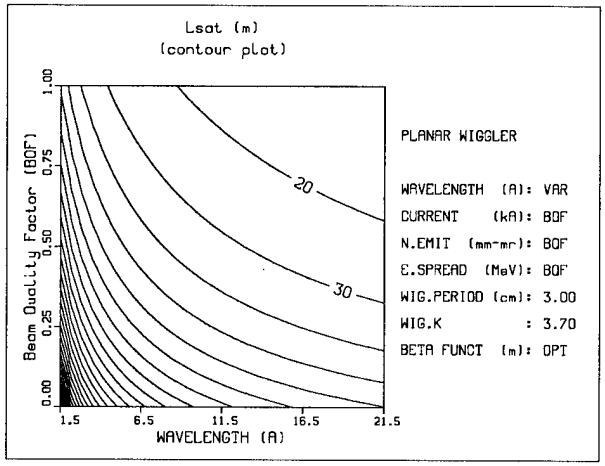


Figure 3. L_{sat} vs. λ and beam quality factor for the hybrid wiggler with $g = 0.6$ cm.

References

[1] H. Winick et al., NIM. A347 (94) 199.
[2] K.-J. Kim, NIM. A250 (86) 396. PRL.57 (86) 1871.
[3] J.-M. Wang, L.-H. Yu, NIM. A250 (86) 484.
[4] R. Bonifacio et al., PRL. 73 (1994) 70.
[5] L.-H. Yu, S. Krinsky, NIM. A285 (89) 119.
[6] L.-H. Yu et al., Phys.Rev. E51 (95) 813.
[7] G. Travish, J. Rosenzweig, Proc. PAC (93) 1548.
[8] R. Bonifacio et al., Opt. Comm. 50 (84) 373.
[9] L.-H. Yu, S. Kringsky, R.L. Gluckstern, PRL. 64 (90) 3011.
[10] Y.H. Chin, K.-J. Kim, M. Xie, Phys. Rev. A46 (92) 6662.
[11] M. Xie, to be published.
[12] K.-J. Kim, M. Xie, NIM. A331 (93) 359.
[13] W.M. Fawley et al., Proc. PAC (93) 1530.
[14] K. Halbach, J.Phys. (Paris) Colloq. 44 (83) C1-211.
[15] S. Caspi, LBL tech-note, SC-MAG-475 (94).

THE FERMI FEL PROJECT AT TRIESTE

D. Bulfone, F. Cargnello, G. D'Auria, F. Daclon, M. Ferianis, M. Giannini,
G. Margaritondo§, A. Massarotti, A. Rindi, R. Rosei, C. Rubbia¥, R. Visintini,
R.P. Walker†, A. Wrulich, D. Zangrando, Sincrotrone Trieste S.c.p.A.
F. Ciocci, G. Dattoli, A. De Angelis¶, A. Dipace, A. Doria, G. P. Gallerano, F. Garosi, L. Giannessi,
E. Giovenale, L. Mezi, P. L. Ottaviani, A. Renieri, E. Sabia, A. Segreto‡, A. Torre, ENEA-Frascati
M. Castellano, P. Patteri, S. Tazzari, F. Tazzioli, INFN-Frascati
F. Cevenini, INFN-Naples and Univ. Naples, Dept. of Physics
A. Cutolo, Univ. Naples, Dept. of Electronic Engineering

† corresponding author; ¶ guest; ‡ study grant holder
§ also at EPFL, Lausanne, Switzerland; ¥ also at CERN, Geneva, Switzerland

The main features of the FERMI project are described, including beam transport design and FEL performance calculations.

I. INTRODUCTION

The FERMI (Free Electron Radiation and Matching Instrumentation) project aims to construct an Infra-Red FEL user facility covering a broad spectral range (2-250 μm) to complement the high brightness radiation from the ELETTRA synchrotron radiation facility at Trieste [1]. A unique feature of the project will be the possibility of carrying out "pump-probe" experiments using synchronized radiation beams from FERMI and ELETTRA on the same sample.

The project was launched at a meeting of Italian FEL experts held in Trieste on the 18th November 1994, chaired by C. Rubbia, as a collaboration between Sincrotrone Trieste, ENEA (Frascati), INFN (Frascati) and the University of Naples (Department of Electronic Engineering).

The facility will make use of an existing linac, that forms part of the ELETTRA injection system, and a hall into which the beam can be extracted. In addition, for the first phase of the project equipment will be used from the suspended INFN/ENEA "SURF" FEL experiment [2], including the undulator, beam transport magnets and optical cavity.

Development of the facility is foreseen in three phases. **Phase 1** will consist of setting up the first FEL (FEL-1) to cover the range 5-20 μm. Initially, the existing optical cavity will be used to demonstrate laser operation at a fixed wavelength of 16 μm. Later, new mirrors will be installed allowing tuneability over the range 5-20 μm with a higher output coupling, permitting a first user experiment to be carried out. In **Phase 2** a second FEL (FEL-2) will be set up for the 15-250 μm region. To allow a full support for user experiments a new building will be constructed (**Phase 3**) hosting several experimental stations. As part of this phase a new linac gun will also be implemented to reduce the emittance, which is necessary to reach the shortest wavelengths on FEL-1 (2-5 μm).

II. LAYOUT

Figure 1 shows the layout of the facility adjacent to the ELETTRA storage ring. The beam from the first 100 MeV part of the 1.5 GeV injector linac will be transported into an existing hall adjacent to the linac tunnel, sufficiently large (32 m x 10 m) to accommodate both FELs as well as space for power supplies etc. and an area for optical diagnostics and pilot experiments. In the final phase the FEL beams will be

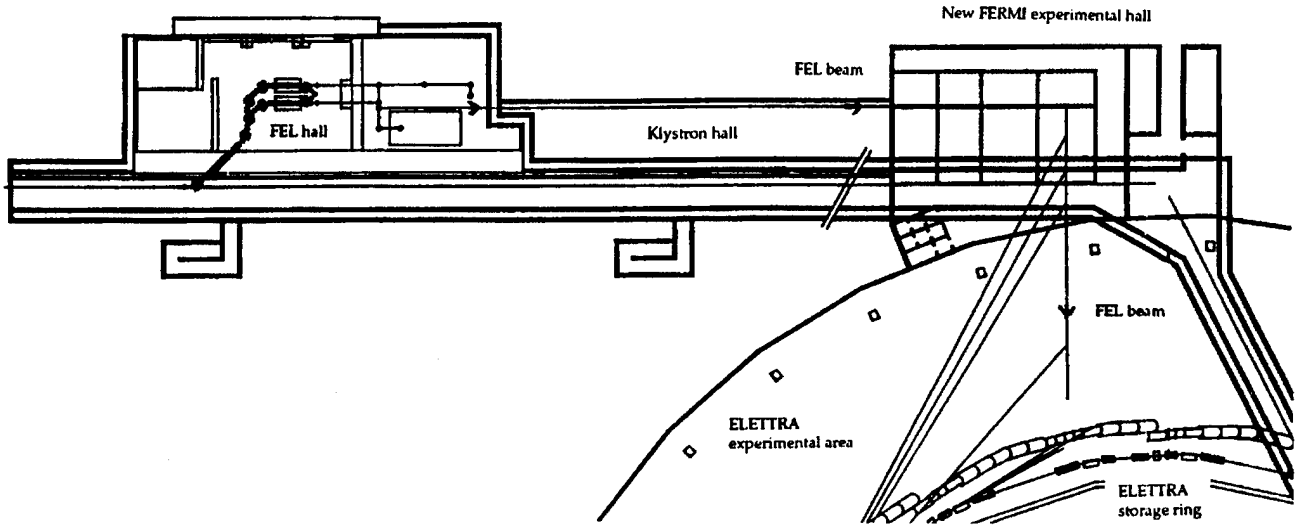


Fig. 1 Layout of the FERMI FEL facility.

0-7803-3053-6/96/$5.00 ©1996 IEEE

transported along the klystron gallery (above the linac tunnel) and into a new FEL experimental area (~ 21 m x 17 m) which will host a number of experimental hutches. The location of the new building will allow the possibility of easily transporting synchrotron radiation beams into the FEL experimental area, or FEL radiation into the ELETTRA experimental hall.

III. LINAC

The low energy part of the linac has been designed to operate in a FEL mode in the 20-75 MeV range with a 10 μs pulse length. First tests in this mode of operation are reported elsewhere in these Proceedings [3]. Table 1 summarises the expected linac parameters, on which the FEL performance calculations were based. It will be seen that the linac performance is not sufficient to allow saturation to be reached below about 5 μm, and therefore possible schemes for upgrading the gun are being evaluated.

Table 1. Main linac parameters in the FEL-mode

Energy, MeV	20-75
Macropulse repetition rate, Hz	10
Macropulse length, μs	10
Charge per micropulse, nC	0.4
Micropulse length (FWHM), ps	10
Peak current, A	37.5
Micropulse repetition rate, MHz	20.8-31.3
Normalized emittance (rms), mm mrad	62.5
Energy spread at 75 MeV, %	± 0.3

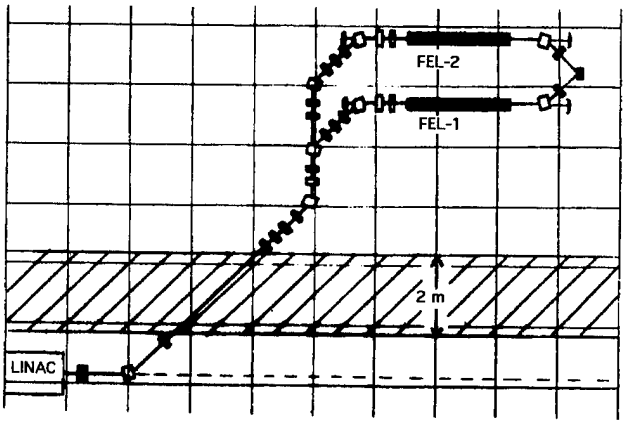


Fig. 2 Layout of the transport line and two FELs

IV. BEAM TRANSPORT

A particular requirement of the transport line is to provide a variable path length dependence with energy, in order to maintain high peak currents or to allow bunch length manipulations in conjunction with linac phase adjustments. Fig. 2 shows a suitably flexible design using four bends for each FEL line. Fig. 3 shows the optical functions for FEL-1 in the isochronous case. The design is compatible with operation over the full 20-75 MeV range using the existing magnets.

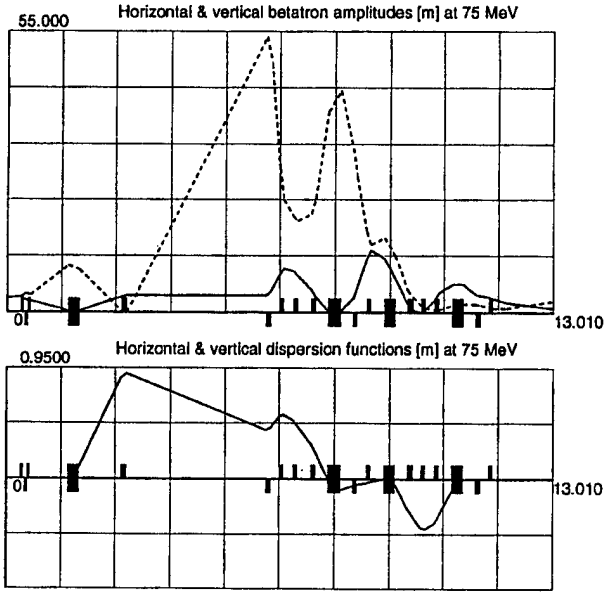


Fig. 3 FEL-1 transport line optics in the isochronous case.

V. UNDULATORS AND OPTICAL CAVITIES

Table 2 summarises the undulator parameters. The undulator for FEL-1 was built by Ansaldo in collaboration with ENEA, Frascati [4]. The minimum gap of 20 mm allows a vacuum aperture of 15 mm which gives minimal diffraction losses at 20 μm. The FEL-2 undulator is designed to have the shortest period allowing 250 μm to be reached at the lowest envisaged energy of 20 MeV, compatible with a vacuum aperture of 40 mm for minimal diffraction losses.

Table 2. Main parameters of the FEL undulators.

	FEL-1	FEL-2
Length, m	2.20	2.28
Period, m	0.044	0.095
Number of periods	50	24
Minimum gap, mm	20	45
Peak field, T	0.35	0.43
K parameter, max.	1.44	3.79

The optical cavity length has been chosen to be 5.4 m, which allows the same bunch separation to be obtained in ELETTRA with a regular filling pattern with 24 bunches. For FEL-1 the mirror adjustment system for the SURF project will be used which has combined PZT and motorized adjustment of mirror tilt and longitudinal position [5]. Mirrors are available for the first demonstration experiment at 16 μm. Thereafter other mirrors will be substituted to cover the 5-20 μm range. No decision has yet been taken about the FEL-2 optical cavity that could employ metal mesh mirrors and a waveguide cavity.

VI. PERFORMANCE CALCULATIONS

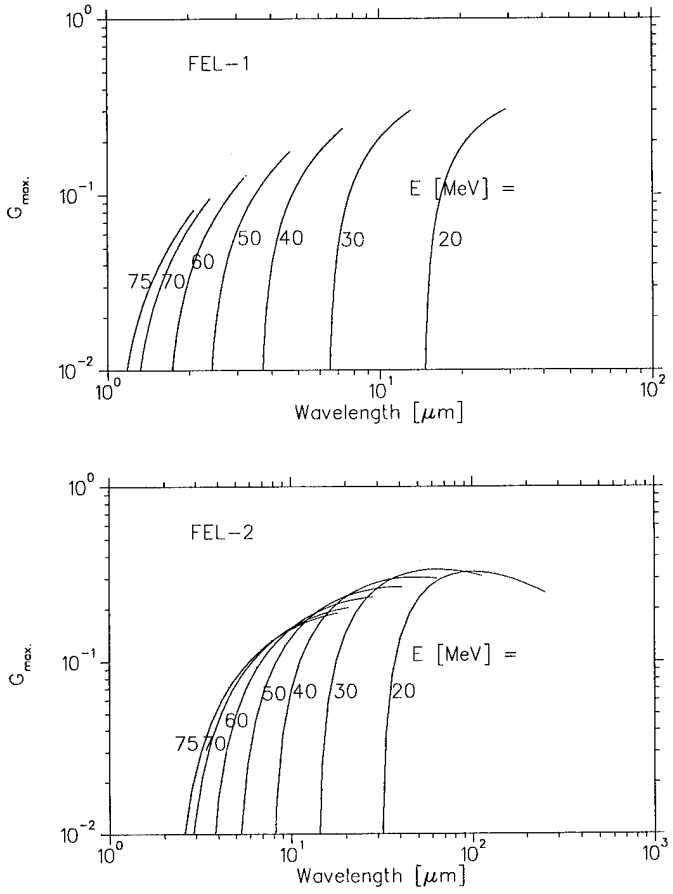


Fig. 4. Small signal gain for FEL-1 and FEL-2.

The estimated small signal gain ($G_{max.}$) , including the effects of emittance, energy spread and slippage is shown in fig. 4 as a function of undulator K value for various electron beam energies. Table 3 presents a summary of the optimized parameters at various wavelengths, assuming 5 % output coupling and 1 % losses. It can be seen that the gain is sufficient above about 5 μm to reach saturation in a sufficiently small time (τ_r) with respect to the macropulse duration. The results indicate that high micropulse energies ($E_{micro.}$) and power ($P_{micro.}$) can be produced, with low average power ($P_{av.}$) due to the low duty cycle.

Table 3. Results of FEL performance calculations.

	FEL-1				FEL-2			
λ, μm	5	10	16	20	20	50	100	250
E, MeV	48	34	27	24	46	30	23	20
$G_{max.}$ (%)	18.3	27.3	31.2	31.4	24.0	33.1	33.6	25.0
τ_r, μs	6.3	3.8	3.2	3.2	4.3	3.0	2.9	4.1
$E_{micro.}$, μJ	27	24	20	18	96	62	40	23
$P_{micro.}$, MW	2.2	2.0	1.6	1.4	9.0	5.8	3.8	2.2
$P_{macro.}$, kW	0.80	0.67	0.56	0.49	2.7	1.7	1.1	0.64
$P_{av.}$, mW	30	42	38	34	152	120	79	38

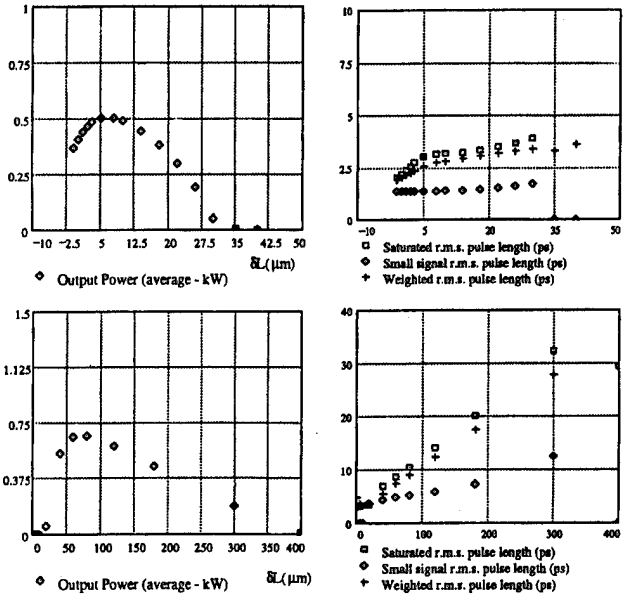


Fig. 5 Results of pulse propagation analysis (see text).

A more accurate numerical analysis of pulse propagation effects has been made, using a code developed by the ENEA group based on the solution of the FEL integral equation including saturation effects. Figure 5 shows the output power averaged over the macropulse and the optical pulse length, near the beginning of the macropulse (small signal value) and at the end (saturated value), as a function of cavity length detuning (δL) for 2 cases : FEL-1 at 16 μm (upper) and FEL-2 at 250 μm (lower). In general the results confirm that saturation is reached in the 5-250 μm range, and that the pulse energy and power is in agreement with the previous calculations. It can also be seen that the pulse length at small detuning is smaller than the electron pulse length (rms = 4.2 ps), but increases with detuning and due to saturation, particularly in the case of large slippage (e.g. at 250 μm).

VII. PRESENT STATUS

The work presented here is a summary of a more detailed Conceptual Design Report that has recently been completed. The present phase of activity concerns the identification of potential users and possible collaborators, as well as sources of funding. A formal collaborative agreement between the Italian partners is also being prepared.

VIII. REFERENCES

[1] C.J. Bocchetta et al., this Conference.

[2] M. Castellano et al., Proc. 3rd European Particle Accelerator Conference, Editions Frontières (1992) p. 611

[3] G. D'Auria et al., this Conference.

[4] F. Rosatelli et al., Proc. 1991 US Particle Accelerator Conference, p. 2760.

[5] M. Castellano et al., Nucl. Instr. Meth. A304 (1991) 204.

Studies on a Free Electron Laser for the TESLA Test Facility

J. Rossbach
for the TESLA FEL Study Group[1]
Deutsches Elektronen Synchrotron, D-22603 Hamburg, Germany

Abstract

We present the layout of a Single Pass FEL to be driven by the TESLA Test Facility (TTF) currently under construction at DESY. The TTF is a test-bed for high-gradient, high efficiency superconducting accelerating sections for a future linear collider. Due to its unrivaled ability to sustain high beam quality during acceleration, a superconducting rf linac is considered the optimum choice to drive a Free Electron Laser (FEL). We aim at a photon wavelength of $\lambda = 6$ nm utilizing the TTF after it has been extended to 1 GeV beam energy. A first test is foreseen at a larger photon wavelength.

1. GENERAL DESCRIPTION

A Free Electron Laser (FEL) in the soft X-ray regime is under study, using the superconducting linac of the TESLA Test Facility (TTF) being under construction at DESY [1]. The FEL at the TESLA Test Facility (TTF FEL) is based on the principle of 'Self Amplified Spontaneous Emission' (SASE) [2]. The key advantage of the SASE scheme compared to other FEL schemes is that neither an input seed laser is required nor mirrors forming an optical cavity. Thus, no known fundamental limitation would prevent operation even down to the Ångstrom region. In the first section of the undulator the electrons radiate independently and the phases of the photons are randomly distributed. Since microbunch formation starts from this „random" noise, a long undulator is needed to achieve laser action with exponential growth in light output. For the TTF FEL an overall undulator length of 30 m is planned.

The photon wavelength λ_{ph} of the first harmonic is related to the period length of a planar undulator λ_u by

$$\lambda_{ph} = \frac{\lambda_u}{2\gamma^2}\left(1+\frac{K^2}{2}\right), \qquad (1)$$

where, $\gamma = E/mc^2$ is the relativistic factor of the electrons and $K = e\, B_u\, \lambda_u / 2\pi mc$ the 'undulator parameter', e being the elementary charge, m the electron rest mass, c the speed of light, and B_u the peak field in the undulator.

The physics program for the TTF FEL requires a photon wavelength of 6 nm. Therefore, for state-of-the-art undulator parameters are assumed, e.g. $\lambda_u = 27$ mm, $K = 1.3$, a beam energy of 1GeV is necessary.

Two beam parameters are essential to reach power saturation within a not too long undulator: A small transverse beam emittance ε_t to provide both small beam diameter and small beam divergence in the undulator, and a small longitudinal beam emittance ε_z to achieve kilo-Ampere instantaneous beam currents at an energy width in the 0.1% range.

The TTF is an ideal accelerator to drive a SASE FEL. There are two main reasons:

- The perturbation of small emittance beams during the acceleration process is smallest with a superconducting linac at lower frequency. Because the resonator volume and the stored energy are big, the accelerating field is hardly affected by the presence of the electron beam. The variation of the effective accelerating voltage over the bunch length („longitudinal wakefield") is minimum and the tendency of beam induced rf deflections („transverse wakefields") is small.
- A superconducting linac provides a large AC power efficiency and a high duty cycle. The TESLA Test Facility will operate at 1 % duty cycle, orders of magnitude larger than a normal conducting linac would do at the TTF nominal gradient of 15 MV/m. In addition to power efficiency, this is another crucial advantage for potential experiments, because it leaves sufficient time between pulses in the bunch train for data handling.

The most expensive single component of a short wavelength FEL is the accelerator. Taking into account,

[1] The TESLA FEL Study Group:
ASC Samara: E.L. Saldin, E.A. Schneidmiller, **CE Saclay:** A. Mosnier, **DESY:** R. Bacher, W. Brefeld, M. Dohlus, H. Edwards, B. Faatz, J. Feldhaus, K. Flöttmann, A. Gamp, P. Gürtler, K. Hanke, L. M. Kiernan, J. Krzywinski, M. Leenen, T. Limberg, G. Materlik, T. Möller, J. Pflüger, D. Proch, J. Rossbach, J. Schneider, S. Schreiber, J. Sekutowicz, M. Seidel, K. Tesch, D. Trines, R. Wanzenberg, H. Weise, S.G. Wipf, B.-H. Wiik, **Fermilab Chicago:** E. Colby, T. Nicol, **Helsinki Univ. of Technology:** T. Åberg, **INFN Milano:** R. Bonifacio, C. Pagani, P. Pierini, L. Serafini, **JINR Dubna:** M.V. Yurkov, **KFA Jülich:** W. Eberhard, G.Ganteför, **Lab. de Photophys. Moléculaire Paris:** G. Comtet, G. Dujardin, L.Hellner, **Lawrence Livermore Natl . Lab.:** T. Scharlemann, **LNLS Campinas:** ,R. DeCastro, **Los Alamos Natl. Lab.:** J. Goldstein, R.L. Sheffield, **Max-Born-Institut Berlin:** H. Rottke, W. Sandner, I. Will, **Max-Planck-Inst. f. Biophys. Chemie Göttingen:** T. M. Jovin, **Max-Planck-Inst. f. Mikrostrukturphys. Halle:** C. M. Schneider, **Polish Acad. of Sciences Warschau:** K. Rzazewski, **TU München:** P. Feulner, D. Menzel, W. Wurth, **UCLA Los Angeles:** J. Rosenzweig, **Univ. Bielefeld:** D. Feldmann, **Univ. Birmingham:** R. E. Palmer, **Univ. Bochum:** K. Al-Shamery, M. Baerns, H. J. Freund, W.Greinert, **Univ. Düsseldorf:** E. Kisker, **Univ. Essen:** C. Westphal, H. Zacharias, **Univ. Frankfurt:** H. Schmidt-Böcking, L. Spielberger, **Univ. Göttingen:** G. Schmahl, **Univ. Hamburg:** C. Kunz, B. Sonntag, H.J. Voß, **Univ. Kiel:** L. Kipp, M.Skibowski, **Univ. Rostock:** K. H. Meiwes-Broer, **Univ. Tomsk, Russia:** Y. Nikitina, **Univ. Würzburg:** H.-P.Steinrück, **Uppsala Univ.:** M. Martensson

0-7803-3053-6/96/$5.00 ©1996 IEEE

that a SASE FEL needs beam parameters similar to those to be realized for a Linear Collider, it is obvious that the TTF linac can be ideally utilized for driving a SASE FEL. For the discussion of the TESLA Test Facility linac and its relation to the TESLA 500 Linear Collider scheme we refer to the TTF Design Report [1].

The TTF design energy is 500 MeV. It has to be upgraded to 1 GeV electron beam energy required for the desired photon wavelength. Figure 1 shows the overall TTF FEL scheme. Table 1 compiles main parameters of the TTF FEL.

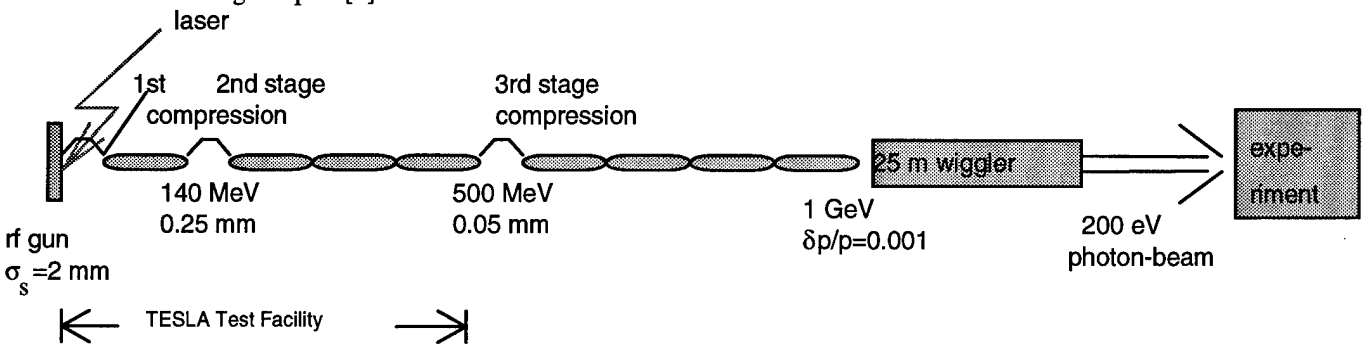


Figure 1: Schematic layout of the TTF FEL based on the TESLA Test Facility (TTF). Four additional TESLA accelerator modules bring the energy up to 1 GeV. The bunch length is reduced from 2 mm to 50 μm within three steps of bunch compression. The SASE FEL process requires an undulator of 25 m effective length. The over-all length of the facility is some 200 meters.

2. ELECTRON SOURCE

The transverse coherence condition imposes a tight requirement on the transverse emittance ε_t of the electron beam [3]:

$$\varepsilon_t^n \leq \frac{\gamma \cdot \lambda_{ph}}{4\pi}$$

ε_t^n is the *normalized* emittance. For λ_{ph} = 6 nm, γ = 2000, this requires $\varepsilon_t^n < 1$ π mrad mm. Actually, as is seen from Figure 2, this condition is not very strict, but the saturation length significantly increases if ε_t^n is larger. Thus, we aim at $\varepsilon_t^n = 1$ π mrad mm for the rms electron emittance of a 1 nC bunch charge from the electron gun, and we allow for a factor of two emittance dilution during longitudinal beam compression and acceleration up to 1 GeV. According to beam dynamics simulations in both the bunch compressors and the accelerator, this seems to be a conservative assumption. These very high phase space densities came into reach due to two major achievements: The development of the rf gun [4] and the concept of space charge compensation [5].

3. UNDULATOR

The undulator is the most prominent FEL specific component. The proposed design avoids technical risks. A planar hybrid undulator is foreseen with period length λ_u = 27 mm and peak magnetic field B_u = 0.5 T, parameters very much like those of existing undulator magnets. The main challenges are the total length of 30 m, the additional quadrupole focusing to be supplied and tight tolerances. To simplify production, measurement and installation, 5m long modules are forseen. This also permits installation of electron and photon beam monitors and correction elements.

VARIABLE	UNITS	VALUE
beam energy	GeV	1.000
λ(radiation wavelength)	nm	6.4 (193 eV)
λ_u (undulator period)	mm	27.3
undulator gap	mm	12
B (undulator peak field)	T	0.497
undulator length	m	25
beam optics β function	m	3
rms beam size	mm	0.05
ε^n (normalized emittance) in the undulator	π mrad mm	2.0
peak electron current	A	2490
number of electrons per Gaussian bunch		6.24E+9
number of photons per Gaussian bunch		4E+13
peak electron beam power	GW	2490
energy spread σ_γ/γ	10^{-3}	1.00
bunch length	μm	50.
L_σ (power gain length)	m	1.00
L_S (saturation length)	m	< 25
P_{sat} (saturated power)	GW	3
average brilliance [photons/s/mm²/mr/0.1%]		up to 6E+21
bunch train length	μsec	800
number of bunches per train		up to 7200
repetition rate	Hz	10

Table 1: Main parameters of the TESLA Test Facility FEL (TTF FEL). The insertion device is assumed to be a planar hybrid undulator. These values should be used as a guideline only since the optimization has not yet been finished and experimental experience has to be gained in this wavelength regime.

4. FEL PROCESS

Various computer codes have been used to investigate the start-up from noise, and the lethargy, exponential and saturation regimes, respectively, e.g. NUTMEG [6], GINGER[7], FS2R[8], TDA[9,10]. There is no essential disagreement between results of all these codes written by different groups and based on different approaches. It should be noted though, that for a complete study of the shot noise startup the time dependence of the input noise and the slippage effects should be taken into account in the theory and in the simulations. The one-dimensional analysis shows that a critical parameter for shot noise analysis is the beam length in units of the "cooperation length" [11]:

$$\lambda_c = \frac{\lambda}{4\pi\rho}.$$

For the TTF FEL the cooperation length is 0.26 μm, and the beam length is 50 μm. In this case bunch-to-bunch fluctuations should be a fraction of a gain length and the use of an equivalent input signal analysis should be adequate. A more careful study with existing time dependent FEL codes (GINGER and FELEX) is in its starting phase and will be reported soon. Figure 2 shows the emitted intensity as a function of ε^n.

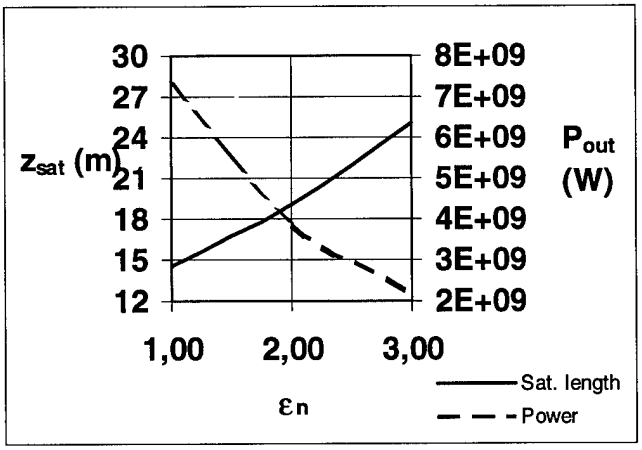


Figure2: Emitted intensity and saturation length at the peak gain as a function of the normalized electron beam emittance, for the nominal energy spread of 0.1%.

In order to determine the performance of the FEL including the undulator field errors, first simulations have been performed with the simulation code TDA3D [10]. The goal is to systematically study the correlation between phase shake and FEL parameters like saturation length and peak power. These simulations will include the undulator plus the superimposed quadrupole focusing. Figure 3 shows the photon flux emitted by the TTF FEL.

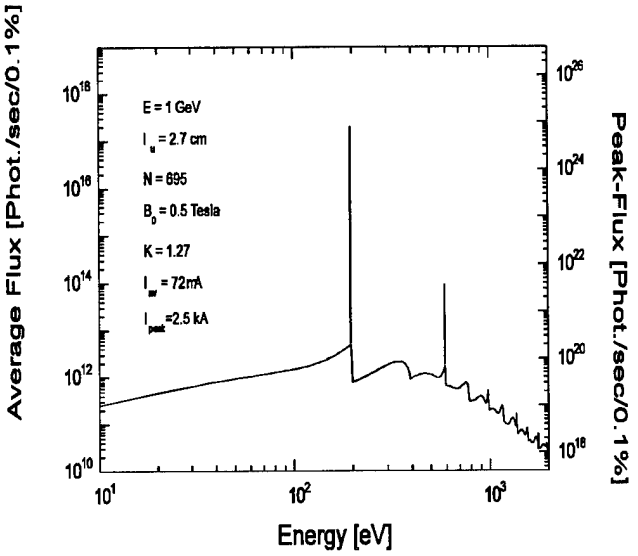


Figure 3: Expected photon flux emitted by the TTF SASE FEL. The two peaks correspond to the FEL emission at the fundamental and 3rd harmonic. The lower curve is the spontaneous emission in the undulator.

REFERENCES

[1] D. A. Edwards (ed.): TESLA Test Facility Linac - Design Report, DESY Print TESLA 95-01 (1995)

[2] R. Bonifacio, C. Pellegrini, I.M. Narducci: Opt. Commun. **50** (1984) 373.

[3] see e.g. W.B. Colson, C. Pellegrini, A. Renieri (eds.): Laser Handbook Vol. 6, North Holland (1990)

[4] J. Fraser, R. Sheffield: Nucl. Instr. Meth. A 250 (1986) 71

[5] B. Carlsten: Nucl. Instr. Meth A 285 (1989) 313

[6] E.T. Scharlemann, W.M. Fawley, SPIE, Vol. 642, 1 (1986)

[7] R.A. Jong, et al.: SPIE, Vol. 1045, 18 (1989)

[8] E.L. Saldin, et al.: DESY Report 94-219 (1994)

[6] C. Travier: Proc. EPAC 94 London (1994) 317

[8] P. Kung, H.-C. Lihn, H. Wiedemann: SLAC-Pub-6507 (1994)

[9] C.-M. Tran, J.S. Wurtele: Comput. Phys. Commun. 54 (1989) 263

[10] P. Jha, J.S. Wurtele: Nucl. Instr. Meth. A331 (1993) 447

[11] R.Bonifacio, et al.: Phys. Rev. Lett., 73 (1994), 70

MIT Microwiggler for Free Electron Laser Applications

P. Catravas, R. Stoner, J. Blastos, D. Sisson, I. Mastovsky, G. Bekefi
Massachusetts Institute of Technology, Cambridge, MA 02139
and
X.-J. Wang and A. Fisher
Brookhaven National Laboratory, Upton, NY 11973

ABSTRACT

A microwiggler-based FEL permits operation at shorter wavelengths with a reduction in the size and cost of the device. The MIT microwiggler is a pulsed ferromagnetic-core electromagnet with 70 periods of 8.8 mm each which generates an on-axis peak magnetic field of 4.2 kG. The pulse repetition rate is 0.5 Hz with FWHM 0.5 msec. The microwiggler is characterized by extensive tunability. We employed a novel tuning regimen through which the rms spread in peak amplitudes was reduced to 0.08%, the lowest ever achieved in a sub-cm period magnetic field. The microwiggler is a serviceable scientific apparatus: spontaneous emission has been observed for wavelengths of 700-800 nm using a 40 MeV beam from the Accerator Test Facility LINAC at BNL.*

INTRODUCTION

In order for the Free Electron Laser to become a practical radiation source at short wavelengths, it is necessary to reduce the size and cost of the device. Reduction in the period of the wiggler from the typical 3-10 cm to below 1 cm permits operation of FELs at shorter wavelengths for a given beam energy.

High field precision in short-period wigglers is difficult to achieve. Mechanical tolerances and other coil-to-coil variations become sufficiently large on the scale of the wiggler period that they translate easily into field errors of harmful amplitude. The severity of the problem compounds with wiggler length, and curtails the FEL efficiency through deleterious increases in electron beam walk-off and energy spread. Various microwiggler designs have been investigated to address these technical challenges. (Table 1) [1-8] We have employed a novel approach to reducing wiggler field errors in which extensive tunability is controlled through a rigorous tuning procedure. The high performance of the microwiggler makes it well-suited for the development of a linac-based FEL in the visible and UV wavelengths.

Table 1. Comparison of some short-period wigglers.

GROUP	TECH-NOLOGY AND STATUS	N_w	λ_w,mm / G,mm	B_w, kG	PEAK RMS ERROR	POLE INT. ERROR
Stoner *et al.*, MIT	Pulsed ferrocore electromag-net; operational	70	8.8/ 4.2	4.2	0.08%	0.14%
Huang *et al.*, Stanford	Staggered ferrocore array in solenoid; test	50	10.0/ 2.0	10.8	1.2%	Not reported
Warren and Fortgang LANL	Permanent magnet; operational	73	13.6/ 1.5	6.5	0.3%	Not reported
Tecimer and Elias CREOL	Hybrid, test	62	8/ Not re-ported	1.0	0.2%	0.6%
Ben-Zvi *et al.*, BNL	Supercon-ducting ferrocore electromag-net; test	20	8.8/ 4.4	>5. 5	0.29%	0.36%

Table 2. MIT Microwiggler parameters.

PARAMETER	VALUE
on-axis magnetic field, B_w	4.2 kG
wiggler period, λ_w	8.8 mm
wiggler parameter, a_w	0.34
wiggler gap, G	4.2 mm
number of periods, N_w	70
rms spread in peak amplitudes, $(\delta B/B)_{RMS}$	0.08%
rms spread in pole integrals, $(\delta I/I)_{RMS}$	0.14%
repetition rate	0.5 Hz

MICROWIGGLER FIELD CHARACTERISTICS

Table 2 summarizes the microwiggler parameters. Wiggler design, construction and tuning algorithm are

* The MIT work is supported by the Office of Naval Research.

0-7803-3053-6/96/$5.00 ©1996 IEEE

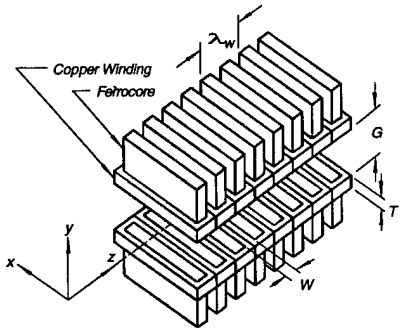


Figure 1. Schematic of the wiggler geometry

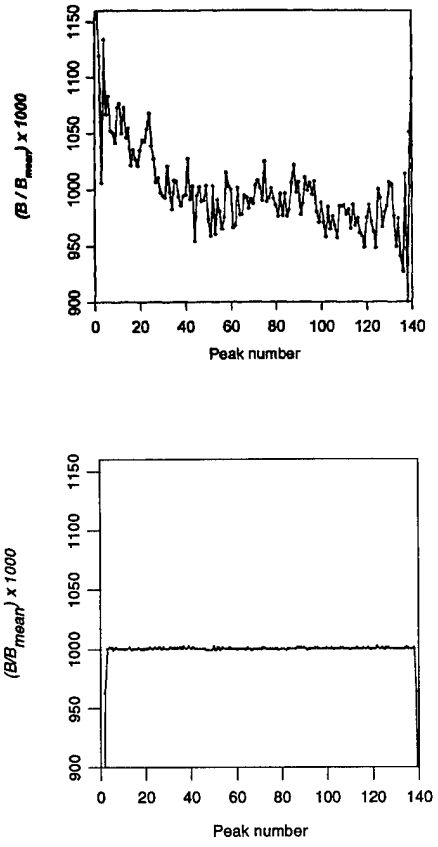


Figure 2. Peak amplitude profile: untuned profile (rms spread 4%) and tuned profile (0.08%).

detailed in our previous work. [9] The measurements of field characteristics described here are for the full 70 periods (excluding tapered end effects) and for a repetition rate of 0.5 Hz.

Each half period in the wiggler is created by a pair of magnets connected electrically in parallel, which are mounted on either side of a stainless steel bore in a precisely formed Aluminum matrix. (Figure 1) Current flows independently to each pair of magnets and is controlled by an variable series resistance.

In order to completely characterize the microwiggler field characteristics, a comprehensive battery of field measurements was performed.

The measurement system

An automated control system monitors the field profile, in which a B-dot loop is pulled through the bore and recorded. Peak amplitudes and peak axial positions are extracted from curve fits to the data. The control system includes feedback to maintain the wiggler total current at a constant level. Complete field scans are repeated from 5-15 times and averaged, so that a single field profile contains the information of over 10,000 field amplitude data points.

Results of tuning

The untuned field profile was dominated by the effects of small inhomogeneities in the wiggler construction and had an rms spread of 4%. (Figure 2) From a consecutive sequence of field profile measurements, tuning iterations reduced the spread in peak amplitudes to 0.08% or better, an improvement of nearly two orders of magnitude. This is an outstanding level of uniformity for a sub-cm period wiggler, and illustrates the power of our tuning algorithm in controlling the field.

Cross-gap field symmetry

Field profile measurements are taken along the axis of the wiggler bore. In order to determine how well the axis of the bore coincides with the wiggler axis, cross-gap field symmetry was measured. The distance between the center of the wiggler bore and the magnetic field center was determined with an axially-oriented B-dot loop positioned at the maxima of the axial magnetic field (nulls of the transverse field.) The voltage on the axial B-dot loop is zero for perfect cross-gap symmetry and is linearly proportional to small displacements. The results determined a spread in the magnetic center displacements of at most 17 μm.

The coils and bore are mounted securely in a precisely formed aluminum matrix. Coil heights relative to the face of this matrix were measured and it was determined that they secure the position of the bore to within 10 μm in the transverse direction. The mechanical measurements are in agreement with the magnetic center measurements, and confirm the straightness of the bore.

Harmonic content of field profile

A high level of purity in the wiggler field harmonic spectrum was measured and provides an independent confirmation of the peak amplitude uniformity. Furthermore, it is important that the design of the wiggler gap dimension, which must be small for large field amplitudes, not result in field harmonics, since the high frequency harmonic emissions can damage optical coatings during lasing. Measurements show that the third

harmonic is down by more than five orders of magnitude from the fundamental, the fifth harmonic is just above the noise level, and the other harmonics are not measurable. [10]

Estimate of spread in pole integrals

The rms spread in pole integrals is an important figure of merit for wigger field uniformity and can be estimated from a precise measurement of the peak amplitudes and positions. Evaluation of errors in the measured amplitude profile, including contributions from stray pick-up, leads to an rms spread in peak amplitudes of 0.08% along the center of the wiggler bore. Contributions to the spread in peak amplitudes due to differing temporal coil response were measured and shown to be negligable. [11] The peak position error spread is currently 10.4 um. As the peak position and peak amplitude spreads are uncorrelated, they add in quadrature, giving an estimated spread in pole integrals of 0.14%.

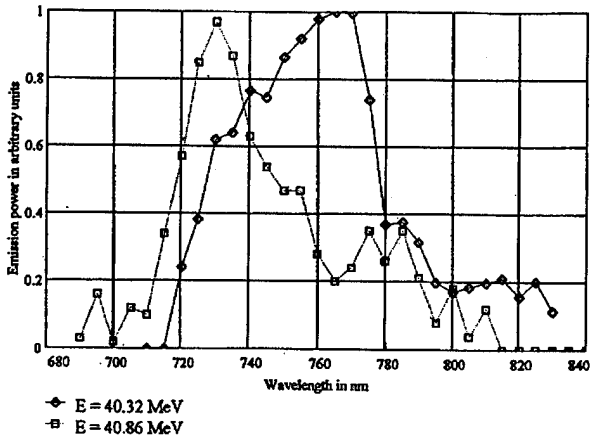


Figure 3. Spontaneous emission spectra for beam energies of 40.32 MeV and 40.86 MeV.

SPONTANEOUS EMISSION MEASUREMENTS

To date, the MIT Microwiggler has been used in measurements of spontaneous emission at the wavelengths of 700-800 nm. (Figure 3). These measurements were taken using a 40 MeV beam produced by the ATF LINAC at BNL. We observed the expected redshift in peak wavelength accompanying a decrease in beam energy. The emissions feature a shoulder at the red wavelengths. An evaluation of possible broadening mechanisms (beam energy spread, off-axis electron propagation and off-axis emission) shows that off-axis emission can easily account for the observed assymetry. Thus, the first steps in extracting information about the electron beam characteristics from the wiggler emissions have been possible.

We are currently working in collaboration with researchers at the Accelerator Test Facility at BNL to lase at 538 nm.

DISCUSSION:

The high precision field profile of the MIT Microwiggler will permit the generation of coherent radiation at wavelengths ranging from the visible to ultraviolet. With our typical observations of an rms spread of 0.08% in peak amplitudes and 0.14% in pole integrals, the microwiggler currently provides the world's most uniform periodic field for any sub-cm period wiggler. Such negligable field errors will permit extraction of information about characteristics of the electron beam from the wiggler emissions.

Acknowledgments:

The authors would like to thank Dr. Ilan Ben-Zvi (BNL) for his support and Dr. Steve Smith (MIT) for useful and enjoyable discussions.

REFERENCES

[1] I. Kimel and R. Elias, "Micro-undulator fields," *Nucl. Instr. Meth.*, **A296**, 611, (1990). G. Ramian, L. Elias, and I., Kimel, "Micro-undulator FELs," *Nucl. Instr. Meth.*, **A205**, 125, (1986).

[2] J. H. Booske, W. W. Destler, Z. Segalov, D. J. Radack, E. T. Rosenbury, J. Rodgers, T. M. Antonsen, Jr., V. L. Granatstein, and I. D. Mayergoyz, *J. Appl. Phys.*, **64**, no. 1, 6, (1988).

[3] R. W. Warren, D. W. Feldman, D. Preston, "High-field pulsed microwigglers," *Nucl. Instr. Meth.*, **A296**, 558, (1990).

[4] N. Ohigashi, K. Mima, Y. Tsunawaki, S. Ishii, N. Ikeda, K. Imasaki, M. Fujita, S.Kuruma, A. Murai, C. Yamanaka, and S. Nakai, "Development of an electromagnetic helical microwiggler," *Nucl. Inst. Meth.*, **A341**, 426, (1994).

[5] J. Vetrovec, "Design of a high-field taperable helical wiggler," *Nucl. Instr. Meth.*, **A296**, 563, (1990).

[6] Y. C. Huang, H. C. Wang, R. H. Pantell, J. Feinstein, and J. Harris, "Performance characterization of a far-infrared, staggered wiggler," *Nucl. Instr. Meth.*, **A341**, 431, (1994).

[7] I. Ben-Zvi, R. Fernow, J. Gallardo, G. Ingold, W. Sampson, and M. Woodle, "Performance of a superconducting, high field subcentimeter undulator," *Nucl. Instr. Meth.*, **A318**, 781, (1992).

[8] M. Tecimer and L. R. Elias, "Hybrid microundulator designs for the Creol Compact CW FEL," *Nucl. Inst. Meth.*, **A341**, ABS125, (1994).

[9] R. Stoner and G. Bekefi, "A 70-Period High-Precision Microwiggler for Free Electron Lasers," *IEEE J. of Quantum Electron.*, **31**, 6, (1995).

[10] *Ibid.*

[11] *Ibid.*

DORIS III AS A DEDICATED SOURCE FOR SYNCHROTRON RADIATION

H. Nesemann, W. Brefeld, F. Brinker, W. Decking, O. Kaul, B. Sarau, DESY Hamburg

Abstract

In May 93 the operation of DORIS for high energy physics was discontinued and the ring became a dedicated source for synchrotron radiation operated at 4.5 GeV. Meanwhile a multibunch feedback system to control beam instabilities had been installed and positrons were stored instead of electrons. The resulting improvements and also the present status are described by discussing some important parameters and their limitations. These parameters include the beam lifetime, the maximum stored currents, the number of bunches, the beam dimensions and aperture, orbit distortions, position control of the photon beams, the reliability and the influence of the 10 insertion devices on the stored beam.

INTRODUCTION

DORIS has been in operation for high energy physics and synchrotron radiation (SR) since 1974. During this period it was rebuilt several times, the last time in 1991. The new ring is called DORIS III and has been described elsewhere.[1] In 1993 it became a dedicated source for SR which now operates with 10 insertion devices (ID). As there have only been minor changes in the magnetstructure in the arcs since 1974, the horizontal emittance is rather large (ϵ_x = .4 $\pi\mu$m at 4.5 GeV) . Thus DORIS cannot be a high brilliance ring, but the photon flux is large. The performance of the ring will be described by discussing some important parameters.

I. BEAM LIFETIME

In Fig. 1 the current of 5 almost equally spaced e^- -bunches is plotted vs time. The lifetime is in general shorter than it would be expected from the vacuum pressure and is also subject to sudden changes. It cannot be increased by varying any machine parameter and the average lifetime of a fill becomes shorter when more current is injected. This limits the maximum current to about 80 mA. The behaviour of the lifetime may be explained by positively charged particles that are captured by the e^- - beam.

According to this hypothesis the polarity of DORIS and of the preaccelerators has been reversed and positrons are now stored instead of electrons. The result is shown in Fig. 2. The lifetime now is in agreement with the vacuum pressure and after some cleaning by beam varies between 15 h and 24 h for currents between 110 mA and 70 mA in 5 bunches.

The lifetime critically depends on the tune for synchrotron and betatron oscillations, especially if the IDs are closed. The maximum field of a 4 m long wiggler is 1.8 T. If the tune variation from the optimum values is larger than .01 for betatron- and .002 for synchrotron oscillations the lifetime is reduced to about 1 h. This is uncomfortable but can be handled. It is not surprising that the area in the tune diagram free from resonances is so small, as the superperiodicity of DORIS III is only 1 and as the IDs generate additional resonances. [2] Moreover satellite resonances

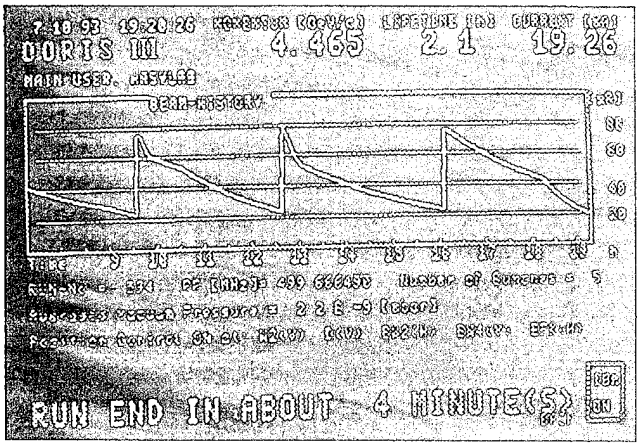


Figure 1. Electron current versus time

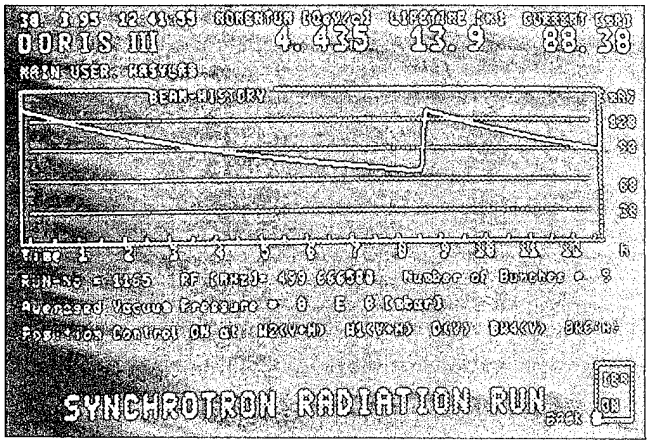


Figure 2. Positron current versus time

are also excited by the horizontal dispersion of about 1.5 m at the cavities and the vertical dispersion of about .15 m at the sextupoles. [3]

II. MAXIMUM CURRENTS AND NUMBER OF BUNCHES

The threshold current for beam instabilities in DORIS III is nearly independent from the number of bunches about 40 mA without feedback system. Therefore a multi-bunch feedback system (MBFB) [4] has been installed that stabilises all focussing oscillations. The distance between successive bunches must be larger than 96 nsec. So a maximum of 10 bunches can be filled out of the possible 482. In table 1 the number of bunches n is given that may be used together with the target and achieved current.

0-7803-3053-6/96/$5.00 ©1996 IEEE

Table 1: Number of bunches and current

n	target [mA]	achieved [mA]
1	35-40	40
2	70-80	80
5	150	160
10	200	-

The target current is limited either according to the MBFB or to higher order mode losses or to the heat load by SR. At 200 mA and 4.5 GeV the vacuum chamber will be loaded by 600 kw, corresponding to a power density of 8 kw/m in the arcs.

At about 150 mA there is at present a current limit due to beam loading. Therefore 10 bunches have not yet been tried seriously. For users 5 bunches are normally filled. That allows high current and time resolved measurements as well.

III. PARASITIC BUNCHES

For time resolved measurements it is important that only the designated RF-buckets are filled. If other buckets contain particles they are called parasitic bunches and may disturb the measurements considerably, at least if their intensity is larger than 10^{-4} of the main bunch.

In DORIS III parasitic bunches have been observed up to 70 nsec, or 35 buckets, behind the main bunch. Their relative intensity varied between 10^{-2} and 10^{-5}. Basically they are generated by an energy mismatch between PIA and DESY II:

Positrons from LINAC II are accumulated in the 450 MeV-storage ring PIA and than injected as single bunches into the 7 GeV synchrotron DESY II. [5] In DESY II they are accelerated to the working energy of DORIS III. [6]

450 MeV is a rather low energy for DESY II. Therefore the dipole current and correspondingly the energy may vary by nearly 1 % from injection to injection. As a consequence there are cycles in DESY II for which the energy deviation of the positrons is so large that they are outside the separatrix, but inside the energy acceptance. Due to their small relative energy loss per turn of 3×10^{-7} [6] these positrons may drift over several buckets until they are finally captured, either by emitting a photon or by the increasing magnetic field of DESY II.

By avoiding the injection of those cycles into DORIS and by setting optimum injection conditions for the other cycles in DESY II, the intensity of parasitic bunches can be made smaller than 10^{-6} of the main bunch. This is shown in fig. 3 [7] which displays the intensity of bunches (arbitrary units) vs time in DORIS. The main bunch is located at t=0. Other bunches are possible every 2 nsec. The intensity extends to about 5 nsec because of the detector's limited time resolution.

IV. ACCEPTANCE AND BEAM DIMENSION

In table 2 the geometrical, horizontal and vertical acceptances of DORIS III are given together with the measured values.

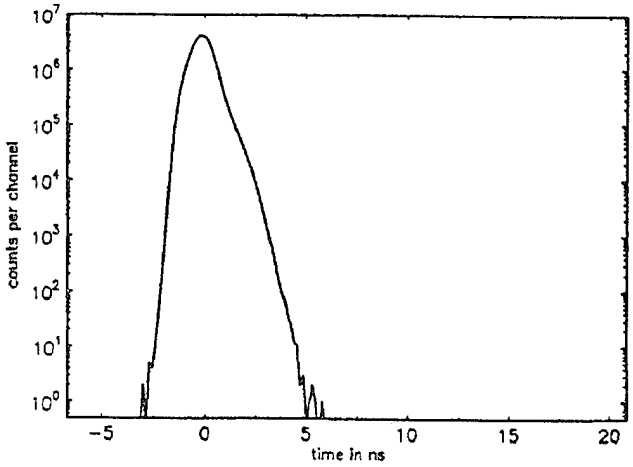


Figure 3. Parasitic bunches

Table 2: Acceptance of DORIS III

	hor [$\pi\mu$ m]	vert [$\pi\mu$ m]
geometrical	80	5
measured without IDs	57	2.4
measured with IDs	43	2.8

The geometrical vertical acceptance is diminished by a factor of 4, compared to the rest of the ring, by the vacuum chamber of the IDs. The free height of the flattest one is 11mm, extending for a length of 4 m. The measured horizontal acceptance is reduced slightly by the IDs whereas there is no influence on the vertical one, which is already small.

Table 3: Beam dimension over aperture

	hor	vert
without IDs	65 %	40 %
with IDs	73 %	63 %

In order to demonstrate that the stored beam needs a great part of the aperture, the ratio of the beam dimension (including the tails required for a lifetime of 1 h) to the measured aperture is given in table 3 instead of the beam dimension itself. With IDs this ratio is increased in the horizontal because the acceptance is reduced, and in the vertical because the beam is enlarged.

V. POSITION STABILITY OF THE PHOTON BEAMS

It has been observed that the position of the photon beams changes typically by $\pm$ 1000 μ horizontally and $\pm$ 150 μ vertically without outside influences in a distance of about 15 m from the source point. This leads to unwanted variations of the photon intensity at the experiments. The reason for the movement is as follows:

The vacuum chamber is heated by SR at the outside and is deformed by the corresponding gradient in temperature. As there are undesirable mechanical contacts with the magnets, especially the quadrupoles are moved by a distance of up to .4 mm. This changes the magnetic fields and causes orbit distortions. For the difference orbit rms-values up to 1 mm have been observed. This may be compared with the rms-value of a well corrected orbit,

namely .8 mm for the vertical and 1.5 mm for the horizontal plane. Orbit distortions finally cause the movement of the photon beam.

To counteract this problem a position control system for the most important beamlines has been installed for frequencies lower than .1 Hz. Out of a total of 22 beamlines, 3 are stabilized horizontally to $\pm$ 50 μ and 4 vertically to $\pm$ 10 μ. In addition the decoupling of some quadrupoles from the vacuum chamber has been improved. By this and similar measures the movement of the photon beams has been reduced to typically $\pm$ 2 % of the beam dimensions (1 STD) for the controlled beamlines and $\pm$ 20 % for the uncontrolled ones.

VI. RELIABILITY

The operational statistics for 1994 are given in table 4:

Table 4: Operational statistics for 1994

Scheduled time for users	4200 h $\hat{=}$ 100 %
usable time	3608 h $\hat{=}$ 85.9 %
time for injection	184 h $\hat{=}$ 4.4 %
time for readjustment	71 h $\hat{=}$ 1.7 %
breakdown time	337 h $\hat{=}$ 8.0 %

During more than 85 % of the scheduled time beam could be delivered to the users. The breakdown time of only 8 % includes the breakdowns of the preaccelerators and also the time without beam that was requested by the users.

References

[1] H. Nesemann et al., First Experience with DORIS III. Proc. 15th Int. Conf. on High Energy Acc., Hamburg, 549 (1992)

[2] W. Decking, Influence of Insertion Devices on the Beam Dynamics of DORIS III. 4th EPAC, London, 1003 (1994)

[3] A. Piwinski, Synchrotron Sidebands of Betatron Coupling Resonances, DESY 93-189, (1993)
A. Piwinski, A. Wrulich, DESY 76/07 (1976)

[4] M. Ebert et al., Compensation of the Multi Bunch Instabilities with Feedback Systems. 15th HEAC Hamburg, 421 (1992)
M. Ebert et al., Transverse and Longitudinal Multi Bunch feedback Systems for PETRA. DESY 91-036 (1991)

[5] A. Febel, M. Nagl, LINAC II and PIA as a Source of Short Electron Bunches with High Intensity. 15th HEAC Hamburg, 430 (1992)

[6] W. Ebeling et al., Acceleration of High Intensity Electron Bunches in DESY II, 15th HEAC 427 (1992)

[7] Data taken by the Mössbauer group at HASYLAB. Private communication.

BEAM LIFETIME AND BEAM BRIGHTNESS IN ALS*

C. Kim, A. Jackson, and A. Warwick, Lawrence Berkeley Laboratory, Berkeley, CA 94720

Beam lifetime in ALS is dominated by the Touschek scattering. Measurements of lifetime in single-bunch mode with estimates of bunch dimensions obtained from undulator radiation data are consistent with expectations (t=1.8 hours at 1.25 mA per bunch). However, the lifetime is significantly longer in multi-bunch mode (t=11 hours at 400 mA per 320 bunches). This discrepancy has been traced to an increase in the momentum spread and bunch length in the beam caused by longitudinal coupled-bunch motions driven by higher-order modes in the rf cavities. The increased momentum spread leads to a significant degradation in the undulator spectral performance. Feedback stabilization of the coupled-bunch motion improves the spectral characteristics of the undulator beam at the expense of beam lifetime. We observe an increase of ~200% in beam lifetime by operating at the betatron coupling resonance.

I. INTRODUCTION

Photon beams with unprecedented spectral brightness from undulators and wigglers are the trademark of the third generation synchrotron radiation sources, such as the Lawrence Berkeley Laboratory's Advanced Light Source (ALS) [1]. Short bunch length, low emittance electron beams are essential for the undulators and wigglers to generate spectral brightness higher than 10^{19} photons /s-mm^2-mrad^2-0.1% bandwidth.

In order to realize the short bunch length low emittance beam, the lattice was designed to have a very strong focusing and a small momentum compaction factor. Longitudinal [2] and transverse [3] rf feedback stabilization was designed to prevent electron bunches from loosing their brightness as a result of various instabilities.

In these storage rings, the beam lifetime is dominated by the large angle intra-beam scattering called Touschek scattering[4]. In this process, transverse momentum is transferred to the longitudinal momentum whereby the particles are lost from the longitudinal momentum acceptance. Measurement of beam lifetime is an indirect way of measuring the brightness of the beam because the lifetime becomes shorter as the electron beam density increases.

The ALS storage ring has been serving the user community without the rf feedback stabilization for some time. Without this stabilization, the longitudinal coupled bunch instabilities grow first and saturate at some larger values of energy spread and longer bunch length. The resulting larger energy spread actually stabilized the transverse instabilities.

*This work was supported by the director, office of the Energy Research, Office of the Basic Energy Science, Materials Science Division, of the U.S. Department of Energy under contract no. DE-AC03-76SF00098.

The ALS lattice and beam parameters are summarized in Table I. We have been operating at the nominal energy of 1.5 GeV with the beam current up to 400 mA and at the ramped energy of 1.9 GeV with the beam current up to 260 mA.

These parameters were experimentally confirmed: the momentum compaction factor was calculated from the measured synchrotron frequency as a function of the cavity voltage; beam emittance and the energy spread were measured at the diagnostics beamline [5].

Table I.. ALS Electron Storage Ring Parameters

Circumference [m]		196.8
Nominal Energy (GeV)		1.5
Revolution Freq. [MHz]		1.52
Harmonic Number		328
Betatron Tune	Horizontal Vertical	14.28 8.19
Synchrotron Freq. (kHz)	1.5 GeV	11.5
Momentum Compaction		0.0016
Natural Chromaticity	Horizontal Vertical	-24.6 -27.3
Natural Emittance (m-rad)	1.5 GeV	3.4×10^{-9}
	1.9 GeV	5.5×10^{-9}
Natural Energy Spread (σ_E/E)	1.5 GeV 1.9 GeV	6.5×10^{-4} 8.3×10^{-4}
Natural Bunch Length (σ_l mm)	1.5 GeV 1.9 GeV	3.7 4.7
Radiation Loss (keV/turn)	1.5 GeV	91.5
Radiation Damping at 1.5 GeV [msec]	Horizontal Vertical Energy	15.3 21.5 13.5

II. LIFETIME MEASUREMENTS

Lifetime in the ALS electron storage ring was measured by measuring the stored current, I(t), using a DC current transformer and using the definition, $\tau(t) = I(t)/(dI(t)/dt)$. Measured lifetime depended on beam energy, bunch current and the number of bunches stored. Measured beam lifetimes at 1.5 GeV are plotted in Figure 1 against stored electron current per bunch for single, 240, and 320 bunches. The rf multi-bunch feedback system was turned off at the time of measurements.

Calculated Touschek lifetimes using the ZAP code [6] are shown in solid lines for different bunch lengths in Figure 1.

For the single bunch mode, the measured lifetime at low current asymptotically approaches the calculated Touschek lifetime for the natural bunch length of 3.7 mm. However, at higher current, the measured lifetime is considerably longer than the expected Touschek lifetime for

the same bunch length indicating bunch lengthening increased energy spread.

Also, longer beam lifetimes were observed for a given beam current per bunch when the number of bunches stored in the storage ring is increased as shown in Figure 1.

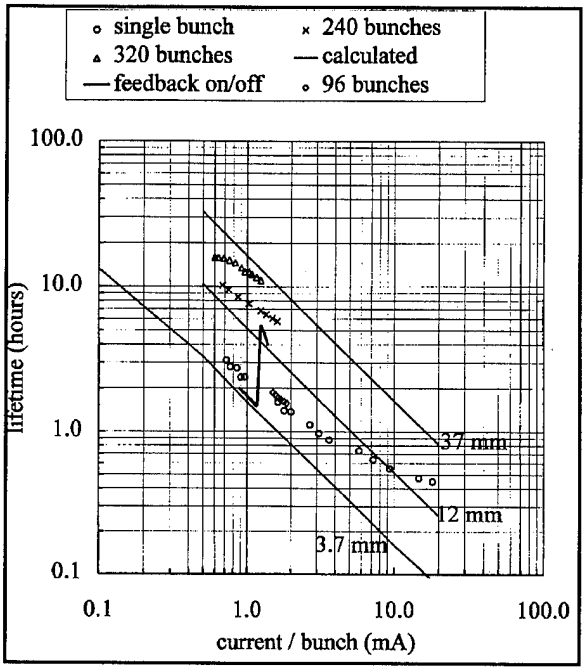


Figure 1: Measured beam lifetimes at 1.5 GeV are plotted against stored electron current per bunch in the ALS Storage ring. Theoretically expected Touschek scattering times at the given bunch lengths are shown in solid lines.

Lifetimes were also measured for 1.9 GeV beam for single and 320 bunch fills. They are plotted in Figure 2 against current per bunch. The rf multibunch feedback system was turned off at the time of measurement.

Calculated Touschek lifetimes are shown in solid lines for three different bunch lengths in Figure 2. The measured lifetime at 1.9 GeV agrees very well with the calculated Touschek time. Significantly less bunch lengthening and energy spread are apparent.

III. SPECTRAL INTENSITY MEASUREMENTS

The effects of the longitudinal beam feedback stabilization on beam lifetime and on the spectral intensity of the ALS undulator Beamline 7.0 were studied. At the time of this study, a prototype of the longitudinal feedback system was able to control up to 84 bunches. The transverse feedback system was not ready. The lifetime is already close to the theoretical minimum with 84 bunches pattern as shown in Figure 1. That would mean that there is no room for further decrease in beam lifetime with the feedback.

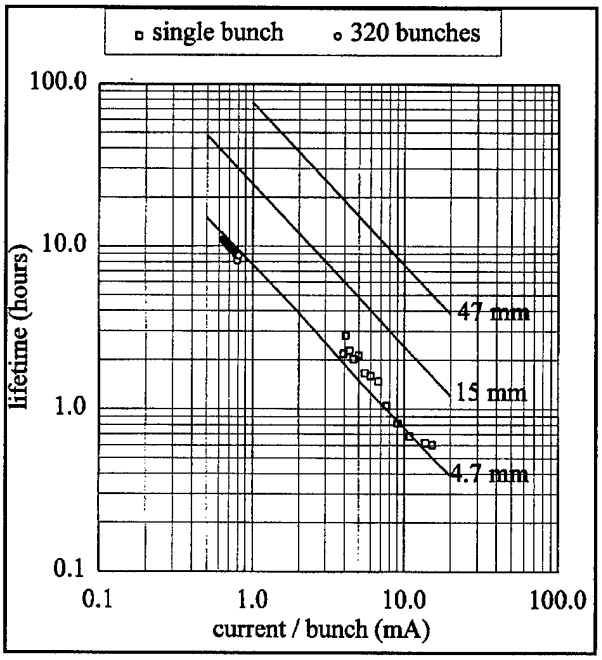


Figure 2: Measured beam lifetimes at 1.9 GeV are plotted against stored electron current per bunch in the ALS Storage ring. Theoretically expected Touschek scattering times at the given bunch lengths are shown in solid lines.

The feedback system was turned on and the storage ring and was filled with 84 bunches up to 2 mA per bunch. When the beam decayed to about 96 mA, the feedback system was turned off. The spectral intensity of the fifth harmonic of the undulator beam at Beamline 7.0 was measured before and after the feedback was turned off. The results are shown in Figure 3. The line with of about 0.7 % with the feedback on is somewhat larger then single bunch spectrum of 0.5 % at a similar current per bunch. The line showed a double peak when the feedback was turned off. The beam lifetime changed from 5.5 hours to 1.5 hours when the feedback was turned off. Both the broader line width and longer lifetime with the feedback came to us as a suprise at first. It is most likely that when the longitudinal feedback system was turned on the transverse feedback system was turned off. Some transverse instabilities apparently were excited which increased the vertical beam size and the lifetime.

This situation, however, has since been shown to be atypical. Usually, the beam lifetime decreases (as expected) when the longitudinal feedback is turned on.

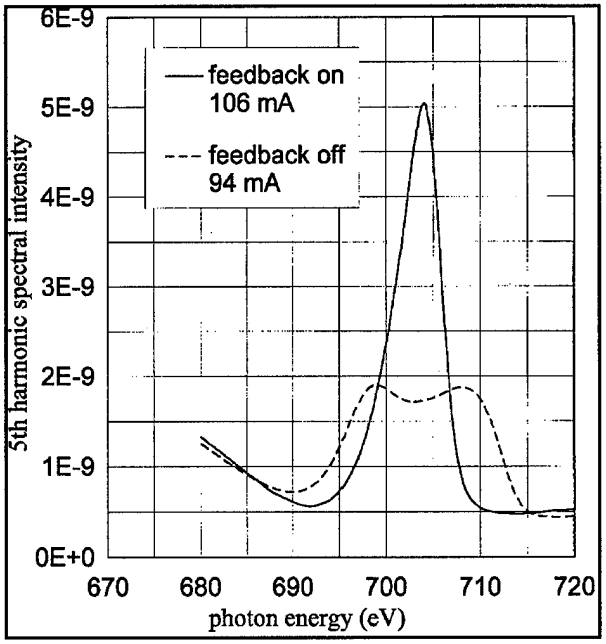


Figure 3: Measured spectral intensity of the fifth harmonic of the photon beam at ALS BL 7.0, with and without feedback.

IV. BUNCH LENGTH MEASUREMENTS

Electron bunch length in the ALS Storage Ring was measured by three methods: measuring the longitudinal structure of the bunch using a streak camera [7], measuring the photon beam pulse duration using a fast photo diode and a sampling scope [5], and measuring the pulse duration using a button-shaped beam position monitor (BPM). The results are consistent. The BPM data is presented here.

A 10 mm button-shaped beam position monitor (IDBPM Sector 4) and the Tektronix CSA803 sampling scope with a 20 GHz bandwidth sampling head were used [8]. The effects of the finite button size and the cable length are subtracted from the measured data by quadratically subtracting a calibrated number. The results are plotted in Figure 4 against the bunch current.

Best fit for the data is of the form $3.7 + 1.04 * I^{0.56}$. Best fit for the data for I > 10 mA is proportional to $I^{0.36}$. These lines are also plotted in Figure 4. Pure microwave turbulent blow-up is expected to give a $I^{(1/3)}$ dependence for currents above certain threshold [9]. Other effects, such as the potential well distortion and a special frequency dependence of the longitudinal impedance, alter the functional dependence.

VII. CONCLUSIONS

We conclude that the beam lifetime in ALS is dominated by the Touschek scattering. We observed significantly shorter lifetimes and brighter spectral intensities as expected for high beam current operations with both the longitudinal and the transverse feedback systems turned on. It is expected that ALS will deliver its full design beam brightness when both the longitudinal and transverse feedback systems become available. Cavity conditions such as the tuner position and the temperature changes the frequencies of the higher order modes and the growth rates of the transverse and longitudinal instabilities and the bunch lengthening characteristics.

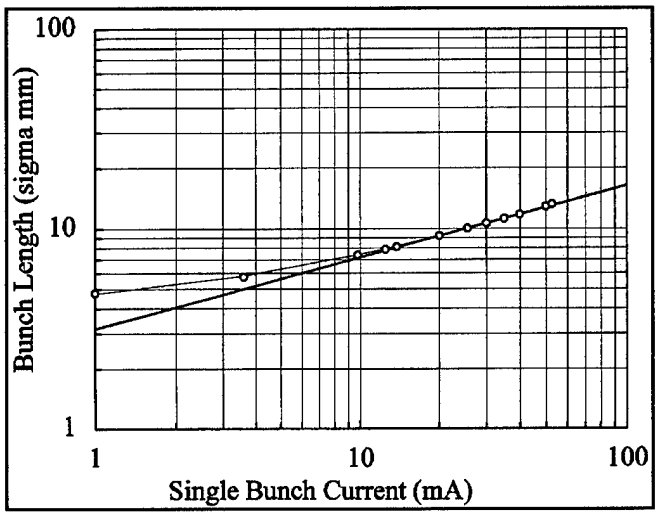


Figure 4: Measured bunch lengths are plotted against the stored electron beam current in the single bunch mode of operation at 1.5 GeV.

VIII. ACKNOWLEDGMENTS

We wish to thank many people who operated various equipment during our measurements. Special thanks are due to J. Hinkson regarding the bunch length measurements using the IDBPM.

IX. REFERENCES

[1] See, for instance, A. Jackson, Proceedings of the IEEE Particle Accelerator Conference, May 6-9, 1991.
[2] J. Fox, et. al., in these proceedings.
[3] W. Berry, J. Byrd, J. Corlett, J. Johnson, G. Lambertson, and J.Fox, in these proceedings.
[4] See, for example, J. LeDuff, *Nucl. Instrum.* Methods A239, 83(1985).
[5] J. M. Byrd and J. N. Corlett, in these proceedings.
[6] M. S.. Zisman, S. Chattopadhyay, and J. J. Bisognano, LBL report, LBL-21270, UC-28 (1986).
[7] T. Renner Private communications.
[8] This beam position monitor system has been developed by J. Hinkson for controlling the beam in the insertion device.
[9] G. Vignola, B. Craft, and S. Chattopadhyay, LBL ESG Tech Note-23, December 1985.

Asynchronized Energy Ramping at SRRC Storage Ring

Gwo-Huei Luo, L.H. Chang, Y. Cheng, K.T. Hsu,
C.C. Kuo, W.C. Lau, Ch. Wang, P.K. Tseng, and Y.C. Liu,
Synchrotron Radiation Research Center
No. 1 R&D Rd VI, Hsinchu Science-Based Industrial Park, Hsinchu, Taiwan, R.O.C.

Abstract

The 1.3 GeV storage ring at SRRC will provide ultra-violet to soft x-ray radiation source to the potential users. The energy ramping of storage ring will push the critical photon energy to the edge of hard x-ray. There are several ways to ramp the electron energy, for example, increasing the extraction energy to 1.5 GeV from booster directly, ramping the magnets' power supplies with synchronized function generators, or asynchronized ramping of magnets at storage ring, etc. The tune drifting during the ramping procedure is expected and should be minimized such that the beam can survive through the ramping process. The betatron frequencies and ramping function of magnets were carefully monitored in order to avoid the betatron tunes cross the resonance line. A successful asynchronized ramping results will be presented in this paper.

I. INTRODUCTION

The storage ring at SRRC is providing an ultra-violet to soft x-ray radiation source to the synchrotron light users. The energy ramping of storage ring will push the critical photon energy to the edge of hard x-ray. A short wavelength will assure the capability of seeing and writing smaller feature. The brightness of the radiated photons will also be improved significantly, due to the increased beam energy, at the edge of the x-ray regime. The likely beneficial research areas include the general x-ray users, micromachining, microscopy, lithography and LIGA application, etc.

With a successful ramping program will also provide a powerful tool for the machine physicist to study the machine performance under different electron beam energy. There are key-signals, the betatron frequencies, which could indicate the characteristic of the ramping process. The betatron frequency is the major indicator for the following up situation for the quadrupoles and the dipoles. If the following up is not good enough, the wiggling of the betatron frequency will be very severe. If the betatron frequency hits the resonance line or stop-band, beam lost will occur.

Two sets of stripline type beam-position-monitor (BPM), which can pickup broad-band signal induced by the electron beam, have been installed at storage ring. The electrons pass through a pair of stripline type BPM will induce a voltage difference, if the beam is off the center of the beam position monitor. The successive analysis of the beam position at fixed BPM can give the information of the fraction of the betatron frequency and the bunch distribution of the electron beam.

The coordinate system was setup as shown in Fig. 1. Considering a single particle case, the description of motion of electron at the storage ring can be written as following [1],

$$\frac{d^2x}{ds^2} + K(s) = f(s)$$

where x(s) is the displacement in horizontal or vertical from the designed orbit. f(s) is the high-order perturbation terms. K(s) is the strength of quadrupoles and satisfies the periodicity relation

$$K(s + C) = K(s)$$

Here C is the circumference of the equilibrium orbit. A similar representation can be found for another transverse direction y.

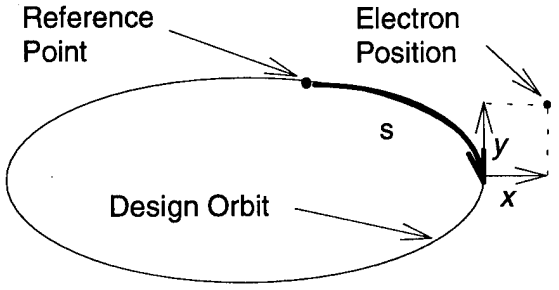


Figure 1. The coordinate system of the storage ring.

For a fixed position observation of the electron beam movement, the description can be rewritten as

$$x_j = a\sqrt{\beta_0}\cos(2\pi j\nu + \phi_0)$$

The $a\sqrt{\beta_0}$ is a constant and the successive passage number is represented by the index j. The initial phase is defined by ϕ_0 and ν is defined as betatron number. Hence the pickup signal by the BPM is a simple sinusoidal oscillation. The Fast Fourier Transform of the observed signal gave us the information of the characteristic of the beam behavior at the storage ring.

To observe the betatron tune we need to excited a coherent oscillation of the entire bunch. The transverse excitation force stimulates the oscillation will be damped by synchrotron radiation. The excitation electrode was fed by the spectrum analyzer which is set to measure the 200th harmonic of the revolution frequency. The setup of the tune measurement system was shown in Fig. 2.

0-7803-3053-6/96/$5.00 ©1996 IEEE

We will utilize the available equipment and software programming tools to achieve energy ramping effect and keep the machine operated within safety margin. We will try to keep the working tune unchanged. The tune drifting during the ramping procedure should be minimized such that the beam can survive through the ramping process. A carefully monitored betatron frequency and ramping function of magnets setting could avoid the betatron tunes cross the resonance line that will induce beam loss during the acceleration.

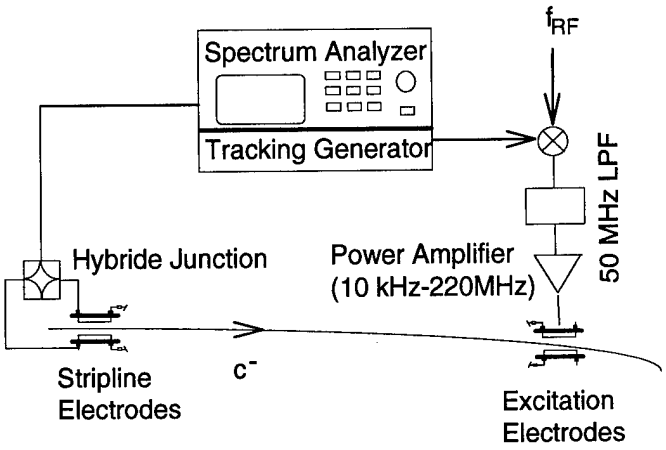


Figure 2. The betatron tune measurement system with transverse excitation.

The non-linearity of the magnet response forces us to use several linear segments to approach the non-linear curve. The non-linear effects are different in each type of magnet, so that the bending magnets, quadrupole magnets must each follow a different current ramp to control the accelerator tunes as function of energy. The concept of multi-knob ramping will be adapted at the first-phase experiment. This asynchronized ramping process is a very slow ramping process, which will take 10 ~ 20 minutes to complete the energy ramping.

II. THE EVALUATION OF BASIC PARAMETERS

Some of the basic parameters that related to the beam energy were listed as following [2,3,4,5]

$$P(kW) = 2.654B(kG)E^3(GeV)I(A)$$

(radiation power loss per turn)

$$\varepsilon_c(KeV) = 0.06651B(kG)E^2(GeV)$$

(critical photon energy)

$$N_{0.1}(\lambda_c) = 1.601\times10^{12}E(GeV)$$

$$photons/sec/mA/mrad/10\%\ BW$$

(photon flux at critical wavelength)

$$\varepsilon_{\min}(m-rad) = 7.37\times10^{-8}E^2(GeV)\varphi^3(rad)$$

(min. emittance for TBA lattice)

where B is the strength of bending magnet, E is the electron beam energy, I is the stored beam current and φ is the bending angle of dipole magnet. The betatron tune was decided by the particle simulation program MAD [6] based on the current setting of lattice.

Some of the major nominal parameters for the storage ring operated at nominal energy were calculated based on above formulations and listed in Table I [7]. The change of these parameters for the 1.5 GeV operating energy was shown in Table II.

Table I. The nominal parameters for the storage ring

Nominal energy	1.3 GeV
Natural beam emittance [3]	1.92 x 10-8 rad m
Radiation loss per turn (dipole)	72.28 keV
Critical photon energy	1.39 keV
photon flux (at critical energy)	$2.08\text{x}10^{12}$ (photons/s/ mrad, 10% BW, mA)
betatron tune	7.18/4.13
bunch length (RF@800KeV)	7.4 mm

Table II. The machine parameters for the 1.5 GeV operation

Nominal energy	1.5 GeV
Natural beam emittance	2.56×10^{-8} rad m
Radiation loss per turn (dipole)	128.1 keV
Critical photon energy	2.14 keV
photon flux (at critical energy)	2.40 x 1012 (photons/s/ mrad, 10% BW, mA)
betatron tune	7.18/4.13
bunch length (RF@800KeV)	9.2 mm

III. THE PREPARATION AND SETUP OF EXPERIMENT

The preparation works for the ramping experiments include the program coding, temperature measurement of dipoles and quadrupoles, and sextupoles. The temperature measurements of dipoles and quadrupole were performed before the experiment of ramping process. The current of dipole and quadrupole magnets were driven to the maximum capacity of the power supplies. From experiments, we could find that the hottest point of the dipole magnet will not exceed 60°C and the hottest point of the quadrupoles will not exceed 40°C. The critical temperature of the magnets interlock system was set at 70°C. If any of the thermal sensors at magnets sensing the temperature exceeds the 70°C limit, the interlock system will interrupt the power supplies to protect the magnet from over heating. The temperature of the vacuum chamber will also protect by the interlock system. Several radiation survey meters also placed around the storage ring to monitor the radiation dosage constantly.

IV. RESULTS

The betatron frequencies were analyzed at spectrum analyzer from which we can find the working tune was set at (7.21, 4.08). We will change the working tune to a difference resonance point, the working tune is (7.11, 4.11), by increasing the first family of quadrupoles. The tune variation during the ramping process was observed around 72 kHz during the slow ramping process. Part of the reason of the tune variation was due to the asynchronized ramping process. A modified control program which will integrate the synchronization feature into the ramping process will cure part of the tune variation problem. The slow ramping is due to the waiting time for the setting process and waiting the power supplies to reach the setting current. A synchronized ramping program is under development. This will shorten the overall ramping time and minimize the tune variation.

The input data file was calculated based on the magnet fitting curve, the detail information could be find in reference [8], and try to keep the difference resonance point as our working tune. The ramping curve for the dipoles was shown in Fig. 3, which were taken from archived file. From the beam current curve, we find there is no significant beam lost during the ramping procedure except the beam lost due to the scattering effects.

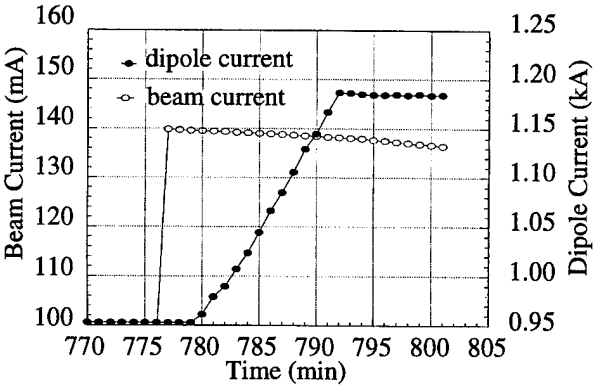


Figure 3. The beam current and the setting current of dipole magnets during the ramping procedure.

The correctors of the storage ring did not ramp with the dipole current setting, hence the closed-orbit-distortion increased at beam energy of 1.5 GeV. The beam dynamic application program was applied to correct the closed-orbit-distortion. The rms value in x-direction is less than .3 mm and in y-direction is less than .2 mm.

The averaged radiation dosage of the 1.5 GeV stored beam was measured around the experimental hall. Comparing with the case in 1.3 GeV, there is no significant increment of the averaged counting rate. The wall shielding is thick enough for the 1.5 GeV operation at the beam current less than 150 mA.

The reasons of the increasing of the gauge reading were 1) due to the change of closed-orbit and induce higher outgassing and 2) part of contribution coming from the increasing of the beam energy. Each of the two RF transmitters could deliver 60 kW power to the cavity. From the power loss estimation, these two transmitters could drive the 1.5 GeV electron beam at beam current as high as 300 mA, if beam instability and beam loading problem is not in our consideration.

V. CONCLUSION

The ramping process from 1.3 GeV to 1.5 GeV has been successfully tested at storage ring using asynchronized ramping method. The testing beam current is set at 140 mA. During the ramping process, there is no significant beam lost except the scattering lost. Some of the critical components have been checked and tested at the high energy operation. The beam line performance will be tested in the near future to verify the resolution and photon flux changing.

The operation of storage ring at 1.5 GeV is possible at SRRC. However, some of the components should be taken more careful examination. A further shorten of the ramping time to seconds is a goal for this ramping program. The necessary tool for this goal is to modify the control program of the power supplies and make the synchronized ramping possible. The slew rate should be able to set to have decimal point of percentage. The synchronized trigger signal should be ready at the time we try.

VI. ACKNOWLEDGMENT

The authors would like to thank all the members in Technical Division that working hard and harmonically to make this experiment possible. The special thanks will go to the magnet and vacuum group with the carefully monitoring the temperature variation of magnets and vacuum chamber.

VII. REFERENCE

[1] E.D. Courant, H.S. Snyder, "Theory of the Alternating-Gradient Synchrotron," Ann. of Phys. 3 (1958) 1-48.
[2] H. Winick and S. Doniach, "Synchrotron Radiation Research," Plenum Press, New York, 1980, p11-25 .
[3] H.Kung, C. Travier and C.C. Kuo, "Emittance Calculation for a TBA Storage Ring," SRRC Internal Memo, SRRC/BD/1987-04.
[4] S. Tazzari, "Electron Storage Rings for the production of Synchrotron," CAS, Vol. II, CERN 85-19, 1985.
[5] H. Wiedemann , "Particle Accelerator Physics," Springer-Verlag, New York, 1993.
[6] H. Grote, F.C. Iselin, "Methodical Accelerator Design," CERN report, CERN/SL/90-13 (AP)
[7] "SRRC Design Handbook", SRRC, 1991.
[8] C.S. Hwang, etc., "The main features and field transfer function of the storage ring magnet," SRRC Internal Memo, SRRC/MM/IM/92-02.

*EMITTANCE MEASUREMENTS IN THE ALS BOOSTER SYNCHROTRON**

D. Massoletti, C.H. Kim, and A. Jackson
Lawrence Berkeley Laboratory, University of California, Berkeley, California 94720

Beam emittance measurements in the Advanced Light Source Booster Synchrotron are presented. Electrons are injected at 50 MeV and extracted at various energies ranging from 150 MeV to 1,520 MeV. The extracted beam is then transported in the Booster-to-Storage-Ring beam transfer line where the emittances are measured. Beam sizes are measured at 7 locations using scintillators and CCD cameras. The measured emittances are then compared with the theory based on intra-beam scattering, betatron coupling, radiation damping, and radiation excitation.

I. INTRODUCTION

The Advanced Light Source (ALS) is a third-generation synchrotron radiation source for UV and soft X-rays at LBL [1]. The Injector consists of a 50 MeV Linac and 1.5 GeV booster synchrotron. Recently several proposals to utilize the Booster synchrotron were made.

One such experiment is the Compton side scattering experiment [2] whereby a femtosecond laser beam collides with the circulating booster beam and generates femtosecond X-rays. The other experiment is to extract the beam at 150 MeV to a specially designed transport line where the feasibility of the optical stochastic cooling will be studied [3].

The following emittance measurements were made on the beam at booster extraction, at various energies, and also at various points in the Booster-to-Storage Ring transfer line (BTS) at a fixed energy. These data were acquired to provide verification of beam characteristics and to obtain data the proposed experiments.

All these proposals use the Booster as a damping ring whereby the beam is ramped to a certain energy where the sychrotron radiation damping is significant, wait at this energy for several damping times to reduce the beam emittance and the energy spread, and ramp down to the desired energy to perform experiments before either the emittance grows too much due to intrabeam scattering or the beam is lost due to Touschek scattering.

II. INSTRUMENTATION

The scintillators used here are 6 % chromate doped alumina (Chromox 6 manufactured by Morgan Matroc Limited in the UK). Linearity of this type of scintillator is not known and expected to be dependent upon the spectral region involved. We did not use any special filters. In the present data analysis, we assumed that the response is linear. CCD cameras are known to have a large linear dynamic range if we do not saturate the pixels. Under the circumstances, the resolution of the measurements is basically the pixel defined image size.

At each BTS scintillator-TV monitor location the image was measured and scaled for pixel to millimeter conversion from the fiducials on each screen The result in each case is on the order of 0.1 mm/pixel. This results in a resolution in emittance for x and y of 1.2E-10 and 2.0E-9 m-rad respectively.

III. EXTRACTED BOOSTER BEAM EMITTANCE AT VARIOUS ENERGIES.

Electrons are injected into the Booster at 50 MeV and then ramped in energy to 1.5 GeV. The beam emittance in the Booster is determined dynamically by the mechanisms comprising synchrotron radiation excitation and damping, intrabeam scattering and adiabatic damping. Intrabeam scattering is negligible during normal operation but might become important for experiments with denser beams, as is proposed for the stochastic cooling experiment.

Initially beam emittances damp adiabatically and above 400 MeV synchrotron radiation damping becomes significant, at energies above 800 MeV quantum excitation causes the emittances to grow. Beam spot size measurements were made on the first scintillator-TV monitor in the BTS at various Booster extraction energies. This monitoring point is immediately after extraction and before any significant transport elements. The emittances were determined from the relationship of beam spot size and the beta functions at TV locations. The measured horizontal emittance, shown in Fig 1, shows a variation consistent with theory.

The larger values at low energy are probably due to mis-matches, energy jitter and kicker fluctuations of the Linac beam into the Booster. Agreement is better at higher energy, where the emittance is dominated by radiation damping rather than initial conditions. The scatter in the data is caused by variations in day-to-day/pulse-to-pulse performance, as well as a sensitivity to beam intensity.

Measured and calculated vertical emittance are shown in Fig 2. In the vertical plane the agreement between measured and predicted values are better at lower energies, suggesting a better match from the Linac into the vertical plane of the Booster (as might be expected from the horizontal injection system).

* This work was supported by the director, office of the Energy Research, Office of the Basic Energy Science, Mterials Science Division, of the U.S. Department of Energy under contract no. DE-AC03-76SF00098.

0-7803-3053-6/96/$5.00 ©1996 IEEE

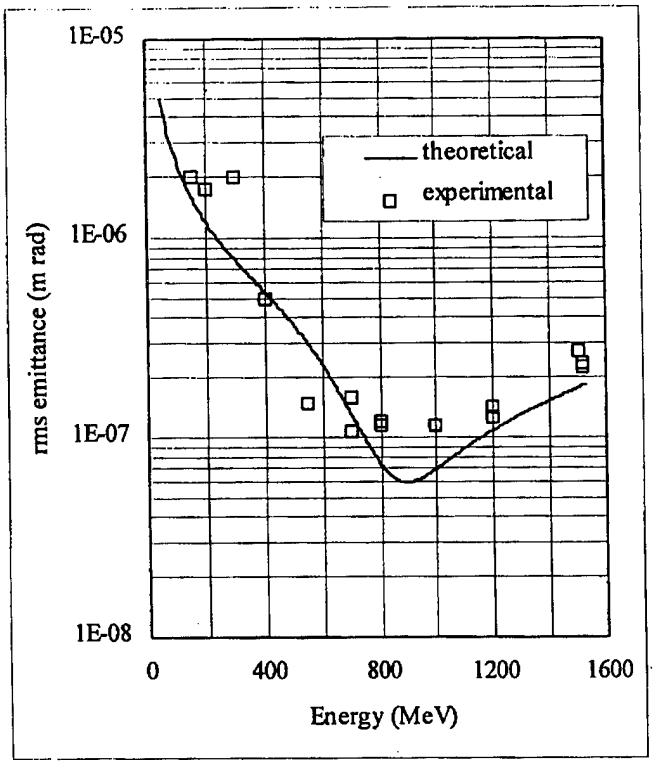


Figure 1. Comparison of measured and calculated transverse emittance as a function of energy.

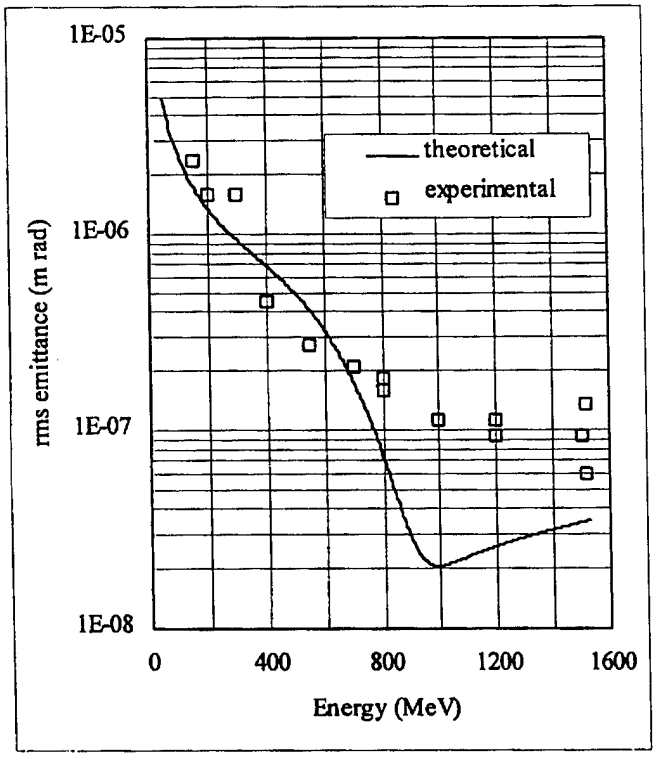


Figure 2. Measured and calculated vertical emittance as a function of energy.

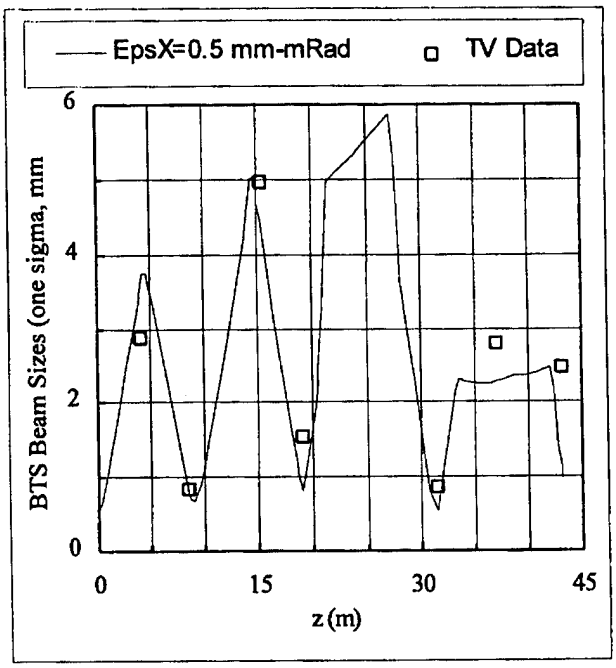


Figure 3. Beam spot size in the horizontal plane at various locations in the transport line.

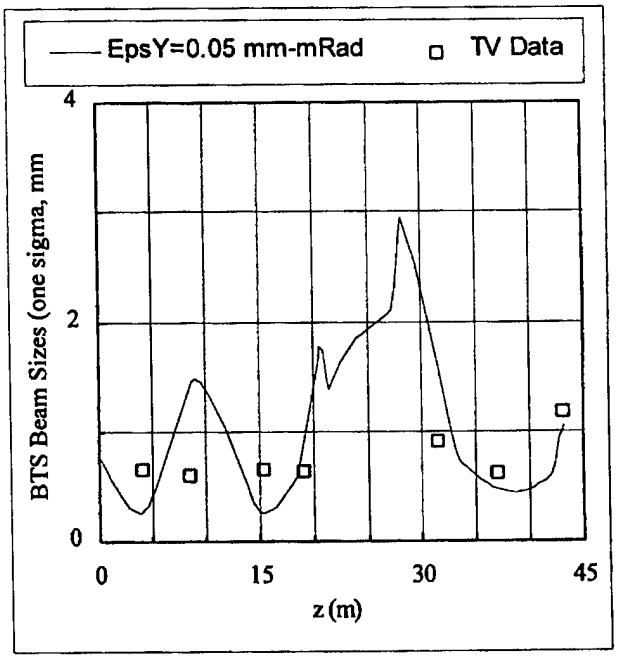


Figure 4. Beam spot size in the vertical plane at various locations in the transport line.

IV. EXTRACTED BOOSTER BEAM SPOT SIZE AT VARIOUS POSITIONS IN THE BTS

Beam spot size measurements were made on the seven scintillator-TV monitors in the BTS and Storage Ring (SR) during typical single bunch operation at the nominal 1.52 GeV level for comparison with theoretical results for optimum transport.

Beam size is fairly consistent with theoretical values in the horizontal plane as shown in Fig 3.

The measured beam spot sizes do not compare as well with theoretical values in the vertical plane, shown in Fig 4.

V. CONCLUSIONS

We have expected that the horizontal-to-vertical emittance coupling is less than 1 % because we used the same techninique that we used for the storage ring to align the booster ring. In the calculation we assumed 10 % coupling to fit the data better.

We notice that the agreement between measurements and the theoretical predictions are good except when the expected spot size is small. This may be due to the fact that the scintillator non-linearity may result in values larger than the actual beam size.

VI. REFERENCES

[1] A. Jackson, "Advanced Light Source - Status Report," Proceedings of the IEEE Particle Accelerator Conference, May 6-9,1991, San Francisco CA, p.2637

[2] C.H. Kim, et al., "Compton Side Scattering at the ALS Booster," in these proceedings.

[3] A. Zholents, et al., "Analysis of Optical Stochastic Cooling," in these proceedings.

COMPTON SCATTERING IN THE ALS BOOSTER*

D. Robin, C. Kim, and A. Sessler, Lawrence Berkeley Laboratory, Berkeley CA 94720 USA

Abstract

Femtosecond x-ray pulses may be generated by 90° Compton side scattering of a short visible laser beam by a well-focused relativistic electron beam.[1] A proof-of-principle experiment is underway using the ALS linac[2]. From this experiment an x-ray pulse of 10^5 photons with a duration of 230 fs in a bandwidth of 10% at 10 Hz is expected. In this paper we explore using the ALS booster instead to increase the average x-ray flux. To generate the small beam size we plan to radiation damp electrons by accelerating them to 600 MeV and decelerate quickly to 50 MeV before intra-beam scattering can increase the beam size. We can achieve a vertical emittance of $< 5 \times 10^{-9}$ m-rad. With a small modification of the booster lattice it is possible to focus the beam to a vertical beta function of $\beta_y^* = 10$ cm. By reflecting the incident laser pulse many times we expect to be able to obtain an increase of the average x-ray flux.

I. INTRODUCTION

At Lawrence Berkeley Laboratory's Advanced Light Source (ALS) there is an experiment in progress to generate short x-ray pulses by colliding short laser pulses with highly focused electron bunches.[2] The electron bunches which are produced in the ALS injection linac are emitted once a second at 50 MeV and with a charge per bunch of >1nC per bunch. Each bunch is then focused to a small transverse size of 50 μm at which time it collides with a laser pulse of ~100 fs duration. In the laboratory frame the laser pulse is traveling in the vertical direction and collides with the electron bunch at a 90° angle. Due to the collision, some of the light is Compton scattered in the direction of the electron beam producing a pulse of x-rays. As a result of the laser pulses short duration and the electron bunches small vertical size the Compton scattered x-ray pulse will have a duration of about 200 fs.[1].

The Compton scattering cross section is very small (6.66×10^{-25}cm^2) so most of the electrons and photons pass through each other unaffected by the collision. These remaining photons and electrons are then deposited in a beam dump and a new bunch of electrons and photons are produced for the next collision. In principle it would be nice to recycle these "unused" electrons and photons and have them recalled many times increasing the average x-ray flux.

There have been several proposals for electron photon recirculating colliders using photon storage rings [3–9]. We investigate the concept in detail for the ALS booster synchrotron.

II. ALS BOOSTER SYNCHROTRON

The booster is normally used to accelerate electrons from an energy of 50MeV to 1.5GeV at which point these bunches are extracted from the booster and injected into a storage ring. The booster has a circumference of 75m and the electron bunches have a revolution time of 4 MHz. Its repetition rate is more than 6 orders of magnitude larger than that of the linac.

A. Decreasing the Vertical Beta Function

To produce femtosecond x-ray pulses the electron bunch must be focused down to < 50 μm. In order to achieve such a small spot size it is necessary to decrease the vertical β-function at the center of a straight section. In the linac scheme β_y is brought down to 4 mm. To reduce β_y in the booster the magnet lattice needs to be modified.

The magnetic lattice of the booster is basically a FODO structure with four fold periodicity where the beam is vertically defocused in the center of the straight section with $\beta_y = 10$ m(see Figure 1). In order to focus the bunch vertically an extra half period is added to the lattice. This requires splitting the quadrupole which is in the center of the straight section and adding two more quadrupoles (see Figure 2). The rings vertical beta function is then reduced from 10 m to 10 cm.

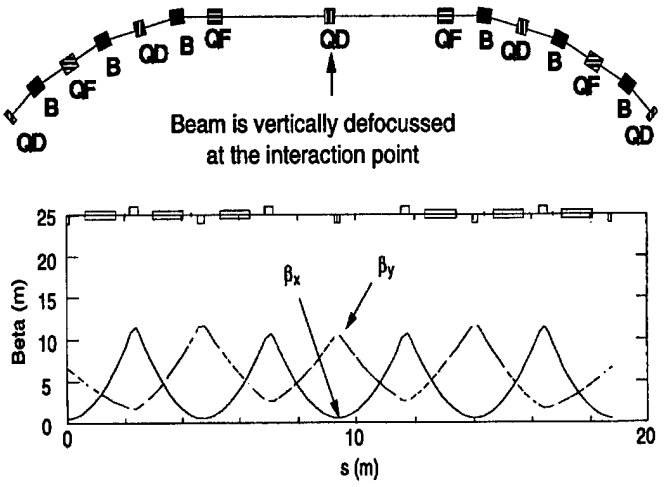


Figure 1. A typical booster cell. The beam is vertically defocused at the center of the straight section.

Reducing the β-function much further requires unrealistically large quadrupole strengths.

Even though β_y is substantially reduced in the modified lattice it is still 25 times larger than in the linac. Therefore in order to get to the same vertical spot size it is necessary for the vertical emittance to be 25 times smaller than that of the linac.

B. Decreasing the Vertical Emittance

The beam emittance in the ALS booster is determined dynamically by the mechanisms comprising synchrotron radiation damping, synchrotron radiation excitation, intra-beam scattering, and adiabatic damping. It is possible to reduce the vertical

*Work supported by the Director, Office of Energy Research, Office of Basic Energy Sciences, Materials Sciences Division, of the U.S. Department of Energy under Contract No. DEAC03-76SF00098

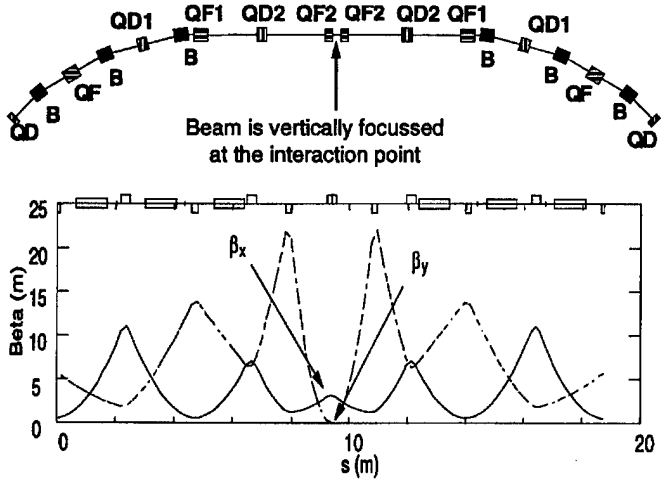


Figure 2. A modified booster cell. The beam is vertically focused at the center of the straight section.

emittance by ramping the bunch to a larger energy where there is a significant synchrotron radiation damping and remain at this energy for several damping times until the vertical beam size is reduced to a small size then ramp its energy down to a lower energy for Compton scattering experiment.

The ultimate beam size will be determined by intra-beam scattering and the coupling of the horizontal motion to the vertical motion by machine imperfections. The shorter Touschek lifetime may determine the usefulness of the beam. Simulations were done using ZAP (modified to include time dependence) to test the feasibility of this scheme. The results of these simulations suggest that there is a broad optimal energy for radiation cooling at about 600 MeV. We assumed a 2 Hz operation with 110 ms for ramping to 600 MeV, 240 ms for damping at 600 MeV, 50 ms to ramp down to 50 MeV, and 100 ms for experiments as shown in Figure 3. The ramping schedule can be easily generated using the present power supply.

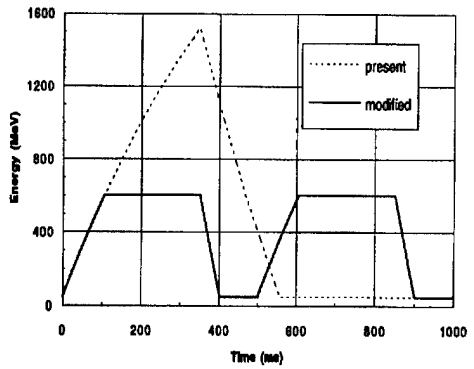


Figure 3. Ramping schedule for the ALS booster. The dotted line is the booster schedule for normal operation.

When the electron bunch is initially injected into the booster its emittance is 0.3 mm-mrad in both the horizontal and vertical plane. If we assume that there is a 1 % horizontal- vertical emittance coupling, the vertical bunch emittance should decrease to smaller than 0.005 mm-mrad, as shown in Figure 4. If we can

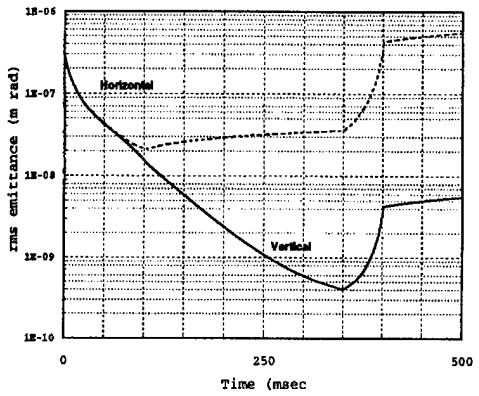


Figure 4. Emittance as a function of time in the booster.

achieve a 0.1 % coupling the corresponding emittance will be less than 0.0002 mm-mrad.

The horizontal bunch size will be much larger than that of the linac. This is a result of the beam being horizontally defocused at the collision point (β_x = 1 m). This increased horizontal size reduces the single pulse x-ray flux in the booster scheme.

C. Colliding at 21° verses 90°

There are two advantages of colliding at a larger energies than 50 MeV. First, the Toushek scattering lifetime is longer at larger energies. As a result one can use a larger fraction of the cycle for colliding beams. Second, the final horizontal and vertical emittances are smaller. Because of the larger energy it is necessary to reduce the scattering angle in order to produce x-rays with the same energy. Reducing the angle will reduce the luminosity of the collision. Therefore there is a balance between energy and angle. In addition to 90° scattering at 50 MeV we have also considered the possibility of colliding at 200 MeV with an angle of 21° and the results are discussed in section IV.

III. LASER

In the case of the linac experiment the laser to be used is a Ti:Al_2O_3 laser with a 10 Hz repetition rate and energy per pulse of 0.175 J. The linac currently operates at 1 Hz so the experiment is not able to take full advantage of the laser. In the future the linac may be able to operate at 10 Hz.

The are several papers which discuss the possibility of storing 100 MW in 100 ps length bunches[8] [5]. Presently the is no optical cavity which can store more than 1 W of energy in a 100 fs pulse. In fact, due to dispersion in the mirrors, even at 1 W the pulse length tends to grow. This stored power is similar to what can be delivered in a single pulse. So even with the boosters high revolution frequency there is no gain in average power by using an optical cavity at this time.

Due to the limitations of short pulse optical cavities a better way to maximize the average x- ray pulse is to simply reflect the incoming laser pulse many times between two mirrors. The path length that the laser pulse travels between the mirrors should be commensurate with the circumference of the booster so that the electron and photon ring could be synchronized to collide every turn. The number of reflections we are able to use will depend upon dispersion and losses in the mirrors. We have assumed that

it may be possible to have 25 usable collisions for each laser pulse.

IV. SYSTEM PARAMETERS

Based upon the above considerations we arrive at table 1. In Table 1 there are four parameter lists given for the booster, 2 at 90° and 2 at 21°. For both the 90° list and the 1° list a "conservative" list and an "aggressive" list is presented. There are several differences between the conservative and aggressive lists. In the conservative lists we assumed 1% emittance coupling whereas in the aggressive lists we assumed 0.1% emittance coupling. This leads to smaller vertical sizes. In addition the horizontal and longitudinal bunch sizes are smaller in the aggressive case resulting from stronger focusing. In the conservative cases the we assume a 1.75 W laser with a 10 Hz repetition rate and a pulse energy of 0.175 J. In the aggressive case we assume a 17.5 W laser.

PARAMETER	LINAC	BOOSTER 90° (Conservative)	BOOSTER 90° (Aggressive)	BOOSTER 21° (Conservative)	BOOSTER 21° (Aggressive)
ELECTRON BUNCH					
Energy (MeV)	50	50	50	200	200
Charge Per Bunch (nC)	1.5	1	1	1	1
Bunch Length (ps)	10	40	10	40	10
Vertical Size (μm)	50	50	20	25	10
Horizontal Size (μm)	50	1000	600	666	400
LASER PULSE					
Wavelength (μm)	0.8	0.8	0.8	0.8	0.8
Energy/Pulse (J)	0.175	0.175	1.75	0.175	1.75
Pulse Length (fs)	117	117	66	85	33
Pulse Width (μm)	35	35	20	25	10
X-RAY PULSE					
Wavelength (Å)	0.4	0.4	0.4	0.4	0.4
RMS Pulse Length (fs)	230	230	120	144	60
Collection Angle (2θ) (mrad)	6	6	6	0.4	0.4
# of X-Rays per Collision (10% bandwidth)	8×10^4	6.8×10^2	3.9×10^4	3.1×10^2	2.1×10^4
# of Collisions per Second	1	50	50	100	100
# of X-Rays per Second (10% bandwidth)	8×10^4	3.4×10^4	2×10^6	3.1×10^4	2.1×10^6

Figure 5. Table 1. Comparison of 0.4 Å radiation produced in the linac and the booster.

We determine the number of collisions per second in the following way. We assume that the electron bunch goes through two ramping cycles as shown in Figure 3. The time between laser pulses is 100 ms. Because the intra-beam scattering time is 40 ms at 50 MeV it is possible to use 1 pulse per ramping cycle (2 per second). In the 200 MeV case the intra-beam scattering lifetime is 100 ms therefore it is possible to use 2 pulses per ramping cycle (4 per second). We also assume that we can reflect the pulse 25 times providing that multiplicative factor. Therefore for 50 MeV case we have 50 collisions per second and in the 200 MeV case we have 100 collisions per second.

A. *Conclusion*

In this scheme we can not gain full advantage of the increased revolution frequency of the electron bunch in the booster because photons storage ring cavities of the required capability have not yet been developed. However with the expected improvements in laser technology and the development of storage ring cavities this approach seems very attractive. We hope that in the future that with advances in short bunch laser technology it may be possible to realize the full potential of an optical cavity scheme which could result in very high average short x-ray pulses.

Acknowledgments

The authors wish to thank W. Barletta and H. Wiedemann whose discussions provided the initial impetus for this work. We thank W. Leemans, R. Schoenlein, K. J. Kim and S. Chattopadyay for useful discussions about Compton scattering and the capability of short pulse laser technology. We thank M. Zisman for helpful discussions for modifying the computer code ZAP.

References

[1] K.-J. Kim, S. Chattopadhyay, and C. V. Shank, Nucl. Instr. and Methods **A 341**, 351 (1994).

[2] W. Leemans, et.al., "Status of the LBL Experiment on Femtosecond X-Ray Generation through 90° Thompson Scattering", Proc. of the European Part. Accel. Conf. (1994).

[3] H. Yamada , "Photon Storage Ring", Japanese Journal of Applied Physics **28**, 1665 (1989).

[4] H. Yamada et al, "Compact hard X-ray source based on the photon storage ring", Rev. Sci. Inst. **63**, 741 (1992).

[5] J. Chen et al, "Development of a compact high brightness X-ray source", Nucl. Instr. and Meth. in Phys. Res. **A 341**, 346 (1994).

[6] P. Sprangle, B. Hafizi, and F. Mako, "New X-ray source for lithography", Appl. Phys. Lett. **55**, 2559 (1989).

[7] P. Sprangle et al, "Tunable, short pulse hard x-rays from a compact laser synchrotron source", J. Appl. Phys. **72**, 5032 (1992).

[8] E. Esarey et al, "Laser synchrotron radiation as a compact source of tunable short pulse hard X-rays", Nucl. Instr. and Meth. in Phys. Res. **A 331**, 545 (1993).

[9] A. Zholents and M. Zolotorev, "A proposal for the generation of ultra-short x-ray pulses", LBL-36061

BEAM STABILITY AT SRRC STORAGE RING *

W.T. Weng †, H.P. Chang, J.R. Chen, Y. Cheng, K.T. Hsu, C.C. Kuo
J.C. Lee, K.K. Lin, Y.C. Liu, G.H. Luo, K.L. Tsang
Synchrotron Radiation Research Center
Hsinchu, Taiwan, Republic of China S.Y. Fu, I. Hsu, C.S. Hsue, J.S. Leu
National Tsing Hua University
Hsinchu, Taiwan, Republic of China

Abstract

To satisfy the need of users of the synchrotron radiation at SRRC, the photon flux at the end station has to be kept at a constant with minimum fluctuation. The sources of flux variation attributable to the electron beam in the storage ring have been carefully studied and the effects on the flux have been investigated. The sources include floor vibration, power supply ripples, cooling water, ion trapping and transverse instability. The cures attempted or in plan include removal of vibration sources, reduction of ripple, local orbit feedback, ion cleaning and damping. A special diagnostic beamline has been constructed and used solely for accelerator studies and improvements.

I. INTRODUCTION

The electron storage ring at the Synchrotron Radiation Research Center (SRRC) [1] was constructed and successfully commissioned in 1993 [2] and routinely operated for research in 1994 and 1995 [3]. All of the design parameters have been realized in the first two years of operation [4]. For reliable and useful operation for scientific research, most users demand a flux stability $\Delta I/I$ of about 0.5% at the end of the photon beam lines. Such a requirement puts a stringent stability condition on the stored electron beam over the useful lifetime, typically five to six hours for SRRC.

The reduction in photon flux has been calculated for a Gaussian beam with rms beam size $\sigma_y \approx 50$ μm passing through a slit with 50 μm opening. Normalized to the flux of beam without orbit deviation, the reduction in intensity as a function of deviation of the beam controid is shown in Fig. 1. It can be seen that to keep the flux reduction to less than 0.5%, the beam has to be kept at a constant position of about 10 mm in the storage ring. This calculation has also been confirmed by an experiment which records the reduction of photon flux as a function of controlled beam offset introduced by a local orbit bump in the storage ring. The found rate of reduction in the photon flux is about 1% per 10 μm offset [5]. In the absence of any feedback system for the photon beam line, any sources capable of generating more than 10 μm oscillation has to be identified and suppressed. Ideally, the beam oscillation can be damped by synchrotron radiation within one damping time. However, some sources of perturbation of a dynamical nature can create beam oscillation and hence flux reduction in the beam line. In this report, five possible sources of perturbation are identified and their effects on the beam stability have been studied.

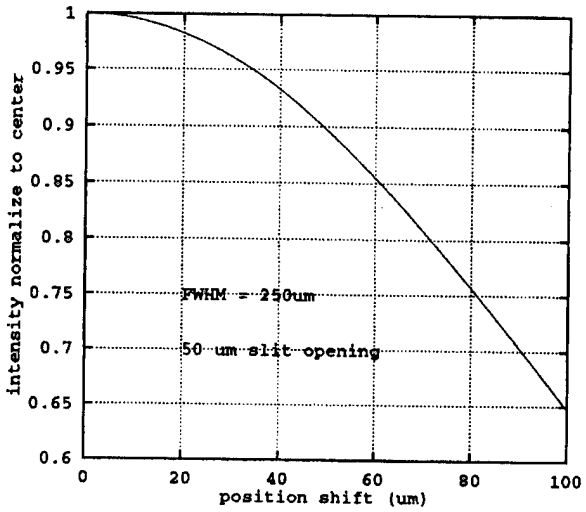


Figure 1. Intensity reduction as a function of beam centroid offset.

II. SOURCES AND CURES OF ORBIT OSCILLATION

A. Power Supply Ripple

The closed orbit correction system in the SRRC consists of 47 beam position monitors (BPM) and 24 horizontal and 30 vertical correction dipoles. The system is capable of correcting the orbit to about 0.15 mm in the vertical plane which is about the resolution of the current BPM system. The power supplies of the correctors have 60 Hz ripple to the order of about 200 PPM which in turn causes photon beam oscillation of about 60 μm. A crash program has been initiated to reduce the 60 Hz ripple to better than 50 PPM which reduced the corresponding photon beam vibration to about 13 μm [6]. In the mean time, the power supplies have also been modified to have bandwidth larger than 300 Hz for the anticipated local feedback application to be discussed later.

B. Vacuum Pump and Water Temperature

A vibration at 29.5 Hz with the amplitude of about 6 μm has been identified and its source traced to be Turbo pumps in the ring. This has been confirmed by turning off the pumps and observing that the spectral peak at 29.5 Hz disappears. Another os-

*Work performed under the auspices of the National Science Council, R.O.C.
†Permanent address: AGS Department, Brookhaven National Laboratory, U.S.A.

0-7803-3053-6/96/$5.00 ©1996 IEEE

cillation at about 0.01 Hz with the amplitude of about 10 μm has been identified as shown in Fig. 2. This oscillation has been attributed to the water temperature variation in the cooling water system of the main magnet supply. Fig. 2 also shows that the ring BPM system is capable of resolution of about 2 μm which is required for future global feedback system.

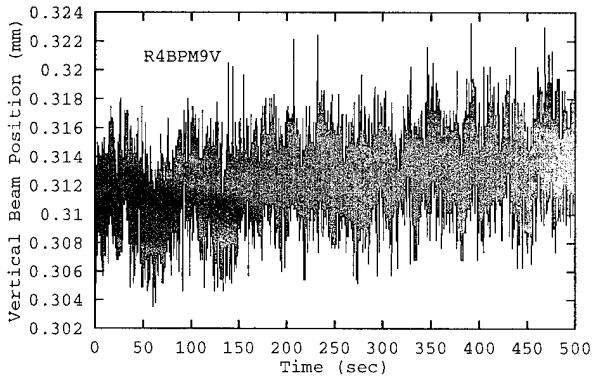


Figure 2. Orbital fluctuation from the beam position monitor system.

C. *Local Feedback System*

To decouple the photon beam stability from the beam oscillation inside the storage ring, a local feedback system has been constructed. Such a system consists of x-ray Photon Beam Position Monitor (PBPM) with resolution of about 1 μm and Local Bump Control and Optimization System. The vibration of the photon beam can be reduced by steering a local bump of the electron orbit. In case that the local bump is not well matched, residual oscillation in other part of the storage ring, hence other beam lines, can be generated. Such a leakage can cause cross-talking of various local bump controls. To reduce the cross-talking, the correlation will be calculated by a digital signal processing (DSP) technique with a gain- bandwidth of 300 Hz [7].

A test of the effect of the prototype system has been carried out in April 1995. The reduction of photon beam by about factor of three vibration and the spectral peak at 29.5 Hz can be seen in Fig. 3.

A final system will be perfected and installed at every photon beam line which requires better than 1% stability. The resolution of the PBPM system is about 1 μm implying that the ultimate beam stability achievable by the local feedback system is about 0.1%. When the cross-talk among various beam line becomes too large for local feedback system to be effective, a global feedback system will be provided.

D. *Transverse Oscillation and Damping System*

Vertical coherent oscillation has been observed since the commissioning time in 1993. When the storage ring current is more than 100 mA and the gap of electron is smaller than 100 bunches, the coherent oscillation can be excited [8]. The strength and threshold of this oscillation depends on gap size, vacuum condition and chromaticity of the ring. For stable operation, large positive chromaticity has to be introduced in both vertical and

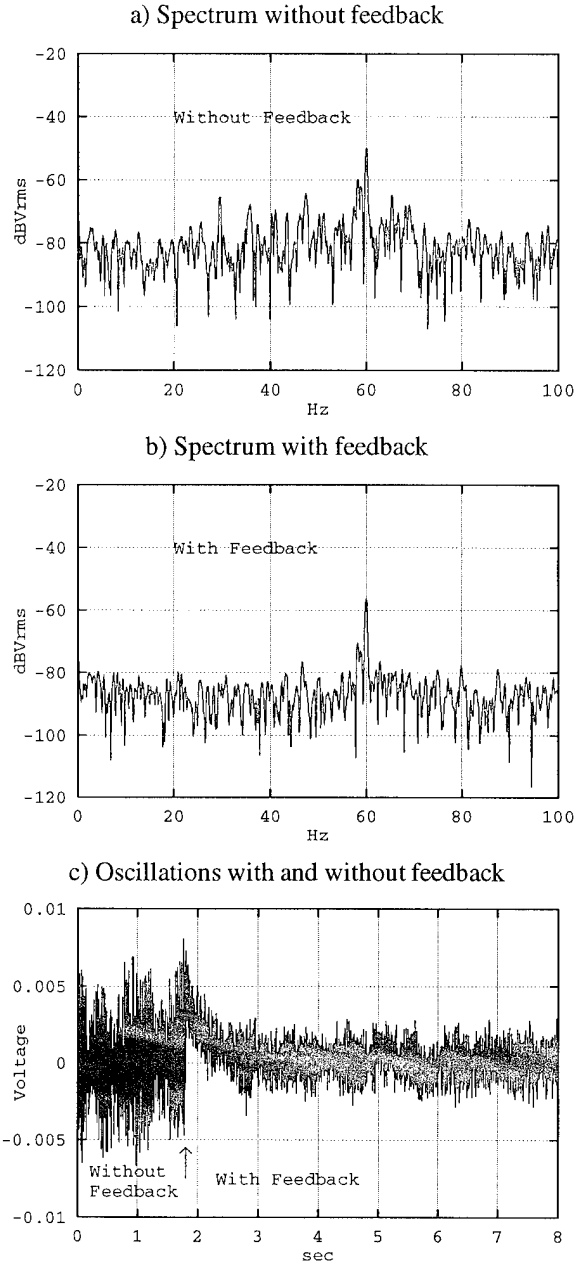


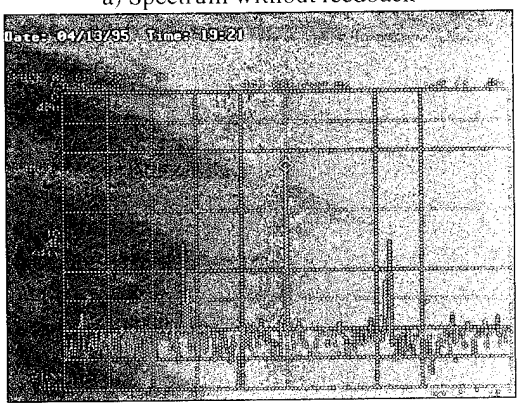
Figure 3. Effects of local feedback system.

horizontal plane. Cleaning electrode and RF-knockout method have been tried to show some effects on the instability.

Although large chromaticity has been shown to be effective in controlling the oscillation, it is not compatible with the injection process. It reduces the dynamical aperture of the stored beam, and finally is not sufficient for higher current of 400 mA anticipated for future operation. Therefore, an active transverse damping system has been introduced to damp the oscillation. Preliminary test of the damping system shows that the beam can be effectively stabilized and also has longer lifetime. In Fig. 4, the sidebands created by transverse oscillation were effectively eliminated with damping system on. In the future operation, the transverse instability will be controlled by the damping system and sextupoles will be used to optimize the lifetime and injection requirement. Gap between the electron train will be reduced to minimum for the reduction of single bunch intensity and the

increase of the total current.

a) Spectrum without feedback



b) Spectrum with feedback

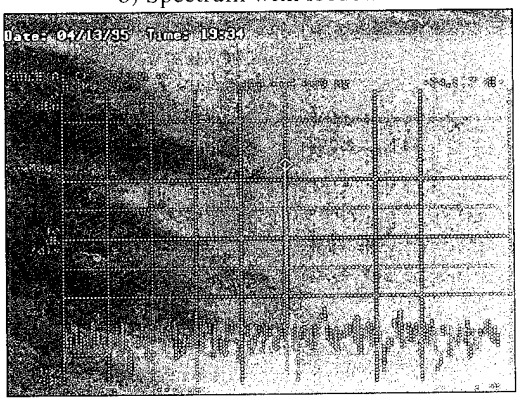


Figure 4. Effect of transverse damping system.

III. OTHER PERTURBATIONS AND FUTURE PLANS

In the longitudinal plane, both the single bunch and couple-bunch instabilities and the beam growth have been observed [9], [10]. Effective method of preventing the single bunch growth is harder to achieve. Fill up the ring with as many bunches of electrons as possible is the operational strategy to stay below the threshold by reducing the single bunch intensity. An active damping system will be constructed to suppress the longitudinal coupled-bunch effect which causes a factor of two growths in momentum spread and hence horizontal emittance and will also spoil the spectral distribution of the future undulator beam line.

At stong users' request, the SRRC intends to raise its operation energy from 1.3 GeV to 1.5 GeV. Besides the hardware and equipment upgrades in order to operate the storage ring at 1.5 GeV reliably, all the beam stabilization methods have also to be able to operate at higher energy.

At present, the SRRC has three bending magnet beamlines. An 1.8 Tesla permanent magnet wiggler was installed and commissioned in March 1995. Three additional x-ray beam lines will be completed in July 1995. Two dedicated beam lines for x-ray lithography and micromachining will also be available in the fall of 1995. The U5 and U10 undulators and their associated beam lines will be completed in two to three years. By that time a self-consistent, user friendly orbit correction, local feedback and global feedback system should be in place to assure beam stability for all users.

IV. ACKNOWLEDGEMENT

The authors would like to thank the assistance given by all staff of the Technical Division of SRRC during the performance of this work.

V. REFERENCES

[1] "SRRC Design Handbook", SRRC, Taiwan, 1989.
[2] E. Yen, "Present Status of SRRC", 1993 IEEE PAC Conf. Proc., p. 1460.
[3] Y.C. Liu, "The Status of SRRC", 1994 EPAC Conf. Proc., p. 110.
[4] C.C. Kuo, et al., "Performance of the SRRC Storage Ring and Wiggler Commissioning", these proceedings.
[5] Ian Hsu, et al., "The Electron Beam Orbit Sensitivity of the Photon Flux of the Photon Beam Line", these proceedings.
[6] Y. Cheng, private communications, 1995.
[7] Y. Cheng, "High Resolution Photon Beam Position Monitor", 1994 EPAC Conf. Proc., p. 1566.
[8] J.C. Lee, et al., "The Study of the Trapped Ion Effects in the SRRC Storage Ring", 1994 EPAC Conf. Proc., p. 1159.
[9] Ch. Wang, et al., "Bunch Lengthening in SRRC Storage Ring", these proceedings.
[10] W.K. Lau, et al., "Study of Longitudinal Coupled Bunch Instabilities in the SRRC Storage Ring", these proceedings.

COMMISSIONING OF THE DUKE STORAGE RING*

V.N.Litvinenko, Y. Wu, B.Burnham, J.M.J. Madey, F.Carter, C.Dickey, M.Emamian, J.Gustavsson,
N.Hower, P.Morcombe, S.H.Park, P.O'Shea, R.Sachtshale, D.Straub, G.Swift, P. Wang, and J.Widgren
Duke University, Free Electron Laser Laboratory , Durham, NC 27708-0319 USA

Abstract

The commissioning of the 1 GeV Duke Storage Ring began in November, 1994 with the demonstration of injection, storage and ramping to 1 GeV at the first attempt. The ring is now operational. The Duke project is unique in that the storage ring and linac were designed, constructed and commissioned by a small new University laboratory, operating on a low budget. The team is comprised of six accelerator physicists and graduate students, eight engineers, and fifteen technicians.

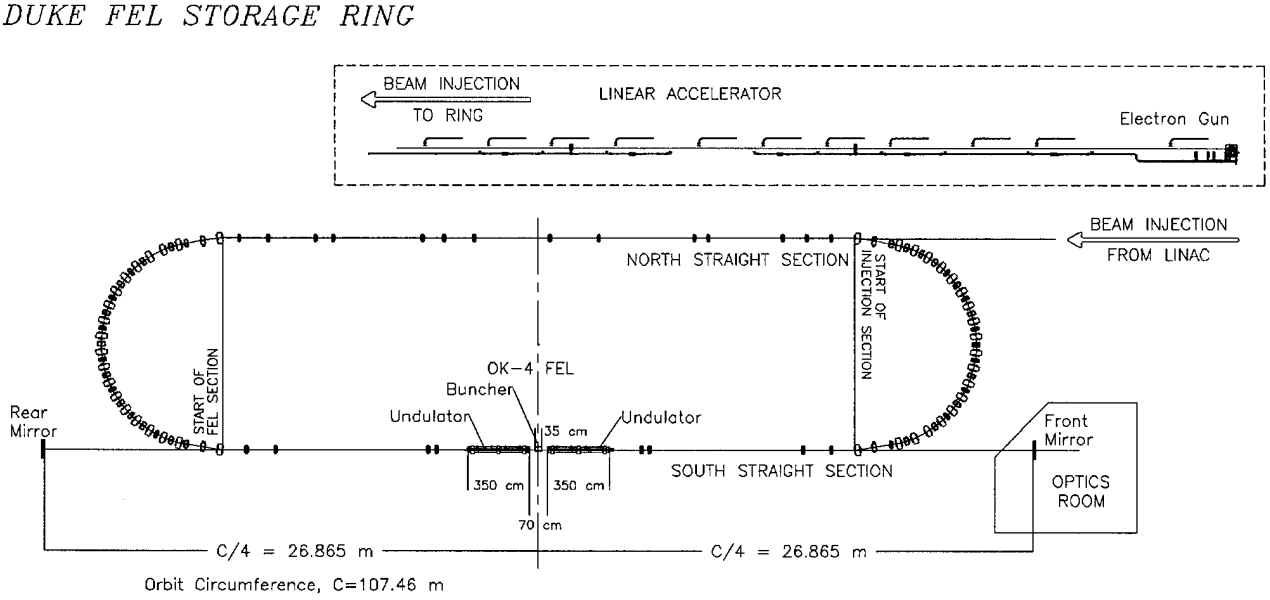


Figure 1. Layout of the Duke FEL storage ring and 280 MeV linac-injector.

I. INTRODUCTION

The new design of the Duke storage ring lattice was initiated in February of 1991 and was completed in October the same year [1,2]. The circumstances leading to the design of the ring's novel modified second-order achromatic lattice is presented elsewhere [3]. Our experience with the Duke storage ring has shown that this lattice is very "tolerant". The use of precise magnetic measurements for control [4,5] in combination with precise alignment [6] was the key to trouble-free commissioning.

II. DUKE STORAGE RING

The unique "third generation" 1 GeV Duke storage ring is designed to drive UV and soft X-ray FELs as well as to produce high brightness synchrotron radiation from the bending magnets and insertion devices. The facility is comprised of the 1 GeV storage ring, the 280 MeV linac-injector and linac-to-ring (LTR) channel.

*Work supported by ONR grant #N00014-94-1-0818

Storage Ring: The layout of the Duke storage ring and linac is shown in Figure 1. The ring itself is a strong focusing race-track with two 34 meter long straight sections. The south straight section lattice is designed to optimize FEL operation with 7 to 28 m long FELs. The north straight section is used for injection and installation of the RF system and synchrotron radiation insertion devices. The main parameters of the Duke storage ring are listed in Table 1.

All dipoles on the Duke storage ring, including those in the injection chicane, are fed by one 560 kW PEI power supply, while all quadrupoles have individual power supplies. This feature provides flexibility for the lattice design.

Arcs: Each arc is divided into ten strong focusing FBDB (FODO) cells to provide low natural emittance of the electron beam. Details of the design are described in [3].

South straight section: The lattice of this section comprising 8 quadrupoles has bilateral symmetry with 3.5 m horizontal and vertical β-functions at its center. This lattice is optimized to facilitate operation of the 8 m long OK-4 UV/VUV FEL [7]. We also designed an alternative lattice for this straight section to accommodate a future 26 m FEL [8].

0-7803-3053-6/96/$5.00 ©1996 IEEE

Table I. Designed Parameters of Duke Storage Ring

Operating energy [GeV]	0.25 - 1.0
Ring circumference [m]	107.46
Arc and straight section length [m]	19.52; 34.21
Revolution frequency [MHz]	2.7898
RF frequency [MHz]	178.547
Number of dipoles and quadrupoles	40; 64
Betatron tunes, Qx and Qy	9.111, 4.180
Orbit compaction factor, α	0.0086
Natural chromaticities, Cx and Cy	-10.0, -9.78
Compensated values, Cx and Cy	+0.1; +0.1
Acceptances [mm mrad], Ax and Ay	56.0, 16.0
Energy acceptance, $\Delta E/E$, of ring	>±5.0%
limited by existing RF	±2.8%
Maximum β-functions [m], x and y	13.6, 21.3
Maximum η-function [m]	0.245

North straight section comprising 14 quadrupoles, is a more diverse lattice: it provides optimal conditions for the 3.75 m NIST undulator (soft X-ray spontaneous source), RF-cavity and injection.

Ring RF system comprising a RF cavity, a circulator, and a 55 kW QEI power amplifier, is described in [9]. ***Duke Storage Ring injection*** system includes a 280 MeV linac, a LTR channel, achromatic vertical chicane, and ferrite kicker. Injection is in the horizontal plane to accommodate insertion devices with small vertical gaps.

The 280 MeV Linac- injector comprising a microwave electron gun, 11 SLAC accelerator sections, and low and high energy spectrometers, was commissioned in October 1994. The linac description can be found elsewhere in these proceedings [13]. A chopper (the gun kicker) installed after the microwave gun forms 25-50 nsec electron bunch trains which define the filling pattern (5 to 10 buckets) in the ring. The linac delivered about 2-2.3 nC of the charge per shot, which transfers to 5-6 mA of average current in the ring.

The ring has one injection kicker (instead of designed three). The ring kicker is described in [10].

The timing system, originally developed at Stanford and adjusted to the new RF frequency at Duke, provides synchronization of the linac and storage ring pulsed systems, namely the gun and ring kickers.

The injection chicane, comprised of three 9° dipoles and a Lambertson type septum magnet, provides a 60 cm vertical bump of the electron trajectory. The chicane dipoles are identical to those on the ring and are fed by the same power supply. This arrangement matches the energies of the ring and chicane which is also used as a spectrometer. The last 3 meters of the chicane employ a vacuum pipe with 8 x 12 mm inside cross-section for differential pumping between the storage ring and linac .

Vacuum system: The ring has stainless steel vacuum chambers with smooth transitions. Synchrotron radiation absorbers are located in the arcs. However, we are presently using temporary end-of-arc vacuum chambers without absorbers and with sudden jumps of the vacuum pipe cross-section. These chambers do not allow operation at full energy with full current. They are also the main source of longitudinal impedance for the ring.

More than fifty vacuum pumps are distributed around the storage ring. Overall vacuum in the ring is $(2\text{-}8)*10^{-10}$ torr without electron beam. Vacuum in the arcs climbs up to $(1.8\text{-}2.8)*10^{-8}$ torr with a 100 mA beam at 280 MeV, and up to $(3.6\text{-}4)*10^{-8}$ torr with a 4 mA beam at 1 GeV. Vacuum is sufficiently good to provide 4 hours lifetime at 1 GeV with 4 mA beam current.

The alignment system is described in these proceedings [6].

Duke Ring diagnostic system comprises the following systems: DCCT for average current measurements with 1 μA resolution (made in BINP); four remotely controlled screens for one-turn tracking; four end-of-arc synchrotron radiation ports equipped with TV cameras, photo-multipliers and a dissector with 20 psec resolution. The tune measurement system is described elsewhere[11].

Duke Storage Ring control system includes advanced intelligent functions for control of lattice modifications, tune and chromaticity controls, magnet normalization, and energy ramp. This system is well described in [4,5].

III . COMMISSIONING OF THE RING

Commissioning of the Duke storage ring proceeded very smoothly and successfully. We did not experience any problems tracking the beam through the LTR, the chicane, and the storage ring from the first shot without use of any correctors. There was no problem storing the beam and ramping the energy from 230 MeV to the design energy of 1 GeV. Later, the beam was ramped to 1.1 GeV as well. This success was achieved with the use of very simple diagnostics.

Table II. Measured Parameters of Duke Ring

Operating energy [GeV]	0.2 - 1.1
Revolution frequency [MHz]	2.7898
RF frequency [MHz]	178.547
Betatron tunes, Qx and Qy	9.118 4.145
Natural chromaticities, Cx and Cy	-10.0, -9.78
Compensated values, Cx and Cy	+0.1; +0.1
Acceptances [mm mrad], Ax and Ay	>56.0, >16.0
Energy acceptance, $\Delta E/E$, of ring	±6.0%
Closed orbit (no correction) x and y, mm	<±5, <±4
Deviation of β-functions , x and y	<±20%
η-function [m] in straight sections	< .005

Table III. Electron Beam Parameters

	Design	Measured
Beam current, mA	100	115
Emittance (@1 GeV) [1]		
Horizontal ,m*rad	$18 \cdot 10^{-9}$	$16\text{-}19 \cdot 10^{-9}$
Vertical,m*rad	$1 \cdot 10^{-9}$	$<1 \cdot 10^{-9}$
Bunch length[2] , ps	33	< 70

The commissioning of the Duke ring has resoundingly demonstrated the effectiveness of the lattice, control system and alignment. Table II comprises the main measured parameters of the ring with the designed objectives.

Stacking the electron beam with 100% efficiency using one kicker (instead of the designed three) was achieved because of the large dynamic aperture of the ring. The measured acceptance of the ring is in very good agreement with physical aperture of the ring [14].

The measured parameters of the electron beam in the Duke storage ring are summarized in Table III.

In addition, two unusual effects were observed during commissioning: capture of 20% of the electrons injected outside the RF separatrix (with higher energy) and stable capture of electrons in a -30 dB level side-band of the RF frequency.

IV. FUTURE PLANS

We plan the following upgrades of the Duke storage ring: 1) smooth end-of-arc vacuum chambers with absorbers to attain the full capabilities of the Duke ring; 2) electronics for the 60 existing strip-line BPMs; 3) reduced injection bunch duration to 5 nsec for single bucket filling; 4.) two additional kickers to simplify injection.

Near term plans include installation and commissioning of the UV/VUV OK-4 FEL and the NIST undulator.

V. ACKNOWLEDGMENTS

We want to thank all those who contributed to the design, installation and commissioning of the Duke storage ring system: all staff from the Duke FEL laboratory, our colleagues from Novosibirsk Institute of Nuclear Physics and Lawrence Berkeley Laboratory. We would like to thank personally C. Pat, R. Cataldo, J. Faircloth, H. Goehring, S. Goetz, M. Johnson, L. Kennard, H. Mercardo, J. Meyer, O. Qakeley, J. Patterson, and R. Taylor at Duke FEL Laboratory; S. Mikhailov, Yu. Levashov, and G. Kurkin at BINP, Novosibirsk; E. Forest, and J. Bengsston at LBL.

This project would not be possible without the wise guidance and support of Dr. Howard Schlossberg and his colleagues.

VI. REFERENCES

[1] V.Litvinenko, Y.Wu, "New Lattice for the Duke Storage Ring", Duke FEL Lab. Report, October 1991

[2] Y.Wu, V.N.Litvinenko, J.M.J.Madey, "Lattice and Dynamic Aperture of the Duke FEL Storage Ring", in Proceedings of the 1993 Particle Accelerator Conference, Washington D.C., p. 218; Y.Wu, V.N.Litvinenko, E.Forest, J.M.J.Madey, "Dynamic Aperture Study for the Duke Storage Ring", Nucl. Instr. and Meth., A331 (1993) 287

[3] V.N.Litvinenko, Y.Wu, B.Burnham, J.M.J.Madey, S.H.Park, "Performance of Achromatic Lattice with Combined Function Sextupoles at Duke Storage Ring", These Proceedings.

[4] B.Burnham, V.Litvinenko, Y.Wu, "Application of Precision Magnetic Measurements for Control of the Duke Storage Ring", These Proceedings.

[5] Y.Wu, B.Burnham, V.Litvinenko, "The Duke Storage Ring Control System", These Proceedings.

[6] M.Emamian, N.Hower, Y.Levashov, "Alignment of the Duke FEL Storage Ring", These Proceedings.

[7] V.Litvinenko, J.Madey, N.A.Vinokurov "UV-VUV FEL Program at Duke Storage Ring with OK-4 optical klystron", Proceedings of the 1993 Particle Accelerator Conference, Washington D.C., p. 1442

[8] Y.Wu, V.N.Litvinenko, J.M.J.Madey, "Study of undulator influence on the dynamic aperture for the Duke Storage Ring", Nulc. Instr. and Meth., A341 (1994) 363

[9] P.Wang, G.Kurkin, P.Morcombe, Y.Wu, "RF System for Duke 1 GeV Storage Ring", These Proceedings.

[10] R.Sachtshale, C.Dickey, P.Morcombe, "Pulsed Power Technology and Accelerators", These Proceedings.

[11]V.Litvinenko, B.Burnham, N.Hower, P.Morcombe "Duke Storage Ring Tune Measurements System using Razor Blade and Photo-multiplier", These Proceedings.

[12] Y.Wu, "A Report on the 250 MeV and 1 GeV Linac Lattice and Alignment Tolerances", Duke FEL Lab. Report, January 11, 1993

[13] P.O'Shea et al., "Accelerator Archaeology - The Resurrection of the Stanford MKIII Electron Linac at Duke", These Proceedings.

[14] Y.Wu, V.N.Litvinenko, B.Burnham, "Experimental Study of the Duke Storage Ring Dynamic Aperture", These Proceedings.

[1] Defined by accuracy of measurements

[2] 3.5 mA, GeV, RF @300kV, required confirmation.

PULSED VUV SYNCHROTRON RADIATION SOURCE

S. H. Kim, Y. S. Cho, T. Y. Kim, K. H. Chung
Dept. Of Nuclear Eng., Seoul National University, Seoul 151-742, KOREA

Abstract

The conceptual design of the pulsed VUV synchrotron radiation (SR) source is reported. This machine has modified racetrack shape (diamond shape) and consist of two superconducting bending magnets, two normal conducting bending magnets, iron yokes, quadrupole magnets and injection system. Maximum magnetic flux density is 7 T. Injector is 100 MeV racetrack microtron and 100 MeV, 10 pps electron beam is directly injected to this SR source. The bending radius is 4.8 cm and critical wave length is 27 nm.

I. INTRODUCTION

Soft x-ray projection lithography using synchrotron radiation, more recently referred to as extreme-ultra violet lithography which has merits in optics is new technology that would lead to the mass production of high-density integrated circuits [1]. The increasing importance of SR for research and industrial applications call for the development of inexpensive and simple source. For this purpose compact superconducting SR rings with small bending radius have been worldwidely proposed and constructed during last several years [2],[3],[4]. Most of these rings use about 3-5 T magnetic flux density.

To study the feasibility of more inexpensive and compact SR source, pulsed VUV SR source which utilizes 100 MeV electron beam from the racetrack microtron which is under construction at Seoul National University is conceptually designed. There is no rf system hence life time of the beam is short, that is pulsed. Electron beam is directly injected to this machine at a field of 7 T. In designing the compact SR ring, nonlinear terms of equations of motion must be considered. Therefore complicated three dimensional magnetic field must be also considered. In this design we use 3-D magnetostatic code TOSCA. The present paper briefly describes the design feature of SR source considering magnet and beam dynamics.

II. INJECTOR

A 100 MeV racetrack microtron (RTM) is under construction. This machine will be used as an injector. Injection to this RTM is provided with 75 keV, 1 A electron gun. Pulsed 2 MW microwave power is delivered to the 5 MeV accelerating column at 2.998 GHz. The field strength of the 180 degree bending magnet is 1.048 T with sufficient uniform area. Its specification is summarized in Table I and figure 1 shows an RTM under construction.

III. DESIGN FEATURE

Compact superconducting SR rings are classified into two types. One is the circular type with single bending magnet using weak focusing, and the other is racerack type with seperated

Table I
Specifications of the RTM

Injection energy	45 keV
Final energy	100 MeV
Beam current	10 mA
Energy gain per turn	5 MeV
Accelerating cavity frequency	2.998 GHz
Maximum flux density of bending magnet	1.048 T
Pulse Width	3 μsec
Repetition rate	10 pps

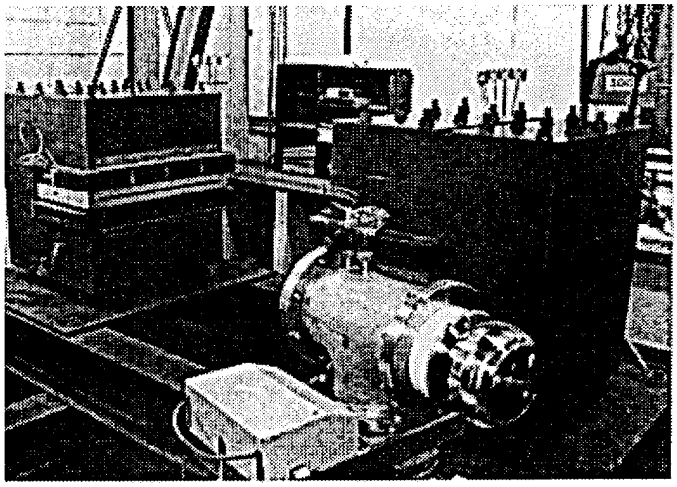


Figure 1. Racetrack microtron under construction

magnet and long straight section using strong focusing or combined focusing.

In case of applying circular type to this design, it has merits of simple structure consequently more compact because the principle of weak focusing is applicable. So auxiliary magnet system is not necessary. But injection is almost impossible because the bending radius correspondence to 7 T magnetic flux density, 100 MeV electron beam is so small (4.8 cm) and fringing field region is wide.

Adapting racetrack type to this design, injection is possible. Because of iron yoke saturation however, electron beam is reflected before it reaches 7 T region. For the more there exists reverse fringing field region. In case of using this reverse fringing field, the orbit is like that of reflex microtron [5] so other optics is not applicable. In order to reduce the reverse fringing field, 'banana'-shape dipole coil which are turned up and away from the beam at each end, it has difficulty to make it small.

To overcome above problems, diamond shape orbit configuration is suggested. The operation scheme is as follows. 100 MeV electron beam from the RTM is injected to this SR source. This

0-7803-3053-6/96/$5.00 ©1996 IEEE

Table II
Designed parameters of Pulsed VUV SR Source

Beam energy	100 MeV
Injection energy	100 MeV
Maximum magnetic flux density	7 T
Critical wavelength	27 nm
Bending Radius	4.8 cm
Circumference	4.2 m

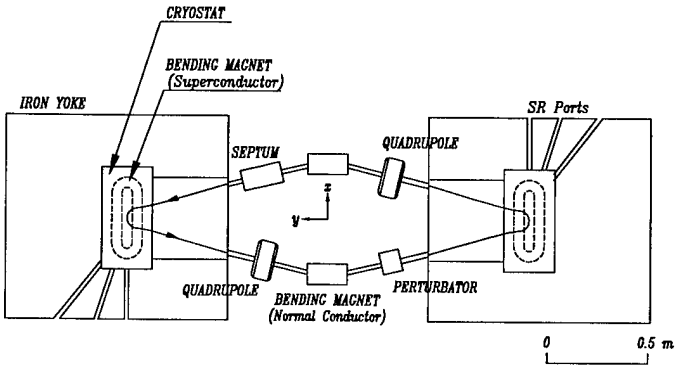


Figure 2. The Schematic Layout of the pulsed VUV SR Source

machine has no RF system, beam loses its energy continuously via radiating SR. Therefore successfully injected beam circulate for few msec. and then decay out. That is pulsed and the repetition rate of pulse is mainly governed by that of RTM. Table II is specifications of this machine and figure 2 shows a rayout of this machine. Located in straight sections are quadrupole magnets, inflector and pertubator. Its circumference is 4.2 m. Its footprint is 0.9 m × 3.2 m.

IV. MAGNET

The magnet system consists of superconducting bending magnets, normal conducting bending magnets and quadrupole magnets. The superconducting magnet have an iron yoke. The maximum flux density is 7 T. The roles of the iron yoke are to reduce magnetomotive force and to shield magnetic field at injection. The design principals of this superconducting magnet are to reduce the fringing field region and to let the field distribution uniform in x-direction (coordinate system is shown in figure 2)

To achieve the former, magnet width should be short. So sub lambda cooling (1.8 K) is selected. NbTi (easy to handle) is chosen as a superconducting material. And to achieve the latter racetrack shape magnet with long straight section is selected. Figure 3 is vertical field component at the center of superconducting magnet in x-direction, and shows good uniformity. Field components are calculated using TOSCA. Figure 4 is the field distributions of the superconducting magnet along the beam axis and figure 5 is schematics of superconducting coil and its cryostat. The location of the normal conducting bending magnet is determined by particle tracking. The bending field of this magnet is about 0.5 T and bending angle is 32 degree. This machine has fairly long straight section compared with bending radius. Therefore quadrupole magnets are necessary.

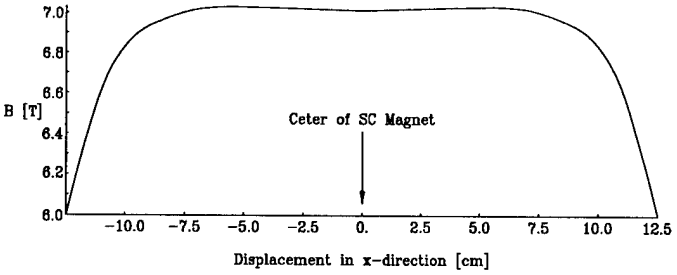


Figure 3. Field distribution at the center of SC Magnet

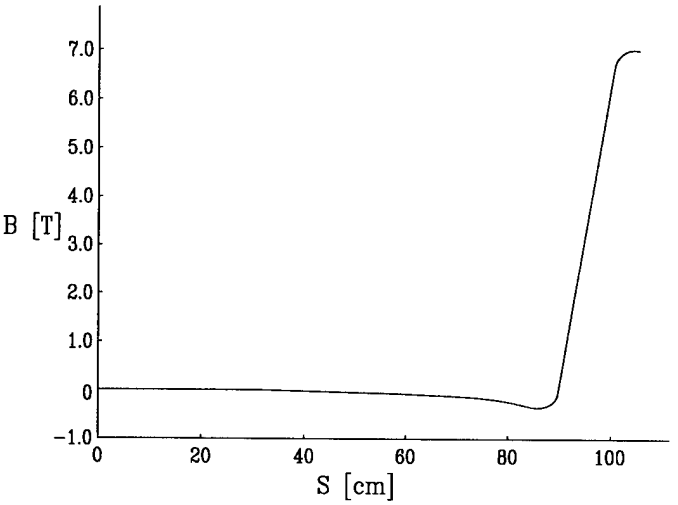


Figure 4. Field Distribution of the SC Magnet along the beam axis

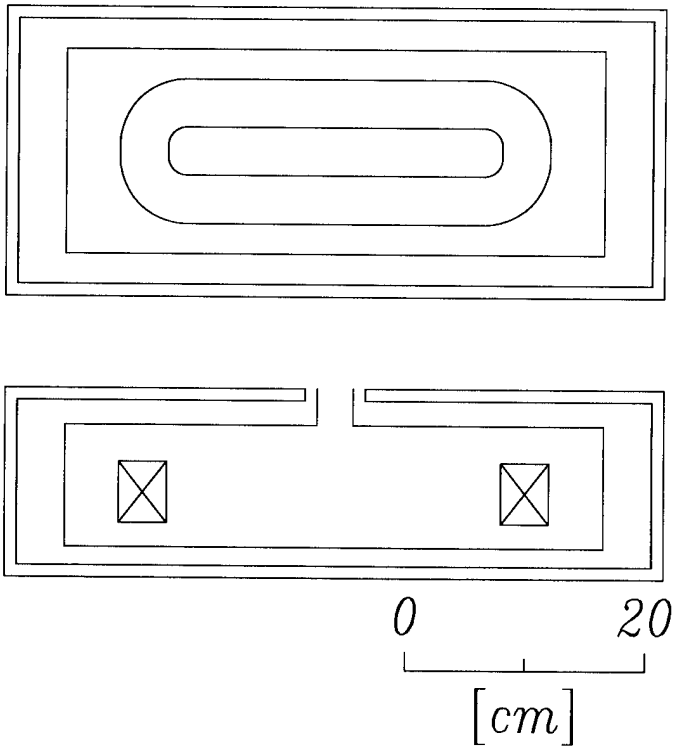


Figure 5. Schematics of SC Magnet and its Cryostat

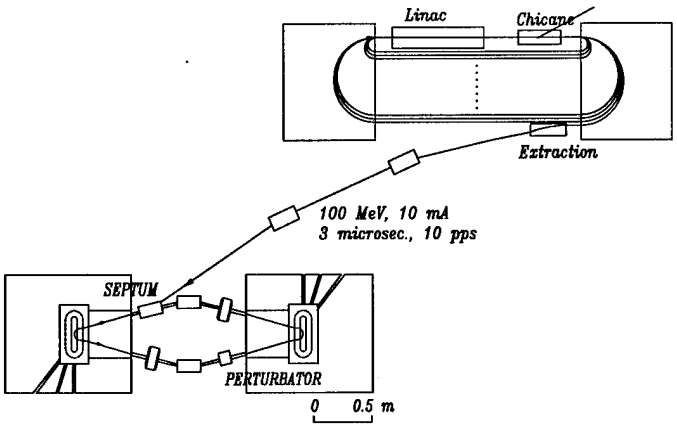


Figure 6. Schematics of Injection

V. INJECTION

In case of using usually used pulse magnet for injection there exist technical problems because of the short revolution time of electron. For recently resonance injection scheme is applied to electron and ion ring [6],[7]. Approximate radial tune of this machine is 1.43. Therefore small pertubation will be enough to create the half resonance condition. Detailed is under calculation. The schematics of injection is shown in figure 6.

VI. CONCLUSION

Pulsed VUV SR source is conceptually designed. It has diamond shape. 3-D magnetic field is calculated (TOSCA) and COD (closed orbit distortion) are determined by particle tracking. Half resonance injection sheme is selected. This paper presents partly calculated results. More presice analysis over the whole of this machine including injection is in progress.

References

[1] W.T.Silfcast and N.M.Ceglio, "Intronduction to special issue of Applied Optics on soft-x-ray projection lithography," Appl.Opt. vol.32 No.34, pp 6895-6900 (1993)

[2] T.Hosokawa et al., "NTT superconducting storage ring-Super ALIS," Rev. Sci. Inst. 60(7), pp 1783-1785 (1989)

[3] N.Takahashi, "Compact superconducting SR ring for x-ray lithography," Nucl. Inst. Meth. in Phy. Res. B24/25, pp425-428 (1987)

[4] U.Trinks, F.Nolden and A.Jahnke, "The table-top synchrotron radiation source ' klein erna'," Nucl. Inst. Meth. 200, pp475-479 (1982)

[5] R.E.Rand, "Recirculating electron accelerators," Harwood Acad. New York, pp 64-66 (1984)

[6] T.Takayama, "Resonance injection method for the compact superconducting SR-ring," Nucl. Inst. Meth. in Phy. Res. B24/25, pp 420-424 (1987)

[7] M.Tomizawa et al., "Injection method using the third order resonance at TARN II," 1993 IEEE Particle Accelerator Conference, Washington,D.C. (1993)

MERITS OF A SUB-HARMONIC APPROACH TO A SINGLE-PASS, 1.5-Å FEL*

W.M. Fawley, Lawrence Berkeley Laboratory, University of California
Berkeley, CA 94720 USA
H.-D. Nuhn and R. Bonifacio†, Stanford Linear Accelerator Center, Stanford University
Stanford, CA 94309 USA
E.T. Scharlemann, Lawrence Livermore National Laboratory, University of California
Livermore, CA 94550 USA

Abstract

SLAC/SSRL and collaborators elsewhere are studying the physics of a single-pass, FEL amplifier operating in the $1-2$ Å wavelength region based on electron beams from the SLAC linac at $\sim$ 15 GeV energy. Hoping to reduce the total wiggler length needed to reach saturation when starting from shot noise, we have examined the benefits of making the first part of the wiggler resonant at a subharmonic wavelength (*e.g.* 4.5 Å) at which the gain length can be significantly shorter. This leads to bunching of the electron beam at both the subharmonic and fundamental wavelengths, thus providing a strong coherent "seed" for exponential growth of radiation at the fundamental in the second part of the wiggler. Using both multi-harmonic and multi-frequency 2D FEL simulation codes, we have examined the predicted performance of such devices and the sensitivity to electron beam parameters such as current, emittance, and instantaneous energy spread.

I. INTRODUCTION

Over the past several years, there has been an on-going study of the feasibility of constructing an FEL operating at x-ray wavelengths (*i.e.* 1-5Å) based on 15-GeV energy electron beams produced by the SLAC linac[1]. The device, provisionally named the Linac Coherent Light Source (LCLS), would operate in a single-pass amplifier configuration employing self-amplified spontaneous emission (SASE). Since the effective shot noise seed for SASE in this case is $\sim$ 10 kW and the expected saturation power is $\sim 1-50$ GW, the wiggler must encompass approximately 15 gain lengths. For peak bunch currents of $\sim$ 5 kA and normalized emittances of $1-2\pi$ mm-mrad, gain lengths are typically 2 m or longer. Hence, the required wiggler length lies in the 30-50 m range unless some means is found to shorten the average gain length. One such possibility is making the first part of the wiggler resonant at a sub-harmonic of the ultimate wavelength sought (*e.g.* 4.5Å as compared with 1.5Å). In this portion of the wiggler, the electron bunches at the resonant (subharmonic) wavelength and shorter wavelength harmonics, thus providing a strong, coherent seed for exponential growth at the resonant, fundamental wavelength of the second part of the wiggler.

This configuration has been suggested previously (see, *e.g.*, [2][3]), although in these cases the input signal was provided by a "master-oscillator" laser. Since SASE's coherence length is relatively short and spectral bandwidth relatively large when compared with those of a master oscillator, the positive results found in [2][3] need to be re-evaluated for the LCLS study. Using the simulation codes GINGER and NUTMEG [4] [5], we have examined the performance of the sub-harmonic approach to a SASE-initiated 1.5Å FEL.

Subharmonic bunching is potentially attractive because of its faster exponential growth rate compared to that of the fundamental. The growth rate scales linearly with the dimensionless FEL parameter [6] ρ where

$$\rho^3 \equiv \frac{\omega_p^2 a_w^2 f_B^2}{16\gamma^3 k_w^2 c^2} \tag{1}$$

Here k_w is the wiggler wavenumber, ω_p is the beam plasma frequency, a_w is the dimensionless RMS wiggler vector potential, f_B denotes the Bessel function coupling term for a linearly-polarized wiggler, and γ is the usual Lorentz factor for the beam electrons. In the LCLS, the dominant focusing will be provided by external quadrupoles (the extremely low beam emittance permits this) so ω_p^2 remains nearly constant in the two wiggler regions. For $a_w \geq 2$, $(\rho_1/\rho_2) \sim [(\lambda_{s,1}/\lambda_{s,2})(\lambda_{w,1}/\lambda_{w,2})]^{1/3}$ where the subscripts 1 and 2 refer to the first and second wigglers respectively. Although the growth rate can be reduced by a number of effects such as instantaneous energy spread, transverse emittance, and diffraction, these play a relatively small role for the adopted LCLS parameters (see Table 1) and we expect the ratio of gain lengths between 4.5Å and 1.5Å to follow closely the ratio in ρ which is about 1.64. Consequently, one might expect to achieve an $\sim$ 30% reduction in overall wiggler length presuming good "coupling" efficiency in bunching from the first to the second wiggler.

There are a number of phenomena which might reduce the coupling efficiency and performance of the second wiggler, in particular when compared to a single wiggler resonant its entire length with $\lambda_s = 1.5$ Å. First, as realized in ref. [2], the instantaneous energy spread induced by the first wiggler will reduce the gain of the second. To limit this reduction, one must limit bunching in the first wiggler to values well below saturation (*e.g.* $b \equiv | < e^{i\theta} > | \leq 0.1 - 0.3$). Second, when starting from broad band noise, the output bandwidth $\Delta\omega/\omega$ of the bunching (and light) of the first wiggler can be larger than the "acceptance" of the second wiggler due to its smaller ρ. On the other hand, the coherence length $c\tau_c \propto \lambda_s/\rho$ induced by the first wiggler may be much longer than the value corresponding to saturation

*This work was supported by the Director, Office of Energy Research, and Office of High Energy and Nuclear Physics, U.S. Department of Energy, under Contracts No. DE-AC03-76SF00098 (LBL) DE-AC03-76SF0015 (SLAC), and W-7405-ENG-48 (LLNL).
† Permanent address: Univ of Milan & INFN, Milan, Italy

0-7803-3053-6/96/$5.00 ©1996 IEEE

Table 1. Parameters and Simulation Results

Standard parameters: $I_b = 5.0\,\text{kA}$ $\gamma = 2.92 \times 10^4$ $\Delta\gamma = 6.0$ $\varepsilon_n(\text{rms}) = 1.0\,\pi$ mm-mrad $\lambda_\beta = 22.4\,\text{m}$				
	Single λ_s Config.		*$3\lambda_s -> \lambda_s$ Config.*	
RUN:	A	B	C	D
λ_s	4.5 Å	1.5 Å	4.5 Å	1.5 Å
λ_w	40 mm	30 mm	40 mm	30 mm
a_w	4.27	2.75	4.27	2.75
L_w	23 m	40 m	16 m	20 m
ρ	2.4×10^{-3}	1.5×10^{-3}	2.4×10^{-3}	1.5×10^{-3}
$\Delta\gamma/\gamma\|_\varepsilon$	5.7×10^{-4}	1.3×10^{-3}	5.7×10^{-4}	1.3×10^{-3}
P_{out}	120 GW	30 GW	1.1 GW	22 GW
$\tau_{1/2}$	0.17 fs	0.14 fs	0.10 fs	0.10 fs
$\Delta\omega/\omega_o$	1.6×10^{-3}	6.7×10^{-4}	2.8×10^{-3}	9.4×10^{-4}

of the second wiggler. If so, the effective input signal for the second wiggler is perhaps more similar to a chirped coherent signal than a broad band, shot noise signal. One might then expect that certain temporal regions of the electron beam pulse, whose local bunching wavelength fall within the nominal gain bandpass of the second wiggler, will have strong exponential gain while those regions, whose local bunching wavelength lies outside, will not.

Moreover, since the bunching at the third harmonic (*ie* $\lambda = 1.5\,\text{Å}$) is proportional to the cube of the bunching at the fundamental (*ie* $\lambda_s = 4.5\,\text{Å}$) in the exponential gain regime of the first wiggler, at the same z one would expect a significantly shorter coherence length at the shorter wavelength. All these effects taken together suggest that the number of spikes that will grow in the second wiggler might be similar to that at the output of the first but whose individual temporal duration will be shorter. Ref. [7] gives additional analysis concerning the evolution of "spikes" in the SASE regime.

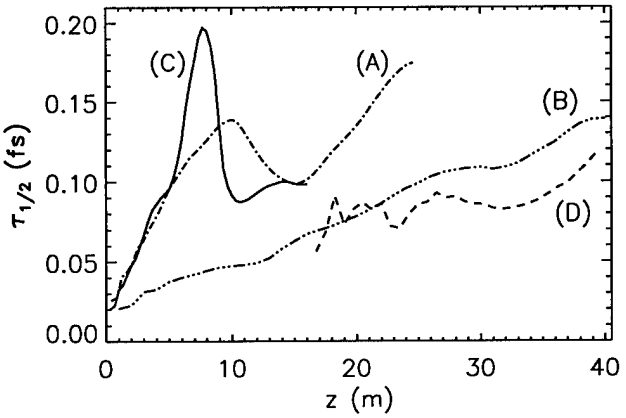


Figure 1. Autocorrelation time $\tau_{1/2}$ vs. z for different GINGER runs. **(A)** SASE-initiated $\lambda_s = 4.5\,\text{Å}$, run to saturation at $z = 23$ m **(B)** SASE-initiated $1.5\,\text{Å}$ run to 40 m, slightly short of saturation **(C)** Same as run A but with only 16 m of wiggler **(D)** $\lambda_s = 1.5\,\text{Å}$ begun at $z = 16$ m using the bunched output electron beam of run C as a subharmonic "seed".

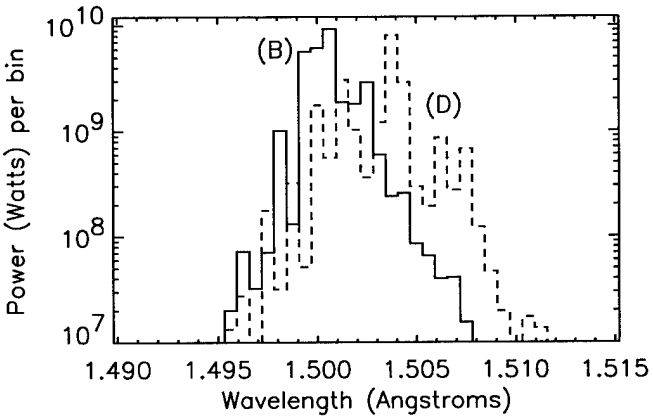


Figure 2. Output spectra for the $1.5\,\text{Å}$ runs B and D.

II. SIMULATION RESULTS

We performed a number of simulations of the subharmonic seeding configuration for a SASE-initiated, $1.5\,\text{Å}$ FEL with the 2D, multiple harmonic code NUTMEG and settled on the wiggler parameters listed in Table 1. Although NUTMEG is not a fully time-dependent code, it gives a reasonably accurate answer for the overall growth in SASE power when initiated with a monochromatic input radiation field quantitatively equivalent to shot noise. The NUTMEG results suggest that the first wiggler should be about 20 m in length at whose end there will be about 1 GW of $4.5\,\text{Å}$ power and a factor of 50 less at $1.5\,\text{Å}$ for a linearly polarized wiggler. All the runs presented here adopted a helically-polarized wigglers and hence the bunching at the odd harmonics will be due only to the radiation field at the fundamental. According to NUTMEG, a second wiggler of 20 m length will result in about 40 GW of power at $1.5\,\text{Å}$ which is not significantly different from what a simpler, single wiggler configuration resonant at $1.5\,\text{Å}$ would give for a total length of 40 m.

The GINGER simulations listed in Table 1 were done with full temporal and radial resolution of the radiation field and electron beam, and thus include the effects of shot noise, diffraction, optical guiding, and betatron motion of the individual beam particles. We adopted periodic boundary conditions in time with an equivalent "window" of 1.2 fs as compared with the slippage length/c of 0.6 fs in the first wiggler and 0.4 fs in the second. After making a number of trial runs for the subharmonic-seeded configuration (*ie* runs C/D), we adopted a first wiggler length of 16 m which is approximately 8 m ($\equiv$ 4 gain lengths in power and 2 in bunching) short of overall saturation at $4.5\,\text{Å}$. This wiggler length is shorter than the value of 20 m suggested by the NUTMEG runs. The difference lies in the fact that at a given z, the particle bunching, instantaneous energy spread, and radiation power have temporal "spikes", with peak bunching values at $\lambda = 4.5\,\text{Å}$ being ≥ 1.6 times greater than the average value of 0.09. Hence, for a given energy spread acceptance of the second wiggler, the allowable output bunching of the first wiggler, when initiated with SASE, will be smaller than that permissible for a monochromatic input field.

At the end of the first wiggler (run C), resonant at $4.5\,\text{Å}$, the

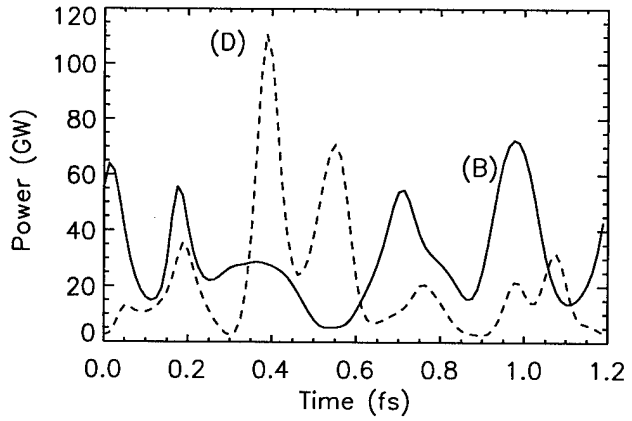


Figure 3. Output power versus time for runs B and D.

average bunching at the third harmonic $\lambda = 1.5\,\mathring{A}$ (which is the "seed" bunching for the second wiggler $\equiv$ run D) is about 0.01. This is about a factor two higher than is produced at $z = 16$ m in run B which employs a wiggler resonant only at $1.5\,\mathring{A}$. Interestingly, the autocorrelation times of runs B and D, as measured by $\tau_{1/2}$ (the point at which the temporal autocorrelation function $C(\tau)$ falls to a value of 0.5), are nearly the same (see Fig. 1) and about a factor of two less than the $4.5\,\mathring{A}$ runs A and C. Over the next 20 m of wiggler, as the power in run D grows by three orders of magnitude, $\tau_{1/2}$ increases by less than 50%; by comparison, the single wiggler $1.5\,\mathring{A}$ run B has $\tau_{1/2}$ double. Comparisons of the output spectra of these two runs (Fig. 2) shows that the single wiggler configuration has a noticeably narrower spectra than that of the subharmonic seeded configuration as would be expected from the differences in the autocorrelation times. It is not clear if the slight redward shift of run D relative to run B is significant or solely due to chance via random number seeds. (Note: The "bump" in $\tau_{1/2}$ in the 6 to 10 m region of the $4.5\,\mathring{A}$ runs does appear to be "real" as it has appeared in numerous runs with different random number seeds.)

The differences in time-averaged output power of the two $1.5\,\mathring{A}$ runs is significant. The single wiggler configuration (B), if run to saturation, would have exceeded 40 GW, while the subharmonic-seeded run (D) saturated at the lower power of 22 GW. Although the difference is probably not critical for most proposed LCLS applications, it is undoubtedly due to the higher instantaneous energy spread induced by the first wiggler resonant at $4.5\,\mathring{A}$. Time-resolved plots (Fig. 3) of the output power of these two runs shows that while the subharmonic seeded run had less average power, it also has fewer spikes and a greater peak output flux within the spikes. As predicted in refs. [7][8], the relative temporal fluctuation of the output power $\delta P / < P >$ is of order 1 which may have undesirable consequences for some LCLS applications.

We have also studied the sensitivity of the subharmonic-seeded configuration to LCLS beam parameters such as emittance. With as little as a 50% increase of normalized emittance to $1.5\,\pi$ mm-mrad, the $4.5\,\mathring{A}$ power at the output of the first wiggler drops to 0.12 GW and the average bunching to 0.03. The $1.5\,\mathring{A}$ output power at $z = 40$ m from the second wiggler drops to 1.4 GW (as compared with 22 GW in run D), the gain length increases to 2.8 m from 2.4 m, and probably another 7-10 m is needed for saturation. Consequently, a longitudinal variation in transverse emittance as small as 30-50% will be transformed into an extremely large variation in output power for a given wiggler configuration. The same sensitivity applies to beam current. To be fair, note that any configuration requiring $\sim$ 15 exponential gain lengths is likely to be sensitive to parameters such as emittance and current. There is less sensitivity to the instantaneous energy spread because of its relatively small value compared to ρ (see Table 1) although it, together with the effective energy spread due to emittance, does appear large enough to prevent LCLS optical klystron configurations working well at $\lambda_s = 1.5\,\mathring{A}$.

Based upon these results, we do not believe that the subharmonic, double wiggler approach to producing a high power $1.5\mathring{A}$ FEL, given its greater complexity, is particularly attractive relative to the simpler, single wiggler configuration for the presently adopted LCLS parameters.

References

[1] H.-D. Nuhn *et al.*, "Short Wavelength FEL's using the SLAC Linac", *Proc. EPAC 94*, London, 1994; also SLAC-PUB-6541 (1994).

[2] R. Bonifacio, L. De Salvo Souza, E.T. Scharlemann, *Nucl. Inst. Meth.*, **A296**, 787 (1990).

[3] L.H. Yu, *Phys. Rev. A*, **44**, 5178 (1991).

[4] R.A. Jong, W.M. Fawley, E.T. Scharlemann, "Modeling and Simulation of Laser Systems", **SPIE 1045**, 18 (1989).

[5] E.T. Scharlemann and W.M. Fawley, "Optical Modeling of Induction-linac Driven Free-Electron Lasers", **SPIE 642**, 2 (1986).

[6] B. Bonifacio, N. Narducci, and C. Pellegrini, *Opt. Commun.*, **50**, 373 (1984).

[7] R. Bonficacio *et al.*, *Phys. Rev. Let.*, **73**, 70 (1994).

[8] W.M. Fawley, A. M. Sessler, and E.T. Scharlemann, "Coherence and Linewidth Studies of a 4-nm High Power FEL", *Proc. 1993 Part. Accel. Conf.*, **93CH3279-7**, 1530 (1993).

OPERATION OF THE ELETTRA INJECTION LINAC IN THE FEL MODE

G. D'Auria, C. J. Bocchetta, M. Plesko, C. Rossi, L. Tosi, R. P. Walker, A. Wrulich

Sincrotrone Trieste, Padriciano 99, 34012 Trieste, Italy

The new FERMI project of an FEL in the infrared will make use of the ELETTRA full energy injection linac. The first part of the Linac was provided with the proper characteristics and an experimental hall to host the FEL was foreseen already from the beginning. The diagnostic measurements on the Linac in the FEL mode are discussed and the performance is presented.

I. INTRODUCTION

The Elettra injector is a linear accelerator composed of a 100 MeV preinjector with a traditional design [1] followed by seven high gradient, backward travelling wave structures equipped with a SLED system[2].

In 1992 the preinjector was successfully commissioned in the injection modes (single bunch and multibunch mode) [3] and since September 1993 the full Linac has been running to inject a 1.0 GeV electron beam into the Storage Ring with an increasing reliability.

At present the injector is used to fill the storage ring once per day and for the rest of the time the Linac would be available to drive an FEL facility extending the light spectrum of ELETTRA, as it was formerly planned. The design characteristics of the preinjector have been chosen to drive also an infrared FEL facility.

Up to now, due to hardware constraints, the switching of the preinjector from injection to FEL operation takes a long time. A single Gun modulator which may support both injection and FEL modes is under design to solve the problem and should be operational by the end of the year.

II. THE MACHINE SET UP

In the FEL mode configuration, the preinjector is capable to accelerate an electron beam to an energy varying from 20 to 75 MeV with a macropulse repetition rate of 10 Hz. The maximum expected pulse width is 10 μs with a micropulse repetition rate variable from 20.83 to 31.25 MHz (32-48 ns in 2 ns steps). During the first initial tests the micropulse repetition frequency has been fixed to 25 MHz (40 ns) and a macropulse width of 5 μs could be reached.

The RF source used is the TH 2132 klystron equipped with two separate RF outputs which feed the two accelerating sections and the bunching section.

The RF peak power has been selected in order to have a beam energy of 30 MeV at the exit of the preinjector to investigate the beam energy spread in the low energy region.

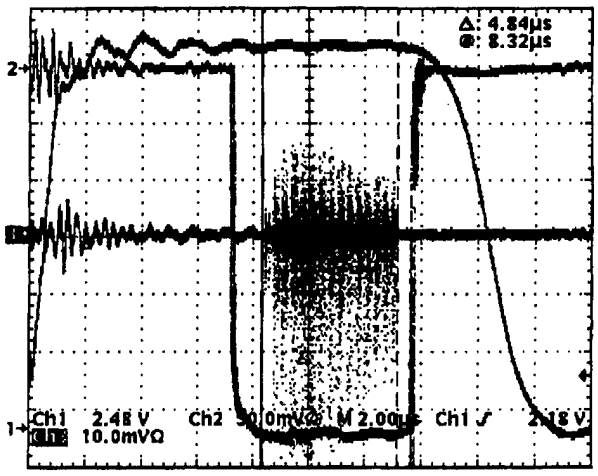


Figure 1: Klystron anodic current (trace 1), RF pulse (trace 2) and beam pulse at Linac output (trace 3).

We have operated the RF generator at roughly 10 MW output peak power. Figure 1 illustrates the klystron anodic current pulse (trace1), the RF pulse detected on one arm (trace 2) and the complete beam pulse at the Linac output (trace 3).

The Gun is a thermionic gridded Pierce type (ϕ 1 cm) which operates at 87 kV and is driven with a burst of micropulses, shorter than 2 ns each. In this first stage we were not allowed to continuously regulate the emitted current due to a fixed grid polarization.

A sample of a 2 μs beam burst is shown in figure 2.

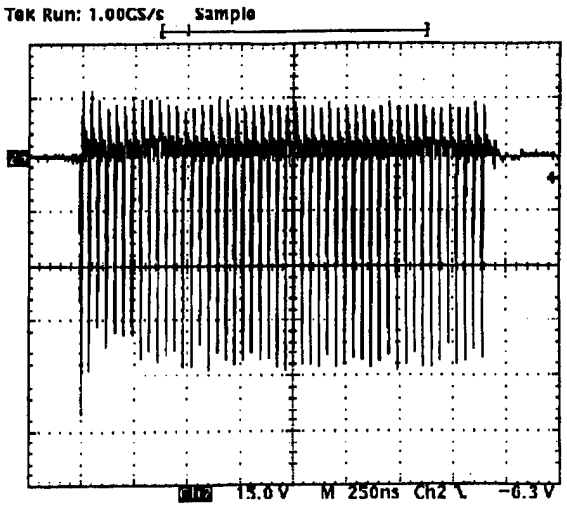


Figure 2: Beam burst from the Gun

0-7803-3053-6/96/$5.00 ©1996 IEEE

Figure 3 shows a detailed image of the beam structure at the exit of the Linac.

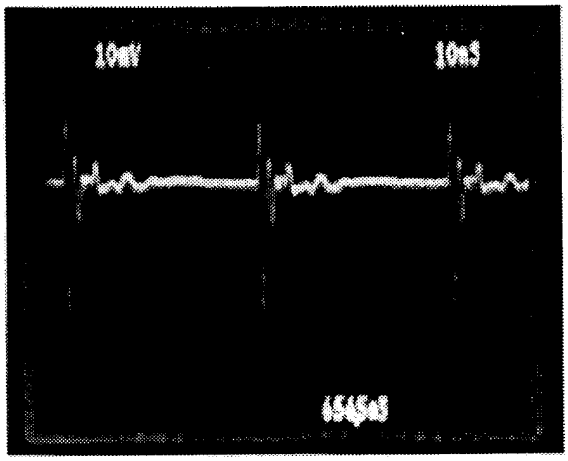


Figure 3: 40 ns structure of the 30 MeV beam

III. TRANSVERSE EMITTANCE AND ENERGY SPREAD MEASUREMENTS

Measurements of the geometrical emittance (defined for 80% of the electrons) and of the energy spread have been performed for the Linac under FEL mode operating conditions. The specifications [4] and the relative measured values are reported in Table 1. Measurements were performed at an energy of 30 MeV for a beam delivering a current of 30 mA in a 5 μs long macropulse measured on a toroid at the exit of the preinjector. Two diagnostic lines, shown in figure 4, were used each of which is terminated with a fluorescent screen [5]. FS1, situated downstream after three bipolar quadrupoles individually powered, is used for the transverse emittance measurement, whereas FS2 placed after a non-normal entry 45 degree bending magnet is used to determine the beam energy and its spread. In order to aid the measurement, two programs based on the high level software philosophy adopted at ELETTRA [6] were prepared. Theoretical details of the adopted measurement methods go beyond the scope of this paper and may be found extensively described in ref. [4].

Parameters	Specified	Measured
Energy	20 to 75 MeV	30 MeV
Charge in bucket	≥ 0.15 nC	-
Central bunch length	≤ 10 ps	-
Emittances at 30 MeV	3.17 π mm mrad 2.85 π mm mrad	3.38 π mm mrad -
Energy spread at 30 MeV	≤ ±0.75%	≤ ±0.60%

Table1: FEL mode Linac beam characteristics.

Both methods are essentially based on measuring the beam width on the fluorescent screens. The resolution error of the destructive monitors is 0.3 mm rms and the error resulting from the method used in finding the width [7] is ±0.2 mm. Given the fairly large amount of beam current in each macropulse, the screens had the tendency of saturating, even though the doping had been kept low [5]. Many measurements with different diagphram settings had to be performed, especially for the emittance, before satisfactory results could be found.

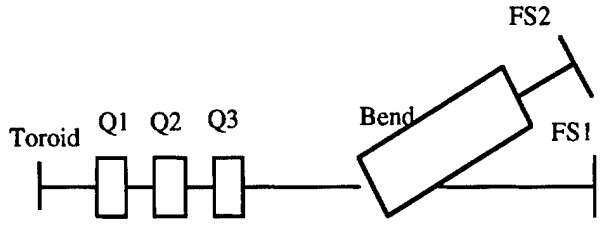


Figure 4: Schematic layout of the diagnostic lines

Regarding the transverse emittance measurement, the technique adopted is based on measuring the transverse dimensions of the beam on FS1 around a minimum as a function of the strength of the last quadrupole in the triplet. A least square fit is then performed to extract the emittance and subsequently the Courant-Snyder parameters for the given emittance at the entrance of the quadrupole. Associated with each measurement there are systematic errors, which can be minimized [4] by a long drift (1.82 m) between the screen and the upstream quadrupole and the proper choice of an optics which gives a small beam size at the entrance of the quadrupole. The two above conditions resulted in a large minimum spot at the screen. Before being measured on the screen, the beam has to traverse a titanium foil, which introduces a systematic error σ_s (0.4 mm for 30 MeV) due to scattering [8]. Since the minimum beam size is more than $1.5\sigma_s$, this error was subtracted from the measured data. Special care was taken to ensure that the beam was passing through the magnetic centers of the three quadrupoles and in the center of the upstream accelerating sections. While the former guaranteed the elimination of spurious dispersion which would give an effective beam size increase, the latter avoided skew effects due to the non-linearities of the accelerating fields which would couple the transverse beam motions. In the design of the optics, care was taken that the beam was always seen entirely on the screen in both planes and that the minimum spot on the screen would occur far from a zero quadrupole strength to avoid undesirable power supply ripple effects. The square of the measured beam size (units in mm^2) together with the fit are shown in figure 5 as a function of the quadrupole current. The measurement was performed with the designed

optics and for each current five measurements of the beam width were averaged. The fit yielded a tranverse emittance of ε=3.38±0.09 π mm mrad and β=0.509±0.02 m and α=0.027±0.04 as the Courant-Snyder parameters at the entrance of the diagnostic lines. The expected values for the latter obtained via simulations [9] was estimated to be β=0.71 m and α=-0.54.

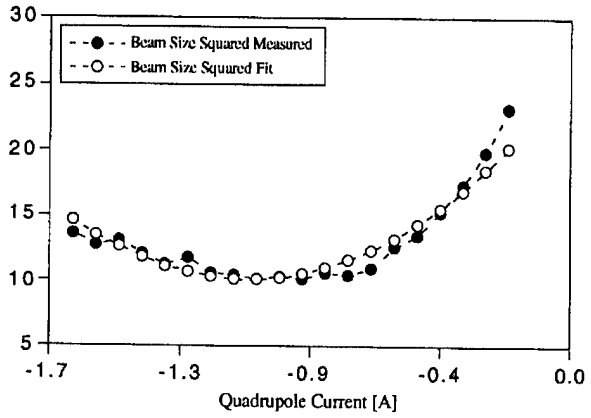


Figure 5: The square of the measured beam size in mm^2 together with the fit as a function of quadrupole current for the transverse emittance measurement.

Regarding the energy spread measurements, the diagnostic line has a dispersion of 1.0 m at the fluorescent screen location. Thus the beam size at FS2 is dominated by the dispersion. Performing an average over ten measurements the energy spread resulted to be ±0.6% assuming a zero emittance beam. Evaluation of the actual natural beam size was found to bring a negligeable contribution to the measurement. It must be pointed out that the image seen on the screen showed a nucleus with a long low energy tail. A very crude method was adopted to estimate that the measured energy spread refered mostly to the nucleus. However at the present date it is not possible to give a precise estimation of how much of the 30 mA macropulse beam measured at the toroid at the entrance of the diagnostic lines was actually in the nucleus.

IV. CONCLUSIONS

The first results obtained during these preliminary tests encourage an FEL operation based on the Trieste preinjector. Several hardware problems have to be solved as soon as possible. A single Gun modulator which can support both the injection and FEL modes is required to simplify the machine operation and to reduce the switching time.

V. REFERENCES

[1] C. Bourat et al., The 100 MeV Preinjector for the Trieste Synchrotron (IEEE Particle Accelerator Conference Proceedings, Chicago, USA, March 1989).

[2] D. Tronc et al., The Elettra 1.5 GeV Electron Injector (IEEE Particle Accelerator Conference Proceedings, San Francisco, USA, May 1991).

[3] C.J. Bocchetta et al., First Measurements of the Elettra 100 MeV Pre-Injector (Linear Accelerator Conference Proceedings, Ottawa, Canada, August 1992).

[4] C.J. Bocchetta, A Diagnostic Line for the Commissioning of the 100 MeV Linac. (Sincrotrone Trieste Technical Note, ST/M-TN-91/16, August 1991).

[5] G.R. Aiello, The ELETTRA Fluorescent Screens. (Sincrotrone Trieste Technical Note, ST/M-TN-91/12, March 1991).

[6] M. Plesko, A Complete Data Structure for the High Level Software of ELETTRA. (European Particle Accelerator Conference Proceedings, London, Great Britain, July 1994).

[7] P. Sereni, Degree Thesis. (University of Trieste, Italy, 1991).

[8] G.R. Aiello et al., Assessment of the Material and Thickness of the Metallic Window in the Housing of the Fluorescent Screen Monitor. (Sincrotrone Trieste Technical Note, ST/M-TN-91/13, March 1991).

[9] J. Gonichon, Beam Dynamics Simulation in the 100 MeV Linac Preinjector for ELETTRA. (Sincrotrone Trieste Internal Report, ST/M-91/9, July 1991).

ACKNOWLEDGEMENTS

The authors are grateful to all the Linac technical staff and in particular to A. Milocco who followed the setup of the gun modulator. Furthermore, the authors wish to acknowledge M. Ferianis, R. Visintini and D. Zangrando for the setup of the diagnostic lines and for useful discussions.

FREE ELECTRON LASER - FEL - STUDY IN INSTITUTE OF NUCLEAR PHYSICS OF MSU

V.K.Grishin, B.S.Ishkhanov, T.A.Novikova, V.I.Shvedunov
Institute of Nuclear Physics, Moscow State University

I. FEL BASED ON THE MSU RACE-TRACK MICROTRON

The possibility of creation of a source of coherent shortwave radiation on the basis of the RM of Moscow State University (MSU) facility was considered. The RM is designed to obtain accelerated electrons with a variable energy of 7-180 MeV at high quality of beam: the homogeneity of energy is 0.0001, the beam emittance is not higher than 0.01 mm.mrad. The beam current is a continuous sequence of electron pulses with the duration of 3-4 ps following at a frequency of 2.45 GHz and the average current of 100 mkA [1]. A special operation mode of the acceleration is provided for duty cycle decreasing by 100 - 300 times and the amplitude of current pulses 1-10 A.

Two operation regimes of the FEL are possible. At the standard undulator parameters (length and number of periods are 2.5 cm and 100, B=5 kGz, undulator factor is K=0.5-1, optical length is 3-5 m) positive gain in the single-particle regime is realised in the 5-170 mkm band [2].

Low emittance permits to provide the collective amplification regime of FEL with channelling radiation [3]. In this case the positive gain may be achieved on the wavelength region of $\lambda_s < 1$ mkm.

II. ESTIMATION OF HIGH-CURRENT FEL TOP EFFICIENCY

High-current FEL are used for the exciting of shortwave electromagnetic radiation (EMR). It operates in collective stimulated EMR regime. Due to the bunching process the efficiency of output radiation is significantly increased. Top efficiency evaluation is obviously acquires remarkable interest.

FEL limiting efficiency is defined by the nonlinear saturation of EMR exciting process. The basis stabilisation process in this case is the capture of beam particles by slow wave of electromagnetic system named as the wave of ponderomotive potential. In a result velocities of electron beam and ponderomotive wave are synchronised. Then energy exchange between beam particles and EMR has only oscillating character. Therefore, analysis of equilibrium condition of particles-wave system allows to estimate the magnitude of FEL top efficiency.

Let us consider one of the perspective FEL schemes with helical undulator. Magnetic field of undulator is described by vector potential $\mathbf{A}=A_0[\mathbf{e}_x\cos(k_0z)+\mathbf{e}_y\sin(k_0z)]$, where $(\mathbf{e}_x,\mathbf{e}_y,\mathbf{e}_z)$ are coordinate orts, $k_0=2\pi/\lambda_0$, λ_0 - undulator period. Injected particles with initial velocity $v_0=\beta_0 c$ acquires a transverse speed $\mathbf{v}_{0\perp}=v_0\mathbf{A}_0/A_0$ in the undulator field. Triggering circularly polarised light wave with the electric field $\mathbf{E}_{si}=E_{0i}[\mathbf{e}_x\cos(\omega_{si}t-k_{si}z)-\mathbf{e}_y\sin(\omega_{si}t-k_{si}z)]$ where ω_{si} is the frequency, k_{si} is initial wave number ($\omega_{si}=ck_{si}$) travels through the laser cavity in the same direction as electrons. Electromagnetic wave is amplified by the oscillating beam of particles. Effective energy exchange requires that the longitudinal velocity of electrons should be equalled to phase speed of the ponderomotive wave: $v_{0z}=v_{ph}=\omega_s/(k_{si}+k_0)$. Particles-wave interaction leads to the bunching of beam and then to the capturing of electrons to "traps" of the ponderomotive potential $U=A_0A_s/(mc^2)$, where A_s is vector potential of EMR. Naturally, the trapped electrons have a speed $\beta_z c=[v^2-v_\perp^2]^{1/2}<\beta_{0z}c$, because of $\gamma_z<\gamma_{0z}$. Interaction of electrons with EMR usually takes place on the beam travelling length $L_{und}=10\div20/\mathrm{Im}(k_s)$, that is 1÷1.5 m with beam current $I_b\sim100$ A÷1 kA.

FEL action for the sufficiently extending system has a permanent character: electron beam are continuously injected to undulator in z=0 and fluxes of particles and EMR run out from the capture area $z=z^*$ Equilibrium equations for the average flows of energy and pulse linear densities of particles (Π_b and G_b) and EMR (Π_s and G_s) through the transverse section of beam are:

$$\Pi_b\big|_{z=0}=\{\Pi_b+\Pi_s\}\big|_{z=z^*}$$
$$G_b\big|_{z=0}=\{G_b+G_s\}\big|_{z=z^*}. \qquad (1)$$

The contribution of EMR wave to the general energetic equilibrium on the beginning stage is assumed slight. Besides, no flows of beam particles and EMR pass through the sides of system. Taking into consideration the ratio $\Pi_b\beta_z=cG_b$ the equilibrium equations permit to make an important formula to limiting efficiency [4]:

$$\eta=(\Pi_s\gamma_0)/[\Pi_0(\gamma_0-1)]=\gamma_0(\beta_{0z}-\beta_z)/[(\gamma_0-1)(cG_s/\Pi_s-\beta_z)] \qquad (2)$$

where magnitude $(\gamma_0-1)\Pi_0/\gamma_0$ is flow density of start kinetic energy of electron. Value of Π_s is equalled to Pointing vector and G_s is equalled to field stress tensor T_{zz} [4].Depended on the Coulomb interaction of particles longitudinal field components are neglectable. Therefore, only the transverse component of EMR wave is included in the equations for Π_s

0-7803-3053-6/96/$5.00 ©1996 IEEE

and G_s . It is notice that phase velocity of radiation wave is decreased: $\beta_s=\omega_s/k_s<1$. Magnitude of β_s is determined by equality of the velocity of the beam electrons and the ponderomotive wave $\omega_s=\beta_z c/(k_s+k_0)$.

After the capturing of the electron the state of system is described by the evolutionary equations . Assuming for the vector potential $A_s=A_{s0}(z)\sin(\int k_s dz-\omega t)$ and for Furrier component of the current density $j_s=\beta_{0\perp} j_b \varepsilon \sin(\int k_s dz-\omega t-\tau)$, where τ is slipping phase to relation to equilibrium point of the ponderomotive potential, ε is Furrier coefficient characterising a bunching agree, j_b is the beam current density, we have:

$$2k_s(\delta A_{s0}/\delta z)=(4\pi/c)\varepsilon\beta_{0\perp} j_b \sin(\tau)$$

$$\Delta_\perp A_{s0}+q^2 A_{s0}=(4\pi/c)\varepsilon\beta_{0\perp} j_b \cos(\tau) \qquad (3)$$

where $\Delta_\perp$ is the transverse part of Laplasian, $q^2=k_s^2-\omega^2/c^2$. It is important to emphasise that after the trapping the magnitude of q^2 remains greater then zero because phase velocity of wave is decreased.

Equations (3) define the alterations of values A_{s0}, ε, q^2 with the oscillating process of phase τ . The change of the phase is determined by the equation of particles moving in the field of the ponderomotive wave. Somewhat conclusions are followed from the physical law-governed nature of trapped bunches and EMR interaction.

After integrating on the transverse section the equations (3) gives the average ratios in which value of $S_A=2\pi\int A_{s0} r dr$ appears in left part. The full beam current I_b and average magnitudes ε and τ are figured in right part. The top value of τ_m corresponds to the capture moment of the beam when electron velocity is equal to phase speed of the ponderomotive wave. Phase value $\tau=0$ conforms with the beam passing over minimum of the ponderomotive potential. The second ratio in (3) acquires a simple form:

$$q^2 S_A=(4\pi/c)\beta_{0\perp}\varepsilon\cos(\tau) \qquad (4)$$

After capturing the electron bunches oscillates with phase $\tau<\tau_m$. From the physical point of view it is clear that the process of energy exchange between beam and EMR prolongs to $\tau\sim 0$. However, the addition to the EMR energy no very appreciable because the EMR wave on the phase area $0<\tau<\tau_m$ passes electron beam. Besides, in the region $\tau=0$ the electron bunches become blurred due to the heterogeneous velocities. Formally this process leads to decreasing of the magnitude ε. Qualitative graphic estimation indicates that $\varepsilon(\tau \approx \tau m)=1.6\text{-}1.8$ and $\varepsilon(\tau\approx 0)=1.3$. In the same time the value of $\cos(\tau)$ increases very small so the value $\varepsilon_1=\varepsilon\cos(\tau)$ is oscillates range from 1.5 to 1.3 [5]. Thus, analysis of the trapped state of system allows to evaluate the practical efficiency of FEL.

Interaction between space-heterogeneous channelling EMR and beam electrons leads to the non simultaneous capturing of the different radial layers of beam. Therefore, the greatest efficiency of particles and EMR interacting are provided by electron beam with the tube configuration. In this case the density of the electron beam is derived from the ratio $n_b(r)=\varepsilon_1 I_b\delta(r-a)/(2\pi ce\beta_z r)$ ($\delta(r-a)$ is Dirac function). The transverse distribution of the EMR field is determined by the second ratio of (3) with the quasi-constant right part (ε and τ change very slowly after trapping).Consequently, solutions of wave equation are given by $A_s(r<a)=A_1 K_0(qa)I_0(qr)$ and $A_0(r>a)=A_1 I_0(qa)K_0(qr)$, where I_0,K_0 are Bessel functions of imaginary values. There is strong channelling structure of EMR [6]. In this way the magnitude of the longitudinal velocity $c\beta_z$ of trapped particles is expressed in terms of the beam current:

$$I_b=[32ak_s I_A\gamma_0(\beta_{0z}-\beta_z)(1-\beta_s^2)^{3/2}(\beta_z/\varepsilon_1\beta_\perp)^2]\times$$

$$\times[(1-\beta_s)^2+2\beta_s(1-\beta_z)]^{-1} \qquad (5)$$

here $I_A=mc^3/e=17$ kA. Taking into account connection between k_s and k_{si} the ratios (2) and (5) give the self-consistent evaluation of top efficiency. In the first approximation on $\delta\beta=\beta_{0z}-\beta_z$ using the coefficient $\varepsilon_1=1.5$ of the limit bunching, we have:

$$\eta=[(I_b/(2I_A a\, k_0\gamma_0^2))^{2/5}]/2 \qquad (6)$$

It is significant that the equation has the same form of the similar ratio of the linear theory but it differs from the later one by the numerical coefficient. The efficiency of the collective FEL is not high and it decreases at more short wavelength. EMR efficiency of FEL in infra-red and optical regions do not exceeds one - two percent for the moderated beam current.

III. HIGH-CURRENT FEL WITH VARIABLE PARAMETERS. THE DEVICE OPTIMISATION

To increase the device efficiency it is necessary to change the initial beam characteristics or the undulator field parameters in the process of the beam passing through the laser cavity [7]. Efficiency estimations are usually based on the numerical methods. Nevertheless, evaluating procedure for system with tapering parameters may be carried out by means of the method stated above.

Consider some examples. The gain magnitude remains enough considerable if the value of β_{0z} differs from the resonance magnitude β_r. It is clear that the surplus of the velocity $\delta=\beta_{zi}-\beta_{z0}>0$ prolongs the process of electron decelerating and delays the particles capturing. In this case the EMR excitation in the same range of frequency is provided by the more high level of the triggering field.

The condition of electron trapping

$$\beta_z(z^*)=\omega_s/(k_s(z)+k_0)c \qquad (7)$$

is not changed and efficiency is estimated by the ratio:

$$\eta=[(\beta_{0z}-\beta_z(z^*))\beta_{0z}\gamma_0]/[(\gamma_0-1)(1-\beta_z(z^*)]. \quad (8)$$

The value of velocities difference $\delta\beta_z=\beta_{0z}-\beta_z(z^*)$ at the beam current is defined from the nonlinear equation that in case using tube design beam is

$$\delta\beta_z(\delta\beta_z-\delta)^{3/2}=I_b/\Lambda I_A, \quad (9)$$

where $\Lambda=2^{7/2}ak_s/\gamma_0^5$. If the initial beam energy exceeds by the 5% from its resonance value the EMR efficiency is higher on the same magnitude. But raising of the efficiency due to the additional part to the initial particles velocity leads to the significant practical difficulties and may be realised to small γ_0 i.e. for the long wave EMR (because $\delta\beta=\delta\gamma/\gamma^3$).

Therefore, other method of the efficiency increasing presents a great interest. We mean the varying of magnetic field parameters of the undulator (B_0 and λ_0). Let us consider the case of alteration of the undulator period. This situation is enough understandable. The decrease of period that follows to the beam passing supports the resonance condition in system. Suitable estimations are determined by the equations (5) - (9) but in later ratio δ is equalled

$$\delta_{und}=[\lambda_0/\lambda_0(z^*)-1]/\gamma_0^2. \quad (10)$$

The magnitude of efficiency is approximated to the corresponding value of δ (or δ_{und}):

$$\eta=\gamma_0^2[\delta+(I_b/\Lambda I_A\delta)^{2/3}]. \quad (11)$$

For example, variation of the undulator length by the 10% allows to obtain the value of the EMR efficiency up to 11% at I_b=200 A and 12% at I_b=600 A (γ_0=30).On the first view the FEL efficiency weakly depends on the beam current. However, the value of L_{und} is inversely proportional to $I_b^{2/5}$.

Consequently, the high-current FEL may operates with high efficiency in the regime of saturation. This conclusion remains true for the arbitrary beam configurations and different undulator designs. Notice that the significant value of the efficiency may be achieved in the only high-current systems. For example, in [8] experimental value of efficiency was not exceeded 3% when undulator parameters was changed to 12% and beam current was 7 A and γ_0=40 (electron energy had been 20 MeV). On the more late experiments [8] electron current was raised to 100 A without quantitative beam deterioration. Nevertheless FEL efficiency was not achieved to optimal value. Indeed the FEL was made for the single-particle amplifying only. For example, when the undulator length was L_{und}=100 cm, then the FEL efficiency appeared to be ~$1/L_{und}$ [2]. For this undulator the collective regime with saturating process may be observed in systems with beam current approximately a few kA. Therefore magnitude of EMR efficiency in these devices may be higher due to using longer undulator or bigger electron current.

Coulomb defocusing of the electron beam is one of problems connecting with the high-current FEL. It may be eliminated by plasma filling of the laser cavity. This method was successfully used at the traditional electronic devices. Plasma at ordinary density $n_p<10^{13}$ do not brings any varieties to the resonance conditions of the FEL. Stimulating processes in system are subjected to more complex influence of neutral gas filled the laser cavity. In this case the resonance interaction of the both fast and slow beam modes are possible. So FEL with plasma filling requires the serious theoretical analysis.

Thus the analysis stated above emphasises that the high-current FEL may be both more powerful and more effective shortwave radiating source.

IV.REFERENCES

[1] S.A. Alimov, A.S. Chepurnov, O.V. Chubarov et al. Moscow Race-Track Microtron, Preprint INP MSU-93, M., (1993)

[2] Pelligrini IEEE Trans. Nucl. Sci, N5-26, (1979), 3731.

[3] J. M. J. Madey. J. App. Phys., v.42, (1971), 1906.

[4] L.D. Landau, E.M. Lifshits. Theory of field. 1988.

[5] N.S. Matsiborko, L.K. Onishenko, V.D.Shapiro, V.I. Shevchenko. Plasma Phys.,v.14 (1972), 561

[6] E.T. Scharlemann, A.M. Sessler, J.S. Wurtels. Nucl. Instr. and Meth. in Phys. A, v.238 (1985), 19.

[7] E.T. Bessonov, A.V. Vinogradov. Uspekhi Fisich. Nauk, v.159, (1989), 143

[8] R.W. Warren, B.E. Newman, J.Q. Wiston et. al. IEEE J. Quant. Electr., (1983), QE-19.P.391.

A CHIRPED-PULSE REGENERATIVE-AMPLIFIER FEL FOR THE GAMMA-GAMMA COLLIDER*

K. C. D. Chan, J. C. Goldstein, D. C. Nguyen, and H. Takeda
Los Alamos National Laboratory , Los Alamos, NM 87545, USA

During a Workshop on Gamma-Gamma Colliders in Lawrence Berkeley Laboratory, it was pointed out that an 1-μm laser that can produce 1-J, 1-ps pulses at a few hundred hertz is required. With high-power scalability and ease of formatting, an FEL can be a promising candidate for such a laser. We propose an FEL scheme based on chirped-pulsed regenerative amplification to achieve this high peak-power laser. The 1-ps pulse of a solid-state laser will be stretched, amplified, and recompressed to achieve the high peak power. The system is relatively simple and consists of mostly components that have already been demonstrated. This paper will describe the proposal and the important issues of such a scheme.

I. INTRODUCTION

For high-rate gamma production in a gamma-gamma collider, a laser that can produce 1-J, 1-ps pulses with wavelength longer than 1 μm is needed. This laser, when Compton-backscattered by a high-energy electron beam, can produce a high-intensity beam of high-energy gamma rays [1].

To achieve the 1-Joule laser pulses, we propose to use chirped-pulsed amplification (CPA) in a free-electron laser (FEL). CPA using solid-state-laser gain media has produced peak powers as high as a few terawatts [2]. In solid-state media, this technique appears to have a maximum average power of 1 watt [3], possibly limited by the thermal characteristics of the gain media. CPA in a FEL has been proposed as a mean to generate femtosecond vacuum-ultraviolet pulses [4] but, thus far, no experimental results on CPA with an FEL have been reported. An FEL is the ideal amplifier medium for CPA because the high-quality electron beams forms a low-distortion, high-gain medium whose gain curve can be tuned to match the input wavelength. Unlike solid-state media, FEL amplifiers are scalable to high repetition rates. Thus, a CPA FEL potentially can be developed into a high-average-power terawatt laser.

Beside tunability and high-average-power capability, an FEL amplifier can be quite efficient, especially if the wiggler is tapered. Efficiencies as high as 4.5% have been demonstrated with tapered wigglers in the infrared [5]. However, a tapered-wiggler FEL amplifier usually has a low single-pass gain. This problem can be circumvented by operating the FEL as a regenerative amplifier. In a regenerative amplifier, an input laser pulse is amplified repetitively by electron pulses in a synchronous cavity. The intracavity power builds up to reach saturation and to efficiently extract energy from electron pulses.

II. PROPOSED SCHEME

The proposed CPA regenerative-amplifier FEL system is shown in Fig. 1. It has the following subsystems: a solid-state laser, a pulse stretcher, an FEL regenerative amplifier, and a pulse compressor. The output of the solid-state laser is a 1-ps, 1-mJ pulse at 1.05 μm. It will be pulse stretched from 1 ps to 50 ps at the pulse stretcher. It is injected into the regenerative-amplifier FEL to be amplified to the 1-J energy level. It is pulse-compressed in the pulsed compressor to the 1-ps pulse length.

The solid-state laser has a Nd:YLF oscillator and a large bandwidth regenerative amplifier. The system is commercially available.

The pulse stretcher and pulse compressor consist of linear dispersive elements that convert between frequency chirp and pulse length. Each of them consists of a pair of gratings [6]. They are different by the stretcher having an extra lens. The grating pair introduces a frequency-dependent temporal delay as given by:

$$\tau(\omega) = \tau_0 - \mu^{-1}(\omega - \omega_0) + \vartheta(\omega - \omega_0)^2 \qquad (1)$$

where τ_0 is the fixed delay at $\omega = \omega_0$, ω_0 is the central frequency of the laser, μ, is the linear dispersion of the grating pair, and ϑ is the higher-order term that is usually negligible. The linear dispersion, μ, is a function of the grating separation b, the groove spacing d, and the angle γ which is the angle between the incident and diffracted beams for a grating

$$\mu = \frac{\omega_0^3 d^2\left(1 - \left(\frac{\lambda}{d} - \sin\gamma\right)\right)}{4\pi^2 c\, b} \qquad (2)$$

Neglecting the higher-order terms, the length of the stretched pulse can be estimated by

$$\tau_{stretch} = \frac{4bm^2\lambda\Delta\lambda}{d^2 c \cos^3\theta} \qquad (3)$$

where m is the grating order, λ is the central wavelength, $\Delta\lambda$ is the bandwidth and θ is the diffracted angle. Estimates using equation (3) show that an 1-ps pulse can easily be stretched to 50 ps.

* This work is supported by Los Alamos National Laboratory Institutional Supporting Research, under the auspices of the United States Department of Energy

0-7803-3053-6/96/$5.00 ©1996 IEEE

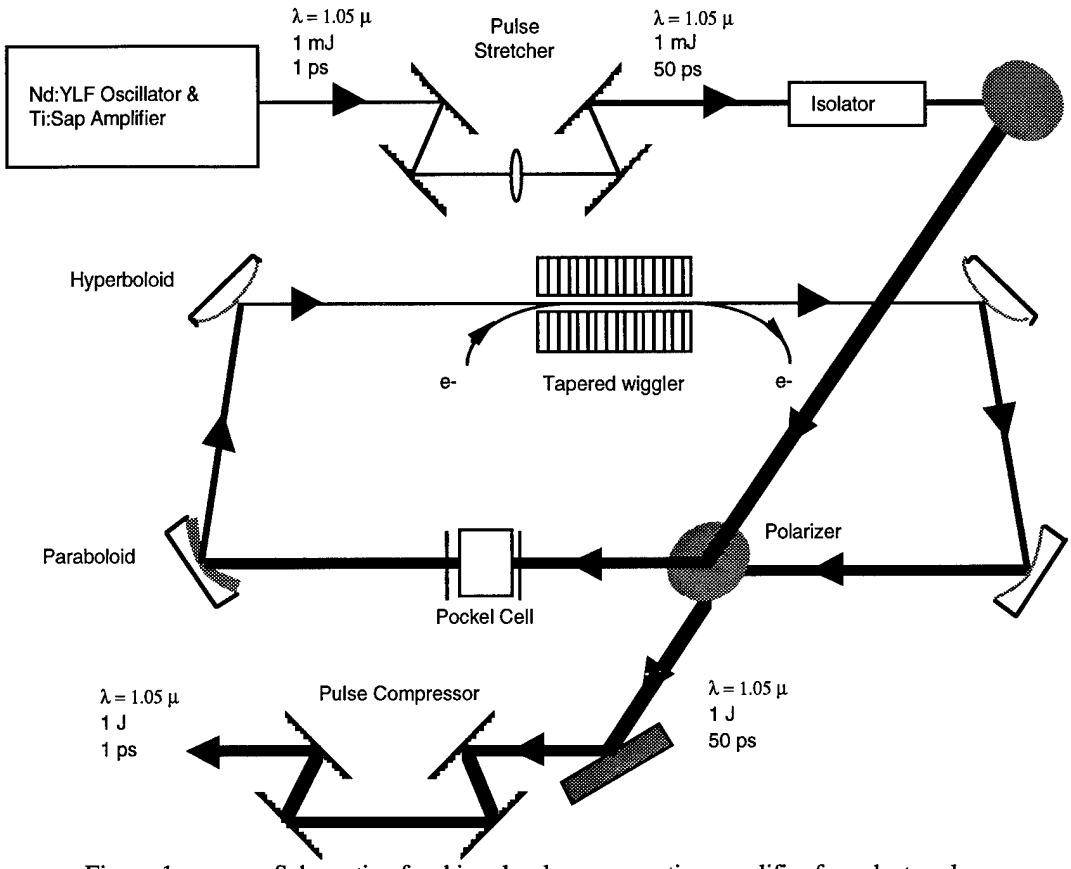


Figure 1: Schematic of a chirped-pulse regenerative-amplifier free-electron laser.

The regenerative amplifier FEL consists of a high-brightness electron beam, a tapered wiggler and a ring resonator. Its parameters are summarized in Table 1. The parameters of the high-brightness electron beam were chosen similar to those of the Los Alamos Advanced Free Electron Laser (AFEL). At a bunch charge of 3 nC, the AFEL electron beam has an rms normalized emittance of 2.5 π mm mrad, an energy spread of 0.5%, and a pulse length of 10 ps [7]. This high-quality electron beam can be obtained at higher bunch charge by lengthening the pulse length. The wiggler is tapered to achieve higher extraction efficiency. The parameters are being chosen similar to a high-efficiency wiggler that was designed for the recent AFEL High-Average-Power-Upgrade Project [8]. The AFEL wiggler will have a length of 36 cm and an extraction efficiency of 7%. The ring resonator consists of 2 hyperboloids and 2 paraboloids with a total cavity loss of 2%. The peak power densities on these optical elements, probably made of dielectric, are kept below 2 GW/cm^2 to avoid damages of the optics. At an optical power of 20 GW, the optical spot on the mirrors needs to have a radius larger than 25 mm. A grazing-incidence ring resonator based on hyperboloids and paraboloids has been designed, constructed, and operated in a high-power FEL [9]. The laser pulse will be switched in and out of the resonator by changing its polarization using an electro-optical switch like the Pockel cell. The Pockel cell has a switch time of nanoseconds that is small compared to the round trip time of the resonator.

III. NUMERICAL SIMULATIONS

To assure the feasibility, we have performed preliminary numerical simulations of the regenerative amplifier FEL performance using a one-dimensional FEL code called FELP [10] using parameters shown in Table I. The input optical pulse is assumed to be a parabolic pulse with 50 ps pulse length and 1 mJ pulse energy, yielding a peak power of 20 MW. The input beam is focused in the center of the 10% tapered wiggler to a waist of 144 μm in radius. If we assume the Rayleigh range to be 50 cm (half the wiggler length), the optical beam waist at the ends of the wiggler is 631 μm.

Over 95 passes, the intracavity power saturates at 20 GW. The high intracavity power allows the optical field to extract energy efficiently from the electron beam. For the 10% quadratically tapered wiggler, the highest extraction efficiency is about 4.5%. In each pass, the extracted energy is a few percentages of the energy of the electron pulses (600 mJ). Over approximately 95 passes, the accumulated optical pulse energy reaches 1 J.

IV. DISCUSSION

The approach described here depends on chirped-pulse amplification (CPA). The frequency chirp has to be preserved in the regenerative FEL amplifier. A compressed pulse of

FWHM of 1 ps has a transform-limited bandwidth of 440 GHz. At 1 μm, this bandwidth corresponds to a relative spectral bandwidth of 0.15%. In an FEL amplifier, the gain bandwidth is determined by the number of wiggler periods N_W. For N_W =100, the FEL gain bandwidth is around 0.5% for a uniform wiggler and will be larger for a tapered wiggler. This bandwidth is considerably larger than the chirp of the 1-ps pulse. Therefore we expect the bandwidth of the laser pulse can be preserved in an FEL amplifier even with an unchirped electron pulse.

Table I: Parameters of Regenerative FEL Amplifier

Electron Beam

Pulse charge	q	15 nC
Pulse width	τ	50 ps nominally
Peak current	I	300 A
Pulse frequency	f	54.167 MHz
Beam energy	E	38.5 MeV (γ = 76.3)
Normalized emittance (rms)	ε_n	2.5 π·mm·mrad
Energy spread	$\Delta\gamma/\gamma$	0.5% (FWHM)

Tapered Wiggler

Taper in k_W		10%
Period	λ_W	1.023 cm
Length	L_W	1 m (N_W = 100)
Full gap	2H	3 mm
Peak magnetic field	B_W	0.585 T
Wiggler parameter (rms)	a_W	0.5586

Ring Resonator

Type		Ring, stable
Cavity length	L_C	5.534 m
Mirror radius of curvature	R_C	70 cm
Rayleigh range	z_R	50 cm (~ L_W/2)
Beam radius at waist	w_O	.378 mm
Beam radius at wiggler end	w	.753 mm
Wiggler clear aperture	2a	2.8 mm
Round-trip loss	α	2%

Table 2: Simulation Results

Wavelength	λ	1.053 μm
Small-signal gain	g_{ss}	100%
Saturated gain	G	2.1%
Intracavity power	P_{cavity}	20 GW
Extraction efficiency	η	≤ 4.5%
Pulse energy	E_p	1 J
Pulse width	τ	15 ps

Special attention is required to insure that the mirrors in the resonator will retain the reflectivity and not be damaged in the high intracavity power. In this design, the peak laser intensity on the hyperboloid mirrors located 1.5 m from the waist is less than 2 GW/cm^2, below the damage threshold of dielectric mirrors.

The design described here is a point design derived from our experience with AFEL showing the feasibility of this approach. Optimized parameters can be derived with respect to specific Gamma-Gamma Collider and further simulations.

V. SUMMARY

We described a point design of a chirped-pulse regenerative-amplifier FEL system that can achieve the 1-J, 1-ps pulse needed for a Gamma-Gamma Collider. This design uses subsystems that are readily achievable with existing technology.

VI. REFERENCES

[1] D. D. Meyerhofer, Nucl. Instr. Meth. **A**355 (1995) 113.
S. Chattopadhyay and A. M. Sessler, (editors), Proceedings of the Workshop on Gamma-Gamma colliders, LBL, Berkeley, CA, USA, March 28-31, 1994, Nucl. Instr. Meth. **A** 355 (1995).

[2] D. Strickland and G. Mourou, Opt. Commun., 56 (1985) 219.

[3] Gerard Mourou, Private communication.

[4] L. H. Yu, E. Johnson, D. Li, and D. Umstadter, Phys. Rev. **E** 49 (1994)

[5] D. Feldman, et al., Nucl. Instr. Meth. **A** 285 (1989) 11.

[6] M. Pessort, P. Maine and G. Mourou, Opt. Commun. 62 (1987) 419.

[7] D. C. Nguyen, et al, SPIE 2118-19 (1994) 260-277.

[8] D. C. Nguyen and R. W. Warren, to be presented in the 1995 International FEL Conference, New York, NY, USA, August, 1995.

[9] D. Dowel, et al, Nucl. Instr. Meth. **A** 304 (1991) 1.

[10] FELP is a one-dimensional FEL code developed at Los Alamos National Laboratory, see J. C. Goldstein, SPIE 453 (1984) 2.

ALIGNMENT AND MAGNET ERROR TOLERANCES FOR THE LCLS X-RAY FEL*

H.-D. Nuhn
Stanford Linear Accelerator Center, Stanford University, Stanford, CA 94309-0210, USA
E.T. Scharlemann
Lawrence Livermore National Laboratory, Livermore, CA 94550, USA
R. Schlüter
Lawrence Berkeley Laboratory, University of California, Berkeley, CA 94720, USA

Abstract

We have examined the influence of misalignments and magnet errors on the predicted performance of the Linac Coherent Light Source (LCLS). Due to the extremely large number of wiggler periods ($> 10^3$) and the small optical mode size (20 μm), alignment and magnet tolerances will be quite demanding. These demands may increase if the wiggler is split into separate sections by the possible inclusion of diagnostic stations, dispersive sections, *etc.* We have attempted to quantify such tolerances using the numerical simulation code FRED-3D.

I. INTRODUCTION

The LCLS is a multi-institutional proposal for a single-pass x-ray FEL operating in the 1-2 Å wavelength region, using electron beams from the SLAC linac at $\sim$ 15 GeV energy [1]. The effect of field and steering errors on the performance of an X-Ray FEL operating at an optical wavelength of 4 nm based on a 7 GeV electron beam from the SLAC linac has been studied before by Kim et. al. [2]. Since then the proposed target wavelength for the LCLS project has been reduced. This change was based on the results of the workshop on Scientific Applications of Coherent X-Rays [3] held at SLAC in 1994.

The change in wavelength required a reduction in electron beam emittance by more than an order of magnitude to stay at the diffraction limit given by $\lambda/2\pi$. This could be achieved by an increase in electron energy and by making use of further progress in the development of low emittance guns, reducing the projected value for the normalized emittance from 3 down to 1 mm mrad. The resulting emittance is still larger than $\lambda/2\pi$ but, as fig. 1 shows, the decrease in FEL performance is expected to be moderate. With the optimum β-function basically unchanged, the transverse beam size is reduced by a factor of about 2.5. The tolerances for field and steering errors should scale approximately by this factor. The present paper presents the results of 3-D simulations for the new LCLS design, also comparing the two wiggler models that are presently discussed.

II. WIGGLER MODELS

The wiggler models that are presently considered include a Superconducting Helical Wiggler [4] and a Planar Neodymium-Iron Hybrid Wiggler. The optimized parameters [5] are listed in table I. The electron beam parameters are listed in table II.

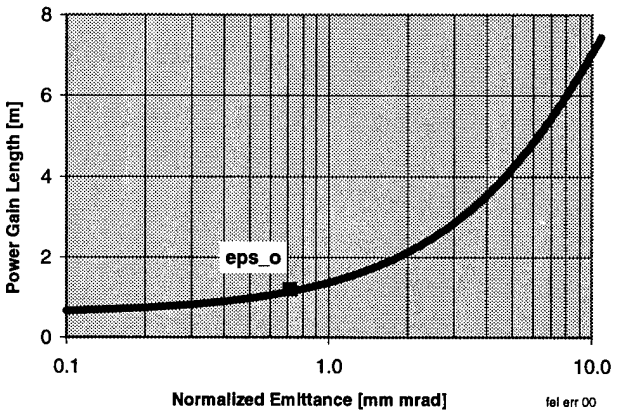


Figure 1. Power Gain Length vs. Normalized Emittance as a result of FRED-3D simulations for the helical wiggler. **"eps_o"** marks the diffraction limited emittance at the optical wavelength of 1.5 Å.

	SC	Hybrid
Type	Helical	Planar
Period Length	2.0 cm	3.0 cm
Optical Wavelength	1.5 Å	1.5 Å
K	3.4	3.7
Peak Field	1.8 T	1.3 T
Gap	0.6 mm	0.6 mm
Number of Periods	1500	1667
Wiggler Length	30 m	55 m
Focussing β	4.9 m/rad	10 m/rad
RMS Beam Radius	19 μm	13 μm
Pierce Parameter ρ	7.4×10^{-4}	7.4×10^{-4}
Gain Length	1.5 m	3.1 m

Table I
LCLS wiggler and FEL parameters

III. WIGGLER ERRORS

Error fields can arise from (1) iron pole, Electro-magnetic coil, and/or Permanent Magnet (PM) positioning/orientation errors, (2) PM strength and global/local easy-axis misorientation errors, and (3) iron non-uniformities, including saturation effects. Symmetric field errors $\Delta B_y(z)$ are perpendicular to the midplane in

*Supported in part by the Department of Energy, Office of Basic Energy Sciences and High Energy and Nuclear Physics and Department of Energy Contracts DE-AC03-76SF00098(LBL) and DE-AC03-76SF0015(SLAC).

0-7803-3053-6/96/$5.00 ©1996 IEEE

RMS Bunch Length	30 μm
R¡S Bunch Length	100 fs
Normalized RMS Emittance	1.5 mm mrad
Uncorrelated RMS Energy Spread	2×10^{-4}
Electron Energy	15 GeV

Table II
LCLS electron beam parameters

the midplane and lead to both a horizontal displacement and steering of the beam. Antisymmetric field errors are parallel to the midplane in the midplane. Those errors $\Delta B_z(z)$ that are also parallel to the electron trajectory have no detrimental effects. Those errors $\Delta B_x(z)$ parallel to the midplane, but perpendicular to the electron trajectory, cause vertical beam steering and displacement. In the ironless helical superconducting wiggler, field errors are dominated by positioning errors of the superconducting coil, which can arise either during the manufacturing process or from magnetic forces during training. There is no iron surface present to channel magnetic flux and thereby govern the field distribution as in the case of the planar hybrid design. Magnetic material placed near the coils can also alter the field on-axis. Mispositioning of the magnetic structure itself or variation of the period length give rise to systematic phase errors. If the electron beam is misoriented with respect to the wiggler magnetic structure or if wiggler sections are not coaxial then steering errors can arise.

IV. FRED-3D SIMULATION CODE

The simulations in this paper have been done with the FRED-3D [6] simulation code on the NERSC computer systems at LLNL. FRED-3D simulates the interaction between the electron beam and optical field in the wiggler of an FEL amplifier. The effects of random pole-to-pole errors in the wiggler magnetic field on the centroid motion of the electron beam and on relative electron-to-radiation phase are included: in each half-period, a transverse momentum increment corresponding to the magnetic field error at that magnetic pole is added to the motion of each particle. The field errors are chosen from a truncated Gaussian distribution. The RMS fractional field error and truncation level are specified as input parameters; for this paper, truncation at three standard deviations is used. The transverse random walk of the electron beam generated by these errors reduces the overlap between the electron and photon beams and causes dephasing of the electrons with respect to the FEL ponderomotive potential wells.

The random walk can be partially corrected in FRED-3D by introducing "steering stations", at which the position of the electron beam is measured and a transverse momentum kick is applied to steer the electron beam onto the axis at the next steering station. The position measurement is assumed to be imperfect, with specifiable errors in the accuracy with which the beam position monitors are aligned and the accuracy with which they can measure the beam position. In addition, an overall displacement and tilt of an average beam position monitor axis from the wiggler axis can be specified. The positions of steering stations along the wiggler axis and the magnitude of the steering errors are inputs to the code.

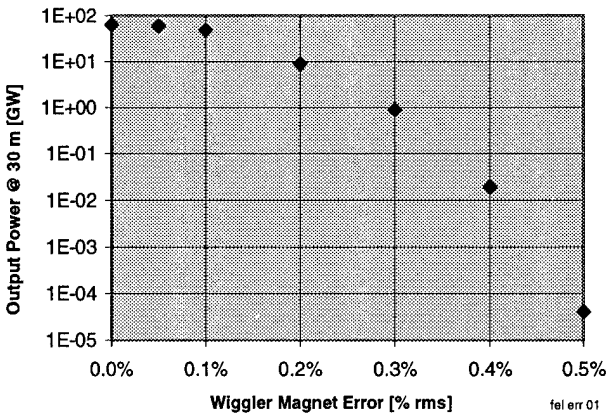


Figure 2. Output Power vs. Magnet Errors for Helical Wiggler

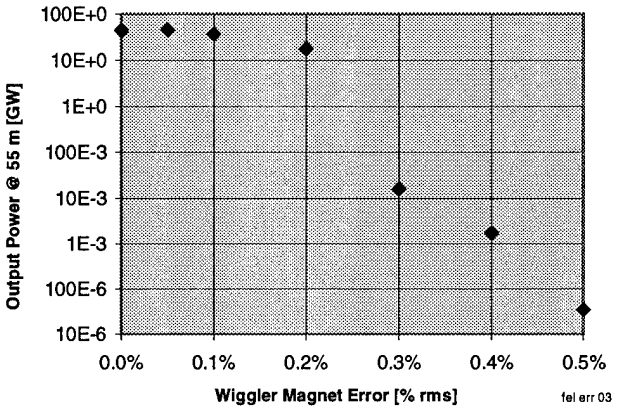


Figure 3. Output Power vs. Magnet Errors for Planar Wiggler

FRED-3D does not explicitly include the phase effects of random fluctuations in the wiggler period, because the cumulative effect of these fluctuations over many periods should be identical to a slight change in wiggler period, which can be simulated by permitting the period to change between wiggler sections.

V. ERROR ANALYSIS

A. *Wiggler Magnetization Errors (Field Errors)*

The sensitivity of wiggler output power on wiggler magnetization errors has been studied.

Figs 2 and 3 show the effect of random fluctuations of the on-axis peak magnetic field on the FEL power when using error-free steering stations separated by 2.5 m. Error bars, which are significant for large values of the rms wiggler error, are not shown. The peak power levels[1] are shown for wiggler lengths at which the error free device would saturate, i.e. at 30 m for the helical and at 55 m for the planar wiggler, *resp.* The output power levels drop by a factor of two for RMS error levels of about 0.15 %.

A detailed analysis of topics such as a comparison of global and local error tolerances and the relative contribution of dephasing of the electrons and reduction in beam overlap has not been done yet. Work by Yu et. al. [7] indicate that the performance

[1] 1 kW of input power has been used in the simulations since FRED-3D does not simulate startup from noise

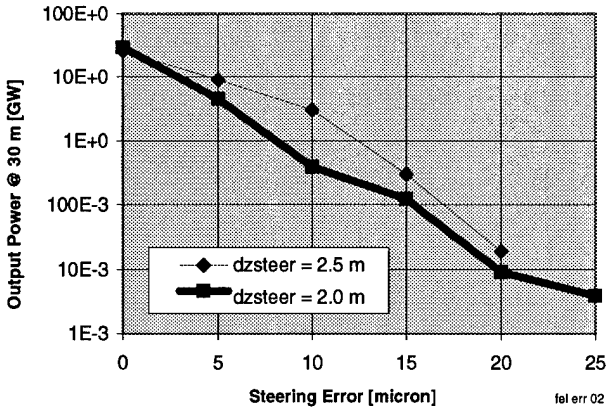


Figure 4. Output Power vs. Steering Errors for Helical Wiggler

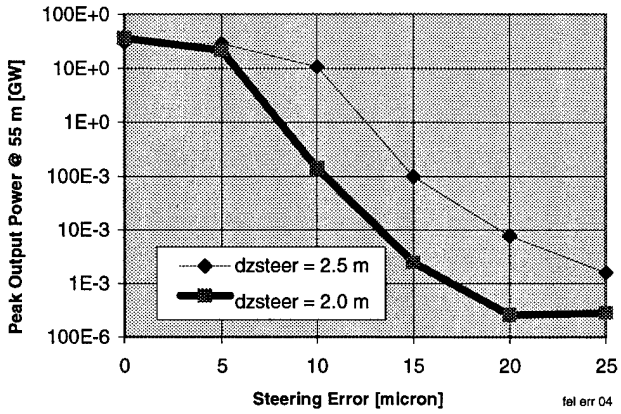


Figure 5. Output Power vs. Steering Errors for Planar Wiggler

reduction due to dephasing should be significantly less than the results that we get for the combined effect.

The natural focussing of the wiggler is not strong enough at the operational energy. Strong external focussing is required to achieve the optimum beta functions as listed in table I. While the simulations used a constant focussing gradient along the wiggler axis, in practice it is more likely that a lattice of separate quadrupole magnets (FODO) will be used. Required integrated quadrupole strengths are 10 T for the helical and 5 T for the planar wiggler. If the electron beam passes off-axis through the quadrupole magnets it will experience additional transverse kicks. To keep these kicks at the same level as those produced by wiggler errors (0.15 %), transverse alignment tolerances for the quadrupoles of a few micro-meter are necessary.

B. Steering Errors

Figs 4 and 5 show the effect of steering errors for the helical and planar wiggler models as result of the simulations. Field amplitude fluctuations of 0.15 % were used in both cases. Each figure shows the result for two different separations of the steering stations: 2.0 and 2.5 m. With steering errors present, FEL performance decreases when steering stations are spaced too closely The optimum spacing of the steering stations for the planar wiggler is between 2.5 and 5 m (for an RMS steering error of 10 μm).

Fig. 6 shows the effect of separating 5 m long wiggler sections

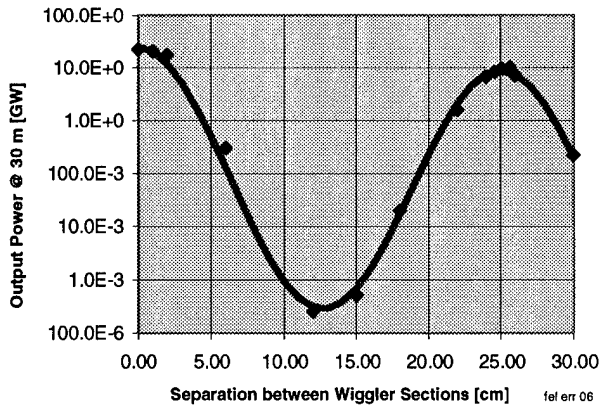


Figure 6. Output Power vs. Section Separation for Helical Wiggler

by short drift spaces to simplify modular assembly and to provide space for diagnostics, vacuum pumps *etc.* The simulations used an rms magnetization error of 0.15 %, a separation of steering stations of 5 m and a steering error of 10 μm.

The performance drops significantly due to phase slippage for separations L_{sep} shorter than about 25 cm, at which point the slippage distance $(1-\beta)L_{sep}$ is equal to one optical wavelength λ_r. Using $(1-\beta) \approx 1/2\gamma^2$ and the FEL resonance condition one gets for the first matching separation $L_{sep}^{match} \approx 2\gamma^2\lambda_r = \lambda_w(1+K^2)$=25.12 cm for the helical wiggler, which for high energies is independent of both the energy and the radiation wavelength. This has been shown by Kim et. al. [8]. Thus, wiggler section separations need not affect FEL tunability, if tuning is done with γ. Tuning cannot be done by using K.

References

[1] H.-D. Nuhn et. al., "Short Wavelength FELs Using the SLAC Linac." Proceedings of the EPAC94, London, England, 1994. SLAC-PUB-6541, SLAC/SSRL-0082, LBL-35905.

[2] K.-J. Kim et. al., "Performance Characteristics, Optimization, and Error Tolerances of a 4nm FEL Based on the SLAC Linac." Proceedings of the PAC93, Washington, DC, 1993.

[3] J. Arthur, G. Materlik, and H. Winick, eds., *Workshop on Scientific Applications of Coherent X-Rays*, February 1994. SLAC-Report-437.

[4] S. Caspi, "private communication," 1994.

[5] M. Xie, "private communication," 1995.

[6] E.T. Scharlemann, "Wiggle plane focusing in linear wigglers," *J. Appl. Phys.*, vol. 58, pp. 2154–2161, 1985.

[7] L.H. Yu et. al., "Effect of wiggler errors on free-electron-laser gain," *Phys. Rev. A*, vol. 45, pp. 1163–1176, 1992.

[8] K.-J. Kim and M. Xie, "Effects Of Wiggler Interruption On LCLS Performance," 1995. CBP Tech. Note-77.

ELECTRON TRANSPORT AND EMITTANCE DIAGNOSTICS IN CIRFEL

J.Krishnaswamy, I.S.Lehrman, and R.Hartley, Northrop Grumman Advanced Technology and Development Center, 4 Independence Way, Princeton, NJ-08540, and R.H.Austin, Princeton University, Princeton, NJ-08544

Electron pulses for the Northrop Grumman Compact Free Electron Laser CIRFEL are produced at a repetition rate of up to 10 Hz by the illumination of a Mg photo-cathode with a photon injector 261 nm seed laser system mode locked to the 20th sub-harmonic of 2.856 GHz. Presently the system is being operated in the 10 to 12 MeV energy range and spontaneous radiation has been observed. We present some preliminary results on electron beam characterization including its energy spread , energy stability, and spontaneous radiation observations.

I. INTRODUCTION

The Compact IR Free Electron Laser facility CIRFEL, under construction by Northrop Grumman Corporation at the Princeton University's Physics Department under a Joint Research Agreement has entered the commissioning phase. When completed it will serve as a platform for advanced research in Physics and Engineering. The facility will be used initially by groups working in the area of biophysics and multi-photon dissociation for pollution control. The CIRFEL system is described, summarizing the progress made with some of the measurements evaluating the electron beam parameters.

II. CIRFEL SYSTEM

The CIRFEL system comprises of the following system components, (1) High brightness photocathode electron gun, (2) Photo-injector laser, (3) 30 MW S-Band RF source, (4) the beam transport system, (5) the FEL microwiggler, (6) the FEL optical cavity, and (7) associated support hardware sub-systems. CIRFEL which occupies two levels with the photo-injector and the high power RF system on one level, and the rest of the system on the ground floor has been previously described [1].

A. High Brightness Photo cathode Electron Gun

The high brightness photocathode gun designed for CIRFEL is an extremely bright source of electron beams and is specified by the parameters shown in Table 1. The Photoelectron source comprises of a 6 mm diameter Mg cathode illuminated by a photon injector and is situated in a 3.5 cell ; Pi mode RF cavity, which produces a very high gradient (60 to 80 MeV/meter) on its surface. The "electrodeless emission" of electrons is controlled by the laser and allows extremely smooth control of the spatial and temporal profiles, and the electron current. The CIRFEL system started with an electron beam bombarded LaB6 cathode, but it was replaced by a Mg cathode operating at room temperature. This has improved the system performance enormously.

Table 1
Electron Beam Specifications

Beam Energy	< 7 - 13 MeV
Total Charge	1 - 2 nC
Pulse Width(FWHM)	5 - 7 psec
Normalized Emittance	< 6 Π mm-mrad
Slice Emittance	~ 1 - 3 Π mm-mrad
Peak Current	> 150 A
Energy Spread	0.2 - 1.5% Selectable

B. Photo-injector Laser

In order to optimize the efficiency of photo-emission and to have control over the characteristics of the emitted electrons, a photo injector laser which meets exacting specifications and repeatable performance has been installed and completely characterized.

A schematic of the photon seed laser system may be found in [1]. The near collimated beam produced by this system is transported to the CIRFEL system at vault level by turning and steering mirrors with reflectivities optimized for 45 degree incidence and p-polarization. The beam is then expanded in a telescope and then focused with long focal length refractive optics followed by a half wave plate so as to optimize polarized light vector on the cathode. Optical elements to correct the geometrical distortion of incoming beam at the cathode illuminated at 65^{o} to the normal at the cathode surface in the form of a cylindrical lens pair have been installed. An optical element is under fabrication to correct the time spread produced by the off-axis illumination of the cathode.

Initial characterization was carried out on the diode pumped Lightwave Nd-YLF oscillator. An average power output of 240 mW at the exit port of this laser was measured with a calorimetric power meter which has remained constant to better than 1% measured several times since it was installed. The Lightwave oscillator is

0-7803-3053-6/96/$5.00 ©1996 IEEE

phase locked to the RF source (20th sub-harmonic of 2.856 GHz=142.8 MHz) derived from the master oscillator driving the RF Linac. Phase stability measurement was carried out by mixing the RF master oscillator signal and the output of the laser oscillator detected by an Antel fast photo diode. D.W.Feldman of Los Alamos Laboratories participated in this experiment. The phase stability was better than 1 psec. The laser oscillator produces a beam with a zero order Gaussian transverse profile. The Gaussian transverse profile remained stable in position and mode structure for periods of observation of several hours. The mode locked pulses from this oscillator have a duration of 6.7 psec which was verified to remain constant over extended periods of time, with an in-line INRAD autocorrelator. The output spectrum of the laser driven by the internal / external oscillator using an Antel photo diode and a spectrum analyzer showed no spurious frequencies in the laser output.

The seed laser macro pulse is designed to have a ~10 msec flat top. In order to maintain the pulse flatness, a feed-forward correction scheme which involves, sampling the 261 nm laser pulse and adjusting the voltage on the Pockel cell as appropriate , has been implemented using the LABVIEW Control system around which the control of CIRFEL system is configured. The amplitude and phase fluctuations of the RF have been controlled to less than a fraction of a percent and less than fraction of a degree respectively using a slightly different algorithm.

The positional stability of the drive laser was characterized by looking at a focused spot with a CCD camera and an image analyzer software. Laser spot centroid movement was determined to be less than ~25 μm. The spot movement of the transported beam on the cathode location was found to be less than ~45 μm measured over a period of 10 minutes. These measurements were carried out at a dummy location of the cathode as the off-axis specular reflection from Mg was found to be too weak.

III. ELECTRON BEAM CHARACTERISTICS

The principal diagnostics used in the CIRFEL system are the current monitors and the pop-up monitor screens at various locations. The current monitors are situated so as to measure the electron current entering the bend section, the current entering the wiggler and the current leaving the wiggler. Gross aperturing of the beam can be easily detected using these monitors. A pop-up monitor before the 90 degree bend helps in centering the beam to the bend entrance. A pop-up monitor in the middle of two 45 degree bends helps to locate beam in a position appropriate for the energy. The three pop-up monitors at either end and the middle of the wiggler monitors to maintain the beam in the center of the wiggler. The HeNe alignment laser also illuminates these monitors so that the electron beam can be made collinear with the FEL laser cavity.

A. Effect of improving the flatness of the RF amplitude & phase

Maintaining the flatness of the cavity fields and the RF phase improves the energy spread of the beam. RF field amplitudes have been flattened to less than a fraction of a percent and RF phase to fractions of a degree. This has improved the energy spread dramatically as shown in Fig.1.

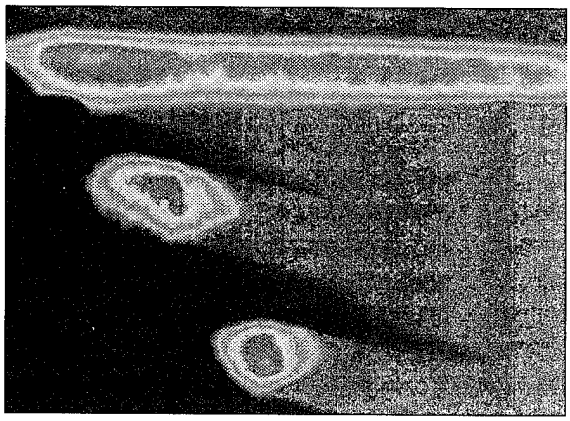


Fig. 1. Electron beam profile on a fluorescent screen in the bend region in CIRFEL. In this composite frame, the TOP profile is that of a beam produced by RF whose amplitude and phase are not flat during the macro pulse. The profile in the MIDDLE is that of beam whose RF macropulse amplitude is flattened to within a fraction of a percent, but its phase not flat. The BOTTOM profile is that one for which both ampitude and phase are flat during the macro pulse.

B. Energy calibration and energy spread of the electron beam

The main diagnostic for energy measurement is the calibrated magnetic field of the bend dipoles and the calibrated electron position monitor screen. Well defined fiducial points imprinted on the screen were used to calibrate the position monitor. Using the calibrated dipole and by producing beams of differing energies, the monitor screen in the middle of the bend was calibrated in terms of energy. The 14.5 mm of monitored reference line in the bend corresponds to 0.54 MeV. This calibration has been used to estimate the energy spread of the beam by measuring the spatial extent of the electron beam on this

monitor, at the appropriate energy. Fig.2 shows the analysis of a typical beam and this does not take into consideration the finite emittance of the beam.

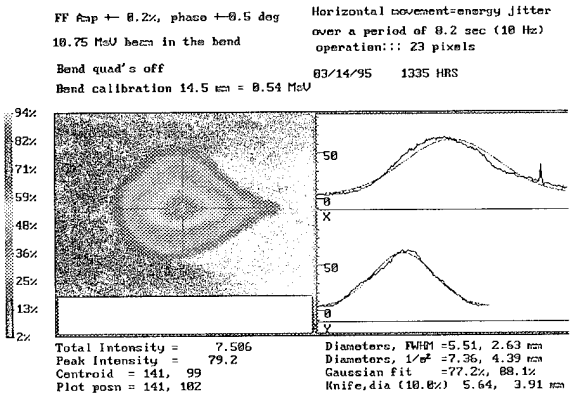


Fig.2 Electron beam profile on a fluorescent screen in the bending region (after the first 45 degree bend) in CIRFEL. The horizontal axis is calibrated in energy

C. Energy jitter of the electron beam

The movement of the electron beam on the bend monitor has been measured using the diagnostic system and the image acquisition & analysis program of Sensor Physics. Using the movie feature of this software, the images are acquired in the framing mode and the soft ware automatically calculates the centroid movement in both axes and adds in a time stamp for each frame. Using this feature the electron spot movement on the bend pop-up monitor screen has been measured. Fig.3 shows the images acquired at 0.3 sec intervals by such a method for a ~11 MeV, 40 mA , 4.75 micro-sec beam. Using energy calibration the jitter in energy of this beam is less than +/- 0.05 MeV.

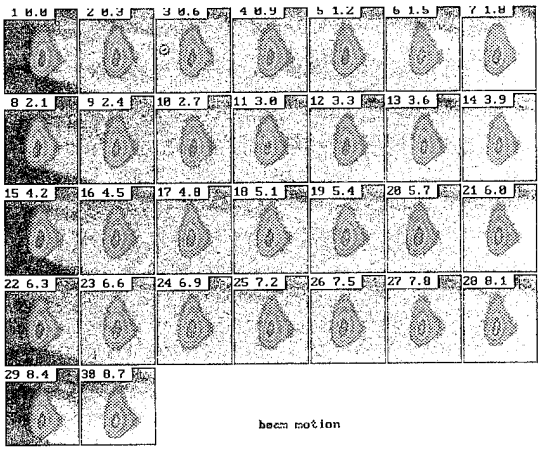


Fig.3. Beam motion in bending plane in framing mode

IV. FEL OPTICAL CAVITY& DIAGNOSTICS

Cavity Parameters of Cirfel for ~10 micron operation has the following parameters:

Near confocal stable resonator
Wiggler asymmetric with respect to cavity

Cavity length	3.1494 meters
Radii mirrors	1.4m & 2.19 m
Coatings	8 to 12 micron
Raleigh range	56.9 cm
Spot sizes on mirrors	< 5mm
Divergence	~2.4 mrad
Waist	2 mm

The Photo cathode gun and the booster cavities have been conditioned up to a maximum energy of 12 MeV with stable continuous operation in the ~11.5 MeV range transporting > 1nC of charge through the wiggler with observation of spontaneous radiation. For this energy range using the wiggler parameters the expected optical radiation is in the 12 to 13 micron range where the original dielectric mirrors do not have adequate reflectivites to obtain FEL operation. Presently, the FEL is being equipped with copper cavity mirrors of the same radii of curvature, but with coupling holes to couple out 1 to 2% of the cavity radiation. Efforts are underway in setting up the cavity length exactly to satisfy the synchronicity condition for lasing.

Preliminary emittance measurements by quadrupole scanning of a ~10.5 MeV beam carrying ~1 nC at an optimum but unspecified launch phase with flat RF, phase, and drive laser excitations gives RMS normalized emittances of ~3.5 mm-mrad which agrees with results of MAGIC simulation.

V. ACKNOWLEDGMENTS

This research is funded by the Northrop Grumman Corporation. The authors would like to thank John Shepherd of Physics Department for preparing the Europium doped Lanthanum Oxysulphide phosphor screens used in this study.

VI. REFERENCES

[1]. I.S.Lehrman, R.A.Hartley, J.Krishnaswamy, P.C.Efthimion(PPPL),andR.H.Austin(Princeton University), " The Grumman Compact Free Electron Laser(CIRFEL)", 16th International Free Electron Conference Aug 21-24, Stanford,CA 1994 (to appear in a forthcoming issue of NIM)

STUDY ON ACCELERATOR NOISE EFFECTS ON A FAR-INFRARED FEL OSCILLATOR *

Shinian Fu, Yinbao Chen, Zhibin Huang
(China Institute of Atomic Energy, P.O.Box 275(17), Beijing,PRC)

A far-infrared free electron laser driven by an L-band RF-linac is developed in our institute. In the linac some kinds of noise exist and they induce beam instability. Optical cavity detuning characteristics and the effects of accelerator noise on the FEL are simulated by an 1-D pulse code. It is found that the time jitter and energy ripple of electron beam during a macropulse modulate the laser power, and even decrease the power. Dependence of the noise effects on cavity detuning and beam parameters are also studied.

I. INTRODUCTION

Extending FEL wavelength to soft X-ray and to far-infrared or submillimeter is now a very interesting subject in FEL research for the reason that FEL in these wavelength ranges may fill in the blank of coherent radiation source. A far-infrared FEL project is launched out at CIAE for science research. The FEL will be driven by an L-band RF-linac which consists of a thermionic pulsed gun, subharmonic buncher, fundamental frequency buncher and an accelerator[1]. It is well known that the good electron beam quality, including intense current, low energy spread and low emittance, is very important for the successful operation of an FEL. And it is also found from the experiment results of Los Alamos National Laboratory FEL oscillator[2,3] that the FEL oscillator performance may be degraded by the e-beam instability generated from the accelerator noise. In the beam test of our injector we also found a serious trouble of time jitter in the gun pulser. Consequently, the phase and energy of the beam fluctuate as the beam passes through the following sections of the linac. The experience of other laboratory and the reality of our facility call for better understanding to the effects of accelerator noise. In this paper, we will investigate the influences of the e-beam instability on the far-infrared FEL oscillator by means of an 1-D pulse FEL code. In the following contents, we will briefly introduce the linac facility and discuss the noise. Then the optical cavity detuning of the FEL is studied to show the sensitivity of the FEL to the cavity length in the case that the bunch length is almost equal to the slippage in the far-infrared FEL driven by RF-linac. Finally the time jitter and energy ripple of the electron micropulse during a macropulse time are simulated to predict the effects of the accelerator noises on the performance of our FEL oscillator, and therefore, to give a requirement on the beam stability. In the simulation study it is also found the effects of accelerator noise are relative to some other beam parameters and the optical cavity detuning.

II. THE LINAC AND ITS NOISES

The grid of the electron gun will be pulsed at the frequency of 108 MHz to provide a string micropulse with length of 3 ns and current of 2.5 A during about 10 μs macropulse time. The electron beam from the gun with energy of 80KeV is injected into the subharmonic prebuncher with frequency of 108MHz. The beam is bunched in the following drift space and then inters the 1300MHz buncher for further bunching and acceleration. Finally the beam is accelerated in the 1300MHz accelerator. According to the PARMELA simulation the beam emerges from the linac with energy of 4-6MeV by varying the input power in the accelerator. The micropulse current is about 75A in length of 45ps.

In each of these components, there may be some kind of instability which can induce beam energy ripple and time jitter at the exit of the linac. In the gun, the fluctuation of pulse time makes the electron bunches emit from the gun at different time and then arrive at the following components on different phases. Fortunately, the subharmonic buncher can function as time stabilizer and therefore the time jitter in the gun can be immediately suppressed several times in the subharmonic buncher according our PARMELA simulation. In the heavily loaded linac, the fluctuation in the emitted current from the gun will induce beam energy change due to beam loading effect by the relation $\frac{\delta\gamma}{\gamma}=0.35\frac{\delta I}{I}$. In the subharmonic buncher a quick variation in bunching voltage or in the bunching phase will result in the beam time jitter at the entrances of the downstream elements and finally at the exit of the linac time jitter and energy ripple appear. For example, when there is a phase fluctuation of 1° in the subharmonic prebuncher, it will induce about 3ps time jitter and 0.7% energy ripple at the exit of the linac. Similarly, the fluctuations in amplitude and phase of acceleration field in the fundamental prebuncher and the accelerator will also result in beam instability, as shown in ref.[1]. All of these fluctuations will affect the interaction between the electron and laser in the FEL oscillator as we will discuss in the following sections.

* The project is supported by National Natural Science Foundation of China (NSFC) and China Science Foundation of Nuclear Industry.

0-7803-3053-6/96/$5.00 ©1996 IEEE

III. CAVITY DETUNING OF THE FEL

The electron beam from the linac will be sent into the undulator through a transport line and a set of bending magnets. In the undulator the first electron bunch generates a spontaneous radiation pulse taking after the form of the electron bunch. This radiation pulse is reflected back on the end mirror of the optical cavity while the electron bunch is deviated out of the cavity to a dump. The optical cavity length is so set that the radiation pulse overrides on the next electron bunch in the forward direction. In FEL mechanism, the electrons in the bunch will interact with the radiation coherently and give part of their energy to the radiation pulse. In many round trips the laser pulse becomes more intense until saturation. But, in fact, there is a slippage between electron bunch and laser pulse as they go through the undulator due to the slower longitudinal velocity of electron than that of laser. The slippage is approximately equal to $N\lambda$, where N is undulator period number and λ the laser wavelength. Therefore in far-infrared FEL the slippage length may be comparable with the electron bunch length. So the overlap between the laser and electron becomes poor and the interaction is week. The leading part of the laser pulse disappears for the gain is mainly obtained at the end of the undulator. And consequently, the laser pulse becomes shorter than electron bunch and the centroid of the pulse lags behind, or equivalently speaking, the speed of the laser pulse is slower than the light velocity in vacuum. Laser lethargy occurs. Slightly shortening the cavity length can ameliorate the case. By solving 1-D pulse self-consistent FEL equations[4], 1-D pulse code traces the evolution of laser pulse in many round trips in optical cavity with certain losses(including output coupling). In the simulations electron beam emittance is taken into account by an equivalent filling factor calculated from small signal theory of FEL. So does for beam energy spread to diminish the run time of the code, even though it can be included in the initial conditions in the simulation by adopting much more sample macroparticles. In our simulation, N=50, λ=200μm, and electron current is 40A in 45ps. So the short pulse effect is obvious, as shown in Fig.1. When the optical cavity detuning length is zero dL=0, the gain is small during the early time and the laser power drops down after 80 passes, and finally vanishes around 200 passes. Slightly shortening the cavity dL=20μm, the laser power increases greatly during the early round trips and then keeps stable level after saturation. If dL is too short there is no obvious improvement comparing with the case of dL=0 because it can not completely offset the lag of the laser pulse. But if the cavity is over-shortened, the laser power decreases quickly after some passes and can not reach a stable level, but the gain is very large during early passes, as shown in curve B of Fig.1. This means there is a good coupling between laser and electrons during early time due to the enough detuning. But as laser becomes stronger in the following passes the gain decreases and the laser pulse lags at a lower speed comparing with that during the early passes, while the detuning offset effect remains the same. Therefore the coupling becomes poor and the laser power decreases. It is found that in our case, dL=20μm is the best detuning length.

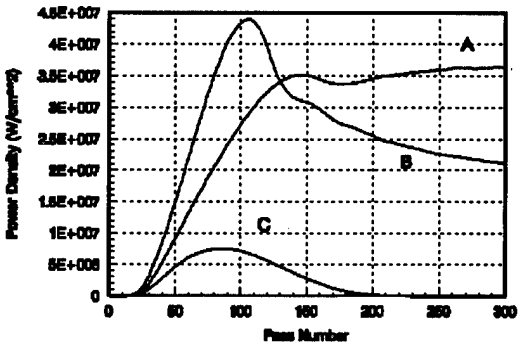


Figure 1. Laser power vs. pass number at different optical cavity detuning length: A--20μm; B--40μm; C--0μm

IV. EFFECTS OF TIME JITTER ON THE FEL

From the previous section we have seen that poor coupling between laser pulse and electron bunch due to slippage can result in a severe degradation of the FEL performance and the FEL is very sensitive to the cavity detuning length. Since 0.1ps time jitter is equivalent to a cavity length change of 15μm, it is necessary to exam the influence of the time jitter on our FEL oscillator in detail and consider the dependence of time jitter effects on some other FEL parameters.

For simplicity, one Fourier component of the jitter noise is taken into the simulations. Because the accelerator has filling time of 0.16μs, only these noise with frequency lower than 6.3MHz can effect the beam instability. Fig. 2 shows the laser power evolution as the pass number in the FEL oscillator under the influence of the noise. It is found that with the same noise amplitude Δt=3ps, different frequency noises result in different modulations in the amplitude of laser power. Noise

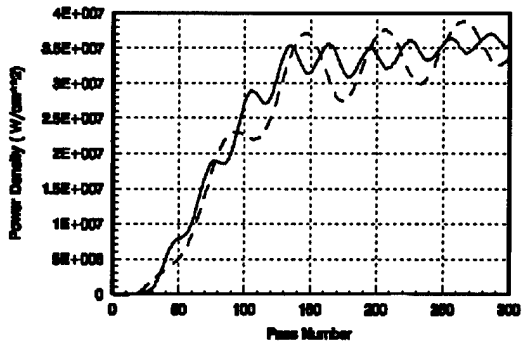


Figure 2. Laser power density vs. pass number with time jitter noise : Δt=3ps, f_1=3.6MHz (solid line) , f_2=1.8MHz (dashed line).

with lower frequency generates deeper modulation in laser power. In Fig.3, the time jitters with amplitudes of 3ps and 10ps induce 7% and 30 % modulations respectively on laser

power at the same frequency of 3.6MHz and at the optimum detuning length. If the FEL does not operate at the optimum detuning, the effect of the time jitter becomes more

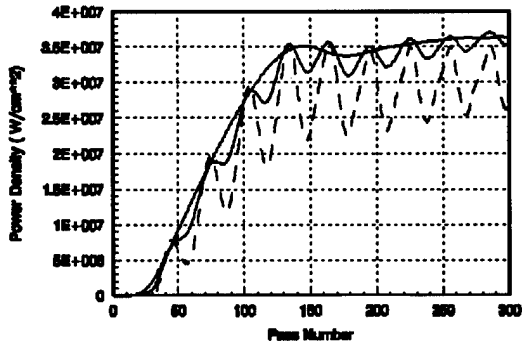


Figure 3. Laser power vs. pass number with time jitter noise at same frequency but different amplitude: f=3.6MHz, Δt_1=3ps, Δt_2=10ps(dashed line)

severe. The time jitter effect also relates to the FEL gain. It is found as the electron current increases 2 times the modulation percent of laser power decreases 2 times. If the electron bunch length is suppressed from 45ps to 30ps while the charge in the bunch keeps the same, no obvious change was found in the effect of time jitter on laser power modulation. But there is a strong modulation at frequency of 3.6MHz up to 70% due to 5ps time jitter when shortening electron bunch to 30ps while keeping the same current.

V. EFFECTS OF ENERGY INSTABILITY ON THE FEL

In the accelerator, the variations in the acceleration field due to instabilities of the input power and beam loading, and changes in acceleration phase can induce the electron energy ripple during a macropulse, as discussed in the second section. From FEL small signal gain curve we know when deviation from the resonant point $\Delta\nu=\pm\pi$, the FEL may work in the absorption or amplification regimes and the gain spectrum has a bandwidth of about π. Therefore electron energy ripple will result in the gain reduction or even absorption according to the relation $\Delta\nu= 4\pi N\delta\gamma/\gamma$. For simplicity, a single fourier component of the noise is again adopted in the simulation. Fig.4 shows the simulation results when the noise amplitudes are 0.5% and 1% respectively with the same frequency. These curves are calculated at the optimum cavity detuning length. It is shown the energy ripple not only modulates the laser power, but also decreases it greatly. Simulations with different noise frequencies but the same amplitudes indicate that as the noise frequency decreases, the noise effects in the power modulation become strong, as shown in the dashed curve B in the figure. Deviation from the optimum detuning length makes the modulation stronger than that at the optimum detuning, as shown in Fig.5.

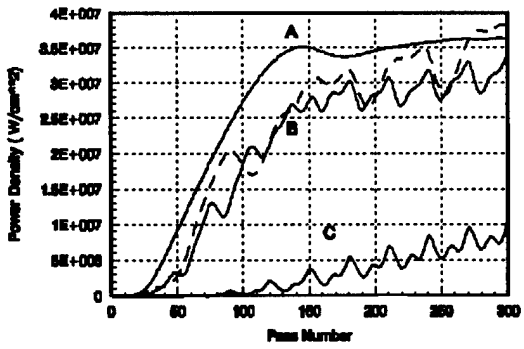


Figure 4. Laser power modulation due to electron energy ripple. A: $\Delta\gamma/\gamma$=0; B: $\Delta\gamma/\gamma$=0.5% , f=3.6MHz and 1.8MHz (dashed line); C: $\Delta\gamma/\gamma$=1% , f= 3.6MHz

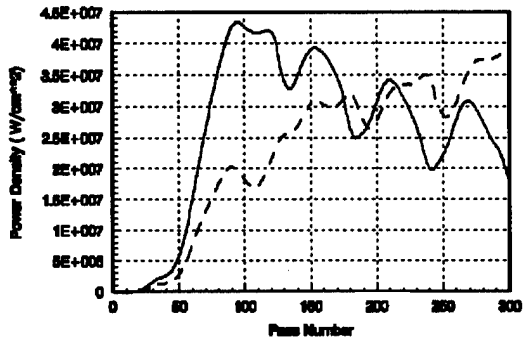


Figure 5. Effect of the same electron energy ripple on laser power at different cavity detuning length ΔL: ——: ΔL=40μm; ------: ΔL=20μm

VI. CONCLUSIONS

The effects of accelerator noise of time jitter and energy ripple on a far -infrared FEL oscillator is investigated by means of an 1-D pulse FEL code. The results show that the time jitter must be less than 3ps and the energy ripple should be controlled under 0.5% for our FEL oscillator. The current ripple should be less than 1.4%. And the optical cavity detuning has the optimum length of 20μm for stable operation during a macropulse.

VII. REFERENCES

[1] Fu Shinian, Chen Yinbao, Yang Tianlu, et. al., Physical design on an RF-linac for far-infrared free electron laser, Proc. of LINAC'94, (1994) 511

[2] M.T.Lynch, R.W.Warren,P.J.Tallerico, The effects of linear-accelerator noise on the Los Alamos free electron laser, IEEE J. of Quantum Electronics, Vol. QE-21(1985)904-908

[3]W.E.Stein,W.J.D.Johnson,J.F.Power,Stability requirements of RF-linac-driven free-electron laser, Nucl. Instr. & Meth. in Phys. Res. A296 (1990) 697-701

[4] W.B.Colson, S.K.Ride, Physics of Quantum Electronics, Vol.7 (1982) 377

STATUS OF THE UCLA HIGH-GAIN INFRARED FREE ELECTRON LASER*

M. Hogan, C. Pellegrini, J. Rosenzweig, G. Travish
UCLA Department of Physics, Los Angeles, CA 90024, USA

A.Varfolomeev
Kurchatov Institute, Moscow, Russia

A compact, infrared (10-20 μm), high-gain FEL is being commissioned at the Particle Beam Physics Laboratory (PBPL) at UCLA. A 60 cm long undulator with a period of 1.5 cm and an undulator parameter K≈1 has been built to be used in conjunction with the PBPL beam. Experiments will focus on FEL physics pertinent to proposed short wavelength devices. Of particular interest is exploration of startup from noise, self amplified spontaneous emission (SASE), beam parameter effects on gain, and output power fluctuations. Beam micro-bunching due to the FEL action will also be measured using coherent transition radiation. Here we present an overview of the relevant diagnostics, FEL simulation results and proposed experiments.

I. INTRODUCTION

The Free Electron Laser has shown potential as a light source in the infrared, UV and, as recent proposals indicate, in the XUV and X-ray regime. While oscillator experiments have provided a number of verifications and enhancements to theory and operational experience, few high-gain amplifier systems have operated in the optical regime. This paper describes the UCLA IR FEL – a system designed to study critical issues in high-gain systems and to improve the operational FEL and accelerator experience with the requisite high-brightness beams.

The UCLA experiment was designed to study issues important to future short wavelength devices at a minimum of cost and space. The short-period undulator, combined with our moderate-energy beam produces radiation in the infrared (IR), where a large number of diagnostics are available, without the added complexity of producing a higher-energy beam necessary for operation at shorter wavelengths. Further, working in the IR does not suffer from the beam noise problems associated with past microwave FELs. The lack of suitable sources at short wavelengths makes the feasibility of start up from noise (SASE) important [1]. Additionally, the difficulty of producing high reflectance mirrors makes an oscillator configuration impractical for short wavelengths, so successful operation in the high-gain regime is a necessary precursor to designing short-wavelength devices. For these reasons the FEL studies will begin from SASE in the high gain regime.

II. OVERVIEW

a. The Beamline

The beam is produced in an S-band RF copper photocathode gun driven by a frequency-quadrupled, pulse-compressed Nd:YAG laser (UV) [2]. Solenoids control the highly divergent beam and provide for emittance compensation [3] into the linac. A Plane Wave Transformer linac (PWT) accelerates the electrons from an injection energy ~4 MeV to a final energy of ~17 MeV [4].

Six of the quadrupoles are used to match the four phase-space parameters needed for injection into the undulator. The magnetic center of the beamline is passively aligned to ~100μm using machined brackets, optical tables, and linear bearings (rails). This tolerance was chosen based on the performance simulations of our FEL. A second dipole after the undulator will bend the electron beam away from the optical pulse to facilitate the IR optics/diagnostics.

b. Diagnostics

An unsaturated high-gain FEL is highly (exponentially) sensitive to certain beam-parameter fluctuations. Thus, beam diagnostics on the UCLA system are designed for single-bunch (shot-to-shot) operation. Beam position, size, charge and emittance are measured using the following:

- Stripline beam position monitors (BPMs) for non-destructive measurements.
- Phosphor screens and video cameras.
- Integrating Current Transformer (ICT).
- Slits (1D pepper pots) to measure the effective transverse emittance of the space-charge dominated beam [5].
- A SLAC-like pulse-length monitor to make non-destructive shot-to-shot pulse-length measurements [6].

The first dipole magnet, in conjunction with the quadrupoles, is used as a spectrometer to measure the energy and the energy spread. The second dipole will also allow for a crude energy measurement after the beam exits the undulator. Other diagnostics include Faraday Cups for charge

*Work supported by US DOE Grants DE-FG03-90ER40796 and DE-FG03-92ER40693.

0-7803-3053-6/96/$5.00 ©1996 IEEE

measurement and Cherenkov radiators, in conjunction with a streak camera, to measure the absolute pulse length.

c. Microbunching monitor

Coherent transition radiation (CTR) can be used to measure the extent of bunching in the FEL. We plan on installing a foil at the exit of the undulator to study the bunching. Calculations indicate that the expected 5% bunching factor should produce CTR in the FEL band comparable to the FEL output itself [7].

d. The Undulator

A planar undulator 60 cm long with a 1.5 cm period, 5 mm fixed gap spacing and a greater than 7 kG peak field awaits installation into the beamline. The undulator was designed to provide IR radiation from modest beam energies (< 20 MeV) while maintaining a strong coupling (K~1). An rms field uniformity of better than 0.18%, measured using both a Hall probe and the pulsed wire technique [8], should assure good FEL performance. Additionally, the second integral of the undulator field satisfies the requirement that the rms electron beam deflection in the wiggle plane (~105 μm) be less than the rms beam waist (~200 μm). It should be notes that the construction of the FEL is not well suited to studying the effects of varying undulator parameters such as field strength and error.

Table 1: Electron Beam and FEL Parameters expected for the UCLA IRFEL.

Electron Beam Parameters [Expected]	
Energy	17 MeV
Energy Spread (uncorr.)	0.1%
Current (peak)	200 Amps
Pulse Length (rms)	~5 psec
Norm. Emittance (rms)	5 mm mrad
Undulator Parameters [Measured]	
Total length	60 cm
Undulator period	1.5 cm
Peak field on axis	7.3 kG
Pole face gap (fixed)	5 mm
Undulator parameter (K)	~1
FEL parameter (ρ) [9]	~1 x 10^{-2}
FEL Parameters [Simulations @10.6 μm]	
Radiation wavelength	10-20 μm
Power gain length	7.2 cm
SASE peak power	3 mW @ 7.2cm ~1 W @ 60cm

III. SIMULATION PREDICTIONS

The lack of experimental work on SASE optical FELs necessitates relying on numerical simulations to predict the performance of our experiment. Earlier work in the IR on the Paladin FEL at LLNL has helped test high gain codes, but has not provided information on startup from noise [10]. Fluctuations in FEL performance, especially from startup, and sensitivities to system parameters are a critical issue in future short-wavelength high-gain systems where output stability and saturation are significant to users. Simulations of the UCLA system have been performed to investigate such sensitivities in hopes of performing experimental comparisons. Most of the following work was performed with TDA3D [11] and includes 3D effects, diffraction, emittance and energy spread.

a. Current

The beam current is our easiest parameter to control and measure. Spontaneous emission can be differentiated from amplified (stimulated) radiation by observing the dependence on current: spontaneous emission is broadband and scales linearly with the current, while amplified radiation power, P, scales as P~Iexp(αI^4/3) where α is a constant and I is the beam current.

Simulations of gain vs. current show that current variations ~ 10% vary the FEL output power +40%/-25%. Current variations of this order are within our ability to measure, and power (energy) fluctuations of a few percent are within our detector / electronics bandwidth. The challenge will lie in deconvolving a variation of beam current from parameters such as beam size, pulse length, energy spread and emittance.

b. Beam Size

Beam-size changes, such as those caused by space charge, affect the beam density as well as the matching into the undulator. The FEL is sensitive to the overall (six dimensional) beam density, however small changes in the transverse beam size should cause predictable changes in the FEL performance. Further, simulations predict FEL performance is insensitive to achievable beam matching. Regardless, matching is a technical issue that needs to be resolved with experience in beam handling. Phosphor screens and BPMs should provide sufficient operator feedback on beam size.

c. Pulse Length

Only a few "finite pulse" simulations have been performed on our system. Slippage is a factor in the performance of this system; however, over the short undulator

being initially used the output power is not degraded severely. Further work is needed to quantify (through simulations and experiment) this effect.

The pulse length is also a factor in much the same way that beam size is. The variation of the pulse length due to laser fluctuations and space charge are still an experimental uncertainty.

d. Energy Spread

Wakefields (primarily from the linac) are expected to produce a correlated energy spread ~ 1%. This spread can be ameliorated by running the linac "off crest". Any residual correlated energy spread will give rise to a broader radiation bandwidth. Our IR detectors are broadband and nearly linear over such linewidths, so that integrating over the wavelengths is inherent in the instrumentation. The expected uncorrelated energy spread (PARMELA [12] simulated and initially measured) of <0.5% does not substantially degrade FEL performance.

e. Emittance

The only single-shot emittance measurements available to us are destructive slits. Hence, we will not be able to measure emittance "on line" with the FEL operating, but by knowing all the other beam parameters it may be possible to calibrate the emittance. Simulations indicate that an emittance much poorer than the design value can still yield measurable gain.

IV. DETECTION OF SASE

The low-level SASE signal (see Table 1.), which can be calculated from numerical integration or simple 1-D theory [13], requires the use of cryogenic detectors to obtain the necessary sensitivity. A non-imaging optic (Winston Cone) will maximize collection efficiency during initial operation, but may degrade the signal-to-noise ratio (SNR) by collecting large amounts of background. Background (blackbody) radiation constitutes a DC offset/pedestal that may be compensated for up to the level of the shot noise. Commercially available IR detectors have relatively long time constants (~nsec) with respect to the pulse (~psec), so that the integrated background noise may be significant. An available copper-doped germanium detector should provide a SNR of $\sim 10^3$, neglecting signal loss in the optics, pre-amplifier noise, and reduction in detectivity due to operating far below the response time of the detector. By removing the Winston Cone and aperturing the field of view of the detector to limit the collected background, the SNR can be increased by several additional orders of magnitude. Other detectors such as Mercury-Cadmium-Telluride photodiodes may offer the advantage of faster response times and/or higher quantum efficiencies, while only needing to be cooled to liquid Nitrogen temperature. Both the spontaneous emission and the amplified signal should be well within our sensitivity, and studies of SASE FEL radiation production should be feasible.

V. ACKNOWLEDGMENTS

The authors thank Dick Cooper for the hyphens. We also thank I. B. Shankin for many useless discussions and Noah Arref and R. Uin, et al. without whom this experiment would be possible.

VI. REFERENCES

[1] H. Winick, *et al.*, Proceedings of the 8th SRI93, Gaithersburg, MD, August 23-26, 1993.

[2] J. Rosenzweig, *et al.*, Nucl. Instr. and Meth. A 341 (1994) 379-385.

[3] B.E. Carlsten, Nucl. Instr. and Meth. A 285 (1989) 313.

[4] R. Zhang, *et al.*, Proc. this conference.

[5] J. Rosenzweig and G. Travish, UCLA Dept. of Physics – CAA–TECH–NOTE #64

[6] E. Babenko, *et al.*, SLAC-PUB-6203 (JUNE 1993).

[7] J. Rosenzweig, G. Travish and A. Tremaine, Submitted to Nuc. Inst. and Meth. A.

[8] G. Travish, UCLA Dept. of Physics, CAA–TECH–NOTE #34.

[9] R. Bonifacio, C. Pellegrini and L. M. Narducci, Opt. Commun. **50**, p373 (1984).

[10] J. T. Weir, *et al.*, Proc. SPIE vol.1133:97-101 (1989).

[11] T. M. Tran and J.S. Wurtele, Computer Phys. Commun. **54** pp. 263-272 (1989) and T. M. Tran and J.S. Wurtele, Physics Reports 195 pp. 1-21 (1990).

[12] K. R. Crandall and L. Young, Computer Codes for Particle Accelerator Design and Analysis, LA-UR-90-1766, Los Alamos (1990).

[13] K. J. Kim, Physical Review Letters **57(13)**, pp. 1871-1874 (1986).

ACCELERATOR DESIGN FOR THE HIGH-POWER INDUSTRIAL FEL*

D. V. Neuffer, S. Benson, J. Bisognano, D. Douglas, H. F. Dylla, D. Kehne, J. Fugitt, K. Jordan, Z. Li, H.-X. Liu, L. Merminga, G. Neil, M. Shinn, C. Sinclair, M. Wiseman, CEBAF, 12000 Jefferson Ave., Newport News, VA 23606 USA, M. Cornacchia, SSRL, Stanford, CA 94309 USA

Abstract

We have developed a conceptual design for an industrial-use kilowatt UV and IR FEL driven by a recirculating, energy-recovering 200 MeV, 1–5 mA superconducting rf (SRF) electron accelerator. In this paper we describe the accelerator design of this FEL. The accelerator consists of a 10 MeV injector, a 96 MeV SRF linac with a two-pass transport which accelerates the beam to 200 MeV, followed by energy-recovery deceleration through two passes to the dump. Technical challenges include high-intensity injector development, multi-pass energy-recovery operation, SRF modifications and control for FEL operation, development of tuneable, nearly-isochronous, large-acceptance transports, and matching of the beam to the FEL wiggler. An overview of the accelerator design is presented.

I. INTRODUCTION

The CEBAF industrial FEL is planned as a prototype and test bed for future high-power, high-efficiency, industrial-use FELs. The purpose of the program is to develop the technology for producing high-power FEL light and to demonstrate the possible uses of FEL light over a broad range of possible applications.[1,2] Applications require tuneable light from the infrared (~20mm) to the ultraviolet (~160nm), at multi-kW power levels. This implies tuneable beam energies up to ~200 MeV, with beam powers of ~1 MW, and peak currents of ~200 A. Practical applications will require cost-effectiveness and energy-efficiency.[3] Therefore, we incorporate multi-pass acceleration and energy-recovery deceleration, and will use our experience in this prototype to develop a cost/reliability optimum. The accelerator must maintain small emittance (ϵ_N< 11 mm-mrad) in the acceleration to the wiggler, and have high acceptance (low losses) throughout.

II. ACCELERATOR DESCRIPTION

Table 1 summarizes the requirements of the FEL driver accelerator. For these requirements we have designed the accelerator system shown in Figure 1, and it consists of a 10 MeV photocathode-based injector, a 96 MV CEBAF-style SRF linac, with a two-pass recirculation transport. The system accelerates the beam from the injector through two passes of the linac to 200 MeV. The beam is compressed and matched into the FEL wiggler where it loses energy and greatly increases its energy spread, while producing coherent light. The resulting beam is decompressed, returned into the linac, decelerated for energy recovery through two passes to ~10 MeV, and then transferred into the dump. The two-pass design is the minimum needed to demonstrate both recirculation and energy-recovery. (More passes would add unwelcome complexity without reducing costs.) In the following sections we describe the accelerator components, and highlight significant features within the design.

Table 1 - FEL Accelerator Parameters

Electron Energy	E	100—200 MeV	
Accelerator type	two-pass SRF recirculator, with two-pass E-recovery		
RF frequency	$f=\omega/2\pi$	1.4997	GHz
Charge/bunch	Q	135	pC
Transverse emittance	ϵ_N	11	mm-mrad
Longitudinal emittance	ϵ_L	60	keV-ps
Rep. rate (start-up)		2.339	MHz
Rep. rate (production)	37.425	MHz	
Total Current	I	5	mA
UV/IR wiggler focus	β	1/2.5	m
rms energy spread	$\Delta E/E$	0.15	%
rms bunch length	$\Delta\phi_{min}$	0.2	ps

A. Injector

The injector must provide high-intensity (large space-charge) bunches, with high beam quality, at 5 mA cw operation. Our design consists of a 500 kV DC laser-driven photocathode gun, a room-temperature 500 kV, 500 MHz buncher, a CEBAF-style quarter-cryomodule providing 10 MV of SRF acceleration, and a transport line matching into the main driver at 10 MeV for acceleration in the linac.[4] Our high-intensity source is designed to deliver 35 ps electron pulses with charges of up to 200 pC. The beam is bunched and accelerated by the buncher and SRF, and then transported into the linac by a 4-quad "zoom-lens" and an achromatic dipole triplet, which permits variable matching. Design calculations show that the injector can produce ~1.5 ps bunches of 135 pC at ϵ_N < 6 mm-mrad, within FEL specs. A significant R&D challenge is to obtain long photocathode lifetimes at the design current, with high beam quality, while handling large space-charge effects. This design will be verified by CEBAF Injector Test Stand [4] experience.

B. Linac

The linac consists of three modified CEBAF cryomodules, with magnetic focussing elements between the cryomodules. Each cryomodule contains eight 5-cell 1500-MHz CEBAF cavities with fundamental power couplers, HOM couplers,

*Research supported by DOE Contract #DE-AC05-84ER40150 and the Virginia Center for Innovative Technology.

0-7803-3053-6/96/$5.00 ©1996 IEEE

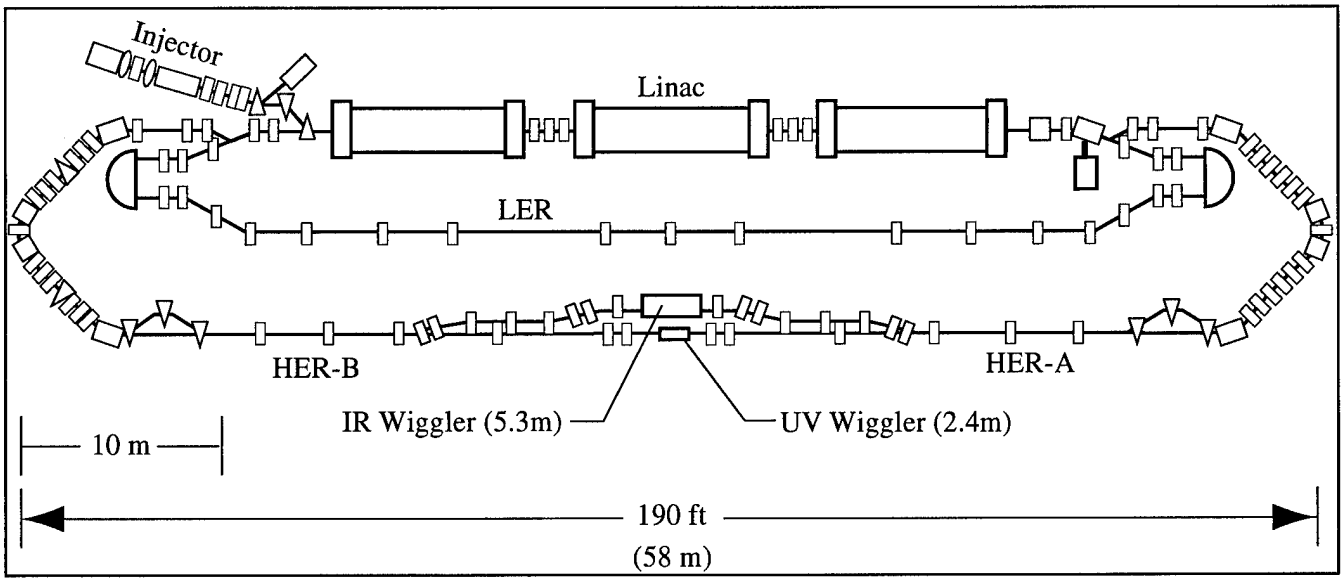


Figure 1. Overview of FEL Driver Accelerator, showing 10 MeV injector, 96 MV linac, low-energy recirculation transport (LER) for 105 MeV beam, and high-energy recirculation transport (HER-A) which takes 200 MeV beam to the UV or IR FEL wiggler and returns it to the Linac for energy recovery (HER-B).

intercavity steps, and cryogenic components. CEBAF experience indicates that each cryomodule should be able to provide at least 32 MV of acceleration. These cryomodules are modified to accommodate the high-peak- current, low-loss FEL operation. HOM load power is dissipated at 50K to reduce thermal loads. The intercavity apertures are enlarged, bellows and ports are shielded, and steps are minimized to reduce impedances. The Linac includes quad triplets and skew-quads between the cryomodules, and a quad doublet after the last cryomodule for multi-pass focusing and matching.

C. Recirculation transport

The recirculation beam transport contains two lines. The low-energy recirculation (LER) transport takes ~105 MeV beam from the exit of the linac and returns it to the entrance in both acceleration and deceleration cycles. The LER is similar to the Bates recirculator [5], and consists of arcs with a 180° bend and two normal and reverse 20° bends which are arranged to obtain isochronous and achromatic motion. The straight section contains three quad triplets, with the overall x-y transport fitted to a -I matrix. The beam is "on-crest" in the first and last linac passes to minimize the momentum width within the LER to $< \pm 1\%$, which maximizes acceptance.

The high-energy recirculation (HER) transport is the outer loop of Figure 1. The HER carries the beam around the high-energy arc from the linac to the wiggler and returns it for energy recovery. The beam is accelerated "off-crest" on the second linac pass and the HER is non-isochronous to enable bunching and debunching. The HER must accept a large energy spread, particularly in the beam exiting the wiggler, and have broad tuneability in transverse and longitudinal focusing. The present design shown in Figure 1 meets these requirements. The arcs are based on a two-cell reverse bend configuration,[6] in which a small negative bend at large dispersion combines with a large bend at small dispersion to provide nearly isochronous motion. The arc quads can be varied to change the chronicity M_{56} by ±0.05 by minor retunings, and to obtain $M_{56} = 0 \pm 0.30$ with larger changes. The transport includes beam-separation chicanes and path-length adjustment chicanes as well as matching transport into both UV and IR wigglers.

The IR FEL requires a separate wiggler from the UV FEL, which is placed in a bypass parallel to the UV FEL. This bypass is an achromatic staircase (see Fig. 1). For longer-wavelength operation, 100 MeV beam is sufficient and it is desirable to have a long, small ΔE/E bunch. This can be obtained in a single on-crest pass of the linac, with dipoles tuned to steer the ~ 100 MeV beam into the HER and into the IR wiggler. Single-pass (off-crest) debunching and energy-recovery follow. This single-pass operation is simpler and has less stringent aperture and stability requirements.

D. Transport to Dump

Following two-pass deceleration the ~10 MeV beam is separated into the dump transport. The separation is obtained in a split dipole at the end of the linac, with the first half extracting the low-energy beam from 105 and 200 MeV beams, and the second half tuned to optimize the 105/200 MeV beam separation. The extracted low-energy beam is transported into a 10 MeV, 50 kW

dump. The split dipole makes it possible to tune the transports to vary the matched beam energies through the system, and enables ~100 MeV single-pass operation.

III. LONGITUDINAL MOTION

The longitudinal motion is critical in the driver design. Conceptually, we take a relatively long, low-energy-spread bunch from the injector and transform it into a short, increased-energy-spread bunch at the wiggler, obtaining high-peak current. At the wiggler, the beam loses energy and greatly increases its energy spread in the FEL interaction. To transport the beam to the dump we must decrease this energy spread, and therefore we must debunch this short, large-energy-spread beam into a long, moderate-energy-spread bunch within the acceptance of the machine.[7] Each of these processes requires rotating the beam in longitudinal phase space.

In our design, the rotations are obtained in a simplest way. The first-pass acceleration to 105 MeV is on-crest and isochronous. The second-pass acceleration to 200 MeV is off-crest, and places a position-dependent energy tilt on the beam ($\Delta E(z) = -eV_{rf} \sin(\phi_2)k\, z$, where V_{rf}, ϕ are the rf voltage and phase, respectively, and $k = 2\pi/\lambda$). The HER transport to the wiggler is slightly non-isochronous and changes particle positions ($\Delta z(\Delta E) = M_{56}\, \Delta E/E$), resulting in a bunching phase-space rotation, if $k\, M_{56} eV_{rf} \sin(\phi_2)/E \approx 1$. Bunching by up to an order of magnitude is obtained.

Following the wiggler, the process is reversed, with a non-isochronous return transport followed by off-crest deceleration to 105 MeV in the third Linac pass, and on-crest deceleration through a fourth Linac pass to 10 MeV, where the spent beam is extracted and deposited the dump.

This scenario requires matched M_{56} throughout the lattice and a large ΔE acceptance, particularly for the beam exiting the wiggler in the HER, where $\Delta E \sim \pm 5$ MeV. Energy width acceptances of $\Delta E \sim \pm 1$ MeV are required in the remainder of the machine. The longitudinal motion is also complicated by nonlinearities due to the rf waveform, the beam transport, and wakefields. These effects are incorporated into the complete design.[2]

IV. ACCEPTANCE AND STABILITY ANALYSES

Particle tracking codes (DIMAD, TLIE, PARMELA) have been used to determine the acceptance and explore the nonlinear and chromatic motion in the lattice. The simulations show that adequate acceptance is obtained throughout the system, with, in particular, linear motion over a large acceptance in the HER transport, and acceptance through the final linac pass into the dump.

The apertures throughout the accelerator have been chosen to enable low losses. Typically, apertures greater than 6σ are allotted, with allowance for energy acceptance and closed-orbit/misalignment errors. Also, the impedance of the accelerator has been minimized to enable high-peak current by removing steps, shielding bellows, using low-impedance beam position monitors, etc. An impedance budget of less than 1 kV/pC per pass has been set.

The FEL accelerator operation is complicated by energy recovery, which must be maintained with the perturbations of FEL operation. With energy recovery, the external energy that must be supplied to the cavities is greatly reduced, to ~1.5 kW/cavity. The relatively small amount of external power also implies a relatively weak degree of external control. Extensive modeling has demonstrated that the CEBAF rf control system can provide adequate control of the accelerating field with modest gains.[8]

Phase oscillations and beam loss can cause an unstable fluctuations in the accelerating field, particularly when coupled through the chronicity M_{56} to fluctuations in the beam phases.[9] A threshold current for this instability can be written as $I \sim E/(eR_s M_{56} k\, S)$, where R_s is the shunt impedance, M_{56} is the total HER chronicity and S is the sum of the sines of the phase differences between the up and down passes. At current design parameters, this threshold is ~0.2 mA. At our design goal of 5 mA, this means that active feedback is required to control the instability.

Alternatively, the lattice can be modified to have opposite signs of M_{56} for the lattice segments entering and leaving the wiggler (so that the total M_{56} is ~ 0) , and the beam phases could be arranged to cancel. An operational mode with these properties has been developed.[2] However, it would require off-crest first pass acceleration, and a much larger LER energy aperture. The lattice can be adapted to accommodate either mode, and the optimum can be determined operationally.

Other instabilities and high-intensity effects have been considered. These include ion trapping, coherent curvature effects and synchrotron radiation, and multibunch beam break-up.[2] None of these presents serious difficulty.

References

1. H. F. Dylla et al., these proceedings (1995 Particle Accelerator Conference, Dallas TX) (1995).
2. CEBAF FEL Conceptual Design Report (1995).
3. G. Neil, S. Benson and M. Shinn, these proceedings (1995).
4. H. Liu, D. Kehne, et al., these proceedings (1995)
5. J. Flanz, G. Franklin, S. Kowalski , C. P. Sargent, MIT-Bates "Recirculator Status Reports", unpublished (1980).
6. A. Amiry and C. Pellegrini, Proc. Workshop on Fourth-Generation Light Sources, SSRF 92/02 (1992).
7. D. Douglas, A. Hutton, C. Leemann, and D. Neuffer, CEBAF TN 95-015 (1995).
8. L. Merminga, J. Fugitt, G. Neil, and S. Simrock, these proceedings (1995).
9. L. Merminga, and J. Bisognano, these proceedings (1995).

FREE ELECTRON LASER AMPLIFIER EXPERIMENT BASED ON 3.5 MeV LINEAR INDUCTION ACCELERATOR

Ding Bainan, Deng Jianjun, Hu Shenzong, Shi Jinsui, Zhu Wenjun, Li Qing, He Yi
Institute of Fluid Physics,CAEP
P.O.Box 523-56. Chengdu,P.R.China.
Post code 610003

INTRODUCTION

Millimeter wave FELs have used beams produced by induction linac [1],[2],Van de Graff accelerator[3],and pulsed diode machines[4].The distinct advantage of the induction linac is its high peak power,capability of producing high current,high energy electron beams with pulse durations ranging from tens of nanoseconds to microseconds. The induction linac at our institute is of 2.5kA,3.5 MeV,90 ns(FWHM) and built in 1991.This accelerator is designed to drive the SG-I free electron laser at our institute for studying the basic physics of FELs.The SG-I facility is divided into three regions, the accelerator ,the beam conditioning section and the interaction region. After the FEL experiments in 1993,in order to satisfy the needs for the FEL experiments and achieve high power FEL output,many modifications have been carried out in the beam conditioning section and RF input way ,resulting in the increase of the current entered the wiggler and microwave output. In this paper the 3.5 MeV LIA and modifications to the linac have been briefly described.Then the FEL experiments and their results are also introduced.Finally discussions on the experiments have been given.

DESCRIPTION OF THE SG-I FEL

A.The Linear Induction Accelerator

The 3.5 MeV linear induction accelerator mainly consists of a 1 MeV injector and 8 identical induction accelerator cavities which are arranged in four module blocks.Each cavity is energized by a Blumlein pulse forming line.Twelve Blumlein PFLs are divided into two groups which are charged through twelve inductances by two Marx generators individually. Each module of the injector is applied to 250kV for a 90ns FWHM pulse.The voltage contributions of the four modules are summed along the hollow steel stem to drive the diode .The surface of the cathode is covered by velvet cloth , the anode aperture is closed off with fine tungsten mesh.

The output beam of the injector is guided through the accelerating cavities by a near-continious array of solenoids that are positioned both internal and external to the accelerating elements.Each accelerating cavity can give about 300 keV of energy to the beam.

B.The FEL Experiments

As we know,the output power of FEL is proportional to the amount of electron beam current which can be trapped in the ponderomotive well,and depends on the brightness of the electron beam as well as the size of the ponderomotive well.In order to obtain a sufficiently bright beam,many modifications have been made. An apparent improvement is made on the beam conditioning section ,the mechanical and magnetic axes have been adjusted carefully and 2-m long conditioning section which consists of three solenoids and one thin magnetic lens has been used. Fig.1 is the experiment arrangement of SG-I FEL.

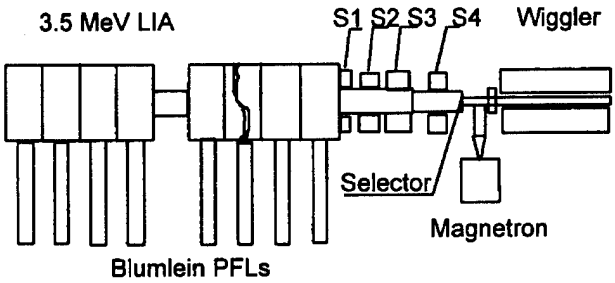


Fig.1 Schematic of the SG-I FEL

Solenoids S1 to S3 are used to transport the beam and S4 focuses the beam to the wiggler field .The space and energy sweep selector is used to provide a well-characterized electron beam for SG-I.The 4-m-long electromagnetic wiggler is composed of specially shaped solenoids with 11 cm period.The pulsed wiggler can provide a peak magnetic field on axis of 3 kG.Each two periods of the wiggler is energized by a separate power supply which allows variation of the strength and the longitudinal profile of the wiggler field.The interaction region consists of a thin-wall stainless steel oversized waveguide(3x10cm),which allows for good penetration of the wiggler field.In the second stage of the SG-I FEL experiment,the beam from accelerator is directly guided and focused into the interaction region after simply conditioning .After being confined , the beam focused transports into the wave guide through the space and energy sweep selector positioned at the entrance and interacts with the wiggler magnetic field to produce the FEL.The input microwave signal to the amplifier is provided by a 34.6 GHz,20 kW pulsed magnetron (pulse length= 500ns).The input signal is injected into the interaction region by means of a waveguide tapers whose angle with the beam line is 90 degree.

0-7803-3053-6/96/$5.00 ©1996 IEEE

EXPERIMENT RESULTS AND DISCUSSION

Modifications to the beam conditioning section and RF input result in the increase of the current and microwave power entered the interaction region. The beam electron energy has been measured with magnetic analyzer to be 3.5 MeV with 1% spread at 1 m from the accelerator output.The emittance is measured to be 0.4 cm-rad with a detector consisting of a pinhole mask and screen spacing 150 mm downstream, the beam brightness is EMBED Equation . The beam current at upstream of the wave guide is measured 2.5 kA with a CVR(current view resistor). The input current into the wave guide is measured 950 A with a Faraday detector., The beam currents in the interaction region are measured with a movable Faraday detector at different positions in the wiggler,and saturated power of 50 MW microwave output has been obtained ,tapered operation results in 140 MW output ,as shown in Fig.2.

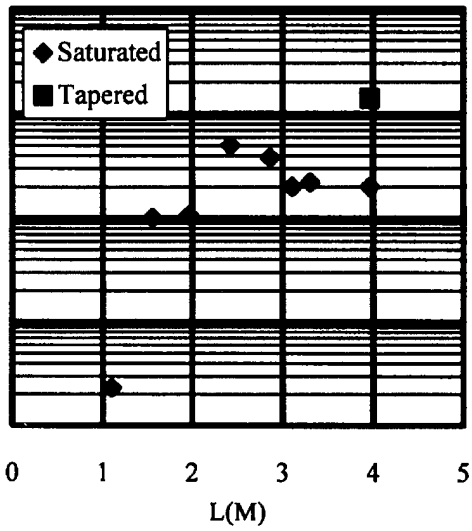


Fig.2 FEL Gain curve

From the experiment results we can find that only a half of the beam current has been input into the wiggler,and the pulse width becomes narrower(40ns),for the corkscrew motion of the beam due to the energy spread and the misalignment of the magnetic axis results in the different displacements at different time of the pulse. The wave guide actually behaved as selector of both emittance and position. This maybe the main reason of the reduced beam current widths. The beam energy in the head and tail of the pulse is lower than that in the middle , in order to let those in the middle with small energy spread have small displacements so that those electrons can entrance the wave guide through the space and energy sweep selector,the magnetic field of conditioning section must be carefully adjusted

REFERENCES

[1] Pasour,J.A, Phys. Rev. Lett., Vol.53,pp.1728-1731,1984.

[2] Orzechowski,T.J. et al, Phys. Rev. Lett.,Vol.54,pp.889-892,1985.

[3] Elias,L.R.,Proc.9th Int. Conf. Infrared and Millimeter Waves,Takarazuka,Japan,Oct.22-26,1984 pp.1-3.

[4] Gold,S.H. et al,Phys.Rev.Lett..Vol.52,pp.1218-1221,1984

[5].Turner,W.C.,Proc.1990 Linac Conf.Albuquerque,NM.Sept. 10-14,1990,pp435-437.

[6].Sampayan,S.E,Proc.1990 Linac Conf. Albuquerque,NM, Sept.10-14,1990,pp417-419

[7] Hui Zhongxi,Deng Jianjun et al,Proc. First Asian Symposium on Free Electron Laser,Beijing,May 26-30,1993.

A High Duty Factor Electron Linac for FEL*

T.D. Hayward, D.H. Dowell, A.M. Vetter, C. Lancaster, L. Milliman, D. Smith,
J. Adamski and C. Parazzoli
Boeing Defense & Space Group
Seattle, Washington

Abstract

An 18-MeV, 433-MHz linac capable of operating at 25% RF duty factor (DF) is being commissioned for FEL applications. Comprising a two-cell RF photocathode injector[1] followed by four new multicell cavities[2], the linac is an extension of the photoinjector which previously delivered 5 nC at 27 MHz micropulse repetition frequency, and 25% DF. The system is constructed using equipment from the Ground Based Laser and the Average Power Laser Experiment (APLE). The linac can serve as the driver for an infrared FEL or as the preaccelerator for a higher energy linac driving a visible FEL [3].

Introduction

The High Duty Factor Electron Linac comprises a photocathode injector, accelerator, beamline, associated controls, vacuum, alignment and beam diagnostics. The present layout of the accelerator and beamline is shown in Fig. 1. At this writing, the accelerator and beamline have been aligned and are under vacuum. The accelerator cavities are ready to accept high power RF and only a few controls, beam diagnostics and the drive laser remain to be implemented prior to starting characterization of the electron beam and related experiments[4]. While the RF power system for this accelerator is only capable of operating to 25% DF, the accelerator structures (photocathode, injector and accelerator) have been designed for CW operation.

Photocathode Injector

The photocathode injector (Fig. 2) was designed and tested previously[1]. It consists of a multialkali photocathode and two vacuum brazed OFHC copper cavities. Each cavity is a standing wave structure, operating in the TM_{110}-like mode. The cavities are iris coupled to the RF power. The dynamic resonance is maintained by computer controlled slug tuners located in each cavity. The RF vacuum interface is provided by a high power half-height WR1800 waveguide (1 MW average, 4 MW peak) alumina ceramic window located approximately 1.7 m from the beam centerline and around a 45^{o} bend, to eliminate any direct line of sight between the electron beam and the window.

The drive laser, a frequency doubled , mode locked Nd:YLF system, is injected by an off-axis mirror into the electron beam transport after the second cavity. This laser illuminates a 5 mm FWHM region of the photocathode. The electric field at the face of the photocathode is 26 MV/m. At the exit of the photocathode injector the beam energy is 2 MeV.

Accelerator

The remainder of the accelerator consists of 16 RF accelerating cells constructed as 4 standing wave cavities operating in the TM_{110}-like mode. These cavities raise the final electron energy to 18 MeV. They were originally designed for APLE.

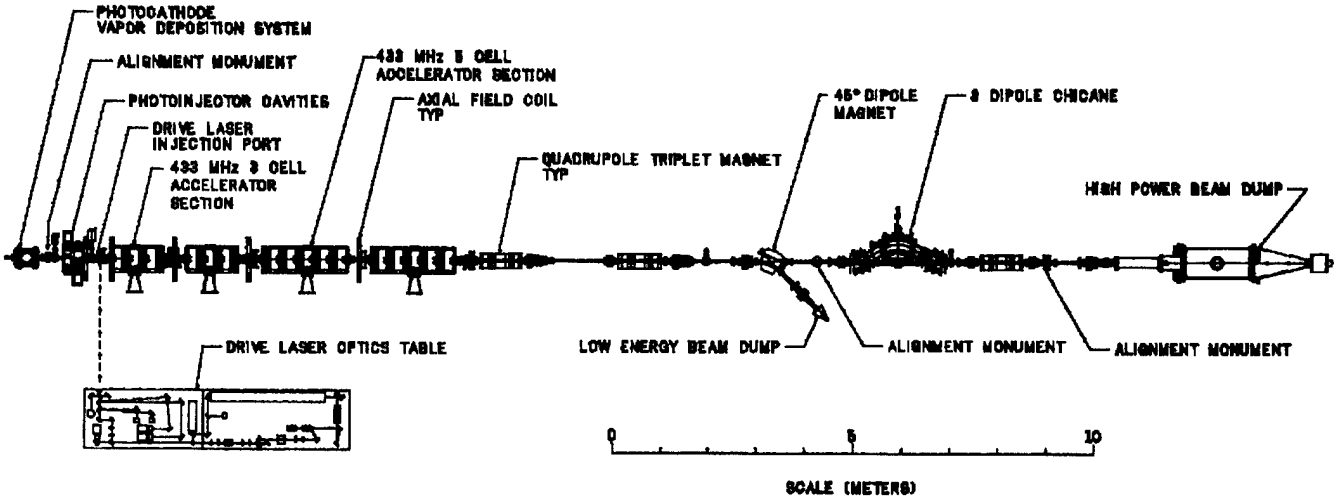


Figure 1. The layout and key elements of the high duty factor electron linac is illustrated in this drawing.

*Work supported by USASSDC under contract DASG60-90-C-0106

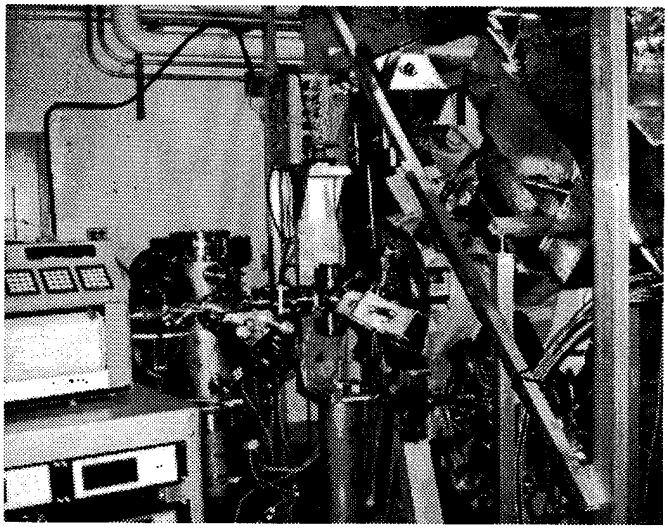


Figure 2. The photocathode fabrication chamber is at the left of the photo. An alignment monument can be seen to the right and immediately to the left of the injector cavities.

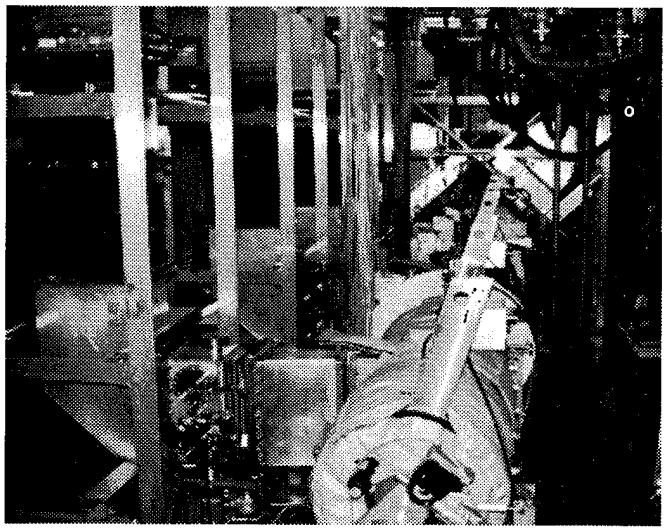


Figure 3. This photograph is taken from the 18 MeV end of the accelerator looking toward the injector. The WR1800 RF waveguide is at the left of the cavities. The bars extending upward to the right of vertical carry the offset alignment targets.

The cavities are constructed from copper plated aluminum cells which are bolted together. The first two cavities each contain 3 cells and the last two cavities each contain 5 cells. RF power is iris coupled into the center cell of each cavity. Dynamic resonance control of each cavity is maintained by two computer controlled slug tuners, one each located in the cells immediately preceding and following the center cell. The RF vacuum interface for each cavity is provided by a full-height WR1800 waveguide (1 MW average, 4 MW peak) alumina ceramic window located 2.4 m from the beam centerline around a 90^{o} bend to eliminate direct line of sight between the electron beam and the windows. Details of the construction and low power RF tests of one of these cavities is reported elsewhere[2]. Figure 3 shows the accelerator and some of its associated equipment.

RF Power

RF power for the accelerating cavities is provided by two 1 MW average, 4 MW peak, 433 Mhz klystrons. The cavities are driven through a system of WR1800 waveguide, hybrid splitters and phase shifters. Phase and amplitude control is accomplished by a Los Alamos GTA[5] RF control system.

The DC power regulator and modulator for each klystron provides DC pulses of up to 115 kV, 10 ms at a pulse repetition of up to 30 Hz. Details of this system are discussed in [6].

Beam Line

The beamline extends from the end of the second 5-cell APLE cavity for 13.7 m to a 1.3 MW high power beam dump. Within this transport are three quadrupole triplet lenses, a 45^{o} dipole magnet leading to a 5 kW beam dump, a magnetic chicane, 8 vertical plus 8 horizontal steering magnet pairs and 12 beam diagnostic stations which will be used to characterize the electron beam, and to conduct various beam conditioning studies. The accelerator beam control is maintained by 7 axial field focusing coils and 5 vertical plus 5 horizontal magnetic steering coil pairs.

Beam Diagnostics

In addition to the beam diagnostics stations in the beam line there are 4 diagnostics stations along the accelerator. The first is located after the photocathode injector and the remaining 3 are located between the four APLE cavities. These diagnostic stations are individually instrumented with a wide variety of devices. In most cases the minimum instrumentation consists of a toroid current monitor and a phosphor or Optical Transition Radiation (OTR) screen. The images produced can be observed with conventional video cameras, intensified gated cameras or a streak camera, depending upon the need of the measurement. Also, in a number of locations nonintercepting beam position sensing detectors are available. The combination of these tools in conjunction with the quadrupole lenses and dispersive elements of the beamline will allow detailed emittance, energy spread, and temporal beam characteristic to be measured.

Vacuum

Vacuum throughout the system is maintained by twelve, 10 cm cryopumps, a 20 cm cryopump mounted on the high power beam dump, two 60 l/s ion pumps, and six titanium sublimation pumps. All of the cavities and their associated vacuum waveguides and the cathode fabrication chamber are provided with provisions for bakeout to 180^{o} C (300^{o} C for the fabrication chamber).

Without bakeout, the injector cavities have been in the low 10^{-9} Torr range and previous experience with these cavities indicate that they will easily obtain the low to mid 10^{-10} Torr range required for long photocathode life after a modest bake. The copper plated aluminum cavities presently are at the required $5x10^{-8}$ Torr vacuum without baking.

Tests were previously conducted on one of the 5-cell cavities. After a 72 hour bake at 180° C, the cavity achieved a base pressure of $5x10^{-9}$ Torr at 20° C. Data collected during these tests on the outgassing rates are well represented by a simple temperature dependant expression
$q = 5.7x10^{-9} \exp(5.6x10^{-2}T)$ Torr-l/s-cm^2
where T is the temperature in degrees Celsius.

Accelerator Support and Alignment

Three alignment monuments have been installed which are used to establish and maintain the accelerator and beamline alignment. These monuments establish the beam center line and an offset line to check alignment of the accelerator without access to the center line.

The APLE accelerator cavities are supported on a three axis kinematic support. The support was designed so that during alignment the vertical, and horizontal motions of bore sight targets placed in opposite ends of a cavity are independently controlled and uncoupled. This greatly facilitates initial installation and final alignment. The cavities have been aligned to better than the required transverse 0.5 mm and longitudinal 3 mm.

Computer Control

The accelerator, RF system, beamline, beam diagnostics and data acquisition are under computer control. The main computers are two micro VAX II's, which control through CAMAC and GPIB, the various magnets, beam diagnostics, and data acquisition. The vacuum systems are controlled by a local Allen Bradly PLC5 and the RF systems are controlled by VME/VXI crates with imbedded 680x0 processors. The operator interface to the RF system is through a SUN SPARC Station 2.

Conclusions

The high duty factor electron linac for FEL is assembled and undergoing initial checkout prior to preliminary operation of the electron beam which is expected soon. Once reliable operation of the electron beam has been established, it will be characterized with regard to beam quality and intensity. After this, the beamline will be modified to conduct an energy recovery experiment, and a beam bunching experiment in preparation for construction of an FEL.

System Characteristics

Characteristics of the main elements of the system are described in Table 1.

Table I.
DESIGN PARAMETERS OF THE HIGH DUTY FACTOR ELECTRON LINAC

Photocathode Performance:	
Photosensitive Material:	K_2CsSb
Quantum Efficiency:	5% to 12%
Peak Current:	132 amperes
Cathode Lifetime:	1 to 10 hours
Angle of Incidence:	0 degrees
Photocathode Laser Parameters:	
Micropulse Energy:	0.47 microJoule
Energy Stability:	1% to 5%
Pulse-to-pulse separation:	37 ns
Micropulse Frequency:	27 x10^6 Hz
Gun Parameters:	
Cathode Gradient:	26 MV/meter
Number of cells:	2
RF Frequency:	433 x10^6 Hz
Final Energy:	2 MeV
Accelerator Parameters:	
Peak Accelerating Gradient:	5.5 MV/m
RF Frequency:	433 x 10^6 Hz
Duty Factor:	25%
Pulse Format	30 Hz x 8.3 ms
Electron Beam Parameters:	
Emittance (four x RMS):	20 to 40 π-mm-mrad
Charge:	1 to 5 nCoulomb
Energy:	18 MeV
Macropulse Current	0.13 Amps
Micropulse Length:	55 ps

References

[1] D. Dowell et al., "First Operation of a High Duty Factor Photoinjector," Proc. of the 1993 Particle Accelerator Conference, Washington, D.C., 2967 (1993).
[2] A. Vetter et al., "APLE Accelerator Prototype Cavity Fabrication and Low Power Tests," Proc. of the 1993 Particle Accelerator Conference, Washington, D. C., 1075 (1993).
[3] J. Adamski et al., "A Kilowatt Class Visible Free Electron Laser Facility," submited to this conference.
[4] D.H. Dowell, A. Vetter "Magnetic Pulse Compression Using a Third Harmonic RF Linearizer," submitted to this conference.
[5] S.P. Jachim et al., "The Los Alamos VXI-Based Modular RF Control System," Proc. of the 1993 Particle Accelerator Conference, Wahsington D.C., 1154 (1993).
[6] L.M. Knox, "The Successful Design and Development of Multi-Megawatt Radio-Frequency Linac Power Modules for Free Electron Lasers," 1992 Twentieth Power Modulator Symposium, Myrtle Beach S.C., 23 (1992).

A KILOWATT CLASS VISIBLE FREE ELECTRON LASER FACILITY*

J. L. Adamski, D. H. Dowell, T. D. Hayward, C. G. Parazzoli, and A. M. Vetter
Boeing Defense & Space Group, Seattle, WA 98124 USA

ABSTRACT

The design for a potential free electron laser (FEL), driven by a 120-MeV linac capable of generating 0.1-A macropulse average current beams at a duty factor of 0.6%, is described. The accelerator will employ a photo-injected, 18-MeV, 433-MHz linac as an injector [1], followed by a 1300-MHz longitudinal phase space "linearizer" [2], a magnetic buncher, and seven sections of 1300-MHz, pulsed traveling wave linac structure. Pulse lengths of 7 ps will be attained with minimal distortion of the pulse profile and normalized 90% emittance of 30 ± 10 π-mm-mr. The magnets used to transport the beam from the linac to the FEL centerline, the wiggler, and the optical resonator will be reclaimed from previous FEL demonstration experiments.

I. A NEW HIGH POWER FEL USER FACILITY

A. Introduction

A design has been developed for a powerful, ultraviolet (UV)-to-infrared (IR) wavelength FEL that can be rapidly completed in the USA/SSDC high average power FEL laboratory at Boeing. The laser design is shown in Fig. 1. A high duty factor electron accelerator is already under construction and is scheduled for test in 1995. The remainder of the laser would be assembled utilizing existing inventory from the SDIO ground-based laser program. This new laser can be ready for test in mid-FY96. The operational characteristics of the laser and its principal subsystems are given in Table 1.

Table 1. Kilowatt FEL Parameters

FEL Output		
Laser wavelength	0.2-4	μm
Peak laser power (0.6 - 0.8 μm)	150	kW
Avg laser power (0.6 - 0.8 μm)	1	kW
Peak electron beam power	12	MW
Avg electron beam power	70	kW
RF System		
Macropulse length	200	μs
Macropulse rep freq	30	Hz
Macropulse duty factor	0.6	%
Electron Beam		
Electron beam energy	120	MeV
Macropulse avg current	0.1	A
Macropulse avg e-beam power	12	MW
Average electron beam power	70	kW
Micropulse		
Micropulse rep freq	27.08	MHz
Micropulse charge	3.5	nC
Micropulse length	7	ps
Micropulse avg current	500	A
Optical Cavity and Wiggler		
Optical cavity length	38.74	m
No. circulating optical pulses	7	
Wiggler length	5	m
Wiggler period	2.18	cm
No. periods	220	
Peak wiggler field	1.0	T
Wiggler parameter (rms)	1.31	
Taper	10 step adjustable	
Extraction	1.4	%

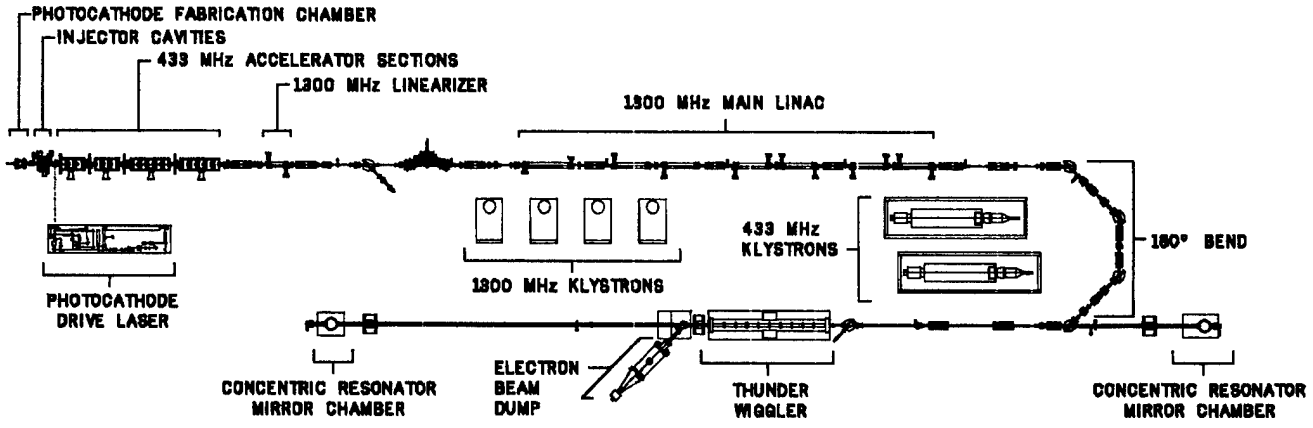


Figure 1. High Power Ultraviolet-Infrared FEL

*Work supported by USA/SSDC under Contract DASG60-90-C-0106

0-7803-3053-6/96/$5.00 ©1996 IEEE

The first operation of the laser will be at visible wavelength. The laser wavelength range can be extended to approximately 4 μm and laser operation on the third harmonic will allow UV wavelengths.

The laser and laboratories will be contained within a 40,000 ft^2 dedicated FEL research complex built with Boeing corporate funds. The FEL facility includes a 12 MW electric power substation, DC power vault, accelerator building with an upper radiation-shielded floor with laser laboratories, and general purpose laboratory space for users. The facility also includes six separate megawatt level thermal control systems for the experiments, full safety systems, and computer control and data equipment.

The 1 kW tunable free electron laser described in this paper builds on both the technical expertise and hardware developed during the defense FEL program. The high electron beam parameter expectations are justified by a series of tests and experiments performed at Boeing and elsewhere. The two-cavity photoinjector has already been operated at 25% duty factor and 32 mA of average current in the 1990-1992 high-duty testing program [3]. These capabilities are nearly 1000 times those of any other photoinjector in time-averaged brightness. In addition, electron beam compression experiments performed in collaboration with the French FEL group at Bruyeres-le-Chatel [4] show high compression factors can be achieved and establish the need to linearize the longitudinal phase space distribution using an RF structure as part of the bunching apparatus.

Comparison with the 0.51 and 0.63 μm FEL experiments conducted at Boeing in the late 1980s shows that the expected kilowatt-level performance of the new laser is quite conservative. An extraction efficiency of 1% with strong side band generation was attained [5] with the much poorer beam quality of a thermionic injector using three stages of RF pulse compression. FELEX simulations show laser efficiencies of 3 to 4%, yielding a laser power of 2.1 to 2.8 kW (based on a 70 kW average power electron beam). Our nominal goal is 1 kW.

The existence of a 1 kW tunable FEL will stimulate the national FEL program tremendously. In addition to advancing high-power accelerator and FEL technologies, this facility will fill an empty niche in the FEL community. Presently there is no other United States FEL operating in the visible-to-near-UV wavelength range, and there is no FEL in the world with 1 kW average power. The combination of wavelength tunability and power will make possible many new and exciting industrial and medical applications; e. g., isotope separation and photo-activation of medical dyes. In particular, the affordable enrichment of a variety of isotopes with high industrial and research value can be the first commercial application of free electron lasers. Finally, the realization of a 1 kW laser will constitute a very important first step to scale the FEL to power levels required for defense applications.

B. Electron Accelerator

The electron accelerator has two separate sections: 1) an 18 MeV, high duty factor, 433 MHz pre-accelerator, and 2) seven 1300 MHz structures to complete acceleration to 120 MeV. The first section, a high average power linac [1] (Fig. 1) presently under construction, comprises a high brightness photocathode injector in two single-cell RF cavities followed by four multicell standing wave accelerator cavities. The six cavities are grouped into two separate RF systems, each energized by its own high voltage power supply, filter, crowbar/regulator, and klystron (Thomson-CSF Model TH-2120). The RF control modules (one set of which has been used successfully in the earlier test of the injector) are furnished by the Los Alamos AOT Division. These modules correct the cavity resonance frequency and stabilize the average cavity field amplitude and phase.

The 18 MeV interface between the 433 MHz pre-accelerator and the 120 MeV, 1300 MHz main linac contains an energy spectrum corrector (which we call a linearizer) and a magnetic buncher chicane that will compress the bunches from the pre-accelerator before acceleration in the main linac. A 10-cell, 1300 MHz, traveling wave structure, requiring about 1 MW RF input, will perform the dual functions of linearizing and tilting the bunch in longitudinal phase space so that it will be compressed in the chicane that follows (Fig. 1). The magnetic buncher is a three-dipole chicane with deflection angles of 30, 60, and 30 degrees; transit time variation with energy is −10 ps/%. The combination of 10-cell structure and chicane will provide beam compression factors of 4-8 to increase the peak current to 500 A and decrease the micropulse width to 7 ps for matching to the 1300 MHz high voltage accelerator [2].

The 120 MeV beam energy is reached after the bunch-compressed beam accelerates through four 1300 MHz pulsed linac modules (Fig. 1). These linac sections and the pulsed RF amplifiers which drive them utilize existing and upgraded hardware from the successful visible FEL tests performed at Boeing in the late 1980s.

The last six 1300 MHz linac sections[6] are configured in series pairs, each driven by one TH-2104/U klystron. Fabrication of these 18-cell sections is 80% complete. The first 1300 MHz linac section differs from the following six. A 25 cell section originally built as a developmental prototype for very high average beam current applications, it was used extensively in earlier visible FEL tests at Boeing. It satisfies the requirement for an additional linac section needed to reach the 120 MeV beam energy required for FEL operation at the shorter visible wavelengths.

To reach that energy with 0.1A average beam current, the linac structures require 12 MW from each of the four klystrons (rated at 15 MW peak, 250 kW average). Since the operating RF duty factor is 0.6%, the average power demanded from each of the RF systems will be only 72 kW, less than one third of the rated average power.

C. Electron Transport, Wiggler, and Resonator

After acceleration to 120 MeV, the beam is brought onto the wiggler axis by the 180° bend (Fig. 1), which consists of four 45° dipole and 14 quadrupole magnets arranged to make the transport doubly achromatic, with all second order geometric aberrations corrected. The bend is also nearly isochronous and is therefore excellent for preserving the short length of the bunches it transports.

Parameters for the THUNDER wiggler [7] appear in Table 1. This wiggler is unique in that its ten 50 cm sections can be individually gapped. The optical cavity [8] for the FEL will be the concentric cavity used with the THUNDER wiggler in earlier oscillator experiments. The vacuum chambers are in place on the wiggler axis, and the mirror mounts and active alignment stabilization optics are available.

II. PERFORMANCE EXPECTATIONS

Performance of the 1 kW design has been simulated using the flat pulse shape of the compressed longitudinal phase space predicted for the linac output [2]. The pulse length after compression is 7 ps with a micropulse average current of 500 A; normalized 4-times-rms emittance is expected to be 30 π-mm-mr. The combination of high peak current, an essentially flat current distribution, and low emittance allow the use of a strong, 10% energy taper in the 5 m THUNDER wiggler. Wiggler field errors and beam jitter are included. The resonator single pass mirror loss is 2.5%, primarily due to scattering. The simulation included a Littrow grating to suppress sideband growth. The FEL output power as a function of resonator outcoupling is shown in Fig. 2. At higher outcoupling the FEL does not start up due to both the high optical outcoupling and the 10% wiggler taper. An electron beam power of 70 kW (see Table 1) produces an average laser power in excess of 3 kW for outcouplings between 20% and 30%, and demonstrates that the 1 kW FEL described here is a very conservative design.

III. REFERENCES

[1] T. D. Hayward et al., "A High Duty Factor Electron Linac for FEL," paper FAA27, this conference.

[2] D. Dowell and A. Vetter, "Magnetic Pulse Compression Using a Third Harmonic RF Linearizer," paper WPR20, this conference.

[3] D. H. Dowell et al., "First Operation of a High Duty Factor Photoinjector," *Proc. IEEE Particle Accelerator Conference, Washington, D.C., 1993*, 2967.

[4] S. Joly et al., "Brightness Measurements of the ELSA Electron Beam," contribution to the 1994 Linear Accelerator Conference, Kobe, Japan.

[5] R. L. Tokar et al., "INEX Simulations of the Boeing FEL System," *Nuclear Instruments and Methods*, **A296**, 115 (1990).

[6] T. Buller, "Design of High Average Power Linear Electron Accelerator Sections," *Proc. IEEE Particle Accelerator Conference, Chicago, IL, 1989*, 231.

[7] K. E. Robinson et al., *IEEE J. Quantum Electron.*, **QE-23**, 1497 (1987).

[8] D. M. Shemwell et al., *Proc. 8th Int. FEL Conf, Nucl. Instr. Meth.Phys. Res.*, (1987).

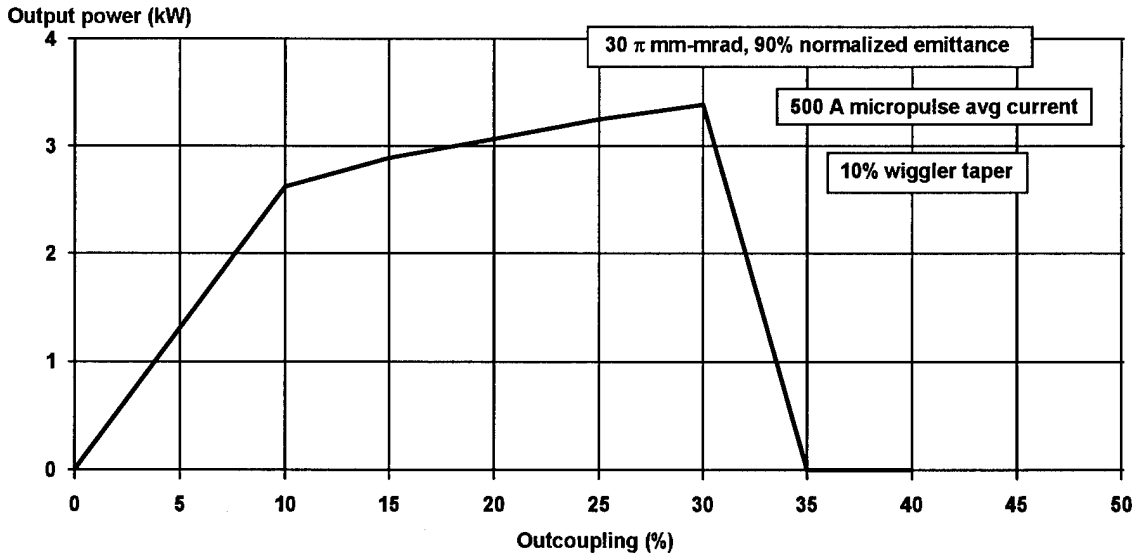


Figure 2. Output power of the proposed FEL as a function of resonator outcoupling.

Self-consistent Analysis of Radiation and Relativistic Electron Beam Dynamics in a Helical Wiggler Using Lienard-Wiechert Fields

M. Tecimer and L. R. Elias, Center for Research and Education in Optics and Lasers (CREOL) and Physics Department
University of Central Florida, Orlando FL 32826

Lienard-Wiechert (LW) fields, which are exact solutions of the Wave Equation for a point charge in free space, are employed to formulate a self-consistent treatment of the electron beam dynamics and the evolution of the generated radiation in long undulators. In a relativistic electron beam the internal forces leading to the interaction of the electrons with each other can be computed by means of retarded LW fields. The resulting electron beam dynamics enables us to obtain three dimensional radiation fields starting from an initial incoherent spontaneous emission, without introducing a seed wave at start-up. In this paper, we present electromagnetic radiation studies, including multi-bucket electron phase dynamics and angular distribution of radiation in the time and frequency domain produced by a relativistic short electron beam bunch interacting with a circularly polarized magnetic undulator.

1. INTRODUCTION

The coherence characteristics of the radiation fields produced by a beam of relativistic electrons moving along a magnetic undulator depend on the degree to which electrons become organized under the influence of the ponderomotive force. Our approach shows that making use of the complete electric and magnetic fields produced by a point charge, the longitudinal beam dynamics of the particles is governed by the "near -" and "far zone" fields. Electric field components in the near zone are composed of terms falling off as R^{-2} and R^{-3} whereas in the "far zone" they vary as R^{-1} corresponding to radiation fields. The latter combined with the undulator fields gives rise to the ponderomotive force. For sufficiently high density electron beams, depending on the pulse length and axial charge distribution within a radiation wavelength, "near zone" fields have considerable effects on the longitudinal motion of the electrons and the associated bunching process, altering the characteristics of the produced radiation.

The purpose of this paper is to point out the way LW fields can be exploited in obtaining spectral and temporal behavior of the radiated fields for the self amplified spontaneous emission (SASE) process. In our formulation, rather than solving self-consistently the paraxial wave equation coupled to the relativistic single-particle equations of motion, we first compute retarded LW fields with few assumptions to drive the electron's motion. Since the fields are evaluated in the time domain, the used approach allows their interaction with the electron beam with no restrictions on the frequency spectrum. Knowing all variables of the motion, such as retarded position, velocity, and acceleration of the charge, amplitude of the fields radiated by individual electrons in the beam are determined and summed at a observer surface far from the source. For simplicity, we consider in our simulations a filamentary sub-picosecond relativistic electron bunch which is substantially shorter than the slippage length.

Many simulation codes of free electron laser amplifiers utilize a single ponderomotive potential well imposing periodic boundary conditions at the bucket ends, thus neglecting slippage effects. Based on the formalism employed here, both the evolution of the multi-bucket electron phase space dynamics in the beam body as well as edges and the relative slippage of the radiation with respect to the electrons in the considered short bunch are naturally embedded into the simulation model.

A description of the particle and field dynamics underlying the code is outlined in section 2 followed in section 3 the numerical results demonstrating the evolution of the radiation in the time domain and its angular distribution. Here we study the evolution of the radiation for a monoenergetic beam with uniformly spaced electrons along the radiation wavelength as well as a pulse with shot noise in the electron phases.

2. PARTICLE AND FIELD DYNAMICS

The electric and magnetic fields produced by a point charge q moving along a trajectory $\vec{r}(t)$ with relativistic energy γmc^2 can be derived from the well known LW potentials. For the electric field strengths we have [1]:

$$\vec{E}(\vec{r},t) = \frac{q}{4\pi\varepsilon_0}\left[\frac{\hat{n}-\vec{\beta}}{\gamma^2\,(1-\vec{\beta}\cdot\hat{n})^3\,R^2}+\frac{1}{c}\frac{\hat{n}\times\{(\hat{n}-\vec{\beta})\times\frac{d}{dt}\vec{\beta}\}}{(1-\vec{\beta}\cdot\hat{n})^3\,R}\right]_{t_r} \quad (1)$$

All quantities in (1) have to be evaluated at the retarded time t_r The retardation condition $t_r = t - (R(t_r))/c$ connects the observation point time t to the source point time t_r where R represents the distance between the two points. The evolution of the three dimensional resultant radiation field can be determined when individual field contributions of all charges in the beam are superimposed in any point at the observer surface. Since LW fields are expressed in terms of particle's retarded position and it's time derivatives, relativistic Lorentz force equations for a coupled electron beam - radiation system have to be solved in a self-consistent way to describe completly particle's motion. The transverse motion is almost entirely determined by the undulator magnetic field, whereas the axial motion of each electron is defined by the combined undulator and the resultant LW field produced by other electrons in the beam. The for the FEL mechanism crucial axial electron dynamics can be obtained directly from the equation for the energy exchange between the electron and LW fields. The equation for the energy change of the i_{th} electron :.

$$d\gamma_i/dt = (q/mc)\,\vec{E}\cdot\vec{\beta}_i \quad (2)$$

The electric field is a resultant field at the position of the ith electron obtained by summing up LW field contributions from the rest of the charges in the beam. The summation is implemented by including Doppler upshifted and downshifted parts of the radiation fields. The latter has, however, much smaller influence on the motion of the particles if the beam is

0-7803-3053-6/96/$5.00 ©1996 IEEE

highly relativistic.

To compute the field contribution of individual electrons to the summation, the retarded values of R, $\hat{n}$, $\vec{\beta}$, and $d\vec{\beta}/dt$ have to be determined from the present position of the particles in the undulator and be inserted into (1). The retarded distance R is given by

$$R = \sqrt{(x-x')^2 + (y-y')^2 + (z-z')^2}$$

where x, y, z and x', y', z' represent the coordinates of the electron's present and retarded positions. At this point we introduce new dimensionless longitudinal position variables $\theta = k_u z$, $\theta' = k_u z'$, retarded distance $\rho = k_u R$, retarded axial distance $\chi_R = k_u (z_i - z'_j)$, and present axial distance $\chi_p = k_u (z_i - z_j)$ where prime denotes evaluation at retarded time and i, j refer to the particle's index in the beam. With the assumption of having a uniform longitudinal motion (β_z constant) during a numerical integration step for the energy exchange and employing the retardation condition, χ_R can be obtained by solving the equation:

$$\chi_R^2 (1-\beta_z^2) - 2\chi_R\chi_p + \chi_p^2 - 2\left(\frac{a_u}{\gamma\beta_z}\right)^2 (1-\cos\chi_R) = 0$$

The solution establishes the relation between the position of the source electrons at the time of emission and the position of the observer electron at the time of reception where the Lorentz force is exerted on that particular electron by the resultant field. Arranged in inverse powers of ρ, the rate of the energy exchange takes the form:

$$\frac{d\mathcal{E}}{d\tau} = r_0 k_u \sum_{j\neq i} \frac{1}{(1-\vec{\beta_j}\cdot\hat{n})^3} \left[\frac{1}{\rho^3} \{ (a_u^2/\gamma^4\beta_{zj})(1+a_u^2)\sin\chi_R - (a_u^4/\gamma^4\beta_{zj})\sin\chi_R\cos\chi_R \} \right.$$

$$+ \frac{1}{\rho^2} \{ (\beta_{zi}/\gamma^2)(n_z - \beta_{zj})(1+a_u^2(1-\cos\chi_R)) + (a_u/\gamma)^4(1+\sin^2\chi_R) - (a_u^2/\gamma^4)(1+a_u^2)\cos(\chi_R) \}$$

$$\left. - \frac{1}{\rho} \{ (1-n_z\beta_{zj})(a_u/\gamma)^2\beta_{zj}\sin\chi_R \} \right] \quad (3)$$

where we introduced the dimensionless time variable $\tau = ck_u t$. ρ and the axial unit vector component n_z are given by:

$$\rho = \chi_R\sqrt{1 + (a_u/\gamma\beta_z)^2 \sin^2(\chi_R/2)/(\chi_R/2)^2}, \quad n_z = \frac{\chi_R}{\rho}$$

respectively. The factor in the denominator, $1-\vec{\beta}\cdot\hat{n}$, can be expressed by $1-\vec{\beta}\cdot\hat{n} = 1 - n_z\beta_z - (a_u^2/\gamma^2\beta_z)\sin\chi_R/\rho$ Accounting for all forces involved in the electron-wave interaction, except for self radiation reaction, (3) gives a complete description of the change of electron's energy along the undulator. The term falling off as ρ^{-1} ($\sim R^{-1}$) contains the combined undulator-radiation fields causing modulation of the beam energy with subsequent bunching of the electron beam. The terms decreasing as ρ^{-2} and ρ^{-3} dominate at a distance close to the source. Thus we refer them as "near zone" fields. The factor $(1/\rho^2)(\beta_{zi}/\gamma^2)(n_z - \beta_{zj})/(1-\vec{\beta_j}\cdot\hat{n})^3$ describes the Coulomb interaction between the particles. It competes with the ponderomotive force reducing the depth of the ponderomotive potential well thus preventing particles from being trapped in the potential buckets. The rest of the "near field" terms are combined with the undulator fields and contributes to the energy modulation of the beam provided that the distance between the electrons are much smaller than the radiation wavelength. These fields would vanish in the abscence of an undulator. The numerical integration of (3) together with the relation $\beta_z = (1-(1+a_u^2)/\gamma^2)^{1/2}$ allows us finally to obtain the longitudinal motion of the electrons.

Having the knowledge of the position of each electron and it's time derivatives we can elaborate on the radiation evolution at a spherical surface of observation making use of the radiative part of (1). Superposition of fields emitted by each electron yields the resultant field:

$$\vec{E}_r(\vec{r},t) = \frac{q}{4\pi\varepsilon_0 c}\sum_i \left[\frac{\left(\hat{n}\cdot\frac{d}{dt}\vec{\beta}\right)_i (\hat{n}-\vec{\beta})_i - (1-\vec{\beta}\cdot\hat{n})_i \left(\frac{d}{dt}\vec{\beta}\right)_i}{(1-\vec{\beta}\cdot\hat{n})_i^3 \, R_i} \right]_{t_r}$$

Introducing the far-field assumption $R(t_r) \cong D - \hat{n}\cdot\vec{r}(t_r)$ where D is the distance from the observer to the entrance of the undulator and the unit vector $\hat{n}$ specifying the observation direction $\hat{n} = \{\sin\theta\cos\phi, \sin\theta\sin\phi, \cos\theta\}$, $1-\vec{\beta}\cdot\hat{n}$ and R(tr) may be approximated as:

$R(t_r) = (D - z\cdot\cos\theta - (a_u/\gamma k_u\beta_z)\theta\sin k_u z)$ and

$1-\vec{\beta}\cdot\hat{n} = 1 - (a_u/\gamma)\theta\cos k_u z - \beta_z\cos\theta$

respectively. We use here the fact that the radiation pattern emitted by a charge in a helical undulator is azimuthally symmetric around z-axis, and confined to angles of the order of $\theta \approx (1/\gamma) \ll 1$. Noticing that $k_u l_b \ll 2\pi$ for the considered short bunch, where l_b is the bunch length, we can evaluate time structure and frequency composition of the radiated field components E_x and E_y at any point over the observer surface. The time evolution of the angular distribution is determined by $d^2W/d\Omega dt = \varepsilon_0 c|R\vec{E}|^2$ The total radiated power can be obtained performing the integral over the solid angle:

$$\frac{dW}{dt} \approx \varepsilon_0 c \int_0^{2\pi}\int_0^{\pi} |\vec{E}|^2 R^2 \theta d\theta d\phi \quad (4)$$

where $d\Omega \approx \theta d\theta d\phi$. The time integration of (4) over the radiation pulse yields the total radiated energy.

Evaluating Jackson's formula for the energy spectrum, we can also determine energy radiated per frequency ω, per solid angle Ω during the time the beam travels through the undulator:

$$\frac{d^2W}{d\Omega d\omega} = \frac{r_0 mc\omega^2}{4\pi^2}\left| \int_0^T \hat{n}\times\hat{n}\times\sum_i \vec{\beta}_i e^{i\omega\left(t - \frac{\hat{n}\cdot\vec{r}_i(t_r)}{c}\right)} dt \right|^2$$

where $\vec{r_i}$ and $\vec{\beta_i}$ are position and velocity of the i^{th} electron obtained from the describtion of the self-consistent motion of electrons.

In order to give a correct account of the conservation of energy, energy loss of each electron due to its self field is included

into (3). Using Lienard formula for the radiated power from a single electron we have:

$$P = \frac{q^2}{6\pi\varepsilon_0 c}\gamma^6\left(\left(\frac{d}{dt}\hat{\beta}\right)^2 - \left(\hat{\beta}\times\frac{d}{dt}\hat{\beta}\right)^2\right)$$

3. NUMERICAL RESULTS

The theoretical derivations presented in the previous section have been implemented in a simulation code to obtain angular and temporal characteristics of the three dimensional radiation fields emitted by a 35 MeV, 14 A, 70 μm subpico- second filamentary electron bunch propagating trough a 4.5 m long, 1.5 cm period helical undulator. The undulator parameter a_u is chosen to be 1.12. To the parameter set corresponding radiation wavelength is 3.5 μm . The code computes the time evolution of the three dimensional field amplitude with no initial bunching and seed wave at start-up. For a typical run ,a flat-top profile electron beam is used. The simulation particles are uniformly distributed along the electron pulse. The bunch , twenty radiation wavelength long , is much shorter than the slippage distance. To study effects of the shot noise in the electron phase , simulations with randomly spaced electrons are carried out.

4. REFERENCES

[1]J. D. Jackson, Classical Electrodynamics,p.657 (J. Wiley & Sons , 1975)

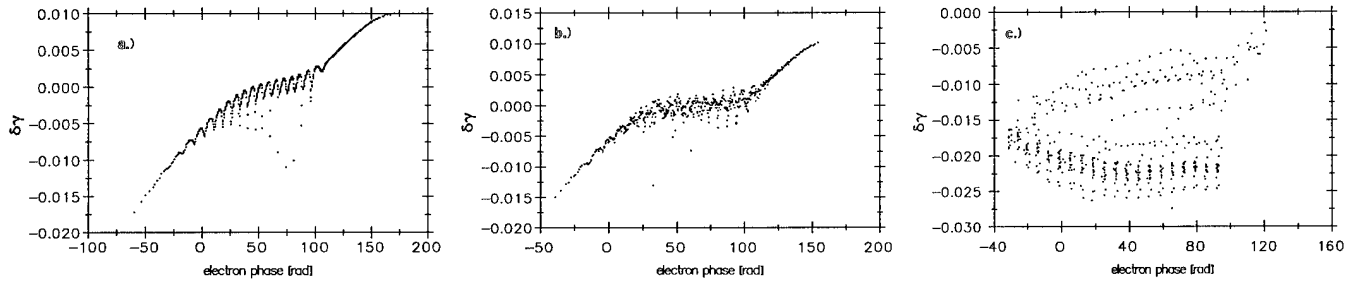
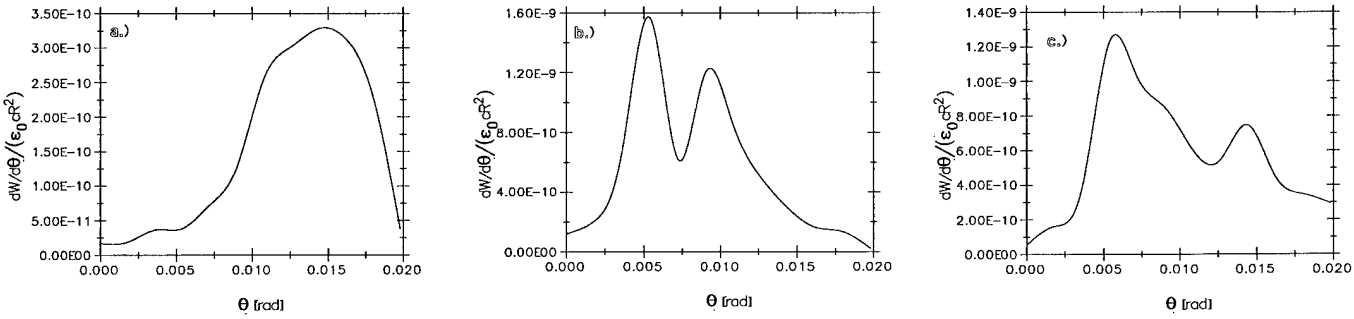
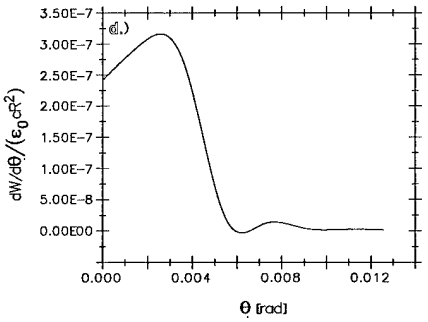


Fig. 1 a-c. show phase versus exchanged energy of initially uniformly and randomly distributed monoenergetic electron beam after traveling trough a 4.5 m long helical undulator. Plot 1.c is obtained from the numerical integration of (19) by considering the 1/R dependent (ponderomotive force) term alone.In plot 1.a-b the influence of the "near-zone" fields on the longitudinal beam dynamics is included. In Plot 1.b the periodicity of the potential wells is perturbed due to the initial random distribution of the charge along the bunch length.





Figures 2. a-c illustrate the angular distribution of the radiated energy by the initially randomly phased electron bunch. The angular distribution observed at a surface far from the source is divided into three different time domains; leading - and trailing edge of the radiation pulse, figures 2a. ,2 c respectively, and the steady state regime fig. 2b, where θ is the observation angle.Due to the (partial) bunching of the electron beam at the end of the undulator, the coherent superposition of radiation pulses from all electrons in the beam produce, as a result of wave interference effects a narrower cone of radiation than the radiation generated by the electrons at the entrance of the undulator.Dependent on the distribution of the electron phases, by summing the amplitude of the fields radiated by individual electrons one can obtain interferece patterns at the observer surface where constructive (destructive) interference takes place for certain observation angles.Fig.2d. shows the angular distribution of the radiated energy in the absence of the "near-zone" fields . Due to the increased coherence in the resultant field, the angular radiation cone becomes narrower than the ones shown in figures 2.a-c.

FIRST LASINGS AT VISIBLE AND IR RANGE OF LINAC-BASED FELs AT THE FELI

T. Tomimasu, E. Oshita, S. Okuma, K. Wakita, K. Saeki, A. Zako, T. Suzuki, Y. Miyauchi, A. Koga, S. Nishihara, A. Nagai, E. Tongu, K. Wakisaka, A. Kobayashi and M. Yasumoto
Free Electron Laser Research Institute, Inc.(FELI):4547-44, Tsuda, Hirakata, Osaka 573-01, Japan

SUMMARY

First lasings at 5.5μm and 1.88μm have been achieved in October 1994 and February 1995 at the FELI using two undulators installed at 30-MeV and 80-MeV undulator beam lines of the FELI S-band linac. Lasing on the third harmonics at 0.64μm has been also observed. A thermionic triode gun of the linac emits 500ps pulses of 2.3A at 23.125MHz. These pulses are compressed with a 714-MHz prebuncher, a 2856-MHz standing wave type buncher, and 3-m long accelerating waveguides to 42A x 10ps. The 24-μs stable RF pulses can increase a conversion efficiency from electron beam power to FEL power at short wavelength FELs. At 5.5μm, 1.88μm and 0.63μm, FEL peak power are 3MW, 2MW and 0.3MW, and FEL spectral widths are 0.5%, 0.3% and 0.3%, respectively.

INTRODUCTION

In the past decade, advances in photoinjector technology have improved the beam quality needed for short wavelength FEL oscillations[1-4]. However, major issues with photo-injectors are short-lifetime of the photocathode and cost and complexity of the drive laser. In these five years, however, two FEL oscillations in the short wavelength have been achieved using rf-linacs with the thermionic gun driven by gride pulsers shorter than 1ns, because of long-lifetime, easy-operation, and low cost of the thermionic gun[5,6].

The purpose of this report is to demonstrate first lasings at 5.5μm, 1.88μm and 0.63μm achieved by using the FELI linac with the thermionic gun and two undulators.

6-MeV INJECTOR WITH A THERMIONIC GUN

The FELI linac for IR-FEL facilities consists of a 6-MeV injector and three ETL type accelerating waveguides. The injector is composed of a 150-kV thermionic triode gun, a 714-MHz prebuncher, and a 2856-MHz standing wave type buncher[7]. The gun with a dispenser cathode (EIMAC Y646B model) emits 500ps pulse of 2.3A at frequencies of 22.3125 MHz. The grid pulser is manufactured by the Kentech Instruments, Ltd., England. The 714-MHz prebuncher is made of stainless steel to reduce wakefield effects introduced by the 500-ps beam from the gun. The rf frequency of 714 MHz is chosen 1) to meet a 9-cm long bunched beam from the gun operated by a 120-kV DC voltage and the 500-ps grid pulser, and 2) to make the cavity as compact as possible.

The 2856-MHz buncher is a standing wave type buncher (SWB) consisting of nine cavities made of copper. The peak electric field is 14MW/m for an rf input of 2MW. In order to reduce space-charge effects in bunched pulses as much as possible, a drift space from the SHB to the first cavity of the SWB is designed to be around 40cm. The axial field distribution from the gun to the SWB has been designed to keep a radius of the bunching beam constant from the SHB to the SWB. The maximum field is about 0.21T near the entrance of the SWB. The field distribution delicately affects FEL oscillations.

The diameter ($2r_b$) of the injector beam was observed to be less than 2mm with a 2-mm slit. The energy spectra of the injector beam were also measured with a 90deg-bending magnet. The energy spread (FWHM) is 150keV (2.5%) for a 5.8-MeV electron beam and the beam emittance ($\varepsilon_n=\gamma r_b\theta$) is estimated to be 12πmm mrad[7].

RF SYSTEM FOR FELI LINAC

An rf system for linac-based FELs requires rf sources with long pulse duration and high stability. Our rf sources are a klystron 1VA88R for the 714-MHz prebuncher and a klystron E3729 for the 2856-MHz buncher and three accelerating waveguides. These are modified for a 24-μs pulse operation [8]. A modulator for the klystron 1VA88R uses MOS-FET modules. However, a modulator for the klystron E3729 consists of 4 parallel networks of 24 capacitors and 24 variable reactors, and it has a line-switch of an optical thyristor stack. The stability of the modulator pulses is 0.067%p-p at 24-μs duration[9].

FELI 80-MeV LINAC AND IR-FEL FACILITIES

The layout of the FELI 80-MeV linac, S-type BT lines for undulators and IR-FEL facilities are shown in Fig. 1. To prevent BBU effects, the linearly narrowed iris type accelerating waveguides are used for the FELI linac. The iris diameter of this type is linearly narrowed from a_1 to a_2 ($a_1>a_2$) along the accelerating waveguide with a length of l_w[10]. For instance, parameters of C3 type are a_1=26mm, a_2=22.8mm, and l_w=3m; those of D3 type are a_1=25mm, a_2=21.8mm, and l_w=3m. The configuration of the injector and these waveguides is the injector-C3-D3-C3. Using screen monitors installed at the inlet and outlet of each accelerating waveguide, quadrupole magnets and steering coils, the electron beam size and position are monitored and controlled to pass through the center of accelerating waveguides. Further, using five screen monitors installed in each BT line, the beam size and position are adjusted along

0-7803-3053-6/96/$5.00 ©1996 IEEE

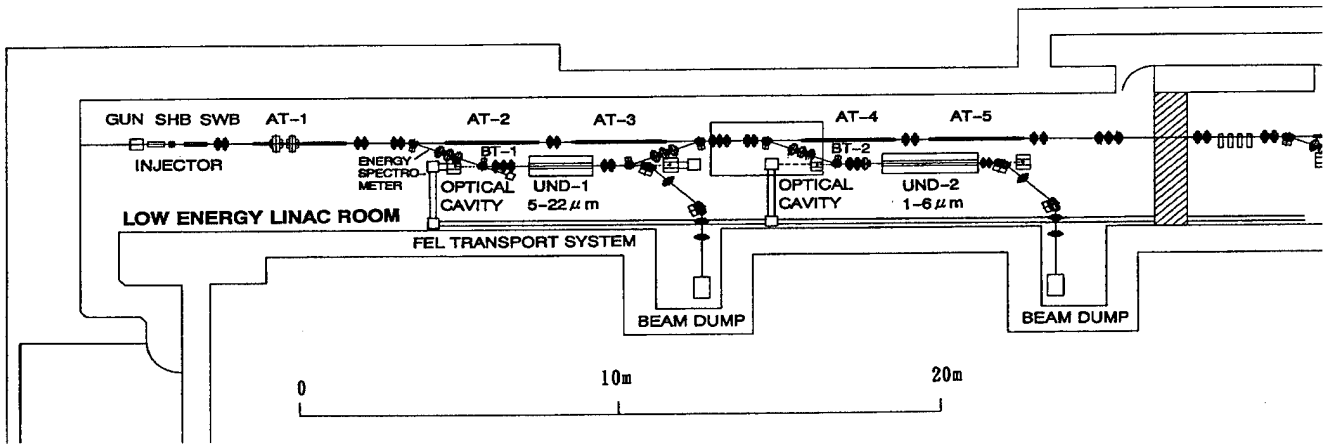


Fig. 1 Layout of FELI Linac, S-type BT lines and IR-FEL Facilities

the axis so as to pass through the center of a narrow vacuum chamber inserted to each undulator[11]. A lattice design of the BT line has been published elsewhere[12]. The beam passing through the undulator is focused and sent to a water dump using two 45deg.-bending magnets. Using variable slit systems installed in the 30-MeV BT line, the first 22.5deg.-bending magnet and a water absorber are used as an energy spectrometer. The energy spread (FWHM) is about 290keV (0.9%) for a 32.2-MeV beams[7]. At the 80-MeV BT line, the energy spread has been also measured but it is about 1% for a 70-MeV beam.

FIRST LASING AT 5.5μm USING THE FEL FACILITY I

First lasing at 5.5μm has been achieved using a 2-m long undulator and a 6.72-m optical resonator installed at the 30-MeV BT line of the FELI linac. Tab. 1 shows the characteristics of the linac beam at the 30-MeV BT line and the undulator 1. Fig. 2 shows a 5.5-μm FEL macropulse shape measured with a HgCdTe detector and an electron beam current pulse measured with a buttom monitor[14]. The laser gain is deduced from the first part of the exponential growth of the FEL pulse. The current pulse is 24μs long. The saturation duration is about 18μs, corresponding to 400 laser micropulses of 10ps. The FEL spectrum was measured with a Czerny-Turner type monochrometer equipped with 120 pyroelectric detectors[15]. The spectrum shown in Fig. 3 is a temporal integration along the laser macropulse.

Tab. 2 shows the characteristics of optical cavities for two undulators[13] and first lasing at 5.5μm.

FIRST LASING AT 1.88μm USING THE FEL FACILITY II

First lasing at 1.88μm has been achieved using a 3-m long undulator and a 6.72-m optical resonator installed at the 80-MeV BT line of the FELI linac. The characteristics of the linac beam at the 80-MeV BT line and the undulator 2 are also shown in Tab. 1, and the characteristics of optical cavity for the undulator 2 and first lasing at 1.88μm are also shown in Tab. 2. Fig. 4 shows a 1.88-μm FEL macropulse shape measured with the HgCdTe detector and a 24-μs, 2856-MHz RF pulse. The 1.88-μm FEL spectrum shown in Fig. 5 is also a temporal integration along the macropulse.

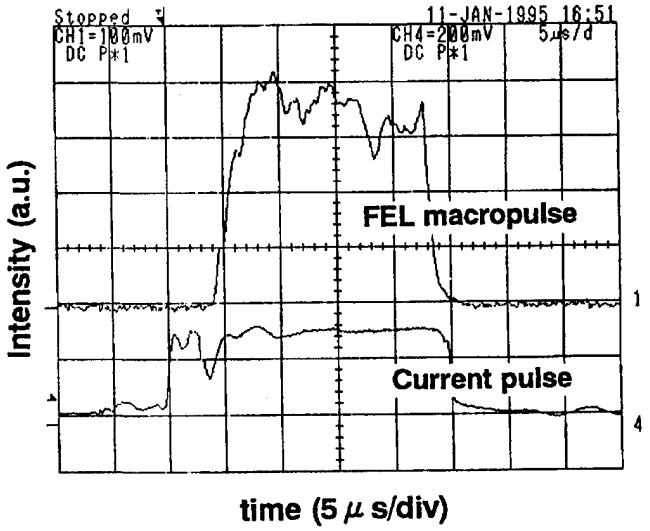


Fig. 2 FEL Macropulse at 5.5μm and Current Pulse

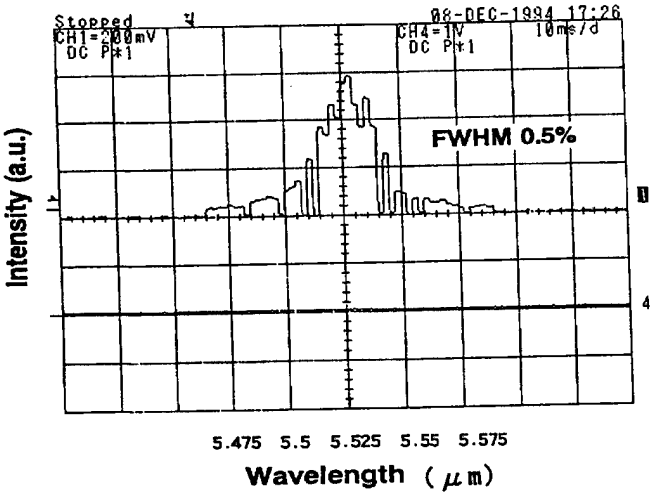


Fig. 3 FEL Spectrum at 5.5μm

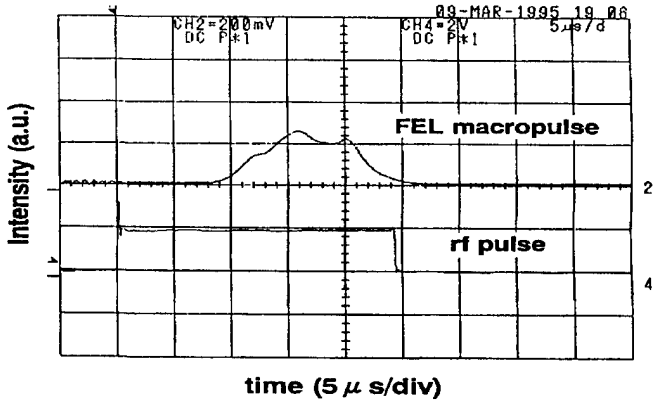


Fig. 4 FEL Macropulse at 1.88μm and RF Pulse

Tab. 1 Characteristics of FELI linac beams and undulators

Accelerator	30-MeV BT Line	80-MeV BT Line
Energy E	33.2MeV	68.0MeV
Peak current I_P	42A	42A
Macropulse duration	24μs	24μs
Macropulse separation	0.1s	0.1s
Micropulse duration	10ps	10ps
Micropulse separation	44.8ns	44.8ns
Energy spread(FWHM)	1.0%	1.0%
Emittance(normalized)	~26πmm mrad	~26πmm mrad
Undulator	No.1	No.2
Type	Halbach	Halbach
Length L_u	2m	3m
Number of periods N	58	78
Period length λ_u	3.4cm	3.8cm
Gap	≧14mm	≧20mm
Magnetic field(peak)	0.49T	0.40T
Parameter K	0.5-1.55	0.5-1.4

Tab. 2 Characteristics of optical cavities and lasings

Optical cavity	No.1	No.2
Type	optical mode	optical mode
Length	6.72m	6.72m
Rayleigh length	1.0m	0.36m
g-parameter	-0.93	-0.80
	-0.76	-1.19
Mirror curvature	3.490m	3.734m
	3.827m	3.062m
Mirror type	Au on Cu	Au on Cu
Aperture of an extraction mirror	0.5mmϕ	0.5mmϕ
Lasing on the fundamental		
Wavelength λ	5.5μm	1.88μm
Spectral width Δλ/λ	0.5%	0.3%
Small signal gain	20%	14%
Total cavity loss	0.8%	2.7%
Peak power at the aperture	3MW	2MW
Date of first lasing	Oct. 31, '94	Feb. 27, '95
Lasing on the third harmonics		
Wavelength	0.63μm	
Net gain	3.3%	
Peak power at the aperture	0.3MW	

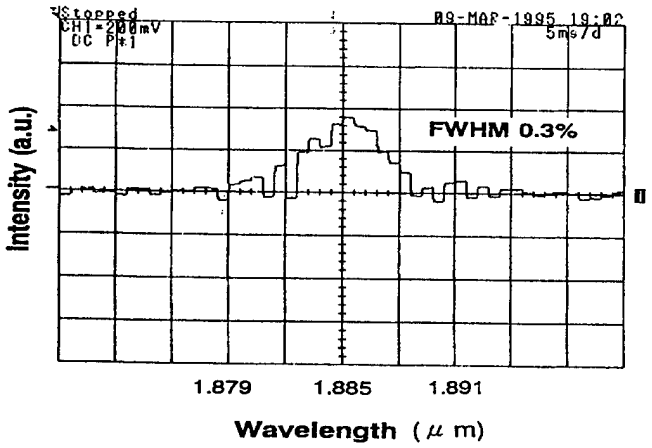


Fig. 5 FEL Spectrum at 1.88μm

CONCLUSION

First lasings at visible and IR range have been demonstrated by using a 68-MeV, 42-A electron beam from the FELI linac with the thermionic gun. A visible FEL oscillation at 0.63μm has been also achieved on the third harmonics. A peak power level at 5.5μm reaches up to 60% of the theoretical limit $EI_P/4N$. However, peak power levels at 1.88μm and 0.63μm are a seventh of the limit. Optical properties of these FELs will be described in details elsewhere.

REFERENCES

[1] M. Curtin, et al., Nucl. Instr. Meth., A296, 127(1990)
[2] P. G. O'shea, et al., Nucl. Instr. Meth., A318, 52(1992)
Nucl. Instr. Meth., A341, 7(1994)
[3] S. Joly, et al., Nucl. Instr. Meth., A331, 199(1993)
[4] R. L. Sheffield, et al., Nucl. Instr. Meth., A341, 371 (1994)
[5] P. W. van Amersfoort, et al., Nucl. Instr. Meth., A318, 42(1992)
[6] R. Prazers, et al., Nucl. Instr. Meth., A331, 15(1993)
[7] T. Tomimasu, et al., Nucl. Instr. Meth., A358, ABS11 (1995)
[8] Y. Morii, et al., Proc. 9th Symp. on Accelerator Science and Technology, KEK, Aug. 25-27, 1993, p.175
[9] E. Oshita, et al., in this proceedings
[10] T. Tomimasu, et al., IEEE Trans., NS-28, No.3, 3523 (1981)
[11] A. Kobayashi, et al., Proc. 6th Int'l Symp. on Advanced Nuclear Energy Res., JAERI, March 23-25, 1994, p.589
[12] Y. Miyauchi, et al., ref. 8, p.416
[13] K. Saeki, et al., Nucl. Instr. Meth., A358, ABS56(1995)
[14] A. Zako, et al., Proc. 1995 Annual Meeting of the Atomic Energy Society of Japan, TIT, March 28-30, p.326
[15] A. Kobayashi, et al., ibid., p.328

THE NORTHROP GRUMMAN COMPACT INFRARED FEL (CIRFEL)*

I. S. Lehrman, J. Krishnaswamy, R. A. Hartley
Northrop Grumman Advanced Technology and Development Center, 4 Independence Way, Princeton, New Jersey 08540, USA
R. H. Austin
Physics Department, Princeton University, Princeton, New Jersey 08544, USA

I. INTRODUCTION

As part of Northrop Grumman's ongoing research in particle accelerators, we have designed and are commissiong a Compact Infrared Free-Electron Laser (CIRFEL) for the study of high-brightness electron beams and free-electron lasers. Besides serving as a tool for FEL development, the CIRFEL laboratory, located at Princeton University, will be used in experiments ranging from basic FEL physics and biophysics to chemistry, materials science and medicine.

The CIRFEL is to lase initially in the 10 – 20 μm range. The pulse format of this FEL is a train of micropulses, 5 - 10 psec is duration, at a repetition rate of 142.8 MHz. The micropulse energy is in excess of 100 μJ. The micropulses comprise a macropulse lasting approximately 10 μsec. The macropulse repetition rate is 10 Hz, thus the average power of the FEL is on the order of 1.5 W.

II. SYSTEM DESCRIPTION

The CIRFEL consists of the following system components: (1) a high-brightness photocathode electron gun, (2) a photocathode illumination laser, (3) a 30 MW S-band RF source, (4) the beam transport system, (5) the FEL wiggler, (6) the FEL optical cavity, and (7) the associated support hardware subsystems. Figure 1. shows the layout of the CIRFEL beamline.

To allow for flexibility and possible future expansion, the beamline components are mounted on a pair of rails. The rails allow the axial positions of the beamline elements to be easily adjusted. The rails are mounted to non-magnetic optical tables which allows additional optics and diagnostics to be fixed to the tables with standard mounts. A description of each of the system components follows.

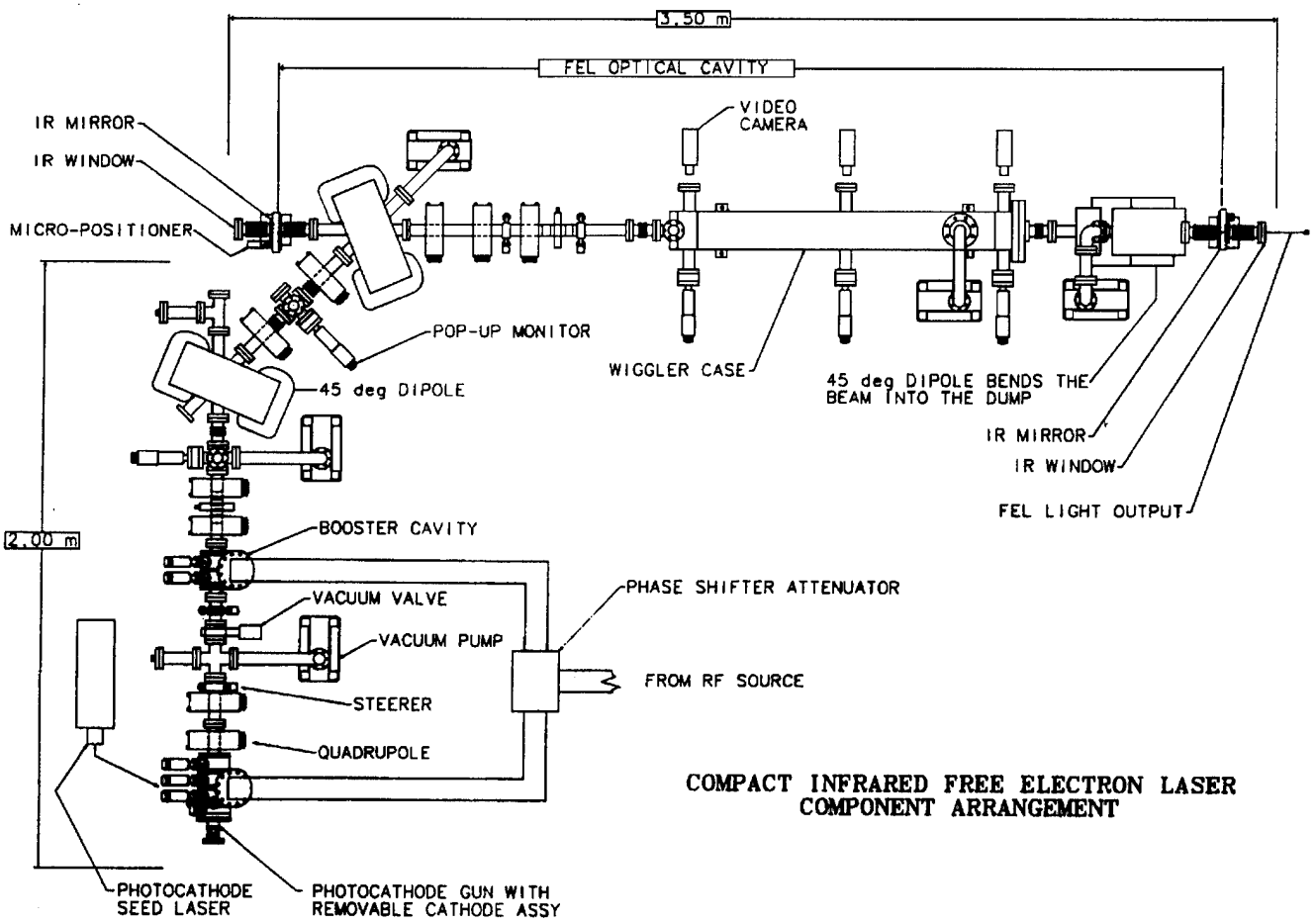


Figure 1. Layout of the CIRFEL beamline.

0-7803-3053-6/96/$5.00 ©1996 IEEE

A. High-Brightness Photocathode Electron Gun

The accelerator for the CIRFEL is a photocathode electron gun shown in Figure 2. The gun is only 20 cm long and produces electron beams with energies up to 9 MeV. The gun consists of $3^1/_2$ cells operated in the π-mode phasing. The gun is fed from a single waveguide which couples power directly to cells 2 and 3. Power is aperture coupled from cell 2 to cell 1 and from cell 3 to cell 4.

The gun has been modeled extensively with the MAGIC[1] particle-in-cell code. These results indicate that the beam emittance (RMS) will be between 2.7 and 10 π mm-mrad depending upon the launch phase. The peak electric field at the cathode will be between 60 - 80 MV/m with gradients up to 100 MV/m in cells 2 through 4.

The photocathode, which is contained in the first cell, is a 6 mm diameter disc of Mg. Approximately 7 μJ of UV (262 nm) is required to release 1 nC of charge.[2]

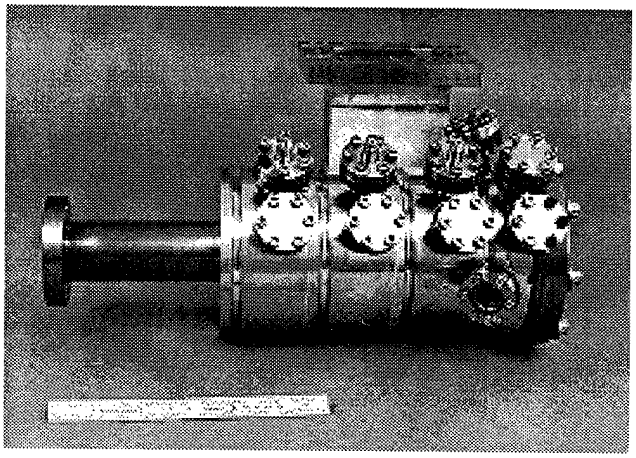


Figure 2. CIRFEL Photocathode Electron Gun

Downstream of the photocathode gun, we have installed a two cell booster cavity to increase the beam energy to 14 MeV. This cavity is identical to the central two cells of the gun.

B. Photocathode Illumination Laser

The photocathode laser for the CIRFEL gun consists of a ND:YLF mode-locked oscillator, a pulse slicer, two double-passed stages of amplification, and harmonic generation. The mode-locked oscillator is a Lightwave Electronics' diode-pumped unit operating at 142.8 MHz. The oscillator produces 7 psec IR pulses (1047 nm) at an average energy of 200 mW. The temporal jitter of the oscillator has been measured to be less than 1 psec.

The oscillator was integrated into a macropulse amplifier by Continuum. A pulse slicer is used to slice out a 10 μsec portion of the beam. The beam is then double-passed through a 7 mm flash lamp-pumped ND:YLF amplifier. After spatially filtering the beam, the beam is passed through another 7 mm ND:YLF amplifier. Second and fourth harmonic generation crystals are used to produce 524 nm and 262 nm radiation. The laser is capable of producing in excess of 16 μJ per micropulse at 262 nm.

C. S-Band RF Source

The RF system consists of a 700 W S-band amplifier (IPA) which feeds a 30 MW ITT 2960 klystron. The modulator for the klystron has a 13 stage pulse forming network (PFN) which produces a video pulse of 12 μsec (FWHM). The klystron has a flattop output of 10 μsec. The RF power from the klystron is split by a power divider to feed both the gun and booster. In order to correct for the PFN ripple, we have implemented Feed-Forward[3] correction for both the RF amplitude and phase. The RF amplitude and phase are sampled in cell 1 of the gun. Amplitude and phase corrections are programmed into arbitrary waveform generators (AWG). The AWG's drive a pin-diode antenuator and phase shifter which are in the low-level RF chain driving the IPA.

D. Beam Transport System

The TRACE3D[4] and PARMELA[5] beam optics/dynamics codes were used to model the CIRFEL beamline. A quadrupole doublet is used to focus the beam from the output of the gun. An achromatic bend is used to allow for mirror access for the FEL optical cavity. Depending upon the longitudinal phase space distribution of the beam, the achromat can act to compress the longitudinal length of the beam, thus increasing the peak current of the bunch.

A quadrupole triplet is used to focus the beam into the wiggler. In order to reduce horizontal defocusing effect of the 45^o bending magnets, the poles were cut with 22.5^o entrance angles. Once a TRACE3D solution was found for the beamline, the PARMELA code was used to determine the effect of space charge. PARMELA simulations indicate there is no significant space charge induced emittance growth for 1 nC bunches. Space charge will cause some slight changes in the effective focal lengths of some of the quadrupoles.

E. FEL Wiggler

Initial experiments will be carried out with a 1.36 cm period, 73 period permanent magnet wiggler loaned from the Los Alamos National Laboratory. The wiggler gap is 7 mm and the RMS wiggler parameter, $A_W = 0.16$. Our calculations indicated that the single pass gain should be in excess of 50%[6].

F. FEL Optical Cavity

The optical cavity is a near concentric, asymmetric stable cavity, with a Rayleigh range of ~ 0.5 m. The cavity utilizes copper mirrors with central holes for outcoupling the radiation. A HeNe alignment laser, which is injected in the upstream mirror, is used to align the electron beam onto monitors that are inserted into the wiggler. The HeNe laser light which is outcoupled through the downstream mirror is used to align the cavity mirrors. ZnSe output windows are used at the vacuum interface.

III. STATUS

Figure 3. shows the CIRFEL device in its present configuration. As of April 1995, we have installed all of the beamline including the wiggler. The cavity length was determined by injecting the ND:YLF mode-locked laser into the cavity and observing interference between sucessive pulses.

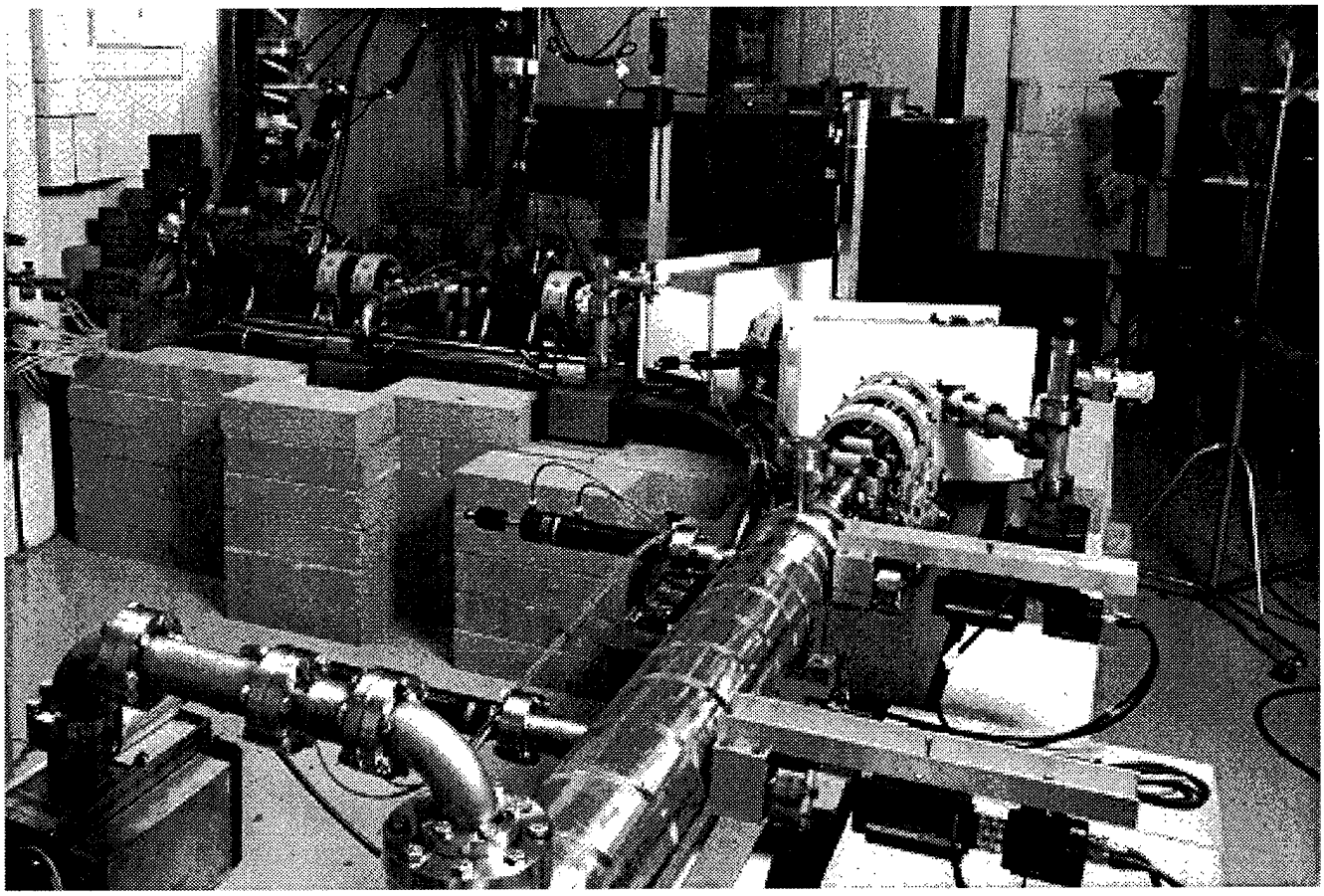


Figure 3. CIRFEL Device installed at Princeton University. The gun is located in the top left corner and the wiggler is contained in the vacuum case in the center of the figure.

From the amplitude of the interference signal, we were able to determine the cavity length to within 50 microns. Using the RF Feed-Forward correction scheme, we have flattened the RF amplitude in the gun to better than 0.1% and the RF phase to 1 degree. In excess of 1 nC of charge at 11 MeV has been transported through the wiggler with 100% transmission. Spontaneous emission has been routinely observed, but we did not see any signs of optical gain.

Beam position measurements indicated that the wiggler axis was not properly aligned to the electron beam and optical cavity axis. An examination of the wiggler revealed a bow in the wiggler structure of 0.75 mm at the center. The wiggler has been removed and will be re-assembled and measured at the Los Alamos National Laboratory. At re-assembly, the wiggler gap will be reduced to 6 mm in order increase the gain from the predicted value of 50% to nearly 100% (including degradation effects due to emittance and energy spread).

Once the wiggler is re-installed, we will be working to observe optical gain and then demonstrate FEL lasing.

REFERENCES

[1]G. D. Warren, L. Ludeking, J. McDonald, K. Nguyen, and B. Goplen, "MAGIC Users Group Software," Proceedings of the Conference on Computer Codes and the Linear Accelerator Community, Los Alamos National Laboratory, Jan 22-25, 1990, Richard Cooper, Ed. LA-11857-Z (1990) 57.

[2]P. G. O'Shea, to be published in the 1994 Proceeding of the International Free-Electron Laser Conference, Nucl Inst and Meth **A**. (1995)

[3] R. Zhang, I. Ben-Zvi and J. Xie, Nucl Inst. Meth **A324** (193) 421-428.

[4] K. R. Crandall, Los Alamos National Laboratory report LA-11054-MS, August 1987.

[5] K. R. Crandall and L. Young, "PARMELA," in the Compendium of Computer Codes for Particle Accelerator Design and Analysis, H. Deaven and K. C. Chan, Eds. Los Alamos Natl. Lab report LA-UR-90-1766, May (1990) 137.

[6] "FEL CAD," D. C. Nguyen, S. Gierman and P. O'Shea, available from Los Alamos National Laboratory, unpublished 1994.

*This work is supported by the Northrop Grumman Advanced Technology and Development Center

A Proposed NSLS X-Ray Ring Upgrade Using B Factory Technology*

E.B. Blum, National Synchrotron Light Source, Brookhaven National Laboratory, Upton, NY 11973

ABSTRACT

A proposed upgrade to the NSLS X-Ray Ring is described that will allow the storage of a 2.4 A, 3 GeV electron beam using technology developed for the PEP-II B factory at SLAC. In this configuration, a peak flux of greater than 10^{16} photons/sec/0.1% bandwidth/5 mrad will be produced. The four existing 53 MHz RF cavities will be replaced with eight 476 MHz cavities. Two 952 MHz cavities will also be used to lengthen the bunch, increasing the Touschek life-time. A copper vacuum chamber will be needed to absorb the increased synchrotron radiation and a feedback system may be needed to prevent multi-bunch instabilities.

I. INTRODUCTION

The third generation synchrotron radiation sources have been designed to produce high brightness beams from undulators. Some experiments may not need brightness (photons / unit time / unit energy bandwidth / unit solid angle / unit source area) as much as flux (photons / unit time / unit energy bandwidth) which can only be provided by a high current storage ring. To meet the need for increased flux, work has already begun to raise the current in the NSLS X-Ray Ring by from 250 to 500 mA at the present operating energy of 2.584 GeV [1]. A much greater increase in the flux can be obtained using technology developed for the SLAC B factory [2] to simultaneously raise the X-Ray Ring energy to 3 GeV and the current to 2.4 Amp [3].

Fig. 1 compares the flux from the proposed upgrade to the X-Ray Ring with the ALS and the APS. Clearly, the flux from the NSLS X17, X21, and X25 wigglers exceeds that from any other source over the entire spectral range. The NSLS undulators (X1 and PSGU) also produce more flux than the third generation sources in the range from 200 to 2000 eV. In that range, the NSLS undulators are even competitive in brightness, filling in the gap between the ALS U5.0 undulator at low energy and the APS UA undulator at high energy by producing over 2×10^{18} photons/sec/0.1% b.w./mm^2/mrad^2. This may benefit the x-ray microscopy experiments underway at the NSLS as well as other brightness-limited soft x-ray experiments.

After the upgrade, the X-Ray Ring will produce twenty times more synchrotron radiation power than is produced today. This qualitative change from today's conditions will place great demands on the RF and vacuum systems. The requirements are similar to those for the SLAC PEP-II B factory. PEP-II will have two rings, one at 3.1 GeV and the other at 9 GeV. The PEP-II RF, vacuum, and multi-bunch feedback systems are adapted for the proposed X-Ray Ring upgrade.

Other problems to be solved in the upgrade include operation of the X-Ray Ring magnets at 3 GeV levels and rapid injection to high current. This paper will describe certain aspects of the upgrade. Enough information will be given to show the feasibility of high current operation of the NSLS X-Ray ring although a complete design will not be presented here.

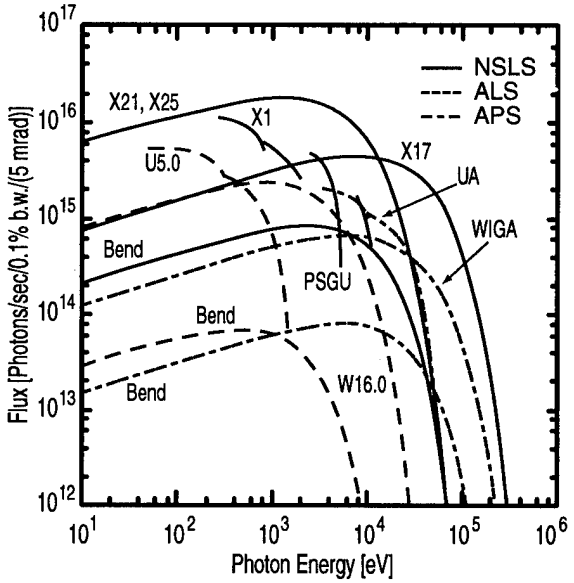


Fig.1: Comparison of the flux from various sources at the proposed upgraded NSLS X-Ray Ring (2.4 A, 3 GeV), the ALS (0.4 A, 1.5 GeV), and the APS (0.1 A, 7 GeV). (Data provided by S. Hulbert [4].)

II. X-RAY RING MODIFICATIONS

Table 1 lists major properties of both the existing and upgraded NSLS X-Ray Ring. The upgrade uses eight 476 MHz cavities to support a 2.42 A, 3 GeV beam. A pair of second harmonic cavities is used to lengthen the bunch from 0.73 cm to 2.64 cm, providing a Touschek lifetime of 184 hours (as calculated by the program ZAP [5]). Each of the storage ring RF systems will be described in the following section.

Both upgrade designs specify 225 of the 270 buckets filled in order to maintain the same length gap in the beam as is now used to prevent ion trapping. The energy acceptance is also preserved. The horizontal emittance is scaled for the higher energy from the 2.5 GeV value but the vertical incorporates the improved decoupling that has recently become operational [6].

* This work was performed under the auspices of the U.S. Department of Energy under contract DE-AC02-76CH00016.

0-7803-3053-6/96/$5.00 ©1996 IEEE

Table 1. Major X-Ray Ring Parameters

	Current	Upgrade
Energy [GeV]	2.5	3.0
Beam Current [A]	0.25	2.42
Horiz. Emittance [nm-rad]	120	173
Vert. Emittance [nm-rad]	1.20	0.29
Fund. Cavity Freq. [MHz]	52.88	475.92
Fund. Cavity Voltage [MV]	0.9	4.26
RF harmonic	30	270
Number of Bunches Filled	25	225
Bunch Length [cm]	4.33	2.64
Synch. Rad. Loss [MeV/turn]	0.50	1.04
Trans. Damping Time [msec]	4.56	2.64
Long. Damping Time [msec]	2.28	1.32
Energy Acceptance	1.82%	1.82%
Synch. Freq. [KHz]	5.91	35.22
Touschek lifetime [hours]	309	184

Table 2. 476 MHz RF System Parameters

		PEP-II Design
Frequency [MHz]	475.92	476
Peak Voltage [MV]	4.26	
Harmonic Number	270	
Synch. Rad. Loss [MeV/turn]	1.04	
Synchronous Phase [Deg.]	19.03	
Number of Cavities	8	
Gap Voltage/Cavity [MV]	0.53	
Cavity Gap [cm]	22.34	
Gradient [MV/m]	2.39	4.5
Shunt Imped./Cavity [MΩ]	3.50	
Wall Loss/Cavity [KW]	40.6	150
Total Wall Loss [KW]	325	
Synch. Rad. Power [KW]	2525	
HOM Power [KW]	417	
Total Power Loss [KW]	3266	
Power Loss/Cavity [KW]	298	
Detuning Angle (Deg)	88.25	
Refl. Power/Cavity [KW]	4.26	
Input Power/Cavity [KW]	413	450
Number of Klystrons	4	
Req. Power/Klystron [KW]	825	1200

Table 3. Harmonic RF System Parameters

		Valvo Klystron
Frequency [MHz]	951.84	1000
Peak Voltage [MV]	2.04	
Synchronous Phase [Deg.]	4.89	
Number of Cavities	2	
Gap Voltage/Cavity [MV]	1.02	
Cavity Gap [cm]	11.17	
Gradient [MV/m]	9.15	
Shunt Imped./Cavity [MΩ]	4.95	
Wall Loss/Cavity [KW]	106	
Total Wall Loss [KW]	211	
Number of Klystrons	1	
Req. Power/Klystron [KW]	211	400

A. RF SYSTEM

The biggest obstacle to raising the X-Ray Ring's energy and current is supplying enough RF power to the beam to replace the synchrotron radiation losses. Only a limited increase in current (perhaps 1 A at 2.5 GeV) can be accomplished with the four existing 52.88 MHz RF cavities. Instead, the upgrade will use the PEP-II single cell, copper RF cavities, operating at a frequency of 475.92 MHz. The operating frequency was chosen because it is exactly one-sixth of the linac frequency, which simplifies injection timing and is close to the 500 MHz frequency used in many other electron storage rings, requiring only small modification of existing klystron designs. Four of the 476 MHz cavities fit in the space now occupied by two of the 52.88 MHz cavities.

Details of the 476 MHz RF system are shown in Table 2. Eight cavities were used in the upgrade design to stay within the PEP-II cavity's limits for gradient, wall losses, and input power (Table 2). As in the PEP-II design, one klystron is used for every two cavities. The klystron output is divided between the cavities using a magic tee. A circulator with water load is placed between each cavity and the magic tee to absorb any reflected power. The maximum power from the klystron is within the PEP-II limits.

The second harmonic system used to lengthen the bunch will have a frequency of 951.84 MHz. Properties for this system are listed in Table 3. Although the cavities have not been designed, the shunt impedance was scaled from the 476 MHz cavities by the square root of the frequency. The peak voltage and synchronous phase were chosen for optimal bunch lengthening. It is assumed that a 400 KW, 1 GHz Valvo klystron can be modified for the lower frequency. One klystron will be used to power both of the cavities.

B. VACUUM SYSTEM

The existing aluminum vacuum chamber in the X-Ray Ring can be operated safely at a maximum current of 500 mA at 2.5 GeV. Increasing the current and energy will have several effects including increased gas pressure, excessive chamber heating, and higher levels of radiation near the chamber. The chamber radiation has contributions from synchrotron radiation as well as from electrons striking the chamber wall. It may or may not be significant here but it has been a concern in B factory design.

Again following the example of PEP-II, the upgraded NSLS X-Ray Ring will use a copper chamber instead of aluminum. This has three advantages as a chamber material: lower photodesorption, improved thermal conductivity, and higher atomic number for improved radiation shielding. The lower photodesorption from copper permits the use of distributed ion pumps instead of the non-evaporable getter (NEG) pumps used in the third generation light sources.

The maximum beam current permitted by the upgrade, 2.4 A, was determined by the synchrotron radiation heat load on the dipole chamber . At that current, the density of the radiation striking the chamber wall is 2.31 KW/cm^2, the same as the maximum power density allowed in the PEP-II high energy ring chamber.

The pressure in the vacuum chamber at the maximum current was calculated from photodesorption of gas molecules from the chamber walls by synchrotron radiation. Desorption coefficients for copper and aluminum were obtained [7] from measurements on an NSLS VUV Ring beamline. Similar pressures of 7 to 8x10^{-9} Torr were obtained for the existing aluminum chamber with 0.25 A at 2.5 GeV and the proposed copper chamber with 2.4 A at 3 GeV for the total pumping speed of 8,880 L/Sec that is now available. This suggests that additional pumping speed will not be needed for the upgrade.

C. FEEDBACK

Running a high current in 225 bunches may produce a multi-bunch instability. SLAC has designed a modular feedback system for PEP-II to damp longitudinal multi-bunch instabilities[8]. The system uses broad-band digital feedback, implemented on digital signal processors (DSPs) to individually control the motion of each bunch. The system is designed so that DSP modules can be added to the system as the number of bunches increases. PEP-II will require 15-20 modules to control 1658 bunches. The upgraded NSLS ring will only need 2-3 modules for 225 bunches.

D. MAGNETS

Most of the X-Ray Ring magnets can be operated at 3 GeV without saturation or power supply problems except for the sextupoles and one of the four quadrupole families. These were built from the laminations designed for the 750 MeV NSLS VUV Ring and are already saturating at 2.5 GeV. They must be redesigned for the upgrade.

III. INJECTION

Electrons are now injected into the X-Ray Ring at 750 MeV before the magnets are ramped to the 2.5 GeV operating energy. Because it is unclear if the ring can stably store 2.4 A at low energy, construction of a full energy injector has been considered as part of the upgrade. The injector can be built concentrically inside of the X-Ray Ring in space that is now used for storage, shops, and power supplies.

The full energy injector will consist of a 10 Hz, 3 GeV synchrotron with a four section, 200 MeV S-band linac for its injector. The synchrotron dipole magnets will need a peak field of 1.47 T in order to fit the injector into the available space. One of the 475.92 MHz PEP-II cavities will be used in the synchrotron. The X-Ray Ring can be filled to 2.4 A in 24 seconds with a current of 10 mA//cycle accelerated in the synchrotron.

IV. CONCLUSION

Examination of the major accelerator systems at the NSLS X-Ray Ring shows that an upgrade to 2.4 A, 3 GeV operation is technically feasible. The improvements needed so that the beamline components can handle the intense radiation are beyond the scope of this paper; however, studies for synchrotron radiation beamlines at the proposed CESR B-factory [9] and elsewhere show that such improvements are possible. A scientific case for the X-Ray Ring upgrade has not yet been made.

VI. REFERENCES

[1] M.G. Thomas, R. Biscardi, W. Broome, S. Buda, R. D'Alsace, S. Hanna, J. Keane, P. Mortazavi, G. Ramirez, and J.M. Wang, *Proceedings of the 1993 Particle Accelerator Conference*, 1419.

[2] SLAC report, LBL-PUB-5379, SLAC-418, CALT-68-1869, UCRL-ID-114055, UC-IIRPA-93-01 (1993).

[3] E.B. Blum, BNL Report BNL-49795 (1993).

[4] S.L. Hulbert and J.M. Weber, *Nucl. Inst. and Meth. in Physics Research* A319 (1992) 25.

[5] M.S. Zisman, S. Chattopadhyay, and J.J. Bisognano, L.B.L. Report LBL-21270, UC-28 (1986).

[6] J. Safranek and S. Krinsky, *Proceedings of the 1993 Particle Accelerator Conference*, 1491.

[7] C.L Foerster, H. Halama, G. Korn, M. Calderon, and W. Barletta, *Vacuum*, 44 (1993) 489.

[8] J.D. Fox, N. Eisen, H. Hindi, I. Linscott, G. Oxoby, L. Sapozhnikov, and M. Serio, *Proceedings of the 1993 Particle Accelerator Conference*, 2076.

[9] Q. Shen and D. Bilderback, SPIE Vol. 1739 *High Heat Flux Engineering* (1992) 191.

A LOW EMITTANCE LATTICE FOR THE NSLS X-RAY RING *

J. Safranek, National Synchrotron Light Source, Brookhaven National Laboratory, Upton, NY 11973

Abstract

A new high-brightness lattice for the NSLS X-Ray Ring is presented. The horizontal emittance of the X-Ray Ring can be reduced by a factor of two to three by allowing nonzero dispersion in the insertion device straight sections and by better controlling the periodicity of the dispersion. Beam was stored in a low emittance lattice during machine studies. The dispersion in the operations lattice lacks the 8-fold periodicity of the magnet structure, because the orbit is offset in the sextupoles. During machine studies the focusing effect of the sextupoles was compensated using trim supplies on the quadrupoles in the dispersive straight sections. Measured results will be presented. A discussion of the hardware upgrade requirements that would be necessary to run the low emittance lattice in operations is also included.

I. INTRODUCTION

In the past the focusing gradients of the NSLS X-Ray Ring magnets were not known to high precision. For example, figure 1 shows the measured horizontal dispersion compared to the accepted model [1] of the ring optics. The work described in references [2] and [3] has enabled us to precisely determine the true focusing gradients in all the X-Ray Ring magnets. With this improved understanding of the ring optics we are now better able to control the horizontal dispersion and beta function. We can now correct for local gradient errors, arising from displaced orbits in sextupoles, that break the periodicity of the dispersion, and we can modify the quadrupole family strengths in order to minimize the horizontal emittance.

The present X-Ray Ring optics give a horizontal emittance of 113 nm*rad. With minimal hardware changes, this emittance can be reduced to 49 nm*rad. The emittance could be further reduced to 38 nm*rad, but this would require replacing the sextupoles used for correcting the vertical chromaticity. This reduced horizontal emittance electron beam would produce a brighter x-ray beam for the NSLS users, adding to other recent increases in the X-Ray Ring brightness [4].

II. MINIMUM X-RAY RING EMITTANCE

A. *Minimum theoretical emittance*

The emittance, ϵ_x, in a storage ring is determined by the horizontal dispersion, η_x, and the horizontal beta function, β_x, in the dipole magnets [5]:

$$\epsilon_x = \frac{CE^2}{\rho} \frac{\int_D (\beta_x \eta_x'^2 + 2\alpha_x \eta_x \eta_x' + \gamma_x \eta_x^2) ds}{\int_D ds}, \qquad (1)$$

where $C = 1.47\text{x}10^{-6}\text{m}*\text{GeV}^{-2}$, E is the electron energy (2.584 GeV in the X-Ray Ring), ρ is the dipole magnet bending radius, $\int_D$ is the integral over all the dipole magnets, $\alpha_x = -\beta_x'/2$, $\gamma_x = (1+\alpha_x^2)/\beta_x$, and s is the longitudinal position around the ring. The X-Ray Ring has four families of quadrupoles, so the gradients in each quadrupole family can be varied to minimize the emittance. The gradients to obtain the minimum emittance were determined by numerical minimization [6]. With the only constraint that the dispersion be zero in the insertion device straight sections, the minimum emittance was found to be 69 nm*rad at 2.584 GeV. When the dispersion is not constrained in the insertion straight sections, the minimum emittance is 21 nm*rad. The increase in horizontal beam size in the insertion straight sections due to dispersion is more than offset by the reduction in emittance, so the beam size is still reduced in the insertion straights

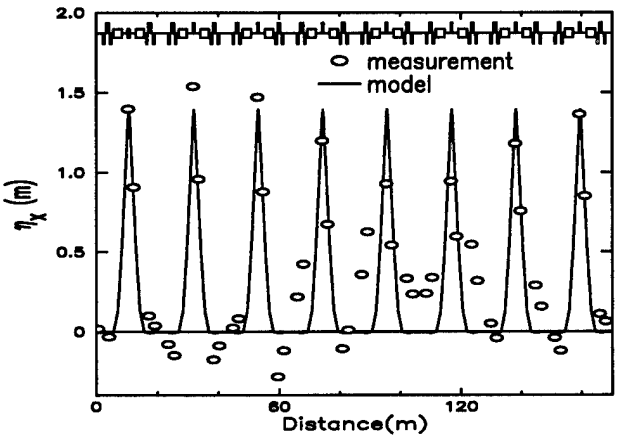


Figure. 1. In the past there was a large discrepancy between the measured and model dispersion, due primarily to focusing in the sextupole magnets.

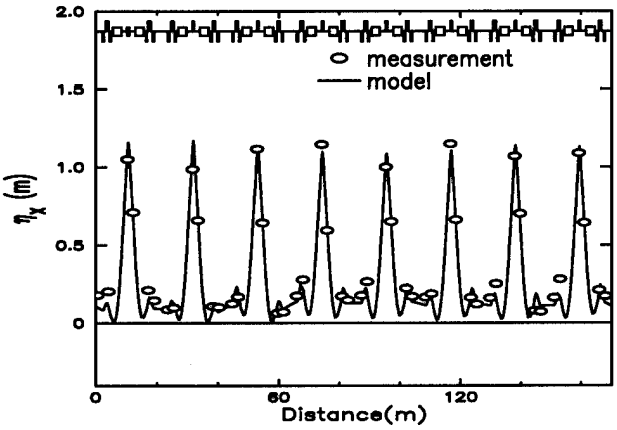


Figure. 2. With our improved understanding of the X-Ray Ring lattice we can adjust the quadrupoles to give η_x the design periodicity and reduce the emittance.

*Work performed under the auspices of the U.S. Department of Energy

0-7803-3053-6/96/$5.00 ©1996 IEEE

as well as everywhere else in such a lattice (see figure 4, for example). The optics for the 21 nm*rad lattice, however, would require huge sextupole strengths which result in a very small dynamic aperture.

B. Minimum practical emittance

Although the minimum-emittance, 21 nm*rad lattice has far too small a dynamic aperture, a dynamic aperture as large or slightly larger than the physical aperture can be achieved with a lattice with a 38 nm*rad emittance. Beam was stored in such a lattice during studies, but the maximum current was only 50 mA and was limited by the head-tail instability. The present sextupoles in the X-Ray ring are not strong enough to compensate the chromaticity of the 38 nm*rad lattice. The iron in the vertical-chromaticity-compensating sextupoles is already in saturation in the present operations lattice, and the 38 nm*rad lattice would require 60 percent stronger sextupoles. To store full current in the 38 nm*rad lattice would require new sextupole magnets or a feedback system to damp the head-tail instability.

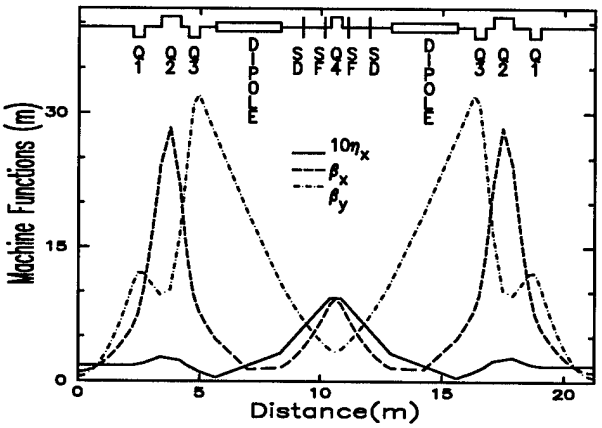


Figure. 3. The optics in the 49 nm*rad lattice for $1/8^{th}$ of the X-Ray Ring. The four families of quadrupole and two sextupole families are shown.

With the limitation that the vertical-chromaticity-compensating sextupole strengths cannot be increased, the horizontal emittance of the X-Ray Ring can still be decreased by more than a factor of two to 49 nm*rad. Figure 3 shows the optics for one superperiod (1/8th) of the ring in this lattice. The tunes of this lattice are 9.70 (ν_x) and 5.45 (ν_y). The dynamic aperture in this lattice is larger than the physical aperture. The reduction in beam size for this 49 nm*rad lattice compared to the present operations lattice is shown in figure 4.

III. EXPERIMENTAL RESULTS

As shown in equation 1, the horizontal emittance is determined by the dispersion in the dipole magnets, so controlling the dispersion is critical for achieving low emittance. The work in reference [3] shows that the primary source of the distortion of the measured dispersion (figure 1) is the focussing in the sextupoles due to horizontal orbit distortions. The easiest way to correct for this would be to steer the electron beam in the sextupoles.

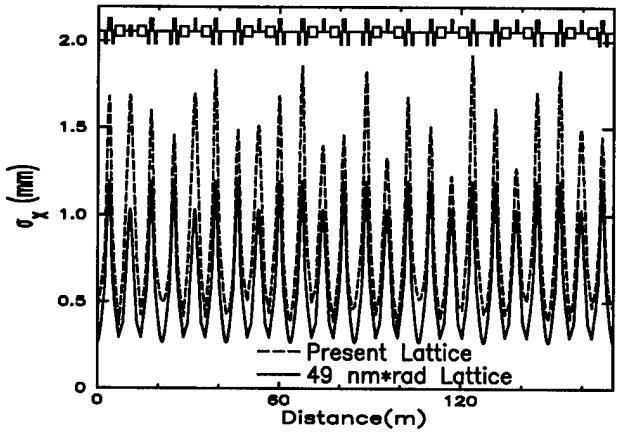


Figure. 4. The horizontal beam size in the 49 nm*rad lattice compared to that in the present operations lattice (113 nm*rad) of the X-Ray Ring.

All the synchrotron radiation users, however, are aligned to the present electron orbit, so changing the orbit is not a viable option. Instead, we added trim power supplies to each of the Q4 quadrupoles, and we adjusted the strength of the Q4's to compensate for the beta-weighted integrated focussing strength associated with the four sextupoles surrounding each Q4.

Figure 2 shows the the improved periodicity of this corrected dispersion. Correcting the dispersion alone reduced the emittance from 113 nm*rad to 71 nm*rad. We were able to store the full current of 250 mA in 25 bunches and 100 mA in 1 bunch in this 71 nm*rad lattice. The emittance was measured at 69 nm*rad by imaging the synchrotron radiation from a dipole magnet using an x-ray pinhole camera. The measured 69 nm*rad agrees with the expected 71 nm*rad to within measurement accuracy.

Once the dispersion distortions are removed, further reduction in the emittance can be achieved by adjusting quadrupole family strengths. No attempt has been made yet to store beam in the 49 nm*rad lattice shown in figure 3. The 49 nm*rad lattice has tunes that differ from the present operational tunes of $\nu_x = 9.14$ and $\nu_y = 6.20$, so storing beam in the 49 nm*rad lattice will require setting up a new injection configuration. A current of 50 mA, however, was stored in the 38 nm*rad lattice, which has tunes approximately the same as the present operations lattice. The expected reduction in beam size in the 38 nm*rad lattice was confirmed by imaging synchrotron radiation.

IV. CONCLUSIONS

We have shown that we can control the X-Ray Ring optics and reduce the emittance. We have stored full current in a lattice in which the emittance has been reduced from 113 nm*rad to 71 nm*rad. In the future, we will work to store beam in the 49 nm*rad lattice and explore the potential of this lattice for operations.

V. ACKNOWLEDGEMENTS

I would like to thank Sam Krinsky for stimulating discussions. Thanks go to Om Singh and the NSLS power supply group for

providing and helping with the Q4 trim power supplies. Also, I would like to thank Julie Leader for her fine work editing this paper.

References

[1] J. Murphy, Synchrotron Light Source Data Book, BNL 42333, 1993.

[2] J. Safranek and M.J. Lee, "Calibration of the X-Ray Ring Quadrupoles, BPMs, and Orbit Correctors Using the Measured Orbit Response Matrix," AIP Conference Proceedings, Vol 315, 1994.

[3] J. Safranek, Experimental Determination of Linear Optics Including Quadrupole Rotations, these proceedings.

[4] J. Safranek and S. Krinsky, Plans to Increase Source Brightness of NSLS X-Ray Ring, proceedings of the 1993 Particle Accelerator Conference, pg 1491.

[5] M. Sands, SLAC-121, November, 1970.

[6] W. Press, B. Flannery, S. Teukolsky, W. Vetterling, Numerical Recipes, Cambridge, 1990.

Design of 1.2 GeV Synchrotron Light Source for X-ray Lithography at Samsung Heavy Industries

Keeman Kim, Bumsoo Han, Kihun Joh, Sungmyun Kim, Byungmun Kim, Heunggyu Park, Jongpil Park, Jinsoo Kim, Wongu Kang, Kyungwoo Kang, Yuri Kim, Sangil Lee, and Younghee Kim
Samsung Heavy Industries Daeduk R&D Center
Yousung-Gu, Moonjee-Dong 326, Daejeon, Korea 305-380

ABSTRACT

An 1.2 GeV electron storage ring being designed at Samsung Heavy Industries Daeduk R&D Center is optimized for X-ray lithography works for high density semiconductor devices and micro-machining. The lattice is a variation of a FODO arrangement with four quadrupole doublets. The circumference of 57.6 m includes four 2.1-m-long straight sections and two 3.09-m-long dispersion-free straight sections making the synchrotron a racetrack shape. Two dispersion-free straight sections are located between the doublets and reserved for diagnostics and insertion devices. The harmonic number is 96 and the corresponding RF frequency is 499.654 MHz. The critical X-ray wavelength from sixteen 1.16-m-long bending magnets is 9.55 Å and a superconducting wiggler is also included in the design considerations. The major features of the light source will be described.

I. INTRODUCTION

Samsung Heavy Industries Daeduk R&D Center is a part of SAIT (Samsung Advanced Institute of Technology) Daeduk site which is located at the central part of Korea. The accelerator laboratory at Daeduk R&D Center is devoted for the development of accelerator technologies and applications. Current research activities include the development of electron accelerators for irradiation processing purpose, applications of electron irradiation processing[1] and the development of a synchrotron light source.

During the past decade, synchrotron radiation has come into wide use as a most powerful source of X-rays for studying the structure of matter and various physical processes. Many synchrotron radiation facilities are operational or under construction throughout the world and 2-GeV PLS (Pohang Light Source), which is located at the southeastern part of Korea, is also operational. An industrial synchrotron light source is also being investigated at Samsung Heavy Industries and the most promising site of the light source will be Daeduk Science Town. The synchrotron light source will be able to generate the X-ray for various scientific and industrial research including spectroscopy, diffraction analysis, chemical analysis, photochemical reaction, and biotechnology. As a matter of fact, from the viewpoint of the X-ray quality, the machine does not offer a definite advantage over PLS except the geographical convenience. Though the importance of opportunity for basic research activity targeted by other third generation synchrotron light sources is not overlooked, the design of the lattice is not optimized for insertion devices or for a low emittance beam. The machine is optimized for semiconductor lithography and MEMS (Micro-Electro-Mechanical System) and the main object of the design is to produce a most adequate photon flux at the most useful photon energy for lithography.

II. DESIGN CONSIDERATIONS

In order to design an efficient lithography light source, the X-ray wavelength from bending magnet[2] is the first thing to consider. Useful X-ray wavelength for semiconductor lithography is 6 ~14 Å. The conventional magnet technology is able to generate the bending magnetic field of 1.5 T without serious saturation problems. When 10% margin of the magnetic field limit is take into account, the bending magnetic field of 1.35 T is a reasonable choice for the normal operation. In order to obtain a critical X-ray wavelength, λ_c, of 10 Å from the bending magnet of 1.35 T, the required energy of the electron beam is 1.18 GeV. A superconducting bending magnet is not excluded from the design consideration. Specially, industry would prefer that the storage ring be as compact as possible. The superconducting magnets can reduce the dimension of the synchrotron itself. In particular, if a storage ring is made to be small enough to be shipped in a fully assembled and almost commissioned state, a significant advantage can be achieved. One can even consider that the storage ring could be replaced during the maintenance period of the ring in manufacturing industries. However, the overall system size is mainly determined by the length of beamlines and the decision was made to use a well established conventional magnet technology also to reduce the possibility of accidents during the normal operation of superconducting magnets without the knowledge of cryogenics at manufacturing industries. Using a mature conventional magnet technology could also help ensure programmatic success. An installation of a superconducting wiggler is also included in the design consideration in order to provide hard X-ray for micro-machining.

Another important design consideration is the lattice structure. The lattice of a storage ring and the characteristic of an electron beam is tightly bonded together. The FODO lattice and the Chasman/Green lattice[3] are the most reasonable lattices for a small size storage ring. The FODO lattice is the

0-7803-3053-6/96/$5.00 ©1996 IEEE

very basic lattice and most of booster synchrotrons employ the FODO lattice. The FODO lattice has relatively a large emittance which is not desirable for insertion devices and the high energy physics research, but does not hurt X-ray lithography. As a matter of fact, the vertical width of the X-ray from a 10-m beamline at 1.2 GeV storage ring is a few millimeter and lithography requires at least a few centimeter, which can be achieved by three methods, the use of a vibrating X-ray mirror, the scanning of target assembly, and the wobbling of the electron beam. However, the X-ray mirror is not only difficult and costly to manufacture but also the uniform irradiation of X-ray is difficult to achieve. Though moving target assembly could be a good solution for LIGA (LIthographie, Galvanoformung, Abformung) process, the mechanical vibration can hurt the high density semiconductor lithography where the resolution of ~0.1μ is required. The wobbling of the electron beam is considered to be a better solution for a dedicated lithography machine. The FODO lattice is suitable for the wobbling of the beam. The Chasman/Green lattice is also one of the most widely used lattices for small size storage rings. The Chasman/Green lattice has undulator-type straight sections with a low emittance. However, the cross section of the beam at bending magnets becomes an upright cigar shape and the beam is difficult to wobble. Therefore, the 1.2 GeV electron storage ring with the FODO lattice using 1.35 T bending magnets seems to be matched to the lithography process.

If the X-ray lithography technique becomes to be put into semiconductor fabrication lines, more than one storage ring are expected to be required and one full energy injector which serves for many storage rings will be an ideal choice. However, a 200~300 MeV linac injector will be the primary choice of the injection system for the storage ring and the storage ring will also have the function of a booster at current stage. In order to prevent instabilities due to ion-trapping, approximately the half of the RF buckets in the ring will be left empty.

III. DESIGN SPECIFICATIONS

Table 1 shows the preliminary design specification of the linac injector. The nominal beam energy of the linac is 200 MeV and the operating frequency is 2.856 GHz. An energy doubler is not included in the preliminary design and the pulse duration of the modulator is 2 μsec. However, the design of the modulator has an expandable structure in order to accommodate the possible upgrade with energy doublers which require a longer pulse duration of modulators.

Table 2 shows the preliminary design specification of the storage ring. The basic structure of the machine is a racetrack type FODO lattice with quadrupole doublets. MAD input for the lattice is listed in Table 3. Here, parameters for magnetic filed strength are not optimized yet. The storage ring has four 2.1-m dispersive straight sections and two 3.09-m dispersion free straight sections. 2.1-m straight sections will be used for injection and RF system. A superconducting wiggler is also planned to be installed at the one of the 2.1-m straight sections. 3.09-m straight sections are reserved for a future insertion device and other purpose such as an optical klystron. The quadrupole doublets at the both ends of dispersion free straight sections make the beta functions at the straight sections suitable for the future expansion of insertion devices. The schematic of synchrotron radiation extraction with the lattice structure is shown in Figure 1. Figure 2 shows Beta functions and dispersion function. The dotted lines in Figure 3 show the bending magnet photon flux of the storage ring per unit horizontal angle as a function of photon energy at the electron energy of 1.2 GeV and 1.4 GeV, respectively and the solid line shows that of PLS for the reference. Here the electron currents are assumed to be 300 mA.

Table 1. Preliminary design specification of the injection linac.

Injection Energy	200 MeV
Energy Spread	< 1 %
Beam Pulse	2 ns x 200 mA
Total charge in SR	60 nC
Time required to fill-up SR	< 5 min
Klystron Frequency	2.856 GHz
Repetition Rate	optimized at 10 Hz
Number of Modulator	2
Modulator Pulse Duration	2 μsec (expandable to 4 μsec)

Table 2. Preliminary design specification of the storage ring.

Nominal Electron Energy	1.2 GeV	
Nominal Beam Current	300 mA	
RF Wavelength	0.6 m (499.654 MHz)	
Harmonic Number	96	
Circumference	0.6 x 96 = 57.6 m	
Straight Sections	2.1m x 4, 3.09m x 2	
Beam Size at 3-m Straight Section	~1.5 mm	
Natural Emittance	0.6 mm mrad	
Dipole Magnet	1.16m x 16	
Bending Radius	18.56/2π = 2.9539 m	
	1.2 GeV	1.4 GeV
Bending Magnet Field Strength	1.356 T	1.581 T
X-ray Characteristics		
λ_c from bending magnet	9.54 Å	6.01 Å
λ_c from 8-T wiggler	1.62 Å	1.19 Å
bending magnet X-ray power (300 mA assumed)	18.66kW	34.56kW

IV. CONCLUSION

The electron synchrotron light source being investigated at Samsung Heavy Industries Deasuk R&D Center is based on

proven light source technologies. A 200~300 MeV linac seems to be the most promising injection system and it could help to improve the basic accelerator technology of our industry. The utilization of well understood technologies together with state-of-the-art diagnostics and feedback system, ensures that the synchrotron light source will perform up to specifications. The soft X-ray from bending magnets will be suitable for lithography works and a superconducting wiggler will be able to provide the hard X-ray for micro-machining. The synchrotron radiation facility will be open to the wide area of scientific and industrial research.

Table 3. MAD input data for the storage ring.

```
TITLE, "STARLIGHT"
DSS  : DRIFT, L=0.47
DS1  : DRIFT, L=0.12
DS2  : DRIFT, L=0.25
DSU  : DRIFT, L=1.545
DSI  : DRIFT, L=2.1
DSP  : DRIFT, L=0.6
DSD  : DRIFT, L=0.6
QV   : QUADRUPOLE, L=0.125, K1=-1.75
QD   : QUADRUPOLE, L=0.25, K1=-1.75
QF   : QUADRUPOLE, L=0.25, K1=2.64
QDD  : QUADRUPOLE, L=0.25, K1=-1.8
QDF  : QUADRUPOLE, L=0.25, K1=3.1
SD   : SEXTUPOLE, L=0.1, K2=0
SF   : SEXTUPOLE, L=0.1, K2=0
BM1  : SBEND, L=1.16, ANGLE=PI/8., E1=PI/16., E2=PI/16.
FODOD : LINE=(DSU, QDD, DSD, QDF, DSP, &
    BM1, DSS,  QD, DSI,  QF, DS1,  SF, DS2, &
    BM1, DSS,  QD, DS1,  SD, DS2, &
    BM1, DSS,  QF, DS1,  SF, DS2, &
    BM1, DSS,  QD, DS1,  SD, DS2, &
    BM1, DSS,  QF, DS1,  SF, DS2, &
    BM1, DSS,  QD, DS1,  SD, DS2, &
    BM1, DSS,  QF, DSI,  QD, DSS, &
    BM1, DSP, QDF, DSD, QDD, DSU)

USE, FODOD, super = 2
beam, particle=electron, energy=1.2
```

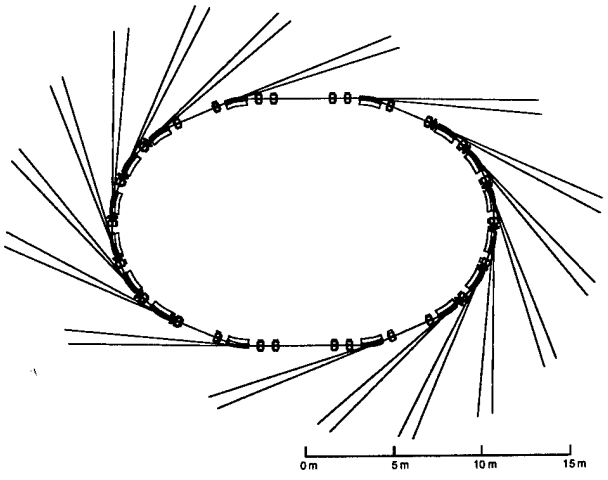


Figure 1. Lattice structure and schematic of synchrotron radiation extraction.

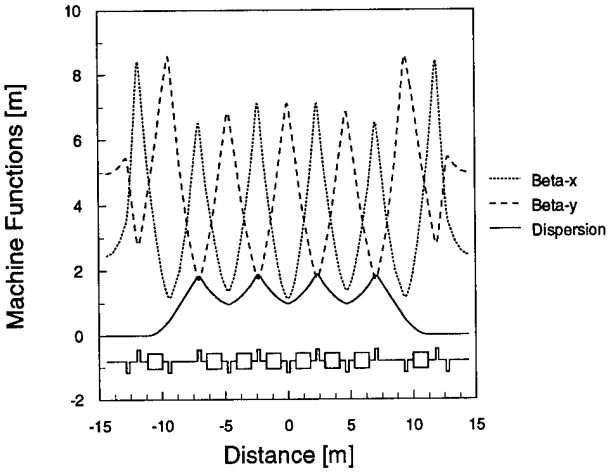


Figure 2. Beta functions and dispersion function for the storage ring under designing.

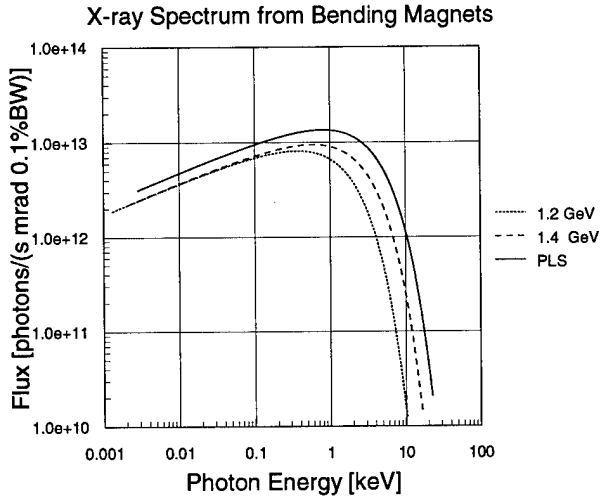


Figure 3. Photon flux per unit horizontal angle as a function of photon energy. The beam current is assumed to be 300 mA. dotted lines are for the storage ring under designing and solid line is for PLS.

V. REFERENCES

[1] B. Han, K. Kim, K. Joh, S. Kim, B. Kim, H. Park, J. Park, J. Kim, W. Kang, K. Kang, Y. Kim, S. Lee, and Y. H. Kim, "Applications of Industrial Electron Accelerators at Samsung Heavy Industries," these proceedings.

[2] A. Hofmann, Stanford Synchrotron Radiation Laboratory ACD-Note 38, 1986.

[3] R. Chasman and G. Green, Brookhaven National Laboratory, BNL-21849, 1976.

ANKA, a Synchrotron Light Source for Microstructure Fabrication and Analysis

H.O. Moser, M. Ballauff[1], V. Bechtold, H. Bertagnolli[2], J. Bialy, P. v. Blanckenhagen, C. Bocchetta[3], W. Bothe[4], C. Coluzza[5], A.N. Danilewsky[6], K. D. Eichhorn[1], B. Eigenmann[1], D. Einfeld[7], L. Friedrich, M. Haller[8], N. Holtkamp[4], V. Honecker, K. Hümmer[1], E. Huttel, J. Jacob[9], V. Kashikin[10], J. Kircher[11], H. Klewe-Nebenius, A. Knöchel[8], A. Krüssel[7], G. Kumpe, K.D. Möller[12], J. Mohr, M. Nagaenko[10], F.J. Pantenburg, M. Plesko[13], J. Schaper[7], K. Schlösser, G. Schulz[6], S. Schuppler, H. Schweickert, I. Seidel, Y. Severgin[10], I. Shukeilo[10], L. Steinbock, R. Steininger[1], M. Svandrlik[3], G. Williams[14], K. Wilson[15], J. Zegenhagen[11]

Forschungszentrum Karlsruhe, Postfach 3640, D-76021 Karlsruhe, Germany

[1]Universität Karlsruhe, Postfach 6980, D-76128 Karlsruhe, [2]Universität Stuttgart, Pfaffenwaldring 55, D-70550 Stuttgart, [3] Sincrotrone Trieste, Padriciano 99, I-34012 Trieste, [4] DESY, Notkestr. 85, D-22603 Hamburg, [5]EPFL, PHB-Ecublens, CH-1015 Lausanne, [6]Universität Freiburg, Hebelstr. 25, D-79104 Freiburg, [7]Fachhochschule Ostfriesland, Constantiaplatz 4, D-26723 Emden, [8] Universität Hamburg, Martin-Luther-King-Platz 5, D-20146 Hamburg, [9]ESRF, BP 220, F-38043 Grenoble Cedex, [10] Efremov Institute, 189631 St.-Petersburg, [11]Max-Planck-Institut für Festkörperforschung, Heisenbergstr. 1, D-70569 Stuttgart, [12]Fairleigh Dickinson University, Teaneck, New Jersey 07666, [13]J. Stefan Institute, Jamova 39, 61111 Ljubljana, [14]NSLS, Brookhaven National Laboratory, Upton, New York 11973, [15]European Molecular Biology Laboratory, Hamburg Outstation, c/o DESY, Notkestr. 85, D-22603 Hamburg

Fabrication of microstructures by X-ray deep lithography (XRDL), galvanoforming, and plastic molding (German acronym LIGA) has made its way from Forschungszentrum Karlsruhe to many labs throughout the world. The acronym ANKA stems from **Å**ngstrom and **Ka**rlsruhe to indicate the main spectral range and the location. ANKA is designed to satisfy the needs of XRDL as well as of X-ray analysis, in particular, of microstructures. Industrial demand of service in both fields will play a major role for ANKA. The main design parameters of the storage ring are an electron energy of 2.5 GeV, magnetic field of 1.5 T, and an ensuing characteristic wavelength of 0.2 nm. The lattice has fourfold symmetry with four dispersion-free straight sections, each about 4 m long. The optics is a double DBA structure with four 22.5° bending magnets per cell resulting in a compact medium-emittance design with a circumference of 97.2 m and an emittance in the range of 40 to 80 nmrad. Four 500 Mhz RF cavities are placed one in the middle of each cell. In this way, only one straight section is needed for injection leaving three for optional insertion devices. Electron current will be 200 mA in a first phase. Lifetime will exceed 17 h. Dynamic aperture is large enough to insert wigglers and wavelength shifters and to double the current when upgrading the RF system. 14 out of 32 available bending magnet radiation ports will be equipped with beamlines in the first phase.

I. INTRODUCTION

After decades of basic research with synchrotron radiation, and development of more and more powerful sources, it is time to bring synchrotron radiation based methods of microfabrication and analysis to the daily use of industry. The ANKA project planned by Forschungszentrum Karlsruhe (FZK) aims at such a transfer in the fields of microfabrication and analysis. An essential element of the philosophy behind ANKA is to commercialise the use of synchrotron radiation in these fields. Mixed beamline groups with members from universities as well as from the service staff will offer a professional full service to customers. More conventional ways of access are, of course, not precluded.

ANKA is a trade-off between low construction cost to keep down operational cost, and finally cost per service hour, and high performance to enable offering high-quality service. In a sense, ANKA is a high-performance, yet „budget-limited" synchrotron light source which could be attributed to the 2.5th generation at the cost of roughly one quarter of a 3rd generation source. A significant number of industrial partners have signed letters of intent for making use of this offer. Thanks to continued marketing their number will grow.

II. GENERAL

ANKA is embedded in the infrastructure of FZK. A 60¥60 m^2 building with additional aisles will house the accelerator and the beamlines with the endstations for microfabrication and analysis. Only this building has to be constructed. Laboratory, workshop, and office space is already available in existing near-by buildings. As far as possible, proven components or designs will be used for the accelerator and the beamlines. All together will help to keep down the construction cost for the accelerator, the beamlines with endstations, and the building.

III. SOURCE

A. Lattice

The lattice is rather compact, featuring four cells with a double Double-Bend-Achromat (DDBA) structure. There are four long dispersion-free straight sections, one for injection, three for optional insertion devices. In the center of each cell is a short dispersion-free straight section which will accommodate an RF cavity. The circumference is 97.2 m to bring down overall cost. Two optics were analysed so far, one with zero dispersion in long and short straight sections,

0-7803-3053-6/96/$5.00 ©1996 IEEE

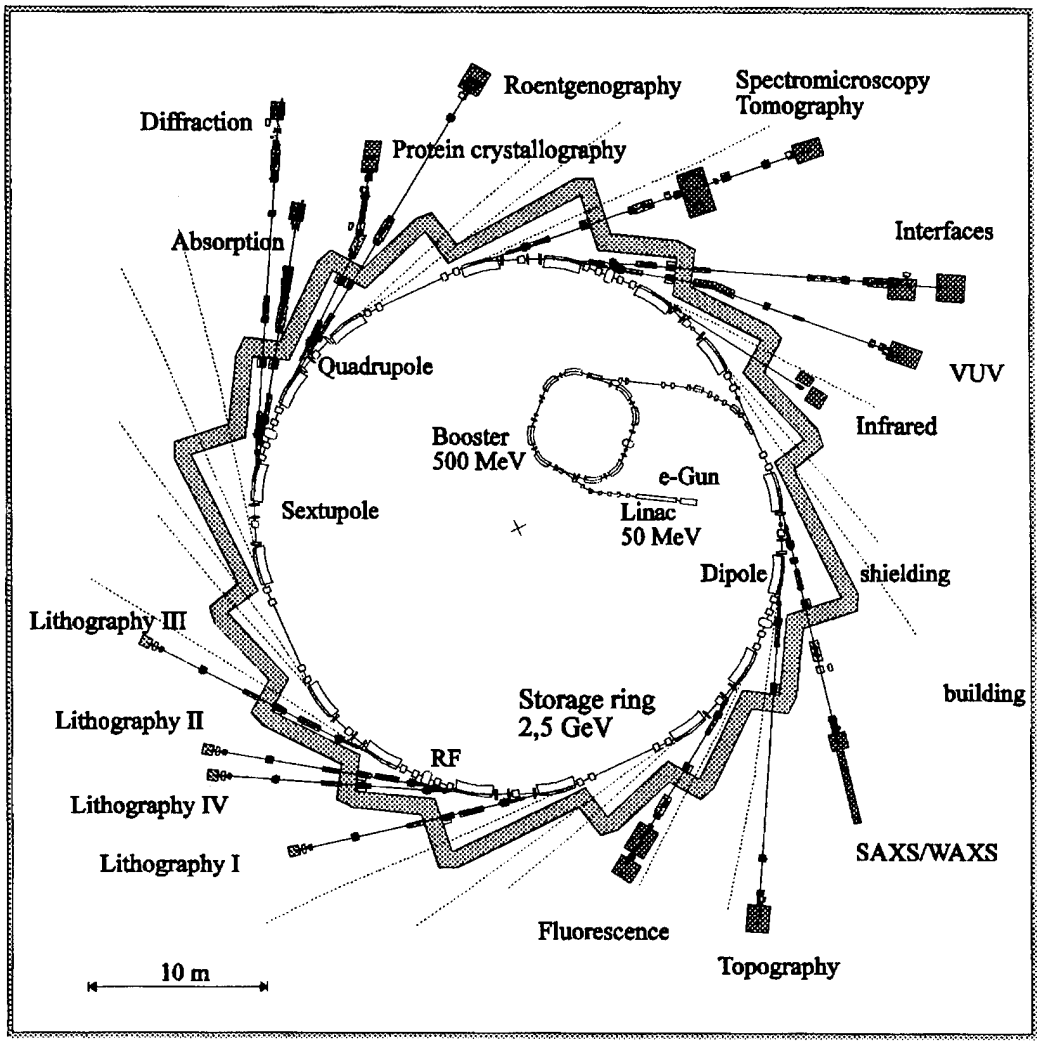


Fig. 1: Layout of the whole ANKA installation

leading to an emittance of 83 nmrad, another one allowing some dispersion in the straight sections with the benefit of reducing the emittance to roughly one half, i.e., 43 nmrad. Chromatic and harmonic sextupoles are used for correcting chromaticity and maintaining a large dynamic aperture. Chromatic sextupoles are separate, harmonic ones are integrated into quadrupoles. An overview of the whole installation is shown in figure 1. Main parameters of the ring are given in table 1. Figure 2 displays the machine functions within a cell in the zero dispersion case.

B. Components

Storage ring dipole magnets are normal conducting and have a bending angle of 22.5°. They produce a uniform field of 1.5 T across a gap 50 mm wide and about 140 mm large. Field uniformity is better than $\pm 1 \cdot 10^{-4}$ within ±35 mm horizontally. The iron yoke is laminated. End faces are parallel. A prototype is about being delivered by Efremov Institute.

Quadrupoles are derived from ELETTRA design with improved pole profiles to enlarge good field region at low power consumption. Open bore is 70 mm diameter. Maximum gradient is 22 T/m, gradient uniformity is better than ±2.3.10-4 within ±32.5 mm horizontally. They come in two lengths, 42 and 35 cm, with a power consumption of 3.6 and 3.2 kW, respectively. They have a horizontal slot 24 mm high to accommodate the vacuum chamber.

Separate sextupoles for chromatic correction are based on the DELTA design. Bore diameter is 75 mm, magnetic length 100 mm, and maximum differential gradient 800 T/m2. Harmonic sextupoles are integrated in the quadrupoles according to the DELTA design.

The vacuum chamber is made of stainless steel with an antechamber design in the dipoles and an octogonal cross section all over the electron beam duct. Synchrotron radiation is absorbed by discrete water-cooled copper blocks. Sufficient pumping capacity (2000 l/s per bend) to reach a dynamic pressure lower than 2 nTorr is provided by NEG and by Ti sublimator boosted ion pumps. Beam lifetime is mainly limited by gas scattering to about 17 h at final energy.

There are up to four RF cavities based on the ELETTRA design. Frequency is 500 MHz. Each cavity will be fed by a commercial 60 kW transmitter allowing for beam currents of

Table 1: Main parameters of ANKA

	$\eta = 0$	$\eta \pi 0$
Electron energy E(GeV)	2.5	
Charact. wavelength λ_c (nm)	0.2	
Circumference C(m)	97.2	
Lattice	4¥DDBA	
Tunes Q_x / Q_y	6.851/2.880	6.851/2.879
Chromaticities ξ_x / ξ_y	-15.3/-7.45	-14.9/-7.32
Natural emittance (2% coupling) ε_x / ε_y(nm·rad)	83 / 1.7	43 / 0.86
Momentum compaction α	$9.2 \cdot 10^{-3}$	0.0107
Beta functions		
Straight section β_x / β_y(m/rad)	18.8 / 6.91	17.5 / 8.53
Center of dipole β_x / β_y(m/rad)	0.65 / 9.25	0.60 / 11.12
Maximum β_x / β_y(m/rad)	19.02/20.20	17.5 / 21.0
Minimum β_x / β_y(m/rad)	0.65 / 1.27	0.60 / 1.30
Dispersion function		
Straight section η_x(m)	0.0	0.60
Center of dipole η_x(m)	0.107	0.13
Damping integral D	0.0255	0.0304
Damping times τ_x / τ_y / τ_s(ms)	2.68/2.61/1.29	2.69/2.61/1.28
Natural energy spread σ_E	$9.035 \cdot 10^{-4}$	$9.024 \cdot 10^{-4}$
Radio frequency system		
Frequency f(MHz)	500	
Number of harmonics h	162	
Energy loss per turn eU_0(keV)	642	
Overvoltage factor q	3	
Electron current I_e(mA)	200 (400 with upgrade)	
Beam lifetime τ(h)	>17	
Beam dimensions		
Straight section Σ_x / Σ_y(mm)	1.25 / 0.11	1.02 / 0.086
Center of dipole Σ_x / Σ_y(mm)	0.25 / 0.13	0.20 / 0.098

about 200 mA. Doubling the number of transmitters as a later option will upgrade the current to 400 mA.

C. Injector

Injection energy is 500 MeV. Two alternative injectors are looked at, namely a booster synchrotron with a linac preinjector and a 500 MeV linac. In this paper, the booster alternative is shown (fig. 1). Lifetime at injection energy is roughly 1.5 h. The injection process will include accumulating a current which can be accelerated by the RF system and, then, ramping it to final energy.

D. Spectra

In the first phase, radiation from bending magnets will be used. Figure 3 shows a comparison of the brightness of operational 2nd generation sources with ANKA. Options for later upgrading include a normalconducting wiggler to enhance flux and a superconducting wavelength shifter to produce harder photons.

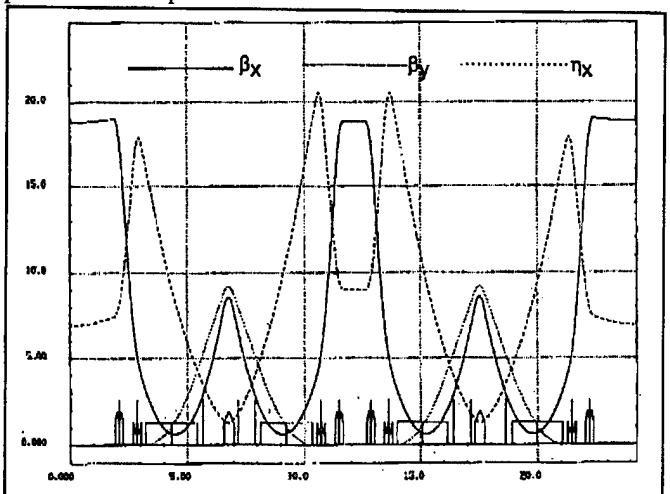


Fig. 2: Beta functions and dispersion within a quadrant.

E. Beamlines and experimental stations

14 beamlines are planned for the initial operation phase as shown in fig. 1. Four of them are for microfabrication with the LIGA process, 10 for various analytical purposes. The latter were selected according to demand expressed by industrial partners and evidenced by operational sources.

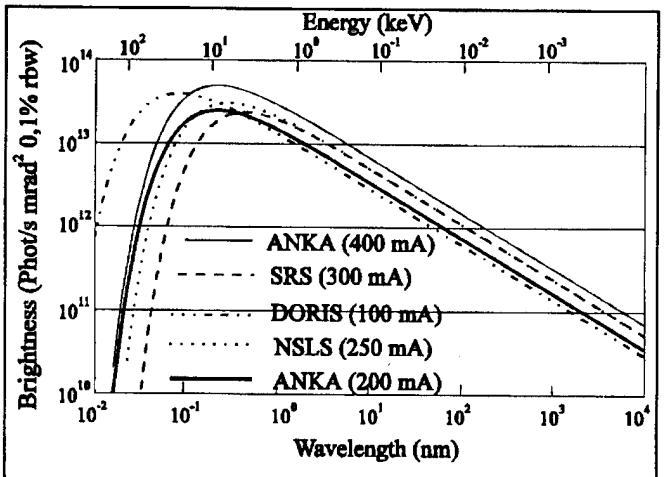


Fig. 3: Brightness of ANKA compared with other sources.

IV. CONCLUSION

Benefitting from the experience available ANKA is designed as a powerful X-ray source at moderate cost. Letters of intent signed by industry indicate that there will be a demand for full service in microfabrication and analysis.

An Undulator at PETRA II - A New Synchrotron Radiation Source at DESY

K. Balewski, W. Brefeld, U. Hahn, J. Pflüger, R. Rossmanith
Deutsches Elektronen Synchrotron, D-22603 Hamburg, Germany

Abstract

PETRA, currently operating as a proton and positron injector for HERA, has been modified to serve also as a synchrotron radiation source in 1995. Running at 12 GeV with currents up to 60 mA the machine will be a unique source. The PETRA injector optic will be changed locally to suit the requirements of an undulator beam. In addition a new low emittance optic has been examined both theoretically and experimentally. The undulator with a period length of 33mm and a maximum field of 0.59 T at a gap of 14mm has been installed in the straight section North East. The photon energy range up to 200 keV can be covered using the 1st, 3rd and 5th harmonics. At 12 GeV, 60 mA and using the low emittance optic a photon brilliance in excess of 10^{18} photons/(s 0.1%BW 0.1 mrad^2 mm^2) will be obtained. To allow for compatibility between injector and synchrotron radiation operation a keyhole shaped vacuum chamber, with both a wide and narrow aperture for the two operational modes respectively has been constructed. The photon beam travels along a 120 m long beamline until it reaches the experimental hall. The beamline includes elements of the beam position control system and the safety system needed to avoid damage to machine components due to the high power undulator beam.

I. INTRODUCTION

The former electron positron collider PETRA has been turned into a preaccelerator for HERA.Since 1988 PETRA has filled HERA-e with both positrons and electrons and since 1991 HERA-p with protons. The major changes to PETRA were the removal of most of the electron cavities and the installation of a bypass in the straight section south so that the protons do not have to traverse the remaining electron cavities[1].Thanks to a powerful feedback system[2] large electron and positron currents can be stored. When operating as the HERA injector PETRA idles in standby mode for approximately 50% of the scheduled time. In 1993 it was therefore decided to use PETRA as a synchrotron radiation source during the idle time. For this purpose an undulator should be installed in the straight section north east. This undulator can produce synchrotron radiation of world wide unique characterictics making interesting experiments possible[3]. In 1994 the experimental hall was built. During the next winter shut down 94/95 the modifications of the vacuum system and the PETRA tunnel were made the undulator installed and the beam line was completed. During the start up of PETRA this year the first undulator beam was observed at the end of the beam line (see fig.1). Parts of the beam position control system and the safety system were tested succesfully.

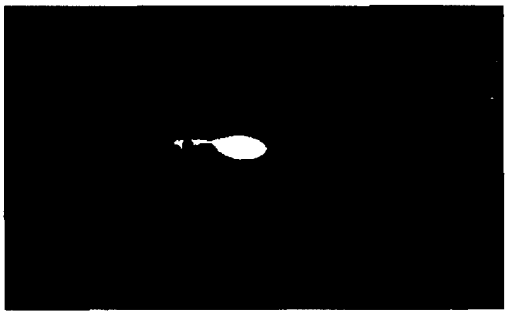


Figure 1 Beam spot at the end of the beamline

II. MACHINE PARAMETERS

The circumference of PETRA is 2304 meters. The energy of electrons and positrons can be varied between 7 and 13 GeV. The upper limit is defined by the available rf power. Currents of up to 55mA can be ramped to 12 GeV but in principle 60 mA should be possible. The current is distributed in 42 bunches but other filling schemes are possible. One constraint is given by the bandwidth of the feedback system which limits the distance between adjacent bunches to 96 ns. Single bunch operation is also possible with currents between 5 to 10 mA. The life time of the beam is at least 5 hours which is sufficient for the foreseen run time of approximately 5 h. During this year a modified injection optic is used for synchrotron radiation operation. The injection optic has a FODO like structure with a betatron phase advance of 45° which results in a horizontal emittance of 18nmrad at 7 GeV. This optic is locally changed to fulfill the requirements for an undulator beam to obtain an electron beam with small divergence. In addition optics were investigated theoretically with a larger phase advance yielding a smaller emittance at 7 GeV for example 5nmrad. At the end of the last machine run in 1994 first experimental tests of a 8nmrad optic were performed and it could be proven that the machine is also working with a phase advance of 70°. Further tests are now in progress.

0-7803-3053-6/96/$5.00 ©1996 IEEE

III. THE UNDULATOR

The object of the PETRA undulator is to provide high brilliance radiation at photon energies well above 100 keV. Fig. 2 shows a comparison between the PETRA undulator with a number of insertion devices in other facilities.

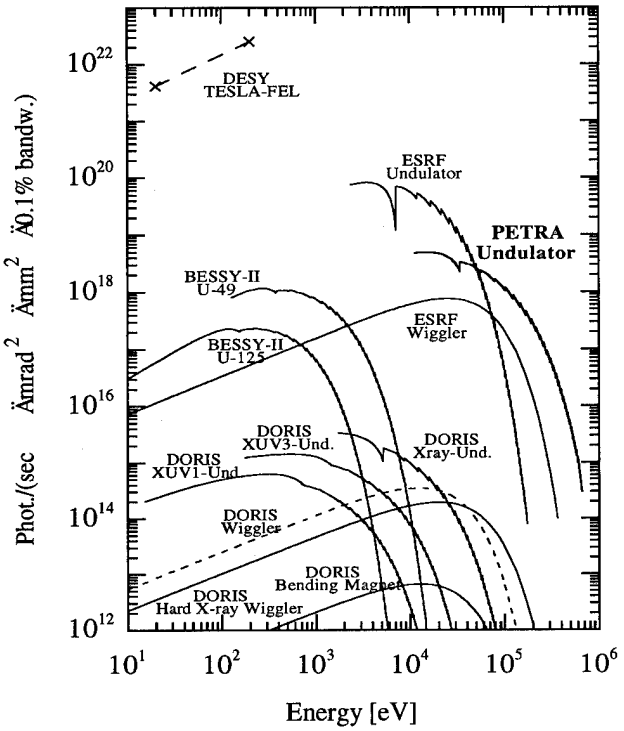


Figure 2: brilliance of the PETRA undulator compared with that of other insertion devices

Above 100 keV it has unique properties[4]. A short period undulator is needed to obtain these radiation properties. Table 1 gives an overview of undulator and relevant storage ring parameters.

undulator parameter	
period length	33 mm
number of periods	121
total length	4 m
min. gap	14 mm
max. field (14mm gap)	0.59 T
max. K-parameter	1.81
total power	6 kW
power density	500 kW/mrad²
storage ring parameters	
hor. emittance	18 nmrad (12GeV)
emittance coupling	3%
σ_x	0.6 mm
σ_y	0.1 mm
$\sigma_{x'}$	24 µrad
$\sigma_{y'}$	4.2 µrad

Table 1: PETRA undulator parameters

As was already pointed out PETRA II is an integral part of the HERA injection system. It has to accelerate electrons as well as protons. For proton operation and for electron injection a very large aperture of 80x80 mm is needed. For synchrotron operation a very small magnetic gap and therefore a very small chamber height is required. In order to solve this aperture problem a keyhole shaped vacuum chamber which can be translated horizontally has been designed and built. Fig. 3 shows its principle.

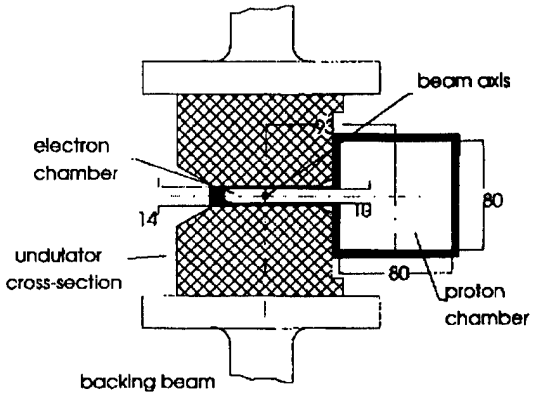


Figure 3: sketch of the keyhole shaped vacuum chamber

The wide region is used for proton operation and for electron injection. To operate the undulator the chamber is translated horizontally and moved over the stored beam. Now the undulator can be closed to its minimum gap position. Great care was taken in the design of the transition regions between the movable keyhole shaped chamber and the fixed PETRA vacuum system. The transitions include bellows, smooth movable RF guiding inserts and smooth tapered sections without discontinuities to avoid higher order mode losses. More details can be found in Ref. [4-6]. The problem of higher order mode losses has been investigated using thermal sensors attached to the tapered sections. No heating could be observed indicating that these losses are indeed negligible. For the first run period a vacuum aperture of 10 mm was allowed with a resultant magnetic gap of about 14mm. In future a new vacuum chamber allowing for a magnetic gap of 11mm will be built.

IV. BEAM POSITION CONTROL AND SAFETY SYSTEM

The power density of the undulator beam is very high (see table 1) so that care has to be taken that no element of the machine or the beamline is hit by this beam. A special monitor has been designed as a beam detector. As long as the undulator beam is detected there is no danger of equipment melting. If there is no undulator beam signal detected by the monitor the positron beam is instantaneously dumped. The detector

consists of a 1mm thick carbon filter and a 50 mm wide carbon foil 0.13 mm thick. The photoemission of this thin foil is measured. Confirmation of undulator beam transmission through the beamline is given when the measured emission exceeds a preset threshold. The purpose of the filter is seen in Fig. 4 which shows a comparison of the PETRA bending magnet spectrum with two undulator spectra for different gap heights (14mm and 28mm). The gap height of 28mm is chosen as the power density limit where misalignments of the beam become dangerous for elements of the beamline and the machine. At this gap height the dump monitor has to detect the beam. The comparison in fig. 4 shows that even at 100m from the undulator source (this is 80m from the bending magnet) the contribution of the bending magnet radiation to the total photoemission yield is higher than that of the undulator. Introducing a carbon filter (1mm thick) between source and detector foil cuts off the low energy radiation and the contribution of the undulator dominates the photoemission yield. These theoretical considerations have been verified experimentally. When the yield is below the threshold the positron beam is dumped.

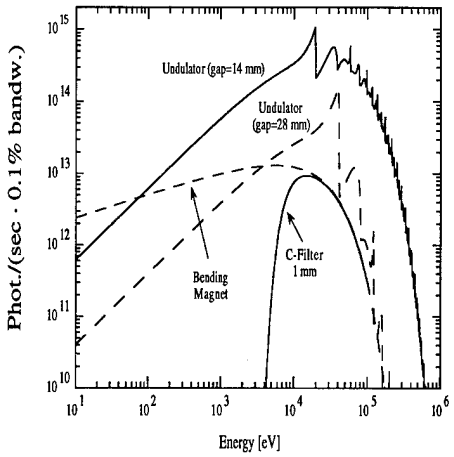


Figure 4: Comparison of spectral flux of the PETRA undulator at different gaps with the flux of the bending magnet (0.8 mrad horizontal width). For the bending magnet the transmission of a 1mm thick C-filter is added.

To keep the undulator beam stable within a small fraction of its size and divergence, a beam position control system for the horizontal and vertical plane was successfully established. It is based on two pick up monitors for the positron beam, two photoemission monitors for the photon beam and four correction magnets for each plane. The pick up monitors, with a position resolution of 50 μm to 100 μm, are located directly in front of and behind the undulator. At the beginning of each run they guide and control the positron beam. Simultaneously the photon beam is guided into the acceptance range of the two photon beam position monitors, which are 57 m and 100 m away from the centre of the undulator. Information from these monitors allows precise on-line control of the positron beam position. The tungsten blades of the photon beam position monitors can measure the beam position with a resolution of a few μm. All adjustments of the positron beam are performed using localised four corrector orbit bumps.

V. REFERENCES

[1] J. Roßbach, DESY HERA 87-06,1987
[2] D. Heins et al., DESY 89-157,1989
[3] J.R. Schneider, Synchrotron Radiation News 8(1995)
[4] J. Pflüger,proceedings of SPIE conference, San Diego,1993
[5] HASYLAB Annual Report 1993
[6] HASYLAB Annual Report 1994

ELECTRON STORAGE RING, KSR FOR LIGHT SOURCE WITH SYNCHROTRON RADIATION

A. Noda, H. Dewa, H. Fujita, M. Ikegami, Y. Iwashita, S. Kakigi,
M. Kando, K. Mashiko[1] H. Okamoto, T. Shirai and M. Inoue
Nuclear Science Research, Facility, Institute for Chemical Research
Kyoto University, Gokanosho, Uji-city, Kyoto 611, Japan

A small electron storage ring (KSR) in a race track shape with the triple bend doubly achromatic lattice and the circumference of 25.7 m is now under construction. Its maximum energy and radius of curvature in the bending section is 300 MeV and 0.835 m, respectively. The critical wave length of the radiation from the dipoles is 17nm. In order to enable future installation of a insertion device for much shorter wave length, two long straight sections, 5.62 m in length are provided. The magnet system consisting of dipole, quadrupole and sextupole magnets are already aligned with precision of a few tenth mm.

I. INTRODUCTION

At Institute for Chemical Research, Kyoto University, a small electron storage ring (KSR) is under construction. Its injector linac with the energy of ~100 MeV has been almost completed[1] and the magnet system of the KSR ring consisting of six dipole, twelve quadrupole and four sextupole magnets has also been aligned precisely. Its layout is shown in Fig. 1. The critical wave length of the light from the dipole section is 17 nm. So as to provide the light with much shorter wave length, possibility to install a superconducting wiggler is being studied. The main parameters of KSR are listed up in Table 1.

Table 1 Main Parameters of the KSR

Maximum Energy	300 MeV
Injection Energy	100 MeV
Circumference	25.689 m
Lattice Structure	Triple Bend Doubly Achromatic
Superperiodicity	2
Bending Angle	60°
Radius of Curvature	0.835 m
n-value	0
Edge Angle	0°
Length of the Long Straight Section	5.619 m
RF Frequency	116.7 MHz
Harmonic Number	10
Number of Betatron Oscillations:	
Horizontal Direction	2.75
Vertical Direction	1.25
Critical Wave Length of the Light from Dipole	17 nm

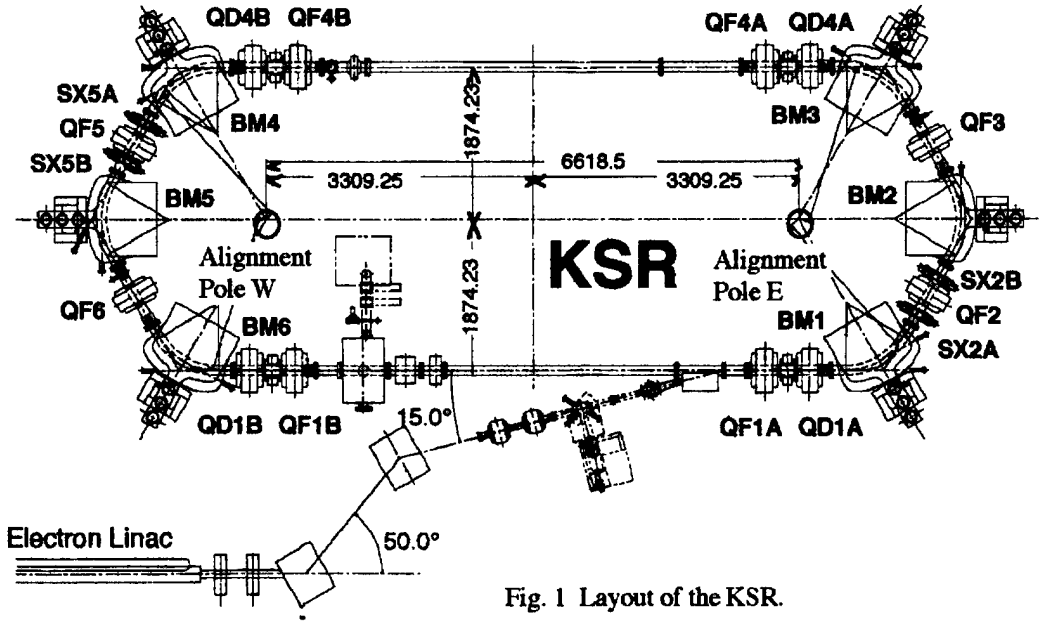


Fig. 1 Layout of the KSR.

[1] Nihon Kensetsu Kogyo Ltd., Shinbashi, 5-13-11, Minatoku, Tokyo 105, Japan

0-7803-3053-6/96/$5.00 ©1996 IEEE

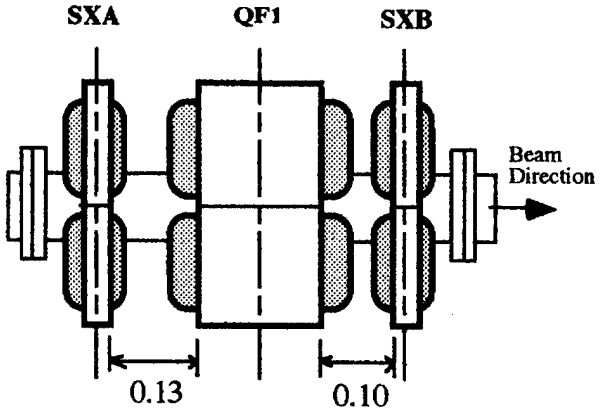


Fig. 2 Positions of the sextupole magnets relative to the quadrupole magnet, QF1. Scales in the figure are given in m.

II. LATTICE DESIGN

The triple bend doubly achromatic lattice with a race track shape including two long straight sections, 5.62 m in length, has already been decided [2]. As the dispersion function is zero in the long straight sections, sextupole magnets for chromaticity correction should be located at the short straight sections between dipole magnets. Keeping the superperiodicity of two, real installation has been made as shown in Fig. 1 taking the spaces needed for vacuum ports and beam monitors into account. Two sets of sextupole magnets are installed at the two short straight sections located at the diagonal positions in the ring. In Fig. 2, detailed positions of the sextupole magnets relative to the quadrupole magnet (QF1) are shown. The operating point with higher vertical tune of (2.75, 1.25) is newly adopted from the point of view of installing an insertion devices as described later. The momentum dependence of the betatron tune is shown in Fig. 3 for the cases of without sextupole correction (a) and with sextupole correction(b). The excitation strength of the sextupole magnet ($B''l/B\rho$) assumed in Fig. 3(b) is -2.34 m^{-2} and 2.05 m^{-2} for SXA and SXB sextupole families, respectively, where the length of the sextupole magnet is 0.065 m.

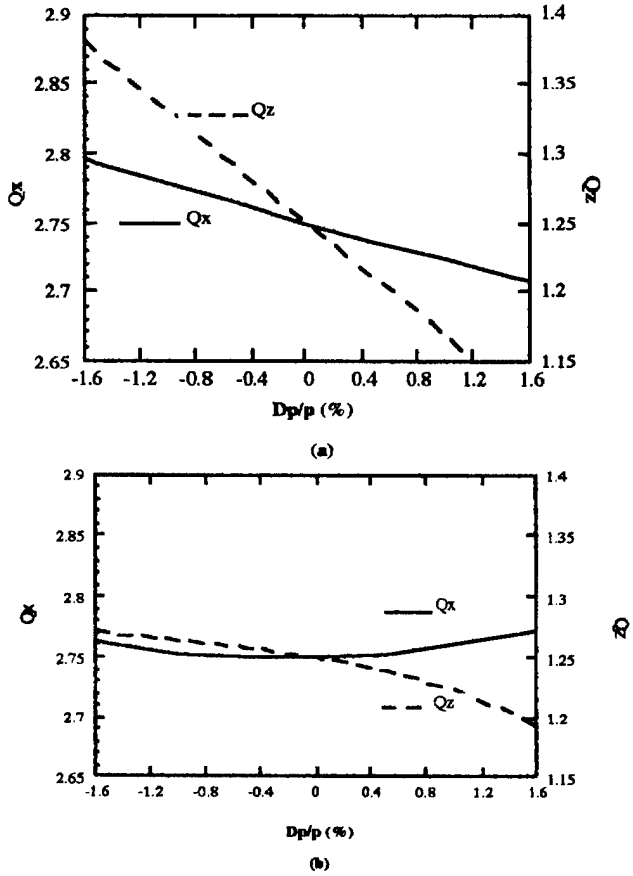


Fig. 3 Momentum dependence of betatron tunes without (a) and with (b) sextupole correction.

The insertion device such as a superconducting wiggler is anticipated to cause undesirable perturbation on beam dynamics[3]. From this point of view, the higher vertical tune might be preferable. The vertical tune is optimal at the value of 0.75 or 1.25 from the point of view of small vertical beam size. The tune value of 1.25 is found more stable against the perturbation from the wiggler. Compared with the case without any insertion device (Fig. 4(a)), the betafunction in vertical direction becomes to have

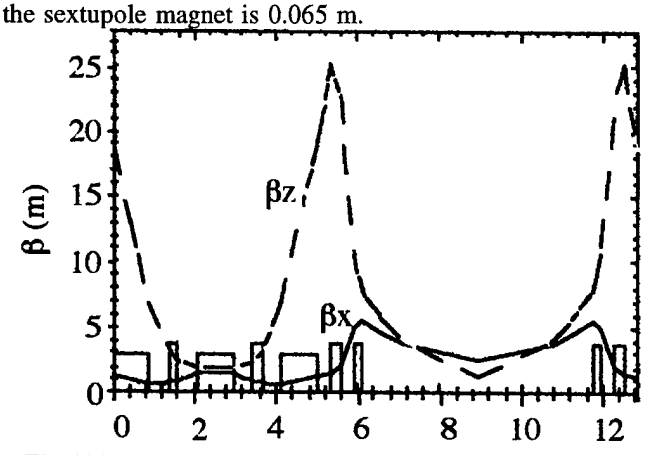


Fig.4(a) Betafunctions without an insertion device.

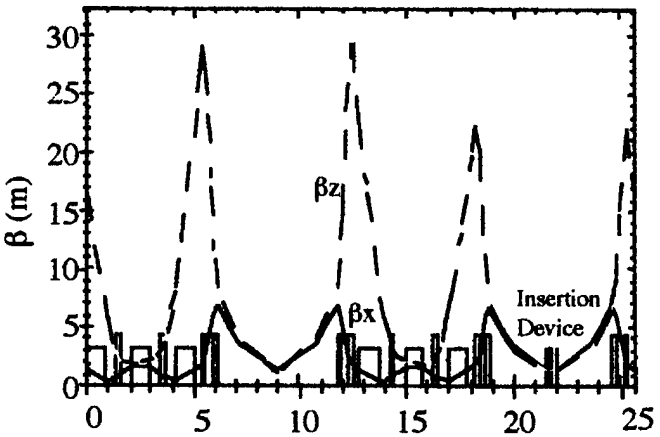


Fig.4(b) Betafunctions perturbed by the three pole wiggler with the strength of 2.5 T.

a beat as shown in Fig. 4(b) due to the wiggler field of 2.5 T,which correspond to the critical wave length of 8 nm. The size of βz beat is ~17% which seems to be comparable with that reported for ELETTRA[4]. The vertical tune shift for this case is 0.03. Further careful studies on beam dynamics are needed.

III. ALIGNMENT OF THE MAGNETS

The procedure of alignment of the magnets has been performed in the following way. (1)Two alignment poles E and W are precisely set at the positions indicated in Fig. 1 with use of optical devices. The pole has a cylinder, the diameter and surface of which are well controlled in precision during fabrication process and the cylinder is set upright with good precision. Further it is possible to attach the positioning table for optical device on the cylinder with good precision. (2)Three dipole magnets in each arc are positioned with measurement of the distances from each alignment pole. Each dipole magnets has three positioning holes whose positions are precisely controlled. The distance between the rods inserted in these holes and the cylinder on the alignment pole is measured with use of an inside-micrometer. Thus the positions of the dipoles are known. The spacing between the adjacent dipoles is adjusted with use of the theodolite which automatically attitude corrected (made by Wild Co. Ltd.) (3) The axes of the quadrupole magnets are adjusted with use of the theodolite set on the line which connects the aperture centers of the two adjacent dipole magnets. Then the distance from the nearest dipole is measured by an inside-micrometer. Thus the positioning of the quadrupole magnets is made relative to the dipole magnets. (4) The sextupole magnets are positioned with the same method as above but relative to the quadrupole magnets. At all stages from (2) to (4), the vertical positions of all the magnets are adjusted with use of an auto-level with optical micrometer.

In order to confirm the precision of this positioning, we measured the distances between positioning rods attached to the adjacent dipoles. The deviations of the measured values from ideal one are less than 60 μm for the distance of 1200 mm. Further the distance between the beam center at the long straight section and the line which connects the centers of the two alignment poles, E and W, is measured to be 1874.17 mm while the designed one is 1874.23 mm (Fig. 1). From these results, we are quite confident of good alignment precision better than a few tenth mm. In Fig. 5, the recent overall view of the KSR after alignment is shown.

IV. SUMMARY

Up to now, the magnets system has already been aligned and some of vacuum chambers have already been also installed into the magnets after their alignment. However, much careful studies about the effects on beam dynamics due to the insertion device is needed. The possible future application of the radiation from the insertion device should also be considered carefully, which requires some more time. Thus, separate evacuating systems for the arc portions will be prepared for the purpose of vacuum aging during such study about insertion devices. The possibility to use the KSR ring as the stretcher of the electron beam from the linac before the completion of the insertion device is also being considered.



Fig. 5 Recent View of the KSR.

V. ACKNOWLEDGEMENT

The authors would like to present their sincere thanks to Drs. Y. Suzuki and C. Kobayashi at Japan Atomic Energy Research Institute for their help through this work. Their thanks are also due to Profs. J. Oda and T. Miyamoto for their encouragements and supports for this work. Cooperation on this work of Nihon Kensetsu Kogyo, leaded by Mr. K. Syoda, is greatly appreciated. One of the authors (A.N.) is also grateful to Mitsubishi Electric Co. Ltd., for their aids during the magnet alignment.

VI. REFERENCES

[1] T. Shirai et al., "A 100 MeV Injector for the Electron Storage Ring at Kyoto University", contribution to this conference.

[2] A. Noda et al., "Design of an Electron Storage Ring for Synchrotron Radiation", Proc. of the 4th European Particle Accelerator Conf., London, U.K. (1994) pp645-647.

[3] G. Wstefeld, private communication.

[4] L. Tosi et al., "Optics and Transverse Beam Dynamics in ELETTRA", ibid., pp1006-1008.

A Lattice for the Future Project of VUV and Soft X-Ray High Brilliant Light Source

H. Takaki, Y. Kobayashi[A], K. Matsuda and Y. Kamiya

Synchrotron Radiation Laboratory,
The Institute for Solid State Physics (ISSP),
The University of Tokyo, Tanashi, Tokyo 188, Japan

[A]Photon Factory,
National Laboratory for High Energy Physics,
Tsukuba, Ibaraki 305, Japan

I. Introduction

Presented in this paper is a lattice for a third-generation VUV and soft X-ray light source[1], which is a future project of the Institute for Solid State Physics (ISSP) of the University of Tokyo and is being designed in close collaboration with the Photon Factory of KEK. The storage ring has an energy of 2 GeV, a circumference of about 400 m, an emittance of less than 5 nm rad, four 13 m long straight sections and twelve 7 m semi-long straight sections. We first present the lattice design of the ring, the chromaticity correction and the dynamic aperture, and next present a new lattice which is now under study to improve the performance.

II. Lattice Design

Table 1 shows the fundamental parameters of the ring, which has a circumference of 374.14 m and an emittance of 4.88 nm. The ring consists of 16 DBA cells. Each cell has two straight half-sections for insertion devices at both ends. The number of the straight sections are 16. Four of them are 13 m long and twelve of them are 7 m long. The 13 m long straight sections are arranged with a four-fold symmetry. A cell with 7 m semi-long straight half-section is called *Normal Cell* and a cell with 13 m long straight half-section at one end is called *Long Cell* (see Table 2). The lattice configuration of a Long Cell is the same as that of a Normal Cell except for three quadrupole magnets (Q1L, Q2L, Q3L), which is used for matching of the betatron functions in the 13 m long straight section. Figure 1 shows the betatron and dispersion functions for an octant of the ring. We have used SAD[2] code for the lattice calculation.

Table 1: Fundamental parameters of the storage ring

Energy	E [GeV]	2.0
Lattice type		DBA
Superperiod	N_S	4
Circumference	C [m]	374.14
semi-long straight section		7m x 12
long straight section		13m x 4
Natural emittance	ε_{x0} [nm rad]	4.878
Energy spread	σ_ε/E	6.66×10^{-4}
Momentum compaction	α	7.13×10^{-4}
Horizontal tune	ν_x	18.410
Vertical tune	ν_y	9.800
Horizontal natural chromaticity	ξ_x	-49.98
Vertical natural chromaticity	ξ_y	-17.75
Horizontal damping time	τ_x [msec]	23.26
Vertical damping time	τ_y [msec]	23.35
Longitudinal damping time	τ_ε [msec]	11.69
Revolution frequency	f_{rev}[MHz]	0.80128
RF voltage	V_{RF} [MV]	1.4
RF frequency	f_{RF} [MHz]	500.0
Harmonic number	h	624
Synchrotron tune	ν_s	0.007
Bunch length	σ_z [mm]	4.04
RF-bucket height	($\Delta E/E$)	0.028

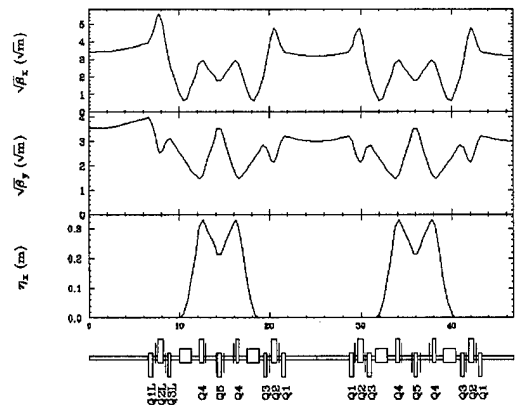


Fig 1: Optics for an octant of the ring.

0-7803-3053-6/96/$5.00 ©1996 IEEE

IV. Chromaticity Correction and Dynamic Aperture

The horizontal chromaticity of the ring is -49.98 and the vertical one is -17.75. The chromaticities have been corrected by using chromatic sextupoles (SF0, SD0) located in the dispersive region of the cell. The strengths of these sextupoles are B''=498 $[T/m^2]$ for SF0 and B''=-392 $[T/m^2]$ for SD0.

These sextupoles, however, introduce nonlinear effects which limit the dynamic aperture. In order to obtain a dynamic aperture as large as possible, the harmonic sextupoles (SF1, SD1, SF1L, SD1L) have been incorporated in the dispersionless region of the lattice. The horizontal dynamic aperture must be larger than the half width of the vacuum chamber (40 mm) at the position where the horizontal betatron function is maximum, while the vertical dynamic aperture must be lager than the half height of the vacuum chamber (10 mm) for an insertion device. A wide momentum aperture (≈±3%) is also required to obtain a long Touschek lifetime. By optimizing the harmonic sextupoles, we have obtained a sufficiently large dynamic aperture as shown in Fig. 2. Here the dynamic aperture is defined as the stable region in which a particle can revolve the ring over 1000 turns.

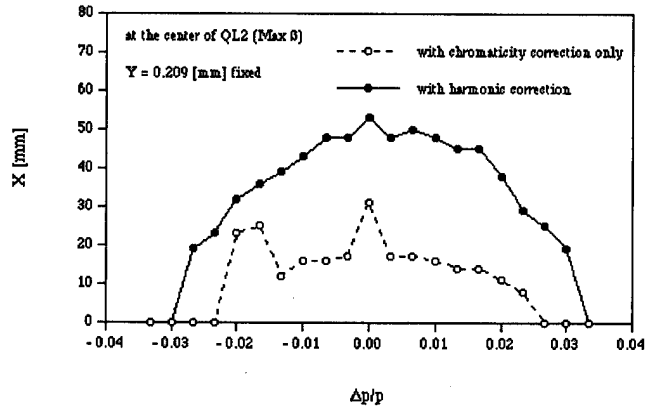


Fig. 2-a: Horizontal dynamic aperture versus momentum deviation

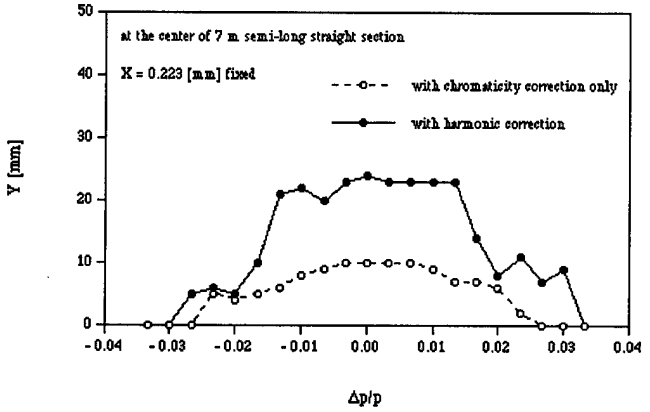


Fig. 2-b: Vertical dynamic aperture versus momentum deviation

Table 2: The lattice of the Normal Cell and Long Cell. The element lengths of the new lattice different from those of the old one are listed in the table. *1 is the symmetric point of 7 m insertion section, *2 the mirror symmetric point of the normal cell, *3 the symmetric point of 12.5 m insertion section. *4 the point where the long cell is connected to the mirror symmetric point of the normal cell.

Normal Cell			Long Cell		
Element	L [m]		Element	L [m]	
	old	new		old	new
*1	-	-	*3	-	-
	3.5	3.3		6.62	6.26
Q1	0.4		Q1L	0.4	
	0.15	0.2		0.15	0.2
SF1	0.15		SF1L	0.15	
	0.15	0.2		0.15	0.2
Q2	0.6		Q2L	0.6	
	0.15	0.2		0.15	0.2
SD1	0.15		SD1L	0.15	
	0.15	0.2		0.2	0.2
Q3	0.4	0.6	Q3L	0.4	
	0.5	0.95		0.95	0.95
B	1.3		B	1.3	
	0.9			0.9	
Q4	0.4	0.6	Q4	0.4	0.6
	0.15	0.2		0.15	0.2
SF0	0.2		SF0	0.2	
	0.9	0.7		0.9	0.7
SD0	0.2		SD0	0.2	
	0.15	0.2		0.15	0.2
Q5 (half)	0.2		Q5 (half)	0.2	
*2	-	-	*4	-	-

V. New Lattice

We are making some modification to the lattice described above to improve the following points;

(1) quadruple magnets should not be C-type,

(2) the access to the BPM should be easier.

For (1), Q3 and Q3L have been shifted away from bending magnets not to touch the beamlines for the synchrotron radiation (see Table 2). For (2), every drift space between a

quadrupole magnet and a sextupole magnet has been lengthened from 0.15 m to 0.2 m.

In order to keep of the betatron functions of 7 m semi-long straight sections to almost the same values as in the old lattice and to obtain a flexibility of optics for long straight sections, the polarities of the quadrupole magnets (Q1, Q2, Q3) have been changed. Since this change causes the magnetic field of Q3 to be saturated, the lengths of Q3 is increased from 0.4 m to 0.6 m.

With these modifications, the circumference of the ring has become from 374.14 m to 388.45 m, the harmonic number from 624 to 648. However long straight sections have become a little bit shorter; from 13 m to 12.5 m for long straight sections and from 7 m to 6.6 m for semi-long straight sections. The new parameters of the ring are listed in Table 3. The betatron and dispersion functions for an octant of the new ring are shown in Fig. 3.

The dynamic aperture for this lattice is now under study. So far, the horizontal dynamic aperture is 30 mm at the maximum position of horizontal betatron function, while the vertical dynamic aperture is 13 mm at the center of the insertion device. It is expected that the dynamic aperture is further improved.

VI. REFERENCES

[1] Y. Kamiya et al., "A Future Project of VUV and Soft X-ray High-Brilliant Light Source in Japan", Proceedings of European Particle Accelerator Conference (London) 1994, p639.

[2] SAD is developed by KEK accelerator group.

Table 3: New parameters of the storage ring.

Energy	E [GeV]	2.0
Lattice type		DBA
Superperiod	N_S	4
Circumference	C [m]	388.45
semi-long straight section		6.6m x 12
long straight section		12.5m x 4
Natural emittance	ε_{x0} [nm rad]	4.582
Energy spread	σ_ε/E	6.66×10^{-4}
Momentum compaction	α	6.87×10^{-4}
Horizontal tune	ν_x	19.410
Vertical tune	ν_y	11.200
Horizontal natural chromaticity	ξ_x	-44.1
Vertical natural chromaticity	ξ_y	-42.9
Horizontal damping time	τ_x [msec]	24.17
Vertical damping time	τ_y [msec]	24.25
Longitudinal damping time	τ_ε [msec]	12.14
Revolution frequency	f_{rev}[MHz]	0.771759
RF voltage	V_{RF} [MV]	1.4
RF frequency	f_{RF} [MHz]	500.1
Harmonic number	h	648
Synchrotron tune	ν_s	0.007
Bunch length	σ_z [mm]	4.04
RF-bucket height	($\Delta E/E$)	0.028

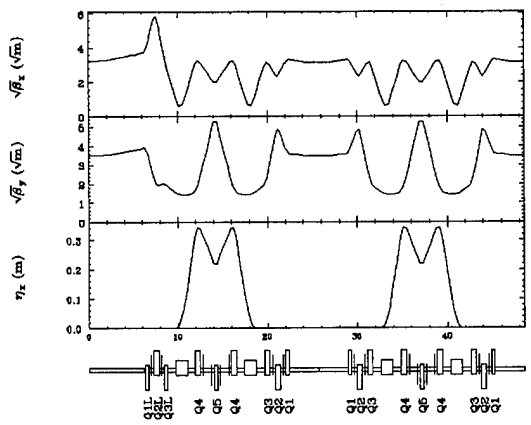


Fig. 3: New optics for an octant of the ring

Millimeter Wave Coherent Synchrotron Radiation in a Compact Electron Storage Ring

J.B. Murphy, E. Blum, R. Heese, J. Keane & S. Krinsky
NSLS, Brookhaven National Laboratory, Upton, NY 11973

ABSTRACT

Installation of a 2856 MHz RF system into the XLS compact electron storage ring would allow the generation of millimeter wave coherent synchrotron radiation. Operating at 150 MeV, one could produce bunches containing on the order of $2x10^7$ electrons with a bunch length σ_{L0} = 0.3 mm, resulting in coherent emission at wavelengths above 0.8 mm. The characteristics of the source and the emitted radiation are discussed. In the case of 100 mrad horizontal collection angle, the average power radiated in the wavelength band 1 mm $\leq \lambda \leq$ 2 mm is 0.3 mW for single bunch operation and 24 mW for 80 bunch operation. The peak power in a single pulse of a few picosecond duration is on the order of one watt. By reducing the momentum compaction, the bunch length could be reduced to σ_{L0} = 0.15 mm, resulting in coherent synchrotron radiation down to 500 μm.

I. INTRODUCTION

Synchrotron radiation in an electron storage ring is a result of incoherent spontaneous emission. The radiated power is directly proportional to the number of electrons in the ring, N. However, if the electrons can be packed into a "small bunch" it is possible to obtain coherent synchrotron radiation proportional to N^2 for wavelengths that are larger than the bunch length ($\lambda \geq \pi\sigma_{L0}$). Numerous authors have discussed the theory of coherent synchrotron radiation including emission from electrons in a storage ring (see reference [1] and the references therein). Experimentally, coherent synchrotron radiation (CSR) has only been observed from linac beams coupled to a bending magnet, it has not been observed in a storage ring.

There is potential for producing short electron bunches in the existing XLS ring at BNL to study coherent synchrotron radiation in a storage ring. A summary of the main parameters of the compact, racetrack style XLS ring is given in Table 1.

Energy, E [MeV]	200
Circumference, C [m]	8.5
Dipole Bending Radius, ρ [m]	0.604
Betatron Tunes, ν_x, ν_y	1.41,0.41
Momentum Compaction, α	0.322
Energy Loss per Turn, U_0 [KeV]	0.234
Longitudinal Damping Time, τ_e [ms]	19
Natural Emittance, ε_0 [nm-rad]	59.2

Table 1: Main Parameters of XLS Storage Ring

According to the theory of electron storage rings, the equilibrium electron bunch length, σ_{L0}, scales as [2],

$$\sigma_{L0} \propto \left(\alpha E^3 / \omega_{rf} V_{rf}\right)^{1/2}. \quad (1)$$

So, to make short bunches implies: 1.) reducing the energy of the ring (E), 2.) increasing the RF voltage (V_{RF}), 3.) increasing the RF frequency (ω_{RF}), and/or 4.) reducing the momentum compaction (α).

In this paper we will discuss the potential for short bunches in the XLS ring using a combination of the first three techniques in the above list. We consider a 2856 MHz RF system with a large RF voltage (V_{RF} = 1.5 MV) at low energy (E = 100-200 MeV) to produce submillimeter electron bunches. In Table 2 the "zero current" bunch length, σ_{L0}, is listed as a function of energy for this RF system. Bunches of 0.2-0.5 millimeters are possible if there are no other deleterious effects to lengthen the bunch. The reduction of the momentum compaction can be used in a second phase of the project to further reduce the bunch length.

Ring Energy [MeV]	σ_{L0} [mm]
100	0.17
150	0.32
200	0.5

Table 2: Bunch Length versus Ring Energy

II. ELECTRON BEAM PROPERTIES

The preceding discussion did not take into account any electron beam intensity dependent effects. It was implicitly assumed that the peak current ($I_p \equiv Nec/\sqrt{2\pi}\sigma_L$) in the electron bunch is below the so called microwave instability threshold as given by the following formula [3],

$$I_p^{th}[A] \leq \frac{2\pi\alpha\sigma_E^2 E[eV]}{(Z_L / n)[\Omega]}, \quad (2)$$

where Z_L / n is the broad band longitudinal coupling impedance of the ring divided by the mode number $n = \omega / \omega_0$. Exactly what the value of Z_L / n should be for short bunches is difficult to answer as this is a subject of active research. In order to proceed we will assume a very conservative value of $Z_L / n = 10\ \Omega$.

Requiring the electron bunch lengths to be those given by the value for the 2856 MHz RF system with V_{RF} = 1.5 MV, the threshold peak currents are calculated and listed in Table 3 along with the equivalent average currents or number of electrons per bunch. The large value of the momentum compaction in the XLS ring (α = 0.322) is

0-7803-3053-6/96/$5.00 ©1996 IEEE

advantageous for increasing the threshold current for low energy operation.

E [MeV]	σ_{L0} [mm]	σ_{E0} [10^{-4}]	I_p^{th} [A]	I_{ave}^{th} [μA]	N^{th} [10^7]
100	0.17	1.0	0.20	10	0.18
150	0.32	1.5	0.66	62	1.1
200	0.49	2.0	1.62	234	4.1

Table 3: Microwave Instability Thresholds for the XLS Storage Ring with $Z_L / n = 10\ \Omega$

The computer code ZAP [4] was used to determine the equilibrium parameters of the XLS electron beam including the effects of intrabeam scattering (IBS). The final properties of the electron beam, accounting for the microwave instability threshold and IBS are listed in Table 4. For energies below 150 MeV, IBS increases even the longitudinal dimensions of the beam. For this reason we focus our attention on energies in the range of 150-200 MeV where bunches with $\sigma_L \approx$ 0.3-0.5 mm and 1-4x10^7 electrons should be possible. The lifetime of the electron beam has been estimated to be ≈ 1.5 hours [1]. This lifetime is more than adequate. In addition, the ring will be injected with a full energy linac, allowing operation in "top off" mode with very little decay in the electron beam current.

E [MeV]	N [10^7]	σ_L [mm]	σ_x [mm]	σ_y [mm]	σ_E [10^{-4}]
100	0.18	0.32	0.34	0.20	2.1
150	1.1	0.32	0.31	0.19	1.5
200	4.1	0.49	0.32	0.19	2.0

Table 4: Final Parameters of the Electron Beam in the XLS Storage Ring

III. 2856 MHZ RF SYSTEM

The key to achieving sub millimeter bunches is the use of a high frequency RF system. Although to date most storage rings have RF systems with frequencies at or below 500 MHz, the MIT-Bates South Hall Ring makes use of a single cell, normal conducting, 3 GHz CW linac structure as its RF system [5]. For a normal conducting cavity, the average accelerating gradient that can be achieved is 2 MV/meter. This limit is set by the ability to remove heat from the copper cavity before excessive distortion detunes the cavity. There would need to be 3 accelerating sections, each having five cells, which is too large to fit in the ring.

To achieve higher gradients and to lower the overall power requirements we propose using a superconducting RF cavity. The present thinking is to stretch the circumference of the ring to 9.6 m to provide more space for the cavity and diagnostics. The properties of the 2856 MHz superconducting RF system to be used in the XLS ring are given in Table 5. A more complete discussion of the RF cavity can be found in reference [6].

Frequency [MHz]	2856
Peak Voltage, V_{rf} [MV]	1.5
Effective Gradient [MeV/m]	5.8
N_{cell}	5
R_{sh}/Q [Ω]	240
Unloaded Q_0	10^9
L_{tot} [m]	0.8

Table 5: Superconducting 2856 MHz RF System

IV. SYNCHROTRON RADIATION

Before discussing coherent emission of synchrotron radiation we briefly outline incoherent emission where the intensity of radiation is proportional to the number of electrons in a bunch. The radiation emitted by a relativistic electron moving in a magnetic field is called synchrotron radiation. The spectrum of the radiation is very broad band but it is usually characterized by a so called "critical wavelength" given by [7],

$$\lambda_c\,[\text{Å}] = \frac{18.64}{B_0[\text{T}]\,E^2[\text{GeV}]}. \qquad (3)$$

Thus for the energies of E = 150 & 200 MeV in the XLS ring the critical wavelengths are λ_c = 1004 Å & 423 Å respectively. The incoherent power (P_{coh}) per milliradian of horizontal arc (θ) and integrated over all vertical angles is proportional to the number of electrons and is given by [7],

$$P_{inc}(\lambda)\left[\frac{\text{watts}}{\text{mrad}\,\theta - \text{mm}}\right] = \frac{8.42\times10^{-8}\cdot\rho^{1/3}[\text{m}]\cdot I[\text{Amp}]}{\lambda^{7/3}[\text{m}]}, \qquad (4)$$

for $\lambda >> \lambda_c$ which is the regime of interest for the present discussion of coherent emission. In this wavelength regime the power is independent of the energy of the ring and depends only weakly on the ring parameters, i.e., $\rho^{1/3}$. As such, for a fixed current, one ring is as good as the next.

V. ESTIMATE OF COHERENT RADIATION

The above discussion of synchrotron radiation ignored any coherence effects that may be present when electrons are packed into small bunches. The qualitative argument for the enhancement of radiation due to coherence effects is as follows. When electrons are bunched into a region with a dimension significantly less than the wavelength of the radiation being emitted, all the charges radiate in phase like one macroparticle and the radiation output is proportional to N^2. Numerous authors have done quantitative analyses of the coherence effects for electrons in a Gaussian bunch of dimensions, σ_x, σ_y & σ_L, the results will simply be reviewed here [8]. The coherent power , P_{coh}, is given in terms of the incoherent power P_{inc} by,

$$P_{coh}(\lambda, \sigma_L) = [1 + (N-1)\cdot H(\lambda, \sigma_L)]\cdot P_{inc}(\lambda) \qquad (5)$$

where $H(\lambda,\sigma_L)=\exp\left[-(2\pi\sigma_L)^2/\lambda^2\right]$ for a Gaussian electron beam. For wavelengths short compared to the electron bunch length the incoherent spectrum is unaffected, but for wavelengths on the order of the bunch length and longer, the radiation output is enhanced by up to a factor of N. For wavelengths larger than a few centimeters the radiation will be suppressed because these wavelengths are below the cutoff of the storage ring vacuum chamber which has a full aperture vertical dimension of 35 mm.

In Figure 1 we plot the coherent spectral power for the wavelength range of 0.1 mm $\leq \lambda \leq$ 10 mm for the electron beam parameters given in Table 4. For comparison the maximum incoherent power assuming a circulating current of one ampere is also plotted in Figure 1. It can be seen that for wavelengths λ > 0.8 mm there is an enhancement of the radiation output beyond what is available on the XLS ring or any other ring for that matter.

To determine how much coherent power is in a given wavelength range we integrated equation (5) over several ranges of wavelength for the two bunch lengths, σ_L = 0.3 & 0.5 mm, and tabulated the results in Table 6.

$\sigma_L = 0.32$ mm, I = 62 μA			
λ_1 [mm] → λ_2 [mm]	0.8→1.0	1→2	2→10
$\int_{\lambda_1}^{\lambda_2} P_{coh}(\lambda,\sigma)\,d\lambda$ [μw / mrad θ]	9×10^{-3}	2.8	8.4
$\sigma_L = 0.5$ mm, I = 234 μA			
λ_1 [mm] → λ_2 [mm]	0.8→1.0	1→2	2→10
$\int_{\lambda_1}^{\lambda_2} P_{coh}(\lambda,\sigma)\,d\lambda$ [μw / mrad θ]	1.7×10^{-3}	4.2	73

Table 6: Coherent Power for Various Wavelength Ranges and Two Electron Bunch Lengths

VI. CLOSING REMARKS

The infrared beamline IR4 on the VUV ring at the NSLS collects radiation from about 100 mrad of horizontal arc. For the racetrack design of the XLS, one could consider collecting radiation from the entire dipole, π radians, if optics of the proper design and reflectivity were available [9].

When a 2856 MHz cavity is used in the XLS ring there can be 81 equally spaced bunches. In this case there exists the possibility of an additional coherence between the various bunches. In practice the stability of multiple bunches in the XLS storage ring against such deleterious effects as ion trapping and multibunch instabilities requires further analysis.

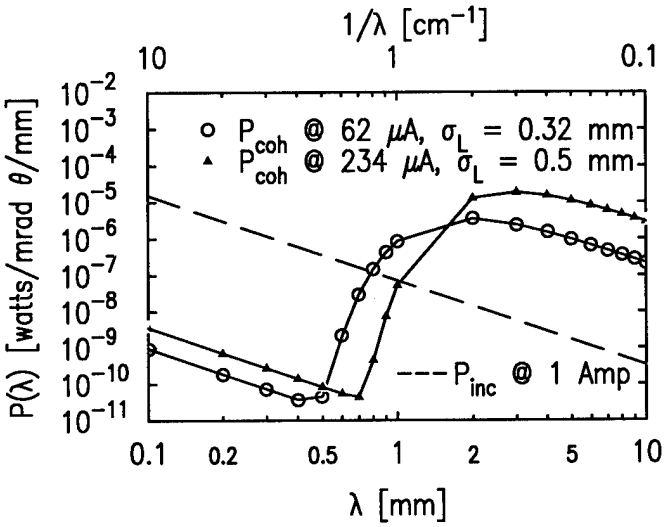


Figure 1: Comparison of Incoherent & Coherent Power versus Radiation Wavelength for the XLS Ring. For incoherent emission, I = 1 ampere, and for coherent emission the currents are taken from Table 4.

VII. ACKNOWLEDGMENTS

The aid of the NSLS RF group in exploring the RF cavity design is gratefully acknowledged. Discussions with Drs. K. Bane & R. Warnock at SLAC on impedance were helpful. Work performed under DOE contract DEAC02-76CH00016.

VIII. REFERENCES

[1] J.B. Murphy & S. Krinsky, "Millimeter Coherent Synchrotron Radiation in the XLS Electron Storage Ring", NIM A346, p.571, (1994).

[2] M. Sands, "The Physics of Electron Storage Rings: An Introduction", SLAC Report 121 (1970).

[3] J. LeDuff, "Current and Current Density Limitations in Existing Electron Storage Rings", NIM A239, p. 83 (1985).

[4] M.S. Zisman, et. al., "ZAP Manual", LBL 21270 (1986).

[5] J.B. Flanz, et. al., "The MIT-Bates South Hall Ring", Proc. IEEE Part. Acc. Conf., p. 34, (1989).

[6] W. Broome, R. Biscardi, J. Keane, P. Mortazavi, M. Thomas & J.M. Wang, "RF System for the NSLS Coherent Infrared Radiation Source", these proceedings.

[7] G.K. Green, "Spectra and Optics of Synchrotron Radiation", BNL Report 50522, (1976).

[8] E. Blum, U. Happek & A.J. Sievers, "Observation of Coherent Synchrotron Radiation at the Cornell Linac, NIM A307, p. 568, (1991).

[9] R. Lopez-Delgaldo and H. Szwarc, "Focusing All the Synchrotron Radiation (2π radians) from an Electron Storage Ring on a Single Point without Time Distortion", Optics Comm., Vol. 19., No. 2, p. 286, (1976).

Commissioning of the Argonne Positron Accumulator Ring*

M. Borland
Advanced Photon Source, Argonne National Laboratory
9700 South Cass Avenue, Argonne, Illinois 60439 USA

Abstract

The Advanced Photon Source (APS) injector consists of a 250-MeV electron linac, a 450-MeV positron linac, a 450-MeV positron accumulator ring (PAR), and a 7-GeV synchrotron. The purpose of the PAR is to accumulate and damp positrons from the 60-Hz linac during each cycle of the 2-Hz synchrotron, thus increasing the fill rate for the main ring. This paper discusses the rapid progress of PAR commissioning. Less than a year was required from first acceptance of beam to transfer of PAR operations to the APS Operations Group. PAR has been well characterized and already meets most of its design specifications. An accurate model has been developed for linear and chromatic properties. Hardware improvements are planned to allow specifications to be fully met.

I. INTRODUCTION

The APS is a 7-GeV positron storage ring that recently delivered "first light" to users. Positron are desirable to eliminate the ion trapping. Because of the inefficiency of positron creation, filling the APS would be slow with the 2-Hz synchrotron. By accumulating charge as the synchrotron ramps and damping the transverse and longitudinal emittances, the PAR increases the fill rate. The principle challenge of PAR was to obtain fast transverse damping and a $\pm 1\%$ energy acceptance, both needed for efficient 60-Hz positron capture.

The PAR design operational cycle lasts 0.5 s. For the first 23/60 s, linac pulses are accepted at a 60-Hz rate. These 0.25-pC, 30-ns FWHM pulses are captured in a first-harmonic, 9.77-MHz rf system. At 1/60 s after injection of the last pulse, a twelfth-harmonic rf system is activated to compress the bunch length from 1-ns to 0.3-ns rms. The bunch is sent to the synchrotron 1/60 s prior to the start of the next cycle.

PAR commissioning began March 7, 1994 using a 177-MeV electron beam from the APS linac, which itself was still being commissioned. Beam was stored at 250 MeV on April 17, 1994, after approximately 35 hours of beam time, on the first shift that had rf available. Due to continuing difficulties with the linac, commissioning has to date used only electrons. Detailed information on the PAR design, a hardware overview, and additional commissioning information are available in the references [1,2]. This paper concentrates on development of the machine model, recent longitudinal dynamics results, septum leakage fields, and upgrade plans.

II. MODEL DEVELOPMENT AND TESTING

When beam was first stored in PAR at 250 MeV, the measured tunes were different from the design values. This was not unexpected, since the ring has 1-m bending radius dipole magnets, with excitation-dependent edge-angles and soft-edge effects [3].

Adjusting the edge-angle largely reconciled measurements and model. Using the adjusted model, a lattice to restore the tunes was created. This worked well, and the method was repeated as the available linac energy increased.

When 450-MeV beam was achieved, the tunes disagreed with the model if the nominal dipole parameters were used. However, adjustment of these parameters was sufficient to produce an accurate model of the linear properties, i.e., of the response matrices and dispersion. The validity of the model in the region around the working point is also good. No other parameter adjustments (e.g., quadrupole strength errors) were found that could explain the measured data as simply.

Figure 1 shows measured and predicted tunes for several lattices. Lattice 1 is the fit point, while the others are test lattices that have (largely) only one of the tunes changed. The model was used to adjust the quadrupoles for each test lattice to give the desired tunes, while limiting changes in the dispersion. Agreement is good except for the horizontal tune for lattice 3; the reason for the problem with lattice 3 is unknown.

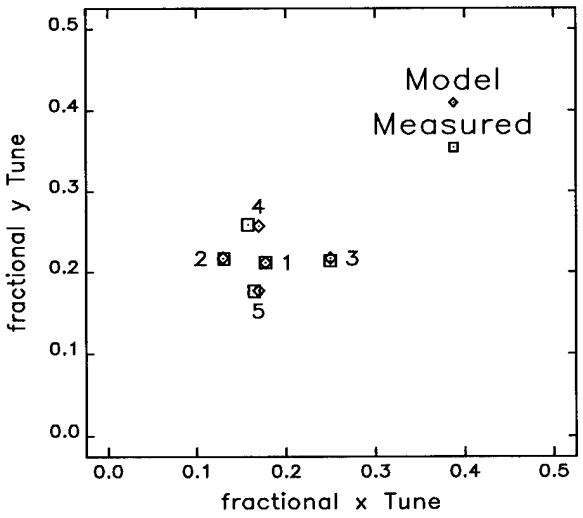


Figure 1: Tune Data and Predictions

Figure 2 shows representative vertical response-matrix data for lattices 1, 3, and 5, which have different vertical tunes. Similar agreement is found for the horizontal plane. Figure 3 shows the measured and model horizontal dispersion. The vertical dispersion is zero to within measurement accuracy. Figure 4 shows the rms normalized deviation of the horizontal (x) and vertical (y) response, and horizontal dispersion. Normalization is to the maximum value of each quantity. The deviations are generally small but statistically significant.

In comparison to the linear model, the chromatic model is relatively simple. The most difficult-to-know parameter is the sextupole, $K_2 = -d^2/dx^2 (B_y/(B\rho))$, in the dipole. This is

* Work supported by U.S. Department of Energy, Office of Basic Energy Sciences, under Contract No. W-31-109-ENG-38.

0-7803-3053-6/96/$5.00 ©1996 IEEE

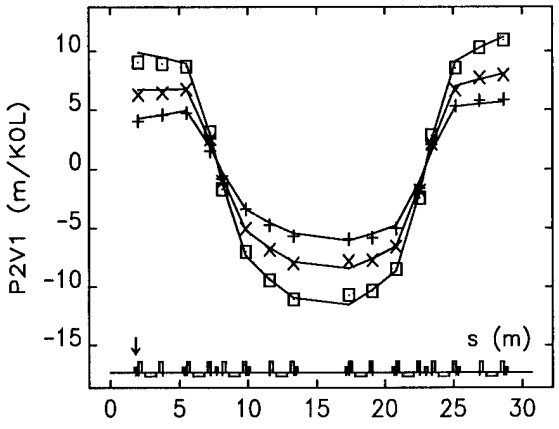


Figure 2: Sample Response Data and Predictions

known to vary between the ends and the center of the magnet. Further, fitting polynomials to the measured field to extract this small term is ambiguous. Turning off all sextupoles gives an easily measured chromaticity for both planes that can be fit reasonably well (see below) by adjusting K_2 . Table 1 summarizes the parameters of the model, along with nominal values from magnetic measurements. The soft-edge parameter K is defined in [3]. Table 2 summarizes the tunes and chromaticities for the nominal and model parameters along with measurements.

Table 1: Nominal and Model Parameters

Parameter	Nominal	Model
E (degrees)	25.50	25.67
K	0.424	0.399
$K_2(m^{-3})$	0.14	0.50

Table 2: Tunes and Chromaticities

Parameter	Nominal	Model	Measured
x tune	2.191	2.177	2.177
y tune	1.140	1.211	1.210
x chrom.	-0.42	-0.89	-0.70±0.05
y chrom.	-6.15	-3.18	-3.08±0.05

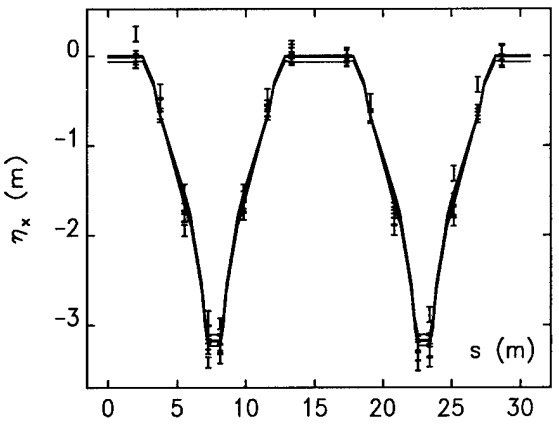


Figure 3: Dispersion Data and Predictions

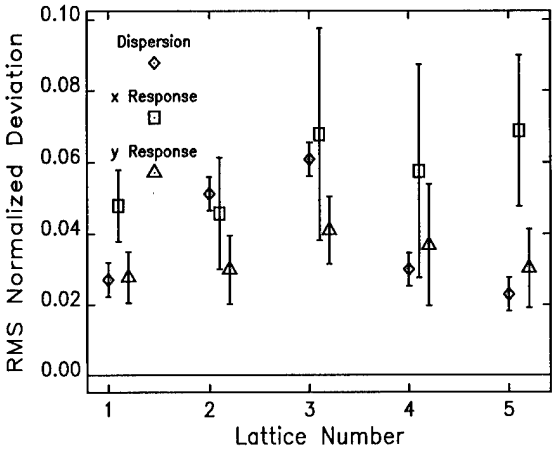


Figure 4: Summary of Model Agreement with Measurements

III. LONGITUDINAL DYNAMICS

Proper functioning of PAR depends on proper functioning of the bunch-compressing harmonic cavity system. During accumulation, the cavity is detuned 150 kHz and deQed fivefold by ferrite loading. This limits beam excitation of the cavity, preventing minibucket formation. Some excitation is desirable to give Robinson damping, which motivated the extent of loading. Early commissioning encountered a longitudinal instability due to deliberately excessive ferrite loading.

Presently, longitudinal instability occurs above about 5-nC stored charge—below the 6-nC goal but above the 3.6 nC specified in the Conceptual Design Report (CDR) [4]. The cause is unidentified; it may be a cavity higher-order mode (HOM) or a feedback problem. Figures 5 and 6 show the bunch length as a function of time (measured with a fast photodiode on a synchrotron light port) during compression for 4.8-nC and 5.9-nC stored charge, respectively. For the latter, the compressed beam is unstable. The time access calibration for these figures is uncertain and hence is not given.

IV. SEPTUM LEAKAGE FIELD

The original PAR septum was a transformer design with a 2-mm copper-iron sandwich for the septum wall. This design had excessive leakage fields. A new direct-drive design is now in use [5]. To measure leakage fields with beam, a single BPM was read turn-by-turn as the septum was pulsed. Since the septum pulse is slow compared to betatron oscillations, the closed orbit follows the leakage field adiabatically. The model was used to compute the leakage field required to produce the observed closed orbit change. By repeating the experiment with the initial closed orbit at different distances from the septum wall, the leakage field vs. distance from the septum wall can be measured. Figure 7 shows three traces of percent leakage field relative to the peak septum field for different initial closed orbits. The traces are labeled by the closest approach the closed orbit makes to the septum. The design places the septum wall 20 mm from the closed orbit. One sees that at 9.7 mm from the septum, the peak leakage field is 0.5%, or 4 G. This is a fourfold improvement over the transformer septum,

and meets requirements. The figure shows the prompt and delayed terms of the leakage field; the dominance of the latter indicates that field is penetrating the septum wall rather than coming from some other source.

V. STATUS AND IMPROVEMENT PLANS

PAR performance relative to the design is good in spite of a few problems. The ring has operated reliably and routinely at the 450-MeV design energy. The damping rate agrees with expectations, and the energy acceptance is better than ±0.8 %. Operation of PAR by non-physicist operators began after less than one year of commissioning. Capture efficiency for electrons with 20-Hz injection is essentially 100%. A single test of 30-Hz injection has been performed, with no loss in efficiency relative to 10 or 20 Hz. Still, several systems require upgrade before PAR can perform complete as designed.

The fundamental rf system delivers 27 kV compared to the minimum 30 kV for "100%" positron capture. The harmonic system delivers 17 kV compared to 30 kV required for the design 0.28-ns rms bunch length. Replacement of solid-state amplifiers with tube amplifiers will provide more power, but improved fundamental-cavity cooling is required.

The septum will shortly be replaced with a direct-drive magnet capable of 60-Hz operation. The present magnet lacks water cooling and is limited to 3 Hz at 400 MeV.

Continued investigation of the rf feedback systems and HOMs will be required to raise the longitudinal instability threshold above 6nC. The energy acceptance appears to be lower than desired, for unknown reasons (it is apparently not rf-related). Resolution of such issues is not urgent in the context of the beginning of commissioning of the APS itself, as PAR easily delivers over the CDR-specified 3.6 nC/cycle.

VI. ACKNOWLEDGMENTS

Design, construction, and commissioning of the PAR was the work of many individuals, whom I am pleased to acknowledge here: C. E. Anderson, J. A. Boggs, J. F. Bridges, J. Curarine, E. A. Crosbie, R. Dame, DANFYSIK Corporation, R. J. Dortwegt, L. Emery, K. Evans, R. Ferry, J. N. Galayda, K. Halbach, R. Holsinger, J. M. Jagger, E. Kahana, Y. W. Kang, R. T. Kmak, M. J. Knott, R. L. Kustom, F. R. Lenkszus, F. Lopez, A. Lumpkin, W. P. McDowell, D. G. McGhee, F. E. Mills, S. Milton, H. J. Moe, P. L. Morton, G. J. Nawrocki, J. R. Noonan, D. R. Paterson, C. Saunders, N. S. Sereno, S. Sheynin, W. Sellyey, T. L. Smith, J. Stepp, L. C. Teng, L. R. Turner, J. Wang, and X. Wang.

VII. REFERENCES

[1] M. Borland, "Update on the Argonne Positron Accumulator Ring," *Proc. of the 1993 Particle Accelerator Conference*, pp. 2028-2030, 1993.

[2] M. Borland, "Commissioning of the Positron Accumulator Ring for the Advanced Photon Source," to be published in *Nuclear Instruments and Methods.*

[3] K. L. Brown, "A First- and Second-Order Matrix Theory for the Design of Beam Transport Systems and Charged Particle Spectrometers," SLAC Report-75, June 1982.

[4] "Annex to 7-GeV Advance Photon Source Conceptual Design Report," ANL-87-15 Annex, May 1988.

[5] S. Sheynin, et. al., "The APS Direct-Drive Pulsed Septum Magnets," these proceedings.

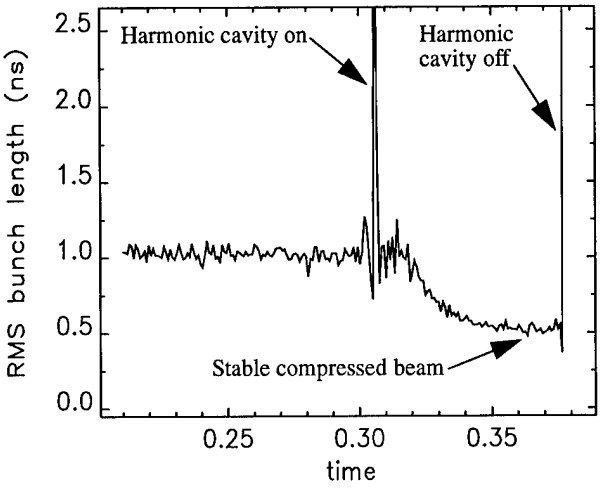


Figure 5: Bunch Length vs Time for 4.8nC Stored Charge

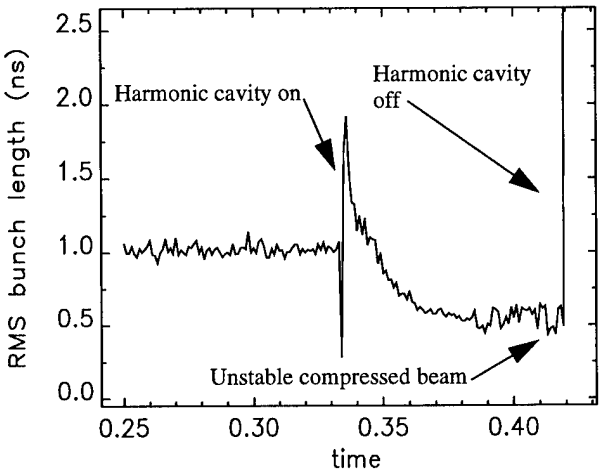


Figure 6: Bunch Length vs Time for 5.9nC Stored Charge

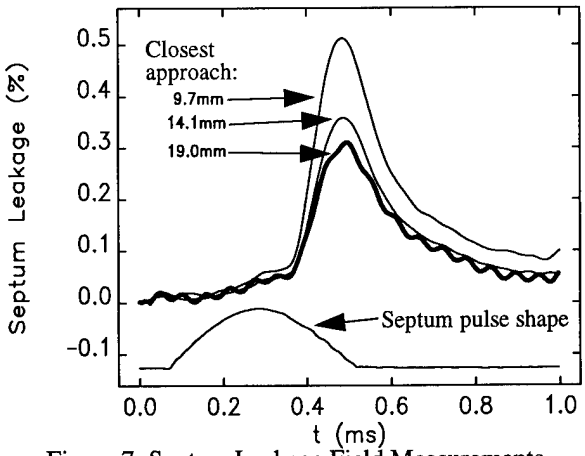


Figure 7: Septum Leakage Field Measurements

APS Storage Ring Commissioning and Early Operational Experience*

G. Decker
Advanced Photon Source, Argonne National Laboratory
9700 South Cass Avenue, Argonne, Illinois 60439 USA

Abstract

The Advanced Photon Source (APS) at Argonne National Laboratory (ANL) uses a 100-mA, 7-GeV positron storage ring to produce high brilliance bending magnet and insertion device x-rays for up to 70 x-ray beamlines. It is 1104 meters in circumference and has a beam lifetime designed to exceed 10 hours with 1 nTorr average ring vacuum at 100 mA. The high brilliance required by the synchrotron light users results from the storage ring's natural emittance of 8.2 nm-rad, together with the requirement that the beam be stable to a level which is less than 5% of its rms size. Real-time closed orbit feedback is employed to achieve the required stability and is discussed elsewhere in these proceedings. Installation of storage ring components was completed early this year, and we report here on the first experiences of commissioning and operation with beam.

I. INTRODUCTION

The first revolution of beam around the APS storage ring took place March 18, 1995, with rf capture demonstrated one week later on March 25. This paper will give a brief description of APS storage ring subsystems and early commissioning activities.

II. SUBSYSTEMS DESCRIPTION

Storage ring subsystems are magnets, vacuum systems, power supplies, rf systems, controls, and diagnostics [1].

Magnets

The APS storage ring magnets consist of 80 C-core dipole magnets with a field of 0.599 Tesla, 400 quadrupoles with peak gradient near 20 Tesla/meter and including three varieties with effective lengths of 0.5, 0.6, and 0.8 meters. There are 280 sextupole magnets in the ring, three chromatic and four harmonic sextupoles in each of the forty sectors. Orbit correction is facilitated via 317 combined function vertical/horizontal correction magnets. A six-pole corrector design wired so as to null the sextupole field components is used to allow clearance for the vacuum chamber photon exit slot and antechamber. Twenty skew quadrupole magnets are also included in the lattice, straddling vacuum spool pieces between girder assemblies. Thirty-eight of the correctors also straddle these thin-walled Inconel spool pieces for improved AC magnet performance which is limited by eddy currents for those correctors having the thick-walled aluminum vacuum chamber in their bore.

Each of the forty storage ring sectors is composed of five girders upon which are mounted the magnets and vacuum chambers. These girders each rest on three wedge jack supports which have two layers of visco-elastic vibration dampening material sandwiched below them.

The lattice is of the Chasman-Green type (Fig. 1), also known as the double-bend achromat. Five-meter-long zero-dispersion straight sections reserved for insertion device installation are located at 35 places around the ring, with the other five reserved for rf cavities and injection hardware.

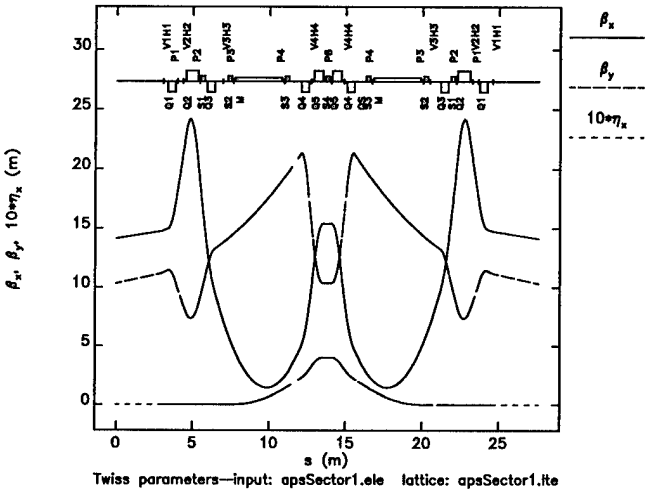


Figure 1: Advanced Photon Source Lattice

Vacuum Systems

The APS vacuum system is composed of 240 extruded aluminum chambers joined with rf-shielded bellows spool piece assemblies. Pumping occurs at the 240 photon absorber locations, one per chamber, with lumped NEG/ion pumps. Each chamber consists of a 41.7 x 84.7 mm roughly elliptical beam chamber and a photon exit slot terminated by an antechamber housing distributed NEG pumping strips. Special small gap chambers (12 or 8 mm vertical aperture) are to be installed in the long straights prior to insertion device installation.

Power Supplies

Storage ring magnets are all individually powered by pulse width modulation regulated DC-DC convertors (20-kHz choppers) with the exception of the main windings of the dipole magnets, which are bus-fed. Eighty raw DC power supplies are distributed around the ring and feed the 1414 choppers. Quadrupole and sextupole magnets have unipolar convertors, while correctors, skew quads, and dipole trim windings employ bipolar designs.

Radio Frequency Systems

Four 1-MW 352-MHz klystrons are used to drive sixteen separately tunable cavities distributed among four of the zero-dispersion straight sections. The commissioning configuration

* Work supported by the U.S. Department of Energy, Office of Basic Energy Sciences, under Contract No. W-31-109-ENG-38.

0-7803-3053-6/96/$5.00 ©1996 IEEE

employs two klystrons to drive a total of 12 cavities. A target 9 MV per turn is required as overvoltage for the 5.45 MV per turn from synchrotron radiation loss at 7 GeV.

Controls and Diagnostics

The Experimental Physics and Industrial Control System (EPICS) software package is used to connect control room-based operator interface (OPI) workstations with remote input-output controller computers (IOCs). Standard EPICS tools are supplemented by in-house physics software tools used for performing a large variety of beam measurements [2]. Initial experience has been excellent.

Commissioning beam diagnostics for the storage ring include 360 AM/PM type monopulse receivers for turn-by-turn beam position monitoring, 10 fluorescent screen stations, a visible synchrotron light monitor, two sets of scraper jaws in each plane, 10 segments of long-ionization chamber style loss monitors, a pulsed and average beam current monitor, and four sets of stripline pickups and drivers for tune measurement and beam damping.

III. COMMISSIONING EXPERIENCE

The six weeks starting mid-January, 1995 were spent primarily commissioning the APS injector synchrotron for 7 GeV electron operation and completing installation of final storage ring components. Prior to this time, 4-GeV injector ramps had been used, for example during the storage ring two-sector test which took place in late October 1994. Positron operation awaits installation of a high repetition rate injection/ejection septum magnet in the positron accumulator ring. The first 7-GeV transfer of beam from the injector synchrotron to the storage ring occurred the morning of February 21, 1995 when beam was transported through the high energy transport line and through two sectors of the storage ring.

The March commissioning run was used for final checkout with beam of the large number of convertor power supplies. Response function measurements using correctors together with the beam position monitors allowed the localization of quadrupole strength errors attributed to malfunctioning power supplies. Although individual power supplies had all undergone pre-installation burn-in and checkout, operation of large numbers coincidentally using the EPICS interface required a significant effort.

First turn in the storage ring at 7 GeV occurred the morning of March 18, 1995, coincident with checkout completion for the 400 quadrupole DC-DC convertors. The next week was spent completing checkout on the sextupoles, which immediately gave up to 40 turns without rf. Strong focusing in this machine inevitably results in a large tune slew per turn if the chromaticity is not corrected.

It was decided to attempt stored beam at 4.5 GeV using a single rf source to simplify phasing This decision was fortuitous, resulting in the first rf capture on March 25, with first extracted x-rays from beamline 1-BM the next morning, March 26. These activities provided proof of principle for storage ring operation, giving confidence in the magnet survey and lattice. First stored beam at 7 GeV occurred after a 10-day shutdown the morning of April 16, now using two rf klystrons. Beam lifetime now exceeds three hours with approximately 1.E-8 Torr average ring vacuum. Vacuum bakeout work is not yet complete and will be finalized this summer.

IV. MACHINE STUDIES RESULTS

Preliminary first-turn orbit correction was performed by adjusting one corrector per sector in such a way as to minimize the mean absolute value for downstream beam position monitor readings. The same algorithm was applied to the closed orbit without rf resulting in an rms orbit relative to the beam position monitor (BPM) zero of 3 to 4 mm. BPM offsets relative to magnetic centers of quads appear to be less than about 1 mm rms, and are still under investigation.

The beam position monitors for the APS storage ring have single turn capability and employ amplitude to phase conversion (AM/PM) monopulse receivers. These have been invaluable to the commissioning efforts, for example during the process of commissioning the 400 quadrupole power supplies. Shown in Fig. 2 is the first turn vertical BPM response resulting from a Sector 2 vertical corrector change. This corrector is located just downstream from the injection point. Note the change in amplitude beginning near Sector 28. This effect was traced to a malfunctioning quadrupole power supply in that sector which was not supplying the required current. This type of problem would be extremely difficult to diagnose with beam without the first-turn capability.

An additional capability of the BPMs are the first-in, first-out (FIFO) beam history modules. Using these, for example, an FFT of the first thousand turns of horizontal beam motion after injection results in a measurement of horizontal tune resulting from the injection transient betatron oscillation. In Fig. 3 the plot is presented in fractional tune units along the x-axis and arbitrary units vertically. The structure near 0.5 is an artifact of the plus/minus shot-to-shot toggling of the BPMs

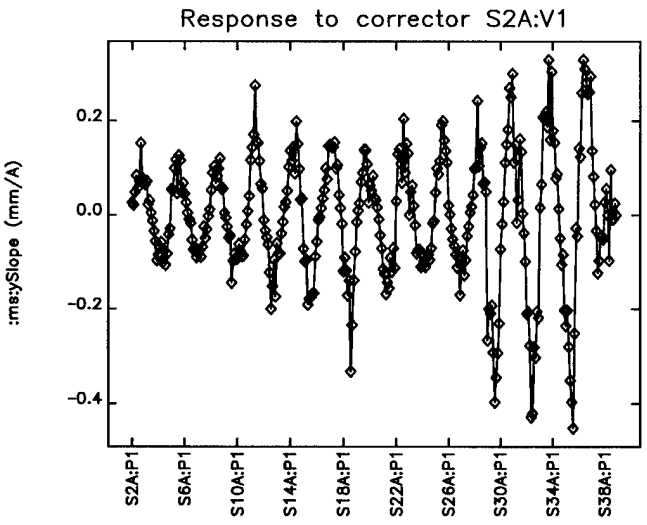


Figure 2: First turn beam position monitor response function.

required for electronic offset compensation. Note the clear signal near $\nu_x = 0.23$ (0.77).

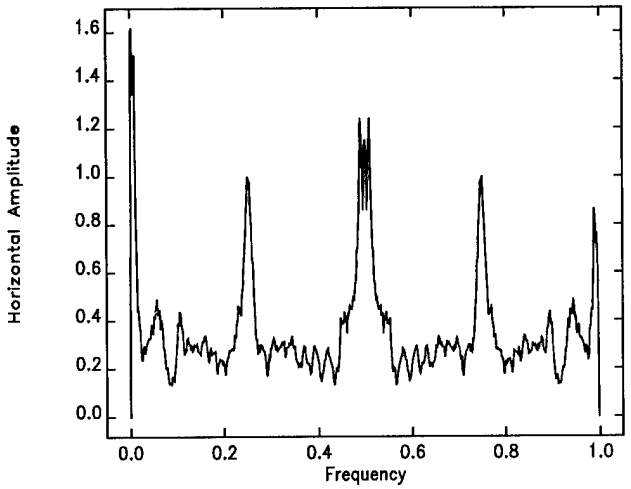


Figure 3: FFT of first 1,048 turns of horizontal beam motion.

Lattice modeling has been confirmed both by tune measurements and closed orbit corrector response function measurements. Shown in Fig. 4 is a comparison between measured and theoretical vertical response functions. In addition to the beam position monitor beam history modules, stripline pickups in conjunction with a vector signal analyzer are used for tune measurement. The beam is excited both with the amplified analyzer source (vertical) and with an injection bumper magnet powered at a low level (horizontal). Spectra similar to Fig. 3 result, and peak detection software is used to automate tune and chromaticity measurement. Figure 5 shows the first chromaticity measurement for the APS storage ring using predicted zero chromaticity values for the sextupoles. Natural chromaticities are $d\nu / d\delta = -58$ and -14 for the horizontal and vertical planes, respectively. The top trace is the vertical tune and the bottom is horizontal.

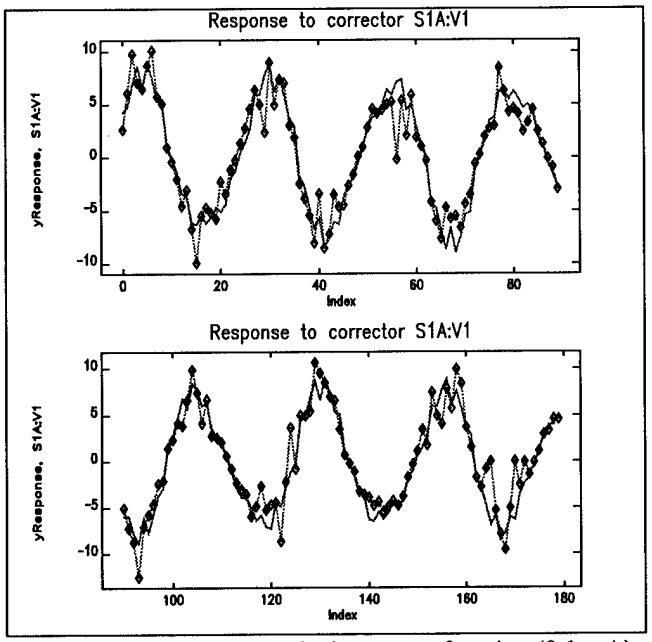


Figure 4: Stored beam vertical response function (0.1 mA).

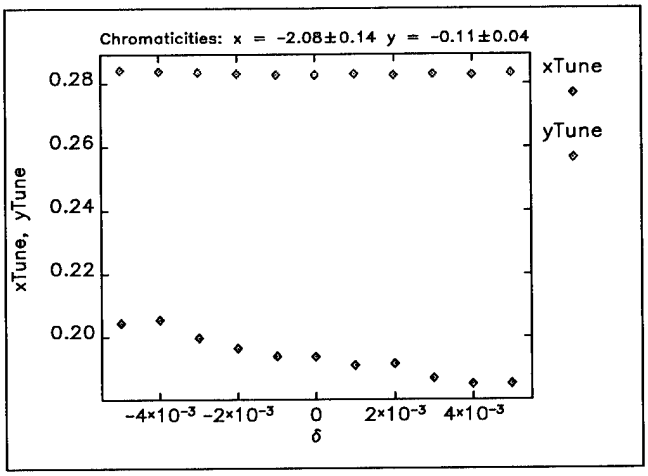


Figure 5: APS storage ring chromaticity measurement.

V. CONCLUSIONS

Commissioning of the APS storage ring is nearing completion. Closed orbit correction algorithms are being implemented at the time of this writing with significant success already. Items remaining are multibunch stacking, high intensity operation, and finally, installation and commissioning of insertion devices together with associated real-time digital closed orbit global and local feedback and beam missteering interlocks.

VI. ACKNOWLEDGEMENTS

This paper would not have been possible without the dedicated efforts of the entire APS Accelerator Systems Division (ASD) over the past two years. Michael Borland and Louis Emery performed the lion's share of data acquisition and machine modeling of which I am primarily the reporter. Steve Milton, John Carwardine, and Nick Sereno have served tirelessly commissioning and operating the injector synchrotron during this commissioning period. Ken Evans generated some extremely useful graphics tools the end results of which are shown here. The ASD Operations Group has been of enormous value providing reliable beam from the linac and positron accumulator ring.

VII. REFERENCES

[1] 7-GeV Advanced Photon Source Conceptual Design Report, ANL-87-15, April 1987.

[2] L. Emery, "Commissioning Software Tools at the Advanced Photon Source," these proceedings.

NEW SPECIFICATIONS FOR THE SOLEIL PROJECT[1]

M.-P. Level, P. Brunelle, A. Nadji, M. Sommer, H. Zyngier
LURE, Centre Universitaire, Bât. 209 D, 91405 Orsay Cedex, France
J. Faure, P. Nghiem, J. Payet, A. Tkatchenko
LNS, Centre d'Etudes de Saclay, 91191 Gif sur Yvette Cedex, France

Continuous interaction with potential users has led to an evolution of the source requirements : maximum brilliance greater than 10^{20} ph/s/mm^2/mrad^2/0.1 % $\Delta\lambda/\lambda$ from undulators in the keV energy range, while keeping the LURE specificities such as temporal structure and FEL operation. To meet these goals an optics tunable from 2 to 30 nm.rad has been optimized. Two kinds of straight sections (14 m and 7 m long) with high and low β functions are available for long undulators or special devices producing various polarizations and different wavelengths.

I. INTRODUCTION

From the beginning of the SOLEIL project studies, the specifications have changed continuously [1, 2]. The basic characteristics remain the same, namely a polyvalent synchrotron radiation source in the 10 eV-20 keV energy range with a large number of undulators, a few special 10-20 keV sources and up to 40 beamlines to satisfy the VUV and soft X-rays communities. However, the performances required are now more ambitious such as extremely high brilliance and possible FEL operation. This paper discusses the choice of the configuration, gives higlights on the optics and presents beam lifetime for different tunings and brilliance calculations for various insertion devices. Detailed studies can be found in a general paper [3].

II. CHOICE OF THE CONFIGURATION

The choice concerns the cell lattice as well as the length and number of long straight sections. Furthermore, as only few 10-20 keV sources are required, short wigglers are preferred rather than superconducting bending magnets, the choice of the configuration takes this into account.

A. Basic cell lattice

Extensive studies have been undertaken in order to choose the best lattice providing the very low emittance (≈ 2 nm.rad) needed to reach the required high brilliance of 10^{20} ph/s/mm^2/mrad^2/0.1 % $\Delta\lambda/\lambda$ from undulators.

In order to allow for a large number of undulators, multiple bend structures were not considered while DB and TB structures were compared as well as bending magnet field index efficiency and various arrangements of multiplets. It turns out that for the same number of periods, TBA and DBA have more or less the same practical minimum emittance, the ratio to the theoretical minimum emittance being larger for the TBA. When the dispersion is distributed, the results are similar. A field index has only a small effect (10 to 20 %) on the value of the final emittance. Both structures require 16 cells in order to reach an emittance around 2 nm.rad. As there is no superconducting bending magnet planned, the simplest DB structure (n = 0) is chosen.

B. FEL dedicated straight section

The aim of the FEL is to provide a powerful tunable (350-100 nm) picosecond source with a practical lifetime (> 10 h) and a reasonable gain (50 %) in order to perform user experiments [4].

The optimized energy of 1.5 GeV results from a compromise between mirror degradation and gain on the one hand and laser power and beam lifetime on the other.

Similarly the length of the straight section was determined as a compromise between the maximum length of the insertion device which defines the gain and the stability of the optical cavity. As the FEL is designed for experimental use, the optical cavity mechanics must be outside the shielding for providing various FEL parameters according to the users requirements. Taking into account the deformation due to local heating, the mirror curvature radius cannot be too large (≈ 30 m) in order to keep the cavity stable. This point leads to an optical cavity length of around 40 m and an optimum length for the straight section of 14 m.

C. Number of long straight sections

Different configurations have been studied with 8, 4 and 2 superperiods. As the symmetry order is decreased the optimization of the optics in terms of optical function matching and dynamic aperture becomes more difficult. For 2 superperiods a unit matrix scheme with 6 additional quadrupole families is needed, which increases dramatically the length of the optical cavity, while for 8 superperiods good results are obtained without additional quadrupoles. After a longer optimization a good solution with 4 superperiods was found and retained for SOLEIL. It offers a better solution for the FEL operation (no additional quadrupole) and two long additional straight sections open for future experiments.

III. OPTICS RESULTS

The energy range for machine operation is 1.5 GeV (FEL and temporal structure operation) to 2.15 GeV (high brilliance operation). Table 1 shows the main machine parameters given at 2.15 GeV.

[1]Work supported by CNRS, CEA, MESR.

0-7803-3053-6/96/$5.00 ©1996 IEEE

Table 1 : Machine parameters.

Energy (GeV)	2.15
Circumference (m)	336
Lattice cell type	DB + 4 long straights
Number of cells, number of superperiods	16, 4
Straight length	14.1 m x 4 + 7.4 m x 12
Dipole : field (T), nb	1.56, 32
Quad. : max gradient (T/m), nb, [nb of families]	18, 160, [8]
Sext. : max strength (T/m^2), nb, [nb of families]	250, 112, [8]
Radiation loss per turn (keV)	410 + 90 [insertion devices]
RF frequency (MHz), max peak voltage (MV)	500, 3

A large number of operating points have been studied in order to obtain low emittance and to provide low vertical beta-functions in straight sections for insertion devices. The horizontal emittance is about 7 nm.rad in the Chasman-Green structure and reaches 2.4 nm.rad with distributed dispersion.

In every case a comfortable dynamic aperture is available even with energy deviation up to ± 4 % for chromaticity $\xi_{x,z} = 0$ and up to ± 3 % for ξ_z = + 1 (high positive chromaticity is expected to increase the single bunch current threshold).

The characteristics for one of the nominal operating points are listed in Table 2. Fig. 1 and Fig. 2 show the corresponding optical functions and dynamic aperture.

Table 2 : Typical operating point characteristics.

Emittance (nm.rad)	2.7
Betatron tunes ν_x, ν_z	18.30, 8.38
Synchrotron tune ν_s	$5.3\ 10^{-3}$
Momentum compaction α	$3.8\ 10^{-4}$
Energy spread σ_ε	$8.6\ 10^{-4}$
Damping times (ms) τ_s, τ_x, τ_z	5.85, 11.7, 11.7
Natural bunch length* (mm), σ_ℓ	3.3
Natural chromaticities (ξ_x, ξ_z)	- 2.98, - 2.90

** (V_{RF} = 1.9 MV for ε_{RF} = 4 %)*

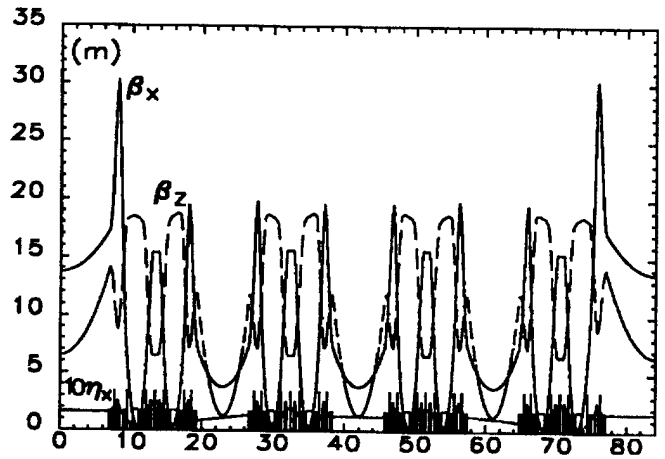


Fig. 1. Optical functions for the typical operating point.

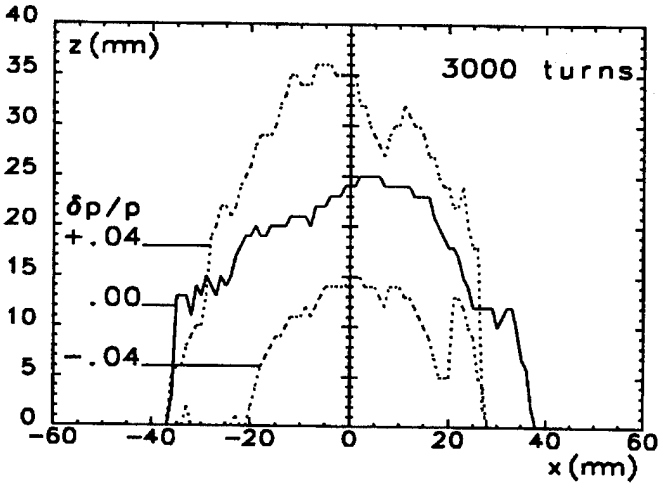


Fig. 2. Dynamic aperture for the typical operating point.

A special operating point has been optimized for FEL operation and temporal structure with an emittance of 30 nm.rad at 2.15 GeV, i.e. 15 nm.rad at 1.5 GeV and zero dispersion in the long straight sections. Its characteristics are given in Table 3 at 1.5 GeV.

Table 3 : FEL operating point characteristics.

Emittance (nm.rad)	15
Betatron tunes ν_x, ν_z	19.40, 6.38
Synchrotron tune ν_s	$15.2\ 10^{-3}$
Momentum compaction α	$1.3\ 10^{-3}$
Energy spread σ_ε	$6.0\ 10^{-4}$
Damping times (ms) τ_s, τ_x, τ_z	17, 34, 34
Natural bunch length* (mm), σ_ℓ	2.8
Natural chromamicitie (ξ_x, ξ_z)	- 2.87, - 3.41

** (V_{RF} = 3 MV for ε_{RF} = 4 %).*

The sensitivity of all the optics has been tested versus standard alignment errors, the machine remains stable over 100 sets of random errors (3 σ). The injection study taking into account those closed orbit distortions led to a beam stay clear of Δx = ± 40 mm ; Δz = ± 17 mm. The individual effect of each multipolar field component was computed, the maximum values retained as tolerances were the ones which kept the dynamic aperture almost

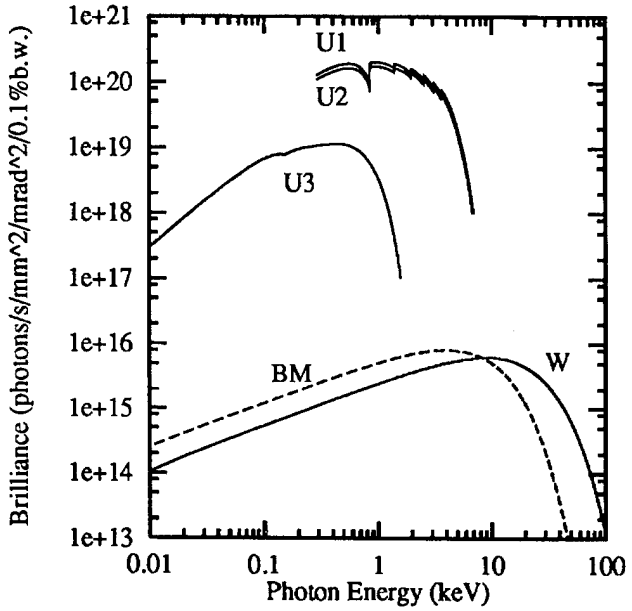
unchanged. The reduction due to the global effect of all systematic and random multipolar field tolerances is about 10 %.

IV. BRILLIANCE AND BEAM LIFETIME

A. Brilliance

Fig. 3 shows the brilliance calculated at the typical operating point with a beam current of 500 mA, and a coupling factor of 1 %, from the bending magnet and several types of insertion devices.

It is worthwhile to remark that the maximum brilliance at about 2 10^{20} ph/s/mm^2/mrad^2/0.1 % $\Delta\lambda/\lambda$, is obtained in both kinds of straight sections (with respectively an undulator length of 10 m and 7 m) due to the fact that β_z can be lower in the shorter straight sections. The longer ones could be dedicated to future developments.



U1 : λ = 4.6 cm N = 220 K_{max} = 2.2
U2 : λ = 4.6 cm N = 150 K_{max} = 2.2
U3 : λ = 20 cm N = 50 K_{max} = 6.7
W : 1 pole superconducting wiggler, B_{max} = 3.5 T

Fig. 3. Typical brilliance for SOLEIL.

B. Beam lifetime

Three modes of operation are expected :

1) High brilliance at 2.15 GeV with 500 mA.

2) Temporal structure at 2.15 GeV with 8 x 10 mA.

3) FEL compatible with temporal structure at 1.5 GeV with 8 x 10 mA.

Beam gas (τ_v) and Touschek lifetimes have been computed for different emittance, coupling and energy values. The pressure taken for the calculation is 10^9 Torr for 500 mA and 2 10^{-10} for 80 mA while the maximum RF voltage is assumed to be 3 MV providing an energy acceptance of 4 %.

Table 4 shows the results for the three modes of operation, the values in bold type correspond to beam lifetime larger than 10 h and maximum factor of merit (brilliance x beam lifetime).

Table 4 : Beam lifetime for three modes of operation.

E (GeV)	2.15		1.5
ε_x (nm.rad)	2.7		15
I (mA)	500	8 x 10	8 x 10
τ_v(h)	33	164	115
τ_{tot} (h), κ^2			
0.01	**12.5**	2	3
0.10	22	6	8
1	27	**11**	**14**

V. CONCLUSION

The SOLEIL parameters optimized in order to reach the targets, are presently completely defined and the ultra vacuum and magnetic element systems detailed studies are now in progress.

The machine offers very high performance at 2.15 GeV with extremely high brilliance from undulators as well as at 1.5 GeV with the FEL providing the possibility of two color experiments as already shown on Super-ACO [5].

SOLEIL associated with the ETOILES project [6], which would cover the whole infrared domain with synchronized FEL, will be a unique multipurpose high performance tool.

VI. ACKNOWLEDGMENT

We are indebted to J.-L. Laclare for fruitful discussions on the machine parameters, M.-E. Couprie and P. Thiry for their implication as designers of insertions and experiments.

VII. REFERENCES

[1] M.-P. Level et al., "SOLEIL, a New Synchrotron Radiation Source for LURE", PAC 93, Vol. 2, p 1465.

[2] P. Brunelle et al., "New Optics for SOLEIL", EPAC 94, Vol. 1, p 615.

[3] P. Brunelle, J. Faure, M.-P. Level, A. Nadji, P. Nghiem, J. Payet, M. Sommer, A. Tkatchenko, H. Zyngier, "Optics and performances of the source", Report APD SOLEIL/A/95-03.

[4] M.-E. Couprie et al., "Projet SOLEIL, Argumentation Scientifique", Les Editions de Physique, Juin 1993, p 257.

[5] M.-E. Couprie, "Applications of FELs in the UV", proceedings of the "Symposium on Ion and Laser Processing for Advanced Materials", Oct. 1994, Keihanna, edited by T. Takagi and T. Tomimasu, pp. 181-186.

[6] J.-M. Ortega et al., "Le Projet ETOILES", to be published.

A COMBINED MAGNET LATTICE OF THE SYNCHROTRON LIGHT SOURCE ISI-800

I.Karnaukhov, S.Kononenko, A.Shcherbakov, National Science Centre "Kharkov Institute of Physics and Technology", Kharkov, Ukraine

V.Nemoshkalenko, V.Molodkin, A.Shpak, Institute of Metal Physics of the Ukrainian Academy of Science, 252147 Kiev, Ukraine

ABSTRACT

The design of an electron storage ring for low emittance mode operation is presented. The parameter optimization is based on the spectrum and on beam source sizes and on general specifications for the machine performance such as dynamic aperture, lifetime. Superconducting magnets in the middle of a TBA cell with a high field are used in the storage ring.

In recent years, great interest has been displayed in basic synchrotron radiation sources whose physical properties along with performance parameters provide a means for handling process problems of X-ray lithography in microelectronics (photon energy ε_c~1 keV), micromechanics (ε_c~ 6 keV) and angiography (ε_c~33 keV). The design of a relatively cheap and compact source with the above-mentioned photon beam parameters is a complicated task, since the compactness of the source sets limits, first of all, on the electron energy, and hence, on the energy of emitted photons. This, in turn, necessitates the mounting, arrangement of special devices such as superconducting wigglers with limiting magnetic-field values of about 10 T. However, the installation of such wigglers in the storage rings with a beam energy lower than 1 Gev is impeded by an impact of magnets on the beam focusing and phase stability of the orbit in the storage ring. This makes necessary long straight sections in the lattice to accommodate the matching elements, and also imposes special requirements on the wiggler design. Furthermore, in consequence of a great distortion of the reference orbit in the wiggler ($\Delta x \sim 5$ cm at an electron energy of 0.8 GeV and a field of 10 T in the wiggler), there arise essential technological difficulties.

One of the ways out of this situation might be the construction of a compact synchrotron radiation (E ~ 1GeV) source with a photon energy up to 33 keV using the storage ring lattice with superconducting magnets as a basis. However, in such a lattice, owing to great beam energy losses by synchrotron radiation, a demand for a powerful RF system arises. Besides, a low emittance (ε_x~10 nm) in the lattice can be provided through a significant increase in the rigidity of the magnet lattice. As a consequence, the natural chromaticity of the ring will increase, and this will result in the reduction of both the dynamic aperture and the beam lifetime [1].

To produce high-brightness photon beams with a sufficiently high energy, it may be reasonable to construct a compact storage ring with the lattice based on the combined TBA (Three Bend Achromat) cell ("warm" and superconducting magnets), where the central dipole magnet of the cell is superconducting.

The minimal emittance in this lattice is given by the formula

$$\varepsilon^*_{x\,TBA} = \frac{55}{32\sqrt{3}} \frac{h}{2\pi m_e c} \frac{\gamma^2}{J_x} \frac{\frac{I_c}{\rho_c^3} + \frac{I_k}{\rho_k^3}}{\frac{\varphi_c}{\rho_c} + \frac{\varphi_k}{\rho_k}} \qquad (1)$$

where h - Planck's constant ($6.6261 \cdot 10^{-34}$ J·s);l

m_e - electron mass ($9.1094 \cdot 10^{-31}$ kG);

c - speed of light in vacuum ($2.9979 \cdot 10^{8}$ m/s);

J_x - damping coefficient of the radial tune,

I_c and I_k - integrals $\int_0^{L_i} H\, ds$

$H = \gamma_x \eta_x^2 + 2\alpha_x \eta_x \eta_x' + \beta_x \eta_x'^2$

α_x, γ_x - Twiss's parameters,

β_x, η_x - amplitude and dispersion functions of the storage ring;

β_x', η_x' - derivatives of β_x, η_x in the longitudinal coordinates, respectively;

ρ_c and ρ_k - radii, φ_c and φ_k are the beam bending angles for central and external magnets, respectively.

As is seen from formula (1), the lowest emittance can be attained only by minimizing I_c, because ρ_c is considerably smaller than ρ_k.

We have analysed the possibility of extending the special range of photon beams from the dipole magnets of the ISI-800 storage ring [2] by replacing the central magnet of the TBA cell with the superconducting one, whose field is 7 times higher than the fields in the outer magnets of the cell. The traditional and modified superperiods of the ISI-800 are schematically shown in fig.1.

0-7803-3053-6/96/$5.00 ©1996 IEEE

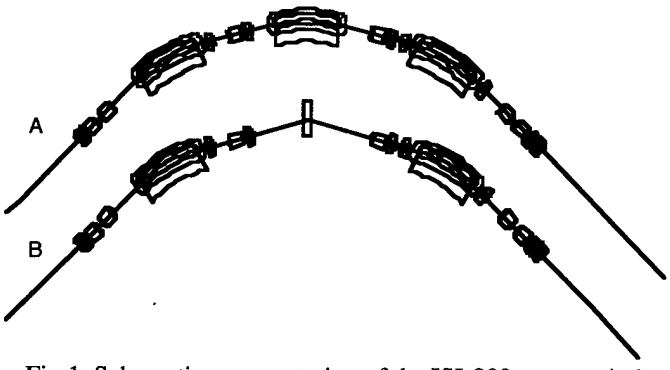


Fig.1. Schematic representation of the ISI-800 superperiod (A - traditional, B - modified).

Substituting the relationships $7\rho_c = \rho_k$ and $\varphi_c = \varphi_k$ into formula (1), we obtain

$$\varepsilon^*_{x\,TBA} = \frac{55}{32\sqrt{3}} \frac{h}{2\pi m_e c} \frac{\gamma^2}{J_x} \frac{343 I_c + 2 I_k}{9\rho^2 \varphi} \qquad (2)$$

The procedure described in [1] can be used to derive the followingexpression for I_c:

$$I_c = \gamma_0 \eta_0^2 \frac{L}{2} - 2\gamma_0 \eta_0 \rho \left(\frac{L}{2} - \rho \sin \frac{L}{2\rho} \right) + \frac{1}{2} \beta_0 \frac{L}{2}$$

$$- \frac{1}{4} \beta_0 \rho \sin \frac{L}{\rho} + \frac{3}{4} \gamma_0 \rho^2 L - 2\gamma_0 \rho^3 \sin \frac{L}{2\rho} + \frac{1}{4} \gamma_0 \rho^3 \sin \frac{L}{\rho} \qquad (3)$$

Proceeding from the condition that in the symmetry plane (in the centre of magnet) $\alpha_0 = 0, \rightarrow \gamma_0 = \frac{1}{\beta_0}$, and finding the minima $\frac{\partial I_c}{\partial \eta_o} = 0, \quad \frac{\partial I_c}{\partial \beta_o} = 0,$ we may obtain

$$\eta_0^* = \rho - \frac{2\rho^2}{L} \sin \frac{L}{2\rho};$$

$$\beta_0^* = \sqrt{\frac{3L\rho^2 - \rho^3 \left(8 \sin \frac{L}{2\rho} + \sin \frac{L}{\rho} \right) - 2L\eta_0^{*2}}{L - \rho \sin \frac{L}{\rho}}} \qquad (4)$$

The substitution of the L and ρ values chosen for the ISI-800 into these expressions gives $\eta_0^* = 0.022$ m, $\beta_0^* = 0.1358$ m.

The contribution of the central magnet to the emittance value at a beam energy of 0.8 GeV is calculated to be $\varepsilon_x^* = 1 \cdot 10^{-8}$ mrad.

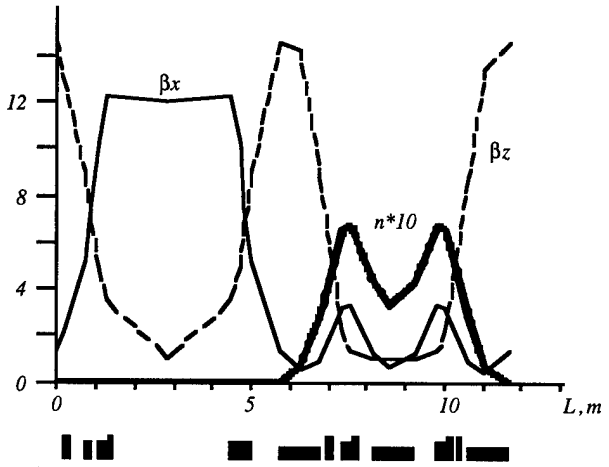


Fig.2. Structural functions of the traditional TBA cell.

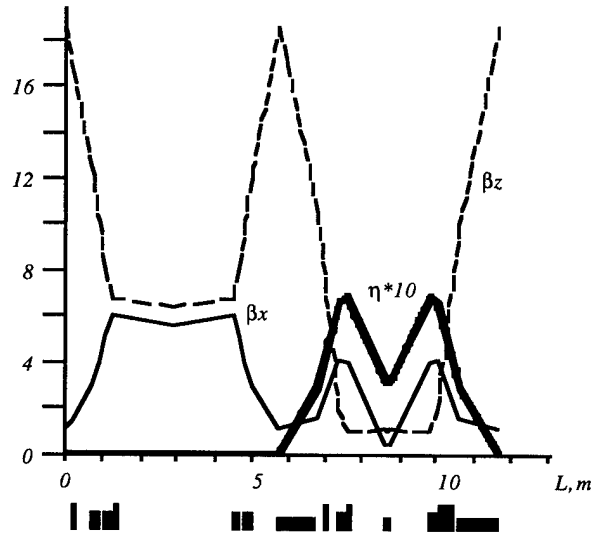


Fig.3. Structural functions of the modified TBA cell.

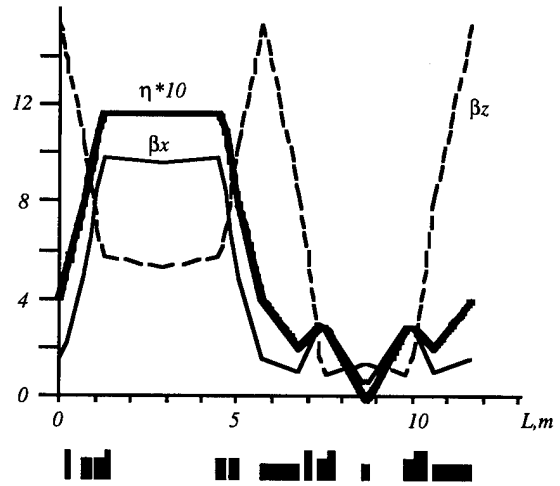


Fig.4. Structural functions of the modified TBA cell under low emittance conditions.

Figures 2, 3 and 4 show the structure functions computed with the DeCA code for the traditional TBA cell and the modified TBA cell of the ISI-800 storage ring [3]. It is seen that in the centre of the middle magnet the relations

$\eta_0 \approx \eta_0^*$, $\beta_0 \approx \beta_0^*$ can be provided only under operating conditions of nonzero dispersion in long straight sections (fig.4). The contribution of the middle superconducting magnet to the emittance value is close to the predicted value ($\varepsilon_x^* = 2 \cdot 10^{-8}$ mrad). For comparison, Table 1 lists the values of the parameters for different variants of the ISI-800 storage ring lattice.

Table 1 Lattice parameters of the ISI-800 storage ring

The simulation of the dynamic aperture of the storage ring with a modified lattice shows that the presence of the superconducting central magnet in the TBA lattice exerts no essential influence on the aperture value.

Thus, from the comparison between the characteristics of the ISI-800 based on traditional "warm" magnets with special inserts (of wiggler type) and the combined lattice with the central The simulation of the dynamic aperture of the storage ring with a modified lattice shows that the presence of the superconducting central magnet in the TBA lattice exerts no essential influence on the aperture value.

Thus, from the comparison between the characteristics of the ISI-800 based on traditional "warm" magnets with special inserts (of wiggler type) and the combined lattice with the central superconducting magnet in the TBA cell it is evident that the latter has the following advantages:

(i) a greater number of channels for photon beams with a hard spectrum;

(ii) a wide range of beam emittance variation with the storage ring tune remaining the same (ε_x=$4 \cdot 10^{-8} \div 6 \cdot 10^{-7}$ mrad);

(iii) physically, the superconducting dipole magnet is considerably easier in manufacture than the wiggler is;

(iv) the influence of superconducting dipole magnets in the centre of the TBA cell on the beam dynamics and the actual aperture is insignificant because of the smallness of the structure functions at the place of magnet location.

The construction of the synchrotron radiation source ISI-800 with the combined TBA cell as a basis will ensure the conduction of photon beam studies in the ranges of vacuum ultraviolet and hard X-ray radiation.

REFERENCES

1. H.Wiedemann "Storage Ring Optimization" 1991' in Handbook on Synchrotron Radiation, vol. 3, ed. G.S.Brown, D.E.Moncton (North-Holland, Amsterdam) ch.1

2. V.Bar'yakhtar, E.Bulyak, et al. "A Source of Synchrotron Radiation for Research and Technology Applications" *Proc.PAC93 (Washington, 1993)*

3. P.G, A.Zelinsky, M.Strelkov "The Application Package DeCA for Calculating Cyclic Accelerators" *Proc.PAC93 (Washington,*

Parameter	TBA	Modified TBA	Modified TBA with a low emittance
Nominal energy, MeV	800	800	800
Stored current, mA	200	200	200
Circumference, m	46.729	46.815	46.815
Number of dipole magnets	12	8+4	8+4
Radius of magnet bend, m	2.005	2.005/0.267	2.005/0.267
Magnet length, m	1.05	1.05/0.14	1.05/0.14
Betatron numbers, ν_x/ν_z	4.26/3.20	4.26/3.20	4.26/3.20
Momentum compaction factor, α	0.025	0.023	0.021
Natural chromaticity, ξ_x/ξ_z	-7.27/-7.24	-6.2/-6.7	-6.2/-6.7
Damping times $\tau_x/\tau_z/\tau_s$,	8.7/13.8/9.8	7.2/7.9/4.1	8.4/9.9/5.4
Emittance, mrad	$2.7 \cdot 10^{-8}$	$6. \cdot 10^{-7}$	$4. \cdot 10^{-8}$
Beam size in the centre of the superconducting magnet σ_x/σ_z		0.54/0.25	0.15/0.07
Energy spread, %	0.058	0.122	0.125
Energy losses per turn, keV	18.3	57.4	57.4
Critical photon energy from the supercoducting magnet, keV		4.2	4.2

PROGRESS OF THE ISI-800 PROJECT

E. Bulyak, S. Efimov, A. Gevchuk, P. Gladkikh, I. Karnaukhov, S. Kononenko, V. Kozin, V. Markov,
N. Mocheshnikov, A. Mytsykov, A. Shcherbakov, Yu. Telegin, A. Zelinsky
Kharkov Institute of Physics and Technology, Ukraine

V. Molodkin, V. Nemoshkalenko, A. Shpak
Institute of Metal Physics Academy of Sciences of Ukraine

ABSTRACT

The general layout of ISI-800, a low emittance third generation machine consisting of a linac injector (120 MeV), a storage ring with 4-period TBA lattice, and intended for research and industrial applications, is presented together with a discussion of most important design considerations. Design features of magnet, vacuum, injection RF systems are described. Three straight sections are available for wigglers and undulators, and up to 24 photon beam lines may ultimately emanate from dipole magnets. The emittance is 27 nm. The dynamic aperture is sufficiently large for the injection and the stable storage of the beam.

INTRODUCTION

The use of synchrotron radiation noted for its broad continuous and highbrightness has brought the research in the fields of molecular physics, physics of condensed states of matter, chemistry, microbiology, etc. to a qualitatively higher level. In recent years, great interest has been displayed in basic synchrotron radiation sources whose physical properties along with performance parameters provide a means for handling process problems of X-ray lithography in microelectronics (photon energy $\varepsilon_\gamma \sim 1$ keV), micromechanics ($\varepsilon_\gamma \sim 6$ keV) and angiography ($\varepsilon_\gamma \sim 33$ keV). The design of a relatively cheap and compact source with the above-mentioned photon beam parameters is a complicated task, since the compactness of the source sets limits, first of all, on the electron energy, and hence, on the energy of emitted photons. This, in turn, necessitates the mounting, arrangement of special devices such as superconducting wigglers with limiting magnetic-field values of about 10 T. However, the installation of such wigglers in the storage rings with a beam energy lower than 1 Gev is impeded by an impact of magnets on the beam focusing and phase stability of the orbit in the storage ring. This makes necessary long straight sections in the lattice to accommodate the matching elements, and also imposes special requirements on the wiggler design. Furthermore, in consequence of a great distortion of the reference orbit in the wiggler ($\Delta x \sim 5$ cm at an electron energy of 0.8 GeV and a field of 10 T in the wiggler), there arise essential technological difficulties. This paper describes the concept of a SR source which can form the basis of creating the National Centre of SR [1]. Ways of realizing this concept are discussed.

MAIN STORAGE RING PARAMETERS

The upper limit of the magnetic-field strength range, at which the magnetic materials can ensure a high-quality field, is about 1.5T. Besides the radiation from bending magnets, the modern SR sources incorporate superconducting wigglers (with the field up to 10 T) to increase the energy of the photons produced. The electron beam energy of about 1 GeV allows the generation of photon beams complying with the requirements of most applications.

We came to conclusion that SR source would be a 1 GeV compact electron storage ring. Injecting energy was chosen to be 120 MeV. The traveling wave linac is intended to employ as an injector. The injector is placed below the ring to provide room for more beamlines. For this purpose the injecting system and the RF cavity share the same long straight section. The general layout of the complex is presented in Fig. 1.

The magnet lattice is responsible for both the efficient operation of the source and the SR beam quality. One of the principal SR beam parameters, i.e., brightness, is proportional to the transverse electron-beam density in the region of radiation. Therefore, it is necessary to have a beam with a minimal cross-sectional area; the lattice must ensure the minimal beam emittance and a low value of the vertical betatron function in bending magnets. The latter allows one to diminish the magnet gap, thereby reducing the cost of magnet manufacture and operation.

We have chosen the TBA lattice as providing low emittance. It consists of four superperiods. The structural formula of each superperiod has the form

$$O_1\ QD\ O_2\ QF_1\ O_3\ QF_1\ O_2\ QD\ O_1\ M\ O_4\ QF_2\ O_4\ M\ O_4\ QF_2\ O_4\ M$$

where QD, QF_i are the horizontally defocusing and focusing quadrupoles; M is the dipole magnet, O_i is the straight section; O_1=0.7 m; O_2=0.15 m; O_3=3.23 m; O_4=0.6 m.

The curvilinear part of the trajectory includes: 3 magnets, each with a bending angle of 30°, the curvature radius R=2.005 m (B=1.34 T at an electron energy E=0.8 GeV, B is the magnetic field strength at the equilibrium orbit), the field

0-7803-3053-6/96/$5.00 ©1996 IEEE

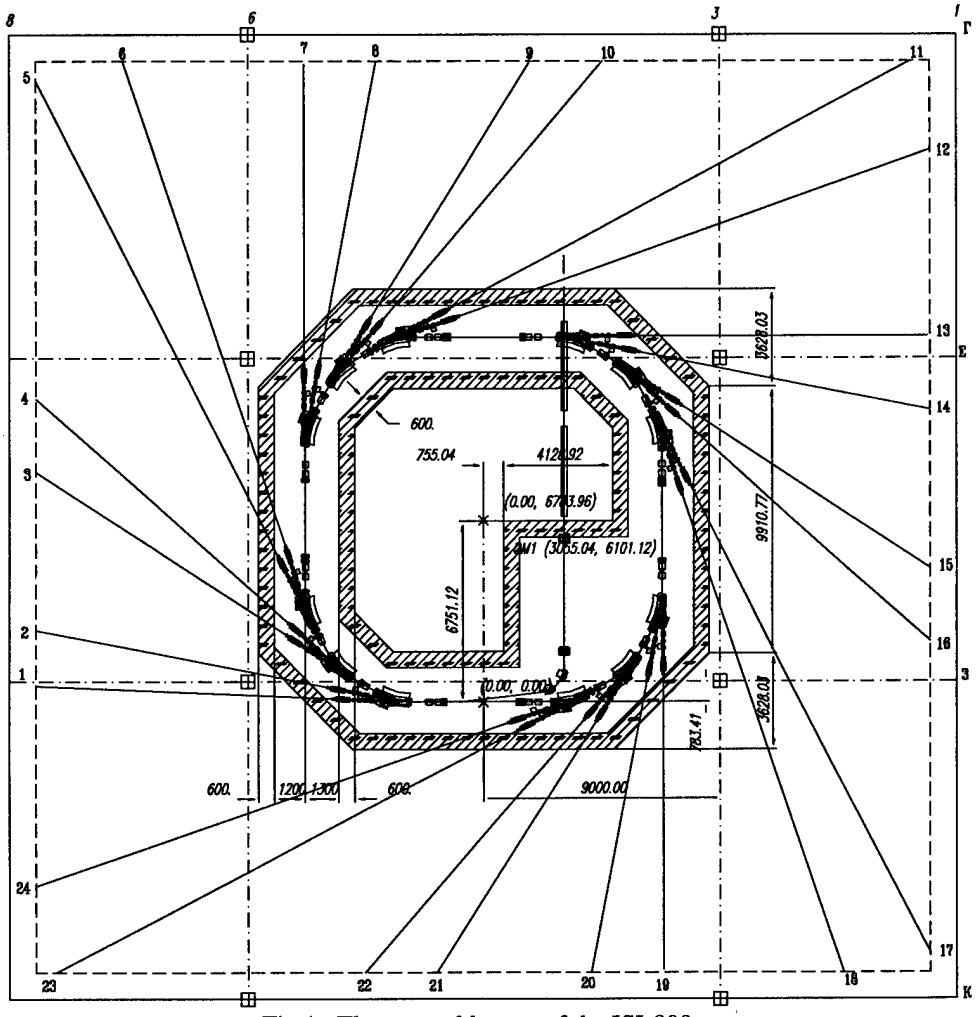


Fig.1. The general layout of the ISI-800

index n=3 and 2 focusing quadrupoles providing the achromaticity of the long straight part of the orbit.

The straight-line part of the trajectory comprises four quadrupole magnets which ensure the stability of radial and vertical motion in combination with two quadrupole magnets and vertically defocusing dipole magnets. Fig. 2 shows the machine functions of the superperiod for the zero dispersion function in the long straight section.

The phase advance for the focusing period is $\mu_x = 6.666$ and $\mu_z = 5.026$ for radial and vertical oscillations, respectively. These values correspond to the tunes $Q_x = 4.25$ and $Q_z = 3.20$. Since the vertical focusing is mainly

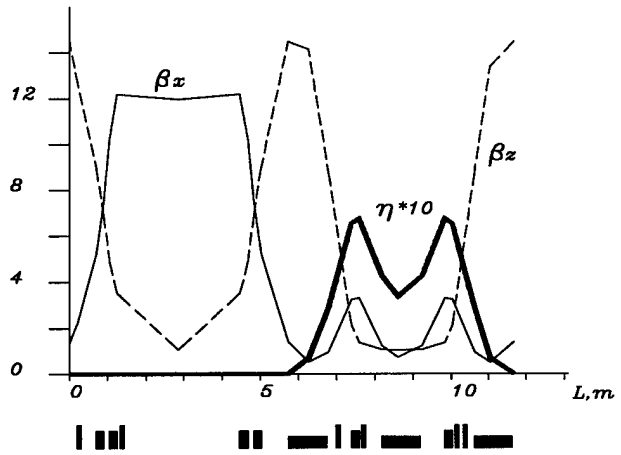


Fig. 2. The machine functions of a superperiod.

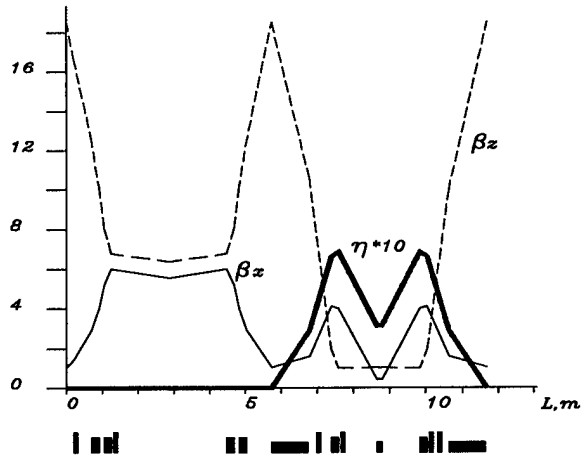


Fig.3 Machine functions of the modified TBA cell.

accomplished by gradient dipole magnets, this provides the smallest value of the betatron radial function β_x in the

magnet, and hence, the minimum radial size of the beam. The radiation emittance is $\varepsilon_x=2.7\cdot10^{-8}$ mrad (E=0.8 GeV) for the steady-state energy straggling $\Delta p/p=5.88\cdot10^{-4}$ (E=0.8 GeV).

The operating conditions of the SR source are characterized by a low radiation emittance attained due to a higher rigidity of the magnet lattice. This has resulted in the increased natural chromaticity, the compensation of which requires the mounting of sextupole lenses arranged in the sections with a nonzero dispersion. At large betatron amplitudes the presence of sextupole fields leads to the occurrence of undesirable nonlinear effects, which significantly decrease the dynamic aperture. The simulation has resulted in the following conclusions:

- the inclusion of sextupole lenses to correct the dynamic aperture appreciably increases the latter both in the absence and presence of sextupole perturbations in the dipole magnet;
- with the corrected equilibrium orbit and the compensation lenses switched on the dynamic aperture exceeds the geometric one, and therefore, will not affect the beam parameters.

The dynamical aperture values calculated at the same conditions by the code DeCA [3] (200 particles, 50 turns) - curves 2. The approach described above considers the effects of sextupoles on the lattice only. To take into consideration other effects such as higher-order multipole errors, excitation and alignment errors numerical tracing simulation is performed with DeCA. The final choice of the sextupole strengths is based on the results of computer simulation.

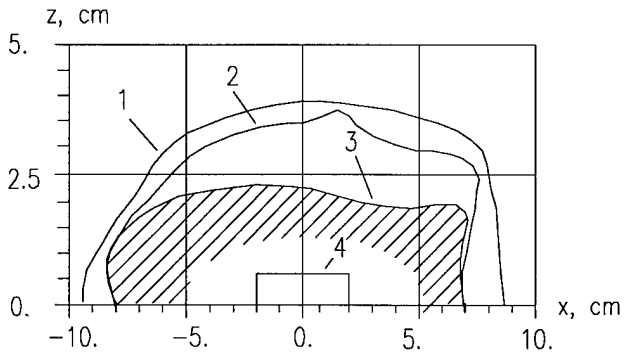


Figure 4. Dynamical aperture in the middle of the insertion straight section for the normal operation mode. 1- Analytical calculations of dynamucal aperture with consideration of the combined action of first-and second-order resonances and the tune shift depending on amplitude. 2- Dynamical aperture obtained by numerical calculations (200 particles, 50 turns) if only regular sextupoles exist. 3- Dynamical aperture obtained by numerical calculations if systematic multipole errors are occur. 4- Geometrical aperture in the middle the straight section. The hatched region corresponds uncertainly region of dynamical aperture.

The multiple injection chosen for this design consists in the following. The beam from the injector is horizontally introduced, via the transport system, to the vacuum chamber of the ring, where it is bent by the necessary angle with the help of the septum magnet. By the moment of injection of the next beam portion the orbit of the ring in the region of injection comes closer to the septum. After trapping the necessary number of turns, the orbit is restored, the initial betatron oscillations are damped.

To produce high-brightness photon beams with a sufficiently high energy, we also considered a compact storage ring with the lattice based on the combined TBA cell ("warm" and superconducting magnets), where the central dipole magnet of the cell is superconducting.

The contribution of the central superconducting magnet (field is 10 T) to the emittance value at a beam energy of 0.8 GeV is $\varepsilon_x=2\cdot10^{-8}$ mrad.

Fig. 3 shows the machine functions for the the modified TBA cell of the ISI-800 storage ring. For comparison, Table 1 lists the values of the parameters for different variants of the ISI-800 storage ring lattice.

Table 1

Parameters of the ISI-800 storage ring

Parameter	TBA	Mod TBA
Nominal energy, MeV	800	800
Stored current, mA	200	200
Circumference, m	46.729	46.815
Number of dipole magnets	12	8+4
Radius of magnet bend, m	2.005	2.005/0.27
Magnet length, m	1.05	1.05/0.14
Betatron numbers, ν_x/ν_z	4.26/3.20	4.26/3.20
Compaction factor, α	0.025	0.021
Nat chromaticity, ξ_x/ξ_z	-7.27/-7.24	-6.2/-6.7
Damping times $\tau_x/\tau_z/\tau_s$,	8.7/13.8/9.8	8.4/9.9/5.4
Emittance, mrad	$2.7\cdot10^{-8}$	$4.\cdot10^{-8}$
Beam size in centre of SC		0.15/0.07
Energy spread, %	0.058	0.125
Losses per turn, keV	18.3	57.4
Crit. energy SC, keV		4.2

The simulation of the dynamic aperture of the storage ring with a modified lattice shows that the presence of the superconducting central magnet in the TBA lattice exerts no essential influence on the aperture value.

The synchrotron light generated by the electron beam with current up to 200 mA and the radiation emittance of $2.7\cdot10^{-8}$ m·rad would be utilized by beam lines. Each line will provide the light beam with spectral brightness of $(2\text{-}9)\cdot10^{20}$ phot /(m^2·rad^2) within 0.01% bandwidth. We have designed the general purpose beamline. This project allows one to assemble dedicated beamline (for, e.g., photolithography, EXAFS, x-ray material analysis, etc.). The radiation from both conventional magnet dipoles and wigglers as well would be utilized through this line.

The beamline is supposed to operate in following modes:

1. X-ray lithography beamline (comprises from no optical elements inside). Transverse beam dimensions could be achieved within the range of 0-30 mm.

2. The line with the turnable flat grid will be applied for experiments in physics and chemistry. This line comprised few optical elements covers photon frequency from VUV to the soft x-ray.

3 The toroidal grid monochromator line will be used in experiments requiring large photon flux and moderate resolution.

4. X-ray transmitting microscope.

5. The coronal angyography line.

The dipole magnet will have a conventional C type cross section. The rectangular magnet will be laminated, the laminates are 1.5 mm thick. The good-field region extends to ± 15 mm horizontally. The dipole parameters are given in Table 2.

Table 2

Parameters of dipole magnet

Number of dipoles	12
Length, m	1.05
Field strength (E=800 MeV), T	1.34
Horizontal good field, mm	30
Vertical good field, mm	20
Field index	3
Gap, mm	36
Pole width, mm	110
Number of turns in the winding	48
Cond cross section (12.5*12.5Ø7.5), mm^2	99.5
Exciting current range, kA	0.16÷1.1
Magnet weight, kG	2000

24 quadrupole magnets are grouped in three families with 8 in each, the lenses in a family being connected in series. The poles of all the lenses are of one and the same profile The bore diameter is 50 mm and length is 20 cm for all quadrupole magnets.

The ISI-800 magnet lattice contains 4 families of sextupoles, total 24 magnets. To compensate the negative chromaticity $\xi_{x,z}$, which is equal to -7.14, -7.36, four sextupole magnets are mounted at the curvilinear part of the trajectory of each superperiod and two sextupole magnets in the achromatic part of each superperiod correct the dynamic aperture. The aperture radius of sextupoles is 28 mm, with a pole width of 28 mm. The magnets are capable of producting a field of 200 T/m^2 over a length of 0.1 m. The sextupole weight is 70 kG. In addition to the main coils mounted on the poles, there are six back-leg coils which, given the correct excitation, can generate vertical and horizontal dipole fields with maximum corrector strength: vertical 3 mTm, horizontal 3 mTm.

The synchrotron radiation facility ISI-800 will have a transfer line which has been designed for transporting 120 MeV electrons from the linac to the storage ring. The transfer line includes 4 dipole magnets (rectangular, C-type, bend angle is 41.5 degrees, length is 29 cm), 9 quadrupole magnets (length is 10 cm, gradient is 15 T/m) and 4 bidirectional steering magnets.

Correction of the storage ring orbit is accomplished by 8 horizontal, 8 vertical sextupole steering elements (combined with the sextupoles) in the curvilinear part of the orbit and 8 bidirectional dipole steering magnets distributed in the straight sections (length is 10 cm, field is 0.03 T).

Beam energy losses by synchrotron radiation and parasitic losses in the vacuum chamber walls are compensated with the help of a 10 kW RF (699.3 MHz) system. The accelerating voltage of 200 kV chosen in view of the Touschek lifetime, is provided by a single half-wave cavity, whose shape has been optimized against the shunt resistance at the main (operating) mode (Ω-cavity). As calculations and measurements indicate, this cavity has lower coupling impedances at higher-order modes than the cylindrical cavity has and, therefore, is less sensitive to the excitation of coupled oscillations of bunches.

Based on the reasonable 6-hour life of the zero-intensity beam we come to the conclusion that the residual gas pressure in the chamber should not exceed $5 \cdot 10^{-9}$ Torr throughout the range of circulating currents at an operating energy of the beam. Pumping is produced by 40 sputtering 400 l/s pumps placed on the dipole magnet chambers and by the end of the defocusing quadrupole magnets.

Sixteen pickup stations and a current transformer are used to monitoring the beam in the storage ring.

CONCLUSION

The design of the magnet, the vacuum, the RF and the indicating systems is completed. Also we have the project of the injector and the building.

Now we work on the modified TBA lattice, the beamlines, the design of the superconducting dipole magnet and the wiggler.

We have got the goverment decision about the construction of the synchrotron radiation source ISI-800 for Ukrainian National Synchrotron Center.

REFERENCES

[1] Bar'yakhtar V. et al., "A Source of Synchrotron Radiation for Research and Technology Applications" PAC93, Washington, 1993; E. Bulyak et al, "Synchrotron radiation source", HEPACC-92, Hamburg, 1992.

[2] E.Bulyak, A.Gevchuk, P.Gladkikh, I.Karnaukhov, S.Kononenko, A.Mytsykov, A.Shcherbakov "The magnet system of the synchrotron radiation source ISI-800", MT13, Vancouver, 1993

[3] Gladkikh P.I. et al. DeCA - code for analysing and designing of cyclic accelerators, Proc. EPAC-90, v.2, p.1234-1236.

Reduction of Open-Loop Low Frequency Beam Motion at the APS*

G. Decker, Y.G. Kang, S. Kim, D. Mangra, R. Merl, D. McGhee, S. Sharma
Advanced Photon Source, Argonne National Laboratory
9700 South Cass Avenue, Argonne, Illinois 60439 USA

Abstract

The Advanced Photon Source (APS) 7-GeV positron storage ring at Argonne National Laboratory (ANL) produces high brilliance bending magnet and insertion device x-rays for up to 70 x-ray beamlines. To efficiently make use of the storage ring's high brilliance, an extremely tight tolerance has been placed on positron beam stability, namely that the beam be stable to a level which is less than 5% of its rms size. This requirement amounts to ± 4.4 microns rms in the vertical plane and ± 17 microns horizontally, assuming 10% coupling. While real-time closed orbit feedback (discussed elsewhere in these proceedings) will be employed to exceed the required stability requirement, efforts are underway to identify and reduce sources of beam motion in the absence of feedback. These sources include ground- and water-system-induced vibrations in addition to power supply jitter and drift. Results to date of this effort will be presented.

I. INTRODUCTION

The low frequency beam stability requirements at the APS are very strict, namely that rms positron beam motion at the insertion device straight sections (β_x = 14.2 meters, β_y = 10.0 meters) be less than 4.4 microns vertically and 17 microns horizontally in a bandwidth 1-50 Hz. Sources of beam motion in this band are magnet vibrations induced by ground motion and water flow, and power supply noise from the large number of corrector power supplies installed in the ring.

The APS magnets are arranged in 40 similar sectors, each including five different girder designs. Three quadrupoles in a defocusing-focusing-defocusing (DFD) pattern, a sextupole, and two combined function vertical horizontal correctors are mounted on the first and fifth girder in each sector. Girder three holds four quadupoles in a DFFD arrangement, one sextupole, and two correctors. Girders two and four each support a dipole, two sextupoles, and a corrector. Each girder additionally supports an aluminum extruded vacuum chamber with a fixed tri-axial support near the center and two leaf-spring-type supports which allow thermal expansion during bakeout but which also constrain transverse chamber motion. The chambers are not mechanically coupled to the magnets except via their attachment to the girder. The particle beam height is nominally 1.4 meters above the floor.

Each girder is supported by three wedge jack supports mounted on two fixed pedestals grouted to the storage ring enclosure floor. Two jacks are near one end of the girder on one pedestal and at the other end is the pedestal with the single jack support. Shown in Fig. 1 is an end view of a girder 5. Visible are the pedestal, two wedge jacks, the box-frame girder, a six-pole combined function vertical-horizontal corrector magnet, and the storage ring vacuum chamber.

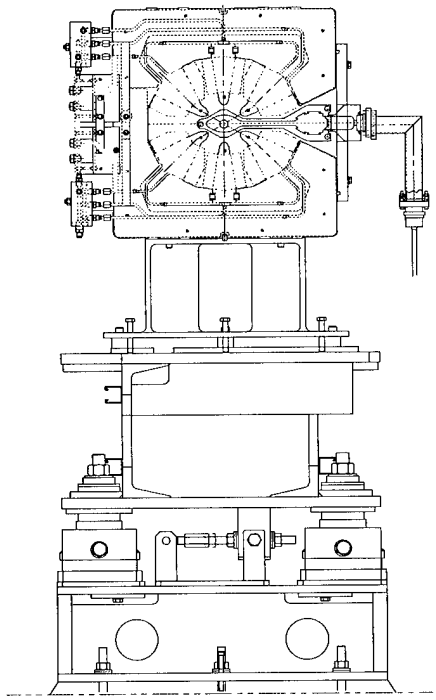


Figure 1: APS Storage Ring girder support structure

Considerable effort has been invested over the past several years toward understanding the ground motion environment at the APS and its impact on magnet motion, primarily regarding the strong focusing quadrupoles which have a large steering effect for even the smallest transverse motion. For this reason, the odd-numbered girders have been studied most extensively, as they support all of the quads.

Lattice modeling [1] indicates that random uncorrelated quadrupole motions of rms amplitude Δx_q result in rms beam motion of amplitude 17.3 $\sqrt{\beta_x}\ \Delta x_q$. Since β_x = 14.2 at the insertion device source points, this amounts to a relatively large amplification factor of 65, a consequence of the strong-focusing low-emittance lattice. Fortunately, because each girder supports a quad triplet (the central two quads on girder 3 are both horizontally focusing), the situation is not quite so severe, since the dominant girder vibration mode involves correlated motion for all magnets on a girder [2]. For random uncorrelated rms transverse girder motion Δx_g, where all quads on the same girder move together, the beam motion is given by $\Delta x_b = 5.2\ \sqrt{\beta_x}\ \Delta x_g$, yielding an amplification factor at the insertion device source point of 19.6.

* Work supported by the U.S. Department of Energy, Office of Basic Energy Sciences, under Contract No. W-31-109-ENG-38.

0-7803-3053-6/96/$5.00 ©1996 IEEE

II. GIRDER VIBRATION

An outside contractor was brought in to measure and analyze ambient and driven girder vibration modes when the first production girders became available. Several girder assemblies were installed in the storage ring enclosure and instrumented with as many as 50 vibration transducers each over the course of a few weeks.

While many vibrational modes were discovered during the course of these measurements, the bottom line was that the quad girders are dominated by their lowest frequency mode at approximately 12 Hz for girders 1 and 5 and 10.5 Hz for girder 3. This mode is a horizontal bending mode, involving the quadrupoles essentially pivoting about the wedge jack supports as viewed in Fig. 1. The Q of these modes was approximately 100. Motion of the quad nearest to the single jack end is larger than at the double jack end of the girder by 50 to 100%. This induces a girder yaw component which was modelled and found to be a factor of 5 less important than the common mode transverse quadrupole motion [1].

Vertical magnet motion is much smaller in comparison to horizontal, the main mode of significance being a 45-Hz "bounce" mode where the end quads are stationary and the center quad(s) move vertically. While this mode shape is damaging given the FDF field pattern, the amplitude is very small and ground motion excitation in this band is also small.

These early studies were performed prior to the introduction of cooling water in the tunnel enclosure, and the ambient motion was exclusively driven by ground motion. Depending on the amount of activity taking place in the tunnel and on the adjacent experiment hall floor, rms ground motion in the tunnel varies from below 5 nm 4-50 Hz in the dead of night to as high as 100 nm during high activity days. This translated into horizontal quad motions as high as 0.5 microns 4-50 Hz which result in exceeding the beam stability specification. The specification for quadrupole motion is that the rms quadrupole motion be less than 113 nm in the band 4-50 Hz. This specification should keep beam motion to less than 19.6 x 113 nm = 2.2 microns, which conservatively meets the beam stability requirements even in the presence of 100% vertical horizontal coupling. Frequencies below 4 Hz were not included in the specification since ground motion is largest here and feedback is expected to work most effectively at low frequency.

Many techniques for reducing the horizontal magnet motion were attempted, with the best overall solution being to introduce a "sandwich" of visco-elastic material between the wedge jack supports and the pedestals. This material is ubiquitous and commonly found on everyone's desktop in the form of transparent adhesive tape. Assemblies of this material sandwiched between steel plates produce excellent damping of low-frequency vibration both under shear and in compression. The configuration chosen for the APS is a "double-decker" sandwich using three steel plates and two 0.006" thick layers of Anatrol 216 visco-elastic material. These vibration pad assemblies are easily installed below the wedge jack supports with minimal impact on girder alignment. The effect of these damping pads is to reduce the Q of the lowest horizontal mode by roughly a factor of 10, and the ground-motion-induced rms motion 4-50 Hz by a factor of about 5. Figures 2 and 3 show typical horizontal magnet motion spectra taken simultaneously at similar locations in adjacent sectors, one with (sector 28) and the other without (sector 27) damping pads installed. The data were collected under operating conditions with magnet coolant water flowing. Figure 2 integrated yields 217 nm rms 4-54 Hz, while Fig. 3 gives 118 nm.

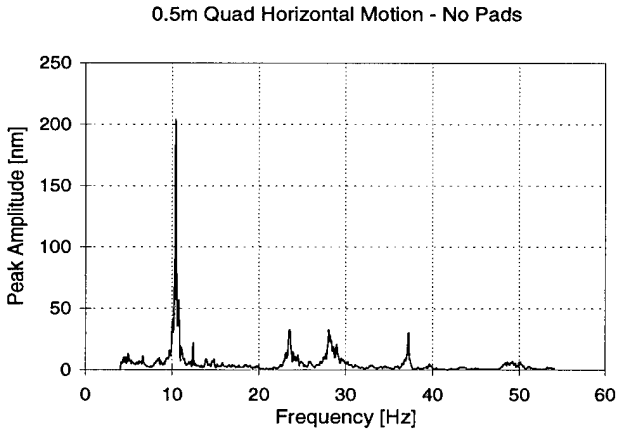


Figure 2: Quadrupole horizontal motion spectrum, no pads.

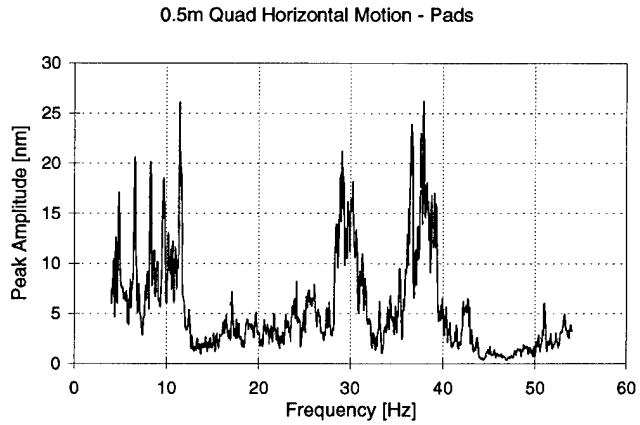


Figure 3: Quadrupole horizontal motion spectrum, with pads.

The integrated motion shown in Fig. 3 with water flowing, damping pads installed, and using the as-built water distribution system, was found to decrease from 117 nm rms to 42 nm rms when the water flow was stopped. This reduction occured primarily in the 6- to 12-Hz bands and at the broad structures seen near 30 and 38 Hz, respectively.

III. WATER-FLOW-INDUCED VIBRATION

Water distribution in the storage ring tunnel enclosure is accomplished via headers mounted to the ceiling and attached to magnets, synchrotron radiation absorbers, and vacuum chambers via both flexible and rigid connections. This is a large source of vibration excitation for the girders, as shown in Fig. 4, which indicates the effects of turning pumps off and back on in two adjacent storage ring sectors, one with vibration damping pads (sector 10), the other without (sector 11). The legend "S10 0.5 m X" conveys that this data is for a 0.5-meter-

long quad in sector 10 in the horizontal plane and similarly for sector 11. Note that the sector without pads shows a strong response to water flow.

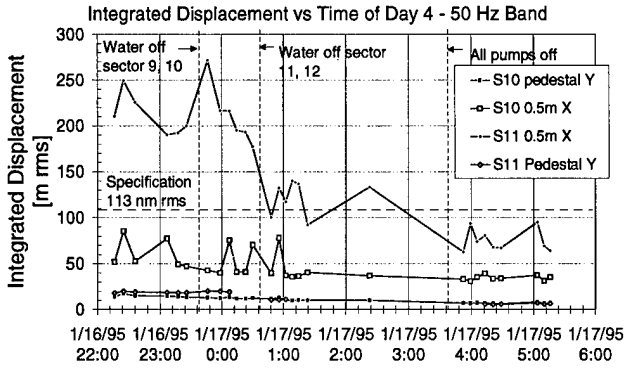


Figure 4: Effect of water flow on rms magnet motion

A major difference between this data and that of Figs. 2 and 3 is that, in addition to the inclusion of damping pads in sector 10, the overhead water distribution headers were reinforced by using closely spaced tabs welded to the pipe which were in turn bolted to the ceiling at approximately 3-foot intervals. This had the effect of reducing the pipe vibration from 12 microns rms 4-50 Hz to 3 microns. The spectrum of pipe motion before reinforcement was dominated by a broad resonance structure, centered in the 6- to 12-Hz band which was found to exacerbate the girder resonances. This feature is virtually eliminated by header reinforcement.

IV. STEERING CORRECTOR NOISE STUDIES

First turn trajectory and closed orbit correction is accomplished in the APS storage ring using 317 corrector power supplies [3] in each plane powering the 317 combined function vertical/horizontal corrector magnets [4]. These correctors are required to be relatively strong, ±150 Amps corresponding to more than ±1 mrad of steering to overcome eddy currents in the aluminum vacuum chamber for AC operation, while at the same time maintaining very low noise so as not to stir up the beam. The very large number of supplies makes this noise requirement even more restrictive since the beam motion noise contributed to by a single supply gets increased by a factor $\sqrt{317}$, assuming that the 317 correctors each make random contributions to beam jitter.

The specification for APS corrector power supplies is that the rms noise current in the band 1-10Hz be less than 0.6 mA. If all correctors operate at this specification and are uncorrelated, resulting beam motion will be less than 1 micron rms in the same band. Additionally, 40 of the correctors have thin-walled Inconel spool pieces in their bore and are to be used for wide-band (up to 100 Hz) orbit feedback. These correctors must generate a low amount of noise in a wider bandwidth. Noise studies on these wide-band correctors is underway.

Early measurements on a few correctors in their final configuration have been performed and indicate that over a large fraction of their dynamic range, the noise specification is met. The spectrum is generally flat in the 1-10 Hz band of interest, i.e. the noise power per unit frequency (power spectral density, or PSD) is constant. Many variables involving the detailed construction of the supplies have been investigated, including changing the regulation from shunt feedback to transductor feedback and employing a linear control power supply in place of the present switching unit. Additionally, the effects of cross talk between power supplies housed in the same cabinet have been investigated. The measurement of electrical noise at these low levels is complicated by the hostile noise environment inside and near the convertor cabinets. In-tunnel measurements of both current and field have been performed, using current transductors and Hall probes. Operating conditions of some units have been found with power supply noise as large as 2.5 mA rms, i.e., 4 times specification. This would imply beam motion near 4 microns rms, which is not in violation of the beam stability specification; however, all sources cumulatively must allow the beam motion specification to be met. Work is continuing in this area.

V. CONCLUSION

Substantial progress has been made in the area of reducing magnet vibrations resulting from ground motion and water flow. A factor of at least ten reduction in the Q of the lowest girder vibrational mode has been achieved by using sandwiched visco-elastic material installed at the girder support pedestal/ jack interface. The vibration specification for girders appears to be achievable. Installation of vibration reduction pads will be complete this year, followed by the effort to reinforce the water header system. Corrector power supply noise-induced beam excitation is under investigation, and measurement techniques are in hand.

VI. REFERENCES

[1] E. Crosbie, ANL, private communication.

[2] "Analysis of the Vibration on the APS," Roush-Anatrol Noise and Vibration Engineering, Cincinnati, OH, Report No. 94092, 1994.

[3] Y. Kang, "Design and Development of a Bipolar Power Supply for APS Storage Ring Correctors," *Proc. of the 1993 Particle Accelerator Conference*, pp. 1268-1270, 1993.

[4] G. Decker, "APS Storage Ring Commissioning and Early Operational Experience," these proceedings.

HORIZONTAL -VERTICAL COUPLING CORRECTION AT ALADDIN

R. A. Bosch and W. S. Trzeciak, Synchrotron Radiation Center
University of Wisconsin, 3731 Schneider Dr., Stoughton, WI 53589

Horizontal-vertical coupling and vertical dispersion can arise from vertical misalignments and tilts of bending magnets, quadrupoles, and sextupoles. Experimental measurements and accelerator code studies suggest that the vertical dispersion from bending magnet errors and quadrupole height errors is largely compensated by optimization of the vertical closed orbit. The majority of the coupling and vertical dispersion remaining after orbit optimization may be the result of quadrupole tilts on the order of 1-2 mrad. A correction scheme is being implemented in which the excitation of skew-quadrupole correctors is determined from measurements of the vertical orbit displacements resulting from horizontal steering bumps and vertical dispersion [1].

I. INTRODUCTION

In an ideal electron storage ring, the horizontal and vertical motions are independent, resulting in an extremely small beam height. In practice, ring imperfections result in a coupling of horizontal and vertical transverse oscillations (betatron coupling) as well as vertical motion associated with energy oscillations (vertical dispersion). The coupling and vertical dispersion then determine the beam height.

The vertical emittance ($\varepsilon_y \equiv \langle y^2 \rangle / \beta_y$) characterizes the excitation of vertical betatron motion. As a result of coupling, both transverse oscillation modes include vertical motion, and both modes are excited by photon emission in bending magnets. With non-zero vertical dispersion in bending magnets, photon emission excites vertical motion even in the absence of coupling. These effects give rise to vertical emittance [2]. In addition, vertical dispersion contributes to the height because of the beam energy spread.

Rotations of bending magnets and quadrupoles and vertical orbit offsets in sextupoles cause betatron coupling and vertical dispersion. Vertical dispersion is also caused by vertical misalignment of bending magnets and quadrupoles.

II. SOURCES

Experiments and modeling have been performed to study the sources of coupling and vertical dispersion. For normal 800 MeV operation ($\nu_x = 7.14$, $\nu_y = 7.23$, optimized orbit, sextupoles on), the rms vertical dispersion is $D_y^{rms} = 0.03$ m, while the emittance ratio ($\kappa = \varepsilon_y/\varepsilon_x$) equals 0.014. The coupling associated with the nearby $\nu_x = \nu_y$ resonance (global coupling) gives rise to a minimum tune separation, $\delta\nu_{min} = 0.009$. The global coupling contribution to the equilibrium emittance ratio is $\kappa_o = 2|\delta\nu_{min}/2(\nu_x - \nu_y)|^2 = 0.005$, about one-third of the total.

With steering magnets and sextupoles turned off, D_y^{rms} increases to 0.26 m; the minimum tune separation was not measurable because of the broadened tune signals without sextupoles. For normal 1 GeV operation, D_y^{rms} increases by 30%, while the beam height, tilt, and $\delta\nu_{min}$ increase by factors of 2-3, compared to 800 MeV values.

For historical reasons, the bending magnets were installed with measured rolls and pitches, where roll is rotation about the beam axis, and pitch is a height difference between the upstream and downstream ends of the magnet. Typical rolls are 2 mrad, and pitches are about one-tenth as great. We measured the beam properties with these errors removed. For normal 800 MeV operation, D_y^{rms} was reduced by 20%, while little or no change was observed in $\delta\nu_{min}$, the beam height or tilt. $\delta\nu_{min}$ was nearly independent of the horizontally-focusing sextupole strength, but depended upon the horizontally-defocusing sextupoles. Reducing their current from the normal 72 A to 40 A caused $\delta\nu_{min}$ to increase from 0.009 to 0.014, while a larger sextupole current of 85 A resulted in $\delta\nu_{min} = 0.007$. For the case where steering magnets and sextupoles are turned off, D_y^{rms} was 70% smaller than its value before correcting the bending magnet rotations.

We used the MAD computer code [3] to model the measured bending magnet rotations. The effects of pitch errors were negligible, but the roll errors resulted in $\delta\nu_{min} = 0.006$. (This is consistent with $\delta\nu_{min}$ equaling 0.009 both before and after removing the bending magnet rotation errors, because coupling adds as a complex number.)

MAD modeling also showed that vertical dispersion resulting from bending magnet rotations, bending magnet height errors, or quadrupole height errors may be reduced by ~ 90% when the vertical orbit is optimized, comparable to the measured reduction from 0.26 m to 0.03 m. However, vertical orbit optimization does not effectively compensate the vertical dispersion from quadrupole rolls or sextupole height errors. This is expected for quadrupole rolls because they do not affect the closed orbit in an otherwise ideal ring. Thus, for a combination of errors, the relative contribution of bending magnet errors to the vertical dispersion is expected to be less on the optimized orbit than the zero-steering orbit, as observed.

The measurements and modeling suggest that misaligned bending magnets, quadrupoles and sextupoles are all important sources of betatron coupling and vertical dispersion during normal operation. First, MAD modeling of the measured bending magnet rotations gives $\delta\nu_{min} = 0.006$, compared to a measured value of 0.009 in the ring. The experimental removal of these errors reduced the vertical dispersion by 20% on the optimized orbit. However, bending magnet rotations do not appear to be the dominant source of coupling and vertical dispersion during normal operation,

0-7803-3053-6/96/$5.00 ©1996 IEEE

since the major portion of the vertical dispersion, height, tilt, and $\delta\nu_{min}$ remained after their removal.

Sextupole current variations on the order of their normal operating current change $\delta\nu_{min}$ by a factor of two, indicating that sextupole positioning errors are also a significant cause of coupling. However, if sextupole errors were the dominant source of global coupling, the coupling would increase with sextupole current, in contrast to the measured decrease. Thus, quadrupole errors are most likely the dominant source of coupling and vertical dispersion during normal operation.

The observed beam height, tilt, and $\delta\nu_{min}$ increase dramatically when the ring energy is increased from 800 MeV to 1 GeV, while the vertical dispersion increases only 30%. This suggests that coupling, and not vertical dispersion, is the dominant source of the beam height. This conclusion is confirmed in the next section by estimates of the beam height from the measured values of $\delta\nu_{min}$ and D_y^{rms}.

We estimated the magnet positioning errors required for the observations. Bending magnet roll errors of order 2 mrad and pitch errors of order 0.2 mrad were measured before the storage ring was assembled. Quadrupole roll errors of order 1 mrad and sextupole height errors of order 1 mm are expected to give a contribution to $\delta\nu_{min}$ and D_y^{rms} comparable to the 800 MeV observations. At 1 GeV, the errors must be 2-3 times as large to account for the observed coupling, perhaps a result of current-induced stress in the quadrupoles.

III. EFFECTS

For a beam whose height results primarily from vertical emittance characterized by the emittance ratio $\kappa = \varepsilon_y/\varepsilon_x$, the height is $\sigma_y^{\kappa} = (\beta_y\varepsilon_y)^{1/2} = (\beta_y\kappa\varepsilon_x)^{1/2}$; its rms value is $\sigma_y^{\kappa,rms} = (\sqrt{\beta_y})^{rms}(\kappa\varepsilon_x)^{1/2}$. For a beam whose height results primarily from the energy spread and vertical dispersion, $\sigma_y^{Dy} = D_y\,\sigma_E$, and $\sigma_y^{Dy,rms} = D_y^{rms}\,\sigma_E$. When both effects contribute, $\sigma_y^2 = (\sigma_y^{\kappa})^2 + (\sigma_y^{Dy})^2$; the rms values combine in the same way.

The vertical emittance has contributions from global coupling, local coupling, and vertical dispersion in bending magnets. When the emittance is primarily a result of global coupling characterized by a minimum tune split, the equilibrium emittance ratio is $\kappa_o = 2|\delta\nu_{min}/2(\nu_x-\nu_y)|^2$. Here, $\kappa_o/2$ is the emittance ratio of the almost-horizontal eigenmode. An equal contribution to the equilibrium vertical emittance arises from excitation of the almost-vertical eigenmode by synchrotron radiation emission [2].

The coupling which is not associated with the $\nu_x = \nu_y$ resonance is termed local coupling. According to [4], errors of sufficient magnitude to cause a minimum tune split of $\delta\nu_{min}$ are expected to produce local coupling with eigenmode roll angle $|\psi| \sim \pi\,\delta\nu_{min}$. Relating this roll angle to the equilibrium emittance ratio by $\kappa = 2|\psi|^2$, we obtain the estimate $\kappa^{local} \approx 2|\pi\delta\nu_{min}|^2$.

Because this estimate is insensitive to the proximity of coupling resonances ($\nu_x \pm \nu_y$ = integer), it must be regarded as a rough approximation. We tested its validity by using MAD to track betatron oscillations in a ring with skew-quadrupole errors. For both cases modeled, elimination of global coupling with skew-quadrupole correctors (so that $\delta\nu_{min} = 0$) reduced the height of the betatron oscillation envelope by 70% for the normal operating tunes. This suggests that $\sigma_y^{\kappa local} = 0.3\,[(\sigma_y^{\kappa local})^2 + (\sigma_y^{\kappa o})^2\,]^{1/2}$, which gives $\kappa_{local}/\kappa_o = 0.10$, versus the estimate of 0.32. Thus, the estimate gives the correct order of magnitude.

When vertical dispersion in bending magnets is the primary source of vertical emittance, the emittance ratio is approximately [2] $\kappa_{Dy} = [D_y^{rms}/(\sqrt{\beta_y})^{rms}]^2/[D_x^{rms}/(\sqrt{\beta_x})^{rms}]^2$. When several sources of vertical emittance are important, an approximate calculation may be performed by combining the above formulas as $\kappa = \kappa_o + \kappa_{local} + \kappa_{Dy}$, so that $(\sigma_y^{\kappa})^2 = (\sigma_y^{\kappa o})^2 + (\sigma_y^{\kappa local})^2 + (\sigma_y^{\kappa Dy})^2$. Combining the effects of emittance and dispersion gives $(\sigma_y)^2 = (\sigma_y^{\kappa o})^2 + (\sigma_y^{\kappa local})^2 + (\sigma_y^{\kappa Dy})^2 + (\sigma_y^{Dy})^2$.

These formulas may be used to estimate the rms beam height before and after global decoupling from measurements of $\delta\nu_{min}$ and D_y^{rms}. At 800 MeV, we measured $\delta\nu_{min} = 0.009$ and $D_y^{rms} = 0.033$ m. The normal operating parameters are $(\nu_x,\nu_y) = (7.14, 7.23)$, $(\sqrt{\beta_y})^{rms} = 3.7\ m^{1/2}$, $(\sqrt{\beta_x})^{rms} = 2.4\ m^{1/2}$, $\varepsilon_x = 0.127 \times 10^{-6}$ m-rad, and $\sigma_E = 4.5\times10^{-4}$. Here, the horizontal rms values are taken over horizontal beam position monitor (BPM) positions, while vertical rms values are taken over vertical BPM locations. From the ring parameters and measurements, we estimate: $\kappa_o = 2|\delta\nu_{min}/2(\nu_x-\nu_y)|^2 = 0.005$; $\sigma_y^{\kappa o,\,rms} = (\sqrt{\beta_y})^{rms}(\kappa_o\varepsilon_x)^{1/2} = 93$ μm. $\kappa^{local} \approx 2|\pi\delta\nu_{min}|^2 = 0.0016$; $\sigma_y^{\kappa local,\,rms} = 53$ μm. $\kappa_{Dy} = [D_y^{rms}/(\sqrt{\beta_y})^{rms}]^2/[D_x^{rms}/(\sqrt{\beta_x})^{rms}]^2 = 0.00057$; $\sigma_y^{\kappa Dy,\,rms} = 31$ μm. $\sigma_y^{Dy,\,rms} = D_y^{rms}\,\sigma_E = 15$ μm. Adding the squares of the height contributions gives $\sigma_y^{rms} = 112$ μm. In the bending magnets, $\sqrt{\beta_y}$ is 68% of its rms value, and the FWHM beam height is 2.35 times the standard deviation, so that $\sigma_y^{rms} = 112$ μm corresponds to a bending magnet FWHM height of 112 x 0.68 x 2.35 = 180 μm. If the global coupling contribution is neglected, an rms height of 63 μm is obtained from the other three contributions, suggesting a 44% reduction may be obtained from global decoupling.

In comparison, we measured FWHM beam heights of 184 and 214 μm in the bending magnets, within 20% of the above estimate. When skew-quadrupole correctors were used to eliminate global coupling, the vertical dispersion was increased by 34%, the beam lifetime was reduced by 28%, and the measured heights in the bending magnets were reduced by 5% and 28%. The lifetime and height reductions are less than the 44% predicted if global decoupling did not change the local coupling or vertical dispersion.

For normal 1 GeV operation, we measured $\delta\nu_{min} = 0.026$ and $D_y^{rms} = 0.043$ m with 1 GeV parameters $\varepsilon_x = 0.15 \times 10^{-6}$ m-rad, and $\sigma_E = 6\times10^{-4}$. We estimate: $\kappa_o = 2|\delta\nu_{min}/2(\nu_x-\nu_y)|^2 = 0.042$; $\sigma_y^{\kappa o,\,rms} = (\sqrt{\beta_y})^{rms}(\kappa_o\varepsilon_x)^{1/2} = 293$ μm. $\kappa^{local} \approx 2|\pi\delta\nu_{min}|^2 = 0.013$; $\sigma_y^{\kappa local,\,rms} = 166$ μm. $\kappa_{Dy} = [D_y^{rms}/(\sqrt{\beta_y})^{rms}]^2/[D_x^{rms}/(\sqrt{\beta_x})^{rms}]^2 = 0.0009$; $\sigma_y^{\kappa Dy,\,rms} = 43$ μm. $\sigma_y^{Dy,\,rms} = D_y^{rms}\,\sigma_E = 26$ μm. Adding the squares of the height contributions gives $\sigma_y^{rms} = 340$ μm, corresponding to a FWHM beam height of 540 μm in the bending magnets. If the global coupling contribution is neglected, an rms beam height of 173 μm is obtained from

the other three contributions, suggesting a 49% height reduction may be obtained from global decoupling.

In comparison, we measured FWHM beam heights of 428 and 439 μm in the bending magnets, within 20% of the above estimate. When skew-quadrupole correctors were used to reduce global coupling by 77%, the vertical dispersion was increased by 16%, the beam lifetime was reduced by 39%, and the measured heights in the bending magnets were reduced by 45% and 54%. The lifetime and height reductions are comparable to the 49% reduction predicted if the global coupling were completely removed with no change in local coupling or vertical dispersion.

Thus, our predictions of the beam height from the measurements of $\delta\nu_{min}$ and D_y^{rms} are in approximate agreement with height measurements in bending magnets and the observed effects of global decoupling. The modeling and experimental results suggest that reducing the height by more than 50% cannot be achieved by global decoupling alone.

IV. CORRECTION

Harmonic correction is a decoupling scheme in which skew-quadrupole correctors are powered to eliminate the driving terms ("harmonics") of important coupling resonances ($\nu_x \pm \nu_y$ = integer) and vertical dispersion resonances (ν_y = integer). For example, global decoupling, in which correctors are used to obtain $\delta\nu_{min} = 0$, is the correction of the $\nu_x - \nu_y = 0$ driving term. The coupling harmonic [5] for $\nu_x \pm \nu_y = p$ is a complex number: $\Delta_p^{\pm} = (4\pi)^{-1} \Sigma\, KL(\beta_x\beta_y)^{1/2} \exp i[\varphi_x \pm \varphi_y - (\nu_x \pm \nu_y - p)\theta]$, while the vertical dispersion harmonic [6] for $\nu_y = p$ is $\Delta_p^{Dy} = (\nu_y/4\pi) \Sigma\, KL\, D_x\sqrt{\beta_y} \exp(ip\varphi_y/\nu_y)$. Here, the sum is over skew quadrupoles with integrated strength KL, where $\varphi_{x,y} = \int dz/\beta_{x,y}$ is the betatron phase and $\theta = z/R$ varies between 0 and 2π around the ring. For Aladdin, the five most important harmonics are expected to be Δ_o^-, Δ_{14}^+, Δ_{15}^+, Δ_7^{Dy}, and Δ_8^{Dy}, where $|\Delta_o^-| = \delta\nu_{min}/2$.

Ten skew-correctors are required to eliminate these five complex terms. For a given set of ten locations, we constructed a 10x10 matrix containing the real and imaginary contributions to the 5 harmonic terms for unit excitations of the skew correctors. Its inverse gives the skew-corrector strengths associated with unit excitations of the 10 harmonic terms (Re Δ_o^-, Im Δ_o^-, etc.). We selected ten locations for which this inverse had elements with small magnitude.

To model the effectiveness of harmonic correction with these locations, we studied two test lattices with rotated quadrupoles. In one lattice, the roll angles were assigned randomly from a truncated Gaussian distribution with $\sigma = 1$ mrad, maximum roll of 3σ; the other lattice was an attempt to fit roll errors to ring data. From the quadrupole roll angles, the 5 harmonic terms were calculated, along with the skew-corrector strengths necessary to cancel them out. To quantify the coupling, we used MAD to track betatron oscillations from an initial horizontal offset, and then measured the envelope height; D_y^{rms} was also calculated.

For the lattice with random quadrupole rolls, the height of the oscillation envelope was reduced by 73% and D_y^{rms} was reduced by 44% with the skew-correctors on. For the lattice fit to data, the envelope height was reduced by 89% while D_y^{rms} was increased by 3%. This indicates that ten skew-correctors can effectively reduce coupling. However, the skew-corrector settings were calculated from known quadrupole roll errors, which is not feasible in practice.

We then modeled the same lattices and corrector locations, setting the correctors to minimize the vertical orbit change resulting from horizontal bumps or an energy offset [1]. Letting K_k equal the k^{th} skew corrector strength, V_{ij} equal the i^{th} vertical BPM deflection from a unit excitation of the j^{th} horizontal steerer (or a unit energy offset for one value of j), and $M_{ijk} = d(V_{ij})/dK_k$, we set the skew correctors according to $\Delta K_k = -(M_{mnk}M_{mnl})^{-1}_{kl} M_{ijk} V_{ij}$. Singular value decomposition or regularization may be used to obtain an approximate inverse that prevents "corrector-fighting".

We found that the coupling correction with this technique improved with iteration. The results after 5-10 iterations were better than harmonic correction with the first test lattice and worse with the second. The height of the betatron oscillation envelope was reduced ~ 70% for both cases. For the first lattice, D_y^{rms} was reduced by 60%. With the second lattice, D_y^{rms} was reduced by 25% with the first iteration, but increased with successive iterations to exceed the uncorrected value.

We plan to study the latter correction scheme experimentally as multipoles which can be wired as skew-correctors become available.

V. SUMMARY

The above results may be summarized as follows:

1) Quadrupole rolls appear to be the dominant cause of coupling, but bending magnet rolls and sextupole alignment errors are also important.
2) Global decoupling can reduce the beam height by less than ~ 50%.
3) Using ten skew-quadrupole correctors, a beam height reduction of ~ 70% appears feasible.
4) Coupling correction may be implemented at Aladdin.

VI. REFERENCES

[1] J. Safranek and S. Krinsky, AIP Conference Proc. **315**, p. 163 (1994).
[2] G. Guignard, CERN 87-03, p. 203 (1987).
[3] H. Grote and F. C. Iselin, CERN/SL/90-13 (1990).
[4] S. Peggs, IEEE Trans. Nucl. Sci. **NS-30**, p. 2460 (1983).
[5] G. Guignard, CERN 76-06 (1976).
[6] G. F. Dell, H. Hahn, S. Y. Lee, G. Parzen, S. Tepikian, Proc. 1991 IEEE PAC, p. 1627 (1991).

ONE AND A HALF YEARS OF EXPERIENCE WITH THE OPERATION OF THE SYNCHROTRON LIGHT SOURCE ELETTRA

C.J.Bocchetta, D.Bulfone, F.Daclon, G.D'Auria, A.Fabris, R.Fabris, M. Ferianis, M.Giannini, F.Iazzourene, E.Karantzoulis, A.Massarotti, R.Nagaoka, N.Pangos, R.Richter, C.Rossi, M.Svandrlik, L.Tosi, R.Visintini, R.P.Walker, F.Wei, and A.Wrulich
Sincrotrone Trieste, Padriciano 99, 34012 Trieste, Italy

Commissioning of ELETTRA started in October 1993. By the end of 1994 the beam time dedicated to experiments was gradually increased to a level of 80%. The performance is presented and developments on the machine are discussed.

I. INTRODUCTION

The commissioning of ELETTRA started on October 4 and has progressed without major problems [1]. On the third day, beam was stored for the first time and in the following days the current level was increased up to 216 mA on October 16. A proof of principle experiment using bending magnet synchrotron radiation could already be carried out on October 25. Table 1 summarises the major commissioning steps. A more comprehensive summary of the achievements and the measurements performed during the first phase of commissioning is given in reference [2].

Date	Achievement
Oct. 4 /1993	Start of commissioning
Oct. 25	Bending magnet experiment
Nov. 7	Radiation seen from U5.6
Dec. 11	410 mA, design current passed
Jan. 24 /1994	2.3 GeV, design energy passed
Feb. 4	Experiment at 1.5 GeV
Mar	Light from U5.6 with low gap and U12.5
Apr	Light from W14.0
May	Light from ID's at 2.0 GeV with low gap

Table 1: Milestones of ELETTRA Commissioning

II. OPERATION AND PERFORMANCE

Injection is performed by a high energy linac [3] at 1.0 GeV. A ramping procedure was installed which allows the selection of any operating energy from injection up to the maximum energy [4]. Currently, the experimental runs are performed at 2 GeV, with three insertion devices closed to a minimum gap of 26 to 28 mm [5]. At the beginning of May this year a fourth insertion device U8 will be installed and operated with a low gap vacuum chamber. The filling time for the storage ring is determined by the cycling, loading of the injection file and final ramp to the operating energy. At present these operations are limited by the configuration of the power supplies. The average time for beam ready of a little more than one hour will be reduced to some tens of minutes at the end of the year with the implementation of hardware and control software changes to the current system. In the multibunch mode a maximum current of 530 mA has been reached, whereas >50 mA has been stored in a single bunch, both at an energy of 1.1 GeV. After improvement of the gas pressure in the vacuum chamber, the lifetime becomes dominated by Touschek scattering and depends therefore strongly on the optical beam conditions. Running the machine with a relaxed vertical optics, i.e., larger vertical beam size, the lifetime is 30 hours at 200 mA and 2.0 GeV. An optics giving the minimum vertical beam size has a lifetime of 14 hours at the same current and energy. Under normal conditions the machine is loaded with a partial filling, leaving a 20% gap.

Machine reliability has increased significantly after one and a half years of operation and already reached a level of 90% at the end of 1994. Major interruptions due to linac unavailability have been reduced by injecting at predefined times. All systems have in general performed well. Downtime due to failures are mostly associated with rf and power supplies.

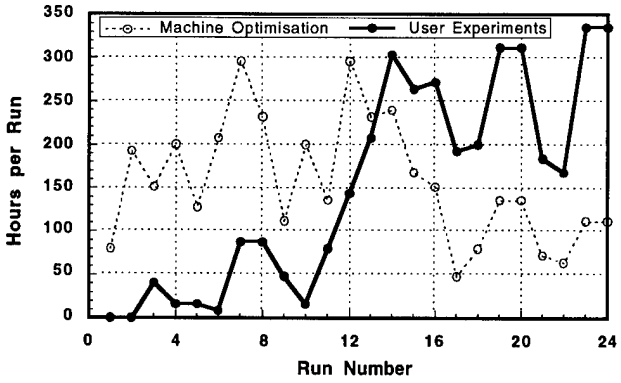


Figure 1: Hours per run for machine and user experiments since the start of commissioning. Run 24 ends June 1995.

Five beamlines are at present installed in the experimental hall. Two of them, the SuperESCA and VUV-Photoemission lines are fully operational and open to external users. Two other lines, X-Ray Diffraction and ESCA-microscopy are close to completion of commissioning and already provide beam for external users. The Spectromicroscopy beamline is still in the commissioning phase. In addition there are two more lines in construction, the Surface Diffraction line (ALOISA) and the Small Angle Scattering line (SAXS). Construction activities have been started for the Spin Polarisation and Spiral Spectroscopy line (using a cross-field undulator [6]) and the Mammography line (using a bending magnet). Go-ahead has been given to an

0-7803-3053-6/96/$5.00 ©1996 IEEE

industrial initiative at ELETTRA, the installation of a Lithography line for micromechanics by the private company Micromore. Excellent results have been achieved with all operating lines. Figure 2 for instance shows recent results of the SuperESCA beam line [7].

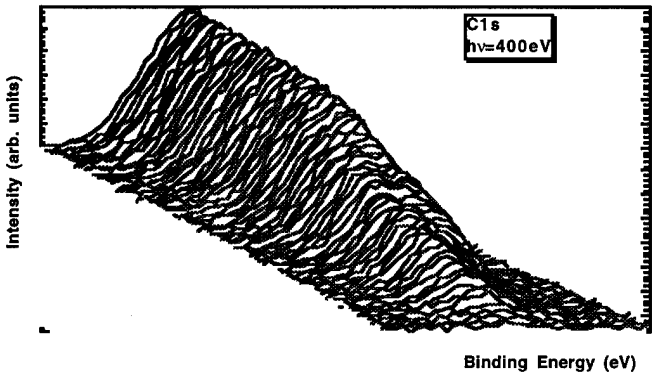


Figure 2: Time resolved X-ray photoelectron spectroscopy (C1s) of CO adsorption on Rh(110). Individual spectra took less than 5 seconds to produce [8].

For the moment three insertion devices are installed in ELETTRA, each of them providing light for two beamlines. Table 2 reports the status of the insertion device installation during the year 1995.

ID - type	N	Gap[mm]	Bo[T]	K	Status
U12.5	36	28	0.506	5.91	operat.
U5.6	81	27	0.444	2.34	operat.
W14.0	30	26 (20)	1.3 (1.6)	17	operat. +)
U8.0	19	20	0.866	6.5	inst. May
U12.5	36	28	0.506	5.91	inst. Dec.
EEW	12	25	0.6 (v) 0.047 (h)	13 1	prototype

+) in parenthesis the numbers for the new 20 mm chamber.

Table 3: ELETTRA Insertion Devices

III. MACHINE DEVELOPMENTS

A series of improvements have been performed during the last one and a half years (the achievements before this time have already been reported in reference [1]).

III.1 Improvement of vacuum chamber cooling

In ELETTRA the beam position monitors are rigidly attached to the adjacent quadrupoles, allowing only a longitudinal motion for thermal expansion of the chamber. It was observed that at 2 GeV and currents beyond the design current (200 mA at 2 GeV, 400 mA at 1.5 GeV) the thermal load creates a transverse movement of the vacuum chamber of which approximately one third is transferred to the quadrupoles via the BPM support system. This occurs only for those BPM's immediately after the bending magnet and in spite of an already existing cooling tube brazed on the outer side of the vacuum chamber. An enhancement of cooling power in this area considerably reduced the transverse movements. Furthermore the thermal desorption was strongly diminished, as shown in figure 3, which increased the lifetime at 2.0 GeV by about a factor of 2 for 200 mA.

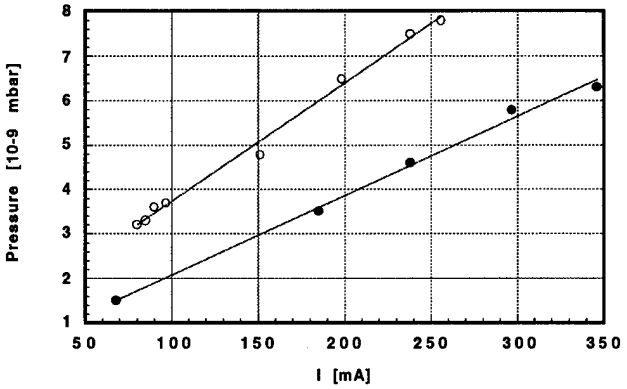


Figure 3: Pressure versus beam current at 2.0 GeV before and after the enhancement of the vacuum chamber cooling.

III.2 Continuous (slow) orbit correction

Residual thermal beam movements have been effectively corrected by a continuous slow orbit correction (once every three minutes) which has been implemented. The orbit displacements in the straight sections are in this way maintained to within a few microns over a 24 hours period.

III.3 Fast local orbit feedback system

The commissioning of the fast local orbit feedback system with synchrotron light monitors has started. Several closed loop tests have been performed which bring encouraging results. The system is expected to be fully active in the second half of 1995.

III.4 Dispersion correction

In ELETTRA the emittance coupling is dominated by spurious vertical dispersion [9]. A scheme has been implemented in association with closed orbit correction which can reduce this dispersion to a level below 0.4 cm rms,

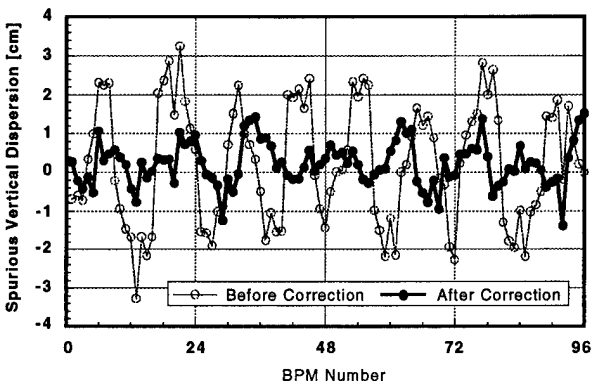


Figure 4. Dispersion correction

corresponding to less than 0.3% effective emittance coupling. Figure 4 shows the vertical dispersion before and after correction.

Such a correction reduces the lifetime due to Touschek scattering. Under normal operating conditions the users would therefore prefer a larger coupling with improved lifetime, since the vertical photon beam size is dominated by diffraction for most of the experiments.

III.5 Cure of multibunch instabilities

Intensive studies were performed to analyse multibunch instabilities and to cure them. The high precision temperature tuning of the cavity is an excellent method to shift dangerous parasitic cavity resonance's away from coupled bunch modes. In this way satisfactory conditions for operation could be achieved for currents up to 230 mA at 2.0 GeV, see these proceedings [10]. For even higher currents and enhanced instabilities the method starts to become critical, therefore the development of a longitudinal multibunch feedback system is envisaged, or alternatively the development of new cavities with higher order mode suppressors.

III.6 Accelerator physics issues

Great progress has been made in the understanding of the machine. A long standing puzzle was the interpretation of low frequency oscillations in the beam from fractions of Hertz up to 50 Hz depending on the machine parameters, i.e., current, energy, cavity temperature, rf-voltage, filling mode, etc. The oscillations were interpreted as an increase of the longitudinal oscillation amplitude due to multibunch instabilities up to a loss of coherence through the action of Landau damping. This fast blow up is then followed by a reduction of the beam size due to radiation damping. Figure 5 shows the beam as seen by a button electrode. The fast blow-up followed by the slower damping is clearly depicted.

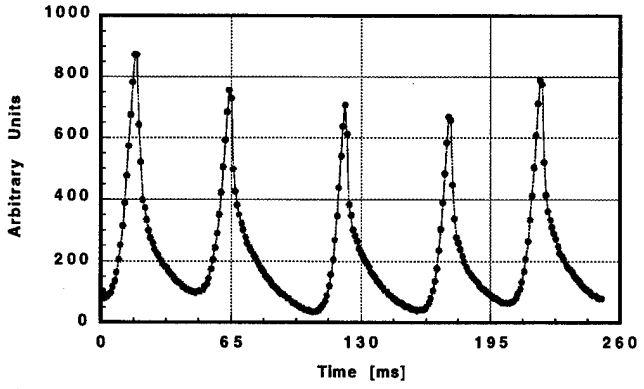


Figure 5: Beam signal on a button electrode which accompanies low frequency beam oscillations.

II.7 Re-alignment

The storage ring magnet positions have been surveyed and realigned after one year of operation. The results confirm the excellent geological conditions and the well constructed storage ring foundation. Figure 6 shows the vertical position of the bending magnet sockets after one year of operation. Eighty percent of the positions were within ±100μm. Maximum deviations only occurred at positions where the transfer line and the service tunnel cross the storage ring.

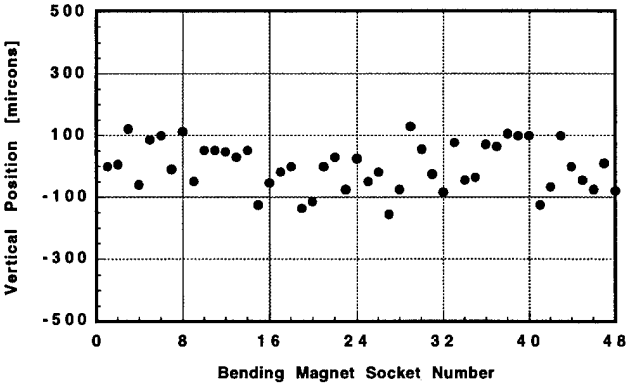


Figure 6. Relative position of bending magnet sockets after one year of operation.

IV. OUTLOOK

Future work will comprise the exploration of higher energies for ELETTRA (2.4 GeV) and the testing of a new optics, that leaves a residual dispersion in the straight sections but considerably reduces the emittance. The development of fast automatic machine preparation and ramping for user experiments. The development of an elliptical insertion device, micro-undulators and the implementation of a new generation of insertion device vacuum chambers with even lower gaps will be continued. Furthermore work is going on for the development of a cavity gun for the linac, the infrared FEL project FERMI [11] and the development of new cavities with waveguide mode suppressors or alternatively a longitudinal multibunch feedback system.

V. REFERENCES

[1] C.J.Bocchetta et al, EPAC-1994, London, pp 579
[2] A.Wrulich, EPAC-1994, London, pp 57
[3] G. D'Auria, et al., these proceedings.
[4] D.Bulfone at al, EPAC-1994, London, pp 1809
R.Nagaoka et al, EPAC-1994, London, pp 1812
[5] R.P.Walker, et al., these proceedings.
[6] R.P.Walker and B. Diviacco, Rev. Sci. Inst. **63**, 332, (1992)
[7] A.Abrami, et al., Rev. Sci. Inst. **66**, 1618, (1995)
[8] G. Paolucci, et al., to be published.
[9] R. Nagaoka, et al, Sincrotrone Trieste ST/M report, to be published.
[10] M. Svandrlik, et al., these proceedings.
[11] D. Bulfone, et al., these proceedings.

FIRST GENERATION ISOL RADIOACTIVE ION BEAM FACILITIES

D. K. Olsen

Oak Ridge National Laboratory,* P. O. Box 2008, Oak Ridge, TN 37831-6368 USA

Abstract

Widespread scientific interest has developed in using accelerated Radioactive Ion Beams (RIBs) for nuclear physics, astrophysics, solid-state physics, and applied studies. Two general methods can be used to produce RIBs: the recoil fragmentation method and the Isotope-Separator-On-Line (ISOL) method. The recoil-fragmentation method requires one accelerator, filters radioactive fragments produced from medium-energy heavy-ion beams incident on thin targets, and is relatively well developed. This method has been pursued vigorously at several laboratories. The ISOL method requires two accelerators, has the promise of lower energies and more intense beams, and is in an earlier state of development. The status, challenges, and plans of the first-generation ISOL accelerated RIB facilities presently operating or under construction will be discussed. These are facilities based in part on at least one existing accelerator and will produce limited RIB beam species, intensities, and energies.

I. INTRODUCTION

A remarkable level of interest has developed with accelerated radioactive ion beams (RIBs) in a short time. This interest has led to the construction, development, and proposed construction of first- and second-generation RIB facilities in Asia, Europe, and North America. This interest stems directly from the scientific opportunities RIBs provide for nuclear, solid-state, and astrophysics and applied research, and the fact that the acceleration of RIBs has become technically feasible over the last two decades.

RIBs will greatly increase the number of nuclei available for study, particularly nuclei with extreme values of neutron and proton number. Altogether, between the proton and neutron drip lines and the fission limits for heavy nuclei, there are approximately 3000 particle-stable nuclei that can be studied. Some information exists on about 40% of these nuclei. Most of our nuclear structure information is from nuclei near beta stability that were first produced with accelerated light-ion stable beams incident on stable targets and then with heavy-ion beams, particularly heavy-ion fusion reactions producing proton-rich nuclei. Much of the nuclear information on neutron-rich nuclei was obtained from reactor produced fission fragments. The development of the RIB facilities presently underway will allow new regions of proton- and neutron-rich nuclei to be studied, providing exciting new research opportunities. Of course not all unstudied nuclei will prove to be interesting; however, much of the new information on new interesting phenomena will come from nuclei studied with RIBs.

Another extremely interesting research area for RIBs is astrophysics, and in particular nucleosynthesis. Most of the heavy nuclei in the universe have been produced in explosive stellar events with short-time scales through nuclear reactions on unstable nuclei. It is only with RIBs that these reaction processes can be studied in detail in the laboratory. The reaction network for explosive hydrogen burning, the rapid proton or RP process, is believed to have produced the proton rich stable nuclei between oxygen and the iron region. The first-generation ISOL facilities described in this paper will be uniquely positioned to produce these proton-rich unstable nuclei for inverse-proton-reaction cross section measurements

In general, RIBs can be obtained by two very different and complimentary methods: The Projectile Fragmentation, PF, method and the Isotope Separator On Line, ISOL, method. The PR method produces RIBs in peripheral collisions between heavy-ion projectiles and light-target nuclei. [1] The incident beam is typically in the 50 to 200MeV/A range and the radioactive fragments recoil in a forward-angle cone with velocities similar to that of the incoming beam. The PF method is fast, so short half-life RIBs can be made, and does not suffer from the severe target-beam-ion-source chemistry constraints of the ISOL method. However, RIBs are produced at high energies and the RIB intensities, because of thinner targets and smaller primary beam intensities, can be several orders of magnitude lower than those from the ISOL method. The PR method requires only one accelerator system.

II. ISOL METHOD

The ISOL method requires two accelerator systems, a driver accelerator to produce radioactive atoms at rest and a post accelerator to accelerate these radioactive atoms to energies of interest. The two accelerators are coupled by a target-ion source and mass separator. This method is equivalent to selecting a low-energy RIB from an on line isotope separator and accelerating this beam to energies of

* Research sponsored by the U.S. Department of Energy under contract No. DE-AC05-84OR21400 with Martin Marietta Energy Systems, Inc.

0-7803-3053-6/96/$5.00 ©1996 IEEE

TABLE 1. FIRST-GENERATION RIB FACILITIES USING THE ISOL METHOD

FACILITY	DRIVER ACC	POST ACC	DONE	COMMENTS
Louvain la Neuve	30MeV-p cycl	K=110 cycl	operating	4E8 pps 13N, 2E9pps 19Ne
ARENAS	K=110, 70MeV-p cycl	K=44 cycl	1996	0.2-0.8MeV/A
INS, Tokyo	K=65, 40MeV-p cycl	RT SCRFQ & IH Linacs	1996	RIBs<1.05MeV/A
HRIBF, ORNL	K=100, 60MeV-p cycl	25MV tandem	1995	RIBs<5MEV/A for A<80
SPIRAL, GANIL	cpl. K=400 HI cycls	K=265 cycl	1998	heavy ion RIB production
EXCYT, Catania	K=800 SC cycl	15MV tandem		heavy ion RIB production
REX ISOLDE, CERN	1000MeV PS Booster	RT RF, IH, 3-7gaps	>1997	RIBs<2.0MeV/A, trap/EBIS inj
ISAC-1, TRIUMF	500MeV-p cyclotron	RT RFQ & IH linacs		RIBs<1.5MeV/A

interest. A good example of the target-ion source and mass-separator technology required for an ISOL RIB accelerator facility is ISOLDE [2] at CERN. In fact, it was realized early by Hansen [3] in 1977 that many of the intense low-energy RIBs developed at ISOLDE, some of them reaching $1x10^{12}$ pps, could be accelerated to energies of interest for nuclear and astrophysics.

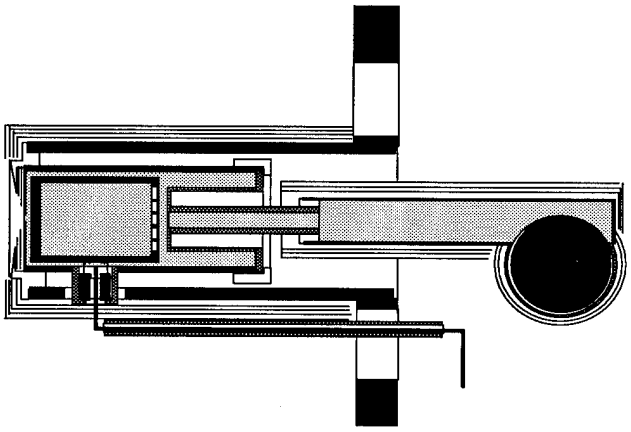


Figure 1. ISOLDE high-temperature FEBIAD target-ion source for the production of RIBs by the ISOL method.

The crucial component for the ISOL method is the target-ion source. Figure 1 shows the ISOLDE high-temperature FEBIAD target-ion source. Radioactive atoms are produced by bombarding thick targets with high-intensity beams of protons or other light ions. The resulting radioactive atoms will diffuse and desorb from the target material, which typically is a refractory ceramic in powder form which is heated to over 2000°C. The radioactive atoms will effuse through a heated transport tube into the FEBIAD ion source where they are ionized by electrons from a heated cathode and accelerated to about 50keV. Following ionization and acceleration, the desired mass can be separated with a magnetic mass separator. A very good separator, with a mass resolution greater than 1/10,000, can separate isobars from a single mass thus providing isotopically pure beams on target.

A significant disadvantage of the ISOL method, is that the diffusion and desorbtion of the radioactive atoms from the target material and the effusion and surface desorbtion in the transport tube and ion source are sensitively dependent on the high-temperature chemistry of the target material, the beam element, and construction materials. The ISOL method is also much slower than the PF method, limiting RIBs to a half-life of at least 100ms or longer. However, for the longer lived species, the ISOL method is capable of producing more intense beams at energies needed for nuclear spectroscopy and astrophysics studies.

III. FIRST GENERATION ISOL FACILITIES

At least seven ISOL RIB facilities are either now funded or nearly funded. These facilities can all be considered first-generation facilities because they all, in some way, are limited, either by RIB species, RIB energy, or RIB intensity. These facilities are also cost effective since they each build on an existing driver accelerator, The facilities are listed in Table 1 and discussed below:

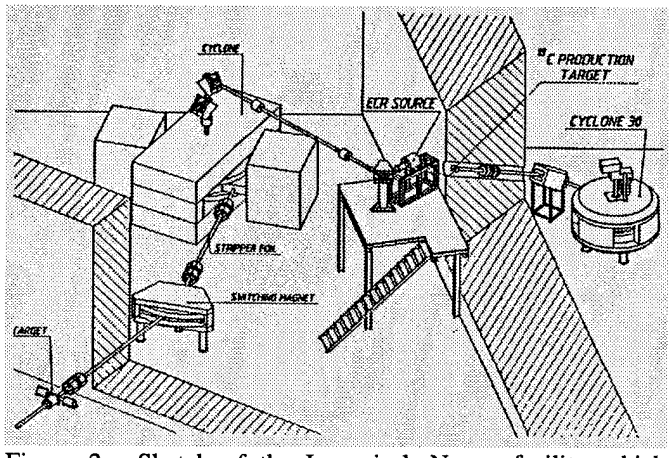


Figure 2. Sketch of the Louvain-la-Neuve facility which produced the first accelerated ISOL RIBs, 13N, used for nuclear astrophysics measurements.

Louvain-la-Neuve Facility

Presently, the only operating RIB facility is at Louvain-la-Neuve where ^{13}N and ^{19}Ne beams have been accelerated for astrophysics research with intensities of $4x10^{8}$

and $2x10^9$ pps, respectively [4]. The driver, CYCLONE 30, is a compact H^- cyclotron designed to produce a 500uA, 30MeV proton beam for PET isotope production. This beam is transported, as shown in fig. 2, to a target located in a 3m-thick concrete shielding wall. For ^{13}N beams, a 50% enriched ^{13}C, thick graphite-powder target is embedded into a graphite rod in good thermal contact with a water-cooled copper cylinder. The resulting ^{13}N activity from (p,n) reactions is extracted on line as ^{13}N-^{14}N gas molecules. The 170μA proton beam heats the target to about 2300°C. The ^{13}N-^{14}N gas is transported to a single-stage ECR ion source that has an 8% ionization efficiency. The resulting $^{13}N^+$ ions are mass analyzed, transported to a second cyclotron, axially injected, and accelerated with a 6% efficiency.

An important problem has been the separation of evaporated ^{13}C from the ^{13}N beam. This separation has been achieved using the high intrinsic resolving power of the CYCLONE magnetic field. The ^{18}Ne beam is produced with a liquid LiF target. Beams of ^{11}C and ^6He are being developed. A 110-minute half-life ^{18}F beam is being developed using (p,n) reactions on enriched ^{18}O water following a batch process very similar to that used for PET isotope production. The ^{18}F is slowly released into the ECR source as CF_4 gas.

The work at Louvain-la-Neuve will be extended with the ARENAS project which is now funded to construct a 25% efficiency, K=44, 0.2 to 0.8MeV/A, cyclotron post accelerator dedicated for astrophysics research. This new cyclotron is scheduled for completion in 1996 and will allow the K=110 CYCLONE to also be used as a driver for higher energy protons and other light ion beams for RIB production.

INS Project, Tokyo

A RIB facility has been constructed at the Institute for Nuclear Studies of the University of Tokyo, [5] originally as a part of the Japanese Hadron Project. RIBs have been made with beams from the existing K=68, 40MeV-proton cyclotron. The new apparatus consists of an ISOL system, a 50m low-energy transport line, and a linac complex. SI, ECR, and FEBIAD target-ion sources have been developed. A sophisticated two-stage mass separator with dipole magnets raised to different voltages to reduce background has been built. A mass resolution of 1/9000 is expected.

The post accelerator linac, shown in fig. 3, consists of a 25MHz Split Coaxial RFQ which is an extended version of a successfully tested prototype. The SCRFQ will accelerate RIBs with Q/A>1/30 from 2 to 170keV/A with a duty cycle between 10 and 30%. The output beam will be stripped to Q/A>1/10 and accelerated to 1.05MeV/A with a 4-cavity, 51MHz inter digital H linac. The cavities will be separated by quadruple triplets providing large horizontal and vertical acceptances. In order to use the RIBs efficiently, a pulsed RIB source has been developed to match the linac time structure. A bunching electrode operating at 300V has been added 1mm from the exit aperture of a Re surface ionization source. Tests with ^{23}Na, ^{39}K, and ^{41}K beams pulsed at 100Hz with 2ms pulses have been completed. A bunching gain of nearly 2.5 for ^{38}K produced from 3He bombardment of a CaF powder target has been measured.

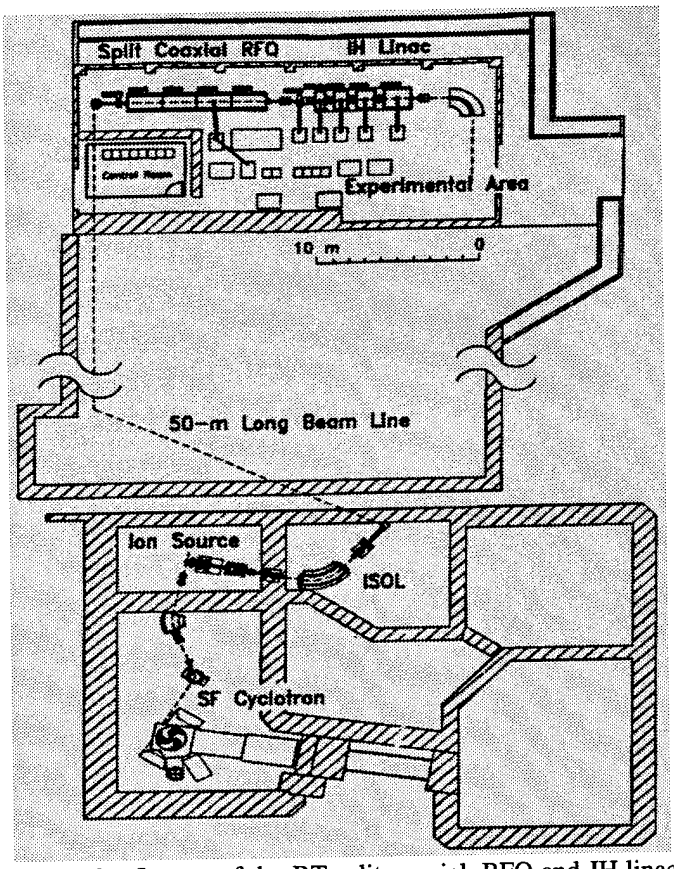


Figure 3. Layout of the RT split-coaxial RFQ and IH linac post accelerator system of the INS RIB facility.

HRIBF Project, ORNL

The Oak Ridge Isochronous Cyclotron (ORIC) and the 25MV tandem accelerator are being reconfigured to provide an economic first-generation RIB facility [6]. In the past ORIC served as an energy booster for stable heavy ion beams from the tandem. For RIBs, this process has been reversed: the tandem will be injected with RIBs produced by light-ion ORIC beams. The tandem presently operates at 25MV, the highest electrostatic accelerator voltage in the world. With single foil stripping, mass-80 beams will be accelerated above 5MeV/A for nuclear structure studies. The tandem is a DC machine, so no bunching is required. There is no low velocity problem as with linacs and its simplicity, reliability, and beam quality, are unmatched. An unusual feature of tandems is that negative ions are required for injection, not highly-charged positive ions.

The accelerators will be coupled by a RIB injector, shown in fig. 4, consisting of an ISOLDE-type target-ion source, mass separator, and charge exchange cell, all mounted on a 300kV platform constructed in an existing shielded room. The neutron fluence from the RIB target has been estimated to be up to $1x10^{15}n/cm^2$ at one meter for 2kW of beam for 2000 hours. This fluence will destroy nearly all unshielded semiconductor devices. Consequently, a split

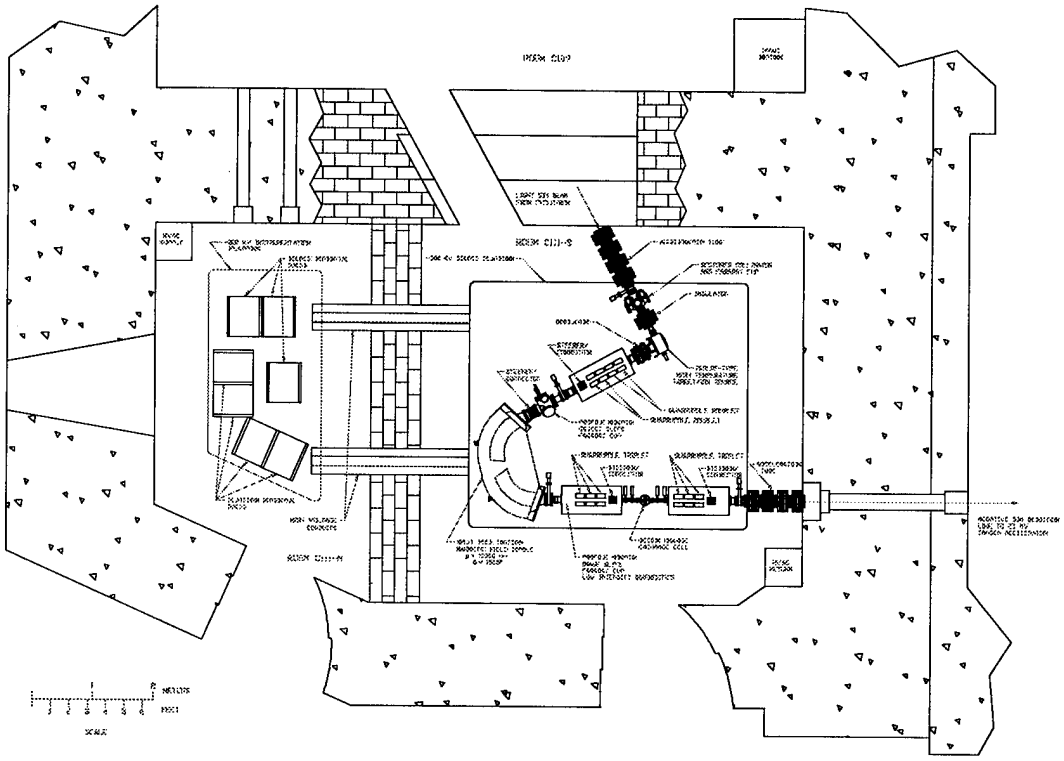


Figure 4. Recently completed HRIBF RIB injector which will mass analyse, charge exchange, and inject negative RIBs at 300KV into the 25MV tandem accelerator.

platform system separated by a shielding wall has been constructed. One platform will hold the target-ion source and mechanical equipment and the other will hold all the electronics. The first-stage mass separator will give a mass resolution of 1/1000 at 50keV and will select a mass to be refocused through a charge-exchange cell. The negative-ion injection line is configured to provide a second stage mass resolution greater than 1/10,000 at an energy of 350keV.

The RIB injector has been tested with stable beams and the remaining components have been ordered. In the summer of 1995, ORIC-produced RIBs from the new injector will be optimized. The first RIBs should be accelerated through the tandem in 1995 and scheduled experiments will start in 1996.

SPIRAL Project, GANIL

As an extension to the existing high-energy PF facility, GANIL has been funded to develop a RIB ISOL facility, SPIRAL [7]. RIBs will be produced with the 95MeV/A heavy ion beams from the existing coupled K=380 RT cyclotrons. A new 14.5GHz ECR source on a 100kV injector has increased the primary beam intensity to 3puA for ions up to Ar. A new rebuncher between the main cyclotrons should increase this intensity further allowing a maximum beam power of 6kW.

Radioactive atoms will be multiply ionized in a permanent magnet ECR source at 20kV and mass sorted with a low resolution spectrometer. There is some debate on the efficiency of light-heavy ions for RIB production. The projectile fragmentation cross sections for RIB production with 95MeV/A light-heavy ions are significantly larger in many cases than target fragmentation, spallation, and fission cross sections for energetic protons; however, this increase in cross section may be more than compensated by a decrease in target thickness. Also, target power density is a concern at the planned intensities. These issues of RIB production are being studied at GANIL with a Caprice-type ECR source and new mass separator, SIRa. The initial measurements have been made with noble gas beams, both primary and radioactive, on a powder carbon target. Yields of 1.0×10^8 $^{76}Kr^{10+}$, 1.2×10^7 $^{34}Ar^{7+}$, and 1.5×10^7 $^{18}Ne^{5+}$ ions/s/puA have been measured. GANIL will have the special ability to vary the primary beam species, in addition to the target material, so as to maximize the intensity of a particular RIB species.

RIBs will be accelerated in a compact K=265 cyclotron, CIME, presently under construction. Beam energies will vary from 2 to 25MeV/A depending on their charge to mass ratio. Mass separation will be performed for the most part with CIME itself. RIB experiments will be done with the extensive experimental areas and equipment at GANIL. The SPIRAL project does not require any major civil construction. The new cyclotron is scheduled for delivery late in 1996 and the first RIB experiments should start in 1998.

EXCYT Project, LNS Catania

The Laboratorio Nazionale del Sud is equipped with a 15MV SMP tandem and a K=800 SC cyclotron. These accelerators will be reconfigured to provide an ISOL RIB

facility, EXCYT.[8] Radioactive atoms will be produced, in a manner similar to GANIL, using projectile fragmentation reactions with heavy ion beams from the cyclotron. In order to increase both the energy and intensity of beams from the cyclotron, a new 14.5GHz, 1.4T, SC ECR source for axial injection is being constructed. Intense heavy ion beams from the cyclotron may be limited by the electrostatic deflector. Negative radioactive ion beams will be produced with a new 150kV RIB injector, similar to the HRIBF concept, and injected into the 15MV tandem. Beams up to mass 40 will be accelerated above the Coulomb Barrier. On December 22, 1994, the first beam at LNS was extracted from the SC cyclotron., 3nA of 30MeV/A $^{58}Ni^{16+}$.

CERN ISOLDE/RAL Projects

An accelerator project REX ISOLDE has been approved to increase the ISOLDE energy from 60keV to 2MeV/A.[9] The scheme directly produces ions with Q/A>1/4.5 with no stripping. ISOLDE presently uses 2uA of time-averaged beam from the 1GeV PS Booster in $3x10^{13}$ proton pulses at a 0.4 to 0.8Hz rate. ISOLDE 1+ beams will be injected a Penning ion trap which will be used as an accumulator-buncher to convert the DC ISOLDE output into 50Hz pulses. These pulses will then be fed into an EBIS acting as a charge state converter. About 100us wide pulses from the EBIS will be injected into a 108MHz linac complex very similar to the Heidelberg TSR high-intensity injector. The linac consist of a 4-rod RFQ for 10 to 500keV/A, a 10 drift tube IH linac for 0.5 to 1.0MeV/A, and three 7-gap resonators for 1.0 to 2.0MeV/A. The system will be pulsed at 50Hz with about a 5% RF duty cycle. The accelerator would be used for experiments in nuclear astrophysics, polarization studies, and solid state applications. A building extension is under design and much of the accelerator equipment is funded. The earliest possible beam will be in 1997.

ISOLDE is also heavily involved with RAL in development of a high-power Radioactive Ion Source Test stand, RIST, as a proof of principle for a very-high-power second-generation RIB target-ion source.[10] Up to 100uA of 800MeV protons from the ISIS spallation neutron source will be used. Intense RIBs will be produced with a thick Ta target consisting of 25um disks with 25um spacing and a hot tungsten surface ionization source. A prototype target-ion source has been successfully tested at ISOLDE with a 2uA beam. High power test will be done at RAL.

TRIUMF ISAC-1 Proposal

A collaboration centered on the TRIUMF high-intensity, 500MeV H^- cyclotron has constructed and tested an on-line mass separator TISOL, installed a single-stage ECR source, and initiated an experimental physics program. Building on this experience, TRIUMF is proposing in their next five-year plan to build a facility, ISAC-1, to accelerate RIBs to 1.5MeV/A.[11] A 10uA beam from TRIUMF will produce RIBs in a new heavily-shielded building extending into the existing proton hall. This building will house all the high activation activities of RIB production. A 60keV beam, from a variety of possible ion sources, will be delivered from this new building to either a 60keV experimental area or the new post accelerator. The first stage of this accelrator will consist of a 35MHz RT CW RFQ which will capture, bunch, and pre-accelerate RIBs, with Q/A>1/30, from 2 to 150keV/A. A foil stripper will increase the Q/A ratio of the beam to at least 1/6 before further acceleration in a second-stage 70MHz RT IH linac. A switching magnet will deliver beam to three experimental areas including a recoil separator. Approval of the five-year plan containing this project is expected in 1995.

IV. CONCLUSIONS

Accelerator-based nuclear physics, which only a few decades ago moved, in part, from light-ion to heavy-ion beams, is now moving, in part, from stable-heavy-ion to radioactive-heavy-ion beams. The exciting physics opportunities presented by accelerated RIBs will lead to the construction of perhaps seven first-generation ISOL facilities. These first-generation facilities all use at least one existing accelerator and are cost effective. However, they are all limited in some way with respect to what is technically feasible, either in RIB species, RIB intensity, or RIB energy. Eventually, at least one second-generation ISOL facility, capable of producing and accelerating almost all masses to energies above the Coulomb barrier, should be developed.

V. REFERENCES

1. T J M Symons et al, Phys. Rev. Lett. 42(1979)40.
2. H L Ravn and B W Allardyce, *Treatise on Heavy Ion Science*, ed. D A Bromley, Vol. VIII, *Nuclei Far From Stability* (Plenum Press, New York, 1989).
3. P G Hansen, Proc. CERN Workshop on Intermediate Energy Physics for Unstable Nuclei and Radioactive Ion Beams, CERN PS-CDI/77-43 (1977).
4. M Loiselet et al., Proc. of the 1993 IEEE PAC, p 1672, 93CH3279-7 (Washington DC, May 1993).
5. I Katayama et al, Proc. Third Int. Conf. on Radioactive Nuclear Beams, East Lansing MI, May 1993, ed. D J Morrissey (Edition Frontiers, France, 1993) p 87.
6. A Proposal for Physics with Exotic Beams at the Holifield Heavy Ion Research Facility, February 1991, edited by J D Garrett and D K Olsen.
7. The SPIRAL Radioactive Ion Beam Facility, May 1994, GANIL R 94--02.
8. R Alba et al, Proc. Third Int. Conf. on Radioactive Nuclear Beams, East Lansing MI, May 1993, ed. D J Morrissey (Edition Frontiers, France, 1993) p 31.
9. Proposal to the ISOLDE Committee, CERN/ISC 94-25
10. J R J Bennett et al, RAL Report RAL-94-095, p 11.
11. A proposal for an Intense Radioactive Beam Facility ISAC-1, TRIUMF 1995, to be published.

RECENT DEVELOPMENTS IN SUPERCONDUCTING CYCLOTRONS

H.W.Schreuder, Kernfysisch Versneller Instituut, Zernikelaan 25, 9747 AA Groningen, Netherlands.

I. INTRODUCTION

Superconducting cyclotrons have come of age: three machines have been operating on a regular basis since several years. These first generation machines have benefited from improvement programs and new equipment, while proposals for further expansion of their capabilities have been elaborated. The most significant events of 1994 have been the first beams in two new machines: the AGOR cyclotron in Orsay (France) and the K800 cyclotron in Catania (Italy). The first beam of the machine in Catania, Ni ions at 30 MeV/A, crowned a long construction effort, requiring transport of the magnet from Milan and assembly of the accelerator at its final location on the island of Sicily. AGOR, the first machine of a new generation, accelerated and extracted α-particles with an energy of 50 MeV/A, proving the validity of a number of novel design features. The vitality of the concept of using superconducting coils in a cyclotron is demonstrated by new proposals for such machines, to be used in cancer therapy.

II. THE FIRST GENERATION

1. Catania

The Catania cyclotron [1], now being commissioned, is certainly the first cyclotron to have traveled more than 1200 km from the place of conception to its final site. Starting in 1992, subsystems have been moved from Milan to Catania for integration with a previously installed tandem accelerator into a dual accelerator. This operation was crowned with success when a Ni beam at 30 MeV/A was extracted on December 22, 1994. An overview of the cyclotron with beamlines for injected and extracted beams is shown is figure 1. Since design work started in the 1980's, the machine can be described as the last member of the first generation of cyclotrons with superconducting coils. Not surprisingly, its design closely parallels those of the MSU machines: several members of the Italian team have intensively collaborated in the MSU design studies. Similarly to the TASCC facility, a Tandem accelerator is used as an injector. However, at Catania the installation of a system for axial injection of the beams is being prepared. In this context, the project SERSE has been started in collaboration with CEN Grenoble (France), with the purpose of constructing an ECR ion source with superconducting coils. Since the cyclotron will predominantly accelerate heavy ions, beam diagnostics is centered on the application of visual techniques, pioneered at MSU [2], which exploit fluorescent screens and ccd camera's.

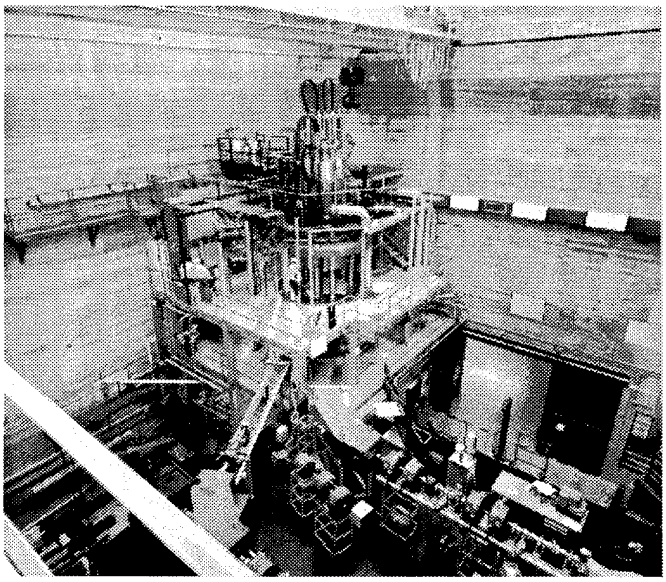


Figure 1: The Catania cyclotron with beam lines for injected and extracted beams.

The lower pole of the magnet is illustrated in figure 2, showing the main beam probe on its guiding track. The cylindrical housing on the probe is the air enclosure of the

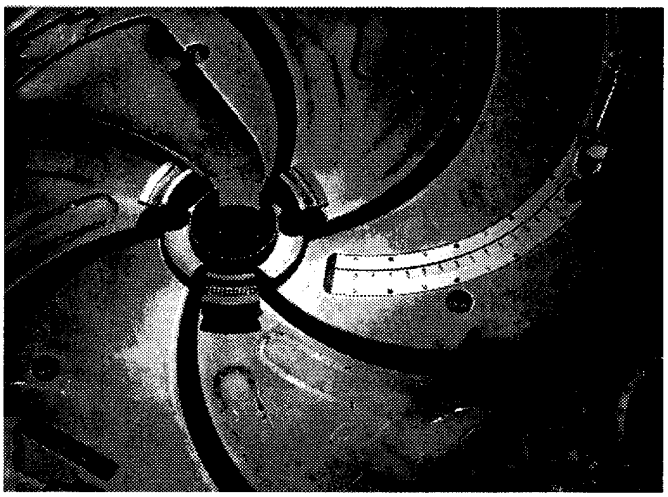


Figure 2: Catania: lower pole with beam probe.

camera and the plate at 45° is the alumina scintillator. Interestingly, a movable copper plate can be made to slide in front of the scintillator. It is driven by a small coil, which rotates in the ambient magnetic field when current is applied to it, as a motor. Since ccd camera's are damaged by a radiation dose in excess of 10^5 Gy, the applicability of these instruments for viewing high-energy beams is limited.

0-7803-3053-6/96/$5.00 ©1996 IEEE

2. *MSU K1200 cyclotron*

The K1200 cyclotron at MSU [3] has started operations in 1989. Its status as the most powerful machine in the class of cyclotrons with superconducting coils remains unchallenged. In recent years, development work has focused on commissioning new beams and approaching the operational design limits of the machine. This work has greatly profited from the successful development program for ECR ion sources. The superconducting ECR source is among the best in the world: it produces completely stripped ions up to Z≈18 and high Z ions with charge states up to 40^+, allowing the acceleration of Uranium ions to energies of 25 and 30 MeV/A. The range for Xenon beams has recently been extended upwards and is now 20-100 MeV/A. The highest energy beams are those with charge state Z/A=0.5, which can be accelerated to a maximum energy of 200 MeV/A: fully stripped O is a typical example. In addition to heavy ions, H_2^+ beams have been produced at that energy, adding the capability for producing proton beams, unexpected in this heavy -ion cyclotron. The machine has therefore demonstrated the capability of covering the entire periodic table. Operational experience has allowed the reduction of the time required for beam changes to typically 4 h. Table 1 presents a summary list of extracted beams as of October 1994.

Ion	Energy (MeV/A)	Ion	Energy (MeV/A)
H_2^+	140, 155	^{48}Ca	55, 100
^{4}He	40-170	^{51}V	50
^{6}Li	65-100	^{52}Cr	60
^{11}B	32	^{55}Mn	70
^{12}C	22-155	^{58}Ni	50-70
^{14}N	35-130	^{84}Kr	22-70
^{16}O	25-200	^{86}Kr	35-100
^{20}Ne	30-170	^{92}Mo	70
^{24}Mg	60	^{106}Cd	60
^{28}Si	50, 80	^{129}Xe	20-70
^{36}Ar	22-160	^{136}Xe	30, 35
^{40}Ar	25-115	^{197}Au	20-35
^{40}Ca	55	^{238}U	20, 25

Table 1: K1200 Extracted beams (summary)

3. *TASCC*

The design operating diagram for this coupled Tandem-Cyclotron accelerator [4] is now fully covered. In fact, as illustrated by figure 3, the diagram has been extended beyond the original specifications by accelerating ^{3}He beams to energies of 20 and 30 MeV/A. In 1994, a reliability of 90% has been obtained for the dual accelerator system. With the aims of increasing beam intensity and adding new elements to the beam list that are not available with the standard sputtering source, the Tandem has recently been equipped with an ECR ion source coupled to a charge-exchange channel. The source is optimized to produce high-intensity, singly charged ions. With a typical charge conversion efficiency of 12%, 15 μA of Bi^{1-} ions are available to date for injection into the Tandem. Improvement by at least an order of magnitude is foreseen [5]. A long-term research and development program, aimed at understanding the problems of holding the high electric fields needed in the electrostatic deflector of a high magnetic field cyclotron, was started in 1991 [6]. The practical success of this research effort is demonstrated by an electric field of 175 kV/cm now being sustained in operating conditions [5].

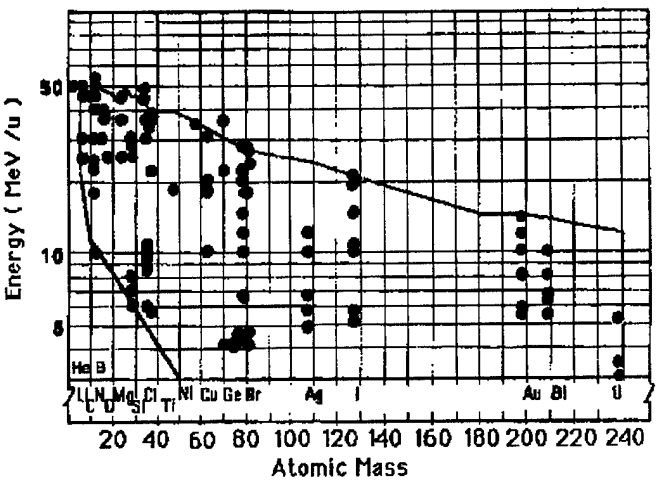


Figure 3: TASCC operating diagram

4. *TEXAS A&M*

Like the other cyclotrons of the first generation, with the exception of the Catania facility, the cyclotron at Texas A&M University is in the phase of active utilization. This phase is characterized by intensive use of the machine and

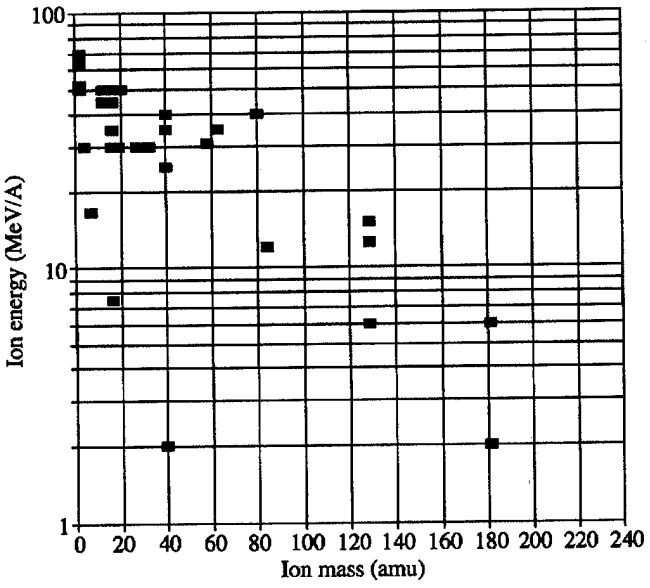


Figure 4: Representative beams extracted from Texas A&M K500 cyclotron.

gradual commissioning of new beams.Little time is available for technical developments, as is to be expected in an efficiently operated facility.

III. SECOND GENERATION: AGOR

This cyclotron, resulting from a French-Dutch international collaboration, can be considered to be the first of the second generation of cyclotrons with superconducting coils [7]. It has been designed to accelerate all elements of the periodic table, including protons. AGOR was constructed at the Institut de Physique Nucléaire (IPN) at Orsay (France) and was successfully tested with its first extracted beam of 50 MeV/A α-particles in April, 1994. The cyclotron was subsequently disassembled and transported to its final destination, the Kernfysisch Versneller Instituut (KVI) of Groningen University (Netherlands). Figure 4 shows the machine during reinstallation. The time schedule calls for final commissioning to start by mid-1995.

AGOR has been designed for a maximum proton energy of 200 MeV, close to the focusing limit of a three-sector cyclotron. The low value of the magnetic field required for proton acceleration, as well as the high rf frequencies needed, have

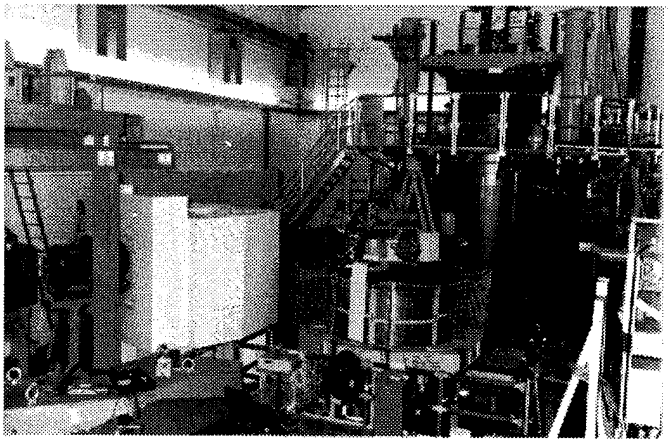


Figure 5: The AGOR cyclotron during reinstallation .

led to unusual design features.

i) It is a desirable analytical as well as operational feature of these cyclotrons that their magnets operate with saturated poles. This allows fields to be accurately calculated and to be obtained with excellent reproducibility. Since 200 MeV protons and a typical pole radius of 1m combine to an average field of only 2 T, the valleys in the AGOR poles are very deep to ensure saturation of the hills. ii) The revolution frequency of 200 MeV protons in a 2 T field is 31 MHz. For efficient acceleration using three RF resonators, the harmonic number should be at least 2, implying 62 MHz as the maximum accelerating frequency. Conventional half-wave coaxial resonators are used, in which the short circuit plate must be placed at about 40 cm from the median plane for obtaining this frequency [8]. This leaves insufficient space for a high-voltage feedthrough insulator. The entire resonator, including the movable short-circuits, is therefore placed in the machine vacuum. Since the stems of the electrodes have a length of 2 m (imposed by the low-frequency limit of 24 MHz), the required position accuracy of the accelerating electrodes of 0.3 mm, as indicated by central region orbit calculations, makes for a difficult mechanical design of the resonators.

Other novel design features are the following:

a) The magnet design aims at perfect three-fold symmetry to avoid conflicting criteria for main coil centering: minimization of radial force on coils versus minimization of the first harmonic in the beam region. For this reason, passive magnetic channels are not employed for beam extraction but active electromagnetic channels are used instead [9]. Such channels can be designed to provide deflecting fields up to 0.4 T and are therefore more powerful than electrostatic deflectors, which are fieldstrength-limited to the equivalent of typically 0.1 T. Their conductor configuration must be designed to provide deflection and focusing, as well as a high degree of cancellation of the magnetic field in the beam extraction region.

b) The arsenal of beam diagnostic equipment is shown in figure 6, representing a cross-section through AGOR's median plane and indicating the location of this equipment.

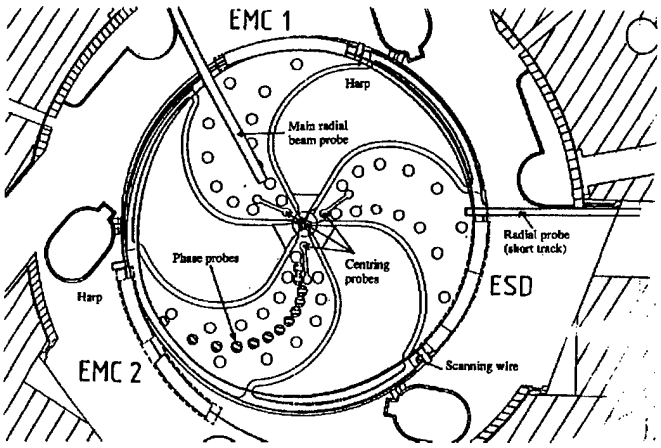


Figure 6: AGOR: cross-section through median plane, showing diagnostic equipment.

Novel features are the centering probes installed at R=0.3 m in each of the hills. Their active element is a tungsten wire scanning the beam density over a circular orbit with a 3 cm diameter. The off-centredness of the beam can be determined from the scans made by the three probes. Figure 7 represents the output of such a scan, demonstrating the ease with which individual turns can be located.

Conceptually simple, but uncommon, is the systematic use of diagnostic elements in the path of the extracted beam: each extraction channel has a diagnostic (harp, scanning wire) at its entrance and a total beam current measuring device at its exit.

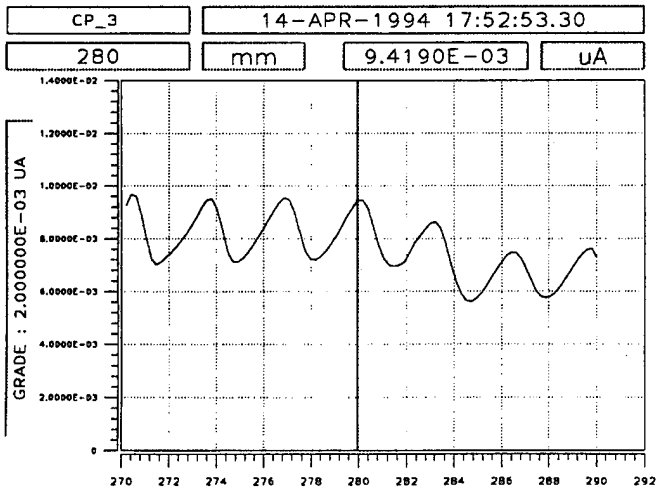


Figure 7: Output of a radial scan with one of the centering probes.

The utility of this arrangement was convincingly demonstrated the first time the beam was threaded through the long - nearly one full turn- path out of the cyclotron.. For beam phase measurements, an array of 13 electrostatic beam pickup probes has been installed, also shown in figure 6. Experiments with the 200 MeV α beam proved that the probes and the associated electronics are capable of producing valid phase information at a beam current as low as 80nA.

IV. UNCONVENTIONAL CYCLOTRONS

1. TRITRON.

The superconducting, separated orbit cyclotron Tritron [10], which has been in construction at the Munich Technical University for some time, is approaching the beam test phase. Tests have already demonstrated that the operation of the rf cavities is not perturbed by the stray field from the superconducting magnets and that their nominal voltage of 530 kV can be obtained. Assembly was completed early in 1994, when faults in the inter-coil connections became apparent. These have been remedied, and Tritron is now being cooled down in preparation for beam. Figure 8 shows the magnet sectors, the RF resonators and the injection magnets.

The concept of the separated orbit cyclotron is intrinsically suited for high-intensity beams, since it provides for longitudinal stability. There is thus more freedom for selecting the transverse focusing frequencies than in the case of the isochronous cyclotron. The very concept of a SOC implying a large energy gain per turn, it is significant for possible future proposals that the recent tests have demonstrated that the very high rf accelerating voltages can be obtained with superconducting cavities. It is remarkable that a design study for a 1 GeV, 10 mA machine seems to present no insurmountable difficulties.

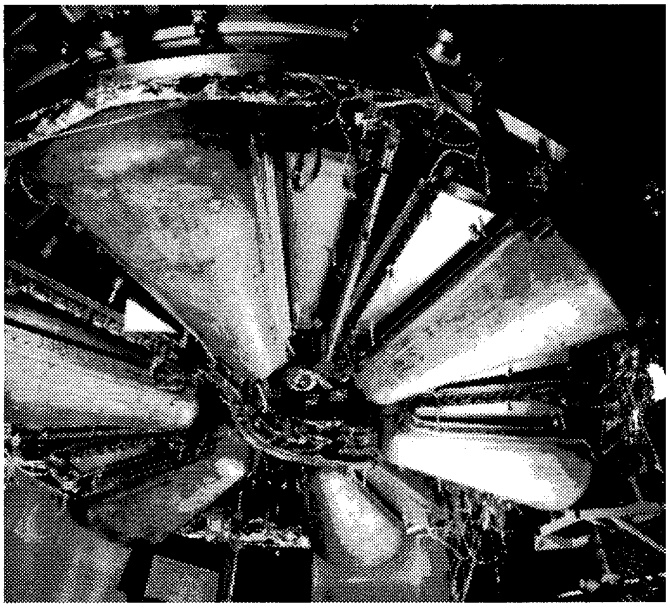


Figure 8: Tritron assembled (as seen from below).

2. OSCAR

The only cyclotron with superconducting coils to be commercially available, Oscar has been on the market since several years [11]. Nine machines of these 12 MeV proton cyclotrons have been installed and a tenth is now under construction. Most machines are used to produce PET isotopes. The beam current has been raised to 150 μA. The design of the machine is based on the magnet technology developed for MRI magnets; the coils are used in persistent mode. The remarkably small size of this cyclotron is demonstrated in figure 9, showing two of these machines side by side.

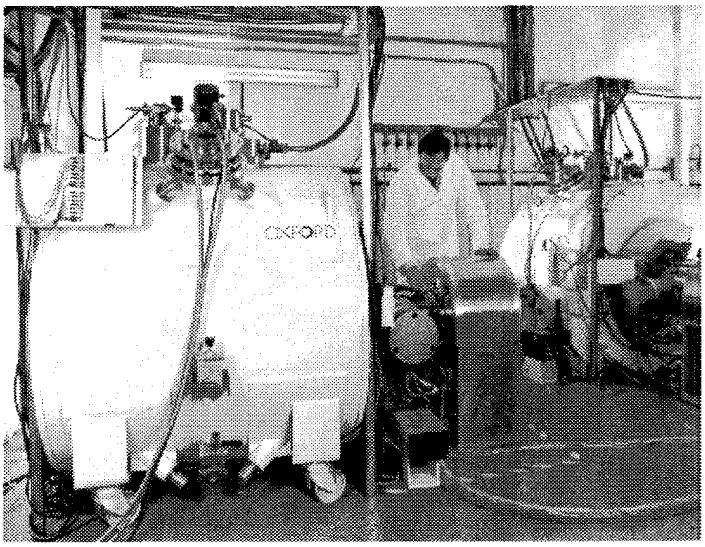


Figure 9: Two 12 MeV Oscar cyclotrons.

V. PROPOSALS

1. Cyclotrons for proton therapy.

There exists a widespread interest in using energetic ion beams for cancer therapy, as illustrated by a large number of conference contributions as well as by proposals for accelerators dedicated to this activity. Because of penetration depth, protons with energies of 200-250 MeV are the projectiles of choice. Indeed, the dedicated proton therapy facility at Loma Linda University is already operational since 1993. The Massachusetts General Hospital in Boston has ordered a 230 MeV proton cyclotron with IBA (Belgium). This machine has copper coils and is scheduled to be operational in 1998.

MSU

Approximately one year ago, the National Superconducting Cyclotron Laboratory at MSU published a design report for a 250 MeV cyclotron for proton therapy [12]. As is to be expected, this machine has superconducting main coils. The cyclotron will have an internal ion source. and its central region will be equipped with slits, so that pencil beams with very sharp time resolution will be accelerated and extracted. The small radial emittance will result in a nearly 100% extraction efficiency and allows the electrostatic deflector to have a small gap, leading to conservative voltage holding requirements. Although the slits will have sub-millimeter apertures, the transmitted current is estimated to be a few μA. Since the required beam current on target is typically 10 nA, the rf accelerating voltage will be pulsed with an appropriate duty cycle.

Milan

The Milan group, after having completed the design and construction of the K800 MeV cyclotron that is now being commissioned at its final site in Catania, has started a design study of a 230 MeV proton cyclotron with superconducting coils, to be used for radiotherapy [13]. The design aims at low costs of construction and of operation. For this reason, the coils will operate in persistent mode. Heat input will be minimized by using two thermal shields at 80 K and 20 K respectively, which are cooled by separate refrigerators of modest capacity. The liquid helium evaporation rate is expected to be only 10 l/day. The magnet has a diameter of 2.8 m and a height of 1.8 m and is therefore very compact.

2. NSCL Proposal

The K1200 cyclotron at NSCL is increasingly used for the production of radioactive beams. Evidently, improvement of the intensity of the primary beam is highly desirable. The laboratory has therefore elaborated a proposal [14], which aims at an increase in intensity with 3 to 4 orders of magnitude and at an increase of the highest attainable energy to 100 MeV/A for heavy ion beams up to A=200. In order to obtain a high charge state after final stripping, high-energy beams from the existing K500 cyclotron are to be injected into the K1200. The proposal calls for upgrades on most K500 subsystems to achieve reliable operation at beam currents up to 10 pμA. The K500 will be injected from one of the available ECR ion sources. Since only modest charge states are required for the K500, the required high intensities can be readily obtained. As a result, the K1200 will produce more intense heavy ions at higher energies.

VI. REFERENCES

The abbreviation ICCA is used for: "International Conference on Cylotrons and their Applications".

[1] F. Alessandria et al. "Status Report on the Heavy Ion Facility at LNS", in Proceedings of the 13-th ICCA, Vancouver, 1992, p.90.

[2] F.Marti et al, "Beam diagnostic Developments at NSCL", in Proceedings of the 12-th ICCA, Berlin 1989, p.268

[3] J.Stetson et al., "Performance of the K1200 Cyclotron at MSU", in Proceedings of the 13-th ICCA, Vancouver, 1992, p.86.

[4] H.Schmeing et al., "Current status of the Superconducting Cyclotron at Chalk River", in Proceedings of the 12-th ICCA, Berlin 1989, p.88

[5] TASCC Newsletter, Vol.8, no.12, Dec.1994, and H.Schmeing, private communication.

[6] W.Diamond et al., " The Electrostatic Deflector for the Chalk River Superconducting Cyclotron", in Proceedings of the 12-th ICCA, Berlin, 1992, p.569

[7] H.W.Schreuder, "AGOR: Recent Achievements", in Proceedings of the 13-th ICCA, Vancouver, 1992, p.40.

[8] S.Brandenburg et al., "The RF system of the Superconducting Cyclotron AGOR", in Proceedings of the 12-th ICCA, Berlin, 1992, p.197

[9] S.Gustafsson, "Etude magnétique des éléments d'extraction des faisceaux du cyclotron compact a bobines supraconductrices AGOR", Thesis, Orsay, 1991.

[10] U.Trinks, "The Superconducting Cyclotron Tritron", in Proceedings of the 13-th ICCA, Vancouver, 1992, p.693.

[11] R.Griffiths, "A Superconducting Cyclotron", Nuclear Instruments and Methods NIM 40/41 B, 1989, p 881.

[12] H.G.Blosser et al. "Proposal for a Manufacturing Prototype Superconducting cyclotron for Advanced Cancer Therapy", MSUCL-874, Feb.1993.

[13] E.Acerbi, private communication.

[14] K.Gelbke et al., "The K500⊗K1200", report MSUCL-939, July 1994

VII. ACKOWLEDGEMENT.

It is a pleasure to acknowledge helpful cooperation of L.Calabretta, F.Marti, H.G.Blosser, D.May. H.Schmeing, W.Diamond, U.Trinks, M.Kruip and E.Acerbi.

SYNCHROTRON-DRIVEN SPALLATION SOURCES

P.J. Bryant, CERN, CH-1211 Geneva 23, Switzerland

1 INTRODUCTION

The use of synchrotrons for pulsed neutron spallation sources is an example of spin-off from the accelerator development prompted by particle physics. The first proposal for an accelerator-driven source with a thermalised neutron facility was in the 1960s (Intense Neutron Generator, ING) [1], but this project was never built. There was earlier work on 'electrical' breeders [2] and the direct bombardment of a heavy-metal target for spallation had already been foreseen by Lewis [3], but the first demonstration of the spallation source concept was at ANL in 1972 (ZGS Intense Neutron Generator Prototype, ZING-P). A spallation source uses a medium-energy accelerator to excite the nuclei of a heavy-metal target (often Ta or W alloy), from which neutrons 'evaporate'. These 'fast' neutrons are slowed in moderators set around the target. Neutrons make excellent probes for condensed matter [4] as their neutrality ensures deep penetration, their magnetic moment reacts to magnetic structures and their weak interaction minimises radiation damage allowing *in vivo* experiments. Neutron sources are widely used in biology, chemistry, materials science and basic physics, as well as for technological applications such as radiography and materials testing. Spallation sources are environmentally friendly compared to reactors. The time structure of accelerator beams offers some experimental advantages and peak neutron intensities can exceed those of reactors. Although, the present demand for neutrons can be met by reactors, this situation is unlikely to continue due to the increasing severity of safety regulations and the policies of many countries to close down their reactors within the next decade or so. At the same time, the demand for neutrons is expected to grow and, consequently, there has been an increasing interest in accelerator-driven sources.

II. BASIC REQUIREMENTS

Figure 1 shows the generic pulsed neutron source. The target receives short (≈μs), high-intensity, proton pulses with repetition rates of typically 10-60 Hz. The intensity should be as high as possible, as the appetite of the users is currently beyond what the accelerator and target designers can provide. The pulses are formed by accumulating protons from an H^- linac by charge-exchange injection into a large-aperture synchrotron, or accumulator ring, that is filled to its space-charge limit. The final energy of the beam needs to be 500 MeV to 4 GeV, but these are soft limits. The synchrotron can be used to perform the major part of the acceleration (*synchrotron-driven source*), or it can be used as an accumulator/buncher leaving all the acceleration to the linac (*linac-driven source*).

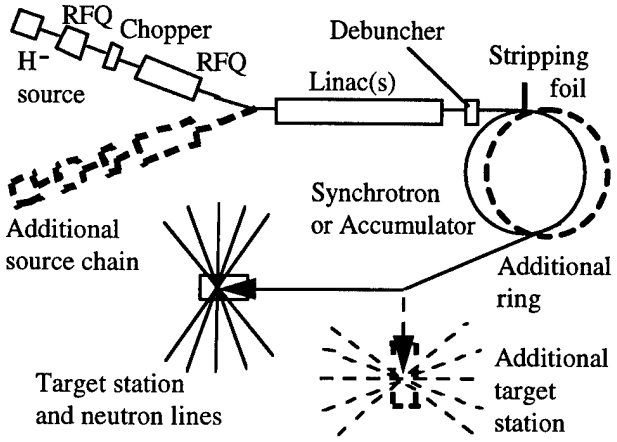


Figure 1: Generic complex for a pulsed source.

When deciding the design of a spallation source, there are a number of practical considerations to be taken into account:

1 In general, it is cheaper to accelerate in a synchrotron than a linac. Fast-cycling synchrotrons typically work over a range of less than 1 to 8 in magnetic field. This keeps the top field below saturation and avoids tracking problems between the different magnetic circuits. By using two synchrotrons of 25 Hz interleaved to produce 50 Hz, many problems can be eased.

2 The higher the injection energy into the synchrotron, or accumulator, the weaker the space-charge and the higher the intensity that can be stored. There is a soft threshold at around 130 MeV, below which the losses are more tolerable from the point of view of induced activity. At this energy, it is also natural to change from an Alvarez to a coupled-cavity linac and go straight to say 800 MeV, or higher. It is true that the injection losses are more potent at higher energies, but it is hoped that a static accumulator is easier to operate than a rapid-cycling synchrotron so that losses can be reduced. At high energies, charge-exchange injection experiences problems with magnetic-field stripping.

3 The targets have a natural threshold at around 200 kW, above which surface cooling is no longer feasible and either the coolant becomes directly irradiated by the beam, or a more complicated dynamic (e.g. rotating) target is needed.

Synchrotron-driven sources should work well up to 1 MW average power with final energies in the range 0.5-2 GeV. Linac-driven sources are planned for 1-5 MW with final energies in the range 0.8-1.5 GeV. For higher powers, one can speculate on the future use of superconducting linacs of 3 GeV or so. Table 1 lists the operating, planned and proposed sources of various types, including the continuous,

0-7803-3053-6/96/$5.00 ©1996 IEEE

cyclotron-driven sources, such as SINQ at PSI. The following sections, however, refer to synchrotron-driven sources, although many of the considerations apply equally to the accumulator ring in the linac-driven option.

III. INJECTION, RF-TRAPPING AND ACCELERATION

The injection into the synchrotron is the natural starting point for the design of the complex. This is a critical point regarding space charge and it determines the intensity, emittance, momentum spread, duty cycle, debunching and chopping to be achieved in the injection chain. It also determines the final beam characteristics and apertures in the synchrotron and extraction line.

A. Charge-exchange injection

Charge-exchange injection was pioneered in Novosibirsk [17] and is now the preferred method for injection into high-intensity machines. A beam of H^- ions is steered onto a closed orbit in the synchrotron between two dipoles (see Figure 2). This is possible, since the dipoles will bend oppositely charged particles in opposite directions. In the drift space where the two beams coincide, both pass through a thin foil, which strips away the weakly-bound electrons from the H^- ions to create protons for the main beam. Those particles that are not stripped, or are stripped to the H^0 charge state, will be separated from the circulating beam by the next dipole. The stripping foil can be made from aluminium oxide. It is a critical element and a good example of the specialised technologies that abound in accelerator engineering. The fringe field of the dipoles is used to guide the stripped electrons onto a collector. The beam could also be injected onto an outer orbit, but the scheme in Figure 2 is more natural, since the injection takes places just before the field minimum and the falling field causes the newly injected beam to spiral outwards from the foil so filling the machine aperture. Making the injected beam cross the main beam also represents a saving in the aperture of the dipoles.

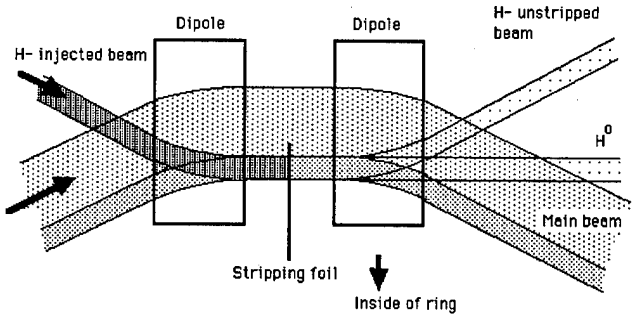


Figure 2: Schematic view of H^- injection.

Typically the stripping foil will be 98% efficient with the 'waste' beams emerging as unstripped ions and neutral H^0 particles (some of which may be in excited H^{0*} states). Figure 2 suggests that the simple solution of collectors placed outside the main beam will lead to a very clean injection. At low energies (< 500 MeV), this is possible, but at higher energies strong (and especially inhomogeneous) magnetic fields can strip H^- ions and H^{0*} excited states leading to distributed losses that cannot be collected cleanly. For this reason, higher energy injection schemes use a single, long, weak dipole. It is desirable at high energies to bring the H^0 beam right out of the machine before collecting it, but the small angle given by a weak dipole makes this difficult. In the European Spallation Source (ESS), a second stripping foil is proposed in the H^0 and H^- beams followed by a septum magnet, once they have left the main beam.

B. 'Painting'

The transverse emittances of the linac beam are small compared to the synchrotron acceptance and 'painting' is used to fill the machine acceptance to its space-charge limit. Ideally, a Kapchinskij-Vladimirskij (K-V) distribution is created by injecting a zero-emittance beam over N turns, on the locus shown in Figure 3(a). The position of the nth injected pulse $[x(n),z(n)]$ with respect to the closed orbit in the synchrotron follows a square-root law as shown in Figures 3(b) and (c). 'Painting' occurs over hundreds of turns (e.g. AUSTRON- 130, SNS-ISIS at RAL- 200, PSNS at BNL - 300, IPNS-Upgrade at ANL- 500 and ESS- 1000 turns).

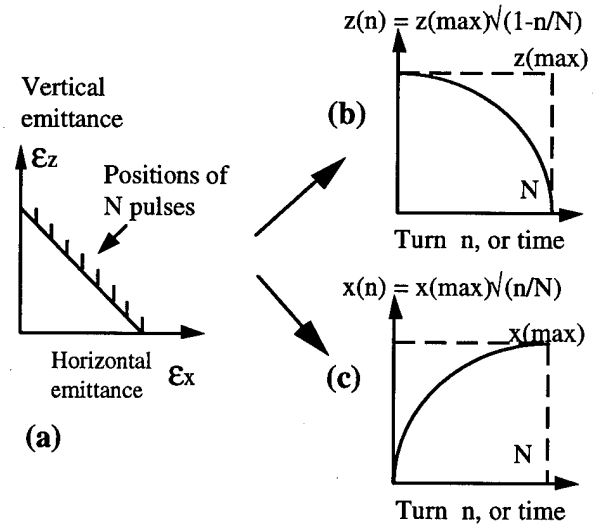


Figure 3: 'Painting' a K-V distribution.

The sinusoidal fall of the main field is not ideal for 'painting' so the position of the beam's equilibrium orbit has to be controlled in another way. This can be done by fast bumpers in both planes, starting with the maximum vertical amplitude and minimum horizontal amplitude and sweeping through to the opposite situation. Two sets of bumpers may be difficult to fit into the synchrotron lattice, so one alternative is to sweep vertically using a bumper in the transfer line. Another possibility is to use a cavity in the injection line to modulate the beam energy while injecting into a region of high dispersion in the synchrotron. This is proposed for the ESS in conjunction with a 'corner' stripping foil (see Section IIIC).

Name	Status	Type	Inj. energy into ring(s) [MeV]	Final beam energy [GeV]	Average beam power [MW]	Energy per pulse [kJ]	Repetition rate [Hz]	Ref.
IPNS [1], ANL, USA	Operational 1981	Synchrotron-driven	50	0.5	0.0075	0.25	30	[5]
KENS-I, KEK, Japan	Operational 1980	Synchrotron-driven	40	0.5	0.005	0.25	20	[5]
SNS-ISIS, DRAL, UK	Operational 1985	Synchrotron-driven	70	0.8	0.16	3.2	50	[6]
LANSCE, LANL, USA	Operational 1977	Linac-driven	800	0.8	0.08	3.9	20	[5]
TNF, TRIUMF, Canada	Operational 1974	Cyclotron-driven	-	0.5	0.15	-	Continuous	[5]
SINQ, PSI, Switzerland	Operational 1996	Cyclotron-driven	-	0.59	0.9	-	Continuous	[7]
LANSCE-II, USA	Study	Linac-driven	790	0.79	1 (5 upgrade)	16.7	20 + 40[2]	[8]
IPNS-Upgrade, ANL, USA	Study	Synchrotron-driven	400	2.0	1	33	30 or 10+20[2]	[9]
PSNS, BNL, USA	Study	Synchrotron-driven	600 (2 rings)	3.6	5	83	60 or 10 + 50[2]	[10]
ANS, Moscow, Russia	Study	Synchrotron-driven	1000	10	5	100	40+10[2]	[11]
AUSTRON III, Austria	Study	Synchrotron-driven	130	1.6	0.41	8.2	40+10[2]	[12]
KENS-II, KEK, Japan	Study	Linac-driven	1000	1.0	0.2	4	50	[13]
ETA-based SNS, Japan	Study	Linac only	-	1.5	15	150 (1 ms)	100	[14]
ESS[3], Europe	Study	Linac-driven	1334 (2 rings)	1.334	5	100	50 or 40+10[2]	[15], [16]

Table 1: Operational, planned and proposed spallation sources.

1) The Intense Pulsed Neutron Source was preceeded by the ZING-P' (1972), which was the proof-of-principle for the spallation source concept.
2) Split frequency indicates pulse sharing between two targets.
3) ESS also has a synchrotron-driven option using two rapid-cycling synchrotrons operating from 800 MeV to 3 GeV with the same overall performance.

C. Stripping foil traversals

Figure 4 illustrates some foil geometries. In Figure 4(a), the equilibrium orbit of the beam is moved to the right by a horizontal bump, so increasing the horizontal emittance, while the injection spot is scanned downwards by a bumper in the injection line. In Figure 4(b), the bottom half of the foil is removed to reduce unwanted traversals. Figure 4(c) shows a 'corner' foil. In this case, bumps move the equilibrium orbit diagonally. More aperture is needed in the injection region, but this case does offer fewer foil traversals.

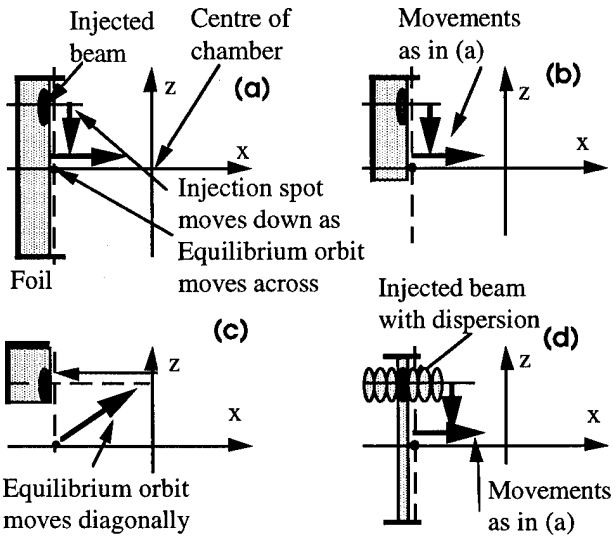


Figure 4: Stripping foil geometries (real space).

Injection usually occurs into a dispersive region of the lattice and the question arises as to whether the linac beam should be dispersion-free or matched to the ring. A dispersion-free beam is smaller and can be drawn off the foil faster, despite the fact that it suffers an emittance dilution due to the dispersion mismatch. On the other hand, the dispersion-matched beam (typically D=5 m, β=1 m) offers a special advantage with the 'strip' foil in Figure 4(d). The 'strip' foil will select a narrow momentum bite from the beam, while allowing the off-momentum halo to leave the machine along the same path as the unstripped ions.

D. RF trapping and acceleration

In synchrotron-driven sources, the rate of energy rise is usually too high for the trapping to be fully adiabatic and a tracking program that includes space charge is needed. When designing the RF programme, the optimisation is directed to reducing particle losses. Apart from the losses that occur directly from the RF bucket, limits have to be set upon the incoherent tune shift that affects losses on non-linear resonances and the momentum spread that affects the aperture. The description below is based on the design experience gained with the AUSTRON, but the basic features should be universal.

The RF cycle splits naturally into four stages starting with the injection and trapping that takes place on the falling magnetic field just before the minimum. The RF voltage is applied smoothly from a very low value and rotation in the bucket is optimised for uniformity of filling. The leading particles rotate by ~90° during injection and reach ~180° at the field minimum. Too much voltage during this first stage will increase the momentum spread in the next step. The second stage starts at the minimum field point and continues to where the momentum spread is maximum (the incoherent tune shift peaks a little earlier). This first critical point occurs typically 1 to 2 ms into the acceleration and, since the adiabatic damping has had little time to be felt, the beam reaches its maximum radial size in the dispersive regions. The smoothness and rate of rise of the RF voltage are optimised to reduce losses. Once this aperture limit is past, the third stage is entered, which runs until the middle of the acceleration cycle when the synchronous phase angle is maximum. During this stage, the RF voltage has to be increased smoothly and rapidly to maintain the bucket area. The fourth and final stage up to the top energy poses no particular problems.

One way to reduce losses during trapping is to pre-bunch the beam by chopping at a much lower energy in the injection line. This scheme features in the proposals for most future machines. Gaps of 25-40% are usually considered.

IV. LATTICE AND RESONANT SUPPLY

In order to keep the voltages applied to the magnet coils within reasonable limits (i.e. <10 kV for safe operation), the lattice should be divided into as large a number as possible of identical cells. One solution is to select an asymmetric cell (to get long and short drift spaces) and to contrive to fit all functions into these cells. SNS-ISIS follows this philosophy with 10 identical cells. At higher energies, a custom-designed lattice with superperiods becomes essential. To keep the voltages down, the upper and lower magnet coils can be separated to increase the number of identical cells as 'seen' by the resonant supply. Magnet lengths are adjusted so that field levels and saturation effects are about equal in quadrupole and dipole circuits. At around 1 GeV, a threefold symmetry is popular (e.g. AUSTRON, ESS). Fast-cycling machines use a resonant circuit with DC-biased, AC excitation known as the 'White circuit' [18,19].

V. RF-CAGE

Fast-cycling machines use insulating (ceramic) vacuum chambers to avoid power loss and field distortions due to eddy currents. To reduce static charging of the chamber walls, define the beam potentials and reduce the longitudinal transverse space-charge impedances, which are proportional to the g-factors, metallic RF shields are used that ideally follow the beam contours. A proven design for RF shields is the stainless steel cage of axial wires with vertical side plates used in the SNS-ISIS machine, but thin metallisation of the

chamber walls has been discussed as an alternative. Recent analytical work on the fields excited by longitudinally and transversely modulated beams in a wire cage can be found in [20] with approximations for the *g*-factors in [12]. The *g*-factors for a beam with elliptical cross-sectional variations in a circular, metallised chamber are also reported in [12].

VI. TRANSFER LINES

The transfer line from the linac to the ring will exhibit strong space-charge forces that will be of importance for the calculation of the debunching cavity. The injection line may also require a bend and a long straight section for momentum and betatron collimation to limit losses at injection (e.g. ESS). Space-charge effects are minimal in the high-energy, large-aperture extraction lines. A transmission target ($\leq 5\%$ interception) may be proposed for a muon experimental area and this will require a zero-dispersion, low-β insertion in the line. The background from a muon-target will need shielding and a bend in the line before entering the neutron experimental area is advisable. In order to have the maximum space for neutron lines, the target can be entered vertically (e.g. SINQ). However, this does complicate maintenance in an area that is likely to have a high level of induced activity.

VII. RADIATION MANAGEMENT

The high intensity and repetition rate of pulsed spallation sources makes radiation management of prime importance. The activation of the exhaust air and waste water must be monitored and kept below limits agreed with licensing authorities. Ventilation systems need low replacement rates (< 2 per hour). High-loss areas can be sealed and the air slowly leaked to lower-loss areas. An under-pressure is needed to prevent out-leaks. Storage of active air may be needed. All exhaust air must be filtered to remove ^{7}Be and other aerosols. Intermediate storage of waste water, shielding of ground water and secondary cooling circuits are all standard considerations. The degradation of materials such as the coil insulation needs to be estimated and radiation-hard elements used in critical places. Remote handling will be needed for the stripping foil. Care must be taken concerning dust, especially from fractured stripping foils, and exhaust air from roughing pumps must be filtered. Tight tolerances and high efficiencies for the collimator and beam control systems will be needed and machine operation should be interlocked to a beam loss measurement system. Where losses are not continuous, aluminium vacuum chambers show less induced activity than steel ones, but for steady losses over many years the reverse can be true due to the build up of ^{22}Na. Similarly, 'heavy' concrete has a shielding advantage, but after many years it can build up more long-lived isotopes than ordinary concrete.

VIII. REFERENCES

[1] P. Tunnicliffe, G. Bartholomew, E.W. Vogt eds., *AECL study for the Intense Neutron Generator*, AECL-2600, (1966).

[2] Livermore Research Laboratory, *Status of the MTA Process*, Livermore Research Laboratory, Report LRL-102 (Del) (1954).

[3] W.B. Lewis, *The significance of the yield of neutrons from heavy elements excited to high energies*, Atomic Energy of Canada Ltd., Report AECL-968, (1952).

[4] J.M. Carpenter, *Pulsed spallation neutron sources for slow neutron scattering*, Nucl. Instr. Meths., 145, 91, (1977).

[5] I.S.K. Gardner, *Review of spallation sources*, Proc. EPAC 1988, June 7-11, Rome, (World Scientific), 65-9.

[6] I.S.K. Gardner, *ISIS status report*, Proc. EPAC 1994, June 27-July 1, London, (World Scientific),3-7.

[7] H.C. Walter ed., *PSI Users Guide*, (PSI, Villigen, March 1994).

[8] A.J. Jason, R. Woods, *The Los Alamos study for a next-generation spallation-neutron-source driver*, Proc. EPAC 1994, June 27-July 1, London, (World Scientific), 2684-6.

[9] Y. Cho, Private Communication, *IPNS Upgrade*, Draft ANL-95/13.

[10] A. van Steenbergen ed., *5MW pulsed spallation neutron source preconceptual design*, BNL 60678, (June 1994).

[11] Y.Y. Stavissky, Y.V. Senichev, *Advanced neutron source for research*, ICANS-XII, RAL Report 94-025, **P**-36.

[12] P. Bryant, M. Regler, M. Schuster eds., *AUSTRON feasibility study*, (AUSTRON Planning Office, c/o Atom-institut der Österreichischen Universitäten, Vienna, 1994).

[13] *Japanese Hadron Project*, (Brochure, Inst. for Nucl. Studies, Univ. of Tokyo, March 1989).

[14] N. Watanabe, *An intense pulsed spallation neutron source using a high-power proton linac for nuclear transmutation*, ICANS-XII, RAL Report 94-025, **P**-21.

[15] H. Lengeler, *Proposals for spallation sources in Europe*, Proc. EPAC 1994, June 27-July 1, London, (World Scientific), 249-53.

[16] H. Klein, *Spallation neutron sources*, Lin. Accel. Conf. 1994, August 21-26, Tsukuba, Japan, 322.

[17] G.I. Budker, G.I. Dimov, *On the charge exchange injection of protons into ring accelerators*, Proc. 5th Int. Conf. on HE Accelerators, Dubna, 1963, (translation Conf-114, US, AEC, Div. of Tech. Info., 1372-7).

[18] M.G. White, F.C. Shoemaker, G.K. O'Neill, *The 3 BeV High Intensity Synchrotron*, CERN Symposium on High Energy Accelerators and Pion Physics, 1956, CERN 56-26, vol. 1, 525. (original single-cell circuit).

[19] J.A. Fox, *Resonant magnet network and power supply for the 4 GeV electron synchrotron NINA*, Proc. IEE 112, no. 6, June 1965. (first multi-cell circuit).

[20] T. Wang, *Electrostatic field of a perturbed beam with RF-screening wires*, CERN/PS 94-08(DI), April 1994.

COMMISSIONING THE MIT-BATES SOUTH HALL RING *

K. Jacobs, R. Averill, S. Bradley, A. Carter, G. Dodson, K. Dow, M. Farkhondeh,
E. Ihloff, S. Kowalski, B. McAllister, W. Sapp, C. Sibley, S. Sobczynski, D. Tieger, C. Tschalaer,
E. Tsentalovich, W. Turchinetz, A. Zolfaghari,
MIT-Bates Linear Accelerator Center,

and

T. Zwart,
Boston University

Abstract

The South Hall Ring at the MIT-Bates Linear Accelerator Center is a 1 GeV electron ring for nuclear physics experiments. It is designed to operate in two modes: as a pulse stretcher to deliver high duty factor beams to external targets, and as a storage ring for internal target experiments. To date we have injected beam into the ring using one and two-turn injection, stored beam with a lifetime of several minutes, and achieved early results performing half-integer resonant extraction from the ring in pulse stretcher mode. Experience in commissioning the ring is presented. Future plans for extraction, improved storage and backgrounds, and spin control and measurement in the ring, are also discussed.

I. INTRODUCTION

The South Hall Ring (SHR) at the MIT-Bates Linear Accelerator Center is now being commissioned. It is an electron stretcher/storage ring designed to serve nuclear physics experiments in two ways: as a pulse stretcher ring, converting the 1 % duty factor beam from the Bates linac into a high duty factor beam, and as a storage ring, providing high average current beams for internal target experiments. Coupled with the existing linac and recirculator, the polarized electron source, and various large spectrometers, as well as the planned large acceptance spectrometer, the SHR provides unique opportunities in medium energy nuclear physics.

The layout of the ring and its associated beamlines is shown in Fig. 1. The ring circumference is half the linac-recirculator circumference, providing for two-turn injection. Each 180° ring bend section is a symmetry corrected second order achromat. The injection straight section has flat beta at the injection point, and low betas at the internal target location. This will help in maintaining good beam lifetimes and low backgrounds with the gas-cell targets we anticipate using. The extraction straight section has a large beta at the extraction electrostatic septum to facilitate extraction. Table 1 gives a summary of ring and beam parameters.

II. COMMISSIONING EXPERIENCE

Commissioning started in early 1993. A staged approach was adopted, with commissioning of the injection line first, followed by storage in the ring, extraction from the ring, commissioning the extraction line, and finally spin control in the ring. Ring diagnostics, when fully implemented, will include 31 BPMs (x, y, and I), 12 retractable flourescent screens, a fast current monitor and a DCCT, loss monitors, and synchrotron light monitors.

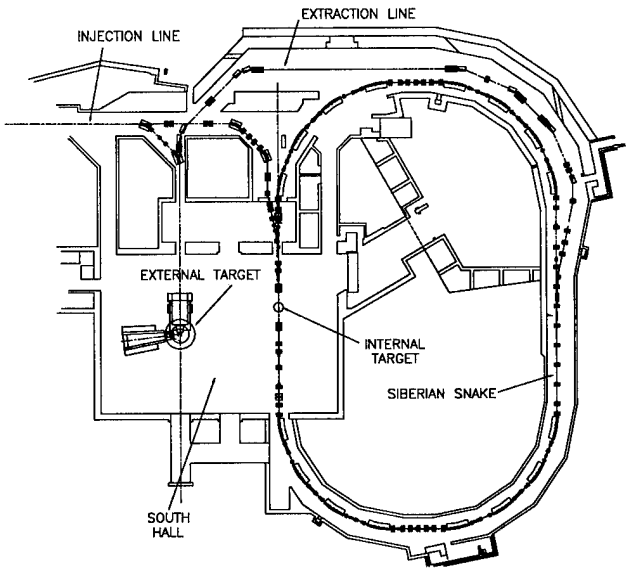


Figure 1. Layout of the South Hall Ring.

A. Storage

Initial commissioning of the ring was done using a single injection kicker and one-turn injection. Figure 2 shows the turn-by-turn current in the ring for the first several turns, demonstrating good capture efficiency. The one-turn injection goal of 40 mA current has been achieved. Using two kickers, we have also demonstrated two-turn injection.

Initially the ring was operated with no RF. In that case, energy loss due to synchrotron radiation gives a short lifetime. Figure 3 shows the beam current measured by a DCCT, for the case of no ring RF. The flat part of the current occurs as the beam is still contained within the beam-pipe, but is moving toward the inner wall of the bend sections as its energy drops. After several milliseconds, the beams starts to be lost on the wall, and the stored current drops.

When CW RF became available, we were no longer limited by synchrotron radiation losses. Lifetimes ($1/e$) of several minutes have now been obtained, as shown in Fig. 4. In order to

*Work supported by the U.S. Department of Energy

0-7803-3053-6/96/$5.00 ©1996 IEEE

Energy range	300–1000	MeV
Circumference	190.204	m
Revolution frequency	1.576	MHz
Bend radius	9.144	m
Stored current (2-turn inj.)	80	mA
Extracted current (average)	50	μA
Extracted duty factor	85	%
Injection frequency	1	kHz
RF frequency	2.856	GHz
Harmonic number	1812	
Momentum compaction	0.029	
Horizontal tune (extr. mode)	7.460	
Vertical tune (extr. mode)	7.798	
Synch. rad. losses (at 1 GeV)	9.8	keV/turn
Energy spread (with ECS)	0.04	%
Emittance (at 500 MeV)	0.01	mm·mr

Table I
SHR design parameters

achieve these longer lifetimes, it was necessary to make controlled bumps in the closed orbit, to move the beam away from apertures (most notably the injection septum). It is likely that further aperture studies will result in increased lifetimes; at this time we know of no other mechanism which should be limiting the beam lifetime. It is worth noting, however, that the lifetimes already achieved are sufficient for the planned experimental programs at Bates.

B. Extraction

Half-integer resonant extraction is used when the ring is operated in pulse stretcher mode. A ramped air-core quadrupole is used to drive the horizontal tune from 7.46 toward 7.50. DC octupoles separate the horizontal phase space into stable and unstable regions. At injection, all of the beam is in the stable region. As the quadrupole is ramped, some electrons become unstable, and eventually pass into the deflecting region of the extraction septa, where they are directed out of the ring and down the extraction beam-line.

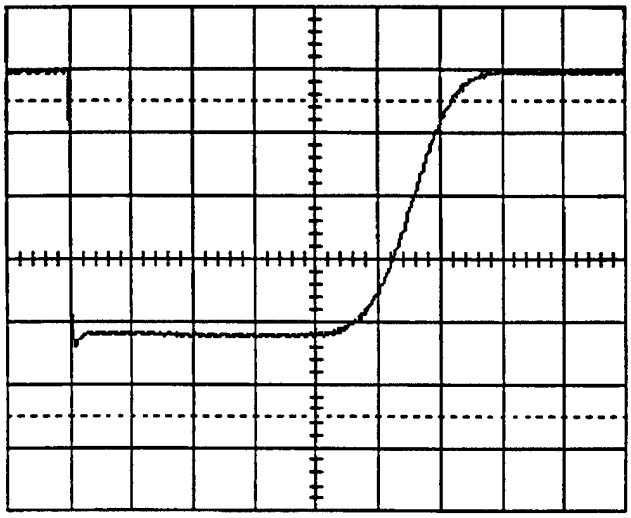


Figure 3. Stored current *vs.* time, without ring RF. The horizontal scale is 1 ms/div.

To date, preliminary extraction results have been obtained. Figure 5 shows the current stored in the ring during the extraction process, as measured by a DCCT, and the current extracted from the ring. The extracted current was measured by a photomultiplier tube aimed at a fluorescent screen in the extraction beam-line. While this does not provide a quantitative measure of how much beam was transported down the extraction line, it does demonstrate successful half-integer resonant extraction. When the fluorescent screen was removed from the beam-line, the PMT signal dropped to noise levels. In addition, the beam spot observed on the screen was well defined.

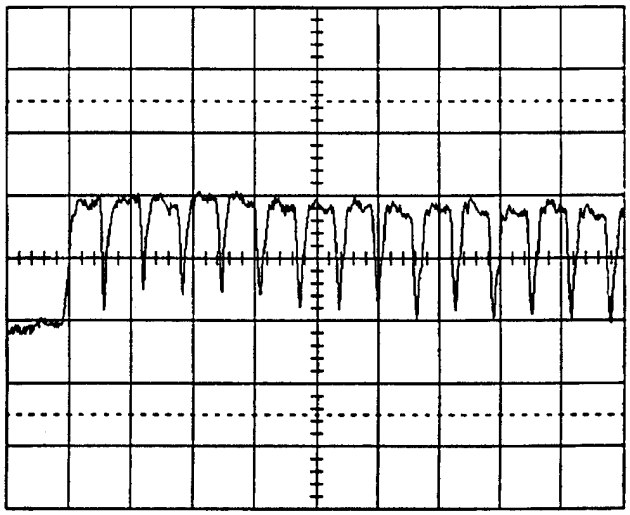


Figure 2. Current in the ring for the first several turns, using single-turn injection. The horizontal scale is 1 μs/div.

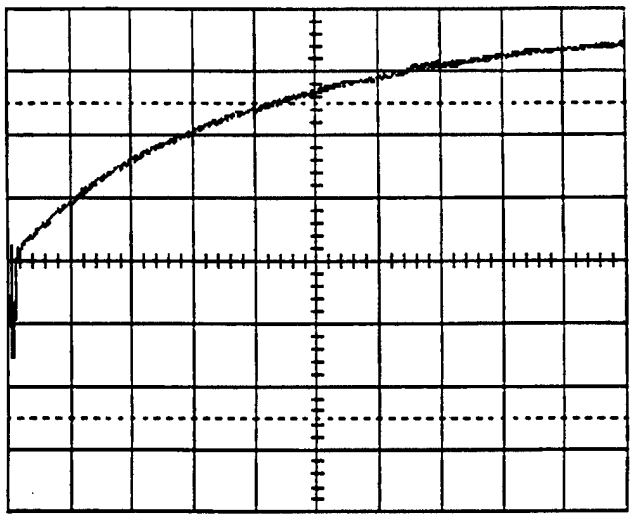


Figure 4. Stored current *vs.* time, with ring RF on. The horizontal scale is 50 s/div.

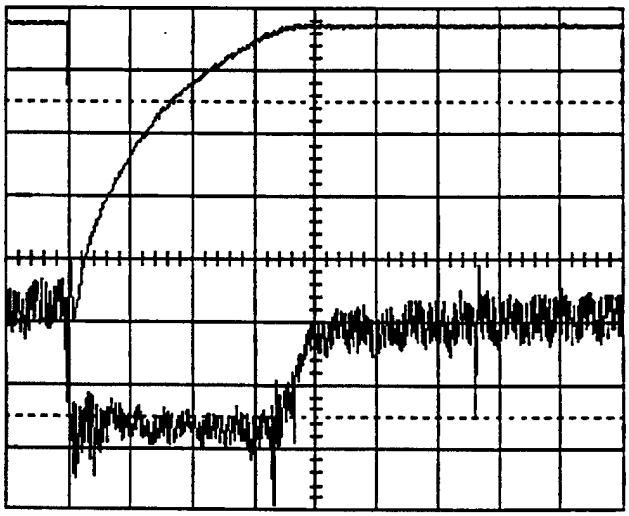


Figure 5. Preliminary results extracting from the ring. The upper trace shows the current stored in the ring, and the lower trace shows the signal from a photomultiplier tube looking at a fluorescent screen on the extraction line. The horizontal scale is 0.5 ms/div.

Beam was recently transported from the ring, through the entire extraction line, to the South Hall fixed target point, for the first time. This was not done with resonantly extracted beam, but rather with beam steered directly down the extraction line.

III. FUTURE PLANS

The work remaining to be done on the SHR falls into three categories: continuation of the work on resonant extraction, studies in storage mode to minimize backgrounds and increase lifetimes for internal target experiments, and the installation and commissioning of spin control and measurement components in the ring.

In the near future we expect to concentrate on further commissioning resonant extraction from the ring. This will include quantitative measurements of both the duty factor and efficiency of the extracted beam, with the ultimate goal being 50 μA of beam on target with good throughput and high ($\sim$ 85 %) duty factor.

Although beam lifetimes are already sufficient for internal target usage, some work remains to be done to determine the sources of backgrounds, and their cures. This encompasses backgrounds associated with injecting beam into the ring ("injection flash"), as well as backgrounds from beam stored in the ring. It is likely that what reduces backgrounds, will also result in increased lifetimes.

Electrons from the Bates polarized source will be injected and stored in the ring with their spins oriented longitudinally. To compensate for $g - 2$ spin precession at arbitrary electron energies, a superconducting solenoid (Siberian snake) will be installed on the straight section of the ring opposite the injection point. The location of this solenoid, indicated in Figure 1, is such that it will maintain longitudinal polarization both for internal targets and for fixed targets utilizing the extracted beam. The optics of the solenoid and its associated skew and normal quadrupoles has been designed such that the beam outside the snake region is not perturbed from unpolarized operation.[1] Installation and commissioning of the snake are expected to take place in late 1995.

We plan to measure the spin of stored electrons utilizing Compton backscattering. Design of the polarimeter is well underway at this time.

IV. SUMMARY

Commissioning of the MIT-Bates South Hall Ring is well underway. We have demonstrated one and two-turn injection, and have stored beam with lifetimes exceeding design goals. Good preliminary results have been obtained for resonant extraction, with more work to be done. Control of electron polarization in the ring is expected to be in place within a year.

References

[1] T. Zwart, P. Ivanov, Yu. Shatunov, R. Averill, K. Jacobs, S. Kowalski, W. Turchinetz, "A Spin Control System for the South Hall Ring at the Bates Linear Accelerator Center", these proceedings.

THE AMPS RING: ACTUAL PERFORMANCE AND FUTURE PLANS

G. Luijckx, R. Bakker, H. Boer Rookhuizen, C. de Jager, F. Kroes, L. Kuijer, J. van der Laan, R. Maas,
J. Noomen, Y. Wu, NIKHEF, P.B. 41882, 1009 DB Amsterdam, the Netherlands

The Amsterdam Pulse Stretcher AmPS is a 300-900 MeV electron storage ring with a circumference of 212 m. The ring operates either in stretcher mode to provide external continuous beams of tens of μA or in storage mode with currents up to 200 mA for internal target experiments. Machine commissioning and simultaneous operation started for nuclear physics started mid 1992. The actual performance is presented. During 1995 a polarized electron source will be added to the linac injector. A "Siberian Snake" acting as a spin flipper will be implemented in the ring; these systems have been made by the Institute for Semiconductor Physics at the Budker Institute of Nuclear Physics both at Novosibirsk as part of a scientific collaboration agreement. Results from a feasibility study on the use of the ring as a free electron laser in the VUV region are also summarized.

I. INTRODUCTION

NIKHEF is a nuclear physics and high-energy physics research institute. Since the early eighties the nuclear physics branch is specialized in electron scattering experiments using several detectors measuring in coincidence. Electron beams with a high duty factor (d.f.) are required to obtain a good real to accidental coincidence ratio. Initially electrons were provided by the 500 MeV 1 % d.f. linac MEA [1]. Meanwhile the pulse stretcher ring AmPS was designed [2] with the aim to improve the duty factor with almost 2 orders of magnitude. Installation of the AmPS facility started early 1991 and the first extracted beam on target was available by mid 1992. The optical design and the first commissioning results were reported earlier [3-5]. The facility is also used in storage mode for experiments with internal targets. Experiments with stored polarized electrons are scheduled from 1996 on. Already before the completion of AmPS the funding agency F.O.M. announced to dramatically reduce the funding of nuclear physics research in the Netherlands from mid 1998 on. As a result the AmPS facility will only be available for nuclear physics until that date. There is obviously a strong pressure on the accelerator group to deliver as much beam as possible for nuclear physics often at the detriment of proper commissioning and accelerator development. Meanwhile plans are developed to convert the AmPS ring to a free electron laser operating in the V.U.V. wavelength after 1998.

II. PERFORMANCE

A. General

AmPS is now in the production phase were it routinely delivers beams for nuclear physics.. The overall reliability has been improving gradually since the first external beam with a high duty factor was generated in 1992. In 1994 beam was available for experiments during 2200 hours: 575 h in storage mode, 1250 h in stretcher mode and 375 hours for commissioning. The unscheduled downtime was 10 %. Once tuned the ring operation normally remains extremely stable during many days but tuning of the beam, especially in stretcher mode, is still an expert process.

Table 1 shows that the obtained beam parameters so far come close to their target values.

Operation mode	Energy (MeV)	Current (mA)	Duty factor (%)
Storage	635	150	100
(internal targets)	**850**	**200**	**100**
Stretcher	600	10μA	94
(external targets)	**700**	**20μA**	**> 80**

Table 1. AmPS beam parameters available on the experimental targets (as achieved until May 1995).
The goals are displayed in ***bold.***

B. Linac

The electron linac MEA operated as a 1 % duty factor (d.f.) 500 MeV machine from 1980 to 1991. Its modulator-klystron units were then modified to provide energies up to 900 MeV at a d.f. of 0.1 % [6]. The maximum energy the linac can provide at i=0 is now 770 MeV.

The 520 pulse forming network (pfn's) units of MEA show some degradation after 15 year of operation. Presently all pfn's are successively refurbished.

Accelerating 0.7 to 2.1 μs beam pulses at currents up to 50 mA requires compensation of the transient beam loading because of the 1.2 μs fill time of the accelerator sections and the beam loading of 2.6 MeV/mA. The compensation technique is based on staggered triggering of individual modulator RF pulses. At MEA the RF triggering of each station can be altered in steps of 10 ns. This compensation method is in use for several years and can "compress" 130 MeV energy spread to approximately 5 MeV by shifted RF triggering on 4 of the 12 klystron modulators. To work satisfactorily the timing generators have to be very stable and the beam transport in the linac has to be well centered to avoid energy dependent steering by the quadrupoles.

Originally MEA was designed and constructed as a 10 % d.f. accelerator. This high d.f. required intensive cooling amongst others of the pfn's. FREON 113, a Carbon Fluor Chlorine (CFC) was chosen as a coolant and was sprayed on the pfn's. Although the present d.f. of MEA is limited to .1 % cooling of the pfn's is still required. Because of environmental requirements the use of CFC is no longer allowed in the Netherlands. Perchloroethane (p.e.r.) showed to be an acceptable substituent and the cooling systems have been adapted accordingly.

C. Ring

1. Operational aspects

Stretcher mode: one turn injection provides a very high

0-7803-3053-6/96/$5.00 ©1996 IEEE

quality beam with a macroscopic d.f. well over 90 %. Fig.1 shows a typical plot of the circulating and extracted current. When the nuclear physics detectors operate at their maximum time resolution (nanoseconds) they "see" a time structure in the beam that corresponds to the revolution frequency ; this effect reduces the d.f. to 70 %. Operation up to 3 turn injection at a horizontal tune (ν_x) of 8.3 is achieved on a regular basis but requires sensitive tuning of machine to avoid beamloss. Also the d.f. is still somewhat lower, 50 %. Stretcher operation at a $\nu_x \sim 8.25$ allowing 4 turn injection has been demonstrated but requires further investigation to ensure sufficient clearance of the beam from the injection septum. The extraction is controlled by 4 extraction sextupoles in the straight sections and by the 2856 MHz RF system. Until now only the amplitude of the RF is modulated but in the future phase modulation will be investigated too.

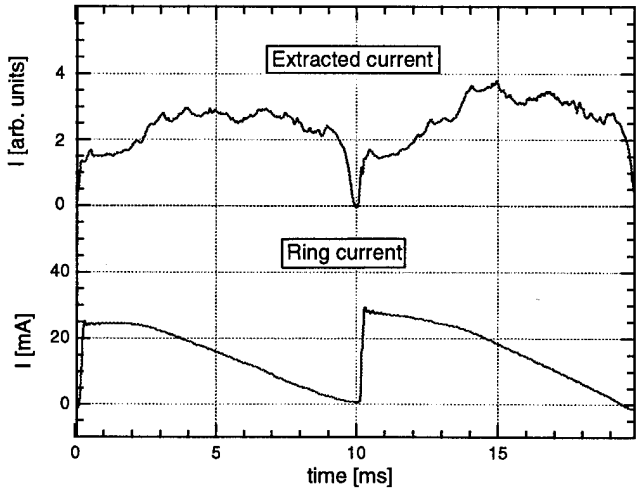


Fig.1. Typical current patterns in stretcher mode.

Storage mode: currents up to 150 mA have been stored an the maximum energy obtained was 630 MeV. Lifetime (1/e) is in the order of 30 minutes and is limited by the relatively high vacuum pressure of $1*10^{-7}$ mbar @ 100 mA beam. This lifetime is sufficient for internal target physics purposes. Up to 500 MeV RF acceleration is ensured by a 2856 MHz system [7&8]. This system normally operates at 30 kW at which level it provides an acceleration voltage of 130 kV. A 476 MHz system is available since early 1995 to allow operation beyond 500 MeV [9]. It consists of a modified single cell Doris cavity and a CW 476 MHz 30 kW transmitter. The ring can be used as a synchrotron to enable to operate at energies above the injection energy. This way an energy of 630 MeV was obtained with an injection energy of 330 MeV. The ramping speed is limited by the data transfer rate of the magnet power supplies. To eliminate this bottleneck part of the serial communication links will be converted to parallel communication in the future.

Circulating currents above 100 mA have been obtained by stacking the injection pulses. Apparently because of the poor vacuum the maximum current is limited to ~ 150 mA. At this current and pressure ions are clearly present and the clearing electrodes have to be powered (4 kV). Also tune shifts as function of the stored current have been noticed. Partial filling of the ring will be tested to increase the maximum current.

2. Machine parameters

Both beta and dispersion functions as obtained from the machine tuning procedure have been measured recently [10]. It appeared that especially the dispersion function deviated strongly from theory: there was even some dispersion in the straights while they were designed to be dispersion free . After a 1 to 2 % correction of the calculated quadrupole settings the machine functions are now close to their theoretical values. The circumference of the central orbit has been measured and appears to be ~ 1 cm shorter than the required 211. 618 m to fit 2016 buckets. In storage mode this effect is counteracted by a slightly higher oscillator frequency. In stretcher mode the RF is locked to the linac frequency so the closed orbit can't follow the central trajectory in the magnets . The linac frequency therefore will be adapted.

3. Hardware performance

Magnets [11] , septa [12] and their power supplies show a very good long-term stability and operate very reliably. Also both the 2856 MHz and the 476 MHz RF accelerator systems operate according to specification. From Fall 1995 the performance of the fast switching kicker power supplies [13] will be enhanced through new deflector insulators and improved pulse power electronics .

Diagnostics: an overview is available in ref [14]. A major drawback is the lack of a reliable closed orbit correction (c.o.c.) tool. The beam position information for the present tool comes from the 2856 MHz stripline monitors [15]. Because the cut-off frequency of the beam pipes is > 2856 MHz the slm's are sensitive to wake fields and require lengthy and tedious calibration of both sensitivity and offset at regular intervals. A new c.o.c. tool is now being developed based on the use of wobbling quadrupoles as beam position monitors [16]. Ion chamber based radiation loss detectors are very helpful in minimizing the beam loss around the ring. This is particularly important in stretcher mode when the average beam power can be as high as 15 kW.

Vacuum: the present pump capacity is based on stretcher mode operation only and is marginal for storage mode at high energy and with high currents. So NEG strips from SAES will be implemented inside of the Varian Star cell pumps mid 1995 to improve the pumping by at least an order of magnitude for light molecules (H_2)

III. FUTURE

A. Polarized electrons

A design for producing a stored beam of longitudinally polarized electrons has been made by NIKHEF in collaboration with the BINP and ISP institutes from Novosibirsk. The polarized electrons are produced by illuminating a strained GaAs photo cathode with circularly polarized light from a flash lamp pumped pulsed 5 kW Ti-sapphire laser. The polarization vector can be rotated to an arbitrary angle with a Z-shaped manipulator consisting of two

electrostatic deflectors and eight solenoids. The polarization degree can be measured with a Mott polarimeter. A 100 keV electron beam with a peak current of 40 mA and a pulse length of 2μs is extracted from the source at a maximum repetition rate of 2 Hz. A two-cavity scheme, one for bunching the electron beam coming out from the Z-manipulator and another for acceleration to 400 keV will be incorporated between the polarized electron source and MEA With this design both the polarized and the existing thermionic source can be used alternatively. The expected capture efficiency of 20 % results in an 8 mA peak current in MEA. By three-turn injection 20 mA is then captured in the AmPS ring. Consecutive pulses accelerated in MEA are stacked into the ring until the desired intensity of over 100 mA is reached. A beam with energy up to 700 MeV can be injected directly into the ring. The stored beam can also be ramped to a maximum energy of 900 MeV.

In order to maintain the polarization longitudinal at the interaction point, a Siberian Snake, consisting of two superconducting solenoids, two pairs oSf skew quadrupoles and one normal quadrupole will be installed in the East straight section of the AmPS ring. The degree of polarization of the stored beam will be measured by using a Compton back-scattering polarimeter, utilizing circularly polarized light at a wavelength of 528 nm produced by a 10 W Ar-ion laser in CW mode. Part of this work was funded by the Human Capital and Mobility program of the EEC under contracts numbered ERBCHBICT930606 and CHRX-CT93-0122.

B. High luminosity.

Luminosity for internal target experiments can be increased by reduction of both the target cell diameter and the beamsize at the IT. The present emittance is 96π mm.mrad at 700 MeV. By lowering the dispersion function η in the curves the emittance becomes 32.π mm.mrad. Of course the Twiss parameters in the curves change and they have to be matched with the straight parameters. Fortunately this results in a decreased β function value at the IT location. In total the beam diameter should be reduced by a factor of 2.7. By splitting the quadrupoles in 3 instead of 2 families this high luminosity scheme can be achieved. This requires only one additional power supply and the associated (re)cabling.

C. Free electron laser

Early 1995 a feasibility study [17] to incorporate a FEL in one of AmPS' straight sections was completed with help of Prof.. V. Litvinenko from the DFELL in Duke. It is shown that this FEL could operate in the Vacuum Ultra Violet (V.U.V.) at wavelengths below 100 nm. To ensure sufficient gain for the lasing in this wavelength region the emittance of AmPS will have to be reduced and also the peak bunch current should be increased. As a first step a 'pilot experiment' has been proposed in which two 1.3 m undulators will be used (as an optical klystron) in conjunction with a reduced-emittance confi-guration of AmPS. It is expected that coherent radiation in the 250 nm range can be produced in this set-up. The two 24 pole electromagnetic undulators with a λ_W = 11 cm are on loan from the Budker Institute of Nuclear Physics of Novosibirsk. By reducing the emittance of AmPS to the 10 nm rad @ E= 900 MeV and extending the undulator length to the range of 8 -15 m, lasing should be feasible down to the 25 nm level. A first zero-order investigation how to modify the ring lattice to enable a low emittance has been already been made [18] but although apparently feasible further detailed analysis is clearly required.

IV. CONCLUSION

The AmPs facility now operates almost completely according to the specifications required for nuclear physics experiments. Both for the near and the far future accelerator physics fun is ensured by challenging new projects.

V. REFERENCES

[1] C. de Vries et al., "The 500 MeV Electron-Scattering Facility at NIKHEF-K" , Nucl. Instr. & Meth., 223 ,pp. 1-25.

[2] G. Luijckx et al.," The Amsterdam Pulse Stretcher Project (AmPS)", Proc. 1989 Part. Accel. Conf., pp. 46

[3] R. Maas & Y. Wu," Optics of the Amsterdam Pulse Stretcher", Proc. 1989 PAC., Chicago, pp. 1689

[4] G. Luijckx et al., "The Amsterdam Pulse Stretcher, first commissioning results", Proc. 1992 HEACC, pp. 464

[5] R. Maas et al., "Commissioning results of the AmPS Ring", Proc. 1993 PAC, Washington, pp. 1998

[6] F.B. Kroes, E. Heine, " Modification of MEA modulator-klystron units enabling short pulse injection into a pulse-stretcher ring" , Proc. 1989 PAC, pp. 205

[7] J. Haimson & B. Mecklenburg, "Design and Operating Characteristics of a CW non-synchronous traveling wave structure for a 900 MeV pulse stretcher ring", Proc. of the 1992 LINAC Conf., Ottawa

[8] F. Kroes et al., "A Fast Amplitude and Phase Modulated RF Source for AmPS", Proc. 1991 PAC, , pp. 684.

[9] F. Kroes et al., "A 476 MHz RF system for the storage mode of the AmPS ring", this conference.

[10] Y.Y. Wu & R. Maas, "Machine parameter measurement of the Amsterdam Pulse Stretcher AmPS", this conference.

[11] H. Boer Rookhuizen et al., "Magnetic Devices of the Amsterdam Pulse Stretcher Ring AmPS", Proc. 1991 PAC, San Francisco, pp. 2366.

[12] A. van der Linden et al., "High Power Density, Thin Magnetic DC. Septa for AmPS", Proc. EPAC 92, pp. 1478.

[13] E. Heine et al., "Pulsed Electrostatic Kickers with Low Beam Impedance for AmPS", Proc. EPAC 92, pp. 1475

[14] J.G. Noomen et al., "Beam diagnostics for the Amsterdam Pulse Stretcher AmPS", this conference

[15] J. Noomen et al., "An over-moded stripline beam position monitor", Proc. 1993 PAC., Washington, pp. 684.

[16] P. Röjsel, "A beam position measurement system using quadrupole magnets magnetic centra as the position reference", Nucl. Instr. & Meth., 343 (1994) pp. 374.

[17] R.J. Bakker et al.," Expected Performance of FELINA, the Dutch VUV-FEL in Amsterdam ", Nucl. Instr. & Meth.in Phys. Res., 358 (1995) pp. 358.

[18] R. Maas & G. Luijckx, "AmPS, the Amsterdam Pulse Stretcher, as Photon Source", Proc. 1992 EPAC, pp. 480.

FEASIBILITY STUDY FOR USING THE FNAL ANTIPROTON SOURCE AS A LOW ENERGY $\bar{P}$ P COLLIDER

Mike Church, Fermilab, Stephan Maury, CERN

During The Fermilab fixed target program, the Antiproton Accumulator is available for internal experiments. We have investigated the possibility of using this machine as a $\bar{p}$ p collider in the energy range of 8.9 to 2.2 GeV. This would require upgrades to the current RF systems, the addition of stochastic cooling systems for the protons, and the installation of electrostatic separators. We calculate luminosities in the range of 10^{28} $cm^{-2}sec^{-1}$ at a single interaction region with beam intensities of $4x10^{11}$ and a beam-beam tune shift of .0015.

I. INTRODUCTION

The lattice of the Accumulator [1] has been designed to accept the injection of antiprotons every few seconds at an energy of 8.9 GeV. These are then momentum stacked and stochastically cooled. The antiprotons are accumulated over a period of several hours to obtain a dense core of antiprotons prior to extracting a high intensity beam towards the Main Ring and Tevatron (Fig. 1). The lattice parameters for one sector of the ring are shown in Fig. 2.

In addition to the standard operation mode described above, we study the possibility of operating the Accumulator in the collider mode, $\bar{p}$ p. We also discuss the possibility of decelerating beam in the Accumulator as low as 2.2 GeV.

II. TUNE SHIFT AND LUMINOSITY

In collider mode, 4×10^{11} antiprotons are stacked and cooled in about 8 hours. Then, 4×10^{11} protons are injected in the opposite direction using the current antiproton extraction line. The main parameters to know in this option are the tune shift and the luminosity. To get an upper limit on the luminosity, we assume head-on collisions of proton and antiproton bunches. We consider a round Gaussian beam [2,5] with n particles per unit length and with a density distribution

$$\rho(r)=\frac{ne}{2\pi\sigma^2}e^{\frac{-r^2}{2\sigma^2}}.$$

The Lorentz force on one particle at a radius r is

$$\overline{F}_r = e(E_r \pm \beta c B_\phi)\hat{r}.$$

The positive sign corresponds to a particle in the other beam and the negative sign to a particle in the same bunch. The radial electric field E_r and the magnetic induction B_ϕ can be obtained from Gauss' theorem and Ampere's law respectively. Then,

$$F_r=\frac{ne^2}{2\pi r\varepsilon_0}(1\pm\beta^2)(1-e^{\frac{-r^2}{2\sigma^2}})$$

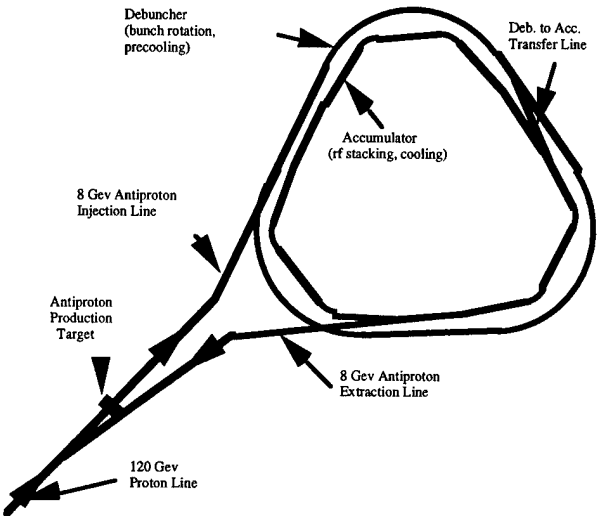


Figure 1: Antiproton Source Layout

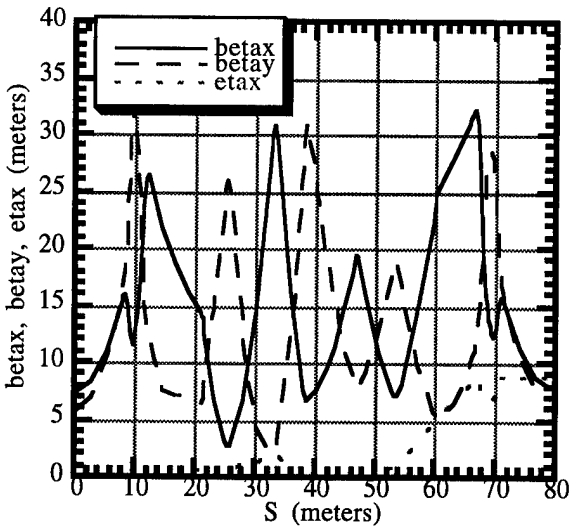


Figure 2: Accumulator lattice -- 1/6th of ring

Intrabeam scattering, Coulomb collisions between particles in the same bunch (negative sign), is counteracted by the stochastic cooling. For particles in the other beam, the effect of electric and magnetic fields is additive. We define an equivalent magnetic field B_{eq} which gives the same force:

0-7803-3053-6/96/$5.00 ©1996 IEEE

$$B_{eq} = \frac{F_r}{e\beta c} = \frac{E_r}{\beta c} + B_\phi$$

$$= \frac{ne}{2\pi r\varepsilon_0 \beta c}(1+\beta^2)(1-e^{-\frac{r^2}{2\sigma^2}}).$$

The linear tune shift $\Delta\nu$ is given by

$$\Delta\nu = \frac{1}{4\pi}\cdot K\cdot\beta^*\cdot\frac{l_B}{2} \text{ where } K = \frac{1}{B\rho}\cdot\frac{\partial B_{eq}}{\partial r}$$

where β^* is the beta function at the interaction point and $l_B/2$ is the effective length of the interaction which is half the bunch length. Putting

$$B\rho = \frac{mc\beta\gamma}{e} \text{ and } r_p = \frac{e^2}{4\pi\varepsilon_0 mc^2} = 1.535\times10^{-18} m$$

gives

$$\Delta\nu = \frac{N}{B}\cdot\frac{r_p}{4\pi\sigma^2}\cdot\frac{(1+\beta^2)}{2\beta^2\gamma}\cdot\beta^*,$$

where N is the total number of particles in the beam, and B is the number of bunches. We can express the tune shift in terms of the measured emittances containing 95% of the beam. Using $\beta^*\varepsilon_{95\%} = 6\pi\sigma^2$, gives

$$\Delta\nu = \frac{3}{2}\cdot\frac{N}{B}\cdot\frac{r_p}{\varepsilon_{95\%}}\cdot\frac{(1+\beta^2)}{2\beta^2\gamma}.$$

The luminosity per bunch [3] is defined as the product of the number of particles per bunch (N_B) of the two beams per cross-sectional area:

$$L_B = \frac{N_B^2}{4\pi\sigma^2} = \frac{3}{2}\cdot\frac{N_B^2}{\beta^*\varepsilon_{95\%}}.$$

The average luminosity is the luminosity per bunch times the collision frequency:

$$L = \frac{3}{2}\cdot\frac{N^2 f_{rev}}{B\beta^*\varepsilon_{95\%}}.$$

We can write the average luminosity as a function of the tune shift:

$$L = N\cdot\frac{f_{rev}}{r_p}\cdot\frac{2\beta^2\gamma}{(1+\beta^2)}\cdot\frac{\Delta\nu}{\beta^*}.$$

The luminosity seen by a detector is:

$$L_{\det} = L\times\frac{l_{\det}}{l_b}$$

where $l_{\det}$ is the effective detector length and l_b is the bunch length.

III. RF SYSTEMS

The bucket area per bunch as a function of RF voltage is

$$A = 16\cdot\frac{E}{H\omega_{rev}}\cdot\left(\frac{\beta^2}{H\eta}\cdot\frac{eV_{peak}}{2\pi E}\right)^{1/2}$$ [4].

We also know that for debunched beam the phase space area is:

$$A = \beta^2\cdot\frac{E}{f_{rev}}\cdot\frac{\delta p_{95\%}}{p}.$$

So, the voltage needed for a full bucket (bunching factor=1) is

$$eV_{peak} = \frac{\pi^3}{32}\cdot H\eta\beta^2\left(\frac{\delta p_{95\%}}{p}\right)^2\cdot E.$$

The voltage required for a bunching factor less than 1 is obtained from numerical integration of the longitudinal difference equations for particle motion in an RF bucket. With the addition of two new H=84 RF cavities in the ring, we can obtain 25 kV of DC RF voltage. At 8.9 GeV $\delta p_{95\%}/p$ can be extrapolated from measured data on σ_p, and at 2.2 GeV $\delta p_{95\%}/p$ is estimated from measurements made at 3.8 GeV.

IV. ACCUMULATOR COLLIDER PARAMETERS

Accumulator parameters, emittances, tune shifts, and luminosities are listed in Table 1 for 8.9 GeV and 2.2 GeV. At 8.9 GeV transverse emittance is extrapolated from the measured data. At 2.2 GeV transverse emittance is estimated from measurements at 3.8 GeV. We have used η=.012 at 8.9 GeV because it is already planned to modify the Accumulator lattice for Main Injector running. We have also assumed a detector length of 1 meter.

E (beam energy)	8.866 GeV	2.210 GeV
N (# of particles per beam)	4×10^{11}	2×10^{11}
B (number of bunches)	84	84
η	.012	-.065
β	.9944	.9053
γ	9.449	2.355
f_{rev} (revolution frequency)	.628840 MHz	.572520 MHz
β^* (effective beta function)	3.0 m	2.6 m
$\delta p_{95\%}/p$	.0008	.0006
$\varepsilon_{95\%}$ (transverse emittance)	$.25\times10^{-6}\pi$	$.17\times10^{-6}\pi$
A (phase space area)	11.1 ev-sec	1.9 ev-sec
eV_{peak} (RF voltage)	25 kV	25 kV
bunching factor	.47	.37
bunch length	3.0 m	2.6 m
$\Delta\upsilon$ (tune shift)	.0015	.0048
L_{det} ($cm^{-2}sec^{-1}$)	2.6×10^{28}	1.1×10^{28}

Table 1: Accumulator parameters in collider mode

V. DECELERATION TO 2.2 GEV

The Accumulator has been operated successfully as low as 3.8 GeV. The passage through transition is accomplished with a γ_t jump of 1.2 units. The deceleration is accomplished in

several steps, to allow for stochastic cooling in all three dimensions to counteract transverse and longitudinal emittance blow up. A deceleration efficiency to 3.8 GeV of 90% has been achieved routinely. The deceleration process has been done with an RF system on harmonic 2 with about 2.5 kV. At 2.2 GeV several issues may be of concern:

A. Stochastic Cooling

At 3.8 GeV the primary limitation to stochastic cooling has been found to be due to beam instabilities caused by trapped ions and longitudinal impedance (Keil-Schnell criterion). We expect this situation to be similar at 2.2 GeV. In cooling systems that are not gain-limited and not noise-limited (Accumulator core systems) the cooling rate is determined by the machine parameter η. At 2.2 GeV this parameter will be 4 times larger than at 3.8 GeV (in favor of better cooling). Adversely, the bad mixing (mixing from pickup to kicker) will be worse. The momentum band for effective transverse cooling in the 4-8 GHz band will be limited to approximately $\delta p_{95\%} / p = 1.0 \times 10^{-3}$ by this effect.

B. Power Supplies

Power supplies will need to be tested for stability and regulation at these low currents. At this time, there is no reason to believe they will not be well-regulated.

C. RF

In the future there will be 5 kV of H=2 RF available for bunching the beam for deceleration above 4.2 GeV. At 2.2 GeV only about half this will be available due to the fact that the cavities will be off resonance. This is adequate to completely bunch the beam provided that DC beam can be stochastically cooled to $\delta p_{95\%} / p = 1.7 \times 10^{-3}$. In operation, typical beam widths at 3.8 GeV have been $\delta p_{95\%} / p = 0.6 \times 10^{-3}$. Variable tuning capacitors could be installed on the cavities if required to increase the RF voltage at low energies.

VI. DISCUSSION

In the collider mode, new core stochastic cooling systems will be required to cool the proton beam. Two new H=84 RF cavities would need to be installed in the Accumulator for RF manipulations of the protons. Space is presently available for these additions.

In calculating the tune shift, we have assumed the beams only cross at one point in the ring (A50). This necessitates the use of electrostatic separators to separate the beams at the other zero dispersion regions (A10 and A30). We have not investigated such a system in detail, and this requires further study; however, we do not foresee any difficulty here. For example, in order to separate the beams by 4 sigma at 8.9 GeV, it would require an electrostatic 4-bump in one dimension with 4 separators, each 1 meter long, running at about 15 kV with a plate separation of 50 mm. To get a good separation in the high dispersion regions requires

$$D \bullet (\Delta p / p) \geq 2\sqrt{\beta_h \varepsilon_{95\%} + \left(D \frac{\delta p_{95\%}}{p}\right)^2}$$

where Δp is the difference in energy between the two beams and $\delta p_{95\%}$ is the beam momentum width. In the high dispersion region D=8.95 m and β_h=15.8 m, so that a separation in energy of the two beams $\Delta p / p \geq 1.7 \times 10^{-3}$ is necessary. Since the momentum aperture of the Accumulator is 1.7×10^{-2} this should pose no problem.

VI. CONCLUSION

In this preliminary feasibility study, the operation of the Fermilab Antiproton Accumulator as a $\bar{p}p$ collider from 8.9 GeV to 2.2 GeV can be envisioned with a luminosity of 2.6×10^{28} cm^{-2}sec^{-1} at high energy and 1.1×10^{28} cm^{-2}sec^{-1} at low energy. The beam separation scheme can easily be implemented. The beam energy can be continually adjusted from 8.9 GeV to 2.2 GeV except near the transition energy (γ_t=5.43). The operation of the Accumulator in this mode would require modest additions to the stochastic cooling systems and RF systems and an extensive R&D program to implement.

The use of LEAR as a $\bar{p}p$ minicollider for beam energies up to 2.2 Gev [6] has been contemplated since 1980 and was recently reconsidered [7], with similar assumptions as those made in the present paper.

VII. REFERENCES

[1] Design Report, Tevatron I Project, Sept. '94

[2] "Beam-beam Effects", LR Evans, J Gareyte, in CERN 87-03, p159

[3] "An Introduction to the Physics of Particle Accelerators", DA Edwards, MJ Syphers in Physics of Particle Accelerators, p13

[4] "Theory of RF Acceleration", G Dome, in CERN 87-03, p110

[5] Donna Siergiej, private communication

[6] Design Study of a Facility for Experiments with Low Energy Antiprotons (LEAR), CERN-PS/DL 80-7, ch 6.4

[7] "LEAR in Collider Mode Preliminary Feasibility Study", P Lefevre, PS/DI/Note 94-09

CIS, A LOW ENERGY INJECTOR FOR THE IUCF COOLER

D.L. Friesel and S.Y. Lee, Indiana University Cyclotron Facility, 2401 Milo B. Sampson Lane, Bloomington, IN 47408

Abstract

Construction has begun on a low energy booster synchrotron to replace the IUCF isochronous cyclotrons for the injection of polarized light ions into the existing 3.6 T-m electron-cooled storage ring (Cooler). CIS (Cooler Injector Synchrotron), with a circumference of 1/5th the Cooler ring, will provide $\geq 2.5 \cdot 10^{10}$ polarized protons (deuterons) per pulse at 1 Hz for Cooler injection. Bucket-to-bucket beam transfer from CIS to the Cooler operating on the 5th harmonic will fill the Cooler with 10^{11} protons in 5 sec. The higher intensity and improved duty cycle will enhance the range and quality of experimental nuclear physics research programs using Cooler beams.

I. INTRODUCTION

In August of 1994, NSF and Indiana University jointly funded the construction of a dedicated, low energy booster synchrotron to inject high intensity polarized proton and deuteron beams into the IUCF 3.6 T-m Cooler. The Cooler, which began operation in 1987[1], is presently filled with light ion beams from the IUCF cyclotrons. Strip injection of $^2H^+$ ions and cooling accumulation produces $\approx 10^{10}$ stored protons in a few seconds. A complex kick injection and cooling accumulation scheme for fully stripped polarized ions yields 10^9 stored particles in several minutes. Although both injection methods have demonstrated stacking factors of 10^3, stored Cooler beam intensities are limited by modest beam intensities available from the cyclotrons ($\approx 2\ \mu$A). Cooler intensities are is also limited (≤ 2 mA) by coherent transverse instabilities aggravated by high peak currents and phase space densities caused by rf bunching and electron cooling[2], both of which provide beam qualities required by most experimental users.

CIS will fill the Cooler with a minimum of 10^{11} protons or deuterons in a few seconds without cooled accumulation techniques, while reducing the overhead and operating expense incurred by the precise cyclotron/Cooler matching requirements presently needed to obtain optimum Cooler performance. While 10^{10} stored polarized ions will enhance the developing spin physics program on the Cooler, 10^{11} stored polarized ions will open new avenues of research. High intensity Cooler beam is also needed to fill a proposed high energy ($\leq$ 20 GeV) Light Ion Spin Synchrotron (LISS), which is currently under design.

II. CIS PERFORMANCE GOALS

The layout of the CIS ring relative to the cyclotrons and Cooler is shown in Fig. 1, and the projected beam performance and ring lattice parameters are summarized in Table I. Details of the CIS ring lattice, strip injection performance and rf accelerator cavity design are provided in separate contributions to this conference.[3], [4], [5]

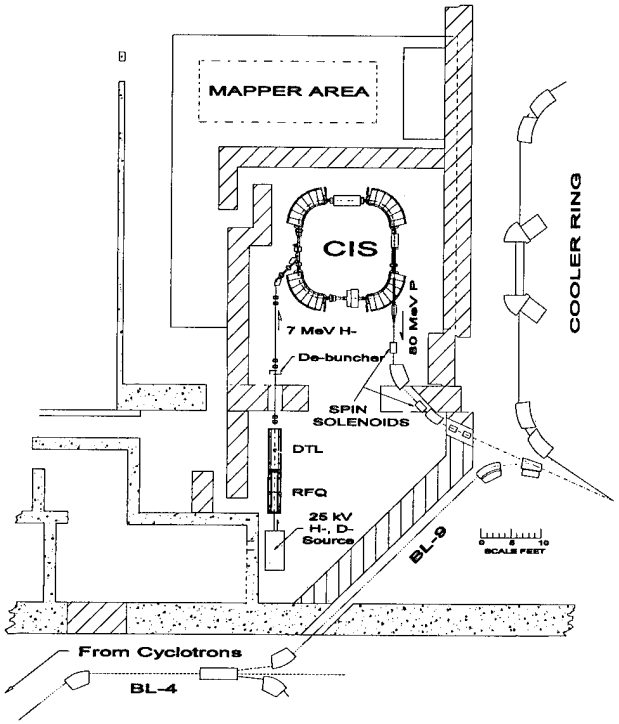


Figure. 1. Layout of CIS ring in IUCF accelerator vaults

A. Sources and Pre-accelerator

Ongoing development activities are rapidly increasing polarized H^- beam intensities towards the 1 mA level. Consequently, the CIS pre-accelerator, injection beam line and ring will be commissioned using a high intensity unpolarized H^- Cusp source to permit intensity development of the ring to its space charge limit. The existing IUCF High Intensity Polarized Ion Source (HIPIOS)[6] can then continue operation with the cyclotrons and Cooler during CIS construction. Installation of either an upgraded HIPIOS or a newer 1 mA polarized ion source will follow the initial CIS ring commissioning effort in 1997.

Polarized or unpolarized, 25 keV H^- ions are accelerated to 7 MeV via a coupled 3 MeV radio frequency quadrupole (RFQ) and 4 MeV drift tube linac (DTL) pre-accelerator operating at 425 MHz. The pre-accelerator will be fabricated and tested by AccSys Technologies, Inc.[7] and IUCF, working together as industrial partners. 25 keV D^- ions can be similarly accelerated using a separate RFQ/DTL pre-accelerator, which is not included in the initial construction program. Beam transmission from the source through the linac decreases with increasing source emittance. While the HIPIOS and Cusp source normalized emittances are less than $1.0\pi\ \mu$m, the 1 mA polarized source emittances are reported to be somewhat larger.

0-7803-3053-6/96/$5.00 ©1996 IEEE

Table I
CIS BOOSTER PARAMETERS

I. Proton Beam Properties	INJ	EXTR
Maximum Design Energy (MeV)	7	200
Initial Operating Energy (MeV)	7	80
Momentum (MeV/c)	114.8	498.2
Rigidity (Tm)	0.383	1.03
Accumulated Emittance (π μm)	34.0	10.0
Orbit Period, 7-80 MeV (μsec)	0.477	0.149
Tune Shift @ $2.5 \cdot 10^{10}$ Part.	0.03	0.006

II. Lattice Parameters	
Circumference (m)	17.364
Straight Section Length (m)	2.341
Dipole Magnet Radius (m)	1.273
Dipole Length (m)	2.0
Dipole Edge Angle	12°
Magnet Field Maximum (T)	1.68
Number of Quadrupoles	4
Hz Tune (Q_x)	1.463
Vt Tune (Q_y)	0.779
β_x (m): Max (mid-bend)	4.373
Min (mid-straight)	1.123
β_y (m): Max	3.786
Min (mid-straight)	3.342
Dispersion (m): Max (mid-bend)	1.759
Min	1.576
Momentum Compaction Factor	0.655
Chromaticity (x, y)	-0.53, -0.16

For our performance estimates, a linac transmission of $\geq$85% was calculated for a 1 mA H^- beam with a normalized emittance of 1.2π μm. The RFQ/DTL will produce beam pulse widths of $\leq$360 μsec at up to 5 Hz.

A 9.7 m injection beam line is used to both de-bunch and phase space match the linac beam to the CIS ring Twiss parameters in the injection straight. The FWHM beam energy spread is $\pm$0.5%, and will be further reduced by a factor of 3 to 5 by a de-buncher located 2.6 m from the linac exit. Space charge induced longitudinal emittance growth in this beam line is small for intensities below 1 mA.

B. Strip Injection Performance

The 7 MeV H^- (D^-) linac beam must be strip injected into the CIS ring to achieve the design goal of $2.5 \cdot 10^{10}$ particles/pulse at extraction. Beam is directed onto a carbon foil strip via a dc magnet chicane located symmetrically about the center of the injection straight section, as shown in Fig. 2. Two bumper magnets, located $\pm 90^o$ in phase advance from the foil in adjacent straight sections, move the closed orbit onto the foil during injection. A critical performance area for CIS is the intensity gain provided by strip injection of relatively low intensity polarized beams ($\leq$200 μA), particularly since the CIS extracted beam emittance cannot exceed the Cooler acceptance of 10 π μm. Detailed ray trace computer simulations using a 7 MeV H^- beam with a normalized emittance of 1.2π μm and a 90% energy spread of 0.5%,

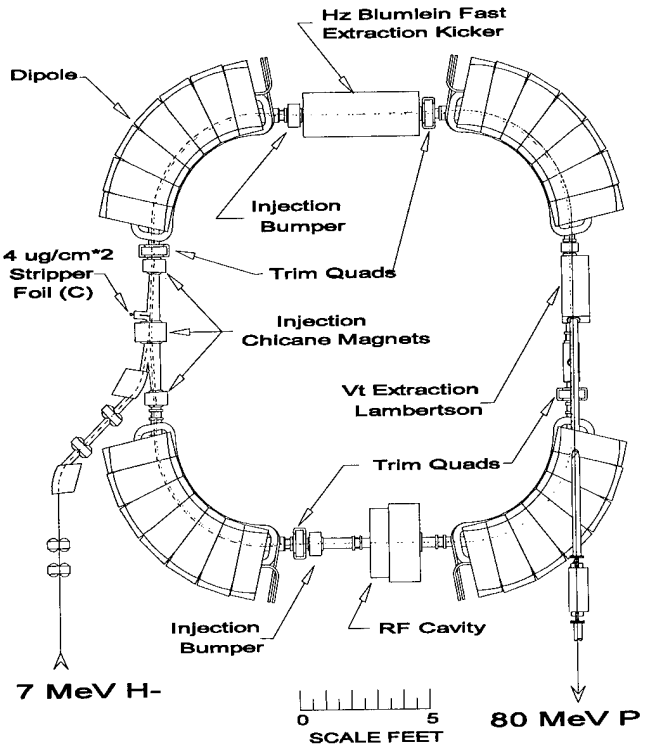


Figure. 2. CIS Ring Plan View

matched to the ring beta functions at a 4 μg/cm^2 Carbon foil strip, predict an intensity gain of 250 [4]. Consequently, a minimum H^- source intensity of 65 μA is required to achieve the design intensity goal, assuming 85% transmission through the linac and 60% transmission through CIS. Accumulation time for this intensity gain is 230 μsec, which matches well with typical beam pulse widths from pulsed polarized sources, and is within the range of the RFQ/DTL pulse structure.

IUCF has recently fabricated several 4.5 μg/cm^2 Carbon stripper foils with one and two unsupported edges of 22 mm. These will soon be tested in the Cooler to determine performance and survivability. Work is continuing to develop thinner foils, although 50% thinner foils may require accumulation times longer than the 360 μsec linac pulse width.

III. Ring Design

CIS is a weak focussing synchrotron with a superperiod of 4 and operates below transition. Primary beam focussing is determined by the C-shaped corner dipole edge angles. Dipole back leg windings and vertical steerers in each straight section are used for orbit centering. Four trim quads are available for small tune adjustments during routine operations, and can also be used to vary ring tunes and the transition energy for accelerator physics studies. The ring dipole magnet design allows acceleration of protons (deuterons) up to 200 MeV (100 MeV) at 5 Hz. However, proton energies will initially be limited to 80 MeV at 1 Hz for budgetary reasons. Future power supply and extraction element upgrades will be required to achieve the maximum design capability of the ring.

The injected beam is adiabatically captured using a VCO controlled, ferrite biased rf cavity similar in design to the IUCF Cooler MPI rf cavity[8]. The cavity operates on the first harmonic of the orbit frequency, which varies from 2.09 to 9.78 MHz for protons from injection to 200 MeV. VCO control is relinquished to beam position monitors (two radial position monitors 180° apart in phase advance) and phase feedback systems (wall gap monitor) during acceleration.

Single turn beam extraction is accomplished via a fast rise time (50 nsec) horizontal counter traveling wave (Blumlein) kicker,[9] which jumps the beam accross a 7 mm wide septum of a vertical extraction Lambertson magnet in the following straight section. An injection bumper and dipole backleg windings move the closed orbit close to the septum prior to firing the kicker.

IV. MAGNET DESIGN

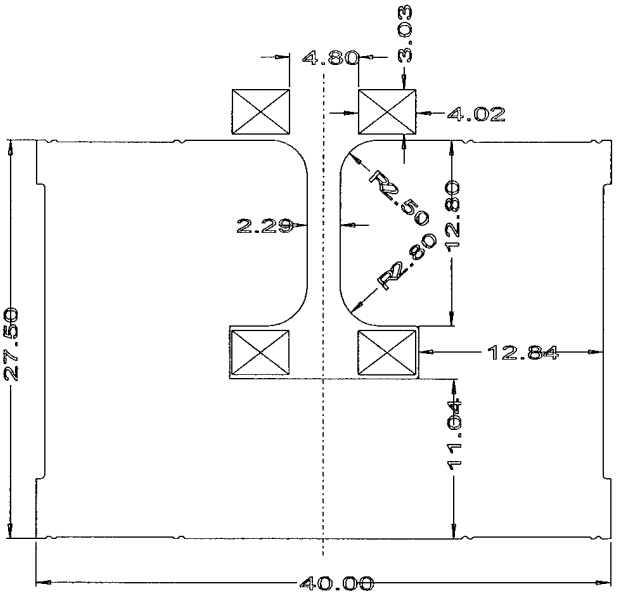


Figure. 3. Dipole Magnet Lamination (inches)

The high energy and small bending radius of CIS (see Table I) requires 90° dipole magnets with a high field (1.68 T) and large sagitta (37 cm), presenting several laminated magnet design challenges. Axially symmetric field calculations (computer code *MagNet*) were used to optimize the radial cross section of the magnet lamination shape, shown in fig. 3. A large pole width to gap ratio was chosen to keep the sextupole component below -0.6 T/m^2 at 1.68 T. No other multipoles are significant in the region ±4.5 cm either side of field center. Since the beam is affected by multipoles in the field integral, 3-d *MagNet* calculations are in progress to optimize the magnet end shape. Also, eddy current effects in the 0.06 inch thick magnet laminations and metallic vacuum chamber in the gap will also be modeled using the time transient solver in *MagNet*.

A practical magnet design was achieved with the aid of magnet experts at the FNAL, ANL-APS, and BNL magnet factories. The magnets will consist of laminated wedge shaped modules, as shown in figure 2. The blocks are fabricated from low carbon steel laminations coated with B-stage epoxy. A stacking fixture is used to assemble and compress the laminations and cured them in a hot air furnace. Strengthening plates are then welded onto the blocks prior to their being machined into wedge shapes. Five wedge shaped blocks and two parallel endpacks are then assembled on a prefabricated base plate to complete the dipole magnet.

V. PROJECT STATUS AND SCHEDULE

An intense CIS design effort beginning in August 1994 culminated in an external design review in February, 1995. Presently, the CIS dipole magnet magnet steel and lamination stamping vendor selection is underway. Detailed magnet and coil fabrication bid packages are nearly complete, with expected vendor selection before June. Field mapping and endpack fine adjustment of the first dipole is planned for January of 1996. In a parralel effort, design of the AccSys Technology RFQ/DTL Linac is complete, fabrication will begin in late May and delivery to IUCF is scheduled to occur in June of 1996. Beam development of the linac and injection beam line should begin in the fall of 1996. Many of the ancillary items required for the injection and extraction beam lines, rf accelerator cavity and de-buncher, and ac power distribution systems are either designed or have been acquired as surplus equipment. The completion of ring assembly and start of beam commissioning is scheduled for the first quarter of 1997.

VI. ACKNOWLEDGEMENTS

Many IUCF staff members provided significant contributions to the CIS design presented here, which are reported elsewhere in these proceedings. In addition, three visiting scientists, Dag Reistad and K. Hedblom from the Svedberg Laboratory, Uppsala, and Boris Sukhina from INP, Novosibirsk, have provided many usefull discussions and ideas which are incorporated into the present CIS design. This work is funded by Indiana University and the National Science Foundation under grants NSF 48-308-30875 and NSF PHY 93-14-783.

References

[1] R.E. Pollock, IEEE 89CH2669-0, 245 (1989).

[2] S. Nagaitsev *et.al.*, Space Charge Effects and Intensity Limits of Electron Cooled Bunched Beams, these proceedings.

[3] D. Li *et.al.*, The Lattice Design of IUCF CIS, these proceedings.

[4] K. Hedblom, D.L. Friesel, Stripping Injection into the New Booster Ring at IUCF, these proceedings.

[5] A. Pei *et.al.*, The Indiana University CIS RF System; A. Pei *et.al.*, The Indiana University CIS RF Cavity, these proceedings.

[6] M. Wedekind *et.al.*, IEEE 93CH3279-7, 3184 (1993).

[7] AccSys Technology, Inc, PO Box 5247, Pleasonton, CA 94566.

[8] A. Pei, IEEE 93CH3279-7, 1421 (1993).

[9] J.F. Power *et.al.*, The Los Alamos Proton Storage Ring Fast-Extraction Kicker System, IEEE NS-**32**, 3021 (1985).

The R&D Works on the High Intensity Proton Accelerator for Nuclear Waste Transmutation

N. Ito, M. Mizumoto, K. Hasegawa, H. Oguri, J. Kusano, Y. Okumura, M. Kawai*, H. Ino**, H. Murata*** and Y. Touchi***
Japan Atomic Energy Research Institute, Tokai-mura, Naka-gun, Ibaraki 319-11, JAPAN

The R&D works of the 10MeV/10mA proton linear accelerator have been carried out for last four years. A high brightness hydrogen ion source, an RFQ and an RF power source have been developed and examined to achieve 2MeV proton beam. A DTL hot test model was also fabricated and a high power test has been carried out. The present status of the R&D works are described in this paper.

1. Introduction

A high intensity proton linear accelerator (ETA: the Engineering Test Accelerator) with an energy of 1.5 GeV and an average current of 10 mA has been proposed for the engineering test of the accelerator-driven nuclear waste transmutation system[1]. To achieve low emittance beam in the low energy portion, the Basic Technology Accelerator (BTA) with an energy of 10 MeV and an average current of 10 mA is planned to be built. Table 1 shows the fundamental specifications of the BTA.

Main accelerator components of a high brightness hydrogen ion source, a radio-frequency quadrupole (RFQ), a drift tube linac (DTL) and an RF power source have been developed as the R&D works for the BTA. The ion source, the RFQ, and the RF power source were fabricated successfully and 2 MeV beam tests have been performed with construction of a beam line. For the DTL development, the hot test model was fabricated and a high power test has been made by feeding RF power. This paper describes the present status of the R&D works.

2. Ion Source Development

Based on the design of the BTA, an ion source is needed to produce hydrogen beam of 100 keV with high current (120mA) and low emittance (0.5 πmm·mrad normalized 100%)[2]. The multicusp type ion source with two-stage beam extractor has been developed to obtain a high brightness beam.

Table 1 Fundamental Specifications of the BTA

Output energy	10 MeV
Ion source	100 keV
RFQ	2 MeV
DTL	10 MeV
Operation mode	pulse
Duty Factor	10 %
Average beam current	10 mA
Peak beam current	100 mA

Beam tests of the ion source have been carried out to confirm the performance[3]. The optimum beam currents providing minimum beam divergence were measured as a function of the extraction voltage; the results are shown in Fig. 1. As shown in the figure, beam current of 140 mA has been achieved at 100 kV, which exceeds the designed value of 120 mA. The normalized emittance was measured using a double slit emittance scanner and estimated to be about 0.5 πmm·mrad (90%). The proton ratio has been also measured to be 85 % at the current of 120 mA by the Doppler-shifted spectroscopy method. The impurities level has been also confirmed to be negligibly small (<1%). The details of the performance tests are presented in Ref.3.

After the performance tests, the ion source was connected with the RFQ through LEBT to carry out the RFQ beam test and has operated stably as an injector. More precise emittance measurements are scheduled to study the beam match for the RFQ.

3. RF Source Development

For the BTA, three sets of 201.25 MHz RF sources are required with output power of about 1 MW; one set with 640 kW (duty 12%) output for the RFQ and two sets with 760 kW (duty 20%) output for the DTL. Each RF power source consists of three-stage amplifier[4], i.e., 1 MW final stage amplifier with the tetrode tube 4CM2500KG (EIMAC), 60 kW intermediate amplifier with the tetrode tube RS2058CJ (SIEMENS) and 3 kW solid state amplifier.

In the R&D works, one set of the RF source has been

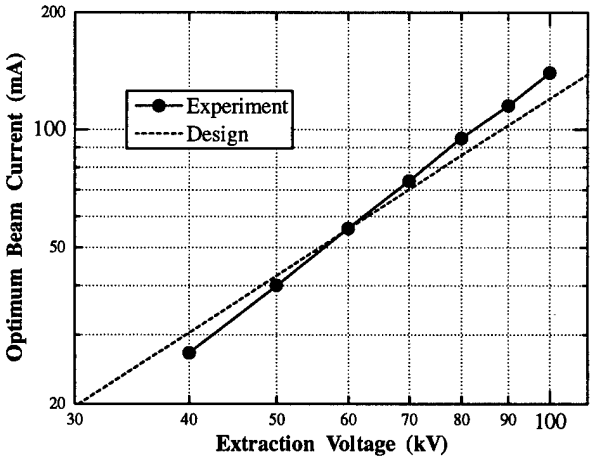


Fig. 1 Measured and designed optimum beam current from the ion source

* Toshiba Corporation
** Mitsubishi Heavy Industries, Ltd.
*** Sumitomo Heavy Industries, Ltd.

0-7803-3053-6/96/$5.00 ©1996 IEEE

developed to provide RF power to the RFQ or the DTL hot test model. The high power test has been made successfully using a dummy load. RF power output of 1 MW was achieved at the duty factor of 0.6%, whereas the measured gain of the final stage amplifier is lower than the designed value. The power efficiency was measured to be 60 % which is in good agreement with the designed value of 62 %. At the high duty operation of 12 %, RF power of 830 kW was generated, which satisfies the requirements of the R&D studies for the RFQ and the DTL hot test model.

The low level controller of the RF system includes feedback circuits to compensate power loss and phase shift due to the beam loading. The performance of the feedback system was examined in the RFQ beam test. The amplitude change was remarkably small to be within 0.5 % even when the beam loading was 110 kW. On the other hand, the phase error was relatively large to be >5 . The feedforward control system, which is also included in the RF system, will be examined to decrease the phase error.

The details of the design and the test are given in Ref. 4.

4. RFQ Development

A prototype RFQ has been developed in the R&D works of the BTA. Parameters of the RFQ are presented in table 2. The low-power tuning, the high-power conditioning and the first beam test were carried out successfully[5] at the test shop of Sumitomo Heavy Industries, Ltd. and the basic performance of the RFQ was obtained. To study further beam properties, the beam test has been made at Tokai site, JAERI since November, 1994.

The layout of the RFQ beam test is illustrated in Fig. 2. The hydrogen beam extracted from the ion source was focused by the two solenoids in the low energy beam transport (LEBT) to match the input beam emittance to the RFQ acceptance. Currents of the input and the output beam were measured by the Faraday cups of FC2 and FC3, respectively, and the RFQ transmission was deduced. The energy of the proton beam from the RFQ was measured by the compact magnetic energy analyzer (MEA) installed in the medium energy beam transport (MEBT) and was confirmed to be 2 MeV.

Figure 3 shows the RFQ output beam current as a function of the ion source extraction current, which includes H_2^+ and H_3^+ as well as H^+. In this beam test, the maximum RFQ output current is 70 mA at the ion source current of 155 mA as shown in Fig. 3. The ordinary RFQ operation with the current of 50 ~ 60 mA has been made at the ion source current of 125 ~ 135 mA to avoid over heat-loading of the ion source electrodes . The beam transmission of the RFQ has been estimated to be around 60%, although it is difficult to make the precise measurement because the net proton ratio of the beam coming into the RFQ is not clear due to the mass separation effects of the solenoids. The maximum duty factor of 5 % was achieved at the first beam test; it is limited by the over heat-loading of the RF contact between the tank and the vane. The improvement of the contact is required to achieve 10 % duty factor and the study is in progress.

Table 2 Parameters of the RFQ

Ion	Proton
Frequency	201.25 MHz
Input/Output energy	100 keV / 2.0 MeV
Beam current	100 mA (peak)
Duty factor	10 %
Number of cells	181
Vane length	334.8 cm
Cavity diameter	36.6 cm
Mean bore radius (r_0)	0.613 cm
Vane voltage	113 kV (1.68 Kilpatrick)
Q-value	9400 (71%Q)
Wall loss	360 kW (71%Q)

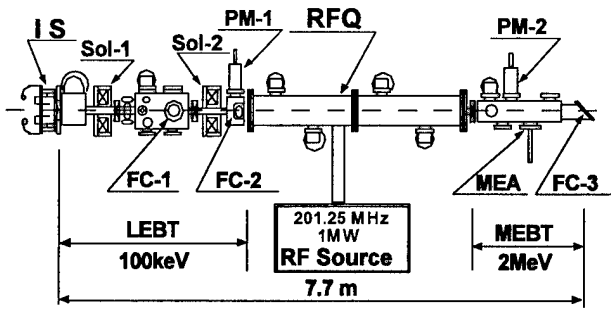


Fig. 2 Layout of the RFQ beam test
FC : Faraday cup
PM : Beam profile monitor
MEA : Magnetic energy analyzer

5. DTL Development

In the R&D works, a hot test model of the DTL with 9 cells, which is a mockup of the low energy portion of the BTA-DTL, has been fabricated to develop a hollow conductor type quadrupole magnet and to study the RF characteristics and the cooling capabilities[6]. Two electromagnetic quadrupoles have been fabricated successfully and installed in the hot test model. The cold test was made to investigate the RF characteristics.

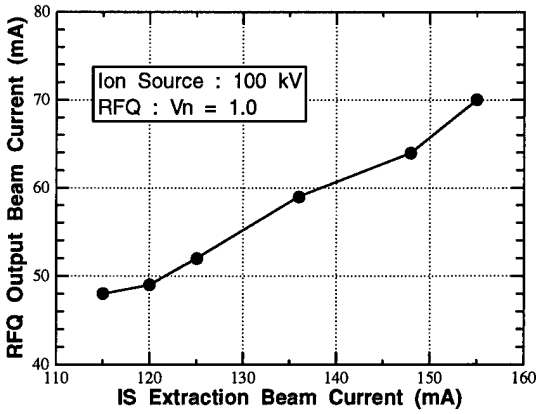


Fig. 3 Beam current accelerated by the RFQ as a function of the ion source extraction current. The ion source current includes H_2^+ and H_3^+ as well as H^+.

Parameters of the hot test model are listed in table 3.

The high power test was carried out with the RF power source. Prior to the cooling capability test, high power conditioning was made with monitoring RF signals from the pickup loop and the directional coupler, temperatures of the cooling water and the vacuum pressure. In the conditioning, the input RF power of 154 kW with duty factor of 12 % was fed to the hot test model, which exceeds the prescribed power of 130 kW as presented in table 3. Spectrum of the bremsstrahlung X-ray from the gap was also measured to estimate gap voltage. The gap voltage was measured to be 195 kV at the prescribed RF power of 130 kW, which was in good agreement with the calculated value of 197 kV by the SUPERFISH code.

As an example of the results of the cooling capability test, Fig.4 shows the power dissipation of the DTL hot test model. In the figure, histograms represent the calculated values by the SUPERFISH code and circles represent experimental results which were obtained from the calorimetric measurement (the temperature rise and flow rate of the cooling water flowing each path). The experimental results are in good agreement with the calculated values. Most of the Q-magnet heating around 7 kW was confirmed to be removed by the cooling water flowing in the hollow conductor, which satisfied our cooling design.

6. Summary

The R&D works with the design and the fabrication of the prototype accelerator components, i.e., the ion source, the RF source, the RFQ and the DTL, have been carried out. The good performance of the components has been confirmed, while some problems are remaining. For the RFQ, it is necessary to increase the duty factor and the transmission. To increase the duty factor, the improvement of the RF contact between the tank and the vane is being studied. For the increase of the transmission, the emittance measurements are being prepared to match the injected beam emittance to the RFQ acceptance. At the same time, the emittance of the RFQ output beam will be measured for the design of the BTA. For the DTL, the operation with the higher RF duty factor of 15~20% is required for the BTA and the high power test is being carried out with the higher duty factor. For the ion source, an examination of the negative hydrogen ion beam extraction is planed. These further R&D works will be performed in FY-1995 and the detailed design of the BTA has already started partly based on the results of the R&D works.

Table 3 Parameters of the DTL hot test model

Cavity	Frequency	:	201.25 MHz
	RF duty factor	:	12 %
	Average field strength	:	2 MV/m
	Number of cells	:	9
	Tank diameter	:	893 mm
	Tank length	:	1005.5 mm
	Q-value	:	42000 (83%Q)
	Wall loss (83%Q)	:	130 kW
Q magnet	Hollow conductor	:	5 ~ 5 mm^2
	Field gradient	:	80 T/m
	Excitation current	:	780 A (DC)
	Number of turn	:	5.5 Turns
	Pole & yoke	:	Fe-Co Alloy

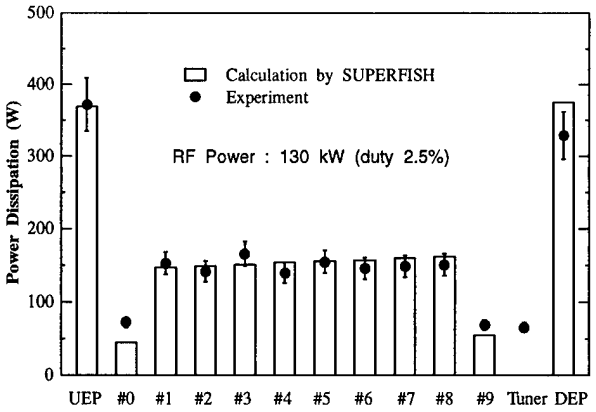


Fig. 4 Comparison of the RF power dissipation between the experimental results and the calculated values by the SUPERFISH code on the high power test of the DTL hot test model.
#0~9 : drift tube and stem
UEP : upstream end plate
DEP : downstream end plate

References

[1] M. Mizumoto et al., "High Intensity Proton Accelerator for Nuclear Waste Transmutation", 1992 Linear Accelerator Conference, Ottawa, Canada, AECL-10728, p.749-751 (1992).

[2] Y. Okumura and K. Watanabe, "Design of a High Brightness Ion Source for the Basic Technology Accelerator (BTA)", Japan Atomic Energy Research Institute Report JAERI-M 92-024 (1992).

[3] H. Oguri et al., "A High Brightness Hydrogen Ion Source for the BTA at JAERI", Proc. of the 1994 International Linac Conference, August 21-26, 1994, Tsukuba, Japan, K. Takata Editor, p.381-383.

[4] Y. Touchi et al., " An RF System for the BTA", 4th European Particle Accelerator Conference, June 27 - July 1, 1994, London, edited by V. Suller and C. Petit-Jean-Genaz, p.1900-1902.

[5] K. Hasegawa et al., "First Beam Test of the JAERI 2MeV RFQ for the BTA", Proc. of the 1994 International Linac Conference, August 21-26, 1994, Tsukuba, Japan, K. Tanaka Editor, p.113-115.

[6] N. Ito et al., "Fabrication and Tests of the DTL Hot Model in the R&D Works for the Basic Technology Accelerator (BTA) in JAERI", ibid., p.119-121.

Development of the RFD Linac Structure*

D.A. Swenson, K.R. Crandall‡, F.W. Guy‡, J.W. Lenz‡, A.D. Ringwall‡, and L.S. Walling‡
Linac Systems, 2167 N. Highway 77, Waxahachie, TX 75165

The new Rf-Focused Drift-tube (RFD) linac structure resembles a drift tube linac (DTL) structure with rf quadrupole (RFQ) focusing incorporated into each "drift tube". As in the conventional DTL structure, these drift tubes are supported on single stems along the axis of a cylindrical cavity excited in the TM_{010} rf cavity mode. Four electrodes of each drift tube couple energy from the primary cavity mode to produce rf quadrupole focusing fields along the axis of the drift tube. The rf properties of this three-dimensional structure are being studied with the aid of HFSS (3D-rf code), CHARGE-3D (3D-electrostatic code), and SUPERFISH (2D-rf code). The beam dynamics of this structure is being analyzed with the aid of a new PARMILA-like beam dynamics code, PARMIR, and TRACE-3D. The results of these studies and descriptions of our target applications are presented.

I. Introduction

The RFD linac structure[1], resembles a DTL with RFQ focusing incorporated into each "drift tube". As in a conventional DTL, these drift tubes are supported by single stems along the axis of a cylindrical cavity excited in the TM_{010} rf cavity mode. These "drift tubes" comprise two separate electrodes operating at different electrical potentials, as determined by the rf fields in the cavity, each supporting two fingers pointing inwards towards the opposite end of the drift tube, forming a four-finger geometry that produce an rf quadrupole field distribution along its axis.

The fundamental periodicity of this structure is equal to the "particle wavelength", $\beta\lambda$, where β is the particle velocity in units of the velocity of light and λ is the free-space wavelength of the rf. The particles, traveling along the axis, traverse two distinct regions, namely gaps between drift tubes where the acceleration takes place, and regions inside the drift tubes where the rf quadrupole focusing takes place.

This structure uses both phases of the rf fields to affect the beam; one for accelerating the beam and the other for focusing the beam. In this case, the "reverse phase" does not decelerate the beam because the fields inside the drift tubes are distorted into transverse focusing fields with little longitudinal component. The orientation of the fingers in the focusing regions alternate so as to create an alternating focusing and defocusing action on the beam in each transverse plane.

The distribution of voltage between an accelerating gap and a neighboring focusing region is inversely proportional to the intra-electrode capacitance of each region. A most interesting feature of this structure is the ability to have a relatively high voltage on the relatively low capacitance accelerating gap while putting an adequate voltage on the focusing region.

II. Evolution of the Geometry

When first conceived, and as originally described, the rf focusing fields were completely contained within a drift-tube-like metallic shell. Indeed, there were some gaps in the shell allowing the fore- and aft-portions of the drift tubes to ride at different potentials, as determined by the axial electric field of the drift tube linac structure, thereby giving rise to a potential difference across the internal four-finger geometry that produced the rf quadrupole focusing field.

Even though a portion of the cell excitation is called upon for excitation of the rf quadrupole lens, the entire cell excitation is available for particle acceleration. The potential differences between the centers of drift tubes in the RFD structure is exactly the same as it is in the DTL structure for the same cell length and axial field.

In the DTL linac structure, the drift tubes concentrate the axial electric fields into the vicinity of the gaps resulting in a net acceleration from the rf fields, expressed quantitatively in terms of a transit time factor. In the RFD linac structure, the rf quadrupole electrodes extend the average potential of the drift tube along the axis towards the gaps, resulting in a concentration of electric fields in the gaps and acceleration from the rf fields, expressed in terms of a transit time factor.

For very short RFD cells, where a substantial portion of the cell voltage is required across the rf quadrupole lens, the original configuration tended to elongate the effective length of the gap fields, which resulted in a reduced transit time factor and acceleration rate. Our principal RFD geometry now involves rf quadrupole lens electrodes that are exposed to the rf gap accelerating fields. This results in transit time factors, for the RFD linac structure, that are similar to those of the more familiar DTL linac structure.

As originally conceived, the rf quadrupole lens electrodes were supported through thin rings of ceramic from a water cooled drift tube body, supported from the tank wall on a single stem as shown in Fig. 1. Recently, we have developed an understanding of the effects of inductive stems on the structure. Circuit-wise, these inductive-stem drift tubes appear as LC circuits in series with the drift tube linac gap capacitances. They offer better cooling for the two essential electrodes and elimination of the ceramic spacers. They still offer a complete drift tube package supported from the tank

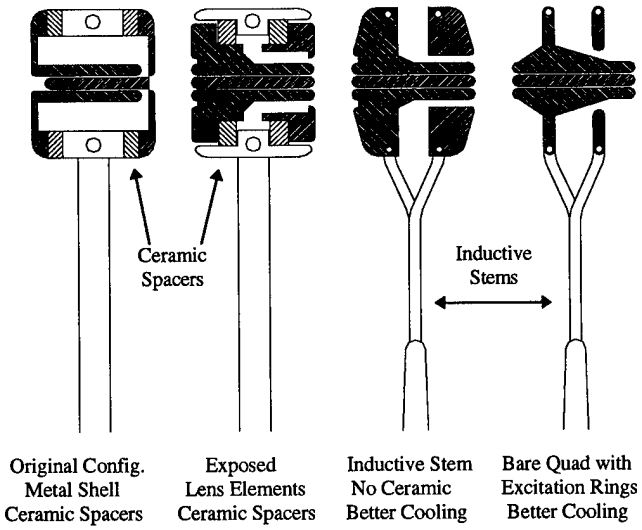
* Supported by SBIR Grants DE-FG03-94ER81797 and MH53750-01.
‡ Consultants to Linac Systems.

0-7803-3053-6/96/$5.00 ©1996 IEEE

wall at a single point. The relative alignment of the four fingers can be inspected "on the bench" and adjusted if necessary. This preserves the simplicity of installation and alignment of our original configuration.

The latest step in the evolution of the RFD geometry involves the development of the "bare quad" configuration, which resembles four bare rods surrounded by two ring electrodes at different longitudinal stations, each of which are attached to an opposing pair of rods. The rods provide a good transit time factor for acceleration of the particles and a minimum capacitive loading to the drift tube linac circuit to insure the highest possible acceleration efficiency for a DTL-like structure. The rings provide a source of excitation for the rf quadrupole lens.

Fig. 1. Evolution of the RFD Geometry.



III. Merits of the Structure

The RFD Linac Structure opens the door to 850-MHz DTLs, just as permanent magnet quadrupoles opened the door to 425-MHz DTLs a decade ago. Each factor of two in frequency brings an order of magnitude reduction in the space available for focusing elements. The electrodes of the RFD are more readily scaleable to small dimensions than are permanent magnet quadrupoles.

Higher frequencies imply shorter cells and require smaller diameter beams for efficient acceleration. RFD linacs, which employ the same rf electric focusing as in RFQ linacs, will have the same small diameter beams that we have in RFQ linacs.

These higher frequencies offer higher efficiencies (shunt impedances), higher acceleration gradients (shorter structures), less rf power to generate, less thermal load on the cooling system, less weight, and less surface area to evacuate. These compact structures will be more transportable that their predecessors and, when required, will be easier to enclose in radiation shielding.

Fig. 2 compares the acceleration efficiencies for several linac structures that have been considered for 850-MHz operation, including the RFD, a permanent-magnet-focused DTL (PMQDTL), bridge-coupled DTL tanks (BCDTL)[2], and Coupled-Cavity DTL cells (CCDTL)[3]. The data are raw SUPERFISH results without any degradation for support stems, post couplers, coupling slots, bridge couplers, joints and/or surface finishes. The gap lengths in all cases were $\beta\lambda/4$. The RFD and PMQDTL, which include provisions for beam focusing within the basic structure, have bore diameters of 3 mm and are assumed to be long structures without significant end effects. The BCDTL and CCDTL structures, which do not provide focusing within the basic structure, have bore diameters of 6 mm and are broken at intervals of $5\beta\lambda$ for insertion of focusing elements with lengths of $1.5\beta\lambda$. The power and real-estate losses associated with these breaks are included in the net results. The drift tubes of all structures, except the PMQDTL, are 20 mm in diameter; the diameter of the drift tubes in the PMQDTL are 50 mm to accommodate the permanent magnet quadrupole lenses.

The RFD Linac Structure is also extendible to lower energies than possible for magnetically focused structures. At all proton energies above 0.5 MeV, the RFD structure, as shown in Fig. 2, is more than competitive with the RFQ structure. At 0.5 MeV, the RFD structure is approximately equal to the RFQ structure in acceleration efficiency; at 1 MeV, it is twice as efficient as the RFQ; at 2 MeV, it is 4 times more efficient; and at 5 MeV, it is 10 times more efficient. The RFD Linac Structure has significant advantages in acceleration efficiency over both RFQs and other DTL-like structures.

IV. Tools for the Development

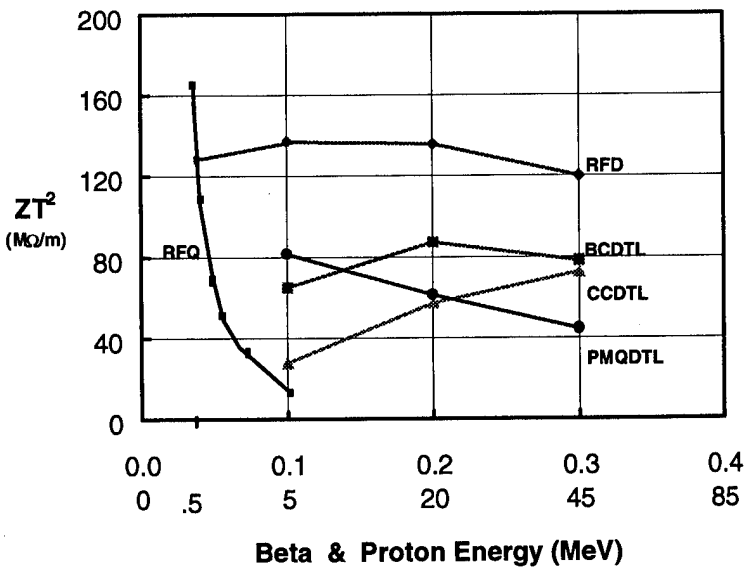


Fig. 2. Acceleration Efficiencies for Several Linac Structures.

The design and optimization of the drift tubes of the RFD Linac structure represents one of the most challenging technical tasks in the development of the structure. As the interior of the drift tubes are highly three dimensional, use of a 3D-RF code is required for precise information on resonant frequencies, field distributions, power dissipation, and other cavity parameters.

Calculations are currently in progress using Hewlett Packard's High Frequency Structure Simulator (HFSS) code, a 3D Finite Element RF and Microwave Modeling Code. It utilizes a solid modeling user interface, has a frequency domain solver, and requires at least one port to excite the structure. Output is in the form of s-parameters, fields, and field derived quantities. The elements of the geometry are tetrahedrons and structures can be developed as many different regions of differing element sizes. This allows accurate modeling, even for small irregular objects within larger structures, with a manageable problem size. The mesh is created and adapted automatically by the code. For complex geometries, the mesh generation process can be enhanced by "seeding" certain regions with user defined meshes. The code supports lossy materials and boundaries.

We have used the results from HFSS to verify that rf energy does indeed get inside the drift tubes, to reveal the field distribution along the axis of the drift tube, to establish the voltage division ratio between the drift tube gap and the rf lens, to get some indication of the strength and distribution of the rf fields inside the drift tube, to get some information on the distribution of the electric fields near the axis of the structure, to establish the frequency perturbation that the drift tube body capacitance imposes on the structure, and to get some idea of the ratio of the rf power losses inside the drift tube to the losses in the rest of the structure.

Once the effective properties of the interior of the drift tubes are determined by three dimensional calculations, effective use can be made of the two-dimensional rf codes, such as SUPERFISH, for further optimization of the structure. We have conceived of a SUPERFISH geometry that presents the correct capacitive loading to the cavity and has the correct effect on the axial field distribution. The resonant frequencies, voltage division ratios, and transit time factors agree quite well with those rendered by HFSS. HFSS has served to verify the utility of SUPERFISH for general RFD Linac design purposes.

The multipole content of the rf fields inside the fingers are essentially identical to what we find for electrostatic excitation of the fingers. Hence, useful approximations of these quantities are determined from the 3D electrostatics code, CHARGE-3D, written by one of the authors (KRC) in the early 1980's, and modified by him to support studies of the RFD linac structure.

The analysis and optimization of the beam dynamics in this structure represent another challenging technical task. A PARMILA-like beam dynamics code, PARMIR (Phase And Radial Motion In RFDs), was written to facilitate the study of the beam dynamics in this new linac structure. PARMIR simulates multiparticle beam dynamics in drift tube linacs that employ rf focusing inside the drift tubes. The formulation includes hard- and soft-edged quadrupole fringe fields and dodecapole effects. This code has been used extensively in our studies of the RFD structure. Recent modifications include a more precise soft-edged fringe field treatment, adjustability of bore size and lens voltage with beam energy, and incorporation of a variety of possible focusing options that may be advantageous for some applications.

Useful information of the performance of these structures can be obtained from the well known linear beam dynamics code, TRACE-3D. The RFD structure can be described to TRACE by using three types of elements; an RFQ with no acceleration, a drift, and an rf gap. Even though it cannot simulate non-linear fields or space charge forces, it can yield valuable information on the properties of the matched beam in the structures and a measure of their relative performance.

Thermal and mechanical analyses of the structures are being conducted with the aid of the finite element analysis code, COSMOS/M.

V. Applications for the Structure

At the present time, we are addressing the development of the RFD linac structure towards three distinctly different proton beam applications, namely;

1) Intermediate Energy (6-14 MeV), High Grad. (10 MV/m), Low Duty (0.5 - 2%), Proton Accelerator for the PET Isotope Production and/or Proton Synchrotron Injector Applications,

2) High Duty (100%), Low Energy (2.5 - 4 MeV), Low Grad. (1.5 MV/m) Proton Accelerator to produce Thermal and Epithermal Neutrons for the Neutron Radiography, Thermal Neutron Analysis (TNA), and Boron Neutron Capture Therapy (BNCT) Applications, and

3) Very High Frequency (3 GHz), High Energy (40-70 MeV), High Gradient (12 MV/m), Low Duty (0.1 %), Low Current (1-mA) Accelerator for the Proton Therapy Applications.

VI References

[1] D.A. Swenson, "Rf-Focused Drift Tube Linac Structure", Proc. of 1994 Linac Conference, p. 804.

[2] R.W. Garnett, D. Liska, G. Lawrence, and T. Larkin, "--BCDTL--", Proc. of 1992 Linac Conf., p. 802.

[3] J.H. Billen, K.L. Krawczyk, R.L. Wood, and L.M. Young, "--CCDTL--", Proc. of 1994 Linac Conf., p. 341.

PROPOSED UPGRADE OF THE NSCL*

R. C. York, H. Blosser, T. Grimm, D. Johnson, D. Lawton, F. Marti,
J. Vincent, X. Wu, and A.F. Zeller
National Superconducting Cyclotron Laboratory
Michigan State University
East Lansing, MI 48824-1321 USA

Abstract

The present nuclear physics program at the National Superconducting Cyclotron Laboratory (NSCL) is based on an ECR-ion-source-injected K1200 superconducting cyclotron. We propose to significantly increase the facility's output intensity for light ions and energy for heavy ions by coupling the existing superconducting K500 cyclotron's output to the K1200. The improved acceleration chain will consist of an ECR-ion-source-injected K500 cyclotron to accelerate ions to $\leq$17 MeV/nucleon followed by radial, charge-stripping injection into the K1200 for final acceleration to 100-200 MeV/nucleon.

	^{11}Li	^{19}Ne	^{32}Mg	^{56}Ni	^{132}Sn
K1200 & A1200	2.5×10^{3}	6×10^{7}	1.2×10^{3}	7×10^{4}	2
K500⊗K1200 & A1900	4×10^{6}	1×10^{10}	3×10^{6}	1×10^{8}	4×10^{4}

Table I

Intensities (ions/sec) of representative radioactive beams achievable with K1200 stand-alone operation compared to those predicted for the K500⊗K1200 coupled cyclotron operation using the A1900 fragment separator.

I. INTRODUCTION

The NSCL proposes to couple its two superconducting cyclotrons (K500 and K1200) and to replace the existing fragment separator (A1200) with one of increased capacity (A1900) as shown in Figure 1. Since the upgrade relies on the existing cyclotrons and incorporates the present experimental facilities, it can proceed in a timely (~4 - 5 years estimated project duration) and cost-effective fashion (~ 19M FY94 US$ in total project costs including labor and materials).

The coupling of the cyclotrons (K500⊗K1200) will provide significant increases in the primary beam intensity and for the heaviest ions, in beam energy permitting a wide variety of experimental programs to be undertaken which are presently not feasible.

II. PERFORMANCE

The maximum theoretically achievable energy is determined by the characteristics of the K1200 cyclotron. The improvements in energy and intensity that come with coupling the cyclotrons result from the lower charge states required from the ECR ion source for the K500⊗K1200 mode. These lower charge states needed from the ECR to achieve the same final energy have significantly more intensity than the higher K1200 stand-alone charge states.[1]

Large gains in intensity are possible for all ions considered, and in addition, there are significant gains in energy for mid and high-mass nuclei. Figure 2 shows these gains and also illustrates the possible trade-off of intensity for energy. Shown are contours of intensity as a function of E/A and A for the K500⊗K1200 operation (solid lines) and the present K1200 stand-alone operation (dashed lines). The intensities are also given at specific points for the K500⊗K1200 operation (solid) and stand-alone operation (open). For heavier beams, the intensity gains for highly charged ions effectively result in higher energy beams (by factors of 2 - 4). Note that energies of over 100 MeV/nucleon are possible for uranium, while intensities up to 6×10^{12} particles/s are possible for lighter ions.

The greater intensities for the lighter ions are an excellent match to the needs of the growing field of nuclear physics research using radioactive ion beams, as they can be converted into very intense, good-quality secondary beams. To fully capitalize upon the increased primary beam intensities for the production of secondary radioactive beams, a large projectile-fragment separator (A1900) is proposed. In order to produce and separate rigid neutron-rich nuclei at optimal production energies, the A1900 will have ~30% greater bending power than that of the cyclotron (K1200), and will have a collection efficiency for fragmentation products approaching 50% compared to the 2-4% for the present NSCL system (A1200). Intensities for some representative ions are given in Table I.

III. DESIGN

Some parameter details for the injection chain are given in Table II. Ions of charge state Q_1 will be produced in an ECR ion source, transported from the ion source area to a point below the K500 and axially injected into the K500 central region. Ion intensities of ~ 10^{13} particles/s will be accelerated in the K500 in approximately 230 turns to energies of $\leq$ 17 MeV/u. The beams will then be transported to the K1200 with a system of magnetic elements and an rf system (used to control the bunch length between the two cyclotrons) and injected through an existing horizontal port to a point at approximately one third of the K1200 extraction radius (~0.33 m) where they will be stripped to a higher charge state Q_2. Finally, the beam of charge state Q_2 will be accelerated in the K1200 to final energies of $\leq$200 MeV/u and extracted. Following the K1200, the extracted beam will be

*Work Supported by Michigan State University and NSF Grant # PHY9214992.

0-7803-3053-6/96/$5.00 ©1996 IEEE

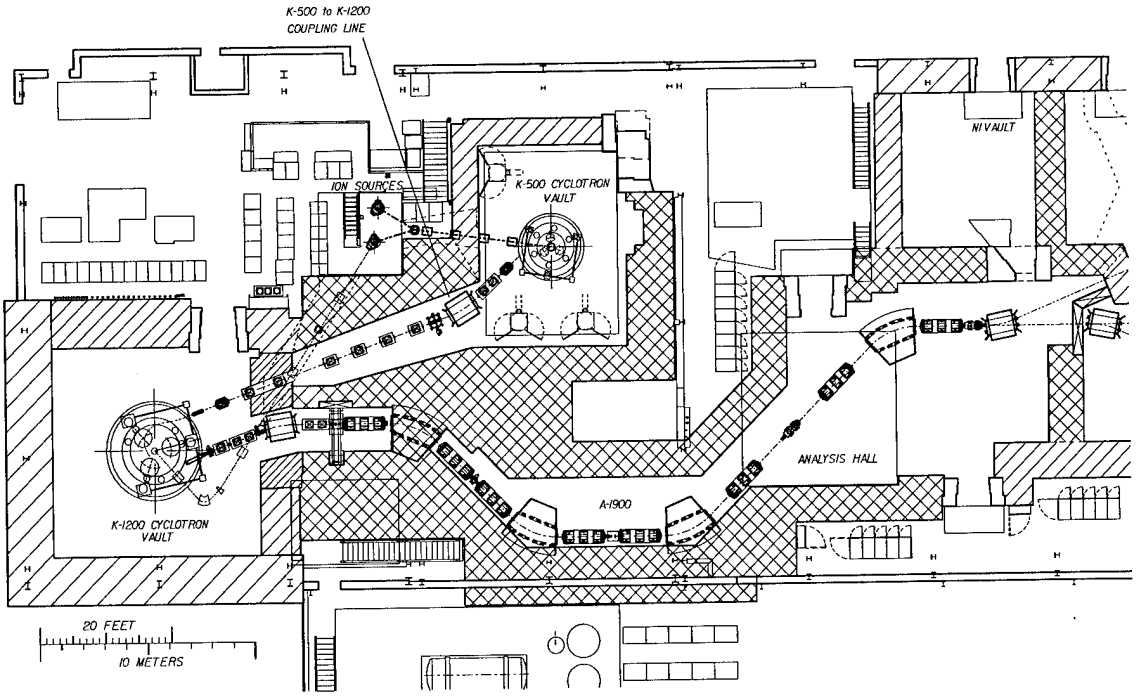


Figure 1. Proposed new accelerator area of the National Superconducting Cyclotron Laboratory.

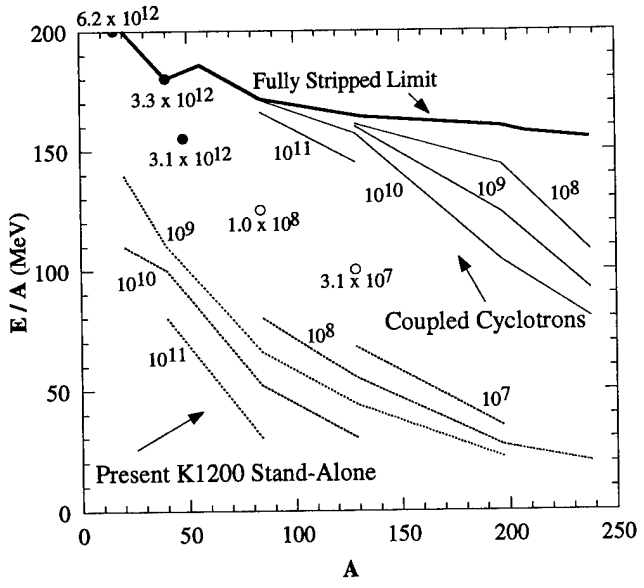


Figure 2. Operating diagram for the present K1200 stand-alone cyclotron and the K500⊗K1200 system. Intensity contours in particles per second are given for the K1200 stand-alone cyclotron (dashed) and the K500⊗K1200 (solid). The intensity is also given at specific points for the K1200 stand-alone (open) and the K500⊗K1200 (solid) operation. The present K1200 stand-alone performance contours are based upon the performance of the room temperature ECR with specific points (open) based upon the superconducting ECR performance.

	K500		Strip.	K1200		
Ion	Q_1	Energy (MeV/u)	Effic. %	Q_2	Energy (MeV/u)	Intensity (part./s)
^{16}O	3	16.7	100	8	200	6.2×10^{12}
^{84}Kr	15	14.7	2.2	36	170	2.1×10^{10}
^{238}U	32	8.6	2	74	90	1.2×10^{9}

Table II
K500⊗K1200 parameter details for selected ions.

optically matched to a new beam analysis system, the A1900. As with the present A1200 analysis system, the A1900 will be positioned as the first element of the switch yard so that any beam, including separated fragments, can be delivered to any of the experimental areas.

IV. PROJECT SCOPE

The operating voltage of the existing superconducting and room temperature ECR ion sources will be increased from ~ 20 kV to ~ 30 kV in order to mitigate space charge effects, increase the beam brightness, and reduce the deleterious effects of the K500 fringe fields on the injection process. The existing coupling line between the K500 and the ECR ion sources will be modified in order to provide for efficient transport of high intensity beams.

The K500 cyclotron will be refurbished to obtain the operating reliability which is currently achieved by the K1200 cyclotron (>90%). During the refurbishing process, the K500 will be disassembled with reassembly in a position rotated 120° from its present position to orient the extraction channel towards the K1200. In addition to the implementation of proven K1200-like engineering solutions, a new central region will be used to allow

Task	Funding Required (FY94 M$)
ECR/Injection Upgrade	0.50
K500 Upgrade	3.08
Coupling Line	2.11
K1200 Upgrade	1.29
A1900	4.46
Building Systems Upgrades	3.67
Commissioning	0.15
Total	15.26
Contingency (~25%)	3.68
Grand Total	18.94

Table III
K500⊗K1200 Costs in FY94 M$.

Item	Achieved	K500⊗K1200 Specification
ECR to K500 Transmision	≥50%	50 %
ECR Voltage	20 kV	≤30 kV
K500 Injection Efficiency	~5%	6 %
K500 Extraction Efficiency	~80%	90%
Overall Transmission	~2%	2.7%
Extracted Emittance (πmm-mrad)	~10	~3

Table IV
Results achieved to date compared to K500 specifications for the K500⊗K1200 system.

more efficient operation at the second harmonic and a higher performance extraction septum will be installed.

A new coupling line between the K500 and the K1200 will be implemented. In the K1200, the injection hardware will be installed and the extraction hardware improved. (The capability to operate the K1200 cyclotron in the stand-alone mode will be retained.) The present fragment separator (A1200) will be replaced with a much higher performance system (A1900).

The NSCL high bay area will be extended by approximately 25 m in order to provide a staging area for magnet construction and refurbishing of the K500. A building addition will be constructed near the present cryogenic plant to house a cryogenic system of increased capacity, and the radiation shielding will be increased.

The total project costs are given in Table III.

V. PRESENT STATUS

The design concept for the K500⊗K1200 was developed during 1993-1994. A conceptual design report was published [2] and a proposal was submitted to the National Science Foundation (NSF) in 1994 in which a cost sharing strategy between Michigan State University (8 FY94 M$) and NSF (11 FY94 M$) was specified. Since that time, research and development projects have begun on certain aspects of the design. MSU has already committed a portion of its contribution (~ 1 M$) for the extension of the high bay area with construction scheduled for completion near the end of 1995.

Detailed design and initial prototyping of programmatic elements such as the coupling line rf system and the stripping foil system to be used in the K1200 are in process.

The superconducting ECR has been tested up to a platform voltage of 25 kV. However, due to limitations in the ECR to K500 transport system only beam energies compatible with a platform voltage of 20 kV can be effectively transported to the K500 at the present time.

A new second harmonic central region for the K500 [3] has been designed and fabricated, and commissioning is well underway. Existing internal beam probes have been refurbished and bunch length diagnostics have been designed and implemented. The K500 extraction system geometry has been modified appropriately for K500 operation in the K500⊗K1200 mode, although the power handling capacity remains to be developed. Recent results of the ECR through K500 extraction system are given in Table IV. These initial results are quite encouraging since the K500⊗K1200 specifications are nearly met even though critical elements such as the improved ECR to K500 injection line remain to be implemented. Bunch lengths meeting design specifications (3° FWHM) and intensities at ~ 55% of the design requirement (6×10^{12} particles/s) have been achieved, although not simultaneously. In the near term, efforts will be directed towards achieving the nearly realized goal of extracting beams from the K500 which meet the K500⊗K1200 specifications.

References

[1] Richard C. York, T.A. Antaya, Henry Blosser, Don Lawton, Felix Marti, D.J. Morrissey, B.M. Sherrill, John Vincent, and A.F. Zeller, "Present Status and Future Possibilities at NSCL-MSU", Proc. 4th European Part. Accel. Conf., London, England,June 1994,pp. 554-556.

[2] "The K500⊗K1200 - A Coupled Cyclotron Facility at the National Superconducting Cyclotron Laboratory", July 1994, Michigan State University, East Lansing Michigan, MSUCL-939.

[3] S. L. Synder and F. Marti, "Study and Redesign of the NSCL K500 Central Region", these proceedings.

ISAC-1: RADIOACTIVE ION BEAMS FACILITY AT TRIUMF

P. G. Bricault, R. Baartman, J. L. Beveridge, G. S. Clark, J. Doornbos, G. Dutto, T. Hodges, S. Koscielniak, L. Root, P. W. Schmor and H. R. Schneider, TRIUMF, Vancouver, B. C. Canada

This paper describes the ISAC-1 radioactive ion beam facility proposed at TRIUMF. A novel approach for the target/ion source station will allow an incident proton beam intensity of at least 10 μA at 500 MeV. This should give high luminosity for the production of nuclei far from stability with a very large isotopic range. After mass separation the beams can be sent to two different experimental areas. One uses the 60 keV energy beam for experiments such as the neutral atoms trap, parity violation, etc. The second one, mainly dedicated to nuclear astrophysics, will use the 0.2 to 1.5 MeV/u post-accelerated beam. Singly charged ion beams, with $A \leq 30$ delivered from the on line mass separator, with an energy of 2 keV/u, will be accelerated in a two stage linac consisting of an RFQ and a post-stripper drift-tube linac up to 1.5 MeV/u. CW operation mode is required to preserve beam intensity. As a consequence of the low charge to mass ratio of the ions a low operating frequency for the RFQ is required to achieve adequate transverse focusing. The main features of this accelerator are: 35 MHz RFQ, stripping at 150 keV/u, and beam energy continuously variable from 0.2 keV/u to 1.5 MeV/u.

I. INTRODUCTION

During the last decade there has been a growing worldwide interest in the use of radioactive ion beams (RIB) for both fundamental and applied sciences. The possibility of producing intense radioactive nuclear beams with N/Z ratios largely different from those of natural isotopes opens a new field of research. Some examples where the use of RIB can be of great interest are:

- In nuclear physics it will be possible for the first time to test the isospin dependence of a large variety of nuclear systems far from stability. Nuclear deformations predicted a long time ago with a variety of models can be tested. This will provide a strong constraint on nuclear models and will improve our understanding of the nuclear interaction.
- In astrophysics, it is believed that the lightest elements were synthesized immediately after the Big Bang. The process of synthesis of heavier elements includes nuclear capture and decay of, often very short-lived, unstable nuclei. Except for a few long-lived elements only a theoretical estimation of these processes can be applied in cosmology. With a RIB facility, empirical determination of crucial reaction rates will permit prediction of production probabilities of the heavier elements at various stages of stellar evolution.
- Atomic physics techniques are commonly used to measure many properties of the nucleus; such as the spin, electromagnetic moment and charge radius. On the other hand, nuclear physics techniques and nuclei far from stability can be used to address fundamental issues in atomic physics such as QED.
- Tests of the Standard Model of elementary particles can be complementary to and, in specific areas, competitive with those performed at high energy. For example, PNC experiments can be performed using unstable ions like Fr.
- In condensed matter RIB can be used for doping new generations of semiconductor material and as a probes to obtain information on their local surrounding on an atomic scale. RIB and muons techniques can be combined to study the dynamics of certain phenomena on a very short time scale. With low energy muons we can study the dynamics of magnetic processes off surface and thin layer. The later is complementary to the solid state physics program that is an active field of research at TRIUMF.

A proposal to install an ISOL (isotope-separator-on-line) and post-accelerator RIB facility at TRIUMF was first made in 1985[1]. Although the full project was not funded at that time, an on-line target/ion source and mass separator test facility was installed on one of the TRIUMF proton beam lines, and has been used since 1987 to provide low energy radioactive beams for experimenters and to develop the target-ion source system.

Radioisotope production by the ISOL method is achieved with an intense beam of energetic light particles, (eg. neutrons, protons, or light ions) incident on a thick target of high atomic mass material. The radionuclides thus formed are stopped within the target, which is heated to high temperature to promote diffusion to and desorption from the target surface. Once free of the target the radionuclides are ionized in an ion source and then mass analyzed with the selected species then delivered the low energy experimental area or to the post accelerator for further acceleration.

Particle fragmentation, employing a high energy heavy ion primary beam, is an alternative production method for radioactive beams. In this case however all ions emerge with velocities close to that of the incoming primary beam (e.g. with particle energies typically >30 MeV/u) with significantly larger emittances than the primary beam. In contrast the ISOL beams have properties similar to those of stable ion beams, such as low emittance, low energy spread, and if required, short pulse widths.

The high energy (500 MeV) and high intensity (>100 μA) of the TRIUMF H^- cyclotron make TRIUMF a time and cost effective choice for a RIB facility in North America. The high proton energy permits the use of a thick target providing a wide mass range of isotopes via a large number of reaction mechanisms. Lower energy machines can instead only produce intense RIB near the stability line, with constraints on the choice of target material set by the higher energy density deposition requirements.

II. TARGET/ION SOURCE SYSTEM

Flexible target handling and containment of the radioactivity are the major considerations in the present design[2]. The target will be placed at the end of a steel shield plug. The target station is to be housed in a new heavily

0-7803-3053-6/96/$5.00 ©1996 IEEE

shielded building which is attached to and extends into the existing proton hall. Figure 1 shows the target/ion source handling concept. All highly activated and potentially contaminated components such as production targets, beam dump, ion sources and initial focusing devices will be located in this building along with the primary radiation shield. Services required to operate the target area components will also be housed in this building. Hot cell, warm cell and a decontamination and storage facility will be included.

III MASS SEPARATOR

There is no universal ion source for the production of all the elements required for the physics program. Beam properties will depend on the type of ion source used. The extraction system will be optimized for each individual ion source to give the highest source brightness and small angular divergence. Space has been allowed in the target module design to incorporate additional optical elements such as steering devices or other optical elements.

The design of a radioactive ion beam mass separator system requires that a number of fundamental issues be addressed and resolved. These issues are the following: extraction from the ion source, matching of the beam to the mass separator, beam emittance and high beam current aspects, multiple beam requirements from the mass separator, high mass resolution (for $6 \leq A \leq 240$) and transport to the user.

In our present design the mass separator consists of two anti-symmetric QQQDDQQQ systems each with a total bend angle of 112°. It will have a source-defining entrance aperture. Aberrations are corrected by four sextupole and four octupole elements placed near each dipole. This separator will have a dispersion at the focal plane of 6 cm/% in DM/M and a mass resolving power of 10,000. A movable slit system will be placed on the focal plane to select the mass to be transmitted. The second bend section can be maintained at an elevated potential to provide additional beam purification if this is required.

IV. ACCELERATOR

Most of the astrophysics and applied program can be achieved within an energy range of 0.2 and 1.5 MeV/nucleon, while higher energies (≤ 10 MeV/u) would be desirable for nuclear structure studies, fusion reactions, etc. This could be viewed as a possible upgrade in the future. At present, for ISAC-1, we are limiting ourselves to the following specifications, (Table 1).

The block diagram in fig. 2 illustrates the two-stage linac that would satisfy the ISAC-1 specifications. Further improvements to this design are being contemplated. For example, the addition of a charge state selector will improve the tuning capability by eliminating other charge states and will prevent radioactive contamination of the drift-tube linac.

A radio-frequency quadrupole operating at 35 MHz provides the initial acceleration of the singly charged ion beam delivered by the ISOL system. Taking singly charged mass 30 as the reference particle we are led to an operating frequency of 35 MHz, with an inter electrode voltage of 85 kV, and r_0 = 0.86 cm. This gives a design value of B = 3.

Table 1 - Basic specifications for ISAC-1.

Input beam	
Energy	60 keV
Ion mass	$A \leq 30$
Ion charge	1
Beam current	< 1 μA DC
Beam emittance	≤ 0.25 π mm mrad (Normalized)
Accelerated beam	
Output energy range	$0.15 \leq E \leq 1.5$ MeV/u
Resolution ΔE/E	≤ 0.1 %
Duty factor	100 %

In the RFQ design the conventional shaper is replaced by a buncher of a few modulated cells, followed by cells with no vane modulation. Then, after one quarter synchrotron oscillation, the synchronous phase is jumped from -90 to -85 degrees. Then the beam is accelerated while the vane modulation parameter and synchronous phase vary smoothly, according to the Yamada prescription, toward final values of m=2.5 and Φ_S = -20°, respectively. The output longitudinal emittance is ≤ 1 π keV.ns/u, the transverse normalized acceptance is 0.55 π.mm.mrad, and the transmission is 92 %3[3].

From a structural point of view, the low frequency of the RFQ dictates that a semi-lumped resonant structure be used to generate the required RF voltage between the RFQ's electrodes. Various RFQ models have been built and the structure proposed for the ISAC-1 accelerator is a variant of the 4-rod structure developed a the University of Frankfurt[4]. A 4-rod RFQ split-ring structure has been chosen because of its relatively high specific shunt impedance, its mechanical stability, and the absence of voltage asymmetries in the end regions [5].

Calculations using MAFIA combined with model measurements have been used to optimize dimensions. For our present design, the rings have a rectangular section (15 cm axially by 8 radially), a mean diameter of 43.5 cm, and are spaced at 40 cm intervals along the RFQ electrodes. The theoretical specific shunt impedance Z_S for this structure when enclosed in a 1 m diameter tank, is 500 kΩ m.

After acceleration to 150 keV/u in the RFQ, the beam passes through a matching and stripper section, where its charge to mass ratio is increased to ≥1/6. Thereafter it is injected into a 70 MHz drift-tube linac and accelerated up to 1.5 MeV/u. To permit variation of the output beam energy, the 48 accelerating gaps of the drift-tube stage are divided into eight independently driven sections of six gaps each. Quadrupole doublets between sections provide the transverse focusing necessary to maintain the beam well focused along the drift-tube linac. Self consistent particle tracking computations through the RFQ, stripper and matching section,

and drift tube linac have been carried out using computer codes. We start with a 2 keV/u, single charged mass 30 ion beam. A random distribution of 5000 particles in the 4 dimensional transverse phase space, with normalized emittance of 0.25 π mm mrad, is used as input. Angular and energy straggling in the stripper carbon foil is assumed having a Gaussian distribution with σ of 8 mrad and 26 keV, respectively. The beam at the output of the linac shows final transverse and longitudinal emittances of 0.94 π mm mrad and 11 π (keV/u) ns. The overall transmission through the linac, excluding losses at the stripper, is 86%.

IV. CONCLUSION

Recent developments in the field of isotopic separation on line can now be combined with the remote handling expertise of meson factories to produce a very attractive RIB facility providing beams with intensity large enough to allow many new experiments. Applications can be performed on a relatively small scale and require modest investment if based on existing facilities. This will provide the opportunity to perform front-line multidiciplinary research. In nuclear astrophysics this opens the possibility to measure reaction cross sections of processes occurring in stellar sites. Ion beams with relatively low energy and submicron dimensions would have important applications in the semi-conductor and computer industries. In material sciences, techniques such as Möβbauer spectroscopy and perturbed angular correlation will become possible with radioactive tracers implanted within bulk material.

The accelerator solution presented satisfies the specifications for the presently envisaged experimental program. It serves as a reference design which will be developed and modified to match physics requirements

Reference

[1] G. E. McMicheal, B. G. Chidley and R. M. Hutcheon, AECL 8960/TRI-DN-85-3.

[2] J. L Beveridge, G. Clark and C. Mark, TRI-DN-94-2.

[3] S. Koscielniak, TRI-DN-95-4R.

[4] Schempp et al., Nucl. Instr. & Meth. B10/11 (1985), p. 831

[5] P. G. Bricault, D. Joffe and H. R. Schneider, this conference

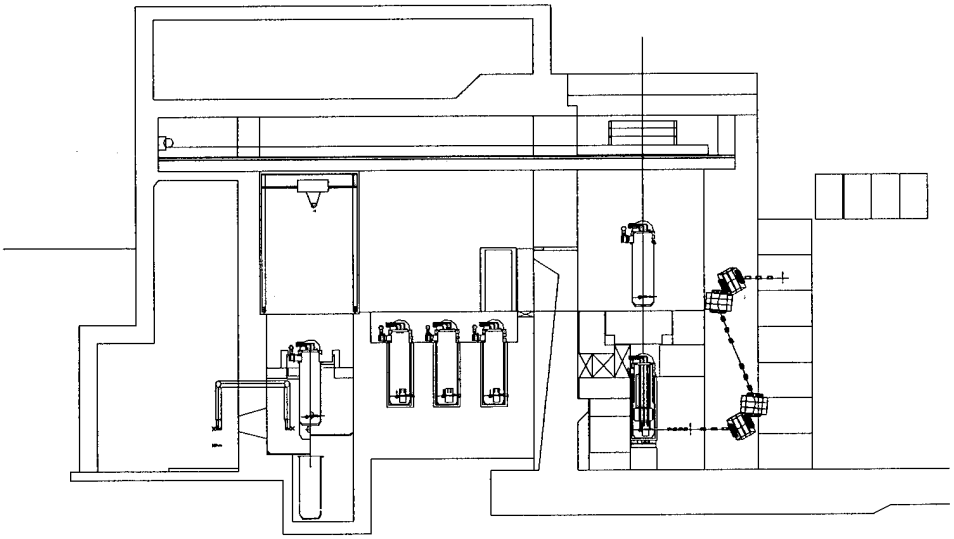


Fig. 1 - Vertical view of the target and remote handling annex.

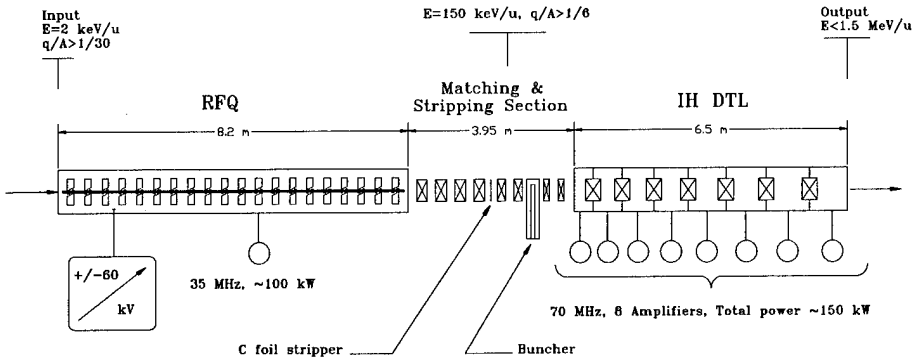


Fig. 2 - Block diagram of ISAC-1 post-accelerator.

FIRST BEAM TESTS OF THE INS SPLIT COAXIAL RFQ FOR RADIOACTIVE NUCLEI

S. Arai, A. Imanishi, K. Niki, M. Okada, Y. Takeda, E. Tojyo, and N. Tokuda
Institute for Nuclear Study, University of Tokyo
3-2-1 Midori-cho, Tanashi, Tokyo 188, Japan

Abstract

A 25.5-MHz split coaxial RFQ has come into operation at INS. This linac was designed so as to accelerate ions with a charge-to-mass ratio greater than 1/30 from 2 to 172 keV/u. The maximum intervane voltage so far achieved is 91 kV. We have conducted acceleration tests by using Ne^+ and N^+ ions. Through N^+ acceleration we obtained the following preliminary results. The output-beam emittances are well in the design ellipses of 0.06 π cm·mrad (normalized). The data of transmission efficiency vs intervane voltage agree well with PARMTEQ results. The transmission at the nominal voltage is measured to be 90%.

I. INTRODUCTION

The split coaxial RFQ presented here is to be used in a radioative-beam facility now under construction in INS [1]. Radioactive nuclei will be accelerated by the 25.5-MHz RFQ and a 51-MHz interdigital-H linac. The beam, whose energy is variable in a range from 172 to 1053 keV/u, is to be used for nuclear physics experiments.

The RFQ was designed so as to accelerate ions with a charge-to-mass ratio (q/A) greater than 1/30 from 2 up to 172 keV/u [2]. The cavity, comprising 12 module cavities, is 0.9 m in diameter and 8.6 m in length. It was set up in the experimental hall in the spring of 1994. We then made low-power tests for tuning of the resonant frequency and field distribution [3]. For the study of the acceleration performance we built a test stand, where a 2.4-GHz ECR ion source is located near the RFQ. In the middle of March, 1995, the cavity underwent aging for high-power operations. On March 22, we succeeded in the first acceleration by using a Ne^+ beam. Through further tests with a N^+ beam we found the beam performance agrees with PARMTEQ predictions. This paper describes the high-power operations and beam tests.

II. HIGH-POWER OPERATION

The rf power source with an EIMAC 4CW150,000E tetrode generates a maximum output power of 350 kW in peak with a duty factor of 30%. Higher duty factors, even 100%, are available at lower power levels. The rf power is transmitted into the cavity through a 6-m coax (WX-120D) and a loop coupler.

Figure 1 shows the progress in achieved intervane voltage (V_{vv}) as a function of the aging time (≡ operation time × duty factor). The duty factor was changed as the rf power increased: 1% → 60% (V_{vv} = 0.2 → 0.56 kV), 80% (0.58 → 70 kV), and 10% (70 → 80 kV). The input power was increased gradually so that the cavity vacuum stayed in a range of $1 \sim 3 \times 10^{-6}$ Torr at a pump head[1] (0.5×10^{-6} Torr without power input). It took a long time to get over the multipactoring level lying between 15 and 20 kV. Through this aging the cavity came into stable operation at V_{vv} = 80 kV (20% duty, peak power = 130 kW). We then carried out the first acceleration with a Ne^+ beam.

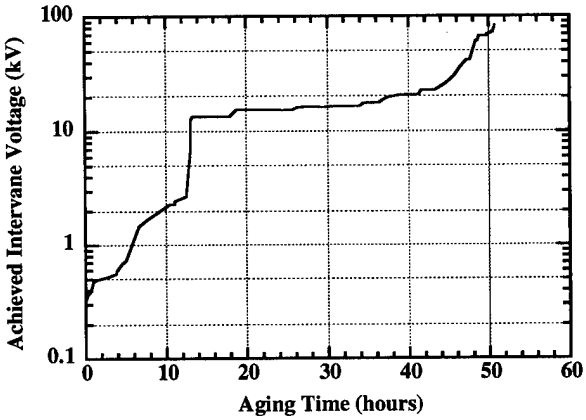


Figure 1. Achieved intervane voltage vs aging time (≡ operation time × duty factor).

We figure out intervane voltage from the output voltage (V_{ML}) of a monitor loop attached to the 12th module cavity. The calibration constant V_{vv}/V_{ML} is 10,388. For the calibration we measured endpoint energy of the X-ray from electrons accelerated between vane tips. A germanium detector cooled by liquid nitrogen, an amplifier, and a pulse height analyzer (PHA) were used. The factor for the conversion from a PHA channel into an energy is 0.10042 keV/ch. This value was obtained from two energy peaks from ^{57}Co: 122.6 keV (1219 ch) and 136.47 keV (1361 ch). The calibration constant V_{vv}/V_{ML} was measured at five V_{vv} values between 44 and 77 kV. The averaged value and rms error of V_{vv}/V_{ML} are 10,388 and 73.

In Fig. 2 the intervane voltage is plotted as a function of the input power (P_{in}) to the cavity. In the figure V_{vv}^M (○, ●) is the intervane voltage derived from the monitor loop voltage, and V_{vv}^X (×) from the X-ray endpoint energy. From the V_{vv}^M values the resonant resistance R_p (≡ $V_{vv}^2/2P_{in}$) is 24.55 ± 0.44 kΩ. This value is higher than 22 kΩ, which we obtained in low power tests [3]. The increase of the resonant resistance may be due to that the cavity Q-value might have increased through the aging.

Our goal is to operate the cavity at V_{vv} = 109 kV (design value for q/A = 1/30 ions, P_{in} = 240 kW) or higher with a duty factor of 30%. The cavity operates now stably at 80 kV (P_{in} = 130 kW, 20% duty). Reducing the duty factor down to 1.5%, we have achieved 91 kV (P_{in} = 170 kW). At this voltage we have now two problems: one is sparking between vane tips, and the other

[1] Four 500-l/s turbomolecular pumps are evacuating the cavity.

0-7803-3053-6/96/$5.00 ©1996 IEEE

is creeping discharge on the ceramic window (atmospheric side) of the loop coupler. These occur once per several minutes. After improving the loop coupler, we will conduct further aging for higher intervane voltages and duty factors.

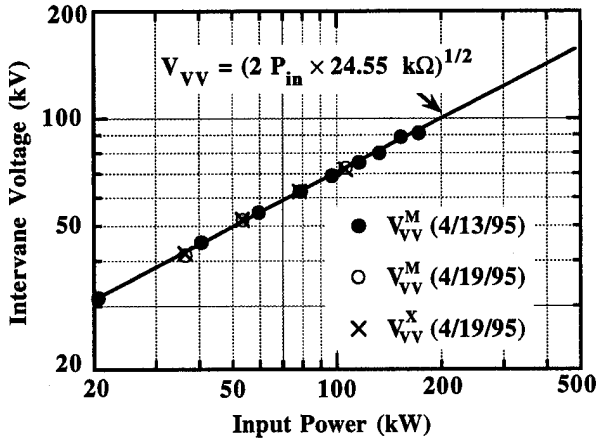


Figure 2. Intervane voltage vs input power into the cavity.

III. ACCELERATION TESTS

A. *Test stand*

Figure 3 shows the layout of the LEBT, which consists of a 2.4-GHz ECR ion source, a 90° bending magnet, two quadrupole magnets (defocusing in the horizontal plane), and four einzel lenses [4]. In front of the 3rd einzel lens, we set an electrostatic steerer, which has four electrode plates and deflects the beam in horizontal and viertical directions. At the entrance of the steerer we set a collimator (aperture radius is 0.65 cm) for ion separation. The collimator is effective in beam shaping also, cutting off beam filaments caused by the einzel lenses Nos. 1 and 2. A double-slit emittance monitor and a Faraday cup (FC1) are installed at the RFQ entrance.

The HEBT is illustrated in Fig. 4. The emittance monitor is separated into two parts: the front slit is near the RFQ exit, and the rear one is between the quadrupole magnets. The Faraday cup FC2 measures the current of drift-through ions (both of accelerated and unaccelerated ions), and FC3 the current of accelerated ions. The quadrupole doublet kicks out unaccelerated ions and focuses acceelerated ones into FC3. According to a beam simulation, less than 1% of unaccelerated ions reach FC3.

B. *Beam performance*

Figure 5 shows emittance porfiles at the RFQ entrance (vane end). The bars indicate measured profiles of a N^+ beam,[2] and the ellipses the designed ones with an area of 29.1 π cm · mrad (ε_n = 0.06 π cm · mrad). The input match is imperfect: the beam center deviates by 0.19 cm in the horizontal (x) plane, and in the vertical phase space (y-y' space) the beam focusing is insufficient. The LEBT parameters deserve further tuning. Figure 6 shows emittance porfiles at the RFQ exit (vane end). The RFQ

[2]Some of the ions may be N_2^{2+}; we cannot discriminate between N^+ and N_2^{2+} ions in our test stand.

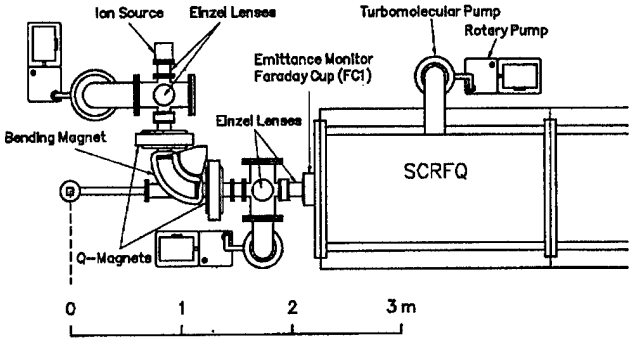


Figure 3. Layout of the LEBT

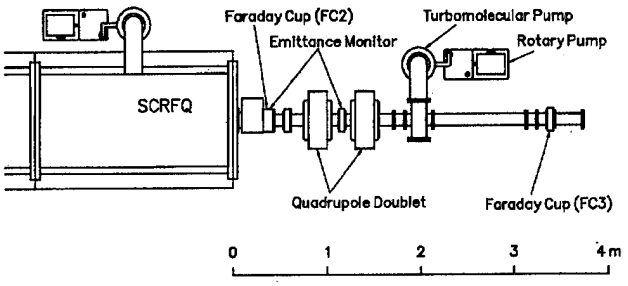


Figure 4. Layout of the HEBT

operated at the nominal intervane voltage, 50.68 kV for N^+. The measured profiles are inside of the ellipses, whose area is 3.11 π cm · mrad (ε_n = 0.06 π cm · mrad) and the Twiss parameters are expected ones from a PARMTEQ simulation.

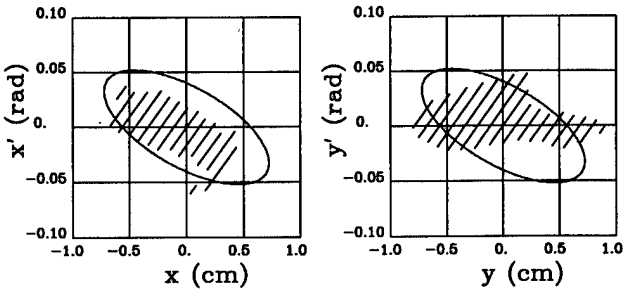


Figure 5. Emittance profiles at the RFQ entrance.

We measured the transmission efficiency as a function of the intervane voltage. The RFQ operated at 25.47 MHz with a duty factor of 5% (0.53 ms × 95 Hz), and the ion source synchronized the RFQ. The N^+ beam had the input emittance profiles shown in Fig. 5, and the current was 0.21 ~ 0.22 mA in peak at FC1. The measurement result is shown in Fig. 7 along with a PARMTEQ prediction. The horizontal scale is the normalized intervane voltage, $V_n = V_{VV}/50.68$ kV. The measured transmission efficiency of drift-through ions (○ in the figure) is defined by I(FC2)/I(FC1), where I(FCi) is the beam current from the Faraday cup i, and that of accelerated ions (●) by I(FC3)/I(FC1). The PARMTEQ simulation was done by using the PARMTEQ-H version, where the electric field has the higher-order mulitipoles calculated by Crandall [2, 5]. The input emittance profiles are ellipses approx-

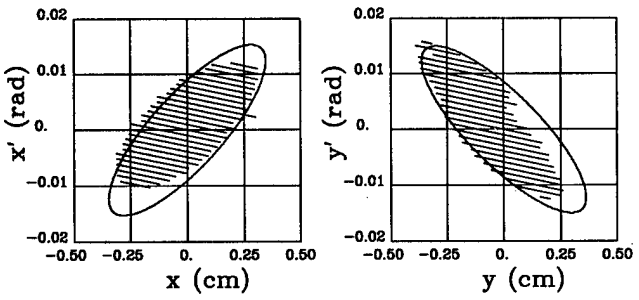


Figure 6. Emittance profiles at the RFQ exit.

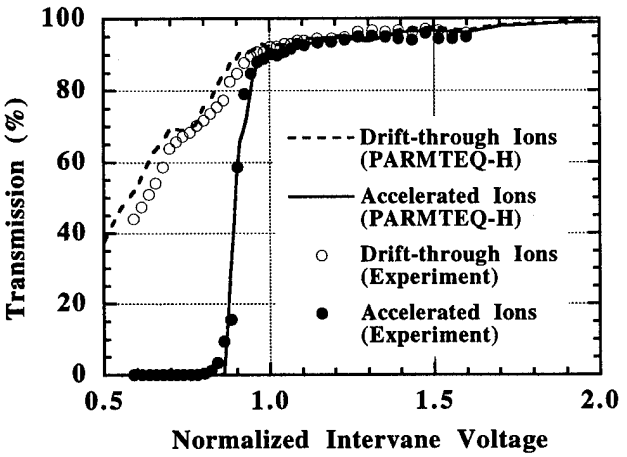


Figure 7. Transmissions vs normalized intervane voltage.

imately same as the measured ones in Fig. 5. Some of the unaccelerated ions have so large divergences that they might miss FC2 (aperture radius = 1.7 cm). The missing rate is 10% or less. This was taken into account in the simulation.

At the nominal intervane voltage ($V_n = 1$) the measured transmission efficiency is 90%. This is close to the design value of 91.4% with a matched input beam with $\varepsilon_n = 0.06\ \pi$ cm · mrad. Though the input match is rather poor in the y-y' space (Fig. 5), we obtained a high transmission. This is due to the RFQ acceptance larger than $0.06\ \pi$ cm · mrad normalized. Running PARMTEQ-H, we get a transmission of 90% for a matched beam with $\varepsilon_n = 0.09\ \pi$ cm · mrad [2].

IV. CONCLUDING REMARKS

The measured output beam emittances and transmission efficiencies show that the performance of the RFQ is close to the designed one. The input power is, however, still low. The maximum averaged power in the above measurement was 6.7 kW (134 kW × 0.05) at V_{vv} = 81 kV (V_n = 1.6 in Fig.7). We are aiming at the operation at V_{vv} = 109 kV with a 30% duty; then the averaged power will be 73 kW (242 kW × 0.3). Under this high-power, high-duty operation, the frequency stabilization is indispensable. For the frequency control, we have already installed eight inductive tuners with stepping motors to the cavity. Our experience with the prototype RFQ tells us that the tuners will keep the frequency under control [6]. Another possible problem with a heated cavity is distortion of the vanes; the beam performance may be affected. From this anxiety we chose a water-pipe diameter larger than that at the prototype RFQ. At the full power operation of the present RFQ, the averaged power loss per cavity length will be 8.5 kW/m (73 kW/8.6 m). At the prototype RFQ we had increased the power up to 7.6 kW/m (16 kW/2.1 m) and observed no appreciable change in the beam performance. From this experience and the increased flow rate of the cooling water, we expect the RFQ will work well under the full power operation.

V. ACKNOWLEDGMENTS

We express our thanks to T. Nomura for his encouragement, M. Imamura and S. Shibata for their help in the X-ray endpoint energy measurement, and M. Tomizawa for his help in the cavity aging. The cavity was fabricated by Sumitomo Heavy Industries, Niihama Work, and the rf power source by Denki Kogyo. The computer works were done on FACOM M780 and VP2100 in the INS Computer Room.

References

[1] S. Kubono *et al.*, "Low-Energy Radioactive Nuclear Beam Project at INS", 3rd INS-RIKEN Symp. on Heavy Ion Collisions, Shinrin-Koen, Saitama, Japan, 1994, INS-Rep.-1084, 1994.

[2] N. Tokuda and S. Arai, "Beam Dynamics Design of the INS Split Coaxial RFQ for Radioactive Nuclei", Proc. 1994 International Linac Conference, Tsukuba, Japan, 1994, p. 762.

[3] S. Arai *et al.*, "Cavity Construction and Low Power Tests of the INS Split Coaxial RFQ for Radioactive Nuclei", ibid., p. 689.

[4] K. Niki *et al.*, "Beam Transport Design for the Linac System in the INS Radioactive Beam Facility", ibid., p. 725.

[5] K. Crandall, "Effects of Vane-Tip Geometry on the Electric Fields in Radio-Frequency Quadrupole Linacs", Los Alamos Technical Report, LA9695-MS, 1983.

[6] N. Tokuda, "Progress in Low Beta, Low q/A RFQ's at INS", Particle Accelerators, Vol. 47, p. 171, 1994.

ACCELERATOR COMPLEX FOR A RADIOACTIVE ION BEAM FACILITY AT ATLAS

J.A. Nolen, Physics Division, Argonne National Laboratory, Argonne, IL 60439

Since the superconducting heavy ion linac ATLAS is an ideal post-accelerator for radioactive beams, plans are being developed for expansion of the facility with the addition of a driver accelerator, a production target/ion source combination, and a low q/m pre-accelerator for radioactive ions. A working group including staff from the ANL Physics Division and current ATLAS users are preparing a radioactive beam facility proposal. The present paper reviews the specifications of the accelerators required for the facility.

I. INTRODUCTION

There is much enthusiasm in the nuclear physics research community for the opportunities for studies which would be enabled by an advanced, high intensity accelerated radioactive beam facility based on the isotope-separator on-line (ISOL) method. There are recent reports from both North American and European study groups [1,2]. A group including many ANL Physics Division staff and ATLAS outside users has discussed the research possibilities and prepared a working paper entiled "Concept for an Advanced Exotic Beam Facilitty Based on ATLAS." This paper is available on the World Wide Web at the ANL Physics Division home page (http://www.phy.anl.gov). This paper summarizes the accelerator complex proposed in the working paper.

A schematic layout of the conceived facility is shown below in Fig. 1. The existing ATLAS accelerators and experimental facilities are in the lower part of the figure, and the proposed driver linac, production target area, mass separators, new low energy experimental areas, and post accelerator injector are in the upper part.

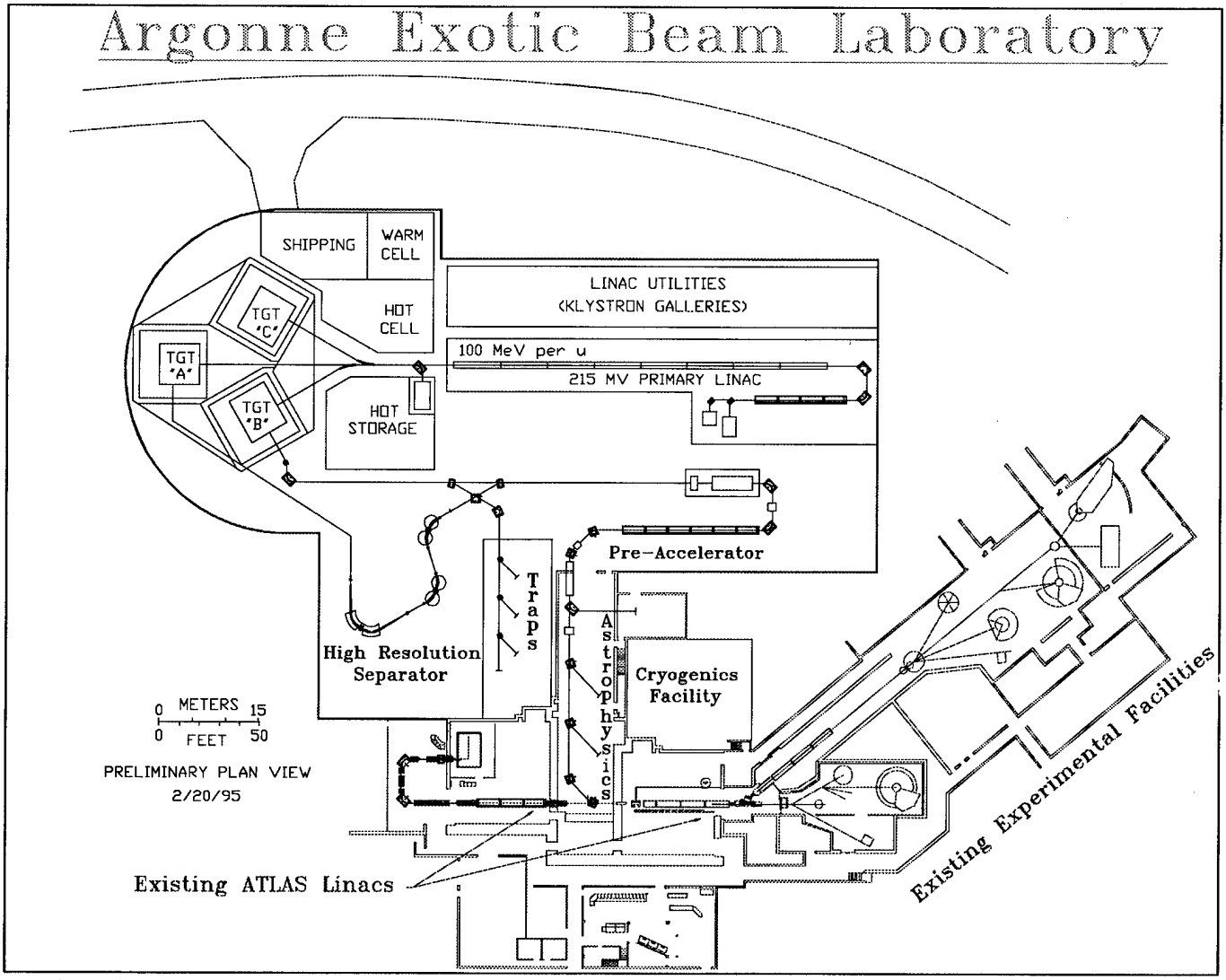


Figure 1. Schematic layout of the present ATLAS accelerators and experimental facilities (lower part of the figure) and the proposed additions to the facility (upper part).

0-7803-3053-6/96/$5.00 ©1996 IEEE

Table I. Beam parameters of the Production Linac

Max Output Beam Energy:	100 MeV per nucleon[sss]
Max Output Beam Power:	100 kW
Typical Light Ions (multicusp ion source):	^{1}H, ^{2}H, ^{4}He
Typical Heavy Ions (pulsed ECR ion source):	$^{12}C^{2+,6+}$; $^{16,18}O^{3+,8+}$; $^{20,22}Ne^{4+,10+}$; $^{36}Ar^{6+,16+}$
Typical Max. Light Ion Currents @100 kW:	^{1}H, 1000 pμA; ^{2}H, 500 pμA; ^{4}He, 250 pμA
Typical Max. Heavy Ion Currents @100 kW:	$^{18}O^{8+}$, 55 pμA; $^{36}Ar^{16+}$, 28 pμA
Typical Heavy Ion Source/Stripping Limits:	$^{18}O^{8+}$, 20 pμA; $^{36}Ar^{16+}$, 3 pμA

As indicated in Fig. 1 the new components for the radioactive beam laboratory will be constructed in a new building just north of the present ATLAS facility. Radionuclides are produced by irradiating targets in well-shielded areas with light ion beams from a modern drift tube linac. The present plan is for the primary linac and production targets to be located below grade level to assist with shielding prompt neutron radiation. Using standard ISOL (Isotope Separator On-Line) target/ion source techniques the radionuclides are extracted and ionized, mass separated, and then sent either directly to an experimental area for research with ion or atom traps, or on to the secondary-beam accelerator. All secondary beamlines will be at the elevation of those in the existing ATLAS facility. Acceleration of these very low q/m ions requires a sequence of three new subsystems: a short, low-frequency RFQ and two new sections of superconducting linac optimized for these low charge-state ions. After initial acceleration to the 0.5-1.0 MeV per nucleon energy range the secondary beams can be delivered to a new experimental area for astrophysics experiments (labeled "Astrophysics", in Fig. 1). This area is in the existing ATLAS building, in the room presently occupied by the tandem injector for ATLAS. For further acceleration to the 1 to 15 MeV per nucleon range, the beam merges into the present ATLAS beamline at the south end of this room. The capability of ATLAS to accelerate stable beams will remain independent of the added radioactive beam capability, both during construction and afterwards.

Table II. Driver Linac Specifications

Injector RFQ/Linac:	5 MeV/u output @ q/m ≥ 1/6, (30 MV)
Main Linac:	100 MeV/u output @ q/m ≥ 8/18, (215 MV)
Duty Cycle:	2% @ 120 Hz
Input Power:	1 MW
Output Energy Variability:	15% increments
Controls:	Pulse-pulse ion source and energy variation possible

II. PRODUCTION METHODS

The basic concept is to use a conventional drift-tube linac with 100 kW beam power available for a variety of light ions as indicated in Table I. The essential specifications of the driver linac are given in Table II.

Secondary beam intensities have been calculated using a variety of production mechanisms, proven target/ion source methods where known [3], and the efficiencies of bunching, stripping, etc. in the post acceleration. A table of specific beam intensity predictions for this facility is given in the working paper discussed above. A common problem for many second-generation radioactive beam facilities is learning to deal with very high power densities in the production targets. A large collaboration is currently preparing to test a new geometry target system with a 100 kW, 800 MeV proton beam at the ISIS accelerator at the Rutherford Laboratory[4]. Continued R&D on high power targets and associated ion sources is important for advanced radioactive beam facilities worldwide.

One production mechanism which has been investigated for this facility is indicated schematically in Fig. 2. This method separates the issue of the primary target which must dissipate the 100 kW beam power from that of the isotope production target/ion source combination. Quantitative yields from such a geometry were measured recently by an ANL/MSU collaboration using a low intensity, 200 MeV deuteron beam at the NSCL. Yields of a variety of short-lived fission products, including ^{132}Sn, were determined. Scaling the measured yields to a 0.5 mA deuteron beam and a 100 g/cm^2 secondary uranium target gives a ^{132}Sn production rate in the ion source/target system of 10^{13}/sec.

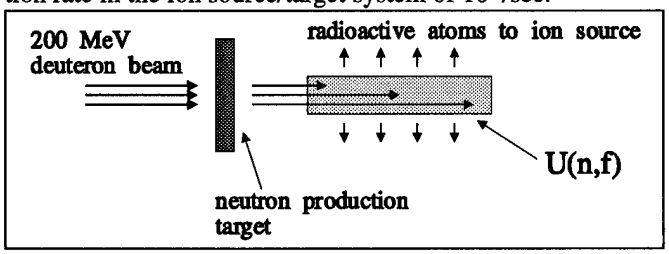


Figure 2. A conceptual layout showing the basic idea of using a 200 MeV deuteron beam to generate an intense secondary beam of neutrons for the production of fission fragments. This separates the problems of the high power in the primary beam from the secondary target/ion source system.

	Worksheet for the Secondary Beam Accelerator for the Argonne Exotic Beam Laboratory									
Driver Accelerator:				200 MV Linac, q/m=0.5, 100 kW beam power, 120 Hz						
Radioactive Beam Accelerator:					^{132}Sn Example		A=	132		
Voltage gain (MV)	q	T/A (MeV/A)	velocity (v/c)	Accel. length (m)	efficiency (this step)	efficiency (cumulat.)	intensity (ions/sec)	intensity (part. na)	Device:	Comments:
							1.0E+13		primary production rate	100 g/cm^2 UC target
0.1	1	0.0008	0.0013		0.03	0.030	3.0E+11	50.0	ion source & release	4π mm-mr
					0.80	0.024	2.4E+11	40.0	isobar separation	resolution ~30,000.
0.3	1	0.003	0.003	1.0	1.00	0.024	2.4E+11	40.0	onto HV platform	
					0.65	0.016	1.6E+11	26.0	prebunch/rebunch	
1.0	1	0.011	0.005	2.0	0.95	0.015	1.5E+11	24.7	RFQ on HV platform	12 MHz RFQ
-0.3	1	0.008	0.004	1.0	1.00	0.015	1.5E+11	24.7	leave HV platform	
0.0	2	0.008	0.004		0.40	0.006	5.9E+10	9.9	strip and rebunch	Gas stripper
2.0	2	0.039	0.009	2.0	0.95	0.006	5.6E+10	9.4	24 MHz linac	SC folded resonator
30.0	2	0.493	0.033	15.0	0.95	0.005	5.4E+10	8.9	48 MHz linac	PII-type, 4 gap
	20	0.493	0.033	1.0	0.20	0.0011	1.1E+10	1.8	strip to q/m=0.15	Foil stripper
	20	0.493	0.033	2.0	1.00	0.0011	1.1E+10	1.8	rebunch	
4.0	20	1.099	0.049	3.0	0.95	0.0010	1.0E+10	1.7	72 MHz matching linac	PII-type, 4-gap
40.0	20	7.160	0.123	25.0	0.90	0.0009	9.1E+09	1.5	out of ATLAS	existing accelerator

The spreadsheet shown above starts with these measured/scaled yields for ^{132}Sn in the production target and then lists the various ionization, bunching, acceleration, and stripping stages of the ISOL and secondary beam complex to illustrate, for a specific example, the predicted beam intensity for this facility. In this example the 3% efficiency for the combined release and ionization of the target/ion source is the established value for Sn isotopes given in reference [3]. Recently developed laser ionization techniques [5] have the potential to increase this number by more than an order of magnitude.

III. POST ACCELERATOR

An essential feature of the post accelerator is to preserve the excellent beam quality currently available at ATLAS for stable beams of any mass up to uranium in the energy range from 6-15 MeV per nucleon. Concepts for the injector stage of the post accelerator are presented in other contributions to this conference [6-8].

As indicated in the spread sheet above, a beam such as ^{132}Sn is first accelerated in the 1+ charge state through a voltage of about 1 MV and then stripped in a thin gas stripper to 2+. The advantage of stripping at this very low energy is that the efficiency is over 40%, whereas at higher energies the peak of the charge-state distribution is typically 20%. The second stripper is at the more typical energy of 500 keV/A where a q/m of 0.15 is reached for final acceleration through ATLAS.

Preliminary estimates of the cost and schedule for this project are given in the working paper discussed above.

This work is supported by the U.S. Department of Energy Nuclear Physics Division.

IV. REFERENCES

[1] The IsoSpin Laboratory, Research Opportunities with Radioactive Beams, LALP report 91-51 (1991).

[2] European Radioactive Beam Facilities Report of NuPECC Study Group (1993).

[3] H. L. Ravn et al., Nucl. Instr. and Meth. B88, 441 (1994).

[4] J. R. J. Bennett et al., "A Test Facility for Radioactive Ions Generated by Intense Beams of High Energy Protons" Proceedings of the Workshop on the Production and Use of Intense Radioactive Beams at the IsoSpin Laboratory, Oak Ridge, TN (1992).

[5] V. I. Mishin et al., Nucl. Instr. and Meth. **B73**, 550 (1993)

[6] K.W. Shepard and J.-W. Kim, paper RPR5 in this conference.

[7] J.-W. Kim and K.W. Shepard, paper RAR21 in this conference.

[8] J.-W. Kim and K.W. Shepard, paper FAQ9 in this conference.

The Lattice Design of Indiana University Cyclotron Facility Cooler Injector Synchrotron

D. Li, X. Kang, D.L. Friesel, S.Y. Lee, J.Y. Liu, A. Pei, A. Riabko, L. Wang
Indiana University Cyclotron Facility
2401 Milo B. Sampson Lane, Bloomington IN 47408

Abstract

This paper reports lattice design studies of a low energy booster at Indiana University Cyclotron Facility (IUCF). This booster will be used as an injector, which is named as Cooler Injector Synchrotron (CIS), for the existing IUCF Cooler ring. The IUCF CIS will be able to accelerate high-intensity polarized protons or deutrons coming from a RFQ linac from 7 MeV (6 MeV) to 200 MeV (105 MeV). The beam bunch then will be extracted and injected into the Cooler ring for further acceleration. The finalized lattice design for the CIS has four superperiods. Each period is composed of a drift space and a dipole magnet which has 90° bending angle and 12° edge angle at both ends. The circumference of the CIS is 17.364 meters, one fifth of that of the Cooler ring. The designed horizontal and vertical tunes are 1.463 and 0.779, respectively. Possible effects from the employment of trim quadrupoles, which will be located between dipoles, are also discussed.

I. Introduction

The Cooler Injector Synchrotron (CIS) at Indiana University Cyclotron Facility (IUCF) was jointly found by National Science Foundation (NSF) and Indiana University in 1994 [3]. The CIS will be replacing the currently running cyclotrons, which are used to fill the Cooler at IUCF, to increase the beam intensity of the Cooler ring. The CIS is designed to accelerate 7 MeV high-intensity polarized protons (or 6 MeV for deutrons) exited from a RFQ linac to 200 MeV (105 MeV). The beam bunch is then injected to the Cooler storage ring for further acceleration [2]. The CIS will be a zero gradient synchrotron with a superperiod of four. Each period consists of a draft space and a dipole magnet. In order to find the best lattice design for the CIS, namely, to locate a good working point in tune diagram, i.e. the tunes are not too close to any possible linear, nonlinear and spin resonance lines, and at the same time to enhance the injection efficiency at a tolerable emittance, and to limit the construction costs of the machine without losing the proposed beam performance, a number of lattice designs have been considered, discussed and compared. Finally a compromised lattice design is reached with the circumference as one fifth of the Cooler ring. The lattice parameters are listed in Table I. The general layout of the CIS is shown in Figure 1.

II. CIS Lattice Design

For such a simple lattice without any quadrupoles, only a limited parameters θ_e, the edge angle, and L, the length of the dipoles can be adjusted. Scanning over θ_e and L of the dipoles,

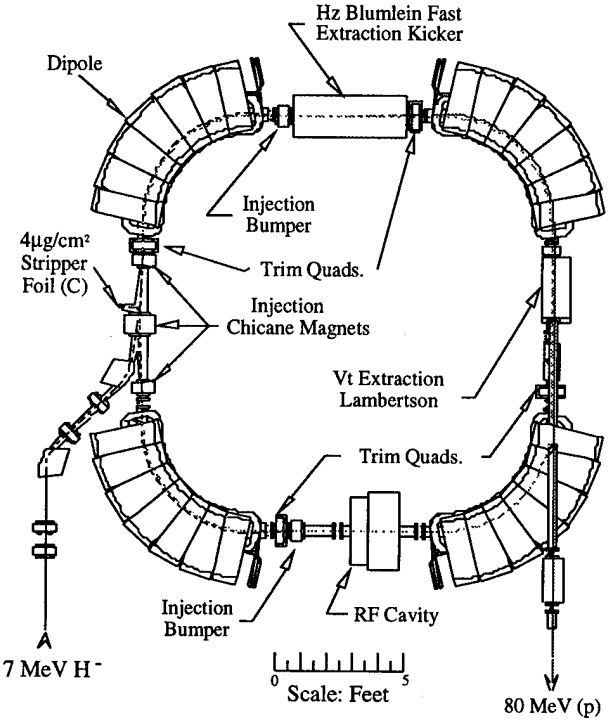


Figure. 1. The general layout of the Indiana University Cyclotron Facility Cooler Injector Synchrotron at IUCF

Table I
IUCF CIS lattice parameters

Parameters	Symbol	Values
Circumference(m)		17.364
Horizontal tune	Q_x	1.4633
Vertical tune	Q_z	0.7788
Dipoles:		
Length(m)	L	2.0
Edge angle	θ_e	12°
Bending radius(m)	ρ	1.273
Transition Energy	γ_T	1.271
Beta x: Maximum(m)	β_x	4.373
Minimum(m)		0.996
Beta y: Maximum(m)	β_y	3.786
Minimum(m)		3.380
Dispersion	D_x	
Maximum(m)		1.759
Minimum(m)		1.617
Chromaticity(x)	C_x	-0.529
Chromaticity(z)	C_z	-0.156

0-7803-3053-6/96/$5.00 ©1996 IEEE

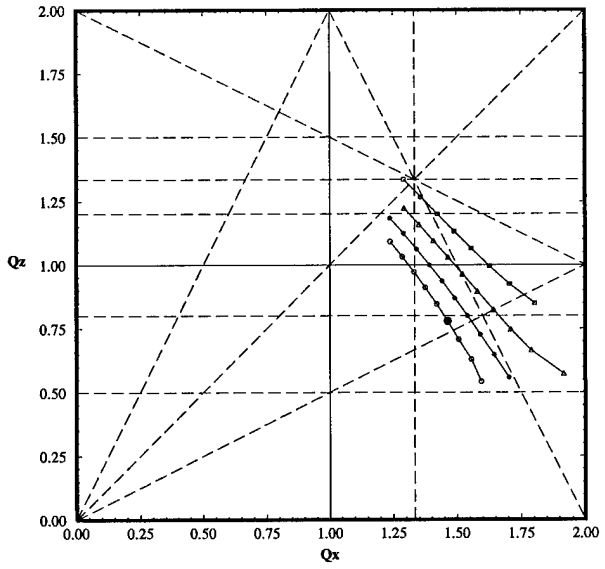


Figure. 2. Tune Diagram of the Cooler Injector Synchrotron of IUCF. Where □ stands for θ_e changing from 12° to 26° for $L = 1.7$m, △ for θ_e from 6° to 24° for $L = 1.8$m, $*$ for θ_e from 6° to 22° for $L = 1.9$ m and ○ for θ_e from 12° to 26° for $L = 2.0$ m. Step between two points is 2°

a number of possible lattice designs were obtained using MAD program [1].

A. *Tune diagram*

Tune changes due to the variations of edge angle θ_e and dipole length L are plotted in tune diagram as shown in Figure 2, where betatron resonances and the spin tune at injection energy are also shown. In particular, the working point is marked by a symbol •, where the horizontal and the vertical tunes are 1.463 and 0.779, respectively.

B. *Betatron Function*

When scanning over the edge angle and the length of dipoles, lattice functions are also changed due to the variations of the effective focusing forces in both planes. Figure 3 shows the lattice function distributions of β_x, β_z and D_x (horizontal dispersion function) at the working point. We note that $\beta_z \approx 3.5$ m and $\beta_x \approx 1.0$ m at the injection stripper location.

C. *Dispersion Function and Chromaticity*

Momentum spread could result in closed orbit changes through the dispersion so as to cause emittance growth during the injection. At a $D_x \approx 1.5$ m, the emittance growth due to energy loss at the stripper thickness of $4\mu g/cm^2$ is tolerable. The final momentum spread of the injected beam is about 2×10^{-3}. Thus the chromaticity of the machine dose not cause large tune spread. The effects of the dispersion and the chromaticities on the variations of θ_e and L are also studied. It becomes clear that the chromaticities of the CIS lattice are small, we do not need to worry them.

D. *Momentum Compaction Factor* α

To avoid passing transition energy problem, we also need to keep tracking the changes of the momentum compaction factor α

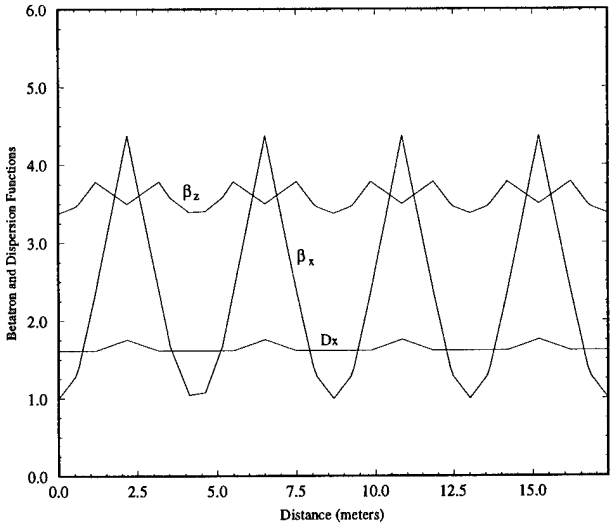


Figure. 3. The CIS lattice function distributions for $L = 2.0$ m, $\theta_e = 12°$

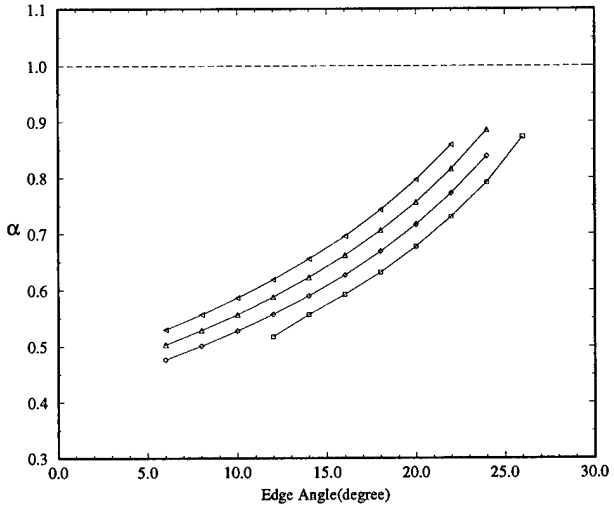


Figure. 4. Momentum Compaction Factor α variation with respect to L and θ_e with the same parameters used in Figure 2

($\alpha = 1/\gamma_T^2$) when other parameters are adjusted. Figure 4 shows the change of α with θ_e and L.

III. The CIS Lattice With Trim Quadrupoles

In order to have the flexibility of adjusting betatron tunes, four trim quadrupoles will be used. However, we do have the options of using two or four trim quads. with their positions adjustable.

A. *Tune Diagram*

Figure 5 shows the tuning range of the CIS with these trim quads.. In the case of two trim quads., machine is stable for the vertical tune below 1.0, which shows in Figure 5 as △s below the line of $Q_z = 1$. In the case of four asymmetrical quads. with superperiod of two, there is a vertical tune gap due to the integer resonance. Within this gap, the vertical motion is unstable as shown in Figure 6. The corresponding lattice function distributions are shown in Figure 7.

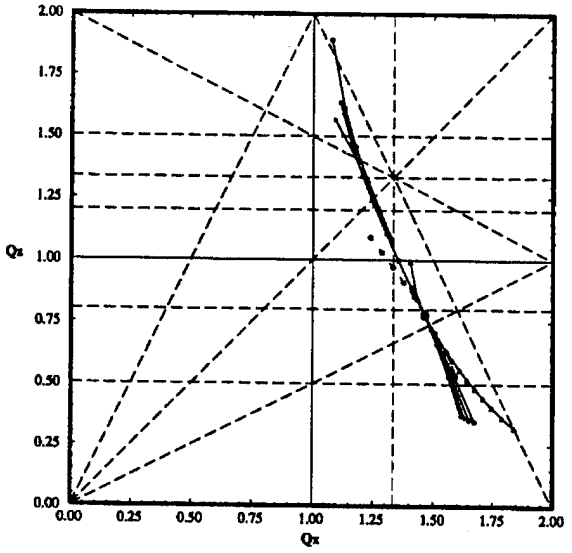


Figure. 5. Tune diagram for the CIS with trim quads.. Where ○ stands for the lattice without trim quads., △ for the lattice with two trim quads. and all others having four trim quads. with their locations adjusted with respect to the the dipoles

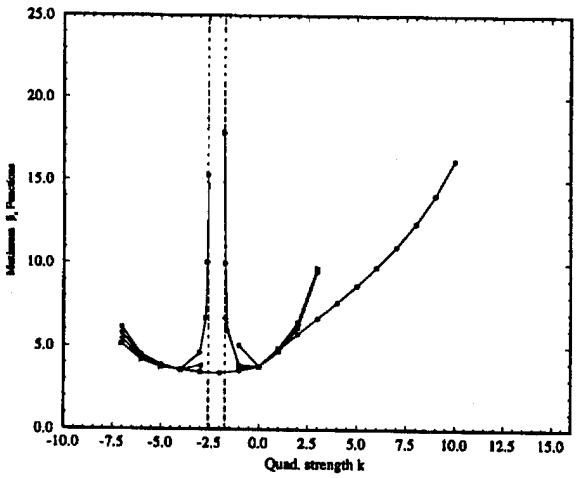


Figure. 6. Maximum vertical betatron functions for the CIS with trim quads. Where the notations and conditions are as same as that we used for Figure 5

B. *Momentum compaction factor* α

Figure 8 displays the variation of momentum compaction factor α. It turns out that α does not change very much for different strengths of the quadrupoles. It, however, offers possibilities of transition crossing lattices. In the case of two trim quads., momentum compaction α changes sign at the quadrupole strength between 7.68 and 7.8. This leads to a possible imaginary γ_T lattice ($\alpha = 1/\gamma_T^2$).

IV. Conclusion

In conclusion, we have studied the CIS lattice by varying parameters, such as circumference, the dipole length, the edge angle, the trim quads. position and strength. We found that the CIS lattice parameters, which are listed in Table I, will meet our proposed requirements for the beam performance. With the employment of trim quadrupoles, the machine possesses flexibility for

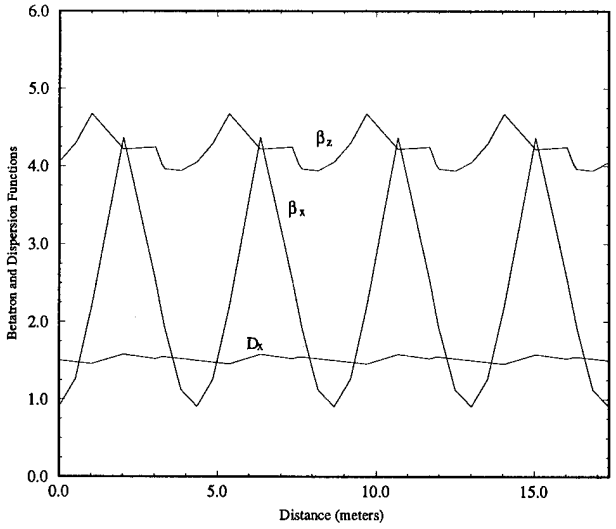


Figure. 7. Lattice functions for the CIS with trim quads. for four trim quads and each quadrupole is 20 cm away from the dipole.

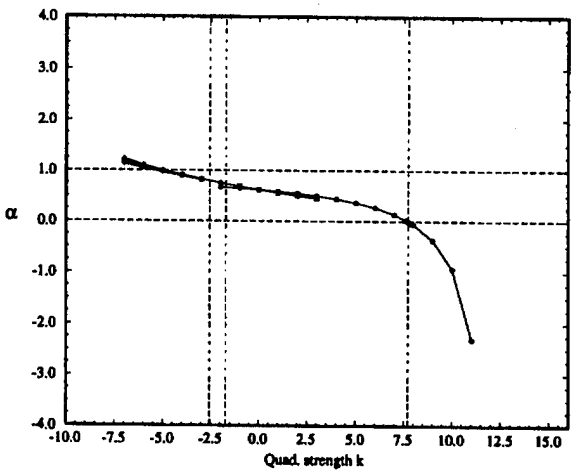


Figure. 8. Momentum compaction factor α for the CIS with Where the notations and conditions are as same as that we used for Figure 5

betatron tune adjustments. Furthermore, γ_T can be also varied by the trim quadrupoles. Thus, the CIS will become an interesting machine for accelerator physics studies such as transition energy crossing and imaginary γ_T lattice in longitudinal beam dynamics studies.

References

[1] H. Grote *et al.*, The MAD Program, User,s Reference Manual.

[2] D. Friesel *et al.*, News Letter, IUCF, April, 1995.

[3] Conceptual Design Manual For CIS, IUCF Internal Report (January 1995).

DESIGN STUDY OF ANTIPROTON ACCUMULATION AND DECELERATION RING IN THE KEK PS COMPLEX

S. Machida and M. Yoshii
National Laboratory for High Energy Physics (KEK)
1-1 Oho, Tsukuba-shi, Ibaraki, 305 JAPAN
Y. Mori and N. Tokuda
Institute for Nuclear Study, University of Tokyo (INS)
3-2-1 Midori-cho, Tanashi-shi, Tokyo, 188 JAPAN
Y. Ishi
Mitsubishi Electric Corporation
2-2-3 Marunouchi, Chiyoda-ku, Tokyo, 100 JAPAN

Abstract

An antiproton accumulation and deceleration ring in the KEK proton synchrotron (KEK PS) complex has been designed. The KEK PS top energy is 12 GeV and it is enough to produce 2 GeV/c antiprotons. As many as 10^5 of them would be collected each synchrotron cycle, that is 2 second. After stacking and stochastic cooling of the beams, 10^7 to 10^8 antiprotons per hour should be available for physics experiments. There are several R&D items such as compression of the nine bunch train in the PS. Preliminary simulation has been done to look at single turn transfer of antiprotons to the proposed ring whose circumference is 1/3 of the PS.

I. OVERVIEW

The complex of rings (ACOL, AA and LEAR) at CERN [1] is the only facility in the world that accumulates and decelerates antiprotons for versatile fields of physics. A lot of interesting work using low energy antiproton beams with this complex has been done and there are still increasing number of proposals. Atomic physics using antiproton beams is one of that growing fields. There is no doubt that if there were another low energy antiproton source in the world, even dedicated for atomic physics, it would be very useful.

At KEK, the proton synchrotron (KEK PS) which provides an intense proton beam at the energy of 12 GeV is in operation. Experiments using antiprotons is nothing new to the KEK PS users. However, there are vigorous demands for higher intensity of antiprotons with good beam quality to carry out more systematic study. A dedicated ring for antiproton accumulation and deceleration is desired, although there are manifest disadvantages compared with the CERN complex such as lower primary proton energy, which will produce less number of antiprotons.

In this report, a preliminary design of the ring for antiproton accumulation and deceleration, necessary change in the KEK PS operation, antiproton yield, and stochastic cooling are described. During the discussions of that ring, we examined simultaneously (not described in this report) whether the same ring could be operated for the acceleration of heavy ions as a booster synchrotron for the KEK PS. By that reason, we name the proposed new ring AA-HIB (Antiproton Accumulator - Heavy Ion Booster).

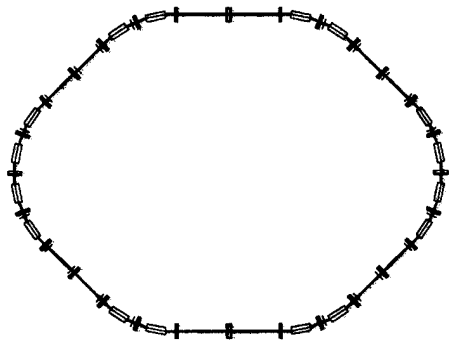


Figure. 1. Lattice layout of the AA-HIB.

II. LATTICE DESIGN FOR AA-HIB RING

In designing the antiproton facility, it is requested that accumulation and deceleration of antiproton beams should be done in one ring at the first stage. That is just because of the limited budget. In designing the lattice of the AA-HIB ring, the following criteria are to be considered.

1. The absolute value of the phase slip factor ($\eta = 1/\gamma_t^2 - 1/\gamma^2$) should be about 0.1 to have a good mixing condition in stochastic cooling.
2. The straight sections for beam injection and extraction should be dispersion free.

The maximum magnetic rigidity of the ring is $(B\rho)_{max} = 6.671$ T·m, where the momentum of accumulated antiprotons is 2 GeV/c. Since antiprotons and heavy ions are to be decelerated and accelerated, respectively, and considering requirement (1.) above, it is desirable that the transition energy should be far above the top energy.

In order to meet those requirements, a lattice based on three DOFO-cell configurations [2] consisting of one missing bending magnet cell between two cells is adopted. In this lattice, dispersion function at the bending magnets are relatively small and, on the other hand, it is large at the missing-bending magnet cell. This is a desirable feature for our purpose. That is, a beam with large momentum spread such as an antiproton beam does

0-7803-3053-6/96/$5.00 ©1996 IEEE

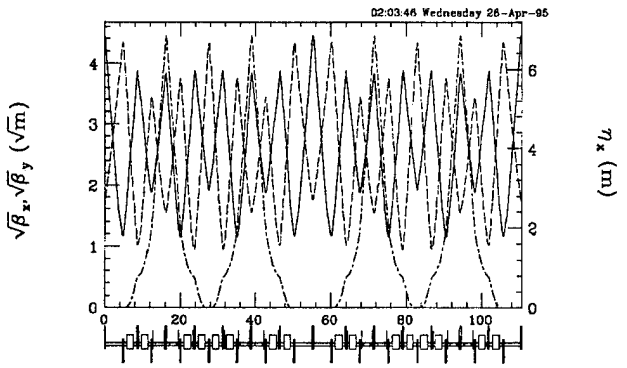


Figure. 2. Beam optics functions of the AA-HIB. β_x:solid line, β_y:dashed line, η_x:dotted line.

not necessarily require large horizontal aperture in the bending magnets.

Superperiod of the ring is two and one arc section consists of the two unit cell of DOFO configuration. There are sixteen bending magnets, and the effective length of each bending magnet is 1.8 m. The distance between the two quadrupole magnets of the unit cell is 3.5 m, which provides enough room for beam monitors and steering magnets for the optics correction. The lattice layout and beam optics function are shown in Fig. 1 and Fig. 2, respectively. An optics code SAD [3] is employed to calculate optics functions.

There are four straight sections which can be used for the injection and extraction systems, the rf cavities and the pick-ups and kicker magnets for stochastic cooling. The length of each straight section is 4.5 m. The dispersion function at both ends of an arc section is zero. The transition energy γ_t is 5.4, which is well above the maximum Lorentz γ of the beam. The operating tune can be changed by varying the field strength of a series of quadrupole magnets placed only in the straight sections. The nominal tune are selected as (ν_x, ν_y)=(3.6, 4.7).

Chromaticity correction can be made by a pair of sextupole magnets placed near the quadrupole magnets in the arc. Dynamic apertures for both horizontal and vertical planes when correcting the chromaticity using these sextupole magnets are evaluated by particle tracking simulation of 5,000 turns. In this simulation, the momentum dispersion of the beam is assumed to be zero. The estimated dynamic aperture for both planes turns out quite large, namely about 1,000 π mm·mrad. That is larger than the acceptance, which is 100 π mm·mrad for horizontal and 90 π mm·mrad for vertical.

The physical aperture of the bending magnets requires 220 mm (hor.) × 70 mm (ver.) because a momentum acceptance of at least ±3% is necessary for rf stacking of accumulating antiprotons. The horizontal beam size becomes maximum at the position of the quadrupole magnet in the center of the unit cell of the arc section and reaches about 400 mm, requiring a large bore quadrupole magnet.

III. MANIPULATION OF BUNCH STRUCTURE IN THE KEK PS

In this section, we review the present beam parameters of the KEK PS and examine the necessary manipulation of the longitudinal bunch structure in order to match the design of the AA-HIB. The circumference of the AA-HIB lattice is about one third of the KEK PS. The transfer of antiproton beams into the AA-HIB should be done by one turn injection. The transverse emittance of antiproton beams is much larger than the primary proton beams so that the transverse ring acceptance is filled with the one turn injected beams; no room for multi-turn injection. If a very fast kicker is developed, and provided that antiproton beams have the same bunch structure as the primary proton beams, multi-turn injection filling the longitudinal phase could be another choice. However, it is not a realistic plan at the moment. To transfer all of the beams in the KEK PS to the AA-HIB with one turn injection, the length of the bunch train should be shortened before the extraction. In the concrete, nine bunches uniformly distributed in the KEK PS is gathered at the top energy so that the beams can occupy only one third of the circumference.

Table 1: Parameters of the KEK PS.

harmonic number	9
rf frequency (at the top)	8.0 MHz
rf voltage	92 kV
bucket height ($\Delta p/p$)	±0.55%
bunch spacing	37.7 m
maximum dispersion	3.8 m
maximum β_x and β_y	20 m
machine aperture (H*V)	145 mm*50 mm
Lorentz gamma	13.8
slip factor	1.67×10^{-2}
longitudinal emittance	3 eV·sec (full)
norm. horizontal emittance	45 π mm·mrad (full)
norm. vertical emittance	20 π mm·mrad (full)

The simplest way employs an additional rf system which has the harmonic number (h) of unity in the KEK PS. After the beams are accelerated to the top energy by the normal rf system with the harmonic number of nine, the normal rf system is turned off and, in turn, the $h = 1$ rf system is turned on. The switching timing of those two rf system gives several options with more detailed differences. Nevertheless, the primary use of the $h = 1$ rf system is to populate most of beams near the center of the rf bucket so that the bunch length can be within the range of one third or less of the circumference.

We examined the scheme in detail using multi-particle simulation. Table 1 shows the rf, lattice, and beam parameters of the KEK PS.

By exciting the $h = 1$ rf system at the top energy, only one rf bucket is made. In the bucket, we want to have less than 113 m (the circumference of the AA-HIB) bunch and its maximum $\Delta p/p$ = 1.5%. The maximum momentum spread was limited by the horizontal aperture in the KEK PS, that is 145 mm. In fact, it is the most optimistic estimate since we assumed that the closed orbit distortion can be perfectly corrected and beam size are simply determined by the transverse beam emittance and the momentum dispersion. Reduction of the useful aperture by sagitta is, though, included.

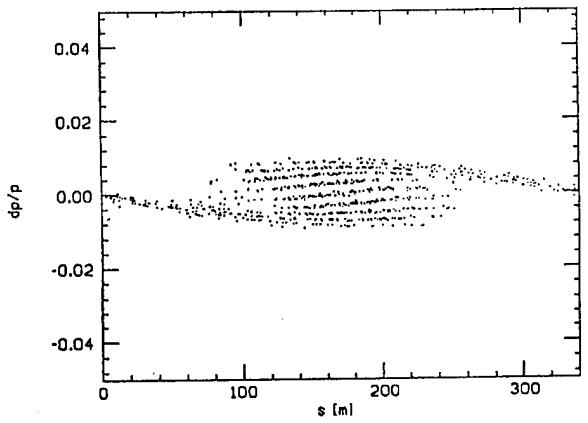


Figure. 3. A bunch from the KEK PS.

The following is the simulation results. The $h = 1$ rf system is excited to 22 kV suddenly (within 1 msec) after the $h = 9$ rf system is turned off. About one quarter of synchrotron oscillation period of $h = 1$, nine bunches, which are mismatched in the $h = 1$ rf bucket, are aligned in the momentum direction so that projection of the beam to the position axis has the narrowest profile as shown in Fig. 3. We counted the number of particles within 113 m in the position direction and $\Delta p/p = 1.5\%$ in the momentum direction. The ratio of the above counted number to the total particles is the capture efficiency and turns out to be 69%. The whole process takes 5.7 msec. Note that the higher voltage can populate more number of beam around the center of the bucket, but at the same time, the momentum spread becomes larger, that is limited by the horizontal aperture.

IV. ANTIPROTON YIELD

We have estimated antiproton yield based on the CERN parameters and scaled them in the following way. The production yield rate of 2.0 GeV/c antiprotons from 12 GeV protons is assumed to be 1/8 of that of 3.5 GeV/c antiprotons from 26 GeV protons. The antiproton yield rate at 24 GeV is 9.1×10^8 per 10^{13} protons and it is scaled to the yield at 26 GeV by multiplying 1.22 [1]. As the acceptance of a horn, we take $24\,\pi \times 10^{-4}$ sterad. The momentum acceptance is assumed to be 1.5%. Therefore, according to the simplified formula in [1] the antiproton into the AA-HIB per incident proton is

$$Y = \frac{1}{8} \cdot 1.22 \cdot (9.1 \times 10^8/10^{13}) \cdot 1.5 \cdot (24\pi \times 10^{-4}) = 1.6 \times 10^{-7}$$

V. STOCHASTIC COOLING AND TOTAL NUMBER OF ANTIPROTONS

The number of protons per PS machine cycle is 4×10^{12}. One cycle takes 4 seconds presently, but 1 to 2 seconds out of 4 seconds is spent for slow extraction. In the operation mode to produce antiprotons, we expect that the KEK PS cycle could be 2 seconds and therefore 4.5×10^5 antiprotons should be injected every 2 seconds, where transfer efficiency (69%) from the PS to the AA-HIB demonstrated above is included.

Once a bunch is injected into the ring, precooling is applied until the next bunch is injected. The momentum spread is reduced from $\pm 1.5\%$ to $\pm 0.5\%$ in 2 seconds. A stripline type pick-up and kicker whose total length is about 3 m each will be used with a notch filter. The pick-up and preamplifier are to be cooled down to 20 K. The required system bandwidth and total gain are 560 MHz and 160 dB, respectively. The power to the kicker is estimated to be 1.2 to 1.3 kW.

After 1,000 bunch injection, which takes about 40 minutes, more than 10^8 antiprotons are accumulated. Additional deceleration down to 100 MeV/c or lower makes one machine cycle of the ring the order of hour. With beam loss in the transport line and deceleration process included, as many as 10^7 to 10^8 antiprotons per hour are expected for physics experiments.

References

[1] P. Bryant and S. Newman (Editors), *CAS* (CERN Accelerator School), Antiprotons for Colliding Beam Facilities, Geneva, 1983.

[2] U. Wienands, R. V. Servranchx, R. C. York, X. Wu, S. Machida, A. A. Garren, F. Botlo-Pilat, E. D. Courant, "The High-γ_t Lattice of the SSC Low Energy Booster", Proc. of 15th International Conference on High Energy Accelerators, Hamburg, 1992.

[3] SAD stands for "Strategic Accelerator Design" code. It is developed by K. Oide and colleagues at KEK.

FEASIBILITY STUDY OF A 1-MW PULSED SPALLATION SOURCE*

Y. Cho, Y.-C. Chae, E. Crosbie, M. Fathizadeh, H. Friedsam, K. Harkay, D. Horan, S. Kim, R. Kustom, E. Lessner, W. McDowell, D. McGhee, F. Mills, H. Moe, R. Nielsen, G. Norek, K. J. Peterson, A. Rauchas, K. Symon, K. Thompson, D. Warner and M. White,
Argonne National Laboratory, Argonne, IL 60439, USA.

Abstract

A feasibility study of a 1-MW pulsed spallation source based on a rapidly cycling proton synchrotron (RCS) has been completed. The facility consists of a 400-MeV H^- linac, a 30-Hz RCS that accelerates the 400-MeV beam to 2 GeV, and two neutron-generating target stations. The design time-averaged current of the accelerator system is 0.5 mA, and is equivalent to 1.04×10^{14} protons per pulse. The linac system consists of an H^- ion source, a 2-MeV RFQ, a 70-MeV DTL and a 330-MeV CCL. Transverse phase space painting to achieve a Kapchinskij-Vladimirskij (K-V) distribution of the injected particles is accomplished by the charge exchange injection and programming of the closed orbit during the injection. The synchrotron lattice uses FODO cells of 90° phase advance. Dispersion-free straight sections are obtained by using a missing magnet scheme. Synchrotron magnets are powered by a dual-frequency resonance circuit that excites the magnets at a 20-Hz rate and de-excites them at a 60-Hz rate, resulting an effective rate of 30 Hz, and reducing the required rf power by 1/3. Details of the study are presented.

I. INTRODUCTION

A proton synchrotron system capable of delivering 1 MW of beam power was designed for the Intense Pulsed Neutron Source (IPNS) Upgrade Feasibility Study at Argonne National Laboratory (ANL) [1]. The RCS and associated research facilities are housed in the 50,000 m^2 of space in the former 12-GeV Zero Gradient Synchrotron (ZGS) area. The ZGS Ring Building houses a 190-m circumference, 2-GeV RCS. Two adjoining experiment halls house two neutron generating target stations, each serving 18 neutron beamlines and instruments. Figure 1 shows the proposed facility layout. Enclosures for the linac and low energy transport line (LET) are the only new conventional facility construction, and are also shown in Figure 1. The choice of 30 Hz as the repetition rate of the fast cycling synchrotron was based on preferences expressed by the users.

II. LATTICE

Required features of the lattice are: 1) To have a large transition energy so that the lattice has a relatively large slip factor, $\eta = \left|\gamma^{-2} - \gamma_t^{-2}\right|$, 2) to have enough straight section length for an radio-frequency cavity system that could have a total length of 20-30 m, and 3) the straight sections should be dispersion-free for implementation of charge-exchange

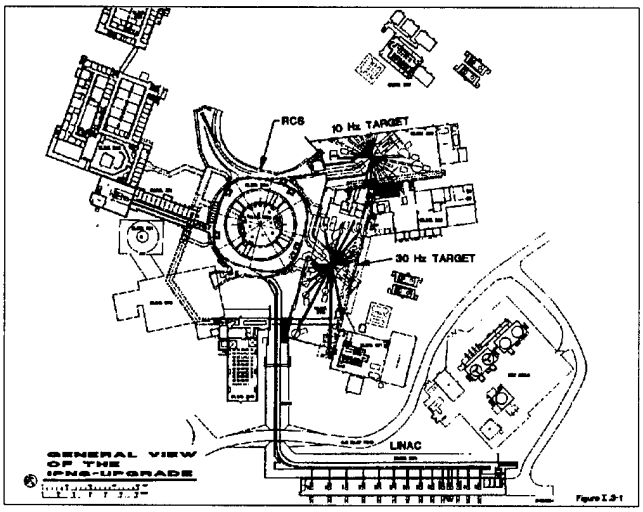


Figure 1: IPNS Upgrade Facility Layout.

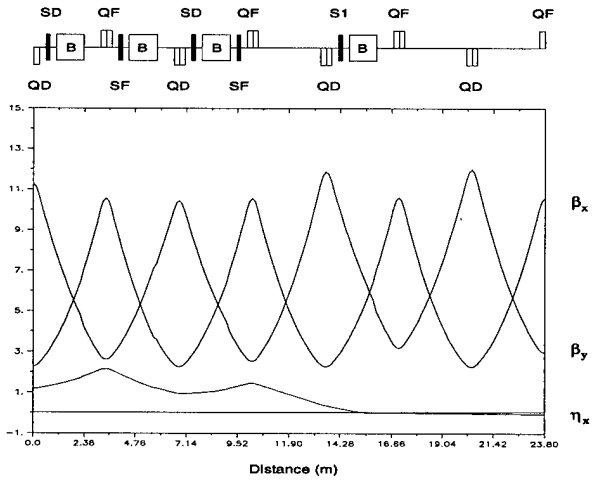


Figure 2: Lattice Functions for 1/2 Superperiod.

injection. Figure 2 shows 1/2 of a super period that has a reflective symmetry at both ends. Each cell of the FODO structure has a phase advance of ~ 90° in both transverse planes. The normal cells, dispersion suppressor cell and the straight section cells are indicated in the figure. The dispersion suppressor cell is made by removing a dipole from a 90° phase advance cell. When the vertical phase advance is slightly less than 90° but the horizontal phase advance is maintained at 90°, the missing dipole scheme suppresses the dispersion function. An advantage of this arrangement is that when the total lattice is put together, the horizontal tune is about one unit higher than the vertical. The dynamic aperture study took alignment and

* Work supported by the U. S. Department of Energy, Office of Basic Sciences under the Contract W-31-109-ENG-38.

0-7803-3053-6/96/$5.00 ©1996 IEEE

construction imperfections into account, and the results are presented elsewhere [2]. Table 1 shows parameters of the normal cell.

Table 1 Normal Cell Parameters
(2.2 GeV, B ρ = 9.989 Tm)

Elements	Length (m)	Strength	Units
QD	0.25	-7.276	T/m
D1	0.3		
SD	0.2	-0.843	m^{-2}
D1	0.3		
B	1.3	1.5088	T
D2	0.8		
QF	0.5	8.267	T/m
D1	0.3		
SF	0.2	0.612	m^{-2}
D1	0.3		
B	1.3	1.5088	T
D2	0.8		
QD	0.25	-7.276	T/m

III. INJECTION

The injection energy was determined by the incoherent space charge limit of the lattice and the defined acceptance of the synchrotron. If the injected beam stack has an emittance of 375 π mm mr in both transverse planes, and the allowed tune shift due to space charge is 0.15, an injection energy of 400 MeV is sufficient to allow a time averaged current of 0.5 mA with a repetition rate of 30 Hz.

The 400-MeV H^- ion injector linac design for this feasibility study was performed by the industrial firm, AccSys Technology, Inc. The linac design specification includes: 1) an rms normalized emittance of 1π mm mr, 2) an energy spread of less than 2.5 MeV, 3) a beam pulse length of 0.5 msec, and 4) beam chopping capability near the ion source so that the beam can be injected into a waiting synchrotron bucket.

Phase space painting in both transverse planes is used to stack 560 turns in the synchrotron. Four bumper magnets provide radial closed orbit displacement, and both injection position and angle can be radially adjusted as shown in Figure 3. A fast vertical steering magnet allows adjustment of the vertical injection angle. Unique features of this injection system include: 1) Trajectories of incoming H^- ions and of the circulating protons are combined by one of the ring focusing quadrupole magnets rather than by the customary dipole magnets. The use of this quadrupole has an added advantage in that the ring focusing quadrupole acts as a defocusing quadrupole for the incoming H^- beam, and it provides an additional bend for the H^- particles. There is ample separation between the incoming beam and the circulating beam. 2) Since each cell has 90° phase advance the bumper magnets, B1 and B4, shown in Figure 3, can displace and restore the closed orbit. However, B2 and B3 are needed to adjust the injection angle of the H^- ions so that H^0 particles emerging from the stripping foil can be collected in a catcher. A discussion of the H^- and H^0 particles associated with this injection system is given in reference [3].

Using the bumper system together with the vertical steering magnet in the transport line, the injected beam can be stacked in a K-V distribution [4].

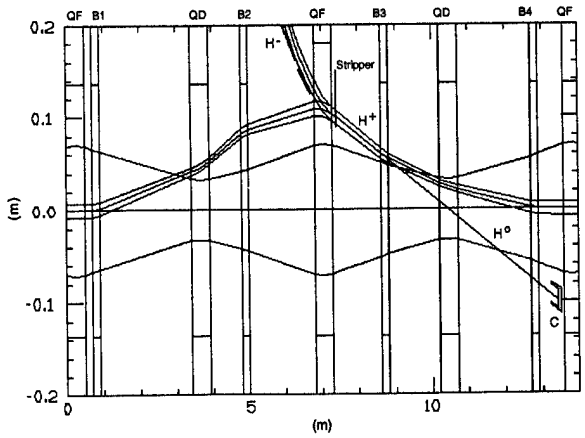


Figure 3: Bumped Orbit Injection, Showing the H^0 Catcher.

IV. RF VOLTAGE PROGRAM

A key goal of the design study was to devise an rf program that prevents beam loss from injection through acceleration to extraction. The rf program was obtained using a Monte Carlo program that tracked the particles from injection to extraction. The tracking study also provided information on optimum chopping of the incoming beam. In the context of bunch rotation, chopping is related to the energy spread of injected beam. Figure 4 shows the rf voltage program and the corresponding bucket and bunch areas. When the first turn arrives at the start of injection, the voltage required to contain the 2.5 MeV energy spread of the linac beam is 40 kV. The injected beam has a bunch area of 3.3 eV sec, and the waiting bucket has an area of 7.3 eV sec, thus the initial dilution of the area is a factor of 2.2. During injection the voltage is raised to 67 kV to compensate for space charge effects and to give a somewhat larger bucket area. Soon after injection, the bunch is well formed. The bucket area is raised to 9 eV sec, and that area is maintained for the next 7.5 msec. The bucket area beyond that point in time is made larger as indicated in Figure 4 for two reasons. The first is to make the momentum spread of the circulating beam large enough to stay below instability thresholds [5,6], and the second is to provide a synchrotron frequency large enough so that the particles in the bunch can follow the rapidly changing synchronous phase angle near the time of extraction.

V. IMPEDANCE AND INSTABILITIES

Impedance of the RCS is dominated by space charge which is capacitive for the both longitudinal and transverse components. The RCS operates below the transition energy of the machine, and therefore it is not expected to have longitudinal microwave instability. However a detailed study of longitudinal impedance and instability was performed, and results are presented in this

conference [7]. Similarly, the transverse impedance and instabilities, were analyzed and details are presented in this conference [8].

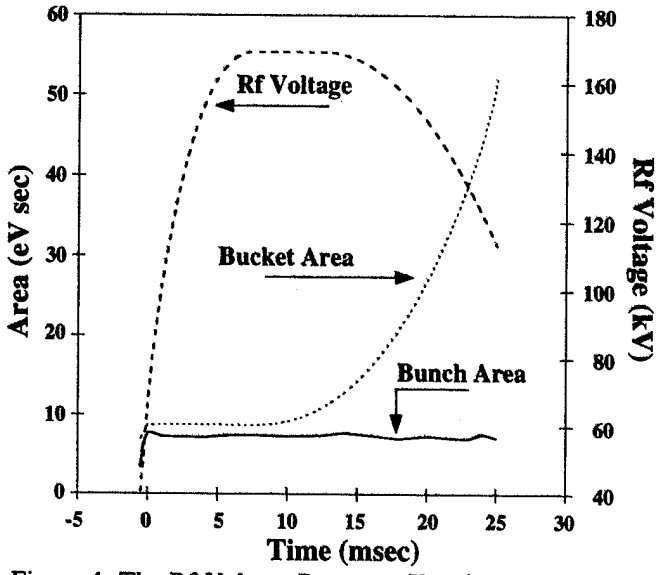


Figure 4: The Rf Voltage Program, Showing Bunch and Bucket Area Over the Complete Cycle.

VI. SYNCHROTRON HARDWARE

The RCS has ceramic vacuum chambers equipped with rf shields constructed of conducting wires. The system is similar to that used at the ISIS facility at Rutherford-Appleton Laboratory [7].

The RCS ring magnets are energized with dual frequency resonant power supplies that excite the ring at a 20-Hz rate and de-energize it at a 60-Hz rate. This method results in an overall repetition rate of 30 Hz, and reduces the required rf accelerating voltage by 1/3. Detailed descriptions of the hardware can be found in Reference 1.

VII. SUMMARY

The IPNS Upgrade Feasibility Study resulted in the design of an accelerator system capable of producing 1 MW of proton beam power. The full power can either be delivered to one of the two neutron generating targets, or can be split between the them. A scheme of phase-space painting using charge exchange allows injection of 500 turns into the machine. Table 2 is a summary of the main RCS parameters.

Table 2: Main Parameters of the RCS.

Parameters	Values	Units
Circumference	190.4	m
Super-periodicity	4	-
Total number of cells	28	-
Number of normal cells	12	-
Nr. of dispersion suppressor cells	8	-
Nr. of straight section cells	8	-
Nominal straight section length	2.9	m
Injection energy	400	MeV
Injection field	0.463	T
Nominal extraction energy	2.0	GeV
Maximum design energy	2.2	GeV
Dipole field at 2.2 GeV	1.5088	T
Bending radius	6.6207	m
Dipole length	1.3	m
Dipole good field region	0.45	m
Dipole gap height	0.182	m
Number of dipoles	32	-
Number of quadrupoles	56	-
Quadrupole length	0.5	m
Quadrupole aperture radius	0.1185	m
Maximum quadrupole gradient	8.8	T/m
Number of sextupoles (F)	16	-
Number of sextupoles (D)	16	-
Number of harmonic sextupoles	8	-
Maximum sextupole strength	1.2	m^{-2}
Sextupole length	0.2	m
Sextupole aperture radius	0.13	m
Horizontal tune, ν_x	6.821	-
Vertical tune, ν_v	5.731	-
Normalized transition energy, γ_t	5.40	-
Natural chromaticity, $\xi_x = (\Delta\nu/\nu)_x/(\Delta p/p)$	-1.06	-
Natural chromaticity, $\xi_v = (\Delta\nu/\nu)_v/(\Delta p/p)$	-1.20	-
Maximum β function	12	m
Minimum β function	2.2	m
Maximum η function	2.2	m
Minimum η function	-0.06	m
Revolution time at injection	890.1	nsec
Revolution time at extraction	665.1	nsec
$\dot{B}_{max}$	64.5	T/sec
Maximum energy gain/turn	81.4	keV

Acknowledgments

We acknowledge D. Haid for help in manipulation of computer graphics and H. Rihel for drawings.

VIII. REFERENCES

[1] "IPNS Upgrade - A Feasibility Study", ANL Report ANL-95/13 (April, 1995).

[2] E. Lessner, Y.-C. Chae, and S. Kim, "Effects of Imperfections on Dynamic Aperture and Closed Orbit of the IPNS Upgrade Synchrotron," in these proceedings.

[3] Y.-C. Chae and Y. Cho, "Study of Field Ionization in Charge Exchange Injection for the IPNS Upgrade," in these proceedings.

[4] E. Crosbie and K. Symon, "Injecting a Kapchinskij-Vladimirskij Distribution into a Proton Synchrotron," in these proceedings.

[5] K. Harkay, Y. Cho, and E. Lessner, "Longitudinal Instability Analysis for the IPNS Upgrade" in these proceedings.

[6] K. Harkay and Y. Cho, "Transverse Instabilities Analysis for the IPNS Upgrade" these proceedings.

[7] G. H. Rees, "Status report on ISIS," in Proceedings of the IEEE Particle Accelerator Conference (March 16-19, 1987).

ORIC CENTRAL REGION CALCULATIONS*

J.D. BAILEY ORNL†/ JIHIR‡ and

D.T. DOWLING, S.N. LANE, S.W. MOSKO, D.K. OLSEN, B.A. TATUM ORNL

Abstract

The central region for the K=100 Oak Ridge Isochronous Cyclotron, ORIC, will be modified to provide better orbit centering, focusing of orbits in the axial direction, and phase selection, in order to improve extraction efficiency, and reduce radioactive activation of cyclotron components. The central region is specifically designed for the acceleration of intense light ion beams such as 60 MeV protons and 15 - 100 MeV alphas. These beams will be used in the production of radioactive atoms in the Radioactive Ion Beam Project at Oak Ridge National Laboratory.

I. RIB PRODUCTION REQUIREMENTS ON ORIC

The Holifield Radioactive Ion Beam Facility, HRIBF, will use the K= 100, Oak Ridge Isochronous Cyclotron, ORIC, as a driver to provide beams of light ions (protons, deuterons, helium, and lithium) ranging from 10 – 65 MeV on target[1]. These will produce proton-rich radioactive atoms for acceleration in the HRIBF 25 MV Tandem. The Target Ion Source on the RIB Platform, presently has a carbon window 170 mg/cm^2 thick. Using the energy loss in this window as a guide, ORIC will need to operate at K$\geq$15 for protons, K$\geq$35 for deuterons and 2-plus helium, and K$\geq$60 with 3-plus lithium. These beams need intensity so as to provide experimenters with sufficient radioactive ions to study nuclear structure and astrophysis. Direct and induced radioactivity produced by these beams, require further constraints on ORIC. The administrative limits for operation as a low hazard facility will be 50μA of 65 MeV protons, and 200μA of 100 MeV alphas. Good extraction efficiency (90+%) is needed to minimize the induced radioactivity produced in ORIC.

II. AN OVERVIEW OF ORIC HISTORY

ORIC was constructed and began operation over three decades ago[2]It was initially used to accelerate light ions. The acceleration of heavy ions in ORIC first took place in 1968[3]. Extraction was achieved by inducing radial oscillations near the center of the cyclotron, and using the precession at 29 in., while ν_r was still $\simeq$ 1.05, to increase the radial separation between turns near the deflector septum[4]. In the early 80's, ORIC was converted to be used as a booster for the 25 MV tandem accelerator. A new magnetic field mapping was performed for this conversion in the range of 12–20 kG. This enabled the writing of a set of cyclotron injection/orbit/extraction codes which accurately predicted machine settings for operating the cyclotron in coupled mode for K$\geq$ 60[6]. A new extraction method soon followed. The injected tandem beam had a small emittance, a 6° RF Phase width, and was injected with very good centering. A first harmonic bump was then used at outer radii to produce radial separation closer to the $\nu_r = 1$ resonance, ($\nu_r \simeq 1.017$). These qualities improved the extraction efficiency from a typical 30% to a typical 70%[5] Calculated turn separation at extraction is .1 in.

III. THE PRESENT ORIC CENTRAL REGION

The ORIC central region has been restored to a configuration similar to central regions used before the coupled operations. A PIG ion source is inserted on a radial arm from the North side of the machine. The source, which was modified to use a smaller chimney, can be positioned in both directions in the median plane. The puller, which is a little hook extending out from the dee, can be positioned in one dimension only, along the edge of the 180° dee. It's position in the other direction can be changed by removing the dee and replacing the puller. A radial clipper has been added. It is a small plate with a slot cut axially, that has been mounted on the dee, and runs parallel to the puller. In addition, the source head has been modified so that two plates can be mounted on them to form an axial slit which will restrict the beam axially within the first few turns[7].

Axial focusing in the central region is provided by two separate mechanisms. The first is geometric. The source chimney is set back from the leading edge of the source head. The electric field, which was calculated with RELAX3D[8], penetrates in to the source. Calculations, made with Z3CYCLONE[9], show that this provides axial focusing over most of the gap between the source and the puller when the electric field is accelerating the ions. This axial focusing in the first gap is extremely strong. It over focuses, causing the beam to expand axially. This expansion was measured using marks that a helium beam left on the axial slits, with the axial spread of the beam increasing from .2 in at the source slit to 1.0 in within two turns. The second method of axial focusing comes from rotating the source counter to the direction of the beam rotation[10]. This makes the beam arrive late with respect to the RF at subsequent gaps, providing vertical focusing. To bring the beam back to isochronism after the azimuthally varying magnetic field is strong enough to provide vertical focusing, the magnetic field begins above the isochronism value, returning to isochronism after a few inches, forming a magnetic cone at the center.

The central region is very open, with up to 100° width of RF phase of beam clearing the back of the source. Much of this time spread is lost after the crossing of the $\nu_r = 1$ resonance found at the transition between the magnetic cone and the isochronous field. Depending on the centering of the source, the relative posi-

*Work supported by the U.S. Department of Energy

†Managed by Martin Marietta Energy Systems, Inc., under contract No. DE-AC05-84OR21400 with the U.S. Department of Energy.

‡member institutions the University of Tennessee, Vanderbilt University, and the Oak Ridge National Laboratory; it is supported by the members and by the U.S. Department of Energy through Contract Number DE=FG05-87ER40361 with the University of Tennessee.

0-7803-3053-6/96/$5.00 ©1996 IEEE

tion of the puller, and first harmonic component of the magnetic field added by the innermost harmonic coils, calculations have shown anywhere from 15° – 45° of RF phase of beam orbiting about the center of the cyclotron after this crossing. The ions remaining outside of that time range orbit about the magnetic hills, subsequently returning to the machine center and being lost.

The properties of this open and variable geometry, a wide phase acceptance, a strong variation of centering with phase, and difficulty finding the optimum positions, are counter to those required for consistent, efficient extraction of the beam[11]. Indeed, the good extraction obtained in coupled operation was dependent on both good centering and a small phase width. Recommissioning runs have found the earlier extraction technique easy to reproduce, with 40% extraction efficiency, but the predictions of the cyclotron codes, lacking information about the source, are now only 'ball park' predictions.

IV. CALCULATED MODIFICATIONS TO THE ORIC CENTRAL REGION

Ideally, the installation of a fixed central region, designed to provide good centering, together with slits to provide fine phase selection, would be the best way to provide these qualities consistently for all operating points. This would entail completely redesigning the source for axial insertion, with accompanying changes in the center plug iron. The RF system, which is now used to provide 70 kV at all operating frequencies, would also need to provide a wide range of voltages to accelerate the various combinations of Q/A and E_f/A which are required.

Table I
Operating K Values for the three Pullers

ρ in	V_{dee} kV	p	$^3He^{2+}$	d,$^4He^{2+}$, $^6Li^{3+}$	$^7Li^{3+}$
1.07	70		100		
	66	65			
	54			100	
	47				100
	43	40	60	80	93
1.34	70	40	60	80	93
	43	25	36	50	60
1.69	70	25		50	
	43	15		33	
K to penetrate C window		12	35	32,46,60	70
Lowest K in first harmonic		7.3	16.4	29.2	39.7

Instead of a fixed central region, it is proposed that ORIC operate with a set of modified pullers, each operating over a smaller portion of the operating diagram as if it were part of a 'fixed central region'. With two such pullers, one where the ions have a radius of curvature after the first gap of 1.07 in, and the other 1.34 in, most of the useful part of the first harmonic operating range can be covered. If lower energy beams are desired, a third puller with a 1.69 in radius of curvature could be used. Table I lists the range of K values over which each puller will operate, with the associated accelerating voltage as a function of the Q/A of specific light ions. Also listed are the minimum K values needed for each ion to penetrate the 170 mg/cm^2 Carbon window, as well as the lowest K for which each Q/A can be accelerated using the first harmonic of the accelerating frequency.

The puller itself will be based on a design developed by Blosser and Marti at MSU[12]. The puller is extended to within .4 in of the source. This will create a maximum electric field of approximately 70 kV/cm, which is still below values routinely achieved in other machines. There is still some sparking concern about the puller penetrating between the two source heads. Proper care must be taken in preparing the surface of the puller. If necessary, the source heads will be redesigned to eliminate this overhang. The axial slit has a primary function as a ground post. Also new is an extension of the dummy dee. Previously, the dummy dee was open for the first 6.0 in above and below the cyclotron center. This allowed the insertion and free movement of the source head. but came at the price of deep electric field penetration about either side of the source. The extension restricts the open region from 1.8 in above machine center to 3.0 in below center. While still allowing the insertion and movement of the the source, it, together with the axial slit, provides better definition of the electric field, balancing the gaps on either side of the source as can be seen in Figure 1.

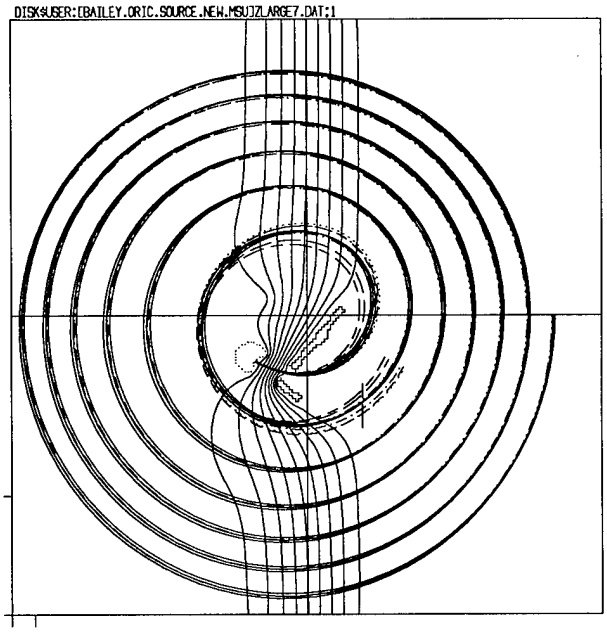


Figure. 1. Central Region Orbits with the New Puller. Depicted are the source, puller, and radial clipper protrusions in the median plane with electric field 10% equipotential lines. The axial slit restricts the gap on the source side above the centerline. Overlaid on the electric field are orbits for central rays for starting times from 200° to 270° RF, as well as displaced rays covering the radial phase space about the central ray which passes through the radial clipper.

The short and well defined gap between the source and puller, .46 in including the knife edge source slit, serves to reduce the energy and centering spreads in the ion beam. There is still enough centering spread that the radial clipper can make a coarse

phase selection, as shown in Figure 1, where central rays for starting RF times of 200°, 220°, 240°, 265° and 270° are shown being stopped by the clipper. The central ray, together with parallel rays displaced ± .01 in and rays diverging ± 90°, all with the starting time of 252.5° RF, are shown passing through the slit in the clipper. For this calculation, the starting times of 245° and 260° begin to slip beam through the slit. Thus, for the K=75 Q/A=1/2 operating point, the clipper will cut out all beam except ±8° about a starting time 17.5° before the peak of the accelerating voltage. This phase cut is not enough to provide single turn extraction, but will provide a well centered beam which will pass through the $\nu_r = 1$ resonance, and improve the extraction efficiency. Further reductions in phase will require the use of additional phase slits.

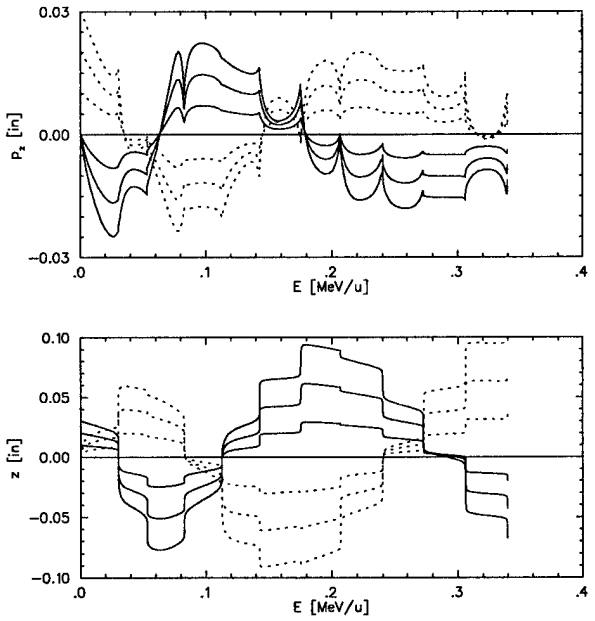


Figure. 2. Axial Motion of the Central Ray from Figure 1. For these starting conditions, $z \leq .03$ in., and $p_z \leq .03$ in. the motion is linear. (Momentum is converted to cyclotron units by dividing by $m\omega$.) Outside of this range it is nonlinear. The axial slit, set at ± .1 in., will pass this range, cutting the rest.

The axial motion is depicted in Figure 2, where z and p_z are plotted versus energy for the first six turns, for three parallel rays displaced in z, and three diverging rays with no z displacement. This motion is linear, except for the outermost orbits, which have small nonlinearities. Calculations starting with larger values of z or p_z quickly become nonlinear. The axial slit, which covers the first five turns will collimate out the nonlinear beam if the slit is set at ± .1 in. Notice the rapid change in p_z in the first accelerating gap, which is the geometrical focussing discussed earlier.

The central region presented here will be implemented in ORIC over the next year.

References

[1] J.D. Garrett and D.K. Olsen. A PROPOSAL FOR PHYSICS WITH EXOTIC BEAMS AT THE HOLIFIELD HEAVY ION RESEARCH FACILITY. February 1991. Table 4.2

[2] R.J. Jones et. al. NIM **18,19** 46-61 (1962).

[3] R.S. Lord et. al. Fifth Intl. Cyclotron Conf. 453-458 (1971).

[4] R.J. Jones et. al. ORNL–3630 Electronuclear Division Annual Progress Report 38-62 (1963).

[5] C.M. Jones et. al. NIM **A244** 7-12 (1985).

[6] R.S. Lord et. al. IEEE **NS-28**, No. 3 2083-2085 (1981).

[7] J.D. Bailey et. al. ORNL–6842 Physics Division Progress Report sec 1. p 10. (1994).

[8] H.Houtman et. al. European Conference, Computing in Accelerator Design and Operation, 98-103 (1983),

[9] F. Marti et. al. Ninth Intl. Conf. on Cyclotrons and their Applications, 465-468 (1981).

[10] W.I.B. Smith. NIM **9** 49 (1960).

[11] H.G. Blosser. Fifth Intl. Cyclotron Conf., 257-273 (1971).

[12] H.G. Blosser, private communication.

AN INTERNAL TIMING PROBE FOR USE IN THE MSU K1200 CYCLOTRON*

J.D. BAILEY ORNL†/JIHIR‡ and J. KUCHAR, F.MARTI, and J.OTTARSON NSCL/MSU

Abstract

A probe was installed in the K1200 to measure the internal beam time structure as a function of radius. Using the fast rise times of a Si detector, which was specially cut to extend the active area to within 150 μm of the detector edge, the time of arrival of the heavy ions on the detector is measured with respect to the accelerating RF voltage. Limited to count rates of several kHz, use of the detector requires attenuation of the injected beam, and permits studies of single particle beam dynamics.

I. THE TIMING DETECTOR

The development and use of a Si PIN diode as an external timing detector to measure the RF time spectra of the MSU K1200 extracted ion beam was previously reported[1]. The success of the external detector was an initial step in developing an internal timing detector for the K1200 cyclotron. The basic idea takes advantage of the large signals produced when heavy ions are incident upon a Si detector. This is possible in the K1200, because the injection beam line has attenuators which can reduce the injected beam current by 6 orders of magnitude[2], which keeps the detector count rate manageable, and increases the life of the Si detector. It is useful in the K1200, because beam intensities of highly charged heavy ions produced in the ECR's are too low for the longitudinal space charge force to alter the beam.

Table I
Detector Characteristics Prior to Cutting.

Device	Bias Voltage	Active Current	Guard Current
Uncut	40 V	65 pA	650 pA
Cut outside inner guard ring	50 V	35 pA	509 pA
Cut inside inner guard ring	50 V	65 pA	560 pA

The small turn separation inherent in a compact, 5 T cyclotron, approximately .6 - .7 mm in the K1200 near extraction, presents a significant challenge in using a Si detector to collect the beam, because the guard rings that shape the electric field inside the detector, create a large dead area around the edge. The Senter for IndustriForskning, in Norway, met this challenge by providing three detectors, one which was cut outside the innermost guard ring, one which was cut inside the innermost guard ring, and a reference detector. The increase in leakage current due to mounting and cutting these detectors is presented in Tables 1 & 2[3]. The detectors were bench tested with an alpha source. The fast signal obtained with an LBL Time Pick-Off from the detector with the inside cut did change, adding a shoulder to the falling edge, but the rise times were unaffected, all at 5 ns. The dead areas of these detectors were estimated to be between .15 – .19 mm for the detector with the outside cut, and between .01 – .10 mm on the detector with the inside cut[3].

Table II
Detector Characteristics after Cutting and Mounting.

Device	Depletion Voltage	Active Current	Guard Current
Uncut	40 V	1.3 nA	2.4 nA
Cut outside inner guard ring	35 V	38 pA	18 μA
Cut inside inner guard ring	40 V	4.0 μA	4.3 μA

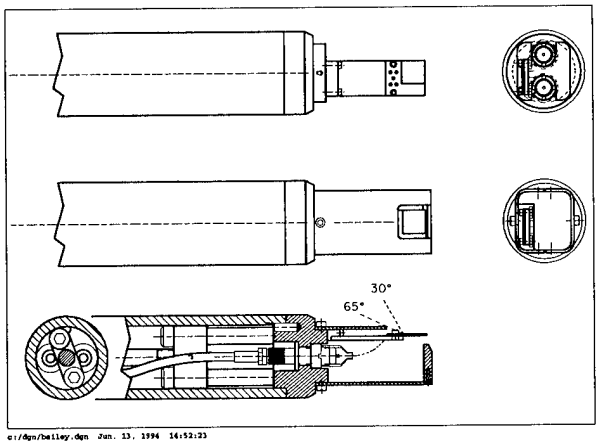


Figure. 1. K1200 Timing Probe Head. The detector mount, and RF shield are depicted above. Th cut away shows vacuum feed throughs, and beam clearance of the RF shield.

The probe head, depicted in Figure 1, inserts the detector into the beam. The cut edge of the detector extends out from the edge of the probe. A copper RF shield around the detector, has a notch cut in it which allows the ions to strike the detector without first hitting the shield. The bias voltage is supplied, and output signal extracted through two vacuum feed throughs. The probe is then inserted into the cyclotron in the hill, which doubles as a dummy dee.

*Work supported by the U.S. National Science Foundation grant PHY-9214992.
†Managed by Martin Marietta Energy Systems, Inc., under contract No. DE-AC05-84OR21400 with the U.S. Department of Energy.
‡The Joint Institute for Heavy Ion Research has as member institutions the University of Tennessee, Vanderbilt University, and the Oak Ridge National Laboratory; it is supported by the members and by the U.S. Department of Energy through Contract Number DE=FG05-87ER40361 with the University of Tennessee.

0-7803-3053-6/96/$5.00 ©1996 IEEE

II. USING A Si DETECTOR INSIDE A CYCLOTRON

There are several concerns when using the detector inside the cyclotron. First, the corner of the detector is pushed into the beam, allowing the ions to traverse only a small part of the detectors active area. To simulate the response of the detector, the energy loss profile for ions incident on the detector was calculated with the program ELOSS[4]. A simple model of the detector, developed by Spieler[5], was used to simulate the charge collection of the detector. The output signal from the program simulates the output of the detector reasonably well. This is passed through a simulation of a constant fraction discriminator. The final result, shows a variation of 40 to 50 ps between the measured time of arrival of ions which hit the edge, and those which hit the center of the detector.

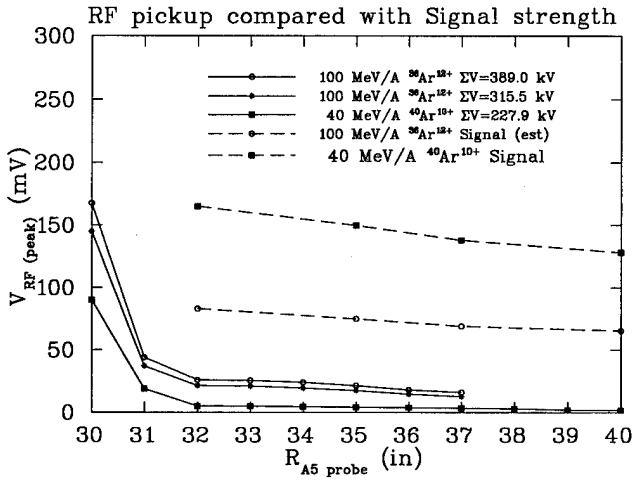


Figure. 2. Relative Strengths of Beam Signal and RF Pickup. The measured RF pickup of the detector from the dees is relatively constant until the probe begins to approach the accelerating gap. The strength of the beam signal is also displayed as a reference.

Second, the notch in the RF shield allows the detector, as a capacitor, to pick up a signal from the accelerating electric field. Since the hills spiral, due to the spiral in the magnetic field, as the detector travels deeper into the cyclotron it begins to approach an accelerating gap. Figure 2 shows the measured strength of the RF pickup, compared to the signal strength of Ar ions as a function of detector radius. It is clear that inside of 32 in the detector won't see any signal. To calculate the effect of the RF pickup on the measurements, the pickup sine wave was added to the detector simulation. Care was taken so that beam followed the calculated phase curve of the cyclotron, and that the phase of the sine wave was correct for the time of arrival of the ion on the probe. The measured time of arrival has a radially dependant shift. The RF stop signal used in the time measurement is relative, and not absolute, so the net shift is unimportant, but radial differences are important. The radial difference varies by 40 ps when the pickup is 6% of the beam signal, but when the difference is 30%, the measured beam time can vary by 800 ps. Also, since the beam has a time spread, a 30% RF pickup will widen the measured beam time by up to 200 ps for $\Delta\phi = 10°$ RF, and 600 ps for $\Delta\phi = 40°$ RF.

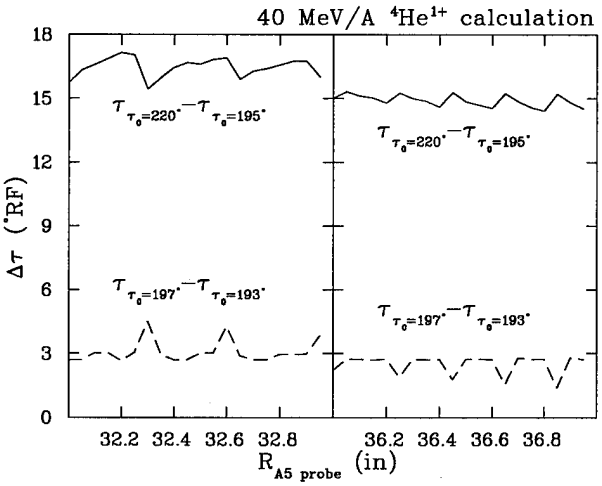


Figure. 3. Calculated Variation in Measured Time Widths Due to Precession. Precession will cause the measured time width of the beam to vary periodically as a function of the radius at which it is measured. The starting time of 220° RF is centered.

The detector collects one beam pulse over many turns. At 32 in, it takes about 20 turns, and at 40 in, it takes 35 turns. This allows multi-turn effects to influence the measurement. The phase slip per turn is small so, except near extraction, this will have little effect. One measurement though show that for extreme conditions this slip is significant. An analog beam that was about to fall out of resonance grew fourfold in width before it was lost. Also, as the energy gain per turn became so small that only the radial precession could clear the detector dead area, the beam spread into several small peaks. Radial precession of off centered beams, though, will have an effect. Figure 3 shows the calculated effect of precession at two different radii for a beam 4° wide and one 25° wide in RF starting times. The phase compression is from the central region, and is real, but the variation in calculated width shows that precession can cause an error as large as 2° RF. The sign of the error corresponds to the slope of the phase curve. This is true for any method of measuring phase widths internally. The solution is to take a measurement in an area where one expects the phase curve to have zero slope, and to move the detector a small amount and repeat the measurement.

III. INTERNAL BEAM TIME MEASUREMENTS

Both of the cut detectors were successfully used as timing detectors in the K1200 cyclotron, performing equally well. Figures 4 & 5 show the versatility of these detectors. In Figure 4, the detector measured the outer portion of the phase curve. Spectra were taken every inch, from 32 to 40 inches. The centroids were calculated, and corrected for travel time of the beam from the dee center to the probe. These were then fixed in absolute phase by a Smith–Garren frequency swinging phase measurement at the three innermost data points. (This technique, which is extremely slow, does not work in the K1200 at radii greater than 34 inches, since the phase diagram has a maxima there.) For comparison, a

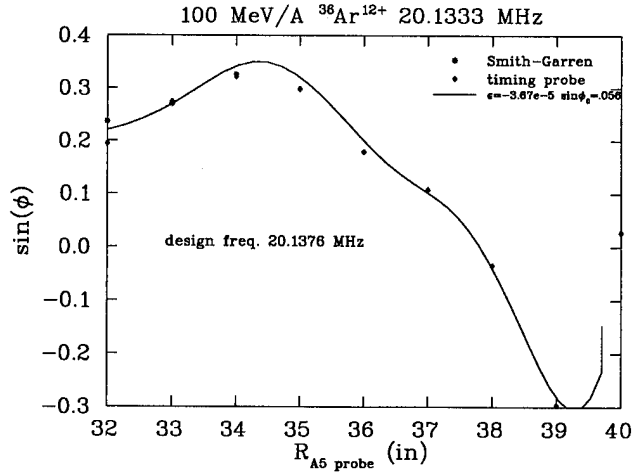


Figure. 4. Phase Curve Measured with the Internal Timing Probe. The phase curve was measured using the internal detector. The timing probe can only measure relative changes, so one point was fixed using a Smith–Garren measurement. The calculated phase curve was then fit to the data, varying frequency and starting time, demonstrating the accuracy of the magnetic field calculations.

phase curve from a calculated magnetic field was fit to the data, with extremely good agreement.

Figure 5 shows several beam time spectra which were taken with the internal probe. The left most, and center spectra show the results of inserting one of the phase slits, while the right most spectra show the results of both slits inserted into the beam. The scale is in channels, at 50 ps per channel. The bottom row was done without the buncher, and the top row was used to emphasize the intensity of the main peak, relative to the other peaks. These spectra show the detectors' ability to resolve fine sub-nanosecond structures, approx 250 ps wide, as well as its usefulness in tuning the phase slits.

In summary, a Si detector was implemented as an internal beam timing detector in the K1200 cyclotron. It proved to be useful in measuring phase curves, and tuning the phase slits, as well as demonstrating a 250 ps resolution. It is ready for use in studying the time aspects of single particle beam dynamics.

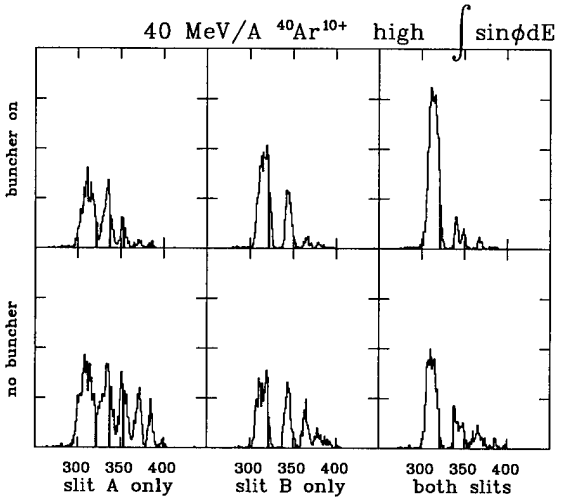


Figure. 5. Time Spectra Measured with the Internal Timing Probe. Time spectra measuring the effects of the phase slits, which are really posts inserted into the beam, and the buncher. One phase slit makes multiple cuts in the beam, and the two together with the buncher are used to select and enhance one peak for transmission, while cutting the others. Each channel is 50 ps. Note the small peak widths, one of which is only five channels wide FWHM.

References

[1] J. Bailey et. al. Proc. 13th Intl. Conf. on Cyclotrons and Their Applications, 431-434 (1993).

[2] D. Cole et. al. Annual Report, MSU/NSCL, 147-148 (1990).

[3] L. Evenson. Private Communication, (1992).

[4] J.A. Winger et. al. NIM B70:380, (1992).

[5] H. Spieler. IEEE Trans. Nucl. Sc. NS-29(3):1142-1157, (1982).

AXIAL INJECTION AND PHASE SELECTION STUDIES OF THE MSU K1200 CYCLOTRON*

J.D. BAILEY ORNL†/JIHIR‡

Abstract

Axial injection into a cyclotron through its iron yoke, a spiral inflector, and the central region electrodes couples the transverse coordinates of motion together, as well as with the longitudinal coordinates. The phase slits in the K1200 cyclotron use the $r-\phi$ correlations inherent in acceleration of ions in a cyclotron. Computer simulations of injection into and acceleration within the K1200 cyclotron encompassing the four transverse dimensions together with time were used to determine beam matching requirements for injection and phase selection in the K1200 cyclotron. The simulations were compared with measurements using an external timing detector.

I. INTRODUCTION

Simulation of the function of the phase slits, which have been installed in the K1200 cyclotron at MSU[1], requires an accurate understanding of the injected beam. The ion source for the cyclotron can be any one of three external ECR sources. A 90° analyzing magnet selects ions with a specific Q/M, which are then brought into the K1200 vault 3 m below the median plane of the cyclotron. Figure 1 shows the portion of the injection line which is inside the cyclotron vault. A bending magnet guides the beam up the axis of the cyclotron, where a solenoid focuses it for inflection into the cyclotron. There is also a buncher in the injection beam pipe, which is used to increase transmission into the cyclotron. A spiral inflector brings the beam onto the median plane of the cyclotron, where it is defined by, and guided about the machine center by the central region electrodes.

While this is an idealized picture of the injection process, it serves as a start for the injection calculations. Starting the beam at the exit of the vertical bending magnet, these calculations ray trace the ions up the yoke of the cyclotron and through the spiral inflector with modifications of the programs MYAXIAL, where bunching has been added, and INFLECTOR[2]. The ray tracing then continues through the central region and out into the cyclotron with Z3CYCLONE[3]. Ions which strike electrodes are removed from the calculation, and the radius and phase of the surviving ions are saved each time they pass by the active area of the slits. A third program was written to sort through the final output, rapidly displaying the number of particles versus phase of the beam which passed the phase slits. This allows an interactive tuning of the simulated phase slits.

*Work supported by the U.S. National Science Foundation grant PHY-9214992.

†Managed by Martin Marietta Energy Systems, Inc., under contract No. DE-AC05-84OR21400 with the U.S. Department of Energy.

‡The Joint Institute for Heavy Ion Research has as member institutions the University of Tennessee, Vanderbilt University, and the Oak Ridge National Laboratory; it is supported by the members and by the U.S. Department of Energy through Contract Number DE=FG05-87ER40361 with the University of Tennessee.

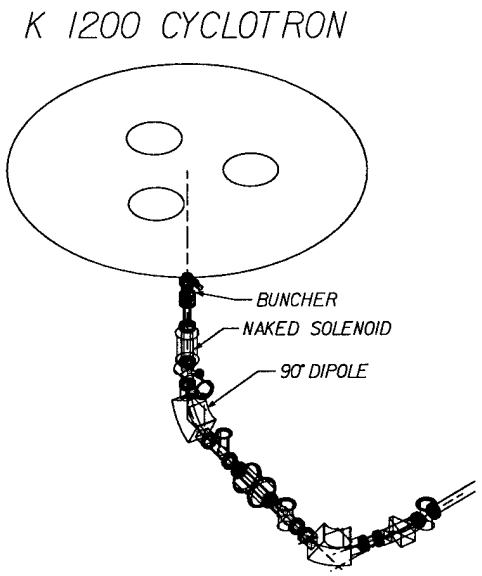


Figure. 1. K1200 Axial Injection Line. Depicted are the buncher, focussing solenoid, and 90° bending magnet. The axial portion is used in the injection studies.

II. CONTINUOUS (DC) BEAM INJECTION

The injection study began with a two dimensional study of the initial coordinate system. Phase space ellipses were followed to the inflector exit. The resulting ellipses were coupled in the transverse coordinates, with distortions existing in both. The solenoid strength, and the initial ellipse shape were varied, and both could reduce but not eliminate this distortion. The radial spot became smaller and more distorted as the solenoid field was increased, while at the same time, the axial dimension was losing its distortions. The point where the solenoid was tuned to inject the largest area in phase space was also a happy compromise between beam quality in the two coordinates. The optimum initial phase space also varied with solenoid strength.

The two dimensional ellipses were changed to a four dimensional lattice, covering 100π mm·mrad in each transverse dimension, so that the couplings could be observed. The solenoid was found to increase transmission by focussing the beam into the entrance aperture of the inflector. Matching the initial phase space ellipse served to minimize distortions caused by traversal of areas in the yoke where the iron suddenly narrowed. Both this, and the solenoid, minimized the divergence of the beam entering the inflector.

Following the beam through the inflector and central region the smaller beam produced by the solenoid, has now become the larger beam in both spot size and divergence. Clear couplings

0-7803-3053-6/96/$5.00 ©1996 IEEE

Table I

K1200 Cyclotron DC Acceptance. Injection efficiencies are presented for four 4–D DC acceptance studies. Transmission are given in percent at the entrance and exit of the inflector, and after the central region of the cyclotron.

Case 1:	I_{infl}	=	60.5%	I_{start}
$B_{sol} = 0.0kG$	I_{exit}	=	89.1%	I_{infl}
circular	I_{CR}	=	11.9%	I_{exit}
ellipses		=	10.6%	I_{infl}
		=	6.4%	I_{start}
Case 3:	I_{infl}	=	99.5%	I_{start}
$B_{sol} = 2.65kG$	I_{exit}	=	100.0%	I_{infl}
circular	I_{CR}	=	12.0%	I_{exit}
ellipses		=	12.0%	I_{infl}
matched		=	11.9%	I_{start}
Case 5:	I_{infl}	=	76.0%	I_{start}
$B_{sol} = 0.0kG$	I_{exit}	=	95.4%	I_{infl}
elongated	I_{CR}	=	12.3%	I_{exit}
ellipses		=	11.7%	I_{infl}
matched		=	8.9%	I_{start}
Case 6:	I_{infl}	=	100.0%	I_{start}
$B_{sol} = 2.65kG$	I_{exit}	=	96.7%	I_{infl}
elongated	I_{CR}	=	11.4%	I_{exit}
ellipses		=	11.0%	I_{infl}
		=	11.0%	I_{start}

have also been found between r and z and r and p_z as well as the expected $E - \phi$ correlations. The transmission of four cases is presented in Table 1.

III. BUNCHED BEAM INJECTION

The time spread of the 4–D pulse was also examined as functions of the solenoid focussing and injection matching of the initial phase space. Matching the beam for traversal up the yoke minimized the spreading of that pulse in time. Focusing with the solenoid made small improvements in the time spread for both matched and unmatched cases. Transmission through the inflector also spread the beam in time, with the final results shown in Figure 2. It rounded off the peaks of the matched cases, and extended all of the bases, but the FWHM's were essentially unchanged. This debunching sets a limit on how tightly the buncher can bunch the beam into the cyclotron. The 4–D studies were extended in time to include the buncher. Figure 3 shows the two extremes of the best and worst calculated bunching.

One final note on bunching: the buncher added a 1% variation in the kinetic energy of the injected beam which is correlated with time. The spiral inflector is electrostatic, bending the less energetic ions more than, and the more energetic ions less than the reference particle, which is bent onto the median plane. Thus all the particles starting at the buncher at any specific time, will be shifted axially, inducing an oscillation about the median plane.

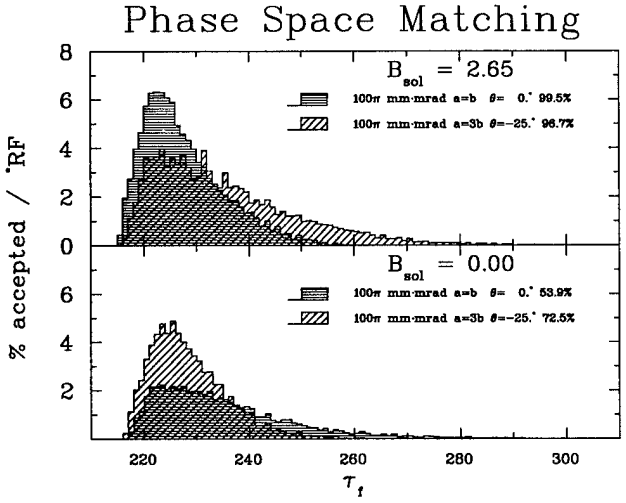


Figure. 2. Debunching Produced by the Yoke and the Inflector. Matching the initial phase space for injection up the yoke will minimize the straggling of the beam.

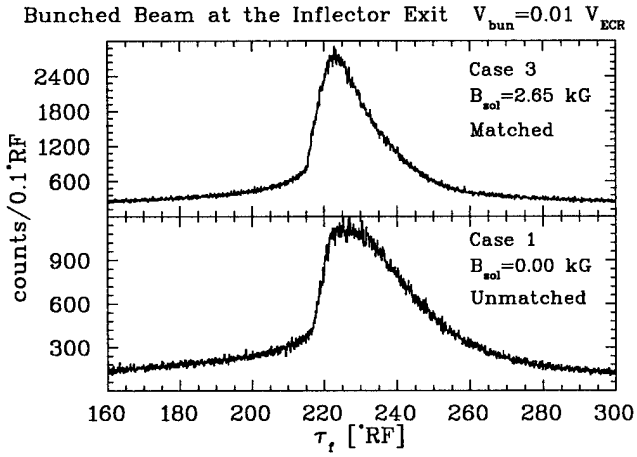
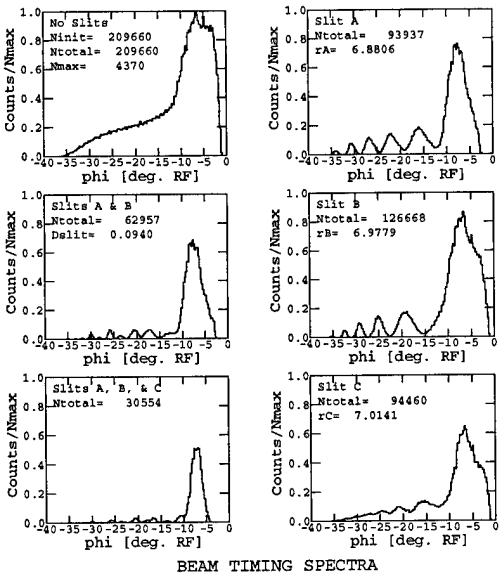


Figure. 3. Bunched Beam at the Inflector Exit. The improvement possible in the bunching efficiency by matching the injected phase space of the beam is depicted above.

IV. PHASE SELECTION

The phase slits are two posts which are inserted axially into the beam at a radius of 7 in, and in the center of two hills. These posts can be shifted over a small radial range, which encompasses about three turns. Each beam pulse takes several turns to clear a post, which cuts out a piece of the beam each pass. A correlation between E and ϕ has built up at this point, turning the radial cuts into time cuts. Figure 4 shows a simulation of this process made on the beam from the 5–D starting lattice, which has survived the injection process. The buncher has been tuned to one side, and the two slits have been tuned to remove as much of the beam outside of the main peak as possible, with beam not cut by one slit being cut by the other. The multi turn process is clearly evident, handicapping the use of the slits to define a clean and narrow phase cut.

Figure 5 shows a measurement made using an internal timing detector[4], and performed under similar conditions as the above calculation. The multi turn cutting of the beam by the phase



8DKA0:[BAILEY.AXIAL.ALPHA.CENTREG]CRS0B1T225SL4.DAT;1
8DKA0:[BAILEY.AXIAL.ALPHA.CENTREG]CRS0B1T225C.DAT;1

Figure. 4. Calculation of Phase Cuts Made with the Buncher Tuned to One Side. The upper left is the uncut phase spectra, with the upper and middle right being the phase cuts produced by the individual slits. The two slits combined are on the middle left, with the lower two showing the effect of a hypothetical third slit.

slit is evident, though the calculation over predicted the phase width and hence the number of phase cuts made. The use of the buncher almost made this a clean phase cut.

The injection into the K1200 has been studied, resulting in a good understanding of the phase selection process being used at the present time. Better phase selection can be achieved by restricting the emittance of the injected beam, and matching its initial phase space. This would allow cleaner bunching of the beam. Clean phase selection will require an initial central region phase cut, eliminating the overlap of turns at the phase slits.

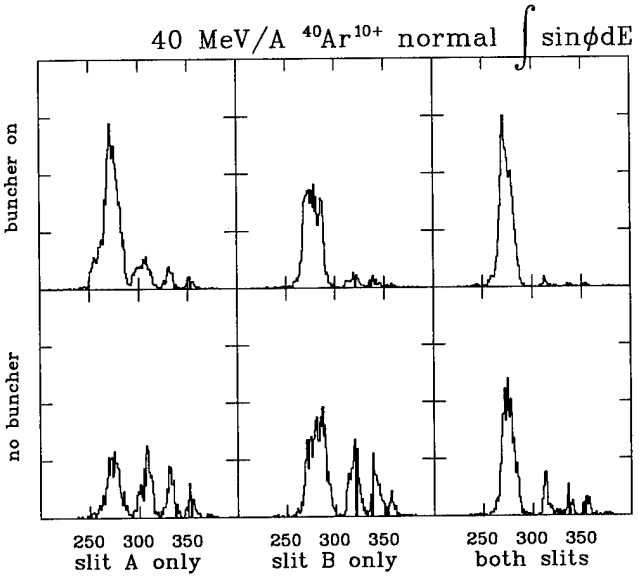


Figure. 5. Measurement of Phase Cuts Made with the Buncher Tuned to One Side. This measurement shows that the calculations, while slightly pessimistic, simulate the actual conditions of the beam at the phase slits.

References

[1] J. Bailey et. al. Proc. 13th Intl. Conf. on Cyclotrons and Their Applications, 431-434 (1993).

[2] F. Marti et. al. IEEE Trans. on Nuc. Sci., NS-32:2450-2452, (1985).

[3] F. Marti et. al. Ninth Intl. Conf. on Cyclotrons and their Applications, 465-468, (1981).

[4] J.D. Bailey et. al. Proc. of this Conference. (1995).

STUDY AND REDESIGN OF THE NSCL K500 CENTRAL REGION*

S.L. Snyder and F. Marti, National Superconducting Cyclotron Laboratory
Michigan State University, E. Lansing, MI 48824-1321 USA

Abstract

The proposed K500-K1200 cyclotron coupling project calls for a redesign of both the inflector and central region of the K500. An increased injection voltage will be needed to reduce space charge effects in the higher intensity beam. In order to obtain stripping injection matching with the K1200, the K500 will operate in the second harmonic rf mode. To meet the requirements of this higher energy beam (and new rf mode) a new spiral inflector and central region geometry were designed. Results of beam orbit calculations and experimental data concerning phase selection and central region acceptance will be presented.

I. Introduction

The NSCL presently operates the K1200 superconducting cyclotron with support from the NSF for nuclear physics research. With the purpose of increasing the intensity of low mass ions (A < 40) and the energy of heavy ions (up to uranium) a proposal to couple the K500 to the K1200 cyclotron has been presented [1]. The ions are produced in an external ECR ion source and axially injected in the K500 cyclotron. After extraction the beam is transported and injected in the K1200 where it is stripped and accelerated to higher energies (5 Tm).

To decrease the deleterious effects of a more intense injected beam, the energy of the ECR produced beam has been increased. In the stand-alone configuration the K500 was used in first harmonic mode to obtain the maximum possible energy (80 MeV/u for ions with Q/A=0.5). In the coupled mode the maximum energy needed is only 16.6 MeV/u for ions with Q/A=3/16. A maximum ECR voltage of 30 kV was selected, this voltage being considered as within easy reach of the present ECR configuration. These parameters define a total energy of 5.6keV for the O^{+3} ion. This higher energy, higher intensity beam requires the design of a new inflector. Additionally, the new 2^{nd} harmonic central region limits the radial extent of the inflector to 2.0 cm and requires flexibility in the positioning of the orbit center of emerging ions. A spiral inflector was therefore studied based on the inflector presently used in the K1200.

II. Inflector Design

An increase in the axial height (for ease in construction) and gap size (for improved acceptance) over the present inflector was studied and comparisons of the two inflectors made. Acceptances in initially uncoupled x,v_x and y,v_y phase spaces were calculated as were the effects of changing the axial field by way of a solenoid along the injection route. The spiral inflector equations described by Belmont and Pabot [2] can be used to determine an appropriate electric field and inflector shape to best match the required machine parameters. An inflector field of 20kV/cm was chosen to maximize the final radius in a 4.6 Tesla central field. This results in a 1.96 cm final (inflector exit) central ray radius and an inflector height of 3.00 cm. The final inflector outline is shown in figure 1 along with the reference orbit as the inflector will sit in the 2^{nd} harmonic central region. The figure was used as input to a RELAX3D [3] run with grid dimensions $\Delta x=\Delta y=.0254$cm and $\Delta z=.127$cm. The vertical grid size is clearly visible as steps in the hill shape.

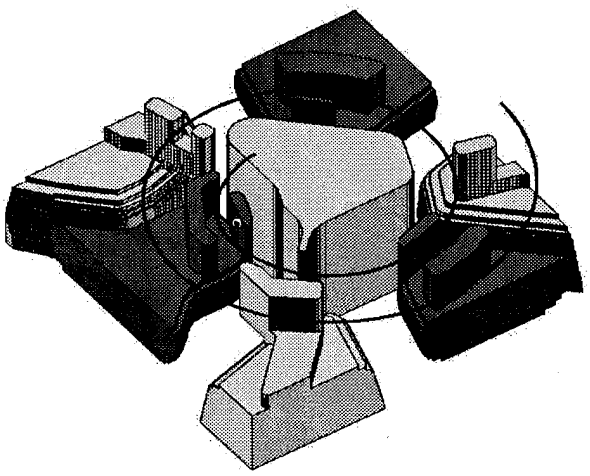


Figure. 1. The 2^{nd} harmonic central region design. The view show a cutaway of the central region electrodes below the magnetic median plane. The dark structures are the dee tips while the large object in the center is the inflector housing. The other light structures are the ground potential hills. The first turn phase slit can be seen in the upper left corner. Also shown is the path of the central ray.

A. Acceptance Calculations

To estimate the acceptance of this inflector design, ions were tracked from 3m below the cyclotron median plane through the inflector. This was accomplished using two ray tracing codes MYAXIAL and INFLECTOR [4] which integrate the equations of motion for ions passing through the axis of the cyclotron magnetic field and the inflector electrodes, respectively.

All ions were started 3m below the median plane and passed through a solenoid field centered at 2.227m below the median plane, the K500 magnet yoke field, a circular aperture at the entrance to the inflector centered on the magnet axis with a diameter equal to the electrode spacing, the inflector and finally an exit aperture centered on the reference ray. The inflector voltage and position were set by requiring the central (axial) ray to emerge with $v_z = z = 0$. Initially uncoupled x, v_x and y, v_y phase spaces were started in order to avoid the complications inherent in dealing with an initially coupled, 4d space. The normalized acceptances for the new inflector are compared to those for the

*Work supported by the U.S. National Science Foundation under Grant No. PHY89-13815.

0-7803-3053-6/96/$5.00 ©1996 IEEE

Table I
Normalized Acceptance (mm-mrad)

Inflector Gap	$\beta\gamma$	x, v_x	y, v_y
6 mm	.0035	5.77	7.80
4 mm	.0030	5.42	3.66

old K500 inflector in table I. Clearly the new 6mm aperture inflector will have a much greater acceptance, as expected.

III. Central Region Design

Once an inflector shape was determined a second harmonic central region was designed. All electrode shapes and positions had to accommodate the new, larger inflector housing and guide the beam through the central region leaving it reasonably well centered. The dee voltage chosen for the O^{+3} test case was 70kV (well below the 80kV which can be reliably achieved) with a chosen minimum electrode separation of 8mm. With these considerations in mind a central region was designed that produced a well centered beam with good vertical focusing properties. Figure 1 shows the central region so obtained as well as the path of the central ray. This figure also shows the first turn phase selection slit (located at θ=110°) which will be used to limit the phase width of the beam.

A. Central Region Acceptance and Phase Selection

In order to determine the acceptance of the new 2^{nd} harmonic central region and inflector system, a set of ions were tracked from 3.0m below the median plane of the K500, up the magnet axis, through a 1^{st}+2^{nd} harmonic buncher, the spiral inflector and out through the first 23cm of the K500. The ion paths up to the exit of the inflector was accomplished using the aforementioned MYAXIAL and INFLECTOR codes , while the motion through the central region of the K500 used a modified version of the Z3CYCLONE [5] orbit code. This modified version extends the number of electric fields from two to three and removes ions whose paths intersect with electrode or dee structures. In addition this new version saves the particle's r and ϕ values at the locations of both the central region slit and the phase selection pins (located at r=17.88cm).

In order to calculate the percentage of the input DC beam which maps into the final 3° bandwidth required by the K500-K1200 coupling project, a range of emittances were tracked up the machine axis and through the spiral inflector. Each set of starting conditions consisted of a uniform circular distribution of points (one point per mm-mrad) spanning the emittance area in x,p_x and y,p_y. Each point in x,p_x space corresponded to a complete set in y,p_y which spanned the entire emittance area. In this way a spatially coupled set of starting conditions was obtained. To simulate the time structure of the incoming beam a series of coupled x,p_x/y,p_y sets were started each separated by 2° RF. This now complete set of starting conditions was then passed through the K500 axis elements (a single solenoid and buncher), through the inflector and out past the K500 phase selection pins.

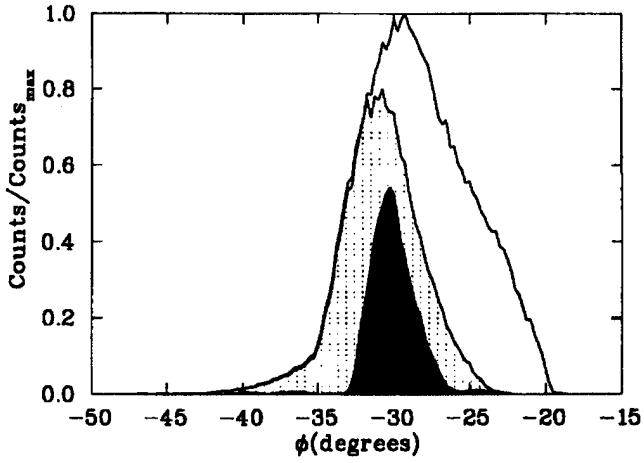


Figure. 2. Timing spectra at r=22.0cm. The three spectra are (white) before the first turn slit, (dotted) after the first turn slit, and (filled) after the 18cm phase selection pins. The peak has been reduced from 10° FWHM to one of only 3°.

Extraction requirements restrict the timing spectra coming out of the central region to 3° FWHM. In order to obtain this, a scheme is necessary to select only those particles whose final phases fit this range. Utilizing the radius dependence on the phase radial slits have been used to select only those ions with the proper phase [7]. Presently, the K500 is equipped with two phase pins located on the 0° and 120° hills at a radius of 18cm. These pins consist of two movable tungsten blades that are used to intersect the beam [6]. As mentioned above, there is a third slit, consisting of a fixed aperture window, located on the first turn. Thus there are three apertures which may be used in phase selection.

To model the effect of these slits a program was used which simulates the effect of various slit combinations. This program accepts r,ϕ orbit data at specified slit positions and a set of final ϕ data. At each slit position a separate pin (labeled A,B, and C) can be inserted. The position of each pin can be adjusted, it can be inserted or removed, and the width of the pin can be set. In this way any combination of pins, pin positions and pin width can be achieved. The program then identifies which ion orbits (if any) intersect with each pin and removes these from consideration. The final collection of surviving ions is then binned according to final phase and a beam timing spectra is produced. Additionally, a variable width, first turn, window slit can be inserted to further reduce the final timing spectra. By using the r,ϕ output of the central region orbit code a measure of the acceptance of the cyclotron into a 3° FWHM timing region which can be expressed as a percentage of the input DC beam (at z=-3.0m) surviving for various starting emittances and buncher modes.

IV. Acceptance Results

A variety of starting emittances were calculated in order to determine the performance of the injection plus central region design. Starting emittances of 25, 50 and 75π mm-mrad in each of the coupled x,p_x/y,p_y phase spaces were tracked through the phase selection process. Additionally, in order to determine the relative gain of the 1^{st}+2^{nd} harmonic buncher system, these

Table II
Percentage of DC Beam in 3° FWHM Peak

Buncher Harmonics	Initial Emittance (mm-mrad)		
	25π	50π	75π
1^{st} Harmonic Only	11.0%	5.8%	2.9%
1^{st} and 2^{nd} Harmonics	16.7%	9.5%	5.5%

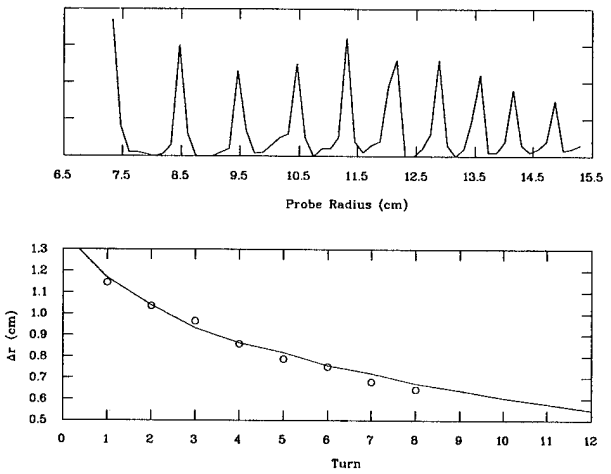


Figure. 3. Top: Differential wire probe trace in the K500. Bottom: Δr vs. turn for the same. Circles represent probe data while the curve was calculated by computer orbit tracking.

starting emittances were run in both buncher modes and the various parameters of the phase selecting slit system were adjusted to give a 3° FWHM peak containing the maximum number of surviving ions. Figure 2 shows the timing spectra before the first turn slit, just after this fixed window, and then the final 3° peak obtained by using the outer phase pins for a 75π mm-mrad emittance using the 1^{st}+2^{nd} harmonic buncher mode. Table II shows the percentage of the injected DC beam which survives in the appropriate bandwidth for a range of buncher modes and initial emittances. As can be seen, using the 1^{st}+2^{nd} harmonic buncher mode provides a 50 to 90 percent increase in the surviving beam.

V. Experimental Results

The new K500 central region and inflector have been built and are currently being commissioned. Early results from runs of 15MeV O^{+4} show dee voltages higher than the design levels. This is due to errors in the placement of the dees in the central region. The planned upgrade calls for a correction of this effect. As a check on the reliability of the orbit code calculations measurements of radius gain per turn were made on the O^{+4} beam. Figure 3 shows a differential probe trace and a comparison of measured values with those obtained from computer runs. By varying starting time of the calculated central ray good agreement between the two can be reached. Measurements of the internal bunch length have been made using both the first turn slit and phase selection pins. A 3° FWHM bunch length has been observed for the internal beam.

VI. Conclusions

A new inflector and 2^{nd} harmonic central region have been designed to meet the specification of the K500-K1200 coupling project. Beam orbit calculations show that a 3° FWHM bunch length, with good transmission properties can be achieved. The new design has been installed and early results support the design's calculated properties.

References

[1] Proposed Upgrade of the NSCL, RC York, H Blosser, T Grimm, D Lawton, F Marti, J Vincent, X Wu, A Zeller, at this conference.

[2] J.L. Belmont and J.L. Pabot, Study of axial injection for the Grenoble cyclotron. *IEEE Trans. Nucl. Sc.*, NS-13:191-193, 1966.

[3] H. Houtman and C. Kost, Proc. of the Europhysics Conference, Computing in Accelerator Design and Operation (Springer Verlag, Lect. Notes in Physics 215, Berlin, 1983) pp. 93-103.

[4] F. Marti, J. Griffin, and V. Taivassalo. Design of the axial injection system for the NSCL cyclotrons. *IEEE Transaction on Nuclear Science*, NS-32:2450-2452, 1985.

[5] F. Marti, M.M. Gordon, M.B. Chen, C. Salgado, T. Antaya, E. Liukkonen. Design calculations for the central region of the NSCL 500 superconducting cyclotron. In *Proc. 9th Intl. Conf. on Cyclotrons Their Applications*, pages 465-468, Caen, France, 1981.

[6] B.F. Milton. *Phase Selection in the K500 Cyclotron and the Development of a Non-Linear Transfer Matrix Program.* PhD thesis, Michigan State Universtiy, 1986.

[7] H.G. Blosser. *IEEE Transactions in Nuclear Science*, NS - 13:1, 1966.

HEAVY ION ACCELERATION STRATEGIES IN THE AGS ACCELERATOR COMPLEX -- 1994 STATUS REPORT*

L.A. Ahrens, J. Benjamin, M. Blaskiewicz, J.M. Brennan, C.J. Gardner,
H.C. Hseuh, Y.Y. Lee, R.K. Reece, T. Roser, A. Soukas, P. Thieberger
Brookhaven National Laboratory, Upton, New York 11973-5000 USA

Abstract

The strategies invoked to satisfy the injected beam specifications for the Brookhaven Relativistic Heavy Ion Collider (RHIC) continue to evolve, in the context of the yearly AGS fixed target heavy ion physics runs. The primary challenge is simply producing the required intensity. The acceleration flexibility available particularly in the Booster main magnet power supply and rf accelerating systems, together with variations in the charge state delivered from the Tandem van de Graaff, and accommodation by the AGS main magnet and rf systems allow the possibility for a wide range of options. The yearly physics run provides the opportunity for exploration of these options with the resulting significant evolution in the acceleration plan. This was particularly true in 1994 with strategies involving three different charge states and low and high acceleration rates employed in the Booster. The present status of this work will be presented.

I. INTRODUCTION

The AGS accelerator complex has supplied Gold ions at a kinetic energy of about 10.5 GeV/nucleon for the annual AGS Heavy Ion Physics run during each of the past three years[1,2]. The present beam is adequate both in intensity and emittance to satisfy the slowly extracted beam (SEB) Physics Users who allow the primary ion beam to interact in their detectors - unlike the High Energy Physics proton users who bring secondary beams (e.g. kaons) into their detectors. However, the beam produced thus far does not meet the intensity goals for injection into the Relativistic Heavy Ion Collider (RHIC)[3]. This situation has both motivated and permitted the exploration of a variety of strategies in the configuration of the accelerator chain, with the setup each year evolving significantly from the previous year. Last year (1994) several modifications occurred during the course of the run. A summary of this evolution will follow a brief description of the major relevant acceleration components and the resulting beam.

II. GOLD ACCELERATION

Gold ion acceleration at Brookhaven begins with the 15 MV Tandem Van de Graaff and then continues through the Booster and AGS synchrotron. Au^{1-} ions produced by a pulsed source are accelerated to the center terminal of the Tandem where they pass through a foil which strips away electrons to produce ions with charge states ranging from +10 to +15. The ions emerge from the Tandem with about 1 MeV/nucleon kinetic energy, and beam currents of a few particle uAmps are possible during the .5-1 msec beam pulse. (The maximum charge output per pulse is roughly constant.) A second foil just downstream of the Tandem may be inserted to allow additional stripping of the ions, thereby increasing the charge state options available for injection into the Booster. Transport, injection, and acceleration of charge states 14,15, and 33 have been explored. For the case of Au^{33+} (which requires the additional stripping after the Tandem) the rigidity is about a factor of two lower than for Au^{14+}, reducing the requirements on the Tandem to Booster transfer line. In addition the final momentum to which the ion can be accelerated in the Booster (for the maximum Booster magnetic field) is increased by the same factor of two. Since the ions must be further stripped to at least Au^{77+} before transfer to AGS a higher momentum at BTA (Booster to AGS) transfer is desirable. For the first gold run, in 1992, the planned charge state in AGS was Au^{79+} - fully stripped - and the higher momentum at Booster extraction was considered necessary. The Au^{33+} beam is also more resistant during acceleration to losing electrons due to interactions with the Booster residual gas (typical pressure $2x10^{-11}$ Torr). Requiring a stripping foil after Tandem does have a cost. It results in the loss of about 80% of the ions accelerated in Tandem since that fraction strip to charge states other than 33+ and are not transported to the Booster. In addition the beam transverse emittances grow slightly due to the additional foil passage. Stripping after the Tandem to Au^{33+} was the plan followed for the '92 and '93 runs. This choice allowed AGS physics program intensity requirements to be satisfied while providing the opportunity for studies of the implications of removing this stripping foil.

The beam produced by the Tandem has excellent emittance properties. Both transverse emittances at Booster injection even with the additional stripping are small (about 1% horizontal and 1.7% vertical) compared to the Booster acceptance, making stacking in transverse phase space effective. The possible number of turns efficiently stacked has been extended further by introducing coupling between the horizontal and vertical betatron oscillations during injection[2]. Typically more than forty turns can be injected with efficiencies

*Work performed under the auspices of the U.S. Department of Energy.

0-7803-3053-6/96/$5.00 ©1996 IEEE

above 70%. The longitudinal emittance of the Tandem beam is negligible relative to the smallest practical emittance associated with capturing the beam in the Booster. The resulting longitudinal emittance is sufficiently small relative to RHIC (or AGS) requirements and relative to the capabilities of the Booster and AGS accelerating systems to allow adiabatic merging of adjacent bunches during the acceleration cycle. Each such merging drops the required accelerating frequency for that momentum as well as the number of bunches in the ring by a factor of two.

The power supply for the Booster main magnets was designed with two operating modes. The "proton" mode allows rapid ramping (up to 9 Tesla/sec) but cannot exceed a magnetic field of about .6 Tesla. The "heavy ion" mode can ramp to more than twice this field but at less than one third the ramp rate. The cycle for high intensity proton operation typically involves four Booster accelerations at a 7.5 Hz rate for each AGS acceleration cycle, with two bunches transferred to AGS each Booster cycle until the AGS ring is filled. (The AGS circumference is four times the Booster circumference.) For heavy ions the original plan was to accelerate the same three bunches first in Booster and then on to extraction in AGS, so the Booster cycle rate was required only to be equal to that of the AGS. The power supply modes described above satisfy this situation. This plan called for three sets of acceleration cavities (with frequency "Bands" I, II, and III) in the Booster to cover the large frequency range required. There were no bunch merges in the plan.

For the first Gold run (1992) only the proton "Band III" acceleration system was available. This system comprises two independent low and high level rf drives and cavities. At this time each system had the capability for little more than a factor of two frequency sweep. From Booster injection to extraction the revolution frequency of the accelerating Au^{33+} would have to increase more than a factor of twelve. Nevertheless Au^{33+} was successfully accelerated with acceleration responsibility handed back and forth between the two cavities; one accelerating and sweeping up through its frequency range while the other reset to the low starting frequency. Longitudinal dilution (beyond the factor of four from the four mergings) was small. This acceleration approach was verified. A second set of rf cavities and drive systems, referred to as "Band II" was in place for the 1993 run. This allowed the rf gymnastics for that run to be simplified to a single merge, from 12 bunches to 6, which were then transferred to AGS. That 6 rather than 3 bunches were transferred to AGS represented another modification to the original acceleration plan.

The capabilities required of the AGS rf have evolved from the original idea of catching and accelerating the three booster bunches in three of the twelve buckets and carrying them to extraction to the present operational mode of debunching the injected Booster beam and then rebunching it as desired. This change has been motivated in part by the present slow extraction work. Spreading the beam around the AGS circumference at injection and capturing equally in twelve buckets yields a smoother spill at extraction than carrying the beam up in only three buckets. The post-Booster evolution of the AGS rf system has also given that system most of the capabilities necessary for bunch merging with the rest to come next year. This will open the option of AGS bunch coalescing for RHIC injection optimization.

III. THE 1994 RUN

By the end of the '93 Gold run, most of the open questions concerning the switch to Au^{14+} at Booster injection had been answered. First, it was still relevant. The efficiencies at each step in the accelerator process were reasonably high and yet the AGS output was only about $3x10^8$ ions per cycle. RHIC requires $1x10^9$ ions per bunch. The factor of six intensity increase possible by removing the post-Tandem stripping foil was very attractive. Second, it had been shown experimentally, using Au^{33+} extracted at the velocity to which Au^{14+} could be accelerated, that stripping at Booster extraction to Au^{77+} had an acceptable efficiency, provided an optimized stripping foil was used. (In this case a carbon foil of thickness 29 mg/cm^2 or 5 mils gives nearly 60% efficiency at 380 MeV/c/nucleon)[4]. Third, vacuum studies in Booster predicted that increased beam loss due to electron stripping during acceleration would be at an acceptable (20%-30%) level. Fourth, the survival of the lower velocity Au^{77+} in the AGS was predicted to be adequate based on beam survival measurements on the AGS injection porch with higher velocity Au^{77+} and Au^{78+}. The transfer line between Tandem and Booster had been upgraded to allow transporting the higher rigidity Au^{14+} beam. Transferring all of the ions accelerated in Booster to AGS would not be possible in 1994, the revolution period of the Au^{14+} ions at the maximum Booster field being longer than the kicker pulses; but the predicted intensity would be adequate for the physics program.

In fact the '94 run began using Au^{15+} rather than the more intense Au^{14+} from Tandem. This slight rigidity reduction allowed a high enough extraction momentum to be achieved (for BTA stripping and for the AGS rf capture at h=12) while significantly reducing the requirements for the maximum Booster magnetic field and for the fields in several other extraction systems. The test of accelerating without a post-Tandem foil was made no less rigorous by this choice. The Booster main magnet power supply was configured in the usual "heavy ion" mode, with a slow dB/dt and a high final field relative to the "proton" mode. The frequency range of the Booster Band II cavities had been extended so that the ninth harmonic of the revolution frequency could cover the entire acceleration range with no merges required. Five of the nine bunches fit within the pulses of the extraction kickers and were transferred to AGS.

Neither the momentum shift nor the momentum spread introduced by the BTA stripping foil for this low momentum beam had been anticipated. The first moved the ratio for the revolution frequencies in the AGS and Booster below the one

quarter predicted by the ratio of machine radii, which was a surprise but not a problem for a single transfer. The deterioration in longitudinal emittance from the foil was reduced by another set of rf gymnastics. Using the second Band III cavity in Booster the nine bunches were held in h=3 buckets for one quarter of a synchrotron oscillation just before extraction and then the two of the resulting three "pseudo-bunches" which fit within the kicker widths were sent into the BTA line. In the AGS they were caught in two of the twelve buckets and allowed to roll another quarter oscillation. At this point the AGS rf was turned off and the beam was allowed to debunch, with a smaller energy spread as a result. Finally the beam was adiabatically rebunched at h=12 filling the twelve buckets equally.

The predictions for survival in Booster and stripping efficiency at Booster extraction were all verified for low ($5x10^8$ ions/cycle) intensities. Slow losses during acceleration with a time dependence consistent with electron stripping were seen at the predicted levels. Additional foil choices available for this run in BTA allowed a slight improvement over the previous stripping efficiency to Au^{77+} using a 4 mil thick carbon foil rather than the 5 mil optimum of the preliminary study. Nevertheless, as the intensity of the beam from Tandem increased the Booster acceleration efficiency decreased with the maximum accelerated beam in Booster less than $1x10^9$ ions. This loss behavior was fascinating but is neither understood nor corrected[5].

IV. THE MULTIPLE CYCLE OPTION

At this point another way to configure the accelerator components offering increased intensity was proposed. The possibility of bunch merging in AGS allows ions accelerated on multiple Booster cycles to contribute to one bunch later in the AGS cycle. To make this useful both from the point of view of survival of the accumulating beam in AGS and of delivering beam either to the SEB program or to RHIC, a fast Booster cycle short compared to the AGS cycle is required. The momentum at Booster extraction obtained using Au^{15+} and the slow "heavy ion" magnet mode could also be obtained using Au^{33+} and the fast "proton" magnet mode. The quite acceptable stripping efficiency to Au^{77+} in BTA for ions with this momentum whether Au^{15+} or Au^{33+} would remain. A "proton mode" magnet cycle was built which maintained unchanged the low field ramping during the multiturn Booster injection and allowed acceleration to a field high enough to produce the same rigidity ion after stripping in BTA with Au^{33+} as was produced with the former magnet cycle and Au^{15+}. The length of the resulting Booster cycle was 200 ms. The idea then is to accelerate and transfer four Booster batches into the AGS and then accelerate and merge them into a few RHIC bunches. The first transfer of Au^{77+} to AGS must wait 600 ms while the other three Booster loads are accelerated and transferred. Survival in AGS was tested while still in the Au^{15+} mode - same momentum in AGS - and found to be satisfactory, though significant losses were observed. This approach gives up the potential intensity gains from eliminating the stripping foil just after Tandem, but at this point the higher current can not be efficiently accelerated in Booster.

The switch to Au^{33+} was successfully accomplished along with the reconfiguration of the Booster power supply and the associated machine functions. The intensity available to the Physics program, with one Au^{33+} Booster cycle feeding the AGS was still adequate and in fact was not much different from the Au^{15+} situation. Of course nearly half the beam was still lost at BTA transfer due to the present kicker lengths. The complex ran in this mode for the second month (the second half) of the Heavy Ion run.

The next step in this approach, and the last change attempted in '94 was to multiple pulse the Tandem and Booster at the 5 Hz rate. This was a new request, well beyond the scope of the instrumentation and controls defined for the Tandem, but nevertheless was accomplished. Four Tandem bursts, coming at 200 msec spacings, were successfully accelerated in the Booster. The reorganizations required to further transfer these cycles into the AGS proved too hard given the short time available, but do not involve exploring new territory since this part of the setup closely resembles normal high intensity proton operation.

V. FUTURE PLANS

The final step of actually transferring four Booster batches of Au to AGS remains for the 1995 run. A further optimization of BTA foils to reduce energy spread is possible. The slow losses observed in AGS still require understanding. Perhaps some of what has been learned about AGS stopbands in accelerating high intensity protons will contribute to this effort. Synchronizing the four transfers of Booster bunches, with their slightly "wrong" frequencies into AGS buckets, and bunch merging in AGS to achieve RHIC bunch intensities still lie ahead.

[1] W.T. Weng, "Operation of the Brookhaven AGS with the Booster", 1993 Particle Accelerator Conf., pp. 3726-3730.

[2] T. Roser, "AGS Heavy Ion Operation with the New Booster", Fourth European Particle Accelerator Conf., pp. 151-155.

[3] M.A. Harrison, "The RHIC Project", Fourth European Particle Accelerator Conf., pp. 156-160.

[4] T. Roser, L.A. Ahrens,and H.C. Hseuh, "Charge Exchange Studies with Gold Ions at the Brookhaven Booster and AGS", Fourth European Particle Accelerator Conf., pp. 2441-2443

[5] M. Blaskiewicz, L.A. Ahrens, H.C. Hseuh, T. Roser, and K. Zeno, "Observation of Intensity Dependent Losses in Au^{15+} Beams", these proceedings.

OBSERVATION OF INTENSITY DEPENDENT LOSSES IN Au(15+) BEAMS*

M. Blaskiewicz, L.A. Ahrens, H.C. Hseuh, T. Roser, Y. Shoji†, K. Zeno,
AGS Department BNL, Upton, NY, 11973-5000,USA

Abstract

During the 1994 heavy ion run at Brookhaven a strongly intensity dependent loss for the Au(15+) beam in the AGS Booster was encountered. Coherent instabilities or space charge induced stopband losses were neither expected nor consistent with the data. It was found that the beam lifetime was an order of magnitude shorter for normal operating conditions than in the low intensity limit with the inverse lifetime increasing monotonically with the injected number of particles. Studies data are presented and the Au(15+) situation is compared with that for Au(33+). Various hypothetical mechanisms are considered.

I. INTRODUCTION

The AGS Booster is a fast cycling proton and heavy ion synchrotron. The beam pipe has an average radius of $r_p = 7$ cm and the Booster's circumference is $C = 202$ m with betatron tunes ≈ 4.8. When accelerating gold, the pressure of the background gas is $P \approx 2 \times 10^{-11}$Torr. The injection momentum of the ions is 9 GeV/c and the final momentum of 70 GeV/c was reached in 0.55 s for Au(15+) and 0.10 s for Au(33+).

During 1992 and 1993, the BNL Tandem Van de Graff delivered Au(33+) to the Booster. This required a low energy stripping foil between the Tandem and the Booster and resulted in a small fraction of Au(33+). For 1994, the foil was removed with the intent of using the more plentiful Au(15+) as the primary beam. The number of ions delivered to the Booster increased by a factor of two but losses in the Booster resulted in a lower extracted intensity than was obtained with Au(33+).

It was found that the losses depended strongly on the injected intensity and the peak extraction intensity was reached at less than peak injected intensity. The Laslett tune shift was estimated to be $\lesssim 0.01$ and instability growth rates were expected to be $\lesssim 0.01$ s^{-1}, well below the values normally needed for collective effects.

II. STUDIES WITH Au(15+)

Two machine studies were conducted in September 1994. The Booster magnet cycle was modified to include intervals of constant field, so that data could be collected at a fixed beam energy. The rf was turned off at the end of the flat top and the beam was lost as the magnetic field ramped down. The data consisted of normalized current transformer traces taken under various conditions. It was found that the instantaneous loss rate $\alpha(t) \equiv -d \ln N/dt$ depended on the particle momentum, the number of particles in the ring N, and the intensity on previous cycles.

*Work performed under the auspices of the U.S. Department of Energy
†permanent address KEK

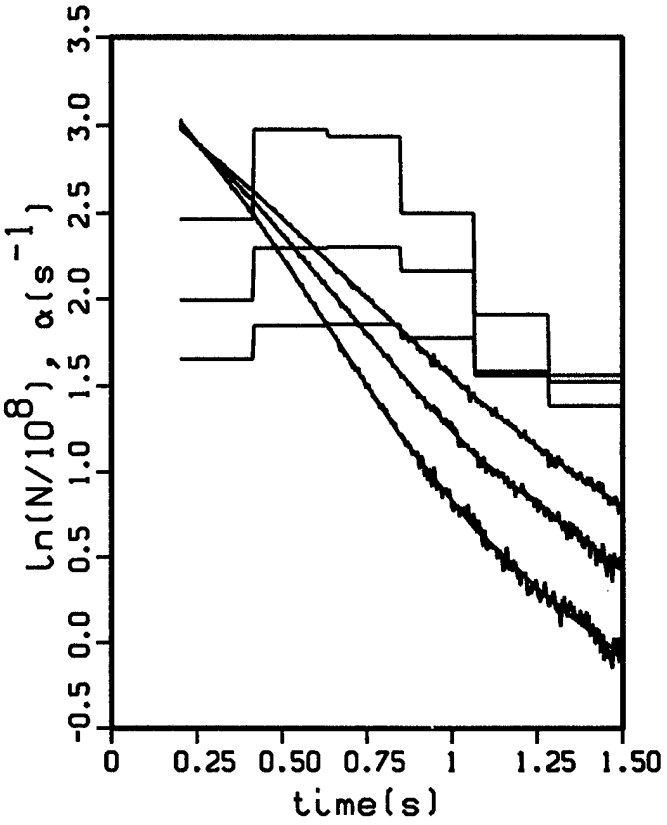


Figure. 1. Typical data for the number of particles and loss rate in the Booster. The largest loss rate and smallest final intensity correspond to equilibrium conditions. The smallest loss rate and largest final intensity correspond to the first cycle after cooling. The intermediate state is for the second cycle after cooling.

Figure 1. shows $\ln N$ and α for a momentum of 15 GeV/c and different machine histories. The initial number of particles were comparable in all three cases but the loss rate varied dramatically. The smallest losses occurred after the machine had been allowed to "cool" for about a minute and intermediate losses occurred on the second cycle after a cool down. The cooling was accomplished by turning off the inflector and allowing the injected beam to crash in the ring without spiraling. Comparable results were obtained when the injected beam was killed farther upstream in the transfer line. This memory effect strongly suggests that the accelerating beam is affecting the residual gas in the ring. Additionally, it was observed that the number of Booster cycles required to reach equilibrium after a cool down increased when the vacuum was intentionally spoiled.

A first pass at parameterizing the data fitted an exponential to the current yielding an average loss rate, $< \alpha >$. Figure 2 shows the average loss rate for equilibrium conditions as a function of

0-7803-3053-6/96/$5.00 ©1996 IEEE

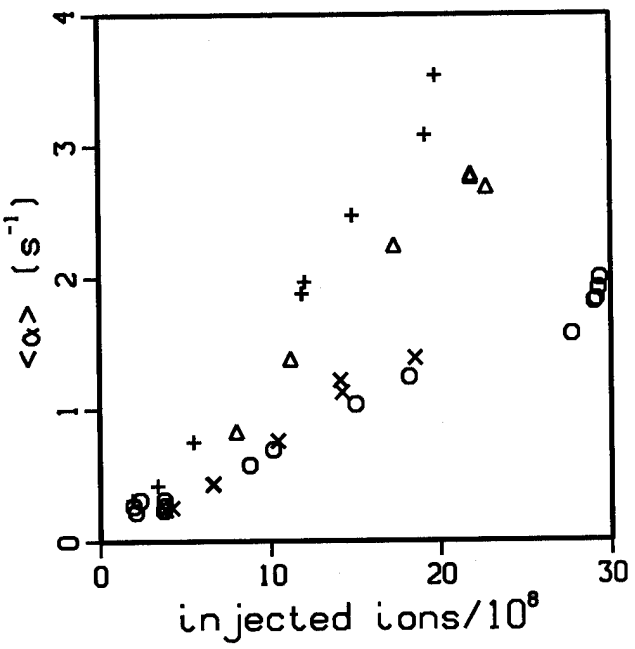


Figure. 2. Average loss rate versus the number of injected ions for momenta of 9 GeV/c (circles), 15 GeV/c (triangles), 30 GeV/c (crosses), and 60 GeV/c (Xs).

the number of injected particles and beam momentum. The loss rate rises monotonically with the number of injected particles and peaks for a beam momentum around 30 GeV/c. Loss rates for normal operating conditions are about an order of magnitude larger than loss rates at low intensity and the low intensity loss rates of $\sim 0.1 s^{-1}$ are comparable to the expected stripping losses due to residual gas at a pressure of 2×10^{-11} Torr.

There were other notable observations. As is apparent from Figure 1 the loss rate is not constant even at constant beam energy. Both increases and decreases in loss rate can occur during a single machine cycle. In most cases any increase in loss rate during a machine cycle occurred before a decrease in loss rate, but not always. When the rf was turned off after reaching the magnetic plateau, the losses were identical to those observed when the beam remained bunched. Radial steering of the beam by changing the rf frequency had little effect on losses.

III. COMPARISON WITH Au(33+) AND POSSIBLE LOSS MECHANISMS

Given the amount of time that had been lost with Au(15+) no dedicated studies were performed using Au(33+). Data on Au(33+) loss rates were obtained using current transformer data over the whole machine cycle. For Au(33+) the peak number of injected ions was 10^9, about a factor of two smaller than was available as Au(15+). The net loss rate for 10^9 injected ions was $\approx 1.7\ s^{-1}$, and this rate did not decrease substantially as the number of injected ions decreased by a factor of two. From Figure 2, the loss rate for 10^9 Au(15+) ions was $\lesssim 1\ s^{-1} < 1.7\ s^{-1}$ so it is difficult to say whether intensity dependent losses, at the level seen with Au(15+), were present with Au(33+). We go on to consider possible mechanisms for the Au(15+) losses.

With a pressure of $P = 2 \times 10^{-11}$ Torr and temperature of $T = 300$ K, the number density of molecules is $6.4 \times 10^5\ cm^{-3}$. For a cross section $\sigma = 10^{-16} cm^2$ with a gold momentum of 9 GeV/c the interaction rate is $0.1\ s^{-1}$ which is consistent with the loss rate in the limit of very low intensity.

The increase in loss rate with intensity suggests that the beam is creating targets with which it subsequently scatters. One possible mechanism is beam induced gas desorption [1]. However, the time scale for desorption must be very fast $\lesssim 0.1$ s since the loss rates can change significantly over that time. Additionally, the number of desorbed molecules would need to be a factor of ~ 100 larger than those normally in the pipe. The increase in equilibration time with pressure is also a consideration, though the number of adsorbed molecules probably varies with average pressure.

As a second process, consider the possibility that the beam is creating a background of electrons. Given the temperature and pressure any ionization present would be caused by the beam, in accord with the increase in loss rate with intensity. In the case of complete charge neutralization of 10^9 ions by electrons, the electron density within the beam is $2.4 \times 10^5 cm^{-3}$. This is less than half the number density of gas molecules. If the intensity dependent loss is due to ambient electrons, then the density of electrons is higher than required for complete charge neutralization or the relevant cross section is $\gg 10^{-16}\ cm^2$. Additionally, we know of no process which would generate such a number of electrons. Other processes we have considered are even less likely.

Since the loss rates did not change when the beam was debunched, charge exchange between the ions in the beam (*eg.* Au(15+) + Au(15+) → Au(14+) + Au(16+)) appears to be ruled out. Space charge induced stopbands and coherent instabilities, which are estimated to be nil, would also be reduced by debunching. Also, these processes would have no "memory", as shown in Figure 1.

References

[1] O. Gröbner, R.S. Calder CERN/ISR-VA/73-15 (1973).

HIGH INTENSITY PROTON OPERATIONS AT BROOKHAVEN *

M. Blaskiewicz, L.A. Ahrens, E.J. Bleser, J.M. Brennan, C.J. Gardner, J.W. Glenn,
R.K. Reece, T. Roser, M.J. Syphers, W. VanAsselt, S.Y. Zhang
AGS Department BNL, Upton, NY, 11973-5000,USA

Abstract

In 1995 the AGS upgrade met its design goal of 60 TP (1 TP = 10^{12} protons) per pulse, made possible by significant improvements in the AGS Booster and AGS. We summarize these improvements and outline strategies for future upgrades.

I. INTRODUCTION

A schematic diagram of the proton accleration complex at Brookhaven is shown in Figure 1. The 200 MeV LINAC produces an average, chopped H^- current of 20 mA which is charge exchange injected for $\sim$ 300 turns into the AGS Booster. The Booster accelerates the protons to a kinetic energy of 1.6 GeV. They are then injected into the AGS via bunch to bucket transfer. This process is repeated four times, filling the AGS ring. The AGS accelerates the protons to a kinetic energy of 24 GeV and they are extracted via the $3Q_H = 26$ sextupole resonance as slowly extracted beam (SEB). While this general scenario has been followed since the Booster began operating in 1992, steady improvements in accelerator technology have resulted in a continual increase in performance [1], [2], [3].

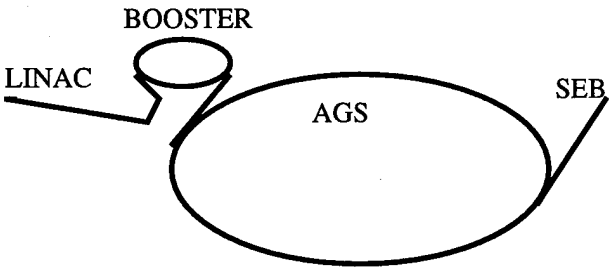


Figure. 1. Schematic of the BNL Proton Acceleration Complex.

II. AGS BOOSTER

In 1994, the AGS Booster repetition rate increased from 5 Hz to 7.5 Hz and the extraction kinetic energy increased from 1.41 GeV to 1.56 GeV. Also, the number of protons per Booster cycle increased from 12 TP to 17 TP which was in excess of the design goal of 15 TP [3]. In 1995 the peak intensity at Booster extraction was 21 TP per cycle. The main magnet current and beam intensity over the four Booster cycles for 1995 operation are shown in Figure 2. This state of affairs was the result of several efforts.

In 1994 the harmonic number of the Booster was switched from $h = 3$ to $h = 2$ [4]. This reduced the possibility of coupled bunch longitudinal instabilities along with increasing the total bucket size. In 1995 the reduced frequency allowed the cavities

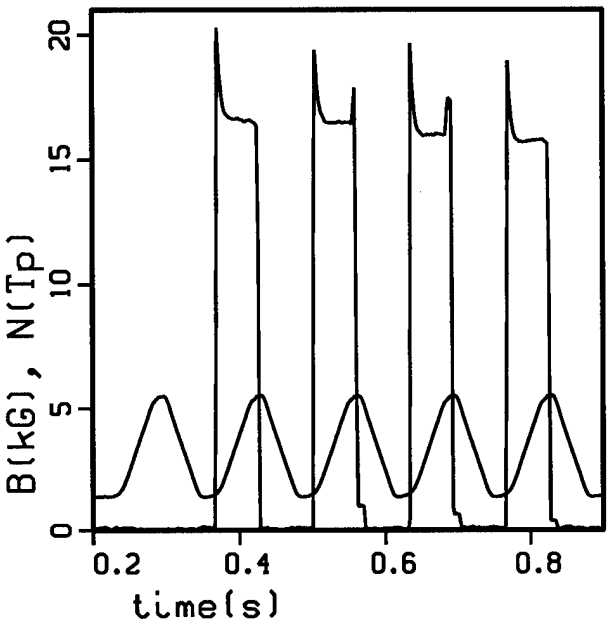


Figure. 2. Booster main magnet field and beam intensity over the four Booster cycles for 1995 operation, the current spikes at the end of the middle cycles are due to a calibration pulse.

normally used during heavy ion operation to operate at $h = 4$ early in the cycle as a second harmonic component.

In 1995 the magnetic field ramp rate at extraction was reduced from $\dot{B} = 8.7$ T/s to $\dot{B} = 2$ T/s. This allowed more freedom in optimizing longitudinal parameters between Booster and AGS. Stopband corrections appropriate to the new cycle were obtained via a previously derived scaling law [5] and worked well without fine tuning. At injection the vertical tune is just below 5, necessitating careful correction of the 5th harmonic of the vertical closed orbit. The horizontal closed orbit requires careful tuning as well. As the beam is accelerated the orbit corrections are scaled appropriately. In particular the "dump bump", which moves the horizontal orbit away from the beam dump, is optimized throughout the cycle so that the horizontal aperture is maximized while keeping the majority of the beam loss at the dump. This is particularly important for high intensity operation when about 15% of the beam is lost during acceleration.

After reaching extraction energy the beam is kicked out of the Booster and through the Booster to AGS (BTA) transport line. The line is quite short with only one major bend, which makes it difficult to match the dispersion and its derivative into AGS. When fully matched, the beam size in certain portions of the line becomes unacceptably large. The large beam size is further aggravated by steering fluctuations in the extracted beam from the Booster. Such considerations, and the losses they imply, have required a transfer line with optical parameters that

*Work performed under the auspices of the U.S. Department of Energy

0-7803-3053-6/96/$5.00 ©1996 IEEE

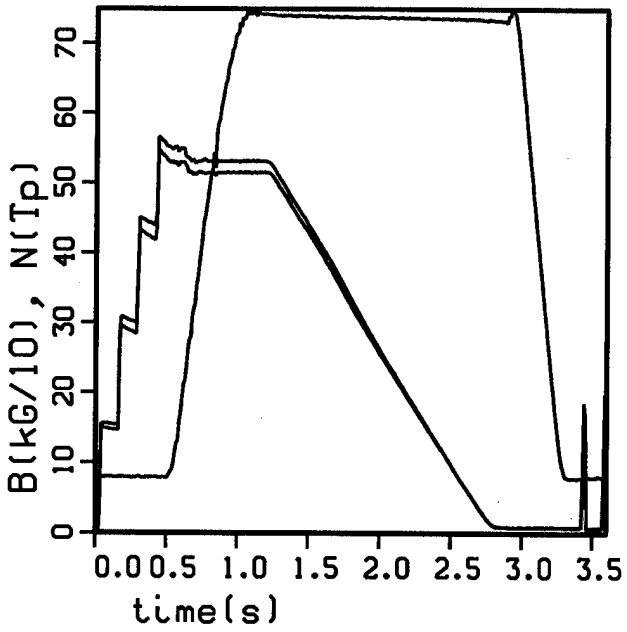


Figure. 3. AGS field and intensity with octupoles on and off.

are mismatched to the AGS. At present the mismatch is not too serious. In fact, the resulting dilution is further enhanced by intentional misteering of the beam at injection to reduce space charge tune spread.

III. AGS

In 1994 the number of protons per cycle surviving to extraction energy increased from 25 TP to a peak of 40 TP. The peak intensity increased to 60 TP in 1995 with intensities of 55 TP typical for normal operations. Figure 3 shows the beam intensity and the main magnet field in AGS for typical 1995 conditions. Several accelerator improvements contributed to this result.

A. AGS Injection Porch

A significant amount of effort has gone toward improving transfer and early survival in the AGS. There are three broad catagories of loss associated with the injection porch: fast losses due to beam oscillations and beam halo scraping in both the transfer line and AGS which occur over the first few turns, intermediate losses that occur over a few milliseconds which are associated with the rise and fall of the injection bump, and slow losses which occur over several tens of milliseconds and are attributed to stopbands. During normal 1995 operations roughly 10% of the beam at extraction energy in the Booster failed to survive for $\gtrsim$10 turns. Intermediate losses, most of which occur after the fourth transfer, are probably due to the imperfect tail-bite on the kicker. Slow losses have been the most insideous in the past and their reduction has been the focus of considerable effort.

To reduce slow stopband losses the beam is longitudinally mismatched between the Booster and AGS and the $h = 8$ rf system is augmented by a higher harmonic dilution cavity ($h \approx 270$) which aids filamentation [3] and increases the emittance. The net result is a bunching factor of $I_{\rm avg}/I_{\rm peak} \approx 0.4$ after 20 ms in the AGS [4] though differences in longitudinal emittance among the bunches persist throughout the cycle. We point out that not only a large bunching factor but also adequate momentum spread appear to be necessary for beam survival on the injection porch and that the dilution cavity creates both. Without it the coherent synchrotron tune shift is well beyond the Landau damping threshold and the bunch simply oscillates without filamenting.

The transverse beam size is aperture limited to $\sigma \approx 9$ mm. For 60 TP in the AGS the resulting space charge tune depression is ~ 0.2 on the injection porch. During the 1994 run there was a significant slow loss on the injection porch which was a major intensity limitation. The slow loss was greatly reduced in 1995 due to a combination of factors.

The ten fast ferrite quads used for tune manipulation during polarized proton operations were removed, locally opening the vertical aperture. Along with opening the aperture, replacing the ceramic chambers with metal ones greatly reduced the beam induced signal outside the vacuum pipe and resulted in a quieter electrical environment. Upgrading and repairing the high pass networks between the main magnet vacuum chambers, which allow image currents to pass while reducing eddy currents, helped as well. The broadband impedance of the AGS undoubtedly decreased.

A vertical survey of the AGS during the summer shutdown of 1994 led to repositioning several combined function magnets. The rms orbit excursions decreased significantly in both planes (*e.g.*, due to skew quadrupole) confining the beam to the clean spectral region in the center of the aperture. The resulting orbit was quite good, but losses were then distributed all around the ring, in particular at the ferrite injection kicker. This led to another magnet move after the 1995 startup which created a horizontal orbit distortion so that losses would go into the "catcher", a 6" thick, 7' long water cooled shield around the beam pipe designed to absorb stray beam.

Two normal octupoles were added to the AGS lattice. While these devices were added to allow study of the normal octupole resonances $4Q_H = 35$, $4Q_V = 35$ and $2Q_H + 2Q_V = 35$, it was found that empirically optimized settings significantly reduced the slow losses on the AGS injection porch (see Fig 3.) and allowed smaller betatron tunes at injection without increasing losses. Perhaps the optimal settings represent a compromise among the various octupole corrections. However, it has been found that losses on the decapole lines going through $Q_H = Q_V = 8.8$ can be largely corrected by the octupoles, ostensibly due to stabilization coefficients [6]. In any case, the high intensity coherent tunes at injection are $Q_H = 8.85$ and $Q_V = 8.80$, down by ≈ 0.05 from 1994. The lower tunes are favorable for the transverse damper, resulting in more beam surviving to be accelerated than previousely achieved. Additionally, the damper algorithm has been modified to employ autoregressive closed orbit subtraction which has resulted in higher gain. However, as the push for intensity with small loss continues it is likely that transverse instabilities will continue to be a prominent issue.

The final improvement, relevant to early survival in the AGS, was a modification of the setpoint function for the main magnet current. The modification was to add a small correction to the setpoint function which tends to cancel residual oscillations associated with the previous cycle. This resulted in a main magnet field which fluctuated by $\lesssim$0.1 G over the injection porch. The

net result of these changes led to a peak of 65 TP surviving to be accelerated.

B. Acceleration, Transition and Extraction

Steady improvement in the acceleration phase of the AGS cycle continued. In 1995 the 10 AGS rf power amplifier individual power supplies were available, which reduced beam loading problems and allowed for more rf power [4]. The magnetic ramp rate at transition increased from 1.8 to 2.2 T/s. Fine tuning of the transition jump system which was commisioned in 1994 [7] continued. After the 1995 startup it was found that the closed orbit was not centered through the transition jump quadrupoles, most notably the one closest to the catcher. When the jump was powered the closed orbit distortions led to signficant beam loss. By moving the offending quadrupole the beam was centered through it, allowing a larger emittance and momentum spread through transition than had been achieved before. Even with the transition jump optimized, the beam size increase associated with deforming the dispersion is a major bottleneck in the cycle. The tradeoff between early beam survival and small momentum spread at transition appears to be a fundamental limit.

After transition an upgrade in the dilution cavity power amplifier allows for bunch dilution as the revolution frequency increases. This additional dilution is required to keep the peak current adequately small for the remainder of the cycle and to smooth out "ripples" in the bunches that are probably caused by longitudinal, chromatic nonlinearities [8]. Removing the previously required dilution porch after transition, reduced the time required for acceleration by ~ 0.1 s increasing the average current to the users.

Acceleration to top energy results in a smoothly bunched beam at 24 GeV. The beam is debunched using rf phaseback where the beam is moved to the unstable fixed point of the rf bucket. This results in a faster debunch than when the rf is simply turned off. For debunching, the rf cavities are counterphased at high voltage. Counterphasing, as opposed to cavity voltage reduction, allows better control over the net voltage per turn by keeping the cavities matched to the power amplifiers [4]. Improvements in beam extraction have also taken place. The peak to peak ripple in the extracted beam was reduced by a factor of four due to three efforts. Voltage dividers on the main magnet power supply were improved and their leads were rerouted to reduce noise pickup. A transformer coupled servo supply was added to sense main magnet voltage ripple and reduce it toward zero. Finally a fast, discrete frequency, spill servo was added which fed spill error signals in narrow band harmonics of 60 Hz to the horizontal tune quadrupole supply during the spill.

IV. FUTURE UPGRADES

Several near term upgrades for the AGS are planned. To reduce transverse emittance and slow losses on the injection porch a set of normal octupole correction magnets is planned. When coupled with the normal and skew sextupole corrections currently available, a significant increase (even 50%?) in beam intensity is imaginable. Without an intensity increase it may be possible to reduce the bunching factor and momentum spread early in the cycle which will lead to fewer problems with the beam size increase due to the perturbed dispersion at transition. Additionally, improved optics in the BTA line and a better understanding of AGS apertures will hopefully reduce losses. Given the possibilities of higher intensity and smaller longitudinal emittance, a damper for coupled bunch longitudinal instabilities will be installed.

Over the long term the possibility of employing barrier buckets in the AGS or even building an accumulator ring are being considered. It is likely that the push toward high intensity with low losses will continue until the experimenters are satisfied. With any luck, human nature will not allow that to occur.

References

[1] W.T. Weng et al., PAC93, 3726, 1993.

[2] R.K. Reece, L.A. Ahrens, E.J. Bleser, J.M. Brennan, C. Gardner, J.W. Glenn, T. Roser, Y. Shoji, W. vanAsselt, W.T. Weng, PAC93 3763, 1993.

[3] L.A. Ahrens, M. Blaskiewicz, E. Bleser, J.M. Brennan, C. Gardner, J.W. Glenn, R.K. Reece, T. Roser, A. Soukas, M. Syphers, W. van Asselt, W.T. Weng EPAC94 485 1994.

[4] J.M. Brennan *these proceedings.*

[5] C. Gardner, Y. Shoji, G. Danby, J.W. Glenn, J. Jackson, A. Soukas, W. van Asselt, C. Whalen, EPAC94, p. 979 1994.

[6] G. Guignard, CERN 78-11 1978.

[7] W. van Asselt *these proceedings.*

[8] J. Wei, A. Warner, L. Ahrens, J.M. Brennan, W.W. MacKay, S. Peggs, A. Ratti, K. Reece, T. Roser, W.A. Ryan, C. Saltmarsh, T. Satogata, D. Trbojevic, W. vanAsselt, EPAC94, p976, 1994.

FAST EXTRACTED PROTON BEAMS AT LOW ENERGIES IN THE CPS EAST EXPERIMENTAL AREA

R. Cappi, L. Durieu, J.-Y. Hémery, M. Martini, J.-P. Riunaud, Ch. Steinbach
CERN, CH-1211 Geneva 23, Switzerland

To provide beams with characteristics required by the Energy Amplifier Test, the CERN PS had to deliver new beams, of low kinetic energy (0.6 - 2.7 GeV), low intensity ($0.5\text{-}5\times10^9$p) and short duration (<500 ns) via the existing slow extraction channel, the transfer line currently used for 24 GeV/c beams and a slightly modified secondary line. These beams were delivered without impairing other CPS operations and, despite large operational differences, the other three East area beam lines could alternatively be supplied with slow extracted beam, for half week periods, thanks to the short setting-up time of a few hours.

This paper describes how such beams were produced: by (i) acceleration or deceleration of the injected beam in the CPS, depending on the requested energy, (ii) fast extraction using the usual slow extraction channel, (iii) careful optics adjustments and reduction of multiple scattering in the transfer line. The range of beam characteristics achieved, as well as the limitations encountered are also reported.

I. INTRODUCTION

An Energy Amplifier Test [1,2] was performed in the CPS East Experimental Area with a calorimeter housing a target hit by a low energy proton beam. For this test the south branch of the beam lines was used to transport a primary proton beam delivered by the PS via the usual slow extraction channel. The far end of the line, the T7 area, was covered and shielded to accept proton bunches of a few 10^9 particles per supercycle of 14.4 s.

II. BEAM IN THE CPS

The basic CPS magnetic cycle used to deliver proton test beams at 2.7 GeV kinetic energy (3.5 GeV/c momentum) to the Antiproton Collector and Accumulator was adapted to this operation. Its flat-top was adjusted to the energy required by the experiment and consequently, the 1 GeV beam from the PS Booster was either accelerated or decelerated to energies ranging from 2.7 GeV down to 0.6 GeV. The usual fast extraction through straight section 16 was inactivated and replaced by a fast extraction via straight section 61 described later.

The relatively low intensity required was obtained by injecting in the CPS a single PSB ring of 2.5×10^{10} protons in five bunches. Although only one bunch was to be extracted, the five bunches were kept in the machine up to the firing of the extraction kicker in order to provide a better intensity signal to the RF beam control.

For each new magnetic cycle the transverse tunes were measured throughout the cycle of the bare machine and adjusted by tuning of the low energy quadrupoles, to provide the proper phase advance for the fast extraction and to avoid resonances.

III. EXTRACTION

Extraction towards the East Experimental Area used the existing elements of the 24 GeV/c slow extraction process with the exception of the electrostatic septum. It included two magnetic septa and a set of 4 local orbit bumpers pushing the beam first near the thin septum SMH57 placed towards the inside of the machine, then near the extractor septum SMH61 located towards the outside as shown in fig. 1. The thin septum having an unfavourable betatron phase advance of $5\times2\pi+3\pi/4$ with respect to the fast extraction kicker KFA71-79, instead of the ideal value multiple of $\pi/2$, a tune adjustment was applied with the low energy quadrupoles to bring the horizontal tune from 6.25 down to 6.1. This provided the required $\pi/4$ phase lag to obtain a maximum horizontal deviation at the thin septum location. The kick duration was adjusted to extract a single bunch, the remaining ones being lost either on a pulsed beam dump or against the vacuum chamber wall during the decreasing part of the magnetic cycle.

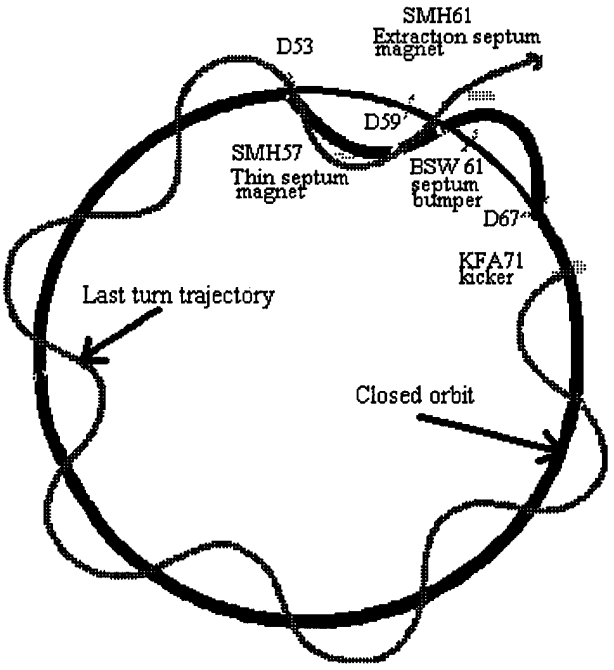


Figure 1. Schematic of the fast extraction scheme, using of 4 horizontal closed orbit bumpers, a fast kicker and 2 magnetic septa.

0-7803-3053-6/96/$5.00 ©1996 IEEE

Transverse emittances of the circulating beam were (at 2σ) 5 μm in the horizontal plane and 2.5 μm in the vertical one. However, as the corresponding extraction channel acceptances are respectively 2 μm and 6.6 μm, transmission efficiency was limited to 30 %. Table 1 shows the main parameters of this extraction scheme.

Horizontal tune, Qx	6.10
Orbit bump in Straight Section 57	-61 mm
Orbit bump in Straight Section 61	43 mm
Kicker KFA71-79 deflection	-1.5 mrad
Septum SMH57 deflection	3.1 mrad
Septum SMH61 deflection	2.2 mrad

Table 1. CPS beam tune, displacement and deflections in the fast extraction process using a fast kicker and elements of the slow extraction.

IV. BEAM TRANSPORT

The extracted beam was transferred to the experiment along the existing primary line FT61S and one of the secondary test line T7, target removed. Modifications of the two lines had to be kept to a minimum owing to time, budget and reusability constraints. However, it was necessary to adapt the primary line designed for slow 24 GeV/c extraction to the low momentum fast extraction scheme used. Moreover, at low energy (1 GeV and below) as some correctors were out of their control range, they had to be turned off, leading to an unavoidable slight trajectory error compensated downstream.

The beam splitter was used to deflect the beam to the south branch but also to control the delivered intensity by adjustment of its gap.

Additional beam instrumentation was installed in the last part of the T7 line, shown in fig. 2:

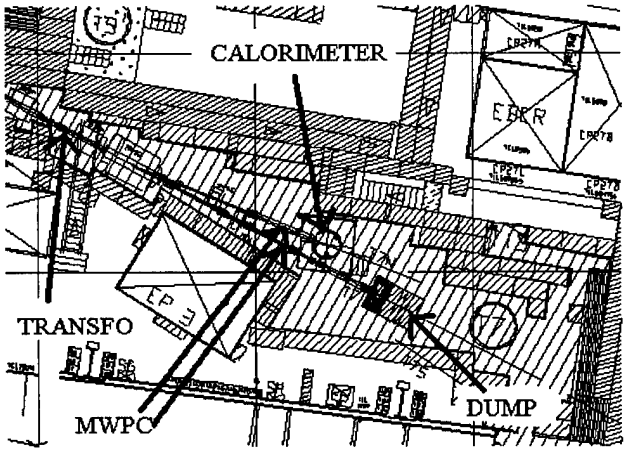


Figure 2. The test area (T7) with the monitoring devices. Beam goes either to a dump, if undeflected, or to the calorimeter, if deflected by the last bending magnet.

- a second beam transformer close to the target, to monitor the beam intensity,
- two scintillator counters close to each of the lines, to provide triggers to the experiment,
- two Multiwire Proportional Chambers (MWPCs) on the dump and target line, to focus and centre the beam, and to estimate its profiles. These MWPCs were used as first ionisation chambers, with a voltage limited to about 100 V, due to the high beam density.

On various occasions films were exposed to the beam, to provide a qualitative assessment of its size and position and aluminum foils were irradiated in order to give a further calibration of the beam intensity, a fundamental parameter in evaluation of the Energy Amplifier gain.

The optics functions of the secondary line were completely changed in order to accommodate a primary beam with very low losses, particularly beyond the beam transformer. Simulations performed with the computer code TURTLE (see Table 2) and a preliminary test showed an excessive contribution of multiple scattering in the target area. Therefore a 4.6 m air drift space was replaced with a helium bag and some 200 μm Al windows changed to 150 μm Mylar ones in order to bring this effect down to an acceptable level.

Transfer Line	**H (mm)**	**V (mm)**
'Standard' optics	20.8 mm	6.3 mm
- with He bag	13.8 mm	4.9 mm
- with Mylar window	10.0 mm	4.3 mm
'Round beam' optics	6.1 mm	5.9 mm

Table 2. Beam sizes (FWHM) at 2.7 GeV estimated by TURTLE. Multiple scattering was reduced by replacing free air space and Al window with He bag and Mylar windows

The 'round beam' optics, giving a better matching to the experiment target, was chosen. It was achieved with a triplet at energies higher than 1 GeV and with a quadruplet at 1 GeV and below. For each energy, matching was adjusted to minimize losses in the beam transformer and beyond. Figure 3 shows the beam optics for energies higher than 1 GeV.

Optical parameters have been carefully matched to minimize losses using all available instrumentation. Special care was taken for the T7 line due to limited diagnostics and the necessity to guarantee the precision of the beam transformer.

The final focus was made on a beam dump location using MWPCs. Switching to the experiment target required one single dipole and no further adjustments. The power supply driving the last switching magnet provided interlocks to the beam request in order to ensure that beam was

delivered to the dump or to the calorimeter only when the appropriate current was settled.

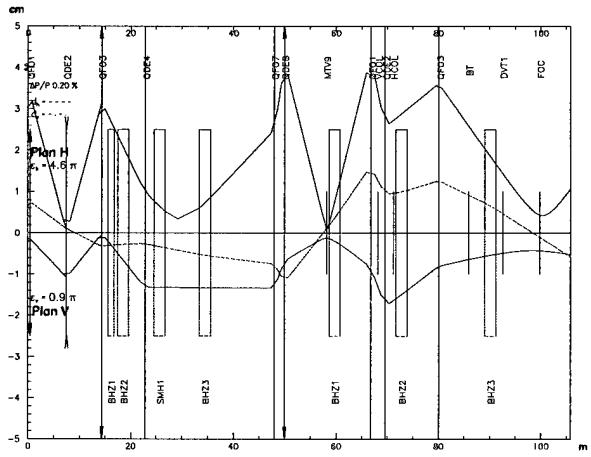


Figure 3. Beam optics for energies higher than 1 GeV.

V. RESULTS

Eight different beam energies were set-up, from 2.7 GeV down to 0.6 GeV, the lowest energy the beam line could properly transport, to allow an estimation of the Energy Amplifier gain as a function of the energy of the beam hitting the target. Transverse beam dimensions measured at target position as in fig. 5, are plotted in fig. 4 as a function of beam energy. The relative mean energy variation had an rms value of 2×10^{-4} at high energy and 7×10^{-4} at low energy. The beam longitudinal emittance was 0.5 eVs and the RF voltage at extraction was adjusted to match the bunch length (70 ns) to the beam transformer bandwidth.

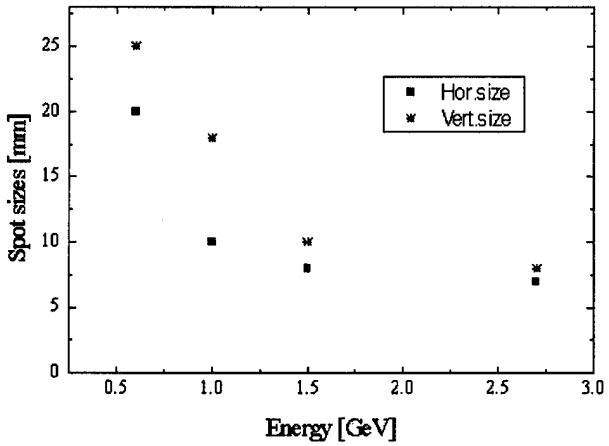


Figure 4. Spot sizes measured on MWPCs (FWHM), for the various beam energies achieved.

At the lowest energies transmission efficiency dropped to 10 % because beam dimensions naturally increase and multiple scattering induces transverse beam blow-up.

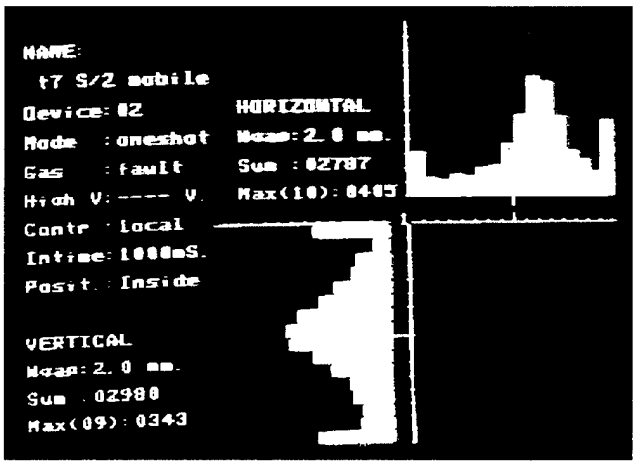


Figure 5. Beam shape on Multiwire Proportional Chambers (MWPCs), at 2.7 GeV. Extreme wires show the sum signal of all other undisplayed wires.

VI. CONCLUSION

Additional new beams were delivered by the CPS to the East area, in fast extraction and in parallel with other operations. The limitations were given by the radiation level allowed by the shielding of the area, the power supply regulation at very low currents and beam dimensions and multiple scattering at low energy. However, these beams could satisfactorily cover the intensity, dimensions and energy range required by the Energy Amplifier Test.

VII. ACKNOWLEDGEMENTS

We are indebted to V. Agoritsas, J.-P. Bovigny, C. Carter and F. Lenardon who provided the necessary instrumentation, to K. Bätzner, R. Coccoli, L. Danloy, J. Delaprison, and M. Zahnd who took care of the unusual modifications of the T7 area and to B. Vandorpe who participated actively in the beam tuning. We also got enthusiastic support from C. Rubbia and his team, and in particular from J.-P. Revol.

VIII. REFERENCES

[1] F. Carminati, C. Gelès, R. Klapisch, J.P. Revol, Ch. Roche, J.A. Rubio and C. Rubbia, " An Energy Amplifier for Cleaner and Inexhaustible Nuclear Energy Production Driven by a Particle Beam Accelerator", CERN/AT/ 93-47 (ET) (1993).

[2] S. Andriamonje & al., "Experimental Determination of the Energy Generated in Nuclear Cascades by a High Energy Beam", CERN /AT/ 94-45 (ET) (1994).

ION-OPTICS SYSTEMS OF MULTIPLY CHARGED HIGH-ENERGY IONS FOR HIGH EMITTANCE BEAMS

V.O.Naidenov, L.A.Baranova, G.M.Gusinskii, A.V.Matyukov, and S.Ya.Yavor.
A.F.Ioffe Physical Technical Institute of Russian Academy of Sciences, St.-Petersburg, Russia

Methods are presented for the calculation of high-emittance ion-optics systems based on magnetic quadrupole lenses for beams of protons and heavy ions with energies from 1 to 10 Mev/nucleon. The strong focusing of the system makes it possible to form beams with linear dimensions less than 0.1 mm. The system for increasing the deflection triples the deflection angle of the beams during scanning. The systems are designed for use with beams from the cyclotron at the A.F.Ioffe Physical Technical Institute of Russian Academy of Sciences, St.-Petersburg.

INTRODUCTION

The development of technological processes based on the use of beams of protons and heavy ions accelerated to energies of 1 to 10 Mev/nucleon, as well as the use of such beams for determining the elemental composition of samples and elemental concentration profiles have stimulated the development of ion-optics systems that form high-energy beams of various configurations. Quadrupole magnetic lenses (QML) are the heart of such systems now. The literature on the basic principles of QML calculation and operation is quite extensive (see, for example, [1,2]). The chief lines of investigations now are optimization of experiments and widening the scope of exploiting of accelerators with high emittance ion beams. Both of these problems have risen during creation of microprobe and nuclear track membrane equipment for our cyclotron.

An analysis shows that the most convenient ion-optic systems that solves these problems are triplet or quadruplet of QMLs. We have derived a system of algebraic equations for the calculation of parameters of the triplet and the quadruplet that provide stigmatic operation. In the thin-lens approximation the system of equation for triplet has the form

$$f_2^2[f_1^2L(L-g)-a^2(s_1+s_2)(L-a)]$$
$$+f_1f_2a[-Ls_1s_2+2s_2(a+s_1)(s_2+g)$$
$$+s_1s_2(a+s_1-s_2-g)]-f_1^2s_2(a+s_1)^2(s_2+g)$$
$$+a^2s_1^2s_2(s_2+g)=0,$$

$$f_3=\frac{g[-f_1s_2(a+s_1)+f_2a(s_1+s_2)]}{as_1(s_2+g)-f_1f_2L}.$$

Here a is the distance from the source of charged particles (or its preliminary image - PI) to the center of the first lens, s_1 and s_2 are the distance between the centers of the first and second and the second and third lenses, respectively; g is the distance from the center of the third lens to the target, $L=a+s_1+s_2+g$ is the total length of the system, and f_1, f_2, and f_3 are the absolute values of the focal lengths of the first, second, and third lenses, respectively.

SCANNING UNIT

The nuclear track membrane production implies uniform irradiation of thin (10 μm) wide (35 cm) film by Ar ions of 40 MeV energy. A transport mechanism advances the film with velocity of 2 - 15 cm/sec, so that the high frequency scanning system is required in another direction.

In scanning a beam in one direction it is possible to arrange the QMLs in such a way that the system, in adding to focusing the beam, which can be scanned at any frequency, also increases the deflection severalfold. This property of lenses is due to the diverging action in the lens and has been previously used in the design of some electron-beam device [3]. The necessary condition for increasing the deflection is that the diverging plane of the last lens coincide with the plane of deflection. The deflection element must be placed in front of the last lens, and therefore a property of these systems is that the distance between the last and the next-to-last lenses is large. As a rule the beam is focused between these two lenses in a plane perpendicular to the deflection plane; i.e., a linear focus is obtained.

The parameters of two systems we have calculated: a triplet and a quadruplet. They increase the deflection by a factor of about three. The beam entering the lenses was in our case astigmatic, with the distance $a=3400$ mm in the deflection plane and $a=2250$ mm in the perpendicular plane. The other parameters for triplet were $s_1=590$ mm, $s_2=3070$ mm, $g=4900$ mm. The beam was focused on the target in both planes, i.e., it was stigmatic at the exit from the system. The focal length of the QMLs were, respectively, $f_1=761$ mm, $f_2=935$ mm, and $f_3=1147$mm. The identical lenses were used, so that their ratios of the number of ampere-turns was 1.50 : 1.23 : 1.0, respectively.

Fig.1 shows a diagram of the path of an undeflected beam in the triplet, where the solid lines represent the beam in the deflection plane and the dashed lines represent it in the perpendicular plane (C means converging, D - diverging). The deflection system was located in front of the third lens, with the distance between the center of deflection and center of this lens equal to 1970 mm.

The deflector is a parallel-plate capacitor 60 cm length (about 100 pf). Voltage amplitude about 40 kV is necessary for our conditions. An inductive coil were added (20 - 200 μ H) to create resonance circuit with Q-factor 500 and to use only 1 kW output generator. The resonance frequency can cover 100kHz - 2MHz. To compensate of non-uniform

0-7803-3053-6/96/$5.00 ©1996 IEEE

irradiation due to sinus law of scanning the amplitude modulation of voltage was used.

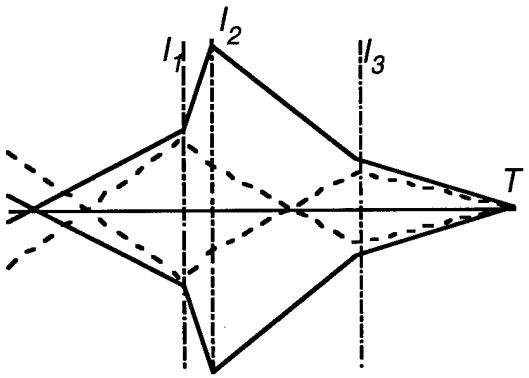


FIG.1 Trajectories in the triplet with increased deflection. Solid lines, the DCD plane (the deflection plane); dashed lines, the CDC plane; dot-dashed line, centers of the lenses; T - target.

For increase the angle of capture of the beam by the lens system we used also a forth quadrupole lens. It was placed in front of the first lens of triplet, with the distance between the center of the first lens and the center of the additional lens equal to $s_0 = 1100\,\text{mm}$ (Fig.2). The geometric parameters of the triplet were kept the same, and in order to maintain the increased deflection the excitation of the last lens was not changed. With optimization of this system it gave the following results. The angle of capture of the beam in the deflection plane could be increased by factor of 1.3 to 1.5. The focal lengths of the QMLs were $f_0 = 2300\,\text{mm}$, $f_1 = 731\text{mm}$, $f_2 = 992\text{mm}$, and $f_3 = 1147\,\text{mm}$ (the subscript 0 refers to the additional lens). The ratios of the ampere turns of the lenses were of 0.5 : 1.57 : 1.17 : 1.0.

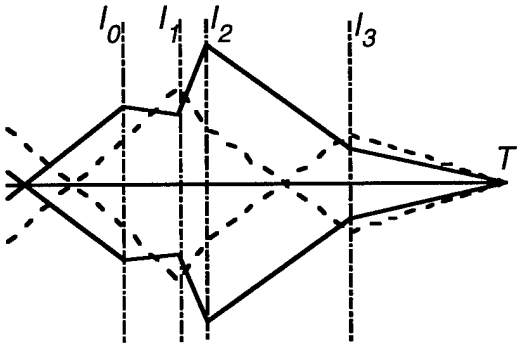


FIG. 2. Trajectories in the quadruplet with increased deflection. Solid lines, the CDCD plane (the deflection plane); dashed lines, the DCDC plane; dot-dashed line, centers of the lenses; T - target.

MICROPROBE UNIT

The lens system forming the microprobe must be located close to the target in order to operate with large linear demagnification. In this arrangement, however, the beam losses a great deal of intensity, particularly if it has a high emittance.

We have found a compromise that gives a probe with a spot size that does not exceed 0.1 mm. The intensity losses can be 96 - 98%. If we take into account the actual intensities of the beams from the cyclotron and the limitations of the permissible current density in the microprobe, this coefficient of use the beam is entirely warranted. In this triplet design the distance L was 5000 mm. The distance a was chosen to be 4626 mm, the distances $s_1 = s_2 = 132\text{mm}$, and $g = 110$ mm. The focal lengths were $f_1 = f_2 = 98\text{mm}$ and $f_3 = 65\,\text{mm}$. This system provides a demagnification factor of 86 in the CDC plane and 24 in the vertical DCD plane. For lenses with a pole length of 100 mm, an aperture radius 10 mm, and pole faces close to hyperbolic, the required field strength at the poles of the first and second lenses is 3500 Oe, and for the third lens it is 5400 Oe for focusing protons with an energy of 7 MeV.

CONCLUSION

Two important problems in formation and control of high-energy ion beams of large initial emittance have been examined. The systems that focus ion beams down to the level of a microprobe and systems that provide effective scanning by means of essential increase in deflection angle have been designed.

REFERENCES

[1] S.Ya.Yavor, Focusing of charge particles by quadrupole lenses [in Russian], Atomizdat, Moscow, 1968.

[2] L.A.Baranova and S.Ya.Yavor, Electrostatic Electron Lenses [in Russian], Nauka, Moscow, 1986.

[3] V.A.Shkunov and G.I.Semenik, Wideband Oscilloscope Tubes and Their Use [in Russian], Energiya, Moscow, 1976.

THE STATUS OF THE FERMILAB MAIN INJECTOR PROJECT

D. Bogert, W. Fowler, S. Holmes, P. Martin, and T. Pawlak
Fermi National Accelerator Laboratory*, P.O. Box 500 Batavia, IL 60510

The Fermilab Main Injector is a new 150 GeV synchrotron now in the fourth year of a scheduled seven year funding profile. An R&D program has been completed, and both civil construction and the production of technical components are well underway. The Main Injector Project is part of a larger upgrade program at the Fermi National Accelerator Laboratory called Fermilab III which is designed to ensure a Collider luminosity in excess of $5x10^{31}$ $cm^{-2}sec^{-1}$ while simultaneously providing a 2 microAmp resonantly extracted 120 GeV beam. The 120 GeV beam will provide unique capabilities in the realm of rare neutral K decays and long baseline neutrino oscillation experiments. The expected performance characteristics of the Main Injector will be discussed, and the status of the construction and the schedule for completion will be reviewed.

I. OVERVIEW

Fermilab III, a program to produce at least a factor of 30 increase in the Tevatron Collider luminosity as compared with a 1988-89 baseline of $1.6x10^{30}$ $cm^{-2}sec^{-1}$ has included several projects at Fermilab of which the Main Injector is designed to produce the final factor of five increase in luminosity. The other projects: new low-Beta focusing systems at both colliding experiments, 22 electrostatic separators to eliminate collisions other than at the experiments, improvements to the antiproton source, and the Linac Upgrade Project have already produced initial luminosities in excess of $2x10^{31}$ $cm^{-2}sec^{-1}$, leading to the hope of achieving a luminosity above $1x10^{32}$ $cm^{-2}sec^{-1}$ with the Main Injector. The present Fermilab accelerator complex is a cascade of four accelerators (400 MeV Linac, 8 GeV Booster, 150 GeV Main Ring, Tevatron) The Main Ring and Tevatron share a single tunnel enclosure. The Main Injector will functionally replace the Main Ring in a separate tunnel enclosure. An ancillary benefit is to remove the 150 GeV accelerator from the vicinity of the Collider experiments where the operation of the Main Ring introduces an undesirable background which can only be avoided by a combination of shielding and gating. The gating reduces the D-Zero experiment live time significantly.

The Main Injector is an accelerator with the two fold symmetry of a sheared oval, the exact shape being dictated by siting considerations. The circumference is 3319 meters, seven times the Booster, or 28/53 of that of the present Main Ring. The lattice is based upon a 90^{o} FODO cell, with zero dispersion straight sections created with short dipoles. The transverse admittance is 40π mm.mrad and the longitudinal admittance is 0.5 eV-sec. β_{max} is 58 meters representing stronger focusing than the Main Ring.

In addition to the 3319 meter Main Injector accelerator, there are five beam lines to provide for: injection from the Booster at 8 GeV, two lines for proton and antiproton transfers from the Main Injector to the Tevatron at 150 GeV, and two lines at 120 GeV for extraction of protons for antiproton production and to the existing fixed target switchyard.

New technical components including 344 dipoles and 12 dipole power supplies, 80 long quadrupoles, 108 sextupoles, 208 dipole correctors, and 18 rf power amplifiers are included in the project. "Recycled" technical components to be relocated from the existing Main Ring include 18 rf cavities, 128 quadrupoles and 6 power supplies, 102 correction magnets, 589 beam line magnets, and assorted power supplies, controls, and instrumentation. A second 345 kVolt substation will be built on the Fermilab site with some back feed capability between the existing substation and the new one.

Transfers to the Tevatron for fixed target physics acceleration cycles, or for Collider operation, are made at 150 GeV. Twelve Booster batches are presently required to fill the Main Ring. The Main Injector will be filled with six Booster batches, requiring two Main Injector acceleration cycles to 150 GeV to fill the Tevatron for fixed target physics at Tevatron energies. Antiproton production at 120 GeV, on the other hand, only requires a single Booster batch. The Main Injector has been designed with a faster cycle time than the Main Ring to increase the rate of antiproton production. If loaded with six Booster batches, one batch is sufficient for antiproton production while simultaneously permitting the direct extraction at 120 GeV of the other five Booster batches for a dedicated fixed target research program at 120 GeV.

When built and operated as a 400 GeV accelerator in the early 1970's the Main Ring had a transverse admittance much higher than the approximately 12π mm.mrad measured today at 8 GeV injection from the Booster. The reduction in admittance is the result of many changes made to the Main Ring since its inception. The most significant of these changes are the introduction of the vertical overpasses at the CDF and D-Zero colliding detectors, a source of vertical dispersion which the original planar machine did not have, and the introduction of more extraction and injection points, especially for antiproton production and Tevatron injection, which has further reduced the aperture of the Main Ring. The reduced admittance of the Main Ring at the 8 GeV transfer from the Booster is the greatest single limitation on luminosity increases left in the acceleration cycle. The Main Injector has been designed to have a minimum of a 40π mm.mrad admittance at 8 GeV. This has been achieved by the design of large aperture magnets and with great care to place injection and extraction devices at advantageous places in the lattice. These considerations, coupled with the requirement

*Operated by Universities Research Association, Inc., under contract with the U.S. Department of Energy

0-7803-3053-6/96/$5.00 ©1996 IEEE

for a 1.5 second cycle time to 120 GeV for antiproton production, or a 1.8 second cycle time for neutrino production, have implied the necessity of designing new conventional copper and iron magnets with a good field quality over a large aperture with a cost effective high ramp rate. Power supplies and rf capabilities matching these requirements have also been developed. The design and prototype production of the dipole magnets, the dipole power supplies, and rf power amplifiers were the subject of the completed R&D Program.

II. DESIGN; R&D PROGRAM; FUNDING

The actual construction of the Main Injector was proceeded by two pieces of the project program, both of which were also necessary in the process of obtaining funding and approval to begin construction. The first was the completion of a design report, which evolved into the Title I design report and later into the Main Injector Technical Design Handbook. The design report was an iterative process that specified the accelerator lattice, the beam transfer lines, injection and extraction techniques, and the necessary equipment: magnets, power supplies, rf, vacuum, instrumentation, controls, utilities, etc. Using the design report, it was then possible for both civil and technical designers to begin detailed designs in each area. Also, the lattice could be checked by tracking programs and then the actual measured values of magnetic fields, with harmonics, could be inserted into the tracking programs used during the initial designs, and the whole process iterated.

On the basis of the design report, it was possible to count the necessary new technical components, as well as to identify those items which could be reused from the Main Ring, such as the main quadrupoles. A complete cost estimate leading to the definition of the project financial baseline was thus generated.

In the course of the design studies, three areas were identified which were the focus of a large R&D effort. These were the main guide field dipole magnets, the dipole power supplies, and an improved rf power amplifier. The R&D program began in FY90 and was completed in early FY95. The first major emphasis was placed upon the demonstration that a reliable large aperture conventional dipole magnet with rapid excitation could be designed and then mass produced at a reasonable cost. The second project was the design, construction, and operation of the necessary 9500 Amp power supply for the dipole guide field, and finally the development of a solid state rf power amplifier using commercially available technology, and a demonstration that it was reliable using the existing Main Ring.

The dipole R&D program consisted of the following activities. First, two dipoles were constructed and completed during FY91. These dipoles were used to first study the body field in the magnet and to assure that the field was adequate at both injection and at 120 GeV and 150 GeV extraction energies. Next, the details of the 'end pack' design were worked out by a combination of design calculations and physical construction, both carried out in iteration. Finally, after consultation with business and procurement personnel from the Department of Energy, a business strategy for the procurement of the dipoles in production quantities was defined, and ten more R&D dipoles were constructed using commercial vendors for all tasks that were not to be done at Fermilab. Additional quadrupoles and sextupoles are also required, and were designed at this time.

A first prototype dipole power supply was constructed and operated with R&D magnets as a test load at site E4R, originally constructed for the 4 cm SSC magnet test string. The prototype design suggested several modifications, and a second dipole power supply was also constructed under the R&D program. Both oil filled and dry type 13.8 kVolt transformers are undergoing evaluation as part of the ongoing testing of the R&D dipole power supply.

A new solid state rf power amplifier using commercial components was constructed and has been operated without failure throughout the most recent Collider run in the Main Ring.

It is not possible to conclude a discussion of the design of the Main Injector without reference to the project funding profile, since this also has a significant iterative impact on the details of the planning for project construction. It was originally conceived that an aggressive funding profile should be assumed since, among other advantages, a rapid funding profile can be easily demonstrated to minimize overall project costs. It was assumed at first that an approximately flat four year profile was both sensible and achievable. In fact, the actual appropriations and the funding profile that has been incorporated in the last three fiscal year's appropriation is not aggressive at all. The project is now shown as a seven year project with a total, then year cost, estimated at $229.6M on the plant line with a total project cost of $259.3M. Now in the fourth year of plant line appropriations, the total appropriated to date (FY92 through FY95) is $94.65M. The actual appropriations have been: FY92 $11.65M, FY93 $15M, FY94 $25M, FY95 $43M, and budgeted amounts for future years are FY96 $52M, FY97 $52M, FY98 $30.60M, with commissioning extending into FY99. It should be noted that in order to start both the technical and civil construction it has been necessary to make extensive use of both phased funding and bids with options to extend, and to divide work which could easily be accommodated into larger contractual obligations into relatively small pieces. This has had an impact on the civil design and on the methodology of technical component construction.

As of April 1, 1995, the cost estimate included $101.1M for technical components, $88.7M for civil construction, $8.2M for project management, $1.4M for G&A, and the remainder ($30.2M) unassigned contingency.

III. CIVIL CONSTRUCTION

The first conceptual civil design for the Main Injector was made by the Fermilab civil engineering group prior to FY91. It was then decided that the detailed Title I design package, the individual Title II bid packages, and a substantial part of the Title III effort would be done by an outside A&E firm in support of the Main Injector Project Office and a small group from Fermilab. Thus in early 1991 an A&E selection board was constituted and as a result Fluor Daniel, a national A&E firm with a substantial Chicago office, was selected as the Main Injector A&E firm. An important early assist to this endeavor was a State of Illinois Challenge grant totaling $2.2M which permitted Fluor Daniel to prepare some advanced Title I designs prior to the formal release of federal funding. The Illinois Challenge grant was also used to help prepare the Environmental Assessment. Details of the approval stages prior to the unrestricted release of funding for construction have been reported previously. [1,2] Fluor Daniel carried out the Title I and Title II design effort on the basis of a negotiated fixed price contract.

The basic civil requirements of the Main Injector are: 1) a Ring Enclosure for the accelerator consisting of 1181 precast units in an inverted "U" shape and cast-in-place tunnel segments at 'non-standard' locations, 2) Tunnel connections for transport of 8 GeV Protons from the Booster to the Main Injector (211 more precast units), and for transfer of 150 GeV Protons and Antiprotons from the Main Injector to the Tevatron, 3) Connections to existing enclosures at the Booster and at MR/Tev F0, 4) Service buildings at appropriate locations around the Main Injector, on the 8 GeV transfer Line, and as necessary for connection to the Tevatron, 5) Site Utilities - water, electrical, new 345 kVolt service, etc., and 6) various other installations.

By the standards of many large civil projects, the Main Injector is not a particularly large construction project. It is possible to consider such a project as either one or a very few construction contracts. The funding profile discussed above, however, led management and the A&E firm to adopt a very different approach. The civil work has been divided into approximately 24 packages for construction and/or procurement. It need hardly be observed that this rather fine subdivision of the work does create a significantly larger number of bid drawings and specifications sets, and even then there is a considerable connection to an assumed obligations profile which, if altered, causes some disruption of assumptions designed and drawn into the many individual bid packages. This all translates into increased EDIA (Engineering, design, inspection, administration) costs as compared with the minimum conceptually possible.

A list of the bid packages (civil construction contracts) and civil procurement items is found in the following table. Projects for which the civil construction is completed are indicated "complete". Details about the scope and bidding of 'completed' projects have been previously reported. [2] Projects in progress are so indicated. Projects to be funded in this or future fiscal years are indicated by the notation of the fiscal year when the obligation is expected.

1) Wetlands Mitigation (complete)
2) Accelerator Enclosure at MI-60 (complete)
3) MI-60 Service Building (complete)
4) Site Preparation, roads, utilities (3 phases)(complete)
5) Substation Hardstand (complete)
6) Ring Enclosure Precast Units (3 phases)(in progress)
7) 8 GeV Line Precast Units (in progress)
8) Main Injector Ring Enclosure (2 phases)(in progress)
9) 8 GeV Line (3 phases)(in progress)
10) Main Injector Service Buildings (8 structures)(FY96)
11) Cable Trays in Enclosures (FY96)
12) 13.8kV Distribution (FY96)
13) 345kV transmission Line (FY96)
14) Kautz Road Substation (FY96)
15) Commonwealth Edison 345kV connection (FY95)
16) Add to MR-F0 Service Building, new F17 (FY97)
17) Cooling Ponds and Cooling System (FY96)
18) Connection of Main Injector at MR/TeV F0 (FY98)
19) Connection of 8 GeV line at Booster (FY98)
20) Landscaping, Road Paving, etc.(FY98)
21) Various Transformer Procurements (FY95)
22) Shielding Steel Procurements (in progress)
23) Survey Monuments (complete)
24) Reconstruction of E4R facility (FY95)

The ring enclosure inverted "U" precast units have been built at the rate of four units per day since early February 1994. The contractor is PBM Concrete of Rochelle, Illinois. Approximately 1140 of 1181 have been completed, and the contract should be finished approximately May 15, 1995. PBM Concrete is also building the 211 precast units for the 8 GeV line. Production will follow immediately upon completion of the ring enclosure precast units and should be completed by July 31, 1995.

The Main Injector ring enclosure was started in April 1994 by the contractor, Wil-Freds of Aurora, Illinois. Approximately 50% of this work is complete and costed. The work consists of excavation following by tunnel construction using precast units set on a cast-in-place base slab, as well as sections of cast-in-place tunnel where non-standard cross sections are required. The work also includes exit stairs and the stairs and backwalls at the locations of future service buildings. The enclosure contract should be completed in early 1996.

The 8 GeV line contract was awarded to Martam Construction of Glen Ellyn, Illinois. Work has just begun on phases 1 and 2 using FY95 funding, the third phase will be funded in FY96. Phase 2 requires an accelerator shutdown which is scheduled to begin July 24, 1995.

Shielding steel procurements subcontracted to Wil-Freds are underway. The use of 'continuous cast salvage slab' steel delivered by rail car to Fermilab has been found to be quite advantageous.

Fluor Daniel has completed the Title II packages for all of the civil construction work with the single exception of some details on the 8 GeV Connection at the Booster. To date, the actual civil construction work has been bid below the Title II estimates, and work completed, including changes to work in progress, has not exceeded the Title I baseline estimates. Civil EDIA has, however, exceeded initial estimates.

The Main Injector civil designs have included a number of capabilities for future utilizations including several possible extraction points, room for Siberian Snakes for polarized protons, and a 'keep away' region for a possible additional ring of magnets in the enclosure. A recently approved addition to the scope of the Main Injector Ring Enclosure added an extraction stub enclosure for a northwesterly extracted beam. This stub was designed at Fluor Daniel and is being added by negotiation to the enclosure contract.

IV. TECHNICAL COMPONENTS

The technical components for the Main Injector Project have been divided into ten "WBS Level 3" areas, each with a "Level 3 Manager" responsible for the cost estimate, scheduling, and overall design and production. These ten areas are: 1) Magnets, 2) Vacuum, 3) Power Supplies, 4) rf Systems, 5) Kickers and Slow Extraction, 6) Instrumentation, 7) Controls, 8) Safety Systems, 9) Utilities and Abort, and 10) Installation.

It was decided at an early point in the project that the work would be accomplished with approximately the following priorities until funding was not an almost absolute restriction: 1) Technical R&D, 2) Technical EDIA, 3) Civil EDIA, 4) Start Civil Construction, 5) Start Dipole Magnets, and 6) Start other technical components. The result of this prioritization coupled with the actual funding appropriations outlined above has been that with the exception of the Wetlands Mitigation which was begun in late FY92, the actual civil construction began in FY93, the dipole magnet production began in FY94, and the rest of the technical components were only funded to start construction in FY95. Even with this slow start, both civil and dipole magnet obligations have been subdivided into small amounts with extensive use of 'phased funding.' In addition, the rate at which work has been scheduled has been generally determined by fiscal constraints rather than a consideration of attempting to maximize parallel endeavors.

In spite of the funding constraints, very considerable progress has been made and the rate of production of technical components being built and the accomplishment of civil construction has now reached approximately the rates projected when the project schedules were baselined, although in both instances with a several month 'start-up delay' offset. In other words, the amount of costs accrued in recent months has reached a steady state supported by the appropriations profile.

The dipole magnet R&D program was designed to flow smoothly into the production of the guide field dipoles, and when the R&D program was finished approximately at the end of the first quarter of FY94 the production of dipole magnets was initiated. Since Fermilab acts as the 'general contractor' for the dipole magnets and only performs the final assembly (about 6% value added) there was a long 'start up' period while all the queues were filled.

Now production has reached a steady state of approximately one dipole completed every two working days. There are two streams of material which meet just prior to final assembly for this to work correctly. The magnets each consist of two insulated copper coils and two steel half cores fabricated from stacked steel laminations. One stream has to provide the insulated coils at the rate of a pair every two days, and the other stream has to provide a pair of stacked half cores every two days.

The copper coils are wound at Everson Electric in Pennsylvania. The bare copper coils are shipped, via Fermilab, to Tesla Engineering in England (via rail and sea) to be insulated, and returned, (via sea and rail) to Fermilab. The steel is fabricated in the form of coils at LTV Steel, shipped to a coil 'slitter', and then shipped to a lamination stamper. The steel production is not a 'continuous process' but rather a series of supposedly reproducible runs. To avoid systematic variations as much as possible, the steel laminations are shipped to the 'stacker' (SVF in Rock Falls, Illinois) according to a 'recipe' selection which the stacker then follows. SVF is also responsible for the manufacture of 'end packs', special small stacks of laminations using non-standard laminations to produce the desired end fields. The completed half cores are then delivered to Fermilab. As of the end of April, 1995, approximately 60 production dipoles have been completed and measured, with sustained production over several months at the rate of one every two working days.

Two issues, neither damaging to the timely completion of an acceptable accelerator lattice, have arisen during the last half year of dipole production. An interruption of the delivery of the insulated coils due to transportation labor difficulties in Canada led to a suspension of production while a larger inventory was accumulated. Without some buffer in the inventory a large exposure to small upsets in the delivery transportation system could too easily again interrupt production. A review of delivery experience led to the decision to create a four week inventory to draw against for the insulated coils. Measurement of the finished magnets revealed a larger than expected, although still acceptable, variation in the higher field (only) performance of the magnets which correlated with steel from different production runs at LTV. When the source of this variation was understood, (variations in magnetic permeability in regions of the magnet far from saturation when the gap was at high field) discussions to insure that greater variations did not occur were conducted with LTV and attention to any source of steel variation is constant.[3]

The Main Injector will utilize 'recycled' quadrupoles from the Main Ring for most of the quadrupole requirements. The recycled quadrupoles will require a change of the mounting system and a change of beam tube. These quadrupoles must be left in the Main Ring until the accelerator shutdown when

the enclosure connections are built at MR/Tev-F0. Eighty additional quadrupoles are required for the Main Injector Ring lattice. These quadrupoles are being fabricated at Fermilab to a larger extent than the ring dipoles. The work at Fermilab for these quadrupoles includes the steps of coil winding, coil insulation, half core stacking, and final assembly. This work also began in FY94 and is continuing. To date the complete complement of 35 254 cm (100") quadrupoles has been assembled, and work on an eventual complement of 52 295 cm (116") quadrupoles is underway with over half of the necessary coils wound and 20% of the half cores stacked. One 295 cm quadrupole is fully assembled. 113 sextupole magnets are required and are also being built at Fermilab. Ten have been completed at the rate of two per month. Essentially all of the completed magnets have been powered and measured at the Magnet Test Facility.[3,4]

Procurement of materials for Lambertson magnets and "C" magnets for the transfer lines has begun, and studies of the Lambertson end field configuration have been completed. Other quadrupoles and trim magnets are in various stages of design.

When the evaluation of the dipole power supply built under the R&D program at E4R is complete later in FY95, parts for the full complement of power supplies will be ordered. Parts are being ordered for the kicker supplies as engineering is completed.

Following the completion of the rf R&D program, approximately $1.25M of parts for the production complement of the rf power amplifiers have been ordered since January 1995. This equipment will be assembled in the MI-60 service building as it is delivered.

Design work for a beam position monitor based upon the cross section of the Main Injector beam tube is in progress, and successful prototyping has been completed.

All of the Technical Component Level 3 project areas have now been allocated funding in FY95 to complete design work and to start acquisition and construction activities to some extent. The utilities installation needed at the MI-60 building has begun, and several tasks each in excess of $100K were started in FY95 and some of the low conductivity water (LCW) piping tasks have been completed. Heat exchangers are being acquired and will be installed also. Design work for vacuum systems, controls, safety systems, and magnet installation equipment is well advanced. An installation test in an approximately 30 meter section of standard tunnel cross section in the completed MI-60 enclosure region is underway.

V. SCHEDULE

The present seven year funding profile is much slower than was originally expected or hoped. When the Main Injector was in the conceptual design stage, a four year schedule was believed to be quite realistic, and considering the original schedule for the construction of Fermilab over twenty-five years ago, such a schedule was considered demonstrated. The actual project schedule has been funding limited since the first appropriation and continues to be funding limited.

It will be necessary to turn off the Fermilab physics program for a period of approximately nine months to connect the Main Injector to the existing complex at the Booster and the Tevatron rf straight section (called MR/Tev F0) involving demolition work at both locations. To minimize the down time of Fermilab all the rest of the civil and technical construction, and the installation of new components, must be completed prior to the final civil interconnections at MR/Tev F0 and the Booster. The connection at the Booster could be accomplished at an earlier shutdown of sufficient length if the funding is available. Technical staff cannot be 'double counted' during the shutdown, so all possible prior work must be completed so staff is available to dismantle, remove, and recondition items such as the Main Ring quadrupoles being recycled into the Main Injector. According to the present funding profiles which require $52M in each of FY96 and FY97 it will be just possible to complete the pre-shutdown work in time to permit the 9 month shutdown to begin in February 1998 so that commissioning should be completed in early 1999. It is absolutely necessary that the present funding profile that has existed in the last three of the President's budget proposals to Congress be maintained if this schedule is to be met.

The Main Injector project management team is very encouraged by the progress of the project to date. Progress on all civil and technical design and construction has been rapid given the available funding, and both obligations and costing of completed work are tracking the original project baseline with a less than three month delay, almost all of which represented a slightly slow startup, some large fraction of which was delays in administrative approvals for the first expenditures. Actual contracts have been placed at favorable pricing. The project is essential for the national physics program, a point repeatedly endorsed even prior to the elimination of the SSC project. Project management is anxious to complete the job and to make this research facility available to the research community.

VI. REFERENCES

[1] D. Bogert, W. Fowler, S. Holmes, and P. Martin, "The Status of the Fermilab Main Injector," XVth International Conference on High Energy Accelerators, Hamburg, Germany, Vol.1, p.492, (July 20-24,1992).

[2] D. Bogert, W. Fowler, S. Holmes, P. Martin, and T. Pawlak, "The Status of the Fermilab Main Injector Project," Proceedings of the 1993 Particle Accelerator Conference, Washington, D.C., Vol.5, p. 3793, (May 17-20, 1993).

[3] D. J. Harding et. al., "Magnetic Field Measurements of the Initial Fermilab Main Injector Production Dipoles", Proceedings of this Conference.

[4] D. J. Harding et. al., "Magnetic Field Measurements of the Initial Fermilab Main Injector Production Quadrupoles", Proceedings of this Conference.

STATUS AND FUTURE OF THE TEVATRON

V. Bharadwaj, Fermi National Accelerator Laboratory*, P.O. Box 500, Batavia, Il 60510

The Fermilab Tevatron proton-antiproton collider is nearing the completion of a long physics run at 1.8 TeV in the center-of-mass with a goal of delivering 100 pb^{-1} each to the CDF and D0 detectors. An 800 GeV fixed target run is scheduled to begin in 1996. Recent performance of the accelerator complex, culminating in the reliable delivery of integrated luminosity in excess of 2 pb^{-1} per week, is presented. The prospects for improving the delivery of integrated luminosity to a level in excess of 10 pb^{-1} per week for the next collider run, presently scheduled to begin with the completion of the Main Injector project, will be presented. Finally, ideas related to extending the luminosity beyond the stated goals of the Main Injector, as well as possible alternate directions for the continuation of Fermilab's successful accelerator R&D program, will be discussed.

I. INTRODUCTION

The Fermilab accelerator complex consists of a 400 MeV Linac, an 8 GeV Booster, a 150 GeV Main Ring, a 900 GeV superconducting Tevatron and associated transfer and extraction beamlines. In addition, there is an Antiproton Source that contains two 8 GeV synchrotrons, the Debuncher and Accumulator. The Main Ring supplies the 120 GeV proton beam to generate antiprotons that are then accumulated in the Antiproton source. The complex has two major modes of running, collider and fixed target. In the former mode, beams of protons and antiprotons are brought into collisions at a center of mass energy of 1800 GeV. In the latter mode, protons are accelerated to 800 GeV and delivered to a number of experiments at the ends of various extraction beamlines. Typically fixed target running alternates with collider running every year or two.

Fermilab is coming to the end of a collider running period that has been designated as Run 1b. Since the initial commissioning of the Tevatron as the world's highest energy proton-antiproton collider in 1985, there have been four collider runs, i.e. the 1987 Run, the 88-89 Run, Run 1a in 1992 and the current Run 1b. There has been a steady increase in the delivered luminosity every run from the 0.07 pb^{-1} delivered in the first three month long collider run in 1987. In the 88-89 Run typical initial luminosities of 0.16 x 10^{31} $cm^{-2}sec^{-1}$ were seen and the integrated luminosity in that 14 month run was 9.6 pb^{-1}. At that point the luminosity in the Tevatron was limited by the beam-beam tune shift. The installation of electrostatic separators prior to Run 1a reduced the number of beam crossings from twelve to two. This enabled the Tevatron to reach typical luminosities of 0.54 x 10^{31} $cm^{-2}sec^{-1}$ and integrate a total of 32 pb^{-1} at two interaction regions (B0 and D0). The collider luminosity was now limited by the available proton beam that could be injected in the Booster and, hence, be used for antiproton production and for proton injection into the Tevatron. The limit in the Booster was due to space charge effects at injection from the 200 MeV linac. The Linac Upgrade project increased this injection energy to 400 MeV, thereby improving the performance of the collider complex. This improved performance has been demonstrated in Run 1b which has seen typical luminosities of 1.89 x 10^{31} $cm^{-2}sec^{-1}$ and which has already delivered more than 100 pb^{-1} to each of the two experiments at the two interaction regions.

Run 1b is presently scheduled to end on July 24, 1995. The next collider run, Run II, will start after the commissioning of the new Main Injector synchrotron. Between the end of Run 1b and then, there is scheduled a total of 68 weeks of Tevatron fixed target running at an energy of 800 GeV as welll as the Tevatron collider studies needed for the success of Run II.

At present the luminosities delivered by the collider are limited by the proton beam intensity coming out of the Main Ring. The Main Injector synchrotron is designed to replace the Main Ring and alleviate these limits. The proton bunch intensities in the Tevatron are expected to increase modestly and the antiprotons injected into the Tevatron increase much more. This is expected to generate another factor of five increase in delivered luminosity. After this, no more gains can be made from increasing the proton bunch intensities in the Tevatron. However further increases in the antiproton accumulation rate can give a factor of up to ten increase in delivered luminosity, i.e. greater than 10^{33} $cm^{-2}sec^{-1}$ typical initial luminosities and 200 pb^{-1} integrated luminosity per week. Ideas for achieving this goal are lumped under the name TEVATRON33.

There is significant effort at Fermilab to look at the very far future and R&D effort is going on looking at the feasibility of higher energy proton-proton colliders, muon colliders and other projects. This work is of a very speculative nature, but it is hoped that project proposals will result for the next generation of high energy accelerators.

---

*operated by the Universities Research Association under contract with the United States Department of Energy

0-7803-3053-6/96/$5.00 ©1996 IEEE

II. RUN 1B STATUS

A. *Stacking and storing choreography*

During collider runs the accelerator complex has two distinct operational modes, i.e. "shot setup" and "stacking and storing". At the end of a store, the beam is aborted out of the Tevatron and shot setup starts. The antiproton beam transfers between the Accumulator and Main Ring and between the Main Ring and Tevatron are checked using "reverse protons". Then the Tevatron is loaded with six intense proton bunches and six intense antiproton bunches. Each intense bunch is generated by coalescing eleven bunches in the Main Ring at flattop. The proton and antiproton bunches are injected onto electrostatically separated orbits. Beam is then accelerated to Tevatron flattop. Strong focusing low beta quadrupoles either side of each interaction region squeeze down the beam spot size and the beams are then brought into collisions at the centers of the two collider detectors. At this point the Tevatron provides collisions at the two experiments, and the Main Ring and the Antiproton Source are reconfigured to produce and accumulate antiprotons. Shot setup typically takes 2.5 hours and the stores last about 16 hours. The luminosity lifetime is such that the luminosity drops by a factor of three during a typical store. It should be pointed out that the exact daily schedule depends on many factors, including component failures. On average the collider provides luminosity for the experiments about two thirds of the time.

B. *Luminosity Formula*

The luminosity in a synchrotron collider is given by

$$\mathcal{L}=\frac{fN_p(BN_{\bar{p}})}{2\pi(\sigma_p^2+\sigma_{\bar{p}}^2)}F(\sigma_z/\beta^*)=\frac{3\gamma fN_p(BN_{\bar{p}})}{\beta^*(\varepsilon_p+\varepsilon_{\bar{p}})}F(\sigma_z/\beta^*)$$

At Fermilab, the convention used is 95%, normalized emittances. For emittances that are roughly equal this equation factorizes as follows

$$L \propto (N_p/\varepsilon_p) \times (BN_p)$$

i.e. that the luminosity is proportional the product of the phase space density of the proton bunches and the number of antiprotons in the collider for a particular store. The ultimate particle phase density is limited by the beam-beam tune shift in the Tevatron. At the design operating point, this limit is approximately 1.5×10^{10} particles per π mm-mrad. The integrated luminosity depends on the initial luminosity and the luminosity lifetime. The length of a store depends on being able to replenish the accumulator stack for antiprotons used in a shot setup and on maximizing to total integrated luminosity delivered to the experiments.

C. *Run 1b highlights*

The Linac upgrade was completed by October 1993 and the accelerator startup began. The Tevatron saw some beam by November, 1993. Between then and July 1994 collider performance was well below what was expected and indeed even below the performance during Run 1a. The problem was finally traced down to a badly rolled low beta quadrupole in the B0 interaction region. This caused the Tevatron beams to be badly coupled leading to large emittances and low initial luminosities. Once this was corrected the performance improved by a factor of three. In October and November, 1994 there was an obstacle in the Main Ring. This obstacle was a sliver of metal that would stand up in the beam every so often as the Main Ring ramped. This reduced performance by 20% and was eventually found by very careful detective work. In February of 1995, additional coalescing RF cavities were installed in the Main Ring and the resulting increased RF voltage improved bunch coalescing significantly. Also, a 2-4 GHz stochastic core cooling system was recommissioned in the antiproton accumulator. When used in conjunction with the standard 4-8 GHz system, there was a marked improvement in the antiproton accumulation rate.

D. *Run 1b Performance*

The present performance in Run 1b is a factor of 3.5 better than in Run 1a. This improvement results from injecting more protons and antiprotons into the Tevatron. Figure 1 shows the steady increase in beam intensities. Data from both Run 1a (before store number 4500) and Run 1b is shown. The figure shows that both the proton and antiproton intensities have gone up by a factor of almost two. Given that there has been no significant increase in emittances, this increased intensity has directly translated into improved performance. After store 5400 the coalescing RF upgrade was made operational and a 10% improvement in proton and 20% improvement in antiproton intensities is seen. With typical proton and antiproton emittances of 24π and 13π mm-mrad the single bunch proton and antiproton phase space densities are 1.0×10^{10} and 0.6×10^{10} particles per π mm-mrad respectively. Comparing these numbers with the beam-beam limit of 1.5×10^{10} particles per π mm-mrad indicates that the number of bunches used in collider operation will have to be increased to get significantly more luminosity.

Figure 1: Proton & Antiproton Bunch Intensities

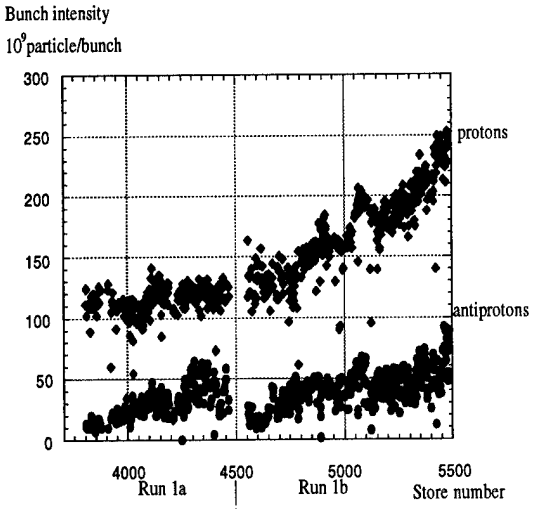


Figure 2: Peak Luminosity Evolution

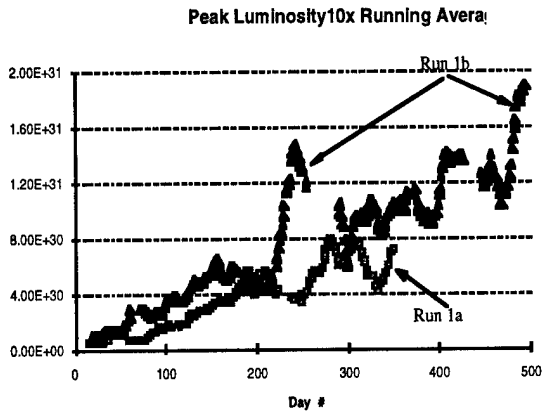


Figure 3: Luminosity per store hour (nb^{-1}/hour)

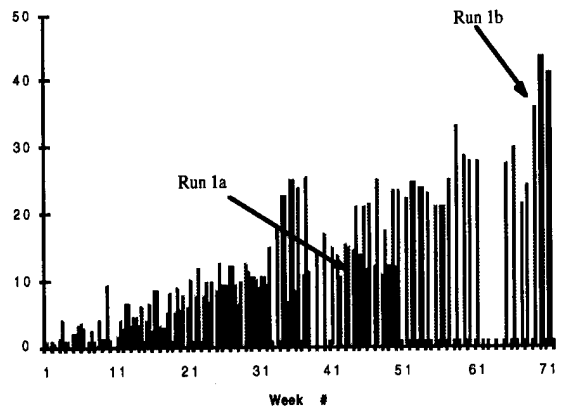


Figure 2 shows the evolution of peak luminosity as a function of days into Run 1b. The Run 1a data is also shown for comparison. The displayed luminosity is a ten times running average and it is seen that recently initial luminosities of 2 x 10^{31} $cm^{-2}sec^{-1}$ are regularly obtained.

Figure 3 shows the luminosity delivered per store hour. This plot is a good measure of performance because the downtime of machines and store length effects are factored out. It is seen that in the last few weeks the per store hour delivered luminosity is greater than 40 nb^{-1} per hour, a number that compares favorably with the 70 nb^{-1} that was delivered in the entire 1987 run. The per store hour luminosity in Run 1a was 11 nb^{-1} per hour.

Table I shows the actual and expected (Run II, Run II+ and TEV33) evolution of parameters at Fermilab. After a slow start, Run 1b has been very successful, delivering greater than 100 pb^{-1} so far. Luminosities of greater than 2 x 10^{31} $cm^{-2}sec^{-1}$ are regularly achieved and the machine reliability has been excellent. It is expected that modest improvements, at the level of 10-20%, to the present performance will be seen by the end of the run. The run goal of 130 pb^{-1} will be easily achieved by the end of the run. Further statistics may be found in reference [1].

III. FERMILAB III

Fermilab III is the generic name given to all the improvements to the accelerator complex that are needed for Run II. The major part of Fermilab III is, of course, the construction and commissioning of a new synchrotron, the Main Injector [2]. Equally important to the success of Fermilab III is the design and construction of new components and the improvements to existing components that are needed to fully exploit the design capabilities of this new ring.

From the discussion above on the Run 1b status, it is seen that the machine performance is now being limited by Main Ring. The Main Ring limits both the proton bunch intensities and the antiprotons accumulated, and hence the antiproton bunch intensity. The Main Injector is designed to alleviate these constraints. Table I shows how Tevatron parameters will change as a result of the Main Injector. The Run II column represents the standard collider parameters using the Main Injctor. Run II+ shows the improvements that can be achieved using new low beta systems and a higher frequency RF system in the Tevatron collider. The Main Injector is in its own enclosure and this has the added benefit of eliminating the backgrounds due to Main Ring losses at the collider experiments. In addition, the Main Injector is also designed to extract beam for fixed target experiments at 120 GeV during collider operation.

Table I: Fermilab Collider Parameters

Collider Parameters	**88-89 Run**	**Run 1a**	**Run 1b**	**Run II**	**Run II +**	**TEV33**
Protons/bunch (10^{10})	7.00	12.00	22.50	33.00	33.00	24.00
Antiprotons/bunch (10^{10})	2.90	3.10	6.50	3.60	3.60	10.00
Proton emittance (π mm-mr)	25	20	22	30	25	18
Antiproton emittance (π mm-mr)	18	12	14	20	20	18
Beta* at interaction point (meters)	0.55	0.35	0.35	0.35	0.25	0.25
Energy (GeV)	900	900	900	1000	1000	1000
Number of bunches	6	6	6	36	36	108
Bunch length (RMS , meters)	0.65	0.55	0.55	0.43	0.17	0.26
Form factor	0.71	0.62	0.62	0.70	0.86	0.75
Typical luminosity (10^{31} $cm^{-2}sec^{-1}$)	0.16	0.54	1.89	8.29	14.20	104.00
Best luminosity (10^{31} $cm^{-2}sec^{-1}$)	0.21	0.92	2.31	12.40	20.00	157.00
Integrated Luminosity (pb^{-1}/ week)	0.32	1.09	3.82	16.72	28.66	210.62
Bunch spacing (nsec)	3000	3000	3000	396	396	132
Interactions/crossing (@ 45 mb)	0.25	0.85	2.98	2.17	3.72	9.13
Antiproton tune shift	0.025	0.009	0.015	0.016	0.016	0.020
Proton tune shift	0.014	0.004	0.007	0.003	0.003	0.008
Average luminosity lifetime (hours)	20	17	15	14	14	13
Typical Antiproton Stack (10^{10})	70	120	180	300	300	900
Antiproton stacking rate (10^{10}/hour)	1.5	3.0	4.5	16	16	80

A. Fermilab III Physics Goals

The physics goals of Fermilab III are

1. Tevatron Collider:
   - precision measurement of of W and top masses
   - b meson production rates of 10^{10} per year
   - search for new phenomena at high mass, high P_T
   - peak luminosities in excess of 5 x $10^{31}cm^{-2}s^{-1}$ (see Table 1 for Run II collider parameters)
   - delivered luminosities greater than 10 pb^{-1}/week
   - 2 TeV energy in the center of mass

2. Main Injector fixed target.
   - short and long baseline neutrino oscillations
   - rare K decays
   - greater than 3 x 10^{13} protons per pulse @ 120GeV, 2 second repetition

3. Tevatron fixed target
   - quark spectroscopy
   - greater than 6 x 10^{13} protons per pulse @ 1000 GeV, 60 second repetition

B. Accelerator Performance Issues

Fermilab III has an ambitious set of physics goals. In order to realize these goals the accelerator complex will have perform better than at present. Some of the needed performance criteria are discussed here.

In the Antiproton Source the stacking rate will have to increase by a factor of three. This will require more protons on the production target and a target beam sweeping system will have to be implemented in order to achieve the needed antiproton stacking rate. Run II will have 36 x 36 bunch operation and the Antiproton Source will have to deliver 36 ensembles of up to 11 bunches.

For collider operation, the Main Injector will need to deliver 5 x 10^{12}, 120 GeV proton batches to the antiproton production target every 1.5 seconds with 20 π mm-mrad transverse emittance and less than 0.5 eV-sec longitudinal emittance per bunch. In addition, the Main Injector will have to supply intense proton and antiproton bunches to the Tevatron. For the Main Injector fixed target operation, various different scenarios are needed such that the needs of the fixed target experiments and the antiproton source are simultaneously satisfied. Most of these needs require a pulse repetition rate of about two seconds and proton beam intensities of 3 x 10^{13} proton per pulse. For the Tevatron fixed target operation, the Main Injector will supply two pulses of 3 x 10^{13} protons to fill the Tevatron to an intensity of 6 x 10^{13}..

In collider mode the Tevatron will accept 36 bunches of protons and antiprotons and accelerate them

to 1 TeV. Beam-beam effects, both short and long range, may become important at this time. In fixed target mode the Tevatron will have to accelerate and extract 6 x 10^{13} protons per pulse.

In collider mode the Fermilab III beam intensities will be a factor of ten larger and in fixed target a factor of three larger than at present. Understanding of beam dynamics and stability will be essential. For the past few years, and continuing until Fermilab III is fully commissioned, there has been a program to design, build and commission active beam damper systems for the various accelerators at Fermilab. This work is critical for the success of the Fermilab III upgrade. In addition there will have to be considerable work done on the accelerator control system to ensure that the various beam transfer scenarios are operational and the accelerator systems are easy to debug.

D. Main injector Schedule

The construction of the Main Injector is progressing well. It will be completed and beam commissioning will start in February 1998. Commissioning for Run II will start in January 1999 with beams for antiproton production. Run II is expected to provide colliding beams for experiments by March 1999 and 120 GeV fixed target beams by the middle of August 1999.

IV. BEYOND FERMILAB III

The Main Injector and the associated Fermilab III upgrade are expected to be fully operational in the year 2000. At this point there are still further improvements in collider performance that may be contemplated. In additional novel accelerator concepts using some parts of the existing accelerator complex are being actively discussed.

A. High Frequency RF in the Tevatron

One way to get as much as a 70% increase in luminosity in the Tevatron collider is to reduce the bunch lengths at collisions in conjunction with new low beta systems to further lower the β^* at the interaction regions. The smaller bunch lengths are most easily achieved by installing a higher frequency, 159 MHz, RF system in the Tevatron. The parameter set for such an option is shown in Table 1 under column Run II+. There is a large increase in the delivered luminosity from 16 to 28 pb^{-1} per week. One important parameter in the table is the interactions at the experiments per beam crossing. This number is uncomfortably large for the HEP detectors. One way to reduce this parameter is to increase the number of bunches in the Tevatron. This will not increase the overall luminosity, indeed it may even reduce the luminosity if a crossing angle is required, but it will reduce the interaction per crossing. This scenario may produce better physics on tape at the collider experiments.

B. TEVATRON33

After Fermilab III is fully operational luminosities of 10^{32} $cm^{-2}sec^{-1}$ will be routine. Looking at the collider parameters in Table 1 it is seen the protons bunch intensity is near the beam-beam limit. The only gain left is to increase the antiproton bunch intensity to the same limit. This requires a factor of ten more antiprotons and hence an antiproton stacking rate that is the same factor of ten larger. Ideas to effect this and increase luminosity to 10^{33} $cm^{-2}sec^{-1}$ range are lumped under the name TEVATRON33 [3]. The improved antiproton accumulation rate is achieved by building a new synchrotron called the "Recycler" in the Main Injector tunnel. This at present is thought to be a permanent magnet ring utilizing electron cooling to achieve very small emittances. In addition the antiproton production rate can be increased by targeting more than one batch of protons from the Main Injector onto the production target or by using a linear debuncher to accept a larger momentum bite out of the antiproton production target. The parameters of the TEVATRON33 upgrade are given in Table 1.

C. 2020

Fermilab is actively pursuing an R&D program to look at the very far future. A large fraction of this R&D is being done in collaboration with other laboratories and institutions. Amongst the ideas being discussed are higher energy "Tevatron" colliders, a very high energy proton-proton collider, muon colliders and TeV scale e^+e^- linear colliders. It is hoped that these discussions will coalesce into proposals that can be presented to the US HEP community.

[1] "Fermilab Collider Run 1b Statistics", V. Bharadwaj et al, proceedings this conference.

[2] "The Fermilab Injector Complex", D. Bogert, proceedings this conference.

[3] "Potential Accelerator Improvements Required for the Tevatron Upgrade at Fermilab", G. Jackson & G. W. Foster, proceedings this conference.

THE RHIC PROJECT – STATUS AND PLANS*

M. Harrison, Brookhaven National Laboratory, Upton, NY 11973 USA

Abstract

The Relativistic Heavy Ion Collider (RHIC) Project is in the 4th year of an estimated 8 year construction cycle at Brookhaven National Laboratory. The accelerator complex is designed to collide a variety of ion species at center-of-mass energies up to 100 GeV/nucleon in a two ring superconducting structure. Industrial magnet production is in progress as well as the other accelerator systems. This presentation will outline the status of the construction effort, near and long term goals.

I. INTRODUCTION

The overriding motivation for colliding heavy ions at ultra-relativistic energies is the belief that it is possible to create macroscopic volumes of nuclear matter as such extreme conditions of temperature and energy density that a phase transition will occur from hadronic matter to a confined plasma of quarks and gluons.

The performance objectives of a heavy ion collider were originally formulated in 1983 by a Task Force for Relativistic Heavy Ion Physics [1]. The main goal is collisions at energies up to 100 GeV/u per beam for very heavy ions, which for the RHIC project is defined to be gold ($^{197}Au^{79}$), but the program outlined also called for lighter ions all the way down to protons. Luminosity requirements for the heaviest ions were specified to be in the 10^{26-27} $cm^{-2}s^{-1}$ range. The higher Au-Au total cross-section results in interaction rates comparable to p-p colliders although this luminosity is several orders of magnitude lower than those machines. A short interaction point length (<20 cm rms) is desirable for optimum detector design. The final, though most influential, experiment requirement was the need for collisions of different ion species (most notably p-Au) at the same center of mass energies per nucleon. This necessitates accommodating charge to mass ratios (A/Z) in the range of 1 (p) to 2.6 (Au). Stabilizing the collision point involves equalizing the rotation frequencies of the two beams which in turn requires the two rings to operate at different magnetic fields. The complications in the interaction region where the beams must pass through common magnets dictate a lattice design different from conventional hadron colliders.

Based on these general requirements the detailed RHIC machine parameters were derived and are outlined in Table 1. Operation of the RHIC collider at relatively low energies together with the enhanced intrabeam scattering, which scales as Z^4/A^2, result in beam of large transverse and longitudinal dimensions. This in turn has ramifications for the lattice (short cells, strong focusing), and magnet aperture. The rf system requirements are also determined by this consideration and the short interaction point. Colliders unlike fixed target machines, are designed to operate for extended periods at high energies. The economics of power consumption argue strongly for superconducting magnets and RHIC is a superconducting machine.

Table 1: Major Parameters for the Collider

Kinetic Ener.,Inj.-Top(each beam),Au	10.8-100	GeV/u
protons	28.3-250	GeV
No. of bunches/ring	57	
Circumference, 4-3/4 C_{AGS}	3833.845	m
Beam separation in arcs	90	cm
Number of crossing points	6	
Free space at crossing points	±9	m
Beta @ crossing,horiz./vert.	10	m
low-beta insertion	1	m
Betatron tune, horiz./vert.	28.18,29.18	
Transition Energy, γ_T	23.60	
Magnetic rigidity,Bρ:@inj.	97.5	T·m
@top energy	839.5	T·m
Bending radius, arc dipole	242.781	m
No. dipoles (192/ring+12common)	396	
No. quadrupoles(276arc+216inser)	492	
Dipole field@100 GeV/u,Au	3.45	T
Arc dipole length, effective	9.45	m
Dipole current	5	kA
Arc quadrupole gradient	71.2	T·m
Arc quadrupole length, effective	1.11	m
Coil i.d. arc magnets	8	cm
Beam tube i.d.	6.9	cm
Operat. temp., He refrigerant	<4.6	K
Refrigeration capacity @ 4 K	24.8	kW
Vacuum, warm beam tube sections	5×10^{-10}	Torr
Beam stored energy	200	kJ
rf voltage, h=342	600	kV
rf voltage, h=2508	6	MV
Acceleration time	80	sec

II. MACHINE LAYOUT AND LATTICE

The complete RHIC facility will be a complex set of accelerators interconnected by beam transfer lines. The RHIC rings are shown schematically in figure 1. It is comprised of two identical, quasi-circular rings separated horizontally by 90 cm, and oriented to intersect with one another at six locations. Having 3-fold symmetry each ring consists of three inner and three outer arcs and six insertion regions joining the inner and outer arcs. Each arc consists of 11 FODO cells with each half cell consisting of a single dipole together with a spool piece assembly containing a quadrupole, sextupole and concentric correction elements. The nominal design magnetic rigidity of the dipoles if 840 T·m which corresponds to a design field of ~ 3.5 T at 100 GeV/u. Injection takes place at 100 T·m. The dipole coil i.d. of 8 cm is determined by the beam size at injection. The quadrupoles run at

*Work performed under the auspices of the U.S. Department of Energy.

0-7803-3053-6/96/$5.00 ©1996 IEEE

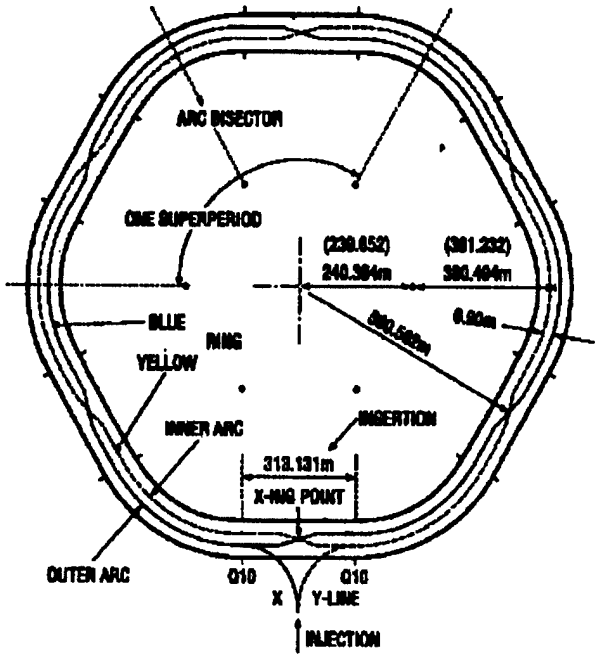


Figure. 1. Layout of the collider and in parenthesis of the tunnel.

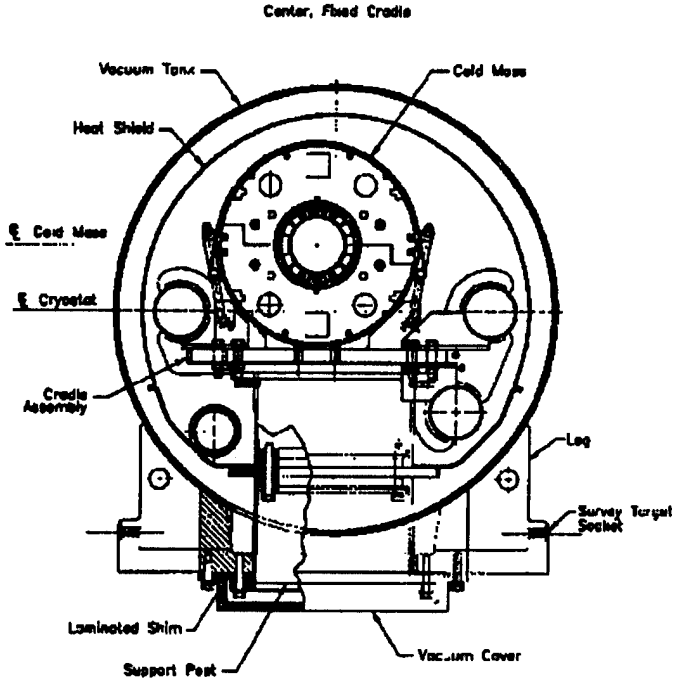


Figure. 2. Arc dipole with cryostat cross section.

a maximum gradient of 72 T·m and also have a coil i.d. of 8 cm. A cross-section of a dipole is shown in figure 2. The magnets are conceptually similar to the HERA dipoles with a 'cold-iron' design and cryogenic transfer lines located in the cryostat. Each dipole is 10.45m long.

Collisions of the beams take place at the crossing point of the insertions. These regions contain the optics necessary for producing a small betatron amplitude function β^*, zero dispersion at the crossing point, and the bending magnets to bring the beams into head-on collisions. The 'non-arc' regions also contain the only warm regions of the machine where the machine utilities reside such as injection, beam abort, rf, collimators and specialized instrumentation. Locations available for these other devices are the 35m between Q3 and Q4, the missing dipole between Q7 and Q8, and the region adjacent to the short D9 dipole. The layout of an insertion, connecting the standard cells to the interaction point, is shown in figure 3. The magnetic elements in the Q10→Q4 region are identical in cross-section to the standard cell but with various lengths. The final focus triplet (Q1, Q2 & Q3), and bending magnets (D0 & DX) are non standard magnets with apertures of 13cm, 10cm and 18cm respectively. The focusing is relaxed at injection with a β^* value of 10m. During collisions at top energy a β^* of 1m can be attained resulting a betamax of 1400m in the triplet quadrupoles. The lattice functions in the IR's are shown in figure 4, for both injection and collisions.

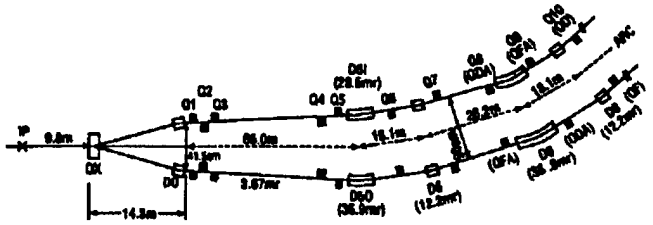


Figure. 3. Expanded layout of RHIC half insertion.

III. COLLIDER PERFORMANCE AND LUMINOSITY LIFETIME

The nominal RHIC bunch parameters range from Au (10^9 ppb, 10πmm-mrad) to proton (10^{11} ppb, 20πmm-mrad) which together with 57 bunches in each ring and a β^* of 2m result in initial luminosities for various ion species as shown in figure 5. The initial luminosity increases with the lighter ion species since the ion source maintains the electric charge (N_bZ) per bunch roughly constant. In contrast to hadron colliders the beam-beam tune shift is relatively small ($\sim$ 0.012 maximum) and does not limit the performance.

Limitations on the average luminosity arise from several effects. As previously mentioned intrabeam scattering growth rates scale as Z^4/A^2 which results in growth times for Au ions an order of magnitude larger than those for protons even though the bunch intensity is two orders of magnitude lower. This effect has been extensively studied in the RHIC scenario [2,3] and the calculations show some quite dramatic effects. Figure 6 shows the estimated longitudinal growth as a function of time during a store. The beam expands to fill the available bucket area during the first two hours and then starts to fall out of the bucket. During the nominal 10 hour store, 40% of the circulating beam is estimated to be lost due to this effect. In addition, transverse emittance growth will also occur with an increase from 10 $\rightarrow$ 40πmm-mrad expected. The initial luminosity lifetime is thus relatively short, 0.9 hr, rising to 11.1 hr by the end of 10

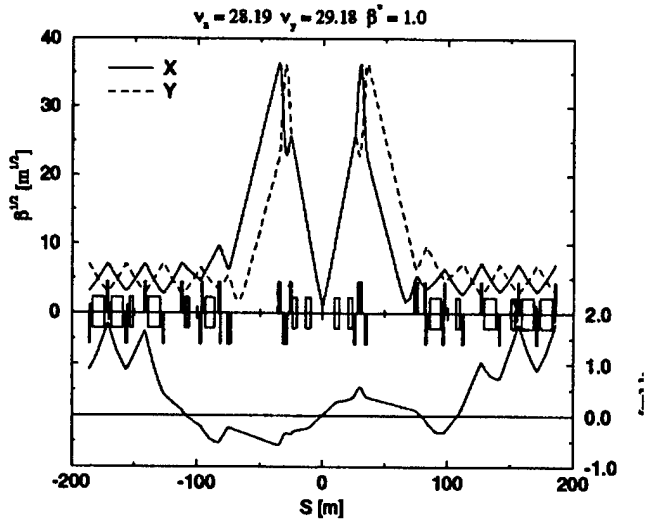


Figure. 4. Betatron and dispersion functions in the insertion region.

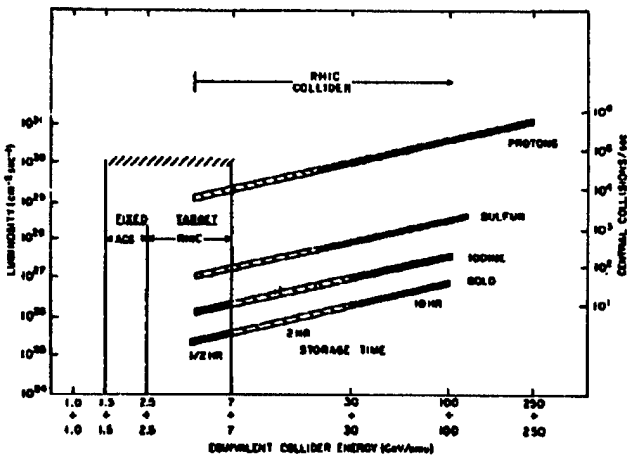


Figure. 5. The initial luminosity, for various ion species, as a function of collision energy over the full range accessible with RHIC.

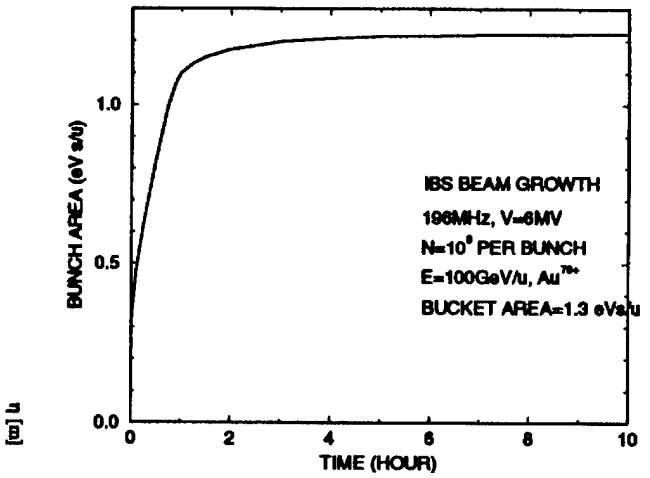


Figure. 6. Longitudinal and transverse emittance growth from IBS v's time in the store.

hours. Significant beam losses are also expected to provide enhanced background rates for the detectors which will require the protection of remote collimation devices. The large transverse emittances also have dynamic aperture implications in the triplet quadrupoles and have been used to define the desired field quality specifications in these elements.

In addition to IBS, significant beam depletion is also expected from the interactions at the crossing point from electro-magnetic interactions. The Lorentz contracted Coulomb field of the Au ions is sufficiently intense to produce large numbers of electron pairs (estimated cross-section 33,000 barns!) as the bunches pass through each other. These are relatively low energy electrons (a few 10's of KeV kinetic) so that pair production itself does not adversely affect the beam. Within this electron cloud however, an ion can capture an electron and change it's charge state by one. These particles will then be lost during the next several turns. Coulomb dissociation is also significant with the ions breaking up into several lighter fragments. Particle depletion cross sections from these effects (and the much smaller rate of nuclear interactions) have been estimated [4] to be 250 barns per high luminosity IR. The reduction in integrated luminosity during 10 hours arising from particle depletion is 15% but becomes more significant for higher luminosity upgrade scenarios.

Compared to proton colliders the beam-gas cross section for Au ions is large (7 barns) which results in a stringent specification on the ring wide average beam tube vacuum in the warm regions of the machine of 5×10^{-10} torr.

IV. COLLIDER STATUS & PLANS

The main focus of the construction project to this point in time has been the magnet program. RHIC will use both in-house and industrially made superconducting magnets. The dipole magnets are currently under fabrication at Northop-Grumman Industries

and the program is well underway with over 100 magnets delivered, accepted and installed on stands in the tunnel. Cold testing has been performed on 40 of these magnets so far and the initial and plateau quench data is shown in figure 7. The magnets exhibit a healthy 30% operating margin and none of the magnets tests to date has quenched below the nominal operating current of 5kA. The field quality has been measured for all dipoles (either warm, cold or both) and is summarized in figure 8 which shows $\Delta B/B$ v's offset for a subset of magnets. The dashed curves show the range of nominal field quality used in the machine simulations. The magnet ensemble lies comfortably inside these values. In addition to the dipoles, 30% of the quadrupoles are at hand (Northrop-Grumman) and show a greater operating margin than the dipoles. Sextupole and trim quadrupole production (Everson Industries) is complete with the majority of elements achieving short sample under cold testing. Magnets produced in house include the nested correction elements (40% complete) and the triplet quadrupoles (66% complete). The remaining magnetic elements for the ring are the splitting dipoles in the IR regions. Of the 2 kinds of magnets, the 10 cm dipole is in mechanical design, the 18 cm one is still in magnetic design.

The AGS to RHIC transfer line(s) is 600m long and requires a total of 143 conventional magnets. This system is complete, installed and has been under vacuum. Cable termination and power supply testing is presently in progress. The transfer line will require the first operation of the RHIC control system.

In addition to installation effort in the transfer line, activities are underway in the main tunnel enclosure. The infrastructure is complete in the arc sections with magnet stands, cable tray, and survey grid in place. Interfacing the superconducting dipoles to the corrector-quadrupole-sextupole assemblies in the arc sections is just getting underway and will represent the major effort for the foreseeable future. The interaction region magnets will be the final elements to be installed. The cryogenic system is supplied from a single large refrigerator (24 kW at 4K) which is available now. Transfer line connections to the tunnel and above ground feeds (valve boxes) will be delivered over a 30 month period which started in March 1995.

The short term schedule is defined primarily by two integrated system tests. The first involves extracting beam from the AGS and transporting it down the transfer line to an internal beam dump and is scheduled for the fall of 1995. This test will validate the AGS single turn extraction system and allow a detailed measurement of the beam and lattice parameters of the incoming RHIC beam. New controls, personnel safety, vacuum and instrumentation systems will be commissioned for this activity. Twelve months later the sextant test will extend this beam transport to include the full injection line and 1/6 of the superconducting ring. This test will represent the first test of the sub-systems associated with the rings: cryogenics, vacuum, power supplies, instrumentation, and controls. The start of full machine commissioning is presently estimated for the beginning of 1999 with partial ring cooldown starting several months earlier.

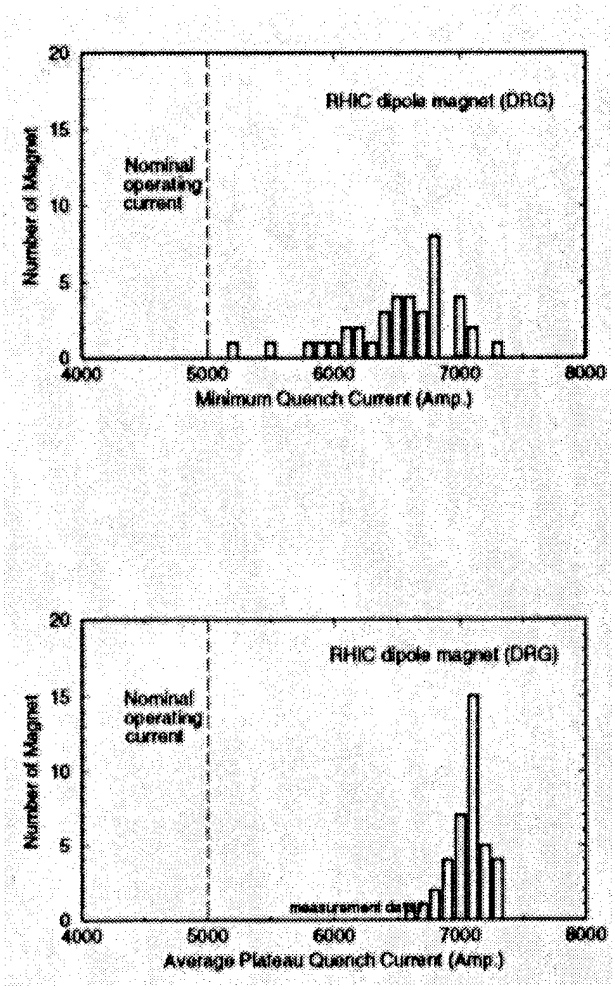


Figure. 7. Initial and plateau quench data.

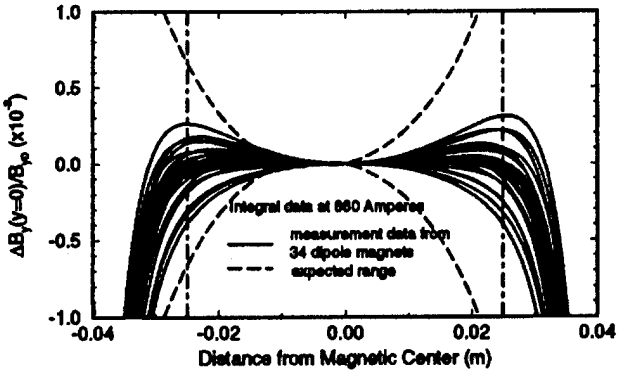


Figure. 8. Field quality.

V. CONCLUSIONS

With the overall machine design stable the RHIC Project is well into the superconducting magnet production program. The magnet quality to date is good and production is achieving the requisite rate. About one quarter of the magnets are in place in the ring enclosure and magnet interfacing is getting underway. In addition to the magnet activities the injection line between the AGS and RHIC is largely complete, and installation of the initial elements of the cryogenic distribution system has started. The medium term schedule is focused around two integrated system

tests. The first involves extracting beam from the AGS and transporting it down the injection line to the ring enclosure. This is scheduled to take place during the Fall of 1995. The following year a similar test involving beam transport through a full machine sextant will permit early operation of the major machine systems in a realistic operating environment. Start of beam commissioning for the Collider is set for the beginning of 1999.

References

[1] T. Ludlam and A. Schwarzchild, Nucl. Phys. A418, 657c (1984).

[2] J. Wei, Proceedings of the XVth International Conference on High Energy Accelerators, Hamburg, 1992, p. 1028.

[3] J. Wei and A.G. Ruggiero, Proceedings of 1991 Particle Accelerator Conference, San Francisco, 1991, p. 1869.

[4] A.J. Baltz, M.J. Rhoades-Brown and J. Weneser, "Convergence of bound-electron-positron pair production calculations for relativistic heavy ion collisions", BNL Report 60532, June 1994.

HERA Status and Plans

R. Brinkmann (for the HERA machine group)
Deutsches Elektronen Synchrotron, D-22603 Hamburg, Germany

Abstract
In 1994, the HERA electron-proton collider delivered an integrated luminosity of 6.1 pb^{-1} to the ZEUS and H1 experiments each, about a factor of six more than in the previous year. The peak luminosity reached 4.7×10^{30} cm^{-2} s^{-1} corresponding to 31% of the design value. This paper reviews the present performance limitations of HERA concerning luminosity operation and the plans for future improvements. After successful commissioning of the spin rotator in 1994 (65% longitudinal polarisation was achieved) the HERMES experiment has been installed during the winter shutdown and will start taking data this year. Further plans concern machine modifications for the installation of the HERA-B internal target experiment in the proton ring (study of CP violation).

I. INTRODUCTION

The Hadron Electron Ring Accelerator HERA operates at DESY for High Energy Physics experimentation since 1992. It consists of a 30 GeV electron ring and a superconducting 820 GeV proton ring, placed in a common tunnel of 6336 m length. The ring geometry has a fourfold symmetry, with experimental halls in the center of each of the four 360 m long straight sections (see fig.1). The two beams are brought into collision in the north and south straight sections, where the H1 and ZEUS experiments, respectively, for the study of e/p collisions are installed. In the east section the HERMES experiment has been installed during the 1994/95 winter shutdown. This new experiment will investigate the nucleon spin structure by studying the interaction of the longitudinally polarized electron beam with an internal polarized gas target. The modifications of the magnet lattice necessary to accomodate HERMES (separation of e- and p-beamlines, installation of a spin rotator pair) were already done during the 1993/94 winter shutdown. The straight section west of HERA has so far been reserved for machine utilities (e.g. p-injection and beam abort systems, collimators, rf-cavities). In the future, this section will house a fourth experiment, HERA-B, which has recently been approved. HERA-B will use protons in the halo of the beam interacting with an internal wire target and study CP violation in the b-quark system.

The construction of HERA started in April 1984 and was finished by the end of 1990. Over 40 institutes from 12 countries participated in the international HERA collaboration, contributing machine components as well as manpower during the design and construction phase of the machine. Commissioning of the e/p collider took place in 1991 and first beam collisions were observed on Oct. 14, 1991. Data taking for the H1 and ZEUS experiments began in June 1992.

In the following, the status of HERA concerning e/p luminosity operation is reviewed, the performance limitations for both rings are discussed and an outlook to future operation is given.

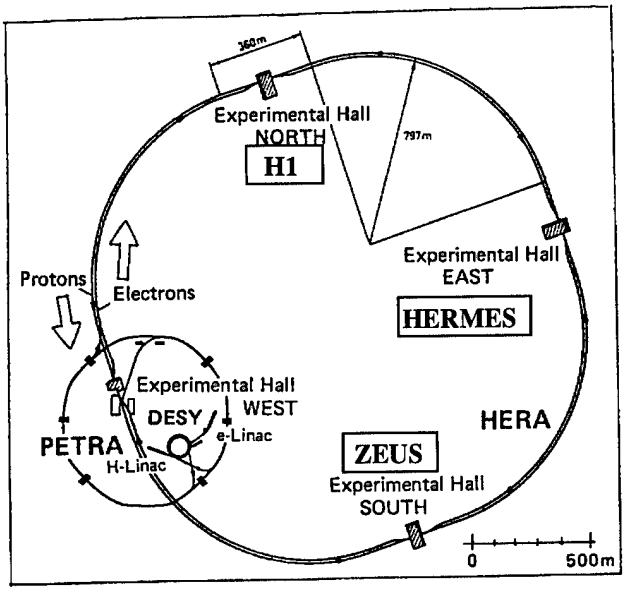


Fig. 1: General layout of HERA

II. LUMINOSITY OPERATION

The improvement in the machine performance over the past three years of luminosity operation is demonstrated by the increase in the yearly integrated luminosity delivered to ZEUS and H1 (see fig.2). In the first phase of the 1994 run the machine performance was significantly limited by lifetime problems of the electron beam at high intensities (see

0-7803-3053-6/96/$5.00 ©1996 IEEE

section 3). This limitation was overcome by switching to positron operation in mid-July 1994, resulting in an increase of integrated luminosity per day by about a factor of two. The main machine parameters for the 1994 run are shown in table 1. HERA was operated with 156 colliding bunches, in addition 12 non-colliding electron and 14 proton bunches were stored to measure the background. The average luminosity at the beginning of a fill reached $2.5\times10^{30}cm^{-2}\ s^{-1}$, 17% of the design value. The main limitations for the luminosity were the proton and electron bunch intensities (typically 30% and 60% of

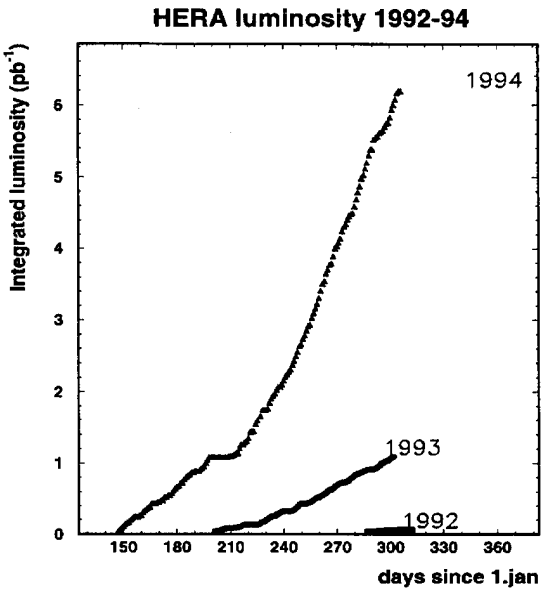


Fig. 2: Yearly integrated luminosity delivered to each of the two colliding beam experiments.

the design value, respectively). The specific luminosity, defined as the luminosity divided by the product of beam intensities, was higher than the design value, a result of the small proton beam emittance and a mini-β optics with $\beta^*_{x,y}$ 30% below the design values. The luminosity lifetime of about 5h was mainly determined by the positron beam lifetime (τ_{e+} = 6...10h, the specific problems with electron operation are discussed in the following section) and the proton emittance growth rate due to the beam-beam interaction (0.5...1 mm×mrad/h for the normalised 2σ-emittances). The proton beam lifetime in collision was typically of the order of 100h, together with an efficient beam collimation system an important prerequisite for low background at the experiments. The operation efficiency, defined as the luminosity time devided by the total time scheduled for e/p operation, was 32%, averaged over the entire 1994 run. This has to be compared to a maximum possible efficiency (limited by the unavoidable magnet cycle, beam filling and energy ramping times) of about 70%. The best monthly figure for the efficiency was about 50% in October 1994.

	94 average	**design**	
# bunches	156 (+12/14)	210	
E_e	27.5	30	GeV
E_p	820	820	GeV
N_e/bunch	2.0	3.6	10^{10}
I_e	27	58	mA
N_p/bunch	3.0	10	10^{10}
I_p	40	160	mA
$\gamma\varepsilon_{x,y}$ (p)	12, 16	25, 25	mm×mrad
$\sigma^*_{x,y}$ (e)	.29, .045	.27, .036	mm
$\sigma^*_{x,y}$ (p)	.20, .055	.27, .08	mm
L_{spec}	4.4	3.4	$10^{29}cm^{-2}\ s^{-1}\ mA^{-2}$
L	2.5	15	$10^{30}cm^{-2}\ s^{-1}$
η_{lumi}	32	≈ 70	%
$\int Ldt$	6.1	≈ 75	pb^{-1}

Table 1: Main machine parameters during 1994 luminosity operation and design goals

The experience concerning machine reproducibility and orbit stability, in particular with keeping the beams in collision, has been very good. Only occasionally (a few times per day) local orbit corrections at the interaction points were applied. This demonstrates the low level of ground motion effects [1], a result not only important for HERA operation but also in view of possible future projects.

III. ELECTRON RING

A. Beam Lifetime Problem

The breakdown of the electron beam lifetime effectively limited the beam intensity during the 1993 run to about 15 mA. At higher beam current the lifetime dropped to typically 1...2 h shortly after ramping the energy from E_{inj}=12 GeV to E_{lumi}=27 GeV and remained low even with decreasing beam current. Studies showed that the breakdown of beam lifetime can be triggered by switching the Ti sputter pumps integrated in the dipole magnet vacuum chambers. The problem could be reduced by lowering the operating voltage of the pumps. This modification allowed to increase the electron beam intensity to 20...25 mA for

the 1994 run, the lifetime typically being 2...3 h, inconsistent with the vacuum pressure of $<10^{-8}$ mbar. After switching to positron operation, the lifetime breakdown effects completely disappeared (see fig. 3).

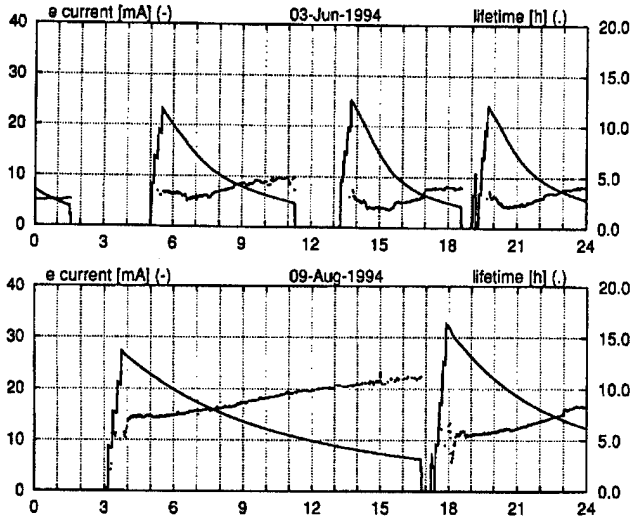


Fig. 3: Behavior of beam current (full line) and lifetime (dotted line, right hand scale) for typical electron fills (upper figure) and after switching to positron operation (lower figure).

The observed effects are most likely caused by the trapping of small (< 1 μm) "dust" particles which are ionized and trapped in the beam. The role of the ion getter pumps is not fully revealed yet, one hypothesis is that the macroparticles are ejected from the pump channels by the electric field of the pump. For a more detailed discussion of this problem, see [2].

B. Intensity Limitations (positrons)

Whereas the single bunch charge in HERA-e is far away from coherent instability limits, the large total intensity stored in up to 210 bunches gives rise to strong multibunch instabilities in both the transverse and the longitudinal planes, driven by the parasitic modes of the accelerating cavities. The instabilities are cured by broadband feedback systems [3], which have been routinely in operation since 1993. During the 1994 e+/p run, the beam intensity was kept below 35 mA, favoring operational stability instead of pushing the rf-system closer to its limit. During machine studies in November 1994 a maximum current of 54 mA was stored. This could, however, only be achieved by deactivating the superconducting rf-system (16 4-cell cavities powered by a 1.5 MW klystron), which during routine operation contributes about 30% (40 MV) of the circumferential voltage. The problem was later traced down to an instability of the cavity phase regulation loop [4] and it is expected that this intensity limitation is no longer present for the 1995 run.

C. Spin Polarisation

In April 1994 the new electron ring beam optics with the modified straight section east was commissioned and a high degree of transverse polarisation (65%) was achieved by applying well established orbit correction and optimisation techniques [5]. The newly installed spin rotator pair was switched on for the first time on May 4, and a longitudinal polarisation of more than 50% was obtained without further optimisation. In subsequent runs up to 65% of longitudinal polarisation was obtained and reproduced later in November during machine studies (fig. 4), see [6] for more details.

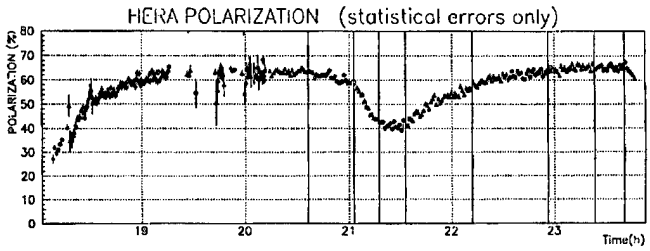


Fig. 4: Positron spin polarisation measured in November 1994 with the spinrotator in the east straight section switched on.

There were no indications that the activation of the rotator causes a degradation of the achievable degree of polarisation.

During part of the 1994 collider run, the influence of the beam-beam interaction on the polarisation was studied. At this time the rotator was switched off (note that the polarisation axis remains vertical at the north and south e/p interaction points in any case, for the present configuration with only one rotator pair installed). Up to the maximum beam-beam tune shift parameter of $\Delta Q_{e,y} = 0.018$ reached in 1994 (at about 40% of the design proton bunch intensity), no significant reduction of spin polarisation was observed. There are indications from tracking simulations with SITROS [7] that depolarising effects may become important at higher beam-beam strength [8], obtained when the proton bunch intensity approaches its design value.

Concerning depolarising effects due to the spin polarisation axis tilt caused by vertical closed orbit deviations, an improvement is expected by applying a beam-based calibration procedure [9] which allows to determine the relative transverse alignment of the beam

position monitors w.r.t. the magnetic center of the nearby quadrupoles with an accuracy of about 0.05 mm. Using this method, up to about 80% of polarisation seems possible.

IV. PROTON RING

A. Preaccelerators and Beam Transfer

The limitation on the bunch intensity in the HERA proton ring was mainly determined by the performance of the preaccelerators. The DESY-III synchrotron routinely accelerated a beam current of 180 mA (12 % above the design value) to 7.5 GeV. The longitudinal instability, which had been observed earlier at high intensity, was successfully cured by a new feedback system [10]. The beam transfer and injection efficiency from DESY-III to PETRA was typically about 70%, another 15% of beam get lost in PETRA during the ramp from 7.5 to 40 GeV. The highest beam current so far accelerated in PETRA was 108 mA in 60 bunches, 85% of the design value [11]. The emittance of the beam stored in PETRA, however, showed a significant correlation with the intensity, see fig. 5, mainly a result of intensity dependent emittance growth in DESY-III.

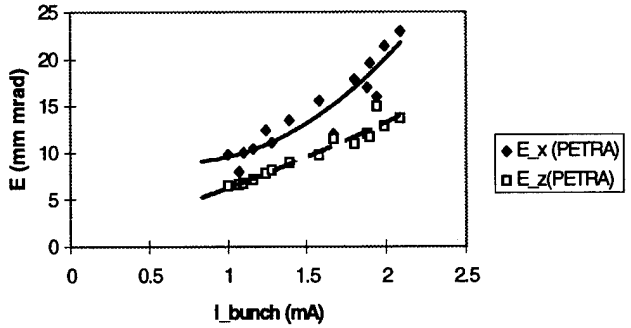


Fig.5: Transverse proton beam emittances in PETRA at 7.5 GeV (injection energy) vs. bunch current [11]. The design bunch current is 2.1 mA.

On average, the bunch intensity transferred from PETRA to HERA was around 40% of the design value. Further losses during transfer, injection and energy ramping in HERA led to an average bunch charge of 3×10^{10} (30% of design) for luminosity operation. The highest beam current stored in the proton ring was 60 mA in 170 bunches ($N_p=4.5\times10^{10}$ per bunch). An improvement of the capture efficiency of the bunches in the HERA 52 MHz rf-buckets was obtained by applying a bunch rotation in longitudinal phase space by suitable manipulation of the PETRA rf-phase and amplitude before transferring the beam.

B. Beam Dynamics

After careful orbit and chromaticity correction, the measured dynamic acceptance in HERA-p at injection energy was 2.4 mm×mrad, in good agreement with tracking simulations [12]. The beam lifetime was above 10h for the well-optimised machine. The variation of the "persistent current" sextupole component in the s.c. dipoles during injection and the early phase of the energy ramp was kept under control by improved automatic procedures, thus minimizing beam losses due to reduced lifetime.

Longitudinal Bunch compression in HERA was done during the energy ramp by raising the voltage in the 2nd (208 MHz) rf-system. During luminosity operation the bunch length was typically σ_s = 20 cm. The 208 Mhz rf-system was operated with low amplitude at injection energy in order to provide stronger Landau damping, which turned out to be necessary for longitudinal beam stability.

In the transverse plane, a single bunch coherent instability was observed during the energy ramp, typically at about 80 GeV. The measured risetime was above 100 ms, to be compared with a measured decoherence time for betatron oscillations of 30 ms. At present the most likely explanation a loss of Landau damping due to an approximate cancellation of non-linear detuning from the sextupoles with amplitude dependent space charge tune shift (note that the latter does not contribute to the measured decoherence) [13]. The pragmatic approach to cure the effect was to turn up the sextupole circuits during the ramp. During machine studies, a broad-band feedback system was successfully tested, which will be used to damp coherent transverse excitations.

Further investigations of beam dynamics concerned the beam lifetime and emittance growth during e/p operation. The frequency spectrum of the beam loss rate at one of the collimators was used as an effective diagnostic tool [14]. Certain frequency components of this loss-spectrum caused by power supply ripple could be minimised by artificially adding tune modulation and adjusting the phase and amplitude properly [15]. Whether this compensation scheme can effectively reduce the observed beam emittance growth with colliding beams, remains to be shown.

V. OUTLOOK

A. Improvement of Luminosity Operation

The most important goal for the near future is to approach the designe/p luminosity in HERA. For the

1995 run the following main improvements are foreseen:

- 170 instead of 156 colliding bunches
- reduction of horizontal e^+ beam size at the IP by ≈20...30% (match p-beamsize)
- higher p-bunch intensity (> 40% on average) with improved transfer efficiencies in the injector system
- achieve design e+ beam intensity with improved rf-system stability

For 1995 an integrated luminosity of 15 pb^{-1} per IP during the run period from May to November is planned. The peak luminosity is expected to reach 10^{31} $cm^{-2}s^{-1}$. Further machine studies are scheduled to investigate the electron beam lifetime problem. In addition, for the 1995/96 winter shutdown an exchange of the Ti sputter pumps with passive NEG-pumps in a significant fraction of the e-ring circumference is planned.

B. Operation with HERMES

First tests with a gas storage cell in 1994 showed that running the HERMES experiment in parallel with e/p operation does not cause an intolerable beam lifetime reduction, in agreement with expectations. Also from 1994 experience, a high degree of spin polarisation seems possible with colliding beams so that data taking of HERMES in 1995 should be compatible with e/p operation. However, with increasing proton intensity in the future, additional spin matching concepts to avoid depolarisation by the beam-beam effect may have to be applied. At higher e^+ intensity, a good match between the e- and the p-beam height at the IP becomes more important and requires to maintain a sufficiently large positron beam vertical emittance. This has been provided in the past by using additional dispersive orbit bumps, a concept which may have to be improved in order to minimise depolarising effects.

C. HERA-B

The internal fixed target experiment "HERA-B" for the study of CP-violation has recently been approved as the 4th HERA experiment. During test runs in 1994 it was demonstrated that with a wire target moved into the halo of the proton beam the required interaction rate of $3\times10^7 s^{-1}$ could be achieved [16]. The influence on the background rates at H1 and ZEUS was tolerable so that operation of the target does not interfere with data taking at the colliding beam experiments. Installation of HERA-B will require to rebuild the straight section west of HERA. The necessary machine modifications have been investigated in detail [17] and are scheduled to be implemented during the 1995/96 winter shutdown. Commissioning of the new beam optics and first tests for HERA-B will take place in 1996. The experiment is scheduled to start taking data in 1998.

VI. REFERENCES

[1] R. Brinkmann and J. Roβbach, Nucl. Instr. Meth. A 350, p. 8 (1994).

[2] D. Kelly et al., "On the Electron Beam Lifetime Problem in HERA", contribution to this conference.

[3] R-D. Kohaupt et al., Proc. EPAC 92 Conf. Berlin, Vol. I, p. 269.

[4] J.Sekutowicz, private communication (1995).

[5] D.P. Barber et al., DESY 93-038.

[6] D.P. Barber et al., "The First Attainment and Routine Use of Longitudinal Spin Polarisation at a High Energy Electron Storage Rings", contribution to this conference.

[7] J. Kewisch, DESY 85-109.

[8] T. Limberg and M. Böge, "Calculations on Depolarization in HERA due to Beam-Beam Effects", contribution to this conference.

[9] M. Böge and R. Brinkmann, "Polarisation Optimisation in the HERA Electron Ring Using Beam-Based Alignment Procedures", High Energy Spin Conference, Bloomington 1994 (in the print).

[10] R.-D. Kohaupt et al., to be published.

[11] K. Balewski, private communication (1995).

[12] F. Willeke, "Comparison of Theoretical Calculations of Dynamic Aperture with Experiment", contribution to this conference.

[13] J. Feikes, private communication (1995).

[14] K.-H. Mess and M. Seidel, Proc. EPAC 94 Conf. London, Vol. II, p. 1731.

[15] O. Brüning and F. Willeke, "Reducing the Particle Loss in Hadron Storage Rings by Generating an Additional Harmonic Tune Modulation", contribution to this conference.

[16] C. Hast et al., DESY 94-119, and J. Spengler, private communication (1995).

[17] B. Parker, DESY M-95-06, in the print

THE CERN HEAVY ION ACCELERATING FACILITY

H. D. Haseroth, CERN, for the Lead Ion Accelerating Facility Collaboration,
CERN CH-1211 Geneva 23, Switzerland

CERN's Lead Ion Accelerating Facility has been operating successfully for its first physics run. The facility, supported financially by some member states and designed, built and installed in a collaboration with several other laboratories (not only from member states), features a completely new linac and a major up-grade of the existing CERN machines. This paper reviews the design philosophy and discusses the present performance and the first operating experience.

I. INTRODUCTION

The work reported here [1] is the result of a collaboration between different laboratories, namely GANIL (Caen, France), Legnaro (INFN, Italy), GSI (Darmstadt, Germany), Torino (University, Italy) and CERN (Geneva, Switzerland), supported by financial contributions from Sweden and Switzerland. and helped with software and some hardware from India (VECC, Calcutta, TIFR and BARC, Bombay), a debuncher from IAP (Frankfurt, Germany) and manpower for installation from Prague (Czech Academy of Sciences).

The scheme [2] followed the model of the successful collaboration [3,4] between GSI, LBL (Berkeley, USA) and CERN for oxygen and sulphur ion acceleration using Linac 1. This collaboration was a consequence of the acceleration of deuterons and alpha particles in the Linac (Linac 1), PSB (Proton Synchrotron Booster), PS (Proton Synchrotron) and the ISR (Intersecting Storage Rings). Deuterons were produced by the conventional duoplasmatron source as used for the protons, alpha particles by stripping a He^{1+} beam after the preaccelerator. O^{6+} beams and S^{12+} beams had required a new (ECR) source and a dedicated RFQ. Pb ions need not only a new Linac but also substantial modifications of the circular accelerators (Fig. 1). Actually about half of the investment went into up-grading the circular machines.

II. BASIC PHILOSOPHY AND DESIGN OF THE LEAD ION ACCELERATING FACILITY

If a brand new facility to accelerate Pb ions to high energies would have had to be constructed, it is clear that the machines to accomplish this task would look drastically different from what has been built at CERN in the context of this project [5,6]. To accelerate ions (heavier than protons) has not been CERN's main goal in the recent past. Ions were dealt with by dedicated laboratories like GSI, GANIL, Berkeley and others. Only a minority of nuclear physicists expressed interest in the higher energies the CERN machines were able to provide. Though they could convince the CERN management to deviate some effort towards ions, it was certain that this effort would remain fairly limited. Without external collaboration nothing would have been achieved. From this it is clear that it was necessary to keep the modifications to the existing machines and the construction of new ones to an absolute minimum.

After the oxygen/sulphur acceleration it was obvious that fully stripped ions could be handled by the existing circular machines without too many problems. The problem was rather how to get fully stripped lead ions. There is no source that could provide the minimum intensity, specified by the interested physicists community: $5 \cdot 10^7$ per SPS supercycle. For reasonable intensities the charge states or rather the more interesting charge to mass ratio is much lower. The compromise selected consisted of an ECR (electron cyclotron resonance) source capable of producing 80 eμA of Pb^{27+}. This choice (charge to mass ratio of 0.13) unfortunately ruled out any further use of the good old Linac1, which had been pushed to 33% higher fields in order to accelerate oxygen and sulphur ions with a charge to mass ratio of 0.375. Being obliged to use a new Linac leaves the question of the desired energy open. To pass through the PSB and the PS with Pb^{27+} would have required up-grading of the vacuum of these machines with large expenses - beyond the scope of this project.

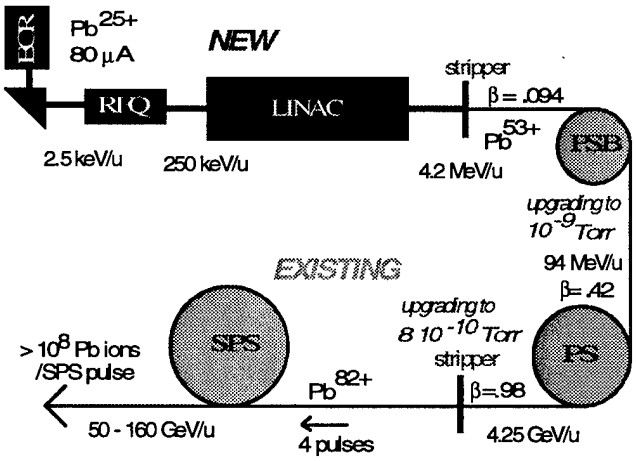


Fig. 1: Layout of the CERN Heavy Ion Accelerating Facility

It was hence necessary to do some intermediate stripping (in spite of the loss in intensity) before the PSB. Inside the circular machine, stripping is impossible because the sudden change of charge to mass ratio can not be accommodated. A higher output energy of the Linac results in a higher charge state after stripping and both make the

0-7803-3053-6/96/$5.00 ©1996 IEEE

vacuum requirements less stringent. Unfortunately, there is a complicated injection line to feed the four Booster rings. A substantial up-grading of this line towards higher energies - still keeping the 50 MeV proton injection from Linac2 on a pulse to pulse basis - would have meant again high expenditure.

The compromise was to aim at 4.2 MeV/u, which, with a foil stripper, yields Pb^{53+} as dominant charge state. With these values the magnetic rigidity is just 13% higher than the one for 50 MeV protons and a very modest up-grading of the injection line elements resulted in the desired performance. Note that up-grading in terms of pulse length for the different pulsed elements in this line was needed in any case to cope with the low velocity of the ions: about a factor 3.5 lower than for the 50 MeV protons.

Basically, existing material has been kept wherever possible, in the circular machines as well as in the beam transfer lines. A new Linac together with its source, however, was unavoidable. We have tried also to standardize, as far as possible within the collaboration, on CERN materials and equipment for ease of maintenance and repairs afterwards. Thanks due to the flexibility of our collaborators, this philosophy has been quite successful.

III. PRESENT PERFORMANCE

The Linac

In spite of the large number of collaborations (all external collaborations were involved in the Linac), construction, installation and running-in worked quite well [5,6]. Though several major components were rather late, the last of a series of milestones (injection into the PSB on June 15, 1995) could finally be kept. Performance of the Linac was close to the design values [6, 7, 8 and references therein] as can be seen from Table 1:

	horizontal emittance [mm mrad]	vertical emittance [mm mrad]	energy spread [keV]	current [eμA]
design	1.0	1.0	2.1	20
achieved	1.2	1.2	2.5	22

Table 1: Linac beam characteristics (at input to PSB)

The Proton Synchrotron Booster (PSB)

As was well known from the very first discussions and presented already [1], the vacuum pressure is a very critical issue in the Booster synchrotron. A general cleaning and replacement of equipment with a very high outgassing rate had been executed [9] together with the installation of additional pumping capacity (Ti sublimation pumps). Unfortunately, several leaks occurred last year causing pressure bumps in two places. The apparent reason has been corrosion due to the decomposition of PVC by the beam induced radiation - after more than 20 years of operation. These leaks have been treated with a plastic sealant which could not yield the ultimate vacuum performance. Though the vacuum has been improved considerably resulting in pressures in the very low 10^{-9} Torr range (gauge reading), it was nevertheless important to accelerate as rapidly as possible to overcome the low energy region. Fig. 2 shows the dependence [1] of lifetime versus energy and demonstrates the importance of fast acceleration.

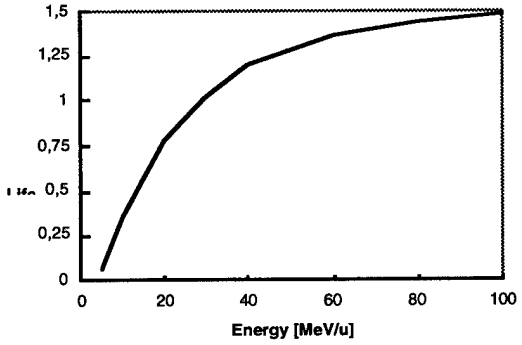


Fig. 2: Lifetime of Pb^{53+} at $9 \cdot 10^{-9}$ Torr (N_2) in the PSB as function of energy

Measurements of the beam lifetime when the Pb ions are injected at constant field showed 30 to 40 ms instead of the assumed 60 ms (Fig. 3).

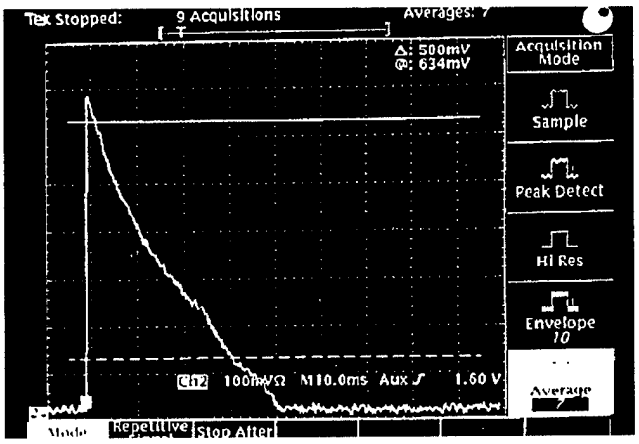


Fig. 3: "Survival" of Pb^{53+} at 4.2 MeV/u in the PSB

It must be stressed that vacuum measurements are extremely difficult as what is of interest is the integrated pressure and the residual gas composition around the closed orbit and not the pressure gauge readings at the positions of the gauges. Beam lifetime measurements are actually a much better indication for the real vacuum pressure - if the relevant cross-sections were known precisely.

The vacuum has not been constant, for example a short time after heating the Ti sublimators, the pressure was lowest and started rising again. Time constants for the pressure rise were between two (in high pressure zones) and ten hours. The resulting intensity variations were

between 1.3 and $1.6 \cdot 10^{10}$ charges. As the PSB had not only to work for the ion users but also for other clients, an unexpected effect was noticed that came from high intensity proton beams for ISOLDE (Isotope On Line separator): These beams produced a pressure increase in the PSB reducing the ion transmission in the next cycle.

Anyhow, by injecting not at a flat field but at the moment where the field is already rising (with 1.8 T/s) together with a fast acceleration, the PSB performance was excellent [10]. Fig. 4 shows oscilloscope traces of the PSB main field (upper trace) and the current in the ring (lower trace - the rising part at the end is not real current but induced noise).

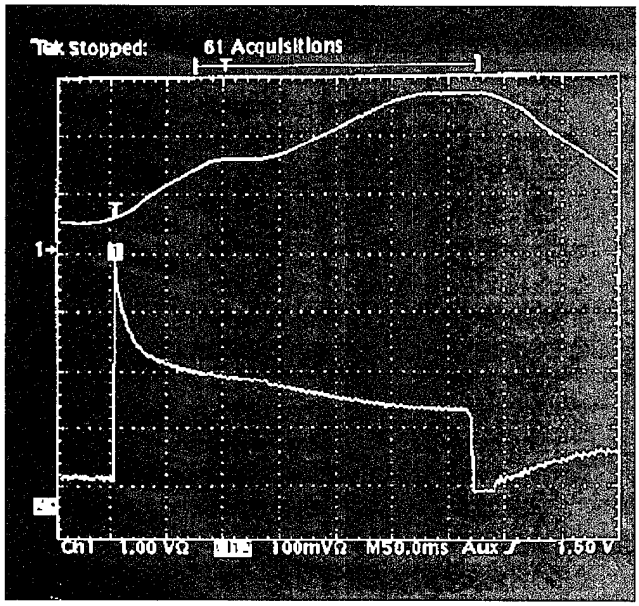


Fig. 4: Field and Pb^{53+} current in the PSB as function of time

It can be seen that losses are highest at the very beginning (injection, trapping and vacuum) and are lower at later times. The intermediate flat top, where debunching and rebunching occurs, does not contribute much to losses. Actually, due to this fact, another debunching/rebunching cycle was added at the top field before ejection. Originally, it had been foreseen to eject 40 bunches. With the second change of the harmonic number to five in the PSB, 20 bunches are injected into the PS avoiding thus any complicated RF gymnastics in the PS.

The Proton Synchrotron (PS)

Several improvements were needed for the PS [10] to cope with the low velocity (β still less than 1/2 at injection, revolution time in the PS: 5μs), the low intensity and the sensitivity to the residual vacuum. To improve the vacuum situation new magnetic septa (bakeable in-situ) were installed together with a large number of Ti sublimators. The low β required lengthened injection kicker pulses and a new digital beam control system uses a radial loop with a sensitive pick-up electrode. Injection takes place at 95.4 MeV/u (magnetic rigidity corresponding to the usual 1 GeV protons) with 20 bunches from the PSB. Although there would have been some interest to strip before injection into the PS (at this energy to a dominant charge state of 80+), it would have meant a loss in intensity of a factor two and some additional losses due to emittance blow-up. Hence no stripping has been envisaged at this position.

With the choice of the parameters, transition (at $\gamma_{tr} = 6.12$) could be avoided with acceleration taking place from $\gamma = 1.1$ to 5.56. Being close to transition at ejection means a strong dependence of the momentum with respect to the RF frequency. To lower the energy spread at ejection the RF voltage is reduced.

One supercycle of 19.2 s is being used with 4 ion batches. As had been anticipated, the leptons (due to their synchrotron radiation) degrade the PS vacuum and hence the ion transmission.

The stripper

The problems with the stripper behind the PS had been underestimated. The construction of it is fairly complicated because the SPS has not only to work for the ions but also as injector for LEP, i.e. the stripper has to move in and out of the beam on a pulse to pulse basis ("ppm"). To avoid bellows, a magnetic coupling mechanism had been chosen. The physics of the stripper, however, was considered as trivial in view of the very high energy of the ions, although special machine development sessions had been foreseen but were lost due to other priorities. Detailed calculations ([11] and in particular [12]) were made and showed two essential facts: energy straggling is negligible and the choice of the stripper material (Al, Cu or Au) is not important; however, its thickness matters very much in terms of transverse emittance blow-up. For fine tuning, the material maybe of some importance. Experimental verification has been difficult, as it seems we have a large emittance blow-up (or mismatch?) in the transfer line towards the SPS independent of the stripper. In fact this blow-up is there also for Pb^{53+} and even for similar proton beams. The homogeneity of the stripper is of course a very significant parameter. With the present choice of 0.5 mm Al, the transverse blow-up is negligible but the stripping efficiency is below 100%, perhaps around 90 %.

The Super Proton Synchrotron (SPS)

The SPS has to deal only with fully stripped ions at high energy and hence does not have any vacuum problems. However, the difficulty of low intensity and even of low velocity remains [13]. The low velocity (β=0.984) does not allow normal acceleration with the SPS travelling-wave cavities. Their frequency swing is not large enough: They can cope with only 0.9 MHz (in 200 MHz); 3.2 MHz

is needed for the lead ions. Their short filling time and the fact that the four PS batches do not fill the whole circumference makes it possible to re-phase the cavities for each batch and each revolution [14]. Thus not only acceleration is possible but at injection batches can be trapped while still waiting for the next ones to arrive from the PS.

Instrumentation

Substantial up-grading of the beam instrumentation has been necessary. Contrary to the situation, for oxygen and sulphur ions, it is now possible to perform closed-orbit measurements with pick-up stations (300 units!) equipped with new high sensitivity preamplifiers. New instrumentation was also integrated into the beam transfer lines to the experiments. The number of FISCs (filament scintillation counters) was increased from 40 to 80. This change (finished in this year's shutdown) became necessary because the normally used SEM grids would spoil the beam quality too much.

Beam performance

Setting-up of the machine has been hampered by the loss of all "long" MD-sessions due to problems with the 400 kV mains and the vacuum. A further boundary condition was the parallel running of LEP, which uses the SPS as injector. Due to the emittance problem mentioned above there were no ideal conditions for high efficiency injection. In addition the 0.5 mm stripper does not give the optimum performance in terms of stripping efficiency.

The intensities achieved per SPS super cycle are compared in Table 2 with the estimated [1]values:

	energy	estimated	achieved
Linac out	4.2 MeV/u	$3.7 \cdot 10^9$	$4.2 \cdot 10^9$
PSB (accel.)	94 MeV/u	$8.9 \cdot 10^8$	$1.2 \cdot 10^9$
PS (accel.)	4.25 GeV/u	$5.9 \cdot 10^8$	$7.5 \cdot 10^8$
SPS (accel.)	160 GeV/u	$3.9 \cdot 10^8$	$2.7 \cdot 10^8$

Table 2: Intensities in ions per SPS super cycle and energy of the accelerators.

The original request from the heavy ion physics community was $5 \cdot 10^7$ ions / supercycle, hence, for the time being, most of our clients are satisfied.

IV. POSSIBLE IMPROVEMENTS

In spite of these excellent results it is very likely that future experiments will require higher intensities. This is in particular true for the LHC (Large Hadron Collider) where lead ions will be accelerated to a few TeV/u. Various possibilities are open to satisfy prospective clients.

Intensity improvements on the source, which are possible, will reflect proportionally on the final intensities. Additional improvements in the vacuum pressure in the PS and especially in the PSB, both done in the 1995 annual shutdown, will also increase the performance. Study of the emittance blow-up or mismatch in the PS - SPS transfer line is of high priority.

For the LHC several means have been studied [15,16] to achieve the required luminosities. The most promising scheme is a faster (10 Hz) repetition rate of the Linac and injection into LEAR (Low Energy Antiproton Ring). Accumulation of several pulses and electron cooling would provide for the intensities and emittances needed for the LHC.

A first electron cooling test with Pb^{53+} ions was performed in LEAR in December 1994 [17]. The test showed, that cooling time constants (1/e) of 50 ms for the momentum and of 300 ms for the transverse emittances can already be reached with the present state of the cooler. However the lifetime of the ion beam decreased to values of 2 s in the presence of an electron beam of 0.4 A. This effect has to be carefully studied in further tests at LEAR and at other cooling rings. The dependence on the charge state of the ion and on the magnetic field of the cooler is of importance in the search of conditions for a lifetime longer than the stacking time of 2 to 3 seconds.

Another possibility, depending on ion source development [18,19], is a high current, short pulse, source (EBIS or Laser source) that could provide the necessary intensity and keep the required low emittance by monoturn injection into the PSB. Work in this field is going on in some labs, e.g. BNL (EBIS) and CERN (Laser source, in collaboration with ITEP and TRINITI).

V. CONCLUSION AND ACKNOWLEDGMENTS

It has been demonstrated that proton machines can be efficiently up-graded for operation with ions, and that a large collaboration of several labs from different countries can not only build experiments, but also accelerators, which are supposed to have a longer life and must be integrated into the existing "accelerator environment".

It is a pleasure to acknowledge the substantial help given to this project by our friends from the collaborating institutions. Their enthusiasm was essential for our success. Thanks are of course also due to the CERN people in the different groups of the PS division, but also from the SL, AT, MT, ST and TIS divisions.

Special thanks go to several of my colleagues in PS and SPS for supplying material for this paper.

VI. REFERENCES

[1] N. Angert, M. P. Bourgarel, E. Brouzet, R. Cappi, D. Dekkers, J. Evans, G. Gelato, H. Haseroth, C. E. Hill, G. Hutter, J. Knott, H. Kugler, A. Lombardi, H. Lustig, E. Malwitz, F. Nitsch, G. Parisi, A. Pisent, U. Raich, U. Ratzinger, L. Riccati, A. Schempp, K. Schindl, H. Schönauer, P. Têtu, H. H. Umstätter, M. van Rooij, D. Warner (Ed.), M. Weiss, CERN Heavy Ion Facility Design Report, CERN 93-01.

[2] R. Billinge, E. Boltezar, D. Boussard, E. Brouzet, R. Cappi, B. de Raad, N. Doble, P. Grafström, H. Haseroth (Ed.), C.E. Hill, K.H. Kissler, J. Knott, T. Linnecar, F. Nitsch, A. Poncet, U. Raich, N. Rasmussen, H. Schönauer, T.R. Sherwood, N. Siegel, U. Tallgren, P. Têtu, D. Warner, M. Weiss, "Concept for a lead-ion accelerating facility at CERN", CERN/PS 88-67 (DL) 1988 and CERN 90-01.

[3] N. Angert, R. Caylor, R.A. Gough, H. Haseroth, C.E. Hill, D. Howard, J. Klabunde, B. Langenbeck, K. Leible, R. MacGill, P. Spädtke, J. Staples, J. Tanabe, P. Têtu, M. Weiss, B.H. Wolf, "Ion acceleration in the CERN Linac 1", Lin. Acc. Conf., Stanford , Calif., 1986 (SLAC-Report-303, Stanford, Calif., 1986), p. 355.

[4] N. Angert, E. Brouzet, R. Garoby, S. Hancock, H. Haseroth, C.E. Hill, K. Schindl, P. Têtu, "Accelerating and separating mixed beams of ions with similar charge to mass ratio in the CERN PS complex", Proc. Europ. Particle Acc. Conf., Rome, 1988, Ed. S. Tazzari (World Scientific, Singapore, 1988), vol. 2, p. 1367.

[5] H. Haseroth, "The CERN Heavy Ion Facility", Proc. of the Fourth European Particle Acc. Conf., EPAC94, London.

[6] D. J. Warner, "The Heavy Ion Linac for the CERN Lead Ion Facility", Proc. of the 1994 International Linac Conf., Tsukuba.

[7] N. Angert, W. Bleuel, H. Gaiser, G. Hutter, E. Malwitz, R. Popescu, M. Rau, U. Ratzinger, Y. Bylinski, H. Haseroth, H. Kugler, R. Scrivens, E. Tanke, D. Warner, "The IH Linac of the CERN Lead Injector", LINAC94, Tsukuba.

[8] M. Crescenti, U. Raich, "A Single Pulse Beam Emittance Measurement for the CERN Heavy Ion Linac", to be published in the Proc. of the Second European Workshop on Beam Diagnostics and Instrumentation for Particle Accelerators, DESY 1995.

[9] M. van Rooij, J-P. Bertuzzi, M. Brouet, A. Burlet, C. Burnside, R. Gavaggio, L. Petty, A. Poncet, "The Vaccum Upgrade of the CERN PS and PS Booster, this conference.

[10] H. Schönauer, F. Blas, P. Bossard, R. Cappi, G. Cyvoct, R. Garoby, G. Gelato, H. Haseroth, E. Jensen, D. Manglunki, K. Metzmacher, F. Pedersen, N. Rasmussen, K. Schindl, G. C. Schneider, M. van Rooij, L. Sermeus, M. Thivent, F. Völker, E. Wildner, "Acceleration of Lead Ions in the CERN PS Booster and the CERN PS", this conference.

[11] R. Cappi, D. Manglunki, B. Vandorpe, "Preliminary Results of Pb^{53+} Total Stripping at 5.2 GeV/u", CERN, PS/PA Note 95-01, 1995.

[12] C. Scheidenberger, H. Geissel, H. Mikkelsen, F. Nickel, T. Brohm, H. Folger, H. Irnich, A. Magel, M. F. Mohar, G. Münzenberg, M. Pfützner, E. Roeckl, I. Schall, D. Schardt, K. H. Schmidt, W. Schwab, M. Steiner, Th. Stöhlker, K. Sümmerer, D. J. Vieira, B. Voss, M. Weber, "Direct Observation of Systematic Deviations from the Bethe Stopping Theory for Relativistic Heavy Ions", Phys. Rev. Lett., Vol. 73, 1, 50, 1994.

[13] A. Faugier, X. Altuna, R. Bailey, R. Blanchard, T. Bohl, E. Brouzet, H. Burkhardt, P. Collier, K. Cornelis, G. de Rijk, F. Ferrioli, A. Hilaire, M. Lamont, T. Linnecar, M. Jonker, C. Niquille, G. Roy, H. Schmickler, "The SPS as Accelerator of Pb^{82+} Ions", this conference.

[14] D. Boussard, T. Bohl, T. Linnecar, U. Wehrle, "Non Integer Harmonic Number Acceleration of Lead Ions in the CERN SPS", this conference.

[15] D. Brandt, E. Brouzet, R. Cappi, J. Gareyte, R. Garoby, H. Haseroth, P. Lefèvre, S. Maury, D. Möhl, F. Pedersen, K. Schindl, T.R. Sherwood, L. Thorndal, D. Warner, "High Intensity Options for the CERN Heavy Ion Programme", Proc. of the 2nd European Particle Acc. Conf., Nice 1990, vol. 1, p.49.

[16] P. Lefèvre, D Möhl, "Lead Ion Accumulation Scheme for LEAR", Workshop on Beam Cooling and Related Topics, Montreux, Switzerland, 1993

[17] S. Baird, J. Bosser, M. Chanel, J. Duran, R. Giannini, P Lefèvre, R. Ley, R. Maccaferri, S. Maury, I. Meskov, D. Möhl, G. Molinari, F. Motsch, H. Mulder, U. Öftiger, J. Perrier, E. Roux, G. Tranquille, F. Varenne, "First electron Cooling Test with PB53+ Ions", CERN PS/AR/Note 95-6, 1995

[18] H. Haseroth, K. Prelec, "Possible Applications of an EBIS in Preinjectors for Large Heavy Ion Colliders", 6th Intern. Symp. Electron Beam Ion Sources and their Applications, Stockholm, June 20 - 23, 1994.

[19] T. R. Sherwood, "Laser Ion Sources for High Energy Particle Accelerators", Proceedings of the 12th Intern. Conf. on Laser Interaction and Related Plasma Phenomena, Osaka, 1995.

UNK STATUS AND PLANS

G. Gurov, Institute for High Energy Physics, Protvino, Moscow Region, Russian Federation

The 3000 GeV proton Accelerating and Storage Complex (UNK) is now under construction at the Institute for High Energy Physics (IHEP), Protvino. 2.7-kilometer UNK Beam Transfer Line was commissioned with a 65 GeV proton beam during March, 1994. An overview of the project's status is given, and the construction progress is reported.

I. INTRODUCTION

Started in 1983, the original project of IHEP Accelerating and Storage Complex (UNK) implied, in its final design, construction of two accelerators in a tunnel of 21 km in circumference [1]. First, a conventional magnet synchrotron (UNK-1) to receive protons from the existing 70 GeV synchrotron (U-70) and accelerate the beam from 70 to 400 GeV. Second, a superconducting accelerator storage ring (UNK-2) to accelerate the beam to 3 TeV. Finally, these 3 TeV protons could collide with 400 GeV protons from the UNK-1, thus aiming at a collider physics with 2.2 TeV energies in the center-of-mass.

In an initial phase of operation, the approved laboratory program gives priority to a 3 TeV fixed target physics. To provide this mode of operation, 3 TeV accelerator option of UNK has been designed. It includes 400 GeV "warm" magnet ring (UNK-1) and a 3 TeV superconducting ring (UNK-2) [2].

Unfortunately, due to financial problems, the 3 TeV UNK-2 superconducting ring construction has been delayed. In January 1993, the Scientific Programme Committee of the Russian National Scientific Programme "High Energy Physics" took a decision to focus efforts on the earliest possible commissioning and running in of the conventional accelerator (UNK-1) which can be run up to 600 GeV for a fixed-target physics, the superconducting programme being kept atR&D level.

In spite of the constrained budget, the fabrication of the 600 GeV accelerator equipment (magnets, vacuum system, beam diagnostics, instrumentation, computer controls etc.) continues slowly but steadily. During March, 1994 the first milestone in the UNK programme has been reached - the commissioning of the new 2.7-kilometer UNK Beam Transfer Line (BTL) with a proton beam [3].

II. BASIC CHARACTERISTICS

Originally, UNK-1 was designed as a slow booster for the UNK-2, the superconducting ring. Certain changes have been introduced during the last years into the design of the first stage of UNK (which is now referred to as UNK-600) in order to ensure its operation both, as a storage ring at 400 GeV and as an accelerator at 600 GeV. The storage ring option will be used

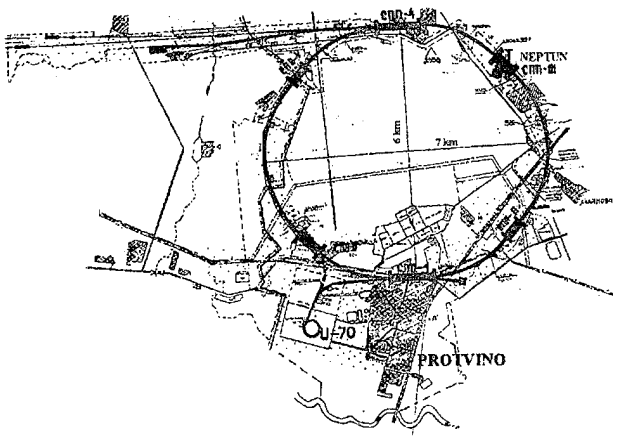


Figure 1: Ring layout.

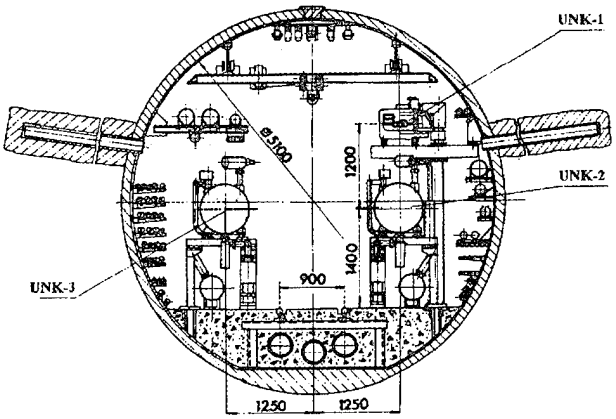


Figure 2: Tunnel cross-section.

for colliding of the circulating beam with an internal jet target placed in Straight Section 3 - experiment "NEPTUN" [4]. The accelerator option will be run for an external fixed target physics at 600 GeV.

During the injection 72 s flatbottom, the UNK-600 orbit will be filled consecutively with 12 beam pulses of the presently existing 70 GeV proton accelerator which will be operated as an injector into the UNK. The maximal intensity to be stacked can be as large as 6×10^{14} protons. On stacking, the beam will be accelerated in UNK-600 up to 600 GeV. The field rise time is 20 s, the extraction flattop is 20 s. The possibility of a slow resonant extraction with uniform spill over a period of 1 to 20 s, a fast resonant extraction in the range of 1 to 3 ms and a single-

0-7803-3053-6/96/$5.00 ©1996 IEEE

turn extraction are planned. The total cycle length is 120 s, the mean beam intensity is 5×10^{12} pps.

The accelerator ring will be installed on top in an underground tunnel of 5.1 m in diameter and 20.77 km in circumference. Fig.1 shows the ring layout and the extracted beam areas for a fixed target physics. Fig.2 shows the equipment installed inside the tunnel.

Specifications of the UNK-600 is given in Table 1.

Table 1. UNK-600 specifications.

Peak energy, GeV	600
Injection energy, GeV	65
Orbit length, m	20771.9
Maximum field, T	1
Injection field, T	0.108
Acceleration time, s	20
Flattop time, s	20
Total cycle duration, s	120
Harmonic number	13860
RF frequency, MHz	200
Peak RF voltage, MV	7
Transition energy, GeV	42
Beam intensity	$6 \cdot 10^{14}$
Average beam current, A	1.4

The space left in the main ring tunnel and surface buildings, power of the substations and the infrastructure available make it possible to consider as a long-term perspective the development of a collider version of the accelerator complex in which 3 TeV protons would collide with 400 GeV protons from the booster ring, and construction, in future, of a second 3 TeV superconducting ring (UNK-3) with a view to arrange 3×3 TeV colliding beams.

III. CONSTRUCTION OF UNK-600

A. Beam Transfer Line

The 2.7-kilometer UNK Beam Transfer Line (BTL) will eventually transfer beam from the U-70 to the UNK-600 (fig.3). BTL was designed for proton energies between 60 and 70 GeV, momentum spread 2×10^{-3} and beam emittance 2 mm.mrad. The U-70 fast ejecton system for BTL includes a full aperture kicker, two septum magnets and a bump system for closed orbit distortion. The BTL consists of a matching section for adjusting the beam to a bend section, a 64-degree bend section and a second matching section to adjust the beam parameters to the UNK lattice. The considerable distance between the UNK ring and U-70 injector is a result of the geological conditions on the IHEP site.

The BTL lattice has a strong focusing FODO structure with 88 quadrupoles, 52 dipoles and 56 corrector magnets. The UNK orbit plane is 6 m below then that of U-70. Beam diagnostics

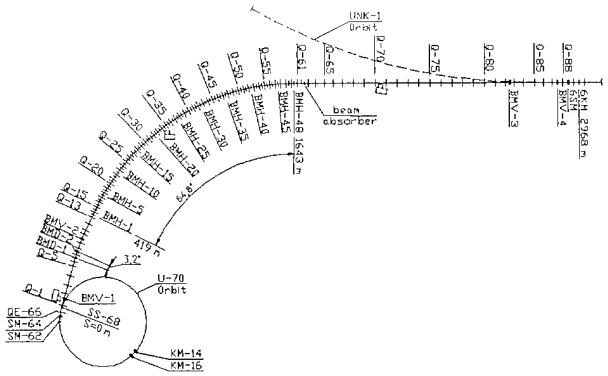


Figure 3: Beam transfer line.

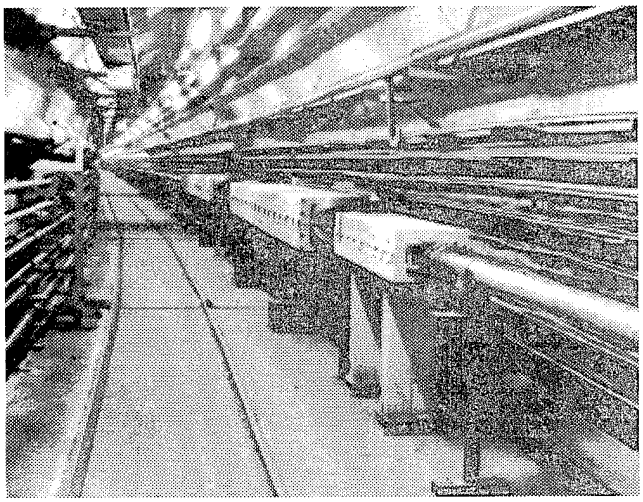


Figure 4: Beam transfer line tunnel.

include beam current monitors, 46 beam position monitors, 26 profile monitors, loss and halo monitors. The final U-70 radiofrequency is 6 MHz, while a 200 MHz accelerating system will be used for UNK. A recapturing station is installed in U-70 to match the extracted beam with the longitudinal phase space of the UNK [6].

The first BTL beam test was successfully carried out on 14 March 1994. A small fraction of normal U-70 beam intensity (5 bunches of 30) was accelerated to 65 GeV and recaptured by the U-70 200 MHz system with some further acceleration. Then U-70 beam was ejected and transferred to the BTL (fig.4). Using corrector magnets and adjusting the bending magnet current, the beam was negotiated through the BTL to a beam stop two kilometers from the ejection point. The beam size was in a good agreement with calculations.

A temporary PC-based control system was implemented for BTL commissioning, with four console computers and equipment controllers connected to the console via serial communication lines and line multiplexers. Magnet power supplies used more then 50 homemade equipment controllers. Beam instrumentation electronics was implemented in CAMAC with Intel auxiliary crate controllers inside.

At the same time a prototype UNK control system, developed in collaboration with CERN, was successfully tested. The system consists of an ULTRIX DEC station and a diskless front-end computer linked through MIL-1553 with equipment controllers. Good operational reliability and perfect flexibility in interface design were demonstrated [5].

B. Ring tunnel

The UNK tunnel shown in Fig.1 is completely excavated. The underground halls designed for the installation of the "NEPTUN" experimental facility and the extraction system equipment are under construction. Two sections of the main tunnel comprising about 1/4 of the ring are nearly finished (with utilities), in preparation for installation and testing of a section of UNK-600 with several hundred magnets. Construction of twenty surface buildings, surrounding the access shafts, now about 1/4 complete, but it is significantly behind schedule and work has nearly stopped because of the very constrained budget of the institute.

C. The equipment for UNK-600

Table 2 shows the current status with the production of the equipment for UNK-600. About 70% of the equipment has already been delivered to IHEP, but due to present financial difficulties further purchase of equipment has nearly ceased.

Table 2. UNK-600 equipment. April 1995

Equipment	Total Required	Available
Dipoles	2226	1500
Quadrupoles	522	522
Correctors	1180	1180
Main power converters	25	13
RF cavities	16	50%
RF power converters	8	8
RF amplifiers	8	3
Vacuum chamber	23.7 km	17 km
Beam pos. monitors	550	150

All the magnets meet the field quality requirements of UNK. These magnets will be tested, preassembled together with vacuum chambers, beam monitors etc. in modular units before being brought into the tunnel for fast installation (fig.5).

The 17 km vacuum chambers for the regular lattice cell with all the auxiliary vacuum equipment (ion getter and turbo pumps, gate valves, power supplies, vacuum measurement systems etc.) have been delivered. Preinstallation assembly and tests of the vacuum chambers are going on at test facilities. An entire period of the regular cell of the vacuum chamber has been tested. The 2×10^{-9} torr vacuum satisfying the requirements even of the collider mode was attained by applying a special technique of treating the chamber with an argon discharge without preliminary baking.

The RF accelerating system consists of 8 independent units. Each unit includes a doublet of cavities coupled by a quadrature hybrid and RF power amplifier located in a ground-level building. Each RF power amplifier delivers 800 KW RF power in CW operation by means four 250 kW power tetrode tubes coupled by hybrid junctions. All power supplies for RF system and 3 of 8 power amplifiers have been delivered from industry. The waveguides and accelerating cavities are manufactured at IHEP. About 50% of the waveguides and cavities components have been manufactured. One accelerating module of this type has been installed at U-70 in order to be used for rebunching the U-70 beam to the frequency of the UNK accelerating field [6].

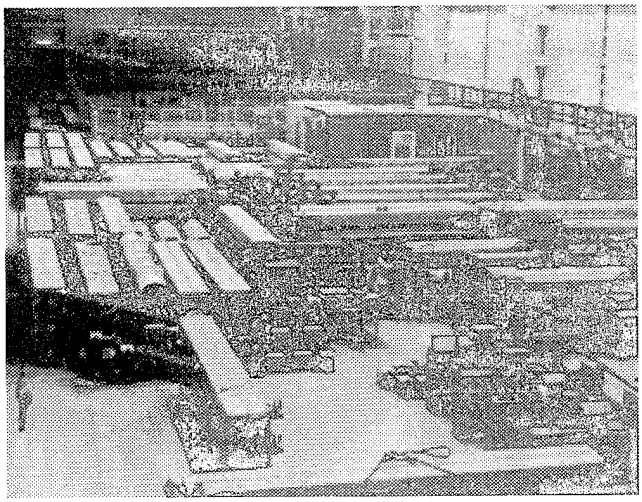


Figure 5: UNK-600 dipoles stored in the test facility building.

A half of the power supply units for the main ring magnet has been delivered. One of them is used to power the bending magnets of the Beam Transfer Line. The tests showed that the power supply requirements have been met.

A large number of relatively low-voltage power supplies for the correction magnets have been ordered from industry. The prototypes of commercial power supplies are undergoing tests and the requirements for their parameters are specified.

IV. THE DEVELOPMENT OF THE SUPERCONDUCTING PROGRAMME

The major elements of UNK-2 are the 2192 superconducting dipoles and 474 superconducting quadrupoles. The design of these magnets is complete [7],[8]. The dipole is a two-layer cold iron design with 80 mm bore. At the design field of 5.1 T the current is 5100 A which is quite conservative since the prototype models reach plateau values of between 6000 and 6400 A at 4.4 K. A pre-production batch of 25 prototype dipoles has been completed and tested and meets specifications [9]. The study performed shows that the magnets do "remember" the training after warmup and cooldown cycles. This ensures the required reserve for reliable operation of the UNK.

The detailed measurements of the field properties of the preserial batch dipoles were made. The results of this analysis show that the field quality is acceptable.

A full-scale SC quadrupole prototype has been manufactured and tested [8]. The first quench current level 6750 A was

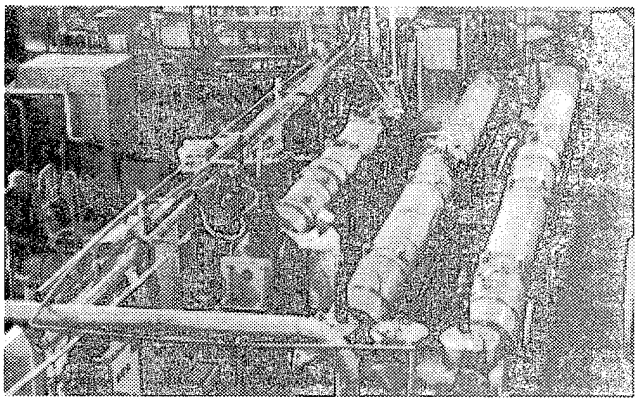


Figure 6: String of UNK SC dipoles.

attained, which is much higher than the maximum operating one in the UNK. The field measurements showed that the normal and skew nonlinearities were within the tolerances.

A large area of the magnet factory has been prepared for mass production of superconducting magnets. All magnets are to be cold tested, measured and trained. The testing facilities are designed to handle this. However, due to decision to cut short the superconducting program at R&D level this work has been brought to stop.

At present, the R&D SC programme is mainly aimed at the study the quench process in the string UNK SC dipoles [1] (fig.6). The programme includes the study of quench origin in some SC elements of the string, energy dissipation, temperature and pressure distribution during the quench, as well as test of prototypes of quench protection system [11]. A new type of quench detector based on magnetic modulator was tested with good results [12].

The first string tests demonstrated a good operation of UNK SC dipoles assembled in two quench protection units. Parameters of quench protection elements (quench stopper, safety leads, quench bypass switches) correspond to the requirements. The description of the string and new test results are presented elsewhere at this Conference [13].

V. UPGRADING U-70

The existing accelerator complex at Protvino consists of a 30 MeV linac, a 1.5 GeV fast cycling booster and a 70 GeV proton synchrotron. The beam produced by U-70 in its present status has a current, longitudinal and transverse emittances which do not satisfy completely the UNK requirements. Therefore, the program of upgrading U-70 has been initiated [14]. It involves extensive modification and up-grade of the 25-year old U-70 accelerator. These modifications include:

- Replacing the corrugated vacuum chamber with a smooth chamber to reduce impedance from 100–200 Ohms to 10 Ohms,
- Upgrading the correction system, including replacing all pole-face windings on magnets,
- Increasing the linac energy from 30 to 60 MeV,
- Constructing a new 20 mA H^- source,
- Replacing the main ring magnet power supply,
- Upgrading the RF system.

These modifications are presently in progress, 1/4 of the vacuum chamber has already been replaced.

VI. CONCLUSIONS

In this brief report the UNK status have been summarized. At the moment, second milestone is to complete the first section of the main ring. The most essential problem now is funding. In case of a sufficient funding (say, at the 1991 level), installation of the UNK-600 could be finished in 1998.

VII. REFERENCES

[1] V.I. Balbekov et al., Proceed. of 12th Intern. Conf. on High Energy Accel., Batavia, 1983, p.40.

[2] K.P. Myznikov, Proceed. of 13th Russian Conf. on High Energy Accel., 1993, V.1, p. 43.

[3] A.I. Ageev et al., Proceed. of the 4th EPAC, 1994, V.3, p. 2426.

[4] V.L. Solovianov, Proceed. of Workshop on the Experimental Program at the UNK (Sept. 14-19,1987), Protvino, 1989, p. 191.

[5] V.T. Baranov et.al., "Beam diagnostics of the UNK Beam Transfer Line", 14th Russian Conf. on High Energy Accel., Protvino, 1994.

[6] O.V. Bujanov et al., Proceed. of 11th Russian Conf. on High Energy Accel., Dubna, 1989, V.1, p.211.

[7] A.I. Ageev et al., Proceed. of the 11 Intern. Conf. on Magnet Technology (MT-11), Tsukuba, Japan, 1989, V.1, p.111.

[8] N.I. Andreev et al., Proceed. of the 4th EPAC, 1994, V.3, p.2280.

[9] A.I. Ageev et al., Proceed. of the 3rd EPAC, 1992, V.2, p.1411.

[10] A. Alexandrov et al., Proceed. of the 4th EPAC, 1994, V.3, p.2313.

[11] O.V. Afanasiev et al., Supercollider 4, Plenum Press, N.Y., 1992, p.867.

[12] I.M. Bolotin et al., Supercollider 4, Plenum Press, N.Y., 1992, p881.

[13] A. Alexandrov et al., "Investigation of the string of UNK superconducting magnets", This conference.

[14] E.A. Myae et al., "Status of 70 GeV accelerating complex IHEP", 14th Russian Conf. on High Energy Accel., Protvino, 1994.

REDUCTION OF PARTICLE LOSSES IN HERA BY GENERATING AN ADDITIONAL HARMONIC TUNE MODULATION

O.S. Brüning *, F. Willeke
Deutsches Elektronen-Synchrotron DESY, Notkestr. 85, 22603 Hamburg, Germany

Abstract

The combined effect of non-linear fields and a tune modulation with fast and slow frequency components results in an enhanced emittance growth and increased loss rate in hadron storage rings. In the proton storage ring of HERA, a fast harmonic tune modulation is caused by ripples in the power supplies and a slow tune modulation by the ground motion in the HERA tunnel. The recognition of the damaging effect of fast tune modulation frequencies on the particle dynamics initiated attempts to compensate for the fast frequency components in HERA. The fast tune modulation frequencies in the proton beam can be measured with a phase-locked-loop and the compensation can be established by generating an additional external tune modulation with the same frequency but with a 180^o phase difference. The following work summarizes the results of recent experiments in the proton storage ring of HERA where the generation of an additional tune modulation led to a significant reduction of the proton loss rate during luminosity operation.

I. INTRODUCTION

During luminosity operation, the beam-beam interaction in the lepton-hadron collider HERA is a source of strong non-linear fields. An additional tune modulation leads to resonance sidebands of the primary beam-beam resonances. For slow modulation frequencies ($f < 50Hz$), the modulation sidebands overlap and give rise to modulational diffusion [1]. For the beam-beam interaction in HERA, the modulational diffusion primarily affects the particles in the beam halo and results in particle loss and increased background rates in the experiments [2]. In order to avoid a modulational diffusion with strong resonances, the working point of the proton beam in HERA is located between the $7th$ and $10th$ order betatron resonance. Without tune modulation, the area between the 7^{th} and 10^{th} order resonances contains no low-order sum resonance lines [2]. Thus, one expects a sufficiently large beam lifetime for any working point between the 7^{th} and 10^{th} order resonances.

For fast modulation frequencies ($f > 50Hz$), the modulation sidebands do not overlap, but might reach the working point of the proton beam even if it is well inside the resonance free area between the 7^{th} and 10^{th} order resonances. The combined influence of such fast modulation sidebands and an additional slow tune modulation results again in modulation diffusion [2]. Thus, with slow and fast modulation frequencies it is virtually impossible to find a working point that does not lie near a non-linear resonance sideband. In HERA, a slow tune modulation is caused by the ground motion in the HERA tunnel and by the longitudinal synchrotron oscillation ($f_{syn.} \approx 30Hz$). The frequency spectrum of the ground motion reaches from $1Hz$ to $20Hz$ with modulation depths of the order of $\triangle Q \sim 10^{-5}$. A fast tune modulation is caused by ripples in the proton power supplies in HERA. All the superconducting main magnets of the HERA-p storage ring are connected in series. The current flows first clockwise from the power supply in Halle West through all the main dipole magnets and then counter-clockwise through all the main quadrupole magnets back to the power supplies. Thus, the first magnets of both chains see the same voltage ripples. Typical ripple frequencies are $50Hz$, $150Hz$, $300Hz$, $600Hz$ and $1200Hz$ and their harmonics and the resulting tune modulation depth is of the order of $\triangle Q \sim 10^{-4}$. The analysis in [2] showed that for the design values of the HERA beam-beam parameters even modulation depths as small as $\triangle Q = 10^{-4}$ result in a significant particle diffusion once the modulation sidebands reach the particle tune. Because the particle dynamics in hadron storage rings has virtually no damping, the resulting diffusion can spoil the long-term stability of the particles and might result in large loss rates [2]. A subsequent experiment in the proton storage ring of HERA confirmed this expectation [3].

II. COMPENSATION OF FAST MODULATION FREQUENCIES

Recognizing the damaging effect of a fast tune modulation due to power supply ripples, it is desirable to minimize either the ripple amplitudes at the power supplies or to actively compensate for the tune modulation in the storage ring by generating an additional external tune modulation with the same frequency spectrum as the tune modulation due to power supply ripples but with an 180^o phase difference. The first approach requires active filters for each power supply and is technically difficult and expensive. On the other hand, the second approach, a compensation of existing modulation frequencies by actively generating an additional tune modulation in the storage ring, requires only minor changes in the existing hardware and presents an interesting new method for improving the quality of the power supplies and improving the beam performance.

In HERA, an external tune modulation can be generated by modulating the current in two superconducting correction quadrupole families. This approach requires only a small modification of the chopper electronics in the proton power supplies and allows a modulation of regular quadrupole magnets in the lattice. In order to achieve a constant phase relationship of the generated signal and the power supply ripples, the modulation signal is triggered by a $50Hz$ signal from the power supplies.

The prerequisite for a compensation of the tune modulation due to power supply ripples is a monitor that allows the measurement of the existing tune modulation frequencies in the storage ring. In HERA, first attempts of a tune modulation compensa-

*e-mail: i02bru@ips102.desy.de

0-7803-3053-6/96/$5.00 ©1996 IEEE

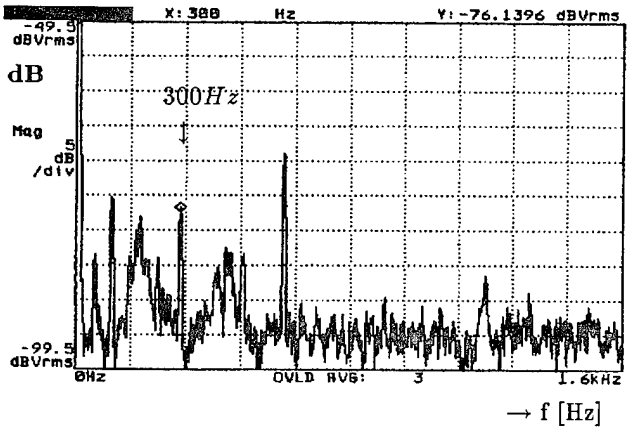


Figure 1. The horizontal phase-locked-loop spectrum at $820GeV$ without and additional external tune modulation.

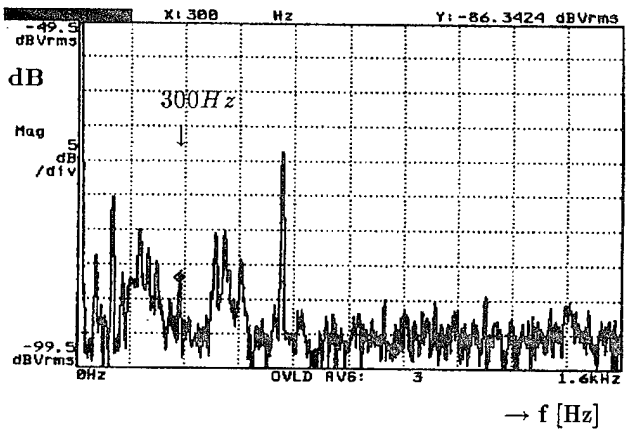


Figure 2. The horizontal phase-locked-loop spectrum at $820GeV$ with an additional tune modulation of $300Hz$ and $triangleQ \approx 10^{-4}$. The additional tune modulation compensates the $300Hz$ line of the original phase-locked-loop spectrum.

tion were made using the loss spectrum at the proton collimators as a monitor for the modulation frequencies in the storage ring [4]. However, even though it is possible to compensate individual frequency lines in the loss spectrum, the compensation does not result in a reduction of the total loss rate [4]. On the contrary, the compensation results in increased loss rates. The increase in the loss rate can be related to three characteristic aspects of the proton loss spectrum: First, the loss spectrum does not allow a distinction between modulation frequencies in the horizontal and vertical plane; Second, the loss spectrum does not allow a distinction between tune modulation, closed orbit motion, and beta-beats; and third, even a tune modulation with only one frequency component results in a whole spectrum of frequency lines in the loss spectrum [5]. Thus, the proton loss spectrum does not allow a reliable measurement of the existing tune modulation frequencies in the storage ring and can not be used as a monitor for the existing tune modulation in the storage ring.

However, the first compensation attempts with the proton loss spectrum illustrated two important aspects of the tune modulation in HERA and motivated further studies. First, the first experiments showed that a tune modulation with amplitudes as small as $\triangle Q \sim 10^{-4}$ does influence the proton loss rate as it is expected from the analytical analysis. And second, the results showed that the fast modulation frequencies in the loss spectrum are phase synchronous with the power supplies.

III. MEASURING THE TUNE MODULATION WITH A PHASE-LOCKED-LOOP

A new approach is to use a phase-locked-loop (PLL) for the measurement of the existing tune modulation in the storage ring. This results in a successful compensation of the individual frequency lines in the PLL spectrum and a substantial reduction in the total proton loss rate. In contrast to the proton loss spectrum, the spectrum of the PLL is neither sensitive to closed orbit motion nor to a modulation of the beam size. Furthermore, each tune modulation frequency leads to one unique frequency line in the PLL spectrum. The PLL consists of a transverse kicker and pickup in the storage ring and a voltage controlled oscillator (VCO). The signal from the beam pickup drives the frequency of the VCO and the signal from the VCO is connected to the transverse kicker. The PLL constantly measures the betatron frequency, adjusts the VCO frequency according to the measurement and excites the beam on the VCO frequency. Once the PLL locked on to the betatron frequency, the excitation amplitude in the kicker can be reduced to small values so that the excitation does not significantly dilute the beam profile. In HERA, the PLL was operated for one hour without measuring a noticeable effect on the transverse beam size.

The difference between the measured betatron frequency and the current oscillation frequency of the VCO provides a sensitive measurement of the fluctuations in the mean betatron frequency. Thus, a Fourier analysis of the difference signal is a measure of the existing tune modulation of the storage ring. Fig.1 shows the spectrum of the horizontal PLL without an additional external tune modulation. In order to compensate a frequency component in the spectrum the frequency line is first calibrated by generating an additional harmonic tune modulation with given amplitude. Once the modulation amplitudes of the frequency lines in the PLL spectrum are known, a compensation of the frequency lines can be achieved by generating an additional harmonic tune modulation with the same frequency and amplitude and varying the phase of the generated signal until the frequency line attains a minimum in the PLL spectrum. Fig.2 shows the corresponding PLL spectrum of Fig.1 for a successful compensation of the $300Hz$ line in the PLL spectrum.

IV. EXPERIMENTAL RESULTS

Fig.3 shows the proton loss rate at the main collimator during the compensation procedure as a function of time. The picture shows three different situations in the compensation process: Part 1, from 5.87 hours to 5.96 hours, shows the loss rate during the calibration of the $300Hz$ line in the PLL spectrum with an additional tune modulation of $320Hz$. As the amplitude of the $320Hz$ signal increases, the loss rate also increases. Once the amplitude of the $300Hz$ line is calibrated, the amplitude of the $320Hz$ signal is set to zero and the loss rate attains again its initial value of $1600Hz$ at 5.88 hours. The frequency of the external signal is now set to $300Hz$ and the phase of the

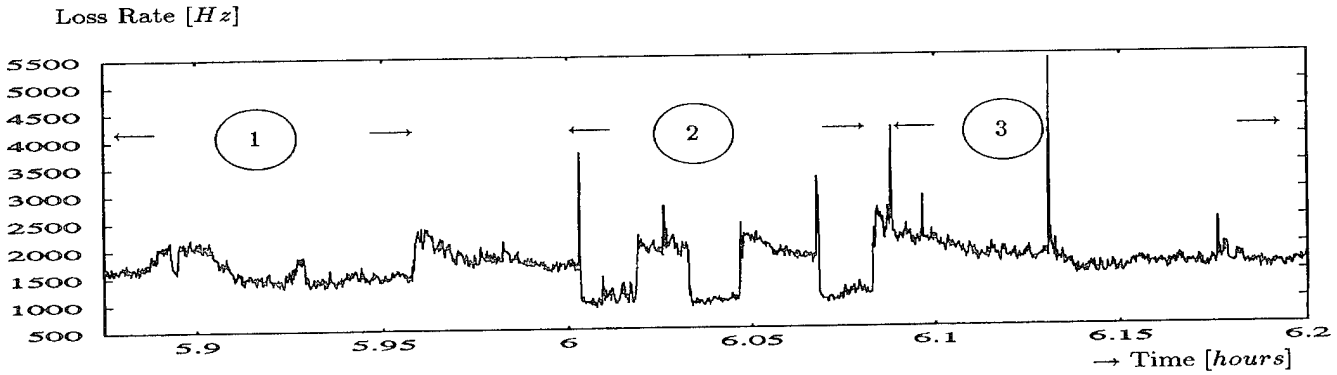


Figure 3. The proton loss rate at the main collimator jaw during the compensation procedure.

signal with respect to the $50Hz$ trigger signal of the power supplies is adjusted. First, the loss rate increases again once the external modulation is turned on and then slowly decreases with the changing phase of the external signal. The loss rate attains a minimum of $1400Hz$ at 5.925 hours when the $300Hz$ line in the PLL spectrum is compensated and increases again once the phase is further increased. At 5.93 hours the phase is set back to its optimum value and the loss rate attains again its minimum value of $1400Hz$. At 5.96 hours, the external modulation is turned off and the loss rate goes up again to its initial value of $1600Hz$.

In the second part, from 6.0 hours to 6.08 hours, a compensation of the horizontal $100Hz$ and $300Hz$ and the vertical $100Hz$ line is turned on and the loss rate drops from $1600Hz$ to $900Hz$. The compensation is then repeatedly turned on and off and the loss rate changes from approximately $1600Hz$ without compensation to $900Hz$ with the compensation on. In all cases, the compensation results in a reduction of the loss rate of approximately 40%.

In the third part, from 6.08 hours to 6.2 hours, the compensation is turned off and the loss rate increases and assymtotically reaches again its initial value of $1600Hz$.

V. SUMMARY

The presented work illustrates how the tune modulation due to power supply ripples can be compensated by generating an additional external tune modulation. First experiments in the proton storage ring of HERA showed that a compensation of the fast frequency components results in a substantial reduction of the proton loss rate during luminosity operation. The reduction in the loss rate is the better, the more frequency lines are compensated. So far, only three frequency lines of a total of approximately 10 dominant lines could be compensated simultaneously. The limitation to only three frequency lines is given by the maximum available modulation amplitude for the external signal and an increase of the total modulation amplitude is expected to allow an even better reduction of the proton loss rate.

By compensating only three frequency lines in the tune modulation spectrum of HERA-p, the proton loss rate could be reduced by almost 40%. This encouraging result led to the construction of a 'tune modulation feedback system', which is now ready to go and will be tested in the 1995 luminosity operation of HERA.

References

[1] B.V. Chiricov, M.A. Liebermann, D.L. Shepelyansky and F.M. Vivaldy, Physica **14D**, 289-04, (1985)

[2] O. Brüning (DESY), DESY 94-085, 1994

[3] O. Brüning, K.-H. Meß, M. Seidel, F. Willeke, DESY HERA 94-01 1994

[4] O. Brüning, F. Willeke (DESY), EPAC'94 London, 1994

[5] O. Brüning, (DESY), Proceedings, Workshop on 'Non Linear Dynamics in Particle Accelerators: Theory and Experiments', Arcidosso (September 1994)

ACCELERATION OF LEAD IONS IN THE CERN PS BOOSTER AND THE CERN PS

F. Blas, P. Bossard, R. Cappi, G. Cyvoct, R. Garoby, G. Gelato, H. Haseroth, E. Jensen, D. Manglunki, K. Metzmacher, F. Pedersen, N. Rasmussen, K. Schindl, G.C. Schneider, H. Schönauer, L. Sermeus, M. Thivent, M. van Rooij, F. Völker, E. Wildner, CERN, CH-1211 Geneva 23, Switzerland

I. INTRODUCTION, BASIC PARAMETERS

The new CERN Heavy-Ion Accelerating Facility [1] implies besides a new linac also important modifications of existing accelerators. They are imposed by the low speed and the low intensity of the ion beam and, crucially at low energy, by the short lifetime of the partially stripped ions due to charge exchange with the atoms of the residual gas.

Once the optimum charge state (Pb^{53+}) and energy of the injector (4.2 MeV/u) had been chosen [2], the operational pulse-to-pulse variability (PPM) of particle species and intensities in the PS and its four-ring Booster (PSB) dictate the main beam parameters (Table I).

Table I: Basic parameters of lead ion and proton beams

Parameter	$^{208}Pb^{53+}$	p
Injection PSB		
Kinetic Energy	4.2 MeV/u	50 MeV
β = v/c	0.0946	0.314
Bending Field B dB/dt	0.141 T 1.8 T/s	0.125 T 0.4 T/s
RF Harmonic Number	17	5
PSB Intermediate Flat		
Kinetic Energy	32.4 MeV/u	
β = v/c	0.257	
RF Harmonic Number	17 / 10	
Ejection flat top		
Kinetic Energy	95.4 MeV/u	1 GeV
RF Harmonic Number	10 / 5	5
Acceleration Time	288 ms	415 ms
PS Harmonic Number	20	20
PS Extraction		
Kinetic Energy	4.25 GeV/u	19.07 GeV
Acceleration Time	0.5 s	0.5 s

II. PSB INJECTION LINE AND INJECTION

The magnetic rigidity of the ion beam being 13% higher than the proton one, all elements of the injection line have to vary in PPM by this amount and keep their values over the 500 μs duration of the linac pulse. While most elements and their power supplies were able to do this with some minor upgrading, a dedicated pulsed staircase magnet (vertical distributor) had to be designed to switch the ion beam to the four Booster rings. The multi-turn injection kicker generators were upgraded to provide in PPM two different negative slopes. The steering of the ion beam through the line is monitored solely by scintillator screens, which had to be made operating in PPM to avoid interference with proton pulses.

III. VACUUM LIMITED LIFETIME AND RELATED HARDWARE UPGRADES

The partially stripped ions are subject to charge exchange processes with the residual gas. Empirical formulae derived from cross-section measurements [3] predicted unbearable loss at the existing PSB vacuum level of $2\ 10^{-8}$ mbar and suggested necessary nitrogen equivalent pressures of a few 10^{-9} mbar, yielding calculated lifetimes (cf. Figure 1 in [2]) of 60 ms at injection and 1.5 s at extraction, with a steep slope at low energies. Therefore the - unbakeable - vacuum system had to be improved. The possible measures were limited to adding 14 ion getter pumps and 40 Ti sublimation pumps in the PSB with the aim to lower the static pressure to $3.7\ 10^{-9}$ mbar ($5\ 10^{-9}$ mbar achieved). In the PS some 90 Ti sublimation pumps reduced the pressure from $5\ 10^{-8}$ to less than $5\ 10^{-9}$ mbar. Further improvements, including more refined instrumentation, are under study [4].

Even with this vacuum pressure, fastest possible acceleration is mandatory for an acceptable transmission in the Booster. The vacuum is less critical in the PS as lifetimes at $4\ 10^{-9}$ mbar are of the order of seconds. The PSB main power converter is now routinely operating with four rectifier groups instead of three to allow for higher induced voltages and dB/dt. Equally, the limitations of d^2B/dt^2 had to be raised in order to reach the dB/dt limit faster. A further, decisive, shortening of the critical low-energy phase is to inject and capture not on a flat bottom but at rather large dB/dt.

IV. PSB CAPTURE AND ACCELERATION CYCLE

Three distinct loss mechanisms prevail during RF capture and initial acceleration (Figure 1): (i) initial fast loss due to transverse scraping of the spiralling beam before being captured, (ii) loss of about 10% (τ_{ini} = 15 ms) due to particles not captured due to the lack of adiabaticity

0-7803-3053-6/96/$5.00 ©1996 IEEE

(k_a = 2.4) [5], and (iii) after 4 ms, slow loss (τ = 39 ms) due the vacuum limited lifetime at low energy. Given this lifetime and the constraints on dB/dt and d^2B/dt^2 from the main power converter, an optimum value for dB/dt at injection was found at 1.8 T/s .

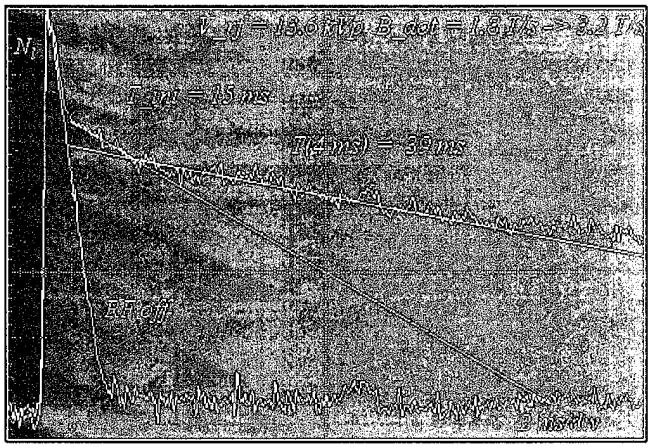


Figure 1: Beam current during horizontal multi-turn injection and capture in the PSB with and without RF.

Initial acceleration is with harmonic number 17. When the 8.3 MHz frequency limit is reached, an adiabatic debunching followed by an adiabatic rebunching with h = 10 takes place at an intermediate flat top followed by further acceleration to maximum energy (Figure 2). A second harmonic number change from 10 to 5 at the ejection flat top serves to facilitate bucket to bucket transfer to the h = 20 RF system of the PS.

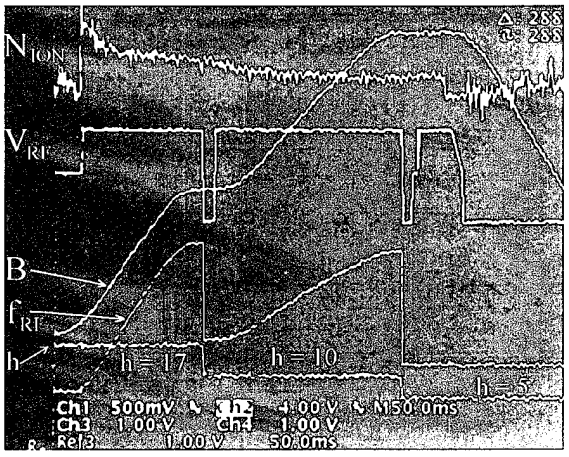


Figure 2: Acceleration in the PSB. From top to bottom: Ion intensity, RF voltage, main B field, RF frequency, harmonic number, vs. time

Four complete, new, digital beam control systems with digitally programmed acceleration frequency (smoothed by an AC-coupled beam phase loop) were built using the new standard modules recently developed for machines in the PS complex [6].

V. TRANSFER TO PS AND PS INJECTION

In order to eject and merge the slow ion beams from the four PSB rings sequentially into the PS, a total of 5 km of new, longer, high quality SF_6-filled PFN cables were installed for the corresponding seven fast kicker pulse generators. The main pulse switches were replaced by more powerful thyratrons to avoid pulse quenching. At PS injection, the double flat-top pulse length is obtained by pulsing two groups of kicker modules sequentially. The magnets of each group are short-circuited (in PPM) to double their strengths.

VI. ACCELERATION IN THE PS

To minimize the SPS filling time the PS cycle length was limited to 1.2 s. This resulted in a maximum energy of 4.25 GeV/u (γ=5.56), just below transition (γ_{tr}=6.12).

The beam control previously used for the acceleration of sulfur ions was upgraded to the new standard recently developed for machines in the PS complex [6]. After adjustment of RF capture and acceleration, about 25 % of the beam was still lost by stripping on the residual gas (Figure 3). These losses increase up to 30-40% when the ion cycle is preceded by a lepton cycle due to outgassing because of synchrotron radiation impact.

The energy stability of the extracted beam proved to be insufficient with the frequency programme alone because of the proximity of transition. A rudimentary radial loop was then assembled and guaranteed a maximum peak deviation $\Delta p/p = 1\ 10^{-4}$.

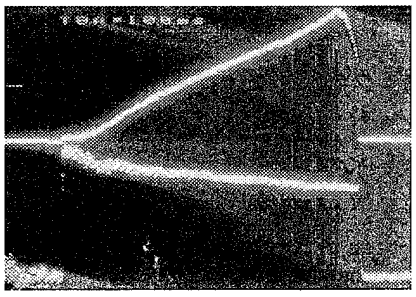


Figure 3: Acceleration in the PS (100 ms/div). Peak (top trace) and DC (bottom trace) beam current.

VII. FULL STRIPPING

Total ion stripping, from Pb^{53+} to Pb^{82+}, is performed with an Al foil situated in the PS–SPS transfer line. The foil is mounted on a mechanism which moves it into the beam only during the ion cycles. Three foil thicknesses were tested, and first preliminary results are shown in Table II.

Table II: Relative momentum loss, approximate stripping efficiency, measured and theoretical transverse emittance blow-up factors as a function of the stripper thickness.

Thick. [mm]	Rel. momentum loss	Stripping eff.	Meas'd B-up		Theor. B-up	
			HOR	VERT	HOR	VERT
0.5	$1.5\ 10^{-3}$	90%	2	3.3	1.2	1.3
1	$3.0\ 10^{-3}$	95%	2.3	4.2	1.5	2
2	$6.0\ 10^{-3}$	100%	2.6	4.7	1.9	2.5

Relative momentum losses and stripping efficiencies were in good agreement with theory [7, 8], but excessive emittance blow-ups (more than a factor two above the theoretical expectations) were measured. This seems to indicate a further optical problem, under investigation, in the transfer line.

VIII. BEAM DIAGNOSTICS

The six beam current transformers in the PSB injection line and the four DC ones in the rings were redesigned to cope (in PPM with high-intensity proton cycles) with the new low-intensity range. Pulse to pulse range switching is used in the injection line, auto-ranging in the rings. The new transformers use multi-layer shielding against external fields. The dynamic range of the PSB orbit measurement system has been extended to measure ion orbits. In the PS, the sensitivity of the wall current monitors has been increased.

Before and after the stripping foil in the PS–SPS beam line, two new identical transformers with a common calibrator help in the evaluation of the stripping efficiency.

IX. PERFORMANCES

Overall performances are summarized in Table III.

Table III: Ion intensities at various stages and characteristics of the extracted Pb^{53+} beam

Machine	Stage	Ions $\times 10^8$	Design$\times 10^8$
Linac3 Pb^{53+}	after stripper	10	9.25
PSB	injected	7.2	
	accelerated	3.0	2.22
PS	injected	2.8	
	accelerated	1.6	1.48

Extracted Beam after Stripping

Number of bunches	20
Intensity	1.5×10^8 ions/pulse
Bunch length	11 ns
Long. emittance	0.037 eVs/u
Momentum spread (2σ)	0.4×10^{-3}
Emittance (2σ), hor., vert.	1.5 μm, 0.6 μm

X. CONCLUSIONS

In the past the PS circular machines proved able to handle ions: deuterons and alphas in the seventies, oxygen and sulfur ions in the eighties. Lead ions, however, required a more substantial upgrading due to their much lower velocity and due to their sensitivity to the residual vacuum. Especially with the latter one is at the limit of what could be achieved at reasonable cost and within a short time. It can be noted that most of the predictions turned out to be fairly accurate, as shown by the successful acceleration of lead ions to more than design intensity in the CERN PS and its Booster.

XI. ACKNOWLEDGMENTS

We would like to thank C. Carter, S. Hancock, J. P. Terrier, J. L. Vallet, and the PS and PSB operation teams, in particular B. Vandorpe, for their efficient support during preparation and operation for physics.

XII. REFERENCES

[1] D. Warner ed., CERN Heavy Ion Facility Design Report CERN 93-01, April 1993.

[2] H. Haseroth, The CERN Heavy Ion Accelerating Facility, this Conference.

[3] B. Franzke, Vacuum Requirements for Heavy Ion Synchrotrons, IEEE Trans. Nucl. Sci. NS-28, 1981, p. 2116.

[4] M. van Rooij, J.-P. Bertuzzi, M. Brouet, A. Burlet, C. Burnside, R. Gavaggio, L. Petty, A. Poncet, The Vacuum Upgrade of the CERN PS and PS Booster, this Conference.

[5] F. Pedersen, N. Rasmussen, H. Schönauer, Fast Capture of Heavy Ions in the CERN PS Booster, Proc. 4th Europ. Part. Acc. Conf., London, June 1994, pp. 1225-1227.

[6] F. Blas, J. Boucheron, B.J. Evans, R. Garoby, G.C. Schneider, J.P. Terrier, J.L. Vallet, Digital Beam Controls for Synchrotrons and Storage Rings in the CERN PS Complex, ibid., pp. 1568-1570.

[7] U. Fano, Penetration of Protons, Alpha Particles and Mesons, Ann. Rev. Nucl. Sci. 13, (1963), p 1.

[8] P. Thieberger, H.E. Wegner, J. Alonso, H. Gould, C. Munger, R. Anholt, W.E. Meyerhof, Fully Stripped Heavy Ion Yields vs. Energy for Xe and Au Ions, IEEE Trans. on Nucl. Sci., Vol NS-32, No.5, October 1985, p. 1767.

Highly Efficient Deflection of the Divergent Beam by Bent Single Crystal

V.I. Baranov, V.M. Biryukov, A.P. Bugorsky, Yu.A. Chesnokov,
V.I. Kotov, M.V. Tarakanov, V.I. Terekhov, S.V. Tsarik
IHEP Protvino, 142284 Moscow Region, Russia.
O.L. Fedin, M.A. Gordeeva, M.P. Gur'yev, Yu.P. Platonov, A.I. Smirnov
PINP St. Petersburg, Russia

Abstract

We have investigated the proton beam deflection in the geometry where the first crystal formed a divergent beam and the second crystal shaped this beam into parallel one. In spite of the aberration influence a high bending efficiency was obtained.

I.

Nowadays the bent single crystals of silicon are applied for bending low-divergent (as compared to channeling angle $\theta_L \sim 0.02 \div 0.002$ mrad at 100 GeV – 10 TeV) high-energy particle beams [1]. The CERN experiment [2] has demonstrated that efficiency of bending proton beam of energy 450 GeV and divergence less than 3 μrad is up to $\sim$ 50%. In Ref. [3] a method was proposed for focusing a beam with a bent monocrystal in the plane of bending. The focusing (parallel to point) was due to the difference of the bending angles of crystal, the end face of which had a special shape. Another important application of a focusing crystal may be related to the reverse motion of particles – transformation of the beam diverging from a point-like source into a parallel. To do this, the crystal entry face must have a special shape. The problem of the focusing a divergent beam is typical for steering of the secondary particle beams, and in particular for their extraction from colliders.

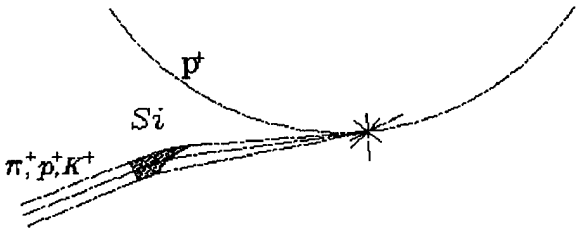


Figure. 1. The scheme of extraction of the secondary-particle beam from accelerator by the focusing crystal

To extract most of the secondary particles produced in the target situated in the vacuum chamber of accelerator (at the crystal focal point, see Fig. 1), certain conditions must be fulfilled. It is known that most of the produced secondaries exit in the angular range

$$\pm\theta = \frac{0.4\ \mathrm{GeV/c}}{P} \qquad (1)$$

where P is momentum. The acceptance of the focusing crystal is

$$\pm\varphi = \frac{H}{2F} \qquad (2)$$

where H is the crystal thickness, F focus distance, should be about $\pm\theta$.

High efficiency of particle trapping into channeling mode may be obtained, if the target size Δx in the bending plane is

$$\Delta x \leq 2\theta_L F \qquad (3)$$

Then the particles entering the crystal are aligned w.r.t. the crystal planes within θ_L, and the trapping efficiency η may be close to the theoretical limit $\sim$ 70%. In the realistic experiment the defects of the focusing device may lower η essentially.

The above conditions for the efficient extraction of secondary particles can be easily met at TeV energies. The estimates for LHC collider (energy of protons is 7 TeV) show that in this way one can extract the secondary particles with intensity of up to $\sim 10^8$/s.

The experimental investigation of the efficiency of capture and deflection of the beam diverging from a point-like source was made at the extracted 70 GeV proton beam of IHEP accelerator. The experimental scheme is in Fig. 2.

The crystal Si_1 (with usual flat faces) bent by 60 mrad was exposed to the 70 GeV proton beam of $10^{11}/s$ intensity, and bent the beam with moderate intensity $\sim 10^7/s$ toward the magnet-optics system $MQ - M$ where two other crystals were placed. The beam formed with the forward part of the magnet system was brought onto the crystal Si_2 which had the focusing end face. This crystal was 2 mm thick 15 mm high 70 mm long and 18 mrad bent. The crystal focused the beam at the distance of 0.5 m into a narrow vertical strip with the width $\simeq$ 80μm FWHM at the crossover and divergence $\pm$2 mrad. The beam formed in this way was used as a source of protons. In order to focus and deflect this divergent beam, the crystal Si_3 with focus distance 2.5 m was used. It had size 2 × 20 × 30 mm^3 and was bent by 6 mrad. (The first and second crystals had orientation (111), the third was cut along the (110) planes.) This crystal had the acceptance of $\varphi = \pm 0.4$ mrad. According to preliminary measurements, it gave for the parallel-to-point focusing the crossover size $\sim$ 200μm FWHM (ideal value is $\Delta x = 2\theta_L F = 125\mu$m). The crystals were aligned to the beam successively. Each of them had an independent goniometer.

The effect of focusing the beam from the divergent to parallel was detected by measuring the intensity of the beam deflected by the third crystal during when the latter was rotated around the vertical axis crossing its entry face. The intensity obtained in this angular scanning is shown in Fig. 3. The scan FWHM approaches to $2\theta_L$ ($\simeq 4\theta_L$ at the base), which attests a good qual-

0-7803-3053-6/96/$5.00 ©1996 IEEE

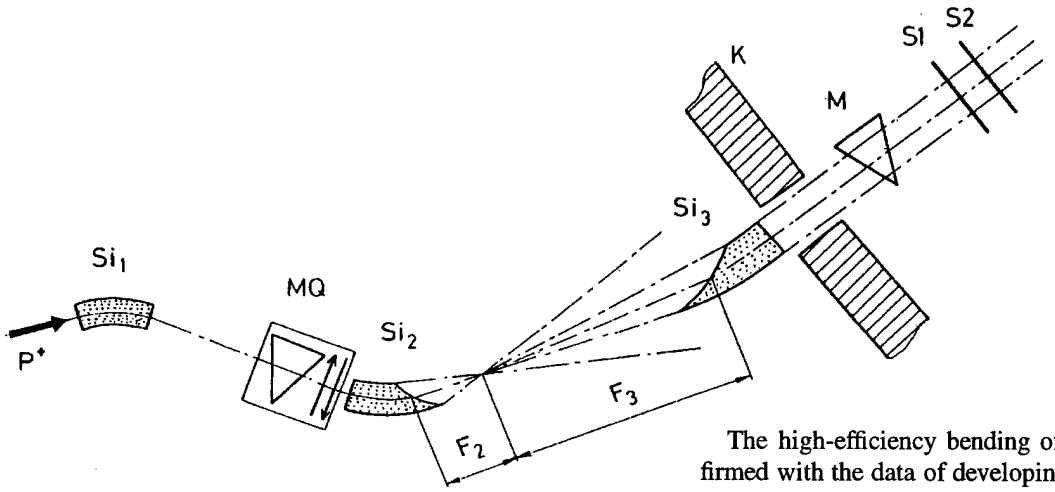


Figure. 2. The scheme of experiment

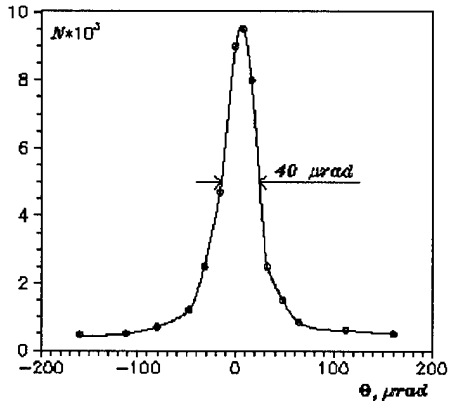


Figure. 3. Angular scan of intensity for the beam bent with the third crystal

ity of focusing. According to measurements with the remoted scintillation counters S1 and S2, crystal Si_3 at the best angle deflected $(15 \pm 2)\%$ of the protons incident on its face, which is factor of ~ 2 lower than the calculation for the ideal focusing.

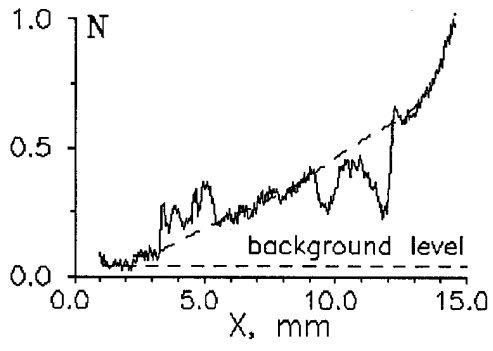


Figure. 4. Beam profile on the nuclear emulsion downstream the third crystal

The high-efficiency bending of the divergent beam is confirmed with the data of developing the beam profile on the nuclear emulsion, which was placed downstream the crystal Si_3 at its optimal alignment. This profile is shown in Fig. 4. The wide beam (excess over the background) corresponds to the divergent beam formed by crystal Si_2. The dip at the right is the shadow of the crystal Si_3, due to the capture of beam fraction in channeling mode. From the ratio of areas one can find that $\sim 30\%$ particles are trapped in channeling mode. On the left of the figure the contribution of particles bent by Si_3 is seen, superimposed on the broad profile of the beam divergent from the crystal Si_2. The bent-beam fraction, according to the figure, is 14% of incident particles. This well agrees with the measurements by scintillation counters. Reduction of the number of bent particles by the factor of 2.2, as compared to the particles trapped in the channeling mode, is explained by dechanneling. It is also seen from the figure, that efficiency of particle bending is not uniform over the crystal thickness (at the edges it is higher than in the middle). Apparently, this is due to defects of crystal Si_3. For focusing the beam with this crystal from parallel to point, there was observed a characteristic split of the beam profile some distance downstream the crossover, similar to the profiles of Fig. 4. Above $\sim$ 500 GeV and for the same crystal size, the fraction of the bent particles will be close to 30%, as in this case the particle losses in the process of deflection are insignificant because of the dechanneling length growth. The obtained efficiency is high despite the defects of both Si_2 (the source) and Si_3. In further studies we suppose to use microstrip detectors to measure precisely the characteristics of the incident and bent beams. We hope with this detailed information to improve the quality of focusing crystals and to bring the bending efficiency closer to the theoretical value.

This work was supported by the grant of the Russian Fund for Fundamental Investigations.

References

[1] V.M. Biryukov, V.I.Kotov and Yu.A. Chesnokov, Physics–Uspekhi, **37** 937 (1994)

[2] S.P. Møller et al, Nucl.Instr.and Meth, **B84** 434 (1994)

[3] A.S. Denisov et al, Nucl. Instr. and Meth., **B69** 382 (1992)

POTENTIAL ACCELERATOR IMPROVEMENTS REQUIRED FOR THE TEVATRON UPGRADE AT FERMILAB

G. Jackson and G.W. Foster
Fermi National Accelerator Laboratory[1], MS 345, P.O.Box 500, Batavia, IL 60510 USA

ABSTRACT

A considerable amount of effort has been dedicated toward understanding what accelerator improvements are required to reach a luminosity per detector exceeding 10^{33} cm^{-2} sec^{-1} at Fermilab. This effort has been popularly named the Tevatron33 project. Collider issues involve long range beam-beam interactions between the 100 or more bunches per beam traveling along separated helical orbits, the necessity of crossing angles at the interaction points, and beam instabilities. The main challenge of the injector chain is to produce more antiprotons at a faster rate. One potential improvement would be to configure the modified antiproton source to recycle the antiprotons left over at the end of each collider store. In this paper the current plan for implementing the Tevatron33 upgrade is reviewed.

I. BEYOND THE MAIN INJECTOR

After the demise of the Superconducting Super Collider, the Fermilab Tevatron Collider again became the highest energy collider in the world. With the discovery of the Top quark, a rich program of excellent high energy physics research has commenced. The possibility of further research aimed at discovering or ruling out the theory of supersymmetry, as well as the search for a possible low mass Higgs particle, has started a grass roots project to increase the Tevatron luminosity to 1x10^{33} cm^{-2} sec^{-1}. This project has been dubbed Tevatron33. The accelerator upgrades required to achieve this luminosity are based on the assumption that the Main Injector upgrade [2] is successfully completed.

The design luminosity of the Main Injector was approximately 1x10^{32} cm^{-2} sec^{-1}. Therefore, the Tevatron33 project calls for a luminosity increase of a factor of 10. The equation describing the luminosity is

$$L = \frac{N_P (N_A B) f_0 (\beta_r \gamma_r)}{2\pi \beta^* \left(\varepsilon_{n_P} + \varepsilon_{n_A}\right)} H\left(\frac{\beta^*}{\sigma_s}\right) \frac{1}{\sqrt{1 + \frac{2\alpha^2 \sigma_s^2 (\beta_r \gamma_r)}{\beta^* \left(\varepsilon_{n_P} + \varepsilon_{n_A}\right)}}} \quad , (1)$$

where N_P is the number of protons per bunch, N_A is the number of antiprotons per bunch, B is the number of bunches per beam, f_0 is the revolution frequency of the Tevatron Collider, $\beta_r\gamma_r$ is the relativistic momentum of each beam, β^* is the value of the focusing function at each of the interaction points, ε_n is the transverse normalized rms emittance, σ_s is the rms bunch length, and α is the crossing half angle between the proton and antiproton bunches at the interaction point. The degradation of the luminosity due to the shape of the focusing function around the interaction point coupled with an extended bunch length is referred to as the hour-glass form factor, which has a round beam closed form solution of

$$H(x) = \sqrt{\pi}\, x [1 - \Phi(x)] e^{x^2} \quad . \quad (2)$$

The ultimate limit to luminosity in hadron colliders to date has been the beam-beam interaction. This limit has been a total beam-beam linear tune shift ξ of approximately 0.025 (where r_p=1.535x10^{-18} m), and is defined by the equation

$$\xi = \frac{r_p}{4\pi} \frac{N}{\varepsilon_n} N_{IP} \quad . \quad (3)$$

The ratio of the proton bunch intensity to emittance is limited by the total beam-beam tune shift suffered at all interaction regions. Plugging the equation for this tune shift into the equation for luminosity per interaction region yields the result

$$L = \frac{(N_A B)}{N_{IP} \beta^*} \frac{2\xi_{max} f_0 (\beta_r \gamma_r)}{r_p \left(1 + \frac{\varepsilon_{n_A}}{\varepsilon_{n_P}}\right)} \cdots \quad , \quad (4)$$

where the factors whose values can be modified appear in the left fraction. The quantity $N_A B$ is just the total antiproton intensity injected into the Tevatron, independent of bunch spacing. The number of interaction points N_{IP} is determined by the high energy physics community, and β^* is probably limited to 25 cm due to lattice control issues. Table 1 contains a list of the parameters which determine the luminosity in the past, present, and proposed future at Fermilab. Figure 1 is a summary of this luminosity history/proposed future in the form of a "Livingston Plot". It is impressive to note that the Main Injector project ensures the continuation of Fermilab's progress on the exponential curve which has as 2.3 year 1/e time.

II. ANTIPROTON PRODUCTION

Since the initial luminosity of a store depends proportionally on the number of antiprotons available for injection, the key to the proposed luminosity upgrades is to increase the maximum antiproton inventory intensity and also to increase the rate of production (stacking rate) of antiprotons. In addition to creating new antiprotons, the ability to reuse the antiprotons remaining at the end of the previous Tevatron Collider store also increases the luminosity.

0-7803-3053-6/96/$5.00 ©1996 IEEE

Table 1: Parameter values for past, present, and proposed future Tevatron Collider runs. The column labeled MI contains the design numbers for the original Main Injector upgrade project. The column labeled Tevatron* is the replacement for the Main Injector scenario in the situation where the 8 GeV antiproton production storage ring in the Main Injector tunnel is built, allowing antiproton recycling from the previous store and storage of excess stacked antiprotons from the Accumulator ring. The Tevatron33 numbers are accessible after antiprotons stacking rate improvements are successfully implemented in addition to the commissioning of the new ring in the Main Injector tunnel. Invariant emittances quoted are in Fermilab units of 95%, which is 6 times the rms emittance.

Parameter	1988/9	1992/3	1995	MI	Tev*	Tev33
Protons/Bunch (10^9)	70	120	240	380	270	270
Antiprotons/Bunch (10^9)	29	31	55	36	45	66
Proton Emittance (π mmmr)	25	20	20	30	20	18
Antiproton Emittance (π mmmr)	18	12	18	15	15	15
Beta @ IP (cm)	55	35	35	25	25	25
Beam Energy (GeV)	900	900	900	1000	1000	1000
Bunches/Beam	6	6	6	36	36	108
Longitudinal Emittance (eV-s)	6.3	4.5	4.5	3.0	0.5	0.3
RMS Bunch Length (cm)	65	55	55	45	20	15
Interaction Regions	12	2	2	2	2	2
Minimum Bunch Spacing (ns)	3500	3500	3500	395	395	132
Luminosity Form Factors	0.71	0.62	0.62	0.58	0.81	0.88
Luminosity (10^{30} cm^{-2} s^{-1})	1.60	5.42	16.2	123	200	1000
Integrated Luminosity (pb^{-1}/week)	0.32	1.1	3.2	25	40	200
Interactions/Crossing (@ 45mb)	0.25	0.85	2.6	3.2	5.2	8.7
Total Antiproton Tune Shift	0.026	0.009	0.019	0.020	0.021	0.023
Total Proton Tune Shift	0.015	0.004	0.005	0.004	0.005	0.007
Antiproton Intensity (10^{10})	17	19	33	130	160	710
Loss Rate (10^{10}/hr @ 90mb)	0.62	0.35	1.0	8.0	13	64
Scenario	actual	actual	actual	design	goal	goal

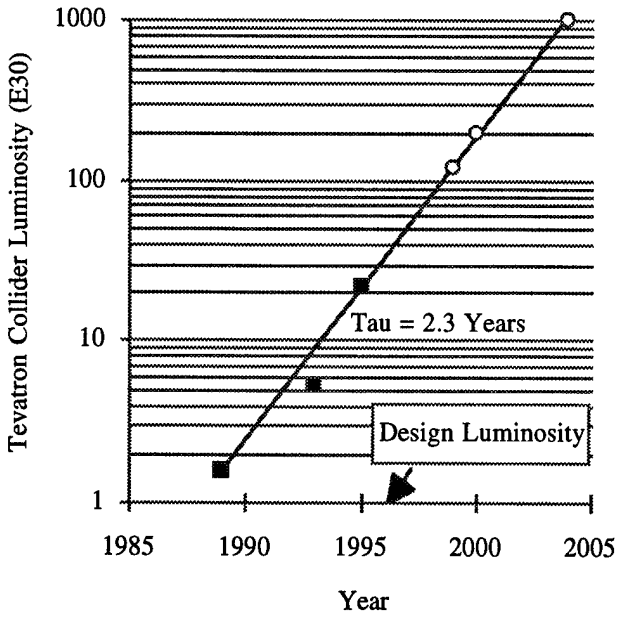


Figure 1: History of Tevatron Collider luminosity as a function of year is contained in the solid squares. The open circles represent design goals for the Main Injector upgrade and the luminosity upgrades presented in this paper (Tevatron* and Tevatron33).

The present Accumulator storage ring employs stochastic cooling to stack antiprotons. Because the cooling electronics can only tolerate a maximum intensity much less than that needed to achieve the Tevatron33 luminosity goal, it is necessary to build an addition storage ring to store the excess antiprotons. Recycling of the antiprotons left over at the end of the previous store can also be made possible by an additional storage ring. Since enhanced reliability is yet a third way to achieve higher effective stacking rates, the present plan is to build this additional ring in the Main Injector tunnel [3] with permanent magnets. This ring has an energy of 8 GeV and employs electron cooling for antiproton stacking and recycling. The electron cooling can also be applied to the protons before injection into the Tevatron.

Recycling of the antiprotons remaining at the end of the previous store is possible because one of the dominant sources of luminosity loss during the store is proton emittance growth due to intrabeam scattering. A numerical simulation of the evolution of the luminosity, beam emittances and intensities has been compared to observations in figure 2. Since the agreement is excellent, the model was applied to the projected parameters for Tevatron33 operations (see figures 3 through 5). Note that the longitudinal emittance of the antiproton bunches has exceeded the longitudinal admittance of the Main Injector, which is 0.5 eV-s. Therefore, deceleration of the antiprotons back down to 8 GeV for recycling is impossible

unless the inverse of coalescing [4], called decoalescing, is employed at 150 GeV.

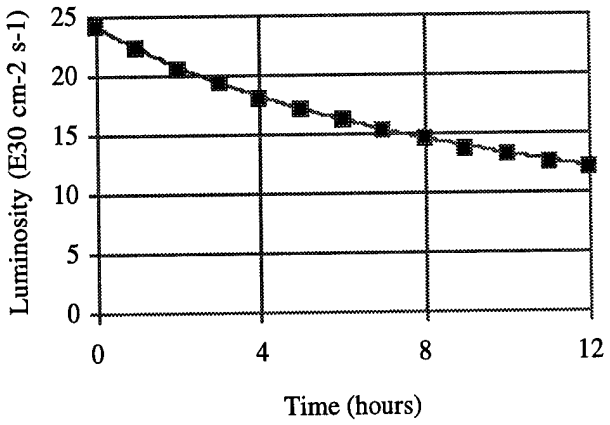


Figure 2: Comparison of measured luminosity (boxes) and a numerical simulation of the evolution of luminosity, beam emittances and intensities.

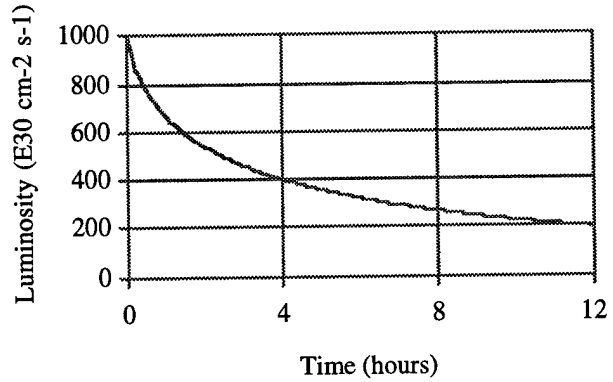


Figure 3: Tevatron33 numerical model prediction.

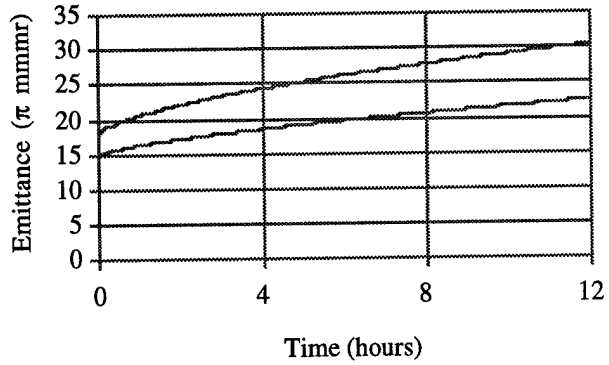


Figure 4: Tevatron33 numerical model predictions.

The initial usage of the permanent magnet storage ring in the Main Injector tunnel for antiproton storage and recycling is called Tevatron*. In that scenario no attempt is made to increase the rate at which new antiprotons are produced in order to achieve a luminosity twice that of the original Main Injector upgrade goal. Table 2 contains the results of calculations of the effect of antiproton recycling on the required stacking rate. Note that recycling alone is responsible for the luminosity increase needed for Tevatron*.

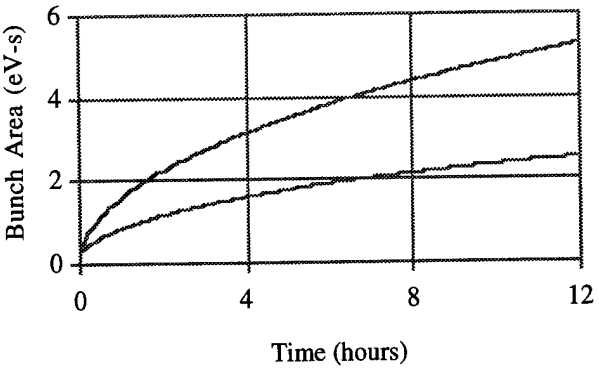


Figure 5: Application of the numerical model to Tevatron33 parameters.

There are a number of methods by which the factor of 5 improvement in stacking rate over that of the Main Injector design of 15×10^{10}/hr is achievable for Tevatron33 operations. The presently favored scheme is to increase the number of proton bunches delivered to the antiproton production target every 2 seconds. The implementation of this concept will require the development of a novel kicker magnet and improvements in the ability of the target and downstream optical system to handle the increased energy density and beam pulse length. Another method which will be employed in the years of adiabatic improvements leading up to Tevatron33 luminosities is the increase in the momentum aperture of the Debuncher ring [5]. Preliminary calculations show that an antiproton capture efficiency improvement exceeding 25% is achievable.

Table 2: Calculation of the required stacking rate of new antiprotons in the 3 upgrade scenarios.

Parameter	MI	Tev*	Tev33
Store Duration (hrs)	12	8	4
Antiproton Remaining (% Inj)	60	70	80
Recycling Efficiency (%)	0	90	90
Injection Eff. to LowBeta (%)	95	95	95
Usable Stack Required (10^{10})	137	168	747
Antiprotons Recycled (10^{10})	0	100	511
New Antiprotons Required (10^{10})	137	68	236
Required Stacking Rate (10^{10}/hr)	11	8	59

III. REFERENCES

[1] Operated by Universities Research Association Inc., under contract with the U.S. Department of Energy.

[2] D. Bogert, "The Status of the Main Injector Project", this proceedings.

[3] G. Jackson and G.W. Foster, "Storage Ring for Enhanced Antiproton Production at Fermilab", this proceedings.

[4] J. Dey, et al., "Improvement in Bunch Coalescing in the Fermilab Main Ring", this proceedings.

[5] D. Olivieri, private communication.

BEYOND THE LHC: A CONCEPTUAL APPROACH TO A FUTURE HIGH ENERGY HADRON COLLIDER*

M. J. Syphers, M. A. Harrison, S. Peggs, Brookhaven National Laboratory, Upton, NY 11973 USA

Abstract

The concept of a post LHC hadron collider operating in the radiation damping regime was discussed in the DPF workshop on future hadron facilities[1]. To date hadron colliders have all operated in a state of insignificant damping, where phase space dilution from any source results in a costly degradation of instantaneous and thus integrated luminosity. The concept of using radiation damping to enhance the integrated luminosity results in an effective decoupling of the machine performance from the initial beam parameters. By relying more heavily on the damping mechanism, the requirements for tight emittance control through the injector chain and during the collider fill process can be relaxed allowing for less stringent injection field quality and the possibilities for looser tolerances in many other aspects of the machine. In this paper we present some generic parameters and machine characteristics before examining options for lengthening the standard cell (quadrupole and spool piece reduction) and highly lumped correction schemes (correction element reduction).

Table I
30 TeV Collider Parameters

Parameter	
Beam Energy (TeV)	30
Peak Luminosity ($\times 10^{33}$ cm^{-2} sec^{-1})	10
Injection Energy (TeV)	1
No. of IR's	2
Dipole Field (T)	12.5
Circumference (km)	60
β^* (cm)	20
Init. Trans. Emittance (rms, mm-mr)	1.5π
Init. Long. Emittance (rms, eV-s)	0.1
Bunch intensity (10^{10})	2.4
No. of bunches	2030
Bunch spacing (ns)	100
No. Events per crossing (@60mb, 10^{34})	60
Init. beam lifetime – burn off (hr)	16
Syn. Rad. power / length / ring (W/m)	0.56
Rad. transverse damping time (hr)	4.3

I. PARAMETERS

Radiation damping implies synchrotron power with the associated problems of cryogenic heat load and gas desorbtion. Constraining the latter to a tractable range while maintaining the former as a useful feature argues for a collision energy in the range of $25 \rightarrow 40$ Tev with a corresponding dipole field of 12.5 ± 2.5 T. We have chosen to use a parameter set based on a 30 Tev design (T30) since this looked a reasonable energy for a post LHC machine and demonstrates the necessary parametric behavior. We have also used a 12.5 T dipole magnet, since this appeared to represent a reasonable goal for a next generation superconducting magnet. A range of dipole fields can be accommodated in this approach.

A partial parameter list is shown in Table I. Minimizing the synchrotron power resulted in a reduced number of protons and beam bunches. The total number of protons was determined largely by the desire for $\sim$ 10 hr stores in spite of significant particle burn-off with 2 IR's operating up to a luminosity of 10^{34} cm^{-2}s^{-1}. The maximum credible cryogenic heat load is considered to be 3 W/m. This parameter set is well below this value. We estimate an average of $\sim$ 60 events per bunch crossing.

The time evolution of the luminosity, transverse emittance, and bunch intensity is shown in Fig. 1. A parameterization of intra-beam scattering (IBS) is used to provide a beam heating mechanism. The luminosity increases by a factor of 2 during the first several hours of a store until the IBS and radiation damping mechanisms come into equilibrium, from which point the luminosity decreases as the bunch intensity is depleted from the interactions. The peak to average luminosity is a healthy $\sim$ 70%. We have assumed a standard FODO cell lattice with an "SSC-like" footprint of 2 IR's and 2 long arc regions. Dipoles occupy 90% of the machine circumference. The machine operating characteristics do not exhibit any undue sensitivity to the details of the assumed parameters but rather are defined primarily by the damping regime itself. This is demonstrated in Fig. 2, which shows the 10 hour integrated luminosity versus the initial transverse emittance. Unlike a conventional hadron collider, the performance is only weakly correlated to the initial beam parameters, but is defined primarily by the equilibrium condition between heating and cooling mechanisms. It is this robust nature of the performance that allows the kind of speculation in the balance of this report which involves simplifying the lattice, and contemplating inferior magnetic field quality, in a more agressive manner than was deemed prudent for the SSC.

II. LATTICE ISSUES

Drawing upon the lessons from the SSC, the number of different types of components must be minimized, long cable runs for correctors are to be avoided, and the number of power leads minimized. This philosophy leads one to a design with "sparse/lumped" correctors, and to have power and vacuum hardware physically attached to the main quadrupole magnet cryostat, avoiding having "spool pieces" in every half-cell.

*Work performed under the auspices of the U.S. Department of Energy.

0-7803-3053-6/96/$5.00 ©1996 IEEE

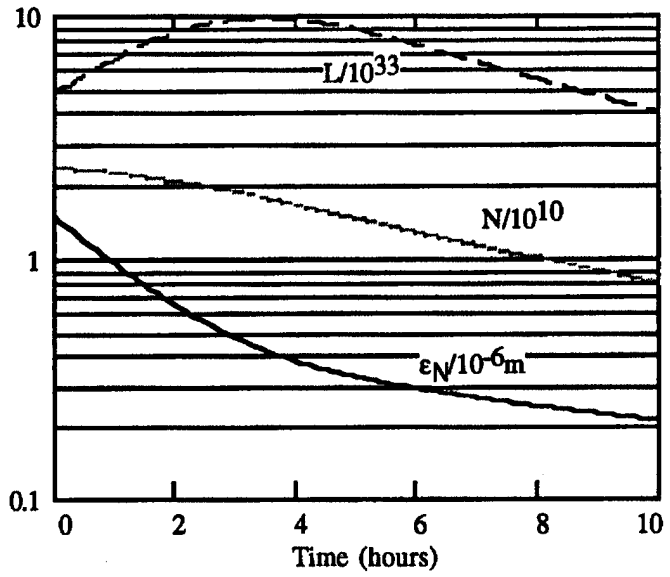


Figure 1. Emittance, luminosity, and bunch intensity vs. time during store.

A. Cell Length Optimization

The optimum half FODO cell length, L, depends on a dynamic balance:

- longer cells save money through fewer quadrupoles, fewer correctors, and fewer spool pieces
- longer cells reduce chromatic sextupole nonlinearities
- shorter cells and thus smaller beams reduce magnetic field quality demands

The magnetic field quality in the arc dipoles dominates the dynamic aperture at injection, the most critical time. The half cell in T30 can become quite long, if the historical trend to improved field quality continues, and the dipole bore is large enough. Figure 3 plots the vertical magnetic field versus horizontal position in the mid-plane of dipoles for which data were available [2].

The dynamic aperture may be crudely represented by the "good field aperture," r_{GF}, in the arc dipoles. In this picture, particle motion is stable so long as the maximum field deviation $\Delta B/B \leq 10^{-3}$, which occurs at a horizontal displacement of r_{GF}. In practice, of course, there are many complications to attach to this simple model, which is nonetheless useful in the spirit of this paper.

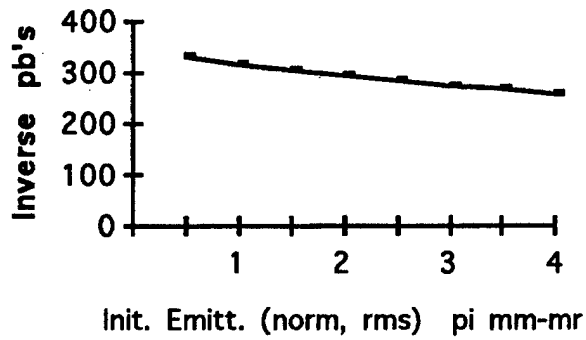


Figure 2. Integrated luminosity (10 hr store) vs. initial transverse emittance.

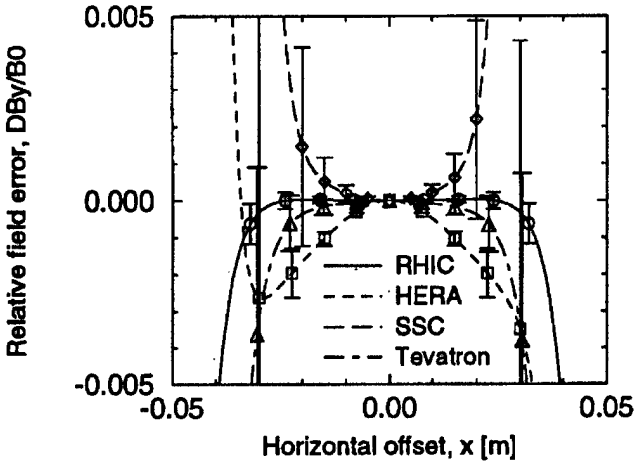


Figure 3. Field profiles of arc dipoles at injection.

For 90° FODO cells the maximum beta function is given by $\widehat{\beta} = 3.41\ L$. The maximum transverse rms beam size at injection, $\widehat{\sigma} = \sqrt{\epsilon\widehat{\beta}/\pi\gamma_I}$, therefore increases with increasing cell length. The maximum allowable beam size occurs when the beam fills the good field aperture, or $r_{GF} = n\widehat{\sigma}$, where a reasonable value for n is 10. This expression ignores the beam size contribution due to finite momentum spread. It is shown, below, that with nominal parameters it is possible to reduce σ_p/p (at the expense of increased bunch length) so that the betatron size continues to dominate. Putting all this together gives a maximum allowable half cell length

$$\widehat{L} = \frac{\pi\gamma_I}{\epsilon}\frac{r_{GF}^2}{3.41\,n^2} \tag{1}$$

Table II applies this expression to existing machines and to T30, assuming that $n = 10$ in all cases. For the SSC [3], the real half cell length appears to be conservatively small, while RHIC is close to the limit predicted by Equation 1.

Table II
Half cell length for different accelerators.

Machine	γ_I	ϵ/π [μm]	r_{GF} [mm]	$\widehat{L}$ [m]	L_{real} [m]
Tevatron	150.0	3.0	20	60	30
SSC	1000.0	1.0	10	290	94.0
RHIC(Au)	12.6	1.7	30	20	14.9
T30	1000.0	1.5	15	440	(400)

Even in a careful and detailed analysis, the good field aperture is the least well known quantity in determining $\widehat{L}$, and the most important, since it enters quadratically on the numerator of Equation 1.

Long FODO cells make $\widehat{\beta}$ unusually large, while the total arc tune $Q_{arc} \approx C/8L$ remains quite modest. The maximum dispersion $\widehat{\eta} = 2.71\ L^2/R$, and the beam width due to momentem increase quadratically with L, faster than the betatron contribution. Assuming a longitudinal rms bunch area of $S = 0.1$ eV-sec,

this results in the rather small momentum spread 3×10^{-5}, determined by setting $\sigma_p/p = \widehat{\sigma}/\widehat{\eta}$ so that the two contributions are equal. The bunch is not unusually long (36 cm), because the injection energy is relatively high. The resultant synchrotron tune is in the range of conventional experience, since the slip factor (approximately $1/Q_{arc}^2$) is relatively high, while the momentum width is relatively low. This high slip factor also makes the beam acceptably resistant to collective effects, such as the microwave instability.

So long as the field quality can be maintained, a much longer half cell (few hundred meters) for this next generation hadron collider must not be ruled out.

B. Sparse Correctors

To take even more advantage of a "simplified arc," every few kilometers the normal FODO lattice is interrupted by a section of cells with free space generated by leaving out a sequence of dipole magnets as a "dispersion-matched insertion." These "free spaces" would contain "empty cryostats," which could then be converted to function as spool pieces as required. An example of such an insertion is shown in Fig. 4.[4]

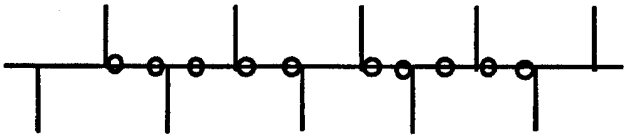


Figure 4. Dispersion-matched free-space FODO region; the circles indicate locations where dipole magnets are missing from the normal cell structure.

The adjustment of the global tunes of the accelerator can be performed by Phase Trombones – one at each end of each arc, supplemented by the placement of trim quadrupoles in the "free-space" insertions. Likewise, sextupoles are placed in these spaces as well. Naturally, the effects on dynamic aperture of such a lumped scheme will have to be studied carefully. But the analysis of the previous section has shown that long half cells help in this regard.

One primary concern of a sparse correction scheme is that of orbit correction. Suppose that "trim" dipoles are used only in our "free space" insertions to bring the orbit deviations to zero at these locations. For a distance d_{sa} between service areas, d_{rms} quadrupole alignment error, and dipole magnets with individual lengths ℓ_b, then in terms of the half-cell length L and bend radius ρ, the rms maximum displacement is

$$\widehat{\Delta x} = 4.8\, L \sqrt{\frac{d_{sa} d_{rms}^2}{L^3} + \frac{(\Delta B/B)^2 d_{sa} \ell_b}{\rho^2}}. \qquad (2)$$

Figure 5 shows the rms maximum orbit distortion and lattice functions versus half-cell length for $C = 60$ km, $d_{rms} = 0.5$ mm, $\ell_b = 20$ m, $d_{sa} = 8$ km, and $\Delta B/B = 10^{-3}$.

Some form of local orbit correction (trim coils, moveable magnets) is still necessary for any reasonable cell length. However, it is feasible that many other major correctors can be sparsely distributed, thus simplifying the arc hardware design.

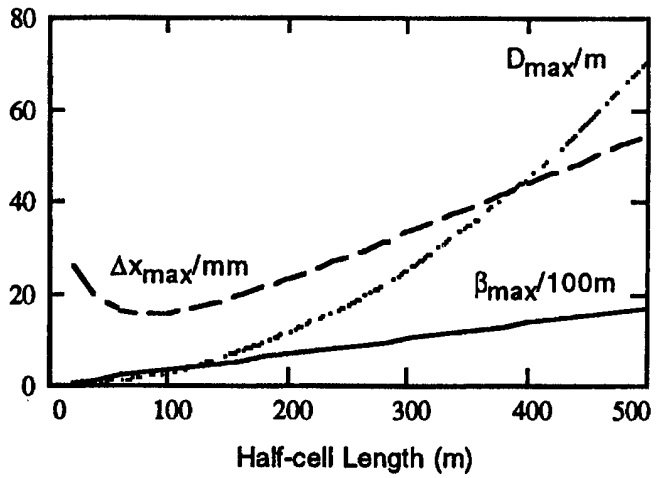


Figure 5. Maximum beta function and dispersion function, and rms maximum orbit error versus half-cell length.

III. CONCLUDING REMARKS

The goal of $\geq$60 TeV in the center-of-mass, with a luminosity of 10^{34} cm^{-2}sec^{-1} is reasonable for a facility following the LHC. The most interesting and promising factor of this energy regime is the utilization of synchrotron radiation to enhance the accelerator performance. Long cells and lumped correctors are an option worth pursuing, as the overall performance of the collider can be maintained or enhanced with such a simplified hardware design. Bending magnets with fields in the range of 12.5 T$\pm$ 3 T will be needed to support these aims. The authors would like to thank all of the participants of the DPF Workshop for their contributions to this effort.

References

[1] "Proc. of Workshop on Future Hadron Facilites in U.S.," Fermilab-TM-1907, 1994.

[2] Tevatron and HERA data are from private communication with N. Gelfand and D. Gall, respectively.

[3] J.D. Jackson (Ed.), "SSC Conceptual Design", Berkeley, 1986

[4] A. A. Garren, reported in "Proc. of Workshop on Future Hadron Facilites in U.S.," Fermilab-TM-1907.

132 NSEC BUNCH SPACING IN THE TEVATRON PROTON-ANTIPROTON COLLIDER

S.D. Holmes, J.A. Holt, J. Johnstone, J. Marriner, M. Martens, D. McGinnis
Fermi National Accelerator Laboratory*, P.O. Box 500 Batavia, IL 60510

I. INTRODUCTION

The Tevatron proton-antiproton collider currently operates at a center-of-mass energy of 1.8 TeV, delivering a luminosity greater than $1.5 \times 10^{31} cm^{-2} sec^{-1}$. This is achieved with six proton and six antiproton bunches colliding at two locations, B0 (CDF) and D0. An electrostatic separator system causes the two beams to pass with approximately 5σ separation at the ten other possible collision points around the accelerator. In this configuration each experimental detector, with a sensitivity to about 45 mb of the total p-$\bar{p}$ cross section, witnesses 2.4 interactions per crossing.

The Fermilab Main Injector is projected to support a Tevatron luminosity in excess of $5 \times 10^{31} cm^{-2} sec^{-1}$. Hardware currently under construction will allow operation with 36 proton and 36 antiproton bunches when the Main Injector comes on-line in late 1998. A representative set of collider parameters for the first Main Injector-based collider run (Run II) is given in Table I. Improvements to the antiproton accumulation rate, to low beta systems, and/or reduction of the rms bunch lengths to 15 cm or less hold the promise of raising collider luminosity above $10 \times 10^{31}\ cm^{-2} sec^{-1}$. Continued operation with 36 bunches would, however, result in 3-4 interactions per crossing at this higher luminosity. Reducing the number of interactions per crossing below 1 will require circulating more bunches as indicated in the right-most column of the table.

This paper summarizes a preliminary conceptual design for a Tevatron collider configuration in which bunches are spaced at 132 nsec. Increasing the number of bunches is not expected to raise the luminosity--the sole motivation is to reduce the number of interactions per crossing by about a factor of three. Multibunch schemes with 72, 108, 96, and 120 proton and antiproton bunches have been studied.

Implementation of any of these multi-bunch scenarios will require new hardware. The introduction of a crossing angle will result in reduced luminosity and the bunch length must be shortened considerably compared to present operations to minimize this impact. This means that a new rf system, operating at 159 MHz, will be required. Other new hardware probably includes 1)upgraded low beta optics; 2)upgraded abort kicker; 3) new coalescing cavities operating at three times the frequency (7.5 MHz) of those currently operational in the Main Ring and also planned for the Main Injector, and; 4) a new 7.5 MHz rf system in the Antiproton Accumulator.

*Operated by Universities Research Association under contract to the United States Department of Energy

II. DESIGN AND PERFORMANCE ISSUES

The proton-antiproton luminosity in the Tevatron is given by the expression:

$$L = \frac{3\gamma f N_p (B N_{\bar{p}})}{\beta^* (\varepsilon_{Np} + \varepsilon_{N\bar{p}})} H\left(\frac{\beta^*}{\sigma_l}\right)\left(1 + \frac{2\alpha^2 \sigma_l^2}{\sigma_p^2 + \sigma_{\bar{p}}^2}\right)^{-1/2} \quad (1)$$

where γ is the relativistic factor, f is the revolution frequency, B is the number of bunches in each beam, N_p ($N_{\bar{p}}$) is the number of protons (antiprotons) in a bunch, ε_p ($\varepsilon_{\bar{p}}$) is the 95% normalized transverse beam emittance, σ_l is the rms bunch length, β^* is the beta function at the interaction point, σ_p ($\sigma_{\bar{p}}$) is the rms transverse beam size at the interaction point, and α is the crossing half-angle. The form factor $H(\beta^*/\sigma_l)$ approaches 1 asymptotically as $\beta^*/\sigma_l \to 0$, clearly indicating that bunch length should be kept as small as is reasonable compared to β^* to minimize the luminosity reduction. A 14 cm bunch length is chosen to minimize the impact of the 190 μrad crossing angle.

A major limiting factor in the Tevatron proton-antiproton collider is the beam-beam tune shift. In the present collider mode, with six proton and antiproton bunches, there are twelve potential collision points around the ring. Through the use of electrostatic separators the beams are made to collide with zero crossing angle at the interaction points, but separated by 5σ (center to center) at the other ten (parasitic) crossings. This basic configuration must be continued as the number of number of bunches increases to 36 and beyond.

The separator nearest to the interaction region is beyond the position of the first parasitic crossing for 132 nsec spacing. It does not appear to be possible to avoid these first parasitic collisions unless a crossing angle is introduced to separate the beams within the low β quadrupoles. An interesting alternative technique for avoiding a crossing angle through the use of rf resonant magnets has been envisioned [1], but, at least with existing technology, a substantial crossing angle seems to be inescapable.

The existence of a crossing angle dictates that the orbits be separated within the low β quadrupoles. The necessary aperture in the low β quadrupoles and, conceivably, changes to the low β optics which minimize this separation need to be considered. Also, although long range beam-beam effects are not significant in the current operating mode, once the number of bunches approach 100 such effects can no longer be ignored.

0-7803-3053-6/96/$5.00 ©1996 IEEE

Table I: Collider Parameters for Run II and options for reduced bunch length or bunch spacing

	Collider Run II: 36 bunches 53 MHz 396 nsec	Option I: 36 bunches 159 MHz 396 nsec new low β	Option II: 108 bunches 159 MHz 132 nsec new low β	
Beam Energy	1000	1000	1000	GeV
Circumference	6283.0	6283.0	6283.0	meters
Protons/bunch	3.3×10^{11}	3.3×10^{11}	2.7×10^{11}	
Antiprotons/bunch	3.6×10^{10}	3.6×10^{10}	1.2×10^{10}	
Bunches	36	36	108	
Total Antiprotons	1.3×10^{12}	1.3×10^{12}	1.3×10^{12}	
Proton emittance (95%, norm)	30π	30π	25π	mm-mr
Antiproton emittance (95%, norm)	20π	20π	20π	mm-mr
β*	0.35	0.25	0.25	meters
Longitudinal Emittance (95%)	3	3	2	eV-sec
rf Frequency	53	159	159	MHz
rf Voltage	1	15	15	MV
Bunch length (rms)	0.43	0.17	0.14	meters
Bunch Length Form Factor	0.70	0.86	0.89	
Crossing Half-angle	0	0	0.19	mr
Crossing Angle Form Factor	1.00	1.00	0.77	
Typical Luminosity	8.3×10^{31}	14.2×10^{31}	10.4×10^{31}	$cm^{-2}s^{-1}$
Integrated Luminosity	16.72	28.67	20.99	pb^{-1}/wk
Bunch Spacing	396	396	132	nsec
Interactions/crossing (@45 mb)	2.17	3.73	0.91	
Antiproton tune shift (2 crossings)	0.016	0.016	0.016	
Proton tune shift (2 crossings)	0.003	0.003	0.001	
Average helix separation (d/σ)	5	5	6.5	
Long Range tune spread (antiproton)	0.008	0.008	0.008	

The length of the luminous region is modified appreciably with the introduction of a crossing angle and shorter bunches. Figure 1 shows the distribution dL/dz that will be seen by an experimental detector for various crossing angles and a 14 cm bunch length. The result is a luminous region of ≈8cm length (rms)--a factor of four shorter than those currently experienced and a desirable experimental feature.

A. Multibunch Loading

The first collider run of the Main Injector era will operate with 36 bunches of protons and antiprotons. A workable configuration calls for three batches of protons and antiprotons containing twelve bunches each, with the batches spaced symmetrically around the ring. For 132 nsec it would be most natural to continue with a threefold symmetric scheme. There are two possible three-fold symmetric loading schemes, resulting in either 72 or 108 bunches colliding. In 72x72 operation two batches of twelve bunches each would be spaced 396 nsec apart, followed by a 3.7 μsec abort gap. This sequence would be repeated twice more around the ring. The abort gap of 3.7 μsec is larger than that for 36x36 operation, and the abort at A0 could be used. The 108x108 scenario calls for three batches of twelve bunches spaced by 396 nsec followed by a gap of 1.8 μsec.

Single gap configurations are also possible. However, these have the disadvantage of not allowing utilization of existing aborts, and of providing unequal luminosity at B0 and D0.

B. RF System

A 14 cm bunch length is required to minimize luminosity loss due to the 190 μrad crossing angle selected for this study. The total voltage required to produce a 14 cm bunch length, with a beam longitudinal emittance of 2 eV-sec, is 15 MV at 159 MHz or 11 MV at 212 MHz. The 159 MHz system is evaluated here. A total of 12 proton and 12 antiproton cavities would be required. Power requirements are estimated at 935 kW for each system, based on providing 1.25 MV per cavity.

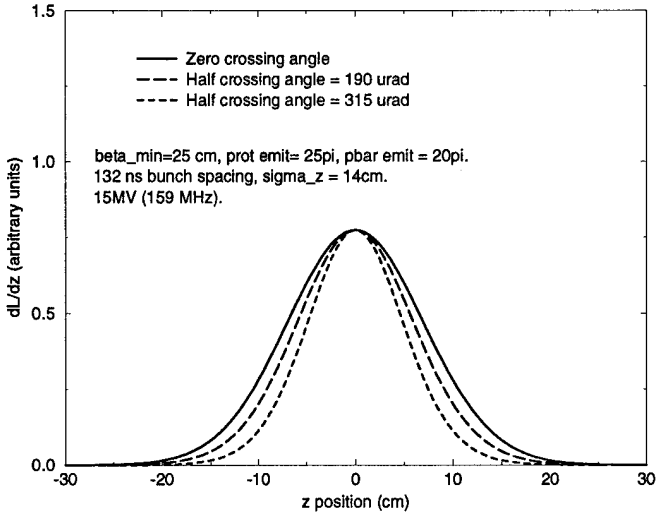


Figure 1: dL/dz for three crossing angles and the Tevatron parameters contained in the rightmost column of Table 1.

C. Interaction Region Optics

Six pairs of high gradient (140 T/m) low β quadrupoles are powered in each Tevatron interaction region. In the present mode of operation dispersion at the IP is zero, but with a non-zero slope, resulting in dispersion reaching its maximum value within the low β triplet - precisely where the beam already reaches its ring-wide maximum from β_{max} ($\geq$1 km). An alternative match to the lattice which gives both η and $\eta' \equiv 0$ throughout the straight section has been found [2] that uses the current IR physical configuration of magnets and gradients compatible with the existing quadrupoles. Extending to $\beta^* = 0.25$m requires a maximum gradient in one of the low β quadrupoles of $\approx$185 T/m. This lies beyond the capabilities of the present system and would require an upgrade to quadrupoles similar to those proposed for the CERN LHC [3].

The dispersion-free solution significantly reduces beam-size in the low-beta quads--particularly at injection. This optics configuration is particularly desirable for 132 nsec bunch spacing since the beams must be separated through the IR triplet and the momentum spread in the beam will be large due to the short bunch length.

D. Electrostatic Separators & IP Crossing Angle

A crossing half-angle of 190 μrad, giving 3σ separation at the first parasitic crossing, has been chosen. Assuming the current physical location of electrostatic separators, an average of 6.5σ separation is maintained at all other parasitic crossings. In general the electric fields are comparable to, or less than, those currently in use.

The primary dynamical consequence of a non-zero crossing angle is thought to be the excitation of synchro-betatron resonances. These resonances were a serious problem at the e^+e^- collider DORIS [4]. The excitation of such resonances in the Tevatron has not been studied in detail, but it is expected that they will be less important than in the DORIS experience because of the relatively low synchrotron frequency. Note, however, that the proposed parameters and crossing angle for the Tevatron Collider are rather similar to those proposed for the LHC.

E. Long Range Beam-Beam Effects

The large number of parasitic beam-beam crossings can lead to significant orbit and tune shifts. If the bunches are not uniformly populated and regularly spaced each bunch will have a different orbit and a different tune. In the Tevatron the bunches can not be regularly spaced because of the requirement for an abort gap. A bunch loading scheme that leads to 72 bunches colliding with a 132 nsec spacing has been considered. This configuration was chosen because it was thought to be as irregular as any that might be used. The maximum orbit shift is about 20 μm, 2/3 of the rms transverse beam size at the interaction point. The bunch-to-bunch range of tune shifts is shown in Table II. The range of tune shifts is less than, but comparable to, the maximum working space of 0.025. The range of linear coupling and the range of chromaticities are neither overwhelming nor small.

Table II. Range of tune shifts for the 72 antiproton bunches

Tune plane	Tune shift
Minimum $\Delta\nu_x$	-.0008
Maximum $\Delta\nu_x$	.0026
Minimum $\Delta\nu_y$	-.0118
Maximum $\Delta\nu_y$	-.0017

III. SUMMARY

A number of scenarios for operation of the Tevatron collider with 132 nsec bunch spacing have been analyzed. Collider parameters are summarized for 108 bunch operation in Table I. The 132 nsec spacing, coupled with a 190 μr crossing angle, produces a luminosity approximately 20% low as compared to bunches spaced at 396 nsec colliding head-on. This results primarily from the crossing angle form factor. Other factors, such as reduced proton bunch intensity due to coalescing of fewer bunches, tend to be ameliorated by the resultant lower longitudinal and transverse emittances.

Luminosity in all scenarios will continue to be limited by antiproton availability. Schemes for increasing the antiproton availability, and hence the luminosity, by an additional factor of ten are currently under study at Fermilab.

IV. REFERENCES

1. Gerald P. Jackson, Beam-Beam Collisions of Bunches Separated by 132 nsec without a Crossing Angle, Internal Fermilab Report, Oct. 22, 1994.

2. John A. Johnstone, Report to the Low Beta Study Group I, Internal Fermilab Report, September 29, 1994.

3. The LHC Study Group, LHC, The Large Hadron Collider Accelerator Project, CERN/AC/93-03(LHC).

4. A. Piwinski, DESY 77/18, 1977.

ALUMINUM BEAM TUBE FOR SUPER COLLIDER: AN OPTION FOR NO-COATING & NO-LINER

W. Chou, Fermi National Accelerator Laboratory,* P.O. Box 500, Batavia, IL 60510, USA

Abstract

This paper proposes to use a single-layer beam tube made of high strength, high resistivity aluminum alloy (such as 7039-T61 or A7N01) to replace the double-layer copper coated stainless steel tube in Super Collider. The merits, technical issues and possible implementation are briefly discussed. For details the readers are referred to Reference [1]. This work was originally done for the SSC. But it may also be useful to future colliders.

I. INTRODUCTION

The baseline design of the SSC Collider beam tube calls for a stainless steel (SST) pipe of about 2-mm thickness with a thin copper (Cu) layer (about 0.1-mm thick) coated on its inner surface. The purpose of the copper coating is to reduce the surface resistance, thus suppressing the possible beam instability caused by the resistive wall and reducing the beam-induced wall heating. This paper suggests a drastic change in the choice of the beam tube, namely, a single-layer aluminum (Al) alloy pipe without coating. The merits are as follows:

- There will be a potential saving of about $2300 per tube, as shown in Table 1, or $23M for a total of 10000 tubes.
- An extruded aluminum tube with a specially designed cross section (with antechambers or plate insertions) will more easily accommodate a distributed cryopump and, therefore, will eliminate the need for a separated liner addition to the tube.
- There is a concern about adhesion in the bi-layer Cu+SST tube over a 25-year lifetime. This will not be a problem for a single-layer aluminum tube.

Aluminum beam tubes have been used in many lepton storage rings. They were ruled out in the early SSC design mainly because of the concerns about eddy currents and mechanical stability during quench, and the technical difficulty of making leak-free joints between aluminum and stainless steel . However, we will show that the recent industrial development of some high strength, high resistivity aluminum alloys (e.g., 7039-T61 or A7N01) can meet performance requirements in a quench, and that the Al-SST joints have been successfully tested and employed in a cryogenic environment at DESY, KEK and LANL.

II. TECHNICAL ISSUES

A. Surface resistance

A.1 Low frequencies — Resistive wall instability problem:

In order to control the beam instability, the requirement on the surface resistance of the beam tube is:

$$\sigma_e \Delta \geq 1 \times 10^5 \quad \Omega^{-1} \tag{1}$$

in which σ_e is the electrical conductivity and Δ the thickness (which is assumed to be smaller than the skin depth δ) of the wall material. Table 2 shows that the product $\sigma_e \Delta$ of a 2.5-mm thick aluminum tube is comparable to that of a 0.1-mm thick copper layer (RRR = 30).

A.2 High frequencies — RF heating problem:

In calculating the parasitic heating due to the beam and wall resistance, the anomalous skin effect (which was overlooked in the early SSC design) plays an important role.[1] The surface resistance ratio $R_s(300\text{ K})/R_s(4\text{ K})$ of copper at high frequencies is significantly lower than the dc value.[2,3] The data measured by LANL using a copper coated stainless steel tube is listed in Table 3.[4] In order to have a realistic comparison between Cu and Al, more measurements are needed in the presence of cold temperature (4 K), high frequency ($\geq$ 1 GHz) and strong magnetic field (6.8 T).

B. Quench problem

B.1 Eddy current:

The eddy current during quench is proportional to the product $\sigma_e \Delta$:

$$I = 2\dot{B}b^2 \cdot \sigma_e \Delta \tag{2}$$

in which $\dot{B}$ is the rate of decrease of the magnetic field B, and b is the beam tube radius. It is seen from Table 2 that the eddy current is comparable for the two tubes.

B.2 Quench stress and tube thickness requirement:

To analyze the stress during quench, three effects need to be taken into account: thermal contraction during the cool down from room temperature to 4 K, the vaporized helium pressure P_{He} (which is isotropic in the radial direction pointed inward) and the Lorentz pressure P_{max} (which is in the horizontal direction pointed outward, has a cos-θ distribution and peaks at the equator). For $P_{\text{He}} = 488$ psi and $P_{\text{max}} = 100$ psi, a stress analysis using the 3D code ANSYS for a 2.5-mm thick aluminum tube gives a maximum stress $\sigma_{\text{max}} = 16.9$ ksi.[5] The critical buckling pressure P_c is 4.57 ksi. According to the American Society of Mechanical Engineers, the allowable stress for membrane loading is:

$$\sigma_{\text{allow}} = 1.5 \times \min\{0.25\sigma_t^u,\ 0.67\sigma_t^y\} \tag{3}$$

in which σ_t^u is the ultimate tensile strength of the tube material, and σ_t^y is the yield tensile strength. For the aluminum alloy

*Operated by Universities Research Association Inc. under Contract No. DE-AC02-76CHO3000 with the U.S. Department of Energy.

[1] When the frequency is high enough such that the mean free path of electrons becomes larger than the skin depth, the normal conduction theory based on electron collisions breaks down and the surface resistance becomes independent of the conductivity σ_e of the material. This is called the anomalous skin effect.

0-7803-3053-6/96/$5.00 ©1996 IEEE

Table 1. Cost Comparison

Cu Coated SST Tube		*Al Tube*	
15-m 304LN tube	\$930	15-m A7N01 tube, extruded	\$240
Copper coating	\$2000	Two Al-SST welding joints	\$200
		Two Al-SST demountable joints	\$156
TOTAL	\$2930	TOTAL	\$596

Table 2. Surface Resistance Comparison

Material	σ_e $(\Omega^{-1}\mathrm{m}^{-1})$	δ (mm)	Δ (mm)	$\sigma_e\Delta$ (Ω^{-1})
Cu	1.8×10^9	0.6	0.1	1.8×10^5
Al	5.6×10^7	3.6	2.5	1.4×10^5

7039-T61 at 4 K, one has $\sigma_{\mathrm{allow}} = 36.75$ ksi. The allowable buckling pressure is:

$$P_{\mathrm{c\ allow}} = \frac{P_{\mathrm{c}}}{4} = 1.14 \quad \mathrm{ksi} \tag{4}$$

To estimate the needed tube thickness, the stress ratio method is employed. The requirement is:

$$\frac{\sigma_{\max}}{\sigma_{\mathrm{allow}}} + \frac{P_{\mathrm{He}}}{P_{\mathrm{c\ allow}}} < 1 \tag{5}$$

For a 2.5-mm thick aluminum tube, this ratio is 0.89. Therefore, it should be safe during quench.

B.3 Quench test:

A convincing evidence of the quench survivability of an aluminum tube comes from a preliminary quench test.[6] The sample is a 2-m A7N01 pipe (1.7-mm thick), which is co-extruded with an A1100 pipe (0.2-mm thick). The eddy current and Lorentz pressure of this clad pipe in a quench are comparable to what is calculated above. The test results showed that the elastic deformation was < 0.1 mm, and the plastic deformation < 0.01 mm.

C. Gas desorption problem

C.1 Photon induced gas desorption:

The main concern of the vacuum problem in the Collider is the photodesorption due to the synchrotron radiation of the protons. Previous measurements at NSLS and CERN showed that the initial photodesorption rate η of aluminum is higher than that of copper and stainless steel. But the rate of decrease is also greater. At sufficiently high photon dose, η for all the three metals tend to similar low values.[7]

C.2 Ion induced gas desorption:

The ionized molecules of the residual gas, which are accelerated by the potential field of the proton beam (about 400 V in the Collider), can desorb gas molecules from the accumulated layer on the tube surface. This effect is usually described by the quantity $\eta_i I$, the product of the ion desorption coefficient and the beam current. Thanks to the low beam current (0.07 A) in the Collider, this effect is small no matter what material (Al, Cu or SST) is used for the beam tube.

Table 3. Surface Resistance of a Copper Plated Tube

Frequency	Ratio $R_s(300\ \mathrm{K})/R_s(4\ \mathrm{K})$
dc	107
0.959 GHz	4
1.865 GHz	3.2
7 GHz	3.7

C.3 Electron multipactoring:

Because aluminum has a high secondary electron emission coefficient, the electron multipactoring could become a problem as has been observed in the ISR. However, the calculations using Gröbner's model show that this should not be a concern due to the low beam current and short bunch length in the SSC.[8]

D. Al-SST joint problem

The Al-SST joint presents a technical challenge in a cryogenic storage ring because of the possible leak of helium at the joint near the end of the coldmass. In recent years, however, it has been successfully used in a helium environment.

- The demountable joint:[9]
  It uses bolted aluminum and stainless steel flanges manufactured by Hakudo/SMC and is employed in a superconducting RFQ at LANL. The pipe contains helium gas at 450 psi. After 100 thermal cycles between room temperature and 22 K, there was no detectable helium leak. The cost is about \$78 per joint.
- The explosion bonded Al-SST transition piece:
  This has been used in cryogenic and vacuum environments at KEK for years and proved reliable and leak-free.
- The friction welding method:
  In the dipoles of the HERA proton ring, the helium cooling tube of the 40 K shield is made of aluminum. It is connected to the stainless steel flanges and bellows by friction welding. The helium pressure is 300 psi. During the past several years of operation, no helium leak from these welds has been found.[10] These joints are manufactured by Thevenet Clerjounie Co. The price is about \$100 apiece for a mass order.

III. IMPLEMENTATION

There are three possible ways to employ the aluminum beam tube in the Collider.

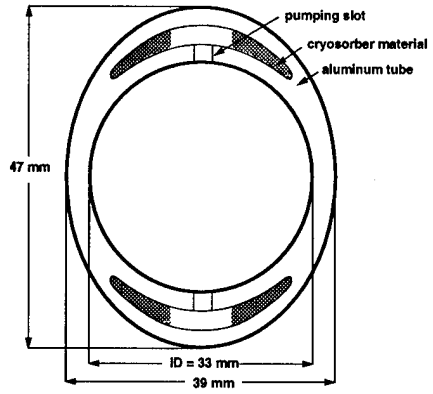


Figure 1. An aluminum tube with antechambers.

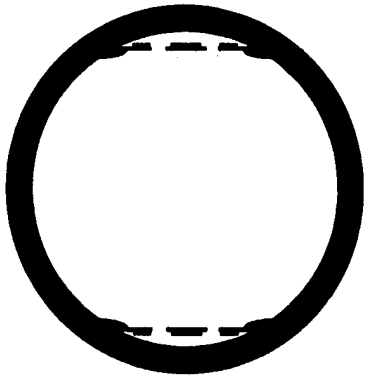


Figure 2. An aluminum tube with two plate insertions.

A. A beam chamber with antechambers

Because aluminum is easy to extrude, one may design a complex cross section to accommodate a cryosorber while eliminating the liner, such as the shape shown in Figure 1. It consists of a beam chamber and two "ears". The "ears" are the antechambers housing the cryosorber material such as coconut charcoal. The chamber and antechambers are connected by a series of pumping slots. The top-bottom symmetry is desirable for reducing the coupling impedance and the multipole magnetic field errors. The extrusion of a 15-m aluminum tube with such a cross section is feasible. There are, however, two potential problems: (1) Machining of the slots is not easy. (2) The two "ears" consume certain radial space that are precious to the magnet measurements.

B. A beam chamber with plate insertions

An alternative is to use a circular tube with two plate insertions as shown in Figure 2. The beam tube is extruded such that there is small bump on the inner surface that can support the plates. During magnet field measurements, the plates are not in place and, thus, a larger aperture is available. After the measurements, the two plates, which are perforated and have cryosorber material on one side, will be inserted into the beam tube for pumping purpose.

C. A beam chamber with an anodized layer

This is proposed in Ref. [11] and is illustrated in Figure 3. The anodized layer serves as a cryosorber. Therefore, no need for a liner. However, there are concerns about the impedance presented by this insulating layer and about the direct exposure of the layer to synchrotron radiation.

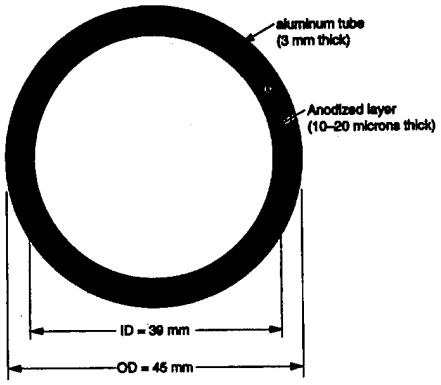


Figure 3. An aluminum tube with an anodized layer.

References

[1] W. Chou, SSCL-649, SSC Laboratory (1994).
[2] Y. Suetsugu and H. Ishimaru, Japanese Journal of Appl. Phys., Vol. 27, p. 1077 (1988).
[3] J. T. Rogers *et al.*, Appl. Phys. Lett., Vol. 52, p. 2266 (1988).
[4] E. Gray, LANL, private communication.
[5] K. Leung, SSCL, private communication.
[6] H. Ishimaru and M. Nilno, "*Result of Quench Test For Aluminum Alloy Clad Pipe,*" unpublished.
[7] A. G. Mathewson *et al.*, American Vacuum Society Series 12, Conference Proceedings No. 236, p. 323 (1991).
[8] W. Chou, "*Bunch Induced Multipactoring at the SSC,*" Internal Technical Note PMTN-0081C, SSC Laboratory (1993).
[9] N. G. Wilson *et al.*, Conference Record of 1991 IEEE Particle Accelerator Conference, Vol. 4, p. 2459.
[10] H. Kaiser, DESY, private communication.
[11] W. Nexsen, internal technical memo to W. Turner, SSC Laboratory, Sept. 27, 1991.

VARIABLE BUNCH SPACING IN SUPER COLLIDER

W. Chou, Fermi National Accelerator Laboratory,* P.O. Box 500, Batavia, IL 60510, USA

Abstract

This paper suggests a variable bunch spacing instead of a fixed value in the SSC. This will give a higher luminosity for a given beam current and provide more flexibility in machine operations. Two possible schemes for varying the bunch spacing, namely, bunch coalescing and beam chopping, are studied and compared. Some of these discussions may be useful to future accelerators.

I. INTRODUCTION

When the beam-beam tune shift limit is not reached, the luminosity $\mathcal{L}$ is proportional to the bunch spacing S_b:

$$\mathcal{L} = \left(\frac{\gamma}{4\pi c \cdot e^2}\right) \frac{I^2}{\beta^* \cdot \epsilon_N} \cdot S_b \qquad \mathrm{cm}^{-2}\mathrm{s}^{-1} \qquad (1)$$

in which γ is the relativistic factor, c the velocity of light, e the electron charge, β^* the β-function at the interaction point, I the average bunch current, and ϵ_N the normalized rms transverse emittance. The average number of events per crossing is:

$$n = \frac{\mathcal{L} \cdot \sigma_{\mathrm{inel}}}{c} \cdot S_b \qquad (2)$$

in which σ_{inel} is the inelastic pp cross section. The baseline parameters are: $\gamma = 21316$, $I = 71$ mA, $\beta^* = 0.5$ m, $\epsilon_N = 1$ mm-mrad, and $S_b = 5$ m. They correspond to $\mathcal{L} = 1 \times 10^{33}$ and $n = 1.7$.

The parameters I, β^* and ϵ_N were chosen based on the limitations of accelerator technology and the costs, whereas the choice of S_b was made by the detector requirement that n should be close to 1. In the following sections, we investigate the merits and penalties of a larger bunch spacing — a multiple of 5 meters — and the means to implement it.

II. MERITS AND PENALTIES

It is seen from Eq. (1) that, when all the other parameters are fixed, a larger bunch spacing will directly translate to a higher luminosity. This fact can be exploited in two different ways: (a) In the first few years during the commissioning stage, we will be on a learning curve. A larger bunch spacing can speed up the pace to reach the design luminosity. (b) When the machine operation is matured, a larger bunch spacing provides one of the easiest ways for a luminosity upgrade.

On the detector side, a larger bunch spacing would be beneficial to the electronics and instrumentation. This is because a lower collision frequency implies simpler electronics, easier synchronization of subsystems and easier bunch crossing identification. Moreover, a larger S_b is preferred by the detectors should the luminosity be below the design value, because it will bring n close to 1. Even when the luminosity reaches the design value, a larger S_b may still be preferred in order to get a higher luminosity in the n-for-$\mathcal{L}$ trade off.

A larger bunch spacing will also have certain negative impact on the pattern recognition of detector subsystems if it results in multiple events per crossing. The main concern is the tracking detector, which is most sensitive to an increase in pile-up per crossing, while the performance of the muon system, the electromagnetic calorimeter and hadron calorimeters will remain unchanged.

It is interesting to note that all the three LHC detectors — ATLAS, CMS, and L3P — claim they can deal with a n much larger than unity.[1-3]

III. IMPLEMENTATION

Assume $\mathcal{L}$ is fixed and S_b increased by a factor of 6. Then n will also be increased by the same factor. Below are two possible scenarios to achieve this bunch spacing.

A. Bunch coalescing

Assuming the coalescing be carried out in the MEB at the flat top (200 GeV), a new 10 MHz rf system (in addition to the main 60 MHz rf) is required. The longitudinal emittance ϵ_L will be increased by a factor of about 6. Because the baseline design includes an intentional ϵ_L blowup by a factor of about 50 when the beam is accelerated from 200 GeV to 20 TeV, the coalescing blowup factor can be absorbed in this process so that the final ϵ_L at 20 TeV will remain unchanged.

The reasons to choose the flat top in the MEB for coalescing are the following:

- The two cold machines, HEB and Collider, are excluded because of the possible quenching that could be caused by the lost particles during coalescing.
- The LEB is a fast cycling machine (10 Hz). It is thus difficult to incorporate the coalescing scheme.
- At the flat bottom (12 GeV), the beam lifetime due to gas scattering is poor, and the rf voltage required to generate the necessary size of the buckets to capture the coalesced bunches is high. In addition, a coalesced bunch with large longitudinal emittance represents a concern during the transition crossing.

The bunch coalescing has been a routine operation at Fermilab (Main Ring) and CERN (PS) for many years. The new features of the MEB coalescing are: (a) Unlike the Main Ring, all the buckets are filled in the MEB; (b) Unlike the PS, more bunches (six) need to be merged.

The procedure is: (a) reduction of the bunch momentum spread by either adiabatic debunching, or rf phase jump, or rf amplitude jump; (b) adiabatic capture and compression by the subharmonic rf system; (c) bunch rotation; (d) recapture of the coalesced bunches by the main rf system; (e) extraction. The simulations show that when coalescing 6 bunches using this scheme, the particles leaking into adjacent buckets are less than 0.5%.

*Operated by Universities Research Association Inc. under Contract No. DE-AC02-76CHO3000 with the U.S. Department of Energy.

0-7803-3053-6/96/$5.00 ©1996 IEEE

B. Beam chopping

This is to chop a gap in a sequence of micro-pulses of particles, i.e., to create a macro-structure. This has to be done when the beam energy is low, namely, in the linac, in order to avoid the radiation problem.

The injection from the linac to the LEB is a 4-turn process. In each turn, there are 9 micro-pulses injected into each LEB bucket. All the buckets are full. To change the bunch spacing from 5 m to 30 m, one has to chop out a gap of 25 m in the linac pulse sequence and fill up only every 6th bucket in the LEB. Meanwhile, each filled bucket has to contain more particles (a factor of 4, see Table 1) in order to maintain the luminosity. The number of injection turns has to be increased accordingly. The transverse emittance will also have to be blown up (by a factor of 3) due to the space charge. Four schemes have been studied:

1. The transverse deflector:
   This is a pulsed electrostatic deflector consisting of a number of pairs of plates. The voltage is applied to the plates sequentially at a rate that matches the beam velocity as a slow wave structure. In the AGS Booster, it is placed after the RFQ where the beam energy is 750 keV. Its length is about 1 m.[4] In the SSC linac, the beam exit energy from the RFQ is 2.5 MeV. Therefore, the deflector would have to be longer. The main concern of this scheme is that the no-focusing long drift space occupied by the deflector will cause a significant transverse emittance growth.
2. The energy chopper:
   This is a new idea proposed by D. Swenson. It is based on the fact that the Low Energy Beam Transport (LEBT) and RFQ are energy-selective. When the beam energy is 35 keV, the transmission in the RFQ is about 90%. When the energy error is ± 6 keV, the transmission is reduced to almost zero. Therefore, if one lowers the ion source energy down to 30 keV and installs a small acceleration device between the ion source and RFQ to provide alternatively $+5$ keV and -1 keV to the beam, then one can chop the beam by switching this device on and off. The device suggested by Swenson is a Betatron using a high permeability ferrite ring. It needs to provide the rise and fall times of 2-3 ns and the peak pulse length 21 ns. The difficulty is that the ferrite must have both high permeability and high frequency response. In the preliminary measurements using the commercial products CMD5005 and CN20, the rise and fall times of the primary are 200 ps, and that of the secondary are 25 ns (CMD5005) and 5 ns (CN20), respectively. The difference comes mainly from the geometry rather than the material. But the voltage of the pulse generator is too low (several volts) to draw any conclusions from the measurements.
3. The rf switch in the ion source:
   To meet the requirement of the neutron spallation source, V. Smith at LANL proposes to pulse the electrically-isolated collar in the Penning source to chop the H^- beam. The goal of the rise and fall times are on the order of 10 ns, which is still too slow compared with 2-3 ns required by the SSC linac.
4. The laser stripper:
   This is based on the observation that the binding energy of the second electron on the H^- is 0.75 eV and can be stripped by a laser beam of wavelength 1.06 μm (corresponding to a photon energy of 1.18 eV). The photoneutralization cross section is large (35 mega-barns). A pair of parallel mirrors of 5 cm length that reflects the laser beam 40 times can give rise to neutralization over 99%. However, if one wants to use this technology to chop 45 out of every 54 micro-pulses, the costs seem prohibitively high.

C. Comparisons

The advantages of the bunch coalescing method are:

1. For the same beam current, it gives more luminosity than that by the chopping method, because it does not have to sacrifice the transverse emittance.
2. For the same luminosity, it can ease the space charge problem in the LEB, because the number of protons per bunch is smaller.
3. It is a proved technology.

The advantages of the beam chopping method are:

1. It is flexible. In principle, it can create any macro-structure in the beam as needed. This is in contrast to the coalescing method, which requires a specific subharmonic rf system for a specific coalescing scenario.
2. It can decrease the current per bunch. This feature will be particularly useful during commissioning.
3. It can reduce the radiation at the LEB extraction.

IV. ACCELERATOR ISSUES

Table 1 lists the changes of the beam parameters when the bunch spacing is increased from 5 m to 30 m by the two different methods. The luminosity is fixed at 1×10^{33} cm^{-2}s^{-1} in these calculations.

1. Space charge in the LEB:
   When the chopping method is used, one has to put about 4 times more particles into a bunch. But this should be okay when one allows ϵ_N to be increased by a factor of 3. The simulation results are supported by the Fermilab Booster measurement data.
2. Injection efficiency in the LEB:
   When the chopping method is used, only a portion of the LEB buckets are to receive particles from the linac. The particles may leak into the neighboring empty buckets and create satellites or cause particle loss. Therefore, one needs to modify the rf voltage profile and inject 7 micro-pulses in each turn instead of 9. Simulation shows the particle loss will be less than 3%.
3. Dynamic aperture in the Collider:
   When ϵ_N is 3 times larger, the dynamic aperture, expressed in terms of the beam size σ, will be reduced. The values listed in Table 1 are obtained by a scaling formula. More accurate data by long term tracking (10^5 turns) gives 9σ.
4. Single bunch instability threshold:
   This should not be a serious problem because there is a relatively large safety margin (about 6) in the design. Furthermore, this margin can be improved by redesigning the longitudinal emittance budget.
5. Beam-beam interaction:
   The head-on tune shift is increased because there are more

Table 1. Beam Parameter Dependence on Bunch Spacing

Parameter	S_b = 5 m $\epsilon_N = 1 \times 10^{-6}$	S_b = 30 m $\epsilon_N = 1 \times 10^{-6}$ Coalescing	S_b = 30 m $\epsilon_N = 3 \times 10^{-6}$ Chopping
Events per crossing n	1.7	10	10
Time interval between crossings Δt (ns)	17	100	100
Events per second (s^{-1})	10^8	10^8	10^8
Average current I (mA)	71	29	48
Protons per bunch N_b ($\times 10^{10}$)	0.81	2.0	3.3
Number of bunches M	17424	2904	2904
Head-on tune shift $\Delta\nu_{HO}$	0.0038	0.0094	0.0053
Long range tune shift $\Delta\nu_{LR}$	0.0067	0.0027	0.0046
Long range tune spread $\delta\nu_{LR}$	0.0020	0.0008	0.0041
LEB space charge tune shift $\Delta\nu_{SC}$	0.38	0.16	0.53
Synchrotron radiation P_s (kW/beam)	9.0	3.7	6.1
Parasitic heating P_{loss} (kW/beam)	1.3	1.3	3.6
Instability threshold $Z_{\|}/n$ (Ω)	3.7	1.5	0.9
$Z_\perp$ (MΩ/m)	250	100	60
Resistive wall instability τ_{wall} (turns)	106	260	155
Dynamic aperture during injection (σ)	13	13	8.0
Dynamic aperture at IR (σ)	11	11	6.2
Beam-beam luminosity lifetime $\tau_{\mathcal{L}}$ (h)	78	32	54
Intrabeam scattering lifetime τ_x (h)	211	86	516
τ_z (h)	120	49	109
Luminosity reduction factor R_r	0.91	0.91	0.97

particles in a bunch, whereas the long range tune shift is decreased because of a larger S_b. The total change is small and the sum is well below the tune shift budget of 0.02.

6. Synchronization during beam transfer:
When the chopping method is used, the linac and LEB need to be phase locked. In addition, the beam transfer must be bucket-to-bucket. The SSC synchronization scheme assures that these can be done.
7. Instrumentation:
The specifications (dynamic range, bandwidth and accuracy) of the orbit and phase measurements need to be revised in order to serve variable bunch spacing.
8. Other issues:
   (a) The average beam current becomes smaller, whereas the peak current becomes larger.
   (b) The synchrotron radiation is proportional to the average beam current. Therefore, it is also decreased.
   (c) The parasitic heating is proportional to the product of the average and peak beam current. It remains the same (in the case of coalescing) or is increased (in the case of chopping). This term may become a dominant loss term if more and more charges are put in a bunch for luminosity upgrades.
   (d) The beam-beam luminosity lifetime becomes shorter because the number of protons is smaller.
   (e) The total number of bunches is reduced by a factor of 6. This will make the machines more stable.

V. ACKNOWLEDGEMENT

This paper represents a collaborated work that involves many people's contributions, in particular, J. Griffin, D. Swenson, R. Shafer, D. Raparia, D. Anderson, S. Machida, N.K. Mahale and F. Pilat.

References

[1] ATLAS Collaboration Internal Note GEN-NO-001, CERN (January 25, 1993).

[2] CMS Collaboration Internal Note CMS-M/93-05, CERN (January 25, 1993).

[3] L3P Collaboration, "L3P Physics Performance and Increased LHC Bunch Spacing," memorandum to the LHC Committee, CERN (1993).

[4] J. M. Brennan *et al.*, Proc. 1989 IEEE Particle Accelerator Conference, March 1989, Chicago, p. 1154.

FERMILAB COLLIDER RUN 1B STATISTICS

V. Bharadwaj, J. Crawford, R. Mau

Fermi National Accelerator Laboratory, P.O. Box 500, Batavia, Il 60510

The present Fermilab Tevatron Collider run, designated as Run 1b, started in October 1993 and will conclude in July 1995. This paper summarizes the parameters and performance of the Fermilab accelerator complex to date. Operational problems encountered during the run are described as well as the factors that limit peak and delivered luminosities.

I. INTRODUCTION

The Fermilab Tevatron is the world's highest energy superconducting proton synchrotron. It has been modified to also run as a colliding beam storage ring in order to study proton-antiproton collisions, presently at 1800 GeV in the center of mass. There have been four collider runs to date i.e., the 87 run, the 88-89 run, Run 1a and Run 1b. More details on the status of the Fermilab collider are given in reference [1].

II. TABLES AND FIGURES

Table I list some parameters for the accelerator complex for the 88-89 Run, Run 1a and Run 1b. There has been a steady improvement in all parameters.

Table II contains performance numbers for Run 1b and compares them to their values in the two previous runs. There has been a factor of ten improvement since the 88-89 Run.

Table III categorizes the stores that ended abnormally. The percentage of stores ending abnormally is smaller now and there is less sensitive to the TeV power supply system and to power glitches and lightning.

Figure 1 shows the evolution of peak luminosity during Run 1b and compares this to Run 1a. A 10X running average is applied to remove the scatter of points.

Figure 2 displays integrated luminosities. The bars represent the weekly delivered luminosity and the lines the run totals.

Figure 3 shows the antiproton stacking rate. Again there has been a steady increase in the stacking rate. The accumulator regularily stacks greater than 6×10^{12} antiprotons in a week, nearly twice the rate for Run 1a.

Figure 4 shows the luminosity per store hour. In the last few weeks before this conference the collider has been delivering greater than 40 nb^{-1} per hour.

[1] "Status and Future of the Tevatron", V. Bharadwaj, proceedings this conference.

Table I : Fermilab Collider Parameters

Collider Parameters	**88-89 Run**	**Run 1a**	**Run 1b**
Protons/bunch (10^{10})	7.00	12.00	22.50
Antiprotons/bunch (10^{10})	2.90	3.10	6.50
Proton emmitance (π mm-mr)	25	20	22
Antiproton emmitance (π mm-mr)	18	12	14
Beta* at interaction point (meters)	0.55	0.35	0.35
Bunch length (RMS , meters)	0.65	0.62	0.62
Typical luminosity (10^{31} $cm^{-2}sec^{-1}$)	0.16	0.54	1.89
Best luminosity (10^{31} $cm^{-2}sec^{-1}$)	0.21	0.92	2.31
Integrated Luminosity (pb^{-1}/ week)	0.32	1.09	3.82
Interactions/crossing (@ 45 mb)	0.25	0.85	2.98
Antiproton tune shift	0.025	0.009	0.015
Proton tune shift	0.014	0.004	0.007
Average luminosity lifetime (hours)	20	17	15
Typical Antiproton Stack (10^{10})	70	120	180
Antiproton stacking rate (10^{10}/hour)	1.5	3.0	4.5
Main Ring Intensity (10^{12} protons per pulse	1.5	2.0	3.2

0-7803-3053-6/96/$5.00 ©1996 IEEE

Table II : Collider Statistics

	88-89 Run	Run 1a	Run 1b
Total Integrated Luminosity (pb^{-1})	9.59	31.70	100.80
Total store hours	4257	3373	5531
Peak luminosity ($10^{31}cm^{-2}sec^{-1}$)	0.21	0.92	2.31
Integrated luminosity rate (nb^{-1}/hour)	3.5	11.0	36.0
Max integrated luminosity in a week (pb^{-1})	0.52	2.33	4.89
Max integrated luminosity in a store (pb-1)	0.14	0.39	0.82
Max antiproton stack	97	150	221
Longest store	53	33	29
Typical shot setup time (hours)	3.5	2.5	2.5
Typical store length (hours)	21	18	16
Total number of stores	295	265	426
Abnormal store ends/total # of stores (%)	55	35	27

Table III: Store End Categories

Store end explanation	**88-89 Run**	**Run 1a**	**Run 1b**
Intentional	133	173	309
Controls	8	19	17
Quench protection system	17	15	17
TeV power supplies (TECAR)	16	5	11
Lightning & power glitches	15	5	6
TeV RF system	11	1	6
Human error	11	6	8
Cryogenics	9	7	8
Experimental areas operations	7	1	1
Correction systems	12	8	5
Vacuum	4	1	3
Low beta quads	4	6	15
Utilities	3	6	7
Instrumentation	0	1	1
Abort kicker prefire	31	0	1
Miscellaneous	14	11	11

Figure 1: Average Peak Luminosity ($cm^{-2}sec^{-1}$) vs. Day

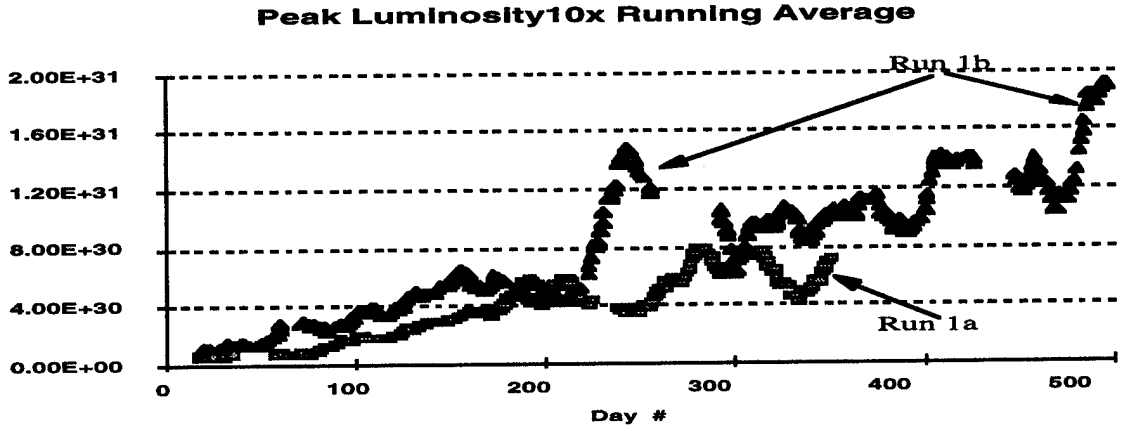


Figure 2: Weekly and Run Integrated Luminosities (nb^{-1})

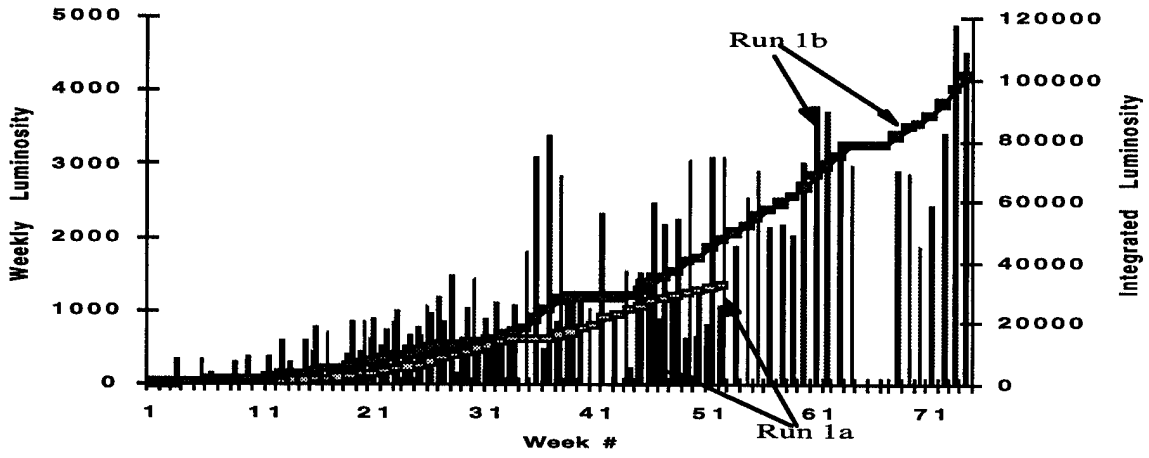


Figure 3: Antiproton Stacking ($x10^{10}$ antiprotons)

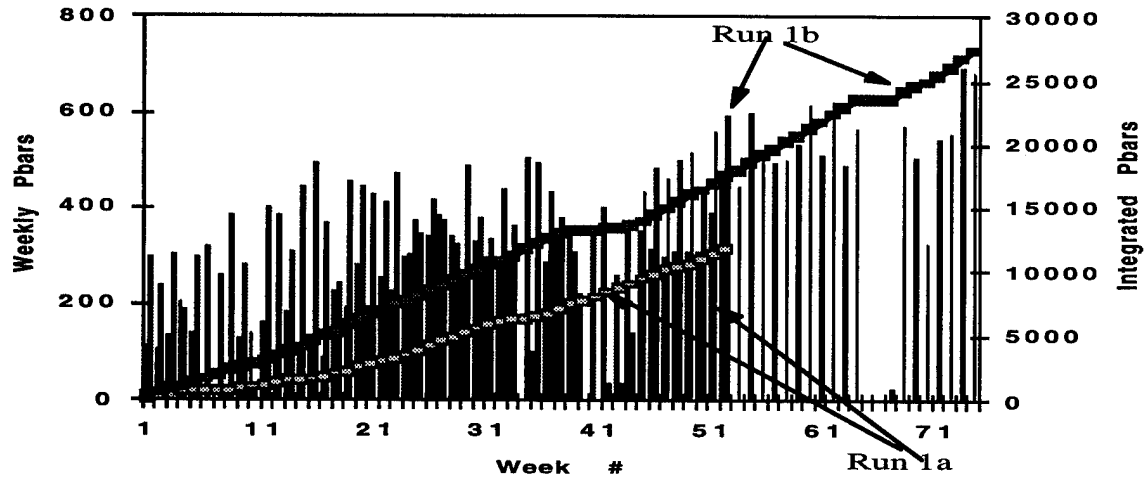
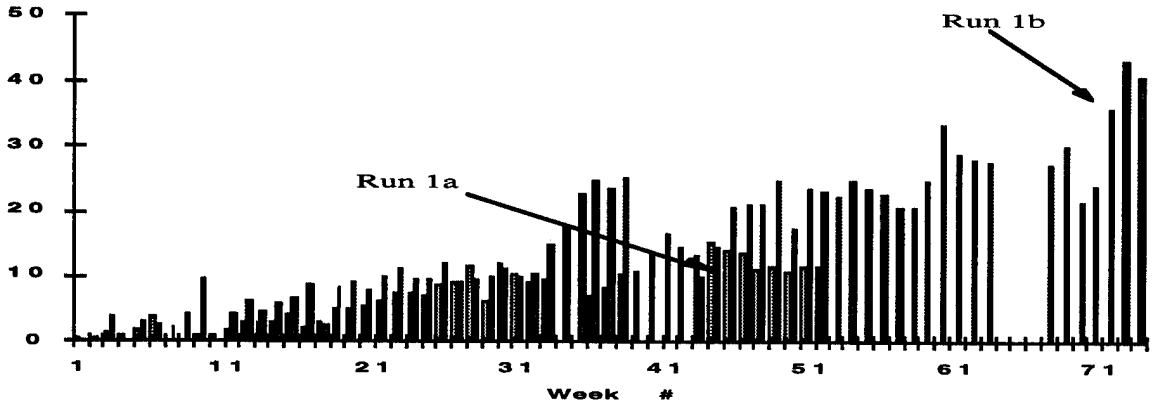


Figure 4: Luminosity per Store Hour (nb^{-1} /hour)



Optimizing the Luminosity in the Tevatron by Independently Moving the Horizontal and Vertical Beta Stars Longitudinally

M. A. Martens, G. P. Goderre
Fermi National Accelerator Laboratory
P. O. Box 500, Batavia, IL 60510, USA

Abstract

The low beta tripplet in the Tevatron is instrumented such that it is possible to move the horizontal and/or the vertical beta star in the longitudinal direction. This control over beta star allows us to minimize the longitudinal separation of horizontal and vertical beta star at each interaction region independently, thus maximizing the luminosity. Results of varying the longitudinal separation of horizontal and vertical beta star are shown and the sensitivity of the luminosity on this parameter is discussed.

I. Introduction

In the Fermilab Tevatron a series of low beta quadrupoles are used to transversely focus the proton and antiproton bunches as they collide in the B0 (CDF) and D0 interaction regions. The Tevatron lattice is designed such that the center of the experimental detectors is aligned longitudinally with both the minimum of β_x and the minimum of β_y. Due to imperfections in the lattice however, the minimum β_x and minimum β_y may not coincide resulting in a lower luminosity and a shift in the longitudinal luminosity distribution. The luminosity may also be reduced if the centers of the proton and antiproton bunches do not collide at the same place as the minimum β. Therefore the luminosity is maximized by aligning the collision point and minimum β.

Changes to the collision point in the Tevatron are easily made by cogging the antiproton bunches with respect to the proton bunches. As we will show in this paper, the positions of the minimum β can also be changed by adjusting the currents in the low beta quadrupoles near the interaction regions. Using a combination of the β moves and cogging changes we have been able to increase the luminosity at CDF and D0 and to better center the longitudinal luminosity distribution in the CDF detector.

In the next section we introduce the α-bumps which are used to change the position of the minimum β. We then give some examples of the sensitivity of the luminosity on mis-alignments of the minimum β and collision point. Finally we give some results of implementing these α-bumps in the Tevatron.

II. α -bump

Figure 1 shows a sketch of the low beta quadrupoles on either side of one of the interaction regions in the Tevatron. For our purposes the currents in these magnets can be thought of as being supplied by four power supplies: 1 on Q3U, 1 on Q3D, 1 on Q2U and Q4U in series, and 1 on Q2D and Q4D in series.* By changing the currents in these magnets in the proper ratio it is possible to change the value of $\alpha = -\frac{1}{2}\frac{d\beta}{ds}$ in the center of the interaction region. The net effect of this α-bump is to move the position of the minimum β without changing the value of the minimum β and without changing significantly the lattice outside of the tripplet magnets.

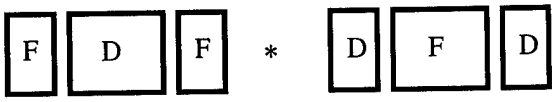


Figure. 1. Sketch of the positions of the low beta tripplet quads around the interaction point (IP). F (D) are focusing (defocusing) in the horizontal plane.

The simplest way to understand how the α-bump works is by first realizing that phase advance $\Delta\psi$ between the upstream set of magnets and the downstream set is nearly 180 degrees. This makes it possible to start a β-wave in the upstream magnets and almost identically cancel the β-wave in the downstream magnets. To determine the ratio of current changes in the quadrupole magnets for a horizontal α-bump, for instance, we use the constraints: 1) start a β_x-wave in the upstream magnets, 2) cancel the β_x-wave in the downstream magnets, 3) create no β_y-wave in the upstream magnets, and 4) create no β_y-wave in the downstream magnets.

The β-wave created by a quadrupole kick of strength $q = B'l/(B\rho)$ at a location where the β has a value of β_1 is given by [2]

$$\frac{\Delta\beta}{\beta} = -q\beta_1 \sin 2\psi_0 + \frac{1}{2}(q\beta_1)^2(1 - \cos 2\psi_0) \qquad (1)$$

where ψ_0 is the phase advance of the unperturbed β function. Since the value of β is large in the quadrupole magnets the phase advance through the tripplet magnets is very small (0.4 degrees) and we can make the approximation that phase advance between the magnets and the center of the interaction region is 90 degrees. This simplifies the calculation of the α-bump since we can treat the quadrupole kicks from the 3 upstream magnets

*In reality the Q2 and Q4 magnets are on one buss with a trim supply to add current to the upstream magnets and the Q3 magnets are on one buss with a trim supply to add current to the upstream magnet.

Operated by the Universities Research Association,Inc, under contract with the U.S. Department of Energy

0-7803-3053-6/96/$5.00 ©1996 IEEE

as single kick with strength

$$\kappa_x = -q_{Q2U}\beta_{x,Q2U} + q_{Q3U}\beta_{x,Q3U} - q_{Q4U}\beta_{x,Q4U} \qquad (2)$$

where the $\beta_{x,Q2U}$, for instance, is the average beta function in the Q2U quadrupole, and q_{Q2U} is the change in gradient strength multiplied by the length of the magnet. The resulting β-wave is then given by

$$\frac{\Delta\beta_x}{\beta_x} = \kappa_x \sin 2\psi_0 + \frac{1}{2}\kappa_x^2(1 - \cos 2\psi_0) \qquad (3)$$

Ignoring any coupling effects, and assuming the unperturbed β function in the interaction region is given by

$$\beta(z) = \beta^* + \frac{z^2}{\beta^*} \qquad (4)$$

we can use Eq. 3 to calculate the new β function with the α-bump in place,

$$\beta_{x,\mathrm{new}} = \beta_x^* + \frac{(z + \kappa_x\beta_x^*)^2}{\beta_x^*} \quad . \qquad (5)$$

As Eq. 5 shows, there is no change in the value of the minimum β and the position of the minimum β is moved by $-\kappa_x\beta_x^*$. A similar expression holds in the vertical plane as well. By choosing κ_x and κ_y in the correct ratio we can change the horizontal beta function and leave the vertical beta function unchanged.

During colliding beam operations the collision point and α-bump strengths are adjusted to maximize the luminosities at B0 and D0 separately.

III. Luminosity dependence on α-bumps

The luminosity of proton and antiproton bunches colliding in the Fermilab Tevatron is given by the luminosity overlap integral [1]

$$\dot{} = \frac{f_{\mathrm{rev}}N_pN_{\bar{p}}}{\sqrt{2\pi}^3\sigma_z}\int \frac{\exp(-(z-z_0)^2/2\sigma_z^2)}{\sigma_x(z)\sigma_y(z)}\,dz \quad . \qquad (6)$$

In this expression it is assumed that the longitudinal and transverse beam profiles are Gaussian and we ignore coupling and differences in the proton and antiproton orbits. As Eq. 6 shows, the luminosity is affected by such things as the collision point z_0, the longitudinal widths of the bunches $\sigma_z^2 = (\sigma_{z,p}^2 + \sigma_{z,\bar{p}}^2)/4$, and the transverse width of the bunches $\sigma_x^2(z) = \sigma_{x,p}^2(z) + \sigma_{x,\bar{p}}^2(z)$. The widths of the particle bunches are a function of the emittances, momentum spread and β function, $\sigma_x^2 = \epsilon_x\beta_x^* + (\eta_x\sigma_\delta)^2$. Therefore the luminosity is also dependent on the β functions.

To demonstrate the effects that offsets in the collision point and position of the minimum beta have on luminosity we use Eq. 6 with a set of typical beam parameters for collider operations. The 95% normalized emittances we use are $\epsilon_{x,p} = \epsilon_{y,p} = 25\pi$, $\epsilon_{x,\bar{p}} = \epsilon_{y,\bar{p}} = 15\pi$, and $\sigma_z = 45$ cm. Fig. 2, for instance, shows the reduction in luminosity as a function of an offset in the β_x. As seen in Fig. 2 the luminosity is 5% below optimum when the minimum β_x is moved by 20 cm. Offsets in the collision point have a similar effect on the luminosity as shown in Fig. 3.

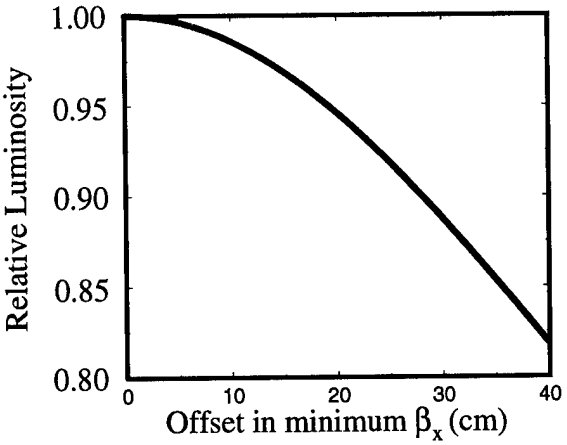


Figure. 2. Luminosity as a function of offset in the minimum β_x for typical collider operations.

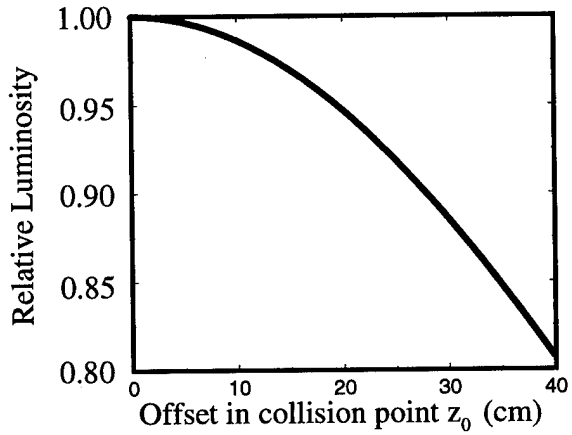


Figure. 3. Luminosity as a function of collision point offset z_0 for typical collider operations.

In addition to lowering the luminosity offsets in the minimum β and collision point also affect the longitudinal distribution of the luminosity $d\dot{}/dz$. Fig. 4 shows the effect of a 20 cm offset in the position of β_x. The dashed line is the luminosity distribution for the nominal parameters and the solid line is the luminosity distribution with the offset β_x. Both the reduction in luminosity as well as the shift in the distribution are apparent.

IV. Conclusions

The α-bumps described above were implemented and used in the Tevatron during collider run IB. An example of a α-bump scan is shown in Fig. 5. In this particlular example the luminosity at D0 was recorded as the magnitude of the horizontal α-bump was changed.

After several iterations of α-bump scans and cogging scans we found that we could increase the luminosity at D0 by 3%, increase the luminosity at CDF by 1% and move the center of the distribution at CDF from +4.5 cm to within 1 cm of the center of the detector. The net changes to the cogging and positions of the minimum β are shown in table I.

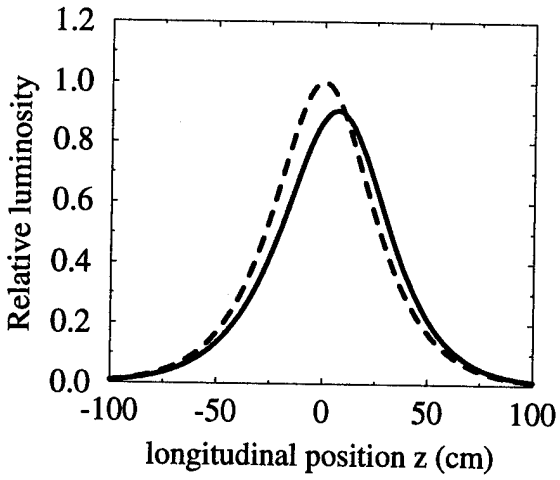


Figure. 4. Change in the luminosity distribution created by an +20 cm offset in the position on minimum β_x. The dashed line is the nominal distribution and the solid is the distribution with the offset.

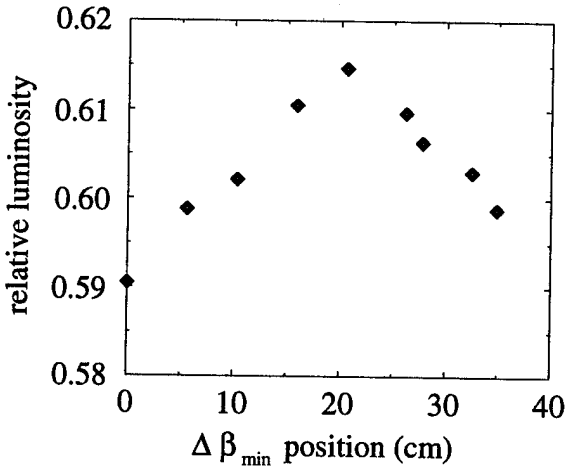


Figure. 5. Measured luminosity at D0 as a function of α_x-bump amplitude. This measurement shows that moving the β_x minimum by +20 cm would maximize luminosity.

Δz_0	-6 cm
$\Delta\beta_x$ at CDF	-11 cm
$\Delta\beta_y$ at CDF	0 cm
$\Delta\beta_x$ at D0	-4 cm
$\Delta\beta_y$ at D0	+13 cm

Table I

Net changes made to Tevatron lattice as a result of cogging and α-bump scans.

References

[1] M. Month, "Collider Performance with Ideal Collisions", "Accelerator Division Report 85–1", (1985)

[2] D.A. Edwards and M.J. Syphers, "An Introduction to the Physics of High Energy Accelerators", John Wiley and Sons, Inc., New York, (1993)

A MODEL OF THE FERMILAB COLLIDER FOR OPTIMIZATION OF PERFORMANCE

Elliott S. McCrory and Peter W. Lucas
Fermi National Accelerator Laboratory*
Batavia, IL 60510, USA

Abstract: A Monte Carlo-type model of the Fermilab Collider has been constructed, the goal of which is to accurately represent the operation of the Collider, incorporating the aspects of the facility which affect operations in order to determine how to run optimally. In particular, downtime for the various parts of the complex are parameterized and included. Also, transfer efficiencies, emittance growths, changes in the luminosity lifetime and other effects are included and randomized in a reasonable manner.

INTRODUCTION

This model is written as a set of C++ classes, which each represent some aspect of collider operations. It is an entirely phenomenological model, with its parameters based only on direct observation of the operation of the Fermilab Tevatron Collider. Parameters in this paper are based on the period from March 1 through April 15, 1995.

A more thorough analysis of this topic can be found in the Reference.

Definition of Parameters

Many aspects of the Collider are randomized in order to realistically reflect present-day operations. The randomization comes from the C routine `srand(3V)` provided by Sun under SunOS 4.1.3. Simple correlation plots of this generator show it to be satisfactory.

The parameters used in this model are summarized in Table 1.

Stacking. Stacking is the creation and accumulation of anti-protons. The stacking rate is observed to be accurately parametrized by the following (surprising?) form:

$$R = R_0 / \cosh(S/S_c)$$

where R_0 is the zero-current stacking rate, S is the present stack size and S_c is chosen to accurately reproduce the stacking rate fall-off at higher stack values. The stacking rate is randomly reduced by upstream studies and/or other programmatic work.

Stacking downtime is parameterized as a fractional "up time" with a randomly varying time down. When in a stacking downtime, there is a probability that this downtime causes the antiproton stack to be lost. The model parameters are adjusted to accurately reflect the present operation: stacking downtime is 5 to 10%, and a stack is lost every 7 to 10 days.

Aspect	Param	Description	Units	Value	Randomize
Model	Δt	Time step in simulation	hours	0.1	-
Stacking	*D1*	Probability that stacking is okay	1/hour	0.99	-
	T1-1	Max time stacking off	hours	10	1-10 hrs
	D2	Probability of keeping the stack	1/hour	0.4	-
	R0	Zero-current stacking rate	mA/hour	7.5	10% less
	Sc	Critical Stacksize	mA	190	-
	Average time between lost stacks		days	8	
Accumulator	ε *pbar*	Zero-stack core emittance, normalized, 95%	mm mr	9.3 π	3 π
	g	Emittance growth per stack size	emit/mA	0.02	-
	f max	Zero-stack extraction fraction	-	0.70	0.08
	w	Extraction fraction reduction	1/mA	0.0011	-
	e all	Overall transmission efficiency (best)	-	0.8	2% per step
Main Ring	εp	Initial Proton Emittance	mm mr	12 π	5 π
	Np	Initial Proton Intensity	E10/bun	25.0	1.0
Tevatron	*D3*	Probability that store is retained	1/hour	0.9801	-
	T3-1	Max recovery time	hours	24	1-24 hours
	B	Number of bunches	-	6	-
	Fraction of stores ended intentionally		%	70	
Collider	$\mathcal{K}$	Conv from Accelerator units to Luminosity	*complex*	4.0	20%
	τ	Initial Luminosity Lifetime	hr	11	5%
	K	Initial Lifetime growth	hr/hr	1	-

Table 1, Overview of Parameters

Luminosity. The instantaneous luminosity is:

$$\mathcal{L} = \mathcal{K} \frac{N_p N_{\bar{p}}}{\varepsilon_p + \varepsilon_{\bar{p}}}$$

If the intensities are in units of E10 particles per bunch, the emittances are in units of 95% π mm mrad and the luminosity is in units of (10^{30} cm^{-2} sec^{-1}), then $\mathcal{K}$ is, numerically, about 4.

Each of the two intensities and two emittances above die out so that the overall luminosity obeys this form:

$$\mathcal{L}(t) = \mathcal{L}_0 e^{t/(\tau + K t)}$$

The lifetime growth factor K is about 1hr/hr initially. A constant growth factor does not make sense for very long stores, so the lifetime growth is a smoothly varying function which is 1.0 hr/hr at the beginning of the store and 0.5 hr/hr at 36 hours.

Downtime in the Tevatron means losing a pbar-p store. When the Tevatron is down, the amount of time down is calculated randomly from 1 to 24 hours. There is no downtime in this model greater than 24 hours. The performance of the Collider is being modelled; incorporating longer downtime would mask the optimizations which are, hopefully, being revealed. The data presented below use 30% of the stores lost by failure.

* Operated by the Universities Research Associations, Inc., under contract with the U.S. Department of Energy, contract number DE SC02 76CH03000

Scheme	Target	Best Targ Val(s)	Error bar	Exp'd Lum
Straight	Duration	21 hours	1 hour	4797 ± 24
	Stack Size	175 mA	10 mA	5054 ± 28
	Min Lum	4.5 E30	0.2	4772 ± 24
	Integrated	1100 (1/nb)	100 (1/nb)	4826 ± 30
	Stack *OR* Duration	190 mA *OR* 22 hours	n/a	5078 ± 23
Figure of Merit	Stack, Min Lum & Integrated	Stack=160 mA MinLum=6E30 Integ'd=850 (1/nb)	unknown	5141 ± 24
Ratio	Luminsoity Ratio	2.6	0.3	4988 ± 27
Difference	Luminosity Difference	10 E30	0.5 E30	5089 ± 26

Table 2, Summary of Scheme Optimizations.

Taking a Shot. We call the two-hour process of preparing the Accumulator for pbar transfers, tuning of the Main Ring and Tevatron and the transference of pbars and protons to low beta in the Tevatron a "Shot." Most of the aspects of this class are randomized. The randomizations are linear.

The average number of pbars per bunch is

$$N_{\bar{p}} = S\ (f_{\max} - wS)/B$$

where S is the stack size, $f_{\max}$ is the maximum fraction of the stack which can be extracted, w is the rate at which this fraction falls off with stack size and B is the number of bunches (6, for the present run). This is randomized by ± 8%.

The transmission efficiency of the pbars from the Accumulator to low beta is a major contributor to the performance of the collider. This transmission is randomized by small, non-unity transmissions on the way to low beta for both the the pbars and the protons.

The emittance of the pbars from the Accumulator is

$$\varepsilon_{\bar{p}} = \varepsilon_0 + gS$$

This emittance and the proton emittance are randomly grown in each of the steps to low beta.

The other randomizations are: The time necessary for shot setup is usually two hours, but 50% of the time, the shot setup is increased by up to four more hours. Also, when a store is lost, stacking stops half the time, too.

How Do We Decide When To End Stores?

The genesis of this analysis was to determine the best criteria for ending stores intentionally. We have, in the past, always ended stores by the wall clock. Three schemes for ending the stores are considered here.

Scheme 1: End when a critical parameter exceeds a target value. The parameters considered are the duration of the store, the stack size, the instantaneous luminosity and the integrated luminosity from this store. We refer to these, collectively, as the "Straight Scheme." Several variations on this scheme have been considered.

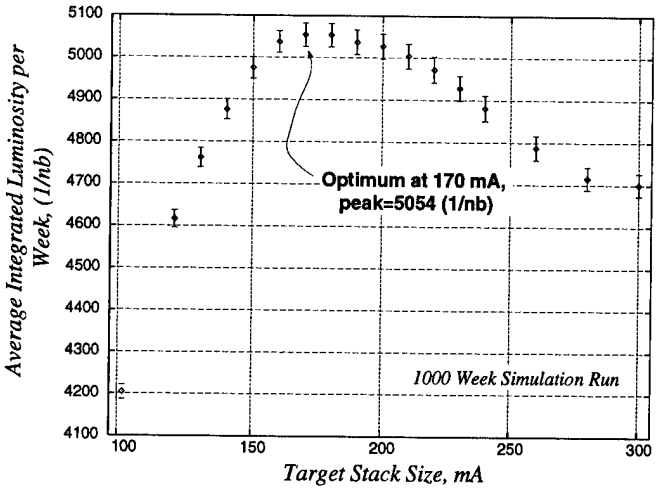


Figure 1, Optimization of the Target Stack Size.

Scheme 2: Calculate a "figure of merit" based on how some of these critical parameters exceed targets. A multiplicative factor is used to convert these (numerically) different quantities to the same basic units. The time to end the store is when the figure of merit exceeds some value, zero is used here. This is the "Figure of Merit Scheme."

Scheme 3: Assuming knowledge of the expected luminosity for a given stack size, then two approaches can be made. Calculate the ratio of the luminosity expected from the current stack size to the luminosity now; end the store when this ratio exceeds some constant. This is called the "Ratio Scheme." Or, alternatively, end when the difference between the expected luminosity and the actual luminosity exceeds some value. This is called the "Difference Scheme."

Analysis

Many analyses have been carried out with this model. They are: Which criterion is the best for ending stores; What is the character of a typical store; What is the character of a typical week; How do changes in downtime affect these results; What is the effect of improved stacking; What is the effect of other Collider improvements; How is the luminosity delivered to the experiments, that is how much luminosity is integrated at each instantaneous luminosity. Only the first three are reported here due to space limits.

Which Criterion is Best? A summary of some of the optimization results from this model is presented in Table 2. The Straight Scheme using only the Target Stack Size is the most consistent and understandable method for producing high weekly luminosities. A simple graph of average weekly luminosity for 1000 weeks of simulated running versus the target stack size is shown in Figure 1. (It has been our experience that we should shoot from stacks slightly larger than the optimum because we, as human researchers, tend to improve perfor-

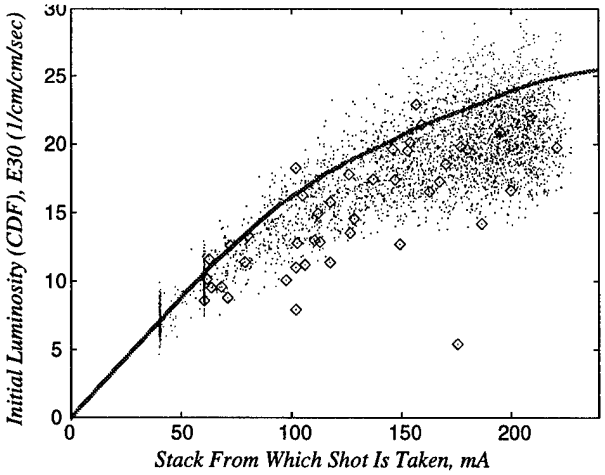


Figure 2, Initial Luminosity versus anitproton Stack Size; model predictions and actual data.

mance, unlike this model which shows the same performance at all times.) This method has the (not-to-be underestimated) benefit of being understood by all observers. Ending a store when either the stack size is bigger than 190 mA OR the store duration is more than 22 hours seems to be slightly better than the stack size criterion alone.

The figure-of-merit scheme produces average luminosities up to 3.5 sigma better than the target stack criterion alone, but many different, unrelated parameter choices give similar results. One such combination is with the following "goals" in the figure-of-merit calculation: Stack=160 mA, end luminosity=6E30, total store integrated=850 nb^{-1}. This investigation is proceeding.

The ratio and the difference schemes are each good criteria for the stable performance assumed in this model.

A definite conclusion drawn from this model is that using the store duration alone is a rather poor criterion for ending stores. The best one can do with this parameterization (21 hour stores) is 10 sigma worse than the best target stack size run. Other suggestions from the "peanut gallery" of observers have been similarly eliminated.

(It should be pointed out that the decision to end a store usually contains some sociological consideration!)

Figure 2 is one which we use in Operations daily: the initial luminosity vs. stack size. The dots are from 200 weeks of this simulation, the diamonds are the real data and the line is the average of the top half of the simulation in 10 mA bins.

What is Typical? A typical store, which is ended intentionally, is characterized by the data in Table 3. Some comparison between using the Target Stack Size criterion (using 180 mA target) versus using a Figure of Merit approach can be made. Also, the difference between all stores and only those stores which are ended intentionally is shown. The sigmas are the calculated first moments of the distributions.

A typical week is characterized by the data in Table 4. Here, again, some comparison can be made between a Target Stack Size criterion and the Figure of Merit approach.

CONCLUSION

A good representation of the Fermilab Collider exists which models the operational features of the Tevatron, the Pbar Source and of shot setup. Conclusions can be made on what criteria are best for determining when to end a store. In particular, strong conclusions can be made about the unacceptability of several possible criteria. Parameters describing a typical store and a typical week can be calculated. Work on this model continues.

A nice benefit of this model has been in developing intuition on the operation of the Collider. In particular, we and the other Run Coordinators for the Fermilab Collider now have a much better idea about what to expect in day-to-day operations. Moreover, recent preformance of the real Collider has been comparable to the optimal preformance predicted here.

REFERENCE

Fermilab Technical Memo TM-1901, "Modelling the Fermilab Collider to Determine Optimal Running," E. McCrory.

			Best Target Stack Size			Best Figure of Merit		
Aspect	**Units**		*Average*	*Median*	*Sigma*	*Average*	*Median*	*Sigma*
Stack Shot From	mA	ALL	158.2	180.9	38.1	163.1	178.3	42.9
Initial Luminosity	E30		18.64	20.52	3.93	18.83	19.99	4.09
Final Luminosity	ditto		8.00	6.55	3.48	7.81	7.75	3.50
Total Integrated	(1/nb)		650.0	695.7	245.7	681.7	734.8	263.9
Store Duration	Hours		17.0	17.8	7.6	17.7	19.6	7.4
Stack Shot From	mA	GOOD	160.6	180.2	36.0	164.7	183.9	41.8
Final Luminosity	E30		6.74	6.22	1.85	6.38	6.24	1.57
Total Integrated	(1/nb)		758.8	749.2	156.7	802.1	806.8	172.6
Store Duration	Hours		20.3	17.1	5.3	21.5	19.2	3.8

Table 3, Data for a Typical Store.

		Target Stack Size			Best Figure of Merit		
Aspect	*Units*	*Average*	*Median*	*Sigma*	*Average*	*Median*	*Sigma*
Integrated Luminosity	(1/nb)	5083.1	5128.0	743.6	5140.7	5202.3	754.7
Store Hours	Hours	132.5	133.4	9.5	133.5	134.1	9.9
Integrated per Hour	(1/nb)	38.32	39.03	4.65	38.47	39.32	4.58
PBars Stacked	mA	736.6	741.1	45.3	728.6	733.6	45.6
Stacking Hours	Hours	132.8	133.9	9.1	133.8	134.3	9.3
Num Shot Setups		7.8	8	1.0	7.5	8	0.9
Hours in Shot Setup	Hours	25.12	26.05	5.37	24.0	24.8	5.1
Tevatron Downtime	Hours	8.92	8.86	5.71	8.98	9.28	5.71
Stacking Downtime	Hours	5.28	2.4	8.21	5.43	3.45	7.94
Num Lost Stores		2.58	2	1.51	2.6	2	1.5
Num Dropped Stacks		0.84	1	0.91	0.85	1	0.87

Table 4, Data for a Typical Week.

Coupling in the Tevatron

Norman M. Gelfand*, Fermi National Accelerator Laboratory, Batavia IL 60510

Abstract

The performance of the Fermilab Tevatron Collider at the commencement of collider run Ib (Jan. 1994) was far below expectations. The poor performance was found to be due to a rolled low-β quadrupole downstream of CDF. This rolled quadrupole coupled the horizontal and vertical motion of the Tevatron beams and significantly reduced the Tevatron luminosity. When the roll in the quadrupole was corrected the performance of the Tevatron improved dramatically. This note will discuss the experimental data indicating the presence of coupling, and subsequent calculations which show how coupling can affect the luminosity.

I. OBSERVATION OF COUPLING

Introduction

Two different kinds of measurements made on the Tevatron beam showed that the Tevatron was coupled. These measurements were of the change in the closed orbit when the strength of a dipole corrector is changed, and the variation in tune as the strength of a quadrupole is changed. [1]

In the case of the closed orbit measurements the coupling manifested itself as the large change in the closed orbit in the crossed plane; the plane orthogonal to the plane of the dipole whose strength was varied. This is shown in figure 1, where the bump was generated using the horizontal correction dipole HE13. (The figure was generated assuming a kick of 30μr.) The rms size of the change in the closed orbit in the vertical plane is ~40% of the rms slope in the horizontal plane. It is possible to understand these data, as well as the data on the tune shift, with a model of the Tevatron lattice which includes a rolled quadrupole downstream of the CDF detector.

With the tune shift measurements the evidence for coupling comes from the anomalously small values of the tune

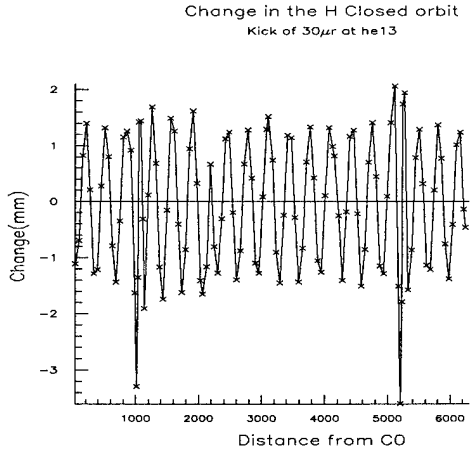


Figure 1a
H bpm
rms= 1.19mm

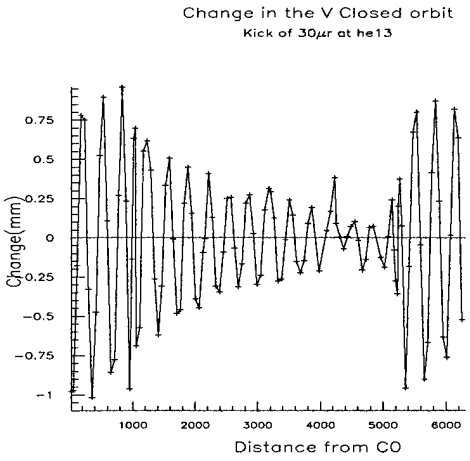


Figure 1b
V bpm
rms= 0.45mm

shift measured for quadupoles outside of the interaction region (IR). The β values that would be imputed from these values would be comparable to those at the interaction point and make no sense with our lattice.

Closed Orbit Measurements

Measurements were made of the change in the closed orbits in both the horizontal and the vertical planes, after applying to the beam a single, known dipole bump. To increase the precision of the resulting data, the measurements, of the changed closed orbit are repeated with a number of different values for the dipole bump, and the slope of the closed orbit value with respect to the size of the dipole bump was calculated. The correction dipoles located at HE11, HE13, VE11 and VE14 are used to produce the bumps. These pairs of correctors are chosen because the phase advance between the locations is large ($\Delta\phi_x$ ~69° and $\Delta\phi_y$ ~95°) and yet is not near a multiple of 180°.

When the measurements were made the horizontal and vertical tunes had been brought together by adjusting the strengths of the skew correction elements in the lattice. The large change in the closed orbit in the crossed plane, which must be due to coupling, was therefore surprising.

The change in the closed orbit in the crossed plane, due to a coupling element of a given magnitude, will be greatest if the coupling element is located at a place in the lattice where the product (β_x β_y) is large. For the Tevatron lattice we find that the maximum values of (β_x β_y) occurs at the outside end of the interaction region triplet. This, together with the fact that the low-β quads are very strong, makes these elements natural ones to look to as the source of the coupling. The closed orbit data unfortunately do not allow the identification of which element is producing the coupling, or even on which side of the IR the coupling occurs.

The normal computer model of the Tevatron contains no skew elements except for the skew quadrupole and skew sextupole elements located in the Tevatron spool packages, and the high order skew moments in the Tevatron magnets.

*This work was performed at the Fermi National Accelerator Laboratory, under contract DE-AC02-76CHO3000 with the U.S. Department of Energy

0-7803-3053-6/96/$5.00 ©1996 IEEE

The high order moments are not strong enough to account for the magnitude of the observed closed orbits in the crossed planes. The values in the skew quadrupoles are adjusted to bring the tunes in the two planes together, i.e., to reduce the coupling, and therefore should not be the source of the coupling. In order to study the source of the coupling we have to introduce coupling into the description of the Tevatron lattice. This has been done by allowing, in the description of the Tevatron lattice, for a roll, about the beam direction, of the low-β quads.

This modified lattice has been used with a version of the tracking code Tevlat [2], which allows fitting experimental data with MINUIT, varying the parameters of lattice elements, such as the roll, during the fit. While this analysis of the data was under way, a limited survey of the low-β magnets was performed which revealed that the outer member of the triplet downstream of CDF (Q2 in the Fermilab nomenclature) was rolled by ~7*mr*.

Since a large roll had been found in a particular magnet I tried to fit simultaneously, the closed orbit data at all four bump locations, by varying the size of the roll of this magnet and the roll of the corresponding magnet at D0. The differences between the measured change and the fitted change in the closed orbit, assuming a kick of 30μr, are plotted in figure 2 for a bump at HE13. With the other bump locations the fits are of comparable quality.

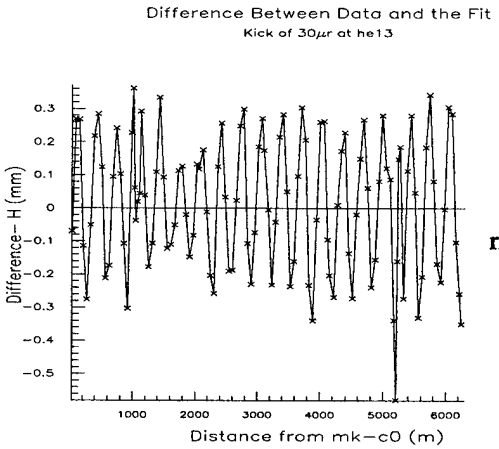


Figure 2a
H diff.
rms= 0.20mm

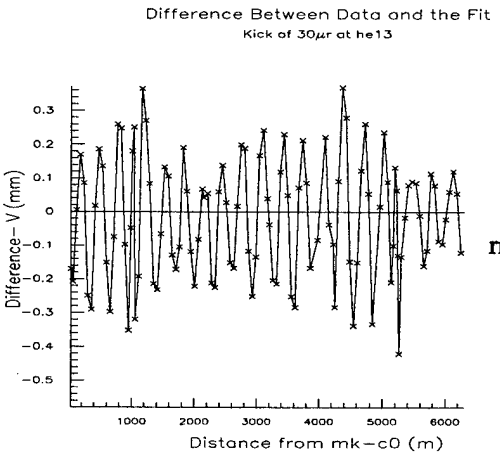


Figure 2b
V diff.
rms= 0.18mm

The fit gives a value of +7.0*mr* for the roll in the downstream Q2 at B0 and -1.4*mr* for the downstream Q2 at D0. I would estimate that the uncertainty in these values is ~1*mr*. The agreement with the survey result is striking and reassuring, but should not be overemphasized. We have represented all the skew effects by the roll in only two magnets which is certainly not the case. We get the correct value in this instance because of the large roll in a single magnet. When the skew effects are distributed among several magnets we cannot expect to so easily find the individual rolls.

The roll in the surveyed magnet was corrected. An immediate result was increase in the luminosity by a factor of two. The closed orbit measurements were repeated. Though the coupling from the interaction regions is considerably decreased there was a fair amount of coupling left in the Tevatron(figure 3). Comparing crossed plane data taken after correcting the quad roll to the original data we find that the crossed plane amplitudes have been reduced by approximately a factor of 2. These data have been fit as before. The fitted value of the roll in the quadrupole at B0 is now 0.3*mr* consistent with our having removed the roll. The fitted value of the roll in the downstream Q2 at D0 did not change from the value found earlier. That is reassuring since the was no change made to that magnet and it gives me some confidence that our fitting procedure has some connection with reality.

Tune Shift

The traditional way of measuring the value of β at a location in an accelerator is to vary the gradient of a quadrupole, $\Delta B'$, of length *l*, at that location and measure the resulting tune shift. In the *absence* of coupling the tune shift $\delta\nu$ is related to the value of β by:

$$\delta\nu = (1/4\pi)\,\beta l\,\Delta B'/[B\rho]$$

The only data available were taken before the unroll of the downstream Q2 at B0. The current in the different correction quadrupoles at B0 was varied and the tunes measured.

In a coupled machine the simple relationship above is no longer true. It is however, possible to fit the measured tune shift, $\delta\nu$, as a function of quadrupole strength, $\Delta B'$, using the model of the Tevatron and MINUIT. The parameters used were the same as the ones used to fit the closed orbit data. The value of the roll in the downstream quad at D0 was fixed at the value comeing from our fit to the closed orbit data. It is used because we have no tune shift data taken by varying the quads near the D0 interaction region.

For the case with the large quad roll, the only case for which we have data, the solution gives +6.5 *mr* for the roll at B0 . This agrees very well with the values found from fitting the closed orbit data. It is reassuring that two independent methods find the same roll for the quadrupole at B0 and that both results agree with the survey measurements.

II. LUMINOSITY

Introduction

With a given intensity in the proton and pbar bunches the

luminosity depends on the sizes of the bunches at the interaction point. The smaller the size of the beams the higher the luminosity. In an uncoupled machine the size, σ, of the beam is given, when either the dispersion η or the momentum spread *dp/p* is zero, by $\sigma_{rms}= (\beta\varepsilon_{rms})^{1/2}$. The luminosity L is then proportional to $1/(\beta_x\varepsilon_{xrms}\ \beta_y\varepsilon_{yrms})^{1/2}$.

In the case where we have a coupled machine it is not possible to use the normal horizontal and vertical β functions to calculate the beam size. In order to see the effect of the coupling on the beam size, and hence on the luminosity Tevlat was used to track a distribution of 1000 particles for a thousand turns. The initial particle distribution was generated assuming the design lattice with no coupling. The values σ_x and σ_y for the distribution were chosen so that the particles had a 95% normalized emittance, $\varepsilon_n = 25\pi$ *mmmr*.

During the tracking, for each turn, the value of σ for the particle distribution was calculated at D0 and B0 for both planes. The σs vary from turn to turn since the original distribution was not a stationary distribution. The values of σ were therefore averaged over 100 turns. The resulting average values for σ, which go into the calculation of **L** are very constant over the several thousand turns for which we have tracked.

Calculations and Results

The computed values of $(\sigma_x\sigma_y)^{1/2}$ at B0 and D0 are plotted in figure 3 for four configurations of the Tevatron:

- The design lattice with β~0.35*m*.
- The solution found for data taken with the downstream Q2 at B0 rolled.
- The solution found for data taken after the roll of the downstream Q2 at B0 was corrected.
- The solution found for data taken after the shutdown in 9/94 during which additional low-β magnets were surveyed and their rolls corrected.

The calculated radius of the beam, $\sim(\sigma_x\sigma_y)^{1/2}$ at B0 after the roll of the Q2 was removed, ~46μ, is ~74% of the calculated radius using the fit to data where the Q2 was rolled. This decrease in radius should translate into an ~80% increase in the luminosity. There is a much smaller change in the beam radius at D0 with the changes in the quad rolls, the unrolled value is ~93% of the value with the rolled Q2.

Using the measured luminosity and bunch intensities it is possible to calculate an equivalent beam radius at the interaction point. Comparing the data from the stores before the unroll of the magnet to the data from stores after the unroll we find that the equivalent beam radius at B0 decreased by ~63±13% after he unroll. The beam size at D0 did not change significantly. This is in good agreement with the change predicted by the calculation in Tevlat of the beam size.

III. Conclusion

The data on the change in the closed orbit with a dipole bump and the change in tune with a change in the strength of a quadrupole can be used to study coupling in the Tevatron. From the measurements it seems possible to construct a reasonable model of the Tevatron which, together with tracking can be used to calculate the Tevatron luminosity.

IV. Acknowledgments

The data analyzed here were obtained by a number of members of the Accelerator Division as part of an extensive series of measurements performed to better understand and improve the Tevatron. Among those responsible for the data used in this note are G. Annala, S. Assadi, G. Goderre, G. Jackson and W. Marsh. I wish to express my gratitude to them first for taking the data with such care, and then for making it available in a form convenient for analysis.

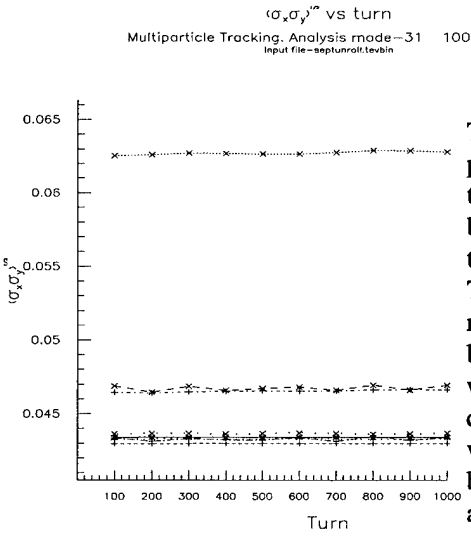


Figure 3. The top most points correspond to the size of the beam at B0 with the rolled quad. The middle points represent the beam size at D0 with the rolled quad which is very similar to the beam size at B0 after the initial unroll of the quad. The lowest group of points represent the beam size at both B0 and D0 after the final unroll and also the design values. As can be seen the current configuration, after correcting for the rolls in the low-β quads, is very close to the design.

V. REFERENCES

[1] A fuller discussion of the data and the analysis is found in Fermilab TM-1916.

[2] A. Russell, Private communication.

Calculating Luminosity for a Coupled Tevatron Lattice

J. A. Holt, M. A. Martens, L. Michelotti, G. Goderre
Fermi National Accelerator Laboratory
P. O. Box 500, Batavia, IL 60510, USA

Abstract

The traditional formula for calculating luminosity assumes an uncoupled lattice and makes use of one-degree-of-freedom lattice functions, β_H and β_V, for relating transverse beam widths to emittances. Strong coupling requires changing this approach. It is simplest to employ directly the linear normal form coordinates of the one turn map. An equilibrium distribution in phase space is expressed as a function of the Jacobian's eigenvectors and beam size parameters or emittances. Using the equilibrium distributions an expression for the luminosity was derived and applied to the Tevatron lattice, which was coupled due to a quadrupole roll.

I. Introduction

The Tevatron lattice for collider operations at Fermilab is designed to give the same lattice functions and luminosity at the two interaction regions CDF and D0. During the first part of Collider Run IB however, the ratio of measured luminosities at CDF and D0 was about $\check{}_{\rm CDF}/\check{}_{\rm D0} = 0.75$. In addition to a lower luminosity, the longitudinal distribution of luminosity at CDF was not symmetric as expected. These discrepancies were reduced when a low beta quadrupole near the CDF interaction region was found to be rolled by 8 mrad and subsequently re-aligned. After the realignment of the low beta quad, the ratio of measured luminosity changed to about $\check{}_{\rm CDF}/\check{}_{\rm D0} = 1.1$ and luminosity distribution at CDF also became symmetric as expected.

Since the effect of a rolled quadrupole on luminosity cannot be explained by using the standard β function treatment of uncoupled machines we develop the formulation for calculating luminosity in a coupled machine. Others have developed a set of general lattice functions which can be used to describe the lattice of coupled machines [2] but we choose instead to use linear normal form analysis. We present the development of an expression for the luminosity in a coupled machine based on linear normal forms and give results of luminosity calculations based on models of the Tevatron with and without the rolled quad.

II. Theory

In this section we will lay out the expressions used to calculate luminosity in the presence of strong coupling.

A. *Linear normal form coordinates*

As usual, we write the state of a particle as an array, $\underline{u}^T = (x, y, c\Delta t; x', y', \delta)$, by referring a coordinate chart to a local "design" fiducial curve in phase space, normally a segment of the closed orbit. $\underline{u}$ contains the coordinates of a particle as it crosses a plane transverse to this local fiducial curve. The coordinates, x, y, x', and y' are the transverse position and momentum* of a particle, relative to the curve, at the instant the particle crosses the plane while $\delta = \Delta p/\bar{p}$ is its momentum offset. The coordinate Δt is the time, relative to the reference time, at which the plane is crossed, so that particles with $\Delta t > 0$ arrive late.

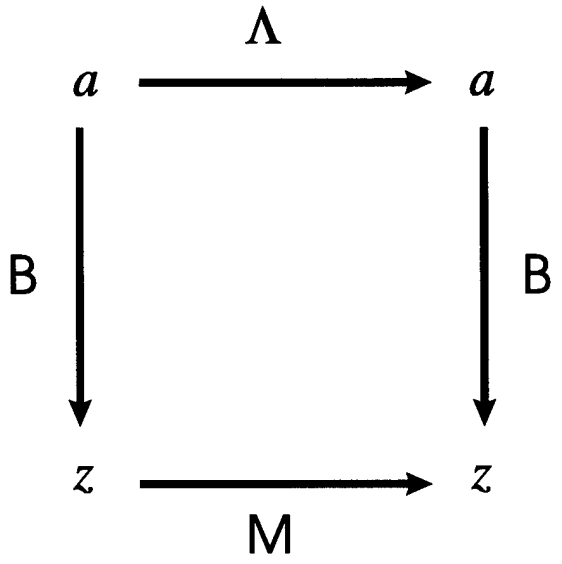


Figure. 1. Commutative diagram showing the action of a one-turn matrix in the normal form representation.

Let $\check{}(\underline{u}; s)$ be the one-turn map at the point marked with arclength coordinate s. That is, in one revolution starting from s, $\underline{u} \mapsto \check{}(\underline{u}; s)$. We are interested in the linear part of $\check{}$ obtained by taking the Jacobian: $\underline{\underline{M}}(s) = (\partial\check{}/\partial\underline{u})_{\underline{u}=0}$, and $\underline{u} \mapsto \underline{\underline{M}}(s) \cdot \underline{u}$, in linear approximation. Let $\underline{\underline{B}}(s)$ be the matrix whose columns are eigenvectors of $\underline{\underline{M}}(s)$, so that,

$$\underline{\underline{M}}(s) \cdot \underline{\underline{B}}(s) = \underline{\underline{B}}(s) \cdot \underline{\underline{\Lambda}} \ , \qquad (1)$$

where $\underline{\underline{\Lambda}} = \mathrm{diag}(e^{\pm i 2\pi \nu_k})$. The conversion to linear normal form (Weyl) coordinates, $\underline{a}$, is given by

$$\underline{u} = \underline{\underline{B}}(s) \cdot \underline{a} \ .$$

These are complex coordinates, and from the commutative diagram (Fig. 1) based on Eq.(1), we see that in one turn, $a_k \mapsto \Lambda_{kk} a_k = \exp(\pm i 2\pi \nu_k)\, a_k$. Thus, each $|a_k|$ is an invariant, and *with proper normalization,* such as either auxiliary condition,

$$-i\,\underline{\underline{B}}^T(s)\,\underline{\underline{J}}\,\underline{\underline{B}}(s)\,\underline{\underline{J}} = \underline{\underline{1}} \ , \quad \text{or} \quad \det \underline{\underline{B}} = 1 \ ,$$

*Actually, $x' = p_x/\bar{p}$ and $y' = p_y/\bar{p}$, where $\bar{p}$ is the reference momentum.

Operated by the Universities Research Association,Inc, under contract with the U.S. Department of Energy

0-7803-3053-6/96/$5.00 ©1996 IEEE

these magnitudes are easily related both to Hamiltonian action coordinates, I_k, and to physical "emittances" of the particle, $\epsilon_k = 2\pi I_k = 2\pi |a_k|^2$.

We want to calculate the state covariance matrix,

$$\underline{\underline{+}}(s) \equiv \langle \underline{u}\,\underline{u}^T \rangle = \underline{\underline{B}}(s) \cdot \langle \underline{a}\,\underline{a}^\dagger \rangle \cdot \underline{\underline{B}}^\dagger(s) \ ,$$

of a stationary, equilibrium distribution. With this condition, the angle variables must be uniformly distributed, so that $\langle a_k a_m^* \rangle = \delta_{km} I_k$, and

$$+_{ij}(s) = \langle u_i u_j \rangle = \frac{1}{2\pi} \sum_k B_{ik}(s) B_{jk}^*(s) \langle \epsilon_k \rangle \ . \qquad (2)$$

Coefficients of the $\langle \epsilon_k \rangle$ in this expression are what *should be* meant by "lattice functions" in a coupled machine. They are the numbers which relate invariant emittances to observable properties: the transverse widths of bunch distributions.

B. Luminosity integrals

We now use $\underline{\underline{+}}(s)$ to evaluate luminosity in the presence of coupling. The general expression for the luminosity of two bunches colliding head on with velocity $v = \beta c$ is given by the overlap integral [1],

$$\mathcal{L} = 2\beta c f_{rev} \int\int f_1(x, y, z; t) f_2(x, y, z; t)\, dV dt \qquad (3)$$

where f_{rev} is the revolution frequency, and $f_1(x, y, z; t)$ and $f_2(x, y, z; t)$ are the volume density distributions of the two colliding bunches.

To simplify Eq.(3) we assume a Gaussian for the equilibrium distribution in $\underline{u}$ phase space,

$$\rho_s(\underline{u}; s) = \frac{N}{\sqrt{2\pi}^3 (\det \underline{\underline{+}}(s))^{\frac{1}{2}}} e^{-\frac{1}{2}\underline{u}^T \cdot \underline{\underline{+}}^{-1}(s) \cdot \underline{u}} \qquad (4)$$

where N is the number of particles in a bunch, and $\underline{\underline{+}}(s)$ is the covariance matrix defined in Eq.(2).

To find the volume density distribution $f_1(x, y, z; t)$ we first need to convert Eq.(4) from the s-representation to the time or t-representation. What we are interested in is the position of a particle at a given instant of time. However the s-representation describes the state of a particle as it crosses the transverse plane at position s. Therefore we need to "propagate" the particle away from the local transverse plane. In a drift space this "propagation" is simple since particles travel in straight lines. Without giving the details, the resulting volume density distribution is

$$f_1(x, y, z; t) = \frac{N_1}{\sqrt{2\pi}^3 (\det \underline{\underline{C}}_1)^{\frac{1}{2}}} e^{-\frac{1}{2}\underline{\zeta}_1^T \cdot \underline{\underline{C}}_1^{-1} \cdot \underline{\zeta}_1} . \qquad (5)$$

In this expression $\underline{\zeta}_1^T = (x, y, \beta ct - z)$ and $\underline{\underline{C}}_1$ is the 3×3 matrix composed of the elements of the position sector of $\underline{\underline{+}}$, – the matrix, $\underline{\underline{C}}$, obtained by projecting out the momentum and energy components – describes the beam footprint in the local fiducial chart, that is, in local transverse coordinates.

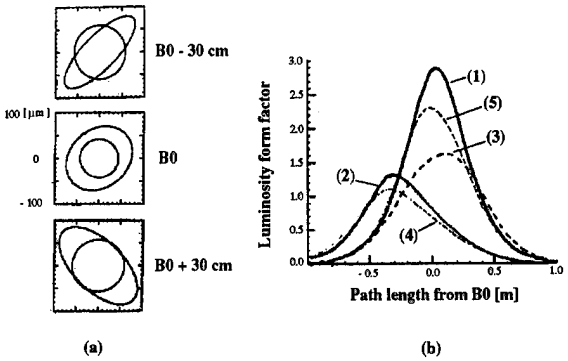


Figure. 2. Astigmatism in the vicinity of B0 resulting from a 9 mrad roll of a low beta quad.

The integrals over x, y, and t in Eq.(3) can be done analytically and the luminosity reduced to an integral over z. First define

$$\underline{d} = \text{third column of } (\underline{\underline{C}}_1^{-1} - \underline{\underline{C}}_2^{-1}) / \sqrt{[\underline{\underline{C}}_1^{-1} + \underline{\underline{C}}_2^{-1}]_{33}}$$

$$\underline{\underline{D}} = (\underline{\underline{C}}_1^{-1} + \underline{\underline{C}}_2^{-1} - \underline{d} \cdot \underline{d}^T)^{-1} \ , \quad \Sigma_z^2 = [\underline{\underline{D}}]_{33}.$$

Then the expression for the luminosity becomes

$$\mathcal{L} = \frac{2 f_{rev} N_1 N_2}{\sqrt{2\pi}^3} \int \frac{(\det \underline{\underline{C}}_1^{-1} \cdot \underline{\underline{C}}_2^{-1} \cdot \underline{\underline{D}})^{\frac{1}{2}}}{\Sigma_z \sqrt{[\underline{\underline{C}}_1^{-1} + \underline{\underline{C}}_2^{-1}]_{33}}} e^{-\frac{(z-z_0)^2}{2\Sigma_z^2}} dz. \qquad (6)$$

where $\underline{\underline{D}}$, $\underline{\underline{C}}_1$, and $\underline{\underline{C}}_2$ are all functions of z. The emittances, ϵ_k, are determined by measuring the beam profile at three different locations in the accelerator s_k, $k = 1, 2, 3$. From our lattice model we have $\underline{\underline{B}}(s_k)$ and from the measurements we have a component of $\underline{\underline{+}}(s_k)$. Thus we have three equations of the form given in Eq.(2) and can calculate the ϵ_k.

III. Calculations and Measurements

A. Astigmatic focus

A first application of Eq.(2) to the vicinity of B0 is shown in Figure 2(a). For simplicity, only the transverse dimensions have been taken into account, and we assume the values $\langle \epsilon_1 \rangle = \langle \epsilon_2 \rangle = 30\pi$ mm-mr $/\beta\gamma$ for the transverse expected emittances appearing in Eq.(2). (These numbers are actually the nominal 95% emittance values.) Drawn at three locations in Part (a) are ellipses corresponding to the projection of the covariance matrix, $\underline{\underline{C}}$, into the transverse position sector. They represent the footprint of the bunch as it passes through a plane at each location. The circular loci were obtained by assuming that the accelerator hardware was perfectly aligned, and the more eccentric ones, by introducing a 9 mrad roll in the upstream B0Q2 quadrupole, (the low beta quad near CDF) that was discovered to have this roll. Two effects occur: (a) the focus itself has expanded, and (b) the orientation of the footprint rotates as one travels downstream – the bunch "twists." Optically, these characterize a condition of astigmatism; the quad roll produced an astigmatic focus.

Of course, the emittances that appear in Eq.(2) do not really refer to the "horizontal" and "vertical" planes. They refer to

invariant planes in six dimensions, with "longitudinal" entering into the mix. For the above example we simply assumed that the emittances were $\langle\epsilon_1\rangle = \langle\epsilon_2\rangle = 30\pi$ mm-mr $/\beta\gamma$. A more correct way of doing this calculation would be to infer the true emittances from three flying wire measurements, as described in the preceding section, but the results would not change significantly.

B. Luminosity Profiles

A more direct way of estimating the effect on luminosity is shown in Figure 2(b). The expression $\exp(-s^2/2\sigma_z^2)/(\det \underline{\underline{C}}(s))^{\frac{1}{2}}$ is plotted within a two meter interval of B0. This profiles the integrand of the luminosity integral at the instant when the centroids of the proton and antiproton bunches meet. The two solid curves correspond to (1) the ideal case of no quad roll and (2) the "actual" case, corresponding to a 9 mrad quad roll with skew quad settings as they actually existed during the run up to July 20, 1995. The dashed curves illustrate three hypothetical scenarios: (3) a "best-case" scenario, in which the effect of the quad roll is compensated by the SQB0 skew-quad correction circuit only, (4) a "worst-case" scenario, in which the SQA0 circuit was not used to compensate, and (5) an attempt to mimic the quad roll with skew quad circuits, without rolling the quad. Notice that (5) comes nowhere near the other dashed curves, or curve (2).

C. Online 6-D Calculation

Eq.(6) has been implemented in conjunction with an online, interactive, six-dimensional model of the Tevatron using the C++ class libraries MXYZPTLK and BEAMLINE [3]. Using the design lattice, a comparison was made using the beam conditions of the present collider run. Two Tevatron collider stores were chosen; one before the quadrupole roll was discovered and one after. In the model the quadrupole was rolled 8 mrad. The invariants (I_k) have been calculated using the sigmas from three Tevatron flying wire measurements. The ratio of measured luminosities at CDF and D0 before the rolled quadrupole discovered was 0.76; the model predicts 0.70. For a store after the roll was corrected the measured ratio was 1.13; the model predicts 1.03. In the rolled quadrupole case, the luminosity distribution at CDF is skewed towards the upstream end of the interaction region. This is in agreement with both the model and with Figure 2.

Several effects have been neglected in the calculation. The electrostatic separators were assumed to be zero and no account was taken of RF bucket cogging. Some of the Tevatron low-β quadrupoles run at values slightly different from the design in order to change the longitudinal position of the minimum β. Inclusion of these effects should bring the model calculation in closer agreement with experimental data.

IV. Conclusions

Linear normal form analysis has been used to develop an expression for the luminosity in a coupled machine. Comparison of calculation with experimental data show that the model can reproduce the qualitative features of the data. Work is in progress to implement a more accurate lattice model of the Tevatron and to include electrostatic separators.

References

[1] M. Month, "Collider Performance with Ideal Collisions", "Accelerator Division Report 85–1", (1985)

[2] D.A. Edwards and L.C. Teng, "Parameterization of Linear Coupled Motion in Periodic Systems" *IEEE Trans. Nucl. Sci.*, vol. NS-20, No. 3, pp. 885–888, June 1973.

[3] L. Michelotti, *MXYZPTLK and Beamline: C++ Objects for Beam Physics.* In *Advanced Beam Dynamics Workshop on Effects of Errors in Accelerators, their Diagnosis and Correction.* (held in Corpus Christi, Texas, October 3-8, 1991) Published by American Institute of Physics, as Conference Proceedings No. 255. 1992.

REMARKS CONCERNING THE γ-PRODUCTION PROBABILITY OF HIGH RELATIVISTIC DIRAC-ELECTRONS IN THE POSITRON BUNCH

Huschang Heydari, Technische Universitaet Berlin, Institut f. Theoretische Elektrotechnik
Einsteinufer 17, EN 2, D-10587 Berlin

Abstract: An exact relation between the γ-production probability in the Dirac-case and the corresponding probability in the Klein-Gordon-case is derived. In addition, several interesting terms are analysed when the Klein-Gordon equation is approximated up to second order in the field derivatives.

INTRODUCTION

As the main result, an exact relation between the γ-production probability occuring in beam-beam radiation in the case of Dirac electrons and the corresponding γ-production probability calculated for scalar electrons (Klein-Gordon-case) is presented. The above found relation enables the transfer of approxiamation schemes applied in the Klein-Gordon-case directly to the Dirac-case.

As an additional result, by using properties of the Airy-function, specific approximate expressions are derived in the case where derivatives of underlying variable forces up to second order are taken into account.

AN EXACT RELATION FOR THE TRANSITION PROBABILITY OCCURING IN BEAM-BEAM RADIATION

The probability for the emission of a photon produced by a high relativistic Dirac-electron traversing mainly in z-direction a positron bunch, as is well known, means considering the three cases.

Case 1: Right-handed electron emits right-handed photon and remains right-handed.

Case 2: Right-handed electron emits left-handed photon and remains right-handed.

Case 3: Right-handed electron emits right-handed photon and flips to the left-handed electron.

Thus giving:

Case 1:

$$\frac{d(W_a)}{dx}=\frac{\alpha_s}{p_{\parallel}^2(1-x)^3}\frac{1}{x}\frac{1}{2x}\cdot\int_{-\infty}^{+\infty}\frac{d^2\vec{k}_\perp}{(2\pi)^2}\cdot \left\|\int_{-\infty}^{+\infty}dz\hbar\tilde{k}'_+(z)e^{-\frac{i}{\hbar}\int_0^z dz's(z')}\right\|^2 \quad (1)$$

Case 2:

$$\frac{d(W_a)}{dx}=\frac{\alpha_s}{p_{\parallel}^2(1-x)^3}\frac{1}{x}\frac{1}{2}\cdot\int_{-\infty}^{+\infty}\frac{d^2\vec{k}_\perp}{(2\pi)^2}\cdot \left\|\int_{-\infty}^{+\infty}dz\hbar\tilde{k}'_+(z)e^{-\frac{i}{\hbar}\int_0^z dz's(z')}\right\|^2 \quad (2)$$

Case 3:

$$\frac{d(W_a)}{dx}=\frac{\alpha_s}{p_{\parallel}^2(1-x)^3}\frac{1}{x}2x\left(\frac{1}{x}-1\right)^2\frac{1}{4}(1-x)^2\cdot \int_{-\infty}^{+\infty}\frac{d^2\vec{k}_\perp}{(2\pi)^2}\left\|\int_{-\infty}^{+\infty}dz\frac{m}{c}e^{-\frac{i}{\hbar}\int_0^z dz's(z')}\right\|^2 \quad (3)$$

where $p_{\parallel}$ denotes the initial momentum (in z-direction) of the electron, $\hbar$ denotes Planck's constant, x denotes Sommerfeld's fine structure constant, x denotes the relative momentum fraction of the photon related to the initial momentum $p_{\parallel}$ of the electron, $\vec{k}_\perp$ denotes the component of the photon wave number vector perpendicular to the z-direction,

$$\tilde{k}_\pm(z):=\tilde{k}'_x(z)\pm i\tilde{k}'_y(z)$$

$$\hbar\tilde{\vec{k}}_\perp(z):=\hbar\vec{k}_\perp-(1-x)\left[\vec{p}_{i\perp}+\frac{1}{c}\int_{-\infty}^{z}dz',\vec{b}_0\right] \quad (4)$$

and where s(z) is defined by

$$s(z):=\frac{m_0^2c^2(1-x)^2+(\hbar\tilde{\vec{k}}_\perp(z))^2}{2x(1-x)p_{\parallel}}. \quad (5)$$

Apart from the above introduced abbreviations and definitions, m_0 denotes the rest mass of the electron, $\vec{b}_0$ denotes the impact parameter, $\vec{p}_{i\perp}$ denotes the perpendicular component of the initial momentum of the electron and $\vec{K}_\perp$ denotes the force the positron bunch exerts upon the electron. It is emphasized, that in the high relativistic limit, because of conservation of helicity there exists a possible fourth case:

Case 4: Right-handed electron emits left-handed photon and flips to left-handed electron
which identically vanishes.

As is well known, the corresponding formula for calculating the probability fo the emission of a photon produced by a high relativistic Klein-Gordon electron traversing mainly in the z-direction a positron bunch reads:

$$\frac{d(W_a)}{dx}=\frac{d\sigma}{dxd^2\vec{b}_0}=\frac{\alpha_s}{p_{\parallel}^2(1-x)^{x3}}\cdot\int_{-\infty}^{+\infty}\frac{d^2\vec{k}_\perp}{(2\pi)^2}\cdot \left\|\int_{-\infty}^{+\infty}dz\hbar\tilde{\vec{k}}'_\perp(z)e^{-\frac{i}{\hbar}\int_0^z dz's(z')}\right\|^2 \quad (6)$$

0-7803-3053-6/96/$5.00 ©1996 IEEE

Equations (1), (2), (3), (6) represent exact relations with regard to arbitrary z-dependence of the force $\vec{K}_\perp(z)$ originating from the positron bunch.

It might be interesting to find relations among (1), (2), (3), (6) or among the corresponding relevant expressions containing the integrals:

$$DR_1 := \left\| \int_{-\infty}^{+\infty} dz \hbar \tilde{\vec{k}}'_-(z) e^{-\frac{i}{\hbar}\int_0^z dz' s(z')} \right\|^2 \tag{7}$$

$$DR_2 := \left\| \int_{-\infty}^{+\infty} dz \hbar \tilde{\vec{k}}'_+(z) e^{-\frac{i}{\hbar}\int_0^z dz' s(z')} \right\|^2 \tag{8}$$

$$DR_3 := \left\| \int_{-\infty}^{+\infty} dz \frac{m}{c} e^{-\frac{i}{\hbar}\int_0^z dz' s(z')} \right\|^2 \tag{9}$$

$$KG := \left\| \int_{-\infty}^{+\infty} dz \hbar \tilde{\vec{k}}'_\perp(z) e^{-\frac{i}{\hbar}\int_0^z dz' s(z')} \right\|^2 \tag{10}$$

By using calculus with complex numbers as well as some vector algebra, the subsequent term can be written as:

$$\tilde{k}'_+(z_1)\tilde{k}'_-(z_2) = \tilde{\vec{k}}'_\perp(z_1)\cdot\tilde{\vec{k}}'_\perp(z_2) - i\vec{e}_3\cdot\left(\tilde{\vec{k}}'_\perp(z_1)\times\tilde{\vec{k}}'_\perp(z_2)\right) \tag{11}$$

so that by using

$$DR_1 = \int_{-\infty}^{+\infty}\int dz_1 dz_2 \hbar^2 \left(\tilde{\vec{k}}'_\perp(z_1)\cdot\tilde{\vec{k}}'_\perp(z_2) - i\vec{e}_3\left\langle \tilde{\vec{k}}'_\perp(z_1)\times\tilde{\vec{k}}'_\perp(z_3)\right\rangle\right) e^{EXP} \tag{12}$$

for the case 1, the exact relation results

$$DR_1 = KG - \hbar^2 \iint dz_1 dz_2 i\vec{e}_3 \left\langle \tilde{\vec{k}}'_\perp(z_1)\times\tilde{\vec{k}}'_\perp(z_2)\right\rangle e^{EXP} \tag{13}$$

and as well for the remaining cases, the exact relations

$$DR_2 = KG + \hbar^2 \iint dz_1 dz_2 i\vec{e}_3 \left\langle \tilde{\vec{k}}'_\perp(z_1)\times\tilde{\vec{k}}'_\perp(z_2)\right\rangle e^{EXP} \tag{14}$$

$$DR_3 = \frac{m^2}{c^2}\iint dz_1 dz_2 e^{EXP} \tag{15}$$

can be presented, where the abbreviation

$$EXP = \frac{i}{\hbar}\int_{z_1}^{z_2} dz' s(z') \tag{16}$$

has been introduced.

In order to arrive at the expression for the total probability, summation over final states (i.e. summation of (1), (2), (3)) has to be performed, thus leading to the central formula:

$$\frac{d(W_a)}{dx} = \frac{\alpha_s}{p_\parallel^2(1-x)^3}\frac{1}{x}\int\frac{d^2\vec{k}_\perp}{(2\pi)^2}\left\{ KG\cdot\left\langle\frac{1}{2x}+\frac{x}{2}\right\rangle - i\hbar^2\int_{-\infty}^{+\infty}\int dz_1 dz_2 \vec{e}_3\cdot\left\langle\tilde{\vec{k}}'_\perp(z_1)\times\tilde{\vec{k}}'_\perp(z_2)\right\rangle e^{EXP}\cdot \left\langle\frac{1}{2x}-\frac{x}{2}\right\rangle + \frac{m^2}{c^2}\int_{-\infty}^{+\infty}\int dz_1 dz_2 e^{EXP}\frac{(1-x)^4}{2x}\right\}. \tag{17}$$

Apart from the middle term

$$MT := -i\hbar\int\frac{d^2\vec{k}_\perp}{(2\pi)^2}\iint dz_1 dz_2 \vec{e}_3\left\langle\tilde{\vec{k}}'_\perp(z_1)\times\tilde{\vec{k}}(z_2)\right\rangle e^{EXP} \tag{18}$$

and apart from the spin-flip term

$$SPFL := \frac{m^2}{c^2}\cdot\int\frac{d^2\vec{k}_\perp}{(2\pi)^2}\iint dz_1 dz_2 e^{EXP} \tag{19}$$

the central formula (17) permits the easy calculation of the transition probability for the Dirac-case simply by multiplying the corresponding transition probability found in the Klein-Gordon-case by the constant factor $\left\langle\frac{1}{2x}+\frac{x}{2}\right\rangle$ thus giving:

$$\frac{d(W_a)^{Dirac}}{dx} = \left\langle\frac{1}{2x}+\frac{x}{2}\right\rangle\frac{d(W_0)^{K.G.}}{dx} + \frac{\alpha_s}{p_\parallel^2(1-x)^3}\cdot\frac{1}{x}\left[\left\langle\frac{1}{2x}-\frac{x}{2}\right\rangle(MT)+\frac{(1-x)^4}{2x}(SPFL)\right] \tag{20}$$

It should be remarked that the above mentioned relation (20) is independent of any considerations of appropriate evaluation methods of the underlying contributing integrals in the case of weakly or (more) strongly z-dependent forces $\vec{K}_\perp(z)$.

In the case of considering derivatives of the force $\vec{K}_\perp(z)$ originated from the positron bunch up to at most second order, as generally known, one arrives at:

$$\frac{d(W_a)^{K.G.}}{dx} = \left\langle\frac{1}{2x}+\frac{x}{2}\right\rangle\frac{\alpha_s m}{\hbar c^2 p_\parallel}\int_{-\infty}^{+\infty} d\bar{z}\int_u^\infty dv Ai(v)\cdot\left[2\cdot\frac{V}{U}-1\right] + 2\alpha_s\frac{l_{coh}}{90\Gamma}\left(\frac{2}{U}\right)A'i(u) + UAi(u)\left\langle\frac{1}{2x}+\frac{x}{2}\right\rangle \tag{21}$$

The corresponding approximate expression for the spin-flip-term reads:

$$\frac{d(W_a)^{\text{Dirac-Fall}}}{dx}\overset{\text{SPFL}}{=:}\frac{\alpha_s}{p_{\shortparallel}^2(1-x)^3}\cdot\frac{1}{x}\cdot\frac{(1-x)^4}{2x}\text{SPFL}=$$

$$=\frac{\alpha_s m^2}{p_{\shortparallel}\hbar c^2}\int_{-\infty}^{+\infty}d\bar{z}\left[\int_U^{\infty}dv\,\text{Ai}(v)\cdot\frac{(1-x)^2}{2x}\right]+$$

$$+\int_{-\infty}^{+\infty}d\bar{z}(-1)2\alpha_s\frac{(1-x)^2}{2x}\cdot\frac{l_{coh}}{90\Gamma}\cdot \tag{22}$$

$$\cdot\left[\frac{\left\|\dot{\vec{K}}_\perp\right\|^2}{\left\|\vec{K}_\perp\right\|^2}+3\frac{\vec{K}_\perp\cdot\ddot{\vec{K}}_\perp}{\left\|\vec{K}_\perp\right\|^2}\right]\left(\frac{2}{U}A'i(u)+uAi(u)\right).$$

Besides the presentation of the central formula (17) as an additional result, the approximate evaluation of the integrals contained in the middle term up to the so far considered order of derivatives in the force $\vec{K}_\perp(z)$ can be treated analagously by using similar arguments leading to (21), (22) as demonstrated briefly below.

Starting from a series expansion in the variable $w = z_1 - z_2$ about $\bar{z}=\frac{1}{2}(z_1+z_2)$ of the subsequent expression:

$$C:=-\vec{e}_3\cdot\left\langle\tilde{\vec{k}}'_\perp(z_1)\times\tilde{\vec{k}}'_\perp(z_2)\right\rangle e^{EXP} \tag{23}$$

enables one to arrive at the following relation for the middle-term:

$$MT=i\hbar^2\int\frac{d^2\tilde{\vec{k}}'_\perp}{(2\pi)}\int d\bar{z}dwC$$

$$TM=i\hbar^2\int_{-\infty}^{+\infty}d\bar{z}\frac{x^2(1-x)^2p_{\shortparallel}^2 i}{\hbar^2}\vec{e}_3\left\langle\vec{K}_\perp\times\dot{\vec{K}}_\perp\right\rangle\cdot \tag{24}$$

$$\frac{1}{\left\|\vec{K}_\perp\right\|^2}\cdot(-2)\cdot U\,\text{Ai}(u)$$

thus yielding the corresponding contribution of the probability:

$$\frac{d(W_a)}{dx}=\int_{-\infty}^{+\infty}d\bar{z}2\alpha_s\left\langle\frac{1}{2x}-\frac{x}{2}\right\rangle\frac{1}{3\Gamma}\vec{e}_3\cdot$$

$$\frac{\left\langle\vec{K}_\perp\times\dot{\vec{K}}_\perp\right\rangle}{\left\|\vec{K}_\perp\right\|^2}\frac{1}{\sqrt{u}}\text{Ai}(u) \tag{25}$$

or

$$\frac{d(W_a)^{\text{Dirac-Fall-MT}}}{dx}=\frac{2\alpha_s}{3}\sqrt{\frac{m^2}{p_{\shortparallel}\hbar c^2}}\cdot\left\langle\frac{1}{2x}-\frac{x}{2}\right\rangle$$

$$\cdot\int_{-\infty}^{+\infty}d\bar{z}\sqrt{\frac{l_{coh}}{\Gamma}}\vec{e}_3\cdot\frac{\left\langle\vec{K}_\perp\times\dot{\vec{K}}\right\rangle}{\left\|\vec{K}_\perp\right\|^2}\frac{1}{\sqrt{u}}\text{Ai}(u) \tag{25a}$$

where within the above presented equations the coherence length l_{coh}

$$l_{coh}:=\frac{m}{\left\|\vec{K}_\perp(z)\right\|} \tag{26}$$

as well as

$$\Gamma:=\frac{p_{\shortparallel}\hbar c^2}{m^2 l_{coh}}=\frac{p_{\shortparallel}hc^2\left\|\vec{K}_\perp\right\|}{m^3},$$

$$\hat{r}=\left[\frac{(1-x)\left\|\vec{K}_\perp\right\|^2}{c^2\cdot 8\cdot\hbar\times p_{\shortparallel}}\right] \tag{27}$$

and $$m=m_0c^2,\qquad \bullet=:\frac{\partial}{\partial z} \tag{28}$$

have been introduced.

Conclusion

In this paper, an exact relation between the probability for the emission of a photon in the Dirac-case and the corresponding probability in the Klein-Gordon-case has been presented in the high relativistic limit.

An additional result, in the case of considering derivatives of the force $\vec{K}_\perp(z)$ up to at most second order, a detailed approximate expression of the middle term comprising the cross product $\vec{K}_\perp\times\dot{\vec{K}}_\perp$ has been obtained by using specific properties of the Airy function Ai. Obviously, this above mentioned approximate expression vanishes in the case of e.g. presupposed cylinder symmetry around the z-axis, evidently implying $\vec{K}_\perp\times\dot{\vec{K}}_\perp=0$.

FIELD QUALITY EVALUATION OF THE SUPERCONDUCTING MAGNETS OF THE RELATIVISTIC HEAVY ION COLLIDER*

J. Wei, R.C. Gupta, A. Jain, S.G. Peggs, C.G. Trahern, D. Trbojevic, P. Wanderer
Brookhaven National Laboratory, Upton, New York 11973, USA

Abstract

In this paper, we first present the procedure established to evaluate the field quality, quench performance,[1] and alignment of the superconducting magnets manufactured for the Relativistic Heavy Ion Collider (RHIC),[2] and then discuss the strategies used to improve the field quality[3] and to minimize undesirable effects by sorting the magnets. The field quality of the various RHIC magnets is briefly summarized.

I. INTRODUCTION

The RHIC magnet system[2] consists primarily of the superconducting dipole, quadrupole, sextupole and corrector magnets for guiding, focusing, and correcting the counter-circulating ion beams into the design orbits in the regular arcs of the machine lattice. A large complement of special magnets is also required for steering the beams into collisions at the six interaction regions where the ion beams interact.

Besides reaching fields with substantial margins above the required range, all of the RHIC magnets must meet stringent requirements on field quality, reproducibility, and long-term reliability. In order to fulfill this goal, a committee of magnet division and RHIC accelerator physics personnel jointly review the field quality, quench test performance, survey and other engineering aspects of the magnets. Subsequently, the magnets are sorted to minimize undesirable effects resulting from unexpected changes in the manufacturing process.

Currently, the arc dipoles (DRG) and quadrupoles (QRG) are built by the Northrop-Grumman Corporation, the arc sextupoles (SRE) and trim quadrupoles (QRT) are built by the Everson Electric Corporation, and other special magnets (corrector magnets (CR), etc.) are built by the BNL magnet division. Table I shows the status of the manufactured magnets. The first 30 dipoles

Table I
Status of the RHIC magnets (April 1995).

No.	DRG	QRG	SRE	QRT	CR
built	127	150	300	55	215
quench tested	42	60	60	12	110
cold measured	42	60	53	12	48
needed	288	372	288	72	420
installed	112	14	14	0	14
spare needed	10	8	12	6	10
spared	2	1	0	0	0

and 20 quadrupoles were fully tested at both room temperature (warm) and superconducting temperature (cold) at various currents including those corresponding to injection (660 A), transition (1450 A), and storage (5000 A) operation. Thereafter, while all the magnets are still warm tested, 10% of them are cold tested to ensure the established warm-cold correlations.

After the magnets are measured and tested, the magnetic field quality data, including transfer function, field angle, multipole harmonics, magnetic center offsets, etc. at all the test currents, is recorded along with the warm mechanical survey measurements of the fiducial positions, sagitta, mechanical length and field angle. The data are transferred from the magnet division into the RHIC database (MAGBASE), formatted into a self-describing standard (SDS) dataset, and then analysed by studying trends, comparing with the expected values, and evaluating the deviation from the mean using the computer program MAGSTAT.[4]

II. REVIEW OF INDIVIDUAL MAGNETS

A. Arc dipole (DRG)

The RHIC arc dipoles are designed to operate at nominal current of 5 kA at top energy for ion beams with magnetic rigidity 840 T·m. Fig. 1 shows that the minimum quench currents during

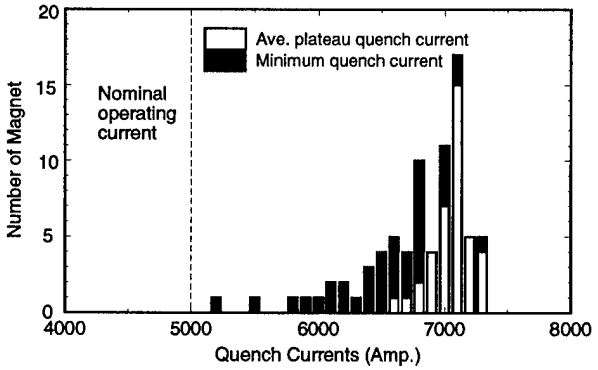


Figure. 1. RHIC dipole magnet quench performance.

the entire testing process for all the tested magnets are above the operating current, while the average quench current after the plateau is reached easily exceeds a 30% margin.

The high quality of the RHIC dipoles is demonstrated by magnetic field profiles at the horizontal ($y = 0$) and vertical ($x = 0$) midplanes (Figs 2a and b), respectively, measured at the top operating current. The overall performance of the magnetic multipole harmonics exceeds nominal operation requirements, as indicated by the expected range shown by the dashed lines for normal (Fig. 2a) and skew (Fig. 2b) multipoles.

The dominant multipoles of the dipole magnets are b_2 (normal sextupole) and b_4 (normal decapole) resulting from the dipole symmetry of the magnets, and a_1 (skew quadrupole) resulting

*Work performed under the auspice of the U.S. Department of Energy.

0-7803-3053-6/96/$5.00 ©1996 IEEE

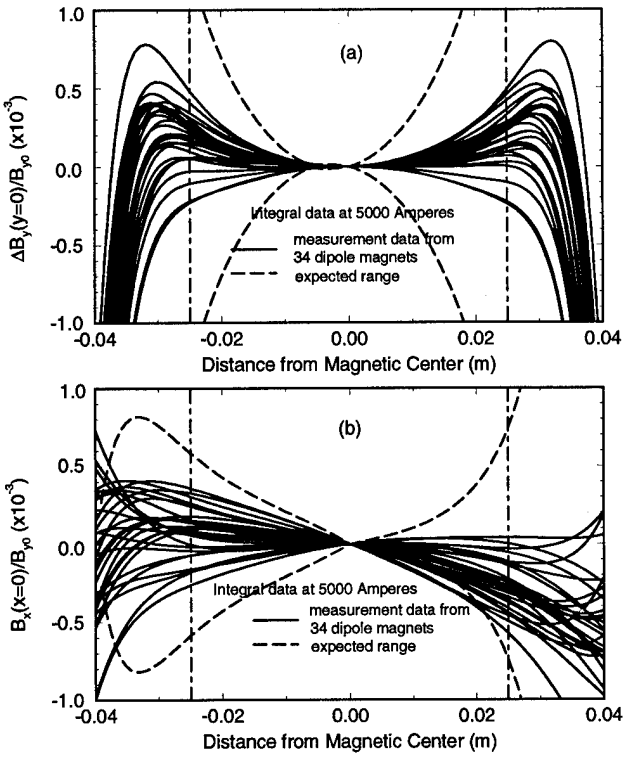


Figure. 2. RHIC dipole magnet a) vertical field profile at horizontal midplane and b) horizontal field profile at vertical midplane.

from the asymmetric vertical placement of the magnet cold mass in the cryostat, as shown in Table II. From a beam dynamics point of view, a large b_2 would require a stronger chromaticity correction, especially at top beam energy when the low β^* lattice is used. Large a_1 and b_4 would require linear decoupling and tune-spread minimization at the injection energy when the beam size is the largest in the arc. Fortunately, due to the relatively high injection energy and the small diameter of the coil filaments, the persistent current is small. Magnet design has minimized b_2 and b_4 (Table II) for both injection and storage currents by optimizing the cross-sections of the coil and the yoke taking into account the persistent current and saturation effects.[3] The minimization of a_1 is achieved by making the lower half yoke heavier than the upper half during the assembly process.

During March 1995, a drop in dipole integral transfer function of about 0.1% was noticed and traced to the narrower width of the phenolic insulator used between the coil and the iron. Although the problem has been corrected, these 20 magnets affected are

Table II

Some integral multipole harmonics of the RHIC dipoles measured at various test currents (mean±standard deviation in prime units[6] at the reference radius of 2.5 cm).

	a_1	b_2	a_2	b_4
30 A (warm)	0.1±1.5	4.8±1.4	-1.0±0.2	0.0±0.4
660 A (cold)	0.7±1.3	1.0±1.4	-1.0±0.2	-0.6±0.5
1450 A (cold)	0.6±1.2	2.9±1.4	-1.0±0.2	-0.4±0.5
5000 A (cold)	-1.3±1.4	1.4±1.5	-1.1±0.2	-0.1±0.5

being sorted,[5] along with all subsequent dipole magnets. The sorting procedure is based on the strength minimization of the horizontal dipole correctors required to compensate for the variation in the integral transfer function. With sorting, the maximum current required for such compensation is decreased from 12 A to about 3 A. Table III presents other field quality issues of the

Table III

Warm measured means and standard deviations (SD) of the integral and body transfer function, integral field angle, body field angle standard deviation, and center offsets of the RHIC arc magnets.

	DRG	QRG	SRE
Integ. trans. func. (relative SD)	3.0×10^{-4}	4.8×10^{-4}	1.8×10^{-3}
Body trans. func. (relative SD)	3.1×10^{-4}	—	—
Integ. field angle (Mean±SD) (mr)	-0.5±0.8	-1.8±0.4	0.0±0.3
Body field angle SD (Mean) (mr)	0.8	—	—
Center offset X_0 (Mean±SD) (mm)	—	0.03±0.06	0.02±0.09
Center offset Y_0 (Mean±SD) (mm)	—	0.13±0.06	0.03±0.03

magnets.

Two dipole magnets (DRG516 and DRG545) have so far been allocated as spare magnets. DRG516 has an excessive twist (2.5 mr standard deviation in body field angle) along the azimuthal axis. DRG545 has a large (−5.9 units) a_1 caused by a known coil size mismatch.

B. Arc quadrupole (QRG)

The arc quadrupoles are also designed to operate at nominal current of 5 kA at top energy. Fig. 3 shows that the average

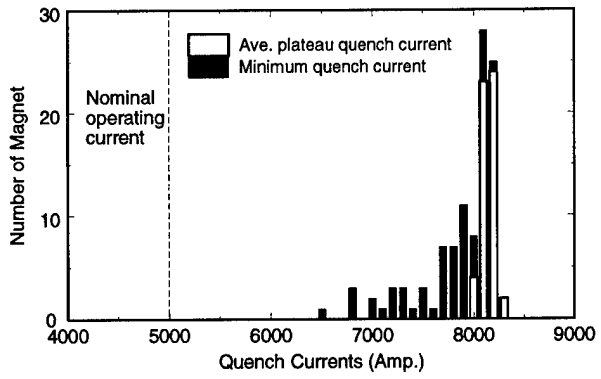


Figure. 3. RHIC quadrupole magnet quench performance.

quench current after the plateau is reached exceeds the operating current by more than 60%.

The dominant multipoles of the quadrupoles are b_5 and a_5 resulting from the quadrupole symmetry of the coil and the end configuration, and b_3 resulting from the asymmetry between the

horizontal and vertical planes, as shown in Table IV. From a beam dynamics point of view, the present values of b_5 and a_5 impose no significant impact on the particle motion due to the relatively small beam size in the arc. b_3 has been compensated in the design by making the coil to midplane gap appropriately asymmetric,[3] while b_5 has been reduced by compensating the body with the ends of the magnet.

During an early stage of industrial manufacture, midplane shims were incorrectly applied on 5 quadrupoles, resulting in a b_3 of about -6 units. These magnets were sorted and assigned to defocusing locations around the two rings to minimize their effects. So far, one quadrupole magnet (QRG156) with excessive b_2 (-5 units) has been allocated as a spare magnet.

C. Sextupole (SRE)

In general, the performance of the sextupole magnets has exceeded the design goal. However, the epoxy contained in about 42 magnet coils is significantly weaker than normal. Consequently, the average quench currents (about 170 A) of these magnets, although exceeding the design operating current (100 A), are lower than the average of the regular magnets (above 200 A). To minimize possible long-term effects, these magnets have been sorted and allocated to the focusing locations around the two rings where the required strength of the sextupoles for chromaticity correction is about 50% of that at the defocusing locations.

D. Trim quadrupole (QRT)

Ten of the trim quadrupoles (QRT) manufactured have been cold tested. The minimum quench currents of all the tested magnets are above 200 A, well exceeding the design operating current of 100 A. The field quality also exceeds the design goal.

E. Arc correctors (CRB, CRC, CRD, CRE, CRF)

All of the five types of arc correctors (CRB, CRC, CRD, CRE, and CRF) will be cold tested. After initial training, all the magnets quench above the design operating current of 50 A. Since the dipole corrector layers are all powered individually, the variation in the integral transfer function (typically 1% standard deviation) is of little concern.

III. MAGNET ASSEMBLY INSTALLATION

Since each arc dipole magnet is individually contained in its own cryostat, the magnet is immediately assigned to the ring for installation after it is approved and sorted. On the other hand, one arc quadrupole (Q), one sextupole (S), and one corrector (C) cold mass share a common cryostat, along with an attached beam position monitor and (for some types) a recooler, becoming the CQS assembly. Individual corrector, quadrupole, and sextupole elements are assigned to CQS assemblies only after they have been reviewed and approved. The completed CQS assembly[7] is then assigned to the ring only after the overall unit has been separately reviewed and approved.

Each CQS is surveyed with the colloidal cell technique[8] to directly correlate the magnetic field center with the externally accessible mechanical fiducial positions. This information, along with the measurement data of the magnetic field angle, is used to align the magnets during and after installation.

Table IV

Some integral multipole harmonics of the RHIC quadrupole magnets measured at various test currents (mean±standard deviation in prime units[6] at the reference radius of 2.5 cm).

	b_3	b_5	a_5
10 A (warm)	-1.4±1.2	1.4±0.5	-3.7±0.3
660 A (cold)	-0.7±1.7	-1.9±0.6	-3.7±0.4
1450 A (cold)	-0.7±1.7	0.5±0.6	-3.7±0.3
5000 A (cold)	-0.7±1.7	5.6±0.6	-3.8±0.3

IV. CONCLUSION

The field quality and quench performance of the RHIC magnets well exceed design goals. Sorting has been applied to the arc dipoles to minimize the required maximum corrector strength, on the 5 arc quadrupoles with incorrectly applied shims, and on the 42 low-epoxy sextupoles to minimize possible long-term effects. By April 1995, 112 dipole magnets and 14 CQS assemblies have been installed in the RHIC tunnel.

Acknowledgment We thank A. Greene, M. Harrison, D. McChesney, S. Mulhall, J. Muratore, S. Tepikian, and P. Thompson for many useful discussions and assistance.

V. REFERENCES

1. P. Wanderer, et al., these proceedings.
2. RHIC Design Manual, Brookhaven National Laboratory, revised Oct. 1994.
3. R. Gupta, et al., these proceedings.
4. S. Peggs et al., computer program MAGSTAT (1994).
5. S. Peggs, computer program SORT_DIPOLE (1995).
6. J.Wei, R. Gupta, and S. Peggs, Proc. 1993 Part. Accel. Conf., p.258 (1993); J. Wei and M. Harrison, Proc. Int. Conf. on High Energy Accel., p.1031 (1992).
7. S. Mulhall, et al., these proceedings.
8. D. Trbojevic, et al., these proceedings.

HIGH INTENSITY PROTON BEAMS IN A MULTI-CYCLED SPS

A. Faugier, X. Altuna, R. Bailey, R. Blanchard, T. Bohl, H. Burkhardt, P. Collier, K. Cornelis, N. Garrel, A. Hilaire, M. Jonker, R. Keizer, M. Lamont, T. Linnecar, G. de Rijk, G. Roy, H. Schmickler, J. Wenninger, CERN

The SPS ran for 247 days during 1994; 64% of this was with high intensity proton beam for physics data taking in the Fixed Target mode of operation, 12% was for a lead run at the end of the year, with the remaining 24% spent in setting up and machine development. The SPS supplied LEP with 8 bunches of electrons and 8 bunches of positrons either in the 14.4 or 19.2 seconds interleaved cycling mode during the operation with protons or lead ions respectively. The new record peak intensity during the year was 3.9×10^{13} protons per pulse at 450GeV. A total of 11×10^{18} proton were delivered to all targets, with an overall average during physics of 2.5×10^{13} protons per pulse at 450GeV. Some 6×10^{18} protons were delivered to both neutrino experiments.

I. SPS FIXED TARGET OPERATION

A. General

The 450GeV proton operation was carried out with a cycle duration of 14.4 seconds, including four 1.2 second lepton cycles. A typical display of the different intensities delivered onto targets is shown Figure 1.

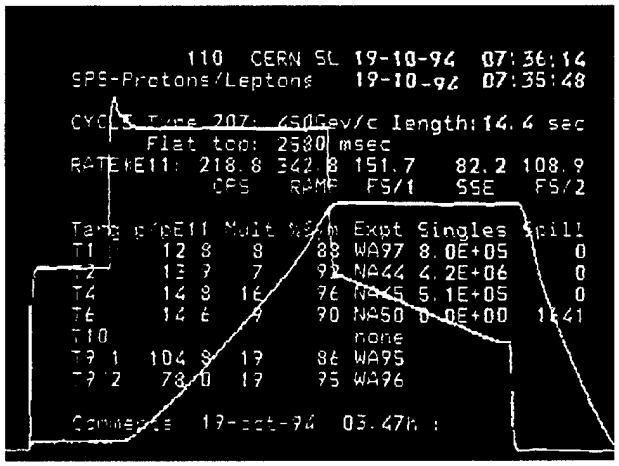


Figure 1: Proton intensities and magnetic cycle display as seen on video screens in the Control Room

The start-up period was difficult for a variety of reasons; dominant were many equipment problems, the unavailability of the injectors, and the new controls and application software following the withdrawal of the obsolete ND100 computers. The major difficulties came first from computer controls and associated software, then from the superconducting cavities, a second bi-module having been installed during the shutdown. Later, when the intensity started to increase, a high sparking rate of the West electrostatic septa (mainly tank4) caused further delays. After a careful systematic commissioning including newly developed extra feedback loops, the superconducting cavities behaved better, allowing to increase the intensity to 2.7 10^{13} at 450GeV, giving 10^{13} ppp for the neutrino experiments. The operation was rather unstable at this moment, due partly to trips of the neutrino interlock system itself, but amplified by numerous data acquisition and controls problems (the equipment protection system philosophy was completely revised before the summer). In May/June, about 4 days of neutrino operation were lost due to numerous vacuum leaks, mainly in SPS, but also in the CPS booster. At the beginning of June, the intensity was 3.2 10^{13} at 450GeV of which 1.8 10^{13} ppp were extracted for the neutrino target. After the June technical stop, significant improvements were observed on the computer front and the sparking in the West electrostatic septa, although not fully understood, was under control. From July, the very good transverse emittances delivered by the CPS allowed the SPS to run high intensity with a good transmission, but with a moderate overall efficiency due to a number of various faults, mainly after a second 400kV failure in July. The observation was made that the sparking rate on the electrostatic septa was directly affected by tiny losses during the acceleration. At the end of summer, a serious difficulty came from the superconducting cavities which suffered from frequent trips during the proton cycle, and necessitated a reduction of intensity one month before the end of the run.

A systematic study of the behaviour of the cavity and its dependence on the beam quality revealed the importance of the 14 GeV longitudinal structure which was improved by fine adjustments of the four booster ring intensities, and of the CPS continuous transfer extraction bumpers. It was then possible to launch the common CPS-SPS intensity increase program, with the aim of finding the maximum intensity acceptable by the neutrino target (and by the machine), with minimum perturbation for the other users. The CPS was able to accelerate batches of 2.4 10^{13} protons under stable conditions and with good transverse emittances; the SPS, after some tuning to accept such a beam, was able to accelerate over 3.5 10^{13} ppp to 450GeV, in stable conditions, reaching the peak intensity of 3.9 10^{13}ppp.

In conclusion, the very high intensity run at the end of the year was a success only after months of continuous effort not only in the SPS but also in the chain of injectors.

B. Acceleration of high intensity proton beams

To maintain longitudinal stability of the intense proton beam against coupled bunch instabilities the various RF cavities in the SPS must be damped, either actively or passively. Four separate RF systems, one for

0-7803-3053-6/96/$5.00 ©1996 IEEE

high intensity proton acceleration and three for lepton acceleration are present in the SPS ring. RF feedback with one turn delay is used on the fundamental passband of the broadband 200MHz travelling wave structures available for proton acceleration, while direct RF feedback is used on the three active 100MHz standing wave cavities used to capture long lepton bunches at injection. The twenty one 200MHz standing wave cavities, which accelerate lepton bunches to about 15GeV, are passively damped in the proton cycle, the damping loop being inserted and removed once every super-cycle. The four 352MHz superconducting cavities, accelerating leptons to top energy, are each heavily damped using short-delay RF feedback supplemented by a one-turn delay RF feedback system [1]. All cavities have higher order mode suppressors.

The superconducting system has proved the most delicate to operate in the presence of the high intensity proton beam. This is not because of beam instabilities but because of the transient beam loading that can occur with non-uniform beams. The RF feedback essentially maintains zero voltage on the cavity, the power amplifiers injecting the current necessary to counteract the beam induced voltage. The cavity frequency, 352MHz is far away from the harmonics of the main accelerating frequency and for uniform beams the amplifiers are not heavily solicited. However, any strong structure on the beam has components at multiples of the revolution frequency which can increase the demand significantly. These components can excite resonances in power supplies etc., care must be taken to filter these effects, but the main problem is the extra power requirement on the amplifiers. With increasing intensity it was necessary to improve the situation in two ways; first by making the amplifiers as robust as possible, i.e. tuning the interlock circuits to the beam characteristics, and secondly by attacking the source, i.e. the beam components. The major source of the latter is the continuous transfer system in the injector which unless carefully adjusted can give beam current components to many times the revolution frequency. A secondary source is the longitudinal emittance blow-up in the injector at top energy done to prevent microwave instabilities. If this is not accurately adjusted losses can occur on parts of the beam again introducing revolution frequency components.

For the next run the current capability of the amplifier system is being increased, more improvements to the protection circuits are being added, and new digital filtering techniques are being examined which will reduce the loop response at the revolution frequency lines thus lowering the demand on the amplifiers while maintaining gain at the synchrotron frequency sidebands to prevent instability. Instrumentation to rapidly analyse the beam structure will also be introduced

C. Neutrino beams

During 1994, the neutrino program was again operational after a 2 year stop. The proton transfer line TT66, the neutrino target T9 and the neutrino beam line were completely re-build during this time. The proton beam is extracted from the machine in 2 extractions separated by 2.76s. Both extractions are combined 2^{nd}-4^{th} order resonant extractions. The first takes place during the round off at the end of the ramp at 446GeV. The beam is bunched with all buckets filled, except for the 220ns holes in between the injection batches. The second takes place at the end of the 450GeV flat top, where the beam is debunched. Both extractions have a length of 6ms. The beam intensity is monitored by a beam current transformer in the first part of the transfer line. The beam positions in the line are measured with secondary emision monitors, on which radiation damage was found to develop. This damage results in a non-uniform sensitivity of these detectors. To monitor the real intensity received on target an additional BCT will be added in front of the target. In the first part of 1994 the maximum allowed beam intensity on T9 for both extractions was $1.3*10^{13} + 0.7*10^{13}$ protons per cycle, respectively. After a careful recalulation of the thermal and stress effects in the target these limits were lifted to $1.5*10^{13} + 1.5*10^{13}$ protons per cycle. During the end of 1994 total intensities of up to $2.8*10^{13}$protons per cycle on target were achieved. During a few days, $2.5\ 10^{3}$ protons were registered, and an inspection of the target, after a 3 months cooldown period revealed no visual damage.

D. Radiation problems

One of the very important factors linked to the high intensity running is the loss of particles in the high energy extraction channels, not only during at the time of the extraction at 450 Gev/c, but also during the acceleration process.

For the survival of the equipment and to limit the personnel dose it is necessary to have the proper tools to optimize the setting-up and analyze the proper functioning of the extraction channel. Intensive studies carried out over the last 5 years have lead to the following recommendations:

1. During the annual shut-down, careful HV conditioning accompanied by minimizing the vacuum pressure by a proper bake-out to reduce the outgassing time during the start-up period;

2. During the setting-up, allow the necessary time to outgas with the beam, components like septum wires and HV electrodes, which receive much radiation and are likely to cause frequent sparking;

3. During operation, constant survey of the beam quality through the whole chain of accelerators involved, in order to take appropriate action at the right moment.

Application software has been developed which will allow carefully monitoring of the beam losses, normalized to the extracted intensity, to spot instantaneous changes in extraction efficiency and abnormal beamloss.

A second system of high gain beamloss detectors has been installed to monitor the evolution of the induced radioactivity and micro beamloss during acceleration.

A pilot system has allowed the development of an algorithm which calculates the present and future induced activity from the time series of the number of

protons extracted per day. It predicts that operation at higher intensities will exponentially lengthen the time before access may be given to the machine in case human intervention is required Figure 2.

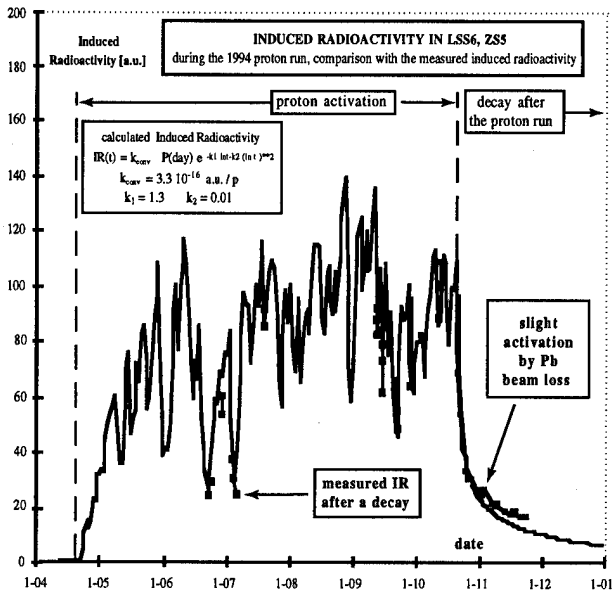


Figure 2: Measured and expected induced activity

II. LEPTON

The SPS and CPS nominally have 4 * 1.2 second cycles dedicated for lepton production and transfer. In 1994 only the middle two cycles (called e+2 and e-1) were used for LEP in 8 bunch mode. The harmonic numbers of SPS and CPS were chosen such that the 8 bunches were equidistant in the SPS and no re-phasing was required by the CPS between extraction the first and second 4 bunch batches. This allowed the 8 SPS bunches to be directly injected into the 8 LEP pretzel bunches within 1 SPS cycle. In the CPS the two spare cycles were used extensively for MD, physics and the setting up and optimisation of lead ion cycles (for the SPS physics program). In the SPS less use was made of the spare time in the supercycle. One of the spare cycles (e-2) was used for commissioning of the newly installed Robinson wiggler and for optimisation of a 22GeV electron cycle. The other spare cycle (positron 1) saw no beam after the initial start-up period. However, the reduction in the number of active cycles in the SPS allowed the operators to concentrate on those that were left.

III. ACKNOWLEDGEMENTS

The work reviewed in this paper is the combined effort of a very large number of persons in the SL and PS division. It is a pleasure to thank them here. B. Desforges is in charge of the statistics; the editing and assembling has been done by M. P. Colin.

IV. REFERENCES

[1] Improved Impedance Reduction in the CERN SPS Superconducting Cavities for High Intensity Proton Operation. D.Boussard, G.Lambert, T.P.R.Linnecar. PAC, Washington 1993

THE SPS AS ACCELERATOR OF PB $^{82+}$ IONS

A. Faugier, X. Altuna, R. Bailey, R. Blanchard, T. Bohl, E. Brouzet, H. Burkhardt, P. Collier, K. Cornelis, G. de Rijk, F. Ferioli, A. Hilaire, M. Lamont, T. Linnecar, M. Jonker, C. Niquille, G. Roy, H. Schmickler, CERN

In 1994 the CERN SPS was used for the first time to accelerate fully stripped ions of the Pb^{208} isotope from the equivalent proton momentum of 13 GeV/c to 400 GeV/c. In the CERN PS, which was used as injector, the lead was accelerated as Pb^{53+} ions and then fully stripped in the transfer line from PS to SPS. The radio frequency swing which is needed in order to keep the synchronism during acceleration is too big to have the SPS cavities deliver enough voltage for all frequencies. For that reason a new technique of fixed frequency acceleration was used. With this technique up to 70% of the injected beam could be captured and accelerated up to the extraction energy, the equivalent of 2.2 10^{10} charges. The beam was extracted over a 5 sec. long spill and was then delivered to different experiments at the same time.

I. SPECIFIC PROBLEMS

In 1994 the SPS was used for the first time to accelerate fully stripped Pb^{82+} ions from 13 GeV/c to 400 GeV/c proton equivalent. The injector, the CERN PS, accelerated Pb^{53+} ions which were subsequently fully stripped in the transfer line to the SPS.

One of the specific problems with the lead ion operation is the low intensities involved (1 10^{10}charges). This requires special monitoring. High gain FET amplifiers had to be installed close to monitors in order to keep the signal to noise ratio to an acceptable level. However, for secondary emission monitors in the transfer lines the signal is high because it is proportional to Z^2. For the same reason, the energy loss in any foil of material, like secondary emission monitors, or luminescent screens is also much higher than for protons. A luminescent screen in the injection line for example, changes the energy by 0.5%, so special care had to be taken during the steering process.

The closed orbit pickups were fully equipped with new amplifiers. This was the first time a complete closed orbit could be measured for the heavy ion intensities. In previous heavy ion runs only a few pickups were equipped with special amplifiers.

The RF frequency at injection is much smaller than that for protons at the equivalent energy. The frequency swing which is needed for the acceleration of Pb-ions is bigger than the bandwidth of the traveling wave cavities. In order to overcome this problem a new technique of constant frequency acceleration is used as will be explained in a subsequent chapter.

II. STRIPPING EFFICIENCIES

The Pb^{53+} ions from the CPS injector where fully stripped by an aluminum-foil in the transfer line to the SPS. First a 2 mm aluminum-foil was used. This gave a stripping efficiency of 100% Pb^{82+} . However, this foil gave a normalized emittance growth of 1π mmmrad in both planes. The resulting normalized emittance of 3π mmmrad in the vertical and 4π mmmrad in the horizontal plane was to big to fit into the acceptance of the SPS which is of the order of 2.5π mmmrad vertical and 3.5π mmmrad horizontal. This resulted in a poor acceleration efficiency of only 25%. Later a stripper of 0.5 mm was used. For this thickness no emittance blow up was observed but, according to profile measurements using a luminescent screen and a camera (fig. 1), a contamination of 20% Pb^{81+}-ions could be observed.

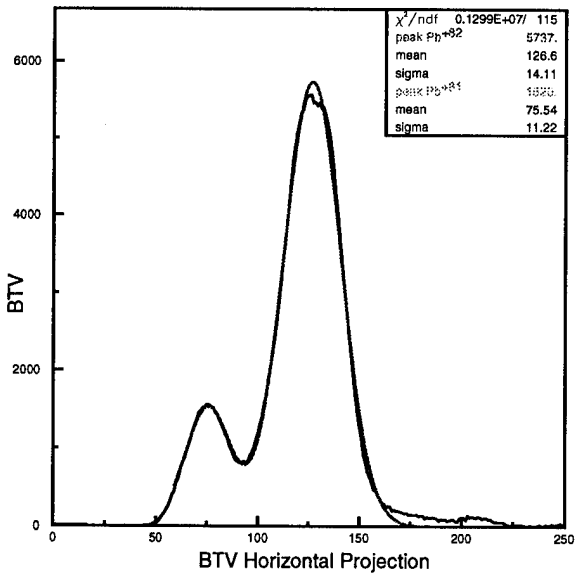


Fig 1. Beam profile measured with a camera showing both the Pb^{81+} (left) and the Pb^{82+}(right) peak.

The response of the screen-camera system is very nonlinear and an empirical calibration against intensity had to be performed. The result of this is shown in Fig. 2. There is still some doubt for the lower part of the curve which seems to show a behavior that is not completely understood. The next period with lead ions we will try to perform the measurements again with a more linear camera. We will also

0-7803-3053-6/96/$5.00 ©1996 IEEE

have current transformers available in order to increase the precision.

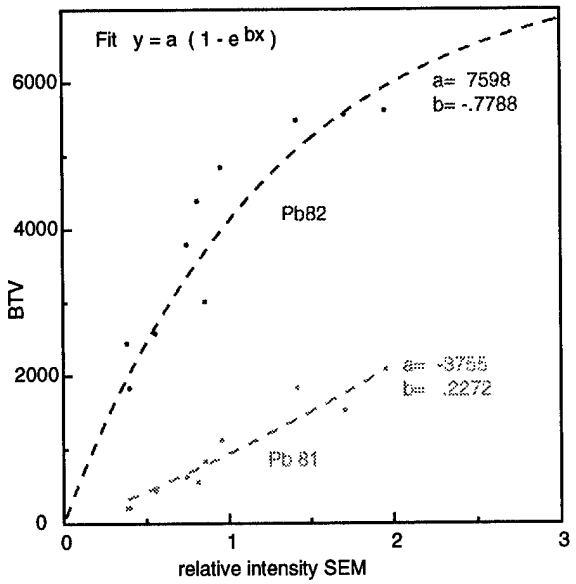


Fig .2: Intensity calibration of the screen-camera response against secondary emission monitors.

At the end of the run a 1mm stripper was also tested. The results can be summarized as follows :

2 mm Al : V normalized emittance 3π mm mrad
H normalized emittance 4π mm mrad
No Pb^{81+}contamination
Momentum loss 0.5%

1 mm Al : V normalized emittance 2.5π mm mrad
H normalized emittance 3.5π mm mrad
5 % Pb^{81+}contamination
Momentum loss 0.2%

.5 mm Al : V normalized emittance 2π mm mrad
H normalized emittance 3π mm mrad
20% Pb^{81+}contamination
Momentum loss 0.1%

III. CONSTANT FREQUENCY ACCELERATION

The RF cavities used to accelerate lead ions and protons in the SPS are of the untuned traveling wave type. Their bandwidth is sufficiently large to allow acceleration of protons at fixed harmonic number but the frequency swing for lead ions is too large. Changing harmonic number on intermediate flat tops in the cycle is one way round this problem but a more elegant method is to use non-integer harmonic number acceleration.

In this scheme advantage is taken of the short filling times of the cavity, 0.8υs compared to revolution period, 22us. The ions are injected and accelerated in short batches, 2υs long, and the cavity frequency is held constant at a value giving maximum voltage each time the batch traverses the cavities. After the batch has passed the cavity, the power is switched off and the frequency of the generator is modulated to adjust the phase of the RF ready for the next transit of the batch through the cavity for which the power is switched on again. Thus the batches always see the same frequency but the average frequency of the generator varies with the revolution frequency of the ions. The system is fast enough to allow four batches of ions spaced around the circumference to be accelerated in this way.

This novel beam control system is described elsewhere [1], but here we mention that the fundamental requirement was the development of a fast switching, voltage controlled oscillator. Considerable modifications to the power amplifiers were also necessary to allow full power switching at 180kHz with rise and fall times of less than 1υs.

The four batches of ions are injected at 1.2s intervals from the injector. Each batch is allowed to debunch for 10ms and is then captured adiabatically and held along the injection plateau at fixed frequency while the other batches are likewise injected and captured. Individual capture of each batch is possible by counterphasing the voltages of two cavities at four times the revolution frequency. When all the batches are in, they are accelerated using a radial loop with sensitive pick-up to control the mean frequency of the oscillator.

After initial setting-up, capture efficiencies of 80% were regularly obtained during this short run. There is some evidence that this figure will be improved by reducing the noise at multiples of the revolution frequency, inherent to this type of oscillator.

IV. PERFORMANCES

For the 2 mm stripper, the transverse emittances were too big for the machine aperture. This resulted not only in transverse losses at injection, but also in capture losses. The horizontal aperture of the machine being limited in the high dispersion regions resulted in a strong reduction of the momentum acceptance so that adiabatic capture became very inefficient. Only 25% acceleration efficiency could be obtained. When the stripper was changed to 0.5 mm, 70% of the injected beam could be accelerated.

The transmission throughout the system for a good cycle can be summarized as follows :

Before stripper :
9 10^9 charges (Current transformer)

After stripper :
13 10^9charges (Current transformer)

TT10:
7 10^9 charges (Secondary emission monitor)

Injected:
7 10^9 charges (Current transformer)

400 GeV (4 injections):
22 10^9 charges (Current transformer)

These numbers indicate that there is a serious loss between the stripper and TT10. However, the calibration of the secondary emission monitors (SEM) against intensity is not obvious. Only with protons could a cross calibration be done with a current transformer. For lead the Z^2 law was used in order to scale the sensitivity of the SEM. For next year two current transformers will be upgraded for measuring low intensities, so we will be able to cross check the calibration for lead-ions.

At the end of the lead running period, which lasted only a month, a total of 7.25 10^{14} charges was accumulated on the targets (Fig.3).

The most striking feature was the stability of the ion source, delivering the same intensity at every cycle.

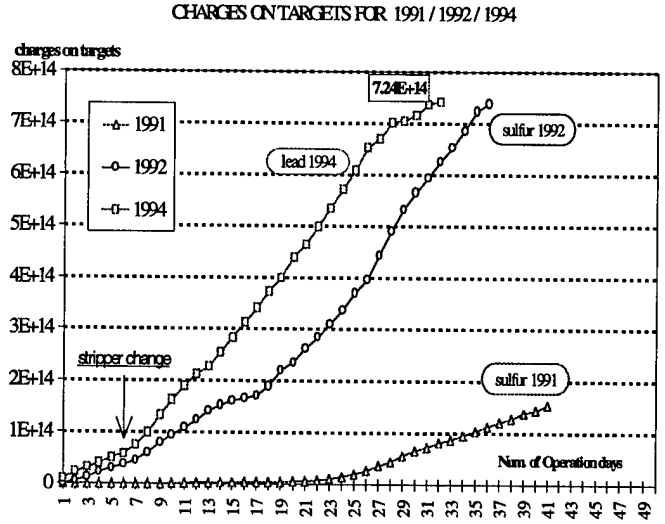


Fig. 3: accumulated intensity of the lead charges on target, compared with previous heavy ion runs.

V. REFERENCES

[1] T. Bohl et al. , "Non Integer Harmonic Number Acceleration of Lead Ions in the CERN SPS", This conference.

EXPERIMENTAL EVIDENCE FOR MULTI-PASS EXTRACTION WITH A BENT CRYSTAL

B. Dehning, K. Elsener, G. Fidecaro, M. Gyr, W. Herr, J. Klem, W. Scandale, G. Vuagnin,
E. Weisse, S. Weisz (CERN); S.P. Møller, E. Uggerhoj (Aarhus University, Denmark);
A. Freund, R. Hustache (ESRF Grenoble); G. Carboni (Roma, Italy);
M.P. Bussa, F. Tosello (Torino, Italy)

I. Abstract

The feasibility of extracting particles from the halo of a circulating proton beam using a bent silicon crystal has been demonstrated experimentally at the SPS for a beam energy of 120 GeV. Presently studies are conducted to understand the extraction mechanisms and the measured efficiencies. In particular the contribution of multi-pass extraction, where the particles can pass through the crystal many times before being channeled and extracted, is investigated. In a recent experiment, using a crystal especially fabricated with a finite amorphous layer on its surface, it has been proven that multi-pass extraction plays an important role. The experiment is described and the implication for further studies are discussed.

II. INTRODUCTION

There is considerable theoretical and experimental activity in order to understand the mechanisms leading to the observed proton beam intensities extracted by means of a bent crystal from high energy accelerators [1], [2], [3], [4]. One aim of this work is to assess the perspectives of using such a crystal to parasitically extract a proton beam from the LHC [5].

While the principles of channeling and deflection of protons in bent silicon crystals are well understood [6], the specific processes leading to the extraction of protons from the halo of a circulating beam are more difficult to assess. The extraction of 120 GeV protons from a beam coasting in the CERN SPS is now regularly achieved with an efficiency of about 10% [3]. Two mechanisms are being discussed, which could be responsible for extraction with a bent crystal: first-pass extraction and multi-pass extraction. The aim of the experiment described in this report was to experimentally demonstrate the existence of the latter.

III. EXPERIMENT AT THE SPS

For the present experiment a 120 GeV coasting beam with an intensity of about $5 \cdot 10^{11}$ protons was used. The lifetime of the beam without external interference can be several hundred hours. The crystal is placed typically at 10 from the closed orbit, some 10 times the transverse beam size, where only very few halo particles are found initially. The beam is then excited horizontally with band limited white noise induced on a pair of condenser plates. Typical kicks produced are of order 0.0005 - 0.005 μrad, and the kick strength can be varied by changing the noise amplitudes. Once the beam has diffused onto the crystal and a steady state is reached, normalized emittances of 60 mm mrad (horizontal) and 10 mm mrad (vertical, unaffected by the noise) are found. Beam lifetimes in this steady state vary from a few minutes to 50 hours depending on the kick strength. The protons extracted by the bent crystal are measured in an arrangement of detectors which is described in refs. [3], [4].

IV. FIRST- AND MULTI-PASS EXTRACTION

First-pass extraction would correspond to the experimental situation found at an external beam-line [6], the only difference being the small impact parameters of the protons onto the crystal (see next section). Therefore, for first-pass extraction the surface quality is of paramount importance.

Multi-pass extraction has been predicted as a possible mechanism by several authors [7], [8]. The term "multi-pass" refers to the situation of protons that are not channeled during their first encounter with the crystal, but rather scattered by a small angle. Thus these protons will have "further chances" at later turns to be channeled and extracted when passing the crystal inside the critical angle for channeling (see [3]) and with larger impact parameters. While for a first-pass extraction with the required high efficiency the surface properties of the crystal are important, the accelerator parameters play a more important role for the multi-pass mechanism [9].

No direct experimental proof of the existence of this mechanism existed so far, although some (model-dependent) conclusions were inferred from recent experimental results. For example, the observation of extracted protons over a very large range of crystal angles with respect to the closed orbit in the SPS experiment [3], but also the enhanced extraction efficiency due to an additional scatterer observed at Serpukhov [10] seem to indicate the importance of multi-pass extraction.

Within the restrictions of an accelerator experiment, the possibility to reach large impact parameters (therefore clear "first-pass" conditions) are limited: the only possibility found is the "kick-mode" [11], but the high instantaneous proton intensities extracted in this mode make it hard to estimate an extraction efficiency. Furthermore, such a mode does not reflect the standard operational conditions and certainly cannot be used for a parasitic extraction in the LHC. Therefore, a different approach was taken here to experimentally prove the importance of multi-pass extraction: a crystal as shown in Fig. 1, with an amorphous layer of 30 μm Silicon oxide, has been installed in the SPS [12].

This layer should prevent any first-pass extraction, the impact parameters being much smaller than the thickness of the layer (see below). An extracted beam would therefore demonstrate the existence of multi-pass extraction and provide a clean sample to study the multi-pass process separately and in detail.

0-7803-3053-6/96/$5.00 ©1996 IEEE

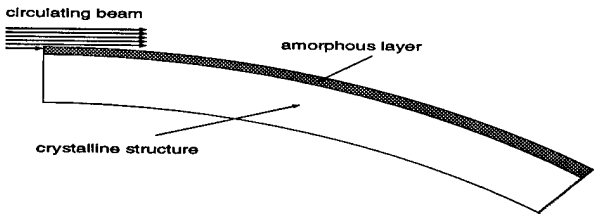


Figure. 1. Schematic view of crystal with amorphous layer

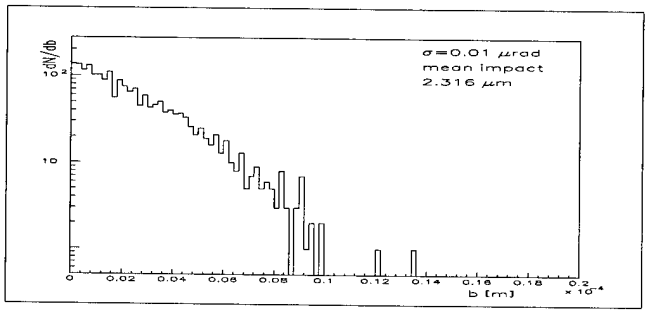


Figure. 2. Impact parameter distribution from simulation

V. COMPUTER SIMULATIONS

The diffusion of particles in our experiment is provoked by random kicks [13]. The amplitudes of the kicks follow a Gaussian distribution with a width σ_k.

For an otherwise linear machine the diffusion speed is then independent of the betatron amplitude and can reach maximum values in the order of mm per minute. The magnitude of the impact parameter b can then be estimated by:

$$b = \frac{D \cdot n_{res}}{\nu_{rev}}$$

where D is the diffusion speed, n_{res} the order of the resonance and ν_{rev} the revolution frequency ($\approx$ 43375 Hz in the SPS) and gives values in the order or a few nm, in any case much smaller than the crystal imperfections.

In order to get a better understanding of the extraction experiment with a bent crystal at the SPS, particle tracking with a computer program was done [13], [14]. A beam of 10'000 particles was followed through the (linear) machine, with parameters close to the ones found in the SPS experiment. Emittance growth due to induced voltage (white noise) on the damper plates was simulated, and the impact parameter and impact angle distributions resulting at the crystal position were recorded. For details of the simulation see [13], [14]. An example is shown in Fig. 2 for a kick strength of 0.01 μrad.

The impact parameters are very small and do not exceed values above 10 μm even for these kick amplitudes 20 times larger than those used in the experiment. The emittance growth is a stochastic process and very slow when the kicks are small. In order to reach an equilibrium state for many particles, the required time for the simulation is very large and depends strongly on the kick strength. Realistic kick strength would thus require huge amount of computer time. However, as has been shown earlier [13], for small kicks the mean impact parameter rises approximately linearly with the kick strength and scaling of the impact parameter distributions obtained is thus permitted. The important result at this stage is that the mean impact parameter (of an exponential distribution) in the experiment is estimated to be about 20 - 50 nm and excludes first-pass extraction.

VI. EXPERIMENTAL RESULTS

Results of the measurements using the bent silicon crystal with its amorphous layer are summarized in Table 1.

Intensity (10^{11} p)	Lifetime (hours)	Extracted rate (10^5 counts/s)	Efficiency (%)
5.8	33.0±1.1	2.07±.02	4.2±.3
4.5	8.1±.2	9.49±.03	6.2±.3
4.4	28.3±1.4	2.38±.03	5.5±.5
1.9	5.11±.2	8.78±.04	8.8±.4
1.8	2.3±.1	13.83±.12	6.5±.3
0.69	0.8±.1	13.76±.06	5.9±.3
0.57	1.7±.1	7.27±.05	8.5±.6
0.36	0.50±.05	11.06±.35	6.5±.4

Table I
Extraction efficiencies for the crystal with an amorphous layer.

Measurements were taken for different kick strengths and a crystal position 10 mm from the closed orbit [15]. The number of particle hitting the crystal is estimated from the beam intensity and the measured lifetime. Extraction efficiencies (defined as the ratio between extracted and lost particles) are rather independent of the kick strength (i.e. impact parameter b) and are in the same order of magnitude as found without amorphous layer [3]. From this result we conclude the existence of multi-pass extraction. The comparable efficiency also indicates that this mechanism plays an important role in the extraction process. The large thickness of the amorphous layer causes proton losses even on later turns, thus reducing the efficiency slightly. A typical angular scan obtained with this crystal is shown in Fig. 3. The width of the scan is approximately 300 μrad and the comparison with an angular scan for the same crystal without the amorphous layer shows a similar result [3] and further supports our conclusion that multi-pass extraction is a dominant mechanism. The profiles of the extracted beam as measured by the scintillator hodoscope at the peak of the angular scan are shown in Figs. 4 and 5. For comparison, measurements were also performed with a so-called "U-shaped" crystal (see [4]), and efficiencies of up to 16% have been found. Detailed results are published elsewhere [15].

VII. FURTHER STUDIES AND IMPROVEMENTS

Once the existence and importance of the multi-pass process is established, one can try to increase the extraction efficiency. It has been demonstrated [9] that the efficiency for pure multi-pass extraction strongly depends on the machine parameters, in particular on the β-function at the crystal position and the tune.

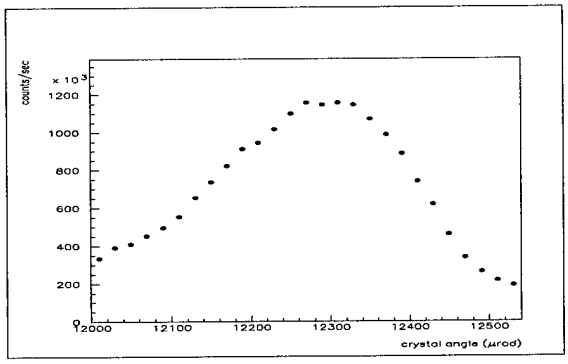


Figure. 3. Angular scan with respect to beam axis

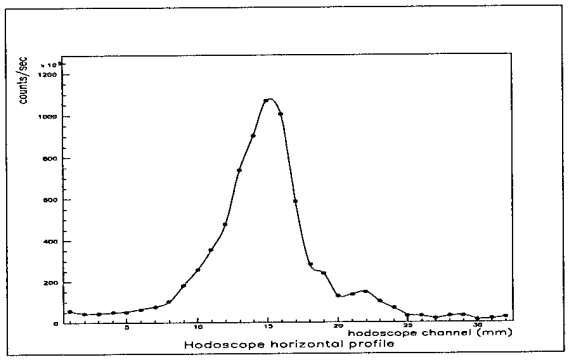


Figure. 4. Horizontal profile of extracted beam

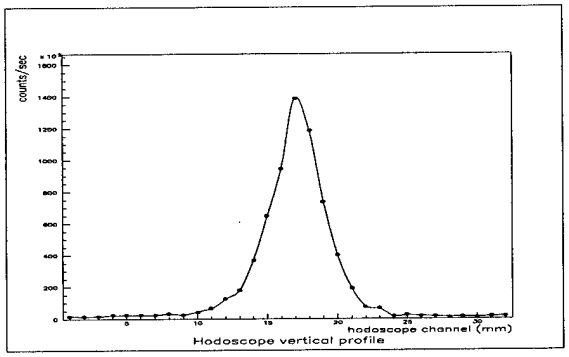


Figure. 5. Vertical profile of extracted beam

These parameters can be optimized to achieve the highest possible efficiency [9]. This could be studied with a simulation program or experimentally using a dedicated insertion at the crystal position.

A further possibility has been suggested to increase the efficiency: the use of an external scatterer at an appropriate location in the machine [10]. We intend to evaluate such a scheme in simulations as well as in our experiment at the SPS.

VIII. CONCLUSION

We have investigated the mechanism of multi-pass extraction using a bent crystal with an imperfect surface and have made the following observations:

- We have measured extracted particles using a crystal with an amorphous layer of 30 μm.

  This can only be explained by a multi-pass extraction mechanism.

- The efficiency and angular scans are comparable to the one obtained without an amorphous layer and prove the importance of this mechanism for the extraction process.

References

[1] A. Asseev et al.; Nucl. Instr. Meth. A330 (1993) 39.
[2] R.A. Carrigan et al.; Nucl. Instr. Meth. B90 (1994) 128.
[3] H. Akbari et al.; Phys. Lett. B313 (1993) 491.
[4] H. Akbari et al.; Proc. EPAC94, (1995) 199.
[5] W. Scandale; Proc. LHC Workshop (Aachen, 1990), CERN 90-10, 760.
[6] S.P. Møller et al.; Nucl. Instr. Meth. B84 (1994) 434.
[7] V.M. Biryukov; Nucl. Instr. Meth. B53 (1991) 202.
[8] A.M. Taratin et al.; Nucl. Instr. Meth. B58 (1991) 103.
[9] S. Bardin; CERN SL/Note 92-52 (AP).
[10] A. Asseev et al.; Nucl. Instr. Meth. A324 (1993) 31.
[11] S. Weisz and the RD22 collaboration; Proc. 1993 IEEE Particle Accelerator Conference, 26.
[12] E.M. Hansen; Private Communication
[13] W. Herr; CERN SL/92-53 (AP).
[14] G. Vuagnin; CERN SL/Note 95-24 (AP).
[15] K. Elsener et al.; SL-MD Note 170 (1995).

STORAGE RING FOR ENHANCED ANTIPROTON PRODUCTION AT FERMILAB

G. Jackson and G.W. Foster
Fermi National Accelerator Laboratory[1], MS 345, P.O.Box 500, Batavia, IL 60510 USA

ABSTRACT

There is interest in the high energy physics community to upgrade the luminosity of the Tevatron Collider to a value greater than $1x10^{33}$ cm^{-2} sec^{-1} per detector. The only feasible means to increase the luminosity by this factor of 10 over the design goal of the Main Injector project is to increase the antiproton production rate by almost the same factor. Using excess space in the Main Injector tunnel it is possible to build an additional storage ring whose purpose is to provide the flexibility necessary to produce and store the increased number of antiprotons. In this paper the motivation for this ring is discussed. The details of the scheme to recycle the antiprotons left over at the end of each Tevatron Collider store is also reviewed.

I. MOTIVATION

Given that Tevatron Collider luminosity is proportional to the initial antiproton intensity, which in turn depends on the rate at which antiprotons are produced (stacked), it is essential to understand how to generate high stacking rates to support the Tevatron33 [2] luminosity goal of $1x10^{33}$ cm^{-2} s^{-1}. The antiproton stacking rate achievable with the Main Ring at this time [3] at small Accumulator stack sizes is $7x10^{10}$/hr. The design stacking rate for the Main Injector [4] in the absence of the Recycler is $15x10^{10}$/hr. The Tevatron33 upgrade has a stacking rate of $100x10^{10}$/hr for the design goal.

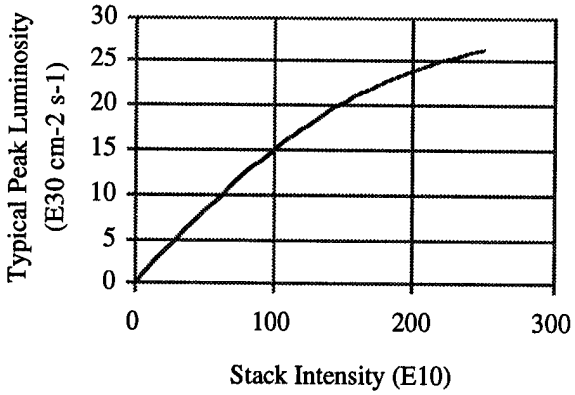


Figure 1 Observed luminosity vs. Accumulator stack size curve for the present Tevatron collider run. Instead of growing linearly, the luminosity saturates due to the increased transverse emittance of the antiproton stack.

The dependence of initial Tevatron luminosity on the antiproton intensity (stack size) in the Accumulator 8 GeV storage ring saturates as the beam current increases (see figure 1). This effect comes from the fact that the transverse emittance of the Accumulator antiproton stack increases linearly with increased current. At higher stack sizes the beam size exceeds the aperture of the Main Ring, thus reducing the antiproton intensity in the Tevatron Collider, and hence the initial luminosity.

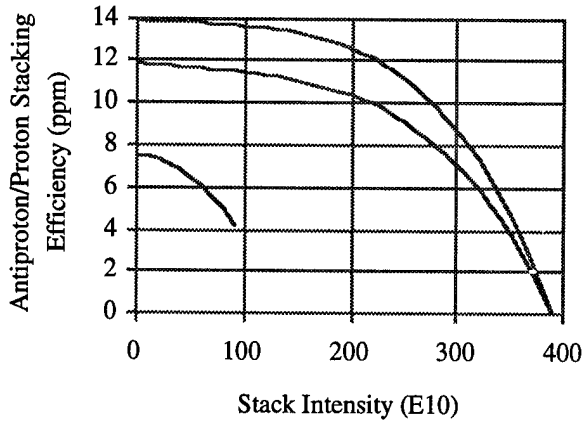


Figure 2 Stacking efficiency as a function of the antiproton stack size in the Accumulator. The lowest curve was measured during the 1988-9 collider run. The middle curve is the expected stacking profile given upgrades of some stochastic cooling systems. Finally, the top curve is the prediction of the stacking rate planned for the Main Injector.

As seen in figure 2, the other repercussion of large stack sizes is a reduced stacking efficiency (defined as the number of antiprotons produced for every proton delivered to the production target). To achieve the Tevatron33 luminosity goal a total stack size of $800x10^{10}$ antiprotons is required. Given that the stacking rate vanishes well before this level, an additional storage ring capable of holding more antiprotons is needed.

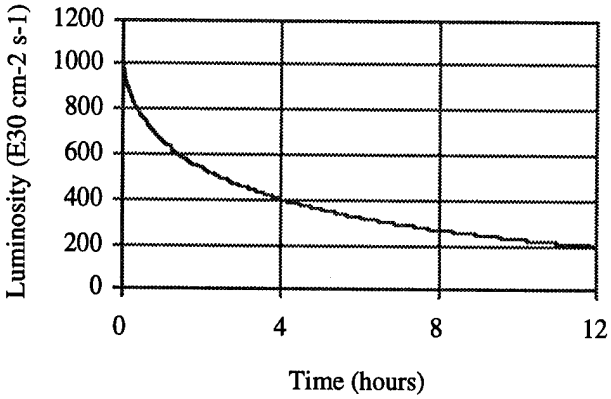


Figure 3: Expected evolution of the luminosity in the Tevatron Collider given the typical Tevatron33 initial luminosity. Note that the useful luminosity occurs in the first 4 hours.

0-7803-3053-6/96/$5.00 ©1996 IEEE

One of the shortcomings of the present Tevatron Collider facility is the fact that the antiprotons are dumped at the end of each store. Given that the luminosity lifetime is quite short at high luminosity due to high particle collision rates and intrabeam scattering induced emittance growth, the required stacking rate could be dramatically reduced if the antiprotons could be recycled after each store. Figure 3 contains the results of a simulation of the anticipated luminosity evolution at Tevatron33 luminosities. By the time that 4 hours have passed, the luminosity has dropped to a point where another store is desired. As can be seen from figure 4, 80% of the antiprotons are still in the Tevatron at that point. Assuming even pessimistic deceleration and recapture efficiencies, the required stacking rate can be reduced by more than a factor of two.

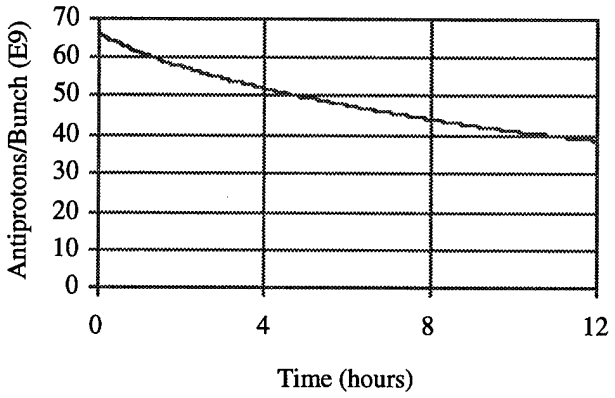


Figure 4: Evolution of the antiproton bunch intensity in the Tevatron during the store assumed in figure 3.

At present the Accumulator is used to store antiprotons. Unfortunately, the antiproton stack is lost on average once per week due to equipment failure, electrical outages, or human error. If the storage ring used to preserve the high intensity stacks had a higher reliability, the average luminosity would increase substantially.

II. ANTIPROTON STORAGE RING

In the last year a number of options have been studied for increasing the number of antiprotons available to the Tevatron Collider. A second storage ring at a kinetic energy of 8 GeV in the Main Injector tunnel was found to provide for the storage, recycling, and reliability criteria outlined above. Because of the added desires of low cost and fast magnet production, permanent magnets [5] were chosen for the entire 3.3 km ring circumference.

A. Lattice

A number of lattices based on the Main Injector design were considered. After weighing the relative merits of separated and combined function, a combined function lattice based on 4 m long gradient sector magnets is presently favored. With a dipole field of 1.5 kG and a 3.5 kG/m quadrupoles field, the standard cell length of 34 m is dominated by empty beam pipe. Straight sections contain 1 m long quadrupoles which have a gradient of 30 kG/m. A sketch of the magnet placement in this lattice is displayed in figure 5, showing the bellows which provide the bend between otherwise straight sections of beam pipe. All magnets are straight, since the sagitta is relatively small. Table 1 contains the parameters for a first pass of such a combined function lattice.

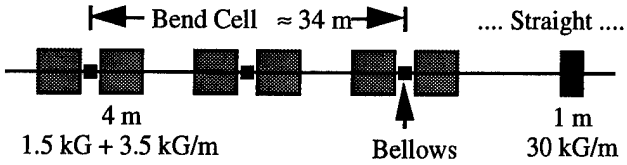


Figure 5: Sketch of the relative magnet placement and lengths in the lattice favored at present.

Table 1: Summary of preliminary lattice parameters for the combined function lattice.

Parameter	Value
Ring Circumference (m)	3319.414
Arc Cell Maximum Beta Function (m)	56.1
Arc Cell Minimum Beta Function (m)	9.75
Maximum Dispersion (m)	2.23
e Cooling Insert Max. Horz. Beta (m)	210
e Cooling Insert Max. Vert. Beta (m)	542
Beta Function in e Cooling Insert (m)	200
Horizontal Tune	25.45
Vertical Tune	25.45
Horizontal Chromaticity	-34.7
Vertical Chromaticity	-36.3

B. Location

Because of the existing transfer lines and RF power amplifiers, the only space available in the tunnel at the same radius as the Main Injector was up on the ceiling. Because the weight of the magnets is approximately 200 lbs/ft, they can be hung from the ceiling using stands bolted into the concrete tunnel roof.

C. Temperature Compensation

Strontium Ferrite, the material to be used in the permanent magnets, has a field which varies with temperature. The magnitude of this dependence is -0.2%/°C. To determine if this level of field variation is a problem, the history of tunnel temperature variations in the Main Ring tunnel was studied. Figure 6 contains a summary of that data, in which the peak air temperature difference around the tunnel is plotted as a function of time. Given a calculated maximum allowable field variation of 1×10^{-3}, it is necessary to reduce either the temperature fluctuations in the Main Injector by an order of magnitude or stabilize the field in the magnets themselves.

To achieve this magnetic field stabilization, an iron/nickel alloy used as a flux shunt was suggested [6] and tested. Figure 7 contains the results of this test. The average temperature variation was reduced to approximately

9 ppm/°C. This level of temperature compensation removes all concerns about stability of the magnetic field in permanent magnets.

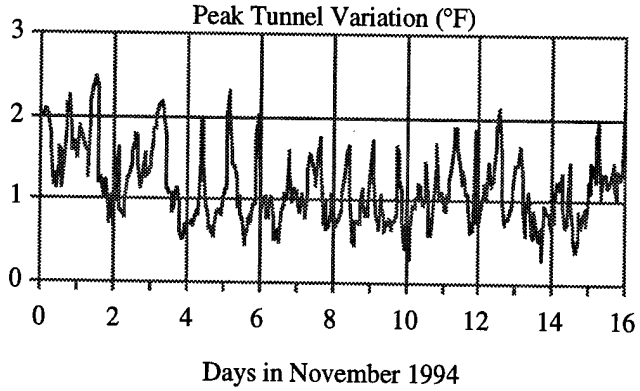


Figure 6: Peak air temperature variation around the Main Ring tunnel as a function of time.

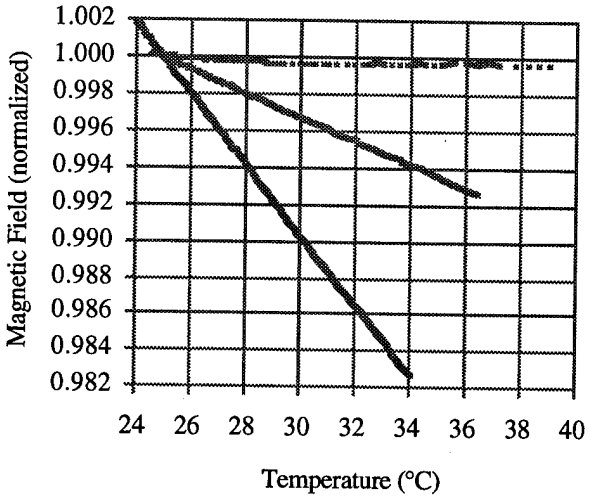


Figure 7: Variation of the magnetic field in a permanent magnet before (lower line) and after (horizontal line) temperature compensation with an iron/nickel alloy.

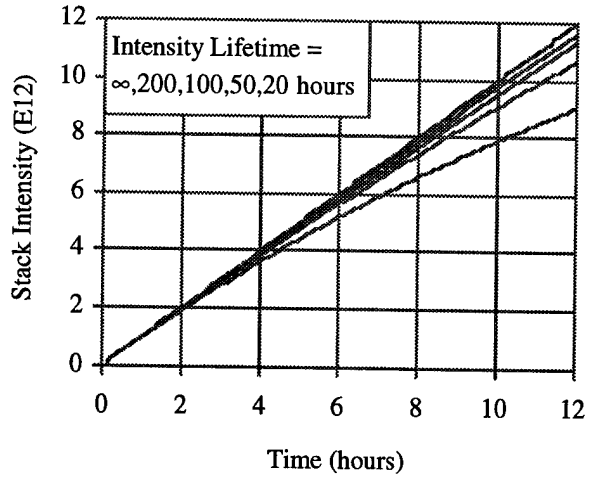


Figure 8: Calculation of the stack size vs. time as a function of the vacuum driven intensity lifetime of the antiprotons.

D. Vacuum

The need to store antiprotons with sufficient lifetime to efficiently produce and store the beam leads to a value for the maximum allowable average vacuum pressure in the storage ring. Because the Tevatron Collider luminosity drops to an insufficient level in about 4 hours, for normal operations an vacuum lifetime of 20-40 hours would be sufficient. Because failures sometimes occur in the proton injector chain or in the Tevatron, the ability to hold beam for extended periods of time is also desirable in this ring. As can be seen from figure 8, in that 4 hours the new antiproton stack is sufficiently large that the combination of recycled antiprotons and the new stack is sufficient to reach the Tevatron33 luminosity design goal.

E. Electron Cooling

The present plan for transverse and longitudinal phase space cooling required to stack and recycle antiprotons is to use electron cooling. Because the kinetic energy of the antiprotons is 8 GeV, the electron beam energy must be 4.5 MeV in order to match velocities. The design current for the electron beam at present is approximately 2 Amperes. The beam is generated and recovered by an electron gun and collector inside of a Pellatron [7] electrostatic accelerator.

One of the unique features of the proposed electron cooling system is that the direction of electron flow is reversible. With an injection scenario which calls for antiprotons transferred into the Tevatron first, the protons destined for the Collider can also be electron cooled. The most significant benefit of this procedure is the elimination of the process of coalescing [8]. By instead forming the collider bunches at 8 GeV in the presence of electron cooling, the longitudinal emittance of the proton and antiproton bunches will be significantly smaller than at present. The allows the Tevatron Collider to run with smaller β^* (and hence higher luminosity) and with crossing angles at the interaction points.

III. REFERENCES

[1] Operated by Universities Research Association Inc., under contract with the U.S. Department of Energy.

[2] G. Jackson and G.W. Foster, "Potential Accelerator Improvements Required for the Tevatron Upgrade at Fermilab", this proceedings.

[3] V. Bharadwaj, "Status and Future of the Tevatron", this proceedings.

[4] D. Bogert, "The Status of the Main Injector Project", this proceedings.

[5] G.W. Foster, et al., "Issues Surrounding the Construction of Permanent Magnet Storage Rings", this proceedings.

[6] K. Bertsche, et al., "Temperature Considerations in the Design of a Permanent Magnet Storage Ring", this proceedings.

[7] National Electrostatics, Middleton WI.

[8] J. Dey, et al., "Improvements in Bunch Coalescing in the Fermilab Main Ring", this proceedings.

LEP STATUS AND PLANS

S. Myers (for the LEP team), *CERN, Geneva, Switzerland*

Abstract

A description is given of the present performance of LEP. The major factors related to the limitations are discussed as are the measures currently used to overcome them.

The results from the "pretzel" scheme operation in 1994 are presented as well as a brief description of the new bunch train scheme. This scheme should ultimately allow the luminosity to be doubled by increasing the number of bunches per beam to sixteen (four trains of four bunches).

The results and limitations from the energy calibration by resonant depolarization are summarized.

A review is then given of the performance limitations, hardware requirements, and machine studies associated with operation of LEP at energies above the W± threshold. Finally the present plans for the LEP2 timescale are given.

I. INTRODUCTION

The CERN Large Electron Positron (LEP) collider is a 26.6km circumference e^+e^- storage ring which has, until the end of 1994, operated with 4 and 8 bunches per beam in an energy range of 20 to 50 GeV (see previous conference reports, [1],[2],[3],[4]).

LEP obtained its first circulating beam in July 1989 and performed collisions one month later in August. Since then, operation has been a mixture of physics data taking around the Z^0 energy (45.6 GeV) and machine studies aimed at performance improvement, beam energy calibration, and future upgrades. During 1994, LEP was operated for physics with a pretzel scheme and 8 bunches per beam and it is foreseen to further increase the number of bunches during 1995 by the use of a bunch train scheme [5].

For the second phase (LEP2) the collider will be operated at an energy of about 90 GeV with an expected luminosity $\sim 7 \times 10^{31}\ cm^{-2}s^{-1}$ to produce W pairs. This will be made possible by the addition of 224 superconducting cavities giving a total voltage of more than 2.2 GV. A total RF-power of about 30 MW will be available for the beam, which, with an energy loss of about 1.9 GeV per turn, will be sufficient to store a current of ~8 mA per beam.

II. PRESENT PERFORMANCE

For LEP1 the most critical parameters are the integrated luminosity, which dictates the number of Z^0s, and the precision with which the beam energy can be calibrated, which determines the mass and the width of the Z^0 interaction. Figure 1 shows the increase in the daily integrated luminosity over the past 6 years. The integrated luminosity has been increasing by about 50% per year over the past 3 years. Since there has been no significant increase in the current per bunch this increase is due to three main factors.

1. Improvements in the operational efficiency,
2. Optimization of the beam-beam tune shift by emittance control, and
3. Increasing the number of bunches by the use of the pretzel scheme.

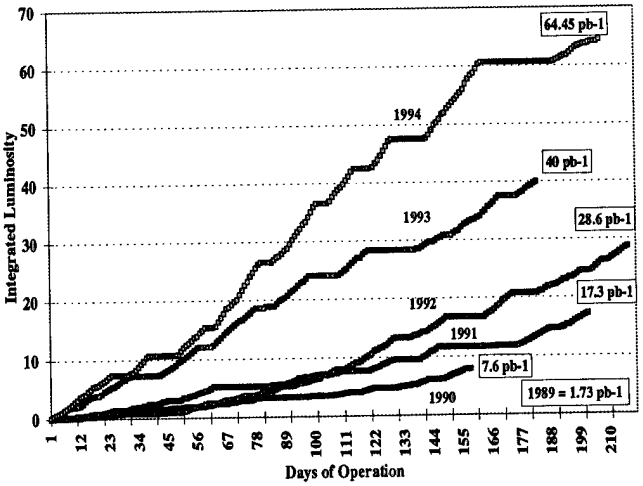


Figure. 1. Daily Integrated Luminosity

A. *Improvements in the Operational Efficiency*

The operational efficiency in LEP (defined as the ratio of the actual hours spent in physics to the scheduled hours) has steadily increased from about 40% in the first year of operation to about 61% during 1994. It should be noted that due to the finite refill time the efficiency can never be 100% (a realistic upper limit is ~ 85%), and that the efficiencies of all injectors in the LEP injection chain are included in this figure. The improvement in the operational efficiency is due to two main components

1. Improvements in the reliability of all hardware. This has been done by identifying the least reliable components and improving their design as well as doing preventative maintenance.
2. Reduction of the refill time. The accumulation time has been reduced by improving the injection efficiency by better diagnostics and by using synchrotron injection [6] [7] . In addition the applications software has undergone enormous improvements which greatly speed up all "measure and correct" manipulations.

B. *Beam-beam Optimization*

The luminosity (L) is directly related to the vertical beam-beam tune shift (ξ_y) i.e.

$$L = \frac{\gamma}{2r_e e} \frac{k_b i_b \xi_y}{\beta_y^*} \qquad (1)$$

0-7803-3053-6/96/$5.00 ©1996 IEEE

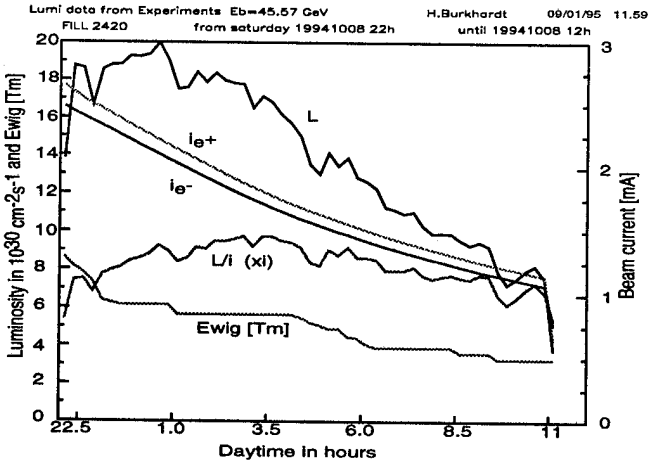


Figure. 2. Evolution of beam parameters during a typical physics run.

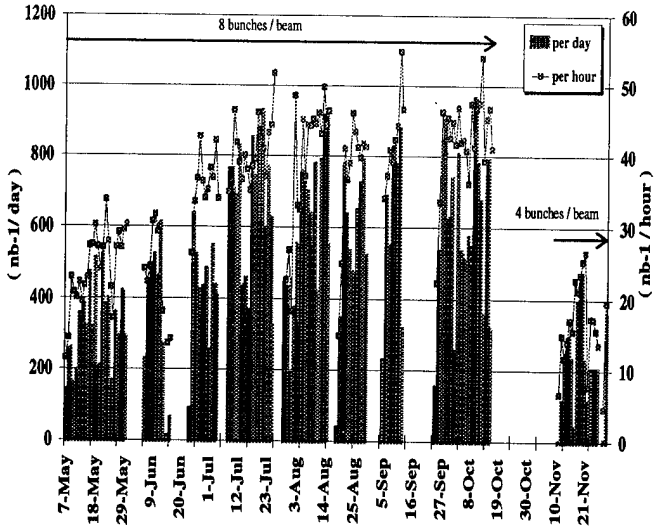


Figure. 3. Daily and Hourly Luminosity during 1994.

where γ is the relative energy, k_b the number of bunches per beam, and i_b the bunch current. The beam-beam strength parameter is approximately given by

$$\xi_y \approx \xi_x = \frac{i_b r_e}{2\pi\gamma e f_{rev}\varepsilon_x} \qquad (2)$$

where ε_x is the horizontal emittance.

Clearly in order to maximize the integrated luminosity during a physics run, it is necessary to maintain the ξ_y at its maximum value independent of the bunch current which decays naturally with time. Consequently the natural emittance must be sufficiently small so that the beam-beam "limit" can still be reached with the low bunch currents at the end of the run. The natural horizontal emittance is approximately given by

$$\varepsilon_x \approx \frac{c_q R\gamma^2}{\rho Q_x^3} \qquad (3)$$

where R is the average radius, ρ the bending radius, and Q_x the horizontal tune value.

In LEP the small emittances are obtained by the use of a 90^0 phase advance per cell lattice instead of the original design of 60^0. It is also clear from equation (2) that, in order to maintain ξ_y constant, larger emittances are needed at the higher currents associated with the beginning of the run. To this end emittance wiggler magnets are excited at the beginning of the run and progressively reduced during the course of the run. The evolution of the beam parameters, during a typical run in 1994, are shown in Figure 2.

C. *Pretzel Operation*

A horizontal pretzel scheme was developed during machine studies periods in 1993 and brought into operation near the end of 1993 [8]. The same scheme was used throughout 1994 for operation for physics and after an initial learning period resulted in an increase in luminosity which corresponded to the increase in number of bunches. This can be demonstrated in Figure 3 where the reduction in luminosity results from reverting to 4 bunch operation at the end of the year. Fine tuning of the machine was more difficult with the pretzel scheme and required very careful control of the closed orbits, the chromaticities, the horizontal and vertical separations, and the tune splits between electrons and positrons [9].

III. ENERGY CALIBRATION

The precise measurement of the mass and width of the Z^0 resonance requires a high integrated luminosity and *a very accurate absolute calibration* of the beam energy. The average beam energy can be measured by resonant depolarization to a relative accuracy of around 10^{-5}[10]. During the physics scan of the Z^0 in 1993, all energy calibrations were performed at the end of the fills, usually with a single beam, and usually with about 12 days between calibrations. In order to estimate the average beam energy on physics fills between calibrations it was necessary to monitor all possible energy changes during the time interval between these calibrations. The average beam energy can be changed either by a modification to the integrated bending field or by a change in the length of the central orbit. The latter phenomenon results from the fact that the beam path length is fixed by the frequency of the RF system which can be held constant to around 10^{-10}. In principle, variations in the bending field should be seen by the reference magnet which is connected in series with the dipoles and equipped with flip-coil and NMR field measuring devices. However due to the large dimensions of LEP, there can be differences in the environment between the reference magnet and the main dipoles (magnet temperatures etc.) which must be carefully monitored and used in correcting the energy estimates from the reference magnet system. In addition, about once every two weeks a measurement of the total integrated dipolar field ("flux-loop") is done in order to cross-correlate with the resonant depolarization measurement. The length of the central orbit is regularly measured by changing the revolution frequency until the beam is centered in all sextupoles. The observable for this centering technique is the change in the tune value when large chromaticities are applied with the sextupoles.

In LEP the beam energy at each interaction point is different

from the average beam energy as measured by the techniques described previously. This difference results from a combination of the energy "sawtoothing" and the geometrical alignment and properties of the RF accelerating system. RF phase errors and voltage asymmetries produce changes in the energies of the two beams at the collision points. The status of the RF system is an important ingredient in the final calibration of the colliding beams.

Despite all these correcting algorithms, considerable variations in the LEP energy were observed during the course of the 1993 scan. The path length variation has been identified with tidal effects and other variations on a longer time scale. More recently, other subtle effects have been investigated, such as the influence [11] of the water level in Lake Geneva and the effect of small values of dispersion at the collision points.

IV. LIMITATIONS FOR LEP1

A. *Beam-beam, Background and Aperture*

The luminosity of LEP1 is limited by the interplay between beam-beam effects, background in the detectors, and the aperture as set by the collimator system. Low background conditions in physics are ensured by a large number of collimators which define the LEP physical aperture, shield from synchrotron radiation and from off momentum particles generated by beam gas interactions. For geometric reasons, it is not possible to collimate a beam with a horizontal emittance greater than 45 → 50 nm. The natural emittance at Z^0 energies is around 13nm, which, at high currents is increased to around 40 nm by the use of emittance wiggler magnets.

From equation (1), with a constant value of ξ_y it appears that the luminosity may be increased linearly with the bunch current (i_b). It is also clear from equation (2) that for constant ξ_x the horizontal emittance (ε_x) increases linearly with current and for LEP reaches around 45nm with a bunch current of ~350μA. Increasing the bunch current beyond this value would require retraction of the collimators to avoid reductions in the lifetime. This has been attempted on several occasions and always produced an increase in the background rates. Consequently the maximum bunch currents which can be collided at Z^0 energy has been limited to around 350μA for several years.

When operating at high values of ξ, the beam parameters (tunes, chromaticities, closed orbits, bunch current inequalities) must be adjusted within very tight tolerances ($\pm$.003 in tune and $\pm$1 in Q′) in order to avoid non Gaussian tails [12]. The creation of these tails reduces dramatically the lifetime due to the aperture reasons given above.

B. *Number of Bunches and β_y^**

For LEP1, when operating at the beam-beam limit, it is clear from equation (1) that the only remaining "free" parameters are the β_y^* and the number of bunches (k_b). The design value for the β_y^* was 7cm and LEP is currently operated with 5cm. On trial runs the β_y^* has been reduced to 3.7 cm but without any increase in the luminosity and resulted in much greater sensitivity of the beam to small perturbations due to the very large β values at the first two insertion quadrupoles.

The number of bunches was doubled to 8, by the use of the pretzel scheme at the end of 1993 and throughout 1994. Although the pretzel scheme could have been extended to a larger number of bunches, the detector electronics imposed a maximum of 8 equally spaced bunches. Consequently two proposals were studied to used trains of bunches. The first, which had a horizontal crossing angle was abandoned because of the large background created by passing off center in the low β quadrupoles near the interaction points. The second proposal involved separating the beams at the unwanted collision points using electro-static separators upstream and downstream of the interaction point. This scheme has been studied extensively during machine study periods [5]. The limitation to the number of bunches in the train came from the detector electronics requirement that the total length of the train be not greater than 750 ns. The minimum bunch spacing is given by the distance from the first separator to the interaction point, which sets an upper limit of 4 bunches per train. It is foreseen to operate LEP1 during 1995 with 4 trains of 4 bunches per beam unless some unexpected critical problems are encountered with this scheme.

C. *Summary of LEP1 Performance*

Table 1 gives a comparison of the LEP design parameters with those achieved in physics or in machine study sessions.

Table 1. Comparison of Achieved with Design

Parameter	Design	Achieved	Units
Peak Luminosity	13	24	$10^{30}cm^{-2}s^{-1}$
Luminosity/day	480*	1000	nb^{-1}
Beam beam ξ_y	.030	.049	
Bunch Current	750	820	μA
β_y^*	.07	.037	m
Total Current	6.0	10.0	mA
Energy calibration	~25	1.7	MeV

V. FUTURE PLANS – LEP2

A. *Beam Energy Limitations*

The most crucial parameters for the physics to be performed above the W± threshold are the *maximum* beam energy and the integrated luminosity. The beam energy is determined by the total installed RF voltage needed to replenish the losses due to synchrotron radiation and to provide an "RF bucket" sufficiently large to provide a quantum lifetime of around 15 hours. Since the radiation losses increase with E^4 the required RF voltage increases dramatically with the beam energy needing more than 2000 MV/turn needed at beam energies of ~ 90 GeV (see Figure 4).

B. *Luminosity Limitations*

Combining equations (2) and (3) gives

$$\xi_y \approx \xi_x \propto \frac{i_b Q_x^3 J_x}{\gamma^3} \qquad (4)$$

Consequently, for all other parameters constant, to maintain identical beam-beam conditions at 90 GeV as at 45 GeV would require an increase in the bunch current by a factor of 8. It is therefore unlikely that LEP2 will be strongly beam-beam limited

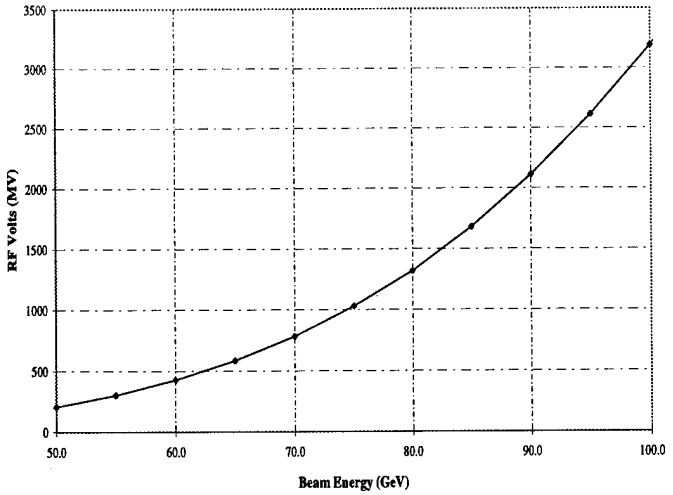


Figure. 4. RF Voltage as Function of Beam Energy.

as is the current operation of LEP1. In this case the luminosity is better written as

$$L \propto k_b \frac{i_b^2}{\sigma_x^* \sigma_y^*} = \frac{i_{total}^2}{k_b \sigma_x^* \sigma_y^*} \tag{5}$$

In LEP2 the *total* current will be limited by the required beam power which is transmitted from the klystrons i.e.

$$P_{klystron} = P_{beam} \propto 2 i_{total} U_0 \propto 2 i_{total} E_b^4 \tag{6}$$

e.g. 30 MW of klystron power allows 8 mA of beam current at 90 GeV. It is evident from equation (5) that with the total current being limited, the luminosity is maximized by storing this current in the *minimum* number of bunches k_b, or in other words maximizing the bunch current. The current per bunch in LEP is limited at injection energy by the Transverse Mode Coupling Instability (TMCI). The approximate threshold for this instability is given by [13]

$$i_{th} = \frac{2\pi Q_s E_b f_{rev}}{e \sum \beta_i k_{\perp i}(\sigma_s)} \tag{7}$$

where Q_s is the synchrotron tune, E_b the beam energy, and β_i the betatron amplitude function at the location of the transverse loss factor $k_{\perp i}$ which decreases with increasing bunch length (σ_s). In order to maximize the current per bunch for LEP2 operation, several schemes have been proposed and tested.

- The "High Q_s" Scheme [14], in which the synchrotron tune is increased at injection energy and reduced in steps as the energy is increased. The highest bunch current reported in Table 1 was obtained [15] using a Q_s of .0125 at injection energy. The main anticipated problem with this scheme is the possible beam loss due to traversing (at higher energies) low order synchro-betatron resonances with high beam intensities.
- Increasing the injection energy from 20 to 22 GeV. Two new superconducting bi-modules have been installed in the SPS which will allow the extraction energy to be raised to 22 GeV. This should increase the threshold current by 10% and the luminosity by 20%. Energies higher than 22 GeV would require substantial changes to the transfer lines and an upgrade of the radiation shielding in the SPS machine.
- Reduction of the transverse impedance ($k_\perp$). The major source of transverse impedance in LEP comes from the 120 room temperature cavities (47% of the present total impedance) which could be replaced by about 32 SC cavities which have a much smaller transverse impedance (1.5%) due to their large bore diameter. This replacement, along with the other mentioned improvements should allow bunch currents of ~0.8 mA at the LEP2 collision energies. Under these conditions and with 8 bunches per beam, a peak luminosity of $\sim 7\times 10^{31}$ cm^{-2}s^{-1} is predicted at 90 GeV.

Further optimization of the luminosity may result from a reduction in the beam size at the IP (see equation (5)). This can be achieved with a higher phase advance per cell lattice which reduces the horizontal emittance (see equation (3)). A lattice with phase advances of 108^0 and 60^0 (H and V) has been tested with beam [16] with very encouraging results. If operation is possible with this lattice and the high bunch currents described previously it is conceivable that LEP2 may produce beam-beam tune shifts of ~.03 with a luminosity of $\sim 10^{32}$ cm^{-2}s^{-1}.

C. LEP2 Hardware

The hardware conversion to re-configure LEP1 to LEP2 has been going on for several years with the final modifications carried out during the last winter shutdown which ended in April 1995. These modifications included

- civil engineering for the new klystron galleries around IP4 and IP8.
- complete re-arrangement of the 8 RF straight sections to physically accommodate the new SC cavities.
- installation of 4 new 12kW cryogenic plants
- replacement of the superconducting low β quadrupoles
- and, an upgrade of power converters for higher energy

The final stage of the energy upgrade will be the installation of more than 200 SC cavities with their associated couplers, waveguides, klystrons and control electronics. This work will be carried out progressively until the spring of 1997 with several milestones (see later).

D. Superconducting Cavities

For the LEP2 SC cavity system three aspects can be identified as being critical.

1. Cavity production and module (4 cavities) assembly (for details see contribution to this conference [17] .
2. Design and performance of the main coupler which must be capable of passing 125kW to the beams (for details see contribution to this conference [18].
3. Higher order mode couplers. The initial design of the output lines from these couplers imposed a current limitation for LEP especially when operation was foreseen with bunch trains. Recent improvements in the design of the output lines have allowed the HOM power per cavity to be increased from the 400W "design" to 1700W which is beyond any powers foreseen with a reasonable set of parameters.

At present there are 7 SC modules (28 cavities) installed in LEP. Two of these modules were installed in Autumn 1994 and

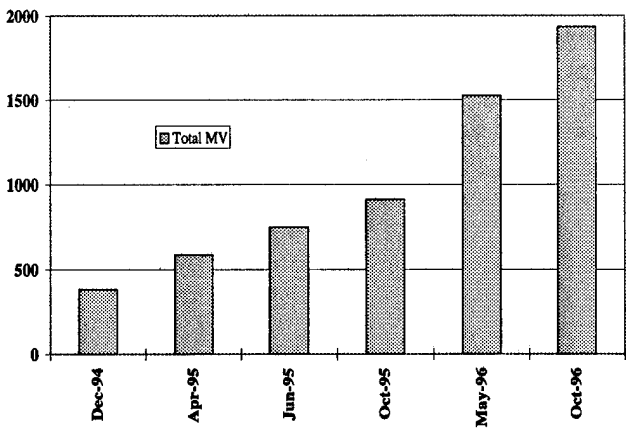


Figure. 5. Planned Available RF Voltage.

could be tested with beam during the last running period of this year. One of these modules was successfully operated for more than 70 hours at its design gradient of 6MV/m and in the presence of the normal operating intensities for LEP1.

E. Installation Plans

The planned installation (see Figure 5) of SC cavities should allow a physics data period with ~70 GeV per beam at the end of 1995 followed by a run at 80.5 GeV in the first part of 1996 which will allow a precision measurement of the mass of the W. In October 1996 the increased RF voltage should allow phyics data taking at energies significantly above the threshold of W± production. In 1997 production physics runs will be started at the maximum possible energy .

F. Summary of Plans

In 1995 LEP1 will continue operation at Z^0 energies but using a bunch train scheme which should significantly increase the luminosity. During the first part of 1996 it is planned to perform physics data taking at 80.5 GeV/beam for precise measurement of the mass of the W. Following a shutdown in Autumn 1996, LEP2 will be operated for the first time at energies above the W± threshold. Following the 1996–1997 winter shutdown LEP2 will start an exciting physics programme at high energies which will extend beyond the year 2000.

References

[1] A. Hofmann; "Performance Limitations in LEP", Proc. of the Fourth European Particle Accelerator Conference, held in London from 27 June until 1 July, 1994. (pp 73– 77), (1994)

[2] L. Evans; "LEP Status and Future Plans", Proc. of the 1993 Particle Accelerator Conference, Washington, p. 1983 (1993)

[3] S. Myers; "LEP Performance and Plans", Proc. 15th Int. Conf. on High Energy Accelerators, Hamburg 1992; HEACC92, p. 66, (1992).

[4] S. Myers; Proc. of the Second European Particle Accelerator Conference, held in Nice from 12 till 16 June, 1990. (pp 13– 17), (1990)

[5] E. Keil, W. Herr, et al.;"Experiments with Bunch Trains in LEP", accepted for oral presentation at this conference.

[6] S. Myers; LEP Notes 334 and 344 (1981)

[7] P. Collier; "Synchrotron Phase Space Injection into LEP", accepted to this conference.

[8] R. Bailey et al., "LEP Operation in 1993 with the Pretzel Scheme", Proc. of the Fourth European Particle Accelerator Conference, held in London from 27 June until 1 July, 1994. (pp 439–441), (1994)

[9] P. Collier et al.; "Operational Procedures to Obtain High Beam-Beam Tune Shifts in Pretzel Operation", accepted to this conference.

[10] R. Assmann et al.; "Energy Calibration with Resonant Depolarization in LEP", Proc. of the Fourth European Particle Accelerator Conference, held in London from 27 June until 1 July, 1994. (pp 935– 937), (1994)

[11] J. Wenninger; "Radial Deformations of the LEP ring", SL Note 95-21 (OP), Feb. 1995

[12] K. Cornelis et al.; "Tail Distributions due to Beam-Beam in LEP", accepted to this conference.

[13] B. Zotter: CERN-SL 92-29 p193

[14] S. Myers; "Synchro-Betatron Resonance Excitation in LEP", Proc. of the IEEE Particle Accelerator Conference held in Washington D.C., March 16–19, 1987, p. 1325.

[15] D. Brandt: CERN SL/94-06 (DI) p149, March 1994.

[16] A. Hofmann et al.; "Low Emittance Lattice for LEP", accepted for this conference.

[17] E. Chiaveri et al.; "Analysis and Results of the Industrial Production of the SC Nb/Cu Cavities for the LEP2 Project", accepted for this conference.

[18] J. Tückmantel et al.; "Improvements to Power Couplers for the LEP2 SC cavities", accepted for this conference.

CESR STATUS AND PLANS *

David L. Rubin for the CESR Operations Group

I. INTRODUCTION

The CESR electron positron collider has been configured to operate with trains of closely spaced bunches that collide with a small horizontal crossing angle. The crossing angle scenario provides for an increase from seven to as many as 45 bunches per beam. Two pairs of electrostatic separators yield differential horizontal closed orbits for the electron and positron beams. The separators are powered antisymmetrically with respect to the two-fold symmetry of the storage ring. The bunches collide with a small horizontal angle of $\pm 2.1 mrad$, that serves to separate the counterrotating bunches at the parasitic crossing points adjacent to the IP. Nine trains, with temporal length of up to 56ns can be accomodated. The storage ring has operated for high energy physics with trains of two bunches spaced 28ns apart and reached peak luminosity of $3.3 \times 10^{32} cm^{-2} s^{-1}$. The Phase II upgrade of the interaction region, now underway, will permit an increase in current to 300mA per beam, and luminosity to $6 \times 10^{32} cm^{-2} s^{-1}$. In Phase III of the CESR upgrade, scheduled for completion in 1995, the room temperature RF system will be replaced with single cell superconducting cavities. The single beam limit will increase to 500mA, and the luminosity to $10^{33} cm^{-2} s^{-1}$.

II. SEVEN BUNCH OPERATION

Prior to the switch to crossing angle operation in March of 1994, beams of seven nearly equally spaced bunches were directed into head-on collisions at a single interaction point. The then symmetrically powered electrostatic deflectors separated the beams at the thirteen parasitic crossing points. The "pretzeled" orbits characteristic of the head-on scheme are shown in figure 1. At the interaction point, $\beta_v^* = 18mm$, $\beta_h^* = 1m$, and $\eta^* = 0$. The integer part of the horizontal tune was chosen to yield differential orbits consistent with seven bunches per beam. The horizontal emittance with permanent magnet wigglers closed was $3.3 \times 10^{-7} m - rad$. Peak luminosity was $2.9 \times 10^{32} cm^{-2} s^{-1}$ at 5.3GeV beam energy, with 112mA/beam, corresponding to a beam-beam tune shift parameter of $\xi_v = 0.04$. The long range interaction of the beams at the parasitic crossings in the arcs precluded a further increase in bunch current, and the proximity of the electrostatic separators to the interaction point, along with the constraint that the beams collide head-on, limited the number of bunches per beam to seven.

III. CROSSING ANGLE OPTICS

The notion that a small horizontal crossing angle might permit a significant increase in the number of bunches in each beam is due to R. Meller [1]. He proposed that we store trains of closely spaced bunches in each beam, and that we take advantage of a horizontal crossing angle to separate the bunches at the parasitic crossings adjacent to the interaction point.

*Work supported by the National Science Foundation

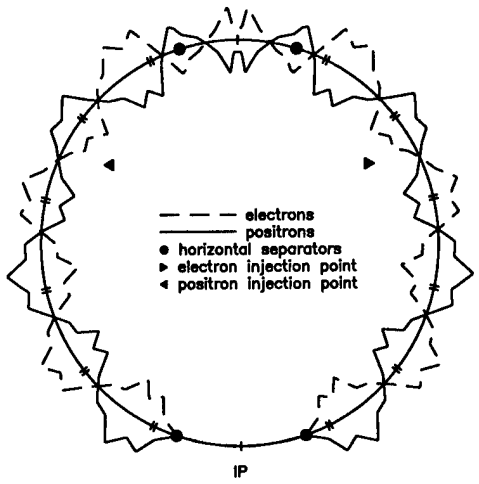


Figure 1. Electron and positron closed orbits for head on collisions. Tic marks along the circumference indicate parasitic crossings with 7 almost evenly spaced bunches per beam. Electrons travel counterclockwise.

Criteria for the requisite separation of the bunches at the parasitic crossings is based on our experience with multiple bunch beams. It was established in seven bunch operation that the bunch current was limited by long range interactions when:

1. The largest long range horizontal tune shift of any of the parasitic crossings was $\Delta\nu_h = 0.00072$
2. The largest long range vertical tune shift of any of the parasitic crossings was $\Delta\nu_v = 0.0011$,
3. and that

$$\frac{1}{I_{bunch}(mA)} > \sqrt{\Sigma_i^N \left(\frac{\epsilon_h (mm - mrad) \beta_i^h(m) \beta_i^v(m)}{s_i^2 (mm)} \right)^2}$$

The last is a phenomonological attempt at including the collective effect of multiple crossings and horizontal tails[2]. The sum is over all of the N parasitic crossings and β_i^h, β_i^v, and s_i are β-functions and separation at each crossing.

A. Linear Optics

The linear optics are designed to maximize the bunch current consistent with the separation criteria. The differential closed orbits that result are shown in figure 2. Nine 56ns long trains can be accomodated in each beam. If the bunches are spaced 28ns apart, then the long range tune shift at each of the parasitic crossings, including the one nearest the IP, are comparable. We expect the long range beam-beam limit at bunch currents over 11mA. For more closely space bunches (14ns), the vertical β at the parasitic crossing nearest the IP (at 2.1m) is large, and may limit bunch current below 11mA prior to the Phase III IR upgrade (see below).

0-7803-3053-6/96/$5.00 ©1996 IEEE

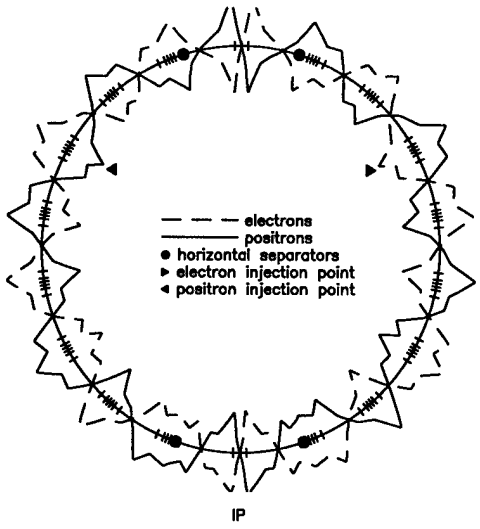


Figure 2. Electron and positron closed orbits in crossing angle operation. The crossing angle is $\pm 2.3 mrad$. Tic marks along the circumerence indicate parasitic crossings with 9 trains with the 2 bunches/train spaced 28ns apart.

A half wave vertical displacement bump (not shown in the figure) separates the beams at the crossing point diametrically opposed to the interaction region. The integer part of the horizontal betatron tune is increased to ten, (as compared to 8 for the head-on pretzel), while the integer part of the vertical tune remains at nine. Fractional tunes are just above the half integer. Note that the orbits are displaced toward the injection septa. A consequence of the increased horizontal tune is a significantly reduced emittance; $\epsilon_h = 2.1 \times 10^{-7} m - rad$ with wigglers closed. The interaction point focusing functions are unchanged ($\beta_v^* = 18mm, \eta^* = 0, \beta_h^* = 1m.$)

The horizontal phase advance the separator just west of the interaction point to the separator just east of the IP is $\frac{11}{2}$ wavelengths. During injection a symmetric voltage is superimposed on these two separators so that the beams are horizontally separated at the interaction point.

Inspection of figures 1 and 2 reveals a complication of the crossing angle versus head-on configuration. In the crossing angle scheme there is no place in the machine where electrons and positrons share a common orbit. In particular, the beams are horizontally displaced in essentially all of the skew quads. Adjustment of the transverse coupling, a critical aspect of luminosity tuning, effects a differential vertical kick to the beams, altering the closed orbits and the vertical overlap at the IP. Luminosity tuning is inevitably more difficult.

B. *Sextupole Optics*

The distribution of sextupole strengths is designed to:

1. Correct chromaticity
2. Minimize the chromatic function, (the energy dependence of the β-function through the arcs as well as at the interaction point)
3. Maximize dynamic aperture for on and off energy particles
4. Minimize the "pretzel" dependence of the β-function.
5. Yield flexibility to differentially adjust betatron tune.

Except for a two-fold symmetry about the IP, all sextupoles are varied independently in the optimization of the distribution[3]. We break the symmetry to generate different tunes for electron and positron beams.

IV. CROSSING ANGLE OPERATION

Initial operation of CESR with beams crossing at an angle (beginning in March 1994) was characterized by poor injection efficiency and poor beam-beam performance. The horizontal displacement of the stored beams in the interaction region forced the injected bunch to large amplitudes. The lost particles found there way into the CLEO detector and through the shielding walls into the experimental area of the synchrotron light facility, effectively limiting injection rate. We observed a significant degradation of luminosity with crossing angle and displacement of the beams in the permanent magnet wigglers. In tests with a single bunch in each beam, the crossing angle was set to zero and a tune shift parameter of $\xi_v \sim 0.04$ was measured. The tune shift parameter fell to 0.03 with a crossing angle of $\theta^* \sim \pm 2.1 mrad$, and with nine bunches in each beam it deteriorated further to $\xi_v \sim 0.023$. Solutions to the various complications peculiar to crossing angle operation were evolved during the Spring and Summer of 1994. There follows a brief description of that work.

A. *Injection*

As noted above, a symmetric eletrostatic displacement bump is superimposd on the crossing angle to separate the beams during injection. Its sign is chosen so that the asymmetric displacement that results in the interaction region quads is greater in the east and smaller in the west. Electrons, which are injected into the horizontal plane with positrons already stored, approach the interaction region from the west (from the left in figure 2). Large amplitude particles in the injected electron bunch are therefore more likely to be scraped leaving the IR than while entering. With attention to the orbit correctors east of the IR, it is possible to reduce electron losses into the synchrotron light experimental area to tolerable levels.

As the electron beam current increases during injection, the long range beam-beam interaction tends to blow up the stored positrons. The tails of the positron beam are typically lost into the CLEO detector as they approach from the east. We discovered that the beam-beam coupling that is responsible for the blow-up can be reduced by introducing a difference in the betatron tunes of the two beams, via an asymmetry in the sextupole distribution. A horizontal tonality ($\Delta Q_h \sim 0.05$) is typical of electron injection conditions. The large tonality is essential to control losses of positrons during injection of electrons. The tonality is restored to nearly zero with beams in collision.

B. *Wigglers*

CESR operates with two $2.5m$, $1.2T$, permanent magnet wigglers for generating intense x-ray beams. In the crossing angle separation scheme beams are displaced $\pm 11mm$ in the wigglers. (The beams are on axis in the wigglers in head-on operation.) At least part of the degradation of the beam-beam performance with crossing angle pretzel was observed to be due to that large dis-

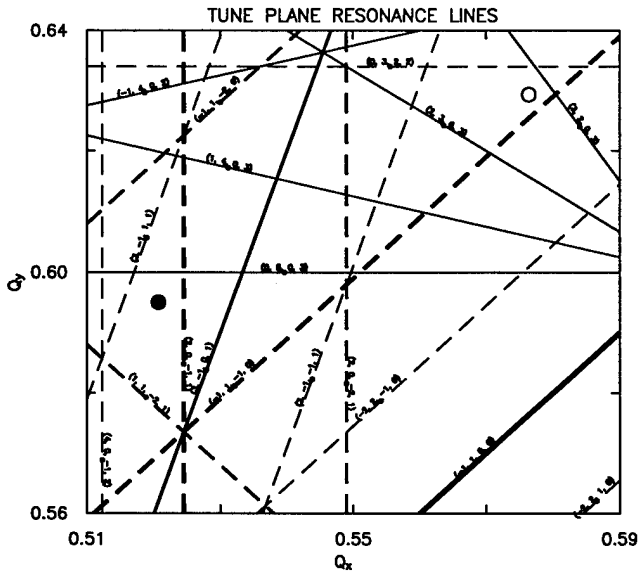


Figure 3. The region of the tune plane in the vicinity of the CESR operating point. The solid circle is the operating point that yields good performance for beams colliding at an angle. The operating point that proved effective in head-on operation is indicated by the open circle. (2,0,-1,1) corresponds to $2Q_h + 0Q_y - 1Q_s = 1$

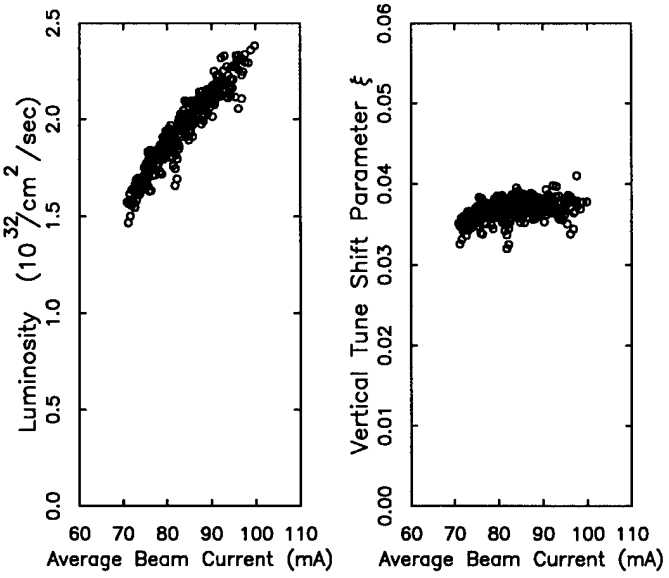


Figure 4. Luminosity versus beam current with nine bunches per beam and crossing angle of $\pm 2.1 mrad$.

placement. In experiments with single bunches in head-on collision we learned that a closed orbit displacement in the wigglers, generated by magnetic steering elements, yields the same degradation as the crossing angle pretzel. Elimination of the sextupole component of the wiggler and implementation of a skew sextupole correction magnet were somewhat effective in compensating the impact of the wigglers. Theoretical investigation of the effects of the wiggler fields on the colliding beam dynamics continue.

C. Operating Point

Exploration of the tune plane by CESR operators[4] with single and multiple bunch colliding beams, lead to the discovery of a new operating point more tolerant of the crossing angle dynamics. The change in the fractional tunes ($\Delta Q_h \sim -0.05$ and $\Delta Q_v \sim -0.04$) brought the operating point very near to the half integer as shown in figure 3.

With careful attention to injection orbits and suitable tonality, repair and compensation of the permanent magnet wiggler, and subsequent tuning at the low operating point, we eventually recovered performance typical of earlier head-on operation. We measured luminosity $L = 2.4 \times 10^{32} cm^{-2} s^{-1}$ with $11 mA/bunch$ as shown in figure 4, with nine bunches per beam colliding at an angle of $\pm 2.1 mrad$. The beam-beam tune shift parameter was 0.038.

V. BUNCH TRAINS

In late October of 1994, 2-bunch trains with 28ns interbunch spacing were introduced into the crossing angle pretzel. Total current in the 18 bunch beams was limited by synchrotron radiation heating of various components of the CESR vacuum system, and by electron injection. Transverse stability of the trains

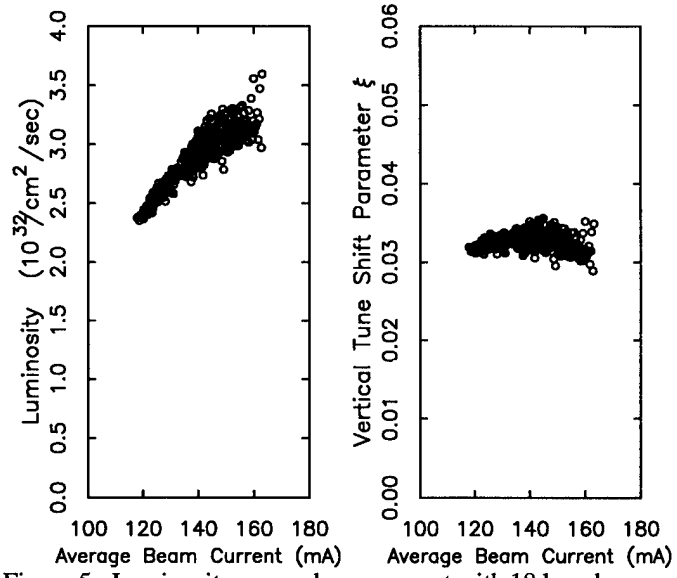


Figure 5. Luminosity versus beam current with 18 bunches per beam and a horizontal crossing angle of $\pm 2.1 mrad$.

of bunches was ensured by a wideband bunch by bunch feedback system[5]. During a three week down period in November and December, cooling was added to overheating flanges and sliding joints, and rebuilds of offending vacuum transitions installed. Following runs with nine bunches per beam at $\Upsilon(1s)$ and $\Upsilon(2s)$ energies, we returned to $\Upsilon(4s)$ (5.3 GeV/beam) and bunch train operation. Total current was gradually increased over a period of several weeks as the CESR operators learned how to tune so as to minimize the effects of parasitic interactions during injection. Tonality and pretzel amplitude were the critical tuning parameters. By mid March of this year we measured a luminosity of $L = 3.3 \times 10^{32} cm^{-2} s^{-1}$ with $160 mA/beam$ and an integrated luminosity of nearly $18 pb^{-1}$ in a single day. The current dependence of luminosity and tune shift parameter are shown in figure 5.

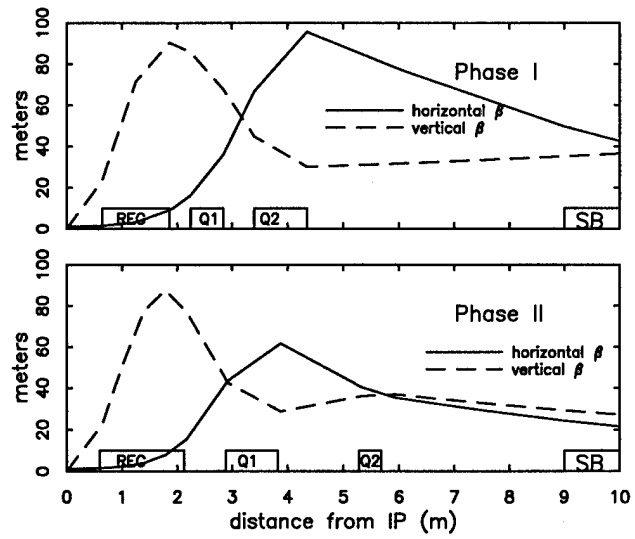


Figure 6. Optical functions in the Phase I and Phase II interaction regions. In Phase I, Q1 and Q2 are vertically and horizontally focusing respectively. In Phase II, Q1 is horizontally focusing and Q2 vertical.

A. *Trains with 14ns spacing and more bunches*

During periods of machine studies we have experimented with three bunch trains with 28ns interbunch spacing, and two, three and four bunch trains with 14ns spacing. At currents of at least 7mA/bunch, with two bunches/train, and nine trains, the beam-beam performance is essentially identical for 14ns and 28ns spacing. Injection may indeed be easier with the shorter train, presumably because the ends of the train are not so far from the pretzel maxima in the arcs. Single train experiments with three and four bunches per beam are consistent with the expectation that the luminosity will scale with the number of bunches.

VI. PHASE II

Beginning in April of 1995 the interaction region has been taken apart for the installation of a silcon vertex detector for the CLEO experiment and a rearrangement of final focus quadrupoles.

A. *Increased Aperture*

As noted above, the horizontal aperture in the interaction region severely impacts injection into the crossing angle pretzel due to the large horizontal displacement of the beams in the horizontally focusing lens. In the Phase I IR (pre-April 1995), the vertically focusing permanent magnet quadrupole is followed by a vertically focusing electromagnet. By eliminating the vertical trim in favor of a lengthened permanent magnet, it is possible to bring the horizontally focusing lens closer to the interaction point. The peak horizontal β and displacement of the beam in the horizontal lens is reduced from nearly 100m to just over 60m as shown figure 6.

In addition to reducing the required horizontal aperture in the IR, the bores of the IR quads, (Q1 and Q2), are being enlarged, increasing the physical aperture. The available aperture will be increased by nearly 2cm at the peak of the orbit displacement in the interaction region. Finally, the rebuild of the shielding walls will reduce radiation rates in the synchrotron light experimental area by factors of 30 to 100.

During the 4-5 month shutdown we will complete the replacement of horizontal separators. The modern separators operate at somewhat reduced electrode voltage and half the broadband impedance of the original equipment. Rebuilt vertical separators will also be installed. The four, 5-cell RF cavities will be retuned for optimal coupling at 600mA total current. (We have stored 220mA in single beams and 350mA in two beams and anticipate with beam processing, to reach 300mA/beam.)

The vacuum chamber through the interaction region is being replaced to accomodate the new vertex detector, the increased aperture IR quads, and to provide better pumping. In addition, beam position monitors are being installed at the IP end of the REC quadrupoles. The beam detectors will provide a direct measure of the overlap of the beams at the collision point.

At the conclusion of the installation of Phase II hardware (September 1995) CESR will operate with two to five bunches in each of nine trains. The number of bunches in each train and the bunch spacing (14ns or 28ns) will be chosen on the basis of operating experience to optimize performance. At currents of 300 mA per beam we expect a luminosity of $6 \times 10^{32} cm^{-2} s^{-1}$.

B. *Phase III*

Installation of Phase III hardware will begin in late 1997. The interaction region quadrupoles will be replaced with a high gradient, 30cm long permanent magnet at 30cm from the IP, followed by a pair of superconducting lenses. The scheme permits reduction of β_v^* to $7mm$ while limiting the value of the β functions at the first parasitic crossing point that occurs 2.1m from the IP. The optical functions for the phase III IR with $\beta_v^* = 1cm$ are shown in figure 7.

At the same time the 20-cell copper RF system will be replaced with 4 single cell superconducting cavities. Each cell is designed to deliver $325kW$. The beam test of the prototype cavity completed in August of 1995, is described elsewhere in these proceedings[6]. The broadband impedance of the superconducting system is approximately %6 of the room temperature system. The superconducting RF system will increase the current limit to 500mA/beam and the luminosity to $10^{33} cm^{-2} s^{-1}$ with $\beta_v^* = 18mm$. Substantial upgrade of the vacuum system will be required to accomodate the higher current.

With the increase of voltage of the superconducting cavities to the design goal of $10MV/m$, ($3MV$/cell), it will be possible to reduce the bunch length and exploit the capability of the superconducting IR to shrink β_v^* and further increase the luminosity.

VII. SUMMARY

Peak luminosity $L = 3.3 \times 10^{32} cm^{-2} s^{-1}$ has been achieved with trains of bunches colliding at a horizontal crossing angle of $\theta^* = \pm 2.1 mrad$. The 2-bunches in each train are spaced 28ns apart and there are nine trains in each beam. The beam current is 160mA. Tests indicate that the extension to at least four bunches per train, spaced 14ns apart is straightforward. During Phase II operation (Fall 1995-Fall 1997) we expect to deliver peak luminosity of $6 \times 10^{32} cm^{-2} s^{-1}$ and with the completion

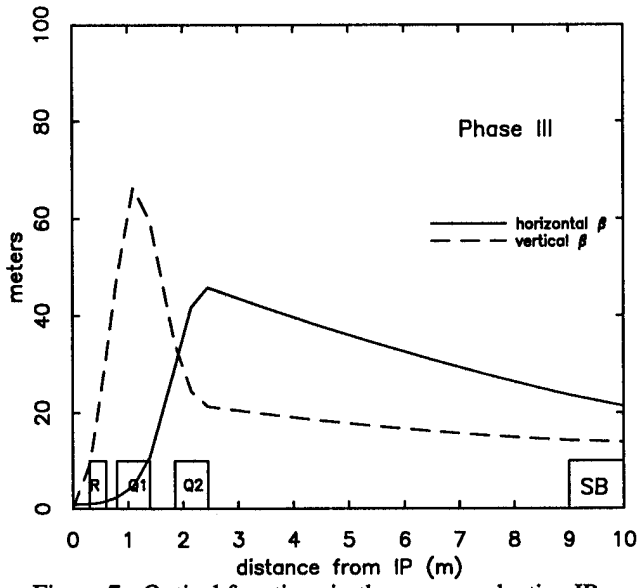


Figure 7. Optical functions in the superconducting IR.

of the Phase III upgrade in 1998 to reach luminosity in excess of $10^{33} cm^{-2} s^{-1}$.

References

[1] Meller,R.E., CON 90-17, July 1990.

[2] A.Temnykh and J.Welch, *Coherency of the Long Range Beam-Beam Interaction in CESR*, these proceedings

[3] T. Pelaia, PhD thesis, Cornell University, January, 1994, p. 31-45.

[4] Exploration of the tune plane and discovery of the low tune operating point is due to J. Hylas.

[5] J. Rogers, et.al.,*Operation of a Fast Digital Transverse Feedback System in CESR*, these proceedings

[6] H. Padamsee et. al., S. Belomestnykh et.al., and J. Kirchgessner, these proceedings.

PEP II STATUS AND PLANS*

John T. Seeman+

Stanford Linear Accelerator Center, Stanford University, Stanford, CA 94309 USA

The PEP II B-Factory[1] project is an e^+e^- colliding beam storage ring complex to be built on the SLAC site. PEP II is designed to provide a luminosity of 3 x 10^{33} $cm^{-2}s^{-1}$ at a center of mass of 10.6 GeV with unequal energy beams of 3.1 and 9.0 GeV. The goal is to study CP violation in the B meson system. The project is being built by a collaboration of the Stanford Linear Accelerator Center, Lawrence Berkeley Laboratory, and Lawrence Livermore National Laboratory. DOE construction authorization was given in 1994. The asymmetric beam energies require two storage rings with the low energy ring (LER) supported above the high energy ring (HER). There will be one interaction point with head-on collisions, requiring magnetic separation of the beams, low values of the beta functions, and magnetic elements inside the solenoid of the BABAR[2] physics detector. The high luminosity necessitates a large number of bunches requiring advances in the vacuum design, damped RF cavities, and bunch-by-bunch feedback systems. The injection scheme uses the high current, low emittance, on-energy beams available from the SLAC linac. At present, the old PEP tunnel has been cleared and installation of the high energy ring has started. Several of the many papers on PEP II at this conference are listed in References 3-23.

I. PARAMETERS

The general PEP II layout is shown in Figure 1 where the two rings are located in the former PEP tunnel. Two injection beam lines are built along the SLAC linac tunnel where the 3.1 and 9.0 GeV beams are extracted, transported, and injected into their respective PEP II rings. The LER magnets and supports are mounted above the HER dipole for ease of installation and maintenance, as shown in Figure 2. The general parameters of PEP II are listed in Table 1.

* Work supported by US Department of Energy contracts DE-AC03-76SF00515, DE-ACO3-76SF00098, and W-7405-Eng-48.

+ Representing the PEP II Staff from SLAC, LBL, and LLNL.

Table 1 Parameters of the PEP II B Factory

Parameter	Units	HER	LER
Circumference	m	2199.32	2199.32
Energy	GeV	9.0	3.1
Luminosity	10^{33} $cm^{-2}s^{-1}$	3	3
Bunch spacing	nsec	4.2	4.2
Crossing angle	mrad	0	0
Energy spread	10^{-4}	0.61	0.77
Bunch length	cm	1.1	1.0
σ_x	μm	155	155
σ_y	μm	6.2	6.2
β_x*	cm	50	37.5
β_y*	cm	2.0	1.5
Tune shift $\xi_{x,y}$		0.03	0.03
x tune		24.57	36.57
y tune		23.64	34.64
τ beam	hours	4.2	5.3
ε_x	nm-rad	48.	64.
ε_y	nm-rad	1.9	2.6
Nb	10^{10}	2.7	5.9
Bunches		1658	1658
Bunch gap	%	5	2
Current	A	0.99	2.14
RF frequency	MHz	476	476
RF Cavities		20	6
Klystrons		5	3
RF voltage	MV	14.	5.5
Loss Per Turn	MeV	3.57	0.77
$\tau_{x,y}$	turns	5400	7200
ν_s		0.045	0.035
# dipoles		192	192
# quadrupoles		290	326
Filling time	min	3	3
Injection rate	Hz	60	60
Injected bunch Q	10^9	1-30	1-30
Number of IRs		1	1
BABAR offset	m	0.37	-0.37
Solenoid field	T	1.5	1.5

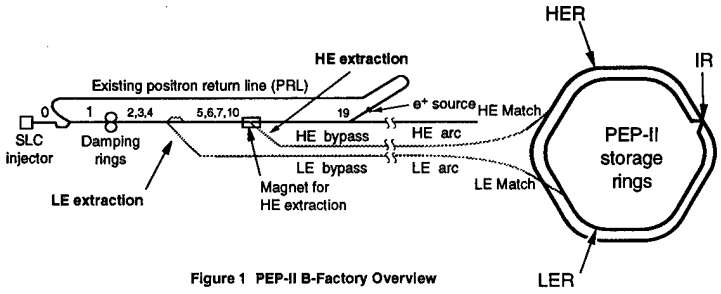


Figure 1 PEP-II B-Factory Overview

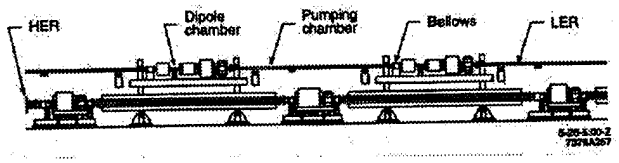


Figure 2 Cell layout

II. HIGH ENERGY RING

The HER has an energy range of 7 to 12 GeV and is designed to store up to 3 A of electrons. The arc dipole magnets and sextupoles are refurbished from the original PEP. The quadrupoles are either refurbished (about half) or reworked magnets from PEP. The old 1 m long laminated quadrupoles are being cut in half which become PEP-II magnets with new end packs and coils. The refurbishing is nearly complete and the magnetic quality is still good. The HER magnets and supports are starting to be reinstalled in the tunnel as shown in Figure 3.

The HER vacuum system has octagonal copper extrusions in the arcs and cooled circular stainless steel pipes in the straights. The chamber cross sections are shown in Figure 4. The copper provides low outgassing and contains the x-ray radiation inside the chambers. The extrusions have started to arrive at SLAC with the e-beam welder to start work in July. A prototype copper chamber has produced the vacuum pressures required (a few nTorr).

The beam position monitor is shown in Figure 4b. MAFIA and measurements have been used to design the button to minimize the narrow band impedance which minimizes the coupled bunch instability. The signal processors are multiplexed between the two rings and operates at 952 MHz. Special electronics are needed to minimize the effects of cross coupling of the bunch signals and to handle up to 50 W of signal power potentially exiting a single button from a 1 cm offset beam. Each monitor can store 1024 single measurements.

The HER lattice has a phase advance of 60 degrees per cell with semi-local chromatic corrections near the IR including a beta bump scheme to reduce the sextupole strengths.

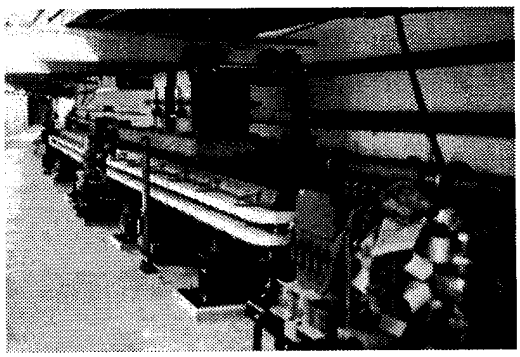


Figure 3 Installation of the first HER arc cell with operating Cu vacuum chamber. A prototype LER raft is mounted above.

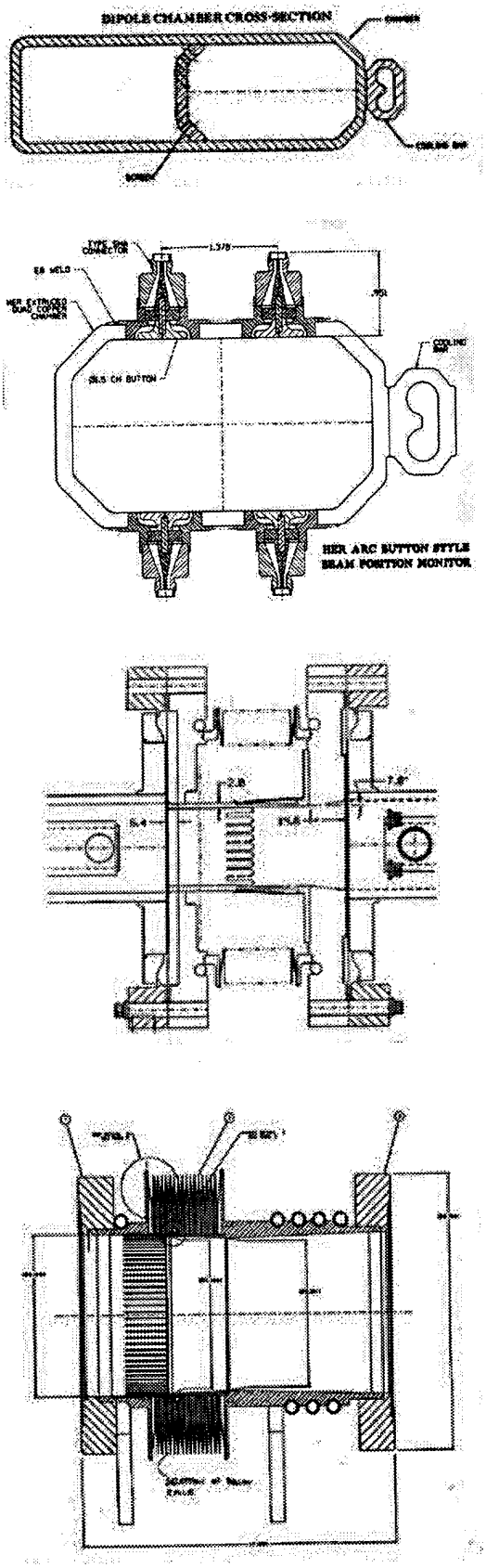


Figure 4 HER Vacuum chambers: a) dipole , b) quadrupole, c) arc bellows, and d) straight section bellows.

III. LOW ENERGY RING

The LER has an energy range of 2.1 to 4.0 GeV and is designed to store up to 3 A of positrons. All the magnets will be new. The dipole magnets are short (0.45 m) to enhance the radiation damping and beam emittance. The quadrupoles will be built with two piece laminations. The magnet designs were recently completed and orders have been placed for most of the dipoles and quadrupoles. The first prototypes will arrive in summer of 1995.

Two special wiggler chicanes are placed in the LER to provide emittance control. Only one of the chicanes will be implemented with a full wiggler on startup.

The LER vacuum system has aluminum extrusions with ante-chambers in the arcs, stainless steel pipes in the straights, and special copper chambers in the wiggler regions. The chamber cross sections are shown in Figure 5. The aluminum chambers are similar to the ALS design at LBL. The radiation from the LER beam strikes an angled copper photon stop in the ante-chamber with a TSP pump below. This arrangement reduces the average gas pressure around the ring increasing the beam life time. The aluminum extrusions have been through design reviews and one of two designs has been ordered.

The LER lattice has a 90 degrees per cell phase advance with a non-interleaved sextupole chromatic correction scheme in the arcs far from the IR with semi-local chromatic corrections near the IR. An octupole scheme to adjust the amplitude dependent tune shift has been designed.

IV. INTERACTION REGION

The layout of the interaction region is shown in Figure 6. The HER remains in the horizontal plane and is nearly straight. It has a few dipoles to make a 15 mrad angle at the interaction point to allow the two beams to collide head-on. Vertical dipoles are used in the LER to lower the ring the 0.8 m to the HER plane. Additional horizontal dipoles in the LER are used to provide the proper angle at the IP and to allow for chromatic corrections. In Figure 7 is shown the +/- 7 m region about the IP where the permanent magnet dipole B1 and quadrupole Q1 are used to separate the beams. At the first parasitic crossing the horizontal beam displacement is about 12 σ_x, adequate to ameliorate the beam-beam effect. The vacuum chambers in the IR region are primarily copper to mask and absorb the radiation power. At the collision point there will be a water cooled Be beam pipe. The detector solenoid field of 1.5T makes it difficult to correct the coupling in the LER and affects the beam trajectories at the millimetor level in the near IR.

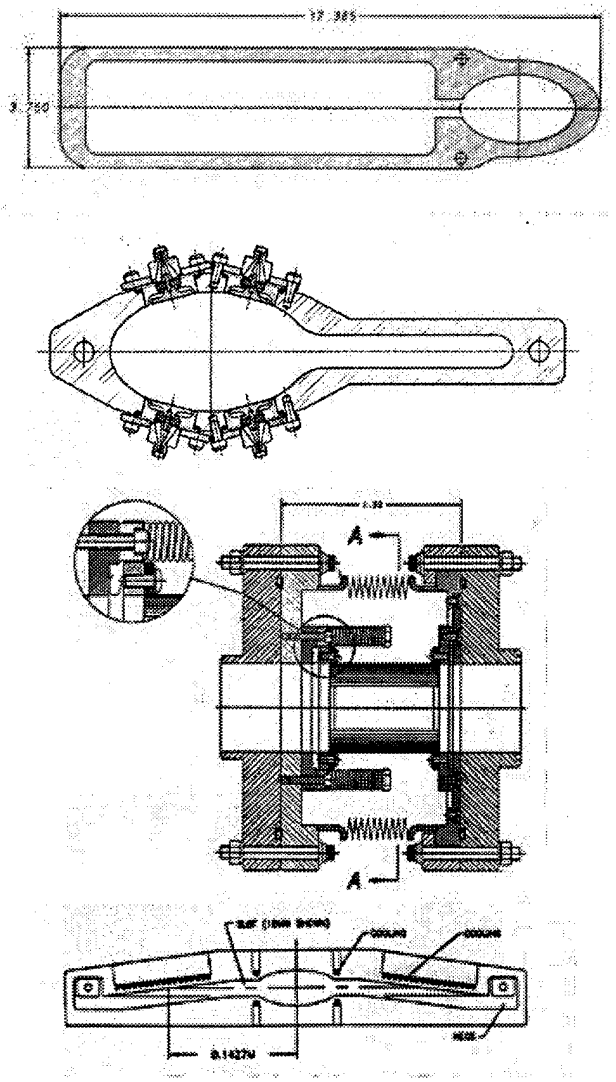


Figure 5 LER vacuum system: a) pumping chamber, b) magnet chamber, c) arc bellow section, and d) wiggler chamber.

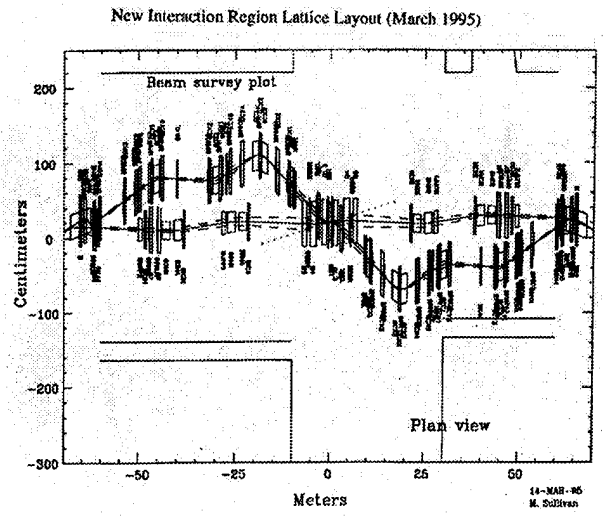


Figure 6 Interaction region lattice layout.

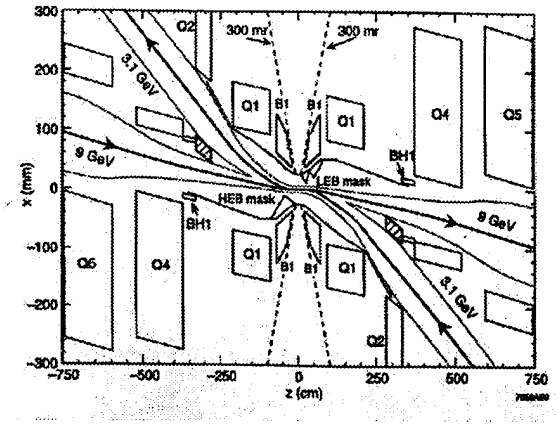


Figure 7 Beam separation at the interaction point.

V. RF SYSTEM

The PEP-II RF systems must support large beam currents 3A in the LER and 1A in the HER, which drives the design. The unique aspects of the klystrons needed for PEP II are the required short delay time of about 150 nsec, a large bandwidth of 3 MHz, and an output power of 1.2 MW. The short delay and band width are needed to provide for feedback of beam loading and longitudinal coupled bunch instability. One of these klystrons has been built at SLAC and has recently started tests (see Figure 8). The remainder of the required klystrons for PEP II will be made in industry.

The RF cavities for PEP II will be copper single cells with three higher order mode damping ports and an aperture coupler. The cavities are designed for 120 kW operation but will be used in PEP II at 80kW or less. The assembly raft with the cavity, the window, and pump is shown in Figure 9. The first production cavity is in machining as shown in Figure 10. This first cavity is nearing completion and will be under full high power tests by mid-summer 1995.

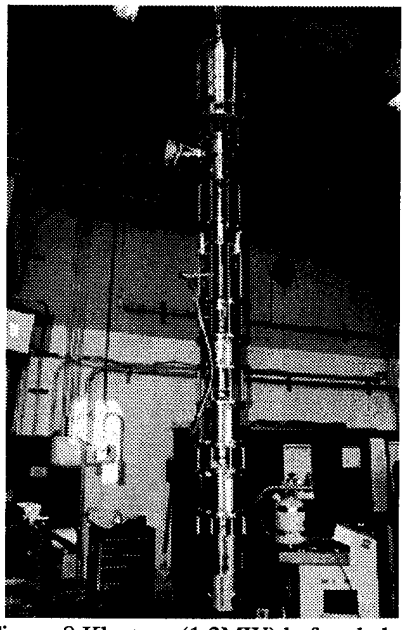


Figure 8 Klystron (1.2MW) before bake.

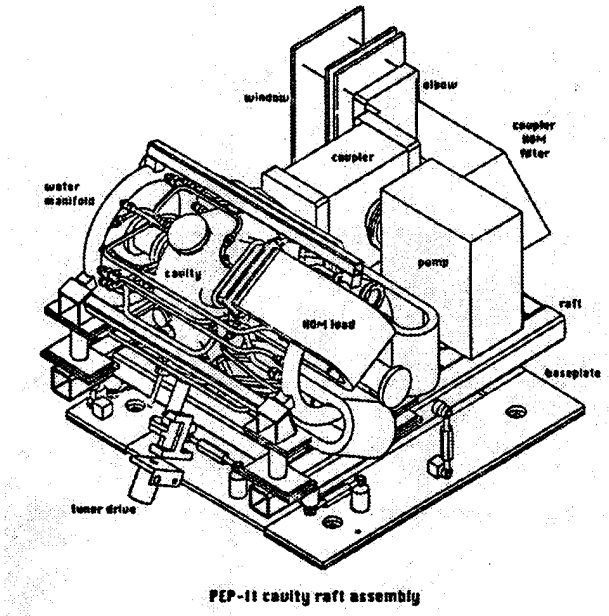


Figure 9 PEP II cavity raft assembly.

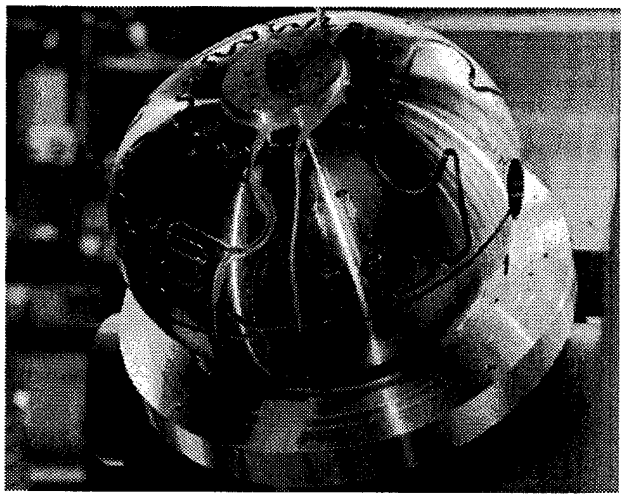


Figure 10 RF cavity during machining of water cooling grooves.

The high power cavity window is made from a circular alumina ceramic. Full scale prototype windows have been made and are in test. A power of over 400 KW have been successfully passed through the window while under vacuum and over 500 KW with nitrogen.

High power tuners are being designed after the successful PEP tuners with modification required of the sliding RF contacts.

VI. FEEDBACK SYSTEMS

The prototypes for the bunch-by-bunch transverse and longitudinal feedback systems for PEP II to be used to control multi-bunch instabilities down to 1 msec growth times are under test in the ALS at LBL. The tests are going very well. After a few final experiments, the full PEP II production of the required beam pickups, digital electronics, amplifiers and kickers will start. The interfaces of these fast digital processors with the PEP II control system are important and under study.

VII. CONTROLS

The control system for PEP II will be an extension of the working and elaborate SLC control system. This VAX-Microcomputer-CAMAC based system will be extended into the PEP II tunnel to provide basic control as well as proven high level application data taking and software analysis. Integration with linac injection is thus automatic. These controls will be broadened by adding VXI control of the PEP II fast bunch by bunch feedback and RF systems using EPICs. The SLC timing system will provide pulse control with an additinal modified trigger module for the PEP ring turn-to-turn needs, such as the position and charge monitors.

VIII. POWER CONVERSION

The large, intermediate, and small power supplies will be controlled via BITBUS through a digital controller local to the power supply. The large magnet string supplies will use the (massively reworked) existing chopper supplies. The intermediate power supplies are switching units used to power strings of a few quadrupoles. The small supplies power sixteen corrector magnets using a modified controller to handle all simultaneously. The controllers are designed to allow magnet ramping for configuration changes with stored beam.

IX. STATUS

The PEP II project is off to a fast start due to the hard work of our staff at the three laboratories. Since the linac is operational throughout our construction phase, we will commission our beam lines as soon as they are ready. The electron extraction line from the linac and the mile long bypass line will be tested with beam in the fall of 1995. The HER is to be complete in spring 1997 and injection and storage tests will then begin. The LER is to be finished in spring 1998 with storage tests to follow. First collisions are planned to be achieved in summer of 1998. The BABAR detector is planned to be placed on-line in early 1999.

X. REFERENCES

[1] "PEP II Conceptual Design Report," LBL-PUB 5379, SLAC-418, CALT-68-1869, UCRL-ID-114055, UC-IIRPA-93-01, June 1993.

[2] "BABAR Technical Design Report," SLAC-R-95-457, March 1995.

[3] M. Zisman and R. Yourd, "Design of the PEP II Low-Energy Ring," PAC, Dallas, May 1995.

[4] U. Wienands, et al, "Design of the High Energy Ring of the PEP II B Factory, PAC, Dallas, May 1995.

[5] D. Hunt, et al, "Design of the PEP II Low Energy Ring Vacuum System," PAC, Dallas, May 1995.

[6] T. Henderson, et al, "Design of the PEP II Low Energy Ring Arc Magnets," PAC, Dallas, May 1995.

[7] W. Barry, et al, "Design of the PEP II Transverse Coupled-Bunch Feedback System," PAC, Dallas, May 1995.

[8] J. Fox, et al, "Operation and Performance of the PEP II Prototype Longitudinal Damping System at the ALS," PAC Dallas, May 1995.

[9] A. Kulikov, et al, "The PEP II High Power Dumping System," PAC, Dallas, May 1995.

[10] U. Wienands, et al, "The Vacuum System for the PEP II High Energy Ring Straight Sections," PAC, Dallas, May 1995.

[11] C.-K. Ng, et al, "Simulation of the PEP II Beam Position Monitors," PAC, Dallas, May 1995.

[12] S. Heifets, et al, "Impedance Budget of the PEP II B Factory," PAC, Dallas, May 1995.

[13] X. Lin, et al, "Impedance Spectrum for the PEP II RF Cavity," PAC, Dallas, May 1995.

[14] Y. Cai, et al, "Low Energy Ring Lattice of the PEP II," PAC, Dallas, May 1995.

[15] M. Donald, et al, "Lattice Design for the High Energy Ring of the B Factory (PEP II), Dallas, May 1995.

[16] Y. Yan, et al, "Nonlinear Analyses of Storage Ring Lattices using One-Turn Maps," PAC, Dallas, May 1995.

[17] F. Zimmerman, et al, "Trapped Macroparticles in Electron Storage Rings," PAC, Dallas, May 1995.

[18] Y. Nosochkov, et al, "Detector Solenoid Compensation in the PEP II B-Factory," PAC, Dallas, May 1995.

[19] L. Jackson, et al, "PEP II Magnet Power Conversion Systems," PAC, Dallas, May 1995.

[20] T. Fieguth, et al, "PEP II Injection Transport, Construction Status and Commissioning Plans," PAC, Dallas, May 1995.

[21] R. Rimmer, et al, "Development of a High-Power RF Cavity for the PEP II B Factory," PAC, Dallas, May 1995.

[22] W. Fowkes, et al, "1.2 MW Klystron for Asymmetric Storage Ring B Factory," PAC, Dallas, May 1995.

[23]A. Chan, et al, "The PEP II Project-Wide Database," PAC, Dallas, 1995.

KEKB STATUS AND PLANS

Shin-ichi Kurokawa
National Laboratory for High Energy Physics, KEK
1-1 Oho, Tsukuba, Ibaraki, 305 Japan

ABSTRACT

The Japanese B-Factory project at KEK (KEKB) was approved by the Japanese government in 1994 as a five-year project and the construction of accelerator and detector started in April 1994. KEKB is an 8 × 3.5 GeV, two-ring, electron-positron collider in the existing TRISTAN tunnel. The luminosity goal is 10^{34} $cm^{-2}s^{-1}$. KEKB has one interaction point where electrons and positrons collide at a finite angle of ± 11 mrad. BELLE detector will be installed around this interaction point. KEKB will be commissioned in JFY 1998.

I. INTRODUCTION

KEKB(B-Factory) is an 8 × 3.5 GeV, two-ring, asymmetric, electron-positron collider aiming at detecting the CP-violation effect at B-mesons. Its luminosity goal is 10^{34} $cm^{-2}s^{-1}$. The project has been approved by the Japanese government as a five-year project and the construction has started from April 1994. Two rings of the KEKB (3.5 GeV low-energy ring, LER, for positrons, and 8 GeV high-energy ring, HER, for electrons) are to be installed in the existing TRISTAN tunnel of 3 km circumference and the infrastructure of TRISTAN will be maximally utilized. Taking advantage of the large tunnel size of TRISTAN, two rings of KEKB will be installed side by side; unnecessary vertical bending of trajectories that may increase the vertical emittance of the beams is minimized.

Figure 1 illustrates the arrangement of two rings. KEKB has only one interaction point, IP, at Tsukuba experimental hall, where electron and positron beams collide at a finite angle of ± 11 mrad. BELLE detector will be installed at IP. The straight section at Fuji is used for injection from the linac and also for installing RF cavities of LER. RF cavities of HER are to be installed in straight sections at Nikko and Oho. These straight sections are also reserved for wigglers for LER. The wigglers reduce the longitudinal damping time of LER from 43 msec to the same value as that of HER, 23 msec. In order to make the circumference of the two rings equal, a cross-over should be made at Fuji experimental hall where two rings pass each other.

To facilitate full-energy injection into the KEKB rings from linac and avoid acceleration of high-current beams, the present 2.5 GeV electron linac will be upgraded to 8 GeV[1]. The upgrade is done by combining the main linac with the positron production linac, increasing the number of accelerating structures, replacing klystrons with high-power ones, and compressing RF pulses by SLEDs. By this upgrade we can increase the energy of electrons impinging on the positron production target from 250 MeV to 4 GeV, thus multiplying positron intensity by 16. The injection time of positrons to LER is estimated to be 900 sec. A new bypass tunnel of 130 m for transport lines between the linac and KEKB rings will be constructed. This bypass tunnel insulates accumulation ring, AR, from KEKB; this is convenient both for KEKB and AR, since upgrade of either accelerator can be done without any large perturbation to the other. The tunnel will be constructed in JFY 1996 and 1997.

II. BASIC DESIGN

A. Beam Parameters

The main parameters of the KEKB accelerators are given in Table 1. HER and LER have the same circumferences, emittances, and the ß functions at IP. The large current, the large number of bunches, small bunch spacing, the small value of ß function at IP and finite-angle crossing of beams are the salient features of KEKB.

B. Noninterleaved Chromaticity Correction and 2.5π Lattice

It is desirable if we can inject beams into KEKB with the same optics as that of collision and avoid changing optics with large stored currents in the rings. We should have large enough transverse dynamic apertures at injection both for LER and HER, and a large enough longitudinal (momentum) aperture to have a sufficiently long Touschek lifetime for LER. Touschek lifetime is not a concern in HER because of

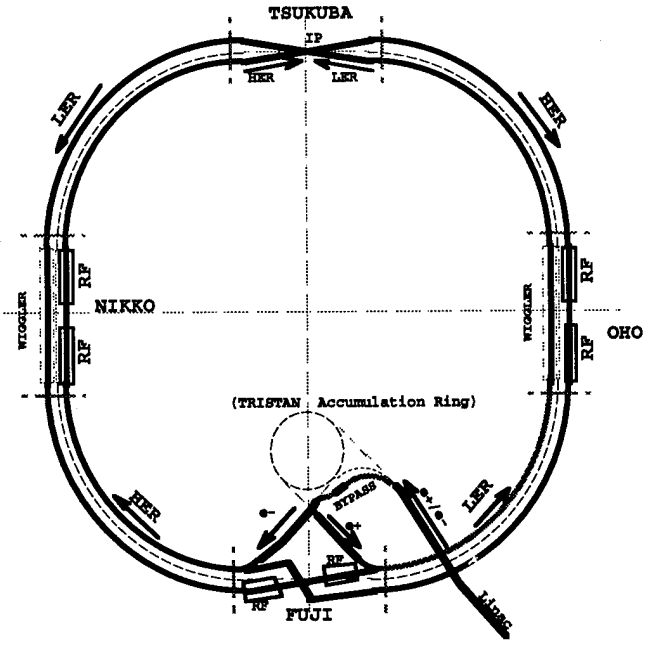


Fig. 1 Configuration of KEKB accelerator system.

0-7803-3053-6/96/$5.00 ©1996 IEEE

its 8 GeV energy. We have decided to adopt a noninterleaved sextupole chromaticity correction scheme to increase the apertures[2]. Between a pair of sextupoles no other sextupoles are installed and the betatron phase advance is π in both horizontal and vertical planes. This scheme cancells out the geometric aberrations of the sextupole by the -I transformation between sextupoles in a pair.

One unit cell of the adopted lattice has a phase advance of 2.5π and includes two pairs of sextupoles, SF and SD, of -I transformation. The addition of extra $\pi/2$ phase advance over 2π cell in this scheme enables effective correction of chromatic kicks and significantly improves the dynamic apertures. The momentum compaction factor can be changed from -1×10^{-4} to 4×10^{-4}. By adding two quadrupoles in a cell we can also have a tunability of the emittance from 50% to 200% of the nominal value. This flexibility of changing the momentum compaction factor and the emittance makes a strong tool to tune the machine.

The local chromaticity correction scheme corrects the large vertical chromaticity produced by the final focus quadrupole magnets within a straight section where IP is located. A few dipole magnets in the straight section produce the dispersion required for chromaticity correction by sextupole magnets. One -I sextupole magnet pair, installed in each side of the IP, corrects the vertical chromaticity. This scheme is applied only for LER where the large momentum aperture is required to imcrease the Touschek lifetime. Since the requirement on the dynamic aperture for HER is less demanding, HER does not employ the scheme.

C. Finite-Angle Crossing of Beams

We have decided to adopt a finite-angle crossing scheme of $\pm$ 11 mrad. In this scheme, parasitic collision is not a concern even though every bucket is filled with beam and we can remove separation dipole magnets that would be necessary for a head-on collision. In the case of a head-on collision, synchrotron lights produced by the separation dipole magnets determine the horizontal width of the beam pipe at IP; this width is minimized in the finite-angle crossing where no separation dipole exists; smaller beam pipe improves the vertex point resolution and permits efficient use of the

Table 1 Main Parameters of KEKB

Ring		LER		HER	
Energy	E	3.5		8.0	GeV
Circumference	C		3016.26		m
Luminosity	L		1×10^{34}		$cm^{-2}s^{-1}$
Crossing angle	θ_x		$\pm$ 11		mrad
Tune shifts	ξ_x/ξ_y		0.039/0.052		
Beta function at IP	β^*_x/β^*_y		0.33/0.01		m
Beam current	I	2.6		1.1	A
Natural bunch length	σ_z		0.4		cm
Energy spread	σ_δ	7.1×10^{-4}		6.7×10^{-4}	
Bunch spacing	s_B		0.59		m
Particles/bunch		3.3×10^{10}		1.4×10^{10}	
Emittance	$\varepsilon_x/\varepsilon_y$		$1.8 \times 10^{-8}/3.6 \times 10^{-10}$		m
Synchrotron tune	ν_s		0.01 ~ 0.02		
Betatron tune	ν_x/ν_y	45.52/45.08		47.52/43.08	
Momentum compaction factor	α_p		$1 \times 10^{-4} \sim 2 \times 10^{-4}$		
Energy loss/turn	U_o	0.81†/1.5††		3.5	MeV
RF voltage	V_c	5 ~ 10		10 ~ 20	MV
RF frequency	f_{RF}		508.887		MHz
Harmonic number	h		5120		
Longitudinal damping time	τ_E	43†/23††		23	ms
Total beam power	P_B	2.7†/4.5††		4.0	MW
Radiation power	P_R	2.1†/4.0††		3.8	MW
HOM power	P_{HOM}	0.57		0.15	MW
Bending radius	ρ	16.3		104.5	m
Length of bending magnet	l_B	0.915		5.86	m

† without wigglers
†† with wigglers

luminosity.

In KEKB we use superconducting final-focus quadrupole magnets in order to have a flexibility of tuning. Since we do not need separation dipole magnets, we can install superconducting solenoid magnets at the place where the separation dipole magnets are to be placed for a head-on collision. One superconducting solenoid and one final-focus quadrupole are contained in the same cryostat. By producing a proper reverse solenoid field, we can make the integrated solenoidal field nearly zero between the pair of the first quadrupole magnets. This cancellation is desirable for asymmetric colliders, where complete cancellation of the solenoidal field is necessary in order not to make the beams rotate by different angles between LER and HER.

By computer simulation we found that the finite-angle crossing reduces usable areas in the ν_x-ν_y plane due to synchro-betatron resonances, and that if we make the ν_s(synchrotron tune) smaller than 0.02, a fair amount of areas in the ν_x-ν_y plane is still free from reduction of luminosity due to resonances.[3] We have also started an R&D work on superconducting crab cavities in order to prepare for unpredictable beam-beam effects due to this finite-angle crossing.

D. Impedance Budget and Single-Beam Instability

Impedance budget of the KEKB was calculated[4] by using ABCI, a newly developed 3D program, MASK30, and analytical formulae. The total inductive impedance and loss factor in LER amount to 0.014 Ω and 42.2 V/pC that corresponds to the HOM power of 570 kW. The total loss factor in HER becomes 60 V/pC. This value is larger than that of LER by 18 V/pC due to the large number of cavities. The total HOM power amounts to 150 kW.

We have found that neither bunch lengthening nor the transverse mode-coupling instability will impose a significant limitation on stored bunch current. The threshold bunch current for the microwave instability was found to be twice as large as the design current. At the design intensity, the bunch lengthens only by 20%[5].

The growth time of the transverse coupled-bunch instability due to resistive wall of vacuum ducts in LER is still as short as 5 msec even though we employ a large duct diameter of 94 mm[5]. This instability must be cured by the fast feedback system.

III. HARDWARE SYSTEM

A. RF System

The RF cavity for the KEKB should have a structure by which higher-order modes (HOMs) in the cavity are damped to the level where the growth times of the coupled-bunch instabilities excited by HOMs become comparable to the damping time. The cavity should have enough stored energy in order to make the dutuning frequency of the cavity due to beam loading small compared with the revolution frequency of the ring. We are now developing two types of cavities for the KEKB. One is a normalconducting cavity called ARES and the other is a superconducting, single-cell, single-mode cavity.

B. ARES

ARES (accelerator resonantly coupled with energy storage) was devised in KEK and extensive R&D works are under way[6,7,8,9,10,11]. If the amount of cavity detuning becomes comparable or larger than the revolution frequency of the ring, strong coupled-bunch instability is excited by the fundamental-mode impedance of the cavity. T. Shintake showed that the amount of the detuning frequency can be drastically decreased by attaching a large volume, low-loss, energy-storage cell to an accelerator cell[12]. On the basis of this proposal, K. Akai, T. Kageyama and Y. Yamazaki proposed a 3-cell structure, where an accelerating cell and an energy storage cell is connected to a coupling cell[13,14]. The system employs a $\pi/2$ mode where almost pure TM010 mode and almost pure TE013 mode are excited in the accelerating cell and the energy storage cell, respectively, and very little field is excited in the coupling cell. Two parasitic modes (0 and π modes) have a field in the coupling cell and can be damped rather easily by a coupler attached to the cell.

In order to suppress HOMs, a choke-mode cavity [15] is used as the accelerating cell of ARES. The choke reflects back the fundamental mode; HOMs propagate out and are absorbed by the SiC absorbers. The first prototype choke-mode cavity was delivered to KEK. It was successfully tested up to 110 kW of wall dissipation which corresponds to a gap voltage of 0.73 MV.

C. Superconducting RF Cavity

A superconducting cavity has a large stored energy due to its high field gradient and is immune to the beam-loading. The superconducting cavity for KEKB is a single-cell cavity with two large-aperture beam pipes attached to the cell[16]. HOMs propagate toward the beam pipes, since their frequencies are above the cut-off frequencies of the pipes. The diameter of the one pipe (300 mm) is made larger than that of the other (220 mm) in order to make a few transverse modes otherwise trapped propagate. The iris between the cell and the larger beam pipe prevents the fundamental mode from propagating toward the beam pipe. HOMs are absorbed by ferrite HOM absorbers.

A full-size Nb model was constructed and tested in a vertical cryostat. The maximum accelerating field obtained was 14.4 MV/m with a Q value of 10^9[17]. The prototype cavity for the AR beam study is under construction and will be teste in AR with beams.

Prototype HOM dampers were made by HIP(hot isostatic press) method: the powder of ferrite is sintered and bonded simultaneously on the Cu surface under high temperature and high pressure. Two HOM dampers, one with an inner diameter of 300 mm and the other with an inner diamter of 220 mm, were high-power tested with 508 MHz RF power upto 14.8 kW and 11.7 kW, respectively. No damage on the ferrite was observed and the outgassing rate was sufficinetly low. A beam test of dampers is in preparation[18].

D. Bunch-by-Bunch Feedback System

Feedback systems that can damp the coupled-bunch oscillations of the beam with a bunch spacing of 2 ns are being developed[19]. Since the number of bunch is large (5000) and the bunch spacing is short (2 ns) at KEKB, the signal processing part of the system needs a lot of R&D. We are trying to develop a 2-tap FIR digital filter system as the kernel of the signal processing unit. The 2-tap FIR filter does not require any multiplication but a substraction of two signals. This kind of filter can be composed of memory chips and simple CMOS logic ICs without relying on DSP chips. By using 500 MHz ADC and DAC, two custom-made 4-bit GaAs 1:16 500-MHz demultiplexers and two 4-bit GaAs 16:1 500-MHz multiplexers, and having 16 parallel 2-tap FIR logics, we can construct a signal processing unit on a single board. This board have a capability of processing 5000 beam bunches with 2-nsec spacing without resort to down-sampling technique. This processing speed makes it applicable also to the transverse feedback system. Prototype transverse and longitudinal pickups that can detect bunch oscillations for the 500 MHz bunch frequency have been completed. Kickers are now being developed.

E. Cu Vacuum System

We have decided to use Cu as material for vacuum ducts by taking into account its low photodesorption coefficient, high thermal conductivity, and self shielding capability of X-rays. In LER the maximum heat load due to synchrotron lights to the duct amounts to 15.3 kW/m and that in HER 12.5 kW/m. The use of aluminum as a material is precluded by these numbers.

The cross section of a LER duct is a circle with an inner diameter of 94 mm. These large duct size and short dipole magnets of LER enable us to have a non-distributed pumping system for LER. NEG cartridges will be used as main pumps. Since the instability due to resistive wall is not strong at HER, a race-tarck shape duct is adopted for HER in order to minimize the gap of the dipole magnets. Long dipole magnets of HER only permit us to adopt a distributed pumping system on the basis of NEG strips.

F. Control System

We have decided that we will build the KEKB control system from the EPICS tool box[20].

IV. SCHEDULE

A. Beam Test of RF Cavities and Feedback Systems at the TRISTAN AR

Three-month long beam test is planned to be held in 1996 by the use of AR. We plan to store more than 500 mA electron beam in AR with a multibunch mode at 2.5 GeV. To accumulate this high current, the existing APS type RF cavities will be removed temporally from the ring and an ARES cavity and a single-cell superconducting cavity for KEKB will be installed. The transverse and longitudinal feedback systems will be also installed and tested.

B. Construction Schedule

Main components of LER such as magnets and vacuum equipment will be procured in JFY1995 and 1996, whereas those for HER in JFY1996 and 1997. TRISTAN will be terminated by the end of 1995 and dismantling of TRISTAN main ring will start from January 1996. By the end of 1996 the TRISTAN tunnel will become ready for installation of magnets. We plan that commissioning will start within JFY 1998.

REFERENCES

[1] A. Enomoto, et al., Proceedings of the 1994 International Linac Conference, p.194.

[2] H. Koiso and K. Oide, Lattice Design in KEKB Colliding Rings, in these proceedings.

[3] K. Ohmi, K. Hirata, and N. Toge, A Study of Beam-Beam Interactions at Finite Crossing Angles for a B-Factory, in these proceedings.

[4] Y.H. Chin, et al., Impedance Budget for the KEK B-Factory, in these proceedings.

[5] Y.H. Chin, et al., Single-Beam Collective Effects in the KEK B-Factory, in these proceedings.

[6] Y. Yamazaki, et al., An Accelerator Resonantly-Coupled with Energy Storage (ARES) for the KEKB, in these proceedings.

[7] K. Akai, E. Ezura, and Y. Yamazaki, Design of the KEKB RF System, in these proceedings.

[8] T. Kageyama, et al., Development of a HOM-Damped Cavity for the KEK B-Factory (KEKB), in these proceedings.

[9] N. Akasaka, et al., RF Characteristics of ARES Cold Models, in these proceedings.

[10] Y. Takeuchi, et al., HOM Absorber for the KEKB Normal Conducting Cavity, in these proceedings.

[11] F. Naito, et al., Input Coupler for the KEKB Normal Conducting Cavity, in these proceedings.

[12] T. Shintake, Part. Accel. 44 (1994) 131.

[13] Y. Yamazaki and T. Kageyama, Part. Accel. 44 (1994) 107.

[14] K. Akai and Y. Yamazaki, Part. Accel. 46 (1994) 197.

[15] T. Shintake, Jpn. J. Appl. Phys. Lett. 31 (1992) 1567.

[16] S. Mitsunobu, et al., A Prototype Superconducting Cavity for KEK B-Factory, in these proceedings.

[17] K. Asano, et al., Stable Performance of Superconducting Cavities for KEKB, in these proceedings.

[18] T. Tajima, et al., Development of HOM Damper for Superconducting Cavities for KEKB, in these proceedings.

[19] E. Kikutani, et al., Recent Progress in the Development of the Bunch Feedback Systems for the KEKB, in these proceedings.

[20] S. Kurokawa, et al., Control System Design for KEKB, in these proceedings.

DAΦNE STATUS AND PLANS

The DAΦNE Project Team*
presented by G. Vignola
INFN, Laboratori Nazionali di Frascati (LNF), C.P. 13, 00044 Frascati, Italy

The $e^+ e^-$ Φ-factory DAΦNE has been approved and funded in 1990; the detailed engineering design started in 1991 and the construction is proceeding steadily.

The beginning of the collider commissioning, with a short term luminosity goal L = 1.3 10^{32} cm^{-2} sec^{-1}, is scheduled for the end of 1996.

I. INTRODUCTION

The main features of the $e^+ e^-$ Φ-factory DAΦNE have been described in detail elsewhere [1]. The project was approved and funded in 1990M and the detailed engineering design started in 1991. The construction of machine and experiments is proceeding steadily.

The accelerator complex layout is shown in Fig. 1. It consists of:

- $e^+ e^-$ LINAC;
- $e^+ e^-$ Accumulator/damping ring;
- twin ring collider (DAΦNE).

The tender phase is almost complete and all the various components are under construction. The beginning of the collider commissioning is scheduled for the end of 1996, and the start of experimental runs for mid 1997.

The design luminosity L = 5.2 10^{32} cm^{-2} sec^{-1} should be achieved in a period of at least 2 years of continuous operation by pushing up the current and, at the same time, by fine tuning all machine parameters.

In the following, we will discuss briefly the main features and the status of the three accelerators and, in some more detail, the vacuum system, the RF cavity and the longitudinal feedback system for the collider.

II. LINAC

The LINAC [2] is an S-band structure with a SLED type pulse compression system capable of accelerating electrons up to 800 MeV at 50 pps. In the positron mode of operation the first part of the LINAC (from the gun to the positron converter) is used to accelerate a 4A-10ns electron pulse at 250 MeV. The high-current performances of the LINAC have been successfully tested [3] at the TITAN Beta factory.

The LINAC (see Fig. 2) is now being installed at LNF and the beam tests are scheduled for May 95. It will be fully operational by December 95.

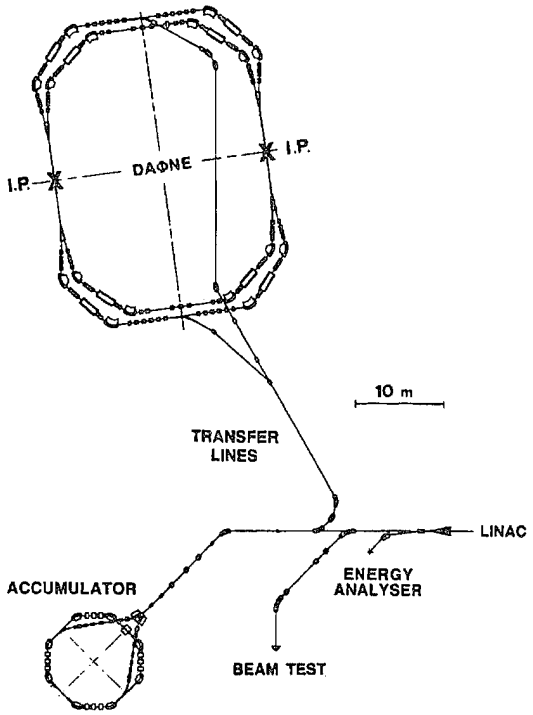


Figure 1: Layout of DAΦNE and its injector.

III. ACCUMULATOR

The main parameters of the Accumulator/damping ring are shown in Table I. It has a compact 4 period structure, with a total length 1/3 of DAΦNE.

Table I - DAΦNE Accumulator Main Parameters

Energy (MeV)	510.0
Circumference [m]	32.56
Emittance, ε_o [mm·mrad]	0.26
Betatron tune, ν_x/ν_y	3.12/1.14
RF frequency, f_{RF} [MHz]	73.65
Bunch average current [mA]	150
RF voltage [kV]	200
Bunch length σ_z [cm]	3.8
Synchrotron radiation loss [keV/turn]	5.2
Damping time, τ_ε/τ_x [ms]	10.7/21.4

The Accumulator is used to store at 50 pps the required number of electrons (positrons) in one RF bucket and to damp the transverse and longitudinal emittance of the LINAC beam. The damped beam is extracted at ~ 1 pps and injected into a single bucket in DAΦNE.

* M. Bassetti, M.E. Biagini, C. Biscari, R. Boni, A. Cattoni, V. Chimenti, A. Clozza, S. De Simone, G. Di Pirro, H. Dong, A. Drago, S. Faini, A. Gallo, A. Ghigo, S. Guiducci, Y. He, H. Hsieh, F. Marcellini, C. Marchetti, M.R. Masullo, M. Migliorati, C. Milardi, M. Modena, L. Palumbo, L. Pellegrino, M. Preger, H. Qu, G. Raffone, C. Sanelli, F. Sannibale, M. Serio, F. Sgamma, B. Spataro, A. Stecchi, L.Trasatti, C. Vaccarezza, M. Verola, M. Vescovi, S. Vescovi, G. Vignola, D. Yao, M. Zobov.

0-7803-3053-6/96/$5.00 ©1996 IEEE



Figure 2: DAΦNE LINAC during installation (April 95).

Oxford Instr. is the main contractor for the construction and the installation of the Accumulator, whose magnets are built by Tesla Eng.

The series production of magnets (designed and measured by LNF), vacuum chambers and other components is complete. The installation of the Accumulator, due to ~ 1 year delay in the delivery of the Transfer Lines, built by Ansaldo Energia, is scheduled for September 95, while the beam tests will begin in January 96.

Due to the excellent magnetic field quality measured on the first Accumulator quadrupole ($\Delta B/B = \pm 10^{-4}$ @ ± 3 cm, instead of $\pm 5 \cdot 10^{-4}$ requested by the Specs), we have decided to use in the DAΦNE long straights the same quadrupoles (60).

IV. DAΦNE

The major physics motivation for the construction of DAΦNE is the observation of direct CP-violation in K_L decays, i.e. the measurements of ε'/ε with accuracy in 10^{-4} range by the KLOE detector [4].

To achieve this result, a luminosity $L = 5\ 10^{32}\ cm^{-2}\ sec^{-1}$ integrated over an effective year of 10^7 seconds is required.

To get such a luminosity DAΦNE is designed as a high current double ring system with a maximum number of 120 bunches/beam.

The high current approach, adopted also by PEP-II [5], allows to use single bunch parameters quite conservative from an accelerator physics point of view, but it moves the difficulties to engineering challenges (vacuum, RF, multibunch).

In DAΦNE electrons and positrons are stored in two separated storage rings laying in the same horizontal plane with horizontal crossing in 2x10m long interaction regions, at an angle of ± 12.5 mrad.

The main DAΦNE parameters are shown in Table II.

The regular lattice of each ring consists of 4 achromats, each housing a 2 m long, 1.8 T normal conducting wiggler to increase beam emittance and radiation damping.

The straight sections orthogonal to the interaction regions are used for injection, RF, feedbacks and a scrapers system [6] optimized for reducing the lost particles background inside the detectors.

The betatron tune working point [7], with equal vertical betatron phase advance between the two interaction points, is almost insensitive to resonances and shows negligible beam blow-up.

The second interaction region is assigned to a smaller size detector, FINUDA [8], for study of hypernuclei formation and decay. The installation of three beam lines for soft X-rays [9] is also planned.

bandwidth required (~180 MHz at least, for 120 bunches operation), the cavity is loaded by 6 ridged waveguides followed by broadband transitions to 7/8" standard coax, very similar to those in the main RF cavity, except that in this case the coupling is extended to the fundamental mode. The 6 waveguides are placed symmetrically with respect to the accelerating mode. Three WGs are used as input ports and the other three as termination loads. In this way, thanks to the symmetry, the system is perfectly matched.

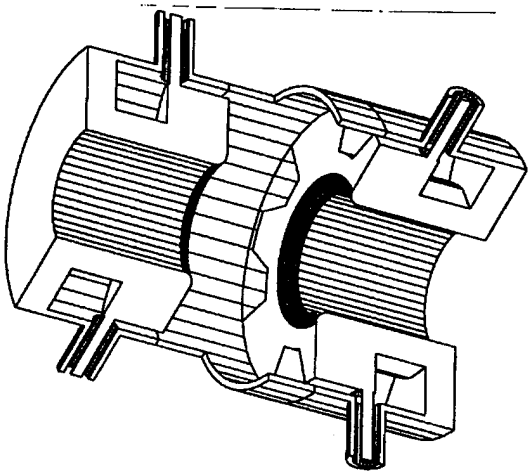


Figure 6: CAD view of the overdamped kicker cavity.

Being broadband, the kicker cavity does not need to be tuned in operation, nor cooled, since almost all the power is dissipated in the external loads. Moreover, the damping waveguides couple out the HOMs as well.

Not being the kicker cavity a directional device like the stripline kicker, it extracts power from the beam. Ferrite circulators are then necessary to isolate the output section of the power amplifier feeding the cavity.

The geometry of the kicker cavity has been defined. A peak shunt impedance of 750 Ω, together with a bandwidth larger than 220 MHz, have been calculated with 3D simulations with the HFSS code by HP. The mechanical design is under preparation at LNF and we intend to place an order to industry for two pieces (one per ring) for the initial operation at a reduced number of bunches. According to simulations with realistic values of the HOM impedances, a large band-width power amplifier of ~ 200 Watt is enough to damp an initial offset of 100 ps of the injected bunch with the other 29 bunches at the full design current. Two cavities per ring will eventually be installed for operation at the full nominal current with a 3x200 Watt power amplifiers per cavity, each feeding separately a waveguide coupler.

VIII. ACKNOWLEDGMENTS

I like to thank the DAΦNE Machine Review Committee (A. Hutton - Chairman, F. Bonaudi, D. Boussard, G. Brianti, J.P. Delahaye, A. Wrülich) for their constant advice; E. Iarocci - LNF Director, D. Federici and F. Pacciani - LNF Administrative Office, for their continuous support to this Project.

I am also pleased to acknowledge all the personnel of the LNF Accelerator Division for their enthusiastic commitment, and the cheerful Pina Possanza for her outstanding secretarial and administrative management.

IX. REFERENCES

[1] The DAΦNE Project Team, "DAΦNE, The Frascati Φ-factory", Proceedings of PAC93, p. 1993.

[2] K. Whitham et al., "Design of the e^+ e^- Frascati Linear Accelerator for DAΦNE", Proceedings of PAC 93, p. 611.

[3] K. Whittam et al., "Installation and Commissioning of the e^+ e^- Injector for DAΦNE at Frascati", these Proceedings.

[4] The KLOE Collboration, "KLOE, a General Purpose Detector for DAΦNE", Frascati Internal Note LNF-92/019 (IR), April 1992.

[5] J.T. Seeman, "PEP II, Status and Plans", these Proceedings.

[6] S. Guiducci, "Background evaluation in DAΦNE", DAΦNE Technical Note IR-6 (1995).

[7] M.E. Biagini, M. Zobov, "A better working point for DAΦNE", DAΦNE Technical Note G-32 (1995).

[8] The FINUDA Collaboration, "FINUDA, a Detector for Nuclear Physics at DAΦNE", Frascati Internal Note LNF 93/021 (IR), May 1993.

[9] A. Balerna et al., "DAΦNE-L: Proposta per l'utilizzazione di DAΦNE come sorgente di luce di sincrotrone", Frascati Internal Note LNF-91/083 (IR), October 1991.

[10] V. Chimenti et al., "The DAΦNE Main Ring Vacuum System", Proceedings of PAC 93, p. 3906.

[11] S. Bartalucci et al., "Analysis of Methods for Controlling Multibunch Instabilities in DAΦNE", Particle Accelerator, Vol. 48, 4 (1995), p. 213.

[12] R. Boni et al., "A Broadband Waveguide to Coaxial Transition for High Order mode Damping in Particle Accelerator RF Cavities", Particle Accelerator, Vol. 45, 4 (1994), p. 195.

[13] G. Oxoby et al., "Bunch by Bunch Longitudinal Feedback System for PEP-II", Proc. of 4-th European Particle Accelerator Conference, London 1994, p.1616.

[14] J. D. Fox et al.: "Operation and Performance of the PEP-II Prototype Longitudinal Damping System at the ALS", these Proceedings.

[15] A. Gallo et al., "Overdamped Cavity for the DAΦNE Longitudinal Feedback", DAΦNE Technical Note, in preparation.

ELECTRON-POSITRON COLLIDERS AT NOVOSIBIRSK

N. Dikansky
Budker Institute of Nuclear Physics, Novosibirsk, 630090, Russia

Abstract

INP has been developing colliders for over 30 years. The first experiments on scattering electrons on electrons at large angles were started at the first electron-electron collider at an energy of 2 x 130 MeV already in 1964. A year later the first in the world electron-positron collider VEPP-2 was put into operation, and in 1966 the first results of the phi-meson decays was published. Since then INP created VEPP-3 and VEPP-4 which were later modernized into VEPP-2M and VEPP-4M. The energy in the centre-of-mass system of these machines ranged from 400 MeV up to 12 GeV. Starting from the first experiments on electron-positron colliding beams we have gone through the luminosity range of $10^{24} cm^{-2} sec^{-3}$ to $310^{31} cm^{-2} sec^{-1}$. A big amount of information and experimental results obtained on these machines have been published in Particle Data.

In 1986 we have started to develop colliders of a new class, i.e. electron-positron colliders, like B- and Phi-factories (VEPP-5). Unfortunately, the beginning of this work coincided with the launch of Perestrojka in Russia, and the rate of financing, and whence, the construction rate of these machines was slowed down.

In 1993 following the recommendation of the International Program Committee for high energy physics of the Russian Ministry of Science the construction of the B-factory was cancelled and it was recommended to develop a C-tau-factory. The present report shows the status of the VEPP-2M, VEPP-4M and VEPP-5 facilities.

I. VEPP-2M

In 1989 due to the modernization of VEPP-2 there appeared a BEP cooling storage ring in the complex and a new VEPP-2M hard focus collider at a maximum enegy of the beam of 2 x 670 MeV. Since then this collider has the luminosity best recorded in the world in this energy range $310^{31} cm^{-2} sec^{-1}$. During the run time of this collider it accumulated an integrated luminosity of 20 reverse picobarn. At present the experiments are carried out at two detectors, KMD-2 and SND. The nearest two years will be devoted to the experiments on the precision measurement of hadron cross sections for estimating the contribution of the hadron polarization to the g-2 muon, as well as the study of rare decay modes of light vector mesons and the preparation for the experiments on the study of CP-violation at the Phi-factory.

A. ROUND BEAMS IN THE VEPP-2M COLLIDER

The Novosibirsk project of the Phi-factory is based on the idea of round beams [1]. There are many agruments in favor of this method of attaining high luminosity. Nevertheless, the final conclusion on the validity of this idea can be made only on the basis of experimental tests. Such a validity test is planned to be carried out at the VEPP-2M facility after its modernization. The necessary changes in the lattice provide for a substitution of superconducting solenoids for quadrupole dublets in the experimental sections (Fig. 1). Like in the Novosibirsk project of the Phi-factory, here the solenoids also perform two functions. First, they allow for obtaining equal betta-functions at the interaction points, second, they turn the betatron oscillation planes by $\pi/2$, which is required for the non-resonant formation of the phase space in both directions. In the case of the round beam optics as compared to the current optics the dispersion function in the experimental sections is equal to zero. In this case it does not only improve the conditions for the beam-beam effects, but also reduces the number of the background particles reaching the detectors. After the modernization the anticipated luminosity at an energy of a phi-meson is $0.5 - 1.0 \times 10^{32} cm^{-2} sec^{-1}$ [2].

Peremeters	flat beam	round beam
Circumference, m	17.88	17.88
RF frequence, MHz	200	200
Momentum compaction	0.167	0.18
Emittances, cm/rad	4.6×10^{-5} 5.5×10^{-7}	1.5×10^{-5} 1.5×10^{-5}
Energy loss/turn, keV	9.1	5
Dimensionless damping decrements	4.4×10^{-6} 3.8×10^{-6} 9.4×10^{-6}	8.2×10^{-6} 8.2×10^{-6} 2×10^{-5}
Energy spread	6×10^{-4}	3.5×10^{-4}
bx at IP, cm bz at IP, cm	48 4.5	4.5 4.5
Betatron tunes	3.05, 3.1	3.1, 3.1
Particles/bunch	2×10^{10}	6.7×10^{10}
Tune shifts	0.02, 0.05	0.1, 0.1
Luminosity, $cm^{-2} s^{-1}$	$\sim 5 \times 10^{30}$ *	$\sim 1 \times 10^{32}$

* Wiggier "on"

In the original project of the VEPP-2M modernization it was supposed to use superconducting solenoids with NbTi windings with a maximum filed at the axis of 10.6 T. In order to obtain such a field in the solenoid it is required to cool its winding from 4.2 K down to 1.8 K. There has been recently found such a version of the solenoid design in which the necessary integral of the magnetic field at an energy of 510 MeV is obtained at a field of 8.7 T. With such a field no additional cooling of the winding is required.

The design and manufacture of the facility is planned for the nearest two years.

II. THE VEPP-4M

The accelerator complex consists of an electron-positron collider at an energy of up to 2 x 6 GeV, a VEPP-3 cooling storage ring at an energy of up to 2 GeV, and an injection complex, see Fig.2 . Since put into operation, the complex was twice modernized. The last modernization was made after fire of 1987. The

0-7803-3053-6/96/$5.00 ©1996 IEEE

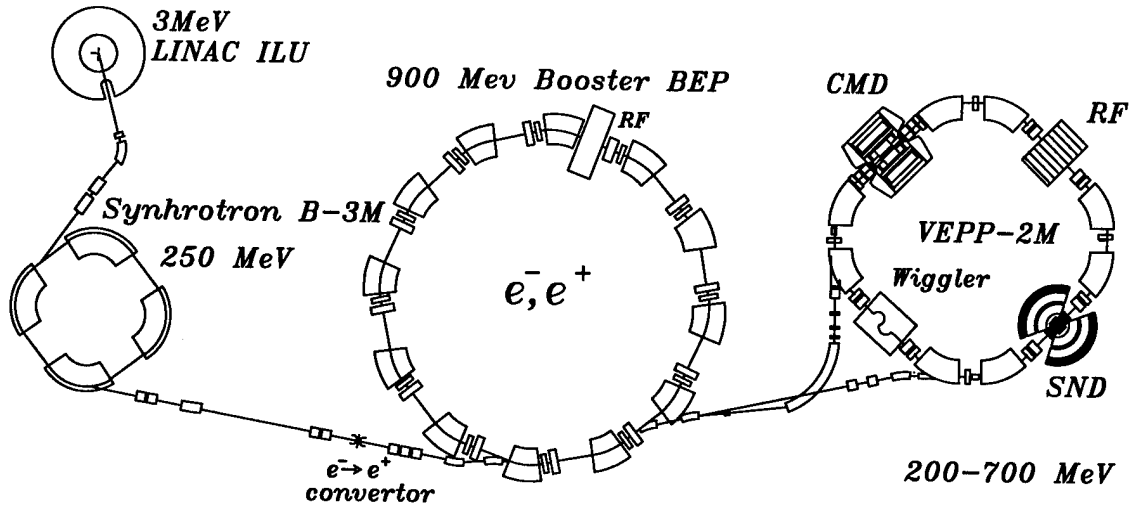


Figure 1. Layout of VEPP-2M complex

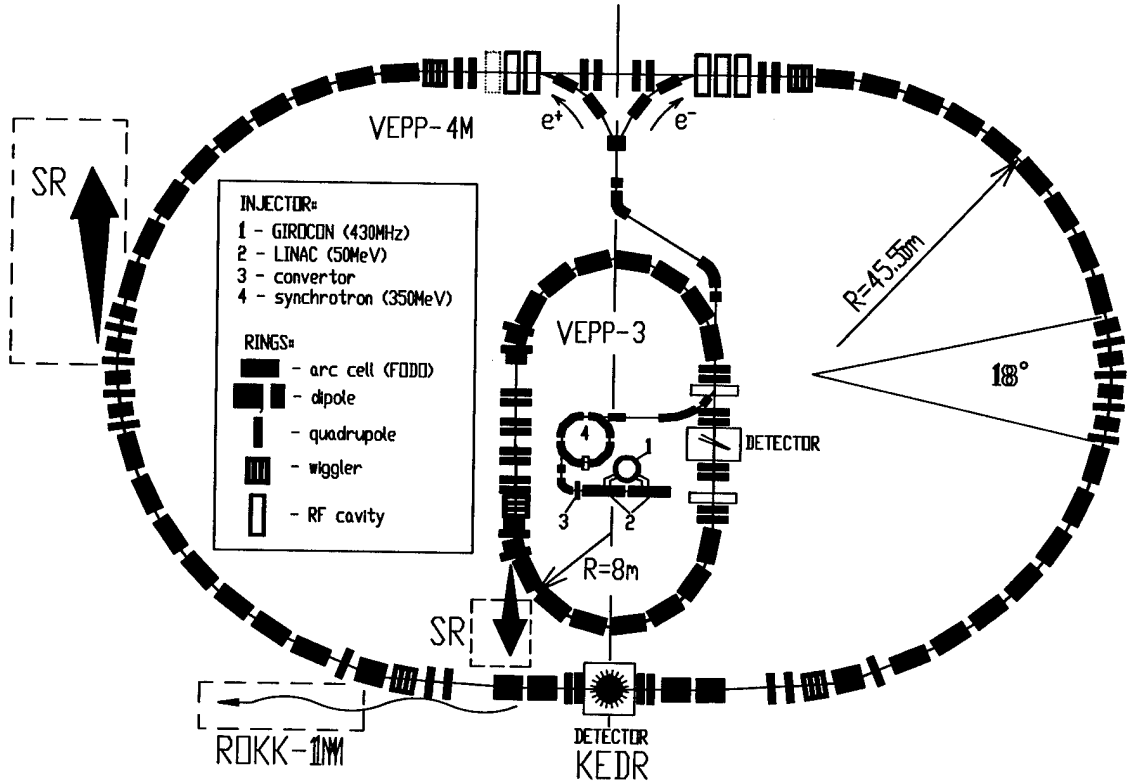


Figure 2. Layout of VEPP-4M complex

design parameters of VEPP-4M are listed in Table 2.

The VEPP-4M collider is mainly designed for carrying out investigations in the epsilon physics on the KEDR detector, and in the two-photon physics on the distributed spectrometer, formed by the collider lattice. Besides, VEPP-4M is equipped with SR beam extraction lines into a $1200m^2$ experimental room with a high-intensity gamma-quantum ROKK-1M setup at an energy range from 50 to 1600 MeV. The gamma-quantum beam is produced by the method of back Compton scattering of a laser light by the electron beam of VEPP-4M.

For increasing the luminosity of the VEPP-4M facility the following modifications are envisaged:

a) reduction of the beta-function down to 5 cm and an operation mode of two electron and two positron colliding bunches;

b) installation of superconducting wigglers in the insertions for increasing the bunch phase space, and correspodingly, the maximum currents with respect to the beam-beam effects;

c) installation of a superconducting cavity for reducing the bunch length, and respectively, the bunch size at the interaction point.

Along with the problem of fabricating the superconducting wigglers and cavity, the problem of positron lack, which were discussed above, there arises the problem of the threshold current in the bunch at VEPP-4M. During 1994 the threshold current was increased from 5 up to 20 mA. Provided 35 mA is obtained in every of the four bunches, the luminosity of $1.4 \cdot 10^{31} cm^{-2} sec^{-1}$ can be attained.

Energy, GeV	6
Circumference, m	366
Average arc radius, m	45.6
Horizontal aperture, cm	6
Vertical aperture, cm	2.7
Bending radius, m	34.5
Betatron frequencies ν_x, ν_z	8.53, 7.57
Compaction factor	0.017
Horizontal emittance, mm*mrad	0.4
Vertical emittance, mm*mrad	0.001
Energy spread, SR loss, MV/turn	4
Synchr. oscill. damping time, msec	2
RF wave length, m	1.65
Harmonic number	222
Accelerating voltage, MV	9
Bunch length, cm	4
RF power for by SR, kW	400
Heat losses in cavities, kW	800
Horizontal beta-function, cm	75
Vertical beta-function, cm	5
Dispersion function, cm	80
Beam sizes X and Z, micron	1000, 7
Space charge parameters X, Z	0.005, 0.05
Number of particles per bunch	2×10^{11}
Number of bunches per beam	2
Beam current, mA	50
Luminosity	7×10^{31}

Table.2

Before modernization VEPP-4 was run in a single bunch mode at currents $I \times I = 8 \times 8$ mA at a luminosity L = 5×10^{30}. The threshold current with respect to the beam-beam effects were of an order of magnitude of 10 mA and were easily obtained by means of a single injection from the VEPP-3 booster storage ring. The possibility of obtaining currents I = 17 mA in one separatrix was limited by the development of the instability appearing due to the interaction of the bunch with the fields induced by the bunch on the vacuum chamber inhomogeneities.

Some steps were taken in the new configuration of VEPP-4M to smoothen the vacuum chamber, in particular there were shut the bellows connections near the electrostatic pick-ups. But at the same time, due to the transit to the two-bunch operation mode, the insertions were additionally equipped with 8 pairs of separation plates, which drastically affected the electro-dynamic properties of the vacuum chamber.

III. EXPERIMENTAL RESULTS OBTAINED AT VEPP-4M BY 1994

By the present time the following results have been obtained at the VEPP-4M collider at an energy of 1.8 GeV: the rated luminosity has been attained, the electrons at currents of up to 15 mA and two bunches at currents of about 1 mA have been raised to an energy of up to 5.1 GeV (the energy is determined by the power of the 1st stage of the RF system), the backgrounds from the SR around the KEDR detector have been studied at this energy.

The magnetic system of the experimental section of VEPP-4M forms a distributing spectrometer for determining the energy loss of electrons and positrons in the two-photon physics experiments. Simultaneously, the ROKK-1M setup (obtaining of a gamma-quantum bunch by the back Compton method) was created and put into operation at the VEPP-4M facility.

These systems complement each other: the sharp edge of the back Compton spectrum provides for the calibration of the scattered electrons detection system. The scattered electrons detection system was calibrated and it showed a high resolution (matching the calculation) with respect to determing the energy. On the other hand, the scattered electrons detection system makes it possible in the experiments with a Compton bunch to mark Compton quanta with reference to energy, which offers outstanding possibilities for the experiments with a bunch of gamma-quanta at an energy range from 50 MeV up to 1.6 GeV.

The first experiments on the photo-nuclear split of heavy elements were performed on ROKK-1M together with teams from Italy and France. It was also on this setup that the experiments on measuring the energy and space resolution of the krypton prototype calorimeter for the KEDR detector were performed.

There were studied the background conditions and demonstrated the feasibility of the following experiments: a) splitting a photon in a strong Coulomb field; b) the Delbrouk scattering of a photon in a strong Coulomb field. These experiments are planned for 1995.

The elements of the ROKK-1M setup make it possible to transform it into a laser palarimeter for VEPP-4M.

A number of systems have been assembled and initially tested at the KEDR detector: the vertex detector, parts of the drift chamber, the end calorimeter, muon chambers.

In full swing is the work for obtaining the luminosity at a high energy and tuning the luminosity monitor.

IV. THE VEPP-5

The VEPP-5 complex consists of an electron and a positron linacs, a cooling storage ring, a Phi-factory and a C-tau-factory (Fig.3-5).

The task of the electron linac is to create an 300 MeV intensive electron bunch for the production of positrons. The electron linac accelerates positorns after conversion and electrons generated by the photo-gun up to an operation energy of the cooling storage ring and the Phi-factory, i.e. up to 510 MeV.

The main parameters of the preinjector are listed in Table 3.

Beam energy	510 MeV
Number of electrons per pulse	10^{11}
Number of positrons per pulse	10^{9}
Pulse repetition frequency	50 Hz
Energy spread:	
of the electron bunch	$\pm 1\%$
of the positron bunch	$\pm 3\%$
Operation frequency	2856 MHz
Pulse power of the klystron	$\sim$ 63 MW
Number of klystrons	$4+1$
Total consumed power	$\sim$ 1 MW

The design of the main elements of the preinjector has been currently completed. There have been manufacture the prototypes of accelerator section, of the subharmonic cavity, and SLED cavities. A number of RF elements have been subjected

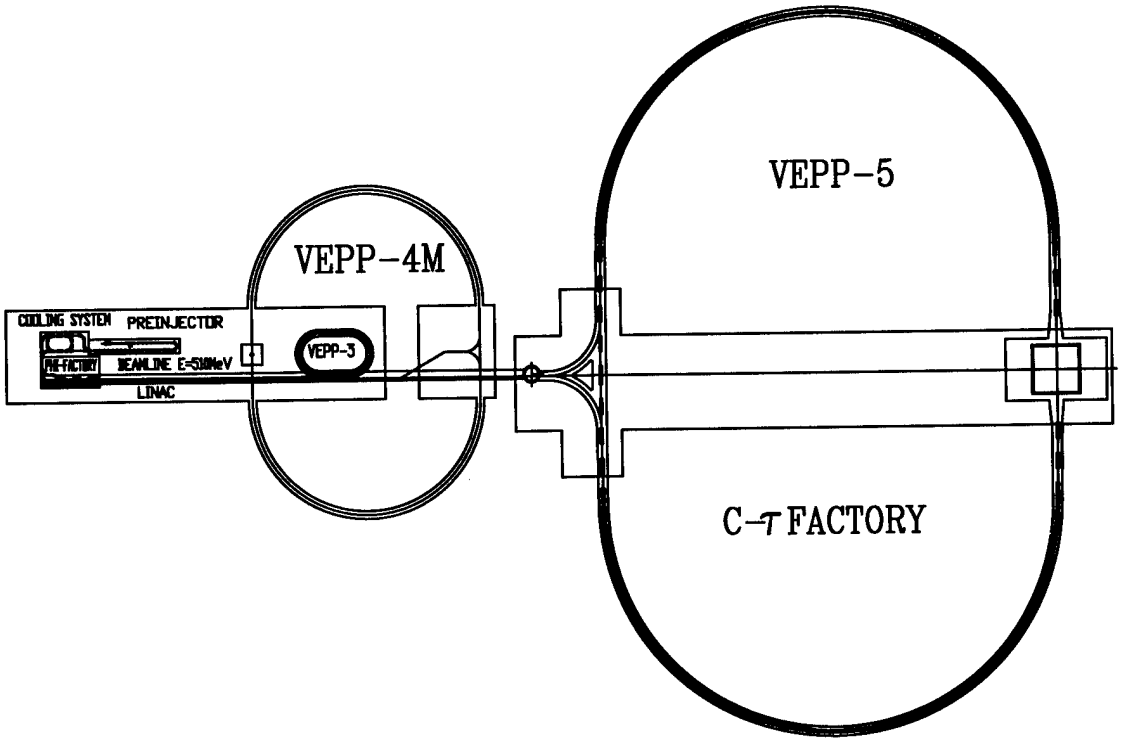


Figure 3. Layout of VEPP-5 complex

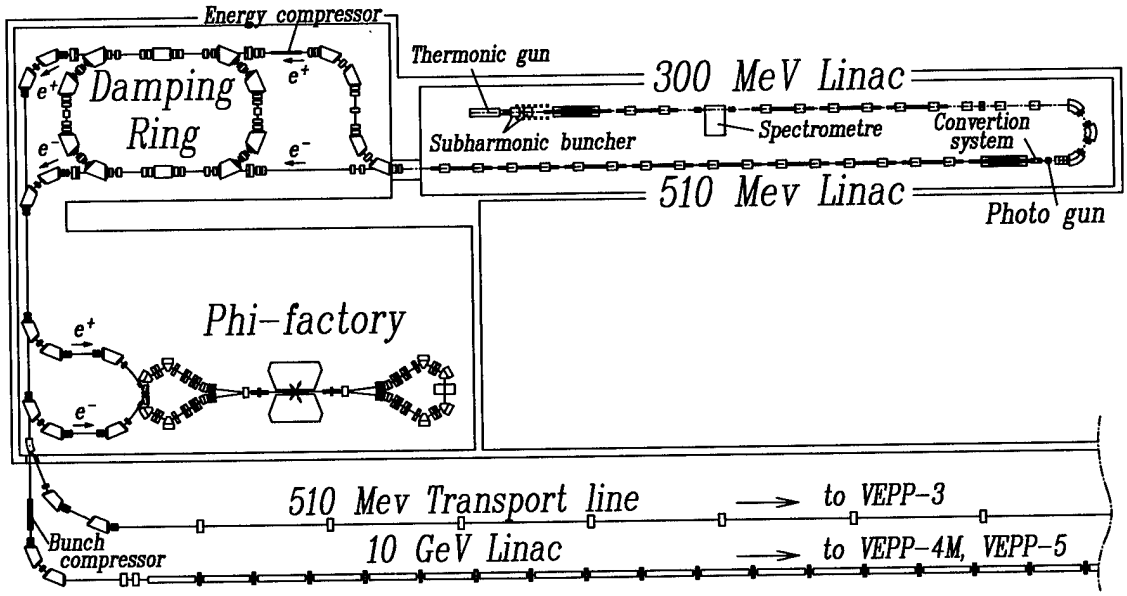


Figure 4. Layout of Injecor complex

to "cold" tests. The first 5045 klystron (product of SLAC) is delivered to Novosibirsk.

The first modulator for the 5045 klystron designed and fabricated at INP has successfully undergone the tests. The tests were performed on a resistive load. After the test run the first 5045 klystron was connected to the modulator and the required parameters, i.e. 60 mW at an RF pulse duration of 4.5 microseconds, were attained. The solution was made to manufacture the rest modulators.

V. COOLING STORAGE RING

The key elements of the ring, that is the pulse generators for injection-ejection are complete, have successfully undergon the tests, and are ready to be installed in the ring; the RF generator and the cavity are 70% complete and will be tested in autumn; the prototypes of dipoles and quadrupoles are manufactured and have been successfully tested; the magnetic system was put into production in December 1994. The yokes for the cooling storage ring and for the beam lines are 90% ready, the manufacture of the coils is delayed by December 1995 due to overlapping with con-

tractual orders. The production of the dipoles and quadrupoles for the injection complex is planned for the end of 1996.

VI. PHI-FACTORY

The Phi-factory project is currently under revision. The main principles remain the same, but in order to expedite the operation in the multi-bunch mode it is decided to separate the rings for electrons and positrons. Besides, we succeeded to reduce the field in the focusing solenoids from 11 T to 9.5 T. The present-day main parameters of the four-wing Phi-factory are listed in the below table 4:

Circumference	47.08 m
Revolution frequency	6368 MHz
Number of rings	2
Number of bunches per beam	11
Number of particles per bunch	$5 \cdot 10^{10}$
Betta-function value at IP	1.0 cm
Bending field B_0	1.79 T
Solenoidal field B_s	9.5 T
Separation field E_y	50 kV/cm
RMS bunch length	0.8 cm
Emittances, ($\epsilon_x = \epsilon_y$)	1.25 10^{-5} cm rad
Betatron tunes ν_x; ν_y	8.1; 6.1
Compaction factor alpha	-0.02...0.06
Energy loss per turn	13.5 keV
Decrements $\delta_x, \delta_y \delta_s$	1.25, 1.25. 2.92 10^{-5}
RMS Momentum Spread	4.310^{-4}
RF harmonic Number q	110
RF frequency	700.4 MHz
RF voltage V	100. kV
Synchrotron tune ν_s ($\alpha = 0.04$)	0.012
Tune shift parameter $\xi_x = \xi_y$	0.1
Beam-beam lifetime	11 min
Design Luminosity	2.510^{33}

Table.4

Schematically the four-wing Phi-factory is shown in Fig.5.

A further optimization of the storage ring parameters is presently under way.

VII. C-TAU-FACTORY

The parameters of the beam for the C-TAU-Factory are determined by the requirement of obtaining a maximum high luminosity of $1.010^{34} cm^{-2} sec^{-1}$ [3] . Along with such a maximum luminosity mode the possibility of obtaining modes of monochromatization of colliding beams is considered as well as of polarized colliding beams. For the operation in these modes it is necessary to have a beam emittance control system. Thus, for obtaining monochromatic colliding beams it is necessary, that the main contribution to the vertical size at the IP is made by the energy spread, while the vertical betatron betatron size is considerably less. For the purpose of control and in order to preserve the polarization one should have rather long solenoids with a magnetic field longitudinal with respect to the beam. As a matter of fact, one can hardly provide all these modes simultaneously, and the transition from one mode to another will be made by replacing magnetic elements in the straight sections. The contribution of arcs (half-rings) to emittances in this case should be as low as possible. In the assumption, that the RF system is used at a frequency of 700 MHz and the distance between the bunches is divisible by the length of the RF wave, one can write down the beam parameters for the ultimate luminosity in the form of Table 5:

Energy (Gev)	2.1
Circumference (m)	773.036
Ring radius (m)	89.63
Interbunch distance (m)	8.14
Straight section lenght (m)	100
Beam radius at IP (μ m)	33
Number of rings	2
Number of bunches per beam	95
Number of particle per bunch	2×10^{11}
b-function at IP (cm)	1
Beams emittance ($\epsilon_x = \epsilon_y$) (cm/rad)	10^{-5}
RMS bunch length (cm)	0.8
Compaction factor	$0.001 \div 0.0017$
Betatron tune ν_x	29.077
Betatron tune ν_y	31.077
Vertical damping time (s)	0.11
RF voltage (kV)	1000
RF frequency (MHz)	700
Energy loss per turn (keV)	100
Energy spread	5×10^{-4}
Harmonic Number	1805
Tune shift parameter $\xi_x = \xi_y$	0.1
Design Luminosity ($cm^{-2} s^{-1}$)	10^{34}

From the point of view of its geometry the C-TAU-factory is located in a tunnel, $3 \times 3m^2$ in cross section, with tunnel floor located at a level of 163 m, and the ceiling at a level of 166 m over the sea. The underground part consists of two arcs, 98.58 m in radius, and interconnected 100 m long straight sections. Here the length of an ideal orbit makes 773.036 m, which corresponds to 1805 RF wave lengths. With the same geometry, each 19th separatrix contains a bunch of particles; altogether the ring will have 95 bunches. The technical section is enlarged up to $3 \times 5m^2$ for housing the injection equipment and the magnetic systems for the emittance control. The tunnel should be enlarged towards the injection beam lines leaving a distance of 1.5 m to the internal wall, and 3.5 m to the external one. The nearest to the surface point in the tunnel is situated at a depth of 10 m, and one of the nearest and in principle accessible points is the bottom of the auxiliary channel, located 168.6 m over the sea, which corresponds to the ground thickness of 2.6 m above the ceiling of the C-TAU-Factory tunnel.

At the present moment the tunnel from the injection complex to the well from where the injection beam line of the C-TAU-Factory starts is complete. The beam line is 200 m long. The construction of these beam lines transporting the electron and the positron bunches into the injection section will be started in the nearest future. The construction is performed by the "Gornyak" company. The construction rate is mainly determined by the financial funds available. Provided the construction rate is preserved at the present level, it will take about 5 years to complete the underground part of the complex.

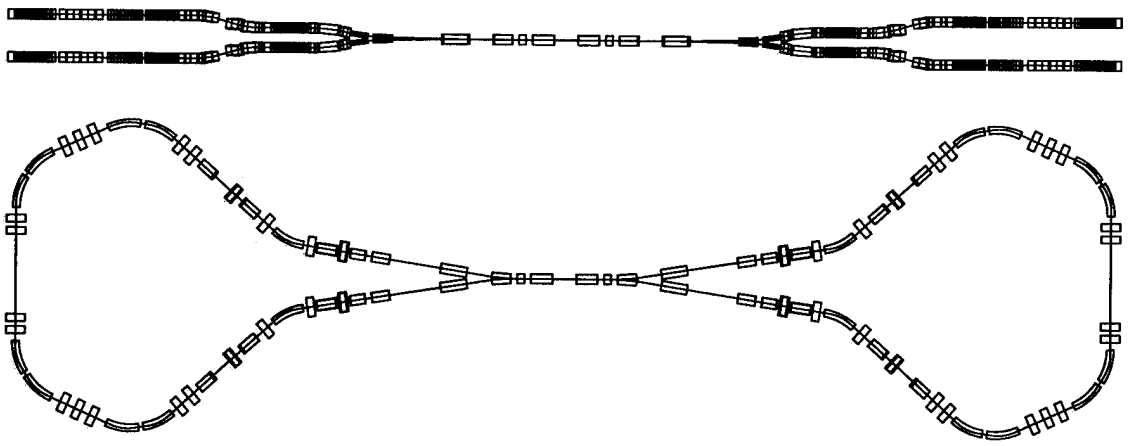


Figure 5. Layout of Phi-factory

Dedicated sections of the magnetic system should be used for the emittance control, where one can change the magnetic field. A well-known element used for this purpose is a wiggler which allows a considerable increase in the synchrotron radiation energy loss. As a rule, the psi-function in the wiggler is low, and as a result, when a strong damping is induced, the magnet does not increase the emittance too high. The magnetic system of the C-TAU-Factory consists of two storage rings, located one over the other and overlapping at the interaction point. For arranging the collision of longitudinal-polarized beams it is proposed to install spin rotators in the arcs. As an example of a particular lattice let us consider a simple system consisting of a dipole magnet, 1.5 m long, with a field of 1042 G and quadrupole lenses, each 0.4 m long, with the parameters listed in Table 6:

	Length (cm)	Field (kG)	Gradient (kG/cm)
Quad	40		1.0631
Gap	30		
Dipole	150	1.042	
Gap	30		
Quad	40		-1.0631
Gap	30		
Dipole	150	1.042	
Gap	30		

For obtaining the ultimate luminosity of the most interest is the arrangement of the interaction point with a small beta-function produced with the help of a strong longitudinal field (9.6 T and a length of 2.18 m). Having a symmetrical focusing in both directions, such a system well corresponds to the idea of operation with round beams and provides for obtaining the space charge parameter $\xi > 0.1$. The main problem in arranging the IP is the necessity of electrostatical beam separation. The total length of the plates with a field of 100 kV/cm is 2 m, and they are located in a place where the value of the beta-function is high, which incurs the problem with providing for the coherent beam stability. A stable strong electrical field under the condition of the plates exposure to the synchrotron radiation also presents a serious problem.

References

[1] Barkov L.M., et al. *PHI- Factory Project in Novosibirsk* Proc. of the 14-th Int. Conf. on High Energy Acc., Tsukuba, Japan, 1989, p.1385

[2] Filippov A.N., Ivanov P.M., Koop I.A., *Proposal of the Round Beam Lattice for VEPP-2M Collider* Proc. of the 15-th Int. Conf. on High Energy Acc., Humburg, Germany, 1992, p.1147

[3] Dikansky N.S., at el. *Status of the VEPP-5 Complex*, Proc. of EPAC94, London, 1994, p.482

BEPC Status and Plans

Shu-Hong Wang of BEPC Group
Institute of High Energy Physics, Chinese Academy of Sciences
P. O. Box 918, Beijing 100039, China

ABSTRACT

BEPC operation status over the past years with the results in exciting physics and integrated luminosity enhancement are summarized. The status of the luminosity upgrade project is described. The future plans on tau-charm factory and new generation light source are presented.

1. OPERATION STATUS

The Beijing Electron Positron Collider (BEPC) [1,2] has been well operated for about 6 years since 1989, serving for High Energy Physics (HEP) as a collider and for Synchrotron Radiation Research (SR) as a light source. It operated 5500 ~ 6000 hrs. each year. The typical operation statistics in a year (e.g. 1994) for HEP, SR, machine study (MD), injection (INJ), recovering & commission (RC) and failure time is listed in Table 1, showing the operation efficiency is higher than 90%.

Table 1. Statistics of BEPC operation in 1994

	HEP	SR	MD	INJ	RC	FALL	Total
Time (hrs)	1928	1182	847	741	818	292	5808
Percent-age	33.2%	20.4%	14.6%	12.8%	14.0%	5.0%	100%

In the HEP runs, due to the high luminosity and the reliable operation, BEPC cooperated with the detector Beijing Spectrometer (BES) has acquired a plenty of data, as shown in Table 2, in which the main operation parameters (Energy, Current, Peak luminosity and the average luminosity per day) are also listed.

Table 2. Operation parameters and acquired data

	J/ψ	$\tau^+\tau^-$	ψ'	$D_s(D_0)$
Energy (GeV)	2×1.548	2×1.777	2×1.843	2×2.015
Max. current (mA)	50	55	60	65
Max. lumi. ($10^{30}cm^{-2}\cdot s^{-1}$)	3 - 4	4 - 5	5 - 6	5 - 7
Int. Lumi. or Event per day	100 K/day	120 nb^{-1}	107 nb^{-1}	161 nb^{-1}
Total Event or Int. Lumi.	9×10^6	4.74 pb^{-1}	3×10^6	23.5pb^{-1}

BEPC/BES is an unique machine which has operated in the tau-charm energy region, and fortunately it has obtained a lot of important experimental results and exciting physics, among which are:

* Having more precisely measured τ lepton mass as [3]

$$m_\tau = 1776.9 \pm 0.2 \pm 0.2 \text{ MeV}$$

It is furthermore precise in statistical error than the one we firstly measured in 1992 by fitting data with likelihood method using more events and more decay modes, and furthermore tend to fit the lepton universality.

* Having confirmed the existence of the ξ(2230), and have discovered its very important new decay modes, $\xi(2230) \to p\bar{p}$ and $\xi(2230) \to \pi^+\pi^-$ with vary narrow decay widths, which is a big progress in understanding its nature and it looks very like a glueball.

In the SR runs, BEPC co-operated with Beijing Synchrotron Radiation Facility (BSRF) has also obtained the rich experimental results in the past years since 1991. About 1000 hrs. and 3500 hrs. beam time per year in dedicated and parasiticmodes respectively are provided to about 80 users units from institutes and universities in China. In the dedicated SR mode, BEPC is operated at 2.2 GeV and 30 ~90 mA with the small horizontal emittance of 70 nm-rad.

In the progress of serving for HEP and SR, BEPC itself has been improved with maintains and machine studies. The main characterization of the improvements is the raise of the integrated luminosity. Table 3 and Fig. 1 show the statistics of BEPC operation at D_s energy (2.015 GeV per beam) in 1992--1994 [4], in which the integrated luminosity per day was significantly increased from 97 nb^{-1} in 1992 to 161 nb^{-1} in 1994, that is with an enhancement factor of 1.65. The main contribution to this enhancement were made by following factors:

Table 3 Statistics of Operation at D_s energy (2.015 GeV) in 1992--1994.

Year	Working days	I_{ini} (mA)	L_{ini} ($10^{30}cm^{-2}\ s^{-1}$)	L_{int}/day (nb^{-1})	L_{int} total (pb^{-1})
1992	68	60.7	5.3	97	6.6
1993	85	56.0	4.0	110	9.3
1994	108	67.0	5.6	161	17.6

* The tunes were optimized and the injection conditions were improved as possible.

* Some beam instabilities related to RF cavities were suppressed by using the HOMs coupler in the BEPC cavities.

* By improving the vacuum situation and the fast protection for RF windows.

* All of the magnets in the ring have been carefully realigned in the summer-shutdown periods, after that much

0-7803-3053-6/96/$5.00 ©1996 IEEE

better closed orbit was obtained and the background was improved.

* By improving the linac operation, e.g. stability and reliability of klystron modulators, so that the injector operation efficiency has been risen.

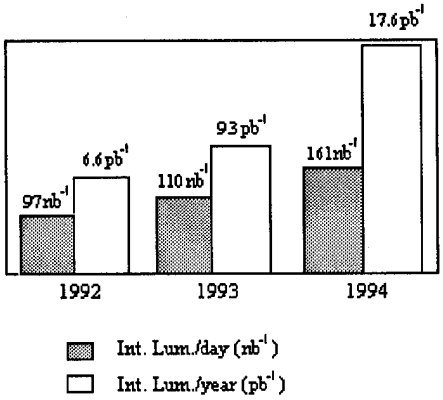


Fig. 1 Integrated Luminosity at Ds energy

2. UPGRADE STATUS

The rich opportunities of high energy physics in BEPC energy region and the exciting physics results obtained with BES encouraged us to upgrade the BEPC luminosity, even though the realized luminosity of 6×10^{30} $cm^{-2}\cdot s^{-1}$ at 2.0 GeV is already met with the design goal. The actions of the upgrade project involve:

* Luminosity upgrade by mainly using mini-β optics, and by using single interaction point collision and by beam emittance control
* Linac energy upgrade
* Control system upgrade and
* Reconstruction of the Detector (BES-II)

The upgrade plan was firstly discussed in 1990. In June of 1991, the workshop on BEPC luminosity upgrade was held in IHEP, and 14 foreign experts were invited to participate this workshop. In May of 1992, IHEP sent an official proposal to the Chinese Academy of Science (CAS), and then to Chinese Government. Finally the upgrade project was officially approved in May of 1993. Since then the project is going well, even facing some technical difficulties.

2.1 Mini-β Optics

The most effective way to get a significant gain of luminosity is to use the mini-β optics. Since keeping the beam current constant, the luminosity is inverse proportional to the vertical β function at interaction point β_z^* in the case of optimum coupling between horizontal and vertical motions.

In the routine operation with low-β optics in BEPC the β_z^* is 8.5cm, and in the primary design of the mini-β optics, β_z^* of 3.6 cm was chosen [5] by using a pair of permanent quadruples which installed inside the detector and very near the interaction point (say 1.3 m away from the IP), as shown in Fig.2.

The most crucial factor for the mini-β optics in BEPC, having a ring with lower energy of 2.0 GeV and smaller circumference of 240 m, is bunch length σ_l and its lengthening. In the routine operation of BEPC the ratio of β_z^*/σ_l would be about 1.2, which makes higher luminosity and better signal to noise ratio. It means the σ_l should be about 3.0 cm in the mini-β optics, while at present σ_l is about 5 ~7 cm.

To shrink the bunch length to about 3.0 cm, a method of having higher RF voltage in the cavities was chosen. By adding two cavities (used in SPS, CERN) and re-grouping the available RF power supplies, together with two BEPC cavities, a total RF voltage of 2.4 MV can be expected. With this mini-β scheme, the luminosity gain factor of 2 ~ 3 was expected.

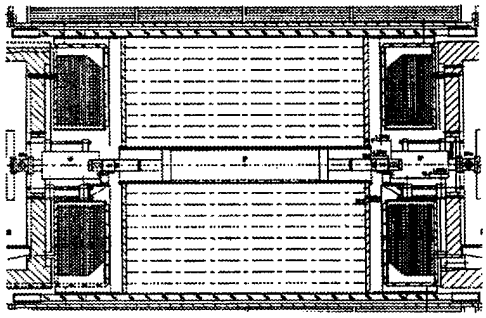


Fig. 2 Mini–β QP in Detector

To measure the real bunch length with higher RF voltage is the most important issue in examining the BEPC mini-β scheme. As the first SPS cavity was put into operation, and the higher RF voltage of 1.5 MV was obtained in the Autumn of 1993, a great number of bunch length data with different RF voltage, different beam energy and currentwere obtained by using streak camera and simultaneously by using beam spectrum analysis method. By fitting all of the measured data, we obtained the scaling law of the bunch length in BEPC storage ring: [6]

$$\sigma_l(cm) = 0.404\left[\frac{I_0(mA)\alpha_p}{E_0(GeV)\upsilon_s^2}\right]^{1/2.80}$$

By this scaling low one find that for E_0 = 2.0 GeV, V_{rf} = 2.0 ~ 2.4 MV and I_b = 35 mA (as the same as in routine low-β operation) then σ_l will be 4.2 ~ 3.9 cm, which is longer than the previously estimated one. If the optimum β_z^*/σ_l is still about 1.2, then the corresponding β_z^* is about 5cm, which is larger than the design value. With β_z^*= 5cm, the luminosity gain factor is only about 1.7.

If one increase the beam current upto 46 mA, which meets the saturated beam-beam parameter $\xi_z = 0.04$, then in the case of $\beta_z^* = 5$ cm, the luminosity gain factor could be reached to about 2, even though the bunch length will be increased to 4.5 cm.

Since the designed BEPC lattice is reliable and flexible, the calculation with $\beta_z^* = 5$cm optics has shown [7] that without adding any hardware in BEPC the $\beta_z^* = 5$cm optics can be reached just by moving the insertion quadruples Q1 and Q2 towards to the interaction point by a distances of 37 cm and 47.7 cm respectively, and a better dynamic aperture can be also obtained.

To finally realize the mini-β optics in BEPC, we should furthermore compress the bunch length, for which one of the possible way is by decreasing the longitudinal coupling impedance of the storage ring. The calculation and mea-surements on impedance with different elements in BEPC have shown that the 4 kickers and 40 bellows made the main contributions to ring impedance. Collaborated with Tsing-hua University a special group has been organized to furthermore study the precise measurement and impro-vement on impedance. The primary results have shown that with the improved bellow, its impedance can be reduced from 0.06Ω to 0.017Ω/each, and with slotted kickers, its impedance can be reduced from 0.35 to 0.074Ω/each [8], so that their contribution to the ring impedance could be reduced by a factor of 3 ~5. We have to make more effort on trying to reduce the ring impedance with machine study and finally realize the mini-β scheme in BEPC.

The mini-β permanent magnet, made of NdFeB, has the length of 500 mm and the field gradient of 8T/m. It consists of 10 magnetic rings longitudinally, and each ring consists of 24 magnet pieces. This configuration makes the harmonic components of magnet much small. The prototype of single-ring and double-ring have been made, and the measured harmonic contents after tuning are about a few of 10^{-4} [9].

The two SPS cavities have been put into operation in the Autumn of 1994. Together with two BEPC cavities, the total RF voltage of four cavities in the operation can be reached to 2.0 MV. The two additional power supplies for Q1 and Q2 were prepared for the mini-β scheme and for the study on single interaction point.

2.2 Linac Energy Upgrade

The linac offers the electron and positron beams with the energy of 1.3 GeV into the storage ring at present. The beams with higher energy from the linac will make the injection more effective. The linac has 16 Klystrons with the average RF output of about 19 MW each in routine operation, and has 13 energy doubles with the energy multiplication factor of 1.4 each.

The procedure of the linac energy upgrade includes[10]:

* Replacing three sets of old Klystrons and old modulators by new constructed 65 MW Klystron and 150 MW modulators. With careful consideration to reliability and EM compatibility, the prototype of the new modulator has been designed and constructed. The measured voltage output shows that it meets with the design requirement. A 3.7 μs wide pulse with 354 kV voltage and 430 A peak current were successfully generated [11]. Other three new modulators have also been fabricated. The prototype of the new Klystron has been made in China and delivered to IHEP in February 1995. The primary test of the new Klystron is being tested on the new constructed test station [12]. Other three new Klystrons are being constructed.

* Increasing the RF pulse width from 3.0 μs to 3.5 μs or more wider so that higher energy multiplication factor can be achieved.

Totally the linac energy will be increased to 1.75 GeV, which can make the full energy injection into ring for J/Ψ and $\tau^+\tau^-$ experiments.

2.3 Control System Upgrade

The BEPC control system has been running safely and reliably for 40,000 hours since it was built at the end of 1987. But the original control system was proved to be undesirable in many aspects, such as low CPU power, limited memory of the VAX/750 control computer and some other hardware problems.

The upgrade of the control system is to transform this system into a distributed one based on DECnet to make it faster in response and more reliable in performance. The new control system is shown in Fig.3.

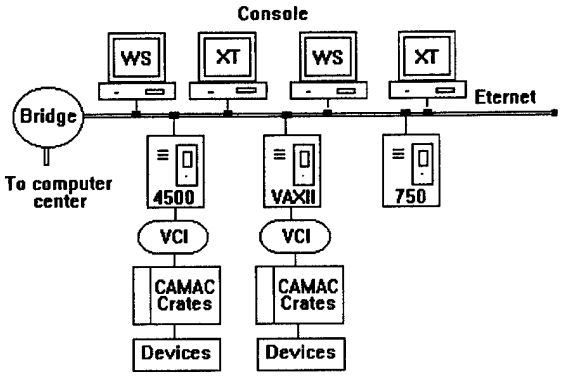


Fig. 3 Upgraded control system structure

With two VAX4090 workstations appended on DECnet used as the new console, the old one and its adapter Grinnell are eliminated. The VAX4500 and Micro VAXII computer are connected with DECnet to carry out the real time control. Replacing VAX750 and the VCC with the Qbus/CAMAC adapter interface, both VAX4500 and VAXII can independently control all BEPC equipment.

The upgrading was carried out without interrupting the normal operation of BEPC, therefore all of the low level CAMAC system have not been changed. A lot of software development have also been done to meet with the upgrade requirement.

The upgrade of BEPC control system has been finished and thenew system was put into use in October 1994[13]. Now, the new BEPC console is a friendly man-machine interface. We use two workstations and two VAX computer systems as on-line control, the system is much more reliable. The CPU power and memory resource have also been increased, so the response time is shortened.

3. FUTURE PLANS

3.1 Tau-Charm Factory (τCF)

Even though there were four τCF workshops in the world since 1989 to 1993, to confirm the necessity and the feasibility of a τCF in existence of two B-factories in the world an international τCF workshop [14] was held again at Stanford, California in August 1994. The meeting has concluded that:" In certain basic areas of particle physics, such as the search for glueballs, possible CP violations in lepton system and the charmonium structure, the τCF provides an unique facility". Since such searches can only be precisely made near their production threshold with a τCF. The meeting also encouraged us to construct a τCF in future at IHEP, Beijing in the frame of international collaboration.

A primary design of a τCF in Beijing has been made [15]. It is a two-ring, one collision electron-positron collider with a design luminosity of 10^{33} $cm^{-2}\cdot s^{-1}$ and an energy range of 3 ~ 6 GeV. Its construction can be carried out on the site of the existing IHEP complex and very near the BEPC as shown in Fig.4, and it can use the existing linear accelerator injector.

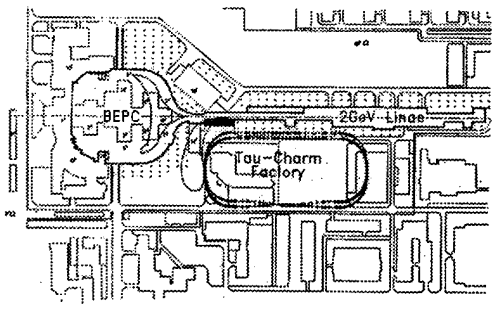


Fig.4 Layout of Beijing τCF

The performance comparison between τCF and BEPC is as shown in Table 4. The main ways to approach the τCF luminosity from the one of BEPC are probably as follows:

* By using a multi-bunch scheme to reach the beam current of 550 mA in τCF, which has a current enhancement factor of 13.75.

* By using a micro-β scheme, so that the β_z^* is 1 cm in τCF, which is 1/5 of the one in BEPC.

Table 4 The comparison between τCF and BEPC

	BEPC	τCF
Number of bunches	1	32
Bunch separation (m)	240.4	11.48
Particles per bunch	2.16×10^{11}	1.32×10^{11}
Bunch current (mA)	40	17.16
Current per beam(mA)	40	550
β- function at IP (cm)	5	1
Bunch length (cm)	4.5	1.0
B-B parameter	0.04	0.04
Luminosity($cm^{-2}\cdot s^{-1}$)	1.5×10^{31}	1.0×10^{33}

So that the total luminosity enhancement factor of 68.75 could be achieved. The construction of Beijing τCF, as the same as CERN design [16], would probably have following three phase program: 1) Standard phase, conventional design with high luminosity at the energy of τ-lepton production threshold. 2) Monochromatic phase at the energy of J/Ψ resonance, with low emittance and a non-zero vertical dispersion at IP, to study the CP-violation. 3) Longitudinal polarization phase, combined with monochromatic collision. For the first two phases, the primary parameters are listed in Table 5.

Table 5 Primary parameters of Beijing τCF

	Standard	Monochromator
Beam energy (GeV)	2.0	1.5
Circumference (m)	367.5	367.5
β_x^*/β_z^* (m)	0.2/0.01	0.01/0.15
Dispersion at IP (m)	0.0	0.35
Momentum compaction	0.022	0.008
Natural emittance (nm)	251	10 (J_x=2)
Energy spread (10^{-4})	5.4	8.0
RF frequency (MHz)	499.58	499.58
RF voltage (MV)	9.0	9.0
Number of bunches	32	32
Current/beam (mA)	550	215
RMS bunch length (cm)	1.0	0.78
B-B parameter (hr)	0.04/0.04	0.031/0.015
Beam life time (hr)	4.8	1.5
CM energy spread (MeV)	1.53	0.105
Luminosity ($cm^{-2}\cdot s^{-1}$)	1×10^{33}	2.2×10^{32}

The design and construction of the τCF should be started with a long term R&D, since it faces a lot of serious challenges in the performance and techniques required both in accelerator and detector. The cost estimation to construct the Beijing τCF is about 120 million USD, a quite big amount for China. Therefore IHEP should make its great efforts, with the national and international collaboration, to prepare this project both in technical and economical aspects. Fortunately the feasibility research of the Beijing τCF was officially approved by Chinese government recently, which will take one and an half year,

making a conceptual design of the Beijing τCF as well. Then it might be followed by a three or four year's R & D. The construction project is expected to start around 1999.

3.2 The New Generation Light Source

Currently the BEPC dedicated SR operation time is only about 20% of the total one, but above 80 users need about 10 ~ 20 times more for their interested experiments. On the other hand, for the parasitic mode it is not easy to well operate the BEPC both as a collider and a light source.

Due to these reasons, a proposal to construct a third generation light source in China [17] (say CLS) is being made at IHEP. The CLS could be built by converting the existing BEPC to a fully SR facility if the Beijing τCF will be constructed in the east side of BEPC, or by constructing a fully new storage ring in the west side of BEPC, and the existing linac can be used as the injector. The another possibility is to construct the CLS in Shanghai, if it could be co-supported by Shanghai city, which is being also discussed recently.

Some principles of designing the CLS have been consi-dered as follows:

* The energy of CLS will be 2.0 ~2.5 GeV, so that will be in median size (190 ~ 250 m in circumference) compared with 0.8 ~1.0 GeV and 6 ~ 8 GeV machines.

* It uses two kinds of bending magnets. One is the conventional magnets with the field of 1.0 ~1.3 T, which produce the photons with the energy of 2.5 ~ 25 keV. Another one is the superconducting magnets, located in the middle of some magnetic periods, with the field of 4 ~5 T, so that the photon's energy will be 10~60 keV, which is equivalent to the one produced from a light source of 5~6 GeV. Therefore the CLS will cover the full spectrum.

* It has two super-straight sections (say about 15 m long each), which remain the rooms behind to develop the new kind of light source, combined probably with free electron laser.

The primary design of the CLS is being made [18]. The Lattice of FBA with 8 periods is preferred to get very small beam emittance (≤5 nm·rad) and enough dynamic aperture as well. In each period there are five bending magnets. In the four periods, there is a superconducting bending magnets in the middle of each period. Due to very small beam emittance, high beam current (~300mA) and well performed insertion elements (undulators and wigglers) in the straight sections, one can get the lights from CLS with the high brightness of 10^{15} from bending magnets, 10^{16-17} from wigglers and 10^{19-20} ph/s·mm^2·mrad^2·0.1% BW from undulator.

The CLS-proposal is going to the Chinese Government, with a proposed schedule of having a two year's R & D and followed by a five year's construction period.

4. CONCLUSION

The BEPC has been well operated for about 6 years. In the HEP runs, due to the high luminosity and reliability BEPC co-operated with the detector BES has acquired a plenty of data and obtained a lot of exciting physics. In the SR runs, BEPC co-operated with BSRF has also obtained the rich experimental results in the different scientific areas. BEPC itself has been improved as well on its integrated luminosity.

The luminosity upgrade project of BEPC, including mainly use of mini-β optics, linac energy upgrade, control system upgrade and reconstruction of the detector, is going well, even facing some technical difficulties. A luminosity gain factor of 1.5 ~ 2.0 is expected in the coming years and of 3.0 ~ 4.0 is also planed in the near future by improving the ring impedance and others.

For the future plans, the Beijing Tau-Charm Factory and the Chinese new Light Source are being proposed.

REFERENCES

[1] S.X.Fang and S.Y.Chen, Proc. 14-th Int. Conf. on High Energy Acc.(1989)51.

[2] C.Zhang of BEPC Group, Proc. 15-th Int. Conf. on High Energy Acc.(1992).

[3] BES Group, High Energy Phys. and Nucl. Phys. 19(1995).

[4] Y.Z.Wu, Internal Report.

[5] Y.Z.Wu et al., Proc. Workshop on BEPC Luminosity Upgrade (1991)184.

[6] Z.Y.Guo, D.K.Liu, Q.Qing, W.R.Liu et al., Internal Report.

[7] Q.Qing et al., Internal Report.

[8] Y.D.Hao, Z.T.Zhao, F.Zhou, G.W.Wang et al., Internal Report.

[9] Z.S.Yin, Y.Yang et al., Internal Report.

[10] J.Wang, Proc. 1994 Int. Linac Conf. (1994).

[11] Q.Han, Internal Report.

[12] D.C.Lin, Internal Report.

[13] J. Zhao et al., Nucl. Instr. and Method in Phys. Res., A352(1994).

[14] Z.P.Zheng, T.Huang et al., Internal Report.

[15] L.H.Jin et al., to be presented in this conf.

[16] J.M.Jowett, CERN SL/93-23 (AP).

[17] D.Z.Ding,S.X.Fang and D.C.Xian, Internal Report.

[18] D.Wang et al., to be presented in this Conf.

The first attainment and the routine use of longitudinal spin polarization at a high energy electron storage ring

D.P. BARBER *
for the HERA Polarization Group
Deutsches Elektronen–Synchrotron, DESY, 22603 Hamburg Germany

Abstract

The HERA electron ring is the first and only high energy electron storage ring at which longitudinal spin polarization has been obtained. This paper describes the spin rotators, the optical set up, the first observation of longitudinal polarization and the plans for its routine exploitation.

I. Introduction

An integral part of the design of the HERA *ep* collider [1,2] has been the provision of longitudinally spin polarized electrons for the high energy physics experiments at the interaction points. Stored electron beams can become vertically polarized due to the emission of spin flip synchrotron radiation–the Sokolov-Ternov (S-T) effect [3]. The maximum polarization achievable is 92.4% corresponding to a planar ring. To provide longitudinal polarization at an interaction point the naturally occuring vertical polarization in the arcs must be rotated into the longitudinal direction just before the interaction point (IP) and back to the vertical just after the IP using special magnet configurations called spin rotators.

Synchrotron radiation not only generates polarization but can also cause depolarization [4]. This is especially the case in the presence of spin rotators. Furthermore the ratio: (depolarization rate/polarization rate) increases strongly with energy. However, the depolarizing effects can in principle be minimized by special choice of the optic called 'spin matching'. Nevertheless, owing to the difficulty of obtaining reliable numerical predictions of the polarization in the presence of rotators throughout the preparatory stage of the project and because of the initially very pessimistic predictions, it was by no means clear that longitudinal polarization could be obtained even after spin matching.

II. The spin rotators.

Dipole spin rotators exploit the prediction of the Thomas-BMT equation [5] for spin precession that for motion transverse to the magnetic field, the spin precesses around the field at a rate which is $a\gamma$ faster than the rate of rotation of the orbit direction. Here, $a = (g-2)/2$ where g is the electron g factor. Thus

$$\delta\theta_{spin} = a\gamma\delta\theta_{orbit} \qquad (1)$$

in an obvious notation. At HERA energies $a\gamma$ is between 60 and 80. So it can be arranged that small commuting deflections of the orbit can result in large noncommuting precessions of the polarization vector. For HERA, the Mini-Rotator design of Buon and Steffen [6] was adopted. In the Mini-Rotators the rotation is achieved by interleaving three horizontal bends with three vertical bends. See figure 1 which shows the ordering of the magnets and the spin precession angles for the chosen running energy of 27.52 GeV. The orbit bend angles are of the order of 10 mrads and the horizontal bends replace the bend angle of one arc cell. The whole rotator is inserted into the end of the arc with minimum disturbance to the rest of the machine. The total vertical bend of this rotator is zero and it is only 56 m long so that no quadrupoles need be included among the constituent dipoles. The vertical orbit excursion is about 20 cm. The required rotator dipole fields and hence the shape of the rotator depend on the energy chosen. By mounting the dipoles on coupled, remotely controlled mechanical jacks and by having flexible joints between sections of vacuum pipe, it is possible to tune the rotator to give the correct spin transformation over the range 27-35 GeV and to obtain both helicities. The vertical bumps in a pair of rotators are antisymmetric with respect to the IP. The first two rotators were installed on either end of the East straight section at the beginning of 1994 so as to provide longitudinal polarization for the HERMES experiment which uses a polarized internal gas target to study the deep inelastic spin structure of nucleons. Figure 2 is a sketch indicating the positioning of the rotators in the HERA ring and the azimuthal spin axis variation. At the chosen energy of 27.52 GeV, the S-T polarization level is reduced below 92.% to about 89% with one pair of rotators by the presence of the vertical bend magnets. This energy corresponds to a fractional spin tune of 0.5 and is thus maximally distanced from resonances. See equation 2.

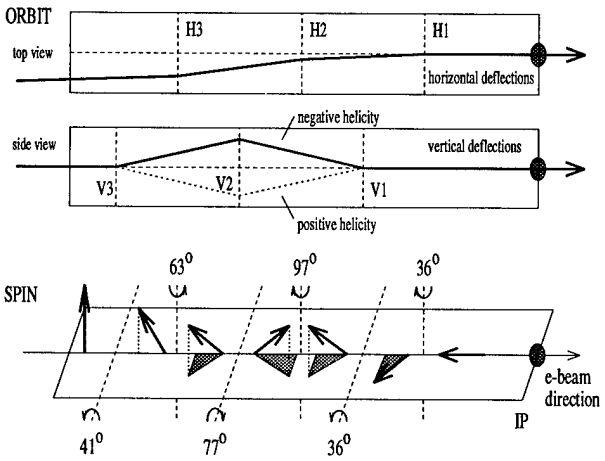


Figure. 1. Layout of the Mini-Rotator bends and the consequent spin configuration at 27.52 GeV.

*e-mail: mpybar@desyibm.desy.de

0-7803-3053-6/96/$5.00 ©1996 IEEE

III. The optics.

In addition to the S-T effect producing the polarization, there can be spin diffusion i.e. depolarization due to the stochastic excitation of the electron orbits by emission of synchrotron radiation photons. The depolarization is especially strong if the resonance condition

$$\nu = k + m_x Q_x + m_z Q_z + m_s Q_s \qquad (2)$$

is satisfied where k, m_x, m_z, m_s are integers, the $Q_{x,z,s}$ are orbital tunes (47.1,47.2 and 0.06 resp.) and ν, called the spin tune, is the number of spin precessions per turn on the closed orbit.
In perfectly aligned planar rings the equilibrium spin axis is vertical, the beam would have almost zero vertical emittance and the depolarization would actually almost vanishe.
But in real rings with their typical misalignments, the closed obit is distorted and the equilibrium spin axis defined along the closed orbit is tilted from the vertical and the spin diffusion can then take hold [1,4]. This depolarization has been successfully combatted by the application of harmonic spin-orbit corrections [1] using special families of closed bumps to return the equilibrium spin axis to the vertical.
However, the installation of spin rotators can result in additional strong depolarization even in an ideal ring. One reason is that between the rotators the spin axis is horizontal and can be considered to be maximally tilted. Another reason is that there is local vertical dispersion inside the rotators so that synchrotron radiation emission in the rotators excites vertical betatron motion. In principle these two consequences of the presence of rotators can, in HERA, be largely eliminated by a special choice of optics called 'strong spin matching'. This consists of arranging the quadrupole settings so that the 2 x 6 matrix describing the coupling of the spin to the orbit in linear approximation vanishes in the section between the rotators straddling the interaction point and in the remainder of the ring [1]. Since the rotators contain no quadrupoles, spin matching inside the rotators is not needed. A spin matched section of ring is said to be 'spin transparent'. As well as minimizing these matrices, the usual optical properties of the machine must be acceptable. At HERA, it has been possible to satisfy these requirements by giving every mirror symmetric pair of quadrupoles in the section between the rotators and in the first seven cells at the beginning of each arc its own power supply.

IV. The first tests.

In the years up to 1994 it had become routine to have obtain over 60% vertical polarization (measured using a Compton polarimeter in the West area– see figure 2)[1]. The first test of the rotators took place in May 1994 with electrons. After achieving about 65% vertical polarization with the vertical bends off and the rotators 'flat', by the usual application of the harmonic spin-orbit bumps, the rotators were activated and a beam was stored without additional orbit adjustment. Then without further ado the polarization as measured at the West area polarimeter rose according to the expected exponential law [1]

$$P(t) = P_\infty \left(1 - e^{t/\tau_{pol}}\right) . \qquad (3)$$

to about 56%. See figure 3. Note that the *value* of the polarization is the same everywhere in the ring but the direction can be changed by rotators. Since a tilt of the polarization vector by more than a few tens of milliradians in the arcs would lead to very strong depolarization we conclude that we had achieved longitudinal polarization at the East IP.

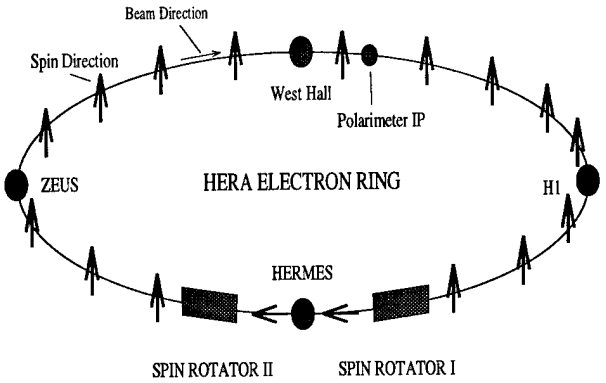


Figure. 2. The locations of the rotators in the ring

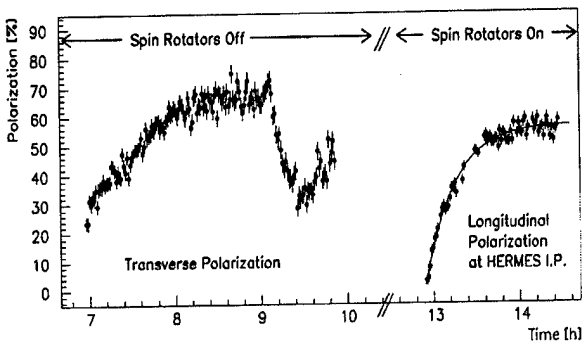


Figure. 3. Longitudinal polarization vs. time (hours) with electrons in May 1994. The dip after 09.00 was due to further attempts at optimization.

This was the first time in the history of high energy storage ring physics that longitudinal spin polarization had been achieved and demonstrated that, with suitable spin matching, it is indeed possible to rotate spins at the machine circulation frequency of 47.35 kHz and in a strongly stochastic environment. In the following days, after further machine optimization, a longitudinal polarization of about 65% was reached consistent with simulations from the Monte-Carlo spin tracking program SITROS [7].

In November 1994 about 65% longitudinal polarization was obtained with positrons.

These measurements with the rotators turned on were made without *ep* beam-beam interaction at the North and South IP's occupied by the experiments H1 and ZEUS (See figure 2). Measurements made in 1994 with the rotators off showed that with up to 40% of design luminosity (beam-beam electron tune shifts of about 0.02) there was no clear degradation of the vertical polarization. This is also consistent with simulations by SITROS [8].

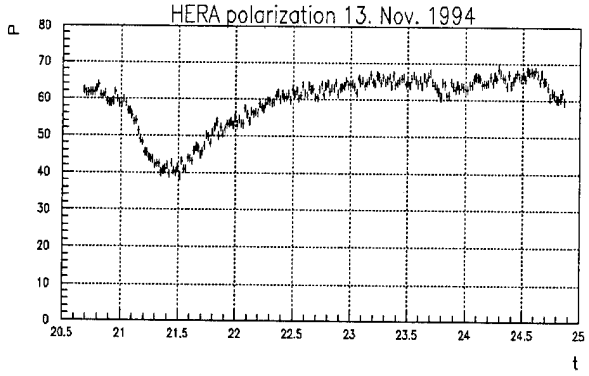


Figure. 4. Longitudinal polarization vs. time (hours) with positrons in November 1994. The dip at 21.30 was due to further attempts at optimization.

V. Plans for 1995.

HERA is now coming online for the 1995 luminosity run and HERMES also. This will be the first time that a physics experiment on a high energy electron storage ring is supplied with longitudinal polarization. SITROS simulations indicate that at full luminosity there could be beam-beam depolarization[8]. In that case extra spin matching will be needed and an algorithm has been prepared. It might also be necessary to increase the vertical emittance by introducing a vertical dispersion bump. The latter can also cause depolarization and the so called 'vertical harmonic dispersion matching' based on the generation of extra dispersion bumps [9] will be needed. Another major source of depolarization is of course the closed orbit distortion. A large reduction in the effect of the latter is expected with the implementation of the beam based calibration of the monitor positions [10]. SITROS simulations suggest that a longitudinal polarization of 80% could then be achieved in the absence of beam-beam effects.

VI. Conclusion and outlook.

At HERA a major milestone in the science of radiative spin polarization in storage rings has been achieved. In 1995 we will supplying longitudinal polarization to an experiment on a regular basis. Two more pairs of spin rotators are in manufacture and will be installed in the '96-'97 shutdown to provide longitudinal polarization for H1 and ZEUS.

VII. Acknowledgements

The author would like to thank colleagues of the HERA polarization group for helpful discussions.

VIII. References

1. Barber,D.P., et al., Phys.Letts.,**B343** (1995) 436.
2. Brinkmann.R., Talk PAC95, HERA Status and Plans.
3. Sokolov,A.A.,Ternov,I.M., Sov.Phys.Dok,**8** (1964) 1203.
4. Barber,D.P.,*Proc.10th Int.Symp.High Energy Spin Physics*, Nagoya,Japan,1992.
5. Thomas,L., Philos.Mag., **3** (1927) 1.
   Bargmann,V.,Michel,M.,Telegdi,V.L., Phys.Rev.Lett., **2** (1959) 435.
6. Buon,J.,Steffen,K.,Nucl.Inst.Meth., **A245** (1986) 248.
7. Böge,M., DESY Report 94-87 (1994).
8. Böge,M.,Limberg,T., Poster session PAC95.
9. Gianfelice-Wendt,E., Private communication.
10. Böge,M.,Brinkmann,R.,4th Euro.Part.Acc.Conf.,London (1994).

EXPERIMENTS WITH BUNCH TRAINS IN LEP

O. Brunner, W. Herr, G. von Holtey, E. Keil, M. Lamont, M. Meddahi, J. Poole, R. Schmidt, A. Verdier, C. Zhang, CERN, Geneva, Switzerland

Abstract

During 1994 tests were made to evaluate the possibility of operating LEP with four equidistant bunch trains in each beam during 1995. A train will consist of up to four bunches with a bunch spacing of some 75 m. The bunch trains collide head-on. They are separated at the parasitic collision points on either side of the interaction points by vertical electrostatic separator bumps. The accumulation of bunch trains in a single beam was studied with magnetically simulated bumps. Following the installation of additional separators late in 1994, the parasitic encounters of the bunch trains near the interaction points were studied for one train of electron bunches colliding with one train of positron bunches in two diametrically opposite interaction points. The higher-order mode losses in the superconducting RF cavities were measured for several arrangements of beams, trains and bunches. The synchrotron radiation background, enhanced by the off-centred beams in the quadrupoles inside the separator bumps, is reduced by super-imposing asymmetric magnetic bumps such that the offset of the incoming beams is reduced.

I. INTRODUCTION

Bunch trains have been considered for the CESR storage ring at Cornell University since 1990 [1], and are now used in operation [2]. Thereafter, bunch trains with a horizontal crossing angle were proposed for LEP [3]. Tests in 1993 revealed insurmountable difficulties with the synchrotron radiation background, caused by the off-centred beams in the quadrupoles next to the LEP detectors [4]. A proposal [5] which overcomes this particular difficulty is described and the results of tests in 1994 are presented. The main changes are an increase of the bunch spacing and a vertical separation scheme which starts beyond the quadrupoles next to the LEP detectors. The orbital effects and background were studied with magnetic bumps, using vertical correctors. With up to four trains in a single beam, possible bunch current limitations, due to collective effects and higher-order mode losses in superconducting RF cavities were investigated. During several technical stops, the extra vertical electrostatic separators were installed [6]. Tests with colliding bunch trains are described and the conclusions are given.

A Bunch Train in LEP consists of up to four bunches. The spacing between bunches, about $s = 74$ m, is much smaller than the spacing between trains. During tests in 1994, one train of electron bunches was collided with one train of positron bunches in two diametrically opposite interaction points, IP4 and IP8. The bunches were vertically separated at the three parasitic collision points near by, on either side.

II. CONCEPT

With the equipment installed for the tests, one bunch train in each beam could be used. The number of bunches within the trains and their spacing is determined by the requirement for sufficient separation at all parasitic encounters and the constraint from the LEP experiments that trains should not exceed a total length of 750 ns [7]. This spacing must be a multiple of λ_{rf} and the final choice was a spacing of 87 λ_{rf}.

A. *Separator bumps*

The separator bumps in the even insertions allow the beams to be separated over the whole length of the bunch train during injection, ramping and squeezing as well as bringing them into collision at the interaction point while keeping the beams separated at the parasitic encounters.

In order to minimize the necessary changes, all existing vertical separators and 4 new ones were used [6]. At each experimental interaction point six separators provide a symmetric electrostatic bump over a length of about 240 m (Figure 1).

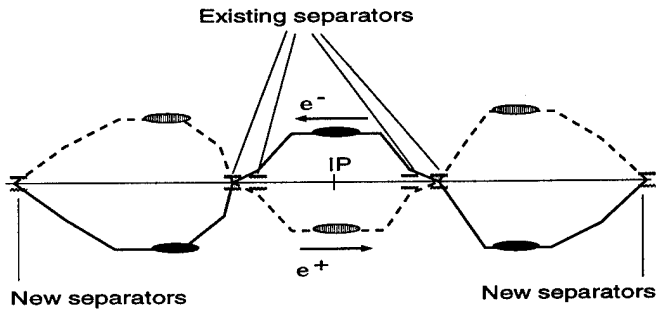


Figure. 1. Separation bump in the even points at injection, full line shows positron orbit and dashed line electrons. The two inner separator pairs are used to cancel the separation for physics.

B. *Side effects*

The amplitude of the electrostatic separator bumps should be large enough to minimize the effects caused by the parasitic beam-beam collisions, i.e. the beam-beam kicks, the beam-beam tune shifts, and their consequences. The bump amplitude should be small to minimize the vertical dispersion D_y and the resulting vertical beam emittance ϵ_y. Practically all these effects also depend on the direction of the bumps in IP4 and IP8 – bumps of opposite direction were used to minimize them. In Pits 4 and 8, $|D_y|$ is less than 1.4 mm, which at an rms momentum spread of 1.2×10^{-3} results in an increase of the vertical beam size of the order of 3%, which is negligible.

Different bunches meet the bunches of the train(s) in the opposite beam at the head-on collision points in IP4 and IP8, and at three different parasitic collision points in their vicinity. Hence,

0-7803-3053-6/96/$5.00 ©1996 IEEE

different bunches receive different beam-beam kicks, travel on different closed orbits, and all their orbital parameters are different. In particular, the simulated vertical orbit position y and the vertical orbit slope y' at IP4 and IP8 are different for all four bunches in a train. The orbit difference between the highest and the lowest bunch is $\Delta y \approx 2.3$ μm whilst the nominal vertical beam radius is $\sigma_y \approx 8$ μm. The difference between the highest and lowest slope is $\Delta y' \approx 60$ μrad which is still small compared to the crossing angle φ above which synchro-betatron resonances [8] are excited: $\varphi = \sigma_y/\sigma_s \approx 0.5$ mrad, where $\sigma_s \approx$ 15 mm is the bunch length. The expected tune and chromaticity splits between the bunches for 0.3 mA/bunch are $\Delta Q_x \approx 0.003$, $\Delta Q_y \approx 0.005$, $\Delta Q'_x \approx 0.01$, $\Delta Q'_y \approx 2.0$. Both ΔQ_x and ΔQ_y should be small compared to the synchrotron tune $Q_s \approx 0.065$ in order to avoid synchro-betatron resonances. We attribute occasionally observed losses on individual bunches to the chromaticity splits.

III. SINGLE BEAM EXPERIMENTS

In order to obtain information on how the separator bumps for the bunch trains affect the beam behaviour, magnetic correctors were first used to excite bumps which follow as closely as possible the proposed electrostatic bumps. The required aperture and optical effects were studied. Bump amplitudes up to 2.7 times the nominal value did not affect the injection or the beam lifetime [9]. The reduced aperture at the beam dump in point 5 was also studied and with bunch train bumps of 1.8 times the nominal value no effects on the lifetime, the intensity and the background were observed [9]. Long bumps extending into the RF cavitites were successfully tested and no effects were observed on the beam. If the relative bump polarity is well chosen, the residual vertical dispersion can be minimized,During one experiment, the vertical rms dispersion was reduced from 48 cm to 20 cm by using alternating polarity.

The injection and accumulation in a single beam were tested by injecting one bunch of each train at a time. The maximum total intensity was obtained when bunches are filled in order, starting at the head of the train. The first injection of four trains of four bunches spaced by $87\lambda_{rf}$ reached a total DC current of 5 mA. After the installation of additional separators, further single beam studies were performed. With four trains of four bunches, 320 μA per bunch were accumulated, limited by transverse mode coupling instabilities (c.f single bunch limit for one beam of 630 μA). The trailing bunches suffered more and saturated at lower levels. The losses were negligible when the beam was ramped to 45.6 GeV and squeezed; the emittances were measured to be $\epsilon_x = 30$ nm and $\epsilon_y = 3$ nm, and there were no noticeable variations amongst the bunches in a train. Longitudinal oscillations, larger for the trailing bunch, and a variation of the synchrotron tune along the trains were observed. These effects were predicted from the beam loading and RF modulation.

IV. HIGHER-ORDER MODE LOSSES

The superconducting (SC) RF cavities are equipped with higher order mode couplers which can extract a few hundred watts of RF power which is sufficient for four or eight equidistant bunches in each beam. The damping due to HOM couplers is, however, too small to damp the HOM losses between bunches in a train. Therefore the knowledge of the HOM losses and frequencies in each cavity becomes crucial since one can not exclude, by design, that any arbitrary bunch spacing is an exact multiple of the wavelength of a higher order mode. When this happens, the HOM fields of the k bunches of a train must be added coherently, instead of simply adding their power (incoherent addition). The same argument holds for the counter rotating beams since the bunch trains in the e^+ and e^- beams pass through the cavities too close in time for damping between passages.

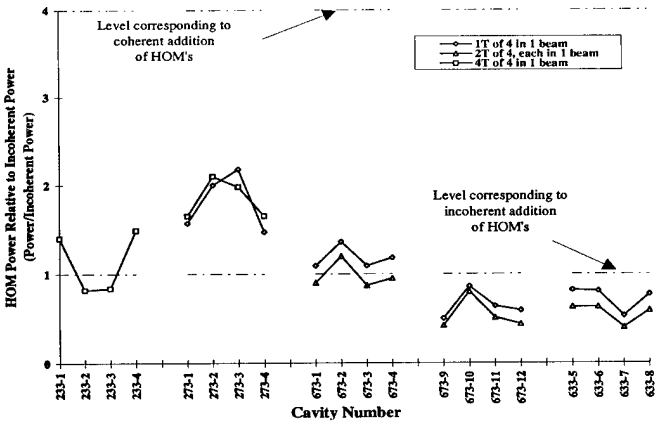


Figure. 2. HOM power measured on 20 cavities with different single beam bunch train configurations.

The results of measurements of the HOM power on 20 SC RF cavities are shown in Figure 2; there is no indication of full positive coherent addition of fields. The HOM power is always about or even below the incoherent value, except for two cavities where the power corresponds to about twice that for simple addition. With the configuration installed in 1994, the effect of the two counter-rotating beams could not be checked because the trains crossed several kilometers away from the RF stations.

V. COLLIDING BUNCH TRAINS

With standard injection conditions the bunch current for one train of four bunches per beam was limited to around 300 μA. Following a low intensity trial during the setup period, the first attempt to establish colliding bunch trains successfully brought 279 - 247 - 221 - 230 μA of positrons and 302 - 303 - 316 - 281 μA of electrons into collision. After appropriate orbit corrections the collimators were moved into position allowing ALEPH and DELPHI to take data. The lifetimes were good and the beam sizes comparable to normal 4 bunch operation.

Physics conditions were established three more times in the following three weeks [9] during which time the luminosity and background were optimised. Luminosity scans using the data for each collision within a train were performed. Figure 3 shows the luminosity for the crossings of bunches a, b, c and d during such a scan. The results confirmed the expected variation in vertical offsets caused by the beam-beam kicks from the parasitic encounters and both experiments gave consistent values for the luminosities of the order of 5 - 6×10^{30}cm^{-2}s^{-1}.

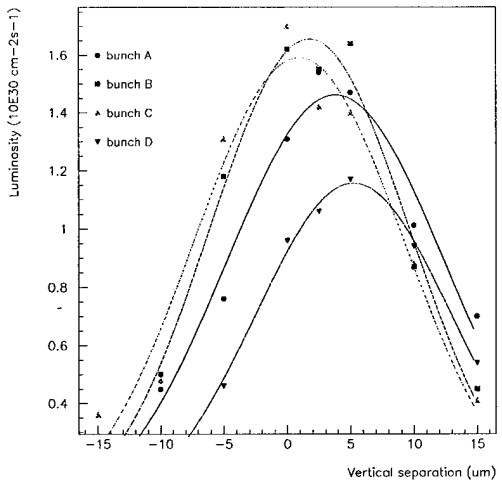


Figure. 3. Luminosity variation during a vertical separator scan in ALEPH.

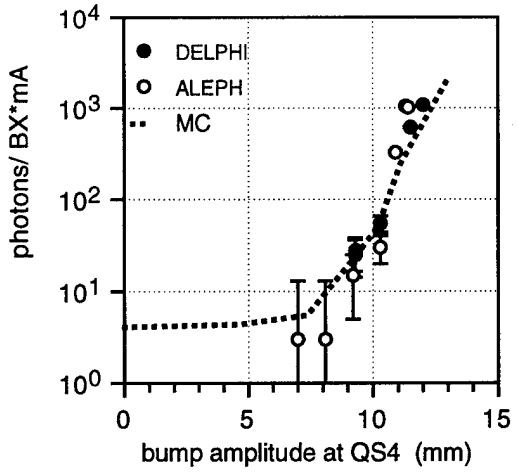


Figure. 4. Measured and simulated (MC) SR photon background in ALEPH and DELPHI as function of the separation.

The experiments had minimal problems and were able to fully explore their ability to take data with colliding bunch trains. Precise luminosity measurements were achieved for each bunch and measured online. Online tagging of the bunch number can also be obtained with high efficiency. The loss efficiency for the ALEPH hadron calorimeter and muon detector, a potential source of concern, appeared to be small and acceptable.

The combination of the vertical separation bump and powering the skew quadrupole magnets caused extremely large beam sizes ($\varepsilon_x \approx 100$ nm) when the beams were brought into collision during physics operation with 4-on-4 bunches. The skew quadrupoles are inside the separation bumps and are used to compensate the solenoidal field of the experimental detectors. This effect was not observed with collisions only in points 4 and 8 during the tests, only when the bunch train bumps were on, the skew quadrupoles in 4 and 8 were powered and there were collisions in all 4 experiments. It was found that removing any one of these three conditions reduced the beam size to normal values.

VI. BACKGROUND

Measurements with two colliding bunch trains [9] have shown no increase of the off-momentum background in the experimental detectors. However, a steep increase of the synchrotron radiation (SR) photon background has been observed in ALEPH and DELPHI for vertical bump amplitudes larger than 10 mm (Figure 4). Monte Carlo (MC) simulations confirm that this is due to photons, radiated from the peak of the bump. These photons strike the jaws of downstream vertical collimators and are back scattered into the detectors. For bump amplitudes below 10 mm most photons from the peak of the separator bump pass the interaction point without hitting downstream collimators and only a small increase of the photon background with amplitude is observed. The SR photon background with large separation bumps can be substantially reduced by superimposing asymmetric magnetic bumps in such a way that the amplitude of the incoming beam is reduced below the critical value of 10 mm, while keeping the separation constant. The increased radiation of photons along the larger amplitude of the outgoing beam does not increase the SR rate, as these photons only strike the vacuum system a long way from the IP. The effect of the asymmetric correction bump has been experimentally verified [9].

VII. CONCLUSIONS

The results of the tests in 1994 were judged encouraging enough for LEP to be adapted during the 1994/95 shutdown, for operation with four trains in each beam. Extra electrostatic separators were installed near IP2 and IP6, the separators near the odd pits were moved [6] and the skew quadrupole magnets were moved outside the separation bump. The application software and databases were modified and most of the other equipment groups also had to make changes to accommodate bunch train operation [9].

References

[1] R.E. Meller, 'Proposal for CESR Mini-B', CESR Operations Note CON 90-17 (1990).

[2] D. Rubin for CESR Operations Group, 'CESR Status and Plans', this conference.

[3] E. Keil, 'Lattice and Interaction Region Design for Z Factories', Proc. of the Joint US-CERN School, Benalmadena, Springer, 1994 - (Lecture Notes in Physics No. 425) 106-126.

[4] R. Bailey et al., 'Studies of Bunch Trains in LEP', Proceedings of the 4th EPAC (1994) 445

[5] W. Herr, 'Bunch Trains without a Crossing Angle', in Proc. 4th Workshop on LEP Performance, ed. J. Poole, CERN SL/94-06 (DI) (1994) 323-332.

[6] B. Goddard et al.,'Modification of the LEP Electrostatic Separator Systems for Operation with Bunch Trains', this conference.

[7] T. Camporesi et al., 'Report from the Bunch Train Working Group', CERN/LEPC 94-13 (1994), CERN/LEPC 94-16 (1994).

[8] A. Piwinski, 'Satellite Resonances due to Beam-beam Interaction', IEEE Trans. Nucl. Sci. **NS-24** (1977) 1408.

[9] C. Bovet et al., 'Final Report of the 1994 Bunch Train Study Group', CERN/SL 94-95 (AP) (1994).

TRAPPED MACROPARTICLES IN ELECTRON STORAGE RINGS *

F. Zimmermann, J.T. Seeman, M. Zolotorev,
Stanford Linear Accelerator Center, Stanford University, Stanford, CA 94309 USA
W. Stoeffl, Lawrence Livermore National Laboratory, Livermore, CA 94551, USA

Abstract

Sudden drops of the beam lifetime ascribed to the capture of positively charged macroparticles ('dust') are observed at many high-energy electron storage rings. A trapped macroparticle has a certain thermal lifetime due to energy transfer from the beam; the interplay of different ionizing and discharging processes gives rise to an equilibrium charge. The beam lifetime is reduced by bremsstrahlung both in the field of the atomic nuclei and in the macroscopic field of the highly charged dust particle. Recent observations at some storage rings can be explained by the capture of a single macroparticle of about micron size, possibly made from silicon dioxide. In the two B factories under construction, PEP-II and TRISTAN-II, trapped macroparticles will be thermally unstable and explode after a few tens of microseconds, thanks to the much higher beam current as compared with other storage rings.

I. INTRODUCTION

Sudden beam loss phenomena, which are ascribed to the capture of positively charged macroparticles of typically micron-size, have been observed in many electron and antiproton storage rings: for example in the TRISTAN accumulation ring [1]; in DCI and Super-ACO [2]; in CESR [3]; in the ESRF storage ring [4]; and in the CERN Antiproton Accumulator [5]. A dust problem is even reported from AdA as early as 1961 [6]. More recently, in 1992 and 1993, the HERA electron ring at DESY has suffered from regular sudden drops of the electron beam lifetime down to 15–60 minutes that have limited the beam current for luminosity runs to values of about 20 mA. A similar phenomenon has been seen at DORIS-III. While in HERA neither a coherent nor an incoherent tune shift could be measured, the lifetime drops coincided with strong localized losses of electrons as a result of bremsstrahlung in certain regions of the machine. The effect is related to the operation of distributed ion pumps, suggesting that macroparticles are generated and ejected from the pumps which are illuminated by (scattered) synchrotron radiation. Both DESY rings are now being operated with positrons rather than electrons and beam-lifetime drops are no longer observed. The successful operation of B factories like PEP-II, under construction at SLAC, or TRISTAN-II, being built at KEK, requires electron currents of 1 A or above a factor 50 higher than what has been achieved in HERA. The higher current is an advantage since, unlike in HERA, trapped macroparticles are expected to melt and explode within a few tens of microseconds. In this report, a possible theory of dust trapping is described. Section II discusses the dynamic and thermal stability of a trapped macroparticle as well as its equilibrium charge. The resulting beam lifetime is calculated in Section III. Section IV is devoted to two different sources of dust: emission from distributed ion pumps and pick-up from the bottom of the beam pipe. In Section V, the theory is applied to HERA, and predictions are made for PEP-II and TRISTAN-II. The results are summarized in Section VI.

*Work supported by Department of Energy contract DE-AC03-76SF00515

II. STABILITY AND CHARGE

In most electron storage rings, single-atomic ions are overfocused and lost in a bunch gap [7]. Only macroparticles whose equilibrium mass-to-charge ratio is sufficiently large can be stably trapped. The minimum ratio required, as determined by simulations, is of the order $A/Q \approx 10^3 - 10^4$, for both HERA and the PEP-II HER. Here, A denotes the mass of the macroparticle in units of the proton mass m_p and Q is the charge in units of the electron charge. We shall see that this condition is easily fulfilled for the estimated masses and equilibrium charges in HERA. A more difficult problem than the dynamic is the thermal stability. Simulations indicate that, once a macroparticle comes close to the beam and is trapped, its transverse oscillation is damped to amplitudes below 1 $\sigma_{x,y}$ in less than a half period of oscillation. The damping is due to ionization and discharging processes. The beam electrons ionize the atoms of the dust particle and thereby deposit a considerable amount of energy. Because high-energetic secondary electrons escape from the charged dust particle, for typical parameters, the total energy deposited is about five times less than the naive estimate based on the Bethe-Bloch result, but still about five to ten times larger than the effect of the incident synchrotron radiation. The energy deposition from the beam is approximately

$$\left.\frac{\Delta E}{\Delta t}\right|_{ion} \approx \frac{1}{5}\frac{2R^3 N_{el}^{tot} f_{rev}\rho}{3\sigma_x\sigma_y}\left.\frac{dE}{dx}\right|_{\min}, \qquad (1)$$

where ρ denotes the mass density of the particle, R its radius, $\sigma_{x,y}$ the rms beam size, N_{el} the total number of beam electrons, f_{rev} the revolution frequency and $dE/dx|_{\min} \approx 1.5$ MeV cm^2 g^{-1} the energy loss of minimum-ionizing particles. The initial temperature rise is exceedingly fast, of the order 10^5–10^8 K/s. If it is not balanced by heat radiation, the dust particle explodes when its temperature reaches the melting point, since it simultaneously acquires a significant charge (see later). Assuming a homogeneous surface charge, a molten particle is stable if

$$4\pi R^2\gamma_{surf} > \frac{Q^2e^2}{8\pi\epsilon_0 R} \quad \text{or} \quad \frac{A}{Q^2} > \frac{r_p c^2\rho}{6\gamma_{surf}} \approx 50\text{–}150\,, \qquad (2)$$

where r_p denotes the classical proton radius, γ_{surf} the surface tension, c the velocity of light, and ρ the mass density of the dust particle. Usually this condition is not fulfilled and thus particles are thermally stable only when their equilibrium temperature is below the melting point. The heat radiation of small particles is

0-7803-3053-6/96/$5.00 ©1996 IEEE

reduced, since, roughly, a particle radiates only at wavelengths smaller than its size. The absorption coefficient for simple geometries can be calculated by Mie theory, for instance using the program BHMIE of Ref. [9]. The calculation involves the complex frequency-dependent dielectric constant of the respective material. The balance of energy deposition and heat radiation determines the equilibrium temperature T which depends on the material, mass, and geometry. A larger surface-to-volume ratio leads to a decreased temperature. At temperature T the evaporation rate $\dot{A}$ of the particle and its thermal lifetime τ_{th} are given by

$$\dot{A} \approx -\frac{4\pi A_{atom}}{\sqrt{2\pi m_p A_{atom} k_B}} \left(\frac{3m_p}{4\pi\rho}\right)^{\frac{2}{3}} \frac{p(T)\ [Pa]}{\sqrt{T}} A^{\frac{2}{3}} \qquad (3)$$

and $\tau_{th} \equiv A/|\dot{A}|$, where $p(T)$ is the vapor pressure, and A_{atom} the atomic mass of the material. A trapped macroparticle gets rapidly ionized by the beam, until discharging effects become so strong that some equilibrium is reached. For large values of Q the ionization rate, due to escaping secondary electrons, is

$$\dot{Q}_{ioniz} \approx 4 \cdot 10^{12} \mathrm{s}^{-1} \frac{N_{el}^{tot} f_{rev} \rho}{\sigma_x \sigma_y} \cdot \frac{R^4}{Q}, \qquad (4)$$

where r_e is the classical electron radius, m_e the electron mass, N_A Avogadro's number, and SI units are used. One discharging effect is the capture of photoelectrons which are created by photoemission from the vacuum chamber wall [3]. For high charge and high temperature, a different discharging process will dominate, namely the field evaporation of ions. It is described by the equation [10]

$$\dot{Q}_{ev} = -\frac{A_{atom} m_p 8\pi^2 R^2 k_B^2}{h^3} T^2 \exp\left(-\frac{U+V-\Phi_-}{k_B T} + \frac{e^2\sqrt{Q}}{4\pi\epsilon_0 R k_B T} - \frac{1}{k_B}\int_0^T \frac{dT'}{T'^2}\int_0^{T'} dT''\, C_p(T'')\right), \qquad (5)$$

where C_p is the heat capacity at constant pressure, U and V the ionization and vaporization energy, respectively, and Φ_- the work function of the material.

III. BEAM LIFETIME

If the beam loss is caused by bremsstrahlung in the field of the nuclei of the macroparticle, the beam lifetime τ_b^n is [11]

$$\frac{1}{\tau_b^n} \approx \left(\frac{16 r_{el}^2}{3 \cdot 137} \ln\frac{E_e}{\Delta E_e} \ln\frac{183}{(Z_{atom})^{\frac{1}{3}}}\right) \cdot \frac{cA(Z_{atom})^2}{A_{atom} 2\pi\sigma_x\sigma_y C} \qquad (6)$$

where $\Delta E_e/E_e \approx 0.01$ is the energy acceptance, Z_{atom} the atomic number, and C the ring circumference. Provided that the equilibrium charge is high enough, bremsstrahlung can also take place in the electric field of the charged dust particle as a whole. This process is similar to the beamstrahlung in linear colliders and may be called "duststrahlung." It can be characterized by a dimensionless parameter Υ [12] which—for a needle-shaped dust particle of transverse radius R and length h, aligned in the beam direction—reads:

$$\Upsilon(b) \approx \frac{\hbar c \gamma^3}{\rho E_e} \approx \frac{\hbar \gamma e^2 Q}{m_e^2 c^3 2\pi\epsilon_0} \frac{\min(b/h, 1)}{\max(R, b)^2}. \qquad (7)$$

The term $\rho \approx (E_e \max(b,h))/(c\Delta p_\perp)$ is the local bending radius and $\Delta p_\perp \approx (2Qe^2)/(4\pi\epsilon_0 c) \cdot \min\left(\frac{1}{b}, \frac{b}{R^2}\right)$ is the transverse momentum transfer for impact parameter b. The average number $N_\gamma(b)$ of emitted photons per electron and per revolution time is $N_\gamma(b) \approx \frac{5}{2\sqrt{3}} \frac{c\alpha\Upsilon(b)}{\lambda_e\gamma} / (1+\Upsilon(b)^{\frac{2}{3}})^{\frac{1}{2}} \cdot \frac{\max(b,h)}{c}$, where we have multiplied the rate of photons per unit time [12] by $\Delta t \approx \frac{\max(b,h)}{c}$. For impact parameters b smaller than $b_{\max}$ defined by $\Upsilon(b_{\max}) = 0.02$ the typical photon energy is so high that each photon emission leads to an electron loss. The beam lifetime τ_b^{ds} due to duststrahlung is

$$\frac{1}{\tau_b^{ds}} \approx \pi \int_0^{b_{\max}} N_\gamma(b)\, b\, db \cdot \frac{c}{2\pi\sigma_x\sigma_y C}. \qquad (8)$$

IV. ORIGIN OF DUST

If charged macroparticles are generated by a vacuum arc inside the (horizontal) distributed ion pumps, they may be accelerated in the direction of the pump slots by the applied voltage U_p (about 5 kV in HERA). Dependent on their initial velocity the macroparticles may or may not be trapped by the beam. One condition for capture is that the particle has not fallen by more than about 8 vertical σ_y when it reaches the horizontal beam position. (The factor 8 comes from a simulation.) For HERA, this condition translates into $A/Q_0 \leq 4 \cdot 10^{10}\, U_p/\mathrm{kV}$, where Q_0 is the initial charge. A second condition is that the particle is ionized highly enough during its first beam crossing. Again, for HERA, it reads $A^{\frac{11}{6}}/Q_0^{\frac{5}{2}} \geq 1.5 \cdot 10^{12} (U_p/\mathrm{kV})^{\frac{3}{2}}$.

Three forces act on a dust particle at the bottom of the vacuum chamber: (1) the attractive force by the beam $F_{beam} \propto Q$ is counteracted by (2) gravity $F_{grav} \propto A$ and, for a conductive chamber surface, by (3) the image charge force $F_{image} \propto Q^2/A^{\frac{2}{3}}$ [3]. Due to the different dependences on mass and charge of the three forces, it is impossible for the beam to pick up any dust particles from the bottom of the beam pipe in most existing storage rings.

V. HERA AND B FACTORIES

In HERA, most metal particles, e.g., those made from copper or aluminum, will explode within a few milliseconds after capture. Needle-shaped titanium particles do not explode, because of their high melting point, but evaporate within about 100 s. More stable is silicon dioxide, which was found in the HERA pumps. Assuming the same complex dielectric constant as for vitreous silica [13], its heat radiation is strongly enhanced at high temperature.

As an example, (see Fig. 1), for a mass $A = 10^{14}$ (or radius $R \approx 2$–$2.5\,\mu$m), the thermal lifetime of a titanium needle is 17 s ($T \approx 1750$ K), while that of a needle-like silica particle is 6 hours ($T \approx 1440$ K). An emissivity $\epsilon \approx 0.5$ is assumed. The lifetime of silica is higher partly due to the smaller temperature and partly due to a much lower vapor pressure. Figure 1 demonstrates that the thermal lifetime increases for decreasing mass until it reaches a maximum at $A \approx 3 \cdot 10^{11}$–$10^{13}$. For smaller mass, the lifetime is shorter due to the reduced heat radiation. The most stable silica particles of mass $A \approx 3 \cdot 10^{11}$ are predicted to melt at a beam current of about 800 mA for a beam energy of 26 GeV, or at 170 mA for 12 GeV. Equation (6) shows that a beam lifetime

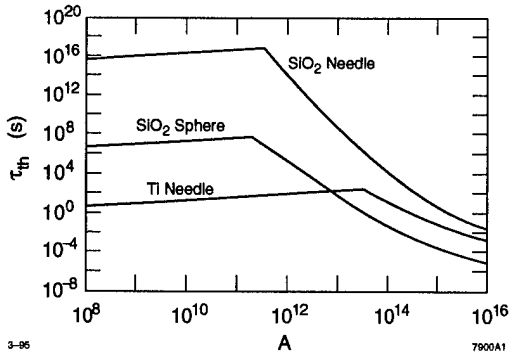


Figure. 1. Thermal lifetime τ_{th} of trapped macroparticles in the HERA electron ring as a function of mass.

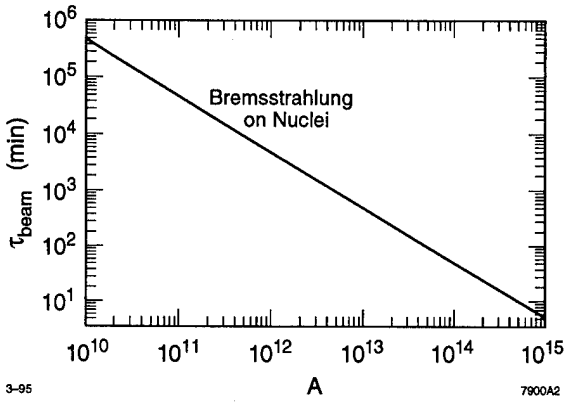


Figure. 2. Predicted beam lifetime in the HERA electron ring as a function of macroparticle mass.

of $\tau_b^n \approx 50$ min. is caused by a trapped silica particle of mass $1.6 \cdot 10^{14}$ ($R \approx 3$ μm). After 0.3 s such a particle has acquired its equilibrium charge of $4 \cdot 10^8$, using Eqs. (4) and (5). For this charge the effect of duststrahlung is insignificant. Figure 2 shows the expected beam lifetime in HERA as a function of the macroparticle mass. Due to the higher operating current in TRISTAN-II and PEP-II, even a trapped silica particle will melt after about 10 μs and 50 μs, respectively. For $A \approx 10^{14}$ the acquired charge at this moment is $Q \approx 5 \cdot 10^7$, so that the particle will explode according to Eq. (2). In the current PEP-II design, the slots of the distributed ion pumps are tilted so as to reduce the incidence of scattered radiation into the pump and to prevent the emission of macroparticles.

VI. CONCLUSIONS

A possible theory of dust trapping was described which seems consistent with the observations at HERA. Application of this theory to PEP-II and TRISTAN-II suggests that dust trapping will not be a problem in these storage rings. However, most of the results presented are quite sensitive to material constants at high temperature and to physical properties of charged hot macroparticles which are either not readily available or not exactly known.

VII. ACKNOWLEDGMENTS

We thank R. Brinkmann, K. Kanazawa, H. Saeki, and G.-A. Voss, for their help, interest, and for sharing beam observations.

References

[1] H. Saeki, T. Momose and H. Ishimaru, *Rev. Scient. Instr.* **62** No.4 1991, 874 and **62** No.11 1991, 2558.

[2] P. Marin, *LURE-RT/***91-03** 1991.

[3] D. Sagan, *NIM* **A330** 1993, 371.

[4] G. Debut et al., *Proc. of the 1994 EPAC, London* 1994; J.M. Filhol and D. Schmied, private communication 1994.

[5] E. Jones, F. Pedersen, A. Poncet, S. van der Meer, E. J. N. Wilson, *IEEE Trans. Nucl. Sci.* **32** 1986, 2218.

[6] M. Placidi, private communication 1994.

[7] Y. Baconnier and G. Brianti, *CERN/SPS/***80-2** (DI) 1980.

[8] R. D. Birkhoff, in S. Fluegge (ed.), "Handbuch der Physik," Bd. 34, 1958, 62.

[9] C.F. Bohren and D.R. Huffman, "Absorption and Scattering of Light by Small Particles," New York, Wiley 1983.

[10] E.U. Condon and H. Odishaw, "Handbook of Physics," 2nd edition, McGraw-Hill 1967.

[11] A. Piwinski, in CERN Accelerator School, Gif-sur-Yvette 1985, *CERN* **85-19** 1985.

[12] K. Yokoya and P. Chen, *KEK* **91-002** 1991; A.A. Sokolov and I.M. Ternov, "Radiation from Relativistic Electrons," AIP, New York 1986.

[13] N.P. Bansal and R.H. Doremus, "Handbook of Glass Properties," Academic Press 1986.

A COMPACT-HIGH PERFORMANCE NLC DAMPING RING USING HIGH MAGNETIC FIELD BENDING MAGNETS

D.B. Cline[1,2], A. Garren[1,2,3], M. Green[3], J. Kolonko[1,2], D. Madura[4]
[1]UCLA, CAA, Phys. Dept., L.A., CA, 90095; [2]Particle Beam Lasers, Inc., [3]LBL, Berkeley, CA 94720, [4]Martin Marrietta

We describe a 1.5GeV damping ring for very low emittance $e^{\pm}$ beams that can be used for the NLC. A key feature of this system is the use of 7T bending magnets to greatly reduce the size and cost of the storage ring as well as the tune and the damping ring while increasing the acceptance. We present only a preliminary study here.

I. INTRODUCTION

There is great interest in the development of the next linear collider, an e^+ e^- collider of 500GeV to 1.5TeV. At least six different designs of this machine exist, all use damping rings to reduce the emittance of the $e^{\pm}$ beams injected into the linear collider. The energy of the damping rings has been chosen to be about 1.5GeV in most cases. In this report we discuss the possibility of using high field superconducting magnets with high quality fields for very compact $e^{\pm}$ damping rings[1,2,3]. We will also discuss a study of a prototype small storage ring and of the superconducting magnets[1]. Such a ring could also be used as part of an asymmetric ϕ factory[4].

II. PREVIOUS STUDIES

In the late 1980's there were several studies of different types of damping rings. In these studies there were cases of very compact damping rings that used superconducting magnets[2,3]. We provide the parameters for the two cases known to us in Table 1 and Table 2.

In the report by R. Palmer there is a formula related to the final emittance that can be reached[2]

$$\varepsilon_{c\eta} \sim \frac{1.2\times10^{-10}}{\xi}\left(\frac{N}{\sigma_z B^2\gamma^2 Fm\sigma_p}\left\langle\frac{H^{1/2}}{\beta_y^{1/2}}\right\rangle\right)^{1/2} \quad (1)$$

where N is the number of particles, B is the bending magnetic field, γ, σ_z, σ_p, β_y all have the normal meaning, H is a lattice function and F_m is related to the fraction of the ring in bending magnets. From this formula we see that increasing the bending magnet field B has the effect of reducing the emittance all other things being equal. Or, one may look at this another way, that increased B could give a smaller damping ring with the same low emittance. The parameter lists in Table 1 seem to bear out this prediction.

Table 1: Palmer (Ref. 2)

	Parameters		E Magnetic Field B ≡ 4 Tesla (2)
ε_n	Equilibrium		10^{-8}
N	Electrons/Bunch		4×10^8
f	Pulse Frequency	kHz	3
P	Power/Beam		3
E	of Ring	GeV	1.1
R	of Ring	m	50
α_1	Wiggler B/B		0.04
l_W	Length Wiggler	cm	13
l_p	Length of Pole	cm	4.5
η	Chromaticity	m	11×10^{-4}
β_x		m	0.23
β_y		m	0.9
Q_x	Horizontal Tune		210
Q_y	Vertical Tune		50
l_{ext}/l_{quad}			0.6
$\hat{\varepsilon}$	Acceptance	m	1.7×10^{-6}
$\hat{\sigma}_y$	Acceptance	μ	27
$\hat{\varepsilon}_n/\varepsilon_n$			170
σ_p	dp/p in Ring		1×10^{-3}
σ_x	in Ring	mm	4.3
τ	Cooling Time	msec	0.5

III. A VERY COMPACT STORAGE RING WITH HIGH FIELD MAGNETS

We have studied a very compact storage ring with special bending magnets. This study will serve as an illustration of the possibility to develop very low emittance damping rings with a similar structure. In Figure 1 we show a schematic of the compact storage ring.

0-7803-3053-6/96/$5.00 ©1996 IEEE

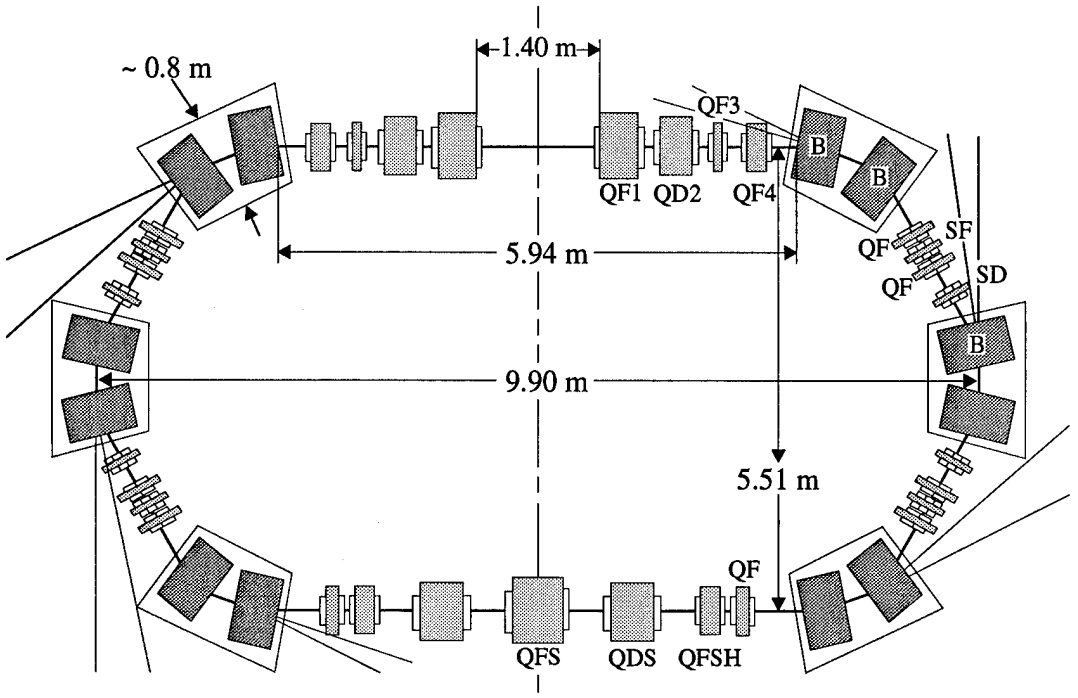


Figure 1: 1.5GeV Superconduction Electron Storage Ring with Conventional Quadrupoles and Sextupoles (Circumference = 26.0m).

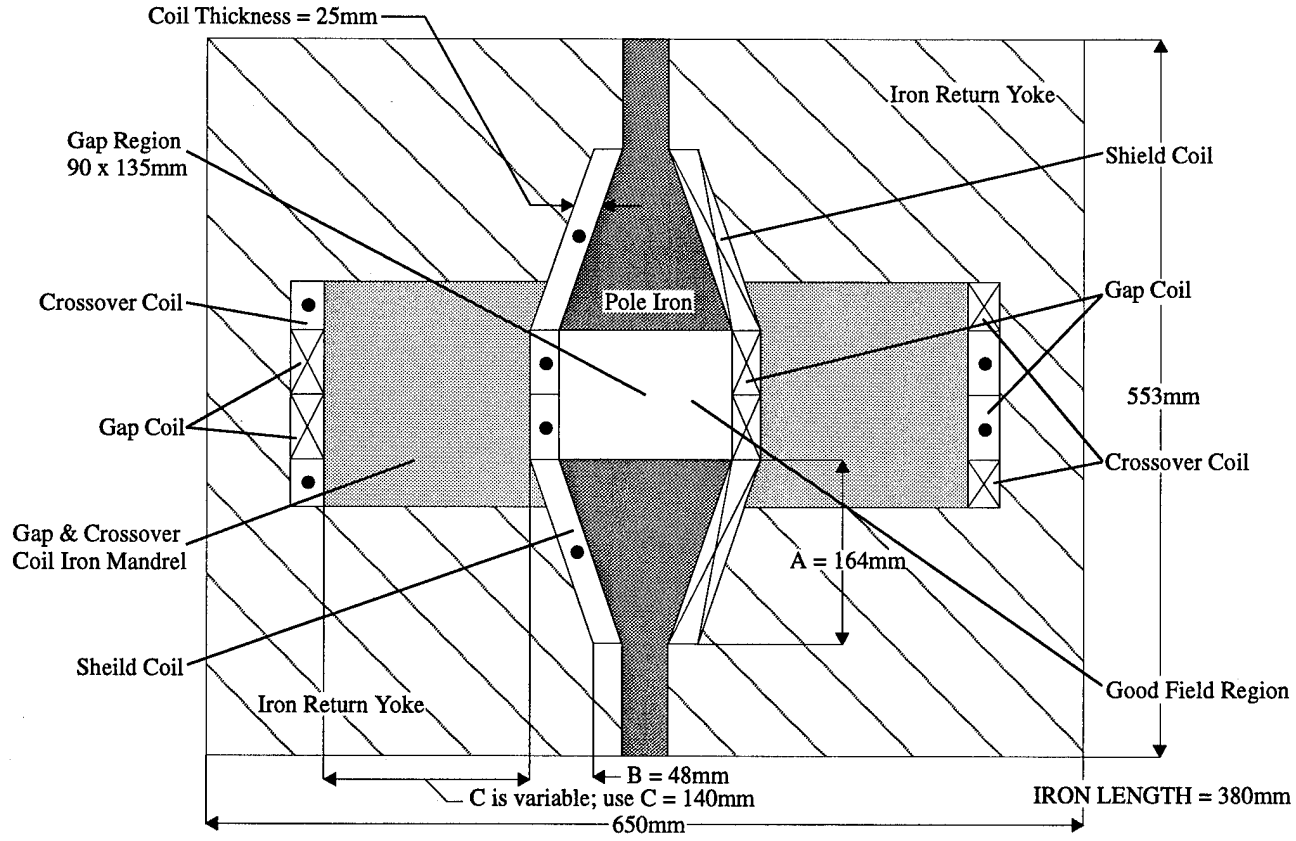


Figure 2: A cross-section view of a 7.2T compact light source dipole. (Quadrupole and sextupole pole face correction coils are not shown.) Each arc consists of three cells with the following cell structure:

The ring has a racetrack shape, shown schematically in Figure 1. It has reflection symmetry about a vertical line through the center of the figure. It consists of two arcs and two straight sections: the straight sections have equal lengths but different beam optics. The magnet layout and orbit functions are shown in Figure 2. The origin is in the center of the insertion-device region. Quadrupoles are represented by rectangles shown above or below the axis, according to whether they are horizontally focusing or defocusing, respectively. Dipoles are shown as rectangles centered on the axis.

QF D B D QF

where QF is half of an F-quadrupole, D is a drift space, and B is a rectangular dipole. The cell closest to the insertion straight section in each arc is missing its first two elements. The cell at the center of each arc contains, in addition, two horizontally focusing sextupoles, SF, which are combined with the QF quadrupoles, and two vertically focusing sextupoles, SD, at the centers of the drift spaces, D.

Table 2: VLEPP (Ref. 3)

Keyword	Units	Achromat
E	GeV	1.54727
Circumference	m	77. (70.)
$\gamma\varepsilon_0$	10^{-6} m-rad	3.
$N_{\text{particles}}$	10^{10}	20.
$\gamma\varepsilon_{\text{INBS}}$	10^{-6} m-rad	6.
τ_x	msec	1.0
τ_y	msec	1.0
U_{RAD}/TURN	kV	760.
RF voltage	MV	0.85
f	GHz	0.5
$\Delta E/E$	10^{-3}	3.0
σ_Z	mm	8. (6)
$\gamma \frac{\partial \nu_x}{\partial \gamma}$		-25.
$\gamma \frac{\partial \nu_y}{\partial \gamma}$		-21
α	10^{-3}	0.6
ν_x		18.35 (25)
ν_y		5.69 (12)
B_0, G_0	T, T/m	1.73; 0.
G_{quads}	T/m	65. (90.)
$\int \text{sext } x, y$	T/m	880.; -253
L_{WIGGLER}	m	0.6 x 20
B_{peak}	T	6.
ε_{inj}	10^{-3} m-rad	1.5 10^{-2}

The calculated x and y damping times are 0.4msec, making this suitable for high repetition rate!

IV. THE HIGH FIELD MAGNET STUDY

The key element for a compact storage ring for any use is the high field bending magnet. This magnet must have a high quality magnetic field, with minimal edge effects and higher multipole moments. We believe the magnet discussed here is likely to satisfy these requirements. The parameters of the magnets are given in Tables 3 and 4.

V. SCALING TO A DAMPING RING

Another approach to the emittance of the damping ring gives

$$\varepsilon_{qn} \propto \frac{1}{Q^3} \qquad (2)$$

where Q is the tune of the machine, Again it is an oversimplification but we may assume that the tune of a compact storage ring can grow as the circumference of the machine

$$Q \propto C \qquad (1)$$

In this case we can study the scaling from our compact ring to the cases illustrated in Table 1 and Table 2. Figure 3 shows this type of scaling.

Table 3: 1.5 GeV Synchrotron Dipole Parameters

Basic Dipole Parameters	
Number of Bending Units	6.0
Number of Dipoles per Bending Unit	2.0
Dipole Bend Angle (degrees)	30.0
X Ray Fan Angle (degrees)	20.0
Integrated Magnetic Induction* (Tm)	2.62
Peak Design Central Induction (T)	7.2
Magnet Iron Length (mm)	376.0
15 sigma Beam Height (mm)	~ 70.0
15 sigma Beam Width (mm)	~ 51.0
Magnet Gap (mm)	90.0
Magnet Pole Width (mm)	135.0
Overall Iron Width (mm)	650.0
Overall Iron Height (mm)	553.0
Slope Coil Height (mm)	164.0
Coil Thickness (mm)	25.0
Cold Mass per 30 degree Dipole (kg)	1070.0
Overall Bending Unit Mass (kg)	2540.0
Estimated Dipole Magnet System Cost (M$)	4.6

* at the peak machine energy of 1.5GeV

Table 4: Parameters for Magnets in a 1.5GeV Compact Synchrotron

Magnet Design	Magnetic Induction or Gradient (T, Tm^{-1}, or Tm^{-2})	Magnetic Length (m)	Pole Aperture Radius (mm)
Superconducting Dipoles			
B	6.894	0.38	67.5 x 45
Conventional Quadrupoles			
QF	22.67	0.125	45.0
QF1	17.65	0.380	60.0
QD2	-24.06	0.340	45.0
QF3	8.43	0.100	45.0
QF4	31.86	0.280	35.0
QFSH	21.83	0.200	45.0
QDS	-21.83	0.400	45.0
QFS	21.83	0.400	45.0
Conventional Sextupoles			
SF	410.2	0.1	45.0
SD	-549.6	0.1	45.0

* The dipole aperture is not a radius.
X and Y half dimensions are given.

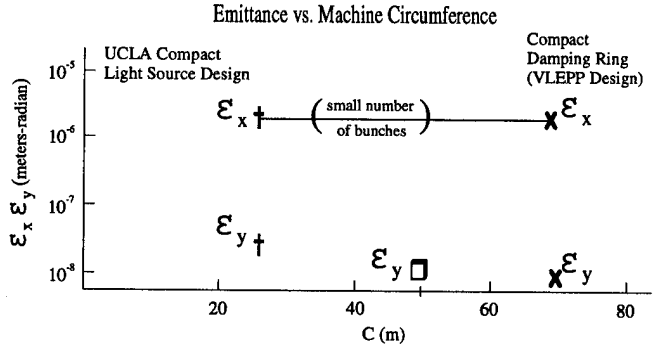


Figure 3: Emittance vs. machine circumference.

In Table 5 we show the general parameters of the storage ring. The vertical emittance is predicted to be ~ 2 x 10^{-8}m, which is in the range of the emittance needed for the NLC. We are now undertaking a study of the effects of increasing the tune of the machine and of the use of multi bunches with trains of bunches.

Table 5 : Parameters for the Compact Synchrotron

Electron Energy (GeV)	1.5
γ	3914
Circumference (m)	26
Tune ν_x	3.17
Tune ν_y	2.57
Horizontal Emittance*, (m-rad)	2.34 x 10^{-6}
Vertical Emittance*, (m-rad)	2.34 x 10^{-8}
Horizontal, β_{max} (m)	3.09
Vertical, β_{max} (m)	6.66
RF Voltage (kV)	2500
FR Frequency (MHz)	499
Momentum Compaction	0.0985
Bunch Length, σ_l (cm)	3

* unnormalized

VI. REFERENCES

[1] D.B. Cline, A. Garren, M. Green, J. Kolonko and D. Madura, A Compact Hard X-ray Source for Medical Imaging and Biomolecular Studies, presented at the 1994 Accel. Appl. Conf., N. Texas Univ., Denton, Texas, and to be published in the proc., NIM (1995).

[2] R. Palmer, Cooling Rings for TeV Colliders, Proc. of 1987 Linear Collider Workshop, SLAC.

[3] Proceedings of the 1988 Linear Collider Workshop, Working Group on Storage Rings for Linear Colliders.

[4] D. Cline, A. Garren, Options for Asymmetric ϕ Factories, publ in the Proc. of the London EPAC Conf.

Application of Precision Magnetic Measurements for Control of the Duke Storage Ring*

B. Burnham, V.N. Litvinenko, Y. Wu
Duke University Free Electron Laser Laboratory
Box 90319 Duke University Durham, NC 27708-0319

Presented at the 1995 Particle Accelerator Conference, May 1 - 5 in Dallas, Texas USA

I. INTRODUCTION

The 1 GeV Duke FEL storage ring is dedicated to drive UV and VUV free electron laser devices. Specifics of this ring include the use of combined function magnets: quadrupole-sextupole and dipole-sextupole. The use of combined function magnets is necessitated by the close spacing of magnetic elements. A discussion on the measurement procedures of these magnets is included in this paper, as well as the data analysis used to create a viable control system for the combined function magnets.

The design of the Duke storage ring was driven by the requirement to use existing hardware manufactured for the original ring design at Stanford. The original design called for the use of "nose" and "dimple" endpieces attached to the dipoles as the main fixed strength sextupole source. In addition, adjustable sextupole magnets were placed in an 18 cm gap between dipoles and arc quadrupoles. In that design the distance between magnetic poles of dipoles, quadrupoles, and sextupoles was less than 2 cm. It was no surprise that this design uncovered major asymmetric saturation of dipoles and sextupoles. Saturation would cause intolerable orbit distortion and high order nonlinearities in the magnetic field.

To solve these problems we decided to:

a) replace odd asymmetric endpieces with smooth and symmetric ones;
b) remove discrete sextupoles which were saturated anyway;
c) create necessary sextupole moments in the quadrupoles using asymmetric excitation;
d) place fixed strength sextupole shims in the center of the dipoles.

II. MEASUREMENT PROCEDURES

Magnetic measurements of all magnets were performed prior to installation on the storage ring. In order to facilitate fast data acquisition of large data sets of magnetic fields accurately we made use of a Hall probe array. Details of the array and its electronics can be found in a previous paper [1].

The high resolution of the array and its electronics yield a magnetic measurement accuracy of better than one part in 10,000 and we can make a two dimensional map with only one pull through each magnet. A set of tracks are used for the precise positioning of the array in each magnet. Since the magnet lattice includes closely spaced elements it is important that all measurements be taken in a real environment. The magnet test bed at Duke has room to place neighboring magnets around the magnet under test as would be the case when the magnet is eventually placed into the storage ring. In this manner we can better understand the fringe field effects and cross-talk of closely spaced elements.

Each dipole magnet is measured with one current ramp using small current increments, and four field maps. Each arc quadrupole is measured with three asymmetric current ramps and five field maps. We use the maps to evaluate magnetic length dependence on current. Then we use interpolated values of magnetic length in combination with the ramping data for precise characterization of magnetic moments.

The normalization curves used to standardize each magnet before measurement are now also used prior to operating the storage ring. This is so that the magnets resemble as closely as possible the same condition they were in when they were measured on the test bed.

To insure consistency with magnetic measurements we calibrated all power supplies and current sensors (shunts, DCCT) using sets of equipment used for magnetic measurements. Controls use individual second order polynomial fits for all power supplies.

III. COMBINED FUNCTION QUADRUPOLES

The arc combined function quadrupoles are wired so that we can independently control the quadrupole and sextupole moments. Quadrupole coils are fed by an individually controlled power supply. An individually controlled shunt regulator is connected to the pair of coils on the inner side of the ring. With no current in the shunt regulator all coils have the same excitation and there is a pure quadrupole moment. By shunting the inner coils we excite dipole and sextupole moments in the magnet. The dipole moment offsets the magnetic center of the quadrupole-sextupole. We have therefore designed the ring so that the electron orbit will pass through this new magnetic center, 2 mm for the design value of the sextupoles.

We have taken large data sets of all of the quadrupole magnets in field mappings and current rampings and created a computer routine to fit the multipole moments using spline interpolation in multi-dimensional space. These data are used in the control system, described below, to achieve the desired strengths in the quadrupole. Graphs showing current settings and field distributions can be found in [1].

The pole tips of the arc quadrupoles (inner radius = 2 cm) have shape corrections to compensate for fringe effects and finite size of the poles. These corrections work as well for combined function quadrupoles. Figure 4 of Reference 1

*This work supported by U.S. Air Force Office of Scientific Research grant F49620-93-1-0590 and U.S. Army Space & Strategic Defense Command contract DASG60-89-C-0028.

0-7803-3053-6/96/$5.00 ©1996 IEEE

shows a plot of the integrated moments above sextupole for both the central part of the magnet and the fringe fields: one curve is the integral of the fields inside the magnet steel without edges, the other for the fringe field. The two very nearly cancel out overall higher order moments. Thus, combined function quadrupoles with asymmetric excitation are nearly perfect; the lowest moment in the integrated field is dodecapole.

IV. COMBINED FUNCTION DIPOLES

We replaced the odd shaped nose and dimple dipole end pieces with new parallel edge smooth symmetric end pieces required to extend dipole magnetic length. This allows us to reach a symmetric magnetic field of 20.5 kGs with excellent quality (15.9 kGs is required for 1 GeV operation). We have devised a way to make the dipole magnets combined function while maintaining a higher level of symmetry by introducing thin steel shim stock in the center of the magnet. These fixed strength sextupoles are not a necessity for the Duke ring. We decided to introduce them in order to simplify quadrupole alignment by maintaining a magnetic center offset of 2 mm in both focusing and defocusing arc quadrupoles. This extra "bump" creates a defocusing sextupole field of the desired strength as shown in Figure 1. In this figure, the peak is 60 Gauss above the baseline field of 3.96 kGs. The steel

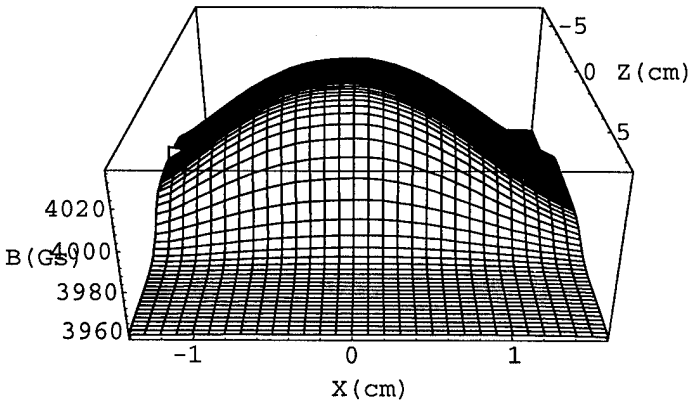


Figure 1. Field map of dipole thin shim stock.

shims themselves are mounted on aluminum strips, so the whole unit is easily replaced if desired. The 0.005 inch thick steel shim stock measures only 6.4 cm long by 2.5 cm wide in a 33 cm long magnet. The measured sextupole moment as a function of longitudinal distance is shown in [1].

V. OTHER MAGNETS

We use standard quadrupoles (inner radius = 3 cm) in the ring straight sections, linac, and linac-to-ring transport channel. These magnets also pass through standard ramping and magnetic measurements. Data analysis for these magnets is much simpler than for the combined function quadrupoles.

The Lambertson type septum magnet used on the Duke ring was measured in a similar manner employing a specially designed curved track to follow the expected orbit of the electron beam. Integrated strengths were calculated from the resulting field ramps and maps.

The data of the measured strengths of all steering dipoles, trim coils, and other small magnets are also used for computer control.

VI. ANALYSIS AND CONTROL

Dipoles:

We have used a special program to track the particles through five 2-D field maps to calculate dipole magnetic lengths as a function of current. Combined with measured ramping curves, the data provides us with individual integrated characteristics of the dipole and sextupole moments:

$$D_i = f_i(I)$$
$$S_i = g_i(I) \qquad (1)$$

Spline fits interpolate these functions between measured points.

All bending magnets and injection chicanes are powered by one 560 kW PEI power supply. For control we use the total dipole moment dependence

$$D_a(I) = \sum_i D_i(I) \qquad (2)$$

This gives us the particle momentum as a function of the PEI current:

$$pc(MeV) = \frac{0.29979}{2\pi} \sum_i D_i(I)[kGs \cdot cm] \qquad (3)$$

The settings of other magnets are based on the ring energy and design lattice.

To insure that each of the 40 dipoles turns the beam 9° we use individual dipole trim currents:

$$\Delta D_i(I_{trim}) = \frac{D_a(I)}{40} - D_i(I) \qquad (4)$$

Individual dipole trims are also used for closed orbit correction and are calibrated in milliradians as are all steering and quadrupole trim magnets.

Standard Quadrupoles:

For the standard quadrupoles we analyzed the integrated quadrupole dependence as a function of coil current:

$$Q_i = A_i(I). \qquad (5)$$

We used the ramping data taken in the center of the magnet along with five field maps to calculate the quadrupole moment versus current curves. Then we use individual cubic spline fits to interpolate between measurement points.

Combined Function Quadrupoles:

Analysis of the combined function quadrupoles assumed that the pole tips are non-saturated and that the filed is a superposition of quadrupole and dipole-sextupole fields. Computer models and data analysis showed that the fields could be fit by the following forms:

$$Q_g = A(\bar{I}) + B(\bar{I})(\Delta I)^2$$
$$S = S_g = C(\bar{I})(\Delta I) \qquad (6)$$
$$D_g = \alpha S$$

where Q_g, S_g, and D_g are the respective quadrupole, sextupole, and dipole moments in the geometric center of the

magnet; Q, S, and D are the respective moments at the magnetic center; A, B, and C are functions of the average current $\bar{I} = (I_1 + I_2) / 2$ through the two halves of the quadrupole, and the current separation is $\Delta I = (I_1 - I_2) / 2$. The dipole and sextupole moments are both odd multipole moments and hence may be closely related. This simple relation is indicated by the coefficient α on the dipole moment. This is due to the fact that the pole tips are not saturated. Saturation occurs farther up the neck of the yoke.

Substitution for ΔI from the equation for S_g into the equation for Q_g shows that the quadrupole moment is proportional to S_g^2. In figure 2 we plot the quadrupole versus sextupole moments where each data point represents a different separation current, but the average current is the same.

The graph shown in figure 2 is repeated for every average current setting used in the measurements. The DC and second order terms of the parabolic fit coefficients are saved as a function of average current. These two functions, then, are $A(\bar{I})$ and $B(\bar{I})$ and are shown graphically in figure 3. The central values for Q and S calculated from the curves in figure 3 are related to the integrated moments simply by multiplying the central value by the effective length of the magnet. The effective length is calculated from the two dimensional field maps and is very nearly a linear function of average current, which is natural for quadrupoles with no chamfers.

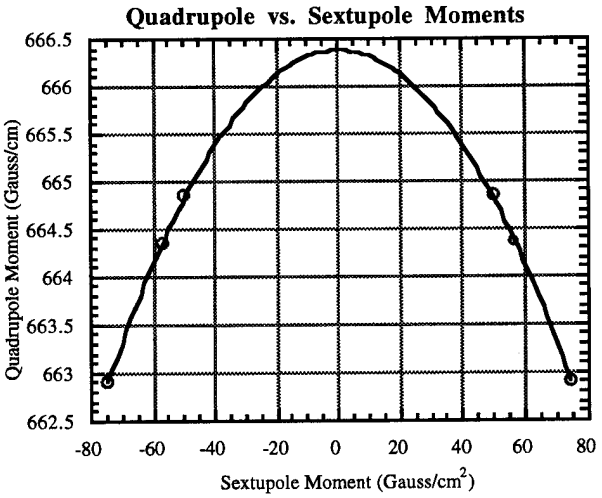


Figure 2. Plot and parabolic fit of quadrupole versus sextupole moments for given average current.

A curve is similarly generated for the sextupole moment coefficient $C(\bar{I})$ using a linear fit to the sextupole moment versus current separation. The dipole proportionality constant α is also determined from the mapping data. These assumptions are confirmed by detailed analysis of magnetic measurement data and computer simulations.

The shift of magnetic center, defined as x_0, is found by a simple change of coordinate system. By definition the dipole

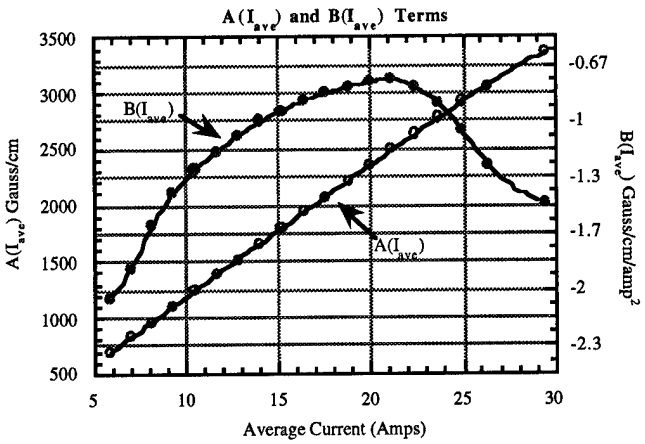


Figure 3. Coefficient curves with spline fits.

moment at magnetic center is zero, and the geometric and magnetic center values of quadrupole moment are related by

$$Q_g = Q - Sx_0 = \sqrt{Q^2 - 2\alpha S^2} \quad (7)$$

Substitution back into the first of equation 6 gives

$$A(\bar{I}) + \frac{B(\bar{I})}{C(\bar{I})^2} S^2 - \sqrt{Q^2 - 2\alpha S^2} = 0 \quad (8)$$

Using this formula it is straightforward to invert the functions of the graph of Figure 3 to find

$$\bar{I} = f(Q,S)$$

$$\Delta I = \frac{S}{C(f(Q,S))} \quad (9)$$

VII. CONCLUSIONS

The effort spent on magnetic measurements and applications which use the magnetic measurement data for control paid off in the end. The commissioning of the Duke storage ring was a great success. We did not experience any problems storing electrons on the first try, or ramping the energy from 230 MeV to 1.1 GeV. All measured parameters of the ring, such as tunes and chromaticity, are very close to the design values [2].

Implementation of magnetic measurements for controls was provided by a set of programs using the EPICS control system and the Tcl-Tk scripting language[3]. Work is in progress to implement these controls at a lower level for greater speed.

VIII. REFERENCES

[1] B. Burnham, N. Hower, V. N. Litvinenko, J.M.J. Madey, Y. Wu, "Specific Features of Magnet Design for the Duke FEL Storage Ring" in Proceedings of the 1993 Particle Accelerator Conference, Washington, D.C., p. 2889.

[2] V. N. Litvinenko, et al., "Commissioning of the Duke Storage Ring", these proceedings.

[3] Y. Wu, et al., "The Duke Storage Ring Control System", these proceedings.

Wiggler Insertion of the PEP-II B-Factory LER

J. Heim, L. Bertolini, J. Dressler, O. Fackler, B. Hobson, M. Kendall, T. O'Connor, W. Stoeffl, T. Swan, Lawrence Livermore National Laboratory

A. Zholents, M. Zisman, B-Factory Project and Center for Beam Physics, AFRD, LBL, Berkeley

Abstract-- The Low Energy Ring (LER) of the PEP-II B Factory at SLAC employs two identical wiggler insertions for emittance control and extra damping with each insertion designed to absorb 400 kW of synchrotron radiation. The wiggler is a set of individual iron core dipoles designed to operate at 1.6 T. The basic variant will include nine 0.4-m length magnets and two 0.2-m length magnets. A copper vacuum chamber is used with continuous antechambers connected to both sides of the beam chamber via slots. Synchrotron radiation dump surfaces and distributed vacuum pumping are located in both antechambers. We describe the design and analysis of the vacuum chamber, dump and magnets.

1-INTRODUCTION

PEP-II B factory LER employs wiggler magnets for beam emittance excitation and synchrotron radiation damping. The beam emittance of this ring without wigglers is only 22 nm·rad, compared to a nominal design emittance of 64 nm·rad. Moreover, an emittance variation of 40—100 nm·rad is envisaged for LER operation in order to provide flexibility of beta-function adjustments at the interaction point and luminosity optimization. Damping associated with wigglers consists in a reduction of damping time from 64 msec to 47 msec with an energy spread of 8.1×10^{-4} in a variant with all wiggler magnets in place. Wiggler magnets are inserted into two LER straight sections with the wiggler centered in a chicane (see Fig. 1). The chicane is formed by four dipole magnets and these chicane bend magnets play an important role in emittance adjustments. By varying the betatron phase advance between pairs of chicane dipole magnets, one can efficiently control excitation of the form factor $H = D_x^2 / \beta_x$ given here in the center of the wiggler section. (As usual D_x is the dispersion function and β_x is the horizontal beta-function). If the chicane bends work together with the wiggler magnets, emittance excitation is controlled by the form factor H, and the wiggler contribution to overall emittance can be maximized. Fig. 2 shows the behavior of beta-functions and the dispersion function along the wiggler straight section for the nominal 64 nm·rad beam emittance case.

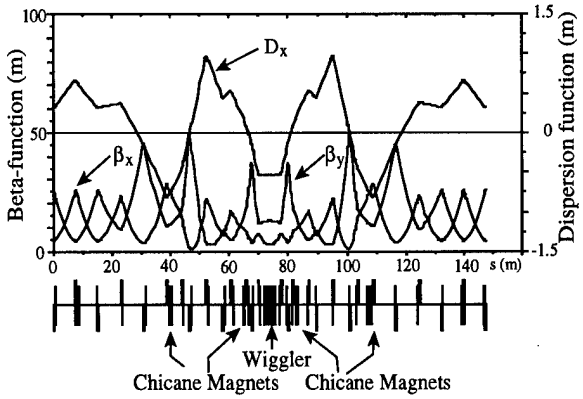


Fig. 2 Wiggler Dispersion and Beta-Functions

2-WIGGLER DESIGN CONCEPT

Beam lattice layout of both wiggler locations are identical with the circulating beam shifted toward the center of the ring with a chicane as shown in Fig.1. The chicane bend angles were chosen to be the same as the standard LER bend magnets (1.875 degrees) as a cost optimization. The chicane standard bend magnets will be connected in series electrically with the LER dipole string magnets.

The wiggler magnets are conventional water cooled iron core dipole magnets designed to operate at 1.6 T. All wiggler magnets are individual "H" magnets which are mounted onto a rigid girder located below the magnets. Our wiggler magnet iron core lengths are longer than most wiggler magnets and the wide angle synchrotron radiation fans deposit most of the synchrotron radiation onto the vacuum chamber sidewalls immediately downstream of the wiggler.

The wiggler vacuum chamber is approximately 25 m long and the material is copper. Synchrotron radiation produced by the wiggler magnets is intercepted by continuous dumps which are an integral part of the copper vacuum chamber sidewall as shown in Fig. 3. Continuous vacuum pumping is also provided on both sides of the vacuum chamber via pumping slots.

Both wiggler chicanes will be installed for start-up, but only one of the wigglers will be installed. A second wiggler will be installed later if necessary.

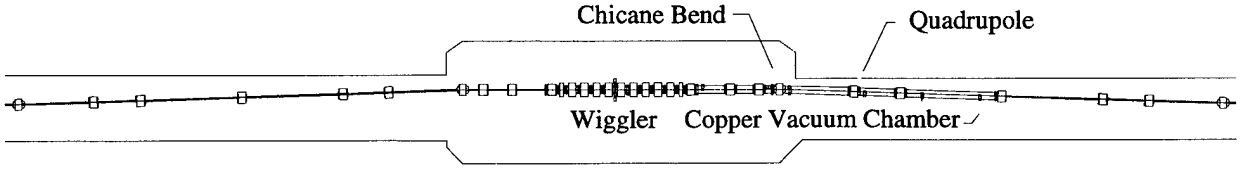


Fig. 1 Wiggler Chicane Layout

0-7803-3053-6/96/$5.00 ©1996 IEEE

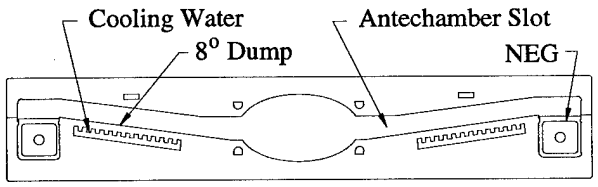


Fig. 3 Wiggler Vacuum Chamber Cross-Section

3-SYNCHROTRON HEATING

A computer program was written to calculate the magnitude and distribution of the synchrotron radiation (SR) incident upon the dump surfaces downstream of the wiggler. Heat flux distribution across the dump surface was also calculated for the peak heating areas. This heating data was then used as an input for temperature and stress calculations. Synchrotron radiation heating distribution is shown in Fig. 4 with the downstream end of the wiggler shown as the origin. Note that for distances less than 6 m downstream of the wiggler, the synchrotron radiation is incident upon both sidewalls, and the distributions are shown as solid and dashed curves. For distances greater than 6 m, one of the sidewalls is shadowed by the chicane bend, and only one distribution curve is shown. Also note that the heating increases by more than a factor of three at the chicane bend into the resume line to a peak of approximately 330 W/cm. The heat flux density at this chicane bend location is approximately 220 W/cm^2, but it is not the peak heat flux. The peak heat flux density of 415 W/cm^2 is located at the highest spike on the sidewall upstream of the bend (see Fig. 4).

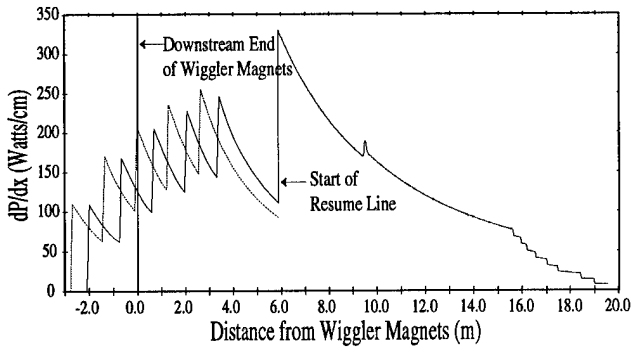


Fig. 4 Synchrotron Heating Distribution

4-VACUUM CHAMBER DESIGN

The wiggler vacuum chamber consists of a 90 mm x 40 mm elliptical beam aperture with continuous SR slots on both sides. The SR slots are sloped at 8° to form water cooled dump surfaces to absorb the SR power. Continuous plenums with distributed Non-evaporable Getter (NEG) pumps are located behind the dump surfaces (See Fig. 3).

The wiggler vacuum chamber top/bottom sections are made from two half-hard C10100 OFHC copper plates which are machined and electron-beam welded together to form the vacuum chamber. After fabrication the chamber will be vacuum baked at 200C for one to two days and then glow-discharge cleaned using an argon/oxygen gas mixture.

Design of the distributed NEG pumps is an innovative departure from conventional NEG designs. SAES ST707 strip is cut into individual "wafers" and stacked onto a stainless steel tube with 2 mm spacers between wafers. The stainless steel tube wall serves as both the vacuum barrier and support for the NEG. A commercial heater is inserted into the tube and used to activate the NEG's with the heater outside of the vacuum space, therefore, penetration of the vacuum wall with an electrical feed-thru is not required. With this design feature, a failed heater can be replaced with the chamber under vacuum. Each pump contains 11.4 meters of NEG strip per meter of length. This provides a distributed pumping speed of 400 l/s/meter of length with a getter capacity of 1.14 Torr-l/meter. Estimates show that this pumping capacity should limit NEG pump reactivations to once per year. The distributed NEG pumps will be supplemented by discrete ion pumps to pump hydrogen during NEG activation.

The LER Wiggler has the potential to experience a pressure bump vacuum instability. This phenomenon occurs when beam and photon produced ions get accelerated toward the chamber walls by the 600 volt average beam potential. These ions can desorb up to 10 new gas molecules on impact. If the pumping speed is too low, this new desorbed gas can lead to an avalanche effect and produce a runaway pressure spike, which leads to beam loss. A high pumping speed and wide distribution of the wiggler vacuum system should eliminate beam-induced degassing problems. The positive effect of this phenomenon is to accelerate the clean-up of the vacuum chamber.

Synchrotron radiation from the wiggler poses two problems for the vacuum system. The first problem is the large gas load caused by photo-desorption which must be effectively pumped by the NEG system. The photo-desorption is 5 x 10^{-6} Torr-l/meter. Our beam-line pressure calculations predict an average vacuum pressure of 3.4 nTorr. This pressure is well within the design goal of the wiggler vacuum system of 10 nTorr.

The second problem is the thermally induced stresses at the dump surface. A thermal/structural analysis of the vacuum chamber was done using a 2D model and the ANSYS finite element code. A 200 psi cooling water pressure, atmospheric pressure and synchrotron radiation heating were applied simultaneously to the thermal/structural model.Thermal analysis results show peak temperatures of 117 C and 87 C on the dump surface and cooling water channel surface respectively. The cooling water channel surface temperature is well below the coolant boiling point and film boiling will not occur.

The highest thermally induced stress is a compressive stress in the longitudinal/beam direction (a principal stress) and it is due to the localized synchrotron heating. The heated stripe would like to grow longitudinally, but the remainder of the vacuum chamber constrains the growth and compressive stresses develop in the heated area. Similar findings were

reported by R. Wong [1] and the PEP-II Conceptual Design Report [2]. A peak longitudinal compressive stress of 22 ksi is developed in the highest temperature region. The two remaining principal stresses in this area are small compared to the longitudinal stress and the resultant von Mises stress of 20 ksi is lower than the longitudinal stress. All stresses due to pressure loading are well below the allowable working stress and their contribution to the combined stresses in the heated zone are not significant. An allowable stress of 2/3 yield stress was used as a static allowable stress.

An analysis was also performed to estimate the fatigue failure safety margin. An axial compression cycle is initiated each time the LER is filled with beam and a maximum of 20,000 fills are expected over the life of the machine. We used the copper S/N curves presented in Z. Wangs et al. paper [3] and a maximum operating stress of 22 ksi to estimate the number of cycles to crack initiation as $30x10^4$ cycles. The number of crack initiation cycles divided by the number of beam fills gives a crack initiation safety factor of 15.

We have concluded that the stress behavior of the dump surface is dominated by the principal stress in the longitudinal beam direction and the peak stresses in the heated area may be estimated to good accuracy with temperature information and the simple expression

$$\sigma=\alpha E\Delta T, \text{ where}$$

σ = Peak compressive stress,
α = Expansion coefficient for dump material,
E = Modulus of Elasticity for dump material,
ΔT =(Tmax - Tavg) for the vacuum chamber cross-section.

6-WIGGLER MAGNET DESIGN

All wiggler dipole magnets are individual "H" magnets using laminated iron cores and water cooled aluminum coils. Aluminum was chosen as the conductor material to be compatible with an existing aluminum cooling water system. Magnet coils are layer wound with an even number of layers so that both leads are located on the side of the coil away from the vacuum chamber. The wiggler magnets are connected in series electrically with alternating polarities. The middle dipole magnets are full magnets (40 cm long) while the end magnets are half magnets (20 cm long). Wiggler end magnets have water cooled aluminum trim coils wound onto the outside of the primary windings. The trim coils are sized to provide a horizontal beam adjustment of ± 2 mr. A wiggler magnet cross-section is shown in Fig. 5.

7-INSTRUMENTATION AND DIAGNOSTICS

Instrumentation and diagnostics for each wiggler include beam position monitors which feed back to corrector magnets for steering, sets of thermocouples every two meters along the vacuum chamber to protect against overheating, and radiation monitors which serve as a fast-response protection system and provide feedback to vertical correctors which keep the synchrotron radiation fan centered on the dump surface. A possible additional diagnostic is an optical monitor which will show the vertical profile of the scattered light from the synchrotron radiation fan.

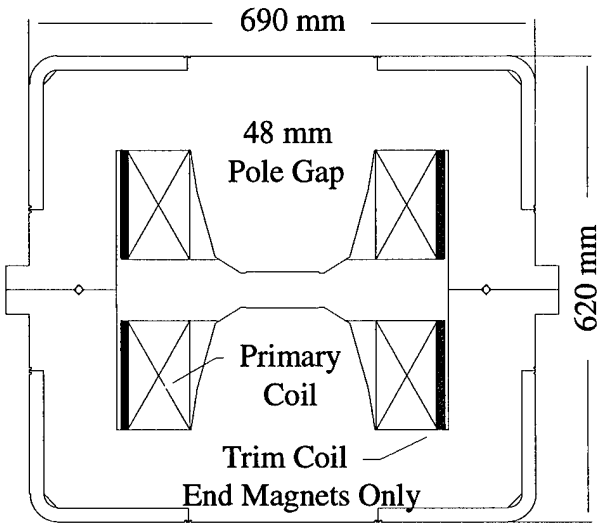


Fig. 5 Wiggler Magnet

8-SUMMARY AND FUTURE PLANS

The preliminary design/analysis of the wiggler has been completed and detailed design is progressing. We will complete detailed design in 1995 and all fabrication work will be done in 1996. A full size cross section of the vacuum chamber 1.5 m long is being built as a fabrication prototype, and the prototype fabrication experience will be evaluated as part of the detailed design. A final design review is planned for this summer.

ACKNOWLEDGMENTS

This work was supported by the Director,Office of Energy Research, Office of High Energy and Nuclear Physics Division, of the U. S. Department of Energy under Contracts DE- AC03- 76SF00098 and W-7405-ENG-48-(LLNL).

REFERENCES

[1] R. Wong, "B-Factory High-Energy-Ring Two-Dimensional Thermal-Stress Analysis", SCMDG 90-5.1-59, LLNL, December 19, 1990.

[2] PEP-II An Asymmetric B Factory, Conceptual Design Report, LBL-PUB-5379, SLAC-418, CALT-68-1869, UCRL-ID-114055, p 326-330, June 1993.

[3] Z. Wang et al., "Low-cycle-fatigue behavior of copper materials and their use in synchrotron beamline components", Nuclear Instruments & Methods in Physics Research, Section A 347, p 651-656, 1994.

STATUS OF THE HIGH ENERGY RING OF THE PEP II B-FACTORY *

U. Wienands, E. Reuter, J.T. Seeman, W. Davies-White, A. Fisher, J. Fox, L. Genova, J. Gracia, C. Perkins, M. Pietryka, H. Schwarz, T. Taylor; SLAC, Stanford University, Stanford, CA 94309
T. Jackson, LBL, Berkeley, CA 94720; C. Belser, D. Shimer, LLNL, Livermore, CA 94550

Abstract

The PEP-II High Energy Ring is a 9 GeV electron storage ring currently under construction at SLAC. It is one of the two rings of the PEP-II B-Factory, an asymmetric high-luminosity e^+–e^- collider. The ring will be housed in the existing PEP tunnel. Main challenges to the design of the ring arise from the high beam current of nominally 1 A. In this paper, overall design and recent progress are presented.

I. INTRODUCTION

The PEP-II[1] storage rings—the 9 GeV High Energy Ring (HER) and the 3.1 GeV Low Energy Ring (LER)—will be housed on top of each other in the existing PEP tunnel (Fig. 1). In order to reach the design luminosity of 3×10^{33} at a moderate beam-beam tune shift of 0.03 relatively large circulating currents of about 1 A and 2.1 A will be accumulated in the HER and the LER, respectively. The bunch length is about 1 cm to take advantage of small values of β^*; the focusing required to achieve these short bunches is provided by a 14 MV rf system at 476 MHz.



Figure 1. First cell of HER underneath LER mockup

II. THE HER MAGNET LATTICE

The geometric layout of the HER lattice fits into the existing PEP tunnel; this determines the sixfold symmetry. A FODO lattice with 60° phase advance/cell and 32 cells/arc has been adopted with three-cell dispersion suppressors to match into dispersion-free straight sections. The beam emittance is set by controlling the dispersion function in the arcs at a nominal value of 48π mm-mrad. A layout of the ring is shown in Fig. 2. A modulation in the β functions is introduced in the arcs adjacent to the interaction region; in this way a semi-local correction of the chromatic aberrations introduced in the final focusing quads is achieved, improving the linearity of the lattice.

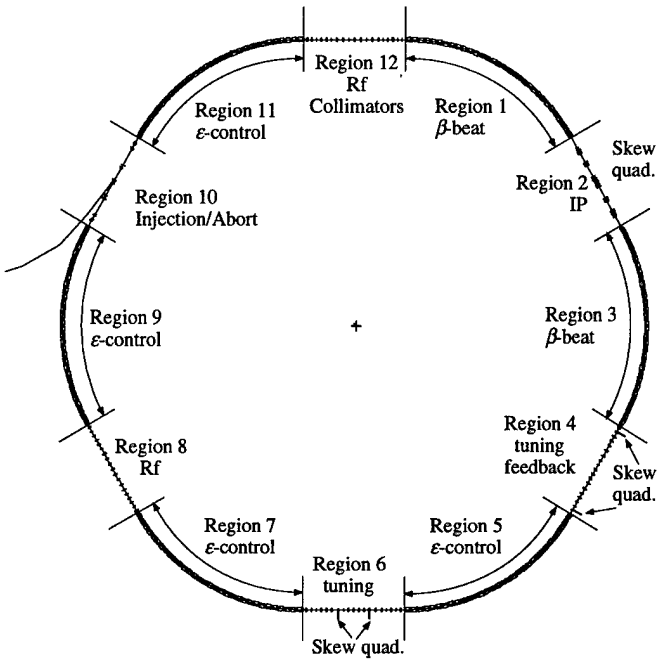


Figure 2. HER Layout

The straight sections have different numbers and structure of focusing cells depending on the functions. Rf systems are located in Regions 8 and 12 with 20 cells each. Injection takes place in Region 10 in a high-β region; 8 cells provide the required lattice functions. The machine tune is controlled with phase trombones in regions 4 and 6. The Interaction Point (IP) is at the center of region 2. While the nominal β^* is 1.5 cm, with the semi-local chromaticity correction values as low as 1 cm can be achieved. Figure 3 shows the acceptance of the ring in the presence of misalignments and field errors but absence of the detector solenoid. A detailed discussion of the HER lattice can be found in Ref. [2].

III. THE HER TECHNICAL SYSTEMS

A. *Magnets*

The HER uses most of the existing PEP magnets, in particular all 192 dipole magnets and all quadrupole magnets with the exception of some of the final focusing quadrupoles. However, since the HER has more focusing cells than PEP had, additional quadrupoles are being built. The additional 560 mm coils needed are being manufactured by BINP, Novosibirsk, under an Interlaboratory Agreement.

*Work supported by US Department of Energy under contract DE-AC03-76SF00515, DE-AC03-76SF00098, DE-AC03-81ER40050, DE-AS03-76ER70285 and W-7405-Eng-48

0-7803-3053-6/96/$5.00 ©1996 IEEE

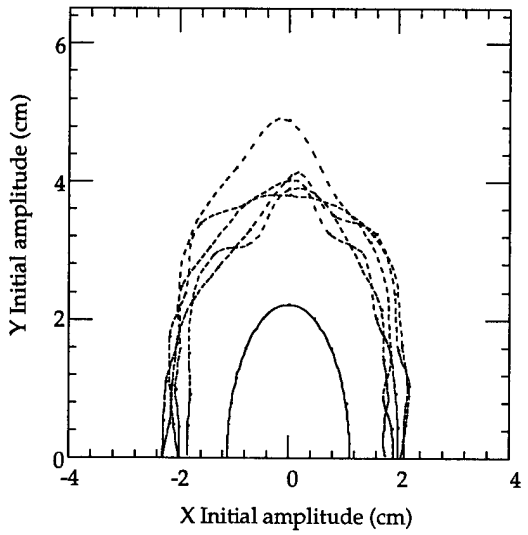


Figure 3. Dynamic aperture of the HER lattice

All existing and converted PEP magnets are being refurbished and tested before acceptance. Dipoles undergo electrical tests, water pressure test and a mechanical straightness inspection before magnetic measurements are being performed. Quadrupoles are being tested electrically and for LCW leaks before magnetic measurements.

The Dipole refurbishment and measurement program has been completed early this year. The magnets have passed the tests and fulfill the magnetic measurement criterion: $\sigma(\Delta \int BdL/I)/(\int BdL/I) < 10^{-3}$. The dipoles will be sorted in three ranges according to their value of $\int BdL/I$ and deployed in a H–L–M– M–H–L pattern (H=high, M=medium, L=low) to reduce horizontal orbit errors due to dipole variations.

The quadrupole refurbishment and measurement program are underway. Measurement data are very close to the values measured during construction of PEP. Since there are many different quadrupole current loops, the quadrupoles will be sorted to reduce the spread in the excitation function for quadrupoles excited by one current loop.

Corrector magnets for the HER are being built in industry. In order to control stray fields on the LER axis these magnets will be of "H" design.

B. Vacuum System

The vacuum system is designed for 3 A beam current to provide margins and an upgrade path. At 3 A beam current, synchrotron radiation power is about 10.5 MW. For beam stability, the impedance presented to the beam is strictly controlled and care is being taken to avoid the possibility of mode trapping in discontinuities of the vacuum chamber.[3]

The arc vacuum system uses octogonal Cu extrusions with cooling channels e-beam welded onto the outside to remove the up to 100 W/cm radiation power.[4] Flanges and bellows are protected from direct hit by synchrotron radiation by masks or chamber offsets.[5] Distributed ion pumps (DIP) are located in each dipole, augmented by lumped ion pumps which also act as holding pumps in the event the main dipoles are turned off. A screen between the DIP and the beam chamber protects the DIP from synchrotron radiation and TEM modes generated by the beam and the beam from particles emanating from the DIP. Prototypes of the DIP and screen are currently under test.[6] Chamber extrusions are starting to arrive and the e-beam welder is scheduled to arrive in June.

The vacuum system in the straight sections uses LCW cooled stainless steel chambers.[7] Here the maximum power dissipation is much less, between 30 W/cm and 5 W/cm, but LCW cooling is still required throughout the straights.

C. Rf System

The RF system for the high energy ring consists of 5 RF stations providing a RF acceleration voltage of 14 MV with a resultant bunch length of 1.15 cm. Each RF station consists of four single-cell cavities, one 1.2 MW klystron and the necessary power splitting waveguide network and an isolating circulator.[8] A low-level RF system provides control of amplitude, phase and tuning of the cavity and includes an elaborate fast feedback system to stabilize the interaction of the cavity with the beam to dampen multi-bunch oscillations.[9] The cavities are normal conducting, reentrant copper cavities with three waveguides for higher order mode damping attached. The HOM loading waveguides are located to achieve optimal damping of longitudinal and transverse resonant modes in the cavity without loading the fundamental accelerating mode. A prototype cavity[10] is 90% complete and will be tested to 150 kW wall dissipation in summer this year. A 10 inch Alumina disk window in a waveguide[11] serves as vacuum barrier to the rf and is designed to transmit up to 500 kW of rf power to cavity and beam. Two prototype windows are under test and show promising results. A prototype klystron with 3 MHz bandwidth and < 150 nsec delay required by the fast feedback loops was constructed at SLAC and is awaiting test to 1.2 MW power.[12]

D. Feedback Systems

The HER relies on bunch-by-bunch feedback systems for both longitudinal and transverse stability. State-of-the-art digital signal processing is used to accomplish the filtering required for loop stability.

D.1 Longitudinal feedback

The longitudinal feedback system uses a dedicated BPM to pick up the beam phase information, which is processed at the sixth harmonic. Down sampled and digitized it is distributed to a farm of 128 DSP modules for signal processing, delay and filtering at a 238 MHz combined rate. The DSP output streams are read into a holding buffer and delivered to an 8-bit DAC. Commercial power amps (2 kW) and modulators will be used to drive the longitudinal kicker at 1.012 GHz. For low-frequency modes the kicker will not have sufficient amplitude and the correction signal is being fed to the low-level rf system, for the main rf cavity to act as longitudinal kicker.

Prototypes of most components of the system have been built and have been successfully tested at the ALS at LBL.

D.2 Transverse feedback

The transverse feedback system is similar in concept, although somewhat more straightforward in implementation. The system is implemented as a one-turn delay system with digital delay

buffer. Two dedicated BPM buttons will provide signals with roughly 90° betatron-phase difference that are processed again at the sixth harmonic. After low-pass filtering and phase adjustment the signal is converted to digital form and delivered to a dual-bank hold buffer. The delayed signal drives base-band kickers.

E. Beam Injection

Vertical injection into the HER takes advantage of the small emittance of the damped SLAC beam ($\epsilon < 10^{-4}\pi$nm-rad). Four slow orbit bump magnets steer the HER orbit to within 8 σ towards the edge of the septum. Two fast kickers, 180° apart in betatron phase, kick the closed orbit such that the injecting beam enters the ring at about 8.5 σ of the fully coupled beam. In this way, the circulating beam can be topped off without significant scraping-off of the circulating beam. 60 Hz operation is foreseen with the possibility of upgrading to 120 Hz. Every bucket in the HER is accessible by suitable programming of the system; allowing to equalize the charges of different bunches. The HER beam has a 5% ion clearing gap; this gap will also be used for "training pulses" to tune up the injection before an attempt to top-off the circulating bunches is made. The system is capable of supporting on-axis injection, which will be an important commissioning tool and also allow for beam-based alignment of the ring.

F. Beam Diagnostics

Several diagnostic systems are being prepared for commissioning the PEP-II HER in 1997. An extensive network of beam-position monitors, one set of four 15-mm-diameter buttons at each quadrupole, will track the beam centroid; the button signals will be combined to provide x or y readout at each focusing or defocusing quadrupole, respectively. Memory in the front-end processors will maintain a 1000-turn history.

Tunes will be measured by driving the beam with a swept-frequency sinusoid while monitoring the beam's spectrum; a phase-locked loop will be added later. This drive signal will be added to the low-level signal for transverse feedback, to share the amplifiers and strip lines.

A DC current transformer will precisely measure the time-average current. The relative charge in each of the 3492 individual buckets (of which typically 1658 will be filled to a charge of 3×10^{10} electrons) will be determined from the sum signal of a set of four buttons.

Visible and near-UV synchrotron radiation will be imaged to profile the beam at two points in the lattice, with low and high dispersion. At each of these locations, the transverse profile will be recorded in the tunnel using CCD cameras; the light from one location will also be transported to a surface building for detailed streak-camera measurements. To study the beam's transverse tails, movable collimators will be used as scrapers.

Beam losses will be monitored by a linear distributed ion chamber ("PLIC Cable") around the tunnel for both HER and LER together. In addition, PIN-diode beam-loss monitors will be distributed around the ring to be able to localize losses.

IV. CONCLUSION

Construction of the HER is on track for a first commissioning run beginning March 1997. At that time, two rf stations (8 cavities) will be available and we expect to be able to commission the ring injection system, store and accumulate beam and perform first tests of the feedback systems.

ACKNOWLEDGMENTS

We thank all the colleagues who have contributed to the design and construction of the HER.

References

[1] J.T. Seeman, "PEP II Status and Plans", these proceedings.
[2] M.H.R. Donald *et al.*, "Lattice Design for the High Energy Ring of the SLAC B Factory (PEP II)", these proceedings.
[3] S.A. Heifets *et al.*, "Impedance Budget of the PEP II B-Factory", these proceedings.
[4] C. Perkins *et al.*, "Vacuum System of the PEP-II High Energy Ring", Proc. EPAC, London, UK, 1994.
[5] M. Nordby *et al.*, "Bellows Module Design for the PEP II B-Factory", these proceedings.
[6] F.R. Holdener *et al.*, "Test Results of Prototype Distributed Ion Pump Design for the PEP II B-factory", these proceedings.
[7] U. Wienands *et al.*, "The Vacuum System of the Straight Sections for the PEP II High Energy Ring", these proceedings.
[8] H. Schwarz *et al.*, "RF System Design for the PEP-II B Factory", Proc. EPAC, London, UK, 1994, pp.1882-1884.
[9] P. Corredoura *et al.*, "Low Level RF System Design for the PEP-II B Factory", these proceedings.
[10] R. Rimmer *et al.*, "Development of a High-Power RF Cavity for the PEP-II B Factory", these proceedings.
[11] M. Neubauer et al, "High-Power RF Window and Coupler Development for the PEP-II B Factor", these proceedings.
[12] R. Fowkes *et al.*, "1.2 MW Klystron for Asymmetric Storage Ring B Factory", these proceedings.

DESIGN OF THE PEP-II LOW-ENERGY RING

M. S. Zisman, R. B. Yourd, and H. Hsieh, for the PEP-II LER Design Team*, Lawrence Berkeley Laboratory, Berkeley, CA 94720 U.S.A.

The PEP-II Project, a collaboration of SLAC, LBL, and LLNL, began construction in January 1994. Since the Conceptual Design Report (CDR) [1] was issued in June 1993, considerable progress has been made at refining and optimizing the Low-Energy Ring. Lattice design has progressed considerably, with solutions obtained for the chromatic correction of the IR and new, more relaxed, parameters for the required wigglers. Based on the latter change, the number of RF stations was reduced from 5 to 4. A new concept for the arc vacuum system has been adopted, based on an antechamber configuration with discrete photon stops pumped by titanium sublimation pumps. Designs for the arc dipoles and quadrupoles have been developed in collaboration with IHEP (Beijing) and these magnets are now being fabricated there. A new configuration for the high-power wiggler photon dumps has been developed and is in the detailed design phase.

I. INTRODUCTION

The PEP-II asymmetric *B* factory collider comprises two storage rings, a High-Energy Ring (HER) with 9 GeV electrons and a Low-Energy Ring (LER) with 3.1 GeV positrons. Main parameters for the LER are summarized in Table I. The requirements of the LER for a large circumference, a low energy, a large emittance, and a short bunch length make the lattice difficult, and substantial effort has been spent on its design. The high beam current requirement is also challenging.

Because the LER is an entirely new ring, all of its technical components must be newly designed and fabricated. LBL is responsible for the arc magnets and supports, the arc vacuum system, and the transverse feedback system, LLNL for the interaction region (IR), the wigglers, and the vacuum system in the straight sections, and SLAC for both the RF and the longitudinal feedback systems. All three labs play a role in the areas of power supplies and diagnostics.

Table I
PEP-II LER main parameters.

Energy [GeV]	3.1
Circumference [m]	2200
Emittance, *y/x* [nm-rad]	2.6/64
Beta function at IP, *y/x* [cm]	1.5/37.5
Beam-beam tune shift	0.03
RF frequency [MHz]	476
RF voltage [MV]	5.1
Bunch length, rms [cm]	1
No. of bunches	1658
Total current [A]	2.1
Energy loss per turn [MeV]	0.8

II. LATTICE DESIGN

To fit in the PEP tunnel, the LER lattice (see Fig. 1) is hexagonal, with six FODO arc sections joined by six long straight sections. The collision straight section is IR-2 (at the 2 o'clock position), with injection on the opposite side of the ring in IR-8. The lattice is mirror symmetric about the axis from the injection point to the interaction point. To simplify the installation and alignment, all magnets in each FODO half-cell are clustered together on a single raft. To keep the overall geometry of the two rings similar in the arc sections, the LER dipoles are centered above the much longer HER dipoles. Emittance control is handled with wigglers located in two straight sections.

The challenges in designing the lattice arise mainly from the low vertical beta function (1.5 cm) at the interaction point (IP) along with the need to produce the relatively large emittance (64 nm-rad) required by the beam-beam interaction. Chromaticity correction is done by means of a "semi-local" scheme [2], with a pair of horizontal sextupoles located in the IR straight section on each side of the interaction point. (Because the two beams collide head on with magnetic separation close to the IP, and because the LER beam must be raised above the plane

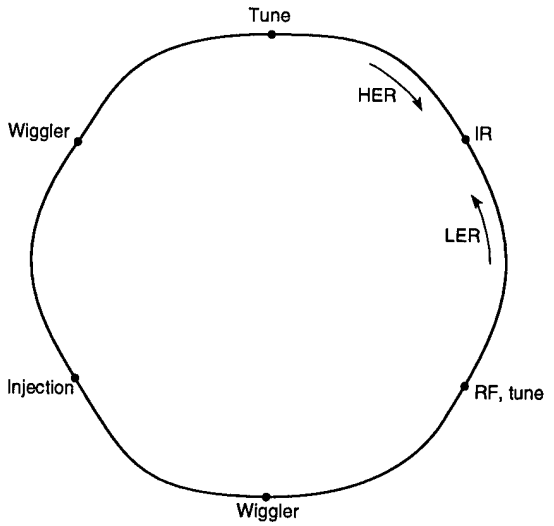


Fig. 1. Functional layout of the LER.

*Supported by the U.S. Department of Energy under contracts DE-AC03-76SF00098 (LBL), DE-AC03-76SF00515 (SLAC), and W-7405-Eng-48 (LLNL).

0-7803-3053-6/96/$5.00 ©1996 IEEE

of the HER in the rest of the collider, dispersion is present in much of IR-2.) Families of sextupoles in the two arcs adjacent to the IR serve to correct the vertical chromaticity. Compared with the CDR design, the resulting simplified layout eliminates 24 magnets in the IR, with substantial cost savings. As part of the optimization, we have also adopted a non-interleaved sextupole scheme in the four arcs remote from the IR. Although this has the disadvantage of constraining the phase advance in the arcs to certain values (90° or 60°) it saves considerably on the number of sextupoles, requiring 80 fewer magnets.

III. MAGNETS AND SUPPORTS

Both the arc dipoles and arc quadrupoles are being fabricated at the Institute for High Energy Physics (IHEP) in Beijing under Attachments to the Interlaboratory Collaborative Agreement between SLAC and IHEP. Both magnets were designed collaboratively by LBL and IHEP engineers [3] and work on prototypes is under way. LER magnets will operate at beam energies up to 3.5 GeV.

The LER quadrupole is a two-piece design (see Fig. 2), modeled on the successful ALS booster quadrupole. Most quadrupoles will be 43 cm in length; a few special needs will be met with 65 cm long magnets. To accommodate the very different operating ranges of quadrupoles in the LER lattice, a number of different coils and cooling topologies are used. Most of the coils use aluminum conductor to match the (existing) magnets of the HER. In cases where the gradient requirements are very high, such as in the IR, a few magnets will use copper coils. The two long arc quadrupole strings are configured with 15-turn coils. The magnets designated for the short magnet strings have 58-turn coils to better match power supply needs. A few magnets in the wiggler straights require a modified version of the 58-turn coil to accommodate the very wide vacuum chamber used in that region. The prototype arc quadrupole will be available this summer.

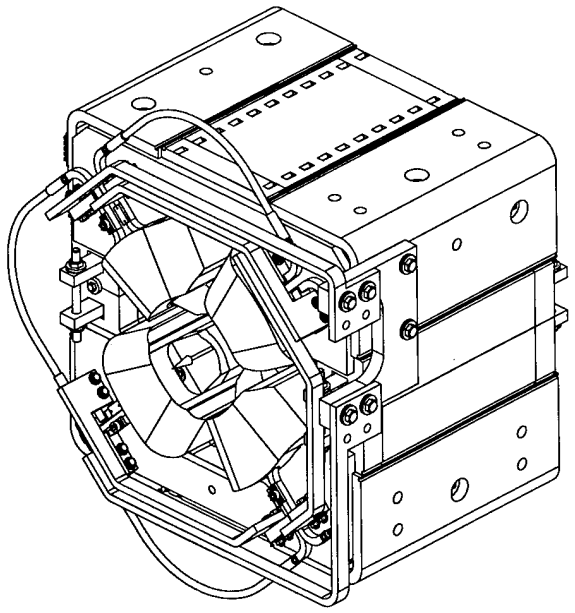


Fig. 2. LER arc quadrupole.

Dipoles are standard H-magnets with a gap of 63.5 mm and an effective length of 45 cm; the operating field at 3.1 GeV is 0.75 T. The aluminum coils of the dipole have a pancake configuration with a large cross section to minimize power consumption. A prototype dipole magnet will be available in the fall.

Designs for the sextupoles are just beginning. We plan to use the same laminations as the original PEP sextupoles. Existing "long" PEP sextupoles will be split into shorter magnets (with new coils that accommodate the larger LER vacuum chamber profile, see below) to meet LER needs.

IV. VACUUM SYSTEM

The LER arc vacuum system is based on an extruded aluminum antechamber, following that of the Advanced Photon Source. Synchrotron radiation exits the beam chamber through a 15-mm high slot. The "magnet chamber" is sized to fit in the magnet bores and has only a clearance slot. In the span between magnet rafts there is a much larger "pumping chamber" containing a photon stop, a titanium sublimation pump (TSP), and a sputter ion pump. The TSP has very high pumping speed and is situated immediately below the photon stop in each half-cell (see Fig. 3). More than 99% of the gas-producing photons are intercepted on the photon stops, which are designed to handle the 15 kW of power from the dipoles at 3.5 GeV and with a 3 A beam. Thermal analysis confirms that the chamber would not be damaged by a worst-case beam missteering event at full power.

Because of the very high beam current of positively charged particles, we must consider the pressure bump phenomenon and the possibility of multipactoring, both of which were originally seen at the ISR [4]. To avoid a pressure bump, we will use glow discharge cleaning (GDC). We expect the GDC to be "remembered" even

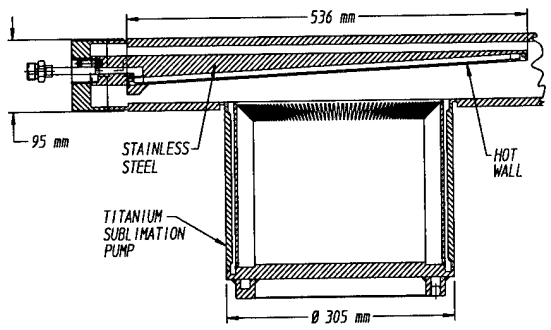


Fig. 3. Photon stop and TSP (elevation view).

after an accidental venting of the chamber, because only a monolayer of impurities is reabsorbed on the surface and this amount is easily removed by either photon or ion scrubbing. (Analysis of the photon distribution shows that some 10% of the emitted photons miss the slot and land within the beam chamber. These are very low energy and do not cause heating but they do serve to scrub the walls of the beam chamber, albeit with low efficiency, because of the high beam current in the ring.)

As concerns multipactoring, our evaluations show that we will be below threshold for nominal running, but we could temporarily reach threshold at some intermediate time during the filling process. The presence of a bunch gap and the ability to fill the bunches unevenly should give sufficient margin against problems. We also contemplate coating the chamber walls (with either TiN or a suitable metal) to reduce secondary electron emission.

V. WIGGLERS

The LER beam emittance is adjusted with wigglers. Although two straight sections are designated for wigglers, we will begin operation with only a single wiggler, located in IR-6. The linear optics in IR-10, where the second wiggler would eventually reside, are kept the same as those of IR-6 to maintain the ring symmetry. To obtain as much damping as possible, the single initial wiggler has five periods, compared with the baseline design of two three-period wigglers. It has been verified that the elimination of one wiggler period will not limit the required range of emittance adjustment and that it has minimal effects on the damping time and on beam-beam performance.

The wiggler is implemented [5] as individual dipoles, similar to the arc dipoles but optimized for higher magnetic field and sized to accommodate the wiggler vacuum chamber and photon dump. The dump comprises a copper chamber with longitudinal slots leading to water-cooled surfaces on both sides that intercept the synchrotron radiation. The dump is capable of dissipating the power from the full five-period wiggler at a 3 A beam current.

VI. RF AND FEEDBACK SYSTEMS

At the time of the CDR, the baseline design [6] called for five 476-MHz RF stations (five klystrons, each powering two single-cell cavities). With the present wiggler length and beam energy spread, it suffices to use only four RF stations. Indeed, an optimized operational scenario calls for running only three stations, with the fourth serving as a "hot spare." At present, we intend to begin operation with a minimum set of three RF stations. We have estimated the bunch length increase and luminosity loss that would result from having a station fail in this circumstance and find these still to be acceptable.

The high beam current and large number of bunches in the LER demand broadband feedback systems. Both longitudinal and transverse feedback systems are employed for the LER. The design for the longitudinal system is based on a digital signal processing approach with downsampling. The transverse system makes use of two pickups with quadrature processing and a broadband kicker driven by a 120 W, 10 kHz–250 MHz, Class A commercial solid-state amplifier. Both systems were tested [7] at the ALS under operational conditions and found to work well.

VII. SUMMARY

The designs of all major LER systems are well along, and many components have now been ordered. The PEP-II commissioning plan calls for a phased approach, with the injection system beginning commissioning this year, the HER in 1997, and the LER in early 1998. An excellent team with members drawn from all three collaborating laboratories is in place and is making excellent progress.

VIII. ACKNOWLEDGMENTS

The professionalism and hard work of the members of the LER team are—and will remain—the key to a successful LER commissioning. We are grateful for their support and enthusiasm.

IX. REFERENCES

[1] PEP-II: An Asymmetric B Factory, Conceptual Design Report, SLAC-418, June 1993.

[2] Y. Cai, *et al.*, " Low Energy Ring Lattice of the PEP-II Asymmetric B Factory," these proceedings.

[3] T. Henderson *et al.*, "Design of the PEP-II Low-Energy Ring Arc Magnets, these proceedings.

[4] R. S. Calder, "Ion Induced Gas Desorption Problems in the ISR," Vacuum 24, 437 (1974); O. Gröbner, "Bunch Induced Multipactoring," in Proc. Intl. Conf. on High Energy Accelerators, July 1977, p. 277.

[5] J. Heim, *et al.*, "Wiggler Insertion of the PEP-II B Factory LER," these proceedings.

[6] H. Schwarz and R. Rimmer, "RF System Design for the PEP-II B Factory," in Proc. of 1994 EPAC, p. 1882.

[7] W. Barry, *et al.*, "Commissioning and Operation of the ALS Transverse Feedback System," these proceedings.

INJECTION ENVELOPE MATCHING IN STORAGE RINGS *

M. G. Minty and W. L. Spence
Stanford Linear Accelerator Center, Stanford University, Stanford, CA 94309 USA

Abstract

The shape and size of the transverse phase space injected into a storage ring can be deduced from turn-by-turn measurements of the transient behavior of the beam envelope in the ring. Envelope oscillations at $2\times$ the β-tron frequency indicate the presence of a β-mismatch, while envelope oscillations at the β-tron frequency are the signature of a dispersion function mismatch. Experiments in injection optimization using synchrotron radiation imaging of the beam and a fast-gated camera at the SLC damping rings are reported.

I. INTRODUCTION

The repetition rate requirements of a linear collider allow the beams to be damped for only a few β-tron amplitude damping times—about 2.3 for the SLC electron beam at 120 Hz. Since the tolerance on the extracted beam emittances is also stringent, the maximum acceptable injected emittance is similarly restricted. It must include effective increases in the injected beam emittance taking place in the ring itself, on time scales short compared to the radiation damping time. Envelope `mismatches' are a potentially serious source of such emittance growth.

II. TRANSVERSE DYNAMICS

A (stably) stored beam envelope will usually asymptotically approach a stationary form, in which its variation around the ring is mainly determined by the magnetic focusing lattice. The stationary envelope is the unique envelope that has the ring's periodicity, and so does not vary from turn-to-turn at any fixed location. Although the shape of the envelope is asymptotically independent of the envelope with which one injects, its size or phase space volume may not be. The time scales for damping and stochastic excitation, which produce initial condition independent equilibria, are typically much longer than those that establish the stationary envelope.

An arbitrary injected beam will not have an envelope shape that `matches' the symmetry of the ring, and will consequently undergo coherent oscillations, `β-beats', at twice the incoherent β-tron frequency. If the phase advance varies with respect to incoherent β-tron amplitude or energy (due to geometric and chromatic non-linearities in the lattice), and the beam contains a spread with respect to these dynamical variables, the β-beat will decohere (Landau `damp') and the phase space volume will filament. The Liouville `invariant' emittance $\epsilon = \sqrt{\langle x^2\rangle\langle x'^2\rangle - \langle xx'\rangle^2}$ increases. The *matched-equivalent* emittance

$$\bar{\epsilon} = \frac{\langle x^2\rangle + \langle(\beta x' + \alpha x)^2\rangle}{2\beta} = B\epsilon \geq \epsilon \qquad (1)$$

where $\beta(s)$ is the unique (ring-turn) periodic, *lattice* determined, `matched' envelope shape function ($\alpha = -\beta'/2$). $\bar{\epsilon}$ is the beam average Courant-Snyder invariant, and since it is *phase advance invariant*, $\bar{\epsilon}$ is conserved in the presence of transport in which there is phase advance spread. If the β-beat decoherence is complete $\epsilon = \bar{\epsilon} = B_0\epsilon_0$, the initial matched equivalent emittance. B is thus the multiplicative factor by which the emittance grows, and $B = 1$ characterizes the `matched' case.

In a dispersion *function* mismatch the off-energy components of the (on-average-energy) injected beam's transverse trajectories are not *closed* orbits in the ring. The beam transverse coordinate-energy correlation coefficients differ from the unique ring-periodic `matched' off-energy function $\eta(s)$. The anomaly

$$\Delta\eta = \eta - \frac{\langle x\delta\rangle}{\langle\delta^2\rangle} \qquad (2)$$

is independent of energy spread in first order, but may contain higher orders. It behaves like a free β-tron oscillation and so has a dispersion-anomaly invariant $||\Delta\eta||/\sqrt{\beta}$, where

$$||\Delta\eta|| = \left\{(\Delta\eta)^2 + [\beta(\Delta\eta') + \alpha(\Delta\eta)]^2\right\}^{1/2} \qquad (3)$$

The matched-equivalent emittance is increased according to $\bar{\epsilon} \to \bar{\epsilon} + \frac{1}{2}||\Delta\eta||^2\langle\delta^2\rangle/\beta$, with $\langle\delta^2\rangle$ the *injected* mean square energy deviation. The effects of anomalous dispersion are damped at the transverse damping rate, and cannot induce synchro-β-tron coupling.

Observation of the evolution of the beam size over several hundred consecutive turns (a time scale short compared to the filamentation time) at a location of non-vanishing dispersion allows a precise and complete diagnostic of the injection envelope. The mean square spot size at a fixed location with β-function β in a ring with a linear lattice and tune ν, will vary with turn number n according to[1]

$$\frac{\langle x^2\rangle}{\beta} = B\epsilon + \sqrt{B^2-1}\,\epsilon\cos\left[2\pi\left(2n\nu + \mu_\beta\right)\right] + 2\eta\frac{||\Delta\eta||}{\beta}\langle\delta^2\rangle\cos\left[2\pi\left(n\nu + \mu_\eta\right)\right] \qquad (4)$$

for an arbitrary β, η mismatch.

III. INSTRUMENTATION[2]

A fast-gated camera manufactured by Xybion Electronic Systems Corporation[3] detects the visible synchrotron radiation from

*Work supported by Department of Energy Contract DE-AC03-76SF00515. Presented at the *16th IEEE Particle Accelerator Conference (PAC'95) and International Conference on High Energy Accelerators*, Dallas, Texas, May 1-5

0-7803-3053-6/96/$5.00 ©1996 IEEE

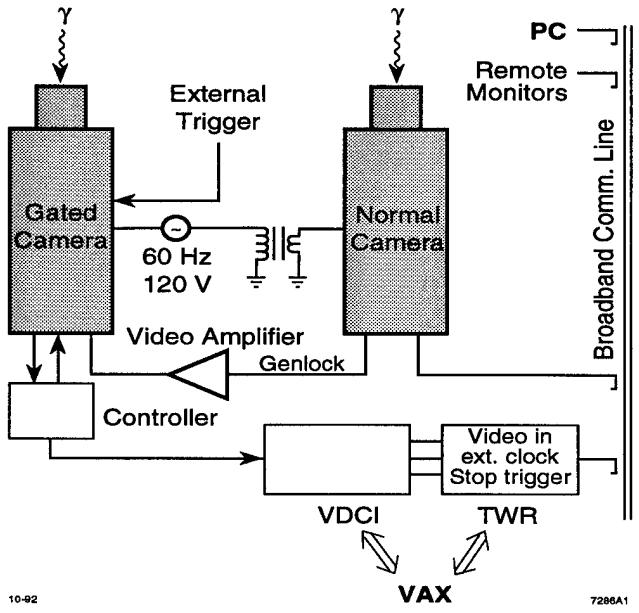


Figure 1. Data acquisition system.

1.19 GeV bunches of $\sim 0.5-3.5 \cdot 10^{10}$ e^- or e^+ in a 2.0 m radius of curvature bending field. The camera's fast gating capabilities allow the imaging of a single bunch on a single ring revolution. Since the system bandwidth limits the data acquisition time, images corresponding to consecutive turns are actually obtained from different machine pulses. Fig. 1 shows a block diagram of the detection apparatus. A line-locked (normal) camera is used to supply composite synchronization for the gated camera. The signals are read out using a SLAC-built video digitizer clock interface (VDCI), and a 30 MHz 8k × 8 bit transient waveform recorder (TWR)—and processed by the SLC control system's VAX using its automated emittance measurement system.[4] Fig. 2 shows digitized data for the first 12 turns. The data are processed by first digitizing a background image, which is then subtracted from a digitized beam image. The x and y-axis projections of the background-subtracted image are found and fit to Gaussians, as shown in Fig. 3.

IV. DIAGNOSTIC AND TUNING EXPERIMENTS

Plotted in Fig. 4 are the measured mean square beam sizes in the x and y planes acquired over the first 100 turns, and their Fourier transforms. The peaks at the betatron frequency and at its second harmonic indicate the presence and size of dispersion and β—mismatches, respectively, in the injected beam. The phase of the mismatch is also obtained by the Fourier transform. The ν values obtained from the 2ν and ν peaks here, agree with the ν peak in the beam centroid data. If ρ is the ratio of the strengths of the $\mu = 2\nu$ to the $\mu = 0$ peaks, the mismatch measure is $B = 1/\sqrt{1-\rho^2}$ according to eq. (4). The equivalent emittance $\bar{\epsilon}$ is just the $\mu = 0$ peak, from which the emittance ϵ follows as $\bar{\epsilon}/B$, which is also the in-quadrature sum of the two peaks. For pure 2ν oscillations the fractional mean square size variations $\left(\langle x^2\rangle^{\max} - \langle x^2\rangle^{\min}\right) / \left(\langle x^2\rangle^{\max} + \langle x^2\rangle^{\min}\right) = \rho$ as well.

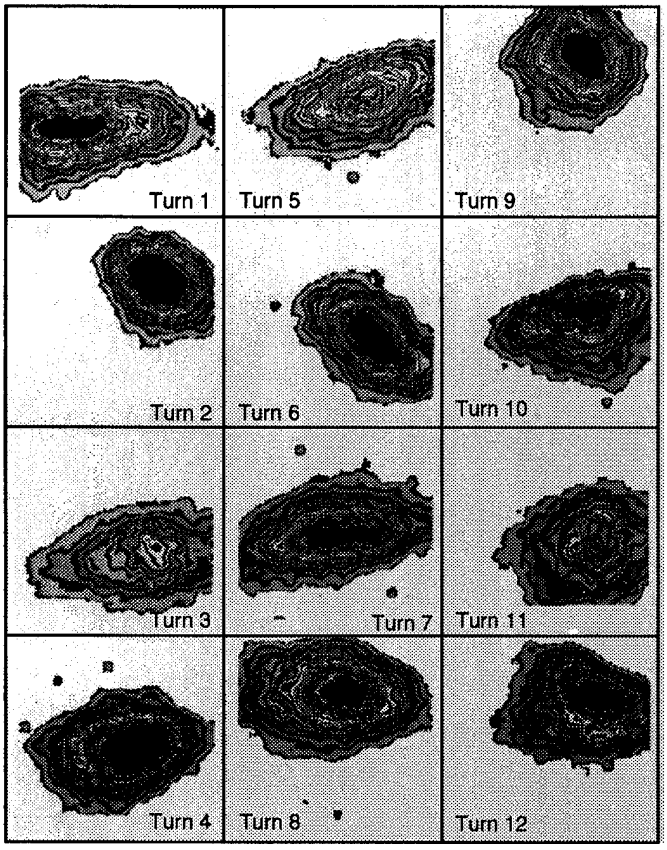


Figure 2. x-y plane beam images for the first 12 turns in the SLC e^- damping ring for $\nu_x \cong \nu_y \approx .25$.

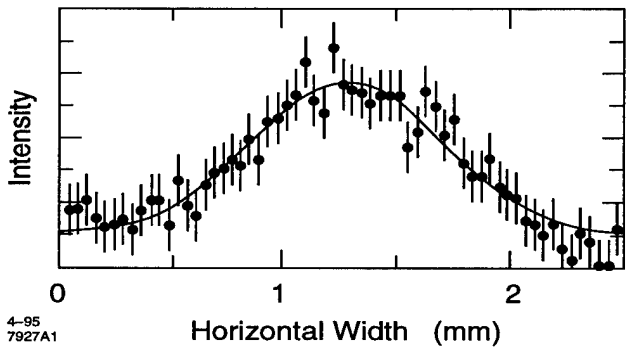


Figure 3. Plane projected data and Gaussian fit.

Even for quite prominent appearing envelope oscillations $B \sim 1 + \frac{1}{2}\rho^2$, corresponding to B values not much bigger than 1. B as determined by this technique is free of any dependence on the length scale calibration of the camera. The absolute emittance depends quadratically on this scale, and on the matched β-function at the observation point—but is otherwise independent of the lattice model.

Optimizing the Match: Gross mismatches can be seen by comparing the beam images corresponding to different turns directly on a tv monitor. The matching quadrupoles in the ring injection line can be used to reduce the differences in the turn-to-turn beam size changes in both the x and y planes. A good match was achieved by measuring the beam sizes after the beam had nearly completely filamented as a function of the strength

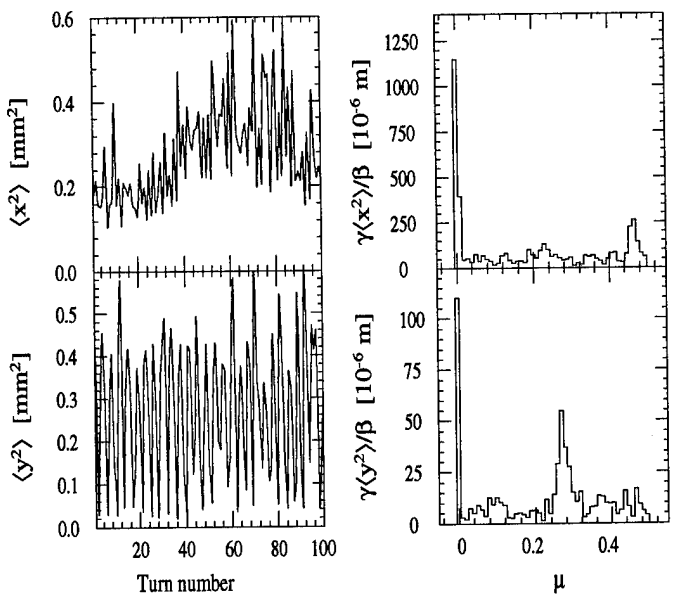


Figure 4. Mean square beam size turn-by-turn data, and its Fourier transform, normalized to have units of Lorentz invariant emittance. Peaks are evident at ν_x and $2\nu_x$ for $\nu_x = .235$, and $1 - 2\nu_y$ for $\nu_y = .365$, indicating a horizontal dispersion function mismatch and β-mismatches.

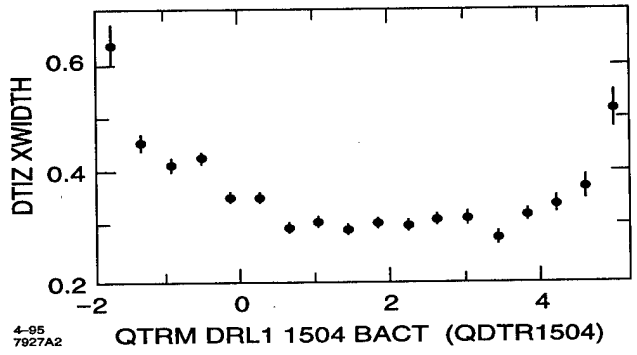


Figure 5. Filamented rms beam size measured as a function of quadrupole strength.

of the matching quadrupoles. Finding the optimum sampling time involved making a coarse scan in which the trigger time was moved in steps of many hundred turns. Plotted in Fig. 5 is the measured size of the filamented beam at about 0.15 ms after injection as a function of quadrupole strength. The minimum width corresponds to the optimum match. Adjustments to this and other quadrupoles yielded a near perfect match as confirmed by the measurements of the first 100 turns shown in Fig. 6.

V. PROSPECTS

The methods developed here have also been used to study the effects of coherent centroid motion on the beam envelope.[5] They could easily be extended to include the x-y correlations in the injected beam as long as the ring is operated off all coupling resonances, and to higher moments $\langle x^3 \rangle$, $\langle x^4 \rangle$, *etc.*. Simultaneous sampling from more that one location in the ring can be used to separately determine the energy spread and the injected dispersion function.[6] The observation of higher betatron harmonics would indicate the presence of nonlinearities in the lattice of the ring and could provide a measure of their strength. Given a suitable signal, alternative to synchrotron light, these techniques can be used in hadron machines.

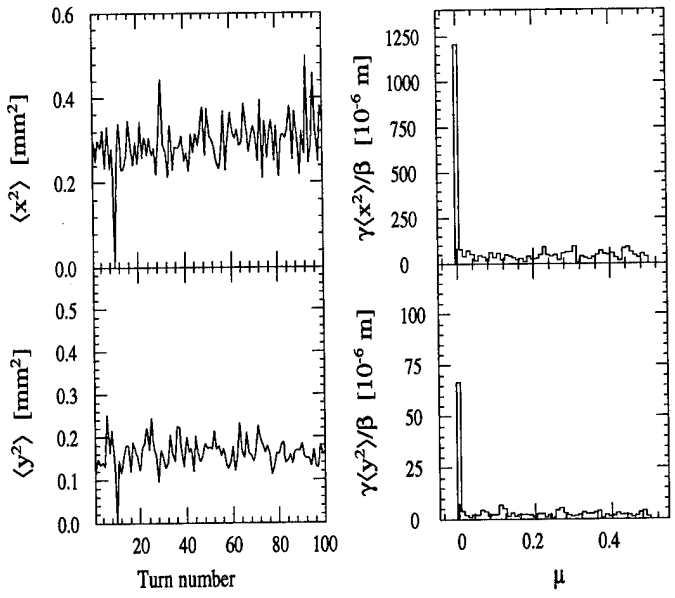


Figure 6. The same measurements as Fig. 4, after optimizing the match.

[1] All orders in $\Delta\eta$ and η require the substitutions: $B\epsilon \rightarrow B\epsilon + \left(\eta^2 + \frac{1}{2}||\Delta\eta||^2 \langle\delta^2\rangle\right)/\beta$ and $\sqrt{B^2-1}\,\epsilon \rightarrow \sqrt{\left(B^2-1\right)\epsilon^2 + \frac{1}{4}\left(||\Delta\eta||^2\langle\delta^2\rangle/\beta\right)^2}$.

[2] M. G. Minty *et al. AIP Conf. Proc.* **281** (1992) 158.

[3] Xybion Corporation, San Diego, CA 92126.

[4] M. C. Ross *et al.*, *1987 IEEE Part. Acc. Conf.*, 725.

[5] M. G. Minty, A. W. Chao, W. L. Spence, these proceedings.

[6] N. Merminga, P. L. Morton, J. T. Seeman, W. L. Spence, *Proc. 1991 IEEE Part. Acc. Conf.* (Chicago), 461.

A MATHEMATICAL MODEL FOR INVESTIGATING CHROMATIC ELECTRON BEAM EXTRACTION FROM A PULSE STRETCHER RING.

Yu.N.Grigor'ev, A.Yu.Zelinsky, Kharkov Institute of Physics and Technology, Kharkov, Ukraine

I. INTRODUCTION

A chromatic beam extraction from a pulse stretcher ring can be realized at a non-zero chromaticity of the machine. The finite chromaticity value stimulates the dependence of the betatron oscillation frequency on the particle energy. This permits one to carry out the beam extraction through the use of the betatron resonance by changing the particle energy.

Considering that during the chromatic extraction the particles are found in the vicinity of the RF separatrix or cross it, the computer code must ensure the simulation of the nonlinear motion of electrons inside and outside of the RF separatrix with due account of the synchrotron radiation effects.

II. A DIPOLE MAGNET WITH A UNIFORM FIELD.

In view of the radiations, the differential equation, the solution of which describes the electron dynamics in the dipole magnet, can be written as [1]:

$$mc\left(\frac{d^2\vec{r}}{ds^2}\right)=\left(\frac{e}{c}\right)\left[\left(\frac{d\vec{r}}{ds}\right)\times\vec{H}+\vec{f}\left(\frac{dt}{ds}\right)\right] \tag{1}$$

where e, m are the electron charge and rest mass respectively, c is the velocity of light, $\vec{r}$ is the electron radius vector defining the particle position in the coordinate space, s is the parameter related to the laboratory time by $ds=cdt\left(1-v^2/c^2\right)^{1/2}$, v is the electron velocity, $\vec{f}$ is the force vector of the radiation reaction:

$$\vec{f}=-\frac{2e^4}{3m^2c^7}\left(\frac{d\vec{r}}{dt}\right)\left[\left(\frac{d\vec{r}}{dt}\right)\times\vec{H}\right]^2, \tag{2}$$

$\vec{H}$ is the magnetic field strength vector.

Under the assumption that $\vec{H}$ comprises only the axial component and is independent of the coordinates and time, eq.(1) can be integrated in the Cartensian system. It is convenient to present the integration results in the cylindrical frame (ρ,φ,z) as:

$$\frac{E}{\varepsilon}=\sqrt{1+c^2\left(1-\frac{\varepsilon^2}{E^2}\right)\Big/\left(2Bs+c_1\right)\left(v_{0\rho}^2+v_{0\varphi}^2\right)} \tag{3}$$

$$\frac{\left(v_\rho^2+v_\varphi^2\right)}{c^2}=\frac{\left(\varepsilon/E_0\right)^2}{\left(2Bs+c_1\right)} \tag{4}$$

$$\left(\frac{v_z}{v_{0z}}\right)=\left[\frac{c_1}{\left(2Bs+c_1\right)}\right]^{1/2} \tag{5}$$

$$z=\frac{v_{0z}\sqrt{c_1}\left(\frac{E_0}{\varepsilon}\right)\left[\left(2Bs+c_1\right)^{1/2}-c_1^{1/2}\right]}{Bc}+z_0 \tag{6}$$

$$\rho=\left[\rho_0^2+\left(\frac{\pi}{BD}\right)\left(\Phi_1^2+\Phi_2^2\right)+\rho_0\sqrt{\left(\pi/BD\right)\Big/ v_{0\rho}^2+v_{0\varphi}^2}\left[v_{0\varphi}\Phi_1+v_{0\rho}\Phi_2\right]\right]^{1/2} \tag{7}$$

$$v_\rho=\left\{\frac{c}{\rho}\left(\frac{\pi}{BD}\right)^{1/2}\left(\frac{\varepsilon^2}{E^2}\right)\left[\Phi_1\sin 2\Omega+\Phi_2\cos 2\Omega\right]+\left(\frac{\varepsilon}{E}\right)\left(\frac{\rho_0}{\rho}\right)\left[\frac{c\left[v_{0\rho}\cos 2\Omega+v_{0\varphi}\sin 2\Omega\right]}{\left(v_{0\rho}^2+v_{0\varphi}^2\right)^{1/2}}\right]\right\}\left(2Bs+c_1\right)^{-1/2} \tag{8}$$

$$\tan\varphi=\frac{M\left[v_{0\varphi}\Phi_2-v_{0\rho}\Phi_1\right]}{M\left[v_{0\varphi}\Phi_1-v_{0\rho}\Phi_2\right]+\rho_0} \tag{9}$$

$$t=\left(\frac{1}{2Bc}\right)\left\{\sqrt{\left(2Bs+c_1\right)\left(2Bs+L\right)}-\sqrt{Lc_1}+N\ln\left\{\frac{\left[4Bs+L+c_1+2\sqrt{\left(2Bs+L\right)\left(2Bs+c_1\right)}\right]}{\left(\sqrt{L}+\sqrt{c_1}\right)^2}\Big/\frac{\left[4Bs+L+c_1-2\sqrt{\left(2Bs+L\right)\left(2Bs+c_1\right)}\right]}{\left(\sqrt{L}-\sqrt{c_1}\right)^2}\right\}\right\} \tag{10}$$

0-7803-3053-6/96/$5.00 ©1996 IEEE

where

$$\Phi_1 = \left[s(u) - s(u_0)\right]\cos u_0 - \left[c(u) - c(u_0)\right]\sin u_0,$$

$$\Phi_2 = \left[c(u) - c(u_0)\right]\cos u_0 - \left[s(u) - s(u_0)\right]\sin u_0,$$

ρ, φ, z are the radius, azimutal angles and axial coordinate, $s(u), c(u)$ are the Fresnel sine and cosine integrals, respectively

$$c(u) = (2\pi)^{-1/2}\int_0^u \left(\frac{\cos\eta}{\sqrt{\eta}}\right)d\eta, s(u) = (2\pi)^{-1/2}\int_0^u \left(\frac{\sin\eta}{\sqrt{\eta}}\right)d\eta$$

$$u = (2Bs + c_1)\alpha \qquad u_0 = c_1\alpha$$

ε is the rest energy of the electron, E is its total energy,

$$v_\rho = \frac{d\rho}{dt}, v_\varphi = \rho\frac{d\varphi}{dt}, v_z = \frac{dz}{dt}, \Omega = \frac{Ds}{2}$$

$$B = \left(\frac{2e^4H^2}{3m^3c^6}\right), D = \frac{eH}{mc^2}, L = \frac{c^2}{\left(v_{0\rho}^2 + v_{0\varphi}^2\right)},$$

$$C_1 = L\left(\frac{\varepsilon^2}{E^2}\right), M = \frac{\left(\pi/BD\right)^{1/2}}{\left(v_{0\rho}^2 + v_{0\varphi}^2\right)^{1/2}},$$

$$\alpha = \left(\frac{D}{2B}\right), N = L\left[1 - \left(\frac{\varepsilon}{E_0}\right)^2\right]$$

The index '0' denotes that the associated quantities refer to the initial moment $t_0 = 0$, $\varphi_0 = 0$. Formulas (4)-(12) enable one to calculate all the necessary quantities.

The procedure of calculating the electron parameters at the exit of the dipole magnet with the angular length φ should be carried out in the following order.

First, the s value is obtained from formula (9) and is substituted into formulas (3-8) and (10). Simultaneously, $E, v_z, \left(v_\rho^2 + v_\varphi^2\right), z, \rho, t$ will be calculated.

Eventually, by the use of formula (4) and the obtained v_ρ value, the v_φ value is calculated.

Formulas (3-10) enable one to calculate all the necessary quantities. However, their employment in the given form is somewhat inconvenient for the computer. Therefore, to simplify the procedure, the following approximations should be made.

By virtue of the fact that the arguments of the Fresnel sine and cosine integrals have large values ($u_0 >> 4*10^{15}\gamma^{-2}H^{-1}$, is in gausses), the s and c can be calculated by using their asymptotic representations [2]:

$$S(u) = \left(1/2\right) - \frac{1}{\sqrt{2\pi u}}\cos u + 0\left(1/u^2\right)$$

$$C(u) = \left(1/2\right) - \frac{1}{\sqrt{2\pi u}}\sin u + 0\left(1/u^2\right)$$

On calculating t as a function of s, in expression (10) we use the condition of smallness of $2Bc/L$ and $2Bs/c$, as compared with the unity: $t \approx \left(s/2c\right)\left(E_0/\varepsilon\right)\left[5 - 3\left(\varepsilon/E_0\right)^2\right]$

III. CYLINDRICAL RF CAVITY.

For the cylindrical Rf cavity operating in the fundamental TM_{010} mode, the electrical and magnetic RF field components in the cylindrical coordinate frame can be represented as:

$$\varepsilon_z = -\varepsilon^0\sin(\omega t + \alpha)I_0(kr), H_\vartheta = -\varepsilon^0\cos(\omega t + \alpha)I_1(kr),$$

where I_0 and I_1 are the Bessel functions; $k = \frac{P}{a}$; P is the first root of the equation $I_0(Pa) = 0$; a is the cavity cylinder radius; r is the polar radius. The z axis is directed along the cavity axis; ϑ is the azimutal angle; $\omega = 2\pi\nu; \nu$ is the RF field frequency.

By solving the differential Newton -Lorents equation $\frac{dP}{dt} = e\varepsilon + \frac{e}{c}\left[\frac{d\vec{r}}{dt} \times \vec{H}\right]$ for the electron moving in the cavity, we can obtain:

$$Er^2\dot{\vartheta} = E_0r_0^2\dot{\vartheta}_0 = C_1 \tag{11}$$

$$E\dot{z} = \left(\frac{e\varepsilon^0c^2}{\omega}\right)I_0(kr)\cos\omega t + C_2, \tag{12}$$

$$C_2 = E_0z_0 - \left(\frac{e\varepsilon^0c^2}{\omega}\right)I_0(kr_0)\cos\alpha.$$

$$\frac{\dddot{\vartheta}}{\dot{\vartheta}} - \frac{3}{2}\left(\frac{\ddot{\vartheta}}{\dot{\vartheta}}\right)^2 + 2\dot{\vartheta}^2 - \frac{2ec\dot{z}H_\vartheta}{\left(EC_1/\dot{\vartheta}\right)^{1/2}} + \frac{\ddot{E}}{E} - \frac{1}{2}\left(\frac{\dot{E}}{E}\right)^2 = 0 \tag{13}$$

$$\dot{E} = e\dot{z}\varepsilon_z \tag{14}$$

Assuming $kr \langle\langle 1$, we put $I_0(kr) \equiv 1$. Under this approximation, we have $I_1(kr) \equiv 0$, and therefore, in eq. (13) should be also set to equal zero.

Using eqs. (11)-(14), we come to the following formulas:

$$E \cong E_0\left\{1+\frac{2eC_2 s^0}{E_0^2\omega}\left[\cos(\omega t+\alpha)-\cos\alpha\right]\right.$$

$$\left.+\frac{e^2\varepsilon^{0^2}c^2}{2E_0^2\omega^2}\left[\cos(2\omega t+2\alpha)-\cos 2\alpha\right]\right\}^{1/2} \qquad (15)$$

$$\dot{z} \cong \frac{\left[\frac{e\varepsilon^0 c^2}{2E_0^2\omega^2}\cos(\omega t+\alpha)+C_2\right]}{E} \qquad (16)$$

$$z \cong \frac{\dot{z}_0+e\varepsilon^0 c^2\cos\alpha}{E_0\omega\gamma_{z0}^2}t-\frac{e\varepsilon^0 c^2}{E_0\omega\gamma_{z0}^2}\left[\sin(\omega t+\alpha)-\sin(\alpha)\right]$$

$$\dot{\vartheta} \cong \dot{\vartheta}_0\Big/\chi_1^2-\frac{\ddot{\vartheta}_0}{\dot{\vartheta}_0}\chi_1\chi_2+\left[\left(\frac{\ddot{\vartheta}_0}{2\dot{\vartheta}_0^2}\right)^2+1\right]\dot{\vartheta}_0^2\chi_2^2 \qquad (17)$$

$$2\vartheta=\frac{\arctan\left[2\chi_2\left(\dot{\vartheta}_0^{-1}\chi_1-\frac{\ddot{\vartheta}_0}{2\dot{\vartheta}_0^2}\chi_2\right)\right]}{\left(\dot{\vartheta}_0^{-1}\chi_1-\frac{\ddot{\vartheta}_0}{2\dot{\vartheta}_0^2}\chi_2\right)^2-\chi_2^2}+2\vartheta_0 \qquad (18)$$

$$\chi_1=\left(\frac{E}{E_0}\right)^{1/2}\left(1-\frac{1}{2}Y\right);\chi_2=(EE_0)^{1/2}Y;(\chi_1\dot{\chi}_2-\dot{\chi}_1\chi_2)=1$$

$$Y=\frac{2}{E_0\omega\sqrt{(1-a\cos\alpha)^2-a^2}}\arctan\left[\sqrt{\frac{1-a\cos\alpha-a}{1-a\cos\alpha+a}}\left(\tan\frac{\omega t+\alpha}{2}-\tan\frac{\alpha}{2}\right)\right],$$

where

$$\dot{\vartheta}_0=\frac{v_{\vartheta 0}}{r_0};\ddot{\vartheta}_0=-\left(\frac{2v_{r0}}{r_0}\right)+\frac{e\dot{z}_0\varepsilon^0 v_{\vartheta 0}\sin\alpha}{E_0 r_0};\gamma_{z0}^2=\left[1-\left(\frac{\dot{z}_0}{c}\right)^2\right]^{-1};$$

$$v_{r0}=\dot{r}_0=\left(\frac{dr}{dt}\right)_0;a=\left(\frac{e\dot{z}_0\varepsilon^0}{E_0\omega}\right);t_0=0$$

By substituting the cavity length value equal to λ/2, where λ is the RF field wave length, into (16), we can calculate the particle transit time

$$\tau \approx \frac{\lambda}{2\dot{z}_0}\left[1-\frac{ec\varepsilon^0\cos\psi}{E_0\omega\gamma_{z0}^2}-\frac{2ec\varepsilon^0\sin\psi}{\pi E_0\omega\gamma_{z0}^2}\right] \qquad (19)$$

It should be noted that at $c_1=0, \dot{\vartheta}\equiv 0$ the $\dot{r}$ and r values are given by

$$\dot{r}=\frac{\dot{r}_0E_0}{E}, r=r_0E_0Y$$

In the general case, the values of $\dot{r}=v_r$ and r should be calculated by formulas

$$v_r=c\left[1-\left(\frac{\varepsilon}{E}\right)^2-\left(\frac{\dot{z}}{c}\right)^2-\left(\frac{v_\vartheta}{c}\right)^2\right]^{1/2} \qquad (20)$$

$$r=\left(\frac{c_1}{E\dot{\vartheta}}\right)^{1/2} \qquad (21)$$

The formulas presented here to calculate the dynamic variables after it traversed the cavity can also be used for the case, where ε^0 and ω are the slow functions of time: $\left(d\omega/dt\right)\Big/\left(\omega/\tau\right) \ll 1$, $\left(d\varepsilon^0/dt\right)\Big/\left(\varepsilon^0/\tau\right) \ll 1$, t is the particle transit time.

IV. Conclusion.

The algorithms described in [3,4] can be used to describe the dynamic characteristics of particles in the other magnetic elements of storage ring. The calculation time of the proposed mathematics model will be considerably longer. However it is supposed that the adequately of the given model to the physical process going at the extraction achromatic regime will compensate this shortcoming.

V. REFERENCES.

[1] L.Landau and E.Lifshits, The field theory. (in Russion), Mir, Moscow,1960.

[2] K.Janke,F.Emde,F.Losch, Tabeln hoherer functionen, Shtutgart,1960.

[3] P.I.Gladkikh,A.Yu.Zelinsky,M.A.Strelkov, Preprint KhFTI 89-44,Moscow, ISNIIAI publ.,1989.

[4] A.W.Chao, Some linear-Lattice Calculations Using Generalized Matrices, Internal Report DESY PET-77/07, July,1977,p.11.

THE DYNAMICAL APERTURE OF ISI - 800

S.Efimov, I.Karnaukhov, S.Kononenko, A.Shcherbakov, A.Tarasenko, A.Zelinsky

National Science Centre 'Kharkov Institute of Physics and Technology',
Kharkov, Ukraine

Beam dynamics studies of the ISI-800 electron storage ring are described in the normal operation mode, the operation mode with a wiggler and the modified lattice with a superconducting magnet. A study of the effects of resonances included by sextupoles and optimization of dynamical aperture is carried out. The effects of magmetic multipole errors, alignment and excitation errors are discussed.

1. ISI-800 LATTICE CHARACTERISTICS

The Ukrainian Synchrotron Light Source ISI-800 is desiged as a dedicated vacuum ultraviolet - soft x-ray radiation source. The photon beams will be provided by bending magnets and insertion devices (wigglers, undulators).

The lattice ISI-800 is a four-fold symmetric three-bend achromat lattice operating with 800MeV electrons [1]. Three-meter of long dispersion-free straight sections are provided for insertion devices.

Figure 1 shows the optical function for the normal operation mode in the superperiod of the ring. Figure 2 shows the optical functions for the operation mode with a wiggler magnet (H_{max}~ 10T) in the dispersion-free straight section. In th-s operation mode the optical functions are the same as in the normal operation mode, except for the straight section with a wiggler. The harmony of optical functions is ensured by two quadrupole triplets in addition. The latest lattice version of ISI-800 is a modified lattice of four-fold three-bend achromat, where the central magnet is superconducting with H~10T [2]. Figure 3 shows the optical functions for the modified lattice.

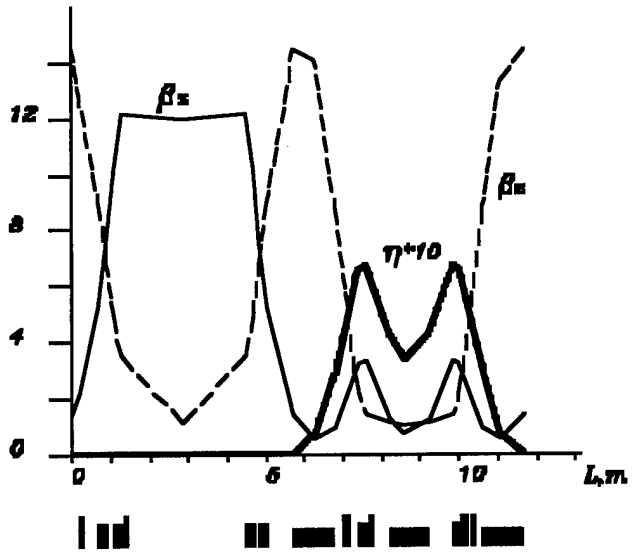


Figure 1. Superperiod of the ISI-800 and focusing function for the normal operation mode. The linear horizontal and vertical tunes are ν_x=4.24, ν_z=3.16.

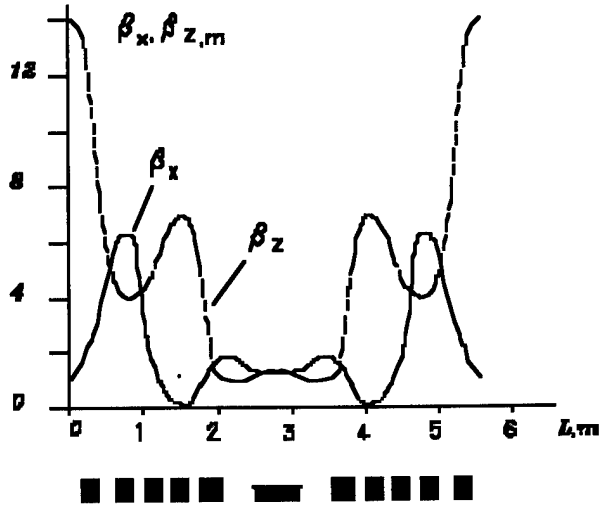


Figure 2. Focusing functions in the straight section with a wiggler. ν_x=5.26, ν_z=3.18.

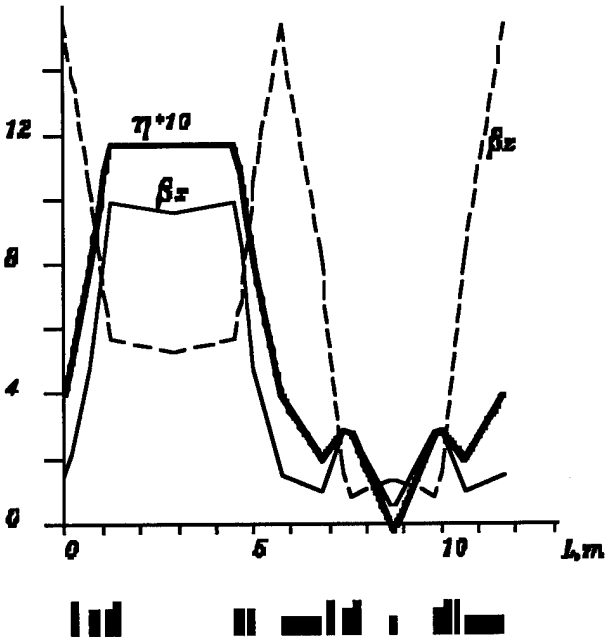


Figure 3. The focusing functions of one superperiod of modified lattice ISI-800 for the operation mode with minimum emittance. ν_x=4.3, ν_z=3.2.

0-7803-3053-6/96/$5.00 ©1996 IEEE

2. RESULTS OF THE ISI-800 DYNAMICAL APERTURE CALCULATION

The dedicated storage ring must be optimized for a small beam emittance. This had lead us to the use of strong focusing lattices, which produce large chromatic aberrations. The natural chromaticity $\varepsilon_0\nu/(\Delta p/p)$ (ε_{0x}= -7.6, ε_{0z}=6.9 for ISI-800 normal operation mode; ε_{0x}= -8.9, ε_{0z}= -10.15 for operation mode with a wiggler; ε_{0x}= -6.2, ε_{0z}= -6.6 for operation mode with a modified lattice) must be compensated. Two families of chromaticity correcting sextupoles are introduced in the dispersive straight sections of the ring. These sextupoles, however, introduce non-linear perturbations which limit the dynamical aperture of the ring.

We try to minimize the effects of these chromaticity correcting sextupoles by introducing two other sextupole families located in the non-dispersive straight section. The theoretical optimization of the sextupoles located in the non-dispersive straight section is based, on the one hand, on the analytically determinated region of stability due to the joint action of the first-and third-order resonances perturbed by sextupole fields [3] for ν_x~4; $3\nu_x$~12 and, on the other hand, on the minimization of the tune shift with amplitude.

In the case where the linear tune is far from resonances, we have:

$$\Delta\nu_x=AJ_x+BJ_z;\ \Delta\nu_z BJ_x+CJ_z\ ,$$

where $\Delta\nu_x$ and $\Delta\nu_z$ are the horizontal and vertical tune shifts; A,B,C are the coefficients determined by the lattice only (they are, thus, dependent on sextupole configuration), and J_x, J_z are the action variables which are the constants of motion and depend on the initial conditions of the particle. The calculations of the tune shift with amplitude are done by the code DeCA [4]. The sextupoles are considered as thin lenses. Figures 4, 5, 6 shows the dynamical aperture analytic calculations based on the joint action of the first-and third-order resonances and the tune shift depending on amplitude [3]. (curves 1).

Table 1 lists the values for the coefficients of the tune shift depending on amplitude for the normal operation mode (N), the operation mode with a wiggler (W) and the operation mode of the modified lattice (M).

Table 1.

	N	W	M
A, m^{-1}	-165	21	-122
B, m^{-1}	-321	721	-5
C, m^{-1}	-133	50	-157

For comparison we give the dynamical aperture values calculated at the same conditions by the code DeCA [4] (200 particles, 50 turns) - curves 2. The approach described above considers the effects of sextupoles on the lattice only. To take into consideration other effects such as higher-order multipole errors, excitation and alignment errors numerical tracing simulation is performed with DeCA. The final choice of the sextupole strengths is based on the results of computer simulation.

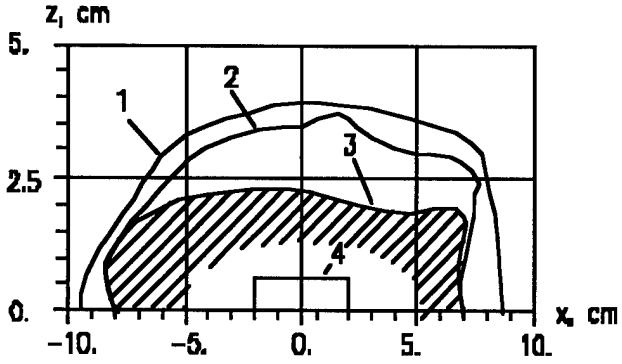


Figure 4. Dynamical aperture in the middle of the insertion straight section for the normal operation mode. 1- Analytical calculations of dynamucal aperture with consideration of the combined action of first-and second-order resonances and the tune shift depending on amplitude. 2- Dynamical aperture obtained by numerical calculations (200 particles, 50 turns) if only regular sextupoles exist. 3- Dynamical aperture obtained by numerical calculations if systematic multipole errors are occur. 4- Geometrical aperture in the middle the straight section. The hatched region corresponds uncertainly region of dynamical aperture.

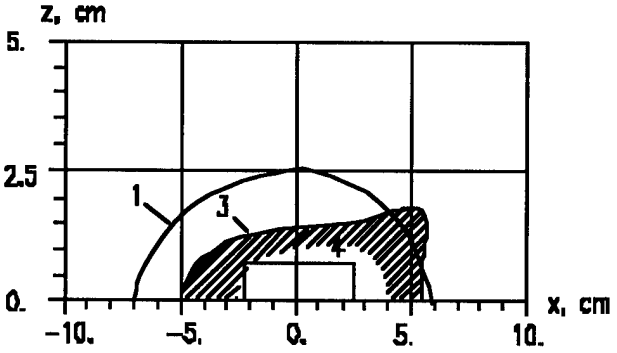


Figure. 5. Dynamical aperture in the middle of the insertion straight section for the operation mode with a wiggler.

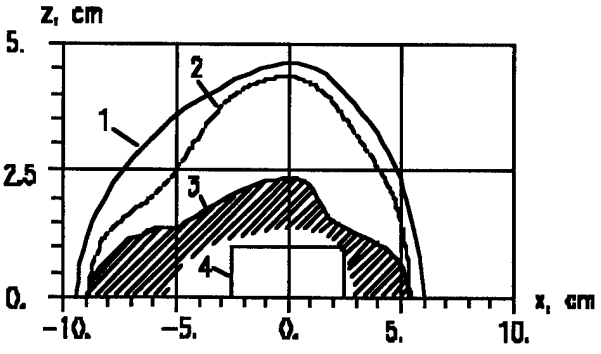


Figure 6. Dynamical aperture in the middle of the insertion straight section for the modified lattice.

The multipole errors are the higher-order terms of the real magnetic field expansion. Multipole errors fall into two categories: systematic and random multipole errors. The systematic errors are those caused by the finite dimensions of the poles and the same for each magnet of the same kind, whereas the random errors arise because of constructional tolerances and are different for each magnet.

Analysis of systematic errors shows that the influence of sextupole and octupole components of dipole magnetic fields is of most vital importance. Sextupole components were determined by calculating the using the Poisson equation. The octupole component of the dipole magnetic field is connected with fringing fields and is determined by the method offered in [5].

Table 2 shows the systematic multipole errors included for simulation (l_m - length of element).

Table 2.

	Normal dipole	Super - conducting dipole	Wiggler
$\frac{\partial^2 H_z}{\partial x^2} l_m$, T/m	4	40	3
$\frac{\partial^3 H_x}{\partial z^3} l_m$, , T/m^2	100	1000	1600

Figures 4, 5, 6 shows the dynamical aperture (curves 3), which was obtained with the DeCA (200 particles, 50 turns) attached to systematic errors. These errors lead to the decrease of the dynamical aperture in vertical. Systematic quadratic nonlinearities are compensated by correcting sextupoles.

After determining the dynamical aperture with systematic multipoles included errors of a simulation involving random multipole errors (table 3) plus distortion of the closed orbit (Δ x, Δz) with one standard deviation Δx, Δz ~2mm was performed.

Table 3.

Multipoles	One standard deviation
$\frac{\partial^2 H}{\partial x^2} l_m$, T/m	3
$\frac{\partial^3 H}{\partial x^3} l_m$, T/m^2	100
$\frac{\partial^4 H}{\partial x^4} l_m$, T/m^3	5000

Particles are tracked using code DeCA for 200 particles and 200 turns. Results for the dynamical aperture calculations in the middle of the long insertion straight section are shown in figures 4, 5, 6. The hatched regions in these figures correspond to the uncertain region of dynamical aperture for three different sets of random errors and closed orbit used.

3. CONCLUSIONS

The dynamical aperture of the ISI-800 storage ring for the normal operation mode, the operation mode with a wiggler and the operation mode of a modified lattice has been optimized using two families of sextupoles in the nondispersive straight section using Hamiltonian formalism. These calculations are used to obtain the first estimate to the values of the correcting sextupoles.

The optimum set of values is found by numerical tracking including higher-order systematic multipoles which are not taken into account in the previous formalism. We have found for ISI-800, that even if other random errors are included, the dynamical aperture remains sufficiently large.

REFERENCES

[1] Androsov V. et al. Synchrotron radiation complex ISI-800, Journal of Electron Spectroscopy and Related Phenomena, 68 (1994),p.747-755.

[2] Shcherbakov A. et al. A combined magnet lattice of the synchrotron light source ISI-800, Proc. of PAC95 (Dallas TX, May 1995).

[3] Ando A. Distortion of beam emittance with nonlinear magnetic fields, Particle Accelerators, v.15(3), 1984, p.177-207.

[4] Gladkikh P.I. et al. DeCA - code for analysing and designing of cyclic accelerators, Proc. EPAC-90, v.2, p.1234-1236.

[5] Bulyak E.V., Efimov S.V. Nonlinear effects occurring due to fringe fields of cyclic accelerators dipoles. Proc. EPAC-90, v.2, p.1455-1457.

The Influence of Residual Vertical Dispersion on LEP Performance

P.Collier & H. Schmickler, CERN, 1211-Geneva, Switzerland

ABSTRACT

During LEP Operation for Luminosity production, the closed orbit is systematically corrected towards a reference orbit which has been empirically found to produce high luminosities. Machine studies have been undertaken to try and understand the mechanism by which the vertical closed orbit affects the luminosity. The dominant parameter has been found to be the residual vertical dispersion, in particular the residual vertical dispersion at the interaction points. This paper reports on studies to investigate how the quality of the closed orbit affects the residual vertical dispersion and especially the residual vertical dispersion at the interaction points.

I. INTRODUCTION

During the LEP operation period in 1994, the operations group found that the luminosity performance of LEP depended critically on the vertical closed orbit [1]. By reloading orbit correctors from a previous 'good' physics fill and correcting back to the orbit measured during this fill, reproducibly good performance for the machine was attained.

Work was started to try and understand the link between orbit and luminosity performance. The vertical orbit in LEP is routinely corrected to a sigma of about 0.6 mm. It was quickly found that 'good' and 'bad' orbits for luminosity were qualitatively the same, in terms of sigma's. The difference between the two being more related to the history of orbit corrections used to achieve the desired result, than the global features of the orbit itself.

The studies made in 1994 concentrated on three main beam parameters which could be affected by the correction of the vertical closed orbit; average residual vertical dispersion, coupling and the local residual dispersion at the interaction points.

Average Residual Vertical Dispersion

The average residual vertical dispersion is an important parameter which can lead to significant increases in beam size and hence, lower luminosity. It is also known to be driven by the specific details of how the orbit is corrected. For example, the correction of the effect of magnet misalignments with non-local orbit correctors and asymmetric bumps across the interaction regions are all known to drive the vertical dispersion. A systematic series of measurements of the dispersion were taken during physics fills. The measured sigma of the residual dispersions were all in the range of 5 to 15 cm. No correlation with the luminosity could be found [2]. A dedicated study of the variation of vertical beam size with dispersion was undertaken. The results are shown in figure 1. For values below 15 cm, the residual vertical dispersion no longer dominates as the source of increased beam size. Thus, the luminosity performance of LEP in physics cannot be explained by vertical dispersion alone.

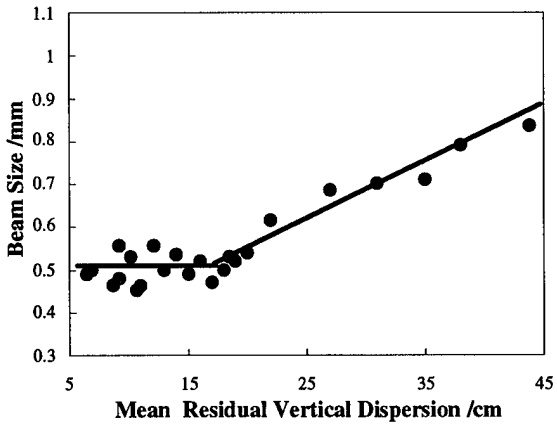


Figure 1: Vertical Beam Size, Measured using a UV monitor in LEP as a Function of rms. Vertical Dispersion

Coupling

Coupling can be driven by discrete sources, such as the experimental solenoids (known as solenoid coupling) and by extended sources, such as the closed orbit in the sextupoles (machine coupling). The latter case could provide the mechanism whereby the vertical closed orbit affects the luminosity performance of LEP. In both cases, the correction of coupling in LEP is made with discrete sqew quadrupoles installed in the straight sections around each LEP experiment.

Studies on the effect of coupling on the luminosity performance have been published [2]. It was found that the machine coupling, characterized by the closest tune approach method, could be changed significantly by the strategy used to correct the vertical closed orbit. The emittance ratio,κ, generated by a given value of coupling is related to the closest tune approach by the equation [3]:

$$\kappa = 1 - \frac{(2r^2+1)}{(4r^2+1)}$$

where

$$r = \frac{\delta q}{2|q_h - q_v|} \qquad [1]$$

Where, $|q_h - q_v|$ is the distance of the working point to the main coupling resonance and δq is the measured closest tune approach. In LEP $|q_h - q_v| = 0.14$. For high luminosity performance the emittance ratio must be kept below the ratio of the betatron functions at the interaction point. In LEP the betatron function ratio is 2% (β^*_h = 2m, β^*_v = 5 cm). For this, a closest tune approach of less than 0.028 is acceptable. It was foundthat, for all correction

0-7803-3053-6/96/$5.00 ©1996 IEEE

strategies tested, the measured closest tune approach value was less than this limit.

It was also speculated that the first synchrotron sideband of the main coupling resonance would have a similar effect to the main coupling resonance. Theoretical studies made since[4], have shown that the synchrotron sideband of the main coupling resonance is not strong enough to significantly affect the emittance ratio, and hence the luminosity performance. However, the coupling remains a parameter which is routinely adjusted by the operators, in order to achieve the highest performance. If the machine is tuned to the highest performance, especially at the end of a physics coast, the emittance ratio is well below the 2% limit mentioned above. For these conditions the tuning constraints for coupling become more strict and a closest tune approach of the order of 0.01 has to be achieved.

II. OFFSETS FROM K-MODULATION

The vertical closed orbit is of critical importance for generating polarized beams in LEP. Polarization is used routinely to measure the LEP beam energy with high precision [5]. In order to improve the quality of the orbit correction and hence polarization levels a system was installed to allow a measurement of the offset of the axis of the orbit pickups to the center of the quadrupole next to it. The system makes use of the technique called k-modulation. So far it has been installed on some of the insertion quadrupoles near to each of the interaction points.

The technique makes use of a low-frequency generator to modulate the strength of a selected quadrupole [6,7]. A sensitive pickup is used to detect the amplitude of the resulting oscillations of the beam at the excitation frequency. The amplitude of the oscillations at the pickup is related to the beam position in the quadrupole which is being modulated and is a minimum when the beam passes through the magnetic center of the quadrupole. Figure 2 shows the amplitude of the beam motion at the k-modulation frequency for various positions of the beam in the modulated quadrupole. The curve has its minimum at 0.13 mm, which is interpreted as an offset between the pickup 'zero' reading and the magnetic center of the quadrupole. All offsets determined this way (the values attain numbers as large as 2 mm) are introduced as additional calibration constants into the orbit measurement system.

Offsets have been measured for several pickups around one of the LEP interaction points and compared with pickup readings taken from a 'golden' orbit, producing high luminosity performance. The data is shown in figure 3. Here the pickup reading for the 'golden' orbit are shown (hatched) together with the same readings after correction for the offsets measured using the k-modulation technique (solid). From the data of figure 3, it seems likely that the 'golden' orbit is just an orbit where the beams pass close to the center of the insertion quadrupoles. This was tested by introducing the offset data, found by k-modulation, into the orbit measurement package. Various techniques were then use to correct the orbit. Without the offsets included, the results, in terms of the performance of the machine, tended to be highly variable. With the offsets in place good luminosity conditions were more easily achieved.

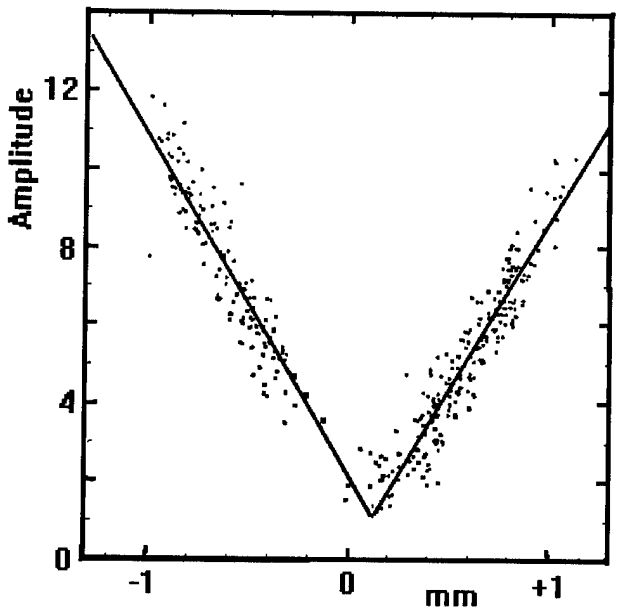


Figure 2: Beam Oscillation Amplitude at a Sensitive Coupler From Modulation of the Strength of a Quadrupole vs. Pickup Reading from the Pickup Next to the Quadrupole.

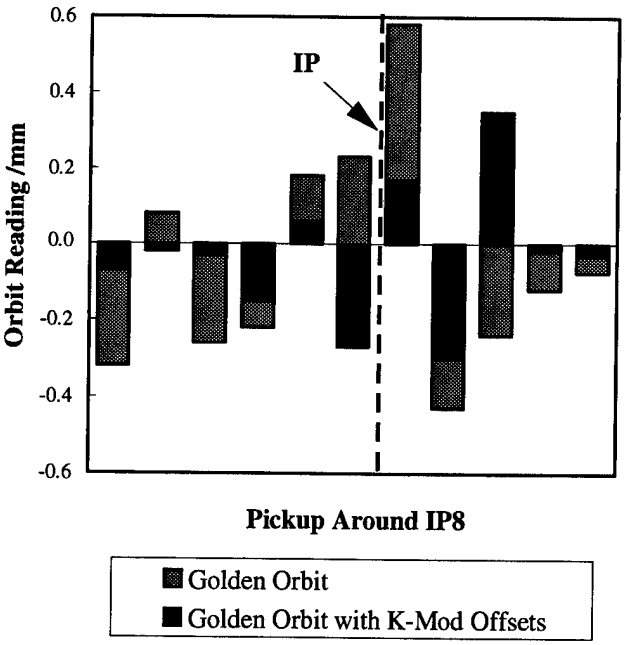


Figure 3: Orbit Readings for a 'Golden Orbit' and the same readings after correction for the offsets measured using k-modulation.

III. THE EFFECT OF BEAM OFFSETS IN THE INSERTION QUADRUPOLES ON LUMINOSITY

From the above chapter it becomes clear that high luminosity performance is achieved by steering the beam through the center of the insertion quadrupoles.

If the beam does not pass through the center of these quadrupoles, the beam experiences a dipole kick. The effect can be corrected with an orbit corrector dipole close by. However, a local dispersion bump in the interaction point can also be produced. This affect has been simulated using the MAD package[8]. Here a 1mm offset was introduced into two symmetric quadrupoles next to an interaction point. The resulting simulated orbit was corrected and the dispersion computed. The results gave a dispersion of around 1cm at the interaction point.

Any dispersion will contribute to the beam size by quadratic addition with the normal beam size from the emittance, using the relation:

$$\left(\sigma_y^*\right)^2 = \varepsilon_y \beta_y^* + \left(\sigma_e D_y^*\right)^2$$

$$ie \qquad [2]$$

$$\left(\sigma_y^*\right)^2 = \left(\sigma_o^*\right)^2 + \left(\sigma_D^*\right)^2$$

Where σ_y^*, $_D{}^{y^*}$ and β_y^* are the beam size, the vertical dispersion and the beta function value at the interaction point, and σ_e is the energy spread of the beam. Table 1 shows the effect of a 1mm local dispersion bump at one of the LEP interaction points with data presented for typical conditions at the beginning and the end of a LEP physics coast.

Table 1: Typical Performance Reductions Expected from the Introduction of 1cm of Vertical Dispersion at one Interaction Point.

Conditions	σ_o / μm	σ_D / μm	Luminosity Change / %
Start of Coast : ε_y ~0.6 nm (Full Wigglers)	**4.0**	**1.6**	**- 8**
End of Coast : ε_y ~0.3 nm (Wigglers Off)	**2.0**	**0.9**	**- 10**

With the symmetry of the LEP machine, the largest effect on vertical dispersion is not in the interaction point where the beam is mis-centered, but in the two adjacent interaction points. Hence all possible offsets in all four interaction points interfere and can increase the above effect.

IV. CONCLUSIONS

Several parameters are affected by the vertical closed orbit correction strategy used during physics coasts. A good control of the coupling compensation and mean residual vertical dispersion are the necessary requisites to obtain high beam-beam tune shifts, above $\xi_y = 0.03$. At this level of tuning, further improvements also need the control of the local dispersion in the interaction points. This dispersion is generated by the beam not passing through the magnetic center of the insertion quadrupoles, due to misalignments of the orbit monitors used for beam steering with respect to the magnetic center of the quadrupoles. Simulations of offsets in a single quadrupole have indicated that such offsets reduce the luminosity performance of LEP significantly. The use of a 'golden' orbit by the LEP operations group has empirically solved the problem of these offsets. This type of reference orbit steers the beam close to the center of the insertion quadrupoles. The offsets have been introduced into the closed orbit measurement system and reproducibly good conditions have proved more easy to obtain. During the next LEP running period, more pickup offsets are planned to be measured to further reduce the problem.

IV. REFERENCES

[1] Bailey, R. et. al., "Operational Procedures to Obtain High Beam-Beam Tune Shifts in LEP Pretzel Operation", This Conference.

[2] Collier, P. & Schmickler, H., "The Influence of the Vertical Closed Orbit on Luminosity Performance in LEP", Proceedings, EPAC-94, London, U.K., 1994.

[3] Guignard, G., "Adjustment of Emittance Ratio by Coupling in e-p Storage Rings", Proceedings, XI High Energy Accelerator Conference, CERN, Geneva, CH., 1980.

[4] Alexahin, Y.I., "On the Strength of the Synchrotron Sideband of the Main Coupling resonance in LEP", SL-Note 94-103 (AP), CERN, CH., 1994.

[5] Kouchouk, J.P. et al., "Energy Calibration with a Polarized Beam at LEP", Proceedings, XVI Conference on High Energy Accelerators, Hamburg, Germany, 1992.

[6] Reichel, I., "Beam Position Measurement by Modulation of Quadrupole Strengths", Diploma Thesis, RWTH of Aachen, PITHA 94154, 1995.

[7] Barnett, I. et al., "Dynamic Beam Based Alignment", SL Note 94-84 (BI), CERN, Switzerland, 1994.

[8] Verdier, A., CERN, Switzerland, private communication.

Operational Procedures to Obtain High Beam-beam Tune Shifts in LEP Pretzel Operation

R. Bailey, P. Collier, T. Bohl, H. Burkhardt, K. Cornelis, G. De Rijk, A. Faugier,
M. Jonker, M. Lamont, G. Roy, H. Schmickler and J. Wenninger,
CERN, Geneva, Switzerland

Abstract

During the running period 1994 the luminosity of LEP has been improved without colliding higher bunch currents. This paper describes the main procedures used by the operations group for luminosity optimization. Separator scans in the vertical plane and orbit interpolations in the horizontal plane are used to adjust settings for electrostatic separators in order to ensure head-on collisions. The closed orbit is corrected towards a reference orbit (called "golden" orbit) which has been found empirically to produce good luminosity. The settings of the skew quadrupoles for coupling compensation is obtained by measuring the closest tune approach of the horizontal and vertical betatron tunes.

I. Introduction

In 1994 LEP was operated since the beginning of the year using a horizontal Pretzel scheme with $8e^+ \times 8e^-$ bunches. The beams are collided at 4 interaction points (IPs) where high energy particle detectors are installed. The horizontal pretzel orbits, used to separate the two beams at 8 mid-arc collision points, are produced with 8 unipolar electrostatic separators operated at a field of 1 MV/m.

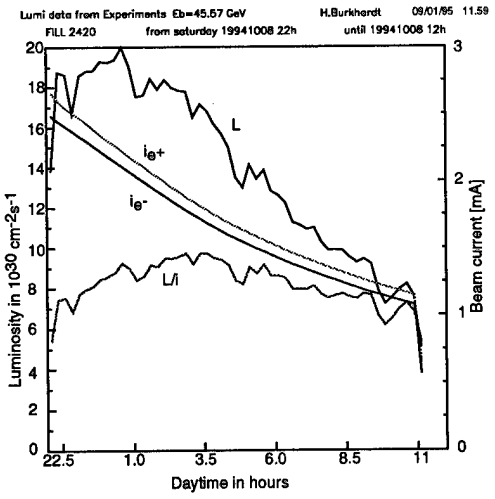


Figure. 1. Evolution of the luminosity, the beam currents and the ratio luminosity over beam current during a good LEP coast.

In 1994 the bunch currents reached typically 0.32 mA at the beginning of the coasts, corresponding to a total beam current of about 5.2 mA. These values are not significantly higher than for the 1993 run [1]. Despite this fact, a total integrated luminosity of 60 pb^{-1} was delivered to each of the four experiments in 1994, 50% higher than in 1993 although the length of the runs and the efficiencies were almost identical. This improvement was achieved mainly by increasing the average vertical beam-beam tune shift ξ_y from 0.03 to 0.04. Peak luminosities of $2.2 \cdot 10^{31} cm^{-2} s^{-1}$ were obtained at the beginning of fills. Figures 1 and 2 show the evolution of the luminosity and ξ_y for a good coast. At lower beam currents the beam lifetimes are limited by beam-beam-Bremsstrahlung and are then correlated with the beam-beam tune shift [2].

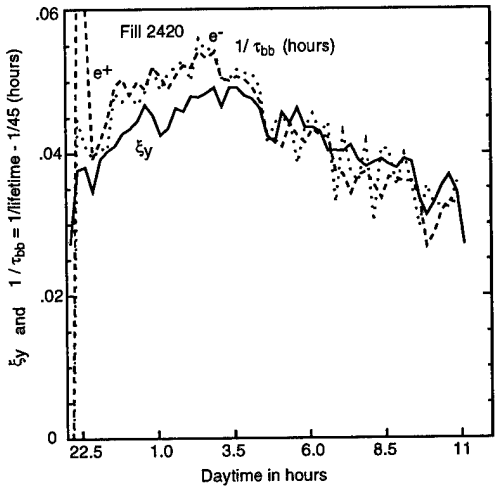


Figure. 2. Evolution of the vertical beam-beam tune shift ξ_y in the same coast that is shown in figure 1. After a short time ξ_y settles down above 0.04. The beam lifetimes in collision τ_{bb} are correlated to ξ_y because they are limited by the beam-beam Bremsstrahlung, particularly at lower beam currents. The single beam lifetime of 45 hours has been subtracted from the lifetimes shown in the figure.

II. Separator Adjustments

The energy sawtooth in LEP together with machine errors induces non-closures of the vertical separator bumps used to avoid collisions in 4 interaction points where no experimental detector is installed. This non-closure as well as coupling of the horizontal Pretzel orbits can lead to vertical collision offsets at the 4 IPs where the beams are put into collision.

To optimize the luminosity, adjustments of vertical trim separators are used to steer the beams against each other to minimize vertical collision offsets. Dedicated luminosity detectors provide fast luminosity measurements in the control room every 20 seconds. This information is used to perform scans or fine tunings of

0-7803-3053-6/96/$5.00 ©1996 IEEE

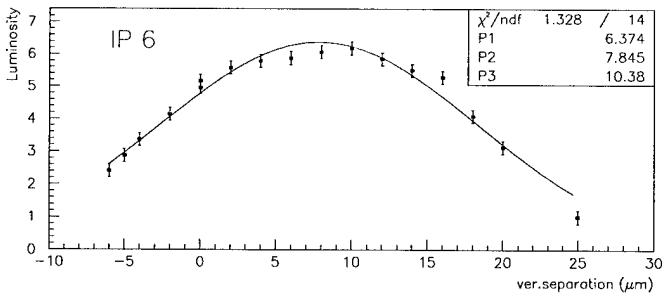


Figure. 3. A complete vertical separator scan around IP number 6. The luminosity is displayed as a function of the vertical separator trim. A Gaussian distribution has been fitted to the data points. The optimum separator settings corresponds to 7.9 μm. The width of the distribution is 10.4 μm

the separator settings. Figure 3 shows an example of a complete scan. Once the optimum position is known, some fine tuning of $1-2\,\mu$m is made on a fill by fill basis, usually while the 4 experiments are already taking data. Typical corrections did not exceed 10 μm at the IP.

The non-closure of the horizontal Pretzel orbits can be corrected to avoid horizontal collision offsets with two horizontal trim separators. A fit of the e^+e^- difference orbit is used to calculate the collision offsets and the correction trim for the separators. An example of an orbit extrapolation is shown in figure 4. This technique allows to reduce the horizontal offsets to less than one tenth of the horizontal RMS beam size at the IP.

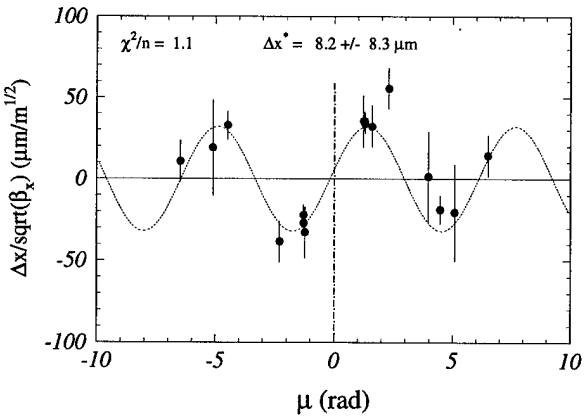


Figure. 4. Example of a fit of the horizontal e^+e^- difference orbit after adjustment of the horizontal trim separators. The horizontal difference orbit, normalized by the square root of the horizontal betatron function β_x, is shown as a function of the phase advance μ with respect to the IP. The fitted horizontal offset Δx^* at the IP is $8.2 \pm 8.3\,\mu$m.

III. Golden Orbit

The LEP quadrupoles were completely realigned for the first time during the winter shutdown 1992/1993. High levels of polarization and a better control of the vertical orbit were achieved as a result of this operation [3]. To maintain this favorable situation all quadrupoles were again aligned vertically in the shutdown 1993/1994 to correct for the continuous position drifts due to ground motion [4].

During the first months of the 1994 LEP run a "golden" orbit yielding very high beam-beam tune shifts of about 0.04 was found empirically. The most common method to find such an orbit was to use 'bare orbit' correction strategies. With this method the theoretical orbit is computed from a measured orbit by reseting to zero all correctors. A MICADO [5] type correction on the result is then used to establish a new set of correctors. It was not sufficient to reach the smallest vertical orbit RMS to obtain the best luminosity performance. The vertical(horizontal) RMS at the pickups of the average e^+e^- beam position for the "golden" orbit is about 0.45(0.5) mm.

In addition to the pickup readings, the corrector settings were found to play a significant role. The corrector settings of both planes were therefore saved at the beginning of each fill to be reloaded at the start of the following fill. The orbit resulting from the reloading was then corrected towards the "golden" orbit. This procedure gave reproducible performances for the whole 1994 run. The importance of the corrector settings is related to the closed orbit correction strategy (bare, number of correctors...). A study performed during the 1993 run [6] demonstrated that a smaller residual machine coupling can be achieved with a "golden" orbit. The same study showed that the average vertical dispersion in the whole LEP ring is not a crucial parameter for a good orbit as long as it is below 10 cm. But in order to achieve the highest possible beam-beam tune shifts the local vertical dispersion at the IPs plays a certain role [6]. This is confirmed by the fact that local dispersion bumps have been successfully used to tune the luminosity.

The vertical orbit at LEP exhibits large and sometimes fast drifts. After periods of 12 hours the RMS drift can reach a few mm. It could be shown that these drifts are caused by vertical motion of the super-conducting low-beta quadrupoles installed next to the experimental interaction points [7], [8]. The instability of their vertical position (a few tens of μm) is related to their support girder which is attached to the ground on one end only because the quadrupoles are embedded in the experimental detectors. To maintain high beam-beam tune shifts, frequent orbit corrections have to be performed. In 1994 a total of about 13200 vertical orbit corrections were made during the running period [7].

A dynamic beam-based alignment technique [9] has been used in 1994 to measure systematic position offsets between the center of the quadrupoles and of the pickups in the regions close to the interaction points. These measurements unveiled large systematic offsets of up to 2 mm. Once the measured beam positions had been corrected for these offsets, it was found that the "golden" orbit had in fact been empirically centered in the quadrupole around the interaction points.

IV. Coupling Compensation

The coupling is measured at LEP using the closest tune approach of the betatron tunes [11]. The two betatron tunes are crossed while the Q-meter is measuring continuously in PLL

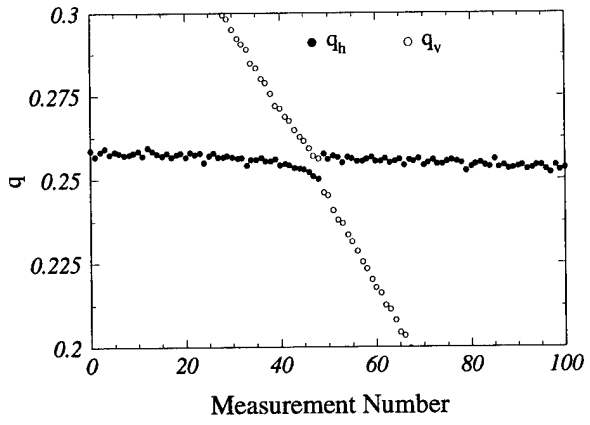


Figure. 5. Evolution of the horizontal and vertical tunes during a closest tune approach measurement. The closest approach can be clearly seen on this figure.

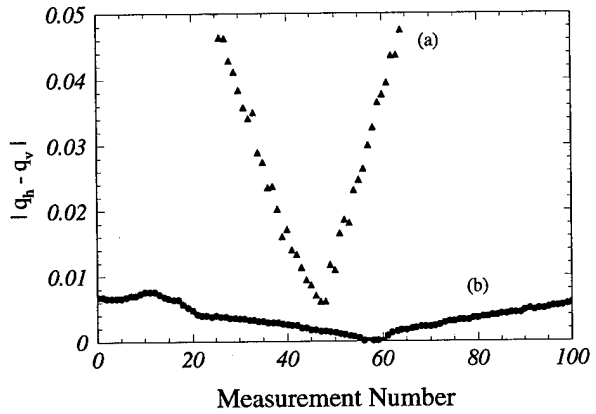


Figure. 6. Difference between the horizontal and vertical tunes for two closest tune approach measurements. Curve (a), where the coupling compensation is poor, corresponds to the measurement shown in figure 5. The lower curve (b) shows a measurement for a machine with low residual coupling between the two planes.

mode as shown in figure 5. The smallest distance Δq between the tunes measures the strength of the coupling resonance. Figure 6 shows the difference between the two betatron tunes for the measurements of a poorly (a) and a very well compensated machine (b). The compensation of the coupling is adjusted with the skew quadrupoles to reach the smallest possible distance between the two betatron tunes during the closest tune approach measurements. As has already been pointed out in the previous section, a very small residual coupling can be achieved with a "golden" orbit [6]. In the absence of vertical dispersion the emittance ratio κ ($\kappa = \varepsilon_v/\varepsilon_h$) is related to the closed tune approach by :

$$\kappa = 1 - \frac{2r^2+1}{4r^2+1} \qquad (1)$$

where

$$r = \frac{\Delta q}{2|q_h - q_v|} \qquad (2)$$

The distance to the main coupling resonance is $|q_h - q_v| = 0.14$ for LEP which is operated in physics with tunes $q_h = 90.3$ and $q_v = 76.16$. To obtain a high vertical beam-beam tune shift, the emittance ratio must be kept below the betatron function ratio at the IP of 2.5% ($\beta_h^* = 2$ m, $\beta_v^* = 5$ cm). This limit is achieved in all cases of vertical orbit correction.

V. Conclusion

The 1994 LEP run has been very successful since it saw a 50% increase of the delivered integrated luminosity over the 1993 run. This was possible with the help of numerous optimization procedures. Collision offsets have been corrected with trim separators using the online luminosity and closed orbit information. Small vertical beam sizes very obtained by a careful minimization of the residual machine coupling. A reproducible performance was achieved by using "golden" orbits. Vertical beam-beam tune shifts larger than 0.04 have been achieved in daily operation.

References

[1] R. Bailey et al., "LEP Operation in 1993 with the Pretzel Scheme", Proc. EPAC, London, 1994.

[2] H. Burkhardt and R. Kleiss, "Beam Lifetimes in LEP", Proc. EPAC, London, 1994.

[3] R. Assmann et al., "Recent Achievements in Transverse Spin-Polarisation at LEP", Proc. EPAC, London, 1994.

[4] M. Hublin et al., "Realignment of LEP in 1993-1994", Proc. EPAC, London, 1994.

[5] B. Autin and Y. Marti, "Closed Orbit Correction of A.G. Machines using a limited Number of Magnets", CERN ISR MA/73-17 (1973).

[6] P. Collier and H. Schmickler, "The Influence of the Vertical Closed Orbit on Luminosity Performance in LEP", Proc. EPAC, London, 1994.

[7] P. Collier, "Overview of Operation in Physics During 1994", Proc. of the Fifth Workshop on LEP Performance, CERN SL/95-08 (DI).

[8] H. Burkhardt, "What Affects the Stability of LEP", Proc. of the Fifth Workshop on LEP Performance, CERN SL/95-08 (DI).

[9] I. Barnett et al., "Do we need K-Modulation in the ARCSs", Proc. of the Fifth Workshop on LEP Performance, CERN SL/95-08 (DI).

[10] P. Collier and H. Schmickler, Contribution to these proceedings.

[11] G.Buur et al., "Dynamic Tune and Chromaticity Measurements in LEP", Proc. EPAC, Gif-Sur-Yvette, 1992.

Synchrotron Phase Space Injection Into LEP

P.Collier, CERN, 1211-Geneva, Switzerland

ABSTRACT

Although LEP was designed to allow both betatron and synchrotron injection, only betatron accumulation has been used up to now. During 1994 tests were made of injection in synchrotron phase space. Results are presented from these machine studies which show that for both 4 bunch and 8 bunch pretzel injection, this form of injection is a more efficient way of accumulating LEP beams. The use of synchrotron injection has several advantages, including faster damping and less sensitivity to injection errors. In addition, the flat trajectories in the straight sections, which are a feature of this type of injection, can lead to lower radiation doses for the LEP experiments and open the possibility of injection into tuned optics. Tests with high phase advance lattices also indicate that high efficiency injection is easier to achieve with synchrotron injection. For the final running period of LEP in 1994, synchrotron injection was used for normal operations and will be the preferred method used in 1995.

I. INTRODUCTION

During the design phase of LEP, the possibility of using synchrotron injection was discussed [1]. In the final LEP design, the placement of the injection elements was made such that synchrotron injection was possible. Since the LEP start-up in 1989, however, no attempts were made to exploit this possibility. Instead, use has been made exclusively of betatron phase space injection.

For each particle type the injection elements of LEP consist of a magnetic septum, which acts on the injected beam together with three kicker magnets, which move the circulating beam close to the septum during injection. The injection points are placed in the arcs, symmetrically around one of the LEP straight sections. Injection is in the horizontal plane on the inside of the main ring.

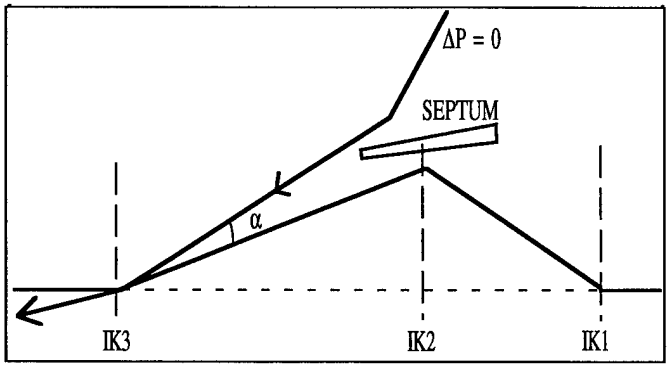


Figure 1: Schematic Diagram Representing Betatron Injection. The angle α is minimized for optimum injection

In betatron injection, the circulating beam is brought as close as possible to the septum with the kickers and the injected beam is steered to minimize the angle between the injected and circulating beams. Due to the finite width of the septum, this angle, α, can never be zero. The injected beam then performs betatron oscillations around the closed orbit of the circulating beam, eventually damping into it. The transverse damping time at injection (20 GeV) in LEP is about 6000 turns. This form of injection is shown schematically in figure 1.

Injection in synchrotron phase space requires that there is a non-zero dispersion, in the plane of the injection, at the injection point. The same use is made of a kicker bump to bring the circulating beam close to the septum. In this case, however, the beam is injected with an offset in energy. As the injection lines to LEP are on the inside of the ring, this offset must be negative. To optimize the injection process the distance between the injected and circulating beam at the injection point is matched to the energy offset of the injected beam, using the relation :

$$x = D_x . \Delta P / P \qquad (1)$$

By adjusting the septum the beam can be injected parallel to the circulating beam and will follow the natural closed orbit that a circulating particle, having the given energy offset, would follow [2]. This is illustrated schematically in figure 2.

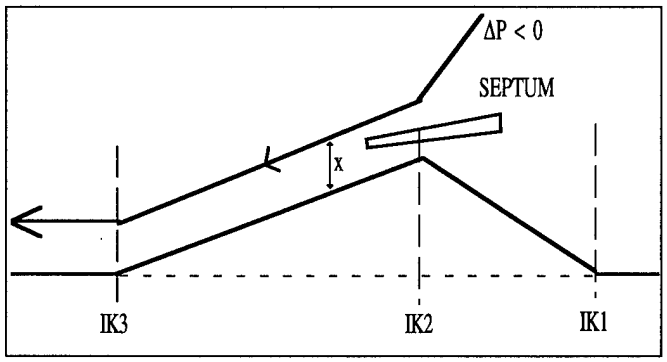


Figure 2: Schematic Diagram Representing Synchrotron Injection with $x = D_x.\Delta P/P$.

In the case of synchrotron injection the angle between the injected and circulating beams can be adjusted to be zero and hence the injected beam will not perform betatron oscillations about the closed orbit. Instead, once injected, the beam oscillates in the longitudinal plane (energy oscillations) at the synchrotron tune (Qs) and slowly damps into the circulating beam.

0-7803-3053-6/96/$5.00 ©1996 IEEE

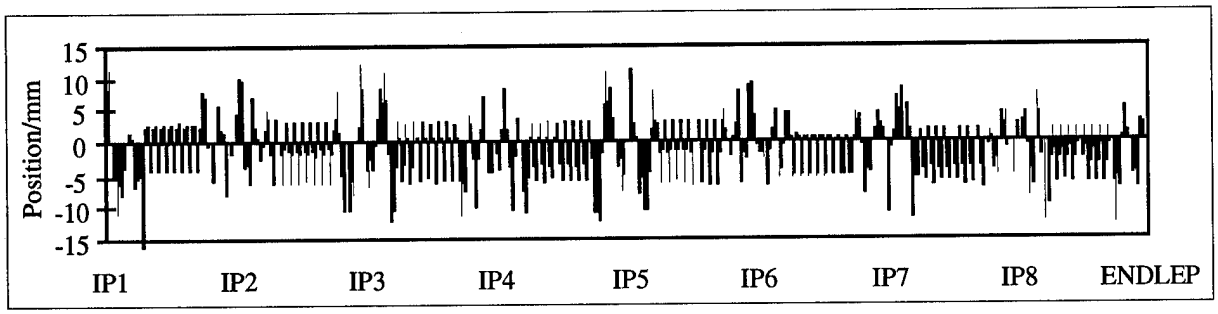


Figure 3: Optimized Horizontal First Turn Trajectory for Betatron Injection of Positrons into LEP.

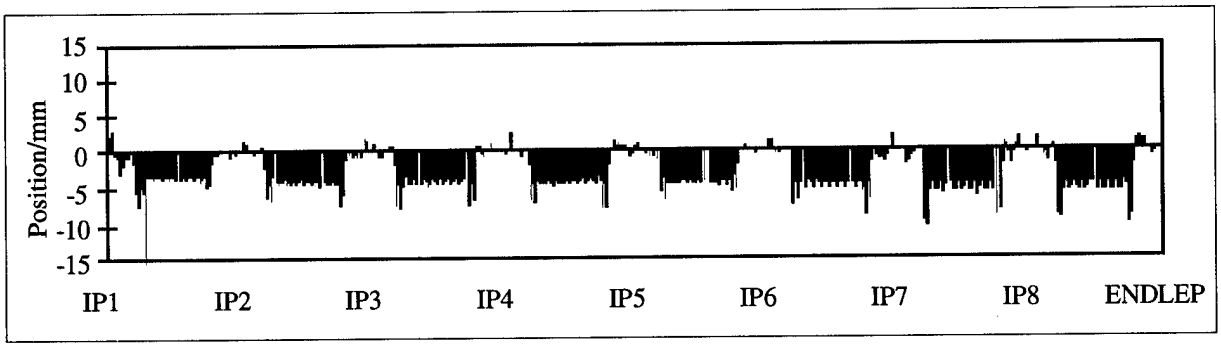


Figure 4 : Optimized Horizontal First Turn Trajectory for Synchrotron Injection of Positrons with ΔP/P at -0.6%

II. INJECTION

In the longitudinal plane the damping time is a factor of 2 lower than in the transverse plane. Therefore, the synchrotron injection oscillations damp out after about 3000 turns in LEP. The injected beam sees non-linear RF fields and different particles thus have different values of Q_s. After a number of energy oscillations the injected beam tends to smear out in longitudinal phase space. This is known as filamentation [1] and is considered to be advantageous as it results in a rapid suppression of any injection oscillation signal.

The main advantage of synchrotron injection is that there are no injection oscillations in the straight sections. This is because the horizontal dispersion is zero in these regions. This allows cleaner injection conditions for the LEP experiments. Figures 3 and 4 compare and contrast the optimized trajectories measured with betatron and synchrotron injection respectively.

Other advantages have been found for synchrotron injection over injection in betatron phase space. Notably, the larger dynamic acceptance in the longitudinal plane allows a very high injection efficiency. Injection into an empty machine routinely produces 100% injection efficiency. In addition the reduced (or zero) betatron oscillations at injection allow the LEP transverse feedback system to operate more easily.

For comparison purposes the data of figures 3 and 4 are plotted on the same scale. In both cases the injection elements were optimized to minimize the betatron oscillations about the closed orbit. In the case of betatron injection this results in an oscillation of +/-4mm in the arcs, but with peaks of 12mm within the straight sections of LEP. In the case of synchrotron injection the betatron oscillations are completely suppressed and the trajectory follows the dispersion function of the machine.

The data of figure 4 was taken with a -0.6% energy offset for the injected beam. This offset can be changed. In order to keep x constant in equation (1), increasing the energy offset allows the kicker bump to be decreased. The limit on increasing the energy offset comes from the variation of the betatron tunes with momentum. For the optics in use for LEP the limit is at about -2% where the horizontal tune drops towards the integer. In figure 5 the injection efficiency into an empty machine is plotted as a function of the energy offset of the injected beam. The efficiency here is defined as the proportion of the beam surviving after 400ms.

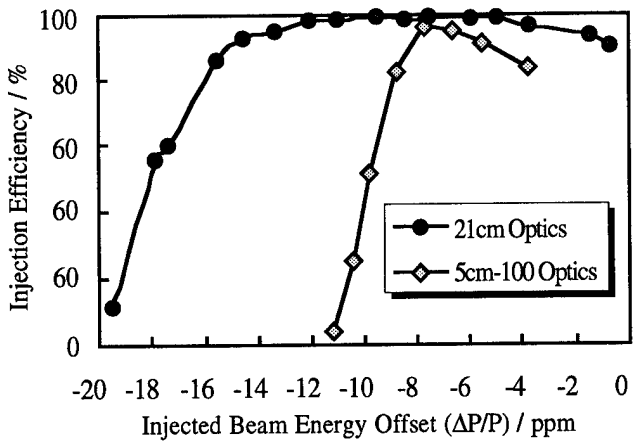


Figure 5 : Variation of the Injection Efficiency into an Empty Machine as a Function of ΔP/P for 21cm and 5cm Optics.

Two curves are shown in figure 5, that for the normal de-tuned injection optics, where β^*_v is 21cm and for the physics optics, where β^*_v is reduced to 5 cm. For the standard injection optics energy, offsets up to 1.5% are possible with good injection efficiencies. Beam can be injected up to 2% off in energy, but the efficiency drops rather steeply. For the physics optics the latitude for changing the energy offset is rather smaller. In this case attempts to inject in betatron phase space were not successful.

The number and arrangement of bunches in LEP has become a variable which changes at regular intervals. Tests of injection onto pretzel orbits (8 bunches per beam) and into bunch trains (with 4 trains of 4 bunches) have been made and in each case the performance of injection in synchrotron phase space proved superior to betatron injection under similar conditions. Attempts have been made to inject using synchrotron injection into other optics configurations. For LEP 2 operation above the W pair threshold, it is desirable to run LEP with a low-emittance lattice. Two optics are under study, one with 108° and the other with 135° horizontal phase advance per cell. In both cases the injection efficiency was much higher when synchrotron injection was used. For the 108 lattice, for example, injection efficiency into an empty machine was above 90%. With betatron injection the efficiency was never higher than about 40%.

III. ACCUMULATION

Figure 6 shows the variation of the injection efficiency with accumulated bunch current, for the case of betatron injection and synchrotron injection, for the same optics configuration. Also shown is the curve for injection into physics optics using synchrotron injection. In this case accumulation was not possible with betatron injection.

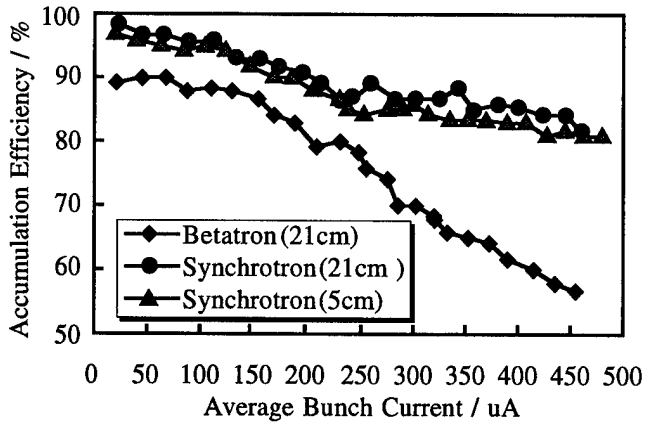


Figure 6: Accumulation Efficiency vs. Accumulated Bunch Current for Betatron and Synchrotron Injection. Note the Suppressed Zero Scale.

A reduction in the efficiency with accumulated bunch current is normal in LEP. The emittance of the beam increases with accumulated current and more losses against the septum are to be expected. In addition, the lifetime of the accumulated beam tends to be lower at high bunch currents.

In the case of synchrotron injection this reduction in efficiency with accumulated current is much smaller; and with 500 μA per bunch (nominal bunch currents for LEP), it is still around 85%. Little, or no, reduction in accumulation efficiency can be seen between the tuned and de-tuned optics.

IV. RAPID SYNCHROTRON ACCUMULATION

LEP plans to operate in 1995 with 4 trains of bunches in each beam. In previous years LEP operated a pretzel scheme and the LEP injectors were modified to allow operation with 8 bunches. The injector chain of accelerators would like to keep the 8 bunch mode operational [3], while still allowing injection into LEP bunch trains. This requires that two bunches from the injectors can be injected into a single LEP bunch within a very short time (a few LEP turns).

Synchrotron injection opens up the possibility of doing this. The method relies on the fact that the synchrotron tune is very low (in LEP Qs is around 0.1). One energy oscillation period is therefore about 10 turns. By waiting some multiple of half a synchrotron period (5,15,25... turns) between injections into the same bunch, the second injection can be made without disturbing the first. This is because the first injected beam will have too much energy and hence be further away from the septum. The method seems practicable [4] and the necessary modifications to the harmonic numbers of the injector accelerators have been made. It will be tried during the start-up of LEP this year.

V. CONCLUSIONS

Synchrotron injection has been found to work well for all machine conditions tested. It is now the preferred operational method of injection into LEP. In general, higher injection efficiencies are normal with synchrotron injection and lower experimental radiation doses are observed. As the trajectory is essentially flat in the straight sections of the machine (the most delicate areas), the performance of the injection process is less sensitive to injection position and angle errors. With no injection oscillations in the straight sections, injection into physics optics has proved to be a practical option. This would avoid the need for a beta-squeeze at high energy and reduce the time needed to set LEP up for physics.

VI. REFERENCES

[1] S. Myers, "A Possible New Injection and Accumulation Scheme for LEP", LEP Note 334, 1981.

[2] P. Collier, "Synchrotron Phase Space Injection into LEP", CERN, SL-MD Note 152, 1994.

[3] P. Collier, "Injectors, Status and Options for 1995", Proceedings, Fifth LEP Performance Workshop, Chamonix, France, 1995.

[4] P. Collier, 'Synchrotron Injection', Proceedings, Fifth LEP Performance Workshop, Chamonix, France, 1995.

SYSTEMATIC STUDIES OF THE LEP WORKING POINT

P. Collier and H. Schmickler,
CERN, Geneva, Switzerland

Abstract

The working point, *i.e.*, the fractional part of the betatron tunes, is one of the key parameters for machine operation. This paper reports on systematic studies in LEP on the dependence of beam sizes and beam lifetimes on betatron tunes. For these studies the horizontal and vertical tunes have been varied by an automatic measurement sequencer over the wide range 0.1 to 0.4 and beam sizes and lifetimes have been recorded in parallel.

I. MEASUREMENT PROCEDURE

During a tune scan the betatron tunes of LEP are changed by trimming the main quadrupole strings. The available trim range is $\Delta q_h = \Delta q_v = \pm 0.15$ with a resolution of 0.001. The maximum number of trim steps is 400 and the time interval between tune changes is 2 seconds, hence a complete scan takes about 12 minutes measurement time. Synchronous to the tune variations several beam parameters are recorded. The tunes themselves are tracked by the LEP q-meter in PLL mode [1]. The transverse beam dimensions are recorded from the UV-monitors and beam lifetimes from the bunch current transformers.

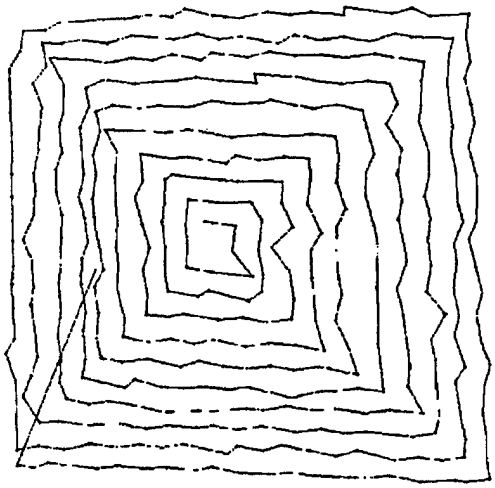


Figure 1. Trace of measured tunes during a tune scan; horizontal axis: measured q_h; vertical axis: measured q_v

Figure 1 shows the measured tunes during a tune scan. Consecutive points of the scan are connected with a line. Optionally the scan pattern could be rotated by 45° in order to cross specific beam resonances faster.

All data sets are retrieved and merged for further processing. More details on the measurement procedure can be found in [2] and references therein.

II. AVAILABLE DATA SETS

During the LEP running period 1994 systematic studies of the working diagram were performed. The following machine conditions were of interest: The untuned lattice at injection energy (beam energy 20 GeV, $\beta_v^* = 21$ cm) and the tuned lattice at collision energy (beam energy 45.6 GeV, $\beta_v^* = 5$ cm). As LEP was operated in 1994 with horizontal pretzel orbits, comparative measurements were done by performing tune scans with the pretzel orbits on or off. None of the available data sets contains beams in collision. Even at moderate bunch currents colliding beams suffer from many more strong resonances and no consistent data set could be recorded over a wide tune range for colliding beams. As an example, Figure 4 on the last page of this paper shows the inverse of vertical and horizontal beam sizes as a function of the measured tunes. In the top picture one can clearly see the main coupling resonance $q_h = q_v$ and its synchrotron sidebands ($q_s = 0.065$). Furthermore, the synchro-betatron resonance $q_v = 2 \cdot q_s$ is strongly seen, and we see an indication of the third order resonances $q_v = 2 \cdot q_h$ and $q_h = 2 \cdot q_v$ respectively.

III. SEARCH FOR A NEW WORKING POINT

The principle goal of the above studies was the search for a working point for physics giving good lifetime conditions and high luminosities. As stated above, tune scans do not give valuable data with beams in collision. Hence the search for a working point has to happen in several steps. First the largest possible area in tune space is measured with single beams and favourable regions in terms of lifetimes and small beam sizes are identified. Thereafter the following considerations are added:

- the working point point for injection energy and collision have to be close in order to avoid the necessity of jumping strong resonances during energy ramping or beta squeezing
- results of compute simulations of the beam-beam effect are considered [4] and [5]
- the working point should be far from the coupling resonance [3].
- beams in collisions do not have unique betatron tunes, but due to the nonlinear nature of the beam-beam force the beams cover a whole area in tune space. The whole area covered should be free of resonances.

The above effect of the beams in collision covering a certain area in tune space (a so-called footprint) has been studied with computer simulations for LEP [6]. Additional information can be obtained from experimental observations. Figure 2 shows a typical spectrum of the transverse tunes of LEP beams in collisions. Several coherent beam-beam modes are visible apart from the undisturbed tunes q = 0.28 and qv = 0.16. Taking this information, a random number generator can be constructed that generates a particle population in tune space according to the distributions measured in Figure 2. The resulting distribution,

0-7803-3053-6/96/$5.00 ©1996 IEEE

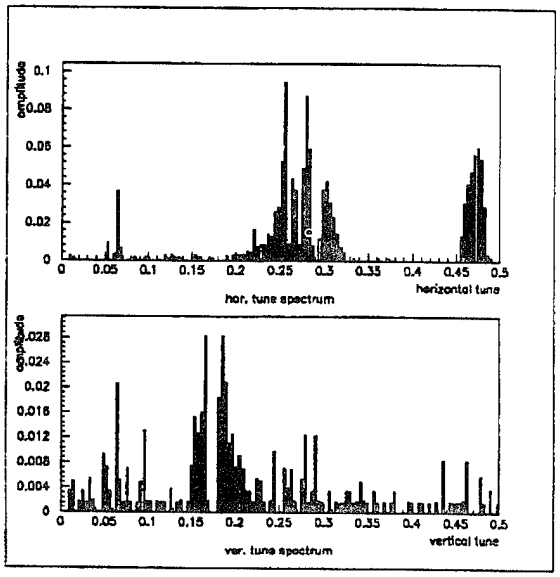


Figure 2. Measured tune spectra with LEP beams in collision.

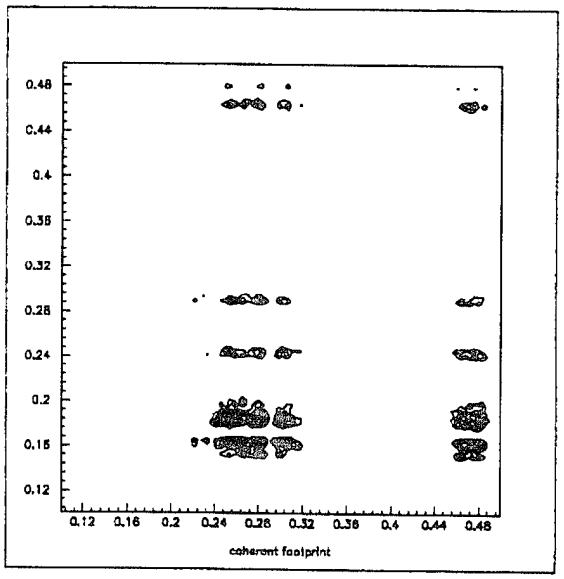


Figure 3. Computer generated distribution of tune space occupied by particles in collision. A random number generator has been constructed to generate a footprint of the particle according to the measured coherent spectra from above.

called a coherent footprint, is shown in Figure 3. An overlay of this information to the measured tune scans gives additional information for the selection of a working point.

Taking together all arguments, the following three working points have been tested experimentally:

1. $q_h = 0.28$ and $q_v = 0.16$
2. $q_h = 0.23$ and $q_v = 0.36$
3. $q_h = 0.36$ and $q_v = 0.16$

Working point 2 and 3 had lower beam sizes with separated beams, but as soon as high bunch currents were collided the beam lifetimes became bad and large particle backgrounds were seen by the LEP experiments. Finally the "standard" working point 1 chosen already for the running period 1992 is still used in daily operation.

IV. CONCLUSIONS

A measurement sequencer that records beam parameters as a function of the betatron tunes is a very valuable for beam diagnostics and the understanding of the machine lattice. It is very difficult to interpret the data for luminosity optimization. Here the measured data provide starting information that has to be complemented with experience and intuition.

References

[1] K. Lohmann, M. Placidi and H. Schmickler, Q-Monitoring in LEP, LEP-BI Note 88-45.

[2] H. Schmickler, "Tune Scans", Proc. of the Third Workshop on LEP Performance, Chamonix 1993.

[3] P. Collier and H. Schmickler, "The Influence of the Vertical Closed Orbit on Luminosity Performance in LEP", Proc. EPAC, London, 1994.

[4] E. Keil, Nucl. Instr. Meth. **188** (1981) 9.
E. Keil, LEP Note 636 Rev. (1991).
E. Keil, LEP Performance Note 86.

[5] S. Myers, "Simulation of the Beam-beam Effect in Storage Rings", Nucl. Instr. Meth. **211** (1983) 263.
Y. Marti, S. Myers, J. Poole, SL Note 92-50 (DI)

[6] Werner Herr, "Can we learn anything from beam-beam footprints?", Proc. of the Fourth Workshop on LEP Performance, Chamonix 1994.

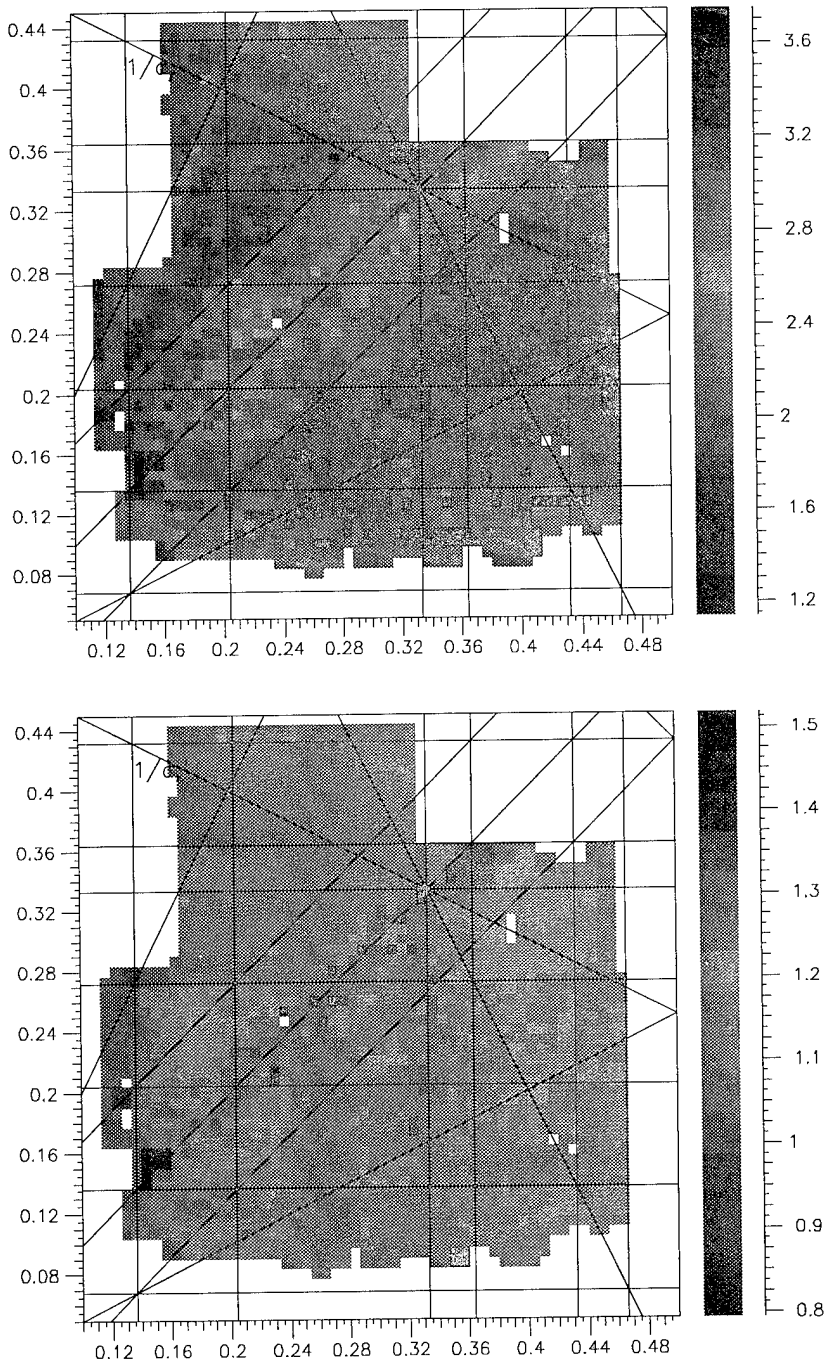


Figure 4. Results of tune scans in LEP at 45.6 GeV beam energy with pretzel orbits on. The top picture shows the inverse of the vertical beam size, and the bottom picture the inverse of the horizontal beam size as a function of the measured betatron tunes.

MODIFICATION OF THE LEP ELECTROSTATIC SEPARATOR SYSTEMS FOR OPERATION WITH BUNCH TRAINS

B.Balhan, A.Burton, E.Carlier, J.-P.Deluen, J.Dieperink, N.Garrel, B.Goddard, R.Guinand, W.Kalbreier, M.Laffin, M.Lamont, V.Mertens, J.Poole, H.Verhagen, CERN, CH-1211 Geneva

To meet the LEP2 luminosity requirements for W-pair production, it is planned to operate LEP with Bunch Trains from 1995 onwards. This new mode of operation entails significant modification both to the existing separator hardware and its control system. The changes have been implemented so as to provide maximum flexibility for the realisation of the Bunch Train scheme, and also make a return to operation with Pretzel separation possible during 1995. Two LEP Interaction Points (IP) were equipped with new separators in late 1994, enabling first tests with the collision of one train of four e^+ bunches with one train of four e^- bunches. During the 1994/95 shutdown, four separators have been installed in the two remaining experimental IPs, and eight separators in the non-experimental IP have been displaced to new positions. Details are given of optics requirements for the separator installations, the polarity of the closed orbit separator bumps, system modifications, and performance considerations. Results are presented of investigations into the effects of separator polarity on High Voltage performance and on the commissioning of the new hardware and software systems during tests of the Bunch Train scheme in 1994.

I. INTRODUCTION

For Bunch Trains in LEP [1] the minimum inter-bunch spacing of 87 λ_{rf} (74.2 m or 247.5 ns) is imposed by the distance from the IP to the first electrostatic separator, with the maximum number of bunches in a train limited to four by the capabilities of the LEP experiments.

To operate LEP with Bunch Trains from 1995 onwards, additional separators have been installed around the even experimental IP, and changes to the separator installations have been made in the odd IPs. The controls software and hardware has been modified accordingly. The changes have been implemented so as to optimize flexibility for operation with Bunch Trains, streamline the controls of the various separator types, and to minimise the level of intervention should a return to Pretzel operation be necessary [2].

II. OPTICS CONSIDERATIONS

A. Tests in 1994

For the initial tests in 1994 [3] it was realised that the polarities of the bumps in IP 4 and 8 should be opposed, in order that the residual vertical dispersion be reduced to acceptable levels. With the convention that a positive (+) bump is defined by an upwards deflection of e^+ in the first separator, the bump in IP4 was installed as positive, and that in IP8 negative. The tests were made with this configuration.

B. Operation in 1995 and beyond

With Bunch Train bumps in all four even experimental IP, numerical simulations show that two of the bumps should be positive and two negative. This combination minimizes both the vertical offsets and slope in the collision of the bunches of a given train, minimizes the residual vertical dispersion and maximizes the possible luminosity [4]. The bump polarities in the odd IPs must also alternate, with the constraints from the LEP beam dumping system fixing the bump in IP 5 to be positive. The variant shown in table 1 was eventually chosen.

LEP IP	1	2	3	4	5	6	7	8
bump polarity	+	−	−	+	+	−	−	+

Table 1: Direction of separator Bunch Train bumps.

III. SEPARATOR LAYOUTS

The separation of a train of bunches requires that a sufficiently long orbit bump is created to separate the individual bunches at all parasitic encounters. In LEP, the minimum inter-bunch spacing of 74.2 m required the addition of two new separators per even IP, and the displacement of two existing separators per odd IP, to accommodate up to four bunches per train. The 1995 separator positions and e^+ e^- trajectories are illustrated for an experimental (even) IP and an odd IP in figures 1 and 2, respectively.

In the even IP, the newly constructed vertical separators (ZL) were placed near quadrupoles QS7 to provide the initial deflection for the separation bump. These separators are powered by the high voltage (HV) generators of the Pretzel ZX separators, with one electrode at HV and one at ground. In the odd IP, the outer separators have been moved further from the IP, to positions near quadrupoles QL8.

The existing horizontal Pretzel separators (ZX) will stay in the machine until sufficient operational experience has been gained with Bunch Trains to make a definitive choice of scheme for LEP2. During this evaluation period a return to Pretzel operation would therefore be possible with around three weeks of machine intervention. On removal from LEP, the ZX units will be transformed into vertical separators (ZY), and redeployed near the existing separators ZL at QS2 in the even IPs to increase the separation available for LEP2.

0-7803-3053-6/96/$5.00 ©1996 IEEE

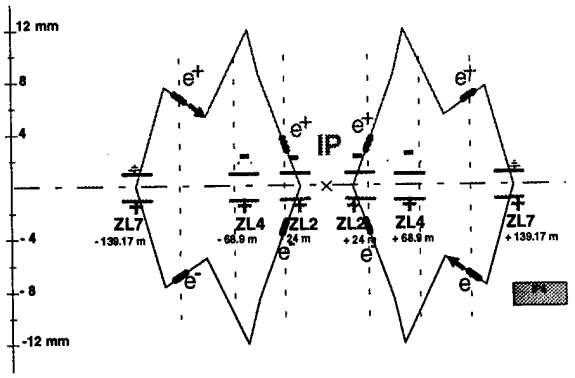


Figure 1: 1995 Bunch Train separator bump in IP4, for colliding beams.

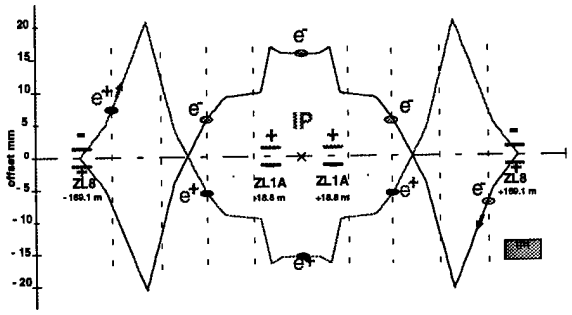


Figure 2: 1995 Bunch Train separator bump in IP1.

IV. HARDWARE CONSTRAINTS

A. Separator voltage changes

In order to allow the bunches to collide head-on at the experimental IP, whilst maintaining the separation at the nearby parasitic encounters, all of the ZL separators in a given IP will remain powered throughout the physics data-taking. This is in sharp contrast to previous years, where the beams were brought into collision by means of a fast discharge switch, which rapidly brought all the separator voltages to zero in a synchronous manner. For Bunch Train operation, the changes of separator voltage are required to be synchronous in order to maintain a properly compensated bump. This can now only be accomplished slowly (in around five minutes), by means of tables of values, since the time-constants of the HV circuits effectively limit the rate at which the voltage can be reduced.

B. Separator polarity considerations

The polarity of the new ZL separators at QS7 in the even IP has to be positive. This is because the spark rate of both horizontal ZX and vertical ZL separators operated with negative polarity is known to be several orders of magnitude higher than for positive polarity when these separators are exposed to high synchrotron radiation fluxes [5,6]. In a ZL unit located near to the LEP arcs, the spark rate with negative polarity at a field of 30 $kVcm^{-1}$ was measured at $4.0\pm2.8\ h^{-1}$, whereas for the units near to the IP operated with both negative and positive polarity the spark rate at a similar field is of the order of $4\times10^{-4}\ h^{-1}$. This effect is believed to result from the charging of insulators under the bombardment of photo-electrons, which results in a space-charge accumulation and leads to surface flashover [7].

The ZL separators are equipped with feedthroughs for both electrodes, so that the field direction can be reversed by simply connecting the HV to the opposite feedthrough. Although such a manipulation invariably requires the separator to be re-conditioned over a period of around one week, this type of change is usually made during the long annual shutdown, and can be planned accordingly, so that flexibility is retained for the choice of field direction and hence the optics.

In contrast, the vertical ZY separators to be installed at QS2 in the 1995/96 shutdown are monopolar, i.e. equipped with only one high voltage electrode, with the other electrode being connected to ground. Thus, once the ZY unit is installed, the only method of reversing the separator field direction will be to power the unit with negative high voltage. A project is now under way to develop prototype insulators which use advanced surface engineering techniques to significantly improve the HV performance in the presence of photon and electron fluxes [8].

C. Vertical adjustment of collisions

Previously, the fine 'vernier' adjustment of the vertical beam offsets to ensure head-on collisions was made using an auxiliary HV generator, to give a minimum step-size of better than 0.05 μm. For Bunch Trains this is no longer possible, as all the main generators must remain powered in order to keep the beams in collision. The average vertical offset of the train can be trimmed by adjustment of the separator voltages; the finest increment possible of around 0.4 μm is imposed by the voltage resolution of the generator [9]. This is deemed adequate when compared with the expected vertical beam size of the order of 10 μm and the inter-bunch spread in the vertical position of up to 7 μm [4].

V. CONTROLS

A. Initial tests in 1994

For the initial tests in 1994, the existing hardware of the Pretzel separators was used to power the newly-installed ZL separators. Shortly before the start of the extended Bunch Train test period, the high voltage cables from the Pretzel tanks were swapped to the new ZL tanks, together with the required control cables.

The setting of the voltage levels for the existing ZL separators was using the present Control Room (PCR) level software ('SloppySoft'). New procedures for the ramp, squeeze, collide and vernier adjustment were defined and incorporated into the control sequencer ('LEPexec'). For the new ZL separators the existing Pretzel separator 'expert software' was used, which has proved adequate since the voltage on these separators remained virtually constant. Prior to the tests proper, the initial modifications to the controls systems were commissioned and the new procedure for vernier adjustment was sucessfully tried [10].

B. Operation in 1995 and beyond

For operation in 1995 and beyond, the two new ZL separator tanks in each IP are powered by the HV supply previously used in Pretzel operation. To render the overall control system more homogeneous, the old SPS type electronics used to control this power supply has been exchanged for a controller of the type used for the vertical separators. This allows the use of the same routines from the PCR to load the tables for ramp, squeeze and collide without writing further software, although it has necessitated slight modifications in the software running in two of the equipment controllers. All other SPS type electronics previously used for the Pretzel separators has been retained.

Because of the many modifications implied by the introduction of the bunch train scheme on all levels of the controls software the opportunity was taken to migrate the process control. This was on PCs running XENIX (used previously for the vertical separators) and VME systems running under OS-9 (used for the Pretzel separators). The new location is a single PC system per IP running LynxOS. With this operation, all systems for which the hardware group is responsible now use this type of controller.

This changeover had several subsequent implications: New MIL-1553 bus controllers were used for the first time [11] to enable the desired block transfer length on LynxOS PCs. New functions to deal with the MIL-1553 message broadcast mechanism used for the vertical separators had to be added in the LynxOS MIL-1553 driver [11]. The reception and redistribution of the timing signals has been moved away from the present G-64 based hardware to a controller card in the LynxOS PCs which offers more direct access and improved monitoring facilities [11]. The 'expert software' had to be modified to deal with the PCs and to account for all modifications in the electronics (new nomenclature, addition of new equipment, removal of obsolete items). This software is used extensively for diagnostic purposes by the separator specialists and also in the PCR for non-standard controls, e.g. during special Machine Development or for commissioning of new operational procedures. It needs to be revised completely before the XENIX PCs can be physically removed since it makes heavy use of the graphics package CGI which is not available under LynxOS.

The alarm and diagnostic software has also been upgraded to take account of the changes, including the addition of new equipment and the removal of redundant items.

The high-level control of the new Bunch Train separators has been included into the 'SloppySoft' environment to properly incorporate the use of tables for bringing the beams into collision, switching between LEP hyper-runs, ensuring updated settings for vernier adjustment, allowing synchronous variation of bump amplitudes, etc. As for other software, the equipment access has been adapted to account for new controllers and redundant equipment.

VI. CONCLUSION

The changes to the LEP electrostatic separator systems following the successful tests in 1994 [3] have been accomplished ready for the machine startup in 1995. A total of eight new separators have been installed, eight other separators have been displaced, and application software at all levels has been updated accordingly.

VII. REFERENCES

[1] C. Bovet et al; "Final report of the 1994 Bunch Train study group", CERN SL 94-95 (AP) (1994).

[2] B. Goddard et al; "Modified LEP separator configurations for operation with Bunch Trains", CERN SL/Note 94-96 (BT) (1994).

[3] O. Brunner et al; "Experiments with Bunch Trains in LEP", this conference.

[4] E. Keil, "Offsets and crossing angles for trains of two, three and four bunches", CERN SL/Note 95-40 (AP) (1995).

[5] N. Garrel et al; "Performance Limitations in High Voltage Devices in the LEP Electron Positron Collider and its SPS Injector", Le Vide: Science, technique et applications, Suppl. to vol. 275, 386-397 (1995).

[6] W. Kalbreier and B. Goddard; "Radiation-triggered breakdown phenomena in high energy e^+e^- colliders", IEEE Trans. Elec. Insul., 28 (4), 444-453 (1993).

[7] G. Blaise and C. Le Gressus; "Charging and flashover induced by surface polarization relaxation processes", J. Appl. Phys., 69 (9) 6334-6339 (1991).

[8] B. Goddard; "Research and development to reduce beam-induced separator sparking for LEP2", CERN SL/Note 94-15 (BT) (1994).

[9] B. Balhan et al; "Separator systems for the LEP Bunch Train project", CERN SL/Note 94-64 (BT) (1994).

[10] B. Goddard et al; "Commissioning of LEP operation with Bunch Train bumps", CERN SL MD Note 160 (1994).

[11] CERN SL-CO group, various private communications.

LOW EMITTANCE LATTICE FOR LEP

Y. Alexahin, JINR, Dubna, Russia,
D. Brandt, K. Cornelis, A. Hofmann, J.P. Koutchouk, M. Meddahi, G. Roy and A. Verdier,
CERN, CH-1211 Geneva 23, Switzerland

Abstract

In order to obtain the largest luminosity with LEP2, it is attractive to make the beam emittance as small as possible because the beam-beam effect is not a limitation at the energy of $E \approx 90$ GeV for the obtained bunch currents. This can be achieved with a high tune lattice. Two possible candidates are lattices with a horizontal phase advance of 108^0 or 135^0 per cell. Both have a vertical phase advance of 60^0. These lattices were developed during 1994 and the results are presented. Tests to reach high intensity for the 108^0 lattice were performed and the bunch current achieved is compared with expectations. For this lattice the detuning v.s intensity and several optics parameters were measured as well.

I. INTRODUCTION

The LEP machine was designed for cell phase advances of $60^0$and 90^0. The resulting transverse beam emittance allows reaching the beam-beam limit at the energy of 85 GeV or higher only with bunch currents considerably larger than the ones possible now. It is therefore beneficial to reduce the emittance of the beam to optimize the luminosity. The smallest emittance is obtained for a cell phase advance of about 135^0. The significant luminosity gain to be expected from a smaller emittance is enhanced by the smaller beam size at the collimators close to the low-β quadrupoles, allowing to decrease β^* and thus further increase the luminosity [1]. Unlike synchrotron light sources, strong chromatic aberrations are generated by the low-β insertions which have to be corrected by the cell sextupoles. To avoid a too strong perturbation to the beam motion, they must be arranged in pairs at an odd multiple of 180^0, constraining the cell phase advance to 90^0, 108^0or 135^0, [2]. The reduced dispersion function demands an increased strength of the sextupoles which enhances the non-linear perturbation to the beam motion. Fortunately the largest chromatic aberration is in the vertical plane, where the cell phase advance can be kept low, thereby reducing somewhat the sextupole excitation. The stronger focusing shortens the bunch length and decreases the threshold for the transverse mode coupling instability. Conversely, the RF bucket is larger, making it possible to slightly increase the beam energy in a critical range. The ultimate gain in luminosity reaching 3.5, a theoretical and experimental study was initiated to investigate the potential of a minimum emittance lattice.

II. HIGH TUNE LATTICES

A. *135/60 lattice.*

In this lattice the arc FODO cells have a horizontal phase advance of 135° and a vertical phase advance of 60°. The horizontal tune is 125.28 and the vertical tune is 75.18. Given the machine super-periodicity, such tunes guarantee that no problem is expected from the non-linear chromaticity and two sextupole families are sufficient [3].

Since early runs in 1993 could not obtain a circulating beam the problems associated with this lattice were studied extensively [4] with the outcome that it is not possible to correct both the third order resonances and the derivative of the horizontal tune with respect to the horizontal emittance. The latter has a value of - $1.6 \times 10^5 \mathrm{m}^{-1}$ for the lattice under consideration. For an rms closed orbit amplitude of 4mm at the BPM's where β_x is about 10m, the associated emittance is about 1.6μrad.m, which makes an associated horizontal tune-shift of -0.26. As the fractional part of the horizontal tune of our machine is 0.28, we see that a badly corrected closed orbit can easily lead to a linear instability. In addition, the orbit excursions in the sextupoles lead to a widening of the second order stop-band which can reach a width of 0.15 for an rms closed orbit deviation of 0.5 mm.

In practice it can be observed that the horizontal tune, estimated from a Fourier analysis of the measurements over several turns, wanders considerably depending on the trajectory corrections applied. It is important to note that applying a tune-shift does not help because of these large tune changes.

In 1994 great care was taken to correct the first turn trajectory so that its r.m.s. value was between 3 and 2mm. Then the orbit closure algorithm [5] was applied and a circulating beam was obtained after having applied it iteratively and having made a systematic horizontal tune-shift of about +0.2 in order to compensate for the anharmonic effects. Another experiment devoted to accumulate more current had various troubles and only 59μA were stored with the damping wigglers on. This is not limited by collective effects.

B. *108/60 lattice*

In 1994, in parallel with the analysis of the problems of the $135^0/60^0$lattice, a $108^0/60^0$lattice was developed from the $90^0/60^0$lattice of 1994, which was the one used for operating LEP at this time. This $108^0/60^0$lattice has now two horizontal and three vertical sextupole families. It was developed for machine developments purposes and is not yet optimized for pretzel or bunch train operation. The derivative of the horizontal tune with respect to the horizontal emittance was 2.26 10^4 m^{-1} the one in the vertical plane was 7.37 10^4 m^{-1}, and the cross term (derivative of the vertical tune with respect to the horizontal emittance) was -7.97 10^4 m^{-1}. For a given orbit distortion the maximum detuning is reduced by 50% compared to the $135^0/60^0$lattice. Although still large, it is sufficiently reduced to obtain easy injection, accumulation in the first experiment.

Five experiments were performed in order to test the performances of the 108^0 lattice. They were very successful and proved the easy operation of the machine with this lattice, from

0-7803-3053-6/96/$5.00 ©1996 IEEE

the injection, accumulation to the ramp and squeeze. Various measurements were done which are developed in the following chapter.

C. Collective effects

One of the problems encountered by the high tune lattices is the small momentum compaction factor α_c. The smaller emittance is obtained by strong focusing resulting in small values of the horizontal dispersion function D_x and consequently in a reduction of the transverse quantum excitation by the emitted synchrotron radiation. This reduces also the momentum compaction α_c and the synchrotron tune Q_s. The bunch current in LEP is limited by the transverse mode coupling instability (TMCI). The tunes of the different head-tail modes are separated at small current by Q_s. At larger current the transverse impedance causes tune shifts which can bring two modes together resulting in an instability. Obviously, a large basic separation Q_s of the modes gives a higher TMCI threshold. The effective impedance involved tends to increase with reduced bunch length σ_s. Since increasing Q_s will at the same time decrease σ_s, the maximum bunch current improves only slowly with Q_s as shown in Fig. 1. Some gain in current can be obtained with wigglers located in dispersion free sections. They increase the energy spread of the beam and therefore also the bunch length. Two groups of such wigglers are available in LEP called damping (DW) and polarization (PW) wigglers according to their original purpose. The beneficial effect of these devices is also indicated in Fig. 1.

D. Phase advance in the vertical plane

The choice of 60^0vertical phase advance per cell was motivated by the need to guarantee a good non-linear chromaticity correction and also a good vertical orbit correction for polarization. This is not without consequence for the collective effects. Moving from 90^0 to 60^0 in the vertical plane increases the average vertical β-function in the arcs by up to 30-40 % when averaging over all the bellow positions in the arcs (e.g. when moving from a $90^0/90^0$ to a $135^0/60^0$ lattice). Since for the present bunch length the bellows represent about half of the total impedance in the vertical plane, the resulting reduction of the maximum intensity at injection (at fixed Q_s) would thus amount to 15-20 %. This is not negligible and could even annihilate the gain expected from the reduced emittances. In the case where a vertical phase advance of 90^0 is not ruled out by polarization considerations, a $108^0/90^0$ optics ($< \beta_y >$=71.0 m in the arcs) would become a very interesting candidate for LEP2.

III. COMPARISON OF THE DIFFERENT OPTICS

A comparison between the different optics presently considered for the operation of LEP2 is presented in Table I. It has been assumed that average β value in the straight sections can be kept the same for all three optics and we concentrate on the variations in the arcs. Similarly, only the horizontal emittance is quoted, since the ultimate value of the vertical one will strongly depend on our ability to correct both the dispersion and the coupling.

Parameter	$90^0/60^0$	$108^0/60^0$	$135^0/60^0$
integer Q_x	90	102	125
integer Q_y	76	76	75
mom. comp. α	0.000186	0.000138	0.000102
β_x in QF [m]	122.0	130.2	178.5
β_x in QD [m]	25.5	18.2	10.2
β_y in QF [m]	41.0	38.7	36.5
β_y in QD [m]	152.7	162.3	175.3
$\langle\beta_x\rangle$ in arcs [m]	64.1	63.2	75.4
$\langle\beta_y\rangle$ in arcs [m]	85.7	87.6	92.5
D_x in QF [m]	1.13	0.88	0.68
D_x in QD [m]	0.60	0.42	0.28
ϵ_x(90 GeV) [nm]	45.6	29.6	22.8
σ_s(90 GeV) [mm]	≈11.0	≈8.2	≈6.0

Table I
Comparison between different LEP2 optics

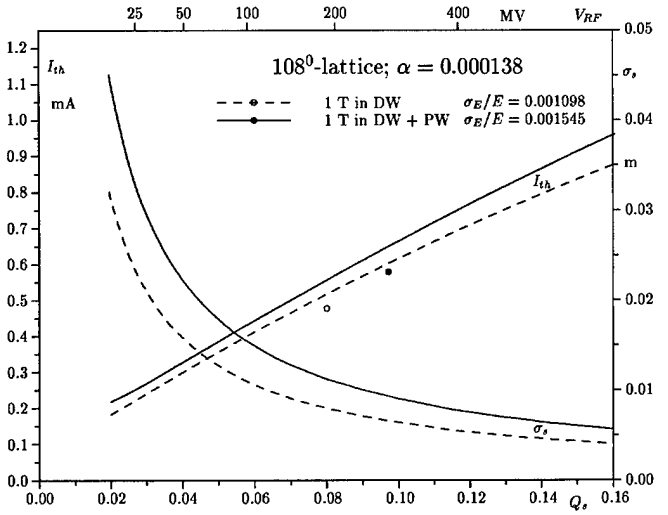


Figure 1. Calculated and measured TMCI thresholds vs. Q_s for two settings of damping and polarization wigglers DW and PW

IV. RESULTS FROM EXPERIMENTS FOR THE 108^0 LATTICE

A. Current limitations and high Q_s

With the damping wigglers alone and a synchrotron tune of 0.08, the maximum intensity reached was 480 μA per bunch. This limit was due to transverse mode coupling instabilities and is not much smaller than the value obtained with the $90^0/60^0$lattice, under the same conditions. Using the polarization wigglers in addition and with a Q_s=0.093, the maximum intensity reached 560 μA per bunch. Increasing Q_s to 0.097 gave a maximum intensity of 580 μA per bunch, which agrees well with the current of 620 μA predicted by simulation for the TMCI as shown in Fig. 1. This value is also very close to the single beam

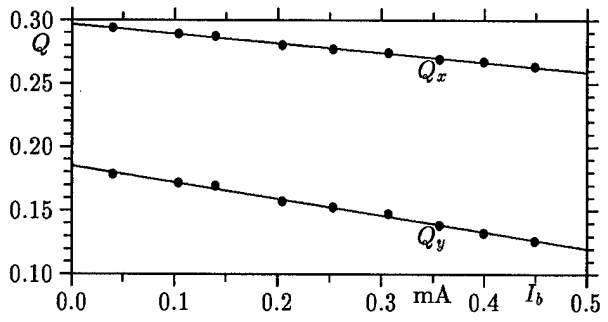


Figure 2. Measured tune change with bunch current

Δf_{rf}(Hz)	Q_x	Q_y	ϵ_x (nm)	ϵ_y (nm)
-50	.259	.181	12.15	1.31
0	.258	.179	9.43	1.24
+50	.257	.177	7.79	1.28

Table II
Measured tunes and emittances for different RF-frequencies

limit of 630 μA obtained presently with the $90^0/60^0$lattice for the same Q_s [6]).

The changes of the betatron tunes with bunch current are good measures for the effective transverse impedances and were measured to be dQ_x/dI_b=-77 A^{-1} and dQ_y/dI_b=-130 A^{-1}, Fig. 2. which are comparable with those of the $90^0/60^0$lattice.

B. Optics and emittance measurements

During the last 1994 experiment, the beam was ramped to 46 GeV. During the ramp, it was observed that each horizontal orbit correction led to a change of both tunes caused by the large sextupole strength as expected. This was as well the case after the ramp and during the squeeze. After few iterations of orbit corrections, the chromaticities were measured to be $Q'_x = 1.1$ and $Q'_y = 1.6$. The vertical rms dispersion was found to be 6 cm.

The emittance, being a significant parameter of this lattice, was measured with the synchrotron light monitor BEUV [7] for different RF-frequencies. The obtained horizontal and vertical emittances are listed in table II. From them, the uncoupled emittance $\epsilon_0 = \epsilon_x + \epsilon_y$ (assuming that vertical damping and coupling are unchanged) and the derivative of the longitudinal damping partition are obtained. These results are compared with calculations by the program WIGWAM [8] and listed in Table III. The fact that the measured emittance value is a little larger than the expected one is not surprising. In a high tune lattice modest orbit distortions can create relatively large spurious dispersions which lead to an increase of the emittance. Very good orbit corrections will be necessary to profit from this optics.

The above measurements were carried out with the injection optics having a vertical β function of β^*_y=0.21m at the four interaction points. An attempt was made to reduce this β^*_y in steps to the value of 0.05 m used in physics runs. Orbit corrections were performed at 0.14 m and 0.09 m without problems. The next step (to 0.07 m) gave a negative vertical chromaticity and the beam

	measurement	calculation
ϵ_0 [nm]	10.67	7.85
$\Delta J/\Delta p/p$	190	240

Table III
Measured and calculated emittance and damping partition derivative at 46 GeV

was lost. This could be corrected easily but further trials were postpone due to lack of time. The easiness with which the ramp and partial squeeze could be performed indicates that no problems are expected for the operations of the $108^0/60^0$lattice.

V. CONCLUSIONS

High tune lattices giving small emittances are promising means to obtain a high luminosity for LEP operation at 90 GeV where the bunch current is limited by instabilities at injection and not by the beam-beam effect in collisions. Solutions have been worked out and tried experimentally for horizontal phase advances per cell of 135^0 and 108^0. The first configuration gives about the smallest emittance possible in a regular FODO-lattice. The strong horizontal focussing obtained in these lattices leads to a small synchrotron tune and bunch length for a given RF-voltage. This reduces the threshold for the transverse mode coupling instability. The wiggler magnets available in LEP have to be used to lengthen the bunch and to keep the current reduction within limits. For the 108^0-lattice a bunch current of over 0.6 mA has been achieved which is close to the expected limit. Furthermore, the emittance measured at 46 GeV is not much above the calculated value. Other parameters have been checked and the β function in the interaction points partially reduced. These results clearly show that high luminosity operation of LEP at 90 GeV is feasible and that the $108^0/60^0$lattice is a good candidate for LEP2.

References

[1] J.P. Koutchouk, "A Superlow Emittance for LEP 2", Proc. of the 3rd workshop on LEP performance, edited by J. Poole, p. 511, CERN SL/93-19 (DI), 1993.

[2] J.R.J. Benett et al., "Design Concept for a 100 GeV e^+e^- Storage Ring (LEP), CERN 22-14, 1977. 1993 Part. Acc. Conf., Washington D.C., 17-20 May 1993.

[3] A. Verdier, "Higher order tune derivatives due to low-β insertions", Proc. 1993 Part. Acc. Conf., Washington D.C., p. 249.

[4] Y. Alexahin, "A study of the low emittance lattice for LEP2", CERN SL/94-46 (AP), 1994.

[5] A. Verdier and F. Richard, "Algorithms to get a circulating beam", This conference.

[6] D. Brandt and A. Hofmann, "Does a high Q_s raise the Maximum intensity to be Accumulated in LEP?", Proc. of the 4th workshop on LEP performance, edited by J. Poole, p. 149, CERN SL/94-06 (DI), 1994.

[7] G. Baribaud, C. Bovet, R. Jung, M. Placidi, E. Rossa and Y. Solberg, "Three Dimensional Bunch Observation in LEP",

Proc. of th 15th Intern. Conf. on High Energy Accelerators, Hamburg 1992, p. 212.

[8] J.M. Jowett, "LEP2 Beam Parameters during Energy Ramping", CERN LEP2 Note 95-27, 1995.

RADIATION DAMPING PARTITIONS AND RF-FIELDS

M. Cornacchia, Stanford Linear Accelerator Center, Stanford, CA 94209 USA,
A. Hofmann, CERN, CH-1211 Geneva 23, Switzerland

Abstract

In his classical paper "Radiation Effects in Circular Accelerators" K.W. Robinson has shown that the damping partitions in a circular machine cannot be changed by a radio-frequency field. The proof given there is quite general and valid for any RF-field, provided it is not so strong that it changes the equilibrium orbit appreciably. However, the physical mechanisms which prevent the possibility to alter the damping partitions is not very transparent. As a consequence, so-called "damping cavities" are still proposed from time to time. Here we want to illustrate the underlying physical principles by going in detail through the beam dynamics for the simple case of a cavity operating in a dipole (deflecting) mode and which is located in a region of finite dispersion in a storage ring.

I. INTRODUCTION

In his famous classical paper on radiation damping [1], K.W. Robinson gives a general proof that the radiation damping partition numbers J_E, J_x, J_y of the three modes of oscillation of particles in a circular accelerator cannot be changed with an RF-field. This is shown in a very general way in the Appendix of his paper, with the only restriction that the radio frequency fields should not be so strong that they change the equilibrium orbit appreciably. The proof is so elegant and complete that not much can be added. However, just due to this generality, it is also not very transparent as far as the underlying physical principles are concerned. Probably for this reason, proposals for so-called "damping cavities" are still made from time to time. K.W. Robinson himself told one of us that he once found such a cavity already in the design stage on the drawing board during a visit to an accelerator laboratory.

The effect of such cavities in linear accelerators and proton synchrotrons has also been investigated by H.G. Hereward [2].

To illustrate clearly the mechanisms which prevent the change of damping partition numbers by RF-fields, we consider here a simple RF cavity operating in a dipole mode. Such a cavity produces a longitudinal electric field with a transverse gradient as shown in Fig. 1. We assume that it is placed at a position with finite horizontal dispersion D , and therefore particles of different energy deviation $\delta\mathcal{E}$ will traverse it at different horizontal offsets

$$x = D\frac{\delta\mathcal{E}}{\mathcal{E}_0} = D\,\epsilon$$

Here $\mathcal{E}_0$ is the nominal particle energy, and the relative energy deviation $\epsilon = \delta\mathcal{E}/\mathcal{E}_0$ has been introduced to make some later expressions more compact. Since the longitudinal cavity field depends on the distance x from the axis, particles of different energy will thus gain different amounts of energy in one traversal. However, there is also a magnetic field associated with this cavity mode. This leads to a transverse deflection which changes the path length of a particle in one revolution. We will show that these two actions of the cavity, i.e. acceleration and deflection, cancel each other as far as their effect on the damping partitions is concerned.

The treatment will not be rigorous or general, but should better illustrate the mechanisms involved. The exact and general proof has already been given by K.W. Robinson.

II. The dipole mode cavity

For acceleration of particles by an RF-field, one normally uses a cavity which oscillates in the so-called monopole mode (m=0). Such a mode has a longitudinal electric field E_z which is - to a good approximation - homogeneous close to the axis.

One can also operate a cavity in a dipole mode (m=1), having a longitudinal electric field with a gradient such that its strength increases with transverse distance from the axis as shown in Fig. 1. In the neighborhood of the axis, the increase is approximately linear and can be written

$$E_z = \frac{x}{a}\hat{E}\cos(\omega_d t) = \frac{\partial\hat{E}}{\partial x}x\cos(\omega_d t).$$

Here ω_d is the frequency of the cavity oscillation which we will choose to be a harmonic of the revolution frequency in the storage ring, and a is an effective cavity radius. We can get the associated magnetic field from Maxwell's equation

$$\dot{\mathbf{B}} = -\mathrm{curl}\,\mathbf{E} \;\rightarrow\; B = B_y = \frac{1}{\omega_d}\frac{\partial\hat{E}}{\partial x}\sin(\omega_d t). \qquad (1)$$

First we calculate the energy gain due to the electric field, and the deflection due to the magnetic field, of a particle with charge e which is going through such a cavity of length ℓ. Both will depend on the distance x from the axis and on the time of traversal t. We phase the cavity such that the synchronous particle with nominal energy $\mathcal{E}_0$ passes through the dipole mode cavity at the synchronous time t_s, when the electric field gradient is at its maximum and the magnetic field goes through zero. Since it is on-axis and synchronous, it will experience neither acceleration nor deflection. Another particle, with a different energy, is now assumed to traverse the cavity at the distance $x = D\epsilon$ from the axis, at a time which deviates by $\tau = t - t_s$ from the synchronous one. The relative energy gain for this particle is

$$\Delta\epsilon = \frac{e\ell\hat{E}}{a\mathcal{E}_0}\cos(\omega_d\tau).$$

We assume now that the bunch length is much smaller than the wave length of the cavity oscillation, i.e. $\omega_d\tau \ll 1$ and approximate the cosine by unity to obtain

$$\Delta\epsilon \approx \frac{e\ell\hat{E}}{a\mathcal{E}_0}x = \frac{e}{\mathcal{E}_0}\frac{\partial\hat{V}}{\partial x}x = Kx, \qquad (2)$$

0-7803-3053-6/96/$5.00 ©1996 IEEE

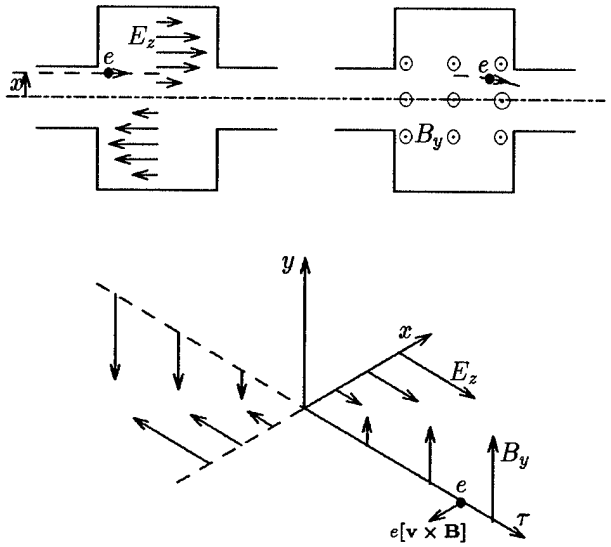


Figure. 1. Dipole mode cavity. Top: The electric field a the synchronous time and the magnetic field a quarter oscillation later. Bottom: Situation of the fields around the synchronous time.

where we used $\hat{V} = \ell\hat{E} = a\partial\hat{V}/\partial x$ and

$$K = \frac{e}{\mathcal{E}_0}\frac{\partial\hat{V}}{\partial x}.$$

Next we calculate the deflection angle $\Delta x'$ due to the magnetic field of the cavity.

$$\Delta x' = -\frac{e\ell B_y c}{\mathcal{E}_0}.$$

With the relation between the electric and magnetic field (1) this can be expressed as

$$\Delta x' = -\frac{ec}{\mathcal{E}_0\omega_d}\frac{\partial\hat{V}}{\partial x}\sin(\omega_d\tau) \approx -\frac{e}{\mathcal{E}_0}\frac{\partial\hat{V}}{\partial x}c\tau = -Kc\tau. \quad (3)$$

III. Longitudinal beam dynamics in an electron storage ring

First we recapitulate some basic longitudinal beam dynamics considerations for a circular accelerator without a dipole mode cavity. For this we consider a model storage ring consisting of two 180^0 arcs with some focusing structure, and an accelerating cavity operating in the monopole mode. We locate this cavity in a dispersion free region in order to avoid any synchro-betatron coupling effects. The accelerating cavity has a peak voltage $\hat{V}_{RF}$, and oscillates with frequency $\omega_{RF} = h\omega_0$, where h is the harmonic number and ω_0 the revolution frequency. The focusing structure in the arcs creates a momentum compaction factor α_c which determines the relative change of the revolution time T_0

$$\frac{\Delta T}{T_0} = \frac{\Delta\tau}{T_0} = \alpha_c\epsilon.$$

The energy gain per revolution of a particle going through the RF-cavity at the time $t = t_s + \tau$ is given approximately by

$$\Delta\epsilon \approx \frac{e\hat{V}_{RF}}{\mathcal{E}_0}\left[\sin(h\omega_0 t_s) + \cos(h\omega_0 t_s)h\omega_0\tau\right].$$

The deviation τ from the synchronous time t_s is assumed to be small such that $h\omega_0\tau \ll 1$. It is convenient to introduce the "synchronous phase angle" $\phi_s = h\omega_0 t_s$, which for electron rings must lie between 90^0 and 180^0 ($\cos\phi_s < 0$) for stability.

We further include the effect of synchrotron radiation which produces an energy loss proportional to the squares of the particle energy and of the magnetic field in the dipoles of the ring $U \propto \mathcal{E}^2B^2$. Calling U_s the energy loss of a particle with nominal energy, we get the loss for a particle with a small relative energy deviation ϵ

$$U = U_s + \frac{2U_s}{\mathcal{E}_0}\epsilon.$$

Putting these equations together, this yields for the relative energy change per revolution

$$\Delta\epsilon = \frac{e\hat{V}_{RF}\sin\phi_s}{\mathcal{E}_0} + \frac{e\hat{V}_{RF}\cos\phi_s}{\mathcal{E}_0}h\omega_0\tau - \frac{U_s}{\mathcal{E}_0} - \frac{2U_s}{\mathcal{E}_0}\epsilon.$$

For the synchronous particle $\tau = \epsilon = 0$, but for equilibrium we should also have $\Delta\epsilon = 0$, which gives the condition

$$U_s = e\hat{V}_{RF}\sin\phi_s.$$

We assume that the changes in ϵ and τ are small over one revolution, such that they can be described by a differential form. We use $\dot{\epsilon} \approx \Delta\epsilon\omega_0/2\pi$ and $\dot{\tau} = \Delta\tau\omega_0/2\pi$ to get the equations

$$\begin{aligned}\dot{\epsilon} &= -\frac{\omega_0}{2\pi}\frac{2U_s}{\mathcal{E}_0}\epsilon + \omega_0^2\frac{he\hat{V}_{RF}\cos\phi_s}{2\pi\mathcal{E}_0}\tau \\ \dot{\tau} &= \alpha_c\epsilon\end{aligned}$$

which have as solution a damped oscillation

$$\epsilon(t) = \mathrm{e}^{-\alpha t}\cos(\omega_s t + \phi).$$

with the synchrotron frequency ω_s and the damping rate α

$$\omega_s = \omega_0\sqrt{-\frac{h\alpha_c e\hat{V}_{RF}\cos\phi_s}{2\pi E}}\ , \quad \alpha = \frac{\omega_0}{2\pi}\frac{U_s}{\mathcal{E}_0}. \quad (4)$$

In this derivation, approximations have been made assuming $\omega_s \ll \omega_0$ and $\alpha_c \ll \omega_s$.

IV. Effects of the dipole mode cavity

We now include the effects of a dipole mode cavity on beam dynamics. This cavity is supposed to be located in a straight section, which may be opposite to the accelerating cavity, and where the dispersion D is nonzero. As we have seen before, such a cavity will give both an energy increase (2) and a deflection (3)

$$\Delta\epsilon = Kx\ , \quad \Delta x' = -Kc\tau \quad \text{with} \quad K = \frac{e}{\mathcal{E}_0}\frac{\partial\hat{V}}{\partial x}.$$

The deflection has also a longitudinal effect which is important. The angle $\Delta x'$, which is created by the cavity, leads to a horizontal orbit distortion, and therefore to a change of the path length L of the trajectory of a particle travelling around the ring[3]. Since this well known effect is an essential part of the mechanism under investigation here, we shall give its detailed derivation in the following.

We study the trajectory of a particle which passes at a radial distance x from the equilibrium orbit through a bending magnet with radius of curvature ρ . Due to the deflection by the magnetic field, its path length will increase by an amount ΔL over that of a particle on the equilibrium orbit

$$\Delta L = \int_0^s \frac{x}{\rho} ds.$$

We will make use of the differential equations for the betatron trajectory $x(s)$ and for the dispersion $D = D_x(s)$

$$x'' + k\,x = 0 \ , \ \ D'' + k\,D = \frac{1}{\rho}$$

where the $x' = dx/ds$, $x'' = d^2x/ds^2$ and $k = k(s)$ is the horizontal focusing function. With these expressions we can rewrite the integral for the path length

$$\Delta L = \int_0^s \frac{x}{\rho} ds = \int_0^s (D'' + k\,D) x ds$$

$$= -\int_0^s (D'' + k\,D)\frac{x''}{k} ds = -\int_0^s \frac{D''x''}{k} ds - \int_0^s Dx'' ds.$$

Introducing for short the quantity $g = D'x - Dx'$, and thus $g' = D''x - Dx''$, we obtain

$$\Delta L = -\int_0^s \frac{D''x''}{k} - \int_0^s D''x ds + \int_0^s g' ds$$

$$= -\int_0^s \frac{D''}{k}(x'' + k\,x) ds + g|_0^s = g|_0^s.$$

since $x'' + k\,x = 0$. Therefore the increase of path length is given by

$$\Delta L = [D'x - Dx']_s - [D'x - Dx']_0.$$

An important application of this expression is lengthening of the closed orbit due to a deflection by an angle θ at the origin. The transverse deflection there is $x'_0 = x'_C + \theta$, where x'_C is the deflection after one turn around a ring with circumference $C = 2\pi R$. Since the closed orbit is stationary, we should have $D_0 = D_C$ and $x_0 = x_C$. The path lengthening due to a stationary deflection at a location with dispersion D becomes

$$\Delta L = (D'x - Dx')_C - (D'x - Dx')_0 =$$
$$= D_0(x'_0 - x'_C) = D\theta.$$

The lengthening of the orbit vanishes for $D = 0$, except for higher order effects in θ which we have neglected.

We now apply this to the deflection $\theta = \Delta x'$ by the dipole mode cavity. We assume again that the synchrotron motion is slow and changes the orbit distortion only adiabatically, and thus we neglect synchro-betatron coupling. In this case we get for the orbit lengthening in good approximation

$$\Delta L = D\Delta x' = -DKc\tau \ \text{ and } \ \Delta\tau = \frac{\Delta L}{c} = -KD\tau$$

Since the orbit is longer there is an increase $\Delta\tau = \Delta L/c$.

Combining the energy and the path length changes caused by the dipole mode cavity, we get for the differential equations

$$\dot{\epsilon} = \frac{\omega_0}{2\pi}\left(-\frac{2U_s}{\mathcal{E}_0} + KD\right)\epsilon + \omega_0^2 \frac{he\hat{V}_{RF}\cos\phi_s}{2\pi\mathcal{E}_0}\tau$$

$$\dot{\tau} = \alpha_c\epsilon - \frac{\omega_0}{2\pi}KD\tau$$

Seeking solutions of the form e^{rt} we calculate the determinant

$$\begin{vmatrix} \frac{\omega_0}{2\pi}\left(-\frac{2U_s}{\mathcal{E}_0} + KD\right) - r & \omega_0^2 \frac{he\hat{V}_{RF}\cos\phi_s}{2\pi\mathcal{E}_0} \\ \alpha_c & -\frac{\omega_0}{2\pi}KD - r \end{vmatrix} = 0$$

and get the characteristic equation

$$r^2 - r\frac{\omega_0}{2\pi}\left(\frac{-2U_s}{\mathcal{E}_0} + KD - KD\right)$$
$$+\omega_s^2 + \left(\frac{\omega_0}{2\pi}\right)^2\left(\frac{2U_s}{\mathcal{E}_0} + KD\right)KD = 0.$$

We see that in the central term, which is responsible for the damping, the two effects of the dipole mode cavity cancel. We find the solution $r = -\alpha_d \pm i\omega_{sd}$ with a slightly changed synchrotron frequency

$$\omega_{sd} = \sqrt{\omega_s^2 - \alpha^2 + \frac{\omega_0}{2\pi}\left(-\frac{U_s}{\mathcal{E}_0} + KD\right)KD}$$

However, the damping rate

$$\alpha_d = \frac{\omega_0}{2\pi}\frac{U_s}{\mathcal{E}_0}$$

is exactly the same as for the case without dipole mode cavity given by (4). Combining the two roots we can write the solution in the form

$$\epsilon = \hat{\epsilon}e^{-\alpha t}\cos(\omega_{sd} + \phi) \approx \hat{\epsilon}e^{-\alpha t}\cos(\omega_s + \phi).$$

where $\hat{\epsilon}$ is the initial relative energy spread.

V. Acknowledgements

We thank L. Emery for pointing out the technique used in calculating the path length change due to a deflection in a dispersive region. The authors would also like to thank B. Zotter for careful proofreading and editing of the manuscript, and J.Poole for help with its electronic transfer.

References

[1] K.W. Robinson, "Radiation Effects in Circular Electron Accelerators", The Physical Review, Vol 111, No. 2, p. 373, 1958.

[2] H.G. Hereward, " Transverse Variation of Accelerating Force", CERN 58-12, June 1958.

[3] A. Piwinski, "Synchro-betatron resonances", CAS CERN Accelerator School Advanced Accelerator Physics, Oxford 1985, CERN 87-03, 1987.

EXPERIMENTS ON BEAM-BEAM DEPOLARIZATION AT LEP

R. Assmann*, A. Blondel*, B. Dehning, A. Drees°, P. Grosse-Wiesmann, H. Grote, M. Placidi, R. Schmidt, F. Tecker†, J. Wenninger

CERN, CH-1211 Geneva 23, Switzerland
** SLAC, Stanford Univ., P.O.Box 4349, CA 94309, USA*
** Ecole Polytechnique, Paris, France*
° Universität Wuppertal, Germany
† Physikalisches Institut III A, RWTH Aachen, Germany

Abstract

The possibility of obtaining transverse polarization with colliding beams was studied at LEP during 1994. A level of transverse beam polarization of 40% was achieved with e^+e^- collisions in one of the experimental interaction points. the collision of one electron and one positron bunch was $1.5 \times 10^{30} cm^{-2} s^{-1}$. The polarization level was not limited by the beam-beam interaction: from three circulating electron bunches only one was colliding with one positron bunch, whereas the beams were separated by electrostatic deflectors at the interaction points of the other electron bunches. No significant difference between the polarization level of colliding and non colliding bunches was noticed. Betatron- and synchrotron frequencies as well as spin tune were chosen in order to avoid beam-beam driven depolarizing resonances.

I. INTRODUCTION

During 1994 a series of experiments were performed to assess the possibility of sustaining polarization with colliding beams at LEP. Polarization in collision would allow beam energy measurement during luminosity fills and future experiments using colliding polarized beams.

To precisely determine mass and width of the Z boson a calibration of the beam energy by resonant depolarization is required. The calibration is performed at the end of a luminosity fill with non colliding beams [1]. A transverse polarization level of at least 10 % with beams in collision would allow to reduce the time required for the energy calibration. The installation of a spin rotator at LEP, although not foreseen for the next years, would allow to collide longitudinal polarized beams and to measure the weak mixing angle θ_w with an accuracy which can not be achieved by other methods. Such an experiment requires a beam polarization of at least 50% [2].

II. MAXIMUM POLARIZATION FOR A SINGLE BEAM

A maximum level of transverse polarization for a single beam of $(57 \pm 3\%)$ has been achieved using various techniques to compensate depolarizing effects [3] :

- the vertical closed orbit is carefully corrected to a rms value of 0.4-0.5 mm.
- the spin rotation due to the experimental solenoid magnetic field of up to 66 mrad/turn which reduces the polarization level to less than 5% is compensated by a proper configuration of vertical closed orbit bumps of both sides of the solenoids [4]
- the beam energy is selected for the spin tune to be close to $\gamma a = n + 0.5$, with n an integer number, in order to minimize the depolarizing effects from integer resonances (γ is the gamma-factor for the electrons, and a is the anomalous magnetic momentum).
- Harmonic spin matching is applied to minimize the spurious tilt of the spin precession axis by compensating those harmonics of the Fourier expansion of the closed orbit which lead to a depolarization [5]. A novel implementation of the harmonic spin matching was developed for LEP by deriving the amplitude of the correcting bumps for the harmonics of interest directly from the beam position measurements [6].

III. BEAM-BEAM EFFECTS

The beam dynamics is strongly affected by beam-beam effects, as one beam acts on the counterrotating particles as a strong nonlinear lens. The strength of the beam-beam effect is characterized by the linear beam-beam tune shift. Beam-beam effects limit the maximum tune shift to a value of about 0.04 per interaction point for e+e- storage rings. If the operating parameters such as betatron and synchrotron tunes are not carefully chosen, the beam-beam tune shift as well as the attainable luminosity is limited to much lower values. Beam-beam effects can lead to an emittance increase and to particle losses. It has also been observed, that the distribution of particle amplitudes, which is Gaussian for a single beam, develops tails in the presence of beam-beam effects [7].

The influence of the beam-beam interaction on the beam polarization is twofold :

- the particle trajectory is deflected by an angle α due to the interaction with the counterrotating beam. The spin vector rotates by an angle : $\gamma a \times \alpha$. This effect can cause higher order depolarizing resonances.
- the excitation of vertical betatron oscillations by beam-beam effects at the beam-beam limit can increase the strength of depolarizing resonances, in particular of those resonances where the condition $\gamma a = Q_y \pm n$ is fulfilled, with Q_y the vertical betatron tune.

At PETRA a decrease of the transverse polarization was observed with increased beam-beam tune shift. At the same time the vertical beam size increased [8].

The influence of the beam-beam interaction on the polarization if not fully understood. Currently both at HERA [9] and at LEP [10] the depolarization by beam-beam effects is experimentally investigated.

0-7803-3053-6/96/$5.00 ©1996 IEEE

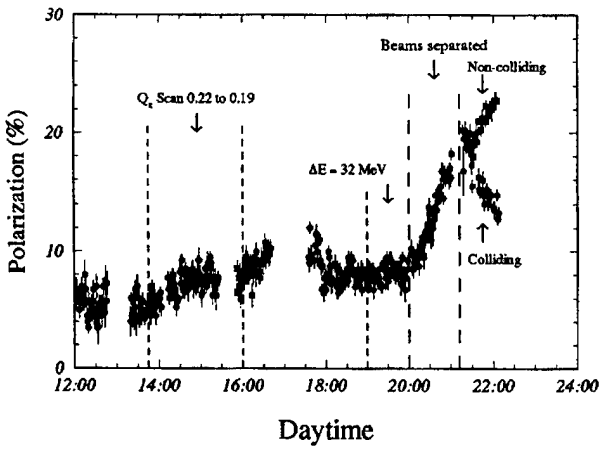


Figure. 1. Polarization level during first experiment

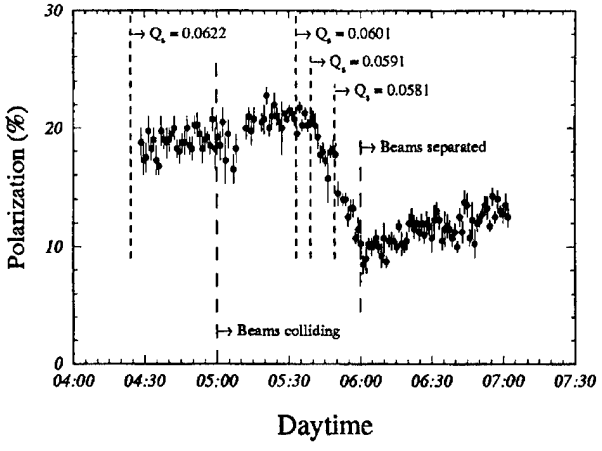


Figure. 2. Polarization level during second experiment

IV. FIRST EXPERIMENT

The first experiment performed at LEP demonstrated a strong depolarization due to the beam-beam interaction. 8 electron and 8 positron bunches were injected into LEP. The bunches were colliding at the four interaction points (IP) where LEP physics experiments are located, and separated at four other points in the vertical plane by electrostatic separators. To avoid collisions in the arcs additional separators are installed to separate the beams in the horizontal plane ("Pretzel scheme") [11]. Even with eight bunches per beam collisions can be avoided: For injection as well as for machine experiments the beams can be separated in the vertical plane at the collision points with LEP physics experiments.

The beam energy was 45.60 GeV, close to the optimum energy for the production of Z bosons. The betatron tunes were adjusted to $Q_x = 90.231$ and $Q_y = 76.153$. The linear beam-beam tune shift parameter was 0.015. Only the polarization of the electron bunches was monitored. As show in fig. 1, the polarization level did not exceed 10% during the first part of the experiment when the beams were colliding at the IPs. An increase of the polarization level was observed when the horizontal betatron tune was changed to $Q_x = 90.187$. A scan of the beam energy from 45.602 GeV to 45.576 GeV had no influence on the polarization level.

Later the beams were separated, and the polarization level increased. Four of the eight positron bunches were dumped and the vertical separation around the collision points with LEP physics experiments was switched off. This left four of the eight electron bunches colliding. For the noncolliding electron bunches the polarization kept increasing, whereas for the four colliding bunches the polarization level decreased.

V. SECOND EXPERIMENT

The second experiment was performed at the end of a luminosity fill at a beam energy of about 45.60 GeV. For energy calibration the beams were separated at all four collision points and a polarization level of 20% was obtained. Then the beams were brought into collision at a single interaction point. The vertical electron beam size increased by about 10% with the beams in collision, but no depolarization due to beam-beam effects was observed. The betatron tunes were $Q_x = 90.226$ and $Q_y = 76.165$ and the noninteger part of the spin tune $\gamma a = 0.48$. After the beams were colliding, the luminosity was increased from $2.0 \times 10^{30}\, cm^{-2}\, s^{-1}$ to $2.4 \times 10^{30} cm^{-2} s^{-1}$ by an optimization of the beam overlap in the vertical plane with electrostatic separators installed left and right of the IPs. During this optimization no change of the polarization level was noticed. The linear beam-beam tune shift reached 0.017.

To better understand the dependence of the beam-beam depolarization on the operating conditions the synchrotron tune was changed from 0.0622 to 0.0591 (see fig.2). The polarization level decreased to about 17%. A further reduction of the synchrotron tune to 0.0581 lead to a strongly decreased polarization level of 10%. When the beams were separated again (leaving the synchrotron tune at a value of 0.0581) the polarization started to rise, indicating that the depolarization was indeed caused by beam-beam effects.

VI. THIRD EXPERIMENT

This experiment was performed at a beam energy of 44.71 GeV. Three electron bunches and one positron bunch were injected. With such a scheme one electron bunch and one positron bunch collide in the interaction points 2 and 6, if the separation bumps are turned off, whereas the other electron bunches meet the positron bunch at points where the beam are separated. This allows a direct comparison of the polarization levels of a colliding and a non colliding bunch.

The aim for this experiment was to achieve the highest possible polarization level with colliding beams. The highest polarization level of 57% was achieved in 1993 with one beam, but during the energy calibrations in 1994 it never exceeded 25% (the reasons for the low polarization level are not well understood, it is assumed that alignment of the magnets and precision of the beam orbit measurement system was slightly degraded during 1994).

All potential depolarizing sources were turned off :

- the solenoid magnets in the HEP experiments

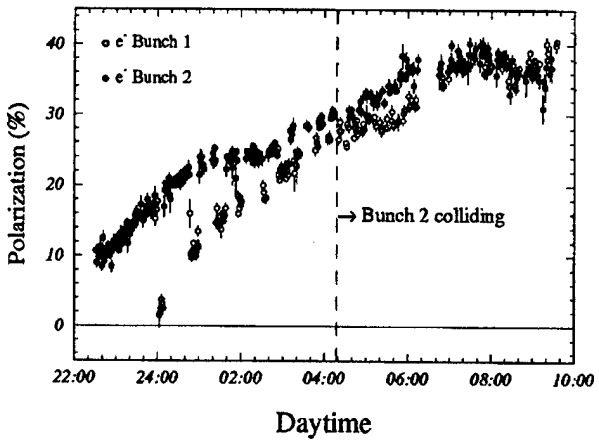


Figure. 3. Polarization level during third experiment

- the separators for the "Pretzel scheme", because the bunches did not meet in the arcs

The polarization level saturated at around 25% after applying the technique of deterministic harmonic spin matching.

Some time was then spend to further increase the polarization level by adopting a new method of "educated harmonic spin matching" [6] [12], leading to a polarization level of more than 30%. At that time electron bunch 2 and positron bunch 1 were brought into collision at interaction point 6. The educated harmonic spin matching was pursued with beams in collision and a polarization level of 40% was obtained for both colliding and non colliding bunches. The luminosity was 1.0 - 1.5 $\times 10^{30} cm^{-2} s^{-1}$ and the linear beam-beam tune shift was 0.04.

VII. ESTIMATION OF BEAM-BEAM DEPOLARIZATION

The asymptotic value for the polarization can be written as :

$$P(t \to \infty) = \frac{0.924}{1 + (\frac{\tau_p}{\tau_d})_{sb} + (\frac{\tau_p}{\tau_d})_{bb}} \qquad (1)$$

$(\tau_p/\tau_d)_{sb}$ includes all depolarizing effects in the presence of only one beam, $(\tau_p/\tau_d)_{bb}$ all depolarizing effects from the beam-beam interaction.

During the third experiment the polarization levels of the colliding and the not colliding bunch were about the same. We can estimate the beam-beam depolarization since the polarization level of the non colliding bunch was 40% and since the difference with the colliding bunch did not exceed 4%. Using the equation above this yields an equilibrium polarization level due to the beam-beam interaction of about 74%, if no single beam depolarizing effects are present.

VIII. SUMMARY

The experimental study is far from being complete. We summarize our observations :

- In one experiment the beams were colliding at four points. The polarization level was limited to less than 10 %. No increase of the electron vertical beam size was observed. The vertical positron beam size increased by about 30 %.
- With the beam colliding at one point, a polarization level of 40 % was achieved. The polarization level was about the same for one colliding and one non colliding bunch.
- It was observed that the polarization level depends critically on the synchrotron tune : when Q_s was changed by 0.005, the polarization strongly decreased.
- In one experiment with the beams colliding at four points at an energy of 45.60 GeV with a linear beam-beam tune shift of 0.015/IP the depolarization was strong. In the last experiment performed at an energy of 44.71 GeV the polarization level was 40 % with a linear beam-beam tune shift of about 0.04/IP. This indicates, that the beam-beam depolarization does not scale with the linear beam-beam tune shift at one crossing point. Other parameters as spin tune and synchrotron tune are also of importance.

The experiments presented here demonstrate that transverse polarization can be maintained in the presence of beam-beam effects, provided that the operational parameters are well selected. The results also show, that experiments with longitudinal polarized beams at least at one collision point are not prohibited by depolarizing beam-beam effects. However it should be kept in mind, that the beam-beam depolarizion with transverse and longitudinal polarized beams might be different.

References

[1] L.Arnaudon et al., Accurate determination of the LEP beam energy by resonant depolarization, CERN SL/94-71 (BI)

[2] G.Alexander et al., -Proposal- A Test of Longitudinal Spin Polarization at LEP, CERN/LEPC94-8, May 1994

[3] R.Assmann et al., Lepton Beam Polarization at LEP, Proc. Conf. High Energy Physics with Polarized Beams, Bloomington, Indiana, 1994

[4] K.Steffen, DESY PET82 (1982) and A.Blondel, LEP Note 629 (1990)

[5] R.Rossmanith, R.Schmidt, NIM A236(1985), 231-248, 1985

[6] R.Assmann, Transversale Spin-Polarization und ihre Anwendung für Präzisionsmessungen bei LEP, Doctoral Thesis, University München

[7] K.Cornelis, Tail production due to beam-beam, Presentation 17, Proc. of the 3rd workshop on LEP Performance, CERN SL/93-19 (DI)

[8] R.Schmidt, Polarisation am Speicherring PETRA, Thesis University Hamburg, DESY Internal Report M 82/20, September 1982

[9] D.Barber, these proceedings

[10] see also : M.Placidi, Transverse Polarization at LEP, Proc. 5th Workshop on LEP Performance, Chamonix, CERN SL/95-08(DI)

[11] R.Bailey et al. PAC 1993, Washington, DC, USA, 17 - 20 May 1993

[12] A.Blondel, to be published

MEASUREMENTS OF IMPEDANCE DISTRIBUTIONS AND INSTABILITY THRESHOLDS IN LEP

D. Brandt, P. Castro, K. Cornelis, A. Hofmann, G. Morpurgo, G.L. Sabbi, J. Wenninger and B. Zotter,
CERN, CH-1211 Geneva 23, Switzerland

Abstract

The distribution of reactive and resistive components of the transverse impedance around the circumference of LEP has been obtained by exciting the beam and measuring the variations of phase advance and of closed orbit displacements with beam current. Tune shifts with current and instability thresholds were determined for two machine lattices with different beta functions and momentum compaction for various values of bunch length and synchrotron frequency. These measurements are particularly interesting for LEP2, which will require larger bunch currents to achieve the design luminosity.

I. INTRODUCTION

In the present operation of LEP near 45 Gev/beam, the single bunch current is limited to less than about 0.6 mA both by the transverse mode coupling instability (TMCI) and by the beam-beam effect. Due to the latter limitation, there is presently no advantage in increasing the single bunch current, and the way to reach higher luminosities is to use a larger number of bunches, such as is done in the "Pretzel" and "bunch-train" schemes. However, for LEP2, operating at higher energies by using superconducting cavities, the **total** beam current will be limited by synchrotron radiation losses which have to be compensated by the available RF power. Also the cryogenic system will provide a limited amount of cooling. On the other hand, the beam-beam limit is expected to be higher in proportion to the energy of operation. Therefore it would be advantageous to operate with a small number of bunches with the highest current possible. For the standard scheme of 4 on 4 bunches, 1 mA per bunch would be necessary to obtain the desired design luminosity. In order to overcome limitations by collective effects, in particular to increase the TMCI threshold, a good understanding of all impedances in LEP is required. The impedances obtained by computer models should be verified on the machine. In addition to measurements of the total values of the impedances, it has now become possible to obtain individual contributions of structures situated around the circumference of LEP.

II. CURRENT DEPENDENCE OF BETATRON PHASE ADVANCE

A. Introduction

The reactive transverse impedance leads to a reduction of the betatron tunes with bunch current which has been measured for several machine lattices[1] in the past. In the present experiment it was tried to distinguish between the tune shift caused by the impedance of the RF-sections and that caused by the rest of the machine which is expected to be dominated by that of the numerous (shielded) bellows. This was done by measuring the betatron phase advance for different bunch currents using the "1000-turn" memory of the pickups[2].

B. Machine Conditions for the First Experiment

A positron beam was accumulated in the $90/60^0$ injection optics, with both damping and polarization wigglers excited. The horizontal and vertical phase advances as well as the tunes were measured for different bunch intensities using a continuous excitation of the betatron oscillation.

C. Analysis of Measurements

First, the tune dependence on the bunch current was measured with the Q-meter. An analysis of the results yielded

$$\frac{dQ_x}{dI_b} = 66\,\mathrm{A}^{-1}\ ,\ \frac{dQ_y}{dI_b} = 133\,\mathrm{A}^{-1}. \qquad (1)$$

All theoretical betatron phase advances were computed with the program MAD [3] and subtracted from the measurements. Several procedures were used to remove the ambiguity in absolute phase, such as considering only the difference in phase between the first and later monitors, or by subtracting the average phase of the first few monitors from the others for each current level. The measurements are presented as the change of the normalized phases per unit bunch current

$$\frac{1}{2\pi}\frac{d\mu_{x,y}}{dI_b}. \qquad (2)$$

For further analysis two different methods were applied. The first one uses some physical insight into the observed effects in treating the results, while the second one makes least square fits through most of the data with as little bias as possible.

First method: To get easily measurable effects, the amplitudes of the betatron excitation were larger at low beam intensities than at higher ones. However, the analysis showed that phases measured with large amplitudes suffer from an additional non-linear detuning effect, which results in a rather poor correlation between those data and the ones taken at high intensity. For this reason, measurements with bunch currents below 200μA were eliminated from the analysis. The results obtained with the remaining data are presented in Table I and II, for both the vertical and the horizontal plane. As can be seen, the relative contributions of the bellows and the RF cavities are rather consistent for different sets of measurements. Moreover, at least in the vertical plane, the accumulated phase shift around the ring is in fair agreement with the values obtained directly with the Q-meter. However, a positive slope of the horizontal phase advance in some of the arcs remains unexplained and is thought to be produced by drifts of the machine parameters and inaccuracies of the measurements.

0-7803-3053-6/96/$5.00 ©1996 IEEE

Second method: A least square fit was applied to all of the data taken in the experiment with the purpose of estimating the accuracy and in order to discover any errors caused by a possible bias in the treatment. Monitors which had very different readings from the adjacent ones were eliminated from the analysis (less than 20 out of a total of over 500). Results which had rather large values for all monitors, probably due to a phase off-set, were also eliminated. To remove ambiguities in the absolute values of the phase, a fit through the first octant was made to find the phase off-set at the beginning of the machine. To investigate the effect of the betatron oscillation amplitude on the measured phase advances, several runs with the same current but different excitations levels were compared.

The results of the second analysis are shown in Fig.1, obtained by linear fitting of measurements performed at 9 different bunch currents. The longitudinal distance s from IP1 is used as horizontal coordinate. We see two large, localized impedances in the two RF-sections at IP2 and IP6. In the arcs, the slopes of individual sections were fitted with dashed lines. A slight variation of these slopes can be seen which may be caused by drifts of the machine parameters or measurement errors: all arcs should have about the same impedance, which is mainly caused by the large number (2800) of uniformly distributed (shielded) bellows. For this reason another fit was made with the same slope for all arcs as shown by the solid line. The fast oscillation of the phase is explained by a beta function mismatch, caused by the defocusing effect of the reactive impedance: this can be understood as the impedance acting as a current dependent quadrupole.

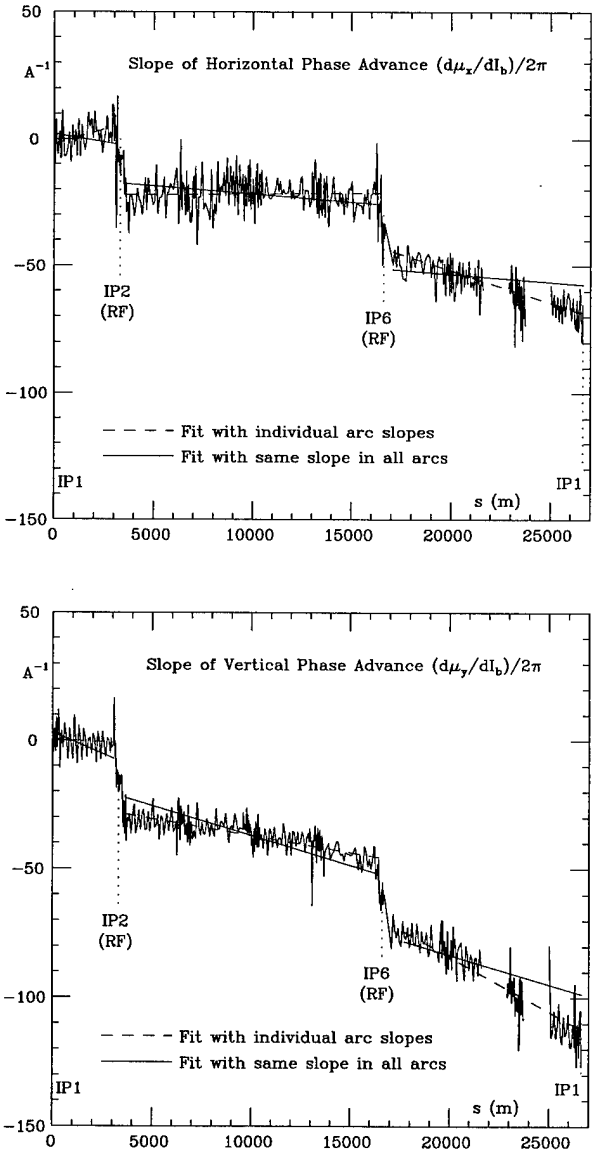


Figure 1. Dependence of phase advances on bunch current

(A^{-1})	First analysis			Second analysis			Average	Q-meter
plane	arcs	cav.	total	arcs	cav.	total	total	total
x	-13.1	-54.3	-67.5	-16.7	-40.5	-57.2	-62.4	-66
y	-63.8	-59.5	-123.4	-64.7	-49.7	-114.4	-118.9	-133

Table I

Measured phase advance per bunch current $d(\mu/2\pi)/dI_b$ for the RF cavities and the rest of LEP

D. Discussion

In Table I, the slopes of the phase advance with current, obtained from the data with the two methods of analysis, are shown individually for the cavities and for the arcs. The averaged sums are compared with those of the direct measurement of the total tune shifts. From the scatter of the values obtained with the different methods we estimate an error about 20%. To estimate the transverse impedance from these measurement, we normalized the phase advance per bunch current with the average beta functions as shown in Table II.

The tables show that the results have variations which depend on the way the fit is made. Measurements taken at large excitation amplitudes always had larger errors than those at smaller ones. In the second analysis, the total phase shifts around the ring were always smaller than the corresponding values obtained by direct measurement with the Q-meter.

E. Comparison with Computation

The effective transverse impedance is the integral over the machine impedance, multiplied by the bunch spectrum squared. For a particular impedance component, it can be found from the measured slopes of the phase shift by inverting the usual expression for the tune shift[4]

$$Z_T^{eff} = \frac{E_o \sigma_s}{eR\langle\beta\rangle} \frac{d\mu}{dI_b} \qquad (3)$$

The resulting values of the various contributions as well as the total effective transverse impedances are shown in Table.II.

From the definition, the effective transverse impedance depends on the bunch length. While it could not be measured in this experiment, it is known from previous experience to be approximately $\sigma_s = 18-19$ mm at injection energy when damping and polarization wigglers are excited and $Q_s = 0.08$. The vertical impedance of LEP is dominated by the 120 five-cell copper RF cavities ($Z_y = 1.2\ \mathrm{M}\Omega/m$ at $f_{res} = 2$GHz) and the 2800 shielded bellows ($Z_y = 0.4\mathrm{M}\Omega/m$ at $f_{res} = 120$GHz) [5], [6]. The horizontal impedance of the cavities with a circular beam

		first analysis		second analysis		average	
	units	arcs	cav.	arcs	cav.	arcs	cav.
$\langle\beta_x\rangle$	m					64.3	39.3
$\langle\beta_y\rangle$	m					84.9	40.7
$\frac{d\mu_x/dI_b}{2\pi\langle\beta_x\rangle}$	$(A\,m)^{-1}$	-0.20	-1.38	-0.26	-1.03	-0.23	-1.21
$\frac{d\mu_y/dI_b}{2\pi\langle\beta_y\rangle}$	$(A\,m)^{-1}$	-0.75	-1.46	-0.76	-1.22	-0.76	-1.34
Z_x^{eff}	$M\Omega/m$	0.11	0.76	0.14	0.57	0.13	0.67
Z_y^{eff}	$M\Omega/m$	0.41	0.80	0.42	0.67	0.42	0.74
Z_x^{eff}	$M\Omega/m$					$\leq$0.2	0.65
Z_y^{eff}	$M\Omega/m$					0.40	0.65

Table II

Normalized phase advance per bunch current divided by the average beta function and effective transverse impedances, measured and computed.

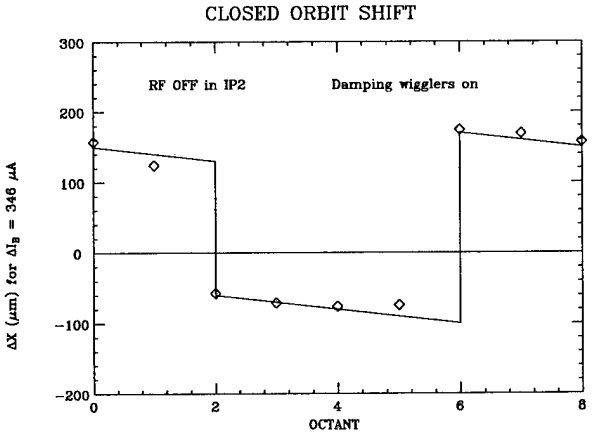


Figure 2. Difference orbits for 2 values of current

hole should be same as the vertical one, while for the flat bellows it is estimated to be less than half that value. All other components (separators, pickup electrodes, collimators, etc.) contribute only about 10 % in total [7] and are neglected.

For a Gaussian bunch in a broad-band resonator, the effective transverse impedance is given by the machine impedance $Z_T = R/Q$, multiplied with a reduction factor $F(\omega_{res}\sigma_s/c)$. The latter can be approximated by[4] $F(x) = 2x^2$ for very small x, and approaches unity for $x \gg 1$. For the cavities the reduction factor is about F(0.8) = 0.54, while for the bellows it is near unity. The effective impedances for the two major impedances in LEP are shown at the bottom of Table II, and - considering the large errors in the phase shift data - compare quite well with the values obtained from the measurements.

III. CURRENT DEPENDENCE OF THE ENERGY LOSS DISTRIBUTION

A. The Second Experiment

By measuring the orbit displacement with current in pickups located in regions with finite values of dispersion, one can obtain the distribution of the energy loss around the machine circumference. In order to eliminate the effects of orbit distortions, only the differences between orbits at a very low bunch current (50μA) and 2 values of higher currents (225 and 500 μA) were measured. During the experiment, only one of the two RF sections (consisting of half the RF cavities) was powered, while the other one was idling (the results were very similar when the other RF section was powered). The data were averaged over each arc in order to eliminate the dependence of the orbit on spurious side effects. The results have been plotted and are shown in Fig.2.

B. Comparison with Computation

The resistive part of the effective longitudinal impedance, i.e. the longitudinal loss factor k_L, can be obtained from the energy loss as function of current. It depends strongly on bunch length which also in this experiment could not be measured. With only the damping wigglers excited, the rms bunch length at injection energy (E_o = 20 GeV) is about 10 - 11 mm for $Q_s = 0.08$.

$$k_L = \frac{E_o f_o}{eD_x}\frac{\Delta x_{co}}{\Delta I_b} \qquad (4)$$

In the idling RF section, the data show an orbit displacement $\Delta x_{co} = 190\mu$ m for a current increase $\Delta I_b = 342\mu$ A. With an average dispersion $D_x = 0.58$ m in the pickups, and the revolution frequency $f_o = 11.25$ KHz in LEP, this expression yields a loss factor of about 210 V/pC. For a bunch length of 11 mm, the computed loss factor of an RF cavity cell is about 0.58 V/pC, or 185 V/pC for one section consisting of 64 five-cell cavities. The rest must be due to all other elements in the RF straight section. The total orbit displacement in both arcs is about 80 μm, corresponding to a loss factor of about 90 V/pC. For $\sigma_s = 10$ mm, one shielded bellows unit has a loss factor of about 8 V/nC, yielding about 22 V/pC for 2800 of them. The loss factor for the resistive wall effect is given by

$$k_L = 0.612\omega_o Z_o \delta_o / \langle b\rangle (R_{arc}/\sigma_s)^{3/2}$$

With R_{arc} = 4.1 km, δ_o = 0.81 mm and $\langle b\rangle$ = 45.6 mm we get k_L = 60 V/pC. The total is quite close to the measured value. Considering the uncertainties in bunch length and shape, the agreement is very satisfactory.

References

[1] D. Brandt et al.: "The LEP Impedance Model", Proc. of 1993 Particle Accelerator Conference; p.3429 (1993).

[2] J. Borer et al.: "Harmonic Analysis of Coherent Bunch Oscillations in LEP", Proc. EPAC, Berlin 1992, p.1082

[3] H. Grote, F. Iselin "The Mad Program"; CERN SL/90-13.

[4] LEP Commissioning Notes 21 (1989) and 75 (1990)

[5] B. Zotter: "Comparison of Theory and Experiment on Beam Impedances", Proc. EPAC, Berlin 1992, p.273

[6] B. Zotter: "Collective Effects", Proc. 3rd LEP Performance Workshop, Chamonix 1993, CERN SL/93-19, p.89

[7] G. Sabbi: "Simulation of Single-Bunch Collective Effects in LEP", CERN SL/94 report in preparation

A Preliminary Lattice Design of a Tau-Charm Factory Storage Ring in Beijing

N. Huang, L. Jin, D. Wang, Y. Wu, G. Xu
Institute of High Energy Physics, Chinese Academy of Sciences
P.O. Box 918, Beijing 100039, China
E-mail: jinlh@bepc5.ihep.ac.cn

ABSTRACT

A preliminary lattice design of a tau-charm factory (τcF) storage ring is described. This storage ring is suggested to be built in the east of the injector, BEL, of BEPC. In addition, some considerations on improving the design will be outlined.

1 INTRODUCTION

Since the initial idea [1] and the machine design [2] of a τcF are proposed, many laboratories have shown great interest in the machine and have studied a lot on it. A τcF is a high performance e^+e^- collider at beam energy range 1-3 GeV with two rings, luminosity reaching up to $1\times10^{33}cm^{-2}s^{-1}$ at 2 GeV. BEPC works at the same energy range as the τcF. In early 1993, we began considering the possibility of upgrading BEPC into a τcF through adding another ring atop the existing one. Unfortunately, the circumference of BEPC tunnel is too short to accommodate the ring of the τcF. Now it is regarded as suitable to construct a τcF storage ring in the east of the injector, BEL, of BEPC, while BEL will be improved as the injector of the τcF. The study of machine feasibility has started up with 5 million RMB yuan investment from the government, which will be finished within one and half year or less. The schematic layout of the τcF is shown in fig.1.

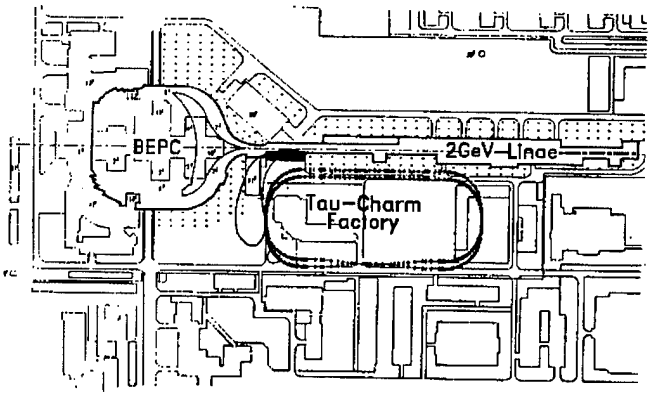


Fig.1: Possible layout of the τcF in Beijing

The preliminary design of the lattice includes both high luminosity scheme (standard scheme) and monochromator scheme. The spread of collision energy is reduced by one order of magnitude in the monochromator scheme, which will be favorable for some physics experiments, especially the study of CP violation at J/ψ resonance. In the monochromator scheme, there must be dispersion functions equal in absolute value but opposite in sign at the IP for electron and positron [3], and the luminosity can be expressed as

$$L = \frac{c}{S_B}\pi\frac{\gamma^2}{r_e^2}\frac{H_y^*}{\beta_x^*}\sigma_\varepsilon^2\,\xi_x\,\xi_y$$

c is light speed, S_B bunch spacing, γ relativistic energy factor, r_e classical electronic radius, H_y^* equal $(D_y^*)^2$ divided by β_y^* (D_y^* is vertical dispersion function at the IP), $\xi_{x,y}$ beam-beam effect parameter, and σ_ε energy spread. To maximize luminosity there need $\beta_x \ll \beta_y$ at the IP and low beam emittance [4].

In addition, we expect the lattice could keep the flexibility of transferring to other promising schemes which could further increase luminosity or improve the machine performance.

2 MAGNET LATTICE

The collider includes two rings with one atop the other one respectively for electron and positron except for the only single interaction region where two rings are incorporated in the same vacuum chamber.

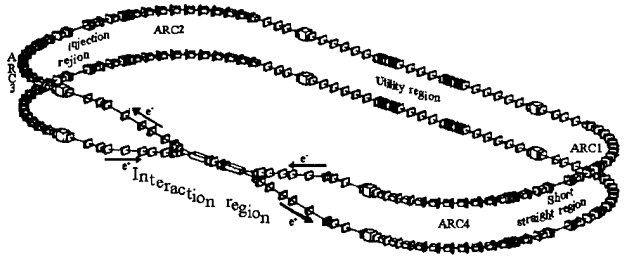


Fig.2: Schematic of the τcF storage ring in Beijing

As shown in fig.2, the circumference is 367.5m with 61.42m wide and 143.49m long, and the two rings are vertically separated 1.46m. There are 32 bunches circulating in each ring. Each ring can be divided into four main parts, including one interaction region, one utility region, four arc regions and two short straight regions one of which is used as the injection region. The main parameters of the machine including monochromator scheme are listed in table.1.

2.1 INTERACTION REGION

The interaction region includes a micro-β insertion, two e^+ e^- orbits separation sections and two β-function matching

0-7803-3053-6/96/$5.00 ©1996 IEEE

sections, which are symmetrically placed on each side of the IP with a length of 95.26m, as show in fig.3.

Table.1: Principal parameters of the τcF in Beijing

Scheme	Standard	Monochr.	Crossing angle
Nominal energy E(GeV)	2.0	1.5	2.0
Ring circumference C(m)	367.5	367.5	367.5
Crossing angle at IP θ (mrad)	0.0	0.0	2.5~4.0
β-function at IP β_x^* / β_y^* (m)	0.2/0.01	0.01/0.15	0.5/0.01
Dispersion at IP D_y^* (m)	0.00	0.35	0.00
Momentum compaction α_p	0.022	0.008	0.022
Natural emittance ε_x (nm·rad)	251	20	251
Emittance with wiggler		10 (J_x=2)	
Vertical emittance ε_{yc}	12	2	4.8
Energy spread σ_ε	5.4×10^{-4}	8×10^{-4}	5.4×10^{-4}
Energy loss per turn U (KeV)	142.6	45.0	427.8
Damping time $\tau_x/\tau_y/\tau_\varepsilon$ (ms)	34/34/17	41/80/80	34/34/17
RF frequency (MHz)	500	500	500
RF voltage (MV)	9.00	9	9.00
Numbers of bunches k_B	32	32	32×3
Bunch spacing s_B	11.48	11.48	11.48/3
Total current per beam (A)	0.55	0.215	1.65
Particles per bunch	1.32×10^{11}	5.14×10^{10}	1.32×10^{11}
Natural bunch length (cm)	1.0	0.78	1.0
Impedance $\lvert Z/n\rvert_{\parallel}(\Omega)$	0.32	>0.32	0.32
Beam-Beam effect ξ_x/ξ_y	.04/.04	.031/.015	.04/.04
Beam life time τ (hours)	4.8	1.5	
Transverse tune Q_x/ Q_y	11.192/ 10.192	13.18/ 9.24	11.15/ 10.18
Synchrotron tune Q_s	0.098	0.068	0.098
Natural chromaticity Q'_x / Q'_y	-26.6/ -32.0	-35.9/ -44.5	-20.0/ -35.09
Luminosity L ($cm^{-2}s^{-1}$)	1×10^{33}	2.2×10^{32}	3×10^{33}
CM energy spread σ_W (MeV)	1.53	0.105	1.53

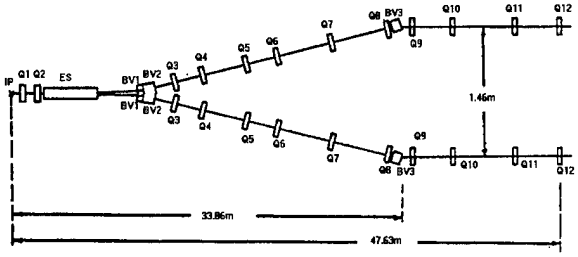


Fig.3: Interaction region of the τcF storage ring

Doublet focusing is used to achieve low β function at the IP with two superconducting quadrupoles distanced 0.8m from each other which are protruded into the detector with their outer radius no greater than 20cm due to the limitation of the detector. Their field gradients are less than 25.4T/m. Q1 is 0.8m away from the IP. The polarities of Q1 and Q2 are adverse in the monochromator scheme and the standard scheme.

After the head-on collision at the IP, the orbits of e^+ e^- are orderly separated by an electrostatic separator ES (0.006rad) with length of 4.7m, two vertical septum bending magnets BV1 (0.006rad) and BV2 (0.02rad) with length respectively 0.5m and 1.0m. The full gap of ES is 48mm and maximum electric field is 3.2MV/m. The magnetic field of BV1 and BV2 are respectively 0.1T and 0.17T and their septum thickness respectively less than 2.3cm and 2.7cm, which seems no difficulty in making. After a 0.8m long vertical bending magnet BV3 (-0.032rad), the orbit is returned to horizon. The vertical separation of e^+ e^- bunches gets $2.5\sigma_x$ for the standard scheme, and $2\sigma_y$ for the monochromator scheme at the parasitic crossing point which is 5.74m away from the IP. There are totally six quadrupoles to finish focusing and vertical dispersion suppressing between BV2 and BV3. In the monochromator scheme, Q7 will be switched off and Q8 changed polarity. The lattice functions in this region is shown in fig.4a and fig.4b.

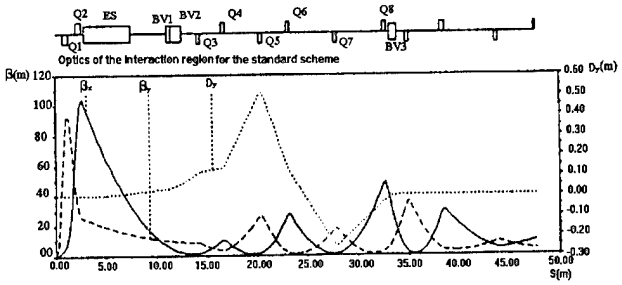


Fig.4a: Lattice functions of the standard scheme in the interaction region

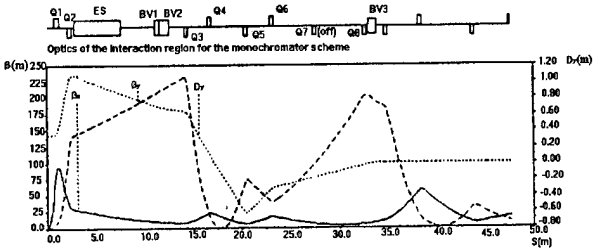


Fig.4b: Lattice functions of the monochromator scheme in the interaction region

2.2 ARC REGION AND UTILITY REGION

Each arc region consists of seven irregular FODO cells in which almost every quadupole has its own independent power supply in order to get more flexibilities. Every bending magnet give the beam bending angle of 7.5°. One magnet is missed in the sixth cell and replaced by a Robinson wiggler. Through the change of the phase advance per cell and adjusting maximum dispersion function in the region, emittance can be varied from maximum 550nm (2.0GeV) to minimum 20nm (1.5GeV). Robinson wiggler can redistribute the damping partition number J_x and J_ε [5,6] ,and so can change emittance. Four Robinson wigglers in arc regions combined with four damping wigglers in the utility region are used to reduce the emittance to 10nm (1.5GeV) in the monochromator scheme, meanwhile concomitant increasing of beam energy spread is good at maximizing luminosity which can be seen from the formula in the introduction.

The utility region consists of ten FOOD cells with a β-function matching section in each side. Some RF cavities

as well as necessary instruments can be installed in this region, and working point also can be adjusted through this region. Fig.5a and fig.5b are lattice functions in half a ring.

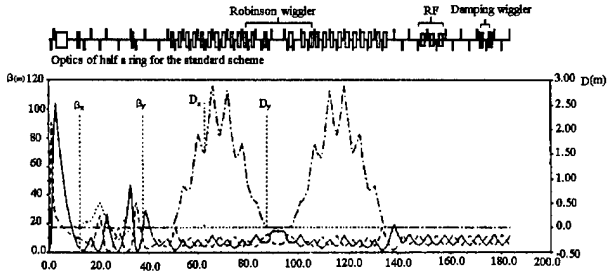


Fig.5a: Lattice functions in half a ring for the standard scheme

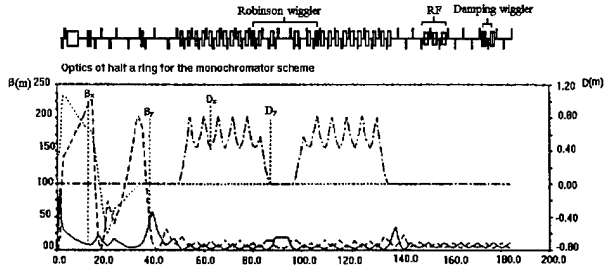


Fig.5b: Lattice functions in half a ring for the monochromator scheme

3 DYNAMIC APERTURE

Six families of sextupoles with total number of 48 are distributed in the arc regions of each ring for chromaticity correction. As to standard scheme, it seems there are no problems about dynamic aperture from the result of tracking studies as shown fig.6. Three different lines correspond to three initial energy oscillation amplitudes. In the range of energy deviation equal $10\sigma_\varepsilon$, β-function deviation at the IP is not greater than 25% and the deviation of working points (Q_x, Q_y) is 0.01.

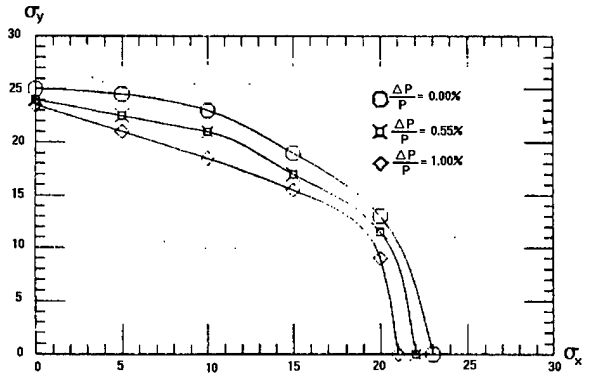


Fig.6: Dynamic aperture with three different initial energy oscillation amplitudes in standard scheme ($\varepsilon_{yc}/\varepsilon_x$=20%)

For the monochromator scheme, the result of tracking studies shows dynamic aperture is 20mm in horizontal direction and 15mm in vertical direction with 0.3% energy deviation at the injection point, which maybe is not sufficient, especially for energy acceptance. However due to existence of vertical dispersion function in the interaction region, additional two sextupoles (electrostatic and 90° rotated) could be installed this region for local chromaticity correction, one between Q1 and Q2 for horizontal chromaticity correction, the other one between BV2 and Q3. The studies on it are under way.

4 FUTURE CONSIDERATIONS

Now a collision scheme with a small horizontal crossing angle (2.5~4mrad) at the IP, which one assumes is too small to drive the synchro-betatron resonance [7] , is being studied on the basis of above design. The crossing angle can be caused by a pair of horizontal deflection dipoles which are symmetrically located just where the phase advance is π or 2π from the IP. To get the two beams are horizontally separated $10\sigma_x$ at the parasitic crossing point, β-function at the IP has to be increased to over 0.5m. The initial study shows bunch spacing can be decreased by three times and so numbers of bunches increased by three times. Obviously luminosity could be expected to close to $3\times10^{33}cm^{-2}s^{-1}$.

Several other versatile lattice designs have been being studied to provided more flexibility in IR and ARC. A complete polarization scheme is also being studied aiming at producing longitudinal polarized colliding beams at 1.55 GeV or 2.087GeV.

5 CONCLUSION

The preliminary lattice design could meet requirements of both standard scheme and monochromator scheme, and keep a possibility of transferring to a crossing angle collision scheme.

REFERENCES

[1] J. Kirkby, " A τ-Charm Factory at CERN", CERN-EP/87-210 (1987).

[2] J. M. Jowett, CERN LEP-TH/87-56 (1987).

[3] M. Bassetti and J. M. Jowett, "Improving the Energy Resolution of LEP Experiments", CERN

[4] A. Zholents, "Polarized J/ψ Mesons at a Tau-Charm Factory with a Monochromator Scheme", Orsay Report, LAL/RT 92-09 (1992).

[5] K. W. Robinson, " Radiation effects in circular accelerator", Phys. Rev. 111, 373 (1958).

[6] Y. Baconnier, et al, Nuclear Instruments and Methods A234 (1985) 244

[7] M. Tigner, private communication

Low Energy Ring Lattice of the PEP-II Asymmetric B-Factory*

Y. Cai, M. Donald, R. Helm, J. Irwin,
Y. Nosochkov, D.M. Ritson and Y. Yan
Stanford Linear Accelerator Center, Stanford University, Stanford, CA 94309 USA
E. Forest and A. Zholents
Lawrence Berkeley Laboratory, 1 Cyclotron Road, Berkeley, CA 94720 USA

Abstract

Developing a lattice that contains a very low beta value at the interaction point (IP) and has adequate dynamic aperture is one of the major challenges in designing the PEP-II asymmetric B-factory. For the Low Energy Ring (LER) we have studied several different chromatic correction schemes since the conceptual design report (CDR) [1]. Based on these studies, a hybrid solution with local and semi-local chromatic sextupoles has been selected as the new baseline lattice to replace the local scheme in the CDR [2]. The new design simplifies the interaction region (IR) and reduces the number of sextupoles in the arcs. Arc sextupoles are paired at π phase difference and are not interleaved. In this paper we describe the baseline lattice with the emphasis on the lattice changes made since the CDR.

I. INTRODUCTION

The LER is the positron storage ring in the PEP-II. It is designed to operate at a nominal energy of 3.1 Gev with a range of 2.4-4.0 Gev. The ring will be newly constructed and situated 0.9 m above the High Energy Ring (HER) in the existing PEP tunnel at SLAC. It consists of six straight sections and six arcs. One of the long straight sections contains the IP with low beta optics and a local chromatic correction module. The straight section on the opposite side of the ring is configured for injection. Two other sections nearest to the IR, with one containing the RF cavities, are used for tune adjustment, and two remaining straights have optics suitable for wiggler.

Parameter	Description	Value
E	Beam energy	3.1 Gev
C	Circumference	2.2 km
β_x^*, β_y^*	Beta value at the IP	50.0,1.5 cm
ϵ_x, ϵ_y	Emittance	64.3,2.6 nm-rad
ν_x, ν_y	Betatron tune	38.57,37.64
U_0	Synch. radiation	0.77 Mev/turn
τ_E, τ_x	Damping time	29.2,60.5 ms
α	Momentum compaction	1.23×10^{-3}
σ_l	Bunch length	1.0 cm
σ_E	RMS δE/E	7.7×10^{-4}

Table 1: Main LER lattice parameters

The six arcs consist of cells with 90^0 phase advance. Beta bumps in the vertical plane are introduced in the two arcs adjacent to the IR to enhance the β values at the locations of sextupole pairs. Selected parameters are listed in the Table 1.

II. OPTICS

A. Interaction Region and Adjacent Arcs

The previous IR design [2] had both x and y chromatic correction sextupoles in the IR. This required two $-I$ optical modules and two beta matching sections per each half IR. This resulted in a large number of magnets in the IR and in several interference problems with the HER beam line. The new design was aimed at reducing the number of magnets in the IR.

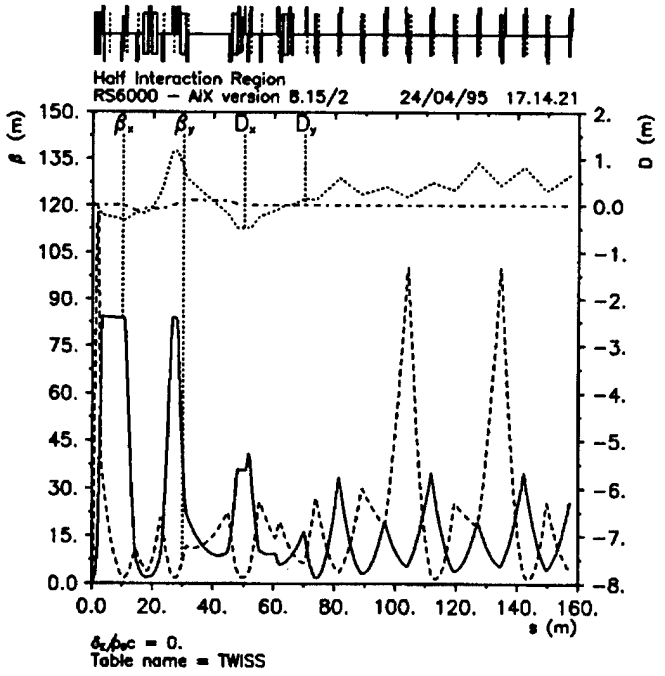


Figure 1. Optical functions for the one half the IR.

The adopted solution was to move the local y-sextupoles from the IR to the beginning of adjacent arcs, as in the HER chromatic correction scheme [7]. This allowed to remove one $-I$ section from the IR. Due to naturally high β_x function after the final focus (FF) doublet the x-sextupole pair was left unchanged. Additionally, the number of vertical dipoles was reduced by a half to provide only one vertical separating step instead of two, and a horizontal dipole was removed after the FF doublet to provide better separation of the LER and HER beam lines. The absence of this dipole resulted in asymmetric dispersion at the local x-

*Work supported by the Department of Energy under Contract No. DE-AC03-76SF00515 and DE-AC03-76SF00098

0-7803-3053-6/96/$5.00 ©1996 IEEE

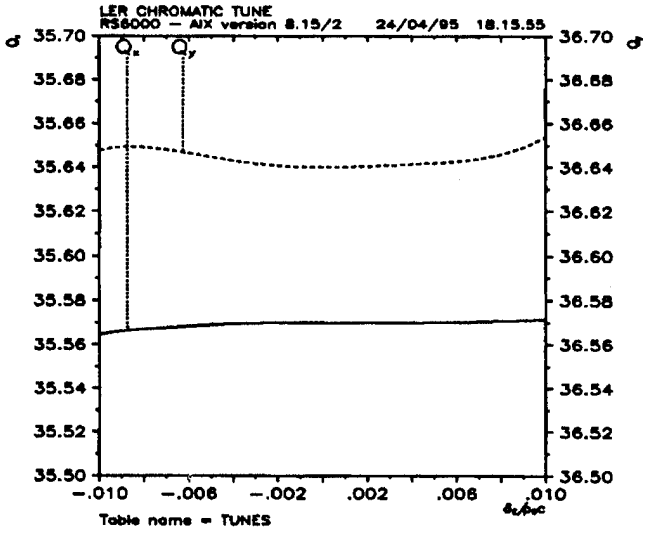


Figure 2. Tune versus relative momentum deviation.

sextupoles, however, this did not degrade the chromatic correction. In total, the number of IR magnets was reduced by 24 magnets.

As in the CDR, each of two arcs near the IR contains two x and two y non-interleaved semi-local sextupole pairs. In the new scheme the first arc pair replaces the effect of the removed y local sextupoles and corrects primarily the linear and second order vertical chromaticity generated from the FF doublet. To optimize its effect on the vertical chromaticity, the vertical phase advance from the FF doublet to this sextupole pair was adjusted to $n\pi$ and the β_y/β_x ratio at the sextupoles was increased by introducing a local beta bump. The other semi-local sextupole families are used as additional variables to minimize the higher order chromaticity. The optics of the one half IR, including the beta bump in the adjacent arc, is shown on Figure 1.

B. Sextupoles in Four Far Arcs

The remaining four arcs, located remotely from the IR, are filled with global sextupoles to correct the linear chromaticity of the machine. With 90^0 per arc cell, the usual scheme of two families of sextupoles located periodically next to each F or D quadrupole has the disadvantage of generating octupole multipoles due to an interaction between interleaved F and D sextupoles. In the LER with interleaved sextupoles the resulting amplitude dependent tune shifts and fourth order resonances are one of the factors limiting the dynamic aperture.

An alternative non-interleaved scheme was studied and adopted for the new LER lattice. It consists of four pairs of non-interleaved sextupoles per arc. Two arcs have only F sextupoles to compensate the horizontal chromaticity, and the other two arcs have only D sextupoles. The typical arrangement of four sextupole pairs is (S_1, S_1)-(S_2, S_2)- (S_2, S_2)-(S_1, S_1), where the transfer matrix between the sextupoles in each pair is $-I$ and the phase between adjacent pairs is $\pi/2$. S_2 sextupoles are as twice as stronger than S_1 sextupoles. This ratio is chosen to minimize the higher order non-linear chromaticity locally in the arcs. Additional (S_2, S_2) pairs can be added in the middle of each pattern depending on the length of the arc. The octupole-like effects in this scheme are minimal and arise only due to finite sextupole length. In this scheme the first order chromatic beta wave is locally canceled, and thus the contribution to the second order chromatic tune shift is suppressed as well. The number of sextupoles is reduced by a factor of 4 compared to the interleaved scheme, and the sextupole strength increases proportionally. Due to a less uniform sextupole distribution the overall chromatic tune shift contains larger higher order chromatic terms, but it is still adequate within the range of $\pm 10\sigma_E$. The LER tune versus relative momentum deviation is shown on Figure 2.

C. Wiggler Straight Section

The LER employs wiggler magnets in one straight section for beam emittance excitation and additional radiation damping. Beam emittance in the ring without wigglers is only 22 nm rad while a nominal value of 64 nm rad is required to match the beams at the IP. Moreover, emittance variation in the range of 40-100 nm rad is envisaged for the LER in order to provide flexibility of beta function adjustments at the IP and luminosity optimization.

Simulations of beam-beam effects for the condition when the damping time in the LER was about 45% larger than in the HER showed that this unbalance in damping times does not compromise the performance of the PEP-II [3][4]. This conclusion allowed us to have a much simpler variant of the LER wiggler sections than in the CDR [1]. Currently, the LER has two identical wiggler straight sections, but only one section has a wiggler. This wiggler consists of nine 40 cm length magnets and two 20 cm length end magnets with the nominal magnetic field of 1.6T. Energy loss to synchrotron radiation in the wiggler at 3.1 Gev is 130 Kev. The optics in the regions has been modified to maintain 64 nm rad nominal emittance.

D. Other Straight Sections

The optics in the injection region remains the same as in the CDR. The beta functions are transformed to large values by a long 90^0 cell acting as a quarter-wave transformer. Bunches are injected into the ring at the center of the straight section by using two identical kickers placed 180^0 apart in betatron phase in the vertical plane. A local DC orbit-bump is introduced to ease the requirement of the kicker magnets.

The tune and RF sections have been modified slightly to accommodate the spacing for RF cavities. These sections provide a change of the betatron tune in the range of ± 1 unit without significant change of β functions. In addition, three 120^0 cells were inserted in the middle of each section to host three families of 18 octupoles for independent adjustment of geometric tune shifts. It is known from the beam-beam effect studies [3][5] that these tune shifts can dramatically affect the beam tails.

III. DYNAMIC APERTURE

One of the important parameters of a lattice is its geometric and chromatic tune shifts. Adjustment of these tune shifts, in order to minimize the effect of lattice imperfections on a dynamic

aperture, is the key to attaining a good lattice performance. For the LER, we have obtained several good lattices with very different chromatic correction schemes. Nevertheless, all these solutions have one common feature: both geometric and chromatic tune shifts are less than 0.01 at a 10σ level in amplitude or momentum.

A. *Lattice Tolerances*

To model the performance of the LER lattices realistically, we introduce alignment, field and multipole errors into ideal "bare" lattices. Since the CDR, alignment tolerances have been relaxed from 0.1 mm to 0.2 mm for quadrupoles and sextupoles because simulations demonstrate that the dynamic aperture and the strength of dipole correctors are still adequate after this modification. The current set of alignment parameters is presented in Table 2. We assumed that all random errors have a Gaussian distribution cut at 2σ. In general, field errors are about 0.1% for most magnets. For the final focus quadrupoles, 0.01% tolerance may be necessary.

Errors(rms)	Displacement(mm)	Roll(mrad)
Dipole	1.0	0.3
Quadrupole	0.2	0.5
Sextupole	0.2	5.0
BPM	0.15	-

Table 2: Alignment tolerances

Multipole content in the magnets is one of important factors that dominate the dynamic aperture. It is crucial that the magnets located at high beta locations have better field quality than those in the arcs. We estimated multipole errors for the magnets in the arcs based on recently refurbished and measured magnets in the HER.

B. *Simulation Results*

After errors are introduced into ideal lattices, we perform many commonly used procedures for correcting closed orbit, dispersion, beta beating and coupling. Typically, after the corrections the residual orbit distortion is reduced to about 0.3mm (RMS) and the vertical dispersion is down to a few cm. The beta values at the IP are controlled to be within 2% to the ideal values while the beating in the other regions is about 10%.

Finally, the dynamic aperture is determined by tracking the positrons for 1024 turns with $10\sigma_E$ synchrotron oscillations. A dynamic aperture plot at the injection point is shown on Figure 3 with the solenoid field of the detector turned off. The results for the solenoid field on can be found in Reference [6].

The damping effect was not included for tracking with 1024 turns. However, it was demonstrated that the dynamic aperture under this condition is about the same as with radiation when tracked for one damping period. The advantage of tracking without damping is a much less required computer time.

In addition, we have studied some lattices with interleaved sextupoles in the four far arcs as alternatives. In the case of 90^0 phase advance per a cell, the dynamic aperture is only about 9σ, which is largely due to the 4th order effects coherently generated by the interleaved sextupoles. For a 72^0 cell, the dynamic aperture increases to 13σ because the non-linear terms from the interleaved sextupoles do not accumulate coherently. We may use the 72^0 lattice if we need to change the momentum compaction.

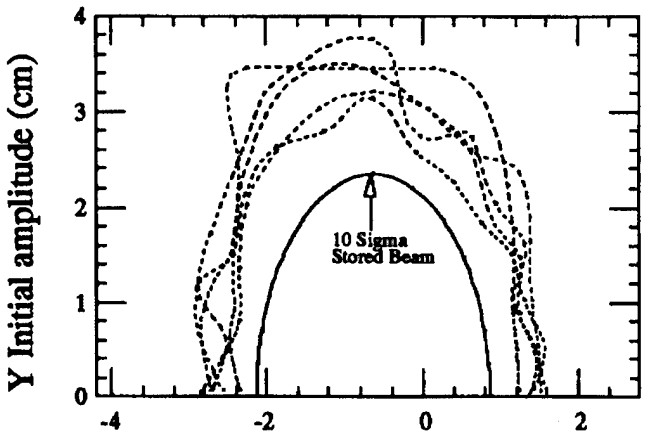


Figure 3. Dynamic aperture for non-interleaved sextupoles and 90^0 cells, 5 seeds with full alignment and multipole errors, $10\sigma_E$ offset.

IV. SUMMARY

We have shown that the new LER baseline lattice has dynamic aperture above 10σ in the presence of the realistic errors. The IR design is simpler than that in the CDR lattice. Furthermore, there is a good backup solution with 72^0 arc cells that provides momentum compaction flexibility.

References

[1] "PEP-II: An Asymmetric B Factory," Conceptual Design Report, SLAC-418, June 1993.

[2] M. Donald *et al.*, "Localized Chromaticity Correction of Low-Beta Insertions in Storage Rings," Proc. of 1993 Particle Accelerator Conference, May 1993.

[3] D.N. Shatilov, A.A. Zholents, "Lifetime and Tail Simulations for Beam-Beam Effects in PEP-II B Factory", these proceedings.

[4] M.Furman, "Scaling of the Luminosity with the Damping Time," these proceedings.

[5] T. Chen, J. Irwin and R. Siemann, SLAC-PUB-6432, Feb. 1994.

[6] Y. Nosochkov, Y. Cai, J. Irwin, M. Sullivan, E. Forest, "Detector Solenoid Compensation in the PEP-II B-Factory," these proceedings.

[7] M.H.R. Donald *et al.*, "Lattice Design for the High Energy Ring of the SLAC B-Factory (PEP-II)", these proceedings.

DAMPING RATES OF THE SRRC STORAGE RING

K.T. Hsu, C.C. Kuo, W.K. Lau, W.T. Weng*

Synchrotron Radiation Research Center
No 1. R&D Rd VI, Hsinchu Science-Based Industrial Park, Hsinchu, Taiwan, R.O.C.

Abstract

The SRRC storage ring is a low emittance synchrotron radiation machine with nominal operation energy 1.3 GeV. The design damping time due to synchrotron radiation is 10.7, 14.4, 8.7 ms for the horizontal, vertical and longitudinal plane, respectively. We measured the real machine damping time as a function of bunch current, chromaticity, etc. To damp the transverse beam instability, especially in the vertical plane, we need to increase chromaticity to large positive value. The damping rates are much larger than the design values. Landau damping contribution in the longitudinal plane is quite large, especially in the multibunch mode. The estimated synchrotron tune spread from the Landau damping is in agreement with the measured coherent longitudinal coupled bunch oscillation amplitude.

I. INTRODUCTION

In the synchrotron storage ring at SRRC, we have observed transverse and longitudinal beam instabilities.[1, 2] It is imperative that the machine provide a stable, high brilliant synchrotron light source to user community so that the users could take full advantage of such a powerful facility. To this end, several measures have been taken to suppress the instabilities.

In the transverse planes, the beam oscillations were attributed to the beam-ion interaction and the most effective and convenient way up-to-date is either to increase the chromaticities by raising the excitation level of the sextupole magnets or to employ the transverse damping system. With overcorrected chromaticities, the major damping sources include head-tail damping and Landau damping. It was found that the growth time of the beam-ion instability could be as fast as a few ms under normal operation condition, i.e., with 200 mA stored beam and 1.5 nTorr vacuum condition. Therefore, typical chromaticity setting is more than 3 in the vertical plane. The increase of the nonlinear field strength in the sextupole magnets not only reduce the dynamic aperture but also cause the injection difficulty. Moreover, it alters the beam orbit and increases the emittance coupling in the transverse planes. Despite of such disadvantages, it is the best way to suppress this instability before other promising cures are applied in the near future, e.g., transverse damping system.

In the longitudinal plane, the higher order modes (HOM) of the rf cavities are responsible for the coupled bunch instabilities. These instabilities have to be eliminated to justify the low emittance, high brightness lattice design. Therefore, we plan to control cavity temperature so that the HOM can be removed away from beam resonance. We also consider to implement a longitudinal damping system.

*Permanent address: AGS Department, BNL Upton, NY, USA.

This article describes the observation of the damping phenomena of the kicked beam in the transverse and longitudinal plane, respectively. The decoherence and recoherence of the kicked beam centroid are discussed. A preliminary transverse damping system in test is briefly described.

II. TRANSVERSE DAMPING

A high current single bunch beam was populated and excited with rf knock-out method in both planes, either simultaneously or independently. The beam signals from the pick-up electrodes were analyzed with spectrum analyzer. The amplitude of the horizontal and vertical betatron sidebands was displayed and recorded in a fast oscilloscope. The decay pattern then was analyzed off-line for different ring parameter settings. Fig. 1 shows a typical decay pattern with different chromaticity.

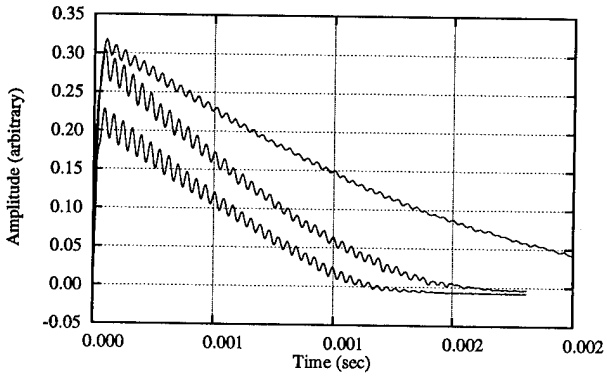


Figure 1: Typical horizontal betatron excitation amplitude of the beam centroid as a function of time. Beam current is 2.4 mA. The upper curve is with $\xi_x = 3.86$, the middle curve is with $\xi_x = 6.097$, and the lower curve is with $\xi_x = 7.71$.

The damping rates as a function of the beam current and chromaticity in both horizontal and vertical planes are shown in Fig. 2 and 3. The measured vertical damping time at zero current is about 11.7 ms which is close to the synchrotron radiation damping time. In the horizontal plane, the damping time at zero current is 4.3 ms. Notice that in the present operation configuration, the design synchrotron radiation damping time τ_x, τ_y, τ_s, is 10.5, 13.75, 8.13ms, respectively. It shows that Landau damping effect is much stronger in the horizontal plane than that in the vertical plane.

In Fig. 1 the decoherence and recoherence modulation amplitude depends on the chromaticity and the frequency is the same as the synchrotron oscillation frequency $\nu_s = 27$ kHz. This is due to incoherent synchrotron oscillation.[3, 4, 5] The modulation amplitude increases as chromaticity is larger. If the bunch purity is not good and hence there exists satellite bunch, we

0-7803-3053-6/96/$5.00 ©1996 IEEE

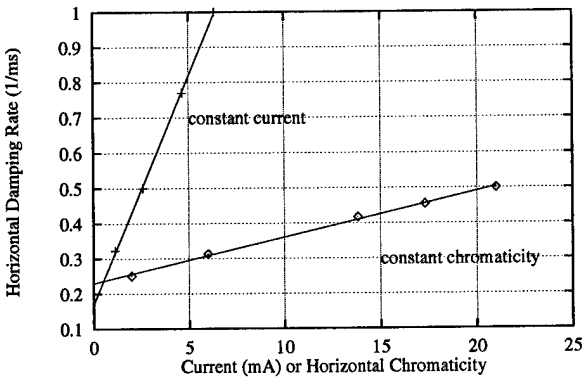


Figure 2: Horizontal damping rate as a function of the horizontal chromaticity with bunch current 2.7 mA or a function of bunch current at constant chromaticity.

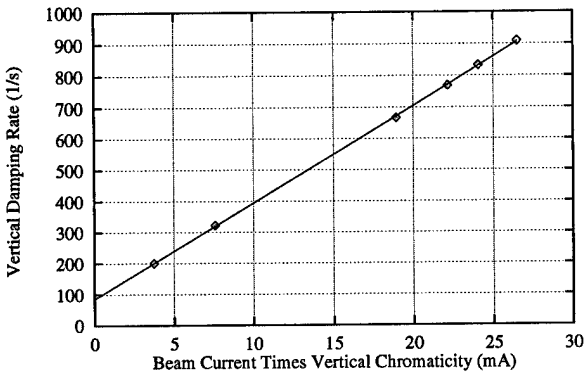


Figure 3: Vertical damping rate as a function of bunch current times vertical chromaticity.

observed some distinct modulation frequency other than the synchrotron frequency, which differed in each plane, corresponding to the frequency beating of the betatron sidebands. The measured vertical tune shift as a function of bunch current was about 0.2 kHz/mA. Hence, the modulation period becomes longer and modulation amplitude is larger as the main bunch current approaches the satellite bunch current. Fig. 4 gives an example of the modulation frequency at different current ratio in the vertical plane.

A transverse damping system is currently under development and test. The system is a wide band damping system. The system shall be of help in the suppression of the transverse beam oscillation in the routine operation at high current mode for the synchrotron light users. Fig. 5 depicts the damping effect with transverse damping system. The stored bunch current was not pure, therefore the distinct amplitude modulation appeared.

III. LONGITUDINAL DAMPING

In the longitudinal plane, we excited the beam with rf frequency modulation at synchrotron frequency for a few μs and then measured the decay rate of the amplitude of the synchrotron sideband. We performed the measurements either in the single bunch mode or in a few-bunch mode. Significant decrease of

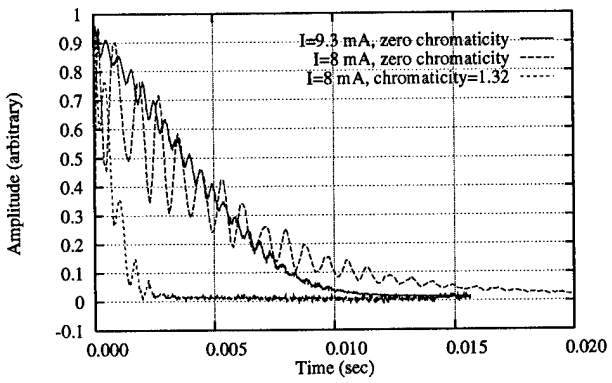


Figure 4: The decay pattern of the vertically excited beam with bunch impurity. In the beginning the beam current is 9.3 mA and then decay to 8mA. The impurity is increased because the main bunch current decay rate is fast due to Touschek scattering. The beating period is increased when impurity becomes larger. The introduction of the high chromaticity increases the decay rate of the excited beam centroid.

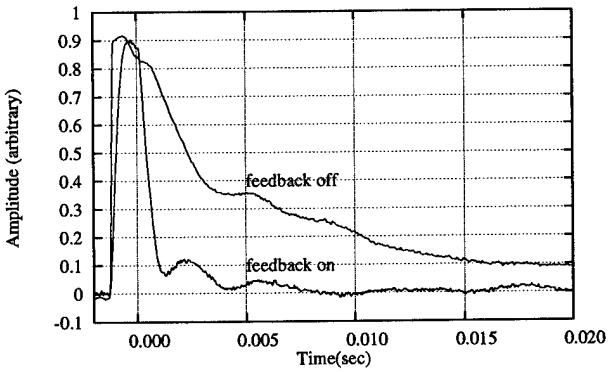


Figure 5: The damping effect of the transverse feedback system.

the damping time in the multibunch mode was observed as compared with that in the single bunch mode as shown in Fig. 6. The reason is that the increase of synchrotron tune spread which is due to the longitudinal coupled bunch instabilities induces Landau damping.[6, 7] Landau damping rate is very large at high multibunch operation current and is consistent with the measured oscillation amplitude in the longitudinal plane. In order to avoid the increase of the emittance and spoiling of the undulator spectral quality, we will implement a bunch-by-bunch longitudinal damping system to realize the low emittance lattice design.

IV. ACKNOWLEDGEMENT

The authors would like to thank H. P. Chang for his assistance in editing of this article.

V. REFERENCES

[1] C.C. Kuo, et. al., "Performance of the SRRC Storage Ring and Wiggler Commissioning", these proceedings.

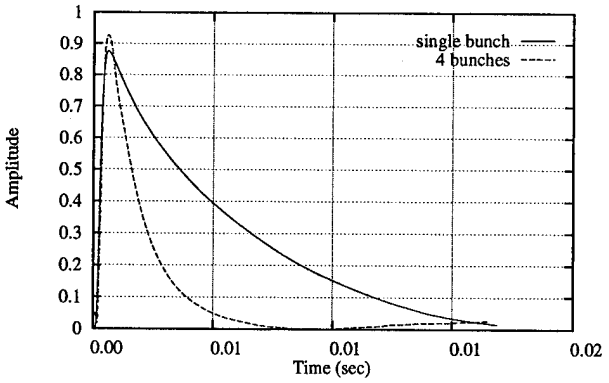


Figure 6: The decay pattern of the synchrotron sideband of the longitudinally kicked beam in the single bunch mode and in the case with four symmetrically distributed bunches. Landau damping is significant with four bunches due to longitudinal coupled bunch instabilities.

[2] W.T. Weng et. al., "Beam Stability at SRRC Storage Ring", these proceedings.

[3] F. Willeke, "Using the Bevatron Beam Position Monitor System to Investigate Transverse Phase Space", Fermilab Report TM-1309 (1985).

[4] R.E. Meller, et. al., "Decoherence of Kicked Beams", SSL-N-360 (1987).

[5] S. R. Mane, "Tuneshifts, Tunespreads and Decoherence", FN-502 (1988).

[6] W.K. Lau, et. al., "Study of Longitudinal Coupled Bunch Instabilities in the SRRC Storage Ring", these proceedings.

[7] M.H. Wang, et. al., "The Observation of Longitudinal Coupled Bunch Motion on Streak Camera at SRRC", these proceedings.

PERFORMANCE OF THE SRRC STORAGE RING AND WIGGLER COMMISSIONING

C.C. Kuo, K.T. Hsu, G.H. Luo, W.K. Lau, Ch. Wang, H.P. Chang,
L.H. Chang, M.H. Wang, J.C. Lee, C.S. Hsue, W.T. Weng*, Y.C. Liu†

Synchrotron Radiation Research Center
No 1. R&D Rd VI, Hsinchu Science-Based Industrial Park, Hsinchu, Taiwan, R.O.C.

Abstract

A 1.3 GeV synchrotron radiation storage ring at SRRC has been operated for more than a year since October 1993. Starting from April 1994, the machine has been open to the user community. In February 1995, We installed a wiggler magnet of 1.8 tesla 25-pole in the ring and successfully commissioned. The machine was scheduled for the users' runs from the middle of April this year. We describe the performance of the machine without wiggler magnet system and then report the wiggler effects on the beam dynamics of the storage ring, e.g., tune shift, beta-beating, orbit change, nonlinear dynamics effect, etc. Some measurements are compared with the model prediction and agreement between them was fairly good. Possible actions to minimize wiggler effects have been taken, such as orbit correction as a function wiggler gap change. The machine improvement projects, such as longitudinal and transverse damping systems as well as orbit stability feedback system are under construction and will be in use soon.

I. INTRODUCTION

The 1.3 GeV synchrotron radiation light source located in Hsinchu, Taiwan, is a storage ring of emittance 1.9×10^{-8} m-rad and circumference 120 m, which has been operated for the VUV users for more than a year.[1, 2] To increase the photon flux in the hard x-ray region of the synchrotron radiation spectrum, a wiggler magnet system was installed and commissioned in the beginning of this year. With such an insertion device, x-ray users would obtain more photon flux at the higher photon energy region.

At users' request, the machine has been scheduled five days per week, 24 hours per day from November 1994. The user beam time is increased to 10 shifts per week. Before installation of the wiggler, the machine was refilled every 8-hour interval to 200 mA. Typical beam lifetime at 200 mA stored current was 6 hours. We report the machine performance and then result from wiggler commissioning.

II. MACHINE PERFORMANCE

We usually run machine in the multibunch operation mode for user beam time with initial stored beam current 200 mA, which is the design value. Typical filling rate was about 5-10 mA/s. A long empty gap in the bunch train was introduced to reduce the ion-related effects. Before we installed a new wiggler vacuum chamber, the base pressure was around 0.4 nTorr and dynamic pressure was about 1-2 nTorr at 200 mA. The Coulomb lifetime was over 20 hours and the lifetime of the stable beam was about 6 hours at 200 mA, which was dominated by the Touschek scattering.

The typical measured horizontal beam size at bending port was about 200-250 μm at 200 mA. The increase from the design value 150 μm was due to the longitudinal coupled bunch instabilities.[3] Some actions to get rid of such instabilities have been planned, e.g., temperature control of the rf cavities to shift the higher order mode frequencies or implementing longitudinal damping system. In the vertical plan, we observed an emittance coupling about 5%, which was mainly due to spurious vertical dispersion.

Up to now, the single bunch operation mode was only for machine studies. A bunch current up to 30 mA could be accumulated in a few minutes and bunch purity could be better than 10^{-3} with bunch purification process.[4]

We observed severe transverse beam instability, in particular in the vertical plane. At least up to present, this instability was attributed to the beam-ion interaction. To cure this instability, several methods were tried, e.g., increase of ring chromaticity, beam shaking, ion shaking, filling pattern control, cleaning electrodes, and transverse damping system. In practice, only the way by increasing the chromaticity or by implementing a transverse damping system demonstrated its effectiveness and feasibility for the routine operation. We usually run the machine with higher positive chromaticity. In the near future, we will use transverse damping system to cope with such instabilities.[5]

We were able to correct the beam closed orbit down to 0.2 mm level in both planes.[6] The on-going study to get precise BPM and quadrupole center position together with the improvement of the BPM precision will enable us to obtain more accurate and reduced closed orbit.

The orbit oscillations around 10-15 μm in both planes were detected both with electron BPM and photon BPM. A slow variation of orbit in about 90 sec was correlated with the water temperature change. An orbit feedback system to reduce orbit fluctuation seen by the synchrotron radiation users is under test .[7]

III. WIGGLER COMMISSIONING

The structure of the wiggler is a hybrid planar type of which permanent magnetic material is NdFeB and pole material is Vanadium permendur. The pole period is 20 cm long and the

*Permanent address: AGS Department, BNL Upton, NY, USA.
†Permanent address: Department of Physics, National Tsing-Hua University, Hsinchu, Taiwan, R.O.C.

0-7803-3053-6/96/$5.00 ©1996 IEEE

effective pole number is 25. The peak field strength is more than 1.8 Tesla at the minimum wiggler gap 22 mm. The overall magnet length is about 3.04 m and located 80 m downstream of the injection point. The wiggler system was manufactured by STI Optronics in Seattle USA. The magnetic field properties were corrected and carefully measured to meet the specifications.

It took about one month in installing the wiggler system, changing and baking the vacuum chamber as well as adding some diagnostics and correction elements. In the end of February, we succeeded in closing the wiggler gap without any beam loss in the first try of the beam test. The poor vacuum and smaller physical aperture of the newly installed wiggler chamber result in less efficient injection rate and poor beam lifetime. Further optimization of the injection process to reduce the beam loss in the wiggler chamber is under way so as to prevent possible damage of the magnet material with mass radiation bombardment. As a result, during the injection the wiggler gap is still open. The vacuum cleaning with synchrotron radiation is necessary to improve the beam lifetime.

The planar wiggler with $k_x = 0$ acts like an extra vertical focusing element and no effect in the horizontal plane. Therefore the vertical optics is distorted and vertical tune shall be shifted, whereas the horizontal optics shall be the same as that without wiggler field. We measured the tunes as a function gap and compared with the model prediction. No change in the horizontal tune is observed while the vertical tune shift is in fairly agreement with the model calculation as shown in Fig. 1. The working point was set at (7.236, 4.088) when wiggler was open. The change of the working point is still away from the systematic resonance lines up to fifth order.

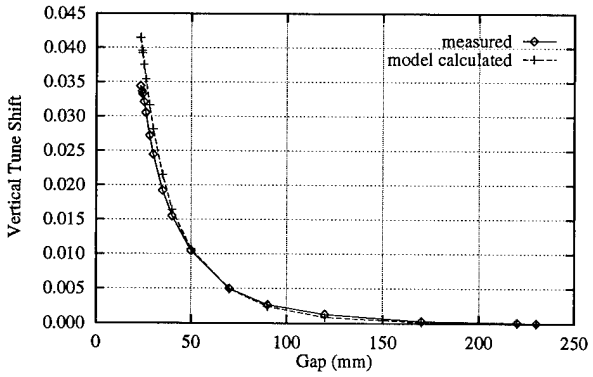


Figure 1: The measured and observed vertical tune shift v.s. wiggler gap.

The betatron function in each quadrupole location was measured with the trim coil in the quadrupole magnet. The measured vertical optics and beta-beat at wiggler gap 23.2 mm are shown in Fig. 2 and 3. Excellent agreement between measured vertical beta-beat and model calculated values are found. In the horizontal plane, the optics is essentially no change. To correct the optics and tune shift with local quadrupoles require some changes in quadrupole strengths. However, quadrupole trim is not large enough and independent quadrupole is not available in the time being.

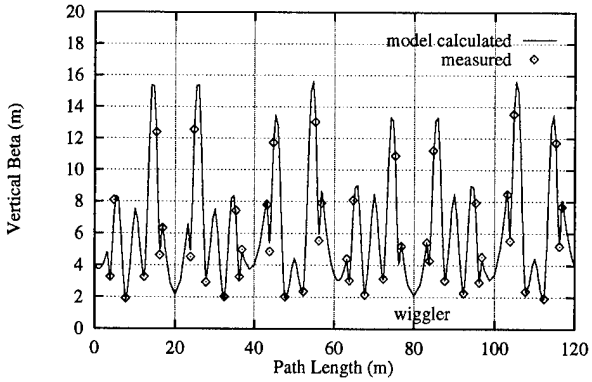


Figure 2: Measured and model calculated vertical betatron function with wiggler gap closed to 23.2 mm. The wiggler center is at 80 m from the injection point.

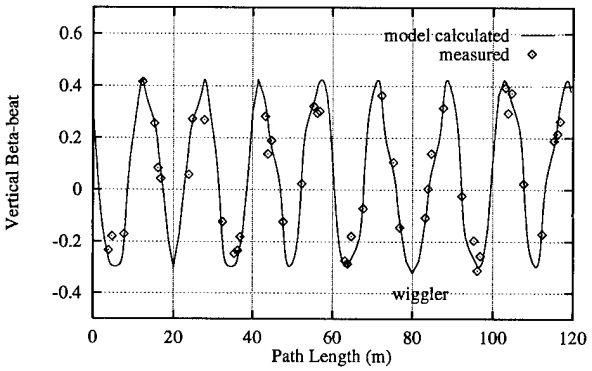


Figure 3: The measured and model calculated beta-beat between no wiggler and with wiggler gap 23.2 mm.

The dynamic aperture, either in the horizontal or vertical plane, is measured and compared between open and close gap. The lifetime of the ring was measured at different scraper setting, which located at upstream long straight section. The physical half aperture of the wiggler chamber is 40 mm × 8.5 mm. There was a slight shrinkage of the dynamic aperture in both planes when the wiggler gap was closed as shown in Fig. 4 and 5. The increase of the sextupole strength to damp the transverse beam oscillation causes larger reduction of dynamic aperture by 1 mm or so in Fig. 6.

The integrated field strength was corrected by the end correctors as a function wiggler gap in order to reduce the orbit change locally and globally. However, we observed a significant change in the vertical orbit which increased when gap became smaller and the error source was traced to be at wiggler position. We re-established a follow gap end corrector setting table and the orbit change has been reduced to some extent as shown in Fig. 7.

IV. ACKNOWLEDGEMENT

The authors would like to thank the help from Wiggler Task Force members C.H. Chang, T.C. Fan, G.F. Lin, C. H. Lee and Control Group member J. Chen, as well as all Technical staff.

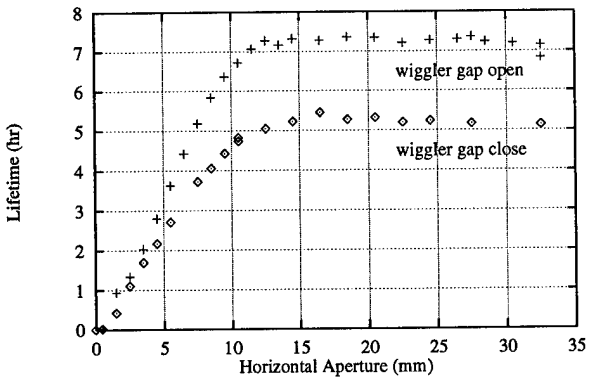


Figure 4: Horizontal dynamic aperture measurement with wiggler fully open and closed to 23.2 mm with SD=107.8 A and SF=91.8 A. The chromaticities are near zero.

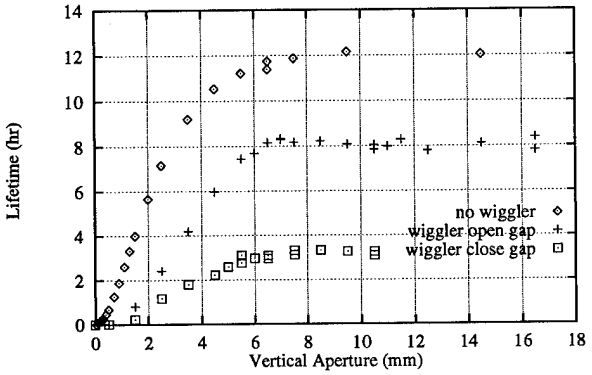


Figure 5: Vertical dynamic aperture measurement with wiggler fully open and closed to 23.2 mm with SD=107.8 A and SF=91.8 A. In addition, a measurement without wiggler is also shown.

V. REFERENCES

[1] E. Yen, "Present Status of SRRC", 1993 IEEE PAC Conf. Proc., p. 1460.

[2] Y.C. Liu, "The Status of SRRC", 1994 EAPC Conf. Proc., p. 110.

[3] W.K. Lau et al., "Study of Longitudinal Coupled Bunch Instabilities in the SRRC Storage Ring", these proceedings.

[4] G.J. Jan et. al., "Bunch Killer System at SRRC", these proceedings.

[5] K.T. Hsu et. al., "Damping Rates of the SRRC Storage Ring", these proceedings.

[6] C.C. Kuo, et. al., "Closed Orbit Measurement and Correction of the SRRC Storage Ring", 1994 EPAC Conf. Proc., p. 1018.

[7] W.T. Weng et. al., "Beam Stability at SRRC Storage Ring", these proceedings.

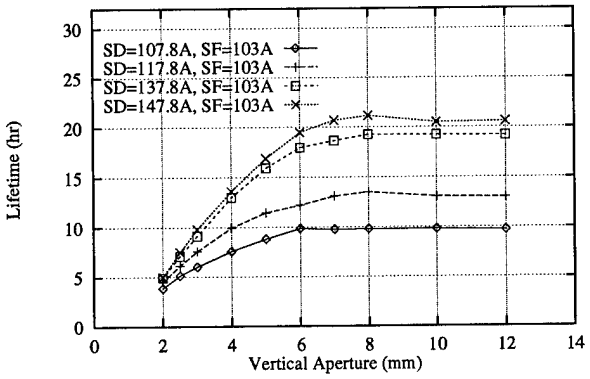


Figure 6: Vertical dynamic aperture measurement at different defocusing sextupole setting (SF=103 A) with wiggler gap fully open. The increase of lifetime with smaller sextupole setting is due to increase of Touschek lifetime of the unstable beam.

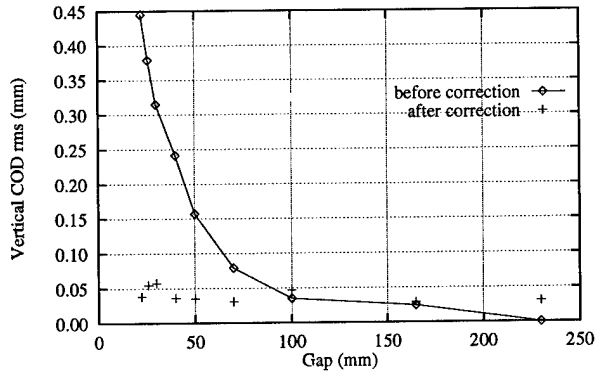


Figure 7: Vertical rms closed orbit change before and after end corrector modification v.s. wiggler gap.

Detector Solenoid Compensation in the PEP-II B-Factory*

Y. Nosochkov, Y. Cai, J. Irwin and M. Sullivan
Stanford Linear Accelerator Center, Stanford University, Stanford, CA 94309 USA
E. Forest
Lawrence Berkeley Laboratory, University of California, Berkeley, CA 94720 USA

Abstract

The PEP-II experimental detector includes a strong 1.5 T solenoid field in the interaction region (IR). With the fringe fields, the solenoid extends over a range of 6 m. Additional complications are that 1) it is displaced longitudinally from the interaction point (IP) by about 40 cm, 2) neither beam is parallel to the solenoid axis, and 3) the solenoid overlaps a dipole and a quadrupole on either side of the IP. In each half IR the correction system includes a set of skew quadrupoles, dipole correctors and normal quadrupoles to independently compensate the coupling, orbit perturbation, dispersion and focusing effect produced by the solenoid. The correction schemes for the Low Energy Ring (LER) and for the High Energy Ring (HER) are described, and the impact on the dynamic aperture is evaluated.

I. INTRODUCTION

The current design of the PEP-II experimental detector calls for a 1.5 T solenoid field. The solenoid length, including fringe fields, is about 6 m, and the total integrated field is 5.7 Tm. The different beam energies, 3.1 GeV for positrons and 9 GeV for electrons, mean that displacing the solenoid center about 40 cm in the direction of the high energy beam (HEB) improves the detector acceptance of the particles produced in the beam collision. The solenoid overlaps a horizontal dipole B1 and the first final doublet (FD) quadrupole QD1 on each side of the IP. Therefore a superposition of magnetic fields exists in these magnets.

The beams are horizontally separated in B1 and in QD1 making the trajectories of the two beams neither identical nor parallel to the solenoid field. The resulting angle between the beams and the solenoid axis leads to a perturbation of the vertical orbit. The low energy beam (LEB), generally, experiences a larger orbit perturbation. With an antisymmetric beam trajectory about the IP, the effect on the LEB can be reduced by adjusting the horizontal tilt angle between the solenoid direction and the beam at the IP. This will bring the LEB closer to the solenoid axis and will provide partial cancellation of the orbit perturbation. The optimum tilt angle for the PEP-II solenoid is about 20 mrad which provides a compromise for the orbits of both beams. The top view of the solenoid with respect to the beam trajectories is shown in Figure 1.

II. SOLENOID FIELD MODEL

In our calculations we used a simplified solenoidal field model which assumes a constant 1.5 T field over the effective length of 3.8 m. Figure 2 shows the shape of the model (solid line) and of the realistic field (dash). The main difference is that the realistic field has an extended soft fringe field while the model solenoid has hard edges.

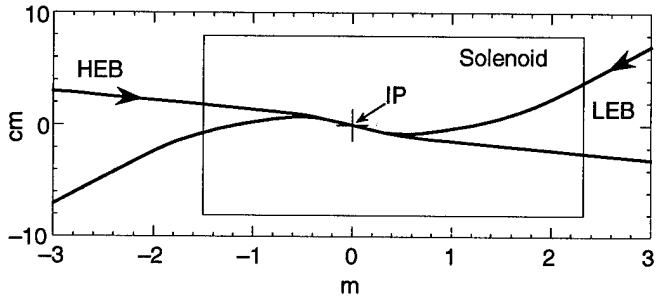


Figure 1. Top view of the beam orbits in the solenoid.

We used the MAD code [2] for numerical analysis. Currently, there is no provision in MAD for a quadrupole or a dipole superimposed with a solenoid, so we used an approximation to model the lattice. Within the solenoid, the B1 and QD1 magnets were replaced by the same length solenoid magnets sliced in 5 cm pieces, and a thin lens dipole or a quadrupole magnet was placed in the middle of each piece to produce the effect of B1 or QD1. The solenoid pieces in the model are aligned along the beam and will not generate orbit perturbations. To simulate the orbit effect, additional thin lens orbit kickers were uniformly distributed through out the solenoid. The kicker strength was calculated according to the beam orientation in the solenoid.

At the end of the solenoid the beams are not centered on the solenoid axis and, thus, receive a vertical orbit kick from the fringe field. In the model we simulated an off-centered fringe field by using a coordinate transformation in MAD.

The orbit effect was verified independently with the code MAGBENDS [3] which uses the superimposed magnetic field from all elements, and a realistic solenoid fringe field. There is

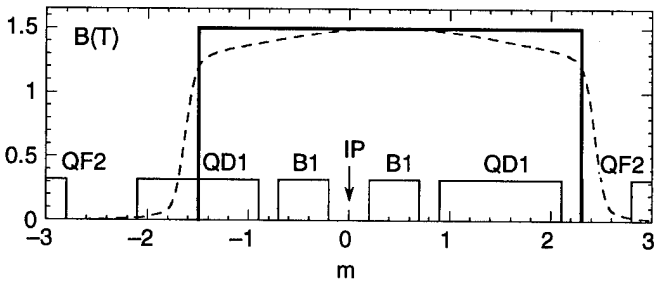


Figure 2. The model and the realistic solenoid field.

*Work supported by the Department of Energy under Contract No. DE-AC03-76SF00515 and DE-AC03-76SF00098.

0-7803-3053-6/96/$5.00 ©1996 IEEE

reasonable agreement between the two models, and the difference can be accounted for by different fringe models.

III. CORRECTION STRATEGY

The following solenoid effects need to be corrected: 1) the coupling between x and y betatron oscillations, 2) vertical and horizontal orbit perturbations, 3) vertical dispersion distortion, and 4) solenoid focusing. Our goal was to cancel these effects at the IP and everywhere outside the IR. The asymmetry of the solenoid requires an independent local correction system on each side of the IP. Generally, for each half IR we need: 1) six skew quadrupoles to compensate the coupling and vertical dispersion, 2) two vertical and two horizontal orbit correctors, and 3) eight variable normal quadrupoles to match the Twiss functions and the horizontal dispersion.

Due to the simplecticity of a transfer matrix there are four independent coupling coefficients. In matrix formalism the betatron coupling is described by the off-diagonal 2×2 matrix in the 4×4 transfer matrix. Therefore, for local coupling correction we need to cancel the (1,3), (1,4), (2,3) and (2,4) terms in the transfer matrix between the IP and the end of the IR. Similarly, the vertical dispersion can be described by (3,6) and (4,6) terms in a 6×6 matrix.

For analysis of the optimum skew quadrupole positions we used the projection method developed in Reference [1]. In this approach, an original lattice with distributed coupling elements is replaced by an equivalent lattice with the same transfer matrix, but with all coupling elements placed at one point, usually the IP. The matrices of the coupling elements have to be modified after this transformation. For instance, an original matrix Q of a thin skew quadrupole will be replaced by a new matrix $R = M^{-1}QM$, where M is an uncoupled matrix from the IP to the original position of the quadrupole. With all coupling elements placed at one point, the rest of the lattice is decoupled, and the coupling terms will add at the IP. It is, therefore, easy to analyze the effect from different coupling elements.

Consider one half of the IR starting from the IP. Suppose the Twiss functions at the original position of a thin skew quadrupole are β, α and μ. The equivalent quadrupole at the IP will have a new transfer matrix with the following terms:

$$
\begin{aligned}
R_{13} &= q\sqrt{\frac{\beta_x^*}{\beta_y^*}}S_xC_y, \quad R_{14} = q\sqrt{\beta_x^*\beta_y^*}S_xS_y, \\
R_{23} &= -q\frac{C_xC_y}{\sqrt{\beta_x^*\beta_y^*}}, \quad R_{24} = -q\sqrt{\frac{\beta_y^*}{\beta_x^*}}C_xS_y, \qquad (1) \\
R_{36} &= fD_x\sqrt{\beta_y\beta_y^*}S_y, \quad R_{46} = -fD_x\sqrt{\frac{\beta_y}{\beta_y^*}}C_y,
\end{aligned}
$$

where $f = \frac{L_q}{B\rho}\frac{dB_x}{dx}$ is a quadrupole strength, $q = f\sqrt{\beta_x\beta_y}$, β^* is a β-function at the IP, $C = cos\mu$, $S = sin\mu$ and D_x is the horizontal dispersion at the original position of a skew quadrupole. The optimum positions for four coupling correctors will be at (μ_x, μ_y) = (π/2, 0), (π/2, π/2), (0, 0) and (0, π/2) (mod π), in which case each skew quadrupole generates only one non-zero coupling term at the IP, thus providing an orthogonal correction. The other two skew quadrupoles will provide an orthogonal vertical dispersion correction if placed at $\mu_y = 0$ and π/2 (mod π) where D_x is large.

In a similar way, the solenoid can be moved to the IP. The projected solenoid transfer matrix, which can be calculated numerically using MAD, is equal to $S = {M_{off}}^{-1}M_{on}$, where M is a matrix from the IP to the end of a solenoid, for the solenoid turned off and on, respectively. For a non-overlapped solenoid only two major coupling terms would exist, (1,3) and (2,4), which is just the rotation angle of the betatron planes. The interaction between the solenoid and the quadrupole gives rise to the other two coupling terms. Figure 3 shows how these terms depend on the overlap with the B1 and QD1 magnets. The results correspond to the longer side of the solenoid in the LER, where the effect on the beam is the largest. In Figure 3 the solenoid starts at the IP and its length L is varied from 0.5 m to the nominal value of 2.3 m, while the integrated field stays constant at 3.45 Tm. For a non-overlapping solenoid (dashed line) the coupling terms are almost constant with L. If the B1 and QD1 magnets are present, then the terms start changing after the solenoid expands into QD1 located at 0.9 m from the IP (solid line).

Figure 4 shows the skew quadrupole terms projected to the IP as a function of position in the IR. The terms vary according to formulas (1), and the skew quadrupole strength was fixed at 10% of the main arc quadrupole strength. The corresponding solenoid term at the IP is shown by a dashed line. Note, that the hardest solenoid term to correct in this case is the (1,4) term. It is generated from the overlapped QD1 and grows quadratically with the overlapped length. This term is much smaller for the shorter side of the solenoid since QD1 is not fully overlapped on this side. In a real lattice it is usually not possible to find the ideal phase positions for the quadrupoles. Therefore, all six quadrupoles may generate all six terms, and a combined set of equations has to be solved.

To locally compensate the orbit at the IP, the general strategy is to use two dipole correctors for each half IR and for each betatron plane, and to locate them at orthogonal phase positions of 0 and π/2 (mod π) from the IP.

Finally, the focusing perturbation has to be corrected with a minimum of eight variable normal quadrupoles in each half IR. The solenoid focuses in both planes. For the LEB it generates a quadrupole component that is about 1% of the QD1 strength. The skew quadrupoles affect the optics as well. More normal quadrupoles can be varied if additional constraints are imposed. For instance, in order to minimize perturbation of the chromatic-

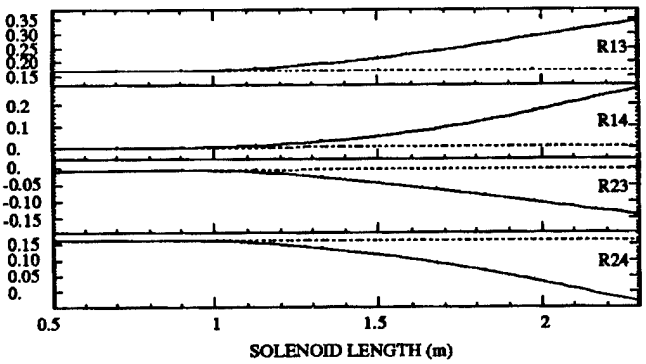


Figure 3. Projected solenoid coupling terms at the IP.

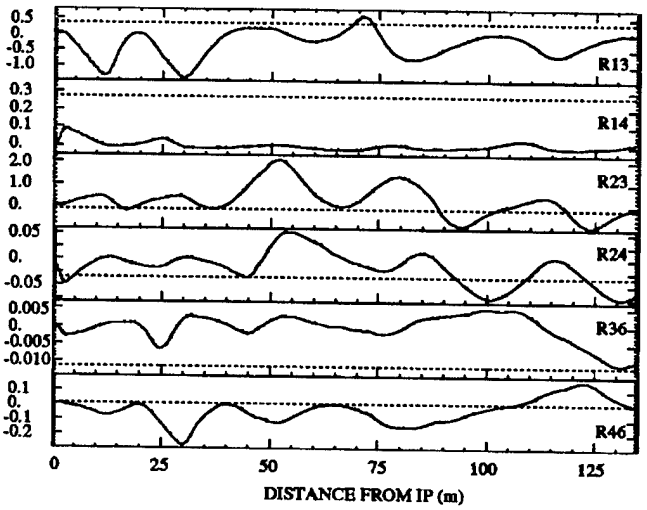


Figure 4. Projected skew quadrupole terms at the IP.

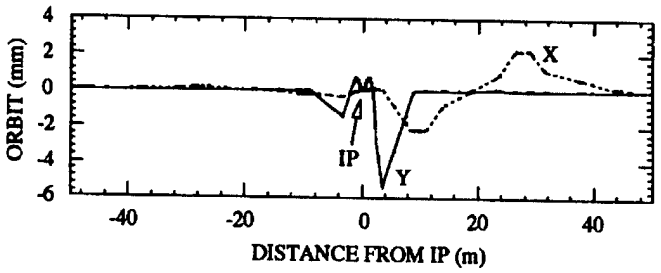


Figure 5. Orbit due to solenoid in the LER.

ity correction, we kept the β-functions and phases unchanged at the local sextupole positions with the solenoid on. In all, in each half IR we adjusted the two FD quadrupoles by 1-2% in strength, 11 normal quadrupoles in the LER, and 9 quadrupoles in the HER.

IV. RESULTS

We tried a variety of possible skew quadrupole positions in order to minimize their maximum strength. Skew quadrupole positions next to the local sextupoles are effective because of the large β function and because the $-I$ transformation between the two skew quadrupoles makes it possible to independently control the coupling and the vertical dispersion. On the longer side of the solenoid the important skew quadrupole position is near the final doublet, where the β values are large and the phase provides the best correction of the (1,4) term. Because of the large orbit perturbation, the first vertical orbit corrector was placed near the FD. We did not place any elements for the solenoid correction between the paired local sextupoles in order to preserve the $-I$ transformation. The positions of the skew quadrupoles and of the orbit correctors on two sides of the IR are symmetric about the IP.

All correction strengths were calculated numerically using MAD. Table 1 shows the skew quadrupole strengths for the two rings that independently compensate the long and the short side of the solenoid. The strongest skew quadrupole occurs in the

Corrector name	LER		HER	
	Long	Short	Long	Short
SQ1	-0.07210	0.01479	-0.00389	0.00076
SQ2	0.02405	-0.00502	0.00369	-0.00110
SQ3	-0.00434	-0.00052	-0.00039	-0.00003
SQ4	0.00271	-0.00110	0.00054	0.00012
SQ5	0.02638	-0.02020	0.00861	-0.00455
SQ6	0.00866	-0.01176	0.00202	-0.00360

Table 1: Skew quadrupole strength $\frac{L_q}{B\rho}\frac{dB_x}{dx}$ (m^{-1}).

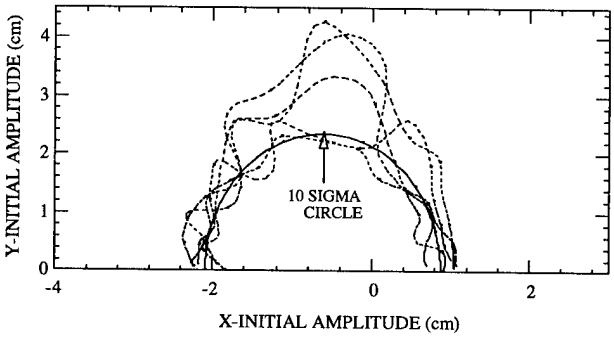


Figure 6. LER dynamic aperture for 5 seeds (dash).

LER near the final doublet, on the longer side of the solenoid, to correct the (1,4) term.

Orbit perturbations caused by the solenoid in the LER are shown in Figure 5. If a soft fringe field is included instead of the hard solenoid edges, then the maximum vertical orbit would be slightly larger than 6 mm.

Finally, the effect of the solenoid on dynamic aperture was evaluated. Typical reduction of the aperture due to the solenoid is about 2-4σ, and the final aperture including machine errors is close to 10σ. An example of the LER short term dynamic aperture with the solenoid is shown in Figure 6.

References

[1] S. Peggs, "The Projection Approach to Solenoid Compensation", CERN/SPS/82-2 (DI/MST) (1982).

[2] H. Grote, F.C. Iselin, "The MAD Program, Version 8.1", CERN/SL/90-13 (AP) (1990).

[3] M. Sullivan, unpublished.

SWAMP PLOTS FOR DYNAMIC APERTURE STUDIES OF PEP-II LATTICES *

Y.T. Yan, J. Irwin, Y. Cai, T. Chen, D. Ritson
Stanford Linear Accelerator Center, Stanford University, Stanford, CA 94309 USA

Abstract

With a newly developed algorithm using resonance basis Lie generators and their evaluation with action-angle Poisson bracket maps (nPB tracking) we have been able to perform fast tracking for dynamic aperture studies of PEP-II lattices as well as incorporate lattice nonlinearities in beam-beam studies[1]. We have been able to better understand the relationship between dynamic apertures and the tune shift and resonance coefficients in the generators of the one-turn maps [2]. To obtain swamp plots (dynamic aperture vs. working point) of the PEP-II lattices, we first compute a one-turn resonance basis map for a nominal working point and then perform nPB tracking by switching the working point while holding fixed all other terms in the map. Results have been spot-checked by comparing with element-by-element tracking.

I. INTRODUCTION

An adequate dynamic aperture is a basic requirement for an acceptable accelerator lattice. Conventionally, to check the dynamic aperture of a lattice one would take the following numerical steps: (1) choose a working point (horizontal and vertical betatron tunes) and make the best effort to optimize the bare lattice; (2) assign systematic and random multipole errors and random misalignment of the magnets; (3) make suitable corrections to the orbit, tunes, and chromaticities; (4) track particles (with synchrotron oscillations) to determine the dynamic aperture.

For the dynamic aperture studies of the PEP-II B-factory[3] High-Energy Ring HER[4] and Low-Energy Ring (LER)[5] lattices, we usually select a working point at $\nu_x = 0.57$ and $\nu_y = 0.64$ and track enough particles (electrons for the HER or positrons for the LER), element-by-element for 1024 turns to determine the dynamic aperture (if a particle survives for 1024 turns after injection, it would survive for longer due to synchrotron radiation damping). Typical dynamic aperture plots can be found in these proceedings[4], [5]. Each of such element-by-element dynamic aperture calculations takes a few hours of CPU time in a RISC Workstation using a tracking program called Despot.

Although a dynamic aperture plot at one working point can help in making an appraisal of lattice nonlinear performance, it offers limited information. For example, during the course of updating and improving the PEP-II lattices, we found, in some cases, that the dynamic apertures were not adequate at the nominal working point (0.57, 0.64) while we would find that they were very good at other working points such as (.78, .82) or (.715, .735). In some occasions, particularly for the HER lattices, we even found that some dynamic apertures were extremely small at (.57, .64) due to synchro-betatron resonances, but were adequate at a working point slightly different from (.57, .64). Thus, it is preferable and even necessary to understand lattice behavior for a broad range of working tunes. Dynamic aperture displayed on a reasonable mesh in the tune plane have been called swamp plots.

However, it is virtually impossible to obtain swamp plots for the PEP-II lattices with element-element trackings since it would require months of computer time. Aimed at not only fast tracking but also understanding in detail the lattice nonlinearities, we developed a fast tracking method using resonance basis Hamiltonians, which we call nPB tracking[1]. The nPB tracking provides a factor of 100 in tracking speed and also offers insight into the underlying physics. Map tracking for proton accelerators[6][7][8] is a different problem since there is no significant synchrotron radiation damping.

II. THE nPB TRACKING

To perform nPB tracking, we first write out a resonance basis map file by taking the following steps: (1) obtain a one-turn transverse Taylor map and a one-turn time-of-flight map at a preset suitable order with respect to the closed orbit, treating the off-momentum δ as a parameter; (2) select terms in the time-of-flight map (neglect insignificant terms) and write them (the coefficients) in a file; (3) calculate the linear normalization transformation matrices and write the two 4 X 5 similarity transformation matrices in the file; (4) perform similarity transformation of the nonlinear one-turn Taylor map and then make a Deprit-type Lie transformation such that in the linearly normalized space, the map can be represented by $Re^{-:H(x,p_x,y,p_y,\delta):}$, where R is a rotation that depends on the transverse and vertical tunes only, and H is a discrete δ-type Hamiltonian for the nonlinear perturbation; write the working tunes in the file; (5) transform the discrete Hamiltonian $H(x, p_x, y, p_y, \delta)$ from the Cartesian coordinate space to the action-angle variable space such that $H = H(\theta_x, J_x, \theta_y, J_y, \delta) = H_T(J_x, J_y, \delta) + H_R(\theta_x, J_x, \theta_y, J_y, \delta)$ and write out all terms (coefficients) in the file, where H_T, in which every term depends on the actions (J_x, J_y) and the parameter (δ) only, i.e. not depend on the angles, contains tune shift information[9] while H_R, in which every term depends on the angles and actions, contains the resonance strength information.

Once the resonance basis map is written in a file, we are ready to perform the nPB tracking by first read in the resonance basis map from the file. After initializing the particle phase-space Cartesian coordinates, we then perform turn-by-turn nPB tracking following the steps: (a) transform the phase-space coordinates into the linearly normalized space (always kept in Cartesian coordinate space); (b) advance the phase of the particles through rotation R that only depends on the working tunes; (c) perform the Lie transformation $e^{-:H(\theta_x,J_x,\theta_y,J_y,\delta):}X$ for nonlinear perturbation of the coordinates by directly making Poisson

*Work supported by the Department of Energy under Contract No. DE-AC03-76SF00515

0-7803-3053-6/96/$5.00 ©1996 IEEE

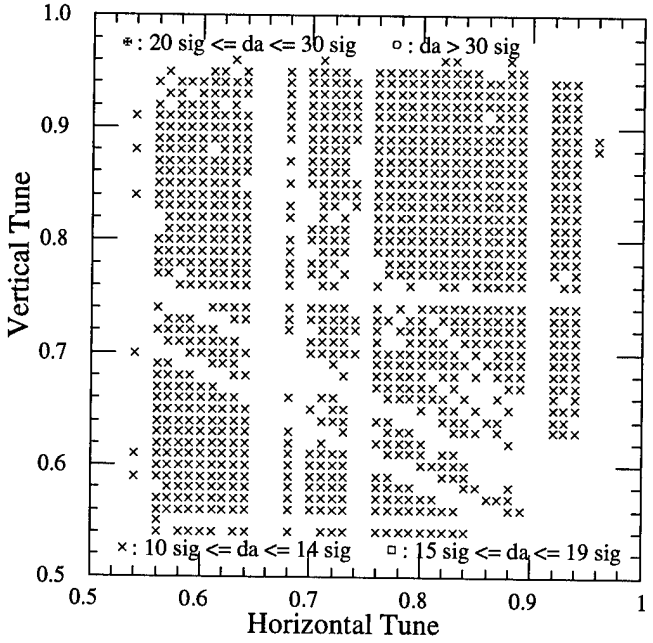


Figure 1. Swamp plot for the HER lattice with interlaced sextupoles, β_y^* = 2 cm

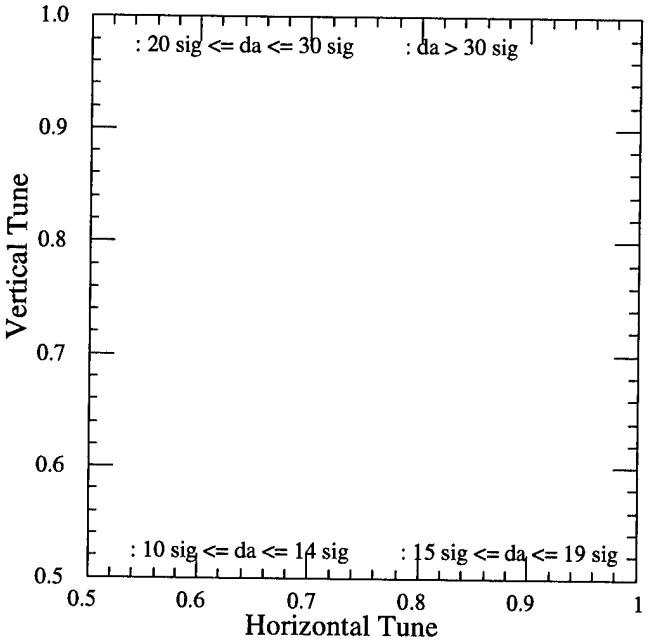


Figure 2. Swamp plot for the HER lattice with beta-bump correction, β_y^* = 1.5 cm

bracket expansions up to a preset n^{th} Poisson bracket (thereby the name of nPB tracking), where X represents each of the phase-space Cartesian coordinates x, p_x, y, p_y which are considered as functions of action-angle variables in Poisson bracket calculations; (d) transform the phase-space coordinates in the linearly normalized space back to the original space; (e) update the off-momentum δ with the time-of-flight map and then go on to the next turn.

III. RELIABILITY OF THE nPB TRACKING

In performing nPB tracking, one has to be careful in two regards. First, it is not 100% accurate since the map is truncated at a moderate order. Second, it is not 100% symplectic since one does not carry the Poisson bracket expansion to the infinite order. Such inaccuracy and non-symplecticity have been controversial in the use of one-turn maps for long-term tracking. However, it is well understood that the required accuracy and symplecticity depend on circumstances[7]. For the PEP-II lattice dynamic aperture studies (only 1024 turns), through numerous testing we have concluded that a map of 10^{th} order in Hamiltonian (9^{th} order in Taylor expansion) is accurate enough and 3 Poisson bracket expansion of the Lie transformation is accurate and symplectic enough. It takes about 1 minute with such 10^{th}-order, 3PB tracking in a RISC Workstation to obtain a dynamic aperture plot at a given working point.

IV. PEP-II SWAMP PLOTS

To obtain swamp plots for the PEP-II lattices, we have followed exactly the nPB tracking procedures described in Section II except that we would increment the working tunes in Step (b) to obtain dynamic apertures throughout the tune plane. It should be noted that except for working tunes, all other linear and nonlinear terms in the resonance basis map are held fixed. This is equivalent to that of the element-by-element tracking by inserting an exactly matched linear trombone to switch the working tunes without further changing the lattice.

Two typical swamp plots of the HER 60^o lattices are shown in Figures 1 & 2. Figure 1 shows the dynamic apertures for a $\beta_y^* = 2cm$ HER lattice with interlaced sextupoles while Figure 2 shows the dynamic apertures for a $\beta_y^* = 1.5cm$ HER lattice with β-beat semi-local correction. Before we performed the swamp plots, we had wondered which lattice was better. Now, it is clear as shown in the figures that $\beta_y^* = 1.5cm$ lattice has better dynamic apertures throughout the tune plane. The predominant dynamic apertures for the interlaced lattice ($\beta_y^* = 2cm$) are between 10σ and 14σ while they are between 15σ and 19σ for the β-beat semi-local correction lattice ($\beta_y^* = 1.5cm$). Note that the dynamic aperture is below 10σ on where no symbol is shown.

Another type of swamp plots we have used frequently is shown in Figure 3 for LER lattices. Dynamic apertures along the diagonal or slightly off-diagonal lines on the tune plane were obtained. As shown in the figure, we can easily conclude that the 90^o noninterlaced-sextupole lattice (dynamic apertures plotted on the left column) is a better choice than the 90^o interlaced-sextupole lattice (shown on the right column). This type of swamp plots is particularly useful during the course of lattice updating and improving since it takes less computer time than that of the full-tune-plane swamp plot while still offers adequate information for comparison of lattice nonlinear performance.

Through use of swamp plots, one can also probe lattice nonlinearities. In particular, betatron and synchro-betatron resonances can be easily observed in a swamp plot with a fine mesh along the diagonal line on the tune plane as shown in Figure 4 for a 72^o semi-local correction LER lattice with interlaced sextupoles. In Figure 4, one clearly sees the strong integer, half-integer and one-third-integer resonances. The one-fourth-

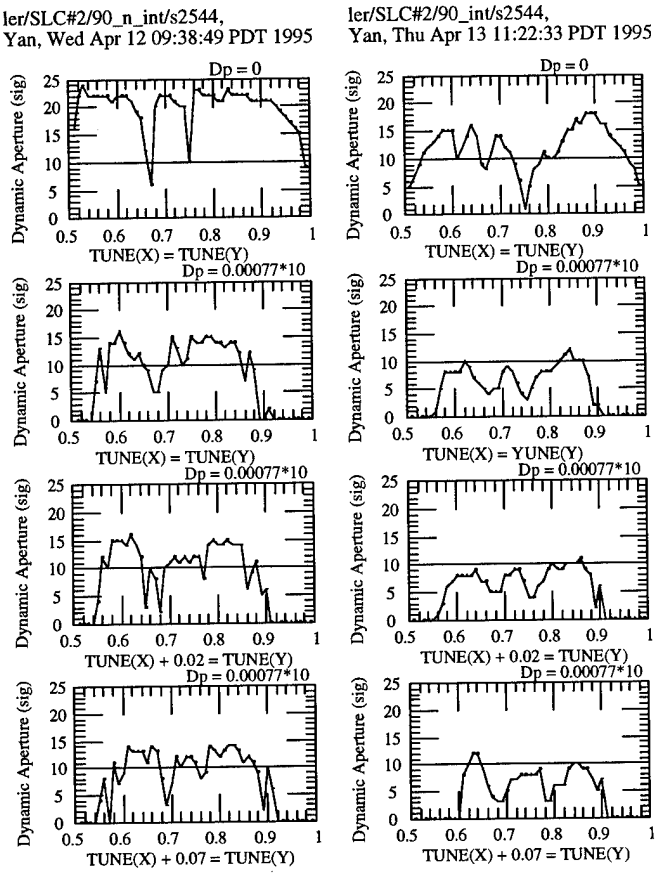


Figure 3. Comparison of dynamic apertures between two lattices. Each column represents a lattice that is identified by the computer working directory shown on the top of the column.

integer resonance is not as strong as the one-third-integer resonance. The plot also shows clearly the side-band resonances due to synchrotron oscillations (the synchro-betatron resonances). The integer and half-integer resonances have strong side-band resonances as the dynamic apertures are 0 or very small for a big range of tunes near the integer and half-integer tunes. The strong one-third-integer resonance and related side-band resonances are a very nice clue for lattice improvement as a 72° lattice can possibly have a weak geometric nonlinearity up to 5th order.

V. SUMMARY

We have shown some typical swamp plots for the PEP-II lattice studies. These swamp plots have helped us in comparing lattices and often led us to the improvement of the lattices.

References

[1] J. Irwin, T. Chen, and Y. Yan, "A fast tracking method using resonance basis Hamiltonians," SLAC-PBU-95-6727.

[2] J. Irwin, N. Walker, and Y. Yan, "The Application of Lie Algebra Methods to the PEP-II Design," SLAC-PUB-95-6779, in Proc. of the 4th EPAC, p. 899 (1994).

[3] "PEP-II: An Asymmetric B Factory," Conceptual Design Report, SLAC-418, June 1993

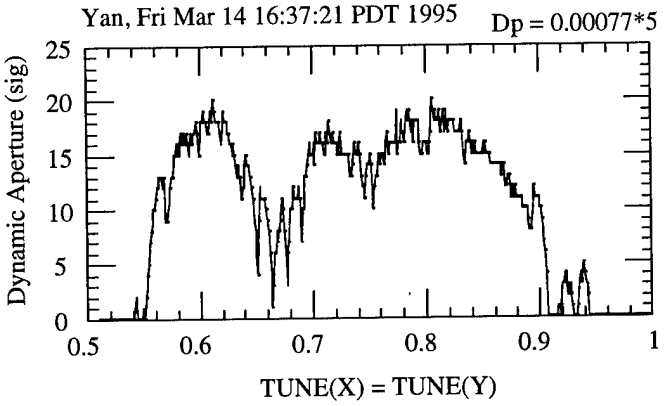


Figure 4. Dynamic apertures along the diagonal line of the tune plane with a fine mesh for a 72° interlaced-sextupole LER lattice

[4] M. Donald, *at al.*, "Lattice design for the high-energy ring of the SLAC B-factory (PEP-II)," in these proceedings.

[5] Y. Cai, *at al.*, "Low-energy ring lattice of the PEP-II asymmetric B-factory," in these proceedings.

[6] J. Irwin, "A multi-kick factorization algorithm for nonlinear maps," in *Accelerator Physics at the SSC*, AIP Conf. Proc. No. 326, edited by Y.T. Yan, J.P. Naples, and M.J. Syphers (AIP, New York, 1995), p. 662.

[7] Y.T. Yan, "Application of differential algebra to single-particle dynamics in storage rings", in *Physics of Particle Accelerators*, AIP Conf. Proc. No. 249, edited by M. Month, and M. Diene (AIP, New York, 1992), p. 378.

[8] R. Kleiss, F. Schmidt, Y.T. Yan, and F. Zimmermann, DESY Report No. HARA 92-01, CERN Report No. SL/92-02 (AP), and SSCL Report No. SSCL-564.

[9] For more accurate tune shift calculation, one should consider use of nonlinear normal form.

Lattice Design for the High Energy Ring of the SLAC B-Factory (PEP-II)*

M. H. R. Donald, Y. Cai, J. Irwin, Y. Nosochkov,
D. M. Ritson, J. Seeman, H-U.Wienands and Y. T. Yan
Stanford Linear Accelerator Center, Stanford, CA 94309 USA

Abstract

The design of the lattice for the High Energy Ring (HER) of the SLAC B-Factory has several special features, notably provision for octupole compensation of amplitude dependent tune shift effects and a beta-beat scheme for semi-local chromaticity correction. In the arcs adjacent to the interaction point (IP) the beta functions are enhanced to allow the use of non-interlaced sextupoles to compensate the chromaticity of the interaction region. A closed bump of beta "mismatch" is generated by two vertically focusing quadrupoles spaced 2 betatron wavelengths apart. The beta-beat has two advantages: it enhances the ratio between the horizontal and vertical beta functions at the sextupoles and, because of the locally higher beta function, allows weaker sextupoles to be used. The standard design uses a 60 degree/cell lattice but a 90 degree/cell lattice may also be used if lower emittances and momentum compaction factor are desired.

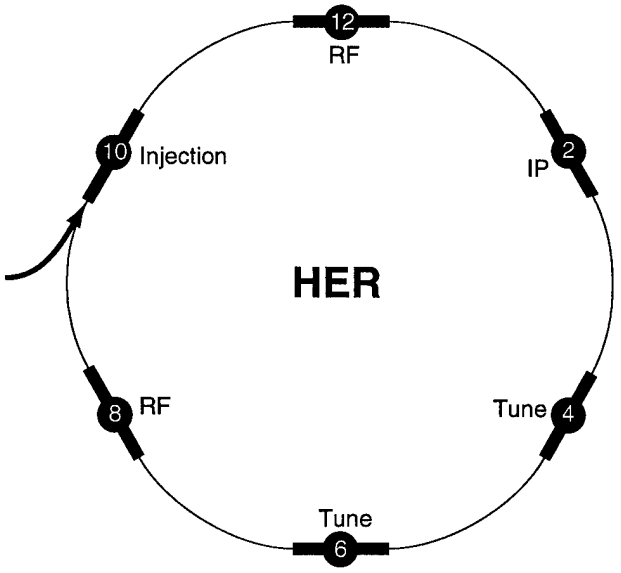


Figure. 1. Schematic of the High Energy Ring of the PEP-II B-Factory

I. INTRODUCTION

The High Energy Ring (HER) of the PEPII high luminosity B-Factory collider is an electron storage ring operating at an energy of 9-12 GeV. The arcs and straight sections are numbered like a clock, the arcs having odd numbers and the straights even numbers. The collisions with the positrons of the Low Energy Ring (LER) take place at the center of straight-2. The separation of the beams from the collision point into the separate rings is done by magnetic fields, relying on the energy difference of the counter-rotating beams[1] (The operating energy of the LER is 2.4-4 GeV). The design of both the LER and HER is described in the conceptual design report[2]. This paper concentrates on new features not described in that report.

To achieve a high luminosity, large currents of closely spaced bunches circulate in the equal-circumference rings and the beta functions at the collision point are made small. The large currents in each bunch require that the transverse emittance of the beams be moderately large to maintain a reasonably small beam-beam tune shift parameter. The magnitude of the horizontal emittance is controlled, in the LER by wiggler magnets[3] and in the HER by tailoring the dispersion function in four of the six arcs.

The low beta functions at the Interaction Point (IP), together with the longitudinal and transverse emittances, make it difficult to correct the chromaticity produced by the large beta functions at the quadrupoles adjacent to the IP. Correction of this Interaction Region (IR) chromaticity is done semi-locally in the arcs closest to the IP (arcs 1 and 3). The global (more linear) chromaticity is compensated by two families of sextupoles SD and SF in the other four arcs.

Injection is in the vertical plane using matched pulsed kickers with a $-I$ transform between them and a current sheet septum to bring the injected beam into alignment with the circulating beam. Four DC bump magnets give further control of the orbit of the stored beam. Good injection efficiency and wide momentum acceptance demands good chromatic correction at the injection point. The demands placed on chromatic correction are more stringent at injection than for colliding beam running.

The RF cavities are located in straight sections 8 and 12 and the beta functions in these areas are kept low. At the center of these straights, away from the RF cavities, are sections where octupoles may be added to control amplitude dependent tune shift effects.

The betatron tune of the HER is controlled by a series of quadrupoles in straight sections 4 and 6. A large tune range may be covered while keeping the beta functions reasonably low.

II. RF AND OCTUPOLE CORRECTION STRAIGHT SECTIONS

Provision has been made for correction of amplitude dependent tune shift effects. At the center of the RF straight sections (straight sections 8 and 12) are three regular cells that may be tuned to 60 degree/cell or 120 degree/cell phase shifts. Three families of octupoles may be placed in each of these sections to adjust the amplitude dependent tune shift terms $\partial\nu_x/\partial\epsilon_x$, $\partial\nu_y/\partial\epsilon_y$ and $\partial\nu_y/\partial\epsilon_x = \partial\nu_x/\partial\epsilon_y$. For each octupole family

*Work supported by the Department of Energy under Contract No. DE-AC03-76SF00515

0-7803-3053-6/96/$5.00 ©1996 IEEE

there are three octupoles, one in each of the cells. The driving terms for each of the quarter-integer resonances cancel within each set for both the 60 degree/cell and 120 degree/cell cases. The octupoles of the family for adjustment of the $\partial\nu_x/\partial\epsilon_x$ term are located close to horizontally focusing quadrupoles, those for adjustment of the $\partial\nu_y/\partial\epsilon_y$ term close to vertically focusing quadrupoles and those for adjustment of the $\partial\nu_y/\partial\epsilon_x$ term are situated mid-cell. The 120 degree/cell arrangement gives better separation of the beta functions and hence more orthogonality, leading to lower strengths for the octupoles but requires stronger quadrupoles and increases the chromaticity.

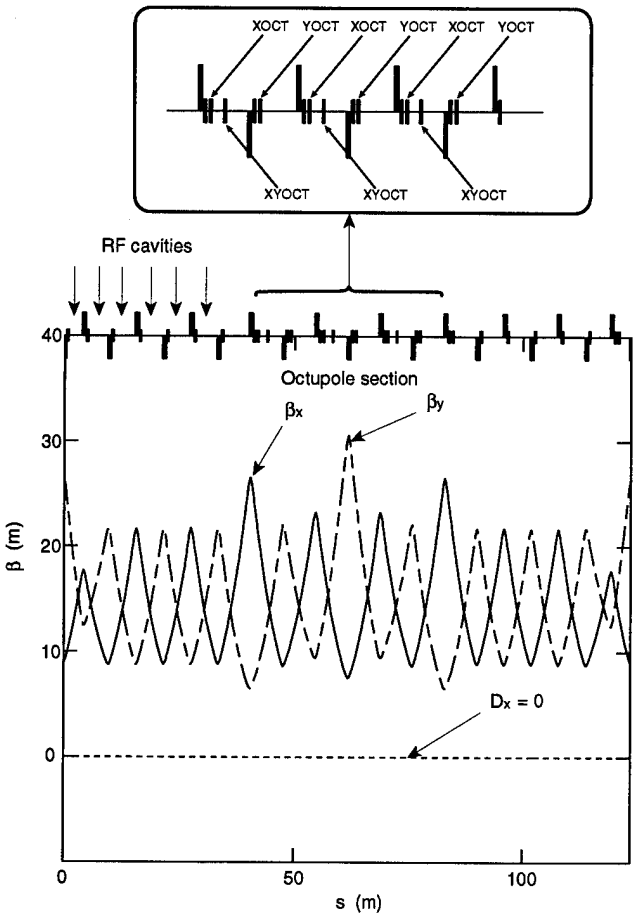


Figure. 2. Lattice functions for an RF straight section, showing positions of the RF cavities and the octupole correction section

III. CHROMATICITY CORRECTION

Initially the semi-local correction of the IR was achieved by many families of sextupoles in arcs 1 and 3. Each of the six arcs are comprised of 12 regular cells with 2 dispersion suppressor cells at each end (The dispersion suppression does encroach slightly into the regular cells). For normal operation the regular cells have a phase shift of 60 degree/cell in both planes. Sextupoles were arranged in pairs three cells apart (180 degrees) in an interleaved manner e.g. SD1,SD2,SD3,SD1,SD2,SD3,SD4... with the SF families interleaved between them.

This arrangement gave very good correction of high order chromaticity but suffered from the geometric effects of the strong interleaved sextupoles. For a β_y^* of 2 cm the dynamic aperture of the HER was adequate, but to gain improvement in dynamic aperture and to reduce the β_y^* down to 1.5 cm alternative correction schemes were investigated.

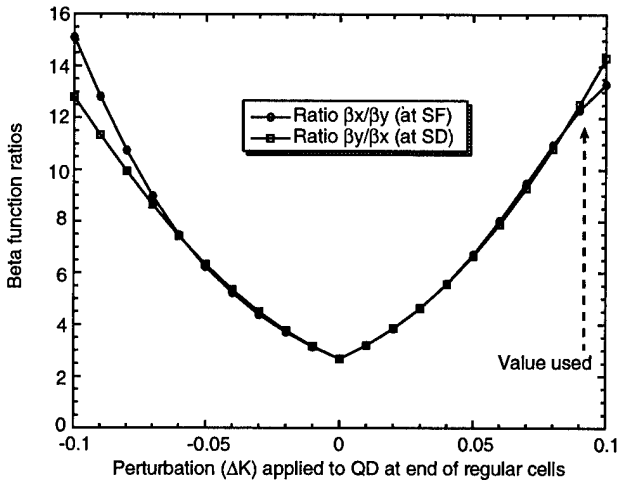


Figure. 3. The ratio of the vertical and horizontal beta functions as a function of the quadrupole perturbations.

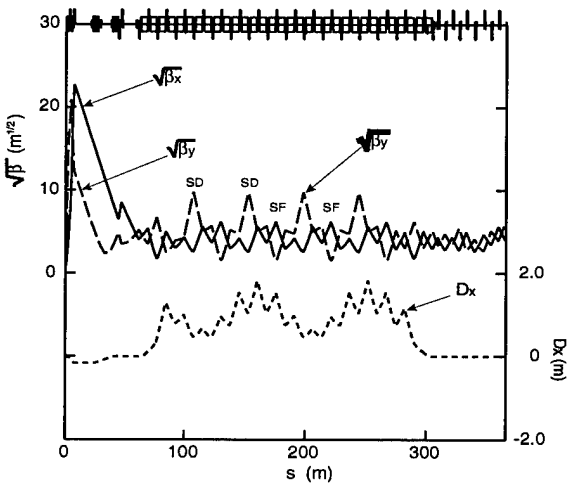


Figure. 4. Lattice functions for sextant 2-4 showing the perturbed beta functions in arc 3.

A fully-local correction scheme such as that used in linear collider final-focus schemes or that formerly used in the LER[4] was not possible because of the limited space in the IR straight and the radiation from the strong bends that would be required for such a final-focus scheme.

Non-interleaved pairs of sextupoles were tried, a pair of vertically focusing sextupoles (SD) three cells apart followed by a pair of SF sextupoles also three cells apart ($-I$ transform), the horizontal and vertical betatron phase shifts from the IP to the sextupoles being adjusted for the best results. The improvement

in on-momentum performance was dramatic but the momentum bandwidth was not acceptable.

It was found that the first correction, vertical in this case, was good but caused bad performance of the second (horizontal) correction. It was deduced that the relatively small ratio of the beta functions (vertical/horizontal) was causing the problem. Cells with 90 degrees of phase shift have a better vertical/horizontal beta function ratio and allow more sets of sextupoles in those arcs. The best arrangement found was Y,X,Y correction but it still was not good enough. The sextupoles were also far too strong (due to the lower dispersion function of the 90-degree cells).

A new idea was then tried. At each end of the block of regular cells (two betatron wavelengths for 60 degree cells) vertically focusing quadrupoles were perturbed to make a region with large beating of the beta functions. A positive perturbation at one end was ended by an equal negative perturbation at the other end. The perturbation that we chose increased the beta function ratio from 2.7 to 13.

The result was enhancement of the vertical beta function in parts of the arcs at the same places as depression of the horizontal beta function, and vice versa, leading to much improved beta function ratios. Due to the higher (wanted) beta functions, where the sextupoles were placed, the strength of the sextupoles was much reduced. The perturbation of the beta functions does cause a perturbation in the dispersion function but this is not a problem. The sum of the dispersion functions at the positions of each of a pair of sextupoles is equal to that of the unperturbed cells. The chromatic effects of the sextupole pair depends (to low order) only on that sum of the dispersion functions. Choosing vertically focusing quadrupoles to make the perturbation minimizes the effect on the dispersion function.

Variations may be made on this beta-beat scheme. When implementing the scheme in a 90 degree lattice some of the enhancement of the beta ratio is lost due to the sextupoles not being at the beta minimum (at the quadrupole positions). This can be countered by making a double beta-beat, first vertical, then changing to the horizontal. There is space to do this with a 90 degree lattice since there are three betatron wavelengths in the 12-cell block of regular cells. The 90 degree cells do require much stronger sextupoles due to their lower dispersion function.

IV. PERFORMANCE OF THE CHROMATIC CORRECTION

The performance of the beta-beat chromaticity correction is much better than that using interleaved sextupoles in the arcs adjoining the IP. The synchro-betatron side-bands of the half-integer resonance $2\nu_x - n\nu_s$ are troublesome due to the imperfect correction of the high order chromaticity. Nevertheless, the performance in those regions equals that of the interleaved scheme and vastly out-performs it elsewhere in the tune diagram[5].

When magnet alignment errors and multipole errors are included in particle tracking the dynamic aperture is found to be more than adequate for both injection and colliding beam running.

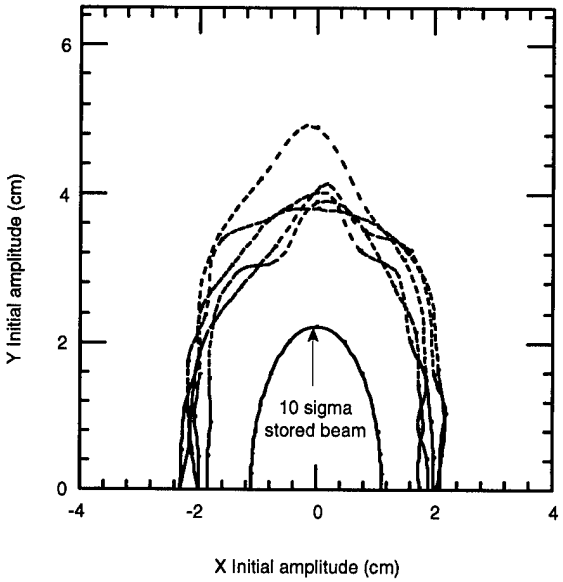


Figure. 5. Dynamic aperture of the HER using 5 seeds for alignment and multipole errors. Particles are stable for initial amplitudes within the curves shown.

V. SUMMARY

Recent improvements have been made to the design of the High Energy Ring. The dynamic aperture has been much improved, allowing for operation at a lower value of β_y^*. Provision has been made for compensation of amplitude dependent tune shifts by the use of octupole sections.

References

[1] Y. Nosochkov, *et al.*, "Detector Solenoid Compensation in the PEP-II B-Factory," these proceedings.

[2] "PEP-II: An Asymmetric B Factory," Conceptual Design Report, SLAC-418, June 1993

[3] J. Heim, *et al.*, "Wiggler Insertion of the PEP-II B-Factory LER," these proceedings.

[4] M. Donald, *et al.*, "Localized Chromaticity Correction of Low-Beta Insertions in Storage Rings," Proc. of 1993 Particle Accelerator Conference, May 1993.

[5] Y. T. Yan, *et al.*, "Swamp Plots for PEP-II Lattices," these proceedings.

The APS Booster Synchrotron: Commissioning and Operational Experience*

S.V. Milton
Advanced Photon Source, Argonne National Laboratory
9700 South Cass Avenue, Argonne IL 60439, U.S.A.

Abstract

The Advanced Photon Source (APS) at Argonne National Laboratory (ANL) was constructed to provide a large user community with intense and high brightness synchrotron radiation at x-ray wavelengths. A 7-GeV positron beam is used to generate this light. Acceleration of the beam from 450 MeV to 7 GeV is accomplished at a 2-Hz repetition rate by the booster synchrotron. Commissioning of the booster began in the second quarter of 1994 and continued on into early 1995. The booster is now routinely used to provide beam for the commissioning of the APS storage ring. Reported here are our commissioning and operational experiences with the booster synchrotron.

I. INTRODUCTION

1.1 The APS

The APS is a synchrotron radiation laboratory built to provide an extremely bright x-ray source for a large user community. Construction and installation of all primary accelerator components is complete. We are now in the process of commissioning the accelerator complex.

There are four accelerators at the APS: the linac, the positron accumulator ring (PAR), the booster synchrotron, and the storage ring. The linac is designed to accelerate an electron beam up to 200 MeV, direct the beam at a tungsten target, and produce positrons. The captured positrons are accelerated in the second stage of the linac up to the nominal energy of 450 MeV, and are then transferred to the PAR. This process is repeated at 60 Hz. The PAR captures the 30-ns bunch train of the linac and damps it down both longitudinally and transversely. After 24 linac pulses are accumulated another 96 ms are allowed to pass before the damped bunch is transferred to the booster for further acceleration. The APS booster synchrotron (booster) raises the energy of a 450-MeV positron or electron beam up to 7 GeV in approximately 230 ms. It is designed to do this at a 2-Hz rate. The 7-GeV beam is then transferred to the storage ring where the light is generated and transported to the users.

This paper is entirely about the commissioning and operational experiences with the booster.

1.2 Description of the Booster

The booster employs a classical FODO lattice structure with four "missing dipole" cells for dispersion suppression in the rf straights. There are two mirror symmetry axes and thus four quadrants. Beam enters the machine nominally at 450 MeV and is ramped up to the full 7-GeV extraction energy in just under 230 ms. Currently this process is repeated at a 1-Hz rate; however, we will be moving to 2-Hz in the very near future.

There are 68 dipoles, 80 quadrupoles, 64 sextupoles, 80 correctors, and 5 pulsed magnets in the booster. The dipoles are all connected in series and are powered by two 12-phase power supplies operating in a master/slave configuration. The quadrupoles and sextupoles are each separated into two families of equal numbers with each family powered by a separate 12-phase power supply. The correctors are powered with separate bipolar DC/DC convertors. Each pulsed magnet is individually controlled. They are used for injection and extraction of the beam.

The lattice functions for one quadrant of the machine are shown in Figure 1, while the main parameters of the booster are listed in Table 1.

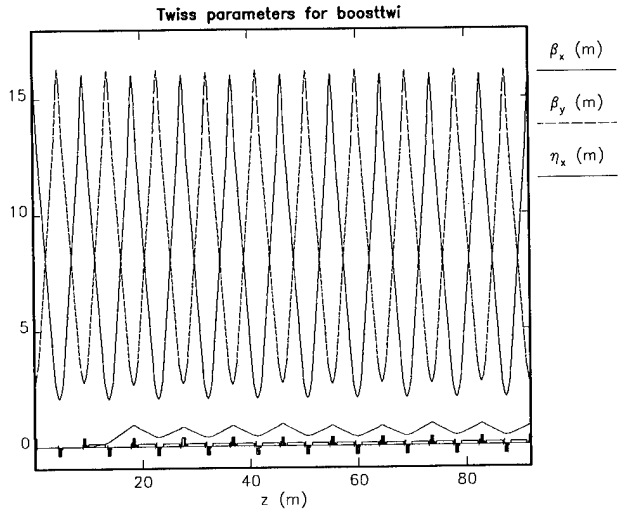


Figure 1: The booster machine Twiss parameters for a quadrant

Table 1: The APS Booster Parameters

Circumference	368	m
Nominal Injection Energy	450	MeV
Design Extraction Energy	7.0	GeV
Maximum Attainable Energy	7.7	GeV
Ramp Repetition Rate	2	Hz
Acceleration Time	230	ms
Tunes: Q_h	11.75	
Q_v	9.80	
Nominal Charge per Ramp Cycle	5.8	nC
Injection Emittance (from PAR)	0.36	mm-mrad
Natural Emittance at 7.0 GeV)	0.13	mm-mrad
Energy Loss/Turn at 7 GeV	6.33	MeV/turn
Energy Spread σ_E/E, at 7 GeV	0.001	
RF Frequency	351.9	MHz
RF Gap Voltage at 7 GeV	8.3	MV
Synchrotron Tune at 7 GeV	0.026	

* Work supported by U.S. Department of Energy, Office of Basic Sciences, under Contract No. W-31-109-ENG-38.

0-7803-3053-6/96/$5.00 ©1996 IEEE

1.3 Ramp Cycle

With the exception of the correctors, a typical magnet current ramp cycle is shown in Figure 2. Injection is on-axis into a single bunch and occurs on-the-fly between 10 - 15 ms after the start of the ramp. The current, and thus energy, continues upward linearly. Single-turn extraction occurs approximately 230 ms after injection and is also done on-the-fly.

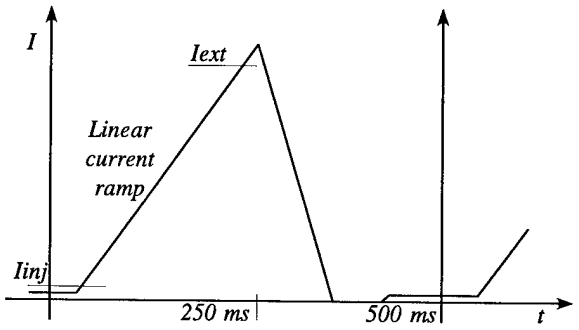


Figure 2: A typical current ramp cycle in the booster.

II. COMMISSIONING AND OPERATIONS

2.1 Chronology

Commissioning of the booster physically began on the 21st of April, 1994, with the first introduction of beam; however, operations were limited to basic systems checks. It was not until August that we attempted acceleration, and then, due to a power supply problem, we were limited to 4 GeV. During the latter part of October the 4 GeV was extracted from the booster and sent to the storage ring for a two-sector test. Preliminary modifications were made to the booster power supplies during the planned down time in the months of November and December. These modifications allowed us to tune the current ramps up to the 7-GeV level. After being off for 2 1/2 months and with modified power supplies, we made the first attempt to accelerate to 7 GeV in the third week of January. Successful acceleration from 400 MeV to 7 GeV was obtained for the first time on the 22nd of January, '95. After some preliminary measurements were finalized, the 7-GeV beam was delivered to the storage ring on the 20th of February. We have had consistent running since then.

2.2 Ramping Power Supplies

A large amount of effort has gone into getting the ramping power supplies to track together with the dipole. Descriptions of their performance and the ramp tuning methods used to achieve the desired tracking tolerances can be found elsewhere [1, 2]. Only a brief description will be provided here.

The power supply currents must all track one another to within tight tolerance; otherwise the beam encounters destructive resonances and is lost before extraction time. The specification is

$$\frac{\Delta I_{q,d}}{I_{q,d}} \leq \pm 0.14\% \ .$$

This is the maximum allowable fractional current deviation of either the dipole or the two quadrupole supplies from the desired programmed currents. Unfortunately, we were not able to achieve the tolerances we required with the original regulator, timing-phase firing card, and ramp function generators. Extensive modifications were done to the ramping control and power supply monitoring systems. We now run the supplies in hardware voltage-control mode with a slower software current control loop. As can be seen in Figure 3, control is now quite good. Injection occurs at the time location of the arrow. A similar level of control has been achieved for both the focusing quadrupole supply and the dipole.

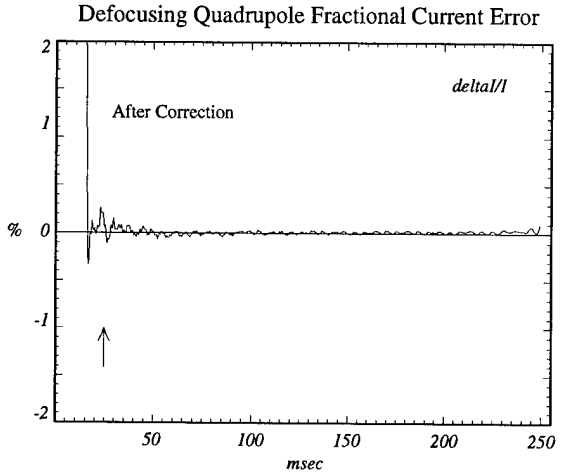


Figure 3: The fractional current error in the quadrupole.

2.3 RF System

There are two sets of two 5-cell 351.9-MHz rf cavities placed symmetrically in the machine. These are driven by a single 1-MW klystron.

The gap voltage varies significanlyt over the course of the energy ramp. At injection the compressed bunch from the PAR takes up a significant portion of the booster rf bucket. During this period the gap voltage is kept as low as required to achieve good capture efficiency. The gap voltage is increased as the energy rises in order to account for the E^4 rise in the synchrotron radiation loses. This is accomplished by varying the drive amplifier amplitude. A typical rf voltage ramp for 7-GeV operation is shown in Figure 4.

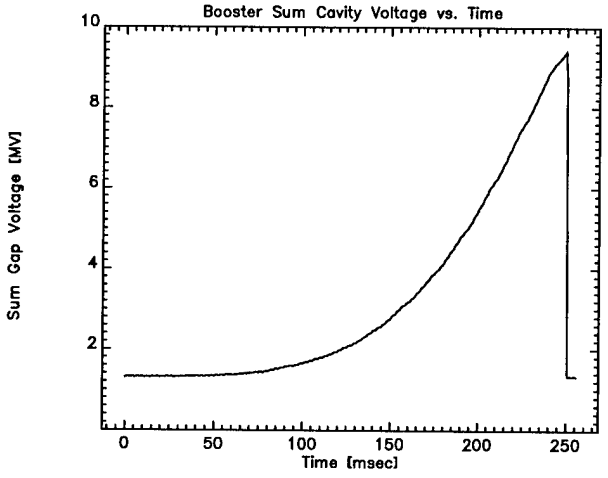


Figure 4: The total sum rf gap voltage in the booster as a function of time during the energy ramp.

2.4 Diagnostics

The primary diagnostics in the booster are the fluorescent screens, integrating current monitor, tune measurement system, and beam position monitoring system. Other secondary diagnostics are the synchrotron light monitor, the beam loss monitor, and the scrapers.

The fluorescent screens are useful only for 1st turn tuning but are quite sensitive (> 20 pC/ pulse visible) and so proved invaluable as an initial injection tuning aid.

We continually monitor the current monitor signal on a scope in the control room. An example of the output is shown in Figure 5. Any losses during the ramp cycle are immediately visible to the operator, providing nearly instantaneous feedback for tuning. The initial drop in the signal is real and is due to some of the PAR charge being lost out of the smaller rf bucket in the booster. The remaining fluctuations are noise.

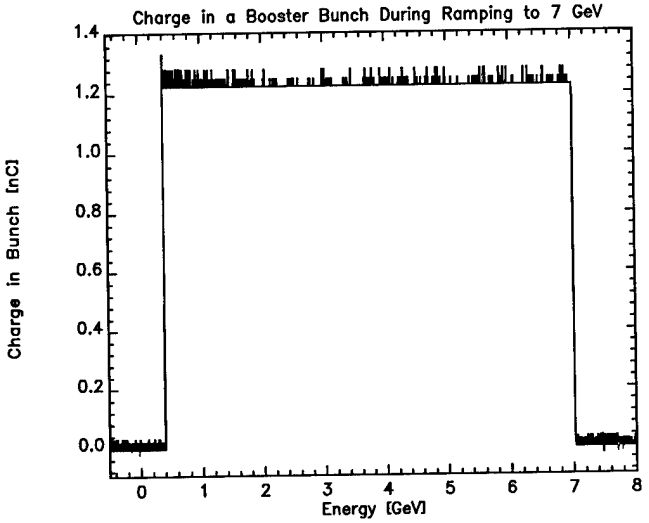


Figure 5: The booster current monitor output as a function of beam energy in the booster.

Measurement of the transverse tunes at injection time and during the ramp cycle also proved extremely valuable in tuning up the machine. The tune measurement system was constructed from stripline beam position monitors and an HP89440 Vector Signal Analyzer (VSA). The VSA came complete with an Ethernet connection and Xwindow software making it useful almost immediately upon hookup. This eliminated the usual troubleshooting delays which are typically found in systems that are designed and built in-house.

Among the many features of the VSA, one came in particularly handy during commissioning: the capture buffer. The VSA has the capability to capture the stripline signal over the course of an entire ramp cycle. This can then be viewed later at ones leisure.

The beam position monitor system (BPM) is nearly identical to that of the APS storage ring. It is capable of measuring the beam position on a single pass. A boxcar averager is used to increase the accuracy, and a timing module and beam history module allow for the possibility of measuring the orbit at any time during the ramp cycle as well as measuring the orbit over a large fraction of a single ramp.

The primary use of the BPM system to date has been to measure the orbit for subsequent processing and application of orbit correction algorithms. Figure 6 shows the measured horizontal and vertical closed orbits before and after correction immediately after injection. It should be noted, however, that we routinely run without correctors on. This is in testimony to the accuracy of the survey and the quality of the magnets and magnet sort.

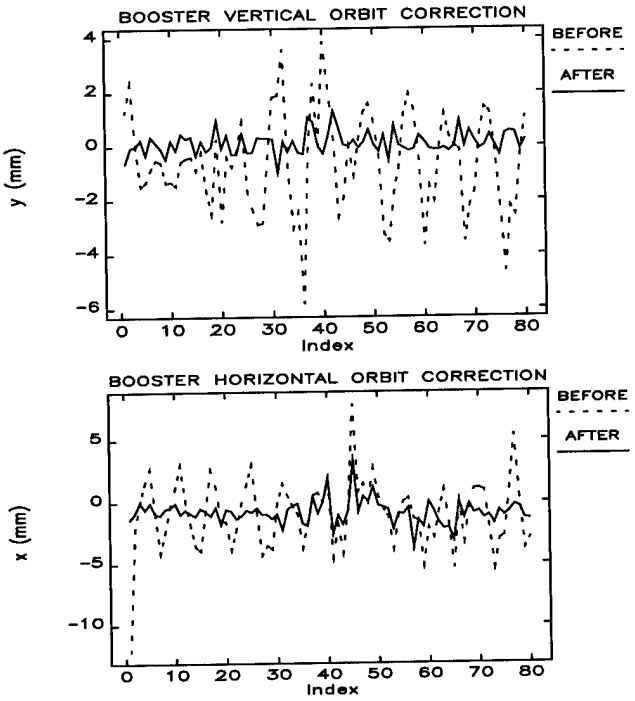


Figure 6: Corrected and uncorrected closed orbits.

III. SUMMARY

The booster has been running reliably since January '95, routinely providing 7-GeV beam upon demand for the storage ring. All systems have now been checked out and tested under actual operational conditions. We are now in the process of finalizing the various systems. The commissioning team fully expects to turn the machine over to the Operations Group within this year.

IV. ACKNOWLEDGEMENTS

As with any project of this nature, many people are responsible for its success; however, special thanks go to the core members of the APS accelerator commissioning team, M. Borland, J. Carwardine, G. Decker, L. Emery, and N. Sereno, for their tremendous support during the commissioning of the booster. A special thanks goes to J. Carwardine for his tenacity in making the ramping supplies work. J. Galayda is also acknowledged for his guidance throughout commissioning and his seemingly endless depth of accelerator expertise.

V. REFERENCES

[1] J.A. Carwardine, S.V. Milton, and D.G. McGhee, "Performance of the Ramping Power Supplies for the APS Booster Synchrotron," these proceedings.

[2] S.V. Milton, "Ramp Tuning of the APS Booster Synchrotron Magnet Power Supplies," these proceedings.

A Preliminary Design for a Tau-Charm Factory*

J. Norem, E. Crosbie, J. Repond, L. Teng
Argonne National Laboratory, Argonne, IL 60439 USA

Abstract

A Tau-Charm Factory (τcF) with a luminosity of 10^{33} /cm^2 /s has been studied to determine the parameters and feasibility of such a facility. We have primarily looked at a system with a circumference of around 380 m, monochromatic optics, superconducting RF, distributed vacuum pumping and electrostatic bunch separation at the single interaction point. A candidate lattice has been developed and we have begun to determine the specifications of magnets and other components

I. Introduction

A Tau-Charm Factory, (τcF), is a high luminosity e^+e^- collider operating near the J/Ψ and τ production threshold, which requires center of mass energies from 3 to ~ 6 GeV. Such a machine would enable a new level of precision in several physics areas such as the tau neutrino mass, rare tau decays, charm decay constants, rare charm meson decays, neutral D^0 meson mixing and charmonium, with high statistics and well understood backgrounds [1]. Such studies, particularly the searches for rare processes such as CP violation, require the highest possible luminosities.

We have made a preliminary design study of the feasibility and cost of constructing such a facility. As described below, we have aimed our lattice design work toward the goal of a simple lattice with monochromatic collision optics. The design is not complete or totally self consistent, however critical and high cost components have been examined in some detail. This paper describes the options considered and the initial conclusions of our study.

II. Parameters

Following other work, this design uses two rings separated vertically, with one interaction region between them [2]. The operational characteristics of the machine are determined by the design of the interaction region and the machine lattice in the arcs.

The goal of producing a luminosity of >10^{33} /cm^2/s based on realistic beam parameters and components can be accomplished in a number of ways. In this design two options have been considered for the interaction region: the monochromatic collision optics [3], in which the beams collide in a region with opposite non-zero vertical dispersions so that the sum of the energies of the two beams is constant; and the standard optics, in which the beams are not dispersed. In the past, it has been assumed that the luminosity for the monochromatic optics was necessarily lower than that for the standard, high luminosity optics. We have shown that, with proper tuning, one may be able to obtain similar luminosities with either optics, thus the need for the difficult retuning might be avoided [4]. We have chosen the monochromatic optics for our design.

The lattice capable of producing the desired luminosity is described in reference [4]. The shape of the rings is determined by the long straight section required by the interaction point optics and the beta and dispersion matching sections which couple the magnet arcs to the IP. The straight section on the opposite side of the ring is used for injection, RF, beam dumps and other functions. The lattice optics are designed to maximize the luminosity at the energy of the J/Ψ while providing beam energy resolution at the IP comparable to $\Gamma_{J/\Psi}$ = 0.088 MeV and large dynamic aperture with realistic components. The primary parameters are summarized below.

Collider Ring Parameters

General		
Center of mass energy	3.0 - 6.0	GeV
Luminosity	10^{33}	/s /cm^2
Current	0.86	A
Electrons (positrons)	$1.8 \cdot 10^{11}$	/bunch
Approximate circumference	385	m
Bend radius	11.7	m
Bunch spacing	~10	m
Momentum compaction, α	0.036	
Bunch length	0.01	m§
Natural emittance, ε_x, ε_y	250 / 3.8	nm§
Beam energy spread, σ_E/E	$3.8 \cdot 10^{-4}$	§
Interaction Point		
Beta functions, β_x*, β_y*	0.01 / 0.03	m
Dispersion, D_y*, (D_x*= 0)	±0.4	m
Beam beam tune shifts, $\xi_x = \xi_y$	0.026	
RF System		
RF frequency	~500	MHz
Required RF voltage turn	3	MV§
Maximum radiated power / beam	530	kW
Cavities	1	/ring§

§ all parameters evaluated at 1.5 GeV, (table and text)

The lattice of the arcs consists of FODO cells with a cell length of 7.4 m and a phase advance of 60° per cell. The dipole magnets operate at 0.71 T and the magnet length is 2.3m. Horizontal dispersion is eliminated in the straight sections by removing the third and fourth magnets from each

* Supported in part by the US Department of Energy, Office of Basic Energy Science and Office of Nuclear and High Energy Physics, Contract # W-31-109-ENG-38.

0-7803-3053-6/96/$5.00 ©1996 IEEE

end of the arcs.

At the collision point the optimized orbit parameters are $\beta_x^* =$ 0.01 m, $\beta_y^* = 0.03$ m, and $D_y^* = \pm 0.4$ m for the two beams. Head-on collisions are assumed, with electrostatic separators near the interaction point producing the initial beam separation. With electrostatic fields of 24 kV/cm at 1.5 GeV, the beams are separated by ~20 σ , at 5 m from the IP, thus a bunch to bunch separation of ~10 m seems adequate.

The proposed lattice can be made to preserve e+/e- polarization with the addition of spin rotators in the straight sections. The injectors must be able to produce polarized positrons to exploit this capability.

To reach higher luminosities it might be necessary to consider the addition of crab crossing cavities and modification of the IP line to permit off axis collisions. This would permit smaller bunch spacings than the ~10 m required for electrostatic separation.

III. Vacuum Chamber

The vacuum chamber determines the stability of the beams as well as the required aperture of the magnets. Synchrotron radiation from the beams in the arcs produces a large heat load on the chamber as well as radiation induced gas desorption. The gas load is given by the relation $Q_{gas} = 24.2\, E\, I\, \eta$ [Torr L/s], where E is the beam energy in GeV, I is the beam current in Amps and η is the desorption constant [5].

Aluminum, copper and stainless steel chambers were considered. Copper seems preferable because it has good vacuum properties, $\eta = 2 \cdot 10^{-6}$ molecules/photon, but aluminum is cheaper and is more easily extruded. We have tried to produce a simple and compact cross section which requires minimal modification to the basic extrusion. Slots will be cut between the beam chamber and the pumping chamber and the structure could then be bent horizontally at a 11.7 m radius using the techniques developed for the vacuum chamber of the Advanced Photon Source (APS) [6]. In normal operation, the chamber would be cooled by water in the outside cooling channel. Heating for bakeout will be accomplished using hot water in the cooling passages.

An arrangement of slots with a conductance of 500 - 1000 l/s will be made parallel to the beam direction. Pumping will be provided by non evaporable getter (NEG) tapes such as SAES ST707 [7]. Three of these tapes 1.5 cm wide will provide ~500 L/s m of pumping, which should be sufficient to produce a vacuum of $\sim 4 \cdot 10^{-9}$ Torr in the arcs, giving a gas scattering lifetime of ~7.5 hours.

Synchrotron radiation near the interaction point causes backgrounds in the detectors as well as heating of the components and perhaps large photocurrents in the electrostatic separators. Masking of these components requires absorbers near the electrostatic separators and IP.

IV. Magnets / Power Supplies

In this design the interaction point quadrupoles have a large gradient and large aperture and therefore must be superconducting.

The design of a 5 cm, warm bore, high gradient, (80 T/m at 3 GeV), superconducting quadrupole would follow the LHC quad designed by Ostojic, Taylor and Kirby and built by Oxford Instruments [8]. The quadrupole would use a NbTi conductor and would have a maximum field on the condutor of only about 5 T.

Conventional magnets were based on designs developed for the APS. In order to study the dependence of cost on the gap, two gaps were considered. Dipoles with gaps of 6 and 8 cm were considered along with quadrupoles of 3.5 an 5 cm radii. The dipoles will be made with laminated C shaped cores and the quads will have demountable laminated cores.

Power supplies for all components would be conventional. All dipoles will be connected in series, as will be the quadrupoles. Shunt power supplies around each quadrupole would permit ±10% tuning capability.

V. RF Acceleration

The cw RF system is required to replace ~600 kW of lost synchrotron power per ~1 A beam and provide longitudinal focusing to keep $\sigma_z \sim \beta_x^* \sim 1$ cm, while presenting the minimum possible impedance to the beam.

A superconducting RF system operating near 500 MHz is a natural choice. At this frequency, a voltage of 2.8 MV/turn is required to bunch the beam to 1 cm at 1.5 GeV, and recent data from Cornell show that 3 MV could be provided by one cavity per ring [9]. A system of coupling out and damping higher order modes has been developed along with a geometry that minimizes wake fields. High power rf windows which can transmit the ~400 kW required by one beam are available at this frequency [9]. High luminosity operation above 1.5 GeV would require more than one cavity to maintain the bunch length and beam energy and these could be added when necessary.

The beam current is limited by the radiated power that can be replaced by the RF system, so it is desirable that more than the minimum power is available. Tubes producing more than 1 MW are available below 500 MHz from a number of sources.

Cryogenic heat loads for the RF system, ~100 W /cavity, and the superconducting quadrupoles on the opposite side of the ring, ~50 W, plus piping, would be 300 - 400 W for a system with one rf cavity per ring.

VI. Injector Options / Injection

The optimum filling frequency can be found by maximizing

the average luminosity as a function of refilling interval. The lifetime of the beams in the machine, τ_t, is limited to about 90 min. at high luminosity, primarily by inelastic e^+e^- collisions and the Touschek effect, and the filling time should be expected to be about τ_f = 2.5 min. The frequency of injection for maximum overall integrated luminosity would then require refilling after operational periods of about $\sqrt{\tau_t \tau_f}$ ~ 15 min. Thus, the injector will be running about 10 - 15% of the time. Topping up the bunches to save injection time might be possible, and it might significantly increase the integrated luminosity if it were done while maintaining the beams in collision.

A high current injector for the τcF would consist of a ~200 MeV electron linac, a positron target, a ~450 MeV positron linac, a positron accumulator ring to store and damp positrons from many electron bunches and a rapid cycling synchrotron with an acceleration frequency of about 5 - 10 Hz [10]. Such a system should be capable of accelerating $2 \cdot 10^{10}$ polarized e^+ /pulse to 2.5 GeV at a frequency of 5 Hz with low losses.

VII. Conventional Facilities

In order to estimate the overall cost and size of such a facility, we have made preliminary estimates of the space required for different systems together with a possible plan of the facility. The collider requires the equivalent of 3 m of earth in order to shield against a worst case beam loss. This seems most easily provided if the rings are underground. We have assumed that the detector, control areas, counting room, power supplies, and assembly areas, as well as injection beamlines and RF could all be in one building. The detector is self shielding, however the storage rings will require some local concrete shielding in the building. One structure, roughly 20 by 60 m should be sufficient for all activities. The injection system would be located in other structures.

VIII. Acknowledgements

We would like to thank F. Mills, K. Thompson, J. Jagger, D. McGhee, J. Goeppner and J. Noonan of the Argonne APS and T. Fields of HEP for their help with this design. G. Kirby of Oxford Instruments has provided helpful advice.

IX. References

[1] Proceedings of the Tau-Charm Factory Workshop, SLAC Report 343, June, 1989

[2] J. M. Jowett, Frontiers of Particle Beams: Factories with e+e- Rings, M. Dienes, M. Month, B. Strasser, S. Turner, eds., Springer Verlag, 1994

[3] A. L. Gerasimov, D. N. Shatilov and A. A. Zholents, Nucl. Instrum. and Meth. A305, (1991), 25

[4] L. Teng and E. Crosbie, these proceedings.

[5] W. Barletta et al, VIth International Conference on High Energy Accelerators, Hamburg, Germany, July 20-24, 1992, 358

[6] G. Goeppner, Argonne National Laboratory, private communication, (1994)

[7] SAES GETTERS / USA., Inc., Colorado Springs, CO 80906

[8] G. Kirby, Oxford Instruments, Oxford England, private communication 1994

[9] CESR B Factory, A Conceptual Design for a B-Factory based on CESR, Cornell 1993

[10] 7 GeV Advanced Photon Source - Conceptual Design Report, Argonne National Laboratory, AN-87-15, 1987

A SPIN CONTROL SYSTEM FOR THE SOUTH HALL RING AT THE BATES LINEAR ACCELERATOR CENTER

T. Zwart, Boston U, Boston MA 02215; P. Ivanov, Yu. Shatunov, Budker INP; R. Averill, K. Jacobs, S.Kowalski,W. Turchinetz; MIT-Bates Linear Accelerator Center

Abstract

An optical design for a spin rotater for the MIT-Bates South Hall Ring is presented. This design maintains longitudinally polarized electrons at both internal and external targets.

I. Introduction

The MIT-Bates South Hall Ring (SHR) was designed and constructed to provide essentially CW extracted beams and stored beams for a unique internal target physics program. [1]. The SHR facility is shown below in Fig.1. An important component of this physics involves measurements with longitudinally polarized electron beams and polarized targets. The measurement of spin observables provides access to interference terms which are directly sensitive to small but important nuclear form factors and excitations.

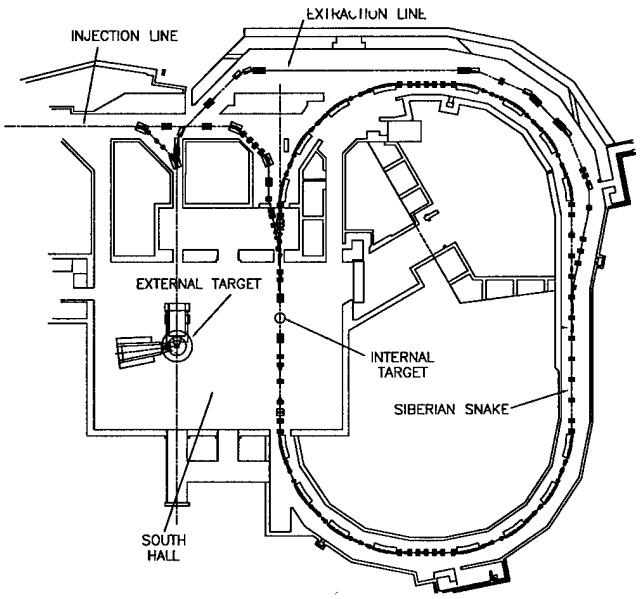


Figure. 1. The MIT-Bates South Hall Floor and South Hall Ring

Maintaining longitudinal polarization for internal target operation and for extracted beam operation is complicated by the fact that for the electron $g-2$ is non zero. Except for 'magic' energies the spin precesses with respect to the momentum over successive circulations in the SHR. A Siberian Snake (SS) approach [2] is being implemented to ensure purely longitudinal polarization at the internal target. The beam is injected with longitudinal polarization on the first pass through the internal target. A superconducting solenoid system on the opposing straight precesses the spin vector by π about the momentum vector. As a result any transverse polarization components are subsequently rotated back into the longitudinal direction by the dipoles in the North half of the SHR. This fixes the spin tune at $1/2$ and eliminates the linear dependence of the spin tune on the beam energy. The magnets in the SS can be scaled to maintain longitudinal polarization at the internal target for any energy.

In the SHR's extraction mode the electron beam is also parallel to the injection line as it passes through the external target on the South Hall floor. Thus the same SS sytem maintains longitudinal polarization on the external target without any additional magnetic elements on the extraction line.

II. Lattice modification

Implementation of the SS scheme requires that the ring lattice be modified because the standard drift length between two quadrupoles (Fig.2) is not long enough to insert a solenoid of reasonable field strength ($10.5\ Tm/GeV$) and the skew quads which compensate for the coupling introduced by the solenoid.

A suitable solution to this problem could probably be achieved in many ways. We developed a new set of machine optics in the extraction straight section that is suitable for the SS insertion and does not affect the beam extraction system. To realize this particular optics it is neccesary to move two quadrupoles (LQ 41 and its symmetric partner, LQ 49) and add two additional quadrupoles (Fig.2). This provides two 4.81 m drift sections. The snake will be in the first drift section and the second is now available for other insertions. Fig.2 shows the matched behavior of the horizontal β_x function along half of the extraction straight section. The solid curve shows the optics of the new lattice. The dashed curve shows the new lattice with the spin rotator elements energized and the dotted line shows the optics of the previous lattice.

This solution satisfies the requirements for both SHR operation modes. There is still optical flexibility to keep the tune away from machine resonances in the storage mode. The optical functions near the extraction septum, between LQ44 and LQ45, are not significantly affected. The positioning of three octupoles for beam extraction is still satisfactory, meeting the requirements of proper phase advance and large values of β_x. In the section for the snake insertion the $\beta_{x,y}$ functions are relatively small and smooth to avoid difficulties in the machine tuning with strong solenoids.

III. Siberian Snake scheme

The SS insertion will not disturb the machine optics if its transfer matrix is equivalent to the drift length physically occupied by the insertion and the betatron tunes are shifted by an

0-7803-3053-6/96/$5.00 ©1996 IEEE

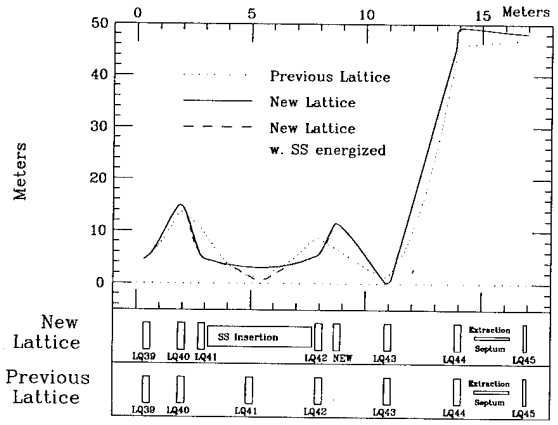


Figure. 2. β_X in the Siberian Snake Region

amount $m \cdot \frac{1}{2}$ where m is an integer. This approach was suggested in [3] and recently applied to the AmPS ring [4].

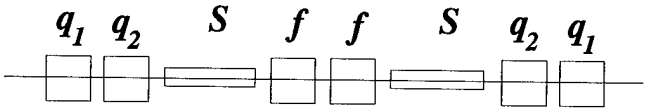


Figure. 3. Siberian Snake scheme

Fig.3 shows a mirror-symmetric SS scheme that consists of two solenoids, a pair of skew quads (q) at each end and two regular quads (f) in the middle. This scheme has four parameters to vary its focusing, three quadrupole strengths and the length of the two solenoids. Of course the solenoid's field integral must be fixed such that the total spin precession angle equals exactly π. A solution for an energy of 1 GeV which satisfies the above requirements is given in Table I.

Note that this solution, which is very economical in number of elements and their strengths, shifts the horizontal tune by integer while the vertical tune will be shifted by an integer and a half. An important feature of these optics is that inside the insertion the β-functions decrease considerably (Fig.2) due to the strong solenoidal focusing dominating over the quadrupole's action. This means that aperture requirements over the insertion are relaxed.

IV. Tolerances and Nonlinearities

An investigation of the effects of errors in positioning, orientation and powering shows that there are not any particularly difficult requirements in alignment and current stability of the snake elements. A possible residual $x - y$ coupling caused by a misalignment of the SS magnets can be easily be compensated by adjusting the skew quadrupoles.

We can use the flat beam approximation to consider the nonlinear effect of the solenoidal fringe field on the extraction process. Certainly the flat beam approximation is valid in the case of the extracted beam where $\epsilon_x >> \epsilon_y$. The beam will see a

Element	Length(m)	Field	α(Deg.)
Skew Quad	0.300	0.61 kG/cm	45°
Drift	0.180		
Skew Quad	0.300	-0.485 kG/cm	45°
Drift	0.175		
Solenoid	0.805	65.00 kG	
Drift	0.175		
Quad	0.300	-1.397 kG/cm	0°
Drift	0.030		
Quad	0.300	-1.397 kG/cm	0°
Drift	0.175		
Solenoid	0.805	65.00 kG	
Drift	0.175		
Skew Quad	0.300	-0.485 kG/cm	−45°
Drift	0.180		
Skew Quad	0.300	0.61 kG/cm	−45°
Total Len.	4.500		

Table I
Position and Strength of Siberian Snake Magnets

non-linear force in the fringe field of the solenoid whose strength can be written:

$$F(s) = \int B(s)B''(s)ds$$

The strength of the non-linear perturbing function, $F(s)$, is a product of the longitudinal field and its second derivative and like the extracting octupole its influence depends on the cube of the radial position. When we compare the kick induced in the fringe field of the solenoids to the kick induced in the extracting octupole we obtain [5]:

$$\frac{\Delta x'_{Fringe}}{\Delta x'_{Oct}} = 0.1$$

Thus we expect that the fringe field focussing will not interfere with the extraction process.

Real field configurations in the solenoids and quadrupole magnets must be taken into account for the actual design.

V. Resonant Depolarization

One concern for the SHR Siberian Snake is that the beam polarization could be destroyed by coupling to the radial betatron motion in the extraction mode. The spin tune and the radial betatron tune are both very close to the half integer. As these two frequencies approach one another the influence of small imperfections in the machine will be maginified and the the polarization could be lost. The magnitude of these imperfections which we expect for the SHR was estimated using the code Apsirin [6]. The strength of this imperfection, ϵ, is a measure of the degree to which the spin eigen vector is not oriented exactly along the beam axis. Using a 10% residual coupling between the radial and vertical betatron motions we obtain a value for

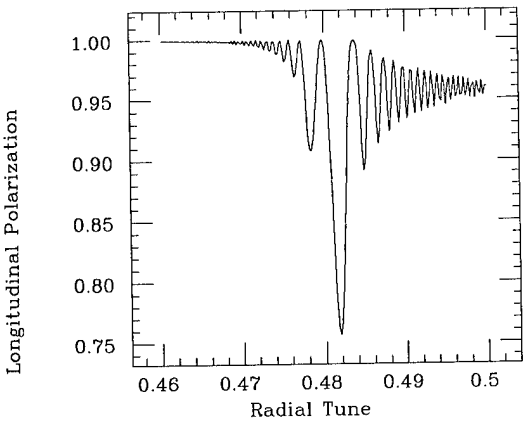


Figure. 4. Polarization over one Extraction Cycle

this intrinsic resonance strength, $\epsilon = 2 \times 10^{-3}$. Following the work of Nghiem and Tkatchenko [7] we have simulated the spin motion in the SHR.

In Fig.4 we use the value of ϵ obtained above and show the average longitudinal polarization over 10 turn intervals while the horizontal tune is ramped from 0.46 to 0.50 over 2000 turns as is done in the extraction process. Note that the polarization is reasonably well preserved until the SHR reaches a tune of 0.48 at which point the polarization drops rapidly to 75% of its initial value. This indicates that some special effort will be neccesary in adjusting the skew quadrupoles to make sure the $x - y$ coupling is kept well below the 10% level.

VI. Conclusion

The Siberian Snake presented here for the SHR will serve to maintain the beam's longitudinal polarization at internal and external targets. This is done with an economy of elements. The solenoids for the spin rotator are now being built at the Institute for Nuclear Physics in Novosibirsk. The lattice on the extraction straight will be modified over the next year and we hope to install the solenoids by January 1996 after which the testing program will begin.

References

[1] J.Flanz, *"South Hall Ring Design Report"*, 1990.

[2] Ya.S.Derbenev, A.M.Kondratenko, A.N.Skrinsky, *Sov. Phys. Doklady*, 15, 1970, p.583.

[3] A.Zholents, V.Litvinenko, *Preprint INP 81-60*, Novosibirsk, 1980.

[4] V.V.Danilov *et al*, *Proc. of 10th Int. Symp. on High Energy Spin Physics*, Nagoya, 1992,p.445.

[5] P.Ivanov, Yu.Shatunov,T.Zwart, *"A Universal Superconducting Spin Rotator for the MIT Bates South Hall Ring"*,Bates Doc. B/SHR 93-10, 1993.

[6] Yu.Shatunov, *Proc. of 10th Int. Symp. on High Energy Spin Physics*, Nagoya,1992

[7] P.Nghiem, A.Tkatchenko, *Nuclear Instruments and Methods in Physics Research*,1993,p.349-366.

Beam-Based Alignment of Sextupoles with the Modulation Method

M. Kikuchi, K. Egawa, H, Fukuma, M. Tejima
KEK National Laboratory for High Energy Physics
1-1 Oho, Tsukuba-shi, Ibaraki-ken, 305 Japan

Abstract

Alignment of sextupoles is vitally important for rings such as B-factory and damping rings. A precision of 100μm or less is required to produce low emittance and large dynamic aperture. Beam-based alignment is crucial for such precision. We present a new technique to measure the magnetic center of sextupole magnet using beam. It is based on the so-called "K-modulation"[2], [3] which has been applied to quadrupoles. We use auxiliary coils on sextupoles which are connected to produce a quadrupole field. By modulating the quadrupole field with some frequency, we observe a sizable modulation of closed orbit whose amplitude is proportional to the offset of beams from magnetic center, thus giving information on the center of the sextupole. In the experiment we could measure the center with a precision of less than 50μm. The present method is applicable to sextupoles connected in series to a common power supply because it induces no voltage to main coils. We report on the experimental results and discuss on the effects of eddy current, asymmetry of chamber and eventual precision.

I. INTRODUCTION

Small emittance in the vertical plane is required to maintain high luminosity in future accelerators such as B-Factories, damping rings for linear colliders. In these machines vertical misalignment of sextupoles has large contribution to the vertical emittance. It is very difficult to keep the alignment of 100 μm against drift of floor levels even though it could be done with high-tech in the commissioning stage. Beam-based alignment (BBA) has been proposed to overcome such difficulties. Several techniques has been proposed for the BBA: for example, π-bump method[1] and K-modulation[2].

K-modulation method has been applied only to quadrupoles[3]. In this paper we discuss on an application to sextupoles and results of a test experiment in TRISTAN. In section II we describe principle of the method. Section III gives detailed discussion on the influence of eddy current in the vacuum chamber, which limits maximum modulation frequency. Section IV gives results of experiment in TRISTAN and discussions on ultimate precisions of the method and on an application to B-Factories.

II. PRINCIPLE OF THE METHOD

In the application of the modulation method, the point is that the kick due to sextupole is too small to detect since it is quadratic to the beam offset at the sextupole. To overcome this we introduced additional quadrupole windings on the sextupole and applied the "K-modulation" to these auxiliary coils. By exciting the auxiliary coils (Fig. 1) numbered 1, 3, 4, and 6, for example, quadrupole field can be produced. Although higher multipoles, mainly octupole, are also excited, quadrupole is still dominant near the origin. If its strength is modulated with some frequency the beam receives, depending on its position, a sizable kick with the same frequency. The amplitude in the resulting closed orbit modulation is proportional to the beam offset, thus giving information of the magnetic center. The merits of this method are: (1)the frequency domain analysis gives high signal to noise ratio, (2)we only need dedicated pickups sensitive to the orbit modulation and (3)it is applicable to sextupoles connected in series to a common power supply because it induces no voltage to main coils. A possible demerit is that the present method gives merely the center of the quadrupole field produced by the selected poles *not* the center of the sextupole field which is generated by all of the poles. Difference between them arises mainly from construction errors of poles. They can be checked by comparing the results with other configuration of poles, (1,2,4,5) and (2,3,5,6).

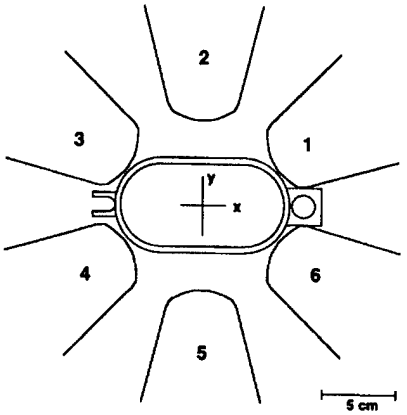


Figure. 1. Geometry of the vacuum chamber and the sextupole for TRISTAN. Auxiliary coils on the poles were excited to produce the quadrupole field.

III. EDDY CURRENT EFFECTS

Since the vacuum chamber has high electric conductivity eddy current driven by the modulated field has significant contribution to the total field.

Consider the equation for the magnetic field in the material with conductivity σ,

$$\nabla^2 B = \mu_0 \sigma \frac{\partial B}{\partial t} . \qquad (1)$$

Here assuming a very low frequency, several ten Hertz at most, we neglected the displacement current term. The total field can be expanded in perturbation series of ω:

$$B = B_0 + B_1 + B_2 + B_3 + B_4 + \cdots , \qquad (2)$$

0-7803-3053-6/96/$5.00 ©1996 IEEE

where $B_0 = \hat{B}_0 \exp^{i\omega t}$ is the external modulation field and B_n $(n = 0, 1, \cdots)$ satisfies following Eqs.

$$\nabla^2 B_1 = \mu_0 \sigma \frac{\partial B_0}{\partial t} = \mu_0 \sigma i\omega B_0 \ , \quad (3)$$

$$\nabla^2 B_2 = \mu_0 \sigma \frac{\partial B_1}{\partial t} \ , \cdots . \quad (4)$$

From Eqs. (3) and (4) we can rewrite B_n as

$$B_n = (i\omega)^n \hat{B}_n \exp^{i\omega t} \ . \quad (5)$$

Real and imaginary part of the total field are given by

$$\Re B = \hat{B}_0 - \omega^2 \hat{B}_2 + \omega^4 \hat{B}_4 - \cdots , \quad (6)$$

$$\Im B = \hat{B}_1 - \omega^3 \hat{B}_3 + \omega^5 \hat{B}_5 - \cdots . \quad (7)$$

We should note that these relations hold for arbitrary geometry and boundary conditions of beam pipe. Eq. (6) implies that in the low frequency the real part (in-phase component) of field always has the form of parabola as a function of the frequency. The strength of high order term depends on the geometry of vacuum chamber.

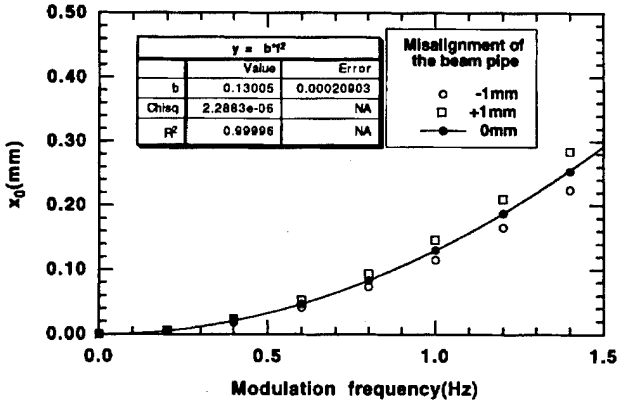


Figure. 2. Horizontal position of the field center as a function of modulation frequency.

Fig. 1 shows the geometry of the beam pipe and the poles of the sextupole magnet of TRISTAN which we used in the experiment. The beam pipe is made of aluminum with race-track shape and at each side a water channel or a slot for heating is attached. The beam pipe has a large left-right asymmetry, thus inducing large asymmetric eddy current. It is enhanced by the fact that the cooling (heating) channels are in the strong modulated field. The left-right asymmetry in the eddy current induces strong dipole field in y-direction (B_1), making the center of quadrupole field shifted in x-direction. The field $B_1$is , fortunately, retarded by 90 degree giving no in-phase component. The in-phase component comes from next order term (B_2). In order to estimate the shift in the center of modulated field in self-consistent manner we made a two-dimensional calculation of the field using a computer code. In the calculation four coils wound on poles (1,3,4, and 6 in Fig. 1) were excited to produce a quadrupole field of 0.032 T/m. The eddy current was calculated under the condition that the total current should be zero in the cross section of the beam pipe. Fig. 2 shows the horizontal position x_0, at which in-phase component of the vertical field $B_y(x, y = 0)$ disappears, as a function of frequency. Filled circles are for the case without misalignment of beam pipe while the squares and open circles are for the horizontal misalignment of $+1$ mm and -1 mm, respectively. In any case parabolic functions of ω fit the results very well.

IV. EXPERIMENTAL

We have installed auxiliary coils on each pole of a existing sextupole magnet of TRISTAN with length of 0.58 m. The cross section of the magnet is sketched in Fig. 1. We excited the auxiliary coils on poles (1,3,4,6) by 40 Ampere-turns(AT) with frequencies ranging from 0.1 Hz to 20 Hz, while the excitation of main coils were kept 615 AT. Beam energy was 8 GeV. Resulting modulation of closed orbit was detected with strip lines in the ring. In the measurement of horizontal(vertical) orbit we used one of strip-line electrodes attached to the horizontal(vertical) side of the chamber. Such selections of the electrodes enable us to separately observe the orbit motion in the horizontal and the vertical plane whenever the beams stay around the central region of the beam pipe. Output signal was processed with the electronic circuit which has been used for the BPM system of TRISTAN[4]. Using an FFT analyzer(HP3562A) we analyzed the pickup signal together with the driving signal that modulated the power supply of the auxiliary coils. We thus obtained both the amplitude and the phase of the cross-spectrum between the two.

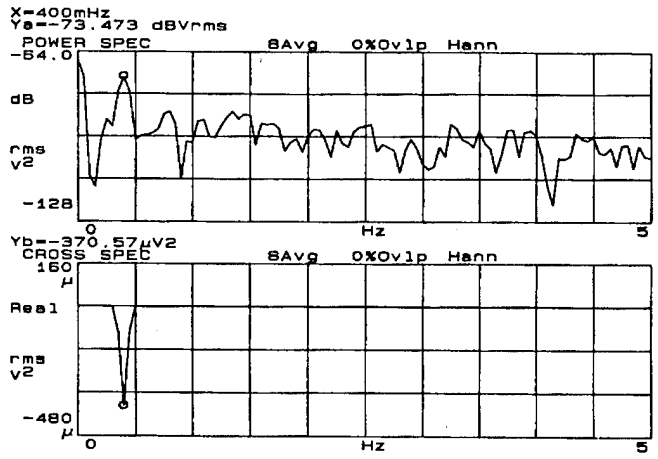


Figure. 3. Raw spectrum in the horizontal plane. Modulation frequency is 0.4 Hz.

Fig. 3 shows an example of spectrum measured with the horizontal electrode. Upper part of the figure shows the power spectrum while the lower part shows the real part of the cross spectrum. Modulation frequency was 0.4 Hz. We made a horizontal bump orbit of 0.9 mm at the sextupole and resulting modulation amplitude of the orbit was about 4 μm at the pickup electrodes. Signal-to-noise ratio was 20 dB in this frequency range. Fig. 4 shows the dependence of the in-phase component of the signal

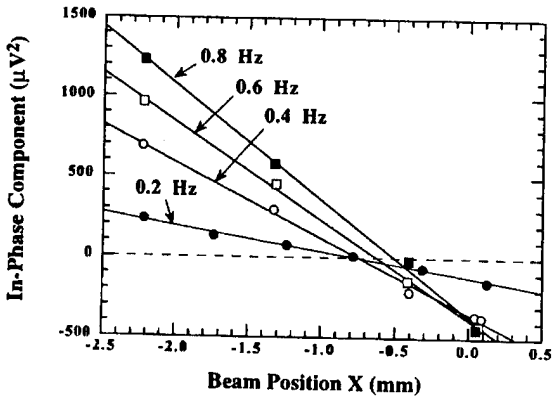


Figure. 4. Dependence of the in-phase component of the signal on the beam position at the sextupole.

on the beam position at the sextupole for the various frequencies. The beam position was scanned by changing height of the local bump orbit at the sextupole while the beam position was measured with a nearest BPM to the sextupole. Distance between BPM and the sextupole was 18 cm. Fitting straight lines to the data we get the BPM offset. From the figure we clearly see that the measured BPM offset depends on the modulation frequency. Fig. 5 shows the dependence of the offset on the frequency. Fitting a parabola to the data, we obtained the offset for the zero frequency with precision of 25μm . The coefficient of the f^2 term is greater by a factor of 4.5 than that of field calculation. This difference could be ascribed to the presence of lead shields in between poles, which was not taken into account in the calculation and possibly could enhance the asymmetry because they were packed not orderly between the pole gaps. Another reason for the difference may be water cooling pipes which bypass the magnet outside the return yoke so that it breaks the condition that the summation of eddy current is to be zero.

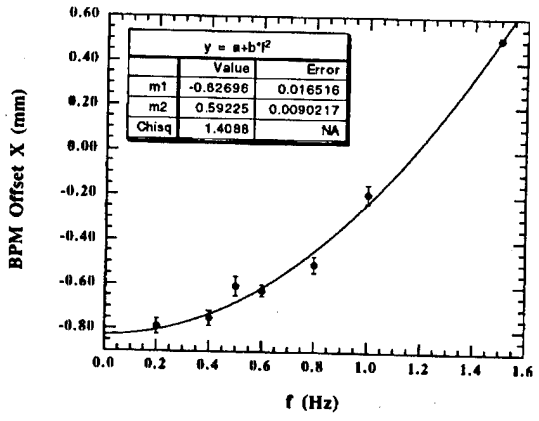


Figure. 5. Dependence of the horizontal offset on frequency

DISCUSSION

We could change the modulation frequency up to 20 Hz without any interference to the main power supply. This is because the induced voltages in the main coils cancel each other as described in section II.

Since the BPM offset for zero frequency is obtained through extrapolation from the data points of higher frequency it is desirable to use lower frequencies as possible in order to get higher precision. In the measurement we did not use frequencies less than 0.2 Hz by the following reason: Firstly there was very large background in the lower frequency part of the spectrum that is not seen in Fig. 1 since the signal was measured with AC-coupling. Secondly lower frequency implies longer time, however, there may be an orbit drift during a single measurement, which will directly degrade the precision. Another approach to get high precision is to make the beam pipe more symmetric: In the design of KEKB, a project of B-factory at KEK, symmetric beam pipe is proposed to take a profit of high frequency although high conductivity of the chamber (copper), unfortunately, induces stronger eddy current than that of TRISTAN.

Uncertainty of construction errors limit the ultimate precision of the method. A conceivable solution is to make a measurement of the difference between the center of the quadrupole filed and that of sextupole filed before the magnet is installed into the ring. Thus the ultimate precision will be limited by the precision of measurement on the filed centers.

V. CONCLUSION

New modulation-method of beam-based measurement on the field center of sextupole was proposed. Eddy current effects were considered in detail. Test experiment demonstrated that the precision is less than 50 μm.

Acknowledgment

The authors owe Satoh Kotaro many ideas and hints on the present work. He is deeply acknowledged.

References

[1] S. Kamada *et al.*, to be published.

[2] D. Rice *et al.*, *Beam Diagnostic Instrumentation at CESR*, IEEE Trans. Nucl. Sci. Vol. NS-30 No4, August 1983, 2190-2192

[3] R. Schmidt, *Misalignments from K-modulation*, Proceedings of The Third Workshop on LEP Performance, Chamonix, January, 1993, 139-145

[4] H. Ishii *et al.*, *Beam Position Monitor System of TRISTAN Main Ring*, Sixth Symp. on Accelerator Science and Technology, Tokyo, 1987, p207

The Stanford Linear Collider*

Paul Emma
Stanford Linear Accelerator Center
Stanford, California 94309

ABSTRACT

The Stanford Linear Collider (SLC) is the first and only high-energy e^+e^- linear collider in the world. Its most remarkable features are high intensity, submicron sized, polarized (e^-) beams at a single interaction point. The main challenges posed by these unique characteristics include machine-wide emittance preservation, consistent high intensity operation, polarized electron production and transport, and the achievement of a high degree of beam stability on all time scales. In addition to serving as an important machine for the study of Z^0 boson production and decay using polarized beams, the SLC is also an indispensable source of hands-on experience for future linear colliders. Each new year of operation has been highlighted with a marked improvement in performance. The most significant improvements for the 1994-95 run include new low impedance vacuum chambers for the damping rings, an upgrade to the optics and diagnostics of the final focus systems, and a higher degree of polarization from the electron source. As a result, the average luminosity has nearly doubled over the previous year with peaks approaching 10^{30} cm^{-2}s^{-1} and an 80% electron polarization at the interaction point. These developments as well as the remaining identifiable performance limitations will be discussed.

I. 1994-95 RUN SUMMARY

In 1994-95 the interaction point (IP) beam intensity has been raised to 3.5×10^{10} particles per bunch (ppb)—an increase made possible through the design and installation of new low impedance damping ring vacuum chambers [1]. The electron polarization has increased to 80% at the IP by using a 100 nm thin strained lattice GaAs photocathode in the electron source [2]. A major upgrade to the final focus optics allows a reduction of the IP vertical beta function which can produce an IP rms vertical spot size of 400-600 nm [3]. Work has continued throughout the run to improve beam stability via feedback refinements, optical modifications and magnet support alterations. The resultant number of Z^0 bosons logged by the SLD has increased from 11,000 at 23% e^- polarization in 1992, and 52,000 at 63% in 1993, to over 100,000 at 80% in 1994-95. Fig. 1 shows Z^0 production over this period. Due to scheduled interruptions and an increased number of various failures, machine up-time has been somewhat lower in 1994-95 (~65%) than in 1993 (~75%). Table 1 lists typical operating parameters at the IP along with an estimate of their variability over the extent of the run. The electron vertical emittance and positron intensity have been the most problematic in terms of variability. Detector backgrounds, which are generally quite low, also vary over the run. They are typically traced to the production of beam tails generated in the main linac.

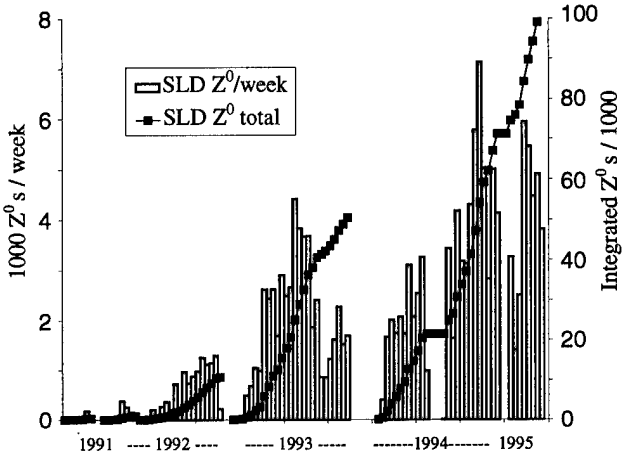


Fig 1. Z^0's per week and integrated Z^0's from 1991 to 1995.

Table 1. Typical IP operating parameters for the 1994-95 run.

beam energy	E	GeV	45.64
e^- intensity	N^-	10^{10} ppb	3.3-3.6
e^+ intensity	N^+	10^{10} ppb	2.9-3.7
hor. rms emittance	$\gamma\varepsilon_x$	mm-mrad	60-90
ver. rms emittance	$\gamma\varepsilon_y$	mm-mrad	10-25
rms energy spread	σ_δ	%	0.09-0.16
hor. rms beam size	σ_x	μm	2.0-2.6
ver. rms beam size	σ_y	μm	0.6-1.2
rms bunch length	σ_z	mm	0.7-1.1
Luminosity	L	10^{30} cm^{-2}s^{-1}	0.4-0.8
Z^0 bosons per hour	—	hr^{-1}	40-80
Repetition rate	f	Hz	120
e^- polarization	P_z	%	78-82
up-time	—	%	55-75

II. POLARIZED ELECTRON SOURCE

Since early 1992 the SLC has been operated exclusively with a polarized electron beam. The electron polarization at the source is now >80%—a significant increase over the 1992 and 1993 values of 25% and 65% respectively. The polarized electron source [2] presently uses a strained lattice GaAs photocathode which is biased at 120 kV and excited with circularly polarized light generated by a pulsed Ti:sapphire

* *Work supported by Department of Energy contract DE-AC03-76SF00515*

0-7803-3053-6/96/$5.00 ©1996 IEEE

laser system. The source intensity is 7-8×10^{10} e^- per bunch (3.5×10^{10} at the IP). During the second half of the run, the cathode quantum efficiency was held below its maximum value in order to yield the highest possible polarization. Periodic cathode recesiations are performed every ~5 days through a simple computer automated process which requires ~20 minutes to complete. The system has been remarkably reliable with <2% unscheduled downtime. The success of the high energy colliding beam physics program at the SLC is due in large part to the success of the polarized electron source.

III. DAMPING RINGS AND BUNCH COMPRESSORS

One of two major SLC upgrades for 1994 was the design and construction of new low impedance vacuum chambers for the damping ring arc-sections [1]. Measurements made in 1992 showed the onset of a bunch length 'sawtooth' instability at beam currents of ~3×10^{10} ppb [4]. This high current instability also appeared as variations (jitter) in the extracted beam phase which produced errant flyer pulses and associated linac collimator losses and detector backgrounds. The net result was to limit the pre-upgrade SLC beam currents to <3×10^{10} ppb. The cause of this instability was the high impedance damping ring vacuum chamber which, prior to 1994, had a computed inductance of 37.5 nH [5]. An interim solution used in 1993 was to ramp the rf voltage down just after injection thereby lengthening the bunch and holding the peak current below the instability threshold [6]. The voltage was ramped up again just before extraction. This procedure necessitated the use of direct rf feedback to compensate increased beam loading at reduced voltage.

The new vacuum chamber has many fewer flexible bellows. Electro-discharge machining (EDM) methods were used to produce smoother transition pieces. The resultant impedance is seven times smaller than that of the old chamber [7]. Measurements show a significantly shorter bunch length and a reduced high intensity lengthening. Fig. 2 shows the measured bunch length at extraction versus beam intensity both for the old and the new vacuum chambers. A single bunch instability is still observed, but it is less severe and no longer limits the SLC operating intensity [1].

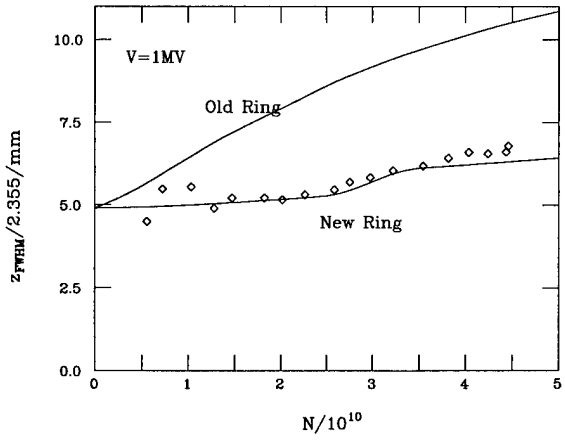


Fig 2. Damping ring extracted bunch length vs. e^- intensity for *old* and the *new* vacuum chamber. Data points represent measurements performed on the new chamber in 1994.

At the nominal machine repetition frequency of 120 Hz the electron store time (~8 msec) is half that of the positron ring (~16 msec). Consequently, the electron damping time is more critical. In 1993 a reduction in transverse partition numbers was achieved by stretching the ring circumference in order to shorten the transverse damping time by ~15% [8]. Recent measurements show damping times of 3.3-3.6 msec horizontally and 4.1-4.2 msec vertically [9]. With an 8.3 msec store the typical extracted electron vertical emittance is 2-3 mm-mrad while it is possible to achieve <1 mm-mrad with a 16 msec store at a repetition rate of 60 Hz.

In the past, effort has been devoted to correcting transverse emittance dilution in the SLC bunch compressors [10-11]. Skew quadrupoles, skew sextupoles and octupole magnets were installed in previous years to correct first, second and even third order anomalous dispersion. The large energy spread (~1%) and the strong bending necessary for a potential ten-fold bunch length compression present severe alignment, construction and multipole field error tolerances. These efforts have been, for the most part, successful. However a 10-30% emittance dilution remains (partially due to an increased compressor voltage—see below). Efforts need to continue here.

The form of bunch compression was changed in 1994. Prior to this, the bunch was 'under-compressed' to 1.3 mm with a 29 MV rf voltage which initiates a <90° longitudinal phase rotation. Starting in 1994 the bunch is now 'over-compressed', also to 1.3 mm, but by using an rf voltage of 41 MV for a phase rotation of >90°. The motivation is to reduce the end-of-linac energy spread by partial cancellation of energy spread due to the longitudinal wakefield in the linac and that due to rf curvature [12]. This technique successfully reduced the end-of-linac energy spread from ~0.25% prior to 1994, to ~0.12% rms. In addition, long low-energy tails in the bunch distribution are no longer generated. A small compromise is made in beam transmission through the compressor beamline where large dispersion and increased energy spread (~1% at 29 MV and ~1.4% at 41 MV) produce a 5-10% beam loss.

IV. MAIN LINAC

The main linac challenge is in high current emittance preservation and stabilization of both the e^- and e^+ bunches in the presence of the inevitable quadrupole and accelerating structure misalignments. The requirements for vertical linac emittance control have become even more challenging with the advent of flat beam operation in 1993 where the linac entrance emittance at 1.2 GeV is now: $\gamma\varepsilon_y \approx$ 2-3 mm-mrad, $\gamma\varepsilon_x \approx$ 30-40 mm-mrad [13]. Beam-based alignment techniques have been used successfully in the past to control transverse quadrupole alignment to ~80 μm rms [14] and new ideas are under investigation to align the disk-loaded wave guides using beam generated dipole wakefields of the accelerating structures as an error signal [15]. Under normal operation, empirical linac emittance correction is accomplished by introducing feedback controlled trajectory oscillations [16] to minimize the measured emittance of wire-scanner phase space monitors [17]

or by observing a set of four off-axis screens [18]. Emittance dilution in the main linac is usually controllable to <60% vertically and <30% horizontally at 3.5×10^{10} ppb. However, temperature dependencies in the linac rf system can generate day to night emittance variations which require constant tuning. Improvements are presently under investigation [19].

A second challenge is pulse-to-pulse and long term trajectory stabilization of both the e^- and e^+ beams [20]. Trajectory jitter not only degrades luminosity but also complicates and slows tuning schemes which rely on phase space monitors requiring many tens or hundreds of pulses. A large source of e^- trajectory jitter, identified in 1994, was due to long range transverse wakefields. With equal e^+ and e^- linac betatron phase advance, the jitter in the leading e^+ bunch is resonantly amplified to the trailing e^- bunch. By introducing a vertical e^+ betatron oscillation initiated in the positron bunch compressor, the trailing electron bunch is seen to accumulate an oscillation due to the long range wakefield [21].

This problem was significantly diminished by introducing a 10°/cell separation between the horizontal and vertical betatron tunes within the linac. Thus the resonant condition is avoided. This linac lattice modification successfully reduced e^- vertical trajectory jitter from ~60% of the nominal rms beam size (observed in the final focus) to ~40%. Some improvement is also observed in e^- horizontal jitter. Fig. 3 shows the initiated e^+ oscillation and its wake induced e^- oscillation both with and without a split tune lattice.

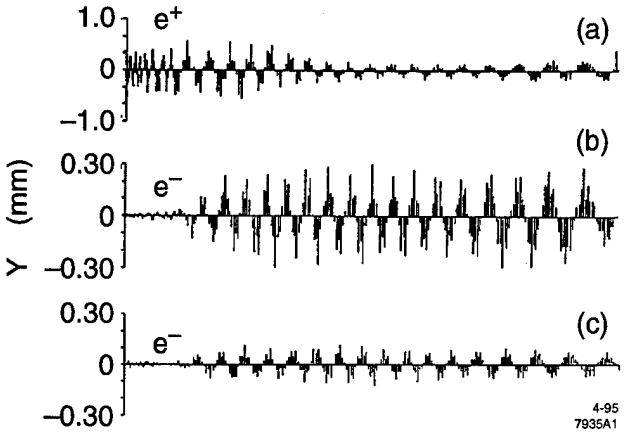


Fig 3. Vertical e^+ oscillation introduced before the linac (a) and long range wakefield induced oscillation for e^- beam of ~300 μm before (b) and ~100 μm after (c) installation of split tune lattice.

However, with the large mid-linac energy spread introduced for BNS damping [22] and the new 'split-tune' quadrupole settings, some increased chromatic emittance dilution within the linac is expected (~10%). Efforts are underway to develop a split-tune linac lattice with less chromatic dilution.

In light of previous successes [23], further efforts to stabilize linac trajectories have centered around modifications of quadrupole magnet support structures. Measurements of quadrupole magnet vibrations using a geophone indicate ~300 nm rms vibrations for frequencies above 1 Hz [24]. Beam response modeling in these conditions predict trajectory jitter which is ~20% of the 10-50 μm nominal vertical beam size. Inspection of the supports has revealed a poorly supported degree of freedom in magnet pitch angle which translates into a significant vertical displacement component due to the longitudinally biased pitch rotation axis of the support. In response, magnet pitch wedges were installed for ~2/3 of the linac quadrupoles.

V. Arcs and Final Focus Systems

Prior to the 1994 run the optics of both final focus systems (FFS)—e^- & e^+—were upgraded in order to allow reduction of the IP vertical beta function [25]. One new quadrupole magnet per FFS was installed between the chromatic correction section (CCS) and the final triplet. This quadrupole optimally adjusts the betatron phase advance between CCS sextupoles and triplet to reduce the dominant 3rd order aberration (U_{3466} coefficient in TRANSPORT notation [26]). In addition, two more quadrupoles—one skew and one normal—were added to the upper transformer section (UT) to provide a full compliment of orthogonal tuning 'knobs' for control of IP beta functions, cross-plane coupling and IP beam waist positions [27]. Four new wire-scanners per FFS were added for emittance and matching diagnostics within the FFS and a fifth wire-scanner was installed at an IP image point in the center of the first CCS bend magnet [28].

The *new* final focus beamlines were commissioned in April and May of 1994 using previously established techniques such as quadrupole and sextupole beam-based alignment methods [29-31]. The new orthogonal UT tuning knobs and image point wire-scanners were employed very successfully to achieve the desired IP beta functions, coupling correction and waist positions. Subsequent low current beam collisions (0.5-1.0×10^{10} ppb) using a twice nominal e^- damping ring store time to achieve ideal emittances produced vertical IP rms spot sizes of 400 nm, clearly confirming the expected performance of the upgrade. The horizontal spot sizes observed were also within the expected value of 1.8-2.0 μm. Fig. 4 shows a 413 nm vertical beam-beam deflection scan [32] measured at low current and long damping ring store.

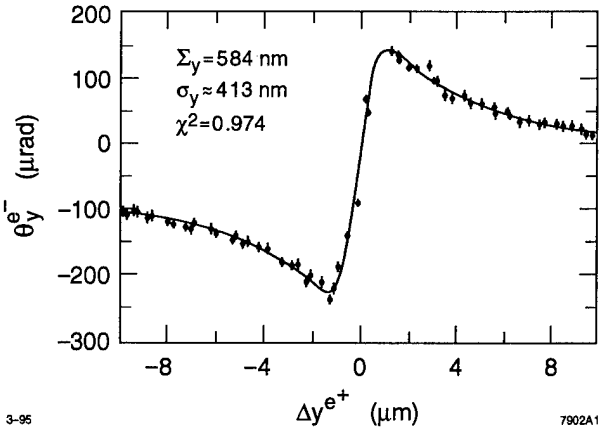


Fig 4. Beam-beam deflection, θ, vs. separation, Δy, fitted with Bassetti-Erskine formula showing 413 nm vertical rms beam size.

At higher beam intensities a significant emittance dilution within the arc/FF systems appears which is not yet

understood. The dilution is usually most evident for the electrons in the vertical plane. At 3.5×10^{10} ppb the observed luminosity is typically 20-40% lower than expectations based on emittance measurements at the end of the main linac. Numerous machine studies have addressed this discrepancy [3]. One probable explanation for high current emittance dilution is collimator generated wakefields. The collimators are used to attenuate detector backgrounds by clipping thinly populated beam tails and are downstream of the end-of-linac wire-scanners used for emittance measurements. Recent studies [33] show clear emittance dilution for some collimators which are routinely closed to within ~3-5 times the rms beam size. However, these measurements have not been reproducible and they are sensitive to varying orbits and beam conditions in the collimator regions.

The addition of new wire-scanners at the entrance to the FFS allowed a first direct observation of the emittance at the end of the 1.2 km, terrain-following collider arcs. At the start of the run the emittance increase through the arcs was found to be independent of both beam current and initial emittance. The vertical increase was $\Delta\gamma\varepsilon_y \approx$ 3-4 mm-mrad while the horizontal was $\Delta\gamma\varepsilon_x \approx$ 10-12 mm-mrad, both of which are in fair agreement with the expected effect of synchrotron radiation and cross-plane coupling calculated from measured betatron oscillation data [34]. Without imperfections the vertical emittance increase in the arcs is expected to be ~1 mm-mrad. However, toward the end of the run, the arc emittance increase showed some sensitivity to beam current, especially for electrons in the vertical plane. It is not yet known if this apparent change was due to a slow degradation of the orbits and optics of the arcs or if it was related to collimator generated wakefields. Careful experiments designed to study current dependencies in the arcs were attempted but are difficult to perform satisfactorily due to problems controlling main linac emittances at varying currents.

Spin transport through the SLC continues to be controlled with vertical orbit 'bumps' in the e^- (north) collider arc [35]. The two post-damping ring spin rotator solenoids have remained switched off. Depolarization in the arcs due to initial energy spread has been reduced in comparison to the previous year by a vertical arc orbit variation method which empirically reduces the effective number of spin precessions through the arc from ~17 'turns' (full precessions) in 1993 to ~10 turns in 1994 [36]. This improvement, in conjunction with the reduction in energy spread using over-compression, has reduced the arc depolarization from ~3% in 1993 to <1% in 1994-95.

VI. Feedback, Controls and Diagnostics

There are approximately 28 different microprocessor controlled fast trajectory feedback loops, as well as several special function loops, in simultaneous operation around the SLC [37]. These loops maintain beam trajectories and energies over a broad band of frequencies up to ~10 Hz. Beam position monitors are used to measure trajectory variations around a previously determined reference orbit and corrections are applied with fast dipole correction magnets or multiple klystron phases in the case of energy corrections. There are seven loops in the main linac which control both e^- and e^+ orbits. These loops are 'cascaded' through a communication link so that loop n+1 nominally corrects only trajectory disturbances incurred after loop n. Furthermore, the loops are 'adaptive' meaning they are able to learn the transport map—the accelerator transfer coefficients—between loops. An added benefit of adaptive-cascaded feedback is the continual measurement of the phase advance between points in the accelerator. This information is recorded every six minutes and can be used to trace and isolate optical errors such as errantly back-phased klystrons. Efforts continue to improve feedback performance through step response testing and modeling [38].

The beginnings of significant progress in machine wide emittance control can be traced to the development and installation of beam profile wire-scanners in the main linac in 1990-91 [17]. Transverse emittance measurements for both beams are now automatically made at three different points in the main linac during colliding beam operations once every hour. In addition, operator initiated measurements are used to direct tuning efforts when necessary. There are now ~50 different wire-scanners in use throughout the SLC from the 40 MeV electron injector to near the final triplet. Most of these wire-scanners are able to measure beam sizes in both planes as well as the x-y correlation. Extensive software controls have been developed which analyze the beam profile data collected and return parameters such as emittance, beta-functions, magnitude and phase of mismatch, coupling magnitudes and beam tails. These parameters, along with raw beam size, are available in history plots for any time interval during the run.

VII. Present Performance Limitations and Future Plans

Table 2 below summarizes 1995 peak operating parameters with respect to the original 1985 'design' expectations. The design expectations are unrealistic, especially in their underestimation of linac wakefield emittance dilution at beam intensities of $>7\times10^{10}$ ppb.

Table 2. Design and peak 1995 parameters most disparate. The intensity difference accounts for a factor of ~8 in luminosity.

PARAMETER	UNITS	DESIGN	1995
Intensity	1×10^{10} ppb	7.2	3.5
repetition rate	Hz	180	120
hor. emittance	mm-mrad	30	60
ver. emittance	mm-mrad	30	10
hor. IP beam size	μm	1.65	2.1
ver. IP beam size	μm	1.65	0.7
energy spread	%	0.25	0.12
Enhancement	—	2.2	~1.15
Luminosity	10^{30} cm^{-2}s^{-1}	6.0	0.8
Z^0 per hour	hr^{-1}	650	80
e^- polarization	%	—	80

The difference between 'design' and 1995 intensities alone, including associated loss in enhancement, accounts for a factor of ~8 in luminosity. Another factor of 1.5 is evident in the repetition rate—not attainable due to modulator limitations. With these past limitations acknowledged, the progress of the SLC is actually quite remarkable. The achieved IP vertical beam sizes have in fact far outperformed the design expectations. This is a result of flat beam operation, not foreseen in 1985, and the 1994 final focus optics upgrade.

The present peak performance parameters are, however, not always maintainable. There are still unexplained variations in the luminosity over all time scales. Some of these variations are traceable to end-of-linac emittances and are partially attributed to temperature variations. However, some variations remain unexplained and are possibly due to an undiagnosed high current dilution mechanism within the collimation, arc or final focus systems. A 20-40% discrepancy still exists between the expected and observed luminosity. This appears to be current dependent and will be the main focus of attention in subsequent collider runs. Efforts are under way to understand and correct the large vertical synchrotron radiation induced emittance growth within the collider arcs.

Future SLC plans include the installation of an IP 'laser-wire' in 1996 which allows single beam size measurements down to ~300 nm [39]. Many smaller projects are in progress which address reliability issues and beam transmission limitations in the various transport lines. The goals for the collider are to record 500,000 Z^0's over the next three years.

VIII. ACKNOWLEDGMENTS

The continuing progress in the performance of the SLC is in a large part due to the persistence of the operations staff who have learned and developed many new ways to deal with the full spectrum of problems encountered in daily operations. Their efforts are fully acknowledged here. Further acknowledgments are extended to the SLC physicists, the engineering groups and the maintenance staff.

IX. REFERENCES

[1] K. Bane et al., *High Intensity Single Bunch Instability Behavior in the New SLC Damping Ring Vacuum Chamber,* these proceedings (1995).

[2] R. Alley et al., *The Stanford Linear Accelerator Polarized Electron Source*, SLAC-PUB-6489, April 1994.

[3] F. Zimmermann et al., *Performance of the 1994/95 SLC Final Focus System*, these proceedings (1995).

[4] P. Krejcik et al., *High Intensity Bunch Length Instabilities in the SLC Damping Rings*, PAC 1993, Washington (1993).

[5] K. Bane, *Bunch Lengthening in the SLC Damping Rings*, SLAC-PUB-5177 (1989).

[6] P. Krejcik et al., *RF Feedback for Beam Loading Compensation in the SLC Damping Rings*, PAC 1993, Washington (1993).

[7] K.L.F. Bane, C.K. Ng, *Impedance Calculations for the Improved SLC Damping Rings*, PAC 1993, Washington.

[8] M.G. Minty et al., *Using a Fast Gated Camera for Measurements of Transverse Beam Distributions and Damping Times*, Accel. Instr. Workshop, Berkeley (1992).

[9] C. Simopoulos, R.L. Holtzapple, *Damping Rate Measurements in the SLC Damping Rings*, these proceedings (1995).

[10] C. Adolphsen et al., *Chromatic Correction in the SLC Bunch Length Compressors*, PAC 1991, San Francisco, CA (1991).

[11] P. Emma, W. Spence, *Grid-Scans: A Transfer Map Diagnostic*, PAC 1991, San Francisco, CA (1991).

[12] F. J. Decker et al., *Over-Compression: A Method to Shape the Longitudinal Bunch Distribution for a Reduced Energy Spread*, Proc. of the 1994 International Linac Conference, Tsukuba, Japan (1994).

[13] C. Adolphsen et al., *Flat Beams in the SLC*, PAC 1993, Washington (1993).

[14] C. Adolphsen et al., *Beam-Based Alignment Technique for the SLC Linac*, PAC 1989, Chicago (1989).

[15] P. Krejcik et al., *Direct Measurement of Transverse Wakefields in the SLC Linac*, these proceedings (1995).

[16] J. T. Seeman et al., *Introduction of Trajectory Oscillations to Reduce Emittance Growth in the SLC Linac*, HEACC'93, Hamburg, (July 1993), p. 879.

[17] M.C. Ross et al., *Wire Scanners for Beam Size and Emittance Measurement at the SLC*, PAC 1991, San Francisco (1991).

[18] F.-J. Decker et al., *Beam Size Measurements with Non-interceptive Off-Axis Screens*, PAC 1993, Washington.

[19] F.-J. Decker et al., *Effects of Temperature Variation on the SLC Linac RF System*, these proceedings (1995).

[20] P. Krejcik et al., *Pulse to Pulse Stability Issues in the SLC*, these proceedings (1995).

[21] F.-J. Decker et al., private communication (1995).

[22] V. Balakin, A. Novokhatsky, V. Smirnov, 12th International Conference on High Energy Accelerators, FNAL, 1983, p. 119.

[23] J.T. Seeman et al., *Induced Beam Oscillations from Quadrupole Vibrations of About 2 Microns at SLC*, PAC 1993, Washington (1993).

[24] J.L. Turner et al., *Vibration Studies of the Stanford Linear Accelerator*, these proceedings (1995).

[25] N. Walker et al., *Third Order Correction to the SLC Final Focus*, PAC 1993, Washington (1993).

[26] K. L. Brown et al., *TRANSPORT*, SLAC-91, (1977).

[27] N. Walker et al., *Global Tuning Knobs for the SLC Final Focus*, PAC 1993, Washington (1993).

[28] D. McCormick et al., *Measuring Micron Sized Beams in the SLC Final Focus*, Sixth BIW, Vancouver (1994).

[29] P. Emma, *Beam Based Alignment of Sector-1 of the SLC Linac*, 3rd EPAC, Berlin (1992).

[30] P. Emma et al., *Beam Based Alignment the SLC Final Focus Sextupoles*, PAC 1993, Washington (1993).

[31] P. Raimondi et al., *Beam Based Alignment the SLC Final Focus Superconducting Final Triplets*, PAC 1993, Washington (1993).

[32] P. Raimondi, F.-J. Decker, *Beam Size Measurement with Flat Beams in the SLC Final Focus*, these proceedings (1995).

[33] K.L.F. Bane et al., *Measurements of the Effects of Collimator Generated Wakefields on the Beams in the SLC*, these proceedings (1995).

[34] T. Barklow et al., *Review of Lattice Measurement Techniques at the SLC*, Proceedings of the Advanced Beam Dynamics Workshop, Corpus Christi, TX (1991).

[35] T. Limberg et al., *The North Arc of the SLC as a Spin Rotator*, PAC 1993, Washington (1993).

[36] P. Emma et al., *Depolarization in the SLC Collider Arcs*, 4th EPAC, London (1994).

[37] T. Himel et al., *Adaptive Cascaded Beam-Based Feedback at the SLC*, PAC 1993, Washington (1993).

[38] M.G. Minty et al., *Optimization of Feedback Performance at the Stanford Linear Collider*, these proceedings (1995).

[39] M.C. Ross et al., private communication (1995).

Options and Trade-Offs in Linear Collider Design

J. Rossbach
Deutsches Elektronen-Synchrotron, D-22603 Hamburg, Germany

Abstract

Four markedly different concepts of linear colliders are presently under investigation. They may be characterised by the keywords 'X-band, S-band, two-beam, and superconducting'. Both the essential differences and the common problems are pointed out in this paper. As a basis of discussion, parameter sets of six collider study groups working on JLC/KEK, NLC/SLAC, VLEPP/BINP, CLIC/CERN, SBLC/DESY, and TESLA will be used.

1. INTRODUCTION

This paper deals with the concepts of linear colliders (LC) in the 300 GeV to 1 TeV center-of-mass energy range as they are presently under discussion. They are based on four distinct approaches: the conventional S-band (3 GHz) approach, the X-band (11 to 14 GHz) approach, the two-beam accelerator approach, and the superconducting L-band approach. Except for the X-band approach, each of them is represented by a single linear collider study group. This does not mean of course, that important R&D work is not done elsewhere. These groups are TESLA as an international effort for the superconducting cavity concept, CLIC(CERN) for the two-beam approach, and SBLC(DESY) putting forward the S-band based design. Use of X-band cavities is proposed by three studies named NLC(SLAC), VLEPP(BINP), and JLC(KEK). Note that JLC also considers an S-band and a C-band version of their collider. The main parameters of these six linear collider studies are compiled in table 1.

The information on the status of the respective activities lies beyond the scope of this paper. It may be useful, nevertheless, to point out some problems which are common to all of the designs, and to compare the different ways proposed to solve them. This comparison is all the more possible since an international committee has been founded to work out a detailed comparison of the various linear collider schemes [1]. The emphasis in the following discussion will be on the optimisation of beam power and vertical beam size. The reason is that, in order to get the desired luminosity, one unavoidably needs very high average beam power, so that power efficiency becomes an essential parameter. Depending on what one feels to be the optimum assumption on these parameters, the choice of rf frequency will have to be different. In addition, since the achievable gradient is connected with the rf frequency, the energy upgrade scenario maybe considered an issue, especially if the total length of the collider will be strictly limited.

2. HOW TO GET THE LUMINOSITY

Due to the small cross-sections of the processes of interest, high energy electron-positron linear colliders need a luminosity L of the order of 10^{33} to 10^{34} cm^{-2} s^{-1}. It is instructive to realize that L can be represented by

$$L = \frac{f_{rep} n N^2}{4\pi\sigma_x^*\sigma_y^*} = \frac{P_b \cdot N}{4\pi E\sigma_x^*\sigma_y^*} \qquad (1)$$

For the meaning of symbols, see Table 1.

Apparently, there are only three free parameters at a given collision energy: P_b, N, and the beam size at the interaction point (IP) $\sigma^*_x \cdot \sigma^*_y$.

The bunch population N cannot be increased beyond the 10^{11} level because of wakefields acting on the tail of each bunch and because of excessive beam disruption caused by the interaction with the large Coulomb-field of the opposing bunch. The vertical disruption parameter D_y scales as

$$D_y = \frac{N \cdot \sigma_s}{\sigma_y^*\left(\sigma_x^* + \sigma_y^*\right)} \qquad (2)$$

Thus, one could - at least in principle - compensate the effect of a large N on beam-beam interaction by a large beam size and a short bunch length. This would be favourable only if one operates at a small rf frequency, because only then are both the longitudinal and transverse wakefields tolerable even at large N. In fact, as is seen from Table 1, all high f_{rf} designs except VLEPP use bunch population numbers below 10^{10}. With VLEPP, one intentionally puts up with both wakefields and a large disruption factor $D_y = 215$, because the BNS damping with 'autophasing' [4] and the 'travelling focus' [5] techniques are considered powerful enough to manage the respective effects. Also, VLEPP considers the γ-γ collision option in the first place, where disruption and beamstrahlung is not an issue. In this scheme[6], two electron beams are collided with very intense laser beams just before interaction thus transferring most of the electron momentum to Compton gammas. These are collided then instead of the electron beams, which are separated by an external magnetic field before collision. Discussion of the challenge of generating the required intense laser beams is beyond the scope of this paper.

A further restriction on parameters is due to the intense synchrotron radiation called beamstrahlung which accompanies the beam disruption. It is characterized by the parameter Υ which scales as $\Upsilon \propto D_y \sigma^*_y / \sigma^2_s$. This limits the possible reduction of σ_s, besides technical

0-7803-3053-6/96/$5.00 ©1996 IEEE

aspects, in the bunch compressor. Since, for a flat beam, Υ depends only on σ_x and not on σ_y , β^*_x is decreased so far that the rms collision energy is smeared by beamstrahlung by just a tolerable amount (say $\delta p/p$ a few %, see Table 1). Afterwards, β^*_y is decreased as far as possible. The limit is given by the bunch length, because a beta function smaller than the bunch length does not increase luminosity (hour-glass effect). In fact, as seen from Table 1, all LC schemes use β^*_y close to σ_s . Another limit on β^*_y that comes into play at very high beam energies is due to the synchrotron

General parameters	**Units**	**Symbol**	**TESLA**	**SBLC**	**JLC(X)**	**NLC**	**VLEPP**	**CLIC**
Initial c.m. energy	GeV	E	500	500	500	500	500	500
Luminosity	$10^{33}\,cm^{-2}\,s^{-1}$		3.6	2.2	5.1	5.3	12	0.7-3.4
total two-linac length	km	l_{tot}	31	36	15	20	10	12.4
rf frequency of main linac	GHz	f_{rf}	1.3	3	11.4	11.4	14	30
Linac repetition rate	Hz	f_{rep}	5	50	150	180	300	2530-1210
Number of particles/bunch	10^{10}	N	3.6	2.9	0.63	0.65	20	0.8
Number of bunches/pulse		n	1130	125	85	90	1	1-10
Damping ring energy	GeV	E_d	4	3.15	1.98	2	3	2.15
Main Linac			**TESLA**	**SBLC**	**JLC**	**NLC**	**VLEPP**	**CLIC**
Avg. beam power/beam	MW	P_b	8.2	7.26	3.2	4.2	2.4	0.8-3.9
Bunch spacing	ns	τ_b	708	16	1.4	1.4	--	0.66
Bunch train length	ns	τ_p	$8{\cdot}10^5$	1984	118	125	--	0 - 6
Unloaded Gradient	MV/m	g_0	25	21	73	50	100	80
Loaded Gradient	MV/m	g_l	25	17	53	38	91	78-73
Length of sections	m	l_s	1.04	6	1.3	1.8	1.0	0.27
a/λ range		a/λ	0.30	0.16-0.11	0.20-0.14	0.22-0.15	0.14	0.2
Section filling time	ns	τ_f	$5{\cdot}10^5$	790	110	100	110	11.6
rf pulse length at cavity	μs	τ_p	1315	2.8	0.23	.24	0.11	0.0116
Pulse compression ratio			--	--	2	3.6	4.5	--
Number of klystrons		n_k	604	2517	3400	3940	1300	'2'
Peak rf power from klystron	MW	P_k	7.1	150	135	50	150	700
Avg. total AC power for rf generation (both linacs)	MW	P_{tot}	88*	142	114	102	57	100*)**
Beam parameters at interaction			**TESLA**	**SBLC**	**JLC**	**NLC**	**VLEPP**	**CLIC**
Horizontal invariant emittance	$10^{-8}\,\pi m$	ε^n_x	1400	1000	330	500	2000	300
Vertical inv. emittance	$10^{-8}\,\pi m$	ε^n_y	25	50	4.8	5	7.5	15
Horizontal β at IP	mm	β^*_x	25	22	10	10	100	10
Vertical β at IP	mm	β^*_y	0.7	0.8	0.1	0.1	0.1	0.18
rms beam width at IP	nm	σ^*_x	845	670	260	320	2000	247
rms beam height at IP	nm	σ^*_y	19	28	3	3.2	4	7.4
Bunch length	mm	σ_s	0.5	0.5	0.09	0.1	0.75	0.2
eff.beamstrahlung parameter		Υ_{eff}	0.03	0.04	0.12	0.09	0.07	0.07
rms δp/p from beamstrahlg.	%	$\sigma_{\delta p/p}$	2.9	2.8	3.2	2.4	13.3	3.5
vertical disruption		D_y	11	8.5	8.2	7.3	215	9.7
Crossing angle	mrad		0	3	6.1	20	0	1

Table 1: Main parameters of linear collider studies at a c.m. energy of 500 GeV [1-3]. For the JLC, there is also a C-band (5.7 Ghz) and an S-band (2.8 GHz) version under consideration. The choice will depend on the maximum beam energy desired in the final stage of upgrade, given a fixed total length of the tunnel. Also, a change of frequency during a later upgrade stage is possible. The luminosity is calculated in accordance to eq. (1). No enhancement due to the pinch effect has been taken into account, and no loss due to the crossing angle. For flat beams, the combination of both effects yields a luminosity enhancement factor of typically 1.5.

)For TESLA and for CLIC (drive beam) the cryogenic power is included.* *)For the single bunch version.*

radiation in the final focus quadrupole magnets [7]. The increasing difficulty with chromatic errors when reducing β^*_y is less a problem since the development of a broad-band final focus optics [8].

If one combines all these scalings and restrictions with eq. (1), it now reads

$$L = A\frac{P_b}{\gamma}\cdot\sqrt{\frac{\langle\delta p/p\rangle}{\varepsilon^n_y}} \quad (3)$$

with $A \approx 10^{36}\,cm^{-2}\,s^{-1}$, if P_b is measured in MW and ε^n_y in rad·m. As $\delta p/p$ is limited by the experiment's requirements, there are only two free parameters left in the luminosity formular: the average beam power P_b and the normalized vertical emittance ε^n_y.

In principle, ε^n_y is determined in the damping ring by misalignment tolerances or, ultimately, by intra-beam scattering. In practice, however, it could be in vain to achieve, with big technical effort, a very small ε^n_y at the exit of the damping ring because it will eventually grow in the linac due to wakefield effects if its value was chosen unreasonably small.

One concludes that, with reasonable numbers on ε^n_y and $\delta p/p$, Megawatts of average beam power are needed to keep L above the $10^{33}\,cm^{-2}\,s^{-1}$ level. Thus, the efficiency of beam power generation from wall plug power becomes an important issue. Facing the fact that there is surely an upper limit of tolerable power consumption, it is a non-trivial statement that the parameter optimization and even the choice of fundamental technical parameters like the rf frequency could have a very much different outcome if the required luminosity would be smaller by say a factor of ten.

2. THE CHALLENGE OF HIGH BEAM POWER

Realization of high beam power involves two problems:

1.
2. One has to generate a large amount of rf power with high power efficiency. Then, again with high efficiency, this rf power must be transmitted to the electron/positron beam.
3. When the beam extracts this large electric power from the accelerating cavities, there will be longitudinal and transverse field distortions induced, called wakefields. They will, in turn, act on the tail of each bunch and may still be present to some extent when the next bunch arrives, thereby causing both single bunch beam break-up and multi-bunch instabilities.

The design net efficiency η_{rf} for production of rf power for the various schemes is listed in Table 2. It is seen that all of these values lie close by in the 25 - 40 % range. It should be noted, however, that the respective values are much closer to the present-day state of the art for the lower rf frequency schemes TESLA and SBLC than for the high frequency ones. The machines differ over a wider range concerning the efficiency η_{AC} of converting ac power to beam power, see Table 2. The reason is, that the efficiency of rf power transmission to the beam is best if the rf pulse is much longer than the cavity filling time, i.e. acceleration of a long bunch train is favoured. In this case, power transmission is in a quasi steady-state. While now most collider schemes foresee the multi-bunch mode, it leads to severe difficulties with CLIC. One concludes from all that, that it is harder for high frequency machines to achieve high beam power.

	TESLA	SBLC	JLC	NLC	VLEPP	CLIC
η_{rf}/%	35	36	30	30	39	26
η_{AC}/%	19	10	5.6	8.2	8.4	1.6

Table 2: Net rf system efficiency for production of rf power [1]. For TESLA and for CLIC (drive beam) the cryogenic power is included. For CLIC, the single bunch version is meant.

With respect to wakefields, the difference is much bigger. The short-range longitudinal wake field causes an energy spread within the bunch, which is undesirable due to the chromatic effects of focusing along the linac. For scaled accelerating structures this spread is proportional to the square of the frequency f_{rf}. This is plausible if one considers the fact that for fixed gradient the stored energy per unit length in an accelerating cavity is inversely proportional to f_{rf}^2. The easiest cure foreseen for this higher order mode excitation is to increase the aperture-to-wavelength ratio a/λ when increasing the rf frequency. Unfortunately, this measure also injures the shunt impedance, i.e. one needs more power to generate the accelerating field (a superconducting linac like TESLA does not have this problem, so it can use a large a/λ value, anyway). Thus one cannot go too far in that direction. What also helps is just to increase the accelerating gradient g_0, because the stored energy scales with g_0^2 while the extracted power only scales linearly with g_0. This is of cause the most favourable way, but it is limited by efficiency considerations. Thus, one has to conclude that low frequencies are preferable also with respect to longitudinal wakefields [9].

The frequency scaling behaviour of transverse wakefields is even more pronounced as they increase with the third power of f_{rf} and linearly with the bunch population N. This is illustrated in Figure 1, where $N\cdot f_{rf}^3$ is plotted in arbitrary units versus N for those frequencies which are considered by the respective linear collider schemes. Note that a logarithmic scale is used. Although TESLA and

SBLC use N considerably larger than the X-band designs and CLIC do (again except for VLEPP), the transverse wakefields would be still smaller by up to two orders of magnitude if the other parameters were unchanged. However, $\vec{E}_\perp$ scales with $\sigma_s^{1/2}$, and the beams suffer on a

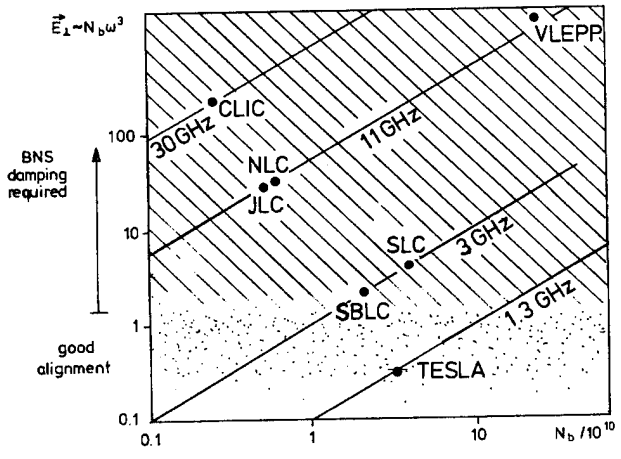


Figure 1: Transverse wakefield $\vec{E}_\perp$ as a function of bunch population N for scaled structures with frequencies as considered by the respective linear collider schemes. The hatched area indicates the region where BNS damping techniques will be indispensable, while for the dotted region good alignment of quadrupole lenses and cavities (in the 10 to 500 μm range) may be sufficient.

longer way if the accelerating gradient is smaller. Also, the cavity shape and the average β function enter. If all these effects are taken into account, the relative transverse emittance growth scales roughly as [10]

$$\Delta\varepsilon/\varepsilon \propto [N^2 \sigma_z ((f_{rf} \lambda/a)^3/g_l)^2/\varepsilon] \beta \Delta y^2_{cav}$$

if cavities are misaligned by Δy_{cav}. Figure 2 illustrates, that the relative vertical emittance growth in fact differs by orders of magnitude between various machines if no counter-measures like BNS damping are taken. The hatched area in Figure 1 indicates the region where BNS damping will be indispensable.

Besides short range wakefields there are also long range effects that can lead to multi-bunch instabilities. These long-lasting distortions are driven by Higher Order Modes (HOM) which are excited by bunches in the front of the bunch train and act on subsequent bunches. A significant reduction of HOMs has been achieved with the development of the 'Choke Mode Cavity'[11], which allows the HOMs to propagate out of the cavity while only the accelerating mode is trapped. Recently a method has been proposed to damp HOMs by stainless steel coating the iris [12].

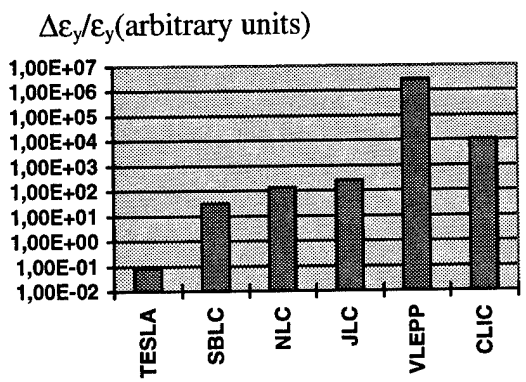


Figure 2: Relative vertical emittance growth (in arbitrary units) from transverse wakefields if cavities are misaligned by Δy_{cav} and if no BNS damping is applied.

To summarize this paragraph, it is seen that low frequency linacs can more easily achieve high beam power while still suffering much less from wakefields. In other words, in spite of higher beam power and significantly relaxed cavity alignment tolerances they can preserve smaller beam emittances. Additional advantages are

- only one stage of bunch length compressor is required
- in case of SBLC, the existing SLC in Stanford/USA, with all its experience, may be considered an existing 20 % prototype of an S-band collider.

There are, however, serious drawbacks if one concentrates on the technology for high beam power alone:

- For accelerating gradients above some 30 MV/m, the power efficiency of a normal conducting low frequency collider drops, because rf pulse compression is required (i.e. η_{rf} gets smaller and the bunch train will be shorter). Thus, an optimized high beam power collider will be very long. This might be, if not an economical, at least a political disadvantage.
- Concerning TESLA, considerable progress has been made with achieving the design accelerating field of 25 MV/m in 5-cell cavities [13], and recently in a TESLA Test Facility series production 9-cell cavity [14]. However, it remains still to be seen if even higher gradients (although not excluded from basic physics) can be supplied routinely in a long linac and if costs can be reduced sufficiently.
- It seems likely that dark currents are more serious at lower frequencies, since they have a higher probability to get trapped there.
- Multi-bunch operation is essential for high beam power operation, and it involves all the complications of multibunch-instabilities. Meanwhile no scheme except VLEPP (and maybe CLIC) is completely free of this complication, but one should be aware that it has ist roots in the requirements of high power efficiency.

3. SMALL VERTICAL EMITTANCE

The vertical beam size achieved with the Final Focus Test Beam installation at SLAC [15] was $\sigma^*_y = 70$ nm at $\varepsilon^n_y = 200 \cdot 10^{-8} \pi$ rad·m and $N = 0.65 \cdot 10^{10}$. Comparing with the respect values of the LC plans (see Table 1), one readily sees that all of them need 'small' vertical beam size at the IP. Some go, however, more than one order of magnitude below the present state of the art. Interestingly, this does not necessarily mean, that alignment tolerances in the respective damping rings are much different, because the TESLA and SBLC damping rings have to be much longer due to the longer bunch train, i.e. more focusing elements are involved.

Techniques beyond well-proven ways of alignment and orbit correction will be needed. As a means of improving the effective beam position monitor alignment, the 'beam based alignment' technique has been devised [16]. To improve cavity alignment, mechanical micro-movers, controlled by signals from HOM antennas, are under construction [17]. All beam-based correction techniques are applicable only for misalignments changing slowly compared to f_{rep}. In this respect, the low f_{rf}, low f_{rep} machines have clearly a disadvantage. On the other hand, especially TESLA can tolerate a much worse cavity misalignment (few tenths of a mm compared to less than 10 μm for X-band) and position monitor resolution because the wakefields are weak enough. Also, its large bunch spacing allows using the first bunch in a train to correct the subsequent ones.

Name	upgrade scenario	l_{tot} for 1 TeV c.m.
TESLA	double the length can still very much reduce ε^n_y	60 km
SBLC	rf pulse compression (reduces η_{AC})	30 km
JLC	start with S-band (?), upgrade with X-band	22 km
NLC	increase both length and gradient	20 km
VLEPP	double the length?	20 km?
CLIC	double the length	14 km

Table 3: Energy upgrade scenarios of LC schemes

4. UPGRADE POTENTIAL

The most essential upgrade of a 500 GeV c.m. linear collider will be a program to increase the collision energy. Table 3 illustrates the various energy upgrade scenarios proposed [1]. It is seen that most groups plan to increase the total length, not only the low f_{rf} schemes. Only the high f_{rf} machines, however, can stay within 20 km for a 1 TeV collider. Also, they have the potential to even further increase the gradient, at the expense though of further reducing η_{AC}. By learning from operational experience how to preserve extremely small ε^n_y, they might then still be able to provide the required luminosity. It is unclear yet if this is realistic and if saving total length pays off compared to the higher power efficiency of, say, a long TESLA collider.

5. CONCLUSION

It is the lesson from many theoretical as well as experimental studies performed over the last two decades, that a linear collider providing the required high luminosity can be built. It remains to be learned, however, from the various test facilities under construction now, what the most economical way and the most reliable technique will be.

REFERENCES

[1] G. Loew, T. Weiland (eds.): Linear Collider Technical Review Committee Report 1995, to be published (1995)

[2] R. Brinkmann: Low Frequency Linear Colliders, Proc. EPAC94, London (1994)

[3] W. Schnell: High Frequency Linear Colliders, Proc. EPAC94, London (1994)

[4] V. Balakin, A. Novokhatsky, V. Smirnov: Proc. 12th Int. Conf. on High Energy Accelerators, Batavia, Illinois (1983)

[5] V. Balakin: Proc. 1991 Linear Collider Workshop Protvino, Russia (1991)

[6] V. I. Telnov, Nucl. Instr. Meth. A 294, 72 (1990)

[7] K. Oide: Synchrotron-Radiation Limit on the Focusing of Electron Beams, Phys. Rev. Lett. 61, No. 15, (1988)

[8] R. Brinkmann: Optimisation of a Final Focus System for Large Momentum Bandwidth, DESY-M-90-14, (1990)

[9] G.-A. Voss: The case for the S-band Linear Collider, Proc. 1992 Lin. Acc. Conf., Ottawa, (1992)

[10] R. Brinkmann, private communication

[11] T. Shintake, et al.: High Power Test of HOM-Free Choke-Mode Damped Accelerating Structures, KEK Preprint 94-82, (1994) and Proc. 17th Int. Linac Conf. Tsukuba (1994)

[12] M. Dohlus, presented on the LC95 workshop, Tsukuba (1995); see also [17]

[13] C. Crawford, et. al.: High Gradients in Linear Collider Superconducting Accelerator Cavities by High Pulsed Power to Suppress Field Emission, Part. Accelerators, 49, 1-13 (1995)

[14] J. Graber: High Gradient Superconducting RF Systems, this conference

[15] V. Balakin, et.al.: Focusing of Submicron Beams for TeV-Scale e^+-e^- Linear Colliders, Phys. Rev. Lett. 74, No. 13 (1995)

[16]. T. O. Raubenheimer; SLAC-report 387 (1991)

[17] N. Holtkamp: The S-band Linear Collider Test Facility, this conference

TEST FACILITIES FOR FUTURE LINEAR COLLIDERS*

Ronald D. Ruth
Stanford Linear Accelerator Center, Stanford University, Stanford, CA 94309, USA

I. INTRODUCTION

For many years now there has been active research around the world towards a future linear collider with an energy of about 1 TeV. This research has led to several test facilities around the world that seek to test key aspects of the various approaches. A comparison of the approaches to the design is given in these proceedings [1]. The purpose of this paper is to review the status of the test facilities.

In Fig. 1 you see a layout of a future linear collider that illustrates all the subsystems common to the various designs. The test facilities focus on three primary areas in the linear collider: creating the low emittance beams in the injector and damping rings, accelerating the beams in the high energy linac, and focusing the beams to a small spot in the final focus.

The damping ring ring and injection is the primary focus of the Accelerator Test Facility (ATF) at KEK. The accelerator technology is the primary focus of the Tesla Test Facility Linac, the S-Band Test Facility, the NLC Test Accelerator and the CLIC Test Facility. Lastly, the Final Focus Test Beam (FFTB) [2] addresses the problems in the final focus system.

We will discuss all the test facilities above except the FFTB which has a paper devoted to it [3]. In addition to all the test facilities above it is very important to note the key experience that has been and is being gained at the SLAC Linear Collider (SLC). Most of the SLC experience is directly applicable to future linear collider designs. For example, in the NLC design the positron source, injector linac, bunch compressors and the preaccelerator linac all draw heavily on the SLC experience. In a sense the SLC is the most important test facility of all! The current status of the SLC is covered in a separate paper in these proceedings [4].

Before beginning the review of the test facilities it is useful to note that their are several other papers in these proceedings (PAC 95) that address each linear collider design, test facility and/or related technology development. We refer the reader to these more detailed accounts. The following should be considered an overview.

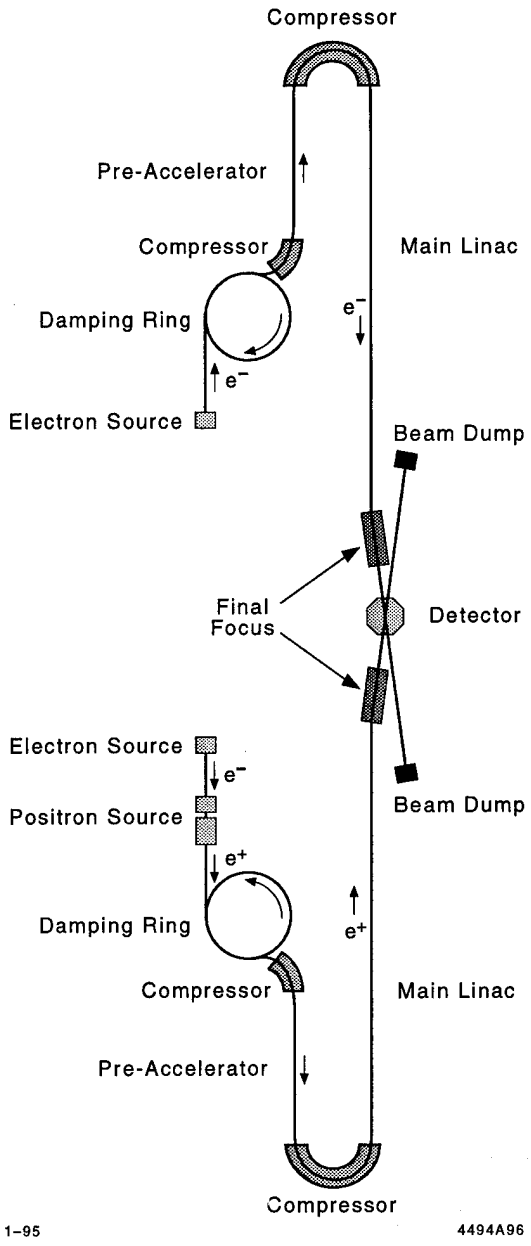


Figure 1. Schematic layout of a future e^+e^- Linear Collider.

II. The JLC: The Accelerator Test Facility (ATF)

The Japanese Linear Collider (JLC) design is based on normal-conducting linac technology. Although several options are being kept open, the initial choice of frequency was 11.424 GHz with accelerating gradients of about 100 MeV/m. Because this technology was not yet developed in the mid 1980s, the initial work began with estabilished S-band technology at 2.8 GHz.

An Accelerator Test Facility (ATF) was founded at KEK in 1988 in order to promote the linac R&D work. At first an S–band rf system was established with several 5045 klystrons sent from SLAC. High gradient tests were carried out for S–band structures. Based upon this infrastructure, R&D work for X–band linac technology was then started. Power source work has been devoted mostly to develop X–band klystrons of 100 MW class. High-gradient tests of X–band structures also were carried out, as klystrons of a few tens of megawatts became available.

In the course of the X–band work and miscellaneous studies, the main purpose of the ATF gradually became construction of a test damping ring. Its energy was chosen to be 1.54 GeV. The injector is an S–band linac of the same energy. Construction of the

*Work supported by Department of Energy Contract DE–AC03–76SF00515.

accelerator complex was started in 1991. The ring is expected to provide electron bunches with their normalized emittance as small as a required value of 5×10^{-8} rad m.

The damping ring must provide beams with the small vertical emittance given above with a repetition rate as high as 150 Hz. A lattice of the FOBO type seems promising to attain the low emittance according to simulations. A long wiggler magnet section is necessary to ensure a fast damping time. The specifications are much more stringent than those for conventional rings; therefore, it is quite desirable to verify the feasibility by constructing a test ring. A fine alignment system for magnets is a key ingredient, since the coupling between vertical and horizontal betatron oscillations must be minimized to achieve the low emittance. The emittances, both transverse and longitudinal, should be as uniform as possible among the bunches for the beam dynamics in the main linac. For this sake, the ring rf system must use damped cavities and energy-compensating cavities. Those technologies will be developed in the ATF damping ring .

Shield walls for both the injection linac and the test ring were completed in 1993. Radiation safety systems were also completed. Construction of high power AC lines and cooling water pipings for the ring was completed by the end of 1994. The injector and the first 3-m accelerator section of the linac have undergone initial tests with beam. Various beam monitors and a choke cavity structure have been also been tested with the beam. In parallel with commissioning, the construction of the linac has continued. Almost all of the accelerator structures, modulators, and klystrons for the injector linac are installed.

In the damping ring one unit section of the arc has been fabricated, comprised of a defocusing dipole magnet, a quadrupole, a sextupole, and steering magnets set on a common table with precision movers. A few wiggler magnets have also been fabricated. Prototype vacuum chambers are under fabrication and a cold test of a damped cavity was completed. A 50 kW, 714 MHz klystron has also been successfully tested. The construction of the damping ring and tests of the injector linac will be continued through 1995 and 1996; at the end of 1996 the damping ring should be completed and ready for initial tests with beam.

III. CLIC: The CLIC Test Facility

CERN is studying the feasibility of building a 0.5–2.0 TeV e^+e^- linear collider, using classical normal-conducting traveling-wave rf accelerating sections, powered by a superconducting drive linac.

The 3–5 GeV high-intensity electron drive linac runs in parallel with the main linac. The bunched drive beam is decelerated in so-called transfer structures where 30 GHz rf power is generated and fed via standard waveguide to the accelerating structures.

Periodic replacement of the energy lost by the beam to the transfer structures is made by short sections of 6 MV/m superconducting cavities driven by 350 MHz 1 MW klystrons. The superconducting cavities and klystrons already developed by CERN for LEP are ideal for this application. Generation of the rf power by a drive linac, rather than by thousands of individual klystrons, is a distinctive feature of the CLIC design and results in a particularly simple tunnel cross-section.

An obvious design aim is to make the linacs as short as possible to keep the cost down. This implies high accelerating gradients, which would normally result in a higher power requirement, but is compensated for by operating at a high frequency to maximize the rf-to-beam power conversion efficiency. CLIC has chosen to work at 80 MV/m and 30 GHz. At this frequency, wakefield effects, alignment tolerances, and fabrication problems seem just manageable, but demand state-of-the-art technology.

Limiting the emittance blowup along the main linacs in the face of strong transverse wakefields is a concern, and sets tight tolerances on the transverse alignment of the components (typically 5 μm on BPMs and accelerating sections for 50 μm initial offsets of the quadrupoles). Such tolerances can only be achieved with a beam-based active alignment system and require in particular micron resolution BPMs. Prototype BPMs based on simple E_{110} cylindrical cavities have been built and their ability to resolve such small displacements has been evaluated on the bench by exciting them with an antenna to simulate the passage of an off-axis electron bunch. The output E_{110} signal as a function of antenna position over a range of ± 1 μm clearly shows a resolution capability of < 10 nm.

CERN has built, and is currently operating, a test facility for linear collider studies (the CLIC Test Facility or CTF) to (i) study the production of short, high-charge electron bunches from laser illuminated photocathodes in rf guns, (ii) generate high-power 30 GHz rf pulses by passing bunch trains through transfer cavities for testing CLIC prototype components, and (iii) test beam position monitors.

Significant amounts of 30 GHz power can only be extracted from the CLIC section by using bunch trains. 76 MW has been generated by a 24-bunch train containing 72 nC of total charge or 3 nC per bunch. This power level corresponds to a decelerating field in the section of 123 MV/m (more than the CLIC nominal accelerating gradient). The charge per bunch which can be transmitted through the structure is at this moment limited by wakefields in the traveling wave accelerating section. The accelerating field in the second CLIC structure is determined from the difference between maximum and minimum energy gain of the beam as its phase with respect to the beam-induced rf accelerating field is varied. An average accelerating gradient of 73 MV/m was measured in this way for the best performance so far. Plans to increase the 30 GHz power generation include (i) raising the gradient in the accelerating section to reduce the effect of wakefields (ii) making shorter bunches using a magnetic bunch compressor (iii) building a new 100 nC/bunch rf gun.

CLIC Alignment Test Facility. An active alignment test facility has been built in an unused underground tunnel at CERN to study the feasibility of making controlled submicron displacements and to try out alignment systems.

The structures to be aligned, dummy accelerating sections for the moment, are supported by V–blocks on 1.4-m-long silicon carbide girders. The ends of two adjacent girders sit on a common platform which ensures continuity of position between units.

The platforms are activated by three stepping-motor-driven precision jacks (two in the vertical plane for vertical displacement and axial rotation, and one in the horizontal plane). The

setup is equipped with linear and angular displacement transducers (0.1 μm and 10 μ-rad resolution respectively) and is piloted remotely from a small computer. After deliberate misalignments of 1 mm, the system which is programmed for automatic alignment with respect to the transducers, settles back to nominal positions within < 1 μm.

The CESTA Test Facility. A collaboration to study the use of an FEM to create the CLIC drive beam exists between CERN and the Centre d'Etudes Scientifiques et Techniques d'Aquitaine (CESTA) in Bordeaux. The aim is to use a helical wiggler to bunch a beam from an induction linac, and in a later phase to use this beam to generate power in a CLIC transfer structure. A preliminary experiment to measure the bunching produced by a helical wiggler using the beam from a gun-diode is already underway.

The MIT Test Facility. CERN is collaborating with MIT to test CLIC prototype components. MIT has a gun- diode driven FEL that produces 20-ns-long, 60 MW power pulses at 33 GHz. This facility is at present being used to test a 25-cell prototype CLIC accelerating section.

IV. The SBLC: The S-Band Test Facility

Among the different design studies for a next generation e^+e^- linear collider, the SBLC approach follows the concept of a relatively low rf-frequency ω_{rf} and a moderate accelerating gradient g. In the SBLC, conventional traveling wave accelerating structures at 3 GHz are used running at a gradient of 17 MV/m. The SBLC linear collider study is pursued at DESY in the frame of an international collaboration with institutes in China, France, Germany, Japan, Netherlands, Russia, and USA contributing to the technical R&D and/or the design of the 500 GeV collider.

The goal of the SBLC test facility under construction at DESY is to construct and test the basic components required for the 2×250 GeV linear accelerators. The test linac consists of an injector providing bunch trains similar to those to be used in the collider. Two 150 MW klystrons (built by SLAC) power four 6-m-long accelerating structures. A beam diagnostics station is foreseen to measure bunch to bunch offsets as well as single and multibunch energy-spread. The injector provides a 6 A pulse out of a 90 kV gun with a duration of 2 ns. This pulse is compressed longitudinally by more than a factor of 200 resulting in a bunch length of $\approx$ 3 mm. Although longer than the final design bunch length, this value is sufficient to study most multibunch and beam dynamics effects. The subharmonic cavities and the vacuum system will be assembled and installed during 1994 and be commissioned early 1995.

Recently, the first klystron has reached its full design parameters in rf tests at SLAC. Conventional line-type modulators are foreseen for pulsing the klystrons. As an alternative solution a hard tube switching device is also under study at DESY. A klystron test stand for the 150 MW klystron with water loads and further required infrastructure is under construction.

The design of the accelerating sections concentrates on the first series production of 5.2-m-long structures for the DESY injector linac, which are very similar to the test facility structures. Nine-hundred cells for 6 sections (from overall 14) have been ordered from industry and are being brazed at DESY. Horizontal or vertical brazing, vacuum- or hydrogen-atmosphere ovens or inductive heating are still being investigated. A cup-tuning machine to match the structure for the accelerating wave after brazing and before final installation is now operating.

Low power test models of the symmetric high power couplers have been manufactured and matched to an accelerating structure while the high power versions are scheduled autumn 1994. Different types of additional couplers required for the HOM damping and/or measurement of the beam induced higher order mode power are being investigated. After brazing and tuning, the sections for the test facility will be mounted on different types of temperature insensitive girders (glass ceramics, carbon fiber composite and heat shielded stainless steel) to keep the six meters of copper waveguide straight within 15 μm rms. Every girder is equipped with micromovers at both ends to allow for ± 1.5 mm offset in both directions.

Magnets, structure supports, and precision movers, as well as methods to compensate ground vibrations, are investigated. The design of the linac quadrupoles completely decouples the coil windings from the iron yoke, which automatically minimizes the vibration effects due to cooling water flow. Although the effects which have been described before will not affect the final emittance in the test accelerator, feedback systems and control loops will be tested on the supports and girders, which have been designed to fit the tunnel requirements and the minimum height for final installation.

V. TESLA: The TESLA Test Facility Linac (TTFL)

The TESLA [5] approach uses a superconducting RF system to accelerate the beam to high energy. The important issues that need to be addressed in the Tesla Test Facility Linac (TTFL) are somewhat different than those in the normal conducting case. There are both cost and technical factors to be considered. On the cost side the achievable gradients need to be raised from the 5 MeV/m typical of existing storage ring cavities to 20 or 25 MeV/m. The cost per unit length of the accelerating cavity plus cryostat needs to be lowered a factor of five to bring the price to about 50k$/m to give a competitive cost per MeV figure. Another source of concern is the relative delicacy of the superconducting state. How reliable would such a system be in the face of the realities of vacuum and cryo system failures? Will it be possible to recover from such a failure by in situ processing? At the long rf wavelength, which is a strength of the SC approach, electrons present in the accelerator vacuum can be more easily captured from rest to make parasitic beams. These parasite beams could perhaps sap energy from the main beam and perhaps cause unwanted cryo losses and beam background in addition to instabilities of the wanted beam. Because of the very high Q of the cavities, small changes in dimension can make large changes in amplitude and phase of the accelerating wave. The pressure caused by the growing stored energy during the pulse can make such changes, the so-called Lorentz detuning. Can an economical cavity stiffening with active control scheme be found? Finally, the large beam power which is on the one hand a virtue implies the need for the most powerful positron source of all the approaches and gives the challenge of safe disposal of the high beam power in addition. Progress in all

of these areas has been made and a plan to demonstrate solutions to many of them put in place.

A 500 MeV TESLA Test Facility Linac (TTFL) is now under construction at DESY. It will consist of four cryomodules of a type that could be used in a linear collider. Each module contains eight 1 m, nine-cell cavity units, plus a focusing doublet assembly with beam monitors. Each cavity subunit has its own couplers. Two cryomodules are driven by one klystron/modulator set. An injector section brings the initial beam up to 15 MeV nominal before introduction into the TTFL proper. A beam analysis station will be installed both after the injector and at the high energy end of the TTFL. The linac will be installed in Halle 3 at DESY adjacent to the recently completed cavity chemical processing area, with cleanrooms, vertical test cryostats, and rf power supply for cavity testing and high power pulse processing (HPP). The first cavities and cryostats have for the first cryomodule have arrived at DESY and initial cavity tests have begun. In a prototype processing and test setup at Cornell, several multicell cavities have been chemically processed and subjected to HPP. Initial tests with HPP at DESY have also been started. HPP has been quite effective in raising the achievable gradient. After exposure to air, HPP was successful in recovering the gradient. How this will apply in a linac environment must await the completion and operation of the TTFL now expected in the 1997–1998 time frame. Experience with the facility will yield information about many of the critical issues cited above; for example, dark current, Lorentz detuning, cost, robustness against vacuum or cryogenic failures, and so on.

VI. The NLC: The Next Linear Collider Test Accelerator (NLCTA)

The NLC uses positron and electron sources similar to those in the SLC. Much of the early acceleration is done with S-Band as in the SLAC linac. The Damping Ring is similar to the ATF Damping Ring described earlier. The FFTB is addressing the Final Focus system issues. The acceleration in the NLC is accomplished with an 11.4 GHz RF system (X-Band) designed to accelerate the beam with gradients in the range of 50-85 MV/m. The purpose of the NLC Test Accelerator is to bring together all the separate developments on X-band in a model of a section of the NLC linac.

The NLCTA is a high-gradient X-band linac consisting of six 1.8 m-long accelerator sections. These sections are fed by three 50 MW klystrons, which make use of SLED–II pulse compression to increase the peak power by a factor of four. This yields an acceleration gradient of 50 MV/m, so that the total unloaded energy gain of the beam in the X–band linac is 540 MeV. The NLCTA parameters are listed in Table 1. The right-hand column of Table 1 lists the parameters for an upgrade of the X–band linac to 100 MV/m by the use of six 100 MW klystrons.

The NLCTA injector will consist of a 150 kV gridded thermionic cathode gun, an X–band prebuncher, a capture section with solenoid focusing, and a rectangular chicane magnetic bunch compressor.

The high-gradient accelerator will be fed with rf power through overmoded circular waveguides which penetrate the shielding blocks above the accelerator. Four 50-MW klystrons will be positioned along the accelerator, outside the shielded enclosure. Each klystron is powered by an independent modulator, allowing the flexibility needed for multibunch energy control and adequate power for an upgrade to a 85-MV/m accelerating gradient with six 75-MW klystrons, as indicated in Table 1. Each klystron feeds a SLED–II pulse compressor. The pairs of delay lines of the SLED–II pulse compressors are overlapped, parallel to the accelerator, outside the shielding. The output of each SLED–II is split to feed two accelerator sections. In the case of the injector, the SLED–II output is split to feed the two short injector sections to provide overhead for beam loading. The first three klystrons have exceeded NLCTA specifications (50 MW, 1.5 μs), and one is presently in regular operation testing the NLCTA pulse compression system and the 1.8 m accelerator section described below.

Table I
NLCTA rf System Parameters.

Parameter	Design	Upgrade
Linac unloaded energy gain	540 MeV	1080 MeV
Linac active length	10.8 m	10.8 m
Unloaded accelerating gradient	50 MV/m	85 MV/m
Injection energy	90 MeV	90 MeV
rf frequency	11.424 GHz	11.424 GHz
Number of klystrons	3	6
Klystron peakpower	50 MW	75 MW
Klystron pulselength	1.5 μs	1.5 μs
rf pulse compression power gain	4.0	4.0
Phase advance/cell	2 π/3	2 π/3

For the NLCTA, we plan to use a detuned structure which is a $2\pi/3$ "constant-gradient-like" structure modified every half meter to include four symmetric pumping holes. These holes lead to parallel vacuum manifolds, which provide sufficient pumping speed despite the small beam aperture. The cavities are machined to provide a precise mechanical reference from the inside dimensions to the exterior of the structure.

In order to achieve the reduced wakefield, the structure is configured to be very nearly constant gradient. The decoherence of the wakefield between bunches will be achieved by a Gaussian distribution of HOM frequencies with a standard deviation of 2.5%, which results in a Gaussian decay in time for the initial wakefield. This distribution can be obtained by tailoring a constant-gradient section so that more cells are near the central frequency, while fewer are near the ends of the frequency band. This choice results in a structure in which the iris size along the structure first decreases rather quickly, then decreases slowly in the middle, and finally decreases quickly along the structure towards the output end.

With this distribution of HOMs, the wakefield decoheres to less than 1% of its peak value. This decoherence is sufficient to eliminate beam breakup in the NLC or NLCTA. Because of

the low injection energy, the NLCTA has a sensitivity to transverse wakefields comparable to the much longer NLC linac. The NLCTA will permit the verification that detuned structures can indeed suppress wakefields to the levels necessary for stable acceleration.

The first detuned accelerator structure has been completed and tested successfully at high gradient. In addition, the resulting wakefield was measured in ASSET in the SLC and was found to agree quite well with theoretical predictions. The second structure plus the two injector structures are presently in fabrication.

A magnetic spectrometer has been designed that will analyze the bunch train after acceleration in the linac in order to determine beam energy, beam-energy spread, and bunch-to-bunch offsets. The optics in the beam analysis region allow for the measurement of emittance in both transverse planes. A vertical kicker magnet upstream of the spectrometer provides a method for separating the bunches vertically so that the energy, energy-spread, and horizontal offsets can be independently measured along the bunch train. After initial commissioning, an extensive set of experiments is planned to verify that the NLCTA can indeed stably accelerate trains of low-emittance bunches suitable for a full-scale NLC.

The NLCTA is proceeding on schedule. The accelerator shielded enclosure is complete and all infrastructure is in place (girders, cable trays, water, lights, racks, and control room). All the magnets are complete and installed in the enclosure, power supplies are installed. The prototypes for the klystron and accelerator structure have performed at NLCTA specifications. Additional klystrons and structures are in fabrication. The prototype of the pulse compression system has been tested up to full power. The injector tests are planned for the fall of 1995, and the full NLCTA should be complete by end of 1996.

VII. SUMMARY and CONCLUSION

During the past several years there has been a tremendous amount of progress on Linear Collider technology world wide. This research has led to the construction of the test facilities described in this report. Some of the facilities will be complete as early as the end of 1996, while others will be finishing up around the end 1997. Even now there are extensive tests ongoing for the enabling technologies for all of the test facilities. At the same time the Linear Collider designs are quite mature now and the SLC is providing the key experience base that can only come from a working collider. All this taken together indicates that the technology and accelerator physics will be ready for a future Linear Collider project to begin in the last half of the 1990s.

VIII. ACKNOWLEDGEMENTS

The information contained in this paper was contributed by many people, K. Takata, I Wilson, J.P. Delahaye, R. Brinkman, N. Holtkamp, T. Weiland, M. Tigner and H. Edwards. I would like to thank them for their input.

References

[1] J. Rössbach, "Options and Trade-Offs in Linear Collider Design," in these proceedings.

[2] The FFTB Collaboration: Deutsches Elektronen–Synchrotron, DESY, Hamburg, Germany; Fermi National Laboratory, Batavia, IL, USA; The Budker Institute for Nuclear Physics, Russia; Laboratoire de l'Accelerateur Lineaire, Orsay, France; Max–Planck–Institute, Munich, Germany; National Laboratory for High Energy Physics, KEK, Tsukuba, Japan; and Stanford Linear Accelerator Center, Stanford University, tanford,CA, USA.

[3] K. Oide and FFTB Collaboration, "Results of Final Focus Test Beam," in these proceedings.

[4] P. Emma, "The Stanford Linear Collider," in these proceedings.

[5] The TESLA Collaboration: CERN, Cornell, CE–S DAPHNIA, DESY, Fermilab, Gesamthochschule Wuppertal, IHEP Beijing, INFN Frascati, LASA Milan, IPN Orsay, Johan-W. Goethe U. Frankfurt, KFK Karlsruhe, LAL Orsay, SEFT Helsinki, TH Darmstadt, TU Berlin, TU Dresden, UCLA Los Angeles.

Channel Guided Lasers for Plasma Accelerators

H. M. Milchberg[a], C. G. Durfee III[a], and T. M. Antonsen[b], and P. Mora[c]
[a]Institute for Physical Science and Technology and [b]Institute for Plasma Research
University of Maryland
College Park, MD, USA 20742
[c]Centre de Physique Théorique, Ecole Polytechnique
91128 Palaiseau France

ABSTRACT

The recent demonstration of optical guiding of high intensity laser pulses in plasma waveguides [C.G. Durfee III and H.M. Milchberg, Phys. Rev. Lett 71, 2409 (1993)] has opened the way to new advances in the development of compact laser-driven electron particle accelerators. We review plasma waveguide properties relevant to intense pulse guiding and electron acceleration and show that the shock driven channels described here are well suited for stabilization of a large class of laser-plasma instabilities deleterious to high intensity guiding over long distances.

1. INTRODUCTION

Calculations show that a typical requirement for producing a 1 GeV/cm laser-plasma wake field is to propagate a 10^{18} W/cm^2 laser pulse for ~1 cm in a plasma of electron density 10^{18} cm^{-3} [1]. Until recently, achieving such extended propagation distances for intense pulses was an unsolved problem. Our demonstration [2] of high intensity optical guiding has made possible the serious investigation of laser-plasma-based accelerator schemes, as well as the development of nonlinear optics based short wavelength light sources [3] and soft X-ray lasers [4]. To date, pulses of intensity above 10^{15} W/cm^2 have been guided up to 90 Rayleigh lengths (~3 cm) in our experiments, and this constitutes the highest intensity-interaction length product ever achieved. Up to this intensity range, guiding has appeared to be approximately linear. However, accelerator applications require the guiding of laser pulses which are short and relativistically intense ($\gtrsim 10^{18}$ W/cm^2 at λ~1μm), where the electron response to the field has relativistic corrections, charge (electron) displacement becomes significant, and strong Raman instabilities can be excited in the underlying plasma medium. We show below show that under conditions characteristic of our plasma waveguides, these instabilities can be greatly reduced or eliminated.

2. PLASMA WAVEGUIDE

As an illustration of how the plasma waveguide is formed, Fig. 1 shows a calculation of gas response under typical pressure and laser conditions used in our experiments. The model [1] includes tunneling ionization in the laser field, inverse bremsstrahlung heating, thermal conduction (gradient based or flux-limited), and collision-based ionization and recombination. The breakdown spark drives a radial shock wave in the ion density, leaving a plasma density minimum on axis appropriate for guiding a laser pulse. The important hydrodynamic timescales of experimental relevance are those for shock generation, $\tau_s = \lambda_{ii}/c_s$, and for column evolution, $\tau_c = w_0/c_s$. Here, λ_{ii} is the ion-ion collisional mean free path, c_s is the local sound speed, and w_0 is the laser spot size. For typical experimental parameters of gas pressure 5-300 torr and laser spot size w_0=1-10μm, τ_s ~10-100 ps and τ_c~0.1-1 ns [5].

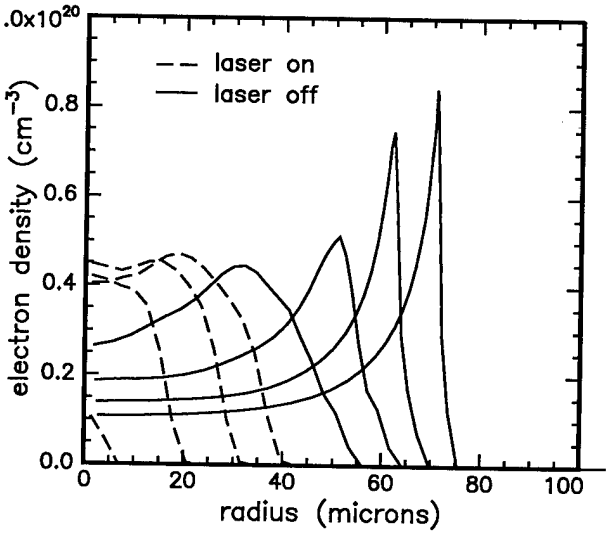


Figure 1: Calculation of 150 torr N_2 response to a 100 ps FWHM pulse of peak intensity 5x10^{13} W/cm^2, spot size w_0 = 10 μm, and λ =1 μm.

The laser used in the initial experiments is a 10 Hz Nd:YAG regenerative amplifier system which can produce 400 mJ, 100ps pulses at λ=1.064μm and 200 mJ, 70 ps pulses at 0.532μm. The pulses are split, with ~200-300 mJ total in 0.532 and 1.064 μm directed to an axicon lens, and up to 100 mJ directed to a waveguide coupling lens. Alternatively, a synchronously amplified dye laser pulse of up to 5 mJ energy at 250fs pulsewidth can be coupled into the plasma waveguide. An optical delay provides -1 to 12 ns delay between the axicon (waveguide generating) pulse and the lens (coupling) pulse. The axicons used are glass cones, with base angles 20° to 35°.

0-7803-3053-6/96/$5.00 ©1996 IEEE

An incident beam refracts at the cone surface, forming a conical wave which interferes with itself, resulting in a Bessel function field profile $E(r,z)=|E_0(z)|^2 J_0^2(krsin\gamma)$, where $|E_0(z)|^2$ depends on the transverse field profile incident on the axicon and γ is the angle with the optical axis of the conical wave normal [5]. The first radial field zero is independent of z for a conical axicon surface and a parallel input beam, resulting in an extended focus of constant spot size. For the 35° axicon, the first zero occurs at r_0~1μm and the focus length is L~1 cm for an input beam radius of 0.8 cm. The $\tau_p < 100$ ps pulses used here are well-suited to the plasma dynamics, since $\tau_p \leq \tau_s$ and $\tau_p < \tau_c$, and the plasma is heated by the channel creation pulse before it evolves hydrodynamically.

3. WAVEGUIDE MODE PROPERTIES

A condition on the modes that will be supported by a plasma channel can be estimated by assuming a refractive index $n(r)= 1- 1/2\, N_e(r)/N_{cr}(r)$ with a parabolic electron density profile $N_e(r)=N_e(0)+N_{cr}(r/a)^2$, where a is a curvature parameter. For a "finite" parabolic channel with constant electron density beyond a radius r_m ($n(r)=n_{min}$ or $N_e(r)=N(r_m)=N_e^{max}$ for $r>r_m$), approximate cutoff and guiding conditions, respectively, are [6]:

$$N_e(r_m) - N_e(0) \geq \frac{(2p+m+1)^2}{\pi r_e r_m^2}\ ; \qquad N_e(w_{ch}) - N_e(0) = \Delta N_e = \frac{1}{\pi r_e w_{ch}^2} \tag{1}$$

Here r_e is the classical electron radius (2.8×10^{-13} cm), $N_e^{min}=N_e(0)$, $\Delta N_e(w_{ch})=N_e(w_{ch})-N_e(0)$, $p\geq0$ and $m\geq0$ are radial and azimuthal mode indices, and w_{ch} is the $1/e$ field radius of the $p=0$, $m=0$ mode. For a non-parabolic infinite channel, these conditions are still a good approximation [6]. From Eqn. (1), lowest order propagation of a spot size $w_0=w_{ch}=10\mu m$ requires $\Delta N_e \approx 10^{18}$ cm^{-3}. Guiding of higher order modes requires a greater electron density difference and/or channel radius r_m. As seen in Fig. 1, the electron density of the real channel decreases beyond the shock for $r>r_m$ so that a mode below but near the cutoff of Eqn. (1) should tunnel or "leak". Waves close to cutoff appear to be guided, but have non-negligible amplitude outside r_m, where the radiation diverges at a small angle with respect to the channel axis [6].

As indicated by Eqn. (1), adjusting the gas pressure and thus the plasma density should determine the mode structure supported by the waveguide. We have demonstrated experimental control over single mode, multimode and leaky mode propagation regimes [6]. Evidence of leaky mode propagation is shown in the logarithmic-scaled lineouts of Fig. 2. The scattered intensity is observed to decrease exponentially along the channel, with reduced attenuation and increased exit scattering as delay increases (indicating greater channel throughput). This attenuation is not due to inverse bremsstrahlung absorption, for which calculations show a bleaching effect as the guided pulse heats the plasma [5]. The enhanced scattering at the entrance and exit is due to Fresnel reflections of the guided pulse from the near-discontinuity in index at the shock wave interface which propagates away from the channel ends. This index change, however, is not enough to refract the entering and exiting pulse [5].

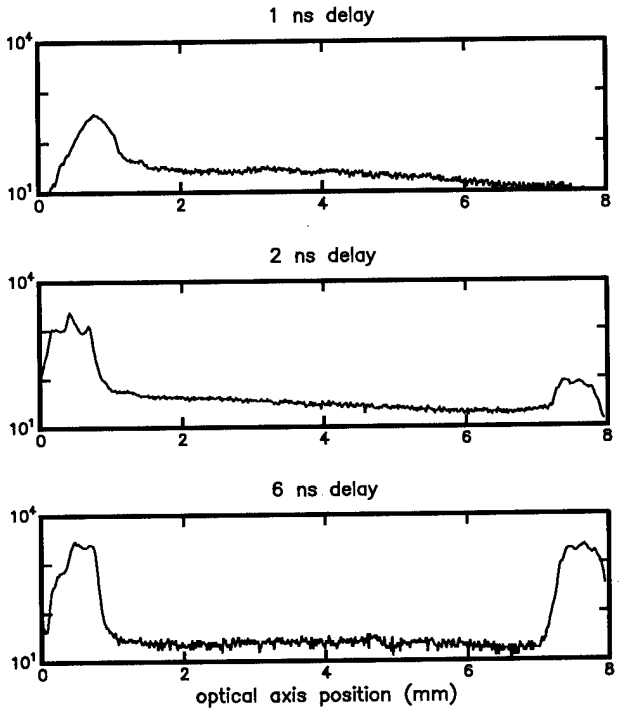


Figure 2: Full channel scattering image lineouts showing leaky mode propagation, for a channel in which the lowest order mode is not well confined at early delays. Confinement improves with increasing delay (and r_m), consistent with Eqn. (1). The injected pulse enters from the left.

4. ULTRA-INTENSE PULSE PROPAGATION

Recently, it has been shown that intense laser pulses suffer from instabilities of the Raman type in which the plasma spontaneously generates modulations at the plasma frequency and the laser light is scattered [7-12]. These instabilities prevent the propagation of smooth pulses of duration significantly greater than the plasma period and have been the subject of theoretical and experimental investigation.

One of the most dangerous instabilities involves the coupling of the Raman and self-focusing mechanisms [7-9]. It results in the scattering at small forward angles of the laser light. If the transverse structure of the laser pulse is initially

the lowest order Gaussian mode of propagation, one can think of the small angle forward scattering of the laser light as the excitation of higher order transverse modes of propagation. To the extent that diffraction is weak these higher order modes are not significantly damped and the instability which excites them is strong. In fact, for pulses of peak power P close to the critical power P_c for self-focusing [12] ($P_c = 16.2(\omega/\omega_p)^2\ 10^9$ W, where ω is the frequency of the laser, $\omega_p = (4\pi N_e e^2/m)^{1/2}$ is the plasma frequency based on the ambient electron density N_e, and e and m are the charge and mass of the electron), the pulse will acquire modulation in a time

$$t_m \approx T_R \frac{1}{k_p L} \frac{P_c}{P} \qquad (2)$$

where $T_R = kw_0^2/2c = z_0/c$ is the Rayleigh time, $k=(\omega^2-\omega_p^2)/c$ is the laser wave number in a uniform plasma, w_0 is the laser spot size ($1/e$ electric field radius), z_0 is the Rayleigh length, L is the length of the pulse and $k_p = \omega_p/c$ is the plasma wave number. Thus, for relativistically intense pulses no shorter than the plasma period, the modulations appear in a Rayleigh time. Propagation of pulses over distances greater than a Rayleigh length will be more effective if these instabilities are avoided.

Recent theoretical studies [13] have shown that propagation in leaky channels has important consequences for ultra intense pulses which might exhibit the previously mentioned side scattering instabilities. In particular, as the instability can be regarded as the excitation of a higher order radial mode of propagation, the instability will be suppressed in a leaky channel where the higher order modes are poorly confined, and essentially damped. This stabilization mechanism can be expected to be important not only for the coupled Raman-self focusing instability, but also for the 'laser hose' instability [11] in which the centroid of the laser light is displaced. The mechanism should not seriously influence the growth of either pure forward [10] or the large angle Raman side scattering perturbations [7]. However, these instabilities are less severe in their effects on the laser pulse. In particular, the large angle side scatter instability is only convectively unstable in the pulse frame and may saturate at low amplitude due to particle trapping, while the growth rate for the pure forward instability is smaller than that of the coupled Raman-self focusing instability in a tenuous plasma.

In order to illustrate the effect of a leaky channel on the propagation of an intense pulse we show the results of a numerical simulation of the laser pulse evolution. The system of equations solved describes the interaction of the laser with a weakly nonlinear, weakly relativistic, cold fluid plasma. The following parameters were chosen: normalized laser amplitude, $a_0 = eA/mc^2 = 0.33$, normalized pulse length $k_pL = 60$, and width $k_pw_0 = 10$, where A is the vector potential of the laser field. These parameters correspond to a 100 femtosecond laser pulse of energy 0.15 Joule and $\lambda = 0.8$ μm (corresponding to the Ti:Sapphire laser under construction at the University of Maryland), focused to a 10 μm radius in a plasma of density $2.83\text{x}10^{19}\text{cm}^{-3}$. Figure 3 shows plots of the laser intensity at four times during the simulation for a case in which the ambient plasma density is uniform. This pulse is moderately long, $k_pL = 60$, and is expected to be subject to the Raman - self focusing instability [7]. Indeed, the plots illustrate the development of the instability and show its detrimental effect on laser pulse propagation. After several Rayleigh times a large fraction of the pulse energy has been scattered out of the simulation region. It can also be seen that the head of the laser pulse diffracts [14] even though the body self-focuses.

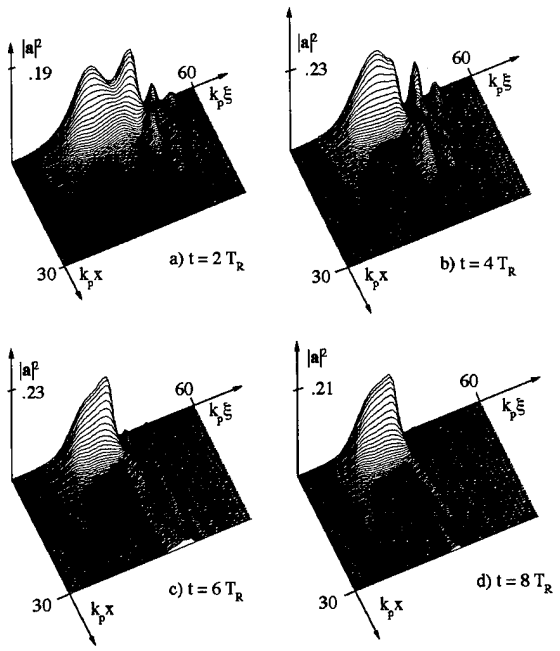


Figure 3: Time evolution of the laser pulse for a uniform plasma. A position coordinate local to the pulse is $\xi=ct-z$. The laser pulse propagates to the left.

Figure 4 shows intensity plots for the same laser parameters for propagation in a leaky channel. Here the peak density is taken to be $2.83\text{x}10^{19}\text{cm}^{-3}$ and the density on axis is 91 % of the peak value. The density profile is quadratic out to a radius $r=r_m=15$ μm, and decreases linearly to zero at $r=21$ μm.

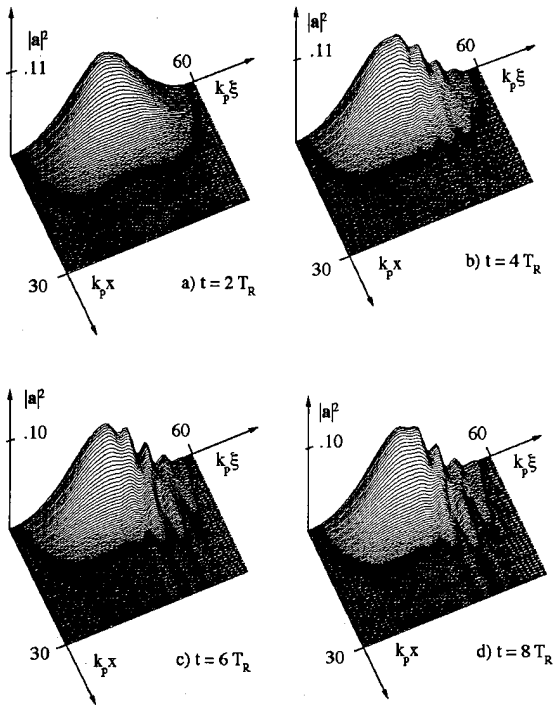


Figure 4: Time evolution of the laser intensity for a leaky channel. The laser pulse propagates to the left.

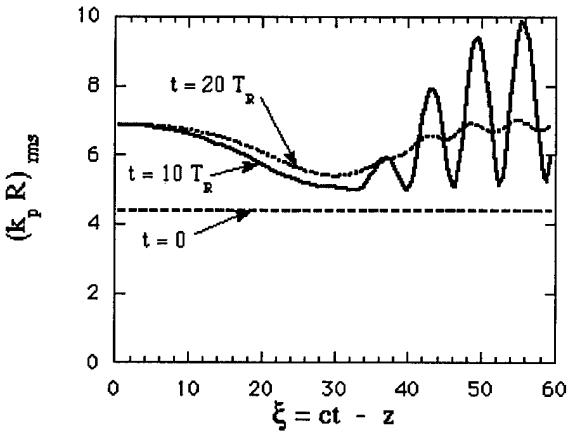


Figure 5: Root mean square radius of laser pulse as a function of distance back from the head for three different times. Here $R=w_0$.

Compared with the simulations of Fig. 3, the laser pulse retains its shape and energy. Small ripples are visible on the trailing edge of the pulse, indicating the presence of some residual instability. However, the pulse propagates intact for a long period of time as seen in Fig. 5, in which the root mean square 1/e field radius is plotted for three different times. By t=20 T_R , the pulse has reacquired a relatively smooth shape with only a slightly reduced amplitude ($|a|^2$ =0.08).

The above simulations are based on a cold plasma fluid model. Use of this model prevents one from treating situations where the plasma motion reaches the wavebreaking limit and where fast electrons are generated in the interaction. In addition, fluid models contain a mathematical singularity at zero plasma electron density which prevents their use when the electrons are totally expelled from the axis of the laser propagation (electron cavitation). Such features are strong limitations of the fluid models in the high intensity regime. An alternative to the fluid models is the particle-in-cell technique [15]. This technique follows the evolution of the laser radiation on the short timescale associated with the laser period, and thus is computationally intensive and restrictive in the parameters that can be studied.

We have developed a novel particle model to describe the long-time plasma behavior under the action of an ultrahigh intensity (of the order of 10^{18} W/cm^2 or more), short laser pulse (1 psec or less). Among the effects we are able to simulate are the following: (i) Relativistic focusing for short laser pulses over long distances (> 30 z_0) with total electron cavitation in the laser channel and strong modification of the Raman type plasma instabilities; (ii) acceleration of plasma electrons to relativistic energies in the wake of the laser pulse; (iii) plasma wave breaking; (iv) electromagnetic plasma wakes; and (v) high field ionization of background gas.

We illustrate this code with the following parameters: a_0 =1, k_pL=40, k_pw_0=4, for propagation in a uniform plasma. The pulse is about twice the critical power for relativistic self focusing [12]. Figure 6 shows a plot of the laser intensity after 8 Rayleigh lengths of propagation. As expected, trailing ripples are seen, indicating that the pulse is subject to the Raman-self focusing instability, and the pulse head diffracts as usual due to a cancellation between the effects of relativistic self-focusing, and forward charge displacement due to the ponderomotive force of the pulse [9]. However, the instability develops slightly slower than predicted by the weakly nonlinear model of Ref. 7. In this case, we observe a total expulsion of the electrons and stabilization of the Raman instability in the bulk of the laser pulse. As a result, the pulse propagates over a large distance (more than 30 Rayleigh lengths). Figure 7 shows the electron density corresponding to Fig. 6. One observes total electron cavitation where the laser intensity is large, enhancement of the density on the sides, and a strong peak behind the laser pulse due to electrons which return towards the pulse axis under the action of the charge separation field. Suppression of Raman instabilities may be attributed to a number of effects.

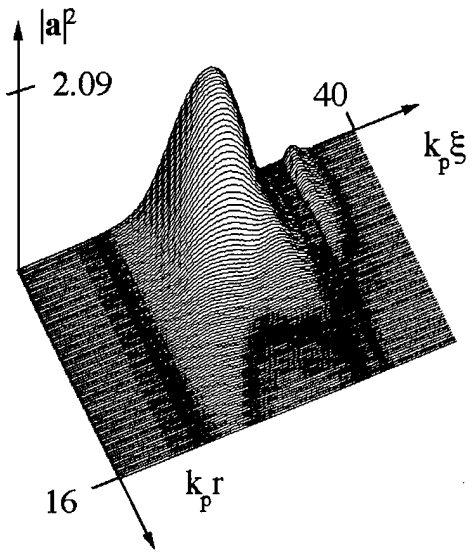


Figure 6: Pulse intensity at $z=8z_0$ for a pulse with initial length $k_pL=40$, width $k_pw_0=4$ and amplitude $a_0=1$.

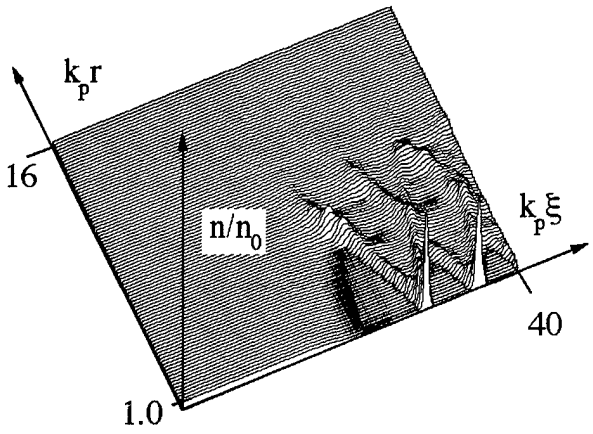


Figure 7: Electron density corresponding to Fig. 6, showing complete cavitation, and leading and trailing peaks.

The electron density is reduced where the laser intensity is greatest so that the plasma channel is inhomogeneous (disturbing the plasma wave resonance), and the channel density has a maximum at a radius just greater than the spot size. This last effect may contribute to enhancing the diffraction of radiation which is sidescattered, and thus suppresses side scattering instabilities as in the leaky channel case shown above in Figs. 4 and 5.

Successful stabilization of Raman instabilities and elimination of diffraction of the head of the pulse via preformed channel guiding will increase the ultimate propagation length of the laser pulse, and both experiments and calculations involving preformed channels are underway. In a tenuous plasma, the laser pulse loses energy while conserving the quantity $\int d^3r\, \omega|A|^2$, the laser "action". In the process, the frequency of the laser light is steadily down shifted and the amplitude of the laser electric field decreases with propagation distance, but the vector potential and plasma electron quiver momentum increases. Thus, as the pulse propagates, the plasma wake becomes more relativistic, as desired for accelerator purposes.

REFERENCES

[1] T. Tajima and J.M. Dawson, Phys. Rev. Lett. **43**, 267 (1979).

[2] C.G. Durfee III and H.M. Milchberg, Phys. Rev. Lett. **71**, 2409 (1993).

[3] H.M. Milchberg, C.G. Durfee III, and T.J. McIlrath, submitted for publication.

[4] H.M. Milchberg, C.G. Durfee III, and J. Lynch, J. Opt. Soc. Am. B. **12**, 731 (1995).

[5] C.G. Durfee III, J. Lynch, and H.M. Milchberg, Phys. Rev. E **51**, 2368 (1995).

[6] C.G. Durfee III, J. Lynch, and H.M. Milchberg, Opt. Lett. **19**, 1937 (1994).

[7] T. M. Antonsen, Jr. and P. Mora, Phys. Rev. Lett. **69**, 2204 (1992) and Phys. Fluids **B5**, 1440 (1993).

[8] N. E. Andreev, L. M. Gorbunov, V. I. Kirsanov, A. A. Pogosova, and R. Ramazashvili, Pis'ma Zh. Eksp. Teor. Fiz. **55**, 551 (1992).

[9] P. Sprangle, E. Esarey, J. Krall, and G. Joyce, Phys. Rev. Lett. **69**, 2200 (1992).

[10] W. B. Mori, C. D. Decker, D. E. Hinkel, and T. Katsouleas, Phys. Rev. Lett. **72**, 1482 (1994).

[11] P. Sprangle, J. Krall, and E. Esarey, Phys. Rev. Lett **73**, 3544 (1994); G. Shvets and J.S. Wurtele, Phys. Rev. Lett. **73**, 3540 (1994).

[12] G. Schmidt and W. Horton, Comments Plasma Phys. Controlled Fusion **9**, 85 (1985).

[13] T.M. Antonsen, Jr. and P. Mora, Phys. Rev. Lett., in press.

[14] P. Sprangle, E. Esarey, and A. Ting, Phys. Rev. Lett. **64**, 2011 (1990).

[15] C. D. Decker, W. B. Mori, and T. Katsouleas, Phys. Rev. E **50**, R3338 (1994).

INVERSE ČERENKOV ACCELERATOR RESULTS

W. D. Kimura, STI Optronics, Inc., 2755 Northup Way, Bellevue, WA 98004 USA

Laser acceleration experiments of relativistic electrons utilizing the inverse Čerenkov effect, whereby a gas slows the phase velocity of the laser light to match the electron velocity, have recently demonstrated >30 MeV/m acceleration gradients over a 12-cm interaction length using a ~580-MW CO_2 laser beam. These experiments were performed at the Brookhaven National Laboratory Accelerator Test Facility (ATF). With a 5-GW laser pulse, an energy gain of >12 MeV is predicted over a 20-cm interaction length corresponding to >60 MeV/m acceleration gradient. Future experiments will examine prebunching the electrons to optical wavelengths and staging the acceleration process. The CO_2 laser is also being upgraded to produce higher peak power. With 250-GW peak power, the goal is to eventually demonstrate 100 MeV net energy gain and an acceleration gradient of >300 MeV/m.

I. INTRODUCTION

Using lasers to accelerate relativistic particles offers the potential for generating >1 GeV/m acceleration gradients. These high gradients are necessary for the next generation of TeV-class (10^{12} eV) electron accelerators needed for high energy physics research. Such high gradients would also make it possible to construct compact accelerators for use in industry and medicine.

The inverse Čerenkov effect was first demonstrated at Stanford University in 1981 [1]. Fontana and Pantell [2] later developed an improved configuration for inverse Čerenkov acceleration (ICA). Their basic scheme is shown in Fig. 1, which is taken from Ref. 2. A radially polarized laser beam is focused by an axicon onto the *e*-beam traveling through a gas-filled interaction region. The light intersects the *e*-beam at the Čerenkov angle θ_C, where $\theta_C = \cos^{-1}(1/n\beta)$, n is the index of refraction of the gas and β is the ratio of the electron velocity to the speed of light.

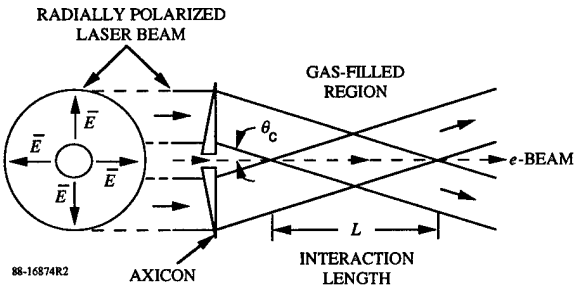


Figure 1: Inverse Čerenkov acceleration configuration [2]. A radially polarized laser beam is focused by an axicon onto the *e*-beam at the Čerenkov angle θ_C inside a gas-filled region, resulting in energy exchange occurring over an interaction length L.

The basic Fontana/Pantell geometry is the one used in the present and planned ICA experiments. This configuration has important advantages over the geometry used during the Stanford experiments. It produces a more efficient coupling of the laser energy into the *e*-beam and the *e*-beam can be focused axisymmetrically. This helps to mitigate some of the detrimental effects of gas scattering by channeling the electrons in the longitudinal direction [3]. This same effect also allows using the inverse Čerenkov effect as a beam focuser.

II. DESCRIPTION OF EXPERIMENT

The experiment [4] is performed on the Accelerator Test Facility (ATF) located at Brookhaven National Laboratory (BNL). This facility features a 40-MeV electron accelerator that uses a photocathode microwave electron gun driven by a Nd:YAG (4ω) laser. This same laser is used to switch out short pulses from a linearly-polarized CO_2 laser ($\lambda = 10.6$ μm) utilizing semiconductor switching. These short pulses are then amplified and are available for laser particle acceleration experiments [5]. Table 1 lists the characteristics of the ATF linac and laser system. (Note that the ATF *e*-beam emittance has been substantially improved since the ICA experiment and is now ~1 π mm-mrad.)

The major components of the experiment are a gas cell where the ICA interaction occurs, an optical system for converting the linearly-polarized ATF CO_2 laser beam into one with radial polarization [6], and an electron beam transport line and diagnostic devices connected to the gas cell.

Figure 2 is a schematic plan view of the gas cell showing the 45° mirror used to direct the incoming laser beam towards the axicon mirror that focuses the laser beam onto

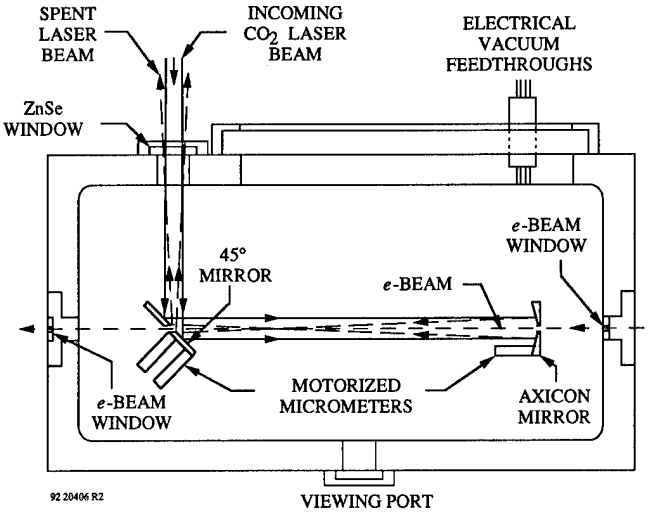


Figure 2: Schematic plan view of gas cell.

0-7803-3053-6/96/$5.00 ©1996 IEEE

the e-beam traveling from right to left in the figure. An axicon mirror is used rather than a lens as depicted in Fig. 1 because of the higher laser damage threshold of metal mirrors. The axicon mirror is remotely adjustable. Table 1 lists the other parameters for the gas cell. Note that θ_C = 20 mrad and that the interaction length is 12 cm.

TABLE 1. ICA Experiment System Parameters

Electron Beam	
Source:	BNL ATF
Beam energy:	40 MeV
Intrinsic energy spread (σ):	≈±0.5 MeV
Normalized emittance:	~20 π mm-mrad
Electron bunch length:	≈10 ps (FWHM)
Charge per bunch:	≈0.1 nC
Pulse format:	Single pulse
Laser Beam	
Laser:	CO_2
Wavelength:	10.6 μm
Pulse length:	220 ps
Peak power delivered to interaction region:	~580 MW
Pulse repetition rate:	Single shot
Interaction Region (Gas Cell)	
Phase matching medium:	Hydrogen gas
Čerenkov angle:	20.08 mrad ± 0.08 mrad
Temperature:	16.7 °C
Length of electron/laser beam overlap:	≈12 cm
Length of gas traversed by electrons:	43 cm
Thickness of diamond film e-beam windows:	2.1 μm

The ATF CO_2 laser is capable of generating ~10 GW of peak output power. However, the amount of peak power that could be delivered to the interaction was limited by one of the optical elements in the ICA optical system. Although this situation was rectified after the experiment, it meant during the experiment the effective peak power delivered to the interaction region was ~580 MW. This effective power includes a correction factor because the delivered laser beam was also only 83% radially polarized. (Normally this is >90%.)

III. EXPERIMENTAL RESULTS

The spectrometer has a momentum acceptance range of ±2.8% of the mean energy. Since the ICA interaction resulted in an energy modulation much larger than this range, it was necessary during the experiment to scan the spectrometer and use multiple shots to obtain subspectra in order to construct the full modulated spectrum. The subspectra are corrected for the spectrometer momentum acceptance and dispersion characteristics based upon separate measurements and modeling performed on the spectrometer.

Some pulse-to-pulse changes in the e-beam and laser beam characteristics occurred during the scan. The largest fluctuations were in the e-beam current ($\sigma \approx 50\%$), which fortunately only changed the magnitude of the spectrometer signal and not the overall shape of the full spectrum. Instabilities of the mean e-beam energy due to RF power fluctuations added a ≈±93 keV uncertainty in the energy values of the full spectrum; but, as will be shown, this is much less than the acceleration imparted upon the e-beam by the laser. Lastly, the laser pulse energy varied with a $\sigma \approx$ 14%; however, since the ICA interaction scales with the square-root of the laser peak power [2], this amount of variation does not appreciably change the shape of the full spectrum. Thus, even though the conditions are not exactly the same for each of the subspectra, an approximate full spectrum can be created by scaling the subspectra to fit end-to-end to compensate for the variations in e-beam current.[1]

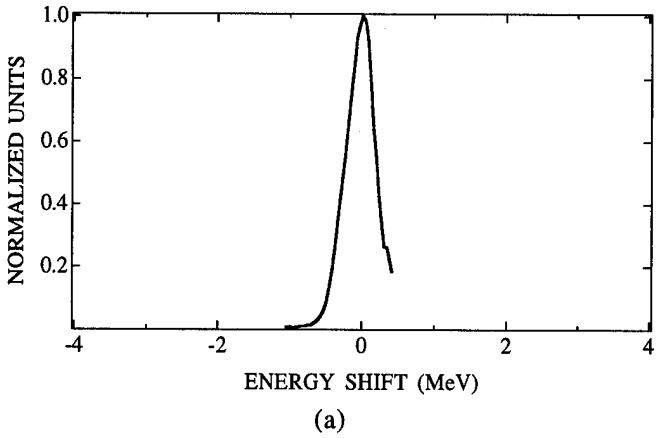
To avoid adding more complications during the scanning process, the gain of the spectrometer detector (image intensifier and CCD camera) was kept constant during the scan. However, this also limited the ability to detect faint signals above the noise level of the CCD camera associated with the highest accelerated and decelerated electrons. These electrons were detected in separate measurements by setting the spectrometer detector to maximum gain. These results will be shown in a later figure.

Figure 3 shows the e-beam energy spectra results for the experimental conditions listed in Table 1. Figure 3(a) shows the energy spectrum after traversing through the gas cell filled with 2.2 atm of H_2 with the laser off. Most of the energy spread is due to the intrinsic width of the e-beam ($\sigma \approx$ 0.5 MeV). Figure 3(b) shows the result with the laser delivering ~580-MW of peak power to the interaction region, where the subspectra have been spliced together to yield an approximate full spectrum. Since the electron bunch length (τ/c ~ 4 mm) is much longer than the laser wavelength, the interaction between the e-beam and the laser beam occurred over all phases of the laser light wave, resulting in both accelerated and decelerated electrons being observed.

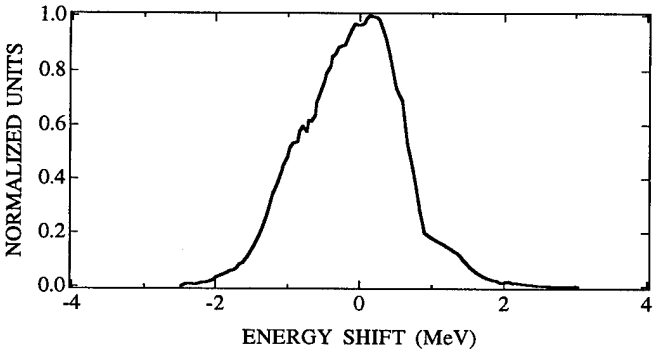
The subspectra obtained at the highest spectrometer detector gain is given in Fig. 4. Electrons at ~3.7 MeV are observed corresponding to an acceleration gradient of ≈31 MeV/m over the 12-cm interaction length. Our model [3] predicted a peak acceleration gradient of 35 MeV/m, which is consistent with the measurements. Note that only a relatively small number of electrons gain high energy. This can be significantly increased by prebunching the electrons before they interact with the laser beam such that the

[1] A Faraday cup was positioned at the output end of the spectrometer for measuring the e-beam current; however, it was limited by noise during the experiment. This limitation also prevented using this current sensor for monitoring fluctuations in the e-beam current.

electron bunch intersects the light wave at the phase point for optimum acceleration. Then most of the electrons in the bunch would gain high energy.



(a)



(b)

Figure 3: Electron-beam energy spectra. (a) With no laser present and after traveling through the gas cell filled with 2.2 atm H_2 at 16.7°C. (b) With ~580 MW of laser peak power delivered to the interaction region and measured at constant spectrometer gain (see text).

Current detector limitations (see Footnote 1) prevented the number of electrons accelerated to higher energies from being quantified during this particular experiment. However, a strong spectrometer signal was obtained which indicated that a significant fraction of the total number of electrons in the *e*-beam pulse were being accelerated with each shot. Based upon the sensitivity of the spectrometer detector system, we estimate that the spectrum shown in Fig. 3(b) corresponds to roughly 10 pC of charge. Based on the shape of the model curve we estimate that $>10^6$ electrons received energy gains >2 MeV.

The pressure was varied to optimize the interaction and, based upon the optimum pressure point, to determine the effective Čerenkov angle of the experiment. Figure 5 shows the measured pressure dependence of the ICA process. Plotted is the width of the normalized central subspectrum (at 80% of the peak) versus pressure. Note that the maximum for the data occurs at a gas pressure that corresponds to a Čerenkov angle of ~19.4 mrad. This may be caused by an imperfectly collimated laser beam at the axicon.

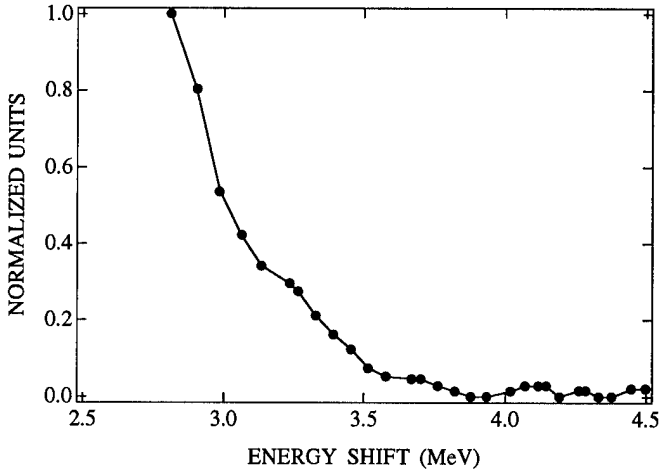


Figure 4: Electron beam energy subspectrum obtained at the highest spectrometer detector gain. The other parameters are the same as in Fig. 3.

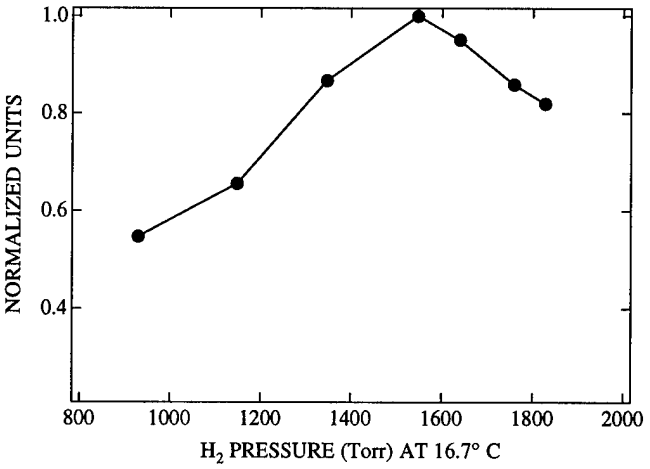


Figure 5: Gas pressure dependence results.

During the next experimental run approximately 5 GW of laser peak power will be delivered to the interaction region and the interaction length will be increased to ~20 cm. Under these conditions the model predicts >12 MeV peak acceleration corresponding to a >60 MeV/m acceleration gradient. The *e*-beam current monitoring capabilities will also be improved.

IV. 100-MeV INVERSE ČERENKOV LASER ACCELERATION EXPERIMENT

The success of the present ICA experiments gives us confidence to improve the process and scale it up to higher energies. We are presently beginning the next phase of the experiments to demonstrate 100 MeV net energy gain using ICA. The goals of the experiment are to: 1) Demonstrate prebunching of the *e*-beam at optical wavelengths. This is

important for efficient acceleration. 2) Demonstrate staging of acceleration sections, where the primary issue is rephasing the light wave with the bunched electrons. Staging is important for scaling to higher energy gains. 3) Compensate for phase slippage within each stage. At high acceleration gradients the electrons gain enough energy that they lose phase matching along the interaction length. Compensation is important for maximizing the net acceleration. And, 4) demonstrate 100 MeV net acceleration of $\geq 5 \times 10^8$ electrons/pulse. While the peak energy gain depends primarily on the laser peak power, the total number of accelerated electrons is affected by many other factors, such as gas scattering, emittance, and trapping efficiency. Hence, reaching the goal of $\geq 5 \times 10^8$ electrons/pulse will require controlling these factors.

Figure 6 shows the conceptual layout for the 100-MeV laser accelerator. The upgraded ATF *e*-beam (65 MeV) is sent into an ICA prebuncher whose output feeds directly into a magnetic chicane (compressor). The magnetic chicane is a device that shortens the distance required to achieve maximum bunching density of the electrons after they exit the prebuncher. Without this device the *e*-beam will diverge too much before optimum bunching has occurred. Hence, the compressor helps keep the overall system short. After the chicane there will be a drift space where magnetic focusing and steering elements refocus the bunched *e*-beam into the ICA accelerator.

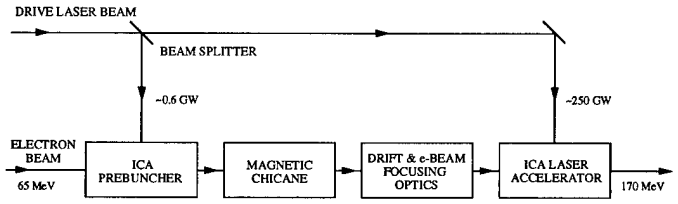


Figure 6: Conceptual layout for the 100-MeV ICA laser accelerator.

The 100-MeV laser accelerator experiment will use most of the existing ICA hardware, including the radial polarization converter system and the present gas cell, which will be modified to act as the prebuncher. The prebuncher will have a much shorter interaction length (~4-5 cm) and roughly 0.6 GW of laser peak power will be used to drive it.

A preliminary design for the experiment is given in Fig. 7. The ICA accelerator will consist of a single-stage, 27-cm long interaction length that is very similar in design to the present gas cell (see Fig. 2). One important difference is that it will use a curved axicon to compensate for phase slippage within the interaction region. Recall that $\theta_c = \cos^{-1}(1/n\beta)$; thus as β increases, θ_c needs to increase in order to maintain the same phase matching condition. This can be achieved by continuously increasing the angle of intersection along the interaction length in a manner analogous to a tapered wiggler. This is depicted in Fig. 8. Note, that for the conditions of our experiment, the actual angle change is very small (~1 mrad).

In order to achieve 100 MeV energy gain, the ATF CO_2 laser needs to deliver ≥250 GW to the ICA accelerator. The ATF has received initial funding to upgrade the laser. Once the upgrade is completed the laser is expected to produce at least several 100 GW output.

Phase synchronization between the prebuncher and the accelerator will be achieved by adjusting the optical delay depicted at the bottom of Fig. 7. Note, that between the prebuncher and the accelerator, the *e*-beam will be traveling through a vacuum tube.

We anticipate that the primary technical issue facing this experiment will be laser damage of optical components. However, we believe the system can be designed to avoid this. Laser-induced gas breakdown should not be an issue based upon calculations using the Keldysh formulas [7].

The experiment will be performed in phases. Phase 1(a) will be occurring after the next experimental run. The objective will be to demonstrate optical prebunching. Tight *e*-beam focusing into the interaction region and minimizing

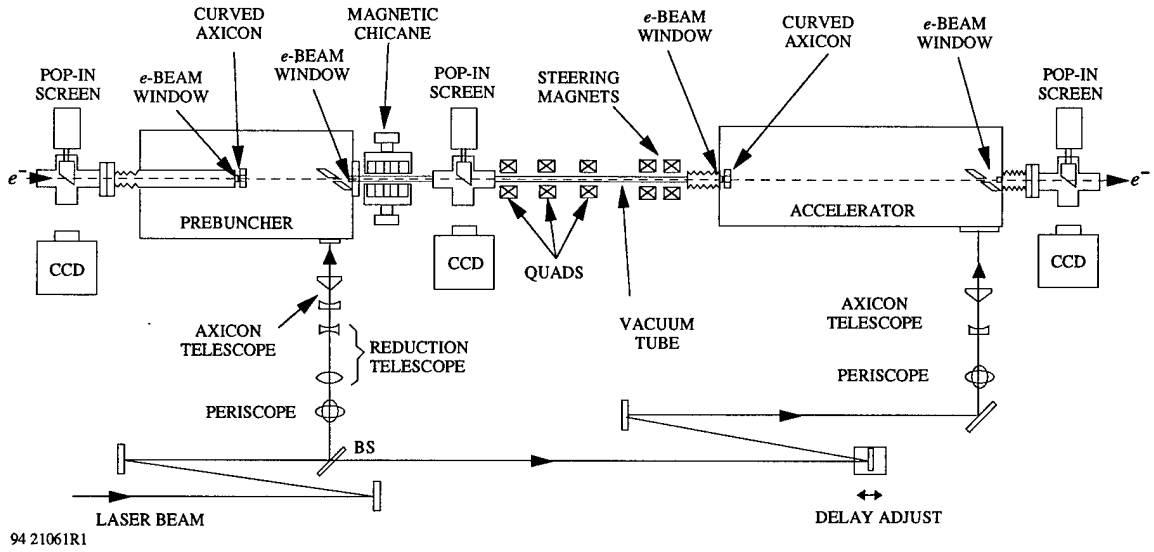


Figure 7: Preliminary design for 100-MeV laser accelerator experiment.

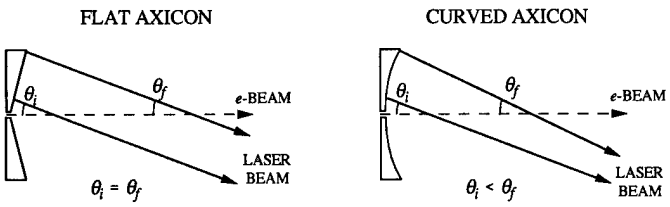


Figure 8: Basic focusing characteristics of flat and curved axicons.

gas scattering will be important. An issue during this phase is determining the best way to measure the bunched *e*-beam characteristics. Examining effects such as enhanced Čerenkov or optical transition radiation are possibilities. Phase 1(b) will incorporate the magnetic chicane and other beamline hardware (e.g., focusing quadrupoles and steering magnets) into the system. We plan to make the chicane using rare-earth permanent magnets and take advantage of the extensive wiggler/undulator design and fabrication experience at STI. Phase 1(c) will add the ICA accelerator to the system and will demonstrate rephasing between the bunched electrons and laser light. To avoid possible laser damage problems, the Phase 1(c) experiments will be performed using the existing 10-GW ATF CO_2 laser beam. Finally, during Phase II the upgraded laser power (≥250 GW) will be delivered to the ICA accelerator for demonstration of 100 MeV energy gain.

The 100-MeV laser accelerator experiment will set the stage for scaling this process to even higher energies by demonstrating important "building block" capabilities, such as prebunching, trapping, staging, and rephasing. The next goal will be to use this knowledge to demonstrate 1 GeV net acceleration. A 100-MeV energy gain over the 27-cm long ICA accelerator corresponds to ~370 MeV/m. Hence, in principle, 1 GeV could be achieved in <4 m. Of course, an actual 1-GeV laser accelerator will be longer than this, but it demonstrates that a 1-GeV ICA system can be reasonable in size. Such a system would probably use multiple ICA stages.

One of the advantages of ICA is that it should be possible to recycle the laser beam to reintersect the *e*-beam and continue the acceleration process. The basic scheme is illustrated in Fig. 9. The cylindrical mirror tube is optically equivalent to the axicon mirror. Recycling the laser pulse helps improve the efficiency of the process.

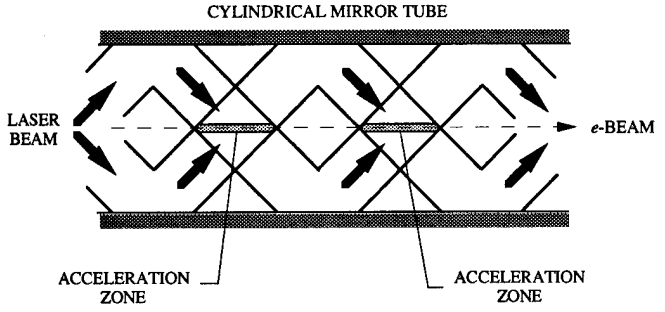


Figure 9: Schematic of possible method for recycling the laser pulse between multiple ICA stages.

V. CONCLUSION

Recent ICA experiments performed on the ATF have demonstrated ≤3.7 MeV acceleration is good agreement with theory. During the next experimental run we anticipate demonstrating >12 MeV energy gain corresponding to an acceleration gradient of >60 MeV/m. Preparations for the 100-MeV ICA laser accelerator experiment on the ATF are underway. The first phase of the experiment will demonstrate prebunching of the *e*-beam at optical wavelengths. This effort will be one of the first in the field of laser acceleration research to demonstrate prebunching and staging. The capabilities demonstrated will directly help in the design of a 1-GeV ICA demonstration experiment.

VI. ACKNOWLEDGMENTS

The author wishes to acknowledge the other collaborators in this research program: G. H. Kim, R. D. Romea, and L. C. Steinhauer at STI Optronics; I. V. Pogorelsky, K. P. Kusche, R. C. Fernow, and X. Wang at BNL; and Y. Liu at the University of California, Los Angeles. This work was supported by the U.S. Department of Energy under Grant No. DE-FG06-93ER40803.

VII. REFERENCES

[1] J. A. Edighoffer, W. D. Kimura, R. H. Pantell, M. A. Piestrup, and D. Y. Wang, "Observation of inverse Čerenkov interaction between free electrons and laser light," Phys. Rev. A **23**, 1848-1854, (1981).

[2] J. R. Fontana and R. H. Pantell, "A high-energy, laser accelerator for electrons using the inverse Cherenkov effect," J. Appl. Phys. **54**, 4285-4288, (1983).

[3] R. D. Romea and W. D. Kimura, "Modeling of inverse Čerenkov laser acceleration with axicon laser beam focusing," Phys. Rev. D **42**, 1807-1818 (1990).

[4] W. D. Kimura, G. H. Kim, R. D. Romea, L. C. Steinhauer, I. V. Pogorelsky, K. P. Kusche, R. C. Fernow, X. Wang, and Y. Liu, "Laser acceleration of relativistic electrons using the inverse Čerenkov effect," Phys. Rev. Lett. **74**, 546-549 (1995).

[5] I. Pogorelsky, "High power picosecond CO_2 laser system for ATF electron accelerator project," in *Advanced Accelerator Concepts*, Port Jefferson, NY, AIP Conference Proceedings No. 279, J. S. Wurtele, Ed., (American Institute of Physics, New York, 1993), p. 608–619.

[6] S. C. Tidwell, G. H. Kim, and W. D. Kimura, "Efficient radially polarized laser beam generation using a double-interferometer," Appl. Optics **32**, 5222-5229 (1993).

[7] L. V. Keldysh, "Ionization in the field of a strong electromagnetic wave, "Sov. Phys. JETP **20**, 1307 (1965).

MEASUREMENTS OF PLASMA WAKE-FIELDS IN THE BLOW-OUT REGIME

N.Barov, M.Conde and J.B.Rosenzweig
Dept. of Physics and Astronomy, UCLA, Los Angeles, CA 90024
P.Schoessow, G.Cox, W.Gai, R.Konecny, J.Power, J.Simpson
Argonne National Laboratory, 9700 S.Cass Ave., Argonne IL 60439

Initial results from nonlinear plasma wake-field experiments at the Argonne Wake-field Accelerator (AWA) test facility are reported. This nonlinear "blow-out" regime is characterized by the complete ejection of the plasma electrons from the beam channel. The wake-fields in this case are of notably high quality for acceleration of electrons, as the acceleration is independent of transverse position, and the focusing is linear and independent of longitudinal position within the electron depleted region, allowing self-consistent guiding of the majority of the driving electron beam. Initial measurements of the energy gain in a witness beam indicate a positive shift in its energy distribution of at least 0.5 MeV.

I. INTRODUCTION

Presently, there is a great interest in experimental evidence of acceleration using the nonlinear plasma wake-field acceleration (NPWFA) concept [1]. In addition to our work, a group at KEK [2] has also been measuring this effect.

The NPWFA an electron drive beam propagates in a plasma whose initial electron density is less than the beam's density (an underdense plasma). When such a beam is short (the rms bunch length, σ_z, is less than 2 collisionless skin depths, k_p^{-1}), it is well-suited to coupling power into a plasma wave in which the plasma electrons' motion is mostly radial. Because of the underdense condition, all of the plasma electrons are pushed out of the drive beam's way, resulting in the extremely strong focusing associated with an ion channel, which guides the drive beam and also the accelerated (witness) beam. This plasma electron depleted region assures that the focusing is linear and the acceleration field independent of radius. This accelerator scheme is exciting for the high acceleration gradient predicted: a 1.5 GeV/m is possible for a plasma density, $n_0 = 1\times10^{14}$ cm^{-3} and a 100 nC beam. The characteristic wavelength of the acceleration field is somewhat longer than 3.3 mm due to relativistic effects, and is suitable for accelerating short electron bunches with collider applications in mind.

The NPWFA concept, however, requires care when considering multiple acceleration sections to increase the final energy. Krall and Joyce [3] are currently studying the electron hose instability in this context. This work suggests that very long, ramped drive beams are not desirable.

II. OVERVIEW OF THE AWA FACILITY

The layout of the Argonne Wakefield Accelerator (AWA) can be found in Ref. 4. The electron source is a single-cell L-band rf cavity, using a copper photocathode to generate the electron pulse, followed by two 1 meter linac sections. The design of this facility is optimized for high charge (up to 100 nC per pulse), and short bunch length.

In the future, an additional electron gun will be added to the AWA to produce a 5 MeV witness beam for probing the wake fields in dielectric structures and plasmas. For the initial measurements, we realized that it was feasible to generate a stably propagating witness beam in the same cavity as the drive beam by delaying a portion (approximately 20%) of the laser pulse. We found that delays as long as 70 picoseconds were possible with laser path differences of about 3 cm. Figure 1 shows a resultant streak camera trace. This data is the result of inserting a 1 mm thick fused silica Cerenkov radiator in the path of the beam (inclined 11 degrees to the normal) and directing the light to a Hamamatsu C1587 temporal disperser. Since the delay time is dependent on the amount of RF compression, and hence on the injection phase of the bunches into the linac cavity, the streak camera was necessary to calibrate this delay time for a specific set of conditions.

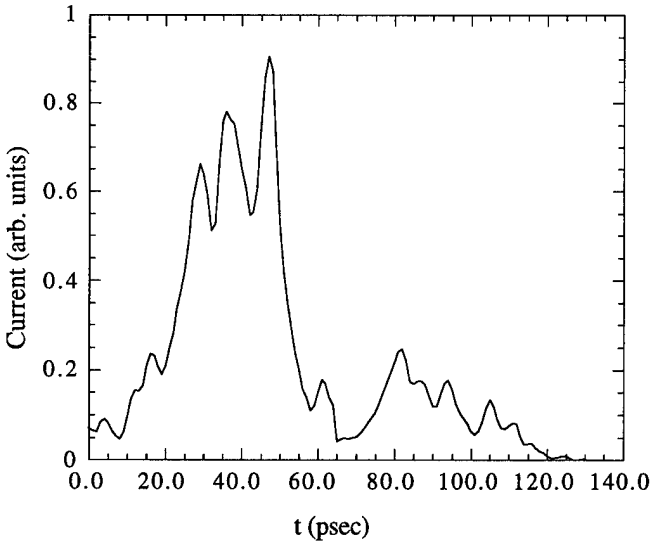


Figure 1. A streak camera image of the current profile of drive and witness beams. The data has been rescaled to reflect the charge in each pulse.

III. THE PLASMA SOURCE AND DIAGNOSTICS BEAM LINE

The plasma source used for this experiment is a modified version of that used in previous linear-regime acceleration [5] and focusing [6] studies (see Fig. 2). It is a

0-7803-3053-6/96/$5.00 ©1996 IEEE

DC hollow cathode arc discharge with a moderate confinement magnetic field (up to 1 kG; typically 200 G,) using Argon at up to 10^{-2} Torr pressures. The plasma electron density is variable between 8×10^{12} and 1×10^{14} cm^{-3}, as measured with a Langmuir probe. The validity of the probe data is also supported by μm-wave (140 GHz) interferometry measurements, which yield an integrated plasma density along a cross section of the plasma; the two techniques agree to within 15%. The length of the plasma column is 13 cm and n_0 is within 25 % of the peak value over 11 cm of this length.

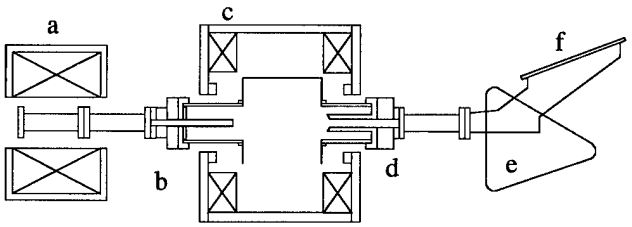


Figure 2. Experimental setup including a) focusing solenoid, b) cathode assembly, c) plasma confinement solenoid, d) anode assembly, e) bend magnet, f) phosphor screen.

In order to access the underdense regime, the beam must be brought to a tight focus - ultimately close to the betatron-matched condition for the ion channel. In order to easily control the location of this focal spot, we chose a solenoid magnet, placed about 40 cm before the start of the plasma. The beam is diagnosed with a phosphor screen before entering the solenoid. In the middle of the plasma chamber, we intercept the beam with a mirrored surface (with no plasma) and use the resulting optical transition radiation (OTR) to measure the solenoid's focal spot. After the plasma, the beam's energy distribution is measured with a spectrometer magnet. This spectrometer was designed in such a way that it has nearly point to point imaging in the bend plane from anywhere inside the plasma to the phosphor screen at the spectrometer's focal plane. The goal of this design is that the energy distribution be accurately measured regardless of the plasma caused focusing and guiding.

IV. MEASUREMENT OF WAKE FIELDS

In the first experimental run (Run I), we did not have use of the witness beam. However, this was a good opportunity to verify that energy was being deposited into the plasma, by observing the beam's deceleration. The charge per bunch was 6-8 nC, the beam was focused by the solenoid to an rms radius $\sigma_r \le 500$ μm and $n_0 = 8\times10^{12}$. Assuming the bunch length to be 7.5 mm FWHM, the underdense factor, $n_b / n_0 = 1$. The result of these measurements is that the low energy half maximum point of the energy moved down by as much as 0.5 MeV, while the high energy half maximum remained within 20 keV of the no plasma case. It is encouraging that this data was shifted primarily toward the low energy side, indicating that the energy distribution was being accurately measured. The lack of the beam's self-acceleration is also supported by computer simulation results (the simulation method is explained in Appendix A.)

By the time of the second experimental run, we had developed the technique of witness beam generation, and there was more charge available from the linac. Also, because of improvements in the beam transport and emittance, the beam could be focused to σ_r=360 μm. To investigate the possibility of particles accelerated by the plasma wave, as predicted by the Run I data and simulations, we recorded images of the high energy end of the spectrometer's phosphor screen. Fig. 3 shows the intensity profiles for all possible combinations of switching on of witness beam and plasma. Each point on this plot is the result of several camera images, averaging the set of energies corresponding to a fixed intensity. With this averaging, we attempt to improve on the energy jitter, probably due to laser injection phase fluctuations in the photoinjector, evident on the phosphor screen. The plasma density for this data was 2.2×10^{13} cm^{-3}, the drive and witness beams combined had Q = 13 - 17 nC, with 20% of this charge belonging to the witness beam. The initial σ_r was 450 μm at athe entrance to the plasma.

With no plasma, the Fig. 3 distributions are identical. This suggests that prior to entering the plasma, the witness beam's high energy tail is at or below that of the drive beam nd does not appear in the plots. Without a method to diagnose the witness beam alone, we can only conclude that the lower limit on the witness beam's gain in energy as a result of the beam-plasma interaction is 0.5 MeV. Note that at lowest intensity, the gain in energy of the tail is approximately twice as large again. Therefore the average acceleration field is at least as large as 4.1 MeV/m, and the peak field measurable is perhaps twice this value.

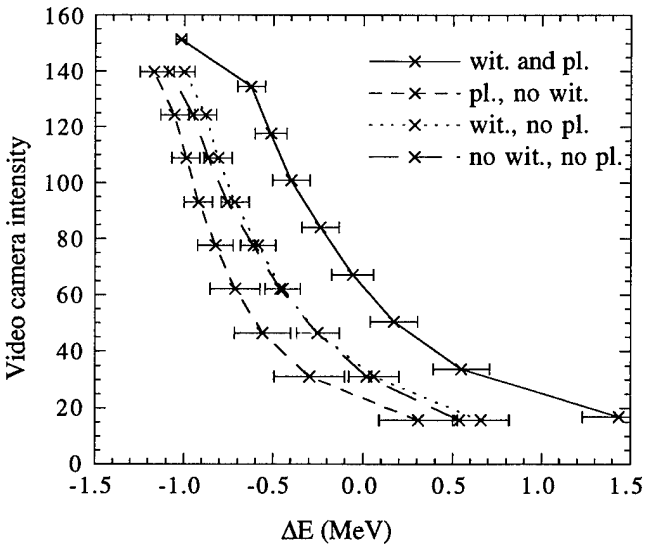


Figure 3. Observation of the high energy tail at spectrometer. In the legend, wit. indicates witness beam and pl. indicates plasma present. The curvature near the top of the plot is due to saturation of the video camera.

We also changed the plasma density to below 1×10^{13} cm^{-3} and above 4×10^{13} cm^{-3} and observed the effect on the energy distribution. From visual observation alone, the energy gain seemed weaker for these conditions.

When trying to compare this data with simulation results, we found that within the range of Q, n_0 and the length of the drive beam, it was possible to cause the acceleration of the drive beam's trailing edge. This, however, does not contradict the fact that the no witness beam high energy tail becomes depressed when the plasma is turned on - the drive beam's energy is initially likely to be negatively correlated with distance from the leading edge, due to space charge and running off-crest in the linac, but the extent of this effect is unknown. Thus, direct comparisons with simulation are not yet feasible. The simulations also reveal that a σ_r = 450 μm beam's core focuses to 180 μm in the plasma and then oscillates, staying below 330 μm. This implies that in places along the propagation the beam is 4 times more dense than the plasma, satisfying the underdense criteria. The witness beam in the experiment was positioned so far back that it overlapped with the second peak in the acceleration field. This simulation resulted in the formation of wake fields of 20 MeV/m averaged over the propagation, assuming a 13 nC drive beam, a number not in disagreement with measurements. A major possible sources of disagreement between the experiment and the simulations is the non-axisymmetry in the beam distribution due to cathode nonuniformity, space-charge and transverse wake-field effects.

V. FUTURE WORK

After improving the longitudinal shaping and transverse focusing of the drive beam, as well as reducing some aperture scraping in our beam transport system, the greater peak density of the electron beam, and more importantly shorter bunch length, should drive much more powerful fields in the plasma - on the order of 200 MeV/m. Even higher gradienst should be possible with the addition of a compressor chicage which is currently under construction. We will accompany this effort with measurements of the beam spot prior to exiting the plasma. A time resolved image of this spot [7] will confirm that the beam is propagating in a well focused state through the plasma, and that phase-mix damping leads a larger equilibrium radius near the beam's leading edge [8].

We also plan to measure the UV and VUV radiation emitted by the plasma as a result of the beam plasma interaction. The plasma wave is characterized by plasma electrons which are mildly relativistic ($v/c \leq .5$). These energetic electrons will further ionize the Ar ions and excite atoms, causing emission of UV line radiation.

APPENDIX A: COMPUTER SIMULATION METHODS

The computer simulations for this paper have used the code NOVO [9], which solves the Maxwell equations, assuming that this solution is unchanging in a frame moving with the beam. The plasma electrons are assumed to behave like a cold fluid and are modeled with the Maxwell-Boltzman equation. We have added a beam model to this code which tracks a set of super-particles, consistent with the NOVO picture [8]. This contradicts the assumption that the fields are static in the beam's frame, but this discrepancy is not very large, if we can assure that the beam changes very slowly compared to a plasma oscillation ($k_p >> 1/\beta$). A similar argument is used with spatial variations in the plasma density. In the most extreme case, the beam crosses a plasma/vacuum boundary, with the method and have been incorporated into the code. causing a transient response, which is neglected in our treatment. More gradual variations in the plasma density, like the droop at the ends of the column, are entirely consistent.

REFERENCES

[1] J.B.Rosenzweig, T.Katsouleas, and J.J.Su, *Phys. Rev. A* **44**, R6189 (1991).
[2] A.Ogata et al., *Proc. of the 6th Workshop on Advanced Accelerators*, Lake Geneva, WI (1994).
[3] J.Krall and G. Joyce, these proceedings.
[4] P. Schoessow et al., these proceedings.
[5] J.B. Rosenzweig, *et al., Phys. Rev. Letters* **61**, 98 (1988).
[6] J.B. Rosenzweig, *et al, , Phys. Fluids B* **2**, 1376 (1990).
[7] N.Barov and J.B. Rosenzweig, *Proceedings of the1993 PAC* , Washington DC.
[8] N.Barov and J.B.Rosenzweig, *Phys.Rev E* **49** 4407 (1994).
[9] B.N.Breizman, T.Tajima, D.L.Fisher, and P.Z.Chebotaev (unpublished).

Experimental Study of Electron Acceleration by Plasma Beat-Waves with Nd Lasers

F.Amiranoff, F.Moulin, LULI Ecole Polytechnique, 91128 Palaiseau, France
J.Fusellier, J.M.Joly, M.Juillard, DSM-DAPNIA-SEA CEA Saclay, 91191 Gif sur Yvette, France
M.Bercher, D.Bernard, A.Debraine, J.M.Dieulot, F.Jacquet, P.Matricon, Ph.Miné, B.Montès,
R.Morano, P.Poilleux, A.Specka, LPNHE Ecole Polytechnique, 91128 Palaiseau, France
J.Morillo, J.Ardonceau, SESI Ecole Polytechnique, 91128 Palaiseau, France
B.Cros, G.Matthieussent, LPGP Université Paris Sud, 91405 Orsay, France
C.Stenz, GREMI Université d'Orléans, 45000 Orléans, France
P.Mora, CPHT Ecole Polytechnique, 91128 Palaiseau, France

Abstract

We have observed the acceleration of electrons by a beat-wave generated in a deuterium plasma by two Nd-YAG and Nd-YLF laser wavelengths. Electrons injected at an energy of 3.3 MeV are observed to be accelerated up to 4.7 MeV after the plasma. The energy gain is compatible with a peak electric field of the order of 1.2 GV/m. The experiment has been performed with different injection energies, from 2.5 to 3.3 MeV, with different plasma dimensions, and with different laser intensities.

I. Introduction

Among new methods to accelerate particles with a large electric field, the beat-wave technique [1] has been investigated by several groups for the last decade. In this scheme two high-intensity laser pulses are focused in a vessel containing hydrogen gas and create a fully ionised plasma. The beating of the two waves provides a longitudinal electric field which oscillates with the frequency difference of the two lasers. If this frequency difference is equal to the plasma frequency, a resonance effect results, and the charge separation produces a field up to several GV/m. A relativistic particle with the right phase can catch the wave and gain energy.

Two types of lasers have been considered for this purpose: the CO_2 lasers at wavelengths near 10 μm, and the Nd lasers near 1 μm. The advantages and drawbacks of CO_2 versus Nd lasers are briefly discussed in reference [7]. Several groups [2], [3], [4] have observed the acceleration of electrons by the first type, with an energy gain of the order of 20 MeV. We already reported [5], [6], [7] on the observation of accelerated electrons with Nd lasers in our experiment at Ecole Polytechnique. Electrons injected at an energy of 3 MeV were observed to be accelerated up to 3.7 MeV.

For the new data taken recently (January 1995) in the same apparatus we were able to vary several experimental parameters. In order to change the plasma dimensions we used two lenses, with different focal lengths, to focus the laser beam on the plasma. The energy of the injected particles were tuned to 2.5, 3.0 and 3.3 MeV, to study the effect of the mismatch between the Lorentz factors of the wave and of the particles. The dependence on the light intensity was measured by comparing several laser shots taken through different absorbers. In this article we describe the energy spectra of the accelerated electrons under these different conditions and we interpret them in the frame of a simple model.

II. Experimental parameters

This paragraph summarises the experimental parameters relevant to the new data sample. The experimental set-up has already been described in details [6], [8].

Two synchronised laser oscillators, Nd-YLF (1.0530 μm) and Nd-YAG (1.0642 μm), deliver two pulses of 90 ps and 200 ps duration (FWHM), of 11.8 J and 4.4 J energy respectively. After amplification in the LULI laser chain, the beam diameter is 65 mm. The two pulses are synchronised in time and then focused by a 1.5 m or 1.2 m focal length lens into the vessel filled with D_2 gas. At resonance, the deuterium density is 1.115×10^{17} cm^{-3} $\pm$2.3%, corresponding to a pressure P_{res} equal to 2.272 mb at 22^{0}C. It can be adjusted in the vessel with a precision of $\pm$0.3%.

The electron source is a pulsed Van de Graaff accelerator delivering electrons with a kinetic energy set to 2.000, 2.500 or 2.800 MeV, i.e. 2.511, 3.011 or 3.311 MeV total energy (in the rest of this article, only total energy will appear). The relative energy fluctuation is 10^{-3}. The pulse duration is equal to 0.4 ms, so the beam can be considered as continuous during the lifetime of the plasma. The current is set to 200 μA, which corresponds to 1250 electrons per picosecond. The geometrical parameters have been measured at the plasma level by monitors detecting the optical transition radiation. We found 25 μm [RMS] for the focal spot in vacuum, 45 μm for the focal spot in 2 mb D_2, and 10 mrad [RMS] for the angular divergence.

The energy spectrum of the electrons after passing the plasma is measured by a magnetic spectrograph and an array of 10 scintillators read by photomultipliers tubes. When the injection energy is 3.011 MeV the lowest detectable channel corresponds to electrons between 3.270 and 3.420 MeV. The other 9 channels are incremented by steps of 0.154 MeV. All these quantities scale proportionally to the injection energy. The angular acceptance for the central channel is 90 mrad horizontally and 110 mrad vertically.

We have found that the noise in the detectors is due mainly to the electrons which scatter on the gas molecules. This noise amounts to about 5 e^-/ns for the current of 200 μA. The photomultiplier signals being gated by 5 ns long electronic gates, this noise corresponds to 25 e^- per channel. The uncertainty on the electron number is partly due to the calibration process ($\pm$15%), and partly to the statistical fluctuation of the noise from scattered

0-7803-3053-6/96/$5.00 ©1996 IEEE

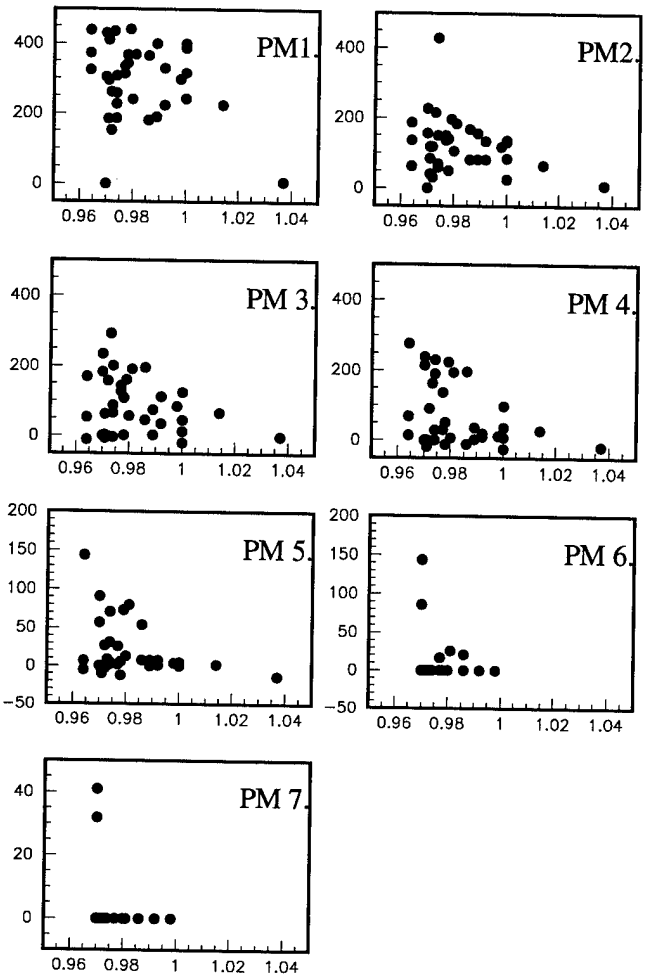


Figure. 1. Number of electrons detected in channel 1 to 7 (3.35 to 4.42 MeV) as a function of the gas fill pressure normalised to the resonant pressure P_{res} (2.272 mbar at 22^0C). The injection energy is 3.01 MeV and the focal length 1.2 m.

electrons ($\pm 5e^-$).

The main proof that electrons are accelerated by the beat-wave mechanism is the fact that, as a function of the gas fill pressure, the number of detected electrons exhibits a peak near the resonant pressure P_{res}. This is evident in figure 1, where we observe also that the width of the resonance peak is narrower for higher energy channels. This can be explained by the high sensitivity of the maximum energy gain to the peak value and to the coherence of the accelerating electric field.

We also performed a number of null tests, consisting of shots with either no electrons, no gas, a single laser wavelength, or two wavelengths separated in time. None of these shots showed a signal of accelerated electrons.

III. Effect of the injection energy

The optimum effect of acceleration is expected when the Lorentz factor γ_p of the plasma wave, determined by its phase velocity, is close to the Lorentz factor γ_e of the injected electrons. The phase velocity of the plasma wave is equal to the group velocity of the laser beat-wave which, in our case, is fixed by the

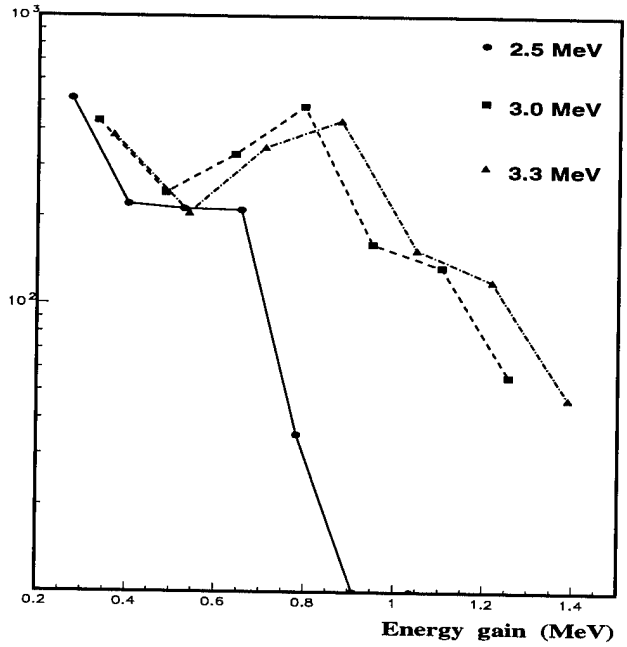


Figure. 2. Number of accelerated electrons, at the resonant pressure, as the function of their energy gain, for three values of the injection energy E_i.

Nd-YLF (1.0530 μm) and Nd-YAG (1.0642 μm) wavelengths. This corresponds to a γ_p equal to 94.5. The maximum energy of the Van de Graaff injector is 3.3 MeV, and the γ_e is equal to 6.5, much lower than γ_p. The consequence of this mismatch is that the electrons get out of phase after travelling a distance l in the plasma:

$$l \approx \gamma_p \gamma_e^2 \lambda$$

where λ is the mean laser wavelength. Figure 2 shows the spectra of the accelerated electrons, for the most efficient laser shots, for three different injection energies, with all other parameters being unchanged. The detector channels are not in correspondence because the magnetic field of the spectrometer magnet is different for each injection energy. One can see clearly that the energy gain is correlated with an increase of the injection energy.

IV. Effect of the laser intensity

Neutral light absorber were positioned in the beam line just upstream of the focusing lens at the entrance of the vessel. The two wavelengths were equally attenuated, successively by factors 0.5, 0.29 and 0.125. The corresponding spectra of accelerated electrons, accelerated over several shots are shown in figure 3. The effect is a rapid decrease of the highest energy channels and a complete disappearance of the detected particles with the last absorber.

V. Effect of the plasma dimension

We were able to monitor the size of the plasma by recording an image for each laser shot. The diagnostic consisted in a lens placed downstream of the vessel, followed by a CCD camera. The diameter of the image of the focal spot gave the lateral di-

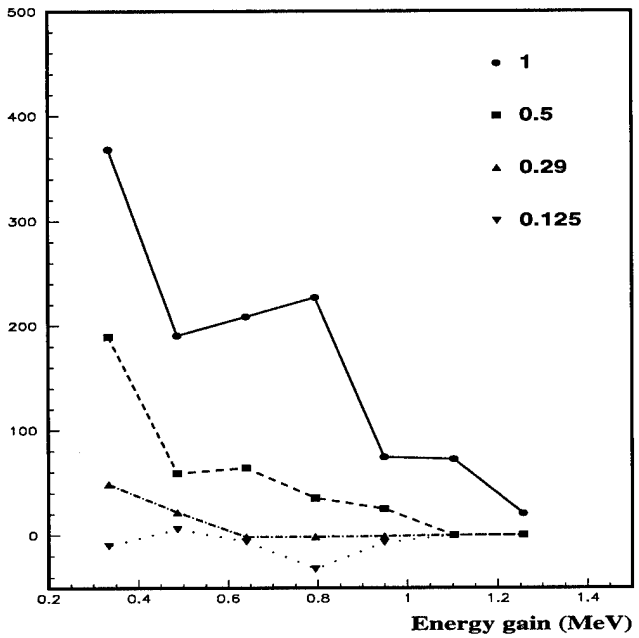


Figure. 3. Number of accelerated electrons, at the resonant pressure, as the function of their energy gain, for four values of the laser relative intensity

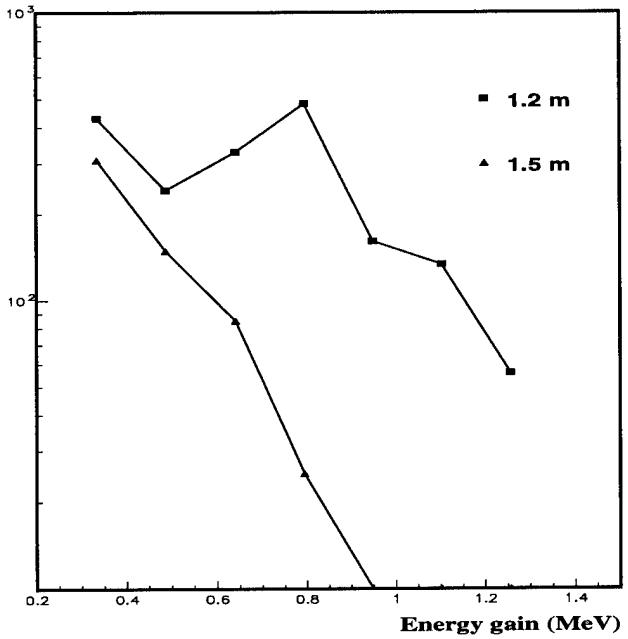


Figure. 4. Number of accelerated electrons, at the resonant pressure, as the function of their energy gain, for two values of the concentrating lens focal length

mension, whereas the longitudinal size was scanned by moving the diagnostic lens between successive shots.

When we changed the concentration lens focal length from 1.5 m to 1.2 m, the longitudinal size scaled. On the other hand the lateral size did not change, probably because the 1.2 m lens has more aberrations. Consequently the variation of the focal length had no effect on the laser intensity in the focal plane.

Figure 4 shows the spectra of accelerated electrons measured with the 1.2 m and 1.5 m lenses. The dramatic improvement of the maximum energy can be attributed to the reduced length of the plasma, which is closer to the optimum value (of the order of 3 mm) for our 3 MeV injected beam.

VI. Conclusion

Our new data confirm our previous observation of the first evidence of the acceleration of externally injected electrons by a relativistic plasma wave, excited by beat-waves of a two-frequency Nd:glass laser. The pressure scan shows that the resonance is sharper for the highest energy channels. Nevertheless the optimum conditions are not fulfilled since the Lorentz factor of the injected electrons, equal to 6, is much smaller than the Lorentz factor of the relativistic plasma wave, equal to 94.5. A clear experimental demonstration of this fact comes from the measurements of the spectra after varying the injection energy or the plasma dimension. A more complete analysis including theoretical simulations is under progress.

VII. Acknowledgments

We gratefully acknowledge the help of the laser and technical staff of LULI, LPNHE and SESI, and of M. Poitevin, S. Simon and Y. Fournier (DAPNIA). This work was financially supported by Ecole Polytechnique, IN2P3-CNRS, SPI-CNRS, CEA, EEC and DRET.

References

[1] T. Tajima and J. Dawson, Phys. Rev. Lett. 43, pp. 267-270, 1979.

[2] C.E. Clayton et al., Phys. Plasmas 1, pp. 1753-1759, 1994.

[3] N.A. Ebrahim, J. Appl. Phys. 76, pp. 7645-7647, 1994.

[4] Y. Kitigawa et al., Phys. Rev. Lett. 68, pp. 48-51, 1992.

[5] F. Amiranoff et al., proceeding of the European Particle Accelerator Conference, pp. 787-789, London, 1994.

[6] F. Amiranoff et al., proceedings of the 6th Workshop on Advanced Accelerator Concepts, Lake Geneva, WI, 1994

[7] F. Amiranoff et al., Electron Acceleration in Nd-laser Plasma Beat-Wave Experiments, submitted to Phys. Rev. Lett.

[8] F. Amiranoff et al., The Plasma Beat-Wave Acceleration Experiment at Ecole Polytechnique, Nucl. Instr. and Meth., in press.

A Broadband Electron Spectrometer and Electron Detectors for Laser Accelerator Experiments

C. E. Clayton, K. A. Marsh, C. Joshi, C. B. Darrow[a)],
A. E. Dangor[b)], A. Modena[b)], Z. Najmudin[b)], and V. Malka[c)]
Department of Electrical Engineering
University of California at Los Angeles
56-125B Engineering IV
Los Angeles, CA 90024

Abstract

We describe the apparatus used to measure the spectrum of accelerated electrons from a laser-plasma acceleration experiment carried out aRutherford Appleton Laboratories (RAL). The source of the broadband, energetic electrons was the forward Raman scattering instability of a high intensity (5×10^{18} W/cm^2) laser. Here the laser beam photons decay into scattered photons and a relativistic electron plasma wave. The plasma wave subsequently accelerates plasma electrons to relativistic energies.[1] The spectrometer and detectors were designed to give a quantitative (in energy and flux) single-shot electron spectrum over as wide a range of energies as possible. In this paper we present some calibration measurements taken prior to the RAL run which agree very well with TRACE3D runs used to model the beam transport. The silicon surface barrier detector (SBD) arrangement and fluorescer-filmpack arrangement are also described. Finally, some preliminary results are obtained which show excellent agreement between the spectra obtained with the SBD's and the film.

INTRODUCTION

The laser is the short pulse VULCAN laser[2] at Rutherford Appleton Laboratories operating at around 25 TW in a sub-ps pulse. The plasma is produced when the laser ionizes a pulsed jet of hydrogen gas exiting a high Mach number nozzle. The typical electron densities of the resultant plasma are in the range of 1×10^{19} cm^{-3} for a jet backing pressure of 20 bar.

ELECTRON SPECTROMETER

The electron spectrometer is shown in Fig. 1(a). It consists of a pair of pole pieces energized by a "C" electromagnet, and a vacuum box. The vacuum box is bolted to the vacuum chamber in the RAL target bay. The exit of the lead aperture is 54 cm from the gas jet and laser focus giving a collection angle of f/60 or 1° full angle. The tilted exit plane of the vacuum box is made so that the different energies are in focus along the length of the exit plane. The detectors are shown placed several cm away from the exit in order to take advantage of the fact that the electrons move in a straight line whereas x-ray noise within the chamber will fall off rapidly as the detectors are moved back. Note that the electron trajectories projected back into the vacuum box tend to intersect at a single point under the pole piece. This is called the "virtual source" for the electron spectrum.

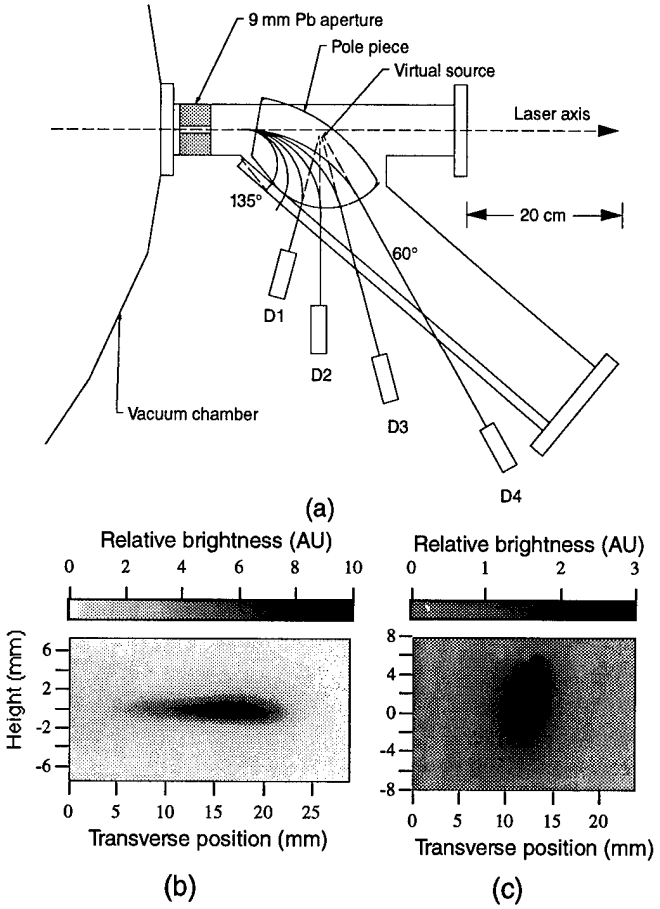


Figure 1: (a) Schematic of electron spectrometer and 4 channel SBD detector array. The pole piece is a Browne & Buechner type[4] with a 10° pole-face rotation at the entrance to provide some vertical focusing. Electron trajectories are shown for bending angles of 135°–60° in 15° steps. (b) focal plane image of stigmatic focal point for "switcher" type pole shape. (c) Focal plane image of the Brownee & Buechner design as shown in (a). Vertical focusing is much weaker with the B&B shape although energy coverage is greater.

Prior to taking the spectrometer to RAL, it was bench-tested with a 2 MeV electron linac at UCLA.[3] Figs. 1(b) and (c) show the results of this test for two different pole pieces. Figure 1(b) shows a nice, stigmatic focus obtained

This work is supported by DOE contract number DE-FG03-92ER40727.

0-7803-3053-6/96/$5.00 ©1996 IEEE

using "switcher" pole pieces[4] (semi-circular shaped). The beam enters on flat side which is rotated by 8° to provide additional vertical focusing. The physical location of this stigmatic focus, i.e., focusing in energy as well as vertically, is within a few mm of the location predicted by TRACE3D runs. Figure 1(b) therefore is the spectrum of the 2 MeV electron beam showing a ≈ 5% droop in the tail. The shape of the same beam using the Browne and Buechner pole pieces, as was used in the RAL experiment, is shown in Fig. 1(c). In this case, the pole pieces are focusing in the energy direction but not in the vertical direction, even with the 10° pole-face rotation. Rather, the beam is approximately collimated vertically at all energies. The location of the energy focal plane lies along the exit to the vacuum box.

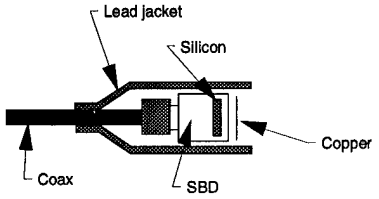


Figure 2: Crossectional view of the shielded surface barrier detectors used for quantitative electron flux measurements. The lead jacket (≈ 3 mm thick) shields the surface barrier detector from background x-rays in the room while the 200 μm thick copper pieces (3 for a total of 600 μm) will transmit energetic electrons but block the soft x-rays exiting the vacuum chamber. With this configuration, the electron signal to x-ray signal was better than 10:1.

THE DETECTOR SETUP

The layout of 4 SBD's is shown in Fig. 1(a). Figure 2 shows a cross-section of one of these detectors. The lead and copper shields are used to reduce the x-ray background to a manageable level. The coaxial cable length was about 10 m which was necessary to move the preamplifiers away from the electrically-noisy environment close to the vacuum chamber. The preamps were EG&G Model 113 "scintillator", charge-sensitive preamps which had a variable integrating capacitor in parallel to the cable capacitance.

Because the expected electron spectrum is exponential in energy, we wanted to configure the detectors so that the sensitivity would be much lower for detector D1 than for detector D4 thereby increasing the single-shot dynamic range of the measurement. The variable capacitor was one of the ways used to vary the sensitivity of individual detectors by switching in extra capacitance. Also, different silicon thickness' were used, with detectors D1 and D2 being 500 μm thick and detectors D3 and D4 being 1 mm thick. Also, each detector has a relationship between bias voltage and "depletion thickness" or active thickness. This, too, can be used to vary an individual detectors' sensitivity by varying the active thickness of the 500 μm detectors to, say, 200 μm by dropping the bias voltage down from it's maximum or fully-deleted value. When a detector is not fully biased, the waveform seen on an oscilloscope will have two distinct components–a fast-rising part due to charge deposited within the depletion region and a slower-rising part due to charge deposited in the field-free region which nevertheless drifts into the detection circuit. Thus by recording the fast-rise portion of the waveform, one is recording the portion only from the thinner depletion region. (This technique was verified at UCLA using the 2 MeV linac to expose the detectors at some middle-scale value. The fast part of the signal was observed to increase linearly with depletion depth. Also measured was the effective parallel capacitance which was found to be about 300 pF for the EG&G 113 preamps attached to 10 m of 50 ohm coaxial cable.) Apertures are not useful as beam attenuators for non-collimated beams at these energies since the range of a 13 MeV electron (the typical value at D1) is nearly an inch in lead.

THE FILM / FLUORESCER SETUP

As an alternative to the electronic detectors discussed earlier, we attempted to acquire a spectrum on film which was sandwiched between two sheets of 3M "Trimax" fluorescer. The fluorescers were cut to the width of the 35 mm film (Ilford HP5 Plus, ISO 400) and the entire 36 cm long sandwich was slid into a black plastic (0.5 mm thick) cassette and the end was sealed against room light with black tape. The cassette was placed either in contact with the exit flange of the vacuum box, i.e., in the energy plane of the spectrometer (near field), or placed 5 cm away from the vacuum box but still parallel to the flange (far field). The film was developed for 5 minutes in D19 developer.

The film data can be obtained on the same shot as the data on the detectors. This is because the areal density of the film + fluorescers + plastic cassette is negligible for the energies measured on the film (13.6–32.6 MeV) being about 1/30 of a stopping range for the lowest energy.

The developed film was converted to "density" using a 12 bit CCD and a calibrated density step-wedge taped up to a lightbox. The estimated density-accuracy of this measurement is ± 0.05. The density was converted to relative exposure using an experimentally-measured replica of a density step wedge taken on the same ISO 400 film and developed in the same way as the data thereby indicating the nonlinear "gamma" of the film. Thus the 2-D image of the film taken with the CCD was converted into Log(Exposure) vs. position on the film. Finally, the horizontal position on the film was converted to electron energy by the known relationship between radius of curvature of the electron (proportional to momentum) and position on the film.

EXPERIMENTAL RESULTS

In this section we present examples of data from both types of detectors–film and SBD's–taken on the very same shot. But first we will look at two images taken with the film which demonstrate that the electrons do indeed appear to come from a "virtual source" under the pole pieces.

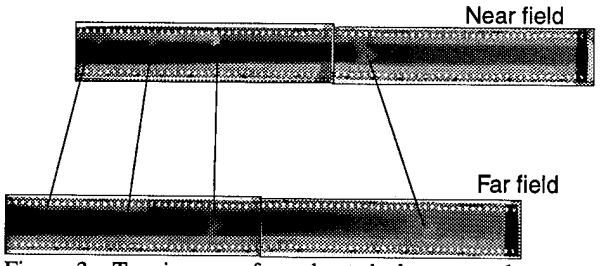


Figure 3: Two images of accelerated electrons taken on two similar laser shots with the film / fluorescer cassette located in two different planes: Near field, against the exit flange of the spectrometer; and Far field, 5 cm away from–and parallel to–the exit flange. Four lead objects were placed against the vacuum window, about 1 cm in front of the near field position. The measurement shows the directional nature of the electrons and the fact that they appear to emanate from a "virtual source".

Film images

Figure 3 shows the near-field and far-field images taken on two similar shots showing single-shot spectra from 13.6–32.6 MeV in the near-field case. Four pieces of lead of various shapes and about 6 mm thick were placed at the exit window (76 μm Mylar) of the vacuum box, about 1 cm in front of the film in the near-field case. For the far-field case, the lead was not moved yet the "shadows" of the electrons have moved in such a was as to indicate that the electrons appear to emanate from a virtual source under the pole piece, just as sketched in Fig. 1(a).

An Electron spectrum

An electron spectrum was taken on both diagnostics on the same shot by putting the film cassette in the near-field position and viewing the SBD signals on the oscilloscopes as usual. Although there will be an energy-dependent scattering angle from the film, the estimated smearing of a beamlet at the low energies is on the order of the beam size so that the net drop in flux seen on the 8 mm diam SBD is small.

Rather than plot the raw signal vs. energy from the SBD's, we have transformed the data into electrons/MeV vs. MeV. Thus the area under the graph is the absolute number of electrons. The conversion to measured volts/detector on the oscilloscope to electrons/detector was made by using the known energy dissipation rate dE/dx into ionization of the silicon detector, the know thickness dx of the detector, the resultant free charge produced (electrons/dE), and finally the known charge-sensitivity of the preamplifiers (V/coulomb). Now, since each detector is about 8 mm wide in the energy direction (0.8 cm/detector), we can use the know dispersion (cm/MeV) to finally put our measured volts/detector into electrons/MeV at the MeV location of the detector. There is one final correction factor needed and that is that the detector is vertically smaller than the beam and this roughly factor-of-two is included to estimate the total flux of electrons, not just those that hit the detector. This is what is plotted in the four points in Fig. 4. A similar routine was performed on a 10 pixel wide lineout down the center of the spectrum taken simultaneously on film. Now one can consider the horizontal pixel discreteness in the same way as discrete detectors and use the transformation: signal/pixel × pixels/cm × cm/MeV = signal/MeV. Finally, the same vertical correction, based on TRACE3D runs, is applied across the energy axis. The only free parameter for comparing this spectrum to the SBD spectrum is the unknown sensitivity, i.e. fluorescence photons per electron. Thus we are free to scale the film data vertically in Fig. 4 and have done so. We see that the two spectra agree very well over an order of magnitude in electrons/MeV.

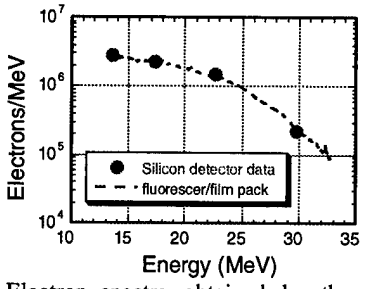


Figure 4: Electron spectra obtained by the SBD detectors (points) and by the film / fluorescer combination (curve) for the same shot in hydrogen gas. The film data was scaled vertically only to overlap the SBD data.

One might question why the agreement. The answer is that both are ionization-based detectors. The amount of light given off by the Trimax fluorescer is proportional to the amount of energy deposited through ionization giving a linear relationship between exposure on the film and electron flux which is completely analogous to the quantity of free charge induced on the SBD's vs. electron flux.

ACKNOWLEDGMENTS

The authors are grateful to Dr. D. Neely, C. Danson and the rest of the Vulcan Laser staff at RAL for their expert assistance throughout this experiment.

[a] Lawrence Livermore National Laboratory, Livermore, USA.
[b] Imperial College, London, U.K.
[c] Ecole Polytechnique, Palaiseau, FR.

REFERENCES

1. A. E. Dangor, A. Modena, Z. Najmudin, C. E. Clayton, K. A. Marsh, C. Joshi, C. B. Darrow, V. Malka, C.N. Danson, "Wavebreaking of Relativistic Plasma Waves", submitted to Nature.
2. C. N. Danson, L. J. Barzanti, Z. Chang, A. E. Demerell, C. B. Edwards, S. Hancock, M. H. R. Hutchinson, M. H. Key, S. Luan, R. R. Mahadeo, I. P. Mercer, P. Norreys, D. A. Pepler, D. A. Rodkiss, I. N. Ross, M. A. Smith, P. Taday, W. T. Toner, K. W. M. Wigmore, T. B. Winstone, R. W. W. Wyatt, and F. Zhou, "High contrast multi-terawatt pulse generation using chirped pulse amplification on the VULCAN laser facility", Opt. Comm. 103, 392-397 (1993).
3. C. E. Clayton and K. A. Marsh, "A 2 MeV, 100 mAelectron accelerator for a small laboratory environment", Rev. Sci. Instr. 64, 728-731 (1993).
4. H. A. Enge, "Deflecting magnets", in *Focusing of Charged Particles*, edited by A. Septier (Academic, Ney York, 1977) ch. 4.2; J. J. Livingood, *The Optics of Dipole Magnets* (Academic, Ney York, 1969).

Photon Acceleration from Rest to the Speed of Light

C. H. Lai, T. Katsouleas, R. Liou, USC, Los Angeles, CA 90089
W. B. Mori, C. Joshi, P. Muggli, R. Brogle, J. Dawson, UCLA, Los Angeles, CA 90024

Abstract

A new mechanism for generating coherent radiation from a laser-ionized gas-filled capacitor array is presented. This scheme directly converts a static electric field of wave number k_0 into coherent radiation pulses. The physical mechanism is analogous to photon acceleration in plasma waves, and in this sense, photons are accelerated from zero frequency (zero energy) to a frequency $\omega_p^2/2k_0c$. The photon frequency is tuned by gas pressure and/or capacitor spacing. In this paper we briefly describe the theory of this scheme and then present the preliminary experimental setup and results.

I. INTRODUCTION

Photon acceleration by using relativistic plasma waves has been investigated by Wilks, *et al*[1]. In this scheme, two short pulses of laser light spaced appropriate plasma wavelengths apart are injected into a plasma. Photons of the second light pulse then absorb energy from the plasma wake excited by the first laser pulse and are accelerated via their frequency upshift (frequency upshifting increases their group velocity in the plasma as well as their energy). It has also been found that the photon frequency can be significantly upshifted by a time-varying medium [2-4],e.g., by a relativistic ionization front rather than a plasma wave. The use of laser-produced ionization fronts have been successfully employed to upshift existing microwave radiation from 35 GHz to over 170 GHz in a plasma.[5].

In this paper, we describe another approach to generating radiation; namely from a static electric field by using a relativistic ionization front.[6]. From the viewpoint of acceleration, photons are accelerated from zero frequency, i.e., zero energy, to the frequency regime of microwaves to possibly IR. First, we analyze the radiation produced when an ionization front moves through a gas-filled capacitor array that is biased to produce a static electric field of wave number k_0 and zero frequency. The frequency and amplitude (output power) of the emitted radiation can be calculated by requiring the continuity of fields at the moving boundary. In the second part, we present he preliminary experimental setup and results.

II. REVIEW OF THEORY

A. Frequency of the Radiation

The geometry of this scheme is shown in Fig. 1. The alternately biased capacitors produce a static electric field of the form $E \approx E_0 \sin(k_0 x)\,\hat{y}$ in a working gas of density n_0, where $k_0 = \pi/d$ and d is the spacing between adjacent capacitor plates. An ionization front (e.g., created by a short laser pulse) moves between the plates in the $+\hat{x}$ direction with a laser group velocity $v_f = c(1 - \omega_p^2/\omega_L^2)^{1/2}$, where ω_L is the laser frequency. To describe the radiation generated, we begin by considering the situation in a reference frame moving with the ionization front. In this frame, the Lorentz transformed electric field approximates an incident electromagnetic wave since the front velocity is close to the speed of light. The front is static in this frame and the incident wave gives rise to reflected and transmitted waves all at the same frequency. The reflected wave will be an extremely short pulse of hard x-rays with the amplitude approaching zero in the lab frame. The transmitted waves will turn out to be the tunable radiation that is the focus of this paper.

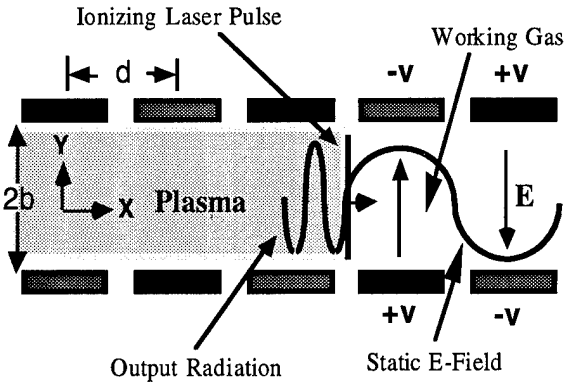


FIG.1 Schematic of a photon accelerator from rest to the speed of light

The frequency of the transmitted radiation can be easily obtained in the lab frame. The frequency follows two conditions: (i) the plasma dispersion relation, and (ii) continuity conditions at the front boundary. The dispersion relation is $\omega^2 = \omega_p^2 + c^2k^2$, while the equation for phase continuity is $\omega + kv_f = k_0 v_f$. When the front velocity is close to the speed of light (i.e., the laser frequency ω_L is much greater than the plasma frequency ω_p), the output frequency can be approximated as

$$\omega \approx k_0 v_f/2 + \omega_p^2/2k_0 v_f \qquad (1)$$

It is instructive to construct graphical solutions to the above two equations[7]. The dispersion equation and continuous phase condition are plotted in Fig. 2; their

0-7803-3053-6/96/$5.00 ©1996 IEEE

intersection, marked by "T1", gives the output frequency and wavelength. Fig. 2 illustrates the case of $k_0 < \omega_p / v_f$ and we notice that the solution (T1 wave) has negative phase and group velocity which indicates that the output radiation moves in the same direction as the ionization front.

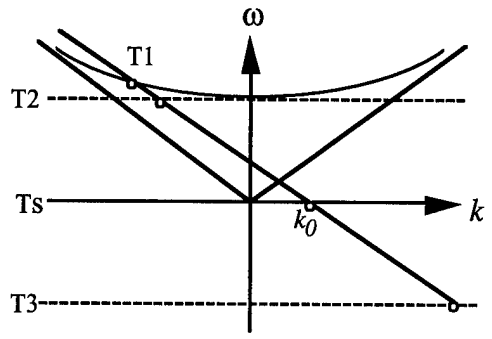


FIG.2 Dispersion diagram for electromagnetic, electrostatic, and free streaming plasma modes intersected by line of constant phase.

B. Output Power of the Radiation

The output power can be calculated by finding the transmission and reflection coefficients at the ionization front boundary. Besides the reflected wave and transmitted radiation, three more modes, i.e., two longitudinal modes and one free streaming mode, can also be excited[6]. They are also shown in Fig. 2, marked as "T2", "Ts", and "T3". The determination of these coefficients requires five boundary conditions. In addition to the usual conditions that (1) $E_{tangential}$ and (2) $B_{tangential}$ be continuous, three more conditions follow from the fact that electrons are 'born' at rest with no initial velocity at the moment they are ionized. As a result, the current density j_y and $j_x = 0$, and the surface charge density $\rho_s = 0$ at the front. The complete set of boundary conditions that follow from these and Faraday's and Gauss' laws are continuity of (1) E_y (2) B_z (3) $\partial B_z / \partial x + (1/c)\partial E_y / \partial t (= 0)$ (4) $\partial B_z / \partial y - (1/c)\partial E_x / \partial t$ (=0) (5) E_x. The details of this calculation have been shown in reference [6]. We simply state the results here: for relativistic fronts and large up-shifts, the coefficient of the T1 mode approaches one. That is, the output radiation amplitude is approximately equal to the amplitude of the static electric field.

III. EXPERIMENTAL SETUP AND RESULTS

A. Setup

An experiment was designed to verify photon acceleration from rest for output frequencies in the microwave range. Fig. 3 depicts the experimental block diagram. A pyrex glass tube and two stainless steel flanges form the vacuum chamber which was evacuated by a turbomolecular pump. Two quartz windows provide the vacuum interface for the laser and microwave radiation. Azulene vapor was chosen to be the working gas because it is easily ionized by a 266 nm laser[5]. In order to achieve sufficient azulene pressure, the experiment was operated at a temperature of 140°C. At this elevated temperature the background pressure was abount 3 mTorr. The entire experimental setup was wrapped with heating tapes (not shown in the figure) to achieve the required temperature. A leak valve was used to control the amount of azulene vapor leaking into the chamber and therefore the gas pressure. A convectron gauge was used to monitor the pressure in the chamber. The structure consists of 12 pairs of copper electrodes (6 periods). The spacing between adjacent electrodes (d) was 4.7 cm with separation (2b) of 1.5 cm. The structure was machined from high temperature plastic kel-F material. The material is mechanically stable and has high dielectric strength. The laser system produces an intense UV pulse (266 nm) with a duration of 50 ps (FWHM) and total energy of 30 mJ. The microwave radiation was detected with a combination of a horn antenna followed by a matched waveguide and a crystal detector in various bands . Three specific bands were used, namely, the X-band (with cut-off at 6.56 GHz), Ku-band (with cut-off at 9.49 GHz) and K-band (with cut-off at 14.08 GHz). The structure was biased with a DC power supply to an operating voltage of 1 kV.

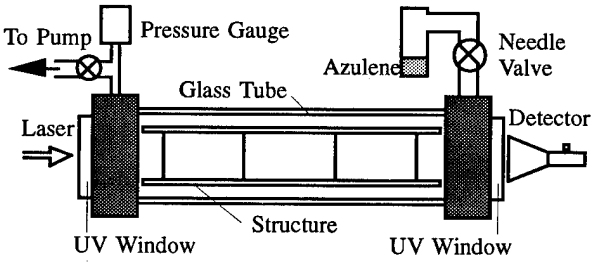


FIG.3 Experimental setup

B. Preliminary results

Null tests showed that the appearance of signals was directly associated with the presence of azulene, DC bias and the ionizing laser. The strength of signals detected on the crystal diode detector increased monotonically with the DC bias voltage and were typically in the range of 2-20 mV, depending on the sensitivity of crystal detectors. Based on cold tests we expect that the detected signal is 0.1 to 1% of the radiation generated within the device (primarily because of large impedance mismatches at the output of the vacuum structure). The signal was coincident with the 50ps laser signal and had a duration less than 5 ns, the instrument limited time resolution of our electronics. The output was also polarized in the direction of the DC bias field typically with a 6 to 1 intensity ratio.

Fig. 4 shows the amplitude of the detected signals measured with three different waveguides as a function of azulene pressure. The amplitudes of signals in this figure were normalized to the maximum signal obtained by the same set of waveguide and crystal detector. As the vapor pressure is increased, one can expected to achieve higher microwave frequencies. The dips occurs between 1.5 and 4 mTorr were thought to be due to the frequency characteristics, i.e., impedance mismatches, of this periodic structure.

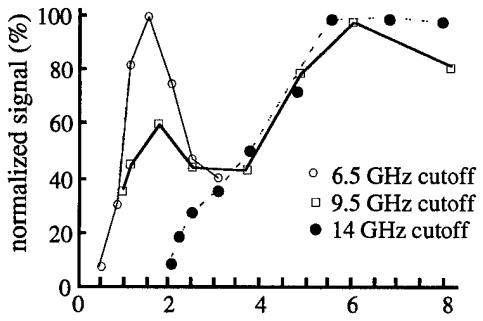


FIG. 4 The normalized intensity of signals vs. azulene pressure

We also converted the azulene pressure to the corresponding plasma density based on a previous experiment done at UCLA with the same laser and similar controlled parameters [5]. The conversion factor was $9x10^{11}cm^{-3}$ per mT of azulene. However, since the laser power in the present experiment was only 75% of the power used in the previous experiment, we expect the conversion factor to be $5.1x\ 10^{11}cm^{-3}$ per mT of azulene because the ionization rate is proportional to the square of laser power for such a two-photon ionization process. With this estimated conversion rate we were able to plot the frequencies of the minimum onset (i.e., the lowest points of the three curves in Fig. 4) vs. plasma density in Fig. 5. The solid line represents the theoretically predicted line given in Eq.(1). The data is in reasonable agreement with the theory.

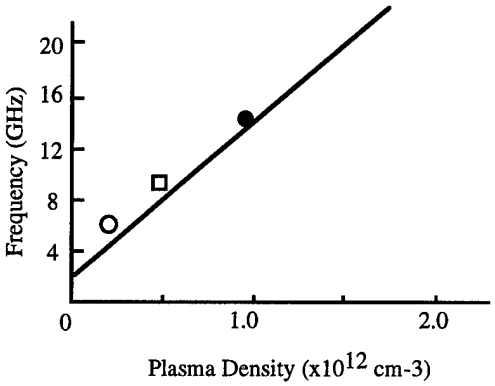


FIG. 5 Output frequency vs. plasma density. The solid line is the theoretical prediction.

IV CONCLUSION

We have described a new mechanism for generating coherent radiation by using an ionization front. This scheme is analogous to photon acceleration in relativistic plasma waves, and in this sense, the output radiation is directly converted from a static field of zero frequency. The output frequency is linearly proportional to the plasma density. In the proof-of-principle experiment we have observed well-polarized signals coincident with the laser signal. We also plotted the relation between the output frequency and the plasma density by applying the conversion factor based on previous work. The preliminary results seem to to be in reasonable agreement with theoretical predictions. However, more accurate measurements on the plasma density and other related tests are necessary in order to further verify this mechanism.

Work supported by AFOSR Grant No. F49620-95-1-0248 and US DOE Grant No. DE-FG03-92ER-40745.
P. Muggli is supported by the "fonds national suisse de la recherche scientifique" grant number 8220-040122.

REFERENCE

1. S. C. Wilks, J. H. Dawson, W. B. Mori, T. Katsouleas and M. E. Jones, Phys. Rev. Lett. **62**, 2600 (1989).
2. V. I. Semenova, sov. Radiophys. and Quantum electron. **10**, 599 (1967).
3. M. Lampe, E. Ott and J. H. Walker, Phys. Fluids **10**, 42 (1967).
4. W. B. Mori, Phys. Rev. A **44**, 5118 (1991).
5. R. L. Savage, R. P. Brogle, W. B. Mori and C. Joshi, IEEE Trans. Plasma Sci. **21**(1), 5(1993); R. L. Savage, W. B. Mori and C. Joshi, Phys. Rev. Lett. **68**, 946(1992).
6. W. B. Mori, T. Katsouleas, J. M. Dawson, and C. H. Lai, Phys. Rev. Lett. **74**, 542 (1995)
7. C. H. Lai, T.Katsouleas, W. B. Mori, D. Whittum, IEEE Trans. Plasma Sci. **21**(1), 45(1993).

A Constant Gradient Planar Accelerating Structure for Linac Use*

Y. W. Kang, P. J. Matthews, and R. L. Kustom
Advanced Photon Source, Argonne National Laboratory
9700 South Cass Avenue, Argonne, Illinois 60439 USA

Abstract

Planar accelerating millimeter-wave structures have been studied during the last few years at Argonne National Laboratory in collaboration with Technical University of Berlin. The cavity structures are intended to be manufactured by using x-ray lithography microfabrication technology. A complete structure consists of two identical planar half structures put together face-to-face. Since microfabrication technology can make a single-depth indentation on a planar substrate, realizing the constant impedance structure was possible but a constant gradient structure was difficult; changing the group velocity along the structure while maintaining the gap and the depth of the indentation constant was difficult. A constant gradient structure has been devised by introducing a cut between the adjacent cavity cells along the beam axis of each half structure. The width of the cut is varied along the longitudinal axis of the structure to have proper coupling between the cells. The result of the computer simulation on such structures is shown.

I. INTRODUCTION

Previously, a planar constant impedance cavity structure was investigated [1,2] and its linac application was investigated [3,4]. The constant impedance structure may be simple and easy to fabricate but may not be the best for accelerator applications, especially this type of microstructure operating at a mm-wave frequency, due to difficulty in heat removal. The heat loading in the constant impedance structure was shown [5]. In a constant impedance structure, the concentration of heat at the structure input can limit the high power rf operation of the structure. In order to have higher shunt impedance of the structure, the thickness of the irises between the cells must be small (say $<0.1\lambda$). However, heating imposes a limit in this case; heating at the center of the irises limits the maximum input power. Successful heat removal and uniform heat loading throughout the structure are important for optimum performance of the mm-wave accelerating structure.

The constant gradient linear accelerating structure has been used in many practical accelerators due to its higher energy gain and better frequency characteristic. The constant gradient structure has higher shunt impedance and more uniform power dissipation, and is less sensitive to frequency deviations and beam break-up when compared to the constant impedance structure [6].

* Work supported by the U.S. Department of Energy, Office of Basic Energy Sciences, under Contract No. W-31-109-ENG-38.

Unlike the circular cylindrical cavity structure, the planar structure at the mm-wave frequency must be manufactured by micromachining technology such as the Lithography, Galvanoformung, Abformung (LIGA, a German Term) process. Since the process can provide the precision required for the accelerator, the structure can be simple without having tuning mechanisms for the individual cavities. However, the one limiting factor in this precision manufactured structure is that it has to have uniform indentations on a planar wafer.

To have a planar constant gradient structure, the cell-to-cell coupling must be controlled. Since the structure needs be manufactured as a single piece on a wafer, this can be done by adjusting the cell width and length with a constant depth within the structure. The control of cell-to-cell coupling in a periodic structure can be made in two different ways for the constant gradient planar structure: 1) with no cut in the irises, the cell dimensions w and g can be varied while the cell-to-cell distance $(g+t)$ and the cell depth d are fixed constant, 2) one or more posts can be used instead of the iris between cells. However, with 1) the cavity Q and the shunt impedance become lower and the maximum voltage limit will be lower; and with 2) heating on the posts will limit the power level.

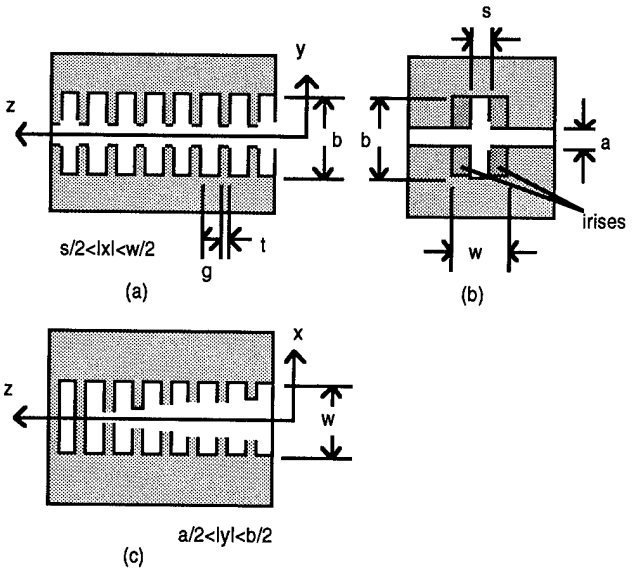


Figure 1: A constant gradient structure with cuts in irises

Figure 1 shows a structure that can be used as a constant gradient structure. The irises between the cells have vertical cuts with a controlled width along the axis. The cutwidth is

greatest at the input side and becomes smaller toward the output.

II. SIMULATION

A $2\pi/3$ traveling wave has been chosen as the accelerating mode. Assuming the shunt impedances and Q-facto are constants throughout the structure, the group velocity of a constant gradient accelerating structure can be shown to be

$$v_g = \frac{\omega l}{Q} \frac{(1-(1-P_l/P_o)z/l)}{(1-P_l/P_o)}, \quad (1)$$

where Q is the cavity quality factor, ω is the angular frequency, l is the length of the section, P_o is the structure input power and P_l is the leftover power at the structure output. For a leftover power $P_l/P_o = 0.15$ at the output of a 7cm-long accelerating structure, the average attenuation constant α=13.6 nepers/m. The number of cells is 84 and the shunt impedance is 300MΩ/m. The required group velocity normalized to the speed of light along the structure is in the range of 0.94 to 0.14.

In the constant impedance structure design [1] the aperture height was chosen to be 0.6mm. In constructing the constant gradient structure, the aperture height needs to be smaller for low cell-to-cell coupling at the end of the structure. It has been found that 0.5mm aperture height can be used for the minimum coupling with a=0.5mm, b=2.2mm, g=0.633mm, and t=0.2mm. The slight reduction in the aperture height may not reduce the effective aperture size, since the vertical cuts are made in most irises.

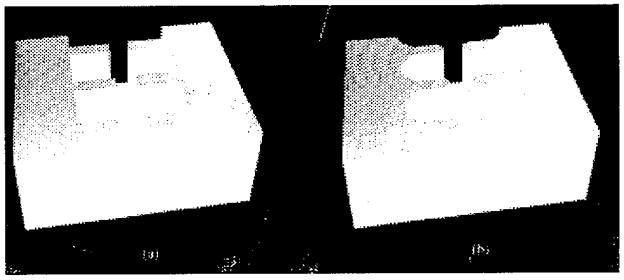


Figure 2: Two types of constant gradient planar structures used in the simulation

Using the MAFIA code [7], the structure was simulated to find the frequencies, field distribution, and shunt impedance. Two different cell shapes were used for comparison: a shape with right angle corners and a shape with half circles. Figures 2(a) and 2(b) show the bottom half of the 3-cell unit structures for the simulation. The structure in Figure 2(b) has rounded corners at the cuts in the irises. For unit structures with various cutwidth s, the group velocity was found. The group velocity vs. the cutwidth with an aperture height of 2a=0.5mm is shown in Figure 3.

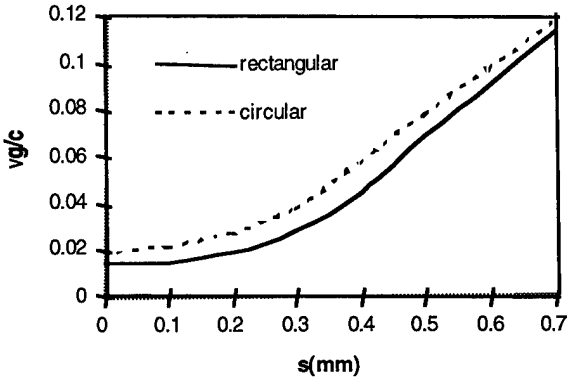


Figure 3: Group velocity vs. cutwidth s in irises

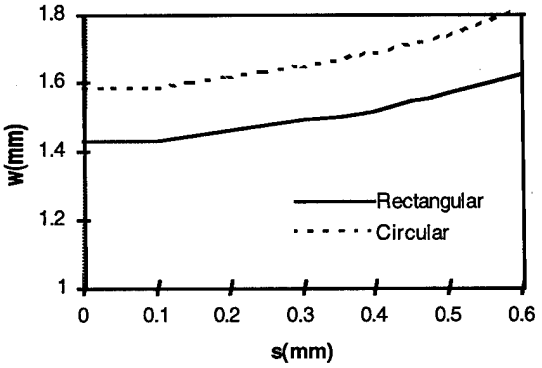


Figure 4: Cell width w vs. cutwidth s in irises

Figure 4 shows the cell width w for different cutwidths for the two differently shaped cases. The Q-factors and the shunt impedances of the structures are shown in Figures 5 and 6, respectively. Note that the cavity with greater cutwidth in the iris has a higher Q-factor but a lower shunt impedance (s>0.1mm) than the cavity with smaller cutwidth in the iris.

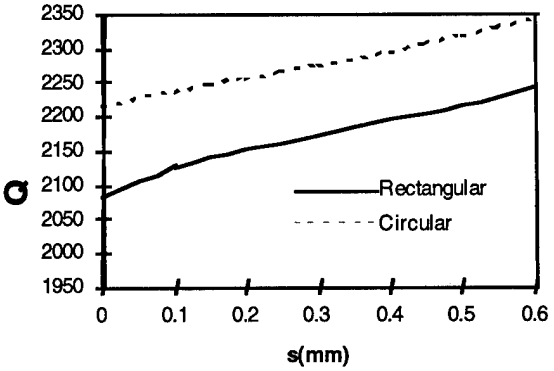


Figure 5: Cavity Q-factor vs. cutwidth s in irises

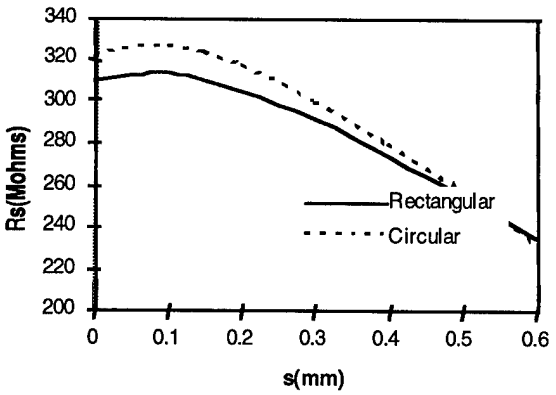


Figure 6: Shunt impedance of $2\pi/3$ mode vs. cutwidth in irises

III. Heat Loading

Figure 7 shows the temperature distribution in a rectangular cell with a cut in the iris due to rf power dissipation. An input power of 29kW and 1% duty cycle were assumed at the input of the structure. For the same input power, that is for a similar energy gain, the heat loadings in the first cell of the constant gradient structure and the constant impedance structure were 34W/cm² and 80W/cm², respectively and their temperatures at the hottest point were 34°C and 45°C, respectively. The area near the beam axis is the hottest area as in the cylindrical cavity. To compare the result with the constant impedance case, the same heat flux of 80W/cm² is used [5]. For the same amount of heat loading, the constant gradient and the constant impedance structures have 47°C and 45°C, respectively, at the tip of the iris. With the same power dissipation at the first cell, the constant gradient structure has 55% more energy gain.

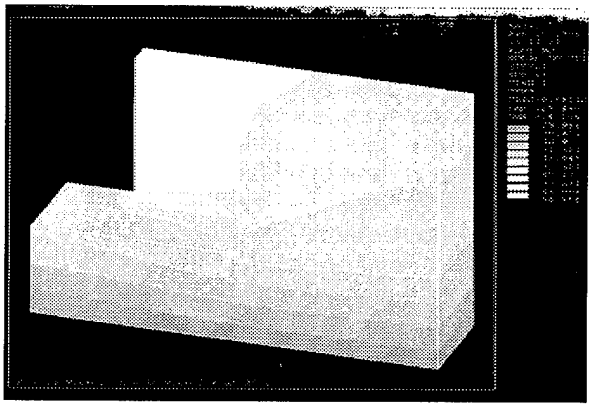


Figure 7: Temperature distribution of a cell with a cut in the iris

IV. Discussion

Previously a planar structure with the aperture only in the x-direction was discussed as the quadrupole-like characteristic [1,3,8]. With additional cuts in the y-direction, the coupling apertures look like cross slots. When the vertical slots are much narrower than the horizontal slots, the focusing characteristic of the structure would be close to the quadrupole characteristic. If the vertical slot width s is comparable to the horizontal aperture height a, the focusing characteristic will become different. At the four corners of the irises facing each other, the electric field concentration is greatest. Thus, the electric and magnetic fields may not be assumed to be rotationally symmetric at near the beam axis; the electric and magnetic forces can not be rotationally symmetric.

With the cross-like aperture, $E_x = 0$ on the *y-axis* and $E_y = 0$ on the *x-axis*. For a particle traveling with the velocity of light at small offsets in x and y, the magnetic forces can be stronger near the iris corners. For small offsets in x and y in the transverse plane, the electric forces due to the electric fields, will be stronger toward the corners of the irises. These forces can be similar to the force in an octupole magnet field.

V. Conclusion

Constant gradient accelerating cavity structures have been computer simulated. It was found that a structure with cuts in the irises can be made with a microfabrication process and used for building a linac system. The calculations shown in the previous sections can provide the physical dimensions of the constant gradient linac structure. The heat concentration at the center of the dividing wall between the cells can be lowered; the input power to the structure can be increased for higher energy gain. Using a pair of half structures in parallel, a precision alignment is a must and is expected to be possible. The input/output couplers of the constant gradient structure can be designed as shown in [9].

VI. References

[1] H. Henke, et. al., private communication.

[2] Y. W. Kang, H. Henke, R. L. Kustom, F. Mills, and G. Mavrogenes, "A mm-Wave Planar Microcavity Structure for Electron Linear Accelerator System", *Proc. of the 1993 IEEE Particle Accelerator Conference*, Vol. 1, pp. 549-551, 1993.

[3] H. Henke, "mm-Wave Linac and Wiggler Structures," *Proc. of the EPAC '94*, London, 1994

[4] R. L. Kustom, et al., "Linear Accelerator Structures," *Linac conference*, KEK, 1994.

[5] P. J. Matthews and A. M. Khounsary, private communication.

[6] G. A. Loew, and R. B. Neal, Linear Accelerators, North-Holland Publishing Co., 1970.

[7] The MAFIA Collaboration, MAFIA User's Guide, July 8, 1994

[8] E. Mills and A. Nassiri, private communication.

[9] Y. W. Kang, "Input/output Couplers for a Planar mm-Wave Structure," *Proc. of the 1993 IEEE Particle Accelerator Conference*, Vol. 2, pp. 1054-1058, 1993.

PULSE TO PULSE STABILITY ISSUES IN THE SLC *

C. Adolphsen, R. Assmann, F.J. Decker, P. Emma, J. Frisch, L.J. Hendrickson, P. Krejcik, M. Minty, N. Phinney, P. Raimondi, M.C. Ross, T. Slaton, W. Spence, R. Stege, H. Tang, F. Tian, J. Turner, M. Woodley, F. Zimmermann, Stanford Linear Accelerator Center, Stanford, CA 94309 USA

ABSTRACT

Although the SLC achieved record luminosity in 1994, a major hindrance to further increases is pulse-to-pulse stability of the machine, often referred to as *jitter*. Raising the intensity of the SLC beams has gained luminosity but the intensity-normalized luminosity has decreased due to additional emittance dilution and to increasing jitter at higher intensities. Precision tuning of the final focus using beam-beam deflection scans is hampered by the pulse-to-pulse variations in both beam position and beam size. These were traced to position, intensity and energy jitter in various subsystems of the collider. Contributions to both the origin and amplification of the jitter have been identified as coming from wakefields in the linac, instabilities in the damping rings, acceptance limitations and feedback performance. The intensity fluctuations from the source can easily be amplified as a result of the SLC configuration of accelerating the two electron and positron bunches in the same linac.

I. INTRODUCTION

Linear colliders are inherently less stable than storage rings, and instabilities on a wide range of time scales must be controlled in order to achieve high luminosity. During the 1994 SLC run [1] the beam intensities were limited to around 3.5×10^{10} particles per bunch at the interaction point (IP) due to the increase of jitter with intensity. The larger effective overlap of the two beams is less important than the fluctuations in estimated beam size (σ). With successive beam size measurements varying by as much as a factor of two, tuning becomes less efficient and may no longer optimally converge. Detector backgrounds may also increase when tails in the beam distributions are intermittently intercepted by collimators.

In addition to orbit (0.3-0.5 σ rms) and IP beam size variations (about 0.4 σ rms), pulse-to-pulse jitter in intensity (1-3% rms) and energy (0.05% rms) may degrade performance. At the SLC there are numerous mechanisms where jitter may be transformed from one type to another and it can be difficult to distinguish between cause and effect throughout the various machine subsystems. A variety of techniques were used to characterize and correlate jitter sources. This paper reviews the measurements and improvements during the 1994 run.

II. JITTER MEASUREMENT

The primary tool for measuring beam stability throughout the SLC is the beam position monitor (BPM) and toroid data acquisition system. In the simplest mode, a few pulses of data are acquired automatically every few minutes and the rms value recorded in a time history. Fig. 1 shows the rms intensity value at different toroid monitors along the SLC, starting at the electron gun and ending at the IP. The jitter is seen to grow steadily along the length of the machine. The two curves represent the separately measured jitter of the positron and electron beams. While intensity jitter is not in itself a critical factor at the IP, it is indicative of other effects.

Another mode of BPM acquisition allows analysis of several hundred consecutive machine pulses. The time dependent data can be displayed along with the mean and rms variation within the sample. Machine-wide data is recorded simultaneously so that correlations can be made between upstream and downstream variations in the beam. The data can also be Fourier analyzed to look for signature frequencies of particular sources of jitter. Commonly observed frequency components are in the range of 10-20 Hz.

Transverse jitter is characterized by fitting the beam trajectory over a range of BPMs. The feedback software that is used to control the orbit at many different points along the machine [2] calculates the rms of angle and position which is recorded in a time history. Trajectory reconstruction of data sampled at the full repetition rate of the beam can be analyzed offline [3]. This technique has been used to fit the coherent betatron oscillations observed at the IP back towards their point of origin upstream. In many instances the amplitude of the jitter is seen to increase uniformly along the linac, indicating a distributed source of jitter within the linac. This data has also been processed with an autocorrelation analysis [4] to quantify the degree of correlation between any two points at given frequencies.

Estimates of both orbit and beam size jitter can be derived from wire scans performed throughout the SLC. Position monitor data acquired as a wire is scanned across the beam is used to correct the centroid position on a pulse-to-pulse basis. This provides an estimate of both the single

* Work supported by Department of Energy Contract DE-AC03-76SF00515.

0-7803-3053-6/96/$5.00 ©1996 IEEE

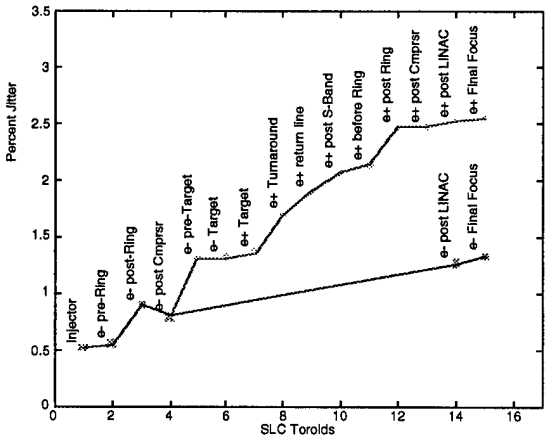


Figure 1: RMS intensity jitter (%) measured at different monitors along the SLC from the gun (left) to the IP (right). Upper trace e+, lower e-. The value plotted at each toroid is the mean of the rms jitter recorded over the entire 1994 run.

pulse beam size and the time averaged beam size over 50-100 pulses. The pulse-to-pulse beam size variations at the IP, as inferred from off-center collisions, are of the order of 200 nm, which is comparable to the IP orbit jitter [5].

III. SOURCES OF JITTER

A variety of sources of instability have been identified throughout the machine from the injector through the collimator region at the end of the linac. Significant improvements were made during the 1994 run.

The polarized electron source operates with an intensity jitter of around 0.5 % for the sum of the two bunches (fig. 1). The effects of laser instability are reduced by operating the photocathode well into saturation. Phase jitter in the injector RF together with changes in beam loading with intensity produce energy errors at the end of the injector linac. The intensity jitter is about the same at this point but then doubles as a result of the finite energy aperture of the damping ring.

The intensity jitter of the positrons at the IP is about a factor of two worse than for the electrons. The intensity jitter of the electron bunch which produces positrons is converted into energy fluctuations due to heavy beam loading in the positron capture and acceleration sections. With a finite energy aperture, these fluctuations are converted back into intensity jitter. A succession of such exchanges creates the amplification mechanism.

The extraction kicker in the electron damping ring operates with a flat top to extract both bunches. Small timing errors can place a bunch on the rising or trailing edge of the kicker pulse, which produces jitter in the extracted kick angle. This typically contributes about 20% of the observed beam jitter. Timing scans are periodically done to minimize this effect and a new feedback has been commissioned to maintain optimal timing.

Jitter in the phase of the extracted beam from the damping rings results in injection energy errors into the linac. In previous runs, a turbulent bunch length instability in the damping rings resulted in a sawtooth behavior in the beam phase above a threshold of around 3.0×10^{10} particles per bunch. This effect has been greatly reduced with the installation of new low impedance vacuum chambers [6].

Energy oscillations, induced by transient beam loading at injection into the damping rings, cause amplification of the intensity jitter via the limited energy aperture of the ring. RF feedback and mismatching the klystron loading angle are used to minimize the transient beam loading [7].

In 1994 bunch overcompression in the transfer line between the damping ring and linac was used to reduce the energy spread at the IP [8]. Clipping of the energy tails reduces the jitter at the end of the linac, however, about 15% of the beam is lost. With reduced energy spread and jitter, detector backgrounds at the IP were significantly reduced.

In the linac, the observed orbit oscillations at 10-20 Hz were caused in part by mechanical vibrations of quadrupoles and RF structures. In 1989 at lower beam intensities, BNS damping [9] was introduced to minimize perturbations caused by short-range transverse wakefields. With BNS, energy spread is introduced at beginning of the linac and taken out at the end. While effective in damping jitter at injection, jitter originating within the linac is not corrected. Measurements indicated amplification of the jitter along the linac by as much as a factor of six. Power supply ripple in the quadrupoles is too small to account for this, but mechanical vibration measurements have shown up to 300 nm vertical motion of the quadrupoles, which is driven by the water cooling systems [10]. Improvements to quadrupole supports and to water systems were made mid-run and further work is in progress.

In the course of studying this amplification, it was observed that the jitter of the electron beam was greatly reduced in the absence of the leading positron beam. An unexpectedly large correlation was also seen between the jitter of the positron and electron beams. The mechanism was studied by inducing an oscillation on the positron beam and measuring the resulting deflection of the electron beam, as shown in figs. 2a,b. The coupling is due to the long range transverse wakefield from the leading positron bunch in the linac. It was possible to map the wakefield kick by varying the timing between the positron bunch and the witness electron bunch. The bunch separation of 59 ns was altered in units of 0.35 ns (one linac S-band bucket).

The coupling between the bunches was greatly reduced by making the transverse phase advance of the two beams dissimilar. The horizontal and vertical tunes were split by

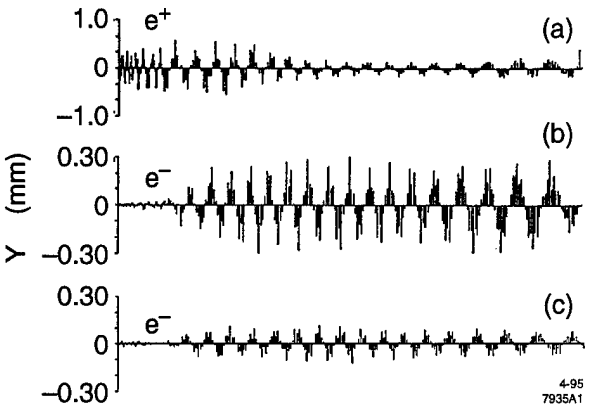


Figure 2: Vertical e+ oscillation introduced before the linac (a) and the long range wakefield induced e- oscillation (b) before and (c) after implementation of the split tune lattice.

about ±5%, to effectively separate the electron and positron tunes in each plane. The reduction in coupling with the new lattice is shown in fig. 2c. The overall electron vertical jitter downstream of the linac was decreased by 30-50%.

Wakefield kicks generated by the linac collimators may distort the beam emittance and create additional jitter. While the jaws are typically set to $\pm 5\sigma$ of the beam, trajectory errors can cause the beam to pass off center through the collimators and receive a wakefield kick. Measurements of the wakefield kick were made as a function of collimator offset and gap at different beam intensities [11]. Periodic checks are required to ensure that the collimators are correctly positioned with respect to the beam. Feedback loops are used throughout the SLC to stabilize the beam intensity, trajectory and energy. Improper compensation or amplification of beam noise at certain frequencies can result from imperfections in the feedback modeling or from frequency aliasing. Performance is degraded by improper characterization of the lattice model, control device dynamics, or assumed beam noise spectrum. With the present feedback loop design, frequencies between about 1 and 5 Hz are amplified. The linac cooling system pumps operate with rotation rates just below the line frequency (at SLC this is one half the pulse repetition rate). The small frequency difference is seen as a 1 Hz beam oscillation due to aliasing. This can be within the anti-damping range of the feedback system for low sampling rates. This year techniques were developed to quantify the performance of a single loop or a succession of loops [12].

Transverse orbit variations affect the luminosity in at least two different ways. First, the average overlap of the two beams is reduced, causing a luminosity decrease by about 5-10% at high current. More importantly, in the presence of orbit jitter, the beam-beam deflection scans become more erratic and are harder to interpret. As a result tuning of the final focus may no longer converge to the optimum IP spot sizes. The beam size variations may be caused by upstream orbit or energy jitter. At the IP, where beam sizes are measured using beam-beam deflection scans, a jitter correction algorithm is also employed [13]. Here the algorithm is more complicated because fitting to the beam-beam deflection curve in the plane of the deflection depends also on the out-of-plane jitter. BPMs in both the linac and final focus are required to effectively sample all phases. The improved fitting algorithm is very useful in simplifying interpretation of the beam-beam scans.

IV. CONCLUSION

In the 1994 run, considerable effort has been devoted to the detection and suppression of orbit and intensity jitter throughout the SLC. Major improvements include the separation of electron and positron phase advance in the linac, a strengthening of the linac quadrupole supports, and the implementation of jitter corrected fits to the beam-beam deflection scans. The recent progress in SLC performance is partly due to these improvements.

IV. REFERENCES

[1] P. Emma, "The Stanford Linear Collider", these proceedings.

[2] L. Hendrickson et al, Proc. 1994 Linac Conf., Tsukuba, Japan, 626-630.

[3] C. Adolphsen, T. Slaton, "Beam Trajectory Jitter in the SLC Linac", these proceedings.

[4] W. Spence, F. Tian, to be published.

[5] F. Zimmermann, et al., "Performance of the 1994/95 SLC Final Focus System", these proceedings.

[6] K. Bane et al, "High-Intensity Single Bunch Instability Behavior in the New SLC Damping Rings Vacuum Chambers", these proceedings.

[7] M. Minty et al, "Operating Experience with High Beam Currents and Transient Beam Loading in the RF of the SLC Damping Rings", these proceedings.

[8] F-J Decker et al, Proc. 1994 Linac Conf., Tsukuba, Japan, 47-49.

[9] V. Balakin, A. Novokhatsky, V. Smirnov, 12th Int. Conf. on High Energy Accel., FNAL (1983) 119.

[10] J. L. Turner et al, "Vibration Studies of the Stanford Linear Accelerator", these proceedings.

[11] K. Bane et al, "Measurement of the Effect of Collimator Generated Wakefields on the Beams in the SLC", these proceedings.

[12] M. Minty et al, "Feedback Performance at the Stanford Linear Collider", these proceedings.

[13] P. Raimondi, to be published.

HOM-FREE LINEAR ACCELERATING STRUCTURE FOR e^+e^- LINEAR COLLIDER AT C-BAND

T. Shintake, [1]K. Kubo*, H. Matsumoto, and [2]O. Takeda
KEK: National Laboratory for High Energy Physics, Oho, Tsukuba, Ibaraki 305 Japan
[1]SLAC: Stanford Linear Accelerator Center, Stanford University, Stanford, CA 94309 USA
[2]Toshiba Co., Yokohama, 230 Japan

HOM-free linear acceleration structure using the choke mode cavity (damped cavity) is now under design for e^+e^- linear collider project at C-band frequency (5712 MHz). Since this structure shows powerful damping effect on most of all HOMs, there is no multibunch problem due to long range wakefields. The structure will be equipped with the microwave absorbers in each cells and also the in-line dummy load in the last few cells. The straightness tolerance for 1.8 m long structure is looser than 30 μm for 25 % emittance dilution limit, which can be achieved by standard machining and braising techniques. Since it has good vacuum pumping conductance through annular gaps in each cell, instabilities due to the interaction of beam with the residual-gas and ions can be minimized.

I. INTRODUCTION

In the future e^+e^- linear colliders, multi-bunch beam operation is essential to get high luminosity. For the same reason, the spot size at the interaction point must be focused into quite small dimension, typically a few nanometer in vertical and a few hundred nanometer in horizontal. To achieve this small spot with multi-bunch beam, it is very important to accelerate low-emittance beam in the main-linac without deteriorating its emittance. Therefore, the wake-field problem in the linear accelerating structure is one of the most important R&D issue to realize the linear collider.

To solve this problem, the choke mode cavity was devised by the author[1]. The concept of this structure is explained in Fig. 1. This structure is made of many copper disks. There are gaps between disks, the beam induced wake-fields (or HOM : Higher-Order Modes) can easily get out from the cavity through the gap, and all of HOM oscillations disappear before the successive bunched beam coming. In order to trap only the accelerating mode inside the cavity, the choke is attached in the gap. Since the choke has sharp notch-filter response, only the selected mode, the accelerating mode in this case, is trapped. On the other hand, all of the HOM power can get out smoothly without reflecting at the choke. Therefore, this structure shows quite effective damping on all HOMs for wide frequency range. If we apply this structure to the main linac for the linear collider, emittance degradation problem due to the long-range wake field can be perfectly eliminated.

In order to demonstrate feasibility of this structure, a hot model of 0.5 m long constant-gradient structure at S-band was fabricated[2,3] in 1993. The completed structure was installed in ATF injector linac at KEK. The high power processing was smoothly performed, finally an average accelerating gradient of 50 MV/m was obtained with 120 MW input power[4]. There was no difficulty on processing due to high voltage break down or multipacting discharges. Also, the beam acceleration test was performed, and the energy gain of 26.2 MeV was observed at 104 MW input power, which was good agreement with the design vale. With this success, the high power capability of this structure was fully proved.

The next step of the R/D program has been started in 1995, a C-band model of this structure is now under developing, in which HOM absorbers will be loaded in each disks and also in-line dummy load will be integrated at the last few cells. In this paper, status of this R/D is reported.

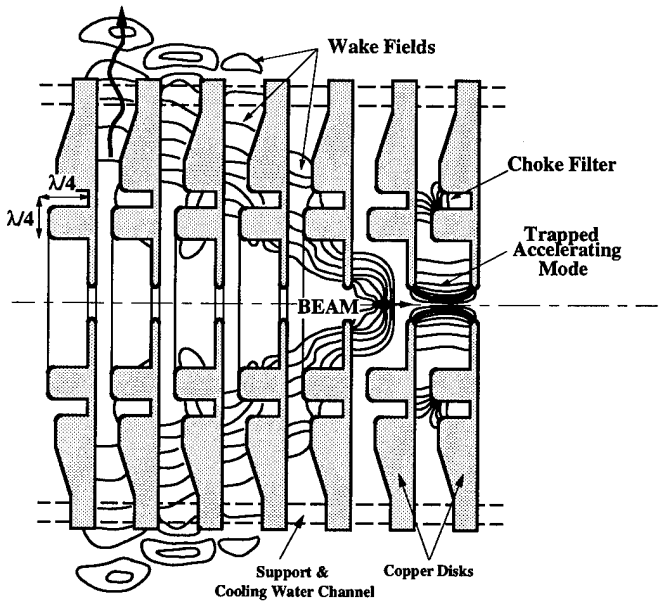


Fig. 1: Conceptual drawing of HOM-free linear accelerating structure using choke mode cavity.

II. C-BAND STRUCTURE DESIGN

We have proposed C-band rf system as one of the best solution to realize the large scale main linac for the e^+e^- linear colliders at 500 GeV to 1 TeV c.m. energy scale with minimum R/Ds and lower construction cost[5,6].

The designed parameter of the C-band structure is listed in Table 1, and its cross-sectional view is shown in

* Visiting from KEK

0-7803-3053-6/96/$5.00 ©1996 IEEE

Fig. 2 The phase shift per cell is $3\pi/4$, whose unit cell length is slightly longer than the $2\pi/3$ mode, which make easy to get more room to fit the choke structure in each cell.

The average shunt impedance in this structure is 55 MΩ/m, which is about 25% lower than that of conventional disk-loaded structure with same 2a, 2b dimensions. It does not mean we have to increase the input rf power by 25%. In a practical operation, the net accelerating gradient is always lowered due to the beam loading effect. This effect is smaller in lower shunt impedance structure, then the loss of the shunt impedance is somewhat compensated. In the C-band system, the pulse beam current is 0.57 A, and the beam loading effect is about 8 MV/m on the nominal accelerating gradient of 40 MV/m. To keep the same accelerating gradient in our structure of 25% lower shunt impedance, the input power has to be increased about 15%. Therefore, the power loss in the choke does not deteriorate the system efficiency so much. If we think about the big benefits of multibunch capability in this structure, this much of the power is not expensive.

Table-1 Electrical Parameters

Operating Frequency	f	5712 MHz
Phase Shift per Cell	βD	$3\pi/4$ TW
Structure Type		const. grad.
Wake field Control		Damping
Damping	Q_e	< 10
Length	L	1.81 m
Number of Cells	N	92 cells
Cell Length	D	19.68 mm
Filling Time	T_F	281 nsec
Attenuation Parameter	τ	0.53
Iris Aperture	a/λ	0.17 ~0.13
Group Velocity (%c)	Vg/c	3.5 ~1.2
Quality Factor	Q	9.5 $x10^3$
r/Q		5.7 kΩ/m
Shunt Impedance	$<r>$	55.0 MΩ/m
Accelerating Gradient at 80 MW input		
Accelerating Gradient(1)	E_a	40 MV/m
RMS Straightens Tolerance(2)		35 μm/92

1) Unloaded gradient for 500 GeV c.m. case.
2) Tightest tolerance on structure straightens over N cells.

III. MICROWAVE ABSORBERS

In the S-band high power model, we did not install the microwave absorber, because the main object in the test was demonstration of the high power capability of this new type of rf cavity. In the C-band structure design, we started R/D study on the microwave absorbers, including survey of material, its quality control, optimization of structure to meet rf matching, and brazing process.

Engineering ceramic of SiC has already been used as microwave absorber. H. Matsumoto developed the first model of waveguide dummy-load for S-band microwave in 1981, and nearly 200 units of this dummy load were successfully used in KEK PF injector linac[7]. Recently, he developed a high-peak power model which can handle 50 MW, 1 μsec at S-band, in which disk shape SiCs(φ20 mm) were directly attached on copper waveguide by brazing. T. Koseki et. al.[8] have recently applied a SiC duct to HOM-damper on beam pipe close to an rf accelerating cavity. They reported the SiC duct made by Toshiba CERASIC-B (resistivity of 20 Ωcm) strongly reduced the Q-values of HOMs in the cavity. Because of these experiences, and also its good vacuum property we will employ SiC in our structure.

We use disk shape SiC (CERASIC-B) of φ15-20 mm, directly attach them on each cell by brazing as shown in Fig. 2. The skin depth in SiC becomes 3 mm at C-band frequency, and the effective surface resistance becomes 6 Ω, which is same order as the characteristic impedance 5 Ω of TEM wave in the radial line at radius of 6 cm with 5 mm gap. Therefore the wakefields will be effectively absorbed in SiCs due to ohomic loss of the wall current.

IV VACUUM CHAMBER DESIGN

In order to simplify the vacuum chamber and reduce number of the components, we will implement the in-line dummy load in the last few cells by coating the cavity with high resistivity metal. This technique has been used long time in medical accelerators[10].

The vacuum conductance from beam line to the tank is quite large, the structure can be pumped down to very low pressure level quickly. This is quite important feature, because recent studies[9] are indicating the existence of new type instability due to wakefield like effect by trapped ions in the residual gas, which can cause emittance dilution in the main linac or in the bunch compressor.

V. CELL COOLING

Since this structure has to be used at high accelerating gradient and high repetition frequency in the liner collider, the cell cooling is one of the most important issue in practical usage. The expected maximum heat-dissipation per unit length is 3.2 kW/m. We assumed cooling water flow of 126 litter/min., and its temperature 21 deg.C, which flows along six cooling water channels of 12 mm inner diameter. We estimated heat dissipation density using SUPERFISH code, then put in these data into I-DEAS code to simulate the heat flow inside the copper-disk and heat transfer into the cooling water. According to this simulation, the maximum temperature at the top of the iris reaches 35.4 deg.C. This is quite high as compared to the traditional design of disk-loaded structure. We will implement a feedback loop which measures the rf phase at the end of the structure, and control the cooling water temperature and also the klystron input phase.

VI. ALIGNMENT TOLERANCE ON ACCELERATING STRUCTURE

The alignment tolerance of accelerating structures can be estimated from an analytical expression of emittance growth. Expected emittance growth due to random misalignment of accelerating structures is approximately[11]

$$< \Delta\varepsilon >= \frac{e^2 q^2 x_{rms}^2 W_{rms}^2 \beta_0 L_a \left(E_f^\alpha - E_0^\alpha\right)}{2\alpha E_f E_0^\alpha g} \qquad (1)$$

where q is total charge, x_{rms} the r.m.s. of misalignment, β_0 initial averaged beta function, L_a length of each structure, E_f final energy, E_0 initial energy, g accelerating gradient and beta-function is assumed to be proportional to E^α., where α = 0.5. $Wrms$ is the r.m.s. of the wakefield effect and

$$W_{rms}^2 \approx 0.91 \frac{W'^2_s \sigma_z^2}{\pi} \qquad (2)$$

for a single Gaussian bunch, where σ_z is bunch length. W'_s is slope of the transverse wake function which is assumed to be a linear function of distance and estimated as

$$W'_s \approx 1.35 \times 10^{19}\ V/C/m^3 \qquad (3)$$

for structures with the aperture radius of 7.77 mm or a/λ of 0.148. Because of the strong damping (Q<10) in our structures, the multi-bunch effect due to the long range wakefield will be negligibly small compared with the single-bunch effects.

We estimated the tolerance for a bunch with 1.1×10^{10} particles and the r.m.s. length of 120 μm[6]. We assumed a linac with the same lattice as the 500 GeV (beam energy 250 GeV) NLC (Next Linear Collider, being designed at SLAC) linac[11], assuming the same beta at the same energy, except different injection energy : 20 GeV in our case and 10 GeV in NLC. The tolerance is 30 μm for each 1.8 m long structure to achieve emittance growth of less than 25%. The tolerances for various length of alignment unit are also estimated by scaling from NLC using a numerical method, which is shown in Fig. 3 comparing with the tolerances for the NLC structures[12]. Because the multi-bunch effect is negligible for our structures, the straightness tolerance of in each structure is loser than the alignment tolerance of each whole structure, which will be achieved by conventional machining and braising techniques.

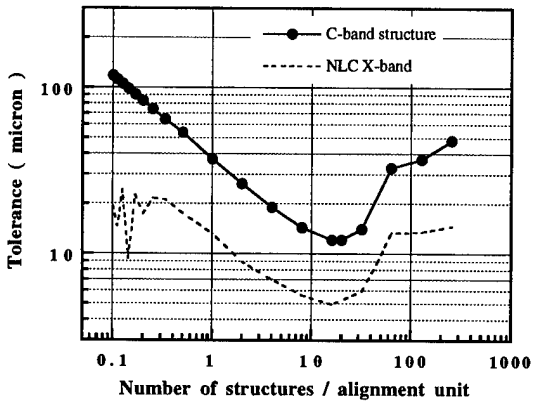


Fig. 3 Alignment tolerance for C-band HOM-free structure comparing with NLC damped-detuned structure.

VII. REFERENCES

[1] T. Shintake, "The Choke Mode Cavity", Jpn. J. Appl. Phys. Vol. 31 (1992) pp.L1567-L1570, Part 2, No. 11A. 1 Nov. 1992

[2] T. Shintake, "Design of High Power Model of Damped Linear Accelerating Structure using Choke Mode Cavity", proceedings of 1993 Particle Accelerator Conference, Washington, D.C., U.S.A., May 1993, pp. 1048 - 1050, KEK Preprint 93-27, May 1993 A

[3] A. Miura, et. al., "Fabrication of HOM-Free Linear Accelerating Structure using Choke-Mode Cavity for Japan Linear Collider", Proc. 17th Int. Linac Conf.(LINAC94), Tsukuba, Japan, August 21-26, 1994, p. 263

[4] T. Shintake, et. al., "High Power Test of HOM-Free Choke Mode Damped Accelerating Structure", Proc. 17th Int. Linac Conf.(LINAC94), Tsukuba, Japan, August 21-26, 1994, p. 293, KEK Preprint 94-82, Sep. 1994 A

[5] JLC Group, "JLC-I", KEK Report 92-16, December 1992, A/H/M, p. 184

[6] T. Shintake, et. al., "C-band linac rf-system for e^+e^- linear collider", presented in this conference.

[7] H. Matsumoto, "Development of the S-band High Power RF Load", Proc. 16th Linear Accelerator Meeting in Japan, Nihon University, Sep. 3-5, 1991

[8] T. Koseki, et. al., "An RF Cavity with SiC Absorbers", 4th European Particle Accelerator Conf. (EPAC94), London, U.K., June 27-July 1, 1994, KEK Preprint 94-60, July 1994, A

[9] T. O. Raubenheimer and F. Zimmermann, "A fast beam - ion instability in linear accelerators and storage rings", SLAC-PUB-95-6740, March 1995, pp. 37

[10] J. Haimson, "Absorption and generation of radio-frequency power in electron linear accelerator systems", Nucl. Instrum. Meth. 33 (1965) pp. 93-106

[11] K.L.F. Bane et. al., "Issues in Multi Bunch Emittance Preservation in the NLC", EPAC'94, SLAC-PUB-6581 (1994)

[12] About the methods and parameters for estimation of the tolerance for NLC, see : K.Kubo et. al., "Alignment tolerance of accelerating structures and corrections for future linear colliders", this conference.

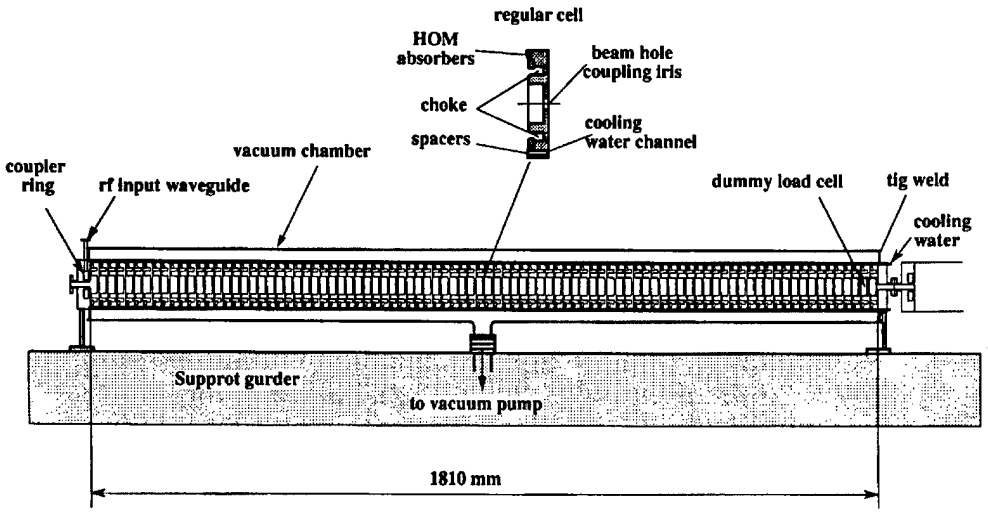


Fig. 2 HOM-Free C-band Structure

SLAC/CERN High Gradient Tests of an X-Band Accelerating Section

J. W. Wang, G. A. Loew, R. J. Loewen, R. D. Ruth, A. E. Vlieks
SLAC, Stanford University, Stanford, CA 94309 USA

I. Wilson, W. Wuensch
CERN, Genève 23, CH-1211

INTRODUCTION

High frequency linear collider schemes envisage the use of rather high accelerating gradients: 50 to 100 MV/m for X-band and 80 MV/m for CLIC. Because these gradients are well above those commonly used in accelerators, high gradient studies of high frequency structures have been initiated and test facilities have been constructed at KEK [1], SLAC [2] and CERN [3].

The studies seek to demonstrate that the above mentioned gradients are both achievable and practical. There is no well-defined criterion for the maximum acceptable level of dark current but it must be low enough not to generate unacceptable transverse wakefields, disturb beam position monitor readings or cause RF power losses. Because there are of the order of 10,000 accelerating sections in a high frequency linear collider, the conditioning process should not be too long or difficult.

The test facilities have been instrumented to allow investigation of field emission and RF breakdown mechanisms. With an understanding of these effects, the high gradient performance of accelerating sections may be improved through modifications in geometry, fabrication methods and surface finish. These high gradient test facilities also allow the ultimate performance of high frequency/short pulse length accelerating structures to be probed.

This report describes the high gradient test at SLAC of an X-band accelerating section built at CERN using technology developed for CLIC.

THE ACCELERATING SECTION

The travelling wave accelerating section has 26 regular cells and 2 coupler cells. Section parameters are summarized in Table 1. Details of the geometry of the disk loaded waveguide are given in Reference [1] which also describes the high gradient test at KEK in September 1992 of a 20 cell version of the same design.

The average and peak accelerating gradients are related to input power by the following expressions:

$$\langle E \rangle [MV/m] = 15\sqrt{P_{in}[MW]}$$

$$\hat{E}[MV/m] = 18.4\sqrt{P_{in}[MW]}$$

The accelerating section was made using the diamond machine and braze techniques developed at CERN for prototype CLIC accelerating sections [4]. After arrival at SLAC, the section was baked out at 250°C for 2 days. It was then stored under a vacuum of 10^{-9} Torr for nine months before being tested.

Beam hole radius	3 mm
Disk thickness	2 mm
Effective length (26+2cells)	.2449 m
Group velocity, v_g/c	1.1% *
Impedance, r/Q	16.0 [kΩ/m]
Shunt impedance, r	106.8 [MΩ/m]
Q	6680*
Attenuation parameter	1.61 [neper/m]*
Filling time, t_f	58 [ns]*
Surface/Accelerating field	1.9

Table 1: Section Parameters (* signifies measured values).

THE TEST FACILITY

The SLAC high gradient test facility was powered by an XC-2 klystron feeding a SLED II pulse compression system. The maximum klystron power was 20 MW with a pulse length of 1 μs, and the corresponding pulse compressor output was 68 MW with a pulse length of 150 nsec. The repetition rate of the system was 60 Hz.

The vacuum levels in the input and output waveguides and in the input beam pipe were measured. Input, transmitted and reflected RF power signals were measured with crystal detectors and captured on a 2 Gsample/sec scope. Upstream and downstream dark currents were measured with Faraday cups. The energy spectrum of the downstream dark current was measured with a spectrometer and a third Faraday cup. The level of radiation produced by the accelerating section was measured with a monitor placed in contact with the side of the accelerating section.

EXPERIMENTAL RESULTS

The accelerating section ultimately achieved an average accelerating gradient of 125 MV/m which corresponds to a peak accelerating gradient of 153 MV/m and a peak surface gradient of 285 MV/m. The highest average accelerating field as function of the number of pulses is shown in Fig. 1. 10^7 shots at 60 Hz corresponds to 46 hours and the entire conditioning process took roughly two weeks.

0-7803-3053-6/96/$5.00 ©1996 IEEE

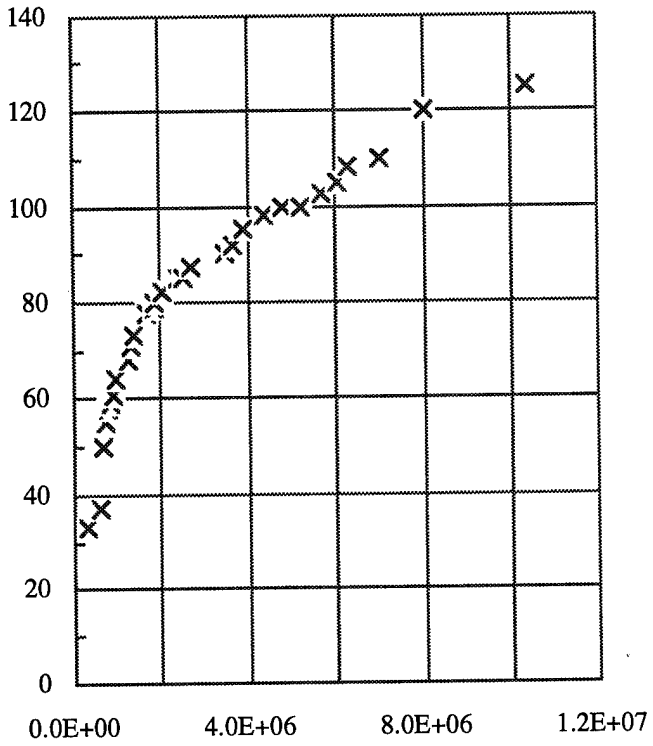


Figure 1: Highest average accelerating gradient [MV/m] as a function of the number of pulses.

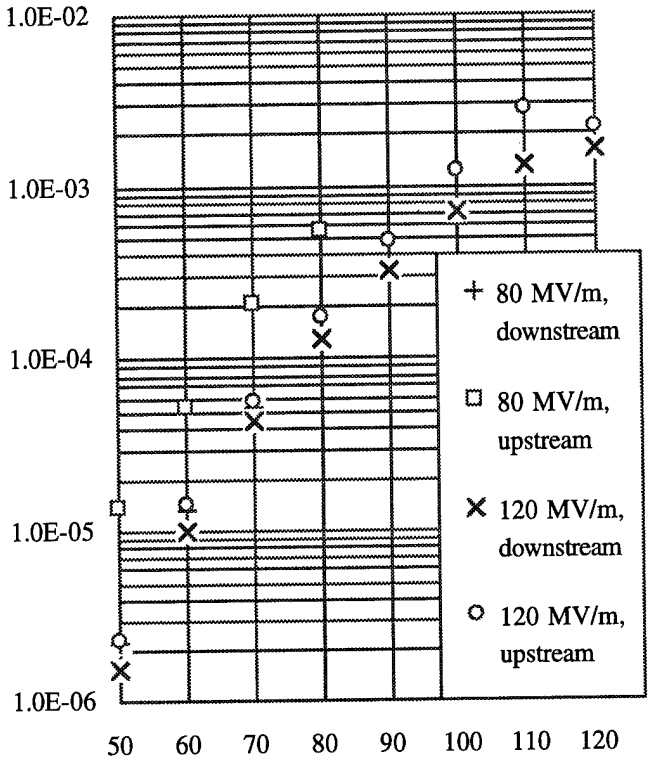


Figure 2: Upstream and downstream dark currents [A] vs. accelerating gradient [MV/m] at various stages of conditioning - indicated by the gradients given in the legend.

After reaching the power level corresponding to about 100 MV/m average accelerating gradient in the section, electrical discharges occurred in both the accelerating section and the test facility components. The recovery time needed for both section and test facility component discharges contributed roughly equally to the slope of data above 100 MV/m in Fig. 1. The experiment ended at 125 MV/m because the gradient in the section was improving very slowly and the klystron was nearly at its power limit.

RF power to the section was interrupted whenever the vacuum level at the section input or output rose above 10^{-8} Torr. After allowing time for the vacuum level to recover, RF was restarted at a reduced power level. The input vacuum level interlock was the most active during conditioning. The reflected RF power level was not used as an interlock input. Dark currents tended to be high and unstable just before a breakdown and thus were used as a rough guide for setting the rate of increase of input power.

The level of dark current as a function of accelerating gradient at different fields and stages of conditioning is shown in Fig. 2.

Throughout the high gradient tests the upstream dark current was greater than the down stream dark current. Below the dark current capture threshold of 60 MV/m the higher upstream dark current is probably due to 33% higher fields at the section input. Why the dark current capture mechanism did not lift the downstream current above the upstream at fields above the capture threshold is not understood.

The upstream dark current for a given gradient decreased as the conditioning process proceeded but the downstream dark current did not.

The downstream dark current spectrometer had a momentum acceptance ($\Delta p/p$) of 2%. Plots of downstream dark current vs. momentum are shown in Fig. 3. The cut-off momenta of 20 and 25 MeV/c correspond to average accelerating gradients of 82 MeV/m and 102 MeV/m respectively.

Dark current as a function of frequency is shown in Fig. 4. The downstream dark current increase with increasing frequency is similar to that observed in other high gradient tests [1,2].

The radiation level measured on the surface of the side of the accelerating section increases roughly exponentially with accelerating gradient as shown in Fig 5.

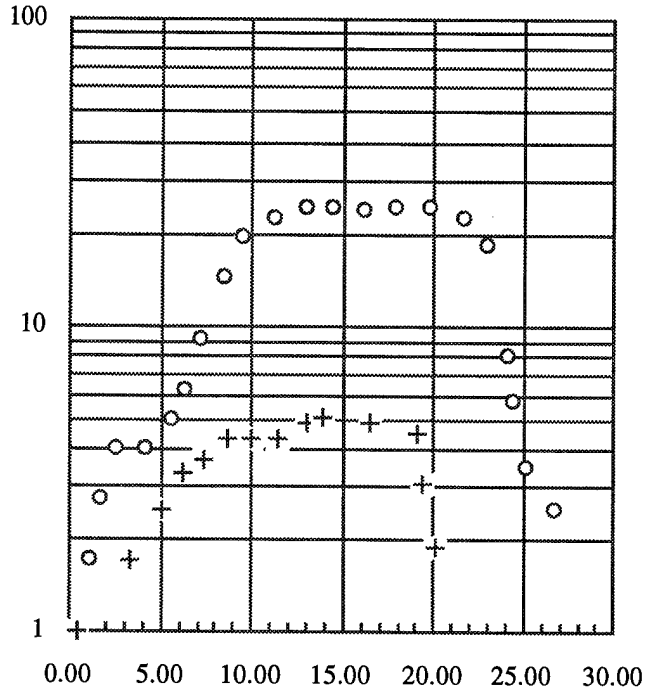


Figure 3: Dark current [pA] vs. momentum [MeV/c]. Circles are for 100 MV/m and plus signs are for 80 MV/m.

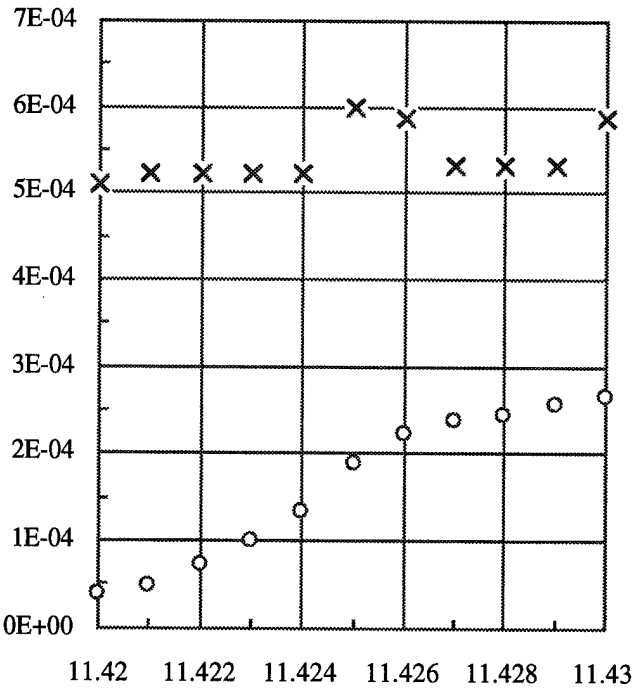


Figure 4: Dark current as a function of frequency for an accelerating gradient of 100 MV/m. x's are upstream dark currents and circles are downstreamdark currents.

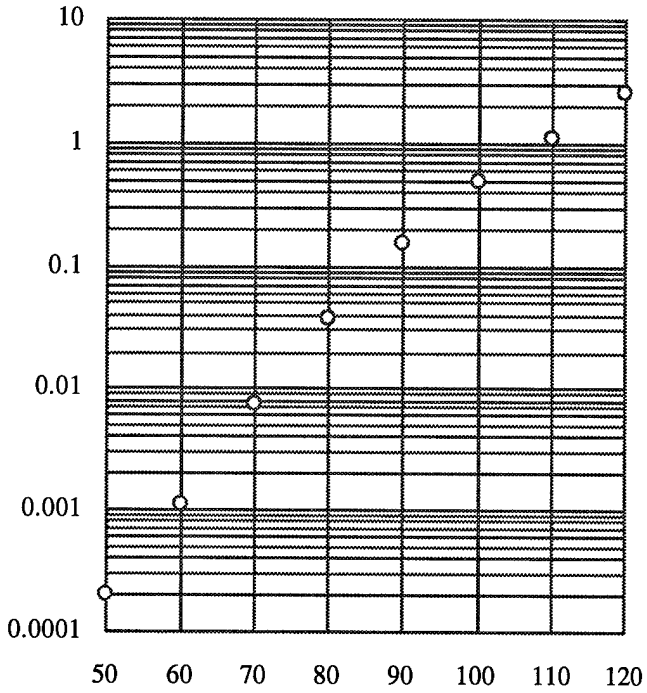


Figure 5: Radiation level [Rem/min] as a function of gradient [MV/m].

ACKNOWLEDGEMENTS

I. W. and W. W. wish to thank C.Achard and S. Leblanc for their help in the design and fabrication of the accelerating section. They also wish to thank the NLC group for making their stay at SLAC enjoyable and successful.

REFERENCES

[1] T. Higo et.al., "High Gradient Performance of X-Band Accelerting Sections for Linear Colliders," *Particle Acclerators*, 1994, Vol. 48, pp.43-59.

[2] J. Wang et. al.,"High Gradient Studies on 11.4 GHz Copper Accelerator Structures," 16th Int. Linac Conf., August 1992, Ottawa.

[3] R. Bossart et. al., "Performances Obtained with the CERN Linear Collider Test Facility (CTF)," European Particle Accelerator Conference, June 1994, London.

[4] I. Wilson, W. Wuensch, C. Achard, "The Fabrication of a Prototype 30 GHz Accelerating Section for CERN Linear Collider Studies," EPAC, June 1990, Nice.

PERFORMANCE OF THE 1994/95 SLC FINAL FOCUS SYSTEM *

F. Zimmermann, T. Barklow, S. Ecklund, P. Emma, D. McCormick, N. Phinney,
P. Raimondi, M. Ross, T. Slaton, F. Tian, J. Turner, M. Woodley, Stanford Linear Accelerator Center,
Stanford University, Stanford, CA 94309 USA,
M. Placidi, CERN, N. Toge, KEK, N. Walker, DESY

Abstract

A major upgrade to the SLC final focus was installed in 1994 to eliminate the dominant third-order aberration of the system, and thereby to reduce the vertical beam size at the IP by a factor of two. At low current, the optimal beam size of about 400 nm is now routinely established, and its sensitivity to orbit variations, to changes of emittance and energy spread, and to other beam parameters has been studied. For intensities above 3×10^{10} particles per bunch, tuning is more difficult due to increased fluctuations of energy, orbit, and emittances. Nonetheless, the expected beam size of about 600 nm has been observed. New procedures and diagnostics allow easier tuning and optimization of the final focus, and also a first measurement of the emittance increase in the arcs.

I. INTRODUCTION

In the Stanford Linear Collider (SLC), electron and positron bunches are accelerated to 47 GeV by the SLAC linac, then transported through two 1200-m-long arc sections, and finally brought into collision at the interaction point (IP). The region between the arcs with the IP at its center comprises the two final foci. Their purpose is to demagnify and collide the two beams. Each SLC final focus consists of two telescopes, called the upper and the final transformer (UT and FT), separated by a chromatic correction section (CCS), which comprises two interleaved $-I$ sextupole pairs [1]. In addition, a dispersion-suppression section is located at the entrance of each final focus. Three superconducting quadrupoles (the final triplet) on either side of the IP provide the last focusing before the beams collide.

II. THE 1994 UPGRADE

In 1993, the smallest vertical single-beam sizes at the IP were of the order of 900 nm. A detailed analysis based on Lie-algebra techniques [2] revealed that the dominant contribution to the beam size (about 700 nm) was caused by a third-order chromatic term (U_{3466} in TRANSPORT notation [3]), the origin of which could be traced back to a non-optimal betatron phase between sextupoles and the final triplet [2]. The aim of the 1994 upgrade has been to correct this phase error by adding a new quadrupole close to the pre-image of the IP at the end of the chromatic correction section.

Furthermore, in the 1994 final focus system, the role of horizontal and vertical sextupoles has been interchanged. A new quadrupole and a new skew quadrupole have been installed in the UT to facilitate an orthogonal tuning algorithm. New wire scanners have been added to measure the beam size throughout the UT.

For rms angular divergences of $\theta_x^* = 300\mu$rad, $\theta_y^* = -200\mu$rad, emittances of $\epsilon_x = 600\mu$mμrad, $\epsilon_y = 60\mu$mμrad, and a relative momentum spread of $\delta = 0.2\%$, the vertical beam size calculated from the linear optics is 300 nm and the largest remaining aberration (U_{3246} in TRANSPORT notation) contributes about 200 nm to be added in quadrature. A third significant contribution of an additional 250 nm is due to synchrotron radiation in the last three bending magnets, which interacts with the uncompensated triplet chromaticity. The expected optimum single-beam spot size in 1994/95 is then of the order of 430 nm, an improvement by about a factor of two compared with the peak value of the previous year.

III. ALIGNMENT AND TUNING

Quadrupole alignment, for which the tolerance may be as tight as 100 μm [4], and the offsets of the beam-position monitors (BPMs) are controlled by a beam-based procedure [5]. The beam is steered through the center of the sextupoles with a precision better than 50 μm, using symmetric and asymmetric orbit bumps for each pair. The magnitude of these bumps is determined by the effect of different sextupole strengths on the IP spot size [7]. UT- and CCS-orbits are maintained by feedback loops. After each opening of the SLD detector and after each change of the detector solenoid field, the final triplet is realigned, again based on a beam-based measurement [6]. A sophisticated orbit-tuning scheme is adopted for the arcs, in order to generate the desired linear transfer matrix while minimizing the effect of synchrotron radiation [8].

In the new final focus, the beam matching is performed in the UT. The incoming mismatched dispersion is corrected by means of two quadrupoles and two skew quadrupoles at the entrance of the final focus. This dispersion-match is typically applied every few weeks. The betatron phase space is matched using six knobs (as suggested by Irwin), which offer orthogonal control over magnification and waist position in both planes, as well as over the coupling from the horizontal into the vertical plane [9]. Each knob simultaneously changes the strength of six quadrupoles and two skew quadrupoles of the UT in a stepwise manner calculated so as to preserve orthogonality. The beam is matched to the design spot size on a wire scanner located at a pre-image of the IP in front of the CCS, which contains 4-μ and 7-μ-diameter carbon wires at different transverse angles [10]. The design spot size at this wire scanner is about 5 times the IP size. The Irwin knobs proved to be sufficiently orthogonal to make the UT-tuning very convenient.

Once the beam is matched in the UT, only fine tuning is necessary to minimize the IP spot size, which is estimated

*Work supported by Department of Energy contract DE-AC03-76SF00515.

0-7803-3053-6/96/$5.00 ©1996 IEEE

from scans of the beam-beam deflection angle, by maximizing luminosity-related signals. The fine-tuning with colliding beams is performed continually by the operators. Small waist shifts are obtained by changing the strength of the triplet and one quadrupole further upstream. Part of the linear coupling is corrected by means of a skew quadrupole at the triplet betatron phase. The residual dispersion at the IP is corrected using two normal and two skew $-I$ quadrupole pairs excited equally with opposite sign in the CCS. Chromaticity is compensated for by the two pairs of CCS sextupoles. Furthermore, several new sextupoles in the FT allow correction of second-order geometric aberrations.

Five new wire scanners in the UT, positioned at appropriate betatron phases, determine the emittances and the beta function mismatch of the incoming beam, as well as its energy spread. The typical rms energy spread in 1994 was of the order of 0.15% for either beam. A wire scanner in front of the final triplet measures the beam divergence, and is used to infer necessary changes of the UT magnification knob.

In order to keep aberrations small, and to preserve the orthogonality of the tuning scheme, it is essential that the phase advance between sextupoles or dispersion-correctors is exactly π. The sum-signal of two horizontal and vertical BPMs, at sextupoles that are nominally separated by a $-I$ matrix, is monitored; it reflects orbit perturbations internal to the CCS. A frequently observed diurnal variation of the sum-signal by up to 80 μm is correlated to changes of the tunnel temperature, and is presumably due to thermal expansion of the magnet supports and the tunnel floor.

IV. BEAM SIZES AND LUMINOSITY

At low current (5×10^9 particles per bunch), the design vertical (horizontal) spot sizes of 420 nm (2.2 μm), are easily achieved, as illustrated by a typical beam-beam deflection scan in Figure 1.

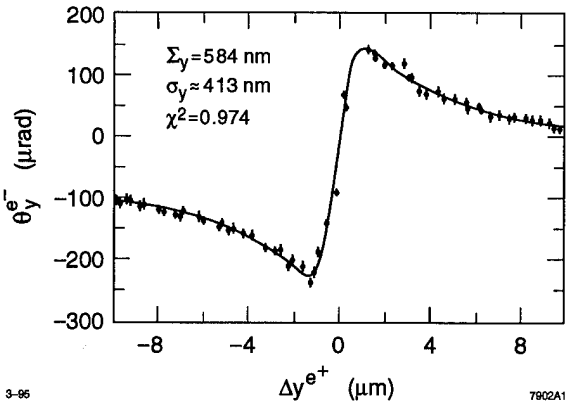


Figure 1. Vertical beam-beam deflection scan at low current, demonstrating a single-beam size of about 410 nm.

The low-current beam sizes correspond to a normalized production rate of 11 Zs per hour per 10^{10} incident particles (the Z cross section is 30 nbarn). At this current, the transverse pulse-to-pulse orbit fluctuation in the final focus is of the order of 0.1 $\sigma_{x,y}$, and the beam-beam deflection scans agree well with the Bassetti-Erskine formula [11], from which the convoluted sizes of the two beams are easily extracted. The small spot sizes at low current were achieved while the electron damping ring was operated at twice the usual store time.

For the usual current of 3.5×10^{10} particles per bunch, the vertical emittances at the end of the linac of about 70 μmμrad are more than twice as large as for the long-store low-current mode. Furthermore, at this current, the vertical orbit variations are much larger, of the order of 0.5 σ_y. Several different sources are currently suspected to cause this transverse orbit jitter, such as magnet and structure vibrations in the linac, long-range wakefields by which a change of positron orbit or intensity affects the 60 ns delayed electron bunch, and variations of bunch length or longitudinal phase [12]. Not only does the transverse orbit motion lower the luminosity by reducing the average overlap of the two beams (a 5% effect), but more importantly it makes tuning more difficult since the beam-beam deflection scans become more erratic in the presence of jitter. Significant efforts have therefore been devoted to optimizing the quality of the fit to the beam-beam scans [13]. Pulses whose intensity, energy, or UT- and CCS-orbit deviations exceed a certain tolerance are now discarded in the scan. A first attempt has been made to adjust the fit to changes of the vertical or horizontal beam position at the IP, which are calculated from the detected beam-positions in the linac and the measured transfer-matrix between the end of the linac and the IP. Partly as a result of improved fitting algorithms, spot sizes as low as 600 nm have been achieved, which correspond to a normalized production rate of 7 Zs per hour or an absolute rate of 80 Zs per hour. The average number of produced Zs was of the order of 50–60 per hour (or 5×10^{29} cm^{-2} s^{-1}).

For typical IP beam sizes of $\sigma_x \approx 2$ μm, $\sigma_y \approx 900$ nm, and $\sigma_z \approx 750$ μm, and 3.5×10^{10} particles per bunch, the expected luminosity enhancement by disruption [14] is about 10%. This is not inconsistent with the ratio of the number of Zs recorded by the SLD detector to the number of Zs estimated from beam-beam deflection scans, which is 1.1 ± 0.1.

In addition to orbit fluctuation, there is also a pulse-to-pulse variation of the beam size. If the beams are collided vertically off center—namely, close to the maximum of the beam-beam deflection curve at about $2.5\sigma_y$—the variation of the deflection angle is insensitive to the orbit, and instead primarily reflects the variations of the beam size. Measurements for off-center collisions are consistent with vertical single-beam-size variations of the order 200 nm. This value is comparable in magnitude to the observed orbit jitter.

The sensitivity of the IP beam size to orbit changes induced at the entrance of the final focus system has also been measured. An orbit change of 2 mm at the vertically focusing sextupoles causes an increase of the vertical single-beam size from 400 nm to 1.8 μm. The measured dependence is consistent with simulation results except for a small asymmetry, which could indicate a skew sextupole component in the final triplet quadrupoles of about $a_3 \sim 2 \times 10^{-5}$ at a radius $r = 21$ mm.

From the dependence of the beam position at the IP wire (or at the pre-image wire) on the beam energy, the second-order vertical dispersion at the IP has been measured. It is of the order of 20 mm and, consequently, its contribution to the vertical spot size is insignificant. The measured beam size is indeed not very sensitive to the relative momentum spread δ in the range 0.1–

0.3%.

Several attempts have been made to measure the single-beam sizes at the IP. One approach has been to greatly enlarge the spot size of the opposing beam (for instance, by increasing its emittance) and then to measure the outgoing divergence of the smaller beam as a function of its waist position. The minimum value of the divergence is a direct measure of the IP spot size, since the density of the large beam is known. At low current, this method gave promising results, but it has not been successful at high current because of the increased orbit jitter and highly distorted beam distributions after collision. In a more recent approach, the single-beam sizes are reconstructed from the measured energy spread and average energy of the two collided beams as a function of their horizontal or vertical distance during collision.

V. ARC EMITTANCE GROWTH

The new wire scanners in the UT allow a direct observation of the emittances in the final focus for the first time. It was found that the emittance-increase along the arcs depends on neither the beam current nor the initial emittance. The increase of the horizontal emittance is about $\Delta\epsilon_x \approx$ 100–120 μmμrad, while the vertical increase is about $\Delta\epsilon_y \approx$ 30–40 μmμrad. These numbers agree well with the expected effect of synchrotron radiation and linear coupling, calculated from measured arc oscillation data [8]. However, a few months after the last arc orbit-tuning, the vertical emittance increase has been much worse, $\Delta\epsilon_y \geq$ 70 μmμrad, which is possibly due to degraded beta functions, coupling, and dispersion. Effort is underway to further reduce the actual emittance blowup by more local arc-tuning schemes. The minimum possible increase of the vertical emittance, due to vertical bending and rolls in the arcs, is about 10 μmμrad. There is some evidence for high-current emittance growth due to geometric or resistive-wall wakefields from collimators in the arcs and at the end of the linac [15].

VI. SUMMARY AND OUTLOOK

In spring 1994, the upgraded SLC final focus system was successfully commissioned. At low current, the new final focus routinely delivers the vertical design spot size of 400 nm. At high current (3.5×10^{10} particles per bunch), the spot size increases to values of 600–900 nm, due to deteriorating upstream emittances and to reduced orbit stability. The peak luminosity achieved corresponds to about 80 Zs per hour. The average production rate was 50–60 Zs per hour. A total of 100,000 Zs were recorded by SLD during the 1994/95 SLC run, translating into an integrated luminosity of 3.3 pbarn^{-1}.

So far, the convoluted transverse sizes of both beams have been inferred indirectly from beam-beam deflection scans. Before the next SLC run in 1996, it is planned to install a laser wire inside the SLD detector [16]. The laser wire will provide a direct measurement of the single-beam sizes at the IP, thus allowing independent fine-tuning of the two final foci, and will make diagnostics much easier.

References

[1] K. L. Brown, "Conceptual Design of Final Focus Systems for Linear Colliders," SLAC-PUB-4159, 1987.

[2] N. Walker et al., "Third Order Corrections to the SLC Final Focus," PAC 1993, Washington, 1993.

[3] K. L. Brown, F. Rothacker, D. Carey, and Ch. Iselin, TRANSPORT manual, SLAC-91 and UC-28, 1977.

[4] F. Zimmermann, "Magnet Alignment Tolerances in the SLC Final Focus System Determined by Lie Algebra Techniques," submitted to *NIM A*, SLAC-PUB-6706, 1994; see also F. Zimmermann, SLAC-CN-398, 1994.

[5] P. Emma, "Beam-Based Alignment of Sector-1 of the SLC Linac," 3rd EPAC, Berlin (1992).

[6] P. Raimondi et al. "Beam Based Alignment of the SLC Final Focus Superconducting Final Triplets," PAC 1993, Washington, 1993.

[7] P. Emma et al., "Beam Based Alignment of the SLC Final Focus Sextupoles," PAC 1993, Washington, 1993.

[8] N. Walker et al., "Correction of the First Order Beam Transport of the SLC Arcs," PAC 1991, San Francisco, 1991.

[9] N. Walker et al., "Global Tuning Knobs for the SLC Final Focus," PAC 1993, Washington, 1993.

[10] D. McCormick et. al., "Measuring Micron Size Beams in the SLC Final Focus," 6th BIW, Vancouver, 1994.

[11] M. Bassetti and G. A. Erskine, "Closed Expression for the Electrical Field of a Two-dimensional Gaussian Charge", CERN-ISR-TH 80-06, 1980.

[12] C. Adolphsen et al., "Pulse to Pulse Stability Issues in the SLC," these proceedings, 1995.

[13] P. Raimondi et al., these proceedings, 1995.

[14] P. Chen, "Disruption Effects from the Collision of Quasiflat Beams," PAC 1993, Washington, 1993.

[15] K. Bane et al., these proceedings, 1995.

[16] M. Ross, Proc. of Advanced Accelerator Concepts Workshop, Lake Geneva, 1994.

*DIRECT MEASUREMENT OF TRANSVERSE WAKEFIELDS IN THE SLC LINAC**

P. Krejcik, R. Assmann, F.J. Decker, S. Hartman, R. Miller, T. Raubenheimer,
Stanford Linear Accelerator Center, Stanford University, Stanford, CA 94309 USA

The transverse wakefields that generate tails in the beam distribution of an off-axis bunch can be viewed as resonant dipole modes in the structure. These same dipole modes were responsible for beam break up of long bunch trains during the early operation of the SLAC linac. This paper describes the excitation of these modes by the single, high-intensity bunches used in SLC operation. Both time and frequency domain measurements were made of the beam induced signals to identify the dipole modes. The amplitude of the measured dipole mode signal is found to be proportional to the bunch's offset in the structure. The utility of this technique for obtaining alignment information of the linac structure is discussed for both the SLC and future linear colliders.

I. INTRODUCTION

The largest contribution to emittance growth at the SLC comes from the transverse wakefields generated when a bunch is off-axis in misaligned accelerating structures. The head of the bunch generates fields which deflect the tail of the bunch and even the following bunches. In frequency domain these deflecting fields can be recognized as higher-order modes excited in the structure. These dipole-mode signals are readily discernible, occurring at a different frequency from the fundamental mode in the structure. This paper covers the techniques used to detect the dipole modes generated by the single bunch SLC beams, and shows that the signals are linearly related to the beam position within the structure.

The presence of dipole modes is well known in the history of SLAC as they were responsible for the beam break-up intensity limit during the early days of long bunch train operation of the linac [1]. The beam break up phenomena is a resonant process whereby the transverse oscillation of the leading bunches amplify along the bunch train as a result of the dipole mode excitation. Structure measurements and calculations of the first-order dipole modes are detailed in ref. [1].

At the SLC our interest has been in directly observing the wakefields responsible for emittance growth and to test whether practical information can be inferred about the alignment of individual accelerating sections. The dipole modes generated in the structure provide a sensitive structure beam position monitor (BPM), compared to normal linac BPM's that typically measure beam position with respect to the center of a discrete quadrupole.

II. ACCELERATOR LAYOUT AND SIGNAL ACQUISITION

It is of interest to observe the signal from both the output end of the structure and from the input end since the dipole modes propagate backwards and can be trapped within a few cells from the end of the structure. The SLAC structure, shown in fig. 1, has a 20 dB coupler attached to one of the four RF loads attached to the ends of the four 10′ accelerating sections driven by one klystron. The signal from the coupler is transmitted via coaxial cable to a phasing station above ground where it was originally used as part of the klystron phasing system. The signals from these cables allow us to sample one in every four of the individual structures at their output end. There are no individual signal couplers on the input couplers to the accelerating sections so we can only observe these signals as they propagate back towards the klystron where the waveguides from four accelerating structures combine. A convenient signal coupler is located on the SLED cavity

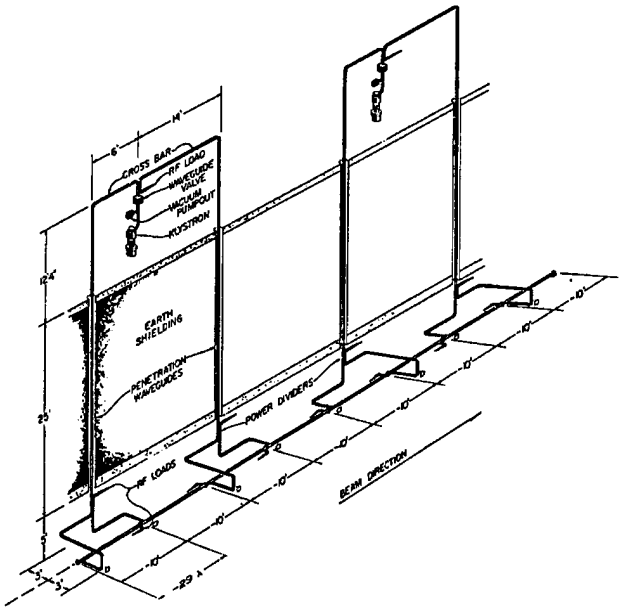


Figure 1: Layout of the accelerator and klystrons (reproduced from ref. 1). Signals were taken from the output load shown at the end of each 10′ accelerator section, and from a coupler on the SLED cavity (not visible) located above each klystron.

* Work supported by Department of Energy Contract DE-AC03-76SF00515.

0-7803-3053-6/96/$5.00 ©1996 IEEE

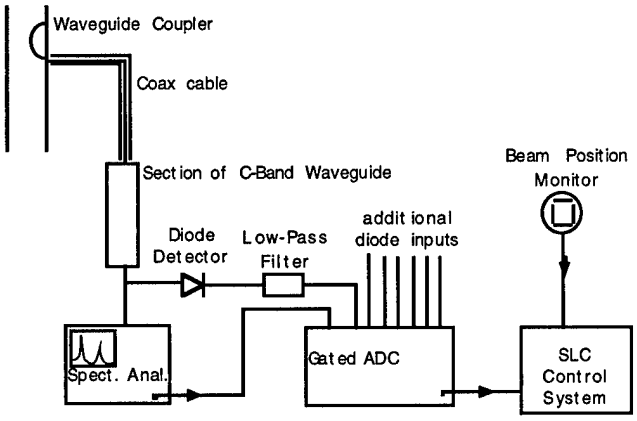


Figure 2: Layout of the instrumentation used for sampling the beam-generated modes in the structure.

(not shown in detail in the figure) which is mounted above the klystron shown in fig. 1.

The signal from the couplers is dominated by the fundamental mode at 2856 MHz. A short section of C-band waveguide, shown in fig. 2, effectively cuts off all of the signal at the fundamental mode giving us good signal to noise ratio for the higher-order modes of interest. As shown in fig. 2, this high-pass filtered signal can be diode-detected immediately and further filtered [2], or it can be analyzed with a spectrum analyzer. The mode spectra can be recorded or the spectrum analyzer can be operated as a narrow band receiver to look at the time and amplitude response of a specific line in the spectrum. In the latter mode the video output of the spectrum analyzer is sampled by a gated ADC (GADC) so that the signal amplitude may be correlated with a BPM signal via the SLC control system. The diode-detected signal is low-pass filtered and

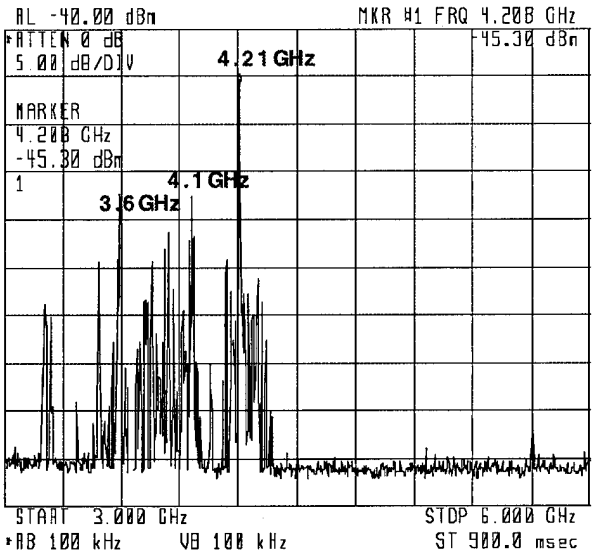


Figure 3: Beam-induced mode spectrum observed from the input couplers, measured from 3 to 6 GHz.

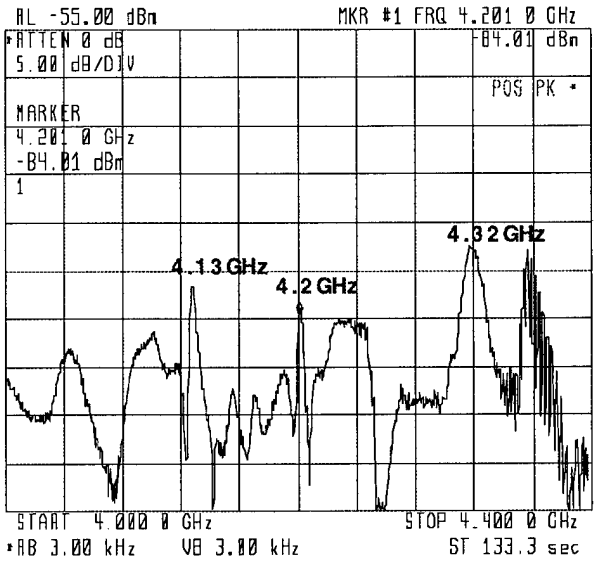


Figure 4: Beam-induced mode spectrum observed from the output couplers, measured from 4 to 4.4 GHz.

also sampled by the GADC for similar correlation measurements. Although this signal is not as selectively filtered as the spectrum analyzer output, it does have the advantage of requiring much simpler instrumentation which can be duplicated to analyze the signals from several sections of waveguide at once.

III. RF MODES GENERATED BY THE BEAM

The spectra of modes induced by a single bunch of 8×10^9 electrons are shown in fig. 3 for the input coupler in the range 3 to 6 GHz and in fig. 4 for the output coupler in the range 4 to 4.4 GHz. The general features common to both spectra are the large number of frequency lines clustered around 4.1 GHz where the dipole modes are expected.

IV. DIPOLE MODE RESPONSE TO BEAM POSITION

The results of the correlation measurement between the horizontal beam position, as measured on an adjacent BPM, and the amplitude of the mode at 4.21 GHz, measured at the input coupler, is shown in fig. 5. The beam was moved with respect to the structure by steering local bumps into the orbit. A linear response is observed and the resolution of the signal is of the order of 20 microns. The standard linac BPM against which the signal is calibrated does not have a resolution much beyond this, so we can not expect to observe a greater resolution in the present experiment. The correlation experiments were repeated at several different mode frequencies at both the input and output couplers for both horizontal and vertical beam motion and are summarized in table 1.

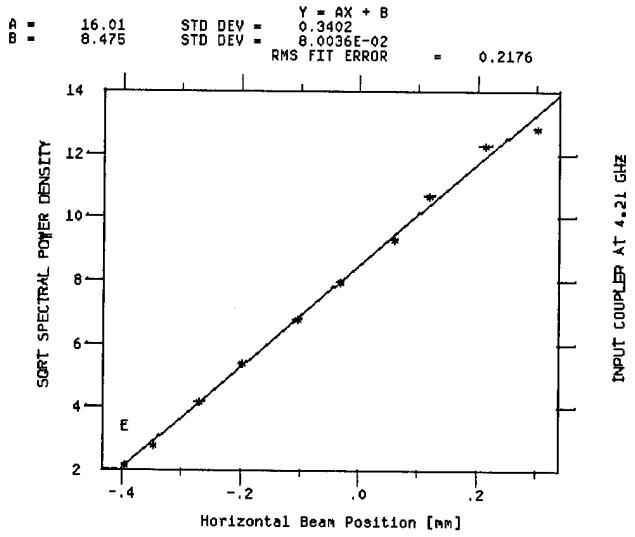


Figure 5: Structure BPM linearity measured at 4.21 GHz at the input coupler.

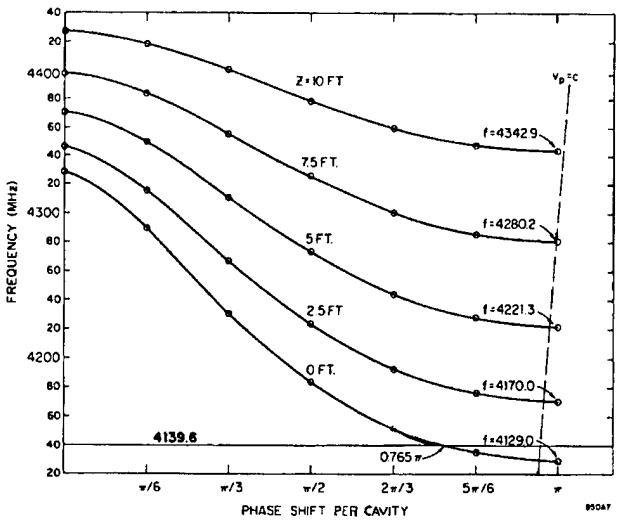


Figure 6: Dispersion diagram for dipole modes in the SLAC structure (reproduced from ref. 1).

The strongest correlations occurred at frequencies with the largest amplitude in figs 3 and 4. The frequencies at which the horizontal correlation was greatest were also those showing the strongest vertical correlation. The vertical signals were much smaller than those generated by horizontal offsets in the beam position. However, if the dipole mode signal was first nulled by appropriate horizontal steering of the beam it was then possible to clearly resolve the correlation to vertical motion of the beam.

Table 1: Measured correlation of mode with beam position.

input coupler	X Correlation	Y Correlation
4.1396 GHz	none	none
4.169	weak	none
4.2105	strong	weak
4.2931	weak	none
8.42	none	none
8.6	none	none
output coupler		
4.1037	strong	none
4.1279	strong	none
4.22525	not measured.	none
4.31463	not measured	none
4.3563	not measured	none

V. COMPARISON TO EXPECTED MODES

The SLAC structure is designed for a constant gradient, so the cells are not exactly periodic. From the dispersion diagram for the dipole modes given in ref. [1], and reproduced in fig. 6, we can see that the dominant 4.21 GHz signal is originating about 4' in from the end of the structure. The solutions found for these dipole modes are for backwards propagating waves. Some of the modes are trapped implying that some of the energy is reflected in the forward direction again, which accounts for their presence at the output coupler.

The horizontal and vertical dipole modes are very close in frequency, as one would expect in an axially symmetric structure, where the only asymmetry comes from the couplers. The couplers are horizontally polarizing and so incapable of transmitting vertical modes. The fact that we still obtain a correlation between the observed dipole mode signal and the vertical beam position indicates that the vertical modes couples some of their energy to the horizontal modes within the structure. The observed strength of the horizontal mode therefore has contributions from both the horizontal and vertical beam offset. This means that if we try and use the signals as a structure BPM it is important to realize that the horizontal and vertical are not orthogonal.

VII CONCLUSION

The structure BPM data is helping us learn to improve the linac alignment and reduce SLC emittances [2]. We have been limited to using existing couplers in the linac to avoid interfering with the ongoing physics program. Future linear colliders, with tighter alignment tolerances, will invariably incorporate structure BPM's, but more efficient higher-order mode couplers can be incorporated in their design.. Never-the-less, these experiments are a significant validation of the technique for future linear collider design.

VIII ACKNOWLEDGMENTS

We gratefully acknowledge Harry Hoag and Marc Ross are for sharing their knowledge and experience of the SLAC linac.

IX. REFERENCES

[1] The Stanford Two-Mile Accelerator, ed. R.B. Neal, 1968 W.A. Benjamin, Inc., N.Y.

[1] D. Whittum et al, to be published.

FEEDBACK PERFORMANCE AT THE STANFORD LINEAR COLLIDER†

M.G. Minty, C. Adolphsen, L.J. Hendrickson, R. Sass, T. Slaton, M. Woodley
Stanford Linear Accelerator Center MS 66, P.O. Box 4349, Stanford, CA 94309 USA

Many feedback loops are used at the Stanford Linear Collider (SLC) to control the orbit and energy of particle beams. Problems with corrector magnet slew rates, actuator calibrations, and computation of the beam transport matrix between loops have resulted in operation of many SLC feedback loops at lower than design gain. The response of various feedback loops to these errors is measured and analyzed in an attempt to improve performance.

I. INTRODUCTION

The SLC feedback system [1,2] is a generalized, database driven system that applies state-space formalisms to stabilize the beam. Feedback has proven to be essential to the successful operation of the SLC. Problems encountered in running high current beams have forced us to adopt tighter tolerances on feedback control parameters and have motivated a stricter evaluation of feedback performance. Of particular concern is the fact that linac feedback loops are routinely operated with lower than design gain.

The design of each feedback loop relies on knowledge of the slew rates of the correctors used to cancel perturbations and of the noise spectrum of the beam. The effect of differences in corrector speeds has been measured and analyzed using high current beams. For a series of loops in succession correction for over compensation, or cascade [3], was found to be necessary, in which information from each loop is passed on to the loop immediately downstream. The transfer matrices between two consecutive cascaded loops are continuously updated, or adapted, using measurements of the natural beam jitter. Measurements of the performance of the adaptive cascade have shown sensitivity to the location of the noise source.

II. SINGLE-LOOP RESPONSE

The SLC beam rate is 120 Hz, while most linac feedback loops sample the beam at 20 Hz due to CPU limitations The most downstream linac feedback loop, which is not cascaded, was upgraded to operate at 60 Hz. However, when the sampling rate was increased, the measured beam jitter downstream of the loop increased. The feedback gain, or the percentage of implemented change relative to the calculated change, was lowered as a result. A lower feedback gain implies less efficient correction.

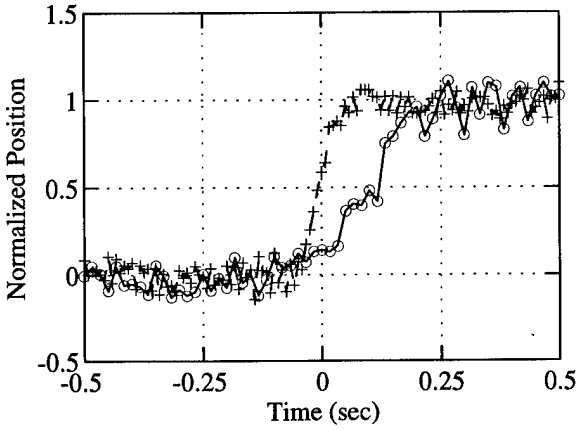


Figure 1: Slew rate measurement for a fast (+) and a slow (o) corrector. A step function was applied to each corrector and the response of the beam as a function of time was measured on downstream BPMs.

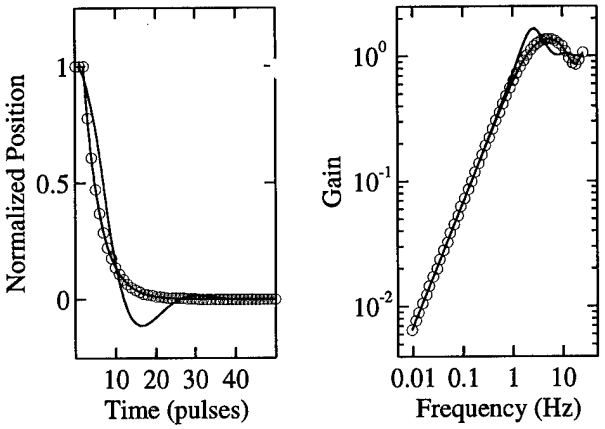


Figure 2: Time and frequency domain simulations of beam response to a step function assuming 8 fast (open circles) or 6 fast and 2 slow correctors (no circles).

Corrector slew rates were a suspected problem. If the feedback design assumed instantaneous correction, then a slow corrector could cause amplification of beam jitter. Slew rate measurements for feedback correctors revealed response times ranging from 7 to 12 beam pulses, compared to the design assumption of 6 pulses. Slew rate measurements are shown in Fig. 1 for two different feedback correctors. Plotted in Fig. 2 are time and frequency domain simulations for the 60 Hz feedback loop

† Supported by D.O.E. contract DE-AC03-76SF00515.

assuming ideal and mismatched correctors. These and similar studies show that slow or mismatched correctors cause feedback to overshoot. Notice also that the unity gain crossover point depends both on the feedback gain and on the corrector slew rates. Currently effort is being devoted to minimizing and matching corrector response times.

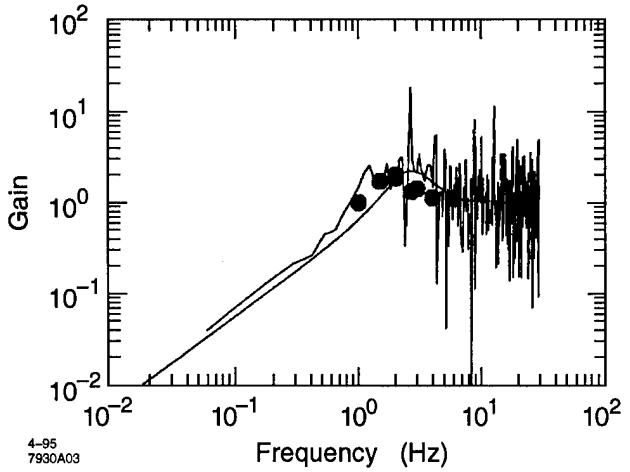


Figure 3: Simulated (smooth curve) and measured frequency response of a feedback loop. The filled circles were obtained from independent measurements using single frequency excitations of an upstream corrector.

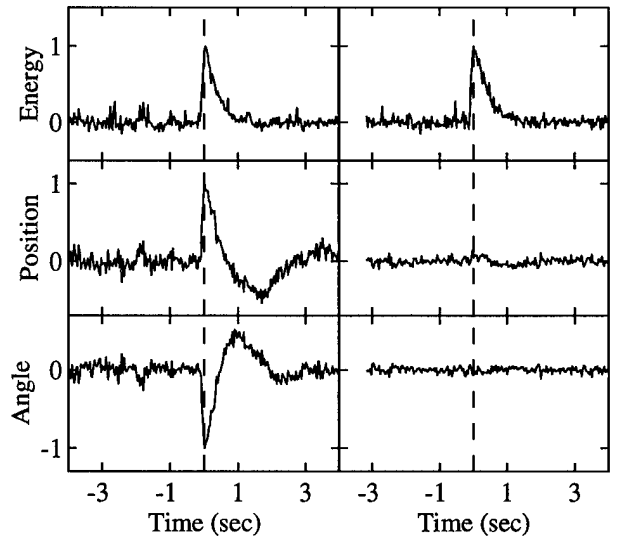


Figure 4: Normalized states computed by RTL feedback before (left) and after (right) including additional BPMs.

To quantify the single-loop response, a step function was applied to an upstream corrector and states were measured for the 60 Hz loop with feedback off, and with feedback on at unity gain. The data were then prepared for FFT analysis by inversion and reflection. The frequency response of the loop, which is given by the ratio of the FFTs of these data, is shown and compared with simulation in Fig. 3. The apparent noise at frequencies greater than about 5 Hz is a result of random noise in the measured states. Separate measurements using single frequency excitations of an upstream corrector are shown as filled circles. These data do not reproduce the occasional spikes observed in the FFT ratio. The solid line is a simulation which assumes that 2 of the 8 correctors are relatively slow. Comparison of Figs. 2 and 3 suggests that the observed structure in the undamped region of the response is due to slow or mismatched correctors.

In the linac, cooling water pumps generate beam jitter at frequencies near 59 Hz. With 60 Hz feedback sampling, 59 Hz oscillations were aliased to near 1 Hz. Depending on the loop gain, the feedback could amplify this 1 Hz oscillation. To avoid this, the feedback sampling rate was reduced to 40 Hz. Ideally, such aliasing effects would best be avoided by sampling at the full beam rate.

Beam energy, as well as orbit angle and position, is measured and corrected in the two SLC damping-ring-to-linac (RTL) transport lines where there is dispersion. It was observed that these loops were having trouble distinguishing changes in beam energy from trajectory changes. This caused conflicting use of energy, angle, and position actuators by the feedback loops and oscillation of the beam. This problem was corrected by including additional beam position monitors (BPMs) in both dispersive and non-dispersive areas of the RTLs. Fig. 4 shows the feedback states computed in response to a step change in the beam ebergy before and after the addition of BPMs; note the improvement in the fitted angle and position (at a non-dispersive point).

III. ADAPTIVE CASCADE

In the current feedback control architecture, cascade passes information from each loop to its nearest downstream successor so that multiple correction of incoming perturbations is avoided. Each feedback loop in the series of loops should therefore correct only those perturbations generated immediately upstream. In adaptive cascade the transport matrix between successive feedback loops is continuously measured using natural beam jitter. Implicit to this procedure is the assumption that perturbations between two loops are uncorrelated with perturbations upstream of both loops. Cascaded feedback loops regulate states that have been adjusted by subtracting off corrections implemented by the nearest upstream loop. For a given loop within the cascade, the ratio of adjusted state to measured state defines the rejection ratio of the loop. This is the fraction of the upstream perturbation perceived by the loop to have been generated between it and its nearest upstream neighbor. Ideally the rejection

ratio should be zero, in which case the cascade is functioning properly. A nonzero rejection ratio indicates poor modeling of the transfer matrix between loops and results in over correction by the downstream loop.

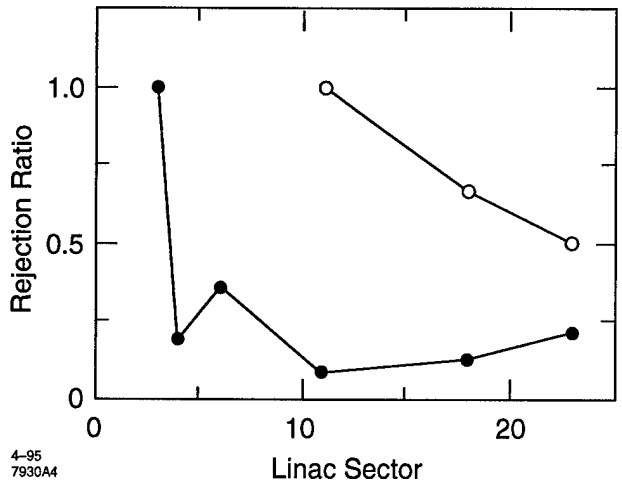


Figure 5: Rejection ratios measured with a pre-linac excitation (closed circles) and a mid-linac excitation (open circles).

Rejection ratio measurements are shown in Fig. 5. The data shown as closed circles were acquired by introducing a single step function perturbation upstream of the linac and measuring the response of all the cascaded feedback loops. These data and other measurements show that the rejection ratios varied from very good (10-20%) to nearly non-cascaded, in which 50-100% of the perturbation was detected and corrected. Also shown as open circles are rejection ratios measured with an excitation made in the middle of the linac. The differences between these measurements indicate that the feedback response is sensitive to the location of the perturbation. A possible explanation for this is that the feedback design assumes linear transport matrices while at high current the transport matrices are actually nonlinear due to wake fields. Poor rejection is still not well understood.

IV. CALIBRATIONS AND MODELING

Imperfections in the lattice model for the beam transport degrade feedback performance. Alternatively, the transport matrices can be measured. Using a recently improved calibration procedure, the position and angle states were measured as a function of feedback corrector magnet settings. Shown in Fig. 6 are measurements of the feedback response using the design SLC lattice model (a,b) and using the calibration (c,d). While the regulation is undoubtedly improved, the time required for calibration (about 1 hour per loop) is significant. Comparison of the online calibration with the linac model is useful in isolating lattice errors. Long term stability of the calibration is coupled closely to the long term stability of the machine.

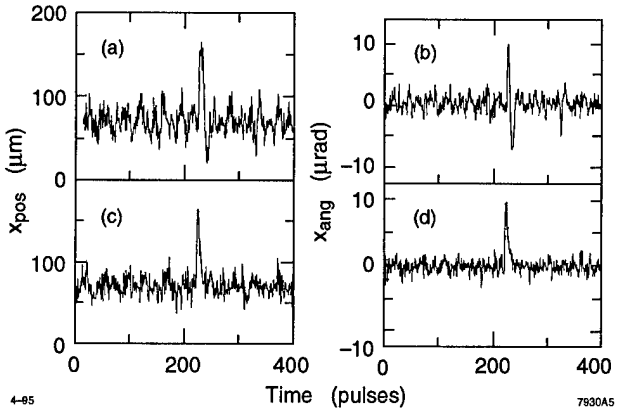


Figure 6: Feedback regulation with lattice model (a,b) and with online calibration (c,d). Feedback states are plotted as a function of time in response to an external excitation.

V. CONCLUSION

Operation of the linac feedback loops at lower than design gain has yet to be fully understood. Evaluations of corrector slew rates, sample rate aliasing, and cascade performance were presented. Future work will include analysis of the effect that wake fields have on beam transport, studying the significance of the location of noise sources, and evaluating how frequently loops should be calibrated.

VI. ACKNOWLEDGMENTS

These studies were made possible by the dedicated work of the SLC controls group, who develop and maintain both the software and the hardware required for feedback. We also wish to thank Tom Himel for his helpful suggestions and support.

VII. REFERENCES

[1] L.J. Hendrickson, et al., "Generalized Fast Feedback System in the SLC", ICALEPCS '91, Tsukuba, Japan, p. 414; SLAC-PUB-5683.

[2] F. Rouse, et al., "A Database Driven Fast Feedback System for the Stanford Linear Collider", *Nucl. Inst. Meth.* **A316**, 343 (1992); SLAC-PUB-5681.

[3] T. Himel, et al., "Adaptive Cascaded Beam Based Feedback at the SLC", IEEE PAC '93, Washington, DC, p. 2106; SLAC-PUB-6125.

VIBRATION STUDIES OF THE STANFORD LINEAR ACCELERATOR†

J. L. Turner, C. Adolphsen, G. B. Bowden, F. J. Decker, S. C. Hartman, S. Matsumoto, G. Mazaheri, D. McCormick, M. Ross, R. Stege, S. Virostek, M. Woodley
Stanford Linear Accelerator Center, Stanford University, Stanford, CA 94309 USA

ABSTRACT

Vibration measurements of the linear accelerator structures in the SLC linac show a 1 micron rms vertical motion. This motion reduces to 0.2 micron rms motion when the cooling water to the accelerator structures is turned off. The quadrupoles have 250 nanometer rms vertical motion with the accelerator structure cooling water on and 60 nanometer motion with it off. These results together with measurements of the correlations as a function of frequency between the motions of various components are presented.

I. INTRODUCTION

During the 1994/95 colliding beam run of the SLC, the measured jitter in the vertical beam position indicated it had a significant impact on the luminosity [1]. Diagnosing the sources of jitter became a priority issue. The possibility of vertical movement of quadrupole magnets or even accelerator structures affecting the beam was considered, and efforts toward modeling and measuring potential sources [2] of beam jitter in the linac ensued. This paper primarily describes measurements of quadrupole and accelerator structure motion in the linac under various conditions and the conclusions reached.

II. SETUP

The system used for most measurements combined Mark L4-C geophones, and a SLAC built integrator and amplifier, with a mobile LabView® data acquisition and analysis system.

The geophone is essentially a mass suspended on a spring that induces a signal on a coil which is proportional to velocity of the ground motion for frequencies above the geophone natural frequency (~1 Hz). The signal is integrated, amplified, then digitized at 4 kilohertz on a quad channel board and analyzed using LabView® on a PC. The combined system as configured for these measurements has good resolution from 2 to 100 Hz. Electrical noise in the geophone measurements was determined to be several orders of magnitude below the measurement data.

Cross checks of the geophones were made using a Hewlett Packard HP3560A Dynamic Signal Analyzer with a PCB Piezotronics model 393B31 accelerometer and an optical linear encoder (Heidenhain model MT60K) with 50nm resolution. They agreed at the 10% level.

III. MEASUREMENTS

Vertical motion of accelerator structures was measured at 1 micron rms, and thought not to be a problem for SLC beams. Quadrupole vertical motion was about 250 nanometers rms, enough to be a problem [2]. Correlation between the motions of two quadrupoles separated by 12 meters was high in the 8-14 Hz range (see figure 1) but not elsewhere in the spectrum.

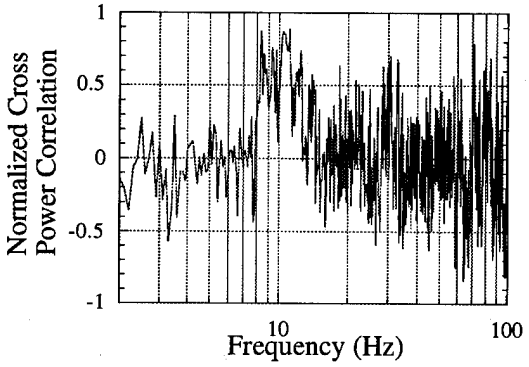


Figure 1. Spectrum of normalized cross power correlation of vertical motion of two quadrupoles.

Turning off water to the quadrupoles themselves had little affect, but turning off the water to the adjacent accelerator structures lowered vibration of the quadrupoles from about 250 nanometers rms to about 60 nanometers rms (see figure 2). Thus most of the quadrupole motion is due to the vibrations that are caused by the cooling water. Much of the motion is at 59 Hz (see figure 2 bottom plot) which can be seen in the jitter of the beam orbits [3]. The 59 Hz motion is believed to be due to the accelerator water pump impeller rotating at 59 Hz. The quadrupole motion in the 8-14 Hz

†Supported by D.O.E. contract DE-AC03-76SF00515.

range, however, was not reduced dramatically with the water off (see figure 2).

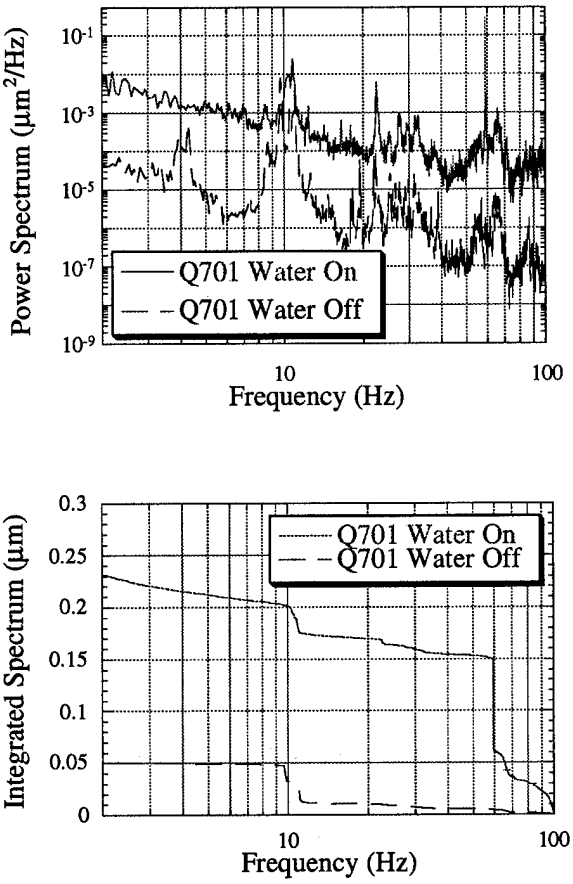


Figure 2. Quadrupole motion spectrum (top) and integrated spectrum (bottom) with accelerator cooling water on and off.

Not all quadrupoles exhibit the same behavior. Figure 3 shows some examples of the integrated spectrum. Note that the fraction of 8-14 Hz motion and 59 Hz motion differs. Oscillations at 28-30 Hz dominate the spectrum of quadrupoles that have upright supports (the so called matching quadrupoles, see Q901 in figure 3) even with the water off. These quadrupoles also have a spike at 59 Hz that disappears when the accelerator water is turned off.

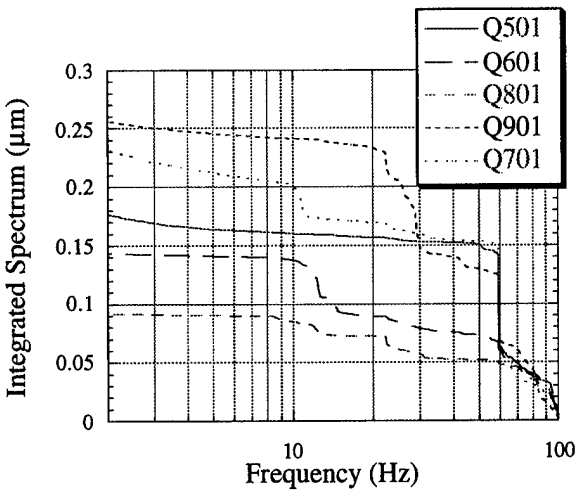


Figure 3. Integrated vertical motion of five quadrupoles with the accelerator water on.

Much of the quadrupole motion is related to the design of its support. The centroid of the quadrupole is offset along the beam direction (Z) which allows the quadrupole to vibrate in an arc in the ZY plane (see figure 4). Clamping the quadrupoles to the adjacent structure reduced the 10-14 Hz motion significantly.

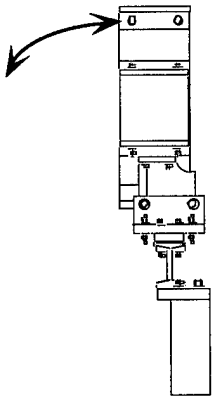


Figure 4. Side view of standard quadrupole with arrows showing direction of movement.

Quadrupoles in different sectors are affected by different accelerator water circuits. Those sampled in sector 12 did not show as large a 59 Hz problem as seen in sectors 14 and 15.

To study the difference, the pipe vibration near the pump was measured in sector 14. The 59 Hz motion was observed. Also, a pressure transducer was used to measure the time variation of the pressure at sector 12 and 14. The pump rotates at 59 Hz, and pump impellers have five vanes which create a large contribution at 295 Hz. Figure 5 shows the integrated spectra of the pressure variations.

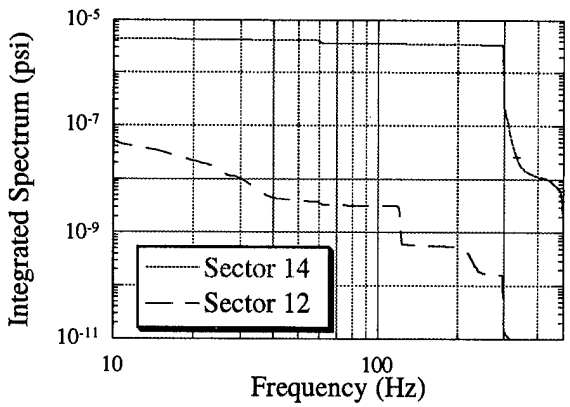
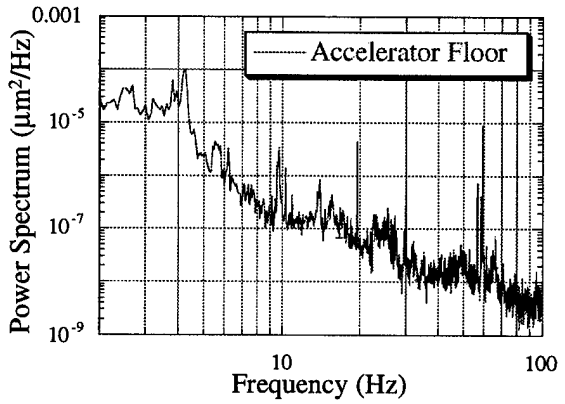


Figure 5. Integrated water pressure variations from two accelerator water systems.



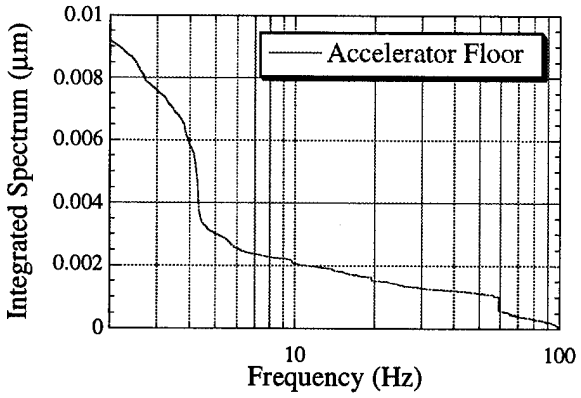


Figure 6. Spectrum and integral of vertical motion on the floor of the accelerator tunnel (about 35' below ground [4]).

Finally, measurements of the accelerator floor motion were made. Figure 6 shows an example. Integrated values (>2 Hz) between 9 and 35 nanometers were observed on different days.

IV. SUMMARY AND CONCLUSIONS

The largest contributor to quadrupole vertical vibration in the SLC is due to the motion of the accelerator cooling water. Much of this motion is at 59 Hz. The 59 Hz is transmitted from the pump by modulating the water pressure. Pump impeller quality may be the cause.

Compounding the problem is a ~10 Hz resonant quadrupole support structure. Its effect was reduced by adding wedge supports. Other types of quadrupoles need similar fixes.

V. REFERENCES

[1] P. Emma, "The Stanford Linear Collider," Contribution WAG01, 1995 PAC

[2] C. Adolphsen and T. Slaton, "Beam Trajectory Jitter in the SLC Linac," Contribution WAB08, 1995 PAC

[3] M. G. Minty *et al*, "Optimization of Feedback Performance at the Stanford Linear Collider", Contribution RPB03,1995 PAC

[4] R. B. Neal, "The Stanford Two-Mile Accelerator," W. A. Benjamin, Inc. 1968

SLAC MODULATOR AVAILABILITY AND IMPACT ON SLC OPERATION*

A.R. Donaldson and J.R. Ashton, SLAC, Stanford, CA 94309 USA

In 1991, the Stanford Linear Collider (SLC) operated, with diverse accelerator systems, at 60% availability. In the more auspicious 1992 and 1993 runs availability improved to over 80%. For the 94/95 run, the availability was also about 80%. Ignoring the eclectic-accelerator, this discussion will assess the dependence of the SLC on the reliability and hence, availability, of 244 klystron modulator systems that provide power to the machine's bunched-particle beams. Klystron modulator availability must be 99% for the accelerator to function at the 75% level. Fortunately, an excess of modulator/klystrons provides some redundancy and, therefore, allows some freedom from the requirement that all 244 systems perform simultaneously. There are, however, 15 specific exceptions. They populate strategic positions at the injector, damping rings, and positron production area of the accelerator complex. These, systems-without-spares, directly influence overall accelerator availability. Their calculated availability as an ensemble is 90%, but by chance they have operated at up to 99% [1]. Individually, a malfunction can bring an experimental program to a halt. The discussion includes a description of several improvements to increase future availability for the modulator system.

TABLE I: Klystron/modulator Deployment in the SLC.

LOCATION	QUANITY	E [GeV][1]
Injector Stations	**5**	0.2
Sector 1 Stations	**5**	1.15
N & S Damping Rings:		1.15
NRTL Compressor[2]	1	
SLTR Compressor[2]	1	
SRTL Compressor[2]	1	
Sectors 2 to 18 Stations	135	32.8
Sector 19 Stations	7	34.5
Positron Source:		
e^- To Target Station[2]	**1**	30.5-31.5
e^+ Accelerate Station[2]	**1**	0.2
Sector 20 Stations	7	36
Sectors 21 to 30 Stations	80	55
Energy to SLC Arcs		47
Energy to Detector		46
Total Station Count	244	

[1] Indicates the maximum possible energy (phase aligned) and does not include losses due to:
15 degree offset for BNS Damping
overhead for energy feedback
modulators down for maintenance
klystrons down for maintenance.

[2] Indicates stations which compress the beam but add no energy gain.

*Work supported by DoE contract DE-AC03-76SF00515

I. MODULATOR/KLYSTRON DEPLOYMENT

The linear accelerator presently uses 244 modulator/klystron stations (in 1991 only 243 stations were used). From Table I it is almost apparent that SLC has more modulators than needed for the required detector energy. This allows modulators to be repaired by substituting operational but off beam modulators to avoid long repair times. At any given time there may be as many as 14 modulators available as spares. However this is not a universal situation, and there are 15 critical modulators (indicated in bold type) which do not have substitutes, hence their critical designation.

Table II offers the specifications for the klystron–modulator station. The modulator operates at high voltage and high current, conditions that essentially stress electronic components.

TABLE II: Klystron and Modulator Characteristics.

Klystron Peak Power Out	67	MW
RF Pulse Width	3.5	μs
Klystron Beam Voltage	350	kV
Klystron Beam Current	414	A
Modulator Peak Power Out	150	MW
Repetition Rate	120	Hz (max)
Thyratron Anode Voltage	46.7	kV
Thyratron Anode Current	6225	A
Pulse Transformer Ratio	1:15	
Voltage Pulse Width	5.0	μs (ESW)
Pulse Flattop Ripple	±0.25	%
Nominal PFN Impedance	4	Ω
Total PFN Capacitance	0.70	μF

II. MODULATOR RELIABILITY

The SLC must operate at 120 Hz with a very high degree of reliability and on a continuous basis. Fortunately, we have a modest excess of modulator-klystron systems which allows some measure of redundancy, and hence some freedom from the constraint that all 244 modulator/klystrons operate simultaneously.

The modulator log books for 1991 through 1995 were poured into a database in order to analyze the reliability and hence availability of the modulators. The log books also recorded station problems associated with the modulator computer interface, klystron (which included rf, water, and vacuum problems), accelerator structure and waveguide problems allied with vacuum and water interlocks, klystron dc magnet circuit, and 600 Vac variable voltage substation operation. The database was designed to

0-7803-3053-6/96/$5.00 ©1996 IEEE

reveal specific modulator problems and the frequency of those problems. Prior to this analysis these revelations existed as only anecdotal recollections among the modulator cognoscenti, the data had not been quantified, accordingly it couldn't be used to provide evidence for improving the reliability of the modulators.

For five years of analysis, we take two approaches. First we compare hours of SLC operation and modulator problem counts to calculate and plot mean time to failure (MTTF) for the various modulator components as part of an entire system. Second, we take all of the reliability data, combine it, calculate availability, and offer the results in Table III with a run by run summary in Table IV.

The plots are divided into three types, the "reset & adjustment" intervention, the "repair then run" occurrence, and finally the component failure situation that requires removal and replacement of a component or sub-system. Consider Figure 1, it shows the "reset & adjustment" MTTF chart for the modulator system. The x-axis displays the category of reset or adjustment and the SLC operating year 1991, 92, 93, and 94/5. The MTTF in hours is on the y-axis. These hours indicate how often the reset or adjustments occur, or require a technician to travel to the Linac gallery. These MTTF's are not based on single modulators, but for the entire 244 station Linac. The modulators operated at 60 Hz for 1991 SLC run. The other three runs were at 120 Hz except for a few weeks of 60 Hz operation in 94/5.

For the "Reset Main CB" category, the MTTF axis indicates how often intervention was required to reset this main modulator circuit breaker over four distinct periods of SLC operation. This circuit breaker can trip for several reasons, but the typical case involves thyratron latch up because of high reservoir voltage or a malfunctioning thyratron. Normally the circuit breaker trips because the over current fault circuit fails to open the primary contactor for the hv power supply. The plot indicates that some improvement in this category has occurred over the years. The installation of a ferro-resonant voltage regulator in 1993 may be responsible for this slight increase in MTTF for the 94/5 run. Until the contactor or control scheme are improved or replaced we will continue to be plagued by these nuisance trips.

III. RELIABILITY AND AVAILABILITY

The five year database contains 7,537 nonscheduled interventions with 3,167 hours of allied repaired time for the 21,840 hour SLC/modulator operating period. This operating period can not be accurately measured as the front end (the first 13 modulators) must always come on weeks before the rest of the modulators down the linac.

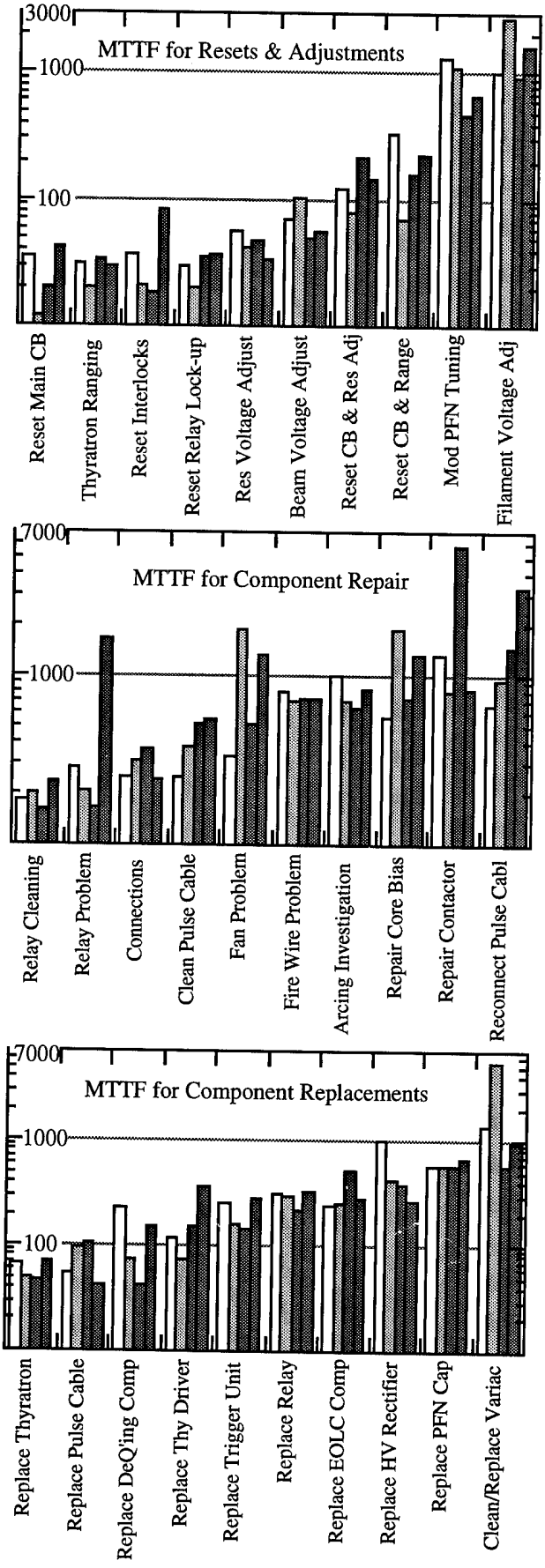


Figure 1. MTTF plots for the 244 modulator system.

The 21,840 hour figure was determined by approximate SLC operating periods for 1991 through 1995 which does not necessarily include front end turn on time or scheduled maintenance periods of less than 24 hours.

Total modulator–hours are then 244 (243 in 1991) modulators times 21,840 hours for 5.33 Mega modulator-hours of operation.

Assuming that a constant failure rate occurs for nonscheduled problems based on the operating hours and a typical Poisson distribution for electronic equipment failure,

Modulator System Failure Rate = 7537/21840 hr

Modulator System Failure Rate = 0.35 problems/hour,

or a problem occurs about once every three hours for the 244 units configured as a "system." This forces the modulator technicians to enter the linac gallery almost every three hours to correct a modulator problem. And these calculations don't include the external problems, e.g., vacuum and water interlocks for the klystron and accelerator waveguide, interface electronics or the 600 V ac utility power.

The modulator "mean time to failure" is then,

Modulator MTTF = 5.33 M hr. /7537

Modulator MTTF = 707 hours,

which when considering the age of modulators, thyratron fault rate, and relay control circuitry seems appropriate (the database error could be as high as ± 5%).

The calculation for the "mean time to repair" with our data gives,

Modulator MTTR = 3167 hr. /7537

Modulator MTTR = 0.424 hr. /problem

or the average modulator problem (a repair or intervention) requires about 25 minutes to correct.

The final calculation of interest to the accelerator operator and physicist is modulator availability, or when can it be depended on to work. The reliability experts give several definitions for availability, we will use the following as it has been applied to other accelerator systems.

Modulator System Availability = 1– (Failure Rate)(MTTR)

Modulator System Availability = 0.854

This would be the "availability" if there were no spares for the modulators, however as mentioned earlier there are up to 14 spares available and they can be activated within 12 minutes to replace a faulty unit. Using the 12 minute or 0.2 hour repair/replacement as the MTTR, then increases the "availability" to 0.931, a respectable increase that verifies the advantages of redundancy and available spares.

SLC operation is compromised when we run out of modulator spares, or when one of the 15 critical modulators fails. The database contained 437 nonscheduled interventions for the 15 critical modulators with a total time for repair of 203 hours. We apply the above calculations for the critical modulators and then compare the data with the entire ensemble of 244 modulators in Table III.

TABLE III: System and Modulator Data for Four Runs.

	244 System	15 Critical	
SLC Operating Period	21,840	21,840	Hr
SLC/Modulator-hours	5.33 e6	3.27e5	
No. of Interventions	7537	437	
Total Repair Time	3167	203	Hr
System Failure Rate	0.345	0.020	P/hr
System MTTF	2.9	50.0	Hr
Modulator MTTF	707	750	Hr
Modulator MTTR	0.424	.464	Hr
System "Availability"	0.855	0.991	
System "A" w/ Spares	0.931	not applicable	

The critical modulator value of 0.990 indicates that their availability was better than either of the above two calculations for Modulator System Availability which offered 0.854 for the no spares case, and 0.931 for the spares case, but it forebodes that the expected availability would be no better than 0.854 since there are no spares for the 15 critical modulators. We are lucky, or we give these modulators more attention when permitted by the schedule.

Finally, we arrive at the comparison of Availability for SLC and the modulator system. Table IV offers this data.

TABLE IV: Availability of SLC and Modulator Systems.

SLC Run Period	1991	1992	1993	94/5
PRR (Hz)	60	120	120	120
SLC Operating Hours	4008	5568	5736	6528
SLC Availability	0.6	0.818	0.828	0.794
244 System Mod "A"	0.884	0.829	0.849	0.863
15 Critical Mod "A"	0.990	0.994	0.992	0.991

IV. CONCLUSIONS

SLC availability increased while the 15 Critical Modulator Availability wavered about 0.99 indicating that the modulator system does not seriously impact SLC performance. We continue to improve the reliability of the system. Presently we are installing a device, an "anode reactor" that extends the life of the pulse cable. It has definitely improved cable lifetimes in six modulators where it has been installed. But even if cable lifetimes improve by a factor of three; "Availability" only increases by 0.9%.

V. REFERENCES

[1] A.R. Donaldson and J.R. Ashton, "SLAC Modulator Operation and Reliability in the SLC Era," 1992 20th Power Modulator Symposium, IEEE Conference Record CH3180-7/92/0000-152.

The SLC as a Second Generation Linear Collider*

J.E. Spencer
Stanford Linear Accelerator Center, Stanford University, Stanford, CA 94309 USA

Abstract

With enough luminosity, the SLC could contribute to most of the high energy physics of current interest such as new hadrons, quark molecules, glueballs and studies of the Standard Model and Minimal Supersymmetric SM in the form of particle searches for the lowest mass Higgs or selectron or tests of the point-like predictions for the W, Z or $\tilde{e}_R$. Some experiments require alternative incident channels such as $e\gamma$ and $\gamma\gamma$ but only modest increases in energy. Just as the SLC was a prototype for the NLC, it could also be a prototype for a general (or gamma) linear collider – a GLC. Because the main problem is luminosity, we give a scaling relation based on multiple bunches per RF pulse. We then ask what is possible for the SLC in terms of bunch and train current, emittance and energy at the IP. The results suggest a phased development with the Higgs as a possible last step requiring a luminosity $\mathcal{L}\geq 10^{32}$.

I. Introduction

The assumption is made that before an NLC is approved, a working prototype is necessary that can demonstrate the feasibility of a general purpose linear collider capable of $\vec{e}^{\pm}\vec{e}^{\pm}$, $\vec{\gamma}\vec{e}^{\pm}$ and $\vec{\gamma}\vec{\gamma}$ incident channels. It is also argued that new physics is available over a range of energies starting at a few GeV by modifying the SLC to provide such channels *and* that this physics is hard to achieve elsewhere [1].

We begin with a discussion of the SLC relative to the next generation of linear colliders. Because the e^+e^- option has been verified, we concentrate on the other channels since positrons are an unnecessary complication for a single linac. While we don't preclude that option, our primary goal is to optimize the $\vec{e}^-\vec{e}^-$ luminosity ($\equiv\mathcal{L}_{ee}$) because this channel is used to produce the others [1].

From the expression for $\mathcal{L}$, one wants to maximize the available charge in a single bunch N_B, then the number of bunches in a train n_B and finally the RF rep-rate f_T:

$$\mathcal{L} = \frac{f_T n_B N_B^2 H_D}{4\pi\sigma_x\sigma_y}\zeta \rightarrow \frac{f_T n_B N_B^2}{4\pi\epsilon_n\beta^*}\gamma \propto \frac{P_b N_B}{\epsilon_n\beta^*}$$

where P_b is beam power and ϵ_n the invariant emittance.

To get more high quality charge through the linac and arcs we consider multibunch operation and coalescence. The reduced energy from beam loading reduces emittance growth in the arcs and is ideal for initial experiments [1]. For subsequent phases, energy can be restored in various ways e.g. by adding 'afterburners' between the arcs and final focus. Other ways to increase the energy and/or the charge/bunch are discussed in terms of a luminosity budget that indicates $\mathcal{L}\geq 10^{32}$ is possible.

*Supported under Dept. of Energy contract DE-AC03-76SF00515.

0-7803-3053-6/96/$5.00 ©1996 IEEE

II. Comparison to the Next Generation

A major concern in the design of the next generation of linear colliders is the effect of transverse and longitudinal wakefields that depend on the characteristics of the bunch and accelerating structure. This arises from the higher beam energies and powers that are required and the fact that to achieve these one is forced to higher RF frequencies and accelerating gradients. Because wake effects depend on the number of apertures, inversely on their area and the amount and distribution of charge in a single bunch, they become increasingly important.

While one would like all the charge/RF pulse in one bunch, this is impractical for incident emittance, energy spread as well as the beamstrahlung. However, the bandwidth of the control system and the stability of the accelerator and its various subsystems relates more to the RF rep-rate f_T. A practical solution would appear to be multibunch trains i.e. to partition the total charge/pulse into a more continuous flow. As a result, most current designs propose to accelerate several bunches per RF pulse with somewhat lower bunch charge N_B than the SLC in order to improve energy efficiency and average luminosity. Any required luminosity then has to come from increasing P_b i.e. P_{RF} and P_{AC} (or n_B and f_T) [2].

Thus, because preceding bunches perturb the effective emittance, energy and spread of the following bunches, multibunch beam loading and phase compensation must be considered to determine the best distribution of charge over each RF pulse. The next question is whether the bunches can be coalesced after acceleration when the physical apertures are larger. This would combine the best aspects of the different designs and reduce the pressure to maximize N_B. Because it is difficult to maintain the emittance with conventional magnetic compression one can consider other methods analogous to FEL bunching structures, fast phase switching techniques [3] or transient wake effects [4].

III. SLC Improvements/Limitations

We now discuss these issues relative to the SLC. We also ask how to avoid the damping rings and take advantage of the arcs for bunch compression/coelescence. One problem in using the arcs is emittance growth which is discussed.

We will assume that we are dealing solely with e^-e^- beams since they provide interesting physics and are used to produce the photon channels. A major advantage of electrons is that they can be polarized so we can control the distribution of energy and polarization in all incident channels [1]. Another advantage is that it allows us to avoid damping rings i.e. simplify multibunch operation if a low emittance RF gun for polarized electrons was available.

A. *The Generalized Luminosity* $\mathcal{L}$

The luminosity given above was for round beams where H_D was the pinch parameter and ζ was the efficiency of the colli-

sion in terms of crossing angles and other parameter conflicts. Since we didn't label this $\mathcal{L}_{ee}$ we could also include the efficiency of converting $e\to\gamma$. For multibunch operation, we introduce a crossing angle and design the FF quads accordingly. This decreases ζ so that we can then introduce variable, crab-crossing cavities or RF deflectors that rotate the beams to the appropriate orientation at the IP or CP (the $e\gamma$ conversion point).

The rms spot size σ at a round focus is

$$\sigma^* = (\frac{\epsilon_n\beta^*}{\gamma})^{\frac{1}{2}} = \frac{1}{\sqrt{\epsilon_1(\mathrm{GeV})}}\,\mu\mathrm{m}\ \ (\epsilon_n = 2\mu\mathrm{m},\ \beta^* = 1\mathrm{mm}).$$

With these characteristics in a 'second generation' collider we would then expect an electron luminosity

$$\mathcal{L}_{ee} \approx \epsilon_1(\mathrm{GeV})\cdot 10^{31}\ \mathrm{cm}^{-2}\mathrm{s}^{-1}\ \ (f_T{=}120, f_B{=}100, N_B{=}10^{10}).$$

Thus, $\mathcal{L}$ varies linearly with incident beam energy if the other parameters are energy independent.

We argue that the product of the parameters H and ζ may be made no worse than 0.2-1.0. Besides simplicity, this is why we consider round beams and ignore H and ζ except for conversion efficiency. To get $\mathcal{L}_{ee}{\geq}5\cdot 10^{32}$ we need an incident e-beam energy $\epsilon_1{\geq}50$ GeV – the nominal energy of the SLC.

We get $\mathcal{L}_{e\gamma}$ or $\mathcal{L}_{\gamma\gamma}$ from $\mathcal{L}_{ee}$ by folding it with the conversion efficiencies and a luminosity coefficient $\eta(z)$. If we can take the e-focus at z=0, then the luminosity coefficient at z relates to the electron size $\sigma(z)$ at that point. Using

$$\beta(z) = \beta^* + \frac{z^2}{\beta^*}\ \Rightarrow\ \sigma(z) = \sigma^*\frac{z}{\beta^*}\ \simeq\ (f/D)\lambda$$

implies small conversion distances for efficient use of laser power or good conversion efficiency and luminosity i.e. $z \approx(\beta^*/\sigma^*)(f/D)\lambda$. Increasing laser intensity increases the strong-field QED processes that we want to avoid.

In Compton collisions and other radiative processes, the lowest energy photons scatter at the largest angles i.e.

$$\theta(\omega) = \theta_\circ\sqrt{\frac{\omega_{max}}{\omega} - 1}\qquad (\theta_\circ = \sqrt{x+1}/\gamma_1)$$

so that

$$\eta(z) \equiv \frac{z\theta_\circ}{\sigma^*}\ \approx\ \frac{1}{2}(\frac{z}{\mathrm{mm}})(\frac{\mathrm{GeV}}{\epsilon_1})(\frac{\mu\mathrm{m}}{\sigma^*})\sqrt{x+1}\ .$$

For $\eta(z){\leq}1$, the higher energy photons collide with the same spot size that the electrons would have had so that $\mathcal{L}_{ee}$ is preserved. If we now get the proper intensity for good conversion efficiency without violating the other z constraint we would expect an optimal GLC. Ref. [1] shows how the luminosity spectrum can be controlled. Experiment E144 in Fig. 1 [5] has verified the possibility of $\vec{\gamma}$ beams from the intense laser beams required for efficient conversion. The SLC could usefully verify crossing angles and crab cavities.

B. The Luminosity Budget

Presently the SLC runs with effectively one bunch/train but having a total current that is 3 times the single bunch value per RF pulse. The simultaneous use of one linac for both beams as well as the scavenger bunch that is used to produce positrons for the next cycle implies an efficiency of 33-67%. Because BNS damping [6] is used to improve the transverse stability of the bunches it is necessary to correct the phase of the scavenger bunch about midway in the linac which implies an additional inefficiency.

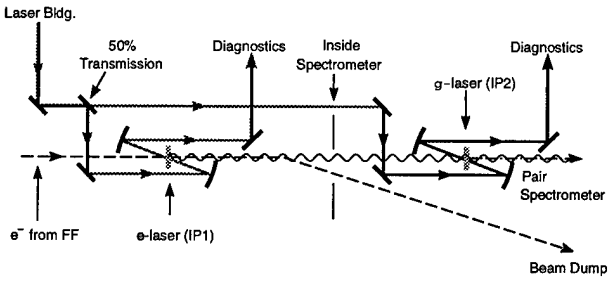


Figure 1. IP1 produces high energy γs and secondary pairs that the 'inside' spectrometer analyzes. Pair spectrometer analyzes the high energy Comptons and pairs from IP2.

Likewise, just as the scavenger imposes overhead, the use of two charge species increases overhead quite apart from the use of one or two damping rings. Thus, the use of only one species in a train that covers some fraction of the RF fill time will be an improvement. Clearly, operation without the damping rings is also more efficient quite apart from any increase in the current/bunch.

The integration of RF beam monitors with the accelerator implies the possibility of significantly higher single bunch currents [7]. Based on better control of transverse wake fields, more efficient use of charge and much simpler operating conditions we estimate a potential 6-fold increase i.e. $\mathcal{L}\approx 6\cdot 10^{30}$ without any emittance improvements or increased total charge/pulse.

Although we expect significantly better emittance from RF guns, we also know that there will be emittance dilution in the arcs e.g.

$$\Delta\epsilon_{n,x}[\mathrm{m}] \approx 4\cdot 10^{-8}E^6[\mathrm{GeV}]\,\mathrm{I}_5[1/\mathrm{m}]\ \geq\ 0.8\cdot 10^{-5}$$

for point beams with no errors at the Z resonance (46.6 GeV). I_5 is the usual synchrotron radiation integral [8].

Assuming an emittance that is a factor of 10 smaller than the SLC ($\epsilon_n\ \simeq 3{\cdot}10^{-5}$ m) for comparable bunch currents, implies it is necessary to run below 40 GeV through the arcs. This implies another acceleration up to final energy even though initial running would be at 10 GeV [1]. Note that a lower energy also allows more total charge. During the final phases it is assumed that either X-Band acceleration at ~100 MeV/m or laser acceleration at ~1 GeV/m would be available to save space or to accelerate more charge in a bunch of the same length for coalescence. With just the emittance improvement but using the present charge/bunch due to emittance constraints gives about a 20-fold increase with wake control and simpler operations.

Increasing the total charge/pulse by a factor of ten is possible [9] with a variety of options. Suppose we allow the increased

loading to modify the energy between bunches to take advantage of the longitudinal dispersion in the arcs:

$$R_{56} = \frac{\delta l_z}{\delta p/p} = \int \frac{\eta}{\rho} ds \approx 15 \text{ cm}/\%$$

where δl is the change in bunch separation with a change in bunch energies. While we want to maximize I_1, we want to minimize I_5 for the emittance. Thus, while it appears that bunches can be coalesced even for S-Band separations of 10 cm, an X-Band linac with $\lambda \approx 2.6$ cm would provide more flexibility in dealing with the wake field problem in filling near-neighbor buckets. It is possible to cancel some of these effects and even provide acceleration [4] but this appears expensive.

C. *Multi-bunch Trains*

Calculations [9] indicate that a sledded RF pulse could accelerate more than 20 times the present, effective charge/pulse with good characteristics. At lower energies we expect a corresponding increase in pulse rep-rate – all without adding any higher power klystrons [2].

If we accelerate 620 mA in a 400 ns train, we increase the total equivalent charge per beam by a factor of 22 assuming 3.5×10^{10} per bunch. This provides a maximum possible luminosity gain of 490. The energy will be reduced by about 10 GeV but this is ideal for preserving the lower emittances from an RF gun. Because we can't coalesce, we have several options to provide a low energy spread e.g. RF amplitude or phase modulation or variation of the beam current with time. In principle, it is possible to get zero energy spread from the acceleration process. This is compatible with lower emittance. Thus, we get another factor of twenty in luminosity from increasing n_B. Anything near this makes Higgs searches possible.

IV. A Physics Example

Several options exist while running up to at least 60 GeV for the Higgs but an interesting and practical one is W^- production via $\gamma_R + e_L$. Of particular interest are the zeros in the differential cross sections predicted by the Standard Model when the W goes in the direction of the incoming electron i.e. when the γ and W are back-to-back in the center-of-mass. Our interest was the sensitivity of these variations to violations of the Standard Model's predictions at *lower* energies.

The important process is the 3 gauge boson vertex. The three coupling parameters that conserve C and P are determined by the W's charge, magnetic dipole moment μ_W and electric quadrupole moment Q_W:

$$\mu_W = \frac{e}{2M_W}(1+\kappa_\gamma+\lambda_\gamma); \quad Q_W = -\frac{e}{M_W^2}(\kappa_\gamma-\lambda_\gamma)\,.$$

Fig. 2 is the SM results for $\sqrt{s}$=109 and 500 GeV where the lower energy is for SLC at 60 GeV. While difficult, there is no advantage at higher energies over this low-cost way to study the heavy gauge bosons and their couplings.

Violations from the lowest order radiative corrections are expected to be of order α and the experiments and machine studies during the various phases are very interesting and have an indeterminant range in energy when we consider future alternatives such as laser acceleration.

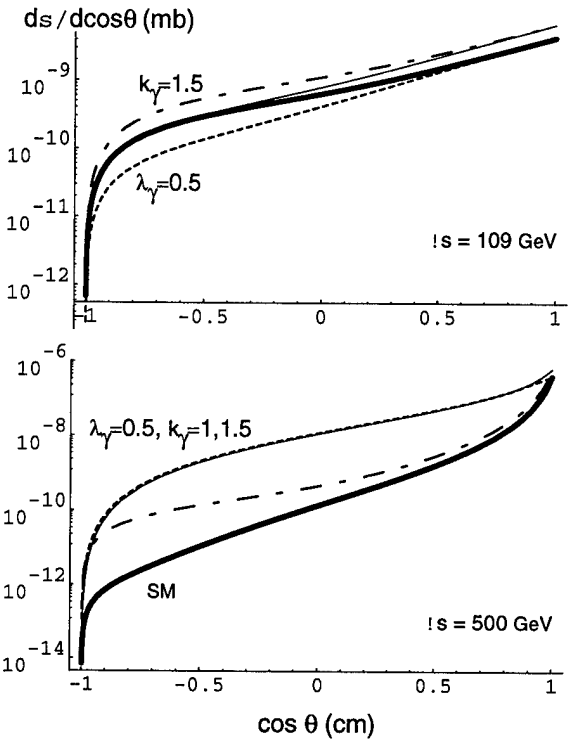


Figure 2. Differential cross sections for $\gamma_R + e_L \to W + \nu$ in the center of mass at $\sqrt{s}$=109 and 500 GeV for the SM prediction of point-like moments (λ_γ=0 and k_γ=1) and some violations showing sensitivity with energy and angle.

References

[1] J.E. Spencer, Uses of a Prototype NLC/GLC, NIM **A355**(1995)184.

[2] The high-power, S-Band klystron development for DESY implies a peak power increase of nearly 2.5.

[3] F.-J. Decker, R.K. Jobe, N. Merminga and K.A. Thompson, Controlling Multi-Bunches by a Fast Phase Switching, Lin. Accel. Conf., Sept. 1990.

[4] C.G. Yao and S. Ecklund, Increasing the Energy of SLC by Transient Wake Field, SLAC-PUB-3751, 1985.

[5] K.T. McDonald and A.C. Melissinos, Spokesmen, Proposal for a Study of QED at Critical Field Strength in Intense Laser High-Energy Electron Collisions at SLAC, Proposal E144, Oct. 1991.

[6] V. Balakin, et al., VLEPP: Transverse Beam Dynamics, 12th Int'l.Conf. on High Energy Accel's., 1983.

[7] D. Whittum, Private Communication.

[8] R. Helm, et al., Evaluation of Synchrotron Radiation Integrals, IEEE Trans. Nucl. Sci., **20**(1973)900 and T.O. Raubenheimer, et al., PAC Proc., (1993)635.

[9] Z.D. Farkas, Sledded SLAC Beam Loading Compensation, AAS-Note 86, Dec. 1994. I thank David Farkas for discussions on this.

Status of the Design for the TESLA Linear Collider

R. Brinkmann, DESY, Notkestr. 85, D-22603 Hamburg
for the TESLA collaboration

Abstract

Among the different approaches towards a next generation 500 GeV (c.m.) Linear Collider the TESLA design uses superconducting accelerating structures operating at 1.3 GHz and a gradient of 25 MV/m. The particular features of TESLA are a high AC-to-beam power transfer efficiency and relaxed tolerances compared to the other approaches. This paper gives an update on the machine parameters and the overall design, including a discussion of the potential for an upgrade to higher center-of-mass energies.

I. INTRODUCTION

The different design studies for a next generation e^+/e^- linear collider fall, roughly speaking, in two categories: the high frequency approaches (NLC, JLC, VLEPP, CLIC), which aim at a high accelerating gradient and the low frequency approaches (SBLC, TESLA) operating at a lower gradient, but having the advantage of reduced rf peak power requirements and smaller wakefield effects in their larger aperture accelerating structures [1,2]. The TESLA design, with an rf frequency of 1.3 GHz at the lower end of this frequency scale, has the special feature of using superconducting cavities for the linac, which allows to accelerate many bunches in a long rf-pulse yielding a high rf-to-beam power transfer efficiency. An accelerating gradient of 25 MV/m with a quality factor (unloaded) of $Q_0=5\times10^9$ at T=2K is foreseen. The choice of 1.3 Ghz is a compromise between surface resistance ($\propto\omega_{rf}^2$) and R/Q (favoring a high frequency). Another argument is the availability of klystrons at this operating frequency. Whereas the advantages of very low wakefields and high acceleration efficiency are obvious, the challenge of TESLA is clearly to demonstrate that stable operation with a gradient of 25 MV/m can be achieved not only within a laboratory experiment but on a large scale. In addition, the costs of the s.c. structures have to be drastically reduced compared to systems built up to now. In order to demonstrate that these goals can be achieved, a test facility is under construction at DESY [3,4] in international collaboration with institutes in China, Finnland, France, Germany, Italy, Poland, Russia and USA contributing to the technical R&D and/or the design of the 500 GeV collider. In the following, the present status of design is described. After a discussion of general parameters, the layouts of the final focus and interaction region, the main linac and the injection system are presented. In section 5, the upgrade potential of TESLA is discussed.

II. PARAMETERS

Using basic relations for the luminosity and the beamstrahlung and assuming an optimum beta-function β_y^* at the interaction point (IP) close to the bunchlength σ_z, the luminosity is in good approximation given by:

$$L = const. \times \frac{P_b}{\gamma} \times \frac{< \Delta E / E >_{rad}^{1/2}}{\varepsilon_y^{1/2}}$$

where P_b is the average beam power, $<\Delta E/E>_{rad}$ the energy loss due to beamstrahlung and ε_y the normalised vertical emittance. With the extremely small wakefields in the s.c. cavities, the TESLA linac is ideal for preserving a small ε_y without excessively tight tolerances (see section 4). Making use of this fact, the TESLA parameters have recently been slightly modified towards a smaller vertical emittance (see table 1 for a comparison of the new with the original [2] TESLA parameters). The main benefit of the new parameter set is a reduced AC-power consumption which is now below 100 MW for the 500 GeV (center of mass) machine at unchanged luminosity. The tolerances in the linac still remain conservative and the vertical spot size at the interaction point (IP) is a moderate extrapolation of the recent achievement of the FFTB experiment [5] by about a factor of 3.5.

III. INTERACTION REGION, FINAL FOCUS, COLLIMATION

Keeping beamstrahlung at a low level is essential for acceptable background conditions and good energy resolution for the high energy physics experiment. The center-of-mass energy spread in TESLA amounts to $<\delta E/E>_{c.m.} = 1.5\%$. It could be further reduced for a top quark threshold scan to $<\delta E/E>_{c.m.} \approx 0.1\%$ by increasing the horizontal beamsize at the IP, still keeping the luminosity above 10^{33} cm^{-2} s^{-1}. With the relatively large spacing between bunches ($\Delta t_b=0.7\mu s$), the experiment can resolve individual bunch crossings. Thus the small numbers of e^+e^- pairs N_{pair} outside a mask with 5cm radius and 100mrad opening angle as well as the hadronic background [6] are easily handable.

For TESLA a head-on collision design with electrostatic separation of the beams after the final doublet is possible [7], see fig.1. This allows to use s.c. quadrupoles which provide a large aperture (a_Q=24 mm) for the disrupted beam and the beamstrahlung γ's emitted at the IP with large angles. A

0-7803-3053-6/96/$5.00 ©1996 IEEE

layout for the separation of the outgoing from the incoming beam and for beamstrahlung collimation is under study [8].

Table 1: New parameters of the TESLA 500 GeV (c.m.) linear collider in comparison with the original design.

	NEW	OLD	
total length	32	32	km
t_{pulse}	800	800	μs
n_b/pulse	1130	800	
Δt_b	707	1000	ns
f_{rep}	5	10	Hz
N_e/bunch	3.63	5.1	10^{10}
$\varepsilon_x/\varepsilon_y$	14/0.25	20/1	10^{-6} m
β_x^*/β_y^*	25/0.7	25/2	mm
σ_x^*/σ_y^*	845/19	1000/64	nm
σ_z	0.5	1	mm
$<\Delta E/E>_{rad}$	2.9	2.9	%
Disr. D_x/D_y	0.2/11	0.4/8.5	
P_b (2 beams)	16.3	33	MW
P_{AC} (2 linacs)	88	154	MW
$\eta_{AC\text{-}to\text{-}beam}$	19	21	%
luminosity L	6	6	10^{33} cm^{-2}s^{-1}

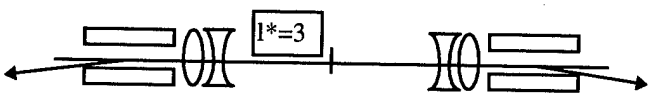


Fig. 1: Basic layout of the interaction region

The magnet lattice between the IR and the main linac consists of the final focus system (FFS) for beamsize demagnification and chromatic corrections, a collimation section to protect the IR quads from large amplitude particles and bending sections for creating a sufficient separation between two beamlines if the collider is to serve two experiments. The bend between collimation and the FFS also helps to reduce background due to muons originating at the collimators [9]. In total this "beam delivery" system is 1.5 km long (per beam). The momentum acceptance of the FFS (±0.6%) is well in excess of the beam energy spread (σ_E/E=0.1%).

The requirements for beam collimation are determined by the condition that synchrotron radiation generated in the doublet before the IP has to pass freely through the aperture of the final quad on the opposite side. This means that particle amplitudes have to be restricted to $12\sigma_x \times 35\sigma_y$ for TESLA. Continuous scraping of beam tails may not be necessary, since in the s.c. linac gas scattering is negligable and wakefields are small so that particles should normally not reach the above defined limits. Following concepts developed at SLAC [10], a design for simultaneous collimation in x,y and dE/E has been worked out [10].

IV. MAIN LINAC

The TESLA linac consists of basic units with one 9 MW klystron delivering rf-power to 32 9-cell 1.3 Ghz s.c. Nb cavities.

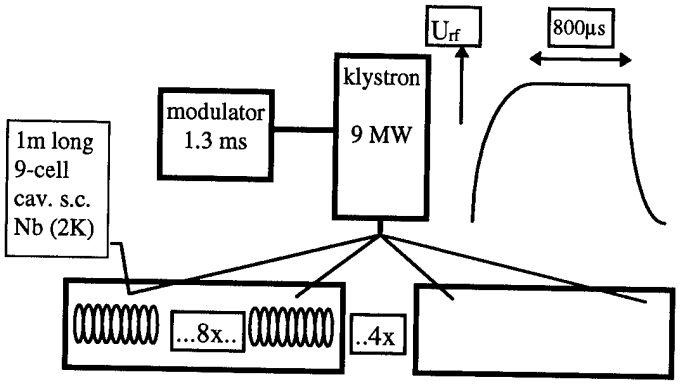


Fig. 2: Basic unit of the TESLA main linac

There are 8 of these 1m long cavities in one kryostat. The modulator produces a 1.3 ms long pulse, yielding a 0.8 ms long flat top accelerating field. The two TESLA linacs require in total 604 klystrons and 19,328 cavities. A focussing scheme using s.c. quadrupoles with scaling $\beta \propto \gamma^{0.2}$ (initial β = 22m) is foreseen [11].

One of the most important accelerator physics issues in a linear collider concerns preservation of a small (especially vertical) emittance in the linac. Emittance dilution caused by chromatic effects (dispersion, filamentation) due to energy spread in the bunch, short range wakefields and long range deflecting modes have been investigated [11]. With HOM-damping provided by two couplers per 9-cell cavity ($Q<10^5$), multibunch BBU leads to an effective emittance growth of only about 1%, assuming rather relaxed transverse rms position tolerances of 0.5 mm for the cavities and 0.1mm for the quadrupoles and beam position monitors (BPM's). A simple "one-to-one" orbit correction algorithm was applied in this computer simulation. With the same assumptions, the calculated emittance growth due to short-range wakefields and chromatic effects amounts to $\Delta\varepsilon_y/\varepsilon_y$ = 20%. A further reduction of emittance dilution is possible applying additional beam-based correction procedures [12]. With its relaxed tolerances, the TESLA linac will be rather insensitive to ground motion. In addition, the large bunch spacing allows to very effectively eliminate pulse-to-pulse orbit jitter. This is done by measuring the position of the first bunch and correct for the following ones with a kicker. Such devices would be installed at the beginning and the end of the main linac. The fast orbit correction method can also be applied to stabilise the beam position at the IP.

V. INJECTION SYSTEM

For TESLA it is necessary to compress the 0.8ms long bunchtrain in order to fit into a damping ring of reasonable size. Two options are presently discussed: A conventional ring with ≈6km circumference (like HERA-e) or a "dog-bone" shaped ring of ≈20 km length [13] which fits almost entirely (except for the arcs at the end) into the linac tunnel. One advantage of the latter design is an increased bunch spacing (80 ns instead of 25 ns for the HERA-e like ring), which relaxes bandwidth requirements for the injection/extraction system and the multibunch feedback. Recent beam optics studies for the dogbone ring show that the required emittances can be achieved with reasonable magnet position tolerances [14]. The possibility to use a rf-photo-gun to achieve the design emittance of the electron beam is being studied [15], which would allow to save one of the two damping rings.

Positrons are produced by converting γ's in a thin (0.4 radiation lengths) target. The required intense photon source is realised by passing the e^- beam after collision through a 30m long wiggler [16]. The method drastically reduces the heat load on the target and opens up the possibility to produce polarized positrons by using a helical undulator.

VI. UPGRADE POTENTIAL

With the relaxed tolerances of the low-frequency approach, TESLA is a very well suited design if one aims to push the vertical emittance towards a smaller value. A small ε_y becomes very important (if not inevitable) when an energy upgrade to 1TeV or higher is considered. How in detail the energy upgrade of TESLA would be realised depends on the progress on cavity development in the longer term future. Under conservative assumptions, the gradient has to be kept at 25 MV/m implying that a 1 TeV version of TESLA would have to double the length of the linac. However, neither this gradient nor the assumed quality factor of 5×10^9 are fundamental limits. Assuming a gradient of 40 MV/m as a future possibility, the machine with twice the length of the 500 GeV design could reach a center-of-mass energy of 1.6 TeV..The parameters for this machine are shown in table 2. A reduced bunch charge is used to facilitate preservation of the vertical emittance (first results of simulation studies show that this emittance can indeed been achieved with still relatively relaxed tolerances). A luminosity above 2×10^{34} cm^{-2} s^{-1} can be reached with an AC-power consumption increased by about a factor of 2.5 compared to the 500 GeV design.

Table 2: Parameters at 1600 GeV (c.m.) with an accelerating gradient of 40 MV/m at $Q_0 = 5\times 10^9$.

	TESLA 1.6 TeV	
total length	62	km
t_{pulse}	800	μs
n_b/pulse	2825	
Δt_b	283	ns
f_{rep}	3	Hz
N_e/bunch	1.8	10^{10}
$\varepsilon_x/\varepsilon_y$	10 / 0.03	10^{-6} m
β_x^*/β_y^*	35 / 0.7	mm
σ_x^*/σ_y^*	474 / 3.7	nm
σ_z	0.5	mm
$<\Delta E/E>_{rad}$	5.2	%
Disr. D_x/D_y	0.15 / 18.8	
P_b (2 beams)	39.2	MW
P_{AC} (2 linacs)	228	MW
$\eta_{AC\text{-}to\text{-}beam}$	17.2	%
luminosity L	23	10^{33} $cm^{-2}s^{-1}$

VII. REFERENCES

[1] J. Roßbach, "Options and Trade-offs in Linear Collider Design", contribution to this conference.

[2] R. Brinkmann, Proc. EPAC 94, London, Vol. I, p. 363.

[3] H. Weise, "The TESLA Test Facility (TTF) Linac- a Status Report", contribution to this conference.

[4] M. Leenen, "The Infrastructure for the TESLA Test Facility (TTF)- a Status Report", contribution to this conference.

[5] D.L. Burke, Proc. EPAC 94, London, Vol. I, p. 23.

[6] D. Schulte, thesis Universität Hamburg, 1995, to be published.

[7] O. Napoly et al., DESY-TESLA 94-31.

[8] A. Drozhdin, DESY-TESLA 94-29

[9] M. Sachwitz and H.J. Schreiber, DESY-TESLA 94-27.

[10] R. Brinkmann et al., to be published.

[11] A. Mosnier and A. Zakharian, Proc. EPAC 94, London, Vol. II, p. 1111 and A. Mosnier, private communication (1995).

[12] T. Raubenheimer, SLAC-PUB-6117 (1993).

[13] K. Flöttmann and J. Roßbach, Proc. EPAC 94, London, Vol. I, p. 503.

[14] R. Brinkmann et al., to be published.

[15] E. Colby et al., "Design and Construction of High Brightness RF Photo injectors for TESLA", contribution to this conference.

[16] K. Flöttmann and J. Roßbach, DESY-M-91-11.

THE TESLA TEST FACILITY (TTF) LINAC – A STATUS REPORT

H. Weise, for the TESLA Collaboration, Deutsches Elektronen-Synchrotron DESY,
22603 Hamburg, Germany

Abstract

The TESLA Test Facility (TTF) Linac, under construction at DESY by an international collaboration is an R&D test bed for the superconducting cavity variant of the TeV scale future linear colliders. The main body of the TTF Linac will consist of four cryomodules, each containing eight 1 meter long nine-cell cavities made from bulk niobium and operated at L-band (1.3 GHz) frequency. The base accelerating goal is 15 MV/m. While a first injector is going to be installed in 1995 and will provide 8 mA beam current within 800 μs long macro pulses at 216 MHz bunch repetition rate, a second injector based on a BNL like RF-gun combined with a standard TESLA cavity as preaccelerator and with a bunch compressor is under development. This injector will need to operate with a bunch charge of 5×10^{10} electrons at 1 MHz bunch repetition rate; the macro pulse length is again 800 μs and the injector output energy approximately 20 MeV. Overview and status of the linac construction will be given. Plans for the future use of the TTF Linac are presented.

I. INTRODUCTION

An electron-positron collider with a center of mass energy of 500 GeV and luminosity above 10^{33} cm $^{-2}$sec^{-1} should be considered as a possibility for the next accelerator facility after the LHC. This is a widespread consensus within the high energy physics community. Such a collider would provide for top analyses via $t\bar{t}$ production and discovery reach up to a Higgs mass of ≈350 GeV.

Worldwide, there are groups pursuing different linear collider design efforts. Several of these R&D groups plan to have working prototype test facilities in the 1997 time scale, this in order to establish well-developed collider designs. The TESLA activity [1] is one of these R&D efforts, differing from the others in its choice both of superconducting (s.c.) accelerating structures and of low operation frequency (1.3 GHz).

The TESLA Test Facility (TTF) is to be located at DESY, with major components flowing in from the members of the collaboration. The facility includes infrastructure to prove the feasibility of reliably achieving acceleration gradients above 15 MV/m in a series production. And the TTF has also to show that the in a LINAC test string (32 s.c. cavities) assembled accelerating structures can be successfully operated; this with the help of auxiliary systems (couplers, frequency tuners, cryogenics) to accelerate an electron beam to 500 MeV.

II. THE 500 MeV TTF-LINAC

In Fig. 1 (see next page) a plan view of the TTFL layout is shown. Being located in one of the DESY experimental halls the linac is within an approximately 100 m long shielded enclosure. From right to left an injector including its gun, a capture cavity, and a diagnostic section, is followed by a first cryomodule housing 8 s.c. cavities. A warm section allows for a later installation of a magnetic bunch compressor (see below, outlook) preceding another three cryomodules. The linac facility is finally completed by a diagnostic area which will be used extensively for beam experiments [2].

The operating parameters of the TTFL are given in Tab. I where the two columns Inj I/Inj II already list two scenarios for different injectors.

Table I
TTFL operating parameter.

Parameter	TTFL	
Linac Energy	500 MeV	
RF frequency	1.3 GHz	
Accel Gradient	15 MV/m	
Q_0	3×10^9	
# Cryo modules	4	
ΔE/E single bunch rms	$\approx 10^{-3}$	
ΔE/E bunch to bunch rms	$\approx 2\times10^{-3}$	
Bunch length rms	1 mm	
Beam current	8 mA	
Beam macro pulse length	0.8 ms	
Lattice β typical	12 m max	
	Inj I	Inj II
Injection Energy	10 MeV	20 MeV
Emittances (x/y), $\gamma\sigma^2/\beta$	$\approx 5\mu$m	$\approx 20\mu$m
Beam size σ, end of linac	250μm	500μm
Beam size σ, injection	1.7 mm	3.5 mm
Bunch frequency	217 MHz	1MHz
Bunch separation	4.6 ns	1μsec
Particles per bunch	2.3×10^8	5×10^{10}

In the first stage of installation the injector area includes a thermionic electron gun [3], a subharmonic prebuncher, the s.c. capture cavity, focusing lenses, and beam diagnostic equipment. The capture cavity is identical to one of the nine-cell structures (see Tab. II below) in the main linac. With its gradient of 15 MV/m the injected 250 keV electron beam will be accelerated to energies above 10 MeV. In the future, Injector I will be replaced by the high bunch charge Injector II [4] based on a laser driven rf gun. This injector comes close to the requirements of the TESLA Linear Collider electron source (5×10^{10} electrons per bunch, $\epsilon_n = 1\ \pi\ mm\ mrad$). The new installation will be located in the same injector area but needs some additional space for the laser and for the klystron/modulator driving the rf electron gun.

0-7803-3053-6/96/$5.00 ©1996 IEEE

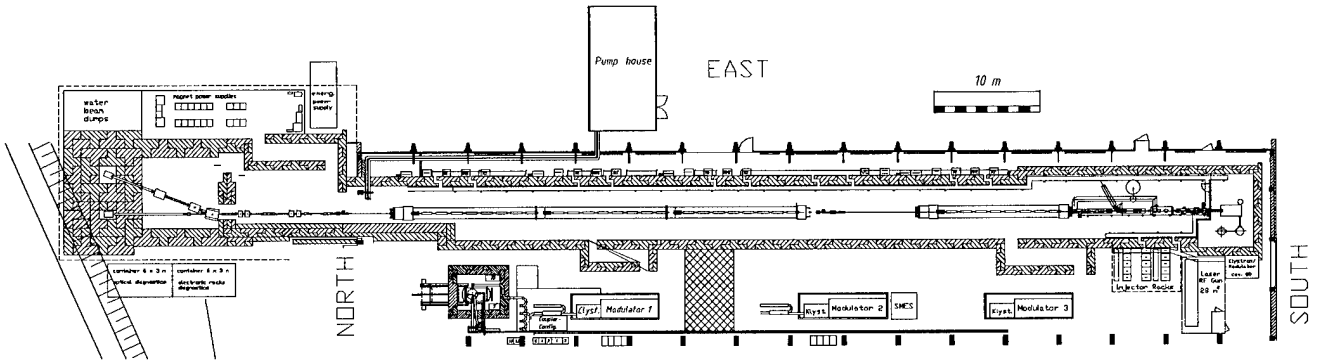


Figure. 1. Plan View of the TESLA Test Facility Linac Layout.

Four cryomodules, each 12.2 m in length, comprise the main body of the linac. Each module contains eight nine-cell π-mode cavities and a quadrupole package. Thus, the beam optics is basically a periodic lattice with a cell length being identical with the module's length; the phase advance in the modified FODO lattice (the quadrupoles come in pairs) is $\pi/2$; matching to the lattice is performed by means of two triplet magnets. Depending on the finally achieved accelerating gradient (15 - 25 MV/m) the energy gain per cryomodule will be between 120 and 200 MeV. Each cavity has a RF power input coupler, two higher-order-mode (HOM) output couplers, a RF fundamental pick up, and a frequency tuning mechanism. Selected parameters of the cavities are given in Tab. II.

Table II
RF cavity parameters for the TTFL

Frequency	1.3	GHz
Cells per cavity	9	
Cavity length	1.036	m
Iris radius	35	mm
R/Q	1011	ohms/cavity
E_{peak}/E_{acc}	≈ 2.0	
RF power @ 25 MeV/m	206	kW/m
HOM k_{long}/cavity	8.5	V/pC (σ_z = 1 mm)
HOM k_{trans}/cavity	18	V/pC/m

The quadrupole package includes a superferric quadrupole doublet, transverse steering coils (two pairs, one each for permanent corrections and for vibration control), a transverse beam position monitor (cylindrical rf cavity), and a HOM absorber. Operation temperature of the quadrupole package is 4 K.

Every s.c. cavity has its own helium vessel and the whole string is supported by a long helium gas return pipe. Shielding against the earth magnetic field will be provided. Therefore, an unloaded quality factor of the cavities well above $Q_0 = 3 \times 10^9$ can be reached at operating temperature (1.8 K). The estimated heat load for all four TTFL modules is approximately 115/115/700 W at 1.8/4.5/70 K, this being calculated for a gradient of 15 MV/m and $Q_0 = 3 \times 10^9$. In this calculation the cold/warm transitions for the bunch compressor section are included. The first module will be equipped with a large number of temperature sensors as well as with vibration sensors. Alignment during cooldown will be monitored using optical methods and in addition to this using a stretched wire system. The latter can be used also during linac operation.

RF power for the main body of the linac will be provided by two klystrons and two modulators. Each klystron/modulator will deliver 4.5 MW with a pulse length of up to 2 ms. The first of these two rf power sources has been commissioned successfully [5]. The injector's capture cavity has its own klystron, the needed RF power within the macro pulse is below 100 kW. The rf gun needed for Injector II requires a few MW of RF power. Here it is foreseen to take advantage of a 10 MW klystron (1.3 GHz) which will be developed as a prototype for the TESLA Linear Collider.

The high energy beam analysis area behind the end of the fourth cryomodule serves as a room to measure the relevant beam parameters, i.e. beam position, beam size and emittance, beam energy and spread, beam current and transmission through the linac, bunch length and shape. Some parameters will be measured as a function of the bunch number in the 800 μs long bunch train, others as an average over some part or for a series of trains. In a first step standard beam diagnostics (scanners, screens and striplines) will be used while commissioning the TTFL. The extensive use of optical transition radiation is foreseen. Space for testing new diagnostic tools developed for TESLA will also be provided. Two beam dumps complete the whole TTF Linac set up.

III. FIRST RESULTS AND STATUS

At present, the commissioning of the TTF infrastructure [6] i.e. a chemical etching facility, a high pressure rinsing station, an UHV oven, and a preparation area/clean room is finished. Two prototype test cavities have been used to commission the cavity processing. Now, a complete preparation procedure includes cavity inspection, a first chemical etching, an UHV oven treatment (with Titanium at 1400°C inside and outside of the cavity), Titanium removal by a second etching, frequency tuning, final etching, and high pressure (100 bar) water rinsing. The first series cavity has been finished in mid March.

In Fig. 2 the shown oscilloscope traces represent the remarkable results of a first operation in the vertical test cryostat. The upper trace gives the field gradient as a function of time while the lower one is the measured forward power, both after some

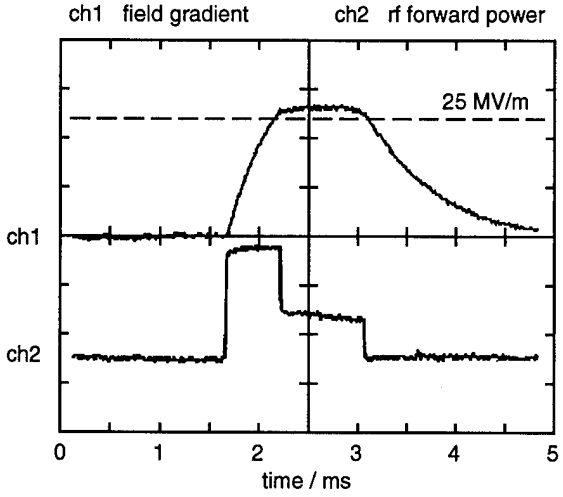


Figure. 2. Field Amplitude and RF Forward Power in the First Series TESLA Cavity.

High Peak Power Processing [7]. The total rf pulse length is 1.3 ms, the first 500 μs are the filling time (exponential groth of the field gradient). At a reduced forward power the gradient was kept above 25 MV/m (the aimed TTF gradient is 15 MV/m) until after 800 μs the exponential decaying gradient relates to the switched off forward power. The decay time corresponds to the loaded quality factor; Q_o has been above 10^{10}.

The assembly of the first cryomodule needs 8 s.c. cavities and will start in summer '95. Injector I is going to be installed in fall '95; at present first tests are carried out at Saclay. The cryomodule installation is also planned for fall this year. It includes the warm/cold transitions and the cryogenic supply lines. A temporary beam line with quadrupoles, steerers, and diagnostics stations will take care of the beam transport between the end of the first module and the high energy experimental area. This area will have its main components installed until the end of the year. Thus, commissioning of the first module of the TTFL can take place by the end of 1995.

IV. OUTLOOK

Further milestones in the TTF Linac schedule are the assembly of the cryomodules #2 - #4 in 1996, the installation of these modules and the above mentioned injector II in early 1997, and the final commissioning with beam in summer 1997. Experiments with the beam will be carried out to study the different components of the linac and their influence on the electron beam quality.

Quite aside from its possible linear collider prospects, the TTF Linac is offering unique beam physics features. As a first application in experimental physics the construction of a Free-Electron Laser (FEL) is under discussion. Due to its exceptional capability to maintain high electron beam quality during acceleration for high charge densities, a superconducting linac might be an optimum choice to drive an FEL based on the Self-Amplified-Spontaneous-Emission (SASE) principle which would allow for the production of coherent radiation tunable in the photon energy range up to 200 eV (6 nm). This kind of FEL has no optical cavity, the electron bunch is just travelling through a long undulator and the spontaneous emitted field together with the periodic undulator field causes an electromagnetic potential (the so-called ponderomotive potential). Further downstream in the undulator the electrons are bunched in this periodic potential and then emit coherently. The achievable peak intensities can be extremely high, and they depend directly on the charge density of the electron beam. A detailed description of studies on such a FEL can be found in [8].

References

[1] The TESLA R&D effort (TESLA = TeV Energy Superconducting Linear Accelerator) is being carried out by an international collaboration. A number of institutions have joined the collaboration and include IHEP Beijing, TU Berlin, Max Born Institut Berlin, CEN Saclay, CERN, Cornell, Univ.Cracow, TH Darmstadt, DESY, TU Dresden, JINR Dubna, Fermilab, Univ.Frankfurt, INFN Frascati, INFN Milano, INFN Roma II, FZ Karlsruhe, LAL Orsay, IPN Orsay, Polish Acad.of Science, IHEP Protvino, SEFT Finland, UCLA Dept.of Physics, Univ.Warsaw, Univ.Wuppertal.

[2] B. Aune, A. Mosnier, Experimental Program with Beam in the TESLA Test Facility, Proc. of the 1994 LINAC Conf., Tsukuba, Japan.

[3] T. Garvey et al., Simulations and Measurements of the TTF Phase-1 Injector Gun, this conference.

[4] E. Colby et al., Design and Construction of High Brightness RF Photo-injectors for TESLA, this conference.

[5] H. Pfeffer et al., A Long Pulse Modulator for Reduced Size and Cost, Proc. 21st Intern. Power Modulator Symposium, 1994, Costa Mesa, CA, USA.

[6] S. Wolff, The Infrastructure for the TESLA Test Facility (TTF) - A Status Report, this conference.

[7] J. Graber, High Gradient Superconducting RF Systems, this conference.

[8] J. Roßbach, Studies on a Free Electron Laser for the TESLA Test Facility, this conference.

THE INFRASTRUCTURE FOR THE TESLA TEST FACILITY (TTF) - A STATUS REPORT

S. Wolff, for the TESLA Collaboration,
Deutsches Elektronen-Synchrotron DESY, Notkestr. 85, 22603 Hamburg, Germany

Abstract

The TESLA collaboration is preparing the installation of a 500 MeV superconducting linear test accelerator to establish the technical basis for a future 500 GeV e^+e^- collider. The setup consists of 4 cryomodules, each containing 8 solid niobium cavities with a frequency of 1.3 GHz. The infrastructure to process and test these cavities has been installed at DESY. The facility includes a complex of clean rooms, an ultraclean water plant and a chemical etching installation for cavity surface preparation and cavity assembly as clean as possible. To improve the cavity performance a firing procedure at 1400°C in an ultra-high vacuum furnace is foreseen. An existing cryogenic plant has been modified to cool down the cavities below 2K and measure them in vertical and horizontal test cryostats. The RF power will be provided by a 4.5 MW klystron (pulse length 2 ms) in connection with a modulator. This system will also be used for a high peak power RF treatment to further improve the cavity performance by eliminating potential sources of field emission. The components of the complete infrastructure for the TESLA Test Facility are described and their status is reported.

I. INTRODUCTION

The theoretical accelerating gradient in a niobium superconducting cavity is limited to around 50 MV/m by the maximum value of the magnetic surface field occuring at the cavity equator. In practice the gradient is limited to substantially lower values by field emission from localized regions of the cavity surface. In the past few years however there has been dramatic progress both in the understanding of field emission mechanism and in its cures. By means of high pressure ultra clean water rinsing (HPR), ultrahigh vacuum baking at 1400°C with titanisation or by high peak power RF processing (HPP) developed at Cornell multicell structures at S- and L-band frequencies have exhibited more than 20 MV/m accelerating gradients.

To develop the surface treatment methods and the fabrication procedures required to produce high gradient multicell cavities on an industrial scale the TESLA collaboration first has started to construct and test forty 9-cell 1.3 GHz solid niobium cavities [1].

The necessary semiconductor standard clean rooms and the surface treatment facilities to process these cavities have been installed at DESY together with the equipment to test the cavity performance.

The most important components of this infrastructure are:

- a complex of clean rooms (300 m^2) for dustfree cavity assembly and treatment, to avoid cavity contamination
- a chemical etching facility complying with the purity standards of semiconductor industry
- an ultraclean water supply for rinsing the inner cavity surface to remove potential sources of field emission
- a high pressure rinsing facility for improved cleaning with ultra pure water of the inside of the cavity
- an UHV furnace to bake out the cavity up to 1500°C to improve the niobium material properties and to eliminate field emitters
- a high peak power RF facility to process cavities for further reduction of field emission
- vertical and horizontal helium cryostats to cool down and test the cavity performance at 1.8 K
- a cryogenic plant to provide liquid helium at 1.8 K and 4.5 K as well as helium gas at 70 K for the cryostats and the planned test linear accelerator

II. COMPONENT STATUS

The TESLA Test Facility (TTF) is located in an experimental hall of about 3000 m^2 surface area, which also houses the planned 500 MeV superconducting linear accelerator[2].

An overview of the TTF is shown in Fig.1.

A. Clean Room and Assembly Area

In order to avoid contamination of the cavity surface during processing and assembly a clean room has been built with an area of approx. 300m^2. The complex is divided into different classes, ranging from class 10000 down to class 10 (Federal standard 209), the last one being used for the most critical operations like mounting the input couplers to the cavity or connecting the cavities to a string for a cryomodule. Integrated in the clean room is the area for chemical etching of the cavity surface, the high pressure rinsing station and the UHV furnace. The clean room is operational since September 93.

B. Chemistry

Inside the chemistry area a cabinet for etching of the niobium cavities is installed. The acid in use is a mixture of $HF(40\%)/HNO_3(65\%)/H_3PO_4(85\%)$ of VLSI quality in a

0-7803-3053-6/96/$5.00 ©1996 IEEE

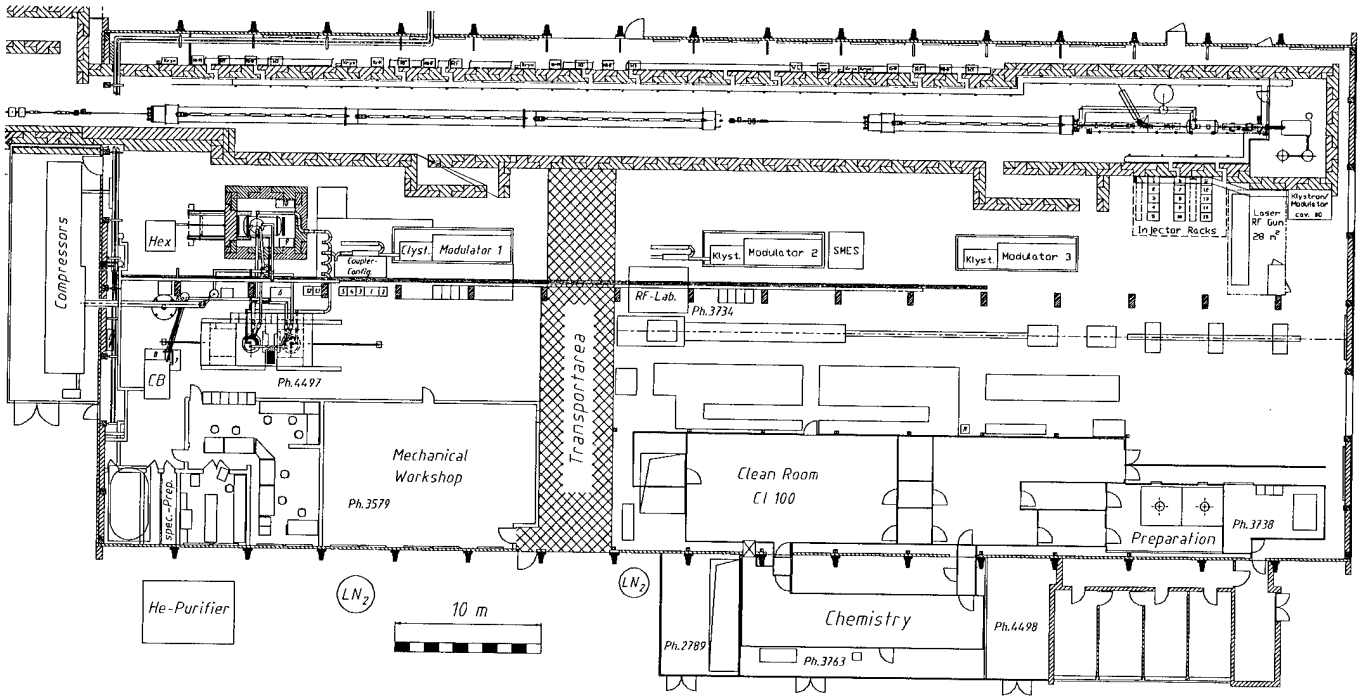


Figure 1: Overview of the TESLA Test Facility (TTF) at DESY.

1/1/2 volume ratio. For etching the cavity can be connected to one of two closed loops. One is operated with acid spoiled from earlier operations performed with a cavity right after reception or after titanisation, the so-called titanium loop. The other is operated with "clean" acid, the so-called niobium loop. In these loops the acid is circulating between the cavity and the storage tanks, which are located in a separate room outside the cleanroom. The pumps, tubes (made from PVDF) and filter elements (0.2µm size) of the chemical distribution system fulfill the standards of semiconductor industry.

The cavity can be etched from inside or from outside separately. For outside etching the cavity is sealed completely and inserted into a vessel which is then connected to the loop.

The standard cavity treatment consists of 5 etching operations. In the first two operations in a precleaning step for later furnace treatment and titanisation about 10 µm are etched off on the inside and on the outside of the cavity just after reception from industry. After titanisation the titanium-niobium surface is removed by etching off about 80 µm on the inside and 30 µm on the outside. Finally after tuning of the cavity outside the clean room a "clean" etching of about 20 µm in the "niobium loop" is performed in order to achieve the highest quality on the inner RF surface. The temperature of the acid can be set between 0° and 20°C with a mass flow of 10 *l*/min (improvement to 20 *l*/min is foreseen). The process itself and the safety interlocks are controlled by a computer to reach high safety and reproducibility standards. After the etching process the cleaning procedure is finished by an ultrapure water rinse. After the last "clean" etching a high pressure rinsing with ultra pure water is performed.

C. Ultrapure Water Supply

An ultrapure water plant supplies the cavity cleaning facilities with water of 18.2 MΩcm specific resistivity under (nearly) particle free conditions. Its first stage consists of a reverse osmosis unit (300 *l*/h), the second stage is equipped with nuclear grade mixed bed ion exchangers, augmented by filters and an ultraviolet light source. The point of use filters have a mesh size of 0.04 µm. A storage tank of 4000 *l* capability allows the use of large quantities of ultrapure water for cavity surface rinsing and cleaning. This plant is in continuous operation since August 93.

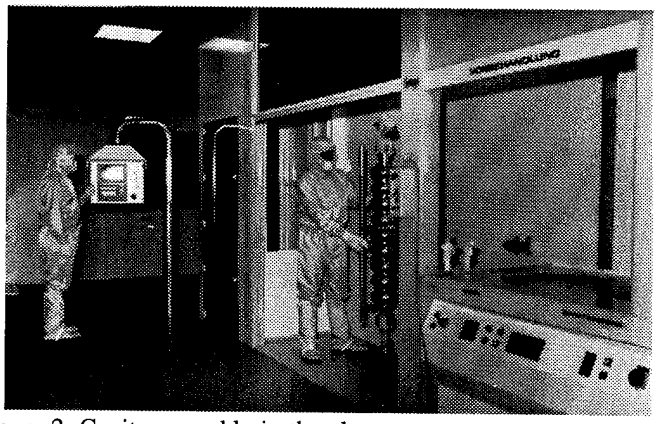


Figure 2: Cavity assembly in the clean room

Added to this facility is a high pressure rinsing station (up to 200 bar), which has been developed and built by CERN.

This unit allows the ultimate cleaning of the inner cavity surface and is in operation since July 94.

Fig. 2 shows the mounting of a cavity in the chemistry. The chemical facility is in operation since April 94.

D. UHV Furnace

Heat treatment of the complete cavity reduces potential sources for field emission and improves the niobium material properties like residual resistivity ratio ($RRR=R_{300K}/R_{10K}$) which is connected to thermal conductivity and homogeneity. During this process (at 1400°C and a vacuum of 10^{-7}mb) titanium is evaporated and builds up as a film on the inner and outer cavity surface. This effect leads to a solid-state gettering process for residual gases, especially oxygen, during high temperature annealing. The furnace for the TESLA cavities is in operation since December 94.

E. High Peak Power Processing (HPP)

Besides heat treatment in an UHV furnace the application of high power RF pulses (≈ 1 MW) for a short time (≈ 1 ms) to the cold cavity has proven as very effective to remove potential field emitters from the inner cavity surface. To apply this method for the TESLA cavities an HPP test stand has been built. It consists of a modulator supplied by FNAL and a klystron with a peak power of 4.5 MW at a pulse length of 2 ms. This setup (shown in Fig.3) is connected through RF wave guides with the vertical and horizontal cryogenic cavity test stands. The HPP facility is in operation since July 94.

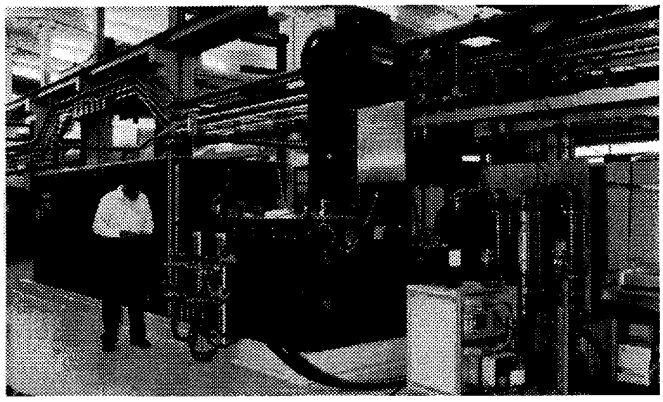


Figure 3: RF setup for HPP treatment

F. Cryogenics

For cooldown and test of the TESLA cavities an existing liquid helium plant has been extensively modified. By adding vacuum pumps and screw compressors a temperature of 1.8 K can be reached, with a refrigeration power of 100 W, which will be increased to 200 W for the test linac operation. The unit, which in addition provides helium at 4.2 K (400 W) and 70 K (2000 W), is connected to two vertical cold test stands built by FNAL and a horizontal test cryostat provided by CE Saclay. The liquid Helium plant is operational since December 93.

G. Cavity Performance

The first 9-cell cavities for TTF have been treated and tested using the above described infrastructure. The cavity treatment consisted of an inner and outer etching of 10 µm, a furnace treatment and titanisation of 4 hours at 1400°C followed by a chemical treatment removing 80 µm on the inside and 30 µm on the outside. After a mechanical tuning a chemical etching of 20 µm on the inside and a high pressure rinsing with 100 bar water pressure was performed. The mounting to the RF coupler was done in the class 10 clean room.

The Q_0 vs $E_{acc.}$ curves during CW operation before and after high peak power processing are shown in Fig.4. As can be seen from the graph the initial Q_0 is about $2*10^{10}$. With high peak power processing it was possible to raise the acceleration field to above 22 MV/m. The decrease in Q_0 value after HPP treatment is due to higher helium temperature.

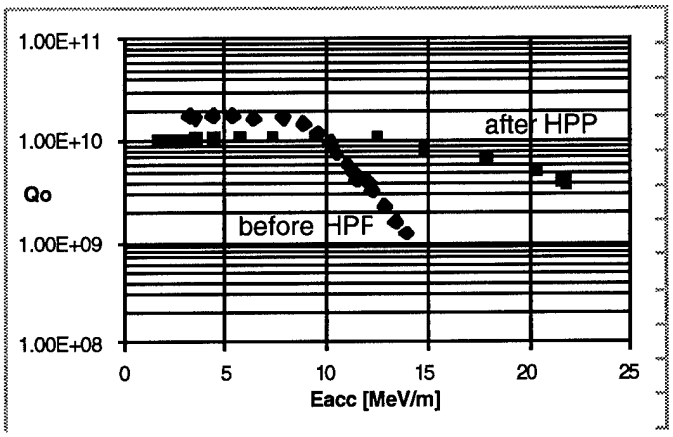


Figure 4: Performance of cavity D2 before and after HPP

III. SUMMARY

For the TESLA Test Facility (TTF) at DESY the complete infrastructure for superconducting cavity processing and testing is in operation. First series cavities have been processed with good results. It is expected that the so far achieved field strength of 22 MV/m during CW operation can still be improved by optimization of the process parameters.

IV. REFERENCES

[1] Proposal of the TESLA collaboration. TESLA Report 93-01.

[2] H. Weise, DESY, for the TESLA collaboration. Contribution to this conference.

THE STATUS OF THE S-BAND LINEAR COLLIDER STUDY

N. Holtkamp for the SBLC study group, Deutsches Elektronen-Synchrotron DESY, Notkestr. 85, 22603 Hamburg, Germany.

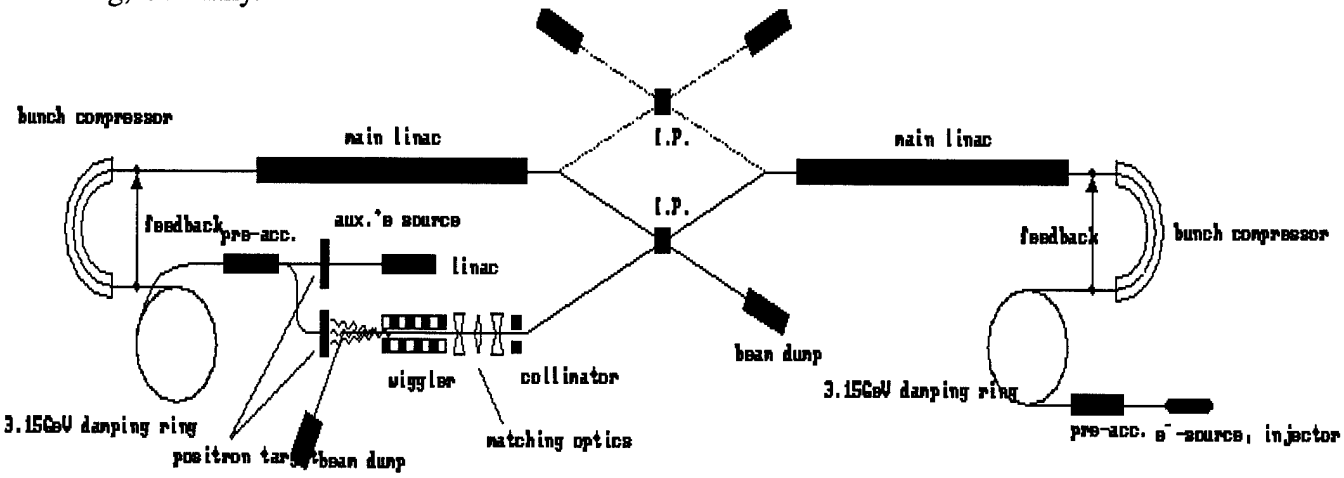


Figure 1 General Layout of the S-Band Linear Collider.

The demand for e^+e^- collisions beyond the LEP 200 energy range up to the TeV region requires the development of linear collider technology and there seems to be international agreement today, that this should be a 2×250 GeV linear accelerator [1]. Different studies around the world concentrate on different designs, all based on partially or non developed technology. The general differences are mainly expressed by the choice of the operating frequency of the rf-power source and the accelerating structure, which varies for the studies (TESLA, SBLC, NLC, JLC, VLEPP, CLIC) between 1.3 to 30 GHz. Based on a number of arguments [2] which mainly summarise the availability, the cost optimisation and the experience gained so far with S-Band technology, a 500 GeV S-Band linear collider design has been worked out at DESY.

I. Introduction

A linear collider consists of two opposing linear accelerators, one accelerating positrons, the other electrons. From the parameters of the proposed S-Band linear collider, which are given in table 1, it can be seen that from today's point of view the operating conditions are close to what has been achieved already[3]. Especially the proposed vertical spot size at the interaction point (I.P.) is only about a factor of two smaller than what has recently been demonstrated in the Final Focus Test Beam [4]. A more detailed description of all the parameters is given in [1] and a summary of the technological developments and the S-band test linac set-up is presented in [5]. The trade-offs in comparison with other approaches are described in detail in [6] and point out other basic advantages of an S-band collider as, for example, the generally lower wakefield due to larger apertures and the smaller peak power required per meter to store sufficient energy for acceleration with good beam quality. The SBLC linear collider study is pursued at DESY in the frame of an international collaboration with institutes in China, France, Germany, Japan, Netherlands, Russia and USA contributing to the technical R&D and/or the design of the 500 GeV collider.

active length 30.2	km	
$t_{beam\ pulse}$	2	μs
n_b/pulse	125	
Δt_b	16	ns
f_{rep}	50	Hz
$\varepsilon_x/\varepsilon_y$	10/0.5	10^{-6} m
β_x^*/β_y^*	22/0.8	mm
σ_x^*/σ_y^*	670/28	nm
σ_z	0.5	mm
$<\Delta E/E>_{rad}$	3.2	%
P_b	2 x 7.2	MW
P_{AC} (2 L's)	139	MW
L (incl H_D)	3.75	$10^{33}cm^{-2}$

Table 1 Main parameters of the S-band 500 GeV (c.m.) linear collider.

II.General Layout

For the overall layout of the linear collider tunnel a number of assumptions have been made to minimise construction costs and toavoid restrictions on the choice of the accelerator site.

- The tunnel has to accommodate all accelerator components otherwise a second tunnel or klystron gallery is necessary.
- Entrance into the tunnel **must** be possible during operation in order to allow maintenance on klystrons and modulators.

0-7803-3053-6/96/$5.00 ©1996 IEEE

From today's point of view this results in a single tunnel 7 meter in diameter with the beam lines and the accelerating structure shielded inside the tunnel (on the bottom under the concrete shielding). A sketch of the cross section is given in figure 2. It should be noticed that only half of the tunnel volume is filled to allow for the energy upgrade (compare following section). In the sketch today's size of the components (modulator, klystron, section support etc) is shown.

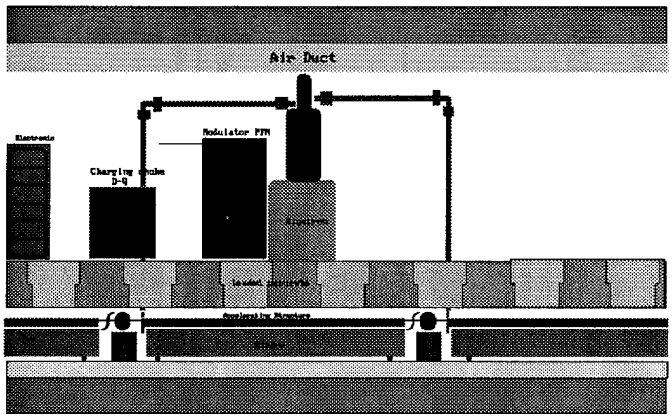


Figure 2 Sketch of the SBLC tunnel with one complete module installed.

A. *Upgrade Path*

In order to upgrade to the S-Band linear collider to 1 TeV it would be desirable not to extend the linac tunnel but to double the accelerating gradient instead (quadruple the peak power). This can only be done on the expense of beam pulse length, if a SLED I type pulse compression scheme is considered for the first factor of 2 in peak power.

active length	30.2	km
n_b/pulse	50	
t_{pulse}	0.5	μs
f_{rep}	50	Hz
N_e/bunch	2.9	10^{10}
$\varepsilon_x/\varepsilon_y$	5/0.05	10^{-6} m
σ_x^*/σ_y^*	572,9	nm
σ_z	0.50	mm
$<\Delta E/E>_{rad}$	4.3	%
P_{AC} (2 l's)	278	MW
L (incl. H_D)	6.17	10^{33} cm^{-2} s^{-1}

Table 2 Parameters at 1000 GeV (c.m.) with reduced vertical emittance

In addition, the number of klystrons have to be doubled (second factor of 2), which automatically would double the ac-power required, if no further increase in klystron and modulator efficiency is assumed. This seems to be unlikely, but so far no save prediction seems to be possible.

Therefore the 1 TeV parameters given in table 2 are based on the same values for the klystron efficiency compared to table 1. From the picture of the tunnel cross section, it can be seen as well that even with this size of the components, the upgrade would be possible

With more relaxed tolerances of the low-frequency approach, the SBLC design is very well suited if one aims to push the vertical emittance towards a smaller value. After gaining experience with the different correction and optimisation procedures, reducing the vertical emittance ε_y by an order of magnitude seems to be conceivable. Further and even more optimistic assumptions on possible reductions of the vertical beam size being transported through the linac could be made, taking into account that the emittance proposed here is still larger than for the higher frequency collider approaches. This could be used to decrease the repetition rate and therefore bring down the average power consumption.

III. FINAL FOCUS & COLLIMATION

In general keeping beamstrahlung at a low level is an essential prerequisite for acceptable background conditions and good energy resolution for the high energy physics experiment. More recently the bunch to bunch distance also became an issue for the high energy physics experiment, because the probability of having underlying events in the detector increases with the number of bunch crossings per unit time [1]. Therefore low frequency linear colliders (and especially sc-linacs) with larger bunch to bunch distances are even more favourable. The most important parameters concerning beam-beam effects are summarised in table 3. In case of the SBLC, beams have to cross at an angle (θ_c=3 mrad) in order to avoid the multibunch kink-instability due to parasitic interactions assuming conventional quadrupoles with a bore radius of 4 mm. A reduction of luminosity caused by an effective increase of the horizontal beam size is avoided by employing a simple crab-crossing scheme with finite dispersion at the IP, making use of a coherent energy spread within the bunch of about σ_E=0.5 %.

$<\delta E/E>_{cm:rms}$	2.7	%
	.04	
Disr. D_x/D_y	0.4/8.5	
angle $\theta_{yx/y}$	1.28/0.55	mrad
bunch to bunch distance	16	nsec
N_{pair}/bunch	7	
N_{hadr}/bunch	0.2	

Table 3 Results of beam-beam simulations

The magnet lattice between the interaction region (IR) and the main linac consists of the final focus system (FFS) for beam size demagnification and chromatic corrections, a section to protect the IR quadrupoles from large amplitude

particles and bending sections for creating a sufficient separation between two beamlines if the collider has to serve two experiments. The momentum acceptance of ±2.0 % ($\sigma_{E,beam}$=0.5%) with an optimised sextupole distribution of the FFS for the SBLC design is far in excess of the beam energy spread. The tight requirements for beam collimation are determined by the fact that synchrotron radiation generated in the doublet before the IP has to pass freely through the aperture of the opposite final quadrupole, which is the main difference compared to other layouts[1] with crossing angles around θ_c=10 mrad. Therefore particle amplitudes have to be restricted to $7\sigma_x \times 7\sigma_y$. The entire lattice from the linac to the IP will require approximately 1.5 km per beam on either side of the IP including the double bend for two experiments [7].

IV.The Linac

The basic linac module consists of one 150 MW klystron driven by one modulator producing a 3 μsec rf pulse which is fed into two 6 meter long accelerating sections (compare fig. 2). In addition each section will have micro-movers which, according to the HOM coupler signal coupled out at the beginning and the end, will align the section. The quadrupoles are equipped with further developed ground motion /vibration pick-ups , which will sample frequencies in the range of 2-50 Hz and feedback on the quadrupole position[8]. This is especially necessary if emittances are considered, smaller than those given in table 1. For the different components the alignment tolerances are around 100 μm for the prealignment of the quadrupoles and the accelerating sections. With a BPM resolution of 4μm the beam orbit will have to be corrected in the quadrupoles applying beam-based correction procedures [9]. Finally the micro-movers correct the electric center of the section with respect to the beam axis to within 30 μm rms.

V.The Injection System

While the design for the damping rings has been done already, the positron source is still one of the main challenges in the collider. The positrons are produce by converting γ's in a thin target to reduce the heat load drastically. While the source is theoretically understood very well [15]. It seems to be impossible to test the new scheme before a linear collider is set up.

VI. Main R & D Activities

The set-up of the S-Band test linac at DESY covers the main effort for the whole technology which has to be developed for a linear collider[5]. In addition for a long linear accelerator the transport and the preservation of a small emittance has to be investigated. From particle tracking results the tolerances mentioned before are determined for the different components of the linac and for the beam quality. More recently a complete simulation of single- and multibunch effects including energy spread, bunch to bunch charge variation, transient beam loading and beam based alignment techniques has been performed with a newly developed code [10]. The results have been compared with a similar code [11] and good agreement was found. At the same time a strong effort to understand and to calculate the Higher Order Mode distribution in accelerating structures has been made[12,13].

VII. Summary and Conclusion

During the last three years of R & D several aspects of the overall layout have been reviewed and discussed. Especially from recent beam dynamics simulation and under the assumption that the multibunch problem has been solved by the technologies mentioned in this paper, the S-Band linear collider is dominated by the single bunch transverse wakefield. In order to optimise the design it will be necessary to reduce the single bunch charge and adjust the number of bunches for the required luminosity.

VIII.Acknowledgement

I would like to thank all the members of the collaboration from the different institutes and countries for their contributions to the S-Band design study. The author is indebted to R. Brinkmann for his contributions and helpful discussions.

IX. References

[1] LC 95, Linear Collider Workshop held at Tsukuba Scientific Center, Tsukuba , March 27th -31st, 1995, to be published.

[2] G.A. Voss, "The Case for an S-Band Linear Collider", 1992 Linear Accelerator Conf. Proc., edit.: C.R. Hoffmann, Ottawa 1992.

[3] J.T. Seeman, "Lessons to be learned from Operating the Stanford Linear Collider", EPAC, London, June 1994.

[4] P.Tenebaum et al, "Beam Based Magnetic Alignment in the Final Focus Test Beam", this conference.

[5] N. Holtkamp, "The S-Band Linear Collider Test Facility", this conference.

[6] J. Roßbach,"Options and Trade-Off's in Linear Collider Design", this conference.

[7] R. Brinkmann et al., to be published.

[8] Ch. Montag et al, "A Mechanical Feedback System for Linear Colliders to Compensate Fast Magnet Motion", this conference.

[9] T. Raubenheimer, SLAC-PUB-6117, (1993).

[10]M.Drevlak et al, "Beam Dynamics Studies for the SBLC", this conference.

[11]A. Mosnier, private communication; Mini workshop on beam dynamics simulation in Linear Colliders, held at DESY, Feb. 1995, no proceedings.

[12]B. Krietenstein et al, "The S-Band 36 Cell Experiment", this conference.

[13]T. Khabiboulline et al,"Measurement of the *H*igher *O*rder *M*ode (*HOM*) Field Distribution in a Linac II Accelerating Section", Internal Report, DESY M-94-02, June 1994.

THE S-BAND LINEAR COLLIDER TEST FACILITY

N. Holtkamp for the SBLC study group, Deutsches Elektronen-Synchrotron DESY, Notkestr. 85, 22603 Hamburg, Germany.

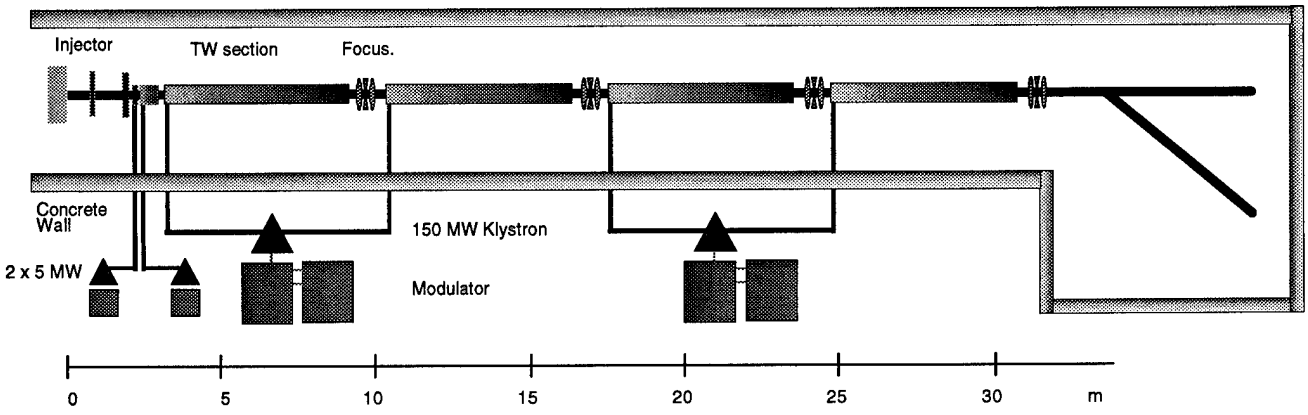


Figure 1: General Layout of the S-Band Test Facility at DESY

The S-Band Linear Collider Test Facility under construction at DESY will serve as a unique test bed for the necessary technical developments of a large scale 2×250 GeV e^+e^- linear accelerator. The test facility consists of two modular units similar to those to be installed in a Linear Collider tunnel (see also [1]). The questions of Higher Order Mode excitation, measurement, damping and feedback on the accelerating cavity and the quadrupole position are especially important and have to be addressed in order to understand the most crucial aspect of a 15 km linear accelerator namely the beam stability. Simultaneously the performance of the newly developed rf-systems will be investigated. The status of this set-up will be presented.

I. INTRODUCTION

Although S-Band linear accelerator technology is well accepted and used around the laboratories, the demands for an S-Band Linear Collider are not a simple extrapolation from any existing accelerator, e.g. the **SLC** [2] at SLAC. Two main reasons lead to the decision, to build and operate an S-Band test accelerator at DESY.

1) The parameters being proposed for the S-Band Linear Collider, even if they are based on well proven and existing linacs, have been pushed to what we think are the limits which can be achieved within the next few years of research and development. Especially for the klystrons and modulators the required peak power (compare **Table 2**) is more than twice as high as compared to the 5045 klystron (65 MW, 3.5 μsec) being in use at the **SLC** right now. Because the modulators and theklystrons are the most expensive single items of a Linear Collider, reliable operation must be proven and the costs for production have to be estimated.

2) A dedicated test accelerator will give the only possibility to prove the feasibility and to a certain extend the reliability of the proposed components and concepts. This is especially true for the HOM cures being proposed for all the future colliders and the feedback's designed to stabilise accelerator components down to rms amplitudes of 10th of nanometers. The whole test accelerator is planned be commissioned by the end of 1996 in order draw a conclusion on the future R & D programs going on at DESY towards a linear collider.

II. THE MODULE LAYOUT

The general layout of the test facility is shown in figure 1. For the S-Band Collider a "linear collider module" consists of one 150 MW klystron driven by one modulator producing a 3 μsec rf pulse which is fed into two 6 meter long accelerating sections. Quadrupoles, beam position monitors and beam diagnostics are part of such a module as well.

Energy at full current	400	MeV
overall length	≅ 40	m
injector energy	≈ 5	MeV
current pulse length	> 2	μsec
modulator & klystrons	2	
number of bunches	1-250	
particles per bunch	1.5,3,5*10	
norm. emittance $\gamma\varepsilon$	$\approx 50 \times 10^{-6}$	π m rad
bunch to bunch distance	8,16,24	nsec
average beam current	> 300	mA

Table 1 Main parameters of the S-Band test linac.

0-7803-3053-6/96/$5.00 ©1996 IEEE

The test facility consists of two similar modules, with an injector in front in order to produce the full charge design bunch train and a beam diagnostics station down stream to analyse the beam energy, emittance and position. The parameter overview is given in table 1.

A. The Modulator and Klystron R & D

Klystrons and Modulators turned out to be the most expensive single components of a linear collider. Therefore as much peak power as possible has to be produced with a single device. In order to satisfy the RF peak power requirements for the S-band linear collider a separate R & D program together with SLAC has been started in 1993. Following an earlier development being done in 1985 when a 150 MW, 1 μsec-klystron with an efficiency of more than 50 % was build [3], the goal now was, to construct and operate a 150 MW klystron with a pulse length of 3 μsec and a repetition rate of 50 Hz. In 1994, only $1^1/_2$ years later, the klystron has been tested meeting the specifications. A second klystron with a slightly modified output circuit geometry and improved HOM damping in the drift tube will be tested during summer 1995. The operating parameters achieved with the first of at least two different klystrons being constructed so far are listed in the next table. This klystron has been shipped to DESY already. Both klystrons have been simulated with 2 D and 3 D codes extensively to optimise the overall layout[4].

	5045	SBLC	
Beam Voltage	350	528	kV
μ-Perveance	2.0	1.8	$A/V^{1.5}$
Output Power	67	>150	MW
pulse length	3.5	> 3.0	μsec
Electronic Efficiency	46	42	%
Drive Power	350	< 400	W
Solenoid Field	0.12	0.18	T

Table 2 Parameters of the 150 MW klystron being tested in 1994 at SLAC and the SLC standard klystron, the 5045.

The modulator considered to drive the 150 MW klystron is a PFN type modulator with pulse forming network connected to a pulse transformer. Such a modulator has been constructed already at SLAC to test the klystron at full power and at a maximum repetition rate of 60 Hz. Two further modulators are under construction at DESY for the S-Band test facility. The modulators are designed for a maximum voltage and current of 550 kV and 700 A. For the test facility, these klystrons will be installed during 1995.

B. The Accelerating Section and the HOM Suppression Techniques to be Applied

The section is a standard 2 π/3 mode constant gradient type section which is designed to have a continuous group velocity taper from the beginning to the end. Because the accelerating section is the main driving force for multi- and single bunch instabilities which deteriorate the beam emittance, not only possibilities to reduce the costs have to be investigated but also HOM damping and alignment is an issue. A first 5.2 meter long accelerating section has been assembled and brazed at DESY by the end of 1994. The high power test ended successfully after approximately 50 hours of rf processing with a maximum gradient of 25 MV/m within the structure. The vacuum pressure achieved so far was of the order of 10^{-8} Torr.

	Linac II	LC	
attenuation	0.5-0.6	0.55	neper
length of the section	5.2	6	m
group velocity	3.3-1.2	4.1-1.3	% c
filling time	750	790	nsec
iris size	1.4-1.25	1.6-1.3	a/λ
alignment toleran.	≅0.200	<0.030	mm rms
aver. power dissip.	0.7	1.4	kW/m

Table 3 Parameters of the accelerating sections build (LINAC II) and proposed (LC).

Other major technical developments being made so far are a very compact symmetric high power input coupler [5] and the collinear load [6]. The collinear load absorbs over the last eight cells of the section the remaining rf-power while still accelerating the beam. Such a load avoids a second high power coupler (costs), is perfectly symmetric (no transverse kicks due to field asymmetries) and absorbs any higher order mode touching the section end as well.

The final required straightness of the section is determined by the tolerable HOM excitation. Assuming an average Q value of the HOM's of 2500 (natural Q≈13.000) with a bunch charge of $3 \cdot 10^{10}$, the tolerance calculated so far is 30μm rms over the full six meter length. The first section has been measured after brazing and maximum deviations from the axis of the order of one millimeter appeared. After correction, the rms. value was of the order of 100 micrometer but nevertheless is to large by almost a factor of 4.

To control the HOM excitation and consequently the beam break-up in a Linear Collider, each section will be equipped with two HOM dampers. One near the front end and one almost at 2/3 of the section length. Definitely two couplers are not sufficient for damping all the modes in the HEM_1 passband because about 2/3 of the severe modes in this passband are trapped at different locations of the section. The HOM couplers, in combination with a set of micromoovers, will have to control the beam induced HOM power. While the HOM couplers are used to couple out as much HOM power as possible, the amplitude of the extracted power will be prepared as a control signal for the micro-movers below the section support. In addition an R & D program has been set up with the MPEI in Moscow to develop symmetric high power couplers which couple out the HEM_{11} modes being trapped close to the input end.

Another method for internal damping is under development [7]. Sputtering a thin (≈20 μm) stainless steel layer onto the

top of the iris strongly damps trapped higher order modes but almost not affect the fundamental mode. First measurements indicate a Q-reduction of the HOM mode by a factor of 5 while the fundamental Q only changes by 5 %. High power tests still have to be done. The combination of both methods will provide the required overall damping and HOM control.

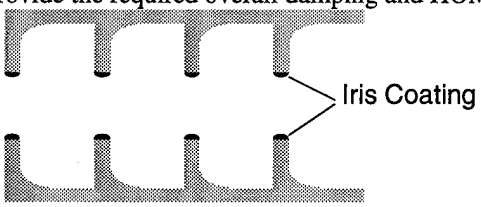


Figure 1 Sketch of the iris coating to introduce losses for the HEM_{11} mode with only little effect on the accelerating field.

C. Ground Motion, Vibration and Feedback

Any kind of quadrupole motion of the order of 20-200 nm within a frequency range of 2-15 Hz can hardly be damped either passive or with beam based feedback techniques. Therefore ground motion detectors (geophones and accelerometers) have been tested and further developed [8]. Each quadrupole in the test facility (and in the Linear Collider) can be equipped with such a detector and either feedback on the vertical quadrupole position via piezo-movers or on the vertical beam position via correction coils. Attenuation with an active feedback between 6 and 12 dB within this frequency range has been achieved so far and corrects the vertical rms quadrupole motion down to the 20 nm range.

In addition a simple and stiff concrete support for the quadrupole has been build and designed which shifts mechanical resonance's well beyond 100 Hz to avoid any excitation driven externally. To decouple the vibration introduced by water flow within the coil windings of the quadrupole, the coils are mounted on a separate aluminium support within the quadrupole yoke. This support can be mounted separately to the floor.

III. THE INJECTOR

The injector under commissioning right now has to produce the full charge bunch train identical to the one planned for the Linear Collider. The small emittance, the single bunch energy spread and bunch length can of course not be achieved in a 3 meter long set-up. Recently the gun part of the injector went into operation and current pulses with the design bunch to bunch distances and burst length (3 μsec and 8,16 or 24 nsec distance; compare table 1) have been produced with a bunch charge of $3.7 \cdot 10^{10}$ per bunch. A complete description of the injector layout, the expected performance and the currents achieved is given in [9].

IV. THE EXPERIMENTAL PROGRAM

To address the beam dynamics questions, the bunch train will mainly be used to perform single- and multi-bunch instability experiments and investigate different beam loading compensation schemes. The questions of Higher Order Mode excitation, measurement, damping and feedback on the accelerating cavity and thequadrupole position are especially important and have to be addressed in order to understand the most crucial aspect of a 15 km linear accelerator namely the beam stability. Especially the concept of measuring the beam induced dipole mode power at the position of the HOM dampers and feedback via the micro-movers on the position of the section is crucial. Therefore a transverse mode cavity will be introduced into the front end of the beam line to modulate the bunch transversely and excite specific frequencies in the accelerating structures.

In order to handle the large number of bunches, various types of monitors for position and beam size are under construction and will be installed in the test facility. Wall current monitors and beam position monitors are going to be checked out, especially for the bunch to bunch resolution within one burst [10].

V. Acknowledgement

I would like to thank all the members of the collaboration from the different institutes and countries for their contributions. The significant progress which has been made during the last 3 years is based on the enthusiasm of the people involved and the willingness of the management to encourage this work.

VI. References

[1] T. Weiland et. al., "The Status of the S-Band Linear Collider Study", this conference.

[2] J.T. Seeman, "Lessons to be learned from Operating the Stanford Linear Collider", EPAC, London, June 1994.

[3] T. Lee et al, "The Design and Performance of a 150 MW Klystron at S-Band", SLAC-Pub-3619, April 1985 (A).

[4] M.Dohlus et al, "Comparison of CONDOR, FCI and MAFIA Calculations for a 150 MW S-Band Klystron with Measurements".

[5] R.F. Koontz, "", LINAC Conference, 1992, Ottawa, pp 740.

[6] V.E. Kaljuzhny et al, "Design and Performance of a Symmetric High Power Coupler..", DESY-M-94-11, 1994, Internal report.

[7] J. Haimson,"Collinear Termination For High-Energy Particle Linear Accelerators", PATENT-US-3264515, Aug 1966. 7pp.

[8] M. Dohlus, private communication.

[9] Ch. Montag et al, "A Mechanical Feedback System for Linear Colliders to Compensate Fast Magnet Motion", this conference.

[10]M. Schmitz et al, "First Tests at the Injector of the S-Band Test Facility at DESY", this conference.

[11] W.Radloff et all, "Beam Position Monitors for the S-Band Test Facility at DESY", this conference.

Beam Dynamics Studies for the SBLC

M. Drevlak, R. Wanzenberg
DESY
Notkestr. 85, 22603 Hamburg, Germany

Abstract

In linear accelerators, wake field effects and dispersion from orbit distortions can lead to considerable emittance dilution. Since the transverse wake fields and the dispersion depend on the orbit in the accelerating structures and quadrupoles, there are constraints on the resolution of the beam position monitors and on alignment tolerances.

The tracking code L, which is affiliated to the family of MAFIA codes, has been developed to simulate both single and multi-bunch dynamics in linear accelerators. By use of this code, the impact of misalignments on the combined single and multi-bunch behaviour of the beam is investigated for the S-band accelerator as envisioned in the SBLC study. Further, the performance of a full machine tuning scheme including beam loading compensation, orbit correction, structure adjustment and emittance correction is examined. From the results, limits for the alignment tolerances are deduced.

I. General Considerations

The SBLC 2×250 GeV linear collider design study considers a bunch train with an average beam power of 7.25 MW (per train), and an invariant (single bunch) emittance of $\gamma\epsilon_x$ / $\gamma\epsilon_y$ = 10.0 / 0.5×10^{-6} m. To achieve a luminosity of $3.75 \times 10^{33}\,(\mathrm{cm}^2\,s)^{-1}$ (with pinch) it is important to preserve not only the single bunch emittance but also to avoid any cumulative beam break-up along the bunch train. It is assumed that 125 bunches with a spacing of 16 ns from bunch to bunch and a bunch population of $N = 2.9 \times 10^{10}$ are injected with an energy of 3.15 GeV into the main linac where they are accelerated to 250 GeV by 2517 S-band structures (each 6 m long, with a loaded gradient of 17 MV/m) [1]. The main parameters of SBLC study are summarized in table I.

The primary sources of emittance growth are wake field effects and dispersive errors caused by small misalignments of the accelerating structures, the lattice quadrupoles and the beam position monitors (BPM's). To avoid single bunch emittance growth and multi-bunch beam break-up the following diagnostics and cures are considered for the SBLC:

- Beam based alignment techniques
- Higher order mode (HOM) dampers at each accelerating structure, lossy cells
- Accelerating structure movers
- Nondispersive trajectory bumps, tuned by emittance measurements
- Active stabilization of quadrupoles
- Fast kickers.

[1] An overhead of 4 % is assumed

General Parameters		
energy (center of mass)	GeV	**500**
luminosity (including pinch)	$(\mathrm{cm}^2\mathrm{s})^{-1}$	$3.75{\cdot}10^{33}$
nominal luminosity	$(\mathrm{cm}^2\mathrm{s})^{-1}$	$2.2{\cdot}10^{33}$
active length (two linacs)	km	30.2
repetition rate	Hz	50
particles per bunch		$2.9{\cdot}10^{10}$
bunches per pulse		125
bunch length (rms)	mm	0.5
bunch spacing	ns	16
normalized vert. emittance $\gamma\epsilon_y$	m	$0.5 \cdot 10^{-6}$
normalized horiz. emittance $\gamma\epsilon_x$	m	$10 \cdot 10^{-6}$
injection energy	GeV	3.15
Accelerating Structure		
loaded gradient	MV/m	17
unloaded gradient	MV/m	21
RF frequency	GHz	3.0
average shunt impedance	MΩ/m	55
iris size a/λ		0.16 - 0.11
structure length	m	6
number of structures / linac		2517
HOM		
frequency	GHz	4.1 - 4.6
number of HOM used in simul.		180
Lattice		
type		FODO
phase advance / cell	°	90
scaling		$\beta \sim \sqrt{E}$
number betatron oscillations		73

Table I

Main parameters of the SBLC design study.

HOM dampers are necessary to damp the dipole modes, which drive the cumulative multi-bunch beam break-up. Furthermore, the accelerating structures can be moved with active structure movers, using the signals from HOM-couplers as a reference. The usefulness of the HOM signals as a diagnostic tool will be investigated at the DESY S-band test facility. The accelerating structure movers can also, like trajectory bumps, be operated in connection with emittance measurements. Once the multi-bunch beam break-up is cured by HOM dampers and structure movers, the single bunch effects determine the alignment tolerances.

II. Longitudinal Dynamics

Transient wake fields cause an energy spread in each bunch, while strong beam loading effects lead to different energies of the bunches in the train. The single bunch energy spread due to the longitudinal wakes amounts to 2.6 % (peak to peak) if not compensated. This spread can be adjusted to a level required for crab crossing by placing the bunch off-crest with respect to the RF. The acceptance of the final focus is $\pm 1.8\%$ [1]. An energy spread can even advantageously be used for BNS damping. The required BNS energy spread is 0.9 % as calculated from computer simulations.

0-7803-3053-6/96/$5.00 ©1996 IEEE

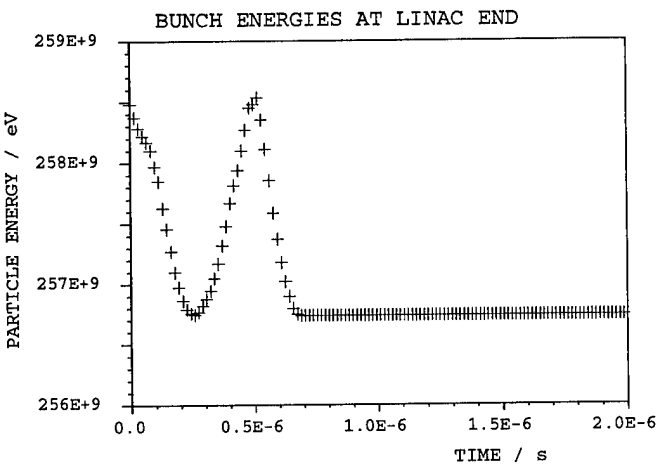


Figure 1. Compensation of the multi-bunch energy spread with staggered timing, results from computer simulations

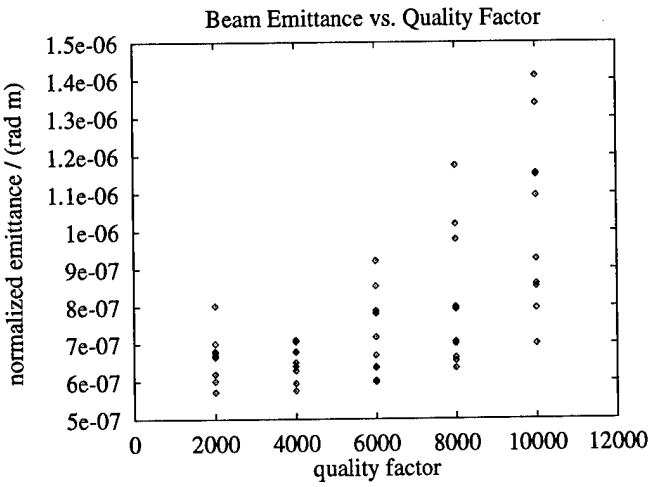


Figure 2. Normalized beam emittance at the end of the linac versus quality factor of the dipole modes. The acc. structures are moved with 30 μm rms to the beam.

A more severe problem is the beam loading leading to a energy spread of 18 % (peak to peak) over the bunch train if not compensated. With staggered timing of the RF-pulses [6] the multi-bunch energy spread can be reduced significantly. This technique exploits the fact that one can produce different profiles of the energy gain in one structure over a bunch train by turning on the RF-power at different times before arrival of the bunch train at the structure. The turn-on times of each klystron are then chosen to minimize the peak to peak energy spread after the structures fed by that klystron. Furthermore it will be investigated at the DESY S-band test facility whether a control of the klystron power over the 2.8 μs long pulse can successfully be used to compensate the beam loading effects. Fig. 1 shows the energies of the 125 bunches at the end of the linac using only the staggered timing of the RF-pulses. The first 50 bunches are affected by the transient beam loading. The residual bunch to bunch energy spread can be reduced to about 1% (peak to peak).

III. Transverse Dynamics

For simulation of the beam dynamics, the bunches are longitudinally divided into slices with charge q_i, phase space moments $\sigma_{11\,i}$,..., and centroids y_i. The projected emittance of the bunch train is given by: $\epsilon_y = \sqrt{\sigma_{yy}\,\sigma_{y'y'} - \sigma_{yy'}{}^2}$ with the phase space moments defined by:

$$\sigma_{yy} = \frac{1}{q_{train}} \sum_{i \in I} q_i \left(\sigma_{11\,i} + (y_i - \langle y \rangle)^2\right), \qquad \sigma_{y'y'} = \ldots$$

The moments of the whole bunch train are calculated as a sum over all slices of all bunches (I = {slices, bunches}) according to the above formula. The bracket $\langle y \rangle$ indicates the average of the bunch centroids over the index set I.

For simulation of the long range dipole wake driving the cumulative multi-bunch beam break-up we used the dipole modes calculated by [5]. It has been assumed that there exist 10 classes of accelerating structures with mutually detuned dipole modes ($\sim$ 3.6 MHz frequency shift from class to class). Each structure itself is a plain constant gradient structure.

Tolerances are given for an emittance dilution of $\Delta\epsilon_y/\epsilon_y \approx$ 30 % if all effects are considered. The full dynamics of a bunch train (i.e. single and multi-bunch) has been studied by computer simulations [2]. With an initial misalignment of the accelerating structures and quadrupoles of 100μm with respect to the machine axis and of the BPM's with respect to the quadrupole centers, it was assumed that the linac was adjusted for luminosity operation along the following steps:

1. Set the klystron ignition times according to staggered timing.
2. Carry out beam based orbit correction using the WF-algorithm outlined in [4].
3. Adjust the axes of the accelerating structures to the beam trajectory with a precision of 30μm with active structure movers. As he signal from the HOM's would be used as a reference, this measure will require the installation of at least two pairs of HOM-couplers per accelerating structure.
4. Fine-tune the beam emittance with non-dispersive bumps [4].

With these assumptions, the total growth of the projected emittance was simulated for quality factors of the dipole modes ranging from $Q = 2000$ to $Q = 10000$ and a constant BPM resolution of 5μm For $Q = 4000$ a emittance growth of $\Delta\epsilon_y/\epsilon_y =$ 31 % $\pm$ 10 % is found from 10 random seeds. Fig. 2 shows the complete result of this simulation.

Further, we looked at the impact of the BPM resolution on the achieved emittance. For this purpose, we simulated the beam dynamics in a machine that was adjusted according to the procedure outlined above with resolution of the BPM's ranging from $\sigma_{res} = 1\mu$m to $\sigma_{res} = 32\mu$m. The quality factor of the dipole modes was kept constant at $Q = 2000$. The result of this simulation is shown in Fig. 3. At a BPM resolution of 4μm the emittance dilution at operation with 125 bunches becomes $(30 \pm 13)\%$.

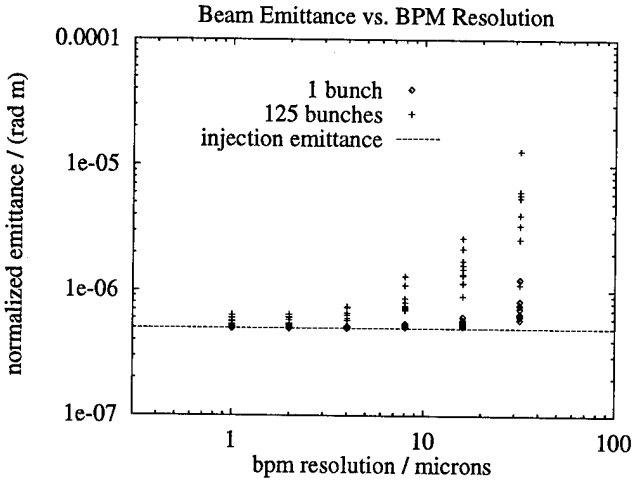


Figure 3. Normalized beam emittance at the end of the linac at single and multi-bunch operation versus BPM resolution. The dipole modes have a constant quality factor of $Q = 2000$. The acc. structures are moved with 30 μm rms to the beam.

IV. Tolerances and conclusion

Including "all" effects, i.e. transient beam loading, single and multi-bunch wake fields, dispersion and chromatic effects the following rms tolerances for an emittance growth of about 30 % $\pm$ 10 % are found from computer simulations:

- Injection jitter	~ 10 μm
- Quadrupoles	
prealignment	~ 100 μm
BPM resolution	$\sim 3-4$ μm
jitter	~ 75 nm
- Accelerating structures	
prealignment	~ 100 μm
with movers	~ 30 μm with respect to the orbit
- Dipole modes	
detuning	~ 10 different structure with $\Delta f_{total} \sim 36$ MHz
damping	$Q \sim 2000 \ldots 4000$ 2 HOM dampers + lossy cells
- Charge jitter	$\leq 5\%$ for single bunches
- Klystron phase errors	$\sim 4°$

The damping of HOM dipole modes is achieved by two pairs of dampers per acc. structure and additional "lossy" cells [3], i.e. the iris region is coated which a lossy material. The accelerating mode is only slightly influence by this type of lossy cells since the quality factor is mainly determined by the fields near the outer cavity walls.

From the computer simulation, which have been done so far, it can be concluded that the effective multi- and single emittance can essentially be preserved if the above mentioned tolerances can be obtained. At the DESY S-band test facility the accelerating structures movers and the HOM signals will be investigated in order to demonstrate that it is feasible to obtain an rms offset of 30 μm between the structures and the beam. Furthermore, it still has to be demonstrated that it is possible to build accelerating structures with a sufficient straightness.

The dipole modes used in our simulations were calculated with a simplified geometry of the acc. structures. Hence, the modes have to be verified. Also, higher passbands could contribute significantly to the multi-bunch beam break-up [3].

The instrumention and control requirements for application of the sophisticated orbit correction techniquess have not yet been considered. The various feedback loops for a linear collider, which may have many interdependencies, are not yet studied for the SBLC design study.

References

[1] R. Brinkmann, *Optimization of a final focus system for large momentum bandwidth*, DESY-M-90-14, Nov. 1990

[2] M. Drevlak, thesis in preparation

[3] M. Dohlus, *HOM in S-band structures* talk at the S-band collaboration meeting, Feb. 1995, and private communication.

[4] T. Raubenheimer, *The generation and acceleration of low emittance flat beams for future linear colliders*, thesis, SLAC-387, Nov. 1991

[5] U. van Rienen, *Higher order mode analysis of tapered disc-loaded waveguides using the mode matching technique* , Particle Accelerators, 1993, Vol. 41, pp. 173-201

[6] K. A. Thompson, R. D. Ruth: "Simulation and Compensation of Multibunch Energy Variation in NLC", May 1993, SLAC-PUB-6154

*S-BAND HOM-DAMPER CALCULATIONS AND EXPERIMENTS**

M. Dohlus, M. Marx, and N. Holtkamp
Deutsches Elektronen-Synchrotron DESY
Notkestraße 85, D-22607 Hamburg, Fed. Rep. of Germany

P. Hülsmann, W.F.O. Müller, M. Kurz, H.-W. Glock, and H. Klein
Institut für Angewandte Physik der Johann Wolfgang Goethe-Universität
Robert-Mayer-Straße 2-4, D-60325 Frankfurt am Main, Fed. Rep. of Germany

I. ABSTRACT

Damper cells for higher order modes are necessary for the S-band linear collider to suppress higher order dipole modes, which are harmful to the beam. It is foreseen to employ two single cell damper stations in the whole 6m-structure. One is posed at cell #25 and the other at cell #106. In order to investigate the effect of a single damper cell within a stack of undamped cells, a 12-cell constant impedance structure loaded by a single wall slotted damper cell was built and analyzed experimentally, numerically and analytically. The goal of the investigations was to optimize the damping effect for the first dipole passband, which contains the (most dangerous) synchronous 11/12π-mode. The first problem is to find the appropriate single damper cell Q-value, which is needed for a certain cell-to-cell coupling to maximize the energy flow into the damper cell. The second problem is to find the optimum tuning position in order to achieve the best over all damping effect for the first dipole passband without disturbing the accelerating mode. Several wall slotted damper cells have been built and examined.

II. INTRODUCTION

In future linear colliders strong higher order mode suppression will be inevitable in order to avoid severe beam break up effects. For S-band linear colliders it is foreseen to suppress higher order modes by detuning [1] and damping [2]. The damper cells are planned to be located at cell #25 and cell #106 of the 6m-section, thus also providing beam position information for the alignment system. The most dangerous higher order modes are known to be trapped within the first twenty cells. But due to the small bandwidth of the first dipole passband (45MHz) which causes very little energy flow due to the small cell-to-cell coupling, damping with a single cell damper is impossible. Therefore damping will be done by coating the iris with lossy material in order to damp every cell. In the chosen geometry the cell-to-cell coupling increases from the front end to the back end of a 6m-structure due to the decreasing iris opening.

III. ANALYTICAL MODEL

The effect of a single damper cell within a channel of undamped cells can be calculated analytically using a simple equivalent circuit model with a serial resistance representing the energy dissipation of the damper cell. For the modes at the outer ends of the passband the dominant change in the field, due to the presence of the damper, turns out to be a phase shift in the argument of the field. With the model described above one can derive the following simple formula for 0- and π-mode:

$$\frac{1}{Q} = K \cdot \sin(\Delta\varphi) \qquad (1)$$

where Q is the Q-value of the simple damper cell, K is the bandwidth of the passband (which represents the cell-to-cell coupling) and $\Delta\varphi$ is the phase shift due to the damper. To achieve a damping effect, $\Delta\varphi$ has to be a real number. Thus

$$K \cdot Q = \frac{1}{\sin(\Delta\varphi)} \geq 1 \qquad (2)$$

K·Q=1 represents the minimal Q-value, which can be applied. We have shown that the relationship (1) is fulfilled by high accuracy for the 0-mode, for which the single cell Q-value can be measured easily by closing the iris openings of the damper cell with metal surfaces. For π-modes the single cell Q-value could not be derived experimentally, because the iris openings would have to be closed by magnetic walls. Generally speaking the single cell Q-value depends on the mode geometrie.

IV. NUMERICAL MODEL

To investigate the properties of a damper cell in a ci or cg structure one can use a field computation program (eg. MAFIA) or a simplified model of coupled oscillators. The effort for the direct field calculation is rather high, but the effects in the first dipole band of a ci structure only depend on few parameters. Therefore it is appropriate to analyze the effects of these parameters in a coupled oscillator model. Due to the mixing of TM- and TE-like modes, for this band a model with two oscillators per cell was used. For the plain cells there are five degrees of freedom to simulate the dispersion charactersistic and two degrees for

* work supported by DESY/Hamburg

0-7803-3053-6/96/$5.00 ©1996 IEEE

the coupling to the beam. These parameters have been evaluated by single cell calculations with the MAFIA periodic eigenvalue solver. To simulate the effect of a damper, losses are introduced in this model. In the damper cell the Q values of the TM- and TE-oscillators can be tuned and damped individually. Introducing losses in every cell (eg. wall losses) or simulating several dampers does not increase the computational effort. The analysis of damping in complete Linac structures with as much as 200 cells is possible.

V. EXPERIMENTS

The slotwidth of the damping cell was varied from 24mm up to 30mm. The slot was of 3mm height. The damper cell (see Fig. 1) was made of brass (Ms58, $\sigma=1.46\cdot10^7\ \Omega^{-1}m^{-1}$) with an inner diameter of 81.6mm and an iris opening of 27.8mm. In order to tune the damped cell with respect to the accelerating mode and the dipole modes of the first dipole passband to some extent independently, six tuning screws (A and B) can be moved into the cell. The waveguides are made of aluminium, they are of 40mm width (3.75GHz cut off frequency) and 9mm height.

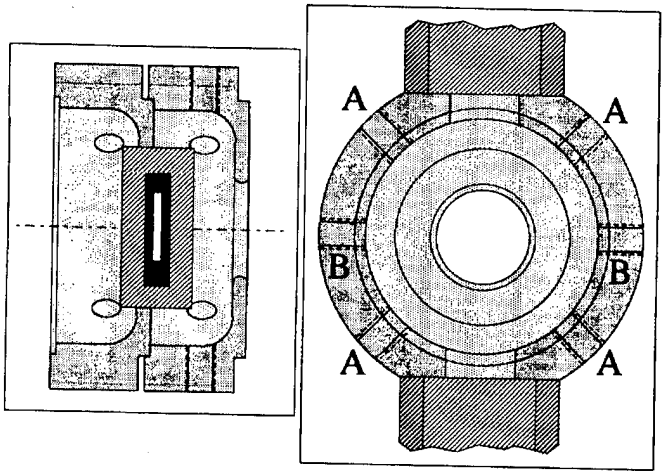


Figure 1: Damper cell with two waveguides.

This damping system was investigated alone, closed with metal plates as shown in figure 2, which shows the dependence of the single cell Q-value upon the slotwidth:

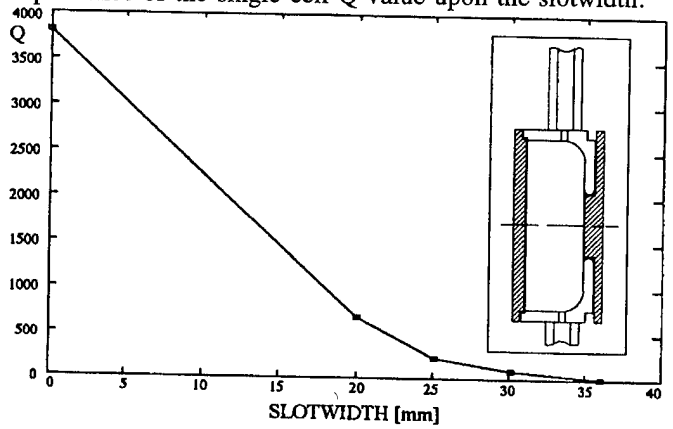


Figure 2: Single damper cell Q-value versus slotwidth.

Then the damper cell was emploid in the 12-cell structure (bandwidth of the first dipole passband is 200MHz) at cell #4 as shown in figure 3:

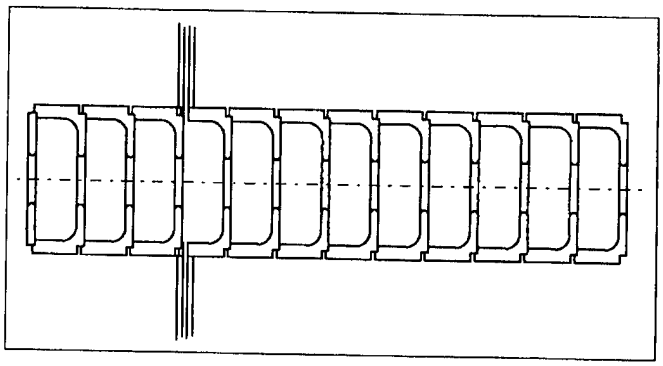


Figure 3: Damped 12-cell structure.

After tuning, the end cells represent electrical boundary conditions, so that the stack shows a proper 0-mode in the TM-monopole passband. In the case of strong damping, the tuning was performed by additional metal pieces, which were attached to the inner wall without affecting the coupling slot geometry. The way of independent tuning was to first tune the 0-mode of the second dipole passband with tuning screws A, which affect monopoles as well as dipoles and then tuning the monopole modes with tuning screws B, which mainly affect the monopole modes. The mode geometry was controlled by bead measurements, using a dielectric bead.

VI. COMPARISON OF NUMERICAL AND EXPERIMENTAL RESULTS

The damping effect of the first dipole passband is shown in figure 4:

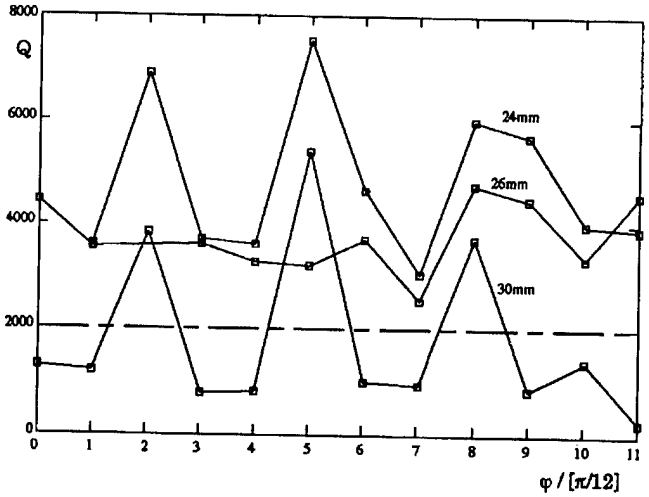


Figure 4: Measured Q-values of the first dipole passband.

The damping effect increases with increasing the slot width. Most of the twelve modes were damped well below 2,000. The three remaining modes show nearly no longitudinal electric field strength at the damper position. The same plot was calculated numerically by the

equivalent circuit model nearly resembling the experimental results (see Fig. 5).

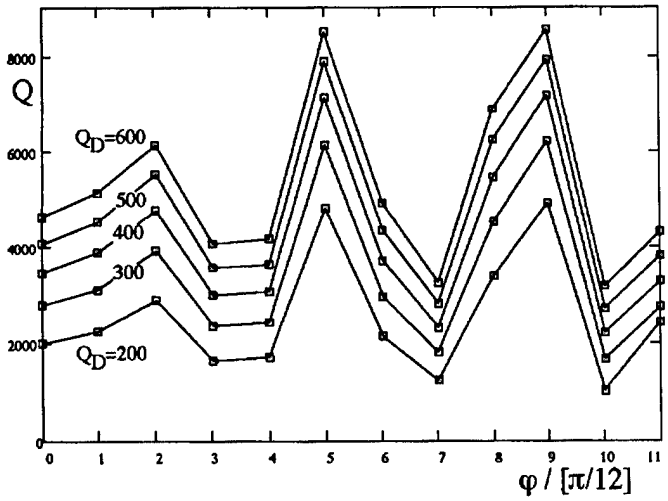


Figure 5: Calculated Q-values of the first dipole passband.

The best overall damping effect was not found in the tuning position where all modes resembles the undamped mode geometry. Exemplary the tuning behaviour of the damping effect was examined for the 11/12π-dipole mode. Tuning the damper cell frequency for this mode to lower frequencies lead to an energy concentration in the neighborhood of the damper cell, maximizing the damping effect (see Fig. 6).

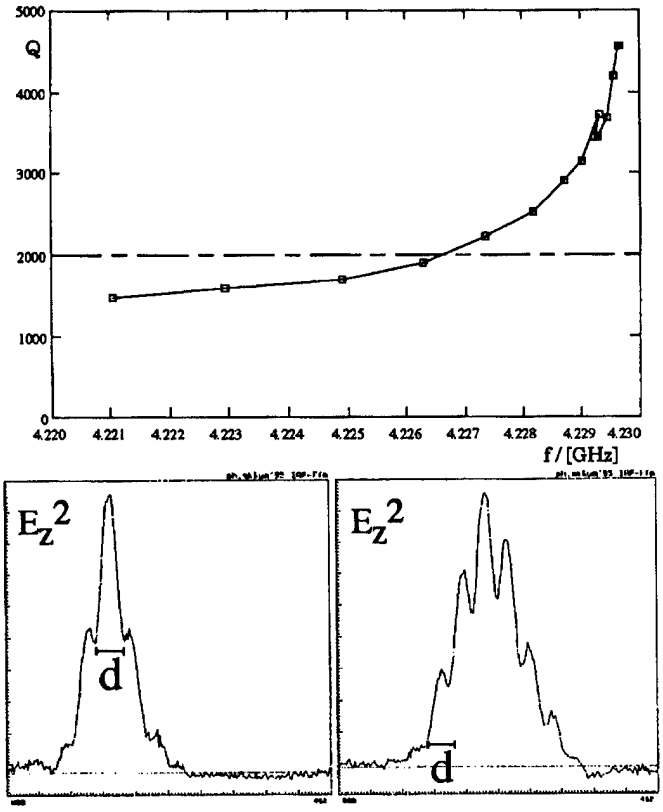


Figure 6: Measured Q-value of the 11/12π-dipole-mode and related field distributions.

This effect can be shown also numerically (see Fig. 7).

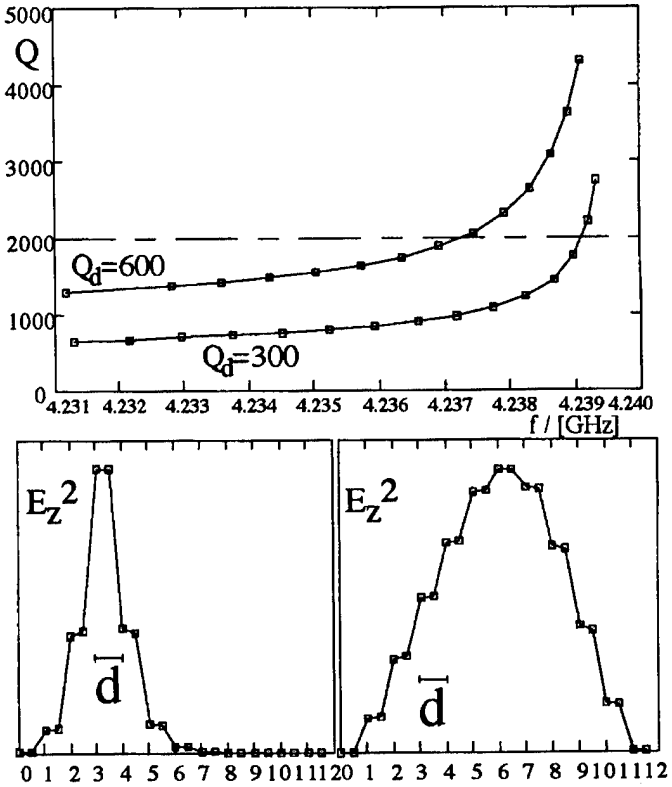


Figure 7: Calculated Q-value of the 11/12π-dipole-mode and related field distributions.

VII. REFERENCES

[1] K. Balewsky et al.: DESY and TH-Darmstadt: Status report of a 500 GeV S-Band linear collider study", DESY 91-153, 1991, D-22603 Hamburg, Notkestraße 85, pp. 1-39

[2] R. Ruth: The status of the NLC", 3rd Int. Workshop on Linear Colliders, LC'91, Vol. 1, Protvino 1991, pp. 141-175

THE S-BAND 36-CELL EXPERIMENT*

B.Krietenstein, O. Podebrad, U. v.Rienen , T. Weiland
Inst. f. Theorie Elektromagnetischer Felder, Technische Hochschule Darmstadt, FRG
H.-W. Glock, P. Hülsmann, H.Klein, M. Kurz, C. Peschke
Inst. f. Angewandte Physik, D-60054 Frankfurt am Main, FRG
M. Dohlus, N. Holtkamp
DESY, FRG

Abstract

In a multibunch collider scheme deterioration of the beam due to long range wakefields is a severe problem to be overcome. While, in principle, it is possible to couple selectively to dangerous Higher Order Modes (HOMs) a different way is to prevent coherent excitation of these wakes by means of modifying a constant gradient accelerator tube such that a structure detuned with respect to HOM modes is obtained. Since the phenomenon of longer interacting dipole modes which are trapped completely in an inner part of the accelerating structure has, to our knowledge, never been studied experimentally – even theoretically it was not notorious – it was decided to design and build a test structure with the characteristics mentioned above. First results of measurements and numerical predictions are presented.

I. INTRODUCTION

The S-Band 2*250GeV Linear Collider Study SBLC forsees 2452 constant-gradient (cg) acceleration structures of 180 cells with a loaded gradient of 17 MV/m. It considers a bunch train of 125 bunches with a spacing of 16ns from bunch to bunch. To achieve a high luminosity any cumulative beam break-up along the bunch train has to be avoided. Wakefield effects driven by HOMs are one of the primary sources of emittance growth. Consequently, the suppression of these HOMs is a very crucial point in all actual linear collider designs. The major interest of calculations was focussed on the modes of the first dipole band since they cause the severest deflecting effects.

Previously first calculations for the SBLC structure were carried out with ORTHO [1] for a somewhat simplified 180–cell structure with 30 landings. The main results were the following:

– The loss parameter curve showed a somewhat oscillatory behaviour which reflects the local periodicity of the structure.

– From the experiences at SLAC a peak was expected in the loss parameter pattern at the lower end of the first dipole passband. Instead of this, the curve showed a nearly flat maximum extended over 2/3 of the first dipole passband.

– Consequently, not only the first π-like dipole modes influence the beam dynamics but about 120 modes. A major part of these deflecting modes is trapped inside the cg structure, that is without contact to the end cells.

Since these results contradicted the usual ideas about the behaviour of HOMs in tapered waveguides and strongly influenced the design plans for damping strategies of the SBLC structure, further studies were set up on the analysis of the HOMs. Mainly these subjects have been treated:

– Development of the double–band coupled oscillator model (MCO).

– Development of a test structure with the following characteristics: a) easy to measure , b) easy to manufacture, c) computable by different numerical methods (MAFIA, URMEL–T, ORTHO, MCO) without geometric approximations, d: appearance of trapped modes.

On principal at least semi-analytical methods, discretization methods and coupled oscillator models could be used for the numerical HOM analysis. While discretization methods are limited to relatively short cg structures semi–analytical methods and coupled oscillator models can handle much longer structures with very small cell–to–cell deviations.

The semi–analytical program ORTHO has been developed in order to calculate the scattering matrices, electromagnetic fields and other parameters for cg structures when roundings of the cells and the irisses are neglected. MAFIA and URMEL–T are well tested codes which consistently solve Maxwell's equations. For this reason the test structure was chosen long enough to show the typical trapped modes but short enough to be computable by MAFIA and URMEL–T. Dohlus developed some special coupled oscillator model (MCO) for the SBLC structure which is characterized by overlapping of the first and second dipole passband: For each cell, a parallel equivalent circuit represents the TM_{110}-like modes and a serial equivalent circuit represents the TE_{111}-like modes. Each circuit of each band is coupled to its adjacent circuits and neigboring circuits of the second band.

Two designs of 36 cells have been compared with MAFIA, URMEL–T, ORTHO, and MCO. One geometry was just every fifth cell of the evenly tapered 180–cell structure. The design, which finally was chosen, has a very strong tapering of the iris, constant outer radius and twice as thick irisses as the original SBLC structure. This structure better fulfilled the demanded characteristics. Comparisons gave a good agreement in the resonant frequencies and in the field distribution, which is very important since a clear appearance of trapped modes inside the structure was found for several modes. Also a very similar shape of the loss parameter curve was found. However, the sensitivity of the loss parameter against any field error has to be stressed.

II. MEASUREMENTS

A. The Test Setup

The structure, made of standard OFHC copper, consists of 36 cells clamped together by truss rods. Overall length is

* work supported by DESY

0-7803-3053-6/96/$5.00 ©1996 IEEE

1300mm, cut-off pipes of 100mm length are atached to each end of the structure. The cell geometry is similar to the one chosen for the SBLC, except for the iris thickness which is 10mm instead of 5mm. The iris openings are evenly tapered from 40mm diameter at the beginning to 20mm at the end.

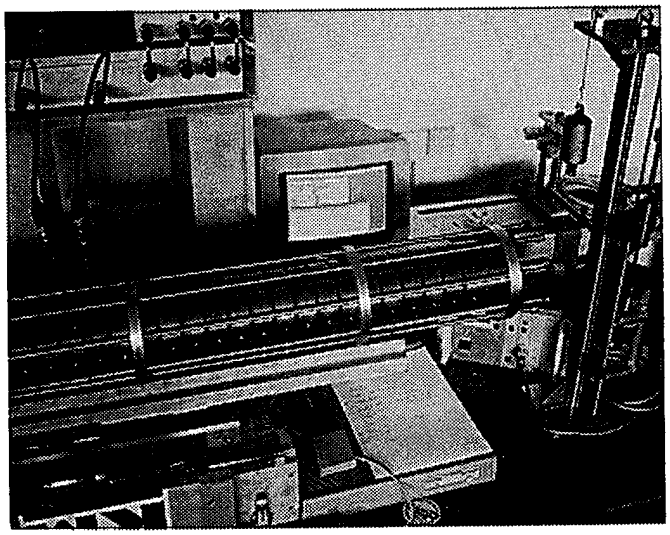


Figure 1: Picture of the test setup

Proper alignment is ensured by laying the structure on top of an optical bench. The field measurements were performed using a modified nonresonant bead pull technique [2, 3]. Data is taken by a HP8753c network analyzer for 801 discrete positions along several paths parallel to the cavity axis. In Figure 1 a picture of the test setup is shown.

B. The Measurement Method

The method applied measures the change of the transmission through a cavity when a bead is moved along a path inside it. Starting from a lumped circuit representation of a resonance one finds expression (1) under the assumption that the bead is sufficiently small to change the resonant frequency of the cavity only by a small amount.

$$\Delta s_{21} = \frac{2\sqrt{k_1 k_2}}{(1 + k_1 + k_2)} i\Omega, \quad \text{with} \quad \Omega = Q_0\left(\frac{\omega}{\omega_0} - \frac{\omega_0}{\omega}\right) \tag{1}$$

Combining equation (1) with Slater's formula [4] leads to the final expression (2). It should be mentioned that (2) provides inherent control of the validity of assumptions and thus information about the accuracy of the measurement since one has only to check for the real part of Δs_{21} not to exceed about 5% of it's magnitude (say).

$$\Delta s_{21} = -i \frac{2\sqrt{k_1 k_2}}{(1 + k_1 + k_2)} \frac{\omega_0}{P_{loss}} \hat{a} |E_0|^2 \tag{2}$$

In the measurements we are interested in both the longitudinal and the transversal component of the electric field. If we use isotropic dielectric material with shapes like rotational ellipsoids the form factor â of the bead becomes a sum of independent quantities. The right end side of (2) can then be written as

$$\hat{a} |E_0|^2 = \sum_v a_v E_v^2 \tag{3}$$

allowing to solve for logitudinal and transversal components individually. Two beads of different shape (e.g. needle and shim) are needed.

$$A \begin{pmatrix} \frac{\Delta s_{21}^{(1)}}{a_z^{<1>}} \\ \frac{\Delta s_{21}^{(2)}}{a_z^{<2>}} \end{pmatrix} = \begin{pmatrix} 1 & f_1 \\ 1 & f_2 \end{pmatrix} \begin{pmatrix} \tilde{E}_z \\ \tilde{E}_\perp \end{pmatrix},$$

$$\text{with } \tilde{E} = \frac{E^2}{P_{loss}}, \; A = \frac{(1 + k_1 + k_2)^2}{2\omega \sqrt{k_1 k_2}}, \text{ and } f = \frac{a_\perp}{a_z} \tag{4}$$

After performing two measurements along the same path using the different beads equation (4) is then solved for $\tilde{E}$.

C. Results

For the measurements two ceramic beads of different shapes (needle, Ø 0.6mm, length 7.5mm and shim, Ø 4.7mm, 0.31mm thick) were used. Both beads were calibrated in a TM_{010}–pillbox for their longitudinal and transversal perturbation constants. The needle consisting of Al_2O_3 showed very stable values of over the period of measurements whereas the shim revealed a significant change. It is believed that this is due to hygroscopic properties of the bead.

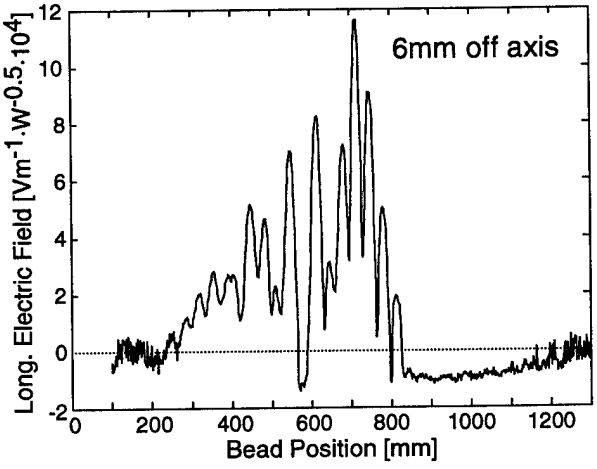


Figure 2: Longitudinal E–field of mode #15, 6mm off axis

Table I.

Mode #16. Transv. Shuntimpedance transittime not included

	MAFIA	Measured
f [GHz]	4.17099	4.17477
R_T/Q [Ω]	521	626
Q	12379	9850

Table II.

Mode #16. Transv. Shuntimpedance transittime not included

	MAFIA	Measured
f [GHz]	4.18557	4.18931
R_T/Q [Ω]	556	605
Q	12471	10150

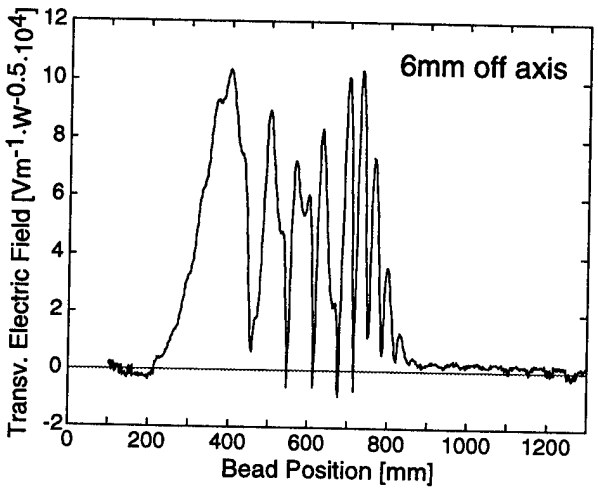


Figure 3: Transversal E–field of mode #15, 6mm off axis

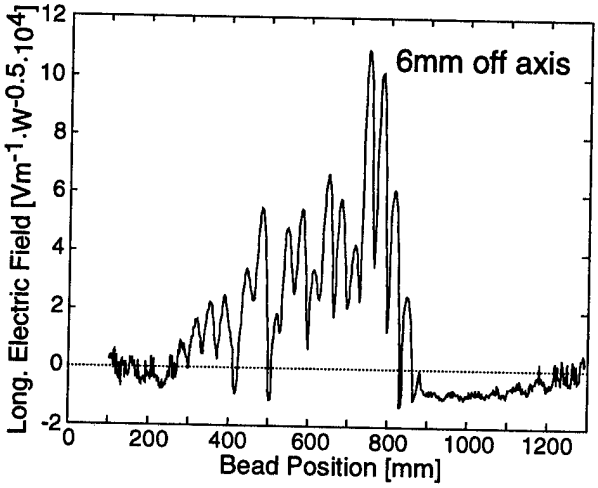


Figure 4: Longitudinal E–field of mode #16, 6mm off axis

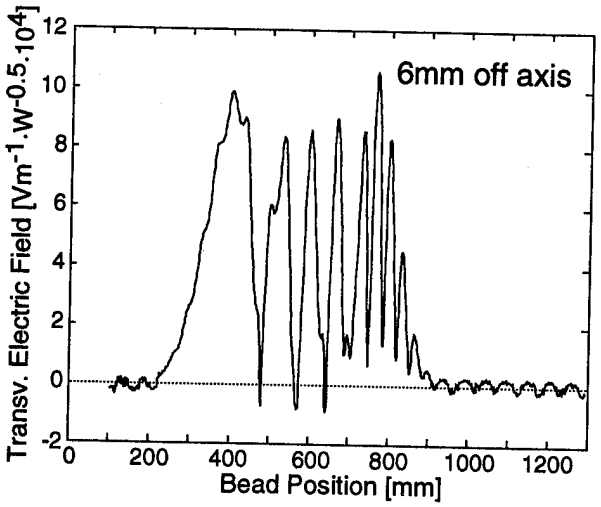


Figure 5: Transversal E–field of mode #16, 6mm off axis

It was decided to repeat the various calculations for the exact geometry of the structure as built. So presently only MAFIA calculations are available to be compared to the results.

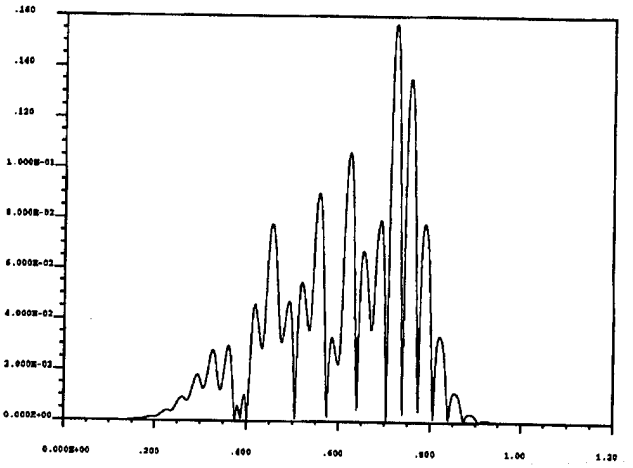


Figure 6: Long. E–field of mode #15, MAFIA, 6mm off axis

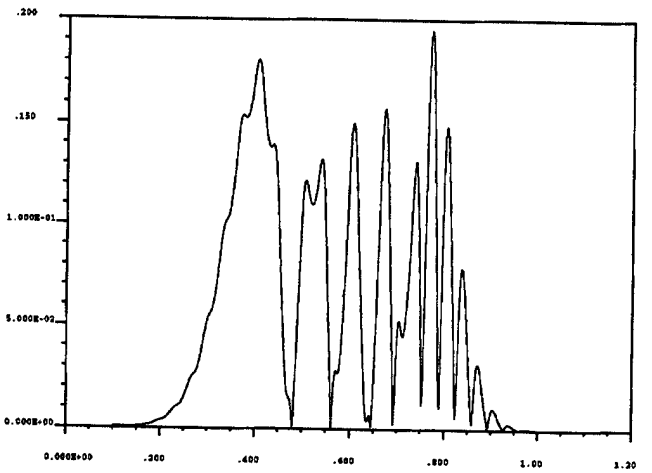


Figure 7: Transv. E–field of mode #16, MAFIA, 6mm off axis

III. CONCLUSIONS

The field geometries calculated and measured showed very good agreement. On average frequencies differ less than 1‰. The Qs measured are about 20% below the calculated values which is an acceptable value for cups clamped together. While for mode #16 the R_T/Qs differ about 8% – which is well inside the estimated 15% accuracy limit of the measurement – results for mode #15 deviate about twice that value.

IV. REFERENCES

[1] van Rienen, U., Higher Order Mode Analysis of Tapered Disc–Loaded Waveguides using the Mode Matching Technique, Particle Accelerators, 1993, Vol. 41, pp. 173 - 201

[2] Steele, C. W., A Nonresonant Perturbation Theory, IEEE Trans. MTT-14 (2), pp. 70-74, 1966

[3] Kurz, M., Untersuchungen zu mikrowellenfokussierenden Beschleunigerstrukturen für zukünftige lineare Collider, thesis, Frankfurt 1993

[4] Maier, L.C., Slater, J.C., Field Strength Measurements in Resonant Cavities, J. Appl. Phys., 23 (1), 1952

Abe, H. FAP13, 1358
Abe, S. TAQ35, 1608
Abraham, W. WPA01, 902
Abramenko, N. RPR10, RPR15, 1143, 1155
Abramsky, P. WPP11, 1681
Adachi, Toshikazu TPR16, 3275
Adamski, J. FAA27, 248
Adamski, J.L. FAA28, 251
Adolphsen, C. WAG11, RPB03, RPB04, RPC01,RAE03,TPQ17, WAB07, WAC18,646, 662, 665, 698, 2389, 2989, 3031, 3112
Adolphsen, Chris WAB08, 3034
Afanasiev, O. FAQ06, 1399
Agafonov, A.V. TPR13, TPR14, 3269, 3272
Ahrens, L.A. TAP11, TAP12, TAP13, WAB04,RAQ22, 378, 381, 383, 3022, 3334
Aizatsky, N.I. WPQ22, TPA14, 1773, 3229
Akai, K. FAE09, WPQ08, WPQ09, WPQ17,WPR05, WPR09, RPQ06,WAC08,1503, 1735, 1738, 1759, 1797, 1806, 2675, 3085
Akasaka, N. RPA20, FAE09, WPQ09, WPQ17,WPR05, WPR09, TPC08,TPC29,TAG01, 1099, 1503, 1738, 1759, 1797, 1806, 2613, 2655, 2742
Akemoto, M. WPR02, WPR03, 1788, 1791
Akimov, V. WAA17, 1263
Akre, J. FAQ24, FAQ25, 1444, 1447
Akre, R. WPR15, WAB12, 1821, 3046
Alessi, J. WPC09, 1013
Alexahin, Y. RAA17, 560
Alexandrof, V.A. TAG01, 2742
Alimov, A. RPA19, 1096
Alimov, A.S. RAR04, 3361
Alinovsky, N.I. TAC06, 143
Allen, C.W. RPA24, 1111
Allen, Christopher K. MPC04, 2324
Allen, J. RAR23, 3406
Allen, L. WPA06, 917
Allen, M.A. WPQ06, 1729
Allen, Ray TPP13, 1645
Alley, R. MPE10, 887
Allison, Paul W. TAE08, 1207
Allison, S. RAE03, 2389
Alonso, Jose R. WPE01, 58
Alton, G.D. MPE05, WPC12, WAQ26, 871, 1022, 1897
Altuna, X. WAP12, WAP13, 464, 467
Amankath, H. RPA26, 1116
Amiranoff, F. WAG07, 634
Anderson, David E. TAE07, 1204
Anderson, K. WAQ22, WAR17, 1888, 1939
Ando, A. RPQ15, 2699
Andreev, V.G. WPP19, 1702
Andreev, V.V. FAC09, 2856
Andriishchin, A. FAQ06, 1399
Anerella, M. TPE04, FAQ04, 1293, 1396
Angerth, B. RPE02, 1999
Ankenbrandt, C. FAG06, 86
Anthouard, Ph. TAE09, 1210
Antonsen, T.M. WAG04, 621
Aoki, T. FAP13, 1358
Arai, S. RPG13, 351
Arbuzov, V. WPP11, 1681
Ardonceau, J. WAG07, 634
Argyrakis, J. FAP03, 1328
Arinaga, M. RAB13, 779
Arnold, N. RPA11, RPA14, MPQ08, 1073, 1082, 2467
Asano, K. TPP03, TPP16, 1620, 1652
Ashton, J.R. RPB05, 668
Assadi, S. TAG10, RAP03, WAB01, 2777, 2886, 3016
Asseev, A.A. WAR23, 1955
Assmann, R. RAA19, WAG11, RPB02, 567, 646, 659
Astapov, A.A. RPE13, 2029
Auble, R.L. WAQ26, 1897
Auch, S. RPR06, 1131
Aune, B. WPB22, 998
Ausset, P. WPQ26, 1781
Austin, R.H. FAA19, FAA31, 234, 260
Autin, B. RPC11, WAE09, 722, 2178
Averill, R. RPG05, RAA31, 327, 600
Azorsky, N.I. TAQ34, 1605
Baartman, R. RPG12, WAQ07, WAC20, 348, 1858, 3119
Baba, T. WAQ06, 1855
Babzien, M. MPE11, 890
Backmor, Rudolf TAQ13, 1550
Bailey, J.D. TAP07, TAP08, TAP09, 366, 369, 372
Bailey, R. WAP12, WAP13, RAA11, 464, 467, 548
Bainan, Ding FAA26, 246
Baiod, R. FAP04, FAP06, FAP07, FAP09,MPB06, 1331, 1337, 1340, 1346, 2285
Bak, J.S. RPA06, 1061
Baker, S. WAR19, 1945
Bakker, R. RPG06, 330
Baklakov, B. TAA01, RAR30, 2078, 3424
Balakin, V. TAG01, 2742
Balewski, K. FAR07, 275
Balhan, B. RAA15, 557
Ball, M. TPB24, RAP21, RAP22, WAC12,RAQ23,RAQ24, 2583, 2934, 2937, 3094, 3337, 3340
Ballauff, M. FAR06, 272
Bamblevski, V.P. RPE13, 2029
Bane, K. RPA04, WAC17, 1058, 3109
Bane, K.L.F. RPA20, TPQ16, TPQ17, WAB07,WAC16, WAC18, 1099, 2986, 2989, 3031, 3105, 3112
Bangerter, R.O. WAQ04, 1852
Baptiste, K. TAR03, 801
Baranov, V.I. MPG10, WAR21, 426, 1949
Baranova, L.A. TAP16, 389
Barber, D.P. WPG08, 511
Bardy, J. TAE09, 1210
Barker, D. MPR13, 2265
Barklow, T. RPB01, 656
Barletta, W. TAA28, 2135
Barlow, T.A. TPC13, 2628
Barnard, J. TAR17, 837
Barnard, J.J. TAR14, TPB14, TPR18, 828, 2557, 3278
Barnard, John J. TPR02, 3241
Barnes, P. FAE13, WPQ02, RAQ04, 1515, 1720, 3294
Barov, N. WAG06, WPB11, 631, 976
Barr, D. MPQ03, RPQ16, TPQ19, 2452, 2702, 2992
Barry, W. RAE13, RPQ08, 2423, 2681
Barts, T. MPB10, 2294
Batchelor, K. MPE11, WPB13, RAE09, WXE03,TPB01,890, 982, 2411, 2432, 2530
Batskikh, G. FAP24, 1387

Batskikh, G.I. RPR07, 1134
Batygin, Y. WPC01, 1001
Batygin, Y.K. TPR06, 3251
Batygin, Yuri K. TPR07, 3254
Beadle, Edward R. TPB08, TPB09, 2545, 2548
Beauvais, P.-Y. RAG07, 3173
Becher, D. MPE05, 871
Bechstedt, U. TPB20, 2574
Bechtold, V. FAR06, 272
Becker, T. FAP02, 1325
Becker, U. TAQ06, WAE13, 1533, 2190
Beebe, E. WPC09, 1013
Behne, D. MPP12, MPP20, 2064, 2075
Beisel, U. WPA04, 911
Bekefi, G. TPG14, RPC15, 192, 734
Belkovets, V. TAC16, 152
Beloglazov, V.I. TAE14, 1225
Belomestnykh, S. FAE13, WPP11, RAQ04,RAR18,RAR19, 1515, 1681, 3294, 3391, 3394
Belov, W. RAQ14, 3315
Belova, Nadya G. WAA01, 1227
Belser, C. RAA04, 530
Belser, F.C. WPQ06, TAA22, 1729, 2129
Belugin, V.M. RPR07, 1134
Ben-Zvi, I. MPE11, WPB13, RAE09, WXE03,TPB01,890, 982, 2411, 2432, 2530
Benesch, J. FAE12, 1512
Benjamin, J. TAP11, 378
Benjegerdes, R. WPA01, FAP17, 902, 1369
Bennett, L. TAE06, 1201
Bennett, Lawrence F. TAE07, 1204
Benson, S. FAG11, FAA25, WPA17, WPC24, 102, 243, 942, 1052
Benvenuti, C. FAE11, TPP12, 1509, 1642
Bercher, M. WAG07, 634
Berenc, T. WPB06, 961
Berezin, A.K. RAB15, 782
Berg, J. TAA22, 2129
Berg, J.S. FAB06, TPQ16, 2804, 2986
Berg, J. Scott TPQ07, WAC05, 2962, 3076
Berg, W. RPA11, MPQ10, 1073, 2473
Berger, D.D. WPQ06, 1729
Bergher, M. RAP19, 2928
Berkelman, K. FAE13, 1515
Bernal, Santiago TAA17, 2117
Bernard, D. WAG07, 634
Bernard, M. WPB01, WPB22, 945, 998
Berridge, S. TAA28, 2135
Bertagnolli, H. FAR06, 272
Bertinelli, F. RPE02, 1999
Bertolini, L. RAA03, 527
Bertsche, K. TPE05, FAP21, WAQ09, MPQ21,TPB19, 1298, 1381, 1864, 2503, 2572
Bertuzzi, J.-P. MPP15, 2069
Berwald, D. RPR20, 1164
Berz, Martin MPC09, 2336
Bessonov, E.G. RAP06, 2895
Beveridge, J.L. RPG12, 348
Beyer, K.A. TPC13, 2628
Bharadwaj, V. MPG02, WAP04, RPC20,RPC21,WPB08, TAG01, 396, 443, 749, 752, 967, 2742
Bhat, C.M. FAP05, WAR02, TAA12, WAC06, 1334, 1903, 2105, 3079
Bialowons, W. RPE08, 2017
Bialy, J. FAR06, 272
Bickley, M. MPA12, MPR19, 2220, 2276
Bieniosek, F.M. WAR17, WAR18, 1939, 1942
Biggs, J. FAP03, 1328
Billen, J.H. RPR08, RPR09, 1137, 1140
Billen, James H. MPB16, 2306
Billing, M. FAE13, FAB12, TPA04, RAQ04, 1515, 2820, 3206, 3294
Billing, M.G. RAE14, 2426
Binns, B. WAA16, TPB04, 1260, 2536
Birukov, I.N. RPR01, 1119
Biryukov, V.M. MPG10, WAR20, WAR21, 426, 1948, 1949
Biryukov, Valery WAR24, 1958
Biscardi, R. TPP06, WPP03, 1626, 1660
Bisognano, J. FAG11, FAA25, WPA17, 102, 243, 942
Bisognano, J.J. RPQ11, 2690
Bisognano, Joseph J. MPC25, RAG12, 2370, 3188
Bizek, Hana M. RAR27, 3418
Bjerklie, S. FAG06, 86
Black, E. FAP03, 1328
Black, W.M. TAE10, 1213
Blanchard, R. WAP12, WAP13, 464, 467
Blas, F. MPG09, 423
Blaskiewicz, M. TAP11, TAP12, TAP13,WAC24, 378, 381, 383, 3131
Blaskiewicz, M.M. RAQ22, 3334
Blastos, J. TPG14, 192
Blazhevich, S.V. FAG12, 105
Bleser, E.J. TAP13, WAR13, 383, 1930
Bloess, D. TPP12, 1642
Blondel, A. RAA19, 567
Bloom, E. WAQ15, 1876
Blosser, H. RPG11, 345
Bluem, H.P. TAA32, 2141
Blum, E. FAR10, 284
Blum, E.B. FAR01, MPQ01, 263, 2450
Bocchetta, C. FAR06, 272
Bocchetta, C.J. FAA13, FAR21, TAG05, 222, 309, 2762
Boehnlein, D. FAG06, 86
Boer-Rookhuizen, H. MPQ17, 2491
Boers, Jack E. MPB18, 2312
Bogacz, A. FAP05, WAR19, RAR17, 1334, 1945, 3388
Bogacz, S.A. RAB20, TAR20, 790, 843
Bogard, D. RAG07, 3173
Bogaty, J.M. TPC12, 2625
Bogdanovich, B. RPR10, RPR15, TAQ24, 1143, 1155, 1575
Bogdanovich, B.Yu. TAB13, TAQ23, 125, 1572
Böge, M. RAP08, 2901
Bogert, D. MPG01, 391
Bohl, T. WAP12, WAP13, RAA11, FAE10, 464, 467, 548, 1506
Bohlen, H. FAE07, 1497
Bohn, C.L. FAG11, 102
Bojon, J.-P. RPE06, 2014
Bolme, G.O. WPA08, RPR19, 923, 1161
Bolotin, I. WPR19, 1833
Bolser, C. MPC01, 2317
Bonati, R. WAR11, 1924
Bondarev, B.I. RPR07, 1134
Bongardt, K. TPA01, TPA02,

TPA03, 3197, 3200, 3203
Boni, R. RPA26, 1116
Bonifacio, R. FAA12, 219
Bonin, B. TPP09, 1632
Bonnafond, C. TAE09, 1210
Bonnafond, Ch. TPC17, 2640
Bookwalter, V. MPR13, 2265
Borden, M. RAR23, 3406
Borland, M. FAR11, WAE11, MPQ10, 287, 2184, 2473
Borodich, A.I. TPA15, 3232
Bortnyansky, A. TAA18, 2120
Bosch, R.A. FAR20, 306
Bosotti, A. TAA07, 2093
Bossard, P. MPG09, 423
Bossart, R. RPC10, 719
Bosser, J. RAP23, RAP24, 2940, 2943
Bostic, D. MPP10, 2057
Bothe, W. FAR06, 272
Botman, J.I.M. WAQ19, WAQ20, RPP04,RPQ31, 1882, 1885, 1970, 2738
Bourdon, J.C. WPB22, 998
Boussard, D. FAE10, TPP12, 1506, 1642
Bowden, G.B. RPB04, RPA23, 665, 1108
Bowers, J. WAC17, 3109
Bowling, B. MPR13, 2265
Bowling, B.A. WAE10, 2181
Bowling, S. RPR19, 1161
Boyd, John K. MPC13, 2339
Boyes, John D. TAE07, 1204
Bozoki, Eva RPQ14, 2696
Brabson, B. RAP21, RAQ23, RAQ24, 2934, 3337, 3340
Bracco, R. FAQ19, 1432
Bradley, S. RPG05, 327
Brandt, D. RAA17, RAA20, FAC03, 560, 570, 2841
Brauer, S.O. RPE09, 2020
Braun, A. RPC21, 752
Braun, H. RPC09, RPC10, 716, 719
Brefeld, W. FAA02, FAR07, 195, 275
Brennan, J.M. TAP11, TAP13, FAE05, MPQ30,RPQ17,RPQ25, WAB04, RAQ22, 378, 383, 1489, 2518, 2705, 2723, 3022, 3334
Bricault, P.G. RPG12, RPR02, RPR03, 348, 1122, 1125
Bridges, J.F. WPP16, 1693
Brillson, L.J. FAG11, 102
Brinker, F. FAA02, 195
Brinkmann, R. MPG04, RPB07, RPE08, 406, 674, 2017
Brodowski, J. WPP07, WPQ19, RPQ17, 1669, 1765, 2705
Brogle, R. WAG09, WPC20, 640, 1039
Broome, W. TPP06, 1626
Brouet, M. MPP15, 2069
Brouzet, E. WAP13, 467
Browman, A. TAR12, TPB13, 822, 2554
Brown, B. TPE05, 1298
Brown, B.C. FAP05, FAP06, FAP07, MPB05,MPB06, 1334, 1337, 1340, 2282, 2285
Brown, D. TPB13, 2554
Brown, K. RPC06, MPR13, 707, 2265
Brown, K.A. TPA06, 3212
Brown, Nathan RPR23, 1170
Brown, R. WPC08, 1010
Brown, V.W. WPA08, 923
Bruhwiler, D. RPR20, TPR07, 1164, 3254
Bruhwiler, D.L. TPR08, 3257
Brunelle, P. FAR14, 293
Brunet, J.-C. RPE02, 1999
Brüning, O. TAG09, 2774
Brüning, O.S. MPG07, 420
Brunner, O. WPG09, 514
Bruns, Warner RPA15, RPA16, 1085, 1088
Bryant, P.J. RPG03, 322
Budilin, V. WPR19, 1833
Budnick, J. RAP21, RAQ23, RAQ24, 2934, 3337, 3340
Bugg, W. TAA28, 2135
Bugorsky, A.P. MPG10, 426
Buhler, S. WPB22, 998
Bula, C. TAA28, 2135
Bulfone, D. TPG11, FAR21, 186, 309
Bulos, F. WAQ15, TAG01, 1876, 2742
Bulyak, E. FAR17, TPA12, TPA13, 299, 3223, 3226
Buon, J. RPC20, TAG01, 749, 2742
Burke, D. RPC01, RPC20, TAA08, WXE07,TAG01, 698, 749, 2096, 2444, 2742
Burkhardt, H. WAP12, WAP13, RAA11, 464, 467, 548
Burlet, A. MPP15, 2069
Burnham, B. FAA08, RAA01, RAB22, MPA10,MPA11, MPQ06, FAC20, 213, 524, 796, 2214, 2217, 2461, 2877
Burnside, C. MPP15, 2069
Burov, A. WAB16, WAB17, 3055, 3058
Burrini, D. RAQ05, 3297
Burton, A. RAA15, 557
Bushuyev, A. WPP11, 1681
Bussa, M.P. WAP14, 470
Butteris, J. FAQ32, 1465
Buxton, W.E. MPA19, 2235
Byrd, J. RPC02, MPC01, RAE12, RAE13,RPQ08,TPQ16, 701, 2317, 2420, 2423, 2681, 2986
Byrd, J.M. WXE06, RPQ09, 2441, 2684
Byrne, M. WPR15, 1821
Cable, M.D. TAR14, 828
Cai, Y. RAA22, RAA25,RAA26, RAA27, 576, 585, 588, 591
Cain, T.D. FAG05, 83
Calabrese, R. RAE05, 2399
Calame, J. TAQ17, 1561
Calame, J.P. TAQ18, TAQ19, 1563, 1566
Calder, R. RPE02, 1999
Calish, S. TAR18, 840
Callahan, D.A. TAR14, TPR19, 828, 3282
Callahan, Debra A. TPR01, 3238
Callin, R.S. TAQ28, 1587
Camas, J. TPC21, 2649
Cameron, P. TAA09, 2099
Cameron, P.R. MPQ05, 2458
Campbell, R. WAA16, 1260
Capone, D. FAQ14, 1417
Caporaso, G. RPC16, MPE14, WPC16, WAA19,TAA20, 737, 899, 1027, 1269, 2123
Cappi, R. TAP14, MPG09, 386, 423
Carboni, G. WAP14, 470
Carder, B. WAA19, TAA20, 1269, 2123
Cardman, L. FAG11, WPA17, 102, 942
Cardman, L.S. WPC17, 1030
Cargnello, F. TPG11, 186
Carlier, E. RAA15, 557
Carlsten, Bruce E. WPB15, FAE06, 985, 1494
Carnegie, D.W. TPE08, 1310
Carrigan, D. WAR19, 1945
Carroll, Frank E. FAG04, 80
Carson, J.A. FAP06, FAP07,

1337, 1340
Carter, A. RPG05, 327
Carter, F. FAA08, RPA17, MPA11, 213, 1090, 2217
Caruette, A. TPP11, TPP14, 1639, 1648
Carwardine, J.A. WAA08, RPP03, RPQ18, 1242, 1967, 2708
Caryotakis, G. FAE07, 1497
Casella, R. RPP02, 1964
Caspers, F. RPE02, RAP24, 1999, 2943
Caspi, S. FAQ23, 1441
Cassel, R.L. WAR06, 1915
Castellano, M. TPG11, 186
Castillo, V. RPQ07, 2678
Castle, M. TAQ18, TAQ19, 1563, 1566
Castro, P. RAA20, FAC03, 570, 2841
Catravas, P. TPG14, 192
Caussyn, D.D. RAP21, RAQ23, RAQ24, 2934, 3337, 3340
Cayla, J.N. WPB01, 945
Celata, C.M. TPA10, 3220
Cevenini, F. TPG11, 186
Chae, Y.-C. TAP05, FAB09, 363, 2811
Chae, Yong-Chul TPQ20, TPQ21, RAR24, RAR25, 2995, 2998, 3409, 3412
Chamouard, P.-A. RAG07, 3173
Chan, A. TAR18, 840
Chan, K.C.D. FAA16, TAR12, 228, 822
Chanel, M. RAP24, 2943
Chang, C.H. FAQ26, 1450
Chang, H.P. FAA07, RAA24, TPQ10, 210, 582, 2971
Chang, L.H. FAA04, RAA24, FAQ26, TPQ08, 201, 582, 1450, 2965
Chang, Peace TAR04, 804
Chang, Y.M. MPQ32, 2524
Channell, P. WAC29, 3146
Chao, A. MPC01, WAC17, 2317, 3109
Chao, A.W. WAB09, WAB11, RAQ02, 3037, 3043, 3288
Chao, Alex FAC02, WAB10, 2838, 3040
Charruau, G. WPQ26, 1781
Chattopadhyay, S. TPG07, RPC16, TAA28, 174, 737, 2135
Chautard, F. RPC10, 719
Chavanne, J. TPE10, 1319
Chehab, R. WPB22, 998
Chen, B. WAB20, 3064
Chen, Bo WAB10, 3040
Chen, C.-I. TPC15, 2634
Chen, D. WAR19, 1945
Chen, J.R. FAA07, 210
Chen, J.S. MPR10, TPB29, 2256, 2592
Chen, Jenny MPR10, MPQ16, TPB29, 2256, 2488, 2592
Chen, P. RPC01, TAA28, RAP15, 698, 2135, 2919
Chen, Pisin RAQ18, 3326
Chen, R.-C. TPC15, 2634
Chen, S.C. MPE12, WPB03, WPB04, 893, 951, 954
Chen, T. RAA26, TAG06, RAP09, RAP11, RAP12, WAC17, 588, 2765, 2904, 2910, 2913, 3109
Chen, Y. RPC16, WPC16, WAA19, 737, 1027, 1269
Chen, Yinbao FAA21, RAQ25, RAQ26, 237, 3343, 3346
Cheng, J. TAQ18, TAQ19, 1563, 1566
Cheng, Wen-Hao RAG09, TPR12, 3179, 3266
Cheng, Y. FAA04, FAA07, 201, 210
Chepurnov, A. RPA19, 1096
Chepurnov, A.S. FAG12, RAR04, 105, 3361
Cherenshchikov, S.A. WPA15, WPA16, 938, 939
Chernikov, V.I. WAR09, 1918
Chernogubovsky, M.A. WPP04, 1663
Chertok, I. TPE09, 1316
Chertok, I.L. TAC06, 143
Chesnokov, Yu.A. MPG10, WAR20, WAR21, 426, 1948, 1949
Chester, N.S. FAP06, FAP07, 1337, 1340
Chiang, R. RAQ04, 3294
Chiaveri, E. FAE11, 1509
Chin, A. TPG07, 174
Chin, Y.H. TPC08, WAC07, WAC08, 2613, 3082, 3085
Chiou, T.C. RAB02, RAB08, 761, 773
Chirkov, P.N. FAB02, 2792
Cho, M.H. TAR07, RPA06, TAQ15, 813, 1061, 1556
Cho, Y. TAP05, TPQ22, TPQ23, 363, 3001, 3004
Cho, Y.S. FAA10, 216
Cho, Yanglai RAR25, 3412
Choi, J. TAR07, RPA06, 813, 1061
Choi, Sewan RPP11, 1985
Chojnacki, E. WPB11, WPB12, WPQ02, RAQ04, 976, 979, 1720, 3294
Chou, P.J. MPQ13, WAC09, WAC10, 2479, 3088, 3091
Chou, W. WAP02, WAP03, MPB10, TPQ15, 437, 440, 2294, 2983
Chowdhary, M. MPR14, RAE11, 2268, 2417
Chu, C.C. MPQ26, RAR05, 2515, 3364
Chu, C.-C. TPC15, 2634
Chu, W.T. RAE04, 2394
Chubar, O.V. RAE06, WXE08, 2402, 2447
Chubarov, O. RPA19, 1096
Chubarov, O.V. RAR04, 3361
Chumakov, S.N. TAC06, RPP08, 143, 1979
Chung, K.H. FAA10, 216
Chung, S.C. RAR05, 3364
Chung, Y. MPQ03, MPQ08, TPC03, RPQ15, RPQ16, 2452, 2467, 2598, 2699, 2702
Chupp, W. TPA10, 3220
Church, M. TAR16, 834
Church, Mike RPG07, 333
Ciardullo, D.J. MPQ30, 2518
Cieslik, W. MPQ11, 2476
Ciocci, F. TPG11, 186
Clark, D.C. WPA08, 923
Clark, G.S. RPG12, 348
Clarke, J.A. TPG09, WAC23, 180, 3128
Claus, J. FAP11, 1352
Claus, R. RAE12, RPQ01, RPQ05, 2420, 2660, 2672
Clayton, C. TPB18, 2569
Clayton, C.E. WAG08, RAB01, RAB02, RAB04, RAB05, 637, 758, 761, 767, 770
Clendenin, J. MPE10, WPC21, 887, 1043
Clendenin, J.E. MPE08, WPC18, 877, 1033
Cleveland, E.K. FAG05, 83
Clifft, B.E. TPC12, 2625
Cline, D. TAA28, 2135
Cline, D.B. TAB06, WPG11, RAB20, TAR21, 119, 520, 790,

846
Codutti, A. FAQ19, 1432
Colby, E. WPB05, WPB08, 957, 967
Colestock, P. WPP01, RAP21, WAB01, RAQ24, 1655, 2934, 3016, 3340
Colestock, P.L. TAG04, WAC01, 2757, 3067
Colestock, Patrick L. WAC02, 3070
Collier, P. WAP12, WAP13, RAA10, RAA11,RAA12, RAA13, 464, 467, 545, 548, 551, 554
Collins, J. TPB24, 2583
Colton, E. WAC29, 3146
Coluzza, C. FAR06, 272
Comunian, M. RPC10, 719
Conde, M. WAG06, WPB08, WPB11, 631, 967, 976
Conkling, C.R. MPA16, 2226
Connolly, R. RPR19, WPP07, 1161, 1669
Connolly, R.C. RPR22, TPC06, 1167, 2607
Cooper, R. WAC29, 3146
Cooper, Ronald WPB15, 985
Corbett, J. RPQ21, RPQ22, RAQ17, 2714, 2717, 3323
Corcoran, P. TAE06, 1201
Corlett, J. RPC02, WPR14, MPC01, RAE12,RAE13,RPQ08, TPQ16, 701, 1818, 2317, 2420, 2423, 2681, 2986
Corlett, J.N. WXE06, 2441
Corley, J.P. TAE06, 1201
Cornacchia, M. FAA25, RAA18, RAQ17, 243, 564, 3323
Cornelis, K. WAP12, WAP13, RAA11, RAA17,RAA20,FAC03, 464, 467, 548, 560, 570, 2841
Corredoura, P. RPQ02, RPQ03, RPQ05, 2663, 2666, 2672
Corsini, R. RPC09, RPC11, 716, 722
Corvin, C. TAA16, 2114
Cosso, R. FAE11, 1509
Couillaud, C. RAG06, 3170
Cours, A. RPA11, 1073
Cours, Alexander TAQ16, 1559
Coverdale, C.A. RAB01, 758
Cox, G. WAG06, WPB11, 631, 976
Craddock, M.K. FAB14, 2823
Craddock, W. TAA28, 2135
Crandall, K.R. RPG10, 342
Crane, G. TAR18, 840
Crawford, J. WAP04, 443
Crawford, K. RPQ29, 2732
Cremer, T. FAP20, 1378
Crofford, M. WXE01, 2429
Cromer, K.D. RAP01, 2880
Cros, B. WAG07, 634
Crosbie, E. TAP05, RAA29, RAG05, 363, 597, 3167
Crosbie, E.A. RAR26, 3415
Crowe, T. TPC04, 2601
Cruikshank, P. RPE02, 1999
Cutolo, A. TPG11, 186
Cyvoct, G. MPG09, 423
d'Amico, E.T. RPC12, 725
D'Auria, G. TPG11, FAA13, FAR21, 186, 222, 309
D'Ottavio, T. MPR20, 2279
D'Yachkov, M. WAC20, 3119
Daclon, F. TPG11, FAR21, 186, 309
Dalin, J.-M. RPE02, 1999
Daly, E. TAA22, MPC01, 2129, 2317
Daly, E.F. MPP08, MPP10, MPP12, MPP20, 2051, 2057, 2064, 2075
Dangor, A.E. WAG08, 637
Danilewsky, A.N. FAR06, 272
Danilov, O. TAQ21, 1569
Danly, B.G. MPE12, 893
Darrow, C.B. WAG08, RAB01, 637, 758
Datskov, V.I. MPP01, 2034
Dattoli, G. TPG11, TPC03, 186, 2598
Davies-White, W. RAA04, 530
Davis, P. WPC20, RPA21, RPA22, 1039, 1102, 1105
Dawson, J. WAG09, TPC16, 640, 2637
De Angelis, A. TPG11, 186
De Brion, J.P. RAG06, 3170
de Groen, P. TAQ12, 1547
de Jager, C. RPG06, 330
de Leeuw, R.W. WAQ19, WAQ20, RPP04,RPQ31, 1882, 1885, 1970, 2738
De Martinis, C. TPC10, 2619
De Mascureau, J. TAE09, 1210
De Rijk, G. RAA11, 548
de Rijk, G. WAP12, WAP13, 464, 467
de Wijs, M.C.J. WAQ19, 1882
Deadrick, F. RPC18, TAR17, WPA02, TAE01, 743, 837, 905, 1178
Deadrick, F.J. TAR14, TPB14, 828, 2557
DeBarger, S. FAP16, 1366
Debraine, A. WAG07, 634
Decker, C.D. RAB01, RAB02, 758, 761
Decker, F.J. WAG11, RPB04, WAC17, 646, 665, 3109
Decker, F.-J. RPB02, WPR15, TPC20, RAP15,RAP16,RAP17, WAB05, WAB07,RAQ03, 659, 1821, 2646, 2919, 2922, 2925, 3025, 3031, 3291
Decker, G. FAR13, FAR19, MPQ03, MPQ08,MPQ10,RPQ16, 290, 303, 2452, 2467, 2473, 2702
Decker, Glenn RAR24, 3409
Decking, W. FAA02, FAB01, FAC19, 195, 2789, 2874
DeCobert, J. WAA16, 1260
Degen, C.M. TPB12, 2551
Dehnel, M. WAQ07, 1858
Dehning, B. WAP14, RAA19, 470, 567
Deitinghoff, H. WPA04, RPR06, RPR18, 911, 1131, 1158
Dejus, R. TPC03, 2598
Delahaye, J.P. RPC10, 719
Delahaye, J.-P. RPC09, 716
delaRama, F. TAE01, 1178
Dell, G.F. MPC05, FAB20, 2327, 2829
Deliwo, J. MPE05, WPC12, 871, 1022
Delsart, Ph. TAE09, 1210
Deluen, J.-P. RAA15, 557
Demko, J.A. MPP01, 2034
Den Hartog, P. MPP16, 2072
Deng, D. WAC24, 3131
Deng, D.P. WPP07, WPQ19, 1669, 1765
Deng, D.-P. MPB08, RAQ22, RAR29, 2288, 3334, 3421
Deppe, G. TPP11, 1639
Derenchuk, V. WPC08, RAP22, RAQ24, 1010, 2937, 3340
Desavouret, E. FAP06, FAP07, MPB06, 1337, 1340, 2285
Desmons, M. WPB22, 998
Despe, O. FAQ18, 1429
Deviatilov, V. WAA18, 1266
Devin, A. TAE09, TPC17,

1210, 2640
Dewa, H. FAR08, RPA13, WAQ01, 278, 1079, 1843
Dey, J. WPP08, WPP09, WPP23, RAQ13, 1672, 1675, 1714, 3312
Di Bona, A. WPC23, 1049
Di Crescenzo, J. RAG06, 3170
Dickey, C. FAA08, RPA17, WAA10, MPA11, 213, 1090, 1248, 2217
Dieperink, J. RAA15, 557
Dieulot, J.M. WAG07, 634
Dikansky, N. WPG06, TAR11, 500, 819
Dikansky, N.S. TAC06, WAA17, 143, 1263
DiMarco, J. FAP06, FAP07, 1337, 1340
Dinehart, M.R. WAQ26, 1897
Dinkel, J. WAA05, WAR01, 1236, 1900
Dinkel, J.A. WAA07, 1239
Dipace, A. TPG11, 186
Diviacco, B. FAQ19, 1432
Dobbe, N. MPQ17, 2491
Dobbins, J.A. RAE14, 2426
Dobeck, N. RPP06, 1973
Dobrovodsky, J. TAA18, 2120
Dodson, G. RPG05, 327
Dohlus, M. RPB15, RPB16, TAQ06, WPP05,WAE13, MPC16, 692, 695, 1533, 1666, 2190, 2345
Doinikov, N. MPC21, 2359
Dolbilov, G.V. WAA20, TAQ34, 1272, 1605
Dolique, J.-M. TPR04, TPR05, 3245, 3248
Donald, M. RAA22, 576
Donald, M.H.R. RAA27, 591
Donaldson, A.R. RPB05, WAA11, WAR06,RPP07, 668, 1251, 1915, 1976
Donaldson, T. WAQ15, 1876
Dooling, J.C. RAQ16, 3320
Doolittle, L. MPR13, MPR14, 2265, 2268
Doornbos, J. RPG12, 348
Doose, C. TPE08, 1310
Doria, A. TPG11, 186
Douglas, D. FAA25, WAQ14, 243, 1873
Douglas, D.R. WXE01, 2429
Dovbnya, A.N. WPA15, WPA16, WPB16, 938, 939, 988
Dow, K. RPG05, 327
Dowell, D.H. FAA27, FAA28, WPB20, 248, 251, 992
Dowling, D.T. TAP07, WAQ26, 366, 1897
Doyle, E. FAE07, 1497
Drago, A. RAE12, RPQ01, 2420, 2660
Drees, A. RAA19, 567
Dressler, J. RAA03, 527
Drevlak, M. RPB14, 689
Drury, M. FAE12, 1512
Du, W. FAP01, 1322
Dugardin, F. TAB04, 116
Dunbar, A. WAB04, 3022
Dunham, B. MPR15, TPC07, 2271, 2610
Dunham, B.M. WPC17, 1030
Dunnam, C.R. RAE14, 2426
Dunning, F.B. WPC21, 1043
Durand, R. TPP04, WPQ02, 1623, 1720
Durfee III, C.G. WAG04, 621
Durieu, L. TAP14, 386
Durkin, A.P. RPR07, 1134
Dutto, G. RPG12, MPE03, WAQ07, 348, 864, 1858
Dykes, D.M. WPQ18, WAC22, 1762, 3125
Dylla, F. WPA17, 942
Dylla, H.F. FAG11, FAA25, 102, 243
Early, R. RPC02, 701
East, G. RAP21, RAP22, RAQ23, RAQ24, 2934, 2937, 3337, 3340
Ecklund, S. RPB01, RPC01, 656, 698
Ecklund, S.D. WPC18, 1033
Edighoffer, J. RPA26, 1116
Efimov, S. FAR17, RAA08, 299, 542
Egawa, K. RAA33, 603
Ehrlich, R. FAE13, 1515
Ehrlichmann, H. RPE08, 2017
Eichenberger, C. WAA19, 1269
Eichhorn, K.D. FAR06, 272
Eigenmann, B. FAR06, 272
Einfeld, D. TPG08, FAR06, WPQ24, 177, 272, 1776
Ekelöf, Tord TPC11, 2622
Elias, L.R. FAA29, 254
Elizondo, J. WAA19, TAA20, 1269, 2123
Elleaume, P. TPE10, 1319
Ellison, M. WPP20, WPP21, RAP21, RAP22,WAC12,RAG10, RAQ23, RAQ24, 1705, 1708, 2934, 2937, 3094, 3182, 3337, 3340
Ellison, T. TPB24, RAP22, 2583, 2937
Elsener, K. WAP14, 470
Emamian, M. FAA08, TAA02, 213, 2081
Emery, L. MPR01, MPB17, MPQ10, 2238, 2309, 2473
Emma, P. WAG11, RPB01, RPC03, RPC06,WAB07, 646, 656, 704, 707, 3031
Emma, Paul WAG01, 606
Emoto, T. TAQ08, 1539
Enchevich, I.B. WPP18, 1699
Engels, O. WPA04, WPA05, 911, 914
Engwall, D. FAG11, WPA17, 102, 942
Enjeti, Prasad N. RPP11, 1985
Enomoto, A. TAQ08, TAQ25, TAA04, 1539, 1578, 2087
Erdman, K. WAQ07, 1858
Eremeev, I.P. FAG10, TAC11, 98, 146
Erg, G.I. FAQ17, 1426
Erickson, R. RPA24, FAP16, 1111, 1366
Ermakov, D. RPA19, 1096
Ermakov, D.I. RAR04, 3361
Erochin, A. FAQ06, 1399
Escallier, J. FAQ03, 1393
Esin, S.K. RPR24, RPR25, RAE08, 1173, 1175, 2408
Estrin, B. WAA17, 1263
Etzkorn, F.J. WPQ26, 1781
Evans Jr., K. MPQ03, 2452
Evans, L.R. FPD04, 40
Everett, M. RAB05, 770
Everett, M.J. RAB04, 767
Evtushenko, Yu.A. FAQ17, 1426
Eyharts, Ph. TAE09, 1210
Eyl, P. TAE09, 1210
Eylon, S. TAR14, WPA02, WPA09, TAE01,TAE11,WAQ04, 828, 905, 926, 1178, 1216, 1852
Ezura, E. FAE09, TPP16, WPQ08, WPQ17,WPR05, WPR09, RPQ06, 1503, 1652, 1735, 1759, 1797, 1806, 2675
Fabris, A. FAR21, WPQ04,

TAG05, 309, 1723, 2762
Fabris, R. FAR21, 309
Fackler, O. RAA03, 527
Fahmie, M. RPQ08, 2681
Fainberg, Ya.B. RAB15, WAA02, WAA03, 782, 1230, 1233
Fallis, M.C. WPR20, 1835
Faltens, A. FAP17, FAP18, TPA10, 1369, 1372, 3220
Fan, T.C. FAQ26, 1450
Fang, C.S. MPQ32, 2524
Fang, S. MPR16, 2273
Fang, S.X. WAB20, 3064
Fang, Si J. FAP05, 1334
Fang, Ye TAR22, 850
Fant, K. WPR08, 1803
Farias, R.H.A. FAP14, 1361
Farkas, Z.D. WPR15, 1821
Farkhondeh, M. RPG05, 327
Farvacque, L. TPG05, 167
Farvid, A. MPP09, 2054
Fateev, A.A. WAA20, TAQ34, 1272, 1605
Fathizadeh, M. TAP05, 363
Faugeras, P. TPE03, 1288
Faugier, A. WAP12, WAP13, RAA11, 464, 467, 548
Faure, J. FAR14, 293
Fawley, W. FAP17, 1369
Fawley, W.M. FAA12, RAB03, FAP18, TPA10, 219, 764, 1372, 3220
Fazio, Michael V. FAE06, 1494
Fedin, O.L. MPG10, 426
Fedotov, A.P. RPR07, 1134
Fedotov, Alexei V. TPR12, 3266
Fedotov, Yu. MPR11, 2259
Feerick, B. WAQ15, 1876
Feldl, E. TPC04, 2601
Feldman, Donald W. WPB15, 985
Fellenz, B. MPQ13, 2479
Feng, W. WAR12, 1927
Feng, W.Q. WAA15, 1257
Ferdinand, R. RPR11, RAG07, 1146, 3173
Ferguson, M. RPP12, 1988
Ferianis, M. TPG11, FAR21, 186, 309
Ferioli, F. WAP13, 467
Fernow, Richard MXG03, 53
Ferrario, M. WAC13, 3097
Feschenko, A.V. RAE08, 2408
Fessenden, R.W. TAB17, 131
Fessenden, T. TAR17, 837
Fessenden, T.J. TAR13, TAR14, TPB14, 825, 828, 2557
Fidecaro, G. WAP14, 470
Fieguth, T. WAQ15, 1876
Field, R. TAG01, 2742
Field, R.C. WXE07, 2444
Fietier, N. FAG09, 95
Filatov, B.A. WAA21, 1274
Filtz, M. MPC28, 2373
Fink, C.L. FAG14, 110
Fiorentini, G. WPB10, 973
Firjahn-Andersch, A. WPA03, 908
Fischer, C. RPC14, TPC21, 731, 2649
Fischer, Henk WAB06, 3028
Fischer, W. TAG07, 2768
Fisher, A. TPG14, RAA04, 192, 530
Fitzgerald, D. WPC10, WAC29, RAR23, 1016, 3146, 3406
Fitzgerald, J.B. TPG09, RAE10, 180, 2414
Flanz, J.B. RPE03, 2004
Flechtner, D. WPC19, 1036
Fleckner, K. RPA26, 1116
Fliflet, A.W. TAQ37, 1611
Flood, R. RPP13, 1991
Flora, R. WAE07, 2172
Flöttmann, K. TAA08, TAG01, 2096, 2742
Flynn, G. FAE13, RAR18, 1515, 3391
Fockler, J. WAA19, 1269
Foelsche, H. FAQ15, 1420
Foelsche, H.W. FAP11, 1352
Foley, M. FAG06, WPP01, 86, 1655
Fomin, M. WPP11, 1681
Fong, K. MPR16, 2273
Forest, E. RAA22, RAA25, FAB06, 576, 585, 2804
Forsyth, E.B. WAA15, WAR10, WAR12, 1257, 1921, 1927
Foster, G.W. MPG11, WAP16, TPE05, 428, 473, 1298
Foster, J. WPB06, 961
Foster, W.B. FAP21, 1381
Fouaidy, M. TPP09, TPP11, TPP14, 1632, 1639, 1648
Fougeron, C. WPQ26, 1781
Fowkes, W.R. FAE07, TAQ28, 1497, 1587
Fowler, W. MPG01, 391
Fox, J. RAA04, RAE12, RAE13, RPQ01, RPQ08, 530, 2420, 2423, 2660, 2681
Fox, T. MPR13, 2265
Frachon, D. FAQ17, FAQ18, 1426, 1429
Franks, R.M. WPQ06, 1729
Franzke, B. MPC15, 2342
Freund, A. WAP14, 470
Fricks, R. MPA11, 2217
Friedman, A. TAR14, TAR15, TAR17, FAQ17, TPR19, 828, 831, 837, 1426, 3282
Friedman, Aharon RPQ14, 2696
Friedrich, L. FAR06, 272
Friedsam, H. TAP05, TAA03, 363, 2084
Friesel, D. WPP20, WPP21, RAQ24, 1705, 1708, 3340
Friesel, D.L. RPG08, TAP03, WAQ08, 336, 357, 1861
Frisch, J. WAG11, MPE10, 646, 887
Fu, Shinian FAA21, RAQ25, RAQ26, 237, 3343, 3346
Fugitt, J. FAG11, FAA25, WPA17, RPQ30, 102, 243, 942, 2735
Fuja, R. RPA10, RPA11, MPQ08, MPQ10, 1070, 1073, 2467, 2473
Fuja, R.E. TPC01, 2595
Fujino, T. TPP07, 1629
Fujita, H. FAR08, RPA13, WAQ01, 278, 1079, 1843
Fukuma, H. RAA33, 603
Fukutomi, M. TPP16, 1652
Fullett, K. WAR17, WAR18, 1939, 1942
Funahashi, Y. TPP07, 1629
Funakoshi, Y. MPQ31, WAC08, 2521, 3085
Furman, M. RPC02, TPQ16, 701, 2986
Furman, Miguel A. RAP14, 2916
Furuya, T. TPP03, 1620
Fusellier, J. WAG07, WPB22, 634, 998
Gai, W. WAG06, WPB11, MPQ11, 631, 976, 2476
Galayda, J. RPQ16, 2702
Galayda, John N. MAD02, 4
Gallardo, Juan C. MXG03, WPB21, 53, 995
Gallerano, G.P. TPG11, 186
Gamo, N. TPP03, 1620
Ganetis, G. TPE04, FAQ02,

FAQ03, FAQ04,FAQ15, 1293, 1390, 1393, 1396, 1420
Ganetis, G.L. TAA09, 2099
Gangeluk, M. WPR13, 1815
Gao, J. RPA03, 1055
Gao, Jie WPQ01, 1717
Garcia, R.C. TPC06, 2607
Gardner, C.J. TAP11, TAP13, 378, 383
Garnett, R.W. RAG11, 3185
Garoby, R. MPG09, 423
Garosi, F. TPG11, 186
Garrel, N. WAP12, RAA15, 464, 557
Garren, A. WPG11, 520
Garren, A.A. TAB06, 119
Garvey, J.D. FAP06, FAP07, 1337, 1340
Garvey, T. WPA14, WPB22, 935, 998
Gavaggio, R. MPP15, 2069
Gavrilov, N.G. FAQ17, 1426
Gay, T. WPC21, 1043
Gayet, Ph. MPP02, 2037
Geisik, C. WPC10, 1016
Gelato, G. MPG09, 423
Gelfand, N.M. RAB19, 787
Gelfand, Norman M. WAP07, 452
Geller, J. WAR11, RPP02, 1924, 1964
Geng, X. MPA01, 2193
Genova, L. RAA04, 530
Georges, J.P. TAB04, 116
Georges, P. WPB01, 945
Geschonke, G. TPP12, 1642
Gevchuk, A. FAR17, 299
Ghiorso, W. TPA10, 3220
Ghosh, A. TPE04, FAQ03, FAQ04, 1293, 1393, 1396
Giacuzzo, F. MPP04, 2042
Giannessi, L. TPG11, 186
Giannini, M. TPG11, FAR21, 186, 309
Gilgenbach, R.M. TAQ32, 1599
Gillespie, G.H. RPR20, 1164
Gillespie, George H. FAG13, MPB14, 107, 2300
Gilpatrick, J.D. RPR19, RPR22, TPB16,TPB22, 1161, 1167, 2563, 2580
Giordano, G. RPC17, 740
Giovannozzi, M. FAC06, 2847
Giove, D. TAA07, TPC10, 2093, 2619
Giovenale, E. TPG11, 186
Gladkikh, P. FAR17, 299
Glass, H. TPE05, 1298
Glass, H.D. FAP05, FAP06, FAP07, MPB05,MPB06, 1334, 1337, 1340, 2282, 2285
Glazov, A. WPC13, WPR19, 1025, 1833
Glenn, J.W. TAP13, WAR13, 383, 1930
Glock, H.-W. RPB15, RPB16, 692, 695
Glover, E. TPG07, 174
Gluckstern, R. RPA04, 1058
Gluckstern, R.L. TPQ14, 2980
Gluckstern, Robert L. RAG09, TPR11,TPR12,RAR12, 3179, 3263, 3266, 3376
Gluskin, E. TPE06, FAQ17, MPP16, 1301, 1426, 2072
Goddard, B. RAA15, 557
Goderre, G. WAP08, 455
Goderre, G.P. WAP05, 446
Godfrey, G. WAQ15, 1876
Godlove, T.F. TAE10, 1213
Godlove, Terry F. TAA17, 2117
Godot, J.C. RPC10, 719
Goffeney, N. RPC17, 740
Gold, C. RPA10, 1070
Gold, S.H. TAQ37, 1611
Goldberg, D.A. WPQ13, 1747
Goldman, M.A. TAA09, 2099
Goldstein, J.C. FAA16, 228
Golkowski, Cz. TAQ01, 1518
Golubev, I.I. WAA20, 1272
Golubev, V. WPC03, 1004
Goncharov, A.D. TAC06, RPP08, 143, 1979
Gonichon, J. MPE12, 893
Gonin, I.V. RPR01, 1119
Goral, J. RPA11, 1073
Gordeeva, M.A. MPG10, 426
Gordon, D. RAB04, RAB05, 767, 770
Gorelov, D.V. RPR01, 1119
Gorev, V.V. MPE06, 874
Gorin, M.Yu. WAR23, 1955
Gorniker, E. WPP11, 1681
Gorski, A. FAP03, 1328
Goto, A. WPC01, 1001
Gougnaud, F. WPB22, 998
Gournay, J.F. WPB22, 998
Govil, R. TPG07, RAB10, 174, 776
Gower, E. RPA26, 1116
Graber, J. FAE03, 1478
Gracia, J. RAA04, 530
Granatstein, V.L. TAQ17, TAQ18, TAQ19, 1561, 1563, 1566
Gras, J.J. TPC21, 2649
Grassi, R. FAC06, 2847
Grau, M.C. MPQ05, 2458
Graves, W.S. FAQ13, 1414
Gray, E.R. RAG11, 3185
Green, M. WPG11, 520
Green, M.A. TAB06, 119
Greene, A. TPE04, FAQ03, FAQ04, FAQ15, 1293, 1393, 1396, 1420
Greenly, John B. TAE07, 1204
Greenwald, Z. FAE13, TPA04, 1515, 3206
Grelick, A. RPA11, 1073
Grelick, A.E. RPA10, RPA14, RPE09, 1070, 1082, 2020
Greth, V.N. WAR20, 1948
Gridasov, V. FAQ06, 1399
Grieser, M. RPR06, 1131
Grigor'ev, Yu.N. RAA07, RAQ28, 539, 3349
Grimm, T. RPG11, 345
Grimmer, J. RPE09, 2020
Grishin, V.K. FAG12, FAA14, 105, 225
Gröbner, O. RPE02, 1999
Gromme, T. RAE03, 2389
Gross, G. WAR06, 1915
Grossberg, P. RAE03, 2389
Grosse-Wiesmann, P. RAA19, 567
Grote, D. TAR17, TAE01, 837, 1178
Grote, D.P. TAR13, TAR14, TAR15, WPA09,TPR19, 825, 828, 831, 926, 3282
Grote, H. RAA19, 567
Grudiev, A. MPB09, 2291
Grunder, Hermann A. MAD01, 1
Gubin, K. WAA17, 1263
Guckel, H. WPE02, 63
Gudkov, K. RPA19, 1096
Gudkov, K.A. FAG12, 105
Guharay, Samar K. MPC04, 2324
Guidi, V. RAE05, 2399
Guignard, G. RPC09, RPC12, RPC13, 716, 725, 728
Guinand, R. RAA15, 557
Guo, H. TAQ17, 1561
Guo, Z. TPQ03, 2955
Gupta, R. TPE04, FAQ04,

FAQ16, TAA09, 1293, 1396, 1423, 2099
Gupta, R.C. WAP10, 461
Gur'yev, M.P. MPG10, 426
Gurov, G. MPG06, 416
Güsewell, D. MPP02, 2037
Gusinskii, G.M. TAP16, 389
Gustafson, Dick TPE05, 1298
Gustavsson, J. FAA08, 213
Guy, F.W. RPG10, 342
Gyr, M. WAP14, WAQ24, 470, 1891
Haber, I. TAR15, TPR19, 831, 3282
Haberichter, W. TPC16, 2637
Habib, Salman RAG01, 3149
Habs, D. RPR06, 1131
Haddock, C. FAQ14, 1417
Haebel, E. TPP12, 1642
Haffmans, A.F. RAG14, RAQ20, 3194, 3329
Hafizi, B. TAQ37, 1611
Haga, K. RPQ23, 2720
Hagedoorn, H.L. WAQ19, WAQ20, RPP04,RPQ31, 1882, 1885, 1970, 2738
Hahn, H. TPQ02, 2952
Hahn, K.D. TPA10, 3220
Hahn, U. FAR07, 275
Haimson, J. RPC22, TAQ03, 755, 1524
Hairapetian, G. WPC20, RPA21, RPA22, 1039, 1102, 1105
Hakota, M. TAQ35, 1608
Hall, P.J. FAP06, FAP07, MPB06, 1337, 1340, 2285
Haller, M. FAR06, 272
Halling, M. RPC20, RPC21, TAG01, 749, 752, 2742
Hamilton, B. TPB24, RAP21, RAP22, RAQ24, 2583, 2934, 2937, 3340
Hammel, E. TPB07, 2542
Han, Bumsoo TAB09, FAR03, 122, 269
Han, D.H. WPR11, 1812
Hanna, B. WAR01, 1900
Hanna, S.M. RPA23, 1108
Hanne, G.F. WPC21, 1043
Haouat, G. RAG06, RAG07, 3170, 3173
Hardek, T. WAC29, 3146
Hardek, T.W. TAQ31, 1596
Harding, D.J. FAP04, FAP05, FAP06, FAP07,FAP09,MPB05, MPB06, 1331, 1334, 1337, 1340, 1346, 2282, 2285
Harkay, K. TAP05, TPQ22, TPQ23, 363, 3001, 3004
Harrison, M. MPG03, TAA09, 401, 2099
Harrison, M.A. MPG12, 431
Hartill, D.L. RAE14, 2426
Hartley, R. FAA19, 234
Hartley, R.A. FAA31, 260
Hartman, S. RPB02, RPC20, WXE07, TAG01, 659, 749, 2444, 2742
Hartman, S.C. RPB04, TPC29, 665, 2655
Hartnagel, H.L. MPC15, 2342
Hartung, W. FAE13, TPA04, RAQ04, RAR18,RAR19, 1515, 3206, 3294, 3391, 3394
Harwood, S.L. WXE01, 2429
Hasegawa, K. RPG09, 339
Haseroth, H. MPG09, 423
Haseroth, H.D. MPG05, 411
Hashimoto, S. FAQ21, 1438
Hathaway, D. MPP12, MPP20, 2064, 2075
Hawkins, A. WAA16, 1260
Hayakawa, A. WXE07, 2444
Hayano, H. RPA20, WPR03, TPC05, TAG01, 1099, 1791, 2604, 2742
Hayashi, E.K.C.S. MPQ33, 2527
Hayashi, S. FAP13, 1358
Haynes, D.L. WAQ26, TPC18, 1897, 2643
Haynes, W. Brian FAE06, 1494
Hays, S. WAE07, 2172
Hays, T. FAE13, TPP02, WPQ02, 1515, 1617, 1720
Hayward, T.D. FAA27, FAA28, WPB20, 248, 251, 992
Hedblom, K. WPP20, WPP21, WAQ08, RAP21, 1705, 1708, 1861, 2934
Heese, R. FAR10, 284
Heifets, S. MPC01, MPC08, TPQ16, 2317, 2333, 2986
Heifets, S.A. TAA22, MPC02, MPC03, MPC18, 2129, 2319, 2321, 2351
Heim, J. RAA03, 527
Heimlinger, G. TAG01, 2742
Heine, E. TAQ12, MPQ17, 1547, 2491
Heinrichs, G. TPB20, 2574
Helm, R. RAA22, RPC06, RPC07, RPC20,TAA08,TAG01, 576, 707, 710, 749, 2096, 2742
Helvajian, H. FAG11, 102
Hemelsoet, G.H WAE09, 2178
Hémery, J.-Y. TAP14, 386
Hemmer, M.F. TAA09, 2099
Henderson, S. FAE13, 1515
Henderson, T. FAP01, 1322
Hendrickson, L. RAE03, 2389
Hendrickson, L.J. WAG11, RPB03, 646, 662
Henestroza, E. RPC16, RPC17, RPC19, WPA02,WPA09,TAE01, TAE11, MPC01,MPC08,TPA10, 737, 740, 746, 905, 926, 1178, 1216, 2317, 2333, 3220
Henke, H. TAQ30, WPQ14, WAB11, 1593, 1750, 3043
Henkel, D.P. FAG11, 102
Hentges, M. MPP01, 2034
Herold, W. WPA12, 929
Herr, W. WAP14, WPG09, 470, 514
Herrup, D.A. TPQ25, TPQ26, 3007, 3010
Hershcovitch, A. WPC09, 1013
Herz, P. TPB07, 2542
Hettel, R. MPQ22, RPQ21, RPQ22, 2506, 2714, 2717
Heutenik, B. TAQ12, 1547
Heydari, Huschang WAP09, 458
Higashi, Y. WPQ15, 1753
Higgins, D.S.G. WPQ18, 1762
Higgins, S. MPR13, 2265
Higo, T. FAQ08, WPQ15, WPR02, WPR03, 1405, 1753, 1788, 1791
Higo, Toshiyasu FAE02, 1474
Higuchi, A. RAQ06, 3300
Higuchi, T. TPP07, 1629
Hilaire, A. WAP12, WAP13, 464, 467
Hill, B.W. RPR20, 1164
Hill, Barrey W. MPB14, 2300
Hill, S.F. WAC21, 3122
Hilleret, N. TPP12, 1642
Himel, T. RAE03, 2389
Hindi, H. RAE12, 2420
Hinode, F. WPQ16, WPR02, WPR03, TPC05, 1756, 1788, 1791, 2604
Hipple, R. WPA01, TAE01, 902, 1178
Hiramoto, K. TAB03, WPQ21,

113, 1770
Hirano, K. TAQ08, 1539
Hirata, K. RAP02, 2883
Hirata, Y. WPR02, 1788
Hirota, J.I. TAB03, WPQ21, 113, 1770
Hizanidis, K. RAQ01, 3285
Ho, C. WPB11, 976
Ho, C.H. WPB07, 964
Hoag, H. RPA04, WPQ05, 1058, 1726
Hoag, H.A. RPA23, 1108
Hobson, B. RAA03, 527
Hodges, T. RPG12, 348
Hodgkins, D. MPE04, WPA08, 867, 923
Hodgson, J. WPR08, 1803
Hoeflich, J. RAE12, 2420
Hoffstätter, G.H. FAB07, 2807
Hofler, A. MPR13, 2265
Hofmann, A. RAA17, RAA18, RAA20, FAC03, 560, 564, 570, 2841
Hogan, B. TAQ18, TAQ19, 1563, 1566
Hogan, M. FAA23, RPA21, RPA22, 240, 1102, 1105
Hogrefe, R. TPE08, 1310
Hohbach, R. TAQ33, 1602
Holdener, F.R. MPP12, MPP20, TAA22, 2064, 2075, 2129
Holmes, C. WAA19, 1269
Holmes, S. MPG01, 391
Holmes, S.D. WAP01, 434
Holmquist, T. RAE14, 2426
Holsinger, R.F. TPE07, 1305
Holt, J. RPC20, 749
Holt, J.A. WAP01, WAP08, RPC21, TAG01,WAC01,434, 455, 752, 2742, 3067
Holtkamp, N. FAR06, RPB12, RPB13, RPB15,RPB16,WPA12, WPP05, MPC16,272, 683, 686, 692, 695, 929, 1666, 2345
Holtzapple, R.L. WXE05, WAB05, WAC04,WAC17,2438, 3025, 3073, 3109
Honda, T. RPQ23, 2720
Honecker, V. FAR06, 272
Hopster, H. WPC21, 1043
Horan, D. TAP05, RPP12, 363, 1988
Hori, T. WPC22, MPA07, 1046, 2208
Houck, T. RPC16, RPC17, WPC16, 737, 740, 1027
Houck, T.L. TAQ03, 1524
Hovater, C. FAE12, TPC26, RPQ29, 1512, 2652, 2732
Howell, J. TAR08, 816
Hower, N. FAA08, RPA17, TAA02, MPQ06, 213, 1090, 2081, 2461
Hower, Nelson WPA13, 932
Hoyer, E. FAQ24, FAQ25, 1444, 1447
Hoyt, E. MPP09, MPP12, MPP20, 2054, 2064, 2075
Hoyt, M. MPP09, MPP12, MPP20, 2054, 2064, 2075
Hseuh, H.C. TAP11, TAP12, MPP11, 378, 381, 2060
Hsieh, H. RAA05, RPA26, 533, 1116
Hsiung, G.-Y. TPC15, 2634
Hsu, I. TAA28, 2135
Hsu, Ian MPQ26, TPC15, RAR05, 2515, 2634, 3364
Hsu, K.T. FAA04, FAA07, RAA23, RAA24,MPR10, MPQ16, MPQ19,MPQ32,TPB29, TPQ08, TPQ09,TPQ10,201, 210, 579, 582, 2256, 2488, 2497, 2524, 2592, 2965, 2968, 2971
Hsu, R.-C. TPC15, 2634
Hsu, S.Y. WPB07, 964
Hsue, C.S. RAA24, TAR04, TPQ09, TPQ10, 582, 804, 2968, 2971
Huang, Gloria MPR10, 2256
Huang, H. TPA06, 3212
Huang, J.Y. TPG06, 171
Huang, N. RAA21, WAC27, 573, 3140
Huang, Zhibin FAA21, RAQ25, RAQ26, 237, 3343, 3346
Huang, Zhirong RAQ18, 3326
Huffman, G. FAE07, 1497
Hughes, Thomas P. TAE08, 1207
Hülsmann, P. RPB15, RPB16, 692, 695
Humbert, J. FAP03, 1328
Hümmer, K. FAR06, 272
Humphries, D. FAQ24, FAQ25, 1444, 1447
Hunt, D. MPP13, 2067
Hustache, R. WAP14, 470
Hutson, R. WAC29, 3146
Hutson, R.L. TAR12, 822
Huttel, E. FAR06, 272
Hutton, A. TPC26, 2652
Hwang, J.I. WPB07, 964
Hwang, O.H. TAQ14, 1553
Hwu, K.H. MPQ19, 2497
Iazzourene, F. FAR21, TAG05, 309, 2762
Ieiri, Takao TPB17, 2566
Igarashi, Y. TAQ25, 1578
Igarashi, Z. WPC07, 1007
Ignatyev, A. TAB13, TAQ23, TAQ24, 125, 1572, 1575
Ihloff, E. RPG05, 327
Iida, S. TPP03, 1620
Ikegami, K. WPC07, 1007
Ikegami, M. FAR08, RPA13, WAQ01, 278, 1079, 1843
Iljinov, A.N. RPR01, 1119
Imai, Y. FAQ08, 1405
Imanishi, A. RPG13, 351
Imel, G.R. TAC12, 149
Inagaki, S. TPP16, 1652
Inaguchi, T. FAQ08, 1405
Ingalls, W. WPC10, 1016
Ingwersen, Pete TAE07, 1204
Inman, T.K. RPA24, 1111
Ino, H. RPG09, 339
Inoue, H. TPP07, 1629
Inoue, M. FAR08, RPA13, RPA18, WPQ21,WAQ01,278, 1079, 1093, 1770, 1843
Irwin, J. RAA22, RAA25, RAA26, RAA27,RPC01,RPC06, RPC07, RPC08,RPC20,TAA08, TAG01, TAG06,FAC18,RAP09, RAP11, RAP12, 576, 585, 588, 591, 698, 707, 710, 713, 749, 2096, 2742, 2765, 2871, 2904, 2910, 2913
Irwin, John MPC31, 2376
Irwin, M. WPQ13, 1747
Isagawa, S. TPP16, 1652
Ishi, Y. TAP04, TPP03, 360, 1620
Ishida, T. MPQ18, 2494
Ishihara, N. TAG01, 2742
Ishii, H. MPQ31, 2521
Ishkhanov, B. RPA19, 1096
Ishkhanov, B.S. FAG12, FAA14, 105, 225
Issinsky, I.B. WAR09, FAC12, 1918, 2863
Ito, I. TAQ35, 1608
Ito, N. RPG09, 339
Itoh, Y. MPA07, 2208
Ivanov, A. TAC16, 152
Ivanov, A.A. WAR20, 1948
Ivanov, A.S. TAE13, 1222

Ivanov, I.N. WAA20, 1272
Ivanov, P. RAA31, 600
Ivanov, P.M. FAQ17, FAQ18, 1426, 1429
Ivanov, S. WPP05, MPC16, TPQ01, TPQ04, 1666, 2345, 2949, 2958
Ivanov, Yu.D. RPR07, 1134
Ivers, J.D. WPC19, TAE12, 1036, 1219
Iverson, R. RPC20, TAA28, WXE07, TAG01, 749, 2135, 2444, 2742
Iwashita, Y. FAR08, RPA13, RPA18, WPQ21, WAQ01, 278, 1079, 1093, 1770, 1843
Izawa, M. TPP03, WPQ07, WPR04, 1620, 1732, 1794
Jablonka, M. WPA14, WPB22, 935, 998
Jackson, A. FAA03, FAA05, RPC02, 198, 204, 701
Jackson, G. MPG11, WAP16, TPE05, WAR19, MPQ13, RAP20, WAC09, WAC10, 428, 473, 1298, 1945, 2479, 2931, 3088, 3091
Jackson, L.T. RPP01, RPP07, 1961, 1976
Jackson, T. RAA04, FAQ24, 530, 1444
Jacob, J. TPG05, FAR06, 167, 272
Jacobs, K. RPG05, RAA31, 327, 600
Jacquemard, B. WPB22, 998
Jacquet, F. WAG07, 634
Jaeschke, E. RPR06, FAQ12, 1131, 1411
Jaffery, T.S. FAQ32, 1465
Jagger, J. FAP03, 1328
Jain, A. WAP10, TPE04, FAQ03, FAQ04, FAQ16, TAA09, 461, 1293, 1393, 1396, 1423, 2099
Jamison, R.A. RPR20, 1164
Jan, G.J. MPR10, MPQ16, TPB29, 2256, 2488, 2592
Jang, J.S. TPG06, 171
Jarvis, H. WPR15, 1821
Jason, A. WAC29, 3146
Jason, Andrew J. TAE02, 1183
Jayamanna, K. MPE03, WAQ07, 864, 1858
Jean, Benedikt FAG03, 75
Jeanjean, J. RPC20, TAG01, 749, 2742
Jeanneret, B. FAC04, 2844
Jenner, D. WPP20, WPP21, 1705, 1708
Jensen, C. WAR01, 1900
Jensen, C.C. WAA07, 1239
Jensen, D. FAQ08, 1405
Jensen, E. MPG09, 423
Jiang, D.M. RPE10, 2023
Jiang, Shicheng TPR11, 3263
Jiang, W.S. MPP11, 2060
Jiang, Y. FAP01, 1322
Jianjun, Deng FAA26, 246
Jin, K. WPP05, 1666
Jin, L. RAA21, WAC27, 573, 3140
Jinsui, Shi FAA26, 246
Jobe, K. WPR15, 1821
Jobe, R.K. WAB05, 3025
Joffe, D. RPR02, 1122
Joh, Kihun TAB09, FAR03, 122, 269
Johnson, B. WPC21, 1043
Johnson, C. RPC09, 716
Johnson, D. RPG11, 345
Johnson, D.E. TAB06, FAP04, FAP09, FAP10, 119, 1331, 1346, 1349
Johnson, J. WPR14, RAE13, RPQ08, 1818, 2423, 2681
Johnson, J.W. WAQ26, 1897
Johnson, K.F. RPR19, RPR22, TPC06, 1161, 1167, 2607
Johnston, M. WPC21, 1043
Johnstone, C. FAG06, 86
Johnstone, J. WAP01, 434
Joho, W. FAB14, 2823
Joly, J.M. WAG07, WPA14, WPB22, 634, 935, 998
Joly, S. RAG06, 3170
Jones, C.M. TPC18, 2643
Jones, G.S. RPP06, 1973
Jones, R.M. TAA33, MPC03, 2144, 2321
Jones, W.P. TPB24, RAQ24, 2583, 3340
Jongewaard, E. FAE07, 1497
Jonker, M. WAP12, WAP13, RAA11, 464, 467, 548
Jordan, K. FAG11, FAA25, WPA17, 102, 243, 942
Joshi, C. WAG08, WAG09, RAB01, RAB02, RAB03, RAB04, RAB05, WPC20, RPA21, RPA22, TPB18, 637, 640, 758, 761, 764, 767, 770, 1039, 1102, 1105, 2569
Judd, D.L. TAR14, 828
Judkins, J. WPQ10, WPR08, 1741, 1803
Juillard, M. WAG07, WPB22, 634, 998
Junck, K. TPQ28, WAB01, 3013, 3016
Jung, R. TPC21, 2649
Junquera, T. WPB22, TPP09, TPP11, TPP14, 998, 1632, 1639, 1648
Juras, R.C. WAQ26, MPA05, 1897, 2202
Juras, S. TPP12, 1642
Jurgens, T.G. MPB15, 2303
Kachtanov, E. FAQ06, 1399
Kadnikov, A. WAA18, WPR13, MPA04, 1266, 1815, 2199
Kadokura, E. MPQ18, 2494
Kageyama, T. FAE09, WPQ09, WPQ17, WPR05, WPR09, 1503, 1738, 1759, 1797, 1806
Kahana, E. MPQ03, MPQ10, RPQ15, 2452, 2473, 2699
Kahn, S. TPE04, FAQ16, 1293, 1423
Kakigi, S. FAR08, RPA13, WAQ01, 278, 1079, 1843
Kako, E. TPP07, 1629
Kalashnikov, V.V. TPB25, 2586
Kalbreier, W. RAA15, 557
Kalfas, C. RAQ01, 3285
Kaltchev, D. FAB14, 2823
Kamber, I. RPC10, 719
Kaminsky, A. TAC16, 152
Kamiya, Y. FAR09, FAP22, WPQ07, WPR04, 281, 1384, 1732, 1794
Kando, M. FAR08, RPA13, WAQ01, 278, 1079, 1843
Kandrunin, V.N. WPR17, 1827
Kaneda, T. FAP13, 1358
Kang, Kyungwoo TAB09, FAR03, 122, 269
Kang, Wongu TAB09, FAR03, 122, 269
Kang, X. TAP03, WPP20, WPP21, RAP21, WAC12, RAG10, RAQ23, RAQ24, 357, 1705, 1708, 2934, 3094, 3182, 3337, 3340
Kang, Y.G. FAR19, FAQ18, 303, 1429
Kang, Y.W. WAG10, WPP16, RPE09, 643, 1693, 2020
Kang, Yoon WPP12, 1684

Kaplan, R. FAE13, WPQ02, 1515, 1720
Karantzoulis, E. FAR21, TAG05, 309, 2762
Karantzoulis, Emanuel MPR12, 2262
Karas', V.I. WAA02, WAA03, 1230, 1233
Karas', Vyacheslav I. WAA01, 1227
Karetnikov, M. RPR10, RPR15, 1143, 1155
Karev, A.I. TAR05, FAP19, WPR17, 807, 1375, 1827
Karl, F.X. TAA09, 2099
Karn, J. MPR15, 2271
Karnaukhov, I. FAR16, FAR17, RAA08, 296, 299, 542
Karpenko, V. TAR17, 837
Karshev, Yu. MPR11, 2259
Kashikin, V. FAR06, 272
Kasuga, T. RPQ23, RPQ26, RAQ06, 2720, 2726, 3300
Katoh, M. RPQ23, 2720
Katoh, T. MPA06, 2205
Katsouleas, T. WAG09, RAB02, RAB08,TAA28,TPB18, 640, 761, 773, 2135, 2569
Kaul, O. FAA02, FAC19, 195, 2874
Kawai, M. RPG09, 339
Kawakubo, T. RAB13, WAR04, MPQ18, 779, 1909, 2494
Kawakubo, Tadamichi TPR16, 3275
Kazarezov, I. WAA17, 1263
Kazimi, R. WXE01, TPC07, 2429, 2610
Keane, J. FAR10, TPP06, 284, 1626
Keeley, D. RPQ21, RPQ22, 2714, 2717
Keffeler, D. TAQ02, 1521
Keffeler, D.R. WPA08, 923
Kehne, D. FAG11, FAA25, WPA17, 102, 243, 942
Keil, E. WPG09, 514
Keith-Monnia, E. WAB04, 3022
Keizer, R. WAP12, 464
Kelley, M.J. FAG11, 102
Kelly, D.R.C. RPE08, 2017
Kelly, E. TPE04, FAQ03, FAQ04, FAQ15, 1293, 1393, 1396, 1420
Kelly, K.W. TAA32, 2141
Kemper, A.H. RPP04, 1970
Kendall, M. RAA03, 527
Kennedy, K. MPP13, 2067
Kerner, T.M. MPA18, 2232
Kerns, C. WPR21, 1838
Kerns, J.A. TAA22, 2129
Kerns, Q. WPR21, 1838
Kerslick, G.S. WPC19, TAE12, TAQ01, 1036, 1219, 1518
Kewisch, J. MPR20, 2279
Khabiboulline, T. WPP05, 1666
Khan, S. FAQ12, WAQ17, WAB03, 1411, 1879, 3019
Kheifets, S.A. MPC18, 2351
Khomyakov, E.A. TAE14, 1225
Khrutchinsky, A.A. TPA15, 3232
Kihara, Motohiro TPR16, 3275
Kijima, Y. TPP03, 1620
Kikuchi, M. RAA33, 603
Kikutani, E. RPQ26, 2726
Kikuzawa, N. TPG02, 159
Kim, Byungmun TAB09, FAR03, 122, 269
Kim, C. FAA03, FAA06, 198, 207
Kim, C.H. FAA05, 204
Kim, G.N. TAR07, 813
Kim, J. TAA11, 2102
Kim, J.W. RPR05, FAQ09, RAR21, 1128, 1408, 3400
Kim, Jinsoo TAB09, FAR03, 122, 269
Kim, K. TPE08, 1310
Kim, K.-J. TPG07, TAG13, RAR02, 174, 2786, 3358
Kim, Keeman TAB09, FAR03, 122, 269
Kim, Kwang-Je RAP06, 2895
Kim, S. FAR19, TAP05,FAB09, 303, 363, 2811
Kim, S.H. FAA10, TPE08, 216, 1310
Kim, Sungmyun TAB09, FAR03, 122, 269
Kim, T.H. FAQ08, 1405
Kim, T.Y. FAA10, 216
Kim, Y.S. WPR11, 1812
Kim, Younghee TAB09, FAR03, 122, 269
Kim, Yuri TAB09, FAR03, 122, 269
Kimura, W.D. WAG05, 626
Kindermann, H.P. TPP12, 1642
Kinkead, A.K. TAQ37, 1611
Kinross-Wright, John M. WPB15, 985
Kinsho, M. WPC07, WAQ06, 1007, 1855
Kinter, R. RAB02, 761
Kirbie, H.C. TAR14, 828
Kirby, R. MPE10, MPP09, 887, 2054
Kircher, J. FAR06, 272
Kirchgessner, J. FAE01, FAE13, WPQ02,RAQ04,RAR18, RAR19, 1469, 1515, 1720, 3294, 3391, 3394
Kirchman, J. RPQ15, RPQ16, 2699, 2702
Kirk, Harold G. WPB21, 995
Kiseljov, V.A. RAB15, 782
Kishek, R. TAQ32, 1599
Kishiyama, K. MPP12, MPP20, 2064, 2075
Kiver, A. MPP03, 2040
Kleffner, C.-M. RPR06, 1131
Klein, H. RPB15, RPB16, 692, 695
Klein, W.B. WAE08, 2175
Klem, J. WAP14, 470
Kleman, K.J. WPR01, 1785
Klewe-Nebenius, H. FAR06, 272
Klippert, T. MPP16, 2072
Klopenkov, M. TAA18, 2120
Kneisel, Peter TPP13, 1645
Knobloch, J. FAE13, TPP04, 1515, 1623
Knöchel, A. FAR06, 272
Knuth, T. TPE09, 1316
Ko, I.S. TAR07, RPA06, MPA02, 813, 1061, 2196
Ko, K. RPA04, RPA11,RPA14, TAQ06, WPQ05,WPQ12, WPR07, MPC01, 1058, 1073, 1082, 1533, 1726, 1744, 1800, 2317
Kobayashi, A. FAA30, 257
Kobayashi, T. RAB13, WPQ17, 779, 1759
Kobayashi, Y. FAR09, RPQ23, 281, 2720
Kodaira, M. FAP13, 1358
Koga, A. FAA30, 257
Kogan, M. TPB04, 2536
Kohaupt, Rolf-Dieter RPQ32, 2741
Koike, S. WPQ15, 1753
Koiso, H. TAG11, 2780
Kokoulin, V. WAA17, 1263

Kokura, S. TPP03, 1620
Kolomiets, A.A. TPA05, 3209
Kolonko, J. WPG11, 520
Kolonko, J.J. TAB06, 119
Komarov, V. MPP03, MPR11, 2040, 2259
Komori, K. TPP16, 1652
Konecny, R. WAG06, WPB11, WPB12, 631, 976, 979
Kononenko, S. FAR16, FAR17, RAA08, 296, 299, 542
Konovalov, V.A. RPR07, 1134
Koontz, R WPR15, 1821
Koopman, J. TPC21, 2649
Korchuganov, V. WAA18, FAP02, 1266, 1325
Korepanov, V.M. WAA21, 1274
Korolev, A.P. TPA05, 3209
Kos, N. RPE02, 1999
Koscielniak, S. RPG12, RAQ15, 348, 3317
Koscielniak, S.R. WAC19, 3115
Koseki, T. FAP22, WPQ07, WPR04, 1384, 1732, 1794
Kößler, V. RPR06, 1131
Kosterin, S.A. FAG12, 105
Kostin, D.V. WPR18, 1830
Kosukhin, V.V. WAA20, 1272
Kot, N. WAA17, 1263
Kotaki, H. WPC22, 1046
Kotov, V.I. MPG10, WAR20, WAR21, 426, 1948, 1949
Kouptsidis, J. RPE08, 2017
Kourbanis, I. WPP08, WPP23, RAQ13, 1672, 1714, 3312
Koutchouk, J.P. RAA17, 560
Koutchouk, J.-P. FAC04, 2844
Kovach, P. TAA18, 2120
Kovachev, V. FAQ14, 1417
Kovalev, V.P. WAA21, 1274
Kowalski, S. RPG05, RAA31, 327, 600
Kozawa, T. RAB13, 779
Kozin, V. FAR17, 299
Kozlov, O.S. WAR09, 1918
Kponou, A. WPC09, 1013
Krafft, G.A. WAQ14, RAE11, WXE01, TPC04,TPC07, 1873, 2417, 2429, 2601, 2610
Krämer, D. TPE09, FAP02, FAQ12, WAQ17, 1316, 1325, 1411, 1879
Kramer, S.L. MPQ23, 2509
Krasnopolsky, V. WPC13, WPR19, 1025, 1833
Krasnykh, A. TAC01, TAC16, 134, 152
Krauter, K. RAE03, 2389
Kravchuk, L.V. RPR24, RPR25, 1173, 1175
Krawczyk, Frank L. MPB16, MPC22, 2306, 2361
Krebs, G. FAB01, 2789
Krejcik, P. WAG11, RPB02, RPC02, WAB07,WAB12, WAC17, 646, 659, 701, 3031, 3046, 3109
Kreps, G. WPP05, 1666
Kriens, W. WPA12, 929
Krietenstein, B. RPB16, TAQ06, 695, 1533
Krinsky, S. FAR10, FAQ17, WXE04, TPQ14, 284, 1426, 2435, 2980
Krishnaswamy, J. FAA19, FAA31, 234, 260
Krivchikov, V.P. TAE14, 1225
Kroc, T. FAG06, 86
Kroes, F. RPG06, TAQ12, MPQ17, 330, 1547, 2491
Krogh, M. WAA19, 1269
Kroll, N. RPA04, 1058
Kroll, N.M. WPQ10, TAA33, 1741, 2144
Kroll, Norman M. WPR10, 1809
Kruijer, A. TAQ12, 1547
Krüssel, A. FAR06, 272
Krutikhin, S. WPP10, 1678
Krycuk, A. RPQ29, 2732
Krylov, Y. MPA04, 2199
Krylov, Yu. WPR13, 1815
Kuba, A. MPA07, 2208
Kubo, K. WAG12, RPC02, RPA20, WPR03,TPQ16,TPQ17, WAC18, 649, 701, 1099, 1791, 2986, 2989, 3112
Kubo, T. MPQ18, 2494
Kuchar, J. TAP08, 369
Küchler, S. FAP02, 1325
Kudo, M. TPP03, 1620
Kuijt, J. MPQ17, 2491
Kukhtin, V. MPC21, 2359
Kulevoy, T. TAC05, 140
Kulikov, A. RPE14, TAA22, 2032, 2129
Kulikov, A.V. WPC18, 1033
Kulipanov, G.N. FAQ17, 1426
Kumada, M. RPP09, 1982
Kumagai, S. TPP16, 1652
Kumpe, G. FAR06, 272
Kunkel, W.B. TPB07, 2542
Kuo, C. RAA24, 582
Kuo, C.C. FAA04, FAA07, RAA23, TPQ08,TPQ10, 201, 210, 579, 2965, 2971
Kuo, C.H. MPR10, MPQ16, TPB29, 2256, 2488, 2592
Kuo, T. WAQ07, 1858
Kuptsov, I. WPP10, WPP11, 1678, 1681
Kurakin, V.G. WAB14, 3049
Kurennoy, Sergey S. RAR11, RAR12, RAR13, 3373, 3376, 3379
Kurita, N. MPP07, MPP08, TAA22, MPC01,MPQ15, MPQ25, 2048, 2051, 2129, 2317, 2485, 2512
Kurkin, G. WPP11, 1681
Kurkin, Grigori WPR22, 1841
Kurokawa, S.-I. MPA06, 2205
Kurokawa, Shin-ichi WPG04, 491
Kurz, M. RPB15, RPB16, 692, 695
Kusano, J. RPG09, 339
Kushin, V. TAC05, 140
Kushnir, V.A. WPB16, 988
Kustom, R. TAP05, WPP13, WPP14, RPP12, 363, 1687, 1690, 1988
Kustom, R.L. WAG10, 643
Kustom, Robert WPP12, 1684
Kuznetsov, M.I. WPP18, 1699
Kuznetsov, N. FAP02, 1325
Kuznetsov, S. WPR13, MPA04, 1815, 2199
Kuznetsov, V.S. TAE13, 1222
Kvasha, A.I. RPR24, RPR25, 1173, 1175
Kwiatkowski, S. WPP07, WPQ19, 1669, 1765
Kwok, P. TAA28, 2135
Kwon, M. TPG06, WPR11, 171, 1812
Kwon, Y.S. WAQ26, 1897
Labrouche, J. TAE09, 1210
Lacarrere, D. FAE11, 1509
Lackey, J. FAG06, 86
Laclare, J.L. TPG05, 167
Laffin, M. RAA15, 557
Lagniel, J.-M. RPR11, RAG07, 1146, 3173
Lagniel, Jean-Michel TPA17, 3235
Lahti, G. MPR13, MPR14, 2265, 2268

Lai, A.-T. TPC15, 2634
Lai, C.H. WAG09, 640
Lai, P. RAB02, TAA28, 761, 2135
Lal, A. RAB04, RAB05, 767, 770
Lam, R. TPC16, 2637
Lambertson, G. MPC01, RAE13, RPQ08, 2317, 2423, 2681
Lamont, M. WAP12, WAP13, WPG09, RAA11,RAA15, 464, 467, 514, 548, 557
Lampel, M. RAB03, RPA21, RPA22, 764, 1102, 1105
Lamzin, E. MPC21, 2359
Lancaster, C. FAA27, 248
Lane, S.N. TAP07, 366
Langdon, A.B. TPR19, 3282
Langdon, A. Bruce TPR01, 3238
Langton, J. MPP08, 2051
Lara, P. MPE04, 867
Lara, P.D. WPA08, 923
Larbalestier, D.C. TPE01, 1276
Lasutin, E.V. FAG12, 105
Latypov, T. FAP24, 1387
Lau, W.C. FAA04, 201
Lau, W.K. RAA23, RAA24, WPB07, TPQ08,TPQ10, 579, 582, 964, 2965, 2971
Lau, Y.Y. TAQ32, 1599
Lauer, E. WAA19, 1269
Launspach, J. TAE09, 1210
Lauritzen, T. RPE12, 2026
Laverty, M. MPR16, 2273
Lavrent'ev, B.M. WAA21, 1274
Lawrence, G.P. FPD03, 35
Lawson, W. TAQ17, TAQ18, TAQ19, 1561, 1563, 1566
Lawton, D. RPG11, 345
Laxadal, R. WAQ07, 1858
Laxdal, R.E. WAR15, 1936
Le Diberder, F. RPC20, 749
Le Goff, A. TPP09, 1632
Le Taillandier, P. TAE09, 1210
Lebedev, A.N. TPR13, 3269
Lebedev, N.I. WAA20, TAQ34, 1272, 1605
Lebedev, O.P. WPP02, 1658
Lebedev, P. TAA01, RAR30, 2078, 3424
Leblond, B. WPB01, 945
LeCroy, C.T. TPC18, 2643
LeDiberder, F. TAG01, 2742
Lee, Edward P. FAC01, 2835
Lee, H.S. RPA06, TAQ14, 1061, 1553
Lee, J.C. FAA07, RAA24, TAR04, TAR06,TPQ09,TPQ10, 210, 582, 804, 810, 2968, 2971
Lee, P.J. TPE01, 1276
Lee, S.Y. RPG08, TAP03, WPP20, WPP21,RAP21, WAC12, RAG10,RAQ23,RAQ24, 336, 357, 1705, 1708, 2934, 3094, 3182, 3337, 3340
Lee, Sangil TAB09, FAR03, 122, 269
Lee, T. TPG06, TAQ06,WPQ05, 171, 1533, 1726
Lee, Terry G. TAQ27, 1584
Lee, Y. TPB07, 2542
Lee, Y.Y. MXG03, TAP11, WAR13, 53, 378, 1930
Leemans, W. TPG07, RAB10, WAQ04, TAA28, 174, 776, 1852, 2135
Legg, R. WAQ14, WXE01, TPC07, 1873, 2429, 2610
Lehrman, I.S. FAA19, FAA31, 234, 260
Lemaire, J.-L. RAG07, 3173
Len, L.K. TAE10, 1213
Lenci, S. FAE07, 1497
Lenisa, P. RAE05, 2399
Lenkszus, F. MPQ07, RPQ16, 2464, 2702
Lennox, A. FAG06, 86
Lenz, J.W. RPG10, 342
Lepeltier, V. RPC20, TAG01, 749, 2742
Lessner, E. TAP05, FAB09, TPQ22, 363, 2811, 3001
Letoumelin, R. TAB04, 116
Letta, P. MPR13, 2265
Leung, E.M. TAB06, 119
Leung, K.N. TPB07, 2542
Levashov, Y. TAA02, 2081
Levchenko, V.D. WAA02, WAA03, 1230, 1233
Level, M.-P. FAR14, 293
Leveling, A. FAG06, 86
Levichev, E. FAP02, 1325
Levy, C.D.P. MPE03, 864
Ley, R. RAP24, 2943
Leyh, G. WAQ15, 1876
Leyh, G.E. RPP07, 1976
Li, D. TAP03, WPA04,WPP20, WPP21, RAP21,WAC12, RAG10, RAQ23,RAQ24, 357, 911, 1705, 1708, 2934, 3094, 3182, 3337, 3340
Li, H. RPC16, RPC17,RPC19, 737, 740, 746
Li, N. FAP01, 1322
Li, Rui WAQ12, MPB11, 1870, 2297
Li, W.M. RPE10, 2023
Li, Xiao-Ping RAP25, 2946
Li, Z. FAG11, FAA25, 102, 243
Li, Zenghai MPC25, RAG12, 2370, 3188
Liang, C. TPC07, 2610
Libault, David TPA17, 3235
Lien, E. FAE07, 1497
Limberg, T. RAP08, WAC17, 2901, 3109
Lin, C.L. MPE12, 893
Lin, G. TPQ09, 2968
Lin, Glory MPQ16, 2488
Lin, K.K. FAA07, MPQ19, MPQ32, 210, 2497, 2524
Lin, Leon C.-L. WPB03, WPB04, 951, 954
Lin, Liu FAP14, 1361
Lin, T.F. TAA14, MPQ16, 2108, 2488
Lin, X. MPC01, 2317
Lin, X.E. WPQ12, 1744
Lin, X.T. RPA04, 1058
Lin, Xintian E. WPR10, 1809
Lindner, M. FAQ04, 1396
Linebarger, W. RPA24, 1111
Linnecar, T. WAP12, WAP13, FAE10, 464, 467, 1506
Linnik, A.F. RAB15, 782
Linscott, I. RAE12, RPQ01, RPQ22, 2420, 2660, 2717
Liou, R. WAG09, TAA28, 640, 2135
Lisin, A. MPP10, WAC17, 2057, 3109
Littlejohn, R.G. RAR02, 3358
Littmann, B. TAQ30, 1593
Littmann, Bengt WPP22, 1711
Litvinenko, V. MPA11, 2217
Litvinenko, V.N. FAA08, RAA01, RAB22,RPA17, MPA10, MPQ06,FAC20, 213, 524, 796, 1090, 2214, 2461, 2877
Liu, H. FAG11, WPA17,WAQ11, 102, 942, 1867
Liu, H.-X. FAA25, 243
Liu, J. TPP16, WPP20,WPP21, WAC12, 1652, 1705, 1708,

3094
Liu, J.Y. TAP03, RAP21, RAG10, RAQ23,RAQ24,357, 2934, 3182, 3337, 3340
Liu, W. MPA01, 2193
Liu, Y.C. FAA04, FAA07, RAA24, WPB07,201, 210, 582, 964
Liu, Y.-C. TPC15, 2634
Liu, Zuping FAQ29, FAQ30, 1456, 1459
Lo, C.C. TAR03, 801
Lobov, I. MPR11, 2259
Loew, G. RPC01, 698
Loew, G.A. WAG13, 653
Loewen, R. RPA23, 1108
Loewen, R.J. WAG13, 653
Lofnes, T. TPC31, 2658
Long, H. WPA14, 935
Longinotti, D. TAR17, 837
Longinotti, D.B. TAR14, 828
Lopez, F. FAP12, 1355
Lorenz, R. TPC14, 2631
Lou, W. FAB12, 2820
Lou, W.R. TPA04, 3206
Lou, Weiran TAA29, 2138
Louie, W. TAA09, 2099
Loulergue, A. RAG06, 3170
Lovato, Richard WPB15, 985
Lu, J.J. TAQ33, 1602
Lucas, Peter W. WAP06, 449
Luccio, A. FAQ28, 1453
Ludmirsky, E. RAB21, 793
Luger, G. WAE08, 2175
Luijckx, G. RPG06, 330
Lumpkin, A. MPQ08, MPQ09, MPQ10, MPQ11,TPC03,RPQ15, RPQ16, 2467, 2470, 2473, 2476, 2598, 2699, 2702
Lund, S. TAR17, 837
Lund, S.M. TAR14, TPR18, 828, 3278
Luo, G.H. FAA07, RAA24, RAR05, 210, 582, 3364
Luo, Gwo-Huei FAA04, 201
Luo, H. MPA01, 2193
Luo, X. FAC04, 2844
Luong, M. TPP09, 1632
Lussignol, Y. WPB22, 998
Lütgert, S. WAE13, 2190
Lykke, Keith R. WPC11, 1019
Lyons, S. TAB17, RPA26, 131, 1116
Lysenko, W.P. RPR19, RPR22, 1161, 1167
Maas, R. RPG06, TPB03, 330, 2533
Maccaferri, R. RAP24, 2943
Macek, R. TPB13, WAC29, RAR23, 2554, 3146, 3406
Macek, R.J. TAR12, 822
MacGregor, I. TAR18, 840
Machida, S. TAP04, WPC07, WAR05, 360, 1007, 1912
MacKay, W.W. WAC24, RAQ22, 3131, 3334
MacKenzie, R. RAE03, 2389
MacLachlan, J.A. WAC06, 3079
Madert, M. RPR06, 1131
Madey, J.M.J. FAA08, RAB22, RPA17, FAC20,213, 796, 1090, 2877
Madlung, J. WPA03, 908
Madsen, J. RPC09, 716
Madsen, J.H.B. RPC10, 719
Madura, D. WPG11, 520
Madura, D.D. TAB06, 119
Magugumela, M. WPC21, 1043
Mahoney, K. TPC26, 2652
Maier, R. TPB20, 2574
Maines, J. FAQ17, 1426
Mair, R. MPE10, 887
Maïssa, S. TPP09, 1632
Maj, J. WPP13, 1687
Makarov, A. RAQ14, 3315
Mako, F.M. TAE10, 1213
Malakhov, N. TAC16, 152
Maletic, D. RAG14, RAQ20, 3194, 3329
Malka, V. WAG08, 637
Malone, R. MPE11, 890
Malygin, A.N. RPP08, 1979
Mamaev, G. FAP24, 1387
Mammosser, J. FAE12, TPC07, 1512, 2610
Manca, J.J. WPR20, 1835
Manca, J.P.J. WPR20, 1835
Mandrillon, P. FAG09, 95
Mane, V. WAC24, WAC25, WAC26, 3131, 3134, 3137
Mangili, P. TPC10, 2619
Manglunki, D. MPG09, 423
Mangra, D. FAR19, 303
Mao, N. WAQ09, 1864
Mapes, M. MPP11, 2060
Margaritondo, G. TPG11, 186
Marhauser, F. WPA05, 914
Mariotti, E. RAE05, 2399
Markiewicz, T. RPC01, 698
Markov, V. FAR17, 299
Marks, S. FAQ24, FAQ25, 1444, 1447
Marneris, I. WAR11, RPP02, 1924, 1964
Marone, A. FAQ03, 1393
Marriner, J. WAP01, TPQ28, WAB01, 434, 3013, 3016
Marsh, K.A. WAG08, RAB01, 637, 758
Martens, M. WAP01, 434
Martens, M.A. WAP05, WAP08, 446, 455
Marti, F. RPG11, TAP08, TAP10, 345, 369, 375
Martin, D. MPQ15, MPQ25, 2485, 2512
Martin, E.J. RPP06, RPP13, 1973, 1991
Martin, K. WAE07, 2172
Martin, P. MPG01, 391
Martin, P.S. FAP04, FAP05, FAP06, FAP07,FAP09,WAR02, TAA12, 1331, 1334, 1337, 1340, 1346, 1903, 2105
Martini, M. TAP14, WAE09, 386, 2178
Martlew, B.G. RAE10, 2414
Maruyama, T. MPE10, 887
Marx, M. RPB15, 692
Masalov, V. WPC13, 1025
Mashiko, K. FAR08, RPA13, 278, 1079
Massarotti, A. TPG11, FAR21, WPQ04, 186, 309, 1723
Massoletti, D. FAA05, 204
Mastovsky, I. TPG14, RPC15, 192, 734
Masunov, E.S. RPR12, 1149
Matheson, R. MPQ22, 2506
Mathewson, A. RPE02, 1999
Matricon, P. WAG07, 634
Matsuda, K. FAR09, 281
Matsumoto, H. WAG12, RPA20, WPR03, 649, 1099, 1791
Matsumoto, S. RPB04, RPA20, 665, 1099
Matsuoka, M. TPP07, 1629
Mattei, P. RPR11, 1146
Matthews, P.J. WAG10, 643
Matthews, Paul WPP12, 1684
Matthieussent, G. WAG07, 634
Mattison, T. RPC02, 701
Mattison, T.S. WAR06, 1915
Matveev, Yu. WAA18, 1266
Matyukov, A.V. TAP16, 389
Mau, R. WAP04, 443
Maury, S. RAP23, RAP24, 2940, 2943

Maury, Stephan RPG07, 333
May, Lisa M. FAE06, 1494
May, M. TPE05, FAP09, 1298, 1346
Mazaheri, G. RPB04, 665
Mazarakis, M.G. TAE06, 1201
Mazur, P.O. FAP06, FAP07, 1337, 1340
McAllister, B. RPG05, 327
McCormick, D. RPB01, RPB04, 656, 665
McCrory, E. FAG06, 86
McCrory, Elliot S. WAP06, 449
McCune, E. FAE07, 1497
McDaniel, B.D. RAE14, 2426
McDaniel, M.R. TAA22, 2129
McDonald, K.T. TAA28, 2135
McDonald, M. MPE03, 864
McDowell, W. TAP05, 363
McGhee, D. FAR19, TAP05, 303, 363
McGhee, D.G. RPP03, 1967
McGinnis, D. WAP01, TPQ26, TPQ28, 434, 3010, 3013
McIntosh, P.A. MPC19, WAC22, 2353, 3125
McInturff, A.D. FAQ07, 1402
McIntyre, Peter M. FAQ31, 1462
McKee, B. WAC17, 3109
McManus, A. WAR19, 1945
McMichael, G.E. TAC12, 149
McMichael, Gerald E. FAG13, 107
Mead, J. TPB12, 2551
Mecklenburg, B. RPC22, TAQ03, 755, 1524
Meddahi, M. WPG09, RAA17, 514, 560
Medvedko, A.S. FAQ17, 1426
Medvedko, E.A. FAQ17, FAQ18, 1426, 1429
Meigs, M.J. WAQ26, MPA05, TPC18, 1897, 2202, 2643
Melekhin, V.N. TAR05, FAP19, WPR17, 807, 1375, 1827
Mencick, M. WPB22, 998
Mendelsohn, S.L. RPR20, 1164
Menshikov, L. TAC16, 152
Méot, F. FAC04, 2844
Meredith, J. TAR17, 837
Meredith, J.W. TPB14, 2557
Merl, R. FAR19, TPE08, 303, 1310
Merle, E. TAE09, TPC17, 1210, 2640
Merminga, L. FAG11, FAA25, RPQ11, RPQ30, 102, 243, 2690, 2735
Mertens, V. RAA15, 557
Merz, W. RPP13, 1991
Meshcherov, R. WPC13, 1025
Meshkov, I. RAP23, RAP24, 2940, 2943
Metz, H. TAQ19, 1566
Metzmacher, K. MPG09, 423
Meuth, H. WPQ26, 1781
Meyer, J. RPQ15, 2699
Meyer, S. TAR18, 840
Meyerer, Thomas WPB21, 995
Meyerhofer, D.D. TAA28, 2135
Meyers, T. RPR20, 1164
Mezi, L. TPG11, 186
Michailov, S. TPE09, 1316
Michelato, P. WPC23, 1049
Michelotti, L. WAP08, 455
Michelotti, Leo FAB15, 2826
Michine, A.V. TAB15, 128
Michnoff, R. MPA17, 2229
Micklich, B.J. FAG14, 110
Miertusova, J. MPP04, MPP05, 2042, 2045
Mikhailichenko, A. TAG01, 2742
Mikhailichenko, A.A. RAB18, 784
Mikhailov, V.A. WAR09, FAC12, 1918, 2863
Milchberg, H.M. WAG04, 621
Milder, M.L. WPA08, 923
Milder, Martin L. WPB15, 985
Miller, H. TAQ11, 1544
Miller, J.M. TPR18, 3278
Miller, R. TAB17, RPB02, RPC01, MPE10, RPA04, RPA26, 131, 659, 698, 887, 1058, 1116
Miller, R.A. WPC18, 1033
Miller, R.H. WPB13, WXE03, 982, 2432
Millich, A. WPQ25, 1779
Milliman, L. FAA27, 248
Millo, D. FAQ19, 1432
Mills, F. TAP05, 363
Mills, G.D. MPE05, WAQ26, 871, 1897
Milton, B. WAQ07, 1858
Milton, B.F. FAG07, 89
Milton, S. MPQ10, 2473
Milton, S.V. RAA28, FAP12, RPP03, RPQ18, 594, 1355, 1967, 2708
Mimashi, T. MPA06, 2205
Minagawa, Y. RPQ26, 2726
Minamihara, Y. FAQ24, FAQ25, 1444, 1447
Minato, T. FAQ08, 1405
Miné, Ph. WAG07, 634
Minehara, E.J. TPG02, 159
Mingalev, B. MPC21, 2359
Minty, M. WAG11, RPC02, RAE03, TPQ16, 646, 701, 2389, 2986
Minty, M.G. RAA06, RPB03, RAP10, WAB09, WAB12, WAC17, TPA09, 536, 662, 2907, 3037, 3046, 3109, 3217
Miram, G. FAE07, 1497
Mirzoev, K. MPP03, 2040
Mishin, A.V. RPA25, 1114
Mishra, C.S. FAP06, MPB05, MPB06, TAG10, RAP03, 1337, 2282, 2285, 2777, 2886
Mishra, S. FAP04, FAP07, 1331, 1340
Mitchell, M. WPR15, 1821
Mitra, A.K. TAQ33, 1602
Mitrochenko, V.V. WPB16, 988
Mitsuhashi, T. RAQ06, 3300
Mitsunobu, S. TPP03, 1620
Miura, T. WPR02, 1788
Miya, K. RAB13, 779
Miyahara, Y. FAQ20, FAQ21, RAQ30, 1435, 1438, 3355
Miyai, Y. TAQ35, 1608
Miyauchi, Y. FAA30, 257
Mizumoto, M. RPG09, 339
Mizuno, A. WPC22, MPA07, 1046, 2208
Mizuno, H. FAQ08, TAQ29, 1405, 1590
Mocheshnikov, N. FAR17, 299
Modena, A. WAG08, 637
Moe, H. TAP05, 363
Moe, H.J. RPA07, 1064
Moffat, D. FAE13, RAQ04, RAR19, 1515, 3294, 3394
Möhl, D. RAP23, 2940
Mohr, J. FAR06, 272
Moi, L. RAE05, 2399
Moibenko, A. WAE07, 2172
Moir, David C. TAE08, 1207
Moiseev, V.A. RPR01, 1119
Moisseev, V. WPR13, 1815
Moisseev, V.I. TPB25, 2586
Mokhov, N.V. RAB19, 787

Mokhtarani, A. FAP06, FAP07, 1337, 1340
Molinari, G. RAP24, 2943
Möller, K.D. FAR06, 272
Møller, S.P. WAP14, 470
Möller, W-D. TPP11, 1639
Molodkin, V. FAR16, FAR17, 296, 299
Montag, C. TAA01, TAA06, RAR30, 2078, 2090, 3424
Montès, B. WAG07, 634
Montjar, B. MPR13, 2265
Moog, E.R. TPE06, 1301
Mora, P. WAG04, WAG07, 621, 634
Morano, R. WAG07, 634
Morcombe, P. FAA08, WAA10, MPA11, MPQ06, 213, 1248, 2217, 2461
Morcombe, Peter WPR22, 1841
Moretti, A. WPA07, 920
Morgan, G. TPE04, FAQ03, FAQ04, FAQ16, 1293, 1393, 1396, 1423
Morgan, J. TAR16, 834
Morgillo, A. FAQ03, 1393
Mori, W.B. WAG09, RAB01, RAB02, RAB08, TPB18, 640, 758, 761, 773, 2569
Mori, Y. TAP04, MPE03, WPC07, WAQ06, WAR05, 360, 864, 1007, 1855, 1912
Morii, Y. TAQ35, 1608
Morillo, J. WAG07, 634
Morpurgo, G. RAA20, FAC03, 570, 2841
Morris, J.T. WAB04, 3022
Mortazavi, P. TPP06, WPQ20, 1626, 1768
Morvillo, M. MPQ05, 2458
Moser, H.O. FAR06, 272
Moshammer, W. RPC02, 701
Mosko, S.W. TAP07, WAQ26, 366, 1897
Mosnier, A. WPB22, WAC13, 998, 3097
Mostowfi, D. RPQ21, RPQ22, 2714, 2717
Moulin, F. WAG07, 634
Mouton, B. WPB22, 998
Mufel, V.B. TAE14, 1225
Mugge, M. MPP12, MPP20, 2064, 2075
Muggli, P. WAG09, WPC20, 640, 1039
Mulhall, S. FAQ15, TAA09, 1420, 2099
Mulhollan, G. MPE10, WPC21, 887, 1043
Muller, H. FAE13, TPP04, RAR19, 1515, 1623, 3394
Müller, W.F.O. RPB15, 692
Munasypov, R.N. WAA21, 1274
Munneke, B. TAQ12, 1547
Murata, H. RPG09, 339
Muratore, J. TPE04, FAQ02, FAQ03, FAQ04, 1293, 1390, 1393, 1396
Murin, B.P. RPR07, 1134
Murphy, C.T. WAR19, 1945
Murphy, J.B. FAR10, TPQ14, 284, 2980
Murray, S.N. MPE05, 871
Mustafin, E. RAP23, 2940
Myakishev, D. RPA12, 1076
Myakishev, D.G. MPC17, 2348
Myers, S. WPG01, 476
Mytsykov, A. FAR17, 299
Myznikov, K. FAQ06, 1399
Nadji, A. FAR14, 293
Nagaenko, M. FAR06, 272
Nagafuchi, T. FAP13, 1358
Nagai, A. FAA30, 257
Nagai, R. TPG02, 159
Nagaitsev, S. RAP22, 2937
Nagaoka, R. FAR21, TAG05, 309, 2762
Nagatsuka, T. FAP22, WPQ07, 1384, 1732
Nagchaudhuri, A. MPA11, 2217
Naidenov, V.O. TAP16, 389
Naito, F. FAE09, WPQ17, WPR05, WPR09, 1503, 1759, 1797, 1806
Najmudin, Z. WAG08, 637
Nakajima, K. RAB13, TAA28, 779, 2135
Nakamura, N. RPQ23, 2720
Nakamura, T. WAC14, 3100
Nakamura, T.T. MPA06, 2205
Nakanishi, H. RAB13, TPP16, TAA28, 779, 1652, 2135
Nakata, K. TAQ35, 1608
Nakayama, H. WAR03, TAG01, 1906, 2742
Nam, S.H. TPG06, 171
Namkung, W. TAR07, RPA06, TAQ14, TAQ15, MPA02, 813, 1061, 1553, 1556, 2196
Naqvi, S. TAQ01, 1518
Nasonov, N.N. FAG12, 105
Nassiri, A. WPB06, RPA10, WPP16, 961, 1070, 1693
Nath, S. RPR08, RPR09, 1137, 1140
Nath, Subrata WAQ02, 1846
Nation, J.A. WPC19, TAE12, TAQ01, 1036, 1219, 1518
Nattrass, L. TAR17, 837
Nattrass, L.A. TAR14, 828
Nawrocki, G. MPQ08, 2467
Nawrocky, R.J. MPQ23, 2509
Neau, Eugene L. TAE03, 1188
Neil, G. FAA25, WPA17, RPQ30, 243, 942, 2735
Neil, G.R. FAG11, 102
Neil, George R. TAC03, 137
Nelson, D. WAQ15, 1876
Nelson, M. TAR17, 837
Nelson, M.B. TAR14, 828
Nemoshkalenko, V. FAR16, FAR17, 296, 299
Nesemann, H. FAA02, FAC19, 195, 2874
Nesterov, N. TAC05, 140
Nesterov, V.V. WAA11, 1251
Nesterovich, A. RPR10, RPR15, 1143, 1155
Nett, D. TAB17, RPA26, 131, 1116
Neubauer, M. WPQ10, WPR07, WPR08, 1741, 1800, 1803
Neuffer, D. FAG11, WPA17, WAQ11, 102, 942, 1867
Neuffer, D.V. FAA25, 243
Neuffer, David MXG03, 53
Newton, M.A. TAR14, 828
Nezhevenko, O. RPA12, TAQ21, 1076, 1569
Ng, C. WPR07, MPC01, MPQ25, 1800, 2317, 2512
Ng, C.K. TAA28, 2135
Ng, C.-K. WPQ10, WPQ12, MPP07, MPQ15, WAB18, WAC17, 1741, 1744, 2048, 2485, 3061, 3109
Ng, K.Y. RAP21, TPQ12, RAQ23, RAQ24, RAR17, 2934, 2977, 3337, 3340, 3388
Ng, K.-Y. TAR20, 843
Nghiem, P. FAR14, 293
Nguyen, D.C. FAA16, 228
Nicol, T. WPB08, 967
Nielsen, R. TAP05, 363
Nieuwenkamp, H. MPQ17, 2491
Niki, K. RPG13, 351
Nikiforov, S. WPC03, 1004

Niquille, C. WAP13, 467
Nishi, M. TAB03, WPQ21, 113, 1770
Nishida, Y. RAB13, TAA28, 779, 2135
Nishihara, S. FAA30, 257
Nishimura, H. MPR03, MPR04, 2244, 2247
Nishimura, Hiroshi WAE04, 2162
Nobel, R.J. WPA07, 920
Noda, A. FAR08, RPA13, RPA18, WPQ21,WAQ01,278, 1079, 1093, 1770, 1843
Noda, K. TAB03, 113
Nogiec, J.M. FAP06, FAP07, MPB06, 1337, 1340, 2285
Noguchi, S. TPP07, 1629
Nolen, J.A. RPG14, FAQ09, TPC13, RAQ16, 354, 1408, 2628, 3320
Noomen, J. RPG06, 330
Noomen, J.G. MPQ17, 2491
Noonan, J. RPE09, 2020
Nordberg, E. FAE13, 1515
Nordby, M. MPP08, MPP12, MPP20, TAA22,MPC01, MPQ25, 2051, 2064, 2075, 2129, 2317, 2512
Nordby, M.E. MPP07, 2048
Norek, G. TAP05, 363
Norem, J. RAA29, TAA28, TPC16, 597, 2135, 2637
Norris, B.L. WAE02, 2152
Norton, M. TAA20, 2123
Norum, B.E. RAP01, 2880
Norum, Blaine E. RAE07, 2405
Nosochkov, Y. RAA22, RAA25, RAA27, 576, 585, 591
Nosyrev, S. WPP10, WPP11, 1678, 1681
Novikov, A. WPP10, 1678
Novikov, S.A. WAR09, 1918
Novikova, T.A. FAA14, 225
Novokhatsky, A. WAA17, 1263
Nuhn, H.-D. FAA12, FAA17, 219, 231
Nusinovich, G.S. TAQ17, 1561
Nyman, M. RPQ08, 2681
O'Connor, T. RAA03, 527
O'Day, S. WAQ22, 1888
O'Shea, P. FAA08, MPA11, 213, 2217
O'Shea, P.G. RPA17, TAQ07, 1090, 1536
O'Shea, Patrick G. WPA13, WPB09, TAG12, 932, 970, 2783
O'Sullivan, M. RPP13, 1991
O'Sullivan, M.K. RPP06, 1973
Obina, T. TPC08, RPQ26, 2613, 2726
Oerter, B. MPA16, 2226
Ogata, A. RAB13, TAA28, 779, 2135
Ogawa, Y. TAA04, 2087
Ogitsu, T. FAQ02, FAQ08, 1390, 1405
Oguri, H. RPG09, 339
Oh, J.S. TAQ15, 1556
Ohgaki, H. MPR04, 2247
Ohmi, K. RAP02, 2883
Ohmori, Chihiro TPR16, 3275
Ohshita, E. TAQ35, 1608
Oide, K. RPC20, RPA20, TAA08, WXE07,TAG01,TAG11, WAB20, WAC08,WAC16,749, 1099, 2096, 2444, 2742, 2780, 3064, 3085, 3105
Oide, Katsunobu WAB10, 3040
Okada, M. RPG13, 351
Okamoto, H. FAR08, RPA13, RPA18, WAQ01, 278, 1079, 1093, 1843
Okamoto, Hiromi TPR11, 3263
Okuma, S. FAA30, TAQ35, 257, 1608
Okumura, Y. RPG09, 339
Okun, L. FPD05, 45
Olivieri, D.N. TAR16, 834
Olsen, D.K. RPG01, TAP07, WAQ26, 312, 366, 1897
Olsen, J. RAE12, 2420
Omeich, M. WPA14, WPB22, 935, 998
Onillon, E. RPQ17, RPQ25, 2705, 2723
Onishchenko, I.N. RAB15, 782
Onken, R. WPQ24, 1776
Ono, M. TPP07, 1629
Opanasenko, A.N. WPA15, WPA16, 938, 939
Oren, W. WXE01, 2429
Oreshnikov, A. TAC05, 140
Orris, D. TPE05, 1298
Orris, D.F. FAP06, FAP07, 1337, 1340
Ortiz, R. MPQ22, 2506
Osborn, J. FAP01, 1322
Oshita, E. FAA30, 257
Ostanin, V.P. RPP08, 1979
Ostiguy, F. TAG04, 2757
Ostiguy, Francois WAC02, 3070
Ostiguy, J.F. WPB08, 967
Ostiguy, J.-F. TAR20, TPE05, FAP10, FAP21,MPC07,843, 1298, 1349, 1381, 2330
Ostojic, R. FAC04, 2844
Ostroumov, P.N. RPR01, RPR24, RAE08, 1119, 1173, 2408
Otake, Y. TAQ29, 1590
Otocki, R. TAA11, 2102
Otocki, R.D. RPE09, 2020
Ottarson, J. TAP08, 369
Ottaviani, P.L. TPG11, 186
Oude Velthuis, R.G.J. RPP04, 1970
Ovchinnikov, V.P. TAE13, 1222
Owen, H.L. TPG09, 180
Oxoby, G. RAE12, RPQ01, 2420, 2660
Ozaki, Y. WXE07, 2444
Pabst, M. TPA01, TPA02, TPA03, 3197, 3200, 3203
Pachnik, J.E. FAP06, FAP07, MPB06, 1337, 1340, 2285
Padamsee, H. FAE13, TPP02, TPP04, WPQ02,RAQ04,RAR18, RAR19, 1515, 1617, 1623, 1720, 3294, 3391, 3394
Pagani, C. WPB10, WPC23, TAA07, RAQ05, 973, 1049, 2093, 3297
Pai, C. MPP11, 2060
Palkovic, J. TPB19, 2572
Palmer, D. RPA26, 1116
Palmer, D.T. WPB13, WXE03, 982, 2432
Palmer, Robert B. MXG03, 53
Palrang, M. MPP10, 2057
Pan, K.T. MPQ16, 2488
Pang, A.W. WPC21, 1043
Pangos, N. FAR21, MPP05, 309, 2045
Pankuch, P. TAE06, 1201
Pantazis, R. MPA11, 2217
Pantenburg, F.J. FAR06, 272
Pappas, G.C. WAR10, WAR12, 1921, 1927
Papureanu, S. RPR06, WPQ26, TPB20, 1131, 1781, 2574
Paramonov, V.V. WPP17, WPP18, WPP19, 1696, 1699, 1702
Parazzoli, C. FAA27, 248
Parazzoli, C.G. FAA28, 251
Pardo, R.C. WAQ03, 1849
Park, H.J. WPR11, 1812

Park, Heunggyu TAB09, FAR03, 122, 269
Park, Jongpil TAB09, FAR03, 122, 269
Park, S. RPA21, RPA22, 1102, 1105
Park, S.H. FAA08, RAB22, TAQ14, 213, 796, 1553
Park, S.S. TAQ15, 1556
Park, Sanghyun WPB02, 948
Parkhomchuk, V. TAR11, 819
Parzen, G. FAB03, FAB04, FAB05, 2795, 2798, 2801
Pasotti, C. WPQ04, TAG05, 1723, 2762
Pasquinelli, Ralph J. RAE01, 2379
Patavalis, N. MPR13, 2265
Paterson, E. RPC01, 698
Patteri, P. TPG11, 186
Patterson, D. MPQ10, 2473
Paulson, C.C. RPR20, 1164
Pavlovets, M. TAA18, 2120
Pawlak, T. MPG01, 391
Payet, J. FAR14, 293
Peacock, M.A. RPR20, 1164
Pearson, C. FAE07, 1497
Pearson, Pauline MPR07, 2250
Peck, S. FAE13, 1515
Pedersen, F. MPG09, 423
Peggs, S. MPG12, TAA09, MPC05, FAB20,FAB22,WAC24, WAC25, WAC26,RAQ21, RAQ22, RAR29, 431, 2099, 2327, 2829, 2832, 3131, 3134, 3137, 3331, 3334, 3421
Peggs, S.G. WAP10, 461
Pei, A. TAP03, WPP20,WPP21, RAP21, WAC12,RAG10,RAQ23, RAQ24, 357, 1705, 1708, 2934, 3094, 3182, 3337, 3340
Pei, Yuan Ji RPE10, 2023
Pekeler, M. TPP11, 1639
Pelaia, T.A. RAE14, 2426
Pellegrini, C. FAA23, RAB03, RPA21, RPA22,RAQ17,240, 764, 1102, 1105, 3323
Pendleton, R. WPR07, WPR16, 1800, 1824
Penicka, M. TAA03, 2084
Pennacchi, R. WPR15, 1821
Perin, R. TPE02, 1282
Perkins, C. RAA04, MPP09, MPP10, MPP12,MPP20, TAA22, MPC01,MPQ25, 530, 2054, 2057, 2064, 2075, 2129, 2317, 2512
Perkins, L. TPB07, 2542
Peschke, C. RPB16, 695
Peters, C. RPC16, RPC18, WPA01, TAE01,FAP17,FAP18, TPA10, 737, 743, 902, 1178, 1369, 1372, 3220
Peters, F. TAG01, 2742
Peterson, K.J. TAP05, 363
Petracca, S. WAE12, 2187
Petrenko, I.I. FAB02, 2792
Petrenko, V. WPR13, 1815
Petrenko, V.V. TPB25, 2586
Petri, H. WPC08, 1010
Petrov, S.P. FAQ17, 1426
Petrov, V. WPP11, 1681
Petrov, V.A. WAA20, TAQ34, 1272, 1605
Petty, L. MPP15, 2069
Pfeffer, H. WAE07, 2172
Pflüger, J. FAR07, 275
Phillips, R. FAE07, 1497
Phinney, N. WAG11, RPB01, RPC01, 646, 656, 698
Phung, B. WPB22, 998
Piaszczyk, C. RPR20, 1164
Piataev, V. TAC16, 152
Pichoff, N. RAG06, RAG07, 3170, 3173
Pickard, D. TPB07, 2542
Pietryka, M. RAA04, WAC17, 530, 3109
Pilat, F. FAQ28, FAB22, 1453, 2832
Pilyar, N. TAC16, 152
Pinto, I.M. WAE12, 2187
Pipersky, P. FAQ24, FAQ25, 1444, 1447
Pirkl, W. WPP07, WPQ19, 1669, 1765
Pirovano, R. TAQ12, 1547
Pisharody, M. FAE13, WPQ02, RAE14, TPA04,RAQ04,RAR18, 1515, 1720, 2426, 3206, 3294, 3391
Piskarev, I. RPA19, 1096
Pitel, Ira J. RPP11, 1985
Placidi, M. RAA19, RPB01, 567, 656
Plass, G. FAG08, 92
Plate, D. FAQ24, FAQ25, 1444, 1447
Plate, S. FAQ15, 1420
Plato, John G. WPB15, 985
Platonov, Yu.P. MPG10, 426
Plesko, M. TPG08, FAA13, FAR06, 177, 222, 272
Plesko, Mark MPR12, 2262
Plotnikov, S. TAC05, 140
Plouviez, E. TPG05, RPQ15, 167, 2699
Plum, M. TPB13, WAC29, RAR22, RAR23, 2554, 3146, 3403, 3406
Podebrad, O. RPB16, 695
Podobedov, B. WAC17, 3109
Poelman, A. MPQ17, 2491
Pogorelsky, I. MPE11, 890
Poilleux, P. WAG07, 634
Poirier, R.L. TAQ33, WPP18, 1602, 1699
Polyakov, V. RAP24, 2943
Poncet, A. RPE02, MPP15, 1999, 2069
Ponds, M. TAQ07, 1536
Poole, J. WPG09, RAA15, WAE03, 514, 557, 2157
Poole, M.W. TPG09, 180
Popik, V.M. FAQ17, 1426
Popov, Yu. TAC16, 152
Popovic, M. FAG06, WPA06, WPA07, WPR21, 86, 917, 920, 1838
Porterfield, D. TPC04, 2601
Portmann, G. FAQ24, RPQ13, FAB01, 1444, 2693, 2789
Potter, James M. FAE06, 1494
Poukey, J.W. TAE06, 1201
Pourre, J.L. TAB04, 116
Power, J. WAG06, WPB11, WPB12, RPR19, 631, 976, 979, 1161
Power, J.F. TPB22, 2580
Powers, T. FAE12, 1512
Powers, Tom TPP13, 1645
Pozdeev, M. TPQ04, 2958
Prabhakar, S. RAE12, 2420
Preble, J. FAE12, 1512
Prelec, K. WPC09, 1013
Prescott, C. MPE10, 887
Price, E. TPC04, 2601
Prieto, P. WAE07, 2172
Primdahl, K. WPP13, WPP14, 1687, 1690
Proch, D. FAE08, TPP11, WPQ24, 1500, 1639, 1776
Prodell, A. TPE04, 1293
Pruyn, J. WPA01, 902
Ptitsin, V.I. RAQ21, 3331
Puchkov, A. RPR10, 1143
Pullia, M. TPC10, 2619
Puntus, V. WPP05, 1666
Puzo, P. RPC20, TAG01, 749,

2742
Qian, Y.L. RPA08, RPA11, 1067, 1073
Qian, Zubao TPP01, 1614
Qin, Q. TPQ03, 2955
Qing, Li FAA26, 246
Qiu, X. MPE11, 890
Qiu, X.Z. RAE09, TPB01, 2411, 2530
Queralt, X. TPG09, 180
Quinn, P.D. RAE10, 2414
Qunell, D. WAR01, 1900
Rackelmann, A. WAC17, 3109
Radloff, W. TPC09, 2616
Radusewicz, P. FAQ08, 1405
Rafael, F.S. MPQ33, 2527
Rago, C. WAC17, 3109
Raimondi, P. WAG11, RPB01, RPC20, TAA08,TAG01,RAP15, RAP16, 646, 656, 749, 2096, 2742, 2919, 2922
Rakowsky, G. FAQ17, WXE04, 1426, 2435
Ramachandran, S. WAR19, 1945
Ramamoorthy, S. MPA15, 2223
Ramamoorthy, Susila MPR07, RPQ14, 2250, 2696
Ramirez, G. WPP03, 1660
Ramirez, J.J. TAE05, TAE06, 1198, 1201
Raparia, D. RAR16, 3385
Rasmussen, J.O. WAQ04, 1852
Rasmussen, N. MPG09, 423
Ratti, A. WPP07, WPQ19, RPQ17, WAC24, 1669, 1765, 2705, 3131
Raubenheimer, T. RPB02, RPC01, RPC03,TPQ16,TPQ17, WAC17, 659, 698, 704, 2986, 2989, 3109
Raubenheimer, T.O. RPC02, TAG03, WAC15,WAC18, RAQ03, 701, 2752, 3102, 3112, 3291
Rauchas, A. TAP05, 363
Ravn, Helge L. MPE02, 858
Razuvakin, V.N. WAA20, 1272
Reece, C. FAE12, 1512
Reece, R.K. TAP11, TAP13, 378, 383
Reed, L. TPC16, 2637
Rees, D. WPA08, TAQ02, TAQ31, 923, 1521, 1596
Reginato, L. RPC16, RPC18, WPA01, TAE01,FAP17,WAQ04, 737, 743, 902, 1178, 1369, 1852
Rehak, M. TPE04, 1293
Reid, J. TAQ11, 1544
Reilly, J. FAE13, WPQ02, 1515, 1720
Reilly, R. WAA05, WAR01, 1236, 1900
Reiser, M. TAE04, TAQ17, TAQ18, TAQ19,TPQ11, 1193, 1561, 1563, 1566, 2974
Reiser, Martin RPR23, TAA17, MPC04, 1170, 2117, 2324
Renieri, A. TPG11, 186
Renken, D. TPP11, 1639
Renner, T. WXE06, 2441
Repnow, R. RPR06, 1131
Repond, J. RAA29, 597
Repose, G. TAR17, 837
Reusch, M.F. RPR20, TPR08, 1164, 3257
Reuter, E. RAA04, TAA22, 530, 2129
Revol, J.L. TPG05, 167
Reymermier, C. RPE02, 1999
Rhoades, J. WAR19, 1945
Riabko, A. TAP03, WPP20, WPP21, RAP21,WAC12, RAG10, RAQ23,RAQ24, 357, 1705, 1708, 2934, 3094, 3182, 3337, 3340
Rice, D. FAE13, FAB12, 1515, 2820
Rich, D. RAQ23, 3337
Richard, Frank FAC07, 2850
Riche, A.J. MPC24, 2367
Richter, R. FAR21, 309
Rimmer, R. WPR07, WPR14, 1800, 1818
Rimmer, R.A. WPQ06, WPQ13, WPR08, 1729, 1747, 1803
Rindi, A. TPG11, 186
Ringwall, A.D. RPG10, 342
Rinolfi, L. RPC10, 719
Rintamaki, J. TPB14, 2557
Risselada, T. FAC04, 2844
Ritson, D. RAA26, 588
Ritson, D.M. RAA22, RAA27, 576, 591
Riunaud, J.-P. TAP14, 386
Rizawa, T. WPR16, 1824
Robin, D. FAA06, RPC02, RPQ13, FAB01, 207, 701, 2693, 2789
Rode, Claus H. RPE01, 1994
Rodger, E. FAP11, 1352
Rodier, J. WPB22, 998
Rogers, J. FAE13, TPA04, 1515, 3206
Rogers, J.T. RAE14, WAB15, 2426, 3052
Rojak, M. MPB09, 2291
Rokni, S. TAG01, 2742
Romanov, G. MPC16, 2345
Romasko, V.P. WPA15, 938
Rookhuizen, H. Boer RPG06, 330
Root, L. RPG12, WAQ07, 348, 1858
Ropert, A. TPG05, 167
Roques, A. TAE09, 1210
Rose, J. WPP07, WPQ19, RPQ17, WAC24, 1669, 1765, 2705, 3131
Rosei, R. TPG11, 186
Rosenblum, B. WAA19, 1269
Rosenzweig, J. FAA23, WPB05, WPB08,RPA21,RPA22, TAA28, 240, 957, 967, 1102, 1105, 2135
Rosenzweig, J.B. WAG06, MPE13, 631, 896
Roser, T. TAP11, TAP12, TAP13, RPQ07,RAG02, 378, 381, 383, 2678, 3154
Rosing, M. WPB11, 976
Ross, M. RPB01, RPB04, RPC01, WPR15,WAQ15, TAA28, 656, 665, 698, 1821, 1876, 2135
Ross, M.C. WAG11, WAC17, 646, 3109
Ross, W. RAE12, RPQ01, 2420, 2660
Roßbach, J. FAC19, 2874
Rossbach, J. TPG12, WAG02, TAA01, TAA06,RAR30, 189, 611, 2078, 2090, 3424
Rossi, C. FAA13, FAR21, 222, 309
Rossmanith, R. FAR07, 275
Rossmanith, Robert RAE07, 2405
Roster, William WAB06, 3028
Rotela, E. MPQ07, 2464
Rotela, R. TAR08, 816
Rothman, J.L. MPQ01, 2450
Roudier, P. WPB22, 998
Roy, G. WAP12, WAP13, RAA11, RAA17,TAG01, 464, 467, 548, 560, 2742
Roybal, W. TAQ02, 1521

Rubbia, C. FAG09, TPG11, 95, 186
Rubin, D. FAE13, RAQ04, 1515, 3294
Rubin, David L. WPG02, 481
Rudenko, V. TAC16, 152
Ruemmler, J. WAR14, 1933
Rufer, C. FAC04, 2844
Ruggiero, A.G. RAG14, RAQ20, 3194, 3329
Ruggiero, F. RPE02, WAE12, 1999, 2187
Ruiz, C. RAG06, RAG07, 3170, 3173
Ruland, Robert E. RPE04, 2009
Rusnak, Brian TPP10, 1636
Russell, A. MPB06, 2285
Russell, A.D. FAP06, FAP07, WAR02, MPB05, 1337, 1340, 1903, 2282
Russell, S.J. TPB22, 2580
Russell, Steven WPB15, 985
Russell, T. RPA11, RPE09, 1073, 2020
Russell, Thomas J. TAQ16, 1559
Rusthoi, D.P. RPR22, TPC06, 1167, 2607
Ruth, R. RPC01, RPA04, 698, 1058
Ruth, R.D. WAG13, TPQ17, 653, 2989
Ruth, Ronald D. WAG03, TAQ26, TAQ27,WAC05,RAQ18, 616, 1581, 1584, 3076, 3326
Ruth, Thomas J. WPE03, 67
Ryan, W.A. MPQ04, 2455
Rybarcyk, L.J. RAG11, 3185
Ryne, Robert D. MPB16, RAG01, 2306, 3149
Ryu, C.M. TAQ14, 1553
Saab, A.H. RPP01, 1961
Saadatmand, K. FAG05, 83
Saba, J. WPQ06, 1729
Saban, R. WAE01, 2147
Sabbi, G.L. RAA20, FAC03, 570, 2841
Sabia, E. TPG11, 186
Sachtschale, R. RPA17, TAQ07, MPA11, 1090, 1536, 2217
Sachtschale, R.J. WAA10, 1248
Sachtshale, R. FAA08, 213
Sackett, J. FAE07, 1497
Saeki, K. FAA30, 257
Saewert, G.W. MPB15, 2303
Sáez, P. MPE10, WPC21, 887, 1043
Safa, H. TPP09, 1632
Safranek, J. FAR02, RPQ19, FAB11, 266, 2711, 2817
Sagan, D. FAE13, TPA04, RAR15, 1515, 3206, 3382
Sagan, David RAP04, 2889
Sah, R. FAG05, 83
Saile, V. TAA32, 2141
Saito, K. TPP07, 1629
Sakae, T. MPE03, 864
Sakai, H. WPQ15, 1753
Sakai, I. WAR05, 1912
Sakaki, H. WPC22, MPA07, 1046, 2208
Sakanaka, S. WPQ16, WPR02, WPR03, RAQ06, 1756, 1788, 1791, 3300
Salah, W. TPR04, 3245
Saltmarsh, C. MPR20, 2279
Sampayan, S. MPE14, WPC16, WAA19, TAA20, 899, 1027, 1269, 2123
Sampson, W. TPE04, FAQ03, FAQ04, 1293, 1393, 1396
Sandberg, J.N. WAR11, RPP02, 1924, 1964
Sander, O.R. RPR19, RPR22, TPC06, 1161, 1167, 2607
Sanders, D.A. RAB20, 790
Sandler, P.H. RAB20, 790
Sandoval, D.P. TPC06, 2607
Sangster, C. TAR17, 837
Sangster, T.C. TAR14, 828
Sannibale, F. RPA26, 1116
Sapozhnikov, L. RAE12, RPQ01, RPQ05, 2420, 2660, 2672
Sapp, W. RPG05, 327
Sarantsev, V.P. TAQ34, 1605
Saraph, G. TAQ19, 1566
Sarau, B. FAA02, 195
Sarstedt, M. TPB07, 2542
Sasaki, S. FAQ21, RPQ15, 1438, 2699
Sasaki, Y. FAP13, 1358
Sass, R. RPB03, RAE03, 662, 2389
Sathe, S. MPR20, 2279
Sato, H. WAR04, WAR05, 1909, 1912
Sato, I. TAQ08, TAQ25, TAA04, 1539, 1578, 2087
Satogata, T. MPR20, TPB21, RAQ22, 2279, 2577, 3334
Satoh, K. WPR02, WAC07, WAC08, 1788, 3082, 3085
Satoh, Kotaro MPQ14, 2482
Satti, J.A. FAP08, 1343
Saulter, Q. WAQ14, 1873
Saury, J.L. WPB22, 998
Sawamura, M. TPG02, 159
Scandale, W. WAP14, FAC04, FAC06, 470, 2844, 2847
Scanlan, R.M. FAQ07, 1402
Schachinger, L. MPR04, RPQ13, 2247, 2693
Schachinger, L.C. TAB06, 119
Schächter, L. WPC19, TAE12, TAQ01, 1036, 1219, 1518
Schaffner, S. MPR13, 2265
Schafstall, P.J. WPA08, 923
Schank, C.V. TPG07, 174
Schaper, J. TPG08, FAR06, 177, 272
Scharlemann, E.T. FAA12, FAA17, 219, 231
Scheidt, K. TPG05, RPQ15, 167, 2699
Schempp, A. WPA03, WPA04, WPA05, RPR06, 908, 911, 914, 1131
Schiffer, John P. RAG04, 3164
Schindl, K. MPG09, 423
Schirm, K.M. FAE11, 1509
Schirmer, D. FAQ12, WAQ17, 1411, 1879
Schlösser, K. FAR06, 272
Schlueter, R. FAQ23, FAQ24, FAQ25, 1441, 1444, 1447
Schlüter, R. FAA17, 231
Schmenk, E.G. TAA32, 2141
Schmickler, H. WAP12, WAP13, RAA10,RAA11, RAA13, 464, 467, 545, 548, 554
Schmidt, C. FAG06, 86
Schmidt, C.W. WPA06, 917
Schmidt, F. TAG07, 2768
Schmidt, R. WPG09, RAA19, 514, 567
Schmieder, R. WPC09, 1013
Schmitz, M. WPA12, 929
Schmor, P. WAQ07, 1858
Schmor, P.W. RPG12, MPE01, MPE03, 348, 853, 864
Schnase, A. WPQ26, TPB20, 1781, 2574
Schneider, G.C. MPG09, 423
Schneider, H.R. RPG12, RPR02, RPR03, 348, 1122,

1125
Schneider, J.D. MPE04, WPA08, 867, 923
Schnell, W. RPC09, 716
Schoenlein, R. TPG07, 174
Schoessow, P. WAG06, WPB11, 631, 976
Scholl, E.H. TPB21, 2577
Scholz, T. RPE02, 1999
Schönauer, H. MPG09, WAQ25, 423, 1894
Schönfeld, Frank WPP22, 1711
Schreiber, S. RPC10, 719
Schreuder, H.W. RPG02, 317
Schulte, Elmar TPC11, 2622
Schultheis, R. MPC15, 2342
Schultz, D. WPC21, WAQ15, 1043, 1876
Schulz, G. FAR06, 272
Schulze, M.E. FAG05, 83
Schumburg, N. RPP02, 1964
Schuppler, S. FAR06, 272
Schwalm, D. RPR06, 1131
Schwandt, P. RAP22, 2937
Schwarz, H. RAA04, WPQ06, WPR07, WPR08,RPQ05,530, 1729, 1800, 1803, 2672
Schweickert, H. FAR06, 272
Scott, B. RPC02, TPQ16, 701, 2986
Sears, J. FAE13, WPQ02, 1515, 1720
Sebek, J. MPQ22, RPQ22, 2506, 2717
Sedlyarov, I. WPP10, WPP11, 1678, 1681
Seeman, J. RAA27, RPE14, MPP12, MPP20,MPC01, MPC02, 591, 2032, 2064, 2075, 2317, 2319
Seeman, J.T. WPG10, RAA04, TAA22, RAQ03, 517, 530, 2129, 3291
Seeman, John T. WPG03, WAB06, 486, 3028
Segreto, A. TPG11, 186
Seguin, S. RAG06, 3170
Seidel, I. FAR06, 272
Seidl, P. TPA10, 3220
Seidl, Peter RAG03, 3159
Selesnev, V.S. WAR20, 1948
Seleznev, D. TAC05, 140
Sellyey, W. MPQ10, TPQ19, 2473, 2992
Sen, T. TAG09, 2774
Senichev, Yu.V. WPP18, 1699
Sennyu, K. TPP03, 1620
Senyukov, V. TAB13, TAQ23, TAQ24, 125, 1572, 1575
Serafini, L. MPE13, WPB10, WAC13, RAQ05, 896, 973, 3097, 3297
Sereno, N. RPA14, 1082
Sereno, N.S. RPA10, RPA11, 1070, 1073
Serio, M. RAE12, RPQ01, 2420, 2660
Sermeus, L. MPG09, 423
Serov, V.L. RPR24, RPR25, 1173, 1175
Sertore, D. WPC23, 1049
Servranckx, R.V. FAB14, 2823
Sessler, A. FAA06, RPC16, RPC17, TAA28, 207, 737, 740, 2135
Sessler, Andrew RAP25, 2946
Sessler, Andrew M. FPD02, 30
Settles, R. TAG01, 2742
Severgin, Y. FAR06, 272
Severgin, Yu. MPC21, RAQ14, 2359, 3315
Sgobba, S. RPE02, 1999
Shalnov, A. TAB13, RPR10, RPR15, TAQ23,TAQ24, 125, 1143, 1155, 1572, 1575
Shapiro, Alan WPB15, TPP10, 985, 1636
Sharma, S. FAR19, TAR08, 303, 816
Sharonov, S.A. FAP06, FAP07, 1337, 1340
Sharp, W. TAR17, 837
Sharp, W.M. TAR13, TAR14, TPR09, 825, 828, 3260
Shatilov, D.N. RAP05, 2892
Shatunov, Yu. RAA31, RAR31, 600, 3427
Shatunov, Yu.M. RAQ21, 3331
Shchedrin, I.S. RPA25, 1114
Shchepunov, V.A. FAC12, 2863
Shcherbakov, A. FAR16, FAR17, RAA08, 296, 299, 542
Shea, D. MPR20, 2279
Shea, T.J. MPQ04, MPQ05, TPB12, WAC24, 2455, 2458, 2551, 3131
Sheehan, J. MPE11, MPA15, 890, 2223
Sheffield, Richard L. MPE09, 882
Shen, Weijun FAQ31, 1462
Sheng, I.C. TAR08, 816
Shenzong, Hu FAA26, 246
Shepard, K.W. RPR05, FAQ09, RAR21, 1128, 1408, 3400
Sheppard, J. RPC01, WAQ15, 698, 1876
Sheppard, R. RPA26, 1116
Sherman, J. MPE04, 867
Sherman, J.D. WPA08, 923
Sherwood, Boyd WPB15, 985
Sheu, R.J. TPQ09, 2968
Sheynin, S. FAP12, 1355
Shibata, H. RAB13, 779
Shiltsev, V. TAA01, TAA21, RAR30, 2078, 2126, 3424
Shimer, D. RAA04, 530
Shimer, D.W. RPP01, 1961
Shinas, M.A. TPC06, 2607
Shinn, M. FAG11, FAA25, WPC24, 102, 243, 1052
Shintake, T. WAG12, RPC20, RPA20, FAE09,WPQ09,WPQ17, WPR05, WPR09,TAA28, WXE07, TPC08,TPC29,RPQ04, TAG01, 649, 749, 1099, 1503, 1738, 1759, 1797, 1806, 2135, 2444, 2613, 2655, 2669, 2742
Shinto, K. WPC07, WAQ06, 1007, 1855
Shirai, T. FAR08, RPA13, RPA18, WAQ01, 278, 1079, 1093, 1843
Shirakata, M. WAR05, 1912
Shishido, T. TPP07, 1629
Shoaee, H. WAE10, RAE03, RAE11, 2181, 2389, 2417
Shoji, Y. TAP12, WAR04, WAR05, 381, 1909, 1912
Shpak, A. FAR16, FAR17, 296, 299
Shu, D. MPQ08, 2467
Shu, Q.S. TPP11, TPP14, 1639, 1648
Shukeilo, I. FAR06, 272
Shumakov, A. RPA19, 1096
Shumakov, I.V. RPR07, 1134
Shurina, E. MPB09, 2291
Shurter, R.B. TPB22, 2580
Shvedov, D. WAA18, 1266
Shvedunov, V. RPA19, 1096
Shvedunov, V.I. FAA14, TAR05, FAP19,WPR17,RAQ01, RAR04, 225, 807, 1375, 1827, 3285, 3361

Shvets, G. RAB08, 773
Shvetsov, V.S. WAA20, TAQ34, 1272, 1605
Sibley, C. RPG05, 327
Siemann, R.H. WXE05, RAP10, RAP11, RAP12, WAB12, WAC17, TPA09, 2438, 2907, 2910, 2913, 3046, 3109, 3217
Sigov, Yu.S. WAA02, WAA03, 1230, 1233
Sikora, J. TPA04, 3206
Sikora, J.P. RAE14, 2426
Sikora, R.E. MPQ05, 2458
Sim, J. FAP05, 1334
Sim, J.W. FAP06, FAP07, MPB05, MPB06, 1337, 1340, 2282, 2285
Simopoulos, C. WXE05, WAB05, WAC04, WAC17, 2438, 3025, 3073, 3109
Simpson, J. WAG06, WPB11, WPB12, 631, 976, 979
Simrock, S. RPQ29, RPQ30, 2732, 2735
Simrock, S.N. MPR14, RAE11, 2268, 2417
Simrock, Stefan MPB11, 2297
Sinclair, C. FAG11, FAA25, WPA17, TPC07, TPC26, 102, 243, 942, 2610, 2652
Sinclair, C.K. WPC17, 1030
Singh, A. TAQ17, 1561
Singh, O. FAQ17, MPA15, RPQ19, 1426, 2223, 2711
Singh, Om V. RPQ27, 2729
Singleterry Jr., R.C. TAC12, 149
Sisson, D. TPG14, 192
Skaritka, J. MPE11, 890
Skarpaas, K. MPP10, 2057
Skrinsky, A. MAD04, TAR11, 14, 819
Skuratov, V. WPR19, 1833
Slaton, T. WAG11, RPB01, RPB03, 646, 656, 662
Slaton, Tim WAB08, 3034
Sloan, T. RAQ23, RAQ24, 3337, 3340
Sloth, K. TAE10, 1213
Sluijk, T. TAQ12, MPQ17, 1547, 2491
Smirnov, A. RAP24, 2943
Smirnov, A.I. MPG10, 426
Smirnov, A.V. RPR13, 1152
Smith, D. FAA27, 248
Smith, D.L. TAE06, 1201
Smith, David L. TAE07, 1204
Smith, G.A. RPQ07, 2678
Smith, H. WPR15, TPC20, 1821, 2646
Smith, I. TAE06, 1201
Smith, J. MPA15, 2223
Smith, J.D. MPR08, 2253
Smith, John MPR07, 2250
Smith, M. RPR22, TPC06, 1167, 2607
Smith, P. WAQ15, 1876
Smith, R. WAQ03, 1849
Smith, S. MPQ15, MPQ25, 2485, 2512
Smith, S.L. TPG09, RAE10, 180, 2414
Smith, T.L. WPP16, 1693
Smithe, D.N. WPC12, 1022
Snyder, S.L. TAP10, 375
Snydstrup, L. MPP11, 2060
Sobczynski, S. RPG05, 327
Sobenin, N.P. TAR05, FAP19, WPR17, WPR18, 807, 1375, 1827, 1830
Solnyshkov, D. WPC03, 1004
Solomon, L. FAQ13, WXE04, RPQ19, 1414, 2435, 2711
Soloveichik, Yu. MPB09, 2291
Somersalo, E. FAE08, 1500
Sommer, M. FAR14, 293
Somov, L. TAC16, 152
Song, J.J. RPA10, WPP16, TAA11, 1070, 1693, 2102
Sotnikov, G.V. RAB15, 782
Soukas, A. TAP11, WAR11, WAR13, RPP02, 378, 1924, 1930, 1964
Specka, A. WAG07, 634
Spence, David WPC11, 1019
Spence, P. TAE06, 1201
Spence, W. WAG11, RPC20, TAG01, WAC17, 646, 749, 2742, 3109
Spence, W.L. RAA06, WAB09, 536, 3037
Spencer, C. WAQ15, 1876
Spencer, C.M. FAP16, 1366
Spencer, J. RPC02, RPC08, TAA28, TPC16, WAC17, 701, 713, 2135, 2637, 3109
Spencer, J.E. RPB06, 671
Spentzouris, L.K. TAG04, 2757
Spentzouris, Linda Klamp WAC02, 3070
Sprehn, D. WAE13, 2190
Spyropoulos, B. TAA15, 2111
Srinivasan-Rao, T. MPE11, 890
Stanek, M. RPA24, TPC20, 1111, 2646
Stefan, P.M. WXE04, 2435
Stege, R. WAG11, RPB04, WAC17, 646, 665, 3109
Steimel, J. TPQ26, 3010
Steimel Jr., James M. RAE02, 2384
Stein, P. TPP11, 1639
Steinbach, Ch. TAP14, 386
Steinbock, L. FAR06, 272
Steinhauser, N. WPQ24, 1776
Steininger, R. FAR06, 272
Stelzer, J.E. WPC10, 1016
Stenz, C. WAG07, 634
Stepashkin, O. RAP24, 2943
Stephenson, E. WPC08, 1010
Stepin, D.L. WPB16, 988
Stepp, J. MPQ08, 2467
Stevens Jr., R. MPE04, 867
Stevens Jr., R.R. WPC10, 1016
Stevens Jr, Ralph R. WAQ02, 1846
Stevens, R.R. WPA08, 923
Stevens, T. MPP13, 2067
Stevenson, G.R. WAQ24, 1891
Stevenson, N.R. FAG07, 89
Stierlin, U. TAG01, 2742
Still, D. RPC21, 752
Stillman, A. TPB15, 2560
Stillman, Arnold MPA09, 2211
Stirbet, M. TPP12, 1642
Stockhorst, H. TPB20, 2574
Stoeffl, W. WPG10, RAA03, MPP12, MPP20, TAA22, MPC01, MPC02, 517, 527, 2064, 2075, 2129, 2317, 2319
Stoker, J. WPA01, 902
Stoker, J.D. TAE01, 1178
Stolyarsky, V.I. TPA15, 3232
Stolzenburg, C. TPP11, 1639
Stoner, R. TPG14, 192
Stovall, J.E. RPR08, RPR09, MPC23, 1137, 1140, 2364
Stover, G. RAE12, 2420
Stover, G.D. WAA14, 1254
Straub, D. FAA08, 213
Striby, S. RAG06, 3170
Strohman, C.R. RAE14, 2426
Strönisch, U. FAP02, 1325
Strubin, P.M. RPE06, 2014
Struckmeier, Jürgen FAC10, 2860
Stuart, M. FAP17, FAP18,

1369, 1372
Studebaker, Jan WPB15, 985
Stupakov, G. MPC01, WAC15, 2317, 3102
Stupakov, G.V. RAQ02, RAQ09, RAQ10, 3288, 3303, 3306
Stupakov, Gennady V. RAR11, RAR12, 3373, 3376
Sturges, Ronald WPB15, 985
Su, J.J. TAA28, 2135
Suberlucq, G. RPC10, 719
Sudan, Ravi N. TAE07, 1204
Sugimoto, M. TPG02, 159
Suk, H. TPQ11, 2974
Sukhina, B. TPE09, 1316
Sukhina, B.N. TAC06, RPP08, 143, 1979
Suller, V.P. TPG09, 180
Sullivan, M. RAA25, 585
Sumbaev, A. TAC16, 152
Sun, D. WPP01, 1655
Sun, Y. FAP01, 1322
Surma, I.V. RAQ01, 3285
Sutter, S. RPA26, 1116
Suzuki, H. FAP13, 1358
Suzuki, S. WPC22, 1046
Suzuki, T. FAA30, TPP07, 257, 1629
Svandrlik, M. FAR06, FAR21, WPQ04, TAG05, 272, 309, 1723, 2762
Svinin, M. WPC03, TAA18, 1004, 2120
Svinjin, M.P. TAE13, 1222
Swan, T. RAA03, 527
Swenson, D.A. RPG10, 342
Swenson, D.R. WPC10, 1016
Swift, G. FAA08, RPA17, TAQ07, 213, 1090, 1536
Symon, K. TAP05, RAG05, 363, 3167
Syphers, M. RAP21, RAQ23, RAQ24, 2934, 3337, 3340
Syphers, M.J. TAP13, MPG12, WAB04, 383, 431, 3022
Syresin, E. RAP23, RAP24, 2940, 2943
Sytchev, V. FAQ06, 1399
Sytchevsky, S. MPC21, 2359
Tachibana, S. TPP03, 1620
Tadano, M. RPQ23, 2720
Tadokoro, M. TAB03, 113
Tajima, T. TPP03, 1620
Takagi, A. WPC07, WAQ06, WAR05, 1007, 1855, 1912
Takahashi, T. TPP03, 1620
Takaki, H. FAR09, 281
Takao, M. FAQ20, FAQ21, 1435, 1438
Takashima, T. RPQ06, 2675
Takashina, H. TPP03, 1620
Takatomi, T. WPQ15, 1753
Takeda, H. FAA16, RPR08, RPR09, MPC23, 228, 1137, 1140, 2364
Takeda, Harunori MPB16, 2306
Takeda, O. WAG12, 649
Takeda, Y. RPG13, 351
Taketani, A. RPQ15, 2699
Takeuchi, Y. FAE09, WPQ17, WPR05, WPR09, TAG01, 1503, 1759, 1797, 1806, 2742
Tallerico, P.J. TAR12, TAQ02, 822, 1521
Talman, R. RAP03, 2886
Tambini, U. RAE05, 2399
Tan, J. TPP09, 1632
Tanabe, J. FAP01, 1322
Tanaka, M. WAR13, 1930
Tang, Cha-Mei WPE05, 70
Tang, H. WAG11, RPC01, MPE10, WPC18, WPC21, 646, 698, 887, 1033, 1043
Tang, J. MPR13, 2265
Tang, Y.N. MPR08, 2253
Tani, N. FAP13, 1358
Taniuchi, T. WPC22, 1046
Taniyama, N. TPP03, 1620
Tantawi, S. WPQ05, 1726
Tantawi, S.G. TAQ28, 1587
Tantawi, Sami G. TAQ26, TAQ27, TAA27, 1581, 1584, 2132
Tarabrin, V. TAC16, 152
Tarakanov, M.V. MPG10, WAR20, WAR21, 426, 1948, 1949
Tarasenko, A. RAA08, 542
Tarnetsky, V. RPA12, TAQ21, 1076, 1569
Tarovik, M. RAQ14, 3315
Tatchyn, R. FAP20, FAQ23, 1378, 1441
Tatum, B.A. TAP07, WAQ26, MPA05, 366, 1897, 2202
Taufer, M. FAE11, 1509
Taurel, E. RPQ15, 2699
Taurigna-Quere, M. WPB22, 998
Tauschwitz, A. WAQ04, 1852
Tavares, Pedro F. RAQ29, 3352
Taylor, B. TAR03, 801
Taylor, T. RAA04, FAC04, 530, 2844
Tazzari, S. TPG11, 186
Tazzioli, F. TPG11, WAC13, 186, 3097
Tecimer, M. FAA29, 254
Tecker, F. RAA19, 567
Tejima, M. RAA33, MPQ31, TPC05, 603, 2521, 2604
Tejima, Masaki MPQ14, 2482
Telegin, Yu. FAR17, 299
Temkin, R.J. MPE12, 893
Temnykh, Alexander B. TAG08, 2771
Tenenbaum, P. RPC06, RPC20, TAA08, WXE07, TAG01, 707, 749, 2096, 2444, 2742
Teng, L. RAA29, 597
Teng, L.C. RAR26, 3415
Teng, Lee C. FAB10, 2814
Tenyakov, I. FAP24, 1387
Tepikian, S. TAA09, MPR20, FAB22, 2099, 2279, 2832
Terada, Y. FAP22, WPQ07, 1384, 1732
Terashima, A. FAQ02, 1390
Terekhov, V. MPP03, 2040
Terekhov, V.I. MPG10, WAR20, 426, 1948
Tereshkin, Y. FAP24, 1387
Terrell, R. MPR14, 2268
Terunuma, N. WAR03, TPC05, 1906, 2604
Tessier, J.-M. WAC13, 3097
Teytelman, D. RAE12, RPQ01, RPQ08, 2420, 2660, 2681
Thern, R. TPA06, 3212
Theuws, W. RPQ31, 2738
Theuws, W.H.C. WAQ19, RPP04, 1882, 1970
Thevenot, M. TAE09, 1210
Thieberger, P. TAP11, 378
Thielheim, K.O. RAR09, 3370
Thiery, Y. WPB22, 998
Thivent, M. MPG09, 423
Thomas, M. TPP06, WPQ20, 1626, 1768
Thomas, M.D. TAB17, 131
Thomas, P. WPB01, 945
Thomas, R. TPE04, TAA09, 1293, 2099
Thompson, K. TAP05, RPC01, RPC02, RPA04, FAP03, 363, 698, 701, 1058, 1328
Thompson, K.A. TPQ16, TPQ17, WAC18, 2986, 2989,

3112
Thompson, P. TPE04, FAQ03, FAQ04, FAQ16, 1293, 1393, 1396, 1423
Thorndahl, L. RPC09, 716
Thur, W. RPE12, 2026
Tian, F. WAG11, RPB01, TPC20, WAC17, 646, 656, 2646, 3109
Tiefenback, M. MPR15, 2271
Tiefenback, M.G. WAQ12, 1870
Tieger, D. RPG05, 327
Tigelis, J. RAQ01, 3285
Tighe, R. RPQ03, RPQ05, 2666, 2672
Tigner, M. FAE13, RAQ04, 1515, 3294
Timmer, Carl WPB15, 985
Timmermans, C.J. WAQ19, WAQ20, RPP04, RPQ31, 1882, 1885, 1970, 2738
Timossi, C. MPR03, 2244
Tinsley, D. WAR01, 1900
Titcomb, Ch. MPP02, 2037
Tiunov, A.V. RPR01, RAQ01, RAR04, 1119, 3285, 3361
Tiunov, M. MPB09, 2291
Tkachev, P.L. RAR04, 3361
Tkatchenko, A. FAR14, 293
Tobiyama, M. RPQ26, RAQ06, 2726, 3300
Todd, A.M.M. RPR20, 1164
Todesco, E. FAC06, 2847
Toge, N. RPB01, RAP02, 656, 2883
Tojyo, E. RPG13, 351
Tokarev, Yu. WAA17, 1263
Tokuda, N. RPG13, TAP04, 351, 360
Tokumoto, S. TAQ29, WPR02, WPR03, 1590, 1788, 1791
Tölle, R. TPB20, 2574
Tolstun, N.G. TAE13, 1222
Tomimasu, T. FAA30, TAQ35, 257, 1608
Tomlin, R. TPQ26, 3010
Tompkins, J.C. FAP06, FAP07, 1337, 1340
Tongu, E. FAA30, 257
Torre, A. TPG11, 186
Torun, Yagmur MXG03, 53
Tosa, M. TPP16, 1652
Tosello, F. WAP14, 470
Tosi, L. FAA13, FAR21, TAG05, 222, 309, 2762
Tosin, G. FAP14, FAP15, 1361, 1364
Touchi, Y. RPG09, 339
Toyama, T. WAR05, 1912
Trahern, C.G. WAP10, MPR20, 461, 2279
Trakhtenberg, E. FAQ17, MPP16, 1426, 2072
Tran, H.J. RAQ15, 3317
Tran, P. RAQ17, 3323
Tranquille, G. RAP24, 2943
Trantham, K. WPC21, 1043
Travier, C. WPB01, 945
Travish, G. FAA23, RPA21, RPA22, 240, 1102, 1105
Trbojevic, D. WAP10, TAA09, FAB22, WAC25, RAQ22, 461, 2099, 2832, 3134, 3334
Treas, P. TAB17, RPA26, 131, 1116
Tremblay, K. WXE01, 2429
Trenkler, T. FAC04, 2844
Trikalinos, C. RAQ01, 3285
Trimble, D. MPE14, WAA19, TAA20, 899, 1269, 2123
Trombly-Freytag, K. FAP06, FAP07, MPB05, MPB06, 1337, 1340, 2282, 2285
Tronc, D. TAB04, 116
Trotz, S.R. MPE12, 893
Trower, W.P. TAR05, FAP19, WPR17, 807, 1375, 1827
Trzeciak, W.S. FAR20, 306
Tsai, H.J. TPQ10, 2971
Tsang, K.L. FAA07, RAR05, 210, 3364
Tsarik, S.V. MPG10, WAR20, WAR21, 426, 1948, 1949
Tschalaer, C. RPG05, 327
Tseng, P.K. FAA04, 201
Tseng, P.-K. TPC15, 2634
Tsentalovich, E. RPG05, 327
Tsoupas, N. FAP11, 1352
Tsuchiya, K. FAQ02, 1390
Tubaev, M. RPR15, 1155
Tückmantel, J. TPP12, 1642
Tuozzolo, J.E. WAR10, 1921
Tupikov, V.S. RPP08, 1979
Tur, Yu. WPB17, 990
Tur, Yu.D. WPB16, TAE14, 988, 1225
Turchinetz, W. RPG05, RAA31, 327, 600
Turner, J. WAG11, RPB01, WAC17, 646, 656, 3109
Turner, J.L. RPB04, 665
Turner, L.R. FAQ17, 1426
Tzeng, K.-C. RAB01, RAB02, 758, 761
Ueda, T. RAB13, 779
Uemura, T. FAQ08, 1405
Ueng, T.S. MPQ19, MPQ32, 2497, 2524
Uesaka, M. RAB13, 779
Ueyama, Y. FAP13, 1358
Uggerhoj, E. WAP14, 470
Uhm, Han S. TAQ04, TAQ05, 1527, 1530
Umezawa, H. TPP07, 1629
Urakawa, J. WPR02, WPR03, WAR03, TPC05, 1788, 1791, 1906, 2604
Ursic, R. TPC26, 2652
Ushkov, V. WPR13, 1815
Uskov, V.V. RAB15, 782
Uythoven, J. TPP12, 1642
v. Blanckenhagen, P. FAR06, 272
v.Es, J. MPQ17, 2491
v.Hartrott, M. WAQ17, 1879
v.Rienen, U. RPB16, 695
Vacca, J.H. RPA07, 1064
Valdez, M. MPR03, 2244
Valentinov, A. MPA04, 2199
Valeri, S. WPC23, 1049
Van Asselt, W. RPQ07, 2678
van Asselt, W.K. WAB04, RAQ22, 3022, 3334
van Bibber, K. MPP12, MPP20, 2064, 2075
v.d.Laan, J. MPQ17, 2491
van der Laan, J. RPG06, 330
van Greevenbroek, H.R.M. WAQ20, 1885
van Oers, W.T.H. MPE03, 864
van Oort, J.M. FAQ07, 1402
van Rooij, M. MPG09, MPP15, 423, 2069
Van Vaerenbergh, P. TPE10, 1319
van Zeijts, J. WAE10, 2181
van Zeijts, Johannes MPR02, MPC20, 2241, 2356
VanAsselt, W. TAP13, 383
Vanecek, D. RPC18, WPA01, TAE01, 743, 902, 1178
Varenne, F. RAP23, RAP24, 2940, 2943
Varfolomeev, A. FAA23, 240
Varisco, G. TAA07, 2093
Vasilevsky, A. MPP03, 2040
Vasiljev, A.A. RPR07, 1134
Vasserman, I. FAQ17, FAQ18, 1426, 1429
Vasserman, S. WAA17, 1263

Vassiliev, L. FAQ06, 1399
Vaziri, K. FAG06, 86
Vella, M.C. FAP18, 1372
Veluri, V.R. RPA07, 1064
Verdier, A. WPG09, RAA17, FAC03, 514, 560, 2841
Verdier, André FAC07, FAC08, 2850, 2853
Verhagen, H. RAA15, 557
Verkooyen, J. TAQ12, 1547
Vescovi, M. RPA26, 1116
Veselov, O. FAQ06, 1399
Veshcherevich, V. WPP10, WPP11, RAR19, 1678, 1681, 3394
Vetter, A.M. FAA27, FAA28, WPB20, 248, 251, 992
Vignola, G. WPG05, RPA26, 495, 1116
Villate, D. TAE09, TPC17, 1210, 2640
Vincent, J. RPG11, 345
Vinokurov, N.A. FAQ17, 1426
Virchenko, Yu.P. RAQ28, 3349
Virostek, S. RPB04, 665
Visintini, R. TPG11, FAR21, 186, 309
Vlieks, A.E. WAG13, RPA23, TAQ26, TAQ27,TAA27, 653, 1108, 1581, 1584, 2132
Vobly, P. MPB09, 2291
Vodopianov, F.A. TAR02, TAQ10, 799, 1542
Voisin, L. TAE09, 1210
Volfbeyn, P. TPG07, RPC15, RAB10, 174, 734, 776
Völker, F. MPG09, 423
von Hahn, R. RPR06, 1131
von Holtey, G. WPG09, 514
Vormann, H. WPA04, 911
Vorogushin, M.F. WPP04, 1663
Voronin, G. WPC03, 1004
Voronin, V.S. TPR13, 3269
Vos, L. RAR07, 3367
Voss, G.-A. TAG01, 2742
Voss, Gustav-Adolf FPD01, 27
Votaw, A. MPQ08, MPQ10, 2467, 2473
Votaw, A.J. RPQ16, 2702
Voykov, G. TPC03, 2598
Vuagnin, G. WAP14, 470
Wachter, J. MPQ22, 2506
Wadlinger, E.A. RPR19, 1161
Wagner, S.R. TAG01, 2742
Wake, M. FAQ32, TPP07, 1465, 1629
Wakisaka, K. FAA30, 257
Wakita, K. FAA30, TAQ35, 257, 1608
Walbridge, D.G.C. FAP06, FAP07, MPB05,MPB06, 1337, 1340, 2282, 2285
Waldschmidt, G. WPB06, 961
Walker, N. RPB01, 656
Walker, R.P. TPG11, FAA13, FAR21, FAQ19,TAG05, 186, 222, 309, 1432, 2762
Wallén, E. RPE02, 1999
Walling, L.S. RPG10, 342
Walters, G.K. WPC21, 1043
Walther, R. WPA12, 929
Walton, J. WAR01, 1900
Walz, D. RPC08, WXE07, TAG01, 713, 2444, 2742
Wan, Weishi MPC09, 2336
Wanderer, P. WAP10, TPE04, FAP11, FAQ02,FAQ04,FAQ16, TAA09, 461, 1293, 1352, 1390, 1396, 1423, 2099
Wanderer, P.J. FAQ03, 1393
Wang, B. MPA01, 2193
Wang, C. MPA01, 2193
Wang, C.J. MPR10, TPB29, 2256, 2592
Wang, C.-P. TPC15, 2634
Wang, Ch. FAA04, RAA24, FAQ26, TPQ08, 201, 582, 1450, 2965
Wang, Chun-xi MPC31, 2376
Wang, Chunxi FAC02, 2838
Wang, D. WAA16, WXE01, TPB04, TPC04,WAC27, 1260, 2429, 2536, 2601, 3140
Wang, D.X. MXG02, 48
Wang, J. RPA04, WAA08, WAA09, 1058, 1242, 1245
Wang, J.G. TAE04, TPQ11, 1193, 2974
Wang, J.M. TPP06, 1626
Wang, J.P. TAA14, 2108
Wang, J.Q. WAB20, 3064
Wang, J.W. WAG13, RPA23, 653, 1108
Wang, L. TAP03, WPP20, WPP21, RAP21,WAC12, WAC27, RAG10,RAQ23,RAQ24, 357, 1705, 1708, 2934, 3094, 3140, 3182, 3337, 3340
Wang, M.H. RAA24, TAR06, TPQ08, TPQ09,TPQ10, 582, 810, 2965, 2968, 2971
Wang, P. FAA08, RPA17, 213, 1090
Wang, Ping WPA13, WPR22, 932, 1841
Wang, Shu-Hong WPG07, 506
Wang, T. WAC29, 3146
Wang, T.S. RAR23, 3406
Wang, Tai-Sen F. WAC28, 3143
Wang, X. MPQ07, MPQ08, MPQ10, 2464, 2467, 2473
Wang, X.J. MPE11, WPB13, RAE09, WXE03,TPB01, 890, 982, 2411, 2432, 2530
Wang, X.-J. TPG14, 192
Wang, X.Q. RPE10, 2023
Wang, Y. TAB17, MPA01, RAP21, 131, 2193, 2934
Wang, Y.L. TAQ08, 1539
Wangler, T.P. RAG11, 3185
Wangler, Thomas P. WAQ02, RAG01, 1846, 3149
Wanzenberg, R. RPB14, 689
Ward, C. TAR17, 837
Warkentien, R. MPA18, 2232
Warner, A. RAQ22, 3334
Warner, D. TAP05, 363
Warnock, R.L. FAB06, 2804
Warnock, Robert L. TPQ07, 2962
Warren, David WPB15, 985
Warwick, A. FAA03, 198
Watson III, William A. WAE05, 2167
Watson, W. WAE10, MPR13, MPR19, 2181, 2265, 2276
Watson, W.A. RAE11, 2417
Webber, Robert C. RPQ10, 2687
Weber, M. TPB07, 2542
Webers, G.A. WAQ19, WAQ20, RPQ31, 1882, 1885, 2738
Wedekind, M. WPC08, 1010
Wehrle, U. FAE10, 1506
Wei, F. FAR21, 309
Wei, J. WAP10, FAB22, WAC24, RAQ22, 461, 2832, 3131, 3334
Wei, Jie RAP25, 2946
Weidemann, A.W. TAA28, 2135
Weihreter, E. TPE09, WAQ17, 1316, 1879
Weiland, T. RPB16, TAQ06, WAE13, MPC01,MPQ15, WAB18, 695, 1533, 2190, 2317, 2485, 3061

Weinberg, J. WAQ15, WAC17, 1876, 3109
Weingarten, W. FAE11, 1509
Weinstein, A. TAR18, 840
Weise, H. RPB08, 677
Weisend, J.G. MPP01, 2034
Weiss, R. RPR22, 1167
Weisse, E. WAP14, WAQ24, 470, 1891
Weisz, S. WAP14, FAC04, 470, 2844
Welch, J. FAE13, 1515
Welch, James J. TAA29, TAG08, FAC14,RAG13,2138, 2771, 2866, 3191
Welton, R.F. MPE05, WPC12, 871, 1022
Welz, J. MPE03, 864
Wendt, M. TPC09, 2616
Weng, W.T. FAA07, RAA23, RAA24, RAG08,RAR05,210, 579, 582, 3176, 3364
Wenjun, Zhu FAA26, 246
Wenninger, J. WAP12, RAA11, RAA19, RAA20, 464, 548, 567, 570
Werkema, Steven J. RAR20, 3397
Wermelskirchen, C. RPQ22, 2717
Wesolowski, W. RPA11, 1073
West, C. MPR13, 2265
Westenskow, G. RPC16, RPC17, MPE14,WPC16,TAA28, 737, 740, 899, 1027, 2135
Westenskow, G.A. TAQ03, 1524
Westervelt, R.T. WAE08, 2175
Wetherholt, D. MPR13, 2265
Wharton, K. RAB04, 767
White, K. MPA12, MPR13, 2220, 2265
White, M. TAP05, RPA07, RPA08, RPA10,RPA11,RPA14, TPC01, 363, 1064, 1067, 1070, 1073, 1082, 2595
Whitham, K. TAB17, RPA26, 131, 1116
Whittum, D. RAB13, TAA28, WAC17, 779, 2135, 3109
Widgren, J. FAA08, 213
Wiemerslage, G. MPP16, 2072
Wienands, H.-U. RAA27, 591
Wienands, U. RAA04, TAA22, MPC01, 530, 2129, 2317
Wight, G.W. MPE03, 864
Wildman, D. WPP08, WPP09, WPP23, RAQ13, 1672, 1675, 1714, 3312
Wildner, E. MPG09, WAE09, 423, 2178
Wilkinson, C. WAC29, 3146
Wilkinson, C.A. TAR12, 822
Willeke, F. MPG07, TAG02, TAG09, 420, 2747, 2774
Willen, E. TPE04, FAQ03, FAQ04, FAQ15,FAQ16, 1293, 1393, 1396, 1420, 1423
Williams, C.E. WAQ26, 1897
Williams, G. FAR06, 272
Williams, M.D. TPB07, 2542
Williams, Mel WPB15, 985
Williams, R. TAA28, 2135
Williams, S. TAG01, 2742
Wilson, I. WAG13, RPC09, RPC10, RPC15, 653, 716, 719, 734
Wilson, K. FAR06, 272
Wilson, P. RPC01, RPC02, RPC06, 698, 701, 707
Wilson, P.B. FAE04, TAA33, TPQ16, 1483, 2144, 2986
Winick, H. WPB13, WXE03, 982, 2432
Winje, R.A. FAG05, 83
Winkler, G. MPP02, 2037
Winn, David MXG03, 53
Wise, M. MPR13, 2265
Wiseman, M. FAG11, FAA25, WPA17, 102, 243, 942
Witherspoon, S. WAE10, MPR13, 2181, 2265
Witkover, R. RPQ07, 2678
Witkover, R.L. TPB26, 2589
Witte, K. MPE10, 887
Wolf, Z. FAP16, FAQ08, 1366, 1405
Wolff, D. WAE07, 2172
Wolff, S. RPB09, 680
Wollnik, H. WAQ26, 1897
Wong, J. TAR18, 840
Wong, V. RPQ07, 2678
Woo, B. MPC18, 2351
Wood, P. TPC04, 2601
Wood, R.L. RPR08, RPR09, 1137, 1140
Woodle, M. WPB13, WXE03, 982, 2432
Woodley, M. WAG11, RPB01, RPB03, RPB04,RAE03,646, 656, 662, 665, 2389
Woods, M. RPC08, 713
Woody, K.A. TPC13, 2628
Wright, D. MPP09, MPP12, MPP20, MPC01,WAC17,2054, 2064, 2075, 2317, 3109
Wright, E. FAE07, 1497
Wright, E.L. TAQ28, 1587
Wrulich, A. TPG11, FAA13, FAR21, TAG05, 186, 222, 309, 2762
Wu, X. RPG11, 345
Wu, Y. FAA08, RPG06,RAA01, RAA21, RAB22,RPA17, MPA10, MPA11,MPQ06, FAC20, 213, 330, 524, 573, 796, 1090, 2214, 2217, 2461, 2877
Wu, Y.Y. TPB03, 2533
Wu, Ying WPR22, 1841
Wuensch, W. WAG13, RPC09, RPC10, RPC15, 653, 716, 719, 734
Wurtele, J. TAA28, 2135
Wurtele, J.S. RAB08, MPE12, WPB03, WPB04, 773, 893, 951, 954
Wüstefeld, Godehard FAC16, 2868
Wyss, C. TPP12, 1642
Xi, Boling RPP04, 1970
Xiao, A. WAC27, 3140
Xie, Jialin TPG04, 162
Xie, Ming TPG10, 183
Xu, G. RAA21, TPQ03,WAC27, 573, 2955, 3140
Xu, J. MPA01, 2193
Xu, S. MPP16, 2072
Yakimenko, V. TAR11, RAR31, 819, 3427
Yakovlev, V. RPA12, TAQ21, 1076, 1569
Yakovlev, V.P. MPC17, 2348
Yamada, R. MPC07, 2330
Yamada, S. MAD03, 9
Yamaguchi, H. MPQ18, 2494
Yamaguchi, S. TAQ25, 1578
Yamamoto, N. RPC20, MPA06, WXE07, TAG01, 749, 2205, 2444, 2742
Yamane, Isao TPR16, 3275
Yamazaki, Y. FAE09, WPQ08, WPQ09, WPQ17,WPR05, WPR09, 1503, 1735, 1738, 1759, 1797, 1806
Yan, Y. RAA22, 576
Yan, Y.T. RAA26, RAA27, TAG06, 588, 591, 2765
Yanagida, K. WPC22, 1046
Yang, B. MPQ09, MPQ10,

MPQ11, TPC03, 2470, 2473, 2476, 2598
Yang, J. RAQ17, 3323
Yang, Ming-Jen MPQ20, 2500
Yang, X.-F. TPC16, 2637
Yano, Y. WPC01, 1001
Yaramishev, S.G. TPA05, 3209
Yarba, V.A. FAP06, FAP07, 1337, 1340
Yarygin, N. FAQ06, 1399
Yarygin, S.N. WPR18, 1830
Yasumoto, M. FAA30, 257
Yavor, S.Ya. TAP16, 389
Yazynin, I. WAR22, 1952
Yee, D. FAP01, 1322
Yeremian, A.D. WPC18, 1033
Yi, He FAA26, 246
Yifang, Wang TAR22, 850
Yin, Yan TPC11, 2622
Ylä-Oijala, P. FAE08, 1500
Yokomizo, H. WPC22, FAP13, MPA07, 1046, 1358, 2208
Yokoya, K. RPA20, WAB20, 1099, 3064
Yokoyama, M. RPQ23, 2720
Yokoyama, S. FAQ08, 1405
Yonehara, H. FAP13, 1358
Yoon, M. TPG06, WPR11, 171, 1812
York, R.C. RPG11, 345
York, R.L. WPC10, 1016
Yoshida, Y. RAB13, 779
Yoshihara, K. TPP16, 1652
Yoshii, J. TPB18, 2569
Yoshii, M. TAP04, WPC07, WAR05, 360, 1007, 1912
Yoshikawa, H. WPC22, MPA07, 1046, 2208
Yoshimoto, S. RPQ06, 2675
Young, E. RAP07, 2898
Young, L.M. RPR08, RPR09, 1137, 1140
Young, Lloyd M. MPB16, 2306
Yourd, R. FAP01, 1322
Yourd, R.B. RAA05, 533
Yu, C.I. MPQ26, RAR05, 2515, 3364
Yu, C.-I. TPC15, 2634
Yu, I.H. WPR11, 1812
Yu, S. RPC16, RPC17,RPC18, WPA01, TAE01, 737, 740, 743, 902, 1178
Yu, S.S. RPC19, TAR14, WPA09, WAQ04, 746, 828, 926, 1852
Yu, Y. MPA01, 2193
Yuan, D. WAQ07, 1858
Yuan, V. RPR19, 1161
Yuan, V.W. RPR22, TPC06, 1167, 2607
Yudin, I.P. MPB19, FAC09, 2314, 2856
Yugami, N. RAB13, 779
Yuldashev, O.I. MPB19, 2314
Yuldasheva, M.B. MPB19, 2314
Yule, T.J. FAG14, 110
Yunn, B. WPA17, 942
Yunn, Byung C. MPB11, RAQ11, 2297, 3309
Yupinov, Y. MPA04, 2199
Yupinov, Yu. WPR13, 1815
Yurkov, M.V. WAA20, TAQ34, 1272, 1605
Zako, A. FAA30, 257
Zakutin, V.V. WPA15, TAE14, 938, 1225
Zangrando, D. TPG11, FAQ19, 186, 1432
Zante, A. TAB17, RPA26, 131, 1116
Zaugg, T. WPA08, 923
Zavadtsev, A.A. WPR18, 1830
Zazula, J.M. WAQ24, 1891
Zegenhagen, J. FAR06, 272
Zelenski, A.N. MPE03, 864
Zelinsky, A. FAR17, RAA08, 299, 542
Zelinsky, A.Yu. RAA07, 539
Zeller, A.F. RPG11, 345
Zenkevich, P. RAP23, 2940
Zenkevich, P.R. TPA05, 3209
Zeno, K. TAP12, 381
Zhan, M. MPA01, 2193
Zhang, C. WPG09, TPQ03, 514, 2955
Zhang, R. RAB03, RPA21, RPA22, 764, 1102, 1105
Zhang, S.Y. TAP13, RAG08, TPA08, 383, 3176, 3214
Zhang, W. WAR10, WAC25, 1921, 3134
Zhang, Zhenhai RAQ25, 3343
Zhao, Aihua FAQ29, FAQ30, 1456, 1459
Zhao, J. MPA01, 2193
Zhao, S. TAA03, 2084
Zhidkov, E.P. MPB19, 2314
Zhiglo, V.F. WPA15, 938
Zholents, A. RAA03, RAA22, FAB01, 527, 576, 2789
Zholents, A.A. RAP05, 2892
Zhou, J. WPB06, TAA11, 961, 2102
Zhou, Ping TPB05, 2539
Zimmermann, F. WPG10, WAG11, RPB01,RPC03,RPC06, RPC07, TPQ16,TPQ17,WAB07, WAC15, WAC17, 517, 646, 656, 704, 707, 710, 2986, 2989, 3031, 3102, 3109
Ziomek, C. TAQ31, RPQ02, RPQ05, 1596, 2663, 2672
Zisman, M. MPC01, 2317
Zisman, M.S. RAA03, RAA05, 527, 533
Zolfaghari, A. RPG05, WAA16, TPB04, 327, 1260, 2536
Zolotorev, M. WPG10, RPE14, MPC01, MPC08, 517, 2032, 2317, 2333
Zolotorev, Max TAQ27, 1584
Zotter, B. RAA20, RPC09, 570, 716
Zubovskiy, V. TAC05, 140
Zwart, T. RPG05, RAA31, 327, 600
Zyngier, H. TPG01, FAR14, 155, 293



